

TN

A5

Vol. 197

N/C

TRANSACTIONS OF THE AMERICAN INSTITUTE OF MINING AND METALLURGICAL ENGINEERS

(INCORPORATED)

Volume 197

*American Institute of Mining, Metallurgical,
and Petroleum Engineers*

INSTITUTE OF METALS DIVISION
IRON AND STEEL DIVISION
EXTRACTIVE METALLURGY DIVISION

1953

PAPERS AND DISCUSSIONS PRESENTED AT MEETINGS HELD AT NEW YORK, FEB. 18 TO 21, 1952; SPOKANE REGIONAL MEETING, MAY 9 TO 10, 1952; PHILADELPHIA, OCT. 20 TO 22, 1952; LOS ANGELES, FEB. 16 TO 19, 1953; CLEVELAND, OCT. 19 TO 21, 1953;* NEW YORK, FEB. 15 TO 18, 1954.*

* Discussion of papers presented at these meetings will be published in Volume 200 (1954).

PUBLISHED BY THE INSTITUTE
AT THE OFFICE OF THE SECRETARY
29 WEST 39TH STREET
NEW YORK 18, N. Y.

COPYRIGHT, 1954, BY THE
AMERICAN INSTITUTE OF MINING AND METALLURGICAL ENGINEERS
(INCORPORATED)
PRINTED IN THE UNITED STATES OF AMERICA

Foreword

We take pleasure in presenting this 197th Volume of the *Transactions* of the American Institute of Mining and Metallurgical Engineers. It contains those papers selected by the Divisional Publications Committees after careful screening and condensation where necessary, from the technical papers and discussions of the Institute of Metals, Iron and Steel, and Extractive Metallurgy Divisions.

As in the past, the JOURNAL OF METALS was paged consecutively throughout 1953. There are eleven interruptions in the pagination of these Transactions because some of the material printed in the JOURNAL OF METALS is not found in this volume. This volume contains all the Metals Transactions for 1953.

There are 149 papers in the volume compared with 107 for the 1952 volume, the increase representing for the most part papers from the Institute of Metals. In this volume there are 19 papers from the Iron and Steel Division, 18 papers from the Extractive Metallurgy Division, and 112 papers from the Institute of Metals Division.

In the past few years there has been increasing use by the members of the opportunity to submit for publication Technical Notes. In this volume you will find 47 Technical Notes, or 13 more than appeared in the 1952 volume.

Discussion to various papers can be readily found by referring to the index for the papers themselves.

I wish to express thanks to the authors and the contributors of discussions. The success of our Institute will depend, in part, on the value received from good papers and discussion resulting from work on timely subjects. The total number of papers printed is limited somewhat by a budget of pages to which the members of the Divisional Publications Committees adhere by careful reading and selection. Thanks are also due to them in their difficult job.

Members of the headquarters staff are to be congratulated for the assembly of the papers into this volume, and also, for the organization of the table of contents which helps to make it possible to find the excellent material contained.

NOVEMBER 30, 1953
ASHLAND, KY.

K. C. McCUTCHEON, *Chairman*
Metals Branch Council, AIME

TECHNICAL PAPERS Institute of Metals Division

	PAGE
Density and Hydrogen Occlusion of Some Ferrous Metals. By J. H. KEELER and H. M. DAVIS.....	44
Bend Plane Phenomena in the Deformation of Zinc Monocrystals. By J. J. GILMAN and T. A. READ.....	49
Preferred Orientations in Iodide Titanium. By C. J. MCHARGUE and J. P. HAMMOND (Discussion, p. 1563)....	57
Forging of Arc-Melted Chromium. By H. L. GILBERT, H. A. JOHANSEN, and R. G. NELSON.....	63
Flow and Fracture Characteristics of the Aluminum Alloy 24S-T4 as Affected by Strain Thermal History. By S. I. LIU and E. J. RIFLING.....	66
Effect of Alloying Elements on the Behavior of Nitrogen in Alpha Iron. By L. J. DIJKSTRA and R. J. SLADEK (Discussion, p. 1560).....	69
Systems Zirconium-Molybdenum and Zirconium-Wolfram. By R. F. DOMAGALA, D. J. MCPHERSON, and M. HANSEN (Discussion, p. 747).....	73
Measurement of Internal Boundaries in Three-Dimensional Structures by Random Sectioning. By C. S. SMITH and L. GUTTMAN (Discussion, p. 1561).....	81
Effect of Tensile Strain at Low Temperatures on Deformation Twinning in Ingot Iron. By G. W. GEIL and N. L. CARWILE.....	213
Absolute Rate Theory Applied to Rate of Growth of Pearlite. By J. H. FRYE, JR., E. E. STANSBURY, and D. L. McELROY (Discussion, p. 1581).....	219
Titanium-Manganese System. By D. J. MAYKUTH, H. R. OGDEN, and R. I. JAFFEE (Discussion, p. 1566).....	225
Titanium-Tungsten and Titanium-Tantalum Systems. By D. J. MAYKUTH, H. R. OGDEN, and R. I. JAFFEE.....	231
Microstructure and Mechanical Properties of Iodide Titanium. By F. C. HOLDEN, H. R. OGDEN, and R. I. JAFFEE (Discussion, p. 1562).....	238
Titanium-Nickel Phase Diagram. By H. MARGOLIN, E. ENCE, and J. P. NIELSEN.....	243
Titanium-Carbon Phase Diagram. By I. CADOFF and J. P. NIELSEN (Discussion, p. 1564).....	248
Constitution of Titanium-Rich Ti-Cr-Al Alloys at 1800° and 1400°F. By J. L. TAYLOR and P. DUWEZ (Dis- cussion, p. 1565).....	253
Mechanism of Plastic Flow in Titanium—Determination of Slip and Twinning Elements. By F. D. ROSI, C. A. DUBE, and B. H. ALEXANDER.....	257
Observation on Scaling of Iron. By W. J. WRAZEJ (Correction, p. 572. Discussion, p. 1570).....	265
Mechanical Properties of High Purity Ti-Al Alloys. By H. R. OGDEN, D. J. MAYKUTH, W. L. FINLAY, and R. I. JAFFEE (Discussion, p. 1561).....	267
System Zirconium-Copper. By C. E. LUNDIN, D. J. MCPHERSON, and M. HANSEN.....	273
System Zirconium-Chromium. By R. F. DOMAGALA, D. J. MCPHERSON, and M. HANSEN.....	279
Kinetics of Thermal Reorientations in Cold Rolled Zirconium. By R. K. McGEARY and B. LUSTMAN (Dis- cussion, p. 1573).....	284
Vanadium-Oxygen Solid Solutions. By A. U. SEYBOLT and H. T. SUMSION.....	292
Cold-Rolling and Annealing Textures of Molybdenum Single Crystals. By N. K. CHEN and R. MADDIN (Dis- cussion, p. 1569).....	300
Grain Boundary Sliding and Migration and Intercrystalline Failure Under Creep Conditions. By H. C. CHANG and N. J. GRANT (Discussion, p. 1579).....	305
Determination of the Absolute Grain Boundary Energy of Gold at 1300°K. By F. H. BUTTNER, H. UDIN, and J. WULFF.....	313
Nature of the Creep Curve. By T. H. HAZLETT and E. R. PARKER (Discussion, p. 1577).....	318
Some Observations on Correlations Between the Creep Behavior and the Resulting Structures in Alpha Solid Solutions. By O. D. SHERBY and J. E. DORN.....	324
Creep Properties of Commercially Pure Titanium. By W. R. KIESSEL and M. J. SINNOTT.....	331
Occurrence of Chi Phase in Molybdenum-Bearing Stainless Steels. By P. K. KOH.....	339
Effect of Small Additions of Oxygen on Lattice Constants and Hardness of Zirconium. By R. M. TRECO.....	344
Development of Mechanical and Magnetic Hardness in a 10 Pct V-Co-Fe Alloy. By R. W. FOUNTAIN and J. F. LIBSCH.....	349
Thermal and Dilatometric Investigation of the Alloys of Cobalt with Chromium and Molybdenum. By A. G. METCALFE.....	357
Residual Stresses Introduced During Metal Fabrication. By K. R. VAN HORN (Institute of Metals Division Lecture, 1953).....	405
Directional Properties of 2S Aluminum. By K. T. AUST and F. R. MORRAL.....	431
Some Applications of the Thermodynamic Theory of Irreversible Processes to Physical Metallurgy. By E. S. MACHLIN.....	437
Measurement of Particle Sizes in Opaque Bodies. By R. L. FULLMAN.....	447
Stabilization of the Austenite-Martensite Reaction in a High Chromium Steel. By S. C. DAS GUPTA and	

B. S. LEMENT.....	530
Effects of Macrostructure on the Performance of Alnico Permanent Magnets. By D. G. EBELING and A. A. BURR.....	537
Vanadium-Uranium Constitutional Diagram. By H. A. SALLER and F. A. ROUGH.....	545
Silver-Cadmium Eutectoid. By G. R. SPEICH and D. J. MACK.....	549
Formation of Deformation Bands in Al-3 Pct Mg Monocrystals During Cold Rolling. By J. HERENGUEL, P. LACOMBE, and P. LELONG.....	559
Statistical Grain Structure Studies: Plane Distribution Curves of Regular Polyhedrons. By F. C. HULL and W. J. HOUK (Discussion, p. 1570).....	565
Effect of Dissolved Sulphur on the Surface Tension of Liquid Copper. By C. F. BAES, JR. and H. H. KELLOGG.....	643
Electron Microscope Study of the Effect of Cold Work on the Subgrain Structure of Copper. By L. DELISLE.....	660
Martensite Habit Plane in Quenched Ti-Mn Alloys. By Y. C. LIU and H. MARGOLIN.....	667
Recrystallization of a Cold-Rolled Copper Single Crystal. By Y. C. LIU and W. R. HIBBARD, JR. (Discussion, p. 1568).....	672
Rate of Formation of Isothermal Martensite in Fe-Ni-Mn Alloy. By R. E. CECH and J. H. HOLLOMON.....	685
Identification of the Precipitate Accompanying 885°F Embrittlement in Chromium Steels. By R. M. FISHER, E. J. DULIS, and K. G. CARROLL.....	690
Densification and Kinetics of Grain Growth during the Sintering of Chromium Carbide. By H. J. HAMJIAN and W. G. LIDMAN.....	696
Deformation of Ferrite Single Crystals. By F. L. VOGEL, JR. and R. M. BRICK.....	700
Vapor Pressure of Silver. By C. L. McCABE and C. E. BIRCHENALL.....	707
Vapor Pressure of Silver over Silver-Gold Solid Solutions. By C. L. McCABE, H. M. SCHADEL, JR., and C. E. BIRCHENALL.....	709
Metallographic Observations of the Deformation of High-Purity Magnesium in Creep at 500°F. By A. R. CHAUDHURI, N. J. GRANT, and J. T. NORTON.....	712
Revealing the Subgrain Structure of Aluminum. By M. S. HUNTER and D. L. ROBINSON.....	717
Alpha Solid-Solution Area of the Cu-Mn-Sn System. By C. W. FUNK and J. A. ROWLAND.....	723
Recrystallization and Stored Energy. By H. P. LEIGHLY, H. L. WALKER, and J. W. MARX.....	809
Magnetic Annealing of a Co-Fe Alloy. By A. H. GEISLER, J. P. MARTIN, E. BOTH, and J. H. CREDE.....	813
Order-Disorder Transformation in Cu-Au Alloys near the Composition CuAu. By J. B. NEWKIRK.....	823
Self-Diffusion of Iron in Iron Oxides and the Wagner Theory of Oxidation. By L. HIMMEL, R. F. MEHL, and C. E. BIRCHENALL.....	827
Electrical Resistance of Titanium Metal. By J. L. WYATT.....	903
Microscopical Examination of Tin Bronzes in the Alpha Range. By E. C. W. PERRYMAN.....	906
Grain Boundary Attack on Aluminum Hydrochloric Acid and Sodium Hydroxide. By E. C. W. PERRYMAN.....	911
Martensite Nucleation in Substitutional Iron Alloys. By J. C. FISHER.....	918
Calculation of Martensite Nucleus Energy Using the Reaction-Path Model. By J. C. FISHER and D. TURNBULL.....	921
Further Progress in the Development of Mg-Zr Alloys to Give Good Creep and Fatigue Properties Between 500° and 650°F. By C. J. P. BALL, A. C. JESSUP, P. A. FISHER, D. J. WHITEHEAD, and J. B. WILSON.....	924
Textures of Rolled and Annealed Iodide Zirconium. By J. H. KEELER, W. R. HIBBARD, JR., and B. F. DECKER.....	932
Anelastic Behavior of Pure Gold Wire. By D. R. MASH and L. D. HALL.....	937
Influence of Aluminum and Silicon Deoxidation on the Strain Aging of Low-Carbon Steels. By W. C. LESLIE and R. L. RICKETT.....	1021
Some Properties of Columbium Containing Nitrogen. By C. Y. ANG and C. WERT.....	1032
System Zirconium-Boron. By F. W. GLASER and B. POST.....	1117
A Study of Some Binary Hafnium Compounds. By F. W. GLASER, D. MOSKOWITZ, and B. POST.....	1119
Creep Behavior of Extruded Electrolytic Magnesium. By C. S. ROBERTS.....	1121
High Pressure Oxidation Rate of Metals—Copper in Oxygen. By W. MCKEYAN and W. M. FASSELL, JR.....	1127
Plasticity of Columbium Single Crystals. By R. MADDIN and N. K. CHEN.....	1131
Electrical Resistivity of Liquid Metals and of Dilute Liquid Metallic Solutions. By E. SCALA and W. D. ROBERTSON.....	1141
A Rationalization of Measured High Temperature Properties of Fe-Cr-Co-Ni Alloys. By J. D. NISBET and W. R. HIBBARD, JR.....	1149
Subgrain Formation in High-Purity Aluminum During Creep at High Temperatures. By A. M. GERVAIS, J. T. NORTON, and N. J. GRANT.....	1166
Inhomogeneity in Creep Deformation of Coarse Grained High Purity Aluminum. By H. C. CHANG and N. J. GRANT.....	1175
Plastic Stress-Strain Relations for Aluminum Alloy 14S-T6 Subjected to Combined Tension and Torsion. By J. MARIN and H. A. B. WISEMAN.....	1181
Deformation Mechanisms in Alpha Titanium. By E. A. ANDERSON, D. C. JILLSON, and S. R. DUNBAR.....	1191
Effects of Solid Solution Alloying on the Cold-Rolled Texture of Titanium. By C. J. MCHARGUE, S. E. ADAIR, JR., and J. P. HAMMOND.....	1199
The Ternary System Ti-Ta-C. By J. G. McMULLIN and J. T. NORTON.....	1205
System Titanium-Chromium-Iron. By R. J. VAN THYNE, H. D. KESSLER, and M. HANSEN.....	1209
Plastic Deformation of Rectangular Zinc Monocrystals. By J. J. GILMAN.....	1217
Variation of Plastic Properties with Annealing Procedure in Zinc Single Crystals. By C. H. LI, J. WASHBURN, and E. R. PARKER.....	1223
Recovery in Single Crystals of Zinc. By R. DROUARD, J. WASHBURN, and E. R. PARKER.....	1226
Plastic Deformation of Single Crystals of Copper. By J. J. BECKER and J. N. HOBSTETTER.....	1231
Orientation Relationships in the Recrystallization of Deformed Copper Single Crystals. By J. J. BECKER and J. N. HOBSTETTER.....	1235
Age Softening of Beta Brass. By H. GREEN and N. BROWN.....	1240
Plastic Deformation of Iron Between 300° and 772°K. By D. F. GIBBONS.....	1245
Rate of Propagation of Martensite. By R. F. BUNSHAH and R. F. MEHL.....	1251
Decay of Lattice Defects Frozen into an Alloy by Quenching. By A. E. ROSWELL and A. S. NOWICK.....	1259
Measurement of Approximately Cylindrical Particles in Opaque Samples. By R. L. FULLMAN.....	1267
The Cold Rolled Texture of Titanium. By D. N. WILLIAMS and D. S. EPPELSHEIMER.....	1378
Neptunium-Aluminum Intermetallic Compounds. By O. J. C. RUNNALLS.....	1460
Diffusion and Solubility of Boron in Iron and Steel. By P. E. BUSBY, M. E. WARGA, and C. WELLS.....	1463
Effects of Temperature on the Flow and Fracture Characteristics of Molybdenum. By J. H. BECHTOLD.....	1469
Bending of Molybdenum Single Crystals. By K. T. AUST, R. MADDIN, and N. K. CHEN.....	1477
Kink Band Formation in High Purity Aluminum During Creep at High Temperatures. By A. M. GERVAIS, J. T. NORTON, and N. J. GRANT.....	1487
The Properties of Sand Cast Mg-Th-Zn-Zr Alloys. By K. E. NELSON.....	1493
Titanium-Rich Regions of the Ti-C-N, Ti-C-O, and Ti-N-O Phase Diagrams. By L. STONE and H. MARGOLIN.....	1498
On the Theory of the Formation of Martensite. By M. S. WECHSLER, D. S. LIEBERMAN, and T. A. READ.....	1503
Diffusionless Phase Change in the Indium-Thallium System. By M. W. BURKART and T. A. READ.....	1516

CONTENTS

PAGE

Some Observations on the Work Hardening of Metals. By E. H. EDWARDS, J. WASHBURN, and E. R. PARKER	1525
Analysis of Molten-Zone Refining. By N. W. LORD	1531
Calculation of Interdiffusion Coefficients When Volume Changes Occur. By M. COHEN, C. WAGNER, and J. E. REYNOLDS	1534
The Molybdenum-Boron System. By P. W. GILLES and B. D. POLLOCK	1537
The Partition of Some Alloying Elements Between Carbide and Ferrite in Steels. By D. A. SCOTT and G. S. FARNHAM	1541
System Titanium-Chromium-Molybdenum. By R. P. ELLIOTT, B. W. LEVINGER, and W. ROSTOKER	1544
After-Effects in Polycrystalline Cadmium. By C. S. BARRETT	1652
Torsional After-Effect Measurement and Applications to Aluminum. By C. S. BARRETT, P. M. AZIZ, and I. MARKSON	1655

Iron and Steel Division

Evaluation of the pH and Conductivity Methods of Slag Control. By P. D. S. ST. PIERRE (Correction, p. 572. Discussion, p. 1552)	41
Accelerated Solidification in Ingots: Its Influence on Ingot Soundness. By E. MARBURG (Correction, p. 572. Discussion, p. 1553)	157
Aluminum-Oxygen Equilibrium in Liquid Iron. By N. A. GOKCEN and J. CHIPMAN	173
Thermal Conductivity Method for Analysis of Hydrogen in Steel. By B. M. SHIELDS, J. CHIPMAN, and N. J. GRANT (Discussion, p. 1551)	180
Reduction of Silicon from Blast Furnace Type Slags. By J. C. FULTON, N. J. GRANT, and J. CHIPMAN	185
Attainment of Equilibrium in Gas-Metal Reactions. By N. A. GOKCEN (Discussion, p. 1550)	191
Effect of Various Elements on Hot-Working Characteristics and Physical Properties of Fe-C Alloys. By C. T. ANDERSON, R. W. KIMBALL, and F. R. CATTOIR	525
Metallic Oxidation in Chromium Steel Melting. By D. C. HILTY, G. W. HEALY, and W. CRAFTS	649
The Influence of the Rate of Deformation on the Tensile Properties of Some Plain Carbon Sheet Steels. By J. WINLOCK (Howe Memorial Lecture, 1953)	797
Further Studies of the Tuyere Zone of the Blast Furnace. By J. B. WAGSTAFF (Correction, p. 1018)	895
Examination of a High Sulphur Free-Machining Ingot, Bloom and Billet Sections. By D. J. CARNEY and E. C. RUDOLPHY	999
Reducing Period in Stainless Steel Melting. By H. P. RASSBACH and E. R. SAUNDERS	1009
Silicon-Oxygen Equilibrium in Liquid Iron—A Revision. By J. CHIPMAN and N. A. GOKCEN	1017
Oxygen Activity in Iron Oxide Slags. By H. LARSON and J. CHIPMAN	1089
Manganese as an Indicator of Blast Furnace Slag Oxidation and Desulphurizing Power. By N. J. GRANT, J. W. DOWDING, and R. J. MURPHY	1451
Diffusion of Calcium Ion in Liquid Slag. By H. TOWERS, M. PARIS, and J. CHIPMAN	1455
Some Observations of Slag-Metal Relations in the Acid Open Hearth Steel Furnace. By G. R. FITTERER	1634
Solid Phase Identification in Partially Reduced Iron Ore. By G. BITSIANES and T. L. JOSEPH	1641
Exchange of Iron Between Liquid Metal and Iron Silicate Slags. By G. DERGE and C. E. BIRCHENALL	1648

Extractive Metallurgy Division

Forging of Arc-Melted Chromium. By H. L. GILBERT, H. A. JOHANSEN, and R. G. NELSON	63
Arc-Furnace Equipment and Its Operation at the Kennecott Utah Refinery. By H. A. SHAW and H. G. G. WHITTON	197
Tristage Crystallization Process for Utilizing Western Ferrophosphorus. By L. H. BANNING, W. E. ANABLE, and R. T. C. RASMUSSEN	423
Kinetics of the Oxidation of Galena in Sodium Hydroxide Solutions under Oxygen Pressure. By J. E. ANDERSEN, J. HALPERN, and C. S. SAMIS (Discussion, p. 1556)	554
Operations at New Cornelia Copper Smelter of Phelps Dodge Corporation. By J. W. BYRKIT	633
Effect of Dissolved Sulphur on the Surface Tension of Liquid Copper. By C. F. BAES, JR. and H. H. KELLOGG	643
Free Energy of Vaporization of Metals from 0° to 2000°C. By J. W. EVANS	655
Vapor Pressure of Zinc in the Reduction of ZnS by Cu and Fe. By A. W. BETHUNE and L. M. PIDGEON (Discussion, p. 1558)	804
Vacuum Dezincing of Desilverized Lead Bullion. By T. R. A. DAVEY	991
Thermodynamic Properties of Molybdenum Dioxide. By N. A. GOKCEN	1019
Constitution of the FeO-Fe ₂ O ₃ -SiO ₂ System at Slagmaking Temperatures. By R. SCHUHMAN, JR., R. G. POWELL, and E. J. MICHAL	1097
Solutions of Metals in Fused Salts. By D. CUBICCIOTTI	1106
Reaction of Silver with Aqueous Solutions of Cyanide and Oxygen. By G. A. DEITZ and J. HALPERN	1109
System Ag ₂ O-B ₂ O ₃ ; Its Thermodynamic Properties as a Slag Model. By G. M. WILLIS and F. L. HENNESSY	1367
Effect of Chloride on the Deposition of Copper, in the Presence of Arsenic, Antimony, and Bismuth. By V. HOSPADARUK and C. A. WINKLER	1375
Hurley Furnace and Boiler Description and Design. By E. A. SLOVER	1435
Preparation of Metallic Iron of High Purity. By G. A. MOORE (Discussion, p. 1449)	1443
Sintering Zinc Concentrates on the Blackwell 12 by 168 Ft Machine. By A. E. LEE, JR.	1631

Technical Notes

A Replica Method for Study of the Structure of Lead-Antimony Alloys. By J. BURBANK	55
Torsion Texture of 70-30 Brass and Armco Iron. By W. A. BACKOFEN and B. B. HUNDY	61
Sintering of Ultrafine Ferromagnetic Powders. By N. I. ANANTHANARAYANAN and J. F. LIBSCH	79
Retained Austenite Determinations by X-Ray Methods. By B. L. AVERBACH	87
Regarding Sigma Phase Formation. By D. S. BLOOM and N. J. GRANT	88
Low Temperature Aging in Titanium Alloys. By W. M. PARRIS, L. L. HIRSCH, and P. D. FROST	178
Lattice Parameter of Beta Titanium at Room Temperature. By B. W. LEVINGER	195
High Temperature Modification of TiCr ₂ . By B. W. LEVINGER	196
Effect of Carbon on the Volume Fractions and Lattice Parameters of Retained Austenite and Martensite. By C. S. ROBERTS	203
Slip and Grain Boundary Sliding as Affected by Grain Size. By N. J. GRANT, I. S. SERVI, and A. CHAUDHURI	217
Allotropy in the Phase ZrCr ₂ . By W. ROSTOKER	304
Preferential Etch for Use in Optical Determination of Germanium Crystal Orientation. By R. H. WYNNE and C. GOLDBERG	436
Grain Boundary Films in Boron Steels. By J. W. SPRETNAC and R. SPEISER	445
Note on Contamination of Silicon Ingots. By G. SANDOZ and H. E. STAUSS	653
Notes on the Plastic Critical Temperature in Strain-Induced Martensite Reactions. By C. D. STARR	654

Simple Devices for Approximating Constant Stress During Tensile Creep Tests. By R. L. FULLMAN, R. P. CARREKER, JR., and J. C. FISHER.....	657
Observations on the Phase TiAg. By R. J. VAN THYNE, W. ROSTOKER, and H. D. KESSLER.....	670
On the Distribution of Sodium in Modified Al-Si Alloys. By A. B. MICHAEL and M. B. BEVER.....	679
Kinetics of Galvanizing. By D. J. BLICKWEDE.....	807
Concentration Gradients Associated with Growing Pearlite. By R. E. GRACE (Correction, p. 1018).....	820
Importance of the Iron Content of High-Purity Aluminum. By M. METZGER and J. INTRATER.....	821
High Temperature Corrosion in Nickel-Chromium Alloys. By N. SPOONER, J. M. THOMAS, and L. THOMASSEN	844
Effect of Nickel and Molybdenum on Stabilization of the Austenite-Martensite Transformation. By D. J. BLICKWEDE.....	922
Isothermal Temper Embrittlement of SAE 3140 Steel. By F. L. CARR, M. GOLDMAN, L. D. JAFFE, and D. C. BUFFUM.....	998
Thermal Conductivity of Nodular Iron. By M. J. SINNOTT.....	1016
Plastic Bending of Zinc Crystals. By G. P. CONARD, II, B. L. AVERBACH, and M. COHEN.....	1036
Modifications of the Schulz Technique for the X-Ray Determination of Preferred Orientation in Rolled Metal. By M. L. FULLER and G. VAUX.....	1038
Some Low Temperature Properties of Titanium Alloy RC-130-B and Stainless Steel. By W. W. TYLER, L. B. NESBITT, and A. C. WILSON, JR.....	1104
Effect of Grain Size upon Temper Brittleness. By L. D. JAFFE, F. L. CARR, and D. C. BUFFUM.....	1147
Crystallographic Angles for Orthorhombic (Alpha) Uranium. By R. B. RUSSELL.....	1190
Filler Material for the Brazing of Titanium. By N. A. DECECCO and H. M. MEYER.....	1197
Structure of the Phase TiMn and the Indexing of Powder Patterns of Sigma-Type Phases. By R. P. ELLIOTT and W. ROSTOKER.....	1203
Detection of Microcracks in Steel. By W. L. JENSEN and R. F. CAMPBELL.....	1222
Relation Between Initial Creep Rate and Resolved Shear Stress in Zinc Single Crystals. By N. BROWN, J. WASHBURN, and E. R. PARKER.....	1229
Thermal Conductivity, Electrical Resistivity, and Thermoelectric Power of Uranium. By W. W. TYLER, A. C. WILSON, JR., and G. J. WOLGA.....	1238
A Corrected Interpretation of the Mechanism of Growth of Magnetite During Oxidation. By M. H. DAVIES, M. T. SIMNAD, and C. E. BIRCHENALL.....	1250
Some Effects of Microstructure upon Temper Brittleness. By D. C. BUFFUM and L. D. JAFFE.....	1373
Notes on a Molybdenum-Rhenium Alloy. By C. J. MCHARGUE and H. W. MAYNOR, JR.....	1382
Change in Ingot Shape During Zone Melting. By W. G. PFANN.....	1441
The Habit Plane of Beta in Alpha Titanium. By P. A. ALBERT.....	1449
The Silver-Cadmium Beta and Zeta Phases. By L. MULDAWER, M. AMSTERDAM, and F. ROTHWART.....	1458
Formation of Sigma Phase in the Mn-Mo System. By B. F. DECKER, R. M. WATERSTRAT, and J. S. KASPER.....	1476
Effects of Sample Surface and X-Ray Diffraction Camera Geometry on the Determination of Retained Austenite in Hardened Steels. By K. E. BEU and D. P. KOISTINEN.....	1529
Notes on the Determination of Retained Austenite by X-Ray Methods. By K. E. BEU.....	1539
The Energy State of Fatigued Copper. By B. WELBER and R. WEBELER.....	1558
A Crystallographic Analysis of the Ductile-Brittle Transition in Body-Centered Cubic Single Crystals. By A. J. OPINSKY.....	1650
Surface Structures on Single Crystals Produced from Melt. By F. D. ROSI.....	1661

Discussions

Institute of Metals Division.....	726, 1560
Iron and Steel Division.....	1549
Extractive Metallurgy Division.....	1556

Index.

Evaluation of the pH and Conductivity Methods of Slag Control

by P. D. S. St. Pierre

IN recent years the use of high sulphur fuels and charges in steelmaking has necessitated rapid methods of slag control in order to insure the production of high quality steel. Several systems of control have been discussed in the literature, and of these the method described by Philbrook, Jolly, and Henry¹ has received the most attention recently. In their process the hydrogen ion concentration of an aqueous slag suspension is determined under controlled, but arbitrary conditions. The basicity of the slag may then be derived from a previously established pH-V ratio curve. Thus, by measuring the pH, some indication of the V ratio is gained, from which significant properties of the slag may be deduced. Philbrook et al. made no claims as to the theoretical justification of their treatment, but simply offered it as a rapid means of slag control. Encouraging results caused others to study the method and publish their findings.²⁻⁵ Although there was fair agreement on the efficacy of the method, no common parameter was evolved against which pH readings could be plotted. The results of the various determinations were related to such V ratios as CaO/SiO_2 and $\text{CaO}/\text{SiO}_2 + \text{P}_2\text{O}_5$ by some,¹⁻³ while others⁵ plotted against "excess lime." Rivet,⁴ however, found a simple proportionality between the hydrogen ion concentration and the sulphur content of the molten steel beneath the slag. Since slag control in North American practice is largely directed toward the efficient removal of sulphur from steel, Rivet's approach to the problem had the advantage of connecting directly a property of the slag with the impurity being removed.

In view of the diversity of parameters used it seemed probable that some fundamental point was being overlooked in seeking a relationship. Examination of the literature revealed that much emphasis had been laid on experimental detail but scant attention paid to the fundamental aspects of the hydrolysis of the aqueous slag suspension. Consequently the present investigation was undertaken with the object of rectifying this deficiency and deriving, if possible, a parameter of general application.

Petrographic studies on several matured Canadian open-hearth steel slags have shown that their major

P. D. S. ST. PIERRE is Metallurgist, Physical and Crystal Chemistry Section, Division of Mineral Dressing and Process Metallurgy, Mines Branch, Department of Mines and Technical Surveys, Ottawa, Ont., Canada.

Discussion on this paper, TP 3417C, may be sent, 2 copies, to AIME by April 1, 1953. Manuscript, May 13, 1952. Los Angeles Meeting, February 1953.

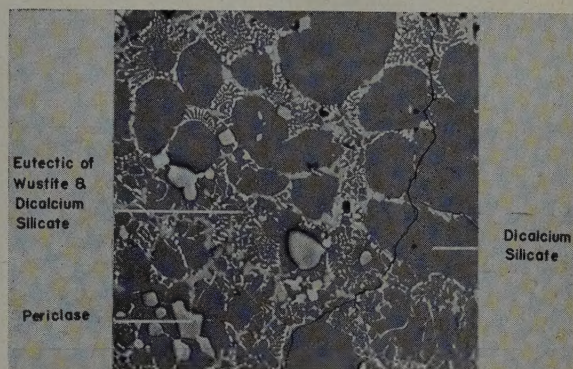


Fig. 1—Polished section of a typical basic open hearth slag. X400. Area reduced approximately 75 pct for reproduction.

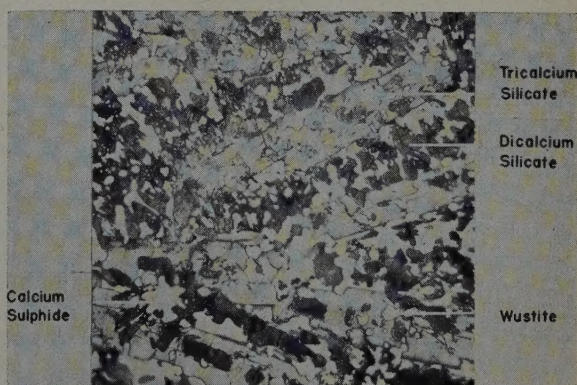


Fig. 2—Polished section of a typical basic open hearth slag. X500. Area reduced approximately 75 pct for reproduction.

constituents are dicalcium and tricalcium silicates set in a complex matrix of iron oxides and ferrites. These phases are shown in Figs. 1 and 2. Free lime is frequently encountered in slags, but is not an equilibrium phase since on continued heating it dissolves forming silicates or ferrites. Thus, it appeared that a study of the hydrolysis of the major phases in steel slags would be profitable.

The experimental technique used in the present work was a modification of that described by the other workers.¹⁻⁵ Electrical conductivity measurements were also made on the suspensions, since Smith et al.³ had claimed advantages for this method in their paper on slag control.

Experimental Procedure

The compounds studied in this investigation were prepared in the laboratory by heating purified oxides

Table I. The pH and Conductivity Values of Aqueous Suspensions of Steel Slag Phases

Compound	Formula	pH	Conductivity, Microhm at 20°C
Wollastonite*	CaO·SiO ₂	10.7	123
Rankinite*	3CaO·2SiO ₂	11.0	192
Dicalcium silicate	2CaO·SiO ₂	11.4	681
Tricalcium silicate	3CaO·SiO ₂	11.9	1810
Lime	CaO	12.6	7800
Fluorite	CaF ₂	6.7	60
Monocalcium ferrite	CaO·Fe ₂ O ₃	9.0	46
Dicalcium ferrite	2CaO·Fe ₂ O ₃	10.5	124
Periclase	MgO	10.1	98

* Not normally found in steel slags, but included in the series to show development of hydrolysis with increasing lime content.

(or carbonates) of the various components to suitable temperatures in platinum crucibles. Samples freshly ground to -100 mesh were used throughout the investigation, the weight taken being varied according to the purpose of the run. After weighing to ± 0.01 g accuracy, the samples were mechanically shaken for a specified time at constant temperature in 100 cc of CO₂-free distilled water. Prior to pH and conductivity determinations, slag suspensions were filtered on Whatman 42 filter papers which previously had been thoroughly washed with CO₂-free distilled water. The first 25 cc of the filtrates was used to wash the electrodes of the instruments, the remainder was used for the actual determinations.

Results

Table I shows the pH and conductivity of the leached elements resulting from shaking 0.50 g of possible open-hearth steel slag phases individually in 100 cc water for 30 min. It should be emphasized that the results relate only to determinations made under the conditions stated and therefore they do not necessarily represent equilibrium values. The pH of wüstite (FeO) was not determined, because it is very difficult to prepare pure ferrous oxide. Although several attempts were made, no really satisfactory product was obtained. There is, however, good reason to believe that its pH would be relatively low, since that of ferrous hydroxide is quoted as only 9.5 in saturated solution. If wüstite caused any pH change at all under the conditions of experiment, it would probably first form hydroxide, in which case it is reasonable to suppose the final pH would not exceed 9.5.

Table II. The pH as a Function of Weight of Steel Slag Phases in Aqueous Suspension

Compound	Formula	Weight, G	pH
Dicalcium silicate	2CaO·SiO ₂	0.05	10.8
		0.10	10.9
		0.25	11.1
		0.50	11.4
		1.00	11.5
		2.00	11.5
Tricalcium silicate	3CaO·SiO ₂	0.05	11.5
		0.10	11.7
		0.25	11.8
		0.50	11.9
		1.00	12.0
		2.00	12.1
Lime	CaO	0.01	11.5
		0.025	11.9
		0.10	12.4
		0.20	12.6
		0.30	12.5
		0.50	12.6

It will be seen from Table I that the lime and calcium silicates are the most easily hydrolyzed compounds and their presence may therefore be considered as the controlling factor in determining the pH of an aqueous slag suspension. Thus, in a mixture of dicalcium and tricalcium silicates the pH will be controlled by the tricalcium silicate, provided there is sufficient quantity present to exceed the maximum pH given by dicalcium silicate. If the tricalcium silicate is present in quantities which exceed that required to produce its maximum pH, there is no means of determining the excess since the pH remains constant.

Because, from a hydrolysis point of view, lime, dicalcium and tricalcium silicates are the most important compounds in a steel slag, data on their hydrolysis as a function of weight were determined. Such data are given in Table II, and the information is shown graphically in Fig. 3. The standard experimental procedure described previously was used to obtain the data. A shaking time of 30 min was found to yield steady pH readings for all the compounds.

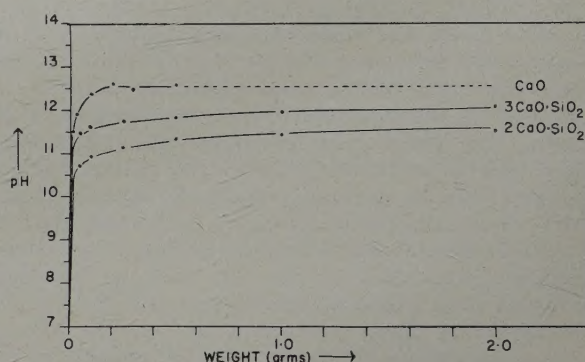


Fig. 3—Effect of weight on the pH of various slag phase aqueous suspensions.

For a given weight of sample the pH increases rapidly in the first few minutes, but after a shaking time of 10 min the rate of increase of pH is very low. Thus, by using 30 min periods of shaking the time factor may be ignored completely.

The curves shown in Fig. 3 immediately reveal the limitations of the pH method of slag control. It will be observed that the curves fall into two parts: at first, pH rises very rapidly with increasing weight of sample, but later the rate of increase is very small. Since slag control implies determination of the calcic mineral content of the slag, pH determinations in general will be either under or over sensitive to variations in such minerals. The choice of weight of slag sample is therefore an important factor in determining the sensitivity of the method. Some workers have used a 0.25 g sample in their investigations, while others have used 0.50 g of slag. Thus in a typical slag containing 30 to 50 pct dicalcium silicate, those using the 0.25 g sample would find the method sensitive to the weight factor and those using the 0.50 g sample would find it insensitive. Clearly in selecting the weight of sample, consideration must be given to the amount of calcic mineral likely to be encountered. If free lime is present it will be seen from the graph that little can be done, since traces of this oxide have considerable effect on the pH of the suspension. If the slag is in equilibrium free lime is generally absent, but in practice it is often found as undissolved material.

The pH of a suspension is controlled by the constituent which will cause the highest pH, and this is a function not only of the intrinsic chemical properties of the compound but also of the quantity present. This latter point may be illustrated by the data given in Fig. 3. It will be seen, for example, that 0.05 g of tricalcium silicate yields almost the same pH as 0.5 g of dicalcium silicate, and there is no way of telling from the pH determination alone which compound is predominant in its effect. If it is known at what stage of the heat the sample was taken, a fairly good guess may be made, for only the late slags are likely to contain tricalcium silicate, see Figs. 1 and 2.

Once the maximum pH of the predominating compound has been reached no determination of the quantity present can be made, for further increases have no effect on the pH. In practice this condition exists as soon as the flat part of the pH-weight curve is reached.

In the case of practical slags a complication exists in that the pH attained by the aqueous suspension will be a function of the surface of mineral exposed, since the calcic minerals may be coated by wüstite (FeO), etc., and can react only through exposed surfaces. This shielding factor may prevent the mineral from hydrolyzing to the value expected for the weight present.

This discussion provides some idea of the inherent difficulties of the pH method of slag control. It has been shown that the mode of hydrolysis of the calcic minerals prevents the hydrogen ion measurement from being an accurate method of estimating the amounts present.

Having shown that the alkalinity of slag suspensions depends on the hydrolysis of certain minerals, it will be apparent that there is no theoretical foundation for relating pH to parameters such as "V ratio" or "excess base." The partial success obtained with some of these parameters might be explained by the fact that they are, to some extent, a crude measure of the calcic minerals present in the slag. Such parameters can therefore be related to pH variations only in a general way.

The information given in Fig. 4 and Tables I and III shows that the conductivity method of control suffers from much the same disadvantages as the pH method.

The conductivity curves of the various compounds are more widely separated than the pH curves and this makes it easier to distinguish between the several phases present in a slag. Equally, however,

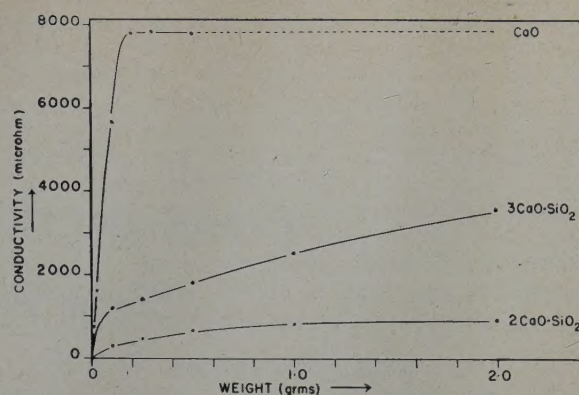


Fig. 4—Effect of weight on the electrical conductivity of various slag phase aqueous suspensions.

it will be seen that very minute quantities of lime present in the slag can upset measurements very considerably. Unfortunately the slopes of these curves render them unsuitable for measuring the amounts of phases present in suspensions. In this respect the conductivity method of control has no advantage over the pH technique.

Discussion

Although pH and conductivity measurements can indicate in a general way the mineralogical development of a slag as the heat proceeds, the nature of hydrolysis of the calcic minerals precludes exact quantitative measurements. In plant practice the method might, however, be used to check the type of slag being made (i.e., whether dicalcium or tricalcium silicate is present or not), provided no free lime is present, and in this application the conductivity measurement would be superior. Thus the pH or conductivity of a good steel slag could be checked and thereafter the composition of all slags adjusted to yield similar results.

Conclusions

1—It is improbable that the pH or conductivity methods of slag control can be improved by refinement of technique or more exact interpretation of results, since both methods are subject to variable sensitivity.

2—The presence of traces of undissolved lime in slag samples has a considerable effect on pH or conductivity measurements.

3—There is little theoretical justification for relating pH or conductivity results to the "V ratios" or "excess base" used by previous workers.

Acknowledgment

The author wishes to acknowledge the valuable assistance of J. F. Tippins, who carried out much of the experimental work, and to thank the Director General of Scientific Services, Department of Mines and Technical Surveys, Ottawa, for permission to publish this paper.

References

- ¹W. O. Philbrook, A. H. Jolly, and T. R. Henry: *Trans. AIME* (1945) **162**, p. 49.
- ²M. Tenenbaum and C. C. Brown: *Trans. AIME* (1945) **162**, p. 60.
- ³W. G. Smith, J. Monaghan, and W. Hay: *Journal Iron and Steel Inst.* (October 1948) **160**, p. 121.
- ⁴J. G. Rivet: *American Foundryman* (December 1950) **18**, No. 6, p. 61.
- ⁵C. W. Sherman and N. J. Grant: *Trans. AIME* (1949) **185**, p. 61; *JOURNAL OF METALS* (November 1949).

Table III. Conductivity as a Function of Weight of Steel Slag Phases in Aqueous Suspension

Compound	Formula	Weight, G	Conductivity, Microhm at 20°C
Dicalcium silicate	2CaO·SiO ₂	0.10	300
		0.25	475
		0.50	681
		1.00	818
		2.00	914
Tricalcium silicate	3CaO·SiO ₂	0.10	1200
		0.25	1420
		0.50	1810
		1.00	2530
		2.00	3560
Lime	CaO	0.01	707
		0.025	1606
		0.10	5650
		0.20	7800
		0.30	7840
		0.50	7800

Density and Hydrogen Occlusion of Some Ferrous Metals

by J. H. Keeler and H. M. Davis

Densities of SAE 1020 (I) and ingot iron (II) decreased with cold rolling to minima at 60 pct reduction, whereas high-purity iron (III) was unaffected. I recovered promptly with annealing; II, sluggishly and incompletely. Hydrogen occlusion of III or II was barely affected by 60 pct cold reduction, but that of I was increased a hundredfold.

IT has been reported of iron that its density is decreased and its occlusive capacity for hydrogen is increased by cold work. One of the most interesting aspects of each of these properties is that the changes brought about by cold work are not necessarily eliminated by annealing and recrystallization. Yet recrystallization is generally accepted as restoring to their original condition the properties or characteristics altered by cold work.

A number of investigators have reported a decrease in density with cold reduction. Two^{1, 2} have shown that annealing after cold reduction may not return the density to its original value. It has been suggested¹ that cracks or flaws in inclusions produced during cold drawing contribute to the lowering of the bulk density of the metal. Extremely high-purity copper has been reported³ as not exhibiting a density decrease with cold reduction. On the other hand, calculations⁴ indicated that grain distortion by itself can produce expansion of the order of magnitude of the changes observable. Maier⁵ showed that both the density of iron and that of copper passed through a minimum with increasing cold reduction.

Although much information is available on the subject of hydrogen in steel^{6, 7} and it is well known that plastic deformation of a metal may increase its

Table I. Chemical Compositions of Materials Investigated

Element	Percentage of Element Present		
	Ingot Iron	SAE 1020	High-Purity Iron
Carbon	0.015	0.17	0.006
Manganese	0.06	0.33	<0.01
Phosphorus	0.004	0.009	0.002
Sulphur	0.025	0.022	0.002
Silicon	0.001	0.024	0.030
Aluminum	0.003	0.004	<0.005
Oxygen	0.066	0.002	0.008
Nitrogen	0.004	0.001	<0.001
Copper	0.04	0.016	<0.005
Nickel	0.018	0.016	0.014
Chromium	0.008	0.010	<0.005
Molybdenum	0.004	0.002	<0.005
Cobalt	0.007		
Tin	0.009	0.001	<0.005
Arsenic	0.006		Faint trace
Titanium	0.0		<0.008
Zirconium			Very faint trace
Magnesium			Trace
Lead			Trace
Strontium	Trace		Very faint trace

occlusive capacity,⁸⁻¹² most of the reports pertain to charging the metal with hydrogen by cathodic deposition or with acid. Darken and Smith,¹² who employed acid charging, emphasized the great influence of cold work on the occlusive capacity of iron for hydrogen and showed the inability of a prolonged high-temperature annealing treatment to restore the occlusive capacity of cold-worked steel to the value exhibited in the hot-rolled condition.

It has been reported¹³ that an "endothermic" metal*

* Endothermic metal refers to metals like iron, nickel, copper, and platinum, which occlude hydrogen with absorption of heat, and for which the occlusion increases with rising temperature.

J. H. KEELER, Member AIME is now Research Associate, General Electric Research Laboratory, Schenectady, and H. M. DAVIS, Member AIME, is Professor of Chemical Metallurgy, The Pennsylvania State College, State College, Pa.

Discussion on this paper, TP 3434E, may be sent, 2 copies, to AIME by April 1, 1953. Manuscript, Feb. 8, 1952; revised, July 31, 1952. Los Angeles Meeting, February 1953.

This paper represents part of a thesis by J. H. Keeler submitted in partial fulfillment of the requirements for the degree of Doctor of Philosophy to The Pennsylvania State College, June 1951.

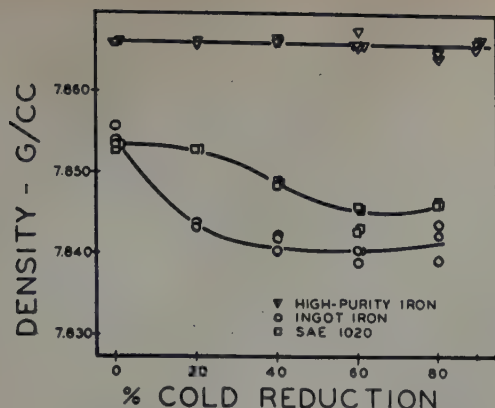


Fig. 1—Relation between density and percentage of cold reduction. The high-purity iron showed no noteworthy decrease in density.

on the other hand, has been said¹⁴ to give to iron at slightly elevated temperatures no "detectable capacity" for absorbing hydrogen. Apparently the influence of cold reduction has been found up to the recrystallization temperature.¹⁶ Tammann¹⁵ has observed considerable evolution of hydrogen from surcharged iron at the recrystallization temperature during heating.

The explanation for the influence of strain (plastic)

Table II. Possible Relation of Area to Density Loss in Annealing

	Area/Volume	Density Loss $\times 10^4$ /Volume
Hot-rolled high-purity iron annealed at 1200°C	19.6	21
Cold-reduced high-purity iron annealed at 1200°C	48.0	40

in the metal upon occlusive capacity is controversial. Whether the hydrogen in molecular form is stored in rifts or lattice imperfections as suggested by Smith¹⁷ and coworkers, and by Zapffe, Sims, and coworkers,¹⁸ or whether hydrogen atoms or protons are held by the lattice imperfections in some manner, has not been fully resolved.

Only indirect evidence has been found showing the influence of cold work or strain in iron on the occlusive capacity for hydrogen at elevated temperatures.

Experiment

Ferrous metals of three compositions were studied in this investigation: a low-metalloid rimmed ingot iron; a rimmed steel, nominally of SAE-1020 grade; and a high-purity iron. The first two were sheets of hot-rolled commercial tonnage alloys, whereas the third was obtained as a 10 lb ingot from the National Research Corp. The chemical compositions are given in Table I.

The heat treatments were done in purified helium in an airtight furnace. The densities were obtained by use of Archimedes' principle, the liquid being monobromobenzene of known density. The overall error was calculated to be possibly as large as 0.00056 g per cc, although separate density calculations for a given specimen have agreed within 0.0002 g per cc. However, the value of 0.00056 g per cc is somewhat less than the variation occasionally found between individual samples of the same material given identical treatments.

The hydrogen occlusion was determined by a technique similar to that of Sieverts. An experiment consisted of heating a metal specimen in an atmosphere of hydrogen at a constant pressure of 710 mm of mercury and measuring over mercury the equilibrium volume obtained at various temperatures. These values were then compared with the volumes obtained at the same temperatures during a blank experiment in which no hydrogen was absorbed. The difference between the volume obtained with metal present and the corresponding value found with the blank showed the amount of hydrogen absorbed by the metal at the particular test temperature.

Results and Discussion

The experiments revealed that neither the density nor the hydrogen occlusion of a ferrous material is necessarily altered appreciably by cold reduction or by subsequent annealing. Each material must be considered individually.

High-Purity Iron: The density of the hot-rolled high-purity iron was found to agree very well with the values cited by Cleaves and Thompson,¹⁹ who reported an average of 7.867 g per cc as obtained by direct determination. The value found in this investigation was 7.866 g per cc. (A density of 7.874 g per cc for exceptionally high-purity iron has been reported by Cleaves and Hiegel.²⁰)

Contrary to the widely accepted opinion that cold working decreases the density of a metal, it was found that sheets of high-purity iron cold-rolled 20, 40, 60, 80, and 90 pct from the hot-rolled condition did not undergo any noteworthy decrease in density, Fig. 1. In no case did the density of this material increase with annealing after cold reduction, Fig. 2. Actually, annealing in helium at a temperature of 1200°C decreased the density, a change which had not been foreseen.

Specimens of hot-rolled high-purity iron (about 0.10 in. thick), annealed with the above material at 1200°C, showed a small decrease in density, although not so large a loss as the thinner, cold-reduced specimens. If the density decrease at 1200°C resulted from a surface phenomenon such as volatilization or reaction with an impurity in the helium, a smaller density loss would be expected for the thicker material than for the thinner sheets. A consideration of the area-to-volume ratios and the density-loss-to-volume ratios of the hot-rolled and the cold-reduced high-purity iron specimens suggested that a surface phenomenon was involved, Table II.

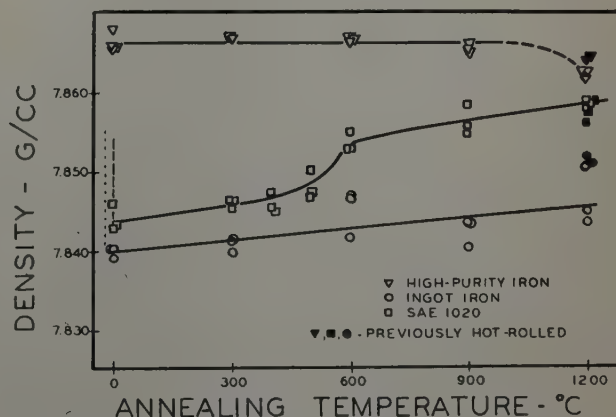


Fig. 2—Relation between density and annealing temperature. The SAE 1020 exhibited a rapid increase in density during annealing at 600°C. The high-purity iron and the ingot iron showed a density decrease after annealing at 1200°C.

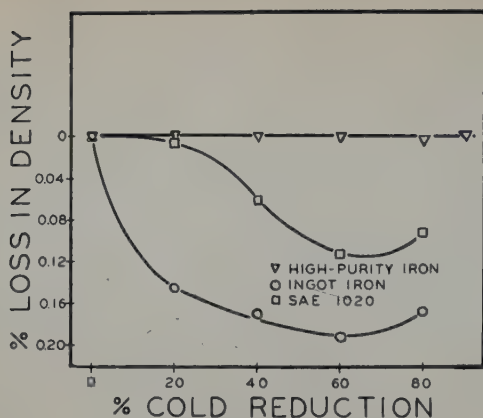


Fig. 3—Relation between percentage loss in density and percentage cold reduction.

Table III contains data showing the lack of influence of either cold reduction or annealing upon the density of the high-purity iron with the exception of the anneal at 1200°C.

Ingot Iron: The density of the ingot iron was found to decrease with increased cold deformation up to 60 pct reduction, as shown in Figs. 1 and 3. A slight increase in density was observed at 80 pct reduction, which is in agreement with Maier.⁵

The density determined for the hot-rolled ingot iron was nearly the same as that obtained for the hot-rolled SAE 1020, Table II. On the basis of purity, it might be argued that, because of the higher oxygen content, the volume of inclusions in the ingot iron would be the greater, giving that material the lower density. It was also suspected that the commercially hot-rolled ingot iron contained some strain, so that the metal was not of maximum density.

The recovery of density by the ingot iron with annealing after cold reduction showed a greater spread in values than was observed in the other materials. Careful rechecking indicated that the measured densities were correct for the individual specimens. Apparently the ingot iron was of a lower degree of homogeneity than were the other metals. In spite of the spread in the data, the recovery of density was clearly shown to be relatively small, inasmuch as the greatest recovery was only about 42 pct of the decrease resulting from cold reduction.

As did the high-purity iron, the hot-rolled ingot iron suffered a density decrease when annealed at 1200°C. The magnitude of this loss was 0.0039 g per cc.

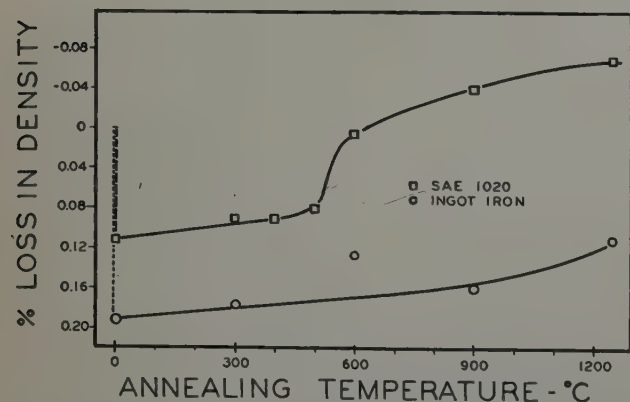


Fig. 4—Relation between percentage loss in density and annealing temperature.

The density of the cold-reduced ingot iron after the 1200° anneal was only slightly increased over that found after the 900° anneal. This may have been the resultant of a density loss (also shown by the hot-rolled material) superimposed on a further recovery from the effects of cold reduction. If it is assumed that the same ratio obtains between the density losses of the hot-rolled and the cold-reduced ingot iron after the 1200° anneal as was observed for the hot-rolled and the cold-reduced high-purity iron, then a value close to the observed density of the un-annealed, hot-rolled ingot iron can be calculated, Table IV.

When the ratios in Table IV are assumed equivalent,

$$\frac{0.0021}{0.0040} = \frac{0.0039}{x}, \text{ and } x = 0.0074 \text{ g per cc.}$$

If the 0.0074 g per cc is added to the experimental density of the ingot iron as cold-reduced and annealed at 1200°C,

$$0.0074 + 7.8463 = 7.8537 \text{ g per cc}$$

the sum is close to the observed density of the hot-rolled ingot iron.

SAE 1020: Although the density of the SAE 1020 decreased as the cold reduction was increased, the rate of density decrease was not so rapid as was that for the ingot iron. The minimum density was reached after a cold reduction of 60 pct and, as with the ingot iron, a slight increase in density above the minimum was observed after a cold reduction of 80 pct, Figs. 1 and 3.

Annealing of the 60 pct cold-reduced SAE 1020 at 300°C for 2 hr provided negligible recovery of density. At a temperature of 400°C an unmistakable increase in the density was found and, after the anneal at 600°C, density recovery was substantially complete. Higher annealing temperatures, 900° and 1200°C, increased the density to a value even greater than that of the nominally hot-rolled condition, Figs. 2 and 4. It was evident from the microstructures of these specimens that little carbon, if any, remained in the metal after the anneal at either 900° or 1200°C. If a straight-line relationship is assumed between the density of cementite, 7.67 g per cc,²¹ and the density of high-purity iron, 7.87 g per cc, the influence of carbon upon density in the SAE 1020 containing 0.17 pct C is approximated at 0.005 g per cc. If 0.0050 g per cc is subtracted from the density of the hot-rolled SAE 1020 annealed 2 hr at 1200°C (7.8574 g per cc), a value of 7.8524 g per cc is obtained. The original hot-rolled and not decarburized material had a density of 7.8534 g per cc, which agrees well with the value obtained by correction for carbon.

The anneal at 1200°C apparently did not produce in the SAE 1020 the density decrease found in the commercially pure ingot iron and in the high-purity iron. The hot-rolled SAE 1020 agreed closely in density with the 60 pct cold-reduced SAE 1020 after both had been annealed at 1200°C.

It was reported previously that the high-purity iron exhibited no decrease in density with cold reduction of as much as 90 pct by rolling. This behavior is contrary to the theoretical prediction that crystal deformation alone can produce a density decrease of the experimentally familiar magnitude. With the same kind of deformation, however, the ingot iron and the SAE 1020 did exhibit a loss of density.

If a decrease in density with cold reduction can be associated with the presence of foreign elements in the metal, a plausible explanation of that relationship is that imperfect or uneven flow of metal occurs at phase boundaries during plastic deformation. Voids in the metal adjacent to inclusions could possibly serve in explanation of the observations.

The presence of voids in cold-worked iron or steel has been indicated by the blistering of such materials by hydrogen after acid pickling. It is also widely observed that such blisters often occur in the vicinity of inclusions in the metal. It is possible that the inability of the metal, during plastic deformation, to flow perfectly about small inclusions would both cause the voids necessary to initiate blistering and contribute to a decrease in the density of the metal.

The wide difference in density recovery with annealing of the SAE 1020 and the ingot iron suggests that different mechanisms are involved in the density decrease induced in these two metals by cold work. It would be instructive to determine the influence of various phases upon the plastic behavior of the surrounding ferrite lattice.

Hydrogen Occlusion: The first experimental values obtained for the occlusion of hydrogen by high-purity iron and by ingot iron in the hot-rolled, the 60 pct cold-reduced, and the annealed condition did not differ significantly from each other. Because this lack of influence of cold work was not anticipated by information found in the literature, several occlusion tests with annealed nickel sheet were conducted to show whether the system was sufficiently sensitive to pick up notable differences in hydrogen occlusion. Inasmuch as the values obtained for the hydrogen occlusion by nickel agreed very well with the data of Armbruster,²² confidence in the measurement was established.

The continued study of the occlusion of hydrogen revealed no large variations in the occlusive capacity of the high-purity iron or of the ingot iron, whether the metal was in the hot-rolled, the 60 pct cold-reduced, or the annealed condition, Figs. 5 and 6. The occlusive capacity of the SAE 1020 in the hot-rolled and in the annealed condition was similar to that of the high-purity iron and that of the ingot iron, Fig. 7. But the 60 pct cold-reduced SAE 1020 exhibited a phenomenal occlusive capacity for hydrogen at the lower test temperatures. At 250°C this material occluded 9.03 cc of hydrogen per 100 g of

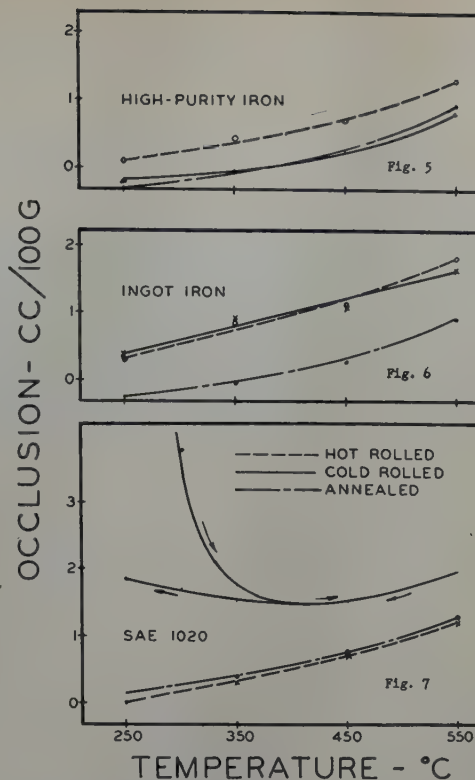


Fig. 5—Hydrogen occlusion vs temperature for high-purity iron in various conditions.

Fig. 6—Hydrogen occlusion vs temperature for ingot iron in various conditions.

Fig. 7—Hydrogen occlusion vs temperature for SAE 1020 in various conditions. The curve for the cold-reduced material is incompletely shown here. See Fig. 8.

metal, about 24 hr being necessary for the attainment of equilibrium. This volume was approximately one hundred times the amount taken up by the hot-rolled SAE 1020, or by either of the other two irons. At 300°C, the occlusion of hydrogen by the cold-reduced SAE 1020 fell to 3.84 cc per 100 g. Here, less than 30 min was necessary for the establishment of equilibrium. A minimum occlusion was reached at 450°C, where 1.50 cc per 100 g was taken up, and the normal solubility rise with a further increase of temperature was observed at 550°C. As the metal was cooled, the curve of occlusion vs temperature did not follow the same path that it took during heating. Apparently some recrystallization (among other possible changes) had occurred at the higher test temperatures, diminishing the occlusive capacity. During cooling, a broad minimum in the hydrogen occlusion occurred at 350° to 400°C, and the amount of occlusion increased slightly at 300° and 250°C. The hydrogen occlusion of the cold-reduced SAE 1020 plotted against temperature is shown in Fig. 8, which also includes, for comparison, selected values from the literature and from this investigation for the occlusive capacity of nickel and of iron.

The density decrease and the large increase in hydrogen occlusion which were exhibited by the

Table III. Densities of Test Materials in Various Conditions

Condition	Density, G per CC at 25°C		
	High-Purity Iron	Ingot Iron	SAE 1020
Hot-rolled	7.8662	7.8549	7.8534
Cold-reduced:			
20 pct	7.8664	7.8435	7.8530
40 pct	7.8663	7.8415	7.8488
60 pct	7.8664	7.8399	7.8445
80 pct	7.8650	7.8418	7.8465
90 pct	7.8664		
60 pct cold-reduced plus:			
2 hr at 300°C	7.8671	7.8409	7.8460
2 hr at 400°C			7.8459
2 hr at 500°C			7.8470
2 hr at 600°C	7.8666	7.8450	7.8537
2 hr at 900°C	7.8655	7.8424	7.8564
2 hr at 1200°C	7.8622	7.8463	7.8587
Hot-rolled plus:			
2 hr at 1200°C	7.8641	7.8511	7.8574

In most instances these values are averages from three specimens in each condition, three determinations per specimen.

Table IV. Comparison of Density Losses in Annealing

Metal	Condition Before 1200°C Anneal	Annealing Loss, G per CC
High-purity iron	Hot-rolled	0.0021
	Cold-reduced	0.0040
Ingot iron	Hot-rolled	0.0039
	Cold-reduced	x

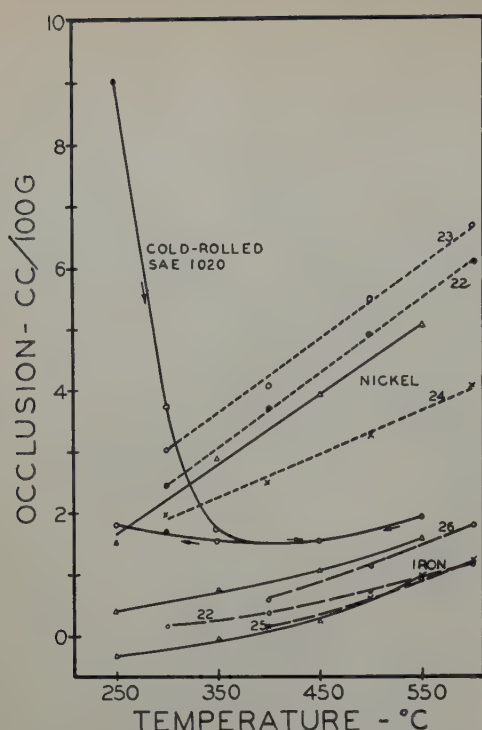


Fig. 8—Hydrogen occlusion vs temperature for nickel (dotted lines 22, 23, and 24) and for iron (dashed lines 22, 25, and 26). The numbers refer to references which are the original sources of the data indicated by broken lines. The solid lines are data from this investigation. The data for iron from this research indicate the wide spread of values. The curve for the cold-reduced SAE 1020 is in remarkable contrast to the other curves.

SAE 1020 after cold reduction were not compatible with the concept of the storage of molecular hydrogen. Approximately 2.9 cc of gas was charged into 4.1 cc of this steel at 250°C, the source of the hydrogen being the gas at a pressure slightly less than 1 atm. Since the observed density decrease of 0.18 pct in this material could provide a calculated storage volume of only 0.00524 cc, storage as hydrogen gas would require a pressure of 516 atm in the voids, or 552 times the charging pressure. Yet the dissociation which makes charging possible at the test temperature, 250°C, would hardly permit the development of void pressures any greater than 1 atm.

The hydrogen-occlusion results for the three ferrous materials in various conditions and for annealed nickel were obtained by subtraction of the observed volumes from the average of the appropriate blank values. Because the blank could vary by as much as ± 1.75 pct, the very small occlusive capacity of iron for hydrogen, particularly at 250°C, occasionally produced a fallacious negative value for occlusion. Obviously, in these instances the slight occlusion of hydrogen was less than the experimental error.

Summary and Conclusions

The high-purity iron showed neither a density decrease nor any noteworthy change in hydrogen occlusion with cold reduction or annealing. Apparently the presence of impurities is necessary for a density decrease with cold reduction.

Cold reduction decreased the density of ingot iron but did not change the hydrogen occlusion of the metal. Annealing after cold reduction restored only 42 pct of the original density loss and did not influence the hydrogen occlusion.

Cold reduction decreased the density of SAE 1020

and increased the hydrogen occlusion at 250°C about 100-fold. This remarkable hydrogen occlusion decreased at higher temperatures, but remained greater than that of the unstrained material. Annealing after cold reduction eliminated the density loss and diminished the large occlusive capacity caused by cold work. The hydrogen-occlusion behavior of the SAE 1020 is not compatible with the theory of occlusion by storage of molecular hydrogen.

To reconcile the various observations, it is proposed that two varieties of voids result from imperfect plastic flow of the ferrite about inclusions or other phases during cold rolling. Hydrogen may be stored in gaseous form in the larger of such voids, which do not disappear with annealing; but it is apparently associated in some other manner with narrower imperfections which are eliminated with annealing or recrystallization.

Acknowledgment

The authors are grateful for materials and analyses provided by the Research and Development Laboratory of the United States Steel Co. Stimulating discussions with personnel of the Research Laboratory of the United States Steel Corp. and of the Research and Development section of the United States Steel Co. lent impetus to this study.

References

- 1 J. H. Andrew, H. Lee, P. L. Chiang, B. Fang, and R. Guenot: *Journal Iron and Steel Inst.* (1950) **165** II, pp. 145-166.
- 2 Toyozo Ishigaki: *Sci. Repts. Tohoku Imp. Univ.* (1926) **15**, pp. 777-794.
- 3 J. S. Smart, Jr., A. A. Smith, Jr., and A. J. Phillips: *Trans. AIME* (1941) **143**, p. 272.
- 4 C. Zener: *Trans. AIME* (1942) **147**, pp. 361-364.
- 5 C. G. Maier: *Trans. AIME* (1936) **122**, p. 121.
- 6 D. P. Smith: *Hydrogen in Metals*. (1948) p. 293. Chicago. University of Chicago Press.
- 7 C. A. Zapffe and C. E. Sims: U. S. Dept. Agriculture Library, Document No. 1255.
- 8 A. Holt, E. C. Edgar, and J. B. Firth: *Ztsch. physik. Chem.* (1913) **82**, pp. 513-540; **83**, p. 501.
- 9 G. Tammann and J. Schneider: *Ztsch. anorg. allgem. Chem.* (1928) **172**, pp. 43-64.
- 10 G. A. Moore and D. P. Smith: *Trans. Electrochem. Soc.* (1937) **71**, pp. 545-563.
- 11 D. P. Smith and G. Derge: *Trans. Electrochem. Soc.* (1934) **66**, pp. 253-270.
- 12 L. S. Darken and R. P. Smith: *Corrosion* (1949) **5**, pp. 1-16.
- 13 D. P. Smith: *loc. cit.*, p. 32.
- 14 D. P. Smith: *loc. cit.*, p. 33.
- 15 G. Tammann: *Ztsch. anorg. allgem. Chem.* (1919) **107**, pp. 89-96.
- 16 D. P. Smith: *loc. cit.*, p. 47.
- 17 D. P. Smith: *loc. cit.*, p. 229.
- 18 C. A. Zapffe and C. E. Sims: *Trans. AIME* (1941) **145**, pp. 225-261.
- 19 H. E. Cleaves and J. G. Thompson: *The Metal-Iron*. (1935) pp. 269-275. New York. McGraw-Hill Book Co.
- 20 H. E. Cleaves and J. M. Hiegel: *R. P. 1472, Journal of Research Nat. Bur. Stds.* (1942) **28**, pp. 643-647.
- 21 F. T. Sisco: *Alloys of Iron and Carbon*. Vol. II, *Properties*. (1937) pp. 568-570. New York. McGraw-Hill Book Co.
- 22 M. H. Armbruster: *Journal ACS* (1943) **65**, pp. 1043-1054.
- 23 J. Smittenberg: *Rec. trav. chim.* (1934) **53**, pp. 1065-1083. (Data extrapolated by ref. 22 used in this paper.)
- 24 L. Luckemeyer-Hasse and H. Schenck: *Arch. Eisenhüttenw.* (1932) **6**, pp. 209-214.
- 25 E. Martin: *Ztsch. physik. Chem.* (1929) **3**, p. 411.
- 26 W. Baukloh and R. Müller: *Arch. Eisenhüttenw.* (1937-1938) **11**, p. 513.

Bend Plane Phenomena in the Deformation of Zinc Monocrystals

by John J. Gilman and T. A. Read

FOLLOWING the deformation of zinc monocrystals, sharply bent basal planes are observed near several types of inhomogeneities. Three of these inhomogeneities have characteristics which are quite regular so that they can be studied and analyzed. These are compressive kink bands, "deformation bands," and the inhomogeneities near end restraints. The present paper describes experiments in which "deformation bands" were artificially produced, and bend plane phenomena are discussed in terms of dislocation theory. Also, two new bend plane phenomena are described.

The importance of bend plane phenomena in the deformation of crystals is not widely recognized. Many phenomena may be explained in a manner similar to the discussion in this paper. Jillson¹ has pointed out that the "punching effect" in zinc is a bend plane phenomenon and is not caused by prismatic slip.² Bowles³ has suggested that they may be involved in diffusionless phase changes. Cahn⁴ has discussed the role of bend plane formation in the polygonization of zinc.

Experimental Work

Tensile Kink Bands: Because of the geometrical similarity between "deformation bands" and "kink bands" (compare Fig. 1 of this paper with Fig. 1 of the paper by Hess and Barrett⁵), the band shown in Fig. 1 of this paper will be called a "tensile kink band," and that shown by Hess and Barrett will be called a "compressive kink band." It is felt that the term "deformation band" should be reserved for banded structures in polycrystalline materials such as iron.⁶

Tensile kink bands seem to form spontaneously in aluminum crystals deformed by tensile loading.⁷⁻¹⁰ In zinc and cadmium crystals they do not form in good, carefully loaded specimens.^{1,9} However, tensile kink bands can be produced artificially in zinc crystals. The present authors did this by scratching one of the flat surfaces of triangular crystals transversely with a sharp needle. Natural tensile kink bands caused by inhomogeneities sometimes appeared in deformed crystals which were identical in appearance with the artificially produced ones.

Zinc monocrystals were grown by the Bridgman method in graphite molds. Chemically pure zinc (99.999+ pct Zn) was used and the molds were sealed inside evacuated pyrex tubes during growth. The crystal cross sections were equilateral triangles with a typical base of 0.210 in. The artificial kink band shown in Fig. 1 is typical of tensile kink bands

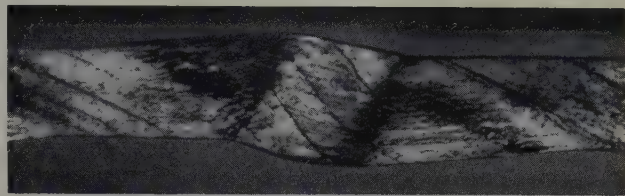


Fig. 1—Tensile kink band in a triangular zinc crystal. X4. Area reduced approximately 25 pct for reproduction.

in zinc. The band lies between two bend planes which run from upper right to lower left and is inclined oppositely to the slip bands which are sharply bent at the two bend planes.

The general form of the artificial tensile kink bands was independent of the scratch depth (1 to 5 mils deep) and also independent of which side was scratched. These variables did cause variations, however. Deep scratches produced more localized kink bands than light scratches. Also, if the angle between the slip plane traces and a transverse scratch varied appreciably among the three sides, then localization of the resulting kink bands also varied. Furthermore, if the slip direction lay nearly parallel to the scratched side, the band was more developed near the scratched side than at the opposite edge. Scratches produced tensile kink bands for crystal orientations from $\chi_0 = 15^\circ$ to $\chi_0 = 75^\circ$.

Fig. 2 shows a scratched crystal after deformation. One triangular side lies in the plane of the photograph. The right hand tensile kink band was produced by a transverse scratch on the upper right side. The next two kink bands were the result of scratches on the front surface. The kink band at the left was caused by a scratch on the lower back side. All four bands have the same general form.

A longitudinal scratch was also made on the crystal shown in Fig. 2 to determine the effect of a scratch on the critical shear stress. The critical shear stress of the scratched region was 33.9 g per sq mm compared to 24.4 g per sq mm for the unscratched region above it.

Fig. 3 shows Laue patterns of the crystal shown in Fig. 2. Fig. 3a shows the pattern of the undeformed crystal. The orientation was $\chi_0 = 21^\circ$, $\lambda_0 = 31^\circ$. After deformation, Fig. 3b was made of the homogeneously deformed portion of the crystal. The spots are compact but split into two halves. This region was elongated 45 pct and its orientation was $\chi = 14^\circ$, $\lambda = 20^\circ$; the sine law predicts $\chi = 14^\circ$, $\lambda = 20.5^\circ$. Fig. 3c was taken near the center of the middle tensile kink band of Fig. 2. The pattern shows a range of orientations and polygonization in this region. The spread in orientation was due to the fact that the basal planes were curved (see Fig. 1) rather than flat as in the ideal case. Some may also have been the result of elastic distortions and "local curvatures." The orientation range was $\chi = 23^\circ$ to 32° , $\lambda = 30^\circ$ to 42° . It is apparent from Fig. 3 that the material inside and outside the kink band rotated in opposite directions with respect to the tension axis during deformation. The orientation calculated from the ideal configuration of Fig. 9,

J. J. GILMAN, Junior Member AIME, formerly with the School of Mines, Columbia University, is now associated with the Research Laboratory, General Electric Co., Schenectady, and T. A. READ, Member AIME, is Associate Professor of Metallurgy, School of Mines, Columbia University, New York.

Discussion on this paper, TP 3443E, may be sent, 2 copies, to AIME by April 1, 1953. Manuscript, Sept. 17, 1951; revised, March 10, 1952. Los Angeles Meeting, February 1953.

This paper represents part of a thesis by J. J. Gilman submitted in partial fulfillment of the requirements for the degree of Doctor of Philosophy to the Graduate Faculties, Columbia University.

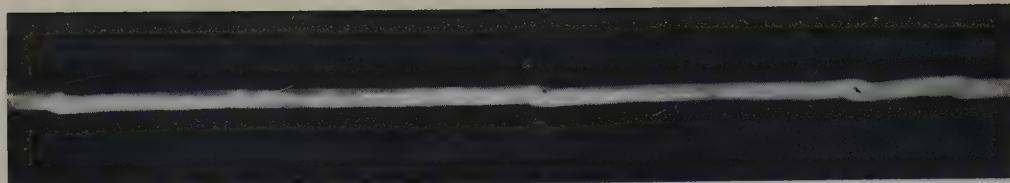


Fig. 2—Tensile kink bands produced in a triangular zinc crystal by scratches prior to elongation. $\times 1/2$. Area reduced approximately 20 pct for reproduction.

$\lambda_{\text{band}} = 2\lambda_0 - \lambda = 42^\circ$, lies at the upper end of the observed range. Thus there is good agreement between the visual and X-ray observations.

To determine whether the effect of a scratch is localized or whether it extends far into a crystal, the following experiment was performed. A crystal was chemically polished and scratched transversely. Then about 0.25 mm of material was removed from each side of the specimen by means of chemical polishing. Another scratch was made on the same side of the crystal at a different place, and it was elongated in tension. An intense tensile kink band formed at the second scratch but only a faint one formed at the first scratch. The same result was obtained with a different crystal. Thus the effect of a scratch is localized initially and spreads across the diameter of a crystal as deformation proceeds.

Artificially produced tensile kink bands do not appear directly at the cross section which is scratched. They appear in the region of the undeformed crystal which is cut by a plane containing the line of the scratch and the normal to the basal planes of the crystal. This plane is one of the bend planes which bound the tensile kink band. Slip is initially inhibited only near the scratch, but after bend planes form the disturbance propagates across the width because of the self-stabilization of the kink band.

The authors have observed natural tensile kink bands near heterogeneities such as included crystals and nonmetallic inclusions. They also occur in mishandled crystals. Artificial tensile kink bands can be induced in zinc and tin crystals by scratches, but scratches have no effect for lead crystals. Schmid¹¹ showed that tensile kink bands can be induced in magnesium crystals by drilled holes. Both natural and artificial kink bands occur in variously shaped zinc crystals. In short, tensile kink bands tend to form whenever one part of a crystal lags in the reorientation process during a tensile test. Once formed, they are surprisingly stable against the large forces which tend to straighten them out. They are not observed when one portion of a crystal is softer than the rest. Two inhomogeneous regions analogous to those at end restraints are found at each end of the soft section instead. Kink bands do not form unless the hard part of the crystal is short

compared to the diameter of the crystal. Thus no kink band formed at the longitudinally scratched region in Fig. 2, although it was harder than the rest of the crystal. If the hard section is long, the large reverse bending moments at the ends do not allow bend planes to form. Finally, tensile kink bands do not form when more than one slip system is active.⁷

New Bend Plane Phenomena: Two new bend plane phenomena have been observed. The first was observed when some crystals cleaved part way through their cross sections during elongation. Tongue-like pieces of the crystals separated from the rest and bent sharply backward upon further deformation, see Fig. 4. Some bending of such a tongue-like fragment would be expected even if the specimen were not a single crystal. The bending here is very lo-

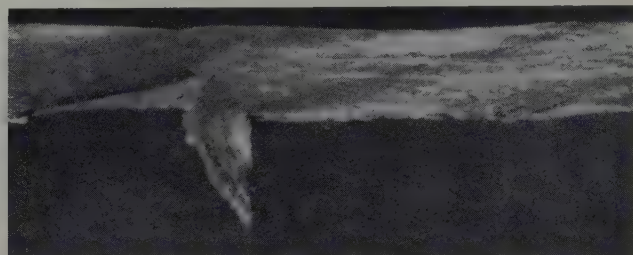


Fig. 4—Bending of a piece of a partially cleaved crystal caused by deformation of the crystal subsequent to the partial cleavage. $\times 2$. Area reduced approximately 25 pct for reproduction.

calized, however. Also, the amount of bending was large compared to the additional deformation given the crystal after the partial cleavage formed. The very sharp angle between the outer edge of the bent piece and the edge of the crystal indicates a bend plane containing the sharp angle and bisecting the angle between the slip direction of the tongue and the slip direction of the rest of the crystal. If the specimen was deformed further, it is expected that the tongue would rotate oppositely to the slip planes in the rest of the crystal in order to maintain the symmetry across the bend plane.

The other new bend plane phenomenon was caused by a longitudinal scratch on one side of a triangular crystal (orientation was $\chi_0 = 74^\circ$, $\lambda_0 = 74^\circ$). Fig. 5a shows the side of the crystal opposite the scratch after deformation, about 50 pct elongation. Fig. 5b shows the cross section. Most of the cross section behaved normally during deformation. This is on the bottom in Fig. 5a. One corner, however, behaved abnormally; its slip planes rotated oppositely to the rest of the crystal. This is on the top in Fig. 5a. Thus, a sort of longitudinal kink band formed in contrast to the transverse kink band of Fig. 1. The anomalous corner did not coincide in location with the longitudinal scratch. If the two locations were connected by lines, these lines would lie near the basal plane normals. From this, and the fact that the specimen axis nearly bisects the angle between the slip directions of the two parts of the crystal, it is concluded that this phenomenon is similar to the effects of transverse scratches. It is believed that slip inhibition near the longitudinal scratch caused

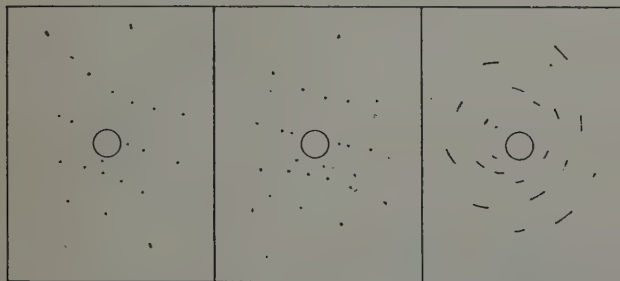
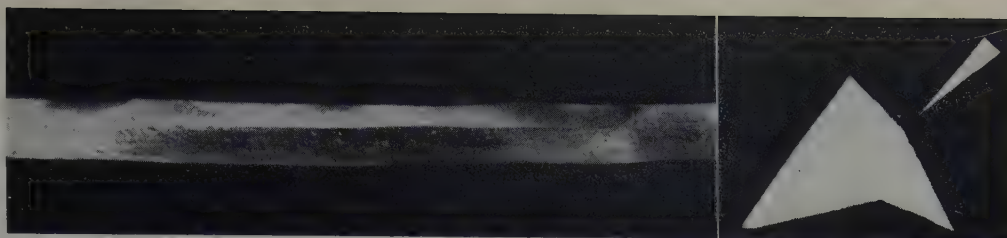


Fig. 3—Tracings of back-reflection Laue patterns. Tungsten radiation. a (left)—As-grown crystal. b (center)—After deformation, 45 pct elongation, homogeneously deformed portion. c (right)—After deformation, near center of deformation band.

Fig. 5a (left)—Side of triangular crystal opposite longitudinal scratch (scratch on back upper side) after 55 pct deformation. X2. b (right)—Cross section of same crystal. Arrow points to scratched side. Area reduced approximately 25 pct for reproduction.



local bending when the crystal was elongated. This caused a longitudinal bend plane making a right angle with the slip direction. After the bend plane was established, the slip planes of the corner on the right in Fig. 5 rotated oppositely to the rest of the slip planes, leading to the configuration of Fig. 5.

Discussion and Theory

Tensile kink bands, compressive kink bands, and the bend planes at end restraints are closely related phenomena. The geometry of these will be discussed after a general dislocation theory of bend plane formation is presented.

Dislocation Theory of Bend Plane Formation: The role of dislocations in the formation of compressive kink bands was discussed by Hess and Barrett.⁵ Their ideas can be extended by use of the dislocation theory of grain boundaries developed by Burgers¹² and by Read and Shockley.¹³ First, it should be pointed out that it is not necessary to invoke dislocation concepts in order to explain bend plane formation phenomenologically. In zinc at room temperature, slip occurs only on the basal planes and therefore is lamellar. Because of this, fact, a discontinuity in shear strain which results from slip must lie in a plane which bisects the disorientation angle between the lattices on either side of the discontinuity. If the shear discontinuity does not lie in the bisecting plane, as shown in Fig. 6a, the thicknesses of the sheared lamellae are reduced; an impossible circumstance. Fig. 6b shows that when a bend plane forms, the strain in the sheared material is given by $2 \tan \theta/2$, where θ is the disorientation angle.

In terms of dislocation theory, bend planes consist of walls of dislocations having the same sign; that is, they are grain boundaries. Defined in physical terms, they are also grain boundaries but are usually discussed as distinct phenomena because they have a different origin than ordinary grain boundaries. Bend planes are rather ideal grain boundaries in that they have only one degree of freedom; the angle between the slip directions on either side of the bend plane.

Bend planes in bent crystals decrease the energy of the system. A plastically bent zinc crystal contains an excess of positive dislocations if it is bent concavely downward. The density of excess positive dislocations is inversely proportional to the radius of curvature.⁴ These excess positive dislocations may be considered to constitute a multitude of small angle grain boundaries. The energy of this configuration may be compared with that of a bent crystal containing a single large-angle grain boundary.

The Read and Shockley expression for the energy of a grain boundary is

$$E = E_0 \theta (A - \ln \theta)$$

where A and E_0 are constants and θ is the disorientation angle. The boundary bisects θ . If ϕ is the angle between the two ends of a bent specimen and it con-

tains $M + 1$ grains, hence M grain boundaries, the orientation difference across each boundary is ϕ/M . Thus the total grain boundary energy of a specimen with variable M will be

$$E = E_0 \phi [A - \ln(\phi/M)]$$

Since ϕ/M must always be small if the theory is to be valid, this expression increases continuously with increasing M . Thus the energy is lowest if the orientation difference between the ends is contained in one boundary. However, if ϕ/M is large, and hence the theory only approximate, there may exist values of ϕ for which the energy will be lower if two twin boundaries are present instead of one large-angle boundary. The bend plane always bisects the angle between the lattices on either side of it. Also, the bend plane contains the normal to the plane containing the slip directions. This position is stable because it yields a maximum of symmetry across the bend plane and a minimum dislocation density in the bend plane. This can be verified by the method of Frank.¹⁴

Although a bent specimen having one large-angle grain boundary has a lower energy than one with many slightly disoriented grains, bend planes do not always form spontaneously in bent zinc crystals. For example, Cahn⁴ found that uniformly bent zinc crystals do not polygonize unless they are heated for several hours near the melting point. The temperature necessary to cause polygonization is lower the smaller the bend radius, and the longer the annealing time. Similar results were found for silicon ferrite by Dunn and Daniels.¹⁵ On the other hand, bend

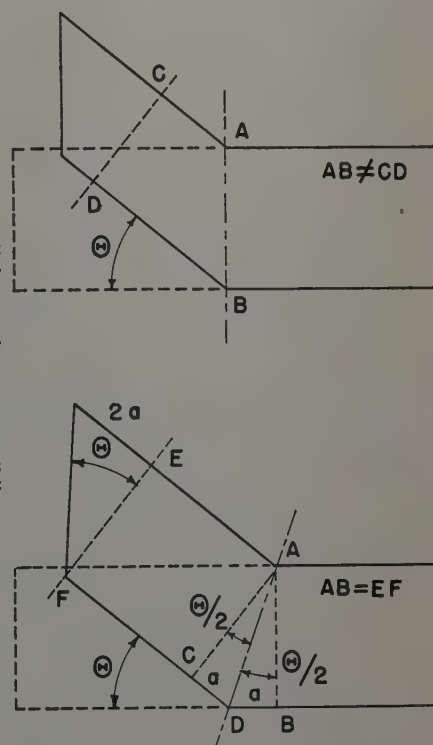


Fig. 6—Showing that the lamellar nature of deformation by slip requires that a shear discontinuity lie in a plane which bisects the disorientation angle between the lattices on either side of the discontinuity.

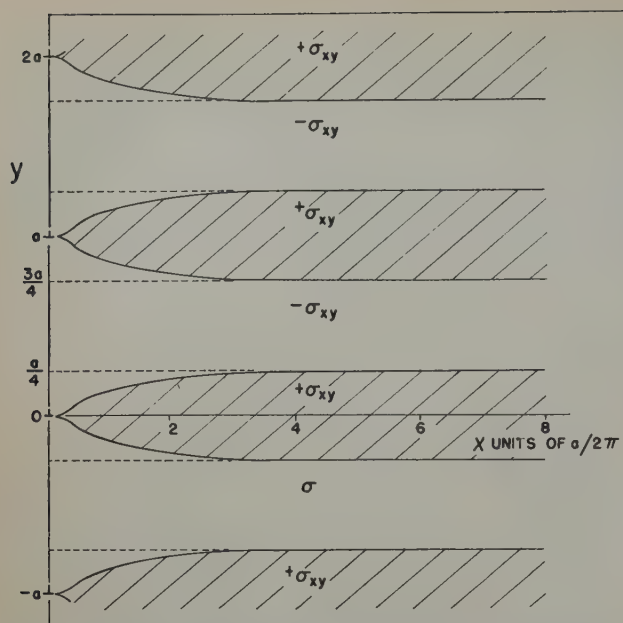


Fig. 7a—Shear stresses caused by an infinite vertical wall of positive edge dislocations. From Burgers' Eq. 13. Regions of positive and negative shear stress over the xy plane.

planes form at room temperature at kink bands and the Laue pattern of Fig. 3c shows evidence of partial polygonization within a tensile kink band.

In a uniformly bent zinc crystal it is presumed that the excess positive dislocations are rather uniformly distributed in a rectangular array. Because of the mutual repulsive forces between them, they tend to remain so distributed. At high temperatures, because of thermally actuated fluctuations, they gradually join into vertical arrays and thus polygonize the bent crystal. If the initial bending is non-uniform, as it is for bend plane formation, the excess positive dislocation density on a given plane is greatest at the point of greatest bending. This configuration is stable and can attract other dislocations to itself. Consideration of an expression which Burgers¹² derived will clarify this statement.

Burgers' expression for the shear stress due to an infinite vertical wall of uniformly spaced positive edge-dislocations is

$$\sigma_{xy} = \left[\frac{G l}{2\pi(1-\nu)} \right] \frac{\pi^2 x}{a^2} \left\{ \frac{\cos h \left(\frac{2\pi x}{a} \right) \cos \left(\frac{2\pi y}{a} \right) - 1}{2 \left[\sin^2 h^2 \left(\frac{\pi x}{a} \right) + \sin^2 \left(\frac{\pi y}{a} \right) \right]^2} \right\}$$

where x, y are Cartesian coordinates; a , the spacing of the dislocations in the wall; G , the shear modulus; l , the magnitude of the slip vector of the dislocations; and ν is Poisson's ratio. The boundaries of regions of positive and negative shear stress in the xy plane are found by setting the numerator of the equation equal to zero, that is, by plotting

$$\cos h \left(\frac{2\pi x}{a} \right) \cos \left(\frac{2\pi y}{a} \right) = 1$$

This has been done in Fig. 7a. At large x the shear stress varies sinusoidally with y . It is positive in the shaded regions from $-a/4$ to $+a/4$, from $3a/4$ to

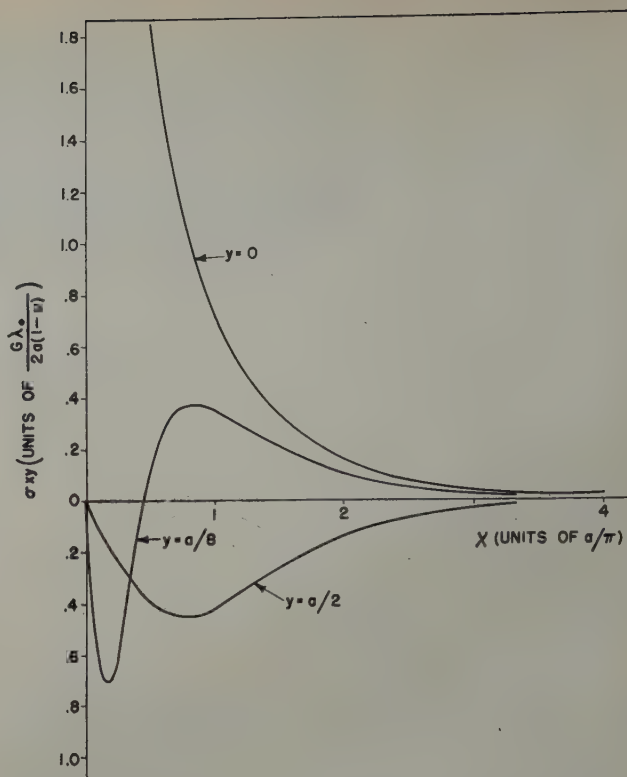


Fig. 7b—Shear stresses caused by an infinite vertical wall of positive edge dislocations. From Burgers' Eq. 13. Variation of shear stresses with x at various values of y .

$5a/4$, etc. Therefore a positive dislocation at large x within those regions would be repulsed from the wall. On the other hand the shear stress is negative in the regions $a/4$ to $3a/4$, $5a/4$ to $7a/4$, etc., and dislocations within those bands would be attracted to the wall. At small x the bands of positive shear stress become very narrow. Therefore a dislocation at small x and almost any y would be attracted to the wall.

The variation of the shear stress, σ_{xy} , with x for various values of y , is plotted in Fig. 7b. For $y = 0$ the shear stress is positive for all x and approaches infinity as $x \rightarrow 0$. For $y = a/8$ the shear is negative for small x but positive for large x .

Since the positive dislocations are inhibited from entering the wall if they lie in planes near those in which the wall already has dislocations, the wall spacing tends to be uniform. Also, a wall of positive edge dislocations is self-stabilizing. As dislocations are added to the wall, a decreases so shear stresses due to the wall become increasingly localized.

All of the bend plane phenomena which have been discussed in this paper began with nonuniform bending of specimens. It is believed that this caused a few excess dislocations of the same sign to assemble in the planes of maximum bending. Thus vertical walls were formed which became increasingly stable as more dislocations attached themselves. The actual experimental configurations are non-ideal, of course. Instead of single dislocations perhaps bend planes may be thought of as assemblies of dislocation bunches. These would behave approximately as single dislocations having large slip vectors.

Bend Planes at End Restraints: Bend planes at end restraints were first described by Mark, Polanyi, and Schmid.¹⁶ Later, Miller¹⁷ studied them systematically. Fig. 8a is taken from Miller's paper. It shows that, at the restrained end of a crystal, the

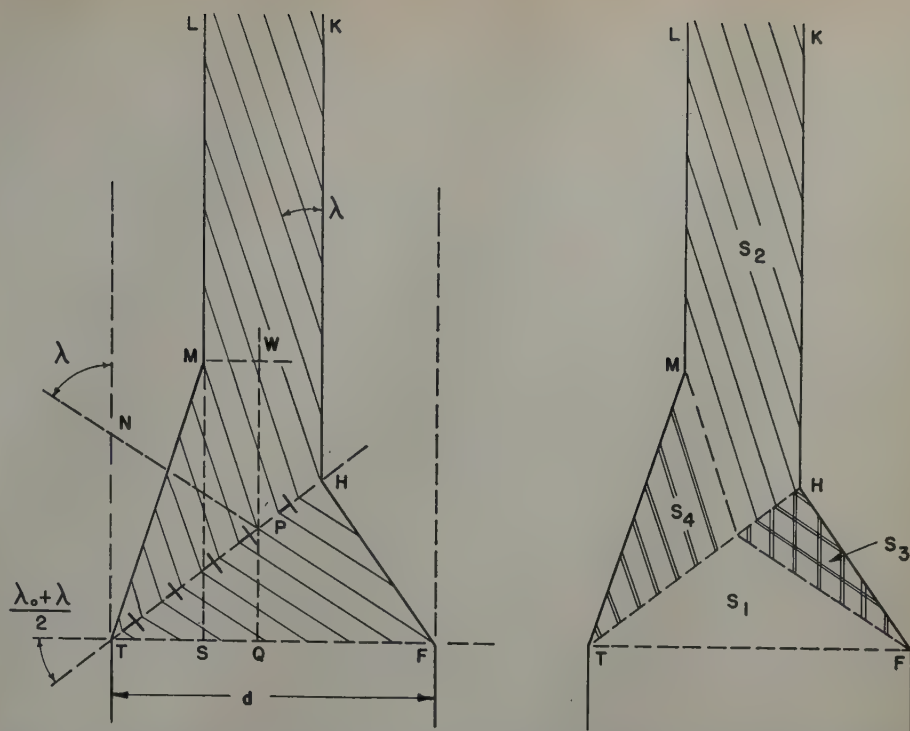
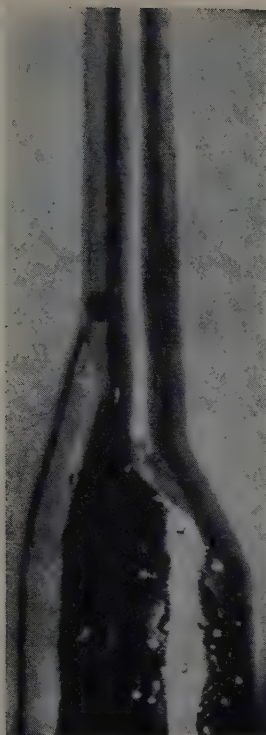


Fig. 8—Bend planes at end restraints. a (left)—Inhomogeneous deformation in a zinc monocrystal near end restrained by polycrystalline portion of rod. (After Miller.) X3. b (center)—Schematic geometry of Fig. 8a. c (right)—Homogeneous shear strain regions in Fig. 8a.

basal planes are bent during deformation. The bending is about an axis lying in the slip plane and normal to the slip direction. The bending moment reaches a maximum at the plane TF , Fig. 8b, but the maximum amount of plastic bending occurs at a plane which is normal to the slip direction and passes through point T because the material within TPF is restrained from slipping by the end restraint. Excess dislocations of the sign shown assemble along TH and form a dislocation wall. Once it is formed, the wall is stable against dispersion and maintains a position such that it bisects the angle MPF between the slip directions of the lattice on either side of it. In order to do this, TH is required to pivot about T , because the planes within TPF cannot easily change in orientation. This pivoting is a rather ideal case of stress-induced, grain-boundary migration.

Actual crystals approach the ideal behavior depicted in Fig. 1b more closely at elevated temperatures than at room temperature.² This happens because recovery (annihilation of dislocations) is rapid at elevated temperatures so that not many excess dislocations pile up adjacent to the bend plane and cause distortion. Miller showed, experimentally, that the bend plane TH always made an angle with TF of $\frac{1}{2}(\lambda_0 + \lambda)$, where λ_0 is the initial angle between slip direction and tension axis. Thus, the position of TH can be calculated for any tensile elongation from the laws of crystallographic slip.¹⁸ Also, it can be seen that the bend plane TH always bisects the angle between the initial and final slip directions, as seen from the geometry of Fig. 6b. The analysis which Miller carried out was incomplete because he did not calculate the maximum distance at which the end restraint affects the crystal, MS . Also, he did not calculate the shear strains in the various regions of the specimen.

The distance MS can be calculated. This derivation was suggested by W. T. Read in a private communication. The suggestion of McKeehan in his dis-

cussion of Miller's paper cannot be used to calculate MS because the axes of the deformed and undeformed sections do not coincide. The calculation is

$$MP = NF - PF \\ = d \csc \lambda_0 - PQ \sec \lambda,$$

and

$$MS = MP \cos \lambda + PQ$$

Miller showed that

$$PQ = d \left[\tan \lambda_0 + \cot \left(\frac{\lambda + \lambda_0}{2} \right) \right]$$

Therefore,

$$\frac{MS}{d} = \frac{\cos \lambda}{\sin \lambda_0} + \frac{1 - \cos \lambda \sec \lambda_0}{\tan \lambda_0 + \cot \left(\frac{\lambda + \lambda_0}{2} \right)}$$

With manipulation this reduces to

$$\frac{MS}{d} = \frac{\cos \lambda}{\sin \lambda_0} - \sin (\lambda_0 - \lambda) \left[\frac{1 - \cos (\lambda_0 + \lambda)}{1 + \cos (\lambda_0 - \lambda)} \right]$$

MS was calculated for Miller's data by means of the last expression and the calculated values agreed satisfactorily with the observed values.

The four regions of homogeneous shear near an end restraint are shown in Fig. 8c. In the region TPF the shear strain S_1 is equal to zero. Consideration of Fig. 6b shows that in the region TMP the shear strain is

$$S_4 = 2 \tan \left(\frac{\lambda_0 - \lambda}{2} \right)$$

The standard expression for the shear strain in the region $LMPHK$ ¹⁸ is

$$S_2 = \cot \lambda - \cot \lambda_0.$$

Since the shear strain discontinuity across TH is constant, then

$$S_2 - S_3 = S_4 - S_1$$

Hence

$$S_3 = S_2 - S_4$$

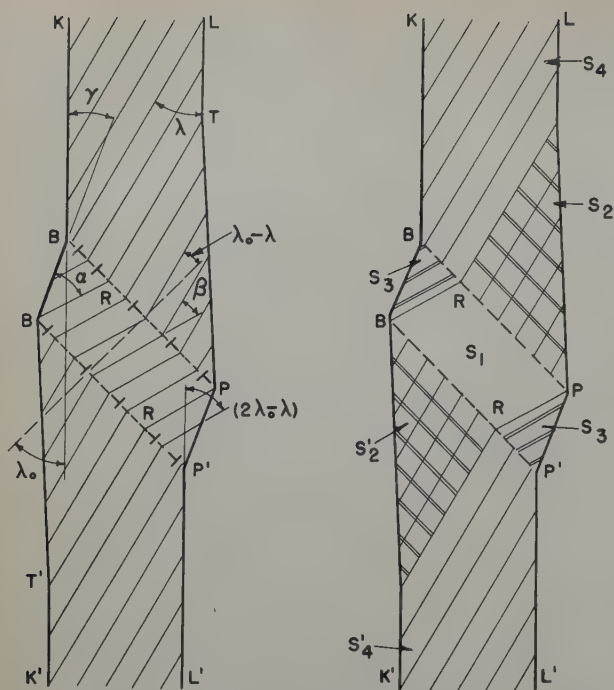


Fig. 9—Schematic drawings of an ideal tensile kink band. a (left) —Schematic geometry. b (right) —Regions of differing but homogeneous shear strain.

Thus the configuration near an ideal end restraint may be completely analyzed.

Tensile Kink Bands: Tensile kink bands in zinc crystals were also first studied systematically by Miller.¹⁰ His interpretation of them was incorrect, however, because he thought they were caused by a new form of twinning. Later authors, notably Andrade²⁰ and Jillson,¹ corrected this mistaken impression, but did not discuss the bands in detail.

If a localized portion of a crystal is harder than the rest, bending moments are created at the edges of the hard portion when the adjacent soft portions slip. The resulting excess dislocation concentrations result in dislocation walls which form along planes BP and $B'P'$, Fig. 9a, cutting the slip planes at right angles to the slip direction. These walls stabilize and tend to maintain equal angles between themselves and the slip directions on either side. As slip causes the basal planes outside the band to rotate counterclockwise, the dislocation walls at BP and $B'P'$ cause the basal planes within the band to rotate equally clockwise. When the bend planes become saturated with dislocations, dislocations of the same sign begin to pile up outside. These cause curvature of the basal planes near the bend planes to give the non-ideal configuration of Fig. 1.

The drawing of Fig. 9a shows the schematic geometry of an ideal tensile kink band. The angle between the slip planes within the kink band and the tension axis is $(2\lambda_0 - \lambda)$ where λ_0 and λ are the initial and final angles between the slip direction and the tension axis respectively.

It should be noted that the rotation of the slip planes within $BPP'B'$ may occur either by means of reverse slip in $BPP'B'$ or by a bulk rotation of the region combined with lateral movement of the bend planes (rotation of the bend planes may occur but it causes no rotation in the region $BPP'B'$). Since no experimental evidence of reverse slip was found, it is believed that the latter mechanism operates when an ideal tensile kink band forms. The rota-

tion of the planes relative to the sides BB' and PP' is the result of normal forward slip in $B'BR$ and $PP'R'$. This latter rotation causes the slip planes within a kink band to take the angle α with the side BB' and the side BB' takes an angle γ with the tension axis. If the angle α is known, γ may be calculated as follows:

$$\gamma = \beta - (\alpha - \lambda_0) \\ = 3\lambda_0 - (\alpha + 2\lambda)$$

Fig. 9b shows the various regions of homogeneous shear strain. The shear strains are

$$S_1 = 0 \\ S_2 = S_2' = 2 \tan \beta / 2 \\ S_3 = S_3' = \cot \alpha - \cot \lambda_0 \\ S_4 = S_4' = \cot \lambda - \cot \lambda_0$$

Since the shear strain discontinuities across BP and $B'P'$ are constant, then

$$S_2 = S_4 - S_3 = S_2' = S_4' - S_3'$$

Thus an ideal tensile kink band is completely determined except for thickness if the angle α , as well as λ_0 and λ , is known.

Actual tensile kink bands deviate from the ideal case because some slip occurs in the region $BPP'B'$ after the band has formed. This was shown by forming a kink band in a specimen, then electropolishing to remove the slip lines, and finally elongating the specimen an additional 10 pct. Slip lines could be seen within the kink band, at the bend planes, and outside the kink band where the deformation was homogeneous. This means that the planes BP and $B'P'$ do not represent static discontinuities since some material passes through them.

Compressive Kink Bands: Compressive kink bands were discovered by Orowan²¹ in cadmium monocrystals which had very low orientation angles. He believed that an entirely new mechanism of deformation was involved, but Hess and Barrett⁵ were able to form compressive kink bands slowly in zinc and thought that the mechanisms of slip and bend plane formation explained their observations. Compressive kink bands differ in their mode of formation from tensile kink bands. Hess and Barrett⁵ showed that buckling is necessary for compressive kink-band formation. This buckling must be that of a beam with restrained ends. If the ends are not restrained, the crystal simply bends uniformly. This is consistent with the theory discussed above. It is expected that a crystal bent with free ends would polygonize if annealed, but bend planes would not form in it during deformation. If the ends of the crystal are restrained, the crystal buckles with two points of inflection in the displacement curve at which the shear stresses are a maximum. Shear yielding occurs here first, according to Hess and Barrett. Thus, positive and negative dislocations flow out of this region along the length of the crystal (the basal planes in this case must be almost parallel to the compression axis) toward the points of maximum bending and minimum shear stress. They stop somewhere in between and assemble into dislocation walls. These oppositely directed walls or bend planes constitute the initial stage in the formation of a compressive kink band.

An important distinction between compressive and tensile kink bands is that the former can be formed in an otherwise homogeneous zinc crystal while the latter form only in crystals containing heterogeneities. Compressive kink bands form in a

particular type of test (compression of thin rod with restrained ends) in crystals having rather restricted orientations. Tensile kink bands form in a particular test (axial tension of thin rod) in crystals with localized heterogeneities. Thus, neither phenomenon is a fundamental mode of deformation. They are the result of the interactions between particular mechanical tests and particular crystals. Their general interest derives from the fact that they involve the formation of bend planes and these seem to be important to our understanding of the behavior of dislocations.

Summary

The inhomogeneities of deformation which occur at the restrained ends of zinc crystals, at tensile kink bands, and at compressive kink bands are described in terms of bend planes which are believed to consist of walls of edge dislocations. The bend plane bisects the angle between the slip directions on either side of it and contains the normal of the plane of the two slip directions. This is used to explain the migration of the bend plane through the lattice at an end restraint, the "anomalous" rotation of the lattice within a tensile kink band, and the geometric conditions which obtain during the formation of a compressive kink band.

Experiments are described in which artificial tensile kink bands were formed by transverse scratches. Scratches cause tensile kink bands in zinc crystals of a range of orientations; which side is scratched is relatively unimportant. It is concluded that tensile kink bands form in zinc if a specimen contains a region of inhibited slip. The lag of the inhibited slip planes in the reorientation process causes bending moments on either side of the inhibited planes. These lead to bend plane formation and thence to a tensile kink band.

Two new bend plane phenomena are described. One of these results when a partially cleaved crystal is elongated. The tongue-like projection resulting from the partial cleavage bends sharply away from the rest of the crystal. This phenomenon is explained by the formation of a bend plane at the base of the projection. The other new phenomenon is caused by a longitudinal scratch on a zinc crystal. Under certain geometrical conditions this causes a bend plane to form parallel to the tension axis of the crystal.

Acknowledgment

The authors wish to thank W. T. Read of the Bell Telephone Laboratories for his helpful discussion of this work and especially Burgers' equation. This work was supported by the Office of Naval Research, Contract N6-onr-27128.

Technical Note

A Replica Method for Study of the Structure of Lead-Antimony Alloys

by Jeanne Burbank

A TECHNIQUE has been developed for the microscopic study of the three-dimensional structure of the Pb-Sb alloys by the formation of a chemical replica in which the internal structure of the metal

J. BURBANK is associated with the Electrochemistry Branch, U. S. Naval Research Laboratory, Washington, D. C.
TN 134E. Manuscript, Aug. 28, 1952.

References

- ¹ D. C. Jillson: An Experimental Survey of Deformation and Annealing Processes in Zinc. *Trans. AIME* (1950) **188**, p. 1009; *JOURNAL OF METALS* (August 1950).
- ² F. Seitz: Prismatic Dislocations and Prismatic Punching in Crystals. *Physical Review* (1950) **79**, p. 723.
- ³ J. S. Bowles: The Crystallographic Mechanism of the Martensite Reaction in Iron-Carbon Alloys. *Acta Cryst.* (1951) **4**, p. 162.
- ⁴ R. W. Cahn: Recrystallization of Single Crystals After Plastic Bending. *Journal Inst. Metals* (1949) **17**, Pt. 2, p. 49.
- ⁵ J. B. Hess and C. S. Barrett: Structure and Nature of Kink Bands in Zinc. *Trans. AIME* (1949) **185**, p. 599; *JOURNAL OF METALS* (September 1949).
- ⁶ C. S. Barrett: Structure of Iron After Compression. *Trans. AIME* (1939) **135**, p. 296.
- ⁷ A. H. Cottrell: Theory of Dislocations. *Progress in Metal Physics* (1949) Vol. 1, p. 77. London Butterworths.
- ⁸ N. K. Chen and C. H. Mathewson: Structural Studies of Plastic Deformation in Aluminum Single Crystals. *Trans. AIME* (1951) **191**, p. 653; *JOURNAL OF METALS* (August 1951).
- ⁹ R. W. Honeycombe: Inhomogeneities in the Plastic Deformation of Metal Crystals, I and II. *Journal Inst. Metals* (1951) **80**, pp. 45, 49.
- ¹⁰ R. W. Cahn: Slip and Polygonization in Aluminum. *Journal Inst. Metals* (May 1951) **18**, p. 129.
- ¹¹ E. Schmid: Beitrage zur Physik und Metallographie des Magnesiums. *Ztsch. Elektrochem.* (1931) **37**, p. 455.
- ¹² J. M. Burgers: Some Considerations on the Fields of Stress Connected with Dislocations in a Regular Crystal Lattice I. *Kon. Neder. Akad. v. Wetten., Proc.* (1939) **42**, p. 293.
- ¹³ W. T. Read and W. Shockley: Dislocation Models of Grain Boundaries. *Physical Review* (1950) **78**, p. 275.
- ¹⁴ F. C. Frank: The Resultant Content of Dislocations in an Arbitrary Intercrystalline Boundary. Symposium on Plastic Deformation Pittsburgh (1950) NAVEXOS-P-834.
- ¹⁵ C. G. Dunn and F. E. Daniels: Formation and Behavior of Sub-boundaries in Silicon Iron Crystals. *Trans. AIME* (1951) **191**, p. 147; *JOURNAL OF METALS* (February 1951).
- ¹⁶ H. Mark, M. Polanyi, and E. Schmid: Processes in the Extension of Zinc Crystals, I. II and III. *Ztsch. Phys.* (1923) **12**, p. 58.
- ¹⁷ R. F. Miller: Influence of a Grain Boundary on the Deformation of A Single Crystal of Zinc. *Trans. AIME* (1934) **111**, p. 135.
- ¹⁸ E. Schmid and W. Boas: *Kristallplastizitat* (1935) Berlin.
- ¹⁹ R. F. Miller: Creep and Twinning in Zinc Single Crystals. *Trans. AIME* (1936) **122**, p. 176.
- ²⁰ E. N. daC. Andrade and L. C. Tsien: The Glide of Single Crystals of Sodium and Potassium. *Proc. Royal Soc., London* (1937) **163**, p. 1.
- ²¹ E. Orowan: A Type of Plastic Deformation New in Metals. *Nature* (1942) **149**, p. 643.

may be seen directly. In the replica process one of the phases present in the structure as-cast is converted into a translucent material, and the second phase remains virtually unaffected, permitting microscopic examination by transmitted light.

Alloys of lead and antimony were made from the chemically pure metals, cast in a sooted and pre-



Fig. 1—Chemical replica of 4 pct Pb-Sb alloy. X160. Area reduced approximately 50 pct for reproduction.



Fig. 2—Chemical replica of 12 pct Pb-Sb alloy showing a crystal of primary antimony. X2000. Area reduced approximately 50 pct for reproduction.

heated brass mold, then air cooled. A vacuum pump was used to draw the molten metal into the mold, producing a sheet 0.003 to 0.004 in. thick. By this technique foils were cast having microstructures similar to those in massive castings except that in most cases the foils were one grain thick. A smooth finish is required on the mold faces to assure ready release of the cast foil and because the specimens may not be polished after casting, owing to their thinness and softness.

The replicas were prepared by prolonged treatment of the as-cast foil specimens with the familiar acetic acid-superoxol etchant.¹ The metal foil, supported on a microscope slide or cover glass, was placed in a shallow dish containing etchant. After a period of several hours the foil was converted to a replica and removed to a slide for microscopic examination. The replica was illuminated by transmitted light and micrographs made. The replicas were also examined with the stereoscopic microscope, which clearly showed the three dimensional distribution of the two phases. Chemical replicas were thus prepared and examined for 1, 4, 9½, and 12 pct Pb-Sb alloys. The replicas are fragile and must be handled with care. It has also been found necessary to make all examinations while specimens are still moist because the translucent material becomes powdery and opaque upon drying.

As evidenced by X-ray diffraction determinations, the replicas are composed of amorphous material and metallic antimony. The white amorphous material contains lead, also trivalent and pentavalent antimony.² This is possibly a mixture of lead metantimonate with tetroxide and trioxide of antimony. The opaque material, which appears black in the accompanying micrographs, is identified by X-ray diffraction as metallic antimony.

Fig. 1 is a chemical replica of a 4 pct Pb-Sb alloy at low magnification showing the dendritic formations present in the cast metal. The translucent material is found in those areas originally occupied

by the lead solid solution. The black portions are the unattacked antimony-rich phase segregated in the interdendritic and intergranular areas. It is evident from this projection of the three-dimensional structure that the entire structure is dendritic, but in many cases the antimony is distributed across dendrite arms; the arms lie at random angles to the specimen surface; and the primary, secondary, and tertiary branches are of varying sizes. For these reasons a metallographic etch of a random cut through such a specimen will often fail to show any recognizable dendritic formation.

At low magnifications, the replica structure of the hypoeutectic alloys resembles that shown in Fig. 1. Examination at higher powers shows that segregated antimony is spheroidal in the low alloys up to approximately 6 pct Sb, and above this concentration the segregated antimony assumes more definite shapes, resembling the eutectic structure commonly seen in metallography. Primary crystals of antimony appear as the eutectic point is exceeded, as in Fig. 2, from a replica of a 12 pct Pb-Sb alloy.

It is intended to use the replica technique to investigate the effects of heat treatment, working, and aging of Pb-Sb alloys. For example, homogenized alloys should produce uniform translucent replicas containing no particles of segregated antimony; annealed specimens should show agglomeration of the antimony into discrete crystals, and the accompanying changes in the lead dendrites; Widmannstätten structure, which is difficult to demonstrate metallographically in these alloys⁴ should be rendered readily visible in the replicas.

References

- ¹ ASTM Standards. Part I-B (1946).
- ² G. P. Haight: Naval Research Laboratory, unpublished work.
- ³ H. W. Worner and H. K. Worner: *Journal Inst. Metals* (1940) **66**, p. 45.
- ⁴ G. Derge, A. R. Kommel, and R. F. Mehl: *Trans. AIME* (1937) **124**, p. 367.

Preferred Orientations in Iodide Titanium

by Carl J. McHargue and Joseph P. Hammond

The wire textures for cold rolled and recrystallized iodide titanium and the sheet textures for this material produced by cold and hot rolling, and recrystallization at a series of temperatures were determined. The effect of the $\alpha \rightarrow \beta$ transformation on the sheet texture was noted.

UNTIL recently it was believed that all hexagonal close-packed metals deformed by slip on the basal plane, (0001), and that rolling should tend to rotate this slip plane into the plane of the rolled sheet. The pole figures of cold rolled magnesium¹ are satisfactorily explained on this basis. There is a tendency for the $\langle 11\bar{2}0 \rangle$ directions to align parallel to the rolling direction, and the principal scatter is in the rolling direction. Zinc² has a rolling texture in which the hexagonal axis is inclined 20° to 25° toward the rolling direction. Twinning is believed to account for the moving of the basal plane away from parallelism with the rolling plane. The texture of beryllium³ places the basal plane parallel to the rolling plane with the $[10\bar{1}0]$ direction parallel to the rolling direction, and the scatter from this orientation is primarily in the transverse direction. Cold rolled textures reported for zirconium⁴ and titanium⁵ show the $[10\bar{1}0]$ directions to lie parallel to the rolling direction and the (0001) plane tilted by approximately 25° to 30° to the rolling plane in the transverse direction.

Rosi⁶ has recently reported that the mechanisms for deformation in titanium are distinctly different from those commonly reported for hexagonal close-packed metals. The principal slip plane is the prismatic plane, $\{10\bar{1}0\}$, with some slip also occurring on the pyramidal planes, $\{10\bar{1}1\}$. However, there is no evidence for basal slip. The slip direction is reported to be the close-packed diagonal axis, $[11\bar{2}0]$. In addition to the twin plane commonly reported for metals of this class, $\{10\bar{1}2\}$, Rosi found the twin planes $\{11\bar{2}2\}$ and $\{11\bar{2}1\}$, with the dominant twin plane being $\{11\bar{2}1\}$.

Information regarding the recrystallization and hot rolling textures of hexagonal close-packed metals is limited. Barrett and Smigelskas report that rolling beryllium at temperatures up to 800°C and recrystallization at 700°C produce textures not differing from the cold rolled sheet texture.³ McGeary and Lustman find that hot rolling at 850°C produces the same basic texture in zirconium as rolling at

room temperature.⁴ These investigators also report that the texture for sheet zirconium recrystallized at 650°C differs from the cold rolled orientation inasmuch as the $[11\bar{2}0]$ direction, instead of the $[10\bar{1}0]$ direction, is parallel to the rolling direction. In the case of titanium, it is not possible to deduce which direction is preferred in the recrystallized state from the pole figures presented by Clark.⁵

The purpose of this paper is to report an extensive investigation of the preferred orientations in iodide titanium. Since the deformation mechanisms for titanium are different from those commonly given for hexagonal close-packed metals, it is not surprising to find distinct differences between the textures of titanium and other metals of this class.

Materials and Methods

This investigation was carried out on iodide titanium obtained from the New Jersey Zinc Co. with an analysis as follows: N, 0.002 pct; Mn, 0.004; Fe, 0.0065; Al, 0.0065; Pb, 0.0025; Cu, 0.01; Sn, 0.002; and Ti, remainder.

The crystallinities of titanium were broken from the as-deposited bar and melted to form 20 g buttons on a water-cooled copper block in a vacuum arc-furnace. Hardness tests conducted on the material before and after melting differed by only two or three Vickers Pyramid Numbers, indicating no or insignificant contamination. The buttons were hot forged, ground, and etched to sizes and shapes suitable for the rolling schedule, and vacuum annealed at 1300°F. Specimens for determination of the wire textures were reduced 91 pct in diameter to 0.027 in. in 24 steps using grooved rolls. In order for the orientation of the central region to be studied, portions of these wires were electrolytically reduced to a diameter of 0.005 in. using the procedure described by Sutcliffe and Reynolds.⁷ The sheet textures were determined on titanium cold rolled 97 pct to a thickness of 0.005 in. A reduction of approximately 10 pct per pass was used, and the rolling direction was changed 180° after each pass.

Specimens used for determination of the recrystallized textures were annealed in evacuated quartz tubes at 1000°, 1300°, and 1500°F. The grain size of the 1000°F specimen was sufficiently small to give satisfactory X-ray patterns with the specimen stationary. However, it was necessary to scan the surface of the other recrystallized specimens. The microstructure of each annealed specimen was that of a recrystallized material. The diffraction rings all showed the break-up into spots typical of recrystallized structures.

C. J. MCHARGUE, Student Member AIME, is Research Associate and J. P. HAMMOND is Associate Professor, Dept. of Mining and Metallurgical Engineering, University of Kentucky, Lexington, Ky.

Discussion on this paper, TP 3364E, may be sent, 2 copies, to AIME by April 1, 1953. Manuscript, April 28, 1952. Los Angeles Meeting, February 1953.

This paper represents part of a thesis by C. J. McHargue submitted in partial fulfillment of requirements for degree of Doctor of Engineering to the Graduate School, University of Kentucky.

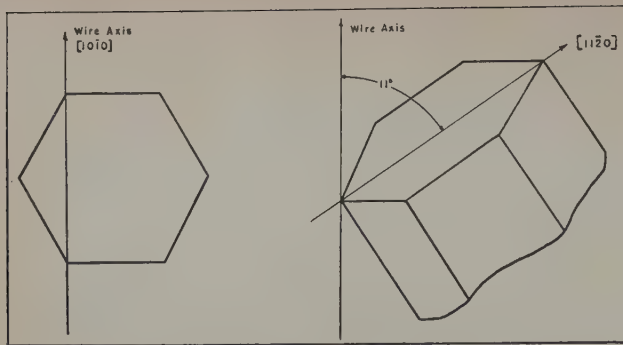


Fig. 1—Fiber axis in iodide titanium.

In order that the orientations in titanium deformed at elevated temperatures could be investigated, annealed ingots were reduced 95 pct in thickness to 0.010 in. at 1050° and at 1450°F. The specimens were heated in air and rolled between sheets of mica to minimize heat losses. The material was reheated after each reduction, which amounted to approximately 10 pct of the sheet thickness. These specimens were etched slightly to remove the surface contamination.

The effect of the $\alpha \rightarrow \beta$ transformation on the preferred orientation was found for a specimen cold rolled 97 pct, heated 5 min at 1650°F in vacuum, and very slowly cooled.

The X-ray specimens were made in the shapes of small rods by polishing strips in a specially constructed jig and etching away the material affected by this polishing. The data for samples of larger grain sizes were obtained by shots on sheet material in a structure integrating camera.⁸ Transmission photograms were taken with molybdenum radiation (45 kv, 18 ma) and a 0.030 in. pinhole. Since titanium fluoresces under these conditions, it was necessary to use a zirconium filter between the

specimen and film. Exposures were made with the beam perpendicular to the rolling direction at 0°, 11°, 26°, 41°, 56°, 71°, and 79° to the cross direction, and with the beam perpendicular to the cross direction at 11°, 26°, 56°, 71°, and 79° to the rolling direction. Additional exposures were then made where necessary. The variations in intensity of the diffraction rings were estimated by eye with the aid of an exposure chart. Intensity readings of 0, 1, 2, and 3 were made on all specimens except those hot rolled, for which intensities of 0, 1, and 2 were used.

Discussion of Results

Wire Textures: The orientation of the cold rolled wire can be described as having the $[10\bar{1}0]$ direction, or type II digonal axis, parallel to the wire axis with all azimuthal position possible. This is shown schematically in Fig. 1a. Burgers, Fast, and Jacobs report the same wire texture for zirconium,⁹ and Morell and Hanawalt report it for Dowmetal.¹⁰

The texture at the surface and the center is essentially the same, varying only in the degree of scatter about the ideal. From a measurement of the spread of the diffraction spots,¹¹ it was found that the $[10\bar{1}0]$ direction has a spread of $\pm 6^\circ$ to the wire axis in the central region and $\pm 15^\circ$ in the surface layers.

The maxima of the diffraction rings for the recrystallized specimens were found to be split and joined by regions of lesser intensity. The average values of the maxima for the (0002), $(10\bar{1}0)$, $(10\bar{1}1)$, and $(11\bar{2}0)$ planes give the average orientation as having the $[11\bar{2}0]$ direction, or type I digonal axis, parallel to the wire axis. However, this orientation is accurately described as having strong concentrations of the basal planes tilted $\pm 11^\circ$ to the wire axis with some basal planes at all positions between these. The $[11\bar{2}0]$ direction is located so that it would be parallel to the wire axis if the basal plane

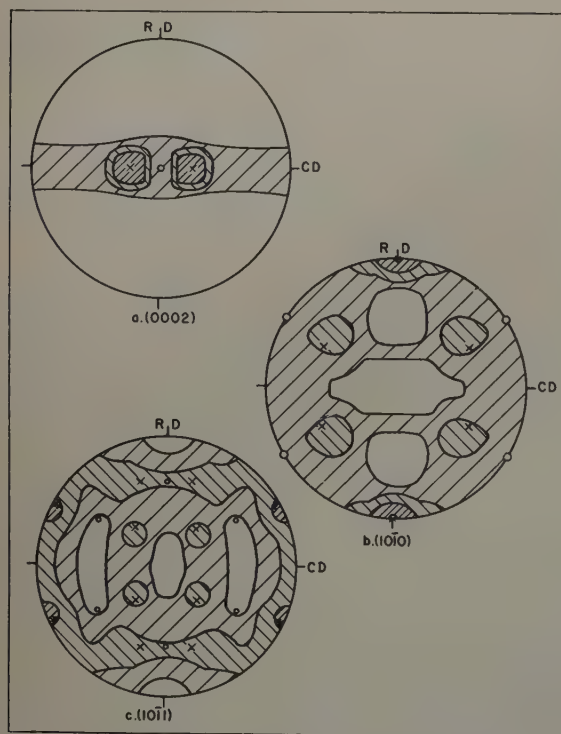


Fig. 2—Cold rolled sheet texture of iodide titanium. $\circ = (0002) [10\bar{1}0]$. $x = (0002)$ rotated 27° about rolling direction.

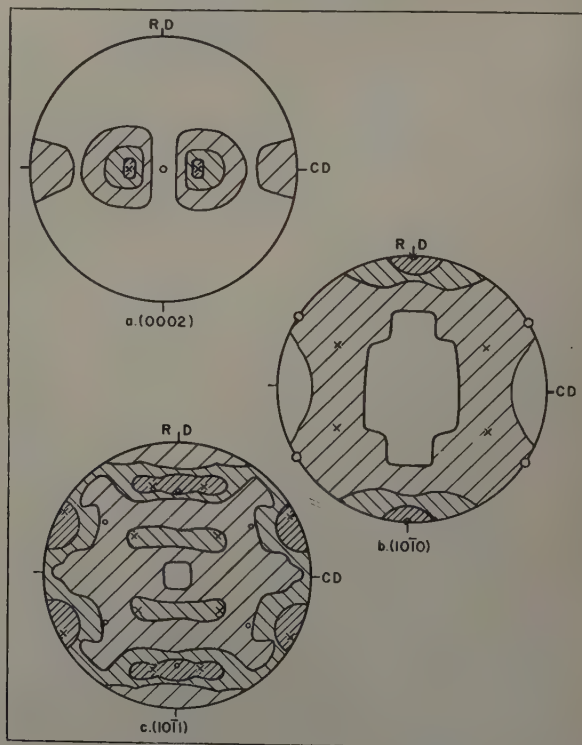


Fig. 3—Cold rolled annealed texture of iodide titanium. $\circ = (0002) [10\bar{1}0]$. $x = (0002)$ rotated 27° about rolling direction.

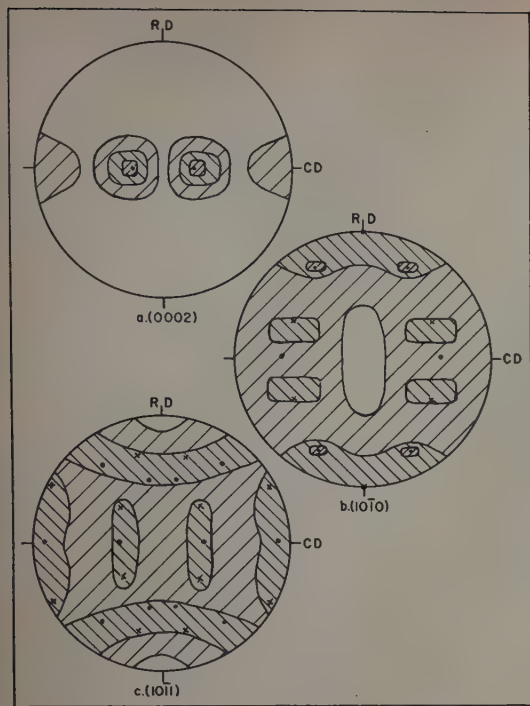


Fig. 4 (left) — Iodide titanium cold rolled 97 pct, annealed at 1300°F. • = (0002) rotated 27°, $[11\bar{2}0]$ parallel to rolling direction. α = (0002) rotated 27°, $[10\bar{1}0]$ parallel to rolling direction.

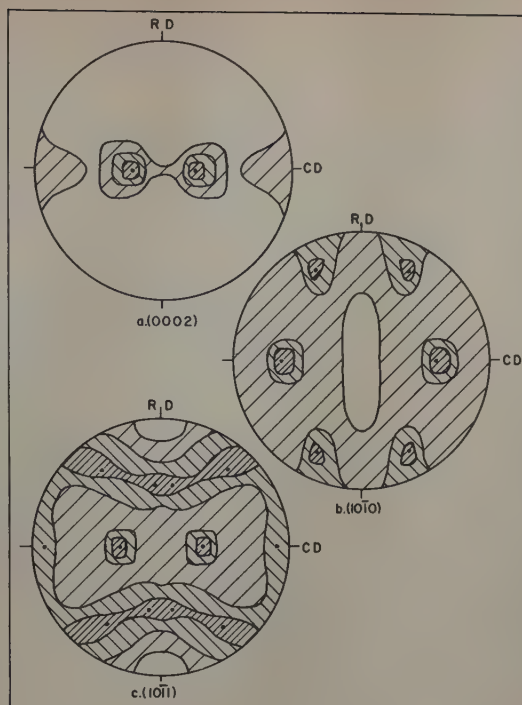


Fig. 5 (right) — Iodide titanium cold rolled 97 pct, annealed at 1500°F. • = (0002) rotated 27°, $[11\bar{2}0]$ parallel to rolling direction.

were to be rotated until parallel to the wire axis. The orientation is such that the $(21\bar{3}0)$ plane is normal to the wire axis, which is shown schematically in Fig. 1b.

Exposures on the surface layer do not show the strong, split maxima, but indicate the average position of $[11\bar{2}0]$ to lie along the wire axis with a spread of $\pm 35^\circ$. The recrystallized wire texture of zirconium⁸ has been found to be $[11\bar{2}0]$.

Cold Rolled Sheet Texture: The cold rolled sheet texture for iodide titanium is presented in Fig. 2. Fig. 2a shows that two high intensity regions are developed for (0002) planes, which correspond to rotation of approximately 27° in the transverse direction from the "ideal" orientation of (0002) $[10\bar{1}0]$ reported for other hexagonal metals. McGeary and Lustman found indications of this tilt in zirconium,⁴ and it has been reported in titanium by Clark.⁵ Fig. 2b shows that the $[10\bar{1}0]$ direction is aligning parallel to the rolling direction, and Fig. 2c confirms the selection of (0002) rotated 27° and $[10\bar{1}0]$ parallel to the rolling direction as the orientation describing the texture. Most of the spread from this "ideal" orientation is in the transverse direction.

Cold Rolled Recrystallized Sheet Texture: Fig. 3 presents the pole figures representing the orientation of the material annealed at 1000°F. These pole figures show that the cold rolled texture is retained for recrystallization at a relatively low temperature, and that there is a slight sharpening of the texture.

An investigation of material cold rolled 97 pct, and vacuum annealed at 1300°F indicates that a dual texture is present in this condition. As is shown in Fig. 4, this texture can be explained in terms of the tilted basal plane and one component having the $[10\bar{1}0]$ direction parallel to the rolling plane, and another component having the $[11\bar{2}0]$ direction parallel to the rolling direction.

The pole figures for iodide titanium cold reduced 97 pct and annealed at 1500°F, Fig. 5, are describable in terms of the basal plane tilted approximately

27° and the $[11\bar{2}0]$ direction aligned with the rolling direction.

Thus, it is seen that the texture obtained upon recrystallization depends upon the temperature of treatment. This work indicates that the cold rolled texture is retained by the material just recrystallized. However, as the temperature is increased and grain growth and secondary recrystallization take place, a new texture is produced.

The texture reported for zirconium recrystallized at 1200°F differs from the cold rolled texture by a rotation of 30° about the normal to the basal plane.⁴ Beck¹² and Kronberg and Wilson¹³ point out that there is a component of the recrystallized textures of face-centered cubic metals which corresponds to a rotation of 30° to 40° about a $[111]$ axis. The results of the present investigation lend added support to Beck's conclusion that in hexagonal close-packed and face-centered cubic metals, the reorientation upon recrystallization corresponds to a rotation about the normal of a close-packed plane.

Hot Rolled Texture at 1050°F: With the exception of beryllium³ and zirconium,⁴ there is no information on the preferred orientation produced by hot rolling hexagonal close-packed metals. These two materials retain their cold rolled textures when rolled at temperatures as high as 1475°F.

The pole figures for titanium hot rolled at 1050°F, Fig. 6, show that this texture can satisfactorily be described in terms of the "ideal" orientation (0002) $[10\bar{1}0]$. Fig. 6a shows a tendency for the (0002) planes to be tilted as in the cold rolled sheet texture, and Fig. 6b shows the tendency for the $[10\bar{1}0]$ direction to be aligned parallel to the rolling direction. The spread of the (0002) plane in the cross direction is $\pm 40^\circ$. The scatter about the normal to the rolling plane brings the $[11\bar{2}0]$ directions parallel to the rolling direction at the ends of this spread. Again, the spread is greater in the transverse direction than in the rolling direction.

That the hot rolled texture is describable in terms of the orientation (0002) $[10\bar{1}0]$ is shown by Fig. 6.

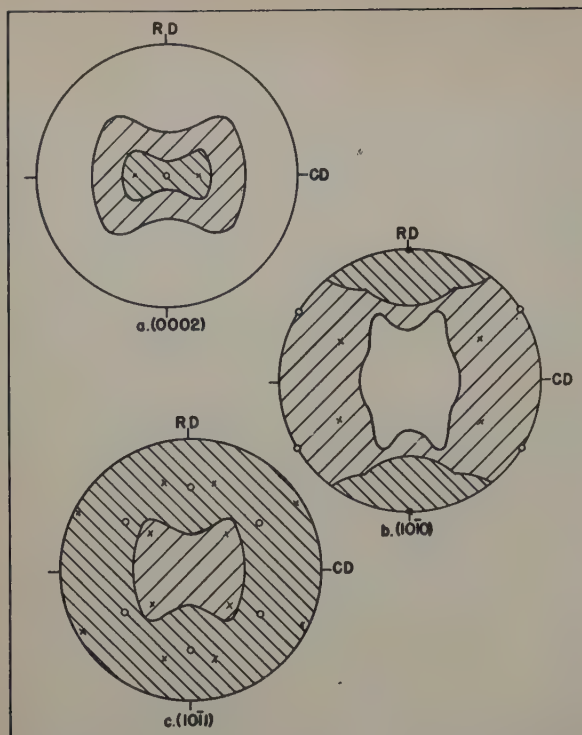


Fig. 6—Iodide titanium hot rolled at 1050°F. $o = (0002)$ $[10\bar{1}0]$. $x = (0002)$ $[10\bar{1}0]$ tilted 27°.

The orientation (0002) $[10\bar{1}0]$ is marked by "o" and this orientation tilted 27°, as in the cold rolled textures, is marked by "x." It can be seen that all regions are satisfactorily explained on the basis of (0002) $[10\bar{1}0]$. It would be possible to describe the hot rolled sheet texture as a great amount of spread about the cold rolled texture. However, it is felt, on the basis of Figs. 6b and c, that the spreads of orientations are better described as deviations from (0002) $[10\bar{1}0]$.

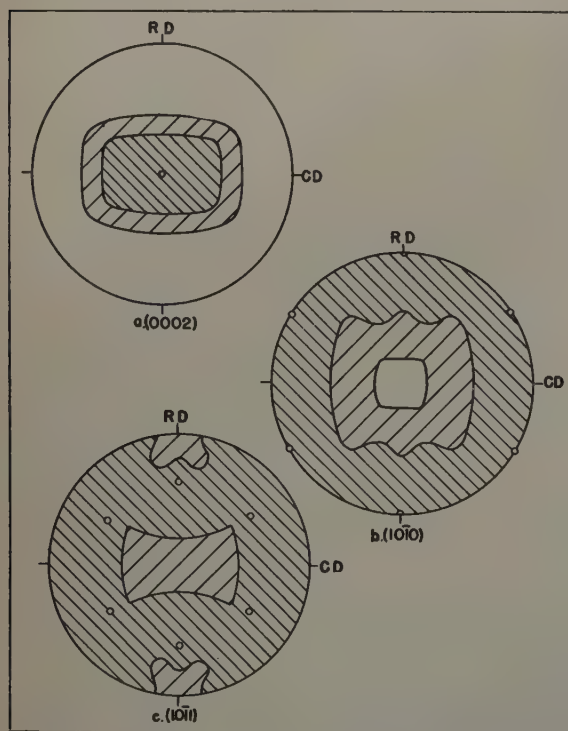


Fig. 7—Iodide titanium hot rolled at 1450°F. $o = (0002)$ $[10\bar{1}0]$.

Hot Rolled Texture at 1450°F: As Fig. 7 shows, the randomness of the texture in the specimen rolled at 1450°F is greater than in that rolled at 1050°F. However, the texture still retains the average position of the (0002) plane parallel to the rolling plane. There is a spread of the (0002) plane $\pm 30^\circ$ in the rolling direction and $\pm 40^\circ$ in the cross direction from this ideal orientation. In this texture, no one direction appears to be preferentially aligning parallel to the rolling direction.

Effects of the $\alpha \rightarrow \beta$ Transformation on Textures: It can be seen in Fig. 8 that a sharp texture is present after the double transformation $\alpha \rightarrow \beta \rightarrow \alpha$. This texture can be described by the 27° tilted basal plane with the $[11\bar{2}0]$ direction parallel to the rolling direction. This is the same orientation reported for iodide titanium recrystallized at 1500°F.

One specimen of cold rolled titanium sheet was cycled five times between the α and β regions, and X-ray shots were made to determine if any change

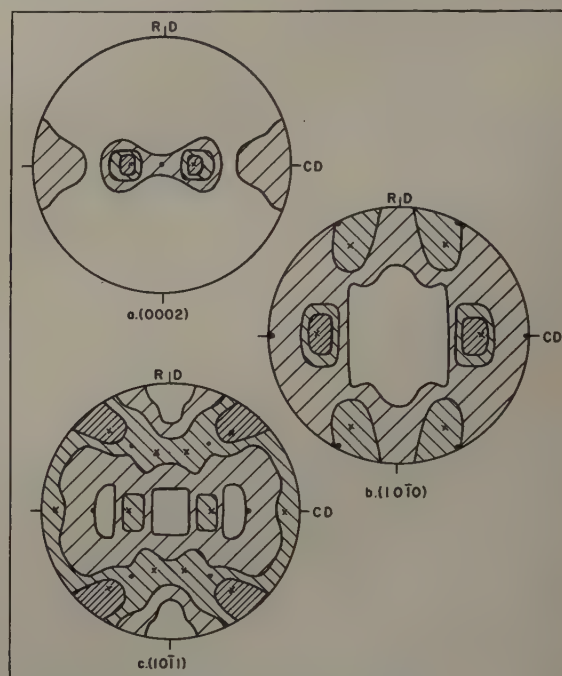


Fig. 8—Texture in iodide titanium cold rolled 97 pct, heated above the $\alpha \rightarrow \beta$ transformation temperature and slowly cooled. $o = (0002)$ $[11\bar{2}0]$. $x = (0002)$ rotated 27° about rolling direction, $[11\bar{2}0]$ parallel to rolling direction.

in the texture resulted. The only difference noted was a slight increase in the spread of the basal planes in all directions. Otherwise, the sharp texture of Fig. 8 was retained.

Summary

1—The wire texture for iodide titanium has the $[10\bar{1}0]$ direction parallel to the wire axis in the cold rolled state. Recrystallized wires have an average orientation containing the $[11\bar{2}0]$ direction parallel to the wire axis, but the actual orientation has the normal to the $(21\bar{3}0)$ plane parallel to the axis.

2—The cold rolled sheet texture is described as having the (0001) planes tilted approximately 27° in the transverse direction to the rolling plane and the $[10\bar{1}0]$ directions parallel to the rolling direction.

3—Sheets annealed in the vicinity of 1000°F retain the cold rolled textures. Those annealed at

1300°F show a component explained by the cold rolled texture, and one explained by this texture rotated 30° about the normal to the basal plane, i.e., [1120] parallel to rolling direction. Annealing at 1500°F produces only the texture containing [1120] parallel to the rolling direction and the (0002) tilted 27° to the rolling plane.

4—Hot rolling at 1050°F develops a (0002) [1010] texture with spread more pronounced in the transverse than the rolling direction. Rolling at 1450°F aligns the (0002) plane parallel to the rolling plane, but does not show a preferred direction parallel to the rolling direction.

5—The texture present after the double transformation $\alpha \rightarrow \beta \rightarrow \alpha$ is the same as the high temperature recrystallization texture.

Acknowledgment

The work described in this paper was done under Air Force Contract AF33(038)-19574 with the Office of Air Research, Wright-Patterson Air Force Base. The authors gratefully acknowledge the aid of S. E. Adair, Jr., graduate student at the University of Kentucky. The authors also wish to thank F. D.

Rosi, of Sylvania Electric Products, Inc., for several stimulating discussions of this work.

References

- ¹ P. W. Bakarian: *Trans. AIME* (1942) **147**, p. 266.
- ² V. Caglioti and G. Sachs: *Metallwirtschaft* (1932) **11**, p. 1.
- ³ C. S. Barrett and A. Smigelskas: *Trans. AIME* (1949) **185**, p. 149; *JOURNAL OF METALS* (February 1949).
- ⁴ R. K. McGeary and B. Lustman: *Trans. AIME* (1951) **191**, p. 995; *JOURNAL OF METALS* (November 1951).
- ⁵ H. T. Clark, Jr.: *Trans. AIME* (1950) **188**, p. 1154; *JOURNAL OF METALS* (September 1950).
- ⁶ F. D. Rosi: Private communication.
- ⁷ D. A. Sutcliffe and J. A. Reynolds: *Metallurgia* (March 1950).
- ⁸ D. W. Smith: *Symposium of Radiography and X-ray Diffraction*. (1937) Philadelphia. ASTM.
- ⁹ W. G. Burgers, J. D. Fast, and F. M. Jacobs: *Ztsch Metallkunde* (1938) **29**, p. 419.
- ¹⁰ L. G. Morell and J. D. Hanawalt: *Journal of Applied Physics* (1932) **3**, p. 161.
- ¹¹ A. Taylor: *Introduction to X-ray Metallography*. (1949) New York. John Wiley and Sons.
- ¹² P. A. Beck: *Trans AIME* (1951) **191**, p. 475; *JOURNAL OF METALS* (June 1951).
- ¹³ M. L. Kronberg and F. H. Wilson: *Trans. AIME* (1949) **185**, p. 501; *JOURNAL OF METALS* (August 1949).

Technical Note

Torsion Texture of 70-30 Brass and Armco Iron

by W. A. Backofen and B. B. Hundy

THE pole figure interpretation in a recent paper¹ on the torsion texture of copper was questioned in discussion,² and a simpler alternative interpretation was proposed. In the hope of reaching a positive decision in favor of one or the other, further studies were undertaken with 70-30 brass and Armco iron. This additional work has not answered all the questions about torsion textures, but the new pole figures do offer support for the original interpretation and show that the texture is more complicated than the alternative suggests.

From the previous paper,¹ the appropriate method of describing the texture in a twisted bar is known to be a pole figure plotted on a plane tangent to the surface of the bar. The axes of the pole figure are chosen to coincide with directions in the tangent plane which are parallel and at right angles to the bar axis (the longitudinal direction, L.D., and the transverse direction, T.D.), for these directions define symmetry axes of the texture. Therefore any ideal orientation that might be selected to represent the texture gives the crystallographic plane parallel to the tangent plane and the crystallographic direction parallel to the axis of the torsion specimen.

A unique texture was assumed in the original interpretation, and the four ideal orientations, (112) [111], (111) [112], (110) [001], and (112) [131], were used in its description. Of the four orientations, the first three provide possible slip directions along the direction labeled T.D. in the pole figure, which is one of maximum shear stress in a specimen being twisted. The alternative, however, simply considered

the texture to be made up of two components, one a [111] alignment along the specimen axis with a random orientation about the axis as in the wire texture, and the other a superimposed orientation (110) [001]. Experimental evidence for this simpler interpretation was derived from two observations: 1—twisting did not alter the orientation of a single-crystal torsion specimen of α brass in which an octahedral plane was perpendicular (and a [111] direction parallel) to the axis, and 2—deformation bands with approximately the (110) [001] orientation were seen to develop in the crystal during the test.

The new pole figures were obtained with a brass and an iron torsion specimen of $\frac{3}{4}$ and 1 in. gage length diameter, respectively. After annealing, polishing, and twisting, seven rods, about 0.030 in. in diameter and with different orientations, were prepared from material near the surface of each specimen; these were required for the method of constructing pole figures by using a Geiger counter as developed by Norton.³ Since the shear strain gradient in plastic torsion is linear, it was readily computed that the material supplying the brass rods had been subjected to a shear strain of about 3.2, and that supplying the iron rods had received a shear strain of about 2. All details concerning specimen design, testing procedure, rod preparation, and use of the Norton technique can be found in ref. 1. Only this procedure was followed in working out the (111) and (100) pole figures for brass, Figs. 1 and 2. However, X-ray photograms were also involved in the construction of the (110) pole figure for Armco iron, Fig. 3. The photograms were made according to the conventional transmission diffraction technique using a small sheet taken parallel to the specimen surface and etched to a thickness of about 0.0025 in. They were especially important in locating the boundaries

W. A. BACKOFEN, Junior Member AIME, is Assistant Professor of Metallurgy, Massachusetts Institute of Technology, Cambridge, Mass., and B. B. HUNDY, formerly at MIT, is now Scientific Officer, British Iron and Steel Research Association, Sheffield, England.
TN 139E. Manuscript, Oct. 6, 1952.

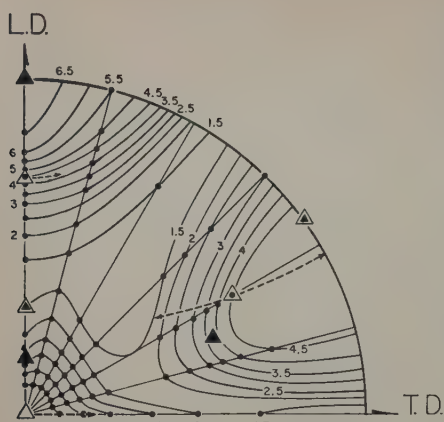


Fig. 1—(111) pole figure of 70-30 brass twisted to a shear strain of 3.2. Ideal orientations indicated as follows: Solid triangle, (112) $[11\bar{1}]$. Open triangle, $(11\bar{1})$ $[112]$. Double triangle, (110) $[001]$.

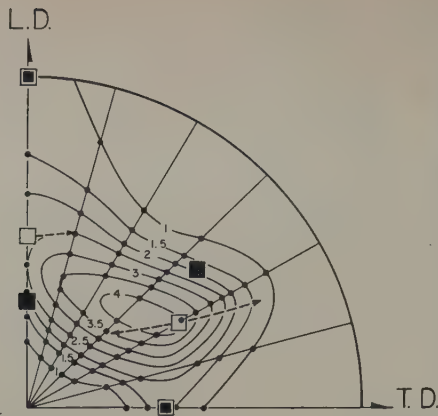


Fig. 2—(100) pole figure of 70-30 brass twisted to a shear strain of 3.2. Ideal orientations indicated as follows: Solid square, (112) $[11\bar{1}]$. Open square, $(11\bar{1})$ $[112]$. Double square, (110) $[001]$.

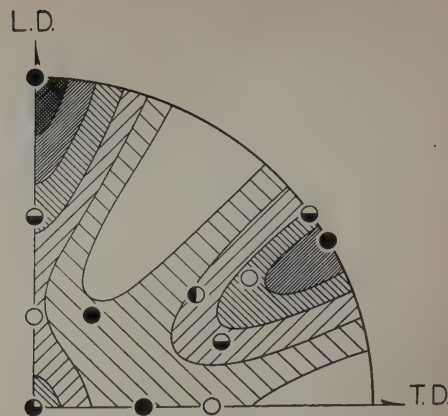


Fig. 3—(110) pole figure of Armco iron twisted to a shear strain of 2. Ideal orientations indicated as follows: Solid circle (111) $[11\bar{0}]$. Open circle (112) $[11\bar{0}]$. Vertical half-solid circle, (110) $[11\bar{0}]$. Horizontal half-solid circle, (110) $[11\bar{2}]$.

of the areas of lowest pole density. Because of the combination of methods, the pole distribution in Fig. 3 has been represented with a precision intermediate between that warranted by the counting data and photograms.

Three ideal orientations, $(11\bar{1})$ $[112]$, (112) $[11\bar{1}]$, and (110) $[001]$, have been selected for the simplest approximation of the torsion texture of brass. The first two help to account for the high concentrations of $[111]$ poles in the polar region, the central region, and, to an important extent, the peripheral region about 60° to 75° from the longitudinal direction; they also position poles reasonably well in the (100) pole figure. The (110) $[001]$ is likewise required by both pole figures, although it is not a particularly strong component of the texture. All three provide a $[110]$ slip direction along the transverse direction of maximum shear stress. There is, of course, much spread about these orientations. A possible rotation of approximately 22° around the $[112]$ direction of the $(11\bar{1})$ $[112]$ orientation is indicated with dashed lines in Figs. 1 and 2. Rotations about the $[11\bar{1}]$ and $[001]$ directions of the other two orientations are much more limited, however. Rotation about the transverse direction is also possible. The (112) $[11\bar{1}]$ can be rotated into the $(11\bar{1})$ $[112]$ and then the (110) $[001]$, although orientations between the last two are not prominent. Further rotation is possible with the $(11\bar{1})$ $[112]$ and (112) $[11\bar{1}]$ around the poles of the $(11\bar{1})$ and (112) planes. There is no need for the fourth orientation, (112) $[1\bar{3}1]$, used in the description of this texture in copper. Considering only the (111) pole figure, the texture might still be interpreted as duplex, consisting of a $[111]$ wire-like component plus the orientation (110) $[001]$; but this possibility is eliminated by the nature of the (100) pole figure.

The torsion texture of iron appears to consist of a strong alignment of $[110]$ directions along the specimen axis, which is limited in its range of orientation around the axis, with (110) $[11\bar{2}]$ superimposed. The spread of the $[110]$ alignment around the longitudinal direction might be taken as the angle between the $[110]$ pole of a (110) $[11\bar{0}]$ orientation and $[112]$ pole of a (112) $[11\bar{0}]$ orientation, or approximately 54° . It seems more reasonable, however, to rule out, or at least not emphasize the

(110) $[11\bar{0}]$ limit and replace it with something closer to (111) $[11\bar{0}]$. Then the spread would be nearer 20° , roughly the angle between $[111]$ and $[112]$ poles. By slighting the (110) $[11\bar{0}]$ orientation, fewer poles from the alignment along the specimen axis appear in the central area of high pole density, which is then accounted for by the (110) $[11\bar{2}]$ orientation. The latter orientation also places poles in the peripheral area of high intensity, and their contribution on top of that from the $[110]$ alignment explains fairly well the intensity variation in that area. Rotations about the transverse direction and an axis perpendicular to the plane of the figure are also possible here. For example, a rotation might be made about a $[110]$ direction perpendicular to the figure to convert (110) $[11\bar{2}]$ into (110) $[11\bar{3}]$. Both the (112) $[11\bar{0}]$ and (110) $[11\bar{2}]$ place a $[111]$ slip direction along the transverse direction of maximum shear stress. And again there appears to be more than a superficial difference between the torsion texture and wire texture.

A few photograms were also taken using transmission specimens prepared from two other bars of brass and iron that had been twisted and untwisted by equal amounts. These indicated that the texture established by twisting is not altered if the direction of twisting is reversed, which is the conclusion reached in the work with copper from comparison of complete pole figures.

To summarize, according to the new pole figures, the torsion texture is not the texture found in cold-drawn wire; it is a unique texture that can be described approximately by a combination of ideal orientations, but one that requires still more study before generalizations about its development, description, and correlation with flow can be made.

Acknowledgment

The authors are indebted to the Office of Naval Research for support of this work and to Walter R. Hibbard, Jr. for reviewing the results.

References

- ¹W. A. Backofen: *Trans. AIME* (1950) **188**, p. 1454; *JOURNAL OF METALS* (December 1950).
- ²W. R. Hibbard, Jr.: *Trans. AIME* (1951) **191**, p. 1062; *JOURNAL OF METALS* (November 1951).
- ³J. T. Norton: *Journal of Applied Physics* (1948) **19**, p. 1176.

Forging of Arc-Melted Chromium

by H. L. Gilbert, H. A. Johansen, and R. G. Nelson

High purity electrolytic chromium plate has been hydrogen-reduced and arc-melted under inert atmosphere to give sound ingots. These ingots may be hot forged to break the as-cast structure and then worked at 500°C to finished form. An intermediate and final high temperature anneal gives best ductility and grain refinement.

THE increasing interest in refractory metals for use in high temperature gas turbines, jets, and rockets has led to great efforts in exploiting the fifth and sixth groups of transition elements. Much of the interest has centered upon production of metals that can be worked and fabricated by normal means to produce various engine parts or components having the high temperature characteristics of oxidation resistance and high creep strength required for such uses. If these pure elements do not exhibit all of the desired characteristics, it may be possible to obtain a high purity alloy that will.

Since, in all cases, development of these transition elements has depended to a large extent upon removal of oxygen and nitrogen as a means for producing ductile metal, the hypothesis has been accepted that oxygen is the normal embrittling material in a high grade electrolytic chromium metal. Various methods have been employed in an effort to remove this oxygen by direct or indirect attack.¹

Many workers have endeavored to produce pure chromium through reduction of the oxide by carbon or active metals, while others have recommended fusion electrolysis of chromium salts or reduction of these salts by active metals, such as sodium or calcium. Hydrogen reduction of the oxide or chloride and thermal dissociation of the iodide have been reported to give high purity metal.

Experimental Work

The U. S. Bureau of Mines, Northwest Electrodevelopment Laboratory, has systematically re-examined the more promising methods and developed two which produce metal having ductility at temperatures lower than heretofore described.

It has been found² that oxide-free chromium chlorides in a NaCl-KCl carrier salt may be mag-

H. L. GILBERT and H. A. JOHANSEN are Chemical Engineers, and R. G. NELSON is Metallurgist, of the Northwest Electrodevelopment Laboratory, U. S. Bureau of Mines, Albany, Oregon.

Discussion on this paper, TP 3442DE, may be sent, 2 copies, to AIME by March 1, 1953. Manuscript, Jan. 28, 1952. New York Meeting, February 1952.

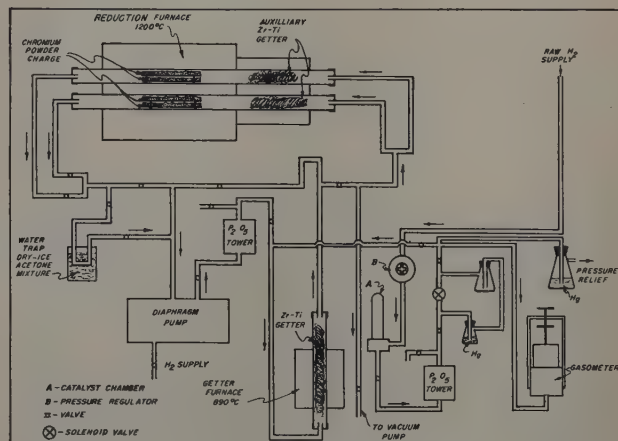


Fig. 1—Hydrogen reduction equipment for chromium powder.

nesium-reduced and the byproduct salts distilled off in vacuo to give a high purity chromium sponge. Fusion analysis conducted under the supervision of W. W. Horton of Knolls Atomic Power Laboratory showed the oxygen and nitrogen both to be below 10 parts per million on a selected sample. A small amount of carbon is carried over in the final metal from the chlorination and reduction steps which are carried out in graphite crucibles. This trace of carbon is not detrimental to hot ductility.

A more practical method for producing ductile metal is through hydrogen reduction of high purity electrolytic chromium. Normal electrolytic chromium will, if "developed" for a few minutes at 1100°C in high vacuum, be found by the method of Adcock³ to contain about 1 pct chromium sesquioxide (Cr_2O_3). This small amount of oxygen may be effectively reduced by hydrogen.^{2, 4}

The method employed was to crush electrolytic chromium plate in a gyratory crusher to pass 60-mesh; finer crushing appears to offer no advantage. A nitric acid leach removed the iron picked up during crushing. The leached powder was rinsed until neutral with distilled water and vacuum-dried.

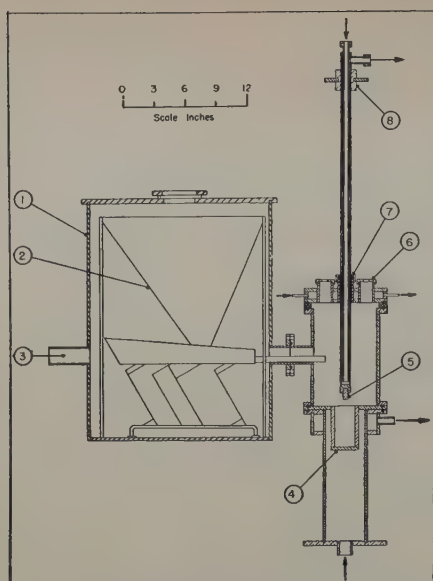


Fig. 2—Description of arc melting furnace.

- | | |
|--------------------------|--|
| 1—Vacuum tight feed tank | 5—Thoriated tungsten electrode |
| 2—Vibrating feeder | 6—Eyepiece |
| 3—Vacuum connection | 7—Packing gland for electrode movement |
| 4—Melting cup | 8—Electrical connection, dc, cathode. |

Charges of chromium powder were loaded in molybdenum boats into the 2-in. diam porcelain tubes of the reduction furnace shown in Fig. 1. The system was then evacuated and checked carefully for leaks. Cylinder hydrogen was admitted through a palladium catalyst tower to convert contained oxygen to water which was removed in the phosphorus pentoxide tower. Hydrogen was added until the gasometer rose, which insured a pressure above atmospheric in the system.

Rapid circulation (25 liters per min at standard temperature and pressure) was accomplished by means of a small commercial diaphragm pump sealed in a steel box under an atmosphere of hydrogen from the furnace system so that pump leakage was no problem. The getter furnace was heated to effect initial purification of the circulating hydrogen gas. A Zr-Ti alloy (50-50 mol pct) getter that has a very high affinity for any contaminating gas present was employed. The cold trap was then filled with dry-

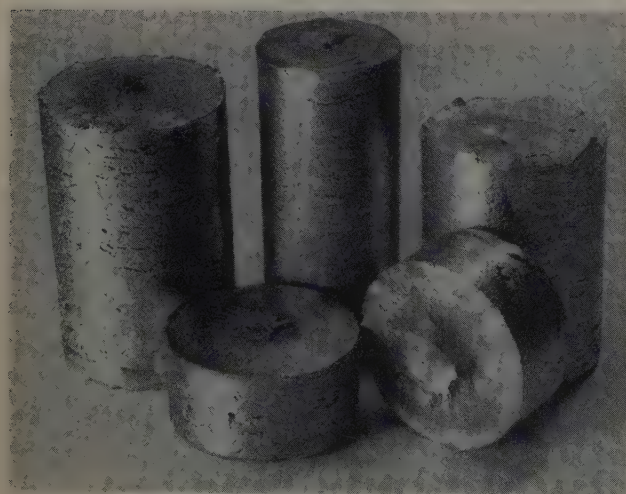


Fig. 3—Arc melted chromium ingots, $1\frac{3}{8}$ to 2 in. diam.

ice-acetone mixture and the reduction furnace turned on. Most of the water formed by reduction was removed from the system by this cold trap, so the metallic getter and phosphorus pentoxide traps had a long service life.

The temperature of the reduction furnace was maintained at a selected point between 1100° and 1200°C . The main getter furnace was operated at 890°C , and small auxiliary furnaces at the inlet end of the reduction tubes were maintained at a like temperature. Considerable hydrogen was absorbed by the getters when they were first exposed, but no further absorption or elimination was encountered under the conditions of operation. After 16 hr at reduction temperature, the furnace was cooled and the metal removed from the molybdenum boats. As some sintering of the chromium powder took place during reduction, it may be sized upon removal. Lumps $\frac{1}{4}$ to $\frac{1}{8}$ in. in size were found best for arc-melting purposes.

Melting was accomplished in an inert-atmosphere arc furnace shown in Fig. 2.⁵ A thoriated tungsten tip $\frac{1}{2}$ in. in diam and 1 in. long screwed into a water-cooled copper electrode holder was used. The



Fig. 4—Half section of chromium ingot, full scale. Etchant, aqua regia.

melting crucible was of pure copper approximately 2 in. ID and 4 in. long. The chromium lumps were loaded into the feed box and the furnace evacuated and backfilled with 80 pct helium-20 pct argon from a getter supply tank. The chromium was fed to the melting cup by a built-in vibrating feeder. An arc of 40 v and 800 amp (dc) will melt 750 g of chromium in 20 min. The ingots as removed from the furnace had a fairly good outer surface, but removal of $\frac{1}{8}$ in. depth on the lathe assured that no cold-shut difficulties would be encountered. Three sizes of ingots are shown in Fig. 3.

Representative analysis of the metal is as follows: Fe, 0.001 pct; Si, 0.05; O, 0.003; N, 0.002; and H, 0.005. In regard to all other metallic impurities, the metal is as pure as the best spectrographic standards available on the market today. Tungsten pick-up during melting was nonuniform and varied from none to

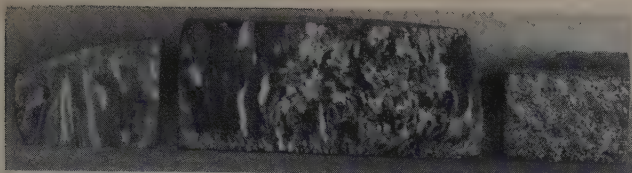


Fig. 5—Chromium ingot. Etchant, aqua regia. X2. Area reduced approximately 75 pct for reproduction. a (left)—As cast. b (center)—Forged 25 pct at 850°C. c (right)—Forged 25 pct, annealed 1 hr at 1200°C in hydrogen.

0.01 pct. Tungsten distribution was very random, and it may be eliminated by use of a consumable electrode of chromium.

Average ingot hardness in the as-cast condition was $R_{\text{c}} 55$ and in the annealed condition $R_{\text{c}} 46$.

The ingots were taken from the arc furnace and given a hydrogen anneal for 1 hr at 1200°C, as severe strains are set up during cooling. After annealing and scalping the ingots may be worked open or sheathed. Owing to the small size of the ingots it was preferred to sheath them in iron pipe to pre-

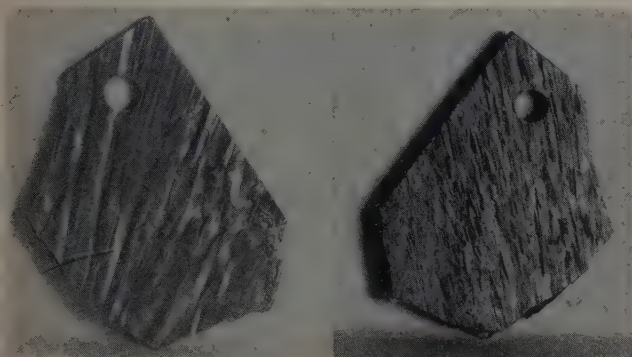


Fig. 6—Sheet rolled from ingot without anneal. Etchant, aqua regia. X15. Area reduced approximately 70 pct for reproduction. a (left)—As removed from sheath. b (right)—Polished and etched.

vent chilling of the chromium on contact with the cold forging hammer or rolls. Initial forging was accomplished at 800° to 850°C with moderate reductions until the cast structure was broken up. This may be followed by heavier reductions at 500°C. After the material had been reduced to final dimension, an anneal in hydrogen at 1200°C gave maximum ductility and grain refinement. This material,



Fig. 7—Swaged rod $\frac{3}{4}$ in. diam and forged and polished disk of chromium.

however, cannot be bent at room temperature without fracture.

It may be seen that this treatment resembles the techniques employed for both arc-melted vanadium⁶ and molybdenum,⁷ although in some respects the behavior of the metal is more like that of tungsten.

Fig. 4 shows a sectioned arc-cast chromium ingot and Fig. 5 the grain refinement effected by forging 25 pct at 850°C followed by a 1 hr anneal at 1200°C. If the arc-cast ingot is worked to finished sheet without an intermediate recrystallization, a very coarse, fibered structure results as shown in Fig. 6. Reductions in area as high as 93 pct have been effected by rotary swaging. As with forging and rolling, an intermediate recrystallization was beneficial in avoiding a coarse-grained product. A rod swaged at 950°C is shown in Fig. 7.

It is felt that the status of development of pure chromium metal is encouraging; but, in view of the lack of cold ductility, despite the many efforts made to overcome this condition, the possibility remains that low ductility may be an inherent property of the metal.⁸ The excellent work on beryllium⁹ has given an extruded metal with fine grain and preferred orientation having an elongation of only 5 to 10 pct in the direction of extrusion. Chromium's sister element, tungsten, seldom displays an elongation better than 6 pct except in fine wire, and there is no reason why chromium may not fall in the same class.

It is believed from the results noted herein that chromium may display the final ductility of tungsten and perhaps even reach the very useful position of molybdenum.

Conclusions

It has been found that a hydrogen-reduced electrolytic chromium powder may be arc-melted to prepare ingots for forging, rolling, or swaging to desired form. Finished forms exhibit ductility at considerably lower temperature than heretofore described. It is possible that in such condition chromium will find wider usage in high temperature applications, either pure or alloyed with other metals of equal purity.

Acknowledgment

Acknowledgment is made to W. W. Stephens, Head of the Rare Metals Branch of the Albany Station, under whose supervision this work has been carried out and to R. A. Beall, Head of the Fusion Section, responsible for production of our ingots. Special acknowledgment is made to W. J. Kroll, formerly consultant to this station, whose enthusiasm and guiding genius permeated this work.

References

- W. J. Kroll, W. F. Hergert, and W. R. Carmody: U. S. Bur. Mines R. I. 4752 (1950).
- W. J. Kroll, W. F. Hergert, and L. A. Yerkes: *Journal Electrochem. Soc.* (1950) **97**, p. 258.
- F. J. Adcock: *Journal Iron and Steel Inst.* (1947) **115**, p. 369.
- J. W. Marden and M. N. Rich: U. S. Patent No. 1,760,367 (1930).
- O. W. Simmons, C. T. Greenidge, and L. W. Eastwood: Report of Titanium Symposium. ONR, Dept. of Navy, p. 77 (1948).
- A. B. Kinzel: *Metal Progress* (1951) **59**, p. 812.
- J. H. Bechtold and H. Scott: Some Mechanical Properties of Arc-Cast and Powder Metallurgy Molybdenum. *Journal Electrochem. Soc.* (1951) **98**, p. 495.
- W. J. Kroll: Unpublished memorandum (1950).
- A. R. Kauffmann, Paul Gordon, and D. W. Lillie: *Trans. ASM* (1950) **42**, p. 785.

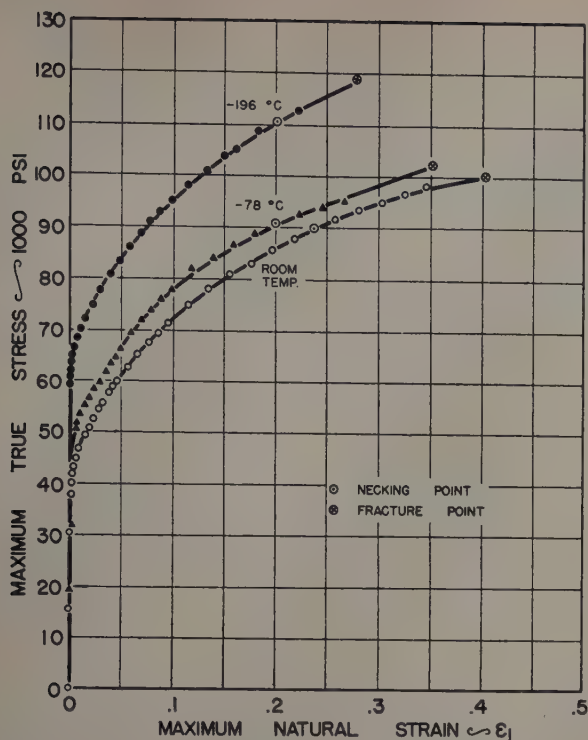


Fig. 2—Stress-strain curves of the aluminum alloy 24S-T4 at different testing temperatures.

the specimen during straining was measured by a radial strain gage reading in ± 0.0001 in.⁵ A strain rate corresponding to a movement of the test machine head of approximately 0.05 in. per min was used for all strains. The concentric tensile testing equipment was modified for low temperature testing as previously described.

Results and Discussion

The effect of testing temperature on the stress-strain behavior of the aluminum alloy is shown in

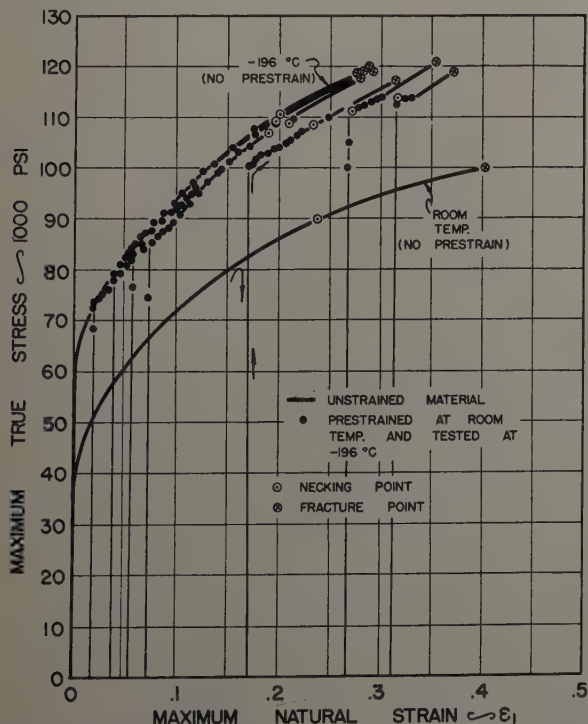


Fig. 3—Effect of prestrain in tension at room temperature on the stress-strain curve in tension of the aluminum alloy 24S-T4 at -196°C .

Fig. 2. Although the difference between the fracture ductility at room temperature and -196°C is not nearly as large as is the case for most steels, the difference is considerably greater than has been reported for a number of other face-centered cubic metals.⁶

Prestraining the aluminum alloy at room temperature and testing at -78° or -196°C produced a lower flow stress curve than would the same total strain at the low temperature. The data obtained by testing at -196°F are shown by the curves in Fig. 3. Again, prestretching at the low temperature pro-

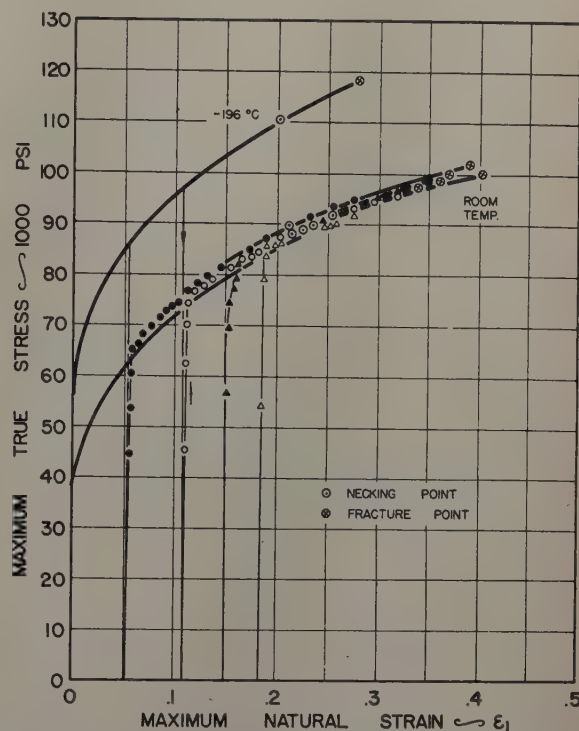


Fig. 4—Effect of prestrain in tension at -196°C on the stress-strain curve in tension of the aluminum alloy 24S-T4 at room temperature.

duced a higher room temperature flow curve than would an equal strain at room temperature, Fig. 4. These curves are quite like those previously obtained on 2S-O aluminum and copper.¹

The fracture stress and fracture ductility possessed by the aluminum alloy at room temperature, -78° , and -196°C after prestraining at room temperature in tension and compression are shown in Fig. 5. Room temperature tensile prestrains apparently have little effect on the low temperature fracture stress, while room temperature compressive prestrains are harmful to the fracture stress only when the magnitude of the precompression is quite large.

When the room temperature prestraining and the low temperature testing were both by tension, the dependence of retained ductility on prestrain can be described by the equation previously presented for steel:

$$\left(\frac{\epsilon_p}{\epsilon_A}\right)^m + \left(\frac{\epsilon_r}{\epsilon_R}\right)^n = 1 \quad [1]$$

where: ϵ , the maximum natural strain, is defined as the natural logarithm of the ratio of the original cross-sectional area to the final cross-sectional area; ϵ_r , the retained ductility in the second straining op-

Fig. 5 (right)—Effect of room temperature tensile and compressive prestraining on the low temperature fracture stress and ductility of the aluminum alloy 24S-T4.

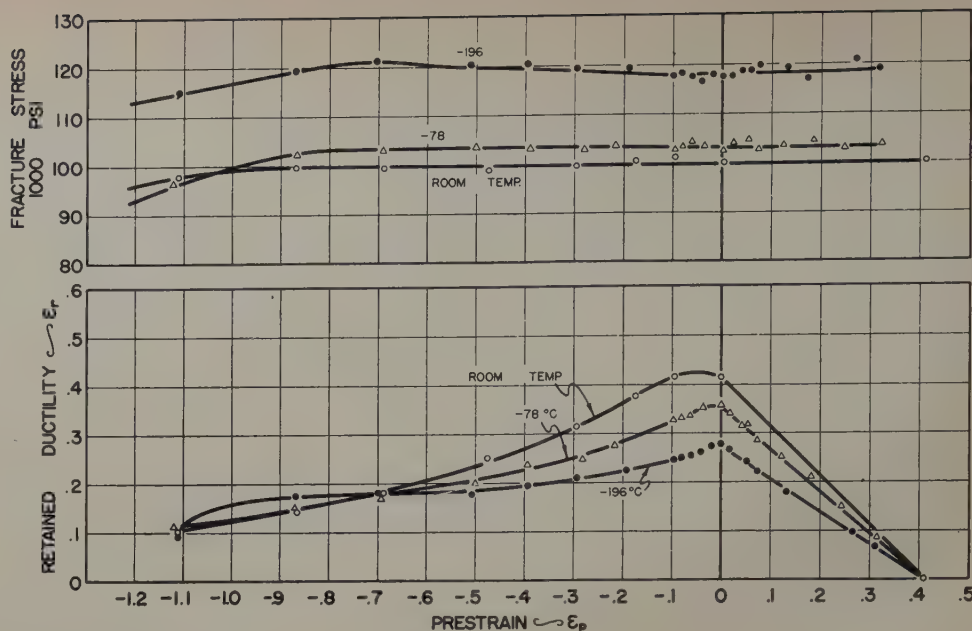
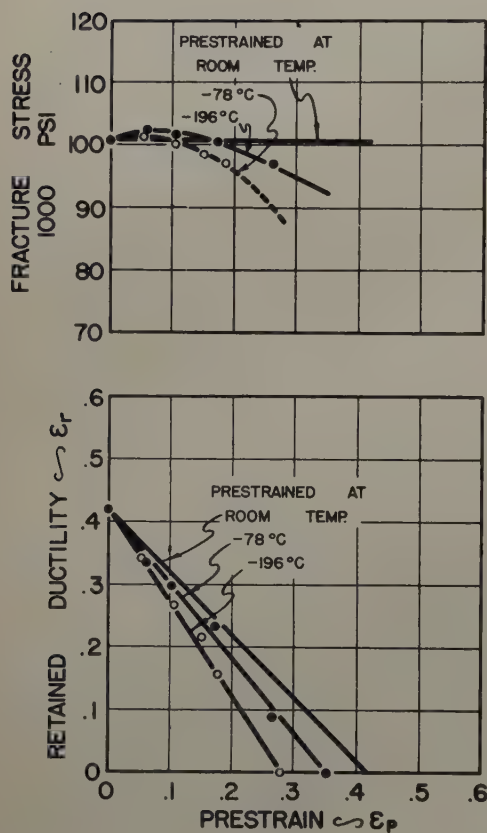


Fig. 6 (below)—Effect of low temperature tensile prestraining on the room temperature fracture stress and ductility of the aluminum alloy 24S-T4.



eration; ϵ_A , the fracture ductility at the temperature of first strain; ϵ_B , the fracture ductility at the temperature of second strain; ϵ_p , the prestrain; and m and n , the material constants.

Since the retained ductility-prestrain curves are straight lines in this case, m and n are equal to one, as is the case for most of the materials investigated to date.

Small compressive prestrains at room temperature were again shown to be unarmful to the tensile ductility both at room and low temperatures. An earlier study showed small compressive prestrains to be helpful to room temperature tensile ductility⁷

and this effect probably persists even with low temperature straining, although data at sufficiently small strains were not collected.

Reversing the order of strains so that the low temperature stretching preceded the room temperature stretching again produced retained ductility-prestrain curves which were straight lines, intercepting the ordinate at the value of room temperature ductility, and the abscissa at the values of low temperature ductility, see Fig. 6. Hence the behavior is again described by Eq. 1.

Acknowledgments

The authors wish to express their gratitude to the Office of Naval Research, U. S. Navy, in cooperation with whom this work was conducted, for permission to publish these data. The authors further acknowledge with pleasure the kind help and guidance given by W. M. Baldwin, Jr., Research Professor, G. Sachs, former director of the project under whom the study was initiated, and to L. J. Ebert. A debt of gratitude is also due the General Electric Co. for supplying the liquid nitrogen used as a coolant in this study.

References

- 1 J. E. Dorn, A. Goldberg, and T. E. Tietz: The Effect of Thermal-Mechanical History on the Strain Hardening of Metals. *Trans. AIME* (1949) **180**, p. 205; *METALS TECHNOLOGY* (September 1948).
- 2 E. J. Ripling and G. Sachs: The Effect of Strain-Temperature History on the Flow and Fracture Characteristics of an Annealed Steel. *Trans. AIME* (1949) **185**, p. 78; *JOURNAL OF METALS* (February 1949).
- 3 E. J. Ripling and W. M. Baldwin, Jr.: Rheotropic Embrittlement of Steel. *Trans. ASM* (1951) **43**, p. 778.
- 4 E. J. Ripling and W. M. Baldwin, Jr.: Rheotropic Brittleness: General Behaviors. *Proc. ASTM* (1951) **51**, p. 1023.
- 5 G. Sachs, J. D. Lubahn, and L. J. Ebert: Notched Bar Tensile Test Characteristics of Heat Treated Low Alloy Steels. *Trans. ASM* (1944) **33**, p. 340.
- 6 E. J. Ripling: Subzero Properties of Metals Surveyed. *Iron Age* (October 19-26, 1950).
- 7 J. J. Lynch, E. J. Ripling, and G. Sachs: Effect of Various Stress Histories on the Flow and Fracture Characteristics of the Aluminum Alloy 24ST. *Trans. AIME* (1948) **175**, p. 435; *METALS TECHNOLOGY* (January 1948).

Effect of Alloying Elements On The Behavior of Nitrogen in Alpha Iron

by L. J. Dijkstra and R. J. Sladek

IN earlier work the effect of manganese on the general behavior of nitrogen in iron was the subject of a careful examination by Fast.¹ Part of the investigation was made, in collaboration with one of the present authors (L.J.D.), by using the internal friction method. This technique, which has been described elsewhere,² showed some significant changes in the properties of Fe-N alloys by the addition of a small amount of manganese namely:

1—Under standard conditions the maximum of the nitrogen peak in pure iron appears around 20°C and the half width is about 27°C. By addition of 0.5 atomic pct Mn a general broadening of the internal friction peak occurs. The half width is increased by about 9°C. Moreover, a shift of the maximum of about 5°C toward a higher temperature takes place, Fig. 2.

2—The precipitation of nitrogen from the supersaturated solution, measured, e.g., at 200°C, was inhibited by the addition of the amount of manganese given in effect 1.

The broadening of the nitrogen peak was confirmed in more recent work³ on samples which were prepared from Westinghouse Puron iron. The effect of manganese on the rate of precipitation, however, was much less striking than in the earlier work¹ based on Philips high purity iron.

Theory

To explain the first change in properties just referred to, effect 1, the following two assumptions were made:¹ First, every manganese atom in substitutional solid solution creates around it six interstices located between an iron and a manganese atom, as is evident from Fig. 1. These interstices, conveniently called Fe-Mn interstices, have for nitrogen a free energy level which is ΔG^* lower than the normal Fe-Fe interstices between two iron atoms. For such low concentrations of manganese as 0.5 atomic pct, the possibility that two manganese

L. J. DIJKSTRA, formerly with the Institute for the Study of Metals, is now associated with the Ontario Research Foundation, Toronto, Ont., Canada, and R. J. SLADEK is associated with the Institute for the Study of Metals, University of Chicago, Chicago.

Discussion on this paper, TP 3403E, may be sent, 2 copies, to AIME by March 1, 1953. Manuscript, May 12, 1952.

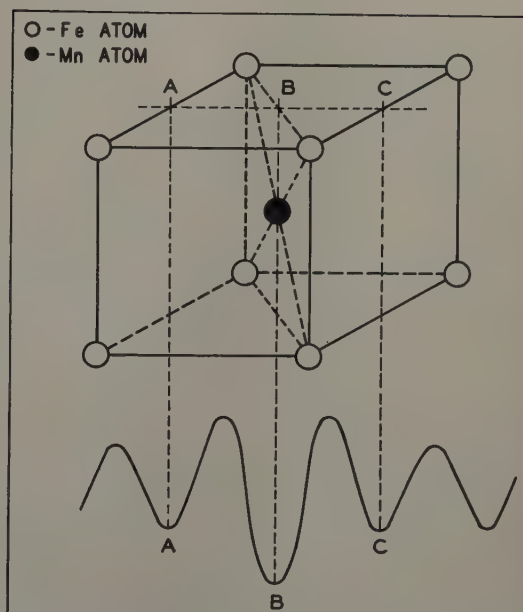


Fig. 1—Assumed modification by a manganese atom of the potential energy of a nitrogen atom in the iron lattice.

atoms will be nearest neighbors can be disregarded.

Second, it is assumed that in addition to the normal relaxation time τ_{Fe} at least one new relaxation time, $\tau_{Mn, Fe}$, enters in the phenomena which is associated with the elementary diffusion jumps between a Fe-Mn interstice and an adjacent Fe-Fe interstice. Fig. 1 gives schematically the free energy for a nitrogen atom as a function of its position along the line ABC. A tentative analysis of the nitrogen peak in a 0.5 pct Fe-Mn alloy based on these assumptions has been made in Fig. 2. The dotted curve with a maximum at 22°C is caused by jumps between Fe-Fe interstices, the dotted curve with maximum at 32°C by jumps between an Fe-Mn and an Fe-Fe interstice. The two effects added together give the dash-dot internal friction curve for the alloy. In the following these two components will be referred to as the normal peak at 22°C and the abnormal one. (The small secondary peak at

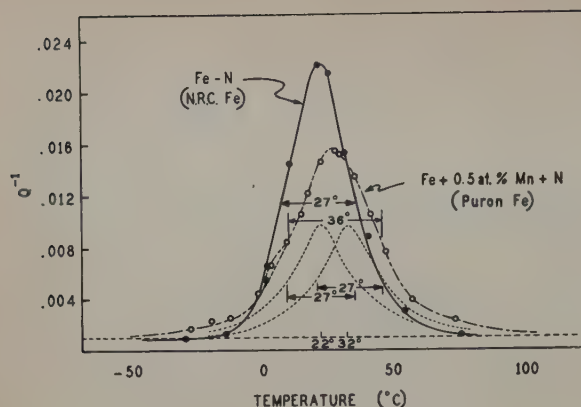


Fig. 2—Influence of manganese upon internal friction due to nitrogen in iron.

3°C is a real effect and increases very much with higher manganese content.)

If by some suitable heat treatment the nitrogen is allowed to precipitate from the solid solution in an alloy, a distinction must be made, in principle, between two different types of equilibria, since the diffusion rates of substitutional and interstitial elements are so widely different. Conditions during precipitation can be such that the alloying element participates in the diffusion, and nitrides of different alloy content from that of the matrix are formed. However, it is also possible that the alloying element does not have an opportunity to diffuse and in that case the nitride inherits its alloy content from the matrix. The terminology introduced by Hultgren will be followed in this paper and the two types of reactions will be called the ortho and the para reactions, respectively.⁴ It will also be convenient to distinguish the nitride and nitrogen-solubilities in both cases by the use of the prefixes ortho and para. In this study the para nitride is practically identical with the normal nitride in pure iron and it is clear from the picture, which was given to explain the effect of manganese, that the para solubility $C_{Fe, Mn}$ of nitrogen in the Fe-Mn alloy is higher than the normal solubility C_{Fe} of nitrogen in pure iron. The ortho solubility of nitrogen in a 0.5 pct Fe-Mn alloy must still be very small at 600°C. For, after tempering this alloy at 600°C in helium for 1 or 2 hr and quenching to room temperature, the internal friction peak has almost disappeared. A short anneal above 900°C in the γ phase is required to dissolve the ortho precipitate, and a subsequent rapid quench to room temperature reproduces the nitrogen peak to its full, original extent.

By standard methods of statistical mechanics it is

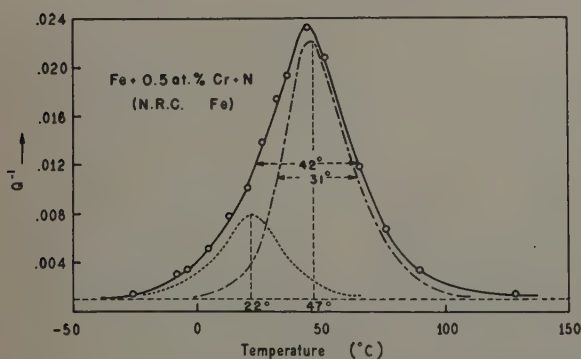


Fig. 3—Influence of chromium upon internal friction due to nitrogen in iron.

found, assuming that the temperature is not so low that saturation of the Fe-Mn interstices with nitrogen occurs, for the para solubility:

$$C_{Fe, Mn} = C_{Fe} (1 + 2c_{Mn} e^{\Delta G^*/RT}) \quad [1]$$

c_{Mn} is the atomic concentration of manganese and is assumed to be small. The factor 2 arises from the fact that per manganese atom there are six Fe-Mn interstices and per iron atom only three Fe-Fe interstices. ΔG^* is the increase in free energy on transferring a mol of nitrogen atoms from Fe-Mn sites to Fe-Fe sites (p and T constant) exclusive of the configurational part of the entropy change. The normal solubility $C_{Fe} = 3e^{-\Delta G'/RT}$ where $\Delta G'$ is the free energy of solution per mol of nitride in iron exclusive again of the change in configurational entropy.⁵ The fraction of the nitrogen atoms at the Fe-Mn interstices is $2c_{Mn} e^{\Delta G^*/RT}$.

Accepting the analysis of Fig. 2, it follows that at $T = 300^\circ K$, $2c_{Mn} e^{\Delta G^*/RT} \cong 1$ or $\Delta G^* \cong 2800$ cal per mol.

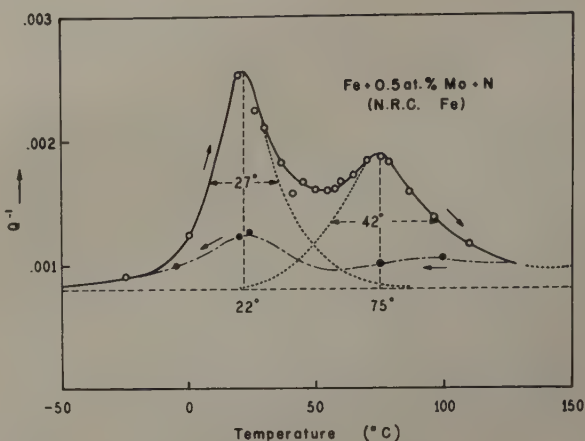


Fig. 4—Influence of molybdenum upon internal friction due to nitrogen in iron.

To explain effect 2, a third assumption appears to be necessary. In general, the rate of para precipitation is governed by three factors, namely: 1—degree of supersaturation with nitrogen; 2—diffusion rate of nitrogen; and 3—number of available potential nuclei.

Using the calculated value of 2800 cal per mol for ΔG^* and substituting this value in Eq. 1, at 200°C the solubility is increased by only 20 pct due to the addition of 0.5 pct Mn. At this temperature, there is only a slight preference for nitrogen atoms to occupy Fe-Mn interstices and therefore the diffusion rate is decreased only by a small amount. The most probable conclusion is that the large influence of manganese on the precipitation of nitrogen in this Philips iron must be a reduction, somehow, of the number of potential nucleation sites.

After cold work (e.g., 50 pct reduction in area) of the Fe-Mn alloy the internal friction peak drops rapidly by aging at room temperature. In other words, dislocations offer a much lower energy level for nitrogen atoms than the Fe-Mn interstices. This is not surprising since it is known⁶ that in pure iron the nitrogen concentration in normal solid solution in equilibrium with the nitrogen phase in the dislocations is very small.

Recent Work on Other Alloys

Recently this investigation has been extended to the alloying elements chromium, molybdenum, and

vanadium. All the alloys contained 0.5 atomic pct of the alloying element. In preparation of these alloys National Research Corp. iron was used with an oxygen content of about 0.003 pct. Furthermore, the Fe-Mn alloy was reinvestigated, this time using Westinghouse Puron iron, which has a rather high O_2 content of about 0.1 pct. In all cases the nitrogen was introduced by nitriding at 600°C for 6 min. The alloys were homogenized, unless otherwise indicated, by an anneal at 1000°C in helium for some minutes and then quenched from this temperature. After this treatment the Fe-V-N and Fe-Mo-N alloys turned out to be very unstable and even at room temperature precipitation was very rapid.

In Figs. 2 to 5 the internal friction Q^{-1} is plotted as a function of the temperature for the various alloys. The Fe-Cr alloy was not homogenized at 1000°C. The dotted curves are single relaxation peaks and are the proposed components of the total internal friction curve. In a first approximation analysis into two single relaxation peaks is indeed possible. The low temperature peak is the normal nitrogen peak at 22°C. The abnormal peak introduced by the addition of the alloying elements is

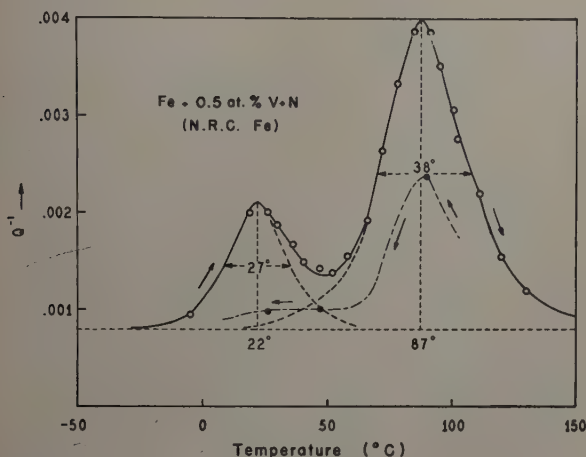


Fig. 5—Influence of vanadium upon internal friction due to nitrogen in iron.

always at a higher temperature. Apart from the theoretical picture given, the analysis in two single relaxation peaks is more or less justified by the curves of the Fe-Mo and Fe-V alloys in which indeed two pronounced peaks occur. The nitrogen peak in the Fe-Mn alloy in Fig. 2 is the exact reproduction of the corresponding peak observed earlier in the Philips iron.¹

Internal friction measurements have two disadvantages. In the first place, since the temperature is changed during the run, the ratio between the number of nitrogen atoms at Fe-Fe and Fe-alloying metal interstices is not constant and the simple analysis in two single relaxation peaks is not quite correct. In the second place, the rapid precipitation is sometimes very disturbing.

The runs of Q^{-1} vs temperature were made in the direction of increasing temperature. On cooling down from the highest measuring temperature, the Q^{-1} was much lower, especially in the Fe-Mo and Fe-V cases; apparently above 100°C para precipitation takes place during the time of measurement. Therefore elastic after-effect measurements were carried out on the Fe-Mo and Fe-V alloys at 0° and 10°C. The method and apparatus which were used

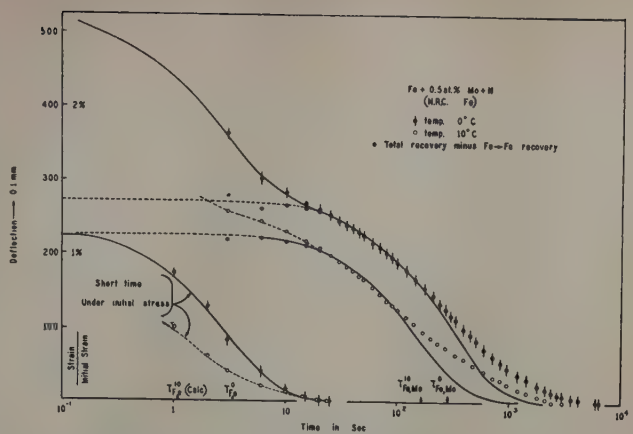


Fig. 6—Influence of molybdenum upon elastic recovery due to nitrogen in iron.

are described in a paper by Wert.⁷ The results are shown in Figs. 6 and 7. The ratio of strain over initial strain (that is, the strain while the external constant stress is applied) is plotted against the logarithm of the time which has passed since the external constant stress has been removed and during which strain recovery has occurred.

In general, the results obtained by the internal friction method are at least qualitatively confirmed insofar as mainly two relaxation times enter in the phenomena. The drawn curves correspond to single relaxation times. The normal effect resulting from jumps of nitrogen atoms between Fe-Fe interstices can be measured separately by keeping the specimen under the constant initial stress only for a time comparable to τ_{Fe} , which is therefore much shorter than $\tau_{Mn, Fe}$. These separately measured curves are shown in the lower left corner of Figs. 6 and 7. They show a discrepancy in that τ_{Fe} at 10°C is not smaller than 0°C, a discrepancy which shows up for both alloys. The accuracy of measurement is not very great for these short times. For the Fe-V alloy the abnormal effect is larger at 10°C than at 0°C. The opposite would be expected. A possible explanation is that at 0°C a state of thermodynamical equilibrium was not quite realized. In order to establish this equilibrium during cooling, the nitrogen atoms must be allowed to escape from the alloying metal atoms. They also have to diffuse over a range of the order of the average distance between the atoms of the alloying element. Because of the many uncertainties involved, more than a qualitative significance should not be attached to these results and

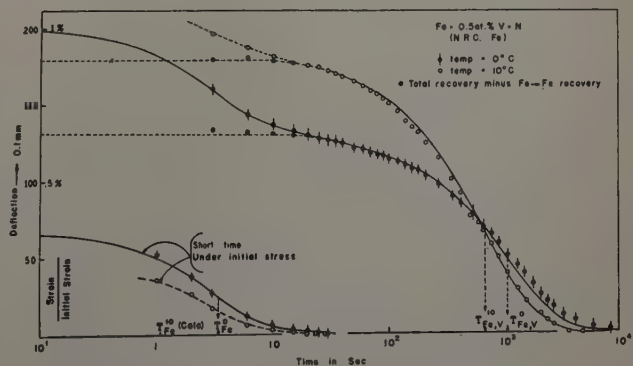


Fig. 7—Influence of vanadium upon elastic recovery due to nitrogen in iron.

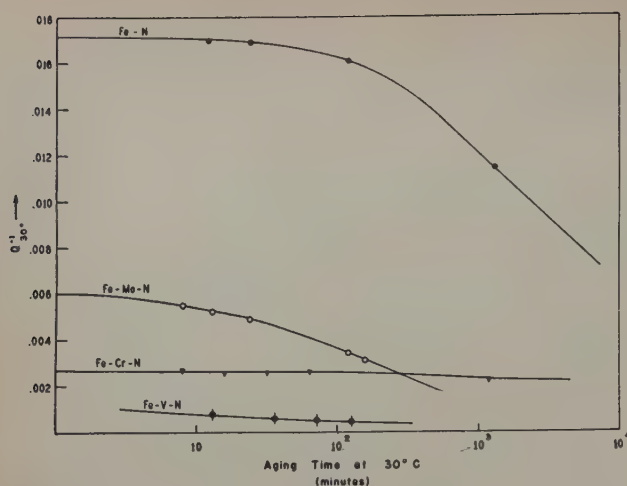


Fig. 8—Effect of alloying elements upon precipitation of nitrogen in N.R.C. iron. Iron quenched from 1000°C before aging.

therefore a further analysis was not made of the internal friction peaks and after-effect curves.

Precipitation

In view of previous results on Philips iron, it was surprising that in this investigation it was found that the rate of precipitation of nitrogen in Puron iron was not affected at all by the addition of 0.5 atomic pct Mn. Nitrogen precipitates for equal concentrations at about the same rate in Puron iron, National Research Corp. iron, Philips iron, and the Puron Fe-Mn alloy. Apparently the high O_2 content of the latter alloy neutralizes the effect of 0.5 pct Mn. The mechanism for this effect is not clear.

Fig. 8 shows the rate of para precipitation of nitrogen at 30°C in various alloys which were all prepared from National Research Corp. iron. The specimens were homogenized at 1000°C in helium for at least 2 min and then quenched from this temperature. Since it was believed that the height of the normal component is the real measure for the degree of supersaturation, the value of $Q^{-1}_{30^\circ}$ as plotted is the height of this component at 30°C. Though no nitrogen analysis has been made, it seems that the Fe-Cr alloys behave abnormally and show a very high rate of precipitation.

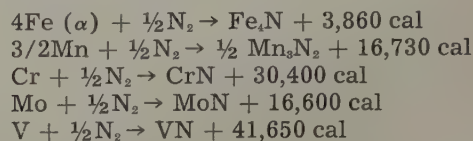
Not much information is available on the ortho precipitation reaction. The following was found for the Fe-V alloy only: Tempering at 600°C for 3 min and quenching to room temperature showed a drop in Q^{-1} of about 50 pct; tempering for 45 min, a drop of about 100 pct; tempering at 700°C for 3 min was sufficient to cause a drop of 100 pct in Q^{-1} . This ortho precipitate is probably submicroscopic at 600°C, for vanadium diffuses very slowly at this temperature. The ortho nitride is stable at 700°, 800°, and 900°C, but starts dissolving at 1000°C in the γ phase. The high rate of precipitation in the Fe-Mo and Fe-V alloys at room temperature might somehow be connected with an insufficient quenching rate through the region 900° to 600°C, where a very finely dispersed ortho precipitate is formed.

Discussion

Apparently the nitrogen atom in solid solution in the body-centered cubic iron lattice is not indifferent to the kind of surrounding metal atoms. If a nitrogen atom is by some means transferred from a monoatomic gaseous state into an interstice in the body-centered cubic lattice, the lattice in the im-

mediate neighborhood of the interstice is strained. It would be expected that the strain energy is larger if the interstice is adjacent to a substitutional foreign atom which is larger than an iron atom, e.g., molybdenum and vanadium. According to Pauling,⁸ the atomic diameters of iron, manganese, chromium, vanadium, and molybdenum for a coordination number 8 are 2.46, 2.48, 2.52, 2.62, and 2.72Å, respectively. That the nitrogen atoms tend, nevertheless, to cluster around the vanadium and molybdenum atoms could then mean only that a second energy term enters which probably is connected with a redistribution of electrons between nitrogen and metal atoms. It is well known that nitrogen is rather strongly electronegative.

Smithells⁹ gives for the heat of formation at 0°K the following values:



The plus sign on the right means that the reaction is exothermal. It must be admitted that these heats of formation are not purely representative for the nitrogen-metal affinity, since the metal lattice is loosened up in the compound formation to a certain extent. This can explain the rather low value for molybdenum, which has a heat of sublimation much higher than the other metals in the table. The heats of sublimation of the latter do not differ very much. The general tendency is that, in going to lower atomic numbers in a transition series, the compound is more stable. This can be understood qualitatively from the rule that the ionization potential for the outer electrons in general decreases with decreasing atomic number in a transition series.

A comparison between heat of compound formation and relative height of the abnormal peak of the various alloys is made difficult by the rapid precipitation during the measurements. Also, strictly speaking, the maxima ought to be compared for the same temperature. Nevertheless, these data seem to indicate a definite correlation. It seems reasonable, too, that the abnormal peak in the internal friction will always appear at the high temperature side of the normal peak, since the energy barrier which must be overcome for a nitrogen atom to break away from the foreign atom will be larger than in a normal interstice. In the case of manganese, chromium, and vanadium, it is apparent that the larger the relative height of the abnormal peak, the further the latter is shifted toward a higher temperature.

References

- ¹J. D. Fast: Aging of Iron and Steel. *The Iron and Coal Trades Review* (1950) p. 837.
- ²T. S. Ke: *Trans. AIME* (1948) **176**, p. 448; *METALS TECHNOLOGY* (June 1948).
- ³A. Josefsson and E. Kula: *Trans. AIME* (1952) **194**, p. 161; *JOURNAL OF METALS* (April 1952).
- ⁴A. Hultgren: *Trans. ASM* (1947) **39**, p. 915.
- ⁵C. Zener: *Trans. AIME* (1946) **167**, p. 513; *METALS TECHNOLOGY* (January 1946).
- ⁶L. J. Dijkstra: *Trans. AIME* (1949) **185**, p. 252; *JOURNAL OF METALS* (March 1949).
- ⁷C. Wert: *Physical Review* (1950) **79**, p. 601.
- ⁸L. Pauling: *Nature of the Chemical Bond* (1945) p. 410. Ithaca, N. Y. Cornell University Press.
- ⁹C. Smithells: *Metals Reference Book* (1949) pp. 428-429. New York. Interscience Publishers, Inc.

Systems Zirconium-Molybdenum and Zirconium-Wolfram

by R. F. Domagala, D. J. McPherson, and M. Hansen

On the basis of metallographic analysis, incipient melting data, thermal analysis work, and X-ray diffraction, phase relationships in the 0 to 50 atomic pct alloy content were carefully resolved. Phase relationships in the higher alloy content regions were outlined. A single intermediate phase, peritectically formed, of the form ZrX_2 was established in each system. A eutectic and a eutectoid were found in the zirconium-rich region of both systems. Appreciable solubility of molybdenum and wolfram was found in β zirconium, but only a slight solubility in α zirconium.

PREVIOUS work on these systems was limited to X-ray investigations of the intermediate phases^{1, 2} and preliminary surveys of the zirconium-rich alloys.³ The diagrams presented were determined principally by metallographic, thermal analysis, and incipient melting techniques. In accordance with the Atomic Energy Commission contract requirements, phase relationships up to 50 atomic pct molybdenum or wolfram were carefully resolved, while only a limited amount of work was done to outline the 50 to 100 atomic pct alloy region.

A description and analysis of the metals used in the preparation of alloys for this study are included in Table I. A "low-hafnium" zirconium crystal bar, produced by the decomposition of a volatile iodide onto a hot filament, was employed for these studies. Westinghouse "Grade 3" crystal bar was used for all alloys. The zirconium, as received, was coated with corrosion product from a standard autoclave test by which its grade designation is determined. This was removed by a sand-blasting and HF-HNO₃ pickling technique developed by the Atomic Energy Commission. The bars were cold rolled to approximately 1/32 in. sheet, pickled for iron removal, sheared to 1/4 in. squares, washed with acetone, and stored for furnace charge.

Molybdenum sheet 0.003 in. thick, 0.001 to 0.005 in. wolfram wire, and 1/2 in. wolfram rod crushed to granular form, from Fansteel Metallurgical Corp., were used as alloying stock.

Melting Procedure

A nonconsumable electrode arc furnace identical to that described in detail by Hansen et al.⁴ was used. The source of power for melting Zr-Mo alloys was a 400 amp dc welding generator, while a 900 amp dc generator was used for preparing Zr-W alloys. Electrode tips of the same material as the alloy addition were employed in both systems, i.e., molybdenum tips were used for Zr-Mo alloys, and wolfram tips for Zr-W alloys. This precluded any possible electrode contamination during arc melting.

Ingots of 20 to 30 g of Zr-Mo alloys were melted under high purity helium in the cavity of a copper block insert in a spun copper crucible. Homogeneity

Table I. Analyses of Metals Used

	Metal		
	Iodide Zirconium*	Molybdenum	Wolfram
Nominal purity, pct	99.8	99.9	99.9
Form	Crystal bar	0.003 in. sheet	1/2 in swaged rod; 0.001 to 0.005 in. wire
Impurities, Pct			
Al	0.007		
Co		0.003 maximum	
Cr	0.002		
Fe	0.03	0.005 maximum	
Hf	<0.05		
Mg	0.0001		
Ni	0.007		
Ti	0.013		
O	0.01	0.045 maximum	
N	0.0087		
C	<0.01		
R ₂ O ₃			0.02 maximum

* Zirconium analysis supplied by The Argonne National Laboratory, Chicago.

was insured by remelting all ingots four to six times without opening the furnace.

Due to the large difference between the melting points of wolfram and zirconium, direct melting of the charged metals as above generally yielded ingots containing unmelted wolfram particles. This was overcome, after many variations in technique, by melting a pure wolfram charge at high power levels (700 to 900 amp) and slowly adding zirconium to form a master alloy. Such master alloys were sectioned and remelted several times, then crushed to serve as melting stock for alloys of lower wolfram content. Master alloys containing 26, 50, 52, 70, and

R. F. DOMAGALA and D. J. McPHERSON, Junior Members AIME, are Assistant Metallurgist and Supervisor of Physical Metallurgy Research, respectively, and M. HANSEN, Member AIME, is Chairman, Metals Research Dept., Armour Research Foundation of Illinois Institute of Technology, Chicago.

Discussion on this paper, TP 3378E, may be sent, 2 copies, to AIME by March 1, 1953. Manuscript, April 11, 1952. Philadelphia Meeting, October 1952.

This paper represents a portion of the work on an Atomic Energy Commission-sponsored project, Contract No. AT(11-1)-149, "Phase Diagrams of Zirconium-Base Alloys."

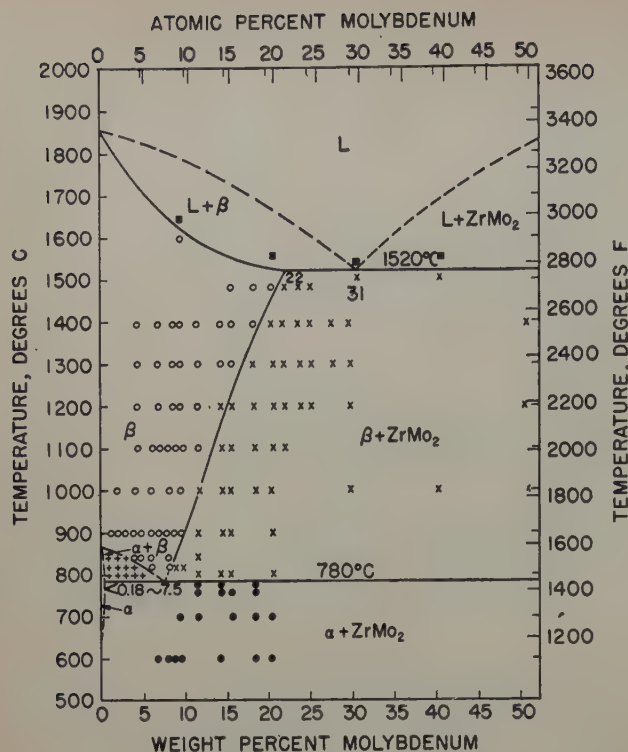


Fig. 1.—Partial diagram of the Zr-Mo system.

90 pct W served for the preparation of all the Zr-W alloys. Calculated weights of zirconium were melted with granules of the analyzed master alloy to yield the desired compositions. Alloys containing up to 50 pct W were arc melted in a copper block insert eight times without opening the furnace, while alloys richer in wolfram were melted ten times in a heavy-wall copper crucible. No unmelted wolfram was detected in any of the alloys prepared in this manner.

Annealing Treatments

Previous studies^{4,6} have shown that Vycor and quartz bulbs are suitable for containing specimens of highly reactive alloys of titanium or zirconium during annealing treatments. Vycor was employed for temperatures up to 1100°C, while quartz bulbs were used above this temperature. Evacuated bulbs were employed at temperatures up to 950°C, but for higher temperatures a partial pressure of argon was admitted to the bulb before sealing. This partial pressure was controlled to produce 1 atm of pressure at the temperature of treatment, in order to balance external pressure. Molybdenum sheet 0.003 in. thick was used as a liner in bulbs scheduled for treatments above 1200°C. These liners served to protect the specimens from direct contact with the bulbs and gave physical support to the bulb walls. All annealing treatments except homogenization were carried out in glazed porcelain tubes in electrically heated furnaces. Resistance alloy-wound furnaces were used up to 1250°C, but for higher temperatures a small Globar tube furnace was employed. Temperature control, in general, was $\pm 3^\circ\text{C}$, but more precise control was achieved for many anneals. Homogenization treatments were carried out in a box-type Globar furnace, with a temperature control of about $\pm 10^\circ\text{C}$. A control sample of pure zirconium was included in each bulb of isothermally annealed specimens. At the conclusion of an anneal, specimens were quenched by breaking the bulb under water.

Solidus Determinations

A high temperature vacuum-induction furnace was used for the determination of solidus temperatures. A description of the unit, details of operation, and temperature calibration have been given.⁴ The technique employed was to heat an alloy of given composition until visual signs of melting were observed, then quench a series of specimens of the same alloy content at approximately 25°C intervals below the temperature of observed melting, and examine them metallographically for evidences of incipient melting.

Thermal analysis was used to check the eutectic temperature in the Zr-Mo system, but was not generally applicable in the present work because of the high temperatures involved. The equipment and techniques employed have been described.⁴

Zr-Mo System

The chemical analyses of alloys prepared for the determination of phase relationships in this system are included in Table II. Table III lists the annealing treatments employed.

Zirconium-rich alloys containing from 0.2 to 28 pct Mo were reduced by cold pressing from 54 to 1 pct, depending upon alloy content, homogenized at 1150°C for 70 hr, and then cold rolled from 75 to 5 pct, prior to isothermal annealing treatments. All other alloys were used in the arc-cast condition.

The phase relationships for the 0 to 50 pct Mo region are presented in Fig. 1, and the entire diagram is shown in Fig. 2. Fig. 1 includes most of the experimental points necessary for the construction of the diagram; some points were omitted for clarity. Preliminary anneals for various times at 700°, 800°, and 900°C indicated that after 250, 150, and 50 hr, respectively, no changes occurred in the relative amounts of phases present in 3, 9, and 16 pct Mo alloys. The results of this program were used to schedule appropriate times for annealing treatments.

It should be noted that a preliminary investigation was undertaken in order to establish the temperature of the allotropic transformation, $\alpha \rightleftharpoons \beta$, in "Grade 3" zirconium crystal bar. Specimens from five random bars, after cold pressing, homogenization and cold rolling, were annealed at approximately 850°, 860°, 870°, 880°, and 890°C followed by water quenching. Two phase ($\alpha + \beta$) structures were observed in certain of the specimens for quenching

Table II. Analyses of Zr-Mo Alloys

Alloy Designation	Mo, Wt Pct	Alloy Designation	Mo, Wt Pct
ZM 0.2-727	0.18	ZM 26-317	25.3
ZM 0.4-724	0.35	ZM 28-316	27.9
ZM 0.5-260	0.60	ZM 29-628	28.7
ZM 0.6-725	0.64	ZM 30-323	30.0
ZM 0.8-726	0.77	ZM 31-629	30.7
ZM 1-240	1.2	ZM 32-630	31.3
ZM 2-243	2.2	ZM 33-631	33.1
ZM 3-242	3.1	ZM 34-632	33.8
ZM 4-244	4.2	ZM 35-324	35.4
ZM 5-245	4.7	ZM 40-325	40.6
ZM 6-246	6.2	ZM 45-328	44.8
ZM 7-247	7.1	ZM 50-335	50.9
ZM 8-239	8.3	ZM 55-330	55.7
ZM 9-237	8.9	ZM 60-221	57.8
ZM 10-235	9.6	ZM 62-331	59.0
ZM 12-315	11.9	ZM 64-332	63.5
ZM 14-322	14.5	ZM 66-333	65.4
ZM 16-321	15.7	ZM 68-334	65.4
ZM 18-320	18.5	ZM 70-220	64.4*
ZM 20-319	20.7	ZM 80-219	79.4*
ZM 22-318	22.1	ZM 90-222	89.3*
ZM 24-314	24.0		

* Analyzed for zirconium, molybdenum by difference.

temperatures between 851° and 868°C. Apparently, then, because of impurities, this grade zirconium transforms over a range of temperatures close to the ideal transition point. The value 862°±5°C, reported by Vogel and Tonn,⁶ was adopted for construction of the diagrams, but it is certain that this departure from ideality must cause corresponding departures from true binary equilibrium in the very dilute alloys.

The eutectic at 31±1 pct Mo and 1520°±15°C was located by the microscopic examination of several as-cast, incipient melting, and thermal analysis specimens in this region. The temperature was fixed as a result of several heating and cooling curves for an alloy of the eutectic composition, as well as by incipient melting. Fig. 3 shows the eutectic structure in a 30.7 pct Mo alloy, quenched from 1535°C in the incipient melting furnace.

Examination of isothermally annealed specimens showed the solubility of molybdenum in β zirconium to decrease from 22 pct at the eutectic level to 7.5±1 pct at the eutectoid temperature, 780°C. Figs. 4 and 5 represent 20.7 and 22.1 pct Mo alloys, respectively, quenched from 1480°C. A typical retained β structure is evident in the former, while $\beta + \text{ZrMo}_2$ phases are present in the latter structure. Figs. 6 and 7 represent 9.6 and 11.9 pct Mo alloys, respectively, quenched from 900°C. The former is 100 pct β , while the latter contains ZrMo_2 . The β phase was retained on quenching alloys containing more than 5 pct Mo, but transformed to acicular α (martensite) in alloys of lower molybdenum content.

The eutectoid decomposition: $\beta \rightarrow \alpha + \text{ZrMo}_2$ proceeds very slowly in this system. The eutectoid level was determined by examination of hypereutectoid alloys annealed at temperature increments of 15°C. The eutectoid level and the sluggishness of the decomposition are illustrated in Figs. 8 and 9. The former illustrates the retained $\beta + \text{ZrMo}_2$ structure observed after annealing a 14.5 pct Mo alloy at 790°C for 610 hr. The latter figure shows the 15.7 pct Mo alloy quenched from 775°C after 380 hr. In this specimen, a small amount of the β adjacent to proeutectoid ZrMo_2 crystals has decomposed. The metastability of β was detrimental to accurate position-

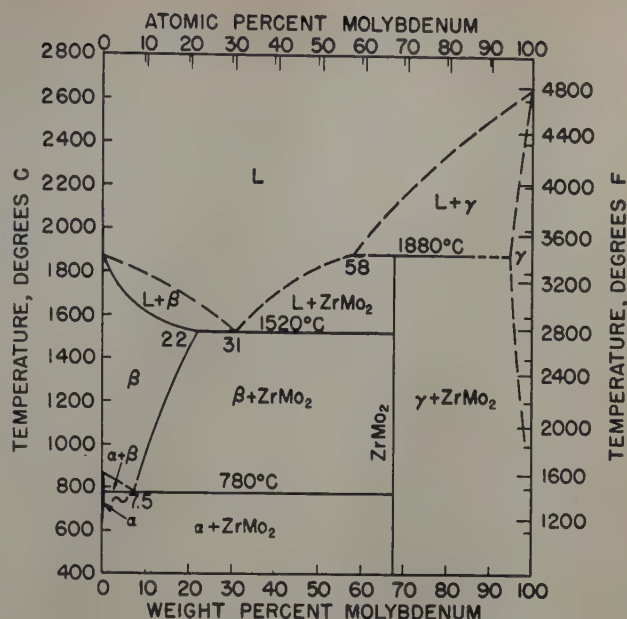


Fig. 2—Zr-Mo system.

ing of the eutectoid composition, but the value presented, 7.5 pct, undoubtedly is within ±1 pct of the equilibrium value. Eutectoid decomposition in hypoeutectoid alloys was never observed.

The solubility of molybdenum in α zirconium is less than 0.18 pct at all temperatures. Fig. 10 shows a 0.18 pct Mo alloy quenched from 775°C after 240 hr. The α plus metastable β phases are present.

The intermediate phase, ZrMo_2 , is formed by the peritectic reaction: Melt + molybdenum-rich solid solution $\rightarrow \text{ZrMo}_2$. The peritectic configuration and the composition of the liquid entering into the peritectic reaction are illustrated in Figs. 11 and 12. A 57.8 pct Mo arc-melted alloy is shown in the former figure. Only two phases, ZrMo_2 and β , are present. Fig. 12, a 59.0 pct Mo alloy, illustrates the initial appearance of the third phase, molybdenum-rich solid solution, as primary crystals. The composition of the peritectic melt is therefore between 57.8 and 59 pct Mo. Heat treatment in the incipient melting furnace brought the peritectic reaction nearly to completion in a 65.4 pct Mo alloy. ZrMo_2 and a small amount of β were present in this structure, supporting the designation of the phase as ZrMo_2 (stoichiometrically, 67.78 pct Mo).

An X-ray pattern of -325 mesh powder from a 57.8 pct Mo alloy was made, using filtered, characteristic $\text{CuK}\alpha$ radiation. Indexing of the pattern indicated that the intermediate phase has a cubic lattice, C15 (MgCu_2 type) with the lattice parameter, $a = 7.59\text{\AA}$. This is in agreement with Duwez and

Table III. Schedule of Annealing Treatments for Zr-Mo Alloys

Annealing Temperature, °C	Annealing Time, Hr	Alloys,* Pct Mo
1480	0.2	16-26, 60-64
1400	1	5-30, 50-68
1300	1	5-30
1204	8	5-30, 50-68
1100	20	5-22
1000	40	2-20, 30, 40, 50, 60, 64
900	48	1-20
840	240	0.5, 1-20
830	240	0.2-0.8
815	240	0.5, 1-12
800	240	0.2-0.8
	150	1-20, 40, 50, 62
790	610†	5-18
775	380†	5-18
	240	0.2-0.8
760	380†	5-18
750	240	0.2-0.8
	208	0.5, 1-24
740	610†	5-18
700	335	0.2-0.8
	256	0.5, 1-24, 40, 50, 60, 64
650	400	0.5, 1-10, 14, 18, 22
600	475	0.5, 1-10, 14, 18, 20, 30, 40, 50, 60, 64

* Alloys were pretreated before annealing as described in the text. Control samples of pure zirconium were included in each annealing treatment.

† Specimens held 17 hr at 900°C, slowly cooled to temperature, and held for indicated time, followed by water quench.

Table IV. Melting Range Determinations for the Zr-Mo System

Alloy No.	Mo, Wt Pct	Thermal Arrest, °C	Melting Observed, °C	No Melting, °C
Zr	0		1852	
YZM10-235	9.6		1640	1590
YZM20-319	20.7		1580	
YZM31-629	30.7		1535	1500
XZM31-791	30.8	1520		
YZM40-325	40.6		1550	1505
YZM60-221	57.8		1965	1855
YZM62-331	59.0		1900	1870
YZM66-333	65.4		1900	1870

Fig. 3—30.7 pct Mo alloy quenched from 1535°C. β -ZrMo₂ eutectic. Etchant: electrolytic K₃Fe(CN)₆ + NaOH in water. X250.

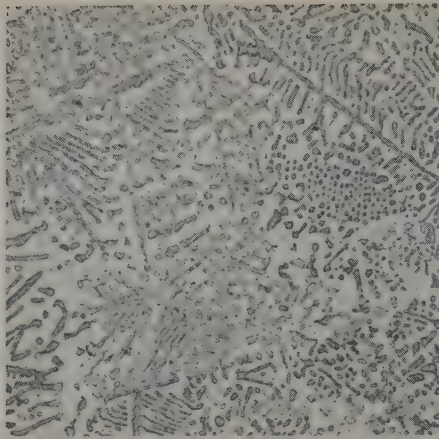


Fig. 5—22.1 pct Mo alloy quenched after annealing at 1480°C. Retained β solid solution plus isothermal ZrMo₂ crystals. Etchant: electrolytic K₃Fe(CN)₆ + NaOH in water. X250.

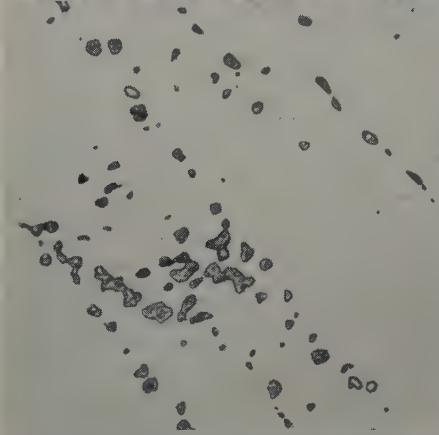


Fig. 7—11.9 pct Mo alloy quenched after annealing at 900°C. Retained β solid solution plus isothermal ZrMo₂ crystals. Etchant: electrolytic K₃Fe(CN)₆ + NaOH in water. X500.

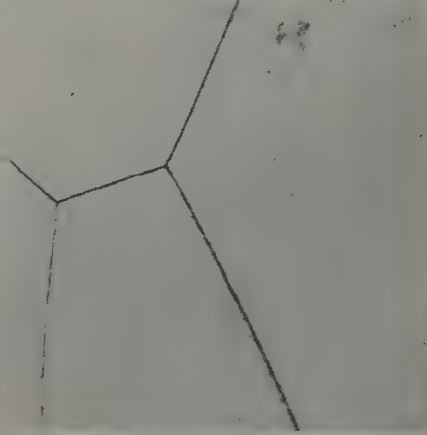
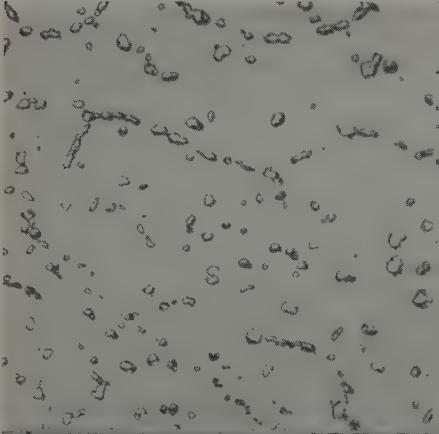


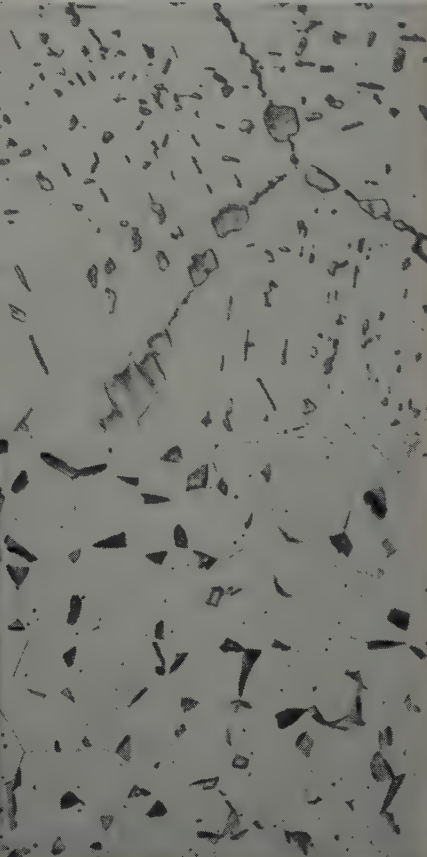
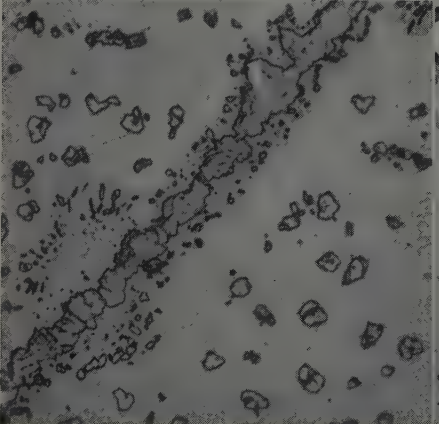
Fig. 4—20.7 pct Mo alloy quenched after annealing at 1480°C. Retained β solid solution. Etchant: 20 pct HNO₃ + 20 pct HF in glycerin. X250.

Fig. 6—9.6 pct Mo alloy quenched after annealing at 900°C. Retained β solid solution. Etchant: 20 pct HNO₃ + 20 pct HF in glycerin. X250.

Fig. 8—14.5 pct Mo alloy quenched after annealing for 600 hr at 790°C. Retained β plus ZrMo₂ structure, annealed above eutectoid level. Etchant: electrolytic K₃Fe(CN)₆ + NaOH in water. X750.

Fig. 10—0.18 pct Mo alloy quenched after annealing at 775°C. The α + metastable β structure here shows the limited α solubility. Etchant: 20 pct HNO₃ + 20 pct HF in glycerin. X500.

Fig. 9—15.7 pct Mo alloy quenched after annealing for 380 hr at 775°C. A small amount of β adjacent to the proeutectoid ZrMo₂ crystals has decomposed into α + ZrMo₂. This places the eutectoid level above 775°C. Etchant: electrolytic K₃Fe(CN)₆ + NaOH in water. X750.



Gordon,¹ who report ZrMo₂ to be cubic, with $a = 7.58\text{\AA}$.

A limited amount of work with molybdenum-rich alloys indicated that less than 10 pct Zr is soluble in molybdenum.

Incipient melting and thermal analysis data used

in construction of the diagram are given in Table IV.

Zr-W System

The phase relationships in the 0 to 50 pct region are presented in Fig. 13, and the entire diagram is shown in Fig. 14. Most of the experimental points

Fig. 11—57.8 pct Mo alloy, as-cast. Primary ZrMo_2 crystals plus β solid solution. Etchant: 3 pct HNO_3 + 2 pct HF in water. X750.

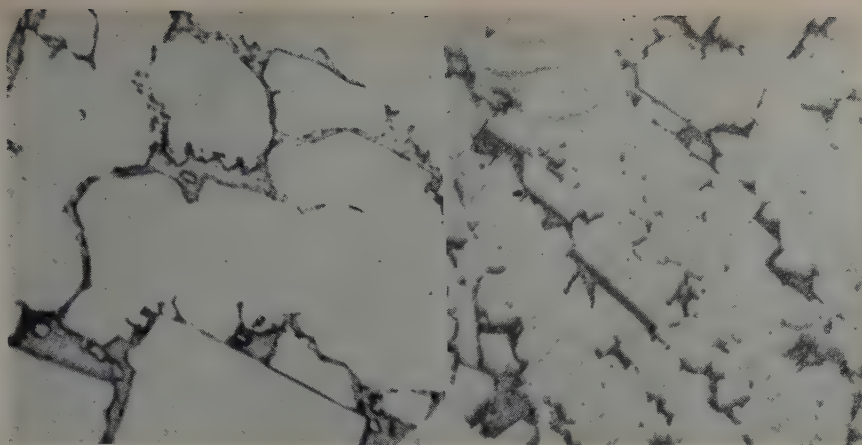


Fig. 12—59.0 pct Mo alloy, as-cast. Primary molybdenum-rich solid solution, peritectic walls of ZrMo_2 and β matrix. Comparing this with Fig. 11 shows that the composition of the peritectic liquid must lie between 57.8 and 59 pct Mo. Etchant: 3 pct HNO_3 + 2 pct HF in water. X750.

necessary for the construction of the diagram are included in the former figure. The chemical analyses of Zr-W alloys are given in Table V. Table VI lists the annealing treatments employed.

Prior to the isothermal anneals, alloys containing 0.5 to 26 pct W were reduced up to 32 pct by cold pressing, homogenized 45 to 70 hr at 1200°C , and cold rolled up to 20 pct. The amount of reduction by cold working was, of course, dependent upon the wolfram content. The Zr-W system is similar in all structural features to the system Zr-Mo.

The eutectic between β and ZrW_2 was positioned at 18 pct W and $1650^\circ\pm 15^\circ\text{C}$ after examining alloys containing 0.5 to 26 pct W in the as-cast condition and quenched in the incipient melting furnace. The eutectic composition is believed to be accurate within ± 2 pct W. The solubility of wolfram in β zirconium decreases from a maximum of 8 pct at the eutectic temperature to about 0.5 pct at the eutectoid temperature, 850°C . Figs. 15 to 18 position the $\beta/\beta + \text{ZrW}_2$ phase boundary at two temperature levels.

Fig. 15, a 3.6 pct W alloy quenched from 1460°C , contains only transformed β , while a 5.3 pct alloy quenched from the same temperature displays $\beta + \text{ZrW}_2$ (Fig. 16). Fig. 17 is a 0.49 pct W alloy quenched from 950°C , illustrating a transformed β structure, and a 1.3 pct W alloy, quenched from the same temperature, Fig. 18, contains ZrW_2 at the boundaries of transformed β grains. No clear retained β structures were observed in this system. Rejection of very fine ZrW_2 particles from β solid solution, even on quenching, masked most structures so that this point was impossible to determine with certainty.

The eutectoid decomposition of β into $\alpha + \text{ZrW}_2$ was placed at $850^\circ\pm 15^\circ\text{C}$. Difficulty was experienced in interpreting some structures because of the low alloy content of the eutectoid (0.5 pct W) and its proximity to the transformation "range" of unalloyed zirconium. Three-phase structures such as that shown in Fig. 19 indicated the proximity to the eutectoid temperature. This is a 1.3 pct W alloy quenched from 850°C .

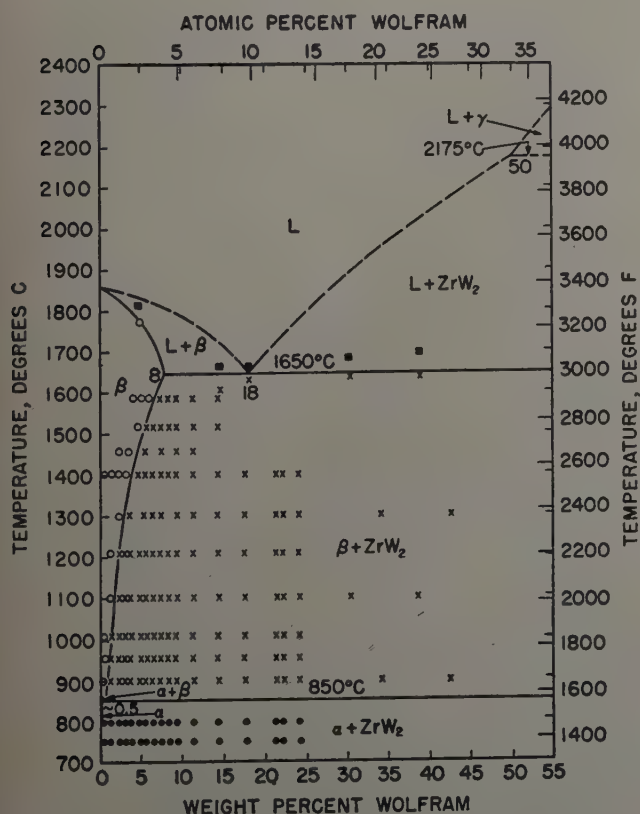


Fig. 13—Partial diagram of the Zr-W system.

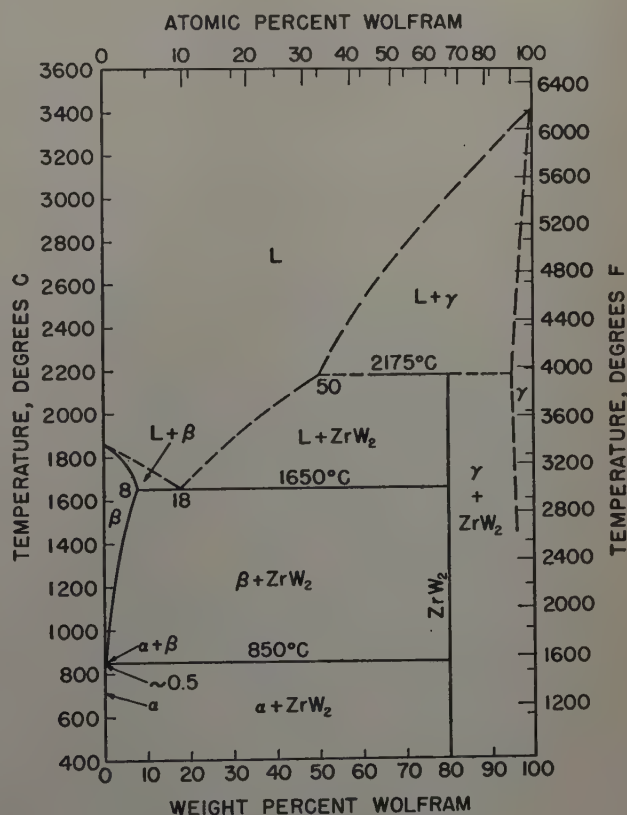


Fig. 14—Zr-W system.

Fig. 15—3.6 pct W alloy quenched after annealing at 1460°C. Transformed β solid solution. Etchant: 20 pct HNO_3 + 20 pct HF in glycerin. X250.



Fig. 16—5.3 pct W alloy quenched after annealing at 1460°C. Transformed β solid solution plus ZrW_2 crystals. Etchant: 20 pct HNO_3 + 20 pct HF in glycerin. X250.

Fig. 17—0.49 pct W alloy quenched after annealing at 950°C. Transformed β solid solution. Etchant: 20 pct HNO_3 + 20 pct HF in glycerin. X250.

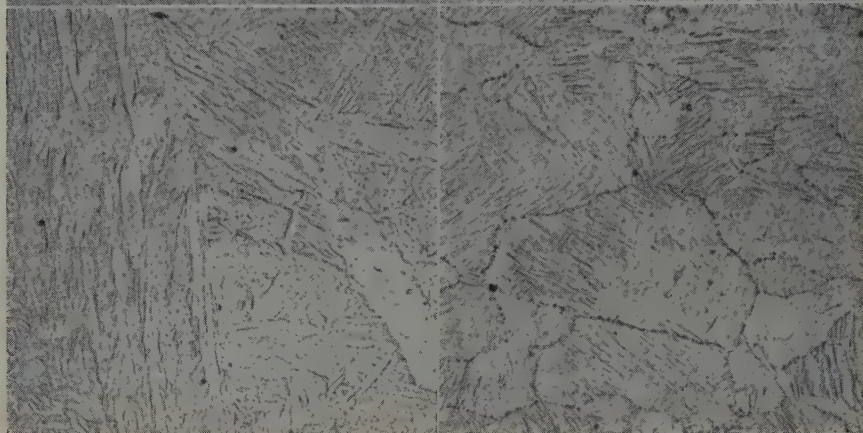


Fig. 18—1.3 pct W alloy quenched after annealing at 950°C. Transformed β solid solution plus ZrW_2 crystals. Etchant: 20 pct HNO_3 + 20 pct HF in glycerin. X250.

The solubility of wolfram in α zirconium is considerably less than 0.5 pct (the most dilute alloy prepared) at all temperatures. A single intermediate phase, peritectically formed, was detected in this system. Claassen and Burgers² have reported this phase to be ZrW_2 (stoichiometrically, 80.13 pct W) having a cubic structure (C15 type) with the lattice parameter, $a = 7.61\text{\AA}$. Figs. 11 and 12, illustrating the peritectic formation of ZrMo_2 , are characteristic of the structures observed in a 48.5 and a 52.3 pct W alloy, respectively. The 48.5 pct W alloy contained only ZrW_2 and β phases, while primary dendrites of wolfram-rich solid solution were observed in the latter alloy. Accordingly, the composition of the peritectic melt has been placed at 50 pct W.

Because of the considerable difference in wolfram

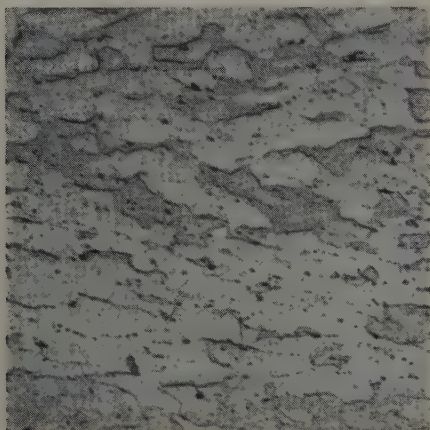


Fig. 19—1.3 pct W alloy quenched after annealing at 850°C. $\alpha + \beta + \text{ZrW}_2$ structure characteristic of alloys quenched from this temperature, indicating the proximity to the eutectoid level. Etchant: 20 pct HNO_3 + 20 pct HF in glycerin. X500.

Table V. Analyses of Zr-W Alloys

Alloy Designation	W, Wt Pct	Alloy Designation	W, Wt Pct
ZW 0.5-784	0.49	ZW 25-646	23.5
ZW 1-783	1.3	ZW 26-766	24.0
ZW 2-782	2.2	ZW 30-647	30.4
ZW 3-781	2.9	ZW 35-648	33.9
ZW 4-780	3.6	ZW 40-649	38.5
ZW 5-779	4.7	ZW 45-650	42.6
ZW 6-778	5.3	ZW 46-783	46.6
ZW 7-777	6.1	ZW 49-782	48.5
ZW 8-768	7.2	ZW 50-652	58.0
ZW 9-776	8.2	ZW 52-781	52.3
ZW 10-775	9.3	ZW 55-801	55.4
ZW 12-774	11.3	ZW 60-800	61.3
ZW 14-773	14.0	ZW 65-799	65.5
ZW 15-644	15.2	ZW 70-798	71.3
ZW 16-772	14.5	ZW 75-796	77.9
ZW 18-771	17.5	ZW 80-795	82.8
ZW 20-770	17.9	ZW 85-794	87.6
ZW 22-769	21.1	ZW 90-765	91.2
ZW 24-767	22.2		

Table VI. Schedule of Annealing Treatments for Zr-W Alloys

Annealing Temperature, °C	Annealing Time, Hr	Alloys,* Pct W
1520†	5 min	5-16
1590†	5 min	5-16
1440	0.2	2, 4, 26, 30, 40, 50
1400	1	1-26
1300	2	2, 4, 26, 35, 45, 55
1204	8	1-26
1100	20	1-26, 30, 40, 50
1006	48	0.5-26
950	50	0.5-26
900	75	0.5-26, 35, 45, 55
850	95	0.5-26
800	170	0.5-26, 30, 40, 50
750	240	0.5-26
700	335	0.5-10, 20, 35, 45, 55
650	450	0.5-10
600	500	0.5-10, 20, 30, 40, 50

* Alloys were pretreated before annealing as described in the text. Control samples of pure zirconium were included in each annealing treatment.

† These treatments were carried out in small molybdenum canisters supported by wolfram wire in the incipient melting furnace.

Table VII. Melting Range Determination for the Zr-W System

Alloy No.	W, Wt Pct	Melting Observed, °C	No Melting, °C
Zr	0	1852	
YZW 5-779	4.7	1815	1775
YZW16-772	14.5	1665	1605
YZW20-770	17.9	1665	1635
YZW30-647	30.4	1695	1645
YZW70-798	71.3	2175	2070
YZW80-795	82.8	2175	2075

content between the peritectic melt and the intermediate phase, and the difficulty in equilibrating the resultant three-phase alloys, nearly single-phase ZrW_2 structures were not obtained. Therefore, X-ray patterns were not made to check the structure of this phase, and the work of Claassen and Burgers has been accepted as valid.

A limited investigation of wolfram-rich alloys indicated that less than 10 pct Zr is soluble in wolfram.

The incipient melting data are presented in Table VII. The results of these studies placed the β - ZrW_2 eutectic temperature at $1650^\circ \pm 15^\circ C$ and the peritectic at $2175^\circ \pm 25^\circ C$.

Summary

The Zr-Mo and Zr-W phase diagrams were carefully determined to 50 atomic pct alloy content. A limited amount of work was done to outline the phase fields in the molybdenum and wolfram-rich regions of the diagrams. Alloys were melted in a nonconsumable electrode furnace using Grade 3 iodide zirconium crystal bar as a base material. These highly reactive alloys were prepared and heat treated under protective atmospheres to prevent contamination.

Zr-Mo: The important features of this system include:

1—Only one intermediate phase, $ZrMo_2$ (ideally 67.78 pct Mo), exists. It is formed by the peritectic reaction: Melt (58 pct Mo) + Mo-rich solid solution $\rightarrow ZrMo_2$ at $1880^\circ \pm 20^\circ C$.

2—A eutectic between β solid solution and $ZrMo_2$ exists at 31 ± 1 pct Mo and $1520^\circ \pm 15^\circ C$.

3—The limit of solubility of molybdenum in β

zirconium is about 22 pct at the eutectic temperature.

4—A sluggish eutectoid decomposition of β into $\alpha + ZrMo_2$ occurs at 7.5 ± 1 pct Mo and $780^\circ \pm 5^\circ C$.

5—The limit of solubility of molybdenum in α zirconium is less than 0.18 pct at all temperatures.

6—Less than 10 pct Zr is soluble in molybdenum.

Zr-W: This system is similar to the Zr-Mo system, and includes the following features:

1—A single intermediate phase, ZrW_2 (ideally 80.13 pct W), exists. It is formed by the reaction: Melt (50 pct W) + W-rich solid solution $\rightarrow ZrW_2$ at $2175^\circ \pm 25^\circ C$.

2—A eutectic between β solid solution and ZrW_2 occurs at $1650^\circ \pm 15^\circ C$ and 18 pct W.

3—The limit of solubility of wolfram in β zirconium is about 8 pct at the eutectic temperature.

4— β decomposes into $\alpha + ZrW_2$ eutectoidally at about 0.5 pct W and $850^\circ \pm 15^\circ C$.

5—The solubility of wolfram in α zirconium is less than 0.5 pct at all temperatures.

6—Less than 10 pct Zr is soluble in wolfram.

Acknowledgments

The authors wish to thank the Atomic Energy Commission, sponsors of this work, for permission to publish this paper. Special thanks are due to C. E. Lundin, who supervised the preparation of alloys, C. A. Johnson, who was responsible for the metallographic work, and W. Rostoker, for interpretation of the X-ray patterns.

References

- ¹ P. Duwez and C. B. Jordan: *Journal ACS* (November 1951) **73**, p. 5509.
- ² A. Claassen and W. G. Burgers: *Ztsch. Kristallographie* (1938) **86**, pp. 100-105.
- ³ C. T. Anderson, E. T. Hayes, A. H. Roberson, and W. J. Kroll: *Bur. Mines, R. I.* 4658 (March 1950).
- ⁴ M. Hansen, H. D. Kessler, and D. J. McPherson: *Trans. ASM* (1952) **44**, p. 518.
- ⁵ M. Hansen, E. L. Kamen, H. D. Kessler, and D. J. McPherson: *Trans. AIME* (1951) **191**, pp. 881-888; *JOURNAL OF METALS* (October 1951).
- ⁶ R. Vogel and W. Tonn: *Ztsch. anorg. allgem. Chem.* (1931) **202**, p. 293.

Technical Note

Sintering of Ultrafine Ferromagnetic Powders

by N. I. Ananthanarayanan and J. F. Libsch

A LITERATURE survey¹⁻⁴ of sintering metal powders and powder compacts indicates that studies have so far been confined primarily to the latter stages of sintering in relatively coarse powders. Presumably this is due to the difficult techniques associated with studies of the early stages of sintering. Recent experimental and theoretical investigations⁵⁻⁹ on the preparation and the magnetic properties of ultrafine ferromagnetic powders suggest the possi-

bility of following the sintering process from a very much earlier stage than has previously been considered.

It is now well-known that ferromagnetic powder particles which are below a critical size behave as single domains and exhibit permanent magnet qualities characterized by a very high coercive force. When the same particles are fully sintered, the coercive force decreases to very low values corresponding to those of the solid metal. Thus the coercive force appears as a sensitive parameter which may be measured to study the early stages of sintering. To determine the feasibility of this technique, experi-

N. I. ANANTHANARAYANAN is a graduate student and J. F. LIBSCH, Member AIME, is Associate Professor of Metallurgy, Dept. Metallurgical Engineering, Lehigh University, Bethlehem, Pa. TN 119E. Manuscript, May 2, 1952.

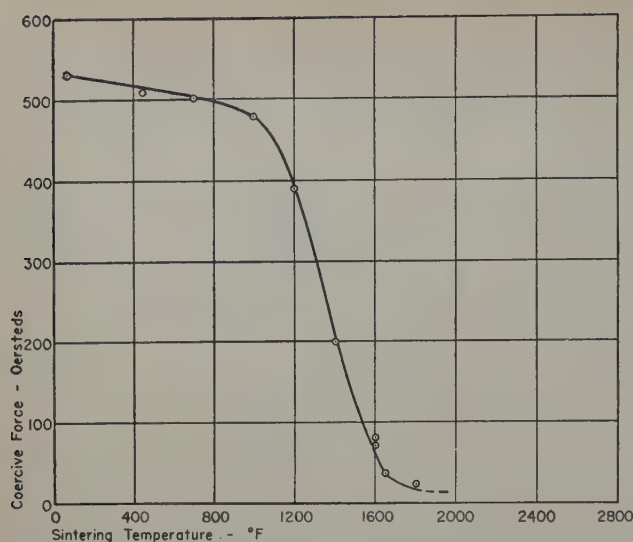


Fig. 1—Variation of coercive force with sintering temperature for ultrafine iron powder compacts.

ments have been initiated on the sintering behavior of ultrafine iron powders.

The present experiments were restricted to powders prepared by the low temperature reduction of finely divided jeweller's rouge, in purified hydrogen. The rouge used contained 98 pct iron oxide and 2 pct SiO_2 , and consisted of particles predominantly one micron or less in size. It has been found that of the powders thus prepared in the temperature range of 600° to 1000°F for 200 min of reduction time and for a hydrogen flow of about 1.5 cu ft per hr per g of oxide, the powder reduced at 700°F exhibited the maximum coercive force, viz., 560 to 600 oersteds. This powder was chosen for the experiments reported, because it provided the maximum variation of the coercive force between the "loose" and fully sintered states. Particle size of the reduced powder was estimated by the electron microscope, X-ray diffraction, and nitrogen adsorption methods, yielding an average particle size of 200 to 250 A.U. Since the powders were pyrophoric and were, therefore, covered with liquids like acetone for protection from oxidation during their subsequent handling, they were pressed wet into bars of approximately $1\frac{1}{4} \times \frac{1}{8} \times \frac{1}{8}$ in. at a single pressure of 40 tons per sq in. The compacts, first evacuated in the sintering chamber to remove all traces of protecting liquid present, were sintered in a stream of dry hydrogen for a period of 2 hr at various temperatures between 450° and 1800°F. The coercive force of the sintered compacts was then measured using a high-H permeameter of the Sanford and Bennet type.¹⁰

The coercive forces of the sintered compacts plotted as a function of sintering temperature are shown in Fig. 1. It may be noted: 1—that up to a temperature of 1000°F there is a very gradual fall of coercive force with sintering temperature; 2—that in the relatively narrow range of temperature between 1000° and 1600°F there is a strikingly rapid diminution of coercive force from about 500 to about 70 oersteds; and 3—that the rate of decrease of the coercive force at the higher temperatures is once again gradual.

The initial slow decrease of coercive force with sintering temperature indicates that little sintering has occurred and that the single domain character of the particles constituting the specimen has been essentially preserved. The relatively narrow range of sintering temperature in which the coercive force undergoes an abrupt diminution marks the exces-

sive formation of domain boundaries between the individual particles by sintering. The subsequent slow decrease of the coercive force with increasing sintering temperatures is to be associated with elimination of the porosity, the slow progress of which, as is well-known, is characteristic of the latter stages of sintering. The final value of the coercive force reported at the highest sintering temperature used, e.g., 25 oersteds at 1800°F, is still high compared with that of massive iron, because of the presence of impurities and the low density obtained, e.g., approximately 4 g per cc.

Any interpretation of the data in terms of the sintering mechanism must recognize the presence of some SiO_2 and some oxygen in the pressed compacts before sintering, since the SiO_2 was present in the rouge used for reduction and reduction of the oxide is not complete at 700°F. The presence of these impurities may have a pronounced influence and would tend to retard sintering by interfering with the formation and lateral growth of point bonds. With pure iron powders completely reduced, the temperature range of sudden decrease in coercive force would be expected to shift to the left.

From the data presented, it appears that the temperature range representing a sudden decrease in coercive force may be an indication of appreciable sintering and the consequent formation of excessive domain boundaries. While the initial and final values of the coercive force may depend chiefly upon the particle size, the purity and possibly the porosity of the powder particles, it is believed the temperature range of sudden decrease in coercive force will depend primarily upon the factors which influence the initiation and progress of sintering. A shift in this temperature range may conceivably be used to show the influence of various nonmetallic films on the powder particles, pressing pressure, and sintering atmosphere upon the initiation and progress of sintering. Experiments to determine the usefulness of this new criterion are presently underway.

The use of coercive force as a parameter for sintering behavior is, of course, limited to ferromagnetic materials. However the electrical resistivity of metals and alloys, another structure-sensitive property, is also known to undergo a large change below a critical size, as evidenced by the many and scattered investigations that have been reported on thin metal films.¹¹ The measurement of electrical resistivity might perhaps form a still more general approach to the study of building up polycrystalline aggregates from ultrafine powders by the powder metallurgy technique.

References

- ¹ F. N. Rhines: *Trans. AIME* (1947) **166**, p. 474; *METALS TECHNOLOGY* (August 1946).
- ² P. Schwarzkopf: *Powder Metallurgy, Its Physics and Production* (1947) New York. Macmillan Co.
- ³ P. Schwarzkopf: *Powder Metallurgy Bulletin* (1949) **4**, No. 2, p. 28.
- ⁴ P. Schwarzkopf: *Powder Metallurgy Bulletin* (1949) **4**, No. 3, p. 64.
- ⁵ C. Kittel: *Physical Review* (1946) **70**, p. 965.
- ⁶ L. Neel: *Comptes Rendus* (1947) **224**, p. 1488.
- ⁷ L. Neel: *Comptes Rendus* (1947) **224**, p. 1550.
- ⁸ L. Weil: *Comptes Rendus* (1947) **225**, p. 229.
- ⁹ E. C. Stoner and P. Wohlfarth: *Trans. Royal Soc., London* (1948) **240A**, p. 599.
- ¹⁰ R. L. Sanford and E. G. Bennet: *Journal of Research Nat. Bur. Standards* (1939) **23**, p. 415.
- ¹¹ See for example J. Krautkramer: *Ann. Physik* (1938) **32**, p. 537.

Measurement of Internal Boundaries in Three-Dimensional Structures By Random Sectioning

by Cyril Stanley Smith and Lester Guttman

It is shown, from a study of geometric probabilities, that the average number of intercepts per unit length of a random line drawn through a three-dimensional structure is exactly half the true ratio of surface to volume. Since the surfaces can be internal or external, the area of grain boundary or of the interface between any two constituents in a microstructure can be measured. Other metric relations are tabulated that may be of use in studies of the microstructure of polycrystalline, cellular, or particulate matter generally.

IN many fields of scientific investigation the structure of cellular aggregates or random arrays of discrete particles imbedded in some matrix is observed on a two-dimensional section and inferences are drawn therefrom as to the real structure in three dimensions. The biologist's microtome slice, the petrologist's thin section, and the metallurgist's plane polished and etched sections are common examples, although the problem is a general one. Scientists have commonly limited their thinking to the same dimensionality as their structures, and the few attempts that have been strictly three-dimensional in character have been laborious and noteworthy.

From a metallurgical standpoint it is often of considerable importance to know, in addition to the volume fraction of two or more components in an alloy, the amount of two-dimensional interface between crystals. Such grain boundaries (which may separate either two identical crystals differing only in orientation or two crystals differing in structure, and possibly also in orientation) have a determining factor upon the mechanical behavior. It is at these boundaries that melting commences, that stress-induced corrosion occurs, and that various precipitates (harmful or otherwise) first appear. The boundary is doubtless of equal importance in nonmetallic crystalline aggregates such as rocks, ceramics, and concrete, and the biologist is deeply concerned with the area of cellular membranes. Many synthetic cellular foams involve similar structural problems. The very term structure usually implies the presence of interfaces and a complete understanding of structure involves nothing but an analysis of the geometrical, metrical, and topological relations between the various interfaces (zero, one and two-dimensional) that exist in a three-dimensional structure. Even systems lacking sharp physical interfaces often have interrelated gradients of composition or velocity (as cored crystals or turbulence cells) in which a neutral surface can be treated as a two-dimensional interface.

C. S. SMITH, Member AIME, is Director and L. GUTTMAN is associated with the Institute for the Study of Metals, University of Chicago, Chicago.

Discussion on this paper, TP 3430E, may be sent, 2 copies, to AIME by March 1, 1953. Manuscript, April 16, 1952.

In an earlier paper by one of the authors¹ the question of cell shape was considered in terms of simple topological principles without regard to physical dimensions. The determination of the actual size of grains in two dimensions is carried out in a routine fashion in innumerable metallurgical laboratories (see, for example, the ASTM standard methods of grain size determination²), though this is done merely to check the uniformity of a product and has no relation to the actual three-dimensional shape or size of the grains. Some authors have discussed the three-dimensional problem but only on the basis of assumptions as to idealized grain shapes.³⁻⁵ Quantitative measurements of microstructures to obtain the volumetric relations of various phases have been carried out by petrographers for many years and are of increasing popularity among metallurgists.⁶

The present paper will show how, on the basis of no assumptions other than randomness of sectioning (usually realizable in experiment), it is possible to learn a great deal about the three-dimensional structure. The relations to be derived will generally be used on random arrays of cells or other particles, although they are equally applicable to ordered arrays and even to isolated objects of complex shape provided that suitable random sections can be made.

Total Area of Interfaces in a Sample

Consider a typical microstructure of a single-phase polycrystalline metal, such as that shown schematically in Fig. 1. The plane cross section shown contains a network of lines which subdivides the area into two-dimensional cells. The lines, of course, represent merely the intersection of the two-dimensional plane of sectioning with the two-dimensional interfaces between adjacent three-dimensional cells. The structure also contains points at which two or more lines intersect; in three dimensions the points are, of course, lines.

In the more general case there may be in three dimensions isolated particles surrounded by a single interface without contact with others, and both two and one-dimensional features which do not necessarily connect with others. On the two-dimensional section these will appear as areas delineated by a closed line (as at *a* and *b*, Fig. 2), as isolated lines

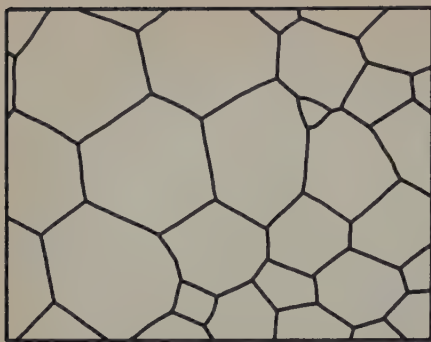
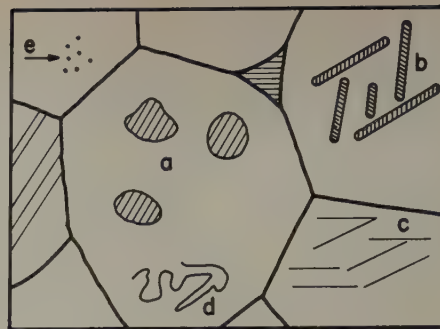


Fig. 1 (left)—Plane section through a polycrystalline body.

Fig. 2 (right)—Plane section through a polycrystalline body containing isolated particles (sectioned at *a* and *b*), isolated surfaces (sections *c* and *d*), and lines sectioned at *e*.



not intersecting others (as at *c* and *d*), or just as isolated points (*e*).

Relations in Two Dimensions: The two-dimensional structure itself will be considered first. It is possible by the use of a map measurer to determine the total length of line in any given area isolated for study. However, this can be done more easily by making use of the probability of intersection of one line with another randomly applied. It is intuitively apparent that the number of intersections will depend in a simple manner on the length of line, and that there will exist a relationship between an area and the length of random line traversing it. By combining these relations it is possible to obtain the ratio of line to area as a simple direct function of the average number of intercepts per unit length of an intersecting straight line (or grid) randomly applied to the structure.

We begin by rederiving the well-known solution to Buffon's "needle" problem:* a line segment of

* Czuber (ref. 7) pp. 84-92. None of the other relations derived in the equations to be given are to be found in their most general forms in the standard works on geometrical probability which have been consulted. Czuber's theorem III (p. 113), IV (p. 115), Problem XXI (p. 116) and Problem III (p. 178) contain formulas similar to ours, but are essentially restricted to convex plane curves. Czuber apparently did not realize that the concept "probability of intersection" could be generalized to "average number of intersections," and thus apply to non-convex curves.

Note added Sept. 30, 1952: After this paper was submitted, there appeared a communication by Campbell and Tomkeieff (*Nature* (1952) 170, p. 117) containing results similar to ours, in which, however, the unnecessary restriction to convex bodies is still made. L. A. Santaló has derived two-dimensional formulas like ours and has stated that the extensions to three dimensions are obvious. Cf. (a) *Abh. Math. Sem. Hansischen Univ.* (1940) 13, pp. 284-294; *Math. Reviews* (1941) 2, p. 13. (b) *Revista Union Mat. Argentina*, (1943) 9, pp. 145-164; *Math. Reviews* (1947) 8, p. 170.

length *l* falls at random on a plane array of parallel lines spaced a distance *d* apart (Fig. 3). What is the probability that the line segment intersects one of the lines (*l* ≤ *d*)?

The probability is clearly the average length of the segment projected on the normal to the array, divided by the distance between the lines, i.e.:

$$p = \frac{\bar{l}_{proj}}{d}$$

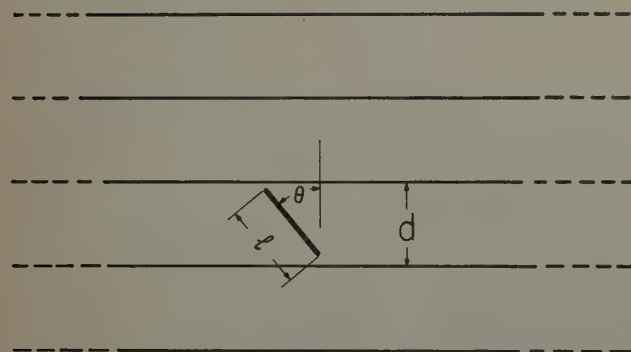


Fig. 3—Diagram to illustrate probability of a line intersecting a grid.

Since all directions of the line segment have equal *a priori* probability:

$$\bar{l}_{proj} = \frac{2}{\pi} \int_0^{\pi/2} l \cos \theta d\theta = \frac{2l}{\pi} \quad [1]**$$

** From this follows an interesting property of all simple plane figures that are not concave. Since each element of the perimeter appears twice within the average projected width, the latter must be exactly $1/\pi$ of the perimeter. It is also to be noted that the average linear intercept across such a figure is $\pi \times \text{area/perimeter}$.

and:

$$p = \frac{2l}{\pi d} \quad [2]$$

If an irregular plane curve is placed at random on the same array, there will in general be *N* intersections; the average value, \bar{N} , can be obtained from Eq. 2 as follows. Divide the curve into short segments of length Δl , each of which is nearly straight. The probability that any one of these segments intersects the array is $p_1 = 2\Delta l/\pi d$, and the product of this with the number of segments is the average number of intersections:

$$\bar{N} = p_1 \cdot \frac{l}{\Delta l} = \frac{2l}{\pi d} \quad [3]$$

l is the total length of the curve. Even though the segments are connected by being parts of the curve, each takes random positions and orientations as the curve as a whole does, hence the additivity of the number of intersections.

In dealing with a given area of a microstructure it is often useful to express the results in terms of ratio of length to area. Consider the limited area***

*** This figure intentionally contains features impossible in any real microstructure to emphasize the independence of the relations on anything but the existence of one and two-dimensional features.

in Fig. 4 crossed by a grid of spacing *d*. If *d* is small, or if a coarse grid is applied many times at random to a fixed area, the total length of grid line, *L*, is *A/d*. Combining with Eq. 3, the following useful relation results:

$$\frac{l}{A} = \frac{\pi}{2} \frac{\bar{N}}{L} \quad [4]$$

In using this relation it is not necessary to utilize a well-ruled grid of parallel lines, but any array of lines repeatedly applied to the structure in a random fashion is satisfactory provided that a sufficient number of intersections is counted. If the structure itself is random, a single line (not necessarily straight) of sufficient length is adequate. Generally, however, it is preferable to use a grid and to apply this successively at various angles between 0° and

180° selected to give the desired total number of counts.

There are no limitations whatever as to the validity of Eq. 4 except for the critically important requirement of randomness.

Relations in Three Dimensions: Consider now the relation between a random two-dimensional section and the three-dimensional structure it represents. Fig. 5 depicts an irregular solid body with closed surface, intersected by a set of parallel planes. This is analogous to the two-dimensional case of Fig. 3. The sections visible in the two-dimensional planes will have an area A and a perimeter of length l . The averages of these, \bar{A} and \bar{l} , are desired for all possible positions of the body. Let the distance between the planes again be d , and assume for simplicity that the surface does not intersect more than one plane at a time. The position of the surface can be specified by the distance z of a fixed point on it from one of the planes, and its orientation by three

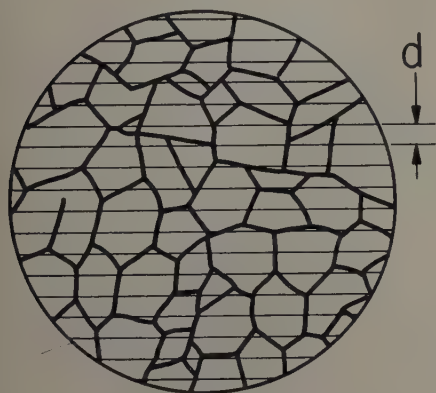


Fig. 4—Isolated area of a two-dimensional structure traversed by a grid of lines.

angles, denoted by ω for brevity. The area of the section is a function $A(\omega, z)$ whose average value is:

$$\bar{A} = \frac{\int d\omega \int dz A(\omega, z)}{\int d\omega \int dz}$$

For a fixed orientation, $A(\omega, z)dz$ is the element of volume of the solid enclosed by the surface. Hence as z varies between the limits $(0, d)$,

$$\int_0^d dz A(\omega, z) = V$$

a result independent of orientation.

$$\bar{A} = \frac{V}{d} \quad [5]$$

There is no restriction on the shape of the surface or on the connectivity of the solid enclosed by it: The distinction between "inside" and "outside" determines what is to be counted as contributing to the cross-sectional area, and conversely.

Consider now a plane figure which intersects one of the planes of the stack in a line of length l (Fig. 6). Again, the average length of intersection is:

$$\bar{l} = \frac{\int d\omega \int dz l(\omega, z)}{\int d\omega \int dz}$$

For a fixed orientation, $l dz$ is just the element of surface of the figure, projected on a plane which includes the intersection and which is normal to the stack of planes, i.e.:

$$l dz = dS \sin \theta$$

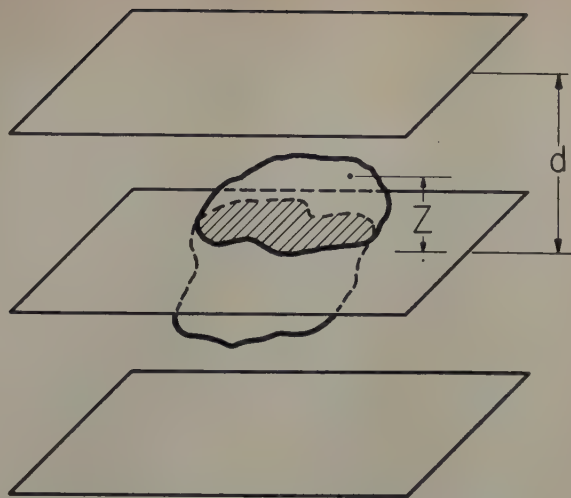


Fig. 5—Diagram to illustrate probable area of intersection of a particle with a set of parallel planes.

where θ is the angle between the normal to the figure and the normal to the stack. Hence, the integration over z gives just the total surface area projected on this vertical plane. The only orientation angle ω which must be specified is θ , and:

$$d\omega = \sin \theta d\theta$$

The range $(0, \pi/2)$ for θ clearly covers all possible orientations, so that:

$$\bar{l} = \frac{S \int_0^{\pi/2} \sin^2 \theta d\theta}{\int_0^{\pi/2} \sin \theta d\theta \int_0^d dz} = \frac{\pi S}{4d} \quad [6]$$

This result is not restricted to plane figures, since any surface can be approximated by plane elements. As before, these elements take random positions and orientations when the figure as a whole does so, and since the contributions to the surface and to the length of intersection are additive, Eq. 6 holds for any surface, however complex.

By combining Eqs. 5 and 6:

$$\frac{\bar{l}}{\bar{A}} = \frac{\pi}{4} \frac{S}{V} \quad [7]$$

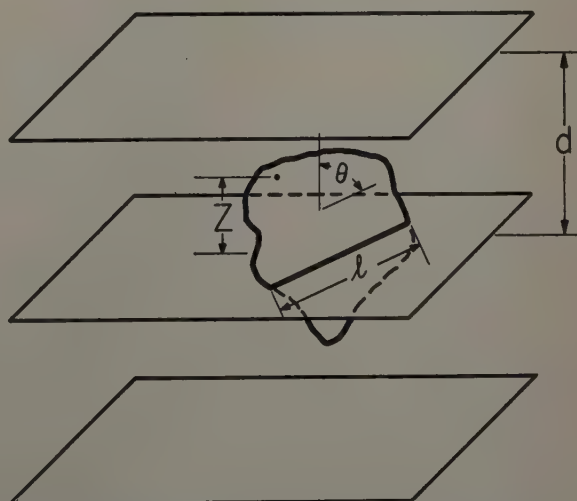


Fig. 6—Diagram illustrating probable length of intersection of a plane figure with a set of parallel planes.

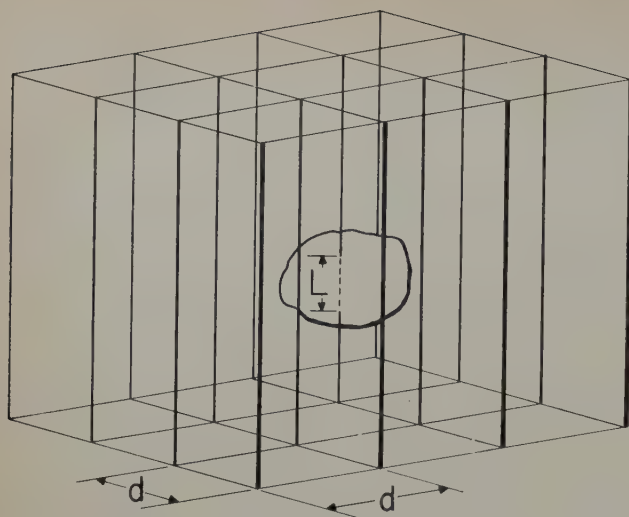


Fig. 7—Intersection of grid of lines with a particle.

This result, being independent of d , means that the stack of parallel planes is no longer needed, and that it is possible to average line length and area of the sections of any solid by a plane oriented and placed at random.

It is desired to apply Eq. 7 to a solid such as a polycrystalline metal, in which the interest is specifically in the internal surfaces (grain boundaries). If the solid is macroscopically homogeneous, the quantity S/V will be a "property" of the specimen in the sense of having the same value for sufficiently large regions, whatever their location. Then it will be possible to obtain its value for the entire specimen from measurements of the average value, \bar{l} , of line length in many equal areas, A , randomly located. If the solid is isotropic as well, a single section will suffice if it is extensive enough, but in general both random directions and random locations of the sections would have to be established.

It is not necessary to measure \bar{l} directly, since Eq. 4 provides a means of determining the length of an irregular curve by random intersections with another of known length. Since the \bar{A} and \bar{l} of Eq. 7 become the A and l of Eq. 4, then

$$\frac{S}{V} = \frac{2\bar{N}}{L} \quad [8]$$

Note that d does not appear in this equation. It means simply that the internal surface in a unit volume of a solid is exactly twice the average number of intersections per unit length of lines drawn at random in the solid.

Eq. 8 can be deduced more directly in another way. Consider a grid of parallel lines spaced a distance d apart in directions normal to each other and to the lines. An irregular solid is placed in the grid (Fig. 7); the average number, \bar{N} , of intersections of its surface with the lines and the average length of line intercepted, \bar{L} , are desired. The position and orientation of the solid are described by the coordinates (x, y) of one of its points in the plane perpendicular to the lines, and by a set of angles, ω , as before. Then:

$$\bar{L} = \frac{\int d\omega \int dx \int dy L'(x, y, \omega)}{\int d\omega \int dx \int dy}$$

For fixed ω , $L' dx dy$ is the volume element, and $\iint L' dx dy = V$, independent of angle. Hence:

$$\bar{L} = \frac{V}{d^2} \quad [9]$$

a result which is intuitively obvious. For a plane figure, whose largest diameter is $\leq d$, the probability of intersection is just the ratio of its average projected area to the area per grid line, i.e.:

$$p = \frac{\bar{A}_{proj}}{d^2}$$

But:

$$A_{proj} = S \cos \theta$$

and:

$$\bar{A}_{proj} = \frac{\int_0^{\pi/2} S \cos \theta \sin \theta d\theta}{\int_0^{\pi/2} \sin \theta d\theta} = \frac{S}{2} \quad [10]^\dagger$$

[†] From Eq. 10 a result of interest for non-concave solids in general can be deduced; on the average, each element of the total surface, S , of such a solid appears twice within the same projected area, so that, for convex solids only:

$$\bar{A}_{proj} = \frac{S}{4} \quad [10a]$$

This theorem has been attributed to Cauchy, but the original publication has not been located.

whence:

$$p = \frac{S}{2d^2} \quad [11]$$

Table I. Properties of a Two-Dimensional Structure

Item	Equation No. in Text	Property	Contiguous Cells of Same Type	Separate Cells Not Sharing Boundaries
1		Average area of cell	$\frac{A}{M}$	$\frac{L_a d}{M_a}$
2		Average linear intercept	$\frac{L}{N}$	$\frac{2L_a}{N_a}$
3	4	Ratio of length of line to total area (perimeter to particle area in separate cells)	$\frac{\pi N}{2L}$	$\frac{\pi N_a}{2L_a}$
4		Ratio of average perimeter of cell to average linear intercept*	$\frac{N^2 A}{\pi M L^2}$	$\frac{\pi N_a^2 d}{4 M_a L_a}$
5		Area fraction of phase α		$\frac{L_a}{L}$

* This dimensionless shape factor is rigorously applicable only if all cells are convex and if there are no lines except those constituting the perimeter of some cell. It is 4 for circles, $24\sqrt{3}\pi$ for regular hexagons, $16/\pi$ for squares, and $36/\pi\sqrt{3}$ for equilateral triangles. (See double asterisk note to Eq. 1.)

Table II. Properties Determinable Rigorously from Random Two-Dimensional Sections of Three-Dimensional Structures

Item	Equation No. in Text	Property	Contiguous Cells	Separate Cells or Particles Not Sharing Boundaries and with No Internal Features
1		Average cross section of cell or particle	$\frac{A}{M}$	$\frac{L_a d}{M_a}$
2		Average linear intercept	$\frac{L}{N}$	$\frac{2L_a}{N_a}$
3	7, 8, 13	Ratio of area of total two-dimensional features to total volume (surface to volume ratio for separate particles)	$\frac{4l}{\pi A}$ or $\frac{2N}{L}$	$\frac{2N_a}{L_a}$
4	14	Ratio of length of total one-dimensional features to total volume (edge to volume ratio for separate particles)	$\frac{2n}{A}$	$\frac{2n}{L_a d}$
5	15	Ratio of total one-dimensional to total two-dimensional features (edge to surface ratio for separate particles)	$\frac{\pi n}{2l}$ or $\frac{nL}{NA}$	$\frac{n}{N_a d}$
6		Volume fraction of particles of α phase		$\frac{L_a}{L}$

A = total area of two-dimensional section examined.
 l = total length of linear features in area A .
 M = total number of grains, cells or particles seen in area A .
 n = total number of points (grain corners) seen in area A .
 M_a = number of separate particles of constituent α .

L_a = total length of line traversing area occupied by constituent α .
 L = total length of line in grid of area A applied to structure.
 d = spacing of lines in grid.
 N = number of intercepts of grid lines with linear features of structure.
 N_a = number of intercepts of grid lines with lines bounding constituent α .

More generally, for any surface:

$$\bar{N} = \frac{S}{2d^2} \quad [12]$$

S being the total surface area, including internal or re-entrant positions. As before, this follows from the possibility of building any surface from plane elements, each of which takes up random positions and orientations as the surface as a whole does so, and to each of which Eq. 11 applies.

Combining Eqs. 9 and 12, then

$$\frac{\bar{N}}{L'} = \frac{S}{2V} \quad [13]$$

The grid is no longer necessary, and if, as for Eq. 8, the number of intersections with random lines of total length L is measured, it may be seen that Eq. 13 leads to the same result.

The three-dimensional structure also may have one-dimensional cells (lines) either defining the limits of various two-dimensional surfaces or existing by themselves without any relation to such. The

number of intersections, \bar{n} , with a set of planes d apart (randomly applied) can easily be shown by the methods used in deriving Eqs. 3 and 5 to be $\lambda/2d$, λ being the true length of the line. Since the total area of the intersecting planes and the volume considered are related as before,

$$\bar{n} = \frac{\lambda A}{2V} \quad \text{or} \quad \frac{\bar{n}}{A} = \frac{\lambda}{2V} \quad [14]$$

This gives directly by the observation of points in random plane sections the length of line in a given volume. This relation can be combined with Eq. 2 dealing with the ratio of line to surface to give directly (on the basis of purely two-dimensional measurements) the ratio of line to surface, which is:

$$\frac{\lambda}{S} = \frac{\pi}{2} \frac{\bar{n}}{l} = \frac{\bar{n}}{A} \frac{L}{N} \quad [15]$$

Use of the Relations

It should be noted that in all of the preceding, L , A , and V are gross values determined by the area

Table III. Properties Determinable on Assumption That Particles Are of One Size and Spherical

Item	Equation No. in Text	Property	Contiguous Cells of Same Type	Separate Particles Not Sharing Boundary
1	16	Average volume of grain or particle	$\frac{4NA^2}{\pi LM^2}$	$\frac{2N_a A^2}{\pi M_a^2 L}$ or $\frac{2N_a}{\pi M_a^2} Ld^2$
2	16	Number of particles per unit volume of whole sample	$\frac{\pi LM^2}{4NA^2}$	$\frac{\pi LM_a^2}{2N_a A^2}$ or $\frac{\pi M_a^2}{2N_a Ld^2}$
3		Average surface area per grain or particle	$\frac{8}{\pi} \left(\frac{NA}{LM} \right)^2$ (See note*)	$\frac{8}{\pi} \left(\frac{N_a d}{M_a} \right)^2$

* Note: If the average surface area of the grains considered as separate polyhedra is desired, this number must be doubled.

selected for study, and the mere counting of intersections within this area gives the total amount of surface and of line. There are no assumptions whatever except that of randomness of sectioning. If the structure itself is random and isotropic a single surface—or even a single line—will suffice provided only that the number of counts is large enough to give satisfactory statistics; if the structure is anisotropic, true averages will only be obtained by combining counts on sections which are randomly oriented and placed.

The factor N/L is the reciprocal of the average linear intercept through the cells assuming them to be convex. Though metallurgists have frequently used this average linear intercept as an index of grain diameter, the fact that it is so simply and exactly related to the ratio of surface to volume seems not to have been previously noticed.

It is possible to experimentally measure on an actual two-dimensional section the total number of intercepts, N , with grain boundaries of a traversing line of a known total length, L (the total being made up of many lines, a distance d apart, repeatedly crossing the area being examined^{††}) as in Fig. 4; the

^{††} In practice d is either the spacing of a grid of parallel lines used for counting or the total area studied divided by the total length of traversing line (i.e., $d = A/L$). Experimentally, it is convenient to use a grid of circular outline which can be applied repeatedly at different orientations to portions of an extended microstructure. The value of A/L is then constant and needs no further measurement. If the specimen area itself is limited and falls always entirely with the grid, its true area is used, and the equivalent L derived from the grid spacing. Counting is easier if, instead of a fine grid in a few orientations, a grid is used of fairly coarse spacing, applied frequently and in many orientations in order to get the necessary counts. To avoid repetition at 180° rotation the grid lines should be displaced from exact symmetry or the grid itself should be moved around randomly within the area available for study. A grid 20 cm diam with lines 1 cm apart has been found satisfactory. With structures on the scale normally used for an 8x10 in. micrograph 12 applications 15° apart give an adequate number of counts.

The counting of intersections or cells is most easily recorded by a counting pencil of the type used by bacteriologists, and may be either electrically or mechanically operated. Instead of using a photograph, measurements may be also made directly on a specimen under the microscope, the grid being either projected optically upon the sample or being laid on the focusing screen of a projection apparatus. A large specimen area may easily be covered in this way by appropriate traversing at properly distributed angles. It would be possible to use a counter operated by a photocell and to record all necessary data automatically, provided that clearly defined boundaries are obtainable and there are no extraneous details in the specimen that would affect local light intensities.

The measurement of the length of linear intercept is most readily obtained by the use of a linear integrating stage of the type used by petrographers, such as that of Hurlburt,⁸ or Wentworth,⁹ or the hydraulic one designed by one of the authors.¹⁰ It is possible to replace these rather elaborate devices by a simple inexpensive stage for point-counting,¹¹ but this seems to be both more tedious in operation and, unless an extremely large number of points are counted, less accurate.

number, M , of particles appearing in section on the whole surface of known area, A ; the number, n , of points ("grain corners") seen in a section. If more than one phase is present, it is possible to measure for each phase the number of intercepts (N_a) of the traversing line with its boundaries, the total length of line (L_a) traversing that phase, and the number (M_a) of α -phase particles seen on an area A .

The results of the preceding paragraphs have been rewritten consistently in terms of the quantities just defined and collected in Tables I and II. The tables also include immediately derivable expressions for the cross-sectional area of a particle or cell, A/M , and the average linear intercept through a particle, L/N . Two sets of formulas must be used, corresponding to the case of one phase or of separate phases. In the latter case, in order to study each phase separately, the actual area of each, $L_a d$, must be used instead of A , and the linear intercept becomes $2L_a/N_a$. If there is more than one phase present the volume percentage of any given phase is precisely determined by the ratio L_a/L_{total} in the now well-known method of linear analysis.⁹

Shape-Dependent Properties

In all of the foregoing it was not necessary to make any assumptions as to the form of the structures under consideration. Therefore very general results were obtained which are true for all shapes, but which cannot for just that reason give information about shape-dependent properties. In this class of properties are the average "caliper diameter" and the average projected area of a particle, neither of which can be measured on a cross section. In this class also, therefore, is the particle volume, which is equal either to the product of the caliper diameter in a certain direction and the average sectional area normal to it, or to the product of the area projected on a certain plane and the average linear intercept in the perpendicular direction.

For the special case of a spherical particle there are simple relations between those properties that are accessible from a plane section and those that are not. If a random arrangement of identical spheres is sectioned, the number of spheres P_a in a volume V can be found from:

$$\frac{P_a}{V} = \frac{\pi}{2} \left(\frac{L}{N_a} \right) \left(\frac{M_a}{A} \right)^2$$

in the notation of the previous section.[‡] It may be

[‡] Relations identical with these have been independently derived by both F. N. Rhines and R. Teitel. These authors discuss the use of these relations in determining grain size or particle size and the distribution of these. Apparently the effect of departures from the rigorous requirement of sphericity is not serious in practice.

assumed that this formula holds approximately for grains which are not too elongated in any particular direction, and which fill space, and thence the volume per particle, V_p , as the reciprocal of the above, may be calculated:

$$V_p = \frac{4}{\pi} \left(\frac{N}{L} \right) \left(\frac{A}{M} \right)^2 \quad [16]$$

the factor two coming from the sharing of boundaries in the present case. By combining Eq. 16 with earlier results, the formulas appearing in Table III are obtained. It should be stressed that these formulas, unlike those in Tables I and II, must be systematically in error, and that they should be used with caution.

Summary

The extent of one and two-dimensional internal boundaries of a solid (e.g., grain edge length and grain boundary area in a polycrystalline metal) can be calculated from measurements on plane sections.

The method involves counting the number of intersections of the boundary with planes of known area or lines of known length oriented and located at random. For example, if a line randomly intersects an array of surfaces or interfaces, then the average number of intersections per unit length is exactly equal to one-half the ratio of surface area to volume. The accuracy of the results is only statistically limited and does not depend on assumptions of shape or isotropic arrangement. True randomness of section is essential.

It is possible to obtain the length or area of a particular kind of feature, for example, the area of interface between any two phases, as well as the surface to volume ratio for any constituent, in addition to the total interface measurements.

It is not possible to derive the volume of the average cell from measurements on two-dimensional sections except on the assumption of a constant shape

and size. Formulas derived for identical spheres are tabulated and may be of some use.

Acknowledgment

The authors wish to express their thanks to the industrial sponsors of the Institute for the Study of Metals for the financial support that has made this work possible.

References

- ¹ Cyril Stanley Smith: Grain Shapes and Other Metallurgical Applications of Topology. Paper in *Metal Interfaces* (1952) pp. 65-113. Cleveland. ASM.
- ² ASTM Classification of Grain Size in Steels, ASTM (a) Tentative Standard E-19-39T.
(b) Preparation of Micrographs of Metals and Alloys (Including Grain Size Standards for Non-Ferrous Metals), ASTM Standard E2-44T.
- ³ E. Scheil: Statistical Investigations of the Structures of Alloys. *Ztsch. Metallkunde* (1935) **27**, pp. 199-208; (1936) **28**, pp. 340-343.
- ⁴ W. A. Johnson: Estimation of Spatial Grain Size. *Metal Progress* (1946) **49**, (1), pp. 89-92.

⁵ J. B. Rutherford, R. H. Aborn, and E. C. Bain: Relation of Grain Area on a Plane Section and the Grain Size of a Metal. *Metals and Alloys* (1937) **8**, pp. 345-348; *ASM Metals Handbook* (1948) p. 405.

⁶ R. T. Howard and Morris Cohen: Quantitative Metallography by Point-Counting and Lineal Analysis. *Trans. AIME* (1947) **172**, pp. 413-426; *METALS TECHNOLOGY* (August 1947).

⁷ Emanuel Czuber: *Geometrische Wahrscheinlichkeiten und Mittelwerte* (1884) Leipzig. B. G. Teubner.

⁸ C. S. Hurlburt: An Electric Counter for Thin Section Analysis. *American Journal of Science* (1939) **237**, p. 253.

⁹ C. K. Wentworth: An Improved Recording Micro-meter for Rock Analysis. *Journal of Geology* (1923) **31**, p. 228.

¹⁰ Lilian Heikkinen Beck and Cyril Stanley Smith: The Copper-Zinc Constitution Diagram, Redetermined in the Vicinity of the Beta Phase by Means of Quantitative Metallography. *Trans. AIME* (1952) **194**, pp. 1079-1083; *JOURNAL OF METALS* (October 1952).

¹¹ F. Chayes: A Simple Point Counter for Thin Section Analysis. *American Mineralogist* (1949) **34**, pp. 1-11, 600-601.

Technical Note

Retained Austenite Determinations by X-Ray Methods

by B. L. Averbach

THE determination of retained austenite by X-ray diffraction uses the following relationship:^{1,2}

$$P_{\alpha} = \text{constant} \cdot RV_{\alpha} A(\theta) \quad [1]$$

where: P is the diffracted power from phase α ; R , the calculated intensity factor; $A(\theta)$, the absorption correction; θ , the diffraction angle; and V_{α} , the irradiated volume of phase α

For a flat sample making a glancing angle ϕ with the incident beam the absorption correction is calculated as:^{*}

^{*} The absorption correction in ref. 1 erroneously contained an extra $\sin \phi$ in the numerator. This error did not influence the results quoted since experimental absorption corrections were used in the retained austenite determinations.

$$A(\theta) = \frac{1}{\mu} \frac{\sin(2\theta - \phi)}{\sin(2\theta - \phi) + \sin \phi} \quad [2]$$

where μ is the linear absorption coefficient.

Beu³ has proposed that the computed absorption correction be combined with the constant and that the experimental observation of the absorption correction used in the original method be eliminated. This procedure is permissible only if: 1—There is no preferred orientation in the sample, and 2—The geometric requirements have been met precisely.

If these conditions are not met the validity of the determination is questionable. Unfortunately the necessary conditions must be tested experimentally for each determination, and this is done most easily by observing whether the apparent absorption has the form of Eq. 2. In practice it may be convenient to plot P/R vs the parameter $\sin(2\theta - \phi)/[\sin(2\theta - \phi) + \sin \phi]$ to obtain straight lines for the ap-

parent absorption correction. Deviations from straight lines indicate either that the sample has not been positioned correctly or that the relative intensities are incorrect.

Geiger counter spectrometer methods also have been used successfully for retained austenite determinations. In the usual spectrometer arrangement the sample makes equal angles with the incident and diffracted beams ($\theta = \phi$); thus the absorption correction is simply $\frac{1}{2}\mu$ and independent of θ . The retained austenite is then easily calculated from integrated intensity measurements on austenite and martensite lines. If the austenite content is not too low and if excessive fluorescence is not encountered it is possible to use filtered radiation and a recording spectrometer. The integrated intensities are then proportional to the areas of the diffraction peaks.

For lower austenite contents the following technique was used: A bent quartz monochromator and a Geiger counter spectrometer are employed. The monochromatic radiation is focused on the front slit, and the counter slit is made broad enough to include the entire line. A series of readings are taken in the vicinity of the diffraction peak. The highest reading includes the diffraction line plus background. The background is obtained from the average of several readings on each side of the peak. The integrated intensity is obtained by subtraction. CrK_{α} and FeK_{α} have been used for such determinations. This technique has been found to be as sensitive and as accurate as the photographic methods.

In the spectrometer methods the ratio austenite/martensite may be obtained from readings on austenite and martensite lines and the application of Eq. 1. It is also possible to use external standards and to obtain the austenite contents from measurements on the austenite lines alone. The small correction for carbides then becomes unnecessary. The best standards are probably samples with known

B. L. AVERBACH, Junior Member AIME, is Assistant Professor, Dept. of Metallurgy, Massachusetts Institute of Technology, Cambridge, Mass.

TN 141E. Manuscript, Sept. 17, 1952.

austenite contents although α brass and rock salt have also been used.

References

¹ B. L. Averbach and M. Cohen: X-ray Determination of Retained Austenite by Integrated Intensities. *Trans. AIME* (1948) **176**, p. 401; *METALS TECHNOLOGY* (September 1947).

Technical Note

Regarding Sigma Phase Formation

by David S. Bloom and Nicholas J. Grant

IN recent reports, Sully¹ and Beck and coworkers² have advanced hypotheses concerning the formation of the σ phase. Both of these hypotheses are based on Pauling's theories of the electronic configuration of the elements of the first transition group. Sully considered that the number of electrons which can be absorbed in filling electron "holes" is the factor which determines whether or not the σ structure can form. Beck suggested that the presence of a certain concentration of electron "holes" is the controlling value.

It can be shown that a similar criterion can be developed without making reference to Pauling's theories. Table I shows the elements of the first transition group and the incidence of the σ structure in the binary systems of these elements according to the data presently available. Also appended is the number of electrons considered to exist in the 3d-4s levels of these elements. If the atomic percentages for the σ phase are listed as shown in Table II, and if the number of electrons in the 3d-4s levels per atom is calculated for the σ boundary values, the results are as shown in the last column. It can be seen that the numerical values are all in the vicinity of 7 electrons per atom. This is true also for the ternary Cr-Mo-Ni σ phase, which occurs in a system in which none of the binary compositions are known to develop the σ phase. In the Fe-Mo binary, the high temperature σ phase, which occurs at a composition of 50 atomic pct of each element, also yields a value of 7 electrons per atom.

From inspection of Tables I and II, it develops that any series of sequential numbers which is assigned to the elements under consideration will result in the numbers pertaining to σ compositions grouping themselves around one specific number. It does not follow, however, that this random number necessarily has physical significance. Such a point has already been discussed by Hume-Rothery.³

One interesting point develops from this study, however, and that is the position of manganese with reference to the other elements and to the σ phase. In the system used here, the formation of σ phase is associated approximately with the value of 7 electrons per atom, which is also the number of electrons per atom that manganese has. Manganese, it will be recalled, exists in three different crystal forms, none of which are the usual, simpler metallic forms; on the other hand, elements just to the left of manganese (in Table I) generally have lower coordination-number structures (body-centered cubic) than do elements to the right of manganese (face-centered

² B. L. Averbach, L. S. Castleman, and M. Cohen: Measurement of Retained Austenite in Carbon Steels. *Trans. ASM* (1950) **42**, p. 112.

³ K. E. Beu: Modifications of an X-ray Method for the Measurement of Retained Austenite Concentrations in Hardened Steels. *Trans. AIME* (1952) **194**, p. 1327; *JOURNAL OF METALS* (December 1952).

Table I. Chart Showing Occurrence of the Sigma Phase in Binary Systems of Elements of the First Transition Group

	V	Cr	Mn	Fe	Co	Ni
V	—	—	σ	σ	σ	σ
Cr	—	—	σ	σ	σ	—
Mn	σ	σ	—	—	—	—
Fe	σ	σ	σ	—	—	—
Co	σ	σ	—	—	—	—
Ni	σ	—	—	—	—	—
No. of electrons in 3d-4s levels per atom	5	6	7	8	9	10

Table II. Electrons/Atom Number for Various Sigma Phases

System	Boundaries for σ Phase in Atomic Pct at Temperatures Indicated	Electrons/Atom Ratio Corresponding to σ Phase Boundaries
V-Mn	24.3 pct V	6.5
V-Fe	37-57 pct V (700°C)	7.3 -6.9
V-Co	40-54.9 pct V	7.4 -6.8
V-Ni	55-65 pct V	7.2 -6.7
Cr-Mn	19-24 pct Cr (800°C)	6.84-6.78
Cr-Fe	43.5-49 pct Cr (600°C)	7.1 -7.0
Cr-Co	56.6-61 pct Cr	7.3 -7.2
Mo-Fe	47-50 pct Mo (1400°C)	7.1 -7.0
Mo-Co	59-61 pct Mo (1500°C)	7.23-7.17
Cr-Mo-Ni	37 Cr, 27 Mo, 36 Ni, 42 Cr, 32 Mo, 26 Ni (1250°C)	7.4 -7.0

cubic). The contribution to a complex crystal structure by the interalloying of elements from opposite sides of manganese is significant in that the σ phase is formed in binary systems including one element from each side of manganese, with manganese capable of participating with both sides.

It is indeed an interesting coincidence that manganese, with 7 electrons per atom, solidifies in complex crystal forms, and that when alloys of the transition elements are made which have seven 3d-4s electrons per atom, they, too, tend to assume a complex crystal form.

From the above, it might be deduced that the study of the σ phase might be advanced by a critical examination of the element manganese and how its structure is affected by small additions of elements which change the 3d-4s electrons per atom number. The role of atom size would also be of interest in σ formation.

References

¹ A. H. Sully: The Sigma Phase in Binary Alloys of the Transition Elements. *Journal Inst. Metals* (1951) **80**, Part 4, p. 173.

² S. Rideout, W. D. Manly, E. L. Kamen, B. S. Lement, and P. A. Beck: Intermediate Phases in Ternary Alloy Systems of Transition Elements. *Trans. AIME* (1951) **191**, p. 872; *JOURNAL OF METALS* (October 1951).

³ W. Hume-Rothery, H. M. Irving, and R. J. P. Williams: The Valencies of the Transition Elements in the Metallic State. *Proc. Royal Soc.* (September 1951) **208A**, p. 431.

D. S. BLOOM, Student Associate AIME, is Research Assistant, and N. J. GRANT, Member AIME, is Associate Professor, Dept. of Metallurgy, Massachusetts Institute of Technology, Cambridge, Mass.

TN 143E. Manuscript, Oct. 3, 1952.

Accelerated Solidification in Ingots: Its Influence on Ingot Soundness

by Edgar Marburg

Most ingots complete solidification vertically rather than transversely. This conclusion is based on complete solidification patterns of big-end-up and big-end-down ingots developed from dumped and split ingots. New mechanisms for segregation in ingots are proposed. Internal soundness in ingots is found to depend upon adequate width of vertical core.

ALTHOUGH it has long been recognized that the internal soundness of ingots is principally dependent on the process of solidification, knowledge of this process is still only fragmentary. The mechanisms causing the several types of segregation in ingots, which mechanisms are necessarily related to the solidification process, are not well understood. In absence of a better conception of the solidification process, it seems hardly surprising that mold design varies widely. Guiding principles for mold design are needed. At stake in the improvement of ingot quality are not only improved properties of steel but also appreciably higher yields of sound steel, which would considerably decrease manufacturing costs.

In the present study, following a general description of the several types of segregation in ingots, Fig. 1, complete solidification patterns of a big-end-up and a big-end-down ingot, including the zones of accelerated solidification, have been reconstructed. In both ingots, a core of vertical solidification extends from the base cone to the hot-top junction. Based on the finding that ingots complete solidification vertically rather than transversely, as has been previously assumed, new mechanisms for segregation in ingots are proposed.

Internal soundness in ingots is found to depend upon the width of the vertical core, which in turn depends principally upon the width to height (w/h) ratio of the ingot. Solidification patterns of ingots are of three general types: 1—those in which vertical solidification does not reach the top, 2—those in which vertical solidification just reaches the top of the ingot, and 3—those in which vertical solidification reaches the top some time before transverse solidification would reach the middle of the ingot, so that a vertical core of definite width at the top of the ingot is developed. Axial defects vary characteristically with the solidification pattern. Examples of ingots of each type are presented.

Dumped ingot data reported by Nelson¹ have been used in developing families of curves of transverse

E. MARBURG is associated with the Research and Development Laboratory, United States Steel Co., Pittsburgh.

Discussion on this paper, TP 3449C, may be sent, 2 copies, to AIME by April 1, 1953. Manuscript, Sept. 17, 1952. Los Angeles Meeting, February 1953.

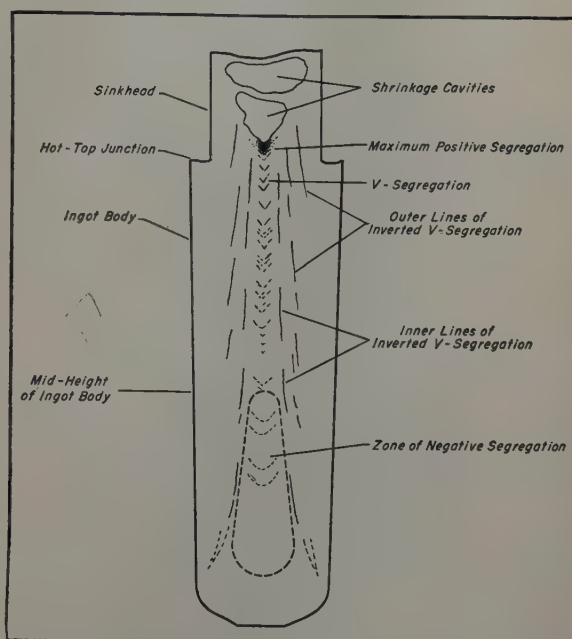


Fig. 1—Typical segregation pattern of a small ingot. Based upon sulphur print of Gary Works' 23x23 in. ingot.

and vertical solidification, and in deriving the effect of the w/h ratio upon the solidification pattern. Photographs of many ingots split at Homestead and at Duquesne Works, United States Steel Co., as well as those published by the British Iron and Steel Institute,² have been studied and analyzed. In the interest of brevity, only typical ingots of each type or classification from the above sources have been reproduced.

Segregation in Ingots

Segregation in ingots falls into three principal classifications: 1—lamellar segregation, as revealed in sulphur prints (Figs. 2 and 3); 2—zone segregation, or broad variations in composition; and 3—interdendritic, or microsegregation. The last class, of minor importance, is not considered here.

When liquid metal cools, according to the theory of differential or selective solidification,³ metal of relatively high purity selectively solidifies first. Liquid segregates (principally carbon, phosphorus,



Fig. 2—Sulphur print of 23x23 in. ingot, AISI 1040 steel. Ladle analysis: C, 0.41 pct; Mn, 0.90; P, 0.016; S, 0.021; Si, 0.24. Ingot split at Gary Works.

and sulphur) diffuse inwardly at definite rates.²⁻⁴ But solidification also progresses at definite rates that decrease inwardly. Hence segregation does not extend far into the liquid, but is restricted to a narrow layer of liquid metal immediately adjacent to the face of solidification.^{2,5} The width of this layer and its concentration of segregation increase inwardly. The several types of segregation in ingots and prevalent theories as to their mechanisms are discussed briefly below.

V Segregation: V segregation, Fig. 1, is a lamellar type of segregation revealed on sulphur prints as imperfectly developed V's centered on the vertical axis. Generally of maximum intensity in the upper portion of an ingot, V segregation may extend well below mid-height, Fig. 3. Ingots of intermediate sizes (15 to 25-in. width) are more subject to this defect than are either smaller or larger ingots. V segregation is less pronounced in big-end-up (Fig.

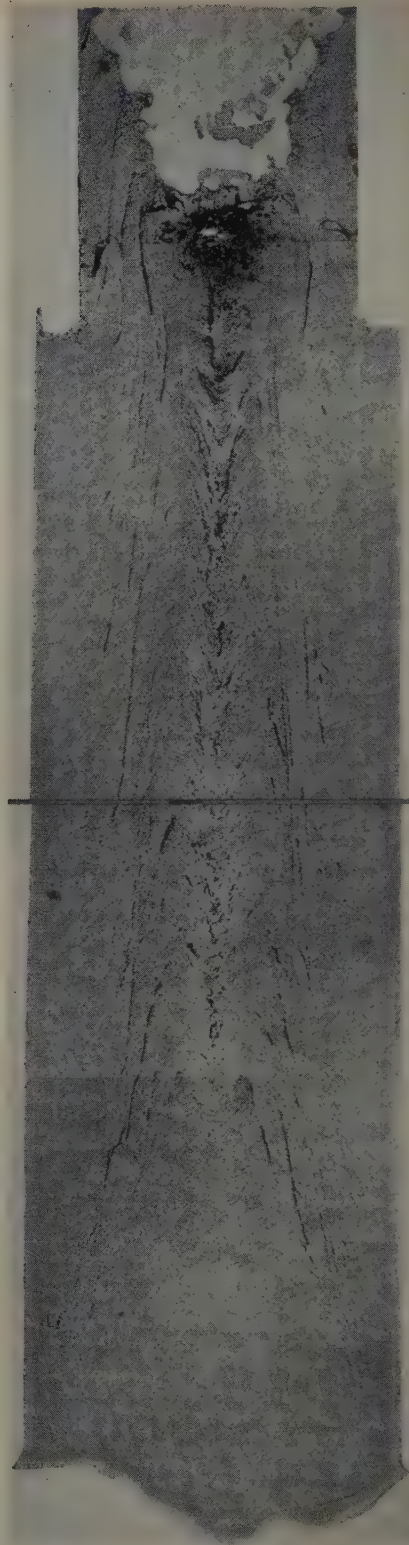


Fig. 3—Sulphur print of 25x25 in. ingot, AISI 1040 steel. Ladle analysis: C, 0.45 pct; Mn, 0.71; P, 0.022; S, 0.037; and Si, 0.20. Ingot split at Homestead Works.

2) than in big-end-down (Fig. 3) ingots. In large ingots, V segregation occurs normally well below the hot-top junction, separated from the latter by a zone of clean sound steel, Fig. 4.

The mechanism proposed by the Heterogeneity Sub-Committee of the British Iron and Steel Institute²—that, in the final stages of solidification, the contraction of the ingot causes segregates to be



Fig. 4—Sulphur print of 52 in. diam ingot, AISI 1040 steel. Ladle analysis: C, 0.45 pct; Mn, 0.66; P, 0.019; S, 0.029; Si, 0.21. Ingot split at Homestead Works.



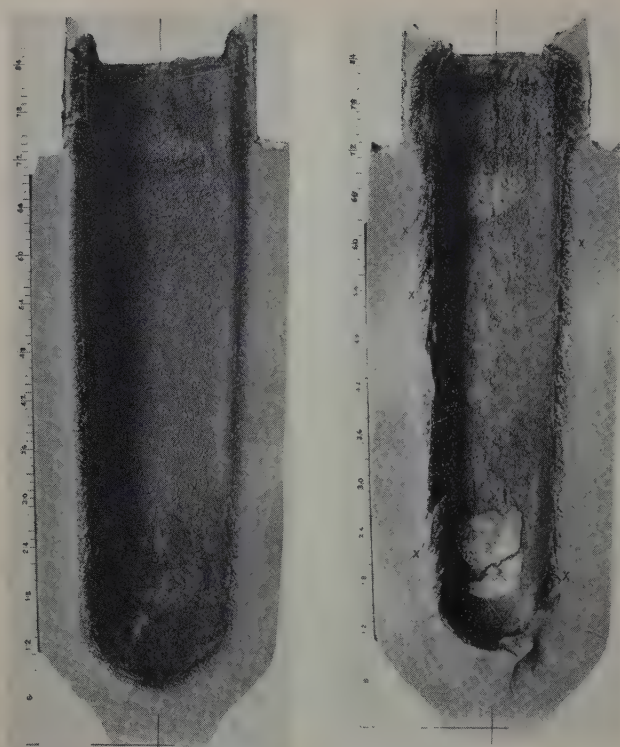
Fig. 5—Macroetch of 27x46 in. ingot, type 347 stainless steel. Ladle analysis: C, 0.08 pct; Mn, 1.26; P, 0.023; S, 0.013; Si, 0.28; Cu, 0.10; Ni, 11.18; Cr, 18.2; Cb, 0.80. Ingot cast at Duquesne Works, rejected on account of hanger cracks, split at Homestead Works.

drawn downwardly from the sinkhead—fails to account for the clean zone mentioned above. Nor does it afford an explanation of the lamellar arrangement of V segregation.

Hultgren⁴ suggests that V segregation results from the entrapment of segregated liquid metal between dendrites in the completion of solidification transversely. In absence of refill metal in final stages of solidification, the unsupported dendrites sag. Sagging plus contraction in cooling, according to Hultgren, cause the V shape of axial segregation. As applied to ingots that do complete solidification transversely (Figs. 22a and 23a), this explanation appears to be sound. As will be discussed later, however, it is not applicable to ingots that complete solidification vertically.

Negative Segregation: In a roughly cone-shaped zone in the lower middle portion of ingots (Fig. 1), segregating elements occur in less than average concentrations. This region is referred to as the zone of negative segregation. The deficiency in segregating elements decreases upwardly to approximately mid-height in an ingot, at which level the steel attains an average or ladle composition.

As segregation normally increases inwardly, the zone of negative segregation in ingot interiors has been difficult to explain. In an attempt to do so, the



a—Ingot No. 1 dumped 34 min after pour. b—Ingot No. 2 dumped 56 min after pour.

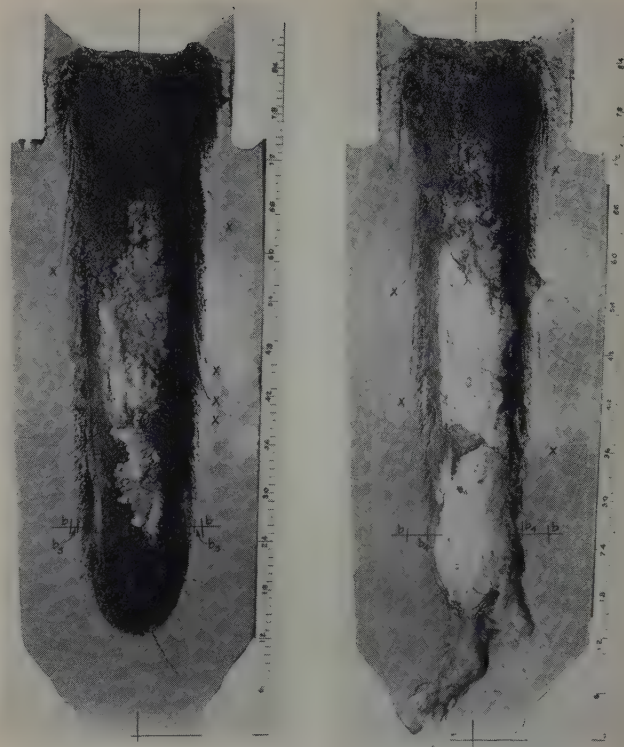
Fig. 6—Shells of 32x32 in. ingots dumped at various time intervals after pour. Ladle analysis: C, 0.83 pct; Mn, 0.77; P, 0.014; S, 0.024; Si, 0.18; Ni, 2.08; Cr, 0.15. Ingots split at Homestead Works.

theory of random nucleation of crystals was proposed speculatively.² According to the random-nucleation theory, crystallites of high purity nucleate, or generate, in the liquid metal in the interior of an ingot. Being of greater density than the surrounding liquid metal, these crystallites purportedly descend to build up a zone of high-purity metal in the lower middle portion of an ingot.

Several considerations make acceptance of the theory of random nucleation of crystals difficult. First, the liquid metal in an ingot quickly attains the liquidus temperature and remains at this temperature until just before solidification occurs, when it drops sharply.^{5,7,8} Second, according to Stokes' law, the rates of descent of crystallites in liquid metal would be so slow that they could not descend the required distance in the available time.⁹ Third, macroetches of ingots show no evidence of a cone of crystals caused by the piling up of descending crystallites. In the 29x66-in. semikilled ingot (Fig. 17), for example, the equiaxed crystals are restricted to a well-defined vertical core above the base cone. If crystals descend in the liquid metal, crystals in the lower middle portion of an ingot should be larger than those above; the reverse is typical, Fig. 5.

In a re-appraisal of their theories some years after they were first proposed, the Sub-Committee on the Heterogeneity of Steel Ingots of the British Iron and Steel Institute held it more probable that the zone of negative segregation occurred as a result of ascent of less pure components away from it than that it was caused by the descent of high-purity crystals into it.⁶

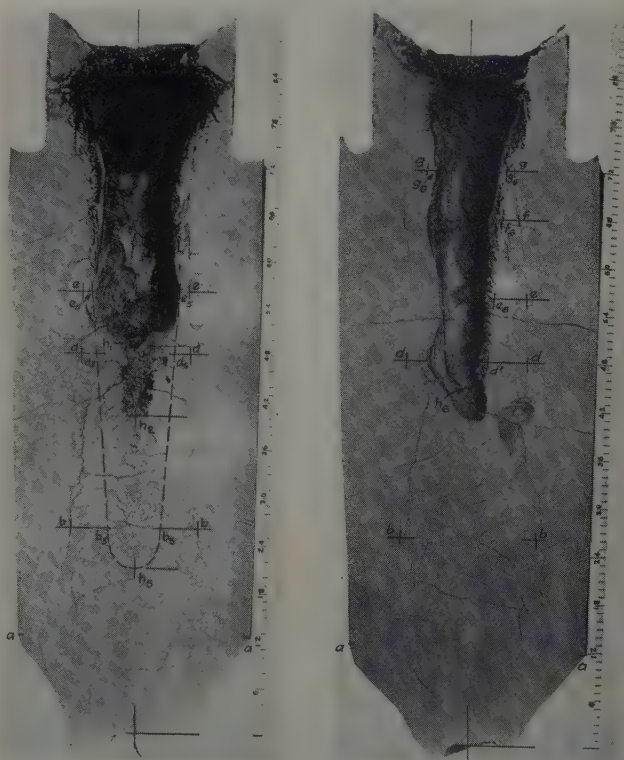
Inverted-V Segregation: Inverted-V segregation is also a lamellar type of segregation, which appears in split ingots as one or a series of discontinuous



a—Ingot No. 3 dumped 73 min after pour. b—Ingot No. 4 dumped 94 min after pour.

Fig. 7—Shells of 32x32 in. ingots dumped at various time intervals after pour. Ladle analysis: C, 0.83 pct; Mn, 0.77; P, 0.014; S, 0.024; Si, 0.18; Ni, 2.08; Cr, 0.15. Ingots split at Homestead Works.

lines outside the V segregation, Figs. 1 to 4. The lines incline slightly toward the vertical axis in an upward direction. Although lines of inverted-V segregation normally increase in number with in-



a—Ingot No. 5 dumped 118 min after pour. b—Ingot No. 6 dumped 150 min after pour.

Fig. 8—Shells of 32x32 in. ingots dumped at various time intervals after pour. Ladle analysis: C, 0.83 pct; Mn, 0.77; P, 0.014; S, 0.024; Si, 0.18; Ni, 2.08; Cr, 0.15. Ingots split at Homestead Works.

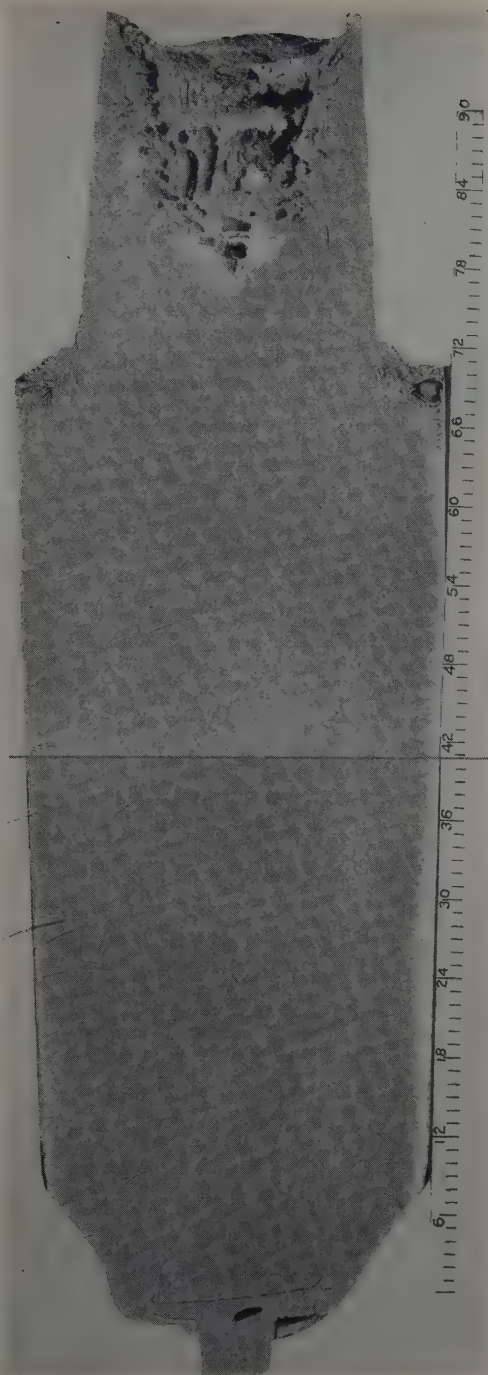


Fig. 9—Macroetch of 32x32 in. ingot, AISI 1020 steel. Ladle analysis: C, 0.22 pct; Mn, 0.52; P, 0.020; S, 0.037; Si, 0.29. Ingot split at Homestead Works.

crease of ingot size, their intensity, unlike that of V segregation, does not vary greatly. In large ingots they flare outwardly near the top to form a bottleneck, Figs. 4 and 24 to 26. In ingots in which such a bottleneck occurs, V segregation is restricted to the region just below the bottleneck, Fig. 4. For present purposes, lines of inverted-V segregation have been differentiated as to whether they are inner or outer lines, Fig. 1.

No satisfactory explanation of inverted-V segregation is found in the literature. According to one theory,² it results from the ascent of segregates along the face of solidification. Another⁹ envisages periodic descent of crystallites, which causes segregates to be swept upwardly in successive waves.

The view is sometimes expressed that lines of in-

verted-V segregation are internal cracks resulting from cooling stresses. Examinations of fractured ingots at Homestead Works, United States Steel Co., have shown that these "lines" are actually narrow zones containing a network of fine dendrites, which indicates that layers of liquid metal were entrapped and solidified with an insufficiency of refill metal. To have been entrapped as a liquid, the metal must have had a lower temperature of solidification than the surrounding metal; that is, it must have been segregated.

Experimental Dumping of Big-End-Up Ingots

In experiments conducted under the supervision of the Metallurgical Department at Homestead Works, six 32x32-in. big-end-up ingots of 2 pct Ni steel were dumped at various intervals from 34 to 150 min after pour. Photographs of the split ingots appear in Figs. 6 to 8. The ladle analysis of the steel was: C, 0.83 pct; Mn, 0.77; P, 0.014; S, 0.024; Si, 0.18; Ni, 2.08; and Cr, 0.15.

The tapping temperature was 2885°F; the pouring temperature 2730° to 2680°F. The mold temperatures were not measured but were reported to be within the range (300° to 400°F) used in normal practice at Homestead Works. The mean mold-wall thickness was 7.75 in., which includes one-third depth of 3/4-in. corrugation. Measurements of thickness were made from the outside of corrugations to the depth completely solidified. This is a close approximation of the depth from the centroidal plane of the corrugations to the mean depth of partially solidified metal at the face of solidification.

No completely solid ingot of the above composition was split. In Fig. 9 is a macroetch of an ingot of this size of 1020 steel.

Transverse Solidification: The depths of solidification as measured in the upper portions of ingot Nos. 1 to 5 (Figs. 6 to 8), which portions are of uniform thickness, are tabulated and plotted in Fig. 10. The equation of a straight-line representation of the five points is $d = -0.50 + 0.93\sqrt{t}$, where d is the depth in inches and t the time in minutes. Thus, initial transverse solidification occurred according

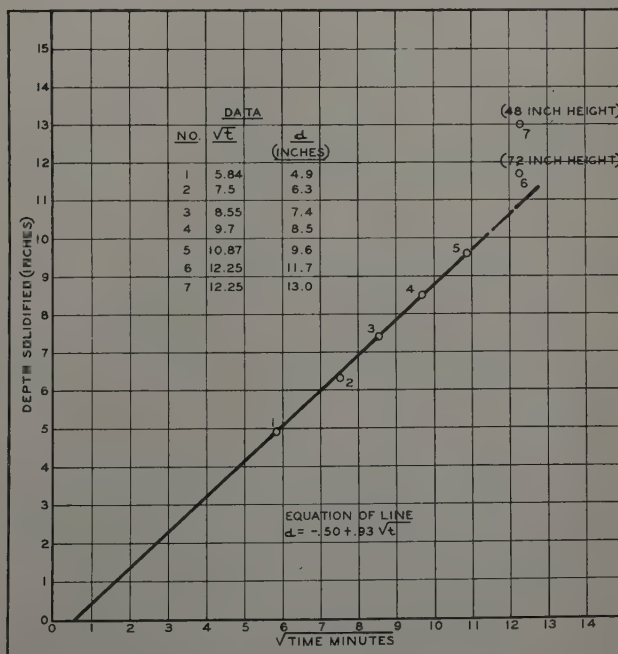


Fig. 10—Transverse solidification in Homestead Works' 32x32 in. ingot.

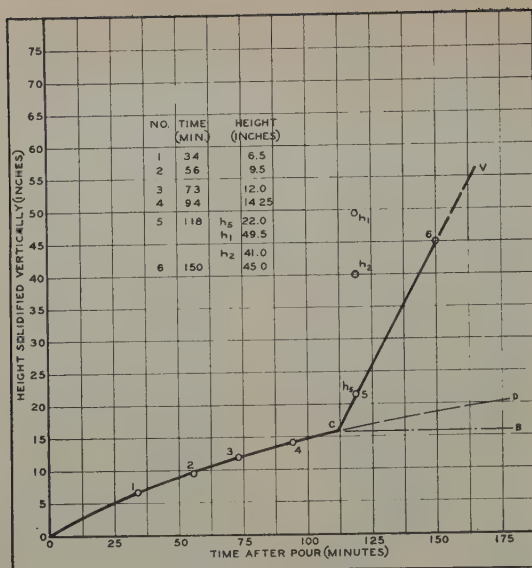


Fig. 11—Vertical solidification in Homestead Works' 32x32 in. ingot.

to the Chipman-FonDersmith equation,¹⁰ $d = -C + k\sqrt{t}$.

* This equation is a modification of Feild's equation, $d = k\sqrt{t}$.¹¹ The negative constant, $-C$, signifies that the curve intersects the abscissa to the right of the origin of coordinates. Dumped ingot data^{1,10,12} (Fig. 10) support the Chipman-FonDersmith equation. Experimental data presented by Bishop, Brandt, and Pellini⁷ indicate that the negative constant in the Chipman-FonDersmith equation increases with superheat.

The face of solidification on the right-hand side of ingot No. 6, Fig. 8b, is not parallel to the side of the ingot. This is evidence of accelerated transverse solidification, which will be discussed later. The depths of solidification at 48 and 72-in. heights in ingot No. 6 have been plotted, Fig. 10.

Vertical Solidification: To allow for the zone of partial solidification, $\frac{1}{2}$ in. has been added to measured heights of complete solidification vertically. The assumed face of vertical solidification in ingot No. 6, which face was gouged by the burning flame, has been represented by a dashed line, Fig. 8b. The measured heights of vertical solidification in all of the ingots are tabulated and plotted in Fig. 11.

The secondary cavity between h_1 and h_2 in ingot No. 5 and the extensive porous zone below this cavity are clearly abnormal. Excessive jarring of the ingot during overturning may have resulted in flash solidification of the liquid metal.** It remained to

** Similar flash solidification has been observed in the interiors of small laboratory ingots that have been jarred excessively in overturning.

decide which height to measure: 1—the base of the wide cavity, h_1 ; 2—that of the narrow cavity, h_2 ; or 3—the height, h_3 , of completely solid metal. As the last point, h_3 , conforms with the pattern established by the other four points, Fig. 11, much more reasonably than does either of the other two points, it was used.

The completed curve of vertical solidification, OCV (Fig. 11), then, consists of two portions, OC and CV, the two intersecting at a wide angle VCD. The significance of this shape will be discussed later.

Effect of Ingot Width on Rates of Transverse and Vertical Solidification

Nelson¹ reported data from dumped 13x13 and 17x17-in. ingots of high-carbon electric furnace steel cast in molds of slightly less and slightly greater than 4-in. mean wall-thickness, respec-

tively. Nelson's data for transverse and vertical solidification are related below to those for the 32x32-in. ingot.

Transverse Solidification: Based upon replots of Nelson's data, the following equations for initial transverse solidification have been derived: for the 13x13-in. ingot, $d = -0.50 + 1.2\sqrt{t}$; for the 17x17-in. ingot, $d = -0.10 + 1.04\sqrt{t}$. The parabolas of initial transverse solidification for these two ingots and that for the 32x32-in. ingot have been plotted in Fig. 12.[†] The plot indicates that the k value of

† As the negative constant in the Chipman-FonDersmith equation is believed to vary with superheat, the same constant, -0.10 , was used in all three equations from which the curves were plotted.

initial transverse solidification varies inversely with ingot width. The reason for this may be considered.

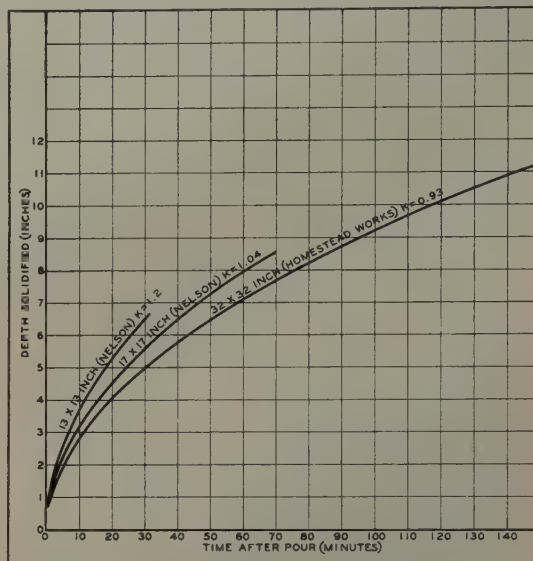


Fig. 12—Effect of ingot width on initial transverse solidification.

Temperature gradients established in mold walls from the middles of the hot sides to the less hot corners affect the k value for solidification across the middle plane. As ingot width decreases, the corner chills become increasingly effective. Thus k varies inversely with ingot width. As ingot width increases above some limiting width, perhaps 35 to 40 in., however, mold corners exert no further influence on heat extraction at the middle plane; that is, the normal k value for a given wall thickness is attained.

In addition to ingot width, mold-wall thickness influences k . Experimental data reported by Bishop, Brandt, and Pellini⁷ indicate that k increases with increase of mold-wall thickness from $1\frac{1}{2}$ to $4\frac{1}{8}$ in. Data reported by Nelson¹ indicate that k increases with increase of wall thickness from $4\frac{1}{4}$ to $6\frac{1}{4}$ in. It seems not improbable that k would increase with further increase of wall thickness up to the maximum thickness used for mold walls.

In mold design, wall thickness is commonly increased with increase of ingot width. Hence the effect of the latter upon k is somewhat moderated by the opposite effect of the former factor. As both influences are reflected in the plotted curves (Fig. 12), however, the k values for transverse solidification of ingots of widths intermediate between 13 and 32 in. may be determined approximately by interpolation between the curves for these two ingots.

Vertical Solidification: Nelson's data for vertical solidification in his 13x13 and 17x17-in. ingots have been replotted on the same chart (Fig. 13), on which has been reproduced also the curve for the

32x32-in. ingot, Fig. 11. As in the last curve, the last plotted point for each of Nelson's ingots lies well above the initial curve through the first three points. Accelerated vertical solidification in the 13x13-in. ingot has been represented as a straight line through the last two points, the slope of which line is the minimum consistent with the data. A pattern for vertical solidification curves clearly emerges. The slope of the line through the last observed point for the 17x17-in. ingot has been determined by interpolation between the final curves for the 13x13 and 32x32-in. ingots. Complete vertical solidification curves for 20x20, 25x25, and 30x30-in. ingots, shown as dashed lines, have been developed similarly by interpolation between the curves for the above two ingots. The slopes of the final portions of the curves are uncertain; they may decrease upwardly a variable amount depending on segregation in ingot interiors.

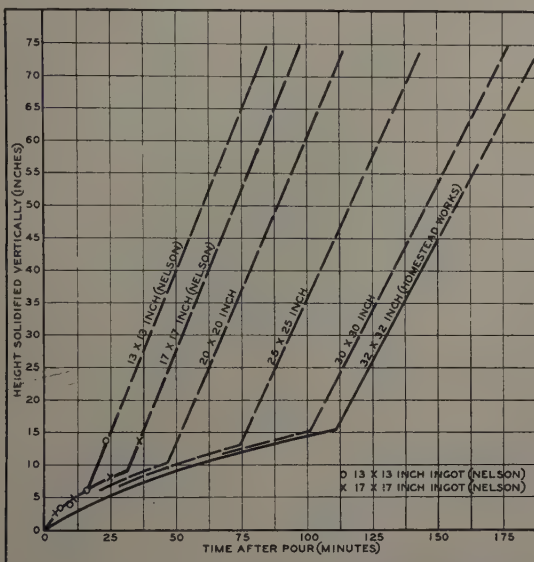


Fig. 13—Effect of ingot width on vertical solidification.

From Fig. 13, vertical solidification curves are apparently composed of two portions: an initial curve approximating a parabola and a final curve of steep slope. The two portions intersect at a height equal to approximately one-half the base width of ingot. The slopes of both portions decrease with increase of ingot width.

Accelerated Solidification in Ingots

As long as heat extraction is unidirectional, that is, all components are parallel, solidification follows the Chipman-FonDersmith equation, $d = -C + k\sqrt{t}$. When components of heat extraction occur in more than one direction, solidification, for the purposes of this paper, is said to be accelerated. Accordingly, solidification from curved surfaces and from ingot corners proceeds at accelerated rates from the start. The face of accelerated solidification widens as it proceeds inwardly in ingots to form zones of accelerated solidification. The zones originating at both side and base corners of ingots are considered below.

Accelerated Transverse Solidification from Side Corners: Nelson¹ noted that the faces of the cavities of 17x17-in. ingots dumped later than 20 min after pour were completely curved; that is, the faces of accelerated solidification arising at the corners had reached the middle planes. With a k value of 1.04 for the latter ingot, solidification would attain a

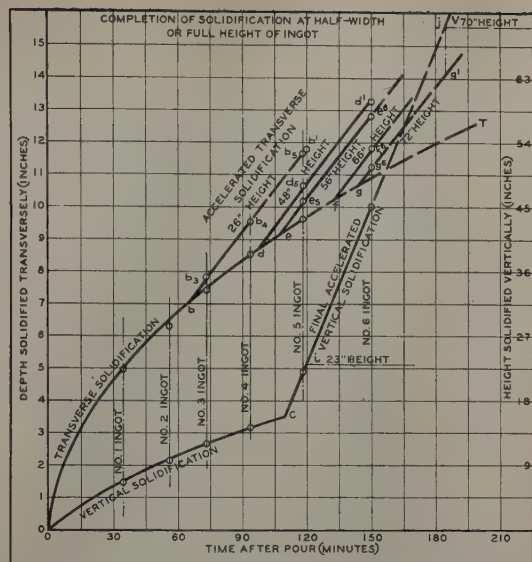


Fig. 14—Solidification curves for Homestead Works' 32x32 in. ingot.

depth of about $4\frac{1}{2}$ in., or approximately one-fourth the face width, in 20 min. This proportionality of depth to face width may be expected to apply approximately to all square and rectangular ingots. Plotted dumped ingot data^{1,10} (Fig. 10), however, fail to show any appreciable acceleration at such depths. It may be concluded, therefore, that acceleration of transverse solidification caused by components of heat extraction to adjacent sides is too slight to be noticeable at the middle planes of ingots of commercial sizes.^{††}

^{††} In small laboratory ingots, acceleration of this type may be quite significant.

Initial Accelerated Vertical Solidification: Analogous to the above, accelerated vertical solidification from base corners may be expected to reach the vertical axis at a height equal to about one-fourth the base width. Evidence that it does is found in the macroetch of Homestead Works' 29x66-in. ingot, Fig. 17. Above line *ada* vertical columnar crystals slope inwardly, which indicates that transverse components of heat extraction became effective along this line. The height, *d*, at which accelerated vertical solidification reaches the vertical axis is about 7 in., or about one-fourth the base width. Zone *adac* (Fig. 17), the upper portion of base cone *aca*, is therefore the zone of initial accelerated vertical solidification.

Vertical solidification from the rounded bases of big-end-up ingots occurs at accelerated rates from the start. If, for example, the data for the first four 32x32-in. ingots (Fig. 11) be plotted on a d/\sqrt{t} basis, the resulting curve increases in slope inwardly. Such a curvature denotes accelerated solidification (the plot of unaccelerated solidification on a d/\sqrt{t} basis is a straight line, Fig. 10).

Accelerated Transverse Solidification from Base Corners: Of much more practical importance than either of these two types of accelerated solidification is accelerated transverse solidification originating at base corners (*a* in Fig. 18) of big-end-down ingots, or at the points of tangency between the straight sides and the rounded bases of big-end-up ingots (*a* in Fig. 15). The loci of this acceleration, *ag* (Figs. 15 and 18), and its effects upon ingot soundness, will be discussed later.

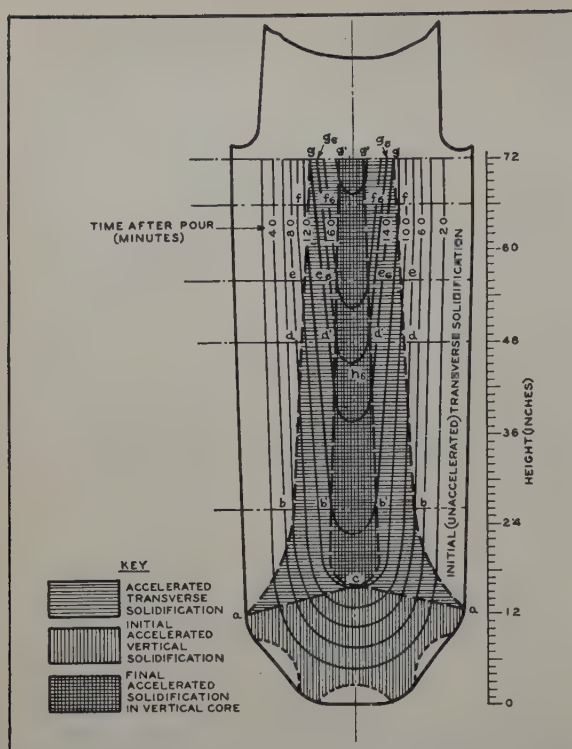


Fig. 15—Solidification pattern of Homestead Works' 32x32-in. big-end-up ingot.

Final Accelerated Vertical Solidification: Analogous to base cone *aca* (Fig. 17), as outlined by crystal structure in Homestead Works' 29x66-in. ingot, so-called base cones of vertical solidification *aca* (Fig. 15) are developed in big-end-up ingots. The height of the base cone is about one-half the base width of an ingot, Figs. 15 and 17. As this is also the height at which sharp acceleration of vertical solidification occurs (Fig. 13), a clue is provided as to the cause of this acceleration. At the tip of the base cone, the faces of transverse solidification from opposite sides first meet at the vertical axis, Figs. 15 and 18. Hence transverse components of heat extraction are here added to the vertical components. The added transverse components appear to be responsible for the high rates of final accelerated vertical solidification.

It has been generally assumed that vertical solidification is confined to the base cones of ingots. In the following, it is hoped to show: 1—that vertical solidification extends above the base cone in most ingots, and 2—that its extent is the determinant of the axial soundness of ingots.

Solidification Pattern of Big-End-Up Ingot: To aid in the development of the solidification pattern of Homestead Works' 32x32-in. ingot, the curves of transverse (Fig. 10) and vertical (Fig. 11) solidification of this ingot have been placed on the same chart (Fig. 14) to the same time scale but to different dimensional scales. The vertical scales have been adjusted so that one-half the top width, 16 in., on the left-hand scale for transverse solidification equals the full height of the ingot, 72 in., on the right-hand scale for vertical solidification. The direction in which solidification is completed, then, is determined according to which curve first attains the top horizontal line denoting completion of solidification in either direction. The curve of vertical solidification, OCV, reaches 72-in. height at V at about 187 min after pour; the curve of transverse solidification, OT, would not reach the same hori-

zontal line, representing 16-in. depth, until much later; that is, solidification of this ingot was completed vertically rather than transversely.

Accelerated Transverse Solidification: Fig. 14 also shows curves of accelerated transverse solidification, plotted from data obtained from the dumped ingots, Figs. 6 to 8. For example, points *b*₃ and *b*₄ represent the wall thicknesses at 26-in. height as measured in ingots Nos. 3 and 4, Fig. 7. A straight line through these points intercepts parabola OT at point *b*; that is, accelerated solidification at 26-in. height began at about 7-in. depth and 66 min after pour.

Similarly, points *e*₅ and *e*₆ in Fig. 14 represent wall thicknesses as measured at 56-in. height in ingots Nos. 5 and 6, Fig. 8. Line *e*₅*e*₆ through these points is approximately parallel to line *b*₃*b*₄, and intersects parabola OT at *e*. Points *b* and *e* have been plotted on the solidification pattern of the 32x32-in. ingot in Fig. 15. Points *b* and *e*, plotted similarly on the split ingots, Figs. 7 and 8, lie on or in line with inner lines of inverted-V segregation, Fig. 1. These coincidences suggest that inner lines of inverted-V segregation are loci of acceleration of transverse solidification from base corners. Additional evidence to this effect is provided by Homestead Works' 29x66-in. ingot. Inner lines *ag* in the sulphur print, Fig. 16, have been reproduced as dashed lines *ag* in the macroetch, Fig. 17. The increased width of columnar crystals beyond these lines and their increased upward slope, particularly in the lower portion of the ingot, are indicative of added vertical components of heat extraction.

In addition to the evidence given, there appears to be a logical reason for the coincidence of inner lines of inverted-V segregation and acceleration of transverse solidification. As solidification rates decrease inwardly, the layer of liquid segregated metal adjacent to the face of solidification increases in concentration.^{2,5} Conversely, when solidification rates accelerate, the concentration of this segregated layer must decrease. The excess segregation above that which can be carried at the higher rates is, therefore, deposited where the rates increase.

In further support of the coincidence of inner lines of inverted-V segregation and acceleration of transverse solidification, inner lines invariably point to the base corners of big-end-down ingots (Figs. 3, 4, and 24 to 26), whence accelerated solidification proceeds.

In view of the above evidence, inner lines of inverted-V segregation have been utilized as loci of accelerated transverse solidification in the construction of the solidification pattern of the 32x32-in. ingot. Thus the depths of the inner line of inverted-V segregation, as measured to points *d*, *f*, and *g* in Fig. 8b at 48, 66, and 72-in. heights, respectively, on the right-hand side of ingot No. 6, have been plotted on both parabola OT in Fig. 14 and the solidification pattern in Fig. 15. The depths of solidification to points *d'*, *f*₆, and *g*₆ at the above heights in ingot No. 6 in Fig. 8b have also been plotted on both the solidification chart and pattern. Through these points have been constructed lines *dd'*, *ff*₆, and *gg*₆, representing accelerated solidification at the above heights, Fig. 14. These lines are approximately parallel with lines *bb*₄ and *ee*₆, previously developed. Accelerated solidification is thus revealed as progressing upwardly in the ingot from the base to the top, its rates not varying greatly. Lines *ag*, Fig. 15, constructed through points *b*, *d*, *e*, *f*, and *g*, then, are loci of acceleration of transverse solidification.

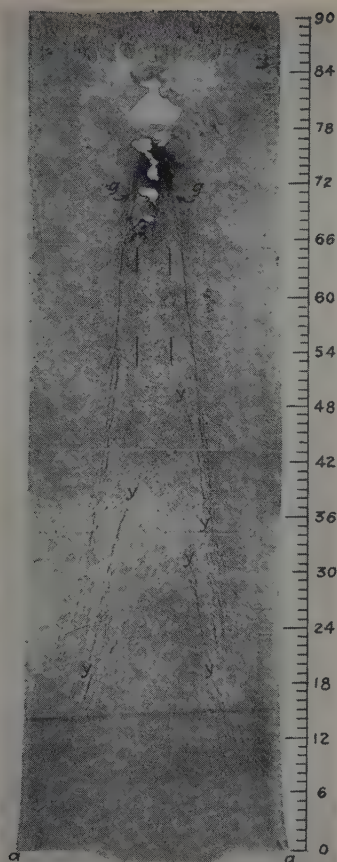


Fig. 16—Sulphur print of 29x66 in. ingot, semikilled steel. Ladle analysis: C, 0.24 pct; Mn, 0.44; P, 0.013; S, 0.033; Si, 0.032. Ingot split at Homestead Works.

In further support of their coincidence, lines ag , Fig. 15, correspond closely with the inner lines of inverted-V segregation faintly visible on the left-hand side of the 32x32-in. ingot, Fig. 9.

The Vertical Core: The vertical core of an ingot in a solidification pattern is outlined by the points of tangency between the faces of vertical and transverse solidification, such as point d' at 48-in. height in ingot No. 6, Fig. 8b. At the time that transverse solidification is completed at d' at 48-in. height, however, vertical solidification has reached a height of only about 45 in. on the vertical axis. Similarly, transverse solidification would be completed at 26-in. height when vertical solidification had reached point i in Fig. 14 at 23-in. height on curve CV of vertical solidification. Accordingly, point b' has been located on extrapolated line bb , vertically above point i . Points b' and d' have been plotted at their proper depths on both sides of the solidification pattern in Fig. 15. As the width of the vertical core apparently decreases upwardly, so does the differential between the heights of vertical and completed transverse solidification. For this reason, point g' has been located on extrapolated line gg , Fig. 14, vertically below point j at 70-in. height on curve CV of vertical solidification. Points g' have also been plotted on the solidification pattern in Fig. 15. As the vertical core of an ingot lies directly above the base cone, Fig. 17, the vertical core in the 32x32-in. ingot has been constructed from the tip of the base cone c (Fig. 15) through points b , d , and g .

The width of V segregation faintly visible in the upper portion of the split full 32x32-in. ingot, Fig. 9, is approximately equal to the width of the vertical

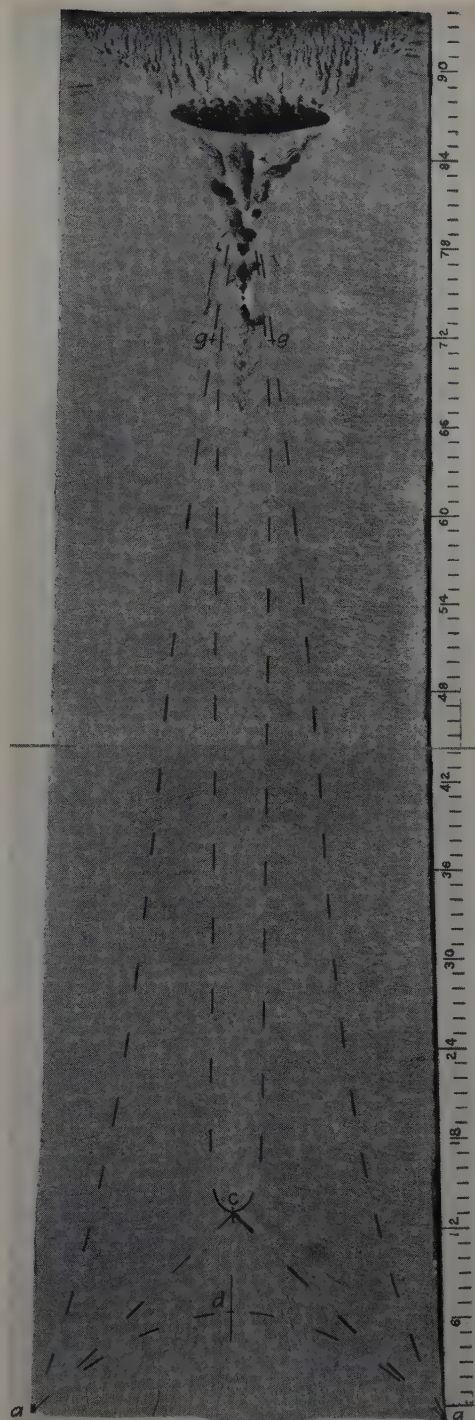


Fig. 17—Macroetch of 29x66 in. ingot, semikilled steel. Ladle analysis: C, 0.24 pct; Mn, 0.41; P, 0.017; S, 0.036; Si, 0.048. Ingot split at Homestead Works.

core in the corresponding location in the solidification pattern, Fig. 15. This indicates that V segregation is developed in vertical solidification in the vertical cores of ingots.

Isochrones: Isochrones at 20-min intervals have been constructed in the outer zone of the ingot in Fig. 15 parallel to its sides at depths as determined from parabola OT in Fig. 14. Curved-line isochrones, spaced on the vertical axis according to the curve of vertical solidification, Fig. 11, have been constructed in the base cone and in the vertical core. The isochrones have been connected by straight lines across the zones of accelerated transverse solidification. Dashed lines g_h correspond in location

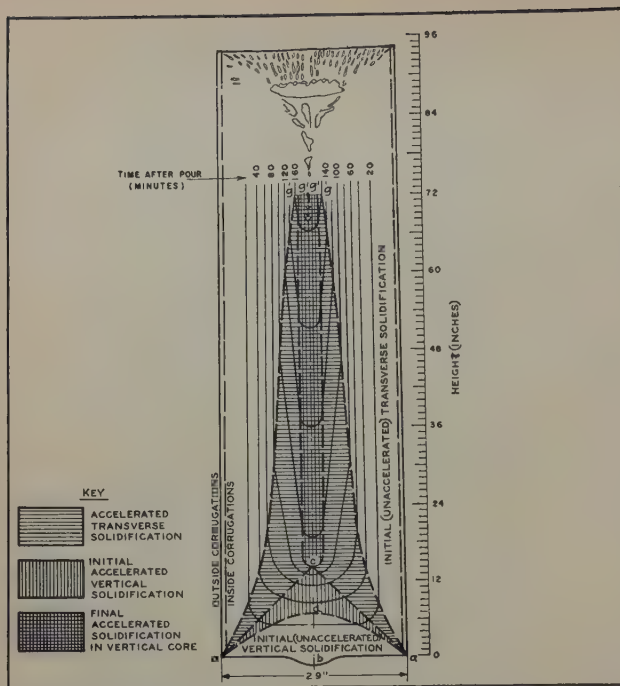


Fig. 18—Solidification pattern of Homestead Works' 29x66 in. big-end-down ingot.

to the actual face of solidification, $g_h c_s$ (Fig. 8b), on the right-hand side of ingot No. 6.

Discussion: With only two points for their establishment, the curves of accelerated transverse solidification, Fig. 14, have been constructed as straight lines. As the spacing of isochrones in the zone of accelerated transverse solidification, Fig. 15, is so nearly uniform, probably little error is involved in this representation.

It is of interest to reconstruct the face of solidification in ingot No. 5, Fig. 8a, from data obtainable from the solidification chart, Fig. 14. As the reconstructed outline $e_h h_s e_s$ closely bounds the porous zone, it appears probable that this would be the normal face of solidification.

Solidification Pattern of Big-End-Down Ingots

Although not of the same ingot, the sulphur print (Fig. 16) and macroetch (Fig. 17) of 29x66-in. big-end-down ingots split at Homestead Works appear

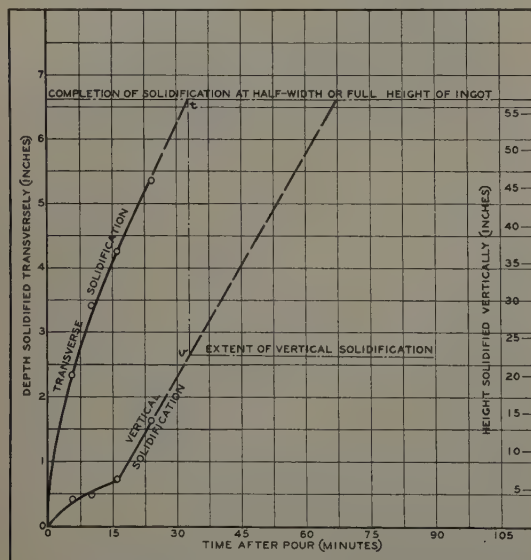


Fig. 19—Solidification curves for Nelson's 13x13 in. ingot.

to match each other closely. The ingots were cast in molds of 9.6-in. mean wall-thickness, having $\frac{3}{4}$ -in. corrugations.

The base cone aca and the vertical core $g'cg'$, Fig. 17, of equiaxed crystals are clearly distinguishable by macrostructure. These zones have been outlined on the solidification pattern in Fig. 18. The width of the vertical core, as indicated by two pairs of short lines in the upper portion of the sulphur print, Fig. 16, is about equal to the width of V segregation just above them. This confirms the evidence from the 32x32-in. ingots that V segregation develops in vertical cores of ingots.

Above line ada in Fig. 17 vertical columnar crystals slope inwardly, which indicates that transverse components of heat extraction were effective. Zone $adac$ in Figs. 17 and 18 is the zone of initial accelerated vertical solidification. As discussed previously, lines ag in Figs. 17 and 18, located similarly to inner lines of inverted-V segregation in the sulphur print in Fig. 16, coincide with crystal structure changes, which changes indicate that solidification beyond these lines occurred at accelerated rates. Hence zones $gacg'$ in Fig. 18 are zones of accelerated transverse solidification.

Based upon rates of transverse and vertical solidification estimated from the curves in Figs. 12 and 13, respectively, isochrones at 20-min intervals have been constructed in the solidification pattern in Fig. 18.

The solidification pattern of the big-end-down ingot, Fig. 18, and that of the big-end-up ingot, Fig. 15, are similar in that both have a vertical core which extends from the tip of the base cone to the top of the ingot. These vertical cores surmount zones of accelerated vertical solidification and are surrounded by zones of accelerated transverse solidification.

Proposed Mechanisms for Segregation in Ingots

Based on the developed solidification patterns of Figs. 15 and 18 and supporting data, the following mechanisms for the several types of segregation in ingots are proposed:

V Segregation: V segregation in ingots appears to result from the entrapment of segregated liquid metal adjacent to the face of vertical solidification by the earlier solidification at higher temperatures of purer metal above the segregated layers. Originally hemispherical, entrapped layers become distorted during cooling, so that they approximate a V shape in ingot sections, Figs. 1, 2, and 3.

In small ingots and in some large ingots of unusual proportions, solidification may be completed transversely rather than vertically. As will be discussed later, the axial characteristics of such ingots differ from those of ingots that develop vertical cores.

Zone of Negative Segregation: Because segregation may ascend readily from the broad face of vertical solidification in the lower portion of an ingot (Figs. 15 and 18), the liquid metal here is relatively pure. Because metal of the highest purity selectively solidifies first,² metal of less than average concentration of segregating elements solidifies in the lower middle portions of ingots. As solidification advances upwardly, the concentration of segregation in the liquid and consequently in the solid metal progressively increases, Fig. 1.

Inner Lines of Inverted-V Segregation: The concentration of segregation in the layer of liquid metal

adjacent to the face of transverse solidification increases as solidification rates decrease inwardly. Conversely, when these rates increase, the concentration of segregation must decrease. Thus the excess segregation above that which can be carried at the higher rates is entrapped along the loci of acceleration.

Outer Lines of Inverted-V Segregation: Although outer lines of inverted-V segregation may originate at various heights in an ingot (Fig. 1), all start at approximately the same depth. The beginnings of outer lines of inverted-V segregation have been indicated by the letter *x* in Homestead Works' 32x32-in. ingots No. 2 (Fig. 6b), 3 and 4 (Fig. 7). According to the theory of selective solidification, there would have been a continuous layer of segregated liquid metal adjacent to the face of solidification in ingot No. 1, Fig. 6a. The presence of termini, *x*, of segregated layers in ingots Nos. 2, 3, and 4, indicates, therefore, that the originally continuous segregated layer was penetrated at random locations by columnar dendrites. Segregation could rise readily from the upper side, but not from the lower side of a penetrating dendrite. As a segregated layer is slightly insulating,³ the upper side of the dendrite would then offer a preferred course for heat flow. Hence solidification could advance upwardly beyond the segregated layer and entrap this layer. As solidification progresses upwardly beyond segregated layers, however, transverse solidification continues inwardly. Hence outer lines of inverted-V segregation slope inwardly in an upward direction.

Fragmentary lines of inverted-V segregation, as designated by letters *y-y* in Fig. 16, sometimes occur inside the prevailing inner lines, *ag*, of inverted-V segregation, that is, in the zones of accelerated transverse solidification. These segregated layers may be entrapped by a mechanism analogous to that described for the entrapment of outer layers of inverted-V segregation. The increased angles of these lines with the vertical, as compared with those of the prevailing inner lines, *ag* in Fig. 16, attest to the higher rates of transverse relative to vertical solidification in zones of accelerated transverse solidification as compared with those in outer zones.

Effect of Ingot Design on Solidification Pattern

As the ultimate objective of ingot solidification studies is to improve ingot soundness and uniformity, it seems important to consider the practical aspects of both ingot and mold design.

In the same manner that the curves of transverse and vertical solidification for Homestead Works' 32x32-in. ingot have been plotted on the same chart, Fig. 14, the curves for Nelson's 13x13 and 17x17-in. ingots, respectively, have been plotted together, Figs. 19 and 20. In these two charts also, the vertical scales have been adjusted so that one-half the top width of the ingot on the left-hand scale for transverse solidification equals the full height of the ingot on the right-hand-scale for vertical solidification. The direction in which solidification is completed, then, is determined according to which curve first attains the horizontal line denoting completion of solidification in either direction. As discussed previously, solidification would be completed vertically in the 32x32-in. ingot, Fig. 14. In the 13x13-in. ingot, on the other hand, solidification would be completed transversely, Fig. 19. At the time of this completion, vertical solidification would have attained a relatively short height of only about 22 in.

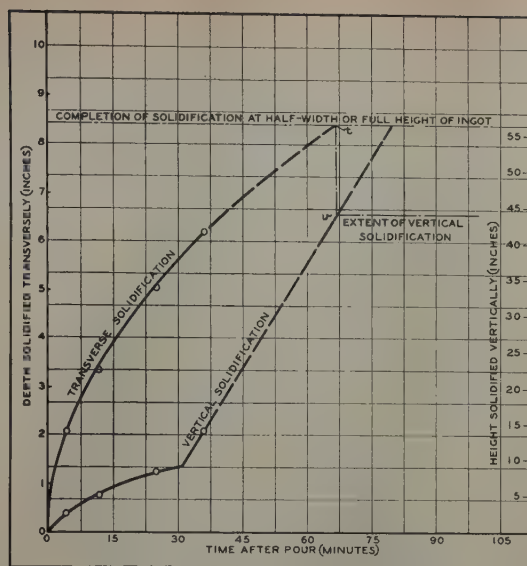


Fig. 20—Solidification curves for Nelson's 17x17 in. ingot.

In the 17x17-in. ingot, Fig. 20, vertical solidification would have reached a height of about 44 in. at completion of transverse solidification across the top. Hence, in an ingot somewhat shorter than the 17x17-in. ingot, or in one of slightly greater top width, transverse and vertical solidification would be completed to the top middle of the ingot at the same time.

Based upon these three charts, then, it appears that three types of solidification pattern may occur in ingots, Fig. 21. An ingot in which transverse and vertical solidification reach the top middle simultaneously, Fig. 21b, may be termed an ingot of critical *w/h* ratio. In an ingot of lower than critical *w/h* ratio, Fig. 21a, vertical solidification does not reach the top of the ingot. The height, *v*, of the vertical core in ingots of this type decreases with decrease of the *w/h* ratio. In ingots of greater than critical *w/h* ratio, Fig. 21c, the width, *V_c*, of the vertical core at the top increases with increase of *w/h* ratio.

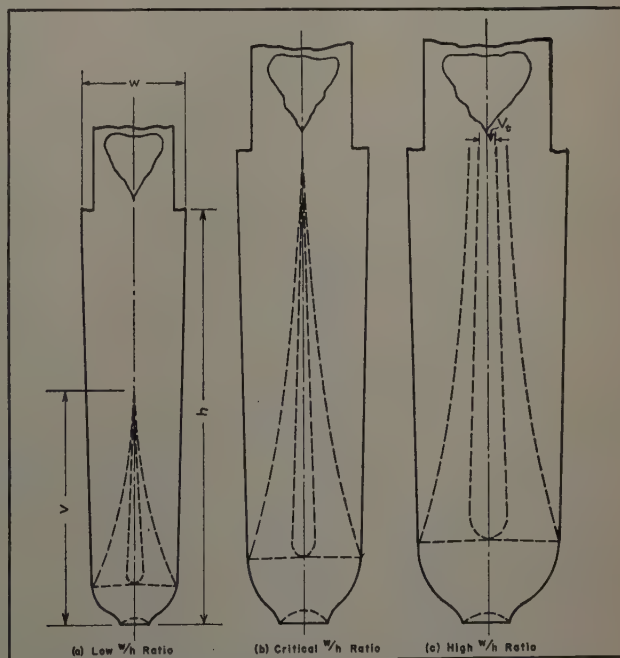


Fig. 21—Typical solidification patterns of ingots of different *w/h* ratios.

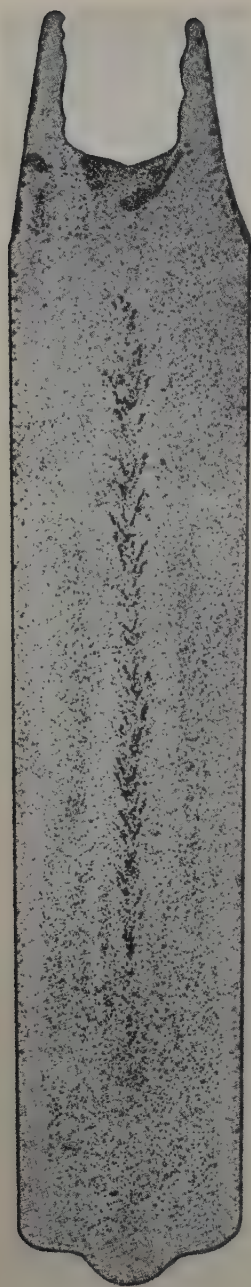


Fig. 22 (above and right)—Sulphur prints of small ingots of low w/h ratio cast in chill and sand molds. Reproduced from the first "Report on the Heterogeneity of Steel Ingots," Iron and Steel Institute, London (1926).

a (above) — Ingot cast in chill mold. Open hearth steel. Ladle analysis: C, 0.50 pct; Mn, 0.83; P, 0.036; S, 0.037; Si, 0.21. Ingot dimensions: 13.8 in. top diameter, 13 in. bottom diameter, 5 ft 5 in. high.

b (right) — Ingot cast in sand mold. Bessemer steel. Ladle analysis: C, 0.48 pct; Mn, 0.82; P, 0.028; S, 0.041; Si, 0.27. Ingot dimensions: 11.9 in. square at top, 10.2 in. square at base, 3 ft 9 in. long.

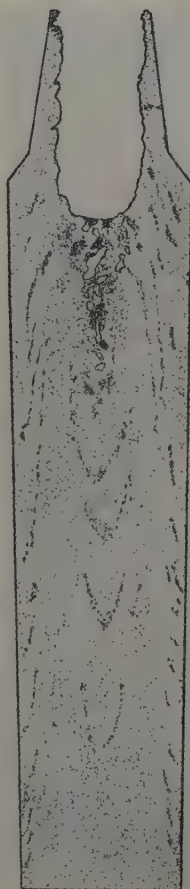
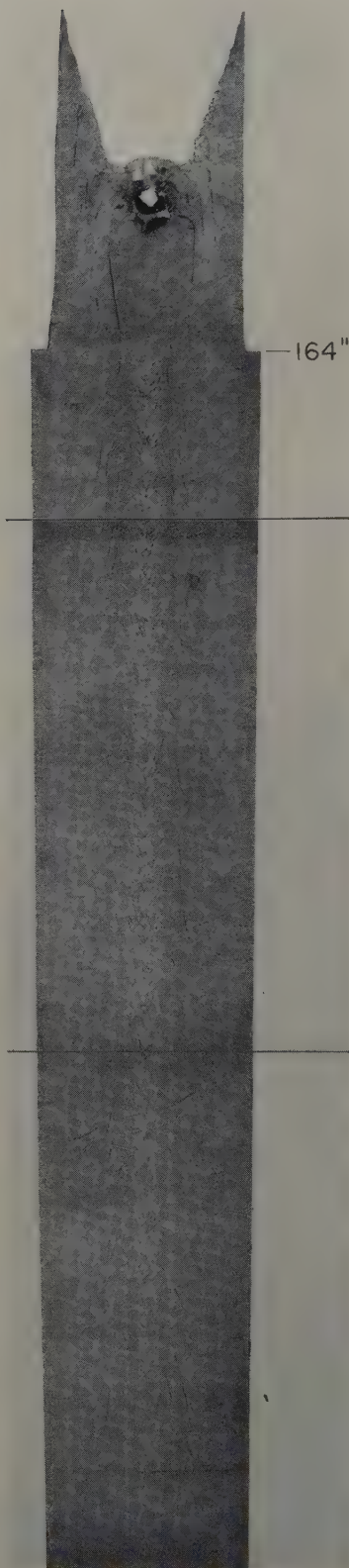


Fig. 23 (below and right)—Sulphur prints of 26 in. diam ingots of low w/h ratio cast big-end-up and big-end-down in same mold. Ingots split at Homestead Works.

a (below)—Big-end-up. Height of ingot, 164 in. Ladle analysis: C, 0.32 pct; Mn, 0.72; P, 0.035; S, 0.035; Si, 0.26; Ni, 3.37.

b (right)—Big-end-down. Height of ingot, 187 in. Ladle analysis: C, 0.32 pct; Mn, 0.90; P, 0.016; S, 0.022; Si, 0.22; Ni, 2.90.



The top width of an ingot of critical w/h ratio may be termed the critical width for an ingot of given height. The critical width of an ingot will vary with both height and type (big-end-up or big-end-down). From calculations based upon the curves of transverse (Fig. 12) and of vertical (Fig. 13) solidification, the critical width of a big-end-up ingot of 65-in. height is estimated to be about 18 in.; the critical width of a big-end-down ingot of the same height would be somewhat greater, perhaps about 21 in.

The type of solidification pattern, as governed by the w/h ratio, has an important effect on the type and extent of axial defects in ingots. Examples of ingots of all three types are discussed in the following.

Ingots of Low w/h Ratios: Ingots of low w/h ratios are usually comparatively small (say, from 9 to 15 in. sq). Because of their relatively rapid rates of solidification, small ingots develop relatively little segregation. For special applications, however, ingots of much larger sectional areas may be abnormally long, hence have a low w/h ratio.

In Fig. 22a is the sulphur print of a small ingot of low w/h ratio, reproduced from the First Report on the Heterogeneity of Steel Ingots of the British Iron and Steel Institute.² The axial characteristics of this ingot are different from those of ingots of higher w/h ratios, Figs. 2 and 3. In the small ingot, the V zone is widest at the top and tapers downwardly to disappearance at about 25 pct above the base. The V-shaped defects are of approximately uniform intensity throughout their extent. The shape of the V zone indicates that the faces of transverse solidification remained parallel to the sides as they advanced inwardly; that is, solidification was completed transversely to the middle of the ingot. Vertical solidification, then, must have been confined to the lower 25 pct of the ingot.

In ingots that complete solidification transversely, the so-called V segregation probably develops according to Hultgren's mechanism⁴ described previously; that is, layers of liquid metal are entrapped interdendritically as the faces of solidification from opposite sides meet at the vertical axis. Regardless of the amount of segregation present, porosity develops upon solidification of entrapped liquid metal. For this reason, it appears that V porosity is a more accurate term than V segregation as applied to axial defects in ingots of low w/h ratios.

That V porosity develops also in large ingots of low w/h ratios is apparent from the sulphur print of the 26-in. diam big-end-up ingot split at Homestead Works, Fig. 23a. The large big-end-down ingot of low w/h ratio, Fig. 23b, was cast in the same mold, inverted, as was the big-end-up ingot, Fig. 23a. Because solidification was completed across the top transversely before it was across the lower portion of this ingot, a central cavity developed. Similar cavities will necessarily develop in all big-end-down ingots of low w/h ratio. For big-end-down ingots to be solid, therefore, they must be of high w/h ratio, that is, they must have a vertical core extending to the top of the ingot, Fig. 17.

The wide V's in the ingot of low w/h ratio cast in a sand mold, Fig. 22b, are indicative of a wide core of vertical solidification. Abnormally slow rates of transverse solidification, caused by casting in a sand mold, appear to be responsible for both the abnormally wide vertical core and the abnormally shallow depths of the lines of inverted-V segregation.

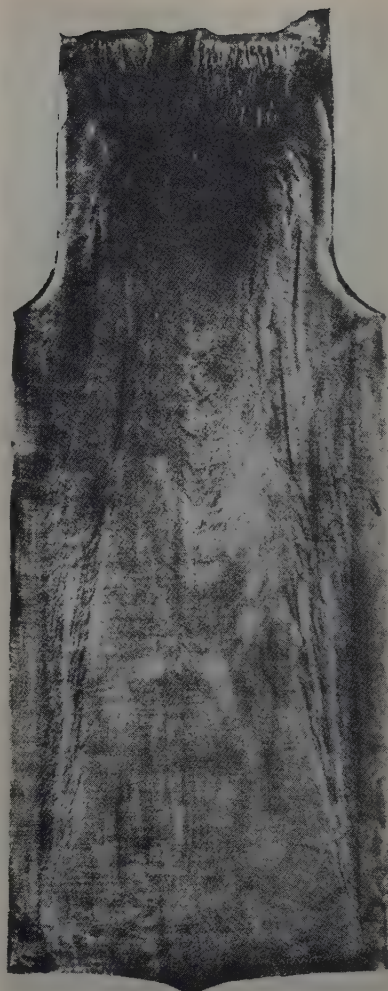


Fig. 24—Sulphur print of 10½ ton big-end-down ingot, electric furnace steel. Ladle analysis: C, 0.30 pct; Mn, 0.74; P, 0.010; S, 0.017; Si, 0.13. Reproduced from first "Report on the Heterogeneity of Steel Ingots," Iron and Steel Institute, London (1926).

Ingots of Near-Critical w/h Ratios: Ingots of near-critical w/h ratios comprise generally those of intermediate sizes, say, from 15 to 25-in. widths. The solidification rates of these ingots are sufficiently slow for a sufficiently long time that appreciable segregation may develop. Since the vertical cores of such ingots are typically narrow (Fig. 21b), segregation may not ascend readily into the sinkhead. For these reasons, V segregation is more prevalent in ingots of near-critical w/h ratios than in ingots of either higher or lower ratios. Big-end-up design effects substantial improvement in the internal soundness of ingots of near-critical w/h ratios, Figs. 2 and 3.

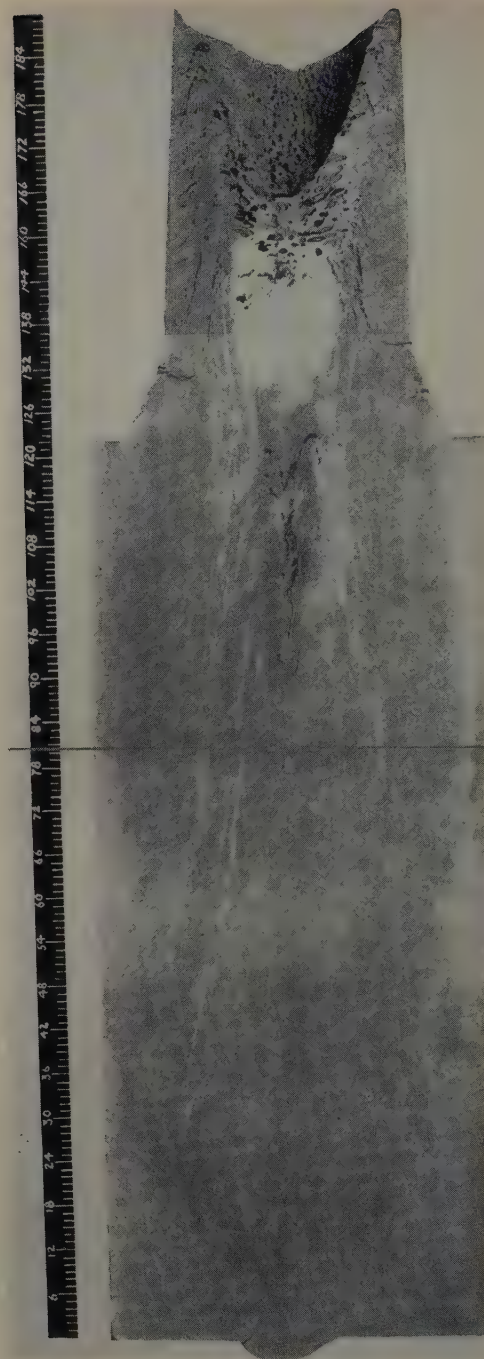
Ingots of High w/h Ratios: Ingots of this type comprise so-called large ingots of over 25-in. width. As the width, V , in Fig. 21c, of the vertical core at the top increases with increase of the w/h ratio above the critical ratio, ascent of segregates from the liquid metal in the ingot body to the sinkhead is facilitated. Thus, even though large ingots normally develop more segregation than do small ingots, the former, Figs. 4 and 9, may be fully as sound as the latter, Fig. 2.

The width of the vertical core is related to the width of the bottleneck or narrowest space between inner lines of inverted-V segregation in ingots, $g-g$



Fig. 25 (above)—Sulphur print of large big-end-down ingot. No data supplied. Reproduced from first "Report on the Heterogeneity of Steel Ingots," Iron and Steel Institute, London (1926).

Fig. 26 (right)—Macroetch of 55 in. diam big-end-up ingot. Ladle analysis: C, 0.37 pct; Mn, 0.57; P, 0.018; S, 0.028; Si, 0.19. Ingot split at Homestead Works.



in Figs. 15 and 18. Large ingots, big-end-up as well as big-end-down, in which the bottleneck is too narrow, are subject to excessive V segregation, Fig. 25, and/or secondary pipe, Fig. 26. Large ingots, big-end-down as well as big-end-up, with bottlenecks of adequate width, are typically sound, Figs. 4, 9, and 24.

Mold Design

As discussed above, ascent of segregates into the sinkhead is facilitated by a wide column of liquid metal in the upper portion of an ingot in the final stages of solidification, Figs. 15 and 18. The width of this column is reflected in both the width of the vertical core and that of the bottleneck between inner lines of inverted-V segregation. Differences in these widths constitute the most significant differences between the solidification patterns of big-end-up, Fig. 15, and big-end-down, Fig. 18, ingots. They are reflected in differences in axial soundness between ingots of the two types, Figs. 2 and 3.

Width V_v , Fig. 21c, of the vertical core at the top of an ingot, which may be measured as the width of V segregation, is a convenient single criterion of

internal quality. Increased width V_v favors improved ingot soundness. Width V_v is principally dependent upon two factors: 1—the w/h ratio, already discussed, and 2—the relative rates of transverse solidification across the top, and of vertical solidification. Decrease of the former and increase of the latter rates, relative to each other, favor increased width V_v . The relative rates in the two directions may be influenced by the following features of mold design: 1—type of mold, whether big-end-up or big-end-down, 2—mold-wall thickness, and 3—mold-wall taper. The effects of each factor are considered below.

Type of Mold: The advantage of big-end-up design arises principally from the fact that the ingot tops are wider than those of big-end-down ingots; that is, the former ingots have normally higher w/h ratios than the latter. But the narrower, rounded bases of big-end-up ingots favor earlier and more rapid rates of final accelerated vertical

solidification in the vertical cores of these ingots as compared with big-end-down ingots, Figs. 15 and 18. The closed bases of big-end-up molds probably also increase the effectiveness of mold walls in extracting heat. Because their molds are closed-based, big-end-up ingots are sometimes advantageously shorter than big-end-down ingots of similar cross section.

Mold-Wall Thickness: Mold-wall thickness affects the rates of vertical as well as those of transverse solidification. The optimum wall thickness is one that will result in a minimum ratio between rates of transverse and of vertical solidification.

In experiments conducted at Duquesne Works, 25x25-in. ingots cast in molds of 3-in. uniform wall-thickness had narrower V's and more center segregation than did ingots of the same size cast in molds of standard 5½ in. mean wall-thickness. Apparently the thin wall reduced the rates of vertical solidification relatively more than it did those of transverse solidification. There is evidence, on the other hand, that excessively thick mold walls may increase rates of transverse solidification relatively more than they increase rates of vertical solidification. For example, the mean wall-thickness of the mold in which the 55-in. diam ingot, Fig. 27, was cast was 15⅜ in. The unsound center in the upper portion of this ingot may have been caused by too rapid rates of transverse solidification.

The service life of a mold appears to be related to its wall thickness.¹⁴ Based on studies of extensive data, Bacon¹⁴ finds an optimum M/I ratio (mold weight/ingot weight) of 0.88 for molds of over 6-ton weight. This ratio would result in a 10-in. wall thickness for the above mold.

In summary, for an ingot of any given size there is probably an optimum mold-wall thickness to result in a minimum ratio between rates of transverse and vertical solidification. From superficial scrutiny, it appears probable that optimum mold-wall thicknesses for quality do not vary greatly from those for maximum mold life.

Mold-Wall Taper: Apparently to facilitate solidification from the base upwardly in ingots, mold walls are commonly made 1 to 4 in. thicker at the base than at the top. But dumped ingot data,¹ Fig. 6a, indicate that, except for accelerated solidification, rates of transverse solidification are uniform throughout the height of ingots cast in molds with tapered walls. The reason that mold-wall taper is ineffective for the purpose intended appears to be that heat flows downwardly in mold walls from the thin, hot, top portions to the thick, less hot, base portions. As a result, the normally slower rates of heat extraction by the thin top portions are increased, the normally faster rates of heat extraction by the thick base portions are decreased, and solidification rates are equalized throughout the height of the ingot. Thus, although thick base portions may advantageously increase final rates of accelerated vertical solidification, mold-wall taper appears to be of limited value in improving ingot solidification patterns.

Alloy Steels

The foregoing discussions apply to molds used in casting carbon steels or steels which solidify similarly to carbon steels. Certain low-alloy steels, cast in molds which produce sound carbon-steel ingots, develop exaggerated axial porosity, Fig. 27. Sykes¹⁸ reports "central looseness" in ingots of an austenitic high alloy steel, R. ex 78. Low-alloy steels have

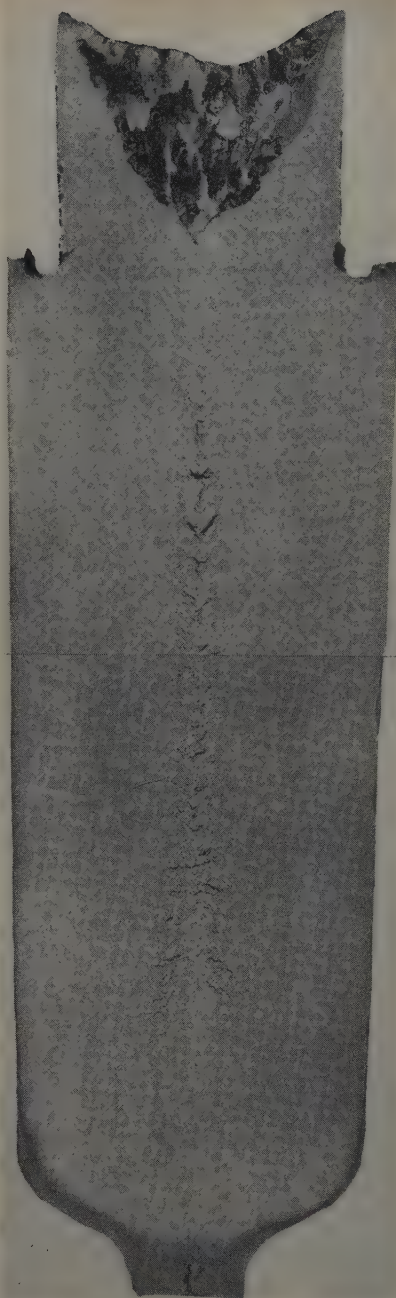


Fig. 27—Macroetch of 22x22 in. ingot, AISI 4340 steel. Ladle analysis: C, 0.40 pct; Mn, 0.68; P, 0.012; S, 0.014; Si, 0.28; Ni, 1.78; Cr, 0.70; Mo, 0.24. Ingot split at Duquesne Works.

strong tendencies toward equiaxed crystals, and austenitic steels toward columnar crystals. Ingots of both types, however, were solid just below the hot-top junction, Fig. 27; that is, solidification was completed transversely across the top before the vertical core was completely solid. Thus the critical w/h ratios, Fig. 21b, for these alloy-steel ingots must be considerably higher than that for carbon-steel ingots.

Sykes determined that exaggerated taper in big-end-up ingots was ineffective in preventing axial porosity. But ingots of R. ex 78 steel cast in sand had completely sound interiors. As shown by the ingot in Fig. 22b, this method of casting results in a wide vertical core. Unfortunately, however, these slow-cooling ingots had excessively large crystals and cracked badly in rolling.

For alloy-steel ingots to be completely sound, it

would be necessary for them to have a higher w/h ratio; that is, to be broader and/or shorter than carbon-steel ingots. From practical considerations, however, the extent to which the w/h ratio may be increased is limited.

Future Trends in Mold Design

As it seems doubtful that w/h ratios of ingots may be increased appreciably above those now used, improved ingot soundness appears to rest upon improved mold design. The benefits to be gained by adjustment of the several factors in molds of conventional design appear to be limited. Although some improvement may be attained by developing the optimum thickness for mold walls, particularly for large molds, there seems to be little prospect for marked gains by adjustment of either ingot or mold-wall taper.

Because of the inherent limitations of molds of conventional design, it seems that departures from conventional mold design should be considered. These should be aimed at increasing rates of vertical solidification and decreasing rates of transverse solidification across the top of an ingot, relative to each other, to the maximum extent practicable. Heat flow in mold walls, which does not appear to have been given adequate attention, needs to be considered.

From viewpoints of both quality and economy, the walls of many large molds in current-use appear to be too thick. Further, as large ingots complete solidification vertically rather than transversely, the purpose of excessively thick walls—to reduce the time for complete solidification—is not accomplished. As the advantage of big-end-up over big-end-down casting decreases with increase of ingot size, large ingots may more advantageously be cast in big-end-down molds of moderate wall-thicknesses.

Conclusions

The following conclusions concerning ingot solidification and hypotheses regarding segregation in ingots appear to be consistent with all of the data examined.

In solidifying, ingots develop a core of vertical solidification above the base cone. The vertical core surmounts a zone of accelerated vertical solidification and is surrounded by zones of accelerated transverse solidification.

In ingots of low width/height (w/h) ratio, the vertical core does not reach the top. Above the vertical core, solidification is completed transversely and V porosity may be developed axially.

In ingots of intermediate w/h ratios (15 to 25-in. widths), the vertical core at the top is narrow. Such ingots are subject to excessive V segregation. Big-end-up casting is most advantageously applied to ingots of these ratios.

The width, V_v , of the vertical core at the top of an ingot increases with increase of w/h ratio above the critical ratio. Sound interiors depend upon development of a vertical core of adequate width V_v .

V segregation is formed in the vertical cores of ingots as a result of entrapment of the layer of segregated liquid metal adjacent to the face of vertical solidification by the prior solidification of purer metal above this layer.

The zone of negative segregation in the lower middle portions of ingots develops as a result of selective solidification vertically of the purest metal available from the relatively pure metal in the lower portion of the contained liquid metal.

Inner layers or lines of inverted-V segregation result from the entrapment of excess segregation above that which can be carried forward at accelerated rates of transverse solidification. Outer layers or lines of inverted-V segregation result from penetration of the segregated layer of liquid metal adjacent to the face of solidification by columnar dendrites. Following such penetration, solidification may progress inwardly and upwardly, and entrap the segregated layer.

Little improvement in internal quality of ingots may be anticipated from increase of ingot taper or mold-wall taper beyond those now used in molds of current design.

There appears to be an optimum mold-wall thickness for each ingot size to result in maximum width of vertical core, V_v , at the top of an ingot. The walls of some molds of current design, particularly those for large ingots, appear to be too heavy from both quality and economy viewpoints.

Departures from current mold design should be considered. These should be aimed at increasing rates of vertical relative to those of transverse solidification in ingots.

Acknowledgments

The interest and cooperation of staff members of the Metallurgical Dept., Homestead Works, in these ingot solidification studies, particularly their permission to use the photographs of the split dumped 32x32-in. ingots and other ingots, is acknowledged. It is desired also to express appreciation of the considerable amount of experimental work performed by the Metallurgical Dept., Duquesne Works, some of which has been mentioned. Thanks are extended to the several members of the staff of the Research and Development Division for their constructive suggestions and criticism in the preparation of this paper.

References

- ¹ L. H. Nelson: Solidification of Steel in Ingot Molds. *Trans. ASM* (1934) **22**, pp. 193-226.
- ² Report on the Heterogeneity of Steel Ingots. *Journal Iron and Steel Inst. London* (1926) **113**, pp. 39-151. First report.
- ³ B. M. Larsen: A Review of Factors Underlying Segregation in Steel Ingots. *Trans. AIME* (1945) **162**, pp. 414-435.
- ⁴ A. Hultgren: Crystallization and Segregation Phenomena in 1.10 Per Cent Carbon Steel Ingots of Smaller Sizes. *Journal Iron and Steel Inst. London* (1929) **120**, No. 2, pp. 69-125.
- ⁵ H. Siegel: Undercooling of Steel in Ingot Molds. *Stahl und Eisen* (1941) **61**, pp. 991-996.
- ⁶ Report on the Heterogeneity of Steel Ingots. Iron and Steel Inst. London (1937) Seventh report, pp. 12-13.
- ⁷ H. F. Bishop, F. A. Brandt, and W. S. Pellini: Solidification Mechanism in Ingots. *Trans. AIME* (1952) **194**, p. 44; *JOURNAL OF METALS* (January 1952).
- ⁸ V. M. Tageev and B. B. Gulyaev: Solidification of Steel Ingot. *Metallurg* (1939) **14**, No. 8, pp. 23-38.
- ⁹ Basic Open Hearth Steelmaking. Committee on Physical Chemistry of Steelmaking, AIME (1944) pp. 434-446.
- ¹⁰ J. Chipman and C. R. FonDersmith: Rate of Solidification of Rimming Ingots. *Trans. AIME* (1937) **125**, pp. 370-377.
- ¹¹ A. L. Feild: Solidification of Steel in the Ingot Mold. *Trans. ASST* (1927) **11**, pp. 264-278, 338.
- ¹² J. W. Spretnak: Kinetics of Solidification of Killed Steel Ingots. *Trans. ASM* (1947) **39**, pp. 569-626.
- ¹³ C. Sykes: Steels for Use at Elevated Temperatures. *Journal Iron and Steel Inst. London* (1947) **156**, pp. 321-369.
- ¹⁴ N. H. Bacon: Mold-Weight/Ingot-Weight Ratio and Its Relation to Mold Consumption. *Journal Iron and Steel Inst. London* (1948) **158**, pp. 81-95.

Aluminum-Oxygen Equilibrium in Liquid Iron

by Nev A. Gokcen and John Chipman

Aluminum and oxygen dissolved in liquid iron were brought into equilibrium with pure alumina crucibles and atmospheres of known H_2O and H_2 contents to study the reactions: $1-\text{Al}_2\text{O}_3(\text{s}) = 2 \text{ Al} + 3 \text{ O}$; $2-\text{Al}_2\text{O}_3(\text{s}) + 3\text{H}_2(\text{g}) = 2 \text{ Al} + 3\text{H}_2\text{O}(\text{g})$; and $3-\text{H}_2(\text{g}) + \text{O} = \text{H}_2\text{O}(\text{g})$. Aluminum strongly reduces the activity coefficient of oxygen and similarly oxygen reduces that of aluminum. Values of the product $[\% \text{ Al}]^2 \cdot [\% \text{ O}]^3$ are much smaller than those found in previous experimental studies and are of the order of magnitude of the calculated values.

ALUMINUM is the strongest deoxidizer commonly used in steelmaking, but the extent to which it removes dissolved oxygen has been debatable. The relationship between aluminum and oxygen has not been determined reliably not only on account of the usual experimental difficulties at high temperatures but also because of uncertainties in the analyses of very small concentrations of oxygen and aluminum.

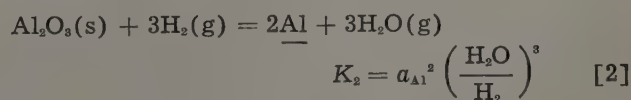
The earliest experimental attempt of Herty and coworkers¹ was followed by a more systematic study of Wentrup and Hieber.² These authors added aluminum to liquid iron of high oxygen content in an induction furnace and considered that 10 min was sufficient to remove the deoxidation products from the melt. Parts of the melts thus obtained were poured into a copper mold and analyzed for total aluminum and oxygen (soluble plus insoluble forms), assuming that the insoluble parts were in solution at the temperatures from which samples were taken. It is conceivable that the furnace atmosphere in their experiments, consisting of mainly air at 20 mm Hg pressure, was a serious source of continuous oxidation and therefore that their oxygen concentrations were correspondingly high. Scattering of their data was explained to be well within the maximum inaccuracy of 10°C in the temperature measurements and errors of ± 0.002 pct each in the oxygen and total aluminum analyses. Maximum and minimum deoxidation values, i.e., values of the product $[\% \text{ Al}]^2 \cdot [\% \text{ O}]^3$ differed by factors of 10 to 15; mean values of 9×10^{-11} and 7.5×10^{-9} were reported at 1600° and 1700°C , respectively.

Hilty and Crafts³ determined the solubility of oxygen in liquid iron containing aluminum, using a rotating induction furnace. Pure alumina crucibles used in their experiments contained the liquid iron which in turn acted as a container for slags of varying compositions consisting mainly of Al_2O_3 , Fe_2O_3 , and FeO . The furnace was continuously flushed with argon, and additions of aluminum and Fe_2O_3 were

made in the course of each experimental heat. The inner surfaces of their alumina crucibles were covered with a substance other than pure Al_2O_3 , containing both iron oxide and alumina. Although frequent slag additions can change the composition of slag in the liquid iron cup formed by rotation, the inner surface of the crucible must depend upon the transfer of oxygen or aluminum through the liquid iron for any adjustment in composition. It is not clear that their metal was in equilibrium with the crucible wall, but it is clear that it was not in equilibrium with Al_2O_3 . Their deoxidation product, $[\% \text{ Al}]^2 \cdot [\% \text{ O}]^3$, varied by a factor of more than 50; the average values of 2.8×10^{-9} and 1.0×10^{-7} were selected for temperatures of 1600° and 1700°C , respectively.

Aside from the experimental determinations, attempts have been made to calculate the deoxidation constant for aluminum indirectly from thermodynamic data. Schenck⁴ combined the thermodynamic data for Al_2O_3 and dissolved oxygen in liquid iron by assuming an ideal solution. His calculated values are 2.0×10^{-15} and 3.2×10^{-13} at 1600° and 1700°C , respectively. Later, Chipman⁵ attempted to correct for the deviation from ideality and derived an expression which led to deoxidation values of 2.0×10^{-14} and 1.1×10^{-12} at 1600° and 1700°C , respectively. The errors in these treatments originate mainly from inaccuracies of thermal data and uncertainties regarding the activity coefficients of dissolved oxygen and aluminum.

The purpose of this investigation was to study the equilibria represented in the following reactions in the presence of pure alumina:



The experimental method consisted of melting pure electrolytic iron, usually with an initial charge of aluminum, in pure dense alumina crucibles under a controlled atmosphere of H_2O and H_2 and holding

N. A. GOKCEN, Member AIME, is Associate Professor of Metallurgy, Michigan College of Mining and Technology, Houghton, Mich., and J. CHIPMAN, Member AIME, is Professor, Dept. of Metallurgy, Massachusetts Institute of Technology, Cambridge, Mass.

Discussion on this paper, TP 3446C, may be sent, 2 copies, to AIME by April 1, 1953. Manuscript, Aug. 6, 1952. Los Angeles Meeting, February 1953.

Table I. Approach to Equilibrium

Heat No.	Hours at Temperature	Al, Pct		O, Pct
		Charge	Analyzed	
205*	5.77	0.00	0.0094	0.0035
204*	10.25	0.00	0.0105	0.0040
207	1.0	0.00	0.011	0.0058
206	3.0	0.00	0.0126	0.0056
208	6.7	0.00	0.013	0.0041
209	2.17	0.017	0.015	0.0052
210	4.17	0.032	0.014	0.0050
211	5.1	0.047	0.015	0.0048
212	5.1	0.060	0.026	0.0053

* Heats 204 and 205 were made at 1680°C and $H_2O/H_2 = 5.12 \times 10^{-3}$. Others were made at 1723°C and $H_2O/H_2 = 3.72 \times 10^{-3}$.

it at a constant temperature until equilibrium was established between gas, liquid, and solid phases. The resulting melts of very small weight were quenched to retain the equilibrium concentrations of aluminum and oxygen and subsequently analyzed for these elements. The apparatus and procedure followed herein were described earlier in detail.⁶

In order to obtain concentrations of aluminum and oxygen high enough for analysis, it was planned to operate at temperatures higher than those used in previous studies.

Experimental Procedure

The procedure employed in these experiments was quite similar to that employed in the previous investigation.⁶ The main differences were as follows:

Slightly lower preheater temperatures were used in order to conserve the heating coil inside preheater. This was necessitated by the relatively dry hydrogen employed which had a strong tendency to embrittle the Pt-Rh alloy.

Experiments were conducted at considerably higher temperatures in order to obtain sufficient amounts of aluminum and oxygen for dependable analysis. At the usual experimental temperature of 1600°C, either the aluminum or the oxygen was always too low for accurate determination.

The temperature control and the accuracy of its measurement were within $\pm 10^\circ\text{C}$ even at the highest temperature used, 1866°C.

Known mixtures of H_2O and H_2 were obtained by passing purified hydrogen through the saturated solution of lithium chloride at various controlled temperatures. The vapor pressure of this solution had been determined previously in the same apparatus.⁷ The saturated hydrogen was mixed with four times its volume of purified argon.

Alumina crucibles used in this work were of the highest purity with less than 2 pct porosity. They were 1 in. high and 1 in. OD with a wall thickness of 0.04 in.

Operation: The charge consisted of 32 g of electrolytic iron containing a small percentage of aluminum in the form of pure Fe-Al alloy. The crucible was inserted in the furnace to the point where the surface of metal was 0.2 in. below the preheater. The preheater was brought to the desired temperature and the furnace flushed for a minimum period of 2 hr. Then the induction unit was turned on and the charge was brought to the desired temperature of 1700°C or more in less than 80 sec in order to preserve the aluminum in the charge. If the charge contained aluminum far beyond the equilibrium concentration, a thin and persistent scum of Al_2O_3 was formed on its surface a short time after reaching the desired temperature. Such heats were rejected, and a very thin grayish white solid scum was observed

on the quenched melts. In the satisfactorily charged heats the surface of melt was uniform and clean, permitting accurate temperature measurements with an optical pyrometer. After the attainment of equilibrium, the melts were quenched with hydrogen as described in the following section. Quenched equilibrium melts were shiny on the top and loosely attached to the alumina crucibles. Crucibles were only slightly discolored at 1866°C and were white at lower temperatures.

Quenching: The crucible was lowered into a position between two groups of orifices through which jets of hydrogen were directed upon it. Dense and very thin alumina crucibles without any radiation shields were used to facilitate the quenching process. It was found that by lowering the crucible into the cold zone of the silica furnace tube without the hydrogen jet the melt required a period of 60 sec to freeze, whereas in hydrogen quenching 7 to 12 sec was sufficient depending upon the temperature of melts.

Occasionally melts were spilled on the brass bottom when the crucibles cracked due to severe thermal shocks, thereby yielding severely quenched sound samples.

Oxygen Analysis: Oxygen analyses were made by the vacuum-fusion technique in the usual manner. The following precautions were taken to minimize the errors in the analytical results: Larger samples of 5 to 8 g were used. Very low and consistent blanks were obtained before proceeding with the analysis. This was accomplished by a long period of degassing of the vacuum-fusion apparatus. The aluminum content of the melt in the vacuum-fusion crucible was kept below 0.03 pct. Independent analyses were made by N. A. Gokcen to check the accuracy in the results.

The reproducibility of the oxygen analyses was generally within ± 0.0005 pct O.

Aluminum Analysis: Determination of aluminum was made by the gravimetric method⁸ in the range of 0.010 to 0.06 pct Al. The colorimetric method of analysis using aluminon as the indicator was used throughout the range investigated, yielding the soluble and insoluble aluminum separately. The agreement between the two methods was usually less than 0.001 pct in aluminum. The insoluble aluminum was approximately constant at each temperature, the average values being 0.0025, 0.0030, and 0.0055 at 1695°, 1760°, and 1866°C, respectively. In the absence of insoluble analyses for a very few heats, the average at each temperature level was added to the soluble aluminum content to obtain the total concentration. Average deviation in the duplicate analyses of total aluminum was always below ± 0.001 pct Al and usually of the order of ± 0.0006 pct.

Experimental Results

Attainment of Equilibrium: The experimental heats in Table I were made in order to ascertain the approximate time required for the establishment of equilibrium between three phases: gas, liquid metal, and solid alumina. Heats 204 and 205 were made at 1680°C under identical atmospheres without any aluminum in the charge. Analysis indicated that most of the aluminum was picked up from the crucible in about 6 hr, but there is no certainty that equilibrium was reached in 10 hr. Heat 208, with no aluminum in the charge, reached a slightly higher concentration than the next three in which the charge was above the final value. These four heats

must be regarded as having reached equilibrium within the limitations of the method.

Aluminum several times higher than the equilibrium value resulted in the formation of a thin and persistent scum of alumina covering the entire surface of liquid iron.

Heats 209, 210, and 211 indicate that by charging aluminum the time required for the attainment of equilibrium was reduced. Generally, heats were charged with an amount of aluminum slightly higher than the expected equilibrium concentration, and a period of time usually exceeding 8 hr was employed to reach equilibrium. Further increase in time was unjustified since the analysis for aluminum is not sufficiently precise to indicate small deviations from equilibrium.

Equilibrium Data: Table II gives the complete data on 20 equilibrium heats at 1695°, 1760°, and 1866°C. Tabulated also are values of the "apparent equilibrium constants" corresponding to Eqs. 1, 2, and 3, namely:

$$K_1' = [\% \text{ Al}]^2 [\% \text{ O}]^3$$

$$K_2' = [\% \text{ Al}]^2 \left(\frac{\text{H}_2\text{O}}{\text{H}_2} \right)^3$$

$$K_3' = \frac{1}{[\% \text{ O}]} \left(\frac{\text{H}_2\text{O}}{\text{H}_2} \right)$$

Thermodynamic Calculations

Oxygen: The equilibrium represented by Eq. 3 has been studied, at higher oxygen levels, by Dastur and Chipman.⁸ Theoretically, the activity coefficient of oxygen in each of the melts reported here is easily found by dividing the value of K_3' by their value of K_3 . This procedure, however, leads to extremely low values for the activity coefficient, so low, in fact, that the present authors are reluctant to put them forward. It seems possible that the results reported here, which are all at very low oxygen concentrations, may contain some small systematic error which makes these values of K_3' a little lower than they should be. In view of this possibility, no attempt will be made to correlate them with Dastur's data.

In Fig. 1 observed values of $\log K_3'$ at the two highest temperatures are plotted against the percentage of aluminum. Dastur's points are plotted

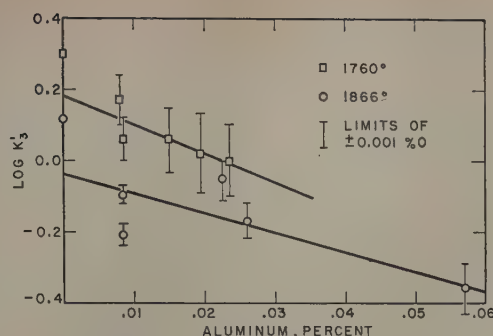


Fig. 1—Experimental values of $\log K_3'$ or $\log (\text{H}_2\text{O})/(\text{H}_2) [\% \text{ O}]$. Limits indicate effect of error of ± 0.001 pct in analysis for oxygen.

at zero aluminum but are ignored in drawing the lines.

The effect of an error of ± 0.001 pct in oxygen analysis is indicated to emphasize the sensitivity of the plot. Actual deviations should be ascribed as much to errors in gas composition as to oxygen analysis. Since the experimental values of $\log K_3'$ are not constant it is evident that the activity coefficient of oxygen varies with the concentration of aluminum. Previous work has shown that in the binary system Fe-O the activity coefficient is constant; hence, variations in the ternary system may be ascribed entirely to the effect of the third component. The slopes of the lines in Fig. 1 represent values of the coefficient $\partial \log f_o / \partial [\% \text{ Al}]$ which shall be designated here by the symbol $e_o^{(Al)}$. Since $\log f_o$ is zero in the absence of aluminum it follows that within the range of concentrations in which $e_o^{(Al)}$ is constant:

$$\log f_o = e_o^{(Al)} [\% \text{ Al}] \quad [4]$$

The slopes of the two lines of Fig. 1 yield values of $e_o^{(Al)} = -5.6$ and -8.0 at 1866° and 1760°, respectively; the data for 1695° agree roughly with those for 1760°. It is evident that the data do not yield accurate values of this quantity but that the figures given are conservative, for if the lines had been drawn to Dastur's points, the numbers would have been about doubled. The uncertainty is regrettable but is inherent in the very low concentrations involved.

Table II. Equilibrium Data at 1695°, 1760°, and 1866°C

Heat No.	Al, Pct		H ₂ O/H ₂ x10 ³ Corrected	Hours at Temperature	O, Pct	K ₂ '	K ₃ '	K ₁ '
	Charged	Analyzed						
At 1695°C:								
235	0.021	0.0038	9.63	7.5	0.0065*	12.9 x10 ⁻¹²	1.48	3.94x10 ⁻¹²
233	0.030	0.0045	7.04	7.5	0.0052	7.03x10 ⁻¹²	1.35	2.84x10 ⁻¹²
234	0.033	0.0073†	5.18	10.7	0.0038	7.48x10 ⁻¹²	1.36	2.92x10 ⁻¹²
226	0.045	0.0125	3.75	11.4	0.0032*	5.27x10 ⁻¹²	1.17	5.11x10 ⁻¹²
221	0.049	0.0164	2.32	12.8	0.0026	3.37x10 ⁻¹²	0.89	4.73x10 ⁻¹²
220	0.051	0.0230	1.95	13.0	—	3.92x10 ⁻¹²	—	—
At 1760°C:								
225	0.027	0.0050	13.03	13.8	—	5.52x10 ⁻¹¹	—	—
224	0.032	0.0080	9.58	12.1	0.0065	5.62x10 ⁻¹¹	1.47	1.76x10 ⁻¹¹
231	0.029	—	7.02	8.0	0.0075	—	0.94	—
232	0.000	0.0080	7.04	8.0	0.0062	2.24x10 ⁻¹¹	1.14	1.52x10 ⁻¹¹
218	0.042	0.0150	5.25	9.0	0.0046	3.26x10 ⁻¹¹	1.14	2.19x10 ⁻¹¹
217	0.042	0.023	3.80	8.7	0.0038	2.90x10 ⁻¹¹	1.00	2.90x10 ⁻¹¹
223	0.056	0.0190†	3.78	10.5	0.0036	1.95x10 ⁻¹¹	1.05	1.62x10 ⁻¹¹
At 1866°C:								
230	0.028	0.0085†	13.03	7.7	0.0164	1.59x10 ⁻¹⁰	0.80	3.19x10 ⁻¹⁰
229	0.026	0.0086†	9.59	8.0	0.0155	0.65x10 ⁻¹⁰	0.62	2.75x10 ⁻¹⁰
216	0.041	0.0230	7.12	6.1	0.0080	1.91x10 ⁻¹⁰	0.89	2.70x10 ⁻¹⁰
228	0.042	0.0335	5.24	6.6	—	1.62x10 ⁻¹⁰	—	—
227	0.049	0.0260†	5.19	9.8	0.0076	0.95x10 ⁻¹⁰	0.68	2.97x10 ⁻¹⁰
215	0.047	0.044	3.50	5.7	—	—	—	—
214	0.061	0.0570	2.45	6.0	0.0057*	0.48x10 ⁻¹⁰	0.43	6.00x10 ⁻¹⁰

* Single analysis.

† Average deviation about 0.0010; in all other cases, less than 0.0006.

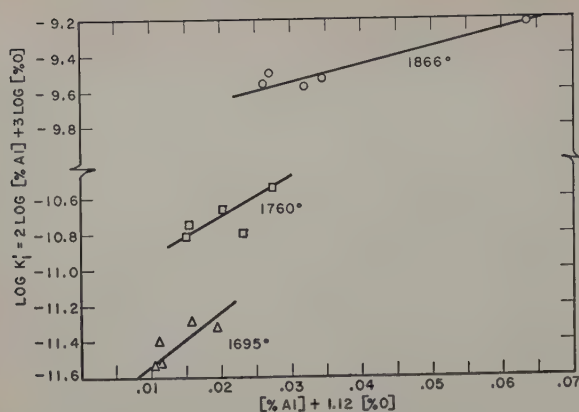


Fig. 2—Effect of concentration on equilibrium product $[\% \text{ Al}]^2 [\% \text{ O}]^3$.

Interaction of Al and O: The attractive forces between dissolved atoms of aluminum and oxygen which give rise to the effect discussed above also lead to variation in values of the equilibrium product $[\% \text{ Al}]^2 [\% \text{ O}]^3$. Before examining the data on this product it will be helpful to review briefly the thermodynamics of ternary solutions which are very dilute with respect to two components.

For the limiting case of a solution which is infinitely dilute with respect to components 2 and 3 in the solvent 1, Wagner⁹ has introduced the coefficients

$$\epsilon_2^{(2)} = \partial \ln f_2 / \partial N_2 \quad [5]$$

$$\epsilon_2^{(3)} = \partial \ln f_2 / \partial N_3, \text{ etc.}$$

and has shown that

$$\epsilon_2^{(8)} = \epsilon_8^{(2)} \quad [6]$$

In the very dilute solutions which are the concern here, it is reasonable to assume that Eq. 6 remains valid and further that $\epsilon_{\text{Al}}^{(\text{Al})}$ and $\epsilon_{\text{O}}^{(\text{O})}$ are negligible. Variations in the activity coefficient of oxygen are ascribed entirely to the effect of aluminum and, reciprocally, variations in f_{Al} are regarded as effects of oxygen. The quantity $\epsilon_{\text{O}}^{(\text{Al})}$ or $\epsilon_{\text{Al}}^{(\text{O})}$ may be re-

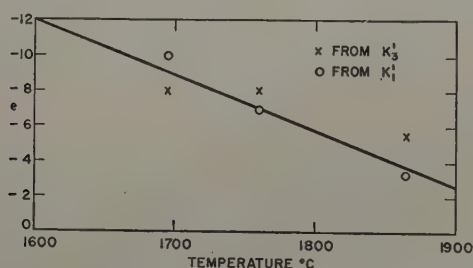


Fig. 3—Effect of temperature on interaction parameter $e_{\text{O}}^{(\text{Al})} = d \log f_{\text{O}} / d [\% \text{ Al}]$.

garded as an interaction parameter which most conveniently represents the effect of one element on the thermodynamic behavior of the other. The parameter is expected to vary with temperature, but at constant temperature the value determined at infinite dilution may remain constant over a considerable range of concentration.

The coefficient $e_{\text{O}}^{(\text{Al})}$ used in the preceding section is related to $\epsilon_{\text{O}}^{(\text{Al})}$ in the manner that atom fraction is related to weight percent. Introduction of the necessary numbers reduces Eq. 6 to the following form which is valid within the composition range in which the e 's are constant:

$$e_{\text{Al}}^{(\text{O})} = \log f_{\text{Al}} / [\% \text{ O}] = \frac{27}{16} e_{\text{O}}^{(\text{Al})} \quad [7]$$

The equilibrium constant for the deoxidation reaction, Eq 1, may be expressed as follows:

$$K_1 = [\% \text{ Al}]^3 \cdot [\% \text{ O}]^3 \cdot f_{\text{Al}}^2 \cdot f_{\text{O}}^3$$

$$\log K_1 = \log K'_1 + 2 \log f_{\text{Al}} + 3 \log f_{\text{O}}$$

$$= \log K'_1 + 2e_{\text{Al}}^{(\text{O})} [\% \text{ O}] + 3e_{\text{O}}^{(\text{Al})} [\% \text{ Al}] \quad [8]$$

which, in view of Eq. 7, becomes

$$\log K_1 = \log K'_1 + 3.37 e_{\text{O}}^{(\text{Al})} [\% \text{ O}] + 3 e_{\text{O}}^{(\text{Al})} [\% \text{ Al}]$$

$$= \log K'_1 + 3 e_{\text{O}}^{(\text{Al})} (1.12 [\% \text{ O}] + [\% \text{ Al}]) \quad [9]$$

In Fig. 2 the experimental values of $\log K'_1$ are plotted against $(1.12 [\% \text{ O}] + [\% \text{ Al}])$. The slope of the line represents $3e_{\text{O}}^{(\text{Al})}$ at each temperature. The intercept would represent $\log K_1$ but a more representative value will be found after establishing average values of $e_{\text{O}}^{(\text{Al})}$ and $e_{\text{Al}}^{(\text{O})}$. The slopes of the three lines correspond to values of $e_{\text{O}}^{(\text{Al})}$ of -3.3 , -7 , and -10 at 1866° , 1760° , and 1695° , respectively.

The two sets of values of $e_{\text{O}}^{(\text{Al})}$ are plotted against temperature in Fig. 3. These are not entirely independent sets since both involve oxygen analyses. The first set derived from Fig. 1 depends upon gas composition, the second does not. An average line is extrapolated to 1600° and the best values of the

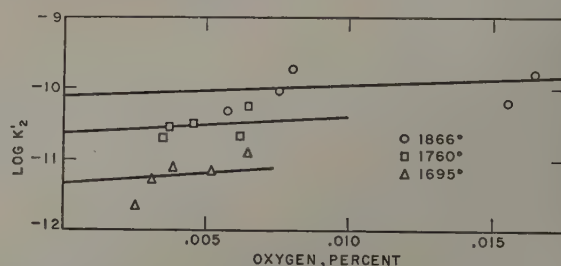


Fig. 4—Experimental values of $\log K'_2$ or $\log [\% \text{ Al}]^2 (\text{H}_2\text{O})^3 / (\text{H}_2)^3$.

coefficients at several temperatures are assembled in Table III.

It is interesting to compare the effects of aluminum on the activity coefficient with those of other elements that have been studied.¹⁰ Both chromium and vanadium diminish the activity coefficient of oxygen and are trivalent, like aluminum, and hence comparable. The order of arrangement of the three is the same as that of the heats of formation of the oxides. Table IV shows the comparison. In a very general way, the effect on the activity coefficient parallels deoxidizing power of the three elements as represented by the free energy change in reactions of the type of Eq. 3. The tabulated values are taken from ref. 10.

Aluminum in Iron: The effect of oxygen on the activity of aluminum has been shown in Table III. The corresponding effect on $\log K'_2$ is shown in Fig. 4 in which the lines are drawn with the slopes required by Table III. It is evident that the data do not afford accurate estimates of these slopes but that

Table III. Interaction Parameters of Aluminum and Oxygen in Liquid Iron

Temperature °C	1600	1695	1760	1866
$e_{\text{O}}^{(\text{Al})} = \partial \log f_{\text{O}} / \partial [\% \text{ Al}]$	-12	-9	-7.0	-3.6
$e_{\text{Al}}^{(\text{O})} = \partial \log f_{\text{Al}} / \partial [\% \text{ O}]$	-20	-15	-12	-6.0
$\epsilon = \partial \ln f_{\text{O}} / \partial N_{\text{Al}}$	-1340	-1000	-780	-400

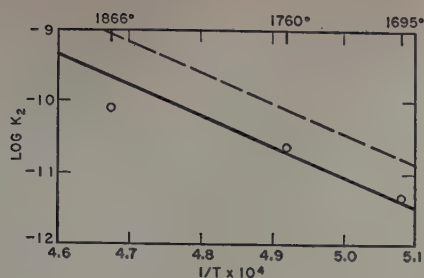


Fig. 5—Effect of temperature on $\log K_2$. Dotted line calculated from ref. 10. Solid line best average.

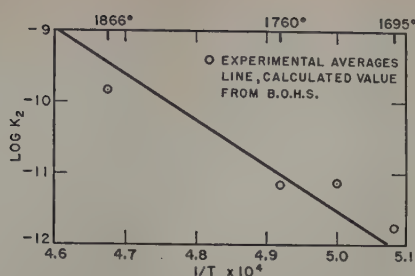


Fig. 6—Effect of temperature on the de-oxidation constant, $a_{Al}^2 \times a_o^3$.

again the effect is estimated conservatively since greater slopes would fit the data equally well.

The limiting values of $\log K_2'$ at zero oxygen represent $\log K_2$ at the three temperatures. It is obvious that these are subject to uncertainties of ± 0.5 or greater. Nevertheless, they are of interest as the only experimental values of this equilibrium constant. In Fig. 5 they are plotted against the reciprocal of absolute temperatures and compared with the calculated values of ref. 10. The calculated slope is probably better than could be obtained from the present data and this is used to draw the solid line whose equation is

$$\log K_2 = -42850/T + 10.37 \quad [10]$$

Eq. 10 deviates from the data of ref. 10 by about 0.6 in $\log K_2$. If this is attributed entirely to deviation in the gas composition, it is equivalent to 0.2 in the logarithm of the ratio $(H_2O)/H_2$, the values of this investigation being low by that amount. Similarly in Fig. 1 the deviations in $\log K_3'$ correspond to ratios that are low to the extent of 0.12 to 0.16 in $\log K_3$ at 1760° and 1866°, respectively. It is not possible at the present time to assign causes of this deviation nor to be sure that it resides in the gas composition.

Deoxidation Constant: Returning to Eq. 1, the equilibrium constant for the deoxidation reaction is calculated in Table V. This includes data on two heats in Table I which appear to have reached equilibrium as well as those in Table II. The average values of $\log K_1$ at each temperature are plotted in Fig. 6. The straight line, which represents the calculated line given in ref. 11, is fitted by the equation

$$K_1 = a_{Al}^2 \cdot a_o^3; \log K_1 = -64000/T + 20.48 \quad [11]$$

The agreement is surprisingly good. Although the new data indicate a slightly smaller temperature coefficient, they are not sufficiently accurate to warrant a change and the equation of ref. 11 is considered satisfactory as it stands. It must be noted that the equation applies to activities rather than percentage concentrations.

Table IV. Comparison of the Effects of Three Elements on Activity Coefficient of Oxygen at 1600°

	Chromium	Vanadium	Aluminum
$e_o^{(s)} = \partial \log f_o / \partial [\% X]$	-0.06	-0.25	-12
$\epsilon = \partial \ln f_o / \partial N_x$	-13	-53	-1340
ΔH for formation of X_2O_3 , kcal at 25°C	-269	-296	-399
ΔF° for reaction $2X + 3O = X_2O_3$			
kcal at 1600°C	-32	-50	-117

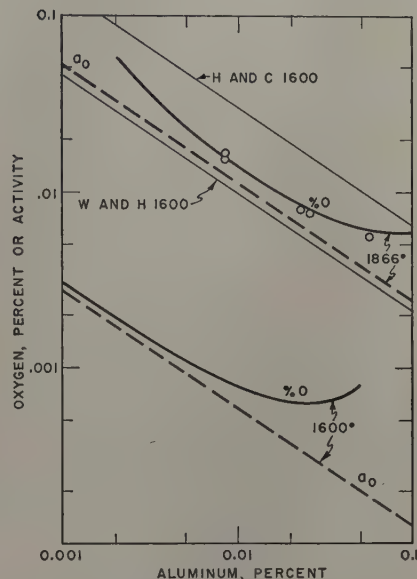


Fig. 7—Comparison of data on aluminum deoxidation. Broken lines show oxygen activities at 1600° and 1866°. Curved solid lines are corresponding percentages. Experimental points at 1866° are shown. Data of Hilty and Crafts and of Wentrup and Hieber at 1600° are shown.

For comparison with other data on aluminum deoxidation, Eq. 11 is used to obtain an extrapolated value of K_1 at 1600° of 2×10^{-14} . This is thought to be a more reliable figure than could have been obtained by a direct experimental approach using our method. To obtain corresponding values for actual concentrations of aluminum and oxygen requires use of the extrapolated interaction parameters of

Table V. Calculation of Equilibrium Constant $K_1 = a_{Al}^2 \cdot a_o^3$

Temperature	Heat No.	$\log K_1'$	$3 \log f_o$	$2 \log f_{Al}$	$\log K_1$
1680°	204	-11.15	-0.30	-0.13	-11.58
1695°	235	-11.41	-0.10	-0.19	-11.70
	233	-11.55	-0.12	-0.15	-11.82
	234	-11.54	-0.20	-0.11	-11.85
	226	-11.29	-0.34	-0.10	-11.73
	221	-11.32	-0.44	-0.08	-11.84
				Average	-11.73
1723°	208	-10.64	-0.43	-0.11	-11.18
	210	-10.60	-0.34	-0.14	-11.08
				Average	-11.13
1760°	224	-10.75	-0.18	-0.16	-11.19
	232	-10.82	-0.18	-0.15	-11.15
	218	-10.66	-0.34	-0.11	-11.11
	217	-10.54	-0.52	-0.09	-11.15
	223	-10.79	-0.43	-0.09	-11.31
				Average	-11.18
1866°	230	-9.50	-0.07	-0.19	-9.76
	229	-9.56	-0.07	-0.18	-9.81
	216	-9.57	-0.24	-0.09	-9.90
	227	-9.53	-0.27	-0.08	-9.88
	214	-9.22	-0.60	-0.07	-9.89
				Average	-9.85

Table III together with Eq. 9. The results of this calculation are shown in Fig. 7 along with the experimental data for 1866°C. Experimental results of Wentrup and Hieber² and of Hilty and Crafts³ at 1600° are included. No attempt will be made here to account for the discrepancy.¹² The low activity coefficients provide only a small correction.

Summary

An experimental study has been made on the equilibrium of liquid iron containing aluminum and oxygen with a gaseous mixture of hydrogen and water vapor and with crucibles of pure Al_2O_3 at temperatures in the range 1695° to 1866°C. The results were used to obtain activity coefficients of aluminum and oxygen in the solution and the equilibrium constants of the several reactions.

The activity of oxygen is strongly reduced by the presence of aluminum and reciprocally oxygen reduces that of aluminum. The effect diminishes with increasing temperature.

Equilibrium constants are in approximate agreement with calculations based on data of "Basic Open Hearth Steelmaking." The "deoxidation constant," $a_{\text{Al}}^2 \cdot a_{\text{O}}^3$ is represented by the equation

$$\log K_1 = -64000/T + 20.48$$

The experimental values of the product $[\% \text{Al}]^2 \cdot [\% \text{O}]^3$ are much lower than results of Wentrup and Hieber or of Hilty and Crafts. The discrepancy is not accounted for by the low activity coefficients.

Acknowledgment

This work was sponsored by the Office of Naval Research under Contract No. N5 ori-78/XVI.

References

- ¹ C. H. Herty, Jr., et al.: The Physical Chemistry of Steel Making. Carnegie Inst. of Tech. and U. S. Bur. Mines, *Coop Bull.* 46 (1930).
- ² H. Wentrup and G. Hieber: Reactions Between Aluminum and Oxygen in Iron Melts. *Tech. Mitt. Krupp, A. Forschungs-Berichte* (1939) 1, No. 2, pp. 47-58.
- ³ D. C. Hilty and W. Crafts: The Solubility of Oxygen in Liquid Iron Containing Aluminum. *Trans. AIME* (1950) 188, p. 414; *JOURNAL OF METALS* (February 1950).
- ⁴ H. Schenck: *Physical Chemistry of Steelmaking*. (English Translation) (1945) British Iron and Steel Research Association.
- ⁵ J. Chipman: Application of Thermodynamics to De-oxidation of Liquid Steel. *Trans. ASM* (1934) 22, pp. 385-446.
- ⁶ N. A. Gokcen and J. Chipman: Silicon-Oxygen Equilibrium in Liquid Iron. *Trans. AIME* (1952) 194, p. 171; *JOURNAL OF METALS* (February 1952).
- ⁷ N. A. Gokcen: *Journal ACS* (1951) 73, p. 3789.
- ⁸ M. N. Dastur and J. Chipman: Equilibrium in the Reaction of Hydrogen with Oxygen in Liquid Iron. *Trans. AIME* (1949) 185, p. 441; *JOURNAL OF METALS* (August 1949).
- ⁹ C. Wagner: *Thermodynamics of Alloys*. (1952) pp. 51-53. Addison-Wesley Press.
- ¹⁰ *Basic Open Hearth Steelmaking*. (1951), Tables 14-12 and 16-4. AIME.
- ¹¹ Ref. 10, p. 672.
- ¹² J. Chipman: Discussion of Ref. 3. *Trans. AIME* (1950) 188, p. 1342; *JOURNAL OF METALS* (November 1950).

Technical Note

Low Temperature Aging in Titanium Alloys

by W. M. Parris, L. L. Hirsch, and P. D. Frost

IT has been established that titanium alloys containing sufficient amounts of β -stabilizing elements, such as iron, chromium, or manganese, can be age hardened.¹ Adenstedt, Pequignot, and Raymer² showed that age hardening occurred in a Ti-15 pct V alloy at room temperature after it was quenched from a temperature in the β -phase region.

During a recent investigation of the heat-treating characteristics of binary Ti-Mn and Ti-Cr alloys at Battelle, further evidence of low temperature aging was found. Appreciable hardening occurred in some of these alloys at aging temperatures as low as 212°F

(100°C). Indeed, the brief heating period employed for mounting metallographic specimens in bakelite resulted in hardening. It was felt that further information on this low temperature aging phenomenon would be of general interest in view of the large amount of work currently being done on titanium alloys.

The alloys examined in this investigation were arc-melted in a water-cooled copper crucible as $\frac{3}{4}$ -lb ingots. Du Pont Process A sponge was used as a base material. The arc-melted ingots were forged at 1700° to 1800°F (927° to 982°C) and hot rolled at 1450°F (788°C) to 14 gage (0.064 in.) sheet. Small specimens were heated in argon at 1742°F (950°C) for 30 min and quenched in various liquid media or air cooled. They were then mounted in a room-temperature-setting resin and given a metallographic

W. M. PARRIS, Associate Member AIME, L. L. HIRSCH, and P. D. FROST, Member AIME, are associated with Battelle Memorial Institute, Columbus, Ohio.

TN 133E. Manuscript, Sept. 2, 1952.

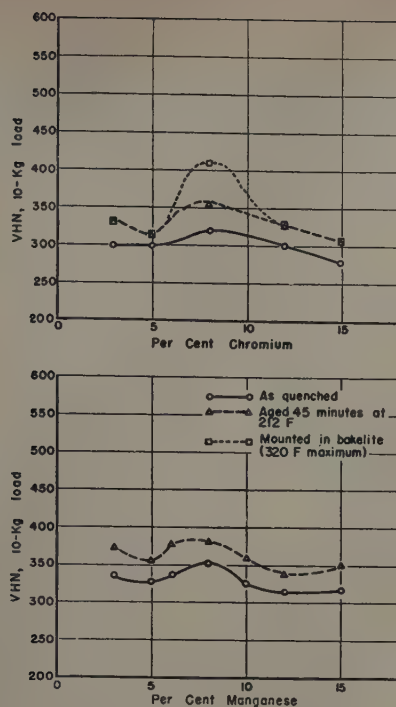


Fig. 1—Effects of low temperature reheating on titanium alloy specimens quenched in ice water from 1742°F (950°C).

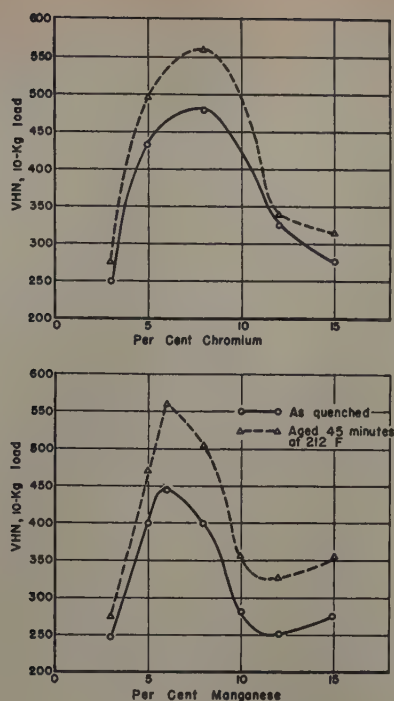


Fig. 3—Effects of low temperature reheating on titanium alloy specimens air cooled from 1742°F (950°C).

polish. After Vickers hardness determinations had been made on these specimens, they were heated in boiling water (212°F) for 45 min and again subjected to hardness tests. Results of these tests are plotted in Figs. 1 to 3. (Each point in the curves represents the average of at least three hardness determinations.) Also included in Figs. 1 and 2 are curves representing the effect of mounting in bakelite on the hardness of the series of Ti-Cr specimens. The maximum temperature attained during the curing of the bakelite mounts was 320°F (160°C). Upon

attaining this temperature, the mounts were rapidly cooled to room temperature.

It is evident that some hardening occurred in all of the alloys under all conditions of prior heat treatment when they were reheated to 212°F. Hardness increases in the water-quenched specimens were moderate, averaging about 25 VHN. However, specimens cooled at the lower rates (liquid-nitrogen quench or air cooled) exhibited hardness increases of over 100 VHN in some cases. The alloys which contain 5 and 8 pct Cr, or 5, 6, and 8 pct Mn, hardened considerably more than those of lower or higher alloy contents. With the exception of the water-quenched 8 pct Cr alloy, the hardnesses of the bakelite-mounted specimens agreed very well with those of the specimens aged at 212°F.

This work demonstrates that it is possible to introduce large increases in hardness in certain titanium alloys by heating in the range 200° to 300°F. The effects of variation in aging time and temperature on the hardness and other properties of the alloys described have not been fully investigated. Likewise, the study has been applied to relatively few alloys. The aging phenomenon warrants further investigation. It will certainly be of interest to those who have been using bakelite mounts for examining the microstructures of titanium alloys. However, it may be of greater future significance in processing alloys for structural applications.

The information in this note was obtained in research on titanium alloys being conducted at Battelle Memorial Institute for the Materials Laboratory of the Wright Air Development Center, Contract AF 33(038)-3736. Permission to publish the data is gratefully acknowledged.

References

- ¹ C. M. Craighead, O. W. Simmons, and L. W. Eastwood: Titanium Binary Alloys. *Trans. AIME* (1950) 188, pp. 485-513; *JOURNAL OF METALS* (March 1950).
- ² H. K. Adenstedt, J. R. Pequignot, and J. M. Raymer: The Titanium-Vanadium System. *Trans. ASM* (1952) 44, pp. 990-1003.

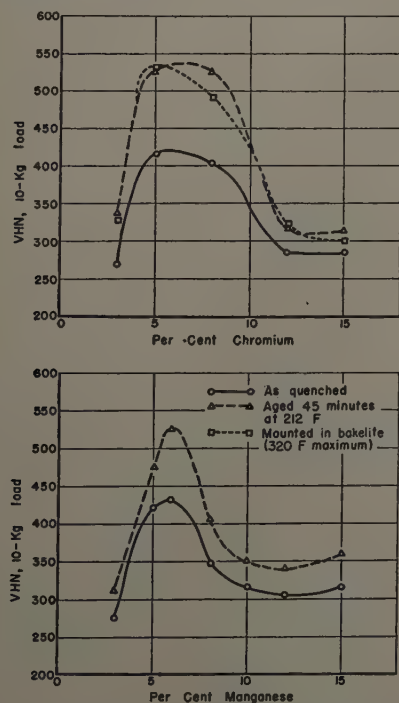


Fig. 2—Effects of low temperature reheating on titanium alloy specimens quenched in liquid nitrogen from 1742°F (950°C).

Thermal Conductivity Method for Analysis of Hydrogen in Steel

by Bruce M. Shields, John Chipman, and Nicholas J. Grant

The vacuum tin-fusion method of analysis for hydrogen, developed by Carney, Chipman, and Grant, has been modified to permit the analysis of the evolved gases for hydrogen by means of a thermal conductivity cell. A properly prepared sample can be analyzed in 10 min with a probable error of ± 0.12 ppm. A study of various methods for storage of hydrogen samples shows that samples can be safely held in a dry ice-acetone bath as long as six days. Storage in liquid nitrogen is necessary for samples to be held one week or more.

THE vacuum tin-fusion method, as developed by Carney, Chipman and Grant,¹ is the only analytical procedure which has shown promise of being fast enough for use in the control of hydrogen during steelmaking. It was felt that further simplification and faster speed of operation could be effected by the use of thermal conductivity measurements for analysis of the gases evolved in the tin-fusion method. The application of conductivity measurements to the tin-fusion method is possible because: 1—the evolved gas is essentially a mixture of hydrogen, nitrogen and carbon monoxide with a hydrogen content usually over 50 pct, 2—the evolved gas is collected at a relatively low pressure, and 3—the thermal conductivities of CO and N₂ are practically identical while that of hydrogen is very much greater. The major part of this research program was devoted to the construction and calibration of a vacuum tin-fusion apparatus which analyzes the evolved gases for hydrogen by means of a thermal conductivity cell.

The second phase of the problem was associated with the development of a procedure for storage of samples prior to analysis. With the rapid quenching method for hydrogen sampling,² which seems to be the most practical for steel mill use, it is necessary that the samples be stored safely during the interval between sampling and analysis if the hydrogen content of the molten metal is to be maintained in the supersaturated solid samples.

The thermal conductivity bridge has been used for a number of years in the analysis of certain gas mixtures. An elementary discussion of the theory and practice of gas analysis by thermal conductivity measurements is given by Minter.³ A more comprehensive discussion of the theory and of the various measuring circuits is presented by Daynes.⁴ A complete knowledge of the theory and properties of

the thermal conductivity of gases and gaseous mixtures can be gained by a study of the standard textbooks on the kinetic theory of gases.⁵⁻⁷ The existing data on the thermal conductivity of single gases are reviewed by Hawkins,⁸ that for a number of binary gas mixtures by Daynes⁴ and Lindsay.⁹

The thermal conductivity method may be applied to the determination of the composition of a binary mixture if: 1—the thermal conductivity of the mixture varies monotonically with composition, and 2—the two gases have measurably different thermal conductivities. The greater the difference between the two gases, the greater the sensitivity of the method.¹⁰ The method is applicable to the analysis of multicomponent mixtures when all of the gases in the mixture except one have nearly the same thermal conductivity. Fortunately, the mixture of hydrogen, nitrogen, and carbon monoxide evolved by the tin-fusion analysis¹ falls in this latter classification. The thermal conductivities of nitrogen and carbon monoxide are practically equal; and the thermal conductivity of hydrogen is approximately seven times that of the other two. Therefore, the thermal conductivity of a gaseous mixture of hydrogen, nitrogen, and carbon monoxide at known temperature and pressure can be related directly to the percentage of hydrogen in the mixture by suitable calibration.

Usually the thermal conductivity of a mixture of gases is measured at atmospheric pressure where the thermal conductivity is independent of pressure over a wide pressure range. At very low pressures (below 1 mm Hg), the thermal conductivity of gases varies with the pressure. This phenomenon has been utilized in the Pirani vacuum gage for the measurement of pressures in the range of 10^{-1} to 10^{-6} mm of mercury.¹¹ Very little has been published concerning the variation of thermal conductivity with pressure at intermediate pressures between 1 mm Hg and 1 atm. However, preliminary measurements indicated that the thermal conductivities did vary with pressure over the range of pressures (up to 10 mm Hg) at which gases are delivered from the vacuum pump. Therefore, the calibration of the thermal conductivity cell had to be planned to include the effects of both gas composition and pressure. Such a calibration chart is shown in Fig. 4.

Most industrial applications of the thermal conductivity method of gas analysis have used a compensated Wheatstone bridge circuit containing two

B. M. SHIELDS, formerly Research Assistant, Dept. of Metallurgy, Massachusetts Institute of Technology, is now Chief Development Metallurgist, Duquesne Works, U. S. Steel Co., and J. CHIPMAN and N. J. GRANT, Members AIME, are Professor and Associate Professor, respectively, Dept. of Metallurgy, Massachusetts Institute of Technology, Cambridge, Mass.

Discussion on this paper, TP 3470C, may be sent, 2 copies, to AIME by April 1, 1953. Manuscript, Sept. 17, 1952. Los Angeles Meeting, February 1953.

This paper is based on a thesis by B. M. Shields submitted in partial fulfillment of the requirements for the Master of Science degree at Massachusetts Institute of Technology.

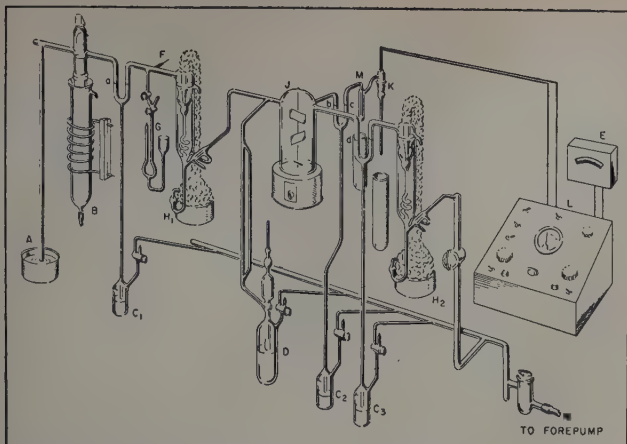


Fig. 1—Apparatus for analysis of hydrogen in steel. A—Mercury lift. B—Furnace. C—Mercury cut-offs. D—McLeod gage. E—Precision ammeter. F—Palladium tube. G—Calibrating pipette. H—Mercury diffusion pumps. J—Mixing chamber. K—Thermal conductivity cell. L—Instrument panel. M—Mercury trap.

or four-cell matched units.¹² Recently Ishihara and Sawa¹⁸ successfully applied a double cell circuit for measuring hydrogen extracted by high temperature vacuum fusion. However, the simplest and theoretically soundest method of measurement utilizes a circuit containing a single thermal conductivity cell¹⁴ maintained at constant temperature. The single conductivity cell circuit was adopted for the vacuum tin-fusion apparatus.

Apparatus

The major modifications to the apparatus of Carney, Chipman, and Grant were the elimination of the copper oxide furnace, the freeze-out traps, and the gas circulating equipment, and their replacement by a conductivity cell, a single cell conductivity bridge, and a mixing chamber. A diagram of the modified apparatus is shown in Fig. 1. Most of the essential parts have previously been described in detail by Carney, Chipman and Grant.¹ A brief description of the new parts is given below.

Known Volume: The known volume extending from the outlet portion of pump H_1 to point b on cut-off C_2 (excluding the conductivity cell) and to point d on cut-off C_2 is equal to 871 ± 2 cu cm.

Mixing Chamber: Previous investigators¹ have shown that the hydrogen in the gases evolved during tin-fusion tends to diffuse out sooner and faster than the carbon monoxide and nitrogen. It was noted in fact that the hydrogen which evolved first could collect in the higher portions of the apparatus while the other heavier gases settled in the lower section. Such a stratification could lead to erroneous thermal conductivity results in view of the rapid determinations made with this apparatus. To guard against such an occurrence, a mixing chamber was installed in the system, the details of which are shown in Fig. 2. Experiments with various gases introduced individually in varying orders showed that the mixing chamber eliminates any possibility of stratification.

Thermal Conductivity Cell: The bottom section of the cell is made of pyrex tubing, 1 cm OD and 8 mm ID, with a closed bottom and a female ground joint on the top, as shown in Fig. 2. The seal between the top and bottom sections is made with picein. A thin piece of pure platinum wire, 0.0104 mm (0.0041 in.) in diameter and approximately 16 cm long, is suspended in the center of the cell from

nickel wire supports. The wire is held taut by a small tungsten spring. The nickel supports are welded to the tungsten rods used to conduct the current into the cell through a glass-metal seal. The electrical leads from the Wheatstone bridge circuit are attached to the tungsten rods. The entire cell up to the side-arm is maintained at 0°C by immersion in an ice and water bath.

Wheatstone Bridge Circuit: In the single-cell thermal conductivity method, the conductivity cell is kept at constant temperature by immersion in ice and water, and the platinum wire is brought to the same temperature each time by the proper adjustment of the current through the wire. The current needed to maintain the wire at the specified temperature is determined by the rate of heat liberation from the wire, which is the same as the rate at which heat is carried away from the wire by gaseous conduction, provided that other sources of heat loss, such as conduction through the ends of the wire, radiation, and gaseous convection, are negligible. Thus the observed current is a measure of the conductivity of the gas.

A diagram of the single-cell thermal conductivity bridge is presented in Fig. 3. The large bridge rheostat P is set at a resistance such that when the bridge is balanced with pure hydrogen in the cell at the maximum pressure to be encountered, the current passing through the external circuit lies within the range of the precision ammeter A . To balance the bridge with a mixture of hydrogen and other gases at known pressure in the cell, the voltage across the ends of the bridge is adjusted by means of the coarse and fine rheostats Rh_1 and Rh_2 . The current recorded on the ammeter can be related to the gas composition after suitable calibration with mixtures of known composition and pressure. It will be noted that virtually all of the current measured by ammeter A passes through the conductivity cell because resistances P and R_2 are so much greater than R_1 and the cell, which has a resistance of approximately 3 ohms. Consequently, very little sensitivity is sacrificed by placing the ammeter in the external circuit where its resistance and temperature variations are not important.

Mercury Trap: The mercury trap between the mixing chamber and the conductivity cell was not originally built into the apparatus. During the calibration it was discovered that the mercury vapor in

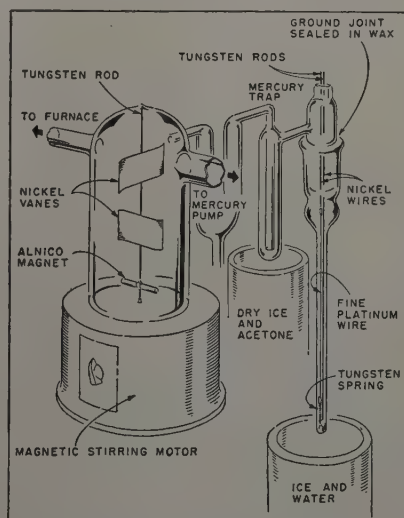


Fig. 2—Detail of mixing chamber and thermal conductivity cell.

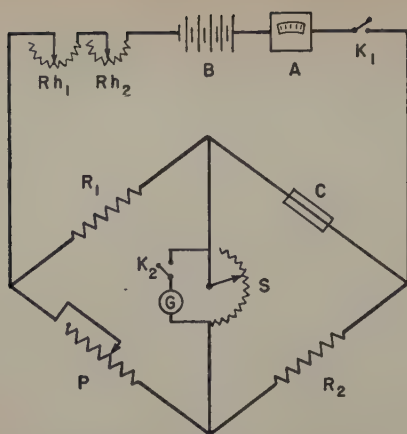


Fig. 3—Diagram of single cell thermal conductivity bridge.

A, precision ammeter, range 0 to 1.000 amp. B, battery, four $1\frac{1}{2}$ v dry cells. C, thermal conductivity cell. G, galvanometer, sensitivity $2\ \mu$ amp per division. K_1 , main switch. K_2 , galvanometer switch. P, bridge rheostat, 0 to 1000 ohms. R_1 , fixed resistor, 1 ohm. R_2 , fixed resistor, 1000 ohms. Rh_1 , rheostat, coarse adjustment, 0 to 20 ohms. Rh_2 , rheostat, fine adjustment, 0 to 2.5 ohms. S, galvanometer shunt.

the vacuum system condensed on the wall of the conductivity cell because it was maintained at a lower temperature than the rest of the system. During a period of two weeks enough mercury condensed upon the wall of the conductivity cell to alter materially the shape of the calibration curves. Damage to the brazed joints was also noted from the mercury present in the cell. The installation of the mercury trap, which is maintained at -80°C by bubbling air through the dry ice-acetone mixture around the trap, eliminated the condensation of mercury vapor in the conductivity cell.

Calibration of Conductivity Cell

It has previously been mentioned that the conductivity of the gaseous mixture in the cell, as measured by the current supplied to the bridge circuit, is a function of both the pressure and the composition of the mixture. Thus, the conductivity cell had to be calibrated with pure gases and mixtures of known composition over a range of measured pressures. Calculations based on a sample size of 1 to 5 g and a hydrogen content in the steel of 1 to 25 parts per million (ppm) indicated that the calibration should cover a pressure range of 0.1 to 3.0 mm of mercury.

A calibration curve of pressure in millimeters of mercury versus conductivity reading in amperes was constructed for pure hydrogen by admitting different amounts of hydrogen into the system through the palladium tube, measuring the pressure in the known volume each time, and determining the current needed to balance the bridge for each pressure. Similar curves were determined for pure nitrogen and pure carbon dioxide by introducing various amounts of the purified gases into the system through the calibrating pipette. The calibration curves are shown in Fig. 4. Because the thermal conductivities of nitrogen and carbon monoxide are practically equal, the calibration curves for the two pure gases are of the same shape and so close together that they can be considered identical. Similar

calibration work with gas mixtures of known compositions showed that direct interpolation between the pure gas calibration curves is possible for gas mixtures. Thus a family of calibration curves for mixtures of hydrogen, carbon monoxide, and nitrogen was plotted from 0 to 100 pct H_2 by interpolation between the pure hydrogen curve and the curve representing pure nitrogen (and/or carbon monoxide).

Analytical Procedure

The clear silica crucible is initially charged with about 130 g of chemically pure tin sticks and 0.7 g of purified silicon metal. The crucible is placed in the bottom furnace section, the entire furnace section is assembled, and the system is evacuated. The furnace is gradually heated up to 1050°C and then "baked out" at this temperature for 2 hr. The degassing time and temperature needed for a low blank have been materially reduced by the use of clear silica crucibles and stick tin as compared to using the satin finish silica.

After the completion of the degassing period, the conductivity circuit is standardized. A small amount of hydrogen is admitted to the system through the palladium tube, the pressure of the hydrogen in the known volume is measured with the McLeod gage, and the hydrogen is permitted to enter the conductivity cell. With pure hydrogen at known pressure in the cell, the current is turned on and bridge rheostat P, Fig. 3, is adjusted so that, with the bridge balanced, the ammeter reading corresponds to the proper reading for that particular pressure on the pure hydrogen calibration curve. At the completion of the standardization, the cell is turned off and all cut-offs are lowered to evacuate the system in preparation for a blank determination. Normally standardization is only necessary at the beginning of a day's run unless there is reason to suspect that the batteries are becoming weaker or the ambient temperature of the instrument panel changes markedly.

The blank is measured by collecting furnace gas in the known volume for 5 min. The pressure of the blank gas is measured by the McLeod gage, and the percentage of hydrogen in the gas is determined in the conductivity cell. At the completion of the blank determination all the cut-offs are again lowered in preparation for the first analysis.

The metal sample is washed in carbon tetrachloride, dried in a current of dry, oil-free air, and weighed on an analytical balance. It is forced beneath the surface of the mercury reservoir and permitted to float to the top of the mercury column. A strong magnet is used to move the sample over to the furnace head. After cut-offs C_2 and C_3 are raised and the gas mixer is turned on, the sample is dropped into the furnace. At the end of the 5-min collection time, cut-off C_1 is raised and cut-offs C_2 and C_3 are adjusted to points b and d respectively. The pressure of the collected gas in the known volume is measured with the McLeod gage, preferably in two of the three calibrated sections to detect any water vapor in the gas.* Cut-off C_2 is lowered to

* Normally water vapor is only present when samples are improperly dried before analysis or when hollow samples contain water picked up during quenching.

permit the gas to enter the conductivity cell and is then raised to point c. The conductivity cell is turned on and the bridge circuit balanced by the proper adjustment of coarse and fine rheostats Rh_1 and Rh_2 . The percentage of hydrogen in the gas can

be read off the calibration chart by utilizing the ammeter reading and the previously measured pressure. The conductivity cell is turned off before the cut-offs are again lowered to prevent overheating of the wire in the cell when it is evacuated. All cut-offs are lowered to exhaust the system in preparation for the next analysis.

Evaluation of the Method

Blanks: After an initial 2-hr bake-out period at 1050°C, the 5-min blank value was reduced to about 0.08 ppm for a 2-g sample. The average 5-min blank correction during the analysis of 50 samples with an average weight of 2.9 g was 0.08 ppm. Blank values were determined several times during a day's run and generally showed a gradual decrease throughout the day.

Evolved Gases: A comprehensive discussion of the gases evolved in the tin-fusion method has been presented by Carney, Chipman, and Grant.¹ The gases evolved from the samples analyzed in this study had hydrogen contents of from 65 to 98 pct by volume and averaged close to 90 pct by volume.

Time for Analysis: The time required for the actual analysis of a single sample is 10 min, although in routine use a total time of 15 min per sample is required to allow for sample preparation, weighing, and introduction of the sample into the melt. The total time required to analyze samples on a routine basis can be further reduced from 15 to 12 min per sample by the use of a direct weighing balance and the installation of a faster McLeod gage. However, the 15-min analysis possible with the present apparatus puts it within the range of many steel mill control analyses.

Precision: The overall precision of analysis by the thermal conductivity method was evaluated by the use of duplicate samples. Each of 10 samples, obtained from a molten bath in the manner described by Carney, Chipman, and Grant,² was cut in half to provide 10 sets of duplicate samples for analysis. The small size of the samples and the sampling technique make it safe to assume that the two halves of each sample contained equal percentages of hydrogen. The results of the analysis of these duplicate pairs by the tin-fusion method in the thermal conductivity apparatus are summarized in Table I. A statistical analysis of the data from these 10 pairs shows the standard deviation of the error of observation to be ± 0.17 ppm. The probable error is ± 0.12 ppm. Using the statistical criterion of three standard deviations, the error in 95 pct of all analyses will be less than ± 0.5 ppm. It should be emphasized that this precision was obtained with 2 to 3-g samples containing approximately 6 ppm of hydrogen. Greater precision can be obtained when analyzing larger samples.

Storage of Hydrogen Samples

With the rapid quenching method for hydrogen sampling,² which preserves the hydrogen content of the molten metal in the supersaturated solid samples, it is necessary that the samples be properly stored to maintain the hydrogen content during the interval between sampling and analysis. Hydrogen is an extremely mobile element and will diffuse out of supersaturated steel samples at room temperature in a relatively short time. Even though the addition of alloying elements to steel may retard the release of hydrogen from quenched samples and although the effusion of hydrogen is slower from austenitic steels than from pearlitic or ferritic steels,¹⁵ it is not

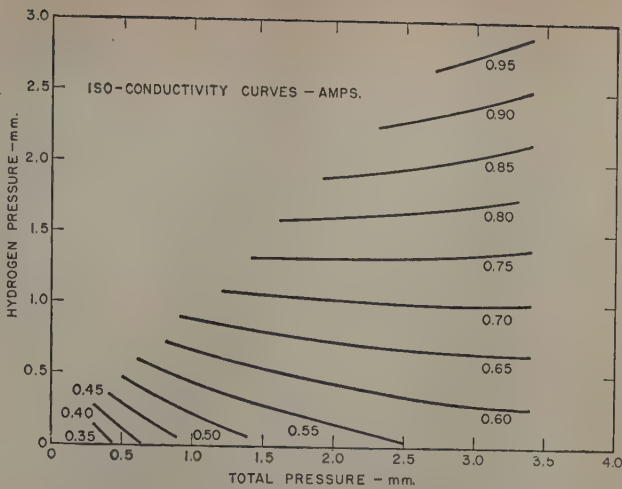


Fig. 4—Calibration curves for conductivity cell.

possible to maintain the hydrogen content of most liquid steels in a quenched sample for any length of time at room temperature. The work by Carney, Chipman, and Grant² includes a complete discussion of storage methods utilized by other investigators together with their own observation that samples could be stored in dry ice for periods of time up to 24 hr with negligible loss of hydrogen. Of the many methods used by previous investigators for either preventing the effusion of hydrogen from the samples or collecting the hydrogen which does diffuse out, the simplest and most practical is the immersion of the samples in a medium at such a low temperature that the diffusion of hydrogen is virtually stopped. It was the purpose of this investigation to determine what storage temperature was necessary to inhibit effectively the effusion of hydrogen from steel samples and how long the samples could be stored at this temperature before a measurable loss of hydrogen occurred.

The samples for this investigation were obtained from heats melted in the controlled atmosphere furnace previously described in detail,² under a mixture of 5 to 10 pct H₂ and the balance helium. The details of the sampling procedure, utilizing a modified Taylor sampling device, have also been described. After thorough quenching in water and then in a dry ice-acetone bath some of the samples were stored in a dessicator at room temperature,

Table I. Precision of Analysis by Duplicate Samples

Sample No.	First Analysis, Ppm	Second Analysis, Ppm	D	($\bar{D}' - D_1$) ²
9	6.74	6.64	0.10	0.0100
10	6.36	5.92	0.44	0.1936
11	6.42	6.95	0.53	0.2809
12	6.04	5.82	0.22	0.0484
14	6.43	6.45	0.02	0.004
21	6.10	5.94	0.16	0.0256
23	5.59	5.63	0.04	0.0016
25	5.96	6.01	0.05	0.0025
00	7.24	7.09	0.15	0.0225
09	5.16	5.31	0.15	0.0225
				0.6080

σ_D = Standard deviation of the difference.
 σ_a = standard deviation of the error of observation.
P.E. = probable error (assuming normal distribution).

$$\sigma_D = \sqrt{\frac{\sum (\bar{D}' - D_1)^2}{n}} = \sqrt{0.0608} = 0.2466.$$

$$\sigma_a = \frac{\sigma_D}{\sqrt{2}} = 0.1744 \text{ ppm.}$$

$$P.E. = 0.6745 \sigma_a = 0.1176 \text{ ppm.}$$

some in an ice and water bath, some in a dry ice-acetone mixture, and the rest in liquid nitrogen.

Prior to analysis, the samples were removed briefly from the storage baths one at a time and cut into 2 to 4-g specimens on an underwater cut-off wheel filled with ice water. After cutting, the specimens were dried and returned to their original storage bath. Throughout the cutting operation suitable precautions were observed to prevent contamination of specimens with grease, oil, or other materials likely to contain hydrogen.

The samples were analyzed according to a time schedule which depended upon the particular storage method being investigated. The results of the analyses for the four storage methods are shown in Tables II to V.

The data in Table II show that it is not safe to keep quenched hydrogen samples at room temperature. The ferritic Armco iron samples used in this investigation showed a gradual decrease in hydrogen content beginning almost immediately after the quenched samples had reached room temperature.

Storage in an ice-water mixture does not retain

Table II. Effect of Time on the Loss of Hydrogen from Samples Stored in Dessicator at Room Temperature (25°C)

Storage Time, Hr	Hydrogen Content, Ppm	Average, Ppm
1	7.8	8.1
1	8.3	
2	7.1	7.7
2	8.2	
6	6.2	6.5
6	6.8	
17	5.6	5.4
17	5.2	

Table III. Effect of Time on the Loss of Hydrogen from Samples Stored in Ice and Water Bath, 0°C

Storage Time, Hr	Hydrogen Content, Ppm	Average, Ppm
4	6.1	6.0
4	5.9	
27	2.8	3.2
27	3.5	
49	2.6	2.5
49	2.3	
73	3.1	

Table IV. Effect of Time on the Loss of Hydrogen from Samples Stored in Dry Ice-Acetone Mixture, -78°C

Storage Time, Day	Hydrogen Content, Ppm	Average, Ppm
1	6.8	6.2
1	5.9	
1	6.1	
2	7.2	
2	6.7	6.9
2	6.6	
2	7.1	
4	6.4	
4	5.6	6.1
4	5.6	
4	6.9	
6	6.6	
10	5.2	5.2
10	5.2	
10	5.3	

Table V. Effect of Time on the Loss of Hydrogen from Samples Stored in Liquid Nitrogen, -196°C

Storage Time, Day	Hydrogen Content, Ppm	Average, Ppm
1	6.4	6.2
1	6.2	
1	6.0	
1	6.4	
1	6.0	6.6
2	6.0	
2	7.2	
4	6.0	
4	6.4	6.0
4	5.9	
4	5.8	
6	6.5	
10	6.1	6.5
10	7.1	
10	5.9	

the hydrogen content much better than does room temperature storage. The analyses reported in Table III indicate that hydrogen samples cannot be stored even one day at 0°C without losing an appreciable portion of their hydrogen content.

It is apparent from the data in Table IV that storage in a dry ice-acetone mixture is satisfactory for periods of time up to six days. If samples are to be stored for as long as a week or more, they must be kept in liquid nitrogen.

It should be emphasized that the results quoted in this study were determined only for Armco iron samples containing about 6 ppm of hydrogen.

Summary

The vacuum tin-fusion method of analysis for hydrogen, developed by Carney, Chipman, and Grant, has been modified to permit the analysis of the evolved gases for hydrogen by means of a thermal conductivity cell. The major advantages of the thermal conductivity method are: 1—elimination of the often questionable conversion of hydrogen to water vapor in the copper oxide furnace, 2—simplification of apparatus, and 3—increased speed of analysis. A properly prepared, weighed sample can be analyzed in 10 min with a probable error of ± 0.12 ppm of hydrogen.

A study of various methods for storage of hydrogen samples shows that samples can be held in a dry ice-acetone bath as long as six days with negligible loss of hydrogen. Storage in liquid nitrogen is necessary for samples to be held one week or more.

Acknowledgments

The authors wish to express their appreciation to W. W. Harvey for his help in the design and construction of the thermal conductivity apparatus and to the Office of Naval Research for sponsorship of the research program (Contract No. N5ori-07816, Task No. XVI NR-031-186).

References

- ¹D. J. Carney, J. Chipman, and N. J. Grant: *Trans. AIME* (1950) **188**, p. 397; *JOURNAL OF METALS* (February 1950).
- ²D. J. Carney, J. Chipman, and N. J. Grant: *Trans. AIME* (1950) **188**, p. 404; *JOURNAL OF METALS* (February 1950).
- ³C. C. Minter: *Journal of Chemical Education* (1946) **23**, p. 237.
- ⁴H. A. Daynes: *Gas Analysis by Measurement of Thermal Conductance*. (1933) London. Cambridge University Press.
- ⁵L. B. Loeb: *Kinetic Theory of Gases*. (1927) New York. McGraw-Hill Book Co.
- ⁶E. H. Kennard: *Kinetic Theory of Gases*. (1938) New York. McGraw-Hill Book Co.
- ⁷Sir J. Jeans: *An Introduction to the Kinetic Theory of Gases*. (1940) London. Cambridge University Press.
- ⁸G. A. Hawkins: *Trans. ASME* (1948) **70**, p. 655.
- ⁹A. L. Lindsay and L. A. Bromley: *Industrial and Engineering Chemistry* (August 1950) **42**, p. 1508.
- ¹⁰H. H. Willard, L. K. Merritt, Jr. and J. A. Dean: *Instrumental Methods of Analysis*. Ed. 2 (1951) New York. D. Van Nostrand Co.
- ¹¹S. Jnanananda: *High Vacua*. (1947) New York. D. Van Nostrand Co.
- ¹²C. C. Minter: Naval Research Laboratory Report 3628, Washington, D. C. (1950).
- ¹³Y. Ishihara and S. Sawa: *Proc. First World Metallurgical Congress*. (1951) Cleveland. ASM.
- ¹⁴Mack and France: *A Laboratory Manual of Elementary Physical Chemistry*. (1934) New York. D. Van Nostrand Co.
- ¹⁵W. Geller and T. H. Sun: *Arch. Eisenhüttenw.* (1950) **21**, No. 11, pp. 423-430.

Reduction of Silicon from Blast Furnace Type Slags

by James C. Fulton, Nicholas J. Grant, and John Chipman

This paper contains data on the distribution of silicon between liquid iron-silicon-carbon alloys saturated with respect to graphite and $\text{CaO-SiO}_2\text{-Al}_2\text{O}_3$ slags under 1 atm of CO at 1600°C . The ranges of slag compositions studied were extended from the dicalcium silicate saturated liquidus composition up to silica concentrations at which SiC appeared as a stable phase.

IN blast furnace operation it is not to be expected that slag and metal reach equilibrium with one another. Nevertheless, the silicon content of the metal varies with slag composition and with temperature in a manner which would be predicted from equilibrium considerations. Similarly, the distribution of sulphur between slag and metal does not attain an equilibrium state, yet the influence of slag composition is strongly analogous to its effect on the distribution equilibrium.

The desulphurizing power of metallurgical slags has been shown to be highly dependent upon the FeO content of the slag. Moreover, the rate of removal of sulphur from slags is influenced by the oxygen potential of the slag-metal system. Thus it was shown by Grant, Kalling, and Chipman¹ that the presence of MnO in slags which are low in FeO causes a marked slowing down of the transfer of sulphur from metal to slag.

This led to the hypothesis that the slow removal of sulphur by blast furnace slags of more acid composition might be due in part to the effect of SiO_2 on the oxygen potential of the system. This was verified in the work of Grant, Troili, and Chipman,² who found that the desulphurizing power of the more acid blast furnace slags could be markedly improved by an increase in the silicon content of the underlying metal. Their explanation of this improvement was that the higher silicon content of the metal decreased the rate of transfer of more silicon and, along with it, of oxygen from the slag to the metal. The slowness of the transfer of sulphur from metal to slag was the result of the slow reduction of SiO_2 from slag to metal. Attempts to study the rate of sulphur removal had in the past resulted in very slow rates corresponding to the rates of silica reduction. It has become evident on the basis of these

studies that further experimental studies on the rate of removal of sulphur must take these factors into consideration if there is to be a clear understanding of the rate of sulphur transfer under conditions simulating those existing in the blast furnace. It will be necessary, at least in a part of such study, to employ combinations of slag and metal in which

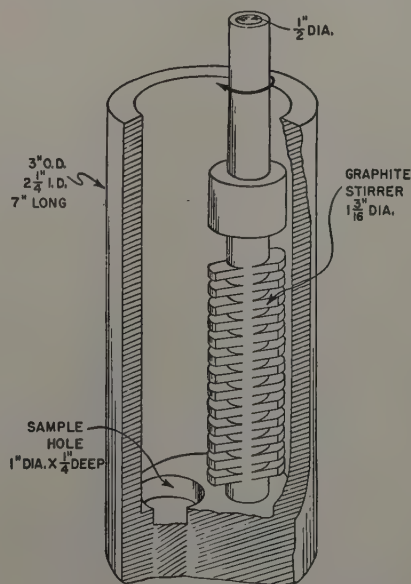


Fig. 1—Schematic drawing of graphite crucible and stirrer.

the disturbing effect of silica reduction has been eliminated; in other words, to employ slag-metal combinations which are already in equilibrium with respect to the transfer of silicon.

In preparation for such studies of desulphurization, a preliminary program of research on the distribution of silicon between slag and metal has been undertaken. This will ultimately include a comprehensive survey of the effects of temperature and slag composition on the equilibrium distribution of silicon between slag and metal. The present paper is a report on experimental methods employed and on

J. C. FULTON, Student Associate AIME, is Research Assistant, and N. J. GRANT and J. CHIPMAN, Members AIME, are Associate Professor and Professor, respectively, Dept. of Metallurgy, Massachusetts Institute of Technology, Cambridge, Mass.

Discussion on this paper, TP 3479C, may be sent, 2 copies, to AIME by April 1, 1953. Manuscript, Sept. 17, 1952. Los Angeles Meeting, February 1953.

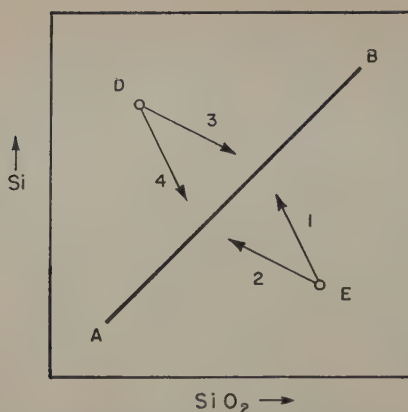


Fig. 2—Schematic representation of changes in composition during reaction. Lines 1 and 2 represent Eq. 1 as written. Lines 3 and 4 represent the reverse reaction.

the results obtained in one series of slag compositions at 1600°C.

Experimental Procedure

The furnace used in this investigation has been adequately described.⁸ The crucible design, initially modified by Grant, Kalling, and Chipman,¹ was used in the first 42 heats of the current study. Beginning with heat 43, the crucible and stirrer arrangement shown in Fig. 1 was substituted. The new design was shown to have not only good thermal characteristics, but also somewhat better mixing qualities.

The temperature of the present set-up is controlled by sighting an optical pyrometer down through the hollow stirring rod and into a centrally drilled $\frac{3}{8}$ in. diam hole in the stirrer. The hole ends 1 in. from the bottom of the stirrer at a point just below the slag-metal interface. By means of a Pt-Pt-Rh thermocouple inserted into the crucible while the stirrer was turning at the usual rate of 600 to 800 rpm, it was found that a temperature difference of not more than 6°C exists between the bottom of the crucible and upper slag surface. Similarly, a thermocouple placed in the pyrometer sighting hole checked the temperature of the optical pyrometer within $\pm 2^\circ\text{C}$. These calibrations served to substantiate the accuracy of the temperature measurements and reaffirm the conclusions of previous investigators who used this apparatus. The main source of temperature fluctuation was the normal variation in control of the induction furnace, yielding a maximum deviation of $\pm 10^\circ\text{C}$ throughout a heat.

The metals used in the heats are listed in Table I. The Armco iron punchings have been used throughout all runs while the source of silicon has changed. In the study of the CaO-SiO₂ slags, silicon metal (A) was used in heats 5, 6, 7, 8, 9, and 12 while silicon metal (B) was used in the remainder of these heats. For the CaO-SiO₂-Al₂O₃ slags, silicon metal (A) was used in all heats up to 97, at which time a 44 pct silicon ferro-alloy was prepared with Armco iron and

Table I. Composition of Iron and Silicon Used in Charge

Armco Iron	Silicon (A)	Silicon (B)	Silicon (C)
0.029 pct C	1.62 pct Fe	0.20 pct	0.90 pct Fe
0.017 pct Mn	1.50 pct Al	(max	0.08 pct Al
0.004 pct P	0.14 pct Ti	impurities)	
0.017 pct S	96.74 pct Si	99.80 pct Si	98.70 pct Si
	(by difference)	(by difference)	

Table II. Chemical Analyses of Slag-Metal Samples for CaO-SiO₂ Slags at 1600°C

Heat and Sample No.	Time at Temperature,* Hr	[Pct Si]	(Pct SiO ₂)	(Pct CaO)
F5	Charge	4.8	55.8	44.2
-1	1.25	5.37	52.36	
-2	2.25	6.47	51.09	
-3	3.25	6.95	50.20	
-4	4.25	7.38	49.34	
-5	5.25	7.82	48.68	
F6	Charge	19.9	50.0	50.0
-1	2.0	20.43	48.03	
-3	4.0	20.21		
-5	6.0	20.60	46.67	
F7	Charge	9.8	44.0	56.0
-1	1.25	9.59	43.37	
-3	3.25	10.14		
-5	5.25	10.42	42.37	
F8	Charge	9.8	59.8	40.2
-1	1.17	13.98	54.62	
-2	2.17	15.14	53.15	
-3	3.17	15.74	51.30	
-4	4.17	16.50	50.37	
-5	5.17	16.79	49.19	
-6	6.17	16.87	48.76	
F9	Charge	14.8	55.8	44.2
-1	1.50	16.33	54.34	
-2	2.50	17.10	51.62	
-3	3.50	17.88	50.55	
-4	4.50	18.26	49.59	
-5	5.50	19.00	48.83	
F12	Charge	21.0	59.8	40.2
-2	1.0	19.00	59.36	
-3	12.0	22.23	51.27	
-4	18.0	21.78	50.78	
-5	18.0	21.56	50.73	
-6	23.0	22.44	48.92	
-7	23.0	22.00		
-8	24.0	22.25	48.62	
-9	24.0	22.29		
F31	Charge	23.0	50.0	50.0
-1	1.5	22.18	50.02	48.75
-2	2.5	22.80	49.44	
-3	8.0	21.74	50.34	49.52
-4	10.0	22.84	50.08	
-5	12.0	21.88	50.24	48.85
F32	Charge	21.0	43.0	57.0
-1	1.08	19.96	43.91	
-2	2.92	19.95	44.04	
-3	7.17	20.05	44.08	
-4	9.33	20.06	44.28	
-5	11.33	19.52	44.02	
F43	Charge	21.8	49.0	51.0
-1	1.0	21.16	48.15	
-2	8.0	21.42	47.87	
-3	9.0	21.84	47.17	
-4	9.5	22.06	47.48	
F44	Charge	21.6	47.3	52.7
-1	1.0	18.63	47.68	
-2	4.0	19.23	46.92	
-4	6.0	19.25	45.68	
-6	8.0	19.07	46.05	
F47	Charge	23.0	52.0	48.0
-1	1.0	22.14	51.18	
-2	3.0	23.00	51.24	
-4	6.0	22.58	50.80	
-5	7.0	23.28		
-6	8.0	22.59	51.22	
F74	Charge	15.3	45.5	54.5
-1	1.0	14.94	45.52	
-5	8.0	15.43	44.28	
F75	Charge	17.9	43.5	56.5
-1	1.6	17.52	43.48	
-5	8.0	17.38	44.04	55.39
F81	Charge	23.0	44.0	56.0
-1	1.0	22.34	44.68	
-3	5.0		44.52	
-5	8.0	22.15	45.40	54.47
F82	Charge	11.8	42.6	57.4
-1	1.0	11.57	42.64	
-3	5.0		42.84	
-5	8.0	11.93	42.76	56.11
F96	Charge	23.0	47.0	53.0
-2	2.0	22.20	46.40	
-3	5.0	22.26		
-4	7.0		46.50	
-5	8.0	22.09	46.30	51.80

* Zero time is taken as that time when the slag and metal are first judged to be molten and at the reaction temperature. The time listed is the time after zero time.

silicon metal (B). This alloy was used in all subsequent heats.

The slags were made by mixing master slags which had been prefused in a graphite crucible. Actual chemical analyses after fusion were used in calculating the various quantities desired.

The "zero-time" used in the tables and figures is a somewhat ambiguous quantity since liquid metal and liquid slag were not mixed to start a run. Si and SiO₂ analyses tended to stray from the calculated composition when samples were taken prior to half an hour after all constituents were in the crucible at 1600°C. For the first 101 heats, about half of the

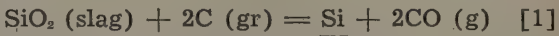
slag and all the metal were placed in the crucible and heated to 1600°C in an atmosphere of carbon monoxide which was purified by passing over ascarite and anhydron. (Nominal gas purity was 97 pct CO, 3 pct N₂.) Generally, it required 15 min to heat the charge to 1600°C and about 10 min more for it to melt in so that the remaining portion of the slag could be added. "Zero-time" for the first 101 heats was taken as that time when all the slag and metal were in the crucible and at the reaction temperature. This is obviously not "zero" reaction time.

Beginning with run 102, a change in melting procedure was made to try to reduce the length of time necessary to fuse the slag as well as to help stabilize the initial silicon analysis. The new procedure consisted of melting only the metal in a nitrogen atmosphere and allowing 5 to 10 min for graphite saturation. All the slag was then added within 5 min, and as soon as the system reached the reaction temperature, the run was considered started. In this procedure the CO atmosphere was established simultaneously with the slag addition. "Zero-time" was again taken when all constituents reached the reaction temperature.

The course of the reaction was followed by slag and metal samples removed during a run. The slag samples were solidified on the end of an iron rod and metal samples were drawn up into a Vycor tube with an aspirator bulb. Slag and metal samples were crushed to -100 mesh. Iron particles were removed from the slag by a hand magnet prior to analysis.

Reaction Studied

The chemical reaction under investigation is given in Eq. 1:



The SiO₂ was dissolved in a CaO-SiO₂ or CaO-SiO₂-Al₂O₃ slag. The metal phase consisted of Fe and Si saturated with graphite.

If a system is considered which is composed of a CaO-SiO₂ slag and the corresponding metal, there are five components and four phases. The components are Ca, Si, O, Fe, and C. The phases are slag, metal bath, gas, and graphite. According to the phase rule this yields two degrees of freedom in a constant pressure system. Thus, if the temperature and the percentage of silicon is fixed, the equilibrium state of the system will be completely described.

Fig. 2 shows schematically how the reaction progresses. Assume line AB represents the equilibrium distribution of Si and SiO₂ at a given temperature. If the initial composition E is selected, there will be silica reduction; that is, Eq. 1 shows a net reaction toward the right (increasing silicon in the metal) along a path such as 1 or 2 in Fig. 2. If an initial composition such as D is selected, there will be silicon oxidation, and Eq. 1 will show a net reaction to the left (increasing SiO₂ content) indicated by path 3 or 4. The steepness of the path from the initial composition depends on the relative quantities (weights) of the two phases charged. Paths 2 and 3 represent higher weight ratios of metal to slag than paths 1 and 4.

Finally, it may be pointed out that these paths are not straight. As the reaction proceeds in either direction, there is a transfer of material between the slag and metal phases tending to increase the weight of the one relative to the other. When silica reduction occurs, there is a loss of 1 g of SiO₂ from the slag for each gain of 28/60 g of silicon in the metal.

Table III. Chemical Analyses for Slag-Metal Samples for CaO-SiO₂ and 10 Pct Al₂O₃ at 1600°C

Heat and Sample No.	Time at Temperature, Hr	[Pct Si]	(Pct SiO ₂)	(Pct CaO)	(Pct Al ₂ O ₃)
F49	Charge	13.9	37.7	51.8	10.5
-1	1.0	15.51	37.80		
-3	5.0	15.22	37.58		
-6	8.0	15.02	38.63		10.60
F50	Charge	22.9	51.3	38.1	10.6
-1	1.0	19.42	48.03		
-3	5.0	20.68	46.05		
-5	7.0	20.68	45.28		
-6	8.0	20.71	45.46	42.24	12.84
F61	Charge	13.8	40.0	50.0	10.0
-1	1.0	13.49	39.00		
-3	5.0	13.50	39.08		
F69	Charge	9.7	41.0	50.0	9.0
-1	3.0	9.67			
-2	5.0	9.86			
-3	7.0	9.93	40.08	49.25	9.64
F72	Charge	14.8	43.0	47.0	10.0
-1	1.0	15.03	41.64		
-5	8.0	15.10	41.12	47.48	11.08
F73	Charge	21.9	43.0	47.0	10.0
-1	1.0	21.65	41.60		
-5	8.0	21.52	42.56	47.45	10.12
F79	Charge	17.9	42.0	48.0	10.0
-1	1.0	18.03	38.96		
-3	5.0		38.68		
-5	8.0	17.96	38.76	49.77	11.20
F80	Charge	23.9	44.0	46.5	9.5
-1	1.0	23.12	43.84		
-3	5.0		44.04		
-5	8.0	23.09	43.84	45.68	10.64
F85†	Charge	19.9	40.0	49.5	10.5
-1	1.0	19.70	39.04		
-3	5.0	19.54	40.40		
-5	8.0	19.36	41.16	47.74	11.56
F97	Charge	18.9	43.0	47.0	10.0
-2	2.0	18.54	42.36		
-3	5.0	18.80			
-5	8.0	18.55	42.65	47.59	9.98
F98	Charge	6.2	38.0	52.1	9.9
-2	2.0	6.42	37.24		
-3	5.0	6.57			
-5	8.0	6.77	36.56	52.50	11.08
F106†	Charge	19.0	44.4	45.7	9.8
-2	2.0	19.33	43.68		
-3	4.5	19.34			
-5	7.0	19.33	43.56	46.42	9.88
F117†	Charge	7.5	35.5	54.2	10.3
-2	2.0	7.84	36.95		
-3	5.0	8.04			
-5	8.0	8.10	36.30		10.65
F118†	Charge	21.0	47.0	43.5	9.5
-1	1.0	23.20	47.00		
-3	5.0	23.07			
-5	8.0	22.92	46.50		10.66
F123†	Charge	15.0	44.0	46.5	9.5
-1	1.0	16.71	43.75		
-3	5.0	17.08			
-5	8.0	17.35	42.72		11.00
F125†	Charge	10.0	36.0	53.5	10.5
-1	1.0	10.23	36.84		
-3	4.0	10.24			
-4	6.0	10.35	36.68		11.52

* See Table II.
† CO bubbled through metal and slag, in all other heats CO flushed over slag surface.

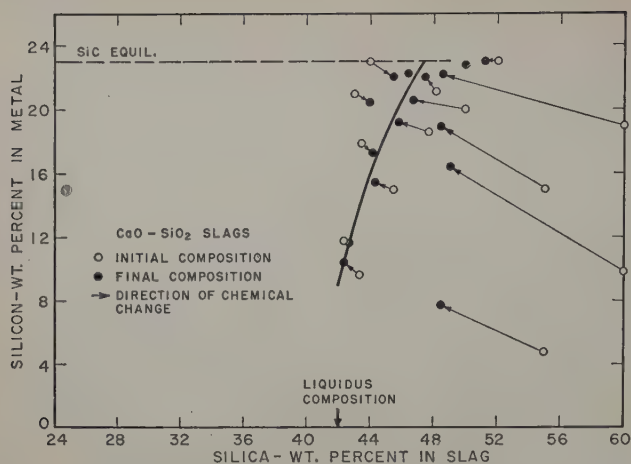


Fig. 3—Silicon distribution at 1600°C for Fe-Si-C alloys saturated with graphite and in contact with CaO-SiO₂ slags under 1 atm of CO. CO gas flushed over slag surface.

Since the iron is saturated with graphite, the only change of percentage of carbon in the metal is that due to the corresponding change of percentage of silicon. In other words, carbon changes due to solubility effects, not stoichiometric considerations.

Results and Discussion

The results of chemical analyses of slag and metal samples taken from heats held at 1600°C are shown in Tables II, III, and IV and are plotted in Figs. 3, 4, and 5 for 0, 10, and 20 pct Al₂O₃, respectively. The final compositions of the binary slags of Fig. 3 are those listed in Table II. The ternary slags of Figs. 4 and 5 have been corrected to even 10 and 20 pct Al₂O₃ as explained below. From preliminary curves similar to Figs. 4 and 5 it was evident that an increase from 10 to 20 pct Al₂O₃ led to a corresponding decrease of from 2 to 7 pct SiO₂, depending on the silicon level. In plotting the final points, therefore, a proportional adjustment was made in the percentage of SiO₂ to correspond to exactly 10 or 20 pct Al₂O₃. This adjustment was not made in the initial points.

Chemical analyses have shown the usual variations for this type of determination. In run 12, Table II, duplicate samples were taken at 18, 23, and 24 hr. The silicon analyses showed a maximum deviation of 0.44 pct Si and the only slag pair that was ana-

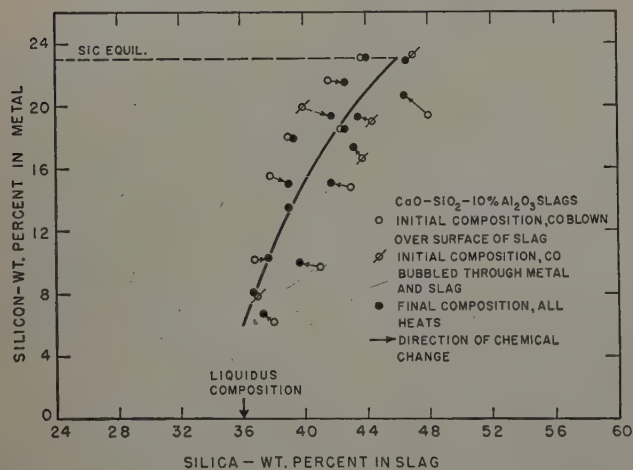


Fig. 4—Silicon distribution at 1600°C for Fe-Si-C alloys saturated with graphite and in contact with CaO-SiO₂-10 pct Al₂O₃ slags under 1 atm of CO.

lyzed in duplicate indicated a deviation of 0.05 pct SiO₂. In run 31, Table II, the silicon dropped 1.06 pct Si from sample 2 to 3 in a run that is not changing composition according to the slag analysis. Thus, there are rather wide variations of results possible due to experimental errors. A more dependable measure of the limits of error can be found in time-averages of the Si and SiO₂ analyses. In general, these plots indicate a deviation of ±0.20 pct Si and ±0.30 pct SiO₂ for any one run.

Material balances on some of the runs indicated serious discrepancies between the SiO₂ lost from the slag and the Si gained by the metal. Table V shows the result of such balances made on runs 5, 8, 9, and 12 (see Fig. 3 and Table II). The charge compositions of slag and metal were taken as the initial conditions. From the final SiO₂ analyses, corresponding

Table IV. Chemical Analyses for Slag-Metal Samples for CaO-SiO₂ and 20 Pct Al₂O₃ at 1600°C

Heat and Sample No.	Time at Temperature,* Hr	[Pct Si]	(Pct SiO ₂)	(Pct CaO)	(Pct Al ₂ O ₃)
F52	Charge	18.9	40.0	40.8	19.2
-1	1.0	18.72	39.78		
-3	5.0	18.78	40.01		
-5	7.0	18.82	39.81	40.71	19.32
F54	Charge	16.8	30.0	50.0	20.0
-1	1.0	16.43	30.44		
-3	3.0	16.60	31.12		
-5	5.0	16.23	31.60		
-6	6.0	16.04	31.80	48.69	19.64
F66	Charge	3.8	30.0	50.0	20.0
-1	1.0	3.91	31.28		
-3	5.0	4.05	30.48		
-6	8.0	4.18	29.64	49.10	20.72
F70	Charge	20.9	44.0	37.0	19.0
-1	1.0	21.07	42.08		
-5	8.0	20.87	42.20	38.04	20.04
F76	Charge	6.2	29.6	50.0	20.4
-1	1.0	6.34	29.46		
-4	7.0	6.46	29.36	49.11	20.28
F78	Charge	11.8	38.0	42.0	20.0
-1	1.0	11.94	37.84		
-3	5.0	12.08			
-5	8.0	12.30	36.92	43.36	19.60
F86†	Charge	11.8	32.0	48.0	20.0
-1	1.0	11.66	31.92		
-3	5.0	11.72	32.12		
-5	8.0	11.70	31.80	47.41	19.24
F87†	Charge	8.8	28.0	52.0	20.0
-1	1.0	8.55	27.72		
-3	5.0	8.43	28.04		
-5	8.0	8.62	28.72	49.78	19.52
F92	Charge	13.8	36.0	44.5	19.5
-2	2.0	13.96	35.32		
-3	5.0	14.08	35.24		
-5	8.0	14.18	34.98	43.90	19.80
F103†	Charge	7.8	33.1	47.7	19.2
-2	2.0	8.34	30.88		
-3	5.0	8.46			
-5	8.0	8.23	30.52	49.77	19.92
F107†	Charge	18.0	35.5	44.0	20.5
-2	2.0	19.48	35.96		
-3	5.0	19.43			
-5	8.0	19.32	36.52	43.41	20.64
F109†	Charge	22.0	45.0	35.2	19.8
-2	2.0	22.86	43.28		
-3	5.0	22.52			
-5	8.0	22.62	43.72	36.44	20.68
F120†	Charge	15.0	32.0	47.8	20.2
-1	1.0	16.76	32.36		
-3	5.0	16.43			
-5	8.0	16.38	33.59		20.97
F121†	Charge	22.0	40.0	39.7	20.3
-1	1.0	23.77	36.41		
-3	5.0	23.47			
-5	8.0	23.20	40.43		21.68
F124†	Charge	6.0	29.0	51.0	20.0
-2	2.0	6.26	29.08		
-3	5.0	6.30			
-5	8.0	6.35	29.60		21.28

* See Table II.
† See Table III.

Si analyses have been calculated, neglecting the weight of slag and metal removed by sampling. Even such checks had limited value. For example, 5 and 12 lost slag due to copious CO evolution which frothed the slag into the system above the crucible. Run 12 is also low in Si for the additional reason that silicon carbide formed as one of the stable phases, as will be explained later.

Pin-pointing the initial composition has been a tedious problem. There are a number of factors that contribute to this uncertainty: 1—lack of homogeneity of master slags, 2—contaminated crucibles from previous runs, 3—dusting losses of slag, 4—errors in weighing, and 5—contamination of metal by entrapped slag. In view of these experimental difficulties, the first sample analyzed, instead of the charged composition, was plotted as the initial composition in Figs. 3 to 5, except when the results extrapolated back to the calculated composition. The final compositions are those listed in Tables II to IV.

It is important that significant chemical changes are detected, for it is the direction of the change as well as the final composition that determines the position of the curves. The greatest difficulty in interpolation of the curves in Fig. 3 to 5 was due to the broad gap remaining between the very slowly converging points from two sides. Silica reduction and silicon oxidation are very slow processes, even at concentrations rather far removed from equilibrium when from 8 to 24 hr were taken to approach equilibrium with vigorous stirring of the slag and metal. This was well illustrated in the curves shown by Grant, Troili, and Chipman.³ Probably the most significant factor in limiting the accuracy of the distribution curves in Figs. 3 to 5 is this sluggishness of the reaction. It seems to place the limits of the distribution curves at ± 1 pct SiO₂ at a given silicon concentration.

The range of SiO₂ concentrations available for study in this investigation were found to be determined by two factors. At the low SiO₂ end, the study was terminated by the liquidus compositions at which dicalcium silicate precipitates. The arrows pointing downward on the abscissas of Figs. 3, 4, and 5 at 42, 36, and 29 pct SiO₂, respectively, represent the liquidus compositions as read from the CaO-SiO₂-Al₂O₃ phase diagram.⁴

As SiO₂ was increased to the upper limit, it was found that the system became saturated with respect to silicon carbide (SiC) when the metal contained 23.0 pct Si, according to the reaction:



The SiC has been identified by X-ray patterns of specimens from the slag and metal and by metallographic examination of metal specimens. Comparison with previous studies on the structure of SiC⁵⁻⁷ revealed that the β modification was formed. It appeared in various colors with blue and green predominating.

The addition of another phase (SiC) to the system, in addition to those listed above, decreases the number of degrees of freedom by one. For the binary

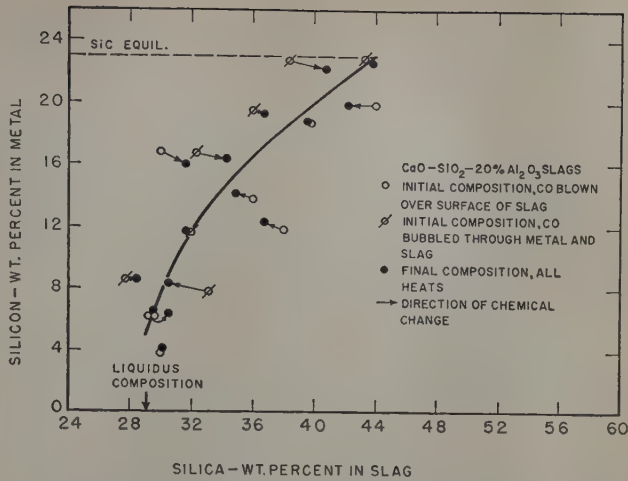


Fig. 5—Silicon distribution at 1600°C for Fe-Si-C alloys saturated with graphite and in contact with CaO-SiO₂-20 pct Al₂O₃ slags under 1 atm of CO.

slags (Fig. 3), there is now only one degree of freedom, namely, temperature. For the ternary slags (Figs. 4 and 5), two degrees of freedom remain, namely, temperature and percentage of Al₂O₃. By fixing the temperature and percentage of Al₂O₃ at 0, 10, and 20 in Figs. 3, 4, and 5, respectively, these systems are completely described. The data are summarized in the three curves of Fig. 6 which extend from the dicalcium silicate liquidus to termini at 23 pct Si, where SiC appears.

It is interesting to compare the present data with the electrochemical study of Chang and Derge.⁸ Briefly, their experimental apparatus consisted of a silicon carbide electrode dipped into a slag held in a graphite crucible. The electromotive force between the graphite and silicon carbide was taken as a measure of the silica activity in the slag. Fig. 7 shows a summary of their data at 1600°C where they have plotted iso-electromotive force (iso-activity) lines as a function of slag composition.

In order to get some comparable results from the present study, it is necessary to return to Eq. 1 and the corresponding equilibrium constant which is

$$K_1 = \frac{a_{\text{Si}} p_{\text{CO}}^2}{a_{\text{SiO}_2}}$$

Since the metal is saturated with carbon, and the

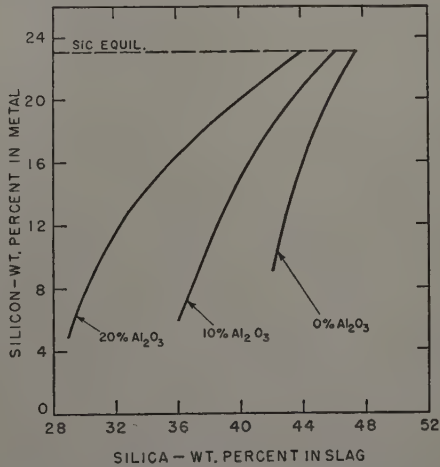


Fig. 6—Summary of silicon distribution curves at 1600°C for liquid Fe-Si-C alloys saturated with graphite and in equilibrium with CaO-SiO₂-Al₂O₃ slags under 1 atm of CO.

Table V. Material Balances on Runs 5, 8, 9, and 12		
Run No.	Final Pct Si Observed	Final Pct Si Calculated
5	7.82	9.46
8	16.87	16.9
9	19.00	18.9
12	22.27	28.6

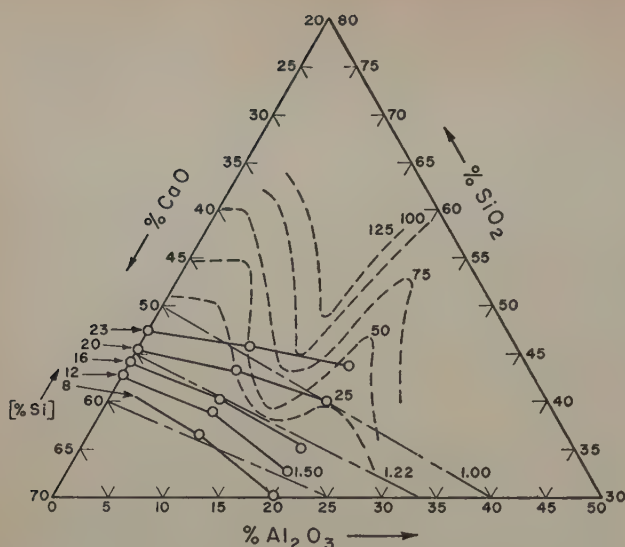


Fig. 7—Ternary isothermal section at 1600°C showing a comparison of iso-activity curves for silica. Dashed lines are electromotive force measurements, Chang and Derge.⁸ Solid lines are silicon distribution, authors. Long and short dashed lines are lime-silica ratios.

pressure of carbon monoxide is constant, any alloy with a given silicon content will have a fixed silicon activity. Thus, if the slag compositions for constant silicon concentration in the metal are picked off Figs. 3 to 5, these points will represent constant silica activities. In this way, lines of constant silica activity corresponding to constant silicon concentrations have been superimposed on the results of Chang and Derge in Fig. 7. It is evident that no agreement exists between the two sets of data. It is the authors' view that the disagreement stems from the interpretation which Chang and Derge put upon their data. A more detailed discussion seems premature at this time and will be deferred until after publication of current work on the activity of silicon in Fe-Si-C alloys.

Based on the lines representing our results in Fig. 7, the following statements may be made concerning the activity of SiO_2 : 1—at constant percentage of silica, its activity increases with increasing Al_2O_3 and decreases with increasing CaO ; 2—the activity of SiO_2 is strongly dependent upon the lime:silica ratio. At a ratio of about 55:45 it is independent of Al_2O_3 or other composition variables. At lower ratios it is decreased and at higher ratios increased by addition of Al_2O_3 . Lines of constant lime:silica ratio have been constructed on Fig. 7 to show this relation.

The question of the rate-controlling step in reaction 1 has been raised by Darken⁹ with respect to the retarding action of SiO_2 reduction on desulphurization in blast furnace type slags. It was suggested that perhaps the rate is controlled by lack of gas bubble nucleation at the slag-metal interface. While most of the heats have been made with CO gas flushing over the slag surface, a sufficient number have been made in which CO was bubbled through the slag and metal in order to be able to detect any appreciable differences. All heats in Fig. 3 had CO flushing over the surface, while a differentiation of the method of gas entrance was made for the heats in Figs. 4 and 5. Qualitatively it appears that there was no improvement of rate by provision of artificial gas bubble nuclei. The similarity of results may be due to the intimate mixing of metal, slag, and gas by the stirring mechanism.

Sawamura and Sawamura¹⁰ recently published some results for the equilibrium of liquid pig iron with $\text{CaO-SiO}_2\text{-Al}_2\text{O}_3$ slags containing 10 pct Al_2O_3 . These workers used small heats consisting of approximately 15.5 g of metal and 6 g of slag. A graphite crucible containing the melt was quenched in water at the end of a run. Their results were not tabulated; however, the plot of a run at 1600°C indicated that equilibrium was obtained with 3.3 pct Si for a slag containing 44 pct SiO_2 , 46 pct CaO , and 10 pct Al_2O_3 . In the present investigation, this same slag was found to require 20.7 pct Si. From their graph it is obvious that silica reduction is still in progress at the end of 4 hr, but they relied on the more slowly changing silicon analyses. It is also worth noting that Sawamura and Sawamura did not stir their heats. This immediately suggests that diffusion of silicon in the metal or of silica in the slag may have been the rate-controlling step.

Conclusions

The results of this investigation may be summarized as follows:

1—The distribution of silicon between graphite-saturated Fe-Si-C alloys in equilibrium with CaO-SiO_2 and $\text{CaO-SiO}_2\text{-Al}_2\text{O}_3$ slags containing 10 and 20 pct Al_2O_3 has been established at 1600°C under 1 atm of CO.

2—The range of silica compositions amenable to study was found to be limited at the high silica concentrations by the formation of β silicon carbide and was extended to the liquidus composition in the low silica slags.

3—Lines of constant silica activity, corresponding to constant silicon in the metal, disagree with conclusions of Chang and Derge based on electromotive force measurements.

4—The silicon of the metal increases as alumina replaces lime at a constant percentage of silica. It is also highly dependent on lime:silica ratio.

Acknowledgments

The authors wish to express their thanks to the American Iron and Steel Institute for their financial support of this work. They also wish to acknowledge the assistance of H. W. Hammond and R. H. Robichaud in the laboratory work and D. L. Guernsey and his associates who carried out all of the chemical analyses.

References

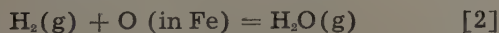
- ¹N. J. Grant, U. Kalling, and J. Chipman: *Trans. AIME* (1951) **191**, p. 666; *JOURNAL OF METALS* (August 1951).
- ²N. J. Grant, O. Troili, and J. Chipman: *Trans. AIME* (1951) **191**, p. 672; *JOURNAL OF METALS* (August 1951).
- ³G. G. Hatch and J. Chipman: *Trans. AIME* (1949) **185**, p. 274; *JOURNAL OF METALS* (April 1949).
- ⁴F. P. Hall and H. Insley: *Phase Diagrams for Ceramists*. Amer. Cer. Soc. (1947) p. 67.
- ⁵N. W. Thibault: *American Mineralogist* (1944) **29**, p. 327.
- ⁶A. Taylor and D. S. Laidler: *British Journal of Applied Physics* (1950) **1**, p. 174.
- ⁷H. N. Baumann: *Journal Electrochem. Soc.* (1952) **99**, No. 3, p. 109.
- ⁸L. C. Chang and G. Derge: *Trans. AIME* (1947) **172**, p. 90; *METALS TECHNOLOGY* (October 1946).
- ⁹L. S. Darken: Discussion to ref. 2, *Trans. AIME* (1951) **191**, p. 1050; *JOURNAL OF METALS* (November 1951).
- ¹⁰H. Sawamura and J. Sawamura: *Memoirs of the Faculty of Engineering*. Kyoto Univ. (1952) **XIV**, No. II, p. 103.

Attainment of Equilibrium in Gas-Metal Reactions

by Nev A. Gokcen

EQUILIBRIA in the reactions between gases and liquid metals have been the subject of many interesting investigations. The experimental realization of true equilibrium, however, is questionable in certain cases due to the lack of conclusive studies in reaction rates. It will be shown here that a systematic interpretation of rate studies with the analysis of prevailing experimental conditions leads to valuable practical information.

The reactions of particular interest are:



The usual and perhaps the most convenient method of investigation may be illustrated with reaction 1. A stream of gas mixture consisting of $\text{H}_2 + \text{H}_2\text{S}$ is passed over or bubbled through the liquid metal at constant temperature. The ratio of $\text{H}_2\text{S}/\text{H}_2$ in the entrant mixture is fixed in each experimental run, and, therefore, the composition of melt varies until the establishment of equilibrium.

The purpose of this paper is to derive a formula

expressing the minimum time required for the establishment of equilibrium and to compare the calculated values from such a formula with the available data.

Equations

Reaction 1 is used for the purpose of illustrating the derivation. Let E represent the equilibrium and X the nonequilibrium sulphur in weight percent at any time t in minutes. For the sake of simplicity, it is first assumed that $E > X$ although the results are of general applicability without restriction. It has been shown by Morris and Williams¹ that within a difference of 1 pct S or less, i.e., $E - X \leq 1.00$, the value of $K'_1 = P_{\text{H}_2\text{S}}/P_{\text{H}_2} \cdot \text{S}\%$ is very nearly constant. The maximum ratio of available $P_{\text{H}_2\text{S}}/P_{\text{H}_2} = \text{H}_2\text{S}/\text{H}_2$, from which sulphur can be absorbed by metal, is equal to $\text{H}_2\text{S}/\text{H}_2$ in equilibrium with E (which equals $\text{H}_2\text{S}/\text{H}_2$ in the entrant gas), minus $\text{H}_2\text{S}/\text{H}_2$ in equilibrium with X . Thus:

$$\text{Available } \text{H}_2\text{S}/\text{H}_2 = EK'_1 - XK'_1 \quad [4]$$

Eq. 4 expresses that sulphur can be absorbed by metal from the $\text{H}_2\text{S}/\text{H}_2$ in the entrant gas until the gas leaving the metal assumes a value of $\text{H}_2\text{S}/\text{H}_2$ which is in equilibrium with the dissolved sulphur X at that time.

H_2S constitutes up to approximately 1 pct of the gas mixture. Its disassociation into H_2 and S_2 is about 1 pct at 1600°C , hence, the $\text{H}_2\text{S}/\text{H}_2$ impinging on the surface of metal is very close to that in the entrant gas. The rate of flow of hydrogen entering the reaction chamber is kept constant experi-

N. A. GOKCEN, Member AIME, is Associate Professor of Metallurgy, Michigan College of Mining and Technology, Houghton, Mich.

Discussion on this paper, TP 3447C, may be sent, 2 copies, to AIME by April 1, 1953. Manuscript, Aug. 20, 1952. Los Angeles Meeting, February 1953.

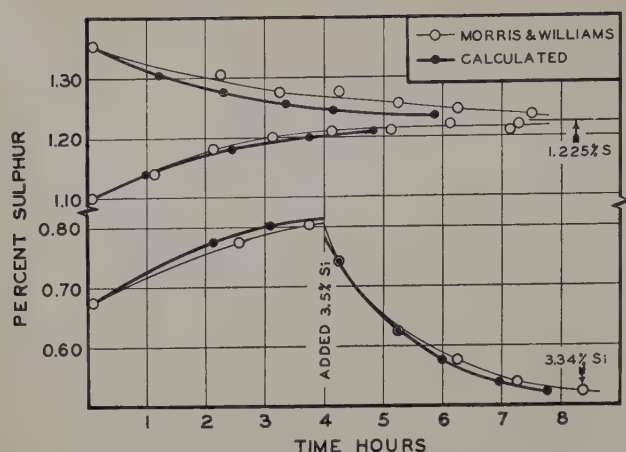


Fig. 1—Reaction rate at 1615°C. Upper curves $H_2S/H_2 = 0.00304$; lower curves $H_2S/H_2 = 0.00220$.

mentally. This is equal to the hydrogen passing through the entire apparatus, because the variation in the amount of hydrogen due to the reaction of part of H_2S with metal is extremely small. Let L represent liters of hydrogen (measured at 0°C and 1 atm) passing through the apparatus. Eq. 4 multiplied by L is equal to the available H_2S in liters per min from which:

$$\text{grams of S available per min} = \frac{32L}{22.4} K'_1 (E - X) \quad [5]$$

is obtained.

It should be emphasized that Eq. 5 represents the maximum amount of sulphur that can be absorbed per unit time by the metal containing X pct S at the time t . The minimum time required to reach equilibrium can be calculated by assuming that the maximum rate of sulphur transfer prevails, i.e.:

$$\frac{32L}{22.4} K'_1 (E - X) = \frac{W}{100} \frac{dX}{dt} \quad [6]$$

where W is the weight of metal in grams and dX the infinitesimal change in composition as the result of sulphur transfer. By rearranging Eq. 6 and integrating with $X = X_0$ when $t = 0$, the following general expression is obtained:

$$\log \frac{E - X_0}{E - X} = \frac{62.1 \times L}{W} K'_1 t \quad [7]$$

It is obvious that for $E = X$ the required time is infinity. Theoretically, this is correct but on account of the limitations in experimental methods, the attainment of equilibrium within 95 to 99 pct of the ideal E value is satisfactory and would require a finite or usually limited period of time. Eqs. 4 and 7 are not limited to the condition of $E > X$; they are also applicable in the exact forms above when $E < X$. It is noteworthy that the algebraic values of Eq. 4 and dX/dt are both negative when $E < X$, and then the value of the former represents H_2S absorbable by the entrant gas or simply the available H_2S/H_2 from the metal.

Applications

Morris and Williams¹ and Morris and Buehl² investigated reaction 1 very carefully by bubbling mixtures of $H_2S + H_2$ through the liquid iron at a rate of 1050 ml per min measured at room temperature (970 ml at standard temperature and pressure). They studied the rate of approach to equi-

librium with melts containing various elements and showed conclusively that the approach to equilibrium is a fairly slow process. During an experimental run, hourly samples of 2 g were taken from the metal, therefore, the weight of melt was constant only between the two successive samples. The weight loss due to splashing was variable, but in general negligibly small for the purpose of these calculations. Table I shows the results based upon their data in the region where the effect of experimental errors in percent sulphur upon Eq. 6 is small; that is, up to 0.98E or 0.99E in sulphur contents. Their data, substituted in Eq. 7, yield:

$$\log \frac{E - X_0}{E - X} = 3.61 \times 10^3 \frac{K'_1}{W} \theta$$

where $\theta = t/60$.

The results are plotted in Fig. 1 together with the original curves of the investigators. The agreement between the calculated and actual curves is remarkably good and, with the exception of the two upper curves, the difference is equivalent to 0.01 pct S or less, which is within the average analytical accuracy of the results. A better agreement between the two curves for run No. E-39 may be obtained by taking the initial sulphur 0.02 pct higher. The choice of the same initial composition and time for both the calculated and actual curves reflects the errors in the initial analysis upon the succeeding experimental points.

The agreement shows that the bubbling technique provides very nearly the maximum rate of sulphur transfer expressed by Eq. 6. Morris and Buehl² actually realized this fact and pointed out that nearly all of the available H_2S reacted with the liquid metal.

Table I. Minimum Time Required for the Change of Composition Toward Equilibrium in the Experiments of Morris and Williams

Run No.	Pct S, $X_{\uparrow\uparrow}$	Time, Hr	
		Actual $\uparrow\uparrow$	Calculated, θ
E-29 (Equil. S=0.86*) (Initial W=61.35 g**)	0.684	0.08	0.08
	0.775	2.56	2.11
	0.801	3.75	3.09
E-29 (Equil. S=0.50*) (W=55.65 g at 4.26 hr)	0.741	4.25	4.25
	0.624	5.25	5.26
	0.576	6.25	5.98
	0.538	7.25	6.96
	0.521	8.37	7.77
E-39 (Equil. S=1.225†) (Init. W=52.1 g)	1.353	0.08	0.08
	1.305	1.25	1.20
	1.275	2.25	2.30
E-44 (Equil. S=1.225) (Init. W=51.65 g)	1.10	0.05	0.05
	1.14	1.12	0.98
	1.18	2.12	2.45
	1.20	3.12	3.75

* Equilibrium sulphur is calculated by using $H_2S/H_2 = 0.00220$ and taking $K_1 = 0.00256$. After the silicon addition, E is computed by using $0.00256 = K'_1/f_s$ where f_s is the activity coefficient of sulphur. Plotting f_s vs pct S by using the four equilibrium runs in ref. 1, it is found that $f_s = 1.72$, from which $E = 0.50$ pct S whereas a short extrapolation of their curve in Fig. 1 gives a value closer to 0.51 pct S. The choice of $E = 0.51$ would shift the calculated curve in Fig. 1 slightly to the right near the equilibrium sulphur and would make the agreement perfect.

** The weight used in each interval is the previous weight minus 2 g of sample, e.g., $W = 59.35$ from 0.08 to 2.56 hr, and 57.35 from 2.56 to 3.75 hr, etc.

† The mean value between the experimental curves for E-39 and E-44 near equilibrium. See Fig. 1.

‡ The values plotted but not tabulated in ref. 1. These, as well as the initial weights, were kindly furnished by J. P. Morris, whose cooperation is gratefully acknowledged.

Run E-39 was made under $H_2S/H_2 = 0.00310$, therefore the reported values of sulphur are corrected to $H_2S/H_2 = 0.00304$ as pointed out by the investigators.

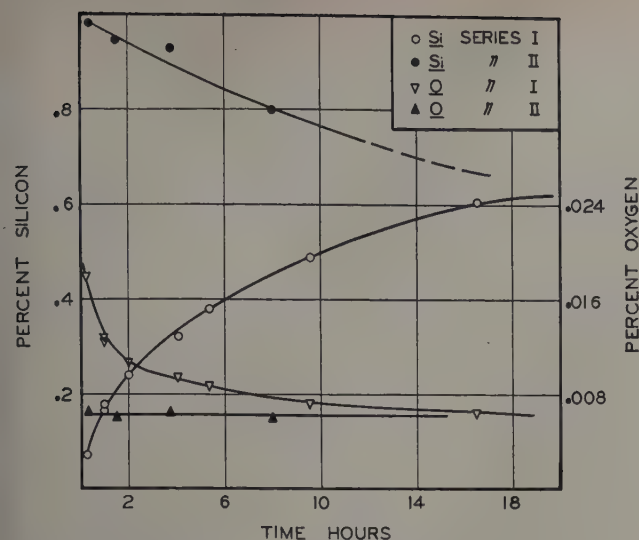


Fig. 2—Reaction rate at 1600°C. $H_2O/H_2 = 0.0182$, data of Gokcen and Chipman.

The earlier investigation of Chipman and Li³ on reaction 1 was later superseded by those of Sherman, Elvander, and Chipman,⁴ Sherman and Chipman,⁵ and Chipman and Sherman,⁶ who used 175 g of metallic charge and passed a mixture of $H_2 + H_2S$ over the melt at a rate of 500 ml per min.⁴ Table II gives the results of calculations by using in Eq. 7, their values for L , W and K' , for each heat in which the only varying dissolved element was sulphur.

In the experimental results of Sherman et al., the initial charge of sulphur, and the time used to obtain equilibrium were not given. It was mentioned, however, that after the melt had been at constant temperature for 1 hr, the first sample was taken and at hourly intervals the metal was sampled and analyzed until the three successive samples yielded identical results and then the melt was "... considered ..." at equilibrium without further proof. The three successive hourly samples limit a period of 2 hr when θ is taken as zero for the first sample. The accuracy of sulphur analysis in their experiments was not given explicitly but it may safely be assumed as ± 0.005 pct whereas Morris and Williams reported that their duplicate samples usually checked within 0.01 pct. Accordingly, an actual change of 0.01 pct S in metal may not be indicated by the three samples which appear to yield identical results when the dissolved sulphur is a substantially lower fraction of the equilibrium value as shown in the last column of Table II. Further, in view of the similarity of apparatus used in these and other investigations,^{8,9} it will be shown later in this paper that the calculated minimum time should be multiplied by a factor of two to three in order to obtain a closer magnitude of their actual experimental time. This is quite likely the result of less intimate contact of the gas with metal than that obtained by the bubbling technique. The gas mixture in their experiments was directed over the metal through a preheater tube located at a certain distance above the surface of the melt and, therefore, a part of the gas must have escaped without reaching to and reacting with metal. (See Fig. 1 or ref. 4 for the arrangement of apparatus and compare with Fig. 2 of ref. 9.) Consequently, the experimental results of Sherman et al. are seriously questionable especially in the range of sulphur below 1 pct.

Eqs. 4 to 7 can be modified to make similar calcu-

lations on the experiments of Rosenqvist and Cox. The calculations show that the required time could have been decreased proportionally by increasing the rate of gas circulation which was of the order of 60 ml per min in their experiments.

Equilibrium in reaction 2 was recently studied by Dastur and Chipman.⁸ The average rate of hydrogen flow was 260 ml per min, the weight of metal 70 g, and the equilibrium constant $K_2 = H_2O/H_2 \cdot O\% = 3.93$ at 1600°C in their investigation. The charge, consisting of electrolytic iron, contained initially $X_0 = 0.080$ pct O as reported by the manufacturer, and the equilibrium heats less than 0.140 pct. The deviation in their oxygen analyses was usually 0.0006 pct, and occasionally 0.0020. These data cannot be used directly in equations similar to 4 and 7, because in this case L varies substantially with time as $L = 0.260 + W 22.4 dX/100 \times 16 dt$. Thus Eqs. 4 and 6 assume the following forms for reaction 2:

$$\text{Available } H_2O \text{ in} \\ \text{liters per min} = 0.260 K_2 E - L K_2 X \quad [4a]$$

$$\frac{16}{22.4} \left[0.260 K_2 E - K_2 X \left(0.260 + 0.98 \frac{dX}{dt} \right) \right] = 0.70 \frac{dX}{dt} \quad [6a]$$

Integration and rearrangement of Eq. 6a gives:

$$(1 + K_2 E) \log \frac{E - X_0}{E - X} + \frac{K_2}{2.3} (X_0 - X) = \frac{16 \times 0.260 \times 100 \times K_2}{2.3 \times 22.4 \times W} t = 0.453t \quad [8]^*$$

* Eq. 7 is a special form of 8 in view of the fact that $K'_1 \cdot E$ and $K'_1 (X_0 - X)/2.3$ are very small for reaction 1 and may be omitted with an error of less than 1 pct.

Eq. 8 gives the minimum time of 4.8 min for the variation in oxygen content from 0.080 to 0.138 when E is taken as 0.140. If 33 pct of the available oxygen was transferred experimentally into the melt as will be shown later, then 14.6 min should be sufficient to establish equilibrium in this reaction. This is in good agreement with their experimental result showing that the equilibrium was established within approximately 15 min.

The application of the preceding equations to the rate studies of Gokcen and Chipman⁹ in reaction 3 is not so simple due to the considerable variation of $K'_3 = (H_2O/H_2)^2 Si\%$ with silicon content and the simultaneous change in oxygen concentration. The variation in dissolved oxygen, however, is small above 0.30 pct Si and it can be estimated from Fig. 2, or calculated by using $[Si\%][O\%]^2 = 2.8 \times 10^{-5}$; the latter gives a total variation of only 0.0004 pct O for a gain of 0.10 pct Si from 0.45 to 0.55, hence, the effect of $d[O\%]/dt$ on the available rate of H_2O is negligibly small in this range. Therefore, equations similar to 4, 5, and 6 may be used to calculate the minimum time for the gain of 0.10 pct Si from 0.45 to 0.55 pct. From their data, $W = 35$ g, $L = 0.260$ liter per min; from a short extrapolation of the lower curve for silicon in Fig. 2, it is found that $E = 0.62$ pct from which $K'_3 = 2.05 \times 10^{-4}$ at equilibrium, and at the average silicon value of 0.50, $K'_3 = 2.12 \times 10^{-4}$. The latter value of K'_3 is found graphically from a curve passing through $\log 2.05 \times 10^{-4}$ and 0.62 pct Si, and parallel to the curve of $\log K'_3$ vs pct Si for the equilibrium runs with fully preheated gas mixtures. The choice of K'_3 in this man-

Table II. Minimum Time Required for the Gain of Sulphur Toward Equilibrium in the Experiments of Sherman Et Al.

Run No.	$K' \times 10^3$	E	Sulphur, Pct**		Minimum Time, Hr, θ^\dagger	Equivalent Time, Morris et al. [‡]	S Pct = x' When Gain = 0.01 Pct S Per 2 Hr	$x' - 100$ Pct E
			Initial X_0	Final X				
S-23*	2.02	4.21	4.00	4.04	4.33	0.64	4.104	97.5
M-1	2.18	2.11	1.985	2.025	7.27	1.07	2.011	95.3
M-4	2.27	1.25	1.16	1.20	10.5	1.54	1.155	92.4
M-17	2.20	0.67	0.603	0.643	17.0	2.50	0.572	85.4
M-27	1.976	0.42	0.363	0.403	25.2	3.71	0.312	74.3
M-36	1.56	0.25	0.20	0.24	42.0	6.18	0.114	45.6
F-3	2.835	0.312 ^{††}	0.259	0.299	20.7	3.04	0.235	75.3

* Runs S-23 and F-3 are from refs. 4 and 6 respectively; others are from ref. 5.

** X/E 100 pct = 96 pct and $X - X_0 = 0.04$ pct S. The substitution of these values in Eq. 7 gives $\log(1 + 1/E) = 10.64K'\theta$. X_0/E 100 pct is 90, 86, and 80 pct for runs M-17, M-27, and M-36, respectively.

† For X/E 100 pct = 96 pct and $X - X_0 = 0.08$ pct S, the time required for the heats of M series is 12.5, 17.2, 25.7, 36.2, and 57.5 hr, respectively.

†† The highest sulphur reported in ref. 6. (See also ref. 5.)

‡ Calculated by using the data in cols. 2 to 4 and the experimental conditions of Morris et al.^{1,2} θ of Sherman et al. divided by θ of Morris et al. equals approximately 6.8 for the same E , X , and X_0 values.

ner, for the runs in reaction rates, is due to the existence of thermal diffusion as the result of insufficient preheating of the entrant gas as pointed out by the investigators. The equation for the maximum rate of silicon gain is then:

$$\frac{d[\text{Si}\%]}{dt} = \left(\sqrt{\frac{2.12 \times 10^{-4}}{\text{Si}\%}} - 0.0182 \right) \frac{0.260 \times 14}{0.35 \times 22.4} \quad [9]$$

The calculation from the integrated form of this equation shows that the increase of silicon from 0.45 to 0.55 should require 1.58 hr, whereas the experimental time is 4.8 hr. The effective fraction of the available oxygen is then 1.58/4.8 or 33 pct, which increases somewhat with increasing silicon. The graphical solution is obtained by determining at 0.50 pct of average silicon, (a) the slope $d[\text{Si}\%]/dt$ from Fig. 2, and (b) the maximum slope $d[\text{Si}\%]/dt$ directly from Eq. 9; the ratio of (a) to (b) is the effective fraction which is 32 to 36 pct depending upon the graphical accuracy of the slope.

Conclusions

Eq. 6 shows explicitly that for a given reaction, W should be small, L large, and X_0 as close to E as possible in order to decrease the time required for the attainment of a final concentration near the equilibrium value. In a series of similar reactions, with the same values of W , L , X_0/E , and X/E , approach to equilibrium is faster for higher values of K (cf. reactions 1 and 2).

It may be pointed out that Eq. 6 is sufficiently accurate for most purposes involving high temperature investigations. The exact form is:

$$\frac{dX}{dt} = AK(a_x - a_x) \quad [10]$$

where A is the combined constants for a reaction of the type 1 or 2 together with the experimental conditions, K is the true equilibrium constant, and a the activity based upon percent concentration, i.e., $a_x = f_x \cdot X$. Substitution of the activity coefficients in Eq. 11 as:

$$\frac{dX}{dt} = \frac{AK'_E}{f_E} (f_E \cdot E - f_x \cdot X) = AK'_E \left(E - \frac{f_x}{f_E} X \right) \quad [11]$$

shows that Eqs. 6 and 11 are identical when f_x/f_E is unity, which is very nearly the case when the initial value of $E - X$ is small. In exceptional cases, such

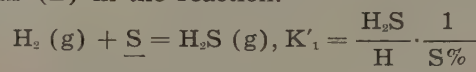
as in reaction 2, $K'_2 = K_2$, hence f_x/f_E is unity. Experimental results are seldom accurate enough to give a ratio of f_x/f_E as a function of X for the integration of Eq. 11. A comprehensive use and discussion of this equation will be in a forthcoming paper together with new data.

The reactions above are being studied by using a cascade-type platinum wound furnace, and by following the technique of Morris and coworkers with some improvements in view of the foregoing considerations regarding the reaction rates.

Summary

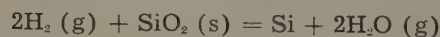
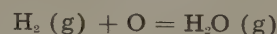
The equation $\log \frac{E - X_0}{E - X} = \frac{62.1 \times L}{W} K'_1$ is de-

rived to relate the time required (t) to the change of percentage of sulphur in liquid iron from (X_0) towards (X) in the direction of the equilibrium sulphur (E) in the reaction:



The constants L and W represent the hydrogen flow rate and the weight of metal respectively.

Similar equations are derived for the reactions:



Available data and experimental methods are analyzed, interpreted, and critically evaluated by using the derived equations.

References

- 1 J. P. Morris and A. J. Williams, Jr.: *Trans. ASM* (1949) **41**, p. 1425.
- 2 J. P. Morris and R. C. Buehl: *Trans. AIME* (1950) **188**, p. 317; *JOURNAL OF METALS* (February 1950).
- 3 J. Chipman and Ta Li: *Trans. ASM* (1937) **25**, p. 435.
- 4 C. W. Sherman, H. I. Elvander, and J. Chipman: *Trans. AIME* (1950) **188**, p. 334; *JOURNAL OF METALS* (February 1950).
- 5 C. W. Sherman and J. Chipman: *Trans. AIME* (1942) **194**, p. 597; *JOURNAL OF METALS* (June 1952).
- 6 J. Chipman and C. W. Sherman: *Rev. Metallurgie* (1951) **48**, p. 613.
- 7 T. Rosenqvist and E. M. Cox: *Trans. AIME* (1950) **188**, p. 1389; *JOURNAL OF METALS* (November 1950).
- 8 M. N. Dastur and J. Chipman: *Trans. AIME* (1949) **185**, p. 441; *JOURNAL OF METALS* (August 1949).
- 9 N. A. Gokcen and J. Chipman: *Trans. AIME* (1952) **194**, p. 171; *JOURNAL OF METALS* (February 1952).

Lattice Parameter of Beta Titanium at Room Temperature

by B. W. Levinger

THE lattice parameter of the β form of pure titanium has been measured at elevated temperature.^{1,2} No attempt was made, however, to correct the parameter obtained to room temperature.

In the course of phase diagram studies at Armour Research Foundation and elsewhere, the variation of β -phase lattice parameter with composition has been established in a number of binary and ternary systems involving titanium. It was possible to extrapolate in these instances to 100 pct Ti to find the apparent lattice parameter of β titanium at room temperature. Table I lists the results thus obtained. The suggested value for the lattice parameter of β titanium is the average of the extrapolated values 3.276 ± 0.003 kX. This suggested value gives an interatomic distance in β titanium of 2.837 kX and

Table I. Apparent Lattice Parameter of Beta Titanium at Room Temperature

System	Extrapolated β Phase Parameter (kX)	Limit of Stable β Phase Wt Pct Ti	Reference
Ti-V	3.275	85	4
Ti-Cr	3.28	85	6
Ti-Mo	3.278	94	7
Ti-Nb	3.276	90	8
Ti-Fe	3.278	64	8
Ti-Mo-Cr	3.275	96	9 Fig. 1
Ti-Mo-Mn	3.277		9 Fig. 2
			9 Fig. 3

for α titanium in a similar range.⁵ It was thus possible to calculate the parameter at 900°C. The value of 3.305 kX agrees well with 3.3065 given by Eppelsheimer.²

The majority of values reported in the literature^{1-4, 8} were given as Angstroms. In at least one case, ref. 8, it was shown that they actually represented kX units. The source of this confusion appears to be that a large number of tables of X-ray emission spectra list wavelengths as Angstroms and give values in kX units. The accepted conversion factor for kX

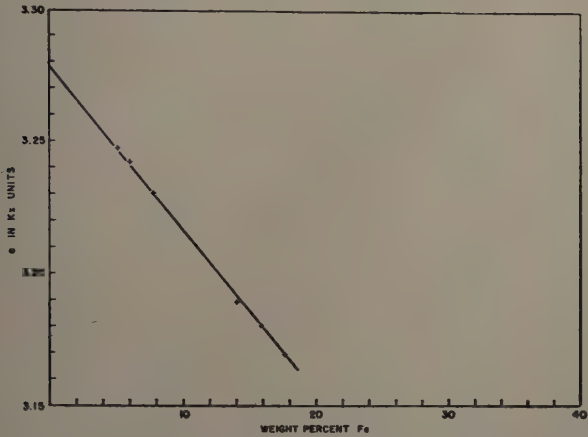


Fig. 1—Lattice parameter vs composition of β phase in binary Ti-Fe alloys.

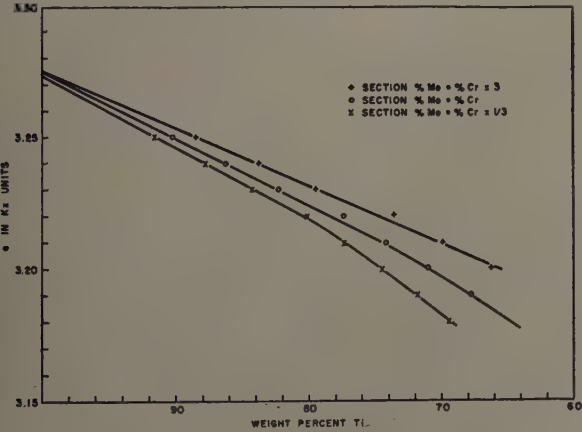


Fig. 2—Lattice parameter vs composition of β phase in ternary Ti-Mo-Cr alloys.

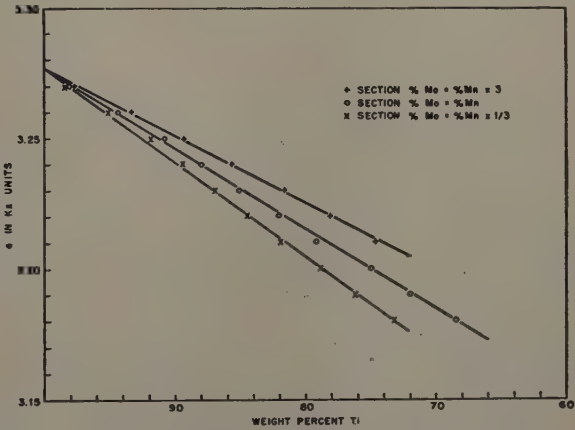


Fig. 3—Lattice parameter vs composition of β phase in ternary Ti-Mo-Mn alloys.

units to Angstroms (10^{-8} cm) is 1.00202. Thus the parameter of β titanium suggested corresponds to 2.828 Å.

References

¹ J. H. de Boer, W. G. Burgers, and J. D. Fast: *Proc. Acad. Amsterdam* (1936) 39, p. 515.
² D. S. Eppelsheimer and R. R. Penman: *Nature* (Dec. 2, 1950) 166, p. 960.
³ W. Hume-Rothery: *The Structure of Metals and Alloys* (1945) London. Inst. Metals.
⁴ H. K. Adenstedt, J. R. Pequignot, and J. M. Raymer: *Trans. ASM* (1952) 44, p. 990.
⁵ *Gmelins Handbuch der Anorganischen Chemie*. Titan, Verlag Chemie, Weinheim (1951).
⁶ P. Pietrokowsky and P. Duwez: *Trans. AIME* (1952) 194, p. 627; *JOURNAL OF METALS* (June 1952).
⁷ P. Duwez and J. L. Taylor: *Trans. ASM* (1952) 44, p. 495.
⁸ M. Hansen, E. L. Kamen, H. D. Kessler, and D. J. McPherson: *Trans. AIME* (1951) 191, p. 881; *JOURNAL OF METALS* (October 1951).
⁹ Unpublished Research, Armour Research Foundation.

hence a Goldschmidt atomic diameter (coordination number 12) of 2.925 kX. The latter agrees closely with the value of 2.93 given by Hume-Rothery.³

From the data of Adenstedt and coworkers⁴ it was possible to determine by extrapolation the mean coefficient of linear expansion for β titanium in the range from room temperature to 1000°C. This value, 10.1×10^{-6} per degree C, compares with about 11×10^{-6}

B. W. LEVINGER, Junior Member AIME, is Assistant Metallurgist, Metals Research Department, Armour Research Foundation of Illinois Institute of Technology, Chicago.
TN 138E. Manuscript, Aug. 27, 1952.

High Temperature Modification of TiCr_2

by B. W. Levinger

THE system Ti-Cr has been studied by several investigators.¹⁻⁴ Though titanium and chromium are completely miscible at high temperatures, an intermediate phase of the approximate atomic proportions TiCr_2 has been identified at various compositions between 60 and 68 wt pct Cr. The structure of this phase was established as the cubic C15 (MgCu_2) type with 24 atoms per unit cell and a lattice parameter 6.929 kX.²

During a study of the ternary system, Ti-Mo-Cr,⁵ the existence of a high temperature modification of the TiCr_2 phase was discovered. In a series of alloys annealed at 1300°C and containing from 60 to 70 wt pct Cr and 5 pct Mo, a new phase was present which did not correspond to either β solid solution or TiCr_2 . By trial, the new phase was identified to be of the hexagonal C14 (MgZn_2) structure with 12 atoms per unit cell. Further work showed that the hexagonal structure was, in fact, also present in binary Ti-Cr alloys quenched from high temperatures.

To make the identification more certain, the intensities of the various reflections were calculated assuming a composition TiCr_2 and C14 structure. Table I lists reflection planes, interplanar distances, calculated intensities, and a comparison of these values with the lines of a binary Ti-Cr alloy (66 pct Cr) annealed for 20 min at 1385°C and water quenched. Since high angle lines were more diffuse, the correspondence between visually observed and calculated intensities was not as good at these angles.

Lattice parameters were computed to be $a = 4.922$ kX, $c = 7.945$, $c/a = 1.614$. The corresponding interatomic distances are: titanium to titanium distance, 3.00, kX, chromium to chromium distance, 2.43, kX, titanium to chromium distance, 2.88, kX. These compare to 3.00, 2.45, and 2.87 kX in the cubic phase, respectively.²

The atomic positions in the C14 structure are as follows:

Titanium $1/3, 2/3, z; 1/3, 2/3, \frac{1}{2}-z;$
 $2/3, 1/3, \bar{z}; 2/3, 1/3, (\frac{1}{2}-\bar{z});$

Chromium $0, 0, 0; 0, 0, \frac{1}{2};$
 $\frac{2x}{x}, \frac{x}{x}, \frac{1}{4}; \frac{2x}{x}, \frac{x}{x}, \frac{3}{4};$
 $\frac{x}{x}, \frac{2x}{x}, \frac{1}{4}; x, 2x, \frac{3}{4};$
 $\frac{x}{x}, x, \frac{1}{4}; x, x, \frac{3}{4};$

The values of x and z were calculated for the alloy mentioned and found as follows: $z = 0.061, x = 0.165$. The values assumed in the intensity calculations were those for an ideal close-packed lattice or $z = 1/16, x = 1/6$.

Work in the Ti-Mo-Cr system indicates that γ_2 , the hexagonal modification of TiCr_2 , is the stable phase above 1300°C, while γ_1 with the cubic structure is stable below 1000°C. X-ray examination of a number of alloys annealed at intermediate temperatures showed that the hexagonal and cubic phases can coexist. Alloys quenched from 1000°C and annealed at 1100° and 1200°C showed small

Table I. Diffraction Data for TiCr_2 (γ_2 Phase)

hkl	d, Calculated* (kX)	d, Observed† (kX)	Intensity Observed‡	Relative Intensity Calculated§	Corresponding Data ² for γ_1	
					d (kX)	hkl
110	2.461	2.454	w	0.14	2.44	220
103	2.250	2.247	wm	0.36		
200	2.131	2.127	vft	0.05		
112	2.092	2.087	m	0.57	2.08	311
201	2.058	2.056	m	0.54		
004	1.986	1.985	w	0.13	1.99	222
202	1.878	1.876	w	0.13		
104	1.800	1.798	vw	0.07	1.73	400
203	1.660	1.657	ft	0.04		
210	1.611	1.610	vft	0.01	1.59	331
300	1.421	1.419	vft	0.02	1.411	422
213	1.376	1.377	wm	0.15		
302	1.338	1.337	wm	0.14	1.333	511
006	1.317	1.323	vft	0.02		
205	1.274	1.272	wm	0.23		
214	1.251	1.251	vw	0.06		
220	1.230	1.229	wm	0.21	1.223	440
206	1.125	1.124	w	0.17	1.167	531
107	1.097	1.095	vft	0.04	1.094	620
313	1.079	1.078	w	0.17		
401	1.056	1.055	vw	0.17	1.057	533
224	1.046	1.045	w	0.27	1.045	622
402	1.029	1.029	vft	0.06		
314	1.016	1.015	ft	0.08		
207	1.002	1.001	vft	0.07	0.9976	444
108	0.9672	0.9686	ft	0.10	0.9708	711
410	0.9301	0.9285	ft	0.06	0.9255	642
217	0.9279			0.08		
323	0.9173	0.9171	vw	0.21		
412	0.9056	0.9052	wm	0.19	0.9021	731
226	0.9014			0.21		
405	0.8850	0.8851	w	0.37	0.8662	800
218	0.8454	0.8453	w	0.34		
406	0.8302	0.8306	vw	0.37		
317	0.8187	0.8186	ft	0.15	0.8168	822
308	0.8139	0.8138	ft	0.13		
332	0.8033	0.8035	w	0.53		
421	0.8014	0.8013	wm	1.00	0.8003	555
0010	0.7945	0.7950	vft	0.11	0.7946	662
422	0.7894	0.7894	vw	0.48		
504	0.7834	0.7837	ft	0.20		
407	0.7769	0.7769	vft	0.61	0.7746	840

* d observed from an alloy containing 66 pct Cr-34 pct Ti water quenched from 1385°C.

† d calculated from lattice parameters: $a = 4.922$ kX, $c = 7.945$. These lattice parameters were obtained by the method of least squares from eight lines of the above pattern.

‡ Observed Intensity: m, medium; wm, weak medium; w, weak; vw, very weak; ft, faint; vft, very faint. In a number of cases, lines were diffuse and it was felt that they represented a pair of lines. This is indicated by bracketing.

§ Relative Calculated Intensity: The values of relative intensity for planes from (110) to (220) are due to Wallbaum.⁶ Actually they represent corresponding values for the isomorphous phase, TiMn_2 ; calculation of a number of lines at higher angles showed that the two values correspond within a few percentage points.

amounts of γ_2 at the higher temperature. A considerable amount of γ_2 seemed present, however, in cast alloys annealed at 1100°C. It further appears that there is a small but definite solubility range for both phases in the ternary system.

Acknowledgment

The results of this paper represent work carried out in conjunction with a project sponsored by Watertown Arsenal, Contract No. DA-11-022-ORD-272.

References

- 1 M. K. McQuillan: *Journal Inst. Metals* (1951) **79**, p. 379.
- 2 P. Duwez and J. L. Taylor: *Trans. ASM* (1952) **44**, p. 495.
- 3 R. J. Van Thyne, H. D. Kessler, and M. Hansen: *Trans. ASM* (1952) **44**, p. 974.
- 4 F. B. Cuff, N. J. Grant, and C. F. Floe: *Trans. AIME* (1952) **194**, p. 848; *JOURNAL OF METALS* (August 1952).
- 5 Unpublished Research, Armour Research Foundation.
- 6 H. J. Wallbaum: *Ztsch. Krist.* **103**, p. 391.

B. W. LEVINGER, Junior Member AIME, is Assistant Metallurgist, Metals Research Department, Armour Research Foundation of Illinois Institute of Technology, Chicago.

TN 137E. Manuscript, Sept. 10, 1952.

Arc-Furnace Equipment and Its Operation

At the Kennecott Utah Refinery

by H. A. Shaw and H. G. G. Whitton

This paper describes the use of the electric-arc furnace for the production of tough-pitch, horizontal cast copper shapes and the production of copper anodes from tank house anode scrap. This installation is the only one of its kind in the United States.

SINCE the initial use of electric-arc furnaces for refined copper melting on a commercial scale at Copper Cliff in 1936, this type of melting has been of extreme interest to everyone in any way connected with copper casting and fabricating. Early in 1948, Kennecott Copper Corp. decided to build an electrolytic copper refinery at Garfield, Utah. One of the major decisions to be made at that time was the type of furnace to be used for melting cathodes for casting into refined copper shapes and for melting anode scrap for the production of anodes. Based on the results obtained from arc furnaces by the International Nickel Co. of Canada, at Copper Cliff, and by the American Smelting and Refining Co., at Baltimore, coupled with certain important economic factors such as having an adequate amount of relatively cheap power available at the Magna Central Power Plant, high cost of poles and oil in the Salt Lake District, and the lack of natural gas at that time, the final decision was to install electric-arc furnaces rather than the standard type of reverberatory furnaces.

Experience has shown certain parts of the original installation to have been inadequate or in need of modification. Although the present status of arc-furnace melting at the Utah Refinery is far from perfect, nevertheless substantial progress has been made.

At the Utah refinery, copper is melted in three 15-ft diam, size "M" Lectromelt furnaces, two of

which are used for melting cathodes and one for remelting anode scrap.

Each furnace is energized from a 13,800-225 v, 3-phase, 60-cycle, 6000-kva (at 40°C rise) oil-immersed water-cooled transformer. Auxiliary equipment for each refined copper furnace includes a charging machine, launders, ladle, 40 ft diam Walker-type casting wheel, bosh, and inspection conveyor. The anode furnace differs in that it is charged by hand from an elevated platform and the anodes are picked off the 24-ft diam casting wheel by a takeoff hoist and loaded directly into specially designed trailers, Figs. 1 and 2.

Electrical Equipment

Electric power to operate the arc furnaces is generated at the Kennecott-owned Magna Central Power Station two miles distant and transmitted to the Refinery outdoor substation at 44,000 v. At this point it is stepped down to 13,800 v and carried through concrete-lined underground tunnels to the switchgear and then to the primary side of the furnace transformers. The power is conducted from the Y-connected secondary bus bars of the transformer to the electrode arms by means of 22 flexible copper cable conductors per phase. Each cable has a cross-sectional area of 1,750,000 circular mils, giving a total area of 38,500,000 circular mils per phase. The power is carried from these cables to the three individual electrode holders by means of water-cooled copper bus tubing. The electrode clamps are incorporated in the electrode holders and are released by air pressure working against a spring in the clamp control cylinder.

The movement of the electrode arms is either automatic or manual. The automatic control is used during melting and is regulated by three Westing-

H. A. SHAW, Member AIME, and H. G. G. WHITTON are associated with the Utah Copper Div., Kennecott Copper Corp., Garfield, Utah.

Discussion on this paper, TP 3495D, may be sent, 2 copies, to AIME by April 1, 1953. Manuscript, Oct. 3, 1952; revised, Dec. 18, 1952. Los Angeles Meeting, February 1953.

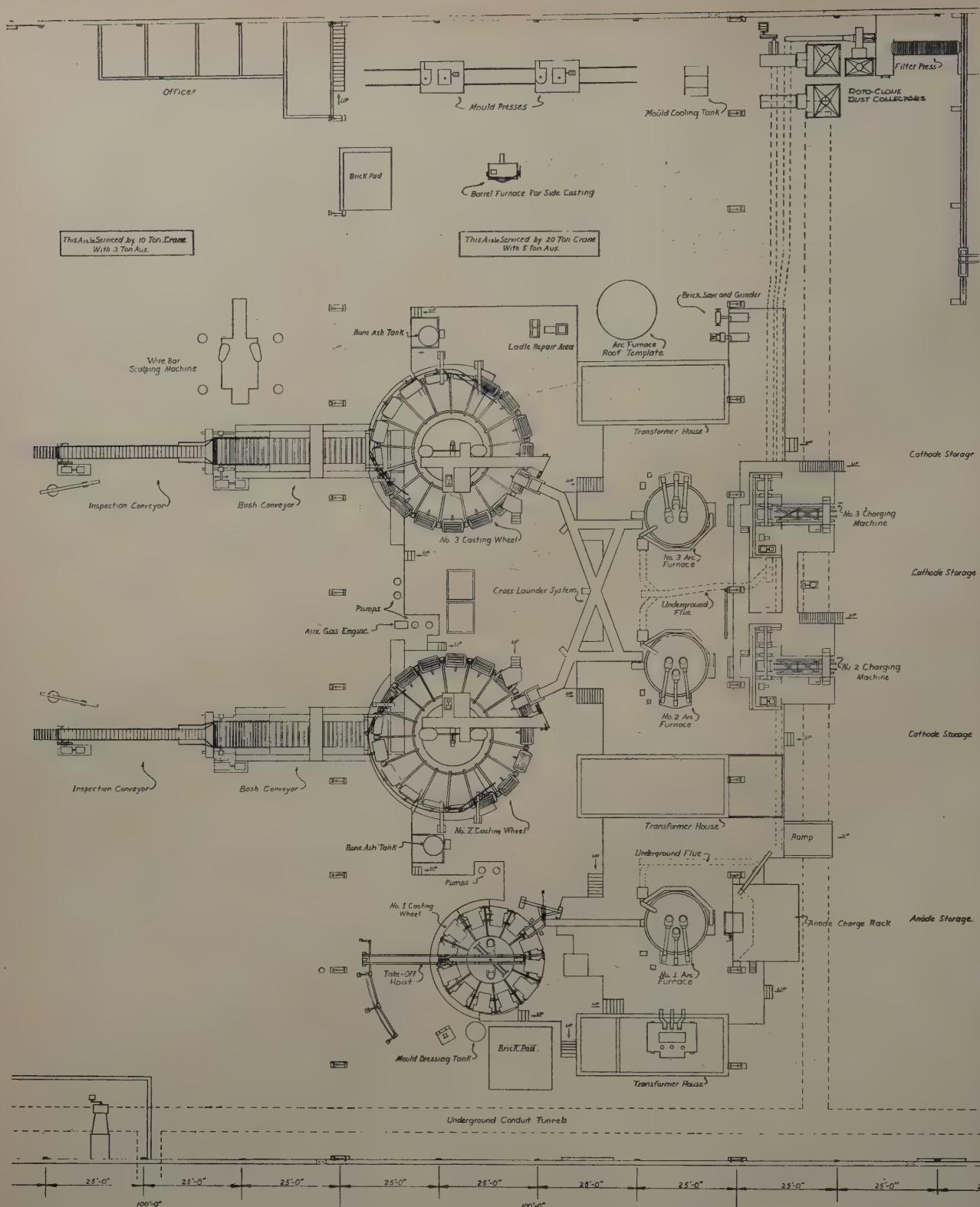


Fig. 1—Diagrammatic layout of furnaces and casting equipment.

house Rototrols which actuate the electrode arm winch motors. The manual control is used whenever it is necessary to raise one or all the electrode arms, such as prior to shutting off the power, or slipping electrodes. The low voltage connections in the transformer provide 13 taps ranging from 85 to 225 v. Suitable connections may be made to a motor operated tap changer which allow the operator to use any one of four selected voltages. Present settings give a selection of 120, 147, 173, or 190 v phase to phase. Most melting is done using 173 v.

A rheostat on each phase provides a limited control of the current for each tap setting.

Data compiled during the two years of operation indicate that 245 kw-hr of power are required to melt one ton of copper.

Description of Furnaces

The three arc furnaces are identical in construction. The walls are fabricated of $1\frac{1}{8}$ in. steel plate, cylindrical in form, having an inside diameter of 15 ft 0 in., and provided with four openings, namely,

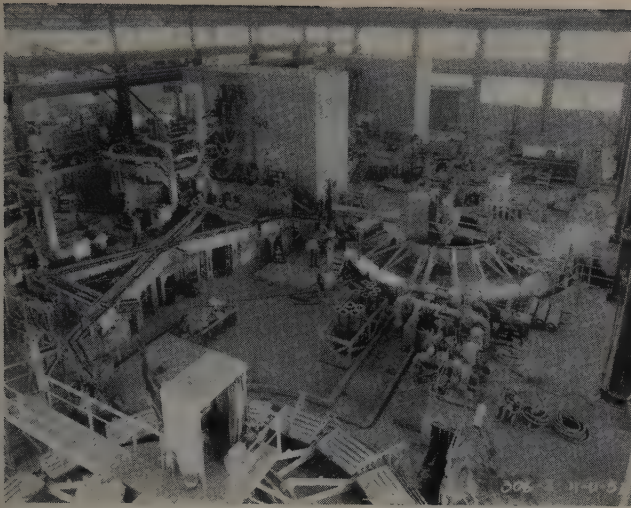


Fig. 2—General view showing the two refined copper melting furnaces and auxiliary casting equipment in the foreground. The anode copper melting furnace and casting equipment is in the background.

charge slot, skim bay, taphole, and a small inspection hole near the taphole. The charge slot is located at the rear of the furnace diametrically opposite the furnace taphole. The skim bay is on the side opposite the masts, 45° from the charge slot. The furnace bottom is also made of $1\frac{1}{2}$ in. steel plate formed on a 14 ft 2 in. spherical radius. For pouring the furnaces are hydraulically tilted about an axis in line with the furnace taphole spout.

The holding capacity of the furnaces when new is approximately 50 tons. The wear on the bottom refractories resulting from operations increases this quantity to about 65 tons before relining of the bottom is necessary.

Furnace Refractory Construction

The furnace lining consists of a refractory cement pad 1 to 8 in. thick formed on the bottom of the empty shell to develop the desired radius for the construction of the superimposed brick bottom. This is followed by two courses of $2\frac{1}{2}$ in. brick keys laid to conform to the desired spherical radius. The third course is constructed from 9 in. special shape, chemically bonded magnesite brick, and the fourth and final course is built from $13\frac{1}{2}$ in. special shape, chemically bonded magnesite brick. The main section of the side walls is built from $9\times 6\times 3$ in. No. 1 keys laid up as headers and backed up by two $4\frac{1}{2}$ in. courses of fireclay brick. An anti-surge ledge projects 9 in. at the metal line. Special precautions are taken to allow vertical expansion to take place without exerting pressure on the roof brick. An annular space between the bottom brick and the sides of the steel shell is allowed. This space is filled either with insulation brick or powdered magnesite to permit expansion of the bottom. Expansion is also provided in the side walls above the metal line by the use of $\frac{1}{8}$ in. corrugated paper between each brick, Fig. 3.

Only basic brick will withstand the corrosive action of the furnace atmosphere due to the concentration of copper oxide fume at high temperature. This fume will react rapidly with silica brick, high alumina brick, and to a lesser extent with refractories of a sillimanite or mullite composition. Silicon carbide brick will withstand the action of the fumes but rapidly breaks down to a silica slag in the presence of oxygen at elevated temperatures that are at times unavoidable.

As low refractory costs and avoidance of operational shutdowns are two of the major objectives of arc-furnace melting, it is necessary that every detail of furnace construction be carefully engineered and that the refractories be selected with due regard to previous results. The actual taphole consists of a 4 in. ID carbofrax tube set in place with magnesite cement in a slot left during the construction of the wall. Accurate location of this tube is important because it determines the level of the molten copper in the furnace, acts as a skimmer, and because it must be positioned so that the furnace can be drained completely. When casting must be interrupted it is only necessary to tilt the furnace back 5° onto safety blocks. This allows the molten copper to drain from the inclined taphole tube. It is possible to hold a furnace full of molten copper in this position for an indefinite period by intermittent application of power.

Arc-Furnace Roof Construction

Roofs are constructed with basic brick using $9\times 4\frac{1}{2}\times 3$ in. series of brick plus some special shapes. When building a roof, the fabricated steel roof support ring is located accurately about a permanent cement template, the surface of which is a dome having a spherical radius of 17 ft 4 in. Wooden templates are set by dowels so that the electrode and vent openings will be located accurately in the finished roof. The roof is developed by constructing a series of brick rings using side arch and wedges to follow the shape of the cement template. Rings of specially shaped, adapter brick are used as needed. The electrode and vent openings are made by using special side arch wedge shapes that form a slightly conical opening with the larger diameter up so that the brick rings are held in position by a definite taper. Circumferential expansion is allowed by the use of a $\frac{1}{8}$ in. corrugated cardboard spacer every eighth brick. At the present time no cement is used in laying the brick. However, after the roof has been installed on the furnace and the temperature raised, the outside surface of the roof is grouted with a thin slurry of magnesite cement to seal the openings between adjacent brick, Fig. 4.

The desirability of roof insulation is being investigated and its use will depend upon results obtained from current experiments.

Since the melting practice requires definite control of the furnace atmosphere, it is necessary that

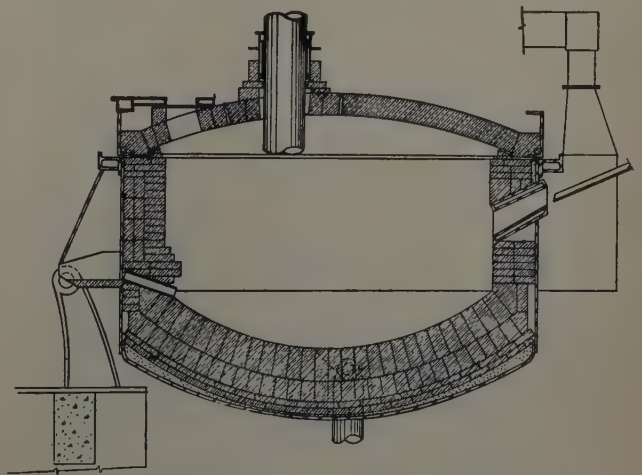


Fig. 3—Section of arc furnace showing arrangement of refractory lining. Diagrammatic section of roof shows section through vent, electrode opening and main portion of roof.

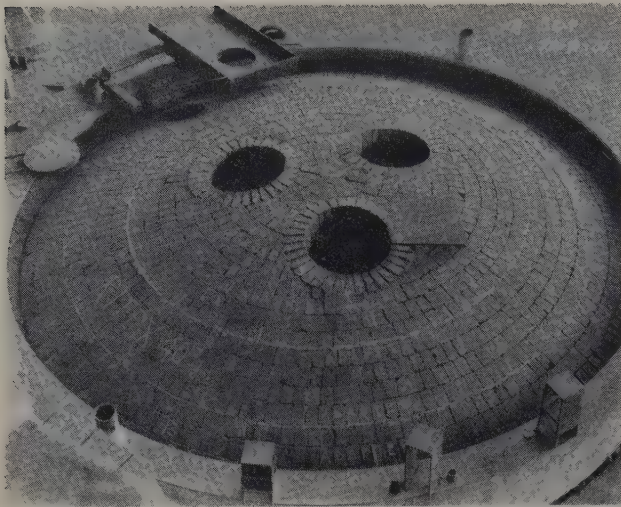


Fig. 4—Arc furnace roof for 18 in. diameter electrodes, showing water-cooled vent plate and water-cooled banjo-type damper.

a gas-tight seal be provided around the electrodes, otherwise "bottlenecking" of the electrode will occur and gas will escape from the furnace. Individual water-cooled glands are used on each electrode. These glands are suspended several inches above the furnace roof. A flat ring of fireclay key brick is set on the roof around each electrode opening so that the small end of the brick comes in contact with the graphite electrode, thus protecting the lower face of the water-cooled electrode gland from copper splash. With a new cold roof, a space of 2 in. is allowed between the lower face of the gland and the fireclay brick pad. This allows the roof to rise due to the expansion of the brick while being brought up to operating temperature, without subjecting the roof to the additional weight of the glands. This opening is sealed by forming a slip joint using a soldier course of fireclay side arch brick strapped to the gland and projecting down so as to come in contact with the fireclay base. The weight of the water-cooled gland is carried from the operating platform by projecting lugs from each gland. These are electrically insulated from the steelwork of the platform by fireclay brick. The glands now in service are fabricated from $\frac{3}{8}$ in. boiler plate. The roof vent opening is built from

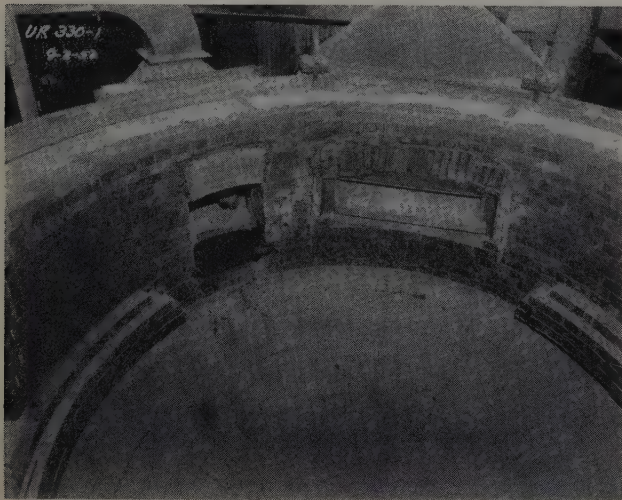


Fig. 5—Refractory lining in refined copper arc furnace showing new brick bottom, anti-surge ledge and water-cooled, boiler plate charge slot.

9x6x3 in. side arch wedge brick to form a slightly conical opening 13 in. in diameter. A water-cooled base plate, constructed from $\frac{3}{4}$ in. boiler plate and containing a 13 in. diam opening, is cantilevered over the vent in such a manner as to allow the weight of the water-cooled section to be carried by the steel roof ring without interfering with the expansion of the roof.

Charge Slot Construction

The original construction of the wirebar furnace charge slot followed previous practice which consisted of a water-cooled copper casting bolted to the outside shell of the furnace and having a minimum opening 44 in. wide x $4\frac{1}{2}$ in. high. The original anode furnace charge slot was similar in design to the standard, copper, water-cooled charge slot casting, but was fabricated from $\frac{3}{4}$ in. boiler plate. The minimum opening was 59 in. wide x 6 in. high, making it possible to charge anode scrap or rejected, full sized anodes. On the outside, a steel door operated by an air cylinder was installed. The refractory portion of the chute consisted of a sill built from special shapes of silicon carbide designed to give a slope of 30° . Trouble was experienced from the start with this construction. The silicon carbide sill brick had a very short life, the extreme heat seriously warped the steel door, and the continual spray of molten metal rapidly formed an objectionable build up of copper skulls on the refractory adjacent to the water-cooled opening of the slot. It was felt that these troubles must be associated with the use of higher arc voltages inherently necessary with 60 cycle power, as such troubles were not encountered on a similar installation using lower voltage and 25 cycle power. As will be discussed later, it was also felt that the 14 in. diam electrodes being used were too small.

It then became necessary to develop a new charge slot construction to meet these conditions. After exhausting the practicabilities of various refractories it was decided to investigate the possibility of using a water-cooled boiler plate slot. In April 1951, a water-cooled boiler plate sill was installed and results were very promising. Development of the idea was continued until at the present time each furnace is equipped with a complete water-cooled charge slot consisting of the sill, two side sections, and a top section. As a safety measure the charge slots have been raised approximately 10 in. to avoid the possibility of the water-cooled section coming in contact with molten copper when the furnace is set back on the low blocks at such times when it may be necessary to stop casting, Fig. 5.

Electrodes

The original furnace installation utilized 14 in. diam graphite electrodes. Shortly after operations started it was realized that the 14 in. diam electrodes would not give the desired melting rate. In spite of every effort it was not possible to obtain melting rates above 15 tons per hour. To obtain this value it was necessary to operate on the higher voltage positions which in turn caused the furnace walls and roof to overheat dangerously to the point of destruction. In an effort to correct this a change was made to 18 in. diam electrodes.

At the time it was reasoned that the larger diameter electrodes would tend to shield the arc to the extent that the sidewalls would not overheat as much, thus making it possible to operate for longer

periods of time on the higher voltage positions. It was also thought that the percentage of down time due to broken electrodes would be decreased because of the greater mechanical strength of the larger electrodes. Experience has proved this reasoning to be correct. Results of the change from 14 to 18 in. diam electrodes are summarized as follows: 1—Melting rate was increased from 15 to 22 tons per hour. 2—Lower wall temperatures enabled the furnace to operate on higher voltages without too much danger of overheating. 3—Less electrode breakage resulted in a decrease in electrode consumption from 5.0 to 4.2 lb per ton. 4—Power factor decrease from 0.7 to 0.6 resulted in greater load on transformer. 5—Stability of the arc at the same current value decreased.

Efforts made to increase the power factor at the furnace by changing the current, voltage, or reactance have not proved successful. While it has been possible to increase the power factor by lowering the current, this has in turn given rise to in-

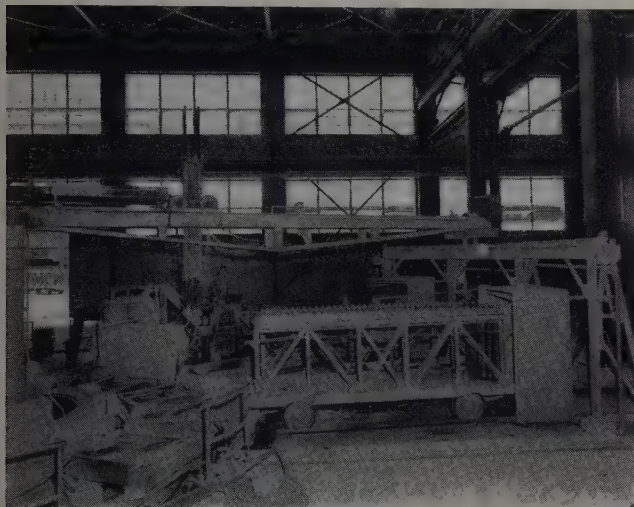


Fig. 6—Anode take-off hoist and cooling sprays used to cool anodes and remove scale after anodes are placed in anode rack cars.

creased arc instability. Likewise, raising the voltage beyond 173 v, phase to phase, gives rise to overheating and instability.

Anode Copper Furnace

As previously mentioned the construction of the anode furnace is identical to the two refined copper furnaces except for a wider charge slot. In contrast to the refined copper furnaces, the anode furnace is hand charged from an elevated platform.

As in the refined furnaces the copper flows from the furnace taphole down the launder into the pouring ladle and is then cast into one of the 12 molds on the 24 ft diam casting wheel. After cooling, the tops of the anodes are raised approximately 2 in. by push-up pins so that the take-off hoist can pick them up and hang them, properly spaced on an anode trailer. Adequate water cooling is provided by overhead sprays through which the loaded trailer is moved so that the anodes will be cooled and some of the scale removed by quenching before they are delivered to the tank house, Fig. 6.

Launders, Ladle, and Wheel

Molten copper from the cathode melting furnace flows from the furnace taphole into launders arranged so that it is possible to cast into either or

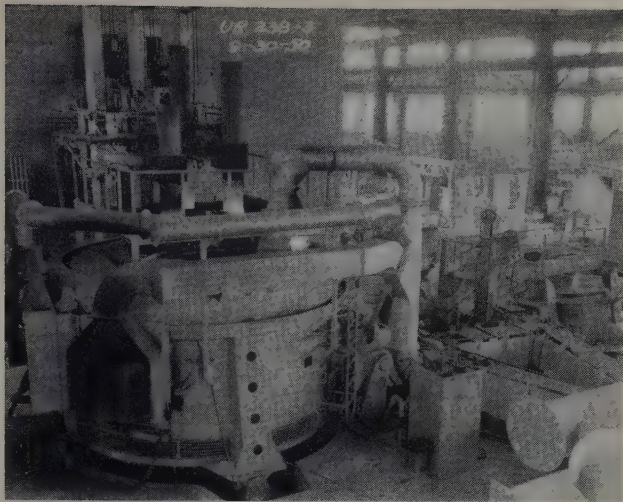


Fig. 7—Arc furnace showing fume recovery system.

both of the two wheel positions. The copper flows from the launders directly into a pouring ladle and then is cast into one of the 17 molds on the 40 ft diam Walker-type casting wheel. The casting wheel revolves continuously with the wire bars being dumped into a water bosh located diametrically opposite the ladle position. After dumping, the molds are automatically righted and then hand sprayed with a slurry of bone ash and water. The refined shapes fall on a steel conveyor in the bosh where they are cooled and then elevated to a second conveyor for inspection and loading.

The original plant construction included a vertical-type, low frequency induction furnace unit at each casting wheel, so arranged that the molten copper could flow down the launder from the arc-furnace taphole and enter the induction furnace through a 5 ft refractory tube set in the hollow trunnion about which the induction furnace was rotated.

Starting February 4, 1951 experiments were conducted in casting molten copper direct from the arc-furnace launder into the pouring ladle. It was found that by close pyrometer control of casting temperature, rate of charging, and condition of the copper at the taphole that casting conditions could be



Fig. 8—Fume oxide recovery system, showing suction fan, two Roto-Clone units. One of the three filter press units is shown mounted over a fume oxide storage bin.

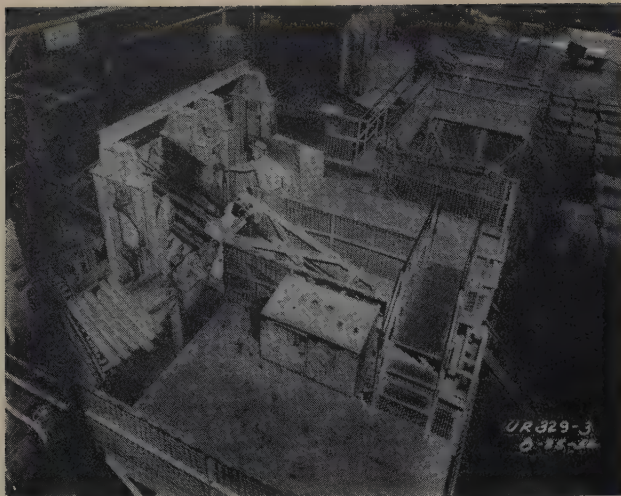


Fig. 9—Charging machine illustrating method of charging cathodes and reject wirebars into the arc furnaces.

maintained more uniformly and casting delays almost entirely avoided with the elimination of the induction units.

Fume Recovery System

The fume recovery system is divided into two parts: one is used to collect the fume oxide from the anode furnace and the other is used to collect the fume oxide from the two refined copper furnaces. This is to keep the anode fume, which must be re-treated to remove the impurities and precious metal values, separate from the relatively pure copper oxide dust recovered from the refined copper furnaces.

The fume that escapes through the roof vent contains from 5 to 6 lb of cuprous oxide for each ton of copper melted. The charge slot skim door and vent are adequately hooded and are connected to a central fume pipe, Fig. 7. The fume is forced through a type N, Roto-Clone collector, the exhaust gases pass through a 25 in. diam stainless steel stack 45 ft high. The slurry containing the copper oxide dust is pumped through a 36 in. filter press, Fig. 8.

Charging

As no refining is accomplished in the usual operation of the arc furnace, every effort is made to insure that the cathodes used for melting are free from nodulation, have a fine grained structure, and are washed to completely remove electrolyte. Special attention is given to washing electrolyte from the pockets formed by the cathode loops. The washed cathodes are stacked directly from the tank house washing machine on to rubber-tired, four wheel, steered trailers. Each trailer carries two piles of cathodes having a total average weight of 15,000 lb. After weighing, the stacks of cathodes are removed from the trailers by use of fork lift trucks and stored in an area directly behind the arc furnaces. Each of the two refined copper furnaces has an independent charging machine, consisting of a structural steel framework which supports a carriage containing two hydraulic tilting magazines, Fig. 9. Each magazine is designed to take a full pile of cathodes. The carriage is operated electrically so that when a charged magazine is lined up with the furnace charge chute a pair of hydraulically operated rams enables the operator to push the slightly inclined cathodes into the charge chute at any desired rate. The charging rate is determined by the furnaceman who takes into consideration the casting rate de-

sired, the pouring temperature, and the average weight of the cathodes being charged. The furnaceman sets the desired charging rate on the dial of a flexopulse, this causes a light to flash at the charging operators stand each time a cathode should be charged. In the meantime a pile of cathodes is being lifted and placed into the empty magazine of the charging machine by means of a 10-ton, overhead crane. As soon as the companion magazine is empty, the carriage is moved over allowing the newly filled magazine to come into charging position.

Cathodes from the charging machine slide down an inclined chute, through the water-cooled charge slot, directly into the bath of molten metal. Reject wirebars are charged back into the furnace by means of a chute that extends from the operating platform of the cathode charging machine to the charge slot.

Furnace Operation

The furnace operating crew consists of a furnaceman for each operating furnace, two chargers for each wirebar furnace, and three chargers for the anode furnace. One overhead craneman services the charging aisle and the crane follower hooks up the charge material for each operating furnace and records the necessary information regarding amount of material charged.

The set and oxygen content of the cast shapes is controlled by regulating the flow of gas and fume through the 13 in. diam water-cooled vent in the roof. A banjo shaped water-cooled boiler plate damper is used to regulate the vent opening. When the vent is closed the reducing action of the volatilized carbon from the electrode arc and the volatilized copper from the superheated copper at the point of arc impingement causes rapid reduction of the oxygen content of the molten copper. When the vent is opened the scavenging action of air which enters at the charge slot removes these elements and allows the molten copper to pick up oxygen. Control of the set of the cast copper shapes is maintained by careful regulation of the vent opening. Spot optical oxygen determinations are made every half-hour on samples taken at the furnace taphole along with block samples taken at the point where the molten copper flows from the furnace taphole into the launder leading to the pouring ladle. In normal operation the furnace is held in a horizontal position, the molten copper flowing from the furnace due to displacement by the incoming cathodes. The tilting mechanism enables the operator to tilt the furnace forward 45° when it is necessary to drain it, or tilt it backward 5° when skimming or during holdovers.

In all arc furnaces used for melting copper the arc strikes on a comparatively bare bath of molten metal. Melting under this condition results in a characteristic wave motion in the molten metal which in turn gives rise to excessive short circuit current surges. Meter readings become wild, sidewall temperatures rise, melting rate decreases and the furnace transformer tends to overheat. To overcome this characteristic a refractory ledge has been built at the metal line and extending in toward the center of the furnace approximately 9 in. This, however, is only a partial cure and it is necessary to cause a refractory slag ledge or shelf to build up and extend in still further to act as a damper to the wave motion. Since there are normally no slag making constituents available in the furnace, except ash from the consumed electrode, it is necessary

to cover part of the bath with magnesite material containing the desired amount of lime and silica. The arc fuses this material to a viscous condition and as the fluid or semifluid slag is formed the action of the arc showers it on to the walls of the furnace. Eventually it flows down the side of the wall and strikes the refractory ledge and extends in over the bath of molten metal, and as the metal temperature is lower than the wall temperature a ledge of slag develops around the metal line of the furnace except at the charge slot and skim bay sections. It has been observed that the melting rate of the furnace increases up to a certain point, as the ledge increases. Any of the brick that spalls from the walls or roof eventually causes the bank or ledge to grow until at times the build up may extend beyond an electrode. An opening may or may not develop which will allow the arc flame to come in contact with the molten bath. In such cases it is necessary to stop casting, open up the skim bay door and break off and remove the excess portion of ledge.

The amount of regular skimming necessary is entirely dependent upon the amount of refractory material that accumulates and is mostly caused by refractory failure. Under normal conditions the so-called slag consists of porous lumps of material, impregnated with small masses of copper. Ideal melting conditions are usually possible only after a good shelf has formed and the surface of the bath partly covered by the so-called slag. It is of extreme importance that the bath should not be allowed to become fully covered so that arcing will occur on the covering of the bath. If this happens a new set of conditions then immediately develops, the meters become stabilized, there is no surging in the low tension leads, the usual crackling noise that is an indication that copper melting is progressing in a satisfactory manner ceases and is replaced by a strong characteristic hum. At the same time copious fumes of volatilized carbon issue from the vent in the roof, and wall and shell temperatures rise at an exceedingly high rate, which in a very short time can

cause destruction of the roof and wall above the metal line. Simultaneously the copper temperature will drop due to the insulating covering on the bath. If the operator attempts to raise the metal temperature by increasing the power input then destruction of the furnace will progress at a still more rapid rate. Under these conditions the copper rapidly becomes oxygen free and is then fouled by the presence of undesirable elements. It will be observed when this happens that the molten copper flowing from the taphole no longer has a bright metallic appearance, but is soon covered by a dull flaky scum.

During the charge slot cleaning operation, also when slipping and adding electrodes, it is of course necessary to shut off the arc power and tilt the furnace forward to provide molten copper for the continuation of casting. Due to these delays an actual furnace melting rate of 22 tons per hour will only result in a continued casting rate of 19 to 20 tons per hour. Tercod pouring lips on the casting ladles enable casting to be continued 24 hr a day for as long as four days, without a shut down. Upon the completion of the tonnage requirements for a certain cast shape, the copper is diverted to the appropriate launder and casting is commenced on the alternate wheel which has previously been loaded with molds for casting the desired shape.

At the present time only horizontal shapes of electrocopper are cast at the Kennecott Utah Refinery, however, the melting equipment is ideal for the production of all types of vertical cast electro and deoxidized shapes if these should be required at some future date.

Acknowledgment

The writers wish to express their appreciation for the considerable time and help in the preparation of this article extended by Stanley Hughes, Assistant to the General Manager of Western Operations for Kennecott, and the entire Casting Department Staff of the Kennecott Utah Refinery, particularly that of M. C. Edlund.

Technical Note

Effect of Carbon on the Volume Fractions and Lattice Parameters Of Retained Austenite and Martensite

by C. S. Roberts

THE advent of a sensitive X-ray method of analysis recently has allowed the determination of retained austenite in amounts as low as 0.3 pct.¹ As a result this phase has been found in quenched low carbon steels where its presence has not been generally suspected.

In the course of a study of the tempering process,²

C. S. ROBERTS, Junior Member AIME, is associated with Metallurgical Laboratories, The Dow Chemical Co., Midland, Mich. TN 142E. Manuscript, Sept. 29, 1952.

retained austenite determinations were made by the X-ray method on a series of high purity Fe-C alloys and plain carbon steels. The chemical analyses of these materials and details of the hardening procedure are given in Table I. Results were obtained after quenching to 72°F (22°C) and -321°F (-196°C). Austenitizing temperatures were between 100° and 150°F above A_s or A_{cm} . All proeutectoid cementite or ferrite was in solution. The combination of the results with those of Averbach, Castleman, and Cohen,¹ and earlier results of Esser

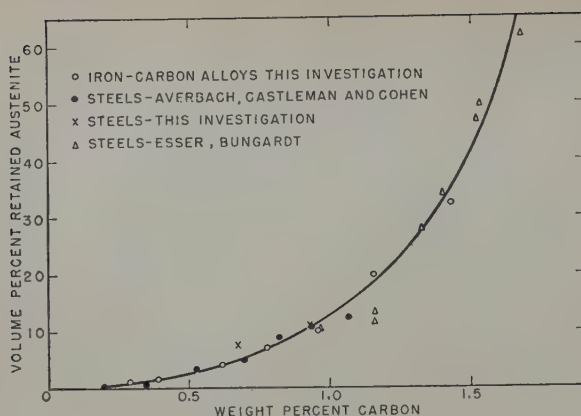


Fig. 1—Effect of carbon content on retained austenite content after quenching to room temperature.

and Bungardt³ are shown in Figs. 1 and 2. The results are better-defined functions of carbon content than have been available previously. The variation is smooth and there is no significant difference between the behavior of the high purity alloys and the plain carbon steels.

Also necessary for this work was a collection of all known data showing the effect of carbon content

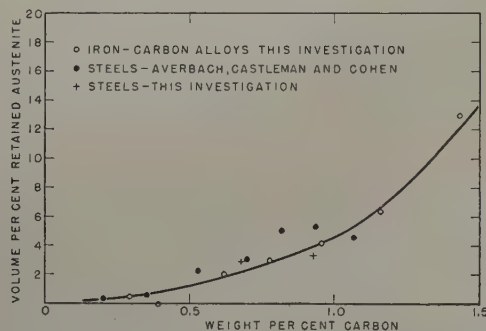


Fig. 2—Effect of carbon content on retained austenite after refrigeration to -321°F (-196°C).

on the austenite and martensite lattice parameters. All of the results which could be found⁴⁻¹² are shown in Fig. 3. The data of Kurdjumov and Kaminsky are apparently low. Neglecting their points, the parameters in kX units may be expressed by the function: Martensite: $c = 2.861 + 0.116x$; $a = 2.861 - 0.013x$; $c/a = 1.000 + 0.045x$; and austenite: $a = 3.548 + 0.044x$; $x = \text{wt pct C}$.

Acknowledgment

The author is grateful to S. G. Lorris, who per-

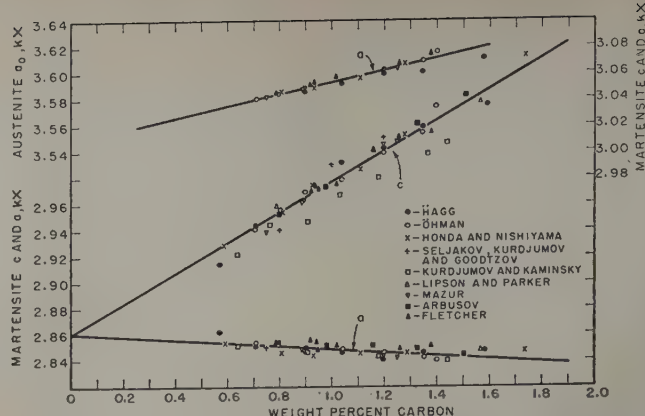


Fig. 3—Variation of martensite and austenite lattice parameters with carbon content.

formed the X-ray determinations and to B. L. Averbach and M. Cohen for guidance of the work.

References

- 1 B. L. Averbach, L. S. Castleman, and M. Cohen: Measurement of Retained Austenite in Carbon Steels. *Trans. ASM* (1950) **42**, p. 112.
- 2 C. S. Roberts, B. L. Averbach, and M. Cohen: The Mechanism and Kinetics of the First Stage of Tempering. To be published in *Trans. ASM* (1953) **45**.
- 3 H. Esser and W. Bungardt: The Heat Effect in Tempering Quenched Carbon Steels. *Archiv. Eisen.* (1934) **7**, p. 585.
- 4 G. Hagg: X-ray Investigation on the Structure and Decomposition of Martensite. *Jern. Ann.* (1934) **118**, p. 173; *Journal Iron and Steel Inst.* (1934) **130**, p. 439.
- 5 E. Ohman: X-ray Investigations on the Crystal Structure of Hardened Steel. *Journal Iron and Steel Inst.* (1931) **123**, p. 445.
- 6 K. Honda and Z. Nishiyama: On the Nature of Tetragonal and Cubic Martensites. *Sci. Rpts. Tohoku Imp. Univ. Ser. 1* (1932) **21**, p. 299; *Trans. ASST* (1932) **20**, p. 464.
- 7 N. Seljakov, G. Kurdjumov, and N. Goodtzov: An X-ray Investigation of the Structure of Carbon Steels. *Ztsch. Physik* (1927) **45**, p. 384.
- 8 G. Kurdjumov and E. Kaminsky: An X-ray Investigation of the Structure of Hardened Carbon Steels. *Ztsch. Physik* (1929) **53**, p. 696.
- 9 H. Lipson and A. M. B. Parker: The Structure of Martensite. *Journal Iron and Steel Inst.* (1944) **149**, p. 123.
- 10 J. Mazur: Lattice Parameters of Martensite and of Austenite. *Nature* (1950) **166**, p. 828.
- 11 M. P. Arbusov: The Structure of Martensite Electrolytically Separated from Hardened Steel. *DAN, SSSR* (1950) **74**, p. 1085.
- 12 S. G. Fletcher: The Tempering of Plain Carbon Steels. Sc.D. Thesis, Massachusetts Institute of Technology, 1943.

Table I. Composition and Metallography of Alloys

Alloy or Steel No.	C, Pct	Mn, Pct	Si, Pct	Austenitizing Temperature, °F	Quenching Medium	Fracture Grain Size	Retained Austenite, Quenched to 72°F, Pct	Retained Austenite, Refrigerated, Pct
122	0.29	*	*	1600	10% brine	6	1.2	0.4
123	0.39	*	*	1550	10% brine	5	1.6	0.1
124	0.62	*	*	1500	10% brine	4½	4.1	2.0
103†	0.68	0.78	0.21	1500	Water	6	7.6	2.9
125	0.78	*	*	1500	10% brine	5½	7.0	3.0
105†	0.93	0.42	0.19	1550	Water	6	11.0	3.3
126	0.96	*	*	1550	10% brine	4½	10.0	4.1
127	1.16	*	*	1650	Water	70% 1, 30% >1	19.9	6.4
128	1.43	*	*	1850	Water	>1	32.3	12.9

* For the high purity alloys, silicon and oxygen <0.01 pct, all other elements <0.001 pct.

† Steel.

Effect of Tensile Strain at Low Temperatures on Deformation Twinning in Ingot Iron

by Glenn W. Geil and Nesbit L. Carwile

A metallographic study was made of deformation twinning (Neumann lamellae) in ingot iron slowly deformed in tension at -196° and -150°C . The results showed that twinning is initiated mainly during the initial stages of plastic deformation. However, the breadth of the twins generally increases with increase in strain up to fracture of the specimen.

THE results of an investigation of the effect of low temperatures on the flow, fracture, strain hardening, and strain aging characteristics, and the true stress-strain relationship for specimens of ingot iron deformed in tension were reported recently.^{1,2} In that study specimens of ingot iron, in different initial conditions, were slowly deformed in tension at various temperatures between -196° and $+100^{\circ}\text{C}$. A phenomenon observed, but only briefly reported, was the formation of deformation twins (Neumann lamellae) in the specimens deformed at the lower temperatures. Preliminary metallographic examination of these specimens indicated that there was apparently some correlation between the deformation twinning and the strain of the specimen and that this factor merited further investigation.

Some recent investigations have indicated a direct association of Neumann lamellae and the fracture of the metal. Bruckner^{3,4} postulated that the twinning immediately precedes the fracture and the latter is initiated by the stopping of the propagation of twins, either at subgrain boundaries or at other structural features. Tipper and Sullivan⁵ postulated that Neumann lamellae are initiated by the shock or a shock wave set up at fracture in the still highly stressed unbroken metal, and that a high rate of deformation is a necessary condition for their formation.

An extensive metallographic examination, therefore, was made of many of the specimens used in the study of ingot iron at this Bureau and of additional specimens deformed to selected strains under various conditions. The present paper summarizes the effects of deformation under these conditions

upon the breadth and scope of the deformation twins. Other features of twinning will be discussed in another paper.

Material and Testing Procedure

All of the specimens were prepared from one lot of ingot iron, as hot-rolled, of chemical composition other than iron as follows: C, 0.02 pct; Mn, 0.02; P, 0.005; S, 0.018; Si, 0.002; Cu, 0.10; O, 0.058; and N, 0.002.

Cylindrical tensile specimens with a 2 in. gage length were used. The reduced section was slightly tapered from each end; the diameter (0.438 in.) at the midsection of the gage length was about 0.003 in. less than at the ends. The specimens were finished to the final dimensions by grinding and polishing in the axial direction. The ends of the specimens were machined with $\frac{3}{4}$ in. x 10 threads and the shoulder fillets were machined to a radius of 0.75 in.

The specimens were extended slowly in tension (deformation rate less than 0.5 pct reduction in area per minute) while immersed in an appropriate cryogenic liquid maintained at the desired temperature. The minimum diameter of the specimen was measured during the test by means of a specially designed reduction of area gage accurate to 0.0001 in.⁶ A detailed description of the testing equipment and the method of maintaining the desired temperature is given in a previous paper.¹

Each specimen, after deformation to a specified strain at a selected temperature, was sectioned longitudinally and examined metallographically. The preparation of specimens for metallographic examination was carried out in the usual manner by mechanical polishing and etching.

Results and Discussion

Deformation twins in specimens of ingot iron extended slowly in tension at -196° and -150°C are shown by the representative micrographs of Figs. 1

G. W. GEIL, Member AIME, and N. L. CARWILE are Metallurgists, National Bureau of Standards, Washington, D. C.

Discussion on this paper, TP 3483E, may be sent, 2 copies, to AIME by April 1, 1953. Manuscript, Sept. 12, 1952; revised, Nov. 26, 1952. Los Angeles Meeting, February 1953.

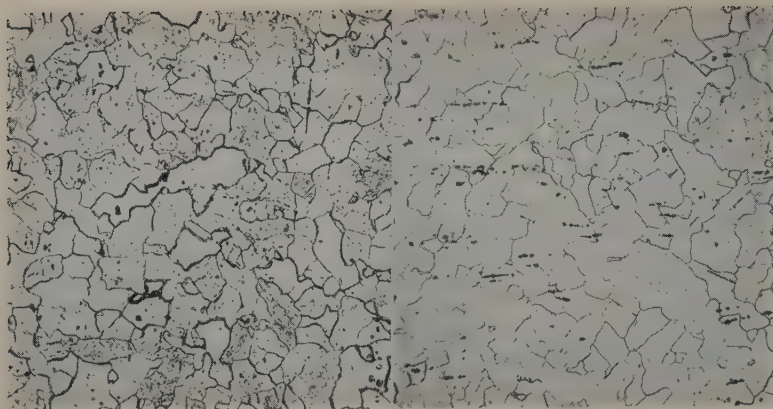


Fig. 1 (a and b, left; c and d, below)—Microstructure of specimens of hot-rolled ingot iron after extension in tension at -196°C to different strains. Etchant: 4 pct solution of nitric acid in ethyl alcohol. Longitudinal sections. X100. Area reduced approximately 50 pct for reproduction.

a (left)—True strain of 0.0019, elastic strain only, (true stress, 91,200 psi).

b (right)—True strain of 0.0037 (true stress, 100,500 psi).

c (left)—True strain of 0.0051 (true stress, 103,600 psi).

d (right)—True strain of 0.0087, upper yield point, (true stress, 110,500 psi).

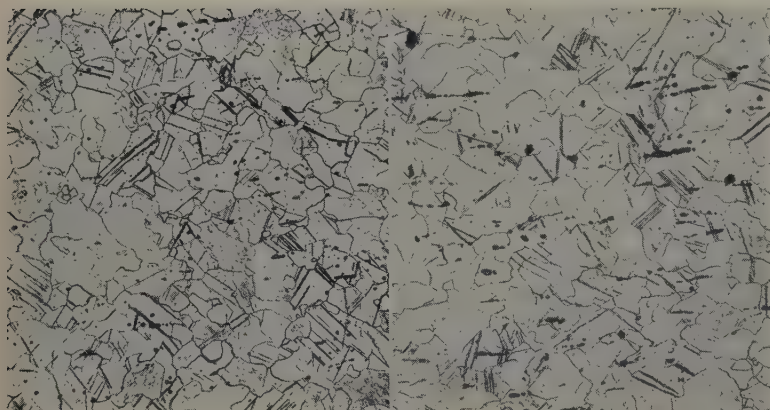
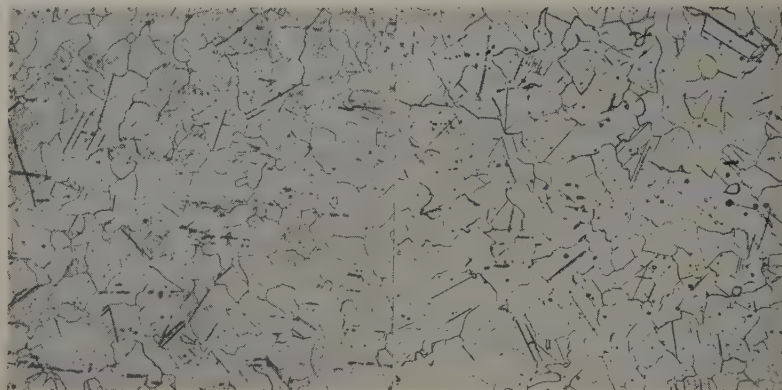


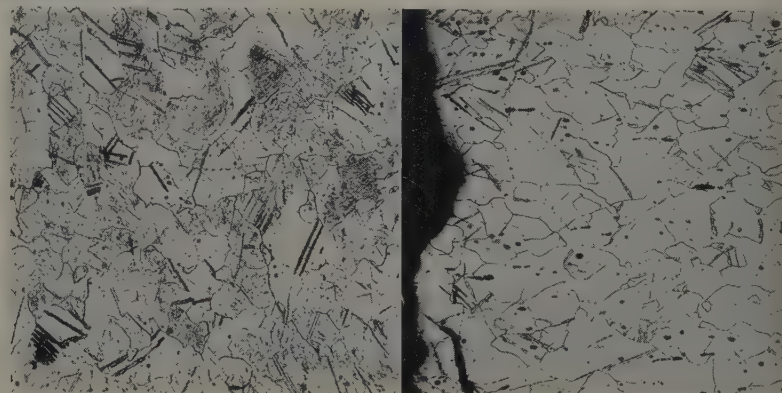
Fig. 2 (a and b, left; c and d, below)—Microstructure of specimens of hot-rolled ingot iron after extension in tension at -196°C to different strains. Etchant: 4 pct solution of nitric acid in ethyl alcohol. Longitudinal sections. X100. Area reduced approximately 50 pct for reproduction.

a (left)—True strain of 0.045, lower yield point, (true stress, 109,800 psi).

b (right)—True strain of 0.115, maximum load, (true stress, 122,600 psi).

c (left)—True strain of 0.166 (true stress, 132,700 psi).

d (right)—True strain of 0.289, fracture, (true stress, 141,000 psi).



to 6. In these figures the horizontal direction lies parallel to the axis of the specimens.

A specimen extended only in the elastic range to a total true strain* of 0.0019 at -196°C showed no

* Total true strain as designated in this paper is determined by $\log_e A_0/A$, in which A_0 and A represent the initial and current minimum cross-sectional areas of the specimen, respectively.

evidence of twinning, Fig. 1a, whereas a specimen extended at the same temperature to a total true

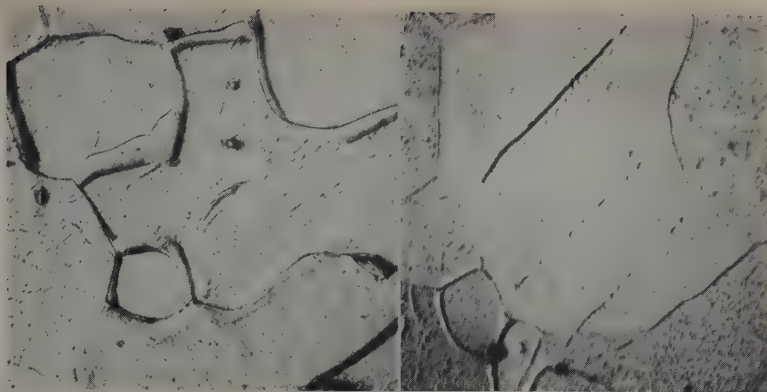
strain (elastic plus plastic) of 0.0037, of which approximately 0.002 was measured as plastic strain, exhibited a very few twins, Fig. 1b. The number of twins per unit area generally increased as the true strain of the specimen was increased through that of the upper yield point, 0.0078† and up to that at

† Tensile specimens of hot-rolled ingot iron may deform plastically to a considerable extent before the upper yield point is reached. This plastic deformation is generally much greater at low temperatures (-196° and -150°C) than at room temperature.

Fig. 3 (a and b, right; c and d, below)—Microstructure of specimens of hot-rolled ingot iron after extension in tension at -196°C to different strains. a, c, and d etchant: 4 pct solution of nitric acid in ethyl alcohol; b, etchant: 5 pct solution of nitric acid in amyl alcohol. Longitudinal sections, oblique illumination (left to right). X1000. Area reduced approximately 50 pct for reproduction.

a (left)—True strain of 0.0019, elastic strain only, (true stress, 91,200 psi).

b (right)—True strain of 0.0037 (true stress, 100,500 psi).



c (left)—True strain of 0.0051 (true stress, 103,600 psi).

d (right)—True strain of 0.0087, upper yield point, (true stress, 110,500 psi).

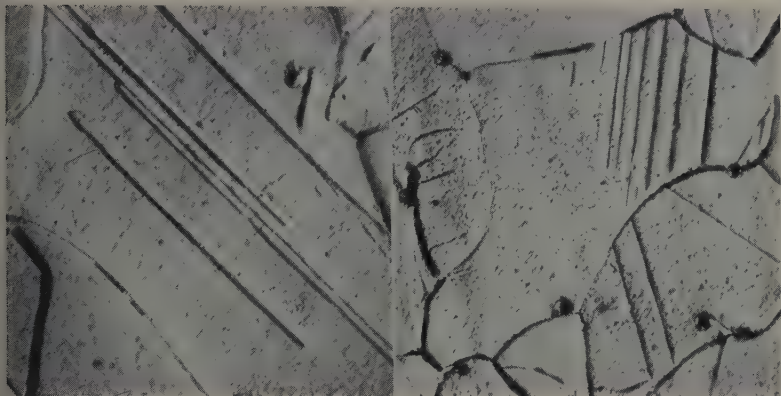
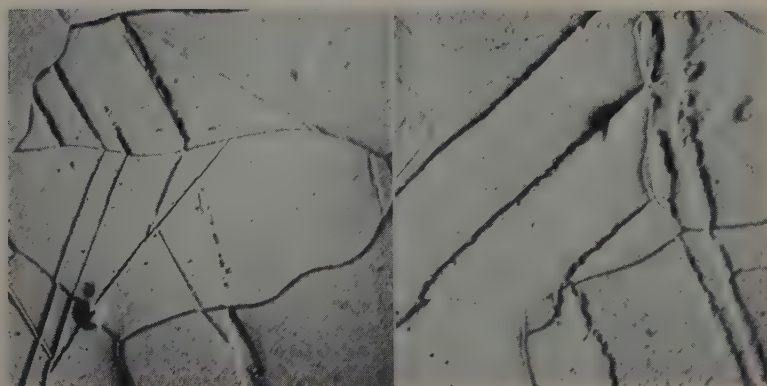


Fig. 4 (a and b, right; c and d, below)—Microstructure of specimens of hot-rolled ingot iron after extension in tension at -196°C to different strains. Etchant: 4 pct solution of nitric acid in ethyl alcohol. Longitudinal sections, oblique illumination (left to right). X1000. Area reduced approximately 50 pct for reproduction.

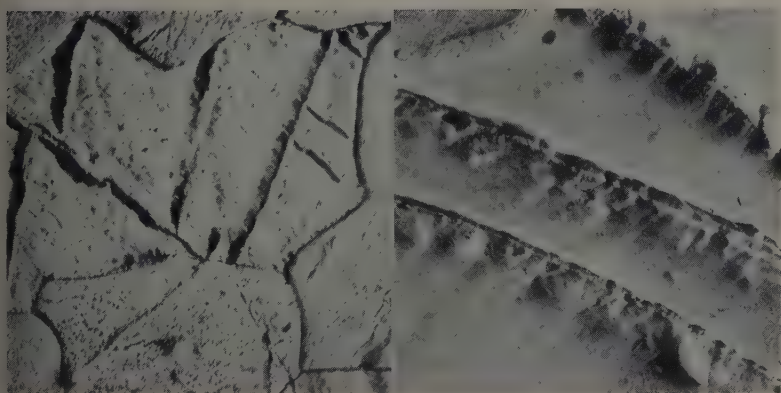
a (left)—True strain of 0.045, lower yield point, (true stress, 109,800 psi).

b (right)—True strain of 0.115, maximum load, (true stress, 122,600 psi).



c (left)—True strain of 0.166 (true stress, 132,700 psi).

d (right)—True strain of 0.289, fracture, (true stress, 141,000 psi).



the lower yield point, 0.045, Figs. 1c and d and 2a. However, no significant increase in the number of twins per unit area was observed as the specimens were further deformed to greater strains even up to fracture, Fig. 2b, c, and d. Furthermore, specimens extended at -150°C to selected strains revealed this same general dependency of deformation twinning on the plastic strain. A very few twins were observed in the specimen extended to the upper

yield point (total true strain of 0.0037) and the number of twins per unit area generally increased with increase in the strain of the specimens up to a total true strain of about 0.06. Further deformation of specimens up to fracture did not significantly increase the number of twins.

The values of strains corresponding to the upper and lower yields, respectively, were smaller in the specimens extended at -150° than at -196°C . The

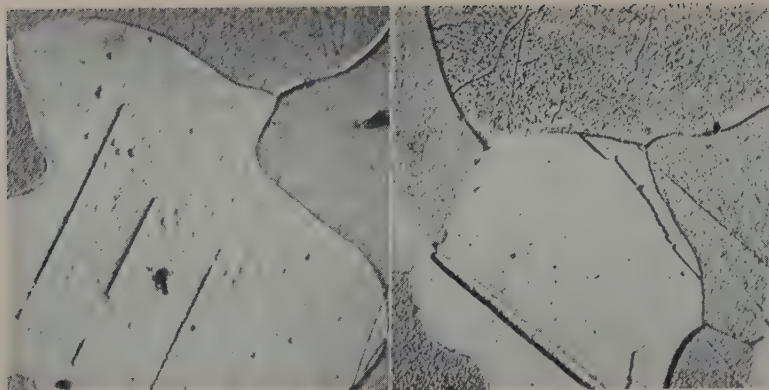


Fig. 5 (a and b, left; c and d, right)—Microstructure of specimens of hot-rolled ingot iron extended in tension at -150°C to different strains. Etchant: 5 pct solution of nitric acid in amyl alcohol. Longitudinal sections, oblique illumination (left to right). X1000. Area reduced approximately 50 pct for reproduction.

a (left)—True strain of 0.0037, upper yield, (true stress, 93,900 psi).

b (right)—True strain of 0.0089 (true stress, 86,200 psi).

c (left)—True strain of 0.040, lower yield, (true stress, 82,300 psi).

d (right)—True strain of 0.063 (true stress, 87,500 psi).

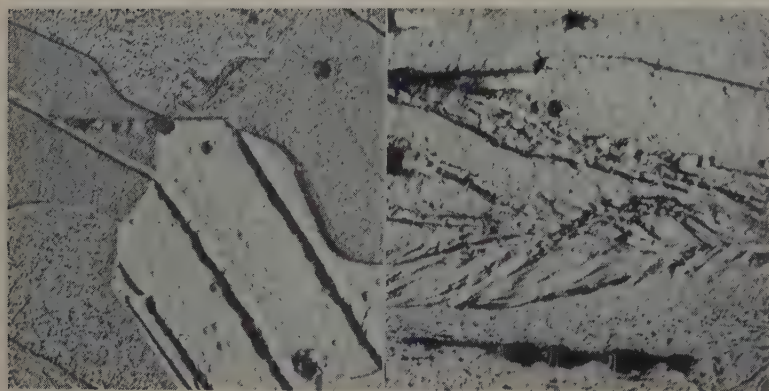
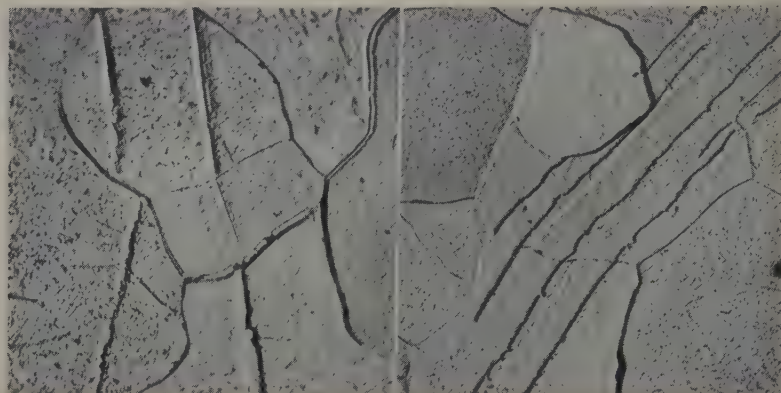


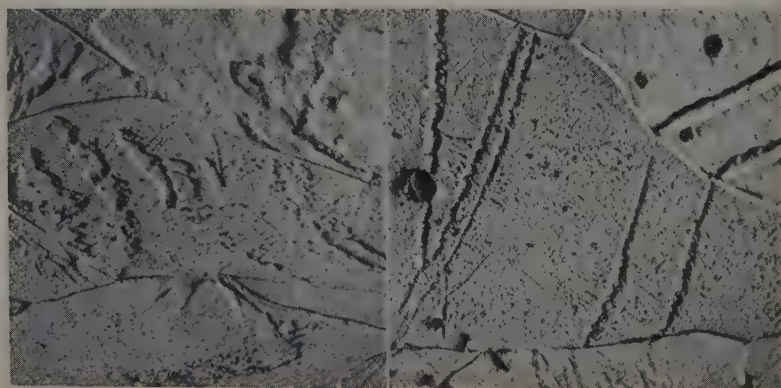
Fig. 6 (a and b, left; c and d, below)—Microstructure of specimens of hot-rolled ingot iron after extension in tension at -150°C to different strains. Etchant: 5 pct solution of nitric acid in amyl alcohol. Longitudinal sections, oblique illumination (left to right). X1000. Area reduced approximately 50 pct for reproduction.

a (left)—True strain of 0.127 (true stress, 95,400 psi).

b (right)—True strain of 1.107, adjacent to fracture, (true stress, 147,200 psi).

c (left)—Same specimen as b, 0.1 in. from fracture.

d (right)—Same specimen as b, 0.6 in. from fracture.



amount of twinning at the upper or lower yield, respectively, was also smaller at -150° than at -196°C . However, the dependency of the number of deformation twins on the degree of strain ($\log_e A_0/A$) was similar at each test temperature. Thus, the deformation twinning apparently occurs with small strains irrespective of the yield-point phenomenon.

The results definitely show that the twinning in hot-rolled ingot iron slowly deformed in tension at

low temperatures is initiated during the early plastic deformation. Furthermore, there was no evidence obtained that indicated any increase in the number of twins per unit area in the deformed specimens as a result of fracture. The number of twins per unit area in the fractured specimens was not significantly greater than that in specimens extended to a strain of about 0.06 or more but not fractured. Therefore, a shock or shock wave set up at complete fracture

is not an essential requirement for the formation of deformation twins in ingot iron at low temperatures.

The micrographs of Figs. 3 to 6, which were taken at high magnification and with oblique lighting, show the effect of strain on the breadth of twins. All of the twins observed in specimens deformed to small strains were relatively narrow (Figs. 3b and 5a) whereas the majority of twins in specimens deformed to greater strains were somewhat broader, although some narrow twins were observed in these latter specimens. Apparently an increase in strain tends to cause a growth in breadth of a twin; however, it is recognized that the observed breadth is also dependent upon the relative orientation of the twin plane to the plane of the section observed.

The thinner twins observed in the same micrograph or even in the same grain with broader twins may be due to a less favorable orientation of the twin plane with respect to that of the parent grain and the direction of loading of the specimen. Examination of a very large number of micrographs revealed that: 1—Twins in the same direction within a grain are, in most cases, approximately the same breadth, and 2—The breadth and irregularity in shape of twins generally increase with increase in the strain up to the fracture of the specimen.

The severe deformation of the ferrite grains in the necked section of the specimen extended to fracture at -150°C (Fig. 6b and c) resulted in a general obscuring and considerable bending of the deformation twins. The bending was caused by deformation of the grains subsequent to the formation of the twins. Bent twins also were observed in other specimens deformed at -150° and -196°C . The ductility of the twins as revealed by degree of bending in tension at low temperatures indicates that deformation twinning is not the cause of low temperature embrittlement of ingot iron.

The data obtained in this study, such as that shown in Figs. 3 to 6 illustrating the growth of deformation twins in ingot iron and in many other micrographs not shown, indicate that the twinning may be a nucleation and growth process and not a simultaneous shear mechanism as often proposed. However, for brevity of the present paper, discussion of these fea-

tures is not included but will be given in detail in a separate paper.

Conclusions

The results of a metallographic study of deformation twinning in specimens of hot-rolled ingot iron slowly extended in tension at -150° and -196°C to selected strains show that twinning is initiated during the early stages of plastic deformation and that a shock or shock wave set up at fracture is not an essential condition for their formation. The number of twins per unit area increases with increase in strain up to a true strain of about 0.05 or 0.06, but greater strains do not appreciably increase the number of twins. The breadth and irregularity in shape of the twins generally increase with increase in the strain up to fracture of the specimen.

The ductility of deformation twins as revealed by the degree of bending in tension at low temperatures indicates that deformation twinning is not the cause of low temperature embrittlement of ingot iron.

Acknowledgments

This work was sponsored by the Ordnance Dept., U. S. Army through the Ordnance Corps, Watertown Arsenal. The authors are also indebted to C. R. Johnson and J. D. Grimsley for assistance in this investigation.

References

- ¹G. W. Geil and N. L. Carwile: Tensile Properties of Ingot Iron at Low Temperatures. *Journal of Research Nat. Bur. Standards* (1950) **45**, p. 129, RP2119.
- ²G. W. Geil and N. L. Carwile: Effect of Strain-Temperature History on the Flow and Fracture of Ingot Iron at Low Temperatures. *Journal of Research Nat. Bur. Standards* (June 1952) **48**, p. 399, RP2329.
- ³W. H. Bruckner: The Micromechanism of Fracture in the Tension Impact Test. The Research Supplement, *Welding Journal* (1950) **29**, p. 467s.
- ⁴W. H. Bruckner: The Micromechanism of Fracture in the Tension Impact Test. Supplementary Report No. 1. The Research Supplement, *Welding Journal* (1951) **30**, p. 459s.
- ⁵C. F. Tipper and A. M. Sullivan: Fracturing of Silicon-Ferrite Crystals. *Trans. ASM* (1951) **43**, p. 906.
- ⁶G. W. Geil and N. L. Carwile: A Reduction-of-Area Gage for Use at Low Temperatures. *Journal of Research Nat. Bur. Standards* (1949) **43**, p. 527, RP2044.

Technical Note

Slip and Grain Boundary Sliding as Affected by Grain Size

by Nicholas J. Grant, Italo S. Servi, and Arup Chaudhuri

IN a recent paper by Servi and Grant,¹ it was illustrated that the slip band spacing and stress based on creep test data were related by the equation:

$$d \cong \frac{1}{\sigma}$$

where d is the spacing in millimeters and σ is the stress in psi, based on a more complete equation proposed by Orowan. It was shown further,¹ that for a given grain size, the slip band spacing became larger with decreasing stress (and was independent of temperature), until such time that the slip band spacing becomes greater than about one-half the grain diam-

eter. When this occurred, the mechanism of deformation in creep of 2S aluminum at high temperature changed from slip to grain boundary deformation (sliding). Additional metallographic evidence is now available which confirms this in a most interesting fashion.

N. J. GRANT, Member AIME, is Associate Professor, Dept. of Metallurgy, Massachusetts Institute of Technology, Cambridge, Mass., I. S. SERVI, Junior Member AIME, and A. CHAUDHURI are associated with Union Carbide and Carbon Research Laboratories, Inc., Niagara Falls, N. Y.

TN 144E. Manuscript, Sept. 18, 1952.

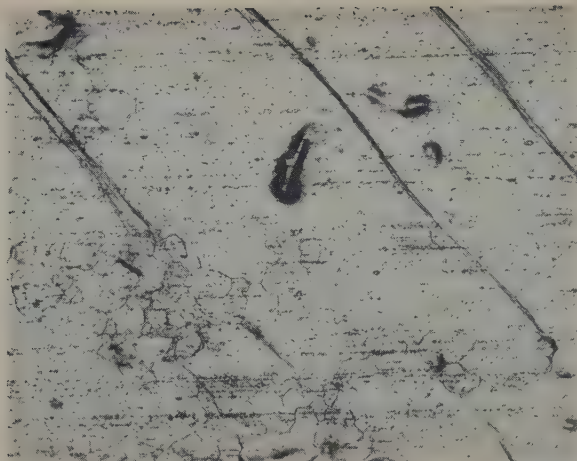


Fig. 1—2S aluminum tested in creep at 900°F, 880 psi, 3.5 pct total elongation. Oblique illumination. Shows slip bands in coarse grain and grain boundary sliding in fine grained zones. Stress in vertical direction. X150. Area reduced approximately 50 pct for reproduction.



Fig. 2—2S aluminum tested in creep at 900°F, 880 psi, 9 pct total elongation. Oblique illumination. Coarse grain shows slip, fine grains show grain boundary sliding, and medium sized grain (upper center) shows both. Stress in vertical direction. X150. Area reduced approximately 50 pct for reproduction.



Fig. 3—2S aluminum tested in creep at 900°F, 880 psi, 9 pct total elongation. Micrograph near necked zone. Shows slip and grain boundary sliding in medium grains and slip in coarse grain. Stress in vertical direction. X150. Area reduced approximately 50 pct for reproduction.

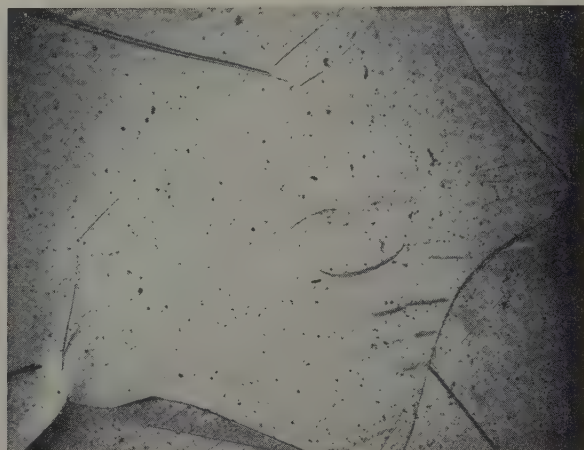


Fig. 4—High purity magnesium tested in creep at 500°F, 670 psi. Shows pyramidal slip of two coarse spacing to be accommodated by fine grain which shows grain boundary sliding instead. Stress in vertical direction. X50. Area reduced approximately 50 pct for reproduction.

The 2S aluminum was recrystallized in a double treatment to yield a mixed grain size. A test bar, similar to that described in ref. 1, was heated at 950°F for 3 hr, producing a rather regular, fine grain size. A second heat treatment of 1150°F for 1 hr then yielded a mixed grain size of such nature that in some parts of the specimen small grains were imbedded in a larger grain, see Fig. 1.

These specimens were tested in creep at 900°F at a stress of 880 psi. Fig. 1, after 3.5 pct elongation, shows that the large crystal deformed by slip. The fine grains located in the large grain do not show slip bands, however, the grain boundaries are "thickened" indicating grain boundary sliding. The lower left slip band is apparently continuous on either side of the fine grained cluster, but does not penetrate these fine grains. The slip band spacing is obviously much larger than the grain diameter.

Fig. 2, after 9 pct deformation, shows slip as the deformation mechanism of the coarse grain and grain boundary sliding as the mechanism of the fine grained cluster in the upper right corner. In the upper center is a grain which is apparently of marginal size since a slip band has developed in it.

Fig. 3 shows another specimen deformed more than 9 pct (near the necked area). Here the slip band spacing is small enough so that many of the finer grains are more than twice the average slip band spacing. These grains also deformed by slip, the spacing being almost the same as that of the coarse grain. At the bottom is a cluster of very fine grains, the larger ones showing one or two slip bands, while the finer ones show some grain boundary sliding.

Similarly, a high purity magnesium specimen, Fig. 4, tested at 500°F and 670 psi when tested in creep shows pyramidal slip bands of uniform spacing in a large grain but no slip bands in the small enclosed grain, the grain boundary of which shows evidence of sliding.

These micrographs clearly support the evidence that grain boundaries have a blocking effect on slip at high temperatures; and at a given grain size, for a given stress, will undergo sliding as a primary mechanism of deformation.

¹I. S. Servi and N. J. Grant: Structure Observations of Aluminum Deformed in Creep at Elevated Temperatures. *Trans. AIME* (1951) 191, p. 917; *JOURNAL OF METALS* (October 1951).

Absolute Rate Theory Applied To Rate of Growth of Pearlite

by J. H. Frye, Jr., E. E. Stansbury, and D. L. McElroy

The rates of growth of pearlite in high-purity Fe-C alloys have been measured as a function of the transformation temperature. These and other data have been correlated in terms of a derived rate equation. Activation energies for the growth were found to be 24,200 cal per mol of austenite for the 0.78 pct C alloy and 27,600 cal per mol for the 0.93 pct C alloy. Theoretical implications are discussed.

AN excellent review of the the theoretical and experimental studies on the mechanism and kinetics of the eutectoid reaction has been presented recently by Mehl and Dube.¹ They have pointed out that these investigations have followed two lines of approach: 1—experimental studies and derivations of expressions for the overall transformation characteristics, and 2—derivation of expressions for the nucleation and growth rates in terms of fundamental

processes. Investigations of the latter type have been concerned for the most part with the nature of the growth at the austenite-pearlite interface in plain carbon and alloy eutectoid steels. They discuss two theories of the rate of growth of pearlite from austenite—those of Brandt and of Zener. Both derive rate equations which are based on the assumption that carbon diffusion is the controlling mechanism. Mehl and Dube,¹ Zener,² and Brandt^{3, 4} have attempted to calculate growth rates by use of these equations together with thermodynamic and diffusion data. The results are encouraging, but agreement is not so good as to constitute verification of the theories.

Furthermore, it is not clear how these equations are to be used to study the effect of alloying elements which apparently exert little influence on carbon diffusion, but markedly decrease growth rates. It is not clear whether or not the addition to iron of an alloying element which does not diffuse during transformation can alter the rate of growth of body-centered from face-centered cubic iron. That it can greatly decrease the overall transformation rate has

J. H. FRYE, JR., Member AIME, is Director, Metallurgy Div., Oak Ridge National Laboratory, operated by Carbide and Carbon Chemicals Corp., Oak Ridge, Tenn., E. E. STANSBURY, Junior Member AIME, is Professor of Metallurgy, University of Tennessee, Knoxville, Tenn., and D. L. McELROY is Graduate Student, Metallurgical Engineering, University of Alabama and Oak Ridge Institute of Nuclear Studies Graduate Fellow.

Discussion on this paper, TP 3489E, may be sent, 2 copies, to AIME by April 1, 1953. Manuscript, May 23, 1952; revised, Sept. 30, 1952. Los Angeles Meeting, February 1953.

This paper is based on research at the Metallurgy Div., ORNL by D. L. McElroy, to be incorporated in a thesis to be submitted in partial fulfillment of the requirements for the degree of Master of Science in Metallurgical Engineering to the University of Alabama.

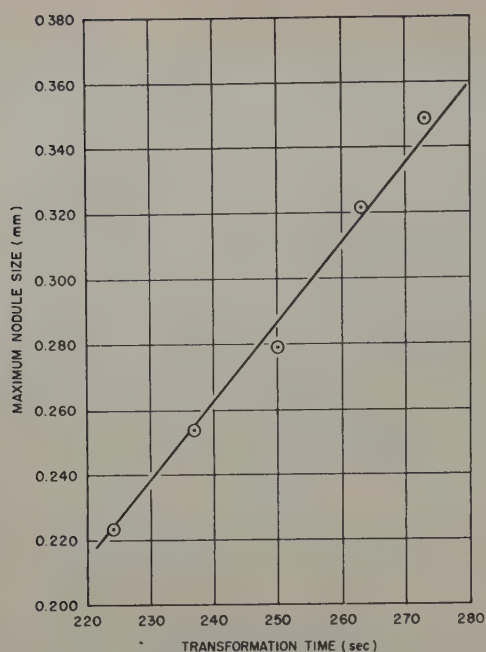


Fig. 1—Growth rate data at 708°C.

been shown by Austin and Pierce,⁵ who investigated a binary Fe-Cr alloy containing 9 pct Cr (carbon less than 0.03 pct). In this alloy, the two-phase region extends over a temperature interval of 5°C. There is no reason to believe that chromium diffuses during transformation below this region. The maximum rate of isothermal reaction occurs at 700°C, with a time for 50 pct transformation of 180 sec. In a high-purity Fe-C alloy containing 0.93 pct C, this time is only 1.3 sec at a temperature of 547°C.⁶ In pure iron, the time is presumably much less. It is possible that the effect of chromium in slowing the transformation rate is entirely in its influence on rate of nucleation and that rate of growth is quite unchanged, but there does not appear to be any reason to suppose that this is the case.

From an examination of the growing eutectoid interface, it is evident that diffusional processes are essential to the growth mechanism; however, it is not evident that diffusion, per se, is the controlling mechanism of the several which must operate across the interface during growth. In the growth of pearlite from austenite, carbon must diffuse in the austenite from the ferrite to the cementite interface. Furthermore, some diffusion of iron must occur to accommodate the volume changes accompanying the formation of ferrite and cementite. In addition, the actual interface mechanisms whereby austenite of the correct carbon content is transformed to cementite and to ferrite must be considered. Unfortunately, little is known of the latter for phase transformations of any type; but it does not seem improbable that they could constitute the rate-determining step in the growth process. Of the many

mechanisms that might be considered, the following are given as examples: 1—atom by atom jumps across the interface, 2—formation of groups of atoms of the proper composition which, by suitable rearrangement, pass from the initial to final phase, 3—shears of either large or small numbers of atoms at the interface, and 4—growth by movement of dislocations. Each of these should operate with a characteristic activation energy.

It appears that additional work in this field is needed and also that a more general approach to the problem might be profitable. Such an approach is the following:

1—Derive a general equation for the rate of growth of pearlite from austenite which assumes no particular mechanism except that the rate is determined by the surmounting of an energy barrier.

2—Measure the rate of growth of pearlite from austenite in a high-purity Fe-C eutectoid, interlamellar spacings, and the necessary thermodynamic quantities to calculate free energy differences between pearlite and austenite. Use these thermodynamic and rate data to calculate the constants in the equation.

3—Measure rates of growth, interlamellar spacings, and thermodynamic quantities for Fe-C eutectoids which contain a third element, and use these data to calculate the constants in the equation.

4—Observe the effect of the alloy additions on the constants of the equation. This should lead to some understanding of the effect of alloying elements on rate of growth.

In this paper, an equation is derived which expresses rate of growth of pearlite from austenite in high-purity Fe-C alloys as a function of the difference in free energy between the two, the activation energy for the reaction, the absolute temperature, and certain constants. Constants in this equation, including the activation energy, are calculated from the following experimental data: 1—heat of transformation and specific heats for the Fe-C system, and 2—rates of growth of pearlite at various degrees of super cooling.

Heats of transformation⁷ and specific heat⁸ data have been taken from the published values for such quantities. Data on the rate of growth of pearlite in a 0.93 pct C high-purity steel have been taken from the work of Hull, Colton, and Mehl.⁶ Growth-rate data on a high-purity steel containing 0.78 pct C have been determined experimentally in this investigation.

Results of measurements of the growth rate of a high-purity, 1 pct Mn eutectoid steel with a similar analysis of the data will be reported in a later paper. It is hoped that these studies will contribute to a better understanding of the effects of alloying elements in steel and of the factors governing hardenability.

Experimental Procedure

The objectives of the experimental work reported herein were to obtain further data on the growth rate of the pearlite-austenite interface in eutectoid Fe-C alloys of sufficient purity to make theoretical interpretations of the data as straightforward as possible. Hull, Colton, and Mehl⁶ have reported the pearlite growth rates for a high-purity Fe-C alloy containing 0.93 pct C. Since such an alloy is slightly hypereutectoid, it was desired to obtain data on an alloy as near 0.80 pct C as possible.

High-purity electrolytic iron previously reduced with hydrogen was melted with high-purity graph-

Table I. Analyses of High-Purity Steels

Steel	C	Si	Mn	P	S	Cr	Ni
0.78 pct C*	0.78	0.03	0.005	0.003	0.013		
0.93 pct C	0.93	0.002	0.004	0.005	0.0001	0.005	0.006

* Spectrographic analysis of the 0.78 pct C alloy indicated that none of the following elements were present in excess of 0.005 pct, and many were sought and not found: Cb, Cr, Cu, Mo, Ni, Ti, V, W, and Zr.

ite in fused zirconia crucibles using induction heating and a purified argon atmosphere. The melt was solidified in the crucible to give an ingot 1¼ in. in diameter and 4 in. long. The ingot was homogenized for 48 hr at 1100°C in vacuum after which it was hot rolled to ½-in. round rod. The analysis of the resulting material is given in Table I, along with the analysis of steel used by Hull, Colton, and Mehl.⁹

The rod was then machined to 7/16-in. diam to remove possibilities of any extraneous effects due to a contaminated surface, and then cut into disks 0.060 ± 0.003 in. thick for transformation studies.

The experimental method of running the isothermal transformations and determining the growth rates was essentially that of Hull, Colton, and Mehl.⁹ It consists of heating the specimen into the austenite range and quenching to a predetermined isothermal subcritical temperature after which it is quenched to room temperature. The transformation is observed to occur by a process of nucleation at the grain boundaries and the subsequent growth of the pearlite as nodules. These nodules are roughly spherical at the higher temperature (20°C subcool), growing from both sides of the boundary from which they are nucleated, and may consume several grains before impinging on other nodules. At lower temperatures, growth is hemispherical from nuclei on one side of the grain boundary, and the relatively greater rate of nucleation prevents growth much greater than the grain radius before impingement occurs.

The rates of growth at the higher temperatures were obtained by examining a large number of nodules and plotting the diameter of the largest nodule as a function of the time. At lower temperatures, the measurements are more difficult, since the growth is hemispherical. In this case, it is necessary to restrict measurements to those grains which are known to have been cut near their center, thus permitting measurements on the nodule perpendicular to the grain surface. A problem encountered in such measurements is the location of the grain boundary when nucleation has occurred with subsequent growth on both sides of the grain boundary. A technique of repeated polishing and etching, followed by examination under polarized light, was developed which revealed the martensite grain boundaries so that their extension through the pearlite could be accurately predicted. The growth rates were obtained from the slope of the maximum nodule-time plots.

Hull, Colton, and Mehl⁹ have reported a half-reaction time for their steel of 2 sec at 599°C for material having ASTM grain size No. 1. Since impingement occurs after 15 pct transformation to an extent making growth measurements impossible, it is evident the accurate growth-rate data are difficult to obtain for specimens undergoing such rapid transformation. In this investigation, an austenitizing temperature of 1300°C for 30 min was used to increase the grain size to No. -1. Under these conditions, the shortest half-reaction time was increased to about 3 sec, thus permitting improved accuracy of measurement.

All transformations were carried out automatically in equipment developed for these studies. The apparatus consists essentially of a small platinum-wound furnace, a stirred lead bath, and mercury quench arranged so that the specimen mounted on the end of a piston rod and activated by pressure-vacuum could be automatically indexed to any posi-

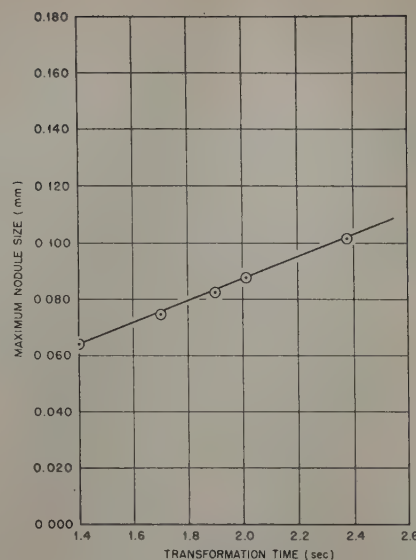


Fig. 2—Growth rate data at 640°C.

tion. The entire space above these three units and in which the specimen moves is filled with purified argon. In this manner, a very clean lead bath is maintained which, with the bright specimens, gives excellent quenching conditions. The transfer time for one position to another is approximately 0.2 sec, and transformation times are probably consistent to about 0.05 sec. The time of transformation is taken as the time interval from quenching into the lead bath to quenching into the mercury. The austenitizing temperature was controlled to ± 5°C and the lead-bath to ± 0.3°C. The lead-bath temperatures are measured with chromel-alumel thermocouples standardized against Bureau of Standards Metals.

Representative plots of nodule radius vs time are shown in Figs. 1 and 2. At the lower temperatures, both a nodular and a feathery constituent are observed. The appearance of the nodular structure was identical with the fine pearlitic structures measured at slightly higher temperatures. No measurements were made on the feathery constituent, but were confined to the nodular constituent.

The growth-rate data for the 0.78 pct C steel are summarized in Fig. 3. The data of Hull, Colton, and Mehl⁹ on a steel containing 0.93 pct C are indicated for comparative purposes. It is evident that the rates are slightly slower for the eutectoid steel and that a definite maximum in the growth rate at a critical degree of undercooling is obtained whereas no maximum appears for the other steel.

A maximum in the rate curve has not been previously reported for the growth of pearlite. Recent electron microscope studies⁹ have shown that pearlite can coexist with bainite as low as 450°C. In the present investigation, growth-rate data at the lower temperatures were taken only on the characteristic hemispherical pearlite regions of the structure.

Theory

It is customary to attempt to describe data on reactions in solids by means of exponential-type rate equations. The usual approach in applying absolute rate theory is to establish a mechanism and compute the constants in these equations, the validity of the resulting equation being established by comparison of calculated and experimental rate data. In our present state of knowledge of rate processes in

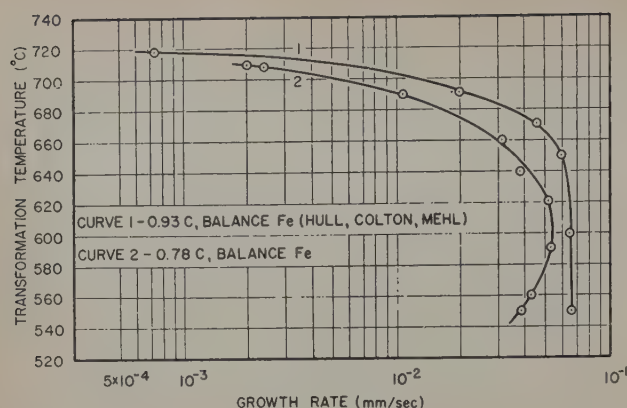


Fig. 3—Summarized growth rate data.

solids, it does not seem possible to carry out these calculations. Therefore, the procedure is followed of deriving an equation which is of the correct form and then of calculating its constants from rate data. Usually, an exponent is calculated, and this is taken to be the activation energy. This procedure may lead to false physical meaning being attached to constants which are merely empirical. This danger is inherent in the use of any of the present rate equations. Nevertheless, it is to be hoped that through such efforts a fuller understanding will eventually be attained of rate processes in solids.

An attempt will now be made to derive a general equation for the rate of growth of pearlite from austenite. This equation will be used in the present paper to calculate the activation energy for this reaction in the Fe-C alloys considered here. Finally, it is hoped that it will be useful in studying the effect of third elements on this rate of growth.

The mechanism of growth of the austenite-pearlite interface is assumed capable of treatment by the Eyring rate theory.¹⁰ With this assumption, it has been found that the Eyring rate equation in the form which takes into account a forward and backward reaction is applicable; i.e.,

$$n = \frac{mkT}{h} \left(\exp \frac{-\Delta F^* +}{RT} - \exp \frac{-\Delta F^* -}{RT} \right) \quad [1]$$

where: n is the net rate of movement of activated complexes; m , the transmission coefficient; k , Boltzmann's constant; h , Planck's constant; R , the gas constant; T , the absolute temperature; $\Delta F^* + = F^* - F_a$; $\Delta F^* - = F^* - F_p$; F^* = the free energy of the activated complex; F_a = the free energy of the austenite; and F_p = the free energy of the pearlite.

In the present application, the transmission coefficient, m , will be assumed to be constant. The linear rate of growth, r , of the pearlite-austenite interface is considered as being proportional to n , the

Table II. 0.78 Pct C High-Purity Fe-C Alloy

Temperature, °K	$10^3/T$, 1/°K	r (exp.) Mm per Sec	$(\Delta F \Delta T/r)$ Cal °K Sec Mm Mol	r (calc) Mm per Sec
983	1.017	2×10^{-3}	9.17×10^4	2.10×10^{-3}
981	1.019	2.46×10^{-3}	9.91×10^4	2.73×10^{-3}
963	1.038	10.3×10^{-3}	11.88×10^4	10.8×10^{-3}
933	1.072	31.7×10^{-3}	15.20×10^4	28.4×10^{-3}
913	1.095	38×10^{-3}	22.80×10^4	38.3×10^{-3}
893	1.120	52×10^{-3}	26.55×10^4	45.1×10^{-3}
863	1.158	52.5×10^{-3}	45.80×10^4	48.9×10^{-3}
833	1.200	43×10^{-3}	87.2×10^4	45.8×10^{-3}
823	1.214	39×10^{-3}	109.8×10^4	44.5×10^{-3}

Table III. 0.93 Pct C High-Purity Fe-C Alloy

Temperature, °K	$10^3/T$, 1/°K	r (exp.) Mm per Sec	$(\Delta F \Delta T/r)$ Cal °K Sec Mm Mol	r (calc) Mm per Sec
993.7	1.006	0.15×10^{-3}	3.83×10^4	0.15×10^{-3}
989	1.01	0.72×10^{-3}	7.34×10^4	1.28×10^{-3}
962	1.04	19.5×10^{-3}	6.68×10^4	20.8×10^{-3}
943	1.06	45×10^{-3}	7.40×10^4	40.3×10^{-3}
923	1.08	59.5×10^{-3}	11.00×10^4	60.2×10^{-3}
872	1.15	65×10^{-3}	31.70×10^4	71.4×10^{-3}
820	1.22	66×10^{-3}	67.3×10^4	53.0×10^{-3}

net rate of movement of activated complexes. Account must also be taken of the fact that the pearlite spacing decreases with decreasing temperature of formation. The work of Pellissier, Hawkes, and Mehl¹¹ has shown that it is difficult to arrive at an exact relationship between interlamellar spacing and temperature of formation. This is due to the difficulty of securing sufficiently precise data. Their published data for plain carbon eutectoids can be correlated linearly, to a rough first approximation, with the number of degrees of supercooling at which the pearlite formed. Furthermore, Roberts and Mehl¹² have shown that the rate of growth of austenite from pearlite is inversely proportional to the number of degrees of supercooling at which the pearlite was formed. It will, therefore, be assumed that the rate of growth of pearlite from austenite is inversely proportional to the number of degrees of supercooling at which the reaction takes place.

Consideration of the above leads to

$$r = cT\Delta T \left(\exp \frac{-\Delta F^* +}{RT} - \exp \frac{-\Delta F^* -}{RT} \right) \quad [2]$$

Where

$$c = \text{constant} \quad [3]$$

This may be rewritten

$$r = cT\Delta T \exp \frac{-\Delta F^*}{RT} \left(1 - \exp \frac{\Delta F}{RT} \right) \quad [4]$$

where $\Delta F = F_a - F_p$

If ΔF is taken as the difference in free energy between austenite and pearlite per mol† and its value

† A mol of pearlite or austenite is defined as 6.023×10^{23} atoms of iron plus carbon.

calculated from the expression derived in the appendix, then for all temperatures within the pearlite range, ΔF is sufficiently small compared to RT to permit close approximation of $\exp(\Delta F/RT)$ by the first term of its series expansion.

Thus,

$$r = cT\Delta T \exp \frac{-\Delta F^*}{RT} \left(1 - 1 + \frac{\Delta F}{RT} - \frac{(\Delta F)^2}{2!RT^2} + \dots \right) \quad [5]$$

or

$$r = C' \Delta T \Delta F \exp \frac{-\Delta F^*}{RT} \quad [6]$$

where C' is a constant.

This constant, C' , must include, among other things, the number of atoms in the activated complex. If the complex contains several atoms, the approximation will be badly in error.

The activation energy, ΔE^* , and the activation entropy, ΔS^* , may be introduced through their relation to the activation-free energy. Thus, neglecting pressure-volume effects,¹³

$$\Delta F^* = \Delta E^* - T\Delta S^* \quad [7]$$

Then the rate of growth will be given by

$$r = C' \Delta T \Delta F \exp \frac{-\Delta E^*}{RT} \exp \frac{\Delta S^*}{R} \quad [8]$$

Finally,

$$r = C \Delta T \Delta F \exp \frac{-\Delta E^*}{RT} \quad [9]$$

where C is a constant.

The relation may be rewritten in the form

$$\ln \frac{\Delta T \Delta F}{r} = -\ln C + \frac{\Delta E^*}{R} \cdot \frac{1}{T} \quad [10]$$

If the derived relation is correct, a semilogarithmic plot of $\Delta F \Delta T / r$ against $(1/T)$ should yield a straight line.

Values of r and T resulting from experimental studies on the 0.78 pct C carried out in this investigation—along with computed values of $10^3/T$, $(\Delta F \Delta T / r)$, and r —have been listed in Table II. Similar values for the high-purity alloy of 0.93 pct C investigated by Hull, Colton, and Mehl⁶ are shown in Table III. The values of ΔF have been obtained from the expression in the appendix by graphical integration.

Fig. 4 shows a plot of $\log (\Delta F \Delta T / r)$ vs $1/T$ for each of these steels. It is evident that a reasonably straight line results in each case. The equations for these two steels are:

0.78 pct C,

$$r = 2.86 \Delta F \Delta T \exp (-24,200/RT) \quad [11]$$

0.93 pct C,

$$r = 31.6 \Delta F \Delta T \exp (-27,600/RT) \quad [12]$$

Discussion

The uncertainties involved in any application of rate equations to solids have been pointed out earlier. For purposes of this discussion, however, it will be assumed that the numerators of the exponents in Eqs. 11 and 12 are activation energies.

From the slopes of the plots in Fig. 4, an activation energy of 24,200 cal per mol of austenite is obtained for the 0.78 pct C alloy and 27,600 cal per mol for the 0.93 pct C alloy. It is evident that the values of these two activation energies are almost within the scatter of the data; and, for this reason, only limited significance may be attached to their relative values. The data for the 0.78 pct C alloy, however, distinctly lie above those of the 0.93 pct C alloy, resulting in a lower value for the constant, C , for the lower carbon alloy. Mehl¹² and coworkers have shown that the interlamellar spacing of hypereutectoid steels is finer at the same ΔT , and this should contribute to faster rates as indicated earlier. Unfortunately, it is impossible without actual measurements of interlamellar spacing to estimate possible changes in the activation entropy.

Activation energies for diffusion of carbon in austenite have been determined.¹⁴ They vary from approximately 36,000 cal for a carbon concentration of 0.22 pct to approximately 28,500 cal for 1.35 pct C. Activation energies found here are low, being 24,200 cal for 0.78 pct C and 27,600 cal for 0.93 pct C. It may be that activation energies for diffusion along the interface are lower than in the austenite used in the diffusion experiments. Thus, these results are not inconsistent with the theory that rate of growth is controlled by diffusion of carbon.

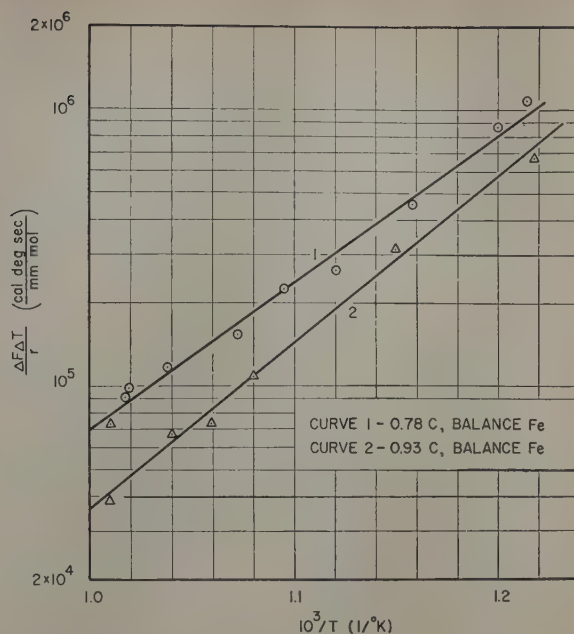


Fig. 4—Plot of $\frac{\Delta F \Delta T}{r}$ vs $\frac{1}{T}$ showing correlation of data according to Eq. 10.

On the other hand, the activation energy for the self-diffusion of γ iron has been reported¹⁵ as approximately 70,000 cal per mol; and it does not seem probable that this would be reduced to the values obtained in the present case by reason of the influence of the stresses or other factors at the interface. Whether the activation energies reported from the present analysis are representative of some interface mechanism of the type previously discussed cannot be stated with data now available. Additional experiments designed to give information on the individual processes are necessary.

Eq. 10 is of approximately the same form as Eq. 11 of Zener's paper,² which was derived on the assumption that the rate of growth is determined by diffusion of carbon. The slight difference is that Zener assumes that the free energy varies linearly with ΔT ; whereas, in the present paper, a more accurate variation with temperature is given. The presentation of this derivation is believed to be desirable for two reasons:

1—Zener has shown that his equation is of correct form to describe the rate of growth of pearlite from austenite, and this implies that the rate is determined by carbon diffusion, since this is the basis of Zener's derivation. It is important to point out that the same equation can be arrived at without any assumption as to the actual mechanism of the reaction beyond the idea that it is controlled by the crossing of an energy barrier.

2—An equation which is not based on a particular mechanism is needed as a guide for the study of the effect of alloying elements on the rate of growth. For example, in work now in progress at these laboratories, it has been found that manganese, which decelerates the growth of pearlite from austenite, does not appreciably partition between cementite and ferrite below a certain isothermal transformation temperature. These results are in general agreement with data reported by Hultgren¹⁶ for a manganese steel. The observation that the degree of partitioning is a function of the isothermal transformation temperature further complicates a theoretical treatment of the kinetics of the austenite-pearlite

Table IV. Free Energy of Formation* of Austenite from Pearlite

Temperature, °K	ΔF, Cal per Mol
996	0
990	6.38
980	17.5
960	41.3
940	67.0
920	94.5
900	123.6
880	154.0
860	185.7
840	218.5
820	252.4
800	287.1

* Calculated by graphical integration of Eq. 6 for $\Delta E = 1050$ cal per mol of austenite.

transformation, for it is now necessary to obtain thermodynamic data on transformations to non-equilibrium products. Thermodynamic and interlamellar spacing measurements are now being made in the hope of analyzing the influence of manganese on rate of growth, in terms of its effect on ΔF , ΔE^* , and possibly ΔS^* .[‡] It is hoped that this work can be

† Qualitatively, it is clear that additions of manganese will decrease the temperature at which the free energy of nonpartitioned pearlite is equal to that of austenite. This follows from the fact that phase diagram work has shown that manganese decreases this temperature for partitioned pearlite and from the fact that the free energy of partitioned pearlite must be higher than that of nonpartitioned. This will result in a smaller ΔF at a given temperature for the transformation to nonpartitioned manganese pearlite than for the transformation to binary pearlites at a given temperature, unless the effect of manganese on heats of transformation and specific heats outweighs the effect on temperature. Furthermore, it seems probable that manganese will increase interlamellar spacing.¹¹ These two effects will tend to result in a lower rate of growth of pearlite from austenite. A quantitative valuation must await the results of work now underway in these laboratories.

extended to a study of the effect of manganese on growth of α iron from γ iron in a binary Fe-Mn alloy. This would be particularly enlightening, since isothermal growth on supercooling should occur without any diffusion of any kind. Again, the influence of manganese would be analyzed in terms of its effect on ΔF , ΔE^* , and possibly ΔS^* .

Conclusions

The rates of growth of pearlite from austenite in two high-purity steels may be represented by the following equations:

$$\text{For 0.78 pct C steel,} \\ r = 2.86 \Delta F \Delta T \exp -24,200/RT$$

$$\text{For 0.93 pct C steel,} \\ r = 31.6 \Delta F \Delta T \exp -27,600/RT$$

As predicted by the theory, data for the steel containing 0.78 pct C show a maximum in the curve of growth rate vs temperature.

Acknowledgment

Eq. 10 was derived by one of us while employed by the Bethlehem Steel Corp. and was included in a report, "Underlying Factors Controlling the Mechanical Properties of Steel," by J. H. Frye, Jr., February 6, 1947.

The writers wish to thank R. F. Mehl, G. M. Pound, and W. C. Hagel for a number of helpful criticisms of an earlier draft of this paper.

One of the writers wishes to thank the Oak Ridge Institute of Nuclear Studies, Inc., for making available one of their fellowships.

Appendix

The free energy of the austenite-to-pearlite reaction can be calculated by means of the following equation:

$$\Delta F = \Delta E (T_i - T)/T_i - \int_{T_i}^T dT' \int_{T_i}^{T'} \Delta C dT''/T'' \quad [13]$$

where: ΔF is the free energy of austenite minus that of pearlite per mol; T_i , the absolute temperature of the transformation at equilibrium; T , the absolute temperature of a given transformation; ΔC , the difference in heat capacity between austenite and pearlite, calories per mol per degree; and ΔE , the internal energy per mol of austenite minus that of pearlite at equilibrium temperature.

A careful search of the literature has failed to yield a reliable value of the heat of the eutectoid transformation, ΔE . Epstein¹⁷ lists values from 875 to 1170 cal per mol of austenite. Analysis of the data of Awbery and Snow⁷ indicates a value of approximately 1000 cal per mol. A value may be estimated from the enthalpy data of pure iron by Darken and Smith,⁸ from the heat of formation of cementite given by Darken and Gurry,¹⁸ and the heat of solution of graphite in austenite by Smith.¹⁹ Considering the transformation as the decomposition of pearlite into ferrite and graphite followed by the transformation of α to γ iron and the subsequent solution of graphite in the γ iron to form austenite gives a value of approximately 1050 cal per mol. Preliminary direct measurements of the heat of transformation by calorimetric methods in these laboratories has indicated that this value is about correct.

The heat capacity of steel below the temperature of transformation appears to be insensitive to large changes in carbon content and small changes in other elements.⁷ In view of this, values of heat capacity of pure α and γ iron have been taken from the work of Darken and Smith.⁸ The last term of the above equation has been integrated graphically. The heat of transformation has been taken as 1050 cal per mol and the equilibrium temperature of transformation as 723°C; the computed values of ΔF are given in Table IV.

References

1. R. F. Mehl and Arthur Dube: *Phase Transformations in Solids* (1951) p. 545. New York. John Wiley and Sons.
2. C. Zener: *Trans. AIME* (1946) **167**, p. 550, and discussion by R. F. Mehl; *METALS TECHNOLOGY* (January, September 1946).
3. W. H. Brandt: *Journal of Applied Physics* (1945) **16**, p. 139.
4. W. H. Brandt: *Trans. AIME* (1946) **167**, p. 405; *METALS TECHNOLOGY* (December 1945).
5. J. B. Austin and R. Pierce, Jr.: *Trans. AIME* (1935) **116**, p. 309.
6. F. C. Hull, R. A. Colton, and R. F. Mehl: *Trans. AIME* (1942) **150**, p. 185.
7. J. Awbery and A. Snow: Iron and Steel Research Committee Special Report No. 24. *Second Report of the Alloy Steels Research Committee* (1939) p. 216.
8. L. S. Darken and R. P. Smith: *Industrial and Engineering Chemistry* (1951) **43**, p. 1815.
9. Second Progress Report by Subcommittee XI of ASTM Committee E-4, *Bull. ASTM* (1952) No. 182, p. 62.
10. Glasstone, Laidler, and Eyring: *The Theory of Rate Processes* (1941) New York and London. McGraw-Hill Book Co.
11. G. E. Pellissier, M. F. Hawkes, W. A. Johnson, and R. F. Mehl: *Trans. ASM* (1942) **30**, p. 1049.
12. G. A. Roberts and R. F. Mehl: *Trans. ASM* (1943) **31**, p. 639.
13. N. F. Mott and H. Jones: *Properties of Metals and Alloys* (1936) p. 26. Oxford.
14. C. Wells, W. Batz, and R. F. Mehl: *Trans. AIME* (1950) **188**, p. 559; *JOURNAL OF METALS* (March 1950).
15. C. E. Birchenall and R. F. Mehl: *Trans. AIME* (1950) **188**, pp. 144, 1374; *JOURNAL OF METALS* (January, November 1950).
16. Axel Hultgren: *Jernkontorets Annaler* (1951) **135**, p. 403.
17. S. Epstein: *The Alloys of Iron and Carbon* (1936) p. 88. New York. McGraw-Hill Book Co.
18. L. S. Darken and R. W. Gurry: *Trans. AIME* (1951) **191**, p. 1015; *JOURNAL OF METALS* (November 1951).
19. R. P. Smith: *Journal ACS* (1946) **68**, p. 1163.

Titanium-Manganese System

by D. J. Maykuth, H. R. Ogden, and R. I. Jaffee

A phase diagram for alloys containing from 0 to 66.9 pct Mn was determined. Two compounds, tentatively labeled δ and γ , were found in this range. The δ compound is located at about 66.9 pct Mn and melts congruently at 1330°C. The γ compound has a composition near 53 pct Mn and originates in a peritectic reaction at 1200°C between liquid and δ . β and γ enter into a eutectic reaction at 1175°C. The β phase field terminates in a very sluggish eutectoid reaction between α and γ at 550°C.

MANGANESE is one of the important alloying addition elements to titanium. As a β -stabilizing addition for α - β and β alloys, it provides high strength with adequate ductility.¹ Two of the earliest commercial alloys contain manganese as a major alloying component.²

The earliest published data on the constitution of Ti-Mn alloys was that of Wallbaum,³ who reported the existence of the compound TiMn_2 . The transformation range of commercial-purity Ti-Mn alloys was investigated by Craighead, Simmons, and Eastwood¹ who found limited α solubility and a lowering of the β transus to about 790°C at 7 pct Mn. Preliminary work by the authors of this paper, using high-purity titanium, confirmed the β -stabilizing action of manganese and showed the existence of several intermediate phases in the Ti-Mn system.⁴ More recently, McQuillan⁵ determined the β transus temperatures for high-purity Ti-base alloys containing up through 4.4 pct Mn. These data are given in Fig. 1.

The present investigation covered alloys made with a high-purity base. The constitution of titanium-rich alloys made with commercial titanium has been reported^{4,6} by Holladay, Kura, and Jackson.

The alloy range covered in the present investigation was from 0 to 69.5 pct Mn. This alloy range extends slightly beyond the composition of the first congruent-melting compound encountered on proceeding from the titanium end of the system. A description of the materials and methods used in the determination of the diagram is given in the Appendix.

The partial phase diagram determined for the Ti-Mn system is shown in Fig. 2. Details on equilibria in the titanium-rich alloys are given in Fig. 3.

Liquid-Solid Relationships

Observations on the cast structures of the arc-melted ingots showed that the terminal solid solution of manganese in β titanium enters into a eutectic reaction with an intermetallic compound labeled γ . As will be shown later, this compound has a composition around 53 pct Mn. The eutectic reaction

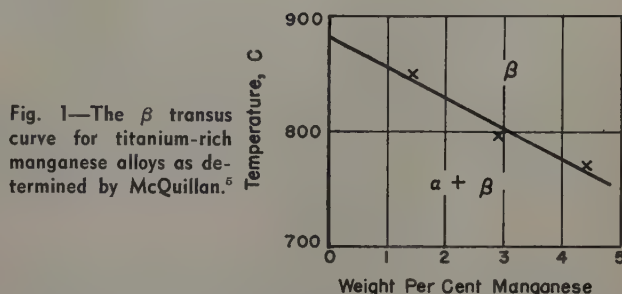


Fig. 1—The β transus curve for titanium-rich manganese alloys as determined by McQuillan.⁵

temperature was determined as 1175°C by thermal analysis which also showed that the γ phase originates in a peritectic reaction at 1200°C. Fig. 4 shows typical eutectic structures for alloy compositions on both sides of the eutectic composition which is located at 42.5 pct Mn.

In alloys over the range of 45.4 through 69.5 pct Mn, a second intermetallic compound, labeled δ , was identified as the primary phase. This phase consistently increased in amount as the manganese content approached 66.9 pct, and, as shown in Fig. 5, an alloy structure containing 66.9 pct Mn consisted essentially of the δ compound. Thermal-analysis data indicate a melting point of about 1330°C for the δ intermediate phase. At 67.0 pct Mn, small quantities of a new, higher manganese-content phase were observed in the form of Chinese-script eutectic particles. Comparison of Fig. 6a and b shows an increasing quantity of this phase as the composition was increased to 69.5 pct Mn.

The formation of peritectic γ in arc-melted alloys containing 45.4 pct Mn and above appears to be almost entirely suppressed, as shown in Fig. 7a and b. This is because of the narrow freezing range available for its formation by peritectic reaction and because of the very high cooling rates obtained in

D. J. MAYKUTH is Research Metallurgist, H. R. OGDEN, Junior Member AIME, is Assistant Supervisor, and R. I. JAFFEE, Member AIME, is Supervisor, Nonferrous Physical Metallurgy Div., Battelle Memorial Institute, Columbus, Ohio.

Discussion on this paper, TP 3471E, may be sent, 2 copies, to AIME by April 1, 1953. Manuscript, Sept. 15, 1952. Los Angeles Meeting, February 1953.

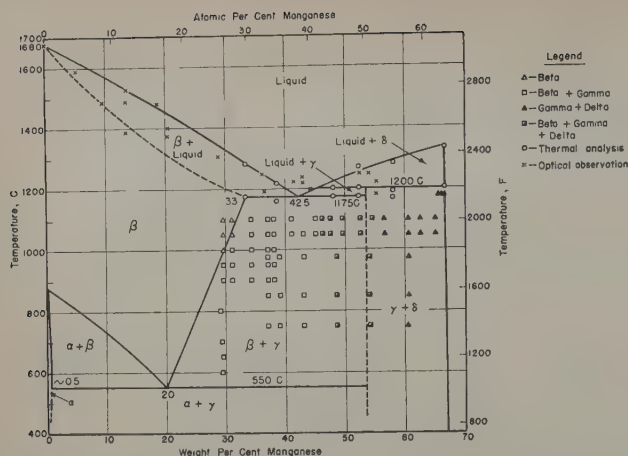


Fig. 2—Partial phase diagram for iodide titanium-manganese alloys.

freezing after arc melting. In fact, these arc-melted alloy structures appear as a "eutectic" series between the β and δ phases.

In an attempt to complete the peritectic reaction, an alloy containing 53.6 pct Mn was melted in graphite and slowly cooled through the solidification range at a rate of about 1°C per min. As illustrated in Fig. 8, this structure clearly shows the peritectic rings of γ around primary δ . Despite this slow rate of cooling, the peritectic reaction was incomplete, and no noticeable quantities of the β - γ eutectic were formed. Instead, the last liquid to solidify formed the nonequilibrium eutectic of δ in β , which characterizes the arc-melted alloy structures in this composition range.

Solid-State Equilibria

Intermediate Alloy Range: Maximum solubility of manganese in β titanium is about 33 pct at the eutectic reaction temperature. At temperatures from 1175° to 550°C , the β -phase field is bounded by a wide two-phase field of β plus γ . Fig. 9a illustrates an alloy within this two-phase region.

All attempts to isolate the γ phase by homogenization treatments were unsuccessful. After soaking 100 hr at 1100°C , alloys containing 45.4 through 54.7 pct Mn show three-phase structures of β , γ , and δ as shown in Fig. 9b. Similar treatment on alloys with slightly higher manganese contents show that the γ - δ phase field extends from at least 56.4 pct Mn (Fig. 10) up to 66.9 pct Mn, which is the composition indicated for δ .

Titanium-Rich Alloys: The addition of manganese to titanium lowers the β transus sharply. McQuillan⁵

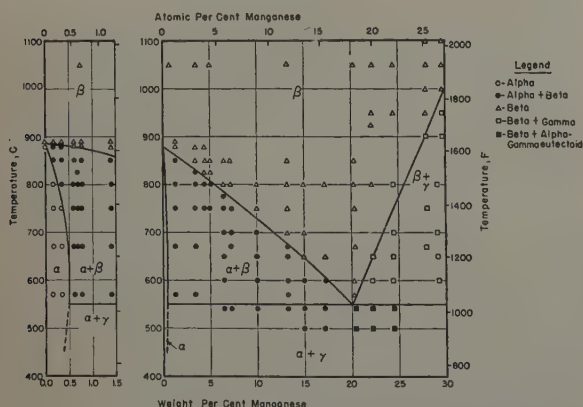


Fig. 3—Partial phase diagram for iodide titanium-manganese alloys.

indicates an even sharper drop in β transus than was found in the present work. Quenching from within the β field of alloys containing up through 5.1 pct Mn, produces acicular or martensitic transformation structures. At manganese contents of 6.4 pct and above, the β phase is retained by water quenching. These observations were corroborated by a determination of M_s temperatures by Duwez on titanium-rich alloys, which showed that the M_s temperature for the 6.4 pct Mn alloy is below room temperature. Fig. 11 illustrates the M_s curve obtained for these alloys.⁷

Manganese solubility in β titanium decreases progressively from a maximum of 33 pct at 1175°C to about 20 pct at 550°C where the β phase decomposes into α and γ in a very sluggish eutectoid reaction.

In an attempt to produce appreciable eutectoidal decomposition, wrought samples containing up through 24.5 pct Mn were annealed for 500 hr at 540°C . Also, several alloys over the range of 15.1 through 24.5 pct Mn were annealed for 1440 hr at 500°C after an initial β -quenching treatment. Neither of these treatments produced any recognizable eutectoid decomposition in the hypoeutectoid alloys containing up to, and including, 17.2 pct Mn. Fig. 12a shows a typical structure for these alloys which consist of the α and β phases. In the alloys containing 20.3 pct Mn and greater, both of the

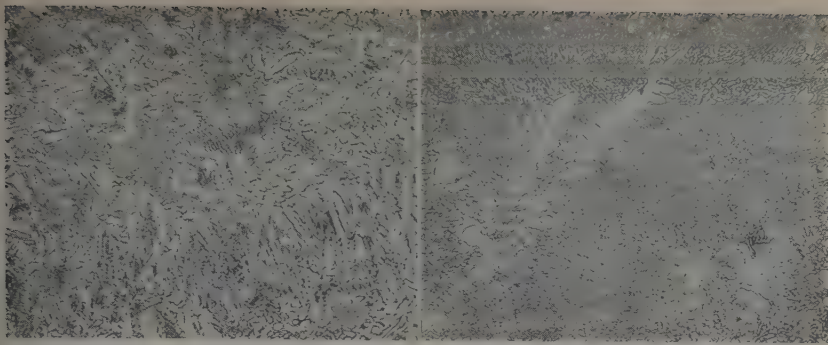
Table I. Inflection Temperatures Obtained from Resistance-Temperature Curves

Manganese Content, Wt Pct	Inflection Temperature, $^\circ\text{C}$
3.66	856
13.3	697
20.5	319

above treatments produced a fine, aggregate structure, illustrated in Fig. 12b, at the β -grain boundaries in addition to precipitating a small quantity of γ particles within the β grains. X-ray diffraction patterns on samples of these alloys did not show a sufficient number of lines for the minor phases to allow positive identification. However, an extrapolation of the β -phase-field boundaries determined at higher temperatures indicates that the β field must terminate at about 20.0 pct Mn in a eutectoid reaction at about 550°C . On this basis, the fine β -grain-boundary aggregate in the hypereutectoid alloys has been identified as the first sign of what must be a very sluggish eutectoidal decomposition. Metallographic data indicate that the α solubility of manganese reaches a maximum of about 0.5 pct Mn at 550°C .

Due to the slow rates of the reactions involved and to contamination incurred in spot-welding, resistance-measurements were not as satisfactory a means of following the phase transformations as were metallographic methods. Resistance-temperature curves obtained for three alloys showed inflections at the temperatures noted in Table I.

The inflections noted for the two lower manganese-content alloys are in fair agreement with the respective β transus temperatures determined metallographically. The inflection noted at 319°C for the 20.5 pct Mn alloy probably represents the beginning of β decomposition for this alloy under these particular conditions and has no direct significance. None of the resistance-temperature curves showed



a—41.9 pct Mn. Proeutectic β plus interdendritic eutectic of β and γ . The proeutectic β also contains Widmanstätten proeutectoid γ .

b—44.8 pct Mn. Proeutectic γ in a matrix of eutectic γ in β .

Fig. 4—Typical cast structures in arc-melted Ti-Mn alloys. Etchant: 1 pct HF, 3 pct HNO_3 in water. X500. Area reduced approximately 50 pct for reproduction.

Fig. 6—Typical cast structures in arc-melted Ti-Mn alloys. Etchant: 1 pct HF, 3 pct HNO_3 in water. Area reduced approximately 50 pct for reproduction. a (left)—67.0 pct Mn. Primary δ plus interdendritic Chinese-script eutectic particles of a new higher Mn-content phase. X500. b (right)—69.5 pct Mn. Primary δ plus interdendritic Chinese-script eutectic particles of a new higher Mn-content phase. X250.

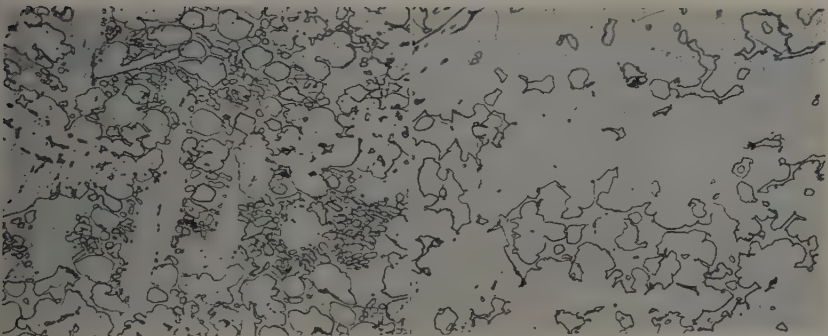
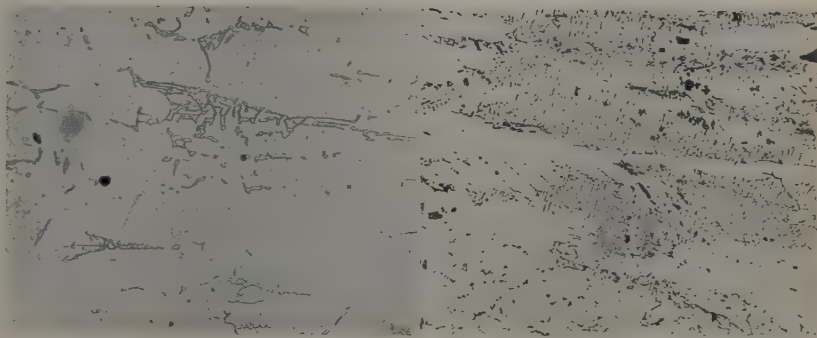


Fig. 7—Typical cast structures in arc-melted Ti-Mn alloys. Etchant: 1 pct HF, 3 pct HNO_3 in water. X500. Area reduced approximately 50 pct for reproduction. a (left)—54.7 pct Mn. Primary δ (large white dendrites) plus an interdendritic mixture of nonequilibrium-eutectic δ (small white particles) in β (gray) and γ (large white crystals). b (right)—65.0 pct Mn. Primary δ (white matrix) plus interdendritic mixture of nonequilibrium-eutectic δ (small rounded white particles), β (gray), and γ (large white crystals).

inflections indicative of the eutectoid reaction temperature.

An interesting side observation from this work was that the apparent temperature coefficient of resistance of the β phase decreases with increasing manganese content until, at some composition between 3.66 and 13.3 pct Mn, it becomes negative.

X-Ray Diffraction

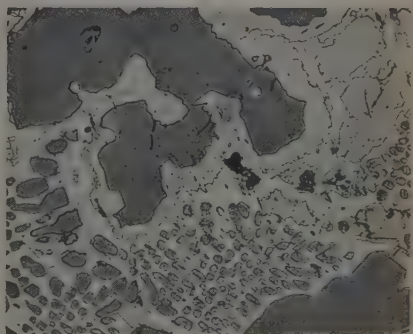
Diffraction patterns on alloys with low-manganese content showed the small amount of manganese taken into solid solution in the α phase had no significant effect on the α lattice parameter of unalloyed titanium.

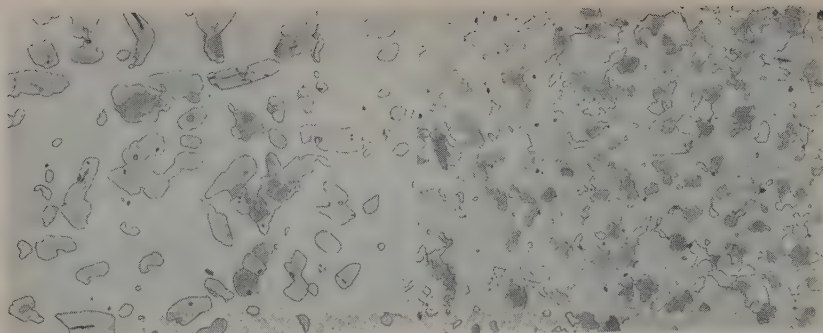
Fig. 13 shows the results of X-ray diffraction measurements of the β lattice parameters of several alloys. The data show some scatter, which is probably due to lack of equilibrium, but indicate a linear relationship between the parameter and composition of the β , in accordance with Vegard's law.

The only one-phase alloy structure directly available for use in X-ray identification of the two Ti-Mn

compounds was that of the 66.9 pct Mn alloy, pictured in Fig. 5, which consisted predominantly of the single-phase δ . However, the diffraction pattern for this alloy gave similar lines to those obtained for alloys containing from 53.6 to 66.9 pct Mn. Metallographic examination showed that both the γ and δ phases were present in these alloys.

Fig. 8—Structure of a 53.6 pct Mn alloy slowly cooled through the solidification range. Primary δ (large dark-gray dendrites) surrounded by peritectic γ (light-gray striated phase) plus interdendritic β (white) containing nonequilibrium-eutectic δ . Etchant: 1 pct HF, 3 pct HNO_3 in water plus heat tinting in air at 425°C for 5 min. X250. Area reduced approximately 50 pct for reproduction.





a—41.9 pct Mn. Grains of γ in β matrix. b—54.7 pct Mn. Nonequilibrium structure of γ (dark gray) and β (white) in δ matrix (light gray).

Fig. 9—Structure for two Ti-Mn alloys quenched after 100 hr at 1100°C. Etchant: 1 pct HF, 3 pct HNO₃ in water plus heat tinting in air at 425°C for 5 min. X250. Area reduced approximately 50 pct for reproduction.

Since all attempts to prepare a single-phase γ structure by equilibration treatments were unsuccessful, a diffusion couple was prepared to isolate the phases. This couple was made by heating contacting samples of electrolytic manganese and a 20 pct Mn alloy in a Vycor capsule under argon for two weeks at 1000°C. Metallographic examination of the original interface between the samples showed that at least two, and perhaps three, compounds are formed between titanium and manganese. An X-ray diffraction film taken from the first compound layer adjacent to the 20 pct Mn alloy (i.e., the γ -compound layer) showed the pattern given in Fig. 14. Subtraction of these lines from the pattern obtained for the 66.9 pct Mn alloy left the lines shown in Fig. 14 as being those characteristic for the δ compound. These patterns were consistent with the metallographic structures and diffraction patterns for alloys containing 53.6 through 66.9 pct Mn.

The pattern for the δ compound is identical to that reported by Wallbaum⁸ for the compound TiMn₂. This investigator found a hexagonal structure of the C14 type (MgZn₂) with a and c parameters of 4.18Å and 7.88Å, respectively. The composition indicated for the δ or TiMn₂ compound by the present work is 66.9 pct Mn rather than 69.6 pct Mn which corresponds to the stoichiometric ratio. As shown in Fig. 6b, an alloy containing 69.5 pct Mn is well within a two-phase field of δ plus a new higher manganese-content phase.

The crystal structure for the γ phase has not been identified. Although the indicated composition for this phase corresponds roughly to TiMn, the diffraction pattern observed does not fit the body-centered cubic CaCl₂-type lattice observed⁸ for the

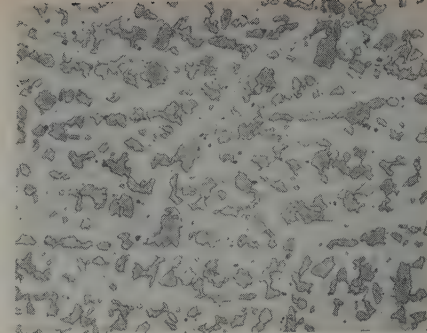
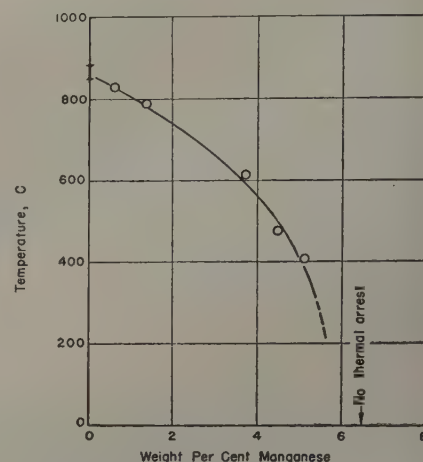


Fig. 10—Structure for a 56.4 pct Mn alloy quenched after 100 hr at 1100°C. Islands of γ (dark) in δ matrix (light). Etchant: 1 pct HF, 3 pct HNO₃ in water plus heat tinting in air at 425°C for 5 min. X250. Area reduced approximately 50 pct for reproduction.

Fig. 11— M_s curve for β solid solution in the Ti-Mn system.⁷



TiX compounds of the neighboring transition elements.

Summary

A phase diagram for alloys containing 0 to 69.5 pct Mn was determined using iodide titanium as the base material. Two compounds, tentatively labeled δ and γ , exist within this composition range.

The δ compound is located at about 66.9 pct Mn and melts congruently at 1330°C. The γ compound has a composition near 53 pct Mn and originates in a peritectic reaction at 1200°C between δ and melt containing 45 pct Mn.

β titanium, containing 33 pct Mn, and γ undergo a eutectic reaction at 1175°C, with the eutectic composition located at 42.5 pct Mn. Manganese solubility in β titanium decreases almost linearly from a maximum of 33 pct Mn at 1175°C to about 20 pct Mn at 550°C where the β phase decomposes,

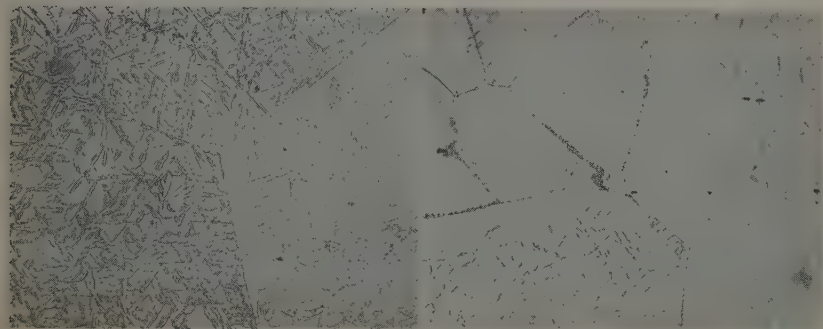


Fig. 12—Structure for a hypo- and hyper-eutectoid alloy quenched from 800°C and reheated to 500°C for 1440 hr. Etchant: 1 pct HF, 3 pct HNO₃ in water. X500. Area reduced approximately 50 pct for reproduction. a (left)—15.1 pct Mn. Widmanstätten α plates in large β grain matrix. b (right)—20.3 pct Mn. Large β grains containing some γ particles plus β eutectoid decomposition at the β grain boundaries.

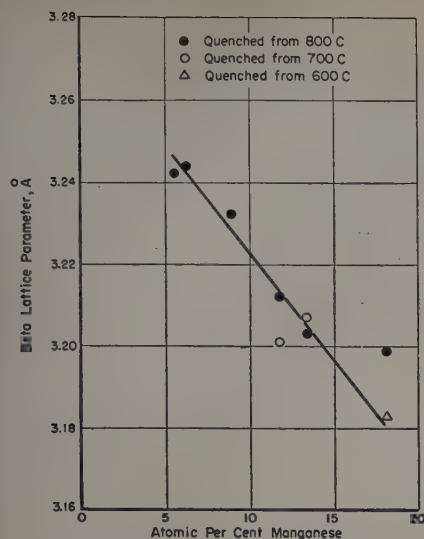


Fig. 13—Lattice parameter - composition curve for β -quenched Ti-Mn alloys.

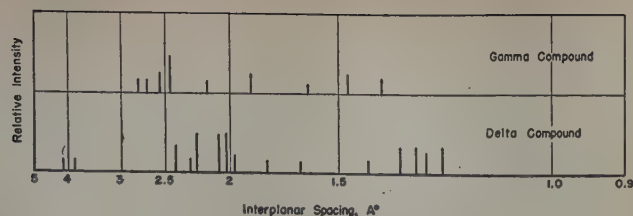


Fig. 14—Interplanar spacing and line intensities for diffraction patterns on the γ and δ compounds.

in a very sluggish eutectoid reaction, into α and γ . Increasing additions of manganese to titanium lower the β transus to 550°C at the eutectoid composition. The solubility of manganese in α titanium reaches a maximum of about 0.5 pct Mn at the eutectoid temperature.

Acknowledgments

The authors are grateful to the Research Division of the Materials Laboratory at Wright-Patterson Air Force Base for permission to publish this work, which was performed at Battelle Memorial Institute under their sponsorship. The authors also wish to thank O. J. Huber and J. R. Doig, of Battelle, for the X-ray diffraction work reported, and M. W. Mallett, of Battelle, for his assistance in the determination of the melting range in the Ti-Mn system.

Appendix—Experimental Methods

Materials: Iodide titanium crystal bar and electrolytic manganese were used in the preparation of these alloys. The titanium was supplied in several lots by the New Jersey Zinc Co. to the specification that the maximum hardness should not exceed 85 Vickers. A typical spectrographic analysis for one of these lots is given in Table II.

Analysis for the as-received manganese was as follows: N, 1 part per million; H, 120 parts per million; sulphide sulphur, 0.014 pct; sulphate sulphur, <0.001 pct; and Fe, <0.001 pct. Prior to use in alloying, the manganese was arc-melted under a total pressure of 10 cm of argon to remove the absorbed hydrogen.

Melting Procedure: All alloys were prepared by direct arc melting of charges of iodide titanium and premelted electrolytic manganese, under a total pressure of 10 cm of argon, and on a water-cooled copper hearth. This furnace and the procedure for con-

tamination-free melting have been adequately described elsewhere in the literature.^{4,9} Ingot size was generally held to about 15 g. In order to minimize manganese losses during melting, current input to the arc was maintained at about 200 amp, and the time of a single melt was limited to about 5 min. Three such melts were generally found adequate to obtain complete melting of all ingots prepared, with each ingot being flipped over between melts. Some weight losses were incurred during melting. Compositions calculated on the assumption that the weight loss was entirely manganese agreed within ± 1.0 pct of the analyzed compositions. However, all compositions were checked by chemical analysis. An excess of 0.5 to 1.0 pct Mn above the desired composition was generally sufficient compensation for losses during melting.

Fabrication: Upset forging and hot rolling in air were used for breaking down the cast ingots wherever possible. Ingots containing through 7 pct Mn were fabricated to 0.060-in. strip by the use of this procedure at 750°C. For the higher manganese-content ingots, 850°C was used. At this temperature, an alloy containing 20.5 pct Mn was the highest manganese-content alloy which could be fabricated. Alloys containing 23.2 pct Mn and above could not withstand forging and cracked badly after the first few passes during attempted hot rolling.

After rolling, each strip was given a 15-min strain-relief anneal at rolling temperature and air cooled. As a precaution against surface contamination, all strips were cleaned by grit blasting and pickling in a 20 parts HF, 80 parts HNO₃ (by volume) bath to remove a total thickness of 0.004 in.

Heat Treatment: All quenching treatments were carried out using chromel-A-wound, Type 304 stainless steel tube furnaces. Gettered argon was admitted through one end of the tube as an atmosphere to protect the samples during treatment. The furnace was mounted in a cradle which pivoted about an axis through the open end of the furnace tube. Samples for treatment were placed in a titanium-sheet sleeve packed with titanium turnings. Quenching of the sleeve and samples were effected by up-ending the furnace and sliding the sleeve out of the tube into a bucket of water. Temperature control in these furnaces was maintained within $\pm 3^\circ\text{C}$.

For homogenization treatments, Globar and molybdenum-wound McDanel tube furnaces were used. These furnaces were adapted to receive argon, and temperatures were controlled within $\pm 10^\circ\text{C}$.

Wherever possible, metallographic samples were cold-rolled before heat treatment to expedite attainment of equilibrium structures. The degree of cold reduction varied from 50 pct, for the lowest manga-

Table II. Spectrographic Analysis for Titanium

Element	Spectrographic Analysis	
	Quantitative, Wt Pct	Qualitative
Mn	0.032	Weak to faint
Al	0.017	Very faint
Fe	0.0041	Extremely faint
Cu	0.0031	Extremely faint
Pb	0.0029	Extremely faint
Sn	0.0018	Extremely faint
Mg	—	Extremely faint
N	0.003*	

* By chemical analysis.

Table III. Time Schedule for Equilibrating Treatments

Temperature Range, °C	Time, Hr
1100	1
1000-1050	2
900-1000	4
800-900	6
775-800	12
750-775	16
700-750	24
570-700	168

nese-content alloys, to 35 pct, for the 20.5 pct Mn alloy. Initially, the time schedule shown in Table III was selected for equilibrating treatments.

Subsequently, several longer time treatments were used to explore critical composition ranges at various temperature levels. Alloys bordering the eutectoid composition were given treatments of 200, 300, 500, and 1440 hr at the respective temperatures of 650°, 600°, 540°, and 500°C. Also, 100-hr treatments were used in equilibrating alloys containing above 25 pct Mn, at temperatures from 925° through 1100°C.

All quenching treatments were carried out under an argon atmosphere. For treatments extending beyond 24 hr, Vycor capsules were used. In these instances, the samples were wrapped individually in columbium foil, and the capsules sealed under a partial pressure of argon.

The alloys containing above 20.5 pct Mn were too brittle to permit either hot or cold-working. Consequently, ingots containing from 20.5 pct to 69.5 pct Mn were given 100-hr homogenization treatments at temperatures ranging from 975° to 1100°C.

Metallography: Samples for metallographic examination were prepared by hand grinding on 240X, 400X, and 600X wet papers. Grinding scratches from the 600X paper were removed by using a slurry of Linde B alumina and chromic acid on either a Forstmann or Miracloth lap on a high-speed (1725 rpm) wheel. Final polishing was done using Linde B alumina on a Microcloth lap on a medium-speed wheel.

An etchant composed of 1 pct HF and 3 pct HNO₃ (by volume) was generally satisfactory for all structures examined. Some difficulty was experienced, however, in differentiating between the phases present in the alloys containing 45 to 55 pct Mn. For these structures, a supplemental heat-tinting procedure proved quite useful. This was accomplished by heating the chemically etched samples for 5 min in air at 425°C. This procedure caused selective oxidation and discoloration of the γ and δ compounds, but left the β phase relatively unchanged.

Resistance Measurements: Electrical resistance measurements were investigated as a means for checking the transformations in the titanium-rich alloys. In this work, a set of current and potential leads were spot welded to a sheet sample surrounded by titanium turnings in a titanium sleeve. This assembly was placed in a tube furnace and heated at a rate of 0.25° to 0.50°C per min, using gettered argon as an atmosphere. Current to the sample was held at 1.00 ± 0.01 amp. Alternate readings of temperature and the potential drop across the sample were taken at intervals of 1 min and used to construct a resistance vs temperature curve for each of the alloys investigated.

X-Ray Diffraction: For precision measurement of the α and β lattice parameters as well as for diffraction work on the γ and δ compounds, samples were photographed in a 114.6 mm Debye camera. The α patterns were prepared using copper radiation with a 1 mm aluminum foil being interposed to reduce the high background normally produced with titanium. The values taken for the wavelengths of the characteristic copper K α_1 and K α_2 radiations were 1.54050 and 1.54434Å, respectively.

For the other diffraction work in the Debye camera, unfiltered vanadium radiation was used. The values taken for the wavelengths of the characteristic vanadium K α_1 , K α_2 , and K β radiations were 2.5072, 2.5034, and 2.2843Å, respectively.

All parameter calculations were based on the Cohen extrapolation method, with the Gauss method being used to calculate the probable error. Spectrometer charts were also prepared on occasional samples to check the metallographic phase identification.

Melting Range Determinations: Initial investigation of the melting range was carried out by observation and optical temperature measurement of block samples induction heated under argon. For fabricable alloys, sheet samples bent into V shapes were used, and

for brittle alloys, wedge-shaped pieces of the fractured ingots were selected. In either case, the sample was placed in a deep-well graphite crucible so that observation could be made on a thin, angular section during heating. Solidus temperatures were approximated by noting the temperature at which rounding of edges or slumping of the sample occurred. Liquidus temperatures were obtained with an estimated accuracy of $\pm 10^\circ\text{C}$ by noting the temperature at which complete collapse of the sample occurred. As a check point, the melting point of electrolytic nickel was determined as 1450°C using this equipment. This compares favorably with the handbook value of 1455°C. Using a similar procedure, the melting point of unalloyed, iodide titanium was determined as 1680° $\pm 10^\circ\text{C}$.

Thermal analysis was used to investigate the liquid-solid relationships in the intermediate alloy range. Samples of approximately 10 g were charged in graphite crucibles 1 1/16 in. in length with an outside diameter of 3/4 in. and a wall thickness of 1/16 in. Temperatures were measured using a calibrated Pt-Pt-10 pct Rh thermocouple inserted in a thin-walled graphite-crucible well. Heating and cooling curves were obtained directly through use of a General Electric recording millivoltmeter. Thermal arrests obtained during the initial run on each sample were rechecked by selecting a higher range of sensitivity on the recorder and repeating the run.

Reaction between the crucible and melts containing from 33.2 to 58.0 pct Mn was largely restricted to the graphite interface, although a small number of carbides appeared scattered through each melt. Reaction between the graphite and melts containing above 63.2 pct Mn was, however, very severe. In the thermal analysis of a 66.4 pct Mn alloy, it was only possible to obtain one cooling curve because of the rapid rate of reaction of the graphite and melt.

Determination of M_s Temperatures: Laboratory work on the determination of M_s temperatures for six titanium-rich manganese alloys was performed in a cooperative effort by Pol Duwez at the Jet Propulsion Laboratory, California Institute of Technology. The equipment and procedures used by Dr. Duwez have been described in detail in a previous publication.¹⁰

References

- ¹ C. M. Craighead, O. W. Simmons, and L. W. Eastwood: Titanium Binary Alloys. *Trans. AIME* (1950) **188**, pp. 485-513; *JOURNAL OF METALS* (March 1950).
- ² D. I. Brown: Two New Alloys Now in Production. *Iron Age* (1950) **166**, pp. 85-88.
- ³ H. J. Wallbaum: *Ztsch. Kristallographie* (1941) **103**, pp. 391-402.
- ⁴ R. I. Jaffee, et al.: The Ti-Mn, Ti-W, and Ti-Ta Phase Diagrams. U.S.A.F., Wright Air Development Center, Wright-Patterson Air Force Base, AF Technical Report No. 6515, Part 1, June 1951, 54 pp.
- ⁵ A. D. McQuillan: The Effect of the Elements of the First Long Period on the Alpha-to-Beta Transformation in Titanium. *Journal Inst. Metals* (1951-1952) **80**, pp. 363-368.
- ⁶ Battelle Memorial Institute: Summary Report on Titanium Alloy Phase Diagrams for the Systems Ti-Mn, Ti-W, and Ti-Ta. To Wright-Patterson Air Force Base, Contract AF33(038)-8544, January 12, 1952, 59 pp.
- ⁷ P. Duwez: Private communication.
- ⁸ P. Duwez and J. Taylor: The Structure of Intermediate Phases in Alloys of Titanium with Iron, Cobalt, and Nickel. *Trans. AIME* (1950) **188**, pp. 1173-1176; *JOURNAL OF METALS* (September 1950).
- ⁹ R. I. Jaffee, H. R. Ogden, and D. J. Maykuth: Alloys of Titanium with Carbon, Oxygen, and Nitrogen. *Trans. AIME* (1950) **188**, pp. 1261-1266; *JOURNAL OF METALS* (October 1950).
- ¹⁰ P. Duwez: Effect of Rate of Cooling on the Alpha-Beta Transformation in Titanium and Titanium-Molybdenum Alloys. *Trans. AIME* (1951) **191**, pp. 765-771; *JOURNAL OF METALS* (September 1951).

Titanium-Tungsten and Titanium-Tantalum Systems

by D. J. Maykuth, H. R. Ogden, and R. I. Jaffee

Phase diagrams for the Ti-W and Ti-Ta systems were determined. The Ti-W system is characterized by a wide, two-phase region of β plus tungsten which is derived from a peritectic reaction between the liquid and tungsten solid solutions. The β field terminates in a eutectoid reaction between α titanium and tungsten terminal solid solution. Tantalum and β titanium form a complete series of solid solutions. Other features of this system are the extensive α - β field at low temperatures and an appreciable solubility of tantalum in α titanium.

BOTH tungsten and tantalum were first thought to form β -isomorphous systems with titanium as a result of early work¹ using powder-metallurgical techniques. Later work² on arc-melted Ti-Ta alloys, made using a commercial titanium base, showed that, in the range of 0 to 10 pct, tantalum was soluble in β titanium and that the α solubility extended to between 2 and 5 pct Ta at 790°C.

The present investigation covered the entire alloy range in both systems and was chiefly concerned with high-purity alloys at the titanium-rich end. The constitution of titanium-rich alloys made with a commercial titanium base was reported by Holladay, Kura, and Jackson.^{3, 4} As will be shown in detail later, the early prediction of β isomorphism was true for the case of the Ti-Ta system, but not for the Ti-W system. The results of this investigation will be presented first. The experimental methods used are described in the Appendix.

Ti-W System

The entire Ti-W phase diagram is shown in Fig. 1. Details of the titanium-rich side are shown in Fig. 2. The chief features of the system are a β eutectoid and a high-temperature peritectic between liquid and tungsten solid solution.

Melting Range: Examination of cast structures of low and medium-tungsten-content ingots showed cored β phase as the primary constituent. Fig. 3a illustrates a typical cast structure for alloys in the range of 20 to 30 pct W. From 30 to 72 pct W, coring was very severe. Alloys containing 72 through 88 pct W, however, showed definite evidence of a peritectic reaction between the liquid and a terminal solid solution of titanium in tungsten. Fig. 3b shows the cast structure for an 80 pct W alloy. A 95 pct W alloy, shown in Fig. 4, consisted primarily of primary tungsten solid solution plus a small quantity of β probably rejected during cooling.

Incipient-melting experiments located the peritectic temperature between 1850° and 1900°C and indicated that the reacting phases are liquid containing about 25 pct W and tungsten terminal solid solution containing about 8 pct Ti. Figs. 5 and 6

D. J. MAYKUTH is Research Metallurgist, H. R. OGDEN, Junior Member AIME, is Assistant Supervisor, and R. I. JAFFEE, Member AIME, is Supervisor, Nonferrous Physical Metallurgy Div., Battelle Memorial Institute, Columbus, Ohio.

Discussion on this paper, TP 3480E, may be sent, 2 copies, to AIME by April 1, 1953. Manuscript, Sept. 15, 1952. Los Angeles Meeting, February 1953.

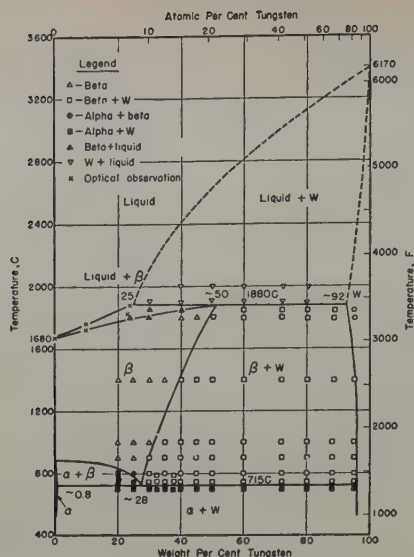


Fig. 1—Phase diagram for the Ti-W system.

illustrate typical structures obtained in these experiments. The peritectic composition was placed at slightly above 50 pct W.

Solid-State Equilibria: Tungsten solubility in β titanium decreases from a maximum of about 50 pct at the peritectic temperature to about 28 pct at about 715°C, where the β phase decomposes eutectoidally. Additions of tungsten to titanium depress the β transus from 882° to 715°C at the eutectoid composition. On quenching alloys containing up through 20 pct W from the β field, martensitic β transformation structures are produced. At compositions of 25 pct W and greater, the β is completely retained on quenching. Metallographic data bracket the eutectoid composition between 25 and 30 pct W, and 28 pct W was taken as the numerical value.

A few spot checks using electrical-resistance measurements have roughly checked the transus temperatures found metallographically. These were done in hypoeutectoid alloys. However, because contamination occurred in spot welding leads to the specimens, and because of the sluggishness of the reactions involved, resistance-measurement did not afford a reliable means of following the phase transformations. No inflections in the resistance-temperature curves were observed at the eutectoid temperature, presumably because of reaction sluggishness. The eutectoid-reaction temperature was bracketed between 700° and 725°C by metallographic examination of heat-treated specimens. The heat treatments used consisted both of isothermal transformation after quenching from the β field to the test temperature and also conventional equilibrating annealing treatments on wrought specimens. Figs. 7 through

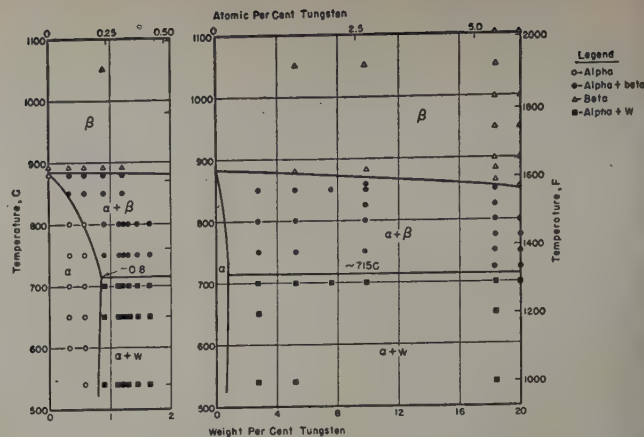


Fig. 2—Partial phase diagram for iodide titanium-tungsten alloys.

11 show typical structures produced in alloys on both sides of the eutectoid by isothermal treatments.

Annealing both hypoeutectoid and hypereutectoid alloys at 700°C and lower temperatures produced the dark-etching structure shown in Figs. 8 and 10. Hypoeutectoid alloys isothermally treated at temperatures within the α - β field contained Widmanstätten α structures of the type shown in Fig. 7.

Hypereutectoid alloys in the range of 30 to 50 pct W showed two distinctive modes of tungsten precipitation as a result of isothermal heat treatments above the eutectoid temperature. The bulk of the precipitated tungsten took the form of small particles or plates. However, as illustrated in Figs. 9 and 11, there was appreciable precipitation of tungsten at the β grain boundaries in the form of fan-shaped colonies. These colonies resemble a eutectoidal decomposition product, but as Figs. 9 and 11 show, the phase within the fan arrangement, adjacent to the tungsten plates, is continuous with the parent β matrix. None of this lamellar-type precipitate was observed in any of the higher tungsten-content alloys at any of the temperatures investigated.

X-ray confirmation on the eutectoid-reaction products was also obtained. Diffraction patterns on samples of an 18.4 pct W sample annealed for 1000 hr at 540° and 650°C showed patterns for α titanium and a body-centered cubic phase with a parameter of 3.164Å. This cubic structure was identified as the terminal tungsten solid solution which has been expanded from 3.158Å by the solution of a small quantity (less than 5 pct) of titanium.

The maximum solubility of tungsten in α tita-

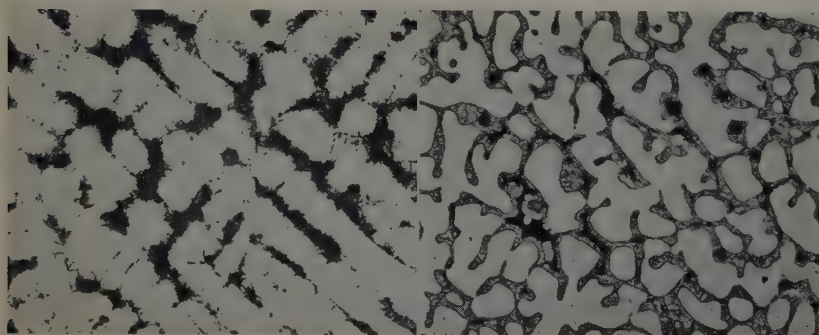


Fig. 3—Typical cast structures for two arc-melted Ti-W alloys. Etchant: 1 pct HF, 3 pct HNO₃ in water. X250. Area reduced approximately 50 pct for reproduction. a (left)—25 pct W cored β phase. b (right)—80 pct W primary tungsten solid solution surrounded by peritectic β and cored β phase.

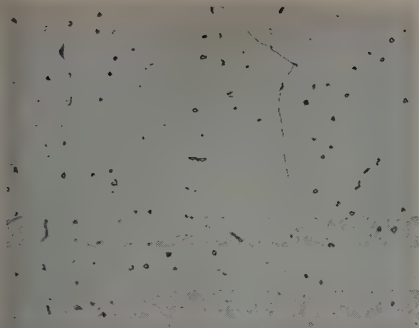
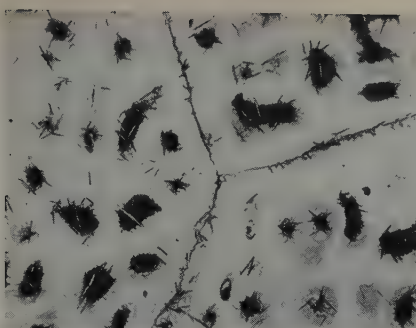


Fig. 4—Cast structure of an arc-melted 95 pct W alloy. Columnar grains of primary tungsten solid solution plus precipitated particles of β . Etchant: 1 pct HF, 3 pct HNO_3 in water. X250. Area reduced approximately 50 pct for reproduction.

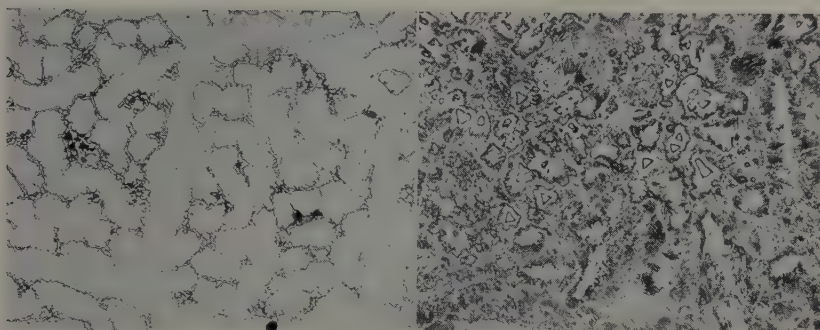


a—30 pct W. Incipient melting indicated by "burnt" spots in large β grains. The grain-boundary precipitate and acicular needles are proeutectoid tungsten solid solution rejected during furnace cooling.



b—40 pct W. Large β grains plus acicular proeutectoid tungsten solid solution precipitated during furnace cooling.

Fig. 5—Structures for two Ti-W alloys held 1 hr at 1800°C and furnace cooled. Etchant: 1 pct HF, 3 pct HNO_3 in water. X100. Area reduced approximately 50 pct for reproduction.



a—30 pct W. Heated to 1850°C for 15 min and furnace cooled. Cored β phase.

b—30 pct W. Heated to 1900°C for 10 min and furnace cooled. Primary crystals of tungsten solid solution surrounded by peritectic β in a matrix of cored β solid solution.

Fig. 6—Liquation in a 30 pct W alloy at temperatures below and above the peritectoid temperature. Etchant: 1 pct HF, 3 pct HNO_3 in water. X100. Area reduced approximately 50 pct for reproduction.



Fig. 7 (left)—Structure of a β -quenched 20 pct W alloy after annealing 250 hr at 725°C . Grain-boundary and Widmanstatten proeutectoid α in β . Etchant: 1 pct HF, 3 pct HNO_3 in water. X500. Area reduced approximately 50 pct for reproduction.



Fig. 8 (right)—Structure of a β -quenched 20 pct W alloy after annealing 300 hr at 700°C . Grain-boundary α plus β eutectoid decomposition product of α plus tungsten. Etchant: 1 pct HF, 3 pct HNO_3 in water. X500. Area reduced approximately 50 pct for reproduction.

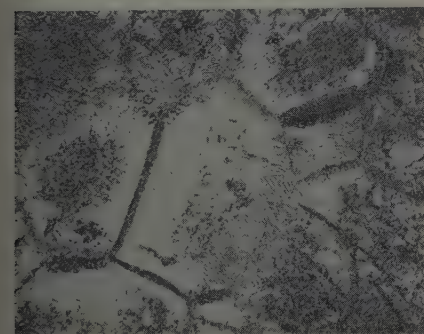


Fig. 9—Structure for a β -quenched 32 pct W alloy after annealing 250 hr at 725°C . Proeutectoid tungsten in β . Etchant: 1 pct HF, 3 pct HNO_3 in water. X500. Area reduced approximately 50 pct for reproduction.

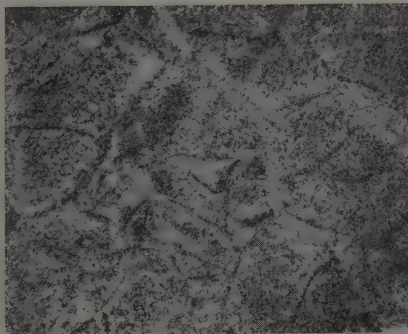


Fig. 10—Structure for a β -quenched 32 pct W alloy after annealing 300 hr at 700°C . β eutectoid decomposition product of α plus W. Etchant: 1 pct HF, 3 pct HNO_3 in water. X500. Area reduced approximately 50 pct for reproduction.

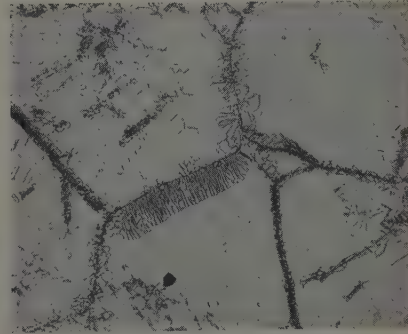


Fig. 11—Structure of a β -quenched 32 pct W alloy after annealing 200 hr at 750°C . Grain-boundary and Widmanstatten tungsten precipitate in β . Etchant: 1 pct HF, 3 pct HNO_3 in water. X500. Area reduced approximately 50 pct for reproduction.

Ti-Ta System

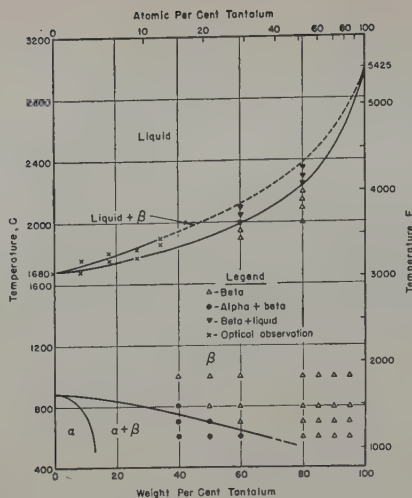


Fig. 12—Phase diagram for the Ti-Ta system.

nium, determined metallographically, is about 0.8 pct at 715°C (cf. Fig. 2). Tungsten in solid solution in α titanium was found to have practically no effect on lattice parameter. Hence, the X-ray method was not useful in determining α solubilities. The solubility of titanium in tungsten decreases from a maximum of about 8 pct at the peritectic-reaction temperature to less than 5 pct at temperatures in the region of the eutectoid. These conclusions are based on microexaminations of as-cast and heat-treated high-tungsten alloys.

Structures in the composition range around the eutectoid were sensitive to heat treatment in that they clearly showed the eutectoid reaction. As the tungsten content increased, however, the β eutectoidal decomposition reaction became increasingly sluggish. Even after isothermal treatment of 300 hr at 700°C, samples containing 36 and 40 pct W showed an increasing amount of undecomposed β phase. Heat treatments at 700°C on alloys containing 88 and 95 pct W showed no metallographic evidence of β eutectoid decomposition.

As mentioned earlier, homogenization treatments failed to produce equilibrium structures in alloys containing above 40 pct W. However, the phase distributions and structures observed were consistent with the lower alloy-content samples over the temperature range investigated.

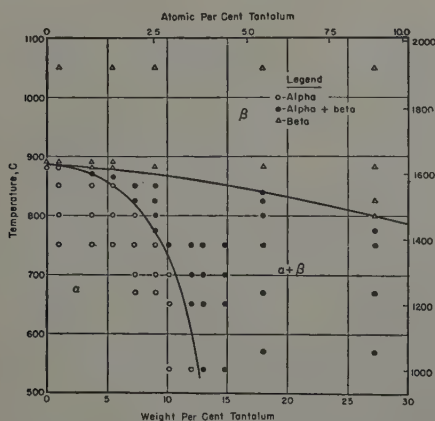


Fig. 13—Partial phase diagram for iodide titanium-tantalum alloys.

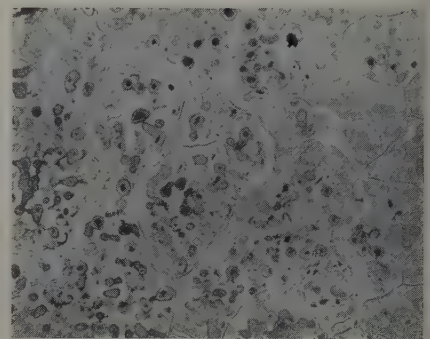
The phase diagram for the entire range of compositions in the Ti-Ta system is shown in Fig. 12. The titanium-rich portion is shown in Fig. 13. β titanium and tantalum form a continuous series of solid solutions. The α field, although closed, has an appreciable range.

Melting Range: Both optical observation and incipient-melting techniques were used to determine the melting range. The solidus curve rises smoothly from the melting point of titanium to that of tantalum. The solid-liquid range is seen to be relatively narrow. Fig. 14 illustrates a typical partially melted alloy, showing how the incipient-melting technique was applied to obtain the solidus curve at the higher alloy contents.

As-cast structures for an alloy series containing 40 to 95 pct Ta were consistent with the isomorphism of β titanium and tantalum in that they consisted entirely of cored β phase.

Solid-State Equilibria: Examination of alloys containing from 0.96 through 95 pct Ta equilibrated at 1000°C confirmed the existence of complete β solid solubility. Fig. 15 shows a typical β -transformation structure and a retained- β structure for alloys quenched from this temperature. Some slight in-

Fig. 14—Incipient melting in a 80 pct Ta alloy heated to 2250°C for 5 min and furnace cooled. Large equiaxed β grains with "burnt" spots indicating incipient melting. Etchant: 1 pct HF, 3 pct HNO₃ in water. X100. Area reduced approximately 50 pct for reproduction.



homogeneity persisted in the alloys containing 40 through 60 pct Ta even after homogenization treatment. This was indicated by nonuniform α precipitation in these alloys at temperatures below the β transus. No evidence of β decomposition was observed in the alloys containing 80 through 95 pct Ta at temperatures down through 600°C.

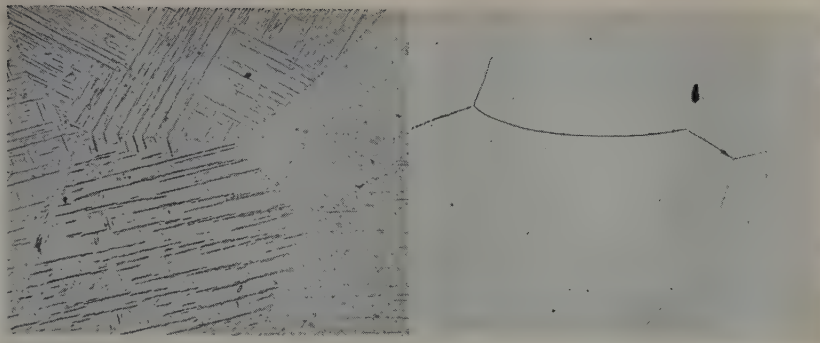
Tantalum additions to titanium depress the β transus gradually. β quenching of alloys containing up to 40 pct Ta produces martensitic transformation structures, like that shown in Fig. 15a. At tantalum contents of 50 pct and above, the β phase was retained on quenching.

As indicated in the phase diagram, tantalum shows an appreciable solubility in α titanium. This increases with decreasing temperature to about a

Table I. Lattice Parameter Data for Three Ti-Ta Alloys

Ta, Wt Pct	Lattice Parameter, Å		c/a Ratio
	a	c	
Unalloyed Ti	2.9503±0.0001	4.6834±0.0001	1.587
0.96	2.9512±0.0001	4.6845±0.0001	1.587
3.70	2.9506±0.0003	4.6858±0.0002	1.588
5.36	2.9502±0.0003	4.6873±0.0002	1.589

Fig. 15—Structures for two Ti-Ta alloys quenched after 24 hr at 1000°C. Etchant: 1 pct HF, 3 pct HNO₃ in water. X250. Area reduced approximately 50 pct for reproduction. a (left)—40 pct Ta. Large equiaxed β grains with martensitic needles of α . b (right)—80 pct Ta. Large equiaxed β grains.



maximum of 12.5 pct Ta at 550°C. α parameters determined for three alloys annealed 14 days at 530°C showed that tantalum expands the α -titanium lattice in the c direction while showing no significant effect on the a parameter. These data are given in Table I. Although the graphical relationship of c parameters to alloy composition was approximately linear, the scatter along this line was too large to permit use of parameter measurements in locating the α transus.

Resistance-temperature curves for three alloys showed inflections at the temperatures noted in Table II. These data provided a rough check for the metallographic determination of the transus tem-

Mines titanium as a base for the intermediate and high-alloy ranges.

Liquid (containing about 25 pct W) and tungsten solid solution (containing about 8 pct Ti) react peritectically at about 1880°C to produce a wide two-phase region of β -tungsten in the intermediate portion of the diagram. The solubility of titanium in tungsten decreases from about 8 pct Ti at 1880°C to slightly less than 5 pct Ti at around 700°C.

Tungsten solubility in β titanium decreases from a maximum of about 50 pct W at 1880°C to about 28 pct W at 715°C, where the β -phase field terminates in a eutectoid reaction between α titanium and tungsten terminal solid solution. Increasing

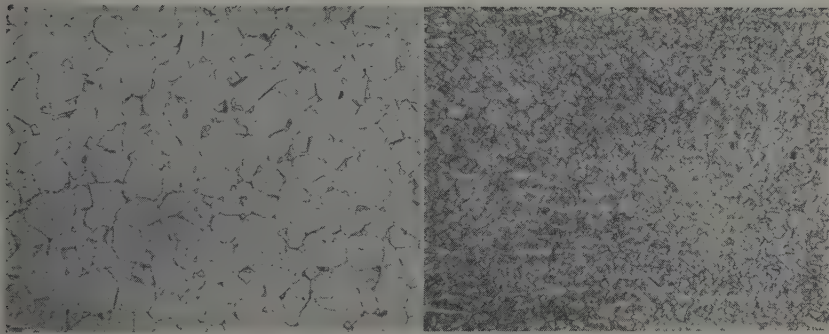


Fig. 16—Structures for two Ti-Ta alloys after a 50 pct cold reduction and 12 hr at 800°C followed by water quenching. Etchant: 1 pct HF, 3 pct HNO₃ in water. X500. Area reduced approximately 50 pct for reproduction. a (left)—9.05 pct Ta. Equiaxed α grains plus intergranular β . b (right)—17.9 pct Ta. α grains (light) in a matrix of small equiaxed transformed β .

perature, which represented a much closer approach to equilibrium conditions. Fig. 16 shows typical two-phase structures for alloys equilibrated within the extensive α - β field.

X-ray diffraction patterns on two alloy samples of a 27.2 pct Ta alloy annealed 1000 hr at 540° and 650°C showed lines for α titanium and a body-centered cubic phase which represented β solid solution. Line intensities of these patterns, however, were not sufficient to permit accurate parameter measurements.

Summary

Binary phase diagrams for the Ti-W and Ti-Ta systems were determined using iodide titanium as a base for the titanium-rich alloys and Bureau of

additions of tungsten to titanium lower the β transus to 715°C at the eutectoid composition. Tungsten solubility in α titanium reaches a maximum of about 0.8 pct W at the eutectoid reaction temperature.

β titanium and tantalum form a complete series of solid solutions. Increasing additions of tantalum to titanium progressively increase the melting range and lower the β transus to 600°C at about 70 pct Ta. Tantalum solubility in α titanium increases with decreasing temperatures to a maximum of about 12.5 pct Ta at 550°C.

Acknowledgments

The authors are grateful to the Research Division of the Materials Laboratory at Wright-Patterson Air Force Base for permission to publish the results of this work, which was done at Battelle Memorial Institute under their sponsorship. They also wish to thank O. J. Huber and J. R. Doig, of Battelle, for the X-ray diffraction work reported in this paper, and M. W. Mallett, of Battelle, for his assistance in the determination of the melting ranges in both alloy systems investigated.

Appendix—Experimental Methods

Materials: Iodide crystal-bar titanium was used in preparing the titanium-rich alloys and U. S. Bureau of Mines powder titanium was used for the intermediate

Table II. Inflection Temperature Obtained from Resistance-Temperature Curves

Ta, Wt Pct	Inflection Temperature, °C			
	Alpha Transus		Beta Transus	
	Heating	Cooling	Heating	Cooling
5.4	833	813	878	854
7.3	830	808	892	859
27.2	—	—	760	680

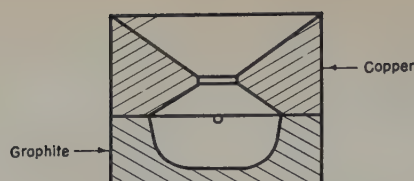


Fig. 17—Crucible design for arc casting of Ti-W ingots.

and high-alloy ranges. The iodide titanium was produced by the New Jersey Zinc Co. to the specification that the maximum lot hardness should not exceed 85 Vickers. A typical spectrographic analysis for one of these lots is given in Table III.

The analysis furnished by the Bureau of Mines for the powder titanium was as follows: Fe, 0.15 wt pct; Mg, 0.30; Ca, 0.036; Si, 0.005; V, 0.012; and H, 0.25 pct or 25 to 30 ml per g.

The tungsten and tantalum used, both of 99.9+ pct purity, were produced by the Fansteel Metallurgical Corp. The tungsten used was in the form of 10-mil wire and as -200-mesh powder. Tantalum was available as 0.006-in. sheet and also as "Standard Reclaimed Powder."

Alloy Preparation: Preparation of homogeneous alloys of titanium with the high-melting, heavy metals, tungsten and tantalum, proved to be a difficult task, and the methods used merit special mention here. Initially, alloys containing up through 18.4 pct W were prepared by direct arc melting charges of iodide titanium crystal bar and 10-mil tungsten wire on a water-cooled copper hearth in a small, tungsten-arc furnace. This furnace and the melting procedure used have been previously described.^{4,5} Because of the refractory nature of tungsten, a rigorous schedule of sectioning and remelting the ingots was necessary to insure complete solution of the tungsten. The total number of melts required was roughly proportional to the tungsten content, with a maximum of 12 melts being required for the 18.4 pct W alloy.

In order to evaluate the higher tungsten-content alloys, samples were prepared using powdered titanium and tungsten. Compacts with compositions ranging from 20 through 95 pct W were pressed and vacuum sintered to remove the magnesium chloride and hydrogen present in the powder. Melting of the compacts containing from 20 through 60 pct W was carried out in a small vacuum-arc-furnace unit with the maximum current capacity of 500 amp being required for the 60 pct W alloy. In order to obtain complete melting of the higher alloys, an arc furnace with a higher current capacity was used. This furnace utilized a spun-copper crucible and operated under a positive pressure of argon. A complete description of the furnace and melting procedure used has been described.⁶

Another method of preparing homogeneous Ti-W alloys was also tried. In hopes of circumventing the arduous sectioning and melting procedure required to insure complete melting of alloys made of tungsten wire and iodide titanium, porous, presintered chunks

of tungsten were used as the alloy addition. Six alloy charges, containing 20 through 40 pct W, were given an initial consolidating melt under argon. The alloys were then given three additional melts under helium, which provides a hotter arc than argon, to complete alloying of the titanium and tungsten. In order to eliminate the freezing segregation, the alloys containing 24 through 40 pct W were given a final melting operation during which they were cast in a cylindrical crucible of the design shown in Fig. 17. Casting was accomplished by placing an ingot over the hole on the split copper block and by directing the arc to the sample until melting occurred. The ingot then flowed into the graphite receptacle below.

Subsequent examination of the arc-cast ingots showed that, while homogeneous and uniform structures were obtained in the 32, 36, and 40 pct W alloys, severe segregation still persisted in the 24 and 28 pct W ingots as a carry-over from the initial melting. Failure of arc casting to overcome this segregation may be because of the lower melting range of these alloys and their increased fluidity.

Alloys containing up through 27.2 pct Ta were prepared by direct arc melting charges of iodide titanium crystal bar and tantalum sheet. Melting of these alloys was only slightly less difficult than for the corresponding earlier Ti-W alloy series. By repeated sectioning and remelting, complete solution of the tantalum was obtained.

Evaluation of alloys in the range of 40 through 95 pct Ta was carried out using samples prepared from titanium and tantalum powders. These powder alloys were processed in the manner described for the similar Ti-W series. All of the Ti-Ta alloys were successfully melted in the small vacuum-arc furnace under a total pressure of 10 cm Hg of argon.

Compositions for the alloys containing up through 18.4 pct W and 27.2 pct Ta were determined by chemical analysis. Because no satisfactory analytical techniques were available for the higher tungsten and tantalum-content alloys, these compositions were determined by weight-change measurements during melting. Weight losses for the alloys containing up through 60 pct W and 95 pct Ta during melting were less than 1 pct, and the use of nominal compositions for these alloys was justified on that basis. The alloys with above 60 pct W were melted in the larger arc furnace, and considerable spattering took place. Here, density measurements were made, and compositions were calculated using the law of mixtures. These checked the intended analyses very well.

Fabrication: Upset forging and hot rolling in air were used, where possible, to break down and homogenize the as-cast structures. Ingots containing up through 9.9 pct W and 9.1 pct Ta were successfully fabricated to 0.060-in. strip at 750°C.

For the 18.4 and 20 pct W alloys, it was necessary to increase the rolling temperature to 850°C to avoid edge cracking. An alloy containing 40 pct W could not be hot worked at 980°C, and fabrication attempts for this and the higher alloys were abandoned.

Alloys containing 17.9 and 27.2 pct Ta were fabricated at 850°C. Experiments on higher tantalum-content alloys indicated that increasingly higher working temperatures were required as the tantalum content increased. At 60 pct Ta, 980°C proved satisfactory, but an 80 pct Ta alloy cracked badly during fabrication attempts at this temperature. In the interest of minimizing contamination, fabrication attempts on alloys containing above 40 pct Ta were abandoned.

After hot rolling, each strip was given a 15-min strain-relief anneal at rolling temperature and air cooled. The rolled strips were then descaled by mechanical grinding and pickling in a 20 pct HF, 80 pct HNO₃ (by volume) bath to remove a total thickness of 0.004 in.

Heat Treatment: Prior to heat treatment, all of the alloys containing up through 20 pct W and 27.2 pct Ta were given cold reductions of 50 pct to expedite equi-

Table III. Spectrographic Analysis of Iodide Titanium

Element	Spectrographic Analysis	
	Quantitative, Wt Pct	Qualitative
Mn	0.032	Weak to faint
Al	0.017	Very faint
Fe	0.0041	Extremely faint
Cu	0.0033	Extremely faint
Pb	0.0029	Extremely faint
Sn	0.0013	Extremely faint
Mg	—	Extremely faint
N	0.003*	

* By chemical analysis.

Table IV. Schedule Adopted for Equilibrating Treatments

Temperature Range, °C	Time, Hr	Temperature Range, °C	Time, Hr
1000-1050	2	800-850	16
950-1000	4	750-800	20
900-950	8	700-750	24
850-900	12	570-600	168

librium structures. In order to minimize the severe coring obtained at the higher alloy levels, the tungsten and tantalum alloys were given a minimum of three, short-time, very high-temperature treatments in the vacuum arc-melting furnace. The currents used were sufficient to heat the ingots close to their melting points. These alloys were then encapsulated in Vycor under a partial pressure of argon and given further homogenizing treatments at 1000°C. A period of 100 hr at 1000°C was used for the Ti-W alloys and 24-hr treatment was given the Ti-Ta series. Examination of these alloys after the above treatment showed that homogeneous structures were obtained in all the Ti-Ta alloys and for compositions up through 40 pct W. At 45 pct W and above, uniform structures were produced, but complete equilibrium between the phases had not been obtained.

Initially, the schedule shown in Table IV was adopted for equilibrating treatments.

After the basic features of the Ti-W system had become apparent, additional treatments for these alloys were given as shown in Table V.

Treatments at 1800°C and above were carried out under argon in a high-frequency induction furnace. Samples were suspended individually by tungsten wires from the cover of a graphite crucible. Temperatures were measured optically, with an accuracy of $\pm 10^\circ\text{C}$, by sighting into a $\frac{1}{8}$ -in. ID hole, 9/16 in. deep, which had been drilled into a graphite pedestal on the crucible base. Unfortunately, no means of quenching samples from temperature was available with this furnace.

At 1400°C, heating was performed in a molybdenum resistance furnace of a design which has been described.⁷ Quenching from this temperature was effected using a silicone oil as the coolant.

All other quenching treatments were carried out in a chromel-A-wound, type 304 stainless steel tube furnace. Samples for treatment were packed in titanium turnings inside of a titanium-sheet sleeve and controlled within $\pm 3^\circ\text{C}$ at temperature. These furnaces were mounted in cradles which pivoted about an axis through one end of the furnace tube. Quenching was effected by up-ending the furnace and sliding the sleeve and samples into a water-filled quench pot.

All treatments beyond 24 hr were made using Vycor capsules and individual columbium-foil wrappers for the samples as protection against contamination by silica. In these and in all of the furnace treatments, gettered argon gas was used as an atmosphere.

Metallography: Metallographic samples were prepared by hand grinding on 240X, 400X, and 600X wet papers. Grinding scratches were removed by polishing with a slurry of Linde B alumina and chromic acid on a Miracloth lap on a 1725-rpm wheel. Final polishing was accomplished with Linde B alumina on a Microcloth lap on a medium speed wheel.

An aqueous solution of 1 pct HF and 3 pct HNO₃, by volume, was satisfactory as an etchant for all structures examined.

Table V. Additional Treatments for Ti-W Alloys

Temperature, °C	Time, Hr	Temperature, °C	Time, Hr
1800	1-4	750	200
1400	6	725	250
775	180	700	300

Resistance Measurements: Resistance measurements were investigated as a means of locating phase transformations in titanium-rich alloys of both systems. Current and potential leads (of molybdenum and Alumel wire, respectively) were attached to sheet-alloy samples by spot welding. The sample was surrounded by titanium turnings in a titanium sleeve and heated in a tube furnace under a gettered argon atmosphere at a rate of 2.0° to 2.5°C per min. Current through the sample was maintained at 1.00 ± 0.01 amp. Alternate readings of temperature and the potential drop across the sample were taken at 1-min intervals and used to construct temperature-resistance curves for the alloys investigated.

X-Ray Diffraction: Films for the α -lattice-parameter determinations on the alloys in both systems were made in a 114.6-mm Debye camera using copper radiation. A 1-mil aluminum foil was interposed to reduce the high background normally produced with titanium. The values used for the characteristic copper $K\alpha_1$ and $K\alpha_2$ radiations were 1.54050 and 1.54434Å, respectively.

In other parameter work, unfiltered vanadium radiation was used, again utilizing the 114.6 mm Debye camera. The values used for the characteristic $K\alpha_1$, $K\alpha_2$, and $K\beta$ radiations of vanadium were 2.5072, 2.5034, and 2.2843Å, respectively.

All parameter calculations were made using Cohen's graphical method. The Gauss method was used to calculate probable errors.

Melting Range: Liquidus and solidus temperatures for titanium-rich alloys in both systems were determined by optical observation on small samples induction heated under argon. Sheet samples of selected alloy compositions were bent into "V" shapes and inserted in deep-well graphite crucibles so that observations at the apex of the "V" could be followed during each run. Pyrometer readings taken at the first sign of rounding at the apex and at the point of the sample's collapse were interpreted as the solidus and liquidus temperatures, respectively. Using a similar procedure, the melting point of unalloyed iodide titanium was determined as $1680^\circ \pm 10^\circ\text{C}$.

Incipient-melting techniques were used to determine the liquid-solid relationships in the intermediate and high-alloy-content ranges. Metallographic samples were suspended individually by tungsten wires from the cover of a graphite crucible, as described earlier, and heated by induction to selected temperatures under argon. After treatment, the samples were mounted and examined metallographically for signs of melting. When melting in a given alloy sample was observed, succeeding samples were heated to progressively lower temperatures to bracket the solidus temperature. In this, as in other optical-pyrometer work, the accuracy of temperature measurement was estimated as $\pm 10^\circ\text{C}$.

References

- ¹ Rand Report RA-15080, April 2, 1948, pp. 13-44.
- ² Research and Development on Titanium Alloys, AF Technical Report No. 6218, Part 2 (1950) p. 40.
- ³ Battelle Memorial Institute: Summary Report on Titanium-Alloy Phase Diagrams for the Systems Ti-Mn, Ti-W, and Ti-Ta. To Wright-Patterson Air Force Base, Contract AF 33(038)-8544, January 12, 1952, 59 pp.
- ⁴ R. I. Jaffee, et al.: The Ti-Mn, Ti-W, and Ti-Ta Phase Diagrams. USAF, Wright-Air Development Center, Wright-Patterson Air Force Base, AF Technical Report No. 6515, Part 1 (June 1951) 54 pp.
- ⁵ R. I. Jaffee, H. R. Ogden, and D. J. Maykuth: Alloys of Titanium with Carbon, Oxygen, and Nitrogen. *Trans. AIME* (1950) 188, pp. 1261-1266; *JOURNAL OF METALS* (October 1950).
- ⁶ C. M. Craighead, O. W. Simmons, and L. W. Eastwood: Titanium Binary Alloys. *Trans. AIME* (1950) 188, pp. 485-513; *JOURNAL OF METALS* (March 1950).
- ⁷ W. E. Few and G. K. Manning: A 4000° Furnace. *Metal Progress* (March 1951) 59, pp. 364-365.

Microstructure and Mechanical Properties of Iodide Titanium

by F. C. Holden, H. R. Ogden, and R. I. Jaffee

RECENT papers dealing with the properties of unalloyed iodide titanium have been directed primarily at the determination of base-line properties for alloy investigations. Early work was limited to a few tests because of the limited availability of iodide titanium at the time. In the results of papers by Campbell et al.,¹ Gonser and Litton,² Jaffee and Campbell,³ Finlay and Snyder,⁴ and Jaffee, Ogden, and Maykuth,⁵ data on mechanical properties are presented for unalloyed iodide titanium in the annealed and cold-worked conditions.

Data are presented in this paper which show the effects of heat treatment on the structure and mechanical properties of commercially produced iodide titanium. Correlation is made between microstructural variables and the mechanical properties.

Experimental Procedures

Melting Stock: The melting stock used was as-deposited iodide titanium, produced by New Jersey Zinc Co. The furnished analysis showed the following range of impurities: N, 0.004 to 0.008 pct; Mn, 0.005 to 0.013; Fe, 0.0035 to 0.025; Al, 0.013 to 0.015; Mo, 0.0015; Pb, 0.0045 to 0.0065; Cu, 0.0015 to 0.002; Sn, 0.001 to 0.01; Mg, 0.0015 to 0.002; and Ni, 0.003. Hydrogen content as determined by vacuum-fusion analysis was 0.0091 wt pct (0.44 atomic pct) after arc melting and fabrication. Nitrogen analysis on the arc-melted and fabricated titanium showed a content of less than 0.002 pct N. The average hardness of the furnished stock was R_t 70, or approximately 85 VHN.

Melting Procedure: The as-deposited rods were rolled, sheared, and degreased in preparation for arc melting. The charge was arc-melted with a tungsten electrode in a water-cooled copper crucible under a positive pressure of high purity (99.96 pct) argon. The final ingot was approximately 2 in. in diameter and showed no increase in hardness over that of the initial stock.

Fabrication: Heating for fabrication was done in air. It was begun by forging the ingot into a $\frac{3}{4}$ in. diam rod, at an initial temperature of 1600°F. Scale was removed by sandblasting. The rod was then swaged to $\frac{1}{4}$ in. diam at room temperature through a series of 20 dies, with approximately 10 pct reduction in area between each die. An anneal of 1 hr at 850°C in air was given after the $\frac{1}{2}$ in. die, such that the final cold reduction was 75 pct. Sections cut from this rod were used for test and microstructure specimens.

F. C. HOLDEN is Principal Metallurgist, H. R. OGDEN, Junior Member AIME, is Assistant Supervisor, and R. I. JAFFEE, Member AIME, is Supervisor, Nonferrous Physical Metallurgy Div., Battelle Memorial Institute, Columbus, Ohio.

Discussion on this paper, TP 3482E, may be sent, 2 copies, to AIME by April 1, 1953. Manuscript, Sept. 15, 1952. Los Angeles Meeting, February 1953.

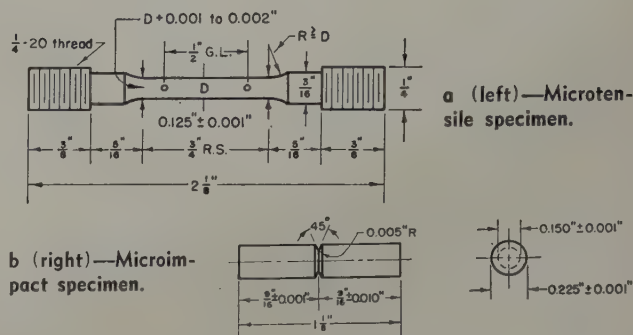


Fig. 1—Specifications for test specimens.

Heat Treatment: Heat treatments were carried out in resistance tube furnaces with stainless-steel linings, under an atmosphere of gettered argon. As further protection against contamination, the specimens were packed in titanium turnings in a titanium sleeve. Control experiments have shown negligible hardness increases with this method, indicating that contamination from oxygen and nitrogen is slight.

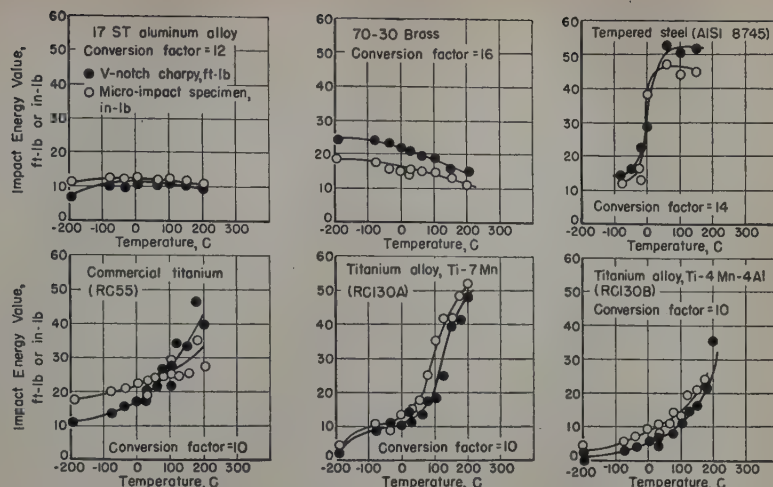
Three cooling rates were employed in this work; these have been designated as water quenching, argon cooling (to simulate air cooling under a controlled atmosphere), and furnace cooling. The cooling rate for an argon cool is 100°C per min for the first minute, with an average cooling rate of 35°C per min over a 15-min period. A furnace cool requires about 10 hr, with an average cooling rate of 3.6°C per min during the first hour, and an average cooling rate of 1.2°C per min over the 10-hr period.

Microimpact Test: The specimen adopted was based on the cylindrical Izod Type Y specimen (ASTM, E23-41T). All dimensions were reduced to half scale, including the notch radius. Specifications are shown in Fig. 1. The specimen is held vertically in an adapter and broken as a cantilever beam. Impact tests were run on a constant-velocity (11.34 ft per sec) Tinius Olsen impact testing machine with a total available energy of 100 in.-lb.

Tests were made to determine the correlation between this microimpact and the standard V-notch Charpy impact test. Curves showing impact energy as a function of temperature for both impact tests are plotted in Fig. 2. Transition temperatures, when they occur, are about the same for both impact tests. All three titanium-rich materials have the same conversion factor, 10.

Tensile Testing: Tensile tests were conducted on Baldwin-Southwark testing machines using the 600, 2400, or 3000 lb range. Specifications for the test specimen were taken from the 1948 edition of the ASM Metals Handbook, and are shown in Fig. 1. Strain measurements were made using an SR-4 resistance gage (Type A-7) cemented to the reduced section in conjunction with a lever-type extensometer. Readings on the SR-4 strain indicator were

Fig. 2—Comparison of microimpact and V-notch Charpy impact energy curves for various materials.



made up to about 2 pct elongation, and from the extensometer in 1 pct elongation increments up to about 50 pct elongation. Crosshead speeds were maintained at not over 0.005 in. per min until the limit of the SR-4 gage was reached, after which the strain rate was increased to 0.01 in. per min.

Metallography: The preparation of metallographic specimens involved mounting and wet grinding

Table I. Effect of Annealing Time and Temperature on the Grain Size of Alpha-Annealed Iodide Titanium*

Annealing Treatment		Average Alpha Grain Diameter, Mm
Temperature, °C	Time, Hr	
600	1	0.01
800	1	0.05-0.07
875	2	0.10
875	100	0.20-0.25

* Tests made on material that had been arc-melted, forged at 850°C to 3/4-in. round, descaled, cold swaged to 1/2-in. round, annealed 1 hr at 850°C in air, descaled, cold swaged to 1/4-in. round (75 pct reduction in area), and given annealing treatments indicated, followed by argon cooling to room temperature.

through 600-grit paper. Polishing was done on a high-speed wheel with an abrasive of jewelers rouge, followed by a final polish on a slow-speed wheel with aluminum oxide. The usual etching reagents consisted of either a 5 pct solution of hydrofluoric acid in water or a 1 1/2 pct hydrofluoric-3 1/2 pct nitric acid solution. Early specimens were mounted in bakelite, but work by Craighead, Lenning, and Jaffee⁶ has shown that bakelite mount-

ing temperatures (up to 350°F) are sufficient to alter the solubility of the hydride phase in titanium, and thus affect the microstructure of the specimen. Accordingly, recent metallographic work was done on specimens mounted in a cold-setting plastic.

Alpha-Annealed Iodide Titanium

In the study of the effect of microstructure on the properties of a pure metal, the variables of interest are the effect of grain size and, for metals exhibiting allotropic transformation, the effect of different transformation structures. In this work the rate of cooling from both α and β anneals was found to influence the mechanical properties and microstructures, and, therefore, cooling rate has been included as a third variable.

Microstructure: Table I details times, temperatures, and resulting α grain sizes. α anneals produce equiaxed α with intragranular markings, which Craighead, Lenning, and Jaffee⁶ have shown to be titanium hydride. Fig. 3, which has been heavily etched to bring out the grain structure, is typical of the slow-cooled α -annealed structures with the Widmanstätten line markings. Figs. 4 and 5 illustrate the difference in dispersion of titanium hydride for α -annealed titanium after quenching and after slow cooling.

Mechanical Properties: The mechanical properties of α -annealed, argon-cooled iodide titanium are presented as functions of α grain diameter in Fig. 6. The effect of α grain size on the flow curves is shown in Fig. 7. These curves are not straight lines, and the flow coefficient B and flow exponent n in

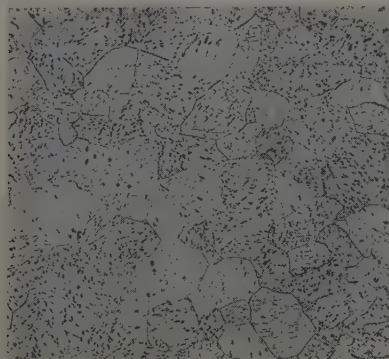


Fig. 3—Specimen TMI-3, cold-reduced 75 pct, annealed 2 hr at 875°C, and argon-cooled. Equiaxed α structure, 0.10-mm average grain size. HF etch. X100. Area reduced approximately 45 pct for reproduction.

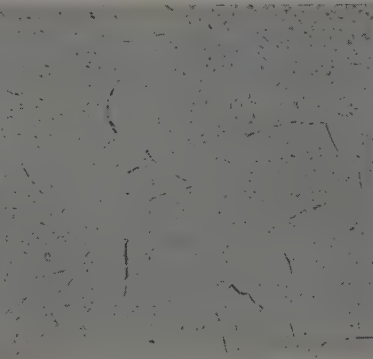


Fig. 4—Specimen TMI-12, cold-reduced 75 pct, annealed 1 hr at 800°C, and quenched. Equiaxed α structure with "salt-and-pepper" markings. HF-HNO₃ etch. X250. Area reduced approximately 45 pct for reproduction.

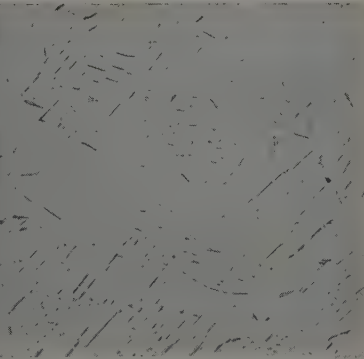


Fig. 5—Specimen TM2-1, cold-reduced 75 pct, annealed 1 hr at 800°C, and argon-cooled. Equiaxed α structure with Widmanstätten markings. HF-HNO₃ etch. X250. Area reduced approximately 45 pct for reproduction.

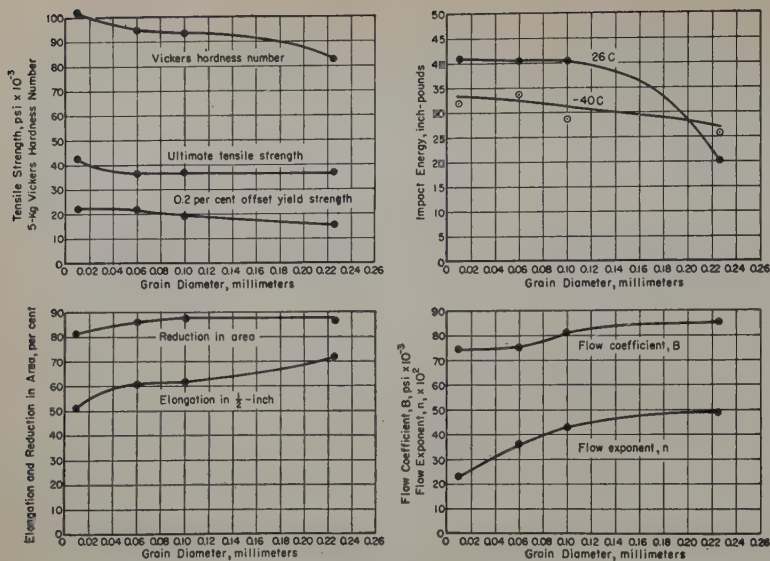
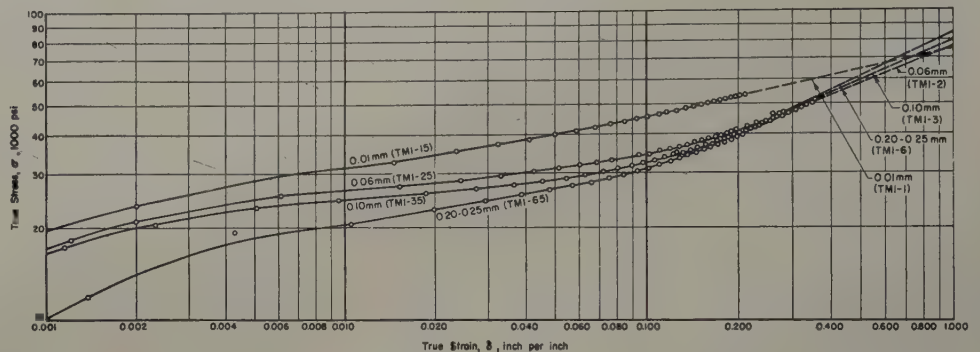


Fig. 6 (left)—Effect of grain size on the mechanical properties of α-annealed, high-purity titanium in the argon-cooled condition.

Fig. 7 (right)—Effect of grain size on the flow curves of α-annealed, high-purity titanium.



the flow equation $\sigma = B\epsilon^n$ are determined from the straight line extrapolation. These data show that, in line with expectation, increased grain size results in lower strength, higher ductility, and higher strain hardening, but the changes involved are relatively slight.

Impact-energy values for equiaxed α-annealed iodide titanium show a greater dependence on grain size, which is illustrated by the room-temperature impact-energy curve in Fig. 6.

The variation of impact energy with temperature can be observed for different grain sizes and cooling rates in Fig. 8. All curves show the same general configuration, with impact-energy values increasing slowly from -196°C up to room temperature, and

increasing rapidly above room temperature. It should be noted that all fractures observed were of the ductile or fibred type, and the impact-energy values are above any brittle-to-ductile transformation temperature. The increase in impact energy observed above room temperature is considered to be caused by an increasing absorption of energy in deforming the test specimen. Bending of the specimens can be observed clearly in those tested at the higher temperatures.

The effects of different cooling rates on the mechanical properties of α-annealed iodide titanium have been investigated. These studies include the effect of quenching as compared with argon cooling in the 0.10-mm and 0.20 to 0.25-mm α grain sizes,

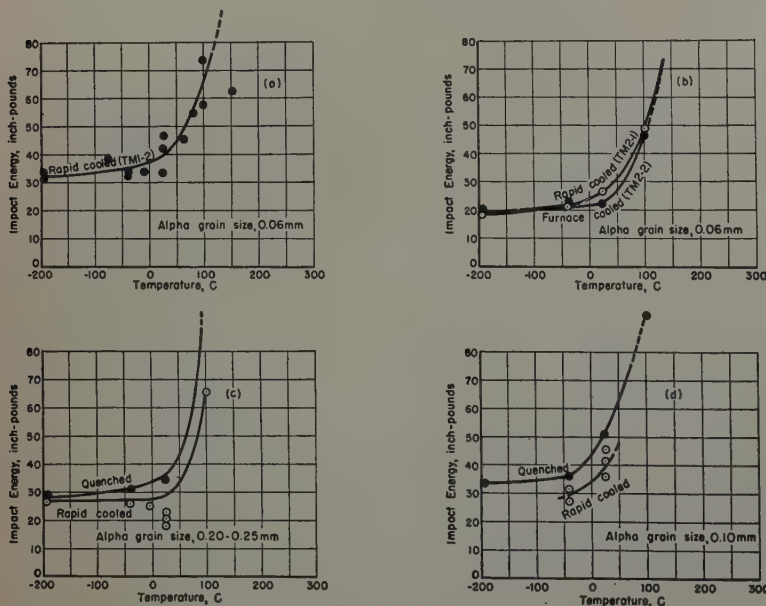


Fig. 8—Effect of grain size and cooling rate on impact energy of α-annealed, high-purity titanium.

Table II. Effect of Cooling Rate on the Tensile Properties of Alpha-Annealed High-Purity Titanium*

Specimen No.	Annealing Treatment			Avg. Alpha Grain Diameter, Mm	Avg. VHN, 5-Kg Load	Elongation, Pct in 1/2 In.	Reduction in Area, Pct	Ultimate Tensile Strength, Psi	0.2 Pct Off-set Yield Strength, Psi	Flow Properties, $\sigma = B\delta^n$		
	Temperature, °C	Time, Hr	Cooling Rate							B, Psi	n	δ_{max} , In. per In.
TM1-3 (Avg.)	875	2	Argon cool	0.10	94.7	62	87.0	36,900	19,500	81,800	0.43	0.35
TM1-8	875	2	Quench	0.10	83.5	—	—	—	—	—	—	—
TM1-6 (Avg.)	875	100	Argon cool	0.20-0.25	83.4	72	86.2	36,600	15,100	85,500	0.49	0.37
TM1-7	875	100	Quench	0.20-0.25	87.9	55	86.5	38,400	21,450	90,000	0.46	0.41
TM2-1	800	1	Argon cool	0.05	98.2	70	88.2	33,300	18,300	68,000	0.35	0.38
TM2-2	800	1	Furnace cool	0.05	100.6	74	87.1	34,000	16,500	69,000	0.34	0.36

* Tests made on material that had been arc-melted, forged at 850°C to 3/4-in. round, descaled, cold swaged to 1/2-in. round, annealed 1 hr at 850°C in air, descaled, cold swaged to 1/4-in. round (75 pct reduction in area), and given annealing treatments indicated.

and the effect of furnace cooling as compared with argon cooling in the 0.05-mm α grain size. Tensile test data are presented in Table II, and impact-energy values are plotted in Fig. 8.

From these data, the quenched equiaxed- α specimens, as compared with those argon-cooled, show increased tensile and yield strengths and less tensile elongation. Greater impact-energy absorption is also found in the quenched condition. No significant difference is found between argon-cooled and furnace-cooled α -annealed specimens.

Transformed-Beta Iodide Titanium

Two cooling rates were used in the study of the transformed- β structures. These were a water quench and a furnace cool. All the anneals consisted of a 1-hr treatment at 1000°C, and the original β grain size was thus the same in each case. Microstructures and mechanical properties resulting from these treatments are presented and discussed in the following sections.

Microstructure: The appearance of the quenched structure is shown in Fig. 9, and that of the furnace-cooled structure in Fig. 10. The irregular outlines correspond to colonies of α plates with similar orientations. It may be observed that the α -colony outlines in the quenched specimen are more irregular than those of the furnace-cooled specimen. Although both maintain the serrated outline, the more slowly cooled structure has had time for growth of the α plates to a more regular outline. The difference in the amount and form of the intragranular marks again points to the presence of the second phase, titanium hydride. In the quenched structure, the marks have a "salt-and-pepper" appearance, being more finely divided than the Widmanstätten line markings observed in the furnace-cooled structure.

The structures observed after heat etching* are

* Heat etching is accomplished by heating a prepolished specimen at the desired annealing temperature in a protective atmosphere and cooling in that atmosphere. The grain boundaries present at temperature are clearly delineated by this method.

shown in Figs. 11 and 12. Fig. 11 shows the result of the formation of α colonies over a background of prior β grains. It should be observed that these α colonies do not conform to the original β grain outlines, as is more clearly shown in the heat-tinted†

† Heat tinting is accomplished by heating a prepolished specimen for a short time in air to stain the surface of the specimen. This stain has a color characteristic of the orientation of the α grain and a very good degree of contrast between α grains may be obtained in this way.

structure in Fig. 12. Here the dark areas conform to the α colonies and do not appear to have a direct relationship to the prior β grains. The rough appearance of the surface is caused by the volume change which accompanies the β -to- α transformation.

Mechanical Properties: Results of tensile tests on the transformed- β structures are given in Table III, and impact-energy values are plotted in Fig. 13. The quenched specimens have higher tensile and yield strengths and lower ductility, as indicated by elongation, than the corresponding furnace-cooled specimens.

Results of the impact-energy tests show a pronounced increase in impact energy for the quenched over the furnace-cooled condition, a result probably associated with the finer dispersion of titanium hydride. This effect was also noted for specimens quenched from the α field. Comparison of the microstructures of these two transformed- β structures shows that the only apparent differences are the regularity of the outlines of the serrated α colonies, and the form and dispersion of the intragranular markings. Since the difference in regularities of the serrated α colonies is small, it would appear that the

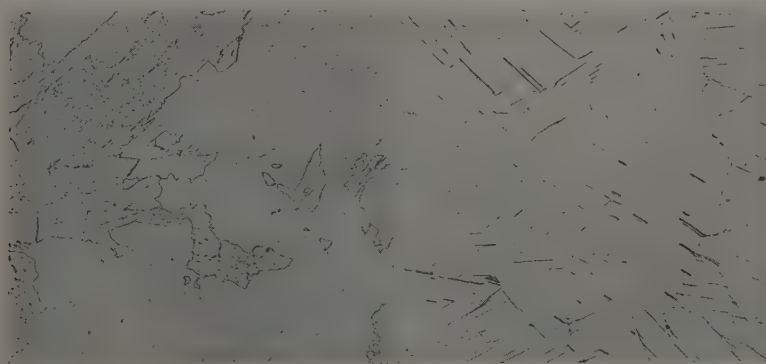


Fig. 9—Specimen TM1-4, cold-reduced 75 pct, annealed 1 hr at 1000°C, and quenched. Transformed β structure with "salt-and-pepper" marking. HF-HNO₃ etch. X100. Area reduced approximately 45 pct for reproduction.

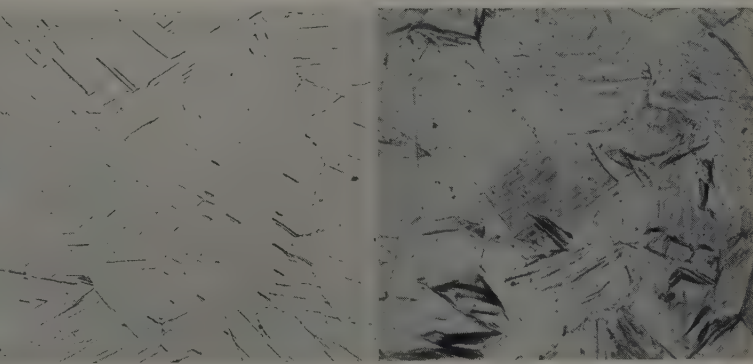


Fig. 10—Specimen TM1-5, cold-reduced 75 pct, annealed 1 hr at 1000°C, and furnace cooled. Transformed β structure with Widmanstätten markings. HF-HNO₃ etch. X100. Area reduced approximately 45 pct for reproduction.

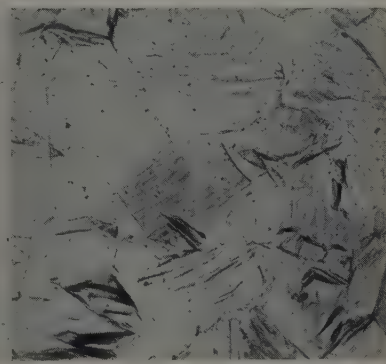


Fig. 11—Specimen 1-5, cold-reduced 75 pct, polished, annealed 1 hr at 1000°C, and furnace-cooled. Transformed β structure. X100. Area reduced approximately 45 pct for reproduction.

Table III. Tensile Properties of Transformed Beta High-Purity Titanium

Specimen No.	Annealing Treatment			Avg. Serrated Alpha Grain Diameter, Mm	Avg VHN, 5-Kg Load	Elongation, Pct in ½ In.	Reduction in Area, Pct	Ultimate Tensile Strength, Psi	0.2 Pct Offset Yield Strength, Psi	Flow Properties, $\sigma = B\delta^n$		
	Temperature, °C	Time, Hr	Cooling Rate							B, Psi	n	δ_{max} , In. per In.
TMI-4 A	1000	1	Quench	0.20-0.30	94.9	60	85.7	41,200	26,900	82,400	0.34	0.32-0.35
TMI-4 B	1000	1	Quench	0.20-0.30	94.1	56	86.4	40,100	26,200	82,000	0.34	0.32
TMI-4 (Avg.)	1000	1	Quench	0.20-0.30	94.5	58	86.1	40,700	26,600	82,200	0.34	0.32
TMI-5 A	1000	1	Furnace cool	0.20	93.5	64	85.7	37,700	20,600	83,800	0.42	0.38
TMI-5 B	1000	1	Furnace cool	0.20	93.8	64	86.5	36,700	20,900	76,500	0.37	0.34
TMI-5 (Avg.)	1000	1	Furnace cool	0.20	93.7	64	86.1	37,200	20,800	80,200	0.40	0.36

* Tests made on material that had been arc-melted, forged at 850°C to ¾-in. round, descaled, cold swaged to ½-in. round, annealed 1 hr at 850°C in air, descaled, cold swaged to ¾-in. round (75 pct reduction in area), and given annealing treatments indicated.

differences in tensile strength and impact energy are caused by the manner in which the second phase, titanium hydride, is distributed. Since the hydride is nearly insoluble at room temperature, but has high solubility above 300°C,⁶ its degree of dispersion will depend upon the rate of cooling through the hydride-precipitation range. Increases in tensile strength and Vickers hardness are slight, as a result of the almost negligible solubility of this phase in



Fig. 12—Specimen 1-5. Same as Fig. 11, followed by heat treating 5 min at 1100°F in air. Transformed β structure. X100. Area reduced approximately 45 pct for reproduction.

α titanium at room temperature. Thus, the dependence of these properties on the degree of dispersion is relatively insignificant. The marked difference in impact energy, however, indicates a considerable dependence of that property on the degree of dispersion of titanium hydride.

Summary

The gross structural features of iodide titanium are its grain size and grain shape, either equiaxed or serrated. In this work, the size of equiaxed α grains has been varied from 0.01 to 0.25 mm. The serrated α structure is the usual result of the β -to- α transformation, and, because of the large size of the β grains, serrated α grains are also quite large. There is also a fine structure in iodide titanium, which is attributed to the formation of titanium hydride whose solubility is very low at room temperature.

The degree of dispersion of the titanium hydride apparently has an important effect on impact-energy values: when the hydride is finely dispersed as a result of quenching, the impact-energy values are

higher than when the hydride is present as Widmanstätten line markings resulting from slow rates of cooling through the hydride-precipitation range.

Variation of the grain size of equiaxed α titanium from 0.01 to 0.25 mm, in the argon-cooled condition, produces relatively small changes in the tensile and impact properties. As grain size increases over this range, the strength and hardness decrease slightly and the ductility in the tensile test increases correspondingly. Flow curves show that the larger grain-size material work hardens considerably more than the fine-grain-size material, starting from a lower initial flow stress. Although all the iodide titanium tested in impact was above any brittle-to-ductile transition for temperatures down to liquid-air temperature, the level of impact energy absorbed did show variations with grain size.

Quenching from the α field, which changes the distribution of the titanium hydride, produced an increase in hardness and strength, particularly in the yield and flow stresses, and also increased the level of the impact energy.

Titanium with a large-grained serrated α structure produced by furnace cooling from the β field had mechanical properties very similar to those of titanium with equivalently large equiaxed- α grains. Quenching from the β field, which changed the intragranular fine structure to "salt and pepper" rather than Widmanstätten markings, produced the same type of increase in strength level and impact-energy level as found for quenching from the α field.

Acknowledgment

The authors wish to express their appreciation to Watertown Arsenal, under whose sponsorship this work was done, for permission to publish this information.

References

1. I. E. Campbell, R. I. Jaffee, J. M. Blocher, J. Gurland, and B. W. Gonser: Preparation and Properties of Pure Titanium. *Trans. Electrochem. Soc.* (1948) 93, p. 6.
2. B. W. Gonser and F. B. Litton: Composition, Structure, and Properties of Iodide Titanium. *Metal Progress* (1949) 55, p. 346.
3. R. I. Jaffee and I. E. Campbell: The Effect of Oxygen, Nitrogen, and Hydrogen on Iodide-Refined Titanium. *Trans. AIME* (1949) 185, pp. 646-654; *JOURNAL OF METALS* (September 1949).
4. W. L. Finlay and J. A. Snyder: Effects of Three Interstitial Solutes (Nitrogen, Oxygen, and Carbon) on the Mechanical Properties of High Purity Alpha Titanium. *Trans. AIME* (1950) 188, pp. 277-286; *JOURNAL OF METALS* (February 1950).
5. R. I. Jaffee, H. R. Ogden, and D. J. Maykuth: Alloys of Titanium With Carbon, Oxygen, and Nitrogen. *Trans. AIME* (1950) 188, pp. 1261-1266; *JOURNAL OF METALS* (February 1950).
6. C. M. Craighead, G. A. Lenning, and R. I. Jaffee: Nature of the Line Markings in Titanium and Alpha Titanium Alloys. *Trans. AIME* (1952) 194, pp. 1317-1319; *JOURNAL OF METALS* (December 1952).

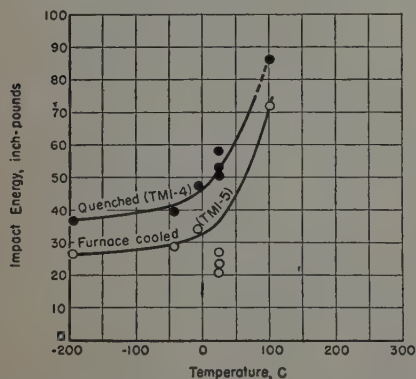


Fig. 13—Effect of cooling rate on the impact-energy values of transformed β , high-purity titanium.

Titanium-Nickel Phase Diagram

by Harold Margolin, Elmars Ence, and John P. Nielsen

The Ti-Ni phase diagram has been investigated up to 68 pct Ni with iodide titanium base alloys by metallographic, X-ray, and melting point methods, and from 68 to 90 pct Ni by examination of as-cast structures of sponge titanium base alloys.

INVESTIGATION of the nickel-rich portion of the Ti-Ni phase diagram was first reported by Vogel and Wallbaum in 1938.¹ This work was subsequently extended to lower nickel contents by Wallbaum² who indicated the possibility of a eutectic reaction for nickel contents below 38 pct. Long et al.³ studied the titanium-rich portion of the phase diagram and found eutectic and eutectoid reactions below 38 pct Ni. However, the temperature of the eutectic indicated by Long et al. was considerably lower than that suggested by Wallbaum. Long and his coworkers synthesized their alloys by powder metallurgical techniques and encountered oxygen and/or nitrogen contamination. Thus the diagram which was obtained did not represent binary alloying conditions. However from these results the features of the binary diagram were predicted. At Battelle Memorial Institute⁴ the Ti-Ni diagram was investigated up to approximately 11.5 pct Ni with sponge titanium alloys. The range of temperatures used was not sufficient to define the eutectoid temperature or composition.

The data of Wallbaum² and Long et al.³ were of particular interest for the present study, and although the work was originally concerned with the region below 40 pct Ni, the investigation was extended to higher nickel contents in an attempt to resolve the differences between these workers.

Experimental Procedure

Preliminary work on the Ti-Ni system was carried out with duPont Process A sponge titanium alloys to reduce the amount of subsequent work to be done with iodide titanium base alloys. The sponge titanium used contained 99.71 to 99.77 pct Ti, 0.1 pct Fe and 0.005 to 0.009 pct Ni. The iodide titanium obtained from the New Jersey Zinc Co. contained 99.9 to 99.95 pct Ti. Nickel used with sponge titanium was 98.9 pct pure. The high-purity nickel alloyed with iodide titanium was cobalt-free with approximately 0.05 pct C and was obtained through the courtesy of the International Nickel Co.

H. MARGOLIN, Junior Member AIME, and E. ENCE, Member AIME, are Research Associates, Research Div., New York University, and J. P. NIELSEN, Member AIME, is Associate Professor of Metal Science, College of Engineering, New York University, New York.

Discussion on this paper, TP 3468E, may be sent, 2 copies, to AIME by April 1, 1953. Manuscript, Sept. 15, 1952. Los Angeles Meeting, February 1953.

The 15 g sponge titanium charges for melting were prepared by compacting in a die or by placing the weighed portions of nickel and titanium directly into the furnace. Iodide titanium charges were made by drilling holes in the as-received rod and inserting the nickel or by wrapping the nickel in sheet.

Sponge titanium alloys containing from 0.2 to 90 pct Ni and iodide titanium alloys containing 0.2 to 68 pct Ni were prepared by these methods. In addition to these alloys several ½ lb sponge titanium alloys were supplied by the Allegheny Ludlum Co.

The charges were melted in an arc furnace under an argon atmosphere. The procedures used were similar to those reported in the literature^{5,6} and the furnace has been described.⁷ Except for iodide titanium alloys with 40 to 68 pct Ni (see section on copper contamination), each alloy was melted for 1 min, then either turned over or broken before remelting for an additional minute. Currents of 200 to 400 amp were used depending on the melting point of the alloy.

Prior to heat treatment, alloys containing less than 14.5 pct Ni were hot-forged at 750°C. With the exception of alloys in the homogeneity range of the compound TiNi, alloys of higher nickel contents could not be hot-forged. Heat treatment of iodide titanium base alloys was carried out in argon-filled quartz capsules which were broken under water at the conclusion of heat treatment to quench the specimens. Temperatures were controlled to $\pm 5^\circ\text{C}$ and annealing times up to 48 hr were used.

For melting point determination, specimens were placed in carbon crucibles which were in turn encapsulated in argon-filled quartz capsules. The start of melting was determined by rounding of corners and by metallographic examination. Complete melting was considered to have occurred at that temperature at which the specimen assumed the shape of the crucible.

Specimens were prepared for metallographic examination by mechanical polishing or by an electrolytic procedure.⁸ For alloys containing up to 80 pct Ni Remington A etch⁹ (50 pct glycerine, 25 pct HNO₃, 25 pct HF) was used. For higher nickel alloys aqua regia and Carapella's etch (5 g FeCl₃, 2 ml HNO₃, and 99 ml methyl alcohol) were employed.

Specimens to be exposed for powder patterns were prepared by filing, by breaking specimens in a



Fig. 1 (left)—As cast, 70 pct Ni (sponge titanium). Primary $TiNi_3$, eutectic of $TiNi_3$ and $TiNi$, and copper contamination. "A" etch. X75.

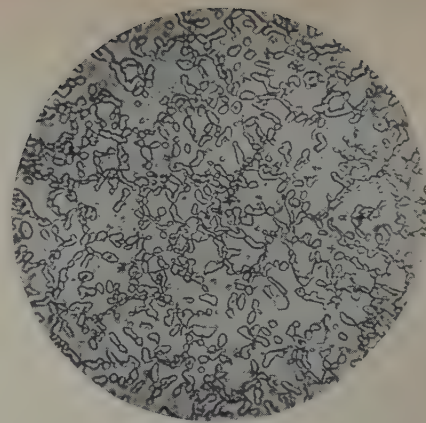


Fig. 2 (right)—64 pct Ni (iodide titanium). 4 hr at 950, 20 hr at 900°C, water quenched. $TiNi$, $TiNi_3$ and copper contamination. "A" etch. X500.

die, or by etching annealed specimens. Molybdenum $K\alpha$ and copper $K\alpha$ radiation were employed.

Homogeneity: Nickel alloys could not be obtained in a completely homogeneous state, despite repeated meltings in a number of cases. Analysis of several samples from the same button showed differences which extended up to 1 pct in alloys below 40 pct Ni. Alloys containing greater amounts of nickel showed differences of up to 2 pct Ni, in one case, between top and bottom of the button, the bottom being nickel-rich. The tendency toward increasing composition differences between top and bottom of the button appears to be due to segregation of titanium to the top of the button. This is suggested by the fact that, after the arc was removed, a solidified island appeared at the top of the melt while solidification proceeded from the bottom upward. This behavior was also reflected in the appearance of as-cast buttons containing up to 90 pct Ni. As compared to the bright uniform surfaces of the low nickels, the high-nickel alloys revealed bright tops, superseded by gray frosted areas in the lower regions.

Since specimens from a given button were generally found to contain within 0.5 pct of the nominal composition, these compositions have been used in plotting data for nickel contents above 14.5 pct. For lower nickel contents the actual chemical analyses*

* Analyses by Lucius Pitkin, Inc., New York.

have been used, with a reported accuracy of analysis of ± 0.2 pct of contained nickel.

Copper Contamination: Sponge alloy buttons (15 g) containing above 40 pct Ni after melting revealed a reddish-brown phase which appeared to be concentrated in considerable quantity at the bottom of the button, see Fig. 1. Since the melting hearths of the furnace were generally wet by these alloys, copper contamination was suspected. Analysis of two alloys containing 64.9 and 70 pct Ni showed copper present in the range 0.1 to 0.5 pct. To overcome this difficulty, the size of the charge was reduced from 15 to 5 g and melting time was reduced from two 1-min periods to four 15-sec intervals. Copper contamination was almost entirely eliminated and very few dendrites of the copper phase could be seen, see Fig. 2. Spectrographic analysis of a 65.9 pct Ni button showed copper to be present in amounts of 0.001 pct.

Phase Diagram

The phase diagram for iodide titanium base alloys is shown in Fig. 3 and the diagram to 15 pct Ni for both iodide titanium and sponge titanium alloys is shown in Fig. 4. The use of sponge titanium and impure nickel in these compositions does not appreciably change the iodide titanium base diagram. The constitution diagram of Fig. 3 below approximately 60 pct Ni is quite different from that of Wallbaum,² see Fig. 5. This discrepancy may be at-

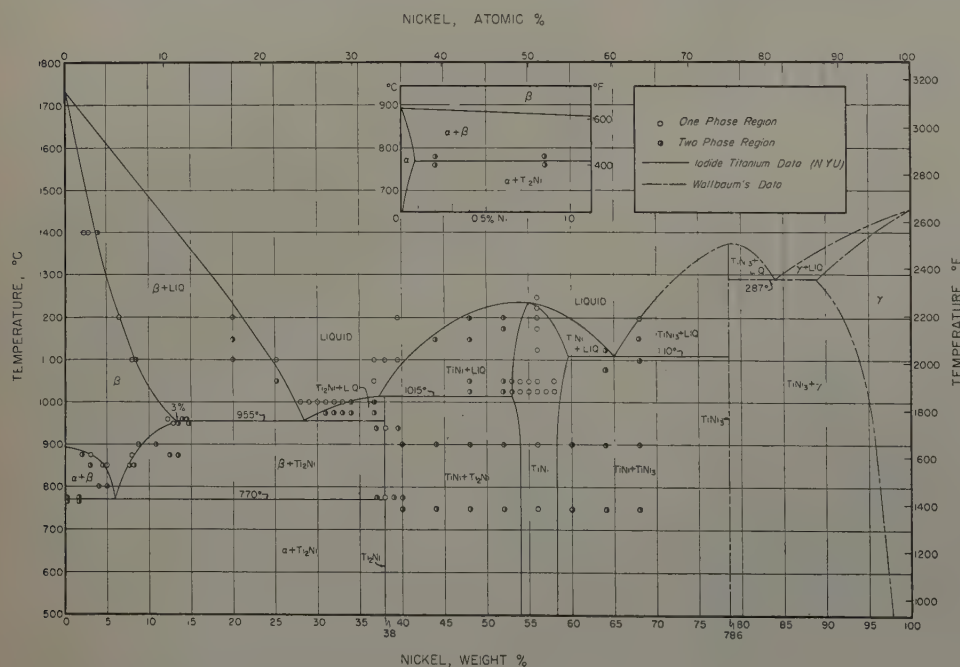


Fig. 3 — Ti-Ni phase diagram (iodide titanium-base alloys).

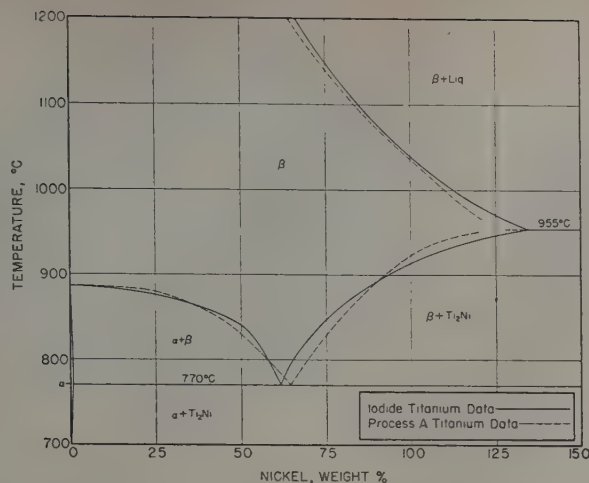


Fig. 4—Partial Ti-Ni phase diagram.

tributed to Wallbaum's use of 95 pct pure titanium and corundum crucibles in which to melt alloys for thermal analysis.

The diagram below the eutectic composition is in good agreement with the prediction of Long et al.³ and the extrapolated data of Battelle⁴ on sponge titanium. A comparison of the data is shown in Table I.

Table I. Comparison of Data

	This Investigation	Long et al. ³	Battelle ⁴ Extrapolated Data
Eutectic temperature	955°±5°C	960°C	
Eutectoid temperature	770°±5°C	765°C	770°C
Maximum β solubility	13 pct Ni	12 pct Ni	
Maximum α solubility	<0.2 pct Ni	<0.5 pct Ni	
Eutectoid composition	6-7 pct Ni	7 pct Ni	7 pct Ni

For higher nickel contents, differences appear in the location of the eutectic point and the compound Ti_2Ni . Based on melting point data and on examination of structures of as-cast alloys, the eutectic composition has been located at 28 to 29 pct rather than at 33 pct Ni. The microstructure of a 33 pct Ni alloy containing primary Ti_2Ni and a eutectic of β and Ti_2Ni is shown in Fig. 6. Long and his colleagues set the γ phase at 41.5 pct Ni "...on the basis of sharp changes in structure between the 39.8 and 44 pct nickel alloys." Laves and Wallbaum¹⁰ suggested that this phase was Ti_3Ni , theoretically containing 38.0 pct Ni, and the d -values for this face-centered cubic compound have been reported by Duwez and Taylor.¹¹ The Duwez and Taylor d -values for this compound have been confirmed in this investigation and examination of microstructures has also located this compound at 38 pct Ni. Although some slight coring was observed in the as-cast alloys of 38 pct Ni, the homogeneity range was found to be quite restricted.

Duweze and Taylor¹¹ have reported that the body-centered cubic compound $TiNi$ decomposes above 800°C, on cooling, into Ti_2Ni and $TiNi_3$. The present authors were unable to obtain evidence for this decomposition in the microstructures of alloys quenched from above and below 800°C (see Fig. 2, characteristic structure for both 750° and 900°C), or in powder patterns obtained from specimens containing 52 and 56 pct Ni annealed at both 750° and 900°C. The a_0 value for $TiNi$, obtained from a 56 pct Ni alloy annealed at 1075°C, is 3.02Å.

The features of the diagram above 68 pct Ni† have

† At the time this work was being prepared for publication additional data on the nickel-rich portion of the diagram was published¹² together with a probable form of the diagram linking the data of Long et al.³ with that of Wallbaum.²

been checked by examination of as-cast, sponge titanium base alloys and several microstructures of as-cast alloys are shown in Figs. 1, 7, and 8. Fig. 7 (90 pct Ni) shows the primary nickel solid solution, a Chinese-script eutectic, the more common eutectic, and the contaminating copper-rich constituent. The presence of the Chinese-script eutectic may be related to the presence of the copper contaminant since the branches of this eutectic are often seen to be emanating from the corners of this phase. If the presence of the Chinese-script eutectic is neglected, then the existence of small amounts of ordinary eutectic may be rationalized from the diagram of Fig. 5.

A typical portion of the as-cast 85 pct Ni alloy is shown in Fig. 8. The white phase is primary $TiNi_3$ and the needle-like structure represents an oriented eutectic according to Vogel and Wallbaum.¹ The presence of primary $TiNi_3$ at a composition somewhat below the eutectic, 16.2 pct Ti, may be due to supercooling. However, Vogel and Wallbaum report uncertainty as to the exact eutectic composition.

In addition to copper contamination, Fig. 1 (70 pct Ni), shows primary $TiNi_3$ and a eutectic of $TiNi$ and $TiNi_3$.

In so far as can be determined from an examination of as-cast microstructures, the data in general confirm the diagram presented by Vogel and Wallbaum.

Observations on the Transformation of β Titanium

The β phase of titanium when alloyed with β stabilizing elements such as molybdenum can transform by nucleation and growth¹³ or by a martensitic reaction.^{13,14} Evidence for both types of β transformation has been obtained in Ti-Ni alloys.

Microstructures of alloys showing transformation of the β phase are shown in Figs. 9 to 15. Figs. 9 to 12 show that increasing nickel contents suppress the transformation of β titanium by nucleation and growth on relatively slow cooling. The transformation of β titanium can be entirely suppressed on quenching when this phase contains approximately 8 pct Ni.

Fig. 13 is a micrograph of an iodide titanium-5 pct Ni alloy slowly cooled from just above the eutectoid temperature. The structure consists of isothermal

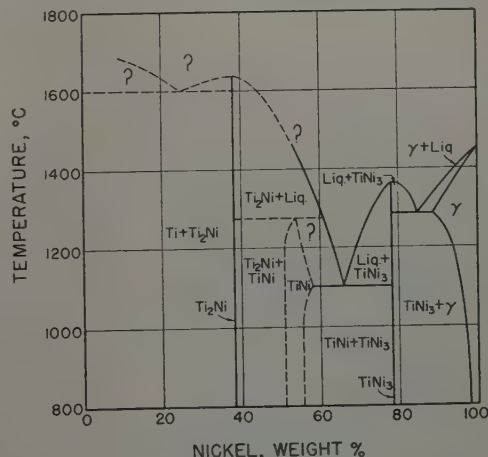


Fig. 5—Ti-Ni phase diagram after Wallbaum (ref. 2).

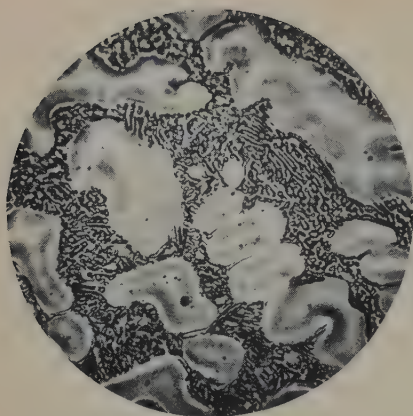


Fig. 6 (left)—As cast, 33 pct Ni (iodide titanium). Primary Ti_3Ni plus eutectic of Ti_3Ni and β . "A" etch. X1000.

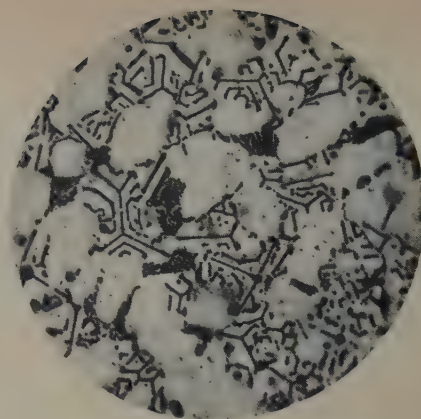


Fig. 7 (right)—As cast, 90 pct Ni (sponge titanium). Primary γ , eutectic of $\gamma + TiNi_3$ and copper contamination. Carapella's etch. X500.

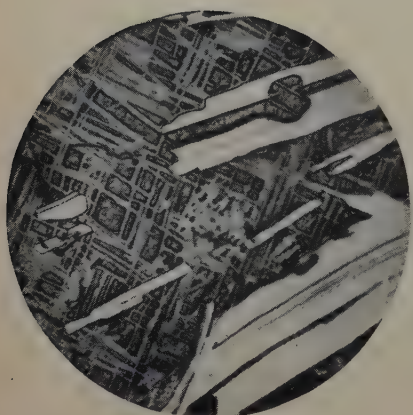


Fig. 8 (left)—As cast, 85 pct Ni (sponge titanium). Primary $TiNi_3$ and oriented eutectic of $TiNi_3$ and γ . Carapella's etch. X1000.

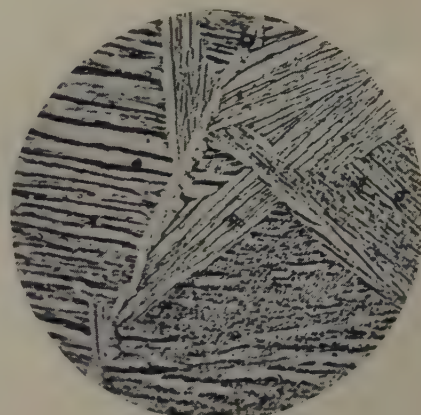


Fig. 9 (right)—As cast, 0.5 pct Ni (sponge titanium). Transformed β . "A" etch. X300.

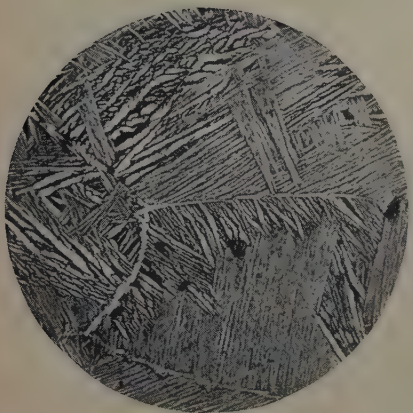


Fig. 10 (left)—As cast, 4 pct Ni (sponge titanium). Transformed β . "A" etch. X300.



Fig. 11 (right)—As cast, 7 pct Ni (sponge titanium). Transformed β . "A" etch. X300.

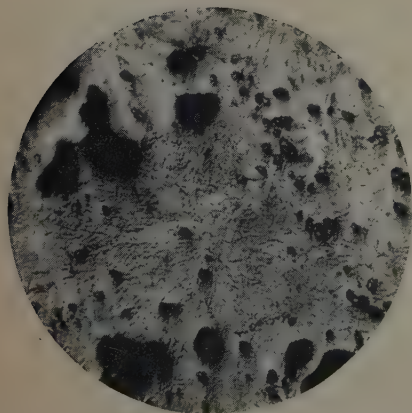


Fig. 12 (left)—As cast, 10 pct Ni (sponge titanium). Retained and transformed β plus eutectic of $\beta + Ti_3Ni$. "A" etch. X300.

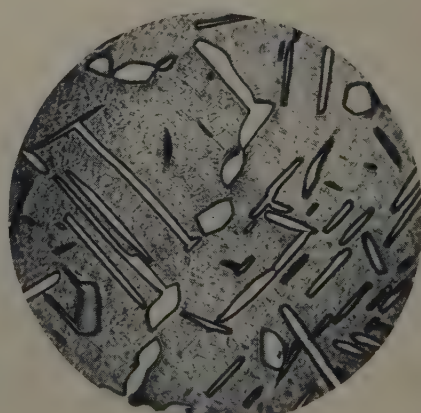


Fig. 13 (right)—5 pct Ni (iodide titanium). 24 hr at $770^\circ C$, furnace cooled. Isothermal α + transformed and retained β . "A" etch. X150.



Fig. 14—5 pct Ni (iodide titanium). Slow cooled from $\alpha + \beta$ field. Isothermal $\alpha + \beta$ transformed β . "A" etch. X1000.

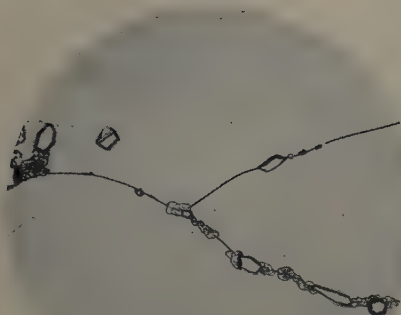


Fig. 15—14.5 pct Ni (iodide titanium). 20 hr at 950°C, water quenched. Retained β , Ti_2Ni and eutectoid of α and Ti_2Ni . "A" etch. X150.

α and transformed plus retained β . The fine transformation needles within the β grains are parallel to the platelets of isothermal α , thus suggesting that transformation of β below the eutectoid temperature occurred by the same mechanism governing the formation of α in the $\alpha + \beta$ field.

Pearlite decomposition has been observed in specimens rapidly cooled from the $\alpha + \beta$ field to 100°C below the eutectoid temperature. This behavior suggests that during the slow cooling below the eutectoid temperature the partial decomposition into α observed in Fig. 12 caused sufficient enrichment of the β phase to stabilize it. Since approximately 8 pct Ni is required to retain β on quenching, the retained β of this 5 pct alloy must contain at least this quantity of nickel.

Both α and Ti_2Ni can stimulate the transformation of β titanium. In the case of α , slow cooling in the $\alpha + \beta$ field develops sharp projections as shown in Fig. 14. In areas adjacent to these α projections transformation occurs most readily and is particularly evident in alloys in which limited transformation takes place. Transformation in areas adjacent to Ti_2Ni is shown in Fig. 15. At higher magnifications these areas can be resolved into a pearlitic arrangement of $\alpha + Ti_2Ni$.

Summary

The Ti-Ni phase diagram has been investigated with alloys of iodide titanium and high-purity nickel up to 68 pct Ni by metallographic, melting point, and X-ray methods and up to 90 pct Ni by examination of as-cast structures of sponge titanium base alloys. The Ti-Ni phase diagram may be summarized as follows:

1—Eutectoid decomposition of β containing 6 to 7

pct Ni into α (<0.2 pct Ni) and Ti_2Ni (38 pct Ni) at $770^\circ \pm 5^\circ C$. 2—Eutectic solidification of liquid containing 28 to 29 pct Ni into β (13 pct Ni) and Ti_2Ni at $955^\circ \pm 5^\circ C$. 3—Peritectic formation of Ti_2Ni from liquid (~ 37.5 pct Ni) and $TiNi$ (~ 53 pct) at approximately $1015^\circ C$. 4—Eutectic solidification of liquid (~ 65 pct Ni) into $TiNi$ (~ 59 pct Ni) and $TiNi_3$ (78.6 pct Ni) at approximately $1110^\circ C$. 5—Eutectic solidification of liquid to form $TiNi_3 + \gamma$.

The β phase may transform by a nucleation and growth process or by a martensitic reaction. The transformation of β may be stimulated in the presence of α or Ti_2Ni or may be suppressed on water quenching alloys containing 8 pct Ni or more.

Acknowledgment

The authors wish to thank the Materials Laboratory, Engineering Division, Air Material Command for permission to publish this work carried out under its sponsorship (sponsored by Wright Air Development Center, Wright-Patterson Air Force Base, Ohio, on Contract No. AF-33 (038)-8725). The authors also wish to express their appreciation to the members of the metallurgy staff who assisted with the experimental work and to H. K. Adenstedt of the Materials Laboratory, Wright-Patterson Air Force Base, for his interest and helpful suggestions.

References

- ¹ R. Vogel and H. J. Wallbaum: The Iron-Nickel-Titanium System. *Archiv Eisenhüttenwesen* (1938) **12**, pp. 299-305.
- ² H. J. Wallbaum: The Systems of the Iron Group Metals with Titanium, Zirconium, Columbium and Tantalum. *Archiv Eisenhüttenwesen* (1949) **14**, pp. 521-526.
- ³ J. R. Long, E. T. Hayes, D. C. Root, and C. E. Armentrout: A Tentative Titanium-Nickel Diagram. *Bur. Mines RI 4463* (1949).
- ⁴ Battelle Memorial Institute: Research and Development on Titanium Alloys. Air Force Technical Report No. 6218, Part 2 (June 1950) p. 42.
- ⁵ C. M. Craighead, O. W. Simmons, and L. W. Eastwood: Titanium Binary Alloys. *Trans. AIME* (1950) **188**, p. 485; *JOURNAL OF METALS* (March 1950).
- ⁶ W. L. Finlay and J. A. Snyder: Effects of Three Interstitial Solutes on the Mechanical Properties of High Purity Alpha Titanium. *Trans. AIME* (1950) **188**, p. 277; *JOURNAL OF METALS* (February 1950).
- ⁷ I. Cadoff and J. P. Nielsen: Titanium-Carbon Phase Diagram. This issue, p. 248.
- ⁸ H. Margolin: Electropolishing of Titanium Alloys. Symposium on Analysis and Metallography of Titanium. Sponsored by Armour Research Foundation, June 1951.
- ⁹ W. L. Finlay, J. Resketo, and M. B. Vordahl: Optical Metallography of Titanium. *Industrial and Engineering Chemistry* (1950) **42**, p. 218.
- ¹⁰ F. Laves and H. J. Wallbaum: The Crystal Chemistry of Titanium Alloys. *Naturwissenschaften* (1939) **27**, pp. 674-675.
- ¹¹ P. Duwez and J. L. Taylor: Structure of Intermediate Phases in Alloys of Titanium with Iron, Cobalt and Nickel. *Trans. AIME* (1950) **188**, p. 1173; *JOURNAL OF METALS* (September 1950).
- ¹² A. Taylor and R. W. Floyd: The Constitution of Nickel-Rich Alloys of the Nickel-Chromium-Titanium System. *Journal Inst. of Metals* (July 1952) **80**, p. 577.
- ¹³ D. J. DeLazzaro, M. Hansen, R. E. Riley, and W. Rostoker: Time-Temperature-Transformation Characteristics of Titanium-Molybdenum Alloys. *Trans. AIME* (1952) **194**, p. 265; *JOURNAL OF METALS* (March 1952).
- ¹⁴ Y. C. Liu and H. Margolin: The Quench Hardening of Ti-Mn Alloys. Interim Report No. 2 to Watertown Arsenal on Contract No. DA-30-069-ORD-207, June 25, 1952.

Titanium-Carbon Phase Diagram

by Irving Cadoff and John P. Nielsen

The Ti-C phase diagram exhibits a peritectic point at 1750°C and 0.8 pct C, and a peritectoid point at 920°C and 0.48 pct C. The maximum solubility of carbon in α titanium is 0.48 pct. The δ region containing the TiC compound (20 pct C) extends to 11 pct C at the peritectic temperature.

THE interest in the Ti-C alloy system stems from the fact that carbon occurs as an impurity in titanium alloys when graphite electrodes or graphite crucibles are used in their melting. Since titanium-base alloys are still in the development stage, some virtue may be found in carbon addition to titanium. The TiC compound is currently emerging as an important powder metallurgy base constituent similar to the WC compound.

Ehrlich¹ identified the phases and structures present in the Ti-C system. The peritectoid region of the phase diagram was investigated by Jaffee et al.² A preliminary diagram based on theoretical considerations was proposed at the outset of this research.³ The TiC compound has been investigated extensively and has been reported on in a large number of papers.

Experimental Procedure

Arc-melted alloys of 24 compositions in the range 0 to 20 wt pct C were investigated using metallography, X-ray diffraction, and, for the liquidus and solidus regions, incipient and complete melting.

All alloys were prepared from iodide titanium (New Jersey Zinc Co., 99.95 pct Ti minimum) and spectroscopic grade carbon (National Carbon Co.). To prevent carbon spattering during arc melting the carbon was encapsulated in titanium. For alloys containing less than 1 pct C the powder was inserted

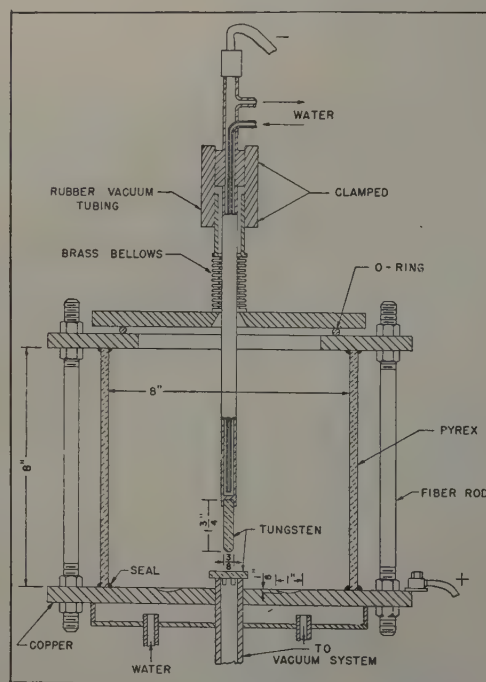


Fig. 1—Multiple hearth arc furnace.

I. CADOFF, Junior Member AIME, is Instructor in Metallurgy and J. P. NIELSEN, Member AIME, is Associate Professor of Metal Science, College of Engineering, New York University, New York.

Discussion on this paper, TP 3469E, may be sent, 2 copies, to AIME by April 1, 1953. Manuscript, Sept. 18, 1952. Los Angeles Meeting, February 1953.

This paper is based on a thesis by I. Cadoff submitted in partial fulfillment of requirements for the degree of Doctor of Engineering Science to the Graduate Division, College of Engineering, New York University.

into a capsule formed by drilling a hole in the as-received rod. For higher compositions, capsules were formed from titanium sheet.

Arc Melting: The charges were melted in the copper-hearth cold electrode furnace shown in Fig. 1. This furnace is similar in principle to the all-metal unit adapted for titanium melting at Battelle Memorial Institute.⁴ The transparent pyrex walls giving unlimited visibility during operation and the multiple-

hearth base allowing for consolidation of six charges per run were modifications developed for the furnace used in the present investigation.

Charges, weighing 15 g, were melted three times, 1 min for each melting, the buttons being turned over between melts. For compositions above 4 pct C the buttons tended to be inhomogeneous after the three melts, and additional meltings were required. Increased melting time was necessary with carbon contents above 4 pct. Direct current power of 150 to 300 amp at arc voltages of 20 to 30 v were sufficient to melt alloys containing less than 7 pct C. Raising the current beyond 300 amp for the higher content alloys caused an excessive weight loss from spattering and vaporization. The spattering and vaporization were significantly reduced by decreasing the current to 200 amp and increasing the melting time to 30 to 45 min. These alloys, because of the high heats developed during melting, could not be successfully melted in the pyrex wall furnace and therefore were melted in an all-metal unit.

Contamination on melting was minimized by evacuating the furnace to less than 10 microns pressure, flushing with high-purity argon several times (99.9+ pct argon supplied by Matheson Chemical Co., N. J.), and melting under a 20 cm partial initial pressure of argon. The leak rate of the furnace chamber was kept below 60 microns per hour. Vickers hardness was used to determine the degree of contamination and 15 g control buttons melted for 1 min increased less than 10 Vickers per melting.

Heat Treatment: To aid in attaining equilibrium during heat treatment, specimens were cold or hot-rolled prior to heat treatment wherever possible. Specimens were heat-treated in sealed quartz capsules for temperatures up to 1400°C. Prior to sealing, the capsules were evacuated to a pressure less than 1 micron and then filled with argon to a pressure corresponding to 1 atm for the heat-treatment temperature. The specimens were wrapped in titanium sheet before capsulating to prevent a specimen-quartz contact. A tabulation of heat-treatment time used at the various temperatures is given in Table I. Where time ranges are indicated, the longer times were used for the higher carbon content alloys. Temperatures were controlled to at least $\pm 3^\circ\text{C}$ with closer control used when necessary. The specimens were quenched by crushing the quartz capsules under water.

Solidus and Liquidus Regions: The unit used to determine the melting range is shown in Fig. 2. The specimen, about $\frac{1}{8}$ in. cube, is placed in the heater boat, as shown. The heater boat, either molybdenum or tantalum, is heated by its own electrical resistance with currents up to 200 to 300 amp, the specimens coming to heat rapidly. Incipient melting was identified by the occurrence of a rounding of corners. Complete melting was assumed to have oc-

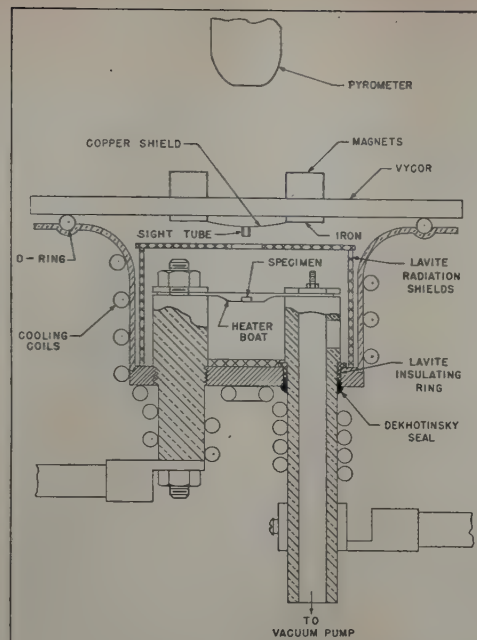


Fig. 2—Melting point determination unit.

curred when the solid specimen appeared to collapse and run along the trough of the heater. Calibration measurements indicated that black-body conditions were attained. Accuracy of a determination was estimated as $\pm 25^\circ\text{C}$. The sight tube may be adjusted by means of the magnets to sight directly on the specimen. The optical pyrometer is fitted with a microscope lens so that the specimen may be observed closely. The unit is operated under vacuum to minimize contamination.

This unit was also used for heat treatments above 1400°C, i.e., beyond the quartz capsule range. A quench was obtained in this apparatus by virtue of the water-cooled electrode leads, which cooled the specimens in less than 2 sec.

Metallography: Metallographic specimens were prepared using an electropolishing technique.⁵ Principal etchants used were Remington A⁶ and cyanide stain,⁷ the latter being useful in identification of carbides.

X-Ray Diffraction: X-ray diffraction patterns were taken with a powder camera (radius of 57.3 mm) using $\text{CuK}\alpha$ radiation. For phase identification powder specimens were prepared by filing or crushing to 230 mesh, the filed powders being subsequently annealed. Lattice parameter measurements revealed that the heat-treated powders had been contaminated to the extent that the data obtained were useless. To overcome this, specimens were etched with HF to a wire diameter of 0.015 in. To eliminate spottiness due to grain size and preferred orientation, specimens were cold-rolled and recrystallized prior to etching. The recrystallization was controlled so that the grain size corresponded to ASTM No. 5 or smaller. The line positions were determined from averages of three measurements and the parameters were calculated using Cohen's method of least squares.⁸

Chemical Analysis: The weight loss of titanium during melting for alloys containing less than 7 pct C was negligible, permitting the use of nominal compositions in this range. Chemical analyses* justified

* Lucius Pitkin, Inc., New York.

Table I. Time of Heat Treatments at Various Temperatures

Heat-Treatment Temperature, °C	Heat-Treatment Time
1400	15 min
1300	30 min
1200	2-48 hr
1100	6-60 hr
1000	9-72 hr
900	18-120 hr
800	36-144 hr
700	72-200 hr
600	144-250 hr
500	350 hr

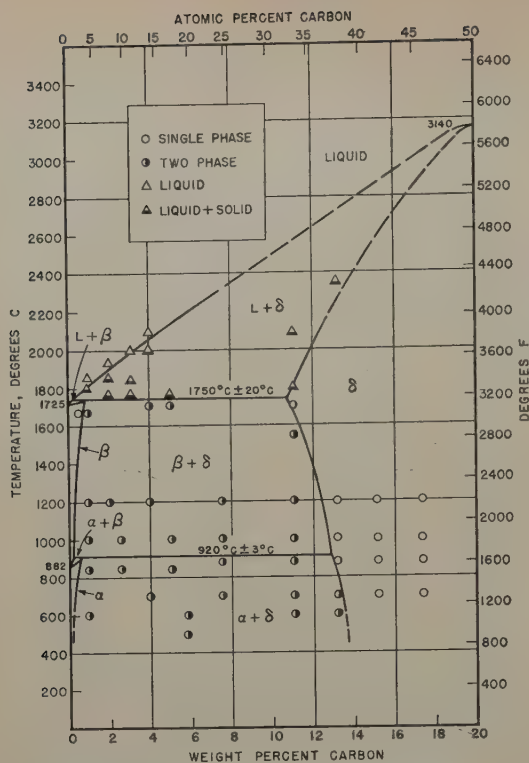


Fig. 3—Iodide titanium-carbon phase diagram.

this procedure. Above 7 pct C the weight loss was excessive and the compositions used are those obtained from chemical analyses.

Results and Discussion

The Ti-C phase diagram in the range 0 to 20 pct C is presented in Figs. 3 to 5.

The region of the α and β solvus lines, the α plus

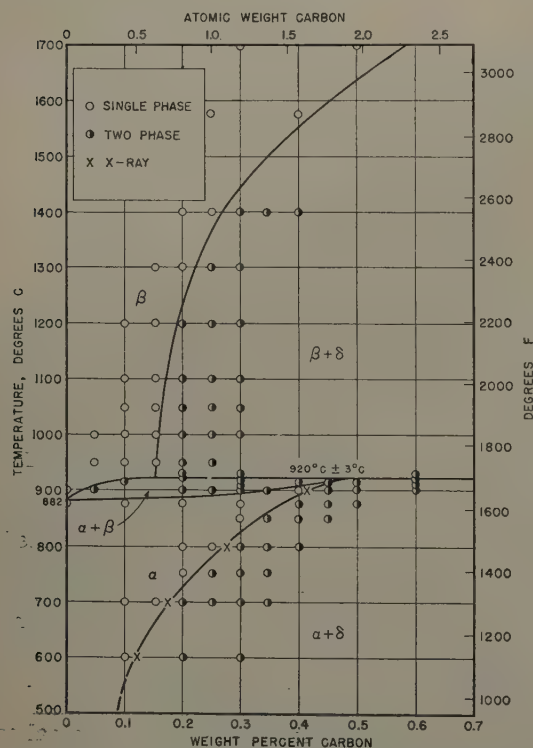


Fig. 4—Iodide titanium-carbon phase diagram detail from Fig. 3.

β field, and the peritectoid point is shown in Fig. 4. The solubility of carbon in α titanium is at a maximum at the peritectoid point, 0.48 ± 0.02 pct C, and decreases with decreasing temperature. In a series of homogenizations designed to bracket the peritectoid reaction temperature, a three-phase structure, Fig. 6, was obtained which confirmed this temperature at $920^\circ \pm 3^\circ\text{C}$. Annealing at 925° and 915°C resulted in structures of δ plus transformed β and α plus transformed β , respectively. The peritectoid point was bracketed between the 0.45 pct C alloy and at 915°C , exhibiting α plus transformed β , and the 0.50 pct C alloy at 915°C , exhibiting α plus δ . The solubility of carbon in β titanium at 920°C is about 0.15 pct C and increases with increasing temperature to about 0.8 pct C at the peritectic temperature, Fig. 5. Ehrlich¹ reported carbon solubility in titanium as high as 2.0 pct C. This high solubility may be attributed to the probable presence of oxygen and nitrogen in his alloys, which contamination increases the solubility of carbon in titanium.⁹ Jaffee, et al.,² using iodide titanium for their alloys, found carbon solubility in both α and β titanium less than 0.45 and 0.1 pct C, respectively.

Fig. 5 is a detail showing the delineation of the phase boundaries in the region of the peritectic reaction. The presence of a peritectic was suspected on the basis of as-cast alloys in which primary δ was found in alloys of carbon content as low as 0.2 pct, Fig. 7. That carbon raised the melting point was further substantiated by relative liquidus temperature determinations of carbon alloys below 0.5 pct. By placing two specimens of slightly different

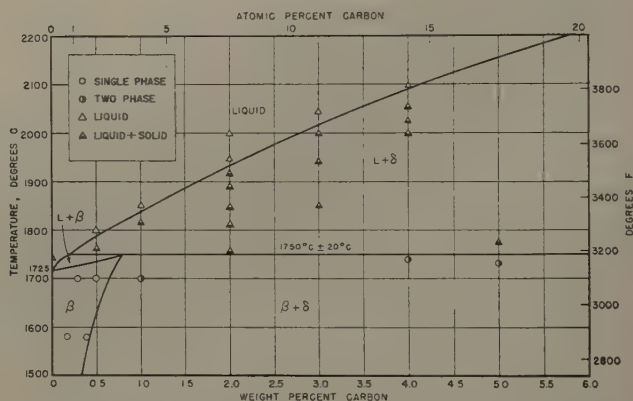


Fig. 5—Iodide titanium-carbon phase diagram detail from Fig. 3.

carbon content on the heater boat of the solidus-liquidus determination apparatus described above and heating until one specimen melted, it was found that the specimen of lower carbon content always melted first. This procedure was necessary since the difference in liquidus temperatures for two specimens of carbon content within 0.1 pct of each other was smaller than the precision of a temperature measurement.

Measurements of incipient melting points indicated that the peritectic temperature was below 1760°C . Assuming a peritectic reaction, the peritectic horizontal would therefore have to be above 1725°C , the melting point of iodide titanium.¹⁰ An absolute measurement of the peritectic temperature on the basis of incipient melting observations within this 1760° to 1725°C range was limited by the instrument, the accuracy of measurement of which was

Fig. 6—0.2 pct C. 6 hr at 920°C, water quenched. α , transformed β and δ . "A" etch. X200.

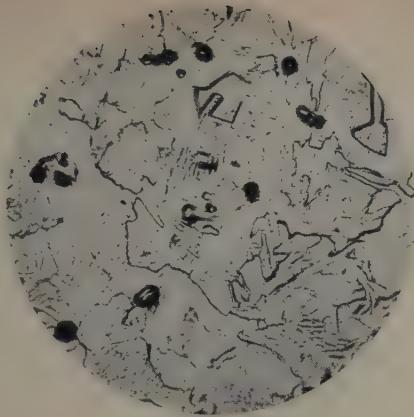


Fig. 7—0.2 pct C, as-cast. δ stringers plus serrated α . "A" etch. X400.

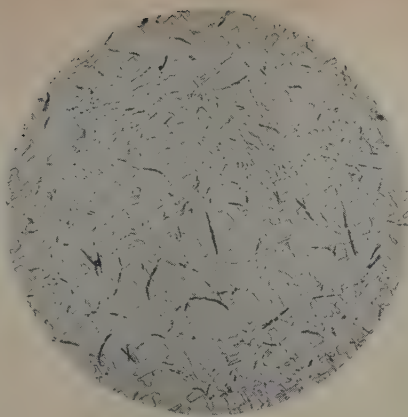


Fig. 8—11.2 pct C. 1 min at 1800°C, quenched. Liquid plus δ . "A" etch. X200.

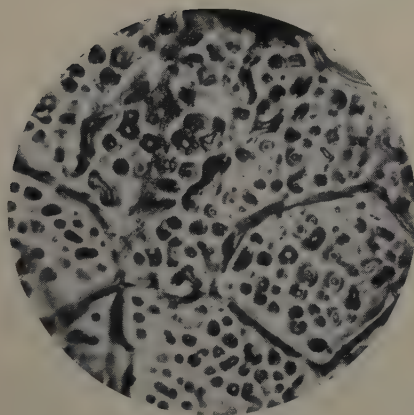


Fig. 9—0.4 pct C. 36 hr at 800°C, water quenched. Equiaxed α plus δ . "A" etch. X150.

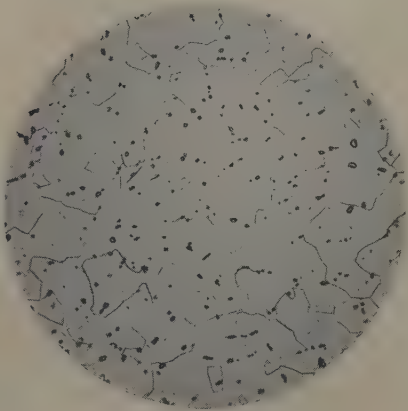


Fig. 10—4.0 pct C. 48 hr at 1200°C, water quenched. Transformed β plus δ . Structure in δ is β . "A" etch. X200.

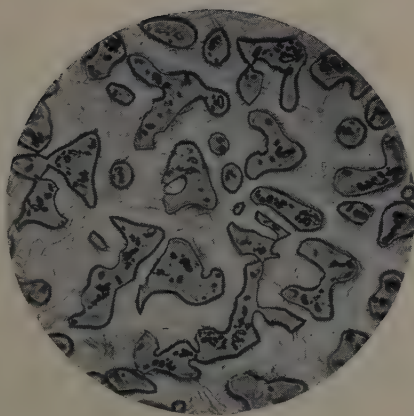


Fig. 11—11.2 pct C. 200 hr at 700°C, water quenched. δ plus α . Structure in δ is α . "A" etch. X500.

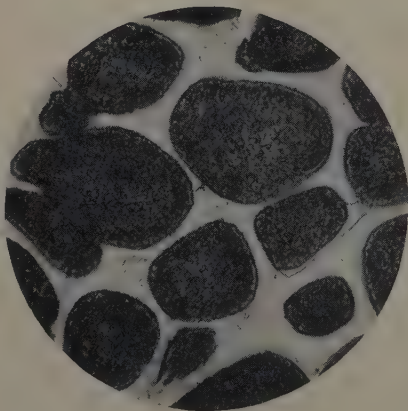
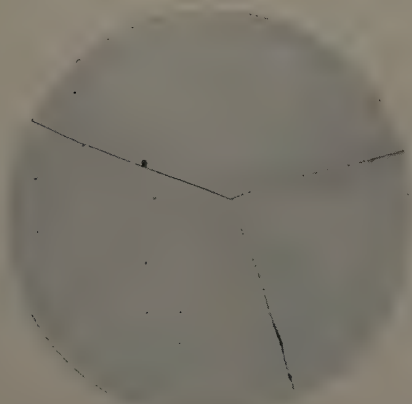


Fig. 12—17.5 pct C. 120 hr at 900°C, water quenched. Single phase, δ . "A" etch. X200.



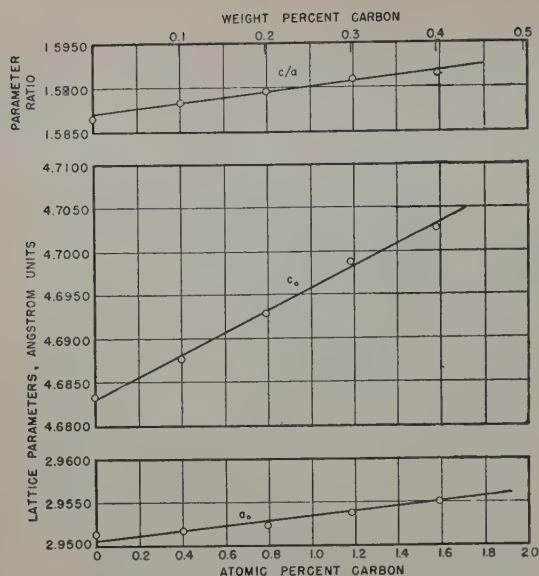


Fig. 13—Effect of carbon on the lattice parameters of iodide titanium.

estimated at $\pm 25^\circ\text{C}$. However, a study of as-cast microstructures indicated that the solubility of carbon in liquid titanium is just under 0.2 pct C at the peritectic temperature. Using this information, the peritectic line was drawn so that it intersected the previously established liquidus line at just under 0.2 pct C, locating the peritectic at 1750°C . It was estimated that the probable error of this temperature value is less than $\pm 20^\circ\text{C}$.

The liquid plus δ/δ boundary (Fig. 3) was confirmed by microstructural examination of the 11.2 pct C alloy quenched from the liquid plus δ region, Fig. 8.

No evidence of an intermediate phase could be found in any of the temperature ranges above 600°C . An alloy corresponding to Ti_3C was treated at 500°C for two weeks with no evidence of compound formation. As shown in Figs. 9 to 12, the amount of δ in the two-phase regions, α plus δ , and β plus δ , increases with increasing carbon content until the δ field is reached.

The phase within the δ in Figs. 10 and 11 is either α or transformed β which has precipitated as a result of the decreasing solubility in TiC with decreasing temperature. It is interesting to note that the surface energy of the δ in contact with the Ti-C liquid solution is significantly different from the surface energy of this phase in contact with the β phase of the same carbon content. In the first case the liquid serves as the matrix with δ as the included phase; and in the second case the δ tends to serve as the matrix for the β , as is indicated by the β precipitates in the δ phase and by the sharp angles the δ constituents have developed at grain boundaries of β , Fig. 10. Fig. 11 gives the appearance of the liquid serving as matrix around the δ phase for a different composition alloy.

The δ phase region extends to 11 pct C at the peritectic temperature and narrows down moderately with decreasing temperature. The melting point of TiC was taken from reported values.¹¹ The δ phase gave a face-centered cubic X-ray diffraction pattern consistent with Ehrlich's¹ report that the compound was a NaCl type. Ehrlich, however, found δ to exist for carbon contents as low as 7 pct. This discrepancy

might be explained by the probable presence of contamination in early titanium work.

Lattice parameter measurements were made on a series of alloys to determine the effect of carbon on the parameters of α titanium and to determine the position of the α solvus. The lattice parameter data of a series of single-phase quenched alloys are presented in Fig. 13. The parameters of iodide titanium agree with those reported by Clark.¹² The effect of carbon on expanding the lattice is more marked than that of oxygen or nitrogen,¹² particularly for the a parameter.

For an independent determination of the α solvus, the α phase parameters of α plus δ alloys, heat treated in the α plus δ region at four different temperatures, were determined. There was good agreement between the X-ray determined α solvus and the α solvus determined microstructurally. The results are presented in Fig. 4.

Summary

Carbon raises the allotropic transformation temperature of titanium from 882°C to 920°C . A peritectoid reaction, $\beta + \delta \rightarrow \alpha$, takes place at 920°C and 0.48 pct C, the maximum solubility of carbon in α titanium. The solubility of carbon in β titanium increases from 0.15 pct at 920°C to a maximum of 0.8 pct at 1750°C . A peritectic reaction, liquid + $\delta \rightarrow \beta$, occurs at 0.8 pct C and 1750°C . The liquidus line rises continuously from the peritectic temperature, with increasing carbon content, to the TiC melting point. Carbon in iodide titanium increases both the c and a parameters of the α form.

Acknowledgments

The authors wish to thank H. Margolin, A. E. Palty, and the staff of the Metallurgy Laboratory at New York University for their assistance in this research. They also wish to thank the Ordnance Corps, Watertown Arsenal, for permission to publish this work, and L. D. Jaffe of the Watertown Arsenal Laboratory for his helpful criticism and comments. This research was performed for the U. S. Army, Ordnance Corps, Watertown Arsenal, Watertown, Mass., under Contracts W-30-069-ORD-4477, DA-30-069-ORD-6, DA-30-069-ORD-76.

References

- ¹ P. Ehrlich: *Ztsch. anorg. allgem. Chemie* (1949) 55/48, pp. 1-43.
- ² R. I. Jaffee, H. R. Ogden, and D. J. Maykuth: *Trans. AIME* (1950) 188, pp. 1261-1266; *JOURNAL OF METALS* (October 1952).
- ³ J. P. Nielsen: Report of Symposium, ONR, p. 155, December 16, 1948.
- ⁴ C. T. Greenidge and L. W. Eastwood: Report of Symposium, ONR, pp. 77-90, December 16, 1948.
- ⁵ H. Margolin: Symposium on Analysis and Metallography of Titanium. Sponsored by Armour Research Foundation, June 1951.
- ⁶ W. L. Finlay, J. Resketo, and M. B. Vordahl: *Industrial and Engineering Chemistry* (1950) 42, p. 218.
- ⁷ Bimonthly Report No. 5, Contract No. NOa(s) 51-331-C, from New York University to Bureau of Aeronautics, November 1951.
- ⁸ M. U. Cohen: *Review of Scientific Instruments* (1935) 6, pp. 68-74.
- ⁹ L. Stone et al.: To be published.
- ¹⁰ B. W. Gonser: Report of Symposium, ONR, p. 66, December 16, 1948.
- ¹¹ M. Hansen: *Aufbau der Zweistofflegierungen* (1936) Springer.
- ¹² H. T. Clark: *Trans. AIME* (1949) 185, pp. 588-589; *JOURNAL OF METALS* (September 1949).
- ¹³ A. D. McQuillan: *Journal Inst. Metals* (1950) 78, pp. 249-257.

Constitution of Titanium-Rich Ti-Cr-Al Alloys

At 1800° and 1400°F

by Jack L. Taylor and Pol Duwez

The phase boundaries in the ternary system Ti-Cr-Al have been established at 1800° and 1400°F for alloys containing more than 60 pct Ti. The martensite transformation temperature has been measured for the titanium-rich alloys.

THE studies of binary alloys of titanium with the transition elements which have been published so far¹⁻⁹ indicate clearly that the solubility of these elements is always much greater in the high temperature body-centered cubic form of titanium (β phase) than in the low temperature hexagonal form. In this category of alloying elements are iron, nickel, chromium, manganese, vanadium, molybdenum, tungsten, columbium, and tantalum. Although studies of the nontransition elements have been rather limited, early work on titanium binary alloys¹⁰ has shown that most of them were not very soluble in the α form, with the exception of aluminum, for which the solubility in α is about 25 pct.^{11, 12} In addition to this large solubility in α , aluminum is also soluble in β titanium to the extent of about 35 pct and the transformation temperature from β to α is raised with aluminum content. This effect is also typical of aluminum, in contrast with that found for the transition elements which lower the β to α transformation temperature. Therefore, it may be anticipated that ternary titanium alloys

with aluminum and any one of the transition elements will constitute a class of ternary alloys having characteristic features absent in alloys involving two transition elements.

Chromium was chosen as a typical transition element for the present study because ternary alloys of Ti-Al-Cr commercially produced have been found to possess very interesting physical properties (MST-3 pct Al-5 pct Cr of Mallory-Sharon).¹³

Binary Systems

The binary systems Ti-Al and Ti-Cr have been established recently by several investigators. The data used in this investigation were taken from the complete diagram of Bumps, Kessler, and Hansen.¹¹ This diagram agrees quite well with earlier investigations.¹² For the Ti-Cr system, the phase boundaries at 1800° and 1400°F were taken from refs. 6 and 7. The binary system Cr-Al has been studied recently by Bradley.¹⁴ This system is rather complex and contains not less than seven intermediate phases. The present study was limited to the titanium corner of the ternary system (less than a total of 40 pct Cr plus Al) and none of the phases present in the Cr-Al binary alloys were found in the ternary alloys investigated.

Experimental Technique

Microscopic observation and X-ray diffraction measurements were used to identify phases and de-

J. L. TAYLOR, Member AIME, is Research Engineer, Jet Propulsion Laboratory and P. DUWEZ, Member AIME, is Professor of Mechanical Engineering and Chief of the Materials Section of the Jet Propulsion Laboratory, California Institute of Technology, Pasadena, Calif.

Discussion on this paper, TP 3478E, may be sent, 2 copies, to AIME by April 1, 1953. Manuscript, Sept. 18, 1952. Los Angeles Meeting, February 1953.

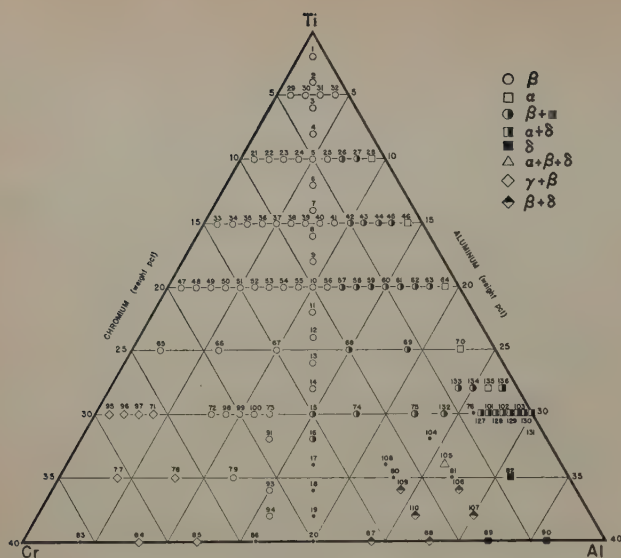


Fig. 1—Partial ternary diagram showing composition of alloys in weight percent at 1800°F.

termine phase boundaries. A total of 130 alloys were prepared by melting in a helium arc furnace on a water-cooled copper plate. The furnace is essentially the same as that described previously.¹⁵ The alloy compositions are shown in Figs. 1 and 2.

The titanium used in this investigation, refined by the iodide process, was received from the New Jersey Zinc Co. According to the manufacturer, a typical analysis of this product is: Mn, 0.0065 pct; Fe, 0.0022; Cu, 0.0015; and Pb, 0.0042. The Vickers hardness number (10 kg load) of the iodide titanium as-received varies between 55 and 80. The chromium powder, obtained from Charles Hardy, Inc., has the following spectroscopic analysis: Na, 0.1 pct; Ca, 0.05; and traces of copper, manganese, silicon, cobalt, and magnesium. The electrolytic chromium powder was first pressed and then sintered in pure dry hydrogen at 2500°F. The aluminum, which was furnished through the courtesy of the Aluminum Company of America, is reported to be 99.99 pct pure.

The three metals were melted together from

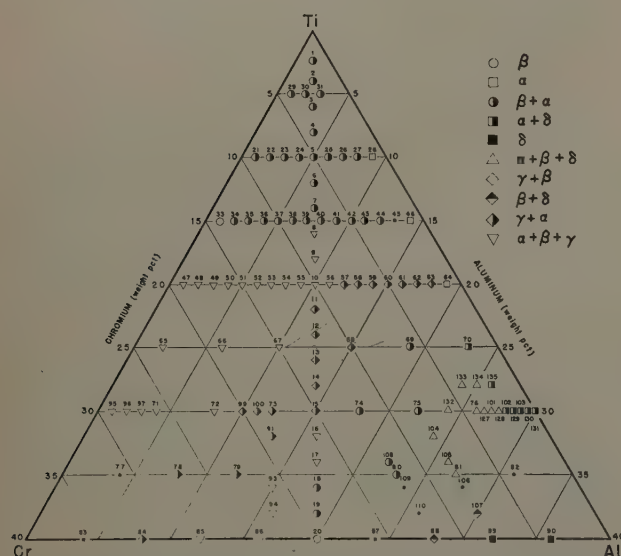


Fig. 2—Partial ternary diagram showing composition of alloys in weight percent at 1400°F.

small pieces to make a 3 or 4 g sample. The homogeneity of the samples was checked microscopically before further work. The prepared composition was accepted if weight losses during melting were less than 1 pct. All samples were sealed in evacuated quartz tubes (10^{-4} mm Hg or better) and homogenized for 4 hr at 1800°F. They were then quenched by breaking the tube under water. Filings from each sample were sealed in quartz vials and quenched in liquid argon after 2 min at 1800°F. The samples for the 1400°F study received the same homogenization treatment as those at 1800°F plus 10 days at 1400°F. Quenching from 1400°F was accomplished by immersing the quartz tubes in water. Filings from these samples were annealed for 4 hr and quenched under water without tube breakage.

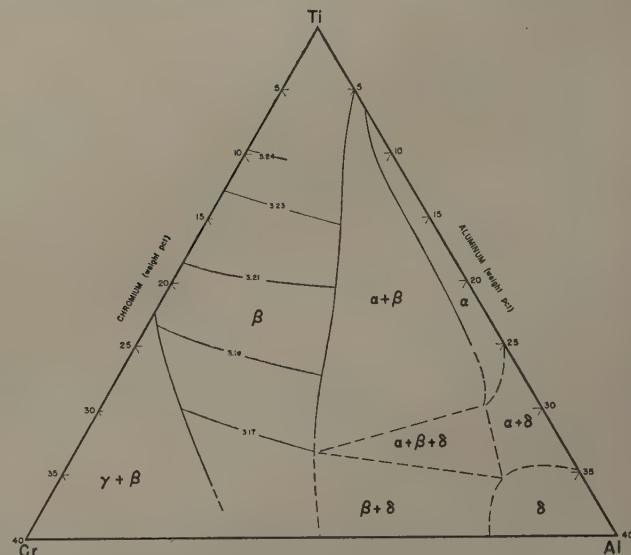


Fig. 3—Phase boundaries in partial ternary Ti-Cr-Al diagram at 1800°F.

Diffraction patterns of the filings were taken on a 14.32 cm camera using Cu K α radiation as filtered through nickel foil. Measurements were taken from film mounted asymmetrically in the camera. This mounting automatically compensates for film shrinkage.

The alloy specimens, mounted in lucite, were polished through a series of successively finer papers and given a final polish on a cloth lap with 2 micron diamond paste. The titanium etching solution consisted of one part nitric acid, one part hydrofluoric acid, and two parts glycerin. The microscopic studies were made at 250 diameters in most cases.

Phase Boundaries at 1800°F

The isothermal ternary phase diagram for Ti-Cr-Al alloys at 1800°F is shown in Fig. 3. The isoparametric lines in the β solid solution region are given in kX units.

The boundary between the β and the β plus α region was established mostly on the basis of microscopic observation, since the beginning of α precipitation can be clearly detected. It is believed that the boundary along alloys No. 32, 25, 10, 11, and 12 between β and α plus β is accurate within 1 pct. The isoparametric lines were based on parameters taken from at least three resolved doublets. Within the β field, there is an area near the titanium apex where β is not retained after quenching. Microscopic ob-

servation was used to differentiate a pure β retained structure from a structure containing some α' (supersaturated α resulting from a martensite type transformation of β). The temperature at which the martensite transformation takes place has also been measured and the results are described in a subsequent section.

The boundary between the β and the β plus γ fields has not been determined with the accuracy of the β to α plus β boundary. The sluggishness of solid state reactions in this composition range adds an element of uncertainty as to correct sampling by filing for X-ray. As for the β boundary near the apex of the ternary region, possible lack of equilibrium, incorrect proportions in X-ray sampling, and the difficulty of detecting a third phase under the microscope are unfavorable factors introducing uncertainties in locating this boundary. The alloys shown by only a dot on the diagram of Fig. 1 are those for which phase identification was most uncertain.

The boundary between the α and the α plus β fields was determined from X-ray measurements. It is interesting to note that the width of the α ternary solid solution is quite narrow. This result demonstrates the strong tendency of chromium toward stabilizing the β phase in titanium. The X-ray patterns in the α plus β field did not have clearly resolved doublets and consequently the tie lines were not determined in the two-phase region.

The boundary between the α plus δ and the α plus β plus δ fields was determined quite accurately to lie between alloys No. 76 and 127. Only one alloy (No. 105) was identified as containing the three phases α , β , and δ . The three-phase region was traced in such a manner that the apexes of the triangle are located on the boundaries of the three one-phase regions.

Phase Boundaries at 1400°F

The phase boundaries at 1400°F are shown in Fig. 4. The limit of solubility of aluminum in the ternary β phase appeared to be of the order of 1 pct, as shown by alloy No. 33. Subsequent findings indicated a more complicated distribution of phases than was expected from considering Fig. 3 at 1800°F.

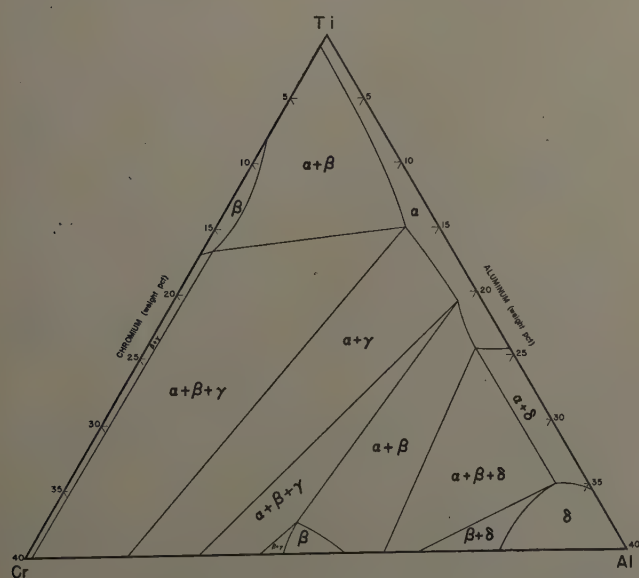


Fig. 4—Phase boundaries in partial ternary Ti-Cr-Al diagram at 1400°F. (The phase boundaries for alloys containing less than 70 pct Ti are only tentative.)

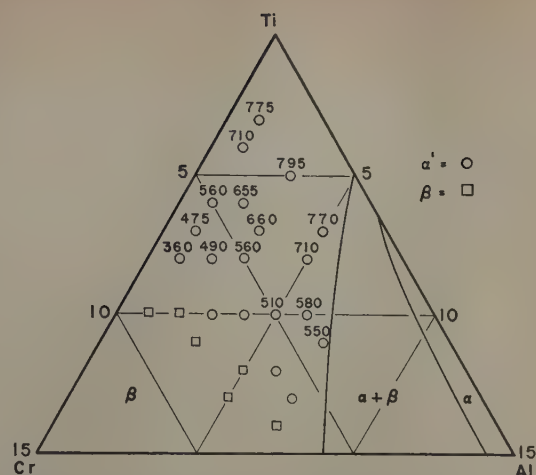


Fig. 5—Composition of titanium-rich alloys and the temperature at which the β phase transforms to α' .

The β phase reappears at alloy No. 20, containing 20 pct each of chromium and aluminum. This result indicated that the β region is split in two at 1400°F.

X-ray diffraction results were the deciding factor in determining boundaries between two and three-phase regions. Assuming TiCr_2 to be the stoichiometric composition, straight lines drawn to the other one-phase regions defined two other split fields, namely α plus β and α plus β plus γ . The X-ray results agree quite well with these requirements, with the exception of those alloys shown as dots (No. 77 and 83).

The apex of the ternary field containing α plus β plus δ , which touches the β region, is beyond the compositions studied in this paper. However, alloys No. 70, 75, 104, and 80 gave fair accuracy in locating the boundary between the α plus β and the α plus β plus δ fields. Similarly, the α plus δ field was defined by alloys No. 70, 128, and 102. The β plus δ boundary location was the least accurate because of the uncertainty in alloys No. 87, 110, 106, and 82, shown as dots.

Martensite Transformation Temperature

A series of alloys whose compositions are shown in the ternary diagram of Fig. 5 were used for the measurements of the temperature at which the β phase transforms, at least partially, to α' . The technique used for the determination of the transformation temperature during rapid cooling was that described by Greninger in his study of martensite in carbon steels.¹⁶ The same technique has been used more recently for the study of some titanium binary systems.^{9, 15, 17} The specimens were about 0.020 in. thick and 1/16 in. square. Chromel-alumel wires, 0.005 in. in diameter, were placed between the two pieces and the assembly spot welded. The specimens were heated by means of a molybdenum coil in vacuum and rapidly cooled by a helium jet. The temperature was recorded on a rotating drum-type oscillograph. The break in the cooling curve due to the heat released by the transformation was quite easy to locate with an accuracy of $\pm 5^\circ\text{C}$. However, the scatter between results obtained on different samples of the same alloy was generally greater than $\pm 5^\circ\text{C}$.

For each alloy at least five measurements were made with rates of cooling in the range of 200° to 600°C per sec (390° to 1110°F per sec). Within this

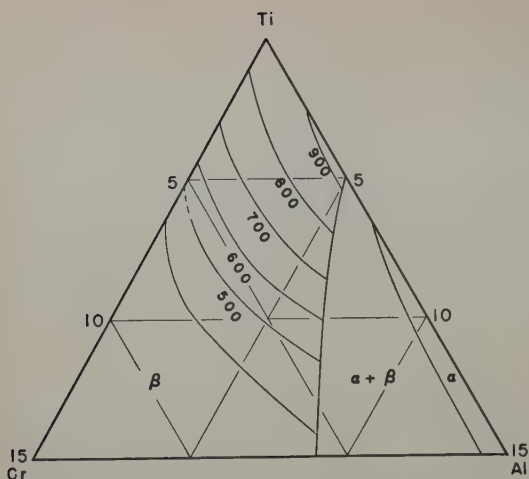


Fig. 6—Isothermal lines showing the compositions at which the β to α' transformation occurs for a given temperature.

range it was found that, as in the case of binary alloys,¹⁷ the transformation temperature was independent of the rate of cooling.

The results of temperature measurements on various ternary alloys are indicated on Fig. 5. The transformation temperatures for the binary Ti-Cr alloys were taken from a previous study.¹⁷ For the Ti-Al binary alloys, unpublished results of measurements made in this laboratory indicate that the Ms temperature increases regularly with aluminum content. In the range from 0 to 5 pct Al, which is the composition corresponding to the boundary of the β phase at 892°C (1635°F), the martensite transformation temperature increases from 882°C (1620°F) to about 940°C (1725°F).

As mentioned in previous studies, the relative amount of β transforming into α' decreases also with increasing concentration; and hence, the thermal arrest becomes weaker and difficult to observe. It is, therefore, not possible, with the sensitivity of the present method of measurement, to establish the Ms curves below approximately 300°C (570°F). Microscopic observation is probably the most reliable method for determining the concentration at which the change occurs from a β plus α' needle structure into a pure β structure. The boundary limiting the compositions for which β is retained, as shown in Fig. 6, is based on microscopic observation. By plotting the martensite temperature vs chromium content for various constant aluminum contents, it was possible to determine compositions having an Ms temperature of 800°, 700°, 600°, and 500°C (1470°, 1290°, 1110°, and 930°F). These plots lead to the tracing of the isothermal lines of Fig. 6, which represent the compositions at which the β to α' transformation takes place at a given temperature. These isothermal lines are roughly parallel to the Ti-Al side of the ternary diagram and hence the amount of chromium in the ternary alloy practically determines the temperature at which the transformation takes place. This result is of course a consequence of the fact that the addition of aluminum to titanium has only a relatively small influence in raising the martensite transformation temperature.

Conclusions

The phase boundaries of the Ti-Cr-Al ternary system have been determined at 1800°F (980°C) and at 1400°F (760°C) in the portion of the diagram

extending from the titanium corner down to compositions containing 60 pct Ti. At 1800°F the β field covers a large portion of the diagram. Within this β field the boundary limiting the field of compositions for which the β phase transforms into the α' supersaturated solid solution has been established. The temperature at which the β to α' martensite transformation takes place has also been determined for the titanium-rich alloys.

Acknowledgment

This work was done at the Jet Propulsion Laboratory, California Institute of Technology, under contract number DA-04-495-ORD-18 with the Army Ordnance Corps, Washington, D. C. The authors wish to thank this agency for permission to publish the results of this investigation.

References

- ¹ D. J. Maykuth and others: Titanium Alloy Phase Diagrams for the Systems Titanium-Manganese, Titanium-Tungsten, and Titanium-Tantalum. Summary Report to Wright-Patterson Air Force Base, January 12, 1952.
- ² M. Hansen, E. L. Kamen, H. D. Kessler, and D. J. McPherson: Systems Titanium-Molybdenum and Titanium-Columbium. *Trans. AIME* (1951) **191**, pp. 881-888; *JOURNAL OF METALS* (October 1951).
- ³ H. K. Adenstedt, J. R. Pequignot, and J. M. Raymer: The Titanium-Vanadium System. ASM Preprint, Pittsburgh, February 1952.
- ⁴ H. W. Worner: The Constitution of Titanium Rich Alloys of Iron and Titanium. *Journal Inst. Metals* (1951) **79**, pp. 173-188.
- ⁵ H. W. Worner: Heat Treatment of Titanium Rich Titanium-Iron Alloys. *Journal Inst. Metals* (1952) **80**, pp. 213,216.
- ⁶ P. Duwez and J. L. Taylor: A Partial Titanium-Chromium Phase Diagram and the Crystal Structure of TiCr_3 . *Trans. ASM* (1952) **44**, pp. 495-517.
- ⁷ M. K. McQuillan: A Provisional Constitutional Diagram of the Titanium-Chromium System. *Journal Inst. Metals* (1951) **79**, pp. 379-390.
- ⁸ R. J. Van Thyne, H. D. Kessler, and M. Hansen: Systems Titanium-Chromium and Titanium-Iron. *Trans. ASM* (1952) **44**, pp. 974-989.
- ⁹ P. Pietrokowsky and P. Duwez: Partial Titanium-Vanadium Phase Diagram. *Trans. AIME* (1952) **194**, pp. 627-630; *JOURNAL OF METALS* (June 1952).
- ¹⁰ C. M. Craighead, O. W. Simmons, and L. W. Eastwood: Titanium Binary Alloys. *Trans. AIME* (1950) **188**, pp. 485-513; *JOURNAL OF METALS* (March 1950).
- ¹¹ E. S. Bumps, H. D. Kessler, and M. Hansen: Titanium-Aluminum System. *Trans. AIME* (1952) **194**, pp. 609-614; *JOURNAL OF METALS* (June 1952).
- ¹² H. R. Ogden, D. J. Maykuth, W. L. Finlay, and R. I. Jaffee: Constitution of Titanium-Aluminum Alloys. *Trans. AIME* (1951) **191**, pp. 1150-1155; *JOURNAL OF METALS* (December 1951).
- ¹³ J. L. Everhart: Titanium and Its Alloys. *Materials and Methods Manual* (May 1952) No. 82, pp. 118-132.
- ¹⁴ A. J. Bradley: An X-Ray Study of the Chromium-Aluminum Equilibrium Diagram. *Journal Inst. Metals* (1937) **60**, pp. 319-336.
- ¹⁵ P. Duwez: Effect of the Rate of Cooling on the Alpha-Beta Transformation in Titanium and Titanium-Molybdenum Alloys. *Trans. AIME* (1951) **191**, pp. 765-771; *JOURNAL OF METALS* (September 1951).
- ¹⁶ A. B. Greninger: The Martensite Thermal Arrest in Iron-Carbon Alloys and Plain Carbon Steels. *Trans. ASM* (1942) **30**, p. 1.
- ¹⁷ P. Duwez: The Martensite Transformation Temperature in Titanium Binary Alloys. ASM Preprint No. 35. Western Metal Congress, Los Angeles. March 1953.

Mechanism of Plastic Flow in Titanium —

Determination of Slip and Twinning Elements

by F. D. Rosi, C. A. Dube, and B. H. Alexander

The slip and twinning planes have been determined in deformed crystals of titanium by an X-ray method of analysis. The slip planes are of the type $\{10\bar{1}0\}$ and $\{10\bar{1}1\}$, while the twinning planes are of the type $\{10\bar{1}2\}$, $\{11\bar{2}1\}$, and $\{11\bar{2}2\}$. In the case of the predominant $\{10\bar{1}0\}$ slip, a type I digonal axis of indices $\langle 1120 \rangle$ was the effective slip direction. Microscopic observations on the appearance of the three twin types disclosed a distinct difference in their shapes, and an attempt was made to correlate this difference with the amount of twinning shear. The slip mechanism was discussed on the basis of the difference in c/a ratios for the common hexagonal close-packed metals.

IT is a general rule that slip in metals occurs most easily on the planes of greatest atomic density and of the largest interplanar spacing, and that the direction of slip is a close-packed direction. Thus, of the hexagonal close-packed metals which have been investigated by the German school in the decade 1925 to 1935 (cadmium, zinc, and magnesium), it has been found that slip occurs on the basal plane (0001) and in a $\langle 11\bar{2}0 \rangle$ direction.¹ In the case of magnesium above 225°C, slip occurs on a first-order pyramidal plane $\{10\bar{1}1\}$ as well as on the basal plane.² The hexagonal metals, moreover, deform in part by twinning, and, again with the exception of magnesium at elevated temperatures, the twinning plane has always been reported to be a second-order pyramidal plane $\{10\bar{1}2\}$.¹

In view of this consistency in the plastic behavior of these metals, it has been supposed that the same slip and twinning elements would be operative in the other important hexagonal close-packed metals (titanium, zirconium, and beryllium), although there are some reasons why this may not be so. Referring to the tabulation in Table I of the axial ratios of the important metals in this structural class, it may be seen that they can be categorized into three distinct groups depending on the value of their c/a ratios. In the first group are cadmium and zinc with large positive deviations from the ideal ratio for closest packing. This expansion in the direction of the c -axis would be such as to accentuate the basal plane as the slip plane, because it increases the interplanar spacing. The second group includes cobalt and magnesium, which closely approximate the ideal ratio. In the third group are zirconium, titanium, and beryllium whose axial ratios are decidedly less than the ideal. The lattice of the elements in this group is compressed along

Table I. Grouping of Important Hexagonal Close-Packed Metals According to Their c/a Ratios

Metal	c/a Ratio	Pct Deviation from Ideal	Group
Cd	1.886	+15.5	I
Zn	1.856	+13.6	I
Ideal c.p.h.	1.633	0	
Mg	1.624	-0.55	II
Co	1.624	-0.55	II
Zr	1.589	-2.69	III
Ti	1.587	-2.81	III
Be	1.568	-3.98	III

the c -axis which, in effect, tends to make the basal plane less favorable for slip inasmuch as it reduces the interplanar spacing and the atomic density of this plane. Thus, for metals in the third group, it may be said that there is a certain indefiniteness about the glide plane, in that planes other than the basal plane may be expected to operate.

The fact that magnesium begins to exhibit planes other than the normal slip and twinning planes at elevated temperatures may indicate that this behavior will become more pronounced in metals of lower axial ratios. For this reason it might be expected that the slip and twinning behavior of zirconium, titanium, and beryllium would be different from that found in cadmium and zinc. One indication that there is a difference is reflected in the recent work which has been done on the deformation textures of these metals.³⁻⁶ As will be shown later, there is a significant difference between the rolling textures of cadmium, zinc, and magnesium on the one hand, and zirconium, titanium, and beryllium on the other, and this difference suggests that the mechanism of plastic flow is not the same in these two groups of metals.

From these considerations, therefore, it may be seen that there are good reasons why it cannot be concluded that titanium will have the same crystallographic elements of slip and twinning as those exhibited by zinc and cadmium. For the complete determination of these elements it would be most advantageous to have single crystals. However, much valuable information can be obtained by using coarse grained polycrystalline specimens, provided the grains are sufficiently large to permit X-ray

F. D. ROSI, Junior Member AIME, is with the Metallurgy Laboratories, Sylvania Electric Products, Inc., Bayside, N. Y., B. H. ALEXANDER, Junior Member AIME, is with the Boston Electronic Div., Sylvania Electric Products, Inc., Boston, Mass., and C. A. DUBE is associated with Laval University, Quebec City, Canada.

Discussion on this paper, TP 3450E, may be sent, 2 copies, to AIME by April 1, 1953. Manuscript, July 18, 1952. Los Angeles Meeting, February 1953.

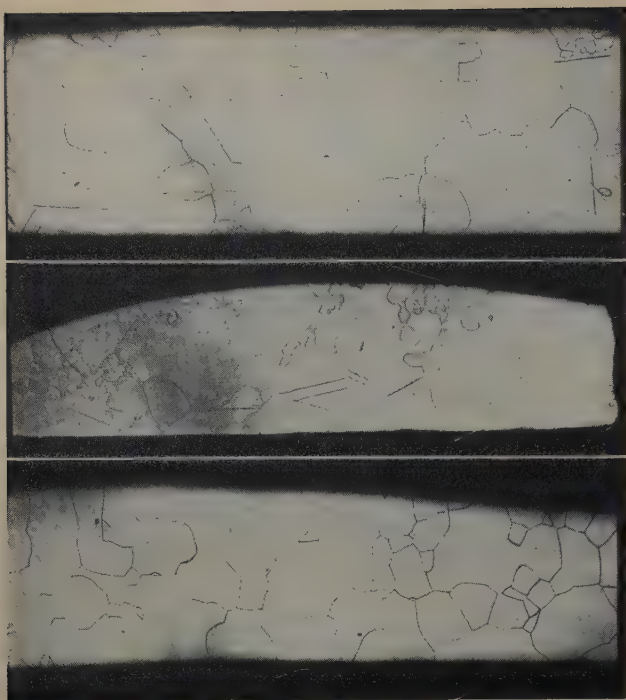


Fig. 1—Titanium specimens critically strained by bending. X30. Area reduced approximately 40 pct for reproduction. a (top)—Bent around 1.5 in. radius, 0.8 pct strain in outer fibers. b (center)—Bent around 1 in. radius, 1.9 pct strain in outer fibers. c (bottom)—Bent around 1/2 in. radius, 2.8 pct strain in outer fibers.

orientation determinations and accurate metallographic examination. In the absence of single crystals, the present study was undertaken using very coarse grains in order to gather as much information as possible concerning the deformation characteristics of titanium.

Production of Coarse Crystals

The titanium used in these experiments was a duPont sponge, which had the following analysis: 99.77 pct Ti, 0.10 pct Fe, 0.009 pct N, 0.05 to 0.08 pct O. This sponge was arc melted in an argon atmosphere into slugs which weighed approximately 25 g each. These slugs were then cold rolled approximately 90 pct to a sheet thickness of 0.05 in. Since the strain-anneal technique was adopted for obtaining the coarse grains, the rolled sheets were annealed to produce a relatively fine, equiaxed and uniform grain size (grain diameter equals 0.04 mm) which is a prerequisite for this method of crystal production.

In order to ascertain the value of critical strain for this material, strips about 0.25x2 in. were cut from the annealed sheets and strained by bending about different radii. The radius of the bend was adjusted to give deformations in the outer fibers of about 1, 2, and 3 pct. The bent strips were then heated in a vacuum at a rate of approximately 150°C per day from 400°C to 840°C, followed by a final anneal at 840°C for two days. The results of these exploratory strain-anneal treatments are

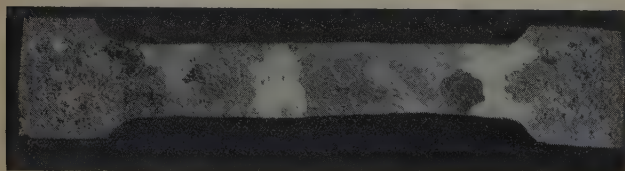


Fig. 2—Coarse grains in titanium produced by controlled recrystallization. X2. Area reduced approximately 20 pct for reproduction.

shown in Fig. 1, from which it may be seen that the optimum deformation for maximum grain size in this material is in the vicinity of 1 pct for a bending type of stress. Consequently, this value of strain was used in a number of specimens to produce two-dimensional growth of grains, which frequently traversed the width of the specimen and facilitated accurate X-ray orientation determinations. For a simple tension type of stress the critical strain was found to be 1.5 pct, and best results were obtained when the annealed structure, prior to the critical strain, consisted of uniform, coarse grains which exhibited a rather strong preferred orientation. A typical example of a coarse grained tensile specimen, with grains averaging 3 to 6 mm in length, is shown in Fig. 2.

Preparation of the surface of these specimens for optical microscopy consisted of mechanically polish-

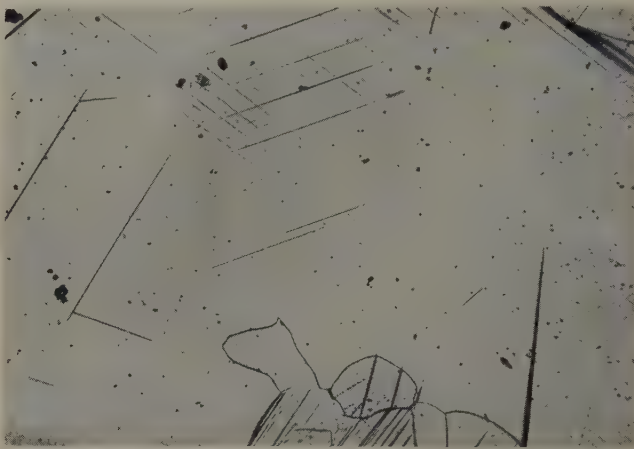


Fig. 3—Nature of slip and twinning in titanium. X100. Area reduced approximately 40 pct for reproduction.

ing through 4/0 metallographic emery paper and then etching with a dilute solution of hydrofluoric acid to remove the cold-worked layer resulting from this mechanical treatment. A final polish on silk and gamal cloths followed again by a light etch produced a satisfactory surface. An annealing treatment in vacuum at a temperature of 850°C for several days indicated that such surfaces were essentially stress-free.

Appearance of Slip Bands and Twins

Coarse grained specimens of titanium, which have been deformed several percent either by extension, bending, or compression in a vise, show well-marked slip bands and twins, as exemplified by Figs. 3 and 4. It is readily apparent from Fig. 3 that the slip bands are rather fine and straight, and show a reasonable regularity in their spacing, which is approximately 1.5×10^{-2} mm. A particularly notable feature of this deformed crystal is the appearance of five distinct slip systems in addition to the twins. Presupposing the presence of basal slip, this observation establishes at once the existence of at least another slip plane in the deformation of titanium at room temperature, since basal slip can only account for one parallel set of slip traces.

Typical appearance of twins in deformed crystals is shown in Fig. 4. These coarse grains were re-polished and etched after deformation for the purpose of removing the slip bands. It may be seen that the twins appear either very thick, similar to those found in zinc⁷ and magnesium,⁸ or as narrow lamellae much like the Neumann bands characteristic of

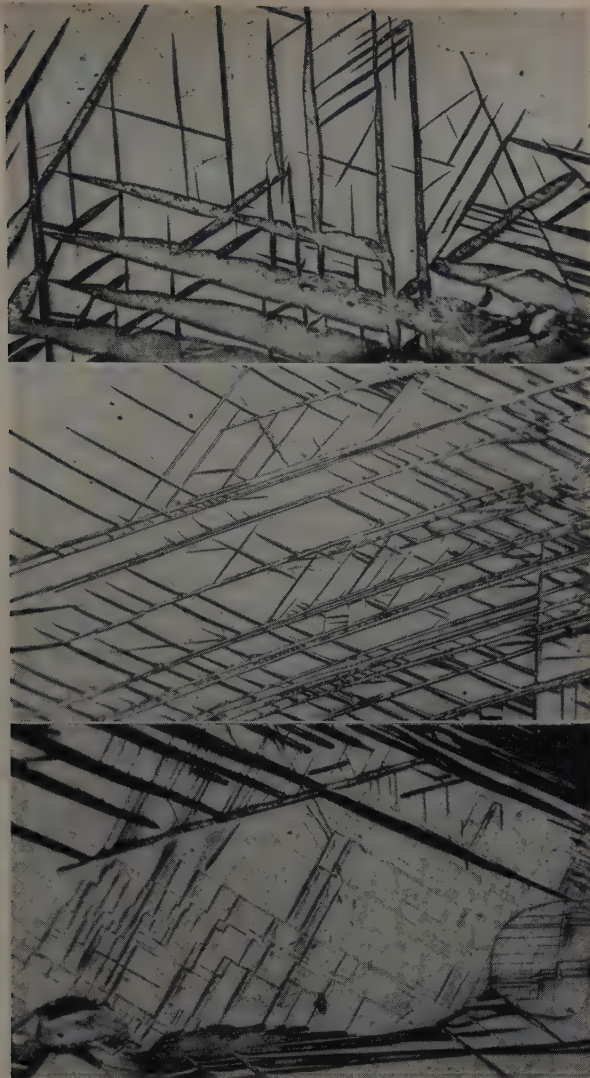


Fig. 4—Nature of twin in titanium. X200. Area reduced approximately 55 pct for reproduction. a, top; b, center; and c, bottom.

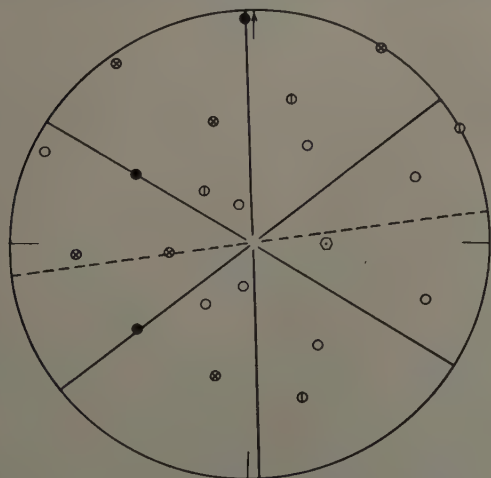


Fig. 5—Determination of slip and twinning planes in titanium.

a (above)—Stereographic projection containing normals to visible traces of slip bands (solid lines) and twins (dashed lines). Hexagon, (0001); solid circle, $\{10\bar{1}0\}$; open circle, $\{10\bar{1}2\}$; vertical line through circle, $\{10\bar{1}1\}$; and circle x, $\{11\bar{2}1\}$.

b (upper right)—Crystal of titanium which was polished, etched, and deformed. X100. Area reduced approximately 20 pct for reproduction.

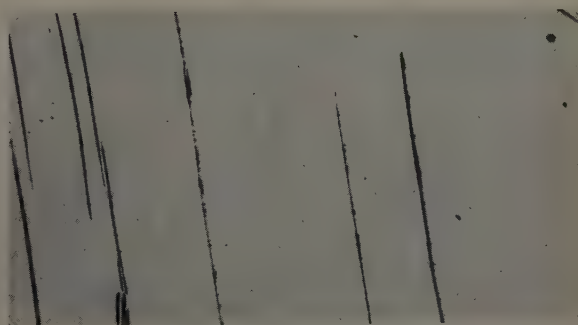
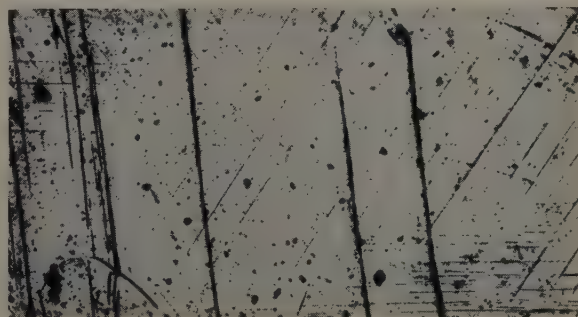
c (lower right)—Same crystal as Fig. 5b but repolished and etched. X100. Area reduced approximately 20 pct for reproduction.

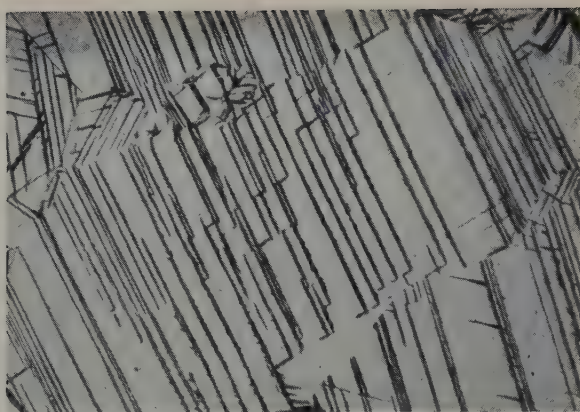
twinning in iron.⁹ This latter form of twins is remarkably illustrated in the stepped twin formation of Fig. 4c. As in the case of slip in Fig. 3, close examination of these micrographs reveals at least seven different sets of twin traces. This suggests that twinning in titanium occurs on at least two different crystallographic planes, since twinning on the conventional $\{10\bar{1}2\}$ planes can only account for six of these traces.

It appears, therefore, from these qualitative observations on the appearance of slip bands and twins in large crystals of titanium that the mechanism of plastic flow in this metal at room temperature is much more complex than that found in the hexagonal close-packed metals, zinc, cadmium, and magnesium.

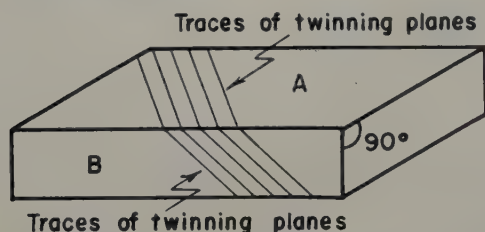
Determination of Slip and Twinning Elements

Experimental Methods: The method of identification of the slip and twinning planes was based on the use of a stereographic plot of a back-reflection Laue photograph describing the region where slip and twinning were observed. Identification resulted from the location in these plots of the poles of the planes responsible for the slip and twinning traces on the surface of the specimen. An example of the application of this method is shown in Fig. 5. The spots from a back-reflection Laue photograph of the crystal, Fig. 5b, (with the incident beam perpendicular to the specimen surface) were transferred to the stereographic diagram, Fig. 5a, on which were plotted the poles of the important planes of low indices. The normal to all visible slip traces (solid lines) and twinning traces (dashed lines) were then shown on the stereographic diagram as great circles passing through the center of the projection. The poles intersected by these great circles identify the slip and twinning planes. In order to distinguish clearly between the slip and twin markings, the specimen, after deformation, was carefully repolished and etched to remove the slip bands, as shown

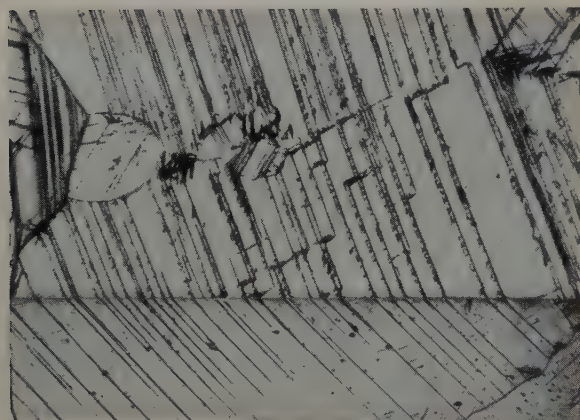




a—Deformed crystal of titanium repolished and heavily etched to remove slip bands. X50.



b—Diagram of traces of twinning planes.



c—Twin markings on mutually perpendicular surfaces, A (top) and B (bottom).

Fig. 6—Two-surface method of analysis for determining twinning plane. Twins are of the type $\{11\bar{2}1\}$.

in Fig. 5c. In using this technique of crystallographic analysis, it is readily apparent that great care must be exercised with regard to reference marks describing the relation of the X-ray beam to the general outline of the specimen surface.

In a number of cases the normals to the twin traces intersected two poles on the stereographic diagram, and this necessitated a two-surface method of analysis to distinguish which pole was responsible for the trace. This technique, illustrated in Fig. 6, involved the preparation of two surfaces at right angles, such that the twin traces in a given crystal could be clearly followed from one surface around the edge to the other surface, Fig. 6c.

In this particular crystal, Fig. 6a, the normal to the long twin traces on the surface A intersected two poles on the stereographic projection describing this surface. By simply rotating this projection 90° on to the surface B, and again drawing the normal to the traces (Fig. 6b), it is relatively easy to distinguish which of the two poles represents the plane responsible for the traces. Since this two-surface

solution is more rigorous in the determination of the slip and twinning planes, it was adopted, whenever possible, to verify the determinations made by the single surface X-ray technique demonstrated in Fig. 5. The surface preparation shown in Fig. 6 also permits a confirmation of these results by the two-surface method which involves measurement of angles of the twin traces with respect to a crystallographically known system of coordinates.¹⁰

Slip and Twinning Elements: More than 40 stereographic analyses of Laue photographs of deformed crystals were made, and the results of these analyses show that two slip planes and three twinning planes are operative in the plastic deformation of these crystals at room temperature. The slip planes are of the type $\{10\bar{1}0\}$ and $\{10\bar{1}1\}$ while the twinning planes are of the type $\{10\bar{1}2\}$, $\{11\bar{2}1\}$, and $\{11\bar{2}2\}$. In the case of slip, the prismatic type $\{10\bar{1}0\}$ is by far the more predominant. It occurred in all but one of the deformed crystals and in this single exception deformation took place solely by twinning. On the other hand, first-order pyramidal slip $\{10\bar{1}1\}$ was observed only in those crystals which exhibited a complex slip process, in that all three prismatic systems were operative. Typical appearance of prismatic slip for two differently oriented crystals is shown in Fig. 7, where it may be seen that the bands are well defined and show a reasonable regularity of spacing. It is interesting to note, however, that the character of the bands differs in the two cases, suggesting an orientation dependence on the appearance of these bands. More will be said concerning the nature of slip bands in another paper on this study, which will deal with manifestations of glide.

It is singularly significant that, no matter how



Fig. 7—Appearance of type I prismatic $\{10\bar{1}0\}$ slip in titanium. X100.

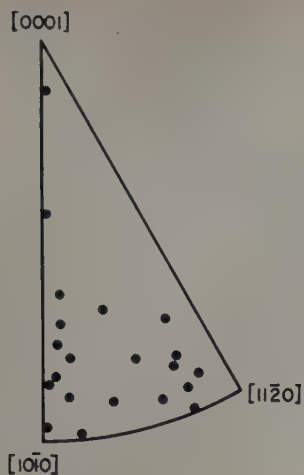


Fig. 8 — Original orientations of coarse crystals studied in tension.

complex the deformation, in no case was slip on the basal plane (0001) established. The absence of basal slip is a glaring contradiction to the general rule of slip behavior in hexagonal close-packed metal crystals (magnesium, zinc, and cadmium). Admittedly, the orientations of a large number of these coarse crystals were similar (as might be expected from the technique used in producing them), yet on the whole the spread appears sufficient to establish $\{10\bar{1}0\}$ prismatic slip as the predominant slip mechanism. The spread in crystal orientations for the tension studies is shown in the standard stereographic triangle of Fig. 8, and it may be seen that there is a paucity of orientations in one region of the triangle. It is not possible, therefore, to rule out definitely an orientation effect with regard to the absence of basal slip.

However, the complexity of the stress pattern in some of these crystals, as a result of the method of deformation and the contiguity of grain boundaries, would be expected to encourage slip on all potential planes. In view of these considerations, it is believed that, with the possible exception of a small range of critical orientations, there is little probability of basal slip in the plastic deformation of titanium crystals of this purity for tests at room temperature.

Unfortunately, the method of stereographic analysis described above does not permit the determination of the slip direction in the planes of slip. Nevertheless, it is noteworthy that both the prismatic $\{10\bar{1}0\}$ and the first order pyramidal $\{10\bar{1}1\}$ planes contain a $\langle 11\bar{2}0 \rangle$, which is both the direction of closest packing and the slip direction in the hexagonal close-packed lattice. In order to determine experimentally the slip direction for $\{10\bar{1}0\}$ slip, it was necessary to follow by X-ray analysis the movement of the specimen axis during extension by ascertaining the crystal orientation at various stages of extension. This follows from the geometrical considerations of glide, which predict a movement of the specimen axis of the crystal toward the operative direction of glide. Fig. 9 shows examples of the application of this method, and it may be seen that in each case a type I digonal axis of indices $\langle 11\bar{2}0 \rangle$ is the effective slip direction. Therefore, the close-packed direction in these crystals is preserved as the slip direction despite the change in the slip plane. This is not too surprising, since it has been established that the slip direction is a more fundamental property of a metal than the slip plane. For example, in aluminum¹¹ and magnesium² at ele-

vated temperatures, and in several body-centered cubic metals¹²⁻¹⁴ slip can occur on more than one plane, but the direction of slip is always the same. In view of this, the assumption will be made that the direction of slip for first-order pyramidal glide is also a $\langle 11\bar{2}0 \rangle$ direction. This could not be determined experimentally in view of the secondary nature of this type of slip.

Twinning on the pyramidal planes type II, order 1 $\{11\bar{2}1\}$ and order 2 $\{11\bar{2}2\}$, as well as on the pyramidal planes type I, order 2 $\{10\bar{1}2\}$, is also a contradiction to the general plastic behavior of hexagonal close-packed metals, where twinning has been found to occur solely on the $\{10\bar{1}2\}$ planes at room temperature. Moreover, the extensive twinning indicates that this mechanism of flow plays an important role in the deformation of titanium. In general, it was found that twinning occurred most frequently on planes of the types $\{10\bar{1}2\}$ and $\{11\bar{2}1\}$; whereas $\{11\bar{2}2\}$ twinning was observed only at specimen edges (see Fig. 10), or in grains which exhibited marked multiplicity of slip and twinning as a result of surrounding stress conditions.

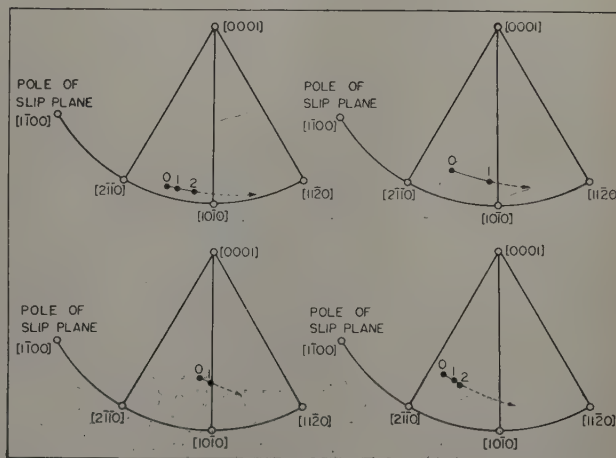


Fig. 9—Determination of the slip direction from the lattice rotation in the course of extension of titanium crystals.

A particularly notable feature regarding the observed twin markings is the considerable variation in their appearance, as typically illustrated in Fig. 11. It may be seen that twins of the $\{10\bar{1}2\}$ type are thick and lens-shaped, similar in habit to those of the same crystallographic form observed in cadmium, zinc, magnesium, and beryllium. In sharp contrast to this, the $\{11\bar{2}1\}$ twins appear as narrow lamellae, much like the Neumann bands characteristic of twinning in iron. The thickness does not appear to vary along the length of these twins and is rarely found to exceed five microns. Moreover, as may be seen from Fig. 6, these twin markings frequently traverse the entire width of the crystal, display an unusual regularity in their spacing, and often exhibit a stepped discontinuity which corresponds to twinning on another plane of the form $\{11\bar{2}1\}$. In these respects, the appearance of these twins is reminiscent of the formation of slip bands, and the stepped character is analogous to the cross-slip observed in α brass¹⁵ and aluminum¹⁶ crystals.

The infrequent occurrence of the $\{11\bar{2}2\}$ type twins does not permit an accurate description of their shape. However, the limited observations do indicate that the nature of these twins represents an

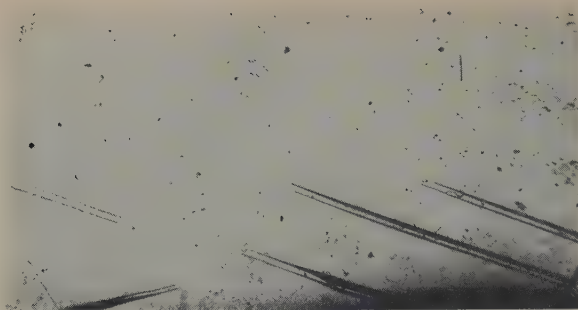


Fig. 10—Appearance of $\{11\bar{2}2\}$ twins at specimen edge. X100. Area reduced approximately 60 pct for reproduction.

intermediate position between the extreme shapes characteristic of the twinning on the $\{10\bar{1}2\}$ and $\{11\bar{2}1\}$ planes. It is interesting to note that the $\{11\bar{2}2\}$ twins of Fig. 10, which were formed at the edge of the specimen, show a distinct preference for appearing in pairs.

A consideration of the variation in the thickness of twin lamellae and their corresponding shear values in different metals suggests that a correlation between the magnitude of shear and the characteristic shape of twins is possible: For example, the thick lenticular deformation twins in zinc are associated with a shear of 0.143 in contrast with a shear of 0.707 for the thin Neumann bands in iron. This variation in twin thickness with magnitude of shear was very recently pointed out by Cahn,¹⁷ who further substantiated this association with his excellent results on the complex twinning behavior in the deformation of uranium. It was argued that the greater the twinning shear, the greater will be the elastic stresses resisting further growth of a twin, so that a new lamella will be started in its immediate vicinity in preference to the continued growth of the old twin. Thus, the greater the value of the twinning shear, the finer will be the twin lamellae. Although this rule is only an approximation, it does explain some experimental observations on the occurrence of twins in some metals, as well as the gross variation in twin shapes from metal to metal.

Unfortunately, in the present investigation the values of shear associated with the three types of twinning cannot be directly calculated, since it was not possible to determine experimentally the necessary twinning elements. However, with regard to the $\{10\bar{1}2\}$ twins, the equivalent $\{10\bar{1}2\}$ plane may be adopted as the "2nd undistorted K_2 plane"¹ in line with the behavior of zinc.⁷ On this basis, the plane of twinning shear is a $\{11\bar{2}0\}$ plane, and the amount of shear is 0.173. For the twins of the form $\{11\bar{2}1\}$ and $\{11\bar{2}2\}$, it is unlikely that their respective equivalent planes are K_2 planes, since the corresponding values for the magnitude of shear would be unreasonably large. However, a consideration of the crystallographic geometry of twinning¹ does permit a speculative evaluation of the shear, which for $\{11\bar{2}1\}$ twins is 0.63 and for the $\{11\bar{2}2\}$ twins is either 0.245 or 0.53. Although these calculated shear values are questionable in view of the many assumptions involved, they do serve to indicate that the thinner twins are associated with greater values of shear, in agreement with the work of Cahn.¹⁷

To summarize the experimental observations of the slip and twinning elements, it may be said that at least nine slip systems and eighteen twinning planes can contribute to the plastic flow of coarse

titanium crystals at room temperature. This is in contrast to three slip systems (basal glide) and six twinning planes (second-order pyramidal planes, type I) in the metals magnesium, zinc, and cadmium. For the purpose of clarification, the slip and twinning planes observed in the deformation of titanium are illustrated in the hexagonal lattice of Fig. 12.

Discussion of Results

Mechanism of Slip: The presence of first-order pyramidal slip $\{10\bar{1}1\}$ as a secondary slip system in titanium is similar to the behavior of magnesium^{2,18} which has a c/a ratio slightly less than the ideal. Slip on these planes in titanium occurs rarely, and the unresolvable nature of their appearance makes their detection difficult. This does not appear to be the case in magnesium at elevated temperatures.¹⁸

The predominance of type I prismatic slip $\{10\bar{1}0\}$, on the other hand, and the apparent absence of basal slip (0001) is significant; since this behavior suggests (in accordance with the general rule for slip) that in the titanium lattice the atomic density and interplanar spacing of the prismatic planes are greater than for the basal plane. This might very well be the case in titanium, if the implications of Fig. 13 are considered. The upper diagram in the figure represents the space pattern of atoms in the close-packed hexagonal structure of titanium, while the lower diagram represents the arrangement of atoms as viewed in the direction indicated by the arrow, i.e., along a $\langle 11\bar{2}0 \rangle$ direction. Therefore, in the lower diagram the arrangement is along alternate prismatic planes of the form $\{10\bar{1}0\}$. For reasons of clarity, the three atomic sites within the body of the cell have been drawn as open circles, while those forming the simple hexagonal lattices have been drawn as solid circles.

If the atoms of the two adjacent prismatic planes are considered as belonging to a single corrugated plane or band, as suggested by the dashed lines in the lower diagram of Fig. 13, it can be shown that both the atomic density and interplanar spacing are greater for the prismatic planes than for the basal planes. This is readily seen from a consideration of

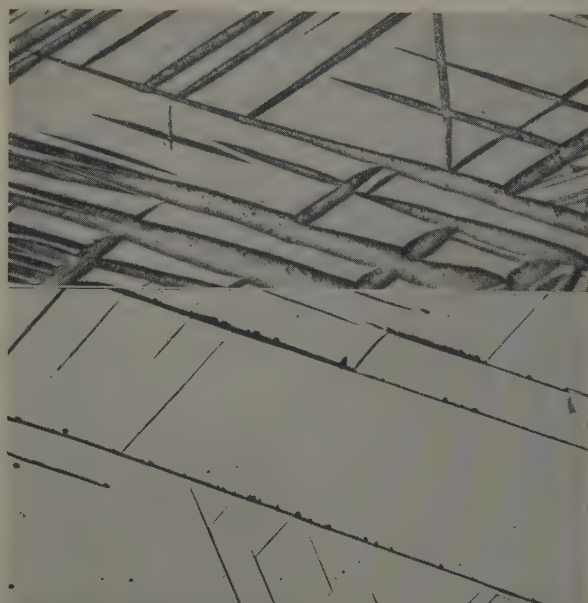


Fig. 11—Appearance of different twin types in titanium. X200. Area reduced approximately 20 pct for reproduction. a (top)— $\{10\bar{1}2\}$ twins. b (bottom)— $\{11\bar{2}1\}$ twins.

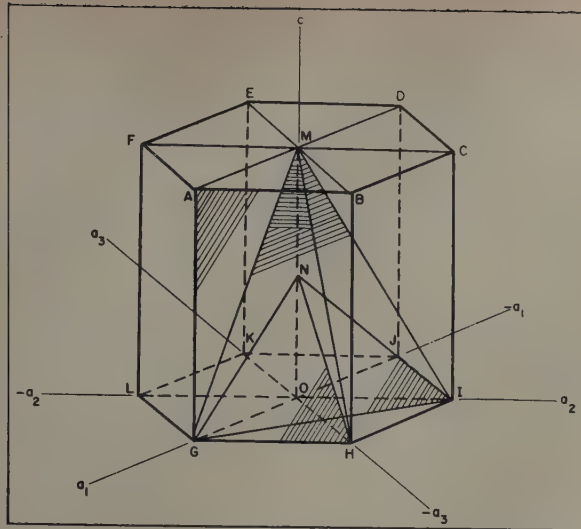


Fig. 12—Hexagonal lattice showing the position of the operative slip and twinning planes and slip direction in the plastic deformation of titanium at room temperature.

Slip planes: ABHG—prism planes, type I; of the form $\{10\bar{1}0\}$. GHM—pyramidal planes, type I, order 1; of the form $\{10\bar{1}1\}$. Twinning planes: GHN—pyramidal planes, type I, order 2; of the form $\{10\bar{1}2\}$. GIM—pyramidal planes, type II, order 1; of the form $\{11\bar{2}1\}$. GIN—pyramidal planes, type II, order 2; of the form $\{11\bar{2}2\}$.

Slip direction: OG—digonal axis, type I; of the form $\langle 11\bar{2}0 \rangle$.

the lattice dimensions and the unit cells depicted to the right of the diagrams in Fig. 13. Values for these properties, which were calculated by taking $a = 1$ and $c = 1.587$, are listed in Table II, which also includes for comparison those for magnesium, zinc, and cadmium. It is evident from the tabulated values that for zinc and cadmium the basal plane still remains the plane of maximum atomic density and interplanar spacing, whereas for magnesium the situation is reversed in favor of the prismatic planes, as in the case of titanium. Therefore, it would appear from the philosophy of this analysis that magnesium should also exhibit prismatic flow. The fact that it does not at once suggests that either the atomic density and interplanar spacing for the corrugated prismatic planes must be significantly larger than for the basal plane for the occurrence of $\{10\bar{1}0\}$ slip, or the nature of the atomic bonding is an important criterion. It might be added that this postulation of a corrugated slip plane in a close-packed crystallographic direction is quite acceptable from the point of view of the present dislocation models of plastic flow.

Mechanism of Twinning: It is apparent from the experimental observations that the twinning habit in titanium, like the slip process, is very different from that generally associated with the hexagonal metals, where for room temperature tests twinning has been found to occur solely on the $\{10\bar{1}2\}$ pyra-

midal planes. In titanium, the situation is much more complex in that twinning takes place not only on the $\{10\bar{1}2\}$ planes, but also on the $\{11\bar{2}1\}$ and $\{11\bar{2}2\}$ type II pyramidal planes. Thus, it would appear that twinning in metals of this structural class always occurs on pyramidal planes of low indices, with a definite constancy in the appearance of the $\{10\bar{1}2\}$ twins. Moreover, on the basis of this difference in twinning behavior it can be empirically stated that metals of the same crystal structure but different axial ratios may not have the same twinning elements nor exhibit the same multiplicity of twinning.

Unfortunately, the present knowledge regarding the dynamics of mechanical twinning is such that it would be difficult to speculate on the reason for the presence of three distinct twin types in titanium, as well as the peculiar choice of the twinning elements. The evidence and arguments advanced by a number of investigators¹⁰⁻²¹ on the general twinning phenomenon are conflicting, and only serve to emphasize the absence of any single criterion which can account for the observed twinning elements. From the apparent complexity of this problem, it is certain that a definite need exists for more systematic investigations and reliable data.

Effect of Slip and Twinning on Ductility: The fact that in titanium there are at least nine possible slip systems (three prismatic type I and six pyramidal type I, order 1) and eighteen twinning planes (six pyramidal type I, order 2, six pyramidal type II, order 1 and six pyramidal type II, order 2) might very well account for the ability of the metal in its pure form to undergo severe amounts of plastic deformation. For example, it is well known that titanium can be cold-rolled above 90 pct reduction in thickness without serious cracking. This is particularly noteworthy in view of the fact that magnesium, which also has a c/a ratio less than the ideal (1.633), can be cold-rolled no more than 50 pct even in its high purity form. In contrast with titanium, this lack of ductility in magnesium at

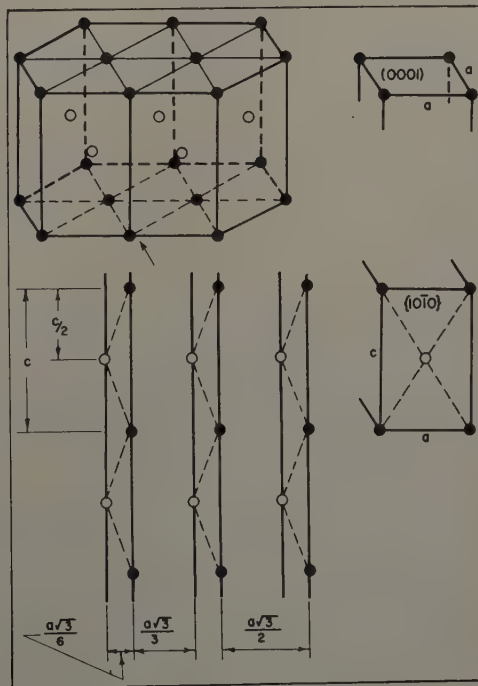


Fig. 13—Crystal structure of α titanium illustrating arrangement of atoms in corrugated configuration.

Table II. Comparison of Atomic Density and Interplanar Spacing for Type I Prismatic and Basal Planes

Metal	c/a Ratio	$\{10\bar{1}0\}$ Plane		(0001) Plane	
		Atomic Density $2/ac$	Interplanar Spacing, $a\sqrt{3}/2$	Atomic Density $2/a^2\sqrt{3}$	Interplanar Spacing $c/2$
Ti	1.587	1.260	0.866	1.155	0.794
Mg	1.624	1.231	0.866	1.155	0.812
Zn	1.856	1.078	0.866	1.155	0.928
Cd	1.886	1.060	0.866	1.155	0.943

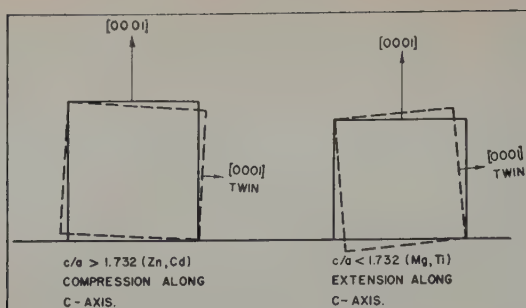


Fig. 14—Sign in the change in length along the c -axis due to twinning on a $\{10\bar{1}2\}$ plane. Solid line, crystal; dashed line, twin.

room temperature can be attributed, in part, to the presence of only three slip systems (basal glide) and six twinning planes (six pyramidal type I, order 2). Certainly, the contribution by twinning to the extent of plastic deformation in titanium is much more important than in the other hexagonal metals (magnesium, cadmium, and zinc).

An equally important consideration which can influence the degree of plasticity, particularly in hexagonal crystals, is the sign in the change in length along the c -axis due to twinning. Considering twinning on the planes of the form $\{10\bar{1}2\}$, it can be shown that depending upon whether the c/a ratio is less or greater than the value 1.732 there results an extension (<1.732) or a compression (>1.732) in the direction of the c -axis, as shown schematically in Fig. 14. Thus, in both magnesium and titanium twinning on the $\{10\bar{1}2\}$ planes cannot occur on cold rolling, since the twinning action can only result in a compression in the flow direction (i.e., rolling direction) as long as the basal plane is either parallel to or slightly inclined to the rolling plane, as is the case in these metals. Unlike magnesium, however, in titanium twinning occurs on the $\{11\bar{2}1\}$ and $\{11\bar{2}2\}$ planes in addition to the $\{10\bar{1}2\}$ planes, and it is expected, therefore, that this would favor greater deformation by rolling than can be hoped for in magnesium which twins only on the $\{10\bar{1}2\}$ planes at room temperature.

Texture Relationships: Another property of titanium which suggests a different mechanism of plastic flow than that found in the more common hexagonal close-packed metals is the preferred orientation developed in severely cold-rolled sheets. According to both Clark³ and McHargue,⁴ the texture in these sheets can best be described as one in which the $[10\bar{1}0]$ direction is parallel to the rolling direction and the (0001) plane is inclined approximately 25° to the rolling plane in the transverse direction. In contrast to this, the metals cadmium, zinc, and magnesium^{22-28, 25-28} have a texture in which there is a definite spread of the basal plane normals in the rolling direction. Moreover, in these metals there is a tendency for the $[11\bar{2}0]$ direction rather than the $[10\bar{1}0]$ direction to be parallel to the rolling direction. Therefore, the essential difference between these textures is in the direction of basal tilting, and in the direction parallel to the rolling direction. On the other hand, in zirconium (with a c/a ratio similar to titanium) McGeary and Lustman⁶ have found that the basal plane is tilted in the same manner as in titanium, and the $[10\bar{1}0]$ direction is also parallel to the rolling direction.

Although it is unwise to predict the mechanisms

of plastic flow from deformation textures, nevertheless this evidence does strongly support the general conclusion deduced from this investigation that the slip and twinning elements in titanium are different from those of magnesium, zinc, and cadmium, which have greater c/a ratios. For example, the coincidence of the $[10\bar{1}0]$ direction with the rolling direction for titanium can very well be explained by the duplex slip rotation resulting from the simultaneous operation of two $\langle 11\bar{2}0 \rangle$ directions on two $\{10\bar{1}0\}$ prismatic planes, whereas for the metals zinc, cadmium, and magnesium the crystallographic significance of the rolling direction results from slip on the basal plane in a single $\langle 11\bar{2}0 \rangle$ direction.

Another interesting consequence develops from the cold-rolled texture of titanium and the observation²⁴ that the strength of severely cold-rolled titanium sheets is greater in the transverse than in the rolling direction. From a consideration of the (0001) pole figure, it is natural to expect that if basal slip occurred in the plastic deformation of titanium, the yield strength of the sheets (because of the direction of tilting of the basal plane) would be much less in the transverse direction. Since this is not the case, it must be inferred that slip occurs more easily on another set of planes, which is what has been established in this investigation.

Conclusion

The slip and twinning elements have been determined in deformed coarse crystals of arc-melted 99.77 pct Ti (diameter of crystals, 2 to 8 mm). The method of identification was based on the use of a stereographic plot of a back-reflection Laue photograph describing the region where slip and twinning were observed. A number of these stereographic analyses showed that at least two types of slip and three twin types are operative in the plastic deformation of these crystals. The slip planes are of the type $\{10\bar{1}0\}$ and $\{10\bar{1}1\}$, while the twinning planes are of the type $\{10\bar{1}2\}$, $\{11\bar{2}1\}$, and $\{11\bar{2}2\}$. In no case was slip on the basal plane (0001) established.

In the case of the predominant $\{10\bar{1}0\}$ slip, the direction of slip was determined by following the movement of the specimen axis during extension by ascertaining the crystal orientation at various stages of extension. In all cases a type I digonal axis of indices $\langle 11\bar{2}0 \rangle$ was the effective slip direction.

Microscopic observations on the appearance of twins disclosed a distinct difference in their shapes. The $\{10\bar{1}2\}$ twins are thick and lenticular, whereas the $\{11\bar{2}1\}$ twins appear as thin lamellae similar to the Neumann bands in iron. A consideration of the geometry of twinning suggests that the characteristic shapes are related to the amount of twinning shear, in agreement with the hypothesis recently proposed by Cahn.¹⁷

The slip mechanism was discussed on the basis of the difference in c/a ratios for the common hexagonal close-packed metals. This led to a postulation of type I prismatic slip on corrugated planes. Some considerations were also advanced regarding the apparent marked ductility of this metal in contrast to the other hexagonal metals.

Acknowledgments

The authors wish to extend their gratitude to F. C. Perkins who carried out much of the experimental program, and to M. Miller who prepared

specimens for metallographic studies. Thanks are also due to V. Hannaford and A. VanRiper for the X-ray orientation determinations. The work reported herein was supported by the Office of Air Research, Contract No. AF-33-038-16031.

References

- ¹E. Schmid and W. Boas: *Kristallplastizität* (1935) Berlin. J. Springer.
- ²E. Schmid: Plastic Deformation of Magnesium Crystals. *Ztsch. Elektrochem.* (1931) **37**, p. 447.
- ³H. T. Clark: The Textures of Cold-rolled and Annealed Titanium. *Trans. AIME* (1950) **188**, p. 1154; *JOURNAL OF METALS* (September 1950).
- ⁴C. J. McHargue: Preferred Orientations in Titanium Resulting from Mechanical and Thermal Treatment. Univ. Kentucky Progress Report (August 1951) Contract AF-33(038)-19574.
- ⁵R. K. McGeary and B. Lustman: Preferred Orientations in Zirconium. *Trans. AIME* (1951) **191**, p. 994; *JOURNAL OF METALS* (November 1951).
- ⁶A. Smigelskas and C. S. Barrett: Preferred Orientation in Rolled and Recrystallized Beryllium. *Trans. AIME* (1949) **185**, p. 145; *JOURNAL OF METALS* (February 1949).
- ⁷C. H. Mathewson and A. J. Phillips: Plastic Deformation of Coarse-Grained Zinc. *Proc. Inst. Metals Div., AIME* (1927) p. 143.
- ⁸E. Schiebold and G. Siebel: Studies Relating to Magnesium and Magnesium Alloys. *Ztsch. Physik* (1931) **69**, p. 458.
- ⁹O. Hugge: Struktur und einfache Schiebungen den Eisens. *Ztsch. anorg. allgem. Chem.* (1922) **121**, p. 68.
- ¹⁰C. H. Mathewson and A. J. Phillips: Twinning in Beryllium, Magnesium, Zinc and Cadmium. *Proc. Inst. Metals Div., AIME* (1928) p. 445; *Trans. AIME*, vol. 78.
- ¹¹W. Boas and E. Schmid: Dependence of Crystal Plasticity on Temperature. III—Aluminum. *Ztsch. Physik* (1931) **71**, p. 703.
- ¹²G. I. Taylor and C. F. Elam: Distortion of Iron Crystals. *Proc. Royal Soc.* (1926) **112**, p. 337; and H. J. Gough: Alternating Torsion of Alpha-Iron. *Proc. Royal Soc.* (1928) **118**, p. 498.
- ¹³C. F. Elam: The Distortion of β -Brass and Iron Crystals. **153**, p. 273.
- ¹⁴L. C. Tsien and Y. S. Chow: The Glide of Single Crystals of Molybdenum. *Proc. Royal Soc.* (1937) **163A**, p. 19.
- ¹⁵R. Maddin, C. H. Mathewson, and W. R. Hibbard Jr.: Unpredicted Cross-slip in Single Crystals of Alpha Brass. *Trans. AIME* (1948) **175**, p. 86; *METALS TECHNOLOGY* (February 1948).
- ¹⁶R. W. Cahn: Slip and Polygonization in Aluminum. *Journal Inst. Metals* (1951) **19**, p. 129.
- ¹⁷R. W. Cahn: Plastic Deformation of Uranium. A.E.R.E. Report (M/R-740); Harwell, Berkshire, England (July 1951).
- ¹⁸P. W. Bakarian and C. H. Mathewson: Slip and Twinning in Magnesium Single Crystals at Elevated Temperatures. *Trans. AIME* (1943) **152**, p. 226.
- ¹⁹H. J. Gough: *Proc. ASTM* (1933) **33**, Part II, p. 3.
- ²⁰E. N. da C. Andrade and P. J. Hutchings: The Mechanical Behavior of Single Crystals of Mercury. *Proc. Royal Soc.* (1935) **148A**, p. 120.
- ²¹A. V. Stepanov: *Journal Exp. Theor. Phys.* (Russian) (1947) **17**, p. 713.
- ²²V. Cogliote and G. Sachs: The Rolling Texture of Zinc and Magnesium. *Metallwirtschaft* (1932) **11**, p. 1.
- ²³P. W. Bakarian: Preferred Orientation in Rolled Magnesium and Magnesium Alloys. *Trans. AIME* (1942) **147**, p. 266.
- ²⁴E. A. Anderson: Private communication (1951). New Jersey Zinc Co., Palmerton, N. J.

Observation on Scaling of Iron

by W. J. Wrazej

THE measurements on the formation of multi-layered scales on pure iron¹ and the metallographic examination of the produced layer of FeO, Fe₃O₄, and Fe₂O₃ shown in micrographs² throw much interesting light on this apparently well-known subject. Professor Paidassi announced³ that in a few months' time further results are going to be published with regard to the growth of Fe₃O₄ and Fe₂O₃ layers on an Armco iron as a function of temperature. Because of the very thin layers of Fe₂O₃ which are

shown by Paidassi (Fig. 10 of ref. 2) when samples were scaled in air at 700°C for 4 hr and because this is not in agreement with the present author's previous observations, the following experiment was recently carried out.

Polished cylindrical samples 13/64 in. in diam and 1/4 in. long from electrolytic iron used for spectrographic work (Hilger, H.S. Iron rods, F.693) and an Armco iron sample 1/4 in. in diam of the same length were suspended in a muffle furnace on Nichrome wire and annealed in air for 4 hr at 700°C \pm 5°C. Because of the known easy peeling off of the Fe₂O₃ layer which is mainly in the form of powder (purple red dust on the surface) the samples were protected against any draft and shock. After annealing, the samples were cooled in air and placed in the mount-

W. J. WRAZEJ is associated with the Physical Metallurgy Div., Department of Mines and Technical Surveys, Ottawa, Ont., Canada. Discussion on this paper, TP 3435E, may be sent, 2 copies, to AIME by April 1, 1953. Manuscript, July 7, 1952. Los Angeles Meeting, February 1953.

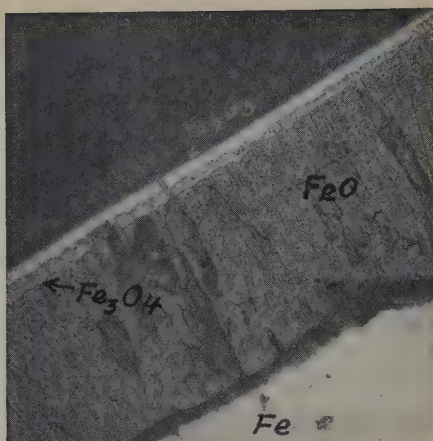


Fig. 1—Layers of Fe_2O_3 , Fe_3O_4 , and FeO on electrolytic iron sample.

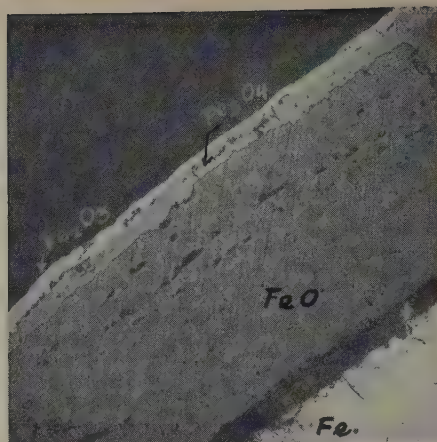


Fig. 2—Layers of Fe_2O_3 , Fe_3O_4 , and FeO on Armco-iron sample.

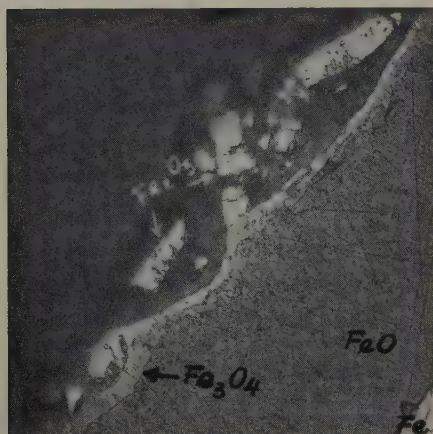


Fig. 3—Other position of sample in Fig. 1 showing the peeling off of Fe_2O_3 .

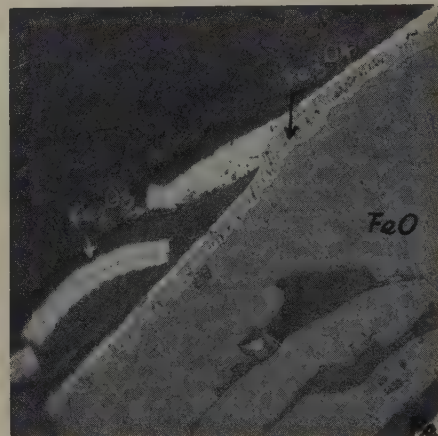


Fig. 4—Other position of sample in Fig. 2 showing the peeling off of Fe_2O_3 .

Figs. 1 to 4—Scales obtained by oxidation of electrolytic iron and Armco iron in air when heated for 4 hr at $700^\circ C$. 4 pct picral etch. X500. Area reduced approximately 50 pct for reproduction.

ing device and mounted in transparent lucite at $150^\circ C$ under a pressure of 5000 psi. The pressure was considered to be essential to retain the deposits of scales on the surface of the sample during the abrading on emery papers, i.e., to make them stick closer to the surface.

After careful abrasion with "no pressure" on emery papers and polishing on nylon with alumina, the samples were examined in unetched and etched (4 pct picral) conditions. The ratio of Fe_2O_3 to Fe_3O_4 (Figs. 1 and 2) appears to be greater than that shown by Paidassi in Fig. 10a.

The examination of the edges of the samples along the circumference revealed distinct and characteristic variations in the thickness of the layers as shown in Figs. 3 and 4, the samples in these instances were additionally etched for 60 sec. This additional etching did not change the appearance of the layer of scales. The ratio of all the three layers along the examined edges in all samples varies considerably.

There were some other important features to be noted. In some places the layers of Fe_2O_3 are extremely thin or entirely missing in spite of careful handling of the samples because of spontaneous peeling off of the scales. In some positions on the samples blisters of Fe_2O_3 are visible which evince that the low coherence of these scale particles is responsible

for the peeling off of this layer. Some pieces of Fe_2O_3 scale are shown trapped by lucite, see Figs. 3 and 4.

It is generally accepted² that a layer of iron scales consists of 85 to 95 pct of FeO covered by Fe_3O_4 layer constituting 10 to 15 pct and a layer of Fe_2O_3 amounting to about 0.5 to 2 pct of the total thickness of the scales. It is of interest to note that this assumption is not in accordance with the observed features. The result of many measurements has indicated that the ratio of the thickness of particular layers in the scale crust is as follows:

$$(Fe_2O_3 + Fe_3O_4):FeO \text{ as } 20:80$$

where $Fe_2O_3:Fe_3O_4$ is at least 1:1 and might be locally as much as 2:1 as evinced in these particular samples.

In showing such features illustrated in Figs. 1 to 4 the purpose is to draw attention to the fact that the technique used in handling the microsamples can greatly influence the apparent thickness of the Fe_2O_3 layer.

References

- ¹ M. H. Davies, M. T. Simnad, and C. E. Birchenall: *Trans. AIME* (1951) **191**, p. 889; *JOURNAL OF METALS* (October 1951).
- ² J. Paidassi: Discussion on ref. 1. *Trans. AIME* (1952) **194**, p. 537; *JOURNAL OF METALS* (May 1952).
- ³ *Metals Handbook* (1948) p. 223. Cleveland. ASM.

Mechanical Properties of High Purity Ti-Al Alloys

by H. R. Ogden, D. J. Maykuth, W. L. Finlay, and R. I. Jaffee

Titanium with up to 7.5 pct Al forms single-phase α alloys that are work hardening, not heat treatable, and ductile as welded. The high aluminum γ phase alloys are not usefully ductile, despite their low hardness, but they have excellent oxidation resistance and hot hardness.

LITTLE has been published on the effect of aluminum on the mechanical properties of titanium, despite the fact that two of the first four commercial alloys released by titanium alloy producers contained aluminum as an important alloying ingredient. These were both α - β type alloys, one containing 4 pct Al and 4 pct Mn and the other containing 3 pct Al and 5 pct Cr. However, neither of these alloys reflects the true alloying nature of aluminum, since each contains important amounts of the β -stabilizing addition, manganese or chromium.

In a previous publication on the constitution of Ti-Al alloys,¹ the authors showed that aluminum had a high solubility in α titanium and was strongly α stabilizing in nature. About 25 wt pct Al is soluble in α titanium at room temperature. With as little as 5 pct added aluminum, the α transus temperature is increased from 882° to 970°C, and the correspond-

ing β transus to 995°C. The first intermediate phase in the Ti-Al system is the ordered face-centered tetragonal TiAl phase, which extends from 34 to 46 wt pct Al.

The present paper presents hardness data over the entire titanium-rich region of the system, through the TiAl phase, and mechanical property data on the alloy range capable of being fabricated.

Methods of Investigation

The materials used and general preparation of alloys, as well as experimental techniques used in the investigation of Ti-Al alloys, have been adequately described.² Briefly, the preparation consisted of arc-melting the desired amount of high purity aluminum (99.99 pct purity) and iodide titanium (maximum hardness 100 Vickers, as deposited) together on a water-cooled copper hearth under a partial pressure of argon. The resulting button ingot was of such form that it could be fabricated without further treatment.

All work was done using ingots weighing 10 to 15 g, which were hot-rolled to strip form whenever possible. Tensile samples were 3.25 in. long, 0.5 in. wide, and 0.040 in. thick, with a reduced section 1.25 in. long by 0.250 in. wide. The gage length used was 1 in. Electrical strain gages mounted on the

H. R. OGDEN, Junior Member AIME, D. J. MAYKUTH, and R. I. JAFFEE, Member AIME, are Assistant Supervisor, Research Metallurgist, and Supervisor, respectively, Nonferrous Physical Metallurgy Div., Battelle Memorial Institute, Columbus, Ohio, and W. L. FINLAY, Member AIME, is Research Manager, Rem-Cru Titanium, Inc., Midland, Pa.

Discussion on this paper, TP 3456E, may be sent, 2 copies, to AIME by April 1, 1953. Manuscript, July 15, 1952. Los Angeles Meeting, February 1953.

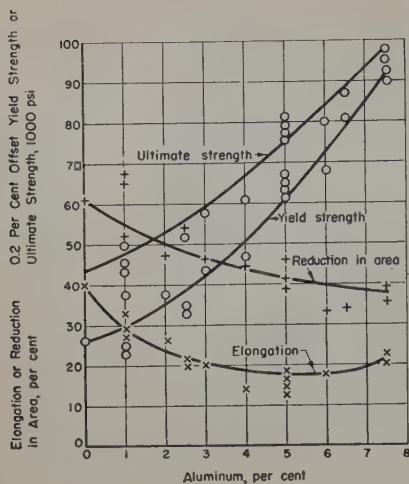


Fig. 1 — Mechanical properties of annealed Ti-Al alloys.

tensile samples were used to obtain stress-strain curves, and data for flow curves were obtained by using dividers to measure the larger strains at each 0.01 in. elongation.

Modulus of elasticity values at elevated temperatures were obtained using the dynamic method described by Andrews.⁸ Samples used in this work were 3 in. long, 0.250 in. wide, and 0.040 in. thick. Subsequent to obtaining dynamic modulus values, the samples were machined into tensile specimens, and the modulus of elasticity was checked in tension using both Tuckerman extensometers and electrical strain gages.

Elevated temperature hardness measurements were obtained using an Amsler-Vickers hardness tester with a small resistance furnace mounted on the anvil and a diamond penetrator mounted in a heat-resistant steel chuck. A protective atmosphere of dried high purity argon was used to prevent oxidation of the specimens. Hardness impressions were taken at the desired temperatures, and measurements were subsequently made at room temperature.

Fabrication and Annealing Characteristics

All ingots were fabricated by hot rolling at 850°C. Since aluminum increases the temperature range of α - β transformation, this corresponded to fabrication in the α field. The alloys with up to about 7.5 pct Al could be rolled to satisfactory strip, although at the higher aluminum contents progressively more severe edge cracking of the strip was noticed. The alloys with more than 7.5 pct Al cracked badly

when rolled at 850°C. At higher rolling temperatures, alloys containing from 8 to 16 pct Al rolled somewhat better than at 850°C, but even at rolling temperatures up to 1250°C, the fabricated sheet was unsuitable for testing. Based on fabrication characteristics alone, the usable range of Ti-Al alloys has been established as between 0 and 7.5 pct Al.

Hot-rolling scale was removed mechanically by grinding on emery cloth. A thin layer of the base metal was also removed by grinding to eliminate any contamination caused by diffusion of nitrogen or oxygen during rolling. It was established by hardness-penetration measurements that the diffusion layer was less than 0.001 in. thick after the rolling operation.

The annealing treatment chosen for these alloys was 3½ hr at 850°C in vacuum, followed by furnace cooling. This treatment produced a completely recrystallized α structure with a grain size between 0.04 and 0.10 mm. All tensile properties were obtained on alloys annealed in this condition.

Aluminum restricts the amount of cold work that can be given to titanium. Thus, although pure

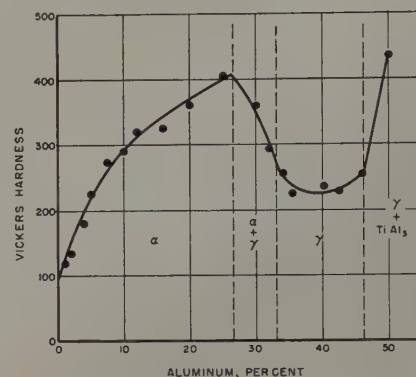


Fig. 3—Effect of aluminum content on the Vickers hardness of titanium.

titanium can be cold-rolled without cracking to reductions greater than 95 pct and Ti-Al alloys with up to 3 pct Al to reductions greater than 80 pct, alloys containing 4 to 5 pct Al edge crack at 70 pct reduction, and the 7.5 pct Al alloy starts edge cracking at 30 pct reduction. Aluminum increases the recrystallization and softening temperatures of titanium. By a series of 1 hr reheats on 40 pct cold-rolled metal, it was found that pure titanium softened and recrystallized at about 600°C, while a 5 pct Al alloy softened and recrystallized at 800°C. Microscopic examination of Ti-Al alloys rolled at 850°C and annealed 3½ hr at the same temperature indicated that finer α grain sizes were obtained with the alloys of higher aluminum content. For these conditions of fabrication, the following approximate α grain sizes were observed: Ti, 0.1 mm; 1 pct Al, 0.075 mm; 4 pct Al, 0.05 mm; and 7.5 pct Al, 0.04

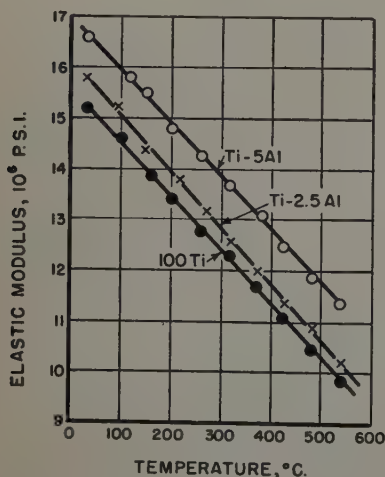


Fig. 2—Effect of temperature on the dynamic elastic moduli of Ti-Al alloys.

Table I. Modulus of Elasticity Values for Ti-Al Alloys at Room Temperature

Composition, Pct (Balance Ti)	Modulus of Elasticity, 10 ⁶ Psi			
	Dynamic Method	Electric-Strain-Gage Method	Tuckerman-Extensometer Method	Tension Method, Average
100 Ti	15.4	15.9	15.8	15.7
2.5 Al	15.8	16.4	16.3	16.1 ^a
5 Al	16.6	16.7	17.3	16.8 ^a

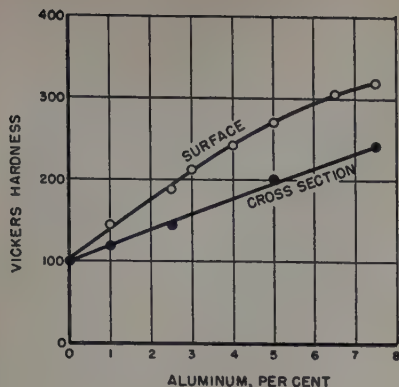


Fig. 4—Cross section and surface hardness of Ti-Al alloys annealed 3½ hr at 850°C after rolling at 850°C.

mm. This effect most probably is caused by the increased recrystallization temperature promoted by aluminum, rather than by any intrinsic grain-refining action of aluminum.

Mechanical Properties

Tensile Properties: Tensile properties of the workable alloys containing between 0 and 7.5 pct Al, as annealed 3½ hr at 850°C, are shown in Fig. 1. Strength increases at a moderate rate up to 4 pct Al, at which point further aluminum additions have a considerably greater strengthening effect. The greatest increase in strength for 1 pct of aluminum added occurs between 4 and 5 pct. The ductility of the alloys remains quite high for alloys containing up through 7.5 pct Al, giving no indication of the poor hot-workability of alloys with the higher aluminum content.

Modulus of Elasticity: The modulus of elasticity values for several alloys are given in Table I. These were obtained using the dynamic and the tension methods. The results obtained using the dynamic method are slightly lower than obtained in tension, but both methods show that additions of aluminum increase the modulus of elasticity of titanium about 200,000 psi for each percentage of aluminum added.

The effect of temperature on the modulus of elasticity of Ti-Al alloys is shown in Fig. 2. These data were obtained using the dynamic method. The modulus values decrease linearly with increasing temperature at a rate of about 1×10^6 psi for each 100°C rise in temperature.

Hardness-Composition Data: The effect of aluminum on the Vickers hardness of iodide titanium is shown in Fig. 3. Hardness increases rapidly with increasing aluminum content up to a peak at about 26 pct Al, the terminal solubility of aluminum in α titanium. In the two-phase α - γ region, the hardness drops linearly until the γ phase is reached. The hardness of the γ phase is quite low and remains fairly uniform throughout the composition limits of this phase.

Anisotropy: When α Ti-Al alloys have been rolled and annealed at temperatures in the α field, the hardness of the rolled strip on the rolling plane is markedly higher than its hardness in planes perpendicular to the rolling plane. This results from the preferred orientation of the hexagonal basal planes parallel to the rolling surface. For Ti-Al alloys rolled and annealed at 850°C, the hardness differential increases from essentially nil for pure titanium to 75 Vickers points for the 7.5 pct Al alloy, as shown in Fig. 4. Anisotropy effects are more pronounced when the alloys are cold-rolled and annealed. For example, a 2 pct Al alloy cold-rolled

and annealed at 850°C had a hardness differential of 97 Vickers points, compared with 38 Vickers points when rolled and annealed at 850°C. Because of these anisotropy effects, it is mandatory to specify the direction of hardness measurements and the prior treatment given to the alloy when considering the hardness of wrought Ti-Al alloys, or, for that matter, of any wrought titanium α alloy.

There appears to be little or no anisotropy in annealed Ti-Al alloy sheet longitudinal or transverse to the direction of rolling. For cold-rolled sheet, the normal anisotropy found with one-phase alloys would be expected, however.

Hardness-Strength Correlations: Correlation between ultimate strength and cross-sectional Vickers hardness for Ti-Al alloys is the same as was found

Fig. 5—Correlation of Vickers hardness and ultimate strength of annealed Ti-Al alloys.

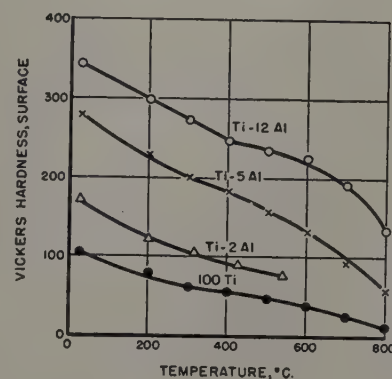
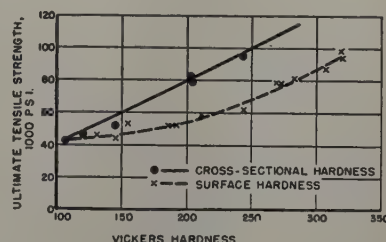


Fig. 6—Effect of temperature on Vickers hardness of Ti-Al alloys.

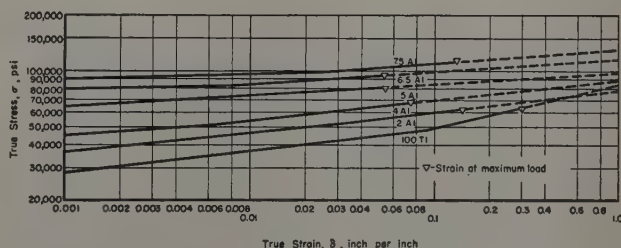


Fig. 7—Flow curves (true stress vs true strain) for Ti-Al alloys annealed 3½ hr at 850°C.

previously for alloys of titanium with oxygen, nitrogen, and carbon.² The ultimate tensile strength is approximately equal to 400 times the Vickers hardness number. The surface hardness vs strength correlation is not a straight line, but is curved concave to the hardness axis, as shown in Fig. 5.

Hot Hardness: The effect of temperature on the hardness of several Ti-Al alloys is shown in Fig. 6. As is characteristic of the elevated-temperature strength properties of titanium alloys, there is no initial plateau in hardness. Starting from room temperature, hardness decreases linearly with increasing temperature up to 600°C, above which a

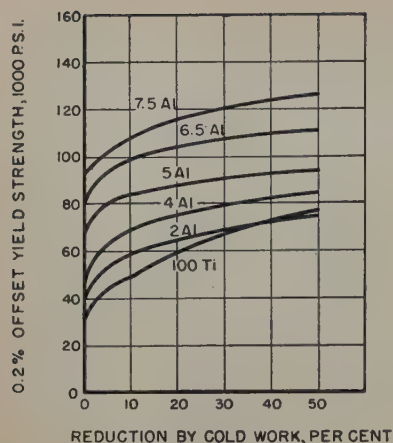


Fig. 8 — Yield strength-cold work curves for Ti-Al alloys calculated from flow curves.

greater hardness decrease occurs with increasing temperature.

Flow Properties: The flow curves of Ti-Al alloys rolled and annealed at 850°C are given in Fig. 7. The flow constants, corresponding to the equation, $\sigma = A\delta^n$, are given in Table II. The strain coefficient, A , which gives an indication of the magnitude of the strengthening effect in the cold-rolled condition, remains about the same as the aluminum content is increased from 0 to 4 pct. For alloys containing more than 4 pct Al, the A values increase rapidly with increasing aluminum content, illustrating the effectiveness of aluminum in quantities over 4 pct. In general, the n values decrease as the aluminum content is increased. Strain hardening, which is directly measured by n as the percentage increase

Table II. Flow Equation Constants for Ti-Al Alloys

Composition	Strain Coefficient, A , Psi	Strain Exponent, n	Strain at Maximum Load, δ_m , In. per In.
100 Ti	84,000	0.25	0.30
1 Al	86,000	0.19	0.24
2 Al	78,000	0.12	0.16
3 Al	84,000	0.11	0.07
4 Al	87,000	0.11	0.08
5 Al	96,000	0.07	0.06
6 Al	112,000	0.09	0.07
6.5 Al	114,000	0.07	0.06
7.5 Al	129,000	0.07	0.14

in flow stress per percentage increase in strain, decreases with increasing aluminum content.

Uniform elongation in tension is recorded in Table II as the observed strain at maximum load. Where the flow equation applies, this is also equal to n for annealed materials. Uniform elongation decreases with increasing aluminum content and is reasonably close to n up to 6.5 pct Al. It appears to increase again at 7.5 pct Al, despite the fact that n remains low. This may be caused by a greater sensitivity of this alloy to the biaxial state of stress or to strain rate after necking occurs.

The effect of cold work on the yield strength can be calculated from the flow-curve data using the relationship, $\delta = \ln L/L_0 = \ln 1/(1-R)$, where R is the fraction reduction in cold working. These data are shown in Fig. 8 and illustrate further how aluminum in solid solution decreases strain hardening of titanium. A comparison of these curves with those previously obtained for alloys of carbon, oxygen, and nitrogen⁸ indicates that the work-hardening charac-

teristics of Ti-Al alloys are very similar to those of the alloys of titanium with carbon, oxygen, and nitrogen.

γ Phase Alloys: All attempts at fabricating alloys within the composition limits of the γ phase were unsuccessful even though this phase has a relatively low hardness, as shown in Fig. 3. The γ alloys were brittle at room temperature, except when deformed by slow compression. They could not be forged or rolled at any temperature up to 1250°C, the highest temperature used in fabricating attempts. These alloys have excellent retention of hardness at elevated temperature. Hot hardness tests conducted at temperatures up to 800°C showed that they maintained a hardness of 200 Vickers up to 500°C without any drop at all, and then decreased slowly to 130 Vickers at 800°C.

In order to obtain information on the mechanical properties of the γ phase, slow compression tests were used to determine the modulus of elasticity, compressive yield strength of the γ phase at room temperature, and some idea of the deformability of these alloys. The test was conducted at a strain rate of 0.015 per min, and was continued until a total reduction of 8 pct was reached. At this point, there were only a few small secondary tensile cracks in

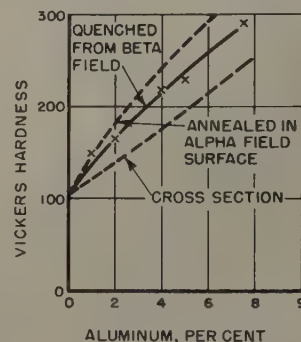


Fig. 9—Effect of quenching from the β field on Vickers hardness of α -annealed Ti-Al alloys.

the specimen. The results are shown in Table III. The high modulus of elasticity is particularly noteworthy. The yield strength is about the magnitude that would be expected from the hardness of γ alloys.

Effects of Heat Treatment

The work on the constitution of Ti-Al alloys¹ showed that the two-phase α - β field was relatively narrow, and it extended to higher temperatures as the aluminum content increased. The β phase can not be retained on quenching, and transforms martensitically to α . However, quenching from the β field would not be expected to produce drastic hardening effects, because the solubility of aluminum in α titanium is greater than that in β . Also, because the terminal α solubility is so much higher than the aluminum contents in the workable alloy range, age-hardening effects would not be expected, either. These probabilities were borne out by experiment.

Fig. 9 shows the Vickers hardness of Ti-Al alloys

Table III. Mechanical Properties of a Ti-37 Pct Al Alloy Tested in Compression. Initial Condition: As-Melted

Modulus of elasticity, psi	20,500,000
Proportional limit, psi	23,000
0.2 pct offset yield strength, psi	58,000
Deformation without cracking	At least 8 pct

rolled and annealed at 850°C and also of the same alloys heated for ½ hr in the β field and water quenched. The hardness of the β -quenched alloys, which are isotropic, is bracketed by the surface and cross-section hardness in the original α worked-and-annealed condition. Clearly there was no hardness increase involved in the martensitic transformation resulting from quenching from the β field. Subsequent aging for long periods of time from 300° to 600°C in the α field after β quenching does not increase hardness by either an aging or transformation mechanism.

The only effective heat treatment of α Ti-Al alloys is the removal of strain hardening by annealing. Annealing characteristics of these alloys were described earlier.

Weldability

The causes for the brittle welds observed in titanium alloys, chiefly of the α - β type, are undoubtedly complex, and are probably the combined result of many factors such as freezing segregation and β -phase transformation. However, like unalloyed titanium, the single-phase Ti-Al α alloys have no heat treating effects and freeze over a narrow range, and would appear to have good potentialities for being ductile in the welded condition. Some exploratory arc welds made on these alloys showed this to be the case.

A series of annealed binary Ti-Al alloys in 0.040 in. sheet form, were arc-welded with the direction

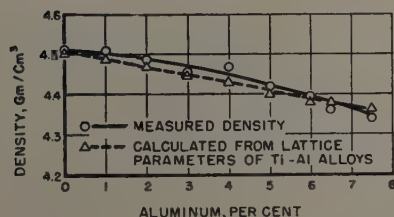


Fig. 10—Effect of aluminum content on the density of high purity titanium.

of the weld in the rolling direction of the sheet. Welding was done in a helium atmosphere chamber using a dc tungsten-electrode arc. The conditions of welding the alloys were identical with those for welding unalloyed titanium and need not be gone into in detail here. Bend tests were conducted on the welds with the weld line perpendicular to the bending axis. This may be termed a longitudinal bend test on the weld, because the bending stresses set up in the weld are in line with the weld itself. Results of these tests are summarized in Table IV. It is apparent that the bend ductility of the weld metal and heat-affected zone is at least as good as the bend ductility of the original equiaxed α base metal.

Density

One of the prime advantages of using aluminum as an alloying addition to titanium is that it decreases the density of an already light metal. Unfortunately, only a relatively small amount of aluminum can be added while maintaining a ductile alloy. Of particular interest is the effect of aluminum on the density of alloys in the usable alloy range (0 to 7.5 pct Al). Fig. 10 shows the measured densities for these alloys and, also, the densities calculated from the lattice parameters of the α phase. The density is decreased significantly with increasing aluminum content at the rate of about 0.02 g per cu cm for each 1 pct Al added. The meas-

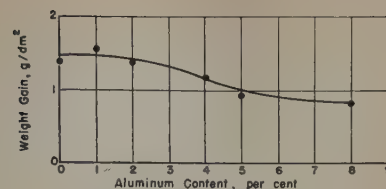


Fig. 11—Weight gain and hardness penetration for Ti-Al alloys heated for 24 hr at 850°C in air.

ured densities and the densities calculated from lattice parameters are fairly close, the measured densities being slightly higher than the calculated densities.

The density of a γ phase alloy (Ti-37 pct Al) was found by weight displacement in water to be 3.80 g per cu cm. This corresponds very well with the density calculated from the lattice parameter of the stoichiometric composition TiAl. The calculated value was 3.80₂ g per cu cm.

Air Oxidation

In the workable α alloy range, up to 8 pct Al, there is a moderate improvement in the oxidation resistance of titanium confirmed by aluminum. Strip specimens were exposed to still air for 24 hr at 850°C. Fig. 11 shows the results that were obtained.* The oxidation rate of titanium is lowered

* The hardness-penetration curve for unalloyed titanium corresponds to 36 hr at 850°C.

by about 40 pct by 8 pct Al. The improvement in oxidation rate by aluminum is not marked until over 4 pct Al is present. Contamination, as measured by hardness penetration into the metal, is not significantly affected by aluminum. The curves in the lower part of Fig. 11 show that the increase in hardness over the original decreases to negligible values at about the same depth, and, also, that the surface hardnesses are high. There may be some significance to the indication that the surface hardness for the 2 pct Al alloy is higher and those for the 5 and 8 pct Al alloys are lower than the surface hardness of unalloyed titanium after oxidation.

The γ phase alloys have markedly superior oxida-

Table IV. Minimum Bend Radii of Arc-Welded Ti-Al Alloys

Composition, Pct Balance Ti	Minimum Bend Radii, T*	
	Weld Zone	Base Metal
0	0	0
1 Al	0	0
2 Al	1.3	1.3
2.5Al	0	1.6
3 Al	0	1.5
5 Al	1.6	1.2
6.5Al	0.9	1.3

* Minimum bend radius is given in terms of thickness of the sheet tested (T value = MBR/thickness of sheet) for a bend through an occluded angle of 75°.

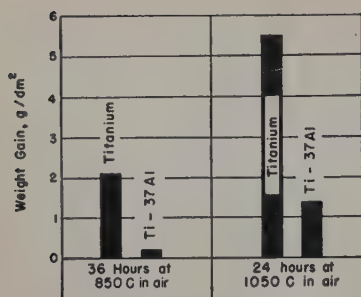
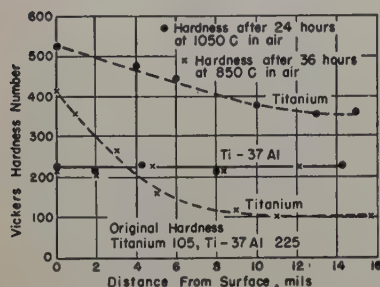


Fig. 12 — Oxidation data for a γ phase alloy.



tion resistance to unalloyed titanium. Still air oxidation tests were conducted on block samples of unalloyed titanium and 37 pct Al alloy, roughly $\frac{3}{8} \times \frac{3}{8} \times \frac{1}{2}$ in. in dimensions, for 36 hr at 850°C and 24 hr at 1050°C. Oxidation rates and hardness-penetration curves under these conditions are shown in Fig. 12. These data show that besides undergoing much less oxidation, the γ alloys are not hardened by oxygen diffusion into the metal.

Discussion

It is surprising to find so small a portion of the α Ti-Al field amenable to fabrication. In this respect, the α Ti-Al alloys bear some resemblances to the α Ti-O and Ti-N alloys. The limited workable portions of the α field found in these alloy systems are readily understandable, however, because oxygen and nitrogen dissolve interstitially in titanium. Aluminum, which is a substitutional solute in titanium, does not suffer this delimitation. X-ray diffraction measurements clearly show changing lattice constants over the entire field, with no evidence of ordering taking place. An associated fact, which may have some as yet unrecognized bearing on the situation, is that all three solutes increase the c/a ratio of the hexagonal close-packed lattice.^{1, 4} Furthermore, when this ratio approaches 1.604, the Ti-Al alloys are no longer sufficiently ductile to be fabricated by hot working. This limiting ratio occurs at about 8 pct Al. In this research, the upper limit of aluminum content that was fabricable was found to be 7.5 pct. In other work, not published, the upper limit of fabricability for binary alloys was 0.7 pct N and 1 pct O. Although data are not available on the c/a ratio of Ti-O and Ti-N alloys at these contents, it is possible that there is a limiting c/a ratio of about the same magnitude reached at about the fabricable limit of these alloys.

The γ phase alloys have some extremely desirable properties, which suggest possible applications as a high temperature material. These are its high modulus of elasticity, its low density, its retention of hardness to high temperature, and its good oxidation resistance. These alloys are limited by their brittleness and inability to be deformed by means other than slow compression.

The good ductility demonstrated for arc-welded Ti-Al α alloys suggests a solution to the problem of the poor weldability reported for titanium alloys. The suggested solution is nonheat-treatable α alloys with a narrow freezing range. The results obtained in this work indicate that the ductility of such alloys in the welded condition is equivalent to that of the annealed wrought material.

Summary

The mechanical properties of high purity binary Ti-Al alloys have been determined using small melts made under contamination-free conditions. The data obtained may be summarized as follows:

1—The workable range of Ti-Al binary alloys lies between 0 and 7.5 pct Al. Alloys containing higher than 7.5 pct are not amenable to fabrication. The γ alloys, around 37 pct, are soft, but have only limited workability.

2—Small additions (up to 3 pct) of aluminum to titanium have a moderate beneficial effect of the properties of titanium. Additions of 4 pct Al or more cause a larger increase in strength. The maximum increase in strength for 1 pct Al added occurs between 4 and 5 pct Al. Ductility remains high over the entire fabricable range.

3—Aluminum was found to decrease the density and increase the modulus of elasticity of titanium about 200,000 psi per pct Al. The increase continues with increasing aluminum content such that the modulus of γ alloy was found to be remarkably high, around 21 million psi.

4—Elevated-temperature hardness and modulus of elasticity determinations are presented which show how the hardness and modulus decrease at elevated temperatures. The γ alloys were found to maintain hardness at elevated temperature much better than the α alloys.

5—The results of heat treatment studies have shown that the fabricable alloys (0 to 7.5 pct Al) are single-phase α alloys which are not heat treatable by β quenching or subsequent aging.

6—Flow properties obtained by true stress-strain analysis have shown that the alloys are strain hardening to a considerable extent, but at a lower rate than is unalloyed titanium.

7—The workable α alloys were found to be ductile in the welded condition.

Acknowledgment

The authors are grateful to Rem-Cru Titanium, Inc., for permission to publish the results of this research, which was done at Battelle Memorial Institute under their sponsorship. They also wish to thank B. W. Gonser of Battelle for valuable suggestions and discussions which aided the progress of the research.

References

- ¹H. R. Ogden, D. J. Maykuth, W. L. Finlay, and R. I. Jaffee: Constitution of Titanium-Aluminum Alloys. *Trans. AIME* (1951) **191**, pp. 1150-1155; *JOURNAL OF METALS* (December 1951).
- ²R. I. Jaffee, H. R. Ogden, and D. J. Maykuth: Alloys of Titanium with Carbon, Oxygen, and Nitrogen. *Trans. AIME* (1950) **188**, pp. 1261-1266; *JOURNAL OF METALS* (October 1950).
- ³C. M. Andrews: Effect of Temperature on the Modulus of Elasticity. *Metal Progress* (1950) **58**, p. 85.
- ⁴H. T. Clark: The Lattice Parameters of High-Purity Alpha Titanium; and The Effects of Oxygen and Nitrogen on Them. *Trans. AIME* (1949) **185**, pp. 588-589; *JOURNAL OF METALS* (September 1949).

System Zirconium-Copper

by C. E. Lundin, D. J. McPherson, and M. Hansen

PRIOR work on the Zr-Cu phase diagram by Allibone and Sykes,¹ Pogodin, Shumova, and Kugucheva,² and Raub and Engel³ was confined largely to copper-rich alloys. The investigations of Raub and Engel were the most recent and seemingly the most complete of these. Alloys from 0 to 68.3 pct Zr were studied principally by thermal analysis and microscopic examination. These authors reported an intermetallic compound ZrCu_3 (1116°C melting point) and two eutectics, one at 86.3 pct Cu (977°C mp) and the other at 49 pct Cu (877°C mp). The solubility of zirconium in copper was reported to be less than 0.1 pct at 940°C.

The zirconium melting stock consisted of Westinghouse "Grade 3" iodide crystal bar (nominally 99.8 pct pure). It was treated by sand blasting and pickling (HF-HNO_3 solution) to remove the surface film of corrosion product, resulting from grade designation tests. The crystal bar was cold rolled to strip, lightly pickled again, and cut into pieces approximately 1/32 in. thick and 1/4 in. square. These were cleaned in acetone, dried, and stored for charging.

The high-purity copper (spectrographic grade) was supplied by the American Smelting and Refining Co. with a nominal purity of 99.99 pct. These copper rods were rolled to strip, cut into squares the same size as the zirconium platelets, cleaned in acetone, dried, and stored.

Equipment and Procedures

The equipment used for melting and annealing the zirconium binary alloys and for the determination of solidus curves has been described in connection with previous work on the Ti-Si system⁴ and in recent papers in this series describing the studies on eight binary zirconium systems.⁵⁻⁷ Techniques employed for preparing and processing the alloys were also similar to those used in the above references.

Ingots of 20 g were melted under a protective atmosphere of helium on water-cooled copper blocks in a nonconsumable electrode (tungsten) arc furnace. The ingots were homogenized and cold-worked prior to isothermal annealing to aid in the attainment of equilibrium. The specimens were heat-treated in Vycor bulbs sealed in vacuo or under argon, depending on the temperature of the anneal. Quenching was accomplished by breaking the Vycor bulbs under cold water. Temperature control was within $\pm 3^\circ\text{C}$ of reported temperatures.

Thermal analysis was primarily relied on to determine eutectic levels, peritectic levels, and compound melting points. The induction furnace incipient melting technique was also used but did not provide the accuracy obtained by thermal analysis

in this system, which involves much lower solidus temperatures than the other zirconium systems. A special technique for the determination of characteristic temperatures was employed in the case of several intermediate phases and their eutectics which displayed very small differences in melting temperatures. Specimens were sealed in Vycor bulbs and annealed at a series of very accurately controlled temperatures. Metallographic examination was then employed to reveal incipient melting. Furnaces and techniques in general were described previously.⁴ The etchant used was 20 pct HF plus 20 pct HNO_3 in glycerine unless otherwise stated.

Results and Discussion

The chemical analyses of the majority of alloys prepared for the determination of phase relationships in this system are given in Table I and a brief summary of the equilibrium anneals employed is given in Table II. In a preliminary program, alloys containing 1, 4, and 7 pct Cu were annealed for three different times at each of the temperatures 700°, 800°, and 900°C. No change in the relative amounts of phases present was detected after 350, 150, and 75 hr at the above temperatures, respectively. The times listed in Table II were accordingly chosen as a result of these preliminary tests.

Zirconium-rich alloys containing from 0.1 to 10 pct Cu were reduced by cold pressing from 58 to 8 pct, depending upon the alloy content, homogenized for 7 hr at 900°C, and then reduced 80 to 13 pct by cold rolling, again depending upon copper content. Other alloys were studied in the cast, or cast and annealed conditions.

The contracted scope of investigation for this system included the range 0 to 50 atomic pct Cu. This approximate region is shown in Fig. 1. Due to evidence of phase relationships departing considerably from those proposed by Raub and Engel³ in the 50 to 100 atomic pct range, the investigation was extended to cover this composition area rather thoroughly also. Fig. 2 is a drawing of the entire diagram. The labeling of some phase fields was omitted in Fig. 2 for the sake of clarity. An expanded view of the zirconium-rich region, with the experimental points necessary for its construction, is given in Fig. 3. The generally accepted value of Vogel and Tonn⁸ for the allotropic transformation $\alpha \rightleftharpoons \beta$, $862^\circ \pm 5^\circ\text{C}$, was employed in the construction of these diagrams. A careful study revealed that the "Grade 3" crystal bar used in this investigation actually transforms over the approximate range 850° to 870°C, due to impurities. It must be expected that this two-phase field in unalloyed zirconium will cause some departures from binary ideality in the very dilute alloys.

Zirconium-rich Alloys: The $\alpha \rightleftharpoons \beta$ transformation temperature is decreased from 862° to about 822°C by increasing amounts of copper. Thus, a eutectoid reaction, $\beta \rightleftharpoons \alpha + \text{Zr}_2\text{Cu}$, occurs at a composition of about 1.6 pct Cu. The eutectoid level was determined to lie between the alloy series annealed at 815° and 830°C. The placement of this eutectoid temperature

C. E. LUNDIN is Metallurgical Engineer, Dow Chemical Co., Rocky Flats Plant, Denver, Colo., D. J. McPHERSON, Junior Member AIME, is Supervisor of Physical Metallurgy Research, and M. HANSEN, Member AIME, is Chairman, Metals Research Dept., Armour Research Foundation of Illinois Institute of Technology, Chicago.

Discussion on this paper, TP 3466E, may be sent, 2 copies, to AIME by April 1, 1953. Manuscript, Sept. 5, 1952. Los Angeles Meeting, February 1953.

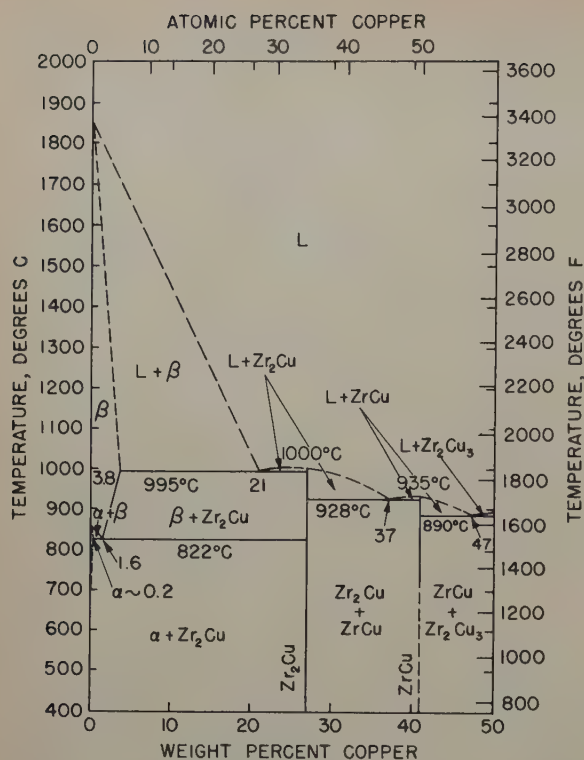


Fig. 1—Partial diagram of the Zr-Cu system.

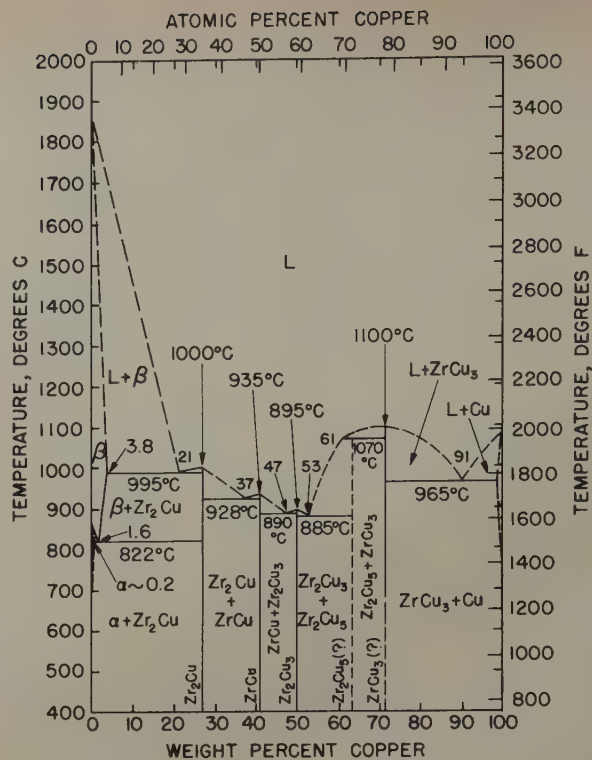


Fig. 2—The Zr-Cu system.

was based principally on the structures of hypereutectoid alloys. The hypereutectoid alloys in the $\beta + \text{Zr}_2\text{Cu}$ region displayed partial eutectoid decomposition during water quenching. This phenomenon is indicated in Fig. 4, a 3.2 pct Cu alloy quenched from 830°C, in which decomposition, probably nucleated by proeutectoid Zr_2Cu crystals, is seen to progress out from the original β grain boundaries. At 815°C, Fig. 5, the structure consists of particles of Zr_2Cu in a matrix of isothermal α . Therefore, at the annealing temperatures of 830° and 815°C, the

specimens were $\beta + \text{Zr}_2\text{Cu}$ and $\alpha + \text{Zr}_2\text{Cu}$, respectively. Partial eutectoid decomposition was also noted in other hypereutectoid alloys quenched from above 822°C.

The convergence of the β solid-solution field toward the eutectoid composition, 1.6 pct Cu, is illustrated by Figs. 6 through 8, of alloys containing 1.05, 1.8, and 3.2 pct Cu, respectively, annealed at 850°C. Structures containing $\alpha + \beta$, β , and $\beta + \text{Zr}_2\text{Cu}$ are evident.

The uppermost experimental placement (980°C) of the $\beta/\beta + \text{Zr}_2\text{Cu}$ phase boundary is illustrated in Figs. 9 and 10. The extrapolation of this boundary to the eutectic temperature, 995°C, indicates a maximum copper solubility in β zirconium of about 3.8 pct.

The maximum solubility of copper in α zirconium is demonstrated by Figs. 11 and 12, showing alloys annealed at 830°C. The former, a 0.09 pct Cu alloy, consists almost entirely of α solid solution. The latter, a 0.18 pct Cu alloy, contains $\alpha + \beta$.

Within a restricted region near the eutectoid, anomalous three-phase structures, stemming from the transformation range in unalloyed zirconium, were sometimes observed. The departure from true

Table I. Analyses of Zr-Cu Alloys

Alloy No.	Cu, Wt Pct	Alloy No.	Cu, Wt Pct
ZC 0.1-363	0.09	ZC 40-259	39.6
ZC 0.2-364	0.18	ZC 41-348	41.1
ZC 0.3-365	0.31	ZC 42-349	42.8
ZC 0.4-366	0.44	ZC 43-350	43.1
ZC 0.5-270	0.47	ZC 44-351	44.2
ZC 0.6-367	0.63	ZC 45-261	44.7
ZC 0.8-369	0.78	ZC 46-361	46.1
ZC 1-272	1.05	ZC 47-353	47.6
ZC 1.25-581	1.1	ZC 48-354	47.9
ZC 1.50-582	1.4	ZC 48.5-478	48.5
ZC 1.75-583	1.6	ZC 49-271	49.3
ZC 2-273	1.8	ZC 50-262	50.1
ZC 2.5-584	2.2	ZC 51-504	50.9
ZC 3-274	3.2	ZC 52-355	52.2
ZC 4-275	3.8	ZC 53-427	52.4
ZC 5-276	5.0	ZC 53-505	52.4
ZC 5-251	5.2	ZC 54-356	54.3
ZC 6-277	5.8	ZC 56-430	55.0
ZC 7-280	6.7	ZC 56-357	55.8
ZC 8-279	7.8	ZC 58-358	57.8
ZC 9-281	8.5	ZC 60-506	59.6
ZC 10-284	9.5	ZC 60-263	59.9
ZC 10-248	10.3	ZC 61-502	60.2
ZC 15-250	15.4	ZC 62-503	62.5
ZC 18-252	17.8	ZC 63-429	62.2
ZC 20-255	19.3	ZC 64-576	63.8
ZC 21-424	20.9	ZC 65-577	64.8
ZC 23-425	23.2	ZC 66-578	65.8
ZC 25-254	25.1	ZC 67.5-264	66.7
ZC 26-256	25.6	ZC 67.5-432	67.0
ZC 27-342	26.9	ZC 69-359	68.6
ZC 29-343	28.9	ZC 70-265	69.9
ZC 30-257	31.2	ZC 71-579	71.6
ZC 33-426	32.2	ZC 72-580	71.5
ZC 35-258	35.7	ZC 80-267	79.4
ZC 37-344	37.0	ZC 86-268	86.0
ZC 38-345	38.3	ZC 90-269	91.1
ZC 39-360	38.6	ZC 95-433	95.2*

*Analyzed for Zr; Cu by difference.

Table II. Schedule of Annealing Treatments for Zr-Cu Alloys

Annealing Temperature, °C	Annealing Time, Hr	Alloys,* Pct Cu
980	25	0.1-10, 15, 20
950	50	0.1-10, 15, 20
900	72	0.1-10, 15, 20
850	100	0.1-10, 15, 20
830	100	0.1-9
815	100	0.1-10, 15, 20
800	150	0.1-10, 15, 20
750	256	0.1-5
700	400	0.1-1, 2, 3, 4, 5
650	450	0.1-1, 2, 3, 4, 5
600	648	0.1-1, 2, 3, 4, 5

*Alloys were pretreated before annealing as described in the text. Control samples of unalloyed zirconium were included with each annealing treatment.

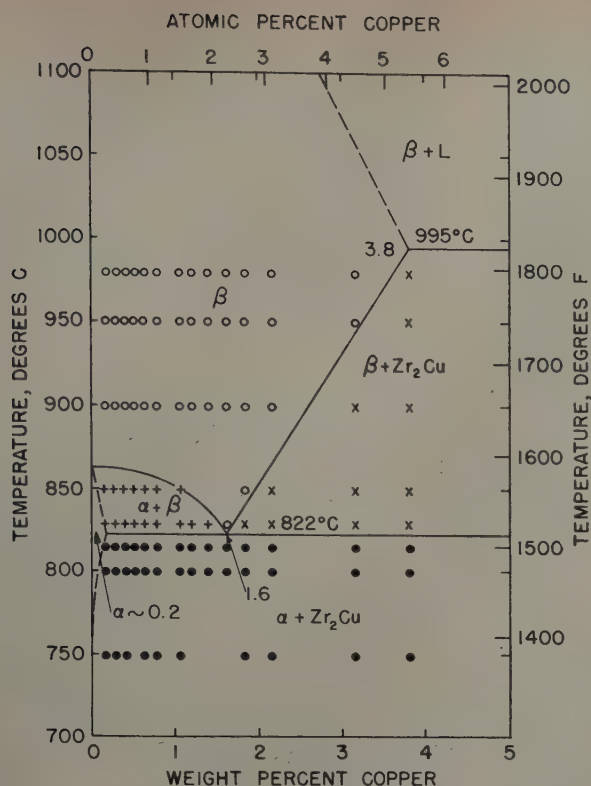


Fig. 3—Expanded diagram of the zirconium-rich region of the Zr-Cu system.

binary equilibrium in this region did not seriously affect the placement of the eutectoid composition and temperature.

Intermediate Phases: Surveying the system in the direction of increasing copper content, the structure in Fig. 9 is that of an alloy with 3.2 pct Cu. The structure represents β solid solution, transformed to acicular α during the quench. Fig. 13, an alloy with 10.3 pct Cu, shows primary β dendrites plus eutectic. At 20.9 pct Cu, the structure consists of 100 pct of the eutectic β -Zr₂Cu; this is depicted in Fig. 14. The intermediate phase Zr₂Cu corresponds to a theoretical composition of 25.83 pct Cu. The alloy which most nearly approaches a single-phase structure analyzed 26.9 pct Cu. Fig. 15 represents this alloy. X-ray diffraction studies indicated the structure of this alloy to be face-centered tetragonal, with the following lattice constants: $c = 3.716\text{\AA}$, $a = 4.536\text{\AA}$, and $c/a = 0.819$. The pattern of this phase is summarized in Table III.

Between Zr₂Cu and the next intermediate phase, there exists a eutectic. Fig. 16 shows this eutectic in a 37.0 pct Cu alloy. Above 37 pct Cu, primary crystals of the new phase increase in amount until, at 41.2 pct Cu, a nearly single-phase structure is ob-

Fig. 4 (left)—3.18 pct Cu alloy, quenched after annealing 100 hr at 830°C. Proeutectoid Zr₂Cu in matrix of transformed β . Quenched from above the eutectoid temperature. X500. Area reduced approximately 40 pct for reproduction.

Fig. 5 (right)—3.18 pct Cu alloy, quenched after annealing 100 hr at 815°C. Two sizes of Zr₂Cu crystals in a matrix of isothermal α . Quenched from below the eutectoid temperature. X500. Area reduced approximately 40 pct for reproduction.

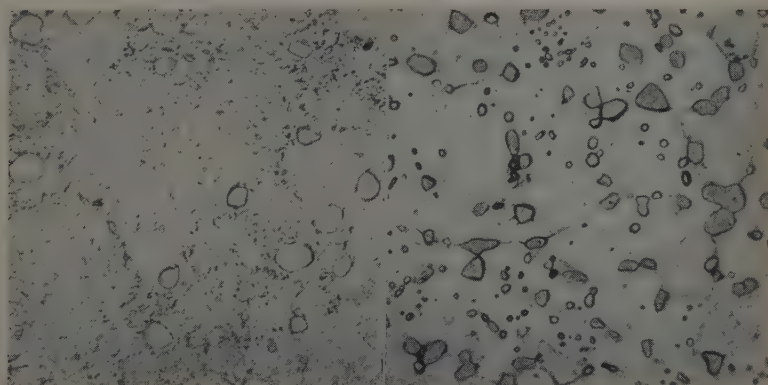


Table III. X-Ray Diffraction Pattern of Zr₂Cu*

I, \dagger Observed	hkl	d , Observed	d , Calculated
ft		2.775	
ms	111	2.416	2.428
wm	200	2.261	2.268
wm	002	1.852	1.858
vw		1.757	
w	220	1.601	1.616
m	202	1.436	1.437
vft		1.386	
m	131	1.336	1.338
w	222	1.215	1.214
w	113	1.155	1.156
vvft	400	1.134	1.134
vft	331	1.028	1.027
vft	240	1.014	1.014
vft		1.001	
vw	402	0.9665	0.9680
w	133	0.9378	0.9375
vft	004	0.9136	0.9240
w	242	0.8910	0.8903
vw	151,204	0.8649	0.8651

* Alloy composition is 27 pct Cu. Structure is face-centered tetragonal with $c = 3.716\text{\AA}$, $a = 4.536\text{\AA}$, $c/a = 0.819$.

† Intensities: ms, medium strong; m, medium; wm, weak medium; w, weak; vw, very weak; ft, faint; vft, very faint; and vvft, very very faint.

tained, Fig. 17. The most probable formula for this intermediate phase is ZrCu (41.06 pct Cu). A pronounced acicularity within the primary ZrCu crystals may indicate a transformation or reaction involving this phase in the solid state. Debye-Scherrer X-ray photographs of the 41.2 pct Cu alloy in the as-cast condition and as annealed at 900° and 700°C, revealed such complicated patterns that no attempts were made to index the structures for the present work.

The next eutectic occurs at 47.6 pct Cu, shown in Fig. 18. The participating phases are ZrCu and an intermediate phase still richer in copper. Nearly 100 pct of this phase is obtained in the cast structure of a 50.2 pct Cu alloy, Fig. 19. The formula Zr₂Cu₃ (theoretically 51.09 pct Cu) was assigned to this phase. X-ray powder patterns of the 50.2 pct Cu alloy in both as-cast and annealed conditions revealed lines too numerous to index within the scope of this program.

An alloy containing 52.4 pct Cu, Fig. 20, represents the eutectic between Zr₂Cu₃ and a new intermediate phase. Between 52.4 and 60.2 pct Cu, primary crystals of this new phase increase in relative amount. Fig. 21 shows a 60.2 pct Cu alloy, consisting of primary compound crystals plus eutectic. In an alloy of 62.5 pct Cu, Fig. 22, a new type of primary crystal (hexagonal habit) appears and is surrounded by a rim of the phase which was primary in the 60.2 pct Cu alloy. Thus, a peritectic reaction takes place between the melt at about 61 pct Cu and primary hexagonal type crystals to form a peritectic phase. Fig. 23 shows the 62.5 pct Cu alloy after annealing. The peritectic reaction has proceeded considerably, but not to completion, since

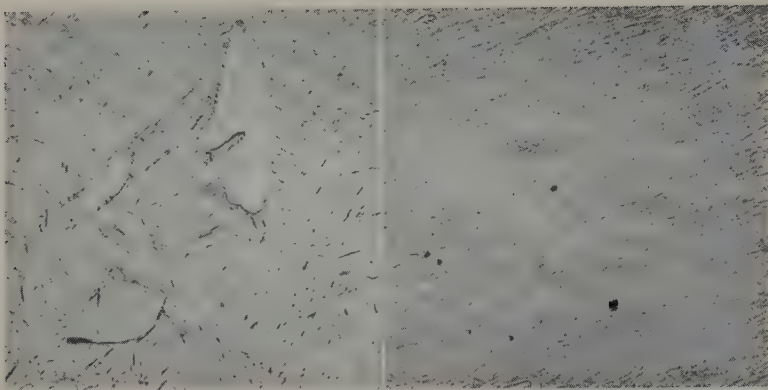


Fig. 6 (left)—1.05 pct Cu alloy, quenched after annealing 100 hr at 850°C. Isothermal α plus transformed β . Annealed in the $\alpha + \beta$ field. X250. Area reduced approximately 40 pct for reproduction.

Fig. 7 (right)—1.8 pct Cu alloy, quenched after annealing 100 hr at 850°C. Single phase, transformed β . X250. Area reduced approximately 40 pct for reproduction.

Fig. 8 (left)—3.2 pct Cu alloy, quenched after annealing 100 hr at 850°C. Proeutectoid Zr_2Cu in transformed β matrix. Annealed in $\beta + Zr_2Cu$ field. X250. Area reduced approximately 40 pct for reproduction.

Fig. 9 (right)—3.2 pct Cu alloy, quenched after annealing 25 hr at 980°C. Single phase, decomposed β . X250. Area reduced approximately 40 pct for reproduction.

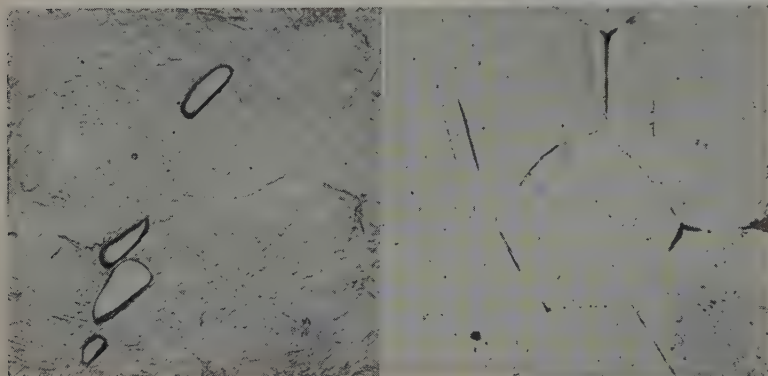


Fig. 10 (left)—3.8 pct Cu alloy, quenched after annealing 25 hr at 980°C. Zr_2Cu plus decomposed β . X250. Area reduced approximately 40 pct for reproduction.

Fig. 11 (right)—0.09 pct Cu alloy, quenched after annealing 100 hr at 830°C. Nearly single-phase α , representing maximum solubility of copper in α . X500. Area reduced approximately 40 pct for reproduction.

Fig. 12 (left)—0.18 pct Cu alloy, quenched after annealing 100 hr at 830°C. Isothermal α plus small amount of transformed β at the grain boundaries. X250. Area reduced approximately 40 pct for reproduction.

Fig. 13 (right)—9.5 pct Cu alloy, as-cast. Primary dendrites of β solid solution in a matrix of eutectic, $Zr-Zr_2Cu$. β phase of the maximum copper content has apparently not decomposed on arc casting. X500. Area reduced approximately 40 pct for reproduction.

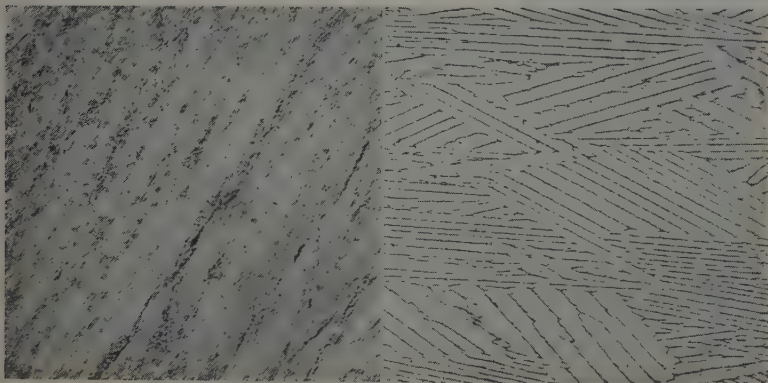


Fig. 14 (left)—20.9 pct Cu alloy, as-cast. Very fine $Zr-Zr_2Cu$ eutectic. X750. Area reduced approximately 40 pct for reproduction.

Fig. 15 (right)—26.9 pct Cu alloy, as-cast. Nearly 100 pct of the intermediate phase Zr_2Cu . X100. Area reduced approximately 40 pct for reproduction.

Fig. 16 (left)—37.0 pct Cu alloy, as-cast. Intimate phase mixture representing the structure of the eutectic $Zr_2Cu-ZrCu$. X750. Area reduced approximately 40 pct for reproduction.

Fig. 17 (right)—41.1 pct Cu alloy, as-cast. Virtually 100 pct primary crystals of the intermediate phase $ZrCu$. Acicularity within the crystals is probably evidence that this phase undergoes a transformation in the solid state. Unetched, polarized light. X75. Area reduced approximately 40 pct for reproduction.

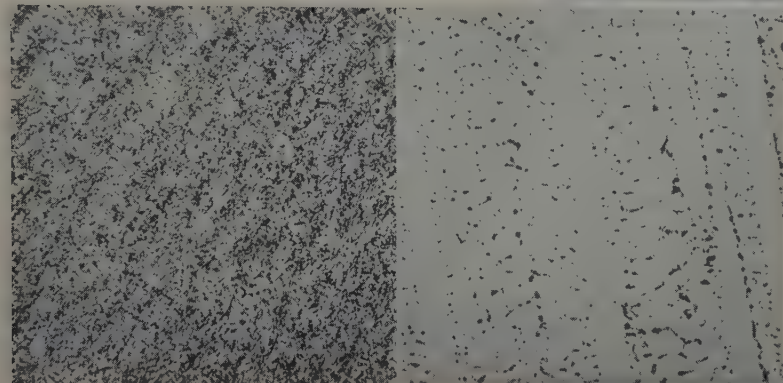
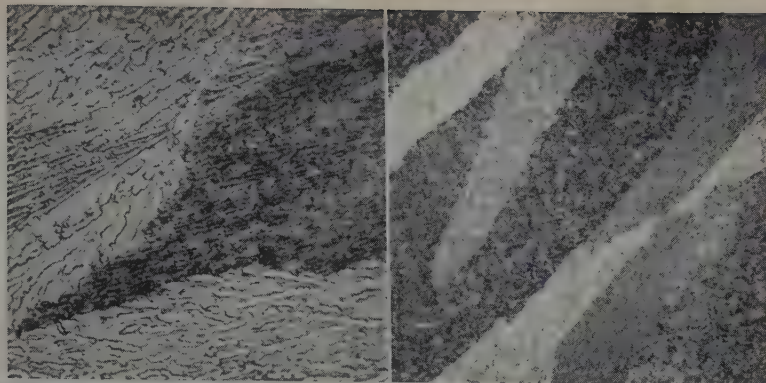


Fig. 18 (left)—47.6 pct Cu alloy, as-cast. Structure of the eutectic $ZrCu-Zr_2Cu_5$. X500. Area reduced approximately 40 pct for reproduction.

Fig. 19 (right)—50.1 pct Cu alloy, as-cast. Nearly single-phase structure representing the intermediate phase Zr_2Cu_5 . X150. Area reduced approximately 40 pct for reproduction.

Fig. 20 (left)—52.4 pct Cu alloy, as-cast. The eutectic structure $Zr_2Cu_5-Zr_2Cu_5$. X500. Area reduced approximately 40 pct for reproduction.

Fig. 21 (right)—60.2 pct Cu alloy, as-cast. Primary crystals of Zr_2Cu_5 in a matrix of the degenerated $Zr_2Cu_5-Zr_2Cu_5$ eutectic. X250. Area reduced approximately 40 pct for reproduction.

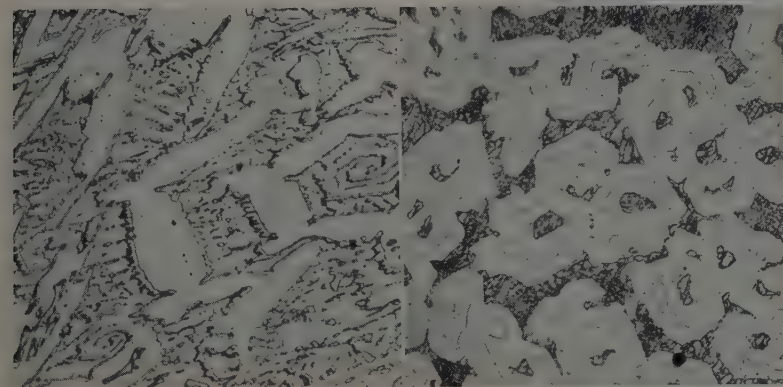
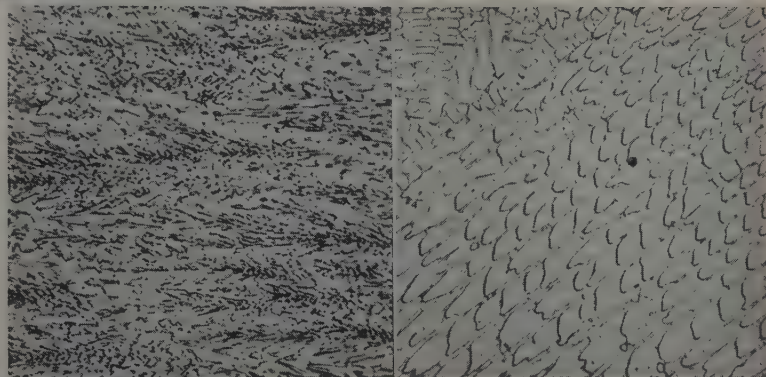


Fig. 22 (left)—62.5 pct Cu alloy, as-cast. A three-phase structure giving evidence of the peritectic reaction: $ZrCu_3 + \text{melt} \rightarrow Zr_2Cu_5$. Primaries of $ZrCu_3$ surrounded by serrated peritectic walls of Zr_2Cu_5 in a matrix of degenerated $Zr_2Cu_5-Zr_2Cu_5$ eutectic. X250. Area reduced approximately 40 pct for reproduction.

Fig. 23 (right)—62.5 pct Cu alloy, quenched after annealing 350 hr at 700°C. As compared to Fig. 22, annealing has caused the peritectically formed Zr_2Cu_5 to grow at the expense of the primary $ZrCu_3$ crystals. X200. Area reduced approximately 40 pct for reproduction.

Fig. 24 (left)—71.5 pct Cu alloy, as-cast. Virtually 100 pct of the intermediate phase $ZrCu_3$. Unetched. X250. Area reduced approximately 40 pct for reproduction.

Fig. 25 (right)—91.1 pct Cu alloy, as-cast. Structure of the eutectic $ZrCu_3-Cu$. X750. Area reduced approximately 40 pct for reproduction.

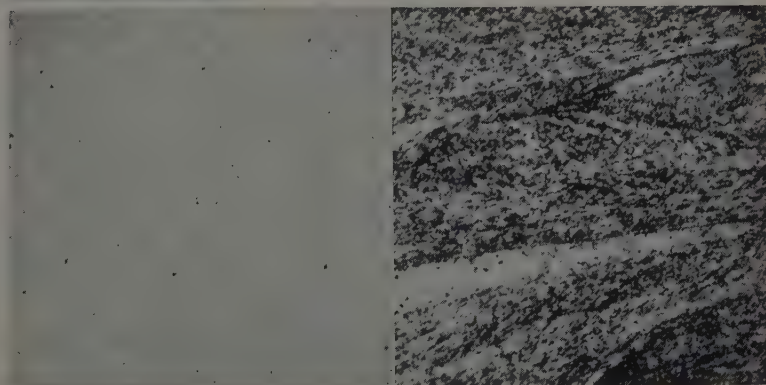


Table IV. Melting Range Determinations for the Zr-Cu System

Alloy	Wt Pct Cu	Thermal Analysis Arrests, °C	Bulb Anneals*	
			Melting Observed, °C	No Melting, °C
XZC 10-790	10.1	1505, 990		
XZC 21-730	21.1	995		
XZC 27-736	27.3	1000		
YZC 27-342	26.9		1006†	
ZC 27-342	26.9		1006	994
XZC 37-735	36.7	935		
YZC 37-344	37.0		930†	
ZC 37-344	37.0		930	925
XZC 41-734	41.3	935		
ZC 41-348	41.1		940	930
XZC 47-750	47.0	890		
XZC 50-732	49.8	895		
XZC 53-731	53.3	885		
XZC 65-747	64.7	1072, 885		
XZC 71-748	71.6	1100		
YZC 71-579	71.6		1121†	
XZC 90-749	89.5	965		

* Isothermal anneals of specimens sealed in Vycor bulbs and held in tube furnaces.

† Vacuum induction furnace incipient melting data.

resorption of the hexagonal habit crystals is not complete. The peritectic phase is tentatively assigned the formula Zr_2Cu_3 (63.52 pct Cu), although it might alternatively be $ZrCu_3$ (67.63 pct Cu).

The next single-phase alloy with an open maximum, Fig. 24, contains 71.5 pct Cu. This is the copper-rich intermediate phase which has been called $ZrCu_3$ (67.63 pct Cu) by previous investigators. This designation is tentatively adopted, although in the present work single-phase alloys persist at compositions closer to the theoretical formula $ZrCu_3$ (73.59 pct Cu). Limited attempts to index the X-ray diffraction patterns obtained from as-cast and annealed (900°C) samples of the 71.5 pct Cu alloy were unsuccessful.

An alloy containing 91.1 pct Cu, Fig. 25, depicts the eutectic between $ZrCu_3$ and the copper solid solution. No alloys were made to study the limited solid solubility of zirconium in copper. This has been rather thoroughly treated in the literature.¹⁻³

Melting Point Determinations: As discussed earlier, the determination of characteristic temperatures in the Zr-Cu system required somewhat different techniques than those employed for other zirconium binary systems, because of, 1—the generally lower solidus, eutectic and peritectic levels, and 2—the very slight differences in certain adjacent characteristic temperatures. Table IV summarizes the melting data for this system. Temperature values shown on the diagrams are thermal analysis or bulb annealing figures and were chosen on the basis of the best reproducible checks.

Discussion of the Literature: There is general agreement between the present authors and Raub and Engel³ on the nature of the system between $ZrCu_3$ and copper. Melting points of the intermediate phase $ZrCu_3$ and the eutectic $ZrCu_3$ -Cu compare favorably, but the compositions are displaced slightly to higher copper contents in the present work.

In the area on the zirconium side of $ZrCu_3$, Raub and Engel reported only a eutectic between $ZrCu_3$ and an unidentified zirconium-rich phase. The present investigation has shown the existence of three intermediate phases, $ZrCu$, Zr_2Cu_3 and Zr_2Cu_5 (?), the last being peritectically formed, and three eutectics in this same region.

It is believed that any investigation based primarily on thermal analysis of these alloys might well fail to find the several structural features because of the previously mentioned close similarity

of characteristic temperatures in this alloy range. An intensive microscopic investigation of cast and heat-treated alloy structures is necessary.

Summary

The Zr-Cu phase diagram has the following features:

1—The maximum solubility of copper in β zirconium is 3.8 pct at the eutectic temperature. The solubility of copper in α zirconium is less than 0.18 pct at all temperatures. A eutectoid reaction occurs at 1.6 pct copper and $822^\circ \pm 10^\circ\text{C}$.

2—A eutectic exists at 21 pct Cu and $995^\circ \pm 10^\circ\text{C}$ between zirconium and Zr_2Cu (25.83 pct Cu).

3—An intermediate phase is formed at about 27 pct Cu and $1000^\circ \pm 10^\circ\text{C}$ which probably corresponds to the formula Zr_2Cu (25.83 pct Cu).

4—A eutectic occurs at 37 pct Cu and $928^\circ \pm 10^\circ\text{C}$ between Zr_2Cu and $ZrCu$ (41.06 pct Cu).

5—An intermetallic compound forms at 41 pct Cu and $935^\circ \pm 10^\circ\text{C}$, corresponding to the formula $ZrCu$ (41.06 pct Cu).

6—A eutectic between $ZrCu$ and Zr_2Cu_3 (51.09 pct Cu) exists at 47 pct Cu and $890^\circ \pm 10^\circ\text{C}$.

7—An intermetallic compound forms at 50 pct Cu and $895^\circ \pm 10^\circ\text{C}$, corresponding to the formula Zr_2Cu_3 (51.09 pct Cu).

8—A eutectic between Zr_2Cu_3 and Zr_2Cu_5 (tentative; 63.52 pct Cu) occurs at 53 pct Cu and $885^\circ \pm 10^\circ\text{C}$.

9—The intermediate phase designated Zr_2Cu_5 is formed peritectically by a reaction between the melt containing 61 pct Cu and $ZrCu_3$ (tentative; 67.63 pct Cu), at $1070^\circ \pm 10^\circ\text{C}$.

10—An intermediate phase exists at about 71.5 pct Cu and melts with an open maximum at $1100^\circ \pm 10^\circ\text{C}$. The formula $ZrCu_3$ (67.63 pct Cu) has been tentatively accepted for this phase on a basis of previous literature.

11—A eutectic between $ZrCu_3$ and copper exists at 91 pct Cu and $965^\circ \pm 10^\circ\text{C}$.

12—The solubility of zirconium in copper is very limited. Previous investigators, although in disagreement on exact values, agree that the solubility is less than 1 pct Zr.

Acknowledgments

The authors are grateful to the Atomic Energy Commission, sponsor of the work under Contract No. AT (11-1)-149 "Phase Diagrams of Zirconium-Base Alloys," for permission to publish this paper. Thanks are due to R. F. Domagala who supervised the heat treatment program, to C. A. Johnson for the metallographic work, and to W. Rostoker for interpretation of the X-ray diffraction patterns.

References

1. T. E. Allibone and C. Sykes: *Journal Inst. Metals*, London (1928) **39**, p. 173.
2. S. A. Pogodin, J. S. Shumova, and F. A. Kugucheva: *Compt. rend. Acad. Sci. U.R.S.S.* (1940) **27**, p. 670.
3. E. Raub and M. Engel: *Ztsch. Metallkunde* (1948) **39**, p. 172.
4. M. Hansen, H. D. Kessler, and D. J. McPherson: *Trans. ASM* (1952) **44**, p. 518.
5. D. J. McPherson and M. Hansen: *ASM Preprint No. 34* (1952).
6. C. E. Lundin, D. J. McPherson, and M. Hansen: *ASM Preprint No. 41* (1952).
7. R. F. Domagala, D. J. McPherson, and M. Hansen: *Trans. AIME* (1953) **197**, p. 73; *JOURNAL OF METALS* (January 1953). See also this issue, p. 279.
8. R. Vogel and W. Tonn: *Ztsch. anorg. allgem. Chem.* (1931) **202**, p. 293.

System Zirconium-Chromium

by R. F. Domagala, D. J. McPherson, and M. Hansen

On the basis of metallographic analysis, incipient melting data, thermal analysis work, and X-ray diffraction, phase relationships in the 0 to 50 atomic pct Cr region were carefully resolved. Phase relationships in the 50 to 100 atomic pct region were outlined. A single intermediate phase, ZrCr_2 , was established in the system. A eutectic and a eutectoid were found in the zirconium-rich region of the system, while a eutectic was located in the chromium-rich region. Limited solubility of chromium in both α and β zirconium was observed.

THIS is another in a series of papers on zirconium-base binary phase diagrams based on a program sponsored by the Atomic Energy Commission. The Zr-Sn,¹ Zr-Si,² and Zr-Mo and Zr-W³ systems have already been published. Previous work on the Zr-Cr system includes a partial diagram by Hayes, Roberson, and Davies⁴ and a complete diagram by McQuillan.⁵ The phase relationships reported by these authors were determined with magnesium-reduced zirconium, whereas those reported herein are based on iodide metal. Some X-ray work on the intermediate phase in this system was also reported by Hayes et al., as well as by Wallbaum.⁶ Comparisons with these data are made in the appropriate sections.

Thermal analysis, metallographic and incipient melting techniques were employed to accurately resolve phase relationships in the 0 to 50 atomic pct Cr region, while the remainder of the diagram is outlined on a basis of cast structures and thermal analysis.

A description and analyses of the metals used in the preparation of alloys for this study are included in Table I. A "low-hafnium" zirconium crystal bar (Westinghouse "Grade 3") was used. This material was produced by the decomposition of a volatile iodide onto a hot zirconium filament. The as-received crystal bar was coated with corrosion product from a standard autoclave test by which its grade designation is determined. A sand-blasting and subsequent HF-HNO₃ pickling treatment was employed to remove this contamination. The bars were cold-rolled to approximately 1/32-in. sheet, pickled again, sheared to 1/4-in. squares, washed with acetone, and stored for use.

Ingot chromium metal from National Research Corp. and electrolytic chromium flakes from Johnson, Matthey and Co., Ltd., were available as alloy additions. The ingot chromium was received in granular form. The large granules were sized by crushing,

R. F. DOMAGALA and D. J. MCPHERSON, Junior Members AIME, are Assistant Metallurgist and Supervisor, respectively, Physical Metallurgy Research, and M. HANSEN, Member AIME, is Chairman, Metals Research Dept., Armour Research Foundation of Illinois Institute of Technology, Chicago, Ill.

Discussion on this paper, TP 3481E, may be sent, 2 copies, to AIME by April 1, 1953. Manuscript, Aug. 26, 1952. Los Angeles Meeting, February 1953.

Table I. Analyses of Metals Used

	Metal		
	Iodide Zirconium*	Johnson-Matthey Chromium	National Research Chromium
Nominal purity, pct	99.8	99.9	99.5
Form	Crystal bar	Electrolytic flakes	Ingot granules
Impurities, pct			
Al	0.007		
Cr	0.002		
Fe	0.03		
Hf	0.05		
Mg	0.0001		
Ni	0.007		
Ti	0.013		
O	0.01	0.005-0.015	0.05
N	0.0087	0.020-0.035	0.045
C	<0.01		0.05
Metallic		<0.005	

* Zirconium analysis supplied by the Argonne National Laboratory, Chicago.

treated for iron removal, rinsed with acetone, and stored. The flakes were broken to approximately 1/8 in. with mortar and pestle, cleaned with acetone, and stored for charging.

Experimental Procedure

A nonconsumable electrode arc furnace identical to that described by Hansen, Kessler, and McPherson,⁷ was used in this work. A 400 amp dc welding generator was the source of power. To insure homogeneity, ingots were melted in a water-cooled spun copper crucible, a total of four times without opening the furnace. No difficulties were encountered in the preparation of these binary alloys. Analyzed chromium contents were found to agree very well with the intended content. Melts of pure zirconium were interspersed in the course of preparing the alloys and their hardness was measured to keep a constant check on the melting technique.

Vycor and quartz bulbs were used to contain the samples for isothermal annealing treatments. Vycor bulbs were employed for temperatures up to 1100°C, while quartz was used above this temperature. For treatments up to 950°C the bulbs were evacuated before sealing, but for higher temperatures a partial pressure of argon was admitted to the

Table II. Analyses of Zr-Cr Alloys

Alloy No.	Cr, Wt Pct	Alloy No.	Cr, Wt Pct
ZR 0.25-401	0.28	ZR 25-392	25.0
ZR 0.50-402	0.48	ZR 30-393	29.7
ZR 0.75-403	0.51	ZR 35-406	34.7
ZR 1-408	0.81	ZR 40-394	37.6
ZR 2-404	1.5	ZR 48-604	48.6
ZR 3-405	2.6	ZR 49-605	49.3
ZR 4-406	4.4	ZR 50-396	50.7
ZR 5-407	4.7	ZR 51-606	51.3
ZR 7-596	6.5	ZR 52-607	52.4
ZR 9-597	8.5	ZR 53-608	53.1
ZR 10-388*	10.0	ZR 55-625	55.4
ZR 15-389	15.2	ZR 57-610	56.6
ZR 16-598	15.6	ZR 59-626	59.8
ZR 17-599	16.8	ZR 60-398	58.5
ZR 18-601	17.6	ZR 70-395	68.3
ZR 19-602	18.9	ZR 80-391	76.8
ZR 20-390	19.2	ZR 90-397	84.9
ZR 22-603	21.9		

* Johnson-Matthey chromium. All other alloys prepared with National Research chromium.

bulb before sealing. This pressure was controlled to produce 1 atm of pressure at the temperature of treatment. Sheet molybdenum, 0.003 in. thick, was used as a liner for bulbs scheduled for treatment above 1200°C. Specimen protection and support to the walls of the bulbs were provided by these liners. All treatments except homogenization were carried out in glazed porcelain tubes in electrically heated furnaces. Temperature control for anneals was held to $\pm 3^\circ\text{C}$ in general, but many runs were held to a smaller deviation. Homogenization treatments were carried out in a box-type Globar furnace. Specimen temperatures were measured with calibrated thermocouples at least twice a day for long time runs and at more frequent intervals for short time anneals. A control sample of pure zirconium was included in each bulb of isothermally annealed specimens. Specimens were quenched at the conclusion of an anneal by rapidly withdrawing the bulb from the furnace and breaking it under water.

A description of the high temperature vacuum-induction furnace and quenching technique used for the determination of solidus temperatures may be found in the literature.⁷ Thermal analysis techniques also described in the literature,⁷ were employed with success in this system because of the comparatively low temperature levels involved. The

Table III. Schedule of Annealing Treatments for Zr-Cr Alloys

Annealing Temperature, °C	Annealing Time, Hr	Alloys,* Pct Cr
1350†	2	1-15,17,19,30,40,48,53-59,70
1300†	2	1-15,17,19,53,55
1200	6	1-10,17,30,40,53,55,60
1100	20	1-10,20,40,53,59,70
994	40	1-7,10,19,30,40,51,53,55,59
950	40	0.25-9,19,70
860	140	0.25-5,9,19,30,51
840	145	0.25-9,17,40,53
840	385†	0.25-5
830	145	0.25-5,9,19,30
820	150	0.25-9,17,40,52,55
820	360†	0.25-5
800	145	0.25-9,17,40,51,53
800	365†	0.25-5
780	360†	0.25-5
750	215	0.25-5,9,20,30,51,60
700	240	0.25-5,30,40,51,53,55
650	310	0.25-5,9,20,30
600	360	0.25-5,30,40,51,53,55

* Alloys were pretreated before annealing as described in the text. Control samples of pure zirconium were included in each annealing treatment.

† Specimens in the region of the eutectic melted.

‡ Specimens held at 900°C for 17 hr, slowly cooled to temperature and held for time indicated, followed by water quench.

1350° and 1300°C isothermal anneals also proved useful in the delineation of the solidus curves in the zirconium-rich portion of the diagram.

Results

Table II includes the chemical analyses of all the alloys prepared for the determination of phase relationships in the Zr-Cr system, while a tabulation of all annealing treatments employed is included in Table III.

Zirconium-rich alloys containing from 0.25 to 15 pct Cr were cold-pressed from 30 to 4 pct depending upon alloy content. Alloys containing up to 40 pct Cr were then given a homogenization treatment at 1200°C for 75 hr. Ingots containing less than 22 pct Cr were then cold-rolled from 74 to 8 pct, depending upon alloy content, prior to the isothermal annealing treatments. All other alloys were employed in the arc-cast condition.

Fig. 1 shows the phase relationships in the 0 to 50 wt pct chromium region of the system. An expanded view of the eutectoid region of this system is given in Fig. 2, while Fig. 3 shows the entire diagram. Figs. 1 and 2 include most of the experimental points necessary for the construction of the diagram; some points were omitted for clarity.

Preliminary anneals of alloys containing 0.5, 2, and 5 pct Cr were made at 700°, 800°, and 900°C. No changes in the relative amounts of phases were observed after 150 hr at 700°C, 100 hr at 800°C, and 48 hr at 900°C. These data were then used to predict the times necessary to approach equilibrium at all temperatures employed in the isothermal annealing schedule.

An investigation, undertaken to establish the temperature of the allotropic transformation, $\alpha \rightleftharpoons \beta$, in "Grade 3" zirconium, manifested a range of transformation for this material. Details of this study may be found in an earlier paper on the Zr-Mo and Zr-W systems.⁸ The value reported by Vogel and Tonn,⁸ 862° $\pm 5^\circ\text{C}$, has been used for the construction of the diagram since the experimentally determined transformation range, 851° to 868°C, bracketed this temperature.

The eutectic at 18 pct Cr and 1280° $\pm 10^\circ\text{C}$ was located by the microscopic examination of as-cast alloys in this region, as well as specimens from the incipient melting and thermal analysis programs. Fig. 4 shows the eutectic structure found in an alloy containing 19.1 pct Cr employed in the thermal analysis program for this system.

Examination of isothermally annealed specimens showed the solubility of chromium in β to decrease from a maximum of 4.5 pct at the eutectic temperature to about 1 pct at 835°C, the temperature of the eutectoid reaction. Figs. 5 and 6 show a 4.4 and a 4.7 pct Cr alloy respectively, quenched from 1300°C. The former is a 100 pct retained β structure, while the latter alloy, also β , shows signs of incipient melting. Fig. 6, therefore, indicates the eutectic temperature is below 1300°C and the maximum solubility of chromium in β is less than 4.7 pct. Figs. 7 and 8 bracket the $\beta/\beta + \text{ZrCr}_2$ boundary at 950°C. The former figure is a 0.81 pct Cr alloy quenched from 950°C showing a typical transformed β structure. Fig. 8, a 1.5 pct Cr alloy quenched from the same temperature, contains crystals of ZrCr_2 in a transformed β matrix.

The eutectoid composition was determined to be 1 pct Cr, while the eutectoid temperature was found to be 835°C. The composition value is believed to be

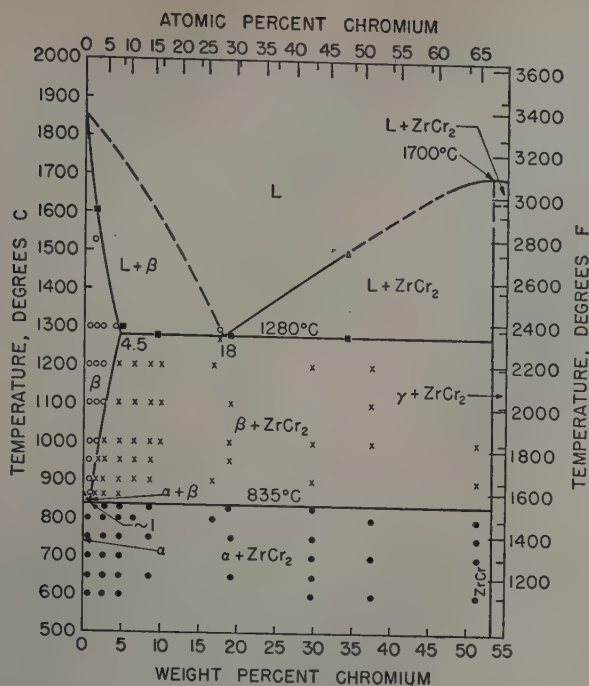


Fig. 1—Partial diagram of the Zr-Cr system.

within ± 0.25 pct Cr of the equilibrium composition, while the temperature level determined by metallographic examination of many specimens is certainly within $\pm 10^\circ\text{C}$ of the equilibrium value. Evidence for the placement of the eutectoid level is shown in Figs. 9 and 10. The former, a 1.5 pct Cr alloy quenched from 840°C , is a typical transformed β plus ZrCr_2 structure, while the latter figure, the same alloy quenched from 830°C , contains α plus ZrCr_2 . Thus the eutectoid level should lie between the two temperatures, and was positioned at 835°C . Due to the transformation range in unalloyed zirconium frequently causing anomalous structures in the region of the eutectoid, the temperature presented is considered somewhat less precise than Figs. 9 and 10 would indicate.

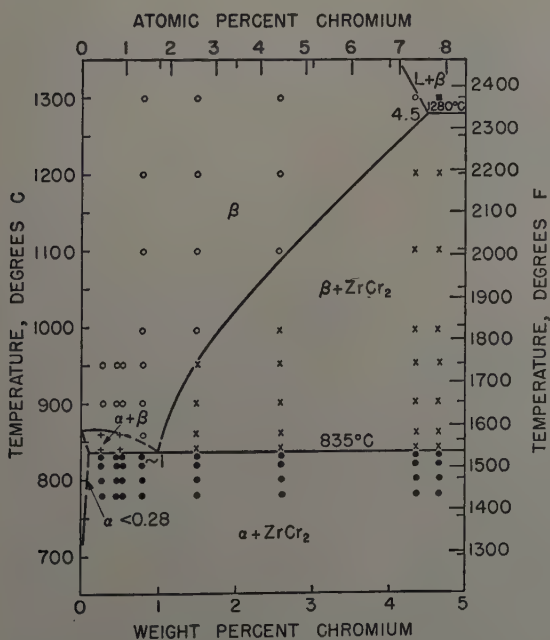


Fig. 2—Expanded diagram of the zirconium-rich region of the Zr-Cr system.

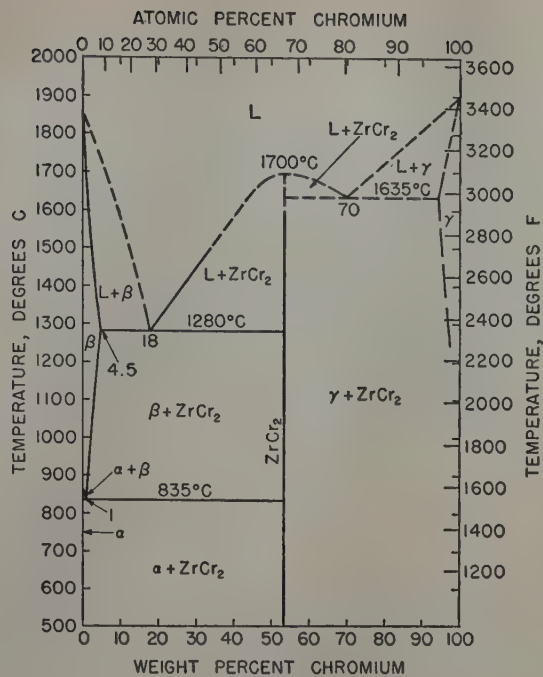


Fig. 3—The Zr-Cr system.

The maximum solubility of chromium in α zirconium was determined to be less than 0.28 pct at all temperatures. Fig. 11 illustrates a 0.28 pct Cr alloy quenched after 360 hr at 820°C . ZrCr_2 particles are present in an α matrix.

Fig. 12, a 53.1 pct Cr alloy, as-cast, is nearly single phase, indicating the proximity to an intermediate phase. This intermediate phase has a maximum melting point and was identified as ZrCr_2 (53.23 pct Cr).

The identification of this phase as ZrCr_2 agrees with Wallbaum⁸ and Hayes et al.⁴ An X-ray diffraction pattern of the nearly single-phase 53.1 pct Cr alloy was made using copper $K\alpha$ filtered radiation. Interpretation of the pattern indicated the structure of the phase to be hexagonal close-packed, with the following lattice parameters:

	Observed	Calculated
c	—	8.262 Å
a	—	5.079 Å
c/a	1.65	1.627

These values compare favorably with an axial ratio of 1.633 reported by Wallbaum,⁸ who classes ZrCr_2 as MgZn_2 type (C14). Hayes et al.,⁴ however, report ZrCr_2 to be cubic of the MgCu_2 type, with $a = 7.21 \text{ Å}$.

The eutectic between ZrCr_2 and the chromium solid solution is illustrated in Fig. 13, a 69.5 pct Cr alloy employed in the thermal analysis work for this system. This alloy was slowly cooled from the liquid field.

On a basis of microscopic examination of unanalyzed as-cast specimens, the solid solubility of zirconium in chromium was shown to be less than 3 pct.

Thermal analysis and incipient melting methods were used to determine solidus curves and eutectic horizontals in this system. The data from this work are included in Table IV.

Discussion of the Literature

Phase diagrams of the Zr-Cr system have been published by Hayes et al.⁴ and McQuillan.⁵ The former authors extended their investigation from zirconium to ZrCr_2 , while McQuillan presented the

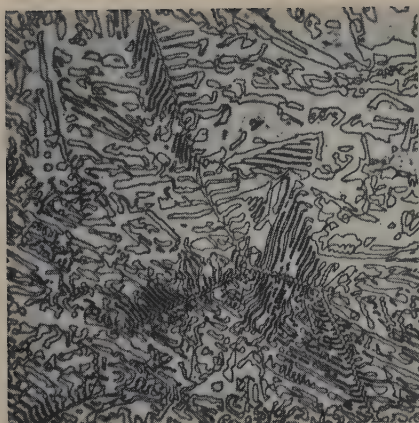


Fig. 4 (left)—19.1 pct Cr alloy employed for thermal analysis. β -ZrCr₂ eutectic. Etchant: electrolytic K₃Fe(CN)₆ + NaOH + H₂O. X500.

Fig. 5 (right)—4.4 pct Cr alloy quenched after annealing at 1300°C. Retained β . Etchant: 20 pct HF, 20 pct HNO₃ in glycerine. X150.

Fig. 6 (left)—4.7 pct Cr alloy quenched after annealing at 1300°C. Retained β + signs of incipient melting. Etchant: electrolytic K₃Fe(CN)₆ + NaOH + H₂O. X250.

Fig. 7 (right)—0.81 pct Cr alloy quenched from 950°C. Transformed β . Etchant: 20 pct HF, 20 pct HNO₃ in glycerine. X500.

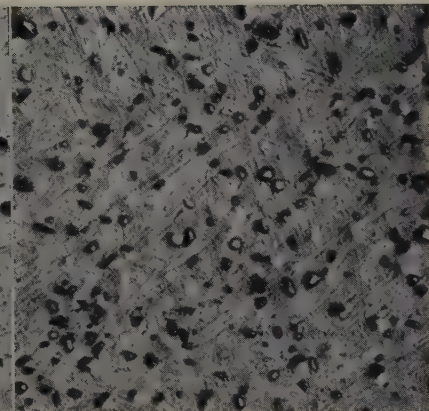
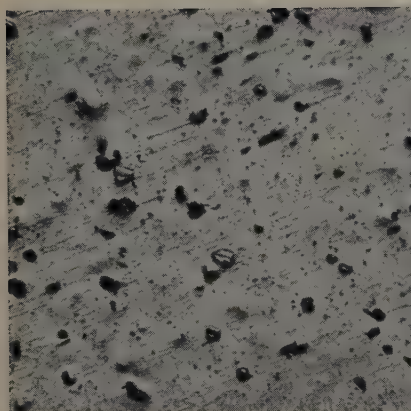
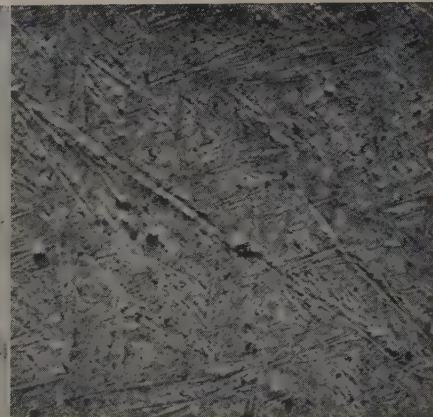
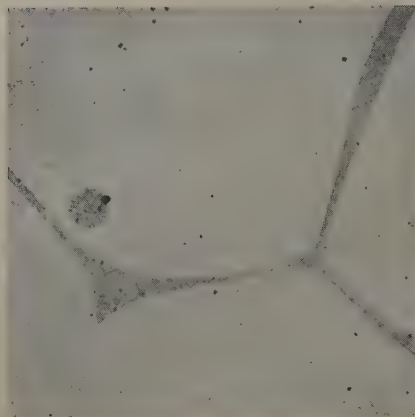


Fig. 8 (left)—1.5 pct Cr alloy quenched from 950°C. Transformed β + ZrCr₂ crystals. Etchant: 20 pct HF, 20 pct HNO₃ in glycerine. X500.

Fig. 9 (right)—1.5 pct Cr alloy quenched from 840°C. Transformed β + ZrCr₂ structure. Etchant: 20 pct HF, 20 pct HNO₃ in glycerine. X500.

Fig. 10 (left)—1.5 pct Cr alloy quenched from 830°C. Isothermal α + ZrCr₂ structure. Etchant: 20 pct HF, 20 pct HNO₃ in glycerine. X500.

Fig. 11 (right)—0.28 pct Cr alloy quenched from 820°C after annealing for 360 hr. α + ZrCr₂ structure. Etchant: 20 pct HF, 20 pct HNO₃ in glycerine. X500.

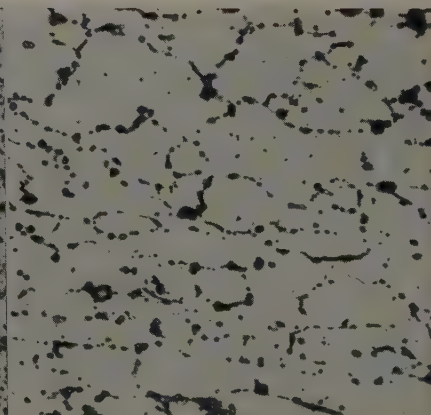
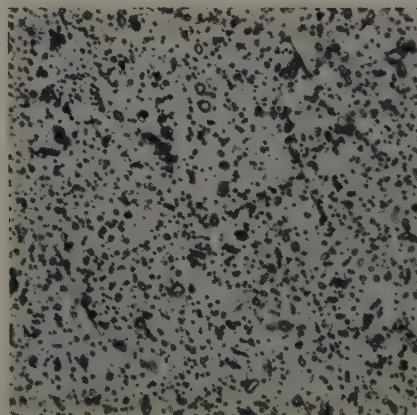
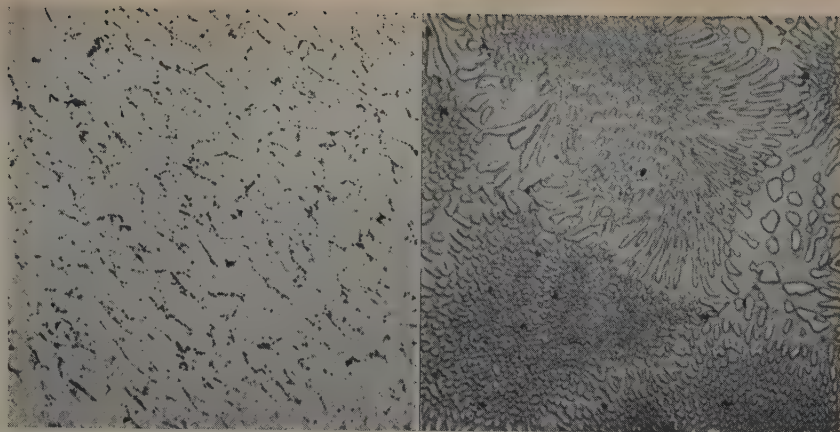


Fig. 12 (left)—53.1 pct Cr alloy, as-cast. Nearly single phase $ZrCr_2$. Etchant: electrolytic $K_3Fe(CN)_6 + NaOH + H_2O$. X200.

Fig. 13 (right)—69.5 pct Cr alloy used for thermal analysis work. The $ZrCr_2$ -Cr eutectic. Etchant: electrolytic $K_3Fe(CN)_6 + NaOH + H_2O$. X750.



entire diagram. The general features of these two diagrams may be summarized as follows:

Hayes et al.: 1—Zr- $ZrCr_2$ eutectic at 18 pct Cr and 1380°C. 2—Maximum solubility of chromium in β zirconium, 6.2 pct at 1380°C. 3—Eutectoid $\beta \rightleftharpoons \alpha + ZrCr_2$ at 1.8 pct Cr and 805°C. 4—Negligible solubility of chromium in α zirconium. 5—Intermediate phase $ZrCr_3$, melting at 1525°C. Crystal structure: cubic $MgCu_2$ type, $a = 7.21\text{\AA}$.

McQuillan: 1—Single intermediate phase at 48 pct Cr, formed by the peritectic reaction $L + \beta \rightleftharpoons C$ at 1650°C. 2—Solubility of chromium in β zirconium decreasing sharply from about 48 pct at 1650°C to about 5 pct at 1350°C, then gradually to about 2 pct at 835°C. 3—Eutectoid: $\beta \rightleftharpoons \alpha + C$ at 2 pct Cr and 835°C. 4—Very limited solubility of chromium in α zirconium. 5—Eutectic between the intermediate phase and chromium solid solution at 70 pct Cr and about 1545°C. 6—Solubility of zirconium in chromium less than 2.6 pct at the eutectic temperature.

Comparing the features established in this work with the literature it may be seen that Hayes et al. and the present authors are in agreement on the general constitution of the zirconium-rich region, whereas McQuillan has determined a greatly different set of phase relationships. The present work, however, agrees with McQuillan that the intermediate phase and the chromium-rich solid solution form a eutectic. To a certain extent, differences in the results may be attributable to the use of different zirconium stock in the three programs. Hayes et al. and McQuillan used magnesium-reduced zirconium metal while the present work is based on alloys prepared with higher purity iodide crystal bar.

Summary

The Zr-Cr phase diagram was carefully determined to 50 atomic pct Cr. A limited amount of work was done to outline the rest of the system. The alloys prepared for this study were melted and

annealed under protective atmospheres to prevent contamination. The principal features of the diagram include:

1—The limit of solubility of chromium in β zirconium is 4.5 pct.

2—A eutectic occurs between β and $ZrCr_2$ at 18 pct Cr and $1280^\circ \pm 10^\circ\text{C}$.

3—A single intermediate phase exists in the system, at 53 pct Cr, corresponding to the formula $ZrCr_2$. This phase melts with an open maximum at $1700^\circ \pm 25^\circ\text{C}$.

4—A eutectoid decomposition of β into $\alpha + ZrCr_2$ occurs at $835^\circ \pm 10^\circ\text{C}$ and 1 ± 0.25 pct Cr.

5—The solubility of chromium in α zirconium is less than 0.28 pct at all temperature levels.

6—A eutectic occurs between $ZrCr_2$ and chromium-rich solid solution at 70 pct Cr and $1635^\circ \pm 15^\circ\text{C}$.

7—The maximum solubility of zirconium in chromium is less than 3 pct.

Acknowledgments

The authors wish to thank the Atomic Energy Commission, sponsors of this work under Contract No. AT(11-1)-149, "Phase Diagrams of Zirconium-Base Alloys," for permission to publish this paper. Special thanks are due to C. E. Lundin who supervised the preparation of alloys, C. A. Johnson who was responsible for the metallographic work, and W. Rostoker for interpretation of the X-ray patterns.

References

- ¹D. J. McPherson and M. Hansen: ASM Preprint No. 34 (1952).
- ²C. E. Lundin, D. J. McPherson, and M. Hansen: ASM Preprint No. 41 (1952).
- ³R. F. Domagala, D. J. McPherson, and M. Hansen: *Trans. AIME* (1953) **197**, p. 73; *JOURNAL OF METALS* (January 1953).
- ⁴E. T. Hayes, A. H. Roberson, and M. H. Davies: *Trans. AIME* (1952) **194**, p. 304; *JOURNAL OF METALS* (March 1952).
- ⁵M. K. McQuillan: Commonwealth of Australia, Dept. of Supply, Aeronautical Research Laboratories Report SM-165 (January 1951).
- ⁶H. J. Wallbaum: *Naturwiss.* (1942) **30**, p. 149.
- ⁷M. Hansen, H. D. Kessler, and D. J. McPherson: *Trans. ASM* (1952) **44**, p. 518.
- ⁸R. Vogel and W. Tonn: *Ztsch. anorg. allgem. Chem.* (1931) **202**, p. 293.

Addendum

Since this paper was submitted, an allotropy has been established for the phase $ZrCr_2$, which involves both the structures reported in this paper and by Hayes, Roberson, and Davies. Details of the allotropy are discussed by W. Rostoker in TN 148E, this issue, p. 304.

Table IV. Melting Range Determinations for the Zr-Cr System

Alloy No.	Wt Pct Cr	Thermal Analysis Arrests, °C	Incipient Melting	
			Melting Observed, °C	No Melt-ing, °C
Zr	0		1852	
YZR 2-404	1.5		1603	1525
YZR 5-407	4.7		1610	
XZR 10-742	9.5	1280		
YZR 18-601	17.6		1295	1265
XZR 18-743	19.1	1280		
XZR 35-744	34.3	1500...1280		
XZR 53-745	52.6	1700		
XZR 70-746	69.5	1635		

Kinetics of Thermal Reorientations in Cold Rolled Zirconium

by R. K. McGeary and B. Lustman

Orientation relationships and rates of annealing of 97 pct cold rolled zirconium have been studied by X-ray techniques, metallography, and by hardness measurements. The process of annealing occurring by the formation of domains, and their subsequent growth without recrystallization, is demonstrated.

NUMEROUS investigators¹⁻⁵ have revealed subgrain formation after annealing cold worked metal single crystals and have generally described the results in terms of a dislocation mechanism of polygonization.^{5, 6} In heavily cold rolled polycrystalline aluminum the first stages of heating cause an apparently spontaneous subdivision of regions of the deformed matrix into a great number of slightly disoriented domains followed or accompanied by rapid growth of certain domains to form a recrystallization texture.^{7, 8}

In the present investigation the isothermal rate of annealing of cold worked polycrystalline zirconium has been studied by X-ray techniques, metallography, and by hardness measurement. It will be shown that, rather than by the usual nucleation and growth mechanism,⁹⁻¹² the process of annealing can best be explained by the formation of domains early in the annealing treatment and the subsequent growth of these domains without recrystallization.

Experimental Procedure

All the experimental work was performed on an arc-melted ingot of high purity zirconium crystal

R. K. McGEARY and B. LUSTMAN, Members AIME, are associated with the Atomic Power Div., Westinghouse Electric Corp., Pittsburgh.

Discussion on this paper, TP 3454E, may be sent, 2 copies, to AIME by April 1, 1953. Manuscript, Aug. 21, 1952. Los Angeles Meeting, February 1953.

bar made by Westinghouse in a production scale deBoer unit. The weight percentage of impurities in the zirconium were as follows: C, 0.04; Fe, 0.05; Hf, 0.014; W, 0.01; Ti, Ni, and Al, 0.003; Si and N, 0.002; Cr and Cu, 0.001. Metallographically the zirconium showed only a single phase. The 4 in. diam ingot was forged at 760°C to a 1½x3 in. plate and was then rolled at 760°C to 0.150 in. thickness and annealed at this temperature for 20 min to produce an equiaxed grain structure of about 0.1 mm average grain diameter. The hot rolled plate was roller-leveled, surface ground to 0.135 in., cold rolled 83 pct reduction in thickness on a two-high mill, and then to a total reduction of 97 pct on a Sendzimir mill. The 0.004 in. strip material so produced received no subsequent mechanical treatment.

Specimens 5/8 in. square were sheared from the rolled strip and isothermally annealed at 10⁻⁵ mm Hg in an all glass vacuum system equipped with a Vycor furnace tube. The temperature data presented are the average temperatures during the runs and did not vary more than about ±3°C.

X-ray Diffraction Methods: When zirconium is drastically cold rolled, a high degree of preferred orientation results in which prism poles, {10 $\bar{1}$ 0}, are perpendicular to the rolling direction. After fully annealing this material an entirely new texture develops which corresponds to a 20° or 40° rotation of the deformation texture about hexagonal axes of



Fig. 1 — $\{10\bar{1}0\}$ pole figure for zirconium cold rolled 97 pct. Circle over cross indicates ideal orientation for $36 \pm 2^\circ$ rotation about R. D.

the annealing texture. In the present work the decrease in transmitted X-ray diffraction intensity from the prism poles perpendicular to the rolling direction has been used as a measure of the rate of thermally induced reorientation in specimens heated at various temperatures for various times. Likewise, for the same series of specimens, the increase of $\{10\bar{1}0\}$ intensity from a low value in the cold rolled

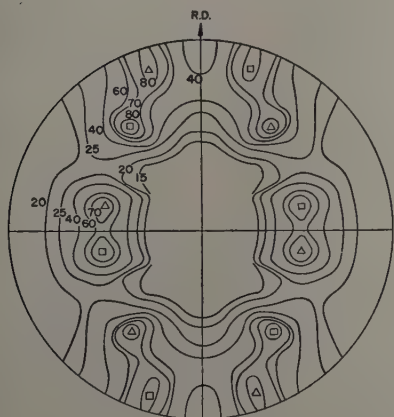
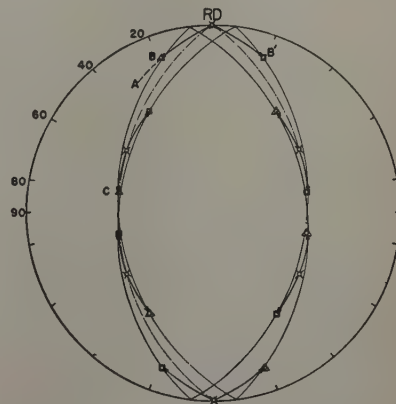


Fig. 2 (left) — $\{10\bar{1}0\}$ pole figure for specimen used for Fig. 1 after annealing at 600°C for 1 hr. Two crystallographically equivalent orientations are represented by the triangle and square symbols.

Fig. 3 (right) — $\{10\bar{1}0\}$ pole figure representing the ideal cold rolling and annealing textures for zirconium. Circle over cross indicates ideal cold rolling texture; triangle and square, the two ideal annealing textures. Heavy lines represent 20° rotations about $\{0001\}$ axes (which are rotated 7° about center of pole figure).



condition to a maximum in the fully annealed condition, for an orientation corresponding to a maximum on the pole figure of fully annealed material, has been used as a measure of the rate of formation of the annealing texture.

A General Electric Geiger counter X-ray spectrometer was used to measure the counting rate of the transmitted $\{10\bar{1}0\}$ diffracted intensity for all the heat treated specimens. This method is similar to that used by Decker and Harker,¹³ and Seymour and Harker,¹⁴ except that transmitted intensity rather than the reflected intensity is measured. In addition $\{10\bar{1}0\}$ pole figures for cold rolled and for fully annealed zirconium were determined.

The final thickness of the rolled strip was chosen as 0.004 in. because for molybdenum radiation the absorption correction due to variable irradiated volume of material^{15, 16} did not vary by more than 2 pct and could therefore be neglected for the 55° of rotation angles used. Therefore, the pole figures could be determined by the transmission method alone without the necessity for making absorption corrections. Counting rates for all of the experimental work in this report are quantitatively comparable since the counting rate was calibrated periodically with a standard sample. Not all of the area

of the pole figures was determined; the symmetry of the figures was established by counting rate measurements for 5° interval rotations of the specimen about an axis perpendicular to the rolling plane of the specimen (corresponding to β or azimuthal angles in the pole figure) from a northeast to a southwest direction, and for 5° interval rotations of the specimen about axes in its own plane (corresponding to α or radial angles from the circumference toward the center of the pole figure) from 0° to 55° from the circumference. The high intensity maxima regions of the pole figures were determined more accurately by 1° or 2° α and β rotations.

Two sets of data were obtained on the heat treated specimens: 1—a decrease from the maximum intensity in the cold rolled condition to a minimum in the fully annealed condition, indicating the decrease in the amount of the old texture; and 2—an increase from minimum intensity in the cold rolled condition to a maximum in the annealed condition, indicating the amount of the new texture formed from the old. The orientation of the specimens with respect to the X-ray beam for these two experimental conditions will be apparent after presentation of the pole figure results in the next section. For heat treated specimens with an average

grain diameter greater than about 10 microns, the X-ray results were erratic, so that a device was used to scan a $\frac{1}{2} \times \frac{1}{4}$ in. area of the specimen. It was experimentally ascertained that satisfactory integrated intensity readings were obtained by using a 0.1° slit to define the X-ray source beam width and a 0.4° slit at the counter. A Soller slit was used to eliminate vertical divergence of the incident beam and

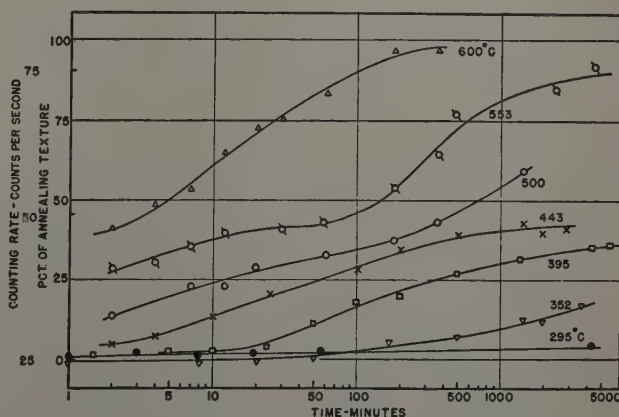


Fig. 4—Isothermal annealing curves for zirconium. Represents increasing X-ray intensity due to formation of annealing texture.

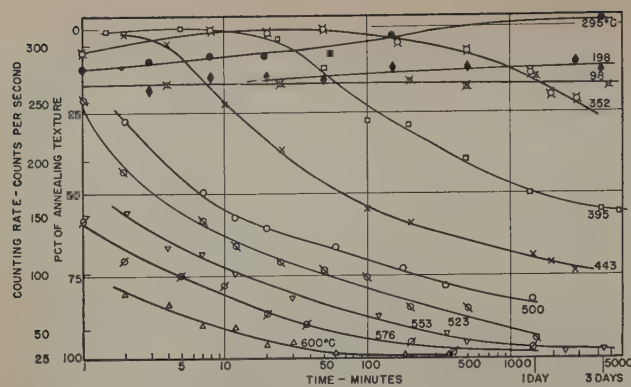


Fig. 5—Isothermal annealing curves for zirconium. Represents increasing X-ray intensity due to perfection of deformation texture and decreasing intensity due to formation of annealing texture.

another Soller slit was used between the 0.4° slit and the Geiger tube to minimize the vertical divergence of the diffracted beam.

Metallographic Techniques: The flat surfaces of the specimens were polished to about half thickness for metallographic examination. All micrographs were taken at 1000X or 1440X. Specimens with the smallest grain sizes had a highly oriented texture and the orientation differences between individual grains were so small that polarized light techniques were not satisfactory. An etching technique was developed in which the degree of surface staining of individual grains was sensitive to the slight existent orientation differences, and the grains were thus observable under bright field illumination. For those heat treated specimens in which some reorientation had occurred, longer immersion in the etchant produced an increasingly clearer delineation of the grain boundaries. The etching technique was as follows: 1—immerse specimen about 10 sec in a solution of 49 pct water, 49 pct nitric acid, 2 pct hydrofluoric acid to obtain a chemically polished surface; 2—etch in a solution of 75 pct glycerine, 23 pct nitric acid, 2 pct hydrofluoric acid for a time sufficient to give the desired staining. Because of the extremely small grain size of many of the specimens an accurate estimation of the grain size was impossible and has not been reported. Accurate grain sizes were obtained for most specimens by counting the grains (40 to 500) in a representative area of the micrographs.

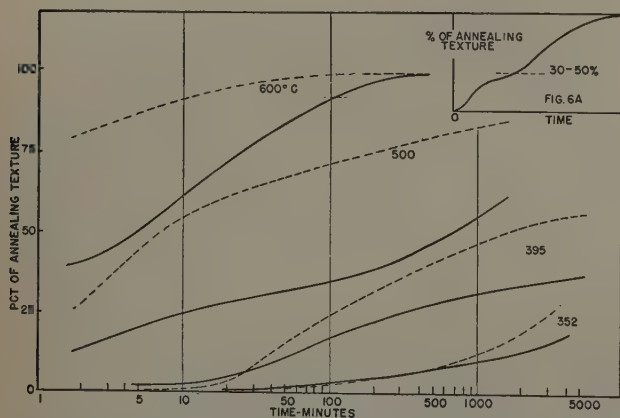


Fig. 6—Isothermal annealing curves for zirconium. Solid lines represent data presented in Fig. 4 and dotted lines that presented in Fig. 5. Fig. 6A is schematic representation of full shape expected for all curves.

Vickers hardness measurements were made with a Tukon tester on the polished edges of all of the specimens using a 100 g load.

Experimental Results

Orientation Relationships: The prism plane $\{10\bar{1}0\}$ pole figure data give the most satisfactory and complete description of the angular relationships of the texture change when cold rolled zirconium is annealed, so that the pole figures for this reflection only have been included.

In previous qualitative texture determinations of zirconium¹⁷ no asymmetry of the pole figures for surface and for inside layers of straight rolled material was found. Likewise, in the present quantitative work no pole figure asymmetry was detected. The last 14 pct of the total 97 pct of reduction on the Sendzimir mill entailed a reversal of the rolling direction of the strip between passes.

A $\{10\bar{1}0\}$ pole figure of the 97 pct cold rolled zirconium is shown in Fig. 1. A pole figure for this material after 83 pct cold rolling differed only in the sharpness of the final texture. The qualitative pole figure determination in the previous investigation¹⁷ is in fundamental agreement with the present results. However, in Fig. 1 all of the six intensity maxima have been resolved and the average rotation of the prism poles about the rolling direction has been established as $36^\circ \pm 2^\circ$ (indicated by the cross symbols in Fig. 1) instead of the approximate 30° rotation previously reported. The small degree of scatter about the transverse direction and the greater degree of scatter about the rolling direction are apparent.

In Fig. 2 is shown the $\{10\bar{1}0\}$ pole figure for the cold rolled zirconium heated so as to produce an annealing texture. This result also is in general agreement with the previous qualitative texture determinations where it was indicated that the "recrystallization" texture could be derived from the cold rolled texture by a 30° rotation about the hexagonal pole figure axes. However, instead of six intensity maxima on the pole figure as previously found, there are six pairs of intensity maxima. One set of the pairs is indicated by triangular symbols and the other set by square symbols in Fig. 2. Annealing of 83 pct cold rolled zirconium produces similar results.

In Fig. 3 all points for the intensity maxima of the pole figures shown in Figs. 1 and 2 have been superimposed to demonstrate that the ideal annealing texture can be related to the ideal cold rolled texture by 20° or 40° rotations about hexagonal axial positions for the annealing texture. The heavy lines emanating from the cross symbols (cold rolled orientation) represent 20° rotations. In the one case 20° clockwise rotations give rise to the square symbols (all of which lie on a line rotated 36° about the rolling direction and counterclockwise 7° about the center point). Counterclockwise rotations of 20° give rise to the triangular symbols (all of which lie on a line rotated 36° about the rolling direction and counterclockwise 7° about the center point). Consequently the angle between any two points shown is about 20° .

Kinetics of Orientation Changes: The temperature dependent rate of change of the orientation has been determined by direct measurement of the intensity of the diffracted X-ray beam for all heat treated specimens. The intensity measured by the

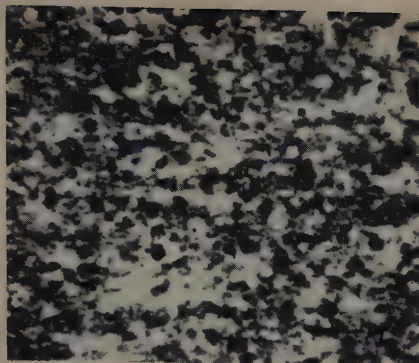


Fig. 7 (left)—Zirconium cold rolled 97 pct and heated at 395°C for 24 min. Shows complete recrystallization "in situ" structure. Slight orientation differences between individual domains revealed by selective staining and bright field illumination. X1440. Area reduced approximately 75 pct for reproduction.

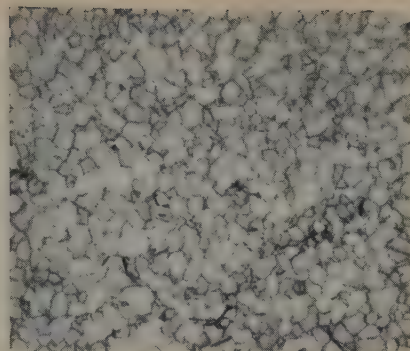


Fig. 8 (right)—Zirconium cold rolled 97 pct and heated at 395°C for 96 hr. Average domain diameter about 2 microns; approximately 55 pct of material has reoriented in the annealing texture. Grain boundary attack by etchant; bright field. X1440. Area reduced approximately 75 pct for reproduction.

Geiger counter located at the proper 2θ angle to receive the $\{10\bar{1}0\}$ diffracted beam was assumed to be proportional to the amount of the particular texture present. In Fig. 4 the rate of growth of an annealing texture from the cold rolled texture, determined by the method described, is shown. The specimens were situated in such a manner that the counting rates at point C on the pole figure of Fig. 3 were obtained. The intensity for this position was low in the cold rolled condition and a maximum in the fully annealed condition. Therefore, ordinate values are shown for both the measured counting rates and for the volume percentage of annealing texture formed. The latter values are calculated assuming that the rate of change of the volume of material in an orientation corresponding to that at point C is the same as that at every other point of the pole figure, and also that counting rate is proportional to the volume.

Counting rates measured for a specimen position corresponding to the cross symbol RD of Fig. 3, (prism planes perpendicular to the rolling direction) are shown in Fig. 5. An initial increase in the counting rate to a maximum at a rate dependent on time and temperature is apparent. The counting rates for the 98°C annealing are identical with the value for the as cold rolled zirconium, but the 198° and 295°C anneals indicate an increase in intensity, or degree of perfection, of the cold rolled texture. At still higher temperatures this maximum intensity is attained in shorter times before the intensity decrease due to gross reorientation takes place. The ordinate values for percentage of annealing texture in Fig. 5 were therefore chosen using as a zero the maximum value of the counting rates. Therefore, this ordinate does not apply to the initial increasing portions of any of the curves.

Corresponding curves for several of the temperatures plotted in Figs. 4 and 5 are replotted in Fig. 6. The dotted lines indicating the decrease in intensity of the cold rolled texture have been inverted so as to be comparable to the solid lines indicating the increase of the annealing texture. It is immediately apparent that there is no appreciable formation of the annealing texture during the period when an increase of sharpness of the cold rolling texture occurs. This plot shows further that not every volume of material leaving the old texture is immediately accounted for in the annealing texture, or else the two curves for a given temperature would superimpose.

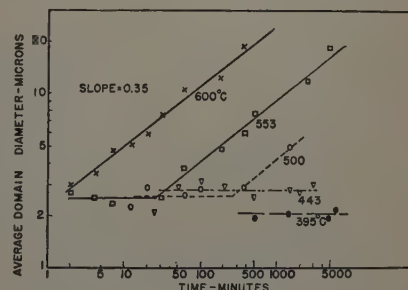
It is suggested that if the full extent of the curves of Fig. 6 were known they would show a double continuous and successive S-shape as indicated

schematically in Fig. 6a. The solid 500°C curve of Fig. 6 illustrates the typical shape expected; the shape of the 600°C curves are an example of what the 500°C curves may look like in the third and succeeding cycles of time, and the 395°C curves illustrate what the 500°C curves may look like in cycles of time less than that shown. This is significant because it will be shown below that grain growth in zirconium occurs at times corresponding to the junction of the two sigmoids. The final increase in the rate of annealing texture formation associated with the second sigmoid of the solid curves is seen to occur also only after about 40 pct formation of the annealing texture regardless of the temperature of the annealing.

Metallographic Observations: Figs. 7 and 8 are micrographs of the two specimens annealed at 395°C for 24 min and 96 hr, respectively. The former corresponds to a stage in the curves of Fig. 5 at which the sharpening of the cold rolled texture has reached a maximum; the orientation differences between individual "grains" or domains (2 microns average diameter) are so small that their boundaries are not clearly delineated. In the case of the latter specimen, formation of the annealing texture is approximately 40 pct complete. For specimens heated for successively longer times orientation differences between the individual domains become more pronounced and the domain boundaries are attacked by heavier etching (Fig. 8) so that the grain size can then be accurately measured. The results of these measurements reproduced in Fig. 9 indicate that there is no appreciable grain growth during the annealing times employed at 395°C. This fact is also apparent in a qualitative way by direct comparison of Figs. 7 and 8. However, grain growth may be noted to occur at times and temperatures corresponding to formation of more than 40 pct of the annealing texture or corresponding to the second sigmoid in Fig. 4.

When domain growth does occur it can be expressed for all temperatures by the usual relation-

Fig. 9 — Isothermal domain growth curves for 97 pct cold rolled zirconium. Initiation time of domain growth corresponds to about 40 pct reorientation to the annealing texture.



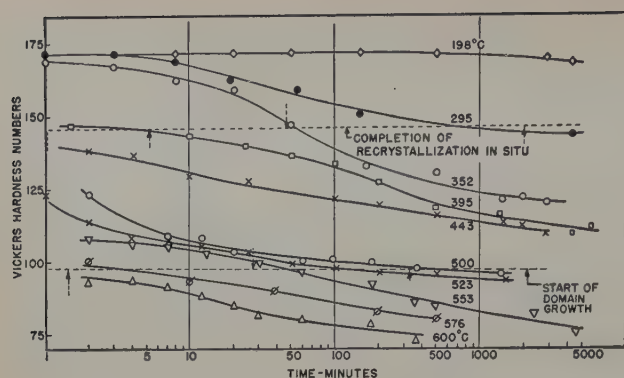


Fig. 10—Hardness decrease curves for isothermal annealing of 97 pct cold rolled zirconium.

ship for isothermal grain growth in pure metals:

$$D = Kt^n$$

where D is the average domain diameter attained in time t ; K , a temperature dependent constant; and n , a constant. Evaluation of the slope of the lines in Fig. 9 gives a value of 0.35 for the constant n . The results of Dunkerley, Pledger, Damiano, and Fulton,¹⁸ for apparently essentially randomly oriented zirconium, in which the second phase was agglomerated in large particles at grain boundaries by annealing prior to the grain growth measurements, give a value of 0.39 for n . The results of Dunkerley et al. give an activation energy for grain growth of 55,000 cal per mol and the present results a value of about 70,000 cal per mol. The difference in activation energies may be caused by differences in purity of the materials and the degree of preferred orientation.

Hardness: The mechanical hardness data of the heat treated specimens are plotted as a function of time at temperature in Fig. 10, and as a function of temperature for 10, 100, and 1000 min of heating in Fig. 11. In Fig. 10 the short, vertical dashed lines indicate the time at the particular temperature for the completion of the sharpening of the cold rolled texture (peak of the curves of Fig. 5) and the upper, dashed horizontal line the average hardness level at which this process occurs. The lower set of vertical lines indicates the times at which domain growth commences (see Fig. 9) and the lower, horizontal dashed line the average hardness level at which such grain growth occurs. Thus, although the shapes of the curves in Fig. 11 appear to be similar to recrystallization curves involving a nucleation and growth process, it is quite apparent that the changes

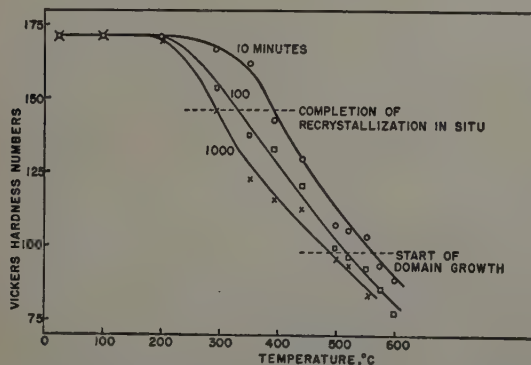


Fig. 11—Hardness decrease curves for 10, 100, and 1000 min of isothermal annealing.

in hardness do not reflect the elementary processes occurring during the annealing of zirconium. For example, the samples appear to be completely recrystallized metallographically after only about 25 pct loss in initial hardness and lose about 75 pct of their initial hardness before grain growth occurs.

Discussion of Results

Formation of "Recrystallization in Situ" Texture: The first stages of recrystallization have been described in terms of the dislocation mechanism of polygonization^{5, 6} in which edge-type dislocations perpendicular to curved slip planes accumulate during annealing leaving a multitude of minute stress-free, unbent regions with essentially the same overall range of orientation as existed in the deformed crystal. With extended annealing certain subgrains grow at the expense of less favorably oriented subgrains and approach an orientation identical to the original orientation of the crystal. The first stage in this process has been termed polygonization and the second "recrystallization in situ"¹⁹ and this terminology has been adopted here.

Since the first stage of the polygonization mechanism is pictured as a fine scale subdivision of the undulated slip planes, a gross change of orientation of the material would not be expected. In the case of zirconium the phenomenon first observed is a gradual sharpening of the cold rolled texture. Only after this process is well along do domains of two microns average diameter appear metallographically and therefore the appearance of these domains is to be associated with recrystallization in situ rather than with the polygonization stage. This evidence suggests that some selective domain growth, corresponding to this maximum ideal orientation condition, has occurred. In the case of heavily cold worked aluminum²⁰⁻²² polygonization is partially complete at the deformation temperature with the formation of domains averaging 2 microns in diameter, and annealing causes a relatively stable state of coarse polygonization, or recrystallization in situ. Some unpublished results of Kulin and Bostrom²³ on electrical resistivity changes in severely deformed zirconium as a function of time at low temperatures indicate that processes occur at temperatures even lower than those used in this work, in fact even at room temperature. These processes are associated with the stages preceding recrystallization in situ and are presumably polygonization or other recovery mechanisms. The methods employed in the present investigation were not capable of detecting any processes preceding the stage known as recrystallization in situ.

Annealing Texture Formation Without Domain Growth: In heavily rolled polycrystalline aluminum, Beck and Hu¹² have metallographically observed domains about 2 microns in diameter after short time, low temperature annealing. These domains did not grow appreciably at the lower annealing temperatures, but at higher temperatures domain growth occurred and the slight orientation differences between domains became more clear cut and the pole figure scatter areas also became sharper. However, during domain growth, consumption of the polygonized domains by rapidly growing grains of an entirely different local orientation (cube texture) occurred.

With continued low temperature annealing of zirconium the X-ray data indicate a gross reorientation from the recrystallization in situ texture to the

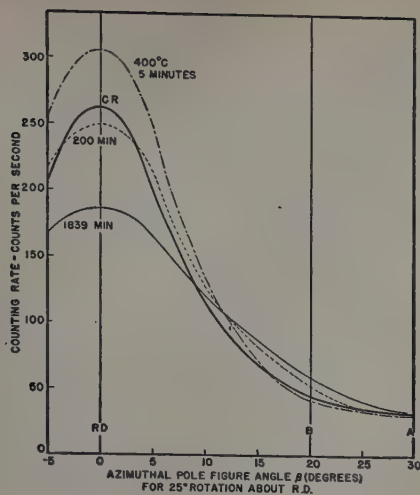


Fig. 12—Changes in integrated X-ray intensity for 97 pct cold rolled zirconium caused by reorientation produced by annealing at 400°C. Measurements correspond to the path A-B-RD-B'-A' shown in Fig. 3.

new annealing texture. However, contrary to the case cited for aluminum, this reorientation takes place initially without any apparent grain growth.

Since no large grains are apparent in any of the micrographs of the annealed zirconium specimens (see Fig. 8), the growth mechanism by which the annealing texture is formed from the recrystallization in situ texture without an increase in average domain size is obscure. In order to ascertain if some larger grains actually were growing at the expense of smaller grains, a certain representative area of an enlargement of Fig. 8 (2 micron average grain diameter, 37 pct annealing texture) was cut up along the grain boundaries and each of the 138 pieces so produced was weighed on a balance. From these measurements average grain diameters were calculated and a frequency plot of grain diameters was made. The distribution was skewed toward small diameters and showed no definite evidence of discontinuous grain growth. The 338 grains in a micrograph of the specimen heated at 553°C for 180 min (5 micron average grain diameter, 55 pct annealing texture) gave similar results. Even for the fully annealed specimens with a complete annealing texture there is no evidence that discontinuous grain growth had occurred.

It is well known that impurities, as well as a high degree of preferred orientation, can inhibit grain growth. The period of no domain growth shown in Fig. 9 could be considered as an induction period during which the mitigating effect of impurities on domain boundary mobility is preponderant. Unfortunately, from the present experiments it is impossible to ascertain which factor, or combination of the factors, is responsible for the inhibition of domain growth. However, the present results for zirconium are believed to be similar to those of Beck and Hu,⁷ who observed no appreciable growth of the domains after recrystallization in situ of deformed aluminum even at temperatures sufficient to cause recrystallization to the cube texture. Dunkerley et al.¹⁸ observed similar induction periods in studies of grain growth in zirconium, but this behavior could be associated with the manner of impurity distribution alone since there was no evidence of a high degree of preferred orientation in their specimens.

A further attempt to understand the enigmatic gross reorientation without apparent domain growth involved the following experiment: A series of cold rolled specimens heated at 400°C were situated

with respect to the X-ray beam in such a manner that counting rate measurements were obtained at 1° or 2° intervals along the arc A-B-RD-B'-A' in Fig. 3 where A' and B' are positions similar to A and B on the arc. The slit system was identical with that used for the integrated intensity and pole figure measurements. From the results shown in Fig. 12 it is apparent that although the intensity increased near the ideal orientation for the 5 min heating time, it actually decreases at angles far from this orientation. In Fig. 13 are plotted the values:

$$100 \times \frac{I_t - I_{cr}}{I_{cr}}$$

for the various angles shown in Fig. 12 where I_t is the counting rate for a certain time of heating at 400°C at a given angle on the arc of Fig. 3, and I_{cr} is the corresponding value for the cold rolled condition. This is simply a representation of the percentage increase or decrease of the counting rate of a heated specimen with respect to the counting rate of a cold rolled specimen measured under identical

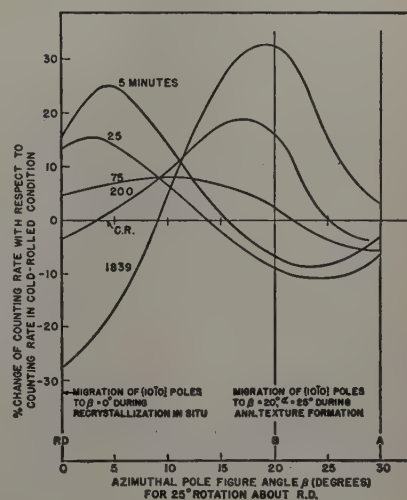


Fig. 13 — Quantitative changes in orientation shown in Fig. 12.

conditions. Polygonization alone would not be expected to account for the appreciable gross orientation sharpening apparent in Fig. 13 (for example, the Laue streaks for deformed single crystals have about the same range of orientation before and just after polygonization⁴). Again it would appear that in very short heating times (i.e. 5 min at 400°) some domains with orientations furthest removed from the ideal orientation are consumed by those closer in orientation to the ideal. Thus, the results of this experiment agree with those previously discussed.

Growth of a new orientation at an orientation corresponding to a maximum for the new texture formation is especially apparent in Fig. 13. Heating for 1839 min has caused about 33 pct of the volume of material to form in the new orientation even though the domain size is not appreciably greater than that for the specimen heated 25 min. A very large decrease in mechanical hardness was shown to occur during this stage of reorientation. The strain energy (hardness) is high after recrystallization in situ but low when domain growth starts. It must therefore be concluded that these domains are highly strained and that this strain energy is relieved only during a period of major change in crystal orientation un-

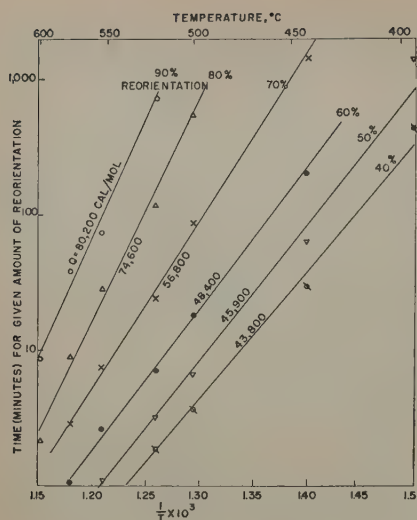


Fig. 14—Time for a given percentage decrease in X-ray intensity due to reorientation produced by isothermal annealing of 97 pct cold rolled zirconium.

accompanied by general nucleation or appreciable domain growth.

Annealing Texture Formation with Grain Growth: From the evidence that has been presented it is evident that the initial stages of annealing texture formation in zirconium are not explainable by the usual concepts of nucleation and growth since no change in grain size occurs. Even during the stage when grain growth does occur, the conventional nucleation and growth mechanism cannot explain the rate of annealing texture formation observed. If it did, the following equation derived by Johnson and Mehl,⁹ expressing the kinetics of general nucleation and growth of grains in a cold rolled matrix when heated so as to cause recrystallization, would be applicable:

$$f(t) = 1 - e^{-\frac{\pi}{8} NG^3 t^4}$$

where $f(t)$ is the fraction of the volume recrystallized in time t , and N and G are the rates of nucleation and growth, respectively. Straight lines are

obtained when $\log \log \frac{1}{1-f(t)}$ is plotted against \log

t ; the slope k is then equal to the power of t . For polyhedral growth in a highly deformed matrix where the rate of nucleation is great (mostly at the beginning of the transformation), a $k = 3$ dependence is predicted by this equation. Avrami¹⁰ has shown that for plate-like and acicular growth of grains a $k = 2$ and $k = 1$ dependence, respectively, would be expected. Decker and Harker¹⁸ have found in the case of primary recrystallization of copper, studied by the same X-ray method as employed in the present work, $4 > k > 3$ for the higher temperatures where polyhedral growth was suspected, and $3 > k > 2$ at lower temperatures where plate-like growth was suspected.

A similar plot of the present results for zirconium gives straight lines with a slope, or k value, of about 0.37 for all temperatures over ranges where at least 40 pct of the volume of the material has formed in the annealing texture; this is the range in which domain growth occurs. If activation energies are determined for this stage in the annealing process

by plotting \log time for given reorientation vs $1/T$ the curves of Fig. 14 are obtained. These curves indicate a continuous change in activation energy with increasing gross reorientation (and also increasing domain size). On the other hand, for copper and an iron-nickel alloy,^{18, 14} where the reoriented material is accounted for only by nucleation and growth of grains in the new orientation, a single activation energy has been found to express the total reorientation.

The almost twofold increase in activation energy from 40 to 90 pct reorientation is an indication that the environmental conditions during the reorientation process change continuously as reorientation occurs. The most obvious change in environmental condition occurring during this stage is domain growth. If the rate of annealing texture formation is assumed proportional to the grain size of the matrix, the equation given previously can be expressed as:

$$f(t) = 1 - e^{-ct^{3n}}$$

where c is a constant and n is the exponent expressing rate of grain growth in the equation $D = Kt^n$. Using the experimental value, $n = 0.35$, a power of t greater than unity would be expected; this is considerably different from the actual power of t obtained, namely 0.37.

In the case of copper¹⁸ and a nickel-iron alloy,¹⁴ the rate of change of the deformation textures and recrystallization textures are equal, but for zirconium a large difference in the two rates has been demonstrated (Fig. 6). In the former case, the recrystallized grains form only in the new texture with a time dependence consistent with the principles of primary recrystallization, but in zirconium the growth of grains in an annealing texture is microscopically indistinguishable from growth in the cold rolled texture.

Textures in Zirconium: The previous qualitative pole figures for the cold worked zirconium¹⁷ are in good agreement with those found in the present work as shown in Fig. 1. In the previous work it was shown that basal slip alone could not account for the cold rolled pole figure. Some recent work on titanium²⁴ indicates that basal slip is not operative in the deformation of single crystals of that material thus substantiating these previous observations on zirconium.

The pole figure for annealed zirconium shown in Fig. 2 is different from the qualitative pole figure previously reported¹⁷ in that the maxima are split into pairs, making an angle of approximately 20° with each other. It is suggested that, following Beck's theory,^{13, 25, 26} the grains formed on annealing may grow at an orientation showing maximum mismatch not only with the matrix but also with already formed neighboring grains of the new texture. Regarded from this point of view, the condition of maximum disorientation can be best met by effective 20° and/or 40° rotations. However, it might be expected that 60° cross rolled zirconium, which has a single texture, should also show 20°, 40° rotations, but recent work shows that only 30° rotations occur.

It was noted in the previous work on this subject¹⁷ that the hot rolling texture of zirconium is similar to the cold rolling texture rather than to the annealing texture. This same behavior has been noted in the

case of iron.²⁷ The observations described previously on recrystallization in situ afford a ready explanation for this fact. If it is assumed that during hot rolling recrystallization in situ occurs concomitant with the deformation, thus releasing part of the strain energy introduced by this working, then sufficient strain energy will not be stored in the matrix to permit the operation of further annealing processes, and a texture will result similar to the deformation texture rather than to the annealing texture.

Summary

1—Quantitative X-ray diffraction techniques have been used to (a)—determine $\{10\bar{1}0\}$ pole figures of 97 pct cold rolled zirconium, as rolled and as fully annealed, in order to establish the exact crystallographic relationships associated with the thermally activated texture changes that have been found to occur, and (b)—determine the rate of the reorientations for specimens heated for appropriate times at temperatures from 98° to 600°C.

2—Metallographic observations, hardness measurements, and other results have been correlated with the X-ray results and the following processes occurring during annealing have been identified: (a)—Polygonization may occur in zirconium during cold rolling or during the very first stages of heating. This polygonization is not accompanied by reorientation nor is it detectable metallographically. (b)—Recrystallization in situ (metallographic evidence of polygonization) occurs after annealing at relatively low temperatures and corresponds to a reorientation in which the ideal cold rolling texture is sharpened; this process may occur by selective growth of favorably oriented domains. (c)—Further annealing causes a complete reorientation corresponding to 20° or 40° rotations about $\{0001\}$ poles. This process occurs in two steps, the one at constant domain size, the latter accompanied by domain growth. Data have been presented to show that the processes do not occur by nucleation and growth of reoriented grains, nor by discontinuous growth of favorably oriented domains.

3—Activation energies for domain growth and for annealing reorientations have been calculated but are limited by conditions described in the text; a single activation energy cannot describe the reorientation process which is a further indication that a simple mechanism, such as nucleation and growth, does not govern the reorientation.

Acknowledgment

The work described in this paper was supported by AEC Contract AT-11-1-GEN-14. The authors wish to express gratitude to Raymond Boyle for the excellent quality of his considerable experimental assistance, G. F. Mechlin for guidance in the development of the X-ray techniques, and F. M. Cain and J. V. Miller for the development of the special metallographic techniques. Thanks are due W. A. Johnson, S. A. Kulin, and E. K. Halteman for advice and reading the manuscript.

References

- ¹ A. Guinier: Substructures in Crystals. N.R.C. Conference on Crystal Imperfections (1950).
- ² R. W. Cahn, A. Guinier, J. Tennevin, C. Crussard, F. Aubertin, B. Jaoul, and G. Wyon: *Progress in Metal Physics II* (Symposium on Polygonization). New York and London (1950).

- ³ P. A. Beck: Interface Migration in Recrystallization. Seminar, Metal Interfaces, ASM (1952).

- ⁴ C. G. Dunn and F. W. Daniels: Formation and Behavior of Subboundaries in Silicon Iron Crystals. *Trans. AIME* (1951) **191**, p. 147; *JOURNAL OF METALS* (February 1951).

- ⁵ R. W. Cahn: Recrystallization of Single Crystals after Plastic Bending. *Journal Inst. Metals* (1949) **72**, p. 121.

- ⁶ A. H. Cottrell: *Progress in Metal Physics*, Chapter 2. (1949) London.

- ⁷ P. A. Beck and Hsun Hu: Annealing Textures in Rolled Face-Centered Cubic Metals. *Trans. AIME* (1952) **194**, p. 83; *JOURNAL OF METALS* (January 1952).

- ⁸ P. A. Beck and P. R. Sperry: Strain Induced Boundary Migration in High Purity Aluminum. *Journal of Applied Physics* (1950) **21**, p. 150.

- ⁹ W. A. Johnson and R. F. Mehl: Reaction Kinetics in Processes of Nucleation and Growth. *Trans. AIME* (1939) **135**, p. 416; *METALS TECHNOLOGY* (August 1939).

- ¹⁰ Melvin Avrami: Kinetics of Phase Change. *Journal of Chemical Physics* (1939) **7**, p. 1103, and (1940) **8**, p. 212.

- ¹¹ J. K. Stanley and R. F. Mehl: Recrystallization of Silicon-Ferrite in Terms of Rate of Nucleation and Rate of Growth. *Trans. AIME* (1942) **150**, p. 260.

- ¹² W. A. Anderson and R. F. Mehl: Recrystallization of Aluminum in Terms of Rate of Nucleation and Rate of Growth. *Trans. AIME* (1945) **161**, p. 140.

- ¹³ B. F. Decker and D. Harker: Activation Energy for Recrystallization in Rolled Copper. *Trans. AIME* (1950) **188**, p. 887; *JOURNAL OF METALS* (June 1950).

- ¹⁴ W. E. Seymour and D. Harker: Recrystallization Reaction Kinetics and Texture Studies of a 50 Iron 50 Nickel Alloy. *Trans. AIME* (1950) **188**, p. 1001; *JOURNAL OF METALS* (August 1950).

- ¹⁵ B. F. Decker, E. T. Asp, and D. Harker: Preferred Orientation Determination Using a Geiger Counter X-ray Diffraction Goniometer. *Journal of Applied Physics* (1948) **19**, p. 338.

- ¹⁶ S. E. A. Beatty: Intensity Correction Factors for X-ray Spectrometer Transmission Pole Figure Determinations. Westinghouse Research Labs., Research Report R-94602-10-J (December 1949).

- ¹⁷ R. K. McGeary and B. Lustman: Preferred Orientation in Zirconium. *Trans. AIME* (1951) **191**, p. 994; *JOURNAL OF METALS* (November 1951).

- ¹⁸ F. J. Dunkerley, F. Pledger, V. Damiano, and J. Fulton: Grain Growth and Recrystallization Characteristics of Zirconium. *Trans. AIME* (1951) **191**, p. 1003; *JOURNAL OF METALS* (November 1951).

- ¹⁹ C. Crussard: Étude du Recuit de l'aluminium. *Rev. Metallurgie* (1944) **41**, pp. 111, 133.

- ²⁰ C. Crussard, F. Aubertin, B. Jaoul, and G. Wyon: *Progress in Metal Physics II*. (1950) p. 193. New York and London.

- ²¹ J. N. Keller, P. B. Hirsch, and J. S. Thorp: An X-ray Micro-Beam Examination of a Plastically Deformed Metal. *Nature* (1950) **165**, p. 554.

- ²² R. D. Heidenreich: Electron Microscope and Diffraction Study of Metal Crystal Texture by Means of Thin Sections. *Journal of Applied Physics* (1949) **20**, p. 943; also: Electron Transmission Through Thin Metal Sections. *Bell System Technical Journal* (October 1951).

- ²³ S. A. Kulin and W. Bostrom: Westinghouse Electric Co., private communication.

- ²⁴ F. D. Rosi, C. A. Dube, and B. H. Alexander: Mechanism of Plastic Flow in Titanium. *JOURNAL OF METALS* (February 1952) p. 145.

- ²⁵ P. A. Beck: Origin of the Cube Texture in Face-Centered Cubic Metals. *Trans. AIME* (1951) **191**, p. 474; *JOURNAL OF METALS* (June 1951).

- ²⁶ P. A. Beck: Theory of Annealing Textures. *Trans. AIME* (1951) **191**, p. 475; *JOURNAL OF METALS* (June 1951).

- ²⁷ M. Gensamer and P. A. Vukmanic: *Trans. AIME* (1937) **125**, p. 507.

Vanadium-Oxygen Solid Solutions

by A. U. Seybolt and H. T. Sumsion

The results of an investigation of vanadium-rich V-O solid solutions are presented, indicating the structure and lattice parameters of two solutions, α and β , and their approximate temperature-composition existence. The α solution is the terminal body-centered cubic one, and contains up to 3.2 atomic pct O. The β solution has an ordered body-centered tetragonal structure, is formed at 1270°C, and exists from about 15 to 22 atomic pct O. From the evidence available, the various phase boundaries have no appreciable temperature dependence. Evidence has been found for a polymorphic transformation in pure vanadium at 1550°C.

IN an earlier investigation¹ dealing with the preparation of pure vanadium by calcium reduction of the oxide, it was found that small amounts of oxygen drastically reduced the ductility of the metal. Because this effect was so marked, it was decided to make a study of the solubility of oxygen in solid vanadium. This report deals principally with this solubility and the nature of the phase relationships in the vanadium-rich region, particularly at temperatures below 1300°C. However, during the investigation enough data on the V-O system were obtained to make it appear worthwhile to present a tentative phase diagram up to the composition VO.

The only significant prior work found on this system are the contributions of Klemm and Grimm,² and Mathewson et al.³ Klemm and Grimm prepared a wide range of V-O compositions by powder techniques including the compositions VO_{0.1}, VO_{0.2}, VO_{0.3} and VO_{0.4} (9.1, 16.8, 23, and 28.6 atomic pct O, respectively). The first three compositions were found to consist of a body-centered tetragonal solid solution, while the last also showed lines of VO (NaCl structure). They found that the parameter c_0 increased and the parameter a_0 decreased with increasing concentration of oxygen. For their composition VO_{0.27}, or about 16.8 atomic pct O, they cite the values $a_0 = 2.948\text{\AA}$, $c_0 = 3.53\text{\AA}$, and $c/a = 1.2$. Klemm and Grimm made no attempt to determine the solid solubility limit nor to construct a phase diagram. They did, however, give some data on the homogeneity range of VO, and they proposed a

structure for the body-centered tetragonal solid solution; these points will be taken up later.

Materials and Preparation of Samples

The vanadium used in this investigation was prepared in the laboratory by the method previously mentioned.¹ A typical analysis is as follows: Fe, 0.007 pct; Si, 0.02; Ca, 0.06; C, 0.224; O₂, 0.044; N₂, 0.0017; H₂, 0.003; and V, 99.34 \pm 0.3 (assay). The vanadium assay is probably low by about the error given. The impurities total about 0.36 which, if subtracted from 100, gives a purity of about 99.6.

At the time material was being prepared for this work no suitable technique was available for melting vanadium without appreciable contamination. The procedure adopted therefore was to cut the calcium-reduced reguli into slices which were then rolled to strip about 0.025 in. thick for oxygen diffusion.

Pieces of rolled vanadium of approximately 0.025x $\frac{1}{4}$ x1 in. and weighing about 0.3 g were suspended in a vertical fused-silica tube which was part of an ordinary gas absorption apparatus. The silica tube was heated by an electric resistance-tube furnace which could be raised around the silica tube or lowered away from it as desired. This apparatus had no novel features which require detailed description. Other than the silica tube and furnace, it consisted of a glass system evacuated by a liquid nitrogen trapped mercury diffusion pump, a mercury-operated gas burette, a McLeod and a Pirani gage, and a mercury manometer. It was also equipped with suitably located stopcocks for isolating various parts of the system; the vacuum ordinarily attained was between 10⁻⁵ and 10⁻⁶ mm of mercury. Oxygen generated by decomposing MnO₂ was passed through anhydrous magnesium perchlorate before introducing it into the gas burette and thence to the absorption chamber.

A. U. SEYBOLT, Member AIME, formerly with Knolls Atomic Power Laboratory, is now associated with General Electric Research Laboratory, and H. T. SUMSION, Member AIME, is associated with Knolls Atomic Power Laboratory, General Electric Co., Schenectady.

Discussion on this paper, TP 3465E, may be sent, 2 copies, to AIME by April 1, 1953. Manuscript, Aug. 19, 1952. Los Angeles Meeting, February 1953.

Various V-O alloys up to about 20 atomic pct were prepared by vertically suspending the vanadium strips in the absorption apparatus at 900° to 1000°C and adding the oxygen gas a few cubic centimeters at a time. It was soon discovered that if a large quantity of gas was added at once, an oxide film was immediately formed on the surface of the metal which required a greater length of time for absorption into the sample than the same quantity of oxygen added a little at a time. After establishing the desired absorption temperature, about 4 cc of oxygen were added to the sample. This caused the pressure to rise to about 3 mm. When the pressure dropped again to the low micron region, it was evident that essentially all of the oxygen had been picked up by the specimen, either in solution or as a surface oxide or both. The time required for the sample to absorb this much oxygen was approximately 5 to 10 min. However, to give the oxygen a chance to diffuse throughout the sample, the sample was held for a period of at least 2 hr before adding the next increment of oxygen. About 12 cc of oxygen could be added per day, or in the neighborhood of 5 wt pct O₂ for a sample weighing 0.3 g. After the last oxygen addition, the sample was held for several hours at the diffusing temperature for further homogenization.

A diffusion constant D was calculated for oxygen diffusing into a vanadium sample at 900°C by making use of the observed drop in gas pressure as a function of time. Since a plot of grams of oxygen absorbed against the square root of time produced a straight line, the oxygen absorption was apparently diffusion-controlled. Then from the observed oxygen flux (grams absorbed into the sample per unit area per unit time) a diffusion constant was calculated where $D = 2 \times 10^{-7}$ sq cm per sec. This value must be regarded as a tentative one until a more precise experiment is carried out.

Samples containing 20 atomic pct O or more were prepared by arc melting vanadium and V₂O₅ in an argon atmosphere using an arc-melting furnace ordinarily utilized for the preparation of zirconium and titanium alloys. While this apparatus was satisfactory for preparing V-O alloys, it was not useful for melting pure vanadium because the melting atmosphere was not under sufficiently good control to avoid vanadium embrittlement by the absorption of small quantities of oxygen.

Many of the alloys were analyzed by vacuum fusion for oxygen content but it was obvious that the synthesis was more accurate than analysis. With oxygen contents of less than about 10 atomic pct, agreement between the amount of oxygen added volumetrically and the amount found gravimetrically was excellent. However, with higher oxygen contents there was usually considerable variance between the two, presumably because of cumulative errors in reading a large number of small volumes in the gas burette. In any case, the gain in weight was always used as the method of determining the oxygen present in the samples. Naturally, this method could not be used with the arc-melted samples; here it was necessary to rely on a chemical analysis for vanadium, taking oxygen by difference. Vacuum-fusion analyses could not be used with the oxygen-rich samples as the volume of gas from even a very small sample was too large to be collected and stored.

The diffusion method of sample preparation worked very satisfactorily, and there was no indication that

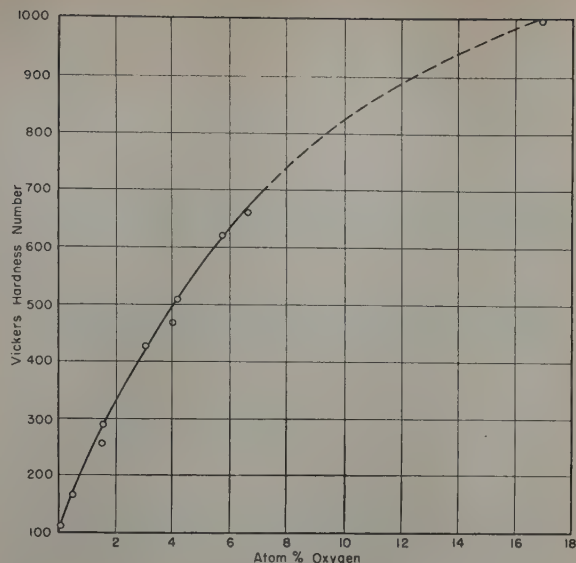


Fig. 1—Vickers hardness number vs atomic percentage of oxygen.

significant concentration gradients were present from the surface inward. Microhardness measurements taken across the thickness of samples and the general reproducibility of test results indicated satisfactory homogeneity. Any sample which showed a surface tarnish after the diffusion preparation was discarded as regards estimating composition. Invariably, however, samples prepared in the standard manner described above emerged from the gas absorption apparatus with a clean surface.

Hardness of V-O Alloys

Fig. 1 shows a plot of Vickers hardness number vs atomic pct O for alloys quenched from 900°C. Slow cooling the alloys instead of quenching them made only a few points difference (lower) in hardness. Vanadium containing more than approximately 0.05 wt pct O (about 0.15 atomic pct) is relatively unworkable or partially brittle at room temperature, but metal containing less than this amount of oxygen is very ductile unless otherwise contaminated.

X-Ray Diffraction Measurements

After examining a few 5.73 cm diam Debye X-ray diffraction films of various V-O alloys, it was clear that many of the alloys were body-centered tetragonal as claimed by Klemm and Grimm.² Also, a trend could be established in which the lattice parameter ratio c/a increased with increasing oxygen content, likewise in agreement with the findings of these authors.

While the X-ray diffraction method was very valuable in the investigation since considerable information was obtained, it turned out to be a tedious and inefficient technique because of the poor quality of films obtained. The only suitable X-ray targets for back-reflection lines were copper and nickel, with copper more generally satisfactory as regards line position for precision measurements of parameters. Unfortunately, copper and nickel radiation cause a large amount of vanadium fluorescent radiation, blackening the film and causing poor contrast. From theoretical considerations, the only target materials which would be free of this defect are titanium, chromium, or metals of lower atomic weight than titanium. A titanium target was not available. Chromium radiation produced no fluorescence and

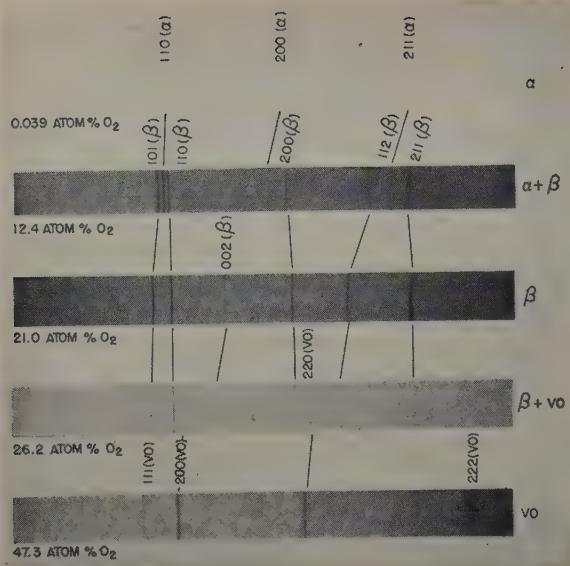


Fig. 2—Debye-Scherrer films of various V-O alloys. (Cr-K α radiation).

gave very good lines, but yielded an insufficient number of lines in the back-reflection region; it was used only for qualitative data, see Fig. 2.

Body-Centered Cubic Measurements: Parameters of body-centered cubic alloys were measured with a 12 cm diam back-reflection focusing camera, using lines of the (321) planes. Film shrinkage was corrected from measurements on fiducial marks. The parameters thus obtained and shown in Table I are considered to be accurate to at least 0.0005Å. Extrapolation methods could not be used with the V-O alloys because of too few lines, but the parameters of the two pure vanadium samples were obtained by 90° extrapolation using Cohen's method.⁴

The calcium-reduced metal used in the investigation gave $a_o = 3.0278 \pm 0.0001\text{Å}$ from an extrapolation of five points, and high purity iodide metal from Battelle Memorial Institute gave $a_o = 3.0258 \pm 0.0001\text{Å}$ on a comparable extrapolation but using only three back-reflection lines. This metal was prepared by the method of Nash et al.⁵ and has the following typical analysis: Fe, 0.07 pct; Al, 0.005; Si, 0.002; Cr, 0.002; O, 0.012; N, 0.008; and H, 0.005. The less precise values from measurement of the (321) planes as described above are reported in Table I in order to show values comparable to the V-O alloys.

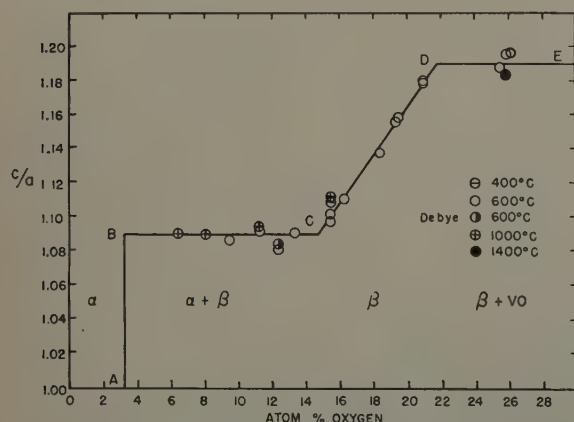


Fig. 3—Lattice parameter ratio c/a vs atomic percentage of oxygen.

Body-Centered Tetragonal Measurements: Most measurements were made with the precision camera; but occasionally the lines were too faint, and recourse was had to the small (5.73 cm diam) Debye camera. In either case, measurements were made on the (321) and (312) lines. Data in Table I for body-centered tetragonal structures are reported to the third decimal place with the probable error less than 0.002Å.

In a few cases where Debye camera measurements are reported, the Straumanis technique⁶ of compensating for film shrinkage was followed.

All films were read on an illuminator equipped with a vernier scale reading directly to 0.02 mm.

Heat Treatments: An annealing temperature of 600°C was used with all specimens as a standard low temperature treatment. The lattice parameters obtained at this temperature level were compared to those after quenching at higher temperatures to find out if the oxygen solubility was a function of temperature. It was standard practice to seal off the -200 mesh powder in a vanadium foil-lined, evacuated, fused-silica tube. The silica tube was suspended in a vertical tube furnace, and at the end of the heat treatment was thrust under water for a quench. While a faster quench could have been obtained by crushing the silica tube under water,

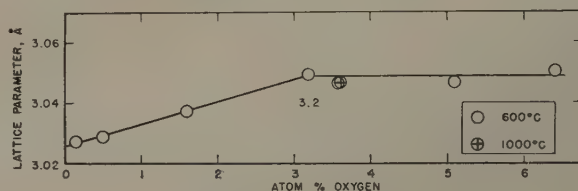


Fig. 4—Lattice parameter of body-centered cubic α phase as a function of oxygen content.

this was not done because of danger of contaminating the vanadium.

By plotting c/a vs atomic pct O for several heat treatments, the graph shown in Fig. 3 was obtained. Since the parameter measurements were about the same after quenching, from various temperature levels, there seemed to be no reason not to show all the data on a single curve. The location of line A-B was determined by plotting the lattice parameter of dilute cubic alloys against concentration, see Fig. 4. Figs. 3 and 4 are interpreted as follows: Oxygen dissolves in solid vanadium up to 3.2 atomic pct without altering the basic structure, but causing a linear lattice expansion of about 0.66 pct. Beyond this point a body-centered tetragonal phase makes its appearance, creating a two-phase region up to 14.7 atomic pct O. No change in c/a occurs during the two-phase interval since the compositions of the two phases (α and β) are fixed.

After passing point C in Fig. 3, the α phase disappears leaving pure β . The c/a ratio for the β solid solution increases with oxygen content, up to point D, the solubility limit of oxygen in the β phase. Further additions of oxygen result in the appearance of VO, a compound of established structure (NaCl) and which according to Klemm and Grimm,² has a homogeneity range from about 47.4 to 56.5 atomic pct O.

Because of lack of precise reproducibility, there was as much lattice parameter variation between different samples of similar oxygen content as in the same sample heat treated at different tempera-

tures. All that can be stated at present regarding the effect of temperature is that if the composition limits of the α and β phases vary with temperature, the variation is apparently not large.

Structure of the Beta Phase

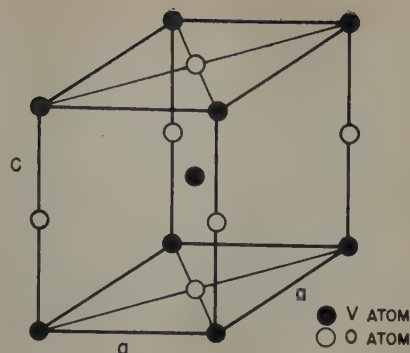
Klemm and Grimm² postulated the structure shown in Fig. 5 for the body-centered tetragonal solid solution. It is interesting to note that this is identical to the structure suggested by Jack⁷ for nitrogen martensite found in the Fe-N system.

Because of the availability today of neutron diffraction as a structure tool, it was considered desirable to locate the oxygen atoms in the β phase directly instead of deducing their position by displacements of the metal atoms. This test was carried out with the cooperation of Dr. E. O. Wollan at Oak Ridge National Laboratory. The neutron diffraction pattern obtained for the oxygen atoms in a 21 atomic pct alloy supported the structure deduced by Klemm and Grimm, Fig. 5, and by Jack for the nitrogen atoms in nitrogen martensite. The details of this investigation will be reported elsewhere.

From the configuration of the atoms in Fig. 5 it can be seen that there are two vanadium atoms and two oxygen atoms per unit cell. The saturated solid solution, if entirely composed of this structure, would reach VO or contain 50 atomic pct O. However, it has been shown in Fig. 3 that the β phase does not reach this concentration but is saturated at approximately 21.8 atomic pct O. Since 50 atomic pct corresponds to two oxygen atoms per unit cell, there is 2/50 or 0.04 oxygen atoms per unit cell for each atomic percentage of oxygen. Hence, multiplying the concentration of an alloy in atomic percentage by 0.04 gives the fractional number of oxygen atoms per unit cell.

In Fig. 6 are plotted the parameters a_0 and c_0 in the range from 14.7 atomic pct for the unsaturated

Fig. 5—Structure of body-centered tetragonal V-O solid solution (all interstitial positions filled).



β solution to 21.8 atomic pct for the saturated solution. From the intersections of the linear plot of the two parameters, normalized a_0 and c_0 values may be read off for these two concentration limits, see Table II. By subtracting the unit cell volume of pure vanadium from the unit cell volume of the two β phase concentrations mentioned above, the increase in average unit cell size may be computed (col. 6 in Table II). The volume occupied by an average oxygen atom may then be approximated by dividing the increase in cell volume by the number of oxygen atoms in that cell.

By assuming that the cell volume increase per oxygen atom is entirely occupied by the atom, an upper limit to the size of the oxygen atom may be calculated by equating the volume to $4/3 \pi r^3$ (volume of a sphere) and solving for r . The radii determined in this way for the unsaturated and saturated β solutions are given in Table II. Obviously, this results in too large an oxygen radius since the oxygen atoms do not fully occupy the extra cell space they create.

Another approach is to calculate the radius of the largest circle in the center of a (001) face using a_0

Table I. X-Ray Data on V-O Alloys After Various Heat Treatments

Oxygen, Atomic Pct	Body- Centered Cubic Parameter, a_0	Body-Centered Tetrago- nal Parameters			Heat Treatment, All Water Quenched		Remarks
		a_0	c_0	c/a			
0.039	3.0255				50 hr	600°C	High purity iodide metal Calcium-reduced metal of analysis is given in text
0.14	3.0275				50 hr	600°C	
0.5	3.0291				50 hr	600°C	
1.6	3.0376				50 hr	600°C	
3.2	3.0495				50 hr	600°C	
3.6	3.0467	*	*	*	2 hr	1000°C	Debye film
3.6	3.0466	*	*	*	2 hr	1000°C	
5.1	3.0474	*	*	*	50 hr	600°C	
6.4	3.0512	2.992	3.263	1.091	2 hr	1000°C	
6.4	*	2.990	3.266	1.092	2 hr	1000°C	
8.1	*	2.992	3.252	1.087	50 hr	600°C	
9.5	*	2.990	3.264	1.092	50 hr	600°C	
11.3	*	2.990	3.275	1.095	2 hr	1000°C	
11.3	*	2.994	3.236	1.081	50 hr	600°C	
12.4	*	2.990	3.241	1.084	50 hr	600°C	
12.4	*	2.989	3.263	1.091	12 hr	1000°C	
13.4	*				2 hr	600°C	
15.5		2.987	3.291	1.102	50 hr	600°C	
15.5		2.987	3.281	1.098	50 hr	600°C	
15.5		2.985	3.312	1.109	7 days	400°C	
15.5		2.985	3.320	1.112	2 hr	1000°C	Arc melted
15.5		2.985	3.315	1.110	50 hr	600°C	
15.5		2.984	3.315	1.111	100 hr	600°C	
15.5		2.984	3.315	1.110	50 hr	600°C	
16.3		2.985	3.314	1.138	50 hr	600°C	
18.4		2.977	3.388	1.156	50 hr	600°C	
19.3		2.958	3.421	1.156	12 hr	1000°C	
19.5		2.980	3.456	1.159	2 hr	600°C	
21.0		2.948	3.476	1.179	50 hr	600°C	
21.0		2.948	3.480	1.181	2 hr	1000°C	
25.5		2.939	3.493	1.188	50 hr	600°C	
25.9		2.943	3.521	1.196	50 hr	600°C	Arc melted, Debye film, VO present
25.9		2.948	3.490	1.184	1 hr	1400°C	
26.2		2.943	3.523	1.197	50 hr	600°C	

* Faint lines present.

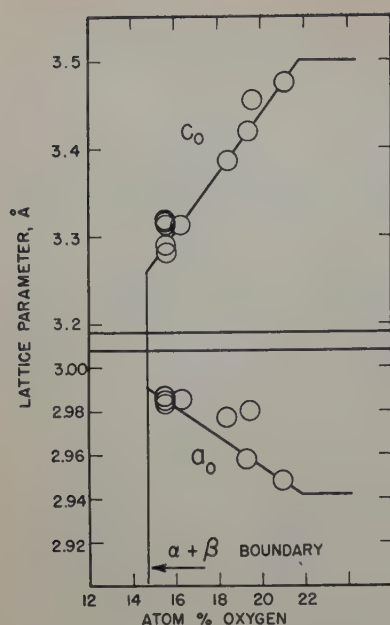


Fig. 6—Effect of oxygen concentration on the lattice parameters of the body-centered tetragonal (β) solid solution.

$= 2.94\text{\AA}$ for the saturated β solid solution and 1.31\AA for radius of the vanadium atom. The solution for this gives an oxygen radius of 0.77\AA , a value which agrees reasonably well with the covalent bond radius for oxygen (0.74\AA) suggested by Schomaker and Stevenson.⁸ The unit cell expansion from the volume of the original vanadium to that of the unsaturated β phase is 5.04 pct, while the corresponding expansion of the saturated β phase is 9.06 pct.

Investigation of Phase Equilibria by Other Methods

Other techniques used in this investigation include electrical resistivity, thermal analysis, thermoelectric effect, microscopic examination, and hydrogen equilibrium. Neither electrical resistivity nor thermal analysis showed any property versus temperature discontinuities in the region where these methods were used (up to 8 atomic pct O and 1200°C). The electrical resistivity method was capable of easily detecting a 1 pct change in this property.

Microstructures: While the microstructures observed in the vanadium alloys were very interesting and instructive in a qualitative sense, it was not feasible to use metallographic evidence in locating phase boundaries. Fig. 7 shows the structure of the vanadium starting material; the particles of constituent visible are VC or V_2C . Fig. 8 shows how 5.7 atomic pct O produces "strain markings" which are caused by the presence of the β phase. Fig. 9 is very typical of alloys in the region near 6 to 7 atomic pct O; here again, more clearly visible bands are apparently deformation markings which have been formed by some cooperative slipping or shearing of the parent α lattice during partial transformation to β . Fig. 10 is characteristic of alloys from the central $\alpha + \beta$ region to the saturation limit of β . At first glance, it resembles a fine-grained austenitic

stainless steel, profusely twinned. Closer inspection indicates some differences and these are: 1—the "twin" bands are not very uniform in width, and 2—there are many areas of extremely fine lamellae, some of which cannot be resolved by the most powerful objective of the light microscope. Fig. 11 shows a particularly clear example of the lamellae in which are seen bands resembling twins, but which contain a lamellar structure, originating possibly by a double shearing action as described by Bowles et al.⁹ for the case of certain In-Th alloys.

It cannot be argued that the alloy of Fig. 11 contains $\alpha + \beta$ since the X-ray evidence is clear that it consists entirely of the β phase. Hence, there is a continuum of metallographic structures from the $\alpha + \beta$ region through the β region such that it cannot be determined by this method whether the alloy contains two phases or one phase. Metallographic structures of similar appearance have been reported by Newkirk et al.,¹⁰ Guttman,¹¹ and Lipson et al.¹²

It is interesting to note that Fig. 12, which shows the structure of an arc melted 21 atomic pct alloy, does not exhibit any banding or lamellae. This suggests that the lamellae, since they are only present in the samples prepared by diffusion, originate during oxygen diffusion. Obviously, with the average unit cell increasing in volume by 5 to 9 pct in the β phase, large amounts of lattice strain are required to create a stable nucleus of the β phase. The creation of nuclei of the β phase might be expected to require a cooperative shearing action in order to produce the displacements necessary to make room for the large β lattice, hence, the bands and lamellae. When the vanadium alloy is converted completely to the β phase, as in Fig. 11, the deformation bands originating during transformation remain even after transformation is complete.

The situation with the arc-melted alloy is quite different as here the β phase originates from the reaction $\alpha + \text{VO} \rightarrow \beta$ at 1270°C (see later). Since this reaction occurs at a comparatively high temperature, there must be considerable stress relaxation, with apparently insufficient stress to cause the deformation markings, or lamellae, during transformation. However, many cracks are observed, which presumably originated at some lower temperature during cooling.

Figs. 13 and 14 show structures observed in alloys containing more than 21.8 atomic pct O (26.2 and 25.9 , respectively). These alloys, like that of Fig. 12, were prepared by arc melting. All of the arc-melted alloys were given various heat treatments from 1000° to 1400°C , but with only minor effects on the microstructure; mainly a somewhat different percentage distribution of the two phases ($\beta + \text{VO}$). The important thing about Figs. 13 and 14 is the Widmanstätten structure in certain areas which suggests the presence of a eutectoid transformation at some elevated temperature. No attempt was made to locate the coordinates of the eutectoid nonvariant

Table II. Geometry of the Unsaturated and Saturated Beta Phase and Approximate Size of the Oxygen Atom

	Atomic Pct Oxygen	a_0	c_0	Unit Cell Volume, \AA^3	Increase in Cell Size, \AA^3 Due to Oxygen	Number of Oxygen Atoms per Cell	Volume per Oxygen Atom, \AA^3	Radius of Oxygen Atom, \AA
Original V	0.14	3.0275		27.749				
Unsaturated β phase	14.7	2.99	3.26	29.144	1.395	0.588	2.37	0.81
Saturated β phase	21.8	2.94	3.50	30.254	2.505	0.873	2.87	0.86
Maximum interstitial radius on (001) plane at saturation ($a_0 = 2.94\text{\AA}$)								0.77

Fig. 7 (left)—Vanadium starting material. X500. Area reduced approximately 50 pct for reproduction.

Fig. 8 (right)—V + 5.7 atomic pct O, 900°C water quenched. X500. Area reduced approximately 50 pct for reproduction.

Figs. 7 and 8—Samples anodically etched in 10 pct HCl.

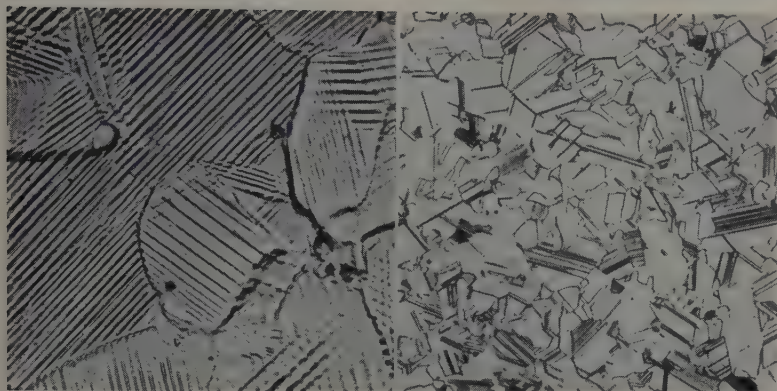
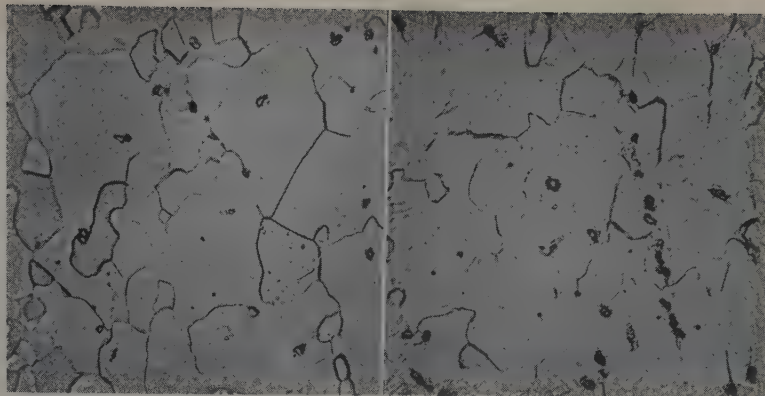


Fig. 9 (left)—V + 6.6 atomic pct O, 900°C water quenched. X1700. Area reduced approximately 50 pct for reproduction.

Fig. 10 (right)—V + 12.4 atomic pct O, 900°C, slow cooled. X500. Area reduced approximately 50 pct for reproduction.

Figs. 9 and 10—Samples anodically etched in 10 pct HCl.

Fig. 11 (left)—V + approx. 18 atomic pct O, slow cooled 1100°C. X1700. Area reduced approximately 50 pct for reproduction.

Fig. 12 (right)—Arc melted V + 21 atomic pct O, slow cooled 1000°C. X250. Area reduced approximately 50 pct for reproduction.

Figs. 11 and 12—Samples anodically etched in 10 pct HCl.

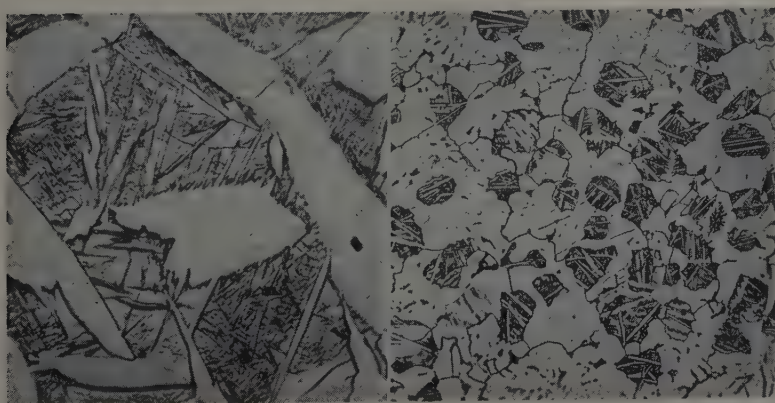
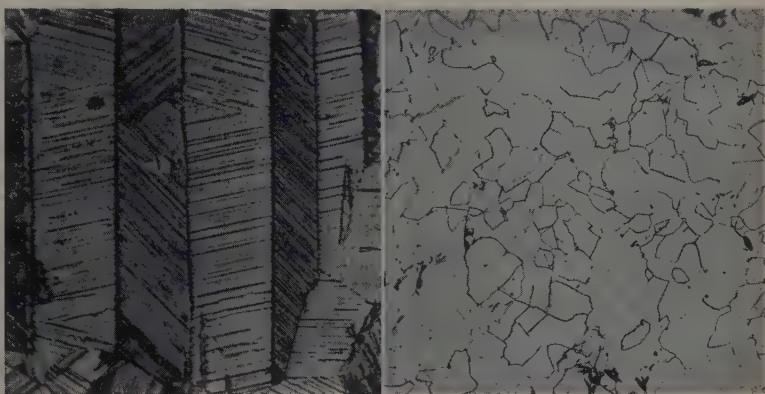


Fig. 13 (left)—Arc melted V + 26.2 atomic pct O, as cast. X1700. Area reduced approximately 50 pct for reproduction.

Fig. 14 (right)—Arc melted V + 25.9 atomic pct O, as cast. X250. Area reduced approximately 50 pct for reproduction.

Figs. 13 and 14—Samples anodically etched in 10 pct HCl.

horizontal, nor to identify the decomposing solid solution, as this was considered outside the scope of this investigation.

Hydrogen Equilibrium: McQuillan⁹ has demonstrated that phase transitions may be detected in metals having a fairly high hydrogen solubility by measuring the equilibrium pressure of hydrogen over the alloy as a function of temperature.

The amount of hydrogen necessary for such

measurements is very small, usually the order of 0.1 atomic pct; the pressure is in the micron range. McQuillan has shown also that if the log of hydrogen pressure is plotted against $1/T_K$, a straight line results as long as the alloy contains one phase, or as long as the relative proportion of two phases remains fixed. However, in going from a single-phase region to a two-phase region, or vice versa, or from one two-phase region to another two-phase region,

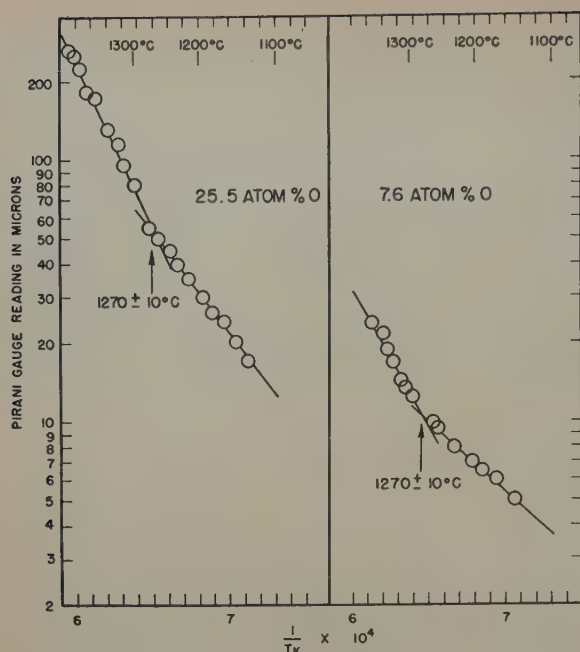


Fig. 15—Hydrogen pressure $-1/T_K$ plot for two V-O alloys.

a discontinuity in the $\log p$ vs $1/T_K$ plot results because of differences in hydrogen solubility in one or more phases.

An advantage of this method in investigating a system like V-O is that it does not involve mechanically attaching a thermocouple or potential leads, etc., to the brittle specimens. The apparatus used consisted of a mullite tube closed at one end about $\frac{1}{4}$ in. ID x 8 in. long attached to the glass vacuum system previously mentioned. Adjacent to the mullite tube was a Distillation Products Pirani gage for measuring the hydrogen pressure. A small platinum-wound resistance furnace was used to heat the sample tube up to 1450°C .

Procedure for Making a Hydrogen Pressure Run: The samples used contained 7.6 and 25 atomic pct O and weighed about 1 to 4 g. After dropping the samples into the mullite tube which had been previously degassed at a temperature higher than that planned for the hydrogen equilibrium run, the sample tube was pumped down to about 10^{-5} to 10^{-6} mm of mercury. The samples were heated to about 1000°C and thoroughly degassed at this level, after which about 1 cc of dry hydrogen was introduced into the gas absorption apparatus open to the mullite tube. After waiting a few moments, the pressure of hydrogen (at first too high to read on the Pirani gage) was reduced to about 5 microns. At this level a stopcock was closed which isolated the sample tube and Pirani gage from the vacuum system. Pressure-temperature readings were taken every 10°C or thereabouts, using a calibrated Pt-Pt-Rh thermocouple.

Several runs were made with both alloys with the result that a single arrest was found at $1270^\circ \pm 10^\circ\text{C}$, see Fig. 15. Apparently the nonvariant horizontal referred to above occurs at this level from at least 7.6 to 25 atomic pct O. Cooling curves were attempted a few times, but without success; the pressure failed to fall in a reproducible way and yielded data of no value. This may have been caused by a mullite-sample reaction, but there was no visible evidence of such a reaction; the samples always dropped out of the tube clean and bright and no discoloration was evident inside the tube. However, since several heating curves all gave the same

value of $1270^\circ \pm 10^\circ\text{C}$, there seems to be no doubt that: 1—there is a reaction at this level, and 2—that this temperature within the error mentioned is correct.

Tentative V-VO Phase Diagram: The phase diagram, Fig. 16, was drawn from the following evidence: X-ray diffraction measurements clearly showed the presence of the α , $\alpha + \beta$, β , and $\beta + \text{VO}$ fields as indicated previously. The limits of these phase fields have also been described, and evidence has been cited for believing that the phase boundaries are essentially vertical. The homogeneity range of VO (47.4 to 56.5 atomic pct O) has been taken from the work of Klemm and Grimm,² and it was assumed that its phase boundaries, as in the other phases, are vertical.

A few optical pyrometer liquidus and solidus points were determined for alloys containing 21, 26, and 48 atomic pct O with the results shown as circles. VO apparently melts congruently in the vicinity of 1900°C . These preliminary results must be assumed to be only semiquantitative, but they suggest a peritectic reaction and such a relation fits in with the deduced existence of the γ phase (see below). Also, no metallurgical evidence for a eutectic was found.

The β phase apparently forms by a peritectoid reaction at 1270°C : $\alpha + \text{VO} \rightarrow \beta$ as already suggested. The nonvariant horizontal is drawn dotted beyond the 25.5 atomic percentage region to VO since no data were obtained in that region.

Since metallographic evidence suggested the existence of a eutectoid reaction, the eutectoid horizontal must evidently be at some temperature above 1270°C . It is also clear that there must be some solid solution fairly rich in oxygen which breaks down to form the eutectoid. Hence, a second terminal solid solution (γ) extending for a considerable distance into the diagram was postulated. However, before this hypothesis could be seriously considered, it was necessary to show that pure vanadium undergoes a polymorphic transformation at some high tem-

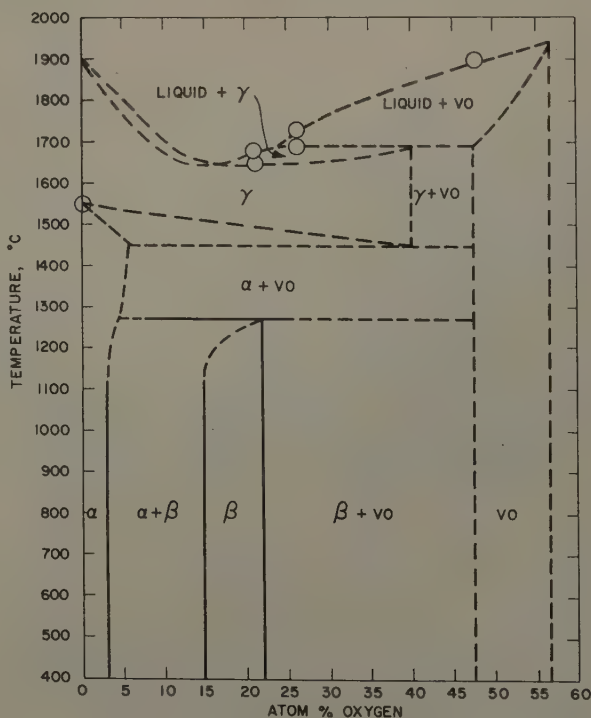


Fig. 16—Tentative V-VO phase diagram.

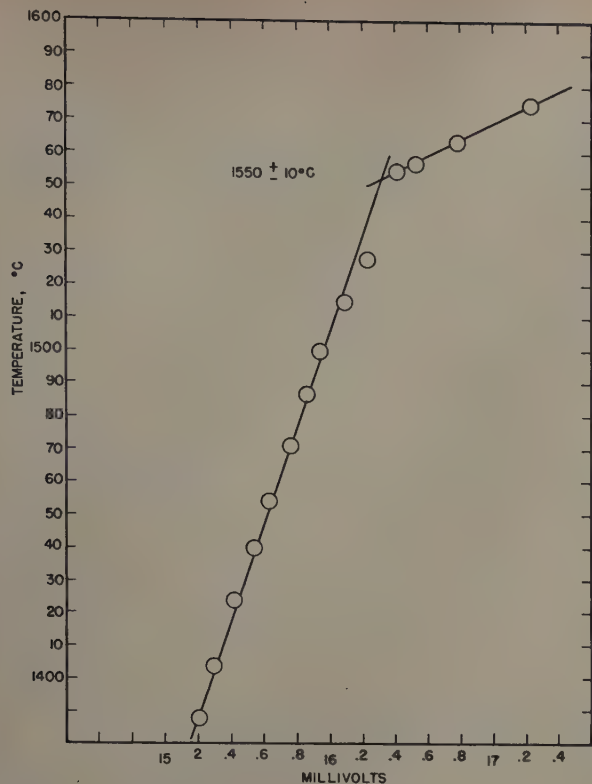


Fig. 17—Electromotive force of V-Mo thermocouple as a function of temperature.

perature, probably above 1400°C. The melting point of vanadium was taken from Adenstedt et al.¹⁴

Evidence for such a transformation at 1550°C is presented in the next section, but no information was obtained on the structure of the new phase.

The location of the eutectoid horizontal at 1450°C is purely arbitrary. The suggested eutectoid point at 40 atomic pct O was estimated from the appearance of microstructures of annealed V-O alloys containing about 25 atomic pct O.

High Temperature Polymorphic Transformation in Pure Vanadium

After considering various possible experimental methods, it appeared that the measurement of the electromotive force generated by a V-Mo or V-W thermocouple as a function of temperature would be experimentally simple and sufficiently sensitive.

Accordingly, two preliminary experiments were made in a high-frequency heated vacuum furnace in which a V-Mo thermocouple junction was pressed into a slot cut in the side of a ½ in. cube of molybdenum. By sighting an optical pyrometer on the molybdenum block and simultaneously reading the thermocouple electromotive force, it was possible to obtain a plot which showed some evidence of an arrest in the neighborhood of 1540°C. Similarly, a V-W thermocouple gave an unmistakable arrest at 1520°C.

Since there was a strong indication of a vanadium transformation, a third run was made in a tungsten resistance furnace using a helium atmosphere and a V-Mo thermocouple. For temperature measurements a Pt-Pt-Rh thermocouple was used which had been previously calibrated at the melting point of electrolytic iron, 1535°C. The data of this run are plotted in Fig. 17. This curve shows clear evidence of a polymorphic transformation in vanadium at about 1550° ± 10°C.

Summary and Conclusions

The results of an investigation of vanadium-rich V-O solid solutions are presented, indicating the structure and lattice parameters of two solutions, α and β , and their approximate temperature-composition existence. The α solution is the terminal body-centered cubic one, and contains up to 3.2 atomic pct O. The β solution has an ordered body-centered tetragonal structure, is formed at 1270°C, and exists from about 15 to 22 atomic pct O. From the evidence available, the various phase boundaries have no appreciable temperature dependence.

A tentative phase diagram is presented from V to VO, but the region above 1270°C is largely speculative. However, there is enough information available about the behavior at these higher temperatures to make it worth presenting as a suggestion to future investigators.

Evidence has been found for a polymorphic transformation in pure vanadium at 1550°C.

Acknowledgments

The assistance and advice of many of our colleagues are gratefully acknowledged. In particular, we wish to mention the help of John Duffy who prepared the samples and assisted with many of the experiments.

References

- ¹ R. K. McKechnie and A. U. Seybolt: Preparation of Ductile Vanadium by Calcium Reduction. *Journal Electrochemical Soc.* (1950) **97**, p. 311.
- ² Wilhelm Klemm and Ludwig Grimm: On the Knowledge of the Lower Vanadium Oxides. *Ztsch. anorg. allgem. Chemie* (1942-1943) **250**, p. 42-55.
- ³ C. H. Mathewson, E. Spire, and C. H. Samans: Division of the Iron-Vanadium-Oxygen System into Some of its Constituent Binary and Ternary Systems. *Trans. Amer. Soc. Steel Treating* (1932) **20**, p. 357.
- ⁴ M. U. Cohen: Precision Lattice Constants from X-Ray Powder Photographs. *Review of Scientific Instruments* (1935) **6**, p. 68.
- ⁵ J. W. Nash, H. R. Ogden, R. E. Durtschi, and J. E. Campbell: The Preparation and Properties of Iodide Vanadium. To be published in the *Journal Electrochemical Soc.*
- ⁶ M. Straumanis and O. Mellis: Precision Debye Scherrer Methods. *Ztsch. Physik* (1935) **94**, p. 184.
- ⁷ K. H. Jack: The Iron-Nitrogen System: the Preparation and the Crystal Structures of Nitrogen-Austenite and Nitrogen Martensite. *Proc. Royal Soc.* (1951) **A208**, pp. 200-215.
- ⁸ V. Schomaker and D. P. Stevenson: Some Revisions of the Covalent Radii, etc. *Journal ACS* (1941) **63**, p. 37.
- ⁹ J. S. Bowles, C. S. Barrett, and L. Guttman: Crystallography of Cubic-Tetragonal Transformation in the Indium-Thallium System. *Trans. AIME* (1950) **188**, pp. 1478-1485; *JOURNAL OF METALS* (December 1950).
- ¹⁰ J. B. Newkirk, A. H. Geisler, R. Smoluchowski, and D. L. Martin: Phase Equilibria in an Ordering Alloy System. *Journal of Applied Physics* (1951) **22**, pp. 290-298.
- ¹¹ Lester Guttman: Crystal Structures and Transformations in Indium-Thallium Solid Solutions. *Trans. AIME* (1950) **188**, pp. 1472-1477; *JOURNAL OF METALS* (December 1950).
- ¹² H. Lipson, D. Shoenberg, and G. V. Stupart: The Relation Between Atomic Arrangement and Coercivity in an Alloy of Iron and Platinum. *Journal Inst. Metals* (1941) **67**, pp. 333-340.
- ¹³ A. D. McQuillan: The Application of Hydrogen Equilibrium Pressure Measurements to the Investigations of Titanium Alloy Systems. *Journal Inst. Metals* (1951) **79**, II, pp. 73-88.
- ¹⁴ H. K. Adenstedt, J. R. Pequinot, and J. M. Rayer: The Titanium-Vanadium System. *Trans. ASM* (1952) **44**, p. 990.

Cold-Rolling and Annealing Textures of Molybdenum Single Crystals

by N. K. Chen and R. Maddin

THE textures of straight-rolled and of cross-rolled molybdenum were first determined with the aid of pole figures by Custers and Riemersma.¹ These authors have shown that for straight-rolling, the main texture was (100) [011] with a considerable spread about the rolling direction. After cross-rolling a second texture was obtained in which there was a [111] axis perpendicular to the rolling plane, possessing a rotary symmetry. Recently Semchyshen and Timmons² in their study of preferred orientation of arc-cast molybdenum sheet obtained similar pole figures. In these two investigations, polycrystalline materials were used. In the main, the textures of molybdenum in these cases are qualitatively consistent with rolling textures of other body-centered cubic metals, such as iron and Fe-Si alloys.³

In the present investigation, single crystals of molybdenum were deformed by rolling with respect to specific crystallographic planes and directions. Since the deformation textures of polycrystalline aggregates have been related intimately to the behavior of individual grains,⁴ a study of possible correlations of final textures with respect to the initial orientations of the single crystals might conceivably lead to a better understanding of the textures. Annealing treatments were carried out after deformation in order to study the recrystallization characteristics as well as the recrystallization texture.

Rolling of Single Crystals

Single crystals of molybdenum (about $\frac{1}{8}$ in. in diam \times 1-in. long), grown by the method previously described,⁵ were cold-rolled without intermediate anneals. Except for specimens MR-1 and MR-2, which were rolled at random in the preliminary test in order to find a proper rate of reduction, all other specimens were carefully documented as to their respective orientation before deformation by means of X-ray Laue back-reflection methods. A stereographic projection was constructed from which it was possible to determine a particular plane and direction to be considered for rolling. Parallel flat surfaces were then polished metallographically with respect to a reference scratch on the specimen which was mounted in sealing wax. These flat surfaces contained the plane chosen for rolling. After etching, a Laue back-reflection photograph was again made of one of the flat surfaces to determine the

N. K. CHEN, Junior Member AIME, is Assistant Professor of Metallurgy and R. MADDIN, Member AIME, is Associate Professor of Metallurgy, The Johns Hopkins University, Baltimore.

Discussion on this paper, TP 3400E, may be sent, 2 copies, to AIME by April 1, 1953. Manuscript, May 19, 1952. Los Angeles Meeting, February 1953.

Table I. Summary of Rolling Results of Molybdenum Single Crystals

Specimen No.	Initial Thickness, In.	Final Thickness, In.	Reduction in Thickness, Pct	Remarks
MR-1	0.082	0.036	56.1	Deformed rapidly; specimen cracked
MR-2	0.092	0.004	95	Small amount of polycrystals present. Cracking occurred
MR-3	0.089	0.0035	96	Polycrystalline section contained in single crystal rolled to 90 pct
MR-4	0.093	0.003	96.8	
MR-5	0.095	0.002	97.9	
MR-6	0.105	0.007	93.3	
MR-7	0.087	0.005	94.3	Severe cracking; cross rolled
MR-8	0.099	0.004	96	
MR-9	0.088	0.004	95.6	
MR-10	0.084	0.011	87	
MR-11	0.087	0.006	93.2	Cross rolled
MR-12	0.082	0.0015	98.2	Cross rolled
MR-14	0.092	0.003	96.8	Compression rolled
MR-15	0.077	0.003	96.2	Compression rolled
MR-16	0.090	0.0015	98.4	Compression rolled

exact plane of rolling. The initial orientations of all the specimens (specified by two elements for each crystal, direction of rolling and the pole of the rolling plane) are summarized in Fig. 1.

The specimens were mounted in plasticene between two hardened Si-Fe plates. The sandwich was then rolled down, keeping the direction constant in the case of straight-rolling. In cross-rolling (MR-10, MR-11, and MR-12) the sandwich was rotated 90° after each pass so that every first and third pass contained the same rolling direction. Specimens MR-14, MR-15, and MR-16 were compression-rolled following the manner of Barrett.⁶ In these cases the direction of the sandwich through the rolls was changed by 3° to 5° for each pass until the specimens were rolled to the desired reduction in thickness. It was found that if extreme care was exercised in rolling, i. e., the amount of deformation per pass was extremely small, the specimens could be rolled to a large reduction in thickness. The rate of reduction used, with a single exception of MR-1, was generally 0.001 in. per 10 passes. Thus, it took about 800 passes to reduce a specimen to a final reduction in thickness of 87 to 98 pct. The results of rolling are shown in Table I.

Cold-Rolling Textures

The final orientations were determined by the conventional Laue transmission method,⁸ using molybdenum radiation, with or without a zirconium filter. Pole figures were plotted from {110} and {200} reflections in which three degrees of intensity—heavy, medium, and light—were determined visually.

Three main types of textures have been observed from the deformed single crystals. These are: 1—a

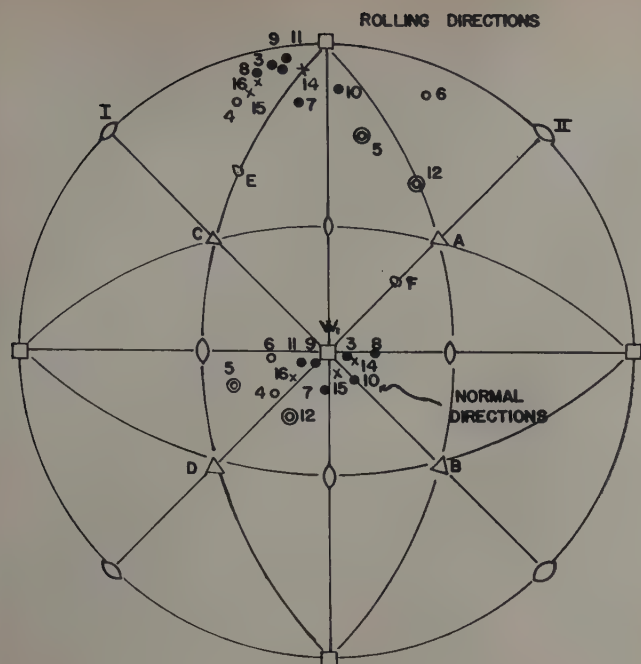


Fig. 1—Initial orientations of molybdenum single crystals used before rolling. Solid circle, crystals developed texture (001) [100]; open circle, crystals developed texture (001) [110]; double circle, crystals developed texture (111) [112]; x, crystals compression-rolled, texture [001].

(001) [110], 2—a (111) [112], and 3—a (001) [100]. A pole figure representing the first type (MR-4 and MR-6) is shown in Fig. 2. It is seen that the main texture is (001) [110], with a spread of 15° about the rolling direction. This type of preferred orientation has generally been observed as the rolling texture of most body-centered cubic metals. A pole figure representing the second type is shown in Fig. 3 for specimen MR-5. The average orientation can be described as a (111) [112] texture, with a spread of 10° about the sheet normal. A minor component, (001) [100], may be noted. A similar preferred orientation, but with a greater spread about the pole

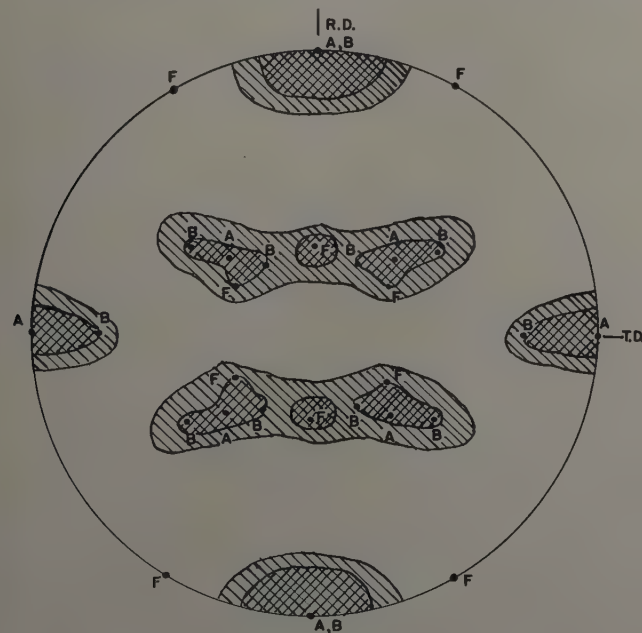


Fig. 2—(110) pole figure for rolled molybdenum single crystal MR-4. Ideal orientations indicated as follows: A, (100) [011]; B, (115) [110]; F, (111) [112].

of the rolling plane, is shown in Fig. 4 for MR-12. A component representing a (001) [100] texture can also be noted.

The third type of texture, (001) [100], has been consistently observed in the present investigation for crystals whose initial orientation had a (001) near the rolling plane and [100] near the rolling direction. Figs. 5 and 6 are pole figures representing this texture. It may be seen that this "cube" texture has a greater spread about the pole of the rolling plane than about both the rolling and transverse directions. The significant point is that there is no [110] in the rolling direction which has generally been observed as the rolling direction of body-centered cubic metals. To check more sensitively the existence of the predominant [100] direction, an X-ray photogram, Fig. 7, was taken with the specimen tilted 13° to the X-ray beam ($\theta = 13.1^\circ$ is the Bragg angle for (200) reflection by molybdenum $K\alpha$ radiation). It is seen, Fig. 7, that the maximum intensity of (200) was obtained and, in addition, all other intensities testify to the existence of [100] as

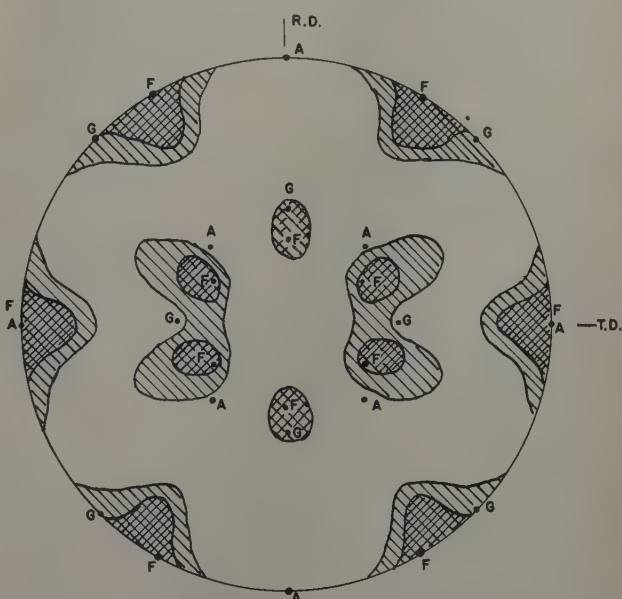


Fig. 3—(110) pole figure for rolled molybdenum single crystal MR-5. Ideal orientations indicated as follows: F, (111) [112]; G, (100) [001].

the rolling direction. These additional photograms were felt necessary, since the existence of a "cube" texture in a deformed body-centered cubic metal has not previously been reported.

The texture resulting from compression rolling can best be described as a [100] fiber coinciding with the compression axis. However, it was also observed that the texture in the rolling plane is not completely random, but contains a cube component parallel to the initial length axis of the specimen. This is considered to be due to the incapability of uniform flow in all directions. Fig. 8 points to this conclusion.

Annealing Textures

The deformed specimens were annealed in argon purified with titanium at a temperature of 950°C for 1 hr. The specimens showed no recrystallization after this treatment as judged by numerous X-ray photograms. A second heat treatment for 3 hr at 1080°C also showed no recrystallization. However, annealing for 14 min at 1350°C resulted in complete recrystallization. The textures after this latter treat-

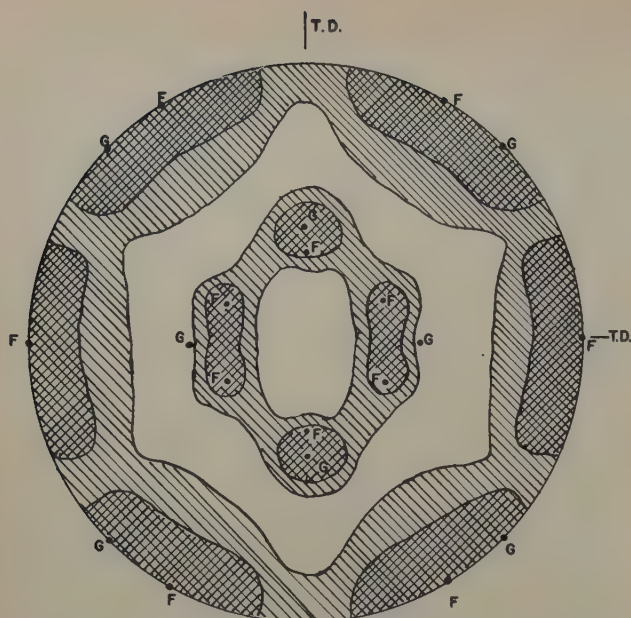


Fig. 4—(110) pole figure for rolled molybdenum single crystal MR-12. Ideal orientations indicated as follows: F, (111) $[11\bar{2}]$; G, (100) $[001]$.

ment are as follows: Those specimens having a deformed texture described as (001) $[100]$ maintained this texture after recrystallization; those specimens having a deformed texture described as (111) $[11\bar{2}]$ also retained this texture upon recrystallization. However, those specimens with (001) $[110]$ as the deformation texture changed into one upon recrystallization which can best be described as (001) in the rolling plane with a direction about 20° from the $[110]$. A pole figure representing this recrystallization texture is shown in Fig. 9.

Discussion of Results

The "cube" texture in the present results is quite different from what has been observed as the rolling

texture of body-centered cubic metals as reported in the literature.¹⁻⁴ Since $[111]$ is the slip direction such a texture is difficult to explain by the existing theories^{7,8} owing to the fact that a $[100]$ direction would not be a stable end position as the direction of rolling.⁷ A possible explanation must be sought from the initial orientations, chosen as the rolling plane and the rolling direction. It is seen from Fig. 1 that all specimens (MR-3, MR-9, MR-10, MR-11, MR-7, and MR-8) which had their rolling direction and pole of the rolling plane very close, within 10° , to a cube axis developed an approximately "cube" texture after rolling, Figs. 5 and 6. This seems to indicate that although a $[100]$ direction should not be a stable end position as a rolling direction during ordinary rolling processes, it could be made metastable in the present case of extremely slow reduction of a single crystal with an initial "cube" orientation.

It is interesting to note that in the rolling of single crystals of iron with the initial rolling direction near $[001]$, Barrett and Levenson⁴ did not observe the

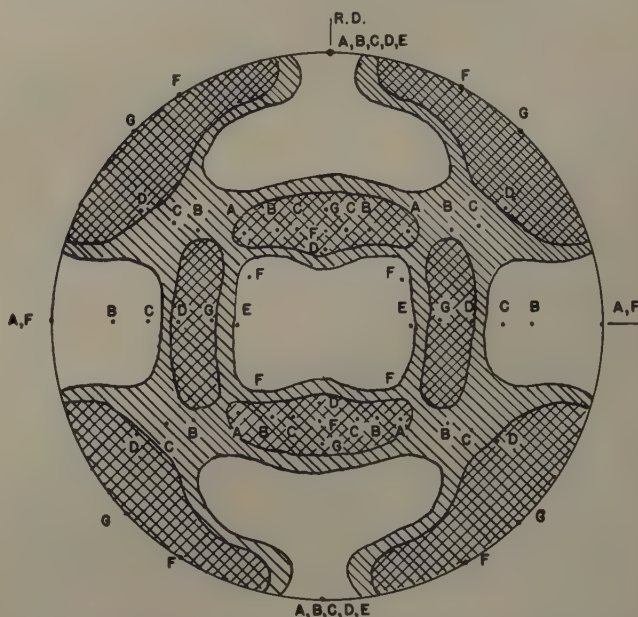


Fig. 6—(110) pole figure for rolled molybdenum single crystal MR-8, and also other crystals with their initial orientations near (100) $[001]$ position. The main orientation is a cube texture; G, (100) $[001]$ with a spread about the normal direction.

existence of a "cube" texture. However, their rolling procedure consisted of reducing the crystals to 82 to 97 pct reduction in thickness in 20 to 40 passes, while in the present case, more than 800 passes were used for the same final reductions. It should also be noted that the theory developed by Decker and Harker⁹ would account for the existence of a "cube" rolling texture in the following manner: While their theory suggests that a grain would keep its initial orientation if: "(1) the slip planes are symmetrical with respect to the normal and transverse plane and, (2) the slip directions nearest the planes of greatest shear stress lie in the plane containing the rolling direction and the normal to the rolling plane," the second condition should be modified to read: "the slip directions nearest the planes of greatest shear stress are symmetrical with respect to the normal transverse plane."¹⁰ It would seem that the conditions modified by Decker are satisfied for crystals having an initial cube orientation. Further emphasis as to the applicability of this theory would appear

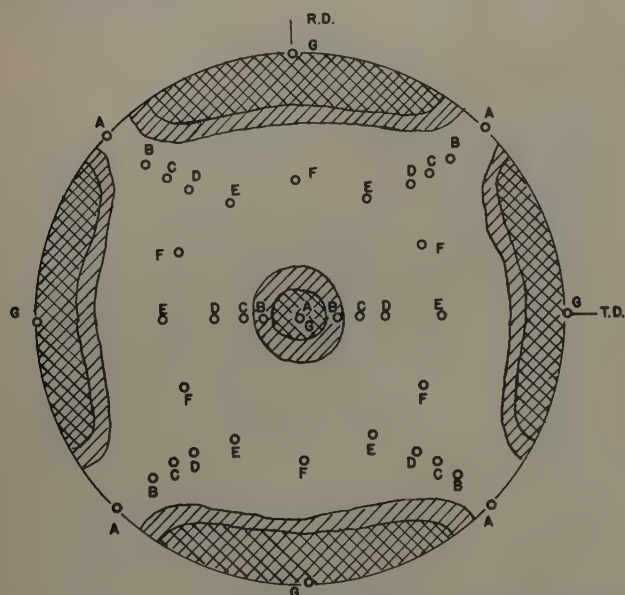


Fig. 5—(110) pole figure for rolled molybdenum single crystal MR-8, and also other crystals with their initial orientations near (100) $[001]$ position. The main orientation is a cube texture, G (100) $[001]$, with a spread about the normal direction. A, B, C, D, E, and F are ideal orientations generally observed for body-centered cubic materials and molybdenum single crystals whose initial orientations are far from (100) $[001]$ position.

to be obtained here since the "cube" texture was retained after recrystallization.

The textures (001) [011] and (111) [$\bar{1}1\bar{2}$] can be explained on the same basis of initial orientation difference as proposed by Barrett and Levenson.⁴ It can be seen in Fig. 1 that for crystals MR-4, MR-5, MR-6, and MR-12 the rolling plane and direction were both distant from a starting (100) [001] position. The development of the preferred orientation in the cases of MR-4 and MR-6 would thus involve mainly a rotation of their initial normal directions toward W_1 , and their initial rolling directions toward I and II, respectively. For crystals MR-5 and MR-12, the rotations would be mainly the movement of the initial normal directions toward D and their rolling directions toward E and F , respectively. Since a co-existence of the two textures was observed in these cases, varying only in their relative amount, fragmentation into deformation bands might be expected. However, no metallographic evidence could be observed.

It should be noted that MR-10, MR-11, and MR-12 were cross-rolled. Since MR-10 and MR-11 had both their initial rolling and transverse direction almost

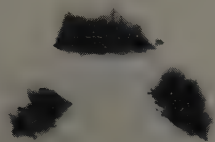


Fig. 7—Pattern for rolled molybdenum single crystal MR-10 showing (100) [001] texture. X-ray beam 13° from the pole of rolling plane, rolling direction vertical. Intense spot (top center) from (200) planes normal to rolling direction. $\theta_{200} = 13.1^\circ$, the Bragg angle for $\text{MoK}\alpha$ radiation.

parallel to the cube direction, a cube texture resulted just as in the other straight-rolled specimens, MR-3, MR-7, MR-8, etc., except for a smaller amount of spread.

MR-14, MR-15, and MR-16 were compression-rolled. The fiber texture was found to be mainly [001] parallel to this axis of compression. This is consistent with Barrett's result on compression of iron single crystals with their initial orientations within 22° of a cube axis.⁶

The general features of the recrystallization texture in rolled iron and steel are: 1—rolling plane (100), rolling direction 15° from [$\bar{1}1\bar{2}$]; 2—rolling plane (111), rolling direction [$\bar{1}1\bar{2}$]; and 3—rolling plane (112), rolling direction 15° from [110].⁸ In the case of molybdenum, the recrystallization texture has been reported as the same as the rolling texture but with less spread.⁹ In the present case, the recrystallization texture apparently depends upon the deformation texture: both (001) [100] and (111) [$\bar{1}1\bar{2}$] textures remain unchanged upon recrystallization, but the (001) [011] texture undergoes a rotation of approximately 20° about the normal direction. Whether or not these differences in recrystallization textures can be explained on the basis of the acquisition of energy during the rolling process¹⁰ as a function of the initial orientation should await

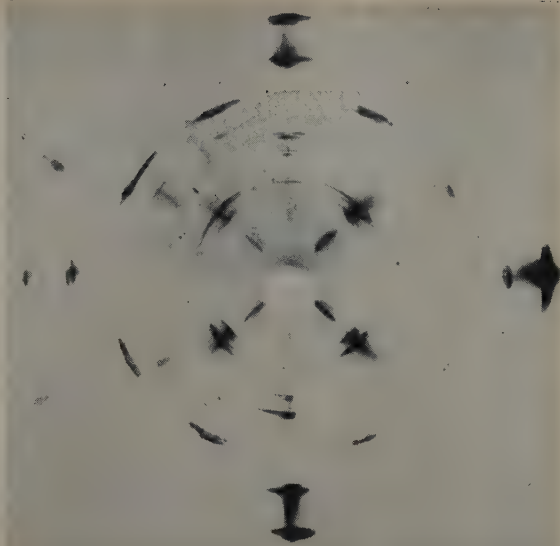


Fig. 8—Pattern for compression-rolled molybdenum single crystal MR-15. X-ray beam 90° from rolling plane. The vertical direction is the initial length-wise direction. Four-fold symmetry of the Laue pattern shows [001] orientation.

further carefully controlled experiments, i.e., a large variation of the initial orientations of single crystals along with a quantitative determination of the resulting textures before and after recrystallization.

Conclusions

1—Those crystals whose initial orientations were remote from a "cube" position developed (001) [110] and (111) [$\bar{1}1\bar{2}$] textures.

2—Those crystals whose initial orientations were close to a "cube" position developed "cube" textures, (001) [100], with a spread about the normal direction.

3—Compression rolling molybdenum single crystals with initial orientation close to the "cube" position gave, generally, a [001] fiber texture.

4—The textures resulting from recrystallization at 1350°C were as follows: the deformation textures, (001) [100] and (111) [$\bar{1}1\bar{2}$], were retained; the

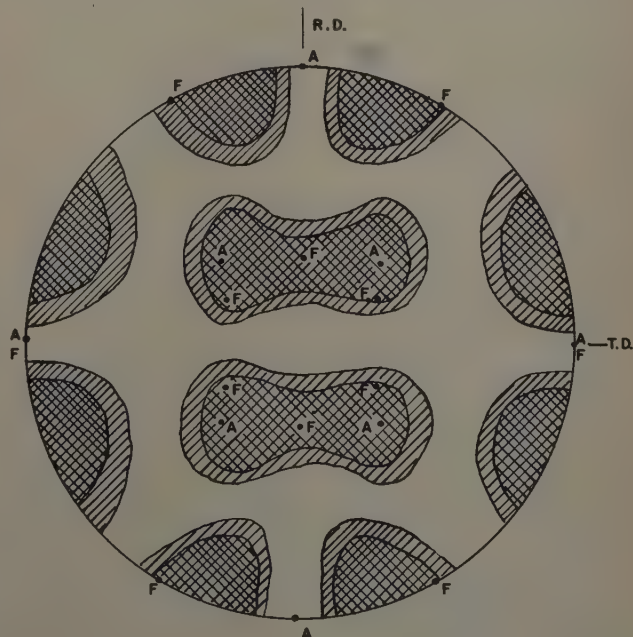


Fig. 9—(110) pole figure for recrystallized molybdenum single crystal after rolling. Ideal orientations indicated as follows: A, (001) [110]; F, (111) [$\bar{1}1\bar{2}$].

deformation textures, (001) [110], underwent a rotation of approximately 20° about the pole of the rolling plane.

Acknowledgments

The authors would like to acknowledge the very careful rolling operations performed by Alexander S. Townes and the assistance of R. B. Pond in the recrystallization experiments. This work was sponsored by the Office of Naval Research under contract Nonr 248(05), NR 034-403.

References

- ¹ J. F. H. Custers and J. C. Riemersma: The Textures of Straight-Rolled and of Cross-Rolled Molybdenum. *Physica* (1946) **12**, pp. 195-208.
- ² M. Semchyshen and G. A. Timmons: Preferred Orientation of Arc-Cast Molybdenum Sheet. *Trans. AIME* (1952) **194**, p. 279; *JOURNAL OF METALS* (March 1952).
- ³ C. S. Barrett: *Structure of Metals* (1943) New York. McGraw-Hill Book Co.

- ⁴ C. S. Barrett and L. H. Levenson: Analysis of the Cold-Rolling Texture of Iron. *Trans. AIME* (1941) **145**, p. 281.
- ⁵ N. K. Chen, R. Maddin, and R. B. Pond: The Growth of Molybdenum Single Crystals. *Trans. AIME* (1951) **191**, pp. 461-464; *JOURNAL OF METALS* (June 1951).
- ⁶ C. S. Barrett: Structure of Iron After Compression. *Trans. AIME* (1939) **135**, p. 296.
- ⁷ W. R. Hibbard, Jr. and Ming-Kao Yen: Wire Textures of Copper and Its Binary Alpha Solid Solution Alloys with Aluminum, Nickel and Zinc. *Trans. AIME* (1948) **175**, p. 126; *METALS TECHNOLOGY* (February 1948).
- ⁸ E. A. Calnan and C. J. B. Clews: The Development of Deformation Textures in Metals—Part II—Body-Centered Cubic Metals. *Philosophical Magazine* (1951) **42**, p. 616.
- ⁹ B. F. Decker and D. Harker: Relations Between Initial and Final Orientations in Rolling and Annealing of Silicon Ferrite. *Journal of Applied Physics* (1951) **22**, 7, pp. 900-904.
- ¹⁰ B. F. Decker: Private communication.

Technical Note

Allotropy in the Phase ZrCr₂

by W. Rostoker

IN the course of the development of the phase equilibrium diagram for the system Zr-Cr,¹ the structure of an as-cast alloy having the composition ZrCr₂ was analyzed and established to be isomorphous with MgZn₂ (C14, hexagonal lattice, 12 atoms per unit cell). In a recent paper on the same system, Hayes, Roberson, and Davies² report for the ZrCr₂ phase an isomorphy with MgCu₂ (C15, cubic lattice, 24 atoms per unit cell). It appeared that this conflict might be resolved by assuming a high and low temperature modification for ZrCr₂. That this was the case with the phase TiCr₂ has recently been demonstrated by Levinger.³ Specimens of ZrCr₂ annealed at 1200°, 1100°, 994°, 900°, 834°, 800°, and 700°C, respectively, and subsequently quenched were

Table I. Structure of ZrCr₂ at Various Temperatures

Temperature, °C	Structure Type
1200	MgCu ₂
1100	MgCu ₂
994	MgCu ₂
900	MgZn ₂
834	MgZn ₂
800	MgZn ₂
700	MgZn ₂

examined by X-ray diffraction analysis. It was successfully demonstrated that a transition from the MgZn₂ structure at lower temperatures to the MgCu₂ structure did occur at some temperature between 900° and 994°C. Table I lists the observed structures at the various annealing temperatures. In Table II, a summary of line spacings and intensities is given for each of the allotropic modifications. The first six lines of the MgCu₂ structures have been located in the table to illustrate the close similarity between the patterns. Lattice parameters of the two modifications were calculated by a least squares solution

Table II. Line Spacings and Intensities of the Two Modifications of ZrCr₂

MgZn ₂ Type			MgCu ₂ Type		
hkl	d, Observed	I,* Observed	hkl	d, Observed	I,* Observed
002	4.136	vft			
003	2.786	vft			
110	2.538	wm	220	2.534	wm
103	2.325	wm			
200	2.197	vft			
112	2.162	m	311	2.163	ms
201	2.125	wm			
004	2.062	w	222	2.071	w
202	1.934	vft			
104	1.863	ft			
210	1.678	vft			
212	1.542	vw			
204	1.510	vvft			
300	1.466	w	422	1.467	wm
213	1.424	wm			
302	1.383	wm	511	1.383	m
205	1.320	wm			
214	1.296	vft			
220	1.271	wm	440	1.270	m
116	1.212	vft			
			620	1.136	vw
			533	1.096	w
			622	1.083	vw
			642	0.9610	wm
			731	0.9364	m
			800	0.8994	vw
			822	0.8480	w
			751	0.8308	m
			662	0.8254	vw
			911	0.8251	ft

* Intensities: s, strong; ms, medium strong; m, medium; wm, weak medium; w, weak; vw, very weak; ft, faint; vft, very faint; vvft, very very faint.

of equations for interplanar spacings for a series of high angle lines. The results are as follows: MgZn₂ type — $c = 8.262$ kX, $A = 5.079$ kX. MgCu₂ type — $a = 7.195$ kX.

It is interesting to note that TiCr₂ behaves in reverse fashion³ in that the MgCu₂ structure is the low temperature modification and the MgZn₂ structure is the high temperature modification.

References

- ¹ R. F. Domagala, D. J. McPherson, and M. Hansen: This issue p. 279.
- ² E. T. Hayes, A. H. Roberson, M. H. Davies: *Trans. AIME* (1952) **194**, p. 304; *JOURNAL OF METALS* (March 1952).
- ³ B. W. Levinger: *Trans. AIME* (1953) **197**, pp. 195-196; *JOURNAL OF METALS* (February 1953).

W. ROSTOKER is Research Metallurgist, Metals Research Dept., Armour Research Foundation of Illinois Institute of Technology, Chicago.

TN 148E. Manuscript, Oct. 30, 1952.

The work reported was done under AEC Contract No. AT(11-1)-149.

Grain Boundary Sliding and Migration and Intercrystalline Failure Under Creep Conditions

by Hsing C. Chang and Nicholas J. Grant

Creep of very coarse grained, high purity aluminum was studied at 400° to 1100°F with an initial stress range of 50 to 1200 psi. The process of boundary sliding and migration was studied. The driving force of boundary migration under creep conditions is shown to be a combination of strain energy and surface energy. A theory is presented regarding the role the grain boundaries play under creep conditions. From this theory intercrystalline failure of commercial alloys can be explained. Also from this theory an optimum grain size should exist for good high temperature properties of high purity materials.

IN the investigation of the creep of very coarse grained, high purity aluminum previously reported,¹ the cyclic nature of the process of grain boundary sliding and migration has been established by microscopic observation of the actual creep process as well as metallographically. It was also substantiated by measuring localized strains across the grain boundaries. In addition, it was shown how extensive subgrain and fold formation may result from boundary sliding and how the slid grain boundary may become sharply wavy as a result of subgrain formation.

Since the publication of those results, additional information on the process of grain boundary sliding and migration has been obtained. It is the purpose of this paper to report on the direction and driving force of boundary sliding and migration, the effect of grain size, and the effect of temperature. Finally the effect of decreasing purity (alloys 2S and 3S) on the process of boundary sliding and migration is noted. From these results, an explanation is presented for the intercrystalline failure of alloys under creep conditions. The effects of grain size on the creep properties of impure and high purity materials are discussed in the same light.

The experimental procedures and technique have been presented elsewhere.¹ It is only necessary to

state how the 2S and 3S aluminum specimens are prepared.

Machined specimens were first annealed at 600°F for about 12 hr. In order to produce a large grain size the specimens were then stretched 3 to 8 pct. The specimens were marked with reference marks, electropolished, annealed at 900°F for 24 hr and at 1150°F for 12 hr, and repolished.

The grain size of 2S aluminum produced by this treatment is comparable to that of high purity aluminum in the direction of its width of the specimen, i.e., there are 2 to 4 grains across the width of the specimen. However, the grains of 2S aluminum are 3 to 10 times longer in the direction of the specimen axis. On the other hand, the grain size of coarse grained 3S aluminum ranges from 10 to 20 grains across the width of the specimen due to the treatment just outlined and therefore is much smaller than that of both high purity and 2S aluminum. As in 2S aluminum, the grains are about 3 to 10 times longer in the direction of the specimen axis than in the direction of the width of the specimen. The arrangements of the grains in 2S and 3S aluminum were generally irregular; therefore it was difficult to follow the course of the grain boundaries.

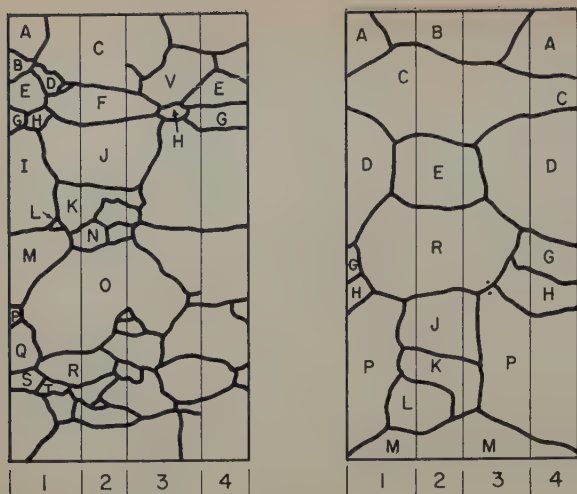
Results

Method of Presentation: In order to show the arrangement of the grains, especially the direction and positions of the grain boundaries, traces of the grain boundaries on the four surfaces of the specimens were unfolded and mapped out after macroetching. Figs. 1 and 2 show the structural development drawings of specimens P-3 and P-8 respectively. The two flat surfaces (of which the front one faces the microscope) and the round-edged surfaces will be called the "front surface" and "back surface" and

H. C. CHANG is DIC Staff Member and N. J. GRANT, Member AIME, is Associate Professor, Dept. of Metallurgy, Massachusetts Institute of Technology, Cambridge, Mass.

Discussion on this paper, TP 3453E, may be sent, 2 copies, to AIME by April 1, 1953. Manuscript, Sept. 15, 1952. Los Angeles Meeting, February 1953.

This paper is based on a thesis by H. C. Chang submitted in partial fulfillment of requirements for the degree of Doctor of Science in Metallurgy to Massachusetts Institute of Technology.



1—BACK SURFACE
2—LEFT EDGE

3—FRONT SURFACE
4—RIGHT EDGE

Fig. 1—Specimen P-3.

Fig. 2—Specimen P-8.

Figs. 1 and 2—Structural development drawings of specimens P-3 and P-8, respectively, tested at 700°F and 85 psi.

the "right free edge" and "left free edge" respectively. Capital letters were used to distinguish individual grains.

The results presented below and the observations made came from eight high purity aluminum, five 2S aluminum, and one 3S aluminum specimens. High purity aluminum specimens were subjected to creep at 400°, 700°, and 1100°F with an initial stress range of 50 to 1200 psi. The 2S aluminum specimens were subjected to creep at 700°, 900°, and 1100°F with a stress range of 200 to 800 psi. One 3S aluminum specimen was subjected to creep at 1100°F with a stress of 300 psi. Several hundred micrographs were taken both during the actual creep tests and after the specimens had been removed from the creep furnace. Many micrographs showing the same phenomena were obtained; however, only the most representative ones are presented here.

Most of the micrographs were taken with oblique light so that maximum details could be shown in the same one. All the micrographs will be so presented in the text that the direction of the applied tension runs from top to bottom of the illustration. Specimen numbers are included after the figure number. The grain letter is indicated on the micrographs and schematic drawings in accordance with the structural development drawings of the specimens.

Direction of Boundary Sliding and Migration: The direction of grain boundary sliding was checked frequently by observing the direction of the granular offset on the specimen surface and along the slid grain boundary surfaces. As a result of many observations of this sort, it can be concluded that the direction of grain boundary sliding is governed by the direction of the shearing stress acting on the boundary surface.

In specimen P-3 (Fig. 1, tested at 700°F) a grain G, bounded by a free edge of the test specimen, passes through the whole thickness of the specimen. This grain slid as a whole in the direction of the thickness of the specimen. As a result of this, the back surface of this grain was depressed and the front surface extruded, as illustrated in Fig. 3. This could be readily observed visually. The direction of

boundary migration is indicated by arrows in Figs. 4a and 5a which are micrographs of the front and back surfaces of grain G, respectively. According to the geometry of this grain, it is natural that it should slide in the way observed in Figs. 4 and 5. After examining many cases of this kind it is necessary to point out that the direction of boundary migration is generally toward the side which is depressed, as shown by the solid arrows of Fig. 3; i.e., away from grain G in Fig. 4 and toward grain G in Fig. 5. This position is also the one which has the least boundary surface area.

That the rate of grain boundary migration is severely nonuniform can be seen clearly in Fig. 6 (specimen P-8 tested at 700°F). A schematic drawing of Fig. 6 is shown in Fig. 7 to illustrate the sequence of steps in the migration of this boundary as observed during the actual test. It should be noted that the migrating boundary tends to approach a position which is perpendicular to the specimen axis. This position of the grain boundary is also the one which has the smallest grain boundary area.

Fig. 8 shows a grain boundary of grains A and B of specimen P-3. From Fig. 1 it can be seen that grain B did not go all the way through the thickness of the specimen. The original doubly curved boundary tended to straighten out. It appears that the inflection point of this migrating boundary divides

Fig. 3—Schematic drawing of the direction of boundary sliding and migration in specimen P-3, grain G. Broken arrow indicates the direction of boundary sliding. Solid arrow indicates the direction of boundary migration. Dotted lines indicate a more stable position of the migrated grain boundaries.



this boundary into two regions in which it migrated in opposite directions, as shown by the arrows in Fig. 8.

The three examples cited above signify a type of grain boundary migration in which the grain boundary tends to reduce its surface energy by reducing its surface area. It must be remembered that all the grain boundaries were stabilized after the annealing treatment (without load) of 24 hr at 900°F and 12 hr at 1150°F. The stability was checked by the fact that no boundary migration was observed even by annealing for another three days at 1150°F. Accordingly, the extensive boundary migration must be attributable only to the applied stress. Boundary sliding caused by the applied stress overcomes the locking effect at the stable triple points. This permits the grain boundary surface energy to come into effect, causing the grain boundary to migrate.

Fig. 9a and b (specimen P-8, Fig. 2, tested at 700°F) shows an interesting case in which the migration of the boundary between grains D and E typifies a case in which the strain energy plays the dominant role. Grain E was apparently under com-

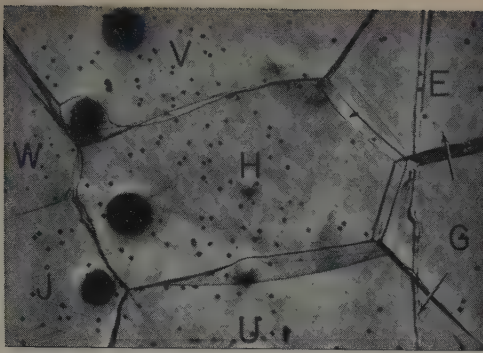


Fig. 4a—Specimen P-3, front surface. The enclosed grain was nonuniformly deformed; grain G slid as a whole. Solid arrow indicates the direction of boundary migration. X50. Area reduced approximately 60 pct for reproduction.

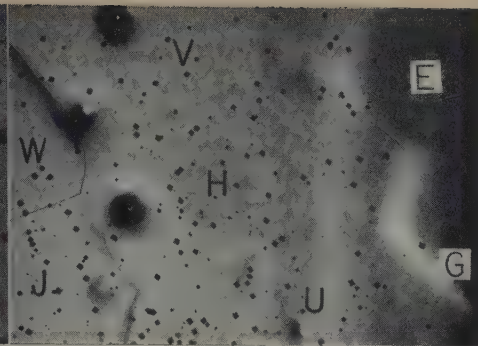


Fig. 4b—Specimen P-3, front surface. Same field as an Fig. 4a, repolished and etched. X50. Area reduced approximately 60 pct for reproduction.

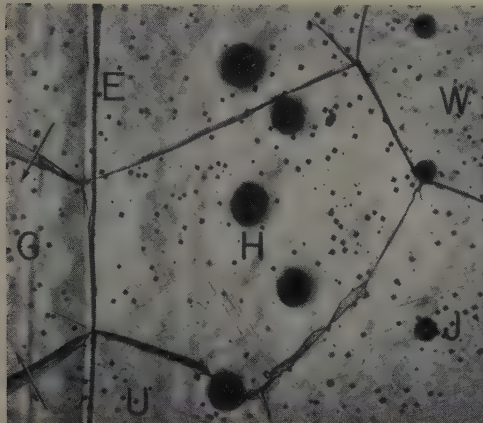


Fig. 5a—Specimen P-3, back surface. Grain G slid as a whole. Solid arrow indicates the direction of boundary migration. X50. Area reduced approximately 60 pct for reproduction.

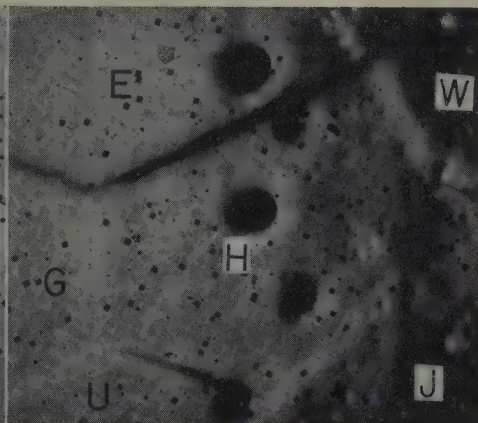


Fig. 5b—Specimen P-3, back surface. Same field as in Fig. 5a. Repolished and etched. X50. Area reduced approximately 60 pct for reproduction.

pression since sliding had taken place along the boundaries of grains C and E, and grains E and R. Furthermore, because of the blocking effect of the triple points of grains C, D, and E, and of grains D, E, and R, on the sliding of the boundaries of grains C and D and grains D and R, the grain boundary between grains D and E is subjected to bending. The compression side of the bending is in grain E and the tension side is in grain D. It is probably due to this stress system and the locking effect of the two triple points that the upper part of the boundary of grains D and E bulges into grain E during progressive boundary migration. Again note how the grain boundaries between grains C and E



Fig. 7—Schematic drawing of Fig. 6 shows the uneven steps of boundary migration. The numbers indicate the consecutive steps of the grain boundary migration.

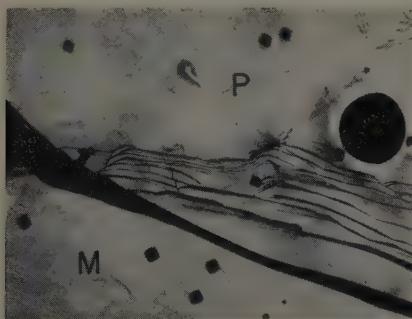


Fig. 6—Specimen P-8, front surface. Uneven nature of grain boundary sliding and migration. X100. Area reduced approximately 70 pct for reproduction.

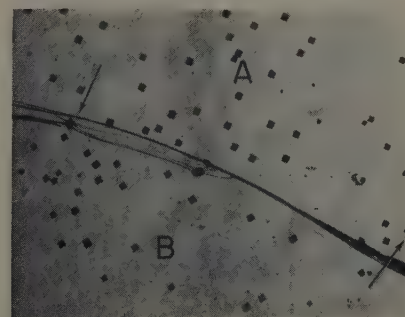


Fig. 8—Specimen P-3, back surface. The boundary migrated in opposite directions, as shown by arrows. Note the attracting effect of the etch pit below the arrow at the left on the migrating grain boundary. X100. Area reduced approximately 70 pct for reproduction.

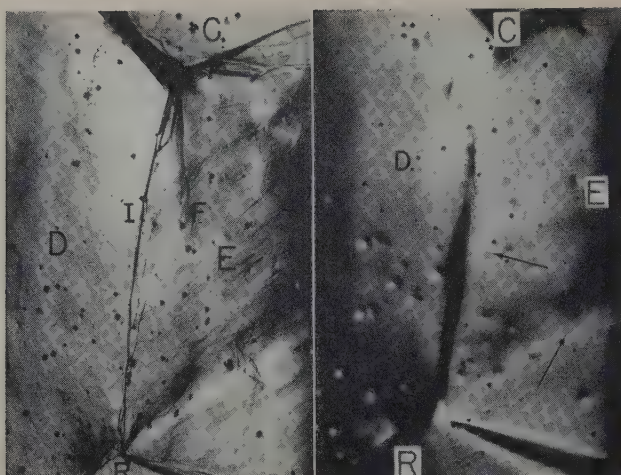


Fig. 9a—Specimen P-8, back surface. Uneven nature of grain boundary migration as a result of non-even distribution of stresses in grain E. I and F indicate the initial and final positions of the grain boundary between grains D and E respectively. Note fold in grain E opposite grain boundary between grains D and R. X50. Area reduced approximately 75 pct for reproduction.

Fig. 9b—Specimen P-8, back surface. Same field as Fig. 9a. Repolished and etched. The rotation of the boundary between grains C and E to a position almost perpendicular to the specimen axis can also be observed. Note subgrain boundaries pointed out by arrows. X50. Area reduced approximately 75 pct for reproduction.



Fig. 10—Specimen P-1. Extensive boundary migration for a case where four grains of comparable size go across the width of the specimen. The zigzag path of the triple point is clearly shown. X50. Area reduced approximately 60 pct for reproduction.

and also E and R have migrated into positions approaching 90° to the stress axis, making grain E bounded by rectangular boundaries.

Effect of Grain Size: It has been shown that the process of boundary sliding and migration is a highly cooperative one. It will be expected that the more the grains go across the width of the specimen, the more extensive will be the boundary migration. The reason for this is that whenever one grain boundary slides, the two triple points at the ends of this slid boundary, and therefore the other two grain boundaries constituting the triple point, must migrate in order to maintain the triple point.

Fig. 10 is a fine example showing the large extent

of boundary migration when four grains go across the width of the specimen (in most cases only two grains go across the width of the specimen). I and F indicate the initial and final positions of the grain boundaries. It should be pointed out that specimen P-1, from which Fig. 10 was obtained, was subjected to creep for 234 hr at 700°F (specimen P-8, for 81 hr at 700°F) and therefore more time was allowed for this extensive boundary migration to take place.

The observation that the path of movement of the triple point is zigzag may be explained as below. Fig. 11a to d (all the boundary surfaces are assumed to be perpendicular to the plane of the paper) shows the stages of the movement of a triple point by the process of boundary sliding and migration. It is considered that the boundary of grains A and B slides first. As a result of this sliding an offset or new surface, as indicated by the dashed line 1-2 in Fig. 11a, is produced between grains A and C. This provides the driving force for the boundary of grains B and C to migrate to form a new triple point, 2, as shown in Fig. 11b. If the other two grain boundaries cannot slide, the traces of the triple point movement would be on the extension of the slid boundary. But this is an unlikely situation because the equilibrium arrangement of grains requires the condition that at least two of the three grain boundaries can slide. If now the boundary of grains A and C slides (Fig. 11c), the boundary of grains A and B must migrate in order to form another triple point 3, as shown in Fig. 11d. Therefore, the traces of triple point movement frequently follow a zigzag path.

Fig. 12a shows an interesting case of how a small surface grain was consumed by three large neighboring grains. This is evident by a study of Fig. 12b, which shows the specimen repolished and etched. The etch pits clearly show the old and new grain change. It can be seen from Fig. 1 that, after the

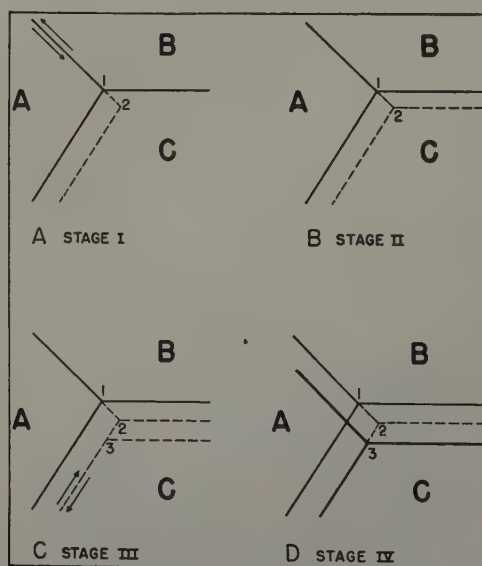


Fig. 11—The stages of the movement of a triple point. A. An offset (1) (2) was produced by sliding along the boundary between grains A and B. B. The boundary between grains B and C migrated from position (1) to position (2) as indicated by the dotted line. C. Offset (2) (3) was produced by sliding along the boundary between grains A and C. D. The boundary between grains A and B migrated from position (2) to position (3) as indicated by the heavy solid line. The heavy solid lines indicate the final arrangement of the grain boundaries.

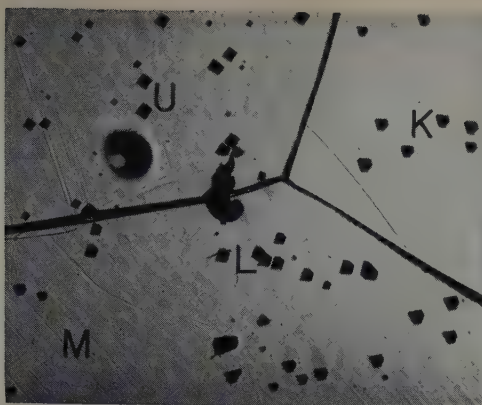


Fig. 12a—Specimen P-3, back surface. Deformed surface. Note how a small surface grain L was eaten up. X150. Area reduced approximately 60 pct for reproduction.

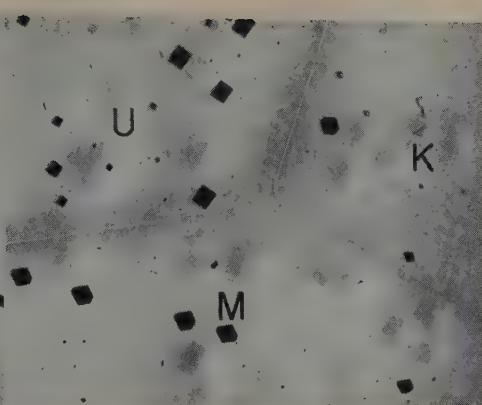


Fig. 12b—Specimen P-3, back surface. Same field as Fig. 12a. Repolished and etched. X150. Area reduced approximately 60 pct for reproduction.

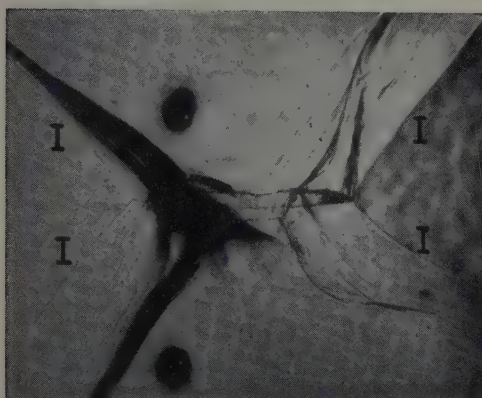


Fig. 13—Specimen P-9. One hour after reaching 1100°F. Two triple points met in the center of the field and then separated in the top-bottom direction. X60. Area reduced approximately 60 pct for reproduction.

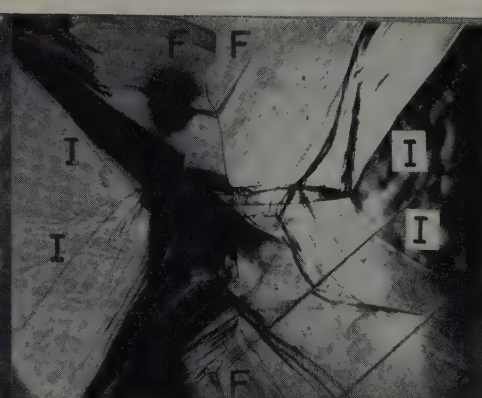


Fig. 14—Specimen P-9. Same field as Fig. 13. One hour and 35 minutes after reaching 1100°F. The grain boundary joining the two original triple points rotated 90°. X60. Area reduced approximately 60 pct for reproduction.

disappearance of the small grain, the grain boundaries of the three large grains went through the thickness of the specimen.

Effect of Temperature: As the temperature increases the atomic mobility (diffusion) increases, and so does the rate of boundary migration. Figs. 13 and 14 were taken from the same field during the creep process of specimen P-9, which was subjected to creep at 1100°F under a stress of about 65 psi. The rate of boundary migration was of the order of 1×10^{-5} cm per sec at the beginning of the test. It is interesting to note how the boundary bounded by the two triple points rotated 90° (from Fig. 13 to Fig. 14).

Fig. 15 is a schematic drawing showing the steps of this rotation process, solid arrows indicating the direction of migration of the triple points. The two triple points must come close to each other, or even meet at point O, before they migrate in opposite directions.

Figs. 16 through 19 show a similar case for specimen P-10, which was subjected to creep at 1100°F under an initial stress of about 50 psi. Each figure represents a successive time interval during the test, namely, 0.5, 3.25, 9.1, and 18.5 hr after reaching the testing temperature, 1100°F.

The specimen fractured after 30.4 hr. The initial positions of the grain boundaries were established before the test by macroetching and are also indicated by the letter I in Fig. 16 (the following dis-

cussion refers to Fig. 16). The triple point marked (1) migrated through a zigzag path in a stepwise manner toward the lower left direction, while the triple point marked (2) migrated toward the upper left direction also in a stepwise manner, as indicated by the solid arrows. They come very close to each other at point A. After point A, the appear-

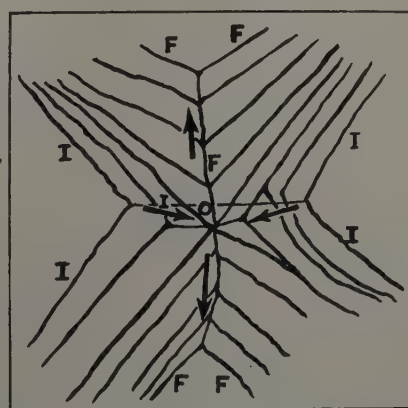


Fig. 15—Schematic drawing of Figs. 13 and 14 showing the steps whereby the grain boundary connecting two triple points rotated about 90°. I and F indicate the initial and final positions of grain boundaries and arrows indicate the directions of the migration of the triple points.

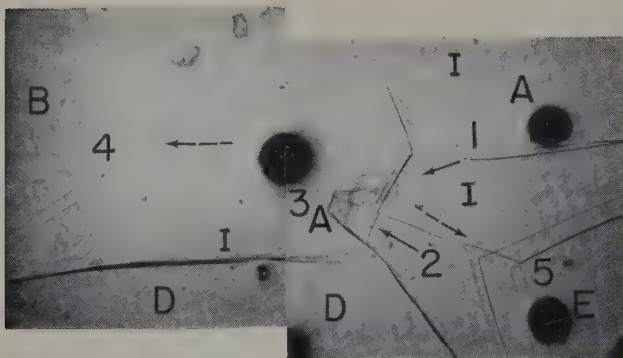


Fig. 16—Specimen P-10. One-half hour after reaching 1100°F. Note the initial grain boundary connecting two triple points, 1 and 2, rotated about 90°; now lying about 68° to the specimen axis. Solid arrows indicate the directions of the migration of the two triple points, 1 and 2, after which they met in the neighborhood of point 3. Dotted arrows indicate the directions of separation of the newly formed triple points to position 4 and 5. X60. Area reduced approximately 60 pct for reproduction.

ance of the traces of the grain boundaries indicated that the two triple points must have separated very rapidly, one to the upper left, marked (4), and the other to the lower right, marked (5), as indicated by the dotted arrows. It has been suggested by Fullman, Burke, and Turnbull² that the two migrating triple points may meet at a common point during grain growth before they separate in a direction different from that which they came to meet. This common point is marked (3). This is a plausible suggestion based on the more exact picture shown in Fig. 13. Once the two triple points occupy a common position, a maximum instability must exist from a grain boundary configuration viewpoint.³ Due to the magnitude of this instability, the two new triple points migrated at a very rapid rate to new positions (4) and (5), indicated by the dotted arrows, leaving no traces of grain boundaries as is usual in a slower process of migration.

The left triple point (4) disappeared at the left free edge of the specimen half an hour after reaching the creep testing temperature at 1100°F, while the right triple point marked (5) continued to migrate toward the right free edge of the specimen to a position (6) in Fig. 17, taken 3.25 hr after reaching 1100°F. The grain boundary connecting the two new triple points now becomes one bounded by one triple point (6), Fig. 17, and the left free edge of the specimen, and is the boundary between grains A and D. This boundary between A and D had migrated in steps, as shown by the arrow in Fig. 17, in approaching a position almost perpendicular to the axis of the specimen. Evidence of sliding of the boundary between grains A and D during consecutive steps of migration can be obtained by observing the offset of the traces of the old grain boundaries (Fig. 16). Fig. 18, taken 9.1 hr after reaching 1100°F, indicates that the boundary between grains A and D swung to a position still closer to 90° to the axis of the specimen, and the new triple point (6), Fig. 17, of grains A, E, and D moved closer to the right free edge of the specimen, as shown by (7) in Fig. 18. At the end of the test (30.4 hr after reaching 1100°F), the grain boundary between grains A and D had migrated to a position almost perpendicular to the axis of the specimen, while the new triple point of grains A, E, and D almost disappeared at the right free edge of the specimen, Fig. 19.

All the results presented above came from high purity aluminum specimens which were subjected to creep at 700° and 1100°F. At 700°F the grain boundaries show very extensive grain boundary sliding and migration before the grains show signs of deformation, and this is even more apparent at 1100°F. However, no appreciable boundary migra-

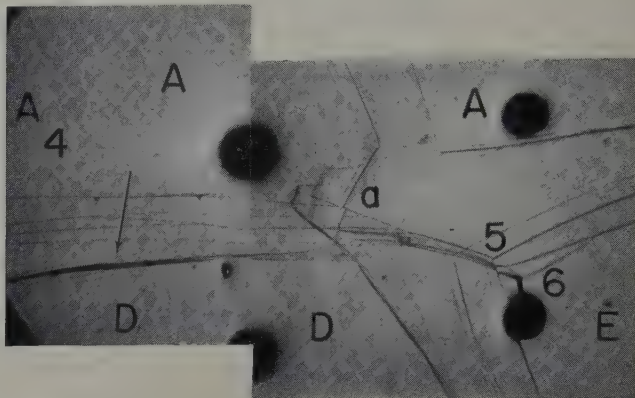


Fig. 17—Specimen P-10. Same field as Fig. 16, 3.25 hours after reaching 1100°F. The triple point 4 disappeared at the left edge of the specimen. The triple point 5 migrated to position 6. The new grain boundary between grains A and D tended to rotate perpendicular to the specimen axis as indicated by the solid arrow. The evidence of sliding of the boundary between grains A and D can be obtained by observing the offset, indicated by a. X60. Area reduced approximately 60 pct for reproduction.

tion was found for specimens which were subjected to creep at 400°F for up to 475 hr, whereas the usual evidence of grain boundary sliding was still observed.

Effect of Impurities: Boundary sliding and migration were observed in 2S aluminum for creep testing temperatures of 900° and 1100°F. This is shown in Fig. 20a and b at 900°F. The extent of grain boundary migration was observed to be a little greater at 1100°F than at 900°F for 2S aluminum. However, the extent of boundary migration for 2S aluminum was very much smaller at 900°F than in the case of high purity aluminum at 700°F (compare Fig. 20a with Fig. 10). It has been observed in high purity aluminum that the grain boundary usually tended to reduce its surface area during migration. It may be seen from Fig. 20 that 2S aluminum behaves in a similar manner but with materially less grain boundary migration. The course of grain boundary migration is more irregular than has been presented above for high purity aluminum. A 3S aluminum specimen subjected to creep at 1100°F for 79.5 hr showed almost no evidence of boundary migration although the usual signs of fairly restricted boundary sliding were observed. Based on these observations, it was quite evident that the alloy and impurity content of 2S aluminum fixes the grain boundary more rigidly, allowing only a small amount of migration, whereas in 3S aluminum migration is restricted almost to the vanishing point. The effect of such grain boundary fixation results in the low ductility noted by Servi and Grant⁷ as the alloy content of aluminum increases from high purity to 2S and then 3S aluminum.

Discussion

Intercrystalline Failure: It has been shown metallographically that grain boundary migration is very structure-sensitive. Boundary migration may be

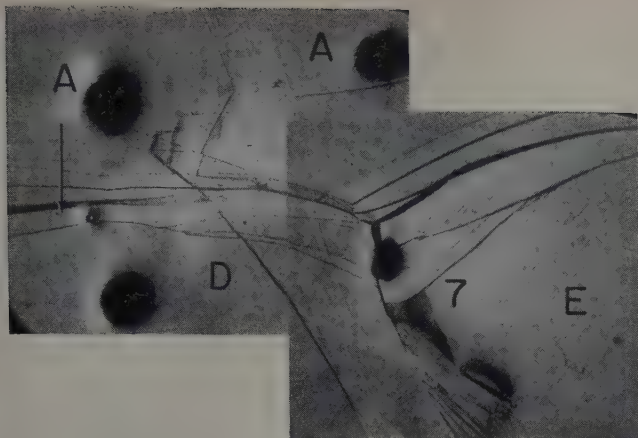


Fig. 18—Specimen P-10. Same field as Figs. 16 and 17. 9.1 hours after reaching 1100°F. The triple point 5 in Figs. 16 and 17 continued to migrate toward the right edge of the specimen. The new boundary continued to rotate perpendicular to the specimen axis as indicated by the solid arrow. X60. Area reduced approximately 60 pct for reproduction.

severely restrained by a second phase as in the case of 2S aluminum, or it may be almost completely stopped with larger amounts of second phase as in the case of 3S aluminum, as predicted by Zener³ on the basis of surface energy considerations. It has also been shown that boundary migration is a kind of recovery process which makes further boundary sliding possible.¹ In impure or alloyed materials, grain boundary migration becomes less significant, and sliding is restricted to a fixed boundary. Since the grains are strengthened by alloying or a second phase, the stresses which are built up around the triple point as a result of boundary sliding cannot be released as readily, if at all, by deformation in the grains. This stress built up by sliding along the same boundary would eventually give rise to cracks at or in the vicinity of the slid boundary. Stress concentration caused by cracks would result in intercrystalline fracture. This is why commercial alloys subjected to high temperature creep show intercrystalline fracture, whereas no sign of intercrystalline failure has been observed for high purity aluminum in the present investigation. In the case of high purity aluminum, boundary sliding not only occurs extensively because of the progressive boundary migration but also causes extensive subgrain and fold formation as shown in ref. 1. Such grain

boundary mobility prevents intercrystalline fracture.

Furthermore, in impure or alloyed materials, the boundaries would be expected to be more irregular and are shown metallographically to be so (see Fig. 20). During boundary sliding an irregular or wavy grain boundary would give rise to local high stress regions not only at the triple point but also at odd positions where the grain boundary is not plane. Therefore, cracks may develop not only at the triple point but also along the slid grain boundary.

Effect of Grain Size on Creep Properties: High Purity Metals: It is interesting to explore the ques-

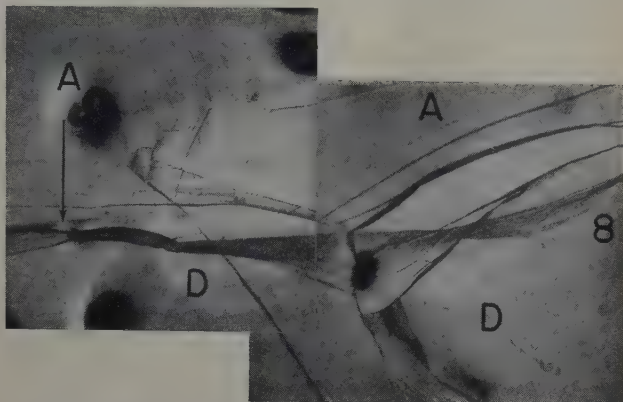


Fig. 19—Specimen P-10. Same field as Fig. 16. 18.5 hours after reaching 1100°F. The triple point 5 in Fig. 16 migrated to point 8. The migration of the new grain boundary indicated by the arrow almost stopped after reaching a position nearly perpendicular to the specimen axis. X60. Area reduced approximately 60 pct for reproduction.

tion of the effects of grain size on the creep properties of a metal on the basis of the observations of the behavior of grain boundaries in this work and in a previous publication.¹ It is stated conventionally that above the equicohesive temperature or transition temperature (the temperature at which the material changes from low temperature behavior to high temperature behavior) the larger the grain size the better the creep properties as measured by minimum creep rate and rupture life. This statement, while generally true, has certain limitations and exceptions. High purity metals do not follow this rule over the entire range of grain sizes,^{4,5} and it is possible that some single-phase alloys may also not conform entirely.⁶ By varying the grain size ten thousand fold for high purity aluminum

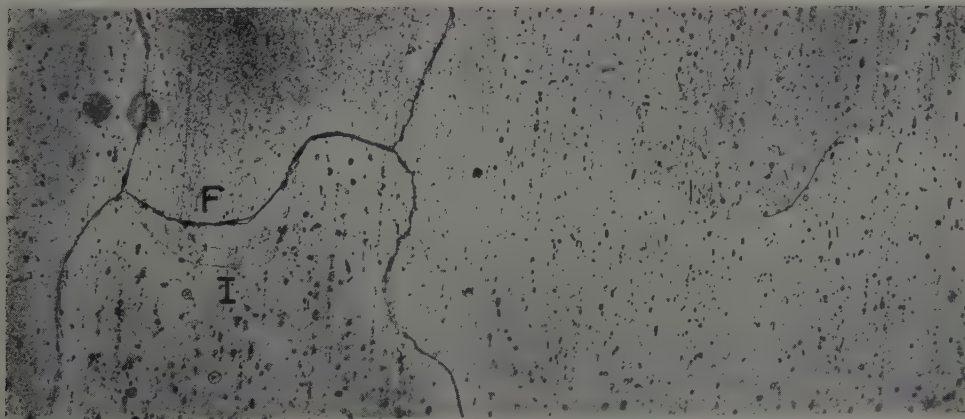


Fig. 20a—Specimen 2S-7. Grain boundary migration in 2S aluminum at 900°F. I and F indicate the initial and final positions of the migrating grain boundary respectively. X150. Area reduced approximately 60 pct for reproduction.

Fig. 20b—Specimen 2S-7. Same field as Fig. 20a, repolished and etched. X150. Area reduced approximately 60 pct for reproduction.

(99.995 pct), Crussard⁴ was able to find an optimum grain size at which the secondary creep rate is a minimum. This conclusion is also proved to be true for zinc specimens.

As shown previously,¹ boundary sliding will inevitably cause deformation in the grains either in the form of subgrains or in the form of folds, or if the grain size is large enough, by slip when sufficient deformation has occurred.⁷ In other words, the ability of the grains to accommodate deformation created by boundary sliding must be taken into account in order to evaluate the resistance to creep for a high purity metal. It should also be remembered that the difference in composition and in strength of the grain and grain boundary in very pure metals is quite small.⁷

For high purity material of a grain size smaller than the optimum, the resistance to creep is small because boundary sliding has many loci, and once such sliding has occurred along boundaries favorably oriented, the grain boundary deformation can be transmitted to other boundaries. The deformation can take place in this manner with less deformation in the grains. In order to deform the specimen as a whole it is not necessary for the deformation to go completely through the grain. For example, folds, one of the noted mechanisms of deformation¹ (see Fig. 9, grain E), cannot develop completely through a grain because of the blocking effects of the grain boundaries. As will be shown in a later paper, the development of folds depends primarily on the length of the sliding grain boundary relative to the length of the grain in the direction of the sliding boundary. In other words, fold deformation depends on the grain size.

For high purity metal of a grain size larger than the optimum, the deformation initiated by boundary sliding can be transmitted to and accommodated by deformation in the grains because the grain deformation is now progressively less influenced by grain boundaries as the grain size increases. Thus while the grain boundary may deform before the grain at elevated temperatures, the grain boundary nevertheless has some blocking effect upon the deformation taking place in the grain. Thus for high purity metals, the resistance to creep is also small for very large grain size materials.

Alloyed or Impure Metals: While it is difficult to predict the effects of grain size on the creep or creep-rupture properties of commercial materials, it can definitely be stated that the effects of grain size are not necessarily the same for both classes of metals. The existence of an optimum grain size, prior to reaching the extreme grain size where orientation effects of the grains become controlling, has not been demonstrated. From fairly limited data on 2S and 3S aluminum it appears that the grains are relatively strengthened more than the grain boundaries. Barring grain boundary precipitates this is probably true of other metals. In 2S and 3S aluminum while it is possible to eliminate slip in the grains for a given grain size, it has not been possible to eliminate grain boundary sliding. If the above is true, then high temperature strength depends on the amount of strain which the grain boundaries can sustain before cracks develop, and on how easily or readily the cracks are propagated. Examination of many hundreds of micrographic structures has clearly demonstrated that the grain boundaries which slide most readily and most extensively are those which are at 45° to the stress

axis and offer a smooth plane boundary. It is readily evident that the fine grained commercial alloys offer many grain boundaries which satisfy the above conditions (see Figs. 22 and 23 of ref. 7). In coarse grained commercial alloys, on the other hand, the grain boundaries are usually curved, are irregular (not plane), and offer only very short sections where the grain boundary can slide readily or extensively (see Fig. 20). But even in these sections the grain, being considerably stronger than the grain boundary, acts to restrain deformation and cracking.

Summary and Conclusions

From creep studies of very coarse grained, high purity 2S and 3S aluminum at 400°, 700°, 900°, and 1100°F, the following conclusions regarding the process of boundary sliding and migration can be drawn.

1—The direction of boundary sliding is primarily governed by the direction of the shearing stress acting on the boundary surface. The driving force which controls the direction of boundary migration is shown to be a combination of strain energy and surface energy. The latter is important at high temperatures.

2—The zigzag nature of the movement of the grain boundary triple point is considered to be a necessary consequence of the highly cooperative process of grain boundary sliding and migration because the direction of boundary migration depends primarily on the direction in which the grain boundary slides as the initial step. The extensiveness of boundary migration during creep of high purity aluminum at high temperatures, particularly of fine grain size, is believed also to be due to the highly cooperative nature of grain boundary sliding and migration.

3—Boundary migration and sliding were observed in 2S aluminum at 900° and 1100°F. As a result of the alloy and excess phase content, the amount of boundary migration was much smaller and its course more irregular than was observed in high purity aluminum. For 3S aluminum at 1100°F, normal boundary sliding was observed (leading to intercrystalline fracture) without any clear evidence of grain boundary migration.

4—A theoretical picture is proposed to explain the superiority of coarse grained structures in commercial alloys.

Acknowledgments

The authors wish to express appreciation to J. T. Norton, A. R. Chaudhuri, A. M. Gervais, and Gloria Johnson, all of whom contributed significantly to this research. Thanks are also due to the Bureau of Ships for sponsoring this research.

References

- ¹H. C. Chang and N. J. Grant: *Trans. AIME* (1952) 194, p. 619; *JOURNAL OF METALS* (June 1952).
- ²R. L. Fullman: *Metal Interfaces* (1952) p. 179. ASM. J. E. Burke and D. Turnbull: *Progress in Metal Physics* (1952) London. Pergamon Press Ltd.
- ³C. S. Smith: *Trans. AIME* (1948) 175, p. 15; *METALS TECHNOLOGY* (June 1948).
- ⁴C. Crussard: *Comp. Rend.* (1944) 219, p. 681.
- ⁵E. R. Parker and C. F. Riisness: *Trans. AIME* (1944) 156, p. 117.
- ⁶P. Shahinian and J. R. Lane: Influence of Grain Size on High Temperature Properties of Monel. ASM Preprint (1952).
- ⁷I. S. Servi and N. J. Grant: *Trans. AIME* (1951) 191, p. 917; *JOURNAL OF METALS* (October 1951).

Determination of the Absolute Grain Boundary Energy of Gold at 1300°K

by F. H. Buttner, H. Udin, and J. Wulff

GRAIN boundaries, the interface between adjacent crystals differing only in respective orientation, have been the object of much experimental and moderate theoretical attention for many years. The earlier experimental work was primarily concerned with the effect that grain boundaries have on the physical behavior of metals, while the basic nature of the boundaries themselves drew only secondary attention. A complete turnabout has been witnessed in more recent years, however, as researchers are now undertaking investigations bearing as directly as possible on the character and physical properties of the grain boundary. Quite comprehensive reviews of the past literature on the subject of grain boundaries have been reported on numerous occasions by various authors, and together these references represent a thorough coverage.¹⁻⁷

It becomes evident in these reviews and other papers⁸⁻¹⁵ that the properties of grain boundaries can be explained by regarding a grain boundary as a crystalline region of transition between two unmatched grains. Studies show that grain boundaries have a definite interfacial energy. By measuring the geometry about a point where three interfaces meet in equilibrium, the energy of any two boundaries can be measured with respect to the third. If the absolute interfacial energy of one boundary is known, the absolute energy of the other two boundaries can be calculated. This apparently holds true for any system of phases and interfaces.¹⁶⁻²⁵

Most studies have been carried out on solid-solid or liquid-solid systems, or systems of both. However, if about the point of intersection one phase is vapor and the other two are disoriented grains, then two interfaces are surfaces, and one is a grain boundary. Investigations leading to relative grain boundary energy for this particular system have been made by Fullman,²³ Greenough and King,²⁴ and Bailey and Watkins.²⁵ Herring²⁶ treats the system mathematically and arrives at an equation, which appears as Eq. 1, in a form consistent with the reference angles indicated in Fig. 1,

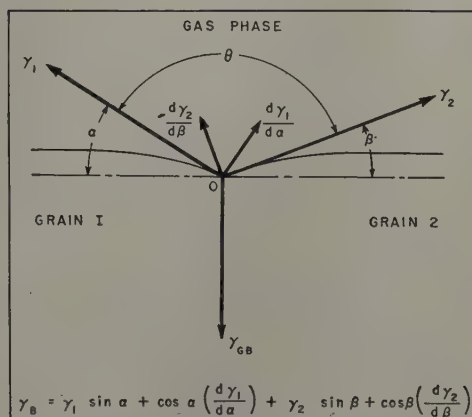


Fig. 1—The interfacial stress pattern about a point in the root of the thermally etched grain boundary groove.

$$\gamma_B = \gamma_1 \sin \alpha + \cos \alpha \left(\frac{d\gamma_1}{d\alpha} \right) + \gamma_2 \sin \beta + \cos \beta \left(\frac{d\gamma_2}{d\beta} \right) \quad [1]$$

As the system of interfaces comes to equilibrium, a groove of angle θ appears at the intersection of the grain boundary with the surface, an effect first observed by Rosenhain and Humfrey.²⁷ Eq. 1 is essentially a summation of the vertical components in Fig. 1 set equal to zero, where γ_1 and γ_2 are surface tension vectors lying along the side of the groove at point O in the groove root. The differential vectors represent the forces tending to rotate the surface into a position that will expose a crystal cleavage surface of lowest energy.

Chalmers, King, and Shuttleworth²⁸ simplify Eq. 1 by assuming the differential vectors equal to zero, $\gamma_1 = \gamma_2 = \gamma_{\text{surface}}$, and arrive at the following equation:

$$\gamma_B = 2\gamma_s \cos \frac{\theta}{2} \quad [2]$$

Greenough and King²⁴ use Eq. 2 for determining the grain boundary energy of silver using prepared bicrystals of known orientation. Bailey and Watkins²⁵ have done the same for copper, as did Chalmers and others on lead. These authors report the grain boundary values as ratios relative to the surface energy.

In the above work, the orientation of grains forming the grain boundary in all cases was controlled so

F. H. BUTTNER, formerly Research Associate, Massachusetts Institute of Technology, is now Staff Metallurgist, Minerals and Metals Advisory Board, NAS-NRC, Washington, D. C., and H. UDIN and J. WULFF, Members AIME, are Assistant Professor and Professor, respectively, Massachusetts Institute of Technology, Cambridge, Mass.

Discussion on this paper, TP 3485E, may be sent, 2 copies, to AIME by April 1, 1953. Manuscript, June 4, 1952; revised, Nov. 25, 1952. Los Angeles Meeting, February 1953.

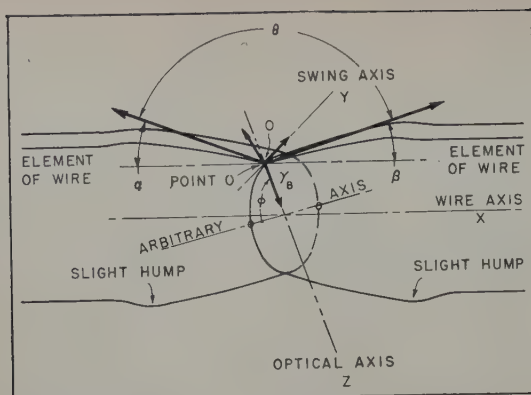


Fig. 2—Perspective of exaggerated grain boundary groove, showing the point O, the force pattern, the angle ϕ , and other important features and dimensions.

as to get disregistry by relative rotation about an axis parallel to the plane of the grain boundary under consideration. This creates "tilt" boundaries consisting of edge dislocations of various concentrations over the surface proportional to the amount of rotation. The generalized results show that the grain boundary energy increases sharply with increasing rotation up to a neighborhood of 15° to 25° , in which region the energy slope tapers off to zero at a saturation level of roughly one third the average surface energy. At still higher angles of rotation where the grains approach a twin orientation, the energy falls off in the same manner. In passing through the twin orientation, the energy falls and rises to form an energy cusp.

The various methods used to measure the groove angle have been critically reviewed by Brooks.⁷ These consist of various techniques of cutting through the groove and observing the root angle on the surface of the cut. Greenough and King²⁴ introduced a goniometric reflected light method, which although imperfect, appears promising from the standpoint of quick and easy measurements of good precision. Essentially, this method is used in the present work.

As was pointed out above, previous investigators studied specially prepared tilt boundaries containing edge-type dislocations. In this paper, boundaries are studied as they appear on 5 mil gold wires recrystallized into a bamboo structure. These boundaries are more or less randomly oriented, since no controlled recrystallization process is involved, except for possible preferential grain orientations arising from the original texture of the cold-drawn

gold wire. The nature of a grain boundary formed at random may be described as a superimposed tilt and twist boundary containing a blend of edge and screw dislocations.²⁰ The purpose of this paper is to outline and discuss the results of a study of random boundaries.

Experiment and Results

In the course of surface tension experiments on copper,³⁰ silver,³¹ and gold,³² conditions of thermal and phase equilibrium were maintained about fine wires held at high temperatures for long periods of time. Grain boundary grooves appear on the surface of these wires during the experimental run and reveal the bamboo structure of the wires. The angular dimensions of these grooves can be used to measure the energy of the grain boundaries. Details of the equipment applied and the procedures followed in the treatment of these fine wires are outlined in detail in the above reports on the surface tension experiments on copper, silver, and gold.

A three dimensional sketch of a wire section showing an exaggerated groove is shown in Fig. 2. The idealized grain boundary running perpendicular to the wire axis produces a groove girding the wire at the surface intersection of the grain boundary. At some angle of rotation, ϕ , from the arbitrary axis, a point O, is observed through a metallurgical microscope. The plane passing through the element of the wire and the wire axis in Fig. 2 is the plane of the paper in Fig. 1. As ϕ changes with rotation of the wire, point O moves along the groove. One of the objects of the experimental procedure is to measure the angles of the force pattern at points along the root of the groove as ϕ rotation passes through 360° . The method used to measure the groove angles employs the goniometric principle introduced by Greenough and King.²⁴

Figs. 3 and 4 show the goniometer apparatus used to measure the important angles. The equipment is in two parts, the goniometer in which a wire is mounted, Fig. 3, and a metallurgical microscope through which light reflections from the wire are observed, Fig. 4. In the goniometer, the wire is strung between two gear linked heads such that the wire axis is perpendicular to the optical axis of the microscope. The gear linked heads are set in bearings in a mounting block. The mounting block has three mutually perpendicular translational degrees

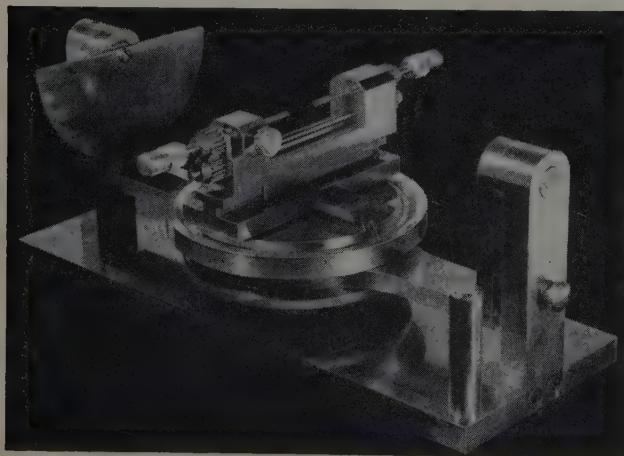


Fig. 3—The goniometer showing wire mount and gear linked head.

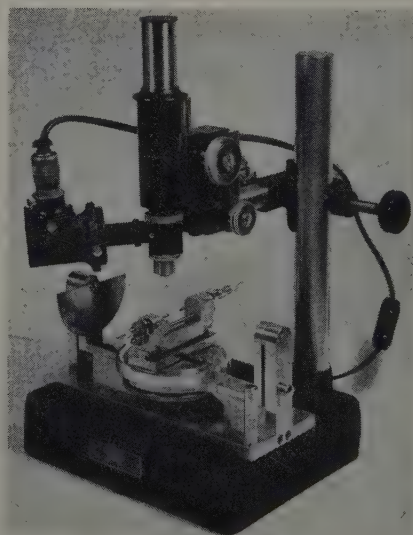


Fig. 4—The goniometer in position beneath the metallurgical microscope.

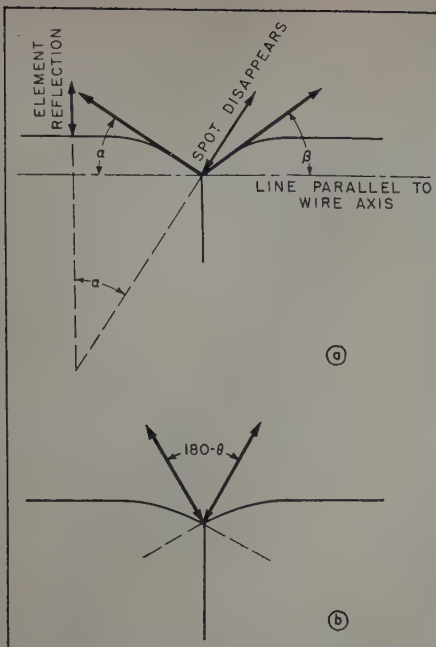


Fig. 5—The geometry about point O showing the principle of angle measurement. (a) Measurement of α and β . (b) Check measurement.

of freedom; up and down in the optical axis, forward and backward from the operator of the device, and sideways along the swing axis. Such freedom makes it possible to station point O at the intersection of the optical axis and the swing axis, Y, Fig. 2.

In order to be able to measure the groove angle by reflected light, and also be able to view the wire from any side through the microscope, three degrees of rotational freedom have been built into the apparatus in the manner of a goniometer. First, the wire can be rotated about the X-axis through ϕ degrees; second, about the optical or Z-axis for measuring the perpendicularity of the boundary trace with the wire axis; and third, about the swing axis, Y, for observing the reflected beam.

For reasons of clarity in describing the measurement procedure, first assume that the microscope sends forth a parallel beam of light. When the wire is properly aligned as described above, a bright line of reflection is seen along the uppermost element of the cylindrical surface with a break at the position of the groove. Upon rotating the "swing" slightly, the line-element reflection disappears and is replaced by a spot reflection at the top of one side of the groove. The rotation is continued through an angle α while the spot travels down the groove side and disappears at the root. The geometry involved here is shown in Fig. 5a. The measurement is taken from a protractor mounted on the side and a pointer rotating with the swing. Reversing the swing and watching for the point where the spot disappears on the other side of the groove produces the angle β . The groove angle is calculated by difference and can be checked as in Fig. 5b by measuring the angle starting where the spot disappears on one slope to where it disappears on the other. That measured angle is equal to $(180^\circ - \theta)$.

The light beam, however, is not parallel, but has a measured divergence at its source of 18° . Thus for the measurement of α and β , the swing must be rotated 9° beyond the point necessary for the reflected spot to disappear if the beam were parallel. Similarly the measurement of θ is 18° too high. These corrections were made in the reported values.

In Fig. 6 several plots of θ vs ϕ are shown. α and β in these cases are not shown, but vary independently of each other.

It became evident that θ varies in a complicated fashion as a function of at least four vectors, Fig. 1. A simple visualization is not only to see θ opening and closing with ϕ rotation, but simultaneously rocking back and forth in the axial direction with the same rotation due to the independent variation of α and β . However, a good average value for θ can be found for a given grain boundary by taking at least four, and preferably more, readings for θ at equally spaced ϕ intervals around the wire. This was done for 69 grain boundaries. The results are plotted as a spectrum in Fig. 7. The average θ for these is 164.5° . Since the differential vectors vary through positive and negative values, they average out to zero in the average vector pattern, wherein also $\gamma_1 = \gamma_2$. Therefore, Eq. 2 applies in the average case. Using the average surface tension for gold, $\gamma_s = 1400 \pm 65$ dynes per sq cm, from Buttner, Udin, and Wulff,³² the average grain boundary energy turns out to be 365 ± 50 ergs per sq cm.

Discussion and Conclusion

Two features of Fig. 7 are deserving of attention. First, the curve is a typical distribution curve with some scatter about the average θ , and second, it contains a few grain boundaries of comparatively high and a few grain boundaries of comparatively low measured average groove angles. The scatter itself may arise from: 1—the probability combinations within the system, 2—errors in the measuring technique, and 3—the limitations inherent in small wire size. The high average groove angles may result from low energy boundaries, lying in an energy cusp, breaking into a cylindrical surface of average surface tension. The low average groove angles may be a result of: 1—the possibility of an average grain boundary breaking into a cylindrical surface of excessively low average surface tension, 2—the likelihood of the differential vectors being negative in direction, or 3—the outside possibility of inverted energy cusps.

The angle θ depends on four surface sensitive vectors, and one grain boundary vector, the magni-

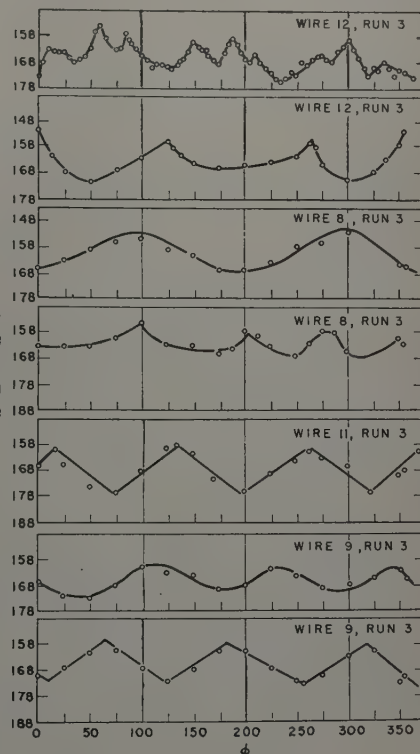


Fig. 6—Several typical plots of groove angle (θ) versus circumferential position of point O in the groove (ϕ).

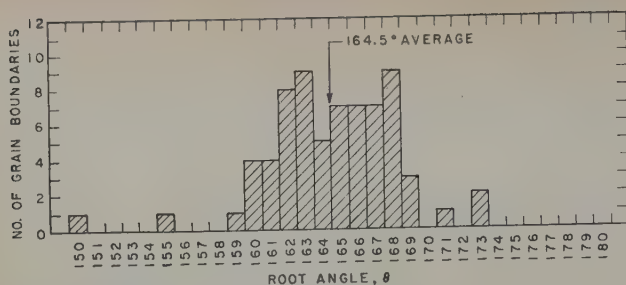


Fig. 7—Spectrum of average grain boundary θ versus number of grain boundaries having that average value.

tude of which, for a given groove, depends on the unique orientation of the two grains concerned. In other words, two grains may expose a high or low average energy surface at the groove wall, while at the same time forming a maximum or sub-maximum grain boundary energy, depending on the relative orientation of the two grains on either side of the boundary. The size of the average groove angle can, therefore, cover a spread of values, resulting from the combinations and permutations of the above possibilities. The number of different recognizable combinations and permutations depends on the resolution of the measuring instrument, or its ability to distinguish between small differences. An example is the above-mentioned combination of a maximum interfacial tension with a low average surface tension, which can lead to shallow grooves or an excessively high θ . This sort of thing can occur to various lesser degrees and lead to a sizable scatter about a mean, as seen in Fig. 7. This is what is meant by probability combinations within the system.

Some error exists in the reflected light method. Since the edge of the light beam is not sharp, a human uncertainty occurs in deciding when, during the swing rotation, the spot disappears. This difficulty did not seem as pronounced as Greenough found it in his measurements. Perhaps a dimly reflecting line is more confusing than an equally dimly lit spot. Precision of repeated measurements fall to within a half of a degree. In deep angle grooves, the ridge that builds up at the brink of the groove can sometimes reflect a spot from its outer side and appear to blend with the spot reflected from the opposite groove wall. This may lead to high values for α and β , and must be carefully watched. It is easily recognized when half the spot disappears at once and the other half remains during a further swing. The check against human error described in the procedure goes far in increasing the precision of measurements.

Although the finer the wire size the simpler it is to get a bamboo structure, there would be a distinct advantage in using the largest diameter wire possible. Point O in Figs. 1 and 2 under the microscope actually appears as the cross-sectional area of the microscope light beam. The beam covers a section of the circumference equal to the diameter of the beam and may be measured in terms of the central angle in terms of ϕ . In the case of 5 mil wires, the edges of the visible light spot is reflected from elements of the wire subtending an estimated central angle of 10° . Therefore, if any local contour irregularity exists, the reflection can come from the same element of the groove wall for positions of ϕ separated as much as 10° . Of course, irregularities that could cover a section of circumference of that extent are noticeable and can be avoided. Those cov-

ering smaller increments are difficult to notice and can account for some error in the θ vs ϕ curves.

In Fig. 6, several groove traverses are plotted in 25° intervals of ϕ , and fairly smooth curves can be drawn through the points. However, in the topmost plot where intervals of $\phi = 5^\circ$ were followed, a suggestion of sharp peaks and curved valleys becomes evident in the circumferential contour of the groove walls, a situation shown by Wulff³⁵ to be the most thermodynamically stable. Energy-wise, this indicates the existence of a corresponding series of curved maxima and cusped minima. A detailed discussion of surface contour and its associated energy is well reviewed by Herring and Nichols.³⁶ It is significant to note that the effect is prominent here when the metal is in equilibrium contact with its own saturated vapor. It is also encouraging to find that the reflected light method appears to have sufficient resolving power to pick up these sharp variations. A more detailed study of these hills and valleys would be desirable, but is hampered by the limitations of wire size in this case.

Another contour feature found in these fine wires is the occurrence of flat spots or facets in the circumferential contour of some groove walls. Facets of this sort in metallic crystals in regions of very small dimensions have never been observed to form in this manner before, to the knowledge of the authors; not even under the critical examination of the electron microscope. Tungsten needle points heated in vacuum have been found to round off into a constant radius at the tip. Although this has been a source of wonder in some circles, it has been suggested that the low free-energy contour would appear in systems of small dimensions where solid-vapor equilibrium exists.³⁸

A detailed theoretical discussion of facets is outside the scope of this paper. However, the existence of facets, like contours, enters in here insofar as they have been observed and as they affect the results of this study.

In some grooves the facets are large and noticeable, while in others they are not. Also variations in average amplitude of hills and valleys appear from groove wall to groove wall. It is generally true that groove walls of high amplitude contours are those in which facets are often noticeable. Measurements of groove angles where the groove wall is a facet are apparently not significant and were discarded.¹⁹ On the other hand, small facets may go unnoticed and cause errors in measurements. For example, in some positions of ϕ , an unnoticed facet may be stationed at some angle far enough from perpendicularity with the X-Z plane to throw the reflected beam off sideways, and out of the range of the microscope. In this case the spot would disappear prematurely and introduce an error in angle measurement. Furthermore, at the edge of a facet, the groove surface in the circumferential direction becomes slightly concave where it blends into the normal average convex contour. In this region, the reflected spot may drift to the right or left and reflect from elements other than the element the optical system is set on. Over a small range of ϕ 's in this region, the spot can very easily be disappearing from the same element, which would result in a horizontal section of the θ vs ϕ plot. In going to a larger wire, the facets as well as the light beam would cover a smaller fraction of the circumference, making it possible to make more certain measurements at smaller ϕ intervals. All of these

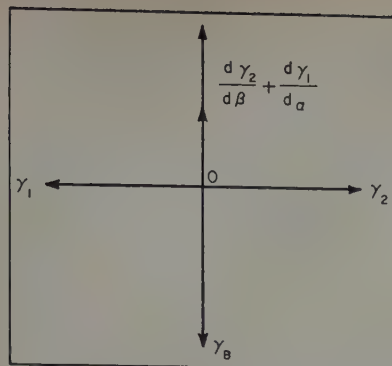


Fig. 8—Force pattern similar to Fig. 1 where $\theta = 180^\circ$.

improvements together should produce a more detailed curve of higher accuracy and greater reliability.

In comparing the relative merits of Eqs. 1 and 2, it appeared that ignoring the differential vectors of Fig. 1 reduces the accuracy of Eq. 1 to an approximation of Eq. 2. This conclusion is based on the findings of Dunn, Daniels, and Bolton, who did their work on tricrystals. Evidence found in the present work indicates that the same is true for the present system involving a vapor phase. Several instances were observed where a fairly deep groove became shallower and disappeared with ϕ rotation at three equally spaced regions about the wire. In places where $\theta = 180^\circ$, the force picture must have been as shown in Fig. 8. In this case, the sum of the two differential vectors equals the grain boundary energy vector. Although the differential vectors can be zero in some cases, they can at times reach fairly sizable positive and negative values, which makes it dangerous to discount them in all cases.

In conclusion, it appears from evidence presented in this paper, that the fine wire technique as described is a suitable method for obtaining the absolute average grain boundary energy for systems where the absolute average surface energy is known. Although the use of fine wires has its limitations as described above, these difficulties have a way of ironing themselves out when the results are computed as averages from a large number of measurements. The method shows the way for making detailed studies of surface tension wherein absolute surface energy values can be found for known free surfaces. This, of course, would require the use of larger wires and possibly X-ray identification of the exposed surfaces.

Summary

In studying the dimensions of the thermal grooves appearing in fine wires with bamboo structure, it was found that the groove angle is a result of independent hill and valley variations in slope of the groove walls with position around the boundary. A given slope in the wall on either side of the grain boundary depends on the magnitude of surface tension vector lying in that wall, and a differential vector standing perpendicular to that surface.

A statistical study of the average groove angle of many grain boundaries produced an overall average of $\theta = 164.5^\circ$. This value leads to an average grain boundary energy of 365 ± 50 dynes per sq cm for gold at 1300°K .

The present work introduces a method whereby the general grain boundary energy of metals in equilibrium at high temperatures can be found, assuming the average surface energy of the material is known for the same temperature.

Acknowledgments

The authors wish to acknowledge their indebtedness to the Office of Naval Research for equipment and supplies purchased under Contract No. N-5-ori-07841.

References

- ¹ R. King and B. Chalmers: *Progress in Metal Physics* (1949) Vol. I, p. 127.
- ² E. H. Bucknall: *Metal Ind.* (London) Vol. 49.
- ³ W. G. Burgers: *Handbuch der Metalphysik*. Vol. 3, No. 2.
- ⁴ Vijay Paranjpe: Solid Solutions and Grain Boundaries. Army Contract No. AT-30-1-Gen-368.
- ⁵ Achter and R. Smoluchowski: *The Physics of Powder Metallurgy*. Edited by W. E. Kingston. (1951) New York. McGraw-Hill Book Co.
- ⁶ D. Turnbull: *Trans. ASM* (1951) **43A**, p. 133.
- ⁷ *Interfaces*. ASM volume to be published.
- ⁸ G. D. Bengough: *Journal Inst. Metals* (1912) p. 149.
- ⁹ F. Hargreaves and R. J. Hills: *Journal Inst. Metals* (1929) **41**, p. 257.
- ¹⁰ W. L. Bragg: *Proc. Phys. Soc.* (1940) **52**, p. 105.
- ¹¹ J. M. Burgers: *Proc. Phys. Soc.* (1940) **52**, p. 23.
- ¹² T. S. Ke: *Physical Review* (1947) **71**, p. 533.
- ¹³ T. S. Ke: *Journal of Applied Physics* (1948) **19**, p. 285.
- ¹⁴ T. S. Ke: *Trans. AIME* (1948) **176**, p. 448; *METALS TECHNOLOGY* (June 1948).
- ¹⁵ N. F. Mott: *Proc. Phys. Soc.* (1948) **60**, p. 391.
- ¹⁶ C. S. Smith: *Trans. AIME* (1948) **175**, p. 15; *METALS TECHNOLOGY* (June 1948).
- ¹⁷ J. W. Gibbs: *Collected Works of J. Willard Gibbs*. (1931) Vol. 1, p. 219.
- ¹⁸ C. G. Dunn and F. Lionetti: *Trans. AIME* (1949) **185**, p. 125; *JOURNAL OF METALS* (February 1949).
- ¹⁹ C. G. Dunn, F. W. Daniels, and M. J. Bolton: *Trans. AIME* (1950) **188**, p. 368; *JOURNAL OF METALS* (February 1950).
- ²⁰ L. H. Van Vlack: *Trans. AIME* (1951) **191**, p. 251; *JOURNAL OF METALS* (March 1951).
- ²¹ G. L. J. Bailey and H. C. Watkins: *Proc. Phys. Soc.* (1950) **63**, p. 350.
- ²² G. W. Sears: Report on an Absolute Measurement of Copper-Copper Interfacial Energy. Gen. Elect. Lab., March 1950.
- ²³ R. L. Fullman: *Journal of Applied Physics* (1951) **22**, p. 448.
- ²⁴ A. P. Greenough and R. King: Report to Royal Aircraft Est., Met. 52, (1950); *Journal Inst. Metals* (1951) **79**, p. 415.
- ²⁵ G. L. J. Bailey and H. C. Watkins: *Proc. Phys. Soc.* (1950) **63**, p. 350.
- ²⁶ Conyers Herring: *The Physics of Powder Metallurgy*. (1951) p. 176. New York. McGraw-Hill Book Co.
- ²⁷ W. Rosenhain and J. C. W. Humfrey: *Proc. Royal Soc.* (1910) **A83**, p. 200.
- ²⁸ B. Chalmers, R. King, and R. Shuttleworth: *Proc. Royal Soc.* (1948) **A193**, p. 465.
- ²⁹ W. T. Read: Role of Dislocations in Crystal Growth and Grain Boundary Phenomena. AIME Seminar on Dislocations, Detroit Meeting, October 1951.
- ³⁰ H. Udin, A. J. Shaler, and J. Wulff: *Trans. AIME* (1949) **185**, p. 186; *JOURNAL OF METALS* (February 1949).
- ³¹ E. R. Funk, H. Udin, and J. Wulff: *Trans. AIME* (1951) **191**, p. 1206; *JOURNAL OF METALS* (December 1951).
- ³² F. H. Buttner, H. Udin, and J. Wulff: *Trans. AIME* (1951) **191**, p. 1209; *JOURNAL OF METALS* (December 1951).
- ³³ R. M. Brick: *Cold Working of Metals*. (1949) p. 102. Cleveland. ASM.
- ³⁴ C. S. Smith: Address at M.I.T., January 1952.
- ³⁵ G. Wulff: *Ztsch. f. Krist.* (1901) **34**, p. 449.
- ³⁶ C. Herring and M. H. Nichols: *Reviews of Modern Physics* (1949) **21**, p. 185, Sect. II-1, and II-2, and Appendix III.
- ³⁷ W. T. Read and W. Shockley: Dislocation Models of Crystal Boundaries. To be published.

Nature of the Creep Curve

by Thomas H. Hazlett and Earl R. Parker

An understanding of the mechanism of creep of metals requires an accurate knowledge of shape of the time-deformation curve. An expression is developed which accurately expresses the creep curve for a number of structurally stable metals and alloys.

VAST strides have been made in the development of high temperature creep resistant alloys; however, no sound understanding of the physical mechanism of creep exists to date. Consequently, creep resistant alloys are still developed by "cut and try" methods formerly so successful but now yielding returns at a continuously diminishing rate. It is apparent to all workers in the field that if the mechanism of creep were understood, much fruitless labor could be avoided. The dearth of fundamental knowledge has not discouraged the theorists. Speculation has flourished and numerous theories of creep have been proposed. A critical review of these theories reveals that, even though there are some general areas of agreement between the majority of the workers, there are many basic questions yet to be resolved.¹

It is generally conceded that theoretical speculation is far in advance of experimental evidence. The shortage of reliable creep data greatly hinders more rapid progress in this field. It is essential that the

effects of different stresses and temperatures on the creep characteristics of metals be quantitatively determined. Once this has been accomplished, it will then be possible to evaluate the effects of alloying additions and, it is hoped, to provide a firm basis of facts for theoretical treatment of the creep phenomenon. The work reported herein was undertaken to determine the effects of such variables as stress, temperature, alloying, and structure on the creep characteristics of some metals.

Material and Equipment

Nickel was selected as the base material for the current investigation and an experimental program was initiated to determine the effects of temperature and stress on the creep characteristics of this material. Since a large quantity of high purity nickel was required for the proposed program and such material was not commercially available, it was decided to refine, cast, and prepare the required metal in our own laboratory. The resulting nickel test bars had the following composition, given in percentage by weight: Fe, 0.030 (1); Si, 0.003 (2); Ca, 0.001 (1); Mg, 0.020 (2); and S, 0.002 (2); to make total impurities of 0.056. The nickel (balance by difference) is 99.944 pct. The details of the purification process are described elsewhere.² This

T. H. HAZLETT and E. R. PARKER, Member AIME, are Research Engineer and Professor of Physical Metallurgy, respectively, University of California, Berkeley, Calif.

Discussion on this paper, TP 3381E, may be sent, 2 copies, to AIME by April 1, 1953. Manuscript, April 17, 1952. Los Angeles Meeting, February 1953.

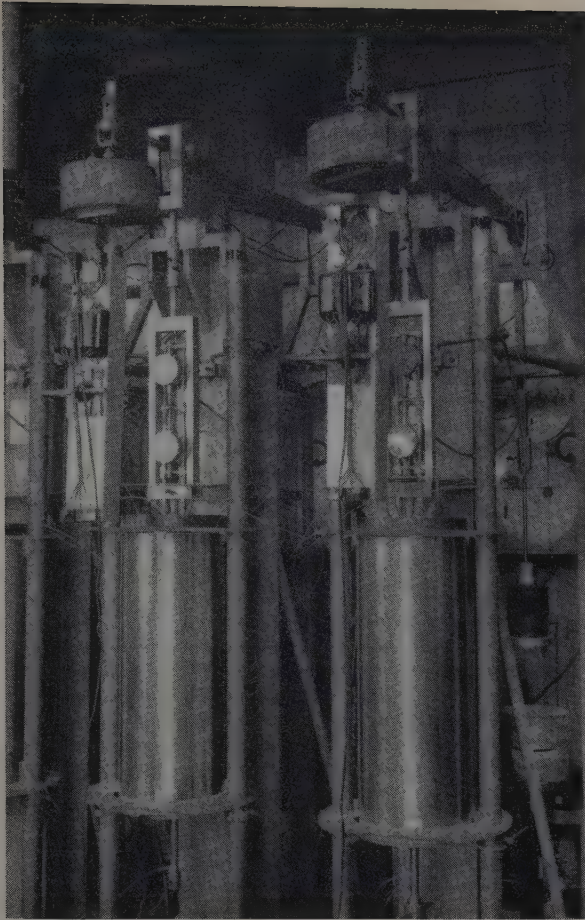


Fig. 1—Single specimen creep units in which tests were performed.

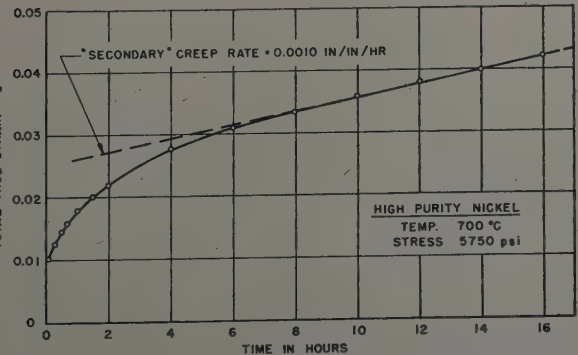
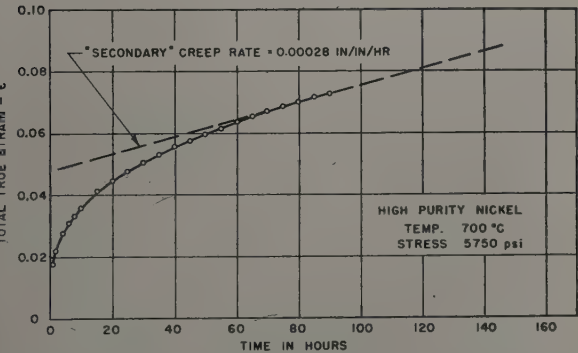


Fig. 3—Expanded initial portion of creep curve shown in Fig. 2.

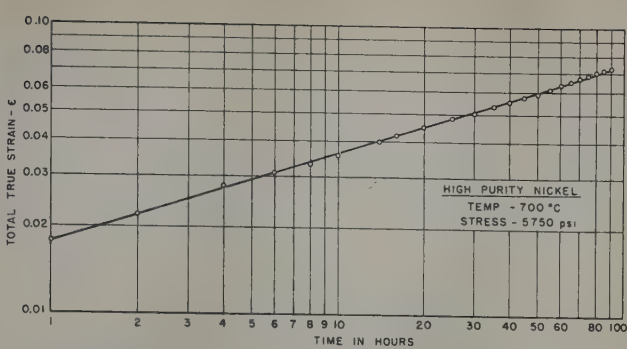


Fig. 4—Typical creep curve of Fig. 2 plotted on logarithmic coordinator.

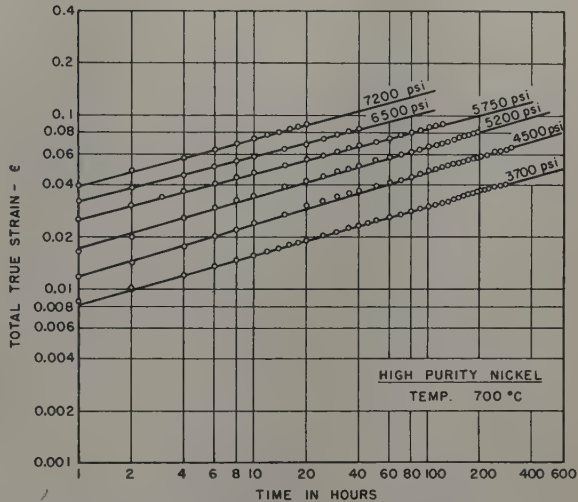


Fig. 5—Constant stress creep curves for high purity nickel at 700°C.

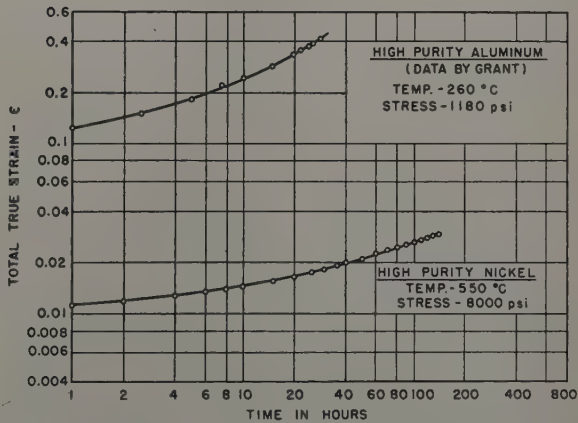


Fig. 6—Nonlinear logarithmic creep curves for nickel and aluminum.

material was also used as the base metal for preparing the alloys mentioned later.

All tests were performed in single specimen creep units similar to those shown in Fig. 1. All units were completely independent of each other to prevent any possibility of shock loading due to failure of another specimen. Load was applied through a knife-edge lever arm system, but since the ultimate

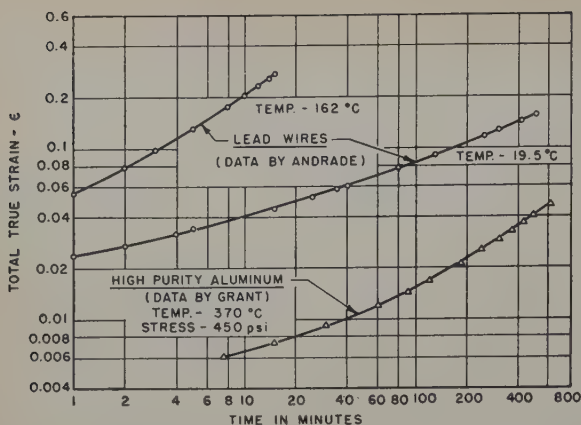


Fig. 7—Nonlinear logarithmic creep curves for lead and aluminum.

goal of the study was to provide data which would be of value for theoretical studies, all tests were performed under conditions of essentially constant stress rather than constant load. The stress variation was held to less than $\frac{1}{2}$ pct by means of modified lever arm system,⁸ which consists of an auxiliary arm attached to the back end of the lever and projecting downward from it at an angle of 90° . The lever systems were counterbalanced and calibrated for several load ranges to correct for possible bending of the lever.

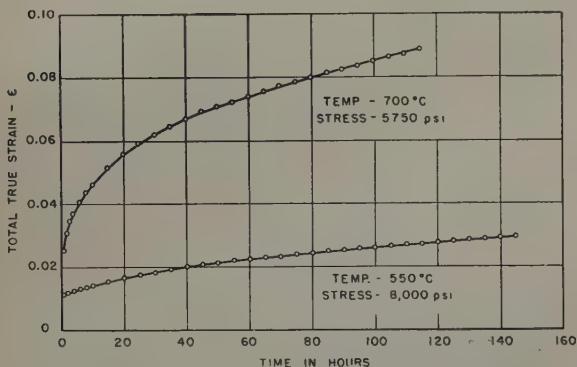


Fig. 8—Creep curves for high purity nickel on rectangular coordinates.

The specimens were heated by tube-type, wire-wound resistance furnaces with three independent windings. The end windings were individually controlled with small auxiliary controllers and the temperature of the center winding was determined and controlled by a thermocouple placed at the center of the specimen. High sensitivity millivolt controllers with an expanded range were used for this purpose. Temperature distribution along the specimens was held constant within $\frac{1}{2}^\circ\text{C}$ and the temperatures of the center of the specimens did not vary more than 1°C during the test.

The specimens were machined with two reduced sections in tandem; one having a reduced length of 1 in. and the other 3 in. Strain measurements were made by means of extensometers pinned to each of the three shoulders of the specimens. The extensometer assembly was made in three portions which were free to move relative to each other in the direction of the specimen axis. The elongation of each reduced section was measured between shoulders and the differences taken as the elongation in 2 in.

Strains were measured with precision dial gages which have been modified to permit automatic recording of all data.

Data and Analysis

The data originally obtained from this program were plotted in the usual manner on rectangular coordinates and the "secondary" or "steady state" creep rate determined for each as illustrated in Fig. 2. This concept of a steady state creep rate has long been accepted and used both by designers and theorists as a reliable parameter to define the creep behavior of materials under given conditions.

However, as pointed out by Lubahn,⁴ such a concept may be unjustified. When the data of Fig. 2 were replotted on a vastly expanded time scale, as shown in Fig. 3, an apparent constant strain rate is

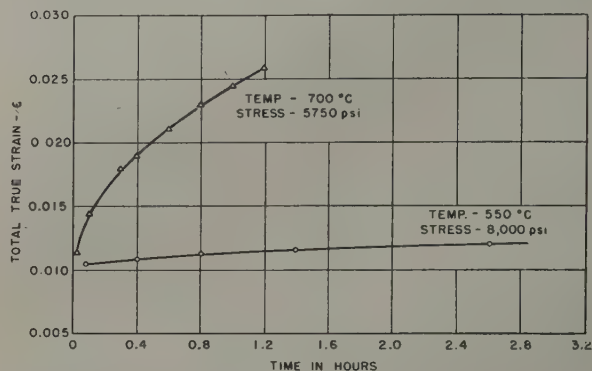


Fig. 9—Initial part of creep curves of Fig. 8 with expanded coordinates.

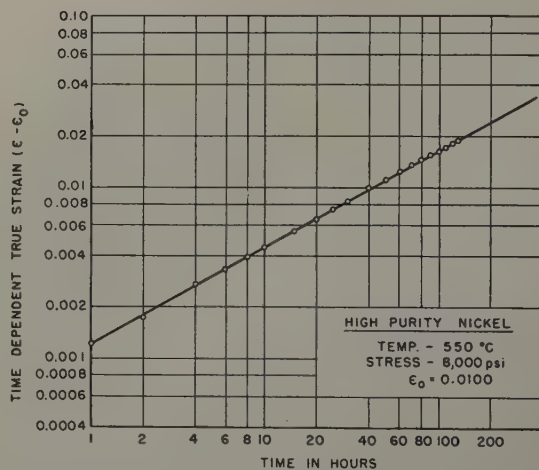


Fig. 10—Linearity of low temperature creep curves for high purity nickel when time-dependent strain only is used.

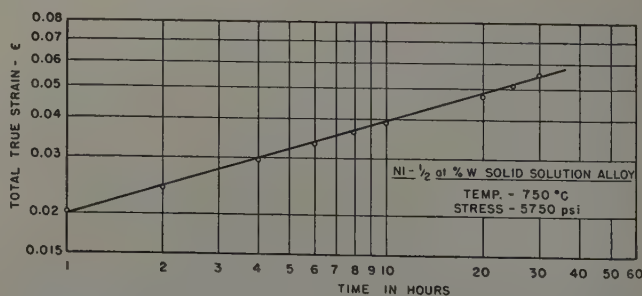


Fig. 11—Linearity of nickel alloy creep curve after first hour of test when total strain, ϵ , is used.

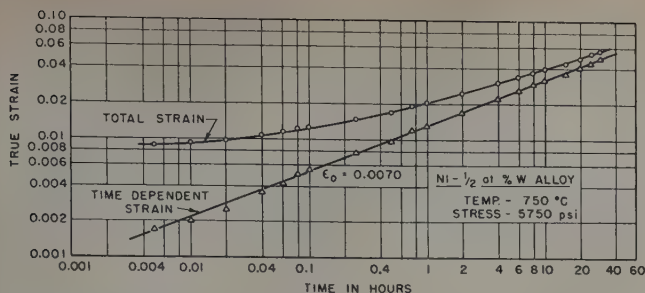


Fig. 12—Logarithmic plots of complete creep curves showing effect of ϵ_0 correction.

again found, but of a magnitude differing from that previously obtained.

Subsequent work by the General Electric Research Group demonstrated that in many cases, creep data obtained from constant stress tests showed a continuous decrease of creep rate up to the point of initiation of failure.⁵ This is illustrated by Fig. 4, which shows that when the logarithm of the strain, ϵ , is plotted against the logarithm of the time, t , the resulting creep curve is linear. Conse-

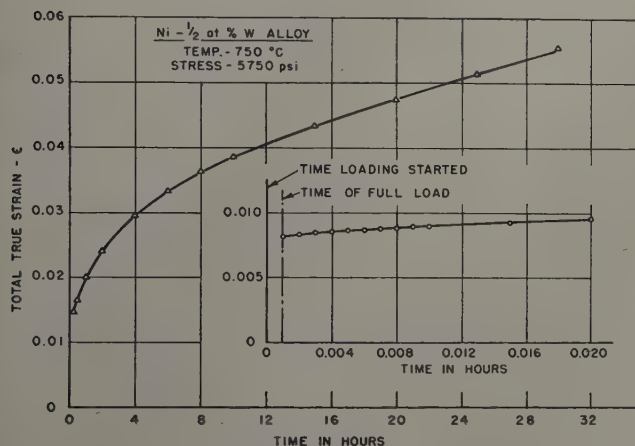


Fig. 13—Rectangular coordinate plot of creep curve shown in Fig. 12.

quently, the data may be represented by the following empirical relationship:

$$\epsilon = At^b \quad [1]$$

where A and b are constants.

A critical re-examination of all available constant stress creep data substantiated the thesis that the creep rate does continuously decrease as postulated by Fisher and Hollomon.⁵ Consequently, it was concluded that the concept that the creep rate eventually becomes and remains constant is incorrect, and the use of such a parameter for correlating constant stress creep data is unjustified.

Since it is highly desirable, if not essential, to utilize some specific parameters when comparing results of creep tests, Eq. 1 was adopted with considerable success as shown by the creep curves for nickel in Fig. 5. This was further substantiated by Lubahn's data on mild steel,⁵ Carreker's results on platinum,⁶ and by Andrade's constant stress creep curves for copper.⁷ However, as the stress and temperature test range for nickel was expanded, it was found that some data did not conform to this simple relationship, but instead produced curved lines which were concave upward on the logarithmic plot. The lack of linearity on the logarithmic plot was also

evident in the data obtained by Andrade for lead and that for aluminum obtained by Grant at M.I.T.⁸ These curves are shown in Figs. 6 and 7.

The nickel curve of Fig. 6, which exhibits this behavior, is shown plotted on rectangular coordinates in Fig. 8, together with a curve obtained from a test performed at 700°C. It may be noted that the total creep strain for the lower temperature test appears to consist of two parts; first, an instantaneous strain and second, a time dependent strain. The region of rapidly decreasing creep rate usually associated with the early portions of the creep curve is not pronounced in the 550°C data, but rather large strains do occur at the time the load is applied. This

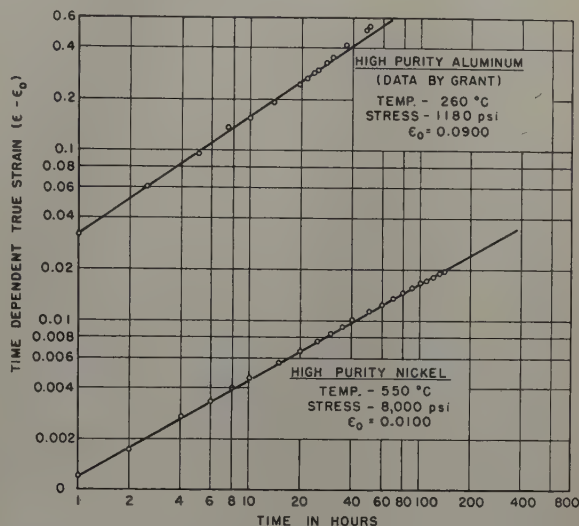


Fig. 14—Time-dependent strain creep curves for nickel and aluminum.

is more clearly portrayed in the expanded scale plots of the same data shown in Fig. 9. The more typical 700°C curve is again shown for comparison. It can be seen that the 550°C curve may be extrapolated to a finite strain at zero time with reasonable certainty, but for the 700°C curve the strain rate is increasing so rapidly with decreasing time that the strain at zero time is very indefinite.

On the basis of data exemplified by the 550°C curve, it was found that if the instantaneous strain

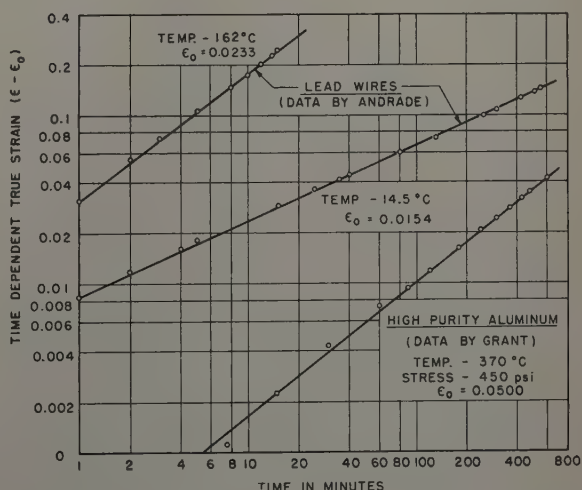


Fig. 15—Time-dependent strain creep curves for lead and aluminum.

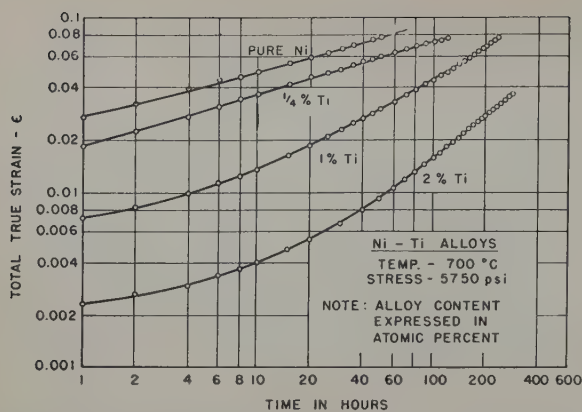


Fig. 16—Effect of additions of titanium in solid solution on creep curves of high purity nickel.

upon loading was subtracted from the total strain, the resulting time-dependent deformation plotted linearly with time on logarithmic coordinates as shown in Fig. 10.

Thus it appears that Eq. 1 should be modified to the form:

$$\epsilon - \epsilon_0 = At^b \quad [2]$$

where: ϵ is the total true strain; ϵ_0 , the instantaneous strain at loading; t , the time; and A and b are constants. However, this does not explain the linearity of the high temperature curves such as the 700°C curves of Fig. 5, since it would appear from Fig. 8 that the zero time intercept of the 700°C curve is of the same order of magnitude as the 550°C curve.

In order to clarify this situation, special high speed strain recording equipment was constructed to determine accurately the initial part of the curve. For times greater than 1 hr, the logarithmic plot of these data yields a straight line as shown in Fig. 11. However, when data at very short times are plotted, the line shows a pronounced curvature as illustrated in the upper curve of Fig. 12. Here it may be seen that the linearity from 1 hr on is merely a very close approximation, the curvature increasing as the time decreases. A value of $\epsilon_0 = 0.0070$ is required to make the total curve straight as shown in the lower curve of Fig. 12. The rectangular plot of these data is given in Fig. 13, including a greatly expanded initial

portion. It may be observed from this curve that the total strain at the time the load was fully applied is $\epsilon = 0.0080$. This is considered very good agreement with the value of 0.0070 determined graphically from Fig. 12. The small discrepancy between the two values may be due to the time-dependent strain which occurred during loading even though this represents a period of only 3.5 sec.

Thus it appears that the value of ϵ_0 obtained graphically is a real quantity having physical significance; i.e., it is the instantaneous total strain at the moment of loading, and the time-dependent strain, $\epsilon - \epsilon_0$, is linear on a logarithmic plot. Further evidence of this fact is presented in Figs. 14 and 15 which are replots of the curves of Figs. 6 and 7 in which the time-dependent strain only is plotted.

The relationship between strain and time of Eq 2 is further substantiated by the creep curves shown in Fig. 16 obtained from a series of solid solution nickel alloys. All of these specimens were tested at the same temperature and applied stress. It may be noted that the degree of curvature increases as the alloy content increases. However, when the instantaneous strain is subtracted from the total strain, all of these curves become linear as shown in Fig. 17. In these cases, the ϵ_0 was determined graphically. It should also be observed that the

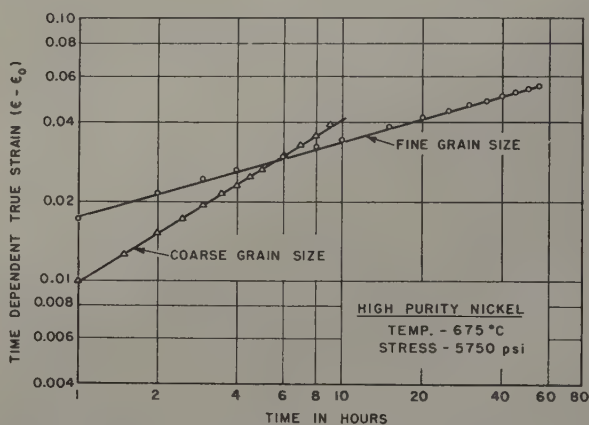


Fig. 18—Effect of grain size on slope of logarithmic creep curves.

slope of the time-dependent strain curves, b in Eq 2, increases as the alloy content increases. Similarly, the slope varies with grain size as indicated in Fig. 18. Observations to date have not revealed any regular variation of b with applied stress and the variation with temperature is not clear at the present time. It may be noted from Fig. 5 that the slope, b , is essentially constant for all stresses from 3700 to 7200 psi at 700°C. Similar results have been found for tests carried out at 675°, 725°, and 750°C. All of these data yield a slope of $b \approx 0.3$ for pure nickel and progressively higher values as the solid solution alloy content is increased. The parameter A of Eq 2 on the other hand, does vary in a regular manner with stress and also varies with structure, alloy content, and temperature. This regular variation of A is illustrated in Fig. 19 in which the logarithm of A is plotted against $1/T$ for a series of pure nickel specimens tested in the temperature range 675° to 750°C. The value of b may be considered a constant for these curves. It may be seen that a straight line may be drawn through the data points with considerable accuracy, indicating that

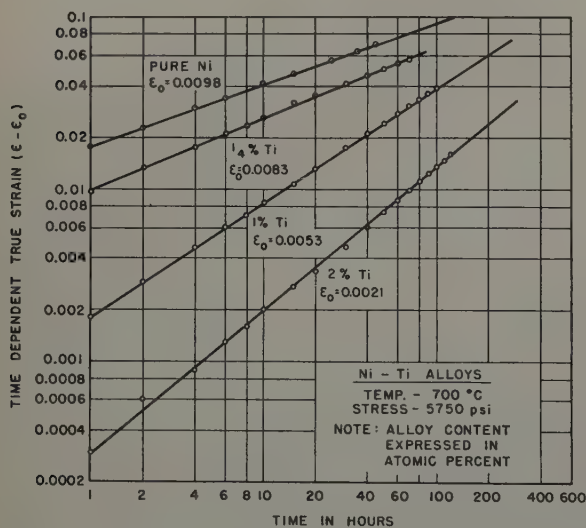


Fig. 17—Time-dependent strain creep curves for Ni-Ti alloys.

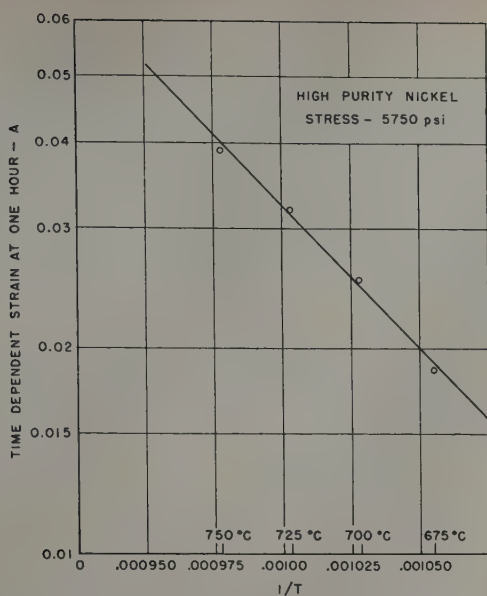


Fig. 19—Variation of the parameter, A , with temperature.

A varies exponentially with temperature so that the following relationship may be written:

$$A = B e^{-Q/RT}$$

where: T is the absolute temperature; R , the gas constant; Q , the "experimental activation energy;" e , the base of natural logarithms; and B , a constant.

Since all of the foregoing data were obtained for polycrystalline materials, it was considered desirable to determine whether the continuously decreasing creep rate required the presence of grain boundaries. In order to resolve this question, creep data on zinc single crystals tested in shear were obtained from O.N.R. project workers of this laboratory. In the typical results shown in Fig. 20, the upper curve

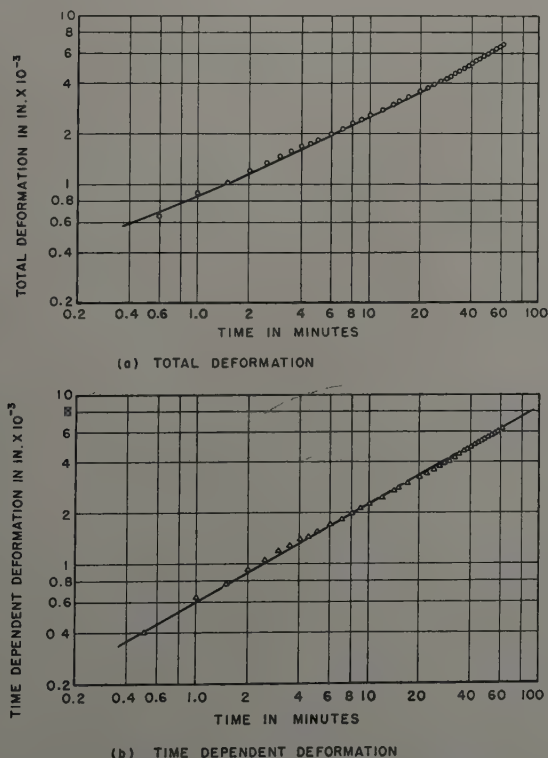


Fig. 20—Logarithmic creep curves for zinc single crystal tested at 24.5°C and 35 psi.

(Fig. 20a) is the total strain and Fig. 20b is the time-dependent strain. It is apparent that single crystals also follow the behavior required by Eq. 2, indicating that the phenomena of continuously diminishing creep rate is not necessarily dependent upon the presence of grain boundaries.

Summary and Conclusions

Results obtained to date may be summarized as follows:

1—The creep rate for structurally stable metals tested under conditions of constant stress decreases continuously until the initiation of failure. There is no region of constant creep rate.

2—The creep curve may be accurately represented by the empirical equation:

$$\epsilon - \epsilon_0 = At^b$$

at constant temperature, or:

$$\epsilon - \epsilon_0 = Bt^b e^{-Q/RT}$$

over a considerable temperature range.

3—The parameter ϵ_0 is a quantity having real physical significance, denoting an instantaneous strain upon loading. The parameter A varies in a regular manner with stress and alloy content and exponentially with $1/T$. The parameter b also varies over a wide range but the correlation of b with temperature, stress, grain size, and alloy content will require many additional tests.

4—The empirical equation given is applicable to both single crystals and polycrystalline materials indicating that the continuously decreasing creep rate is not solely a grain boundary phenomena.

5—Accurate determination of the parameters A , b , and ϵ_0 requires strain measurements beginning at very short times after applying the load. In many cases readings must begin only seconds after loading.

Acknowledgments

The authors wish to thank the U.S. Atomic Energy Commission for sponsoring the work on which this paper is based and for permission to publish these data. We are sincerely appreciative of the conscientious work of Mrs. R. Hansen and her valued assistance in all phases of the work; we also want to thank Paul Langston for his careful work in the preparation of metals used in these tests and C. D. Nail for his valued assistance in the testing laboratory.

References

- ¹M. W. Nathans, E. R. Parker, and T. H. Hazlett: A Survey of Theories of Creep of Metals. University of California Institute of Engineering Research, Series No. 28, Issue No. 2, AEC No. C00-2, November 15, 1949.
- ²Victor F. Zackay and Thomas H. Hazlett: The Melting and Refining of Relatively High Purity Nickel. To be published.
- ³Suggested through private communication by members of the Metallurgy Section of General Electric Research Group.
- ⁴J. D. Lubahn: Creep of Metals. *Cold Working of Metals*. Cleveland, A.S.M.
- ⁵J. C. Fisher and J. H. Hollomon: Wanted: Experimental Support for Theories of Plastic Flow. A Symposium on the Plastic Deformation of Crystalline Solids, Mellon Institute, Pittsburgh, May 1950.
- ⁶R. P. Carreker, Jr.: Plastic Flow of Platinum Wires. *Journal of Applied Physics*, 21, No. 12, p. 1289.
- ⁷E. N. da C. Andrade: The Viscous Flow in Metals and Allied Phenomena. *Proc. Royal Soc.* (1910) A84, p. 1.
- ⁸N. J. Grant: Private communication.

Some Observations on Correlations Between the Creep Behavior And the Resulting Structures in Alpha Solid Solutions

by Oleg D. Sherby and John E. Dorn

For elevated temperature-constant load creep tests of α solid solution alloys, the creep strain is a function of a temperature-compensated time parameter $\theta = \int e^{-\Delta H/RT} dt$. The activation energy ΔH is equal to a constant of about 36,000 cal per mol. The substructures resulting from a given creep stress condition are functions of the creep strain independent of temperature. Each new creep stress gives a new unique set of grain substructures; this is one of the factors responsible for the failure of the mechanical equation of state for creep.

IN this report an attempt is made to correlate the creep properties of dilute α solid solutions in aluminum with the subgrain structures that are developed during creep. The possibilities of such correlations have already been suggested by Wood et al. and others¹⁻⁶ who demonstrated that the subgrain structures are functions of the creep stress, creep strain, rate of creep, and temperature.

Investigations by Sherby and Dorn⁷ have shown that the creep strain, ϵ , at constant load for dilute α solid solutions of aluminum is given by the functional relationship:

$$\epsilon = f(\theta, \sigma_c) \quad [1]$$

where: θ equals $te^{-\Delta H/RT}$ = temperature-compensated time; t , time; ΔH , activation energy, $\sim 35,800$ cal per mol; R , gas constant; T , absolute temperature, above 400°K; and σ_c , initial creep stress.

Consequently, it was anticipated that the subgrain structure that develops during a constant load creep test should also correlate with any two of the three significant variables ϵ , θ , and σ_c .

Another possible correlation between the subgrain structure and the creep variables is obtained by differentiating Eq. 1 with respect to time, whence the creep rate, $\dot{\epsilon}$, becomes:

$$\dot{\epsilon} = \left(\frac{\partial f}{\partial \theta} \right) \left(\frac{d\theta}{dt} \right) = f'(\theta, \sigma_c) e^{-\Delta H/RT} \quad [2]$$

or:

$$\sigma_c = F(\dot{\epsilon} e^{\Delta H/RT}, \theta) \quad [3]$$

For the minimum creep rate, $\dot{\epsilon}_s$, θ is solely a function of σ_c as revealed by Eq. 1. Consequently, at the minimum creep rate Eq. 3 reduces to:

$$\sigma_c = F(\dot{\epsilon}_s e^{\Delta H/RT}) \quad [4]$$

Correlations between σ_c and $\dot{\epsilon}_s e^{\Delta H/RT}$ were found valid for solid solution alloys of aluminum where ΔH was a constant of about 35,800 cal per mol. The parameter $\dot{\epsilon}_s e^{\Delta H/RT}$ is identical to the Zener-Hollomon parameter^{8,9} used by them in evaluating the tensile properties of copper and other metals.

O. D. SHERBY, Junior Member AIME, is Research Engineer and J. E. DORN, Member AIME, is Professor of Physical Metallurgy, University of California, Berkeley, Calif.

Discussion on this paper, TP 3405E, may be sent, 2 copies, to AIME by April 1, 1953. Manuscript, June 2, 1952; revised Sept. 24, 1952. Los Angeles Meeting, February 1953.

Table I. Composition of α Solid Solutions*

Alloying Element	Atomic Pct	Wt Pct of Impurities					Mean Grain Diameter, mm
		Si	Fe	Cu	Mg	Mn	
	(99.987)	0.003	0.003	0.006	0.001		0.25
Mg	1.617	0.003	0.004	0.006			0.26
Cu	0.101	0.003	0.003		0.0006	0.001	0.29

* The authors wish to acknowledge their indebtedness to the Aluminum Co. of America Research Laboratories for preparing these alloys and for determining their chemical compositions.

Eq. 4 suggests that the subgrain structure developed during secondary creep might be correlatable with either of the two variables $\dot{\epsilon}_s e^{\Delta H/RT}$ or σ_c .

Some of the solid solution aluminum alloys which were discussed in an earlier report⁷ were also used in the present investigation. Sheets of these alloys were homogenized, cold rolled from 0.100 to 0.070 in. in thickness and then recrystallized to about the same grain size. Their chemical composition and grain size are recorded in Table I. Creep specimens were selected with their tensile axes in the rolling direction. The details for creep testing have been described¹⁰ and will not be repeated here. All creep tests were performed under constant load conditions.

Experimental Results and Discussion

Metallographic Structure of Creep Specimens: In order to obtain a preliminary concept of creep on the metallographic structure of high purity aluminum, the various ruptured specimens previously used to obtain the creep data for pure aluminum were polished and etched electrolytically in a dilute solution of fluoroboric acid. Oblique illumination was used to reveal the substructures which, for convenience, are shown in correlation with the σ vs. $\dot{\epsilon}_s e^{\Delta H/RT}$ curve in Fig. 1. It is necessary to emphasize that the data for the curve refer to the various secondary stages of creep whereas the micrographs refer to the fractured creep specimens. Nevertheless a regular and systematic correlation is observed between $\dot{\epsilon}_s e^{\Delta H/RT}$ (or the creep stress) and the microstructure at fracture. For $\ln(\dot{\epsilon}_s e^{\Delta H/RT}) = 42.3$, which refers to creep at a high creep rate and a low creep temperature, the fractured aluminum specimen, as shown by the micrograph in the upper right-hand corner of Fig. 1, exhibited extensive deforma-

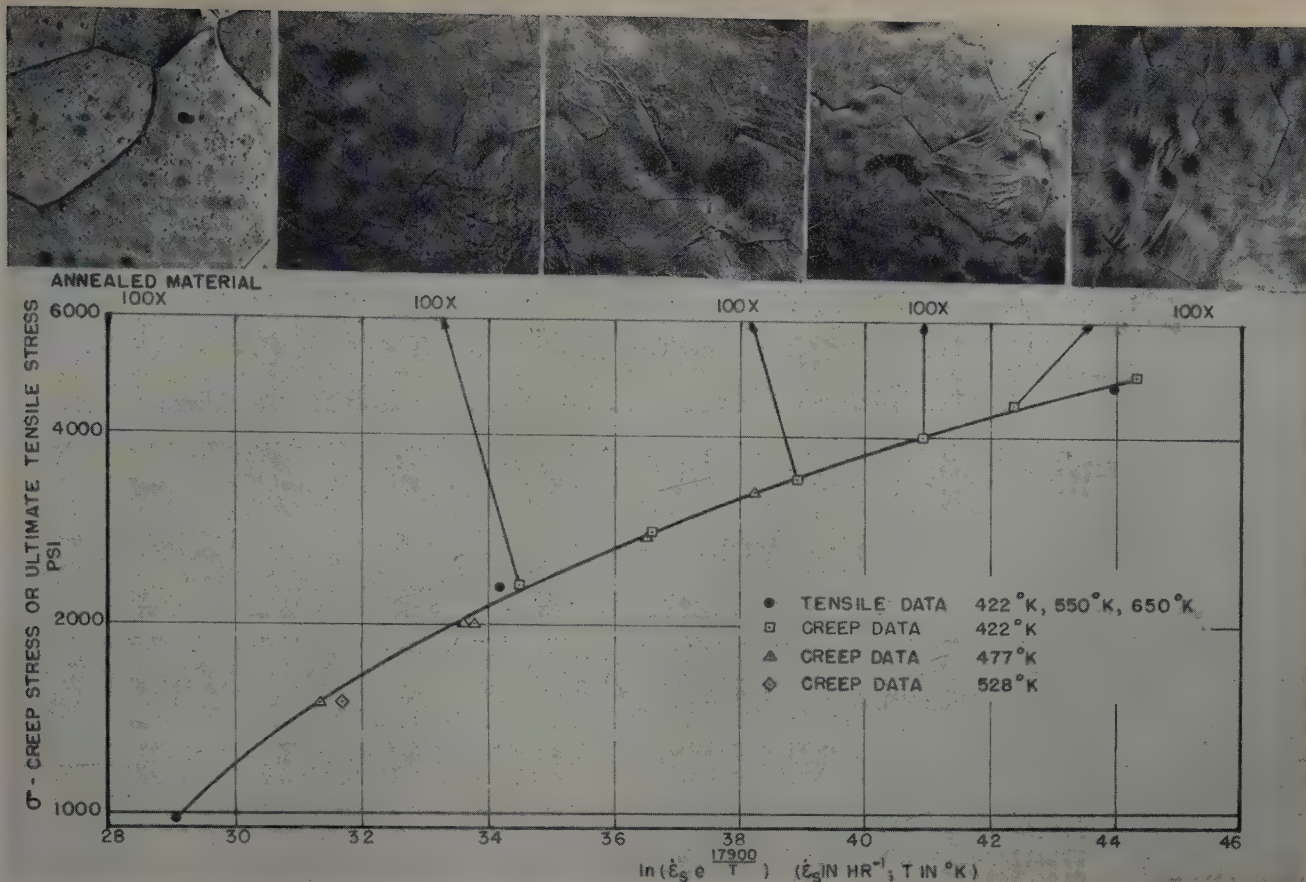


Fig. 1—Metallographic examinations of fractured creep specimens of high purity aluminum as a function of the parameter $\dot{\epsilon}_s e^{\Delta H/RT}$. Area reduced approximately 75 pct for reproduction.

tion banding. Such banded regions are distinguishable from the subgrain structures formed during creep at higher temperatures. This distinction will be more clearly revealed by the X-ray diffraction evidence which will be described in the following section.

At the opposite extreme where $\ln(\dot{\epsilon}_s e^{\Delta H/RT})$ was low, the micrograph of the fractured specimen was completely free from evidence of deformation banding. In lieu of deformation bands, the individual grains appeared to exhibit a fine polygonized structure. For intermediate values of $\ln(\dot{\epsilon}_s e^{\Delta H/RT})$ intermediate types of structures were obtained in the fractured specimens. Thus a regular trend was observed between the creep parameter $\dot{\epsilon}_s e^{\Delta H/RT}$ and the microstructure of the fractured specimens. Similarly, the metallographic structure of the fractured specimens appears to be a function solely of the creep stress, independent of the remaining test condition of temperature.

X-Ray Structure of Creep Specimens: The metallographic techniques necessary to reveal the substructures of creep specimens were found to be tedious and somewhat difficult for the Al-Mg alloy that was investigated. Consequently it was deemed advisable to obtain confirmation of the metallographic data by means of X-ray diffraction studies similar to those previously used by Wood and his colleagues.¹ For this purpose Debye-Scherrer back-reflection radiograms were taken of all the ruptured creep specimens of pure aluminum using a copper target tube operated at 40 kv. Representative samples of the various X-ray diffraction photographs for pure aluminum are reproduced in Fig. 2 and appropriately documented in terms of the creep or ultimate tensile stress and $\ln(\dot{\epsilon}_s e^{\Delta H/RT})$.

The X-ray structure of the original unstrained creep specimens used in this investigation is shown in the upper left-hand micrograph of Fig. 2. In view of the small pinhole (0.27 mm diam) relative to the grain size (0.25 mm diam) only a few grains contribute to the resulting diffraction spots. These spots are small and sharp, revealing that the original annealed specimen consisted of large, almost perfect strain-free grains. The fractured specimens for high values of $\ln(\dot{\epsilon}_s e^{\Delta H/RT})$ exhibited diffuse X-ray diffraction arcs somewhat typical of cold worked metals. These X-ray photographs are associated with the banded metallographic structure that was described in the previous section, and the arcing of the diffraction spot must be attributable to the range of orientations induced in a single grain due to lattice bending during creep. At the other extreme where $\ln(\dot{\epsilon}_s e^{\Delta H/RT})$ is small, the diffraction photographs of the fractured specimens clearly exhibit arcs consisting of a series of sharp, distinct diffraction spots. Undoubtedly each spot represents the diffraction from an almost perfect subgrain and the arc represents the range of orientations of the assemblage of subgrains which originated from one or, perhaps at most, two original grains. Thus X-ray diffraction evidence for subgrain formation at low values of $\ln(\dot{\epsilon}_s e^{\Delta H/RT})$ is directly correlatable with the confirming metallographic evidence which was described in the preceding section. Over the intermediate values of $\ln(\dot{\epsilon}_s e^{\Delta H/RT})$ a regular trend of the X-ray photographs of the fractured specimens were obtained, ranging from the diffuse Debye-Scherrer arcs for high values of $\ln(\dot{\epsilon}_s e^{\Delta H/RT})$ to sharp arcs composed of distinct spots for low values of $\ln(\dot{\epsilon}_s e^{\Delta H/RT})$, in complete harmony with the analo-

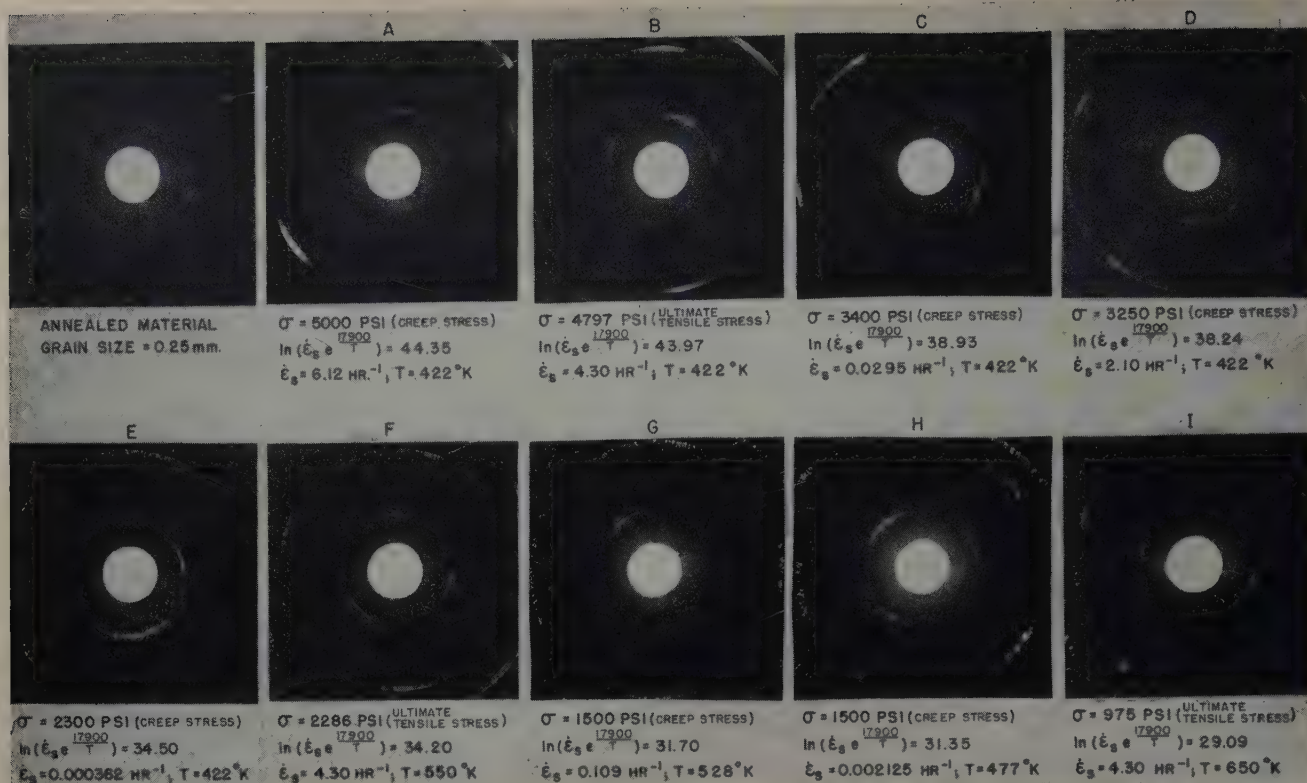


Fig. 2—X-ray back-reflection photograms of high purity aluminum as a function of the parameter $\epsilon_s e^{\frac{17900}{T}}$.

gous trends in the previously discussed metallographic structures.

The structure of fractured creep specimens appears to be a function of the creep stress independent of test temperature. The similarity in the diffraction photograms E and F and also G and H of Fig. 2 support this contention. The specimens whose diffraction photograms are reproduced in G and H were tested at the same stress at two different temperatures; they have about the same values of $\ln(\epsilon_s e^{\frac{\Delta H}{RT}})$ and, within the precision of the experimental techniques, they exhibit about the same diffraction effects. X-ray diffraction photograms E and F were obtained from fractured specimens subjected to only slightly different stresses at two different temperatures and they exhibited only slightly different values of $\ln(\epsilon_s e^{\frac{\Delta H}{RT}})$; they also reveal almost identical X-ray diffraction effects. Thus the structures and the creep properties of metals appear to be directly correlatable.

Effect of α Solid Solution Alloying on the Creep Properties and Structure: As shown by the creep data recorded in Fig. 3, the activation energy for creep is independent of dilute alloying additions.

The primary factor that is responsible for the improved creep resistance of α solid solutions probably arises from the slower crystal recovery rates induced by alloying.¹¹ This fact suggests that alloying elements restrain the migration of dislocations and therefore the α solid solutions should exhibit deformation banding down to somewhat lower values of $\ln(\epsilon_s e^{\frac{\Delta H}{RT}})$ than the pure element. The type of back-reflection X-ray photograms obtained from the series of fractured aluminum plus 1.6 atomic pct Mg creep specimens are shown in Fig. 4. Each photogram is documented in terms of the applied stress, temperature and $\ln(\epsilon_s e^{\frac{\Delta H}{RT}})$ to permit rapid comparison with the σ_c vs. $\ln(\epsilon_s e^{\frac{\Delta H}{RT}})$ data recorded in Fig. 3. The only significant difference between these correlations and those for high purity aluminum is discerned in the greater diffuseness of the diffraction arcs in the Al-Mg alloy for the same value of $\ln(\epsilon_s e^{\frac{\Delta H}{RT}})$.

Constant Load Creep Curves and Metallurgical Structure: In order to check more thoroughly the possible validity of Eq. 1, a series of three creep tests on three newly prepared specimens from a new sheet of high purity aluminum were made at 422°, 477°, and 528°K at a creep stress of 2000 psi. The results of these tests are given in Fig. 5. These tests correlate very well when the creep strain is plotted as a function of the temperature-compensated time. The obtaining of a slightly lower activation energy of $\Delta H \approx 17,000$ R cal per mol in lieu of the former value of $\Delta H \approx 17,900$ R cal per mol is probably attributable to a minor influence of sampling on the apparent activation energy. This difference however, is not conspicuous and will be disregarded for the present.

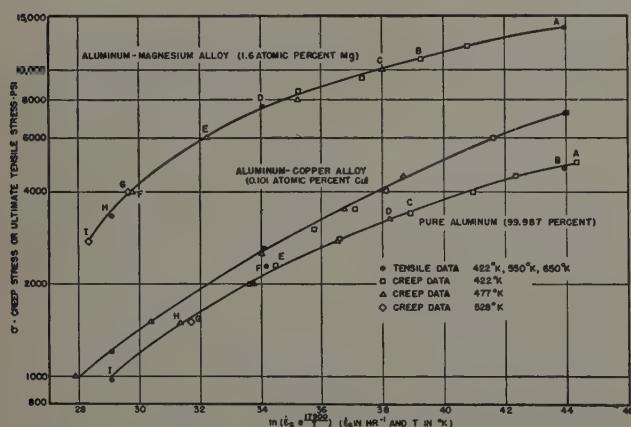


Fig. 3—Correlation of creep and tensile data of various aluminum solid solution alloys by the equation $\sigma \cong \sigma(\epsilon_s e^{\frac{17900}{T}})$.

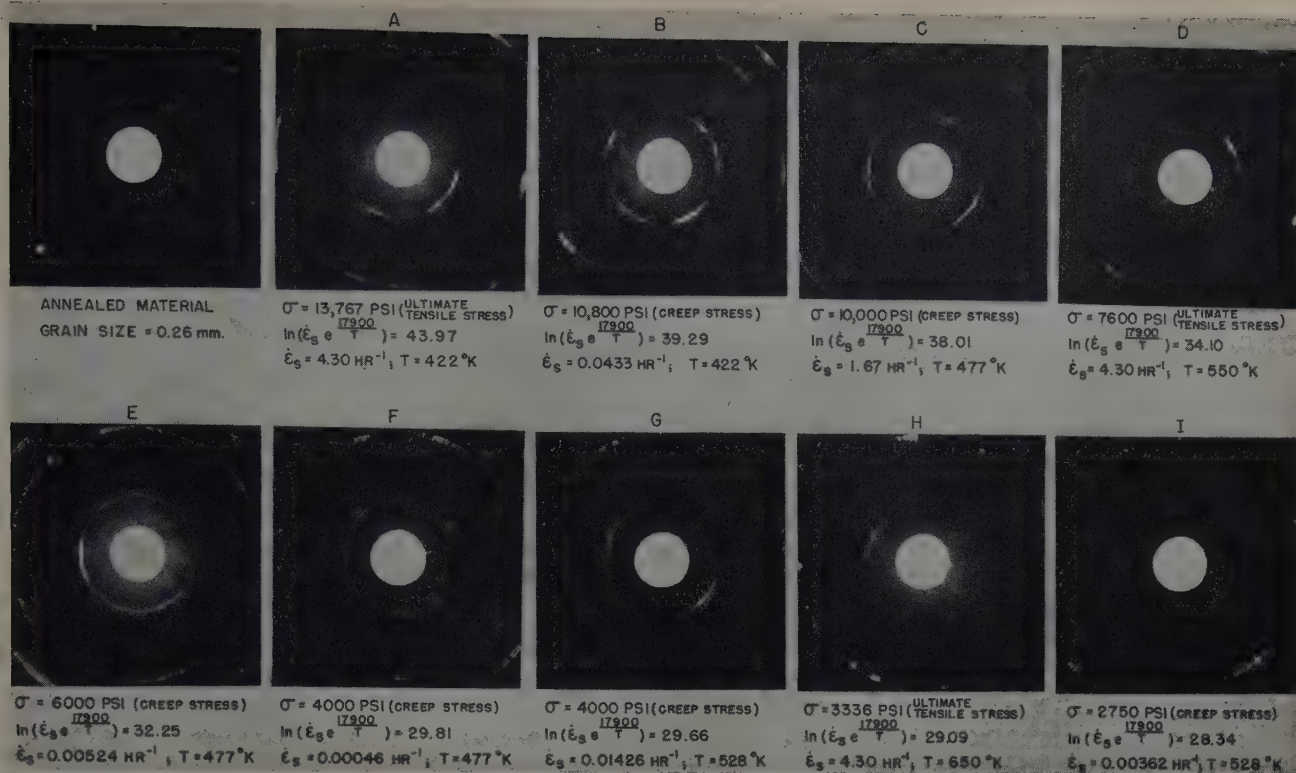


Fig. 4—X-ray back-reflection photographs of an Al-Mg solid solution alloy as a function of the parameter $\dot{\epsilon}_s e^{\frac{17900}{T}}$.

The correlations obtained in Fig. 5 suggest that if long time creep data are desired for a given stress and temperature, they might easily be predicted from two short time creep tests at two somewhat higher temperatures. For the same strain on these two tests:

$$t_1 e^{-\frac{\Delta H}{RT_1}} = t_2 e^{-\frac{\Delta H}{RT_2}} \quad [5]$$

from which ΔH can be obtained. The same strain will be obtained for a creep test at the desired temperature, T , at time:

$$t = \frac{t_1 e^{-\frac{\Delta H}{RT_1}}}{e^{-\frac{\Delta H}{RT}}} = \frac{t_2 e^{-\frac{\Delta H}{RT_2}}}{e^{-\frac{\Delta H}{RT}}} \quad [6]$$

Thus it becomes a simple matter to calculate the entire creep strain, ϵ , vs time, t , curve for any temperature within the realm of validity of the temperature-compensated time concept.

The correlation mentioned between the creep strain and the temperature-compensated time suggests that the metallurgical structure should also correlate with the temperature-compensated time independent of the actual test temperature. In order to examine the validity of this concept, a series of creep tests were run under a creep stress of 2000 psi at each of the temperatures of 422°, 477°, and 528°K. At each temperature the specimens were removed for diffraction examination at the following strains: $\epsilon = 0.085, 0.15, 0.25$, and immediately following fracture. Since the creep curve at a given stress was shown to be a function of the temperature-compensated time, the constant strain values selected are identical with constant values of the temperature-compensated time. The strain $\epsilon = 0.085$ is approximately in the center of the primary creep interval; the secondary creep stage begins at about a strain of 0.15, and the tertiary stage begins at a strain of about 0.25 for the selected stress of 2000 psi. The X-ray diffraction photographs

which were obtained are shown in Fig. 6. Because of the limited number of grains which were sampled by the X-ray beam, small deviations were obtained in the diffraction patterns. Within the sensitivity of the diffraction technique, however, the same structures were obtained at identical strains for the various creep temperatures.

The substructure appears to be independent of test temperature for the same creep strain under a constant stress, but it changes markedly throughout the primary stage of creep. At a strain of 0.085 small diffuse Debye-Scherrer arcs are obtained, whereas at the conclusion of the primary stage longer and less diffuse Debye-Scherrer arcs are in evidence. Minor changes in the Debye-Scherrer arcs occurred over the secondary range of creep from $\epsilon = 0.15$ to $\epsilon = 0.25$ leading to slightly less diffuse and longer arcs. Additional metallurgical changes leading to less diffuse Debye-Scherrer arcs can be observed to occur over the tertiary stage of creep.

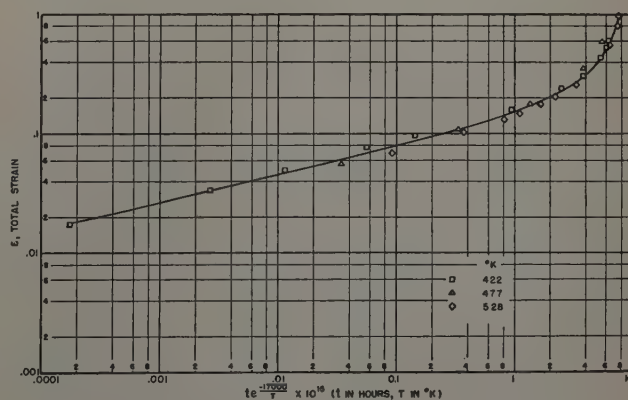


Fig. 5—Correlation of creep strain-time data of high purity aluminum by the equation $\epsilon \cong \epsilon(t e^{-\frac{17900}{T}})$ at a stress of 2000 psi.

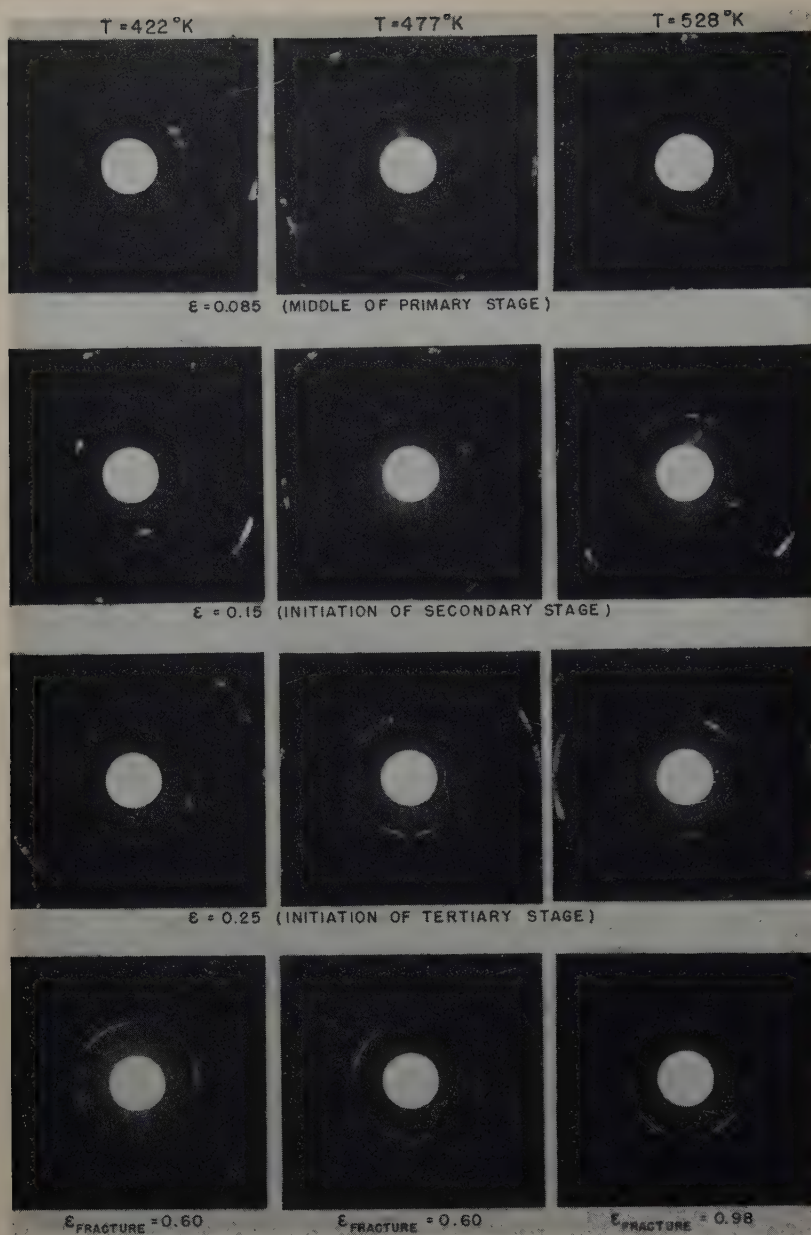


Fig. 6—X-ray back-reflection photograms of high purity aluminum under a creep stress of 2000 psi for various temperatures as a function of strain.

As shown in Fig. 5, ϵ is a function of $te^{-\Delta H/RT}$ where ΔH is a constant, independent of temperature, over the entire creep curve; hence, it must be assumed that ΔH is independent of the structure over the entire range of structures revealed by the diffraction photograms in Fig. 6.

In view of the somewhat insensitive and qualitative nature of comparisons of the Debye-Scherrer photograms, some doubt might yet persist concerning whether exact identity of subgrain structures is achieved at identical strains, independent of the creep temperature, during constant load creep tests. Inasmuch as the plastic properties of metals are quite sensitive to their substructure, it was thought that unqualified proof of this thesis could be established by investigating the true stress-true strain curves at atmospheric temperatures following creep. The atmospheric temperature true stress-true strain diagrams of specimens precrept to the various structures previously recorded in Fig. 6 are shown in Fig. 7. As the creep strain of previously annealed specimens increases, the plastic properties at atmospheric temperatures improve, and the resulting stress-strain curves for constant load creep tests are iden-

tical for identical creep strains independent of the creep temperature. The thesis that the structural changes attending a constant load creep test depend only on the total creep strain independent of the creep temperature is therefore well established.

Creep Under Conditions of Variation in Temperature: In many technological applications the temperature under which creep occurs is not constant. It would indeed reduce the amount of testing if the creep curve for any prescribed program of temperature could be calculated from isothermal creep data. The basic correlations necessary for such a calculation are contained in the correlations between the creep strain and the temperature-compensated time. Assume that a metal is to be subjected to any arbitrary temperature-time history such as that given in the upper graph of Fig. 8. The activation energy can be obtained as outlined by Eq. 5 from two isothermal creep tests at the desired stress. Consequently the temperature-compensated time can be calculated from:

$$\theta_1 = \int_0^{t_1} e^{-\Delta H/RT} dt \quad [7]$$

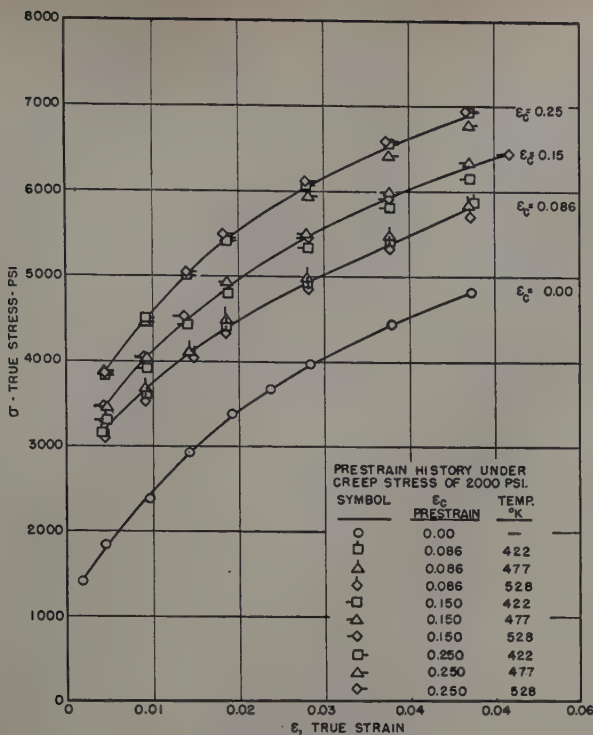


Fig. 7—Tensile properties at 298°K following the series of creep histories shown in Fig. 6.

where T is the prescribed function of t . The value of the integrand of Eq. 7 is given in the second curve of Fig. 8. Thus the value of θ_1 for any time t_1 is merely the area under this curve from $t = 0$ to t_1 . The appropriate creep strain for the value of θ_1 can be read off of a chart based on the isothermal data, such as that given in Fig. 5. This sequence of operations can be repeated for other times until the entire creep strain vs time curve is predicted.

In order to test the above method of predicting creep for constant stress variable temperature conditions, two creep tests at 2000 psi were performed on high purity aluminum for the identical temperature history given in the upper curve of Fig. 8. The actual creep curves which were obtained are shown by the solid curves in the two lower graphs of Fig. 8; the predicted creep curves are illustrated by the dashed curves. The agreement is within the usual variations in creep data from sample to sample. Thus the practical utility of the concept of the temperature-compensated times is well established for the simple metallurgical systems which have been investigated here.

Creep and Resulting Structures: The success of the correlation of the creep strain in a constant stress test with the temperature-compensated time, as described previously, arises from the fact that the metallurgical structure is also a continuous function of the temperature-compensated time independent of the creep temperature. These correlations then allow the simple analyses of creep data for any temperature history. From both the theoretical and practical aspects of the problem on creep it is equally important to be able to describe the creep behavior of metals under any condition of stress history. By direct analogy with the problem of temperature history on the creep of metals, it is clear that the latter correlation would be readily feasible if the same metallurgical structures are developed in creep tests at various stresses. The complete solution of this problem has not yet been achieved but the results of some preliminary in-

vestigations, which will now be described, suggest that the resolution of the problem will be affected by several complicating factors.

The data contained in Figs. 2 and 4 clearly reveal a distinct difference between the structures of fractured creep specimens as a function of the creep stress. As shown in Fig. 1, specimens tested at the higher stresses exhibit deformation bands at fracture whereas those specimens tested at the lower stress levels exhibit a fine subgrain structure. Similar trends are observed in the X-ray diffraction photograms shown in Fig. 4. This suggests that the higher stress test specimens acquire a more severely deformed structure immediately upon loading, and due to their more rapid creep rate retain a more severely worked structure throughout their creep history; the less severely stressed specimens acquire an initially less deformed structure and exhibit greater grain perfection and recovery at the same values of the temperature-compensated time.

In order to study more thoroughly the differences in structures for creep tests conducted at different stress levels, a series of creep tests were conducted at two alternate stress levels 3400 and 2000 psi. Specimens were removed for X-ray diffraction studies at strains of 0.085, 0.15, 0.25, and at fracture. The higher stress tests exhibited greater initial deformation and continued to exhibit such greater deformation at the same strains and same values of the temperature-compensated time throughout the entire creep history. Also, at no point in the higher stress tests was a structure achieved which was in any way similar to the structures obtained at the lower stress level. These observations, then, reveal one source of

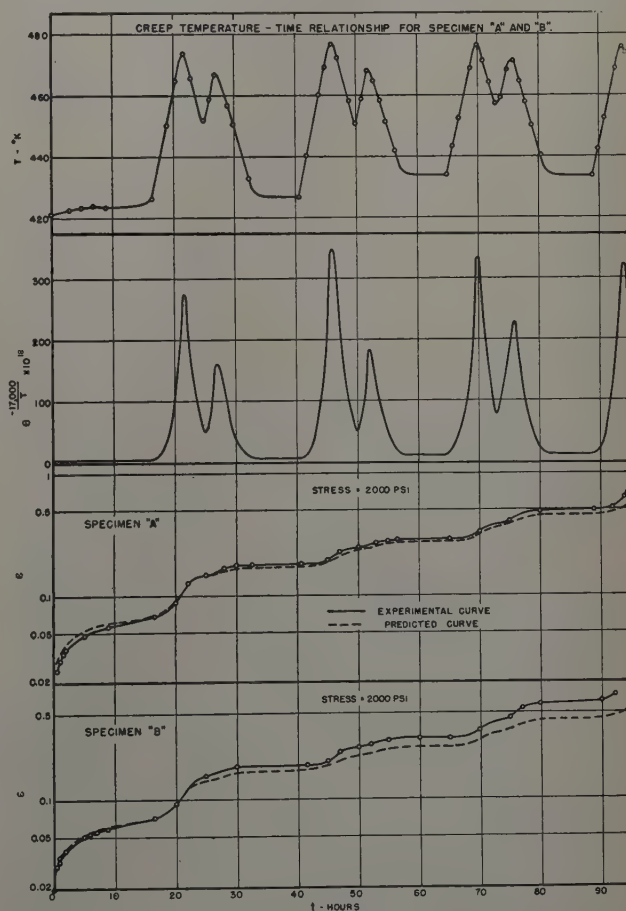


Fig. 8—Predicted and experimental creep curves for high purity aluminum when the temperature is changed as a function of time under constant load conditions.

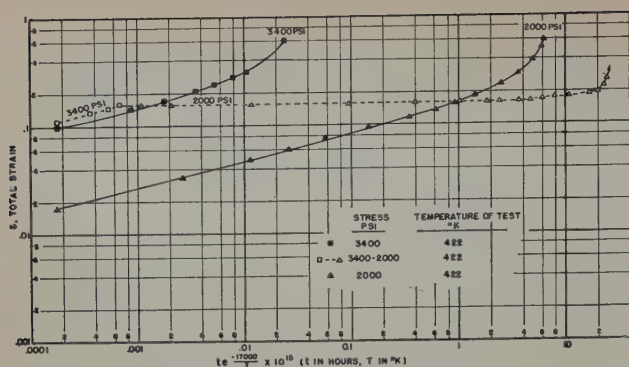


Fig. 9—Effect of change of stress on the creep of high purity aluminum.

the failure of the mechanical equation of state for creep.

If at some stage in a low stress creep test the stress is suddenly increased, the additional tensile deformation that results will introduce changes in the structure of the specimen, bringing the structure into closer agreement with that obtained at some stage of the higher creep stress test. But inasmuch as the structural changes that are introduced upon increasing the load are superimposed on the substructure obtained during creep at the originally lower stress, it is improbable that the resulting structure will coincide exactly with that obtained at any stage of creep in a specimen subjected exclusively to the higher stress. Thus the past stress history modifies the structure of metals in such a way as to modify their subsequent mechanical properties. These discussions are also pertinent to cases wherein the stress is lowered at some stage of creep. The instant the stress is lowered the structure remains essentially that which was developed at the higher stress excepting for the minor modifications induced by creep recovery. At the lower stresses this structure might undergo crystal recovery and polygonization so that eventually the structure begins to approximate that of a specimen exclusively subjected to the lower stress. But inasmuch as the structure upon lowering the stress is reasonably different from that of any structure which is developed exclusively at the lower stress, it is unlikely that exact coincidence of structure can be achieved. The creep data recorded in Fig. 9 illustrate this point. The solid squares refer to creep of high purity aluminum under 3400 psi at 422°K, whereas the solid triangles refer to creep under 2000 psi at the same temperature. A third creep test was conducted at 3400 psi, represented by the open squares, and then the stress was lowered to 2000 psi, represented by the open triangles. The small differences in the solid and open square data for 3400 psi are attributable to sampling differences. After the stress was lowered to 2000 psi a very low creep rate was obtained. The shape of the 2000 psi curve for the specimen prestressed at 3400 psi is very dissimilar from the shape of the curve for the specimen stressed exclusively at 2000 psi. This implies that the structure of the specimen prestressed at 3400 psi probably never achieves the same structure developed in the specimen stressed exclusively at 2000 psi.

Conclusions

1—For α solid solution alloys the creep strain for a constant stress creep test is a function of the temperature-compensated time $\theta = \int e^{-\frac{\Delta H}{RT}} dt$ where: t is the time; T , the test temperature, °K; R , the gas constant; and ΔH , the activation energy.

2—The activation energy for high temperature creep is relatively insensitive to the test temperature, stress, grain size, small concentrations of alloying elements, and metallurgical structure of α solid solutions. ΔH was found equal to approximately 35,800 cal per mol.

3—If the creep curves for a constant stress are known for two temperatures, ΔH can be evaluated. Using this value of ΔH , the creep strain vs time curve can be calculated for any variable high temperature program for creep.

4—The creep behavior of α solid solutions is directly correlatable with the grain substructures that are developed. For a given creep stress the substructures are functions of the creep strain independent of the test temperature.

5—For each new creep stress a unique set of grain substructures is developed as a function of creep strain. This is one of the factors responsible for the failure of the mechanical equation of state for creep.

Acknowledgments

This investigation was sponsored by the Office of Naval Research. The authors wish to thank the ONR staff for their continued interest and full cooperation throughout the conduct of this and related studies on the plastic properties of aluminum alloys. The materials used were supplied by the Aluminum Research Laboratories together with their chemical analyses.

In addition the authors wish to thank Stewart Frederick and Warren Giedt for assistance in the X-ray and creep testing programs, M. Kawaguchi for the micrographic pictures, and C. Dean Starr for his interest in and contribution to this study. To G. Pelatowski sincere appreciation is extended for her careful preparation of the figures in this report.

References

- 1 W. A. Wood, G. R. Wilms, and W. A. Rachinger: Three Basic Stages in the Mechanism of Deformation of Metals at Different Temperatures and Strain Rates. *Journal Inst. Metals* (May 1951) pp. 159-172.
- 2 W. A. Wood and R. F. Scrutton: Mechanism of Primary Creep in Metals. *Journal Inst. Metals* (1950) 77, pp. 423-434.
- 3 D. Hanson: Creep of Metals. *Trans. AIME* (1939) 133, pp. 15-57.
- 4 I. S. Servi and N. J. Grant: Structure Observations of Aluminum Deformed in Creep at Elevated Temperatures. *Trans. AIME* (1951) 191, pp. 917-922; *JOURNAL OF METALS* (October 1951).
- 5 G. Wyon and C. Crussard: Modifications of the Structure of Aluminum During Creep. *Revue de Metallurgie* (1951) 48, (2) pp. 121-130.
- 6 G. B. Greenough and Edna M. Smith: The Mechanism of Creep as Revealed by X-ray Methods. *Journal Inst. Metals* (1950) 77, pp. 435-443.
- 7 Oleg D. Sherby and John E. Dorn: Creep Correlations in Alpha Solid Solutions of Aluminum. *Trans. AIME* (1952) 194, pp. 959-964; *JOURNAL OF METALS* (September 1952).
- 8 C. Zener and J. H. Hollomon: Plastic Flow and Rupture of Metals. *Trans. ASM* (1944) 33, pp. 163-235.
- 9 C. Zener and J. H. Hollomon: Effect of Strain Rate on the Plastic Flow of Steel. *Journal of Applied Physics* (1944) 15, pp. 22-32.
- 10 A. E. Flanagan, L. F. Tedsen, and J. E. Dorn: Stress-Rupture and Creep Tests on Aluminum Alloy Sheet at Elevated Temperatures. *Trans. AIME* (1947) 171, pp. 213-245; *METALS TECHNOLOGY* (September 1946).
- 11 A. T. Robinson, T. E. Tietz, and J. E. Dorn: The Functions of Alloying Elements in the Creep Resistance of Alpha Solid Solutions of Aluminum. *Trans. ASM* (1952) 44.

Creep Properties of Commercially Pure Titanium

by W. R. Kiessel and M. J. Sinnott

The creep characteristics of commercially pure titanium sheet in the annealed state, cold-worked state, and cold-worked and recovered state in the temperature range from 75° to 750°F have been determined. Titanium has been found to exhibit strain aging characteristics. The effect of strain aging on creep has been determined. A possible explanation for the poor creep properties of titanium is proposed.

THE metal titanium exhibits many desirable properties but results on its creep properties have been somewhat disappointing. The creep strength is low even though the material has a very high melting point.¹ The present work was undertaken to determine the creep strength of titanium in various conditions; annealed, cold-worked, and cold-worked and recovered and to determine why titanium shows such relatively poor creep properties.

The general procedure followed in this research consisted in obtaining the usual mechanical prop-

erties such as creep strength, short time tensile strengths, and hardness on materials treated to a controlled degree of internal strain, as determined by X-ray diffraction measurements, and their subsequent interpretation in terms of this internal strain.

The material used in this work was sheet stock taken from one heat of commercially pure titanium. As-received, this sheet was 0.060 in. thick. The analysis was given as 0.037 pct C, 0.023 pct Si, 0.50 pct W, 0.063 pct Ni, 0.08 pct Fe, and the remainder titanium. The oxygen and nitrogen were unreported but generally are about 0.2 pct in commercial heats.

In order to put the material in a state of minimum internal strain all the sheet was given an anneal in a static argon atmosphere for 1 hr at 1600°F prior to processing and testing. The microstructure of the material after this treatment was essentially a single-phase solid solution of uniform equiaxed grains.

For the studies on the cold-worked sheet, the material was reduced by rolling in a two high, 5 in. mill. Rolling was done at room temperature in passes

W. R. KIESEL is associated with Ford Motor Co. Scientific Laboratory, Dearborn, Mich., and M. J. SINNOTT, Member AIME, is Associate Professor, Chemical and Metallurgical Engineering, University of Michigan, Ann Arbor, Mich.

Discussion on this paper, TP 3473E, may be sent, 2 copies, to AIME by April 1, 1953. Manuscript, Sept. 5, 1952. Los Angeles Meeting, February 1953.

This paper is based on a thesis by W. R. Kiessel submitted in partial fulfillment of requirements for the degree of Doctor of Philosophy to the Horace H. Rackham School of Graduate Studies, University of Michigan.

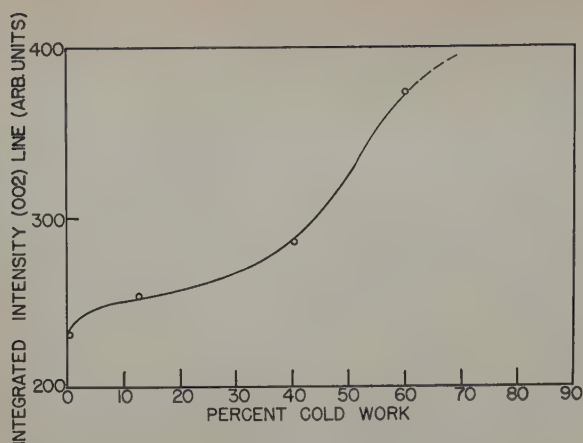


Fig. 1—Effect of cold working on the integrated intensity of the diffracted (002) X-ray line.

of not more than 10 pct reduction per pass, the material being cooled after each pass.

In determining the recovery characteristics of the cold-reduced stock, the material was annealed at temperatures of 210°, 400°, and 600°F for time intervals of 1, 100, and 1000 hr. All creep and tensile specimens were annealed or treated in a similar manner. Specimens that were treated at other temperature levels will be indicated.

Test Procedures

Tensile test and creep data at room temperature were obtained by the use of electric strain gages. For elevated temperatures a modified Martens extensometer was used. Strain rates of 0.001 and 0.050 in. per in. per min were used in taking the tensile data. All tests were run in air and temperatures were controlled to $\pm 3^\circ\text{F}$ as measured by thermocouples attached to the specimens. In the creep tests the specimens were placed in a furnace operating at the test temperature and, after thermal equilibrium was established, the load was applied through a lever

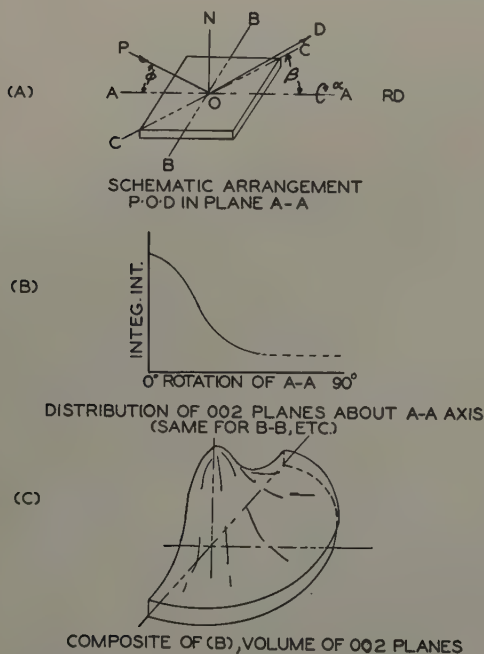


Fig. 2—Pictorial description of preferred orientation correction of integrated intensity measurements for sheet textures.

system which placed the material under constant stress rather than constant load. In most cases complete time-elongation data were obtained but in some instances readings could not be taken until 0.1 hr had elapsed, due to the abnormally large first-stage creep component. Total strain was measured in all cases but is not reported in this paper. Creep test durations were on the order of 1000 hr. In some cases this time interval was insufficient for steady state creep conditions to be reached and in those cases the minimum rate was taken as the steady state creep rate. Longer duration tests showed that this introduced only a small error in the creep rates. The least creep rate obtainable was dictated by the accuracy of the extensometer system, 3×10^{-6} in. per in., and the maximum rates by the rupture properties of the metal.

X-ray diffraction studies using $\text{CuK}\alpha$ radiation were made on etched surfaces of the titanium sheet, the diffracted beam being filtered. For line intensity

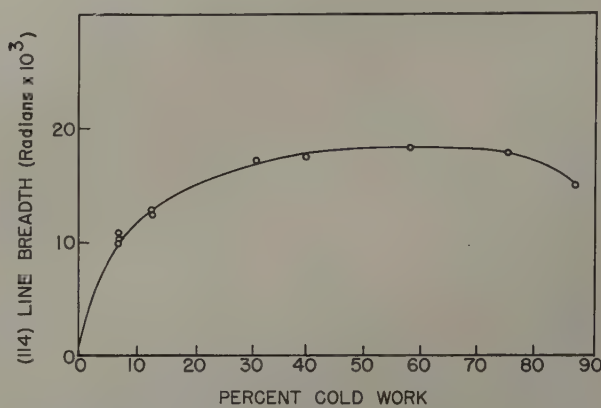


Fig. 3—Effect of cold work on the internal strain as measured by the line breadth of diffracted (114) beam.

measurements the (002) line, $2\theta = 38.8^\circ$, was studied using a Norelco spectrometer with a Geiger-Mueller tube and counting circuit to record the diffracted energy. Orientation corrections were made on these specimens by determining the integrated intensity distribution in all positions with a Shultz fixture.² This is essentially the method used by Frey³ after modification for sheet textures. Diffracted line breadth studies were made on a high angle Norelco spectrometer on the (114) planes, $2\theta = 114.6^\circ$, which were aligned parallel to the rolling direction.

Corrections for instrumental broadening were made on all spectrometer traces by the use of Fourier analysis.⁴ Generally ten harmonics were used although in cases of small strain the number was extended to as many as twenty. As a measure of the amount of line broadening, and hence the amount of internal strain, the breadth was determined in units of radians at the half peak.

Internal Strain Measurements

Mechanically working a metal can result in two phenomena occurring in the lattice; fragmentation^{5, 6} and changing of the interplanar spacings.^{7, 8} Both of these processes can cause broadening of the X-ray diffraction beam. Fragmentation, however, will cause no appreciable broadening unless the crystallites are 10^{-5} cm or less in thickness.⁹ Since line broadening is used in this work to determine the internal strain or changes in interplanar spacings,

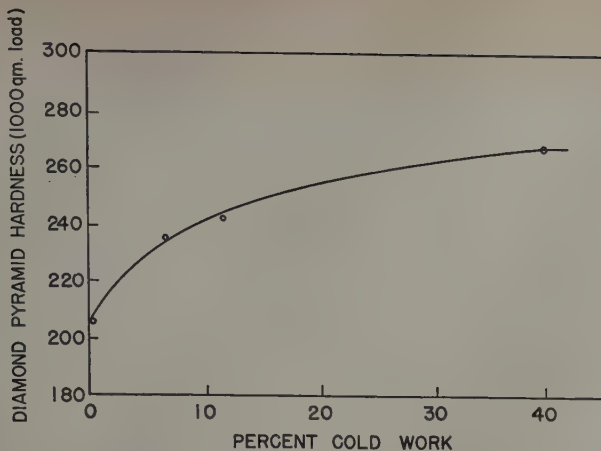


Fig. 4—Effect of cold work on the diamond pyramid hardness of rolled titanium sheet.

it was necessary to evaluate the fragmentation effect if it existed. This was done by the use of integrated intensity studies. The amount of fragmentation that has occurred will be reflected in the degree of primary extinction.

Primary extinction, the power loss of a diffracted beam due to the rediffraction of energy in any one fragment, can be expressed by means of the Darwin term applied to the integrated intensity of the diffracted beam.¹⁰ It is stated as follows:

$$P' = P \frac{\tanh(\text{Constant} \cdot \csc 2\beta \cdot F_{hkl}^2 \cdot d^3 \cdot \cot \beta)^{1/2}}{(\text{Constant} \cdot \csc 2\beta \cdot F_{hkl}^2 \cdot d^3 \cdot \cot \beta)^{1/2}}$$

where P is the integrated intensity of an extinctionless sample; P' , the corrected integrated intensity; β , Bragg angle; F , the structure factor; and d , the thickness of the mosaic fragment.

The correction term approaches unity as d , or β approach zero. If a measurable increase of the integrated intensity of an X-ray diffracted beam occurs at a given Bragg angle from samples cold-worked to various degrees, then the fragment size is such as to cause no broadening of the diffracted beam.

Test pieces of annealed titanium, and sheet rolled 13, 40, and 60 pct were analyzed using the (002) line. The results, as presented in Fig. 1, showed that the integrated intensity of this line, after corrections for preferred orientation effects, increased quite markedly over the entire range, thus indicating that the particle size was not contributing to the broad-

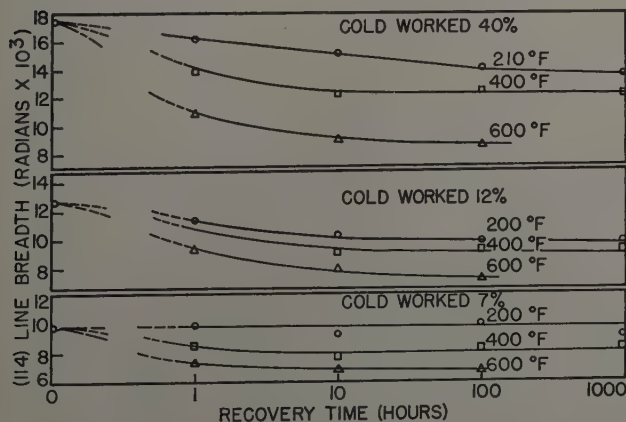


Fig. 5—Effect of recovery time and temperature on internal strain, as measured by line breadths, for titanium cold-reduced 40, 12, and 7 pct.

ening of the diffracted beam. Such broadening as did occur, less instrumental effects, was due to internal strain. This is in general agreement with Smith and Stickley¹¹ and Brindley and Ridley¹² although their investigations were carried out on metallic powders.

The method used for the orientation corrections of the diffracted line integrated intensity measurements can best be explained by reference to Fig. 2. Consider a specimen arranged as shown in Fig. 2a. The X-ray primary beam, which strikes the specimen at the Bragg angle θ , and the diffracted beam lie in the same plane as the axis A-A. If the specimen is rotated to various angular positions α , about A-A, and the integrated intensity measurements made, all the (002) planes lying parallel to the axis will have a chance to diffract. Similarly, if the specimen is rotated about the specimen normal N , to angular position β , as C-C, between A-A and B-B, and if at each such position the specimen is rotated about C-C, as was done about A-A, then all the

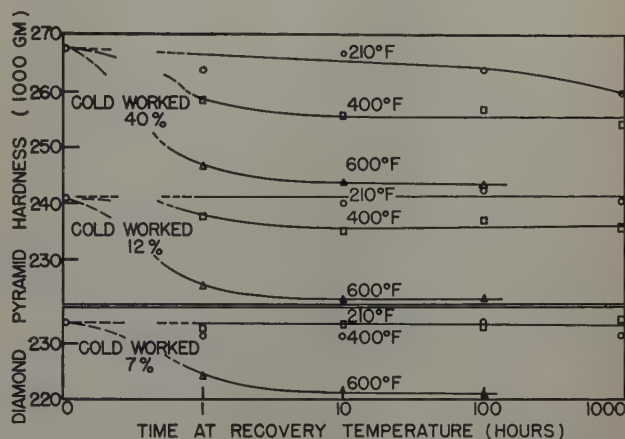


Fig. 6—Effect of recovery time and temperature on the diamond pyramid hardness of titanium rolled 40, 12, and 7 pct.

(002) planes can be accounted for. A series of plots as shown in Fig. 2b, one for axis A-A, axis B-B, and each β angular position of C-C, can be drawn. Combining these plots gives a volume as shown in Fig. 2c, and from the volume an average integrated intensity can be found.

Since titanium exhibits a symmetrical pole pattern, the intensity distribution was determined in one quadrant only; the determinations being made for 15° increments in β and 5° and 10° increments in α . No extinctionless standard was available for absolute intensity or extinction measurements. The relative values, however, were sufficient for this investigation.

Line Breadth Studies

Since broadening of the diffracted X-ray line was found to be caused by internal strain, the effect of varying amounts of cold working on the state of the internal strain was measured. As shown in Fig. 3, cold work up to 30 or 40 pct produces the near maximum of internal strain; further working resulting in only a slight increase, but this is followed by a decrease because of the onset of self-recovery. The data shown in Fig. 3 were taken within 6 hr of rolling. Additional aging at room temperature for four months showed recovery occurring only in specimens reduced 60 pct or more. These facts, coupled with the difficulty of testing thin sheet

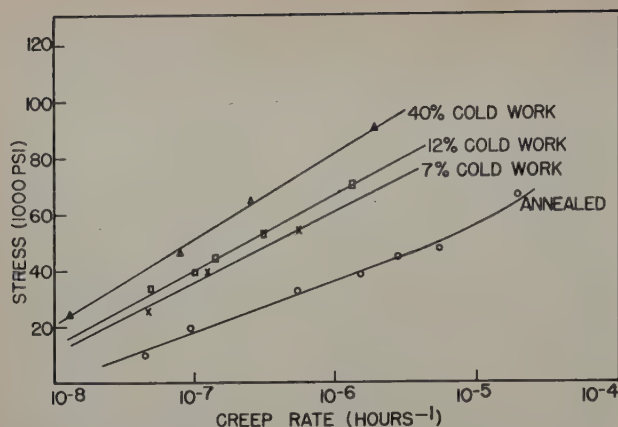


Fig. 7—Second-stage creep rate at 76°F of annealed and cold-reduced titanium sheet as a function of stress.

specimens, resulted in the selection of 40 pct cold work as being the maximum state of internal strain in subsequent studies.

For comparative purposes the effect of cold working on the diamond pyramid hardness is shown in Fig. 4. Its response to changes in internal strain is less sensitive than the X-ray procedure. A metallographic examination of the cold-worked samples showed an elongation of the grains but no deformation bands or twins.

Recovery Studies

The recovery process in cold-rolled titanium was observed by X-ray line breadth measurements and by hardness determinations. Sheets rolled 7, 12, and 40 pct were recovered at temperatures of 210°, 400°, and 600°F for time intervals of up to 1000 hr. The results of the line breadth measurements are shown in Fig. 5, while Fig. 6 shows the results of the hardness measurements.

Recovery did not occur at 210°F on the titanium reduced 7 pct and was incomplete on the sheet reduced 12 and 40 pct. A constant value of internal strain for each condition of previous cold work was reached after 20 to 50 hr at either 400° or 600°F. The hardness measurements showed the same trends as the line breadth studies but did not respond as readily.

Creep Studies

Creep tests were conducted on the annealed, the cold-worked, and the cold-worked and recovered

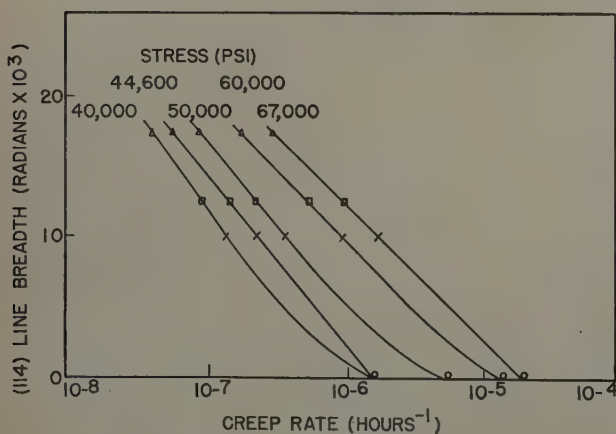


Fig. 8—Correlation between line breadth and second-stage creep rate at 76°F of annealed and cold-reduced titanium at various stress levels.

titanium. Fig. 7 is a plot of the stress vs second-stage creep rate for tests conducted on the annealed stock at 76°F.

Line breadth studies conducted on these completed creep specimens showed only a slight change in internal strain. These increases can be attributed to strain hardening. The specimens tested under high strain rates showed between 5 and 6 pct total elongation after testing. Measurements of the internal strain in these specimens, when compared with the internal strain of samples rolled to this extent, were identical.

The effect of varying degrees of cold work on the creep rate of titanium at 76°F is shown in Fig. 7. Small amounts of cold work are more effective in increasing the creep resistance from the annealed state than from higher degrees of cold work. This follows the trend developed in the internal strain measurements vs cold work, as shown in Fig. 3.

Fig. 8 shows that a logarithmic relationship exists between the line breadth measurements made prior to testing and the creep rate developed at 76°F on the stock cold-reduced to varying degrees. This correlation appears to be valid regardless of the stress level considered. Some of the annealed material shows higher creep rates than would be

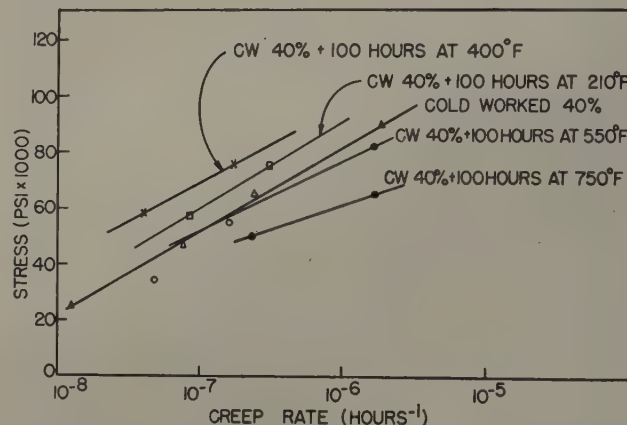


Fig. 9—Second-stage creep rate at 76°F of titanium sheet cold-worked 40 pct and recovered 100 hr at various temperatures.

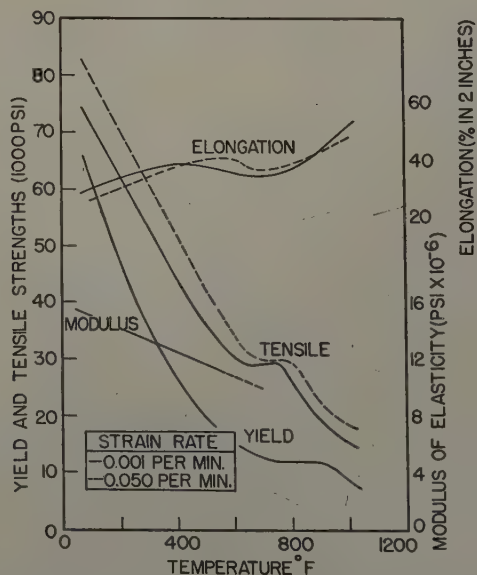


Fig. 10—Short-time tensile properties of annealed titanium sheet as a function of temperature.

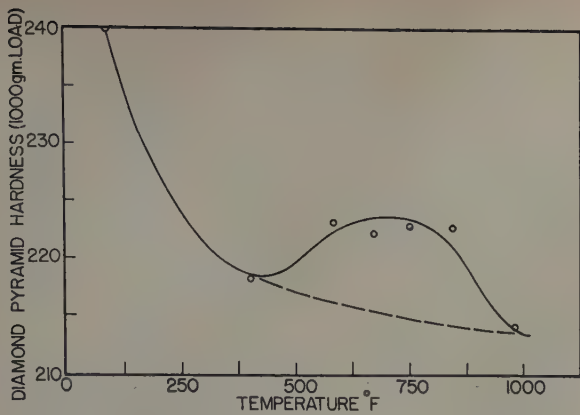


Fig. 11—Diamond pyramid hardness at room temperature of completed short-time tensile specimens.

predicted from a consideration of the cold-worked material only. The reason for this is that the true second-stage creep rate was not reached in the time interval used. Other tests for periods up to 2300 hr (see 44,600 psi data of Fig. 8) yielded data which agree with the correlation obtained on the cold-worked stock.

Fig. 9 presents the results of the creep studies at 76°F on titanium cold-worked 40 pct and recovered 100 hr at temperatures of 210°, 400°, 550°, and 750°F. It will be noted that the creep resistance does not decrease with increasing recovery temperature. Instead the creep strength increases as the recovery temperature increases and reaches a maximum at 400°F.

No correlation between internal strain, as measured by line breadths, and the creep properties at 76°F was obtained on these cold-worked and recovered samples. It is believed that the redistribution of the internal strains during recovery is such as to cause a strengthening effect which is greater than would be predicted from the line breadth measurements.

Strain Aging

The inversion that occurred in the creep properties of the cold-worked and recovered samples is believed to be due to strain aging, since no evidence could be found metallographically for the presence of precipitation. Since strain aging is generally indicated by the following characteristics of: 1—general strengthening, 2—yield point phenomena, 3—decreased strain rate sensitivity in the region of strengthening, and 4—a serrated stress-strain curve,¹⁴ these criteria were investigated by making short time tensile test studies on the annealed material. The studies were made at strain rates of 0.001 and 0.050 in. per in. per min at temperatures to 1000°F. At the faster strain rate it was not possible to determine the stress-strain curves and the yield strengths were not obtained. Fig. 10 summarizes the mechanical properties as determined by these tests. The data show that there is a decrease in tensile strength with increasing temperature but in the range of 600° to 800°F the tensile strengths are constant while the elongation decreases. Over the same temperature range the strength is approximately constant regardless of the strain rate. This is not the case at higher or lower temperatures. An examination of the stress-strain curves showed the presence of a yield point in the tests conducted at temperatures from 210° to 650°F and the presence of serrations. In view of these data, it is concluded

that the titanium tested is subject to strain aging. The basic cause is as unknown as in any of the other metals in which this phenomenon has been detected. The same elements which are variously believed to cause the effect in other metals are present in the titanium, namely, carbon and nitrogen.

In order to obtain some indication of the order of increase in hardness attributable to strain aging, measurements were taken on the completed tensile specimens 1½ in. from the fracture. The results are shown graphically in Fig. 11. The greatest hardening occurred at the lower temperatures because of strain hardening. Increasing temperatures caused a decrease in the strain hardening component, but in the range of 600° to 800°F strain aging is present and its effect must be added to the effect of strain hardening. If it is assumed that the strain hardening component follows the dotted line of Fig. 9, then the maximum hardness increase that can be caused by strain aging is approximately 8 DPH.

Elevated Temperature Creep Tests

Fig. 12 is a plot of the stress vs second-stage creep rate for the annealed titanium tested at 210°, 400°, 600°, and 750°F. These data show that the creep resistance does not continue to decrease with increasing temperature, as might be expected, but instead show a maximum at 400°F. Fig. 13 is a cross-plot of the effect of temperature on the stress required for a given creep rate and more clearly shows this effect.

An interesting feature was noted in the time-elongation curves of these tests. Generally the elevated temperature tests yielded long sweeping

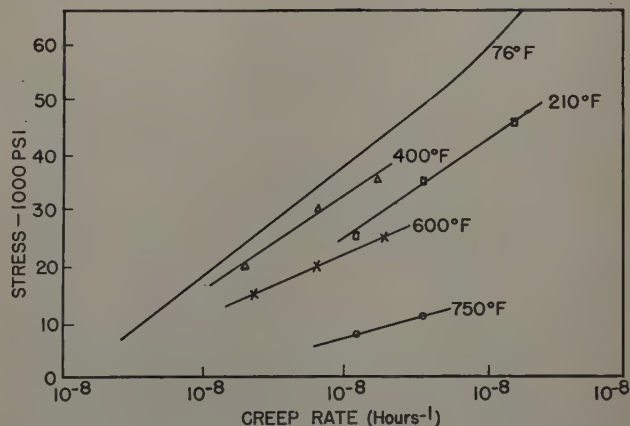


Fig. 12—Second-stage creep rate of annealed titanium sheet as a function of stress and temperature.

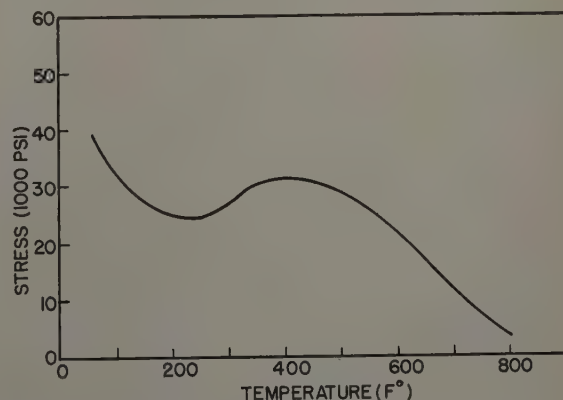


Fig. 13—Effect of temperature on the stress to cause a creep rate of 10^{-6} per hr in annealed titanium sheet.

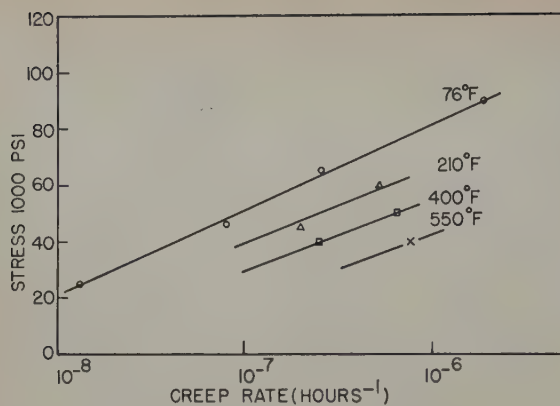


Fig. 14—Second-stage creep rate as a function of stress and temperature for titanium sheet cold-worked 40 pct.

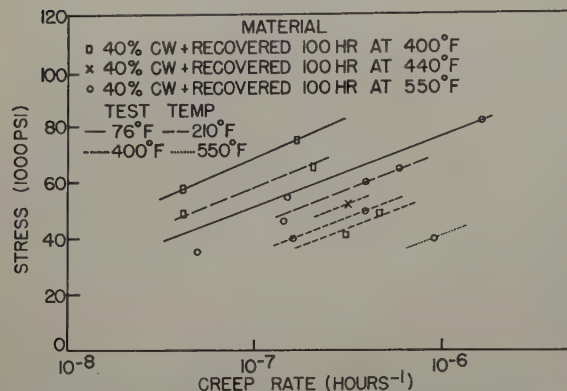


Fig. 15—Effect of stress and temperature on the second-stage creep rate of titanium sheet cold-reduced 40 pct and recovered at various temperatures.

curves with the true second-stage creep rate being established very late in the testing period. In the tests conducted at 400°F however the second stage of creep was established much sooner. At any one stress level the total amount of extension at 400°F was greater than at 210°F because of the higher initial plasticity, but the second-stage creep rate at 400°F was established sooner and was less because of strain aging.

Line breadth studies and hardness measurements were made on the completed creep test specimens of the annealed material tested at elevated temperatures. The results showed that there was an increase in internal strain in the material due to the testing. Some of this strain is due to strain hardening but the samples tested at 400°F had a higher residual internal strain than corresponding specimens tested at the same stress at 210°F. Strain aging is believed to be the cause of this increase.

The maximum effect of strain aging occurred at approximately 400°F, regardless of how it was induced. The increased creep resistance of the annealed and the cold-worked and recovered titanium at the temperature of 400°F is analogous to the increased tensile properties noted at 600°F of Fig. 10. The difference in temperature for the maxima in the two tests can be explained on the basis of the work of Nadai and Manjoine.¹⁵ They showed that with increased rates of straining the temperature of the strain-aging effect is raised and that the extent of the effect is diminished.

The results of creep testing titanium cold-worked 40 pct at elevated temperatures are shown in Fig. 14. The cold-worked material has a higher creep

resistance than the annealed material tested at the same temperatures (see Fig. 12). As the temperature of testing is increased, the creep resistance of the cold-worked material decreases regularly. A possible explanation for the behavior of this material is that the cold working introduces internal strain which strengthens the matrix. During testing at elevated temperatures recovery occurs and this decreases the strength, but the higher temperatures also induce strain aging which strengthens the material. The net result of these last two processes is that essentially they nullify one another.

In the static recovery tests, a constant state of internal strain was reached after approximately 40 hr at temperature. This was not true on materials recovered under stress, since internal strain measurements and hardness measurements on cold-worked 40 pct completed creep specimens tested at elevated temperatures showed values that were lower than the values obtained on the samples recovered under no-load conditions.

In order to study the effect of strain aging induced prior to creep testing on the creep characteristics of titanium, a set of specimens cold-worked 40 pct was recovered at 400° and 550°F prior to testing at temperatures to the recovery temperature. The results are summarized in Fig. 15. Recovery at 400°F produced the greatest strain-aging effect on the creep resistance at 76°F (see Fig. 9), so it was assumed that the same treatment would result in the best creep properties at elevated temperatures; an assumption that is verified in tests at 210°F as shown in Fig. 15. When, however, the material was tested at the same temperature as the temperature of recovery, the strength decreased due to the addi-

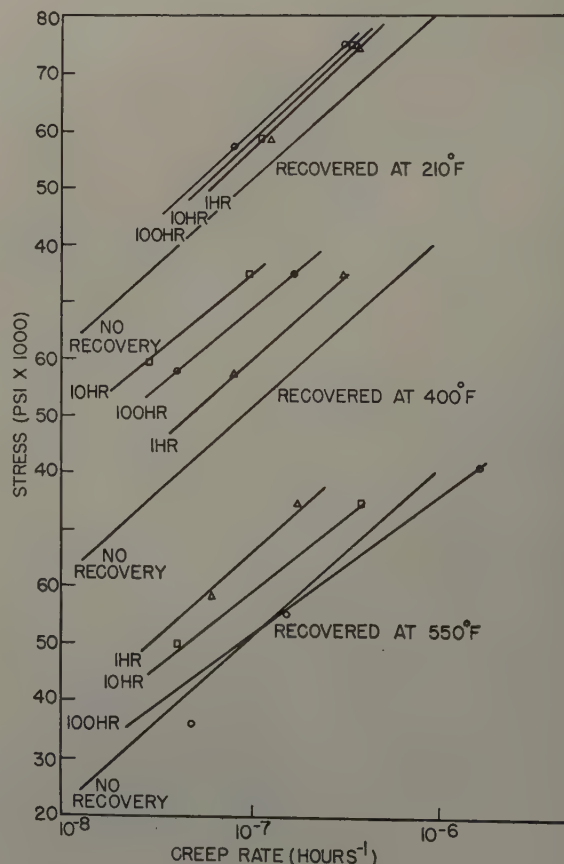


Fig. 16—Effect of stress and recovery time on the second-stage creep rate at 76°F of titanium sheet cold-worked 40 pct and recovered at various temperatures.

tional recovery taking place under stress. As verification of this, the treatment of a specimen cold-worked 40 pct and recovered 100 hr at 440°F was sufficient to prevent any further recovery during subsequent testing at 400°F. The internal strain measurements and hardness measurements made on the above specimens showed that there was no change in these parameters as long as the creep testing temperature was below the temperature used for the prior recovery.

In order to determine the effect of time, as well as temperature, on the strain-aging process, titanium cold-worked 40 pct was recovered 1, 10, and 100 hr at temperatures of 210°, 400°, and 550°F and creep tests made at 76°F. The results are shown in Fig. 16. The results are more graphically illustrated in Fig. 17 where the stress necessary to produce a creep rate of 10⁻⁷ per hr at 76°F is plotted against the log of the time at the recovery temperature. The results are typical of an aging process.

Tensile tests at 76°F were made on the material cold-worked 40 pct and recovered at 400° and 550°F

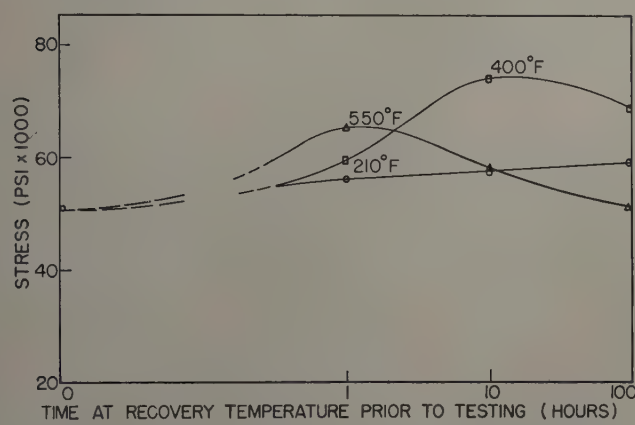


Fig. 17—Stress required to cause a second-stage creep rate of 10⁻⁷ per hr at 76°F in titanium sheet cold-reduced 40 pct and recovered at various temperatures for indicated times.

for varying time periods. The results, shown in Fig. 18, parallel those of the creep data and a correlation between these tensile strengths and the creep resistance for a constant stress was found to exist as shown in Fig. 19. Similar tests on the material cold-worked 40 pct and recovered 100 hr at 210° and 750°F were made and the results agreed with this correlation.

Strain aging has a marked effect on reducing the amount of overall extension by reducing the transient creep component. This fact is quite vividly shown by comparing the total extension at 76°F of specimens cold-worked 40 pct and cold-worked 40 pct and recovered 100 hr at 550°F prior to testing. These two materials had the same second-stage creep component but the strain-aged material had only one-half the total extension, after 1000 hr under test at the same stress, as the cold-worked stock.

Applications of Creep Theories

Andrade¹⁶ has found that creep is mainly of the transient type if the test temperature is low relative to the melting point of the metal and mainly of the quasi-viscous type if the test temperature is high relative to the melting point of the metal. It was thought that at 76°F titanium might exhibit mainly transient creep and this hypothesis was supported qualitatively by the behavior of the annealed ma-

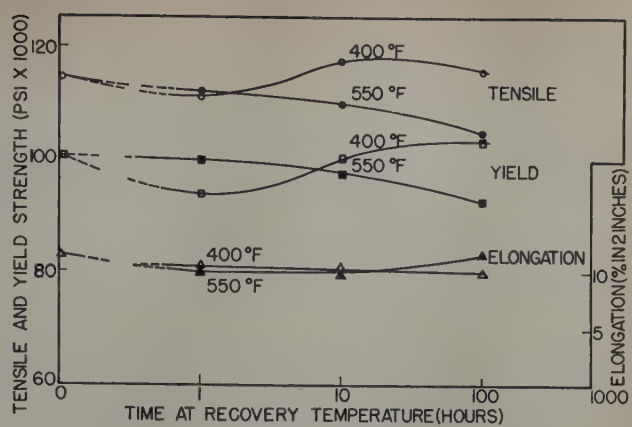


Fig. 18—Effect of time and temperature of recovery on the tensile properties of titanium sheet cold-worked 40 pct.

terial, since quasi-viscous or second-stage creep was not always reached in the time interval considered. An attempt was made, therefore, to correlate existing theories of transient creep with the data collected at 76°F on the annealed and on the cold-worked materials. The data were examined in accordance with the Orowan theory of transient creep,¹⁷ the modification of Smith,¹⁸ and the theory of Mott and Nabarro¹⁹ by noting the mathematical relationship existing between time and strain. In no case did the existing theories describe the creep behavior found for titanium. Deviation from the predicted curves occurred after a time interval of from 50 to 200 hr, depending on the theory and material under consideration. It would seem that second-stage creep becomes active after a relatively short testing time and any further consideration that titanium exhibits chiefly transient creep at room temperature is fallacious.

The analysis of the second-stage creep component was made in accordance with the rate process theory of Eyring and others.²⁰ The process, according to this theory, is assumed to be the result of the activation of small units of flow and their subsequent movement under the applied shear stress over energy barriers. These considerations lead to the following equation:

$$\dot{\epsilon} = \text{Constant} \times T \times e^{\Delta S/R} \times e^{-\Delta H/RT} \times e^{qV\sigma/kT}$$

where $\dot{\epsilon}$ is the creep rate; T , the absolute temperature; σ , the applied stress; S and H , the entropy and enthalpy of activation process; R and k , constants, gas and Boltzmann; V , the flow volume; and q , the stress concentration factor.

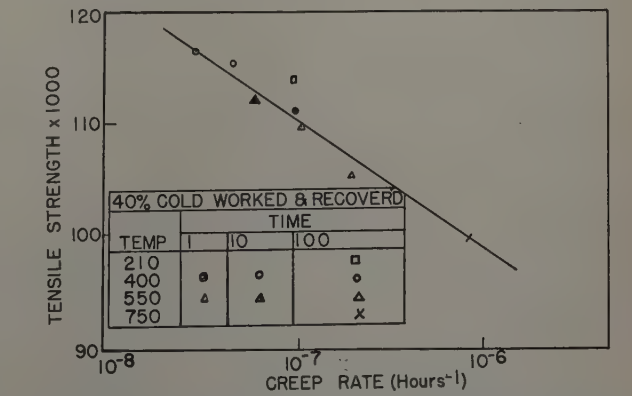


Fig. 19—Correlation between the tensile strength at 76°F and the second-stage creep rate at 76°F under a stress of 60,000 psi of titanium sheet cold-reduced 40 pct and recovered at various times and temperatures.

The usefulness of the theory lies in the fact that, by fitting it to experimental data, some idea of the values of ΔH , ΔS , and V can be determined for comparative purposes.

The flow volume, V , can be determined if several assumptions are made; namely that ΔH and ΔS are not functions of stress and that q is approximately unity. The above equation then reduces to:

$$\log \dot{\epsilon} = \log C_1 + V\sigma/2kT$$

From a plot of the log of the creep rate at 76°F vs stress the slope was found for the materials worked 0, 7, 12, and 40 pct and the values of V found. They varied from 148Å³ to 90Å³ in going from 0 to 40 pct cold work. This is the same order of magnitude as those reported for brass and extrapolated for steel and about ten times less than those reported for zinc.²¹

An estimation of ΔH can be made by plotting C_1 vs $1/T$ since,

$$C_1 = \text{Constant} \times T \times e^{\Delta S/R} \times e^{-\Delta H/RT}$$

It was assumed that temperature has little effect on ΔH over the range considered. The instability of the material prevented the use of data taken above the range of 76° to 210°F. The ΔH for the annealed titanium was found to be 3550 cal. The value of ΔS , as determined graphically, was -99.4 cal per degree per mol.

Combining ΔH and ΔS , as in equilibrium theory, a value of ΔF can be obtained for the free energy of activation. For the annealed titanium a value of 33,000 cal per mol results. This is in the range of values encountered in the soft metals such as tin, zinc, and lead; the ΔF values for steels are greater, being on the order of 50,000 cal per mol.

A similar analysis of the creep data taken on the material cold-worked 40 pct gave a ΔH value of 3000 cal per mol, a ΔS of -105 cal per degree per mol, and a ΔF of 34,500 cal per mol. Obviously there is little difference between the thermodynamic properties of the annealed and cold-worked titanium and the differences in properties between the two states are attributed to the size of the flow volume.

In view of the above, the following generalized statements can be made. Although the free energies of activation are approximately the same for titanium and the soft metals, which have poor creep resistance, titanium is somewhat superior due to its smaller flow volume. On the other hand, titanium and steels have the same flow volume, but the higher free energy of activation of the steels gives them better creep properties than the titanium.

The correlation of internal strain, as measured by X-ray line width studies, with the creep properties of the titanium is not an unexpected phenomenon. Another form of the Eyring rate equation might be as follows:

$$\dot{\epsilon} = \text{Constant} \times T \times e^{\Delta S/R} \times e^{-\Delta H/RT} \times e^{qV(\sigma - \sigma_i)/KT}$$

where σ_i is introduced to describe the internal stress caused by cold working; the other terms are as described previously. This relationship allows for the introduction of internal stresses into the material which oppose the externally applied stress. If, for a constant applied stress and a constant temperature, ΔS and ΔH can be assumed as constant, an assumption that appears to be valid, then the above equation can be reduced to:

$$\log \dot{\epsilon} = \text{Constant} - \text{Constant} \times \sigma_i$$

This is the relationship actually found and graphically shown in Fig. 8.

Conclusions

1—Cold working commercially pure titanium sheet, up to 40 pct by rolling, improves the creep resistance because of the residual strains left in the lattice.

2—Recovery of titanium sheet rolled more than 60 pct occurs at room temperature; sheet rolled 40 pct, between room temperature and 210°F; sheet rolled 7 pct, between 210° and 400°F.

3—Titanium sheet exhibits strain aging.

4—Strain aging markedly improves the creep resistance.

5—A correlation exists between the amount of internal strain induced by cold rolling, as measured by X-ray prior to testing, and the creep resistance at temperatures below which recovery occurs.

6—There appears to be a correlation between the short time tensile strength and creep resistance for titanium which has been cold-worked and recovered.

7—Cold working and/or strain aging reduces extensively the amount of first-stage creep.

Acknowledgment

The writers wish to acknowledge their indebtedness to the United States Air Force, Wright Air Development Center, for their support of this work. This publication represents only part of an overall investigation of the creep properties of titanium and its alloys in progress at the University of Michigan under contract AF-33(038)-14111.

References

- ¹ H. Adenstedt: *Metal Progress* (1949) **56**, p. 658.
- ² L. G. Shulz: *Journal of Applied Physics* (1940) **20**, p. 1030.
- ³ D. N. Frey and J. W. Freeman: *Trans. AIME* (1951) **191**, p. 755; *JOURNAL OF METALS* (September 1951).
- ⁴ A. R. Stokes and A. J. C. Wilson: *Proc. Physical Soc.* (1949) **56**, p. 174.
- ⁵ J. H. Gough and W. A. Wood: *Proc. Royal Soc.* (1936) **154A**, p. 510.
- ⁶ D. McLean: *Journal Inst. Metals* (1952) **80**, p. 507.
- ⁷ V. Cagliotti and G. Sachs: *Ztsch. Physik* (1932) **74**, p. 647.
- ⁸ J. S. Rodgers: *Journal Iron and Steel Inst.* (1938) **138**, p. 91.
- ⁹ W. H. Bragg and W. L. Bragg: *The Crystalline State*. (1949) Vol. I, p. 191. London. G. Bell and Sons, Ltd.
- ¹⁰ C. G. Darwin: *Philosophical Magazine* (1922) **43**, p. 800.
- ¹¹ C. S. Smith and S. Stickley: *Physical Review* (1943) **64**, p. 191.
- ¹² G. W. Brindley and P. Ridley: *Proc. Physical Soc., London*. (1938) **50**, p. 501.
- ¹³ J. E. Wilson and L. Thomassen: *Physical Review* (1934) **46**, p. 337.
- ¹⁴ J. D. Lubahn: *Trans. ASM* (1952) **44**, p. 643.
- ¹⁵ A. Nadai and M. J. Manjoine: *Journal of Applied Mechanics* (1941) **66**, p. 77.
- ¹⁶ C. N. daC. Andrade: *Proc. Royal Soc.* (1914) **90**, p. 329.
- ¹⁷ E. Orowan: *Journal West Scotland Iron and Steel Inst.* (1947) **54**, p. 45.
- ¹⁸ C. L. Smith: *Proc. Physical Soc., London* (1948) **61**, p. 201.
- ¹⁹ N. F. Mott and F. R. Nabarro: *Rept. Conf. Strength of Solids*. Physical Soc., London (1948) 1.
- ²⁰ S. Glasstone, K. J. Laidler, and H. Eyring: *The Theory of Rate Processes*. (1941) New York. McGraw-Hill Book Co.

Occurrence of Chi Phase in Molybdenum-Bearing Stainless Steels

by P. K. Koh

Chi phase (body-centered cubic, $a = 8.89\text{\AA}$) was found in as-cast 23 pct Cr-10 pct Mo-Fe alloy as well as in heat-treated 316, 316L, 317, and modified 446 stainless steels. Chi phase resembles sigma phase in its metastability, chemical composition, and brittleness. Microstructure and some of physical properties of chi phase were developed.

MOLYBDENUM has been established as a desirable alloying element for the enhancement of corrosion resistance in Cr-Ni steels and creep and rupture strength in high temperature alloys. On the debit side, however, the molybdenum addition has been known to stimulate σ formation. When the molybdenum-bearing steels were subjected to prolonged heating at elevated temperatures, losses of corrosion resistance and/or ductility have been observed.

Andrews^{1,2} first found the existence of a new phase among the anodic FeCl_3 extracts from type 316 stainless steel solution treated and then reheated from 800° to 1100°C . This phase was designated χ and was identified by diffraction patterns as of body-centered cubic structure with a value equal to 8.89\AA and similar to that of α manganese. He found that the χ phase in this steel always coexisted with σ phase, but failed to distinguish one from the other by metallographic technique. No definite conclusion was drawn regarding the equilibrium temperature ranges of these two phases.

The appearance of Andrew's work recalled an un-

explained structure observed several years ago at the Allegheny Ludlum Research Laboratories during the investigation of an experimental alloy containing 25 pct Cr, 10 pct Mo, and balance Fe. X-ray diffraction patterns on the as-cast material revealed the presence of a body-centered cubic phase having a lattice parameter of 8.89\AA . The structure was sufficiently similar to that of γ chromium that for a time it was thought that the structure might be caused by the presence of some undissolved electrolytic chromium particles. The alloy as-cast was so brittle that it shattered after the slightest hot reduction by hammer cogging.

This paper gives the results of some metallographic and X-ray diffraction studies on χ phase as found in several experimental alloys as well as a few molybdenum-bearing commercial stainless steels. The analyses of materials studied were as shown in Table I.

Experimental Procedure

Metallography: Solid specimens were polished mechanically and etched in boiling 50 pct HCl solution in order to best delineate χ and σ phases in the alloys studied.

X-Ray Diffraction: The difficulty of satisfactorily developing diffraction lines for σ phase in solid specimens has been previously reported by Bindari, Koh, and Zmeskal.³ For this reason all specimens used in this investigation were subjected to anodic

P. K. KOH is associated with the Research Laboratories, Allegheny Ludlum Steel Corp., Brackenridge, Pa.

Discussion on this paper, TP 3464E, may be sent, 2 copies, to AIME by April 1, 1953. Manuscript, June 18, 1952; revised, Dec. 22, 1952. Los Angeles Meeting, February 1953.

Table I. Analyses of Alloys Studied

Chemical Analyses												
Heat	Type	C	Mn	Si	Cr	Mo	Ni	Co	Fe	Ti	Al	W
Iron-base Alloys												
CM 68	Experimental	0.035	0.25	0.21	23.26	9.37			Bal			
CT 60	Experimental	0.11	0.42	0.34	19.56	12.75	0.10		Bal			
A 748	Modified 446	0.04	1.10	0.98	26.70	1.62			Bal	1.84		0.91
34476	316	0.064	1.82	0.56	17.56	2.63	13.91		Bal			
49754	316	0.044	1.17	0.55	17.24	2.10	13.68		Bal			
93867	316	0.080	1.36	0.48	17.83	2.72	13.35		Bal			
42011	316L	0.028	1.48	0.50	17.76	2.35	13.24		Bal			
67227	317	0.051	1.89	0.41	18.37	3.70	13.92		Bal			
64025	317	0.053	1.58	0.32	18.74	3.68	13.54		Bal			
F-178	Experimental	Low	0.25	0.25	25.0	10.0			Bal			
F-181	Experimental	Low	0.25	0.25	25.0	5.0			Bal			10.0
Nickel-base Alloys												
F-179	Experimental	Low			25	10	Bal					
Cobalt-base Alloys												
F-180	Experimental	Low	0.25	0.25	25.0	10.0		Bal				

extraction in ferric chloride solution. X-ray studies were carried out on the extracted residues.

A wedge powder specimen was adopted for the Debye camera because of convenience in preparation. Accurate determination of lattice parameter was found to be difficult due to absorption of the diffracted beam by the wedge specimen and because of mechanical difficulties in centering the specimen in the camera. Lattice parameters are therefore reported to only two decimal places.

Electrolytic Extraction: The electrolytic extraction cell consisted of an alundum crucible, a 3000 cc beaker, an 18-8 stainless steel sheet cathode with the specimen as anode. Copper lead wires were soldered onto both anode and cathode, the soldered joints being covered with paraffin. The cathode was placed inside the alundum crucible which rests on the bottom of the beaker. The anode is placed outside the alundum crucible which serves as a diaphragm to prevent the extracted residue from being contaminated by the reaction products formed around the cathode. The pH value of the FeCl_3 electrolyte varied between 1.1 at the beginning to 0.1 toward the end of a run. The electrolyte dissolved the matrix at a reasonable rate depending upon the exposed area of the anode and the voltage drop across the cell. The extract was recovered by filtering through a frit-glass bottom filter, and was subsequently dried at 220°F.

Heat Treatment: Specimens were protected from oxidation during heat treatment by electroplating

with chromium. Specimens $\frac{1}{4}$ in. thick were cut from ingots or bars of the alloys under study for metallographic examination and extraction after heat treatment.

Occurrence of Chi Phase

Iron-Base Alloys: Fe-Cr-Mo Experimental Alloys: Experimental heats CM 68 and CT 60 were melted as part of an independent investigation of the resistance of certain alloys to attack by molten metals. When attempts were made to forge the alloys, they both cracked under light hammer blows. The explanation of the observed hot-shortness lay in the presence of χ phase as shown in the microstructures of Figs. 1 and 2.

While both heats exhibited the presence of χ phase (Table II), in heat CT 60 the phase was inclined to

Table III. Diffraction Data on Anodic Extract from Heat-Treated Type 316 and Type 316L Stainless Steel Sheets

Heat	Original Condition of Steel Sheet	Heat Treatment	Diffraction Data on Anodic Extract from Heat-Treated Steel Sheets*
42011	Hot rolled, annealed, and pickled as-received	100 hr at 1200°F 100 hr at 1400°F 100 hr at 1600°F 50 hr at 1800°F	austenite austenite + Cr_{23}C_6 + χ + σ austenite + χ + σ + Cr_{23}C_6 austenite
42011	Cold rolled 85 pct	100 hr at 1200°F 100 hr at 1400°F 100 hr at 1600°F 50 hr at 1800°F	σ + austenite σ + Cr_{23}C_6 σ + Cr_{23}C_6 + austenite austenite
34476	Cold rolled 82 pct	100 hr at 1200°F 100 hr at 1400°F 50 hr at 1800°F	σ + austenite σ + austenite Cr_{23}C_6 + austenite
49754	Hot rolled, annealed, and pickled as-received	100 hr at 1200°F 100 hr at 1400°F 100 hr at 1600°F	austenite χ + Cr_{23}C_6 + austenite Cr_{23}C_6 + χ + austenite
49754	Cold rolled 80 pct	100 hr at 1200°F 100 hr at 1400°F 100 hr at 1600°F	austenite + σ + Cr_{23}C_6 σ + Cr_{23}C_6 + austenite σ + Cr_{23}C_6 + austenite
93867	Hot rolled, annealed, and pickled as-received	100 hr at 1200°F 100 hr at 1400°F 100 hr at 1600°F	austenite Cr_{23}C_6 + austenite + χ χ + Cr_{23}C_6 + austenite
93867	Cold rolled 80 pct	100 hr at 1200°F 100 hr at 1400°F 100 hr at 1600°F	σ + austenite + Cr_{23}C_6 σ + Cr_{23}C_6 + austenite σ + Cr_{23}C_6

* Phases present are listed in the order of decreasing line intensity.

Table II. Diffraction Data on Anodic Extracts from Heat Treated CM 68 and CT 60 Alloys

Solid Specimen from which Extraction Was Made		
Heat	Heat Treatment	Diffraction Data on Anodic Extract*
CM 68	As-Cast 100 hr at 1200°F 100 hr at 1400°F 100 hr at 1600°F 5 hr at 1800°F 2 hr at 2000°F 2 hr at 2200°F 1 hr at 2400°F	χ + ferrite + Fe_2N χ + ferrite χ + Fe_2N χ + ferrite + Fe_2N χ + ferrite + Fe_2N χ + ferrite ferrite ferrite
CT 60	As-Cast 100 hr at 1200°F 100 hr at 1400°F 100 hr at 1600°F 5 hr at 1800°F 2 hr at 2000°F 1½ hr at 2200°F 1 hr at 2400°F	χ + ferrite χ + ferrite χ + Fe_2N χ + Fe_2N χ + ferrite χ + ferrite χ + ferrite χ + ferrite

* Phases present are listed in the order of decreasing line intensity.

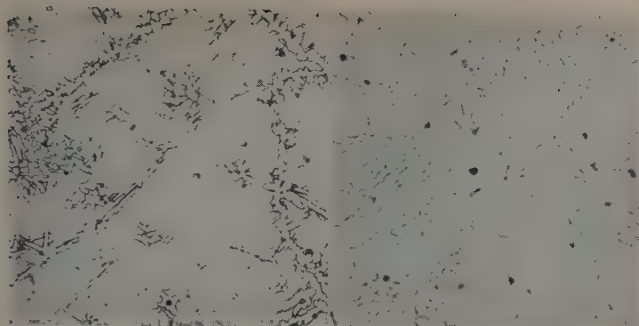


Fig. 1a—CM 68, as-cast. Primary χ phase in ferritic matrix. 50 pct boiling HCl etch. X500.

Fig. 1b—CM 68, 100 hr at 1200°F. Primary plus precipitated χ phases in ferritic matrix. 50 pct boiling HCl etch. X500.

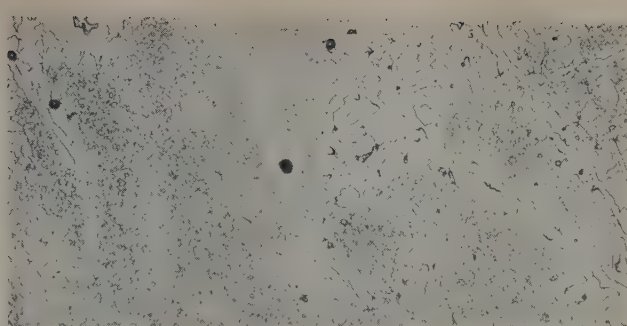


Fig. 1c—CM 68, 100 hr at 1400°F. Primary plus agglomerating precipitated χ phases in ferritic matrix. 50 pct boiling HCl etch. X500.

Fig. 1d—CM 68, 5 hr at 1800°F. Primary plus precipitated χ phases in ferritic matrix. Solution of χ phase begins. 50 pct boiling HCl etch. X500.

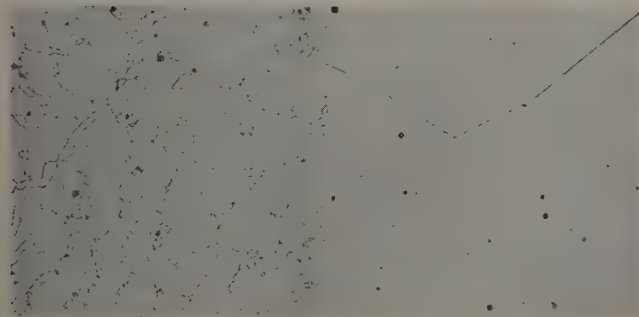


Fig. 1e—CM 68, 2 hr at 2000°F. Primary plus precipitated χ phases in ferritic matrix. Solution of χ phase proceeds to an advanced degree. 50 pct boiling HCl etch. X500.

Fig. 1f—CM 68, 2 hr at 2200°F. χ phase almost completely dissolved in ferritic matrix. 50 pct boiling HCl etch. X500.

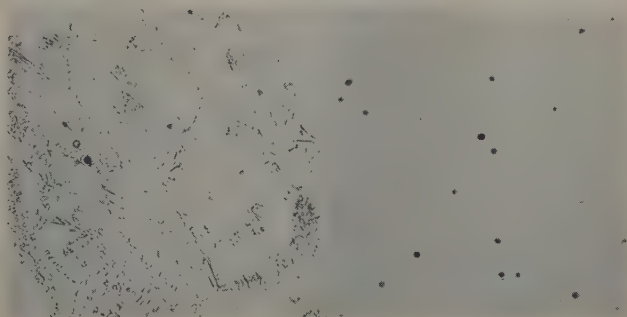


Fig. 2a—CT 60, as-cast. Primary χ phase in ferritic matrix. χ phase in more or less nodular formation. 50 pct boiling HCl etch. X500.

Fig. 2b—CT 60, 1½ hr at 2200°F. Solution of χ phase into ferritic matrix proceeds to an advanced degree. 50 pct boiling HCl etch. X500.

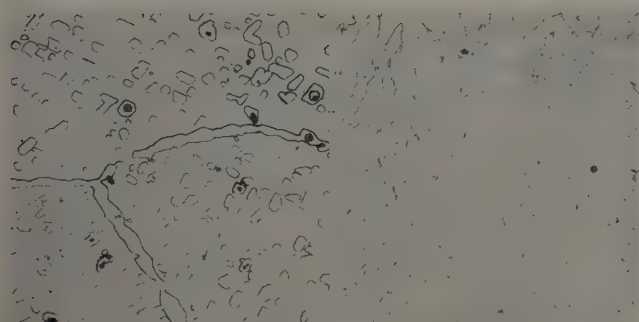


Fig. 3—Heat A-748, modified type 446 stainless steel. Ferrite + mostly χ + some σ . 50 pct boiling HCl etch. X1000.

Fig. 4—Heat F-178, Cr-Mo-Fe alloy as-cast. χ phase in ferritic matrix. Electrolytic etch 25 sec in 5 pct NaCN solution. X500.

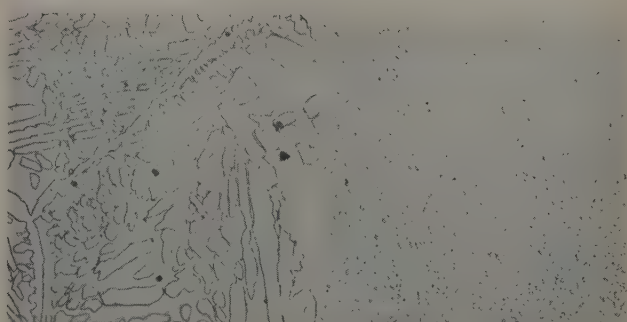


Fig. 5—Heat F-181, Cr-Mo-W-Fe alloy as-cast. χ phase in ferritic matrix. Electrolytic etch 25 sec in 5 pct NaCN solution. X500.

Fig. 6—Type 317, heat 64025, cold rolled 85 pct + 100 hr at 1600°F. σ phase in austenitic matrix. Boiling 50 pct HCl etch. X500.

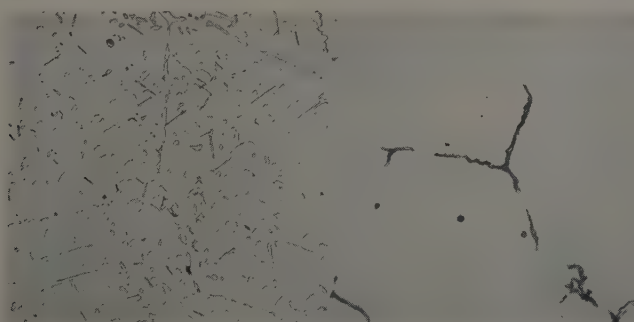


Fig. 7—Type 317, heat 64025, solution treated at 2000°F + 100 hr at 1600°F. χ phase in austenitic matrix. Boiling 50 pct HCl etch. X500.

Fig. 8—Heat F-179, 25 pct Cr-10 pct Mo-Ni alloy. Face-centered cubic matrix. Electrolytic etch, 5 sec in 5 pct NaCN solution. X500.

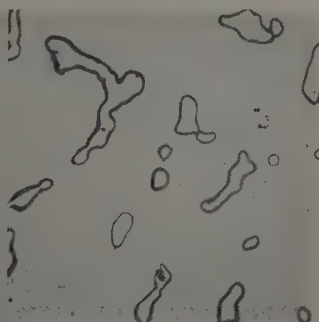


Fig. 9—Heat F-180, low C, 0.25 pct Mn, 0.25 pct Si, 25.0 pct Cr, 10.0 pct Mo, balance Co. As-cast. Electrolytic etch 5 sec in 5 pct NaCN solution. X500.

Area reduced approximately 50 pct for reproduction for these illustrations.

Table IV. Diffraction Data on Anodic Extract from Heat-Treated Type 317 Stainless Steel Sheet

Heat	Original Condition of Steel Sheet	Heat Treatment	Diffraction Data on Anodic Extract from Heat-Treated Steel Sheet*
64025	Hot rolled, annealed, and pickled as-received	100 hr at 1200°F 100 hr at 1400°F 100 hr at 1600°F 50 hr at 1800°F	austenite + Cr ₂₃ C ₆ χ + Cr ₂₃ C ₆ + σ + austenite χ + Cr ₂₃ C ₆ σ + χ + austenite
64025	Cold rolled 85 pct	100 hr at 1200°F 100 hr at 1400°F 100 hr at 1600°F 50 hr at 1800°F	σ + austenite + Cr ₂₃ C ₆ σ + Cr ₂₃ C ₆ σ + Cr ₂₃ C ₆ + austenite σ + austenite
67227	Cold rolled 85 pct	100 hr at 1200°F 100 hr at 1400°F 100 hr at 1600°F 50 hr at 1800°F 10 hr at 2000°F	σ σ σ σ austenite

* Phases present are listed in the order of decreasing line intensity.

be somewhat more nodular. Additional quantities of χ phase were precipitated from the ferritic matrix on reheating to temperatures as low as 1200°F. Agglomeration of the phase took place with prolonged heating at 1200°F or reheating to higher temperatures. Solution of χ phase in heat CM 68 became evident after 5 hr heating at 1800°F, solution being practically complete at 2200°F. In the case of heat CT 60, solution of χ phase occurred after 2 hr heating at 2000°F, the more stable χ phase being of higher molybdenum content.

Concentrated Murakami's solution (30 g K₃Fe(CN)₆ and 30 g KOH in 60 cc of water) failed to stain χ phase in heats CM 68 and CT 60, although it had been reported to be effective in staining σ phase in 19-9-W-Mo steel.³

As the CT 60 alloy was heated from 1200° to 2200°F the lattice parameter of the χ phase increased from 8.89 to 8.92Å.

Modified Type 446 Stainless Steel: Fig. 3 shows the microstructures of heat A-748, a type 446 stainless steel modified by the addition of molybdenum and tungsten. The specimen was heat-treated for ½ hr at 2000°F plus 40 hr at 1600°F. The diffraction pattern of the extracted residue showed strong lines of χ and some weak lines of σ .

According to Andrews,² the least amount of molybdenum for the appearance of χ phase in Cr-Ni-Fe alloys was about 3 pct. The fact that heat A-748 contained 1.62 pct Mo and 0.91 pct W leads to the conclusion that tungsten and molybdenum act similarly in promoting χ formation. This conclusion is supported by the presence of χ phase in extracted residues from heats F-178 (25 pct Cr, 10 pct Mo, balance Fe) and F-181 (25 pct Cr, 5 pct Mo, 10 pct

W, balance Fe). Microstructures of these samples are shown in Figs. 4 and 5.

Type 316, Type 316L, and Type 317 Stainless Steels: Commercial heats of types 316, 316L, and 317 stainless steels were chosen at random from mill production. Tables III and IV show the diffraction data on anodic extracts from specimens of the heats in various conditions as-received and heat-treated.

From the compiled experimental data the following deductions seem to be logical: 1—Cold working accelerates σ formation. 2—Cold working suppresses χ formation. 3—The maximum temperature for stable σ phase is under 1800°F for type 316 steel or under 2000°F for type 317 steel. 4— χ phase forms from solution-treated steels at the temperature range of 1400° to 1800°F. The rate of χ formation seems to reach the maximum around 1600°F. χ phase disappears after heating type 316 steel for 50 hr at 1800°F or after heating type 317 steel to 2000°F.

Comparing diffraction patterns on extracts from type 317 steel with those from type 316 (Tables III and IV), it appears that increasing molybdenum content promotes stability of both χ and σ phases.

Figs. 6 and 7 show respectively the microstructure of σ and χ phases in the austenitic matrix of type 317 stainless steel. Although no reagent has been found to differentially stain σ and χ phases, the differences in characteristic microstructures shown in Figs. 6 and 7 permit some degree of distinction, since χ phase tends to form along preferential atomic planes of the matrix of the annealed material, whereas a general precipitation of σ phase was observed in the cold-worked material.

Experimental Nickel-Base Alloy: Fig. 8 shows the as-cast microstructure of 25 pct Cr-10 pct Mo-Ni alloy which contains a very slight amount of an extraneous phase. The X-ray diffraction pattern of the solid specimen showed no trace of χ phase. No residue was recovered after the as-cast alloy was subjected to anodic FeCl₃ extraction.

It is therefore evident that there is no corresponding χ phase in the nickel-base Cr-Mo alloy.

Experimental Cobalt-Base Alloy: Fig. 9 shows the microstructure of an as-cast 25 pct Cr-10 pct Mo-Co alloy. No residue was recovered from the anodic FeCl₃ extraction of the alloy. Diffraction pattern on the solid specimen showed only face-centered cubic β and hexagonal close-packed α cobalt phases.

Observed Properties

Chemical Analysis: The chemical analyses in Table V on isolated phases indicate that χ phase is essentially an intermetallic compound of chromium, molybdenum, and iron. In this tabulation the total weight percentage of reported elements is so close to 100 pct that the analyses reported represent those of the isolated phases.

Table V. Chemical Analyses on Isolated Phases

Heat	Solid Specimen Prior to Anodic FeCl ₃ Extraction	Phase*	Composition, Wt Pct						
			C	Cr	Mo	Fe	Ni	Mn	Total
CM 68	Experimental	100 hr at 1400°F	All χ	0.51	24.48	17.46	56.44		98.89
CT 60	Experimental	5 hr at 1800°F							
67227	317	Cold rolled 82 pct plus 100 hr at 1400°F	Nearly all χ	0.87	17.98	18.58	61.97		99.40
64025	317	Mill annealed plus 100 hr at 1600°F	All σ	0.82	25.06	9.41	57.70	5.56	99.90
			Nearly all χ	0.97	25.40	10.02	57.48	4.08	99.30

* Based upon Debye diffraction lines. Other phases present due to very weak lines are estimated to be less than 5 pct.

Table VI. Diffraction Lines of Chi Phase*

(hkl)	Relative Intensity†	Sin ² θ		(hkl)	Relative Intensity†	Sin ² θ	
		Observed	Calculated‡			Observed	Calculated‡
(321)α	w	0.2321	0.2325	(622)α ₂	w	0.7329	0.7326
(411)β, (330)β	ms	0.2473	0.2477	(721)β, (633)β,			
(400)α	w	0.2653	0.2658	(552)β	m	0.7439	0.7430
(411)α, (330)α	vs	0.2985	0.2990	(631)α	w	0.7647	0.7631
(332)β	vw	0.3027	0.3027	(642)β	vw	0.7717	0.7706
(422)β	w	0.3310	0.3302	(444)α ₁	m	0.7973	0.7963
(332)α	ms	0.3655	0.3654	(444)α ₂	mw	0.8001	0.7992
(442)α	m	0.3991	0.3986	(710)α ₁ , (550)α ₁	ms	0.8304	0.8295
(431)α, (510)α	m	0.4322	0.4319	(543)α ₁			
(600)β, (442)β	vw	0.4960	0.4954	(710)α ₂ , (550)α ₂	m	0.8333	0.8325
(521)α	vw	0.4997	0.4983	(543)α ₂			
(611)β, (532)β	vw	0.5241	0.5229	(651)β	w	0.8548	0.8531
(530)α, (433)α	vw	0.5658	0.5647	(721)α ₁ , (633)α ₁	vs	0.8959	0.8959
(600)α, (442)α	mw	0.5985	0.5980	(552)α ₁			
(622)β	w	0.6057	0.6054	(721)α ₂ , (633)α ₂	s	0.8993	0.8991
(611)α, (532)α	m	0.6321	0.6312	(552)α ₂			
(444)β	w	0.6618	0.6605	(741)β	w	0.9086	0.9082
(710)β, (550)β	mw	0.6889	0.6880	(642)α ₁	mw	0.9291	0.9290
(543)β				(642)α ₂	w	0.9325	0.9324
(541)α	w	0.6992	0.6976	(644)β	w	0.9359	0.9357
(622)α ₁	mw	0.7307	0.7300	(730)α ₁	m	0.9623	0.9622
				(730)α ₂	mw	0.9658	0.9657
				(660)β	m	0.9898	0.9907

* The specimen was anodic FeCl₃ extract from CT 60 cast alloy and the crystal structure was body-centered cubic, $a = 8.89\text{\AA}$.
† vs, very strong; s, strong; ms, medium strong; m, medium; w, weak; mw, medium weak; vw, very weak.
‡ Calculated according to body-centered cubic, $a = 8.888\text{\AA}$.

Molybdenum tends to concentrate in both χ and σ phases of Cr-Mo-Fe and Cr-Ni-Mo-Fe alloys. There are significant amounts of nickel in both χ and σ phases in type 317 steel. No significance was attached to the reported carbon content because of possible carbon pick up with the technique employed.

It is significant that the χ phase has practically the same chemical composition as the σ phase in type 317 stainless steel.

Crystal Structure: Table VI shows the X-ray diffraction data on χ phase isolated electrolytically in FeCl₃ solution from as-cast CT 60 alloy. The lattice parameter of χ phase isolated from all the alloys studied showed variation from 8.89 to 8.92Å.

The observed similarity in composition between χ and σ phases in type 317 stainless steel leads to some speculation as whether χ may be an ordered structure of σ which is known to be of a distorted body-centered cubic structure.

Microhardness: Table VII shows the microhardness of χ phase formed under various conditions of heat treatment.

Summary

1— χ phase was found in as-cast 23 pct Cr-10 pct Mo-Fe alloy as well as in heat-treated 316, 316L, 317, and modified 446 stainless steels.

2— χ phase resembles σ phase in its metastability, chemical composition, and brittleness.

3—There is no corresponding χ phase in either nickel or cobalt-base Cr-Mo alloy.

4—In stainless steels of the 316 and 317 types, cold working appears to promote σ but suppress χ formation. For applications involving extended time at elevated temperatures, the formation of χ or σ phase appears to depend upon whether the previous history involved solution treatment or cold work. In welded sections, riveted joints, or other strained areas of a large vessel where solution treatment is not possible, σ formation will be unavoidable, possibly without even partial χ formation.

Acknowledgments

The author wishes to acknowledge the assistance of staff members of the Allegheny Ludlum Research Laboratories in various phases of this work. J. A. Berger of the University of Pittsburgh furnished samples of some of the experimental alloys and Laurence C. Hicks, Director of Research, Allegheny Ludlum Steel Corp., has given very helpful suggestions.

References

- 1 K. W. Andrews and P. E. Brookes: Chi Phase in Alloy Steels. *Metal Treatment and Drop Forging* (July 1951) pp. 301-311.
- 2 K. W. Andrews: A New Intermetallic Phase in Alloy Steels. *Nature* (December 10, 1949) No. 4180, p. 1015.
- 3 Ahmed El Bindari, P. K. Koh, and Otto Zmeskal: Sigma-Phase Formation in a Wrought Heat Resisting Steel. *Trans. ASM* (1951) 43, p. 226.

Table VII. Microhardness Data

Heat	Heat Treatment	Vickers Micro-Hardness with 100G Load	Remarks
CT 60	As-cast	322	Within area of primary χ particle
	100 hr at 1200°F	448	Directly on a large primary χ particle
	100 hr at 1400°F	488	Directly on a large primary χ particle
	100 hr at 1600°F	508	Directly on a large primary χ particle
	5 hr at 1800°F	483	Directly on a large primary χ particle
	2 hr at 2000°F	397	Directly on a large primary χ particle
	1½ hr at 2220°F	322	Within area of grain boundaries partially occupied by χ
	1½ hr at 2220°F	256	χ -free matrix
	1 hr at 2400°F	339	Within area partially occupied by redistributed and refined χ particles
CM 68	As-cast	405	On a group of closely packed χ particles
	100 hr at 1200°F	433	On a group of closely packed χ particles
	100 hr at 1400°F	429	On a group of closely packed χ particles
	100 hr at 1600°F	351	On a group of closely packed χ particles
	5 hr at 1800°F	383	On a group of closely packed χ particles
	2 hr at 2000°F	297	On widely scattered χ particles in clear matrix
	1½ hr at 2200°F	330	On almost clear matrix with very little χ
	1 hr at 2400°F	360	On almost clear matrix with very little χ

Effect of Small Additions of Oxygen on Lattice Constants And Hardness of Zirconium

by R. M. Treco

The effect of small additions of oxygen on the hardness, density, and lattice parameters of high purity zirconium has been investigated. Precision parameter values and density of oxygen-free zirconium are given as: $a_0 = 3.2258$ kX units, $c_0 = 5.1373$ kX units, $\rho_{25} = 6.507$ g per cc.

THE effect of oxygen on the hexagonal-phase lattice constants of pure zirconium is of interest for several reasons. The extensive hardening effect of oxygen noted by previous investigators¹ must be due in part to the lattice distortion accompanying its introduction and possibly to the preferred position of the oxygen atoms. De Boer and Fast² have shown that oxygen is taken into solid solution in large amounts, appearing to occupy an interstitial position. These authors also found that expansion of the lattice was not uniform since the a axis attained a constant value after the addition of 10 atomic pct while the c axis continued to expand. It was thought in the present work that this expansion of the zirconium lattice with increasing amounts of oxygen

Table I. Typical Data for Zirconium Using Back-Reflection Focusing Camera

Co $K\alpha_1 = 1.78529$ kX. Co $K\alpha_2 = 1.78919$ kX.

Line No.	Emission K-Series	hkl	$S(\text{cm})$ Average	Maxi-mum Deviation	Maxi-mum Error, PPM	$\sin^2\theta$
1	α_1	212	21.328	0.0025	117	0.8338500
2	α_2	212	21.087	0.0016	76	0.8373665
3	α_1	105	19.845	0.0010	50	0.8550006
4	α_2	105	19.570	0.0020	102	0.8587910
5	α_1	204	17.151	0.0059	344	0.8902808
6	α_2	204	16.854	0.0032	190	0.8939075
7	α_1	300	14.767	0.0027	183	0.9178539
8	α_2	300	14.377	0.0038	265	0.9220207
9	α_1	123	6.064	0.0028	462	0.9858184
10	α_2	123	5.036	0.0037	735	0.9902049

Note: $a_0 = 3.22624$; $c_0 = 5.13928$; $c/a = 1.59296$

Specimen No.—Z62-7B

X-ray Unit—Picker

Potential—33 kv

Temperature— $26.8^\circ \pm 0.3^\circ\text{C}$

Oxygen—0.083 wt pct

Film—Single emulsion

Current—10 ma

Time—3 hr

R. M. TRECO, Junior Member AIME, is Research Project Leader, Bridgeport Brass Co., Bridgeport, Conn.

Discussion on this paper, TP 3367E, may be sent, 2 copies, to AIME by April 1, 1953. Manuscript, May 1, 1952; revised, Nov. 26, 1952.

should lend itself to the determination of oxygen in the metal in the absence of other impurities. Also present-day production of iodide metal has resulted in much higher purity, so that a new check on the lattice constants of unadulterated zirconium appeared desirable.

Zirconium has been found to differ in some properties, particularly hardness and density, depending on the specific refining process employed. Some data on metal prepared by different methods are included here.

Experimental Procedure

A series of oxygen alloys of increasing gas content were prepared from very pure, degassed crystal bars in a high vacuum glass system of special design as described elsewhere.³ The alloys thus prepared were cold-rolled into strip and thoroughly annealed to produce a fine-grained recrystallized structure with a minimum of residual strains. Fig. 1 illustrates a typical microstructure in which the absence of inclusions is indicative of metal purity. Samples were electropolished and etched heavily, then placed in a back-reflection focusing camera of 5 in. diam in such a way as to allow continuous rotation during a run. Cobalt radiation was used for the exposures and exposure times varied from 3 to 6 hr on single-emulsion film. Temperature measurements were taken during each run to establish room temperature corrections.

Parameter Calculations

The films thus obtained usually consisted of 10 α doublets which were measured three times and averaged. Typical data obtained from a single film are assembled in Table I along with the calculated maximum reading error for each line.

Calculation of the lattice constants for each sample was carried through by Cohen's method⁴ with error determinations as outlined by Jette and Foote.⁵ This method results in a least squares solution of the lattice constants and in the present case was modified to include a correction for systematic errors, the equations being set up to avoid the loss of significant figures in subtraction. The notation for the equations employed should be clear from ref. 5, these equations being:

$$\Delta A \Sigma \alpha_i^2 + \Delta C \Sigma \alpha_i \gamma_i + \Delta D \Sigma \alpha_i \delta_i = \Sigma \alpha_i v_i \quad [1]$$

$$\Delta A \Sigma \alpha_i \gamma_i + \Delta C \Sigma \gamma_i^2 + \Delta D \Sigma \gamma_i \delta_i = \Sigma \gamma_i v_i \quad [2]$$

$$\Delta A \Sigma \alpha_i \delta_i + \Delta C \Sigma \gamma_i \delta_i + \Delta D \Sigma \delta_i^2 = \Sigma \delta_i v_i \quad [3]$$

($i = 1, 2, 3 \dots n$)

Table II. Analysis of Zirconium Sample Z62-1A

Element	Weight Percentage	Atomic Percentage
Carbon	0.0640	0.484
Oxygen	0.0260	0.147
Nitrogen	0.0010	—
Iron	0.0280	0.0455
Hafnium	0.0280	0.0142
Aluminum	0.0030	—
Calcium	0.0012	—
Chromium	0.0015	—
Copper	0.0010	—
Magnesium	0.0008	—
Manganese	<0.0005	—
Nickel	<0.0050	—
Lead	<0.0020	—
Silicon	0.0040	—
Tin	<0.0020	—
Titanium	0.0045	—
Vanadium	<0.0100	—

In this particular case of varying composition the difference terms (ΔA , ΔC , etc.) change progressively with the addition of oxygen.

The calculated lattice constants were plotted against oxygen concentration, and with the assumption of linear relations, a least squares equation was obtained for each parameter as a function of oxygen content. All lattice parameter values were corrected to a temperature of 25°C using the data of Russell⁶ for pure zirconium.

Zirconium Analysis

Zirconium used for the oxygen series consisted of five crystal bars from one selected lot, all of which were found to be of similar analysis. Table II gives the complete analysis of the control sample. The only substantial impurities found were carbon and oxygen of which the former was neglected in the

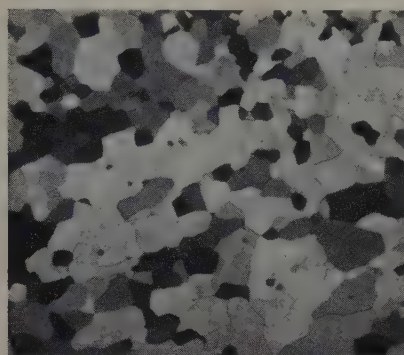


Fig. 1—Zr-O alloy cold-reduced 5.6 pct and annealed to produce fine-grained structure. Polarized light. X100. Area reduced approximately 50 pct for reproduction.

lattice parameter calculations since carbon concentration varied only slightly and its quantitative effect on lattice parameter was not known.

Determination of oxygen in very small amounts in zirconium is most successful with the hydrogen chloride method.⁷ Initial oxygen content of the bars before controlled oxygen additions was most difficult to obtain since it was small and varied slightly from sample to sample. In order to determine this initial oxygen, it was necessary to analyze several samples from a given bar. Since the amount of oxygen added to each sample was known accurately by two other independent checks, namely, weight gain and gas volume, these values could be plotted against the values obtained from chemical analysis, producing a linear plot. The curve obtained was easily shifted to correct each individual analysis for initial oxygen. This method minimized, but did not eliminate, the uncertainties in total oxygen content of each sample.

The atomic percentage of oxygen for each alloy of the series was calculated on the basis of oxygen and zirconium only. The first value listed in Table III was based on the known addition of oxygen, while the second value was corrected for initial oxygen. The correction is shown to be small in most cases, the corrected value being used for discussion purposes.

Results and Discussion

The calculated values of the zirconium hexagonal close-packed lattice constants are given in Table III together with the corresponding oxygen content. A plot of a and c axes as a function of the atomic percentage of oxygen is shown in Fig. 2, while Fig. 3 shows a corresponding plot of axial ratio and unit cell volume. These plots indicate a linear expansion of the lattice with increasing oxygen content as is usually found in dilute primary solid solution alloys. Within the range investigated there is no apparent effect on the axial ratio which remained constant.

The best value of the lattice constants for the

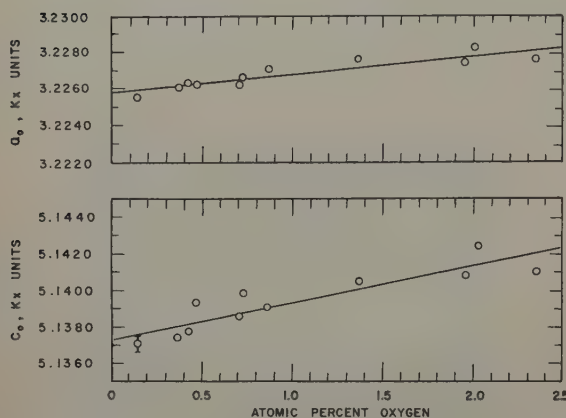


Fig. 2—Zirconium lattice parameter change with oxygen.

initial high purity crystal bar of the composition given in Table II is as follows:

$$a_0 = 3.2256_2 \pm 0.00014 \text{ kX units}$$

$$c_0 = 5.1370_0 \pm 0.00036 \text{ kX units}$$

$$c/a = 1.5926$$

An extrapolation of the two lattice parameter curves was achieved by a least squares solution of the lattice parameter-percentage of oxygen data with the resulting equations:

$$a_0 = 3.22580 + 0.0010184 \times (\text{atomic percentage of oxygen}) \text{ Standard deviation} = \pm 0.00095$$

$$c_0 = 5.13732 + 0.0019967 \times (\text{atomic percentage of oxygen}) \text{ Standard deviation} = \pm 0.00156$$

Lattice parameters for oxygen-free zirconium obtained from these equations together with their probable errors are as follows:

$$a_0 = 3.2258_0 \pm 0.00064 \text{ kX units}$$

$$c_0 = 5.1373_2 \pm 0.00105 \text{ kX units}$$

$$c/a = 1.5926$$

The standard deviations of the two parameter equations proved disappointingly large. Despite the precision of individual parameter calculations, the equations for oxygen concentration did not prove sufficiently accurate to justify their use in chemical analysis. It will be noted that the parameter values for samples 2C and 2B appear to be lower than expected, and if these data are neglected, the remain-

ing parameter values result in a good linear relation. However, exhaustive checks on all the data failed to show any statistical or other justification for discarding the results from these samples. In addition, the hardness of these samples was consistent with other hardness data, see Fig. 4.

Comparison of these data for zirconium with a similar study on titanium by Clark⁸ is of interest because of the similarity of the two metals. In his work, Clark showed that the a_0 parameter remained relatively constant while the c_0 parameter, hence the c/a axial ratio, increased linearly with oxygen concentration. This is at variance with the present results for zirconium and somewhat surprising since the smaller unit cell of titanium would be expected to expand to a much greater extent than zirconium. Lattice strains ($\Delta V/V_0$) calculated from the respective data for 0.35 wt pct oxygen are 0.128 pct for titanium and 0.200 pct for zirconium.

Hardness: Oxygen dissolved in zirconium produces a large increase in hardness. This is shown in Fig. 4 in which average hardness values of oxygen alloys from the original five bars are plotted against oxygen content, and the X-ray samples are seen to be consistent with the curve.

Although zirconium dissolves as much as 40 atomic pct of oxygen,² the presence of as little as 2.0 atomic pct embrittles the metal to such an extent that cold working and machining are impossible. Some success has been achieved with grinding, though the elimination of chipping is difficult. The remarkable decrease in ductility with such small additions suggests that the first oxygen atoms occupy preferred positions in the lattice thus interfering with the normal slip processes. In addition, it was also observed in this work that oxygen alloys show little tendency to form mechanical twins, in marked contrast to pure zirconium.

In view of these observations, it is of interest to

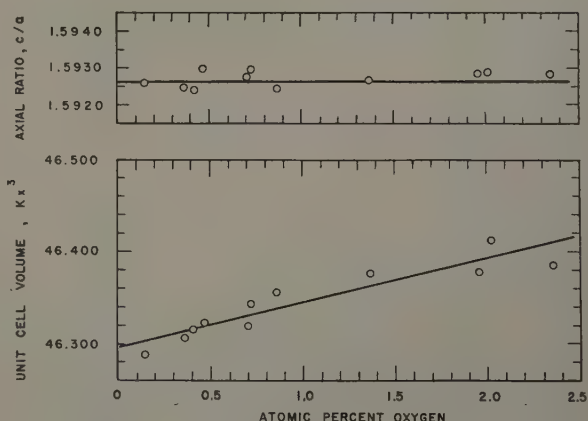


Fig. 3—Zirconium lattice change with oxygen.

consider the recent work of Rosi et al.,⁹ which appears to show that slip and twinning in α titanium do not occur in the usual hexagonal basal plane, but instead slip occurs in the $\{10\bar{1}0\}$ and $\{10\bar{1}1\}$ planes and the direction $\langle 11\bar{2}0 \rangle$; while twinning occurs in the planes $\{10\bar{1}2\}$ and $\{11\bar{2}2\}$.

Since titanium and zirconium have similar axial ratios ($\text{Ti} = 1.587$, $\text{Zr} = 1.592$), exhibiting marked

similarities in their deformation patterns, it appears likely that the titanium mechanism may also apply to zirconium. While these novel slip and twinning systems allow greater ductility in plastic deformation than basal slip, it is also apparent that the presence of interstitial solute atoms are more likely to interfere with prismatic or pyramidal slip. Considered in this light the observed decrease in ductility and lack of twinning in Zr-O alloys are not surprising, although solute size is but one of the factors affecting mechanical properties.

The hardness of zirconium has also been found to vary with the refining process and this has been attributed to variations in residual constituents.

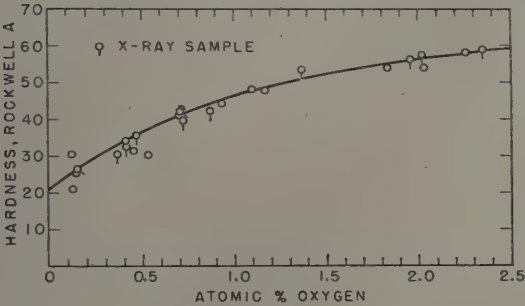


Fig. 4—Zirconium hardness change with oxygen.

Metal produced by magnesium reduction is considerably harder than iodide crystal bar despite extensive efforts to improve purity. These improvements have resulted in metal substantially free of metallic impurities. Removal of the last traces of the three elements, hafnium, carbon, and oxygen, has not been possible by metallurgical methods. Residual hafnium does not appear to be responsible for the gross hardening effect since it also occurs in similar concentration in soft crystal bar and is nearly identical to zirconium in lattice constants and atomic diameter. Carbon, oxygen, and to a lesser extent nitrogen remain as the principal hardening agents. Since all three elements normally form interstitial solid solutions, the hardening effect is apparently caused by strain in the crystal lattice.

In order to examine this hardening effect, the strain induced in the crystal lattice by increasing amounts of oxygen has been calculated from the

Table IV. Effect of Oxygen on Zirconium Density

Atomic Pct Oxygen	Density, G per CC	Source
0	6.541	de Boer and Fast ²
2	6.555	de Boer and Fast ²
10	6.601	de Boer and Fast ²
0	6.507*	Present work
0.147	6.509	Present work
1.961	6.517	Present work

* By unit-cell volume extrapolation.

unit cell volume of each of the X-ray samples as shown in Table III. Since oxygen content was the only significant variable in this series (carbon and nitrogen being relatively constant), a direct correlation between hardness and lattice strain should be apparent. Fig. 5 shows a plot of these data in which a reasonably good linear correlation was obtained for the amount of data available.

Density and Composition: Scattered density values given for zirconium in the literature are not entirely consistent. This may be attributed to the presence of impurities, particularly hafnium, carbon, and

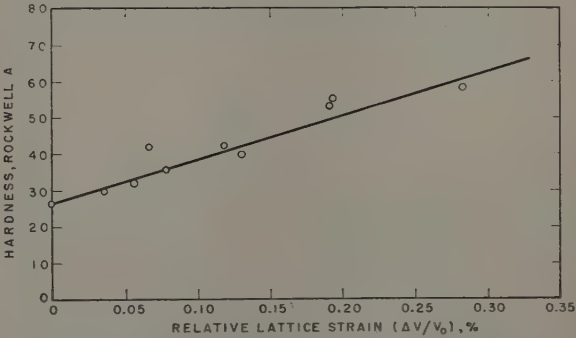


Fig. 5—Zirconium hardness relation to lattice strain.

oxygen, in unknown amounts, which produce significant density differences. A precise calculation of X-ray density requires not only correct parameter measurement and quantitative chemical analysis, but also, in the case of metals, the characteristic dis-

Table III. Lattice Constants of Zr-O Alloys at 25°C

Sample Number	Wt Pct Oxygen	Atomic Pct Oxygen		a_0 , kX	c_0 , kX	c/a	Volume of Unit Cell, kX ³	Relative Strain $\times 10^6$
		Added	Corrected*					
Z62-1A	0.026	0	0.147	3.22562†	5.13709†	1.59259†	46.2884†	0
Z62-8C	0.064	0.166	0.364	3.22611	5.13743	1.59245	46.3054	368
Z62-8A	0.074	0.222	0.420	3.22634	5.13746	1.59235	46.3129	531
Z62-7B	0.083	0.376	0.471	3.22624	5.13926	1.59296	46.3245	761
Z62-8B	0.125	0.536	0.708	3.22619	5.13858	1.59277	46.3191	664
Z62-5D	0.128	0.756	0.725	3.22662	5.13994	1.59298	46.3424	1181
Z62-8D	0.153	0.708	0.866	3.22711	5.13877	1.59238	46.3468	1266
Z62-2A	0.244	1.27	1.38	3.22760	5.14046	1.59266	46.3765	1904
Z62-2C	0.350	1.91	1.96	3.22749	5.14093	1.59286	46.3772	1919
Z62-3A	0.361	2.11	2.02	3.22845	5.14246	1.59248	46.4186	2813
Z62-2B	0.422	2.32	2.36	3.22765	5.14096	1.59279	46.3819	—

* Added oxygen corrected for initial oxygen.

† Final digits uncertain.

Table V. Density and Composition of Several Types of Zirconium

Material	Iodide Crystal Bar, Low Hf	Mg- Reduced Purified Sponge, Low Hf	Iodide Crystal Bar, High Hf	Mg- Reduced Graphite- Melted High Hf
Atomic pct Zr	99.325	99.050	98.423	95.428
Atomic pct O	0.147	0.566	0.130	1.450
Atomic pct C	0.468	0.226	0.084	1.493
Atomic pct Hf	0.014	0.040	1.239	1.310
Atomic pct Fe	0.046	0.117	0.119	0.114
Atomic pct Ti	*	*	*	0.058
Atomic pct Al	*	*	*	0.146
Atomic pct Pb	*	*	0.005	*
Archimedes density at 25°C (g per cc)	6.518	6.492	6.578	6.634
X-ray density at 25°C (g per cc) corrected for composition	6.509	6.497	6.574	6.605
X-ray density at 25°C (g per cc) not cor- rected for composition	6.504	6.489	6.497	6.502
a_0 , kX units	3.2256	3.2279	3.2267	3.2264
c_0 , kX units	5.1371	5.1415	5.1388	5.1356

* Not detected.

persion of impurities, e.g., substitutional or interstitial atoms in solid solutions. Densities in the present work have been calculated from atomic percentages according to the relation

$$\rho = \frac{2(\Sigma A_s + \Sigma A_i)}{NV}$$

where: ρ is the density in g per cc; ΣA_s , the sum of substitutional atomic weights; ΣA_i , the sum of interstitial atomic weights; N , Avogadro's number; and V , the unit cell volume.

Density values determined as above are shown in Table IV for increasing oxygen content. Based on the extrapolation of unit cell volume, see Fig. 3, and interstitial solution of carbon and oxygen, the best density value for oxygen-free, low hafnium crystal bar is 6.507 g per cc. Increased oxygen caused an increase in density despite the observed linear increase in unit cell volume. Comparison of these data with similar work of de Boer and Fast also included in Table IV shows that the present values are significantly lower than previously found, the previous data also showing a decided density increase with added oxygen. The observed difference in absolute density is satisfactorily explained by the much lower hafnium content of the present metal (0.014 vs 0.50 atomic pct O). In addition, the relative change in density per atomic percentage of oxygen is in good agreement with the previous work.

The effect of composition on density and lattice constants of four selected types of zirconium is shown in the data of Table V in order of decreasing purity. The separation of hafnium to produce low hafnium metal results in lower density and higher zirconium assay. Low hafnium iodide crystal bar had the highest purity with a zirconium content of 99.325 atomic pct. Magnesium-reduced sponge purified by vacuum melting with separation of hafnium was also found to be of very high purity.

Observed agreement between calculated corrected densities and measured densities is consistent with the initial assumptions of interstitial solution of oxygen atoms and substitutional solution of hafnium atoms. The necessity of including minor elements in the density calculations whenever true values are desired is shown by the lack of agreement between uncorrected and measured densities included for comparison in Table V. The spread of density values obtained in this work explains the previous lack of consistent results in the literature, since minor impurities may cause the density to vary from about 6.45 to 6.65 g per cc.

Summary

A series of oxygen alloys of high purity zirconium crystal bar examined by X-ray diffraction showed a marked expansion of the hexagonal lattice with increasing oxygen. Precision lattice constants of this zirconium (analysis of Table II) were as follows: $a_0 = 3.22562 \pm 0.00014$ kX units; $c_0 = 5.13709 \pm 0.00036$ kX units. Extrapolated lattice parameter values were also obtained for oxygen-free zirconium. Oxygen is shown to be an active hardening agent in zirconium, occupying an interstitial position in solid solution.

The effect of minor impurities on density was found to vary with the specific elements. X-ray density of oxygen-free, high purity crystal bar was found to be 6.507 g per cc.

A comparison of purity and density of various types of zirconium is included.

Acknowledgment

The author wishes to express his appreciation to A. R. Kaufmann for his enthusiastic support of this work, and to H. Sawyer for his part in preparing and measuring the diffraction data. This work was carried out at the Massachusetts Institute of Technology Metallurgical Project under Contract AT (30-1)-981 with the U. S. Atomic Energy Commission.

References

- W. J. Kroll, A. W. Schlechten, W. R. Carmody, L. A. Yerkes, H. P. Holmes, and H. L. Gilbert: *Trans. Electrochemical Soc.* (1947) **92**, p. 99.
- J. H. de Boer and J. D. Fast: *Rec. Trav. Chim.* (1940) **59**, p. 161.
- R. M. Treco: Some Properties of High-Purity Zirconium and Dilute Alloys with Oxygen. *Trans. ASM* (1953) **45**.
- M. U. Cohen: *Review of Scientific Instruments* (1935) **6**, No. 3, p. 68.
- E. R. Jette and F. Foote: *Journal of Chemical Physics* (1935) **3**, p. 605.
- R. B. Russell: Private communication.
- E. B. Read and L. P. Zopatti: Determination of Oxygen in Zirconium Metal. (1950) AECD No. 2798.
- H. T. Clark, Jr.: *Trans. AIME* (1949) **185**, p. 588; *JOURNAL OF METALS* (September 1949).
- C. A. Dube, F. D. Rosi, B. H. Alexander, F. C. Perkins: Mechanism of Plastic Flow in Titanium. Report No. YE 51-0443, Sylvania Electric Products (October 1951).

Development of Mechanical and Magnetic Hardness in a 10 Pct V-Co-Fe Alloy

by Richard W. Fountain and Joseph F. Libsch

CONSIDERABLE time and effort have been expended recently in research designed to provide a better understanding of the solid state transformations leading to the permanent magnet qualities of many commercial alloys. The knowledge derived from these investigations has resulted in the development of new magnetic materials as well as improvements in some of the older materials. The permanent magnet qualities of the newer alloys having high residual inductions and high coercive force values, have been attributed to the precipitation of a second phase or an order-disorder transformation in a solid solution.

The ternary Co-Fe-V alloys provide an interesting group of magnetic materials having a wide range of magnetic properties. The low vanadium alloys¹ possess soft magnetic properties similar to the binary Co-Fe alloys, while at higher vanadium contents (about 10 pct) interesting permanent magnet properties are obtained.^{2,3} Previous work by Nesbitt⁴ on the ternary Co-Fe-V permanent magnet materials, resulted in the conclusion that the precipitation of a second phase, γ , was responsible for the permanent magnet qualities of these alloys. However, unlike the conventional precipitation hardening alloys, the γ phase, which is stable at high temperatures, is precipitated in the low temperature α phase upon aging. Recent work by Geisler and Martin^{5,6} has established that the order-disorder reaction inherent in the binary Co-Fe alloys is also present in the ternary Co-Fe-V alloys. On the basis of their investigation, it was proposed that ordering of the α phase is also a possible explanation of the mechanical and magnetic hardening in these alloys. Thus, it appears that the Co-Fe-V alloys are rather unique in that two solid state transformations are taking place which may account for the properties of these alloys.

R. W. FOUNTAIN, formerly Graduate Student, Lehigh University, is now associated with the Research Laboratories, Union Carbide and Carbon Corp., Niagara Falls, N. Y., and J. F. LIBSCH, Member AIME, is Associate Professor of Metallurgy, Lehigh University, Bethlehem, Pa., and Director of the Magnetism Project sponsored by the Signal Corps Engineering Laboratories, Fort Monmouth, N. J.

Discussion on this paper, TP 3404E, may be sent, 2 copies, to AIME by March 1, 1953. Manuscript, April 9, 1952; revised, Sept. 22, 1952. Philadelphia Meeting, October 1952.

In view of these facts, the present investigation was undertaken to study the mechanism of mechanical and magnetic hardening in the 10 pct V-Co-Fe alloy with particular reference to the role of the γ phase; and to correlate the results of this study with other magnetic properties. In addition, the influence of increasing vanadium contents on the transformation of Co-Fe alloys was also undertaken to supplement the main objective of the investigation.

Experimental Procedure

The Co-Fe-V alloys used for study consisted of: 1—a commercial lot of Vicalloy I, a 10 pct V alloy, and 2—alloys prepared by powder metallurgy and containing 52 pct Co and 0 to 14 pct V, balance iron. The commercial alloy was received in the cast and forged condition and was used primarily for the detailed study of hardness, electrical resistivity, and magnetic properties of the 10 pct V alloy.

The powder metallurgy alloys were prepared from electrolytic iron, commercial cobalt, and ferrovanadium powders. The processing cycle was as follows:

1—Elemental powders were weighed and mechanically mixed for 24 hr.

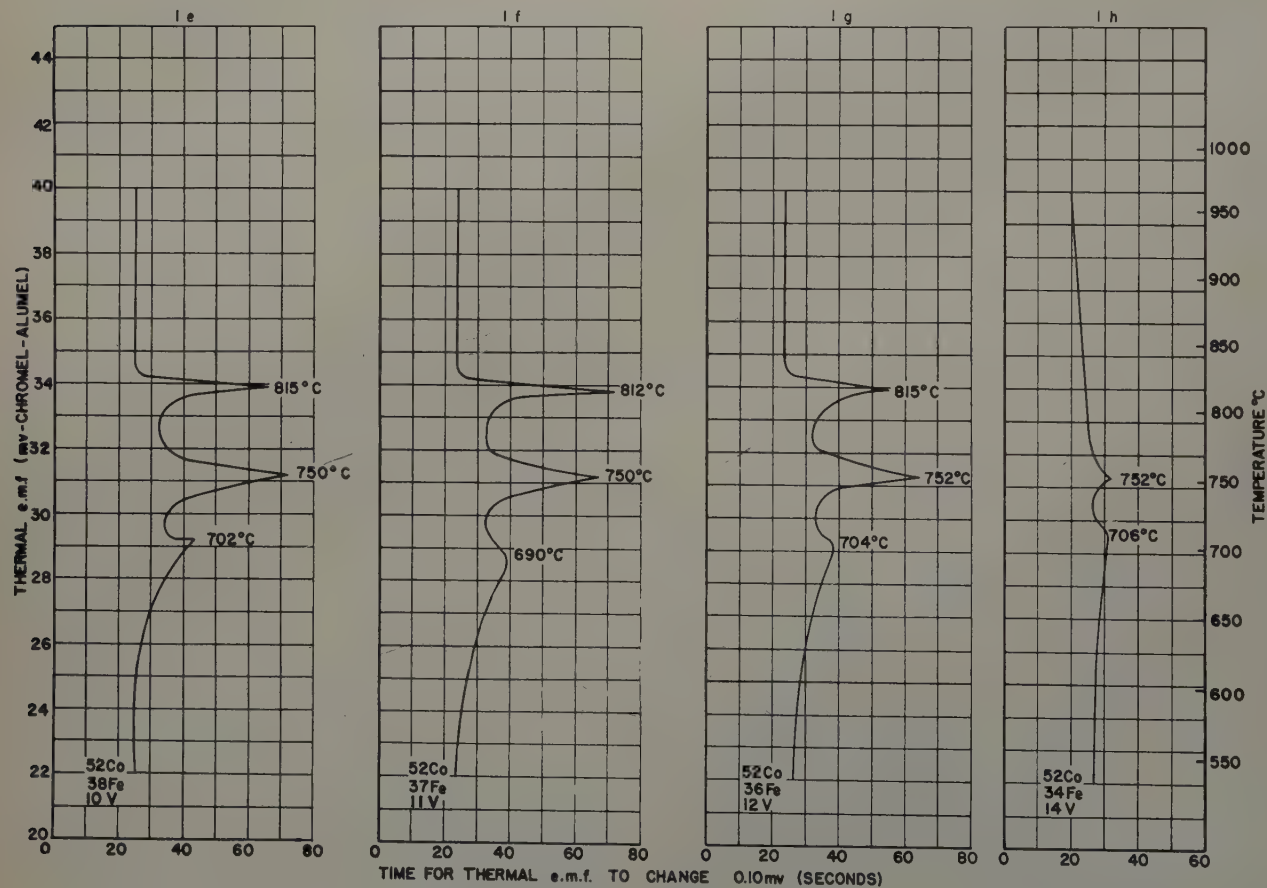
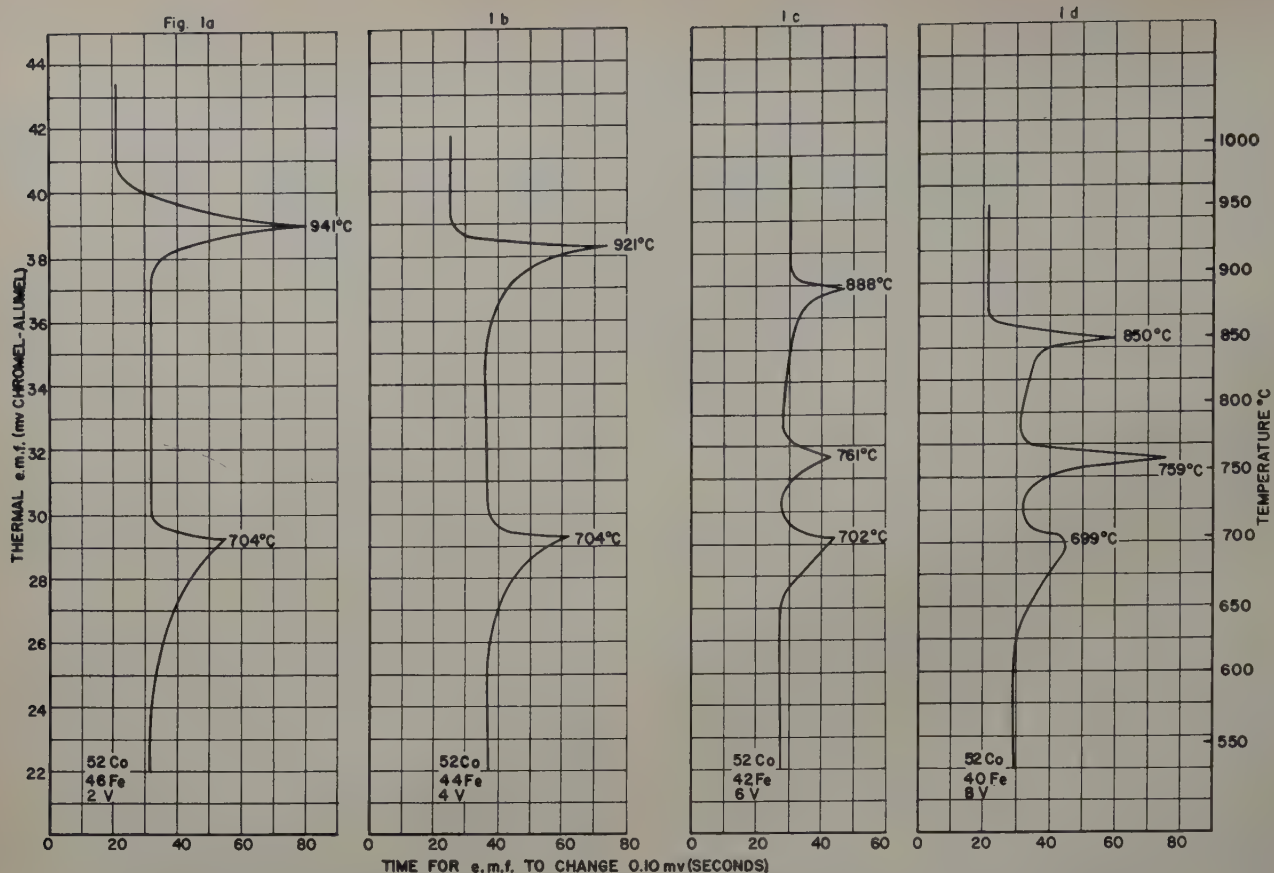
2—Mixed powders were pressed at 60,000 psi into the form of bars $\frac{5}{8} \times \frac{5}{8} \times 5$ in.

3—Bars were sintered in an atmosphere of purified dry hydrogen for 24 hr at temperatures ranging from 1380° to 1340°C, depending upon the vanadium content. The as-sintered bars were cut in half; and one half was machined to $\frac{7}{16}$ in. diam for thermal analysis. The remainder of the bar was hot forged to approximately 0.050 in. for X-ray diffraction analysis.

Additional details of sample preparation are presented subsequently according to the type of test performed.

Thermal Analysis Measurements

One of the simplest and most widely used tools for determining phase relations as they change with temperature and composition is to study the rate of change of temperature of a material as heat is supplied or extracted at a constant rate. The thermal analysis method used in this investigation is the inverse-rate method described by Smith.⁷



The specimens for thermal analysis were solution treated at 1100°C for 1 hr followed by oil and liquid nitrogen quenching. The liquid nitrogen quench was used in an effort to transform any retained γ phase, thus providing a single-phase alloy at the start of the analysis.

Fig. 1a is the thermal analysis curve obtained upon heating an alloy containing 52 pct Co, 46 pct Fe, and 2 pct V. The discontinuities in the curve at the critical temperature of order and at the α - γ transformation temperature are clearly shown in this example.

Thermal analysis curves similar to that of Fig. 1a were obtained for alloys containing less than 6 pct V. In alloys containing 6 pct or more vanadium a curve similar to that of Fig. 1c was obtained. The striking difference between these two curves is at once observed as an additional peak lying between the critical temperature of order and the α - γ transformation temperature of the 2 pct V alloy. This additional peak is present in all the curves for specimens ranging from 6 to 12 pct V. This peak is interpreted as the beginning of the α - γ transformation, while the second peak at 888°C has been interpreted as the completion of the α - γ phase transformation. However, recent preliminary X-ray diffraction tests with chromium radiation indicate the possible presence of a hexagonal phase in aged samples. If substantiated by additional work, this may serve as an alternative explanation for the additional peak in the thermal analysis curves.

Another significant feature of these curves is the continued decrease in intensity of the ordering peak as the vanadium content is increased. Although no quantitative relation can be obtained from these curves, there are two qualitative implications. First, the increased vanadium content may directly prevent the formation of the ordered structure by blocking diffusion processes, or second, it may enter into a second phase with the iron and cobalt and thus may change the ratio of Fe-Co necessary to form the ordered structure. The second possibility seems to be more likely as the continued additions of vanadium lower the α - γ transformation indicating that the vanadium is promoting the formation of the γ phase. At 14 pct V the alloy shows a very small transformation peak indicating that very small amounts of the α phase are present.

X-Ray Diffraction Analysis

X-ray diffraction analysis was used principally to determine the phase relations of Co-Fe-V alloys heat-treated to produce nonequilibrium conditions, in the hope that the results would provide more information regarding the actual mechanism of mechanical and magnetic hardening.

The diffraction studies were carried out using a General Electric XRD-3 X-ray diffraction apparatus for direct measurement of diffracted intensities. The results obtained by this method were checked in many cases by the use of conventional film techniques.

As was mentioned earlier, the as-sintered bars were forged to 0.050 in. for X-ray diffraction analyses. The samples were solution treated individually by placing them in a stainless steel tube and providing a purified dry hydrogen atmosphere. The specimens were held for 1 hr at 1100°C and quenched in oil. When the sample had reached room temperature the atmosphere was discontinued and the sample was removed from the tube and

Table I. Results of the X-Ray Diffraction Analyses* on 52 Pct Co-Fe-V Alloys

Weight Pct		Aging Temperature, °C	Aging Time, Hr	Phases	Parameters	
V	Fe				α	γ
0	48	As quenched	0	α	2.858	
		400	8	α	2.857	
		600	8	α	2.858	
2	46	As quenched	0	α	2.858	
		400	8	α	2.856	
		600	8	Ordered α	2.859	
4	44	As quenched	0	α	2.861	
		400	8	α	2.860	
		600	8	Ordered $\alpha + \gamma$	2.857	3.572
8	40	As quenched	0	α	2.863	
		400	8	α	2.862	
		600	8	Ordered $\alpha + \gamma$	2.856	3.568
10	38	As quenched	0	α	2.864	
		400	4	$\alpha + \gamma$	2.860	3.567
		400	8	$\alpha + \gamma$	2.861	3.581
		500	8	$\alpha + \gamma$	2.861	3.567
		600	8	Ordered $\alpha + \gamma$	2.857	3.575
		700	8	Ordered $\alpha + \gamma$	2.856	3.573
12	36	As quenched	0	$\alpha + \gamma$	2.862	3.574
		400	8	$\alpha + \gamma$	2.860	3.577
		600	8	$\gamma + \alpha$	2.856	3.574
14	34	As quenched	0	$\gamma + \alpha$		3.577
		600	8	$\gamma + \alpha$	2.851	3.578

* X-Ray Data: Filtered Co radiation (Fe_2O_3 filter). Tube operated at 34 kva and 9 ma. Spectrogoniometer speed 0.2° per min—1° X-ray defining slit—0.2° X-ray detector slit.

quenched in liquid nitrogen. Aging was carried out in lead and the specimens were water quenched from the aging temperature. Filtered cobalt radiation was used in this investigation.

In the early stages of the diffraction study, it was found that due to the sluggishness of γ - α transformation in the higher vanadium alloys, many samples would appear to be entirely α phase, but when etched to remove the surface layers, traces of γ phase were detected. For this reason, all subsequent samples were etched until no change in the diffraction pattern occurred.

The results of the X-ray diffraction study are reported in Table I. Two main conclusions can be drawn from these data. First, a face-centered cubic γ phase can be precipitated from the body-centered cubic α phase at temperatures as low, in the higher vanadium alloys, as 400°C. Second, ordering in the

Table II. Influence of Vanadium upon the Phase Relations of 52 Pct Co-Fe-V Alloys as Determined by X-Ray Diffraction*

Weight, Pct		Pct α	Pct γ	Parameters	
V	Fe			α	γ
As Quenched:					
0	48	100	0	2.858	
2	46	100	0	2.858	
4	44	100	0	2.861	
8	40	100	0	2.863	
10	38	100	0	2.864	
12	36	50.7	49.3	2.862	3.574
14	34	12.3	87.7		3.577
Aged 8 hr at 400°C:					
0	48	100	0	2.857	
2	46	100	0	2.856	
4	44	100	0	2.860	
8	40	100	0	2.862	
10	38	96.5	3.5	2.861	3.581
12	36	74.5	25.5	2.860	3.577
Aged 8 hr at 600°C:					
0	48	100	0	2.858	
2	46	100	0	2.859	
4	44	96.5	3.5	2.857	3.572
8	40	93	7	2.856	3.568
10	38	86	14	2.857	3.575
12	36	40.5	59.5	2.856	3.574
14	34	6	94	2.861	3.578

* X-Ray Data: Filtered Co radiation (Fe_2O_3 filter). Tube operated at 35 kva and 9 ma. Spectrogoniometer speed 0.2° per min—1° X-ray defining slit—0.2° X-ray detector slit.

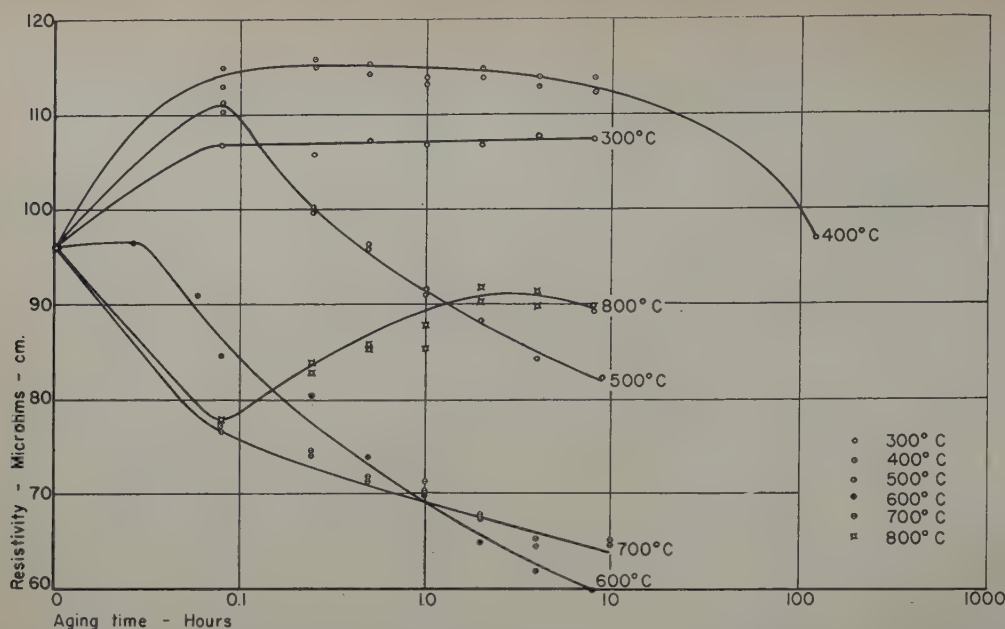


Fig. 2—Influence of aging time and temperature upon the electrical resistivity of Vicalloy I.

α phase can take place in the temperature range of 600° to 700°C. This fact was also established by the thermal analysis data. However, the detection of the ordered phase was very difficult and for this reason any change in lattice parameter due to ordering could not be determined.

Table II presents data for the amounts of the α and γ phase present with various vanadium contents and aging temperatures. From this table it can be seen that the additions of vanadium up to 10 pct to the Co-Fe alloys cause a gradual increase in the lattice constant of the α phase in both the as-quenched alloys and those aged at 400°C. This increase is observed to take place until the γ phase begins to precipitate at which point the lattice constant tends to decrease. This increase of the lattice constant would, of course, be expected, but the decrease of the constant due to the precipitation of γ suggests that the vanadium is going primarily into the γ phase. In addition to the change of the lattice constant due to γ precipitation, additional broadening of the peaks on the diffraction patterns occurred indicating that considerable strain was being introduced into the system due to the γ precipitate. This broadening was observed to take place even before the γ phase could be detected. Although no such trend in the lattice constants was observed at the 600°C aging temperature, additional broadening of the diffraction peaks was observed. The presence of more γ phase in the 12 pct V alloys as-quenched than when aged at 400°C is probably due to the sluggishness of the γ - α transformation on quenching. When the specimen was aged at 400°C, the retained γ phase was unstable at this temperature and consequently transformed to the α phase. This process is very familiar in the case of tempering alloy steels which contain retained austenite after quenching.

Mechanical and Magnetic Hardening in 10 Pct V-Co-Fe

From the results presented thus far, it has been established that suitable heat treatments can cause the precipitation of a γ phase as well as ordering in the α phase. However, the ordering reaction is confined mainly to the temperature range of 600° to 700°C for practical heat treatments which develop best magnetic properties. Thus, it seems that two mechanisms are available to explain the hardening

characteristics and permanent magnet qualities of the 10 pct V-Co-Fe alloy. The precipitation of the γ phase is certainly a possible explanation, as many binary⁸ and ternary⁹ permanent magnet alloys develop their properties by this process. On the other hand, however, an order-disorder reaction is responsible for the permanent magnet qualities of the well-known Co-Pt alloys.¹⁰ Thus, the problem presented is to separate the effects of these two reactions.

Hardness and Electrical Resistivity Measurements

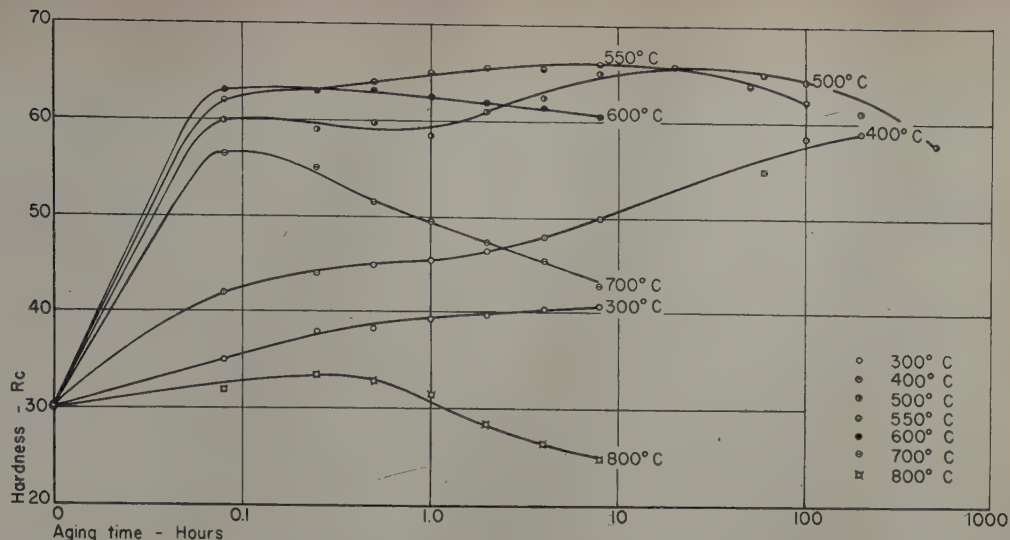
In an effort to provide an answer to the problem just referred to, an extensive survey of electrical resistivity and mechanical hardness was made on a commercial Co-Fe-V alloy of the Vicalloy I composition. The analysis of the alloy used for this purpose was as follows: C, 0.034 pct; Mn, 0.60; P, 0.014; S, 0.005; Si, 0.32; Co, 52.06; V, 9.10; and balance Fe.

The material for resistivity measurements was received in the form of hot rolled strip 0.055x $\frac{5}{8}$ x5 in. The resistivity samples were solution treated at 1100°C for 1 hr, first quenched in oil and subsequently into liquid nitrogen. The samples were aged in lead or salt at temperatures ranging from 300° to 800°C for varying time periods and water quenched from the aging temperature. The resistivity measurements were made using the well-known voltmeter-ammeter technique. The technique was checked thoroughly against known standards and a Kelvin double bridge and found to be capable of producing results accurate to within 1 pct.

The hardness measurements were made on $\frac{3}{8}$ in. sq samples cut from a $\frac{3}{4}$ in. hot forged bar of the same heat. Hardness samples were heat-treated in the same manner as resistivity samples.

The results of the electrical resistivity and hardness measurements are presented in Figs. 2 and 3. These data in conjunction with the X-ray diffraction data permit the drawing of some very interesting conclusions. The most striking feature of the resistivity curves is the sudden increase at aging temperatures below 600°C. This occurrence has been observed in the early stages of both precipitation hardening and ordering systems. As time is increased at temperatures below 600°C, the resistivity begins to decrease, although the hardness

Fig. 3—Influence of aging time and temperature upon the mechanical hardness of Vicalloy I.



is still increasing. These results are not contradictory as a change in electrical resistivity can be caused by slight variations in structure, whereas a macroproperty such as hardness is less subject to slight structural changes. The rapid decrease in the resistivity curves at temperatures of 600° to 800°C may be determined by two phenomena: 1—the coalescence of the γ precipitate, and 2—the effect of ordering in the α phase. As the temperature is increased to 800°C, a sudden reversal is observed in the resistivity curve. This result is most probably caused by the large amounts of γ phase present and disordering in the α phase.

The hardness curves of Fig. 3 are very revealing and need little explanation. The sudden rise in hardness at temperatures up to 600°C is almost certainly due to the precipitation of the γ phase, as at these low temperatures and short times the formation of the ordered phase was not detectable by X-ray diffraction or thermal analysis. Extremely long time periods at these low temperatures are also reported by Geisler and Martin⁶ before the ordered phase could be detected by diffraction analysis.

These time periods are much longer than those required to produce a substantial increase in hardness.

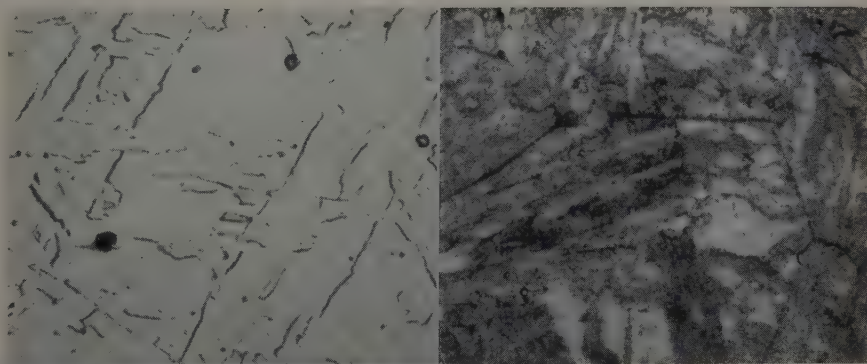
The characteristic shape of the curves of 300°, 400°, 500°C, and to some extent 550°C, suggests the existence of two stages in the precipitation process. The hump of the hardness curves is also observed in many of the common precipitation hardening systems such as Al-Cu. On increasing the aging temperature from 600° to 800°C, the maximum hardness is attained much more rapidly as would be expected, but the hardness decreases after very short time periods, indicating that overaging is taking place very rapidly.

The change in microstructure of this alloy on aging at 600°C for increasing time periods is shown in Fig. 4a to d. The metallographic samples were heat-treated according to the same cycle used in the hardness tests, except that they were subzero cooled in liquid oxygen rather than liquid nitrogen during quenching. All samples were water quenched from the aging temperature. The structure of Fig. 4a is for a sample in the as-quenched condition. According to X-ray diffraction analysis, this sample is all

Fig. 4—Vicalloy I solution treated at 1100°C for 1 hr. Electrolytically etched in 5 pct solution of HCl in alcohol. X2000. Area reduced approximately 65 pct for reproduction.

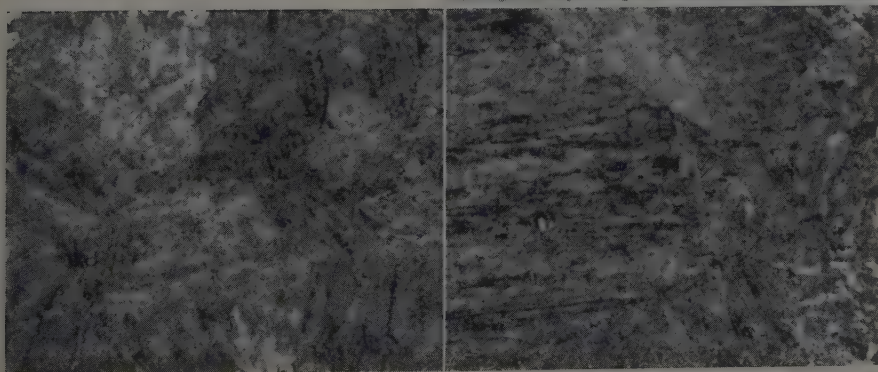
a (left)—Oil and liquid oxygen quenched.

b (right)—Aged 8 hr at 600°C and water quenched.



c (left)—Aged 24 hr at 600°C and water quenched.

d (right)—Aged 72 hr at 600°C and water quenched.



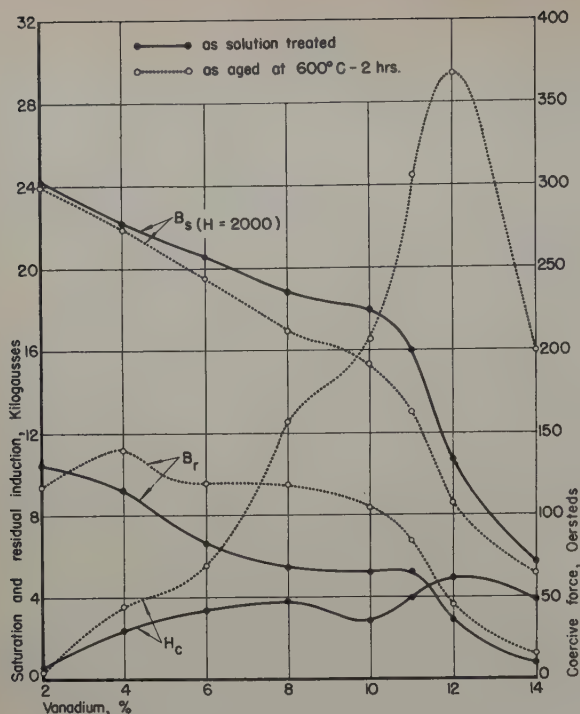


Fig. 5—Magnetic properties vs vanadium content.

α phase. The slightly gray areas may be due to a difference in orientation on etching. After 8 hr at 600°C, Fig. 4b, grain boundary precipitation can be observed. On increased times, Fig. 4c and d, the precipitating phase seems to have completely enveloped the grains and has become quite massive. From Fig. 4d, the general intragranular precipitation can be seen. This sample is completely over-aged. Thus, from this series of micrographs, the course of precipitation of the γ phase can be observed.

Magnetic Properties

The influence of increasing vanadium content upon the magnetic properties of the 52 pct Co-Fe alloy prepared by powder metallurgy was determined. These tests were restricted to a single aging temperature of 600°C and an aging time of 2 hr. However, an extensive survey was also made on the influence of aging time and temperature upon the cast Vicalloy I alloy which was used previously in this investigation.

Experimental Procedure: The vanadium series of alloys was prepared using the same processing cycle

as that outlined for the thermal analysis samples. In addition, however, the magnetic test samples were hot forged to approximately 0.400 in. sq. Subsequently, the samples were solution treated at 1100°C for 1 hr and quenched in oil and liquid nitrogen. In all cases, the samples were aged in lead at 600°C for 2 hr and air cooled from the aging temperature. It should also be mentioned that after forging, the density of the powder magnets was 98 pct of the density of the cast material, and that the magnetic properties were very similar.

The Vicalloy I material was received in the form of hot forged bars $\frac{3}{4}$ in. sq. Test samples $\frac{1}{2}$ in. sq were machined from the as-forged bar and solution treated in the same manner as the powder parts. The test samples were aged at temperatures from 400° to 800°C for various time periods. The magnetic properties were determined on a General Electric saturation permeameter. All saturation values reported are for $H = 2000$ gauss.

Effect of Composition: The influence of increasing vanadium content on the magnetic properties of the 52 pct Co-Fe alloy in the as-quenched and aged condition is presented in Fig. 5. Several interesting conclusions can be drawn from these data. In the as-quenched condition, the saturation induction and residual induction decrease with increasing vanadium content. The highest values of saturation and residual induction are observed in the lower vanadium alloys, where the composition is closest to that of the high saturation binary Fe-Co alloy. The coercive force increases slightly with the vanadium additions, and this result would be expected merely from a composition standpoint.

On aging at 600°C, however, a striking change in properties occurs. The coercive force increases rather slowly with increasing vanadium content to 6 pct V after which it increases very rapidly. The highest values of coercive force are obtained in alloys containing 52 pct Co, 36 to 38 pct Fe, and 10 to 12 pct V. As vanadium content increases, the saturation induction decreases more rapidly in the aged condition than in the quenched condition. This occurrence is to be expected as Nesbitt⁴ reports that the γ phase is nonmagnetic and it was shown in the X-ray diffraction study that the γ phase began to precipitate at about 4 pct V. The residual induction values do not follow the same trend after aging as they did in the as-quenched condition. This difference in the values of residual induction is probably associated with a structural change in the α phase that will be discussed in greater detail later.

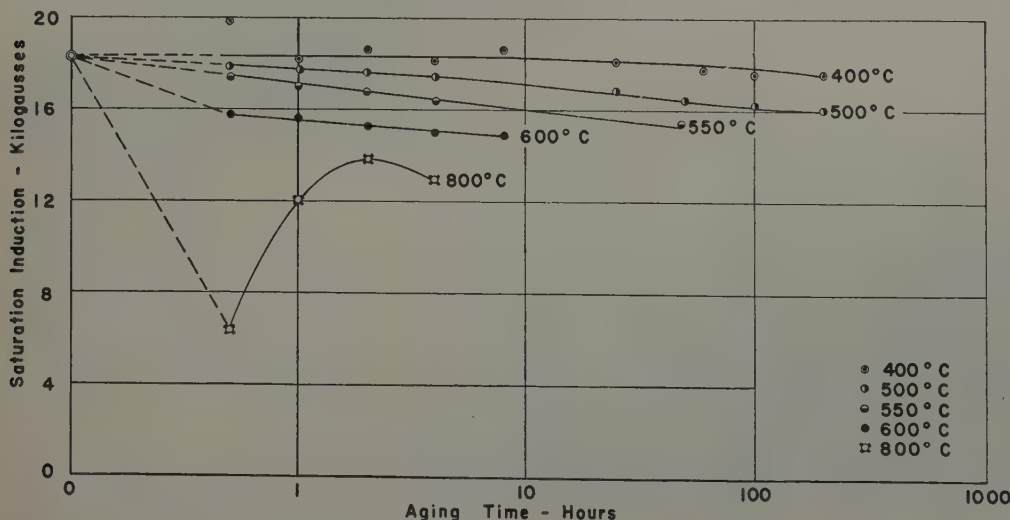
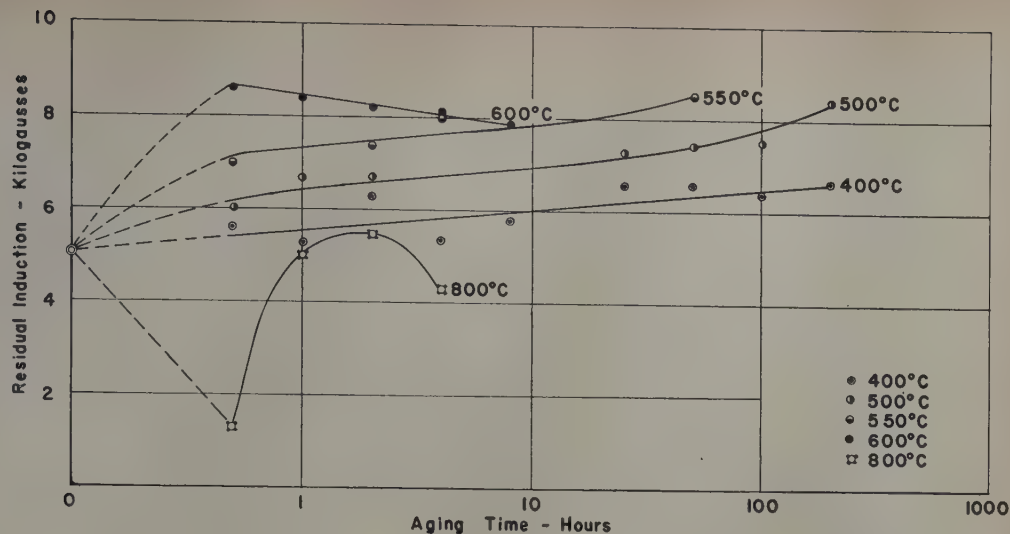


Fig. 6—Influence of aging time and temperature upon the saturation induction of Vicalloy I.

Fig. 7—Influence of aging time and temperature upon the residual induction of Vicalloy I.



Magnetic Properties of 10 Pct V Alloy: The results of the more extensive survey of the magnetic properties of the Vicalloy I alloy are presented in Figs. 6 to 8.

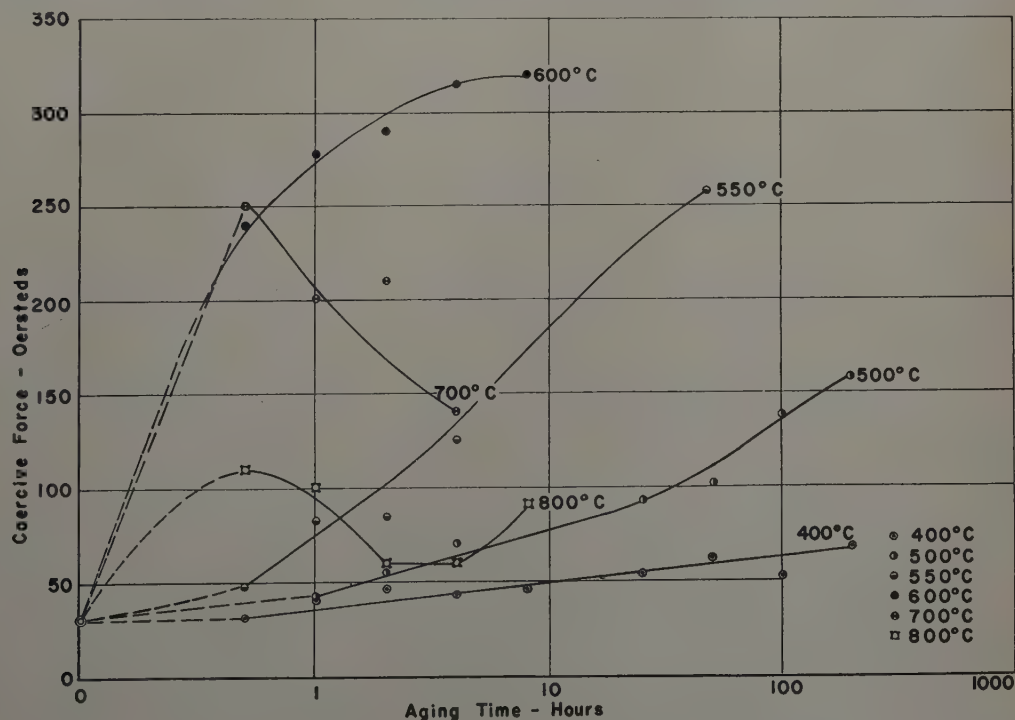
The saturation induction values, Fig. 6, show a general decrease as a function of time and aging temperature. The highest values of saturation are obtained by aging at 400°C. This would be expected because at this low temperature the amount of the γ phase present would be a minimum.

The initial low value of saturation induction after aging at 800°C is probably caused by large quantities of γ phase precipitated even at these very short aging times. The sudden reversal of the saturation induction is very interesting and provides some information concerning the kinetics of the reaction taking place. It appears, for example, that the primary difference between the 600° and the 800°C curve is the amount of γ phase precipitated. At 800°C, as the γ phase precipitated agglomerates, it reaches a large enough size to become an equilibrium state and then transforms on cooling to α by a martensite-like reaction. In this connection, it may be noted in Fig. 1e that 800°C is very near the critical temperature for the 10 pct V alloy.

The data of Fig. 7 show the changes in residual induction on aging. The residual induction increases with aging time in the temperature range of 400° to 550°C. At 600°C the rapid rise and decrease of the residual induction is most probably due to the rapid precipitation of the γ phase. The influence of ordering in the α phase may be playing an important role in the residual induction value for the 600°C aging temperature and for the longer time periods at 500° and 550°C. The behavior of the residual induction on aging at 800°C is similar to that exhibited by the saturation induction.

The values of coercive force obtained on aging are shown in Fig. 8. The general increase in coercive force as the aging time and temperature are increased does not seem to correlate with the mechanical hardness values reported earlier. The behavior of mechanical and magnetic hardness is, however, understandable. A very small nucleus of precipitate should be enough to affect the mechanical hardness sufficiently since such a nucleus and the strained area about it will impede the motion of a dislocation, which is the cause of hardness. On the other hand, the effect on H_c may not be felt until the precipitate is much larger. It appears al-

Fig. 8—Influence of aging time and temperature upon the coercive force of Vicalloy I.



most as though there is some critical diameter to the precipitate which is why at 700°C, H_c begins to get smaller. Such an effect has been found by Dijkstra and Weert in the Fe-C system.¹¹ The most interesting point observed from these data is the increase in the coercive force at the longer times at 500° to 550°C, and, of course, the shorter time periods at 600°, 700°, and 800°C.

Correlation of Structure and Mechanical Hardness

The existence of a γ phase precipitate can be detected by X-ray diffraction analysis in samples aged at 400° to 600°C. At temperatures of 600°C, the first sign of the γ phase is detected at 4 pct V. At lower temperatures, 400°C, small quantities of the γ phase are detected at 10 pct V. The existence of the ordering in the α phase was found to take place in the temperature range of 600° to 700°C. By electrical resistivity and hardness measurements it has been established that the γ phase precipitate is responsible for the mechanical hardening of this alloy in samples aged in the temperature range up to 600°C. In some cases, the maximum hardness obtained is equal to that of fully hardened steel. Above 600°C it is difficult to distinguish between the contribution of the γ phase and ordering in the α on mechanical hardening. However, the very rapid increase in hardness at the short aging times at all the aging temperatures, seems to be more characteristic of an age hardening system. It is certainly possible that the ordering in the α phase is contributing to the mechanical hardening at 600°C and higher aging temperatures.

Concerning the magnetic properties, the influence of the formation of γ phase on the saturation values is quite clear. The presence of the γ phase results in a decrease in the saturation induction due to its nonmagnetic character. It is also possible that the precipitation of this phase may produce a composition change in the magnetic α phase, which detracts from its magnetic properties, thus aiding in the decrease in saturation induction.

The increase in residual induction with aging time and temperature is most probably due to γ phase precipitation and possibly ordering in the α phase at the higher temperatures. It would be expected that the precipitation of the nonmagnetic γ phase would result in a decrease in residual induction similar to the decrease observed in the saturation induction. However, it should be remembered that residual induction is a structure sensitive property. Therefore, it appears that the strain accompanying the γ phase precipitation is resulting in a more favorable domain structure, so that during magnetization a greater degree of domain orientation is obtained. At the higher aging temperature, 600°C, ordering in the α phase probably contributes to this mechanism, resulting in the very rapid initial increase in the residual induction. As the aging time at 600°C increases, the γ phase increases to a size where it loses its efficiency to orient the domain structure and merely acts to decrease the residual induction by its nonmagnetic character.

In regard to the high values of coercive force obtained on aging, the presence of the γ phase appears vital. The large coherency strains associated with the formation of the γ phase and its subsequent precipitation in the grain boundaries and along certain crystallographic planes would appear capable of producing a coercive force of the magnitude reported, i.e., 300 oersteds. In this connection it may

be noted that there is an appreciable difference in the lattice parameter of the α and γ phases.

On the other hand, the lattice constant of the Fe-Co ordered phase differs so slightly from that of the disordered phase, that it would hardly seem possible that this slight difference would cause sufficient disregistry to produce such a large change in coercive force.

Summary and Conclusions

The results of this investigation may be summarized as follows:

1—Increasing vanadium additions to Co-Fe alloys lower the $\gamma \rightarrow \alpha$ transformation, thus promoting the formation of the nonmagnetic γ phase. The vanadium additions also decrease the intensity of the ordering reaction as determined by thermal analysis.

2—Precipitation of the γ phase is primarily responsible for the mechanical hardening in this system. Above 600°C it is felt that ordering in the α phase may be contributing to the mechanical hardening.

3—Increasing vanadium additions to Co-Fe alloys lowers the saturation and residual induction and increases the coercive force. The highest values of coercive force were found in alloys containing 52 pct Co, 36 to 38 pct Fe, and 10 to 12 pct V.

4—The increase in residual induction of the Vicalloy I alloy on aging was attributed to the production of a more favorable domain structure accompanying the γ phase precipitation.

5—The high values of coercive force obtained for this alloy have been associated primarily with the formation and precipitation of the γ phase in the magnetic α phase.

Acknowledgment

The authors wish to express their thanks to the Signal Corps Engineering Laboratories, Fort Monmouth, N. J., for permission to publish this paper.

References

- ¹ J. H. White: Workable Magnetic Compositions Containing Principally Iron and Cobalt. U. S. Patent 1,862,559 (June 14, 1932).
- ² G. A. Kelsall and E. A. Nesbitt: Permanent Magnet Alloy (Co-Fe-V). U. S. Patent 2,190,667 (February 20, 1940).
- ³ E. A. Nesbitt: Permanent Magnet Alloy (Co-Fe-V). U. S. Patent, 2,298,225 (October 6, 1942).
- ⁴ E. A. Nesbitt: Vicalloy—A Workable Alloy for Permanent Magnets. *Trans. AIME* (1946) **166**, p. 415 and **167**, p. 222; *METALS TECHNOLOGY* (February 1946).
- ⁵ A. H. Geisler: Structure of Permanent Magnet Alloys. *Trans. ASM* (1951) **43**, pp. 70-101.
- ⁶ D. L. Martin and A. H. Geisler: Constitution and Properties of Cobalt-Iron-Vanadium Alloys. *ASM Preprint 1* (1952).
- ⁷ C. S. Smith: A Simple Method of Thermal Analysis Permitting Quantitative Measurement of Specific and Latent Heats. *Trans. AIME* (1940) **137**, pp. 236-245.
- ⁸ Seljesater and Rogers: *Trans. Amer. Soc. Steel Treating* (1931) **19**, p. 553.
- ⁹ W. Koster: Mechanical and Magnetic Precipitation Hardening of Fe-Co-W and Fe-Co-Mo Alloys. *Arch. Eisenhütten.* (1932) **6**, pp. 17-23.
- ¹⁰ J. B. Newkirk, A. H. Geisler, D. L. Martin, and R. Smoluchowski: Ordering Reactions in Cobalt-Platinum Alloys. *Trans. AIME* (1950) **188**, pp. 1249-1260; *JOURNAL OF METALS* (October 1950).
- ¹¹ L. J. Dijkstra and C. Weert: The Effect of Inclusions on Coercive Force of Iron. *Physical Review* (September 15, 1950) **79**, pp. 979-985.

Thermal and Dilatometric Investigation of the Alloys of Cobalt With Chromium and Molybdenum

by A. G. Metcalfe

Observations at temperature are used to investigate the phase changes in alloys containing more than 50 pct Co and above 1000°C. The nonsuppressible transformations in cobalt above 1120°C and in the intermetallic compound Co_2Cr_3 are studied. The liquidus and solidus surfaces are determined. Insufficient data is obtained to complete the constitution diagram.

A REVIEW of some of the earlier work on cobalt¹ and on the binary systems with chromium²⁻⁴ and with molybdenum,⁵ showed that one likely source of differences might be attributed to the presence of phases at high temperatures which could not be retained by quenching. Consequently, the decision was made that only methods of examination at temperature should be used in this work. The correctness of this decision was confirmed during the course of the work by the investigation of the martensitic nature of the transformation in cobalt⁶ and by the decomposition of the high temperature form of the phase Co_2Cr_3 on quenching.⁷

The use of high temperature methods, including dilatometry and thermal etching led to the postulation of the existence of a high temperature form of cobalt with a probable hexagonal close-packed structure, transforming from cubic cobalt over a range of temperature from 1119° to 1145°C.⁸ One of the important pieces of evidence for this transformation was that it was observed in alloys with chromium and molybdenum which were nonmagnetic at this temperature so that confusion with magnetostriction effects was impossible. These results were not reported in this earlier paper, so that the data given here supply further evidence for the existence of a second allotropic transformation in cobalt.

A. G. METCALFE is Research Metallurgist at Deloro Smelting and Refining Co., Deloro, Ont., Canada.

Discussion on this paper, TP 3401E, may be sent, 2 copies, to AIME by March 1, 1953. Manuscript, April 14, 1952. Philadelphia Meeting, October 1952.

This paper represents part of a thesis by A. G. Metcalfe submitted in partial requirements for the degree of Doctor of Philosophy to the University of Cambridge, December 1950.

High temperature observations are necessarily much slower in producing results than the examination of quenched specimens at room temperature by conventional means such as X-ray diffraction or microexamination. The investigation has only covered a limited part of the field, as a result, extending from the liquidus down to about 1050°C and from the cobalt corner up to 50 pct alloying elements.

The differences between the various reported diagrams for the constitution of the Co-Mo and Co-Cr systems have already been mentioned. The best available diagram in the first system is due to Sykes and Graff⁹ which is shown in Fig. 1. Fig. 2 shows the latest Co-Cr diagram due to Elsea, Westerman, and Manning.⁷ A comparison reveals that these are incompatible because of the disagreement with regard to the number of allotropes of cobalt. Elsea, Westerman and Manning took their liquidus and solidus curves from Wever and Haschimoto.² The temperature horizontal in the two-phase field beneath the eutectic was placed 35° to 39°C higher than in earlier work^{2,4} with a new interpretation of the nature of this transformation. This interpretation also required a peritectic horizontal at about 1470°C, which has been confirmed here for an alloy with 53 pct Cr.

No investigation had been made of the ternary system until after this work had been terminated, when a section at 1200°C was published.⁹ In this work a ternary compound was found by the X-ray diffraction examination of quenched alloys. This compound contained less than 50 pct Co, and was thus outside the field investigated here. However, some reactions were found dilatometrically which could not be fitted on the diagram and are now believed

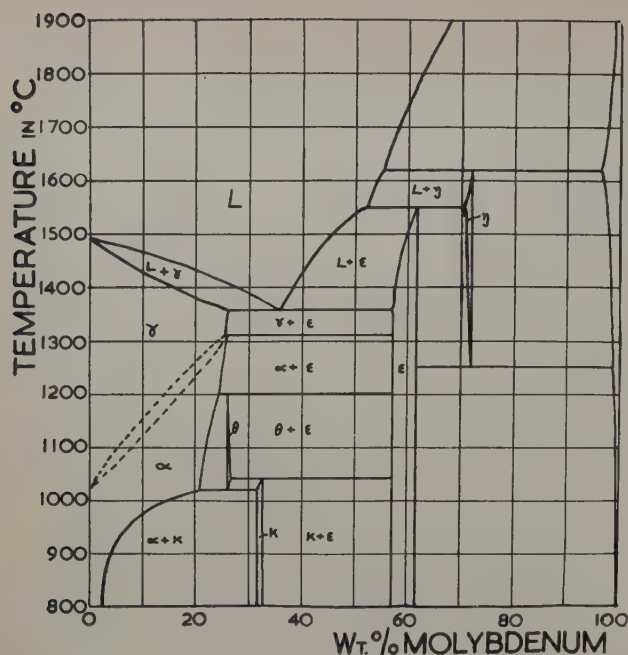


Fig. 1—Co-Mo constitution diagram according to Sykes and Graff.⁶

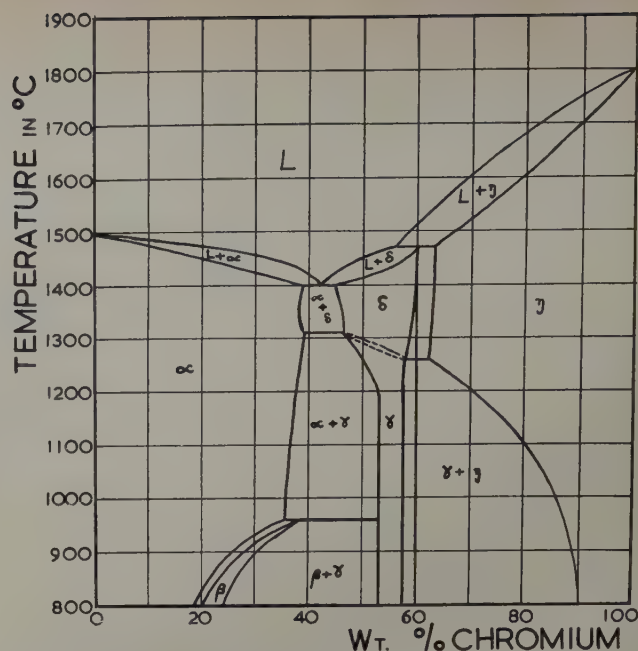


Fig. 2—Co-Cr constitution diagram according to Elsea, Westerman, and Manning.⁷

to be connected with this compound. Although this compound was observed in alloys of lower purity, its existence has had to be considered.

Apparatus

Vacuum Furnace: A sectional view of the vacuum furnace is shown in Fig. 3. The furnace consisted of either a single or a double alumina tube wound with either molybdenum or tungsten wire. The alumina crucibles were 6 in. long and 1 in. diam, with an auxiliary heater consisting of about 20 turns of tungsten wire at the top to prevent bridging of the charge. The vacuum vessel tipped about the trunnions shown in Fig. 3 to cast the alloy into a wrought iron mold, which could be heated. Pumping was continuous by means of a 1½ in. diam pipe leading through one of these trunnions to a taper giving direct connection with an oil diffusion pump. This can be seen in Fig. 4. The pressure could be kept below 1 micron of mercury throughout the melting and casting of both nickel and cobalt up to the highest temperature reached, 1710°C, but tended to be somewhat higher for melts containing chromium.

The temperature of the melt was measured by a thermocouple which could be lowered into the crucible by an Archimedean screw inside the vacuum vessel. The furnace was tipped mechanically to obtain reproducible conditions, see Fig. 4. A small refractory tundish at the top of the mold reduced the initial chill.

Thermal Analysis—Solidus: Thermal analysis on cooling was made in the vacuum furnace, followed by rapid remelting, and casting (after stirring well), in order to minimize composition changes due to evaporation. After homogenization of these ingots, small samples were heated inside a block of the type shown in Fig. 5. The position of the platinum thermocouple is shown by the dotted outline of the sheath. A W-Mo-W thermocouple recorded the difference in temperature between this thermocouple and the specimen which was insulated by coarse alumina powder. The thermocouple junction was pressed into a slit cut in the specimen. This block was then heated

Table I. Composition of Alloys

	Cobalt (As Cast)	Chromium (Electrolytic)
Carbon		0.05
Sulphur		0.04
Silicon		Trace
Iron	Trace	0.01
Nickel	0.025	0.01
Copper	0.025	0.01
Sodium	0.02	Trace
Cobalt	Balance	Absent
Chromium	0.01	Balance

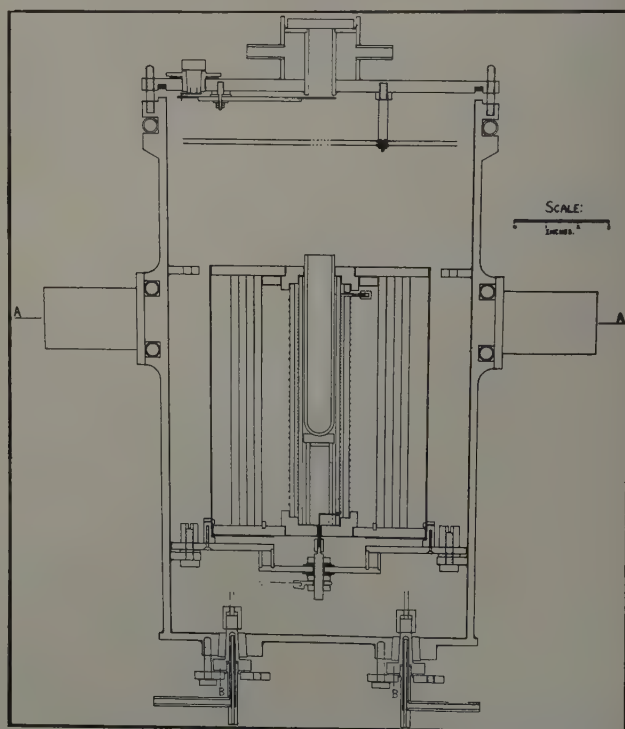


Fig. 3—Section of vacuum casting furnace.

at a constant rate inside a tube through which hydrogen was flowing. Nickel, wrought iron, and stainless iron were used for these blocks.

Dilatometer: A section through the dilatometer is shown in Fig. 6. The outer concentric tube was evacuated to improve temperature uniformity in the inner tube and to prevent leakage of air into it. A short piece of metal bellows took up any differential expansion. The specimen was short and of large diameter to reduce internal thermal gradients and can be seen in the lower drawing. The details of the adjustment device and of the transmission through the metal bellows to the dial gage can be seen in the upper diagram. The temperature range in which readings were taken was 1000° to 1425°C , for which mullite was found to be satisfactory, although trouble was experienced with creep before suitable supports were designed to take the weights of the ends.

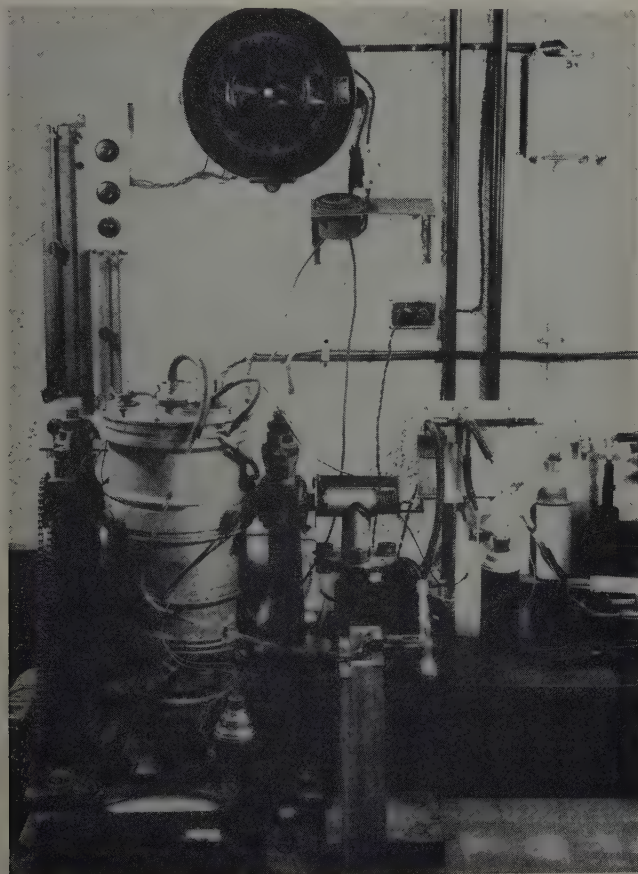


Fig. 4—General view of furnace.

Measurements were made in vacuo and argon, although the latter was preferred for ease of working. One defect was found to be that the contraction of the specimen was not followed smoothly. However, the hysteresis on cooling was considerably greater than on heating, in agreement with general experience,²⁰ so that no advantage was lost by neglecting the cooling curves.

Creep of the specimen was encountered in the initial experiments with nickel,²¹ but was overcome by careful adjustment of the pressure.

Preparation of Alloys

The alloys were vacuum melted and cast using metal of the composition given in Table I. The following elements were also absent from both the cobalt and the chromium: Mo, Pb, Bi, Sb, As, Ag,

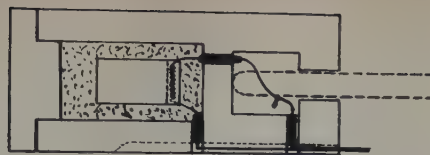


Fig. 5—Block for thermal analysis on heating.

Al, Mn, Sn, Zn, W, Nb, Ta, V, and Ti. No analysis was made for oxygen, hydrogen, or nitrogen. The cobalt had been made electrolytically although the analysis is for a sample after casting. The molybdenum metal powder was not analyzed, but was better than 99.8 pct pure.

It was assumed that all of the metals contained a certain amount of oxygen, and in addition it seemed likely that hydrogen might be present in the chromium. Some preliminary experiments revealed that if the pressure in the system was used to follow the evolution of carbon monoxide, deoxidation by means of carbon could be made. If too little carbon was added the pressure rose when carbon monoxide began to be evolved, but soon fell back to a low value when the carbon was exhausted. On the other hand if too much carbon was added, the pressure remained high owing to the reaction with residual oxygen in the system. At near the critical amount the pressure fell back to the usual value, but rose slightly if the melt was stirred.* Under these pres-

* This method was suggested by E. A. G. Liddiard and A. H. Sully of Fulmer Research Institute, England.

ures and temperatures the product of the concentrations of oxygen and carbon must be extremely low, so that analyzed carbon figures of 0.01 and 0.02 pct must mean low oxygen contents. The carbon content was always analyzed when it was believed to be higher than usual, on the basis of the above tests, so that where no result is reported it is probably below 0.02 pct. The best results were obtained by additions of carbon on the basis that the chromium contained 0.45 pct and the molybdenum 0.15 pct oxygen, confirmed by examination of the ingots for inclusions. These inclusions were solely chromic oxide which had been as high as 0.10 pct before the deoxidation technique was used, but dropped to below 0.01 pct with a residual carbon content of 0.01 to 0.02 pct. It was felt that the "carbon boil" would carry away any hydrogen or nitrogen in the alloy. No chromium nitride was ever detected in any alloy.

The alloys were superheated 100° to 150°C and then stirred well by means of the lateral and vertical movement of the thermocouple sheath. Cooling curves were then made, but were only taken to a little below the liquidus in most cases in order to avoid segregation. The previous superheating made it possible to remelt and cast quickly so as to avoid

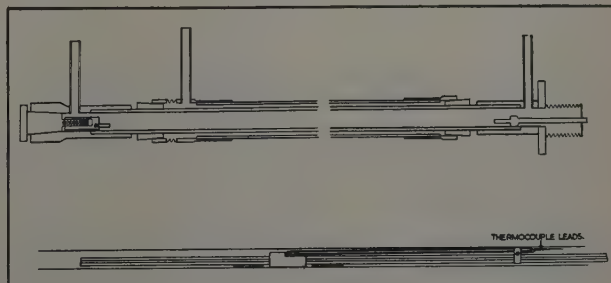


Fig. 6—Dilatometer.

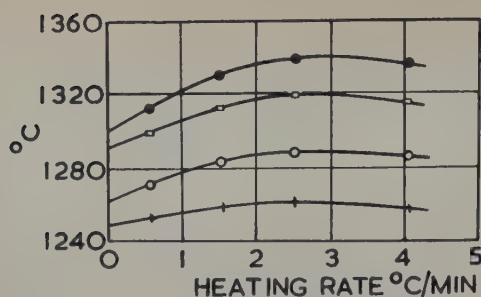


Fig. 7—Extrapolation of dilatometer results to zero rate of heating.

composition changes. The mold was heated to a temperature between 300° and 400°C for casting.

Composition changes due to evaporation were not serious in most of the alloys. The nominal 55 pct Cr alloy had the highest melting point and the highest chromium content, but in spite of extending the cooling curve to below the solidus, the alloy analyzed 53.3 pct Cr against 54.8 pct actually added. Much of this composition change would have occurred from the chromium metal before alloying, so that the change between the thermal analysis and casting was probably under 0.5 pct. Once the alloys had melted down, the small area of the crucible tended to restrict evaporation.

Alloy 2020 (a nominal composition of 20 pct Cr and 20 pct Mo) was allowed to cool in the crucible instead of being cast. The analysis figure quoted in Table II is for a sample taken from the bottom of the ingot and reveals the extensive segregation which can result. On the other hand alloy 3010 which was cast in the normal way, contained 28.2 pct Cr and 11.7 pct Mo at the top, against 28.2 pct

Cr and 12.0 pct Mo at the bottom of the ingot. In other cases where analyses were made at the top and bottom of the cast ingots, similar agreement was obtained.

The ingots weighed about 50 g and were checked for soundness and inclusions by density determinations and microscopic examination. Very little porosity was found (chill-cast cobalt had a density of 8.87 g per cc). Cracking was noticed on many alloys containing much chromium, which was later found to be connected with the transformation in the compound Co_2Cr_3 , see Fig. 2.

The ingots were homogenized by 36 to 48 hr heating at 1300° to 1325°C in a "gettered" vacuum.

Thermal Analysis

Cooling Curves: The temperatures were measured by means of a thermocouple, but as experience was gained many changes were made which increased the accuracy of measurement. The work on the Co-Cr binary was regarded as confirmation of existing diagrams^{2,7} rather than exploratory, so that when it was found that the technique used was not completely satisfactory, only a portion of it was repeated because the data obtained agreed with the earlier results, within its limits of accuracy.

Table I gives these thermal analyses results in the first group. The temperatures were determined by means of a W-Mo thermocouple in alumina insulators and sheath of 6 mm OD. This had been annealed at 1700°C and calibrated in situ against a Pt vs Pt-13 pct Rh thermocouple up to 1400°C, supplemented by melting point determinations at the Ni-Cr eutectic at 1342°C¹² and at the melting points of nickel at 1453°C and of cobalt at 1493°C.¹³ Agreement was within 3°C by these two methods of calibration and

Table II. Composition and Thermal Analysis of Co-Cr-Mo Alloys

Nominal	Alloy, Pct			Thermal Arrests, °C		
	Cr	Mo	C	Cooling		Heating
				Liquidus	Others	Solidus
Group 1						
2000	16.0	—	—	1480±4		
2500	23.1	—	—	1473±6		
3000	28.4	—	—	1464±6	1442±6	
3500	26.9	—	—	1448±8		
4000	26.8	—	—	1420±8		
4500	38.1	—	—	1445±8	1400±3	
1020	9.8	18.65	—	1408±5	1373±5	
Group 2						
2010	—	—	—	—	—	1408
2020	13.9	27.35	—	1355	1337	
1535	13.7	33.4	—	1330	None	1323,1322
2530	22.1	27.7	0.01	1402	None	
3020	27.8	22.0	—	1387	1348.5	1341.5,1342.5
3010	28.2	11.8	0.02	1383	1347	1349
0530	4.1	32.0	—	1357	1333	1333
0540	4.1	38.0	—	1389	1334	1332,1330, 1329
0550	4.05	49.7	—	1471	1333	
1050	10.3	47.3	—	1476	1442.5,1349, 1322.5	
4010	38.2	10.0	0.09	1381.5	1356	1329
3015	29.5	14.7	0.07	1356	1352,1330	1343
1530	14.4	29.6	0.03	1336	1331,1327	1324,1324
2030	19.2	29.7	0.04	1370	1327.5	
4020	38.3	20.5	—	1437.5	1400,1306	1390,1392
2040	19.9	38.4	—	1455	1381	
0520	4.8	20.1	—	1411	1336	1353
5500	53.3	—	0.04	1473.5	1472,1445	
5010	47.9	14.3	—	1459	1426	
1510	14.7	14.4	—	1440	—	
Group 3						
4200	42.4	—	0.01	1411	1403	1400
0021	—	20.3	0.01	1435	—	1389
0036	—	35.6	0.03	1353	—	1342,1342.5
0512	—	—	—	1448	1348	1410
0822	7.3	22.3	0.01	1402	—	1334
2214	—	—	—	1392	—	1361
2905	—	—	—	1421	—	—
3805	—	—	—	1384	—	—
1520	—	—	—	—	—	1347.5

Table III. Co-Cr Alloys

Composition, Pct Cr	Transformation Temperature		Length Change, 10 ⁻⁵ Cm per Cm
	Start	Finish	
10		1190	—
20.2*	1170	1190	+12
23.1	1203	1232	+7
26.9	1275	1325	+20
38.1	1312	1322	+5
42.4	1284	1287	+10
	1322.5	1324	+2
53.3	1270	—	—

* Sand-cast alloy containing also 0.39 pct Mn and 0.06 pct C, kindly supplied by B.S.A. Research Laboratories, Sheffield, England.

fell between the calibration curves of earlier workers.^{14, 15} The agreement between these calibration curves seemed to justify the use of this thermocouple for a series of Co-Cr alloys. After four alloys had been investigated, a second calibration at the melting point of cobalt was made, when it was found that the calibration had changed by 31°C. A similar rise in the electromotive force at the melting point of cobalt was found when another couple was used for two more of these alloys. Most of these thermal analyses were made in duplicate at rates of cooling between 1° and 5°C per min before the primary arrest, but it was found almost impossible to prevent much supercooling which reached a maximum of 57°C for pure cobalt. This could not easily be remedied because this thermocouple was fixed in the melt, an arrangement which also led to the production of ingots of uncertain composition. Subsequent papers^{16, 17} have reported consistent results with this thermocouple, but as it appeared to be necessary to stir the molten alloy, this couple was not investigated further.

The second series of thermal analyses was made with the Pt vs Pt-13 pct Rh thermocouple which could be lowered into the melt when desired. It was found¹⁸ that the calibration varied with time, being at the rate of 3°C per hr at the melting point of cobalt and so occasional checks were made at the melting point of pure nickel or cobalt. In addition to these, the thermocouple was calibrated before and after each thermal analysis at the melting point of silver under standard conditions in a separate furnace. The movement of the thermocouple sheath was sufficient to give adequate stirring and to discourage supercooling which was usually zero and

Table IV. Co-Mo Alloys

Composition, Pct Mo	Transformation Temperature		Length Change, 10 ⁻⁵ Cm per Cm
	Start	Finish	
20.3	1221	1226	8
35.6	1205	1240	—

never more than 5°C. The rate of cooling at the primary arrest varied between 0.9° and 6.5°C per min, although it was usually between 3° and 6°C per min. The thermal analyses results obtained with this thermocouple are considered to have an accuracy of $\pm 3.5^\circ\text{C}$.

A separate investigation of the causes of the change in the calibration of the standard platinum thermocouple¹⁸ led to the use of the Pt-1 pct Rh vs Pt-13 pct Rh thermocouple. The rate of change of calibration of this thermocouple at the melting-point of cobalt was 0.35°C per hr against the 3°C per hr of the

standard couple. The thermoelectric power was greater than 12 microvolts per °C over the range in which it was used. During the course of eight thermal analyses, the electromotive force at the melting point of nickel was observed to fall from 14.085 to 14.061 microvolts or a change of a little under 2°C. This increased stability allowed slower rates of cooling to be used which were between 1.7° and 4°C per min. The results obtained with this thermocouple are given in the third group in Table II. The accuracy of these results is considered to be $\pm 1.5^\circ\text{C}$.

Heating Curves: The whole ingot was used for dilatometry so that the specimens could not be cut until this work had been completed. Some of the determinations were repeated once, or twice, and all of these results are included in Table II.

Dilatometry: The specimen was heated to 1000°C and allowed to anneal at this temperature for a period of several hours before heating curves were determined. The first heating curve was at a rapid rate and was extended to a temperature approaching the solidus. Any irregularities in this curve were then investigated at two or three slower rates of heating which were usually between 0.5° and 4°C per min. The temperature of the start and the finish of each transformation was then plotted against the heating rate and extrapolated by a smooth curve to zero rate of heating. Fig. 7 illustrates this method of extrapolation for alloy 3805. Both of the reactions are peritectoids, and it was found that this type of variation of the transformation temperature with the rate of heating was a characteristic of some peritectoid transformations. It was observed where the composition of the product of the reaction changed rapidly as the transformation temperature was approached. At fast rates of heating, this adjustment of the solubility was largely incomplete, but a reaction was possible when the unsaturated terminal

Table V. Co-Cr-Mo Alloys

Alloy	Transformation Temperature		Length Change, 10 ⁻⁵ Cm per Cm
	Start	Finish	
α/γ Transformation			
0512	1150	1180	+6
1010	1110	1118	+9
0520	1092	1126	+40
2010	1160	1170	+3
1515	1140	1172	+6
0822	1120	1140	+60
2905	1212	1234	+10
1520	1135	1170	+7
0530	1160	1185	+35
2214	1174	1197	+8
3010	1235	1244	+7
3805	1248	1261	—
3015	1188	1198	+4
1530	1078	1080	+35
0540	1162	1174	+10
σ/δ Transformation			
3805	1289	1300	—
3010	1279	1286	—7
4010	1260	1265	—
3015	1275	1278	+7
3020	1272	1278	+4
4020	1270	1310	+16
0822	1271	—	—
1530	1278	—	—
2530	1269	—	—
Other Transformations			
3010	1132	1138A	—6
4010	1150	1160B	+4
2214	1049	1069C	+65
1520	1076	— A	—
3020	1180	— B	—
1530	1198	1199D	+6

Key: A— $\alpha/\alpha + \sigma$ boundary.
C— β/α transformation.

B— $\sigma/\alpha + \sigma$ boundary.
D—Unknown.

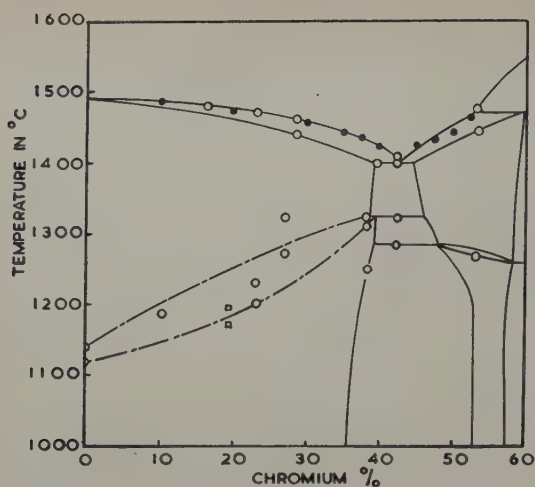
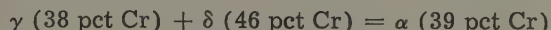


Fig. 8—Co-Cr diagram with proposed modifications. Solid circles due to Wever and Haschimoto.² Open circles, this work.

solid solution crossed into a two-phase field at a temperature below that of the peritectoid reaction.²⁰ The adjustment of the composition of the terminal solid solution was more complete at the slower rates of heating, and a corresponding contraction before the start of the peritectoid transformation was found at the slower rates of heating.⁸ Extrapolation curves of the opposite curvature have been found, for which similar explanations can be advanced. However, most of the curves have not shown a maximum (as in Fig. 7) or a minimum, but the explanations of the shape of the extrapolation curves have given greater confidence in the interpretation and the accuracy of the results.

Only the extrapolated dilatometer results are given in Tables III to V. The results for all of the Co-Cr alloys in Table II are not completely satisfactory because of the segregation in some of these alloys discussed earlier. In every case, however, the transformation of the face-centered cubic cobalt (α) to the high temperature form (γ) was observed at temperatures which increased with the chromium content. The alloy with a nominal content of 35 pct Cr (which analyzed 26.9 pct at one end) transformed over the range 1275° to 1325°C, suggesting that at some point the composition extended sufficiently far on the chromium side to include the peritectoid reaction at 1323°C:



δ is the high temperature form of the compound Co_2Cr_8 shown in Fig. 2. Single crystals of alloys 5500 were examined by Dickins, Douglas, and Taylor²⁰ and shown to have the same structure as the σ phase in the Fe-Cr alloys, leaving γ available for the high temperature form of cobalt.

The alloy 4500 contained 37.3 pct Cr at one end and 38.8 pct at the other after casting, and this is reflected in the more consistent results. The last two alloys in Table II were uniform in composition and hence gave the most reliable results. The length changes refer to the change over the transformation on heating.

The structure of the 35.6 pct Mo alloy confirmed that it was very near the eutectic composition, in agreement with the diagram of Sykes and Graff shown in Fig. 1. Hence the temperatures of the start and the finish of the transformation must be

for two different reactions because if they referred to the same reaction these two temperatures should be the same at zero rate of heating. Comparison with Fig. 1 shows that the 1205°C reaction must be the peritectoid by which θ phase forms, placed at 1200°C by Sykes and Graff,⁵ and the reaction at 1240°C must be the formation of α cobalt from γ cobalt by a peritectoid reaction, which was placed at 1310°C by Sykes and Graff. This temperature is consistent with the α/γ transformation in cobalt and in the 20.3 pct Mo alloy.

Co-Cr Diagram

Fig. 8 shows the changes proposed in the Co-Cr diagram. The liquidus agrees well with the earlier results of Wever and Haschimoto² used by Elsea, Westerman, and Manning.⁷ The solidus was placed a little higher on the basis of one result, but this seems likely because Wever and Haschimoto used a cooling rate of 60°C per min. The eutectic has been placed at 1401°C with a composition of 42.5 pct Cr, because the microstructure of alloy 4200 showed γ cobalt to be present in very small quantities as the primary phase. The peritectic at 1472°C by which δ phase forms was first suggested by

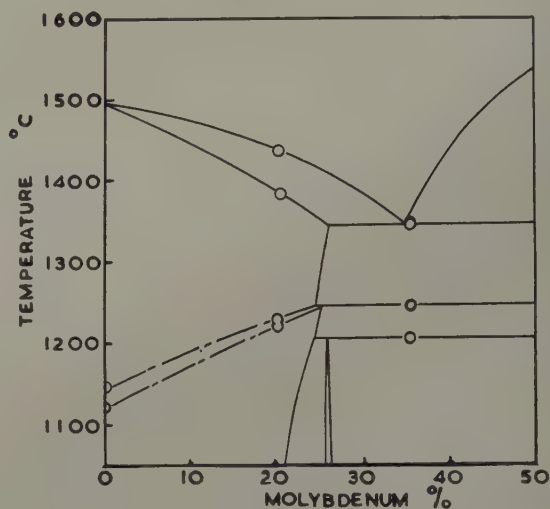


Fig. 9—Co-Mo diagram with proposed modifications.

Elsea, Westerman, and Manning. The composition of the liquid taking part in this reaction is 53 pct Cr.

The α to γ transformation temperatures were not reliable in all cases because of segregation in the ingots used (only the thermal analysis results on alloys with approximately the nominal composition have been plotted in Fig. 8). The dilatometer results for a 20 pct Cr alloy containing manganese and other impurities has also been plotted by open circles. The peritectoid temperature has been placed at 1323°C as stated earlier. The existence of this peritectoid explains the apparent minimum in the solubility of δ phase in the cobalt solid solution at 1325°C which was shown in Fig. 2. The peritectoid by which σ phase forms from δ phase has been placed at 1285°C, against 1310°C given by the earlier investigation,⁷ but the latter was determined by quenching experiments in which the δ phase was not retained. Strong thermal arrests have previously been reported at 1271°C⁴ and 1275°C,² although on alloys of lower purity. A peritectoid at 1285°C is consistent with the transformation starting at 1270°C in a σ phase alloy containing 53.3 pct Cr.

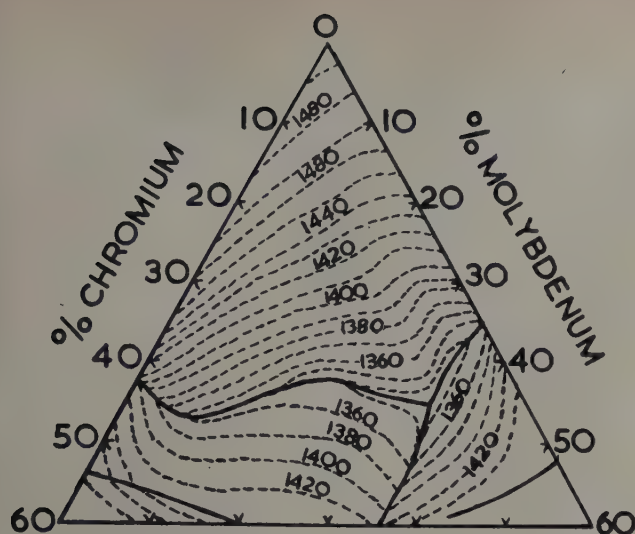


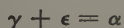
Fig. 10—The liquidus surface.

The solid solubility boundary of α and $\alpha + \sigma$ found by Elsea, Westerman, and Manning⁷ has been confirmed at one point.

Co-Mo Diagram

Only two alloys were made in this system and were intended to check the position of the α/γ transformation. The liquidus and solidus at 21 pct Mo were placed 5°C higher than in earlier work,⁶ but the eutectic temperature was placed 15° lower, at 1345°C. The eutectic composition was on the cobalt side of the alloy containing 35.6 pct Mo and was placed at 35 pct.

The dilatometer results were interpreted to indicate that the α to γ transformation temperatures rise with an increase in the molybdenum content, through 1221° to 1226°C at 20.3 pct Mo to the peritectoid at 1240°C:



This was consistent with the solid solubility boundaries fixed by Sykes and Graff.⁵ The transformation at 1205°C must be the peritectoid reaction by which θ phase forms (see Fig. 9), by comparison with the earlier diagram.

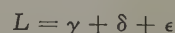
Ternary System

In all cases the dilatometric investigation at the fastest rate of heating was made to a temperature a little below the solidus unless this was in excess of 1400°C. The thermal analysis on cooling was usually stopped at a temperature a little below the liquidus, and the solidus temperature was determined by thermal analysis on heating. In one case, however, a transformation was detected by both methods. Thermal analysis placed the σ/δ transformation at 1306°C on cooling for alloy 4020 (see Table II) which was later found to be between 1270° and 1310°C by dilatometry. In view of this lack of overlapping in other cases it is possible to consider these results in four groups: the liquidus surface; the solidus surface; the α/γ transformation, and the σ/δ transformation. Although indications were obtained directly of some of the solid solubility boundaries, these were inadequate for the construction of a complete ternary diagram.

Liquidus Surface: This is shown in Fig. 10 and includes the results from 34 alloys. One characteristic of the surface at which γ cobalt begins to sepa-

rate is the double valley, running approximately parallel to the 5 and 20 pct Cr compositions.

Arrests due to the composition of the liquid reaching a eutectic valley were observed in alloy 3015 at 1352°C and in alloy 1530 at 1331°C. A prolonged arrest was observed in six alloys: 0530 (1333°); 0540 (1334°); 0550 (1333°); 1530 (1327°); 1535 (1330°); and 2030 (1327.5°C). The arrest at 1330° in alloy 1535 was the only one observed suggesting that this alloy approximates to the ternary eutectic composition. On the other hand, the systematic decrease in the eutectic temperature with increase in the chromium content was also found in the heating curves; 0530 (1332°); 0540 (1330°); 1530 (1324°); and 1535 (1322.5°C). However, a preliminary survey by X-ray diffraction on the chill cast alloys had not revealed the presence of any ternary compounds so that it was assumed that alloys 0530, 0540, and 0550 were outside the ternary fields. The ternary eutectic was placed at 1325°C and at a composition of 11 pct Cr and 34 pct Mo, where the reaction was:



The publication⁹ of details of a new intermetallic compound at a composition surrounding 20 pct Cr-

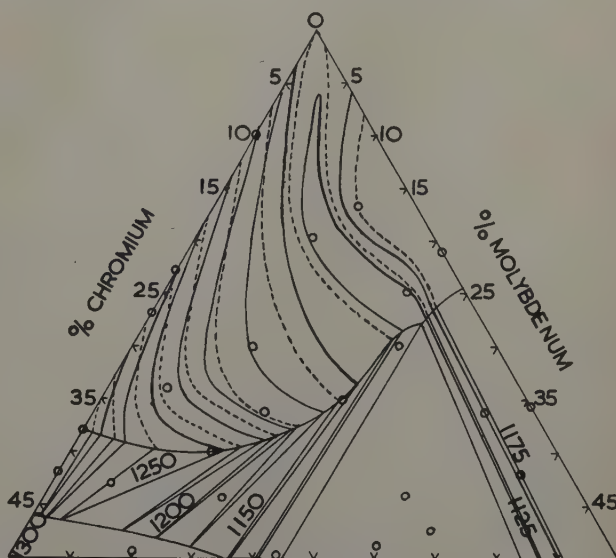
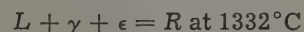
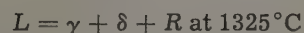


Fig. 11—The α/γ transformation surfaces. The solid lines represent the γ side and the dotted lines the α side of the $\alpha + \gamma$ field.

40 pct Mo makes it necessary to reconsider this assumption. It might be possible for two invariant points to exist, for example:



and:



where R is the new intermetallic phase.⁹ These two nonvariant points would be close together and would require a second break in the surface running towards the Cr-Mo binary system. The liquidus surface was not investigated in detail in this area because the investigation was restricted to cobalt-rich alloys, so that no evidence is available from this source and confirmation of this question must await further work. Two pieces of evidence which did not support the existence of a second invariant point were the absence of a eutectic arrest in alloy 2530 and the X-ray diffraction examination of chill-cast alloy 2040 which revealed only σ and ϵ phases.

The only other arrest recorded in Table II is at 1442.5°C in alloy 1050. This is believed to be the same peritectic as that found earlier in the Co-Mo system at 1550°C where:

$$L + \gamma = \epsilon \text{ (see Fig. 1)}$$

The α/γ transformation is plotted in Fig. 11 which shows the projection of isothermal sections at 1300°, 1275°, 1250°, 1225°, 1200°, 1175°, 1150°, and 1125°C on to the diagram (the 1150° and 1200°C sections on the molybdenum-rich side are omitted for clarity). The falling temperatures and length changes suggested a ternary eutectoid at 1079°C, but this viewpoint will have to be examined anew in the light of the recent claim that a ternary compound exists.⁹ The unexplained yet marked reaction at 1198°C in alloy 1530 (see Table V) and the inconclusive results obtained with alloy 2530 which was also expected to be in the ternary field and exhibit the 1079°C reaction, both suggested that the ternary field was more complicated than that shown in Fig. 11. The transformation surfaces between the γ and α fields will be unaffected by any small changes in this region, however.

The σ/δ transformation was detected in nine alloys by dilatometry and in one of these (4020) it was confirmed by thermal analysis. Although a slight rise in the transformation temperature was found on moving from alloy 4200 to 3805 (from 1285° to the range 1289° to 1300°C), the general tendency was for a fall in temperature on the δ side of the transformation field. The flatness of the lower surface of this field makes it impossible to predict the reactions by which σ forms from δ in the two or three-phase alloys. The solubility of molybdenum in σ phase appears to be between 20 and 25 pct at these temperatures, in agreement with the measured expansion of the plane spacings of the σ phase in chill-cast alloy 2040.

Discussion of Results

The liquidus and solidus surfaces at the cobalt corner of the diagram are characterized by a marked depression along the 5 pct Cr composition line, revealed by alloys 0512 and 0520. With higher chromium contents the liquidus and solidus surfaces diverge giving a maximum freezing range of 68°C in alloy 0822. Towards the Co-Cr side of the diagram, the surfaces approach each other again so that the freezing range of alloy 2905 is 15° to 20°C. This is in conformity with the observed smaller freezing range in which γ phase solidifies from Co-Cr melts.

The valleys in the transformation surfaces of γ to α phase running down from the cobalt corner were confirmed by three alloys with transformation temperatures below those for pure cobalt (1119° to 1145°C). These were 1010, 0520, and 0822 and these point towards the 1079°C reaction in the alloy 1530 being the ternary eutectoid by which γ decomposes to α plus two other phases. The reaction which extrapolated to a starting temperature of 1198° and to a finishing temperature of 1199°C is also believed to be that of another four-phase, nonvariant, equilibrium. The phases involved may be θ (see Fig. 1), γ , ϵ , σ , or R . The absence of any reaction involving θ in alloys 0530, 0540, and 0550 suggests that it is an equilibrium between the last four phases, probably involving the formation, or the decomposition, of R phase.

The temperature of the peritectic reaction $\gamma + \delta =$

α which is at 1323°C in the Co-Cr binary system, falls sharply with the addition of molybdenum, whereas the peritectic reaction $\alpha + \delta = \sigma$ at 1285°C in the binary system occurs at slightly higher temperatures as small amounts of the third element are added. This leads to a nonvariant point of equilibrium between the four phases at 1288°C, and at a composition of 42 pct Cr and 1.5 pct Mo.

Conclusions

In this work particular attention has been paid to the α to γ , and to the σ to δ transformations. Both of these transformations are easily overlooked in quenched specimens, although Sykes and Graff⁵ published micrographs of the α phase in the Co-Mo system drawing attention to the marking on the grains, and Elsea, Westerman, and Manning⁷ observed the precipitate left as a result of a change of solubility of α phase during the decomposition of δ to σ in the Co-Cr system. Both methods are of restricted use and, even then, uncertain.

These results, then, support the widely accepted view that more than one method of examination should be used in the study of constitution diagrams and reaffirm a corollary that one of these methods should involve observations at temperature.

Acknowledgment

This work would not have been possible without the active interest and encouragement of Professor Wesley Austin to whom considerable thanks are due. It is a pleasure to acknowledge the help provided by many outside organizations, especially the financial assistance provided by the Rhokana Corp.

References

- ¹ O. S. Edwards and H. Lipson: *Journal Inst. Metals* (1943) **69**, p. 177.
- ² F. Weber and U. Haschimoto: *Mitt. K. W. Eisenforschung* (1929) **11**, p. 293.
- ³ W. Koster: *Arch. Eisenhüttenwesen* (1932) **25**, p. 22.
- ⁴ Y. Matsunaga: *Kinzoku no Kenkyu* (1931) **8**, p. 549.
- ⁵ W. P. Sykes and H. F. Graff: *Trans. ASM* (1935) **23**, p. 50.
- ⁶ A. R. Troiano and J. L. Tokich: *Trans. AIME* (1948) **175**, p. 728; *METALS TECHNOLOGY* (April 1948).
- ⁷ A. R. Elsea, A. B. Westerman, and G. K. Manning: *Trans. AIME* (1949) **180**, p. 579; *METALS TECHNOLOGY* (June 1948).
- ⁸ A. G. Metcalfe: *Proc. World Metallurgical Congress, Detroit* (1951).
- ⁹ S. Rideout, W. D. Manly, E. L. Kamen, B. S. Lement, and P. A. Beck: *Trans. AIME* (1951) **191**, p. 872; *JOURNAL OF METALS* (October 1951).
- ¹⁰ J. S. Marsh: *Alloys of Iron and Nickel* (1938) Vol. I, p. 143. New York, McGraw-Hill Book Co.
- ¹¹ A. G. Metcalfe and M. J. Olney: *Metal Progress* (November 1950) **58**, p. 733.
- ¹² C. H. Jenkins, E. H. Bucknall, C. R. Austin, and C. A. Mellor: *Journal Iron and Steel Inst.* (1937) **136**, p. 187.
- ¹³ *Metals Handbook* (1948) Cleveland. ASM.
- ¹⁴ B. Osann and E. Schröder: *Arch. Eisenhüttenwesen* (1933) **1**, p. 89.
- ¹⁵ L. S. Chang and G. Derge: *Trans. AIME* (1947) **172**, p. 90; *METALS TECHNOLOGY* (October 1946).
- ¹⁶ R. D. Potter and N. J. Grant: *Iron Age* (March 31, 1949) p. 65.
- ¹⁷ H. T. Greenaway, S. T. M. Johnstone, and M. K. McQuillan: *Journal Inst. Metals* (1951) **80**, p. 109.
- ¹⁸ A. G. Metcalfe: *British Journal of Applied Physics* (1950) **1**, p. 256.
- ¹⁹ A. G. Metcalfe: Ph.D. Thesis, University of Cambridge (1950).
- ²⁰ G. J. Dickens, A. M. B. Douglas, and W. H. Taylor: *Nature* (1951) **167**, (4240), p. 192.

Residual Stresses Introduced During Metal Fabrication

by Kent R. Van Horn

RESIDUAL stresses in metals operate under a cloak of mystery, as they have neither been seen in the laboratory nor detected by means of the microscope. In spite of their phantom-like nature, they frequently exert metallurgical effects that cannot be ignored. In some cases the results have been detrimental, causing rejections or premature failures, but frequently the effects have been highly beneficial to the producer or consumer of metal products. First, however, what is a residual stress?

When a metal is plastically deformed by bending, rolling, pressing, or by a phase transformation or precipitation from solid solution, or by a sharp temperature gradient resulting from nonuniform cooling, quenching, or welding, it remains in a state of strain. The strains or strain gradients produced by such operations and retained after all external forces are released are known as residual strains, and the accompanying stresses as internal or residual stresses.

Many defects or failures in metal products have been ascribed to residual stresses, sometimes erroneously, because there was no other apparent explanation after the usual metallurgical tools of diagnosis had been applied. For example, during World War II, the forged aluminum alloy aircraft cylinder head in the reciprocating engine began to replace the cast head with the familiar cooling fins. The fins were machined in the solid forged head by an ingenious milling operation. One plant reported an epidemic of excessive distortion during the delicate

high-speed milling. A thorough examination revealed that the composition, heat treatment, mechanical properties, and metallurgical quality of these heads were comparable to those of forgings that machined satisfactorily. It was then claimed that the cause of the machining difficulties was connected with residual stresses resulting from the quenching during the solution heat treatment. An elaborate stress analysis actually demonstrated, however, that the magnitude of residual cooling stresses was lower in the cylinder heads which machined poorly than in those which were satisfactory in this respect. Subsequent tests proved that the machining problems in this case originated from variations in the tools and tool design.

Sources of Residual Stresses in Metals

Residual stresses are of two origins—mechanical and thermal. Thus, stresses may be produced in a metal by any cold-working process. The distribution and magnitude of these mechanically produced stresses can be calculated in a satisfactory, although approximate, manner for such simple cases as bending, torsion, and expanding of tubes. However, most manufacturing processes are too complex, and the original stress-strain relations in the products are not sufficiently known to permit calculation of the resulting residual stresses. Also, a specific process, such as wire drawing, may vary in complexity or uniformity of working, and large or small residual stresses may result, depending on the conformation of the dies and other features of the working process. Neither substantially unidirectional deformation, such as can be imparted by stretching a metal product having essentially the same mechanical properties throughout the cross section, nor deformation

K. R. VAN HORN, Member AIME, is Director of Research, Aluminum Research Laboratories, Aluminum Company of America, New Kensington, Pa.

TP 3462E. Manuscript, Nov. 14, 1952. Los Angeles Meeting, February 1953.

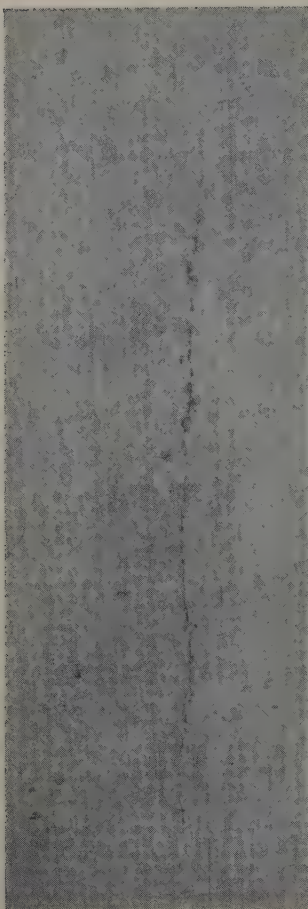


Fig. 1a—Stress corrosion crack in surface of tubular spar chord cold-worked after heat treatment. X5. Area reduced approximately 35 pct for reproduction.

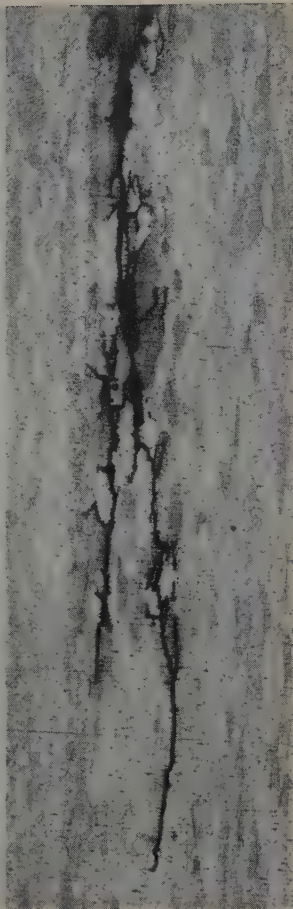


Fig. 1b—Macrograph of crack revealed in (a) just below the surface. Crack is parallel to axis of tube. E. H. Dix, Jr.⁵ X20. Area reduced approximately 35 pct for reproduction.

at sufficiently high temperatures followed by slow cooling will create appreciable residual stress.

At sufficiently high temperatures, residual stresses are relieved by plastic flow. Thus, stresses introduced by cold working during fabrication are erased during a high temperature heat treatment; but the subsequent cooling may or may not produce new stresses, depending on the rate of cooling. A metal piece heated and then cooled very slowly remains free from appreciable stresses. Furthermore, as long as the magnitude of any stress is less than the elastic limit at the specific temperature, the stresses are dependent only on temperature gradients and disappear completely on cooling to room temperature or an equalized temperature. The distribution and magnitude of the stresses may be appreciably affected if some sections yield during either heating or cooling. These direct thermal stresses are an important cause of the cracking in steels, which may occur in an article undergoing temperature changes. During quenching the colder surface zones are stretched beyond the yield strength because their normal thermal contraction is restricted by the retarded contraction of the hotter interior zones. When the temperature of the interior zones subsequently approaches that of the surface layers, the previous permanent stretch results in compressive stresses in the outer zones when they attempt to follow the delayed thermal contraction at the interior. This leads to the im-

portant generalization that the portions which cool more rapidly retain compressive stresses, whereas the portions which are the last to attain room temperature contain balancing residual tensile stresses; that is, in a rapidly cooled part the surface layers generally contain residual compressive stresses and the core or center tensile stresses. Thus, solution heat-treated aluminum alloy products and many heat-treated products of other metals contain compressive stresses in the exterior layers. This is a highly advantageous stress distribution for the accommodation of external service loads, whereas residual surface tensile stresses, on the contrary, would normally be additive to the service stresses and contribute to cracking or failure. Of course, the residual stress pattern of heat-treated and quenched products may be rearranged by subsequent machining or cold-working operations. Also, the conventional distribution resulting from thermal contraction during quenching may be considerably distorted if a phase transformation interferes with the thermal contraction, as in some carbon steels. Thus, residual tensile stresses can be produced in surface layers of certain quenched steels and, depending on the magnitude, may even cause quenching cracks.

A variety of residual stresses are derived indirectly from deformations produced during cooling. These cooling stresses may originate from, 1—quenching, 2—phase transformation, 3—constituent precipitation, 4—welding, and 5—casting (generally low compared to other sources). All of these stresses result from nonuniform thermal contraction or a volume change during a phase transformation, within the temperature range of cold work.

There are, of course, many comprehensive surveys of the origin of residual stresses in metals available in the literature.^{1, 2}

Beneficial and Detrimental Residual Stresses

Residual stresses are frequently suggested as likely sources for some of the difficulties encountered in the machine shop or fabricating plant. In fact, many designers consider residual stresses to be undesirable and believe that procedures should be initiated to eliminate residual stresses in metal products at any cost. Whether or not the residual stresses are actually undesirable can only be ascertained by stress analysis, which may be expensive and sometimes impossible. Castings, extrusions, or forgings generally have complex shapes that do not permit analysis of the stress distribution. The measurement of residual stresses in metals is more difficult, as a general rule, than the determination of the effects of external or service loads.

Residual stresses may have a beneficial as well as a deleterious effect. Some of the advantages of residual stresses that have been commercially utilized have been summarized by your lecturer and Dr. G. Sachs:¹

1—Stresses produced by plastic expansion are used to increase the strength of gun barrels and pressure vessels (auto fretting). The strength of rotating wheels can also be enhanced by a previous overloading.

2—Stresses imposed by shrink fitting are also employed to increase the strength of gun barrels.

3—Stresses formed by shrink fitting or the introduction of inserts are utilized to improve the service life of extrusion cylinders, forging dies, and drawing dies.

4—Stresses introduced by the quenching of most metal parts probably have a beneficial effect on the fatigue strength.

5—Stresses derived from local deformations produced by mechanical surface treatments, such as surface rolling, shot or hammer peening, ball pressing, etc., reduce to a considerable extent the injurious effects of notches, corrosion, and chafing on the fatigue strength.

6—Stresses resulting from stretching, bending, twisting, and overloads in various types of service applications are used to advantage.

In most of these applications residual compressive stresses are formed in the surface layers where high tensile stresses may be produced by the service loads. The beneficial stresses decrease the magnitude of the resultant surface stress in the case of a static loading; and in fatigue the mean stress in the fatigue cycle is displaced toward the compression side of the stress diagram, resulting in an improvement in fatigue life.

The principal detrimental effects that may accompany residual stress are briefly enumerated:

1—Warping or distortion during machining is related to the magnitude of the residual stresses, their distribution, and the quantity and location of the removed metal or the overloading of the part in the fixture.

2—Fire cracking and stress cracking may occur during the soldering and brazing of cold-worked steels and copper alloys.

3—Materials quenched for the purpose of hardening, such as steels and the aluminum alloys, may crack during or after quenching.

4—Castings and ingots may crack on cooling, storing, or reheating.

5—Fusion-welded structures may crack during welding or in service.

6—Certain alloys, subjected to mild corrosion, crack when sufficiently high surface tensile stresses are present.

7—Steel boilers, subjected to corrosion under stress, crack around riveted or otherwise deformed locations.

The different types of cracking originating from residual stresses have been traced in every case to the presence of high tensile stresses at the point of failure. Some of the cracking phenomena, however, are the result of stresses created by external forces.

Wishart³ and Richards⁴ have recently published comprehensive descriptions of the residual stresses in certain metal products and the mechanical or thermal procedures for producing beneficial or detrimental stresses.

Typical Examples of Residual Stress

Investigation in Metals

Many investigations have been conducted to determine the magnitude and distribution of residual stresses in metal products, to develop methods of stress analysis, to discover practices to reduce or eliminate detrimental stresses, and to develop procedures to impose the type of stresses that would improve the serviceability of the part. Most of this work probably has been done by mechanical engineers rather than by metallurgists. Thus, since 1928, when the papers of the Institute of Metals Division were assembled in a separate volume, there have been only seven papers published on this subject.



Fig. 2—Season cracking in a brass tube. Courtesy of D. K. Crampton.

The record of the *Transactions* of the American Society for Metals is six papers from 1928 to 1951. This is indeed surprising because of the acute and continuous interest over the years in residual stresses in so many plants that produce, fabricate, or use metals.

Most of the investigations were probably initiated because a part had failed in service and procedures had to be developed to remedy the situation. Several typical investigations of specific interest to the majority of the readers and to the important air-frame industry will be described.

Aluminum alloy square tubes were used in the main spar trusses of four-engine airplanes. For ease of fabrication these tubes were manufactured originally as round tubes and then sunk (without a mandrel) to the square shape. With the objective of obtaining maximum tensile properties, this sink from the round to the square tube was performed at room temperature on the completely heat-treated material, thus introducing additional cold work, which resulted in high mechanical properties. However, the plastic deformation also produced a high level of residual tensile stresses on the external surface of the tubes.* The tubes met all chemical and me-

* In contrast to the high stresses in tubes produced by cold sinking after solution heat treatment, 24S-T36 sheet which is cold-rolled after solution heat treatment possesses a low level of residual stress.

chanical property specifications and seemed entirely satisfactory for service. Unfortunately, mysterious longitudinal cracks developed in service, Fig. 1. Subsequent fatigue tests of full sections of tube, employing a beam-type specimen with two-point loading, revealed no deleterious effects from the residual stresses.

A laboratory examination of the tubes revealed that the cracks were of an intergranular nature, which suggested that stress corrosion was the cause.⁵ This was confirmed by stress corrosion tests which duplicated the type of crack that occurred in service. Also, stress analysis was possible because of the

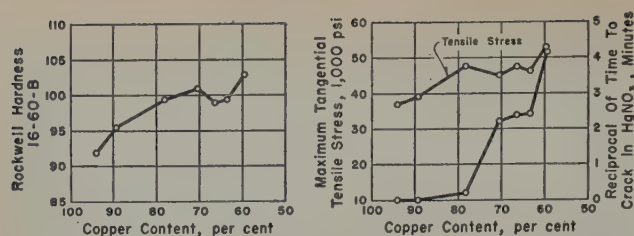


Fig. 3—Effect of copper content on the magnitude of the residual tensile stress, the Rockwell hardness, and the tendency to season crack in brass tubes sunk from 1.0x0.060 in. to 0.813 in. D. K. Crampton.⁶

relatively simple shape of the tube. The investigation revealed that the residual stress level in the tubes, resulting from the manufacturing process, was extremely high, in many cases as high as 65,000 psi tension, the yield strength of the alloy. This level of residual stress was so high that cracking occurred after a period of time, even when painted tubes were exposed only to ordinary atmospheric conditions. All efforts to prevent cracking by protective films proved futile, and this problem was solved by altering the manufacturing practice to reduce the magnitude of the residual stresses. The change involved was to heat treat after the tube was drawn square, so as to alleviate the residual stresses introduced by drawing from the round to the square shape. No further cracks were encountered in service after this practice was adopted; however, some reduction occurred in the final mechanical properties of the tubes.

This example concerned residual stresses in an aluminum alloy product. However, the occurrence of detrimental residual stresses is not restricted to aluminum alloys but may be characteristic of any metal subjected to certain fabricating conditions. In fact, probably the first recognition of residual stress effects and the principal impetus to the early work in this field resulted from the premature failure in service of brass products possessing residual stresses. Cracking was observed to be most pronounced in cold-worked brasses and to occur occasionally even in the absence of applied loads. This phenomenon, known as season cracking, was detected in brass and copper alloy tubes, Fig. 2, but later was found to occur occasionally in other metals.

Season cracking in brass may be initiated by vibration, oxidation, weathering, and especially by attack of ammonia or compounds of mercury. The cracking tendency in brass increases with the content of zinc (with brasses containing over 20 pct zinc) and depends upon the magnitude of residual stresses.⁶ Fig. 3 from Crampton shows the relation of the composition of brass tubes to the tendency to crack, while Fig. 4 illustrates the effect of the degree of sinking on the magnitude of the residual tensile stress (mechanically produced) and the tendency to season crack in high brass tubes.⁶ Because of the unsatisfactory character of the data procured from the earlier mechanical sectioning methods of stress analysis, the exact relation between the magnitude or distribution of the residual stress and the tendency to crack has not yet been determined. One expert claimed that a certain type of stress is significant, while another considered that a specific type of stress distribution is detrimental. However, the practical solution to the problem was attained by the selection of immune brass compositions and the introduction of annealing treatments at temperatures that did

not produce appreciable softening but reduced the residual stresses to values which were within safe limits.

Residual stresses are produced in the cold drawing of steel rods, and may be high under certain conditions. They may even cause failure of the rods when service stresses are imposed along with even slight corrosive attack, or during machining. The residual stresses can be decreased by slight heating (softening) after drawing; however, this may result in an undesirable reduction in the strength and hardness which were provided by the drawing. A recent investigation⁷ revealed that a different distribution of residual stresses could be obtained in drawing steel rods than was previously experienced. Thus, compressive stresses in the interior and tensile stresses in the exterior zones of drawn rods were observed in former experiments. However, Bühler found that the reverse could be obtained, with slight reductions in cross section, by drawing in the opposite direction or pushing through the die. This practice was utilized to reduce the magnitude of residual stresses of drawn rods without any sacrifice in the mechanical properties. Thus, a 0.19 pct carbon steel possessed an 80,000 psi longitudinal tensile stress and 46,000 psi tangential tensile stress at the surface after drawing from 1.9 to 1.8 in. diameter. A subsequent cold reduction of 2.2 pct obtained by pushing through the die, reduced these values to 15,000 and 10,000 psi, respectively.

Among the frequent sources of failure in hardened steel are quenching cracks, Fig. 5. The origin of cracks during quenching of tool steels from the heat-treating temperature was investigated by Scott,⁸ who demonstrated that the cracks occurred at surface locations where tensile stresses existed. Scott concluded that tensile stresses at the surface were the result of expansion during the transformation. This effect was more prominent in the specific steels investigated than the stresses formed by deformation arising from contraction on cooling. Scott was able to recommend practical expedients for the control of residual stresses in tool steels and to minimize the quenching cracks. The familiar grinding cracks in steels were also demonstrated by Scott to be the result of tempering of the surface under the grinding wheel, reducing the volume of surface metal and thereby producing surface tensile stresses. Again the cracks occurred in surface layers where high tensile stresses existed.

Methods of Measuring Residual Stress

Residual stresses are generally measured by either mechanical or X-ray methods, although other means have been employed. Unfortunately, the mechanical methods, although extensively used, are destructive in that the procedures consist of removing metal by machining, sawing, drilling, grinding, or etching, and measuring the resulting elastic deformation of the remaining section. X-ray analysis of residual stresses, although nondestructive, has the disadvantage of giving only approximate surface stresses. Surface stresses are often important, but in many applications it is equally necessary to determine the distribution and magnitude of residual stresses in the interior of the section.

In this lecture it is only possible merely to enumerate the available methods for measuring residual stresses, and not to give a detailed description of the theory and techniques of the various procedures. Excellent reviews have been published by Barrett,⁹

Ford,¹⁰ Baldwin,¹¹ Horger,¹² Sachs,^{1, 13} and Lynch,¹⁴ and in the other references to be subsequently cited. Emphasis will be directed toward the methods that are applicable to differently shaped fabricated products, such as solid cylinders, thick or thin-wall tubes, rods, bars, or plates, and to an appraisal of the accuracy of the methods.

Methods for Solid Cylinders and Thick-Wall Tubes: The residual stresses in solid cylinders and thick-wall tubes have been successfully determined by numerous investigators by the Sachs method.^{1, 13, 15} The procedure consists of boring on a lathe or drilling out, in small cuts, the interior of a solid cylinder or tube having a length at least three times its

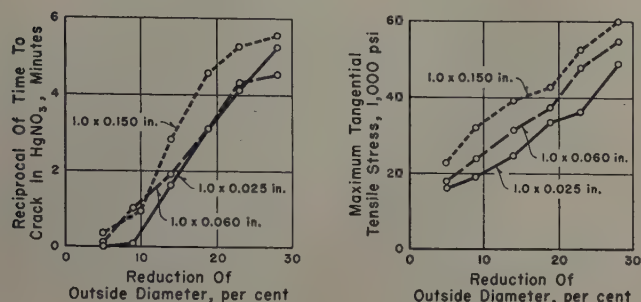


Fig. 4—Effect of degree of reduction by sinking on the magnitude of the residual tensile stress and the tendency to season crack in high-brass tubes. D. K. Crampton.⁹

diameter, and measuring the elastic deformation resulting from each boring operation. The recent use of SR-4 electrical strain gages, cemented longitudinally and circumferentially on the exterior surface of the cylinder, has appreciably improved the accuracy of the measurements.

This method permits determination of the three principal stresses in a cylinder. The equations formulated for these stresses are based on the slopes of the curves obtained by plotting deformation (measured changes in dimensions) against bored-out cross section, and are, therefore, subject to some error. Bühler and Schreiber¹⁶ developed a procedure wherein an analytical rather than graphical development of the curves from the data points was employed in an effort to obtain more precise values for the slopes.

With appropriate modifications, the method can also be applied to the removal of metal from the outside surface of a tube or partially bored-out cylinder. Hanslip¹⁷ developed a technique for locating SR-4 gages on the inside surface.

Method for Longitudinal Stresses in Rods, Tubes, and Rails: Where the dominant residual stresses in rods, tubes, and rails are longitudinal in direction, the stresses can be determined easily, although only approximately, by slotting the member longitudinally into many strips of small cross section and measuring the change in length of each strip individually.¹⁸

Methods for Thin-Wall Tubes: Residual stresses in thin-wall tubes can be obtained by rather simple methods,¹⁹ if the stresses consist of high tensile stresses at the inner or outer surface and high compressive stresses at the other surface. Tangential stresses are evaluated from the change in diameter that occurs at mid-length when a section of tube having a length of at least three diameters is split longitudinally. The deflection resulting from the cut-

ting of a circumferential tongue can also be used. Longitudinal stresses can be obtained from the deflection of a longitudinal tongue. It is generally accepted that the results procured by this procedure permit only an approximate evaluation of the stresses in the tube even when the stresses approach a linear distribution through the thickness. The results are considered to be inaccurate for nonlinear stress distributions.

A more elaborate quantitative method for the determination of residual stresses in thin-wall tube extends the simple procedure described to specimens from which successive surface layers have been removed by machining or etching.

Methods for Bars and Plates: Various methods have been proposed to investigate the stresses in bars and plates. Where the stresses are reasonably uniform through the thickness of a plate, a suitable number of small pieces, oriented in the direction of the principal stresses, are cut from the plate. Each section should contain appropriate gage marks or SR-4 strain gages on which measurements are made before and after the removal of the pieces.^{20, 21} If each piece contains only a single gage line, the sections should always be cut in pairs normal to each other, in order to evaluate the biaxial stress conditions in the plate. Another practice is to employ double gage lines, perpendicular to each other, inscribed on each piece. When the directions of the principal stresses are unknown, a rosette method is used with three or more strain measurements made at appropriate angles to each other to permit determination of the magnitude and direction of the principal stresses. Agreement has not yet been reached as to the most satisfactory type of cut-out pieces for this method.

When the stress distribution through the thickness of a bar is desired, the usual procedure is to remove layers from one side of the bar by machining or etching and measure the elastic deformation of the bar after the removal of each layer.^{22, 23} The deformation of the bar can be determined either by a

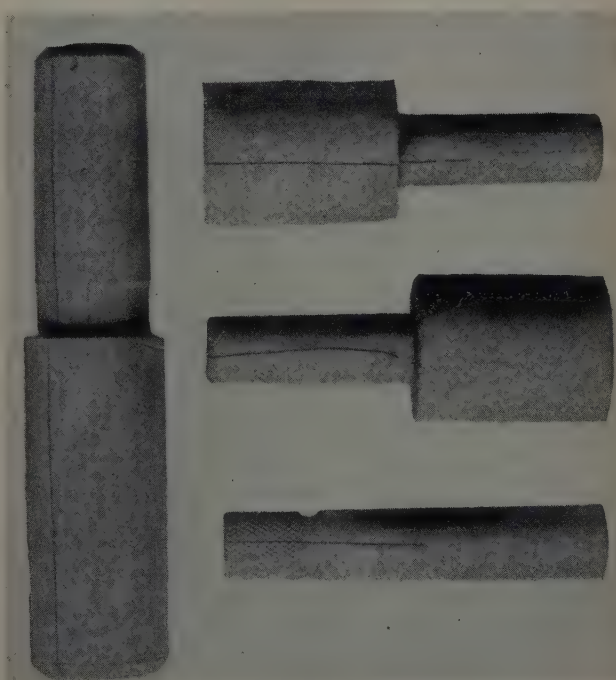


Fig. 5—Quenching cracks in hardened steel plug gages. Cracked from tensile stress at the surface. Deep etched to develop cracks. H. Scott.⁸

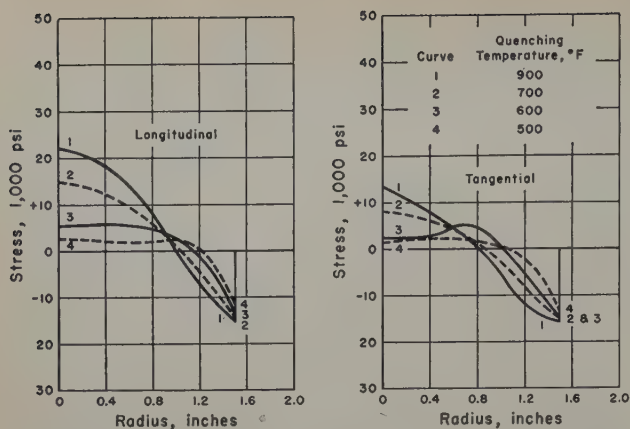


Fig. 6—Effect of quenching temperature on the magnitude of the residual stresses in alloy 56S cylinders, 3.0x9.0 in., quenched in water at 76°F.

sagitta gage, which measures the middle ordinate of a known chord, or by SR-4 gages cemented to the side opposite to the one being machined.

Combinations of these methods can also be adapted for the determination of residual stresses throughout the thickness of a plate.²⁴ Narrow blocks are removed from the plate in the directions of the principal stresses, and then the strains remaining in the blocks are relaxed by removing thin layers from one side. By adding to the residual strain distribution (obtained from the layer-removal method) the strain distribution relieved when the block is removed from the plate, it is possible to calculate the residual stresses. By selecting blocks in two or more directions, the biaxial stress conditions in the original plate can be evaluated.

In the case of sheet, the magnitude and distribution of biaxial stresses through the thickness may be determined by removing thin layers from one surface of the sheet and measuring the change in curvature of the sheet in the direction of the principal stresses.²⁵

Methods of Determining Residual Stresses by Measuring Deformation Around Drilled Holes: A mechanical method for determining residual stresses which does not completely destroy the part to be investigated was devised by Mathar.²⁶ Basically, the procedure consists of drilling a hole and measuring the deformation on the surface of the metal adjacent to the hole. Mathar employed a mechanical extensometer, and therefore the precision of the results may be questioned. Subsequent work indicated that the use of electrical-resistance strain gages offers more promise for this method. At present, the procedure is restricted to surface stresses or to applications where the stresses are approximately uniform through the thickness.^{26, 27} The method has not as yet been extended to the determination of stress distribution where the values vary with depth.

A rapid qualitative survey of residual stresses can be obtained by the use of brittle lacquer to reveal the nature of the stresses relieved by drilling a hole.²⁸ This procedure will indicate the locations of appreciable residual stresses, the directions of the stresses, and the type of stress at each point.

X-ray Diffraction Methods: The X-ray diffraction method for measuring residual stresses has received considerable attention in recent years.²⁹⁻³¹ In this procedure it is possible to measure the distance between atoms in metal crystals; the interatomic dis-

tance is then used as a gage length for the determination of elastic strains. There are numerous modifications that permit the measurement of the sum of the principal stresses at the surface, or the stress component in any direction in the surface layer, or the direction and magnitude of the principal stresses at the surface. The method has the advantage of being nondestructive but is limited to determining the stresses at the metal surface. At-

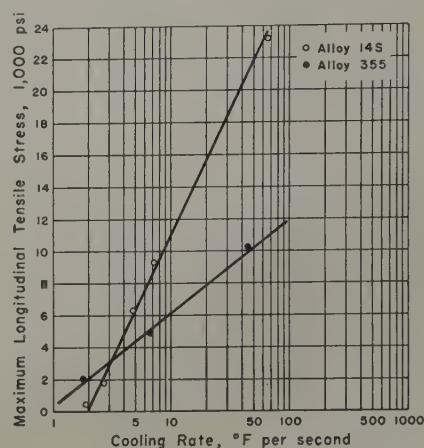


Fig. 7—Effect of quenching rate on the maximum residual longitudinal tensile stress in alloy 14S and 355 cylinders, 3.0x9.0 in., quenched from 935° and 980°F, respectively, in various media.

tempts have been made to measure stresses below the surface by determining strains at the bottom of a drilled hole, but it is thought that such a procedure is not reliable because of the stresses relieved by drilling the hole, and the possible localized deformation of the metal during machining.

Other Methods: Methods other than mechanical or X-ray diffraction have occasionally been utilized to determine residual stresses. Measurements of magnetic properties, electrical resistivity, and internal friction have been used and are, in general, qualitative in nature.³²

Critical Appraisal of Methods for Measuring Residual Stresses

The mechanical methods of determining residual stresses require that the stress equilibrium be disturbed and readjusted by removing metal, and the resulting elastic deformation of the remaining section measured. It is realized, of course, that the mechanical methods are accurate only if no stresses are introduced or relieved by the removal operation itself. Since the metal is generally removed by machining, sawing, drilling, boring, or grinding, some doubt exists as to the reliability of the results obtained from these methods.³³ Etching has been employed to remove metal, but there is the possibility of chemical attack along the grain boundaries of a surface containing residual tensile stresses, which would relieve stresses to a greater depth than intended.

The machining operations used in the mechanical methods tend to increase the temperature of the part being machined. Precautions should be exercised to reduce to a minimum any change in temperature. It is also important that the strains be measured at a constant temperature or that adequate

corrections be applied for any room temperature variations.

Where residual stresses are determined by the removal of successive layers, it is assumed that the stress is uniform throughout the thickness of the layer. This assumption may cause erroneous results where a sharp stress gradient exists. Such gradients occur, for example, at a shot-blasted surface where the stress changes from a high residual compressive

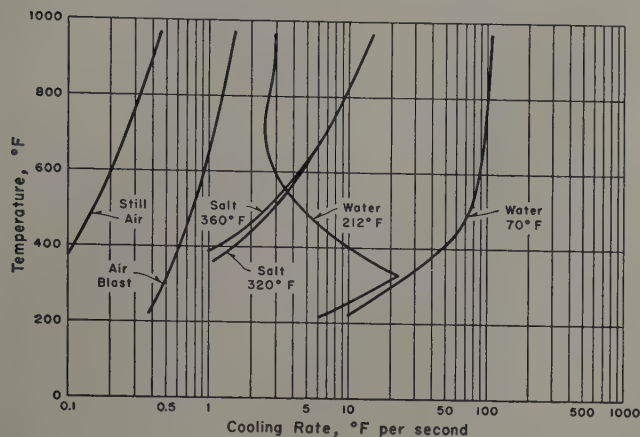


Fig. 8—Cooling rates on alloy 61S sections, 2.25x3.0x7.0 in., quenched from 970°F in various media.

stress at the surface to a relatively low tensile stress at a distance of about 0.020 to 0.030 in. below the surface. Steep stress gradients may also exist on the surface of roller leveled plate. When the stresses in such a plate are determined by removing small sections from the plate, it is desirable that the piece be as small as possible. One limitation on the length of the piece is the gage length by which the strains are measured. For this reason, electrical-resistance strain gages, having an effective gage length as small as 0.06 in., offer a decided advantage over the hand-type mechanical strain gages, where the smallest gage length available for this type of work is about 2.0 in.

The mechanical methods of measuring residual stresses are based on various assumptions, and therefore it is imperative that the limitations of the different procedures are recognized. For example, the Sachs boring-out method, requiring the selection of a cylinder or tube having a length at least three times its diameter, assumes that the stresses have rotational symmetry about the axis and are uniform along the length. If this were not the case, the results would represent only some mean value of the actual stresses.

Not only will the accuracy of the results obtained by the mechanical methods vary with the procedure employed, but the accuracy will also be affected by the dimensions or geometry of the piece to be investigated and the magnitude and distribution of the stresses. For example, the residual stresses were determined in a 0.5x0.75x6.0 in. block from alloy 75S-W as-heat-treated rolled plate by the layer-removal method. Successive layers were machined from the 0.5x6.0 in. surface, the thickness of the first layer being 0.025 in. The strain relaxed on the side opposite the one being machined by the removal of the first layer was 100 microin. per in., equivalent to an average of 14,000 psi compression in the layer removed. Calculations revealed that if the error in

this measured strain was ± 10 microin. per in. and the error in measuring the thickness of the block before and after the removal of the layer was ± 0.0005 in., the residual compressive stress in the layer removed would be between 12,000 and 16,000 psi.

Since the X-ray method is restricted to the measurement of stresses on the surface, and the mechanical methods require extrapolation of stresses to the surface, it is difficult to compare the two procedures and appraise the relative accuracy. The X-ray method requires a refined technique in preparing the metal surface and in making the measurements. The metal must be fine-grained, of uniform composition, and free of minute stress variations. If the grain size is too large, the diffraction lines are spotty or not of uniform width, and therefore cannot be measured precisely. On the contrary, a grain size which is too fine produces broad lines and consequent inaccuracy. Thomas³⁰ compared the stresses measured by X-rays in steel with mechanically imposed stress values and found that the stresses obtained from the X-ray were about 30 pct higher than those calculated from the actual loads. Some of the possible sources of error in the X-ray method were encountered in this investigation, so that the total discrepancy may not be representative of the optimum conditions for X-ray diffraction. Under conditions giving sharp diffraction circles, the line widths can be measured with a precision of about ± 0.01 in., representing an accuracy in stress values of $\pm 1,500$ psi. As the line becomes broader, the precision decreases considerably.³⁰

Effects of Fabricating Practices on the Residual Stresses in Aluminum Alloys

The majority of the investigations involving the determination of residual stresses in fabricated metal products was initiated because of the failure, cracking, or excessive distortion of a part, and the possibility that residual stresses contributed to, or were responsible for, the difficulty. Thus, exhaustive qualitative investigations have been conducted on axles, gears, propellers, spars, tubing, and weldments. In general, mechanical methods of stress analysis were employed, and usually the results culminated in the adoption of a different fabricating practice. There have been few quantitative investigations of the effects of various fabricating conditions and metallurgical factors on the magnitude and distribution of residual stress in metals published in this coun-

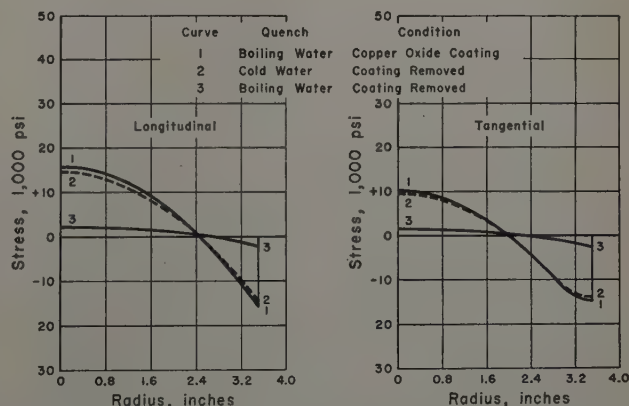


Fig. 9—Effect of surface treatment on the magnitude of the residual stresses in alloy 14S cylinders, 7.0x7.0 in., quenched from 940°F in boiling or cold water.

try. However, the literature reveals that there have been extensive investigations conducted on various steels in Germany.

This lecture will report briefly on an investigation of the effects of quenching temperature, quenching rate, section size, composition, and tensile properties on the magnitude of residual stresses in cast and wrought aluminum alloy products. In addition, the effects of reheating time and temperature on the magnitude and distribution of retained stresses will be discussed. Although the work was performed on aluminum alloys, the significance of the various fabricating factors and the general conclusions should apply to all metals. In the investigation, several hundred cylinders were analyzed by the Sachs¹⁵ boring-out method. The length of most of the cylinders was generally three times their diameter. The curved surfaces of the cylinders were machined and ground to a fine finish, while the bases were machined and finished on a lapping plate. The cylinders were measured in a constant temperature room on a comparator, standardized by the most precise type of gage blocks available. Special jigs were constructed

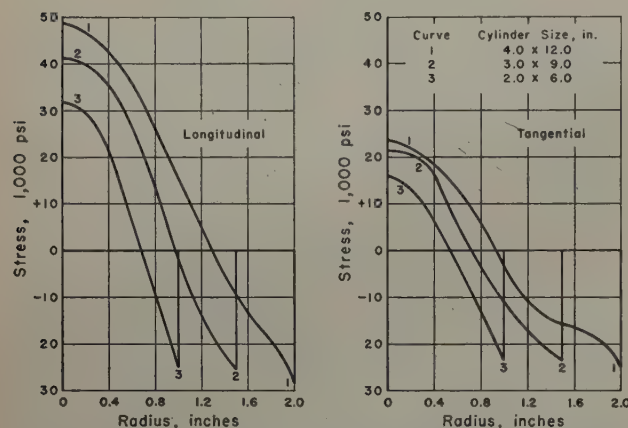


Fig. 10—Effect of section size on the magnitude of the residual stresses in alloy 14S cylinders quenched from 940°F in water at 70°F.

to hold the various sized cylinders rigidly during the boring operations. Care was exercised to use light cuts during boring, and auxiliary cooling was employed to prevent heating of the cylinders. The use of small cuts increased the number of measurements, thereby improving the accuracy of the data, although this practice added appreciably to the cost of the tests. The measured elastic deformations, resulting from the readjustment of stress equilibrium produced by the boring operations, were converted by the equations formulated by Sachs to longitudinal, tangential, and radial stresses. The stress distribution diagrams were all checked by planimeter measurements to determine if the stresses balanced.

Inasmuch as the high strength aluminum alloys are solution heat-treated at relatively high temperatures, the residual stresses formed during the fabrication of castings, bars, extrusions, forgings, etc. are relieved during the heat treatment. However, the quenching or cooling from the solution heat-treating temperature produces residual stresses which may be either large or negligible, depending on the various factors which will be discussed. The resulting stress pattern or distribution is always the same and relatively simple. Longitudinal and tangential compressive stresses exist in the exterior or

surface layers of solid shapes or cylinders, and tensile stresses in the core or center. The radial stresses are tensile at the axis and zero at the surface. The residual stress pattern of heat-treated hollow cylinders reveals longitudinal and tangential compressive stresses on both the exterior and interior surfaces with tensile values between. The residual stress distribution in sunk tube is, of course, different from that in quenched tube. The longitudinal and tangential stresses are tensile in the surface layers and compressive on the interior surface. The radial stresses are compressive in the intermediate layers and zero at the interior and exterior surfaces.

Effect of Quenching Temperature: The effect of quenching temperature on the magnitude of the residual stresses in alloy 56S** solid cylinders, 3.0x9.0

** The alloy and temper numbers in this paper refer to Aluminum Company of America designations. The compositions and temper treatments of the alloys are printed in the 1948 edition of *Metals Handbook* published by the ASM.

in., quenched in cold water at 76°F, is illustrated in Fig. 6. Alloy 56S, essentially a solid solution alloy at all temperatures, was selected for this experiment in order to eliminate precipitation effects during quenching. Varying the quenching temperature from 900° to 500°F decreased the rate of quenching and reduced the longitudinal and tangential compressive stresses in the surface layers of the cylinders by 25 and 13 pct, respectively, and both the longitudinal and tangential tensile stresses in the center by approximately 88 pct. The distribution diagrams also revealed that when the quenching temperature was 600°F or lower, the maximum tensile stress was displaced from the center of the cylinders.

Effect of Quenching Rate: The magnitude of the residual stresses in the quenched aluminum alloy cylinders depended directly on the cooling rate prevailing during the quench from the solution heat-treating temperature. The relation between the quenching rate and the magnitude of the residual stresses in alloy 14S and 355 solid cylinders, 3.0x9.0 in., quenched from 935° and 980°F, respectively, is represented in Fig. 7. In this illustration, only the maximum longitudinal tensile stress at the center of the cylinder was plotted. The highest residual stresses were produced when the cylinders were quenched in cold water, intermediate values when quenched in hot oil, molten salt, or hot water, and very low stresses when quenched in boiling water or by an air blast. The various quenching media employed (cold water, boiling water, oil, moving air, etc.) produced different cooling rates ranging from approximately 100°F per sec to 2°F per sec. Fig. 8 shows the cooling rates obtained for alloy 61S sections, 2.25x3.0x7.0 in., quenched from 970°F in various media.

The significant effect of the quenching rate on the magnitude of the residual stresses was again clearly demonstrated in an investigation of surface treatments on alloy 14S solid cylinders. A cylinder with a surface layer of black copper oxide, produced by the reaction of an alkaline etchant, was found to have the same cooling rate when quenched in boiling water as that of a cylinder with the coating removed when quenched in cold water. The cylinders were quenched from 940°F. Stress analysis revealed that the magnitude and distribution of the residual stresses in the two cylinders were identical, Fig. 9. This marked effect on cooling rate and stress magnitude is attributable to the wettability of the copper oxide coating. The residual stress pattern for a

similar sized cylinder with the coating removed, that was quenched in boiling water, is also included in Fig. 9.

Effect of Section Size: The effect of section size on the magnitude of the residual stresses was investigated in 2.0x6.0, 3.0x9.0, and 4.0x12.0 in. alloy 14S cylinders quenched from 940°F. Increasing the section size of cylinders quenched in water at 70°F appreciably increased the maximum longitudinal, tangential, and radial tensile stresses, and to some extent the maximum longitudinal compressive stress. The maximum tangential compressive stress values remained about the same, Fig. 10.

This effect of section size on the magnitude of the residual stresses is partially explained by the data³⁴ in Fig. 11, which records the temperatures at the center of a 0.75 in. diam rod, and at the center and other locations in a 4.0 in. diam rod, of alloy 75S during quenching from 875°F in water at 70°F. The curves show a marked temperature gradient in the 4.0 in. rod during the quench. It is revealed that the center of the 0.75 in. rod cooled much more rapidly than the center of the larger rod, in fact even faster than the surface zone of the larger rod. It may be

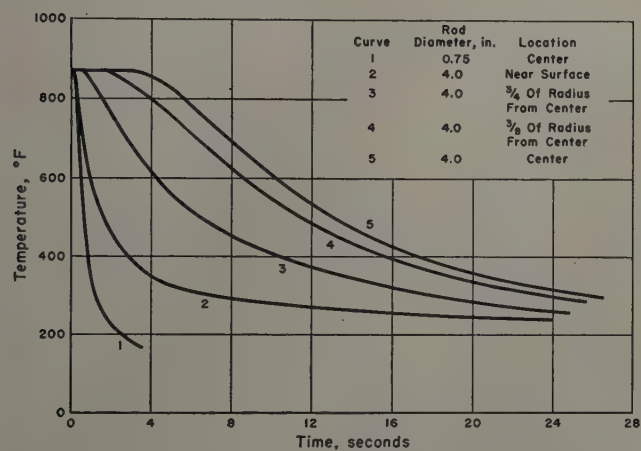


Fig. 11—Cooling curves for 0.75 and 4.0 in. diameter extruded alloy 75S rods quenched from 875°F in water at 70°F. Thermocouples located at various distances from center of 4.0 in. rod. W. L. Fink and L. A. Willey.³⁴

concluded that this would result in a greater, and certainly more prolonged, differential in temperature between the surface and interior zones in the larger rod than in the smaller. Thus, higher stresses would be expected in the larger rod, since the temporary difference in temperature between the center and surface zones is the basis of the formation of thermal stresses, as explained in the introductory pages of this lecture.

The effect of section size can be definitely minimized by employing a slow quenching rate, such as that provided by boiling water, Fig. 12. A comparison of Figs. 10 and 12 demonstrates the advantage of a boiling water quench for obtaining a low level of residual stress. The benefit of the boiling water is ascribed to the slow cooling rate in the critical cooling range, resulting from the prolonged occurrence of the vapor phase or envelope surrounding the cylinder.

Effect of Composition: The magnitude of the residual stresses in the solid cylinders varied considerably with the different cast and wrought aluminum alloys. Cylinders, 3.0x9.0 in., of all the alloys were quenched from the respective commercial

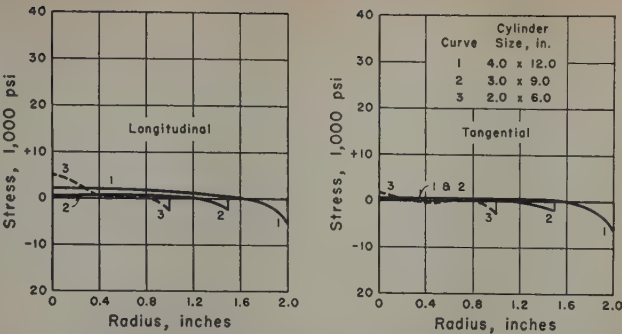


Fig. 12—Effect of section size on the magnitude of the residual stresses in alloy 14S cylinders quenched from 940°F in boiling water.

heat-treating temperatures in boiling water or water at 70°F.^{***} The stresses developed were considered

^{***} The cold water quench at 70°F was employed to evaluate the effect of composition factors and does not represent commercial practice for aluminum alloy castings and forgings. Therefore, the residual stresses indicated in Figs. 13 and 14, resulting from quenching alone, are appreciably higher than expected in commercial castings and forgings.

to depend on several properties or characteristics of the specific alloy. Thus, for a given strain, the higher the value for Young's modulus of elasticity, or the greater the proportional limit and yield strength of the alloy, the higher were the residual stresses, providing the other properties did not vary. Other properties which would be expected to contribute to a large strain, and therefore higher stresses, are: a high coefficient of thermal expansion, a low thermal diffusivity,[†] and a high elevated temperature yield strength.

$$\dagger \text{ Thermal diffusivity} = \frac{\text{Thermal conductivity}}{\text{Specific heat} \times \text{density}}$$

The composition factors appeared to vary in their relative influence on the magnitude of the residual stresses that were developed in the various aluminum alloy cylinders. The coefficient of thermal expansion seemed to be one of the most significant properties. For example, alloys 32S and A132 have fairly high yield strengths and the highest modulus of elasticity values, but the lowest coefficients of thermal expansion, and the stresses developed in these alloys by a water quench at 70°F were the lowest for any of the aluminum alloys investigated (17,900 psi and 20,700 psi maximum longitudinal tensile stress, respectively). Furthermore, alloy 220 with the lowest modulus of elasticity value but the highest coefficient of thermal expansion, developed high residual stresses (39,400 psi maximum longitudinal tensile stress).

The elevated temperature yield strength also appeared to be one of the potent factors. For example, alloys 14S and 142, with average values for the coefficient of thermal expansion, modulus of elasticity, and thermal diffusivity, but very high elevated temperature yield strengths, developed the highest residual stresses, when quenched in water at 70°F; of any of the aluminum alloys tested (41,250 psi and 42,950 psi maximum longitudinal tensile stress, respectively).

Effect of Tensile Strength: It is recognized that the yield strength of an alloy at that temperature during quenching, when plastic flow is completely arrested, is a significant factor affecting the magnitude of residual stresses, but such data are not available. However, some engineers may raise the

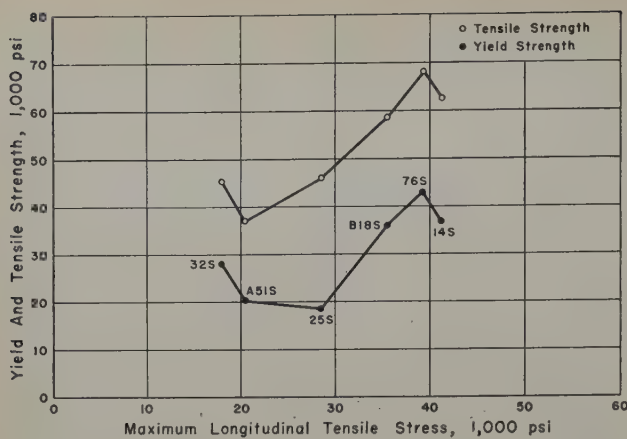


Fig. 13—Relationship of yield and tensile strength (-T4 condition) and maximum residual longitudinal tensile stress in cylinders, 3.0x9.0 in., of various aluminum forging alloys quenched from the respective commercial heat-treating temperatures in water at 70°F.

question of a relationship between residual stresses and the tensile and yield strength at room temperature. Therefore, tensile data were also obtained during the investigations of the effect of fabricating conditions on the magnitude of the residual stresses. Additional cast or wrought solid cylinders of the size used for stress analysis were simultaneously subjected to the same heat-treating, quenching, and room temperature aging procedures. Tensile test bars were machined from identical locations in the cylinders. In general, the tensile properties decreased as the rate of quenching was reduced and as the section size was increased. The magnitude of the decrease varied with the alloy. The results seemed to reveal a trend that the alloys having the higher tensile values, that is, those in the T4 condition,† contained the higher residual stresses, Figs. 13

† Quenched from solution heat-treating temperatures in water at 70°F and aged at room temperature. The aging time was three days for the casting alloys and five days or more for the wrought alloys.

and 14. This relationship was more apparent for the forging than for the casting alloys.

Distortion During Machining: When the balance between relatively high residual stresses in metal products, especially those having heavy or thin sections, is disturbed by machining, undesirable distortion or dimensional changes may result. Thus, for example, airplane cylinder muffs of alloy 142 distorted to such an extent during rough machining that the final finishing operations could not be performed. Measurements of residual stress revealed a maximum tangential compressive value of 14,000 psi in the 8.5x5.5 in. cylinders, quenched from 960°F in water at 90°F and stress-relieved 9 hr at 525°F, Fig. 15. Adoption of a boiling water quench reduced the residual stresses to a negligible amount and eliminated the distortion problems.

Difficulties were experienced by several customers in the textile industry, from distortion during the machining of extruded shapes of some of the heat-treated aluminum alloys. In some cases, the distortion was so severe that the shape was unsuitable for the intended use. An investigation was therefore conducted on the aluminum alloys 14S-T6, 61S-T6, and 75S-T6 to evaluate various methods of reducing the residual stresses which were thought to be the cause. The effect on residual stresses of quenching rate from the solution heat-treating temperature was investigated for the following quenching media:

cold water, cold water spray, boiling water, light oil at temperatures ranging from 70° to 264°F, and an air blast. Different degrees of stretching before artificial aging and reheating treatments after aging were also evaluated.

Since this investigation was concerned principally with deformation during the machining operation, no attempt was made to determine the residual stresses quantitatively. Instead, a procedure was developed which permitted the direct measurement of the distortion of specimens (a complex extruded shape 10 in. in length) resulting from a longitudinal saw cut. All samples were subjected to the same sequence of saw cuts, and the average deformation of several cuts on several specimens was used to measure the tendency to distort during machining.

The type of quench was found to be highly important, with the boiling water quench best and the cold water quench the poorest from the standpoint of distortion. Unfortunately, however, the boiling water quench, because of section size involved, appreciably lowered the mechanical properties of the alloy. Stretching the product was found to be generally effective in reducing the distortion, but stretching alone was in no case sufficient. Reheating

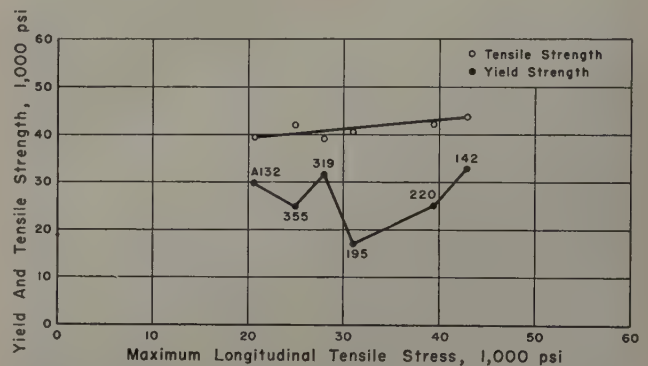


Fig. 14—Relationship of yield and tensile strength (-T4 condition) and maximum residual longitudinal tensile stress in cylinders, 3.0x9.0 in., of various aluminum casting alloys quenched from the respective commercial heat-treating temperatures in water at 70°F.

the product after artificial aging, in the range where the tensile properties would not be seriously impaired, did not significantly decrease the distortion.

After an appraisal of the results of this investigation and considerable experimental work in the fabricating plants, a special metallurgical technique was devised which resulted in sufficiently uniform mechanical properties throughout the cross section so that a controlled stretching operation gave an acceptably low degree of distortion during machining without affecting the final strength of the product. The temper produced by this process is known as -T64 and it applies only to alloy 14S extruded shapes. This product can be used with the assurance that machining operations will not produce any serious distortion.

The cylinder muff and the extruded shape problems illustrate applications where rather high residual stresses were responsible for distortion or change in dimensions of the part during machining. The extent of warpage resulting from residual stresses is also influenced by the design or size of the part. Important factors are a large variation in sectional thickness or high ratio of width to length dimensions and the character and sequence of the machining

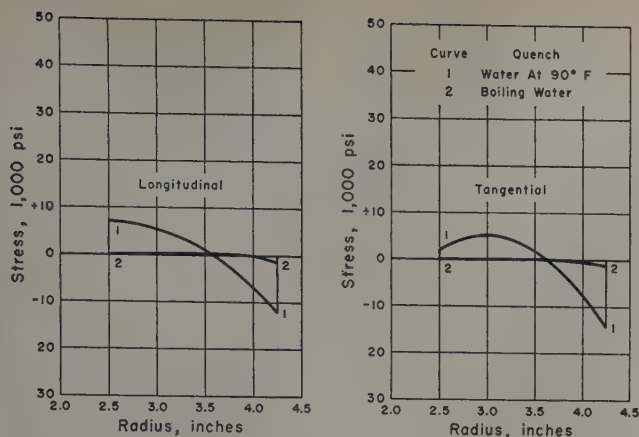


Fig. 15—Effect of quenching rate on the magnitude of the residual stresses in alloy 142 airplane cylinder muffs, 8.5x5.5 in., quenched from 960°F in water at 90° and 212°F and subsequently stress relieved 9 hr at 525°F.

operations. In such instances, intermediate straightening may be necessary, and it is preferable to avoid machining to finished dimensions from one side only. An attempt should be made to balance the machining operations, leaving sufficient allowance to compensate for any final straightening found necessary. However, the residual stress level may be relatively low, but nevertheless substantial warpage may occur during machining or on removal of the part from the clamping device as the result of improper tools or machining practices.

In addition to residual stresses, there are several other sources of distortion or change of dimensions during machining. Careful consideration should be given to cooling the part during machining operations if precise dimensions are to be attained. Aluminum alloys have a high coefficient of thermal expansion, and therefore adequate cooling practices should be employed.

An important cause of distortion in many machining operations is improper jiggling or chucking of the part, so that it is elastically deformed or sometimes even stressed beyond the yield strength. Since a good mechanic would adequately tighten the clamps that hold the part during the machining operation, the fixture should be so designed that such tightening does not deform the part. Very high stresses can be produced by improperly designed fixtures, and the stresses may be redistributed in subsequent machining operations. If the part is overheated during machining, the yield strength is reduced by the temperature and, furthermore, the strains imposed by the fixture may be higher. The distortion occurs during machining or upon removing the part from the fixture. Considerable experience in the field has indicated that more distortion or warpage in cast aluminum alloy parts and some forgings has resulted from this cause than from any of the other sources.

Distortion or change in dimensions of parts as the result of permanent growth in aluminum alloys is thought by some to occur at room temperature or on reheating to temperatures up to 300°F. Growth is caused by an advanced stage of precipitation of constituents in the alloy, and definitely does not occur at room temperature. In fact, extensive tests have demonstrated that no significant changes in dimensions have been detected in aluminum alloys from growth, at room temperature or at slightly elevated temperatures. Therefore, the tendency to

grow is not a source of change in dimensions during machining or in subsequent storage.

Stress Corrosion Cracking: High residual stresses are known to be an important contributing factor in the phenomenon of stress corrosion cracking. Several applications were previously described where the presence of excessive residual stresses contributed to premature cracking or failure of the part in corrosive or natural environments. An interesting example of a quantitative stress analysis, that revealed high residual stresses promoting stress corrosion cracking, will be discussed.

An unusual type of failure was encountered in the early use of Alcoa 76S, an aluminum-zinc-magnesium forging alloy, for aircraft propeller blades of high strength and hardness with improved abrasion resistance. The propeller blade, having about a 6.0 in. diam shank, was forged solid, solution heat-treated, and artificially aged. Then a tapered hole about 17 in. in length was bored in the center of the shank with the diameter gradually decreasing from about 3.0 in. at the end of the shank as illustrated⁵ in Fig. 16. Large cracks occurred during service and were detected when oil from the variable pitch propeller mechanism leaked through the oil-retaining



Fig. 16—Stress corrosion fracture (within the dotted lines) of shank of a forged alloy 76S propeller, caused by high residual tensile stresses in surface layers of bored hole resulting from rapid quenching from 860°F. E. H. Dix, Jr.⁶

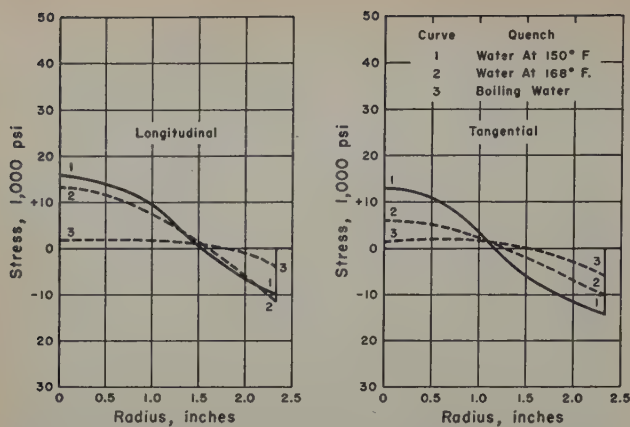


Fig. 17—Effect of quenching rate on the magnitude of the residual stresses in alloy 76S propeller hubs, 4.0 in. diameter x 4.0 in. long, quenched from 860°F in water at various temperatures.

ring into the bore. A crack and the stress corrosion fracture (within dotted lines) are shown in Fig. 16. An investigation revealed that the central portion of the original propeller hub contained high tensile stresses produced by the rapid quenching from the solution heat-treating temperature of 860°F in water at 150°F. The machining of the bore exposed layers at the surface of the hole having high circumferential tensile stresses.

Analysis of residual stresses in sections from alloy 76S propeller hubs, 4.0 in. diameter x 4.0 in. long, quenched from 860°F in warm water at 150° or 168°F and in boiling water revealed that the first two quenches produced a relatively high level of stress, whereas the boiling water quench resulted in low tensile stresses in the center, Fig. 17. Fortunately, alloy 76S is comparatively insensitive to the rate of quenching, and satisfactory mechanical properties can be obtained with the less drastic boiling water quench. This investigation resulted in the commercial adoption of a boiling water quench. As an additional precaution, the propeller manufacturer shot-peened the surface of the drilled bore. The shot peening reduced any possibility of a high interior surface tensile stress and may have imposed a compressive stress. After the introduction of the two procedures, no stress corrosion cracking was experi-

enced, and hundreds of thousands of 76S-T61 propeller blades have been in successful service, beginning in 1942.

Relief of Residual Stress by Thermal Treatments

To insure proper selection of conditions for obtaining optimum combinations of mechanical properties, resistance to corrosion, volumetric stability, and freedom from residual stress problems in heat-treated aluminum alloys, it is desirable to acquire data on the effect of time and temperature on the rate of relief of residual stress. The magnitude of the residual stress can be reduced to a satisfactorily low level by reheating to a temperature at which sufficient plastic flow can occur. However, such stress-reducing methods are not practical in all cases because of the sacrifice in other important engineering properties.

It is recognized that the relief of residual stress involves the phenomenon of flow or creep. Creep characteristics, however, ordinarily are determined by measurement of rate of deformation at constant stress. The relief of residual stress is concerned with flow conditions at relatively constant deformation and decreasing stress. Flow under these conditions is sometimes referred to as relaxation. Relatively little investigational work has been done in this field. There are some indications of a quantitative relationship between relaxation and creep, but the data available at the present time are too meager to permit the definition of any correlation.

The Sachs boring-out method of stress analysis can be applied to the determination of the rates of relief of residual stress in metals. Thus, Kempf and Van Horn³⁵ presented curves showing the rate of stress relief in heat-treated solid cylinders of alloy 122 and in 52S-H34 drawn tubes for several reheating periods at a specific temperature. The curve for the tubes is reproduced in Fig. 18. Both stress-relief curves revealed that the initial reheating resulted in a rapid decrease of 25 to 50 pct of the original[‡] re-

‡ The original maximum residual stress was about 47,500 psi tension in the 122 alloy cylinders and 15,650 psi tension in the 52S-H34 tubes. Subsequent tests demonstrated that the time required to relieve a certain percentage of the residual stress at a specific temperature was independent of the magnitude of the original stress.

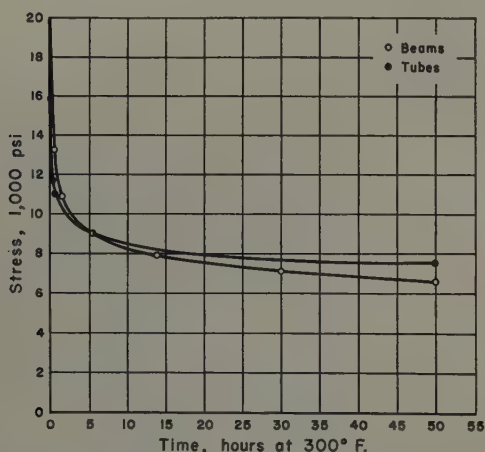


Fig. 18—Relief of stress at 300°F in 52S-H34 drawn tubes and externally loaded 52S-H34 beam specimens, original stresses 15,650 and 27,000 psi, respectively. Tubes 2.75 in. ID, 3.75 in. OD, 6.0 in. long. Beams, 0.25x0.06x12.0 in. Kempf and Van Horn.³⁵

sidual stress, and that further reduction occurred much more slowly on extended heating. In general, the higher the temperature of reheating, the greater the initial reduction in stress and the greater the rate of subsequent relief. It is important to observe that these stress-relief curves resemble the relaxation curves reported in the literature.^{86, 87} This immediately suggests that a measurement of the relaxation characteristics might be a convenient and more economical means than the Sachs method for determining rates of relief of residual stress in metals. Obviously, the Sachs method would require the careful boring and measurement of a large number of cylinders representing many different periods of heating at various temperatures for all the aluminum alloys. However, the quantitative determination of rates of relaxation is by no means simple, involving as it does the accurate measurement of a varying stress under conditions of relatively constant deformation; also determinations must usually be made at elevated temperatures.

Kempf and Van Horn³⁵ considered it sufficient to determine at room temperature the variations in stress, with time at elevated temperature, of specimens maintained during the entire operation at a constant deformation. To achieve this end, a fixture

was utilized that was developed by Dr. W. L. Fink. The fixture⁸⁵ consisted merely of a means for maintaining a small beam of rectangular cross section under constant deformation during reheating, the remaining stress to be measured subsequently at room temperature. Many measurements for different periods of time at a specific temperature can easily be obtained on the same specimen. These tests can be continued until the desired relaxation of stress is achieved. Thus, it is possible to determine the rate of stress relief in a relatively inexpensive manner for different temperatures and periods of time, and for various amounts of imposed stress. Fig. 19, reproduced from this investigation,⁸⁵ illustrates data obtained for the relief of several imposed stresses in alloy 122 beams at 435°F for various time periods. Data for several aluminum casting alloys heated at different temperatures were also included in this paper.

Similar stress-relief surveys can be obtained for any metal. Thus, Fig. 20 from Stewart⁸⁸ represents the effect of tempering temperature on carbon steel

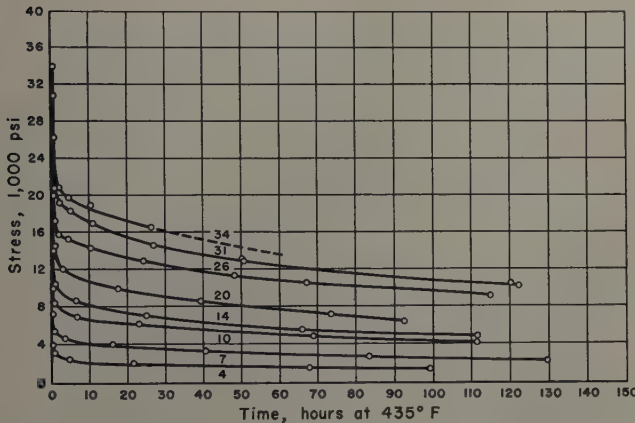


Fig. 19—Relief of stress in beam specimens, 0.25x0.06x12.0 in., of alloy 122 at 435°F. Curves show stress-time relationship for different original loads indicated. All specimens air-cooled from 930°F. Kempf and Van Horn.⁸⁵

boiler plate prestressed in tension to 25,000 psi for various periods of time. In Fig. 20, the stress was constant, while in Fig. 19 the temperature of stress relief was the same for different imposed stresses.

A comparison of the results of the relaxation procedure with those of the Sachs method for determining the rate of stress relief is also shown in Fig. 18. Beam specimens were prepared from 52S-H34 sheet, stressed to about 27,000 psi and reheated for various periods of time at 300°F. The results are represented by open circles in Fig. 18. The curve for the rate of relief of residual stress in hard-drawn 52S-H34 tubes (stress 15,650 psi), determined by the Sachs method, is included in Fig. 18. The resemblance between the two curves is apparent, and undoubtedly is a result of essentially linear distribution of stress in the wall of the tube and, of course, in the stressed beam. Apparently a relationship exists between the rate of relief of residual stresses produced in the cold drawing of the tube and of the stresses imposed by external means in the beam method.

An even better correlation between the Sachs and beam methods for the determination of the rates of stress relief was obtained for alloy 14S. In this case, the residual stresses were produced by quenching

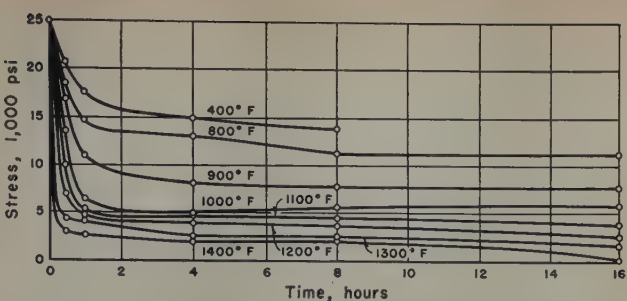


Fig. 20—Relief of stress in 0.5 in. diameter carbon steel specimens of boiler plate prestressed to yield (25,000 psi) before tempering. Curves illustrate stress-time relationship for different tempering temperatures. Stewart.⁸⁸

rather than by mechanical means. These stresses were relieved, measured, and compared with similar stress values in beams imposed by external loads. Fig. 21 shows the results for solid cylinders of 14S quenched from 940°F in water at 150°F and beams stressed to 24,600 psi. The maximum residual longitudinal tensile stress in the quenched 14S cylinders was the same, 24,600 psi. Both cylinders and beams were heated at 437° and 500°F for different periods of time. It was concluded that the beam method should have some utility in arriving at qualitative data for selecting optimum aging or annealing treatments for the various cast and wrought alloys.

Stress-time measurements have now been completed by the beam method for the majority of the cast and wrought aluminum alloys. The amount of stress relief was determined for initially applied stresses of 4,000, 7,000, 10,000 and 14,000 psi at various temperatures, depending on the alloy, for time intervals of minutes up to 100 hr. A typical example of the results for all the original stresses is represented in Fig. 22, including a number of cast and wrought alloys heat-treated at the respective commercial temperatures, quenched in boiling water, and reheated at 482°F, for different time periods. The alloys exhibited different rates of stress relief, showing that composition has an important effect.

In all cases, an appreciable proportion of the stress relief occurred during the first hour of heating. The higher the temperature the greater was the rate of stress relief, both during the initial and subsequent

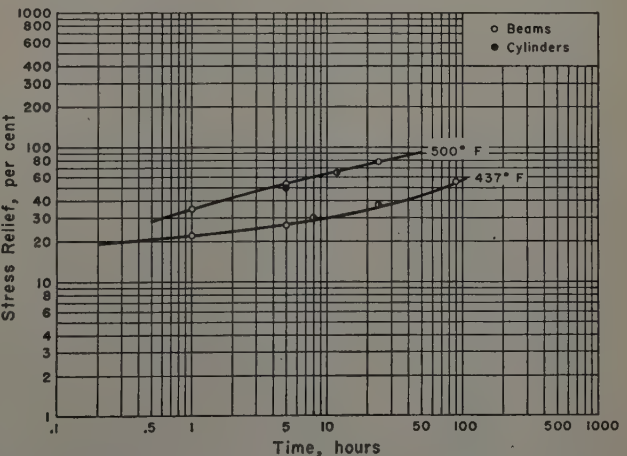


Fig. 21—Stress relief at 437° and 500°F for alloy 14S cylinders, 3.0x9.0 in., and beam specimens, 0.25x0.06x12.0 in., quenched from 940°F in water at 150°F. Maximum residual longitudinal tensile stress in quenched cylinders 24,600 psi and original tensile stress in beams 24,600 psi.

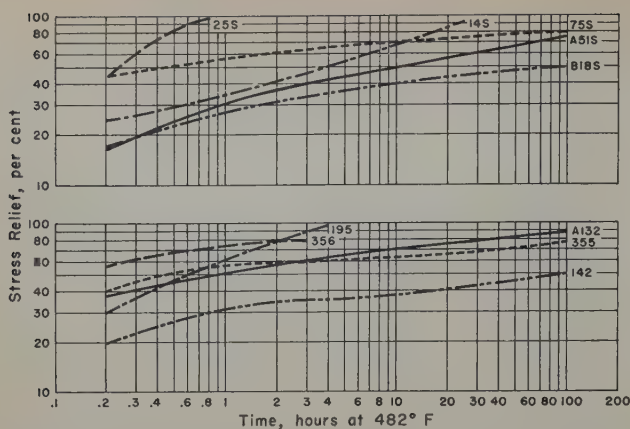


Fig. 22—Relief of stress in beam specimens of various cast and wrought aluminum alloys at 482°F. Original stresses were 4,000, 7,000, 10,000, and 14,000 psi. Beams 0.25x0.06x12.0 in., quenched from the respective commercial heat-treating temperatures of the alloys in boiling water.

heating periods. The stress-time data obtained at the various temperatures for all the alloys demonstrated that in order to obtain a low level of residual stress by relaxation heat treatments, the temperature is more important than the time factor. The effect of temperature on the relaxation rate of three aluminum alloys for a 10-hr heating period is illustrated in Fig. 23. The higher the initial stress, the more rapid was the rate of relief in terms of actual stress. However, the time required to relieve a certain percentage of the residual stress at a specific temperature was independent of the magnitude of the initial stress.

The rate of stress relief varied considerably with the different cast and wrought alloys. The rate of relief was relatively rapid with the essentially binary aluminum-copper and aluminum-magnesium alloys (122, 195, and 220) and with alloys 14S, 25S, 75S, 32S, A132, and 356. The slowest relaxation rates were exhibited by alloys 18S, B18S, 76S, and 142. The very slow rates of relaxation of alloys 18S, B18S, and 142 seemed to indicate that the alloys possessing a high strength at elevated temperatures would also have a slow rate of stress relief. However, this is not always true, because alloys 14S and 122 have rapid relaxation rates.

The close agreement between the stress-relief rates of the wrought alloy 32S and cast A132 of similar composition, and of wrought B18S and cast

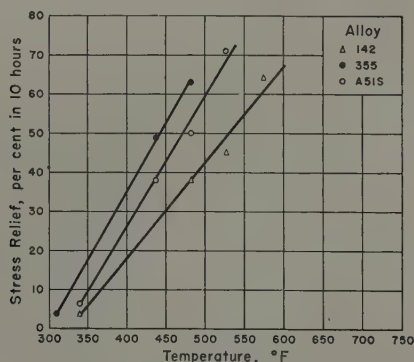


Fig. 23—Effect of reheating temperature on the rate of stress relief in 10 hr of alloy 142, 355, and A51S beam specimens. Beams, 0.25x0.06x12.0 in., were quenched from the commercial heat-treating temperatures into boiling water and stressed 4,000, 7,000, 10,000, and 14,000 psi.

alloy 142 of the same analysis, indicated that the rate of relaxation is not affected by the type of microstructure or the method of fabrication.

It was thought that a correlation should exist between the relaxation rates and the high temperature creep values for the various aluminum alloys. However, from the limited creep data now available it appears doubtful that such a relation can be established.

The effectiveness of the commercial artificial aging treatments in relieving a substantial percentage of the residual stress depends on the rate of relaxation of the specific alloy. If the alloy is one that exhibits a rapid rate of stress relief, a relatively large percentage of the stress will be released, al-

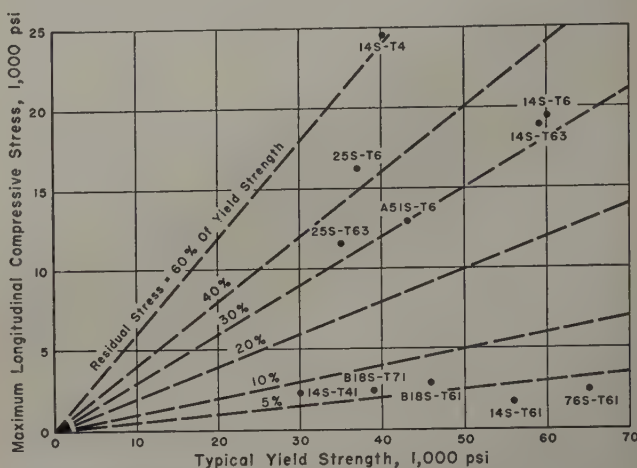


Fig. 24—Relationship of maximum residual longitudinal compressive stress to typical yield strength for aluminum forging alloys in various commercial tempers. Data for 3.0x9.0 in. cylinders.

though the aging temperature may be as low as 300° to 400°F. However, if the alloy is one that has a slow relaxation rate, the low temperature generally employed for aging treatments will relieve only a small percentage of the residual stress.

Residual Stresses in Various Aluminum Alloys With Different Commercial Heat Treatments: The effects of quenching rate, quenching temperature, section size, and alloy composition on the residual stresses resulting from quenching various commercial wrought and cast aluminum alloys have been described. The progressive boring method of Sachs was employed to determine the magnitude and distribution of the stresses. Only a limited number of residual stress determinations were made on cylinders which had been given commercial heat treatments involving aging at elevated temperatures subsequent to quenching because of the expense and time involved in the Sachs method.

It was considered desirable to compile the relative magnitudes of the stresses which could be expected in the various alloys in their respective commercial tempers, the effects of all other factors such as section size remaining constant. Fortunately, cylinders of a standard size were employed for a large proportion of the program. In order to obtain such data, it was necessary to combine the results of the stress determinations on as-quenched cylinders with information on the percentage of stress relief effected by the various aging treatments. The latter information on the rates of stress relief of cast and wrought aluminum alloys was described in the previous section. Rates of stress relief determined by the relaxation beam method were com-

pared with rates measured by the Sachs analysis and found to be identical, Figs. 18 and 21. Thus, the combination of the information obtained by the two experimental methods should provide valid data for determining the stresses present after complete heat treatment.

In some cases results were available for 3.0x9.0 in. cylinders which had been subjected to a commercial heat treatment and artificial aging before stress analysis. Values obtained from such measurements were, of course, valuable and served as a confirmation of the procedure adopted.

The primary objective of this work was to provide data on the comparative residual stresses which

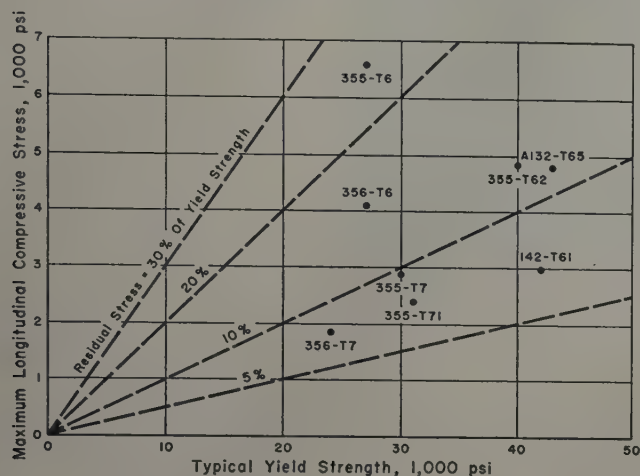


Fig. 25—Relationship of maximum residual longitudinal compressive stress to typical yield strength for aluminum permanent mold alloys in various commercial tempers. Data for 3.0x9.0 in. cylinders.

might prevail in commercial forgings or castings after complete heat treatment. The data revealed differences between alloys as well as between various tempers of a specific alloy. It was apparent from the results that the stresses developed in actual forged or cast parts are affected to a considerable degree by the section size and geometry of the part. However, the results should permit valid conclusions concerning the relative stresses in parts of equivalent size and shape in different alloys and tempers.

Probably the greatest value of such information is its application to the problem of distortion on machining. The character of the stress state, involving triaxial stresses and some variations in the distributions of the three stresses, is so complex that no simple relations have been discovered between the anticipated distortion for a certain machining operation and any of the calculated or measured maximum stress values. However, if a casting or forging of large size were to be bored so that the hole diameter were relatively small in proportion to the external dimensions of the piece, it is probable that the amount of distortion per inch would be approximately proportional to the magnitude of the tensile stresses at the center of the section. The distortion in this case would be expressed by an expansion in the external dimensions. However, if the machining operations removed stock from the surface, the distortion would appear as a contraction, and the relative amount of the contraction would be related to the magnitude and distribution of the surface compressive stresses. Difficulties arising from the release of residual stresses are frequently encountered in slotting. In such operations

the magnitude of stresses in both the surface and center layers would be of importance. The commonest manifestation of these changes is the bending or warping of the part.

Maximum longitudinal compressive stresses in various tempers of the forging alloys ranged from 1,600 psi for 14S-T61 to 24,500 psi for 14S-T4, other alloys and tempers investigated having intermediate values. Similar stresses in casting alloys varied from 200 psi for 195-T7 to 6,800 psi for 355-T4. Among the factors affecting the level of residual stresses in heat-treated parts, the quenching rate was indicated to have an influence considerably greater than that of the alloy composition or the elevated temperature aging treatment, and in all cases a heat-treating practice which involved quenching in boiling water produced a much greater reduction in residual stresses than in the tensile properties. Thus, for example, the residual stresses in alloy 14S varied by a ratio of 12 to 1 or more, depending upon whether the quenching water was at 150° or 212°F. Decrease in the magnitude of the residual stresses with elevated temperature aging treatments of the -T6 type varied from 7 to 44 pct among the various forging alloys.

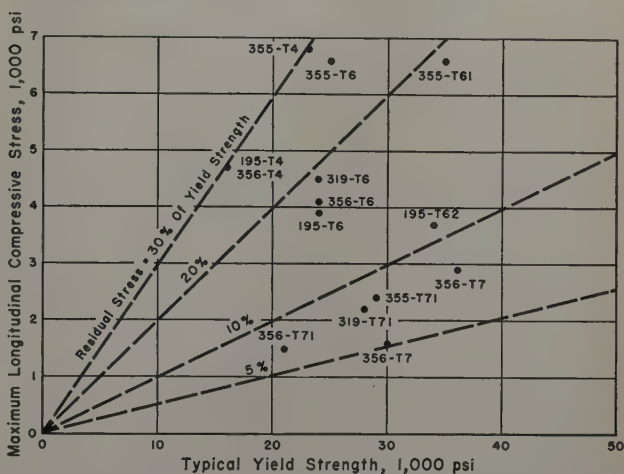


Fig. 26—Relationship of maximum residual longitudinal compressive stress to typical yield strength for aluminum sand casting alloys in various commercial tempers. Data for 3.0x9.0 in. cylinders.

In general, the magnitude of the residual stresses in casting alloys was lower than in forging alloys, because of the prevalence of boiling water quenching for casting alloys. As a result, less variation was encountered among the different casting alloys than among forging alloys in commercial tempers. The percentage of stress relief effected by the elevated temperature aging portions of the -T6 heat treatments varied from 3 pct for casting alloy 355-T6 to 30 pct for 355-T62. The aging cycle of the -T7 type treatments provided stress-relief values of from 43 pct for casting alloy 355-T7 to 96 pct for 195-T7. With the substantial reductions in the magnitude of the residual stresses provided by -T7 type treatments, measurable improvements with respect to distortion on machining can be expected. Generally the most favorable combinations of tensile properties and residual stress values were provided by a low quenching rate followed by artificial aging to the -T6 temper.

Engineers responsible for the design of parts and the selection of suitable alloys and tempers are concerned with relations between the anticipated re-

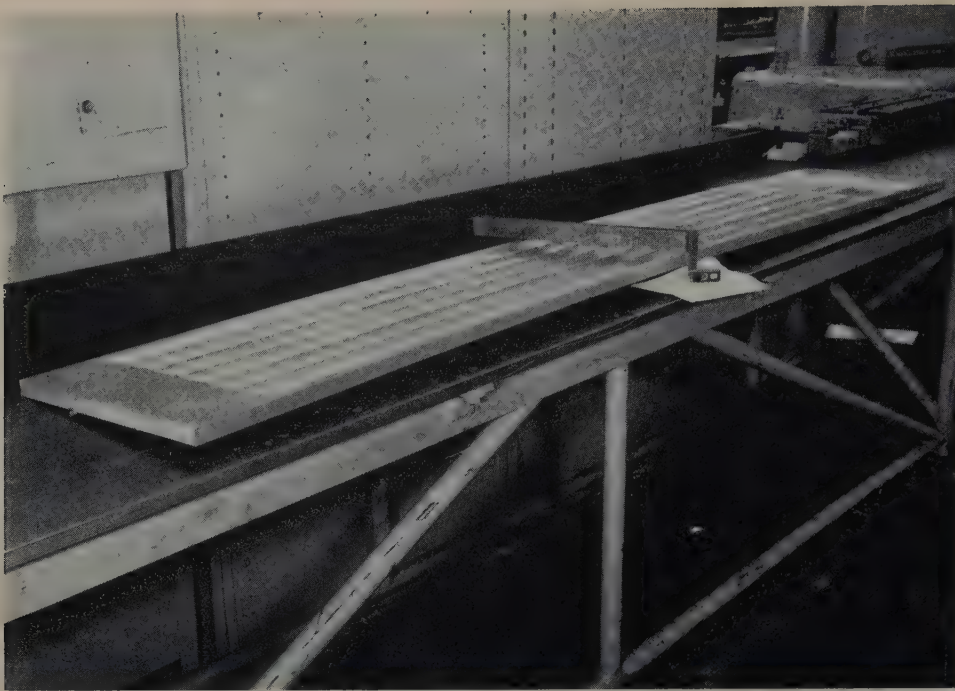


Fig. 27—Machined alloy 75S-T6 test specimen representing the integrally stiffened structure of the Lockheed Super Constellation airplane. Specimen was not stretched after quenching.

sidial surface stresses and the fatigue characteristics of the parts. In some cases the allowable range for fatigue stresses applied in service is restricted by the presence of residual stresses developed in the heat-treating operation.

Consequently, various commercial tempers have been developed for aluminum alloys with the primary objective of fabricating products having a low level of residual stress. These tempers usually do not represent maximum strength properties, but the reduction is modest, considering the degree to which residual stress problems are eliminated. It is, of course, necessary to establish the relation between the typical strength properties of the different tempers of the various alloys and the associated residual stresses. It was decided to express the maximum longitudinal residual compressive stress as a percentage of the typical yield strength. In the case of forging alloys, the longitudinal compressive stress ranged from about 3 pct to as high as 61 pct of the yield strength. This relationship depended not only on the severity of the quench, but also to an appreciable degree on the effects of elevated temperature aging, since a considerable change in yield strength values accompanies the aging treatments.

The relation between the maximum longitudinal residual compressive stress values and the typical yield strengths for the forging alloys is illustrated in Fig. 24. It was apparent that the value of the maximum longitudinal compressive stress in alloys receiving a quench in cold or warm water amounted to 30 to 40 pct of the typical yield strength of the fully hardened temper (-T6 type). When boiling water quenches were employed, the residual stress values were less than 10 pct of the typical yield strengths.

It is of interest that the maximum tangential residual compressive stress was indicated, by the available data from the cast and wrought cylinders, to be approximately equal to the maximum longitudinal compressive stress. Thus, the ratio of the maximum longitudinal compressive stress to the maximum tangential compressive stress varied from 0.79 to 1.21, and the average of this ratio was 0.98. Therefore, the values shown graphically in Fig. 24

can be considered to represent the tangential as well as the longitudinal residual surface stresses. For many purposes the surface longitudinal compressive stresses are undoubtedly the most important; and this consideration, along with the fact that the surface stresses are probably established with greater accuracy and apply to the greatest incremental volume of any cast or forged parts to be machined, was the reason for the selection of the maximum longitudinal compressive stress as providing the most significant data.

The relation of maximum longitudinal residual compressive stresses to the typical yield strengths of various permanent mold casting alloys and tempers is represented in Fig. 25. Similar data for sand casting alloys are presented in Fig. 26.

Relief of Residual Stress by Mechanical Treatments

Mechanical treatments have been used for many years to relieve or realign residual stresses in commercial metal products such as sheet, plate, tube, extrusions, rod, and bar. The mechanical operations employed are stretching, repeated bending, and coining. Stretchers up to 3,000,000 lb capacity, roller levelers, and various other types of roll straightening devices, gag presses, etc. are widely used throughout the metal industry, not only for straightening and forming metal products, but also for reducing the magnitude or improving the distribution of residual stresses in these products. Forgings are often straightened cold in the die.

The mechanism by which the various mechanical treatments reduce residual stresses is perhaps best illustrated by the stretching procedure. Consider a long length of extruded shape in which the outside fibers have a high longitudinal residual compressive stress and the interior layers a correspondingly high longitudinal tensile stress. When the ends of this piece are gripped and the entire piece stretched beyond the elastic range of the alloy, the inner fibers begin to take a permanent set first, because the superimposed tensile stress is added to the residual tension already present. As the stretching force is increased further, the exterior fibers finally begin to assume permanent set, so that the entire cross

section becomes stressed well beyond the limit of elastic action. When the stretching force is removed, both the outer and inner fibers recover nearly the same amount. However, the plastic flow of metal is greater in the interior fibers than in the exterior layers, so that after removal of the stretching force only a small fraction of the initial difference in the residual stresses remains between the inner and outer fibers. One factor controlling the degree of this final difference is the amount of plastic action imposed during the stretching operation. Fortunately, the initial plastic action in such a treatment is more effective than the later stages of plastic flow, so that it is unnecessary to stretch to so high a degree of permanent set that fracture of the piece during the stretching operation might be imminent. Again, fortunately, the amount of stretch required to satisfactorily straighten a part is almost enough to adequately release the residual stresses, and so the minimum required for straightening, or slightly more than this, is the usual amount applied in commercial stretching operations.

The effectiveness of stretching in relieving residual stresses depends also on the uniformity of the mechanical properties, especially yield strength, of the alloy product being stretched. If the cross section is not initially uniform in mechanical properties, stretching can actually produce residual stresses in an otherwise stress-free piece. Of course, the stresses so formed are usually of a smaller magnitude than those produced by quenching in cold water, so that the net effect of stretching is beneficial, even though some minor differences exist in mechanical properties across the cross section. Nevertheless the maximum benefits in relieving residual stresses by stretching can be attained only in a material which has substantially uniform mechanical properties across the cross section.

Tests have repeatedly demonstrated the beneficial effect of stretching on the relief of residual stresses. In one investigation, for example, 75S-T6 extruded shapes after stretching showed only 10 pct as much

warping on machining as was characteristic before stretching. In another test, illustrated in Fig. 27, a 75S-T6 specimen representing the integrally stiffened structure on the Lockheed Super Constellation was machined without having been stretched after quenching. The distortion of the specimen is apparent on the inspection surface plate. In contrast, Fig. 28 reveals the flatness of a similar machined specimen that was stretched between quenching and artificial aging.

Stretching operations are used commercially today on many aluminum alloy products covering a wide range of sizes. Spar chords for airplanes provide another example of aluminum alloy products straightened by stretching after heat treatment that show greatly reduced warpage on machining because the residual stresses have been largely eliminated. Airplane spar chord sections with a cross section of 60 sq in. can be successfully stretched. Very satisfactory results both as to straightness and freedom from warpage on machining have been obtained by such mechanical treatments in many commercial applications.

Relief of Residual Stresses by Combinations Of Thermal and Mechanical Treatments

Mechanical treatments followed by a thermal stress relief are frequently employed to obtain the desired combination of mechanical properties and reduction in residual stresses. An example is the flattening procedure applied to magnesium-base alloy sheet, where a combination of dead load and thermal treatment was used to produce flat, stress-free sheet. Another application is the relatively new method being used by North American Aviation Co. for simultaneously forming, quenching, and stretching high strength aluminum alloy parts by a die quenching process.

Closure

Two objectives have been reached in this exploration of the field of residual stresses in metals. Both the beneficial and the injurious effects of these

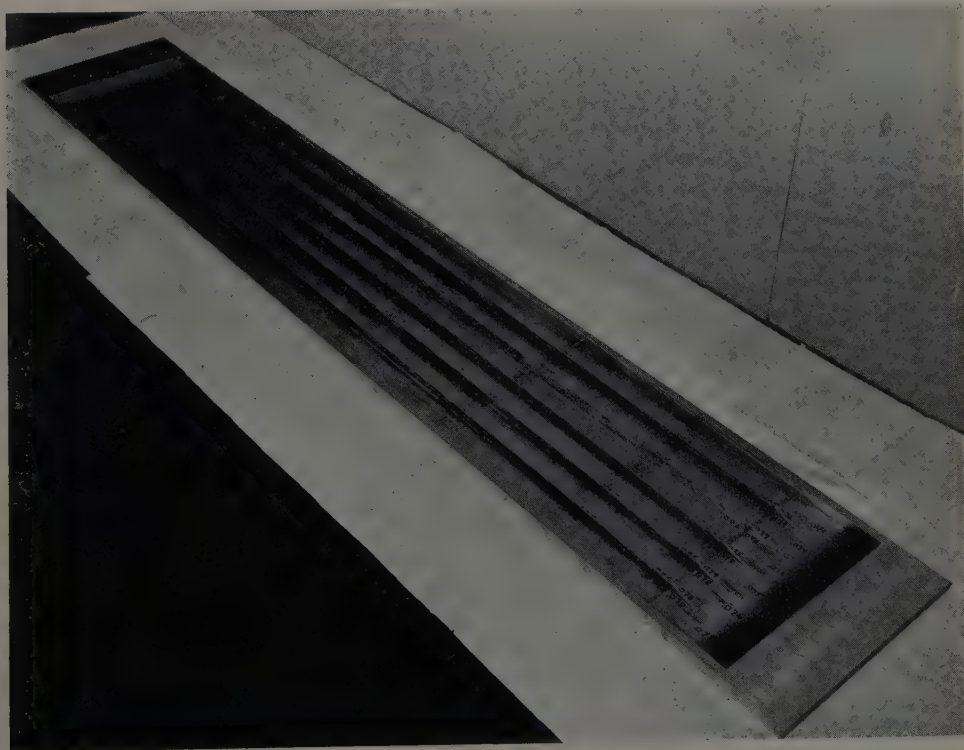


Fig. 28—Machined alloy 75S-T6 test specimen representing the integrally stiffened structure of the Lockheed Super Constellation airplane. Specimen was stretched after quenching but before artificial aging.

stresses have been presented in a qualitative and quantitative manner. Numerous examples from commercial experience illustrate the location of these residual stresses and the practical effects which they introduce. Much experimental work remains to be done in this field, however, and it is hoped that this report will provide a useful background of information which will stimulate others to acquire more of the fundamental knowledge necessary for the control of these forces.

Acknowledgment

The majority of the experimental data was obtained by C. M. Tucker and H. B. Carlsen. The author is indebted to R. A. Kelsey and H. Y. Hunsicker for assistance on the preparation of the sections on methods of stress analysis and the magnitude of stress in commercial tempers of forgings and castings, respectively.

The manuscript has been reviewed and many constructive suggestions were contributed by M. W. Daugherty, E. H. Dix, Jr., J. D. Edwards, F. C. Frary, E. C. Hartmann, R. L. Templin, and W. E. Sicha, of the Aluminum Research Laboratories, H. J. Rowe, of the Castings Division, and K. F. Thornton, of the Development Division of Aluminum Company of America.

References

- ¹ G. Sachs and K. R. Van Horn: Practical Metallurgy. ASM (1940) pp. 165-166, 178-182.
- ² R. G. Treuting: Origin of Residual Stresses. *Residual Stress Measurements*. (1952) pp. 1-41. Cleveland. ASM.
- ³ H. B. Wishart: Residual Stress States in Metals. *Residual Stress Measurements*. (1952) pp. 97-128. Cleveland. ASM.
- ⁴ D. G. Richards: Relief and Redistribution of Stresses. *Residual Stress Measurements*. (1952) pp. 129-204. Cleveland. ASM.
- ⁵ E. H. Dix, Jr.: Aluminum-Zinc-Magnesium Alloys. *Trans. ASM* (1950) 42, pp. 1057-1127.
- ⁶ D. K. Crampton: Internal Stress and Season Cracking in Brass Tubes. *Trans. AIME* (1930) 89, pp. 233-255.
- ⁷ H. Bühler and E. H. Schulz: Reduction of the Internal Stresses Produced in Metal Rods in Cold Drawing by Subsequent Drawing. *Metall* (1951) 5, No. 9-10, pp. 147-156.
- ⁸ H. Scott: Origin of Quenching Cracks. *Scientific Papers*, Bur. Standards (1925) 20, pp. 399-444.
- ⁹ C. S. Barrett: Internal Stresses, A Correlated Abstract. *Metals and Alloys* (1934) 5, pp. 131-135, 154-158, 170-175, 196-198, 224-226. Critical Review of Various Methods of Residual Stress Measurements. *Proc. Soc. Expt. Stress Anal.* (1944) 2, No. 1, pp. 147-156.
- ¹⁰ H. Ford: Mechanical Methods for the Measurement of Internal Stresses. Symposium on Internal Stresses in Metals and Alloys. Inst. Metals, London. *Monograph No. 5* (1948) pp. 3-11.
- ¹¹ W. M. Baldwin, Jr.: Residual Stresses in Metals. *Proc. ASTM* (1949) 49, pp. 539-583.
- ¹² O. J. Horger: Residual Stresses. *Handbook of Experimental Stress Analysis*. Edited by M. Hetenyi. (1950) pp. 459-578. New York. John Wiley & Sons.
- ¹³ G. Sachs and G. Espey: The Measurement of Residual Stresses in Metals. *Iron Age* (1948) 148, No. 12, pp. 63-71; (1948) 148, No. 13, pp. 36-42.
- ¹⁴ J. J. Lynch: Measurement of Residual Stresses. *Residual Stress Measurements*. (1952) pp. 42-96. Cleveland. ASM.
- ¹⁵ G. Sachs: The Detection of Internal Stresses in Bars and Tubing. *Ztsch. Metallkunde* (1927) 19, pp. 352-357; Internal Stresses in Piston Rods of a Large Diesel Engine Ocean Liner. *Trans. ASM* (1939) 27, pp. 821-836.
- ¹⁶ H. Bühler and W. Schreiber: Compensation for Errors in Measurement in the Boring Process According to G. Sachs, for Detecting Internal Stresses in Rods and Tubes. *Metall* (1951) 5, No. 3-4, pp. 53-57.
- ¹⁷ R. E. Hanslip: Residual Stresses in Surface Hardened Oil Field Pump Rods. *Proc. Soc. Expt. Stress Anal.* (1951) 10, No. 1.
- ¹⁸ J. Johnston: Time as a Factor in the Making and Treating of Steel. *Trans. AIME* (1942) 150, pp. 13-29.
- ¹⁹ G. Sachs and G. Espey: A New Method for Determination of Stress Distribution in Thin-Walled Tubing. *Trans. AIME* (1942) 147, pp. 348-360.
- ²⁰ W. Spraragen and G. E. Clausen: Shrinkage Stresses in Welding. *Supplement, Journal Amer. Welding Soc.* (1937) 2, No. 11, pp. 2-62.
- ²¹ J. L. Meriam, E. Paul DeGarmo, and Finn Jonassen: A Method for the Measurement of Residual Welding Stresses. *Welding Journal* (1946) 25, pp. 340s-343s.
- ²² D. G. Richards: A Study of Certain Mechanically-Induced Residual Stresses. *Proc. Soc. Expt. Stress Anal.* (1945) 3, No. 1, pp. 40-61.
- ²³ S. Timoshenko: *Strength of Materials*. Part II. 2nd Edition (1941) pp. 379-383. New York. D. Van Nostrand Co.
- ²⁴ D. Rosenthal and J. T. Norton: A Method of Measuring Triaxial Residual Stresses in Plates. *Welding Journal* (1945) 24, pp. 295s-307s.
- ²⁵ R. G. Treuting and W. T. Read, Jr.: Mechanical Determination of Biaxial and Residual Stress in Sheet Materials. *Journal of Applied Physics* (1951) 22, No. 2, pp. 130-134.
- ²⁶ J. Mathar: Determination of Initial Stresses by Measuring the Deformation Around Drilled Holes. *Trans. ASME* (1934) 56, pp. 249-254.
- ²⁷ W. Soete and R. Vancrombrugge: An Industrial Method for the Determination of Residual Stresses. *Proc. Soc. Expt. Stress Anal.* (1950) 8, No. 1, pp. 17-28.
- ²⁸ C. W. Gadd: Residual Stress Indications in Brittle Lacquer. *Proc. Soc. Expt. Stress Anal.* (1946) 4, No. 1, pp. 74-77.
- ²⁹ J. T. Norton and D. Rosenthal: Stress Measurement by X-Ray Diffraction. *Proc. Soc. Expt. Stress Anal.* (1943) 1, No. 2, pp. 73-76; Application of the X-Ray Diffraction Method of Stress Measurement to Problems Involving Residual Stresses in Metals. *Ibid.* pp. 77-81; J. T. Norton: X-Ray Methods in the Field of Residual Stresses. *Ibid.* (1944) 2, No. 1, pp. 157-160.
- ³⁰ D. E. Thomas: Measurement of Internal Stresses by X-Rays. Symposium on Internal Stresses in Metals and Alloys. Inst. Metals, London. *Monograph No. 5*, (1948) pp. 25-30.
- ³¹ L. Frommer and E. H. Lloyd: The Measurement of Residual Stresses in Metals by the X-Ray Back-Reflection Method, with Special Reference to Industrial Components in Aluminum Alloys. *Journal Inst. Metals*, London. (1944) 70, pp. 91-124.
- ³² R. King: The Investigation of Internal Stresses by Physical Methods other than X-Ray Methods. Symposium on Internal Stresses in Metals and Alloys. Inst. Metals, London. *Monograph No. 5* (1948) pp. 13-24.
- ³³ Residual Stresses in Machined Surfaces. *Engineers' Digest* (blue pages) (1951) 12, No. 3, p. 71; Residual Grinding Stresses. *Ibid.* No. 6, pp. 175-176.
- ³⁴ W. L. Fink and L. A. Willey: Quenching of 75S Aluminum Alloy. *Trans. AIME* (1948) 175, pp. 414-427; METALS TECHNOLOGY (August 1947).
- ³⁵ L. W. Kempf and K. R. Van Horn: Relief of Residual Stresses in Some Aluminum Alloys. *Trans. AIME* (1942) 147, pp. 250-265.
- ³⁶ J. Boyd: The Relaxation of Copper at Normal and at Elevated Temperatures. *Proc. ASTM* (1937) 37, No. 2, pp. 218-232.
- ³⁷ C. C. Davenport: Correlation of Creep and Relaxation Properties of Copper. *Journal of Applied Mechanics* 5, No. 2, pp. A55-A60.
- ³⁸ W. C. Stewart: Residual Stress. *Journal Amer. Soc. Naval Engrs.* (1937) 49, pp. 307-323.

Tristage Crystallization Process For Utilizing Western Ferrophosphorus

by Lloyd H. Banning, Wallace E. Anable, and R. T. C. Rasmussen

In the rapidly growing industry of elemental-phosphorus production from western phosphates, most of the vanadium and chromium contained in the phosphate rock collect in the byproduct ferrophosphorus. Results are presented of a completed laboratory project, which developed a tristage crystallization and hydrolysis process for recovering strategic vanadium and chromium, as well as a valuable phosphorus product, after extracting these elements from the ferrophosphorus by roasting and leaching.

THE Phosphoria formation in Idaho, Montana, Wyoming, and Utah contains the Nation's largest reserve of phosphate rock. A unique feature of the Phosphoria beds is their content of a fraction of a percentage each of vanadium, chromium, nickel, and molybdenum. Vanadium is the most important as to quantity and value.

Small-scale tests by the Bureau of Mines at Albany, Oregon, in 1947, indicated that most of the vanadium in the phosphate rock collects in the ferrophosphorus product of smelting. Subsequent electric smelting operations to produce elemental phosphorus from western phosphate rock (experimentally by TVA and industrially at Pocatello, Idaho) have shown that the vanadium and other metals in the rock are to a large extent recovered in concentrated form in the ferrophosphorus byproduct.

This paper reports the results of completed laboratory research on the recovery of vanadium from ferrophosphorus, which was undertaken by the Bureau of Mines at Albany in 1948 as the first phase of a project entitled, "Vanadium and Fluorine from Western Phosphates." The various vanadium-recovery methods investigated, including the roast-leach method that showed most promise and was studied in greatest detail, are discussed in an earlier publication.¹ Subsequent systematic study of the roast-leach method of extracting vanadium from western ferrophosphorus developed the more effi-

L. H. BANNING, Member AIME, is Metallurgist, W. E. ANABLE, Junior Member AIME, is Chemical Engineer, Northwest Electrodevelopment Laboratory, U. S. Bureau of Mines, Albany, Oregon, and R. T. C. RASMUSSEN, Member AIME, formerly Chief, Ferrous Metals Branch, Northwest Electrodevelopment Laboratory, is now associated with Quebec Metallurgical Industries, Billings Bridge, Ont., Canada.

Discussion on this paper, TP 3477D, may be sent, 2 copies, to AIME by May 1, 1953. Manuscript, July 21, 1952. Spokane Regional Meeting, May 1952.

Papers by authors on the U. S. Bureau of Mines staff are not subject to copyright.

Table I. Test Lots of Western Ferrophosphorus

Lot	Analysis, Pct				
	V	P	Fe	Cr	Ni
TVA 1	3.26	26.6	60.8	3.4	0.84
TVA 2	3.85	26.0	59.9	4.0	0.95
Westvaco A	4.0	25.9	60.7	5.7	0.98
Westvaco B	5.2	24.7	58.5	5.2	1.0

cient tristage crystallization process, which is the subject of this paper.

Process Development

The investigations were made on ferrophosphorus produced in the electric smelting of elemental phosphorus from western phosphate rock. The TVA provided two sample lots of ferrophosphorus produced in pilot plant smelting of phosphatic shale from the Fort Hall Indian Reservation in Idaho. The Westvaco Chemical Div. of the Food Machinery & Chemical Corp. supplied two sample lots of ferrophosphorus produced by its phosphorus smelter at Pocatello, Idaho. The analyses of all four lots are shown in Table I. Westvaco lot B was the starting material for the more recent tests.

The roast-leach process for recovering vanadium from western ferrophosphorus, as originally developed, employed the following principal steps: Roasting of a mixture of pulverized ferrophosphorus, soda ash, and salt; extraction of the water-soluble vanadium, phosphorus, and chromium compounds from the calcine by leaching, settling, and decantation of the pregnant solution; primary crystallization of trisodium phosphate from the pregnant solution; purification of the trisodium phosphate crystals by dissolution in water and secondary crystallization; purification of the pregnant vanadium solution from the primary crystallization step by adding calcium chloride to precipitate calcium phosphate; and hydrolysis of vanadium red cake from the puri-

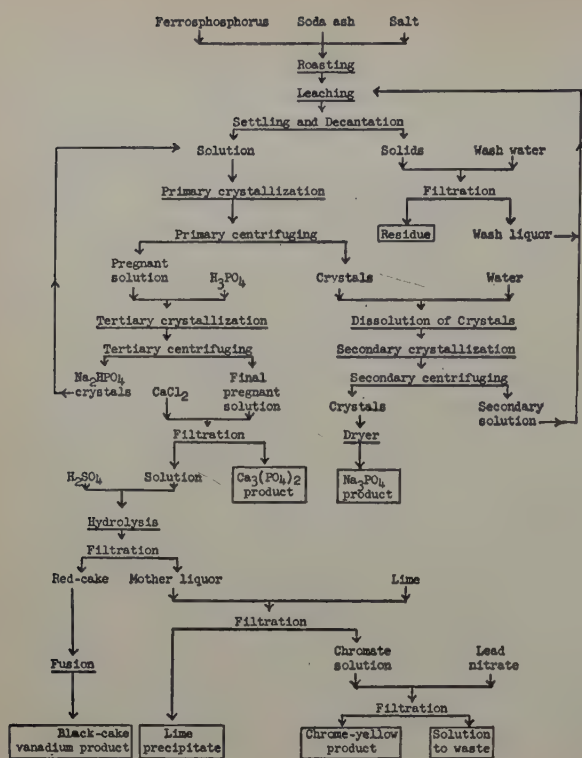


Fig. 1—Flowsheet of tristage crystallization process for recovering vanadium, phosphorus, and chromium products from western ferrophosphorus.

fied pregnant solution. It was recognized that more detailed and systematic study of the several unit operations was desirable, particularly with respect to making a more complete separation of phosphorus from vanadium-bearing solution by crystallization. Methods of recovering chromium remaining in solution after hydrolyzing vanadium also needed to be investigated.

The tristage crystallization process developed in subsequent research is illustrated by the flowsheet of Fig. 1. It differs from the original roast-leach process principally by the addition of a tertiary crystallization step to remove much of the phosphorus remaining in the pregnant vanadium solution from the primary crystallization step. Instead of crystallizing trisodium phosphate, as in the primary and secondary crystallizations, disodium phosphate is brought down by addition of phosphoric acid to the solution before cooling for the tertiary crystallization. This step brings the phosphorus content of the pregnant vanadium solution to a much lower figure than was previously obtainable and also permits recovery of a larger proportion of the phosphorus in a high-purity sodium phosphate product.

As shown on the flowsheet, the more recent studies included tests on conversion of the red-cake product to black-cake and developed one method of recovering chromium as a marketable compound. A more detailed study also was made of the controlling variables in other steps of the process.

Each of the several unit operations comprising the tristage crystallization process will be described individually.

Roasting of Ferrophosphorus with Soda Ash and Salt: The object of roasting is to oxidize the metallic ferrophosphorus and form water-soluble vanadium, phosphorus, and chromium compounds, while avoiding formation of soluble iron compounds. Roasting variables investigated were: soda ash-ferrophos-

phorus ratio, salt-ferrophosphorus ratio, fineness of the ferrophosphorus, temperature, time, degree of oxidation, and amount of rabbling. Most of the roasting tests were carried out in a small rotary kiln.

The optimum quantity of soda ash in the roasting charge was found to be approximately the sum of the quantities theoretically required to react with phosphorus to form trisodium phosphate (Na_3PO_4), with vanadium to form sodium metavanadate (NaVO_3), and with chromium to form sodium chromate (Na_2CrO_4). A satisfactory ratio of dry soda ash to Westvaco ferrophosphorus was 1.45:1. A small quantity of salt (NaCl) in the roasting charge was beneficial, but an excess of salt caused the charge to become plastic below the optimum roasting temperature and resulted in mechanical difficulties. One part of salt to 10 parts of Westvaco ferrophosphorus gave satisfactory results.

Grinding of the ferrophosphorus to -35-mesh provided roaster feed of optimum particle size. Finer grinding accelerated the roasting reaction but increased dust losses, whereas coarser grinding resulted in a less soluble calcine.

The related roasting variables of temperature, time, degree of oxidation, and amount of rabbling must be balanced to obtain calcine having good leaching characteristics, and their control depends to a large extent upon the type of roaster employed. The preferred maximum roasting temperature in the small rotary kiln was between 780° and 800°C . At higher temperatures the charge became plastic, resulting in the formation of nodules that were not properly calcined throughout. The best leach extractions were obtained from calcine that was in the hot zone of the furnace for about 2 hr. Enough oxidation must be attained to produce pentavalent vanadium and phosphorus and hexavalent chromium. Excessive oxidation apparently produces water-soluble sodium ferrate, which causes difficulties in subsequent leaching and crystallization. The degree of oxidation is a function of the roaster atmosphere and of gas-solids contact produced by rabbling, or by tumbling in the rotary kiln, for a given time at roasting temperature.

The best combination of roasting conditions attained in the rotary kiln tests produced calcine in which 95 pct each of the vanadium and phosphorus, 70 pct of the chromium, and virtually none of the iron in the ferrophosphorus were rendered water-soluble.

Leaching of Calcine and Separation of Dissolved Values from Residue: In the early batch leaching tests 500 g of calcine was ground for 5 min in a laboratory ball mill with 2 liters of secondary solution from a previous test. The ground pulp was transferred to a leaching vessel and gently boiled with agitation for 1 hr. After leaching, the solids were settled at a temperature high enough to prevent crystallization. The solution usually was clear enough to decant after settling for 3 hr. The decanted primary solution was sent to the primary crystallization step, while the solids were repulped with water, releached, filtered, washed, dried, and sampled for analysis. The filtrate and washings were combined with the secondary solution from the secondary crystallization step of the process for use in leaching the next batch of calcine.

Later investigations revealed that it was not necessary to grind the calcine before leaching. The procedure subsequently used in simultaneous roasting and leaching tests was to discharge calcine from

the kiln directly into a vigorously agitated boiling leach solution. The specific gravity of the pulp in the leaching vessel was adjusted by frequent small additions of water and recycled solution. When the leaching vessel became full, part of the pulp was removed and filtered.

Occasionally iron was present in the clarified leach solutions in high enough concentration to precipitate during crystallization and discolor the sodium phosphate product. Furthermore, high iron concentration appeared to retard crystallization. The clarified leach solution was acceptably low in iron when the following conditions were met: The solution was alkaline enough so that trisodium phosphate crystals formed on cooling, the pulp was kept vigorously boiling during the leaching operation, the specific gravity of the pulp was kept below 1.27, and the calcine was leached for at least 1 hr.

The leach pulp was kept above the crystallization temperature of trisodium phosphate, which is a function of the phosphorus concentration, until the solution and solids were separated. No trouble was experienced with sodium phosphate crystallizing from solution when the temperature was maintained above 60°C.

Primary Crystallization and Centrifuging: In the primary crystallization and centrifuging operations trisodium phosphate is crystallized and separated from the pregnant solution. The purpose of the step is to make the optimum separation of phosphorus from vanadium and chromium; complete separation cannot be attained as the trisodium phosphate crystals include small amounts of vanadium and chromium, and the remaining solution contains some phosphorus. In the development work on the process a study was made of the relationship between vanadium and phosphorus content of solution and temperature of crystallization. A typical 1500 milliliter sample of primary solution, analyzing 12.1 g V and 54.0 g P per liter, was cooled in the laboratory crystallizer to 20°C and held at this temperature 30 min. A sample of the mother liquor was then drawn from the crystallizer through a submerged fritted glass filter and analyzed for phosphorus and vanadium. The same procedure was repeated for the following temperatures: 15°, 12°, 9°, 6°, 3°, and -3°C. The vanadium and phosphorus analyses and the ratios of vanadium to phosphorus of the mother liquor after each crystallization are shown in Table II.

Results of the crystallization studies indicate that the optimum crystallization temperature for a primary solution containing 12 g of vanadium per liter is between 3° and 6°C, as the vanadium-phosphorus ratio is highest in this temperature range. The relationship between vanadium and phosphorus content of pregnant solution and temperature of crys-

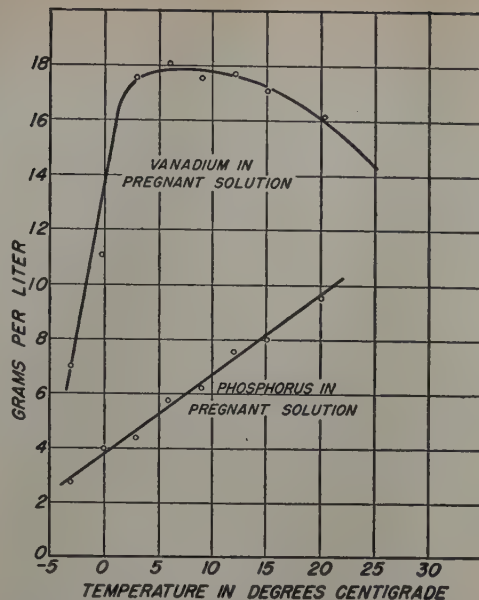


Fig. 2—Effect of crystallization temperature on vanadium and phosphorus content of pregnant solution.

tallization is shown graphically in Fig. 2. It is evident from the graph that the phosphorus content of pregnant solutions decreases linearly as the crystallization temperature is lowered. Conversely, the vanadium content increases to a maximum at about 6°C, then rapidly decreases at lower temperatures. These studies indicate that, if the primary solution were higher in vanadium, the optimum crystallization temperature would be higher, as sodium vanadate would start crystallizing from solution at higher temperature. On the other hand, if the vanadium content were lower, the optimum crystallization temperature would be lower. Hence, the optimum crystallization temperature for a primary solution of known vanadium concentration can be estimated from these data.

Centrifuging has proved superior to filtration for separating crystals from solution, mainly because a drier crystal product can be recovered. In some of the early tests using filtration, the crystals always contained appreciable percentages of vanadium and chromium. By centrifuging, a drier crystal product low in vanadium and chromium was recovered.

Optimum separation of crystals from solution by centrifuging is made only when the minimum crystallization temperature is maintained until the separation is complete. The procedure used in the laboratory test work was to cool the 12-in. basket of the suspended-type centrifuge with ice water before introduction of the crystal-solution mixture. With the basket loaded, the centrifuge was raised to a speed of 3000 rpm. After spinning for 2 min, the crystals were washed with a small amount of ice water, then spun dry in about 1 min.

Purification of Trisodium Phosphate Crystals by Secondary Crystallization: The vanadium and chromium contents of the primary trisodium phosphate crystals vary from 0.1 to 0.2 pct, and the crystals are slightly yellow. To produce a commercial grade of trisodium phosphate the primary crystals must be freed of vanadium and chromium by dissolution in water and recrystallization. Therefore, studies were made to determine optimum conditions for the recrystallization procedure.

A series of eight secondary crystallization tests indicated that a linear relationship exists between

Table II. Effect of Primary Crystallization Temperature on Vanadium and Phosphorus Content of Pregnant Solution

Temperature, °C	Analysis, G per Liter		V-P Ratio
	V	P	
60	12.1	54.0	0.22
20	16.1	9.5	1.7
15	17.1	8.0	2.14
12	17.7	7.6	2.32
9	17.5	6.1	2.87
6	18.1	5.9	3.06
3	17.5	4.4	3.98
0	11.1	4.1	2.70
-3	7.0	2.8	2.50

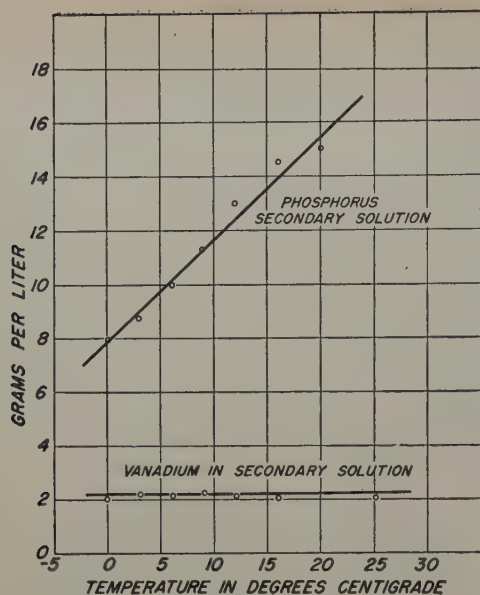


Fig. 3—Effect of crystallization temperature on vanadium and phosphorus content of secondary solution.

the minimum crystallization temperature and the phosphorus content of the secondary solution. The vanadium content of the crystals did not increase at lower crystallization temperatures, as it did in the primary crystallization step. The results of these tests, shown graphically in Fig. 3, indicate that the optimum crystallization temperature is just above the freezing point of the solution.

The effect of phosphorus concentration of solution on the purity of the trisodium phosphate product was investigated in eight recrystallization tests. Solutions with phosphorus concentrations ranging from 27 to 68 g per liter were prepared by dissolving wet primary crystals that contained 0.09 pct V and 6.2 pct P in water. The tests were conducted by cooling 1500 milliliter batches to -1°C and holding at this temperature for 30 min before centrifuging. The crystal products and solutions were measured and analyzed for vanadium and phosphorus. The result of these tests is shown graphically in Fig. 4.

A study of the results of the secondary crystallization tests indicates that under specific conditions a tenfold reduction of the vanadium content of primary crystals can be obtained while recovering 88 pct of the phosphorus in the purified trisodium phosphate crystals and 91 pct of the vanadium in the secondary solution. The graphs also indicate that a choice must be made between high crystal yield and low vanadium content of trisodium phosphate crystals in the secondary crystallization operation. However, low crystal yield in this operation does not necessarily mean low overall phosphorus recovery as the secondary solution is recycled to the leach tank. Only the phosphorus in the residue and in the purified pregnant solution is lost. In plant practice it should be possible to obtain a high overall recovery of phosphorus as trisodium phosphate crystals of low vanadium content.

Purification of Pregnant Solution: When the optimum vanadium-phosphorus separation is made in the primary crystallization and centrifuging operations, the phosphorus content of the pregnant solution is 6 to 8 g per liter. The solution for the vanadium hydrolysis operation must contain no more than about 1 g of phosphorus per liter in order to get a satisfactory recovery of vanadium as red cake

of acceptably low phosphorus content. The conventional procedure for reducing the phosphorus content of pregnant solution is to neutralize with acid and add sufficient calcium ion to precipitate phosphorus as calcium phosphate. The precipitate invariably contains appreciable vanadium and, hence, the more phosphorus that is precipitated from solution as calcium phosphate the lower is the vanadium recovery.

Investigations revealed that disodium phosphate could be crystallized from pregnant solution to the extent that less than 1 g per liter of phosphorus remained in solution. Disodium phosphate was crystallized from pregnant solution by adjusting the pH to 8.8 with phosphoric acid before cooling. Tests have shown that phosphoric acid is the most desirable reagent for the pH adjustment, as the use of other acids introduces foreign ions into the solution which show up in crystals and contaminate the final

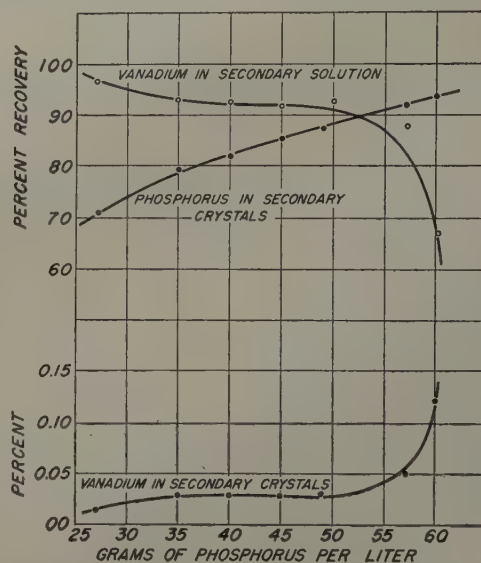


Fig. 4—Effect of dilution on the purification of primary crystals.

trisodium phosphate product. To determine the relationship between temperature of crystallization and phosphorus content of pregnant solution, a series of eight tests was made, the results of which are shown graphically in Fig. 5.

When the third crystallization and centrifuging operation is carried out under favorable conditions, the resulting solution may be used directly for hydrolysis. The crystals from these operations are dissolved in the clarified solution from the primary leaching step; and the phosphorus, including that added as phosphoric acid, is recovered in the trisodium phosphate product. If a higher purity vanadium red-cake product is desired, the solution can be further freed of phosphorus by precipitation with calcium ion before hydrolysis.

Recovery of Vanadium by Hydrolysis: Vanadium recovered from ores is usually sold as fused black vanadium oxide. For grade A fused black vanadium oxide (suitable for manufacture of ferrovanadium and special alloys, direct addition to alloy steel, or the manufacturing vanadium chemicals) the Army and Navy Munitions Board specifies a minimum of 86 pct V_2O_5 (48.2 pct V) and a maximum, in percent, of: P, 0.05; S, 0.15; Cu, 0.05; Sb, 0.05; As, 0.05; Ni, 0.10; Pb, 0.15; Zn, 0.15; and insolubles, 1.0. When recovering vanadium from ores, phosphorus is probably the most troublesome impurity to eliminate

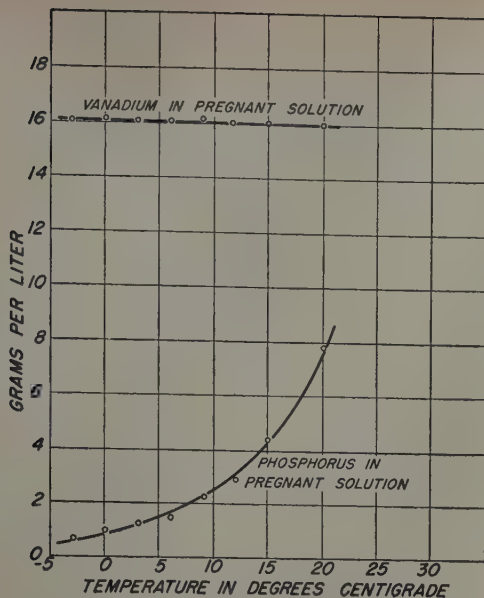


Fig. 5—Temperature relationships when crystallizing disodium phosphate.

from the final vanadium product. The ferrophosphorus used in the test work contained from 4 to 5 pct V and 24 to 25 pct P; so the problem of separating phosphorus from the vanadium product was particularly difficult. By the three crystallization and centrifuging operations described in the foregoing, the vanadium-phosphorus ratio was raised to 15 to 1 in the final pregnant solution, and in some tests the pregnant solution contained as little as 1 g of phosphorus per liter. Still more of the phosphorus can be eliminated from solution prior to hydrolysis by neutralization with sulphuric acid and precipitation of phosphorus as calcium phosphate, thereby increasing the vanadium-phosphorus ratio to as high as 60:1. The final separation of vanadium from phosphorus takes place in the hydrolysis operation.

The apparatus in which hydrolysis tests were first successfully carried out consisted of a 3-neck, 1-liter flask, equipped with a reflux condenser, a thermometer, a mechanical stirrer, and a constant level water bath. Later, to simulate plant conditions more closely, a 3-liter stainless steel beaker was substituted for the 3-neck glass flask. Then, in some of the last tests, a 7-liter stainless steel beaker was used. Equally satisfactory recoveries and grades of red-cake product were obtained in the stainless steel beakers as in the all-glass apparatus.

In making the hydrolysis tests, the pH of the solution was adjusted, after which the solution was heated to the desired temperature while being agitated. In most of the tests the solution was heated to the boiling point, and the volume of solution was kept constant by condensing the vapors and returning them to the hydrolysis vessel or by the addition of water. Samples of the solution were checked at frequent intervals for pH and for vanadium content.

Table III. Results of Some Hydrolysis Tests

Test No.	Red-Cake Analysis, Pct			V Yield, Pct
	V	P	Cr	
17	45.4	0.01	0.7	96.2
18	43.8	0.01	1.1	98.1
19	42.4	0.01	0.8	84.4
20	42.9	0.22	0.8	92.8

Note: Spectrographic analysis of red cakes from tests 18 and 20 indicated no impurities over specifications.

Although the hydrolysis of vanadium from solution is a known procedure, some variables of the hydrolysis operation were given careful study. These studies indicated the following trends:

1—The rate of the hydrolysis reaction and the percentage yield are dependent upon the vanadium concentration of the solution.

2—High phosphorus concentration in the hydrolysis solution depresses the reaction rate, lowers the yield, and contaminates the red-cake product.

3—The hydrolysis reaction rate is accelerated by raising the temperature.

4—Small acid additions at intervals of 15 min until the pH is stabilized accelerate the reaction rate.

The manner in which some of the foregoing trends were determined may be graphically illustrated. To study the effect of hydrogen ion concentration (pH)

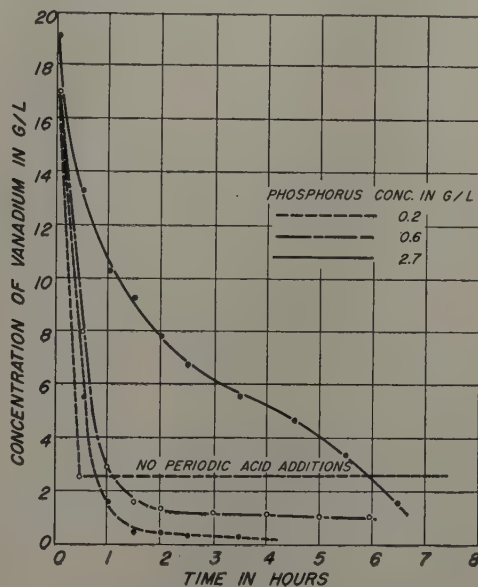


Fig. 6—Hydrolysis of vanadium solutions.

on hydrolysis rate, two tests were made on identical pregnant solutions containing only 0.2 g of phosphorus per liter. In one test (No. 18), after the initial adjustment of the pH to 3.0, 2 milliliter additions of sulphuric acid were made at 15-min intervals. Thirty minutes after the test was started the pH of the solution had increased to 4.6, but after 2 hr it had dropped to 3.1 and the acid additions were stopped. In another test (No. 19), no acid additions were made after the initial adjustment of the pH to 3.0. After a half hour of operation the pH of the solution had increased to 4.9 and precipitation of vanadium apparently ceased. The results of these tests are plotted in Fig. 6. To illustrate the effect of phosphorus concentration in the solution on the rate and completeness of vanadium yield, the results of tests 17 and 20 are also plotted in Fig. 6. In these tests small acid additions were made frequently as described for test 18. The phosphorus content of the solution in test 17 was 0.6 g per liter, and in test 20, 2.7 g per liter. The analyses of the red-cake products from these tests are shown in Table III.

Red cake is a light, fluffy precipitate, and for most commercial uses fused black vanadium oxide is preferred. Red cake is converted to the fused black form by heating to 800°C and then tapping into a suitable mold. Laboratory tests have indicated that the fused black vanadium oxide is higher in vanadium and lower in phosphorus than the red cake from which it was produced. In a typical test the vanadium

content increased from 45.1 pct in the red cake to 47.9 pct in the black cake and the phosphorus content dropped from 0.15 to 0.029 pct. In another test the vanadium content increased from 41.8 pct in the red cake to 50.2 pct in the black cake. Spectrographic as well as chemical analyses indicated no objectionable quantities of undesirable impurities in the fused, black-cake products.

Recovery of Chromium: After recovery of phosphorus as trisodium phosphate and vanadium as red cake, almost all of the chromium leached from the calcine remains in solution at a concentration of 10 to 14 g per liter. The most promising method investigated for recovering chromium from this solution was precipitation as chrome yellow (lead chromate). The object of the investigation was to determine whether pigment-quality chrome yellow could be recovered. The composition requirements for commercially pure lead chromate pigments, according to the ASTM Specification D211-47, are shown in Table IV.

Before pigment-quality chrome yellow could be recovered from the vanadium hydrolysis filtrate, it was necessary to free the solution of 0.02 to 2.0 g of phosphorus per liter, 0.25 to 1.0 g of vanadium per liter, and some of the excess sulphate radical.

Table IV. Requirements for Composition, Chrome Yellow and Chrome Orange

	Type				
	I	II	III	IV	V
Lead chromate (PbCrO ₄) minimum, pct	50	68	93	60	55
Total matter soluble in water, maximum, pct	1.0	1.0	1.0	1.0	1.0
Total of all substances other than insoluble compounds of lead, maximum, pct	8.0	8.0	7.0	3.0	3.0
Moisture and other volatile matter, maximum, pct	1.0	1.0	1.0	1.0	1.0
Coarse particles, total residue retained on a No. 325 (44-micron) sieve, maximum, pct	1.0	1.0	1.0	1.0	1.0

Lime was used to precipitate these impurities. Upon the addition of lime, phosphorus precipitated first; when enough lime was added to raise the pH of the solution to 10.9, vanadium precipitated. Lime added in excess of that required to precipitate phosphorus and vanadium precipitated the sulphate radical. Part of the sulphate in the solution resulting from the hydrolysis of vanadium may be used to good advantage in the chrome yellow, as it precipitates as insoluble lead sulphate.

The main constituent of the lime precipitation product was calcium sulphate. Tests have indicated that less than 4 pct of the chromium was lost in this product and that excess lime caused no additional loss of chromium.

After the solution was freed of phosphorus, vanadium, and excess sulphate radical, chromium was precipitated as chrome yellow with lead nitrate or lead acetate. The effects of varying lime and lead acetate additions were demonstrated in a series of tests. In some, the lime used to precipitate impurities from solution was varied from 12.5 to 25 g per liter and the theoretical amount of lead acetate was used for precipitating chrome yellow. In others, the lime additions were held constant at 12.5 g per liter and the lead acetate additions were varied from 50 to 150 pct of the theoretical. In still others, the lime additions were held constant at 25 g per liter and the lead acetate additions varied the same as in the second series.

Table V. Chromium Recovery from Purified Hydrolysis Filtrate

Chromium, G per Liter	Lime Used, G per Liter	Pb(Ac) ₂ Used, G per Liter	Chrome Yellow Recovered, G	Chromium Recovery, Pct	Chrome-Yellow Product, Analysis, Pct	
					PbCrO ₄	PbSO ₄
9.85	12.5	30.7	36.5	58.6	101.9	Nil
9.56	25.0	29.9	37.0	54.6	93.8	Nil
9.85	12.5	46.1	66.0	86.5	95.7	2.3
9.56	25.0	44.8	52.0	80.2	101.9	Nil
9.85	12.5	61.5	76.5	97.5	93.2	4.5
9.85	16.7	61.5	77.5	97.5	93.8	2.5
9.85	20.8	61.5	74.0	99.4	93.2	1.2
9.56	25.0	59.8	76.5	98.1	95.7	1.9
9.85	12.5	76.9	84.0	98.9	81.4	16.5
9.56	25.0	74.8	79.0	98.3	87.6	15.6
9.85	12.5	92.2	96.0	98.9	63.4	31.1
9.56	25.0	89.7	93.0	99.5	70.8	22.4

It was assumed that all of the chromium in the chrome yellow precipitate was present as PbCrO₄ and that all of the sulphur was present as CaSO₄. In some tests, the calculated lead chromate added up to over 100 pct. In others the calculated lead chromate plus the calculated calcium sulphate added up to over 100 pct. These results indicate that the assumption as to compounds present may not be altogether correct. Nevertheless, this series of tests shows that, by proper lime control in the precipitation of impurities and subsequent controlled lead acetate additions, it may be possible to produce any type of pigment-quality chrome yellow from the chromium in the hydrolysis filtrate. The results of these tests are shown in Table V.

Simulated Plant Test

The object of this test was to simulate plant operating conditions and to determine the recovery of vanadium, phosphorus, and chromium in finished products under such conditions. The first step in the process, roasting, was done in a small rotary kiln of 8-ft length and 5-in. ID. The kiln was set on a slope of 1/2 in. per ft and rotated 1 1/4 rpm. Temperature in the kiln was automatically controlled between 1430° and 1450°F.

The charge for the test was a mixture of 18 lb of -35-mesh ferrophosphorus, 26.1 lb of soda ash, and 1.8 lb of salt (NaCl). The mixed charge was fed continuously to the kiln. After normal operating conditions were established, the calcine was discharged into agitated pulp in a leaching vessel. The specific gravity of the pulp was maintained between 1.25 and 1.30 by frequent water and solution additions. Heat was applied to the leaching vessel to keep the pulp boiling. When the leaching vessel became full, part of the pulp was removed, filtered, and the filter cake washed with water. The filter cake was then repulped with water and releached. During the two-day operation, seven batches of pulp were processed. The results of the leaching operation are shown in Table VI, and a materials balance for the roasting and leaching operations is shown in Table VII.

Table VI. Results of Continuous Leaching of Calcine

	G or Milli-liter	Analysis, Pct or G per Liter			Distribution, Pct		
		V	P	Cr	V	P	Cr
Primary solution	29,840	8.17	41.0	6.69	88.3	90.2	71.7
Washings	5,970	2.69	8.6	0.93	5.8	3.8	2.0
Releach solution	4,620	1.02	4.1	0.50	1.7	1.4	0.8
Residue	4,508	0.25	1.4	1.57	4.2	4.6	25.5

The materials balance indicates that 98.1 pct of the vanadium, 96.0 pct of the phosphorus, and 100 pct of the chromium contained in the materials that went into the test were accounted for in the products. The retention of vanadium, phosphorus, and chromium in the combined kiln and dust-box clean out was high, as the calcine that was discharged from the kiln before normal operating conditions were reached was included in this product. Under continuous operating conditions this loss would be almost negligible. Disregarding the loss in the combined kiln and dust-box clean out, 94.5 pct of the vanadium, 93.9 pct of the phosphorus, and 69.3 pct of the chromium were extracted from the ferrophosphorus. The primary solution contained 91.1 pct of the extracted vanadium, 93.2 pct of the extracted phosphorus, and 95.0 pct of the extracted chromium.

The primary crystallization operation was carried out by cooling 1600 milliliter batches of primary solution to 5°C in a laboratory crystallizer. Four batches were crystallized and stored in a refrigerator, then combined before centrifuging. Four batch centrifuging operations were required to treat all of

Table VII. Materials Balance for Roasting and Leaching Operations

Product	G or Milli-liter	Analysis, Pct or G per Liter			G		
		V	P	Cr	V	P	Cr
To Process							
Ferrophosphorus	8,161	5.2	24.7	5.2	424.4	2016	424.4
Solution 1	6,000	4.67	27.0	4.25	28	162	25.5
Solution 2	6,000	4.06	27.0	3.70	24.4	162	22.2
Total to process					476.8	2340	472.1
From Process							
Kiln and dust-box clean-out	9,456	2.01	9.4	2.05	192.0	889	193.8
Combined residues	4,508	0.254	1.4	1.57	11.4	63.1	70.8
Primary solution	29,840	8.17	41.0	6.69	243.8	1223	199.6
Filter washings	5,975	2.69	8.6	0.93	16.1	51.4	5.6
Releach solution	4,620	1.02	4.1	0.50	4.7	18.9	2.3
Total from process					468.0	2245.4	472.1

the crystallized product. The crystal-solution mixtures were introduced into the centrifuge at temperatures of from 4° to 6°C. The pregnant solution warmed to about 10°C in the centrifuging operation. The results of the individual centrifuging tests and the calculated composite results of the tests are shown in Table VIII.

The primary crystals contained 8.15 pct of the vanadium, 85.18 pct of the phosphorus, and 11.22 pct of the chromium present in the primary solution. To free the primary crystals of vanadium and chromium the crystals were dissolved in water, trisodium phosphate was crystallized from the solution, and the crystals separated from solution by centrifuging. Three series of crystallization and centrifuging tests were required to handle all of the solution. The phosphorus content of the solution to the first series of crystallization tests was 54 g per liter, but in the last two series the phosphorus content was adjusted to 45 g per liter. In each 1600 milliliter batch crystallization run the batch was cooled to -1°C and then stored in the refrigerator until the four batches required for the centrifuging test had accumulated. In the first centrifuging test the crystal-solution mixture was introduced into the centrifuge at 4°C, and secondary solution discharged from the centrifuge at 11°C. The crystals were washed in the centrifuge with 200 milliliters of ice water. In the second centrifuging test the crystal-

Table VIII. Results of Primary Crystallization and Centrifuging Tests

Test	Product	G or Milli-liter	Pct or G per Liter			Distribution, Pct		
			V	P	Cr	V	P	Cr
1	Crystals	4,199	0.13	5.5	0.07	8.62	83.68	8.13
	Solution	5,360	10.8	8.4	6.2	91.38	16.32	91.87
2	Crystals	3,379	0.16	6.8	0.19	9.46	85.80	14.75
	Solution	4,580	11.3	8.3	8.1	90.54	14.20	85.25
3	Crystals	3,379	0.14	6.9	0.09	8.72	86.41	7.92
	Solution	4,420	11.2	8.3	8.0	91.28	13.59	92.08
4	Crystals	1,391	0.05	5.5	0.21	3.15	84.25	15.77
	Solution	1,880	11.4	7.6	8.3	96.85	15.75	84.23
Composite	Crystals	13,348	0.13	6.24	0.12	8.15	85.18	11.22
	Solution	16,240	11.1	8.2	7.5	91.85	15.82	88.78

solution mixture was introduced into the centrifuge at 1°C and the secondary solution discharged at 9°C. The conditions for the third centrifuging test were the same as for the second.

The crystal product from this step in the process is the final trisodium phosphate product, and in this test it contained 1.08 pct of the vanadium from the primary solution. Chemical analysis of a sample of the dried crystal product showed a phosphorus content of 18.3 pct. The results of the secondary crystallization tests are shown in Table IX.

Assuming that all of the phosphorus extracted from the calcine is recovered in the form of trisodium phosphate except that lost in the final pregnant solution, the calculated phosphorus recovery for this test is 91.7 pct.

Perhaps the most noteworthy feature of this process is the addition of phosphoric acid to the pregnant solution from the primary crystallization step so that the solution can be freed of about 90 pct of its phosphorus by crystallization. For every gram of vanadium in the pregnant solution there was 0.74 g of phosphorus. Phosphoric acid was added to the pregnant solution to adjust the pH to 8.8 so that disodium phosphate would crystallize from solution on cooling. In this test the phosphoric acid addition amounted to approximately ½ g of phosphorus per gram of contained vanadium. After the tertiary crystallization and centrifuging operations, the vanadium-phosphorus ratio in the final pregnant solution was 1:0.078.

The adjusted solution was crystallized and centrifuged in the same manner as previously, with three centrifuging tests, each on the combined product of four 1600 milliliter batch crystallization runs. The crystallization temperature was -3°C. The crystal-solution mixtures were introduced into the centrifuge at 6° to 7°C. In this centrifuging operation the

Table IX. Results of Secondary Crystallization and Centrifuging Tests

Test	Product	G or Milli-liter	Pct or G per Liter			Distribution, Pct		
			V	P	Cr	V	P	Cr
1	Crystals	3,575	0.03	5.5	0.05	21.0	87.4	52.8
	Solution	3,720	1.08	7.6	0.43	79.0	12.6	47.2
2	Crystals	4,001	0.005	6.2	0.03	4.3	87.6	65.2
	Solution	4,275	1.05	8.2	0.15	95.7	12.4	34.8
3	Crystals	2,412	0.017	6.5	0.05	13.5	88.7	49.6
	Solution	2,660	0.99	7.5	0.46	86.5	11.3	50.4
Composite	Crystals	9,988	0.017	6.02	0.041	13.2	87.8	54.8
	Solution	10,655	1.04	7.82	0.32	86.8	12.2	45.2

crystals were not washed. The disodium phosphate crystal product of continuous plant operation would be recycled to the primary solution storage tank, and the solution would go to the hydrolysis operation. The results of the tertiary crystallization and centrifuging operations are shown in Table X.

The phosphorus content of the composite pregnant solution from the tertiary crystallization step was 0.98 g per liter. After further precipitation of phosphorus from this solution with lime and/or calcium chloride in three batch operations, red cake was recovered from each of the batches by hydrolysis. The results of the hydrolysis tests are summarized in Table XI.

The calculated overall recovery of vanadium as black cake for the entire test is 84.4 pct, if the recovery obtained in hydrolysis test 3 is applied to the entire hydrolysis operation and if it is assumed that all of the vanadium leached from the calcine is recoverable as black cake, except that in the trisodium phosphate product, the calcium phosphate product, the barren solution, and the red-cake washings.

Most of the test work on the recovery of chromium from barren solution was done on solution from this test, although the tests are described in a preceding section. The results indicated that as much as 99 pct of the chromium was recovered from the barren solution in a chrome yellow product that contained over 93 pct PbCrO₄. In the initial leaching, 69.3 pct of the chromium in the calcined ferrophosphorus was extracted. There were small chromium losses in the trisodium phosphate, black-cake, and calcium phosphate products. Assuming that 99 pct of the chromium could be precipitated from barren solution, as some of the batch tests indicated, the overall recovery of chromium as chrome yellow would be at least 65 pct.

Conclusions

The largest phosphate reserve in the United States occurs in the Phosphoria formation of Montana, Idaho, Wyoming, and Utah. An unusual feature of this great reserve is its content of small percentages of vanadium, chromium, and other metals. In the production of elemental phosphorus by electric furnace smelting most of the vanadium and other metals collect in the byproduct ferrophosphorus. To the authors' knowledge, the western ferrophosphorus currently produced is not being treated to recover vanadium or other values contained in it. By use of the tristage crystallization process described in this paper, vanadium black-cake, chrome yellow, and a valuable trisodium phosphate product could be recovered from western ferrophosphorus.

The tristage crystallization process starts with roasting of the vanadiferous ferrophosphorus with

Table X. Results of Tertiary Crystallization and Centrifuging Tests

Test	Product	G or Milli-liter	Analysis, Pct or G per Liter			Distribution, Pct		
			V	P	Cr	V	P	Cr
1	Crystals	1,288	0.35	4.0	0.25	11.7	95.2	11.6
	Solution	4,030	11.7	0.9	8.40	88.4	4.8	88.4
2	Crystals	1,100	0.29	2.7	0.15	9.4	90.7	6.9
	Solution	2,335	13.1	1.3	9.46	90.6	9.3	93.1
3	Crystals	2,335	0.33	3.3	0.33	11.4	94.8	14.8
	Solution	4,690	12.9	0.9	9.55	88.6	5.2	85.2
Composite	Crystals	5,243	0.33	3.4	0.27	11.1	94.3	12.1
	Solution	11,055	12.50	0.98	9.12	88.9	5.7	87.9

Table XI. Results of Hydrolysis Tests

	Test Number		
	1	2	3
Vanadium loss in calcium phosphate precipitate, pct	0.2	0.6	6.2
Analysis of red cake, pct: V	31.6	38.6	41.8
P	0.11	0.10	0.20
Cr	0.79	2.05	1.09
Na	5.8	8.3	8.9
Analysis of barren solution, g per liter: V	2.48	1.36	0.25
P	0.7	0.5	0.20
Vanadium precipitated by hydrolysis, pct	81.3	88.9	97.2
Analysis of black cake, pct: V	50.5	48.9	50.2
P	0.01	0.01	0.01
Cr	0.008	0.001	0.005
Mo	0.45	0.57	1.0
Na	11.5	12.2	11.0
Vanadium recovery in black cake from final pregnant solution, pct	81.1	88.3	91.0

soda ash and salt, followed by water leaching to extract vanadium, phosphorus, and chromium. Commercial grade trisodium phosphate is produced from the primary leach solution by two crystallization and centrifuging operations. The pregnant solution from the primary crystallization step contains the recoverable metal values and more phosphorus than can be tolerated in the vanadium hydrolysis step. A third crystallization and centrifuging step, involving addition of phosphoric acid to the pregnant solution, removes about 90 pct of the remaining phosphorus as disodium phosphate and leaves only about 1 g per liter of phosphorus in the final pregnant solution. The disodium phosphate crystals are recycled to the primary solution, increasing the yield of the trisodium phosphate product. After further phosphorus purification by addition of calcium ion, the final pregnant solution is hydrolyzed to precipitate vanadium as red cake. The red cake is fused at 800°C to produce black cake, which is the usual form of vanadium for use in the production of ferrovanadium and vanadium chemicals. Chromium is precipitated as chrome yellow by addition of lead nitrate or acetate to the solution remaining after hydrolysis of the vanadium. Results of a simulated plant test indicate that about 85 pct of the vanadium, 65 pct of the chromium, and 91 pct of the phosphorus contained in western ferrophosphorus can be recovered in valuable products.

Acknowledgments

The research reported in this paper was done by the Ferrous Metals Branch, Region II, Bureau of Mines, at the Northwest Electrodevelopment Laboratory. It was part of the general program of the Bureau of Mines to develop and conserve the Nation's mineral resources. The authors acknowledge the advice of Stephen M. Shelton, Regional Director, under whose general supervision the investigation was made. Credit is due Mark Wright, now Assistant Regional Director, W. F. Holbrook, Head of the Chemical Section, and other members of the analytical staff for the many analyses of test products.

The cooperation of J. G. Miller, Resident Manager, Westvaco Chemical Div., Food Machinery & Chemical Corp., in supplying ferrophosphorus produced at the division's Pocatello, Idaho, phosphorus smelter is gratefully acknowledged.

¹ Lloyd H. Banning and R. T. C. Rasmussen: Process for Recovering Vanadium from Western Phosphates. Bur. Mines R.I. 4822 (1951) 44 pp.

Directional Properties of 2S Aluminum

by K. T. Aust and F. R. Morral

The preferred orientation and earing characteristics of 2S aluminum were studied. An empirical correlation was obtained relating earing behavior and variation of mechanical properties for face-centered cubic metals. Strain-ratio measurements for 2S were found to be in good agreement with Hill's theory of plastic anisotropy.

DIRECTIONALITY in sheet metals may be revealed by earing in a cupping test, or by the variation of mechanical properties of tensile specimens taken at different angles to the rolling direction. However, no simple correlation appears to exist between earing and variation in mechanical properties in metals and alloys studied.¹⁻⁵

Aluminum of commercial purity (known as 2S, with a specified minimum of 99.0 pct Al) cast by the direct casting process was chosen in the present investigation since ears at 45° or 0°, 90° can readily be obtained. Preferred orientation is often the principal cause of uneven metal flow, such as earing, and variation in mechanical properties. Consequently, the preferred orientation characteristics of 2S aluminum were initially studied using both X-ray diffraction and micrographic techniques. The variation of mechanical properties with angle to the rolling direction was next determined in an effort to clarify the apparent lack of correlation of earing behavior with mechanical properties for face-centered cubic metals. Strain-ratio^{6,7} measurements

* The strain-ratio values are obtained by deriving the slope of the curve $\ln W/W_0$ vs $\ln T/T_0$ where W_0 and T_0 are the initial width and thickness respectively of the tensile specimen and W and T are the width and thickness at an arbitrarily chosen percentage of elongation.

were finally conducted to determine first, if the maximum values of the strain ratio occurred at the earing positions, and second, if Hill's theory of plastic anisotropy⁷ is applicable to other face-centered cubic metals such as aluminum.

Detailed treatments, working, and heat treating are not given in this paper since this study is not concerned with the methods to produce earing, but to correlate earing with other properties and characteristics of the material. The percentage of earing was measured using the formula specified by the

Aluminum Association, $\frac{x-y}{x} \times 100 = \text{pct earing}$,

K. T. AUST, Junior Member AIME, formerly with Kaiser Aluminum & Chemical Corp., is now associated with Johns Hopkins University, Baltimore, and F. R. MORRAL, Member AIME, is Head, X-Ray Dept., Div. of Metallurgical Research, Kaiser Aluminum & Chemical Corp., Spokane, Wash.

Discussion on this paper, TP 3475E, may be sent, 2 copies, to AIME by May 1, 1953. Manuscript, Sept. 9, 1952. Los Angeles Meeting, February 1953.

where x is the height of the ear and y is the height of the valley from the bottom of the cup.

Preferred Orientation Characteristics of 2S

X-ray Studies: Beck and coworkers⁸ have determined that the rolling texture of 2S after 95 pct cold reduction may be approximately described by four equivalent ideal orientations near (123) $[\bar{1}\bar{2}1]$. Also, the recrystallization or annealing texture of 2S aluminum consists of four components of the (123) $[\bar{1}\bar{2}1]$ type, retained from the rolling texture, and of a (100) $[001]$ or cube texture component.⁹ Fig. 1 illustrates the typical appearance of deep drawn earing cups with the corresponding X-ray diffraction patterns. The X-ray patterns were taken with copper radiation using the structure-integrating method¹⁰ in which the specimen is scanned during the X-ray exposure. The rolling direction was vertical and the rolling plane was perpendicular to the horizontal X-ray beam. It was found that an increase in the retained rolling texture component resulted in a greater 45° ear height, while an increase in the recrystallization texture component (i.e., cube texture) caused greater 0°, 90° earing.

X-ray diffraction studies of 2S cold rolled to final thickness followed by a final anneal have shown that the rolling texture, and also the retained component of the rolling texture after annealing, are increased with greater cold-rolling reduction.

The preferred orientation characteristics of 2S sheets given an intermediate anneal between cold rolling followed by a final anneal were found to depend on the position of the intermediate anneal during cold rolling. For instance, three identical samples of 2S homogenized ingot, each 1 in. thick, were given the following cold-rolling and annealing treatments: 1—50 pct reduction, intermediate anneal, 96 pct reduction to 0.020 in. and a final anneal; 2—75 pct reduction, intermediate anneal, 92 pct reduction to 0.020 in. and a final anneal; and 3—90 pct reduction, intermediate anneal, 80 pct reduction to 0.020 in. and a final anneal. The intermediate and final annealing treatments consisted of a 70°F per hr heating rate, held 6 hr at 800°F and air cooled.

Typical X-ray patterns after each of these treatments are shown in Fig. 2. It was evident that after treatment 1, the retained rolling texture component predominated; after treatment 2, the retained roll-



a—Typical for rolling texture.

b—A mixture of 1a and 1c.

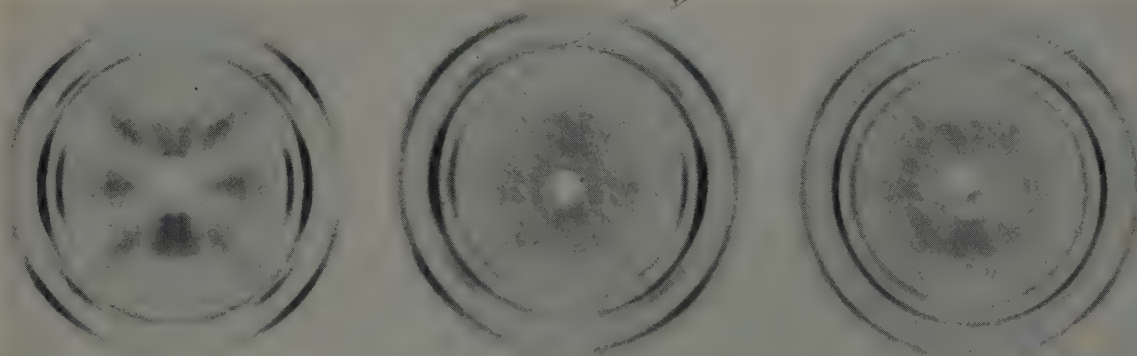
c—Typical for recrystallization texture of rolled 2S.

Fig. 1—Earing cups from annealed 2S sheets with typical corresponding X-ray patterns.

ing texture component decreased and the cube texture component increased. After the treatment outlined in 3, the rolling texture component again decreased with very little cube texture, approaching a random orientation texture. These results illustrate the changes in the amounts of preferred orientation which may occur when the position of a single intermediate anneal is varied.

The importance of final annealing temperature on the preferred orientation and earing characteristics of many face-centered cubic metals and alloys has been demonstrated by various investigations.¹¹⁻¹⁴ For instance, it was determined that the $0^\circ, 90^\circ$ ears of copper¹⁴ and cupronickel¹² increased in size as the final annealing temperature was raised. The height of 45° ears in brass also increased with the temperature of the final anneal.^{11, 13} The effect of final annealing temperature on the earing behavior of 2S was determined and is shown in Fig. 3. The multi-

ple curves of Fig. 3 were obtained by various cold-rolling and intermediate annealing treatments prior to the final anneal. Therefore, the ear height and ear direction at any one final annealing temperature depended on the previous treatment. Generally, a decrease of 45° ear size and an increase of $0^\circ, 90^\circ$ ear size resulted with higher final annealing temperatures. X-ray studies have revealed an increase of the cube orientation texture in 2S after annealing at higher temperatures. For both copper¹⁴ and brass,^{11, 13} it was believed that the increased grain size with resulting greater ease of plastic flow was the more important influence on increase in ear height with temperature of the final anneal. However, if the larger grain size was a contributing factor to the ear height of 2S, then both 45° and $0^\circ, 90^\circ$ ear sizes would be expected to increase as the final annealing temperature was raised. Since this was not observed, the more perfectly developed



50 pct reduction, intermediate anneal,
96 pct reduction.

75 pct reduction, intermediate anneal,
92 pct reduction.

90 pct reduction, intermediate anneal,
80 pct reduction.

Fig. 2—Typical X-ray patterns of 2S sheets which were annealed as shown.

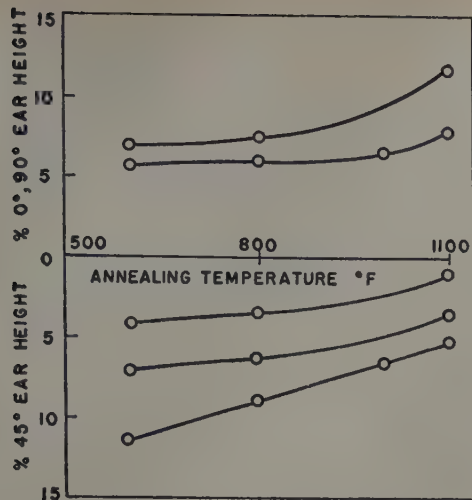


Fig. 3—Effect of final annealing temperature on the ear height of annealed 2S sheets given different cold rolling and intermediate annealing treatments.

cube orientation texture is believed to be the primary reason for the variation of ear size of 2S with change in final annealing temperature.

Micrographic Studies: The orientations present in aluminum sheet were studied micrographically, by using the new technique with an anodized film and polarized light.^{9, 15, 16}

It was observed that the cube grains appeared black under polarized light and remained black even though the microscope stage was rotated through 360°. However, the other orientations changed colors from white to gray to black, and vice versa, for each 45° rotation of the stage. It was,

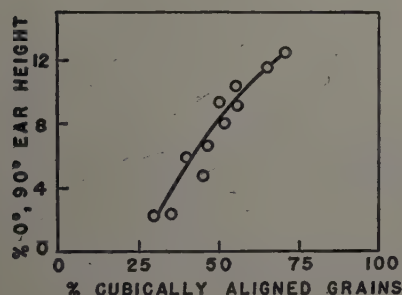


Fig. 4—Relationship between percentage of 0°, 90° ear height in drawn cup and percentage of cubically aligned grains in microstructure.

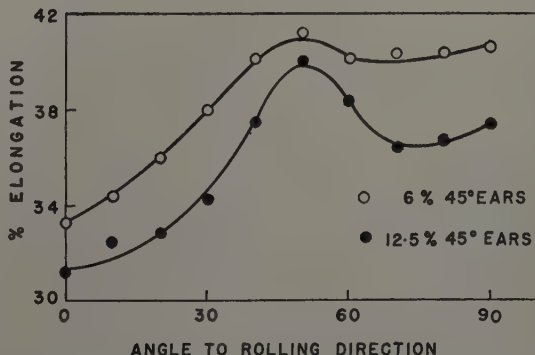
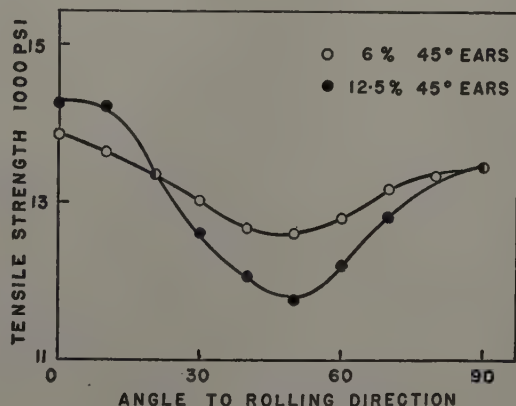
therefore, possible to determine the percentage of cubically aligned grains. Two micrographs were taken from the same locations of a specimen before and after a 45° rotation of the microscope stage. The two negatives were superimposed such that identical grains coincided. A photographic print was then made from the two superimposed negatives. Those grains which were now black on the print possessed the cube orientation texture. The percentage of cubically aligned grains was then determined from the photographic prints using grain count techniques to an accuracy of approximately ± 5 pct. These determinations were carried out near the center of the cross section of annealed 2S sheets having different 0°, 90° ear heights. The percentage of 0°, 90° ear height was plotted as a function of the percentage of cubically aligned grains in Fig. 4. A similar relationship was also found by Baldwin¹⁷ for annealed copper strip. It is noteworthy for annealed

2S that sheets containing less than 40 pct cubically aligned grains still can produce ears at 0° and 90° to the direction of rolling.

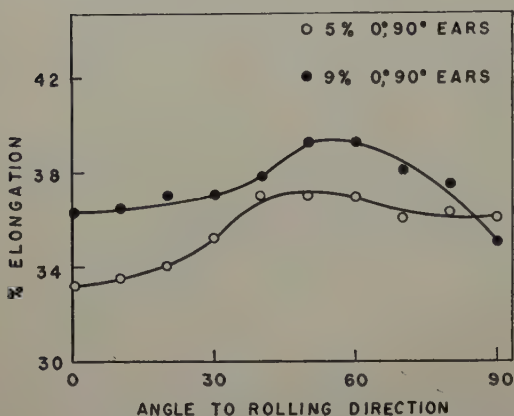
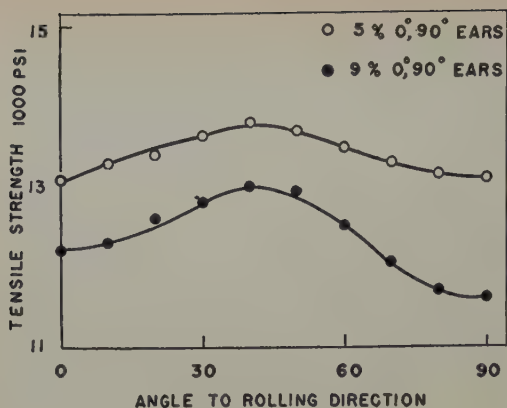
Variation of Mechanical Properties of Annealed 2S

Tensile tests were conducted at every 10° from 0° to 90° to the direction of rolling, for annealed 2S sheets having different earing characteristics. The results are shown in Figs. 5 to 8. Differences in grain size produced by the treatments given influenced the actual values of the mechanical properties. However, the variation of tensile strength and percentage of elongation was a function of the angle the axis of the tensile specimen made with the rolling direction.

When 45° ears occurred in the cups, minimum tensile strength and maximum elongation was obtained in approximately the corresponding position in the sheet, i.e., at 45° to the rolling direction (Figs. 5 and 6). These results therefore agreed with those on brass,⁸ also having 45° ears. When the crests of ears were located in the 0° and 90° positions the tensile values were approximately a minimum and the elongation values generally approached a minimum in the corresponding positions (Figs. 7 and 8). The results for the variation in elongation of 2S were somewhat obscured by the effect of mechanical fibering. However, the general correlation of earing and variation in tensile strength was apparent. The minimum elongation in 2S and copper⁸ occurred in approximately the corresponding positions of 0° and 90° earing. The minimum elongation of copper was attributed to the high proportion of (100) [001] texture.¹⁸ It was shown in the present work that 2S annealed sheets having 5 pct and 9 pct 0°, 90° ear heights (as in Fig. 8) contained a large proportion of cube texture. Therefore, it is believed that the cube texture component of the annealing texture



Figs. 5 (upper) and 6 (lower)—Directionality of tensile properties of annealed 2S sheets with different 45° ear heights.



Figs. 7 (upper) and 8 (lower)—Directionality of tensile properties of annealed 2S sheets with different 0°, 90° ear heights.

was also responsible for the minimum elongation values in annealed 2S having 0°, 90° ear directions.

One obvious anomaly still remained; namely, with 0°, 90° earing, 2S aluminum showed a minimum tensile strength and copper a maximum tensile strength, in the 0° and 90° directions of rolling. Richards¹⁸ has indicated that the 0°, 90° positions of ears in copper corresponded to the direction of minimum true tensile strength. Richards pointed out that an approximate estimation of the true tensile stress at fracture can be made by multiplying the

tensile strength value by a factor, $1 + e$, where e is the elongation of the test piece expressed as a fraction of the gage length. By applying the $1 + e$ approximation, the true tensile strength of 2S was also determined to be a minimum at 0° and 90° to the rolling direction. Therefore, the 0°, 90° earing behavior of both copper and 2S can be correlated with the minimum true tensile strength values in corresponding 0° and 90° positions. The same relationship held for annealed brass and 2S having 45° earing positions, since the directions of maximum and minimum true stress values are identical with the positions of the maximum and minimum tensile strength values.

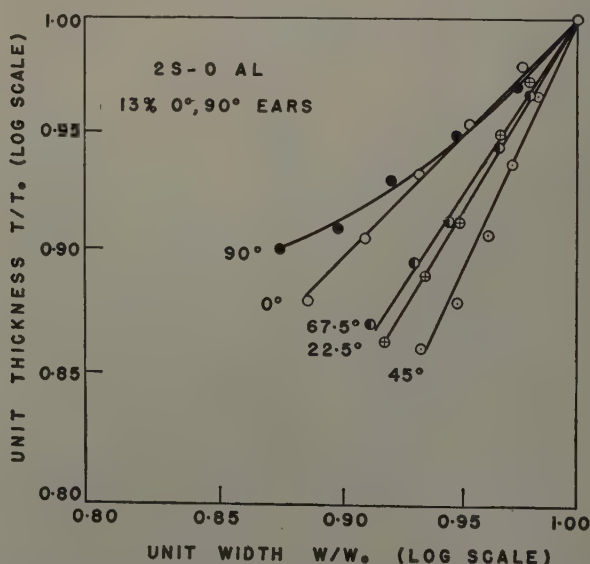
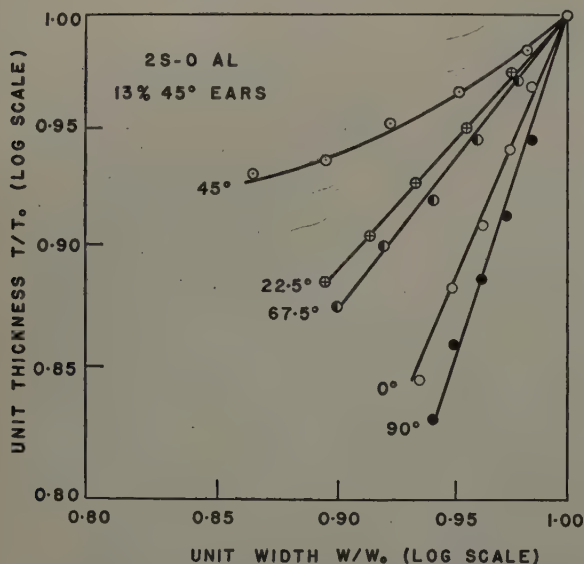
Therefore, a general empirical correlation exists between earing and variation of mechanical properties for face-centered cubic metals. The general tendency with 0°, 90° or 45° earing directions is the occurrence of minimum true tensile strength in approximately the same direction of ear formation. With 45° earing, the elongation is usually a maximum at about 45° to the rolling direction. However, with 0°, 90° earing, the elongation generally approached a minimum in the 0° and 90° positions.

Strain Ratios of Annealed 2S

The previous correlation of directionality and earing tendencies is still only qualitative. The theory of plastic anisotropy advanced by Hill⁷ appears to be a promising quantitative approach to the problem. According to this theory, the important factor controlling the positions of the ears is the relation between the ratios of the components of the stress and the plastic strain increment. The relevant test is the measurement of strain ratios in tension tests. The theoretical treatment, described by Bourne and Hill,⁶ resulted in the following equation:

$$\frac{\ln W/W_0}{\ln T/T_0} = \frac{H + (2N - F - G - 4H) \sin^2 \alpha \cos^2 \alpha}{F \sin^2 \alpha + G \cos^2 \alpha} = r(\alpha) \quad [1]$$

W_0 and T_0 are the initial width and thickness respectively of the tensile specimen and W and T are the width and thickness at an arbitrarily chosen



Figs. 9 (left) and 10 (right)—Contraction of unit width and unit thickness during tensile tests of two samples of annealed 2S having 45° ears and 0°, 90° ears.

percentage of elongation (usually every 5 pct). F , G , H , and N are parameters specifying the constant state of anisotropy. The term r is the strain ratio at an angle α to the rolling direction.

The validity of the theory expressed in Eq. 1 can be checked by comparing it with the experimental results of strain ratios at various angles to the rolling direction. According to Bourne and Hill, if N is less than both $F + 2H$ and $G + 2H$, the ears are in the 0° and 90° positions. However, if N is greater than both $F + 2H$ and $G + 2H$, the ears are in the 90° positions where γ may be obtained from

$$\tan^2 \gamma = \frac{N - G - 2H}{N - F - 2H} \quad [2]$$

The above theoretical considerations were found to be in good agreement with the experimental data for copper and brass having four ears.⁶ The following experiments were conducted to determine if Hill's theory of plastic anisotropy may be generalized to include other metals, such as aluminum.

Two sheets of annealed 2S aluminum (0.020 in. thick) were used throughout these tests, one sheet having four ears of 13 pct height at 45° and the other having four ears of 13 pct height at $0^\circ, 90^\circ$ to the rolling direction, after deep-drawing. Standard tensile specimens in duplicate were milled from these sheets at various angles to the rolling direction, $0^\circ, 22.5^\circ, 45^\circ, 67.5^\circ$, and 90° . The gage length was 2 in. and the width 0.5 in. Width and thickness measurements of the tensile specimens were taken with a micrometer reading to 0.0001 in., at every 5 pct elongation from 0 pct to the stage at which necking began. The values of the width and thickness were expressed in terms of unit width (W/W_0) and unit thickness (T/T_0).

The unit width and unit thickness values for the two sheets of annealed 2S having 45° and $0^\circ, 90^\circ$ ears were plotted logarithmically in Figs. 9 and 10. It is evident that the rate of contraction of thickness with respect to that of the width is a function of the angle between the axis of the tensile specimen and the rolling direction.

Values of strain ratios (r) were plotted as a function of the angle α between the rolling direction and the axis of the tensile specimen in Fig. 11. The maximum values of r were found to occur in the same positions as the ears; i.e., for 45° ears, r is a maximum at 45° and for $0^\circ, 90^\circ$ ears, r is a maximum at 0° and 90° . It is concluded that the occurrence of maximum values of the strain ratio at the actual earing positions is not only true for copper and 70:30 brass but is also the case for 2S aluminum and perhaps for all face-centered cubic metals. Baldwin et al.⁵ have explained the relationship between unit width and unit thickness, for copper samples cut at 45° to the rolling direction, by the manner in which the crystallites deform.

The theoretical relation of Hill (Eq. 1) was checked with the experimental results of r for annealed 2S over the whole range of angles to the rolling direction. The parameters giving four ears at 45° corresponding to the curve in Fig. 11 are: $F:G:H:N = 1:0.8:0.35:3.2$. According to the theory of Hill, if N is greater than both $F + 2H$ and $G + 2H$, as is true in the present case, the ears are in the 90° positions. The angle γ was determined to be 47° from Eq. 2, i.e., the ears should form at 43° . This agrees well with the experimental value of 45° ears.

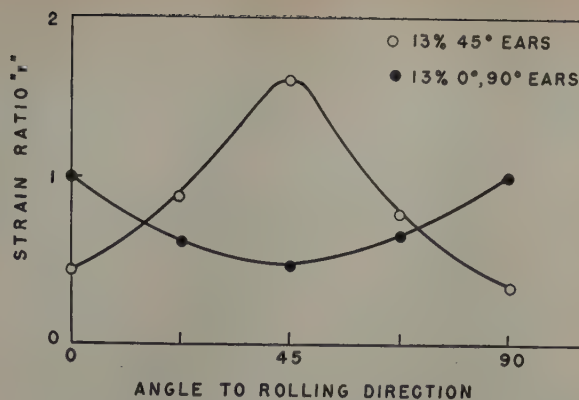


Fig. 11—Variation of strain-ratio " r " with angle to the rolling direction for annealed 2S sheets having 45° and $0^\circ, 90^\circ$ ears.

The results shown in Fig. 11 for the annealed 2S sheet having $0^\circ, 90^\circ$ ears were found to give the following parameters: $F:G:H:N = 1:1:1:1.6$. The theory predicts ears in the 0° and 90° positions when N is less than both $F + 2H$ and $G + 2H$, which is again in agreement with experiment.

Thus, the theory of plastic anisotropy advanced by Hill was found to be in good agreement with the experimental data for annealed 2S sheets. Since similar conclusions were reached for copper and 70:30 brass,⁶ it is concluded that Hill's theory may be applicable to all face-centered cubic metals. Consequently, Hill's method of predicting earing positions from measurements of strain ratios in tension tests is regarded to be of more fundamental significance than the usual empirical attempts to correlate rupture properties with the earing tendency of a metal.

Summary

The occurrence of $0^\circ, 90^\circ$ earing in annealed 2S sheet was related to the cube texture component, while 45° earing was associated with the retained rolling texture component. The preferred orientation characteristics of the final annealed 2S sheet were found to depend on the amount of reduction before the anneal, and on the position of an intermediate anneal during the cold-rolling cycle.

Micrographic methods revealed a definite relationship between the $0^\circ, 90^\circ$ earing tendency of 2S aluminum and the percentage of cubically aligned grains. The amount of cube orientation texture increased with higher final annealing temperatures.

The tensile strength and true stress at fracture were a minimum and the elongation a maximum at 45° to the rolling direction when 45° ears occurred in 2S. However, the tensile strength and true stress were minima and the elongation generally approached a minimum at 0° and 90° when ears formed in the 0° and 90° positions. The variation of mechanical properties with earing behavior of annealed 2S was correlated with similar variations for other face-centered cubic metals.

The strain-ratio values were a maximum at 45° or 0° and 90° for annealed 2S sheets that eared at 45° or 0° and 90° , respectively. The theory of plastic anisotropy advanced by Hill was found to be in good agreement with the experimental results for annealed 2S sheets.

Acknowledgment

The assistance given by F. M. Krill, W. Y. Bleakley, W. H. Falk and various members of the Division of Metallurgical Research, Kaiser Aluminum and

Chemical Corp., is acknowledged. The authors also wish to thank D. W. Smith and J. B. Hess for valuable discussion, and P. P. Zeigler, Director of Research, for permission to publish this work.

References

- ¹ J. D. Jevons: *The Metallurgy of Deep Drawing and Pressing* (1942) p. 89. Chapman & Hall.
- ² M. Whitaker: *The Deep Drawing of Non-Ferrous Metals. Sheet Metal Industries* (1950) **27**, No. 281, p. 815.
- ³ M. Cook and T. LL. Richards: The Structural Changes Effected in 70:30 Brass Strip by Cold Rolling and Annealing. *Journal Inst. Metals* (1943) **69**, p. 351.
- ⁴ M. Cook and T. LL. Richards: Directional Characteristics of Single-Texture-Structure Copper Strip. *Journal Inst. Metals* (1943) **69**, p. 201.
- ⁵ W. M. Baldwin, Jr., T. S. Howald, and A. W. Ross: Relative Triaxial Deformation Rates. *Trans. AIME* (1946) **166**, p. 86; *METALS TECHNOLOGY* (September 1945).
- ⁶ L. Bourne and R. Hill: On the Correlation of the Directional Properties of Rolled Sheet in Tension and Cupping Tests. *Philosophical Magazine* (1950) **41**, p. 671.
- ⁷ R. Hill: A Theory of the Yielding and Plastic Flow of Anisotropic Metals. *Proc. Royal Soc.* (1948) **193A**, p. 281.
- ⁸ H. Hu, P. R. Sperry, and P. A. Beck: Rolling Textures in Face-Centered Cubic Metals. *Trans. AIME*

- (1952) **194**, p. 76; *JOURNAL OF METALS* (January 1952).
- ⁹ P. A. Beck and H. Hu: Annealing Textures in Rolled Face-Centered Cubic Metals. *Trans. AIME* (1952) **194**, p. 83; *JOURNAL OF METALS* (January 1952).
- ¹⁰ D. W. Smith: Symposium of Radiography and X-ray Diffraction. (1937) ASTM Philadelphia.
- ¹¹ E. W. Palmers and C. S. Smith: Effect of Some Mill Variables on the Earing of Brass in Deep Drawing. *Trans. AIME* (1942) **147**, p. 164.
- ¹² W. H. Bassett and J. C. Bradley: Ears on Cupro-Nickel Cups. *Trans. AIME* (1933) **104**, p. 181.
- ¹³ F. H. Wilson and R. M. Brick: Textures, Anisotropy, and Earing Behavior of Brass. *Trans. AIME* (1945) **161**, p. 173.
- ¹⁴ M. Cook and T. LL. Richards: The Influence of Crystal Structure on the Cold Rolling and Annealing of Copper Strip. *Journal Inst. Metals* (1941) **67**, p. 203.
- ¹⁵ A. Hone and E. C. Pearson: Grain Orientation in Aluminum Revealed by Anodic Film. *Metal Progress* (1948) **53**, p. 363; also *Metal Progress* (1950) p. 713.
- ¹⁶ P. Lacombe and L. Beaujard: Etude Microscopique de l'écrouissage et de la recristallisation de l'aluminium extra-pur. *Revue Metallurgie* (1947) **44**, p. 71.
- ¹⁷ W. M. Baldwin, Jr.: Effect of Rolling and Annealing upon the Crystallography, Metallography, and Physical Properties of Copper Strip. *Trans. AIME* (1946) **166**, p. 591.
- ¹⁸ T. LL. Richards: Preferred Orientation in Non-Ferrous Metals. *Progress in Metal Physics* (1949) Vol. 1. London. B. Chalmers.

Technical Note

Preferential Etch for Use in Optical Determination Of Germanium Crystal Orientation

by R. H. Wynne and Colman Goldberg

WHEN using an optical goniometer to determine crystal orientation¹ it is advantageous to use a preferential etchant so that the etch pits have plane faces which are parallel to crystallographic planes, all of which are of the same "form."

"Westinghouse Silver Etch" (WAg), a preferential etch for germanium, is made up as follows: 40 ml of 49.7 pct hydrofluoric acid, 20 ml of 70.7 pct nitric acid, and 40 ml of distilled water containing 2.0 g of silver nitrate. Examination of metallographs of WAg etched surfaces (Fig. 1, for example) indicates that, regardless of crystal orientation, the faces of the etch pits are (111) surfaces. Optical goniometer examination of these WAg etched surfaces also indicates that the faces of the etch pits are (111) surfaces, i.e., all bright reflections are from (111) planes.

When using an optical goniometer of the type described by Barrett,¹ not only (111) reflections from a WAg etched germanium surface but also other reflections of lower intensity will be observed. These latter reflections can cause confusion. We have used an optical goniometer made from a war surplus astrocompass and a galvanometer lamp. The reflections are observed by using the goniometer in a darkened room and letting the reflected light be in-



Fig. 1—WAg etched germanium surface. Approximately (111) orientation.

cident upon a piece of white paper. The resulting decrease of goniometer sensitivity enables (111) reflections only to be observed. This in turn permits the crystal orientation to be determined in a matter of minutes, since only two measurements are necessary.

The authors wish to acknowledge the help received from R. E. Davis who assisted in making the metallographs and aided the authors in the interpretation of the metallographs.

R. H. WYNNE and C. GOLDBERG are associated with the Electronics and Nuclear Physics Dept., Westinghouse Research Laboratories, East Pittsburgh, Pa.

TN 146E. Manuscript, Oct. 16, 1952.

¹ C. S. Barrett: *Structure of Metals* (1943) pp. 173-177. New York. McGraw-Hill Book Co.

Some Applications of the Thermodynamic Theory of Irreversible Processes to Physical Metallurgy

by E. S. Machlin

An extension of the thermodynamic theory has been made for the case of irreversible growth processes occurring by the motion of an interface. The theory is applicable to such diverse phenomena as diffusion, growth in recrystallization, continuous grain growth, growth of carbides, etc., growth of eutectoid products, growth in solidification, recovery, "slipless" flow, etc.

THE publication of a recent book¹ has served to focus attention on a very powerful means of treating certain irreversible processes. This method which has been formally described as the thermodynamic theory of irreversible processes is applicable to processes which involve an approach to equilibrium and for which the deviations from equilibrium are small. The irreversible processes can be classified into three groups: chemical reactions, transport processes (diffusion, heat and electrical flows), and relaxation phenomena involving a degradation of internal energy to more stable states. The limits of applicability of the theory can be precisely defined^{1, 2} for each type of irreversible process. For example, in a chemical reaction at constant temperature and pressure, the Gibbs free energy released per mol in the process should be less than the thermal energy, RT .

Another type of irreversible process, which sometimes involves a combination of the first two of the above-mentioned groups, is treated in this paper. This process is one characterized by the motion of an interface separating two regions having different values of free energy and may be briefly described as a growth process. Prigogine² and Herring³ have treated special cases of this type of process.

Previous conscious applications of the theory in metallurgy have been limited to the field of diffusion, one of the transport processes. Darken,⁴ Bardeen,⁵ Prigogine² and others have made significant contributions in this respect. Some other applications of the theory are described in this paper.

The Theory

The thermodynamic theory of irreversible processes is based on the work of Onsager,⁶ DeDonder,⁷ Prigogine² and others. A resume of the theory has been given by Prigogine² and DeGroot.¹ A brief description of the theory follows, although for a complete understanding the reader is urged to read the references.

E. S. MACHLIN, Member AIME, is Assistant Professor of Metallurgy, School of Mines, Columbia University, New York.

Discussion on this paper, TP 3431E, may be sent, 2 copies, to AIME by Dec. 1, 1953. Manuscript, Jan. 18, 1952; revised, Sept. 18, 1952. Cleveland Meeting, October 1953.

It is first assumed that the change in entropy, even for a system removed from equilibrium, is given by

$$dS = [dU + pdV - \sum_i \mu_i dn_i - \sum_k P_k dx_k] T^{-1}$$

Using this expression, the irreversible entropy production in the system is calculated by subtracting the contribution to the change in entropy of the system by transfer of heat, work, or matter from the surroundings. Thus, for example, the irreversible entropy production of a system at constant temperature and pressure is given by

$$d_i S = -\frac{1}{T} dG \quad (\text{DeDonder}^7)$$

Now it has been shown by Prigogine,² DeDonder,⁷ and DeGroot¹ that the rate of irreversible entropy production $d_i S/dt$, when calculated in the manner suggested, can be written as a sum of products of conjugate forces X_k and fluxes J_k , i.e.,

$$\frac{d_i S}{dt} = \sum_k J_k X_k \quad [\text{I-1}]$$

The assumption is next made that a linear relation exists between a given flux and the forces, obtained from Eq. I-1, i.e.,

$$J_i = \sum_k L_{ik} X_k \quad (i = 1, 2, \dots, n) \quad [\text{I-2}]$$

Generally, there is a degree of freedom in choice of the fluxes and forces. However, for all the choices consistent with Eq. I-1 the Onsager⁶ relations, based on the principle of microscopic reversibility, namely, $L_{ik} = L_{ki}$, are valid. The coefficients L_{ik} , depending upon the choice of the conjugate fluxes and forces, may be more or less dependent upon the parameters defining the state of the system. In general, the proper choice of fluxes and forces utilizing Eq. I-1, makes the coefficients L_{ik} independent of time. Also, because many of the three classes of irreversible phenomena have already been treated,^{1, 2} a proper choice can be made by analogy. In any case, the validity of Eq. I-2, from whatever choice made using Eq. I-1, must be tested by experimentation.

The theory, thus, comprises the following steps: 1—The irreversible entropy production is calculated to yield Eq. I-1. 2—The terms in Eq. I-1 are grouped

to yield what seems to be a logical compilation of conjugate fluxes and forces. 3—The linear relations, Eq. I-2, are set up using these definitions of fluxes and forces. 4—These linear relations are then tested experimentally. 5—The reciprocal relations $L_{ki} = L_{ik}$ are also checked experimentally.

Upon experimental verification of the predicted results for a large number of diverse types of irreversible processes, it has been found that the theory provides a neat, concise description of irreversible phenomena in the state not too far removed from equilibrium.* Thus, the theory fulfills one of the

* The limit of applicability of the theory can be made precise for each type of irreversible process.

goals of scientific endeavor. It is beyond the scope of this paper to illustrate the breadth of applicability of the theory. However, an attempt will be made in this paper to illustrate how the theory rationalizes growth phenomena on the basis of the simple principles just described.

Before concluding this section it is worthwhile to note that the thermodynamic theory in each case comprises the first approximation of the corresponding kinetic description. The thermodynamic theory of irreversible processes is valid, therefore, only when the second term in the expansion of the kinetic description is an order of magnitude smaller than the first term. This situation, for the example of an irreversible process at constant temperature and pressure, exists only when the free energy per atom released in the irreversible process is less than the thermal energy kT . A major advantage of the thermodynamic theory as compared to the statistical mechanical treatment is that the former is independent of any assumption about model. Within its realm of applicability, the theory gives an accurate phenomenological description of nature, quite analogous to the description ordinary thermodynamics gives of the state of equilibrium. An appreciation of this fact can only be gained by reading DeGroot¹ and Prigogine.²

Extension of the Theory

Previous considerations of growth phenomena in the light of the theory have been few. All of these treatments^{2,3} have considered some specific growth process as the resultant of the one or two basic types of irreversible phenomena (transport and chemical reactions) rather than as an entity itself. It occurred to this author that a consideration of the growth process as a separate type of irreversible phenomenon would be extremely simple as compared to previous treatments and would involve no assumption about mechanism.

Growth phenomena at constant temperature and pressure are characterized by the motion of an interface separating two regions having different values of free energy. The basic equation for the rate of production of irreversible entropy per unit area of interface is given by

$$\frac{d_i s_A}{dt} = - \frac{1}{TA} \frac{dG}{dt} \quad [I-3]$$

where G is Gibbs free energy for system; A , the interfacial area; and T , the absolute temperature. In order to use Eq. I-3 in the sense desired (assuming that Eq. I-2 can be applied to the result), the rate of decrease of the free energy must be expressed in terms of the interface. For example, consider the case of a sphere of phase i growing out into the less

stable phase o , and assume that the interfacial energy σ is isotropic. In this case,

$$\frac{dG}{dt} = \frac{\partial G}{\partial R} \frac{dR}{dt} = \{(-g_o + g_i) 4\pi R^2 + 8\pi R\sigma\} \frac{dR}{dt} \quad [I-4]$$

where R is the radius of sphere, and g_o, i the free energy per unit volume of phases o, i , respectively. It should be noted that Eq. I-4 corresponds to the situation where no other parameter that is descriptive of the interface varies with time. For example, in one conceivable growth process—the growth of spheres of cementite from supersaturated ferrite—two additional parameters might vary with time, namely, the thickness of the diffusion layer normal to the interface and the free energy g'_o of that part of the diffusion layer adjoining the interface. In this case two additional terms need to be added to the expansion of dG/dt . Unless otherwise specified the growth phenomena treated in this paper correspond to the situation described by Eq. I-4.

Substituting for dG/dt and A in Eq. I-3, using Eq. I-4, the following equation is obtained:

$$\frac{d_i s_A}{dt} = \frac{1}{T} (\Delta g - 2\sigma/R) \frac{dR}{dt} \quad [I-5]$$

where $\Delta g = g_o - g_i$.

As expected, Eq. I-5 has the form of a product of a force, $\frac{\Delta g - 2\sigma/R}{T}$, and a conjugate flux, dR/dt .

The force is the free energy released per unit advance of a unit area of interface. The flux is the rate of advance of the interface normal to itself. The next step in the theory is to assume that the flux is linearly related to the force, or

$$\frac{dR}{dt} = L_R \frac{\Delta g - 2\sigma/R}{T} \quad [I-6]$$

In words, this assumption of the phenomenological theory is that the rate of advance of an interface is proportional to the free energy released per unit advance per unit area of interface. Eq. I-6 should be applicable to all situations meeting the conditions assumed in the derivation and also the limitation that $(\Delta g - 2\sigma/R) \times \text{atomic volume} \ll kT$.

If now it can be shown that the Eqs. I-3 to I-6, or equivalent equations derived from Eq. I-3, are consistent with experiment, then one use of the thermodynamic theory of irreversible processes will have been demonstrated. Although it is true that Eq. I-6 could have been assumed *a priori*, so could any of a number of other relations have been assumed. The function of the thermodynamic theory in this respect is to provide a criterion which relations of the type Eq. I-6 must satisfy in order to be consistent with the theory. The value of this, or any other, phenomenological theory is the existence of a formalization that describes what appear to be diverse phenomena in terms of some language common to all the phenomena.

Theory Applied to Grain Boundary Migration

Growth of a Recrystallized Grain in a Strained Matrix: Consider the case of a single, spherical, strain-free, monocrystalline grain growing in a polycrystalline strained matrix. Let g_o be the free energy per unit volume of the strained matrix, and

g , the free energy per unit volume of the unstrained matrix. Eq. I-6 applies directly to this case, hence the rate of nucleus growth is given by Eq. I-6, i.e.,

$$\frac{dR}{dt} = \frac{L_r}{T} (\Delta g - 2\sigma/R) = G - B/R \quad [\text{II-1}]$$

This equation states in effect, that after a time t_0 (nearly equal to the induction period), B/R becomes very much smaller than G , and hence that after this time, t_0 , the growth rate is apparently constant. Reasonable estimates of Δg and σ lead to the minimum R for this range as about 10^{-3} cm. This result checks the experimental observations of Mehl and coworkers^{8,9} upon the growth of strain-free crystals in a strained matrix; that is, from observations of strain-free crystals larger than 10^{-2} cm, the growth rate is a constant.

An approximate relation between the induction period and the growth rate can be derived by integrating Eq. I-6 and making suitable approximations. The result is that the induction period is approximately inversely proportional to G , i.e.,

$$t_0 \approx \frac{10 \sigma}{\Delta g G}$$

Thus, a plot of $\log t_0$ vs $\log G$ should yield a straight line having the slope, -1 and the intercept $10 \sigma / \Delta g$ at unit growth rate. Data taken from Anderson and Mehl⁹ have been plotted in this manner in Fig. 1. As shown by the figure, the data for various temperatures and percentage of prior elongation do approximately obey the predicted relations.**

** This result implies that the induction period does not correspond to a time for nucleation, contrary to the assumptions of Anderson and Mehl⁹ and Turnbull.¹⁰

Further, a comparison of the experimental and theoretical intercepts yields a value of 400 for the ratio $\Delta g / \sigma$. Assuming a value of $\sigma = 500$ ergs per sq cm, a value of $\Delta g = 2 \times 10^6$ ergs per cu cm is obtained. This value compares favorably with the value estimated, on the basis of the stored strain energy using 5 pct as the ratio of the energy stored to the work of deformation, namely,

$$\Delta g \text{ (estimated)} = 0.05 \times (\text{work done}) = 0.05 \times 3.5 \times 10^7 = 2 \times 10^6 \text{ ergs per cu cm}$$

If this estimate is meaningful, then about 90 pct of the energy stored during cold work is relaxed by recovery prior to recrystallization. Both these energies when related to one atom are much less than kT . Thus, the application of Eq. I-6 to nucleus growth in recrystallization is justified.

Another interesting result is obtained by considering the contribution of the grain boundaries in the strained phase to Δg . For the data of Anderson and Mehl, this energy corresponds to about $500 \sigma_{s-o}$ (corresponding to a grain size of 530 grains per sq mm). Inasmuch as σ_{s-o} is expected to be of the order of magnitude of σ , but less than σ , this result, when compared to the previously calculated value of $\Delta g = 400 \sigma$, implies that the surface energy contribution to Δg is as important as the strain energy contribution. The fact that both the initial grain size and the amount of deformation affect the growth rate is confirmation of this conclusion.

It is instructive to separate the strain energy term, Δg_s , from the surface energy term, Δg_b , in Δg proper. Whenever, the growing strain-free and

internal, boundary-free, material is surrounded by a matrix comprising both strain and grain boundaries, then Eq. I-6 becomes

$$\frac{dR}{dt} = \frac{L_r}{T} (\Delta g_s + \Delta g_b - 2\sigma/R) \quad [\text{II-3}]$$

where

$$\Delta g = \Delta g_s + \Delta g_b$$

When R is much larger than the average diameter of the grains surrounding the growing grain, then

$$\Delta g_b = A \cdot \sigma_{s-o}$$

where A is the grain boundary area per unit volume, sq cm/cu cm, and σ_{s-o} is the interface energy between strained grains per unit area.

Secondary Recrystallization: The growth of exaggerated grains in secondary recrystallization can be understood on the basis of Eq. II-3. For the case of secondary recrystallization, $\Delta g_s = 0$. Hence, the equation becomes simply

$$\frac{dR}{dt} = \frac{L_r}{T} \left(\Delta g_b - \frac{2\sigma}{R} \right)$$

This dependence of growth rate upon the radius has been obtained experimentally by Rosi et al.¹¹ in the secondary recrystallization of silver. In their case, measurements of growth rates have been made during the induction period which confirm Eq. II-4 qualitatively. More information is required before a quantitative check can be made. They found that R^* defined by

$$R^* = \frac{2\sigma}{\Delta g_b}$$

was about twice the average matrix grain radius. R is the smallest grain radius of the secondary type which can grow spontaneously outward. Thus, as expected, the necessary and sufficient condition for secondary recrystallization is that the secondary grain radius R obey the criterion

$$R > R^* = \frac{2\sigma}{\Delta g_b} = CD_{\text{avg.}} \quad [\text{II-5}]$$

where $D_{\text{avg.}}$ is the average matrix grain size (diameter) and C is a constant (equals 1 for two dimensional recrystallization); while the secondary grain is surrounded by primary grains. If the average grain diameter is restricted in its growth, then secondary growth can occur at a fast rate. If on the other hand the matrix grains can grow, the rate of growth of secondary grains will either be small or nonexistent.

No limit is placed by the theory on the origin of the secondary grains. They can be formed by growth of existing grains which obey the growth criterion Eq. II-5, or a similar criterion derived from Eq. II-3 whenever Δg_s is not zero across some grain boundaries (some internal strains exist), or by a true recrystallization. It is believed however, that the first two alternatives are the most reasonable.

Continuous Grain Boundary Migration: The last case that can be treated under the general classification is that defined by $\Delta g_s = \Delta g_b = 0$. This is the case of grain boundary migration under a surface energy gradient. For this special case

$$\frac{dR}{dt} = \frac{L_r}{T} (-2\sigma/R) \quad [\text{II-6}]$$

Thus, grain boundary migration of this type is characterized by a decreasing dR/dt , rather than an increasing dR/dt . In other words, migration is always in the direction of the center of curvature. An extension of this concept to the continuous grain growth that occurs after recrystallization implies, as expected, that grain growth occurs by the disappearance of grain boundaries.

An interesting effect is predicted if impurities travel with the grain boundary, such that, as the total boundary area decreases, the concentration of impurities at the grain boundary increases. In this event, the differentiation of the free energy in Eq. I-4 introduces another term into the bracketed term of Eq. II-6, namely,

$$-\sum_i \frac{\partial \sigma}{\partial C_i} \frac{\partial C_i}{\partial R}$$

But

$$C_i = N_i/4\pi R^2$$

where N_i is the total number of impurity atoms of type i traveling with the grain boundary. Thus,

$$\frac{\partial C_i}{\partial R} = -N_i/2\pi R^3$$

Let

$$K_i = \frac{\partial \sigma}{\partial C_i} \frac{N_i}{2\pi}$$

then Eq. II-6 becomes

$$\frac{dR}{dt} = \frac{L_r}{T} (\sum K_i/R^3 - 2\sigma/R) \quad [\text{II-7}]$$

For positive values of $\partial \sigma / \partial C_i$, because the net effect of grain boundary migration in ordinary grain growth is to produce grain boundaries having larger R , there will be a limitation to the size of the grains produced, given by

$$\sum_i K_i/R^3 = 2\sigma/R$$

For negative values of $\partial \sigma / \partial C_i$, when $\sum_i K_i/R^3$ is large compared with $2\sigma/R$, the approximate law of grain growth predicted by Eq. II-7 is***

*** This method follows the assumption made by others that $D \sim R$, or that $dD/dt = -2 dR/dt$.

$$D = \left(\frac{4L\sum K_i}{T} \right)^{1/4} t^{1/4}$$

When $\sum K_i/R^3 \ll 2\sigma/R$, the corresponding result is

$$D = \left(\frac{L4\sigma}{T} \right)^{1/2} t^{1/2}$$

Experimentally, it is found that the exponent of the time, t , varies between $1/4$ and $1/2$ as just predicted. Thus, the explanation for the time dependence of grain growth may involve an effect of grain boundary composition upon the surface energy. It is significant in this respect that the exponent is found to approach $1/2$ with increasing temperature of grain growth and with increasing purity of the matrix. This former trend is what would be expected, because as the temperature is increased the concentration of impurities at the boundary is decreased. The exponent $1/2$ corresponds to no impurities in the grain boundary.

Finally, the result obtained by Zener, namely that the limiting grain diameter depends upon the particle impurities according to

$$D = \frac{2r}{f}$$

where r , the average radius of particles, and f , the volume fraction of particles, is also obtained from Eq. I-4, when the grain boundary area intersected by the particles is taken into account.

Effect of Diffusion across Boundary on Grain Boundary Migration Rate: In view of the fact that both grain boundary migration⁸ and diffusion² occur as a result of vectorial forces, interaction effects are to be expected whenever these phenomena occur simultaneously. The phenomenological equations should then take the form

$$\frac{dR}{dt} = \frac{-L_{11}}{T} \frac{2\sigma}{R} - \sum_i L_{1i} \frac{\partial \mu_i}{\partial R}$$

$$\frac{dm_i}{dt} = \frac{-L_{i1}}{T} \frac{2\sigma}{R} - \sum_k L_{ik} \frac{\partial \mu_k}{\partial R}$$

$$L_{11} = L_{11}$$

where dm_i/dt is the number of atoms of kind i flowing across unit area of the boundary per second. These equations apply to the cases of cylindrical or spherical symmetry in μ_i and the grain boundary and isotropy in σ . Equivalent equations can be derived for nonsymmetrical configurations.

The qualitative implications of these equations are rather obvious. The grain boundary migration behavior should be materially affected by diffusion across the boundary, especially for the case of unequal diffusion rates (a net current of vacancies). No quantitative data are as yet available to check the equations. One of the predictions that can be made on the basis of Eq. II-8 is that for sufficient net diffusion into a spherical grain, the grain may be made to grow rather than disappear.

Effect of Temperature Gradient, etc. on Grain Boundary Migration: Another interesting interaction should occur between grain boundary migration and either a flow of electrical charge or heat across the boundary. These effects should be second order compared to the effect of diffusion across the boundary. The stationary states of zero flow of charge or heat imply that a nonzero electric potential and temperature differential, respectively, will exist across the moving interface and will be proportional to the curvature and to the interface energy σ . In particular, for the flow of heat, the phenomenological equations are

$$\frac{dR}{dt} = \frac{-L_{11}}{T} \frac{2\sigma}{R} - \frac{L_{1u}}{T^2} \text{grad } T$$

$$\frac{dQ}{dt} = \frac{-L_{u1}}{T} \frac{2\sigma}{R} - \frac{L_{uu}}{T^2} \text{grad } T \quad [\text{II-9}]$$

The stationary state $dQ/dt = 0$, yields the equation

$$\Delta T = - \frac{L_{u1}}{L_{uu}} T \frac{2\sigma}{R}$$

Here ΔT represents the temperature increase due to the transfer of energy across the grain boundary analogous to the Dufour effect¹ in diffusion. The magnitude of ΔT is expected to be less than 10^{-3} °C.

Theory Applied to Rate of Growth of Stable Phase

Consider a spherical region of the stable phase growing in a supercooled or superheated matrix. If the theory is applicable to this phenomenon, then the

rate law should be given by Eq. I-6, where g_o is the free energy per unit volume of the supercooled or superheated matrix and g_i is the free energy per unit volume of the stable phase. Here again σ is the interfacial energy per unit area.

For the case of uniform growth of a crystal comprising a single component from the vapor phase, the bracketed term of Eq. I-6, $\Delta g - 2\sigma/R$, is proportional to the difference between the actual and equilibrium values of the vapor pressures. The experimental observations are in agreement with this rate equation for the case of uniform growth.¹² In experiments, such as those just described, whenever the change in free energy per unit volume in the presence of plane interfaces can be determined with a given accuracy, then it should be possible to determine σ with the same percentage accuracy. It is necessary, however, in order that the term $2\sigma/R$ be significant that Δg be small, i.e.,

$$\Delta g = \Delta h \Delta T/T_o$$

where Δh is the enthalpy of phase change per unit volume and T_o is the temperature of equilibrium for phase change. In this case errors in σ are likely to be large.

Whenever two irreversible processes such as diffusion and chemical reactions are involved in the motion of an interface, Eq. I-6 must be re-examined to see whether it applies to the physical situation being considered. For certain special cases, where the diffusive flux is linearly related to the rate of motion of the interface (as a result of the conservation of mass), Eq. I-6 can still be applied. However, there are many examples of growth processes where this simple picture is inadequate and a more detailed treatment is required. In all these cases it should be remembered that a chemical reaction involves a scalar flux while diffusion involves a vector flux. There can be no interactions between them in the sense of the theory; that is, in the event of a homogeneous distribution in the unstable phase having the correct stoichiometric relationship between components, the heterogeneous chemical reaction, proceeding by an interface motion, will not induce diffusion. An example of such a situation is the growth of an ordered phase within a disordered lattice, which incidentally should conform to Eq. I-6. These complex processes are outside the scope of the present treatment, but within the scope of the thermodynamic theory.

Theory Applied to Growth of Stable Phase in Supersaturated Matrix

As indicated in the last section, whenever a growth process involves both a chemical reaction as well as diffusion, it is worthwhile deriving the rate equations from first principles, Eq. I-3. In general, the growth of a stable phase from a supersaturated matrix involves both these irreversible processes.

Growth of Noncoherent Precipitates: Consider the growth of a spherical precipitate. There are two fluxes to consider. Namely, a diffusive flux and a chemical reaction. The rate of growth is directly proportional to the rate at which the chemical reaction $o' \rightarrow i$ proceeds, and is given by

$$\frac{dR}{dt} = \frac{L_o}{T} (\Delta g - 2\sigma/R)$$

where $\Delta g = g_o' - g_i$, the difference in free energy per unit volume (for a plane interface) between the

regions just before and just after the interface. The free energy g_o' may vary with time.

The assumption will be made that there are at most only two constituents which can diffuse (in addition to vacancies). For each constituent the diffusive flux will be given by

$$J_i = -L_{ii} \frac{\partial \mu_i}{\partial x} - L_{ik} \frac{\partial \mu_k}{\partial x}$$

where $\partial \mu_i / \partial x$ is the gradient of chemical potential of species i normal to the interface. As pointed out by Bardeen and Herring⁵ the term $L_{ik} \frac{\partial \mu_k}{\partial x}$ involves a factor which is generally an order of magnitude smaller than the diagonal factor. Hence, it will be neglected in the following. Now, for the case of diffusion adjacent to the interface, because diffusion is normal to the interface, by the conservation of mass

$$-J_i = \frac{d}{dt} \frac{(C_o)_i - (C_o')_i}{2} h = \frac{(C_o)_i - (C_o')_i}{2} \frac{dh}{dt} - \frac{h}{2} \frac{d(C_o')_i}{dt}$$

where $(C_o)_i$ is the concentration of i in phase o ; $(C_o')_i$ is the concentration of i in phase o' at interface, and h is the distance normal to interface where gradient of concentration of i exists. In this equation the second factor will be assumed small compared to the first factor. Thus, to a first approximation, the relation

$$\frac{(C_o)_i - (C_o')_i}{2} \frac{dh}{dt} = L_{ii} \frac{\Delta \mu_i}{h}$$

is obtained by equating the two expressions for J_i . Now,

$$\Delta \mu_i = (\mu_o)_i - (\mu_o')_i$$

Although both $(\mu_o')_i$ and $(C_o')_i$ should vary slightly with time, it will be assumed that the variation is sufficiently small as to leave the ratio $\Delta \mu_i / \Delta C_i$ invariant with time compared to the variation of h with time. Hence, separating variables and solving for h ,

$$\frac{h^2}{t} = 4L_{ii} \frac{\Delta \mu_i}{\Delta C_i}$$

This is the relation obtained from diffusion theory, i.e., the variable $x^2/t = \text{constant}$.

One more relation exists as a result of the conservation of mass, namely,

$$-J_i = \{(C_i)_i - (C_o')_i\} \frac{dR}{dt}$$

where $(C_i)_i$ is the concentration of i in phase i . Equating this expression for J_i to $L_{ii} \Delta \mu_i / h$, and substituting for h , then

$$\frac{dR}{dt} = K/t^{1/2} \tag{II-10}$$

where

$$K = (L_{ii} \Delta \mu_i \Delta C_i)^{1/2} \{(C_i)_i - (C_o')_i\}$$

In this equation K is slightly dependent on time.

Eq. II-10 has been obtained independently by Zener¹⁸ and is consistent with the data on growth of spherical carbides in supersaturated ferrite. It is interesting to note that if $(C_o')_i$ is assumed to be the composition of i in equilibrium with the stable

phase, then $\Delta g - 2\sigma/R$ equals zero, and the interface would not move. Hence, $(C'_e)_i$ cannot be the equilibrium composition, contrary to some previous treatments of this problem.

Growth of Pearlite: In order to obtain an expression for the growth rate of pearlite it is necessary to consider three irreversible processes: diffusion, the chemical reaction austenite \dagger to ferrite and the chemical reaction austenite \dagger to cementite. From

\dagger The austenites in these cases differ from the nominal eutectoid composition.

such a consideration it can be shown that the linear growth rate of pearlite per unit area of interface is given by $\dagger\dagger$

$\dagger\dagger$ The driving force $\Delta g - 2\sigma'/S_p$ times the atomic volume is less than the thermal energy kT .

$$V = \frac{L_p}{T(a + S_p)} \left(\Delta g - \frac{2\sigma'}{S_p} \right) \quad [\text{II-11}]$$

where Δg is the free energy released on converting 1 cu cm of austenite to ferrite plus cementite neglecting interfacial energies; σ' , the interface energy per unit area between ferrite and cementite; S_p , the interlamellar spacing of pearlite; and a , a factor comprising the three mobilities for the three irreversible processes.

An interesting result of the theory is the denial of the validity of Zener's derivation for the maximum growth rate. According to Zener¹⁴ the maximum rate of growth occurs when half the available free energy is used to produce ferrite-cementite interfaces, the remainder being dissipated in the irreversible process of diffusion. It is apparent that if no free energy is dissipated in the chemical reaction, austenite (at interface) to pearlite, then the rate of the chemical reaction would be zero. Hence, not all of the free energy is irreversibly dissipated by diffusional processes. Further, the value of the interlamellar spacing corresponding to the maximum rate of growth is given by

$$(S_p)_{\text{max}} = \frac{4\sigma'}{\Delta g} + a/2 \quad [\text{II-12}]$$

to a good approximation. Zener's result corresponds to $a = 0$. Because the parameter a comprises a positive combination of nonzero constants it cannot equal zero. It is on the order of magnitude of S_p . In fact, if the assumption is made that as much free energy is dissipated irreversibly in the chemical reaction austenite (at interface) to pearlite as in the associated diffusion process, then

$$a = S_p$$

There is no reason however for making this assumption, because a is a well-defined parameter that is independent of such assumptions. Specifically,

$$a = \frac{L_d}{L_1} + \frac{L_d}{L_2}$$

where L_d is the mobility for the diffusion process; L_1 , the mobility for the reaction austenite (at interface) to ferrite; and L_2 , the mobility for the reaction austenite (at interface) to cementite.

Thus, the parameter a to a good approximation is exponentially dependent on temperature through an activation energy term, i.e., $\exp(-Q/RT)$, where Q , the activation energy, is equal to the activation energy for diffusion of carbon in austenite less the

activation energy for the reaction austenite at interface to ferrite. (The assumption is made here that the activation energy for either chemical reaction is about the same.) Thus, the temperature dependence of the interlamellar spacing may be either that suggested by Zener¹⁴ if the second term of Eq. II-12 is small compared to the first or that found by Mehl¹⁵ if the first term is small compared to the second term.

Because the interlamellar spacing is a function of the free energy dissipated in the transformation, the velocity of motion of the interface in this case is not simply proportional to the free energy dissipated per unit advance of the interface, see Eq. II-11. Thus, the simple statement that the motion of an interface is proportional to the free energy released per unit advance of the interface is not always equivalent to results derived from the thermodynamic theory of irreversible processes; see also the results of the last section.

Theory Applied to Plastic Deformation

Growth of a Dislocation Ring: Consider that at its inception a dislocation ring defines a circular region in a plane across which shear stress has been relaxed. The ring itself comprises the interface region. There is a linear tension τ associated with the ring equivalent to the surface tension associated with a grain boundary. The tension of a ring comprising a single dislocation singular line, for example, is approximately given by

$$\frac{Gd}{2\pi} \ln R/2d \text{ ergs per cm}$$

where G is the modulus of rigidity; d , the atomic spacing; and R , the radius of ring.

Instead of using Eq. I-6 for this problem, the fundamental Eq. I-4 may be employed. The rate of decrease of free energy is simply the rate of performing work on the specimen less the rate of storing energy in the ring. Analytically, this relationship is

$$\frac{dG}{dt} = -F \frac{dl}{dt} + \tau \frac{dR}{dt} = -\sigma A_s \frac{dl}{dt} + \tau \frac{dR}{dt}$$

where F is the applied tensile load; σ , the applied tensile stress; and A_s , the cross-sectional area of specimen. In this case, it is assumed that only one dislocation ring is growing and that there are no other contributions of plastic origin to the lengthening of a specimen pulled in uniaxial tension. Further it is assumed that

$$\frac{dl}{dt} \sim \frac{d(\pi R^2)}{dt}$$

(i.e., an increase in length is due to a proportional increase in the area across which slip has occurred). Also, it is desired to calculate the entropy production per unit length of ring. Using the DeDonder relation,

$$\frac{d_i s_l}{dt} = \frac{1}{T} (C_1 \sigma - \tau/2\pi R) \frac{dR}{dt}$$

Using Eq. I-2 and assuming the thermodynamic theory to apply to this case, then

$$\frac{dR}{dt} = \frac{L}{T} (C_1 \sigma - \tau/2\pi R) \quad [\text{II-14}]$$

This equation is limited to the situation where σ

times the volume per atom is less than kT . For $\sigma = 10,000$ psi, then the temperature range where Eq. II-14 is applicable is above about 1000°C . This equation should be equally applicable to the rate of growth of a slip band. Unfortunately only indirect methods are available to check this result and these methods do not yield definitive answers.

"Slipless" Flow: The irreversible process of slipless flow investigated recently by Udin and associates¹⁸ can be treated by this theory. Herring¹⁷ has already given one treatment based on the flow of vacancies under a chemical potential gradient, an alternate and equivalent treatment makes use of Eqs. I-2 and I-1. Using the DeDonder relation the rate of production of irreversible entropy per unit volume of specimen is

$$\frac{d_i s}{dt} = \left\{ \frac{W - \pi R (\gamma_s - \gamma_b R N/L)}{\pi R^2 L} \right\} \frac{dl}{dt} = \sigma \frac{d\epsilon}{dt}$$

where W is the external force on specimen; γ_s , the surface free energy per unit area; γ_b , the interface free energy per unit area; R , the radius of specimen; L , the gage length of specimen; N , the number of grain boundaries in length L ; σ , $\frac{W - \pi R (\gamma_s - \gamma_b R N/L)}{\pi R^2}$ = "apparent" stress; and

$d\epsilon = dL/L$ = natural strain. The limitation that σ times the volume per atom be much less than kT is obeyed for the experiments of Udin. Hence, by the assumption of the thermodynamic theory

$$\frac{d\epsilon}{dt} = L_s \sigma \quad \text{[II-15]}$$

where L_s is the mobility related to the migration of vacancies. These results are the same as those already derived by Herring¹⁸ and checked by Udin.

Recovery: For the phenomenon of recovery occurring uniformly over a macroscopic volume, the thermodynamic theory states that the rate of approach to equilibrium is proportional to the deviation from equilibrium. The appropriate state variable for recovery is the average[‡] internal strain,

[‡] Root-mean-square average is more appropriate than the arithmetic average which equals zero.

hence

$$\frac{d\epsilon}{dt} = -L\epsilon \quad \text{[II-16]}$$

This equation is checked by experience with recovery phenomena¹⁸ where the limitation that the average internal stress times the volume per atom is less than the thermal energy, kT , is obeyed.

Discussion of Results

The fact that many of the irreversible processes that interest metallurgists are within the scope of the thermodynamic theory of irreversible processes is fortunate, because the theory is very useful in providing a brief and general method of classifying diverse rate phenomena. If nothing else is obtained from the application of the theory, the pedagogic advantage of having a simple analytic description of growth phenomena justifies its consideration. The analytic description in one equation of nucleus growth during primary recrystallization, secondary recrystallization, and grain boundary migration is a case in point.

The fact that a wide variety of irreversible phenomena falls within the limitations of the theory

should stimulate a search for still other irreversible processes that may be so characterized and, more important, it should stimulate experimentation in the fields of interaction effects, such as thermal diffusion (diffusion due to a temperature gradient, boundary migration due to diffusion across the boundary, etc.). With respect to the latter suggestion the reader is cautioned to read DeGroot,¹ for there are limitations to the theory which should be understood. One such limitation is that no interactions in the sense of the theory would be expected to occur between a scalar flux, such as recovery, and a vector flux, such as diffusion.

A discussion of the assumptions involved in the method used to derive the rate of interface motion is in order. The unique assumptions of this method were: 1—that the production of irreversible entropy was confined mainly to the interface region, hence, by analogy with the theory as previously developed, the specific irreversible entropy production per unit area of this interface region would be quadratic in the "forces" causing motion of the interface region, and 2—that the irreversible entropy was uniformly produced over the unit area of interface considered. Whenever two fluxes of different tensor rank are involved in the interface motion, the statement that the velocity of interface motion is proportional to the free energy released per unit advance of the interface must be examined carefully. For example, in the pearlite transformation the velocity of growth is not simply proportional to the free energy released per unit advance, but is a more complex function of the dissipated energy. Finally, the theory should be applied only to those cases where the free energy released per mol traversed is less than RT .

This mode of description of boundary migration has an interesting implication; namely, that the phenomenological equations can be made mechanism-sensitive by describing the mode of nonuniform entropy production. For example, in the growth of a crystal from the vapor, there are at least two mechanisms of growth which can be considered. These mechanisms are uniform deposition on the surface at high saturation of the vapor phase and preferred deposition on the spirals emanating from screw dislocations at low saturation. In the former case the growth law is given by Eq. I-6, in the latter case a spiral migration rate must be calculated on the basis of an interface localized at the spiral: the irreversible entropy production is localized to lie in some region adjacent to the spiral. (Incidentally, the expression obtained for the rate of migration of the spiral normal to itself is proportional to the right hand side of Eq. I-6.) Then the rate of growth of the crystal must be expressed in terms of the rate of advance of the spirals. Thus, the theory will give correct results, if it is applicable to the microscopic processes that occur, and if the particular mode of nonuniform entropy production ("plane" interface of constant or varying thickness normal to the plane, "line" interface, etc.) is taken explicitly into account in the equations describing the phenomenon as it appears macroscopically. Another example illustrating this point is the process of sintering. Herring¹⁹ has considered the rate laws obtained for many different assumptions of the mechanism of sintering using the proper forces obtained from the thermodynamic theory in each case. This aspect of the mode of production of irreversible entropy must be considered in the process of applying the thermodynamic theory.

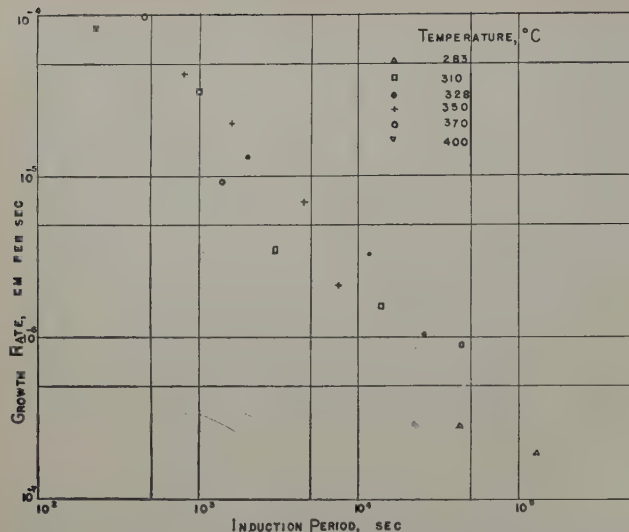


Fig. 1—Growth rate vs induction period for aluminum. Data from Anderson and Mehl.⁹

Finally, the significance of some of the results should be described here. First, it is apparent because of the correlation described in Fig. 1, that the incubation period in primary recrystallization is a consequence of slow growth and not of nucleation or transient nucleation. Second, it seems reasonable in view of the quantitative agreement obtained that the variation of the exponent in the grain growth law, $D = Kt^n$, is due to the migration of impurities along with the migration of the grain boundaries. This result is worth checking into further.

Summary and Conclusions

It is found that the thermodynamic theory of irreversible processes predicts that for many growth processes boundaries (interfaces) shall move at a rate proportional to the Gibbs free energy released per unit volume swept by the interface. However, this description is not generally true and each particular application must be considered separately in terms of the theory.

The equation applicable to growth in primary recrystallization, secondary recrystallization, or grain growth is

$$\frac{dR}{dt} = \frac{L_r}{T} \left(\Delta g_s + \Delta g_b - 2\sigma/R + \frac{\sum_i K_i}{R^3} \frac{\partial \sigma}{\partial C_i} \right)$$

where Δg_s is the difference in strain free energy across interface; Δg_b , the difference in free energy due to grain boundary area per unit volume on both sides of interface; σ , the interface energy per unit area; R , the radius of boundary; C_i , the concentration of i atoms in boundary; L_r , the mobility; T , the absolute temperature; K_i , a constant times number of i atoms migrating with grain boundaries; Δg_s is 0 for secondary recrystallization and grain growth;

Δg_b is 0 for grain growth; and $\sum_i \frac{K_i}{R^3} \frac{\partial \sigma}{\partial C_i} = 0$ for pure metals.

Three results derived from this equation should be emphasized: 1—the induction period in primary as well as secondary recrystallization is due to slow growth; 2—the grain growth law $D = Kt^{1/2}$ corre-

sponds to the case of impurities traveling with the boundaries such that $\partial \sigma / \partial C < 0$

$$\sum_i \frac{K_i}{R^3} \frac{\partial \sigma}{\partial C_i} >> 2\sigma/R$$

and 3—a limitation to grain growth due to impurities at the boundary is predicted for the case where $\partial \sigma / \partial C > 0$.

An interesting interaction effect is predicted between boundary migration and diffusion across the boundary, or heat and electrical flows across the boundary.

The equation applicable to the growth of spherical particles in a superheated or supercooled one component matrix is

$$\frac{dR}{dt} = \frac{L_o}{T} (\Delta g - 2\sigma/R)$$

where the terms have the same significance as for the previous case.

The equation applicable to the growth of a spherical particle of one stable phase in a supersaturated matrix is

$$\frac{dR}{dt} = K/t^{1/2}$$

where K is a function of chemical potentials and concentrations (see text), and t is time. The other terms have the same significance as before. The equations applicable to the growth of pearlite are

$$V = \frac{L_p}{T} \frac{(\Delta g - 2\sigma'/S_p^*)}{(a + S_p^*)}$$

and

$$S_p^* = 4\sigma'/\Delta g + a/2$$

where V is the velocity of growth; σ' , the ferrite-cementite interface energy; S_p^* , the interlamellar spacing corresponding to maximum rate of growth; and a , the sum of ratios of mobilities (see text) which is exponentially dependent on the reciprocal of the absolute temperature. These equations are obtained by considering that not only does diffusion occur but also a chemical reaction occurs. These two processes are complementary—neither is the limiting process because the boundary conditions for one are controlled by the other.

The rate of propagation of a slip band is also treated in the text with the following result:

$$\frac{dR}{dt} = \frac{L_s}{T} (C\sigma - \tau/2\pi R)$$

where σ is the applied stress, and τ , the linear tension at spearhead of slipped region.

The relation between flux and force given by the theory for a uniform approach to equilibrium in the specimen is that the rate of change of some state parameter is proportional to the partial derivative of the Gibbs free energy with respect to the conjugate state parameter. In simple words, the rate of approach to equilibrium is proportional to the deviation from equilibrium. An example of this relation is found for recovery where

$$\frac{d\epsilon}{dt} = -\frac{L}{T} \epsilon$$

Here ϵ is some average internal strain. A description of slipless flow alternate to that of Herring is also given in the text. Almost all the processes

treated are specialized examples of the general theory which treats the case of more than one flux acting simultaneously.

The situation described by a continuous variation of a state parameter has not been treated in this paper because of adequate coverage elsewhere. In this case, the "force" is a gradient of a thermodynamic potential such as chemical potential, temperature, pressure, etc.

The conclusion is made that a multitude of irreversible phenomena studied in metallurgy are described by the language of the thermodynamic theory of irreversible processes. For all these processes the limitation of the theory to processes where the driving energy per atom is less than the thermal energy, kT , is obeyed.

Acknowledgment

The author gratefully acknowledges financial support by the Office of Naval Research under Contract N-onr 266(07) and permission to publish this paper.

References

- ¹ S. R. DeGroot: *Thermodynamics of Irreversible Processes*. (1951) New York. Interscience Publishers Inc.
- ² I. Prigogine: *Etude Thermodynamique des Phenomenes Irreversibles*. (1947) Liege. DeSoer.
- ³ C. Herring: *The Physics of Powder Metallurgy*. (1951) p. 143. New York. McGraw-Hill Book Co.
- ⁴ L. S. Darken: Formal Basis of Diffusion Theory. *Atom Movements* (1951) p. 1. Cleveland. ASM.
- ⁵ J. Bardeen and C. Herring: Diffusion in Alloys and

the Kirkendall Effect. *Atom Movements*. (1951) p. 87. Cleveland. ASM.

⁶ L. Onsager: Reciprocal Relations in Irreversible Processes. *Physical Review* (1931) **37**, p. 405; (1931) **38**, p. 2265.

⁷ Th. DeDonder and Van Rysselberghe: *Thermodynamic Theory of Affinity*. (1936) Stanford University Press.

⁸ J. M. Stanley and R. F. Mehl: *Trans. AIME* (1942) **150**, p. 260.

⁹ W. A. Anderson and R. F. Mehl: *Trans. AIME* (1945) **161**, p. 140.

¹⁰ D. Turnbull: Transient Nucleation. *Trans. AIME* (1948) **175**, p. 774; *METALS TECHNOLOGY* (June 1948).

¹¹ F. D. Rosi, B. H. Alexander, and C. A. Dube: Kinetics and Orientation Relationships of Secondary Recrystallization in Silver. *Trans. AIME* (1952) **194**, p. 189; *JOURNAL OF METALS* (February 1952).

¹² D. Turnbull: Principles of Solidification. *Thermodynamics in Physical Metallurgy*. (1950) p. 282. Cleveland. ASM.

¹³ C. Zener: Theory of Growth of Spherical Precipitates from Solid Solution. *Journal of Applied Physics* (1949) **20**, p. 950.

¹⁴ C. Zener: Kinetics of the Decomposition of Austenite. *Trans. AIME* (1946) **167**, p. 550; *METALS TECHNOLOGY* (January 1946).

¹⁵ Pellissier and other: *Trans. ASM* (1942) **29**, p. 1049.

¹⁶ H. Udin, A. Shaler, and J. Wulff: *Trans. AIME* (1949) **185**, p. 186; *JOURNAL OF METALS* (February 1949).

¹⁷ C. Herring: *Journal of Applied Physics* (1950) **21**, p. 437.

¹⁸ J. E. Burke: *Grain Control in Industrial Metallurgy* (1948) p. 1. Cleveland. ASM.

¹⁹ C. Herring: *Journal of Applied Physics* (1950) **21**, p. 301.

Technical Note

Grain Boundary Films in Boron Steels

by J. W. Spretnak and Rudolph Speiser

IT has been suggested that boron in steel may form a film entirely around the austenite grain and that this film is responsible for the boron hardenability effect. In this connection, it is of interest to examine some of the ramifications of the concentration range of boron usually employed in hardenable steels, namely 0.0005 to 0.003 pct in a grain size range of ASTM grain size No. 1 through No. 10.

The ratio of the iron to boron atoms and the number of unit cells of γ iron per boron atom are listed in Table I. Even at the highest concentration considered, there are 1600 unit cells of γ iron per boron atom, assuming a uniform distribution of boron.

To investigate the possibility of the boron film formation, the number of boron atoms required to cover the grain surface completely must be calculated. With some transition elements, boron crystallizes in sheets composed of equilateral hexagons very much like graphite.¹ The selected value for the length of a side is 1.80Å. A simple calculation shows that two boron atoms cover an area of 8.4×10^{-18} sq cm. Table II lists the number of atoms of boron required for the formation of the monatomic film and Table III lists the number of boron atoms per grain.

J. W. SPRETNAK, Member AIME, and R. SPEISER are Associate Professors, Dept. of Metallurgy, Ohio State University, Columbus, Ohio.

TN 150E. Manuscript, Nov. 28, 1952.

This work on the boron hardenability effect is sponsored by The Office of Flight Research under Contract No. AF 18(600)-94.

The hypothetical cases of 100 pct and 10 pct adsorption are calculated (all boron atoms in a grain and 10 pct of all boron atoms in a grain are located at the grain surface respectively). In Table III, all combinations of grain size and composition below and to the left of the solid line (100 pct adsorption) and the dashed line (10 pct adsorption) are excluded as to the possibility of covering the grain surface with a continuous boron film. Thus, even for 100 pct adsorption, the smaller grains can form the film only at the higher concentrations. For the best case, grain size No. 1 and 0.0030 pct B, the required degree of adsorption is 3.9 pct.

The above calculations deal only with the number of boron atoms required to form a monatomic film and do not take into account the mechanism of concentration of boron at the grain surface and the possible limitations to the extent of this concentration at a constant temperature, as for example in the austenitizing process. The question next arises as to how this surface concentration can occur during an isothermal treatment. Such surface enrichment of boron must occur through the phenomenon of surface adsorption, i.e., the concentration of solute atoms in solid solution in the vicinity of the surface without precipitation. A solute atom will tend to concentrate at the grain boundary if it reduces the interfacial tension. The possibility of adsorption effects involving both boron and carbon in iron has been discussed.² In general, the tendency for a sol-

Table I. Ratio of Iron to Boron Atoms and Number of γ Iron Unit Cells Per Boron Atom for Various Concentrations of Boron

Wt Pct B	Ratio of Iron to Boron Atoms	No. of γ Fe Unit Cells per Boron Atom
0.0005	3.87×10^4	9.97×10^3
0.0010	1.93×10^4	4.83×10^3
0.0015	1.29×10^4	3.22×10^3
0.0020	9.68×10^3	2.42×10^3
0.0025	7.75×10^3	1.94×10^3
0.0030	6.65×10^3	1.66×10^3

Table II. Data on ASTM Grain Sizes

ASTM Grain Size No.	Mean Planar Grain Diameter,* Microns	No. of Unit Cells of γ Fe per Grain	Surface Area per Grain, Sq Cm	No. of Boron Atoms per Grain Required for Monatomic Film
1	286	2.55×10^{17}	2.57×10^{-3}	6.12×10^{12}
2	200	8.98×10^{16}	1.28×10^{-3}	3.05×10^{12}
3	143	3.20×10^{16}	6.44×10^{-4}	1.53×10^{12}
4	100	1.13×10^{16}	3.21×10^{-4}	7.64×10^{11}
5	71	3.99×10^{15}	1.61×10^{-4}	3.83×10^{11}
6	50	1.41×10^{15}	8.04×10^{-5}	1.91×10^{11}
7	35	4.99×10^{14}	4.02×10^{-5}	9.57×10^{10}
8	25	1.79×10^{14}	2.03×10^{-5}	4.83×10^{10}
9	18	6.36×10^{13}	1.02×10^{-5}	2.43×10^{10}
10	13	1.88×10^{13}	4.52×10^{-6}	1.08×10^{10}

* Mean area of grain considered as circular area.

be 0.003 pct at 970°C^* ; therefore the enrichment of

* Unpublished research.

boron in the region of the grain surface at this constant temperature is limited to this concentration. The thickness of the surface phase enriched by adsorption is not known. Assuming grain size No. 6 and that the adsorption effect is limited to a surface shell ten unit cells thick, the maximum possible adsorption for an average concentration of 0.005 pct B is 0.25 pct† for isolated grains and 0.50 pct for con-

† The number of unit cells in the shell is 0.61×10^{12} , which at saturation would contain 3.67×10^8 boron atoms. A single grain contains 1.46×10^{11} boron atoms. Therefore the percent adsorption is $(3.67 \times 10^8 \div 1.46 \times 10^{11}) 100$.

tiguous grains. From Table III, essentially 100 pct adsorption is required to form the film in this case. Considering only the surface layer of atoms enriched by adsorption, this amounts to 0.01 pct adsorption‡ for isolated grains and 0.02 pct for con-

‡ Each cell face at the surface has two iron atoms. The number of boron atoms is at saturation $2(0.609 \times 10^{11}) = 0.1832 \times 10^8$; the percent adsorption is $(0.1832 \times 10^8 \div 6.65 \times 10^8) 100 = 0.01$.

tiguous grains. Thus, from the above arguments, it is extremely unlikely that continuous or extended boron films form on austenite grain surfaces and are responsible for the hardenability effect. It is evi-

Table III. Number of Boron Atoms per Grain

ASTM Grain Size No.		Boron, Pct					
		0.0005	0.0010	0.0015	0.0020	0.0025	0.0030
1	10%	2.63×10^{13}	5.27×10^{13}	7.90×10^{13}	1.05×10^{14}	1.32×10^{14}	1.58×10^{14}
		9.29×10^{12}	1.85×10^{13}	2.79×10^{13}	3.72×10^{13}	4.64×10^{13}	5.58×10^{13}
		3.31×10^{12}	6.62×10^{12}	9.93×10^{12}	1.32×10^{13}	1.66×10^{13}	1.99×10^{13}
		1.17×10^{12}	2.34×10^{12}	3.50×10^{12}	4.67×10^{12}	5.84×10^{12}	7.01×10^{12}
		4.13×10^{11}	8.27×10^{11}	1.24×10^{12}	1.65×10^{12}	2.07×10^{12}	2.48×10^{12}
6	100%	1.46×10^{11}	2.92×10^{11}	4.38×10^{11}	5.84×10^{11}	7.30×10^{11}	8.76×10^{11}
		5.17×10^{10}	1.03×10^{11}	1.55×10^{11}	2.06×10^{11}	2.58×10^{11}	3.10×10^{11}
		1.85×10^{10}	3.69×10^{10}	5.54×10^{10}	7.39×10^{10}	9.24×10^{10}	1.11×10^{11}
		6.58×10^9	1.32×10^{10}	1.97×10^{10}	2.63×10^{10}	3.29×10^{10}	3.95×10^{10}
		1.95×10^9	3.89×10^9	5.84×10^9	7.79×10^9	9.74×10^9	1.17×10^{10}

ute atom to concentrate at the grain boundary would be expected to increase with an increase in temperature. Since adsorption is concentration in solid solution without precipitation, the limitation to the extent of concentration at a particular temperature is the solubility of the solute atom at this temperature. Any further concentration of boron would require the precipitation of the compound Fe_2B from solid solution. The precipitation of this compound would require that the solid solution become supersaturated with respect to boron. This supersaturation cannot occur by the adsorption mechanism at constant temperature, and such precipitation usually occurs on reducing the temperature with resulting decrease in solubility. The only possibility of precipitation at constant temperature is the case in which a second solute element such as carbon is present and also undergoes grain boundary adsorption along with boron. Thus the solubility product for boron carbide in iron could be exceeded at the grain boundary without exceeding the solubility limit of either solute atom. Such precipitation would deplete the solid solution at the grain boundary and allow further adsorption to take place.

The solubility of boron in γ iron is estimated to

dent that the distribution of boron and Fe_2B precipitates at the grain boundary will be localized and spotty.

Although it is quite unlikely that a grain boundary film is the underlying boron hardenability mechanism, the possibility of adsorption effects involving boron in solid solution in austenite appears to be of primary importance in explaining some aspects of the boron hardenability effect. For example, the metallographic test for boron⁸ and the optimum austenitizing range^{3,4} for boron steels can be rationalized in terms of adsorption effects.

References

- ¹ R. Kiessling: The Borides of Some Transition Elements. *Journal Electrochem. Soc.* (1951) **98**, pp. 166-169.
- ² J. W. Spretnak and Rudolph Speiser: Grain and Grain Boundary Compositions: Mechanism of Temper Brittleness. *Trans. ASM* (1951) **43**, pp. 734-747.
- ³ R. A. Grange and T. M. Garvey: Factors Affecting the Hardenability of Boron-Treated Steels. *Trans. ASM* (1946) **37**, pp. 136-174.
- ⁴ T. G. Digges and F. M. Reinhart: Influence of Boron on Some Properties of Experimental and Commercial Steels. *Journal of Research, Nat. Bur. Standards* (1947) **39**, pp. 67-131.

Measurement of Particle Sizes in Opaque Bodies

by R. L. Fullman

IN the investigation of metallurgical transformations and the relationships between microstructure and properties of metals, it frequently is desirable to obtain a measurement of the relative amounts of the various phases present and of the mean size of particles into which each phase is dispersed. The relative amounts of the phases can be measured by the classical methods of area, lineal, and point analysis,¹⁻⁵ in accordance with the principle that the volume fraction of a phase, the fraction of a polished cross section occupied by the phase, the fraction of a random line occupied by the phase, and the fraction of randomly arrayed points occupied by the phase are all equal. The validity of this relationship depends only on the attainment of a truly random sample of area, length, or points, and not on the size, shape, or distribution of the particles constituting the phase. Smith and Guttman⁶ have derived a relationship between the interface area per unit volume S_v and the measurable quantities L_s , the interface length per unit area on a cross section, and N_L , the number of interfaces per unit length intersected by a random line. Their equation,

$$S_v = \frac{4}{\pi} L_s = 2N_L$$

is also valid regardless of the distribution of particle sizes and shapes.

In contrast to the situation concerning measurement of relative fractions of phases and of interface area, the measurement of particle sizes in opaque samples has not been subjected to a complete analysis. It has been common to measure some lineal or area dimension of particles on a polished cross section and to use the mean value as a qualitative measure of particle size. In the present paper, quantitative relationships are established among the various mean dimensions on a polished cross section and the actual dimensions of the particles present.

Particles of Uniform Size

Spheres: If a metal sample contains particles of a phase α dispersed in the form of spheres of uniform size, a polished cross section through the sample will reveal circular areas of phase α with radii from 0 to r , the radius of the spheres. Consider a cube of unit dimensions to be cut from the sample. If a cross section parallel to one of the cube faces is examined, the average number of particles per unit area (N_s) equals the number of particles per unit volume (N_v) times the probability p_1 that the plane would intersect a single sphere positioned at random within the unit cube. Since, of the various possible positions for the cross-sectional plane over the unit length from top to bottom of the cube, only those positions existing over the length $2r$ would lead to the plane intersecting the sphere, the probability of intersecting a single sphere is just $2r$.

R. L. FULLMAN, Junior Member AIME, is associated with the Research Laboratory, General Electric Co., Schenectady.

Discussion on this paper, TP 3432E, may be sent, 2 copies, to AIME by Dec. 1, 1953. Manuscript, April 8, 1952. Cleveland Meeting, October 1953.

$$N_s = N_v p_1 = N_v \cdot 2r \quad [1]$$

Applying the equality of area and volume fractions, the relationship is found between sphere size and average area \bar{s} of uniform spheres intersected by a random cross section,

$$f = N_v V = N_v \cdot \frac{4}{3} \pi r^3 = N_s \bar{s} = N_v \cdot 2r \bar{s} \\ \bar{s} = \frac{2}{3} \pi r^2 \quad [2]$$

A similar analysis reveals the average traverse length across spheres of uniform size when random lines are passed through the sample. If a randomly oriented unit cube is cut from the sample and a randomly positioned line is passed through the cube parallel to a cube edge, the number of spheres intersected by the line (N_L) equals the number of spheres per unit volume times the probability p_1 of the line hitting a single randomly placed sphere in the cube. Since possible positions of the line occupy unit area, and possible positions for which it will pass through the sphere occupy an area of πr^2 , the probability of the line hitting a randomly placed single sphere is πr^2 .

$$N_L = N_v p_1 = N_v \pi r^2 \quad [3]$$

Combining this relationship with the equality of volume and lineal fraction, the desired relationship is obtained between radius and mean lineal traverse length \bar{l} , for spheres of uniform size.

$$f = N_v V = N_v \cdot \frac{4}{3} \pi r^3 = N_L \bar{l} = N_v \cdot \pi r^2 \bar{l} \\ \bar{l} = \frac{4}{3} r \quad [4]$$

Circular Plates: Consider a sample containing particles of a phase α in the form of circular plates of uniform radius r and thickness t , where $r \gg t$. If the plates are randomly oriented, as in a sufficiently large sample of a fine grained polycrystalline material, area and lineal analysis may be carried out with parallel cross-sectional planes and lineal traverses. If the plates are not randomly oriented, it is necessary to randomize the orientation of the cross-sectional planes and traverse directions. Let a unit cube be cut from the sample, and a cross-section plane be passed through the cube parallel to one of the cube faces. The number of plates cut by the cross-sectional plane per unit area is equal to the number of plates per unit volume times the probability of a plate intersecting a single randomly positioned and randomly oriented plate in the cube. If J is the component of the plate diameter in the direction normal to the cross-sectional planes, the probability of a plane cutting a single randomly oriented plate is equal to \bar{J} , the mean value of J for all possible orientations of the plate.

Let ϕ be the dihedral angle between a plate and the cross-sectional plane, and let $p_\phi d\phi$ be the probability that a plate makes an angle between ϕ and $\phi + d\phi$ with the cross-sectional plane. Then for ran-

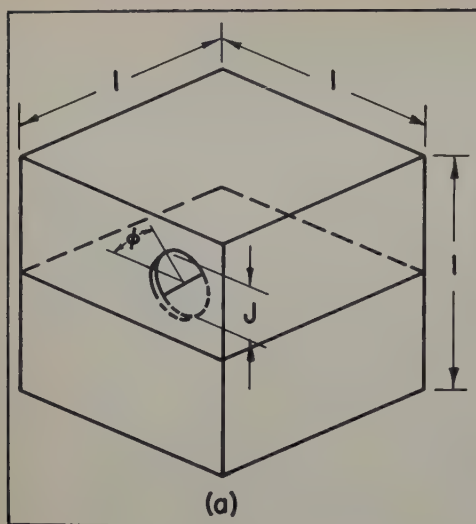
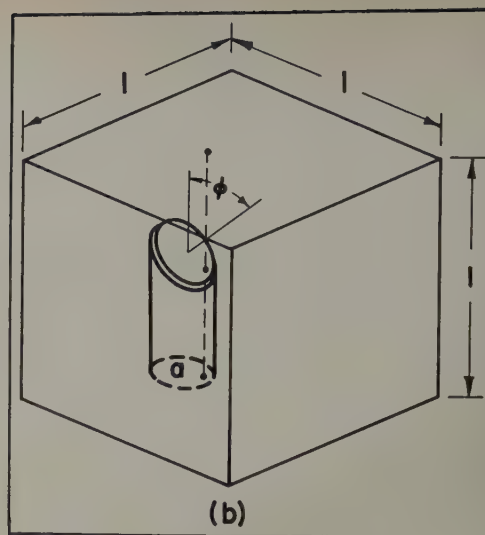


Fig. 1—Intersections of a circular plate in a unit cube with (a) a cross-sectioning plane and with (b) a lineal traverse.



domly oriented plates, $p_\phi = \sin \phi$. Let $p_J dJ$ be the probability that a given plate has a diameter component perpendicular to the cross-sectional plane between J and $J + dJ$. Referring to Fig. 1a,

$$J = 2r \sin \phi$$

$$p_J = p_\phi \left| \frac{d\phi}{dJ} \right| = \frac{\tan \phi}{2r}$$

The average value of J for all orientations is equal to the integral, over all possible values of J , of the product of J and its probability.

$$\bar{J} = \int_0^{2r} J p_J dJ = \frac{\pi}{2} r$$

$$N_s = \bar{J} N_v = \frac{\pi}{2} r N_v \quad [5]$$

Combining Eq. 5 and the equality of volume and area fraction, the desired relationship is obtained between plate size and average area of particles intersected by a random cross section.

$$f = N_v V = N_v \pi r^2 t = N_s \bar{s} = \frac{\pi r^2}{2} N_v \bar{s} \quad [6]$$

$$\bar{s} = 2rt$$

If random lines parallel to an edge of the unit cube are passed through a sample, the number of plates per unit length intersected by the lines is equal to the number of plates per unit volume times the probability that a line will intersect a single randomly positioned and randomly oriented plate in the cube. If a is the apparent area of a plate as viewed from the direction of the lines, the probability of a line cutting a single randomly positioned and oriented plate is equal to the mean value of a , averaged over all possible plate orientations. If ϕ is the angle between the lineal traverses and the normal to a plate, this angle is completely equivalent to that defined above, with respect to its probability of existence. Referring to Fig. 1b,

$$a = \pi r^2 \cos \phi$$

$$p_a = p_\phi \left| \frac{d\phi}{da} \right| = \frac{1}{\pi r^2}$$

Again integrating to find the mean value of the apparent area, \bar{a} , the result is

$$\bar{a} = \int_0^{\pi r^2} a p_a da = \frac{1}{\pi r^2} \int_0^{\pi r^2} a da = \frac{\pi r^2}{2}$$

$$N_L = \bar{a} N_v = \frac{\pi r^2}{2} N_v \quad [7]$$

Combining Eq. 7 with the equality of volume and lineal fractions, the desired value is obtained of the mean traverse length \bar{l} for plates of uniform size.

$$f = N_v V = N_v \pi r^2 t = N_L \bar{l} = N_v \frac{\pi r^2}{2} \bar{l}$$

$$\bar{l} = 2t \quad [8]$$

Rods: Consider a sample containing a phase α in the form of randomly oriented rods of radius r and length H , where $H \gg r$. A unit cube cut from the sample is cut by a plane parallel to a cube face. Let J be the component of rod length in the direction normal to the cross-section planes. Then the number of rods per unit area on the cross section is equal to the number of rods per unit volume times the probability that a single randomly positioned and oriented rod is cut by a plane. Hence, the number per unit area is equal to the number per unit volume times the mean value of J , averaged over all rod orientations. Let ϕ be the angle between a rod and the direction perpendicular to the cross-section planes. Referring to Fig. 2a,

$$J = H \cos \phi$$

p_ϕ is again equal to $\sin \phi$, so that

$$p_J = p_\phi \left| \frac{d\phi}{dJ} \right| = \frac{1}{H}$$

$$\bar{J} = \int_0^H J p_J dJ = \int_0^H \frac{J}{H} dJ = \frac{H}{2}$$

$$N_s = N_v \bar{J} = \frac{N_v H}{2} \quad [9]$$

Combining Eq. 9 with the equality of volume and area fractions, the desired value is found of the mean area of rods intersected by a random cross section.

$$f = N_v V = N_v \pi r^2 H = N_s \bar{s} = \frac{N_v H}{2} \bar{s}$$

$$\bar{s} = 2\pi r^2 \quad [10]$$

If straight lines are passed through the unit cube parallel to one of the cube edges, the number of rods per unit length intersected along the line is equal to the number per unit volume times the probability p_1 that a single line hits a single randomly positioned and oriented rod. The latter probability is equal to the average area \bar{a} presented by randomly oriented rods viewed from the direction of the lines. Let ϕ be the angle between the axis of a rod and the direction of the lines. Then, referring to Fig. 2b,

$$a = 2rH \sin \phi$$

p_ϕ is again equal to $\sin \phi$, so that

$$p_\phi = p_\phi \left| \frac{d\phi}{da} \right| = \frac{\tan \phi}{2rH}$$

$$\bar{a} = \int_0^{2rH} a p_\phi da = 2rH \int_0^{\pi/2} \sin^2 \phi d\phi = \frac{\pi rH}{2}$$

$$N_L = \bar{a} N_v = \frac{\pi rH}{2} N_v \quad [11]$$

Combining Eq. 11 and the equality of lineal and volume fractions, the desired value of the mean lineal traverse across randomly oriented rods of uniform size is found.

$$f = N_v V = N_v \pi r^2 H = N_L \bar{l} = \frac{\pi rH}{2} N_v \bar{l} \quad [12]$$

$$\bar{l} = 2r$$

Note that neither the average cross-sectional area nor the average lineal traverse of particles in the form of long thin rods depends on the length of the rods. It does not appear possible to measure the length of particles in this shape by any of the usual measurements on polished cross sections. This fact demonstrates immediately the impossibility of finding a relationship between measured quantities and any sort of "average particle dimension" that would apply regardless of particle shape.

Combinations of Point, Lineal, and Area Analysis for Particles of Uniform Size: While the measurement of average lineal traverse or average particle area sectioned is sufficient to describe the particle size, as shown in the preceding sections, some other simple relationships may be established which are useful in that they sometimes permit the use of simpler experimental methods. For example, combining Eqs. 1 and 3, the result is

$$r = \frac{2}{\pi} \frac{N_L}{N_s} \quad [13]$$

This relationship permits measuring the radius of uniform spheres by merely counting the number of spheres intersected per unit length of traverse and the number of spheres intersected per unit area of cross section. The necessity for actually measuring either lineal traverse lengths or areas intersected on the cross section is eliminated. For the special instance of grain size measurement, where the volume fraction equals 1, either count alone is sufficient. Then

$$r = \frac{3}{4N_L} = \sqrt{\frac{3}{2\pi N_s}} \quad [14]$$

Eqs. 1 and 3 may also be combined to yield the number of particles per unit volume

$$N_v = \frac{\pi}{4} \frac{N_s^2}{N_L} \quad [15]$$

or to provide a means of measuring the volume fraction of a phase dispersed as uniform spheres.

$$f = \frac{8}{3\pi} \frac{N_L^2}{N_s} \quad [16]$$

For circular plates, Eqs. 5 and 7 may be combined to permit measurement of several quantities of interest.

$$r = \frac{N_L}{N_s} \quad [17]$$

$$t = \frac{f}{2N_L} \quad [18]$$

$$N_v = \frac{2}{\pi} \frac{N_s^2}{N_L} \quad [19]$$

For rods a similar combination of Eqs. 9 and 11 leads to the following relationships:

$$r = \frac{1}{\pi} \frac{N_L}{N_s} \quad [20]$$

$$f = \frac{2}{\pi} \frac{N_L^2}{N_s} \quad [21]$$

Another quantity of frequent interest in quantitative metallography is the mean free path between

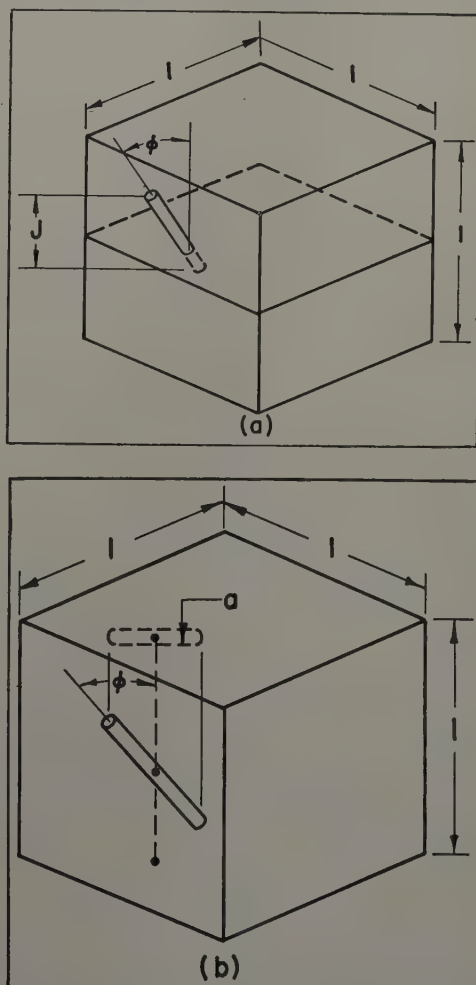


Fig. 2—Intersections of a rod in a unit cube with (a) a cross-sectioning plane and with (b) a lineal traverse.

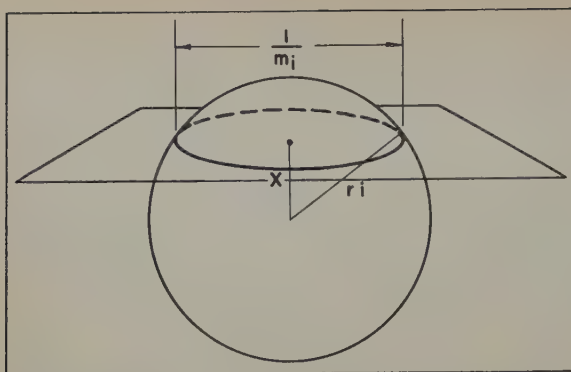


Fig. 3—Intersection of a sphere with a cross-sectioning plane.

particles. The mean free path P may always be found from the relationship

$$P = \frac{1-f}{N_L} \quad [22]$$

which is valid regardless of the shape or distribution of sizes of the particles. Other measures of the mean free path may be obtained by combinations of the relations already found for particles of uniform size and shape, but these do not appear to offer any significant advantage over the general formula.

Particle Size in Samples with Nonuniform Size Particles

The simple relationships developed in the previous section apply precisely only if the particle size is uniform, but they may be used for approximate measurements provided that the range of particle sizes is small. If more accurate measurements are desired, or if there is a large range of particle sizes, the variation in particle size must be taken into account. The necessary analysis for determining the complete distribution of particle sizes present when the particles are in the form of spheres has been carried out by Hagermann,⁷ Scheil and coworkers,⁸⁻¹⁰ and Huber.¹¹ The equations presented above for plates and rods may be combined with the general methods of approach used by these authors to develop methods for measurement of the complete distribution of particle size for these shapes as well. However, the measurement of mean particle sizes for samples containing a distribution of sizes can be measured more easily than the complete distribution function, and these mean values frequently provide an adequate description of the structure. For example, a complete description of the kinetics of a transformation occurring by nucleation and growth is obtained if the number of particles per unit volume, as well as the volume fraction occupied by a new phase, is determined as a function of the transformation time and temperature.

Spheres: Consider a sample containing particles of a phase α in the form of spheres of various radii. If the particles are divided into groups according to their radius, then for each group with radius arbitrarily close to some value r_i , equations analogous to Eqs. 1 to 4 may be written

$$N_{s_i} = 2r_i N_{v_i} \quad [1a]$$

$$\bar{s}_i = \frac{2}{3} \pi r_i^2 \quad [2a]$$

$$N_{L_i} = \pi r_i^2 N_{v_i} \quad [3a]$$

$$\bar{l}_i = \frac{4}{3} r_i \quad [4a]$$

Combining these relationships and summing over all values of the radius r_i , the following expressions for \bar{s} and \bar{l} are obtained:

$$\bar{s} = \frac{\sum_i N_{s_i} \bar{s}_i}{\sum_i N_{s_i}} = \frac{\sum_i N_{v_i} V_i}{2 \sum_i N_{v_i} r_i} = \frac{\bar{V}}{2 \bar{r}} \quad [23]$$

$$\bar{l} = \frac{\sum_i N_{L_i} \bar{l}_i}{\sum_i N_{L_i}} = \frac{\sum_i N_{v_i} V_i}{\pi \sum_i N_{v_i} r_i^2} = \frac{4 \bar{V}}{\bar{A}} \quad [24]$$

where \bar{A} is the average surface area of the spheres.

In order to separate the mean values of r , A , and V from Eqs. 23 and 24, it is necessary to add a new measurement. Let m_i be the reciprocal of the diameter of the circle of intersection of a sphere of radius r_i with a cross-section plane. Then, referring to Fig. 3,

$$m_i = \frac{1}{2 \sqrt{r_i^2 - x^2}}$$

where x is the distance of the cross-section plane from the center of the sphere. If $p_x dx$ is the probability that a cross-section plane cuts a sphere of radius r_i at a distance x to $x + dx$ from its center, then

$$p_x = \frac{1}{r_i}$$

If $p_{m_i} dm_i$ is the probability of finding a reciprocal diameter between m_i and $m_i + dm_i$,

$$p_{m_i} = p_x \left| \frac{dx}{dm_i} \right| = \frac{1}{2 m_i^2 r_i \sqrt{4 m_i^2 r_i^2 - 1}}$$

The mean value of m_i is equal to the integral, over all possible values of m_i , of its value times the probability of its existence at that value.

$$\bar{m}_i = \int_{\frac{1}{2r_i}}^{\infty} m_i p_{m_i} dm_i = \frac{\pi}{4 r_i}$$

Summing these mean values of \bar{m}_i over all sphere sizes and dividing by the total number of observations, an expression is obtained for the mean value \bar{m} for the whole sample.

$$\bar{m} = \frac{\sum_i N_{s_i} \bar{m}_i}{\sum_i N_{s_i}} = \frac{\pi \sum_i N_{v_i}}{4 \sum_i N_{v_i} r_i} = \frac{\pi}{4 \bar{r}} \quad [25]$$

Combining Eq. 25 with Eqs. 23 and 24, the necessary relationships between various mean dimension descriptions of the spheres and the several measurable quantities \bar{l} , \bar{s} , \bar{m} , and f are obtained.

$$\bar{r} = \frac{\pi}{4 \bar{m}} \quad [26]$$

$$\bar{V} = \frac{\pi \bar{s}}{2 \bar{m}} = \frac{\pi f}{2 \bar{m} N_s} \quad [27]$$

$$\bar{A} = \frac{2 \pi \bar{s}}{\bar{m} \bar{l}} = \frac{2 \pi N_L}{\bar{m} N_s} \quad [28]$$

$$N_v = \frac{2 \bar{m} f}{\pi \bar{s}} = \frac{2 \bar{m} N_s}{\pi} \quad [29]$$

Circular Plates: When the particles under consideration are in the form of circular plates with a

distribution of radius r and thickness t , this distribution may be divided into a number of arbitrarily small ranges of particles of radius r_i and within each such range of radii the plates may be further subdivided into arbitrarily small ranges of thickness t_j . Then for each range of particle size, equations equivalent to Eqs. 5 to 8 may be written.

$$N_{s_{ij}} = \frac{N_{v_{ij}} V_{ij}}{\bar{s}_{ij}} = \frac{\pi}{2} N_{v_{ij}} r_i \quad [5a]$$

$$\bar{s}_{ij} = 2 r_i t_j \quad [6a]$$

$$N_{L_{ij}} = \frac{N_{v_{ij}} V_{ij}}{\bar{l}_{ij}} = \frac{\pi}{2} N_{v_{ij}} r_i^2 \quad [7a]$$

$$\bar{l}_{ij} = 2 t_j \quad [8a]$$

Adding the contributions of all particle size ranges to the total number per unit area and per unit length observed, the following is obtained:

$$\frac{\bar{s}}{s} = \frac{\sum_i \sum_j N_{L_{ij}} \bar{l}_{ij}}{\sum_i \sum_j N_{s_{ij}}} = \frac{2 \sum_i \sum_j N_{v_{ij}} V_{ij}}{\pi \sum_i \sum_j N_{v_{ij}} r_i} = \frac{2 \bar{V}}{\pi \bar{r}} \quad [30]$$

$$\bar{l} = \frac{\sum_i \sum_j N_{L_{ij}} \bar{l}_{ij}}{\sum_i \sum_j N_{L_{ij}}} = \frac{2 \sum_i \sum_j N_{v_{ij}} V_{ij}}{\pi \sum_i \sum_j N_{v_{ij}} r_i^2} = \frac{4 \bar{V}}{\bar{A}} \quad [31]$$

In order to separate the various mean dimensions from these equations, and in order to find a measure of the mean plate thickness, it is necessary to introduce three more measurable quantities.

Let E be the reciprocal of the length of intersection of a plate with a cross-sectioning plane. Then referring to Fig. 4,

$$E_i = \frac{1}{2 \sqrt{r_i^2 - x^2}}$$

where x is the distance from the center of the plate to its intersection with the cross-sectioning plane. If $p_s dx$ is the probability that the plate is intersected by the cross-sectioning plane at a distance between x and $x + dx$ then

$$p_s = \frac{1}{r_i}$$

Let $p_{E_i} dE_i$ be the probability that the reciprocal of the intersection length lies between E_i and $E_i + dE_i$. Then

$$p_{E_i} = p_s \left| \frac{dx}{dE_i} \right| = \frac{(r_i^2 - x^2)^{3/2}}{r_i x}$$

The mean value of E_i is equal to the integral of the product of E_i and the probability of its existence, over all possible values of E_i .

$$\bar{E}_i = \int_{\frac{1}{2r_i}}^{\infty} E_i p_{E_i} dE_i = \frac{\pi}{4 r_i}$$

Summing the values of \bar{E}_i over all values of the plate radius r_i the following is obtained:

$$\bar{E} = \frac{\sum_i N_{s_i} \bar{E}_i}{\sum_i N_{s_i}} = \frac{\pi \sum_i N_{v_i}}{4 \sum_i N_{v_i} r_i} = \frac{\pi}{4 \bar{r}} \quad [32]$$

In order to find a measure of the average plate thickness, a quantity F is defined as the reciprocal of the width of an intersection of a plate with a cross-sectioning plane. Then, referring to Fig. 4, if

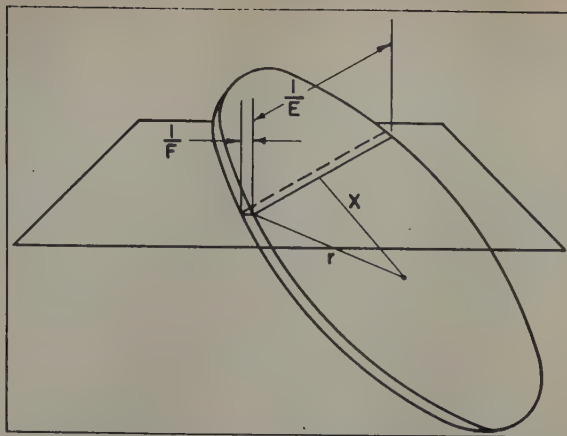


Fig. 4—Intersection of a circular plate with a cross-sectioning plane.

ϕ is the dihedral angle between the plate and the cross-sectioning plane,

$$F_{ij} = \frac{\sin \phi}{t_j}$$

In the present instance the probability function of ϕ required is the probability of cutting a plate at angle ϕ with the cross-sectioning plane, so that it is the probability that a plate lies at an angle ϕ with the sectioning plane times the probability that a plate lying at this angle will be cut by the plane. Since both of these probabilities are proportional to $\sin \phi$,

$$p_\phi = K \sin^2 \phi$$

If $p_{F_{ij}} dF_{ij}$ is the probability that the reciprocal of cross-section width lies between F_{ij} and $F_{ij} + dF_{ij}$, its value is

$$p_{F_{ij}} = p_\phi \left| \frac{d\phi}{dF_{ij}} \right| = K t_j \frac{\sin^2 \phi}{\cos \phi}$$

where the constant K may be evaluated from the fact that the sum of the probabilities of all possible values of F_{ij} must equal 1.

$$\int_0^{1/t_j} p_{F_{ij}} dF_{ij} = K \int_0^{\pi/2} \sin^2 \phi d\phi = \frac{\pi}{4} K = 1$$

Therefore,

$$p_{F_{ij}} = \frac{4}{\pi} t_j \frac{\sin^2 \phi}{\cos \phi}$$

The mean value of F_{ij} is equal to the integral, over all possible values of F_{ij} , of the product of F_{ij} and its probability.

$$\bar{F}_{ij} = \int_0^{1/t_j} F_{ij} p_{F_{ij}} dF_{ij} = \frac{4}{\pi t_j} \int_0^{\pi/2} \sin^3 \phi d\phi = \frac{8}{3 \pi t_j}$$

Summing the values of F_{ij} over all values of the plate radius and thickness and dividing by the number of observations of all plate sizes,

$$\bar{F} = \frac{\sum_i \sum_j N_{s_{ij}} \bar{F}_{ij}}{\sum_i \sum_j N_{s_{ij}}} = \frac{8 \sum_i \sum_j N_{v_{ij}} \frac{r_i}{t_j}}{3 \pi \sum_i \sum_j N_{v_{ij}} r_i} = \frac{8}{3 \pi} \frac{\left(\frac{\bar{r}}{\bar{t}} \right)}{\bar{r}} \quad [33]$$

If the ratio of radius to thickness of the plates is

independent of the plate radius, Eq. 33 provides a measure of the mean plate thickness, since, under these conditions,

$$\bar{F} = \frac{8}{3\pi t} \quad [33a]$$

However, if the radius-to-thickness ratio is not independent of plate size, the mean plate thickness may still be found by measurement of the ratio of width to length of intersections of plates with the cross-sectioning plane. Let G be this ratio; then

$$G_{ij} = \frac{t_j}{2 \sin \phi \sqrt{r_i^2 - x^2}}$$

where ϕ and x have the same meanings as previously. As before the probability functions for ϕ and x may be written as follows:

$$p_\phi = \frac{4}{\pi} \sin^2 \phi$$

$$p_x = \frac{1}{r_i}$$

In this case the probability function for G depends on both the probability functions of ϕ and x .

$$p_{G_{ij}} = \int_0^{\sqrt{r_i^2 - t_j^2/4G_{ij}^2}} p_\phi \left| \frac{\partial \phi}{\partial G_{ij}} \right| p_x dx = \frac{t_j^2}{2r_i^2 G_{ij}^3}$$

The mean value of G is equal to the integral, over all possible values of G , of the product of G and its probability.

$$\bar{G}_{ij} = \int_{t_j/2r_i}^{\infty} G_{ij} p_{G_{ij}} dG_{ij} = \frac{t_j}{r_i}$$

Summing over all plate sizes,

$$\bar{G} = \frac{\sum_i \sum_j N_{ij} \bar{G}_{ij}}{\sum_i \sum_j N_{ij}} = \frac{\sum_i \sum_j N_{ij} t_j}{\sum_i \sum_j N_{ij} r_i} = \frac{\bar{t}}{\bar{r}} \quad [34]$$

Combining Eqs. 30 to 34, the desired relationships between the mean values of plate dimensions and the mean values of the several measurable quantities are obtained.

$$\bar{r} = \frac{\pi}{4\bar{E}} \quad [35]$$

$$\bar{t} = \frac{\pi\bar{G}}{4\bar{E}} \quad [36]$$

$$\bar{V} = \frac{\pi^2 \bar{s}}{8\bar{E}} = \frac{\pi^2 f}{8\bar{E} N_s} \quad [37]$$

$$\bar{A} = \frac{\pi^2 \bar{s}}{2\bar{E} \bar{l}} = \frac{\pi^2 N_L}{2\bar{E} N_s} \quad [38]$$

$$N_v = \frac{8\bar{E} f}{\pi^2 \bar{s}} = \frac{8\bar{E} N_s}{\pi^2} \quad [39]$$

$$\left(\frac{\bar{r}}{\bar{t}} \right) = \frac{3\pi^2 \bar{F}}{32\bar{E}} \quad [40]$$

If the ratio of plate radius to thickness is independent of plate size,

$$\left(\frac{\bar{r}}{\bar{t}} \right) = \frac{\bar{r}}{\bar{t}}$$

so

$$\frac{1}{\bar{G}} = \frac{3\pi^2 \bar{F}}{32\bar{E}} \quad [41]$$

This relationship provides a means of checking on whether or not the radius-to-thickness ratio depends on plate size.

Rods: Since the analysis of rods, even of uniform size, does not permit separation of the rod length from the number of rods per unit volume, it does not appear profitable to pursue the analysis of rods of nonuniform size. Fortunately, most metallurgical transformations lead to the formation of particles in the form of either spheres or plates so that our inability to analyze the particle size of rod-shaped particles is not a serious limitation.

Summary

Methods have been developed for the analysis of particle size measurements by area and lineal analysis when the particles are in the form of spheres, plates, or rods. Methods that are valid when there is a wide range of particle sizes were developed, as well as simpler methods which apply when the particle size is uniform. It was shown that the usual types of observation do not permit measurement of the length of rod-shaped particles. For such particles there is a negligible probability that a cross-sectioning plane will cut along the rod length, so that statistical observations of the dimensions of intersections of the particles with a cross-sectioning plane depend only on the rod's radius. Despite this limitation, the method permits description of the distribution of phases present in commonly encountered metallurgical samples.

Acknowledgment

The author had frequent discussions with J. C. Fisher, who also read the manuscript.

References

- ¹ A. Delesse: Procédé Mécanique Pour Déterminer la Composition des Roches. *Annales des Mines* (1848) **13**, p. 379.
- ² H. C. Sorby: On Slaty Cleavage, as Exhibited in the Devonian Limestones of Devonshire. *Philosophical Magazine* (1856) **11**, p. 20.
- ³ A. Rosiwal: Über Geometrische Gesteinsanalysen. Ein Einfacher Weg zur Ziffermaessigen Feststellung des Quantitätsverhältnisses der Mineralbestandteile Gemengter Gesteine. *Verhand. der K. K. Geologischen Reichsanstalt* (1898) **5-6**, p. 143.
- ⁴ E. Thomson: Quantitative Microscopic Analysis. *Journal of Geology* (1930) **38**, p. 193.
- ⁵ R. T. Howard and M. Cohen: Quantitative Metallography by Point-Counting and Lineal Analysis. *Trans. AIME* (1947) **172**, p. 413; *METALS TECHNOLOGY* (August 1947).
- ⁶ C. S. Smith and L. Guttman: One and Two Dimensional Sections of Three Dimensional Structures. *JOURNAL OF METALS* (February 1952) **4**, p. 150.
- ⁷ T. H. Hagermann: *Geologiska Föreningens i Stockholm Förhandlingar* (1924) **46**, p. 325.
- ⁸ E. Scheil: Die Berechnung der Anzahl und Größenverteilung kugelförmiger Kristalle in undurchsichtigen Körpern mit Hilfe der durch einen ebenen Schnitt erhaltenen Schnittkreise. *Ztsch. anorg. allgem. Chem.* (1931) **201**, p. 259.
- ⁹ E. Scheil: Statistische Gefügeuntersuchungen I. *Ztsch. Metallkunde* (1935) **27**, p. 199.
- ¹⁰ E. Scheil and H. Wurst: Statistische Gefügeuntersuchungen II—Messung der räumlichen Kristallgrösze. *Ztsch. Metallkunde* (1936) **28**, p. 340.
- ¹¹ A. Huber: Zur Kinetik von Kristallisationsvorgängen. *Ztsch. Physik* (1934-1935) **93**, p. 227.

Effect of Various Elements on Hot-Working Characteristics And Physical Properties of Fe-C Alloys

by C. Travis Anderson, Robert W. Kimball, and Francis R. Cattoir

ONE of the principal impurities in all steels is sulphur. Sulphur-bearing, manganese-free steels exhibit hot shortness. Manganese is added to steel to improve the hot-working properties. If no sulphur were present in steel, it is probable that hot shortness would be nonexistent.

This paper is the first of a series to be issued by this Laboratory reporting the measurements of hot forgeability tests and the physical properties of Fe-C alloys to which additions of various alloying elements have been made. The present paper describes the results obtained by the addition of varying amounts of sulphur to Fe-C alloys.

To obtain control over residual elements in the various charges melted in the arc furnace, it was considered advantageous to use sponge iron from one source as the melting stock rather than scrap metal having an unknown history. Small amounts of unwanted alloying elements might be introduced into the charge when scrap was used, thereby influencing the results of the various heats.

A sponge iron having a high silica-lime ratio was used. Ore from Sunrise, Wyo., had been reduced to sponge iron and briquetted at the Bureau of Mines sponge-iron plant at Laramie, Wyo. The briquettes were 5 in. in diam and 2 to 3 in. in thickness, and weighed about 10 lb each. The chemical analysis of the sponge iron is as follows: C, 0.67 pct; Mn, 0.10; SiO₂, 4.75; CaO, 1.4; P, 0.044; S, 0.72; MgO, 0.4; Al₂O₃, 1.1; total Fe, 87.5; Fe metallic, 79.2; and reduction, 90.5 pct.

Where a reducing agent was required, crushed graphite electrodes usually were used. The charcoal available contained 0.20 pct S. An analysis of the available coke showed it to contain 0.70 pct S. Where high sulphur heats were required, elemental sulphur additions were made to the ladle.

Limestone of good quality was obtained locally and had the following analysis: CaO, 53.7 pct; MgO, 0.8; ignition loss, 42.4; R₂O₃, 0.2; SiO₂, 3.0; and P₂O₅, 0.014.

Melting Procedure

Sponge iron was melted to produce metal stock for the experimental alloys in a silica-lined, three-phase, direct-arc, size ST, Moore Rapid Lectromelt

C. T. ANDERSON, Member AIME, is Chief, R. W. KIMBALL is Technologist, and F. R. CATTOIR is Chemist, Ferro-Alloy Research Branch, Region III, U. S. Bureau of Mines, Redding, Calif.

Discussion on this paper, TP 3448C, may be sent, 2 copies, to AIME by June 1, 1953. Manuscript, June 30, 1952. New York Meeting, February 1952.

Papers by authors on the Bureau of Mines staff are not subject to copyright.



Fig. 1—Electric arc furnace installation.

furnace with a 500 kva rating. Fig. 1 shows this furnace installation. About 25 tons of sponge iron was melted in 75 heats, averaging 927 lb of sponge iron to the heat. An addition of carbon was required to complete the reduction of a portion of the iron oxide remaining in the sponge to prevent high losses of iron oxide in the slag and a low carbon content in the resulting metal. As reducing agents in preparing the melting stock, charcoal, coke, and a carbon product resulting from the thermal decomposition of natural gas were used. The quantity varied from 20 to 60 lb per furnace charge, with an average of 38 lb. An average analysis of the metal obtained gave 0.52 pct C, about 0.01 pct Mn, 0.070 pct P, and 0.092 pct S. The average yield of metal was 647 lb with 241 lb of slag, the sponge-iron recovery being 70 pct. The metal obtained in melting the sponge iron was cast into pigs weighing about 20 lb each to facilitate recharging into the furnace for further refining. The pouring of the pigs is shown in Fig. 2. The average power consumption for the production of the 24 tons of metal obtained was 1704 kw-hr per ton.



Fig. 2—Pouring of pigs from lip pouring ladle.

No slag-making or alloy additions were made to these heats, as the metal was subsequently remelted to remove manganese, silicon, phosphorus, and sulphur in a basic-lined furnace under a high-lime oxidizing slag.

A series of 22 heats was made on the melting stock in the basic-lined furnace under the oxidizing slag. After the metal had melted, the oxidizing slag was removed and a reducing slag formed for additional sulphur removal. Considerable sulphur is removed from high-sulphur metal under an oxidizing slag, but the reducing slag removed it much more rapidly.

The results obtained in these 22 heats on the removal of phosphorus are clearly observed in Table I. Temperature control in the furnace had considerable influence on sulphur and phosphorus. High temperatures were necessary to obtain the reductions de-

sired. Where the melt-down carbon is very low, removal of phosphorus is excellent, but where melt-down carbon is high, phosphorus removal is very poor, indicating the oxidizing conditions necessary for good phosphorus removal. This table also shows the phosphorus pick-up in the metal during the reducing-slag treatment. Even though great care was taken in removing the oxidizing slag as completely as possible, some reversion of phosphorus took place during the reducing-slag treatment. After every other possibility was eliminated, it was concluded that the pick-up was obtained from the fireclay roof. It may be noted that a considerably larger pick-up than normal occurred in heat 26B. The reducing slag in this heat was held on the metal much longer than normal. The average increase in phosphorus during the reducing-slag treatment was 0.017 pct. During the latter part of the experimental work a virtually phosphorus-free basic roof was installed, and this phosphorus pick-up was eliminated.

The average sulphur removed by the oxidizing slag was 0.017 pct, whereas 0.067 pct was removed by the reducing slag.

These 22 heats were remelted under an oxidizing slag to remove further manganese, silicon, phosphorus, and sulphur. The results of the remelting are shown in Table II.

Heats 44, 47, and 48 did not receive further treatment. Heat 44 was tapped from the furnace and a 200-lb ingot with a hot top poured. The metal was killed by the addition of aluminum pellets. Carbon was added to the molten-metal bath of heat 47 to produce a material containing 3.72 pct C. Pigs from heat 47 were added to heat 48 to raise the carbon content to 0.20 pct. No reducing slag was used on these three heats. Table III shows the results of remelting the heats shown in Table II to produce the alloys used in the tests described in this paper. Heat 17 was remelted to produce heat 18, which in turn was remelted to produce heat 19. Heat 46 had no aluminum added for deoxidation. Heat 64 was remelted for phosphorus removal to produce heat 65 having a sulphur content of 0.002 pct.

Fabrication of Samples

One ingot with a hot top was poured from each final heat shown in Table III. The ingots weighed 200 to 220 lb and were 6x6x24 in. in length including

Table I. Removal of Phosphorus and Sulphur from Metal

Heat No.	Melt-Down Carbon	Phosphorus, Pct				Pick-Up from Melt Down	Sulphur, Pct				
		At Start of Heat	Melt Down	Removed	At Tap		At Start of Heat	Melt Down	Removed	At Tap	Removed from Melt Down
1	0.024	0.072	0.017	0.055	0.040	0.023	0.099	0.090	0.009	0.033	0.057
2	0.034	0.071	0.013	0.058	0.029	0.016	0.097	0.094	0.003	0.014	0.080
3	0.030	0.073	0.006	0.067	0.027	0.021	0.098	0.076	0.022	0.011	0.065
4	0.024	0.072	0.007	0.065	0.020	0.013	0.097	0.073	0.024	0.015	0.058
5	0.036	0.071	0.003	0.068	0.022	0.019	0.104	0.065	0.039	0.018	0.047
6	0.032	0.070	0.004	0.066	0.020	0.016	0.096	0.071	0.025	0.011	0.060
7	0.050	0.070	0.004	0.066	0.027	0.023	0.097	0.070	0.027	0.010	0.060
8	0.088	0.073	0.006	0.067	0.027	0.021	0.095	0.066	0.029	0.010	0.056
20	0.078	0.068	0.022	0.046	0.030	0.008	0.097	0.072	0.025	0.010	0.062
21	0.108	0.069	0.024	0.045	0.043	0.019	0.093	0.076	0.027	0.022	0.054
22	0.046	0.072	0.008	0.064	0.031	0.023	0.100	0.072	0.028	0.008	0.084
23	0.043	0.071	0.007	0.064	0.024	0.017	0.093	0.076	0.017	0.010	0.066
24	0.066	0.073	0.011	0.062	0.036	0.025	0.095	0.087	0.008	0.007	0.080
25	0.081	0.074	0.028	0.046	0.038	0.010	0.090	0.085	0.005	0.010	0.075
26	0.058	0.070	0.009	0.061	0.044*	0.035	0.092	0.080	0.012	0.007	0.073
27	0.031	0.069	0.003	0.066	0.027	0.024	0.098	0.079	0.019	0.009	0.070
28	0.038	0.073	0.014	0.059	0.030	0.016	0.098	0.081	0.017	0.005	0.076
29	0.162	0.065	0.045	0.020	0.055	0.011	0.089	0.089	0.000	0.005	0.084
30	0.102	0.071	0.038	0.033	0.052	0.014	0.094	0.093	0.001	0.011	0.082
31	0.031	0.071	0.009	0.062	0.027	0.018	0.096	0.081	0.015	0.005	0.076
32	0.036	0.073	0.007	0.066	0.030	0.023	0.098	0.077	0.021	0.006	0.071
33	0.150	0.069	0.042	0.027	0.052	0.010	0.093	0.089	0.004	0.010	0.070

* Long heat.

Table II. Results of Remelting Heats in Table I

Heat No.	Remelt of Heat No.	Melt-Down Carbon	Phosphorus, Pct					Sulphur, Pct			
			At Start	Melt Down	Removed	At Tap	Pick Up	At Start	Melt Down	Removed	At Tap
9	1	0.067	0.040	0.004	0.036	0.013	0.009	0.033	0.029	0.004	0.007
10	2	0.063	0.029	0.002	0.027	0.015	0.013	0.014	0.012	0.002	0.003
11	3	0.046	0.027	0.004	0.023	0.017	0.013	0.011	0.012	0.001	0.004
12	4	0.071	0.020	0.002	0.018	0.012	0.010	0.015	0.014	0.001*	0.004
13	5	0.078	0.022	0.004	0.018	0.012	0.008	0.018	0.015	0.003	0.003
14	6	0.057	0.020	0.003	0.017	0.009	0.006	0.011	0.010	0.001	0.005
15	7	0.050	0.027	0.005	0.022	0.017	0.012	0.010	0.012	0.002*	0.004
16	8	0.078	0.027	0.008	0.019	0.016	0.008	0.010	0.012	0.002*	0.004
34	26	0.032	0.044	0.005	0.039	0.018	0.013	0.007	0.015	0.008*	0.004
35	21	0.027	0.043	<0.001	0.043	0.020	0.019	0.022	0.025	0.003*	0.003
36	29	0.037	0.055	—	—	0.020	—	0.005	0.009	0.004*	0.003
37	33	0.088	0.052	0.018	0.034	0.025	0.007	0.010	0.026	0.016*	0.005
38	30	0.039	0.052	<0.001	0.051	0.015	0.014	0.011	0.012	0.001*	0.003
39	32	0.027	0.030	0.002	0.028	0.019	0.017	0.006	0.016	0.010*	0.004
40	28	0.043	0.030	<0.001	0.029	0.017	0.016	0.005	0.007	0.002*	0.003
41	22	0.026	0.031	<0.001	0.030	0.020	0.019	0.008	0.009	0.001*	0.005
42	31	0.031	0.027	<0.001	0.026	0.009	0.008	0.005	0.006	0.001*	0.002
43	23	0.024	0.024	<0.001	0.023	0.010	0.009	0.010	0.007	0.003	0.004
44†	27	0.027	0.027	<0.001	0.026	<0.001	0.000	0.009	0.007	0.002	0.005
45†	24	0.025	0.036	<0.001	0.035	<0.001	0.000	0.007	0.007	0.000	0.004
47†	20	0.019	0.030	<0.001	0.029	<0.001	0.000	0.010	0.009	0.001	0.006
48†	25	0.036	0.038	<0.001	0.037	0.002	0.001	0.010	0.007	0.003	0.006

* Increase.

† No reducing slag was used. In heat 48 final carbon was obtained by addition of pig iron.

‡ In heat 47 final carbon was 3.72 pct.

the hot top. These hot tops were cropped by sawing. The cropped portion of the ingot weighed about 50 lb, leaving about 150 lb to be worked into test specimens. The ingots were heated in a butane-gas-fired furnace to about 2300°F and forged under an air hammer to approximately 1-in. rounds. The rods were then cold-swaged in a rotary swager to 5/8-in. rods, samples being removed at 3/4-in. diam for tensile and other physical tests. The rods were annealed at intervals during the swaging to relieve the hardening induced by the cold-working operation.

Evaluation of Hot-Working Characteristics

The "hot-twist test" was selected as the most suitable means of conducting the elevated temperature tests in the hot short range. This method has recently been described by Clark and Russ¹ and Ihrig.² While not entirely satisfactory, the test yields reproducible results that serve as an indication of the hot-working properties of the metal. The equipment used is rather simple; and, as Clark and Russ pointed out in their studies, the test requires very little time and is a torsion test in which the predominating stresses are in shear.

Fig. 3 shows the equipment used for the test. It consists of a furnace for heating and maintaining

the specimen at the desired temperatures. The furnace has upper and lower sections which are hinged to allow easy placement and removal of the bar being twisted, and also to facilitate chucking the test pieces. A 3-hp motor with a reduction gear is attached to a chuck for holding and rotating the specimen. At the opposite end of the chuck end of the furnace the sample is held firmly by a dog, which prevents the specimen from rotating. All results except as otherwise noted were carried out at about 200 rpm and at 50° temperature intervals from 1550° to 2000°F. The temperatures used covered the red short range. By means of an electrical circuit, an automatic counter records the number of turns before failure. Table IV gives the analysis for carbon, manganese, silicon, phosphorus, and sulphur of the rods used in the experiments.

Table V shows the results of the twisting tests obtained on the rods containing varying amounts of sulphur. These results clearly show that, as the sulphur content of the metal decreases, the number of twists to failure increases. Heat 65, having only 0.002 pct S, shows very good hot-working properties. Hot-working properties of materials above 0.010 pct S are uniformly poor. Of two ingots containing 0.017 pct S, only one could be forged to produce rod for testing.

Fig. 4 shows the results of an attempt to forge an ingot from heat 55 containing 0.021 pct S. A few blows by the forging hammer fractured the ingot.

Table III. Results of Remelting Heats in Table II

Heat No.	Melt-Down Carbon	Phosphorus, Pct		Sulphur		
		Melt Down	At Tap	Melt Down, Pct	Added Grams	At Tap, Pct
17	0.059	0.002	0.008	0.007	—	0.003
46*	0.029	<0.001	<0.001	0.004	—	0.004
49	0.025	<0.001	0.002	0.005	—	0.006
50	0.024	<0.001	<0.001	0.007	—	0.007
51	0.043	<0.001	0.002	0.004	—	0.004
52	0.029	<0.001	0.003	0.013	—	0.009
53	0.021	<0.001	0.003	0.010	225	0.032
54	0.042	<0.001	<0.001	0.018	—	0.011
55	0.042	<0.001	0.002	0.008	100	0.021
56	0.031	<0.001	0.001	0.013	50	0.017
57	0.034	<0.001	0.003	0.010	32	0.017
58	0.034	<0.001	0.002	0.010	30	0.015
59	0.028	<0.001	0.002	0.007	25	0.011
60	0.025	<0.001	0.001	0.010	32	0.013
61	0.040	<0.001	0.001	0.010	27	0.014
62	0.034	<0.001	0.001	0.009	25	0.012
63	0.041	<0.001	0.001	0.010	10	0.010
64	0.030	<0.001	0.010	0.005	—	0.002
18†	0.068	0.002	0.007	0.004	—	0.002
65‡	0.048	<0.001	0.004	0.005	—	0.002
19§	0.075	0.002	0.002	0.003	—	0.004

* No reducing slag.

† Remelt of heat 17.

‡ Remelt of heat 64 for phosphorus removal.

§ Remelt of heat 19.

Table IV. Analyses of Ingots

Ingot No.	Analysis, Pct				
	C	Mn	Si	P	S
65	0.23	0.003	0.115	0.004	0.002
51	0.21	0.004	0.004	0.002	0.004
48	0.20	0.003	<0.001	0.002	0.006
49	0.32	0.003	0.002	0.002	0.006
50	0.30	0.002	0.002	<0.001	0.007
52	0.17	0.001	0.001	0.003	0.009
63	0.26	0.002	0.002	0.001	0.010
54	0.37	0.003	0.004	0.001	0.011
59	0.24	0.003	0.005	0.002	0.011
62	0.29	0.002	0.002	0.001	0.012
60	0.16	0.003	0.003	0.001	0.013
61	0.22	0.002	0.003	0.001	0.014
58	0.23	0.003	0.004	0.002	0.015
57	0.24	0.003	0.003	0.003	0.017
56	0.27	0.003	<0.001	0.001	0.017
55	0.24	0.002	<0.001	0.002	0.021
53	0.23	0.004	0.004	0.003	0.032
19	0.061	0.004	0.002	0.002	0.004
46	0.019	0.001	0.002	<0.001	0.004
44	0.024	0.002	<0.001	<0.001	0.005

2# Al/ton furnace

No Al

Al to mold

Table V. Twists to Failure

Ingot No.	Temperature, °F										S, Pct	C, Pct
	1550	1600	1650	1700	1750	1800	1850	1900	1950	2000		
65	238	215	209	200	227	261	283	305	317	440	0.002	0.23
51	45	31	27	23	22	20	23	25	29	39	0.004	0.21
48	14	14	7	5	4	4	5	6	7	10	0.006	0.20
49	23	18	15	14	12	12	16	18	30	37	0.006	0.32
50	17	12	11	9	11	10	13	16	27	32	0.007	0.30
52	9	8	7	7	6	7	8	11	17	22	0.009	0.17
63	8	7	5	4	3	3	3	3	6	8	0.010	0.26
54	6	5	4	4	4	4	4	6	7	8	0.011	0.37
59	8	6	5	4	3	3	4	5	6	8	0.011	0.24
62	5	5	4	3	2	2	2	3	3	5	0.012	0.29
60	7	6	4	3	3	3	3	4	5	6	0.013	0.16
61	6	5	3	3	3	3	3	3	4	5	0.014	0.22
58	6	4	5	3	2	2	3	3	4	6	0.015	0.23
57	7	7	5	3	3	2	2	3	3	3	0.017	0.24
56					Broke on forging						0.017	0.27
55					Broke on forging						0.021	0.24
53					Broke on forging						0.032	0.23
19	30	25	21	20	22	20	18	27	50	55	0.004	0.061 2# Al/ton furnace
46	17	15	10	7	6	6	7	8	11	13	0.004	0.019 No Al
44	16	18	12	8	7	7	7	11	16	45	0.005	0.024 Al to mold

In all samples tested, a minimum number of twists was obtained in the hot-short range from about 1725° to 1825°F.

To determine whether the size of the rod influenced the results obtained in the test, rods of heat 19 were swaged to 5/8, 9/16, 7/16, and 3/8 in. in diam. The number of twists to failure for the rods of the various diameters is shown in Table VI. While these results indicate that the size of rod does not greatly influence the number of twists to failure, it is significant to note that, as the diameter of the rod decreases, the number of twists before failure increases.

To determine whether rate of twisting influenced the results of the twisting tests, a four-speed transmission was connected to the chuck used for twisting the rods. Rates of 47, 96, 180, and 290 rpm were obtained with this arrangement. Rods used were swaged to 3/8-in. diam for this series of tests. The results obtained are shown in Table VII. These re-

sults indicate that, as the rate of twisting increases, the number of twists to failure also increases.

Physical Testing

During the working-down schedule of the rods, samples for physical testing and metallographic examination were removed when the rods reached 3/4 in. in diam. The specimens were cut to length for heat treating. The samples were heat-treated and measured or examined in the normalized and annealed conditions. The normalized samples were heated to such a temperature that the material was in the austenitic range, held at that temperature for 1 hr, removed from the furnace, and allowed to cool

Table VI. Results of Twisting Tests on Rods of Various Diameters

Temperature, °F	Number of Twists to Failure				
	3/8 In.	7/16 In.	1/2 In.	9/16 In.	5/8 In.
1550	53	48	40	31	30
1600	52	52	37	29	25
1650	48	49	26	28	21
1700	37	30	25	27	20
1750	30	23	23	25	24
1800	28	22	24	18	21
1850	29	27	26	23	18
1900	35	34	33	30	27
1950	67	46	43	31	50
2000	71	48	54	53	55

Table VII. Results of Twists on 3/8-In. Rods in Which Rate of Twisting is Varied

Temperature, °F	Number of Twists to Failure			
	47 rpm	96 rpm	180 rpm	290 rpm
1550	62	65	85	94
1600	46	58	74	76
1650	37	45	50	65
1700	27	31	41	50
1750	15	26	32	42
1800	15	21	28	33
1850	12	16	24	29
1900	12	15	24	34
1950	15	19	26	41
2000	19	28	42	56

in still air. The annealed samples were given this same treatment but in addition were returned to the furnace after cooling, held for 30 min, the furnace heat turned off, and the specimens allowed to cool in the furnace. Duplicates were prepared on all samples.

Impact specimens were standard Charpy keyhole notch-type, with a breaking section of 0.197x0.394 in. Specimens were broken in a Tinius Olsen impact testing machine of 264 ft-lb capacity with a striking velocity of 16.5 ft per sec.

Rockwell-hardness measurements were made on all samples.

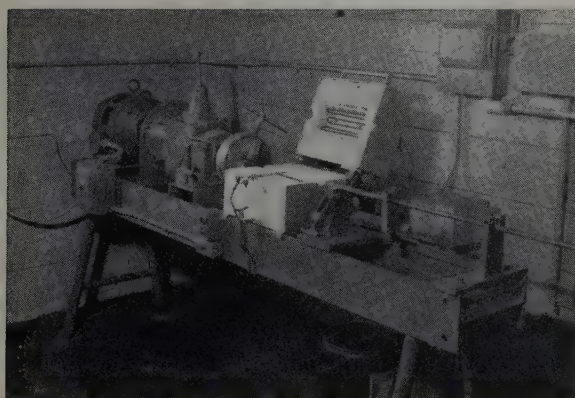


Fig. 3—Equipment used for hot-twist testing.



Fig. 4—Cracking of ingot due to hot shortness.

Table VIII. Charpy Impact Values and Rockwell B Hardness of Normalized and Annealed Samples

Alloy No.	Charpy Impact, Ft-Lb		Hardness, Rockwell B	
	Normalized	Annealed	Normalized	Annealed
65	44	33	60	45
51	46	27	60	51
48	50	27	58	49
49	32	20	65	59
50	29	13	65	56
52	44	10	61	55
63	41	30	55	43
54	26	20	71	56
59	43	29	53	42
62	40	29	58	48
60	43	28	60	41
61	50	31	60	42
58	48	35	54	36
57	48	30	59	40
19	65	59	44	42
46	45	18	55	48
44	56	24	56	46

The Charpy impact values and the Rockwell B hardness of the samples are given in Table VIII.

Tensile specimens were tested by standard methods, using a threaded 0.505-in. diam test bar in a Baldwin-Southwark testing machine. The yield point was determined by the drop of the beam. The proportional limit and yield strength values were determined from stress-strain diagrams drawn by a Templin recorder.

The mechanical properties of the samples in the annealed condition are given in Table IX, while the results obtained on the normalized specimens are given in Table X. From the results of the various physical properties of the Fe-C-S alloys, it appears that the carbon content exerts the principal influence on these properties. All samples were exam-

Table IX. Mechanical Properties of Annealed Samples

No. Heat	Thousands of Pounds per Square Inch					Red Area, Pct
	Proportional Limit	Yield Point	Yield Strength, 0.1 Pct Off	Ultimate Tensile Strength	Pct Elongation in 2 In.	
65	23.0	32.0	28.0	54.0	34.5	62.4
51	15.4	22.0	23.0	52.0	36.5	66.5
48	16.7	22.0	23.0	50.1	39.5	66.0
49	16.9	25.0	25.0	57.0	32.8	57.0
50	15.0	23.0	23.0	57.1	34.0	55.0
52	34.0	37.5	37.1	51.0	39.0	68.2
63	16.9	24.2	24.1	54.6	35.5	62.9
54	20.4	28.5	28.5	60.4	32.5	56.2
59	16.7	20.9	23.9	54.0	33.0	55.0
62	13.8	24.8	24.8	57.0	33.0	61.0
60	13.3	25.0	24.0	53.6	35.0	63.4
61	15.6	22.4	23.1	52.5	38.0	65.0
58	22.0	28.0	28.0	54.0	36.5	63.9
57	14.8	18.7	18.9	51.5	38.8	64.2
19	30.3	38.8	32.3	44.4	47.2	76.4
46	24.8	26.1	24.1	45.6	35.5	62.4
44	27.2	34.6	32.6	45.2	43.2	79.2

Table X. Mechanical Properties of Normalized Samples

Heat No.	Thousands of Pounds per Square Inch					Red Area, Pct
	Proportional Limit	Yield Point	Yield Strength, 0.1 Pct Off	Ultimate Tensile Strength	Pct Elongation in 2 In.	
65	36.3	42.1	39.3	62.4	35.8	63.4
51	28.4	40.2	35.3	57.9	38.8	65.7
48	32.4	37.9	35.5	56.1	40.5	66.7
49	36.7	45.8	45.6	66.4	33.5	56.0
50	32.5	45.8	41.0	66.4	34.5	71.0
52	29.7	45.8	45.0	59.0	36.0	68.5
63	39.7	50.7	43.8	63.8	31.5	48.4
54	33.0	45.4	40.9	69.7	29.8	54.5
59	40.8	47.4	47.0	62.7	36.5	60.6
62	38.1	47.9	41.2	64.3	33.5	59.9
60	32.8	47.9	41.4	58.8	38.2	66.2
61	31.0	43.4	37.5	60.0	37.2	65.7
58	45.1	47.3	46.1	60.6	37.0	65.6
57	35.7	44.6	41.8	60.5	38.8	65.2
19	38.4	40.5	34.8	47.9	45.0	76.3
46	31.2	35.3	32.4	50.9	34.1	59.5
44	35.9	40.4	38.3	50.4	41.2	77.0

Fig. 5—Typical normalized specimen of Fe-C-S alloy. X700. Area reduced approximately 50 pct for reproduction.

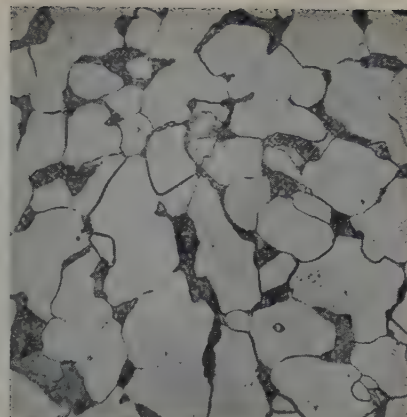
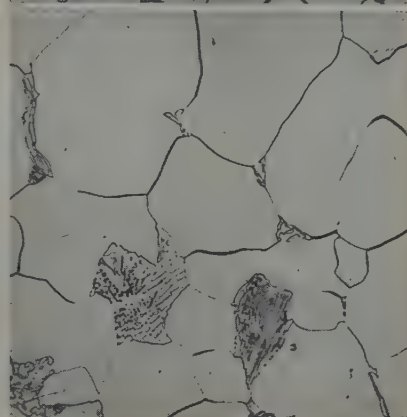


Fig. 6—Typical annealed specimen of Fe-C-S alloy. X700. Area reduced approximately 50 pct for reproduction.



ined under the metallographic microscope. The annealed samples in all cases contained larger grains and more, coarse lamellar pearlite than the normalized specimens. Fig. 5 shows a micrograph of Heat 50 in the normalized condition, while Fig. 6 shows the same alloy in the annealed state.

Summary

A series of Fe-C alloys has been prepared at the Redding, Calif., Station of the Federal Bureau of Mines in which the manganese is 0.004 pct or less with low phosphorus and silicon contents but with varying percentages of sulphur. The experimental alloys have been hot-forged and swaged to rods. Hot-twisting tests have been conducted on 5/8-in. rods. The physical properties of the alloys have been determined. Manganese-free Fe-C alloys with more than 0.017 pct S could not be hot-forged. Alloys with more than 0.010 pct S possess very poor hot-working properties. As the sulphur content of the alloys decreases below 0.009 pct, the hot-working properties of the alloys improve. Alloys containing 0.002 pct S exhibit excellent hot-working properties.

Acknowledgments

Acknowledgment is made to John L. Morning, Dean R. Myers, Edward Knakal, and A. G. Pike, former employees, who assisted in the work; to R. G. Dutton, who constructed the hot-twisting equipment and prepared most of the samples for the physical tests; and to E. D. White, who worked on the electrical equipment and conducted a number of hot-twisting experiments.

References

- 1 C. L. Clark and J. J. Russ: A Laboratory Evaluation of the Hot-working Characteristics of Metals. *Trans. AIME* (1946) **167**, pp. 736-748; *METALS TECHNOLOGY* (December 1945).
- 2 Harry K. Ihrig: The Effect of Various Elements on the Hot-workability of Steel. *Trans. AIME* (1946) **167**, pp. 749-790; *METALS TECHNOLOGY* (December 1945).

Stabilization of the Austenite-Martensite Reaction In a High Chromium Steel

by S. C. Das Gupta and B. S. Lement

No appreciable stabilization of the austenite-martensite reaction occurs in a 15 pct Cr-0.7 pct C steel unless some martensite is initially present. Stabilization is induced by interrupting the subcool below M_s ; however, disappearance of the stabilization effect as manifest by burst formation of martensite may occur on continued holding at the final sub-zero reaction temperature. The higher the temperature of intermediate cycling after the initial subcool, the more permanent is the stabilization effect at the final reaction temperature. Appreciable conditioning of retained austenite occurs on reheating to about 500°C. These phenomena are explainable on the basis of the reaction-path theory.

A RECENT investigation¹ carried out by the authors has shown that isothermal transformation of austenite to martensite definitely takes place in a 15 pct Cr-0.7 pct C steel and that appreciable amounts of martensite can form in this fashion. Investigations²⁻⁶ carried out on other steels and iron alloys make it seem probable that isothermal formation of martensite is a phenomenon of fairly general occurrence. The reaction-path theory of Cohen, Machlin, and Paranjpe^{5, 7} explains isothermal transformation on the basis of thermal activation of strain embryos which generate martensite plates with a velocity approaching that of sound. On the other hand, the nucleation and growth theory of Fisher, Hollomon, and Turnbull⁸ regards isothermal transformation as due to growth of athermally formed martensite nuclei. The experimental evidence obtained thus far favors the reaction-path theory in that the martensite reaction seems to be nucleation-controlled rather than growth-controlled.

Stabilization is another phenomenon of importance with respect to the austenite-martensite reaction. According to the reaction-path theory, stabilization is a result of relaxation of strain embryos. It is postulated that strain embryos are

present at the austenitizing temperature in the form of dislocations or lattice imperfections in the austenite which vary in the extent to which the lattice is displaced along the strain reaction path leading to martensite. On quenching from the austenitizing temperature, athermal martensite starts to form as soon as the M_s is reached, because the activation energy of the transformation which decreases with decreasing temperature is lowered to below the level of the highest energy strain embryos. Martensite plates are generated during the cooling below M_s from embryos possessing energies above the activation energy corresponding to the temperature at which the cooling is stopped. The distribution of lower energy embryos is changed because of the elastic and plastic strains produced in the remaining austenite as a result of the transformation. This effectively increases the number of strain embryos at all levels of energy below the activation energy and tends to stimulate further martensite formation either isothermally or on subsequent cooling. However, if the temperature at which the cooling is stopped is high enough for relaxation of strain embryos to occur, some degree of stabilization against further transformation may be induced. Whether stabilization will be observed on subsequent cooling will depend on the extent of decrease of activation energy with temperature. If the activation energy decreases sharply with temperature, it is possible that transformation will appear to continue with decrease in temperature in spite of the loss of embryos by relaxation. However, with a more gradual decrease in activation energy, stabilization will be manifest by no further transformation on cooling over a measurable temperature range until the

S. C. DAS GUPTA, formerly Research Associate, Dept. of Metallurgy, Massachusetts Institute of Technology, is now in Calcutta, India, and B. S. LEMENT, Associate Member AIME, is on the Research Staff, Dept. of Metallurgy, Massachusetts Institute of Technology, Cambridge, Mass.

Discussion on this paper, TP 3399E, may be sent, 2 copies, to AIME by Dec. 1, 1953. Manuscript, April 14, 1952. Cleveland Meeting, October 1953.

This paper represents part of a thesis by S. C. Das Gupta submitted in partial fulfillment of requirements for the degree of Doctor of Philosophy in Metallurgy to the University of Notre Dame.

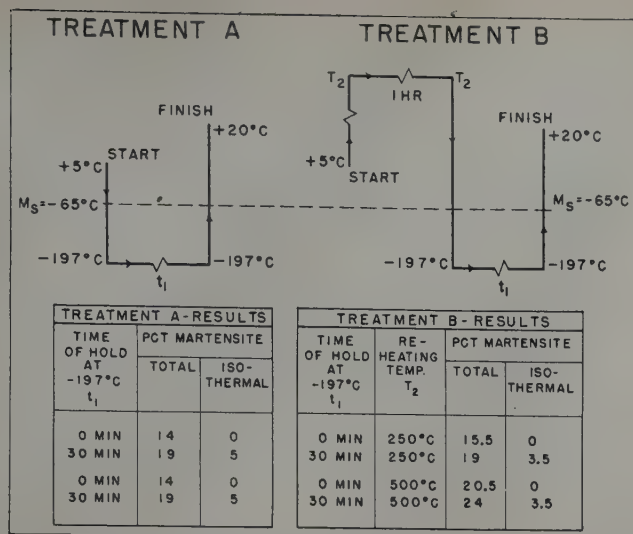


Fig. 1—Effect of reheating prior to cooling below M_s on isothermal transformation at -197°C .

activation energy is decreased below the level of the highest energy embryos that survived relaxation.

Two mechanisms by which relaxation of strain embryos can occur have been proposed by the authors of the reaction-path theory. Relaxation could occur by a recovery process similar to that which occurs prior to recrystallization of cold-worked metals. Another possibility is diffusion of solute atoms such as carbon into strain embryo regions, which results in an increase in the activation energy associated with such regions because of increase in carbon content.

The present investigation was carried out in order to learn more about the characteristics of the austenite-martensite reaction in the 15 pct Cr-0.7 pct C steel. Experiments were designed primarily to study various aspects of stabilization; however, other effects were encountered. These experiments involved prior treatments such as reheating quenched specimens before cooling below M_s , interrupting the cooling below M_s , and cycling from temperatures below M_s to above M_s . The effects of these prior treatments on subsequent athermal and isothermal martensite formation at relatively low subzero temperatures were investigated as further tests of the adequacy of the reaction-path theory.

Experimental Details

The chemical composition of the steel investigated is as follows: C, 0.73 pct; Mn, 0.28; Si, 0.20; S, 0.02; and Cr, 14.84. Specimens approximately $1/16 \times 1/8 \times 1/4$ in. were sealed in an evacuated quartz tube and then austenitized for 2 hr at 1275°C which resulted in a grain size of ASTM No. 1 to 2 and virtually complete carbide solution. The M_s corresponding to this treatment was found to be $-65^\circ \pm 5^\circ\text{C}$. Quenching was carried out in a 10 pct brine solution maintained at 5°C . The quartz tube was broken under the surface of the quenching liquid. The details of the subzero furnace used to attain temperatures down to -150°C have been given previously.¹ Liquid nitrogen was used to attain -197°C . Quantitative determination of the extent of martensite formation was carried out by the method of lineal analysis.⁹ The precision measurement is estimated to be ± 1 pct martensite.

The common starting point for most of the experiments in this investigation was the as-quenched state of specimens quenched from 1275° to 5°C . The

specimens were completely austenitic at 5°C . Comparisons were made of isothermal transformation at temperatures of -130° to -197°C with and without prior treatments. The amount of martensite formed as a result of cooling directly to these temperatures was found to be higher than previously reported;¹ however, there was no measurable change in M_s temperature. This could be due to either a slight variation in chemical composition of the bar stock used or some undetermined variable in heat treatment. In order to make the comparisons more reliable, specimens were taken from approximately the same locality in the bar stock. Furthermore, these specimens were austenitized and quenched at the same time before being subjected to the comparative treatments of each experiment. For each experiment, the basis of comparison is treatment A, which consisted of subcooling specimens from 5°C to a subzero temperature, holding for a definite length of time, and upquenching to 20°C in water.

Results

Effect of Interrupting Cooling Prior to Subcooling below M_s : The M_s temperature, -65°C , as well as the amounts of martensite formed on cooling to subzero temperatures, was found not to be affected to any appreciable extent by holding specimens quenched from 1275°C even as long as 500 hr at 20°C prior to subzero cooling. These results seemed to be at variance with the findings of Klier and Troiano¹⁰ who concluded that stabilization occurs in this steel as a result of holding above M_s prior to cooling below this temperature. However, there was still the possibility that the stabilization process at 20°C is completed so rapidly that detection is difficult. Further experiments were carried out in order to check this point by duplicating Klier and Troiano's procedure in detail. Specimens $1/32 \times 1/32 \times 1/2$ in. were austenitized for 5 hr at 1200°C in purified nitrogen atmosphere. Quenching the specimens directly into refrigerated mercury from 1200°C resulted in an M_s of about $-35^\circ \pm 5^\circ\text{C}$. However, interrupting the quench from 1200°C for 1 hr at 20°C followed by subcooling also gave the same M_s ; thus, no stabilization effect was found. Microscopic examination of specimens austenitized at 1200°C revealed an appreciable amount of undissolved carbides, which means that both the carbon and alloy content of the austenite were lower than for the case of virtually complete solution obtained at 1275°C . This would account for the higher M_s (-35°C as compared to -65°C) resulting from the 1200°C treatment.

Effect of Reheating Prior to Cooling below M_s : In these experiments, specimens were reheated to temperatures as high as 500°C after quenching from 1275°C in brine at 5°C . These specimens were air cooled to room temperature and subsequently subcooled to -197°C . The amounts of martensite formed after holding zero and 30 min at this temperature were then measured. The effect of not reheating (treatment A) is compared with that of reheating to 250° and 500°C (treatment B) in Fig. 1.

It was found that reheating as high as 500°C does not have any appreciable effect on subsequent isothermal transformation at subzero temperatures. Likewise, reheating to below 250°C does not appreciably affect the amount of athermal martensite formed; however, a 500°C reheat does result in an increase in the amount of transformation formed on subsequent cooling to -197°C . It is possible that the increased athermal transformation is due to some

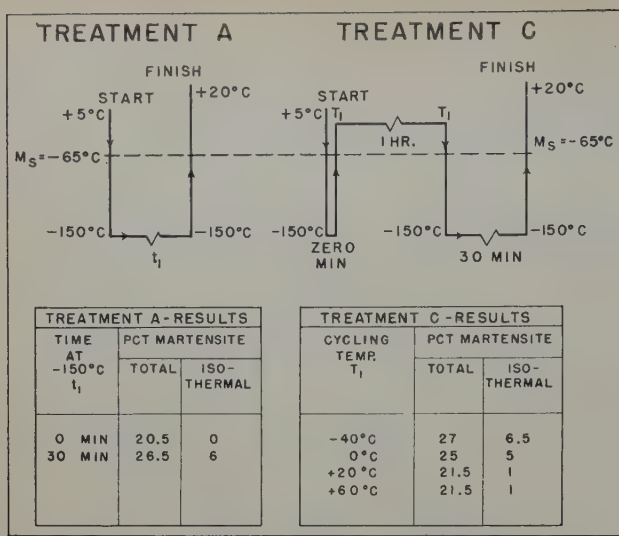


Fig. 2—Effect of cycling temperature on subsequent isothermal transformation at -150°C .

type of conditioning process that occurs in the retained austenite. This conditioning was not found to result in any noticeable increase in the M_s temperature; however, it is possible that a change less than 5°C would not have been detected with the metallographic method employed.

Effect of Cycling from below M_s : The effect of cycling between subzero temperatures below M_s to temperatures as high as 60°C on subsequent isothermal transformation was studied. The results of treatment C shown in Fig. 2 for a subzero temperature of -150°C and a 30 min hold indicate that virtually complete stabilization against isothermal transformation is obtained provided that a cycling temperature of 20°C or above is employed. Similar results were obtained for isothermal transformation at -197°C again using a 30 min hold.

This stabilization effect with respect to isothermal transformation was also found to depend on time at the cycling temperature. Using shorter times than 1 hr at 20°C was found to decrease the extent of stabilization at both -150° and -197°C .

Curiously enough, the stabilizing effect which is noticeable for comparatively short holding times at the final reaction temperature is somehow overcome

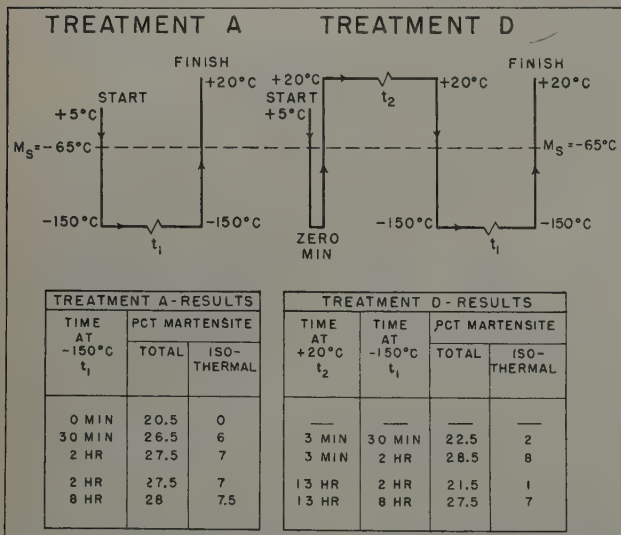


Fig. 3—Effect of time of hold at -150°C on extent of isothermal transformation following cycling treatment.

if longer times are employed. This phenomenon is shown in Fig. 3 for isothermal transformation at -150°C (treatment D). For example, the stabilization effect observed on holding 30 min at -150°C after cycling at 20°C , 3 min hold, appears to be completely overcome on continued holding for a total of 2 hr at -150°C . Similarly, after cycling at 20°C , 13 hr hold, the stabilization effect found on holding 2 hr at 150°C seems to disappear on continued holding for a total of 8 hr at this temperature. Further experiments at both -150° and -197°C established that the stabilizing effect tends to become more permanent the higher the cycling temperature or the longer the time at a given cycling temperature. For example, following 1 hr at 60°C , complete stabilization was found even after holding 6 hr at -150°C .

Effect of Interrupting Subcooling below M_s : In order to determine the effect of interrupted subcooling, specimens were first cooled to intermediate subzero temperatures in the range of -70° to -80°C , held to produce various initial amounts of martensite, and then further cooled to and held at lower subzero temperatures. The results of this procedure (treatment E) are given in Fig. 4.

As shown in Fig. 4, the total amount of martensite formed by treatment E which involved interrupted subcooling to and isothermal holding at either -130°

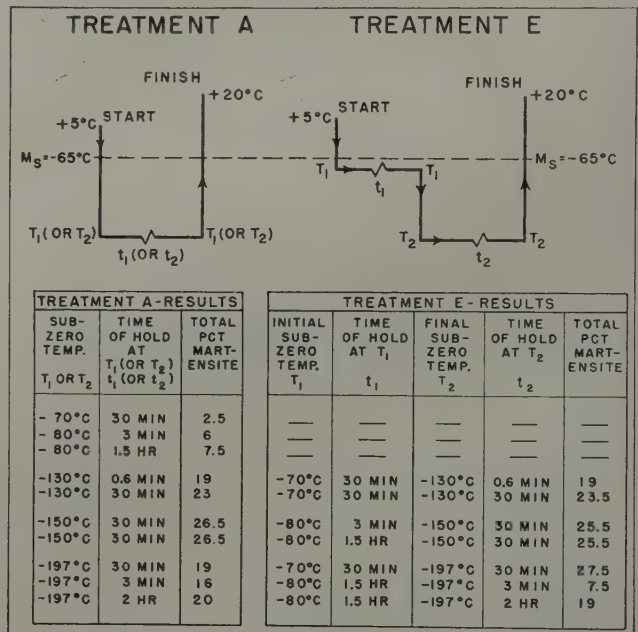
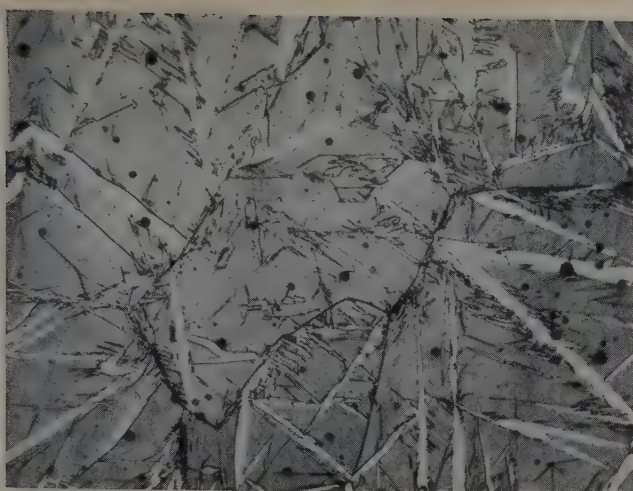


Fig. 4—Effect of interrupting subcooling below M_s on total transformation following holding at -130° , -150° , and -197°C .

or 150°C , is approximately equal to that formed by treatment A which involved direct subcooling to and isothermal holding at these temperatures. Apparently, the initial amount of martensite such as was formed at -70° or -80°C does not affect the total amount of transformation obtained on cooling to and holding at -130° or -150°C .

On the other hand, the situation is different if a final subcool to -197°C is used. The formation of about 2.5 pct martensite by an interrupted subcooling at -70°C for 30 min actually results in a greater total amount of martensite after subsequent cooling to and holding at -197°C for 30 min (treatment E) than after direct cooling to and holding at this temperature for the same time (treatment A). It would seem that the formation of a small amount of mar-



a—Normal formation of martensite resulting from direct subcooling to and holding for 30 min at -197°C .



b—Burst formation of martensite resulting from subcooling to and holding 3 min at -80°C , cycling to 20°C , and finally subcooling to and holding 30 min at -197°C .

Fig. 5—Micrographs showing normal and burst formation of martensite. Etched with modified Villela's reagent. X250. Area reduced approximately 50 pct for reproduction.

tensite by interrupted cooling has a stimulating effect on subsequent transformation on cooling to -197°C . However, if the amount of initial martensite is increased to about 7.5 pct by first cooling to -80°C and holding for 1.5 hr, essentially no further transformation takes place on subsequent cooling to and holding 3 min at -197°C . This indicates that the formation of a sufficiently large quantity of initial martensite can result in stabilization against further transformation on subsequent cooling to -197°C . However, if the time of holding at -197°C is increased from 3 min to 2 hr, the stabilizing effect of interrupted subcooling is overcome and approximately as much total martensite results as in the case of direct cooling to -197°C and holding for 2 hr. This is the same phenomenon that was observed as a result of treatment D, Fig. 3.

In order to study in more detail the stimulating effect associated with initial amounts of martensite, additional experiments were carried out. Specimens were subcooled to -70°C , held for 3 min to produce about 1 pct martensite, and finally cooled to -197°C . It was found that no further martensite formation occurred during the cooling to -197°C . However, on holding at -197°C for only 3 min about 14 pct martensite formed. This indicates that the stimulating effect is a complex phenomenon, first inducing stabilization against subsequent transformation on cooling from -70° to -197°C and then facilitating the formation of a relatively large amount of martensite on holding at -197°C for only a short time.

Microexamination of the specimens used in these experiments revealed that the small amount of martensite that formed during the initial subcool was mainly concentrated in the vicinity of the center of the specimen and was normal in appearance. On the other hand, the much larger amount of martensite that formed on holding at -197°C was found situated mainly in the region between the center zone and surface of the specimen. Furthermore this outer zone of martensite was found to possess a marked "zig-zag" appearance. It is believed that this type of martensite formation is due to the burst phenomenon reported by Machlin and Cohen¹¹ and Kulin.¹² The burst type of martensite formation was observed in all cases of stimulation associated with small initial amounts of martensite in the present

investigation. Micrographs in Fig. 5 show the difference between normal formation and burst formation of martensite.

The normal formation shown in Fig. 5a, which resulted from direct subcooling to and holding at -197°C , is typical of the entire specimen area except for occasional "zig-zag" martensite configurations which occur to a minor extent. The burst formation shown in Fig. 5b, which resulted from interrupted subcooling followed by cycling prior to the final subcool to and hold at -197°C , is typical of the major portion of the specimen area except for a small region at the center which possesses a normal appearance. The effect of cycling following interrupted subcooling is discussed in more detail in the next section.

Effect of Cycling Following Interrupting Subcooling below M_s : In these experiments, specimens were cooled to a subzero temperature such as -80° or -90°C to form some martensite initially, reheated

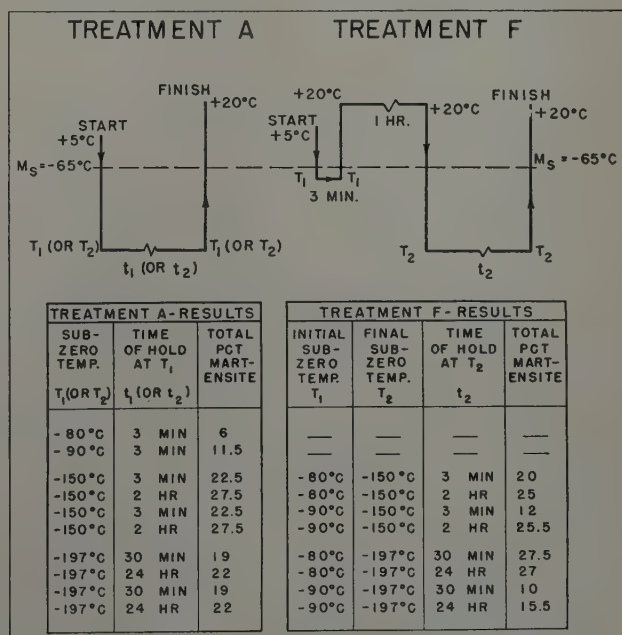


Fig. 6—Effect of cycling at 20°C following interrupting subcooling below M_s on total transformation after isothermal hold at -150° and -197°C .

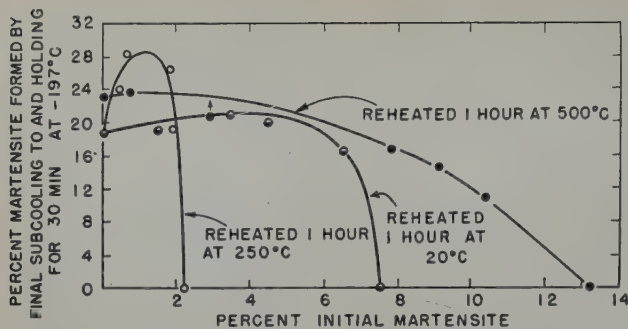


Fig. 7—Variation of amount of martensite formed by final subcool to -197°C with initial amount present and reheating temperature employed.

to 20°C , and finally cooled to -150° or -197°C . In Fig. 6 the effect of this cycling (treatment F) on total amount of martensite formed is compared with that of direct subcooling to and holding at the same final temperature (treatment A). Starting with 6 pct martensite (3 min at -80°C), cycling up to 20°C and back to -150°C results in a slightly lower amount of martensite as compared with treatment A. However, if the final subzero temperature is -197°C , a significant increase in total amount of martensite occurs. This indicates that it is possible to start with the same amount of martensite and incur either stabilization or stimulation depending on whether the final reaction temperature used is -150° or -197°C .

Variation of Critical Amount of Martensite with Reheating Temperature: Experiments were carried out to determine how the amount of initial martensite that is critical with respect to obtaining stimulation or stabilization is affected by reheating temperature. The procedure used is similar to treatment F except that reheating temperatures of 250° and 500°C as well as 20°C were employed. When reheating was carried out at temperatures of 250° and 500°C , the initial martensite was tempered but no transformation of the retained austenite took place. The tempering of the initial martensite provided a means of distinguishing in the same specimen between initial martensite and martensite formed on subcooling following the reheating treatment. The final subzero temperature used was -197°C and specimens were held 30 min at this temperature. The variation in the amount of initial martensite was produced by the initial treatments shown in Table I.

The results of reheating are shown in Fig. 7, which is a plot of amount of martensite formed subsequent to the initial treatment as a function of the amount of martensite initially present. These results confirm that for each temperature of reheating there is a critical limit of initial amount of martensite above which complete stabilization is induced against further transformation on subsequent subcooling to -197°C . For initial amounts of martensite below

these limits, stimulation of the austenite apparently occurs and even more total martensite forms than for the case of zero initial martensite. These limits and the possible experimental errors are 7.5 ± 1.5 pct, 2.5 ± 1 pct, and 13 ± 1 pct for reheating temperatures of 20° , 250° , and 500°C , respectively. Thus it appears that the critical limit first decreases with increase in reheating temperature from 20° to 250°C and then increases again somewhere in the range of 250° to 500°C .

It was shown in Fig. 1 that by reheating to 500°C without any initial martensite present, there results an increase in the subsequent transformation on cooling to -197°C and this was attributed to the phenomenon of conditioning. It is also believed that the marked increase in critical amount of martensite required for complete stabilization using a reheating temperature of 500°C as compared to 250°C , as shown in Fig. 7, is also due to conditioning. This would mean that two opposing effects, stabilization and conditioning, occur as a result of reheating above about 250°C .

Discussion of Results

Relation of Partial Transformation to Stabilization: Whether partial transformation must occur before austenite can be stabilized against further transformation on cooling is still open to question. Although Harris and Cohen¹³ and Machlin and Cohen⁶ report that stabilization occurs only if the cooling is interrupted below M_s , Klier and Troiano¹⁰ and DeLazaro et al.¹⁴ report that stabilization can be induced if the cooling is interrupted above the M_s , determined by continuous cooling. Attempts made in the present investigation to duplicate in detail the experiments of Klier and Troiano¹⁰ on the same heat of 15 pct Cr-0.7 pct C steel failed to give the same results.

The reaction-path theory does not preclude the occurrence of stabilization as a result of interrupting the quench from the austenitizing temperature prior to cooling below M_s . If it is assumed that the distribution of strain embryos existing at the austenitizing temperature is retained on quenching to a temperature above M_s , relaxation of such embryos would not be expected to occur by the process of recovery. After all, these embryos survived exposure to the austenitizing temperature where recovery would be much more potent. It is possible, however, that relaxation could occur by diffusing of carbon atoms into strain embryo regions. At the high austenitizing temperature, the tendency for such clustering of carbon atoms would be opposed by the increased entropy associated with a random carbon distribution. After quenching to above M_s , the entropy effect would be reduced, and an overall decrease in free energy could result if carbon atoms diffuse into strain embryos. Such regions offer a greater amount of interstitial space than the more perfect regions of the lattice and a decrease in distortional energy would be expected. In order to account for the failure to observe stabilization in the present investigation as a result of interrupting the quench at room temperature or reheating the as-quenched austenite to as high as 250°C , it seems necessary to assume that the rate of diffusion of carbon in the austenite of the 15 pct Cr-0.7 pct C steel is too slow to have any appreciable effect in the temperature range studied.

On the other hand, stabilization was found to take place as a result of heating in the same temperature range provided that partial transformation of austenite to martensite had previously occurred. On the

Table I. Amount of Martensite Formed by Initial Subcooling Treatment

Initial Treatment	Range of Pct Martensite Formed
Cooled to -70°C and held for 3 min	Trace to 1
Cooled to -70°C and held for 30 min	1 to 3
Cooled to -80°C and held for 0 min	2 to 4
Cooled to -80°C and held for 3 min	4 to 7
Cooled to -90°C and held for 0.6 min	5 to 8
Cooled to -90°C and held for 3 min	10 to 13
Cooled to -100°C and held for 3 min	12 to 14

basis that diffusion of carbon atoms into strain embryos results in relaxation, this would mean that for some reason the rate of diffusion of carbon in austenite is increased when some martensite is present. According to the reaction-path theory, generation of martensite plates results in the simultaneous formation of new strain embryos in the vicinity of these plates where both elastic and plastic deformation of the remaining austenite has occurred. Since the activity of carbon in martensite is presumably higher than in austenite even of the same composition, there would be a pronounced tendency for carbon atoms to diffuse from the edges of the martensite plates into strain embryos in the adjoining austenite.

Partial transformation appears to be a prerequisite for stabilization against both athermal and isothermal transformation of austenite to martensite. Stabilization against isothermal transformation was induced by first cooling to a subzero temperature below M_s and then cycling to 20°C or above before returning to the same subzero temperature for observance of isothermal transformation. It was found that the degree of stabilization increases with increase in both cycling temperature and time at a given cycling temperature. This would be expected on the basis that relaxation of strain embryos whether due to recovery or diffusion of carbon would be greater the higher the temperature or the longer the time.

Burst Formation: It has been shown that with small initial amounts of martensite formed by interrupting the subcool below M_s , it is possible to end up with more total martensite after subsequent cooling to and holding at -197°C than by direct subcooling to and holding at -197°C for the same length of time. This stimulating effect associated with small amounts of initial martensite is attributed to stabilization against transformation on subsequent cooling to -197°C followed by burst formation at this temperature. Stabilization as induced by interrupted cooling below M_s may be due to a decrease of high energy strain embryos resulting from both relaxation and isothermal transformation. In view of the small amount of isothermal transformation involved, it seems likely that relaxation plays the major role in inducing stabilization.

The burst phenomenon has been described by Machlin and Cohen.¹³ The activation of a sufficient number of strain embryos simultaneously either during cooling or at constant temperature is believed to create sufficient momentum to start a chain reaction. This results in a relatively large increment of transformation occurring practically instantaneously. The temperature at which this phenomenon first occurs on cooling is called the martensite burst point and is designated as M_b . It is apparently necessary to cool the austenite of the 15 pct Cr-0.7 pct C steel to approximately -197°C in order to lower the activation energy sufficiently to facilitate burst formation of martensite.

In the present investigation it was found that the tendency for burst formation is markedly inhibited if the initial martensite content exceeds a critical amount. Interrupting the subcool below M_s results in initial formation of martensite in the region of the center of the specimen. This location is to be expected since the specimen in the as-quenched condition has a residual stress distribution varying from compression at the outside to tension at the center, and Kulin¹² has shown that martensite for-

mation is aided by residual tension and hindered by residual compression. With increase in the amount of martensite that is allowed to form as a result of the initial subcool, the zone of transformation which has a normal appearance spreads out from the center of the specimen. When the specimen is subsequently cooled to -197°C, it is observed that burst formation is restricted to the remaining rim of untransformed austenite. By allowing the formation of sufficient initial martensite, it is possible to virtually eliminate the untransformed rim and thereby suppress burst formation of any appreciable magnitude on subsequent cooling to and holding at -197°C.

That burst formation is mainly restricted to the rim of untransformed austenite is probably due to the constraints resulting from subdivision of austenite by the martensite plates formed initially at the center zone of the specimen. The degree of cooperation required for burst formation is probably lowered by the obstructing action of martensite plates with respect to the propagation of strain associated with a burst. These plates probably act as the walls of partial enclosures in which triaxial compressive stresses are set up when a transformation strain is encountered. Kulin¹² has shown that such a stress condition externally applied to the specimen as a whole can result in a lowering of both M_s and M_b .

It was found that the critical amount of initial martensite required for complete suppression of burst formation over a period of 30 min at -197°C decreases as a result of intermediate cycling to increasing temperatures up to about 250°C. By cycling to 250°C, the critical limit was reduced to about 2.5 pct, which is not a sufficient amount to allow the central zone of normal martensite to encompass the entire volume of the specimen. In this case, the failure to observe the occurrence of burst formation in the untransformed rim may be due to the high degree of relaxation resulting from heating to 250°C. Sufficient relaxation of strain embryos situated at the outside fringes of the center zone of normal martensite formation might prevent them from triggering off bursts on subsequent cooling to and holding at -197°C.

Disappearance of Stabilization: As has been previously discussed, stabilization induced by interrupting the subcool below M_s is more pronounced the greater the initial amount of martensite formed prior to cooling to and holding at the final subzero reaction temperature. With small amounts of initial martensite, stabilization is apparently overcome in very short periods of time at -197°C by burst formations of relatively large magnitude which occur discontinuously. With larger amounts of initial martensite exceeding what is called the critical limit, stabilization seems to be more permanent. However, after sufficient time at the final reaction temperature, the stabilization effect tends to disappear. Disappearance of stabilization is manifest by isothermal formation of martensite starting after what may be either an incubation period or else a period during which the rate of transformation is too slow to be detected with the metallographic method employed. If the holding time at the final reaction temperature is sufficiently long, the original handicap in martensite content can apparently be overcome and about the same total amount of transformation results as formed by direct cooling to and holding at the same reaction temperature for the same period of time. However, the higher the cycling temperature used prior to cooling to the final

reaction temperature, the more permanent is the stabilizing effect.

In the previous investigation the authors found that the rate of isothermal transformation is maximum at the start and then decreases with time. According to the reaction-path theory, the initial rate of isothermal transformation is maximum because at zero time the distribution of strain embryos is most favorable; with increase in time the higher energy embryos are used up in generating martensite and the rate decreases.

Apparently the situation is different with respect to isothermal transformation following stabilization since the initial rate is definitely not maximum and may even be zero. The results of microexamination of specimens in which disappearance of stabilization occurred indicate that this phenomenon may be due to both normal and burst formation of martensite. Machlin and Cohen¹¹ report the occurrence of a series of bursts either with or without periods of gradual transformation at constant temperature. Such a complex behavior is difficult to analyze.

Conditioning: On reheating to temperatures of above 250°C, the phenomenon of conditioning is encountered. This results in more martensite being formed at a subzero temperature than is the case for subcooling without an immediate reheating treatment. Conditioning appears to occur whether or not some martensite is initially present.

In the tempering of high speed steel, conditioning of the retained austenite results from precipitation of carbides which lowers the carbon and alloy content of the austenite and makes it susceptible to transformation to martensite on cooling from the tempering temperature to room temperature. No actual precipitation of carbides from austenite was observed microscopically as a result of heating the 15 pct Cr-0.7 pct C steel to temperatures as high as 500°C; however, it is believed that local changes in chemical composition on a microscopic scale do occur in preparation for formation of isothermal products such as bainite. These segregations within solid solution could yield low carbon regions which are more unstable with respect to transformation into martensite than high carbon regions. On cooling, the low carbon regions should facilitate martensite formation and thus yield a greater amount of transformation on reaching low subzero temperatures. Since both conditioning and stabilization tendencies become stronger the higher the temperature of reheating, the actual martensite formation on subsequent subcooling depends on the relative potency of the two opposing effects.

Summary

The results of this investigation of the austenite-martensite reaction in a 15 pct Cr-0.7 pct C steel are as follows:

1—No appreciable stabilization against athermal or isothermal transformation results unless partial transformation has occurred previously.

2—By interrupting the subcool below M_s and forming small amounts of martensite, stabilization is induced on subsequent cooling. If the final cooling is to -197°C , burst formation of martensite results on holding for very short times at this temperature.

3—When the amount of martensite as formed by interrupting the subcool below M_s exceeds a critical limit, the stabilization effect induced on subsequent

cooling to low subzero temperatures is more marked. However, disappearance of the stabilization effect eventually occurs on continued holding at such temperatures.

4—For a given amount of initial martensite, the higher the temperature of intermediate cycling the more permanent is the stabilization effect at the final subzero reaction temperature.

5—Appreciable conditioning of retained austenite results from reheating to about 500°C with or without the existence of prior transformation.

The reaction-path theory has proved extremely fruitful in providing general explanations for the above phenomena.

Acknowledgments

The authors wish to thank the Union Carbide and Carbon Corp. for the pre-doctoral fellowship and the Studebaker Corp. for the financial aid which made this work possible. The assistance of Professor Morris Cohen in the interpretation of the experimental results on the basis of the reaction-path theory is gratefully acknowledged.

References

- ¹S. C. Das Gupta and B. S. Lement: Isothermal Formation of Martensite at Subzero Temperatures in a High Chromium Steel. *Trans. AIME* (1951) **191**, p. 727; *JOURNAL OF METALS* (September 1951).
- ²B. L. Averbach, M. Cohen, and S. G. Fletcher: The Dimensional Stability of Steel-Part III Decomposition of Martensite and Austenite at Room Temperature. *Trans. ASM* (1948) **40**, p. 728.
- ³B. L. Averbach and M. Cohen: The Isothermal Decomposition of Martensite and Retained Austenite. *Trans. ASM* (1949) **41**, p. 1024.
- ⁴G. V. Kurdjumov and O. P. Maksimova: Kinetics of the Transformation of Austenite to Martensite at Low Temperatures. *Doklady Akad. Nauk, SSSR* (1948) **61**, p. 83.
- ⁵E. S. Machlin and M. Cohen: The Isothermal Mode of the Martensitic Transformation. *Trans. AIME* (1952) **194**, p. 489; *JOURNAL OF METALS* (May 1952).
- ⁶S. A. Kulin and G. R. Speich: Isothermal Martensite Formation in an Iron-Chromium-Nickel Alloy. *Trans. AIME* (1952) **194**, p. 258; *JOURNAL OF METALS* (March 1952).
- ⁷M. Cohen, E. S. Machlin, and V. J. Paranjpe: Thermodynamics of the Martensite Transformation. ASM Seminar on Thermodynamics in Physical Metallurgy (1950) p. 242.
- ⁸J. C. Fisher, J. H. Hollomon, and D. Turnbull: Kinetics of the Austenite-Martensite Transformation. *Trans. AIME* (1949) **185**, p. 691; *JOURNAL OF METALS* (October 1949).
- ⁹R. T. Howard and M. Cohen: Quantitative Metallography by Point Counting and Lineal Analysis. *Trans. AIME* (1947) **172**, p. 413; *METALS TECHNOLOGY* (August 1947).
- ¹⁰E. P. Klier and A. R. Troiano: Ar¹¹ in Chromium Steels. *Trans. AIME* (1945) **162**, p. 175; *METALS TECHNOLOGY* (February 1945).
- ¹¹E. S. Machlin and M. Cohen: Burst Phenomenon in the Martensitic Transformation. *Trans. AIME* (1951) **191**, p. 746; *JOURNAL OF METALS* (September 1951).
- ¹²S. A. Kulin, M. Cohen, and B. L. Averbach: The Effect of Stress on the Martensitic Transformation. *Trans. AIME* (1952) **194**, p. 661; *JOURNAL OF METALS* (June 1952).
- ¹³W. J. Harris and M. Cohen: Stabilization of Austenite-Martensite Transformation. *Trans. AIME* (1949) **180**, p. 447; *METALS TECHNOLOGY* (September 1948).
- ¹⁴D. J. DeLazaro, M. Hansen, R. E. Riley, and W. Rostoker: Time-Temperature-Transformation Characteristics of Titanium-Molybdenum Alloys. *Trans. AIME* (1952) **194**, p. 265; *JOURNAL OF METALS* (March 1952).

Effects of Macrostructure on the Performance Of Alnico Permanent Magnets

by Dolph G. Ebeling and Arthur A. Burr

The effects of casting texture, grain orientation and grain size upon the performance of Alnico permanent magnets is described. Single-crystal specimens were produced by special sintering and grain coarsening techniques to study the effect of crystal orientation. In addition to texture and orientation effects, an analysis of the results indicates that the permanent magnet performance is impaired by a refinement of the grain size.

AN excellent historical review of the development of Alnico permanent magnets has been prepared by Bozorth.¹ The desirable permanent magnet characteristics of Fe-Ni-Al alloys were discovered in 1932 by Mishima.^{2,3} The work of Ruder⁴ showed that the alloys were age-hardenable, and Betteridge⁵ defined the best composition and heat treatment for the magnetically isotropic alloy known as "Alnico 3." Horsburgh and Tetley⁶ increased the energy product by the addition of cobalt and copper, "Alnico 2," and Oliver and Sheddon⁷ demonstrated that cooling in a magnetic field improved the residual induction of this alloy. Jonas^{8,9} then disclosed the great practical benefits of heat treating an alloy of higher cobalt content in a magnetic field and the resulting alloy, "Alnico 5," has become the standard of the industry. This paper describes the fundamental aspects of a procedure which can be used to further improve the properties of these anisotropic permanent magnet alloys.

A study of the casting techniques used in the production of anisotropic Alnico permanent magnets

D. G. EBELING, Member AIME, is associated with the Research Laboratory, General Electric Co., Schenectady, and A. A. BURR, Member AIME, is Associate Professor of Metallurgy, Rensselaer Polytechnic Institute, Troy, N. Y.

Discussion on this paper, TP 3433E, may be sent, 2 copies, to AIME by Dec. 1, 1953. Manuscript, April 16, 1952. Cleveland Meeting, October 1953.

This paper is based on a thesis by D. G. Ebeling submitted in partial fulfillment of requirements for a Doctor of Philosophy degree to the Department of Metallurgical Engineering of Rensselaer Polytechnic Institute.

indicated that the magnetic quality was affected by the as-cast macrostructure. Improved performance was observed in magnets containing a high percentage of columnar grains whose long axes were parallel to the magnetic axis of the casting. McCaig¹⁰ studied the effect of such columnar grain structures upon the magnetostriction characteristics of similar alloys, however no data was presented showing the effects on other magnetic properties. The following paragraphs describe two experiments which were conducted to determine the effect of various grain orientations upon the energy product.

Special composite molds were prepared of highly conductive and highly refractive components to remove the heat of solidification from the casting in a controlled manner. Representative macrostructures produced by these techniques are shown in Fig. 1, along with the relative volumes of favorably oriented columnar grains. The alloy, Alnico 5, has the highest permanent magnet performance of any commercial magnet material. It has the nominal weight composition of 8 pct Al, 14 pct Ni, 24 pct Co, 3 pct Cu, and 51 pct Fe. A heat of this material was cast into molds producing the type A and B grain structures shown in Fig. 1 and pairs of the resulting magnets were placed in heat-treating boats so as to eliminate any biasing effects of boat position. After a standard heat treatment the type A magnets, with 16 pct of the volume composed of favorably aligned grains, had a maximum energy value of 3,940,000 gauss-oersteds, while the type B magnets with 73 pct aligned grains averaged 5,090,000. This large im-

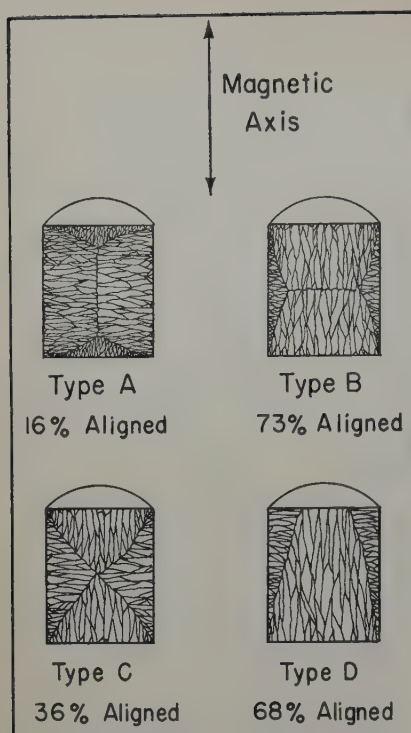


Fig. 1 — Macrostructures developed in directionally chilled, cylindrical castings of Alnico.

provement was obtained with a 57 pct increase in the volume of aligned grains, which indicated a difference of two million in the energy product between the fully aligned and fully unaligned macrostructures.

In another experiment, a portion of an 800 lb heat of Alnico 5 was cast into two types of molds so as to produce magnets of the types C and D shown in Fig. 1. A total of 236 pairs of these magnets were heat-treated in such a manner as to eliminate any spurious effects of loading. The results showed that the type C magnets with 36 pct of the volume composed of favorably aligned grains had a maximum energy value of 4,470,000, while the type D magnets with 68 pct aligned grains averaged 4,950,000. This 480,000 improvement in energy was realized with a 32 pct increase in the volume of aligned grains. This ratio extrapolates to a one and one-half million energy change between the two extreme types of macrostructure. Other experiments substantiated these indications of an important crystallographic factor affecting the quality of these permanent magnet alloys and after a study of the production aspects of the problem, a means of achieving controlled macrostructures was successfully reduced to practice.¹¹ Although the beneficial effects of certain grain structures had been demonstrated, it was of interest to establish an explanation for this behavior.

Theory

Two explanations were proposed for the previous observations. To facilitate a discussion of these proposals it is appropriate to review the magnetic characteristics that are important in the evaluation of permanent magnet materials. For this purpose, reference is made to Fig. 3.

B_r : The "ferric induction" is the peak induction, or B value, minus the peak magnetizing field, or H value.

B_c : The "residual induction" is the magnetic induction corresponding to zero magnetizing force after the material has been magnetized to saturation.

H_c : The "coercive force" is the magnetizing force required to bring the induction to zero after the material has been fully saturated.

BH_m : The "maximum energy" is the commonly accepted criterion of the excellence of a permanent magnet, and it is the product of B and H at the point in the demagnetization curve where this product is a maximum.

C : The "curvature ratio" is a dimensionless number which serves as a useful measure of the squareness of the hysteresis loop and it is defined by the

$$\text{relation: } C = \frac{BH_m}{B_r \cdot H_c}.$$

This relationship emphasizes the simple dependence of the magnet quality on three basic factors, namely: 1—The ferric induction which is controlled by the chemical composition; 2—the coercive force which is largely dependent upon the structures and lattice strains developed by the precipitation hardening reaction; and 3—the curvature ratio which will be shown to be related to crystallographic factors, such as grain orientation and grain size. In terms of these basic parameters the principal effect of the favorably oriented macrostructures was found to be an increase in the curvature factor, that is to say, to produce a square-shaped hysteresis loop. The proposed explanations of these columnar grain effects will now be presented.

In one hypothesis it was assumed there was a crystallographic "direction of easy magnetization" in these permanent magnet alloys. Single-crystal studies have shown that hysteresis curves measured in the direction of easy magnetization are rectangular in shape, whereas measurements in other crystallographic directions produce skewed hysteresis loops.¹²⁻¹⁴ The high curvature factors and energy values of these directionally chilled Alnico magnets could be explained if the crystallographic textures developed in these chilled castings corresponded to the direction of easy magnetization. There were good grounds for this supposition since all body-centered cubic metals solidify with [100] casting textures and this is just the direction of easy magnetization in soft magnetic alloys having a body-centered cubic structure.

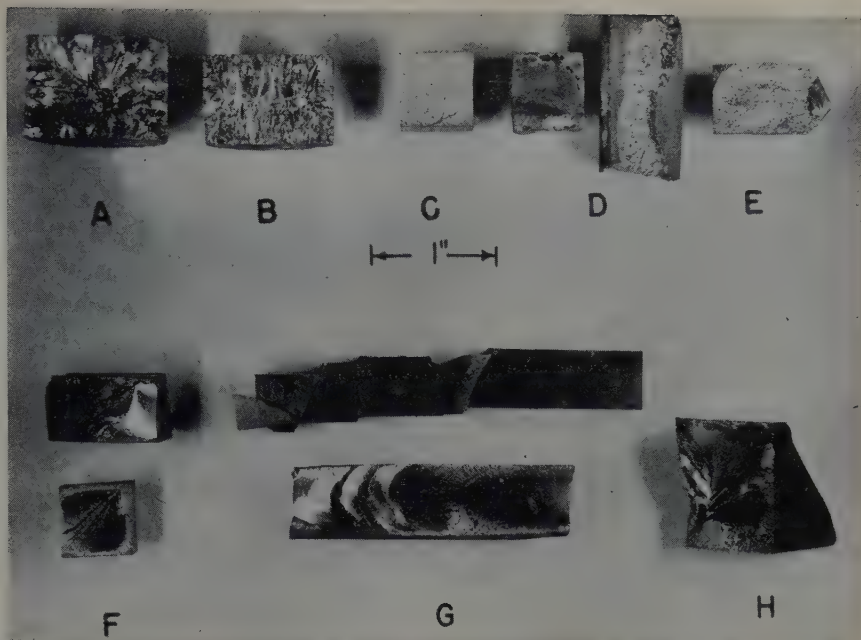
The second explanation of the columnar grain effects was based upon different grounds. Aside from the postulated difference in texture, the macrostructures shown in Fig. 1 differ greatly in the number of grain boundaries intercepted by the magnetic axis. At each grain boundary, the stable direction of magnetization must change and, hence, the internal magnetic path must be discontinuous. In magnets composed largely of favorably aligned columnar grains there are fewer interruptions in the domain path than in an unfavorably aligned structure. Intuitively, it appears that the fewer the interruptions, the more stable will be the resulting domain configuration. This paper describes an investigation which was conducted to examine the validity of these proposed mechanisms.

Procedure

Single crystals were required to study this problem. The standard techniques for growing single crystals from the melt and in the solid state were applied to these alloys without success. Crystal growth from the melt had been found impractical due to the excessive loss of aluminum while holding these 8 pct Al alloys in the molten state for a period of time

Fig. 2—Examples of macrostructures produced in cast and sintered Alnico.

- A. Normal as-cast structure produced by sand mold
- B. Directional grain structure produced in mold by the use of metal chills at the pole faces
- C. Normal sintered structure
- D. First sintered crystal showing distorted surface, cavities and fine grained skin
- E. Longitudinal fracture showing initiation of massive crystal growth
- F. Typical fractures in sintered crystals
- G. Fractures in sintered crystals indicating extent of grain growth
- H. Crystal developed in a sintered bar of $\frac{3}{4} \times 1$ in. cross section



sufficient to grow massive crystals. Grain growth in the solid state did not appear promising, since prolonged exposure to high temperatures resulted in only slight grain coarsening.

An investigation of the powder metallurgy technique was then conducted, since abnormal grain growth had been observed in a few samples of sintered Alnico 5. In the first experiment a heat of 50 pct Al-50 pct Co was prepared in a small induction furnace and subsequently reduced to -200 mesh powder. This powder was made into an Alnico 5 mix and pressed into $\frac{1}{2} \times \frac{1}{2} \times 3$ in. test bars. These bars were placed in sintering boats containing burnt alumina powder and mechanically pushed through a hydrogen atmosphere sintering furnace at such a rate that the bars were at a maximum temperature of 1380°C for 4.5 hr. These bars were fractured after sintering and all but one exhibited the normal, fine-grained macrostructure. As shown in Fig. 2 this remaining specimen contained a massive crystal surrounded by numerous cavities and a badly distorted, fine-grained surface layer. Microscopic examination revealed a fine, flocculent white powder on the surface of these voids which was taken to be alumina.

To minimize the formation of oxide films at the particle boundaries, an attempt was made to reduce the oxygen content of the powder compact. Two additional Al-Co heats were melted; in one the Al:Co ratio was 50:50 while in the other it was 25:75. These heats were ball-milled to -200 mesh under liquid toluene in which was dissolved a small amount of paraffin. The toluene was added to minimize oxidation during milling and the paraffin was expected to provide protection against oxidation during subsequent handling and pressing operations. Bars were prepared from these mixes and, after sintering, it was found that all the bars containing the 50:50 mix were fine-grained, porous, and distorted, whereas the 25:75 mix produced bars having smooth surfaces, practically no distortion, and massive crystals. There was still a thin layer of fine-grained material on all external surfaces which varied in thickness from 0.010 to 0.050 in. This performance was repeated a number of times and,

at one point, 48 out of 50 consecutive bars developed massive crystals.

Having achieved a successful method of producing large crystals, several subsidiary investigations were conducted. A study of the sintering times showed that the growth of the massive crystals occurred in only 30 pct of the bars if the time at temperature was reduced from 4.5 to 2.6 hr. Other experiments were conducted to eliminate the thin surface layer of fine-grained material. Surface treatments, protective shields, and the addition of "getters" to the burnt alumina were investigated and although getter powders were partially effective, this fine-grained skin was never completely eliminated. In all subsequent work this thin surface layer was removed by surface grinding.

The orientations of a large number of grains were determined by X-ray methods to learn if there were any possibility of controlling the orientation of the large crystals. It was found that no characteristic textures were developed about either the pressing or sintering directions. In view of these results, larger compacts were prepared and single-crystal

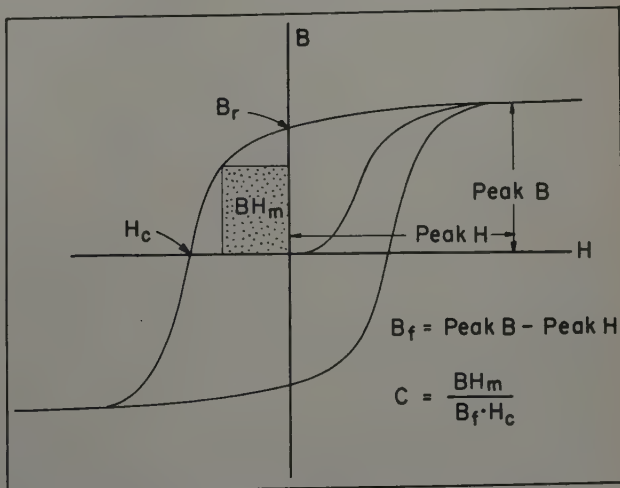


Fig. 3—Hysteresis curve showing the properties of interest in permanent magnet materials.

Table I. Sintered Alnico 5

Test No. Specimen	16 1	17 2	18 3	19 4	20 5
Orientation*	0°-0°	10°-7°	22°-13°	21°-15°	27°-12°
B_f	13,100	13,200	13,100	13,175	13,100
B_r	12,300	12,400	11,950	12,125	11,800
H_c	700	685	665	665	650
C	0.69	0.69	0.60	0.59	0.59
$BH_m \times 10^{-3}$	6,320	6,200	5,280	5,200	5,050

* Angles (a-b) in Fig. 4.

specimens of suitable size and orientation were obtained by cutting and grinding operations.

These larger bars measured about $\frac{3}{4} \times 1 \times 7$ in. Upon removing the fine-grained skin they were found to contain a number of large grains. The surfaces were polished and etched to delineate the grain boundaries and the orientations of the individual grains were determined by the Laue technique. All sides of each crystal were ground on a surface grinder to obtain the parallel faces which were necessary for accurate magnetic testing. These crystals fractured on the cube planes very readily and great care was required to avoid overheating or stressing during the cutting and grinding operations. The final specimens were not identical in shape but a representative size was $\frac{1}{4} \times \frac{3}{8} \times \frac{3}{4}$ in. Laue photograms were taken on each end of each specimen to determine the orientation of the magnetic axis and to detect the presence of any spurious grains.

These crystals had to be heat-treated in a magnetic field to develop their maximum magnetic properties. Above the Curie temperature the permeability of Alnico is roughly that of air and the magnetic lines of flux inside the directionalizing coil are essentially parallel. Upon cooling below this temperature the permeability of the Alnico increases sharply and this causes the lines of flux to be focused toward the higher permeability material. If not corrected, the divergent flux pattern created at the ends of the magnet would cause the material to be permanently directionalized in this manner with a resulting loss in performance. To combat this condition, Alnico pole pieces were placed at the ends of the magnets to concentrate the lines of flux and focus a parallel magnetic field on the magnet under treatment.

Each crystal with its carefully matched pairs of Alnico 5 pole pieces was aligned in a heat-treating boat, blocked in position with pieces of firebrick, and covered with sufficient burnt alumina to provide the proper cooling rate in the magnetic treatment. Unless otherwise noted, the heat treatment consisted of a 30 min, 1300°C solution treatment in a hydrogen atmosphere followed by a cooling treatment in a magnetic field of 1400 oersteds under

such conditions that the cooling rate in the region from 1100° to 800°C was about 100°C per min. These crystals were removed from the field when black and aged at 600°C for 6 hr. Finally, the crystals were demagnetized, polished, dimensioned, and prepared for test by carefully wrapping and cementing a "B" coil about the center cross section of the specimen. The magnetic tests were conducted in an electromagnet using a standard magnetizing field of 3000 oersteds.

Near the end of this program, it was found possible to grow large single crystals in two cast materials having compositions which differ from the straight Alnico 5 by the addition of minor amounts of titanium, silicon, and zirconium. The addition of a few percentages of titanium to Alnico 5 greatly increases the coercive force, and this high coercivity grade is commonly known as Alnico 6. The other

Table II. Sintered Alnico 5

Test No. Specimen	42 11	43 12	44 13
Orientation	40°-0°	6°-2°	0°-0°
B_f	13,100	13,500	13,450
B_r	11,600	12,700	12,650
H_c	589	659	662
C	0.54	0.66	0.67
$BH_m \times 10^{-3}$	4,200	5,900	6,000

modification of Alnico 5 is achieved by the addition of minor amounts of silicon and zirconium.¹⁵ These additions retard the precipitation hardening reaction to such an extent that overaging of the casting while cooling in the sand molds is prevented and therefore the 1300°C solution treatment is not required.

The production of large grains in castings of these modified compositions warrants comment, since this had not been possible in the case of the straight Alnico 5. In addition to their other specific effects, the titanium, zirconium, and silicon additions in these alloys tend to refine the as-cast grain size, presumably as a result of the nucleation effects of compounds formed by these elements. The resulting increase in the grain boundary area greatly increases the grain boundary energy responsible for grain growth, and it also reduces the concentration of impurities in these grain boundaries. This increase in grain boundary energy coupled with the decreased resistance to growth offered by the less contaminated boundaries is believed responsible for the formation of the massive crystals. This view of the abnormal grain growth experienced in these materials is supported by the behavior of the relatively fine-grained, sintered Alnico. In this case, the grain boundary area is extremely large and the impurity content of the boundaries is low because there is no segregation

Table III. Sintered Alnico 5

Composition in Wt Pct	Al 8.24	Ni 13.75	Co 20.88	Cu 3.20	Si 0.02	Zr 0.00	Ti 0.00	Fe Balance
Test No.			45	46	47	48	49	50
Specimen No.			14	15	16	17	18	19
Orientation			45°-0°	43°-2°	43°-1°	44°-1°	2°-0°	44°-35°
B_f			13,400	13,300	13,400	13,800	13,550	13,500
B_r			11,400	11,500	11,600	11,700	12,650	11,300
H_c			559	540	550	562	648	541
C			0.53	0.57	0.57	0.55	0.68	0.51
$BH_m \times 10^{-3}$			3,990	4,100	4,200	4,300	6,000	3,750

of foreign atoms such as occurs during the selective solidification of a melt. The necessity for the extreme precautions against surface contamination of the powder particles may also be explained in terms of this impurity concept.

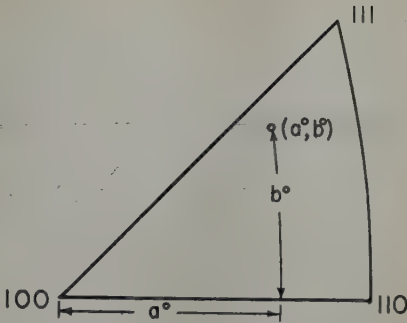
Results

The data obtained in this work is presented so as to show the correlation between the crystallographic orientation of the magnetic axis and the various magnetic properties. For this purpose, the orientation of the magnetic axes in these single crystals is represented by a point in the unit stereographic triangle. The coordinates of this point are given by a pair of angles (*a-b*), the first measured along a [100] zone from the [100] pole to the meridian of the magnetic axis, while the second angle is measured along this meridian between the magnetic axis and this [100] zone, Fig. 4.

Sintered Alnico 5 Crystals: One set of five crystals was cut from sintered bars made from the same mix; these pieces were heat-treated simultaneously and tested in the direction of the magnetic field during heat treatment with the results shown in Table I. These results show a large variation in the maximum energy value as the angle between the magnetic axis and the cube pole is increased. The 25 pct variation in the maximum energy can be attributed primarily to the change in the curvature factor, since the saturation values are unchanged and the coercivity is increased by only 8 pct.

Eighteen additional determinations were obtained on crystals of random orientations, and while the

Fig. 4—Unit stereographic triangle showing the coordinate system used to identify the orientation of the magnetic axis.



cipal crystallographic directions. These crystals were cut from adjacent grains of the same sintered bar so the chemical compositions and the pressing and sintering conditions were identical for all specimens. They were heat-treated simultaneously using six sets of carefully matched flux collectors. The results of the wet chemical analyses taken on pieces of these crystals and the magnetic data are summarized in Table III.

These data, particularly those obtained in tests 45, 49, and 50, demonstrate the marked dependence of the magnetic properties upon the crystallographic orientation of the magnetic axis.

Cast Alnico 6 Crystals: The fracture of a large Alnico 6 casting indicated that grain coarsening had occurred in one section of the piece during heat treatment at 1260°C. This casting was surface ground, polished, and etched to reveal several large grains from which suitable single-crystal specimens of the desired orientations were obtained. In addition, a similar shaped specimen was prepared from a fine-grained portion of the same casting. The chemical and magnetic results are given in Table IV.

The same orientation effects are found in this material as in the case of the sintered Alnico 5, however, the difference between the highest and lowest energy values is greater: 3,650,000 for Alnico 6 vs 2,250,000 gauss-oersteds, in the case of Alnico 5.

Cast Alnico 5 Crystals: In view of the previous results, an attempt was made to develop the ultimate properties of an Alnico permanent magnet. The Si-Zr modification of Alnico 5 was selected for this purpose because this material has a higher intrinsic magnetization than either the porous sintered Alnico 5 or the titanium-bearing Alnico 6. A large casting of this material was subjected to a grain coarsening treatment which consisted of 12 hr at 1300°C followed by 50 hr at 1200°C. This treatment produced large grains from which were obtained two single-crystal specimens. When the 900°C directionalizing treatment was applied to these specimens, the resulting energy product was very low, possibly as a

Table IV. Cast Alnico 6

Al	Ni	Co	Cu	Si	Zr	Ti	Fe
6.68	14.64	23.16	3.09	0.08	0.00	1.65	Balance
Test No.		51	52	53		57	59
Specimen No.		1	2	3		31	32
Orientation	2°-1°	5°-0°	4°-2°	44°-34°	Fine grain		
B _r	14,100	14,000	13,800	12,700	13,200		
B _r	12,600	13,000	12,700	9,800	10,600		
H _c	765	740	745	690	684		
C	0.60	0.63	0.63	0.33	0.44		
BH _m x 10 ⁻³	6,500	6,550	6,450	2,900	4,000		

data confirmed the trend toward high values in the [100] region and low values near the [111] axis, there was some scatter in the results. This variation was due partly to the fact that the specimens did not come from the same mix and had not been sintered or heat-treated at the same time. There was an abnormal variation in the ferric induction values and this was traced to a significant variation in the density of the specimens. Microscopic examination revealed minute voids in these sintered single crystals and this porosity accounted for the variations in density which ranged between 94.4 and 98.7 pct of the theoretical value.

At this point in the program the crystal preparation techniques had improved, and it was possible to cut specimens with any desired orientation. The orientations of major interest were at the corners of the unit triangle and the next set of crystals afforded a comparison of a cube oriented specimen with one having nearly a [110] orientation. The detailed results are given in Table II and they demonstrate the appreciably greater curvature and maximum energy values associated with the cube orientation.

To amplify these results another set of six specimens was prepared which covered the three prin-

Table V. Cast Alnico 5

Al	Ni	Co	Cu	Si	Zr	Ti	Fe
7.79	13.61	22.99	2.07	0.43	0.27	0.00	Balance
Test No.		64	65				
Treatment		900° and 600°C	Plus 1300° and 900° and 600°C				
Orientation	2°-1°	2°-1°					
B _r	14,350	14,300					
B _r	12,650	13,700					
H _c	608	690					
Pct C	0.46	0.71					
BH _m	3,980,000	7,020,000					

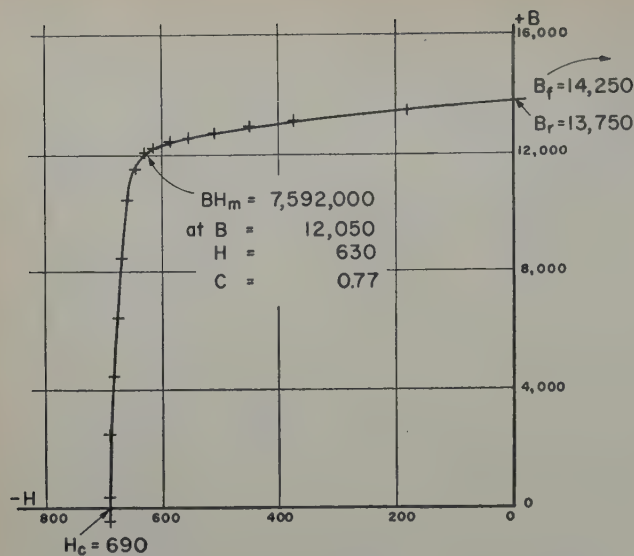


Fig. 5—Demagnetization curve obtained on a single crystal of cast Alnico 5-S.

result of excessive precipitation during the 1200°C coarsening treatment. Consequently, the material was subjected to a 1300°C solution treatment which was followed by another 900°C directionalizing treatment and a 6 hr age at 600°C. The results obtained on the more favorably oriented crystal after these treatments are given in Table V.

Although this seven million energy value was about 50 pct greater than the normal values obtained on this material, an attempt was made to improve the performance still further. In the course of this and other investigations on Alnico magnets, it was found that very deleterious surface conditions could be developed on magnets by prolonged exposures to high temperatures. Microscopic examination of these layers showed that they were heavily precipitated and such a structure is known to produce a very low coercive force. The existence of such a surface layer appeared likely on this reheat-treated specimen, so 0.020 in. was ground off all sides of this crystal. The following results were obtained on this reground specimen: B_r , 14,250; B_r , 13,750; H_c , 690; C , 0.77; and BH_m , 7,590,000. The actual test results are presented in Fig. 5, which illustrates the extreme "squareness" of the demagnetization curve. The curvature ratio of 0.77 was the highest observed in this work, as was the energy value of 7,590,000 gauss-oersteds.

Cast Textures: A large cylindrical slab of Alnico 5 approximately 10 in. in diameter and 2 in. thick was cast using a metal chill on the bottom surface. A uniformly oriented, columnar grain structure was

produced in the center of this casting and the individual grains were of sufficient size to obtain Laue photograms. The orientations of the prominent grains in a sample cut from this structure were determined by James¹⁶ and the results are reproduced in Fig. 6 in the form of a distribution plot showing the orientation of the cooling direction in the various grains of this directionally chilled casting. The concentration of points near the cube pole, particularly those obtained on the ten longest columnar grains, demonstrates the existence of a cube texture in these directionally chilled castings.

Discussion

Crystal Orientation Effects: The results of the investigations on sintered Alnico 5 and cast Alnico 6 are summarized in Table VI.

These values conclusively demonstrate the dependence of the curvature ratio and the coercive force upon the orientation of the magnetic axis. Further, since both of these properties increase simultaneously in the region of the cube direction, there results a very marked improvement in the maximum energy. Although the table adequately summarizes these data, it was of interest to pursue the analysis to establish if the high and low values are approached asymptotically or whether there are cusps in the energy function. For this purpose, the data contained in Tables I to III were plotted on the unit stereographic triangle. Each set of data indicated a slow

Table VI. Crystal Orientation Effects

Magnetic Axis	Maximum Energy Gauss Oersteds	Ferric Induction Gauss	Coercive Force Oersteds	Curvature Ratio
Sintered Alnico 5				
[100]	6,000,000	13,550	650	0.68
[110]	4,100,000	13,500	550	0.55
[111]	3,750,000	13,500	540	0.51
Cast Alnico 6				
[100]	6,500,000	14,100	750	0.62
[111]	2,900,000	12,700	690	0.33
Fine Grain	4,000,000	13,200	680	0.44

approach to the maximum value of the energy at the cube pole, but the data in the region of the octagonal pole were not conclusive.

When a saturating magnetizing field is removed, the directions of magnetization in the individual domains tend to return to the crystallographic axes of maximum stability, [100] in this case. If a cube axis is aligned with the direction of the magnetizing field, there will be relatively little loss in induction when the field is removed. Conversely, there will be a significant loss in induction if the crystallographic directions of easy magnetization are inclined at an appreciable angle to the axis of the magnetizing field. This concept suggests that the induction for any value of the applied field—and hence the energy product—should decrease continually as the angle between the magnetizing field and the crystallographic axis of easy magnetization is increased. Fig. 7 shows the result of fitting the simplest function of this type to the data obtained on all the Alnico 5 specimens. The scatter in the results is not excessive in view of the fact that the plot includes three separate sets of crystals which might be subject to composition and heat-treatment differences. This cosine relationship was adopted in the construction of a contour plot showing the variation in energy for all

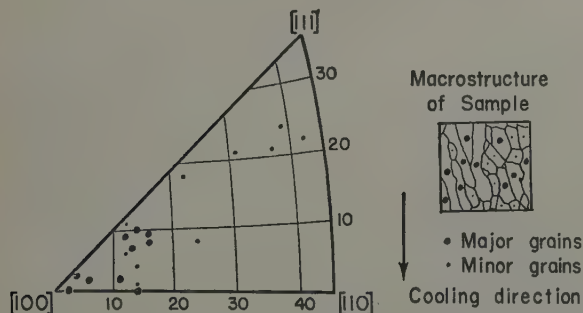


Fig. 6—Distribution plot showing orientation of the cooling direction in a directionally chilled casting.

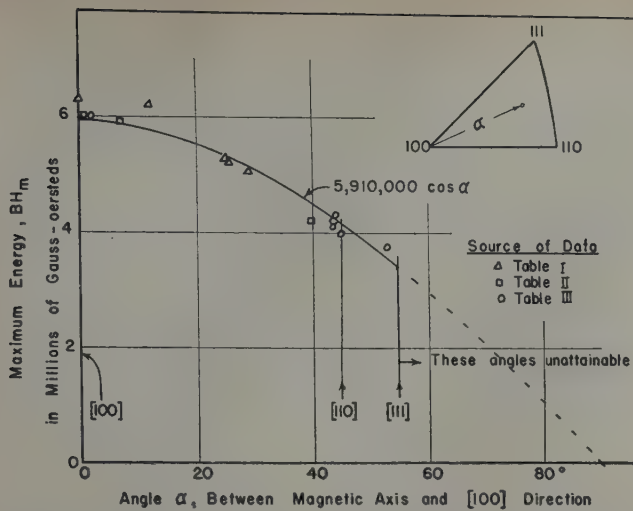


Fig. 7—Correlation of maximum energy values with the orientation of the magnetic axis in sintered crystals of Alnico 5.

intermediate orientations, Fig. 8. The nature of this energy relation is such as to produce flat maximums at the cube poles, saddles at the diagonal poles, and low cusps at the octagonal poles. This same construction was applied to the Alnico 6 data, and on the basis of the limited data, it appeared that the magnetic properties fell off somewhat more rapidly than a simple cosine law.

Grain Size Effects: Having obtained an estimate of the magnitude of the crystal orientation effects an attempt was made to apply these relationships to other phases of the problem. There is no preferred

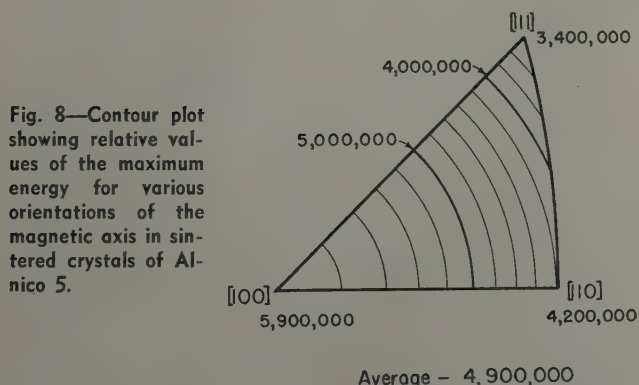


Fig. 8—Contour plot showing relative values of the maximum energy for various orientations of the magnetic axis in sintered crystals of Alnico 5.

orientation in the fine, equiaxed grain structure of the normal sintered material which has an average grain diameter of 0.15 mm or an ASTM grain size of 2 to 3. Thus, if no factors other than the crystallographic orientation are involved, then the maximum energy of this material should be equal to the average value of the energy surface shown in Fig. 8. A mean value of 4,900,000 gauss-oersteds was obtained by a graphical integration of this figure in which the lateral contraction of the stereographic plot was considered by multiplying the unit areas by the cosine of the latitude. The fact that this calculated value is so much greater than the value of 3,500,000 usually obtained for sintered material suggests that a fine-grain structure may be detrimental *per se*, a conclusion which has been suggested by other observations.

For example, a similar analysis using a cast Alnico 6 contour plot yields an average value of 4,780,000

gauss-oersteds for randomly oriented polycrystalline material. This compares with a maximum energy of only 4,000,000 as measured on the fine-grained cast Alnico 6 specimen which had an average grain diameter of 0.5 mm, ASTM grain size -1, and is additional evidence of a detrimental grain size effect. This behavior is rationalized on the basis of the inherent instability of a fine-grained, multidomain structure. In such a structure the misalignment of the directions of easy magnetization between the neighboring grains will facilitate the formation of closed magnetic circuits within the material with a corresponding loss in the useful induction.

Columnar Grain Effects: In the light of these investigations it was of interest to review the original experiments on the columnar grain structures. The grain orientation survey definitely indicated the existence of a cube texture in this material. Actually a perfect alignment is not obtained in any cast texture, but rather the cube axes of all the grains will be distributed about the cooling direction. To characterize the degree of concentration of the cube axes about any given direction, it is convenient to think in terms of an equivalent, uniform distribution of cube axes confined to a cone of revolution about this chosen axis. The degree of concentration can be represented as the half angle of the cone which is required to produce the same resolved component of the [100] axes on this reference axis as exists in the actual casting. On the basis of the distribution plot presented in Fig. 6, it is estimated that the columnar grain structures could be represented by a half angle of 15°. Using this concept and the stereographic contour plots, the theoretical estimates of the fully aligned and the fully unaligned columnar grain structures can be compared. As shown in Fig. 9, the fully aligned structure would be represented by the average of all the energy values within a 15° cone about the [100] axis, while the cross aligned specimen would encompass all values within a 15° band on either side of the [100] zone. Using the same averaging procedure as before, the contour plots gave the values shown in Table VII.

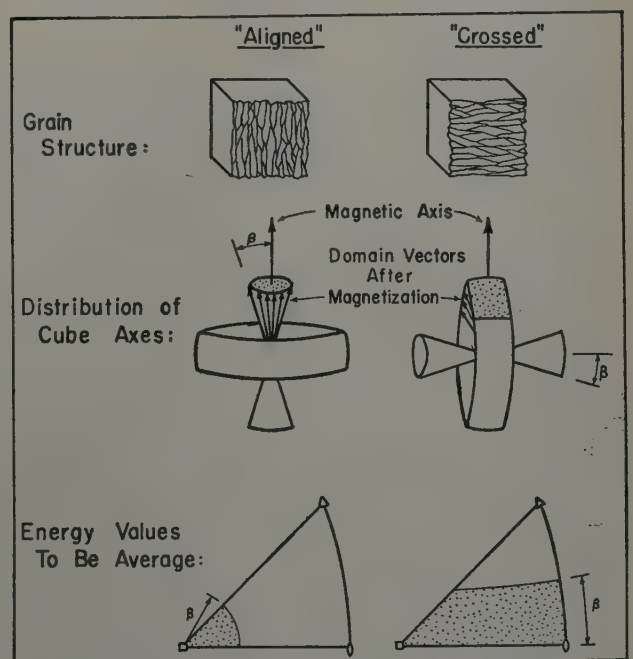


Fig. 9—Method of estimating the relative energy values of two extreme types of columnar grain structures.

Table VII. Estimates of Columnar Grain Effects

Material	Fully Aligned	Cross Aligned	Difference
Alnico 5	5,790,000	5,180,000	610,000
Alnico 6	6,190,000	5,150,000	1,040,000

These crystallographic considerations predict an energy difference of a million gauss-oersteds or less between a casting composed completely of long columnar grains parallel to the magnetic axis and one in which all the grains are perpendicular.

Actually a much greater difference was found and therefore the columnar grain effects cannot be explained solely in terms of the crystal anisotropy. The remainder of this improvement may be a grain size effect. The "effective" grain sizes in a columnar grain casting were determined by measuring the mean distance between grain boundaries in two mutually perpendicular directions. Measuring parallel to the direction of growth, the distance between grain boundaries was found to average 3.0 mm, whereas in the perpendicular direction the mean path was only 0.4 mm. On the basis of these results, it appears that roughly two-thirds the improvement in the magnetic properties of a favorably aligned columnar grain structure may be attributed to the magnetic anisotropy factor, while the remainder is due to the reduction in the number of grains which are intercepted by the internal magnetic path.

Optimum Values: The values obtained in the [100] directions on these alloys are of special interest, since they demonstrate the degree of improvement which can be realized by proper control of the crystallographic variables. Table VIII presents a comparison of the best energy values obtained on the favorably oriented crystals along with the values that are usually quoted for these alloys.

Conclusions

1—Massive crystals of Alnico alloys can be produced either by the slow sintering of fine, non-oxidized powders or by the coarsening of relatively fine-grained castings.

2—The results obtained on single-crystal specimens show that the orientation of the magnetic axis has a marked effect on the performance of Alnico permanent magnets. The squarest demagnetization curves and the highest coercive force and maximum energy values are obtained in the cube direction, while the octagonal direction is the lowest in these respects. With a [100] magnetic axis, the maximum energy of sintered Alnico 5 crystals was about 6,000,000 gauss-oersteds which is appreciably greater than the [111] orientation value of 3,500,000 gauss-oersteds. Cast Alnico 6 crystals under similar circumstances gave values of 6,500,000 and 2,900,000 gauss-oersteds.

3—An analysis of the results obtained on single-crystal and polycrystalline specimens indicates that

Table VIII. Optimum Energy Values

Alloy	Nominal Value	Best Value
Sintered 5	3,500,000	6,320,000
Cast 6	4,000,000	6,550,000
Cast 5	4,500,000	7,590,000

the maximum energy value is reduced by a refinement in the grain size.

4—Cube textures are developed in castings of these alloys and desired orientations of this texture can be realized by the controlled extraction of the heat of solidification. A cast texture in which the columnar grains are aligned parallel to the magnetic axis will produce significantly higher maximum energies than the normal, randomly oriented, grain structure. These pronounced orientation effects can be explained partially on the basis of a cube texture coupled with the pronounced magnetic anisotropy and partially as the result of a larger effective grain size as measured in the direction of the magnetic axis.

5—A cube oriented, cast Alnico 5 crystal produced an energy value in excess of 7,500,000 gauss-oersteds.

Acknowledgment

The authors are indebted to the personnel of the General Electric Co. who supported or assisted in these programs over a three-year period. Particularly, we wish to acknowledge the support of Z. Jeffries and E. E. George who authorized certain phases of this work and the assistance of R. J. Studders for his invaluable contributions on the crystal preparation techniques. The many valuable discussions contributed by staff members of the Rensselaer Polytechnic Institute and the General Electric Research Laboratory contributed greatly to the progress of this work.

References

- ¹R. M. Bozorth: *Ferromagnetism*. pp. 385-396. New York. D. Van Nostrand.
- ²T. Mishima: Nickel-Aluminum Steel for Permanent Magnets. *Ohm* 19, p. 353.
- ³T. Mishima: Magnet Steel Containing Ni and Al. U. S. Patent 2,027,994 (Appl. March 9, 1931).
- ⁴W. E. Ruder: Permanent Magnet and Method of Making It. U. S. Patent 1,947,274 (Appl. February 1, 1933).
- ⁵W. Betteridge: Nickel-Iron-Aluminum Permanent Magnet Alloys. *Journal Iron and Steel Inst.*, London. 139, pp. 187-208.
- ⁶Horsburgh and Tetley: Improvements in Alloys for Permanent Magnets. British Patent 431,660 (Appl. May. 23, 1934).
- ⁷D. A. Oliver and J. W. Sheddon: Cooling of Permanent Magnets in a Constant Magnetic Field. *Nature* 142, p. 209.
- ⁸Philips Gloeilampen Fabrieken: Permanent Magnet Material. British Patent 522,731 (Appl. December 7, 1938).
- ⁹B. Jonas and A. J. M. Emden: New Kinds of Steel of High Magnetic Power. *Philips Technical Review* 6, pp. 8-11.
- ¹⁰M. McCaig: Magnetostriction of Anisotropic Permanent Magnet Alloys. *Proc. Phys. Soc.*, London. B62, pp. 652-656.
- ¹¹D. G. Ebeling: Method of Making Cast Alnico Magnets. U. S. Patent 2,295,082 (Appl. January 10, 1948).
- ¹²H. J. Williams: Magnetic Properties of Single Crystals of SiFe. *Physical Review* 52, pp. 747-751.
- ¹³S. Kaya: On the Remanence of Iron Single Crystals. *Ztsch. Physik* 84, pp. 705-716.
- ¹⁴S. Kaya and H. Takaki: Hysteresis Loops and Magnetostriction of Fe Crystals. *Sci. Repts. Tohoku Imp. Univ.* pp. 314-328.
- ¹⁵J. R. Hansen: Production of Permanent Magnets and Alloys Therefore. U. S. Patent 2,499,861 (Appl. March 16, 1948).
- ¹⁶W. James: Rensselaer Polytechnic Institute Thesis, June 1948.

Vanadium-Uranium Constitutional Diagram

by H. A. Saller and F. A. Rough

Studies of the V-U system have been made to determine the constitutional diagram. The diagram is fairly simple, since no intermediate phases are formed. Additions of vanadium lower the uranium melting point and allotropic transformation temperatures. The maximum solid solubility of vanadium in uranium is 12 atomic pct and the maximum solid solubility of uranium in vanadium is about 4 atomic pct.

WITH the advent of high purity iodide vanadium,¹ it became of interest to study the alloying characteristics of vanadium and uranium. Alloys were prepared covering the entire system and were studied using a combination of metallographic examination and thermal and X-ray analyses. As a consequence of this work, the V-U constitutional diagram was evolved.

In order to prepare suitable alloys for equilibrium-phase studies, it is desirable to have the purest possible starting materials. For this investigation, calcium-reduced vanadium, de Boer process crystal-bar vanadium, and good Mallinkrodt Chemical Co. uranium were used. The first work was done using the best vanadium then available, that being calcium-reduced vanadium produced at Knolls Atomic Power Laboratory. Subsequently, the important features of the diagram were checked using alloys made with crystal-bar vanadium produced at Battelle. These checks are in agreement with the earlier work.

Analyses of the starting materials are contained in Table I. Only minor amounts of any impurities were present in either the vanadium crystal bar or uranium. Nevertheless, care was exercised in selecting the uranium for the alloys. The procedure followed was to section the stock into suitable pieces for melting, and macroetch each piece. Only those pieces which appeared to be clean by macroetch examination were used for alloying.

Experimental Procedure

Melting: Alloys with 0 to 50 atomic pct V were induction melted in beryllia (BeO) crucibles under vacuum of 10 microns pressure or better. A number of remelts was frequently required to insure uniformity of the individual ingots. Although no visible reaction between the alloy and crucible was found in any of these operations, the alloys were checked by spectroscopic analysis. Only trace amounts of beryllium were detected in the alloys.

Table I. Impurities in the Starting Materials

Element Detected	Uranium, Pct	Iodide Vanadium, Parts per Million
Fe	<0.01	150-250
Ni	<0.01	50
Al	<0.01	20-100
Mo	<0.01	50
Cr	<0.01	Trace
W	—	200
Cu	<0.01	50
V	<0.01	—
Si	<0.01	50-150
P	<0.01	—
Mg	<0.01	50
O ₂	—	280-370
H ₂	—	6-17
N ₂	—	40-60

Alloys containing 50 to 100 atomic pct V were arc melted in a water-cooled copper crucible under an atmosphere of helium. A tungsten electrode was used. Ingots of 10 to 15 g were produced readily by turning and remelting a few times. Such small ingots were necessary because high purity vanadium was not available in appreciable quantities at this time. After melting, the ingots were examined metallographically for segregation and were consolidated by remelting before fabrication was attempted. Spectroscopic analyses showed that only small amounts of tungsten were picked up during the arc-melting process.

Fabrication of Alloys: Alloys containing up to 20 atomic pct V could be fabricated by rolling in air at 600°C with 5 min between passes. After each pass through the rolling mill the alloys were returned to

H. A. SALLER and F. A. ROUGH are Supervisor and Assistant Supervisor, respectively, in metallurgy, Battelle Memorial Institute, Columbus, Ohio.

Discussion on this paper, TP 3402E, may be sent, 2 copies, to AIME by Dec. 1, 1953. Manuscript, June 16, 1952. Cleveland Meeting, October 1953.

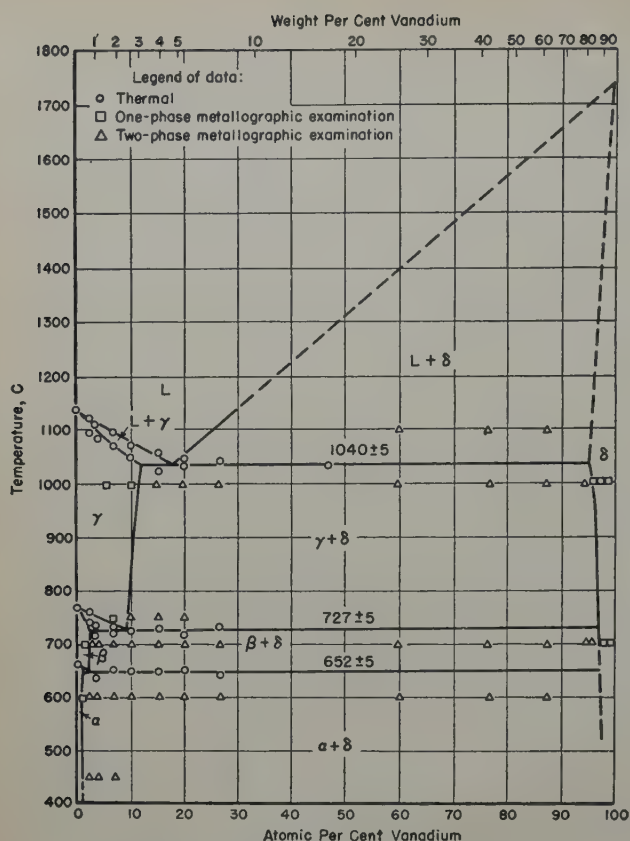


Fig. 1—V-U constitutional diagram.

a furnace that had an atmosphere of argon. The alloys around 20 atomic pct V appeared to be less amenable to this procedure than were the lower alloys, however the fabrication was satisfactory for this work.

High vanadium alloys containing up to 10 atomic pct U were fabricated by jacketing in stainless steel and rolling at 1000°C with 5 min between passes through the rolling mill. No attempts were made to fabricate alloys of intermediate compositions, since preliminary work had shown that two-phase regions extended across the system with no intervening com-

pounds. It is expected that these intermediate two-phase alloys would also be workable, especially if jacketing techniques are used.

Sampling for Chemical Analysis: Samples for chemical analyses were cut from the top and bottom of each of the small induction-melted ingots of high uranium alloys. Since the high vanadium ingots were quite small, sampling techniques in this case were limited. Usually, whole metallographic samples of these alloys were submitted for analysis after thorough examination.

Heat Treating: All heat treating was done under vacuum of one micron pressure or better. The procedure followed was to homogenize the as-rolled alloys by soaking for 40 hr at 1000°C. Subsequent heat treatments at various temperatures were carried out as indicated in a later section of this paper.

Metallography: Specimens were cut using Allison, No. 46A3, cutoff wheels 0.020 in. thick. The samples were then ground wet through the usual rough papers and were finished wet on 240, 400, and 600 grit abrasives.

Alloys with 0 to 30 atomic pct V were polished and etched in a solution of chromic and acetic acids, Table II. Polishing was usually complete after 30 sec to 1 min at 50 v with a current density of approximately 20 amp per sq in. Etching was obtained by dropping the voltage to 6 to 10 v in the same solution. Relief, sometimes troublesome in two-phase alloys, was readily avoided by polishing mechanically with stannic oxide on a wheel covered with billiard cloth. This was followed by etching at 6 to 10 v in the chromic and acetic acid electrolyte. The same etch also served as a macroetch.

High vanadium alloys, 30 to 100 atomic pct V, were prepared for examination by grinding through the same series of abrasive papers, finishing on a billiard cloth with stannic oxide abrasive, and electropolishing for a few seconds at 10 to 20 v. The solution for this operation consisted of sulphuric acid and methyl alcohol. The exact composition is shown in Table II. This polish served to remove scratches and worked metal and also to etch two-phase alloys. Solid-solution-type high vanadium alloys were further etched by swabbing with a solution of hydrofluoric and nitric acids in water, Table

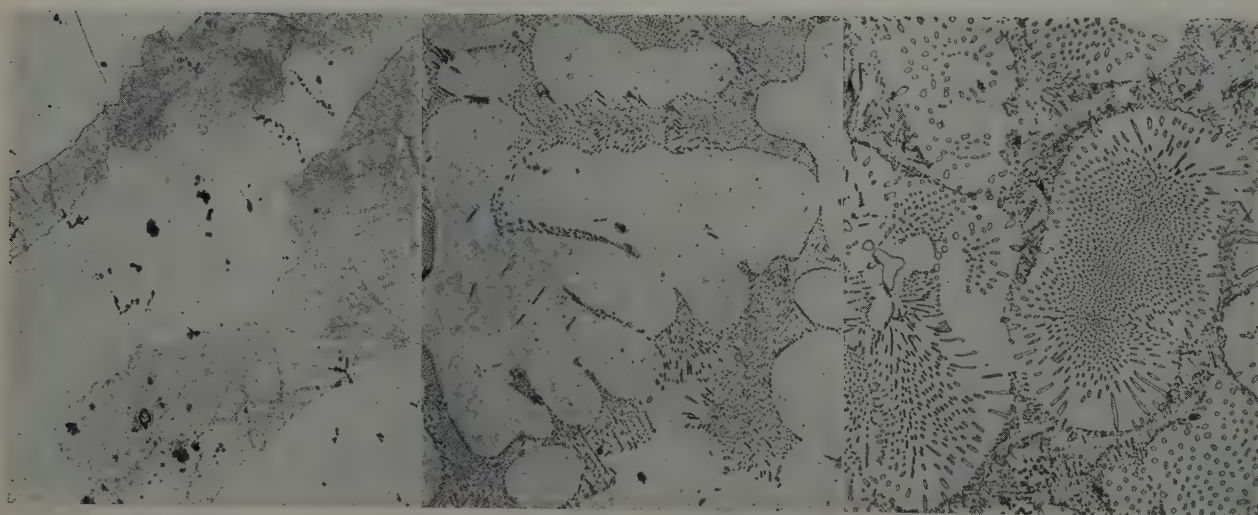


Fig. 2—100 pct U as cast. X100.

Fig. 3—7 atomic pct V alloy as cast. X250.

Fig. 4—15 atomic pct V alloy as cast. X250.

Figs. 2 to 4—Area reduced approximately 25 pct for reproduction.



Fig. 5—20 atomic pct V alloy as cast. X250.

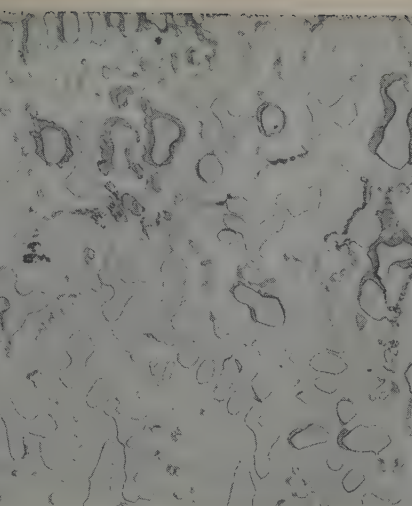


Fig. 6—27 atomic pct V alloy as cast. X250.

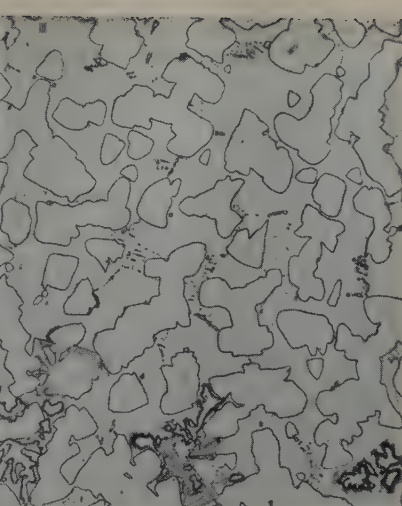


Fig. 7—47 atomic pct V alloy as cast. X250.

Figs. 5 to 7—Area reduced approximately 25 pct for reproduction.

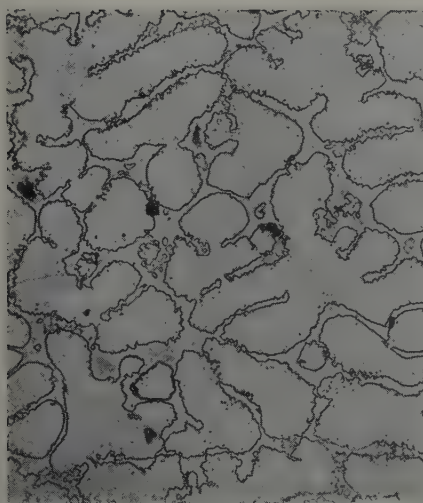


Fig. 8—80 atomic pct V alloy as cast. X250.

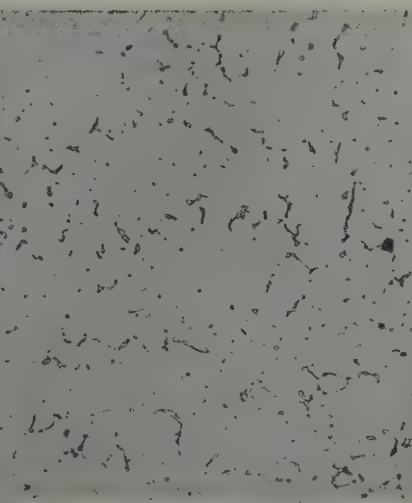


Fig. 9—95 atomic pct V alloy as cast. X250.



Fig. 10—96.2 atomic pct V alloy as cast. X250.

Figs. 8 to 10—Area reduced approximately 25 pct for reproduction.

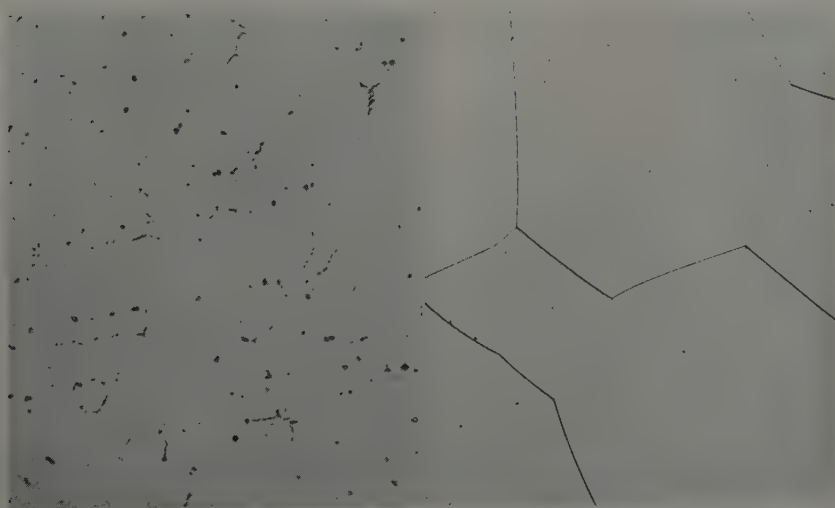


Fig. 11—97.5 atomic pct V alloy as cast. X250.

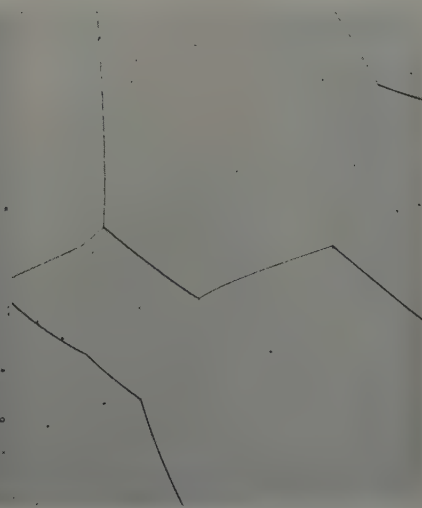


Fig. 12—100 pct V as cast. X250.

Figs. 11 and 12—Area reduced approximately 25 pct for reproduction.

Table II. Polishing and Etching Solutions

- 1—Electrolyte for high uranium alloys:
1 part base solution—100 g CrO_3 and 118 ml H_2O
3 parts glacial acetic acid
- 2—Electrolyte for high vanadium alloys:
20 vol pct concentrated H_2SO_4
80 vol pct methyl alcohol
Few drops H_2O
- 3—Acid etching solution for high vanadium alloys:
1 part concentrated HNO_3
1 part concentrated HF
1 part H_2O

II. This etch brought out grain boundaries which were not visible after the electropolishing operation.

X-Ray Examination: A general survey of the alloy system was not made by X-ray examination. However, a number of confirming checks were made on the results of other studies by making X-ray diffraction patterns from metallographic sample surfaces.

Thermal Analysis: To determine solid-phase transformations, thermal analyses were performed on alloys across the constitutional diagram. Runs were also made for liquidus-solidus data on the high uranium alloys. Standard techniques of analysis were employed for this work using the differential-thermocouple arrangement.² The temperature differential between the neutral and active samples was plotted against the temperature of the active sample under test. Solid-phase transformations were then readily detectable in alloys containing appreciable amounts of a high uranium phase. Best results were obtained by cycling through transformation temperatures one or more times. The data obtained by heating appeared to be most reliable and were little affected by variations of heating rates between 1° and 5°C per min. Cooling data are not considered to be reliable, since difficulty was encountered with supercooling.

In all of this solid-phase work, the thermocouple bead was protected from the uranium by refractory insulators. A piece of refractory in the specimen hole prevented contact between the thermocouple bead and specimen, but allowed radiation directly between them. By using a fine wire, 30 gage thermocouple, this arrangement was found to give good sensitivity at the temperatures of testing.

The best data on the liquidus-solidus determinations were obtained by heating once through the melting range. After the first melting, alloys were usually segregated and unusable. During this work, the thermocouples were protected by using small specially prepared BeO protection tubes.

Results

Constitutional Diagram: The V-U constitutional diagram has been established and is shown in Fig. 1. Since no intermediate phases are formed, the diagram is relatively straightforward. It is characterized, generally, by a high temperature eutectic and lowering of the uranium allotropic transitions by additions of vanadium. The eutectic reaction occurs at $1040^\circ \pm 5^\circ\text{C}$ and 18 atomic pct V. The solubility of vanadium in γ uranium is a maximum of 12 atomic pct at the eutectic, and decreases to 9 atomic pct at the eutectoid temperature of $727^\circ \pm 5^\circ\text{C}$, Fig. 1. The β -uranium region is more restricted than the γ field with 2.0 atomic pct V being soluble at 700°C . The α region is restricted still further. In this case, a solubility of less than 1.5 atomic pct V at 600°C was found.

The solid solubility of uranium in vanadium is limited at all temperatures. The solid-solution line is a maximum at the eutectic temperature, Fig. 1. Here the solubility is 4 atomic pct, 15 wt pct, uranium. At lower temperatures somewhat lower solubilities were observed.

Microstructures of Cast Alloys: Many of the general features of the V-U system are apparent from the series of micrographs of as-cast alloys shown in Figs. 2 to 12. The first micrograph of the series, Fig. 2, shows the structure of arc-melted uranium. Addition of 7 atomic pct V alters the uranium structure producing primary uranium islands surrounded by transformed eutectic, Fig. 3. A somewhat similar structure is found in a 15 pct alloy, Fig. 4. However, in this case precipitation has occurred in the primary-uranium islands. In these two structures the eutectic was altered by the γ and β eutectoid transformations.

Primary dendrites of vanadium are present in a 20 atomic pct alloy indicating that it is on the vanadium-rich side of the eutectic composition, Fig. 5. Structures of additional alloys on the vanadium-rich side of the eutectic composition are shown in Figs. 6 and 7. The eutectic in these alloys is not evident as a two-phase structure. This is assumed to be due to precipitation of vanadium on the primary-vanadium particles during the eutectic reaction.

A decreasing or disappearing uranium phase is observed as the vanadium content increases from 80 to 97.5 pct, Figs. 8 to 11. In the 80 pct alloy considerable uranium-rich material is present while in the 95 pct alloy only scattered uranium-rich particles remain to be observed. A scattering of tiny particles of uranium-rich material also appears to be present in the 96.2 and 97.5 atomic pct alloys, Figs. 10 and 11.

Thermal Data: Some of the general features of the diagram have been illustrated by metallographic structures. As much, or perhaps more, data are also observable from a survey of thermal studies, Fig. 1. The eutectic, γ eutectoid, β eutectoid, and even approximate solubilities might be determined from these data alone, although the diagram is the result of combined studies.

Metallographic Studies of Solid Solubilities: The results of metallographic studies are summarized and plotted in Fig. 1. Data are shown for high uranium alloys quenched from temperatures of 1000° , 750° , 700° , 600° , and 450°C , and for high vanadium alloys from 1100° , 1000° , and 700°C .

Alloys for this work were homogenized by holding for 40 hr at 1000°C and quenching. Samples thus treated were held for appropriate times and quenched from the temperatures of interest. In determining the solubilities of vanadium in α uranium and of uranium in vanadium, the alloys were cold worked before heat treatment to accelerate the approach to equilibrium.

Acknowledgment

The work reported in this paper was performed under Contract W-7405-eng-82 for the Atomic Energy Commission.

References

- ¹ J. W. Nash, R. E. Durtzsch, I. E. Campbell, and H. R. Ogden: The Preparation and Properties of Iodide Vanadium. Electrochemical Society Meeting, Philadelphia. May 7, 1952.
- ² Nat. Bur. Standards TP 170 (1921).

by G. R. Speich and David J. Mack

APRIL 1953, JOURNAL OF METALS—549

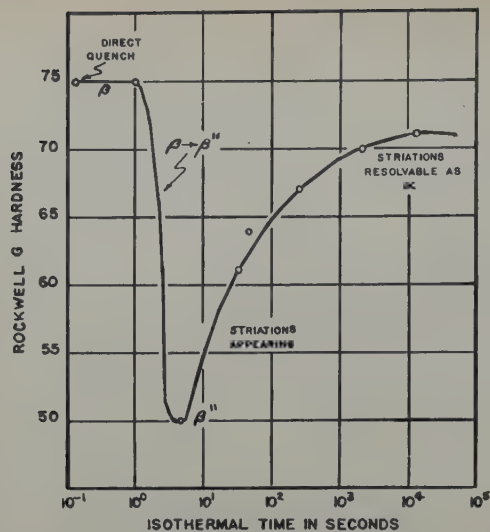


Fig. 2—Hardness of specimens isothermally transformed at 400°C.

was allowed to proceed. Specimens withdrawn from the salt bath were quenched in cold water.

The progress of the transformation was followed by metallographic methods and also by the use of hardness measurements. Specimens were given a preliminary polish on broadcloth using No. 600 alundum, final polishing being on felt using magnesia at slow speed. The only etching reagent that produced satisfactory results was one containing: chromium oxide, 20 g; sodium sulphate, 1.5 g; and water, 100 ml. The etchant was applied by swabbing and gave better results for specimens transformed at lower temperatures when diluted with 5 parts of water.

Experimental Results

The nature of the isothermal transformation of the β phase changes with temperature although the change is gradual from near eutectoid temperatures, 440°C, to the alleged polymorphic transformation at 240°C. There are certain features of the transformation that are common to all temperatures in this range. These are as follows:

1—The β phase transforms sluggishly enough so that it can readily be retained at room temperature. The retained β is very coarse grained and is readily recognized microscopically by its salmon-pink color after etching. This makes the alloy appear pink to the naked eye. Since the β can be easily retained to room temperature,¹ it presumably also exists for a short time in the isothermal bath.

2—The large grained β then rapidly transforms into fine grained β'' * which can be recognized by its

* The following terminology will be used for the various phases formed in this Ag-Cd alloy:

- α — terminal solid solution, silver rich, face-centered cubic.
- β — high temperature intermediate solid solution, body-centered cubic.
- β'' — metastable transition phase, supposedly hexagonal close-packed.
- β' — equilibrium phase, ordered body-centered cubic.
- ζ — low temperature, equilibrium phase, hexagonal close-packed.

light yellow color. This change is accomplished by a pronounced drop in hardness, as shown in Fig. 2.

3—The fine grained β'' develops striations, as illustrated in Fig. 3. The striations seem to start at the grain boundaries and grow completely across the β'' grains. They are straight, parallel, and regularly spaced, usually only one set appearing in a β'' grain. They cause an increase in the hardness of the β'' as shown in Fig. 2. As the transformation temperature decreases, the striations become finer and more profuse as can be seen by comparing Figs. 3 and 8. At lower temperatures there is an increasing tendency for the striations to form along more than one set of crystallographic planes of the β'' giving less regular appearing striations. This is illustrated in Fig. 4. The striations are always associated with the light etching, yellow β'' .

4—Coincident with, or shortly after the striations appear in the β'' , a rejection of white α begins to take place as indicated in Fig. 5. This rejection decreases in amount with decreasing temperature of transformation and virtually ceases below 350°.

While the sequence of changes just described is common to the isothermal decomposition of β at all temperatures between 440° and 240°C, subsequent changes vary with temperature.

With further holding time in the range from about 440° to 400°C, the striations disappear and the amount of white α increases. This is shown in Fig. 6. At the same time the dark etching purple-pink colored phase, β' , appears in the regions where the striations have disappeared. Ultimately the striations and the β'' in which they originally formed disappear completely, the equilibrium structure of α and β' remaining. The equilibrium structure is shown in Fig. 7.

At about 400°C the striated β'' begins to break down by nucleation and growth of pearlitic ($\alpha + \beta'$) nodules, Fig. 8. Not all of the β'' is consumed by these nodules, some of the striations apparently developing the proper composition to form silver-rich α . When this composition is reached, an interface develops and the striations break away from the parent β'' , forming flat plates of white α . While this

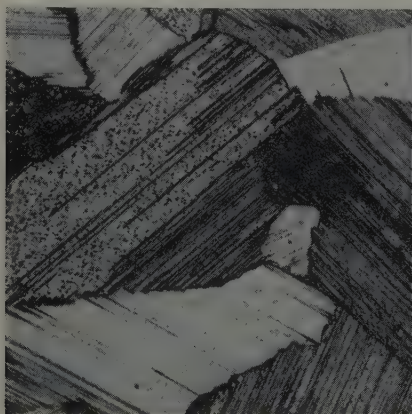


Fig. 3—5 min at 400°C. Striated β'' grains with traces of α at the boundaries. X250.

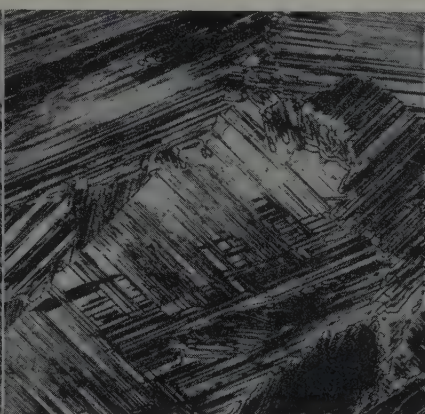


Fig. 4—2 hr at 350°C. Striated β'' with some α at the boundaries. X250.

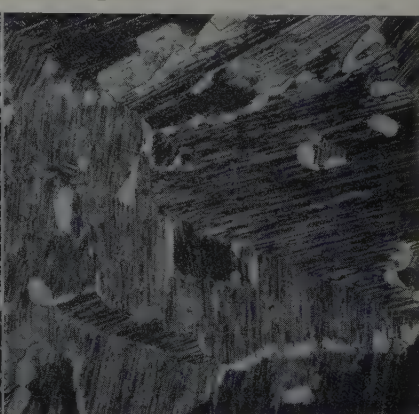


Fig. 5—30 min at 420°C. White α in striated β'' . X250.

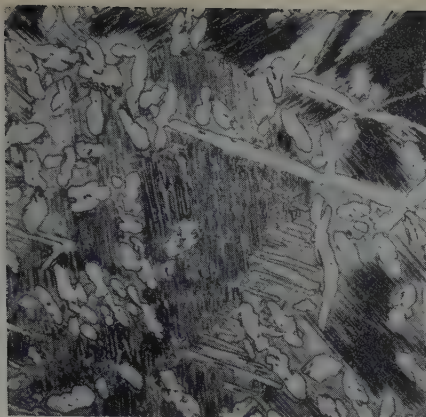


Fig. 6—16 hr at 420°C. α in the form of Widmanstätten precipitate and as rounded particles. Matrix is residual striated β'' plus β' . X250.

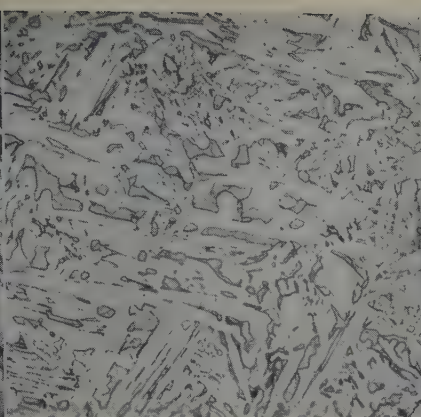


Fig. 7—144 hr at 420°C. Almost all α and β' . Traces of β'' still exist. X250.

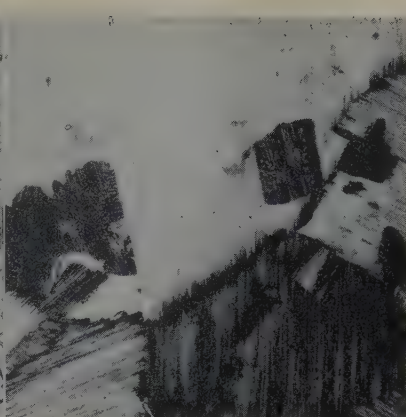


Fig. 8—30 min at 370°C. Pearlitic nodules growing in β'' . X250.

compositional adjustment is occurring, the remaining β'' is developing the composition of cadmium-rich β' . To complete the transformation, $\beta'' \rightarrow \beta'$, an ordering must also take place. Thus the final equilibrium structure in this temperature range of 400° to 350°C consists of α and β' , being similar to Fig. 7. It is interesting to note that no lamellar pearlite is ever found in the structure of this alloy after long holding times at any temperature. This pearlite does not spheroidize. It just gradually disappears, its place being taken by the Widmanstätten distribution of α in β' . When the transformation occurs in the neighborhood of 350°C, there seems to be less tendency for the β'' to transform by the nucleation and growth of pearlitic nodules. Instead, the decomposition of the β'' is by growth of the striations. They become wider, sharper, and better defined and ultimately develop a definite interface with the β'' matrix as shown in Fig. 9. At this point the striations

are readily seen to be α . While the striations are developing into α , the β'' matrix is transforming to β' in a very interesting manner. The yellow β'' first changes color to that of the purple β' , there being a definite color interface but not a phase interface. This is illustrated in Fig. 10. Then suddenly a discrete phase boundary appears where only the color interface previously existed. Fig. 11 shows α platelets, and the β' growing into the β'' . The $\beta'' \rightarrow \beta'$ reaction is only partially completed.

Around 300°C and below, the transformation of the striated β'' takes place entirely by the nucleation and growth of two phase ($\alpha + \beta'$) pearlitic nodules, Fig. 12. The pearlitic nodules consume the striations before they can become discrete α plates; the pearlite in turn giving way to the structure shown in Fig. 7.

It should be kept in mind that the change in the character of the transformation with decreasing tem-

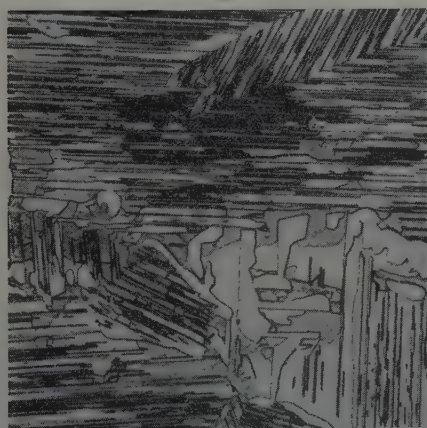


Fig. 9—89 hr at 350°C. Striated β'' with α and β' . X250.

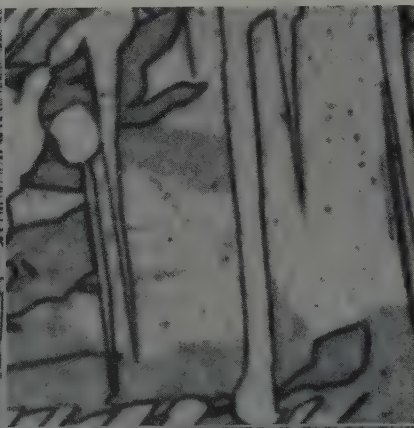


Fig. 10—144 hr at 350°C. β'' transforming to β' . X750.

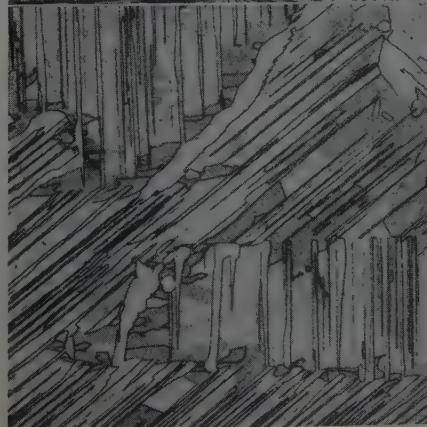


Fig. 11—144 hr at 350°C. α platelets in matrix β'' . Some β' has formed. X250.

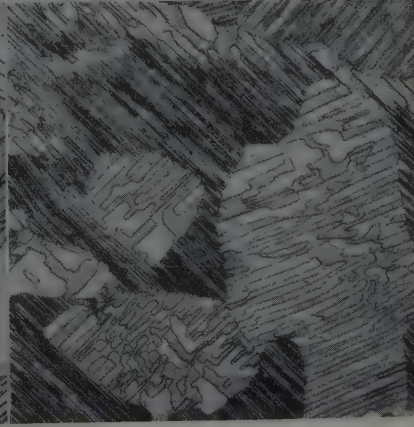


Fig. 12—3 hr at 300°C. Striated β'' with pearlitic ($\alpha + \beta'$) nodules. X1000.

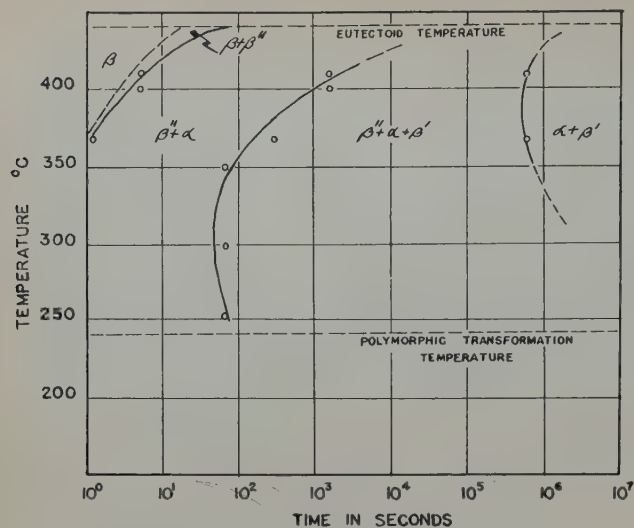


Fig. 13—T-T-T diagram for the Ag-Cd eutectoid alloy.

peratures is gradual, there is no definite temperature where one transformation sequence is suddenly replaced by a different sequence. The time-temperature-transformation characteristics of the β phase for temperatures above 240°C are shown in Fig. 13.

As previously mentioned, the existence of a polymorphic transformation at 240°C is somewhat in doubt. Its existence was not confirmed in this work.

The transformation as just described, continues essentially unchanged down to about 234°C . When the eutectoid specimens are quenched into the isothermal bath below this temperature, only a part of the β quickly transforms into β'' , which is striated as formed, Fig. 14. Some thin platelets of α also appear within a few seconds. In about an hour at 200°C , pearlite nodules appear in the β'' as indicated in Fig. 15, and they grow until the β'' is entirely consumed. Once the β'' is consumed, there is no tendency for the growing pearlite nodule to grow into the surrounding β . This is shown in Fig. 16. During this time the α platelets start to spheroidize.

After the β'' has been consumed by the growing pearlite the remaining retained β transforms slowly to striated β'' , which in turn transforms to pearlite. While this β'' is transforming to pearlite, the pearlite which had formed previously is disappearing, its place being taken by the coarser Widmanstätten α in the β' and a structure similar to that shown in Fig. 7 is obtained.

The transformation was not followed to lower

temperatures because of the very long times required for transformation. The retained β is stable for at least 16 months at room temperature.

Discussion

Any mechanism for the eutectoid decomposition in this alloy must explain:

1—The isothermal formation of a fine grained, yellow etching β'' from a coarse grained, pink etching β .

2—The appearance of striations in the β'' , and the parallelism of the striations.

3—The disappearance of the striations with time, and the subsequent appearance of α platelets in a matrix of β'' or of two-phase nodules of α plus β' , depending on the temperature of transformation.

4—The transformation of the residual light etching β'' to the dark etching β' .

5—The fact that the β' , when first developed, differs in color from the β'' , but ultimately develops a sharp boundary with the β'' .

6—Why the pearlite nodules formed below 240°C consume only the β'' and do not continue growing into the surrounding β .

7—The continuous disappearance of lamellar pearlite with no evidence of spheroidization and the appearance of the coarser $\alpha + \beta'$ mixture in its place.

The mechanism of this eutectoid decomposition may be as follows: The high temperature, body-centered cubic β phase is retained by quenching into cold water. Some evidence of this is shown by the fact that etch pits on the surface of quenched specimens are cubic. Durrant¹ has also reported that the β phase, when quenched, shows no sign of decomposition. The β phase is also retained at high temperatures for a few seconds in the isothermal bath.

The β phase transforms rapidly by nucleation and growth into the metastable β'' in the temperature range of 440° to 240°C . This transformation explains the drastic change in grain size that the specimens undergo when held for only a few seconds in the latter temperature range. The presence of a metastable phase in the alloys near eutectoid composition has been reported by several investigators.^{2,4} There is however, some disagreement as to the true crystal structure of the metastable phase. It has been reported as hexagonal or rhombohedral⁴ and also as ordered body-centered cubic like the β' phase². The authors attempted some X-ray analysis of these structures, but were unable to successfully interpret the patterns obtained. It is not believed that the metastable phase is cubic; the structure of the meta-

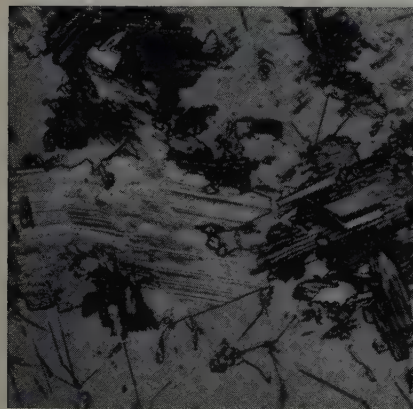


Fig. 14—4 sec at 200°C . Patches of striated β'' in retained β . Some Widmanstätten α . X250.

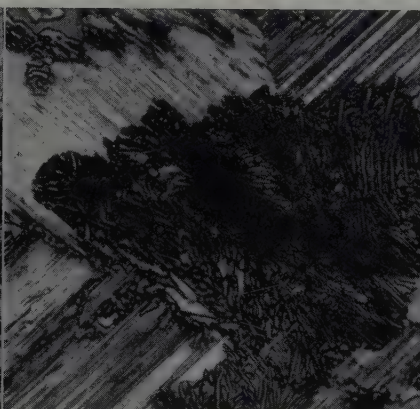


Fig. 15—1 hr at 200°C . Pearlite growing in striated β'' . X750.

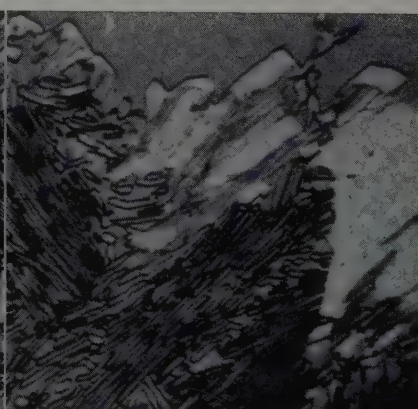


Fig. 16—1 hr at 200°C . Pearlite growing in striated β'' . Note α rim which has formed between the β'' and the retained β . X2000.

stable phase is probably hexagonal. This is supported by the fact that etch pits in the β'' were indicative of a hexagonal structure.

The striations which appear in the β'' are probably the result of a "bainite-type" reaction of the type found in steels⁸ and certain Cu-Al alloys⁹. The "bainite" mechanism in this alloy may possibly be explained as follows:

1—The silver atoms segregate by diffusion to form regions in the β'' of high silver content surrounded by regions of low silver content. This is the point at which the striations first appear and coincides with the rapid increase in hardness, Fig. 2.

2—The β'' of high silver content usually transforms into α platelets above 300°C. At lower temperatures the striated β'' transforms only into pearlite ($\alpha + \beta'$).

3—Above 350°C the residual β'' matrix then transforms into β' .

It may be asked why the striations should appear on only one set of crystallographic planes of the β'' . A possible explanation of this phenomenon is that given by Barrett¹⁰ in his discussion of Widmanstätten precipitates. If it is assumed that the striations are concentration gradients which are formed prior to the precipitation of α , and that the metastable β'' is hexagonal close-packed, then it would be expected that the striations would form on only one set of crystallographic planes of the β'' . This is due to the fact that the (111) plane in the α (face-centered cubic) and the basal plane in the β'' (hexagonal close-packed) are planes of closest matching. A precipitate of α on the basal plane of the β'' would therefore be anticipated, since precipitation takes place in such a way that matched planes occur at the matrix-precipitate interface. The striations form on the same planes where the α is going to precipitate. This may explain the formation of α and striations on preferred crystallographic planes. This, however, does not explain the formation, in some cases, of Widmanstätten needles of α on crystallographic planes different from those on which the striations form, Fig. 6, nor the tendency to form more than one set of striations within a single β'' grain at transformation temperatures below 300°.

Above 300°C the striations transform into α platelets. At this and lower temperatures, however, the striations do not form platelets, but are consumed by two phase pearlitic nodules. This means that at about 350°C the surface energy requirement of a platelet cannot be met and therefore it does not form. The pearlite which consumes the striations at these temperatures is in turn replaced by a structure of lower energy, coarse $\alpha + \beta'$.

The consumption of the β'' by the β' is an ordering reaction. The type of reaction suggested in this paper, $\beta \rightarrow \beta'' \rightarrow \beta'$, has also been suggested by Kosolapov and Trapeznikov⁴. The presence of only a color boundary between the β'' and β' probably indicates that the necessary adjustment in chemical composition has been made but coherency still exists between the two phases. As the β'' becomes ordered, coherency is lost and a sharp interphase boundary is formed.

Item 6, given previously, relating to the fact that below 234°C the growing pearlite nodule will consume only the striated β'' and will not continue growing into the surrounding β is a very important observation on the growth of this pearlite. The α rim which forms around the β'' , Fig. 16, and which might be considered as a mechanical obstruction to the

growth of the pearlite is not the important factor. Areas in the structure can be found where this α rim fails to form and yet the growing pearlite stops at the β'' - β interface. This results from inherent differences of the β and β'' .

The fact that the lamellar pearlite continuously disappears in favor of a coarser aggregate of α and β' has also been observed in other eutectoid alloys. This phenomenon has an important bearing on the morphology of the pearlites and will be discussed in detail in another paper.

Summary

The isothermal transformation of the Ag-Cd eutectoid alloy has been studied at subeutectoid temperatures. Although certain features of the transformation, i.e., retention of the high temperature β , its subsequent transformation to fine grained β'' and the formation of silver-rich striations in the β'' are common to all temperatures below 440°C, the subsequent features of the transformation change with temperature. At high temperatures the striated structure disappears forming a heavy Widmanstätten pattern of α in β' ; around 370°C, the striated β'' begins to decompose by nucleation and growth of pearlite as well as by the formation of α platelets from the striations. Below 300°C the transformation takes place only by means of the pearlite reaction. But at all temperatures, the final result is the same, a coarse structure of α in β' .

The presence of the polymorphic transformation at 240°C was not confirmed by the metallographic methods employed.

Acknowledgment

The authors wish to express their appreciation to R. B. Caples, of Anaconda Copper Mining Co., who donated the cadmium for this study; for the advice of V. W. Meloche, of the Chemistry Department, in regard to the chemical analysis of the alloy; for the financial assistance of the Wisconsin Alumni Research Foundation, under RF50:315, to carry out this investigation; for the aid of R. C. Wiggins in the construction of the experimental apparatus; and for the helpful criticism offered by S. A. Kulin.

References

- ¹ P. J. Durrant: Constitution of the Cd Rich Alloys of the Ag-Cd System. *Journal Inst. Metals*. Advance copy No. 549. 15 pp. (1931).
- ² G. F. Kosolapov and A. K. Trapeznikov: X-ray Studies of the Structures of the Beta Phases of Ag-Cd at High Temperatures. *Journal Tech. Phys. USSR*. (1936) 6, pp. 1131-1134.
- ³ E. A. Owens, J. Rogers, and J. Guthrie: X-ray Study of Ag-Cd Alloys. *Journal Inst. Metals* (1939) 65, 16 pp. Advance copy No. 837.
- ⁴ G. Natta and M. Freri: X-ray Analysis and Crystal-line Structures of Ag-Cd Alloys. *Atti. accad. Lincei*. (c) (1928) 7, pp. 406-410.
- ⁵ W. Fraenkel and A. Wolff: Die Umwandlungen im Festen Zustande bei Silber Cadmiumlegierungen. *Ztsch. anorg. allgem. Chem.* (1930) pp. 189-190.
- ⁶ *Metals Handbook* (1948). Cleveland, A.S.M.
- ⁷ W. W. Scott: *Technical Methods of Metallurgical Analysis* (1923) New York. D. Van Nostrand and Co.
- ⁸ E. P. Klier and Taylor Lyman: The Bainite Reaction in Hypoeutectoid Steels. *Trans. AIME* (1944) 158, p. 394.
- ⁹ E. P. Klier and S. M. Grymko: The Transformations in β -CuAl Alloys. *Trans. AIME* (1949) 185, pp. 611-621; *JOURNAL OF METALS* (September 1949).
- ¹⁰ C. S. Barrett: *Structure of Metals* (1943) New York. McGraw-Hill Book Co.

Kinetics of the Oxidation of Galena in Sodium Hydroxide Solutions Under Oxygen Pressure

by J. E. Andersen, J. Halpern, and C. S. Samis

In the presence of oxygen, galena is oxidized in an aqueous medium containing sodium hydroxide, in accordance with the following reaction:



A novel method was devised for following this reaction which takes place in an autoclave under oxygen pressure, by measuring the concentration of HPbO_2^- in the solution with a cathode ray polarograph employing stationary platinum electrodes. Using this procedure a study was made of the kinetics of the reaction, in which the effect of a number of variables, including temperature, oxygen pressure, NaOH concentration, and agitation, on the rate, were determined. The results of this study are described and discussed, in terms of possible mechanisms for the reaction.

IT is known that sulphide minerals can be oxidized in aqueous media in the presence of oxygen under pressure. Reactions of this type can be classified in two categories depending upon whether the products of oxidation are insoluble or soluble in the aqueous medium. An example of the first type of reaction is the oxidation of pyrite in alkaline solutions, giving rise to an insoluble iron oxide. The kinetics of this reaction have been investigated and its mechanism established.¹ It has been applied in the oxidation of iron sulphides present in refractory gold ores to improve the subsequent recovery of gold by cyanidation.² The second type of reaction finds application where it is desired to recover the metal by leaching during oxidation. In this case a medium is selected in which the oxidized mineral is soluble. For example, nickel, copper, and cobalt sulphide ores can be treated by oxidation in the presence of a solution of ammonia dissolving the nickel, copper, and cobalt as the metal ammine sulphate salts.³ A similar treatment has also been reported to apply to zinc sulphide ores.⁴

It is known that lead sulphate is soluble in solutions of sodium hydroxide or ammonium acetate. It should therefore be possible to dissolve the lead from galena ores by aqueous oxidation with oxygen under pressure using either of these solutions. The applicability of the ammonium acetate treatment has been investigated and confirmed in a recent study.⁵

The present paper describes the results of a similar study in which the kinetics of the oxidation of galena in sodium hydroxide solutions have been investigated. The object of this investigation was pri-

marily to obtain information of a fundamental nature relating to the kinetics and mechanism of this reaction.

The use of pulps of comminuted ore in a study of this type is undesirable because of the difficulty in controlling and measuring the surface area. The measurements were therefore made using galena crystals of measured surface area and in this way absolute reaction rates were obtained.

The reaction was found to proceed as follows:



The products are sodium plumbite and sodium sulphate salts which dissolve in the aqueous solution.

The reaction studies were carried out in an autoclave in which a desired pressure of oxygen was maintained. The reaction was followed by measuring the concentration of lead in the solution with a cathode ray polarograph. The results obtained in this investigation are presented and discussed in the present paper.

Experimental

Materials: The crystals of galena were obtained from Violamac Mines, Sandon, B. C. The following impurities were indicated by spectrographic analysis carried out by the Provincial Assay Office, Victoria, B. C.: Sn, 0.02 to 0.2 pct; Sb, 0.07 to 0.7; Zn, 0.01 to 0.1; Si, Fe, Mg, As, less than 0.05 pct; Ag, 126 oz per ton, the latter determined by standard fire-assaying procedure.

After cutting a specimen measuring approximately 5x7x12 mm, the crystal surfaces were ground parallel to the 100 axes using No. 2 emery, washed with water, and the dimensions were measured with a micrometer. Oxygen gas was of commercial grade and supplied in cylinders by Canadian Liquid Air. Solutions were made up with chemicals of chemically pure grade and distilled water.

Equipment: Autoclave: The autoclave used in these studies was constructed of stainless steel and

J. E. ANDERSEN is Graduate Student and Holder of the Cominco Fellowship, J. HALPERN is Assistant Professor of Metallurgy, and C. S. SAMIS is Associate Professor of Metallurgy, Dept. of Mining and Metallurgy, The University of British Columbia, Vancouver, B.C., Canada.

Discussion on this paper, TP 3407D, may be sent, 2 copies, to AIME by June 1, 1953. Manuscript, June 9, 1952; revised, Dec. 1, 1952. Spokane Regional Meeting, May 1952.

is shown schematically in Fig. 1. The inside dimensions were 2 in. diam x 6 in. high. The autoclave was equipped with a thermometer well and an external heating jacket. The contents were stirred with a cylindrical steel rotor, driven by a 2.5 in. Alnico magnet, rotated externally below the autoclave. The speed of rotation could be varied from 80 to 250 rpm. A Bourdon gage was used to measure the pressure.

Polarograph: The cathode ray polarograph used to determine the concentration of lead in the solution, as the reaction proceeded, was essentially similar to that described by Randles,⁶ and included a cathode ray oscilloscope to amplify and record the vertical (current) and horizontal (voltage) signals. Additional units included an electronically stabilized

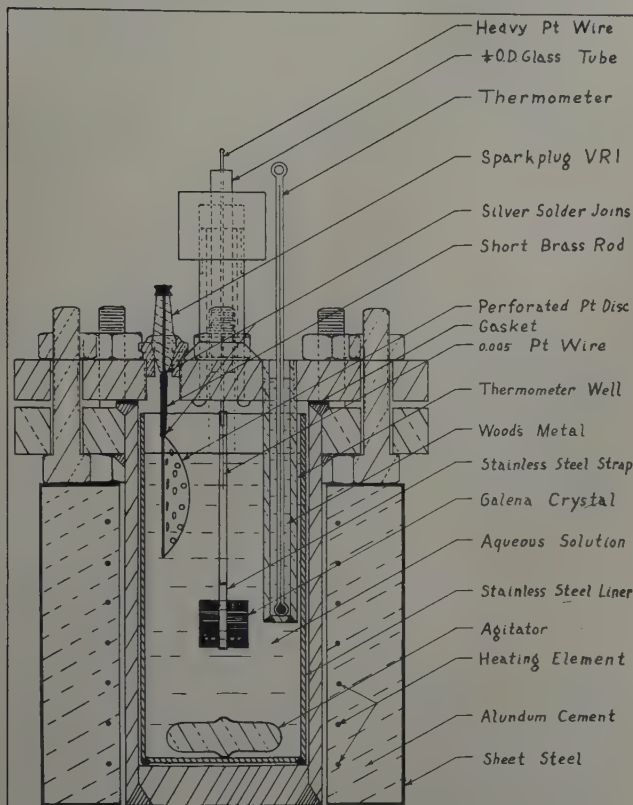


Fig. 1—Schematic drawing showing construction and parts of the autoclave.

voltage supply and a synchronizing unit to control voltage sweep.

The use of a dropping mercury electrode was not feasible under the experimental conditions used (i.e., in an autoclave under pressure) and stationary electrodes were substituted. A small bead of platinum at the end of a 3 mm length of 0.1 mm platinum wire immersed in the solution constituted the polarizable micro electrode (cathode). The unpolarized electrode (anode) was a 2.5 cm disk of perforated platinum foil. Each electrode was connected to an insulated platinum wire which was sealed through the top of the autoclave.

The theory relating to the use of this instrument is given by Randles.⁷ A rapid voltage sweep (about 1 v per sec) was used with an interval of 10 to 15 sec between sweeps. A drawing of a typical polarogram is shown in Fig. 2. The height of the lead peak, measured from the level of the preceding oxygen wave, as indicated in the figure, is proportional to the concentration of HPbO_2^- in solution. The valid-

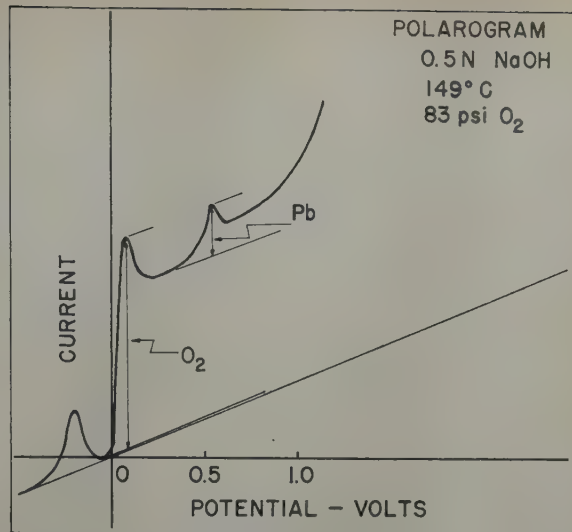


Fig. 2—Drawing of a typical polarogram showing peaks corresponding to oxygen and lead.

ity of this analytical method was confirmed by experimental calibration.

Experimental Procedure: 155 milliliters of an aqueous solution of sodium hydroxide of the desired concentration was placed in the autoclave and a crystal of galena, prepared as described earlier, was mounted in a stainless steel holder and suspended below the surface of the solution in the autoclave. The stirrer was turned on and the autoclave heated to a desired temperature. A desired pressure of oxygen was introduced and maintained. Polarograms were obtained at 15 min intervals by photographing the oscillograph screen. At the end of the experiment the concentration of lead in the solution was determined by the ammonium molybdate gravimetric method. This value was used to calibrate the polarographic measurements. Rate curves were plotted, using values for the concentration of lead determined from the polarograms.

Results and Discussion

Reaction Products: Analysis of the solutions indicated that equimolar concentrations of $\text{SO}_4^{=}$ and HPbO_2^- were formed during the reaction. No other forms of lead or sulphur were observed in the solution. The reaction appears to be represented accurately by Eq. 1.

After the reaction, the crystal surface generally showed some etching in the form of lines and pits, apparently formed by intersecting 111 planes. A

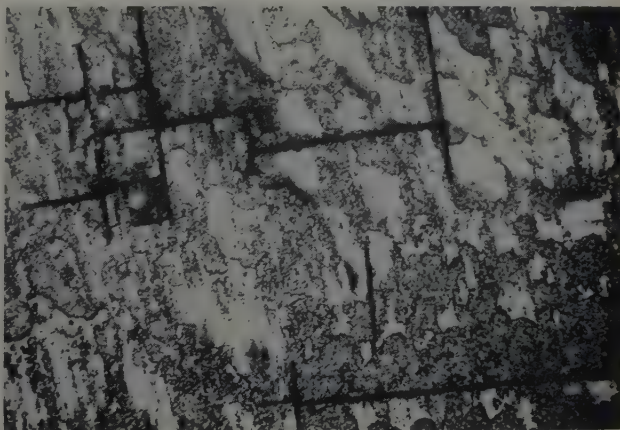


Fig. 3—Micrograph of galena crystal after oxidation in 0.5N NaOH at 150°C for 200 min. X35.

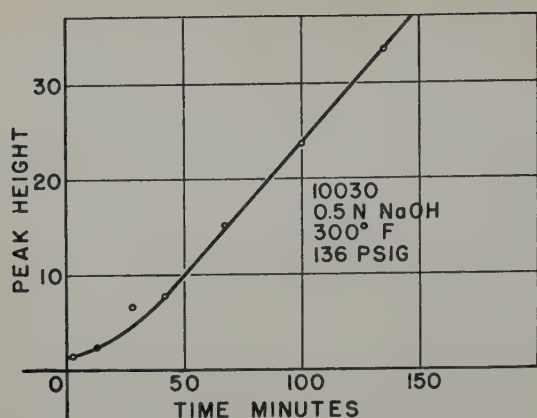


Fig. 4—Typical rate curve for the oxidation of a galena crystal.

micrograph illustrating this effect is shown in Fig. 3. In general there was no evidence of a phase change (formation of solid products) on the galena surface. In a few cases where high NaOH concentrations were used, a loosely adherent yellow coating, believed to be hydrated PbO, was observed to form after cooling.

The Rate Curves: A typical rate curve for the reaction is shown in Fig. 4. An initial induction period was generally present and is believed to be due to the slow dissolution of an oxidized film on the galena surface formed during exposure to air and polishing of the crystal.

Following this induction period, the rate curves were generally linear for the duration of the experiments (60 to 300 min). Reaction rates were calculated from the slopes of these linear plots. It was found that under given experimental conditions, this rate was proportional to the surface area of the galena crystal used. This is shown in Table I. The amount of galena dissolved during any experiment was small, in all cases less than 4 pct of the initial weight of the crystal, so that the apparent surface area remained substantially constant during each experiment. This accounts for the linear reaction rate curves. Reaction rates determined in this way were found to be reproducible to within ± 5 pct even when different galena crystals were used.

Effect of Oxygen Partial Pressure: Experiments were made at 123°C in 0.5N NaOH, using different partial pressures of oxygen ranging from 0 to 11 atm. The results are shown in Fig. 5.

It is seen that the rate of oxidation and solution of galena is proportional to the square root of the partial pressure or concentration of oxygen. This indicates that the oxygen participating in the rate controlling step of the reaction is in a dissociated state.

Table I. Rate of Oxidation of Galena in NaOH Solution

NaOH concentration — 0.5 mols per liter Temperature — 149° C O ₂ partial pressure — 83 psi (5.64 atm) Stirrer speed — 48 cm per sec				
Galena Surface Area, Sq Cm	Dissolution Rate of PbS			
	Mg per Min	Mg per Sq Cm per Min	Mols per Sq Cm per Sec	Deviation, Pct
4.02	0.845	0.210	1.47×10^{-3}	+2.1
4.56	0.935	0.205	1.44×10^{-3}	0
8.71	1.745	0.204	1.42×10^{-3}	+1.4
Mean value		0.206	1.44×10^{-3}	

Effect of Sodium Hydroxide Concentration: The effect of the sodium hydroxide concentration on the kinetics of the reaction was investigated in a series of experiments at 149°C. The concentration of NaOH was varied from 0.5 to 6N. The results are given in Table II and plotted in Fig. 6, using arbitrary units.

It was found that increasing the concentration of NaOH from 0.5 to 6.0N results in a marked lowering of the reaction rate. The shape of the curve is similar to that depicting the change in the square root of the solubility of oxygen with increased NaOH concentration at 25°C, also shown in Fig. 6 and based on data by Geffcken.⁸ The similarity of the two relations suggests that the effect of NaOH on the rate can be at least in part accounted for by the decreased solubility of oxygen with increasing NaOH, since it has already been established that the rate is proportional to the square root of the concentration of oxygen.

Effect of Stirring: The effect of the stirrer velocity on the reaction rate is also shown in Table II and

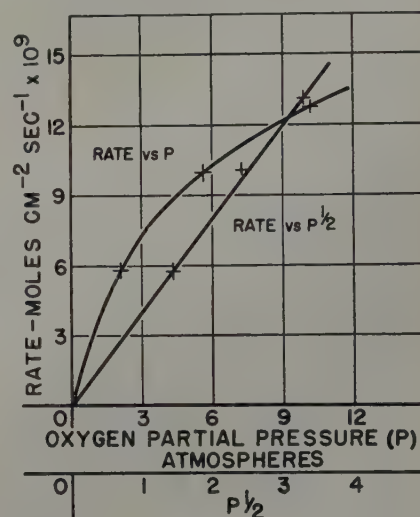


Fig. 5—Effect of the pressure of oxygen on the rate of oxidation of a galena crystal. Solution 0.5N NaOH. Temperature 123°C.

Fig. 6. At low concentrations of NaOH (0.5N) it was found that varying the velocity of the stirrer from 9 to 48 cm per sec had no effect. At higher NaOH concentrations, however, the rate increased markedly with the stirring speed. This effect can be explained in terms of the increase in the viscosity of the medium at higher NaOH concentrations, lowering the rate of diffusion of oxygen to the galena surface. The concentration of oxygen at the reacting surface becomes depleted and the reaction rate is controlled in part by the transport of oxygen to the surface, the rate of which depends on stirring. At low NaOH concentrations the transport of oxygen to the surface is more rapid and the rate of reaction becomes activation controlled and independent of the stirring velocity.

A more quantitative correlation of these effects is impossible in the absence of data relating to the solubility of oxygen and the viscosities of the solutions under the conditions used.

Effect of Temperature: The effect of temperature on the rate of reaction was investigated in the range 93° to 175°C using a 0.5N NaOH solution and an oxygen partial pressure of 5.64 atm. A concentration of 0.5 NaOH was selected for the study of this variable since it has already been demonstrated that under these conditions the reaction rate and therefore the measured activation energy is independent of the stirring velocity.

A good Arrhenius plot was obtained as shown in Fig. 7. The slope corresponds to an apparent activation energy, E , of 6300 cal per mol.

Conclusions

Summary of Kinetic Results: The kinetic results, described above, permit the following conclusions to be drawn regarding the mechanism of the reaction and the nature of the slow or rate controlling stage.

1—The rate controlling step of the reaction is a heterogeneous process occurring at the galena surface and not a homogeneous reaction in solution. This is indicated by the fact that the rate is proportional to the galena surface area.

2—Although four atoms of oxygen are involved in the overall oxidation of one molecule of PbS (Eq. 1), only one atom participates directly in the rate controlling step. This is indicated by the dependence of the rate on the square root of the oxygen pressure.

3— NaOH has only a secondary effect on the kinetics of the reaction, arising from its influence on the solubility and transport of oxygen in the solution. Although OH^- occurs as a reactant in the equation

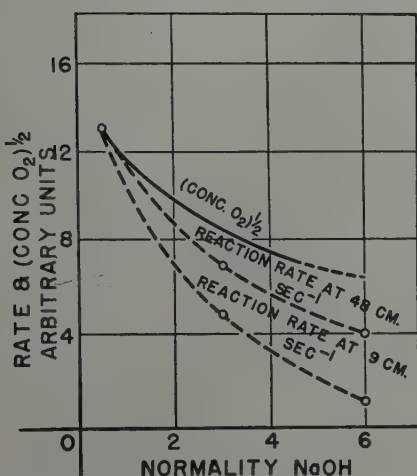


Fig. 6—Effect of the concentration of NaOH on the rate of oxidation of galena and on the solubility of oxygen. Temperature 149°C . O_2 partial pressure 5.64 atm.

tion for the overall reaction, it does not appear to participate directly in the rate controlling step, over the range of conditions investigated.

4—Water is known to participate in the reaction, since the products are hydrated ions. This reactant cannot be studied as a kinetic variable since its concentration remains effectively constant. However the participation of water in the rate controlling step is indicated by quantitative examination of the kinetic data as shown later.

5—The activation energy for the reaction is 6300 cal per mol.

6—The experimental results show that the transport of oxygen through the solution to the galena surface or the diffusion of reaction products away from the surface do not constitute the rate determining steps under the experimental conditions used, although they may influence the rate at high NaOH concentrations.

7—The rate controlling step of the reaction may involve the oxidation of a lead and sulphur atom simultaneously or alternatively the oxidation of only one of these followed by rapid reaction of the other. Both these possibilities are consistent with the observed fact that the lead and sulphur are always oxidized and dissolved in equimolar concentrations and it is impossible to distinguish between them on the basis of the kinetic measurements.

Proposed Mechanism of the Reaction: A mechanism

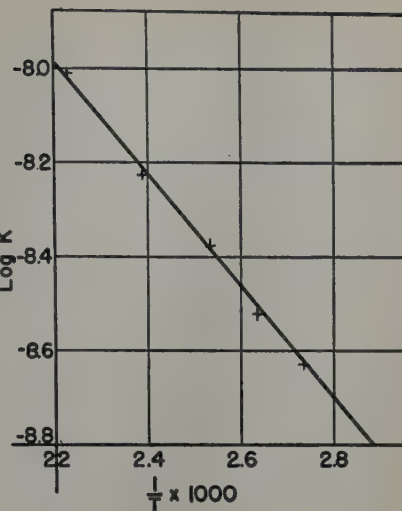


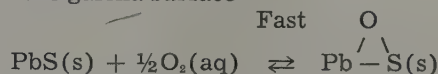
Fig. 7—Arrhenius plot showing the effect of temperature on the rate of oxidation of galena. Solution 0.5N NaOH . O_2 partial pressure 5.64 atm.

nism for the overall reaction involving the following sequence of steps is consistent with all these observations:

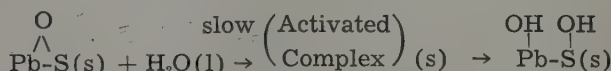
Step 1: Solution of gaseous oxygen in the aqueous medium



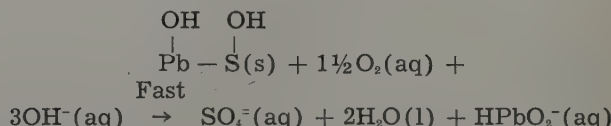
Step 2: Adsorption and dissociation of oxygen on the galena surface



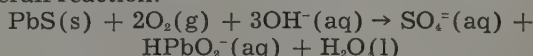
Step 3: Hydration of oxygen atom adsorbed on galena site



Step 4: Formation of reaction products



Overall reaction:



The states of the reacting species are represented by the following symbols: (g), the gaseous state; (l), the liquid state; (s), the solid surface state; and (aq), the aqueous solution.

In the above sequence, steps 1 and 2, the solution of oxygen and its chemisorption on galena sites are assumed to be reversible, the equilibrium in each case being rapidly established. The fraction of

Table II. Effect of NaOH Concentration and Stirrer Velocity on the Rate of Oxidation of Galena

Temperature — 149°C
 O_2 partial pressure — 5.64 atm

Stirrer Velocity Relative to PbS Surface	NaOH Concentration	Rate Constant (K) Mols $\text{Cm}^{-2} \text{Atm}^{-1/2} \text{Sec}^{-1}$
9 cm sec^{-1}	0.5N	6.17×10^{-9}
	3 N	2.44×10^{-9}
	6 N	0.53×10^{-9}
	0.5N	6.17×10^{-9}
48 cm sec^{-1}	3 N	3.47×10^{-9}
	6 N	2.01×10^{-9}

galena sites covered with oxygen is small. Step 3 is the slow stage, determining the rate of reaction. The activated complex is formed through the reaction of water with a galena site on which an oxygen atom is adsorbed. The further oxidation of this complex and the formation of the observed products by reaction with OH^- (step 4) then follow rapidly.

The Eyring theory of absolute reaction rates⁹ expresses the rate of a chemical reaction as follows:

$$\text{Rate} = \frac{kT}{h} C_1 C_2 \frac{\gamma_1 \gamma_2}{\gamma^\ddagger} \exp \left[\frac{-\Delta F^\ddagger}{RT} \right] \quad [2]$$

where k is the Boltzmann constant; h , Planck's constant; C_1 and C_2 are the concentrations of the reactants; γ_1 and γ_2 , the corresponding activity coefficients; γ^\ddagger is the activity coefficient of the activated complex; and ΔF^\ddagger , the free energy of activation.

Application of this equation to the rate controlling step (step 3) in the above sequence gives the following expression for the specific rate constant per unit area of galena surface. As a first approximation the activity coefficients have been assumed to be equal to unity.

$$\text{Rate} = \frac{d(\text{PbS})}{dt} = \frac{kT}{h} C_{\text{O}}^{\text{Pb-S(s)}} C_{\text{H}_2\text{O(l)}} \exp \left[\frac{-\Delta F^\ddagger}{RT} \right] \quad [3]$$

where (PbS) is the number of mols of PbS reacted in time, t ; ΔF^\ddagger , the free energy of activation ($= F^\ddagger - F_{\text{O}}^{\text{Pb-S(s)}} - F_{\text{H}_2\text{O(l)}}$); $C_{\text{H}_2\text{O(l)}}$, the concentration of liquid water; and $C_{\text{O}}^{\text{Pb-S(s)}}$, the concentration of oxygen atoms chemisorbed onto galena surface sites.

The concentration term, $C_{\text{O}}^{\text{Pb-S(s)}}$, can be obtained in the following form by thermodynamic consideration of the equilibria involved in steps 1 and 2:

$$C_{\text{O}}^{\text{Pb-S(s)}} = C_{\text{PbS(s)}} C_{\text{O}_2(\text{g})}^{1/2} \exp \left[\frac{-\frac{1}{2}(\Delta F_1 + \Delta F_2)}{RT} \right] \quad [4]$$

where $C_{\text{PbS(s)}}$ and $C_{\text{O}_2(\text{g})}^{1/2}$ are the concentrations of galena surface sites and of gaseous oxygen molecules, respectively; ΔF_1 is the standard molar free energy of solution of gaseous oxygen in the aqueous solution, i.e., of step 1 ($= F_{\text{O}_2(\text{aq})} - F_{\text{O}_2(\text{g})}$); and ΔF_2 , the standard molar free energy of adsorption of dissolved oxygen on galena, i.e., of step 2 ($= 2F_{\text{O}}^{\text{Pb-S(s)}} - 2F_{\text{PbS(s)}} - F_{\text{O}_2(\text{aq})}$).

Combining Eqs. 3 and 4 gives the following expression for the specific reaction rate:

$$\text{Rate} = \frac{kT}{h} C_{\text{PbS(s)}} C_{\text{O}_2(\text{g})}^{1/2} C_{\text{H}_2\text{O(l)}} \exp \left[\frac{-(\frac{1}{2}\Delta F_1 + \frac{1}{2}\Delta F_2 + \Delta F^\ddagger)}{RT} \right] = \quad [5]$$

$$\frac{kT}{h} C_{\text{PbS(s)}} C_{\text{O}_2(\text{g})}^{1/2} C_{\text{H}_2\text{O(l)}} \exp \left[\frac{-(F^\ddagger - F_{\text{H}_2\text{O(l)}} - \frac{1}{2}F_{\text{O}_2(\text{g})} - F_{\text{PbS(s)}})}{RT} \right] = \quad [6]$$

$$\frac{kT}{h} C_{\text{PbS(s)}} C_{\text{O}_2(\text{g})}^{1/2} C_{\text{H}_2\text{O(l)}} \exp \left[\frac{\left[\frac{(S^\ddagger - S_{\text{H}_2\text{O(l)}} - \frac{1}{2}S_{\text{O}_2(\text{g})} - S_{\text{PbS(s)}})}{R} \right] - \left[\frac{-(H^\ddagger - H_{\text{H}_2\text{O(l)}} - \frac{1}{2}H_{\text{O}_2(\text{g})} - H_{\text{PbS(s)}})}{RT} \right]}{RT} \right] \quad [7]$$

since $F = H - TS$

where S , H and F are the standard entropies, enthalpies, and free energies of the denoted species.

Eq. 7 can be further expressed in terms of the experimental activation energy, E , as follows:⁹

$$\text{Rate} = e^2 \frac{kT}{h} C_{\text{PbS(s)}} C_{\text{O}_2(\text{g})}^{1/2} C_{\text{H}_2\text{O(l)}} \exp \left[\frac{S^\ddagger - S_{\text{H}_2\text{O(l)}} - \frac{1}{2}S_{\text{O}_2(\text{g})} - S_{\text{PbS(s)}}}{R} \right] \exp \left[\frac{-E}{RT} \right] \quad [8]$$

Assuming the entropies of the solid surface states (i.e., S^\ddagger and $S_{\text{PbS(s)}}$) to be equal to zero (since these correspond to vibrational degrees of freedom only, their values will be negligible in comparison with the other terms) and evaluating the remaining terms in Eq. 8 by standard procedures, the rate of reaction at 123°C is calculated to be

$$6.5 \times 10^{-6} \text{ mols cm}^{-2} \text{ atm}^{-1/2} \text{ sec}^{-1}$$

The experimentally observed rate under these conditions is

$$4.2 \times 10^{-6} \text{ mols cm}^{-2} \text{ atm}^{-1/2} \text{ sec}^{-1}$$

This agreement between the observed and calculated values of the rate is considered very good in view of the approximations involved in the calculations and lends further support to the general mechanism which has been proposed, in which the rate controlling step is the reaction of a water molecule with a galena surface site on which an oxygen atom is adsorbed.

Acknowledgment

This work was supported by a Research Grant and a Fellowship from the Consolidated Mining and Smelting Co. of Canada, Ltd.

References

1. J. F. Stenhouse and W. M. Armstrong: The Aqueous Oxidation of Pyrite. *The Canadian Mining and Metallurgical Bulletin* (1952) **45**, p. 49.
2. R. Carter and C. S. Samis: The Influence of Roasting Temperature upon Gold Extraction by Cyanidation from Refractory Gold Ores. *The Canadian Mining and Metallurgical Bulletin* (1952) **45**, p. 160.
3. F. A. Forward, C. S. Samis, and V. Kudryk: A Method of Adapting the Ammonia-Leaching Process to the Recovery of Copper and Nickel from Sulphide Ore and Concentrate. *The Canadian Mining and Metallurgical Bulletin* (1948) **41**, p. 350.
4. V. Tronev and S. Bondin: Oxidation of Zinc Sulphide and Transference of Zinc into Aqueous or Alkaline Solution under Air Pressure. *Comptes Rendus Acad. Science URSS* (1939) **23**, p. 541.
5. D. P. Seraphim: Oxidation of Galena in Ammonium Acetate Solutions under Oxygen Pressure. M.A.Sc. Thesis, Dept. of Mining and Metallurgy, University of British Columbia, May 1952.
6. J. E. B. Randles: A Cathode-Ray Polarograph. *Trans. Faraday Soc.* (1948) **44**, p. 322.
7. J. E. B. Randles: The Current Voltage Curves. *Trans. Faraday Soc.* (1948) **44**, p. 327.
8. G. Geffcken: Beitrage zur Kenntnis der Loslichkeitbeeinflussung. *Ztsch. Phys. Chemie* (1904) **49**, p. 257.
9. S. Glasstone, K. J. Laidler, and H. Eyring: *The Theory of Rate Processes*. (1941) New York, McGraw-Hill Book Co.

Formation of Deformation Bands

In Al-3 Pct Mg Monocrystals

During Cold Rolling

by J. Herenguel, P. Lacombe, and P. Lelong

IN previous studies on the effect of orientation on the rate of anodic oxidation of Al-3 pct Mg monocrystals of high purity, certain anomalies were observed on the cold-worked metal. These anomalies were shown to correspond to regions of changed orientation within the grains resulting from plastic deformation.¹ In fact, they are deformation bands revealed by differences in rate of oxidation and produced by more or less continuous bending of the lattice about a [111] axis common to the original crystal and the band.^{2,3} Preliminary observations made after relatively large degrees of cold working revealed an approximate twin relationship between the bands and the surrounding crystal. Fig. 1 shows the etch figures formed on such a band and on the original monocrystal after a 67 pct rolling reduction. It is evidently not a true twinning, since there is a broad transition zone between the two systems, however the two extreme orientations are nearly in a twin relationship.

It was decided to investigate these preliminary observations by progressive rolling-reductions on monocrystals of varied initial orientation. From these studies, which form the subject of the present article, it became apparent that the initial observation of an approximate twin relation between the bands and the monocrystal was simply a special case.

Our experiments show that deformation in rolling proceeds by a mechanism analogous to those which have already been observed in the simpler cases of tension and compression. Micrography—in particular, the formation of etch figures—has been applied to the quantitative study of these orientations. In addition, observations have been made of slip lines, of thin oxide films yielding interference colors, of thick films in polarized light, and of etchants giving “engraving.” These micrographic methods for studying orientation have established the orientation relationship without any ambiguity, whereas X-ray methods would have given only a statistical result

J. HERENGUEL is Director of Research and P. LELONG is Metallurgist, Centre de Recherches of the Trefileries et Laminiers du Havre Society, Antony, Seine, France, and P. LACOMBE is Professor at the Ecole des Mines, Paris, France.

Discussion on this paper, TP 3451E, may be sent, 2 copies, to AIME by June 1, 1953. Manuscript, July 23, 1952.

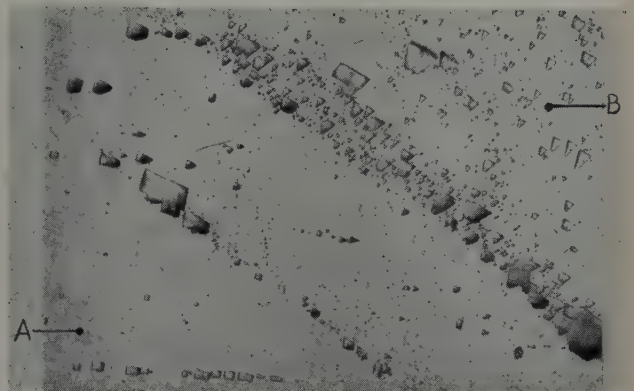


Fig. 1—Al-3 pct Mg monocrystal cold rolled 67 pct and etched for etch-figures. The two extreme portions A and B, in near-twin relation, are connected by a zone of transition pits. X600. Area reduced approximately 50 pct for reproduction.

because we were often dealing with thin bands (2 to 100 microns) and even narrower connecting zones covering a maximum of 20 microns.

Specimen Preparation and Methods

The Al-3 pct Mg alloy was prepared from 99.95 pct Al and is of the type used industrially in France for brilliant anodized finishes under the name of Brillalumag. This material combines the normal commercial properties with an enduring brilliance due to the protection of a thick, but perfectly transparent, film of alumina.⁴

The monocrystals were prepared by the method of critical deformation followed by prolonged annealing. Great care was taken to insure perfect homogeneity of composition, to eliminate included crystals,^{6,7} and to avoid the formation of undulations during oxidation.⁵ The critical deformation for this alloy is about 1.2 pct ($(l-l_0/l_0 \times 100)$) and the subsequent annealing was for one week at 500°C after gradual increase of temperature (35°C per hr). The crystals thus prepared had a section of 10x5 mm and a length of 20 to 40 mm. Each of these crystals was polished electrolytically and etched for the formation of etch-figures with the classical reagent.⁸ The orientation was then calculated from their angles, as measured with a goniometer microscope.

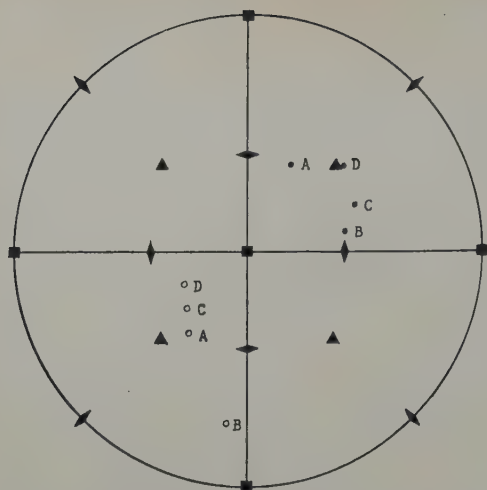


Fig. 2—Stereographic projection on a (100) plane showing the poles of the plane and direction of rolling for crystals A, B, C, and D. Solid circle, pole of the rolling plane. Open circle, pole of the rolling direction.

Rolling was done with cylindrical rolls of 100 mm diam which were degreased before each operation with trichloroethylene. The roll gap was closed progressively and observations were made after each stage. The specimens were always introduced in the rolling mill by the same end and the cold-work required was obtained by several passes.

For microexamination, the specimens were polished mechanically and finished electrolytically. They were then etched for the formation of etch-figures with the reagent maintained at an optimum temperature of 7° to 8°C. For observations on thin oxide films, anodic oxidation was carried out under conditions already published.⁹ For thick films, oxidation was effected in sulphuric acid (10 pct by volume) at a current density of 1 amp per sq dm for 30 min at 20°C. Etching for "engraving" was produced by the action of the electrolytic-polishing mixture of phosphoric-sulphuric acids at 60° to 70°C without applied current,⁶ or alternatively by 20 pct caustic soda at 40° to 50°C. Such etching gives a surface appearance which depends on orientation and can be profitably examined in polarized light.

Experimental Results

Several crystals were cold-rolled. The results on each will be described at successive stages of reduction.

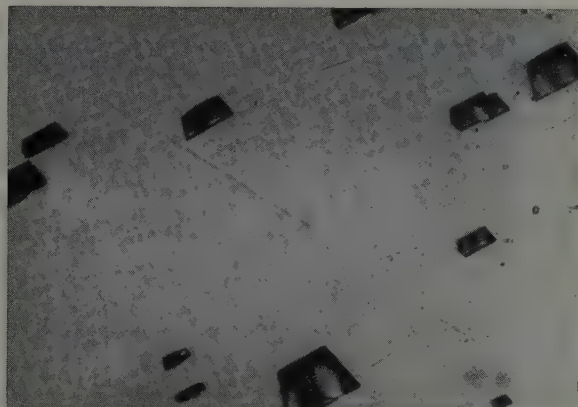


Fig. 3—Appearance of crystal A etched for etch-figure formation after 10 pct reduction. Note the lines which cross the micrograph diagonally. X1000. Area reduced approximately 50 pct for reproduction.

Crystal A: The orientation with respect to the plane and direction of rolling is shown in Fig. 2 which also gives that of the other crystals. The following phenomena were observed as a function of cold working.

1—Rolling Reduction 5 to 10 Pct: Slip lines were visible on the surface of the specimen. After electrolytic polishing of the rolled surface, no local regions of changed orientation were found by any of the different micrographic methods. However, after 10 pct reduction, there appeared certain lines different in character from the classical slip lines. They reappeared even after several successive polishings (removing 0.02 to 0.03 mm of metal) and became more pronounced after etching for the formation of etch-figures, Fig. 3. In addition, they were parallel to the trace of a (111) plane—a plane which later plays an important role.

2—Rolling Reduction 18 Pct: The lines seen after 10 pct reduction disappeared completely but deformation bands began to appear. None of them completely traversed the width or thickness of the specimen, and they were visible on only one of the two rolled surfaces after the different etching treatments.

These bands may be defined in the following manner: the orientation relationship between them and

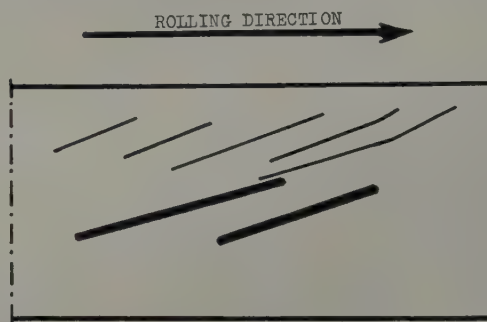


Fig. 4—True position of deformation bands of crystal A as seen in the rolled surface after 18 pct reduction. Sketch magnified approximately 3 times.

the surrounding crystal corresponds to a rotation of 5° to 7° around a [111] axis, which lies almost in the rolling plane and makes a large angle with the rolling direction. The interface between band and crystal was parallel to a (110) plane of the actual crystal, this having been established by observations on two perpendicular faces—the rolled surface and the lengthwise surface. This (110) plane contains the [111] axis of rotation which makes the initial crystal pass from its orientation to that of the bands. In the present case, this (110) plane was slightly inclined to the rolling plane. Figs. 4 and 5 illustrate these observations.

The bands had a thickness covering the range of 5 to 75 microns but were often 30 microns thick. The connecting zones spread over 1 to 2 microns rendering their analysis impossible at this stage of rolling.

3—Rolling Reduction 25 Pct: Increased change, corresponding to rotations up to 10°, and a slight broadening of the transition zones were observed. However, no new bands appeared.

4—Rolling Reduction 45 Pct: The original system of bands continued to change and other systems appeared.

Within the original bands, further local changes of orientation occurred by a mechanism identical

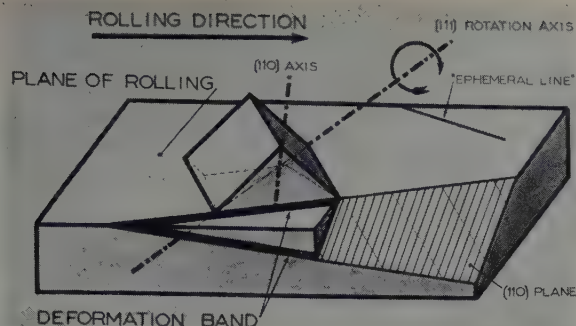


Fig. 5—Diagram showing how the cube representing the crystal lattice in its initial position is oriented with respect to the plane and direction of rolling. Note the conspicuous position of the (110) interface plane and of the [111] axis of rotation. "Ephemeral line" is that observed after 10 pct reduction but which later disappears.

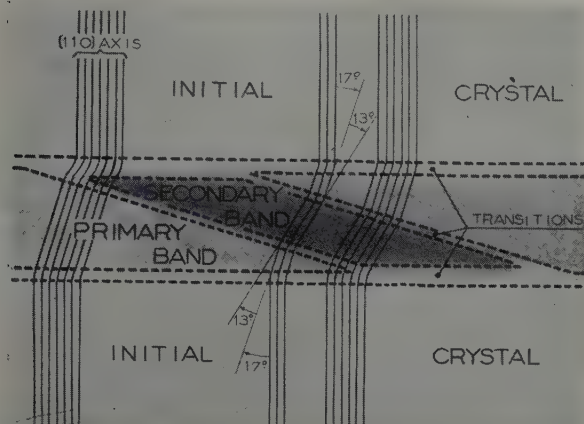


Fig. 6—Diagram showing the formation of a primary band and of a secondary band by double curvature about a [111] axis normal to the paper, becoming localized on a (110) plane.

with that which functioned initially; that is, by rotation about a [111] axis which is therefore common to the original crystal in its present position, to the primary band, and to the secondary band which it contains.

The rotation was 17° between the initial crystal and its primary bands, and 13° between the primary bands and their secondary bands. The total rotation between secondary bands and the initial crystal was thus $13^\circ + 17^\circ = 30^\circ$.

The interface between primary and secondary bands is the (110) plane of the primary band lattice which still contains the [111] axis of rotation. Thus in the diagram of Fig. 6, the plane of the paper is the (111) plane perpendicular to the [111] axis of rotation. The [110] axes which are in fact curved in the connecting zones by the mechanism of band formation are also shown. Fig. 7, taken in polarized light, shows the actual appearance of the surface after "engraving."

The connecting zones between the primary bands and initial crystal now became wider and reached about 6 microns. At high magnifications, these zones were seen to be finely striated in saw-tooth form, of the order of one micron, Fig. 8.

New systems appeared, though on a scale much smaller than the previous ones, but this time covering the whole of the specimen. It was possible to distinguish:

a—Certain systems close to the primary bands and between them. These consisted of thin lamellae (10 microns) of slightly differing orientation (2° to

3°) and regularly alternating. Their interfaces were still straight but it was not possible to identify their direction in relation to the lattices, nor the mode of rotation. Fig. 9 shows such complex systems after "engraving," as seen in polarized light. The fine striations on the primary and secondary bands may be noted also, while Fig. 10 shows this effect in greater detail.

b—In the portions of the crystal which, until now, were free of bands, another system developed made up of alternating lamellae about 10 microns thick and differing slightly in orientation. The general direction of the interfaces was still a (110) plane of the actual crystal, but it was no longer the same one as before, Fig. 11.

Examination of the slip lines on the surface of the polished specimens before the last rolling operation confirmed particularly clearly the existence of the bands and of gradual curvature in the connecting zones. Fig. 12 shows one of these first bands with the secondary bands. At a higher magnification the curvatures appear still more clearly and it will be noted on Fig. 13 that the connecting zone is wider on the upper front than on the other. The secondary bands also appear.

All these descriptions are naturally somewhat schematic. In reality, the initial crystal undergoes a change of orientation as a whole which varies slightly from one point to another and which cannot be explained by the geometry of deformation alone. Fig. 14 is a stereographic projection on a (100) plane of the poles of the rolling plane and

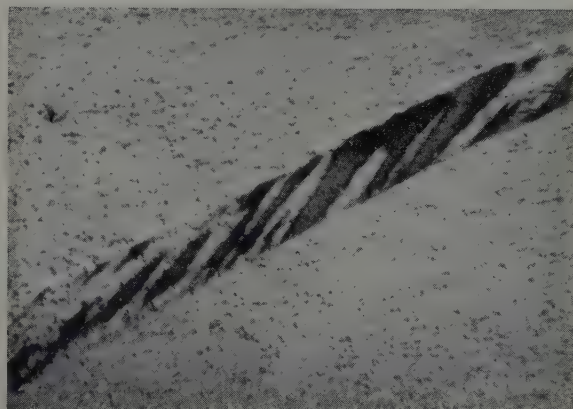


Fig. 7—Appearance of a primary band broken up by secondary bands. The surface was examined in polarized light after etching for engraving. X75. Area reduced approximately 50 pct for reproduction.

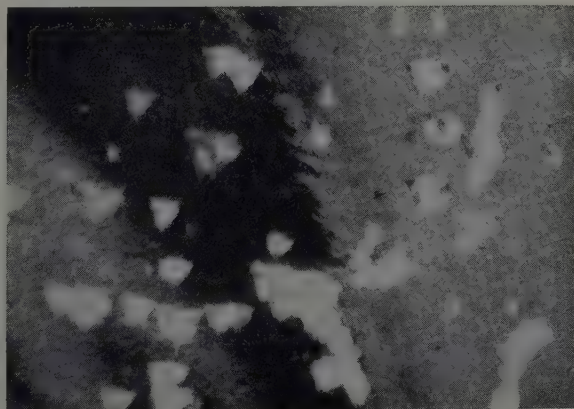


Fig. 8—Saw-tooth striations from the transition zone. Etch pits combined with "engraving." Examination in polarized light. X600. Area reduced approximately 50 pct for reproduction.

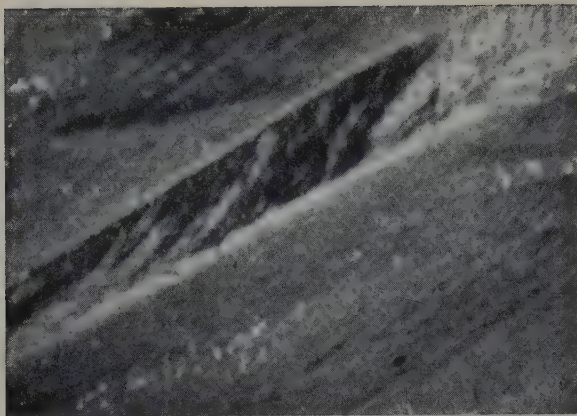


Fig. 9—Complex systems of fine bands in the neighborhood of a large band. Same preparation and examination as in Fig. 7. X75. Area reduced approximately 50 pct for reproduction.

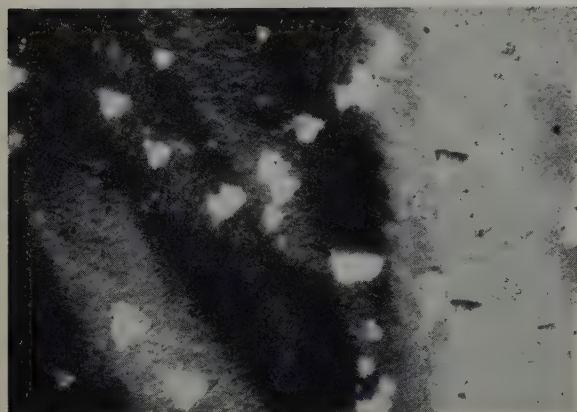


Fig. 10—Fine striations of the primary and secondary bands. See Fig. 7. X600. Area reduced approximately 50 pct for reproduction.

rolling direction after different degrees of cold working for a zone of the crystal judged to be typical of the average behavior.

5—Rolling Reduction 65 Pct: Successive polishing operations made the initial bands disappear. These were approaching nearer to the rolling plane. The complex systems are to be found close by but interpretation is still not possible.

In contrast, far away from these, the system already described, which possesses a (110) plane of the initial crystal as an interface, was still present.

Up to 65 pct reduction, it is striking that the rolled monocrystal was very far from being entirely affected by the bands described. Indeed, they only penetrated up to one fifth of the specimen thickness and from only one surface, in the case of the larger bands, while the finer systems penetrated from one surface only from one third to one half the thickness. This is evidently due to the very great heterogeneity of forces in rolling. These forces applied to the lattice vary through the thickness of the specimen and are very different at each rolling surface.

6—Rolling Reduction 208 Pct: Close to the previously formed large bands, interpretation remains impossible. There were at least two systems which could not be related to the orientation of the initial crystal with any certainty. On the whole of the opposite face, the face on which no system had been previously observed, there now appeared one made up of lamellae 15 microns thick. Interpretation was not possible however.

Far from the initial bands, the system already described was found again but it had not progressed

toward the interior. Thus both faces were now covered with fine bands and with several entangled systems. Between these two zones, at the center of the specimen, was a zone which, having undergone only rotation as a whole and simple slipping, was not fragmented.

Crystal B: This crystal was chosen to have an orientation close to that of crystal A, see Fig. 2.

Up to 5 pct reduction, nothing was noticed. After 13 pct reduction, bands appeared again with an interface corresponding to a (110) plane of the initial crystal, but this time making a large angle with the rolling plane, in contrast to the case of crystal A. The orientation difference was small but increased with increasing rolling reduction. After 20 pct reduction, a rotation of about 12° had occurred about the [111] axis contained by the (110) interface plane. The connecting zone was about 20 microns wide at this stage and the bands 70 microns thick. Analogy with the first-formed bands of crystal A is therefore very satisfactory. The presence of distinct bands mixed up with previously formed ones is worth noting. These are much more numerous on the other face of the specimen. This second system was more complex. Its interface, appearing on the large surface, was built up of straight portions, parallel to the trace of a (110) plane but connected by curved portions. On the other hand, the interface was linear on the side surface and still parallel to the same (110) plane. It therefore seems that the interfaces are (110) planes or ruled surfaces and



Fig. 11—Systems of bands in alternating lamellae in a portion of the crystal free of large bands. See Fig. 7. X75. Area reduced approximately 50 pct for reproduction.

show a certain analogy with cross slip. The width of the bands was 50 to 60 microns, the connecting zones were spread over about 20 microns, and rotation occurred around the same [111] axis as before, contained in the (110) interface plane (different from that of the system on the other face).

This crystal presented certain marked analogies with crystal A. The mechanism by which the bands formed was identical.

Crystal C: The orientation of crystal C is given in Fig. 2. After 5 pct reduction, nothing was observed and there was still nothing on the large faces after 15 pct reduction. However on the side surfaces of the crystal, a system of fine bands 20 microns thick was visible. These alternated regularly forming a layer approximately parallel to the rolling plane. This layer was made up of bands of differing orientation. The orientation of the portion of the crystal free of bands, was present also in the disturbed regions where it formed one element of the pattern. However, there was a slight rotation which

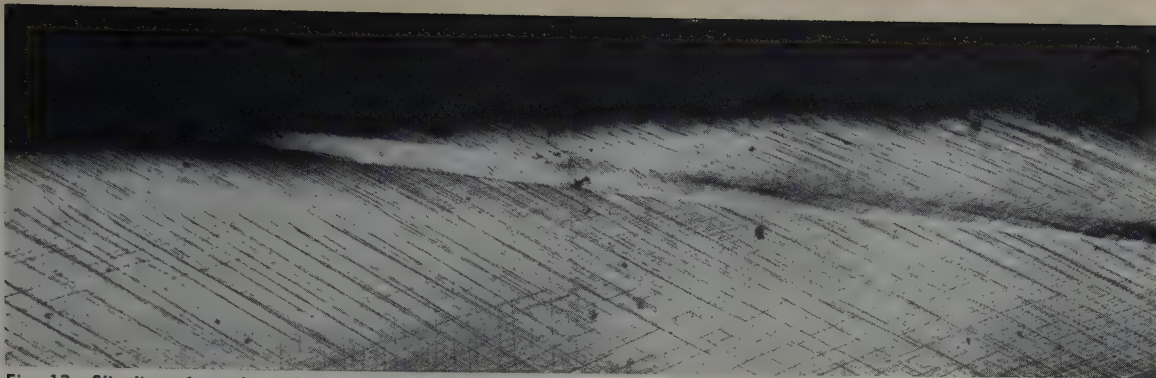


Fig. 12—Slip lines formed on the section of the crystal when the degree of reduction was increased from 25 pct to 45 pct. The primary and secondary deformation bands are revealed by the curvature of the slip lines and by relief on the metal surface. X75. Area reduced approximately 60 pct for reproduction.

made crystallographic identification of the interfaces very uncertain.

In the whole system, three principal orientations were established: one close to that of the surrounding crystal, and two others of slightly differing orientation.

In searching for orientation relationships between neighbors, these seem to be related by rotations of

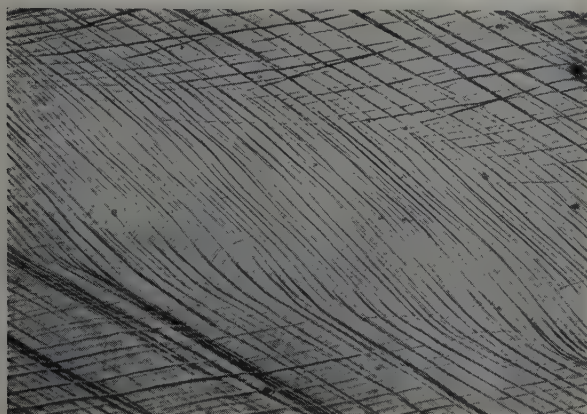


Fig. 13—Portion of Fig. 12 at X600. Note the continuous curvature in the connecting zone and substructure of the band. Area reduced approximately 50 pct for reproduction.

about 5° to 10° around the axes $[112]$, $[110]$, and $[100]$. These axes cannot be determined with precision however. In like manner, it is not possible to see if the general direction of the interface between the bands themselves is a simple crystallographic plane of the original crystal.

The rotation around a $[112]$ axis has already been observed by Chen and Mathewson¹⁰ by X-ray examination on aluminum monocrystals cold-worked by extension. The interface of the deformation bands was a (110) plane as it is for the rolled crystals A and B described in this paper.

Crystal D: Crystal D was chosen to have a (111) plane almost parallel to the plane of rolling.

1—After 8 Pct Reduction: The etch-figures did not undergo any orientation change but they grouped together in wide zones of high density (20 to 250 microns). The interfaces of these zones appeared to be well defined and, in the plane of rolling, were parallel to the sides of the etch-figures (equilateral triangles almost).

On the rolled surface, thin oxide films and "engraving" revealed deformation bands once more. The orientation of these could not be deduced from angle measurement of the etch-figures. The interfaces were also confirmed.

On the side surfaces, no trace of deformation was

revealed by any of the micrographic methods.

2—After 15 Pct Reduction: The intensely attacked regions became more complex. They were to be found in the form of entangled bands formed by two crossing systems.

By measuring a large number of the etch-figures and plotting the orientations on a stereogram, it was found that they were grouped in two principal orientations. One was close to that of the original crystal and the other appeared to be related by a rotation about a common $[110]$ axis. In fact, the great complexity made orientation determination very uncertain.

Discussion and Summary

From the preceding experiments, it may be concluded that when a monocrystal is subjected to progressive rolling-reductions, not only is a general change of orientation produced, but also deformation bands become increasingly numerous and complicated. Such bands, at least those formed during progressive rolling, do not involve the whole thickness of the specimen at the beginning. In certain cases, they form either on only one face in contact with the rolls and then on the other; on both faces at the same time; or they may appear in the interior of the monocrystal. These peculiarities probably arise from variations in the resulting forces and from the orientation of these forces with respect to the induced lattice.

The first two specimens described were most suited



Fig. 14—Positions of the plane and direction of rolling after different degrees of reduction. Stereographic projection on a (100) plane. Solid circle, pole of the rolling plane. Open circle, pole of the rolling direction.

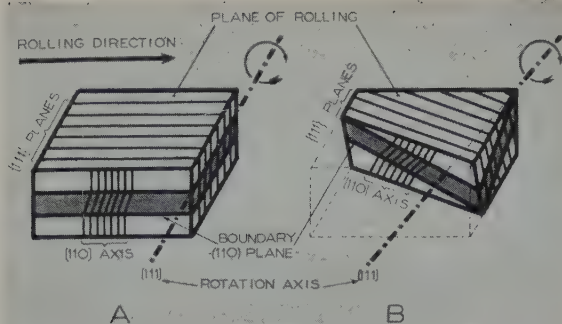


Fig. 15—Bending in crystal A. A—Idealized bending of a lattice oriented with a $[111]$ axis in the plane of rolling and perpendicular to the rolling direction. A (110) plane is thus parallel to the plane of rolling. B—Actual bending which occurred in the case of crystal A.

to precise analysis, as the bands formed initially were few in number, and were relatively large and well separated. In addition, the difference in orientation between bands and crystals was considerable. These bands are formed by progressive curvature of the lattice due to rotation around a $[111]$ axis (the start of the curvature is restricted to a (110) interface plane which contains this $[111]$ axis). The deformation band is thus contained between two parallel planes (110) of the original crystal. For the two specimens of closely similar orientation with respect to rolling, it is the same $[111]$ axis which functions as the axis of rotation. This axis is differentiated from others of the same index $[111]$ because it is that which is most nearly parallel to the rolling plane and perpendicular to the rolling direction. In other words, it corresponds to those $\{111\}$ planes most nearly perpendicular to the rolling plane and parallel to the direction of rolling. This will be easily appreciated since, under the mechanical conditions of rolling, such $\{111\}$ planes are literally blocked and prevented from undergoing normal slip.

There is here a fairly close analogy with the mechanism of kinking in hexagonal crystals which occurs when the active direction is parallel to the only slip plane possible. Fig. 15A shows the manner in which bending of the lattice is produced according to this mechanism. Fig. 15B shows the actual arrangement in the case of the first specimen. It is worth pointing out that bending occurs in the only way which permits a shortening of the $[110]$ axes, that is to say, a decrease in thickness of the specimen. In Chen and Mathewson's experiments,¹⁰ the glide direction was in the plane of the tension axis just as it is in the plane of the compression axis in our own experiments.

In the second specimen, bending is no longer given by the curvature of the $[110]$ axis which is the most nearly vertical, but instead by the two other axes almost equally inclined with respect to the rolling plane. Interpretation of the band formation appears more complicated if only the geometric process is considered.

Within the bands themselves, the same mechanism of orientation change in localized regions operates. The rotation occurs about the $[111]$ axis contained by the (110) interface plane of the new lattice. This $[111]$ axis is common to the initial crystal, and the primary and secondary bands. Therefore the orientation changes are simply additive.

In the first stages of deformation it appears clear that certain planes and axes play a somewhat special role which can be expressed in two ways: 1—Crystal-

lographically—it can be said that the $\{110\}$ planes are planes of high dislocation density, the dislocations being propagated on the $\{111\}$ planes in the directions $[110]$. 2—Mechanically—this amounts to recognizing the directions $[110]$ as having minimum elastic resistance to elongation or to shortening.

The formation of the present deformation bands is comparable from the point of view of crystallography with that observed by Cahn¹¹ and Honeycombe¹² in the tensile extension of aluminum single crystals.

Multiple and complex systems of deformation bands appear as deformation continues, or for certain initial crystal orientations. Only some of these systems have been defined as exactly as the bands already described. It seems they can only be distinguished from them by their more numerous and finer distribution, the rotation axis excepted.

For other systems of thin multiple-lamellae, when the deformation is over a certain limit, it is not possible to identify their positions even relative to one another, with any certainty. Their multiplicity must, without any doubt, finally define the crystallographic properties of rolling textures. It is striking to observe the formation of multiple, superposed patterns, each of them being formed by lamellae of alternating orientation. It is very evident that for texture studies, X-rays can produce only supplementary information, the interpretation of which would appear very difficult in the light of the complex phenomena which have been described for the simpler cases.

References

- ¹ J. Hérenghuel and P. Lelong: Variation de la vitesse d'oxydation anodique avec l'orientation de la face cristalline. *Comptes Rendus* (1951) **232**, p. 2218.
- ² J. Hérenghuel and P. Lelong: Etude des désorientations internes au monocristal d'alliage aluminium-magnésium soumis à une déformation plastique. *Revue de Métallurgie* (1951) **48** (11) pp. 875-878.
- ³ J. Hérenghuel and P. Lelong: Etude des désorientations internes au cours de la déformation plastique d'un monocristal métallique. *Comptes Rendus* (1951) **233**, p. 53.
- ⁴ J. Hérenghuel and R. Segond: Alliages légers spéciaux pour le polissage électrolytique. *Revue de l'Aluminium* (1948) **25** (148) pp. 306-310.
- ⁵ J. Hérenghuel and R. Segond: Emploi de l'oxydation anodique pour l'étude de l'homogénéité des solutions solides Aluminium-Magnésium. *Revue de Métallurgie* (1949) **46** (6) pp. 377-382.
- ⁶ W. Way, T. J. Tiedema, and W. G. Burgers: Inclusions in Aluminium Crystals. *Nature* (1948) **162**, pp. 740-741.
- ⁷ P. Lacombe and A. Berghézan: Relations d'orientation entre monocristaux métalliques de recristallisation et petits cristaux inclus. *Métaux et Corrosion* (1949) **24** (281) pp. 1-6.
- ⁸ P. Lacombe and L. Beaujard: The Application of Etch-Figures on Pure Aluminium (99.99%) to the Study of Some Micrographic Problems. *Journal Inst. Metals* (September 1947) **74**, (1).
- ⁹ P. Lacombe and L. Beaujard: Etudes sur les aspects des pellicules d'oxydation anodique formées sur l'Aluminium et ses alliages. (Published by La Commission Technique des Etats et Propriétés de Surface des Métaux) pp. 73-89, Paris (1944).
- ¹⁰ N. K. Chen and C. H. Mathewson: Structural Studies of Plastic Deformation in Aluminum Single Crystals. *Trans. AIME* (1951) **191**, p. 653; *JOURNAL OF METALS* (August 1951).
- ¹¹ R. W. Cahn: Slip and Polygonization in Aluminium. *Journal Inst. Metals* (May 1951) **79**, (3) pp. 129-158.
- ¹² R. W. K. Honeycombe: Inhomogeneities in the Plastic Deformation of Metal Crystals -I-II. *Journal Inst. Metals* (October 1951) **80**, (2) pp. 45-56.

Statistical Grain Structure Studies: Plane Distribution Curves of Regular Polyhedrons

by F. C. Hull and W. J. Houk

To clarify interpretations of grain structures and to assist in calculations of spatial grain size distributions, plane distribution curves have been determined for random sections through four regular polyhedrons approximating the shapes of metal grains. The characteristics of the distribution curve for the average metal grain are predicted.

IT was realized early in the history of metallurgy that metals are polycrystalline aggregates and that the size and shape of crystals affects the properties of the material. Réaumur¹ in 1722 employed the microscope to examine the fractured surfaces of steel and of white and gray cast iron and suggested a polyhedral arrangement of the crystals. The first extensive investigation of the form of crystal grains was carried out by Desch.² He examined the disintegrated grains from a β brass sample and noted that the number of faces per grain ranged from eleven to twenty and that the number of edges per face varied from three to eight and the maximum occurred at five.

While it has been found practical to examine isolated grains only in exceptional cases, it is always possible to make a plane section through the metal and examine the shape of the grain sections on the plane of polish. Desch² tried to determine the relation between the form of a polyhedron and that of its plane sections for comparison with distribution curves of numbers of sides per grain section of actual metal samples. The polyhedrons investigated were the rhombic and pentagonal dodecahedrons and the orthic tetrakaidecahedron. However, the frequency distributions of the number of sides of plane intersections were not sufficiently characteristic to decide which polyhedron most closely approximated the average grain in a metal.

Determination of Statistical Shape of Grain in Space

Scheil³ was interested in the problem of calculating the distribution of grain sizes in space from the easily measured distribution of grain section sizes on the plane of polish. Assuming that the grains were spheres and using the plane distribution curve for a sphere shown in Fig. 1, he employed a successive subtraction method to calculate the spatial distribution.

In order to evaluate the accuracy of these calculations, Scheil and Wurst⁴ determined the actual distribution of grain sizes in space in their sample of ingot iron by polishing off successive layers and following every individual grain in a series of micrographs. From curves of mean radius of intersection

of a given grain vs thickness of metal removed in polishing, Scheil and Wurst attempted to derive the statistical shape of a grain in space. Their calculated plane distribution curve for this shape is compared with the distribution curve for a sphere in Fig. 1. A table of values based on this curve was prepared for calculating spatial distributions of grains. The calculated and measured spatial distributions of their sample then agreed much better than when a spherical shape had been assumed.

In the present paper, an attempt has been made to learn something about the average metal grain by studying in detail the effect of the shape of regular polyhedrons on the plane distribution of areas and shapes of areas produced by random sections through them. From the data presented below, it can be concluded that the plane distribution curve for the average metal grain differs in three fundamental respects from the curve derived by Scheil and Wurst.

Polyhedrons Selected for Study

The polyhedrons selected for the statistical study are illustrated in Fig. 2 and consisted of a cube, a figure formed by cutting off the corners of a cube at the midpoints of the original edges, a tetrakaidecahedron, and a pentagonal dodecahedron. The length of edge on any one figure is a constant. For the above models the edge lengths were 3.50, 4.00, 2.00, and 2.08 in., respectively.

A cube was selected for one of the polyhedrons because of its simple geometry, because it is a form that by repetition can completely fill space, and because it represents a convenient degree of departure from compactness beyond which the shape of

F. C. HULL, Member AIME, is Manager, Metallurgical Section and W. J. HOUK is Research Engineer, Research Laboratories, Westinghouse Electric Corp., East Pittsburgh, Pa.

Discussion on this paper, TP 3499E, may be sent, 2 copies, to AIME by June 1, 1953. Manuscript, Sept. 15, 1952; revision, Jan. 7, 1953. Los Angeles Meeting, February 1953.

A portion of the work described herein was part of a thesis by F. C. Hull submitted in partial fulfillment of requirements for the degree of Doctor of Science at Carnegie Institute of Technology, June 1941.

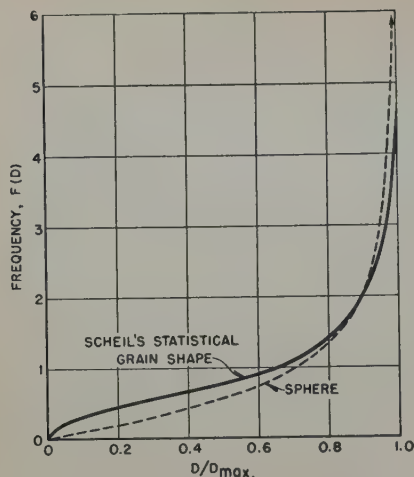
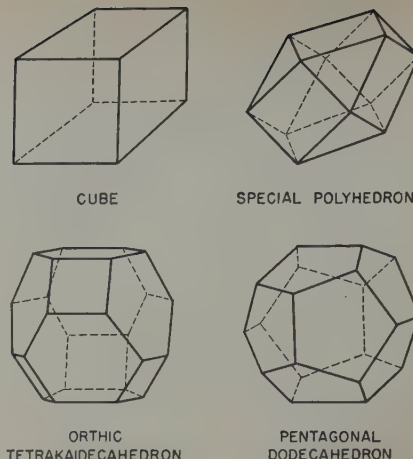


Fig. 1 (left)—Comparison of plane distribution curves of section diameters for a sphere and Scheil's statistical grain shape.

Fig. 2 (right)—Polyhedrons selected for study of plane distributions of area and shapes of sections.



equiaxed metal grains would not be expected to extend. The "special polyhedron," with six square faces and eight triangular faces, represents an arbitrary step in the direction of greater compactness. It is not a space-filling polyhedron.

The tetrakaidecahedron of minimum area, which has eight six-sided faces with double curvature and six four-sided plane faces, is the only polyhedron that satisfies all surface-tension requirements. For ease in constructing the model and evaluating the areas of intersections, this shape has been approximated by the orthic tetrakaidecahedron. Although the form with plane faces and straight edges does not fulfill the surface-tension requirements, the difference in the figures, insofar as the plane distribution curve is concerned, is negligible.

The pentagonal dodecahedron is not in itself a space-filling figure, as is the tetrakaidecahedron. With its twelve five-sided faces, this figure approaches the characteristics of the average metal grain closer than does any other regular polyhedron. However, this comparison is only an approximation because a metal grain has variety in size, shape, and number of faces. By considering the characteristics

of all the polyhedrons, some generalizations can be drawn that are applicable to the average metal grain.

Experimental Procedure

Preliminary calculations and measurements of plane distribution curves of a cube and the "special polyhedron" were carried out by one of the authors at Carnegie Institute of Technology in 1940.⁶ The experimental procedure involved lowering wire models into water, using fifteen different orientations, and measuring the area of intersection as a function of depth of immersion. More recently at the Westinghouse Research Laboratories, the analysis was extended to the tetrakaidecahedron and the pentagonal dodecahedron and to a re-evaluation of the cube, using a more accurate and convenient procedure which was suggested by Roy L. Anderson. The technique is illustrated in Fig. 3.

A wire model of the polyhedron mounted on a rod was held in a tilting bench vise supported by an elevating table borrowed from a Rockwell hardness tester. Vertical displacements of the table and model were read on a dial gage. As the model was raised, it passed through a circular opening in a plywood panel. The top of the panel was parallel to the surface of the elevating table. The shapes and sizes of sections were obtained by sliding templates made of cardboard into contact with each face of the polyhedron intersected by the plane of the panel. The templates were temporarily held in place with masking tape. The panel was then transferred to a desk, a smooth-topped circular blank replaced in the opening, and the area of intersection evaluated with a planimeter.

As the model was raised, the shapes of the intersections were noted. Every time a corner passed the plane of the panel, the intersection polygon gained or lost a side. The elevation was then measured, and the number of sides was counted. From the point of first reaching the panel level, area measurements were made at 0.2-in. intervals up to and including an elevation corresponding to the center of the polyhedron. Because of the symmetry of the figure it was not necessary to go beyond the midpoint. A typical curve of area of intersection and number of sides of the intersection vs elevation, for the tetrakaidecahedron, is shown in Fig. 4.

The procedure used in selecting orientations of the sectioning plane with respect to the polyhedrons was as follows: The polyhedron, for example the cube, was assumed to lie in the center of a stereographic projection reference sphere with a face

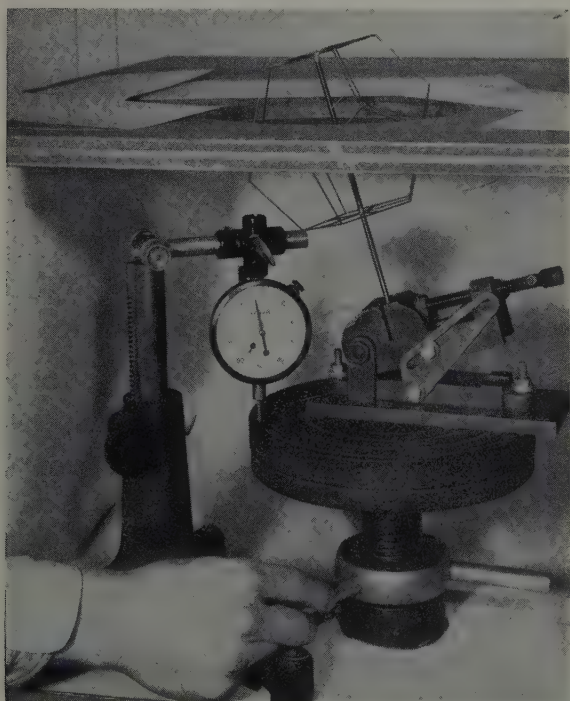


Fig. 3—Position of pentagonal dodecahedron being adjusted with elevating screw.

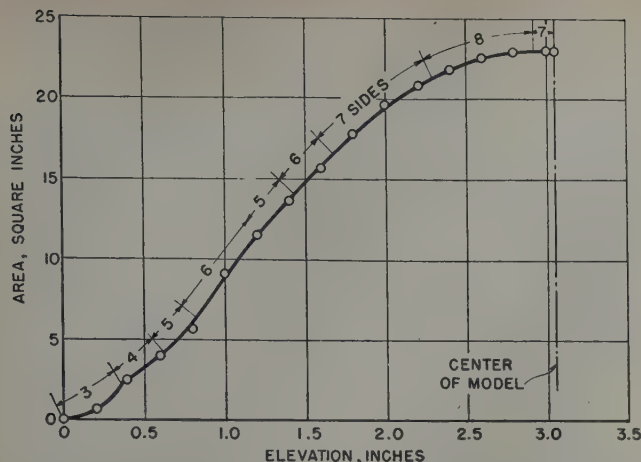


Fig. 4—Area and shape of intersection vs elevation for tetrakaidecahedron of orientation No. 26.

parallel to the projection plane. All possible orientations of a plane with respect to the cube (identified by a normal to the plane passing through the center of the cube) can be represented by a point on the reference sphere and the corresponding point on the stereographic projection. However, because of the symmetry of the cube, it is only necessary to consider orientations lying within one of the twenty-four equivalent stereographic triangles defined by poles of the (001), (011), and $(\bar{1}11)$ planes. The orientations of the sectioning plane with respect to the cube are illustrated in the polar stereographic net plot in Fig. 5 and were selected to give as complete and representative sampling as possible with only twenty-six points. As an aid to distributing the orientations uniformly over the surface of the reference sphere, circles were drawn around each point with a diameter equivalent to a 5° solid angle. The distortion resulting from the method of plotting leads to a much smaller circle for the [001] direc-

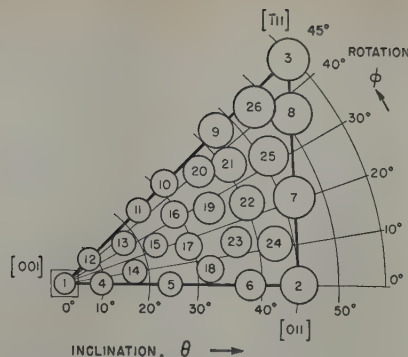


Fig. 5—Polar stereographic plot of orientations of sectioning plane with respect to cube.

tion, for example, than at $[\bar{1}11]$. Angular relationships are listed in Table I for the cube and the other polyhedrons. θ represents angular inclination of the normal to the sectioning plane with respect to the [001] direction and ϕ represents angular rotation about [001]. If an orientation lies on an element of symmetry, it must be weighted as less than one in accordance with the number of equivalent stereographic triangles shared by the orientation. This consideration accounts for the weight factors listed in Table I.

Analysis of the Data

The data obtained by curves of the type illustrated in Fig. 4 have been analyzed to provide curves of frequency of occurrence of intersections with a given number of sides, distribution of areas resulting from intersections with certain numbers of sides, distribution curves of areas, and distribution curves of section diameters. Assume that a polyhedron is cut by a plane of a given orientation and that the area of intersection is A . A parallel plane displaced a distance Δx from the first will have

Table I. Orientations of Normal to Intersecting Plane for Various Polyhedrons

Cube (C.I.T.) and Special Polyhedron				Cube			Orthic Tetrakaidecahedron			Pentagonal Dodecahedron		
Position No.	θ	ϕ	Weight	θ	ϕ	Weight	θ	ϕ	Weight	θ	ϕ	Weight
1	0°	0°	1/8	0°	0°	1/8	0°	0°	1/6	0°	0°	1/10
2	12	24	1	45	0	1/4	10	0	1/2	8	0	1/2
3	22	45	1/2	54.7	45	1/6	21	0	1/2	13	0	1/2
4	18	14	1	9	0	1/2	29	0	1/2	23	0	1/2
5	35	45	1/2	24	0	1/2	35	0	1/2	27.7	0	1/4
6	31	29	1	38	0	1/2	54.7	0	1/8	5	36	1/2
7	27	10	1	46	21	1/2	46	13	1/2	14	36	1/2
8	45	43	1/2	51	37	1/2	42	21	1/2	23	36	1/2
9	40	31	1	42	45	1/2	39	30	1/2	31	36	1/2
10	38	16	1	31	45	1/2	36	43	1/2	38.5	36	1/6
11	37	0	1/2	24	45	1/2	36	53	1/2	30	11	1/2
12	54.7	45	1/6	8	45	1/2	32	60	1/2	31	30	1
13	50	33	1/2	17	35	1	26	60	1/2	29	21	1
14	47	20	1/2	17	10	1	19	60	1/2	27	4	1
15	45.5	7	1/2	23	23	1	12	60	1/2	26	14	1
16				28	37	1	7	38	1	45	26	1
17				29	17	1	13	35	1	22	18	1
18				32	6	1	15	12	1	19	6	1
19				35	28	1	20	20	1	19	29	1
20				37	40	1	20	39	1	16	18	1
21				41	36	1	25	47	1	11	11	1
22				40	24	1	26	34	1			
23				37	14	1	26	24	1			
24				42	11	1	26	10	1			
25				46	31	1	31	16	1			
26				48	43	1	32	28	1			
27							31	38	1			
28							31	48	1			
29							36	33	1			
30							37	22	1			
31							36	10	1			
32							40	4	1			
33							40	13	1			
34							44	8	1			
35							48	4	1			

θ is the inclination of the normal to the [001] direction.
 ϕ is the rotation of the normal around the [001] direction starting from the [010] direction.

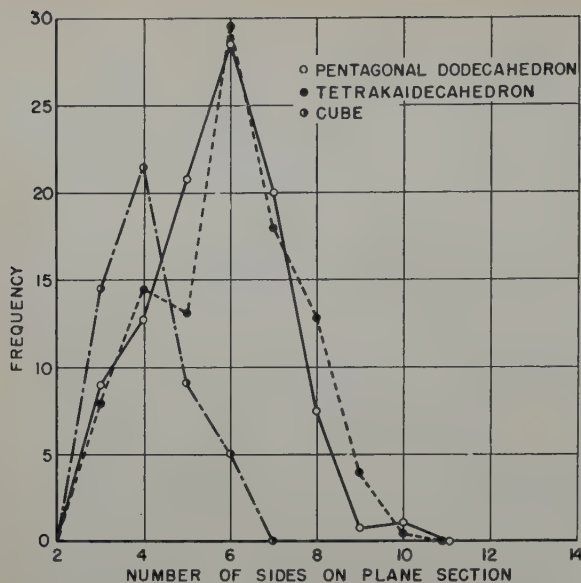


Fig. 6—Distribution of number of sides on plane sections of three polyhedrons.

an area of intersection of $A + \Delta A$. The probability of getting an intersection of area A to $A + \Delta A$ from the given orientation is proportional to Δx . If this probability is summed for all possible orientations and positions of the plane with respect to the polyhedron capable of producing such an area, a frequency distribution of areas is obtained. Orientations lying on an element of symmetry receive less weight, as has been explained.

The frequency function, $F(A)$, has the characteristic that the area under the curve between any two values of area is proportional to the number of intersections per unit area in that size range. In the present paper the "diameter" of an intersection has been defined as $D = \sqrt{A}$. Since it is frequently useful to express distribution functions in terms of diameters, the following relationship is defined:

$$F(A)\Delta A = F(D)\Delta D$$

Since

$$\Delta A = 2D\Delta D$$

then

$$F(D) = 2F(A)\sqrt{A}$$

Discussion of the Distribution Curves

The distributions of number of sides on intersections of the cube, tetraikaidecahedron, and pentagonal dodecahedron are shown in Fig. 6. These curves were obtained by summing the weighted values of Δx , irrespective of areas of the intersection, for each number of sides of the plane section. The cube has a maximum of four-sided sections, with no intersection having more than six sides. In spite of the considerable difference in shape between the other two polyhedrons, both exhibit a pronounced maximum at six sides per plane section, and show surprising similarity over the whole range of the frequency plot. The shapes of these curves are more reasonable than those obtained by Desch's more approximate sampling technique.² From the cube with only six faces to the other twelve and fourteen-faced figures, there is a shift to larger numbers of sides on the plane sections, as would be expected.

When the geometry of a polyhedron is considered, it is readily seen that the area of an intersection generally increases with the number of sides of the

section. It is difficult, however, to visualize the frequencies and ranges of areas possible for each number of sides of a section. A quantitative presentation of the distribution of areas for each shape of intersection possible is made for the cube, the tetraikaidecahedron, and the pentagonal dodecahedron in Figs. 7 to 9.

For the cube (Fig. 7), small three-sided intersections are very frequent, but the number decreases to zero at 10.4 sq in. Four-sided intersections are found from the smallest up to the largest area. The maximum in the distribution function at 12 to 13 sq in. results from the large number of positions of the sectioning plane that produce the same area when the plane is approximately parallel to a cube face. Five and six-sided intersections have reasonably normal frequency distributions of areas. The maximum area is the same as for the four-sided intersections, but the minimum and average areas increase with number of sides.

The tetraikaidecahedron curves in Fig. 8 exhibit similar trends but extended to intersections with up to ten sides. Although the minimum and average areas increase with the number of sides, the largest section possible has only eight sides. The double maximum in the frequency for six sides is comparable to the curve for four-sided intersections of a cube. It results from the shape and symmetry of the

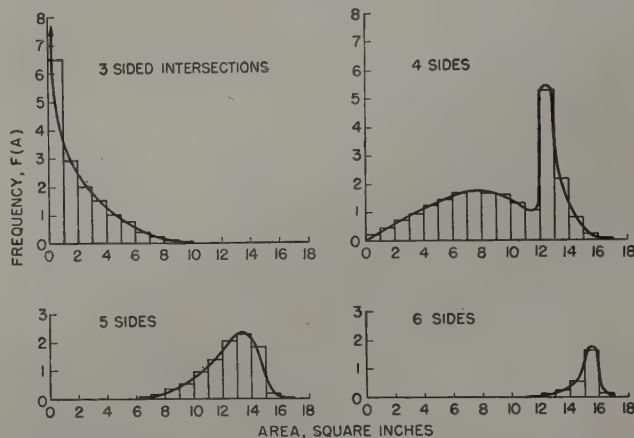


Fig. 7—Distribution of areas for 3, 4, 5 and 6-sided intersections of a random plane with a cube.

figure and thus has no particular significance for irregularly shaped polyhedrons.

The minimum, average, and maximum areas of the pentagonal dodecahedron (Fig. 9) increase with the number of sides of the section. Distribution curves for six and eight-sided intersections are slightly skewed as a result of a geometrical coincidence.

The curves for these three regular polyhedrons are useful in predicting the types of curves that might be obtained for the average metal grain. It is clear that the larger the number of faces on a grain, the larger will be the possible number of sides on an intersection. Since the faces on a metal grain are not necessarily parallel and are different sizes and have from three to about eight edges, there are fewer possibilities for the peculiarities in distribution that arise in regular polyhedrons. For the average grain, the minimum, average, and maximum area would increase more regularly with the number of sides of the intersection, and the frequency distribution of areas would be more normal. For polyhedrons of twelve to fourteen faces, the fre-

quency of occurrence of five, six, and seven-sided intersections would still be high, and intersections of ten or more sides would be exceedingly rare.

The plane distribution curves of areas, irrespective of the shapes of the intersections, are obtained by summing the above curves. For the four polyhedrons illustrated in Fig. 2, the distribution curves of areas are plotted in Figs. 10 to 13. All four curves are characterized by a rapid rise in frequency, $F(A)$, at small areas of intersection. Furthermore, each curve has a pronounced maximum in frequency at a value of $A/A_{\max.}$, somewhere between 0.7 and 0.9, with the frequency dropping to zero at the largest area possible.

For direct comparison with plane distribution curves of the sphere and Scheil's statistical grain shape (Fig. 1), these frequency curves, evaluated experimentally in terms of areas, have been converted by calculation to frequency distributions of section "diameters" using the relationship derived earlier in this paper. One strikingly similar feature of the four plane distribution curves of section diameters in Figs. 14 to 17 is that the frequency does not gradually drop to zero as D approaches zero. Such a behavior is theoretically correct for a sphere, but is not to be expected in the case of polyhedrons or grains with edges meeting at sharp corners. This can be demonstrated in the following way.

For polyhedrons having three straight edges meeting at every corner, the small intersections will be triangles except for a few unique orientations of the cutting plane. For a given orientation, the intersections at a series of elevations are similar triangles whose areas increase with the square of the eleva-

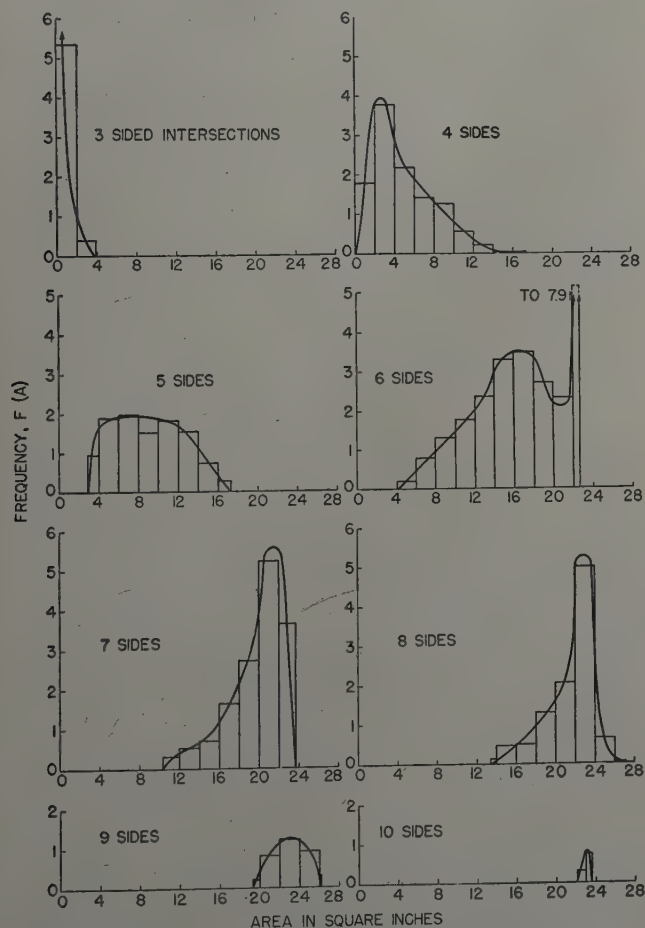


Fig. 8—Distribution of areas for 3 to 10-sided intersections of a random plane with a tetrakaidecahedron.

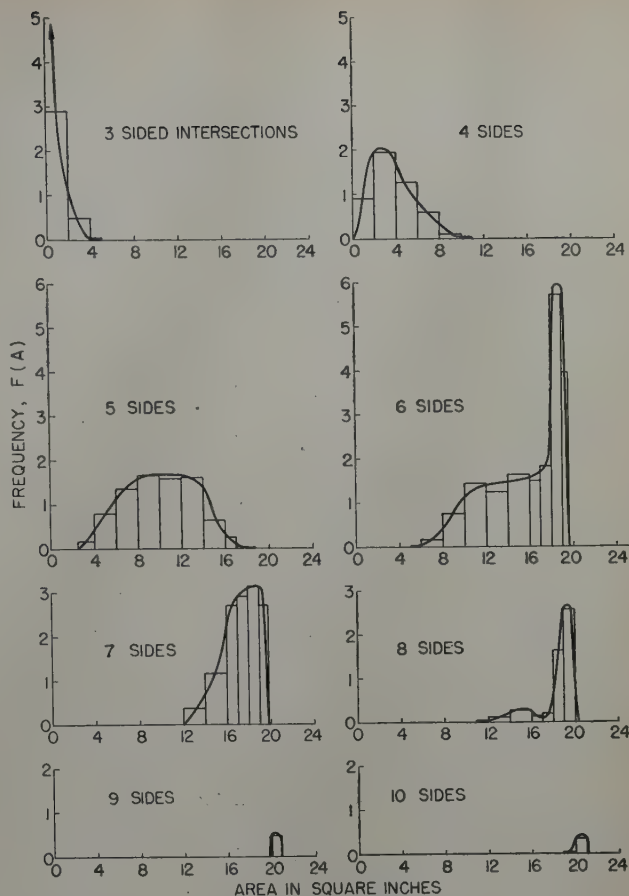


Fig. 9—Distribution of areas for 3 to 10-sided intersections of a random plane with a pentagonal dodecahedron.

tion and whose linear dimensions increase proportionally with distance,

$$D = k_1 x$$

The frequency of occurrence of areas with diameter D to $D + \Delta D$ from orientation 1 is proportional to Δx , that is $F_1(D) \sim \Delta x$ but

$$\Delta x = \Delta D / k_1$$

Therefore

$$F_1(D) \sim \Delta D / k_1$$

For equal increments of ΔD , $F_1(D)$ is a constant. The entire frequency curve at small values of D is obtained by summing such expressions for all orientations, and since the sum of a series of constants is still a constant, the $F(D)$ curve has a finite intercept and approximately zero slope at $D = 0$.

Distribution curves for the polyhedrons studied show a pronounced maximum in frequency at values of $D/D_{\max.}$, between 0.85 and 0.95, and again the frequency drops to zero at the largest diameter of section possible. The detailed shapes of the frequency curves over the whole range of section diameters reflect differences in the compactness of the polyhedrons and their degree of symmetry.

The plane distribution curve for a statistical metal grain must have the four characteristics outlined above:

$$F(D) = \text{finite at } D = 0$$

$$\frac{dF(D)}{dD} = 0, \text{ at } D = 0 \text{ and } D/D_{\max.} = < 1$$

$$F(D) = 0, \text{ at } D/D_{\max.} = 1$$

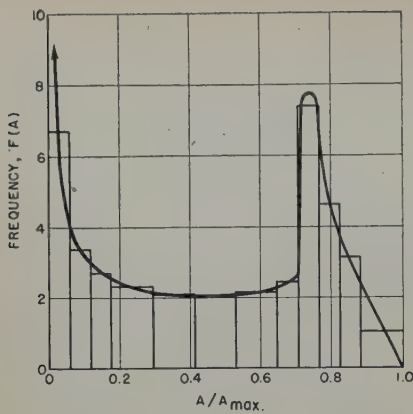


Fig. 10 — Plane distribution curve of areas for a cube.

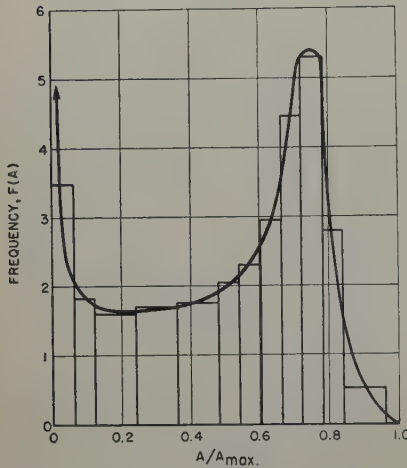
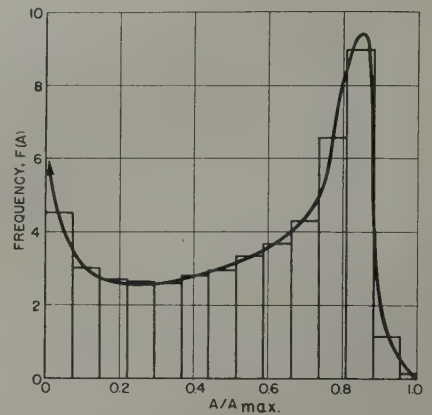


Fig. 11 (left) — Plane distribution curve of areas for special polyhedron.

Fig. 12 (right) — Plane distribution curve of areas for tetrakaidecahedron.



However, it would be expected from the lack of symmetry in the average metal grain that the maximum in frequency would not be as high or as narrow as in the case of the regular polyhedrons and that it would occur at a smaller value of the ratio D/D_{max} . Since occasional small faces are possible on a metal grain, the frequency curve of the average grain would rise more rapidly in the range of small values of the diameter. Aside from these generalizations, little can be said quantitatively about the plane distribution curve of the average metal grain until experimental data are obtained on grains from disintegrated samples to serve to evaluate such a curve.

Characteristics of Polyhedrons

In order to compare characteristics of the polyhedrons on a uniform basis, the dimensions of each were selected so that all the models had the same volume. For simplicity, it was assumed that the number of grains per unit volume, N_v , was equal to

1. The second entry in Table II gives the surface area of each polyhedron. The sphere naturally has the minimum surface per unit volume, but this represents an unattainable minimum in so far as metal grains are concerned because stacked spheres by themselves cannot completely fill space. A cube might be considered as an extreme in the opposite direction according to Kaiser,⁶ excluding consideration of elongated or columnar grains. The three other more compact polyhedrons all have about the same surface per unit volume, indicating that the value is not too sensitive to actual shape for regular polyhedrons with twelve to fourteen faces. Since there is only about a 20 pct spread in areas between the sphere and the cube, it is reasonable to conclude that the surface area of actual grains can be approximated very closely by assuming them to be tetrakaidecahedrons, as was done by Rutherford, Aborn, and Bain.⁷

Fig. 13 — Plane distribution curve of areas for pentagonal dodecahedron.

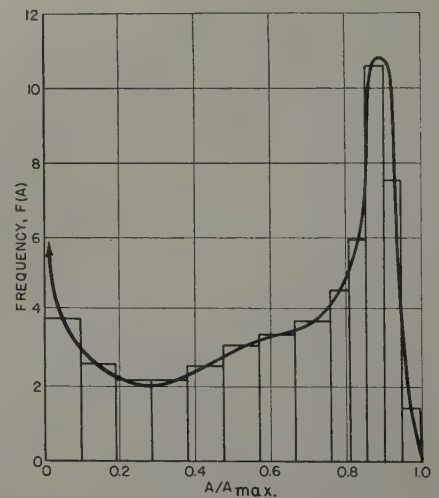


Table II. Characteristics of Several Polyhedrons

	Cube	Special Polyhedron	Tetrakai-decahedron	Pentagonal Dodecahedron	Sphere
Volume	1	1	1	1	1
Surface of figure	6.00	5.34	5.31	5.30	4.83
r of inscribed sphere	0.50	0.53	0.54	0.56	0.62
Average r_i (based on intersections)	0.76	0.70	0.66	0.66	0.62
r of circumscribed sphere	0.87	0.75	0.70	0.71	0.62
Average cross-section area from distribution curve, \bar{A}	0.66	0.72	0.77	0.78	0.81
Maximum cross-section area, A_{max}	1.41	1.47	1.40	1.31	1.21
A_{max}/\bar{A}	2.14	2.05	1.83	1.69	1.50
Number of intersections per unit area, n	$\left. \begin{array}{l} 1/\bar{A} \\ 2r_i \end{array} \right\}$	1.51	1.30	1.29	1.24
		1.52	1.32	1.32	1.24

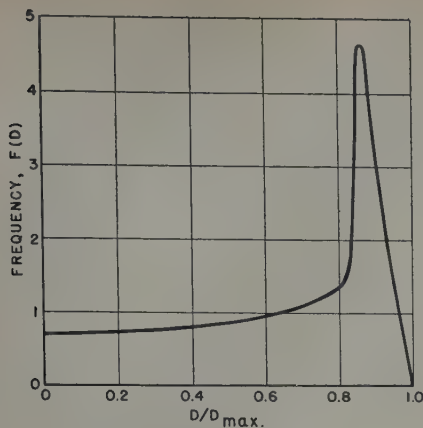


Fig. 14 — Plane distribution curve of section diameters for cube.

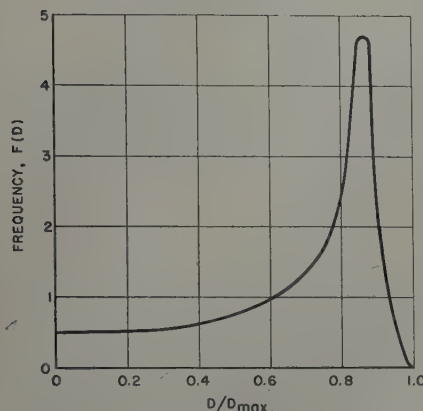


Fig. 15 — Plane distribution curve of section diameters for special polyhedron.

The entries for radii of inscribed and circumscribed spheres give a measure of the extent to which the corners of the polyhedrons protrude. The radius r_i is obtained by averaging the maximum elevation for all orientations of the polyhedron, giving each position its proper weight. On the average, grains whose centers lie within a distance r_i on either side of a sectioning plane will produce intersections. For unit area on the plane, the number of such intersections, n , is equal to the number of grains lying in a volume of $2r_i \times 1 \times 1$, which is $2r_i N_v$. Since $N_v = 1$ by choice in the present instance, $n = 2r_i$.

One of the valuable uses of the distribution curves is that the average area of intersection, \bar{A} , produced by a given polyhedron can be calculated:

$$\bar{A} = \frac{\int_0^{A_{\max.}} F(A) A dA}{\int_0^{A_{\max.}} F(A) dA}$$

From the dimensions of a polyhedron, the maximum area of an intersection, $A_{\max.}$, may be calculated. Sauerwald⁸ and Gulliver⁹ have pointed out that the ratio $A_{\max.}/\bar{A}$ on the plane of polish of a metal sample is a measure of the uniformity of grain size in space. Formerly, there was no information on which to base an estimate of what this ratio should be for grains, except the value of 1.5 for spheres. For polyhedrons reasonably approaching actual grain shapes, it is seen in Table II that $A_{\max.}/\bar{A}$ should lie in the range 1.8 to 2.0. The more the ratio for a given sample exceeds this theoretical minimum (for a single size in space) the greater is the range of sizes in space.

The number of intersections per unit area, n , equals $1/\bar{A}$ and also $2r_i$. Values of these quantities are listed in the last two rows of Table II. By the two independent methods of evaluation, n agrees closer than 3 pct, serving as a check on the accuracy of the distribution curves.

Interpretation in Terms of ASTM Grain Size Numbers

It has been long recognized that even with a constant grain size in space there would be a distribution of section sizes on a plane of polish. This fact was first expressed in quantitative terms, assuming grains were all spheres of a single size, by the plane distribution curve in Fig. 1. Rutherford, Aborn, and Bain⁷ analyzed this curve in terms of ASTM grain size numbers in order to permit a clearer interpretation of its significance in terms readily understandable to the metallographer. In a similar manner, from the plane distribution curves in Figs. 14 to 17 and the known relation between grain section diameter and ASTM grain size numbers, the percentage of grain sections in different ASTM grain size groups has been determined for the various polyhedrons. The results for the polyhedrons, the sphere, and Scheil's statistical grain shape presented in Table III permit an evaluation of the extent of error introduced by the assumption that grains are spheres. As was expected, the latter assumption leads to predicting more large sections and fewer small ones than produced by polyhedrons approaching the shape of the average metal grain. The distribution curve for the cube obtained at Carnegie Institute of Technology resulting from only fifteen orientations leads to values in Table III that agree reasonably well with those based on the more accurately determined curve for the cube.

A person making a visual estimate of grain size is impressed not so much by the relative numbers of

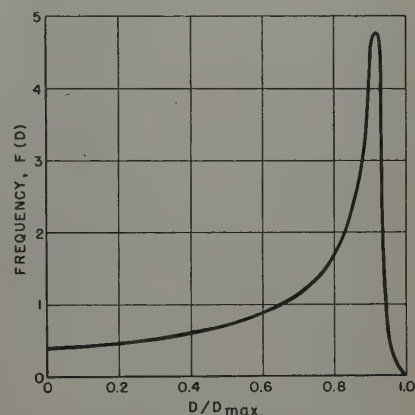


Fig. 16 — Plane distribution curve of section diameters for tetraikadecahedron.

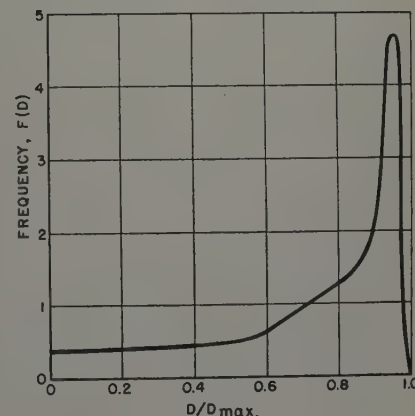


Fig. 17 — Plane distribution curve of section diameters for pentagonal dodecahedron.

Table III. Interpretation of Plane Distribution Curves of Several Polyhedrons in Terms of ASTM Grain Size Numbers

Shape	Intersections of ASTM Grain Size, Pet				Area Occupied by ASTM Grain Size, Pet			
	N	N+1	N+2	N+x	N	N+1	N+2	N+x
Cube	51	18	10	21	80	14	4.3	2.1
Cube (CIT)	53	16	10.5	20.5	81	13	4.4	1.4
Special polyhedron (CIT)	56	20	9.5	15	79	15	3.6	2.0
Tetrapentacahedron	58	19	9.5	13.5	81	14	3.2	1.5
Pentagonal dodecahedron	63	17	8	12	87	10	2.1	0.5
Sphere	71	16	7	6	87	10	2	1
Scheil's statistical grain shape	59	18	9	14	84	12	2.5	1.1

each grain size present as by the relative areas occupied by each. Using the plane distribution curves again, it is possible to calculate the percentage of the section area occupied by grains in certain ASTM grain size groups. The results for the various polyhedrons also appear in Table III. Even with the extreme range of shapes from a cube to a sphere, the area occupied by the grains covering two ASTM grain size groups N and $N+1$ is between 94 and 97 pct of the total cross section. The large proportion of small grain section sizes usually seen on polished metallographic specimens can thus only be accounted for by a distribution of grain volumes in space. Actually, in all cases in which spatial distributions have been determined, a considerable spread about a mean size has been found.^{4, 20}

Conclusions

1—The average and maximum number of sides on a plane section of a polyhedron increase with the number of faces on the polyhedron.

2—The distribution of plane section shapes of a polyhedron depends primarily on the number of faces and is not much affected by the shapes of the faces on the polyhedron.

3—With minor exceptions, the minimum, average, and maximum areas of intersections with a given polyhedron increase with the number of sides on the intersection.

4—Experimentally and theoretically, it has been shown for polyhedrons that the distribution of section diameters is a constant at small values of the diameter.

5—All four of the polyhedrons studied have a pronounced maximum in the plane distribution curve at less than the maximum diameter, and the frequency at the largest section possible is zero.

6—The plane distribution curve for an average metal grain would exhibit the same general characteristics found for the regular polyhedrons, except that the maximum in the frequency curve would be much broader because of the lack of symmetry in the grain shape.

7—If a material has a completely uniform equiaxed grain size in space, then on plane sections, 94 to 97 pct of the area will be occupied by grain sections covering only two ASTM grain size groups N and $N+1$, regardless of the spatial shape of the grains.

References

- ¹ Réaumur: *L'Art de convertir le fer forge en acier*. (1722) Paris.
- ² C. H. Desch: The Solidification of Metals from the Liquid State. *Journal Inst. Metals* (1919) No. 2, p. 241.
- ³ E. Scheil: Statistische Gefügeuntersuchungen I. *Ztsch. Metallkunde* (1935) **27**, p. 199.
- ⁴ E. Scheil and H. Wurst: Statistische Gefügeuntersuchungen II, Messung der räumlichen Kristallgrösse. *Ztsch. Metallkunde* (1936) **28**, p. 340.
- ⁵ F. C. Hull: Reaction Kinetics of the Austenite to Pearlite Transformation. Doctor of Science thesis submitted to Carnegie Institute of Technology, Pittsburgh, Pa., May 15, 1941.
- ⁶ H. F. Kaiser: The Estimation of Inter-Granular Surfaces and Volumes in Metals. *Metals and Alloys* (January 1938) p. 23.
- ⁷ J. J. B. Rutherford, R. H. Aborn, and E. C. Bain: Relation Between the Grain Areas and the Grain Size of the Metal. *Metals and Alloys* (December 1937) p. 23.
- ⁸ F. Sauerwald: *Lehrbuch der Metallkunde* (1929) p. 51.
- ⁹ G. H. Gulliver: Note on Grain Size. *Journal Inst. Metals* (1918) **19**, p. 145.
- ¹⁰ W. M. Williams and C. S. Smith: A Study of Grain Shape in an Aluminum Alloy and Other Applications of Stereoscopic Microradiography. *Trans. AIME* (1952) **194**, p. 755; *JOURNAL OF METALS* (July 1952).

Corrections

In the January 1953 issue: TP 3417C. *Evaluation of the pH and Conductivity Methods of Slag Control* by P. D. S. St. Pierre, Pp. 42 and 43, in Tables I and III and in Fig. 4 the word microhm should read micromho.

In the February 1953 issue: TP 3449C, *Accelerated Solidification in Ingots: Its Influence on Ingot Soundness* by Edgar Marburg. P. 165, col. 1, 4th line from bottom, "b, d, and g" should read "b', d', and g'." P. 171, col. 1, paragraph 3, line 13, "Fig. 27" should read "Fig. 26."

In the February 1953 issue: TP 3435E. *Observation on Scaling of Iron* by W. J. Wrazej. P. 265. The following acknowledgment should be made: "This paper was published by permission of the Director-General of Scientific Services, Department of Mines and Technical Surveys, Ottawa, Ont., Canada."

Operations at New Cornelia Copper Smelter Of Phelps Dodge Corporation

by James W. Byrkit

Design features and operating methods at the new Ajo smelter are described in detail. Successful operation of a novel method of handling and charging wet concentrates to a deep bath type reverberatory furnace contribute to the daily production of 200 tons of anodes with good results from the standpoint of both metallurgy and economy.

THE New Cornelia Branch of the Phelps Dodge Corp. is located at Ajo, Ariz. Large scale mining operations were started at Ajo in 1917, when a 5000 ton leaching plant was put in service to treat the copper carbonate ore that overlaid the sulphide orebody. In 1924 a 5000 ton flotation plant was built to treat the sulphide ore and the leaching operation was abandoned a few years later. Changes in practice and additions to plant facilities have resulted in a gradual increase in the milling rate which now approaches 30,000 tons daily.

Prior to the erection of the Ajo smelter, flotation concentrate was shipped by rail to Douglas, Ariz., where it was treated in the Phelps Dodge smelter. Construction of a one reverberatory furnace smelter to produce an average of about 200 tons per day of copper anodes at Ajo was started early in 1949. Initial heating of the reverberatory furnace was begun on June 21, 1950. Charging the furnace was started on July 8, and the first anodes were cast on July 14. Neither the anode furnace nor the reverberatory furnace has cooled since the initial firing. Fig. 1 is a photograph of the new smelter.

Built primarily to eliminate the 300 mile haul of concentrate to the Douglas plant, the new smelter was designed to treat the Ajo concentrate, with a minimum of capital investment. A novel, and relatively simple, method of concentrate handling and furnace charging made unnecessary the installation and operation of expensive storage facilities and reclaiming equipment, and obviated the necessity of holding in storage large quantities of copper-bearing materials. (Patents are pending in the United States and abroad on the Ajo process.) In the selection and arrangement of equipment, consideration was given to the full utilization of all smelting facilities, reducing the amount of idle equipment to a minimum. The layout of the smelter is shown in Fig. 2. The

J. W. BYRKIT, Member AIME, is Smelter Superintendent, New Cornelia Branch, Phelps Dodge Corp., Ajo, Ariz.

Discussion on this paper, TP 3515D, may be sent, 2 copies, to AIME by July 1, 1953. Manuscript, Nov. 3, 1952. Los Angeles Meeting, February 1953.



Fig. 1—The new copper smelter, designed to treat the Ajo concentrates, eliminated the shipping of flotation concentrates to the Phelps Dodge Smelter at Douglas, Ariz.

important problem of internal transportation was minimized by arranging the reverberatory furnace, converters, and anode furnace in a compact group and providing storage bins inside the smelter building, within reach of overhead cranes, for fluxing materials and other supplies needed in the daily operation. This can be seen in the sectional view of the smelter given in Fig. 3. Incorporated in the design were many innovations in smelting equipment intended to facilitate operations and effect economies in maintenance expense and manpower requirements. Table I gives operating data of the entire plant.

Metallurgy

The metallurgical practice at Ajo is based essentially upon the use of a single, deep bath reverberatory furnace for smelting wet concentrate, without concentrate storage facilities. The large reservoir of slag and matte maintained in the furnace serves to equalize, to some extent, the day to day variations in the nature and grade of concentrate and permits

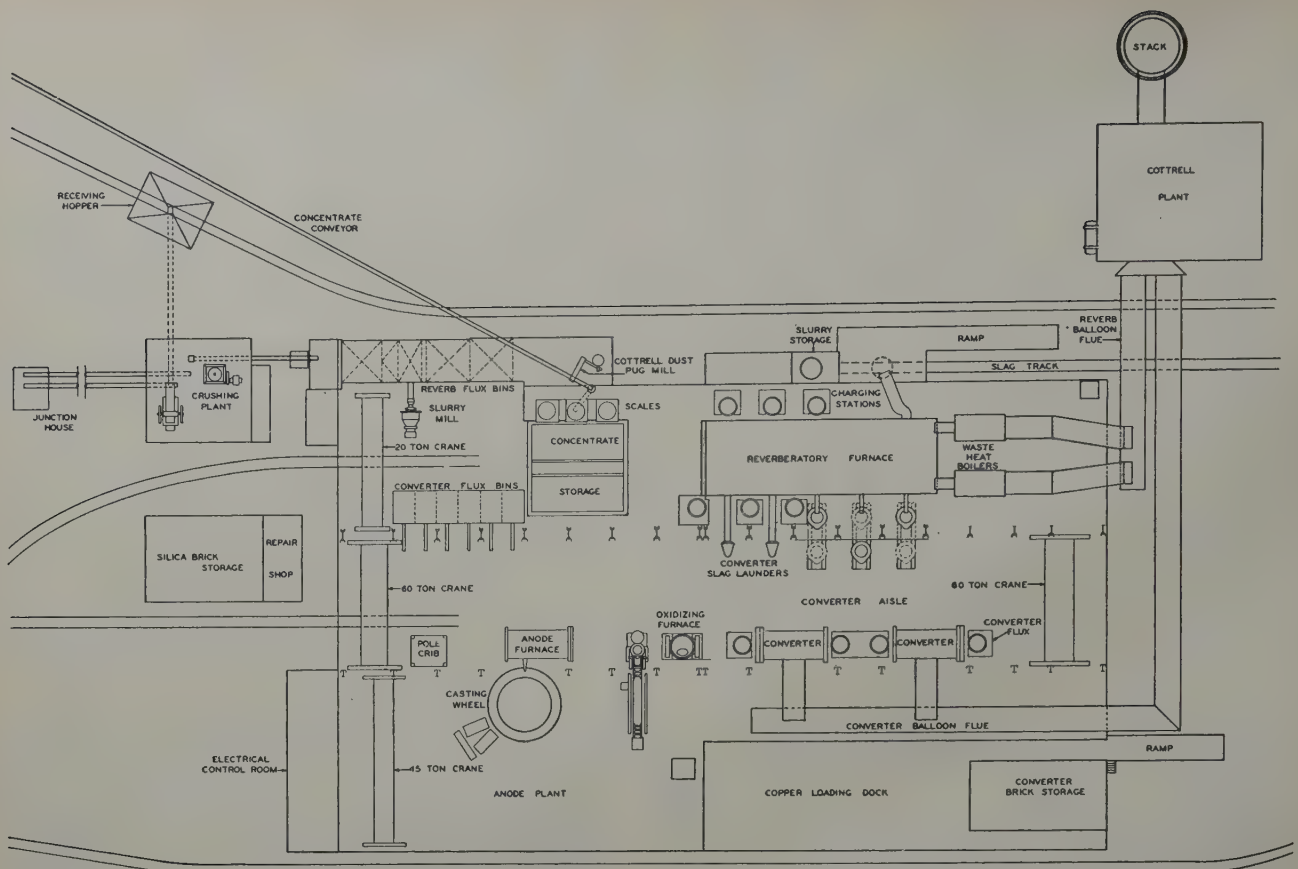


Fig. 2—Arrangement of equipment can be seen in this layout drawing of the smelter. The design permits full utilization of all smelting facilities, and the amount of idle equipment was kept to a minimum.

utilization of converting and refining facilities to the best advantage. The smelter flowsheet is presented in Fig. 4.

Concentrate is taken from flotation plant filters and transported to the smelter on a conveyor belt. Fine crushed limestone is added to the concentrate on the conveyor at a predetermined rate. Ordinarily no other fluxing material is used on the reverberatory furnace charge, which averages 95 pct concentrate. All siliceous fluxing material is charged to converters. The bulk of converter flux is tailing from the old leaching operation. This tailing is about $\frac{1}{3}$

in. in size and contains approximately 67 pct silica and 14 pct alumina. Barren quartz from a local quarry is crushed and blended with tailing to maintain a silica-alumina ratio of about 6 to 1. Custom shipments of siliceous ore constitute a minor portion of converter flux. All converter reverts are resmelted directly in converters.

Copper in the Ajo concentrate is present mainly as chalcopryite, with some bornite and occasional small amounts of chalcocite and native copper. The grade of concentrate varies from day to day, over a considerable range, with accompanying changes in

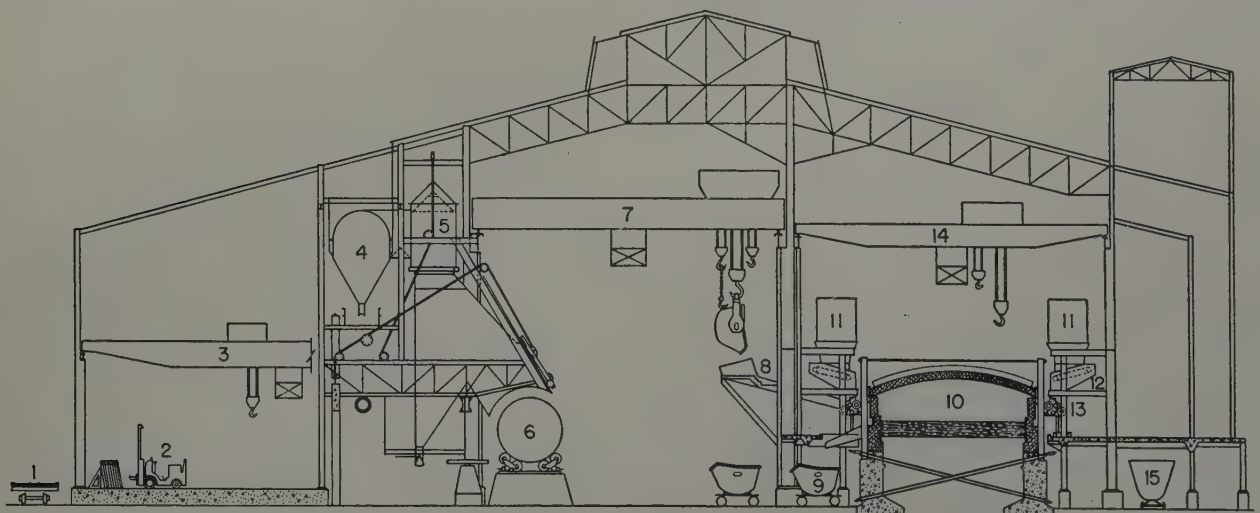


Fig. 3—This sectional view of the smelter shows the positioning of service equipment intended to facilitate internal transportation and operations. 1—Railroad flat car to refinery. 2—Fork lift truck for loading anodes. 3—Anode handling crane, one, 15 ton. 4—Balloon flue, converter. 5—Jug damper. 6—Converters, two. 7—Converter cranes, two, 60 ton. 8—Converter slag return launder. 9—Matte ladles. 10—Reverberatory furnace. 11—Concentrate "can." 12—Concentrate feeder belt. 13—Concentrate slinger. 14—Reverberatory cranes, two, 20 ton. 15—Slag pots.

iron and insoluble material content, depending upon the grade and nature of the mill feed. Matte grade varies with the copper content of the concentrate, ranging from 25 to 35 pct, averaging about 30 pct. Copper content of matte is usually 7.0 to 8.0 units higher than that of concentrate. Slags are fairly uniform in character and composition, copper content varying with matte grade and to some extent influenced by iron carried out in slag.

In the absence of intermediate storage, concentrate is smelted before analyses are available but lack of analyses before charging to the furnace has not been a handicap. Minor adjustments in converter fluxing are made on the basis of analyses of concentrate and final slag for the previous day. When visual appearance of the bath indicates the need, small additions of limestone or silica are made directly to the furnace. Charging of all siliceous flux to converters causes the formation of high-silica slags, but this practice has not perceptibly affected converter linings and has reduced the amount of magnetite returned to the furnace. Furthermore, smelting in converters of practically all silica flux used results in increased furnace capacity for concentrates, which at Ajo is an important factor.

Crushing Plant and Flux Storage

The smelter crushing plant was designed to prepare fluxing materials for converters and reverberatory furnace and to crush reverts and other materials used in the smelter operation. Coarse materials, such as barren quartz and custom ores, are received in either side or bottom dump railroad cars and are dumped into a 75-ton capacity bottom discharge concrete receiving bin. Materials are fed from the bin by pan feeder and belt conveyor into a 36x48 in. jaw crusher, the 3-in. product of which is conveyed to a 4x8 ft mechanically vibrated screen. The screen oversize falls into a 4 ft standard cone crusher set at about $\frac{1}{2}$ in. and remains in closed circuit until reduced to screen undersize. The screen undersize is transported by conveyor and bucket elevator to storage bins.

The leached tailing siliceous flux is loaded by shovel from the dump, which is about one mile from the smelter, into railroad cars and is passed through the plant without crushing. The desired blending of converter flux is accomplished by adding crushed barren quartz in the correct proportion. Limestone, received from an outside source as screened product, likewise requires no crushing. An auxiliary screen is provided inside the smelter building, over which barren quartz is passed, the oversize being used for converter flux, while the 6-mesh undersize is stored for use as furnace patching material.

Storage bins for both reverberatory and converter fluxes are so located in the smelter building that materials may be withdrawn through chutes into

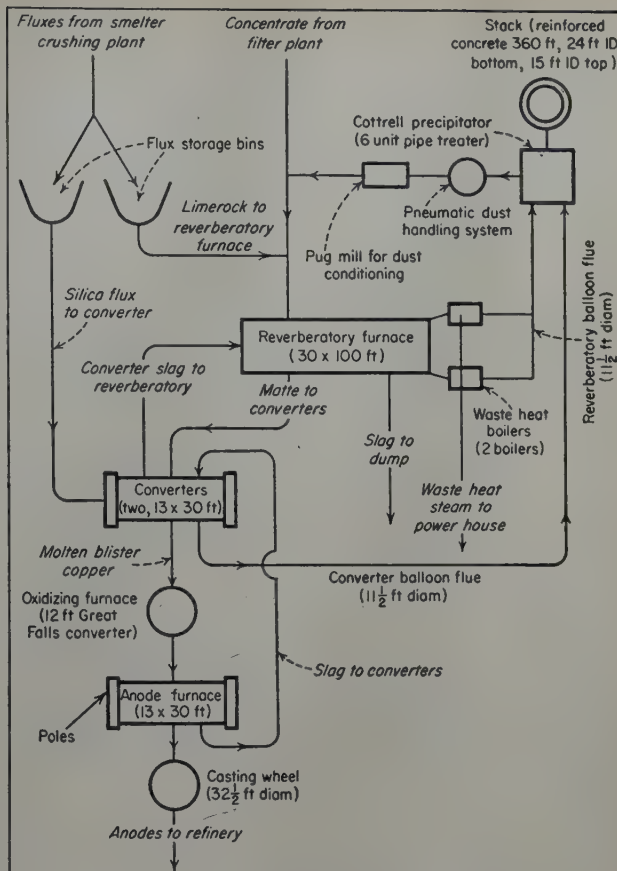


Fig. 4—The processing of the concentrate from the filter plant is diagrammed in the smelter flowsheet. The only fluxing material added to the reverberatory charge is limestone; all siliceous flux is charged to converters.

boats or containers for handling with overhead cranes.

Reverberatory Furnace

Design and Construction: The design and construction of the reverberatory furnace embodies several unusual features. The furnace, 100 ft long and 30 ft wide inside the brick walls, is mounted on a heavily reinforced monolithic concrete foundation which rests on a slab of concrete 5 ft thick. The walls of the foundation are $4\frac{1}{2}$ ft thick, with footings $8\frac{1}{2}$ ft wide that extend 2 ft below plant floor level. The top of the foundation is 11 ft above floor level. The foundation, as well as the furnace itself, is isolated on all sides, thereby avoiding transmission of expansion forces to the smelter structure that surrounds it.

The construction of a 10 ft subbase for the furnace hearth was accomplished by tamping in 3-in. layers of crushed diorite rock from the open pit, mixed with 20 pct mill tailings to fill voids. Above the subbase a $4\frac{1}{2}$ ft layer of granular magnetite, a product removed from the tailing of a New Mexico copper concentrator by magnetic separation, was tamped to dense compaction, followed by an 8 in. layer of material composed of 90 pct crushed magnetite slag and 10 pct granular magnetite. A 4 in. veneer of fire clay brick was laid on a corbel inside the foundation wall, for protection of the upper 30 in. of concrete against furnace heat.

The details of sidewall and furnace arch brick work are shown in Fig. 5. The basic crucible was tamped in 10-ft sections, using a mixture of granular periclase with minor amounts of ground periclase

Table I. Operating Data Total Plant

	Average per Mo. Tons N.M.B.M.* Treated	Pct. Copper Input, N.M.B.M.	Actual Production Average Month Salable Copper	Power Used Kw-Hr Per Ton, N.M.B.M.
1950 (6 mos.)	15,810	28.89	8,692,161	15.79
1951	21,384	25.21	10,541,756	11.21
1952 (6 mos.)	22,822	24.89	11,133,730	11.44

* New metal-bearing material.

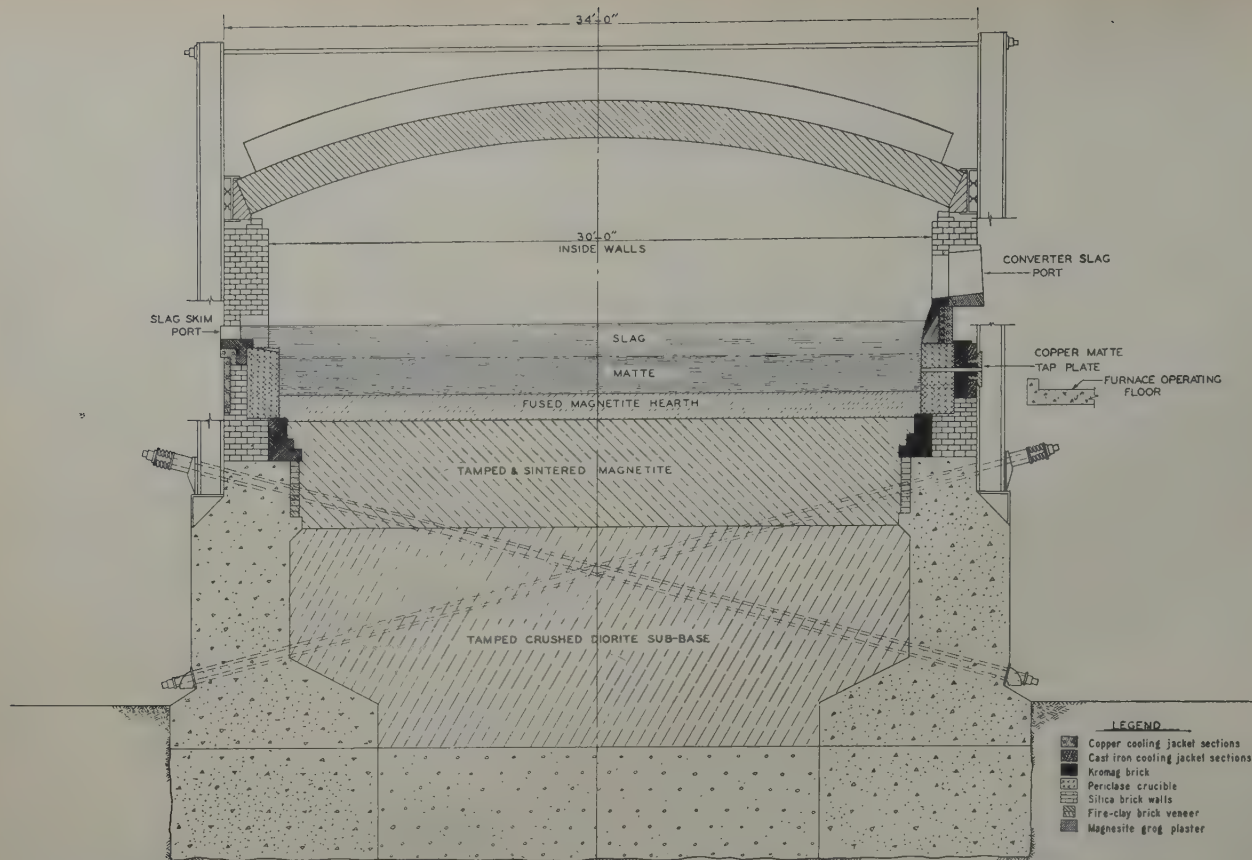


Fig. 5—Sidewall and furnace arch brickwork details, as well as the novel method of buckstay retention, are shown in this composite cross section of the reverberatory furnace. Furnace binding is of unusually heavy construction.

and fire clay, wetted with a controlled amount of sulphuric acid. Immediately above the crucible a row of copper water jackets, 20 in. high, replaces silica brick in the sidewalls extending as far as the skimming bay on one side and through the last matte tap hole on the tapping side. The 20-in. silica brick sprung arch has a span of $31\frac{1}{2}$ ft between skew-backs. The 15-in. ribs, spaced alternately 4 and 6 ft apart, permit installation of a relieving arch through two-thirds of the furnace length, if needed. Above the verb arch, uptake walls are of silica tile sectionally supported construction, and the suspended uptake arch is silica tile.

Furnace binding is of unusually heavy construction. Lateral buckstays are heavy H-beams, resting on an offset in the concrete foundation at the bottom and joined at the top to the opposite buckstay with a $2\frac{1}{4}$ in. square tie rod, threaded on both ends. Bottom thrust is taken by a heavy channel and angle box beam, running the length of the furnace, which is retained by spring loaded 2-in. tie rods extending diagonally through the furnace subbase to the bottom of the concrete foundation on the opposite side. This novel and effective method of buckstay retention is shown in Fig. 5. End binding is retained by heavy buckstays at each corner, which are tied at the bottom by $3\frac{1}{2}$ -in. rods anchored in the concrete foundation and at the top by $3\frac{1}{2}$ -in. tie rods running the length of the furnace, all of which are heavily spring loaded.

The magnetite bottom was fused in with an oil fire by regulating the admission of secondary air along the furnace walls and increasing the fuel until the entire surface had become liquid. Additional magnetite tailing was then charged through the sidewalls until a liquid pool had been formed, the surface of

which was at the desired final bottom level, about 11 in. below the center line of the matte tap holes. Firing was reduced and the magnetite bottom was allowed to solidify. At this point, molten converter slag, prepared by melting and converting concentrate in converters, was charged through converter slag launders and spread over the chilled bottom. Charging of concentrate was started at once.

Reverberatory Operations: Concentrate is received continuously during operating periods from the mill filter plant over a 24-in. conveyor belt, to which a predetermined amount of crushed limestone is added. Mixed concentrate and limestone are discharged into containers, called cans, resting on a platform scale by means of which the can and contents are weighed and the weights tape recorded. The can resembles a concrete bucket, with heavy lifting bails and sloping inner walls, at the bottom of which are double, air-operated arc gates. The capacity of a can is approximately 10 tons of charge, as-received. When the can has been filled, it is removed from the scale platform by a 20-ton overhead crane, and either set aside until needed, or transported at once to one of the six charging stations. When the charge can is in place over the charging station the bottom gates are opened and the charge fills the small hopper immediately below. A 1200-ton surge bin inside the smelter building is used to equalize mill production against smelter consumption. Concentrate delivered to this surge storage is reclaimed as needed with clamshell and overhead crane.

When the operator is ready to charge the furnace, he raises the door covering the charge port in the furnace sidewall and starts the short feeder conveyor under the charge hopper. Concentrate from the feeder falls into the feed hopper of the charging machine,

locally called the slinger. This machine is a short, high-speed portable belt conveyor pivoted on a vertical shaft that permits lateral swinging. The concentrate falls through the feed hopper onto the rapidly moving belt and, as it moves over the head pulley, is discharged into the furnace. This is illustrated in Fig. 6. The trajectory of the concentrate stream may be varied by elevating or depressing the head pulley, by means of an adjusting device, or by regulating the speed of the belt which is driven by a variable speed dc motor. The average charging rate is about 1 ton per min and the usual charge is 2 to 4 tons. Selection of charging station and timing of the charging period is largely a matter of judgment on the part of the operator, who attempts to keep the surface of the bath covered with a thin layer of unsmelted material. When visual appearance of the bath indicates the necessity, either limestone or silica fluxing material is charged to the furnace directly from cans used for that purpose. As the result of this method of charging small amounts of wet concentrate at frequent intervals, explosions caused by contact of wet charge with molten matte are completely avoided.

The normal liquid bath depth is about 42 in., with 24 to 28 in. of matte. Matte is tapped as required by converters into 175 cu ft ladles resting on electric motored trucks that are energized through the rails with 32 v dc. During the tapping period matte ladles are enclosed in cubicles located under the tap holes below the furnace operating floor which are provided with air-operated hinged doors. Two exhaust fans, one connected to the cubicle and the other to an enclosure around and above the matte launder, effectively remove all fumes from the tapping area, venting the gas to atmosphere outside the smelter building. Matte fall amounts to about 83 pct of concentrates charged.

Slag is skimmed through the furnace sidewall near the verb arch and is laundered into 225 cu ft pots. Fig. 7, a view of the reverberatory from the skimming end, shows the closing of the skimming hole. The usual practice is to skim a train load, consisting of three pots, in succession. Slag is hauled to the dump, about one half mile distant, with 25-ton diesel-electric locomotives. The slag dump is graded with bulldozers and new alignment is made with track shifters. Slag fall amounts to about 75 pct of concentrates smelted.

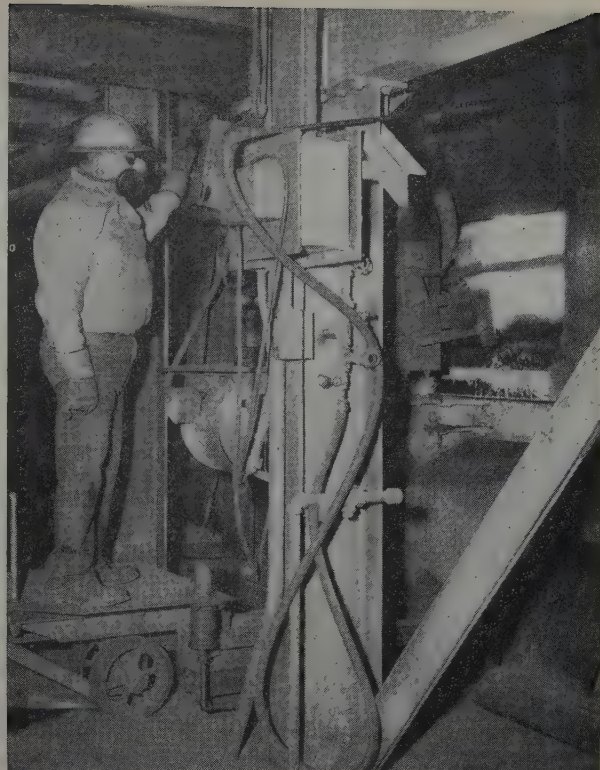


Fig. 6—Concentrate, in 2 to 4 ton charges, falls through a hopper onto a rapidly moving belt and is discharged into the reverb at a rate of about 1 ton per min. The operator regulates charging times and aims at keeping the surface of the bath covered with a thin layer of unsmelted material.

Converter slag is returned to the furnace through duplicate launders in the sidewall near the firing end. Slag inlet ports are formed by heavy, cast copper water jackets set in the brick furnace wall and are equipped with air-operated cast steel gates.

The reverberatory furnace is fired with natural gas. The original installation consisted of multiple jet burners, which functioned well except when a high firing rate was necessary. They were replaced with high pressure, locally made, barrel-type burners. Seven of the barrel-type burners spaced across the burner wall normally burn 185,000 cu ft per hr with good combustion. A view of the furnace from the burner end is shown in Fig. 8. Natural gas is received from New Mexico fields at 300 psi at the plant and



Fig. 7—After slag is skimmed through the furnace sidewall near the verb arch, the skimming hole is closed. Usually three 225 cu ft pots, a train load, are skimmed in succession.

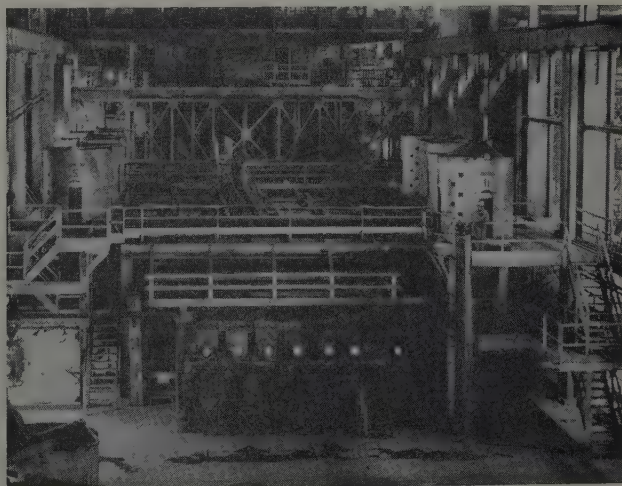


Fig. 8—Seven barrel type burners, firing 185,000 cu ft of natural gas per hr, can be seen in this view of the reverberatory furnace. Standby oil burning equipment is available for emergencies.

Table II. Reverberatory Furnace Data (Dry Ton Basis)

	1950, 6 Mos.	1951	1952, 6 Mos.
Concentrate	91,057	212,298	112,584
Limerock	6,550	12,742	4,987
Silica Flux	5,722	5,387	694
Plant Cleanup	3,085	2,364	960
Solid Charge, total	106,414	232,791	119,225
Furnace Days	175	339	170
Solid Charge per Furnace Day (dry)	608	687	701
Btu per Ton Charge x 1,000,000	6.878	6.674	6.421
Btu per Ton Net x 1,000,000	3.223	3.171	3.002
Converter Slag	51,702	135,103	78,478
Reverberatory Slag	68,857	169,401	89,822
Reverberatory Matte	70,610	168,416	92,140
Steam per ton Concentrate, lb	3,851	3,515	3,422
Waste Heat Recovery, pct	53.14	52.49	53.25

is reduced to 42 psi at the burners. The gas contains about 1100 Btu per cu ft. Standby oil burning equipment is provided for use during periods when the natural gas supply is interrupted. Low pressure oil burners are constructed to fit inside the barrel-type gas burners. Firing can be changed from gas to fuel oil in about 20 min. Furnace combustion is checked frequently by Orsat analysis and a recently installed continuous oxygen analyzer indicates the oxygen content of furnace gases at all times. Effective use of the oxygen analyzer was made possible by the development of a successful method of sampling and cleaning furnace combustion gases by Leonard Klein, research metallurgist. Furnace draft is controlled automatically through dampers in back of each waste heat boiler. An automatically operated butterfly damper was installed in the converter balloon flue to regulate distribution of draft between converter and reverberatory operations. A curtain damper across the furnace at a distance of 10 ft from the verb arch, extends from the furnace roof to about 36 in. above the normal surface of the bath. The damper is constructed of 16 water-cooled panels joined together and covered with silica slurry. The damper serves to stabilize furnace draft, checks flow of dust into boilers, and tends to box in furnace heat.

Furnace sidewalls and arch are maintained by patching with silica slurry, a method developed at Phelps Dodge Corp.'s United Verde branch. Silica is ground and slurried to 65 pct density in a modified Hardinge ball mill and the mill discharge is conveyed through a high pressure blow tank and piping system to an agitator-storage tank located above the furnace operating floor. During patching operations slurry is withdrawn from storage tank into 10 cu ft pressure tanks, to which compressed air is applied, forcing the slurry through hose and pipeline to a nozzle suitable for spraying arch or sidewall. Meas-

urements of arch thickness made twice weekly through 11 measuring holes furnish information as to location in need of patching.

Reverberatory furnace operating data are shown in Tables II and III.

Converters

The general arrangement of the converter aisle is shown in Fig. 2, and a view of the converter aisle is given in Fig. 9. The aisle is 396½ ft long and 63 ft wide. Two cranes, each equipped with a 60-ton main hoist and two 20-ton auxiliary hoists, have a span of 60 ft with crane rails 55 ft above the floor of the aisle. Main hoist dc motors are 135 hp and auxiliary hoist motors are 75 hp. All hoist drives are equipped with two magnetic brakes, one on the armature shaft extension and one on the motor pinion shaft extension. All hoisting ropes are 1 in. preformed plow-steel, with independent wire rope center construction. Crane repair platforms are provided at each end of the aisle, above which are mounted 5-ton repair cranes.

Two 13x30 ft Peirce-Smith converters were moved from the Clarkdale smelter to Ajo over Arizona

Table IV. Converter Data (Dry Ton Basis)

	1950, 6 Mos.	1951	1952, 6 Mos.
Matte	70,610	168,416	92,140
Reverts	9,707	24,735	16,550
Barren Quartz	0	6,707	6,060
Leached Tailing	18,721	43,285	22,110
Other Flux	1,717	1,603	2,094
Net Stand Days	161.75	312.60	161.60
Tons Bullion per Stand Day	164.54	202.90	207.34

highways by motor truck. These converters are spaced on 60-ft centers and are opposite the reverberatory matte tapping area. The converter shells are 1¼-in. plate, welded in 10-ft sections. Welded joints are reinforced with heavy butt straps welded to the shell on both sides. The 1-in. end plates are each stiffened with four I-beams and are retained in place with bolts and springs. Riding rings are mounted at the ends, clear of the tuyere section, and are riveted to the shell. Details of brick lining are shown in Fig. 10. Full insulation of converter shell and ends is believed to result in the retention of sufficient heat to resmelt all reverts and relatively large amounts of siliceous material in converters.

Converters are driven by 75-hp ac motors, direct connected to speed reducers and intermediate gears with a heavy pinion engaging a large gear bolted to one of the riding rings. Drive motors are equipped

Table III. Analyses of Reverberatory Operations (Pct)

	Cu	SiO ₂	Al ₂ O ₃	Fe	CaO	S	H ₂ O	Oxygen Ratio	Fe ₃ O ₄
Reverberatory Solid Charge									
1950 (6 mos.)	26.57	12.3	2.7	22.8	3.6	26.2	6.62		
1951	28.02	10.2	2.6	23.3	3.0	27.8	7.62		
1952 (6 mos.)	28.78	7.6	2.2	25.4	2.5	29.3	7.50		
Concentrate Smelted									
1950 (6 mos.)	30.27	8.0	2.5	25.7	0.5	30.3			
1951	30.41	8.5	2.6	25.3	0.3	30.4			
1952 (6 mos.)	30.21	7.2	2.2	26.8	0.2	31.8			
Reverberatory Slag									
1950 (6 mos.)	0.469	37.3	7.5	43.0	5.2	1.0	2.11		
1951	0.478	37.8	7.7	42.9	4.8	0.5	2.17		
1952 (6 mos.)	0.466	37.5	7.0	44.7	4.1	0.7	2.08		
Reverberatory Matte									
1950 (6 mos.)	38.21			33.1		25.2		8.8	
1951	38.10			32.4		25.7		7.4	
1952 (6 mos.)	37.31			33.3		25.9		6.3	

Table V. Analyses of Converter Operations (Pct)

	Cu	SiO ₂	Al ₂ O ₃	Fe	S	CaO	Fe ₃ O ₄	MgO
Converter Slag								
1950 (6 mos.)	4.42	22.3	4.5	47.1	1.8	0.7	31.7	
1951	4.74	26.6	4.9	43.5	1.7	0.8	20.4	
1952 (6 mos.)	4.76	29.8	4.7	41.9	1.6	0.6	14.8	
Leached Tailing for Converter Flux								
1950 (6 mos.)	66.7	13.9	4.2			0.8		0.9
1951	67.1	14.7	4.2			0.9		1.4
1952 (6 mos.)	67.2	14.5	4.1			0.9		1.3
Barren Quartz for Converter Flux								
1951	94.1	2.7	1.3			0.9		0.4
1952 (6 mos.)	94.8	1.7	1.3			0.7		0.3
Mixed Converter Flux								
1950 (6 mos.)	68.0	13.2	4.0	0.8		0.9		
1951	70.8	12.6	3.7	0.1		1.0		
1952 (6 mos.)	73.4	11.6	3.4	—		0.9		

with magnetic brakes and are controlled from the operating platform.

Each converter is equipped with 52 ball valve tuyeres, with 2-in. pipes rolled into the seat. The middle 16 tuyere pipes are reduced in diameter by seating a 1½-in. pipe inside the 2-in. tuyere pipe. Converter air is supplied by two 30,000 cu ft steam-driven turboblowers, located in the plant power house. Air is delivered at converters at a normal pressure of 13 psi, which may be varied by a system of controls on the converter operating platform. A warning signal is sounded when pressure drops below normal, giving the operator time to turn the converter out of stack if it is blowing. Air volume to converter will average about 25,000 cu ft per min with 30,000 cu ft per min maximum. Main blast valve is pneumatically operated and is controlled from the skimming platform. Air volume is indicated by a flow meter near the punchers platform and is recorded continuously on a meter in the converter office. Blowing time for each converter is recorded by a timing device in the office.

Converter hoods are of welded steel with cast iron liners. A sliding apron, covering the hood while the converter is blowing, is operated through an air cylinder and heavy wire ropes. A cast steel bell damper in each converter uptake just ahead of the balloon flue is raised and lowered by a motor-driven wire rope hoist. Adjustable punchers platforms are raised and lowered with a hydraulic lift. Punchers platforms and operators platforms for both converters are connected by hand-railed walkways.

Tuyere blocks are 18 in., four piece, hard-burned chrome-magnesite. Tuyere line campaigns will average about five months, finishing 12,000 to 15,000 tons of copper per set. When tuyere repair is made, brick immediately above and below tuyere line is renewed and brick is replaced in arches around the mouth, in the ends, and in the converter bottom when necessary. Steel work around the mouth is overhauled during repair periods and necessary repairs are made to silica feeders, stack, and tuyeres. Cast steel pour-

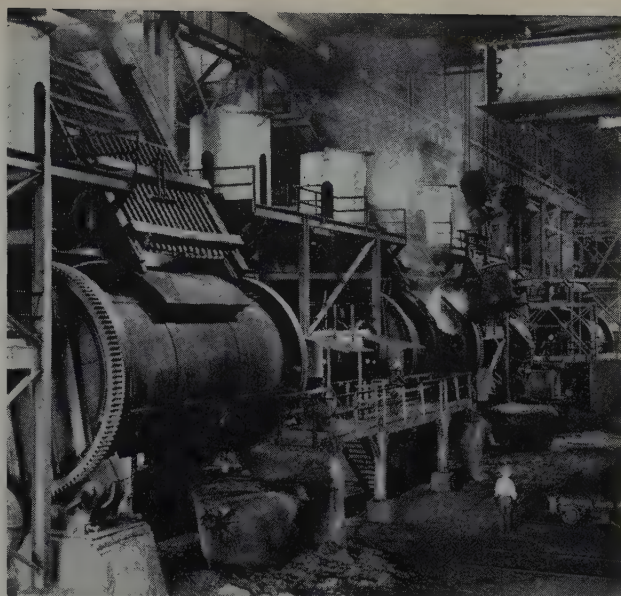


Fig. 9—Two 13x30 ft Peirce-Smith converters, finishing four charges of blister copper daily, are located in the converter aisle.

ing lips are covered with several layers of hard facing and usually last through two or three campaigns.

Normally, converters are charged with four 15-ton ladles of matte which is fluxed, blown, and skimmed, and sufficient additional matte is added to make up a charge of approximately 50 tons of blister copper. Four charges of blister copper are finished daily. Both converters are operated on the day shift and one converter only is blown on the afternoon and night shifts. Converter operating data are given in Tables IV and V.

Mixed converter flux is drawn from storage bins into cans similar to those used for handling reverberatory charge. The cans are transported by overhead crane to a platform above the converters where a charging station is located at either end of each

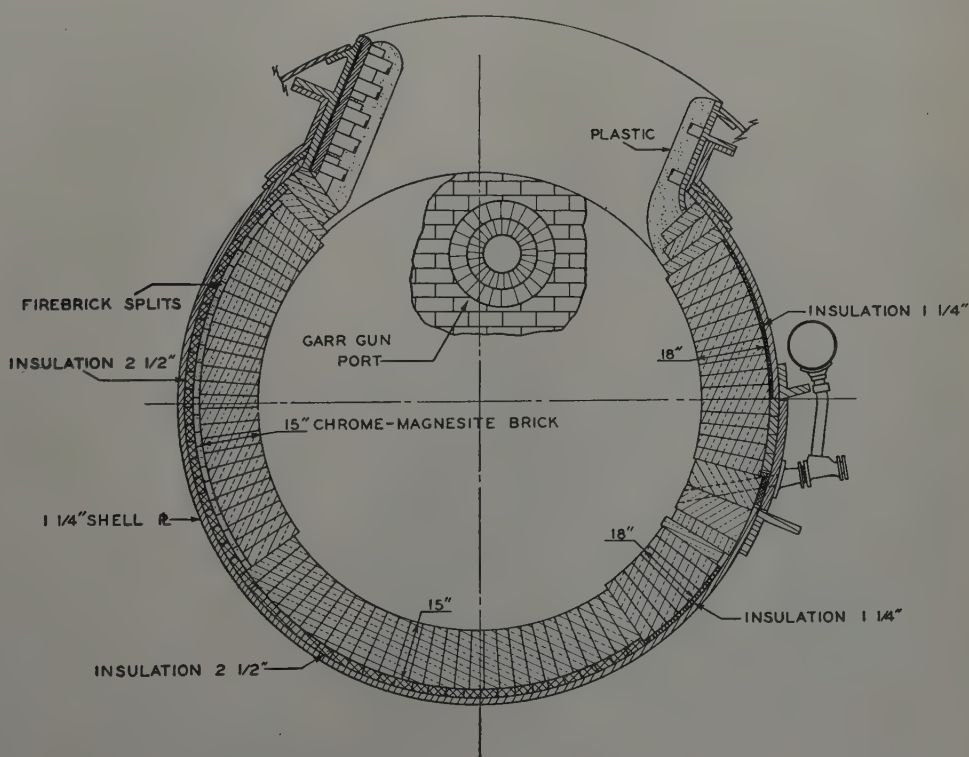


Fig. 10—Sufficient heat is retained by the full insulation of converter shell and ends, as shown in the detailed drawing of the brick lining, to resmelt all reverts.

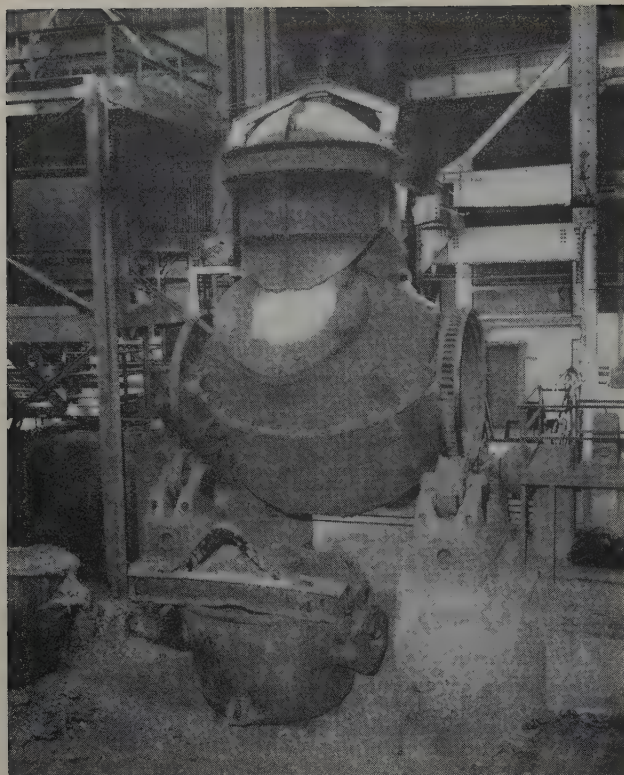


Fig. 11—Blister copper is overblown in this oxidizing and holding vessel, a remodeled 12 ft Great Falls converter. Blowing copper high in this vessel, it is believed, results in longer brick life in the large converters.

converter. The flux flows through the can bottom discharge gates into a hopper which feeds Garr guns at each end of the converter. Additional storage bins make available fluxing materials with high silica content when needed. This method of handling converter flux has been entirely satisfactory and affords considerable flexibility in regulating this phase of the operation.

Converter aisle cleanup is accomplished to a large extent with a small bulldozer. The bulldozer operator cleans the aisle itself and the area under the converters before the start of the day shift, pushing the accumulated slop and spill into a pile at one end of the aisle. Ladle shells are loosened on a copper bumping block, dumped on the revert pile, and broken up with a drop ball. The entire accumulation is loaded into 10-ton boats by crane-operated clam-shell and charged to converters as needed. Dust from converter hoppers and from the converter balloon flue is drawn into a dump truck, dumped into a large boat, and charged to converters as operating conditions permit.

Oxidizing Furnace

A departure from conventional converter practice was made at Ajo, sometime after the smelter was started, by overblowing blister copper in a separate oxidizing and holding vessel. An old 12-ft Great Falls converter was slightly remodeled and installed for this purpose, equipped with a close fitting swinging hood and a stack vented to atmosphere, as shown in Fig. 11. The converter is lined with 9-in. chrome-magnesite brick and all but four of the sixteen 2-in. tuyeres are blocked off. The opening in the converter cap was reduced in size and, to make a closer fit with the hood, the normal position of the cap on the shell was reversed. An opening was made on one side of the cap through which a gas burner is inserted for heating the vessel and the copper charge.

When a copper charge is blown to light blister in one of the Peirce-Smith converters, the final slag is dammed off with cold reverts to permit the copper to be withdrawn clean into ladles and transferred to the oxidizing furnace. The charge is blown with converter air at about 13 psi under a fairly heavy gas fire. Complete sulphur elimination in a 50-ton charge is reached in about 30 min. No slag is formed in the oxidizing operation and the overblown copper carries an average of about 5 pct cuprous oxide. Further blowing in the anode furnace is not necessary.

It is believed that blowing copper high in a separate vessel results in longer brick life in the large converters, as it generally has been felt that conditions reached during the overblowing period were destructive to converter lining. The elimination of oxide slag in converter operation is a distinct advantage, as this material is dangerous to handle and slows down the operation while being skimmed and returned to converters. When needed as such, the vessel also may be used as a holding furnace, thereby permitting greater flexibility in the operation of closely designed converting and refining equipment.

Anode Plant

The anode plant is located in and adjacent to the converter aisle, with the single anode furnace in line with the converters. Design and construction of equipment used in both the refining and the casting operations included many innovations which have contributed largely to the effective performance and economical operation of the anode plant. Anode operating data are given in Table VI.

The anode furnace, shown in Fig. 12, is 30 ft long and 13 ft diam. The shell is 1½-in. plate, welded construction. The heads are dished ¾-in. plate with a heavily reinforced ring around the circumference 11 in. wide, making a slip fit inside the shell. The heads are fastened to the riding rings with eight spring-mounted bolts to accommodate expansion. A 4-ft round opening in the shell near one end serves as a charging port for copper and as an outlet for combustion gas; the copper pouring spout is located about 90° below the charging port near the opposite end of the furnace. Unlike most rotating anode furnaces, which have a common opening for poling and release of combustion gas, the poling door of the Ajo furnace is in one end, about 3½ ft above the center line of the furnace. The 30-in. opening is provided with a heavy steel ring bolted to the head, for the protection of brick lining during the poling operation. A hinged door is closed except during the time the furnace is being poled. Small ports in either end of the furnace serve for blowing with high pressure air when necessary, or for gas burners. The anode furnace drive is similar to converter drives, except that direct current is used.

The anode furnace is equipped with a swinging hood that covers the charge opening during the poling operation and is elevated when copper is

Table VI. Anode Copper Data

	Cu, Pct	S, Pct	O ₂ , Pct	Anode Plant Data Per Ton Anode Copper	
				Poles, Lb	Fuel, Million Btu
1950 (6 mos.)	99.77	0.01	0.156	69.9	1.686
1951	99.75	0.01	0.129	64.3	0.856
1952 (6 mos.)	99.69	0.01	0.130	73.0	1.179

charged. The hood is connected to a steel stack which vents combustion gas to atmosphere through the roof of the building. The furnace is lined with chrome-magnesite brick with a 2½-in. layer of insulating material between the brick lining and the steel shell and ends. Retention of heat in the anode vessel by complete insulation results in better fuel economy as well as improved working conditions on the furnace operating floor.

As sulphur is completely eliminated from the copper charge during the blow in the oxidizing furnace, blowing in the anode furnace is limited to cleaning up the charge and skimming off a minor amount of slag just before the charge is poled.

Oak poles are unloaded from cars into a pole crib at the poling end of the furnace. Poles are raised to the operating floor with an air-operated derrick as needed and are manipulated in the furnace with a small air hoist. A heavy concrete pier immediately below the poling door is provided with rings holding a heavy chain which passes over the pole and takes the strain exerted by the hoist, thereby protecting the poling door and brick lining from damage during the poling operation.

The 700 lb anodes are cast on a 22-mold gear and pinion driven wheel. Copper from the furnace pouring spout is received in a hydraulically operated spoon and poured from it into molds at a normal rate of about 40 tons per hr, as can be seen in Fig. 13. The two dc motors driving the casting wheel are controlled on the Ward-Leonard principle, receiving power from a special dc generator. The armatures of the two 115-v motors are connected in series across the generator terminals.

Control of the casting wheel is semiautomatic. Started by push button, the wheel stops automatically when the next mold is in position under the spoon. The start of motion and acceleration is smooth enough that the wheel can be moved immediately when the mold is filled and cooling of liquid copper with an air blast is not necessary. Cooling water is applied through a series of sprays starting after the surface of an anode has chilled. Lifting pins to raise the top of the anode from the mold are actuated by a lever and roller arrangement that moves over an inclined track under the wheel. Anodes are lifted from molds by pneumatically operated tongs and dropped into one of two bosh tanks, each of which holds 44 anodes. Cooled anodes are lifted from the bosh tanks by a 15-ton overhead crane.

Because of the smooth operation of the casting wheel, rolled edges are seldom formed and little trimming is required. Anodes are carefully inspected and loaded on railroad cars with vertical-lift storage battery trucks. The concrete floor adjacent to the casting wheel, armored with cast iron grids cast into the concrete, affords ample floor space for inspection and loading and an adjoining large concrete platform is available for anode storage when copper shipments are interrupted.

Copper pouring spoons are relined after each pour with a sand-cement mixture and pouring lips are renewed. The newly lined spoon is cured several days under a gas flame and is warmed up to operating temperature before being put into service. Anode molds, weighing about 5000 lb, are cast on the wheel as required, usually before the start of a regular pour. The average life of a mold is about 450 tons of anodes. During the copper pour, molds

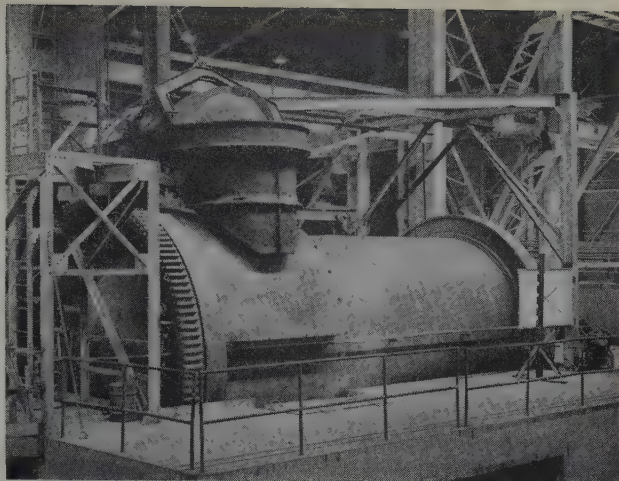


Fig. 12—The rotating anode furnace, located in and adjacent to the converter aisle, has separate openings for poling and release of combustion gas. Blowing in this furnace is limited to cleaning up the charge and skimming off some slag before poling, as all sulphur is eliminated in the oxidizing furnace.

are sprayed while hot with a silica wash to prevent anodes from sticking to the molds.

The operation of the anode plant has been satisfactory in all respects. Repairs to refining and casting equipment have been light and production of high quality anodes has been consistent. Rejection of imperfect anodes has been negligible.

Waste Heat Boilers

Combustion gases from the reverberatory furnace pass through two waste heat boilers, the inlets to which are provided with water-cooled cut off dampers, making it possible to isolate completely either boiler for inspection or repairs. The boilers are not baffled and operate with a draft loss of 0.10 in. of water from inlet to outlet. Design pressure of the boilers is 950 psig, with superheater outlet conditions at 800 psig and 750°F.

Water walls in the furnace section have a heating area of 3730 sq ft per boiler and the boiler section 11,200 sq ft, making a total of 14,930 sq ft of heating area. Normal evaporation is 50,000 lb of water per hr per boiler, with a heat recovery representing 53.0 pct of total fuel used in the reverberatory furnace. Boiler feed water temperature is maintained at 325°F and enters the boiler at 1000 psig.

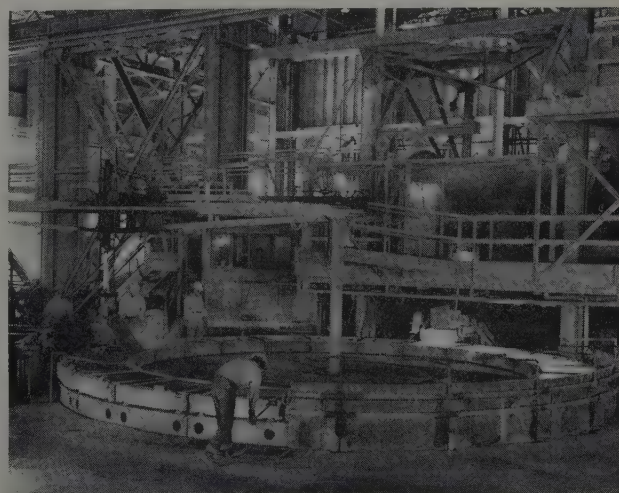


Fig. 13—Copper is cast at a rate of about 40 tons per hr into 700 lb anodes on this 22 mold anode casting wheel. Anode molds are cast on the wheel as required, and have a life of about 450 tons of anodes.

Water wall and slag screen tubes are cleaned with 24 soot blowers, while superheater elements and boiler tubes are equipped with 9 soot blowers in each boiler. Soot blowers are operated automatically from the boiler control panel, using superheated steam at 500 psig. Little hand lancing of boilers is required. Dust trapped in boilers is collected in gated hoppers and is dropped to the ground below where it is moistened with water and loaded into dump trucks. Reclaimed dust is mixed with converter flux in the crushing plant receiving bin and is resmelted in converters.

Flue System, Cottrell and Stack

Converter and reverberatory gases are discharged into separate steel balloon flues, 11½ ft in diameter. The two flues enter a common junction box at the Cottrell inlet, where a baffle system mixes the gases before entering the precipitation chamber. Heavy dust that settles to the bottom of the flues is removed by drag chains, reverberatory dust being discharged to the Cottrell blow tank system, while the converter dust is collected in a hopper from which it is removed by dump truck and returned to the converter aisle for resmelting. Stack and Cottrell temperatures have not as yet indicated the necessity for insulating either of the balloon flues.

Cottrell precipitation consists of six units of pipe treaters, each unit containing 120 12-in. vertical pipes 16 ft long. All units are parallel and down draft. The discharge electrode is a small chain suspended in the center of the 12-in. pipe. All units are hand rapped. Exit gases pass upward around the pipes and then laterally to and through the outlet flue into the chimney. A bypass flue, closed by a jug damper, may be used to pass gases directly into the treater outlet flue uptake, if necessary. Treater walls are acid-proof brick laid with acid-proof mortar.

Power to the treaters is furnished by two mechanical disk rectifiers, each of which is coupled to a 25-kva motor generator set, driven by a 40-hp motor. A third rectifier unit is available as a spare. An exciter furnishes the field for the generator. Two of the four leads from rectifier stationary shoes are connected to terminals of high voltage transformers which have taps ranging from 50,000 to 100,000 v. Normally the 62,500-v tap is used.

Converter gases entering the Cottrell treater vary over a fairly wide range, because of intermittent operation, having an average of 475°F. Reverberatory gas temperature is fairly uniform at about 495°F. Temperature of Cottrell outlet gas averages 430°F. Under present operating conditions, the volume of gas treated is approximately 340,000 cu ft per min, somewhat higher than the normal capacity of the precipitator. However treater efficiency is satisfactory, stack testing showing consistently a loss of less than ¼ of 1 pct of total plant copper input.

Cottrell dust is collected in hoppers, one under each treater unit. The dust is periodically dropped into McLeod blow tanks located under the hoppers and is pneumatically transported from one tank to another in series until it reaches the sixth tank. From the last tank in the series the dust is transported with high pressure air several hundred feet to a cyclone collector, which is equipped with wool filter bags, and is stored in a small bin. Once each shift the dust is withdrawn from the bin, moistened with spray water, put through a horizontal pug mill and delivered to the conveyor belt carrying concentrate into the smelter. Average dust recovery is about 6 tons per day.

The chimney is of tapered reinforced concrete construction, lined with acid-resisting brick laid in acid-proof mortar, and has 2 in. of fiber glass insulation between the concrete and the brick lining. The stack is 360 ft high, 24 ft ID at the bottom and 15 ft at the top. It is protected by lightning rods with copper cables to ground. A testing station is located 127 ft from the ground. At 425°F stack inlet temperature and 60°F outside temperature, total stack draft is 1.70 in. of water. Draft drop through the Cottrell plant is 1.10 in., and the remainder is divided between reverberatory and converter operation by automatically regulating the butterfly damper in the converter balloon flue.

Smelter Organization and Maintenance

Smelter operation is under the control of the general smelter foreman. The reverberatory, converter, and anode departments each have a general foreman, with shift foremen on each of the operating shifts. The crushing plant, mason crew, and Cottrell plant each have a day shift foreman. Testing work is carried on by the smelter engineer.

The reverberatory furnace floor is flushed with water each shift. Grated drainage openings connect with a launder system which discharges all floor cleanings into a concrete sump. A motor-driven pump, actuated by a float switch, delivers the accumulated washings to a concentrate storage tank from whence it is pumped periodically to the mill filter building and joined with current concentrates for return to the smelter. The concrete anode operating and trimming floor, the copper loading dock, and the area behind converters is swept daily with a power sweeper. The area under converters and the converter aisle is cleaned daily with a small bulldozer.

A small repair crew is maintained to take care of running repairs and minor alterations. Major repairs and alterations are handled by the general plant shops which also take care of mine and mill heavy maintenance work.

Summary

After more than two years of entirely successful operation, performance of the Ajo smelter, both from a metallurgical and an economical standpoint, clearly demonstrates that the original objectives have been satisfactorily achieved. Day to day smelting of concentrator output has resulted in a straight flow of copper-bearing material from the mine to finished anodes. Attainment of a relatively high smelting rate through the single reverberatory furnace and a high rate of copper production per man-shift has resulted in an overall cost of producing anodes from concentrates that is favorably comparable with costs achieved in the Corporation's multifurnace copper smelters.

Acknowledgments

The author of the general plan of the Ajo smelter was Charles R. Kuzell, General Manager of Phelps Dodge Corp., who also was responsible for the introduction of numerous innovations in smelting practice and design of smelter equipment. The development of these ideas was carried out by the Western Engineering Dept., under the direction of H. V. Kruse, Chief Mechanical Engineer. Structural design, and the design or selection and arrangement of electrical and auxiliary mechanical equipment and the construction program was under the direction of Wilbur Jurden, Consulting Engineer, New York. Mr. Jurden was represented in the field by Stewart Carpenter, Construction Engineer.

Effect of Dissolved Sulphur on the Surface Tension Of Liquid Copper

by C. F. Baes, Jr. and H. H. Kellogg

The effect of dissolved sulphur on the surface tension of liquid copper has been measured by a sessile-drop method at 1120°C. Sulphur is highly "surface active" in liquid copper; the surface tension lowering is about 650 dynes per cm for a sulphur content of 0.6 pct. The degree of adsorption of sulphur on the liquid copper surface has been calculated, and various models of the surface layer have been tested against the results.

THE science and technology of surface chemistry and physics at room temperature are relatively advanced, and the engineer possesses a background of information that allows him to predict and control many phenomena—such as frothing, emulsification, wetting of solids by liquids, flow through capillaries, adsorption, mineral flotation, penetration of porous bodies by liquids—which are related to the behavior at interfaces. Surface phenomena in high temperature systems are probably of equal importance to the metallurgist and ceramist, but at present are incompletely understood. Frothing of liquid slags, penetration of refractories by liquid metals and slags, infiltration of powder metallurgy "skeletons" by liquid metals, bonding of metals to ceramic oxides in the manufacture of "cermets," wetting of one metal by another for purposes of soldering and welding, are but a few of the many phenomena of metallurgy that are controlled by surface behavior.

Concerning the most elementary of surface properties—the gas-liquid surface tension—the existing data on liquid metals are inadequate. For the surface tension of "pure" metals the results of different investigators differ by 10 or 20 pct. The role of surface-active agents in liquid metals is relatively unknown, and it is not unlikely that the discrepancy in the values for the surface tension of pure metals is due to the presence of traces of surface-tension-lowering impurities in the samples. Based on analogy to room-temperature systems, the highly surface-active impurities in liquid metals should be

elements or compounds of limited solubility in the liquid metal and possessing considerably weaker intermolecular bonding forces than the metal itself. The nonmetals of the V, VI, and VII groups of the periodic table might be expected to act in this way.

The experimental work in this paper represents a study of the surface tension of pure liquid copper in hydrogen at 1120°C, and the effect of dissolved sulphur (which is a strongly surface-active agent in liquid copper) on the surface tension of copper. The Gibbs equation has been applied to the results and an attempt made to correlate the surface tension behavior with two models of the interfacial layer.

The sessile-drop method for surface-tension measurement at high temperatures which was used in this investigation has been described by several investigators.^{1,2} It involves the measurements of the dimensions of a stationary liquid drop on a horizontal surface. From these dimensions and the liquid density, the surface tension of the liquid may be calculated either by means of various approximate formulas, or more accurately by means of the Bashforth and Adams tables.³ For liquid drops which exhibit a contact angle greater than 90°, by far the simplest dimensions to measure are those indicated in Fig. 1, i.e., the diameter of the maximum horizontal cross section ($2X$) and the maximum height (Z) above this plane. In order to calculate the contact angle and the volume of the drop, the diameter at the base of the drop ($2a$) and the total height (h) also must be measured.

Upon investigation of the literature, the authors failed to discover a concise statement of the accuracy of the method when used in conjunction with the Bashforth and Adams tables, hence a careful examination of the tables was made and the curve shown in Fig. 2 was constructed. The "error factor," plotted as the ordinate, is the factor by which the

C. F. BAES, JR. is Research Chemist, Oak Ridge National Laboratory, Oak Ridge, Tenn., and H. H. KELLOGG, Member AIME, is Associate Professor of Mineral Engineering, School of Mines, Columbia University, New York.

Discussion on this paper, TP 3497DE, may be sent, 2 copies, to AIME by July 1, 1953. Manuscript, Oct. 10, 1952. New York Meeting, February 1952.

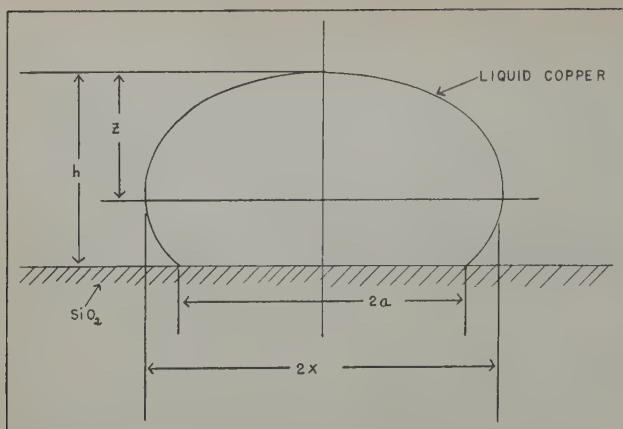


Fig. 1—Diagrammatic representation of a sessile drop of liquid copper on a solid surface.

uncertainty in the experimental measurement X/Z (Fig. 1) is multiplied to obtain the uncertainty in the calculated surface-tension value (assuming no error in the liquid density). The curve clearly indicates the desirability of using drops of the maximum convenient size (thus of the maximum X/Z value).

Experimental

The experimental method involved the following steps: 1—the formation of a sessile drop (of approximately known sulphur content), at 1120°C under hydrogen, in a vacuum-tight furnace tube; 2—photographing the incandescent sessile-drop by means of a fixed-focus camera; 3—measurement of the resulting plates by means of a microcomparator; 4—microanalysis of the solidified drop for sulphur.

Apparatus: The furnace-tube assembly (Fig. 3) consisted of a fused-silica tube ($1\frac{3}{8}$ in. ID, $1\frac{3}{4}$ in. OD x 30 in.) with standard taper, 45/50 male joints ground at each end, which provided a vacuum-tight seal when assembled with the water-cooled female joints. The lubricant used in these joints (Apiezon "N" grade stopcock grease) retained its consistency when the furnace was in operation, provided cooling water was passed through the water jackets continuously. The temperature of the central portion of the furnace tube was controlled to $\pm 3^{\circ}\text{C}$ by means of a Brown temperature-controller activated by a chromel-alumel thermocouple inserted in a silica thermocouple tube. The thermocouple tube

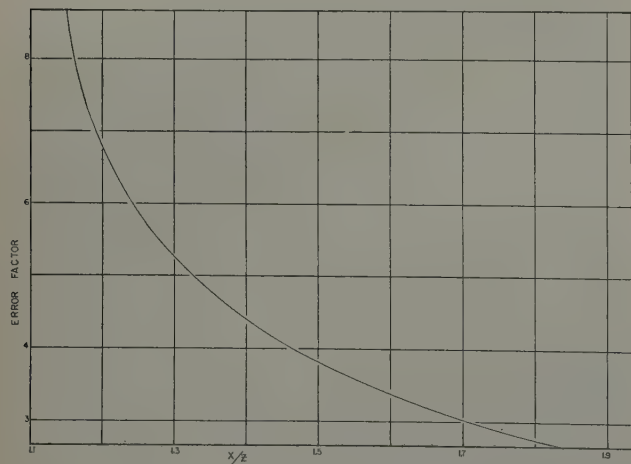


Fig. 2—Error factor as a function of the drop dimensions, X/Z .

contained a silica-pyrex graded seal near the ground joint. The thermocouple was repeatedly checked by noting the temperature reading at which the copper sample began to melt (melting point, 1083°C). The resistance furnace was constructed of a nichrome-wound alumina core packed in insulating brick. The pumping system consisted of a fore pump and a three-stage oil diffusion pump. The all-glass vacuum system, used in conjunction with the vacuum furnace, contained a CaSO_4 and a P_2O_5 drying column through which H_2 was introduced, a Töpler pump for regulating gas pressures, and a McCleod gage. The entire system could be easily pumped down to a "stick" vacuum when the furnace tube was at room temperature; however, when the furnace tube was at 1120°C , the ultimate vacuum obtainable, as indicated by the McCleod gage, was of the order of 10^{-5} mm of Hg.

The Optical System: The incandescent sessile drop was viewed through an optically flat window (surfaces parallel to 30 sec of arc) cemented at the end of the furnace-tube assembly with "Glyptal" cement. For the production of a well-corrected image, it is essential that such a window have optically flat surfaces of good parallelism. The camera, which was mounted directly behind the furnace-tube assembly, consisted of an F:9 "Artar" apochromatic photoengraving lens of focal length 14 in., and a plate holder mounted at opposite ends of a brass tube. Focusing was accomplished by means of a screw-thread adjustment which permitted the entire camera assembly to be moved parallel to the optical axis. The plate distance was fixed at about 42 in., giving an object distance of approximately 21 in., and a magnification of about 2.

Due to the sensitivity of the highly fluid molten drops to vibration, it was found necessary to place the bench, on which the apparatus was mounted, upon sponge-rubber mats.

Preparation and Purification of Materials: All of the copper samples used in these measurements were cut from a single piece of highly purified electrolytic copper, supplied by the Research Dept. of Phelps Dodge Corp. The reported analysis indicated that all impurities other than oxygen totaled 0.0053 pct. Each sample was first cleaned in 1:1 HNO_3 , then in 1:1 HCl , and finally rinsed in distilled water. Copper-plated tools were used in all subsequent handling of the sample. The Cu_2S was prepared by first precipitating CuS from dilute sulphuric acid solution of reagent grade $\text{CuSO}_4 \cdot 5\text{H}_2\text{O}$ with H_2S . The filtered and washed precipitate was then mixed with sulphur and ignited in an alumina crucible at 1200°C for 30 min. Analysis of the resulting matte indicated 21.7 pct S.

Experimental Procedure: The weighed sample strip (1 to 3 g) was wound into a tight spiral and placed on the plaque, a 1x1 in. clear-silica plate polished to a mirror finish. A weighed amount of Cu_2S was deposited within the center of the spiral, the plaque and sample were placed on the silica plaque support and moved to the center of the furnace tube. The apparatus was assembled, opened to the vacuum pumps, and the heating current was turned on. During the heating period, the plaque surface was carefully leveled by rotating the furnace tube about its axis until tests of the image on the ground glass, using a small level, indicated the surface of the plaque to be horizontal in the direction at right angles to the optical axis. Leveling of the plaque along the optical axis could be accomplished by

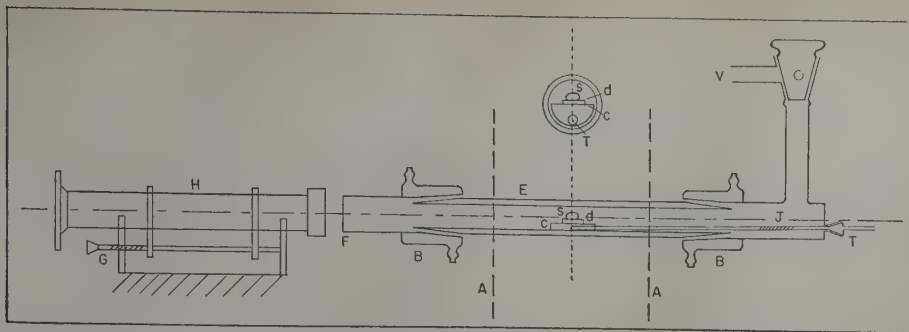


Fig. 3—Sketch of the apparatus for sessile-drop measurements. (Not to scale)

- | | |
|-------------------------------|-------------------------|
| A—Section enclosed by furnace | F—Optical window |
| B—Water-cooled pyrex joints | G—Camera focusing-screw |
| C—Plaque support (silica) | H—Camera |
| D—Silica plaque | T—Thermocouple well |
| E—Silica furnace-tube | |

slightly raising or lowering the free end of the furnace-tube assembly, and then focusing on the ground glass the front and back edges of the plaque to check their relative heights. The system was pumped out continuously until the temperature reached 700° to 800°C and then was flushed with several batches of dry hydrogen. The hydrogen pressure was finally adjusted to 50 mm Hg. The heating rate was decreased when the melting point was reached since it was found that movement of the sample, caused by rapid and uneven melting, often resulted in the sample falling off the plaque. The drop was maintained at 1120°C for 15 min before the first photograph was taken. The image of the drop was very carefully focused on the ground glass with the aid of a 15-X microscope eyepiece placed on the clear central portion of the glass. Focusing at full aperture could be done with an accuracy of at least $\pm \frac{3}{4}$ turn of the focusing screw (± 0.64 mm) which permits a reproducible magnification to within ± 1.2 parts per thousand. Usually two photographs were taken at a 15-min interval. Immediately after the last exposure, the heating current was turned off and the system cooled to room temperature. Kodak "M" plates ($3\frac{1}{4} \times 4\frac{1}{4}$ in.) were used with an exposure of $\frac{1}{2}$ sec at f:16, and were developed in Kodak "Microdol."

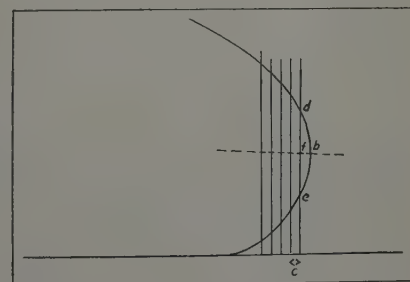
Measurements and Calculations: The microcomparator (a "Toolmaker's Microscope," manufactured by Bausch and Lomb) used in this work was provided with micrometer screw adjustments for measuring both horizontal and vertical distances on the plates. The plate to be measured was mounted on the instrument with the base of the drop-image parallel to the horizontal axis of the stage. The only measurement which presented any difficulty was that of Z (Fig. 1). Because of the uncertainty in locating the vertical coordinate of the tangent point, it is by far the less accurate of the two measurements required for the surface tension calculation. The procedure which was used to locate the point b is as follows (cf. Fig. 4): The horizontal micrometer screw was adjusted until the vertical cross hair was coincident with the edge of the drop in the region of the tangent point. The plate was then moved horizontally a distance c (e.g., 0.005 in.), such that the vertical cross hair intersected the drop surface above and below the tangent point. The vertical coordinates (d and e) of these intercepts were measured; then the stage was again moved horizontally the fixed distance c in the same direc-

tion and the new intercepts read. The process was repeated until five sets of coordinates were obtained for each side of the drop. The coordinate f in Fig. 4 is the mean value of the coordinates d and e . Corresponding f values for each edge of the drop were averaged and plotted against the distance the vertical cross hair had been displaced from the edge of the drop. The resulting nearly straight line was extrapolated to zero to obtain b . The reproducibility of the Z values obtained in this way was about 4 to 6 ppt (parts per thousand), while the X values could be measured to at least 1 ppt. The accuracy of the $2a$ and h values (Fig. 1) was limited to approximately 5 ppt by the relatively poor definition of the image in the region of the base of the drop. The calculation of the data, while straightforward, is too lengthy to be presented here. The method is described by Ellefson and Taylor.¹ A liquid-density value of 7.90 g per cu cm was used in all the calculations.⁴ While the presence of 0 to 0.8 pct S in liquid copper will quite probably change the density, it is believed that this effect will be quite small. Attempts were made to determine the density of the individual liquid drops by calculation of the volume and measurement of the weight of the solidified drops, but the results were scattered and generally low. The lack of precision, while caused in part by the poor accuracy of the a and h values, resulted mainly from gas bubbles trapped within the drop at the liquid-solid interface (*vide infra*).

Experimental Results: Surface tension measurements of liquid copper drops containing 0.0055 to 0.83 pct S, as well as measurements on pure copper drops, are presented in Table I. The surface tension lowering, F , is plotted as a function of final sulphur concentration in Fig. 5.

Preliminary sessile-drop measurements, made by means of a less refined apparatus, served to show that the surface tension of copper in vacuo is not

Fig. 4—Sketch showing method of locating the vertical coordinate of the tangent point on a liquid drop.



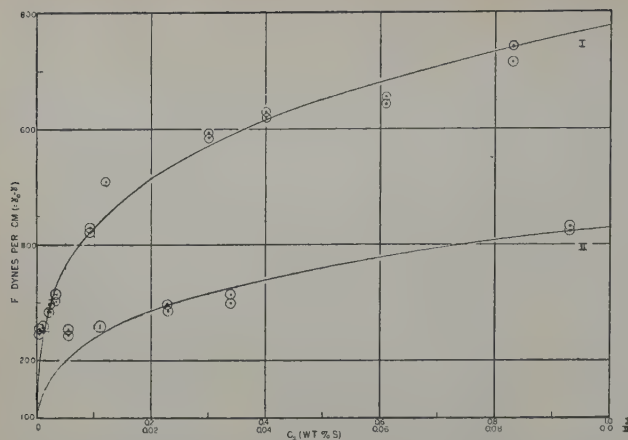


Fig. 5—Surface-tension lowering, F , of liquid copper as a function of the sulphur content. Circles are experimental points; the solid line is calculated from the relation: $\log C_s = 3.9 \log F - 11.27$.

greatly different from the values shown in the table for the sulphur-free samples. Measurements in the presence of nitrogen and argon were inconclusive because of traces of oxygen in the system, partly as impurities in the gases and partly from the permeability of the silica tube to air at the operating temperature. The presence of a trace of oxygen in the system led to irreversible slagging at the copper-silica interface and a dull appearance of the cooled drop. This slagging was a remarkable effect in that the cooled drop adhered to the plaque so strongly that when it was pried loose a quantity of silica adhered to the base of the drop. On the basis of the less accurate measurements, it appears that in cases of appreciable slagging, the surface tension of copper is lowered about 100 to 300 dynes per cm. Only when the sample was melted in hydrogen was slag formation eliminated. While the cooled drop often adhered to the plaque, it usually could be removed easily, leaving the silica surface unaffected, and the copper surface smooth and shiny. The variability of the contact angles listed in the table may be caused in part by traces of slag formation, but the agreement among the three runs on pure copper indicates the surface tension effect to be small.

With one exception, chemical analyses* of the

* These microanalyses were performed by Dr. C. Tiedcke, Teaneck, N. J. An accuracy of ± 2 pct of the absolute value is claimed.

cooled drops indicate that an appreciable loss of sulphur occurred during the course of each run. Rough calculations, based on the Cu_2S volatility data of Hsiao and Schlechten,⁶ indicate that losses due to volatilization and decomposition of Cu_2S during the heating period, prior to the introduction of hydrogen were not appreciable.

While considerable losses of sulphur to the gas phase may be expected as a result of the reaction



calculations based on the data of Sudo⁶ and Rosenqvist⁷ for the equilibrium of the reaction



indicate that after the sample has melted the total amount of H_2S in the gas phase would, in general, decrease to less than 2 pct of the sulphur content of the drop. However, inspection of the furnace tube after each run revealed small deposits of copper and copper sulphide which had condensed on the cooler

portions of the inner wall. In addition, appreciable amounts of material were thrown off from the sample during the melting process, even when the heating rate was reduced to a practical minimum. It is probably this effect, along with transfer of sulphur to the cooler portions of the furnace tube, which is primarily responsible for the generally lower final sulphur contents, especially since the undissolved Cu_2S in a partially melted sample floats on the molten surface as small crystals which are easily thrown off by surface eruptions. To decrease transfer of sulphur to and from the walls, the tube was frequently cleaned (with only partial success) and generally the runs were made in order of increasing sulphur content. An exception to this procedure was run No. 4. While this run was preceded by careful cleaning of the tube, it is apparent that sulphur was transferred to the drop during the run. The final sulphur content of the samples has in every case been taken as that corresponding to the measured surface tension values, since the good agreement between the duplicate surface tension measurements for each run indicates that no appreciable change in sulphur content occurred after the sample had melted, and since little change in composition could occur after the cooling drop had solidified.

The dimensions of a given drop often changed considerably between successive photographs in such a way as to suggest that a gas bubble was trapped in the drop. Indeed upon examination of the solidified drop, large cavities were often found at the metal-silica interface. In view of the large contact angles found for these drops, it is not surprising that such gas bubbles are stable. However, their presence would not be expected to affect the measured surface tension of these drops and, indeed, this is borne out by the general agreement between the values found for a given sample at successive time intervals.

It is clear from Fig. 5 that the presence of sulphur as an impurity in the pure copper samples would affect the surface tension values, and make necessary an additive correction to all of the F values. However, such a correction would not affect the

Table I. Surface Tension of Liquid Copper

Temperature = $1120^\circ \pm 3^\circ\text{C}$ Atmosphere = 50 mm (Hg) of H_2

Run No.	Sulphur, Pct		Surface Tension, Dynes per Cm	Surface Tension Lowering, Dynes per Cm, F	Calculated Contact Angle, Degrees
	Start	Final			
1	—	—	1250 ± 20	1269 ± 20	132
2	—	—	1288 ± 20		138
3	—	—	1290 ± 20		131
			1264 ± 20	0	152
4	0.00065	0.0055	1250 ± 20	244	163
			1025 ± 13	253	
5	0.0126	0.011	1016 ± 13	257	172
			1012 ± 15	260	172
6	0.0225	0.023	1009 ± 15	286	164
			983 ± 13	298	171
7	0.0429	0.034	971 ± 13	301	158
			968 ± 14	316	
8	0.122	0.093	953 ± 14	430	155
			839 ± 11	422	156
9	0.227	0.12	847 ± 11	511	167
			758 ± 9	510	167
10	0.375	0.30	759 ± 9	593	155
			676 ± 11	586	154
11	0.564	0.40	683 ± 11	630	169
			639 ± 9	618	166
12	0.754	0.61	651 ± 9	656	165
			613 ± 9	642	164
13	1.06	0.83	627 ± 10	740	154
			529 ± 7	714	156
			555 ± 7		

quantity dF/dc , which appears in the Gibbs equation. Impurities other than sulphur in the pure copper sample, will likewise have a negligible effect on dF/dc , since they are present in virtually the same concentration in all of the samples.

The uncertainties indicated in the table for the surface tension values have been obtained by use of the curve in Fig. 2. The corresponding uncertainties in the surface tension lowering, (F), are represented approximately by the size of the circles in Figs. 5 and 6.

Discussion of Results

The value listed in Table I for the surface tension of pure copper in hydrogen at 1120°C (1269 dynes per cm) is considerably higher than previously reported values. Thus, Sauerwald, et al.⁸ report 1150 dynes per cm at 1115°C; Becker, Harder and Kornfeld,² who used the sessile-drop method with the sample in argon, find 1038 dynes per cm at 1150°C. Since the effects of various gases such as nitrogen, hydrogen, and argon on liquid-metal surface tensions are by no means well known, it is not possible at this time to compare critically these different values for copper. However, when conflicting values of surface tension of a pure liquid are encountered, the highest value should be preferred, since traces of impurities may well lower the surface tension appreciably, but can have only a negligible effect toward raising it.

Application of the Gibbs equation to the system Cu-S-H at constant temperature leads to the result

$$-d\gamma = dF = \Gamma_1 d\mu_1 + \Gamma_2 d\mu_2 + \Gamma_3 d\mu_3 \quad [3]$$

wherein Γ_1 , Γ_2 , and Γ_3 denote the excess surface concentrations of copper, sulphur, and hydrogen, and μ_1 , μ_2 , and μ_3 denote the partial molal free energies of the three components. For the dilute solutions of sulphur used in the present experiments it may be assumed that the activity of copper is constant. The results of Schuhmann and Moles⁹ establish that even in a saturated solution of sulphur in liquid copper at these temperatures, the H_2S/H_2 ratio in equilibrium with the solution is approximately 4×10^{-3} . Since the present experiments were conducted at a constant H_2 pressure (50 mm Hg), the hydrogen activity in the system may reasonably be assumed constant. Thus, Eq. 3 reduces to

$$dF = \Gamma_2 d\mu_2 \quad [4]$$

By incorporating the approximate proportionality of the sulphur activity to the sulphur concentration, reported by Rosenqvist⁷ and Sudo,⁶ Eq. 4 becomes

$$dF = \Gamma_2 RT d \ln C_2 \quad [5]$$

where C_2 denotes the pct S in the liquid copper. This is the so-called approximate form of the Gibbs equation. Two rearrangements of Eq. 5 will aid in the correlation of the data:

$$\frac{dF}{dC_2} = \frac{\Gamma_2 RT}{C_2} \quad [6]$$

$$\frac{d \ln C_2}{d \ln F} = \frac{F}{\Gamma_2 RT} \quad [7]$$

In low temperature systems it is often the case that F is proportional to C_2 at low concentrations. Thus in Eq. 6 dF/dC_2 may be replaced by F/C_2 and the following relation is obtained:

$$\frac{F}{\Gamma_2} = RT, \text{ or } FA_2 = RT \quad [8]$$

where A_2 is the reciprocal of Γ_2 , or the area per mol of adsorbed material. Systems which behave according to Eq. 8 have been interpreted on the basis of a surface film of the order of one molecular diameter in thickness in which the adsorbed substance behaves as an ideal two-dimensional gas.

It is evident from Fig. 5, where F is plotted as a function of C_2 , that even in the very low concentration region, the relation of F to C_2 is far from linear. The ideal two-dimensional gas model, represented by Eq. 8, is, therefore, not applicable to these data.

In Fig. 6, the data are plotted as $\log C_2$ vs $\log F$. Within the uncertainty of the data, the relation is

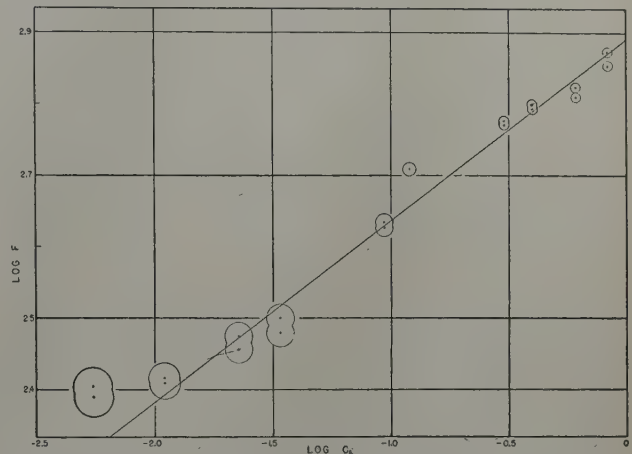


Fig. 6—Log F vs $\log C_2$. Circles are experimental points. The straight line is expressed by: $\log C_2 = 3.9 \log F - 11.27$.

linear with a slope of 3.9. The deviation shown by the lowest point is not serious in view of its uncertainty. The deviation of the point at 0.12 pct S might well be disregarded on the grounds that the sulphur analysis for this sample is anomalous; thus, it is much lower relative to the starting composition for this run than are any of the other analyses. The curves in Fig. 5 have been constructed from the straight-line plot in Fig. 6 ($\log C_2 = 3.9 \log F - 11.27$) and the fit is quite satisfactory except for the two points already mentioned.

If the experimentally found value of $d \ln C_2 / d \ln F$ is now incorporated in Eq. 7, the following relation is obtained:

$$3.9RT = \frac{F}{\Gamma_2}$$

or

$$3.9RT = FA_2 \quad [9]$$

Eq. 9, which correlates the present data, bears a formal relationship to the Schofield and Rideal equation¹⁰

$$F(A_2 - B) = iRT \quad [10]$$

which purports to describe the behavior of a non-ideal gaseous adsorbed-film on a liquid surface. In Eq. 10 B is a constant which represents the limiting area of the surface-active material, and $1/i$ is a measure of the lateral molecular-cohesion. Eq. 9 reduces to Eq. 10 if B is zero and i is 3.9. A value of i greater than unity is meaningless, however, since it would indicate a molecular repulsion rather than a cohesion, hence the Schofield-Rideal equation does not aid in the interpretation of the present results.

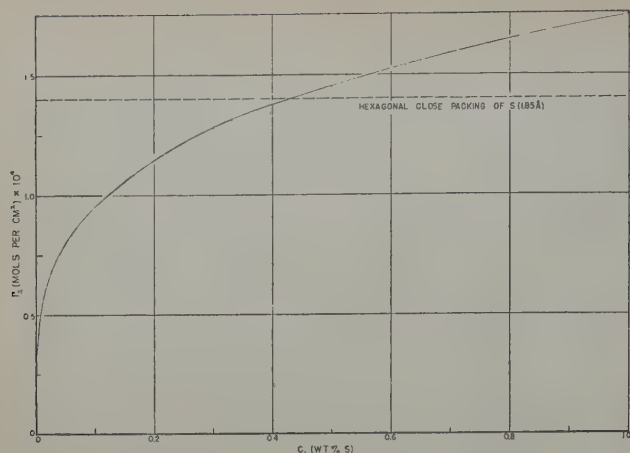


Fig. 7—The surface-excess concentration of sulphur, Γ_2 , as a function of the bulk concentration of sulphur, C_2 . Calculated from the relation: $\Gamma_2 = KC_2^{1/3.9}$. The horizontal dashed line represents the surface-excess concentration of sulphur which would result from a close-packed monolayer of sulphur atoms.

The relation between the bulk concentration, C_2 , and the surface excess-concentration, Γ_2 , which applies to the present data may be derived as follows:

From Eq. 9

$$\log \Gamma_2 + \log 3.9RT = \log F \quad [11]$$

If Eq. 11 is combined with the experimental relation

$$\log C_2 = 3.9 \log F - 11.27$$

the result is

$$\log \Gamma_2 = \frac{1}{3.9} \log C_2 - \log 3.9RT + \frac{11.27}{3.9}$$

or

$$\Gamma_2 = KC_2^{1/3.9} \quad [12]$$

where $K = \frac{782}{3.9RT}$ and has the value 1.74×10^{-9}

when R is expressed in ergs per mol per °K. Fig. 7, which shows graphically the relation between C_2 and Γ_2 , was calculated from Eq. 12.

Based on the recent measurements of Rosenqvist⁷ and Schuhmann and Moles⁸ the solubility of sulphur in liquid copper is probably about 1 pct at 1200°C. If this value is used without correction for the present work at 1120°C, then Fig. 7 indicates the maximum surface excess of sulphur to be 1.74×10^{-9} moles per sq cm. This compares favorably with the value expected for a hexagonal close-packed monolayer of sulphur atoms — 1.4×10^{-9} moles per sq cm (calculated with a van der Waals radius of 1.85Å), represented by the horizontal dashed line in Fig. 7. In all probability the surface excess of sulphur is not confined to a monolayer, hence the fact that the calculated surface excess exceeds the amount that can be held in a close-packed monolayer does not invalidate the results.

The adsorption equation (Eq. 12) found to apply to the present data is identical to the Freundlich adsorption isotherm, and is similar in form to the equation which represents the distribution equilibrium of a solute between two phases when the solute is associated in one phase into groups of n atoms (n is 3.9 in Eq. 12). This suggests one possible model which would correlate the results in the Cu-S adsorption system. If the sulphur in the bulk solution is associated into groups containing four atoms of sulphur, while the sulphur in the surface film is un-

associated, then the distribution between the bulk and the surface would take the form

$$k = \frac{\text{activity of sulphur in bulk}}{(\text{activity of sulphur in surface})^4}$$

Assuming a Henry law relationship to apply,

$$k' = \frac{C_2}{\Gamma_2^4}, \text{ or } \Gamma_2 = k'' C_2^{1/4} \quad [13]$$

Association of sulphur into groups of four atoms is unlikely, however, in view of the results of Sudo⁶ and Rosenqvist⁷ on sulphur activity.

A further correlation that may be significant is the near equality of the free-surface energy of ad-

sorption per atom of sulphur, $\frac{3.9RT}{N_{\text{avg}}}$, which is

7.5×10^{-13} ergs, and the free surface energy of pure liquid copper per atom of copper, which is 7.8×10^{-13} ergs.[†] The agreement between these values suggests

[†] The number of copper atoms per sq cm of surface = $0.918 \left[\frac{N_{\text{avg}} \cdot d}{M} \right]^{2/3} = 1.63 \times 10^{15}$, where d is the liquid density and M the atomic weight of copper. The factor 0.918 is a packing factor for hexagonal closest packing.

$$\frac{\text{Surface tension of pure copper}}{\text{No. of copper atoms per sq cm}} = \frac{1269}{1.63 \times 10^{15}} = 7.8 \times 10^{-13} \text{ ergs.}$$

that, atom for atom, the adsorbed sulphur dissipates nearly all of the free electrovalent forces of copper which give rise to the surface tension.

More experimental data on this and similar systems are needed in order to establish a consistent model for the surface-active behavior of the group VI elements in liquid copper. Preliminary experiments with selenium as an impurity¹¹ have shown this element to behave in a manner almost identical to sulphur. Experiments with oxygen as the impurity have failed due to inability to find a solid surface which is inert towards liquid copper containing dissolved oxygen.

Acknowledgment

The authors wish to express their appreciation to the Eugene Higgins Trust, for the financial assistance which made this work possible. Thanks are due to M. D. Hassialis and N. Arbiter who criticized the manuscript.

References

- 1 B. S. Ellefson and N. W. Taylor: *Journal Amer. Ceramic Soc.* (1938) **21**, pp. 193-205.
- 2 G. Becker, H. F. Harders, and H. Kornfeld: *Arch. Eisenhüttenw.* (1949) **20**, p. 363.
- 3 F. Bashforth and J. C. Adams: *An Attempt to Test Theories of Capillarity*. (1883) Cambridge University Press.
- 4 *Metals Handbook* (1948) p. 903. Cleveland. ASM.
- 5 C. M. Hsiao and A. W. Schlechten: *Trans. AIME* (1952) **194**, p. 65; *JOURNAL OF METALS* (January 1952).
- 6 K. Sudo: *Sci. Rep. Res. Inst. Tohoku Univ.* (1950) **A2**, No. 3.
- 7 T. Rosenqvist: *Trans. AIME* (1951) **191**, p. 535; *JOURNAL OF METALS* (July 1951).
- 8 G. Drath and F. Sauerwald: *Ztsch. anorg. allgem. Chem.* (1927) **162**, p. 301.
- 9 R. Schuhmann, Jr. and O. W. Moles: *Trans. AIME* (1951) **191**, p. 235; *JOURNAL OF METALS* (March 1951).
- 10 R. K. Schofield and E. K. Rideal: *Proc. Royal Soc.* (1925) **A109**, p. 58.
- 11 A. Tuzun: Master's Thesis, School of Mines, Columbia Univ., February 1952.

Metallic Oxidation in Chromium Steel Melting

by D. C. Hilty, G. W. Healy, and Walter Crafts

By means of a theoretical extension of the Cr-C temperature relation in molten chromium steels to low chromium contents and by a correlation of the ratios of chromium to iron in the slag and metal, a method has been developed for estimating the amount of metallic oxidation during the oxidizing period of a chromium steel heat. Application of this method has indicated that due to temperature limitations metallic oxidation may be excessive for very low carbon steels charged with more than a small amount of chromium.

IN the melting and refining of chromium steels the oxidation of carbon to a low level is accompanied by the oxidation of chromium and iron in considerable amounts. For the subsequent recovery of chromium and associated iron from the slag, the amounts of metal oxidized must be known for efficient reduction and control of composition. Further, in order to arrive at an accurate understanding of the process, so that chromium-bearing scrap can be used effectively, information is required on the relation between composition of the charge and weight of metal oxidized to reach the desired carbon content.

Crafts and Rassbach¹ recently developed an empirical relation between chromium, iron, and manganese oxidized per ton of steel charged, and final carbon content and temperature. This relation did not show any dependence on amount of chromium charged. However, it was felt that such a dependence might be present, so a further analysis of the data was undertaken.

Cr-C Relation at Low Chromium Levels

Crafts and Rassbach's results were based on temperatures estimated from the Cr-C relation previously established experimentally by Hilty,² and on a single temperature observation (immersion thermocouple) on a heat made at low temperature from a charge of carbon steel scrap containing only a small amount of residual chromium. The temperatures estimated from the Cr-C relation were for heats charged with chromium-bearing scrap and which contained substantial amounts of chromium (2 to 10 pct) at the end of the oxidizing period. No

D. C. HILTY and W. CRAFTS, Members AIME, are Research Metallurgist and Associate Director of Research, respectively, Union Carbide and Carbon Research Laboratories, Niagara Falls, N. Y., and G. W. HEALY is Research Metallurgist, Metallurgical Dept., Electro Metallurgical Co., a Division of Union Carbide and Carbon Corp., Niagara Falls.

Discussion on this paper, TP 3516C, may be sent, 2 copies, to AIME by July 1, 1953. Manuscript, June 11, 1952. New York Meeting, February 1952.

data, other than that from the low temperature heat just mentioned, were available for the low and intermediate chromium ranges.

In order to extend the range in which temperature may be estimated, the Cr-C relation requires further consideration. The Cr-C relation, expressed as

$$K = \frac{\% \text{ Cr}}{\% \text{ C}}; \log K = -\frac{15,200}{T} + 9.46 \quad [1]$$

suggests that carbon is zero at zero chromium in the bath. This is obviously absurd, because as chromium approaches zero the carbon content must approach the limit established by the Fe-C-O equilibrium. It is evident, therefore, that the Cr-C relation as defined by Eq. 1 is not valid below some minimum chromium content that may vary with temperature. On the other hand, it is probable that any such limiting chromium content is less than 4 pct at 3200°F, since the experimental data from which the Cr-C relation was derived included several observations at that level with no deviation. In any event, it is apparent that further evaluation of the results presented by Crafts and Rassbach is dependent upon a means for estimating the Cr-C temperature relation in the low chromium region.

From the observations of Chen and Chipman³ and thermodynamic data given in *Basic Open Hearth Steelmaking*,⁴ the following relation can be calculated for melts containing small amounts of chromium and carbon assuming a carbon monoxide pressure of 1 atm:

$$K^1 = \frac{\% \text{ Cr}}{(\% \text{ C})^2}; \log K^1 = \frac{-21,250}{T} + 13.88 \quad [2]$$

Moreover, by plotting Eq. 2 for any given temperature on cartesian coordinates, it can be extrapolated graphically to the limiting carbon content at zero chromium for the specified temperature without serious complications.

By means of Eq. 2 and its extrapolation, the Cr-C temperature relations originally established experi-

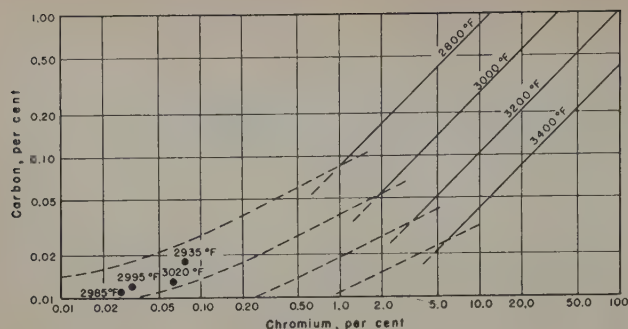


Fig. 1—Approximate Cr-C-temperature relations for all chromium contents of interest in the melting of chromium steels.

mentally at moderate to high chromium levels can be extended through the range of low chromium concentration as shown in Fig. 1. It is emphasized that the dashed curves of Fig. 1 are only approximations of the true Cr-C relations at low chromium contents. Nevertheless, they appear to be of a rea-

Table I. Analytical Results on Samples

Temperature, °C	Carbon, Pct	Manganese, Pct	Chromium, Pct
2934	0.018	0.010	0.058
3020	0.013	0.006	0.048
2995	0.012	0.006	0.026
2985	0.011	0.006	0.021

sonable order and are considered quite useful for practical purposes.

Effect of Manganese

The similarity in the relative deoxidizing powers of manganese and chromium in liquid iron is demonstrated by the work of Hilty and Crafts⁵ on manganese and that of Chen and Chipman on chromium. Moreover, Hilty pointed out the resemblance between the heat of formation calculated for the chromous oxide assumed in order to explain his experimental results and that of manganous oxide. In

addition, arc-furnace heats made by oxygen-blowing practice from charges containing several percentages of manganese as well as chromium-bearing scrap have contained total chromium plus manganese contents at the end of the oxidizing period equal to the chromium contents alone in similar heats made in the same furnace from low manganese charges oxidized to the same carbon levels with the same rate of oxygen input. Consequently, it is considered that the moderate concentrations of manganese usually found in chromium-steel heats are substantially equivalent to similar quantities of chromium and should be added to the chromium for practical applications of Fig. 1. They have been so considered in the arc-furnace data described below.

In this regard it is notable that the four data points spotted in at the very low chromium level in Fig. 1 refer to a laboratory heat that contained a small, but presumably effective, amount of manganese. These data were obtained from a 100-lb induction furnace heat charged with Armco iron and a small amount of high carbon ferrochromium. The heat was held at relatively constant temperature in the open. Samples were taken by the Taylor sampling technique and temperatures were measured by means of Pt-Pt-10 pct Rh thermocouples. Analytical results on the samples are given in Table I. These results agree fairly well with the curves in Fig. 1. The agreement, however, may be fortuitous because of analytical uncertainty and limited understanding of the controlling reactions.

Effect of Metal Composition on Ratio of Cr + Mn to Fe in Slag

Fairly complete data for 27 arc-furnace heats described by Crafts and Rassbach were available. These heats were made in a 2000-lb capacity, magnesite-lined, arc furnace from charges containing various amounts of chromium and nickel as shown in Table II. After meltdown, all heats were blown with oxygen in order to lower their carbon contents. Analytical results from slag and metal samples taken at the end of the oxidizing period are tabulated in Table II.

Table II. Experimental One Ton Steel Heats

Heat	Charge Composition				Metal Analysis after Oxygen Blow, Pct				Slag Analysis after Oxygen Blow, Pct					Lb Cr+Mn+Fe Oxidized per Ton		
	Charge Weight, Lb	Cr Charged, Lb*	Mn, Pct in Charge†	Ni Charged, Lb	Ni	Cr	Mn	C	Cr	Mn	Fe	SiO ₂	MgO			
1	2099	242	0.50	208.0	10.86	6.16	0.21	0.018	29.25	5.54	12.22	18.76	10.28	8.86	—	190
2	2063	241	0.50	208.5	10.95	7.23	0.23	0.036	19.35	4.08	8.96	15.06	13.16	19.35	—	168
3	2109	241	0.50	207.0	10.13	9.39	0.54	0.065	11.37	5.05	4.45	30.20	17.41	22.54	—	86
4	2045	231	0.50	257.0	12.84	8.80	0.38	0.048	14.04	2.76	4.47	24.48	14.22	29.67	1.36	80
5	2075	230	0.50	257.0	13.07	7.92	0.26	0.048	15.10	1.52	6.14	19.38	26.54	19.74	1.50	108
6	2070	231	0.50	257.0	13.37	8.33	0.40	0.034	20.38	3.86	6.25	21.16	14.77	20.86	4.98	103
7	2070	232	0.50	260.0	13.12	8.65	0.40	0.044	12.42	2.74	4.42	24.38	22.43	21.70	3.53	92
8	2090	232	0.50	257.0	13.23	8.44	0.36	0.060	15.68	1.90	5.37	21.50	17.53	22.60	2.45	96
9	2014	164	0.50	257.0	14.17	3.34	0.14	0.016	22.80	3.40	19.50	13.58	10.44	13.29	0.96	206
10	2026	164	0.50	257.0	13.91	3.89	0.15	0.020	18.82	2.74	17.50	14.18	18.62	10.09	4.32	188
11	2014	164	0.50	257.0	14.21	2.80	0.08	0.015	24.42	3.19	22.72	15.50	7.54	9.14	—	236
12	2038	166	0.50	260.0	14.02	3.36	0.12	0.022	14.41	2.20	17.42	14.08	22.40	9.76	—	240
13	1795	111	0.50	235.5	15.06	1.59	0.05	0.016	18.19	2.78	28.60	14.72	3.95	13.12	1.26	262
14	1891	133	0.50	236.5	13.60	2.93	0.11	0.017	17.27	3.42	20.13	17.40	8.09	17.50	2.08	201
15	1760	123	0.50	—	—	1.98	0.05	0.020	17.44	1.55	26.35	16.36	14.36	6.62	1.66	272
16	1681	98	0.50	—	—	1.83	0.07	0.026	9.08	1.49	17.20	16.60	30.34	15.03	4.46	260
17	1660	98	0.50	—	—	2.28	0.06	0.022	13.22	1.36	21.50	16.94	20.18	12.66	2.10	212
18	1640	98	0.50	—	—	2.20	0.07	0.015	11.90	1.39	23.85	15.58	16.32	14.22	2.40	250
19	1576	9	0.50	—	—	0.03	0.02	0.018	2.82	1.43	37.0	15.00	16.84	12.83	1.80	230
20	1576	9	0.50	—	—	0.16	0.03	0.020	1.88	1.94	41.3	12.56	12.90	11.06	2.30	213
21	1576	9	0.50	—	—	0.16	0.04	0.013	1.50	1.81	38.8	15.06	17.61	8.28	2.04	239
22	1576	9	0.50	—	—	0.06	0.02	0.018	0.50	1.32	45.1	10.80	18.52	7.86	2.40	303
23	1576	9	0.50	—	—	0.08	0.02	0.018	0.89	1.32	43.5	11.80	16.30	8.64	4.60	269
24	1576	9	0.50	—	—	0.04	0.04	0.012	0.75	1.62	45.5	12.00	13.26	9.98	2.80	249
25	1576	9	0.50	—	—	0.14	0.02	0.014	2.10	1.03	34.2	12.40	21.81	10.43	6.80	307
26	1576	9	0.50	—	—	0.18	0.03	0.012	2.20	1.56	40.3	15.58	15.58	9.87	2.12	243
27	1322	4.1	0.34	35.8	3.47	0.02	0.01	0.017	0.52	0.59	47.4	14.70	13.19	5.27	5.84	525

* Charge weight plus 9 lb average pickup from lining except Heat 27, obtained from material balance.

† Estimated 0.50 pct Mn in charge except Heat 27, obtained from material balance.

Ratios of the chromium plus manganese to iron contents of the slag were plotted as a function of those of the metal with the result illustrated by Fig. 2.

The data are adequately represented by the line of regression whose equation is

$$\log \frac{(\% \text{ Cr} + \% \text{ Mn})}{(\% \text{ Fe})} \text{ in slag} = 0.812 \log \frac{[\% \text{ Cr} + \% \text{ Mn}]}{[\% \text{ Fe}]} \text{ in metal} + 1.238 \quad [3]$$

Although it appears that the points might be fitted better by two intersecting lines, such a representation is not justified statistically.

The excellent correlation evident in Fig. 2 is rather surprising, especially since the heats covered rather broad ranges of both composition and, presumably, temperature. Apparently however, the relative proportions of chromium (plus manganese) and iron in the slag are controlled almost entirely by the amounts of chromium (plus manganese) and iron in the metal without regard to carbon content or apparent temperature.

Weight of Metal Oxidized

The relation shown in Fig. 2 considerably simplifies the task of calculating the weight of metallics oxidized during the oxidizing period of a chromium-steel heat. In order to perform such a calculation, it is necessary to know only the amounts of chromium and manganese in the charge in addition to the metal composition at the end of the oxidizing period according to the following formula, the derivation of which is shown in the Appendix:

Pounds (Cr+Mn+Fe) oxidized per ton of charge

$$= 2000 \frac{(\text{Cr}_1 + \text{Mn}_1) - (\text{Cr}_2 + \text{Mn}_2)}{\frac{100S}{1+S} - (\text{Cr}_2 + \text{Mn}_2)} \quad [4]$$

where Cr_1 is the percentage of chromium in the charge; Mn_1 , the percentage of manganese in the charge; Cr_2 , the percentage of chromium in the bath after oxidation; Mn_2 , the percentage of manganese

in the bath after oxidizing; and $S = \frac{(\% \text{ Cr} + \% \text{ Mn})}{(\% \text{ Fe})}$

in slag after oxidation which can be calculated from the bath composition by Eq. 3 or read from Fig. 2.

In Fig. 3 is shown the correlation of metallic oxidation of the heats in Table II calculated by Eq. 4 with the observations of Crafts and Rassbach. In general, the correlation is good. The deviations are easily explained by the rather arbitrary assumption of 0.50 pct Mn in the charge for most of the heats and by the lack of adequate tracers such as nickel to assist in calculating material balances for most of the low chromium, low nickel charge heats.

With the additional help of Fig. 1, for estimation of residual chromium after the oxygen blow, the amount of metallic oxidation can now be calculated for charges of varying chromium contents oxidized to specified carbon and temperature levels. The results of such calculations are shown in Figs. 4 and 5 for 0.015 and 0.05 pct C, respectively.

The substantial effect of charged chromium as well as the effects of the carbon content and temperature attained on the oxidation losses is apparent.

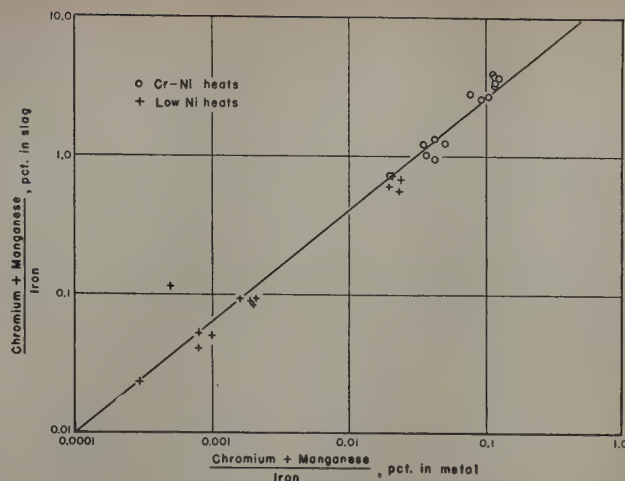


Fig. 2—Correlation of rates of chromium plus manganese to iron in slag and metal.

These illustrations strongly imply that avoidance of excessive oxidation loss in making very low carbon steel from a high-chromium charge may involve temperatures beyond the scope of usual steelmaking furnaces. Consequently, it would appear desirable to regulate the amount of chromium in a charge with due regard to the carbon content of the steel being made and the maximum safe operating temperature of the furnace.

In rationalizing the above results, it is presumed that the Cr-C temperature relation of Fig. 1 refers approximately to a state of equilibrium wherein the metal phase is saturated with an oxide of chromium as well as carbon monoxide. If, however, the chromium content of the bath after oxidation is less than that specified by the carbon content and temperature so that the metal is not saturated with a chromium oxide—as may well be the case in heats made at fairly high temperatures from low chromium charges—then Fig. 2 and Eq. 4 do not apply. Under such conditions, the chromium content of the bath may be controlled by other factors such as slag basicity, etc., in a manner analogous to the case of residual manganese in the open hearth. It would also appear that the relations shown in Figs. 1 and 2

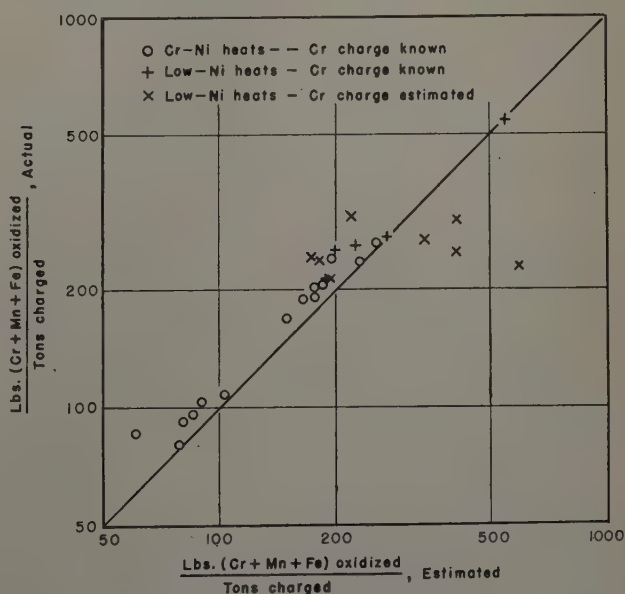


Fig. 3—Correlation of estimated with actual metallics oxidized.

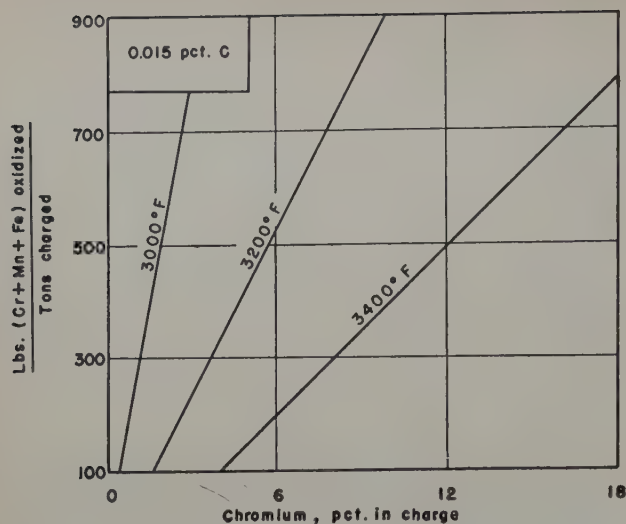


Fig. 4—Estimation of metal oxidized in blowing with oxygen to 0.015 pct C.

are of practical significance only when oxidation is carried out to such a degree that a significant proportion of the charged chromium is oxidized. For this reason the minimum amount of metal oxidized has been limited to 100 lb per ton in Figs. 4 and 5.

The temperature dependence of metallic oxidation indicated by Figs. 4 and 5 differs somewhat from the empirical relation reported by Crafts and Rassbach. Moreover, it is indicated to vary with the amount of chromium charged. A probable explanation of the differences is that among the heats used by Crafts and Rassbach to estimate the temperature coefficient most of the heats with higher chromium charges also reached higher temperatures at the end of the oxidizing period. Such a result would be expected for heats made under the same conditions with regard to oxygen input, etc., because of the relatively higher heat of oxidation of chromium. Thus, under practical operating conditions, the effect of increased chromium in the charge on metallic oxidation would be offset by the higher temperature attained during oxidation. The relation presented by Crafts and Rassbach is believed to illustrate the net result of regulating the amount of chromium in a charge with regard to the carbon content of the steel being made as suggested by Figs. 4 and 5 of this paper.

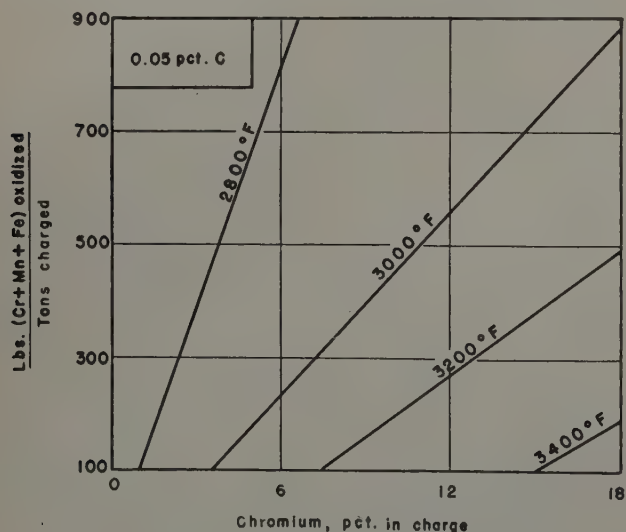


Fig. 5—Estimation of metal oxidized in blowing with oxygen to 0.05 pct C.

Summary

By means of published thermodynamic data an approximate Cr-C temperature relation for molten chromium steel under oxidizing conditions has been derived for the range of low chromium concentrations where the relation established experimentally at higher chromium levels is believed to be invalid.

The ratio of chromium (plus manganese) to iron in the slag of a chromium steel heat has been shown to depend almost entirely on the ratio of chromium (plus manganese) to iron in the metal. Through this relationship an expression for calculating the metallic oxidation during the oxidizing period of a heat has been derived.

It has been demonstrated that the amount of metallic oxidation is dependent upon the amount of chromium in the charge and the carbon content and temperature of the bath at the end of the oxidizing period. It is inferred that for steels oxidized to very low carbon contents from charges containing more than a small amount of chromium, metallic oxidation may be excessive because of maximum temperature limitations imposed by operating conditions.

Acknowledgments

The authors wish to express their appreciation for the valuable suggestions and criticism of John Chipman, Head, Dept. of Metallurgy, Massachusetts Institute of Technology, for the assistance received from H. J. O'Connor, Electro Metallurgical Co., in statistical studies, and particularly for the stimulating appraisal of the practical aspects of the problem by H. P. Rassbach, Electro Metallurgical Co.

Appendix

Derivation of Formula for Pounds of Metal Oxidized

Assume a charge weight of 2000 lb. Let the percentage of chromium plus the percentage of manganese in the charge be Cr_1 . Then the pounds of chromium plus manganese in the charge are

$$\text{Lb Cr + Mn charged} = 2000 \times \frac{Cr_1}{100} = 20 Cr_1 \quad [5]$$

Let X equal the pounds of chromium and manganese oxidized, and Y the pounds of iron oxidized. Then the weight of metal after oxidation will be

$$\text{Lb metal after oxidation} = 2000 - X - Y \quad [6]$$

It was shown that the ratio of chromium plus manganese to iron in the slag after oxidation can be estimated from the ratio of chromium plus manganese to iron in the metal (Fig. 2). Let S be the ratio of chromium plus manganese to iron in the slag. Then

$$\frac{\text{Lb Cr + Mn in slag}}{\text{Lb Fe in slag}} = \frac{X}{Y} = S \quad [7]$$

Eq. 6 can then be written in the form

Lb metal after oxidation =

$$2000 - X - \frac{X}{S} = 2000 - X \frac{1 + S}{S} \quad [8]$$

Let Cr_2 be the percentage of chromium plus manganese in the metal after oxidation. The weight can then be calculated from Eq. 8.

Lb Cr + Mn in metal after oxidation =

$$\left(2000 - X \frac{1 + S}{S} \right) \frac{Cr_2}{100} \quad [9]$$

But the amount of chromium plus manganese in the bath is also equal to the difference between the amount

originally charged (Eq. 5) and the amount oxidized designated by X .

$$\text{Lb Cr} + \text{Mn in metal after oxidation} = 20 \text{ Cr}_1 - X \quad [10]$$

Combining Eqs. 9 and 10, it is possible to solve for X

$$\begin{aligned} 20 \text{ Cr}_1 - X &= \left(2000 - X \frac{1+S}{S} \right) \frac{\text{Cr}_2}{100} \\ &= 20 \text{ Cr}_2 - X \frac{1+S}{S} \frac{\text{Cr}_2}{100} \end{aligned} \quad [11]$$

Hence

$$X \left(1 - \frac{1+S}{S} \frac{\text{Cr}_2}{100} \right) = 20 (\text{Cr}_1 - \text{Cr}_2)$$

$$\begin{aligned} \text{Lb Cr} + \text{Mn oxidized: } X &= \frac{(\text{Cr}_1 - \text{Cr}_2)}{1 - \frac{1+S}{S} \frac{\text{Cr}_2}{100}} \\ \text{or} \end{aligned}$$

$$X = 2000 \frac{\text{Cr}_1 - \text{Cr}_2}{100 - \frac{1+S}{S} \text{Cr}_2} \quad [12]$$

Since total weight oxidized is $X + Y$ and since $S = X/Y$, the total weight oxidized becomes

$$X \left(1 + \frac{1}{S} \right) = X \frac{1+S}{S} \quad [13]$$

Multiplying Eq. 12 by this factor $\frac{1+S}{S}$ then results in

$$\text{Lb metal oxidized} = 2000 \frac{\text{Cr}_1 - \text{Cr}_2}{\frac{100S}{1+S} - \text{Cr}_2} \quad [14]$$

In this equation Cr_1 is known from charge composition, Cr_2 from the analysis after oxidation, and S can be estimated from $[\% \text{ Cr} + \% \text{ Mn}]/[\% \text{ Fe}]$ in the metal after oxidation, using Fig. 2.

Example: A heat containing 11.5 pct Cr and 0.5 pct Mn in the charge is blown with oxygen to 0.05 pct C, reaching a temperature of 3200°F. From Fig. 1 $\text{Cr}_2 = 4.7$ pct is obtained. If there is no nickel in the heat,

$$\frac{\% \text{ Cr} + \% \text{ Mn}}{\% \text{ Fe}} = \frac{4.7}{100 - 4.7} = 0.049$$

Entering Fig. 2 at 0.049, S is estimated as 1.47. Then weight oxidized is

$$W = 2000 \frac{(11.5 + 0.5) - 4.7}{\frac{100 \times 1.47}{1 + 1.47} - 4.7} = 266 \text{ lb per ton charged.}$$

References

- ¹ W. Crafts and H. P. Rassbach: *JOURNAL OF METALS* (January 1952) pp. 20-25.
- ² D. C. Hilty: *Trans. AIME* (1949) **185**, pp. 91-95; *JOURNAL OF METALS* (February 1949).
- ³ H-M. Chen and J. Chipman: *Trans. ASM* (1947) **38**, pp. 70-113.
- ⁴ *Basic Open Hearth Steelmaking* AIME (1951).
- ⁵ D. C. Hilty and W. Crafts: *Trans. AIME* (1950) **188**, pp. 425-436; *JOURNAL OF METALS* (February 1950).

Technical Note

Note on Contamination of Silicon Ingots

by G. Sandoz and H. E. Stauss

THE purpose of this note is to draw attention to the possibility that a melt may be contaminated by a material not in direct contact with it by means of gaseous intermediate agents. In recent years silicon has assumed a position of importance because of its use in rectifiers and transistors and close attention has been required to control of both purification and contamination during all stages of preparation.¹ This note reports the observation that a graphite heater may have contaminated silicon ingots without direct physical contact through reactions that developed gaseous products.

Several ingots made with the equipment of Hino and Stauss,² using a graphite heater in a dried helium atmosphere, were found to have a small amount of a very hard substance on the free surface. X-ray analysis by F. W. von Batchelder showed the sub-

stance to be SiC. Similar contamination was not found when the heater was tantalum, indicating that the carbon had not come from an original impurity in the silicon powder.

One source of the carbon could have been volatile matter released from the graphite heater. This heater had been used about ten times at the time of the observations. A second source of carbon could have been a direct reaction between the quartz crucible and the graphite heater to form CO, or an indirect reaction involving a crucible-melt interaction and volatile SiO as an intermediate product. Such reactions should have developed SiC on the heater; and in fact a yellow powder did form on the inside of the graphite heater although its composition could not be determined.

References

G. SANDOZ, Junior Member AIME, and H. E. STAUSS, Member AIME, are associated with the Naval Research Laboratory, Washington, D. C.

TN 155E. Manuscript, Jan. 30, 1953; revision, March 6, 1953.

- ¹ H. C. Torrey and C. A. Whitmer: *Crystal Rectifiers* (1948) Chapter 10. New York. McGraw-Hill Book Co.
- ² J. Hino and H. E. Stauss: *Trans. AIME* (1952) **194**, p. 656; *JOURNAL OF METALS* (June 1952).

Notes on the Plastic Critical Temperature In Strain-Induced Martensite Reactions

by C. Dean Starr

IT is well known that the martensite reaction can be induced to occur isothermally above the M_s temperature by plastic deformation of an alloy in its austenitic state, and also that as the test temperature is increased above the M_s temperature, plastic deformation under a given set of conditions merely causes additional slip with a corresponding tendency toward the formation of less martensite per unit of strain. Thus it appears that a maximum temperature exists above which martensite cannot be formed isothermally by plastic deformation. This temperature is commonly designated as the equilibrium temperature T_E .

Attempts to determine experimentally the equilibrium temperature have indicated that a critical temperature is observed, under a given set of conditions, above which martensite cannot be formed isothermally by plastic deformation. But the observation of a "so called" critical temperature, T_D , should not be confused with the equilibrium temperature, T_E .

In order to clarify this anomaly, true stress-strain curves were obtained for a series of type 304 stainless steel specimens (manufacturer's analysis, 0.08 pct C, 18 to 20 pct Cr, 8 to 10 pct Ni, balance Fe) over the temperature range 67° to 300°K.¹ Since martensite is magnetic, a quantitative measure of the amount of martensite that was produced by plastic deformation was obtained by determining the magnetic permeability as a function of strain. The results of these tests are given in Fig. 1. They appear to indicate that a plastic critical point does exist at about 240°K for the stainless steel under investigation here. But that 240°K is not the equilibrium temperature nor even a true plastic critical temperature can be seen from Fig. 2 wherein the permeability of the same material is shown to increase with cold rolling at 293°K.

Consequently the observation of a "so called" plastic critical temperature is dependent on the mode of deformation and has no theoretical significance.

Acknowledgment

This work was sponsored by the Office of Naval Research. Permission to publish this note is gratefully acknowledged.

C. D. STARR is Research Engineer, Dept. of Engineering, Institute of Engineering Research, University of California, Berkeley, Calif. TN 153E. Manuscript, Nov. 21, 1952.

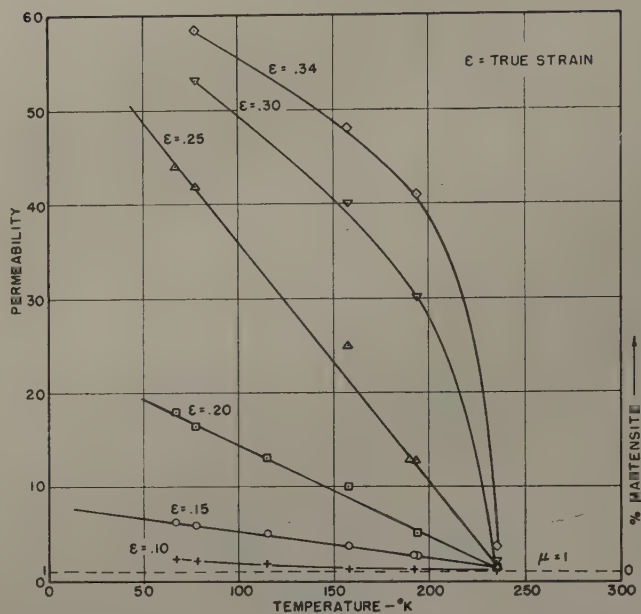


Fig. 1—An apparent plastic critical point as determined by simple tension testing.

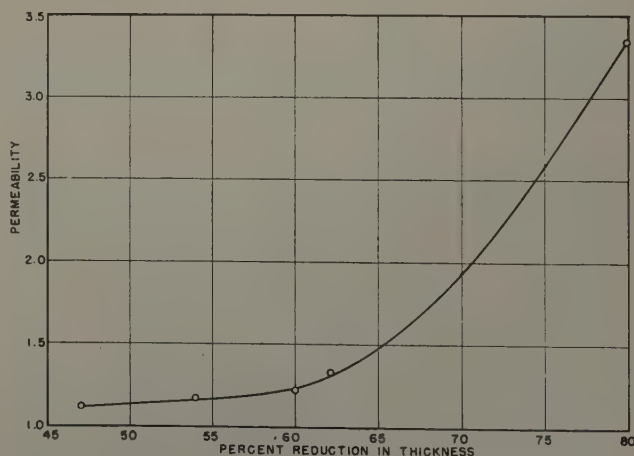


Fig. 2—Formation of martensite during cold rolling of 18-8 stainless steel at 293°K.

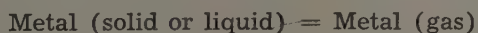
¹ C. Dean Starr, M. Reporter, J. E. Dorn: Investigations on the Mechanism of the Strain Induced Martensitic Reaction in 18-8 Stainless Steel. Univ. Calif. Inst. of Engineering Report, Series No. 22, Issue No. 15, June 1951.

Free Energy of Vaporization of Metals from 0° to 2000°C

by J. W. Evans

ONE of the most important and frequent calculations that the extractive metallurgist is called upon to make is that of the standard free energy change of a reaction (ΔF°). For many reactions of metallurgical interest, the lengthy arithmetical calculations have been eliminated by the use of free energy-temperature diagrams which have been constructed by Ellingham,¹ Richardson and Jeffes,² Kellogg,³ and Osborn⁴ (e.g., for oxides, sulphides, halides) from critical surveys of existing data. The speed and simplicity of making calculations with these graphs make them of great practical value and, this should be stressed, in the majority of cases no greater accuracy is obtained by the individual calculations from specific heat data, entropies, and heats of reaction.

With the increasing industrial application of vacuum methods to the winning of metals, notably at present magnesium and the alkaline earth metals, it is necessary to calculate low metal vapor pressures above reaction mixtures. The existing free energy diagrams usually give values where the solid and liquid metals are at unit activity. To obtain the free energy change associated with the reaction

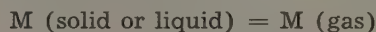


it is customary to calculate this from either vapor pressure equations or from the appropriate free energy functions. This paper presents graphically the free energies of vaporization of a number of metals of economic importance which can be used in conjunction with other free energy diagrams. Certain metals have been excluded on the following grounds: titanium, tungsten, molybdenum, and platinum have very high heats of vaporization and

boiling points and the uncertainty of these values arising from difficulties of high temperature measurements makes free energy values of doubtful accuracy; the data for cobalt, vanadium, and zirconium are uncertain; finally, arsenic, antimony, and bismuth could not be conveniently included because of the presence of mixtures of polyatomic and monatomic vapors in the temperature range considered.

Free Energy Diagram

In Fig. 1, the standard free energies of vaporization per mol (ΔF°_T) have been plotted for the temperature range 0° to 2000°C for the reaction



The data have been obtained from the free energy functions $-(F-H_{298})/T$ for the solid, liquid, and gaseous elements and the heats of vaporization at 298°K, i.e., ΔH_{298} (vapor). The values of these functions have been taken without change from the recent critical survey by Brewer;⁵ the bulk of this data is from Kelley⁷ with adjustments in the light of more recent work. Values of the function $-(F-H_{298})/T$ at $T = 298^\circ, 500^\circ, 1000^\circ, 1500^\circ$, and 2000°K were employed. Where possible, a further independent value was obtained by using the boiling point, i.e., where $\Delta F^\circ_T = 0$. All calculations are based on the assumption that the metal vapors are monatomic and that the boiling points refer to those temperatures at which the partial pressure of the monatomic vapor above the metal is 760 mm. For the alkali metals, e.g., sodium, potassium, and lithium, diatomic gas molecules are present as minor species; details of these are discussed by Brewer.⁵

On the basis of the above values and allowing for the change in slope at the melting point, straight line graphs were constructed and extrapolated to 2000°C. The deviation from a straight line did not exceed ± 500 cal, which in all cases appears less than the probable error in the ΔF°_T values.

J. W. EVANS is associated with the Research Dept., International Nickel Co. of Canada, Copper Cliff, Ont., Canada.

Discussion on this paper, TP 3476D, may be sent, 2 copies, to AIME by July 1, 1953. Manuscript, Aug. 20, 1952; revised, Dec. 30, 1952. Los Angeles Meeting, February 1953.

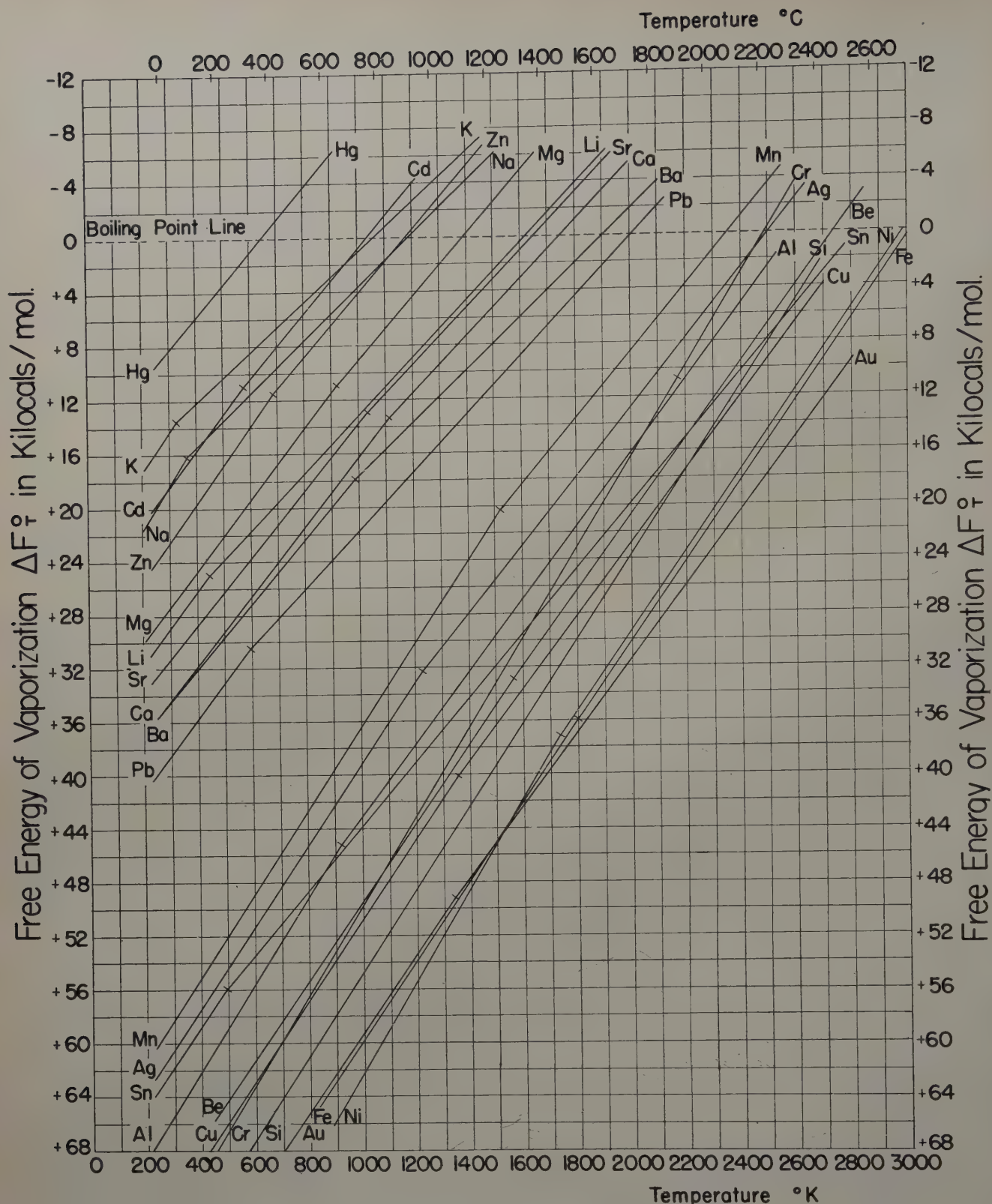


Fig. 1—Free energies of vaporization of solid and liquid elements (ΔF°_T). Break in line occurs at melting point.

It will be noted that the slopes of the free energy lines are approximately the same; this slope corresponds to the temperature dependent term in the expression $\Delta F = \Delta H - T\Delta S$, i.e., the entropy change which, as it involves the simple physical change from liquid or solid to monatomic gas, would be approximately the same for all metals. The relative positions of the free energy lines and, hence, of the volatilities are determined by the heats of vaporization which clearly vary considerably from one metal

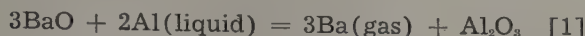
to another. For metals boiling below about 2000°K, the heats of vaporization are probably accurate to within one or two kilocalories per mol, but for the higher boiling metals, the heats of vaporization may be in error by ± 5 kcal or more.

Use of the Diagram

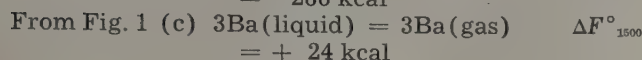
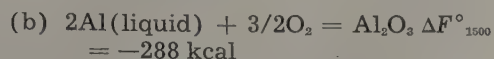
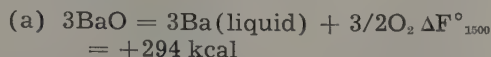
To those familiar with other free energy diagrams, the application of this present diagram will be fairly clear. One example, however, will be given by con-

sidering the thermal reduction of barium oxide with aluminum at 1500°K, i.e., 1227°C, and calculating the equilibrium barium gas pressure over this reaction.

The essential reaction is



From Osborn's data⁴



Adding reactions (a), (b), and (c) gives Eq. 1 for which

$$\Delta F^\circ_{1500} = +30,000 \text{ cal}$$

The equilibrium constant for Eq. 1 is given simply by $K = p_{\text{Ba}}^3$ if it is assumed that there is no interaction between barium and aluminum and that liquid aluminum, barium oxide, and alumina are at unit activities.

By definition, $\Delta F^\circ_T = -RT \ln K$

so that $\Delta F^\circ_T = -3RT \ln p_{\text{Ba}}$

By substituting $\Delta F^\circ_{1500} = +30,000 \text{ cal}$, $T = 1500^\circ\text{K}$, and $R = 1.98 \text{ cal}$, the calculated equilibrium vapor pressure of barium over Eq. 1 is about 27 mm Hg, which is a suitable pressure for the vacuum production of the metal commercially.

Vapor Pressures

Although the main purpose of the diagram is for free energy calculations, the diagram shows at a glance the relative volatilities over the whole temperature range, those with the greatest volatility having the lowest positive free energy change. The actual vapor pressure in atmospheres is related to

the free energy of vaporization by the formula

$$\Delta F^\circ_T = -RT \ln p$$

This may be conveniently written:

$$\log_{10} p \text{ (mm Hg)} = \frac{-\Delta F^\circ_T}{4.57 T} + 2.88 \quad [2]$$

Eq. 2 gives values for the vapor pressures which agree quite well (within 10 to 20 pct) with the three or four term equations usually quoted in the literature. For the more volatile metals, however, e.g., sodium and potassium, quite small errors in the ΔF°_T values of the order of only 500 cal give rise to substantial errors in the calculated vapor pressures. Where the ΔF°_T value is less than about +5000 cal, the calculated vapor pressure as obtained from Eq. 2 should be used with caution and the use of the more accurate multiterm equation is recommended.⁵

Acknowledgment

This work was carried out at the University of Toronto during the tenure of a Fellowship from the Research Council of Ontario, which is gratefully acknowledged. I wish to thank Professor L. M. Pidgeon, Head of the Department of Metallurgical Engineering, for his encouragement of the work.

References

- ¹ H. J. T. Ellingham: *Journal Soc. Chem. Ind.* (May 1944) p. 127.
- ² F. D. Richardson and J. H. E. Jeffes: *Journal Iron and Steel Inst.* (1948) **160**, p. 261.
- ³ H. H. Kellogg: *Trans. AIME* (1950) **188**, p. 862; *JOURNAL OF METALS* (June 1950).
- ⁴ C. J. Osborn: *Trans. AIME* (1950) **188**, p. 600; *JOURNAL OF METALS* (March 1950).
- ⁵ L. Brewer: *Chemistry and Metallurgy of Miscellaneous Materials: Thermodynamics*. Edited by L. L. Quill. (1950) p. 13. New York. McGraw-Hill Book Co.
- ⁶ See, for example, *Metals Reference Book*. Edited by C. J. Smithells (1949) p. 449. London. Butterworth.
- ⁷ K. K. Kelley: *Free Energies of Vaporization and Vapor Pressures of Inorganic Substances*. U. S. Bur. Mines *Bulletin* 383 (1935).

Technical Note

Simple Devices for Approximating Constant Stress During Tensile Creep Tests

by R. L. Fullman, R. P. Carreker, Jr., and J. C. Fisher

CREEP tests are usually constant load tests. As deformation occurs, the cross section of the specimen changes so as to maintain approximately constant volume. Until necking starts,

$$\frac{A}{A_0} \cong \frac{l_0}{l}$$

where A is the cross-sectional area, l is the specimen length, and the subscript 0 indicates initial values. Thus, during a tensile creep test under

constant load, the stress increases in proportion to the elongation.

$$S = \frac{F}{A} \cong \frac{F}{A_0} \frac{l}{l_0}$$

where S is the stress and F the load applied to the specimen.

R. L. FULLMAN, R. P. CARREKER, JR., and J. C. FISHER, Junior Members AIME, are associated with the Research Laboratory, General Electric Co., Schenectady.

TN 154E. Manuscript, Jan. 29, 1953.

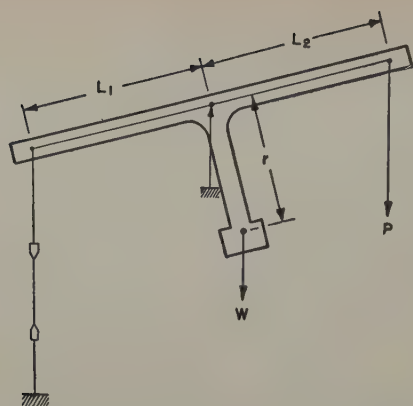


Fig. 1—Schematic diagram of loading beam with center of gravity below fulcrum.

It has been repeatedly emphasized in the literature that, while constant load tests are convenient and may approximate some types of service conditions, constant stress tests are needed to gain an understanding of the nature of the deformation process. Constant load creep behavior can be calculated from constant stress data, but the reverse is much more difficult.

Andrade has described three methods of maintaining constant stress during creep tests,¹⁻³ none of which is as simple, from an equipment standpoint,

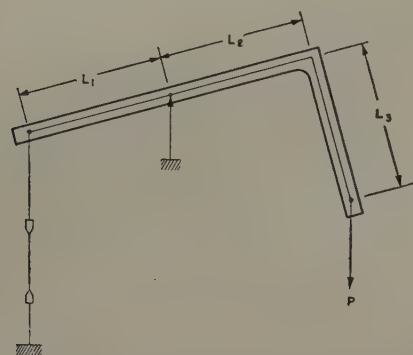


Fig. 2—Schematic diagram of loading beam with knife edges not collinear.

as the usual constant load test. Fisher and Carreker have described a method which maintains an approximately constant stress with relatively simple equipment.⁴ The method described below maintains a more nearly constant stress than that of Fisher and Carreker, while retaining the simplicity of the constant load test. The method requires only slight modification of most constant-load creep testing machines employing a beam loading arrangement. The mechanical advantage of the beam loading device is retained, permitting large stresses to be applied with relatively small weights.

Within the authors' knowledge, the method to be described originated in their joint discussion.⁵ It has been used successfully in their laboratory for several years and is now being used in other laboratories. Its simplicity and utility seem to warrant description.

If the fulcrum of a beam does not lie on a straight line containing the other knife-edges and the beam's center of gravity, the force transmitted by the beam is a function of the angle between the beam and the horizontal. When approximately horizontal, a simple beam having its fulcrum in a straight line contain-

ing the other knife-edges will maintain nearly constant stress in a tensile specimen if the center of gravity is located a distance r directly below the fulcrum, such that

$$r = \frac{P L_1 L_2}{W l_1} \quad [1]$$

where P is the applied load, L_1 and L_2 are the beam dimensions as shown in Fig. 1, W is the weight of the beam, and l_1 is the specimen length when the beam is horizontal. For optimum results, the initial angle of the beam should be such that it reaches a horizontal position when the specimen has attained half the maximum elongation of the test. Constant

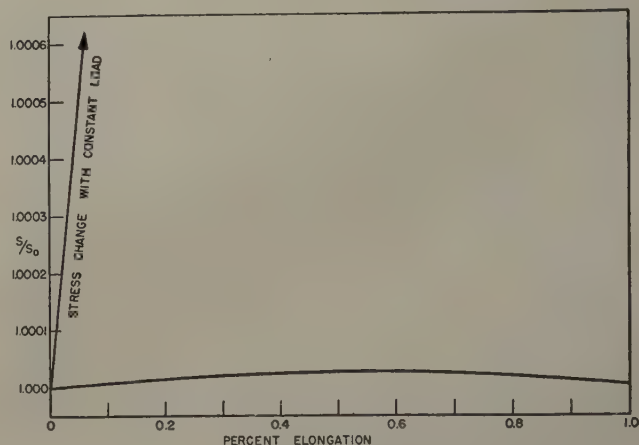


Fig. 3—Stress change in tensile creep test.

stress is not maintained after the specimen starts to neck.

Existing creep machines employing a loading beam may be modified to make use of this method by a change in position of the beam center of gravity. With some equipment this change may be accomplished by the adjustment of existing counterweights. However, the method is somewhat inconvenient in that the position of the center of gravity or the beam weight must be changed for every change in load.

A more convenient application of the same principle may be obtained with a slight modification of the beam. In this case the center of gravity of the beam is placed at the fulcrum, but the fulcrum is not located on a straight line containing the other knife-

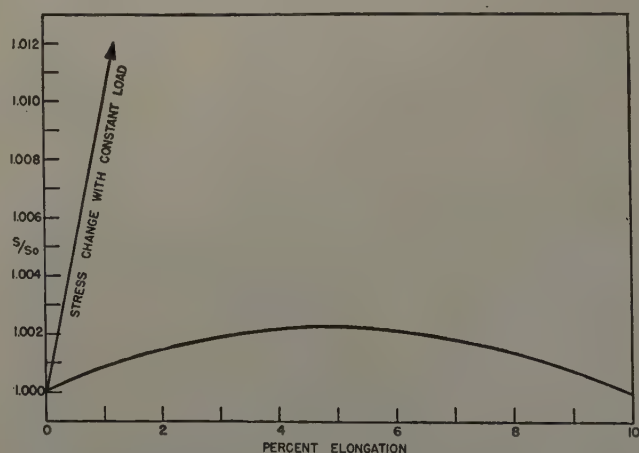


Fig. 4—Stress change in tensile creep test.

edges. Regardless of load, when the beam is approximately horizontal, a tensile specimen is deformed under nearly constant stress if

$$L_3 = \frac{L_1 L_2}{l_1} \quad [2]$$

where l_1 is the specimen length when the beam is horizontal, and L_1 , L_2 , and L_3 are the beam dimensions, as shown in Fig. 2. For optimum results, the initial angle of the beam should again be such that it reaches a horizontal position when the specimen is at half the maximum elongation of the test.

Figs. 3 and 4 show the variation of stress as a function of strain for maximum elongations of 1 and

The resolved shear stress, RSS, is given by the relationship⁹

$$\text{RSS} = \frac{F}{A} \sin \chi \cos \lambda$$

where χ is the angle between the tensile axis and the active slip plane and λ is the angle between the tensile axis and the active slip direction. During deformation by single slip, the crystal orientation and shape change in such a manner that

$$\frac{l}{l_0} = \frac{A_0}{A} = \frac{\sin \chi_0}{\sin \chi} = \frac{\sin \lambda_0}{\sin \lambda} \quad [4]$$

Combining this relationship with the geometry of the loading beam shown in Fig. 2, it is found that the resolved shear stress is maintained at approximately constant value if

$$L_3 = \frac{L_1 L_2}{l_1} \tan^2 \lambda_1 \quad [5]$$

where λ_1 is the value of λ at half the maximum strain of the test (i.e., the value of λ at $l = l_1$, as computed from Eq. 4). The resolved shear stress will then change during deformation in accordance with

$$\text{RSS} = \frac{P \sin \chi_0}{A_0 L_1} \left(L_2 - \frac{L_3 (l - l_1)}{\sqrt{L_1^2 - (l - l_1)^2}} \right) \left(\frac{\sqrt{l^2 - l_0^2 \sin^2 \lambda_0}}{l} \right) \quad [6]$$

Fig. 5 shows the influence of initial orientation of the crystal upon "percentage improvement" in constancy of resolved shear stress, defined by

$$\left(\frac{\Delta S_1 - \Delta S_2}{\Delta S_1} \right) \times 100 \text{ pct}$$

Here ΔS_1 is the maximum change in resolved shear stress during a constant load test and ΔS_2 is the maximum change in resolved shear stress during a test using a loading beam with dimensions that satisfy Eq. 5. The curves of Fig. 5 were computed for strains of 1 and 10 pct, and with $L_1 = L_2 = l_1$. Other dimensions would lead to similar results.

Conclusions

Proper choice of dimensions of a simple loading beam permit maintenance of very nearly constant stress during creep testing of polycrystalline materials or of nearly constant resolved shear stress during creep testing of single crystals.

References

- ¹ E. N. daC. Andrade: On the Viscous Flow in Metals, and Allied Phenomena, *Proc. Royal Soc.* (1910-1911) **84A**, p. 1.
- ² E. N. daC. Andrade and B. Chalmers: The Resistivity of Polycrystalline Wires in Relation to Plastic Deformation, and the Mechanism of Plastic Flow. *Proc. Royal Soc.* (1932) **138A**, p. 348.
- ³ E. N. daC. Andrade: A New Device for Maintaining Constant Stress in a Rod Undergoing Plastic Extension. *Proc. Phys. Soc.* (March 1948) **60**, p. 304.
- ⁴ J. C. Fisher and R. P. Carreker: A Simple Constant Stress Creep Test. *Trans. AIME* (1949) **185**, p. 178; *JOURNAL OF METALS* (February 1949).
- ⁵ R. L. Fullman, R. P. Carreker, and J. C. Fisher: A Simple Device for Approximating Constant Stress During Tensile Creep Tests. G. E. Research Laboratory Report RL 109 (October 1948).
- ⁶ E. Schmid and W. Boas: *Kristall Plastizität*. (1935) Berlin. Julius Springer.

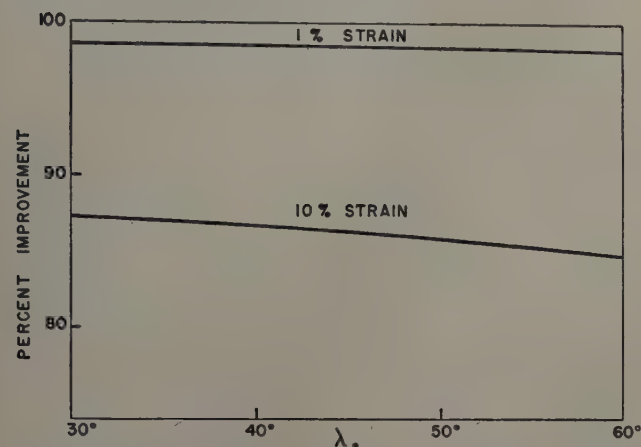


Fig. 5—Influence of crystal orientation on constancy of resolved shear stress.

10 pct, if $L_1 = L_2 = L_3 = l_1$. The same result is obtained using a beam with a low center of gravity, if $W = P$ and $r = L_1 = L_2 = l_1$. The efficiency of the method can be expressed in terms of "percentage improvement" in constancy of applied stress, defined as

$$\left(\frac{\Delta S_1 - \Delta S_2}{\Delta S_1} \right) \times 100 \text{ pct}$$

Here ΔS_2 is the maximum stress change using the type of beam described and ΔS_1 is the maximum stress change with a constant load. For the case considered in Figs. 3 and 4, the percentages of improvement are: for 1 pct total elongation, 99.75 pct; and for 10 pct total elongation, 97.76 pct. A different choice of dimensions causes only a slight change in the efficiency of the method, provided Eq. 1 or Eq. 2 is satisfied. For any choice of dimensions which satisfies one of these equations,

$$S = \frac{Pl}{A_0 l_0} \left[\frac{L_2}{L_1} + \frac{L_2 (l_1 - l)}{l_1 \sqrt{L_1^2 - (l_1 - l)^2}} \right] \quad [3]$$

where l_0 and l are initial and other values of specimen length, and A_0 is the initial cross-sectional area of the specimen.

In tensile creep testing of single crystal specimens, it is desirable to maintain at a constant value the shear stress component on the active slip plane and in the active slip direction.* By suitable choice

* Hereafter this stress component will be called simply the "resolved shear stress."

of the beam dimensions, the loading beam just described can be used to maintain approximately constant resolved shear stress during creep of single crystals.

Electron Microscope Study of the Effect of Cold Work On the Subgrain Structure of Copper

by Laurence Delisle

This work represents the first step of an attempt to test the applicability of the electron microscope to the study of subgrain structures in copper. Observations on annealed and deformed single crystals and polycrystalline samples of copper are described.

IN the course of study of the structure of fine tungsten wires and tungsten rods with the electron microscope, well defined subgrain structures were observed. The size, size distribution, and orientation uniformity of the etch figures varied widely in different samples. Figs. 1 and 2, electron micrographs of a tungsten wire and of a tungsten rod, respectively, are illustrations of the difference in size and size distribution of the etch figures in different samples of the same metal. The observed differences, as pointed out in a previous paper,¹ appeared to be related to the heat and mechanical treatments of the samples. They were also consistent with the results reported in the literature on the mosaic structure of metals.² For that reason a program of research was initiated in an effort to obtain more systematic evidence of the possible relation of heat and mechanical treatments to the subgrain structure of metals as observed in the electron microscope. The purpose of this paper is to present observations made on the effect of cold work on the subgrain structure of copper.

Procedure

Starting Materials: Copper was the metal studied because it can be obtained in a high degree of purity, much information is available in the literature on its properties and its response to cold work and heat treatment, it shows no allotropic change, and it is sufficiently hard to be handled without great difficulty. Two groups of specimens were used: 1—single crystals cast from spectroscopically pure copper and 2—polycrystalline samples of oxygen-free high conductivity copper. Single crystals were studied because it was hoped that the elimination of a number of variables, such as grain boundaries, orientation differences, degree of purity, would simplify the problem and perhaps permit a better understanding of the phenomena that would be observed. The polycrystalline samples were designed to give a general picture of the changes considered.

The single crystals were made of copper which analyzed spectroscopically to better than 99.999 pct

L. DELISLE, Member AIME, formerly with Sylvania Electric Products Inc., is now associated with American Cyanamid Co., Stamford, Conn.

Discussion on this paper, TP 3528E, may be sent, 2 copies, to AIME by July 1, 1953. Manuscript, Nov. 17, 1952.

Cu. They were cast in vacuum, by the Bridgman method, in crucibles made of graphite with a maximum ash content of 0.06 pct. The mold design is shown in Fig. 3. It permitted casting crystals of the size and shape required for the experiments, so that the danger of introducing cold work in the original samples by cutting or other machining would be eliminated.

The polycrystalline samples were pieces, $\frac{3}{4}$ in. long, cut from a rod of oxygen-free high conductivity copper, $\frac{3}{8}$ in. in diameter. A flat surface, $\frac{1}{4}$ in. wide, was milled along the rods, polished, and etched. The samples were then annealed in vacuum at 850°C for 1 hr.

Polishing and Etching: Work previously done on tungsten,¹ polished mechanically and etched chemically,* had shown that: 1—the general appearance

* By "chemical etch" is meant attack of the surface of the specimen simply by flooding with or immersion into the etchant..

of the etch figures of a given sample was not altered by repeated polishings and etchings under similar conditions; 2—variations in the time of etching and the concentration of the etchant changed the definition of the etch figures, but did not alter their general size nor orientation distribution within the limits of observation. Further work confirmed the reproducibility of the subgrain structures observed in, 1—single crystals and polycrystalline samples of copper when polishing and etching were repeated under similar conditions, and 2—specimens of tungsten and polycrystalline copper when electrolytic polishing and etching were substituted for mechanical polishing and chemical etching, respectively. On the strength of these observations, it was felt that, if conditions of polishing and etching were kept constant, changes observed in the subgrain structure of a sample upon deformation and annealing would be attributable to such treatments. For that reason the conditions of polishing and etching were kept as constant as possible.

The single crystals were polished electrolytically in a bath of orthophosphoric acid in water, in the ratio of 1000 g of acid of density 1.75 g per cc to 1000 cc of solution, under a potential drop of 1.6 to 1.8 v. Electrolytic polishing was selected to prevent the formation of distorted metal in polishing. The same samples were etched by immersion in a 10 pct aque-

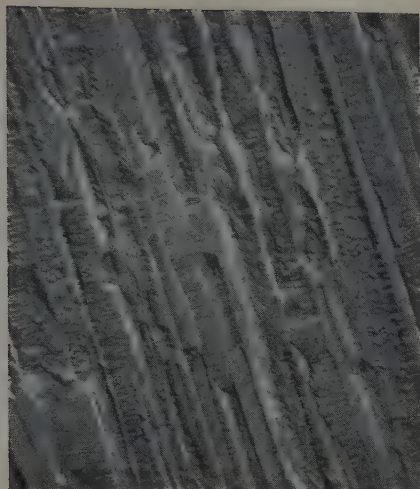


Fig. 1 (left)—Longitudinal section from tungsten wire 0.003 in. in diam. X10,000. Area reduced approximately 50 pct for reproduction.



Fig. 2 (right)—Tungsten rod. X10,000. Area reduced approximately 50 pct for reproduction.

ous solution of $(\text{NH}_4)_2\text{S}_2\text{O}_8$. They required a long etching time, of the order of 1 hr. As was already observed in the case of tungsten, shorter etching time brought out poorly defined structures. As the etching time was increased, the structure gradually became clear. At such a point a steady state of solution was approached since no changes could be observed upon prolonging the etching time by as long as 1 hr. For that reason the sharpness of the struc-

Table I. Amount of Compression Applied to Specimens

Specimen Designation	Degree of Compression, Pct
Single Crystals	
SO	17.0
S1	20.0
Polycrystalline Samples	
PO1	15.0
PO2	23.0
P1	12.4
P2	22.0

tures, rather than the etching time, was used as a guide in etching the single crystals.

The polycrystalline samples were polished mechanically and etched for 5 min by immersion in a 10 pct aqueous solution of $(\text{NH}_4)_2\text{S}_2\text{O}_8$. Mechanical polishing was chosen because it permits a better control of the flatness of the surface. The polishing of the original machined samples was carried out on emery paper, through No. 40, and on silk and velvet wheels. The specimens were repolished after the 850°C anneal prior to deformation. Polishing in this case, as well as polishing subsequent to deformation, was done only on silk and velvet. In both cases, alternate final polishing on velvet and etching were repeated three times.

Deformation: The specimens were deformed in compression. The strains produced are given in Table I.

Examination with the Electron Microscope: Parlodion replicas, stripped dry from the surface of the specimens and shadow cast with manganese were the specimens observed in the electron microscope.

Prior to examination with the electron microscope, polishing and etching were controlled as far as possible with the light microscope. Within the limit of resolution of the light microscope, there was always agreement between the structures observed in the light and in the electron microscopes.

Observations on Single Crystals

Fig. 4 is representative of the structure of one of the single crystals as cast and etched. The structure consists of blocks with edges that are practically straight and faces that appear smooth. Fig. 5, a stereographic projection of the crystal, obtained from an X-ray back-reflection pattern by the Geringer method, shows that a $\{111\}$ plane is nearly parallel to the plane of Fig. 4, an orientation consistent with the three-fold symmetry exhibited by triangular areas between the blocks shown in the micrograph. Goniometric measurements indicated that etching took place on $\{110\}$ and $\{111\}$ faces.

Slip lines appear on the surface of the single crystals after deformation (Figs. 6, 8, and 9). The spacing and intensity of the slip lines that could be observed are not uniform. The closest visible spacing of the flow lines is of the order of 0.1 micron in the plane of the figure. A fine structure is also visible on the surface of some of the blocks. It shows a parallel arrangement along lines closer than 0.1 micron, suggestive of slip lines. Upon repolishing and etching the deformed single crystals, a block structure appears as in the cast samples. Within these larger blocks, however, the fine structure which was faintly visible before repolishing and etching is clearly brought out, Fig. 7. After deformation, the edges of the larger blocks are neither as straight nor as smooth as they appeared in the cast single crystals.

Observations on Polycrystalline Samples

Figs. 10 and 11 illustrate the structure after repolishing and etching, of the polycrystalline specimens annealed for 1 hr at 850°C. Within the grains a block structure appears, but the blocks are smaller than those observed in the single crystals. As will be shown further, by comparison with the subgrain structure in deformed samples, the subgrain blocks of the fully annealed specimens are uniform in size and orientation, and that uniformity extends from

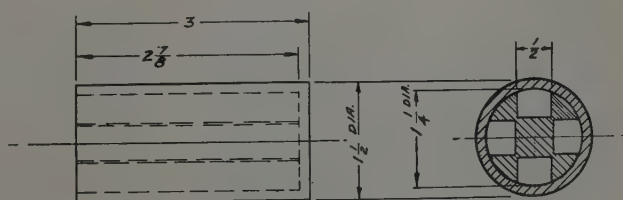


Fig. 3—Graphite mold used to cast single crystals.



Fig. 4—Copper single crystal S1, as cast and etched. X4000. Area reduced approximately 50 pct for reproduction.

the center to the boundaries of the grains. In Fig. 12 the blocks within a grain are shown. As in the case of the cast single crystals, the blocks have edges that are nearly straight lines and the faces of most of them show no structural details.

As a result of deformation, slip lines appeared on the surface of the specimens. As is to be expected, the direction of the slip lines changes with the orientation of the grains, Figs. 13 and 14. In some grains, a multiplicity of slip lines indicates that several slip

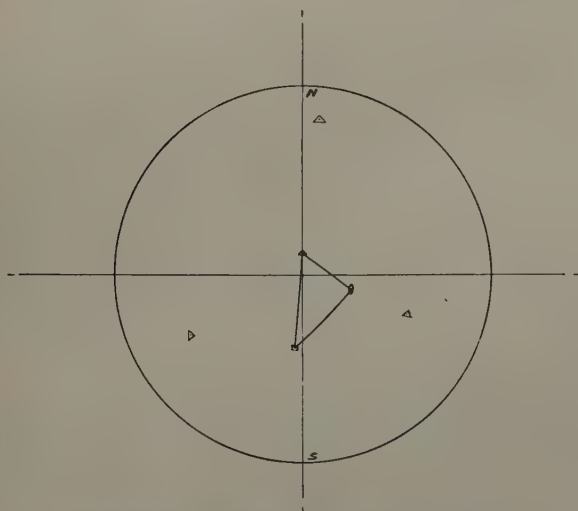


Fig. 5—Stereographic projection of single crystal S1, as cast.

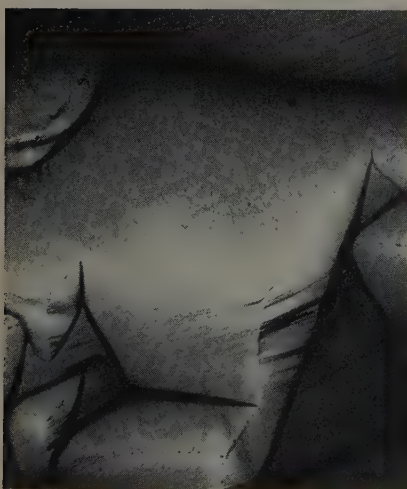


Fig. 6 (left)—Copper single crystal S1, deformed 20 pct. No repolishing nor etching after deformation. X4000. Area reduced approximately 50 pct for reproduction.

Fig. 7 (right)—Copper single crystal S1, deformed 20 pct. Repolished and etched after deformation. X4000. Area reduced approximately 50 pct for reproduction.



systems were operative, Fig. 15. The slip lines that can be seen within a grain are not evenly spaced, and are often crowded at grain boundaries, Fig. 16. The slip lines within a grain stop at the grain boundaries, Figs. 16 to 18, and slip lines in a different direction are sometimes visible in adjacent grains. In Figs. 16 and 17, one set of slip lines appear clearly in one of the grains and a second set, marked F, is faintly visible in the adjacent grain.

Upon repolishing and etching the polycrystalline samples, the slip lines disappear, but other evidences of deformation remain or become visible:

1—Some of the subgrain blocks are severely deformed, especially near grain boundaries, Figs. 19 and 20.

2—The uniformity of orientation of the subgrain blocks that was observed within most grains of the annealed material is destroyed by cold work, Figs. 21 to 23. Within grains, cold work seems to produce shifts in orientation. Such shifts manifest themselves by a change in the appearance of the subgrain blocks that look as if they were seen from different angles in different parts of the grains. The orientation shift is visible across Fig. 21 from the bottom left-hand corner to the top right-hand corner. A comparison of Figs. 10 and 21 brings out the difference in orientation uniformity before and after deformation, respectively. The change in orientation produced by cold work within individual grains is even more pronounced at grain boundaries, Fig. 22. A comparison of Figs. 22 and 18 suggests that the regions of a deformed grain that appear differently oriented after repolishing and etching may be bounded by glide planes.

3—A structure, much finer than the original blocks, of the order of 1000Å, appears, after cold working, at grain boundaries, on the surface of the blocks that had a smooth surface after annealing, and often in the angles formed by meeting subgrain blocks, Figs. 24 and 25. This fine structure is of the same order of size as the fine structure observed in deformed single crystals after electrolytic repolishing and etching, Fig. 7.

4—Some subgrain blocks broke completely into lamellae, Fig. 26. The subgrain blocks shown in the upper and in the lower parts of Fig. 26 are differently oriented within the same grain. They are separated by a region of blocks consisting of lamellae. The arrangement suggests that rotation of the lamellae of the intermediate blocks permits a fit between the two regions of differently oriented blocks of the same grain.

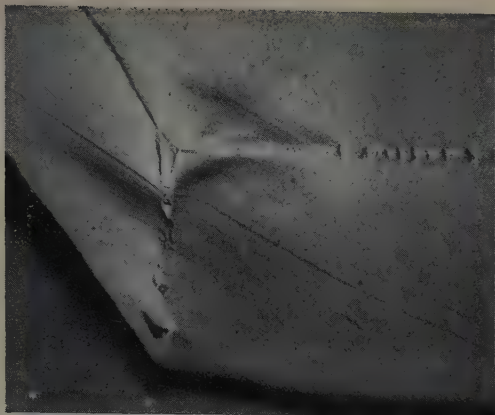


Fig. 8 (left)—Copper single crystal S1, deformed 20 pct. Face other than that shown in Fig. 6. No repolishing nor etching after deformation. X10,000. Area reduced approximately 50 pct for reproduction.

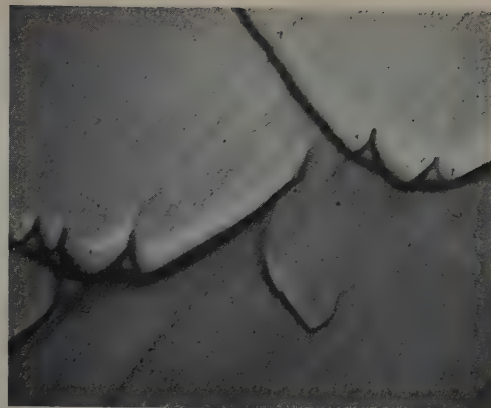


Fig. 9 (right) — Copper single crystal S0, deformed 17 pct. No repolishing nor etching after deformation. X10,000. Area reduced approximately 50 pct for reproduction.



Fig. 10 (left)—Polycrystalline copper, annealed, polished, and etched. Blocks within a grain. X5000. Area reduced approximately 50 pct for reproduction.



Fig. 11 (right)—Polycrystalline copper, annealed, polished, and etched. Blocks in adjacent grains. X5000. Area reduced approximately 50 pct for reproduction.



Fig. 12 (left)—Polycrystalline copper, annealed, polished, and etched. Blocks within a grain. X10,000. Area reduced approximately 50 pct for reproduction.



Fig. 13 (right)—Polycrystalline copper, deformed. No repolishing nor etching after deformation. X10,000. Area reduced approximately 50 pct for reproduction.



Fig. 14 (left)—Polycrystalline copper, deformed. No repolishing nor etching after deformation. X10,000. Area reduced approximately 50 pct for reproduction.

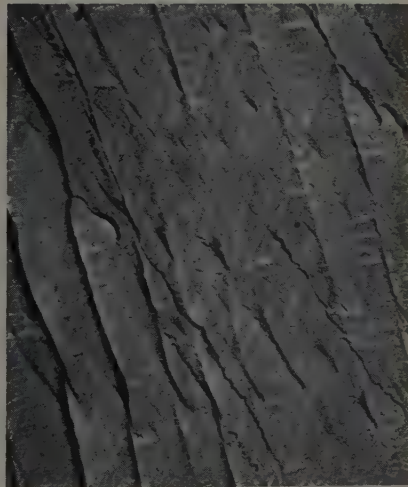


Fig. 15 (right)—Polycrystalline copper, deformed. No repolishing nor etching after deformation. X10,000. Area reduced approximately 50 pct for reproduction.



Fig. 16—Polycrystalline copper, deformed. No repolishing nor etching after deformation. X10,000. Area reduced approximately 50 pct for reproduction.

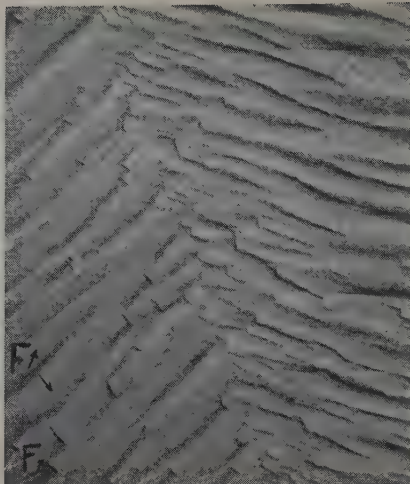


Fig. 17—Polycrystalline copper, deformed. No repolishing nor etching after deformation. X10,000. Area reduced approximately 50 pct for reproduction.



Fig. 18—Polycrystalline copper, deformed. No repolishing nor etching after deformation. X10,000. Area reduced approximately 50 pct for reproduction.



Fig. 19—Polycrystalline copper, deformed 22 pct. Polished and etched after deformation. X10,000. Area reduced approximately 50 pct for reproduction.



Fig. 20—Polycrystalline copper, deformed 22 pct. Polished and etched after deformation. X10,000. Area reduced approximately 50 pct for reproduction.



Fig. 21—Polycrystalline copper, deformed. Polished and etched after deformation. X5000. Area reduced approximately 50 pct for reproduction.

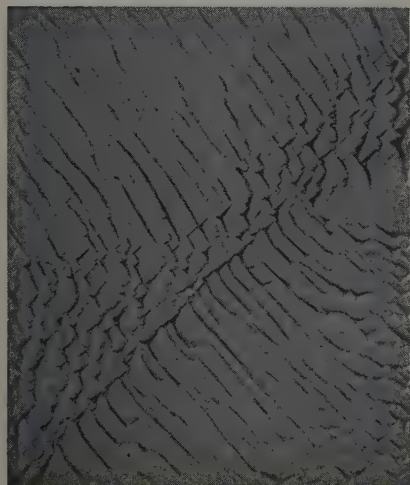


Fig. 22—Polycrystalline copper, deformed. Polished and etched after deformation. X5000. Area reduced approximately 50 pct for reproduction.



Fig. 23—Polycrystalline copper, deformed. Polished and etched after deformation. X5000. Area reduced approximately 50 pct for reproduction.

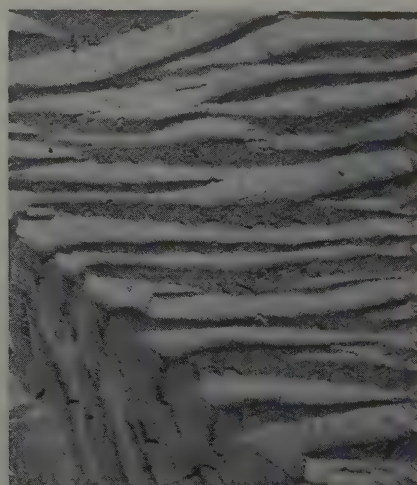


Fig. 24—Polycrystalline copper, deformed 22 pct. Repolished and etched after deformation. X10,000. Area reduced approximately 50 pct for reproduction.

Discussion of Results

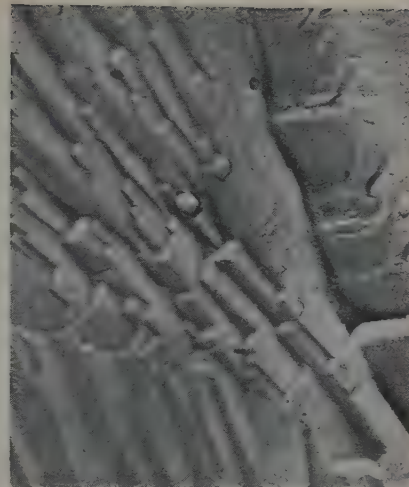
The electron micrographs presented in this paper add support to the existence of a complex subgrain structure in metals. The size of the smallest subgrain units observed in copper, like those previously observed in tungsten,¹ of the order of 1000Å, corresponds to that calculated by Bragg, Darwin, and James³ for the units of a mosaic structure from measurements of intensity of reflection of X-rays by crystals, by Wood⁴ for the limiting size of crystallites from line broadening, and by Born⁵ for a perfect lattice from quantum mechanics considerations. Such a dimension was used by Bragg³ to compute a satisfactory value for the elastic limit of strain of many metals. The size of the larger units of the subgrain structures observed in copper in this paper, and in tungsten previously,¹ is of the order of magnitude calculated by Taylor⁷ for the length through which a dislocation travels before being stopped by a surface of misfit. There seems to be therefore a size relationship between the subgrain structures observed with the electron microscope and the mosaic structures proposed by a number of authors.

On the other hand, there appears to be a relationship between mosaic structures and dislocations. According to Cottrell,⁸ it is "reasonable to suppose that the more macroscopic irregularities in crystals, e.g. mosaic structure and crystal fragmentation in the cold work state, are built up from assemblies of dislocations." If dislocations exist, the metal in the vicinity of a dislocation is stressed and for that reason its rate of etching should be faster than that of the stress-free material. If the blocks of the subgrain structure are considered as separated by arrays of dislocations, they should be brought out by etching. Read and Shockley⁹ explain that veining obtained by Lacombe¹⁰ is the result of etching that starts at dislocations. Once started, the etching proceeds on the planes that dissolve fastest. The same planes have slightly different orientations in different blocks and that difference accentuates the effect of etching. On a different scale of magnitude and disorientation, the phenomenon is similar to the etching of grains as ordinarily applied in metallography. The sizes of the subgrain blocks in the cast single crystals and in the annealed polycrystalline samples of copper studied in this paper agree with the calculations of Read and Shockley⁹ for small angles of misfit.

The number of dislocations should be a function of internal stresses and degree of purity.^{7, 8, 11-14} The single crystals used in these experiments were made of spectroscopically pure copper, they were cast in graphite of high purity, in vacuum, and they were cooled very slowly. They were therefore freer from impurities and internal stresses than the polycrystalline samples, made of commercial copper, and they should have a lower density of dislocations. The subgrain blocks of the cast single crystals are indeed much larger and therefore seem to represent a higher degree of perfection than those of the polycrystalline samples, Figs. 4 and 11.

The number of dislocations should be increased by cold work. The appearance of a fine structure within the blocks of the subgrain structure of the single crystals and the polycrystalline samples upon deformation, Figs. 7, 25, 26, could be explained by an increase in the number of dislocations. In Fig. 7, the alignment of the fine structure within the larger blocks suggests traces of slip planes. Such a structure was not visible in the cast crystals. It seems therefore that it was brought out by cold work. It

Fig. 25—Polycrystalline copper, deformed 22 pct. Repolished and etched after deformation. X10,000. Area reduced approximately 50 pct for reproduction.



is visible after etching, so that it is not a form of slip lines. It could be a structure that existed in the cast crystals,^{3, 5} but could not be resolved because the degree of disorientation of its units was too small. Deformation increased the degree of disorientation and permitted differential etching. It could also be recrystallized crystallites formed, according to Wood,⁴ when cold work on a slip system reaches a certain value. This fine structure has the characteristics of the strain markings reported by Burke and Barrett.¹⁵ If the evidence produced by Burke and Barrett that the strain markings are traces of slip planes rather than mechanical twins is accepted, the etching of such markings could be the result of the presence of the recrystallized crystallites proposed by Wood.

The individual subgrain blocks of the cold-worked samples, after repolishing and etching, often appear bent by the deformation, Figs. 19 and 20. Their size is comparable to the size they had before deformation, Figs. 12 and 20, and they can easily be visualized as the original blocks strained individually by different amounts in different regions of the grains. Such a mechanism seems possible only if the subgrain blocks revealed by etching are a real structure like the grains themselves.

It has been proposed by Burgers,¹⁶ Kochendorfer,¹⁷ and Laurent¹⁸ that dislocations during cold work are created at crystallite boundaries which produce notch effects. The stress field of the new dislocations counteracts the notch effect so that the production of new dislocations becomes more difficult and strain hardening occurs. In the single crystals, the more clearly visible flow lines often pass through the angles formed

Fig. 26—Polycrystalline copper, deformed 15 pct. Repolished and etched after deformation. X10,000. Area reduced approximately 50 pct for reproduction.



by meeting subgrain boundaries that could act as notches, Fig. 9. When several slip systems are operative, the dislocations connected with the first slip system should be an obstacle to the motion of the dislocations on a second slip system. In Fig. 15, the prominent, more widely spaced slip lines appear to have been stopped at places by a finer structure. In the single crystals, no grain and fewer subgrain boundaries hindered slip than in the polycrystalline samples. For that reason perhaps deformation proceeded in one slip system more extensively and slip lines in single crystals are often found to be closely spaced, Figs. 6 and 8. The latter figures are reminiscent, although on a different magnification scale, of electron micrographs of slip lines in aluminum published by Heidenreich and Shockley.¹⁹

On account of the glide in different directions, a slip plane becomes a grid of dislocations which, according to Cottrell,⁸ "constitutes a transition surface between two crystals rotated with respect to each other about an axis normal to the transition surface." The formation of such transition surfaces would explain the presence, upon deformation, of regions differently oriented within individual grains of the polycrystalline samples, Figs 21 to 23 and 26.

This paper described part of the results of an attempt to apply the electron microscope to the study of the changes in the subgrain structure of metals produced by cold work and recovery. Because its scope was wide and it represented a relatively new method of approach, the work was intended to be in the nature of a survey. For that reason no claim was made at conclusiveness and only possible relationships between accredited theories and the structures observed were indicated. It is hoped, however, that the possibility of the relationships pointed out will be considered sufficient to arouse interest in the potentialities of the electron microscope for the study of subgrain structures in metals.

Conclusions

1—A subgrain structure was observed, by means of the electron microscope, in single crystals of spectroscopically pure copper and in polycrystalline samples of oxygen-free high conductivity copper.

2—A study was undertaken in an effort to find out whether consistent changes would be produced by cold work and recovery in the subgrain structures observed in copper. Observations on the changes produced by cold work are reported.

3—The subgrain blocks observed in the cast and slowly cooled single crystals, as well as in the annealed polycrystalline samples, appear to have relatively straight edges and smooth surfaces.

4—The subgrain blocks observed in the cast single crystals are larger than those observed in the annealed polycrystalline samples.

5—Repolishing and etching of the deformed single crystals and polycrystalline samples brought out, within blocks that appear to correspond to the subgrain blocks observed prior to deformation, a finer structure, the size of which is of the order of 1000Å.

6—The degree of disorientation of the larger subgrain blocks within a single crystal or individual grains of the polycrystalline samples is increased by cold work. The larger subgrain blocks also appear individually deformed by cold work.

7—The larger and finer subgrain structures observed differ in size by an order of magnitude. They both correspond to crystallite dimensions reported in the literature on the basis of entirely different observations.

8—Comparable structures were previously observed in tungsten.

Acknowledgments

The author wishes to express her gratitude to: Sylvania Electric Products Inc. who generously financed this research and supplied the laboratory facilities; Walter E. Kingston, Manager, Metallurgical Laboratories, Sylvania Electric Products Inc., whose encouragement and patient assistance made this research possible; George L. Kehl, School of Mines, Columbia University, for his continued guidance; J. S. Smart, Jr., Superintendent of Copper Developments, American Smelting and Refining Co., who courteously supplied the high purity copper; I. N. Zavarine, Sylvania Electric Products, Inc., for the preparation of the copper single crystals; Carol C. Gauger, Sylvania Electric Products, Inc., for her unfailing and very capable assistance with the photographic work; and Virginia Hannaford and Patricia Van Etten, Sylvania Electric Products, Inc., for the X-ray diffraction patterns.

References

- ¹ Laurence Delisle and Gordon A. Davis: Examination of Sub-Grain Structures with the Electron Microscope. *The Physics of Powder Metallurgy*. (1951) New York. McGraw-Hill Book Co.
- ² Ch. Crussard and A. Guinier: Symposium sur la Structure Mosaïque des Métaux. *Revue de Métallurgie* (February 1949) p. 61.
- ³ W. Lawrence Bragg, C. G. Darwin, and R. W. James: The Intensity of Reflexion of X-Rays by Crystals. *Philosophical Magazine* (1926) **1**, p. 897.
- ⁴ W. A. Wood: The Lower Limiting Crystallite Size and Internal Strains in Some Cold-Worked Metals. *Proc. Royal Soc.* (1939) **172A**, p. 231.
- ⁵ Max Born: The Free Path for the Transfer of Energy in Crystals. *Proc. Math. Phys. Soc., Egypt* (1946) No. 3, p. 35.
- ⁶ Lawrence Bragg: Effect Associated with Stresses on a Microscopic Scale. *Symposium on Internal Stresses in Metals and Alloys*. Inst. Metals (1948) p. 221.
- ⁷ G. T. Taylor: The Mechanism of Plastic Deformation of Crystals. *Proc. Royal Soc.* (1934) **145A**, p. 362.
- ⁸ A. H. Cottrell: Theory of Dislocations. *Progress in Metal Physics*. (1949) p. 77. New York. Interscience Publishers, Inc.
- ⁹ W. T. Read and W. Shockley: Dislocation Models of Crystal Grain Boundaries. *Physical Review* (May 1950) p. 275.
- ¹⁰ P. Lacombe: "Sub-Boundary" and Boundary Structures in High Purity Aluminum. *Report of Conference on Strength of Solids*. Phys. Soc., London. (1948) p. 91.
- ¹¹ J. M. Burgers: Geometrical Considerations Concerning the Structural Irregularities to be Assumed in a Crystal. *Proc. Physical Soc., London*. (1940) **52**, p. 23.
- ¹² J. S. Koehler: *Physical Review* (1941) **60**, p. 397.
- ¹³ W. F. Brown: *Physical Review* (1941) **60**, p. 139.
- ¹⁴ F. C. Frank: On Slip Bands as a Consequence of the Dynamic Behaviour of Dislocations. *Report of Conference on Strength of Solids*. Phys. Soc., London (1948) p. 46.
- ¹⁵ J. E. Burke and C. S. Barrett: The Nature of Strain Markings in Alpha Brass. *Trans. AIME* (1948) **175**, p. 106; *METALS TECHNOLOGY* (February 1948).
- ¹⁶ W. G. and J. M. Burgers: *Second Report on Viscosity and Plasticity*. Acad. Sci., Amsterdam (1938) p. 200.
- ¹⁷ A. Kochendorfer: *Ztsch. Phys.* (1938) **108**, p. 244.
- ¹⁸ P. Laurent: *Revue de Métallurgie* (1945) **42**, pp. 79, 125, 194, 230.
- ¹⁹ R. D. Heidenreich and W. Shockley: Study of Slip in Aluminum Crystals by Electron Microscope and Electron Diffraction Methods. *Report of Conference on Strength of Solids*. Phys. Soc., London (1948) p. 57.

Martensite Habit Plane in Quenched Ti-Mn Alloys

by You Chao Liu and Harold Margolin

Investigation of martensite habit plane in water-quenched Ti-Mn alloys was carried out in the range of manganese contents between 4.35 and 5.25 pct. On the basis of 22 measurements, the poles were observed to fall into two groups, indicating the existence of two habit planes. The Miller indices of the poles close to these two groups were found to be $\langle 334 \rangle_{\beta}$ and $\langle 344 \rangle_{\beta}$.

TITANIUM has an allotropic transformation at $882.1^{\circ} \pm 0.5^{\circ}\text{C}^1$ by which the high temperature β (body-centered cubic) phase changes to α (hexagonal close-packed) phase. It is well known, as in the case of low carbon steel, that the unalloyed high temperature β phase cannot be retained no matter how rapid the cooling rate. However, the addition of alloying elements usually lowers the transformation temperature continuously and stabilizes the β phase to a temperature much lower than the allotropic transformation temperature in pure titanium. A typical example of this behavior is found with manganese-alloying of titanium.

Fig. 1 shows the titanium-rich Ti-Mn equilibrium diagram as established by Battelle Memorial Institute.² The addition of manganese lowers the β transus line and the eutectoid reaction takes place at 550°C , the eutectoid composition being 20 wt pct Mn. However, upon quenching to room temperature from the β field, the β phase can be completely retained with much less manganese, see Fig. 2. If the composition is less than that required to stabilize the β phase completely, a plate-like structure, similar to that of martensite in other alloy systems, appears as shown in Fig. 3. Much lower alloying content merely intensifies the amounts of these transformed structures, as shown in Fig. 4.

This paper presents the results of an investigation of the habit plane of these martensitic structures in Ti-Mn alloys.

Experimental Procedure

Investigation of the pole of a given platelet was made using the two-surface method of analysis.³ In

Y. C. LIU, Student Associate AIME, and H. MARGOLIN, Junior Member AIME, are Research Associates, Engineering Research Div., New York University, New York.

Discussion on this paper, TP 3498E, may be sent, 2 copies, to AIME by May 1, 1953. Manuscript, Sept. 15, 1952; revised, Jan. 27, 1953. Los Angeles Meeting, February 1953.

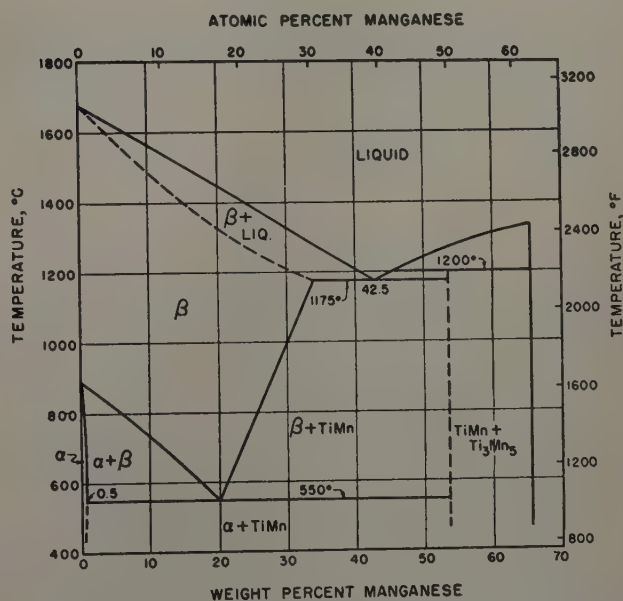


Fig. 1—Titanium-rich Ti-Mn equilibrium diagram. After Battelle Memorial Institute.

order that a given martensite trace on two surfaces be readily recognized both at low and high magnifications, it is desirable that only a small amount of martensite be present. From a review of the data obtained at Battelle Memorial Institute⁴ on quench hardening in Ti-Mn alloys and the results of Duwez⁵ on transformation in Ti-Mo alloys, it was decided that the most appropriate Ti-Mn composition for this study would be about 6 pct Mn. A group of alloys containing from 3 to 10 pct Mn was made to bracket this composition. The choice of the 6 pct alloy was apparently proper, since it was later learned that approximately 5.5 to 6 pct Mn is required to stabilize the β phase on water quenching.

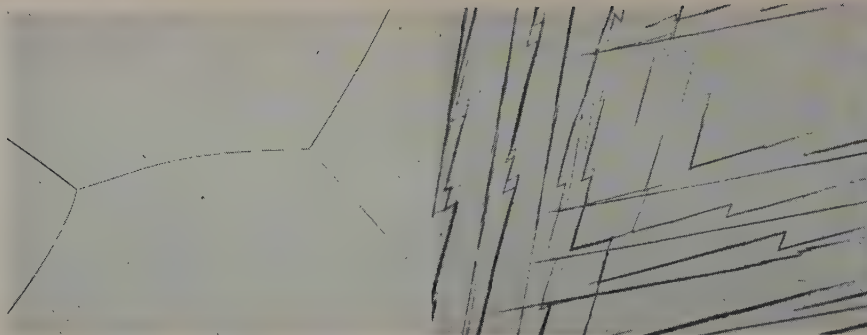


Fig. 2—Ti-Mn alloy (8 pct Mn), water-quenched from 1200°C. Retained β . X75. Area reduced approximately 60 pct for reproduction.

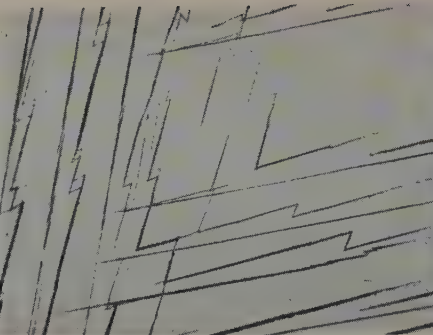


Fig. 3—Typical martensitic structure in Ti-Mn alloys in the range of compositions investigated. X150. Area reduced approximately 60 pct for reproduction.

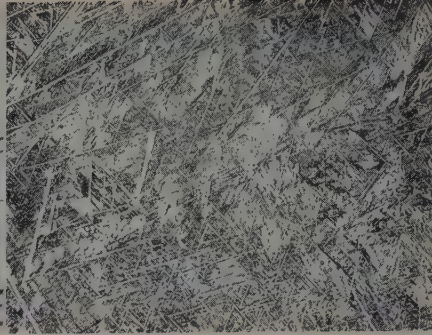


Fig. 4—Ti-Mn alloy (1 pct Mn) water-quenched from 1200°C. Transformed β . X100. Area reduced approximately 60 pct for reproduction.

Five different specimens with a nominal manganese content of 6 pct were finally used in this investigation. The actual compositions of these specimens varied from 4.35 to 5.25 pct Mn. In the case of the 4.35 pct specimen, transformation was so extensive that angular relations of selected platelets could be measured only by first taking photographs of two surfaces and then matching them. A specimen with a nominal manganese content of 3 pct produced Laue spots so broad as to make orientation determination impossible.

All specimens, $\frac{3}{8} \times \frac{3}{8} \times \frac{3}{4}$ in. in size, were heat-treated for 60 to 70 hr at 1200°C, in argon atmospheres to obtain grains of 0.8 to 1 cm in diameter, which proved to be adequate for this investigation.

Three polished surfaces* around the specimen

* The standard procedures for polishing and etching titanium and its alloys as employed at the New York University Metallurgical Laboratory⁶ have been followed.

corner were prepared in each specimen. This arrangement had the dual advantage that many traces

across the edges were available and that the angles between polished surfaces could be measured by manipulation of the stereographic projection.

The stereographic method used in the measurement of the angles between surfaces is described as follows: Fig. 5 shows three polished surfaces at corner O. Angles α , β , and γ were measured with the graduated circle on a metallograph. With surface A as the plane of the stereographic projection and corner O at the center, azimuthal angle α is located as shown in Fig. 6. The intersection of planes B and C, MN, is then represented in Fig. 6 as point M in the projection. The pole of surface C (which is defined by the edges OP and MN) is designated C and is located 90° from the great circle PMP'. Pole B is similarly located and represented. The three polished surfaces, A, B, and C in Fig. 5 are thus represented in Fig. 6 by their respective poles O, B, and C. The angles between the planes are equal to 180° minus the angle between the corresponding

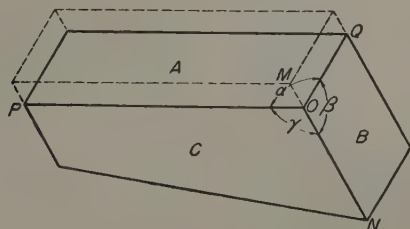


Fig. 5—Schematic diagram of intersection of surface planes A, B, and C at specimen corner.

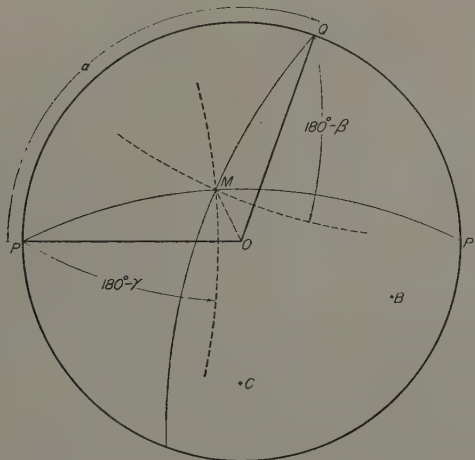
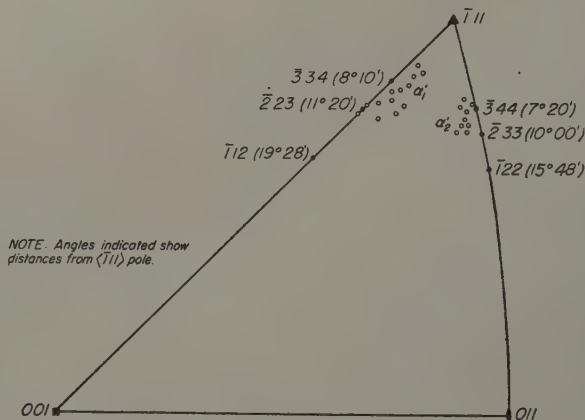


Fig. 6—Stereographic plot of Fig. 5.



NOTE. Angles indicated show distances from $\langle 111 \rangle$ pole.

Fig. 7—Location of poles of habit planes in a standard stereographic triangle.

poles; the latter angle can be measured along great circles in the projection.

The grain orientations were determined from Laue patterns by the back-reflection X-ray method.⁷ In the early stage of this work, difficulties were encountered due to the peculiar nature of the back-reflection X-ray photographs obtained. These showed high intensity spots, not related to any zones, and a scarcity of zones. The number of Laue spots was limited due to the fact that titanium has a very high absorption coefficient with respect to copper radiation. By using an exposure time of 18 hr with a current of 20 ma at 35 kv, sufficient spots for orientation determination were produced. The high in-

tensity spots could not be accounted for and were not considered. The orientations of two polished surfaces of a grain were checked against the value for the angle between these two planes as determined by the stereographic method described earlier. The difference between these two orientations, when brought into coincidence, was about one degree.

After it was learned that two habit planes occur in the present alloy system, it seemed appropriate to attempt to correlate the microstructure with habit plane. The fineness of the transformed structure in most cases ruled out the possibility of using the two-surface method; consequently a single-surface method was employed. The validity of the latter analysis then depended on the consistency of a large number of measurements.

In the single-surface analysis the orientation of the grain where the microstructure is to be studied, as shown in Fig. 8, is plotted on a stereographic projection. All permutations of the two habit planes, a



Fig. 8—Stereographic plot of single-surface analysis of traces of fine transformed needles.

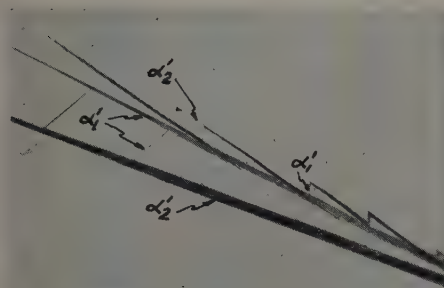


Fig. 9—Intimate association of α'_1 and α'_2 platelets. X400. Area reduced approximately 60 pct for reproduction.

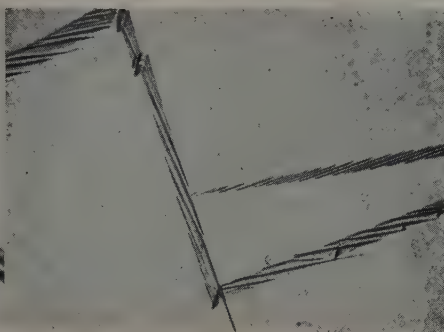


Fig. 10—"Twins" within martensite. X650. Area reduced approximately 60 pct for reproduction.

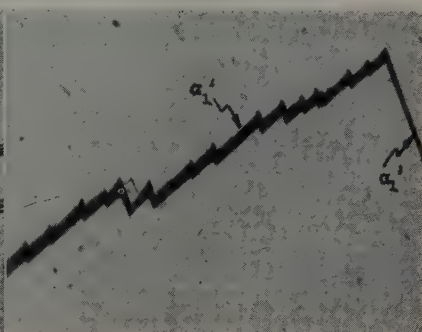


Fig. 11—Change in direction of propagation of martensite. X650. Area reduced approximately 60 pct for reproduction.

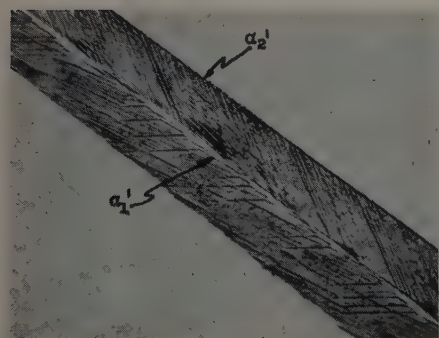


Fig. 12—Two parallel bands of martensite. X650. Area reduced approximately 60 pct for reproduction.

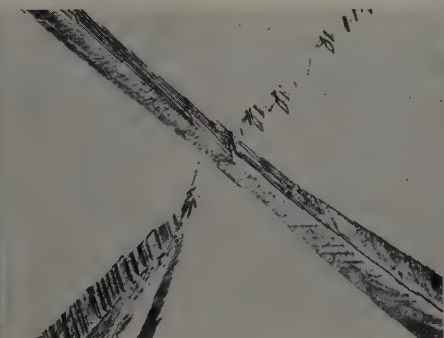


Fig. 13—Same two bands shown in Fig. 12 at point of separation. X650. Area reduced approximately 60 pct for reproduction.



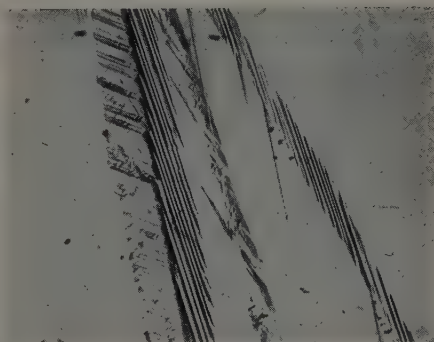
Fig. 14—Parallel array of martensitic platelets. X650. Area reduced approximately 60 pct for reproduction.

total of 12 each, are therefore plotted as the area corresponding to the original data obtained, Fig. 7. The trace normal of the investigated traces is then superimposed on the projection. If the habit plane of these traces corresponds to either of the two habit planes found, the trace normals must pass through one of these 24 areas.

Experimental Results and Discussion

Based on 22 measurements (two-surface) made on six grains in five crystals, the poles of the habit planes were found to fall distinctly into two groups, designated as α'_1 and α'_2 in Fig. 7, thus indicating the

Fig. 15—Another view of parallel martensitic platelets. X650. Area reduced approximately 60 pct for reproduction.



existence of two habit planes. The indices of these two habit planes were determined to be close to $\{334\}_\beta$ and $\{344\}_\beta$.

The martensite corresponding to the α'_1 habit occurs most frequently and appears as fine straight lines, Fig. 9. In more than 40 measurements on this type of structure, it was found that the trace normals, without exception, passed through the α'_1 region.

Figs. 10 and 11 show that the martensite platelet changes its direction of propagation quite readily. From 11 analyses, it has been found that the component parts of this type of structure always follow the α'_1 habit plane and that the poles of these two α'_1 planes always have an angular separation of 60° to 64° as measured on the stereographic projection.

A number of these interesting microstructures, in addition to those shown previously were also encountered during the present investigation. Some of these structures are shown in Figs. 9 to 15. Fig. 12 shows two parallel bands, one with smooth boundaries and the other jagged. These platelets generally are found together and the habit plane along which they occur is indicated. However, the submarkings within the bands cannot be accounted for on the basis of α'_1 or α'_2 planes of the matrix. This type of structure is the thickest observed, the estimated thickness being less than 0.001 in. Fig. 13 shows the same structure as Fig. 12. At the end of this coupled structure, the platelets tend to separate. The thickness of the platelets is reduced when they meet other martensitic transformation products.

Other types of substructure are often found in the martensite platelet. In one type, the substructure frequently extends into the untransformed matrix and in others it resembles twin formation in hexagonal close-packed metals. Fig. 9 shows dark-etching needles which are not confined to the main platelet, but other parallel markings which are confined are also visible. Fig. 10 shows "twins" within a martensite platelet.

The transformation structure is sometimes seen as a cluster of closely-separated parallel lines, as shown in Figs. 14 and 15. These markings can run either transverse or almost parallel to the direction of propagation.

In addition to the above, the following observations on the martensitic structure have also been made:

1—The mid-rib structure, characteristic of mar-

tensite structure in steel, does not occur in the Ti-Mn system.

2—Any boundary between the platelets and matrix corresponds, without exception, to one of the two habit planes found.

3—Submarkings within martensite cannot always be accounted for on the basis of α'_1 or α'_2 .

Summary

1—Two habit planes of martensite with Miller indices close to $\{334\}_\beta$ and $\{344\}_\beta$ were determined in the Ti-Mn system.

2—A variety of martensite microstructures have been found in the present alloy system. Many of these are quite different from the martensitic structures observed in steel, and in none of the structures is a mid-rib observed.

Acknowledgments

This paper is based on part of an investigation sponsored by the United States Army Ordnance Corps, Watertown Arsenal, Watertown, Mass., on Contract No. DA-30-069-ORD-207.

The authors also wish to express their appreciation to E. S. Machlin of Columbia University for his helpful discussions, and to L. D. Jaffe of Watertown Arsenal Laboratory for his interest and encouragement.

References

- ¹ A. D. McQuillan: Some Observations on the Alpha-Beta Transformation in Titanium. *Journal Inst. Metals* (November 1950) p. 249.
- ² Battelle Memorial Institute: Summary Report on the Phase Diagrams of the Titanium-Tantalum, Titanium-Tungsten, and Titanium-Manganese Alloy Systems, for Wright Air Development Center, Contract No. AF33(038)-8544, Jan. 24, 1952.
- ³ C. S. Barrett: *Structure of Metals*. New York. McGraw-Hill Book Co.
- ⁴ Battelle Memorial Institute: Research and Development on Titanium Alloys. Contract No. AF-33(038)-3736, July 30, 1940 to April 30, 1951.
- ⁵ Pol Duwez and J. L. Taylor: Effect of Rate of Cooling on the Alpha-Beta Transformation in Titanium and Titanium-Molybdenum Alloys. *Trans. AIME* (1951) 191, p. 765; *JOURNAL OF METALS* (September 1951).
- ⁶ H. Margolin: Electropolishing of Titanium Alloys. Symposium on Analysis and Metallography of Titanium, sponsored by Armour Research Foundation, June 1951.
- ⁷ A. B. Greninger: Determination of Orientations of Metallic Crystals by Means of Back-Reflection Laue Photographs. *Trans. AIME* (1935) 117, p. 61.

Technical Note

Observations on the Phase TiAg

by R. J. Van Thyne, W. Rostoker, and H. D. Kessler

THE existence of the phase TiAg has not been reported previously. Other investigators have denied the existence of compounds in the Ti-Ag system.^{1,2} However, phases of equi-atomic proportion have been reported by Raub, et al.¹ in the (similar) systems of titanium with gold and copper and zir-

conium with silver. Raub's work indicated that titanium and silver are immiscible in the liquid state. No evidence of this was found although a very wide melting range exists which makes the preparation of homogeneous alloys difficult. TiAg is apparently formed by a peritectic reaction between β

titanium and a silver-rich liquid phase.

The 68 pct Ag-Ti alloys were melted in a nonconsumable tungsten electrode arc-melting furnace. A detailed description of the melting techniques may be found elsewhere.³ Two alloys were prepared. Iodide titanium and a very pure grade of silver were used in the preparation of one alloy and sponge titanium was used for the other alloy. Fig. 1 illustrates the single phase microstructure of the alloy prepared with iodide titanium, annealed at 900°C for 24 hr.

The hardness of TiAg is quite low for an intermediate phase. A hardness value of 130 diamond pyramid hardness was obtained for both the higher and lower purity alloys. The alloy prepared with sponge titanium was cold-pressed 75 pct although edge cracking resulted.

The structure of the TiAg phase was determined by X-ray diffraction analysis. Powder patterns were taken on a 14 cm diam camera using filtered K α copper radiation. By trial it was found that the lines could be indexed on a tetragonal Hull-Davey type chart for a unit cell having an axial ratio just less than unity.

The relative intensities of the lines indicated a CuAu ordered face-centered tetragonal structure in which the atoms of one species are located at the

intensities were measured with aid of a Norelco type Geiger counter spectrometer.

The dimensions of the unit cell were computed by a least squares solution of equations for interplanar spacing of five high angle lines. The results were as follows: $a = 4.096$ kX, $c = 4.069$ kX, $c/a = 0.993$. Using these values, the interplanar spacings of each of the indexed lines were calculated and compared to the observed values. Table I summarizes the calculated and observed d values and relative intensities of the indexed lines.

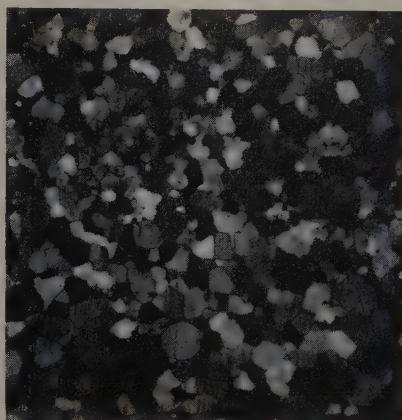


Fig. 1—68 pct Ag-Ti alloy annealed at 900°C for 24 hr and water-quenched. The intermediate phase, TiAg. Unetched, polarized light. X250. Area reduced approximately 50 pct for reproduction.

Table I. Comparison of Calculated and Observed Values of Line Spacings (kX Units) and Relative Line Intensities

hkl	d (Observed)	d (Calculated)*	I (Observed)	I (Calculated)
110	2.728	2.896	15	16
111	2.357	2.360	100	100
200	2.050	2.048	29	35
002	2.030	2.039	16	18
112	1.634	1.665	5	6
220	1.449	1.448	10†	7
202	1.443	1.443	18	23
311	1.235	1.234	14	14
113	1.228	1.228	8	13
222	1.182	1.180	7	12
312	1.090	1.093	2	3
004	1.014	1.017	2	2
331	0.9380	0.9394	8	7
420	0.9166	0.9159	6	7
204	0.9117	0.9111	6	7

* Calculated from the least squares solution for the c and a parameters.

† Intensity is anomalously high because of superposition on (202) line.

(0, 0, 0) and $(\frac{1}{2}, \frac{1}{2}, 0)$ positions and of the other species, at the $(0, \frac{1}{2}, \frac{1}{2})$ and $(\frac{1}{2}, 0, \frac{1}{2})$ positions in the unit cell. On the assumption that this was the correct structure, the relative intensities of the lines were calculated by means of the familiar equation

$$I_{hkl} \propto p \cdot F^2 \cdot \frac{1 + \cos^2 2\theta}{\sin^2 \theta \cos \theta}$$

where p is the multiplicity factor; F , the structure factor; and θ , the Bragg angle. Actual relative line

R. J. VAN THYNE is Assistant Metallurgist, Nonferrous Metals Research Section, W. ROSTOKER is Senior Metallurgist, Physical Metallurgy Section, and H. D. KESSLER, Junior Member AIME, is Supervisor, Nonferrous Metals Research Dept., Armour Research Foundation of Illinois Institute of Technology, Chicago.

TN 156E. Manuscript, Jan. 23, 1953.

Acknowledgments

This work was sponsored by the Ordnance Corps, U. S. Army, Watertown Arsenal, Watertown, Mass., whose financial assistance on Contract No. DA 11-022-ORD-288 and permission to publish is gratefully acknowledged. The authors also wish to express their appreciation to C. A. Johnson for the metallographic work.

References

- ¹ E. Raub, P. Walter, and M. Engel: Die Legierungen des Titans mit Kupfer, Silber und Gold. *Ztsch. Metallkunde* (April 1952) **43**, pp. 112-118.
- ² F. Laves and H. J. Wallbaum: *Naturwissenschaften* (1939) **27**, pp. 674-675; also H. J. Wallbaum: *Naturwissenschaften* (1943) **31**, pp. 91-92.
- ³ M. Hansen, H. D. Kessler, and D. J. McPherson: The System Titanium-Silicon. *Trans. ASM* (1952) **44**, pp. 518.
- ⁴ H. R. Ogden, D. J. Maykuth, W. L. Finlay, and R. I. Jaffee: Constitution of Titanium-Aluminum Alloys. *Trans. AIME* (1951) **191**, pp. 1150-1155; *JOURNAL OF METALS* (December 1951).
- ⁵ Pol Duwez and J. L. Taylor: Crystal Structure of TiAl. *Trans. AIME* (1952) **194**, pp. 70-71; *JOURNAL OF METALS* (January 1952).
- ⁶ E. S. Bumps, H. D. Kessler, and M. Hansen: Titanium-Aluminum System. *Trans. AIME* (1952) **194**, pp. 609-614; *JOURNAL OF METALS* (June 1952).

Recrystallization of a Cold-Rolled Copper Single Crystal

by Y. C. Liu and W. R. Hibbard, Jr.

Based on pole figure data and microstructural observations, the recrystallization orientation found in a copper strip previously cold-rolled 99.5 pct from a single crystal with an initial (110) [112] orientation may be described as: a 30° rotation, clockwise and counterclockwise, about octahedral poles of the cold-rolled texture such that all four poles function at a low annealing temperature (400°C) and only three of them function at high temperatures (500° to 1050°C). The relative intensity of deformation stresses on various slip planes can be correlated with the choice of poles affecting the rotations found in the recrystallized orientations.

ROTATIONAL reorientation about the poles of densely packed crystallographic planes is an important characteristic of secondary recrystallization¹⁻⁴ in face-centered cubic metals. Some evidence has also been interpreted to show that such a rotational relationship also exists in the primary recrystallization process.⁵ In an investigation of the crystallographic relationships in the recrystallization process, several aspects of the experimental procedure should be considered. With cold-rolled polycrystalline metal as the initial material, pole figure analysis leaves many ambiguities as to whether or not simple indices can be assigned to adequately represent its orientation. The rolling texture does not consist of a single texture. Minor deformation textures are usually present. In all cases, twin textures are present. The presence of both minor and twin deformation textures influences the recrystallization texture. In order to study the recrystallization mechanism, a more precise knowledge of the history of the material before recrystallization is necessary. Tensile deformation of a single crystal usually produces residual stresses which are concentrated at slip bands. Since the exact nature and orientation of these potential nuclei sites cannot be experimentally evaluated, the tensile deformation of a single crystal was not considered adequate.

From the work done by Barrett and Steadman⁶ on copper, it appeared that cold rolling of a single-crystal specimen with an initial (110) [112] orientation would yield a specimen which fulfills the

conditions required for the present investigation, namely a highly preferred single rolling texture with relatively homogeneous stress distribution. By investigating the recrystallization texture of this material, additional details of reorientation during recrystallization might be obtained. The purpose of this paper is to describe such an investigation.

Experimental Procedure

Copper used in the present investigation was cathode sheet with a purity of 99.94 to 99.97 pct. A copper single-crystal specimen, 1.15x0.8720x0.5322 in. (thickness) was cut from a cylindrical crystal which was grown in a Bridgman furnace.⁷ The cutting was accomplished on a horizontal milling machine operated at a very slow speed to obtain a (110) plane in the rolling plane and a [112] direction in the rolling direction. The disturbed surface was removed by electrolytic polishing in dilute orthophosphoric acid (H_3PO_4) with a specific gravity of 1.14, and a current density of about 1 to 2 amp per sq cm. A 3-min polishing was needed to eliminate the disturbed surface causing Debye-Scherrer rings and a 45-min polish produced a surface which yielded sharp rounded Laue spots. It was estimated that about 1/16 in. of metal was removed from the original cut surface. The final orientation of this specimen before rolling was about 2° from the (110) plane in the rolling plane with a [112] direction aligned in the rolling direction. It is possible that a small amount of strain was still present in the cube despite the fact that the Laue spots seemed very sharp. It is doubtful, however, that this would be an important factor after a subsequent rolling reduction of 99.5 pct.

This copper specimen was rolled on a laboratory rolling mill with two highly polished rolls 3 3/8 in. in diam in the following manner: 0.010 in. per pass to 50 pct reduction, 0.005 in. to 70 pct, 0.002 in. to 85 pct and, finally, 0.001 in. per pass to a 99.5 pct reduction.

Specimens, about 1 in. sq with the rolling edges intact, were cut from the rolled strip by the electrolytic method previously described, after the strip

Y. C. LIU, Student Associate AIME, formerly Graduate Student, Yale University, is now Research Associate, Research Div., New York University, New York, and W. R. HIBBARD, JR., Member AIME, formerly Associate Professor of Metallurgy, Yale University, is now with the Research Laboratory, General Electric Co., Schenectady.

Discussion on this paper, TP 3527E, may be sent, 2 copies, to AIME by July 1, 1953. Manuscript, Sept. 10, 1952; revision, Feb. 10, 1953. Los Angeles Meeting, February 1953.

This paper represents part of a thesis by Y. C. Liu submitted in partial fulfillment of requirements for the degree of Doctor of Engineering to the Faculty of the Engineering School of Yale University, May 1952.

was covered with electroplater's masking tape, with the exception of a thin slit at the place where it was desired to cut the specimen.

Annealing was carried out in an electrically heated liquid metal or salt bath where possible. Each specimen was dusted with alumina powder and placed between two copper sheets 0.020 in. thick. The assembled sandwich was wrapped with several layers of copper foil 0.002 in. thick. A thermocouple was fastened to each envelope, so that the exact temperature of the envelope could be measured. In all cases, the temperature variation during annealing was controlled within $\pm 5^\circ\text{C}$. In the annealing of the specimen at 1050°C in an air furnace, it was found that the furnace temperature dropped to 980°C upon the introduction of the specimen. A 30-min (1800-sec) reheating period was required prior to the 300 sec at 1050°C .

Cold-rolling textures were determined by ordinary pole figure construction^{8,9} with the help of the glancing X-ray method¹⁰ to complete the center portion of the pole figure. An integrating camera¹¹ was employed in the construction of the recrystallization pole figures because of the large grain size. Since all the recrystallization pole figures were asymmetrical about either the rolling direction or transverse direction, the ordinary basic chart for the construction of pole figures was modified to cover all four quadrants.

Metallographic specimens were electrolytically polished and etched according to the ASTM method for copper and its alloys.¹² Tracings of microstructures were made after each heat treatment and the percentage of recrystallization was determined by averaging 15 measurements of the number of squares of cross-section graph paper encompassed.

Results and Discussion

A single-crystal specimen of copper, with a (110) plane parallel to the rolling plane, was rolled in a [112] direction lying in the rolling direction. The resulting pole figure, Fig. 1, shows that even after 99.5 pct reduction in thickness, the rolled strip still retained essentially its original orientation with about 8° of scatter. The cold-rolled texture has no twin component. This experiment confirms earlier work done under the similar conditions in copper⁶ and in brass¹³ and recently in a Cu-Si alloy.¹⁴ Since the specimen, after 99.5 pct reduction, was less than 0.003 in. thick, it was not expected that there would be a distinct difference of cold-rolled texture on the specimen surface and in the interior of the specimen as had been reported.¹⁵⁻¹⁶

Table I. Recrystallization Measured in Annealed Specimens

Annealing Temperature, $^\circ\text{C}$	Annealing Time	Percentage of Recrystallization
200	One week	Less than 1 pct
300	300 sec	None observed
300	1000 sec	First trace of recrystallization visible at 400X
400	100 sec	No observation
400	300 sec	67.8
400	1000 sec	68.0
500	30 sec	78.1
500	100 sec	88.2
500	300 sec	95 (estimated)
700	300 sec	100
900	300 sec	100
980-1050	1800 sec	100
1050	300 sec	100

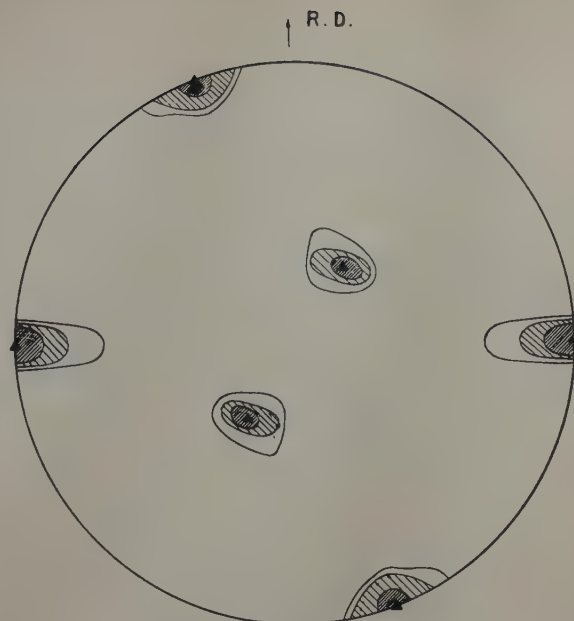


Fig 1—Octahedral pole figure of cold-rolled copper strip after 99.5 pct reduction in thickness.

A series of specimens from the same rolled strip was annealed at temperatures ranging from 200° to 1050°C . The percentage of recrystallization measured in the annealed specimens is listed in Table I. These data show that the range of annealing temperatures and times includes the entire recrystallization process.

The recrystallization texture of all annealed specimens was plotted in the form of conventional octahedral pole figures in Figs. 2 to 10. In general, successive pole figures are quite consistent within the experimental error and possess one center of symmetry, namely a 180° rotation about the center of the figure. Specimens annealed at lower temperatures yielded pole figures containing more high intensity areas than those annealed at higher temperatures. In the latter case, however, these areas were more compact and of somewhat higher intensity. The range and the complexity of the results make it impossible to describe the recrystallization textures adequately by means of simple Miller indices. The predominately cubic recrystallization texture of polycrystalline copper strip was not found in the present specimens.

By careful analysis of the pole figures, a relationship was found between the orientation of the recrystallized grains and the deformation texture. If the deformation orientation is rotated about each one of its octahedral poles, 30° both clockwise and counterclockwise, the resulting ideal orientations were found to best fit the high intensity areas of the pole figures of recrystallized specimens. The theoretical orientations obtained from the rotations described above are plotted in Fig. 11 and these orientations are also plotted as circles (both open and solid) in the individual pole figures in Figs. 4 to 10. The results fit the data very well, especially for the specimens annealed at lower temperatures. The 30° type rotation about the (111) type pole is similar to prior results on a rolled copper single crystal¹⁷ recrystallized at 450°C , although the latter was not rolled in the critical (110) [112] orientation.

The selection of the 30° rotation, both clockwise and counterclockwise, was made on the basis of the fact that the resulting ideal orientations were then

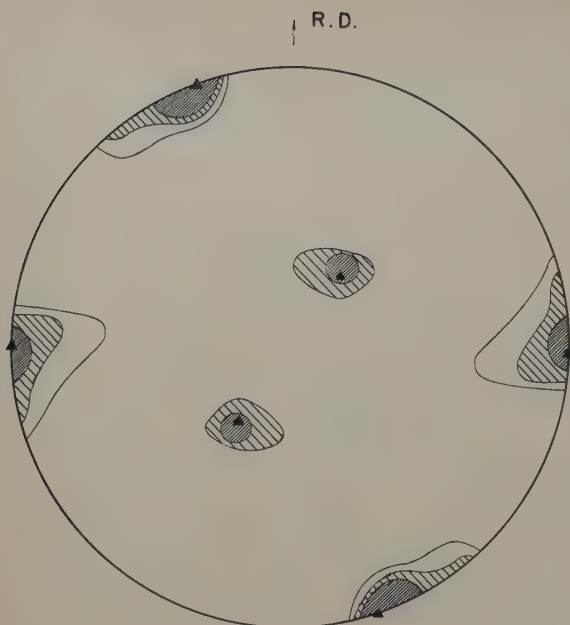


Fig. 2—Octahedral pole figure of copper specimen annealed one week at 200°C.

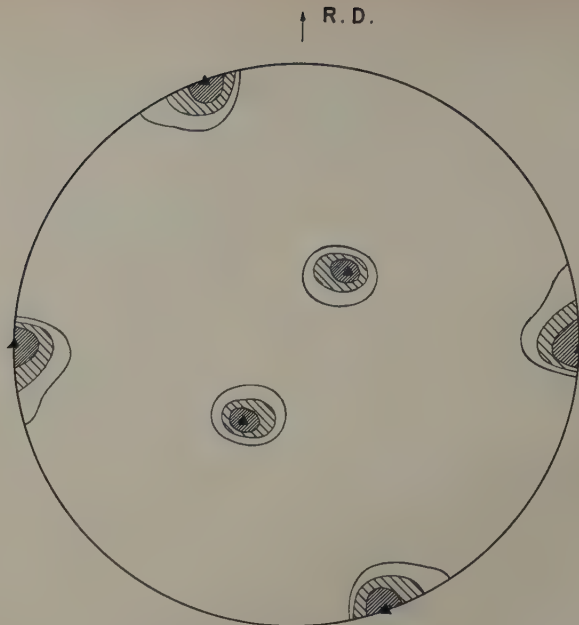


Fig. 3—Octahedral pole figure of copper specimen annealed 300 sec at 300°C.

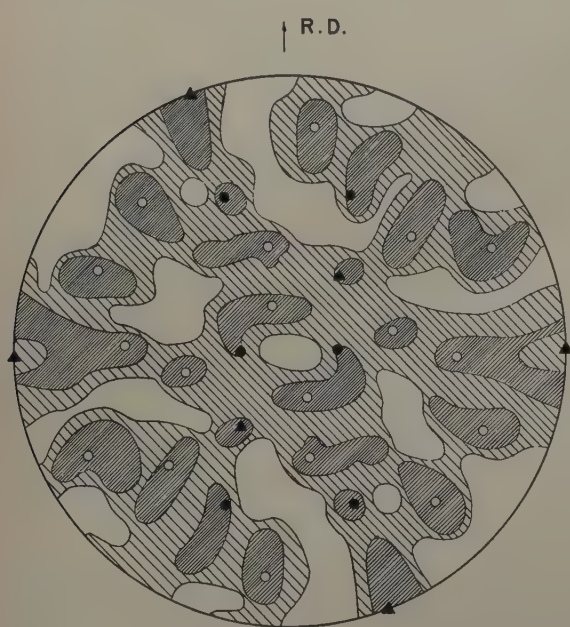


Fig. 4—Octahedral pole figure of copper specimen annealed 100 sec at 400°C.

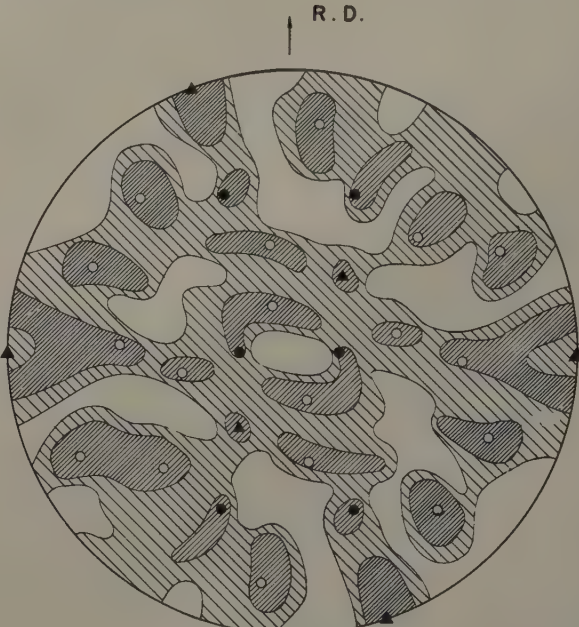


Fig. 5—Octahedral pole figure of copper specimen annealed 300 sec at 400°C.

located for the most part at the center of these intense areas. Actually, any combination of pairs of opposite rotations in the range of 26° to 34° , totaling 60° would be suitable. Opposite rotations totaling 60° about an octahedral pole will generate a twin orientation across the plane of this octahedral pole in face-centered cubic metals. It is possible that orientations, other than those resulting from the rotations suggested, will also fit the data, but it is doubtful that these orientations will satisfy all of the intense areas and also have a simple relationship among themselves.

For annealing temperature at and above 500°C , differences between the ideal orientations and the experimental data occur as shown in Figs. 7 to 10. Two relatively intense areas near the periphery at 1 and 7 o'clock have not been accounted for and six (solid) circles of the theoretical orientations result-

ing from rotations about octahedral pole IV, are not in intense areas. The failure of the recrystallized grains to include an orientation relationship about octahedral pole IV at higher annealing temperature might be interpreted as the result of either: 1—the recrystallized grains resulting from the rotational reorientation about pole IV being absorbed during grain growth, or 2—the rotational reorientation process not functioning with respect to octahedral pole IV.

The first alternative, that grains related to pole IV are actively generated at the start of recrystallization but are absorbed by other growing grains, requires that this absorption occur between 400°C (Fig. 6) and 500°C (Fig. 7) as indicated by the loss of intensity about the orientations with the solid circles. Such a selective absorption from the four equivalent groups of orientations is considered im-

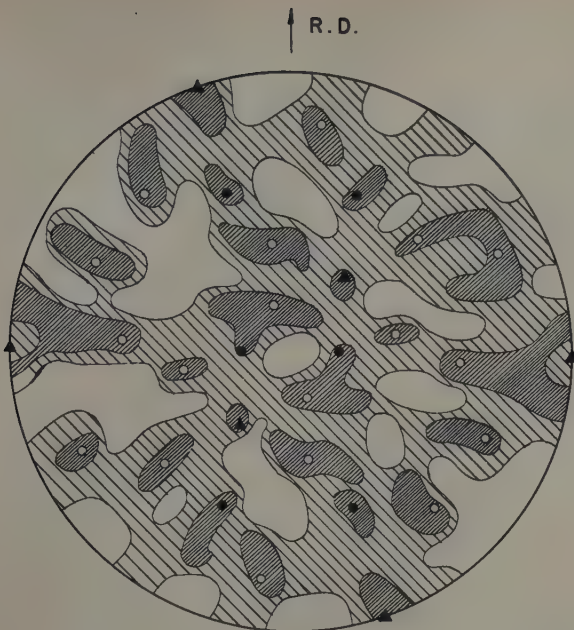


Fig. 6—Octahedral pole figure of copper specimen annealed 1000 sec at 400°C.

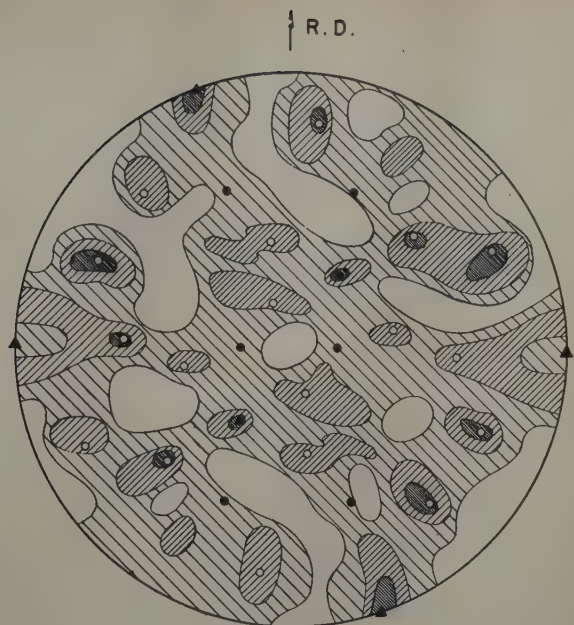


Fig. 7—Octahedral pole figure of copper specimen annealed 300 sec at 500°C.

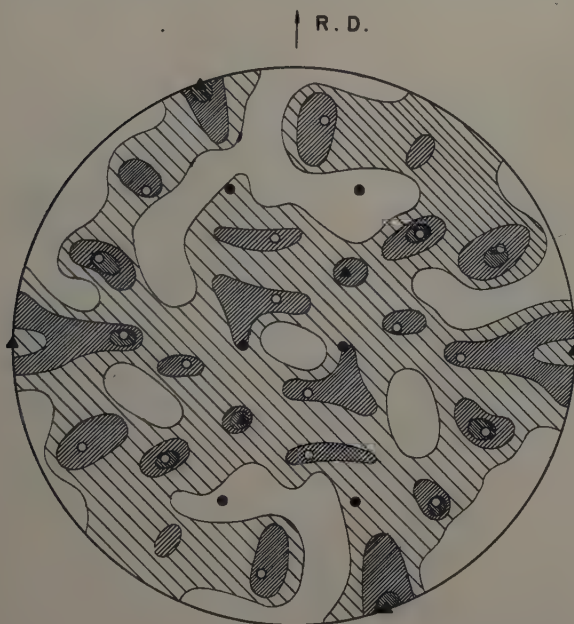


Fig. 8—Octahedral pole figure of copper specimen annealed 300 sec at 700°C.

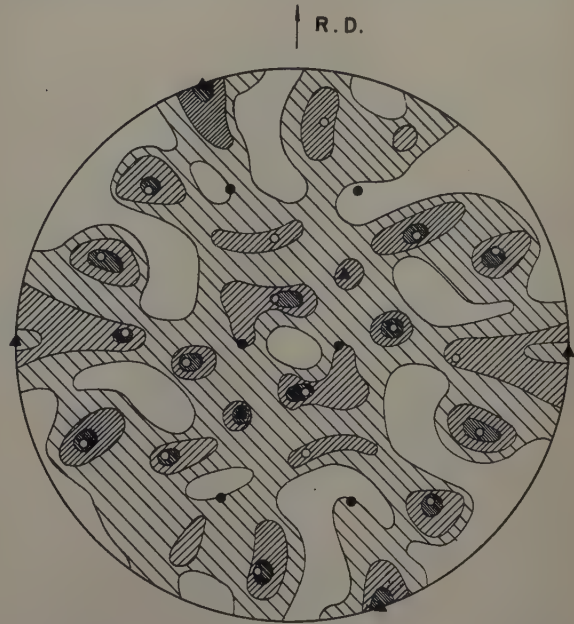


Fig. 9—Octahedral pole figure of copper specimen annealed 300 sec at 900°C.

probable. Therefore, it is suggested that the difference between the recrystallization textures for high and low temperatures is the activation of nuclei related to pole IV at low temperatures, but not at high temperatures.

The second possibility mentioned above may be considered in terms of deformation stresses on the octahedral slip planes based on single-crystal behavior during cold-rolling and correlated with subsequent recrystallization. Maddin, Mathewson, and Hibbard, working on brass,¹⁸ and Chen and Mathewson, working on aluminum,¹⁹ have reported that the orientations of recrystallized grains may be related to the orientation of the deformed crystals by rotations about poles of the active slip planes.

Fig. 12 shows the positions of $[111]$ poles and $[110]$ directions for the starting orientation, $(110)[112]$. The equation for resolved shear stress is

written as

$$S = \frac{F}{A} \cos \phi \cos \lambda \quad [1]$$

where ϕ is the angle between stress axis and normal of the slip plane and λ is the angle between stress axis and slip direction.

If slip takes place during cold rolling in accordance with the resolved shear stress considerations based on plane parallel compression, it is clear that the plane IV, which is perpendicular to the rolling plane and parallel to rolling direction, has a resolved shear stress equal to zero. Theoretically, this slip plane should not operate during cold rolling and at most it would be expected that this slip plane functions least in comparison with the other three octahedral planes. If the factor of stresses on an octahedral plane is assumed to influence recrystal-

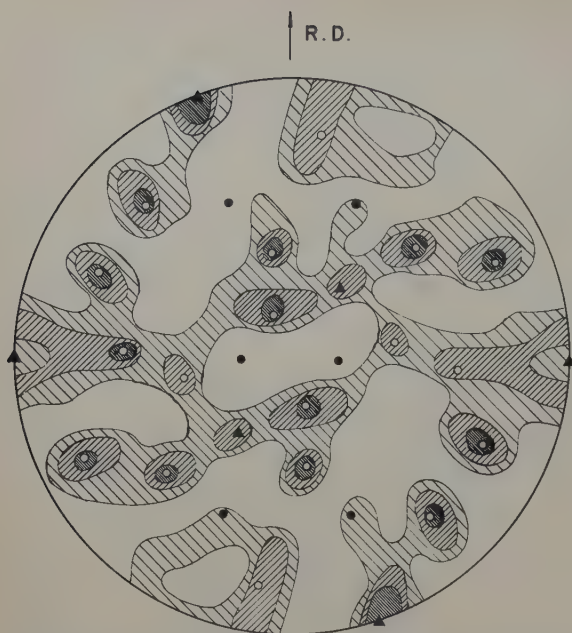


Fig. 10—Octahedral pole figure of copper specimen annealed 1800 sec at 980° to 1050°C and 300 sec at 1050°C.

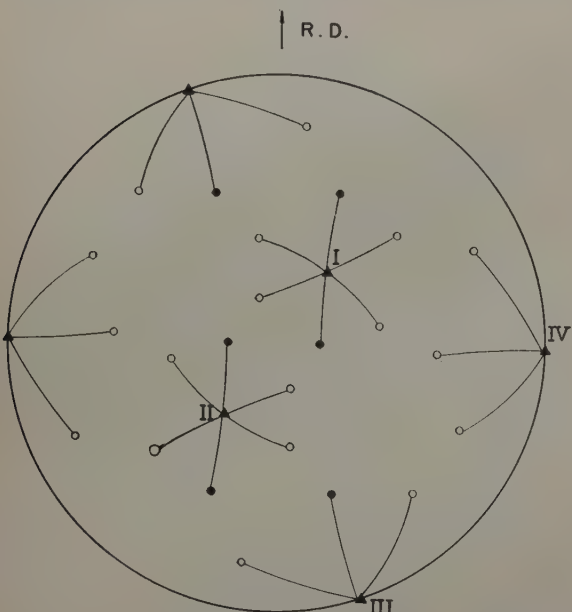


Fig. 11—Ideal orientations resulting from the proposed recrystallization rotations.

lization, then it follows that the low stresses on plane IV rendered the plane least potent in the recrystallization process. The stresses on plane IV, then, may be sufficiently large to cause plane IV to contribute to recrystallization below 500°C, but yet small enough so that they are relieved at temperatures above 400°C rapidly enough and to the extent that plane IV does not contribute to recrystallization at these temperatures.*

* This interpretation is consistent with the results of Maddin, Mathewson and Hibbard¹⁸ and Chen and Mathewson¹⁹ that, after annealing at high temperatures (800° and 600°C), new orientations could be related only to the poles of those planes which were active during deformation. These findings suggest a significant dependence of the activation of nuclei on stress configuration and a competitive relation between the rate of stress relief and the nucleation frequency at the annealing temperature. It has been reported that the nucleation frequency is dependent upon both the amount of strain and stress relief.^{20,21} These factors also affect the incubation time for recrystallization, and therefore the time available for stress relief. Thus, it is more probable that stress relief can occur during the incubation period for potential nuclei in regions of small strain and low residual stress such as along plane IV, provided the temperature is sufficiently high.

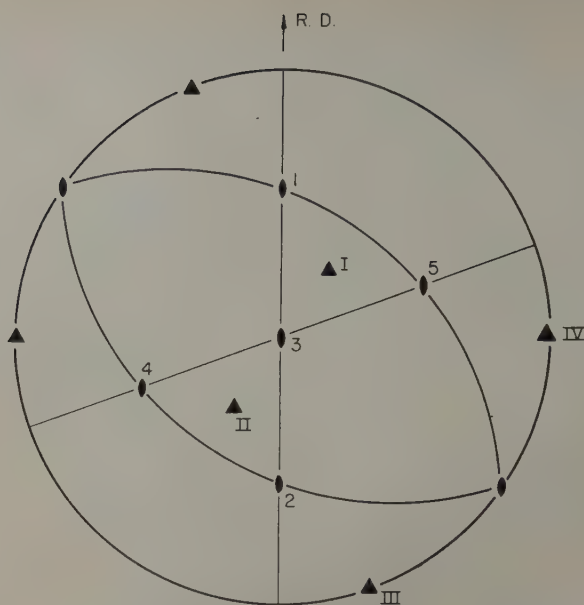


Fig. 12—The positions of octahedral poles and dodecahedral directions in a (110) [112] orientation.

Fig. 10 is the pole figure plotted for the specimen annealed 1800 sec at 980° to 1050°C and 300 sec at 1050°C. The area around [111] poles I and II are less intense than the area around [111] pole III. If this phenomenon is dependent on a stress factor, then it would be expected that the stresses are higher on plane III than on planes I and II.

Hibbard and Yen²² suggested that the stable end orientation of cold-rolled polycrystalline strips of face-centered cubic metals is (110) [112]. The slip systems that operate in a grain rolled in this orientation are systems I-2 and II-1 in Fig. 12. The combination of slip on these two operative slip systems produces a "flow" phenomenon, such that a grain rolled in (110) [112] orientation can experience further cold rolling without changing its orientation.

The role which the (111) plane III plays during cold rolling is complex. According to theory,²² owing to the unfavorable orientation of slip directions in

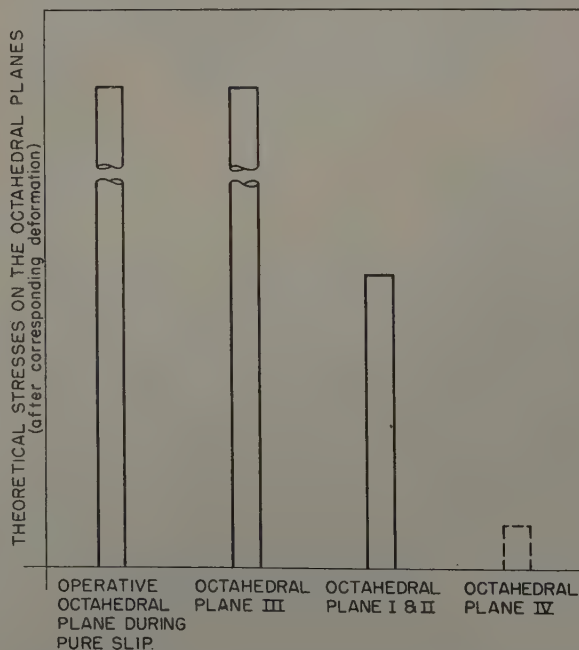


Fig. 13—Schematic representation of comparative amount of residual stresses on the individual octahedral planes.

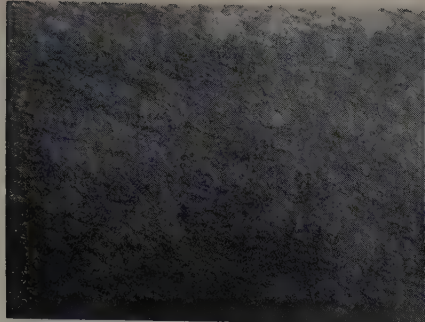


Fig. 14—Cold-rolled structure. Rolling direction is vertical. X500. Area reduced approximately 60 pct for reproduction.



Fig. 15—Specimen annealed 300 sec at 900°C. X500. Area reduced approximately 60 pct for reproduction.



Fig. 16—Specimen annealed 300 sec at 700°C. X500. Area reduced approximately 60 pct for reproduction.

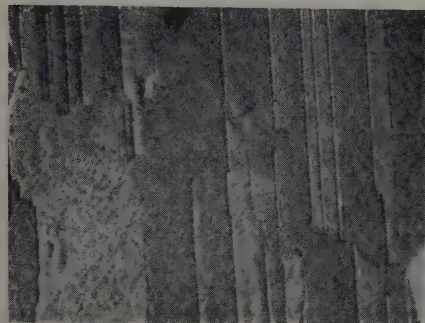


Fig. 17—Specimen annealed 300 sec at 900°C. X500. Area reduced approximately 60 pct for reproduction.

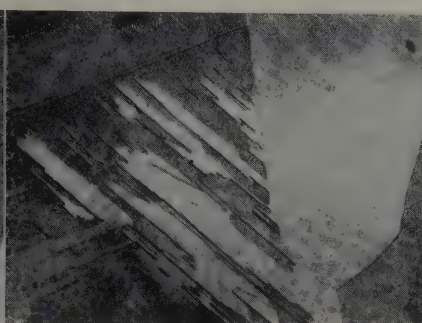


Fig. 18—Specimen annealed 300 sec at 700°C. X500. Area reduced approximately 60 pct for reproduction.

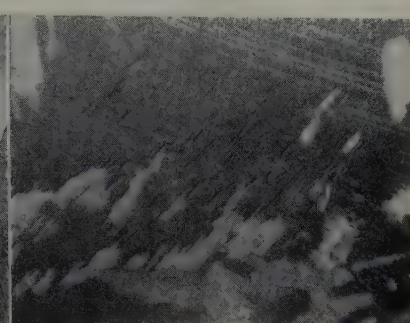


Fig. 19—Specimen annealed 1000 sec at 400°C. X500. Area reduced approximately 60 pct for reproduction.

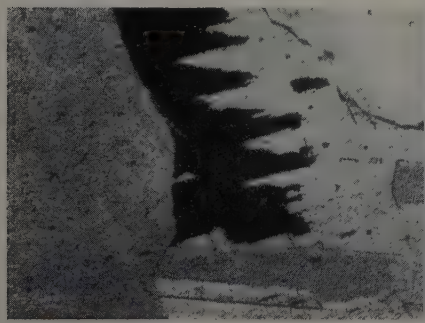


Fig. 20—Specimen annealed 300 sec at 500°C. X500. Area reduced approximately 60 pct for reproduction.

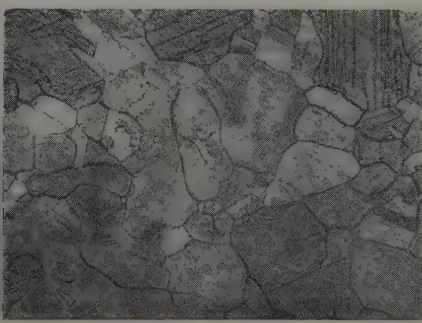


Fig. 21—Specimen annealed 300 sec at 900°C. X500. Area reduced approximately 60 pct for reproduction.

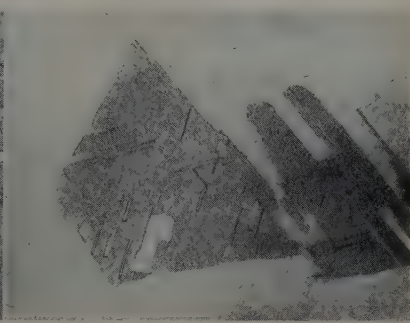


Fig. 22—Specimen annealed 300 sec at 700°C. Rolling direction is vertical. X500. Area reduced approximately 60 pct for reproduction.

this plane, III, with respect to the rolling direction, this slip plane should not operate during cold rolling without a change in orientation. The location of the slip plane causes the $\cos \phi$ value in Eq. 1 to become large with respect to the tensile component in the rolling direction due to cold rolling. In that way, the plane itself would be subjected to large stresses built up during deformation, but the unfavorable position of the slip directions with respect to flow restricts slip. Under such conditions a high stress is built up on plane III. Slip on planes I and II may relieve a portion of this stress, but that remaining on plane III is probably higher than that on planes I and II subsequent to their yielding. The role of slip plane III in this situation might be analogous to that of the cross slip plane in tensile specimens. As reported by Maddin, Mathewson, and Hibbard in brass¹⁸ and Chen and Mathewson in aluminum single crystals,¹⁹ the subsequent anneal of those specimens yielded the recrystallized grains which were more frequently related crystallographically to the poles of cross slip planes than to the poles of primary and conjugate slip planes.

A schematic representation of the comparative

amount of stress on the individual [111] planes of the deformation texture is shown in Fig. 13. The relatively high stresses existing on the [111] plane, III, is believed to be responsible for the observation that the most intense areas of the pole figures of recrystallized specimens may be related to rotations about the pole of this plane III.

The presence of intense areas around the solid triangles in Figs. 8 and 9 may lead to the conclusion that some of the recrystallized grains may have an orientation similar to the deformed matrix, since, at these annealing temperatures, it has been found that these specimens have experienced full recrystallization. The analysis of the pole figure intensities at the four [111] poles of the deformed structure (solid triangles) is not a true way of estimating the number of recrystallized grains with this orientation. Since each of these four poles acts individually, in a crystallographic sense, as a center of rotation to develop the recrystallized orientations, these four [111] poles are therefore each associated with other orientations of newly formed grains and are not necessarily combined into a single orientation. It is not known whether (110) [112] type grains, if they

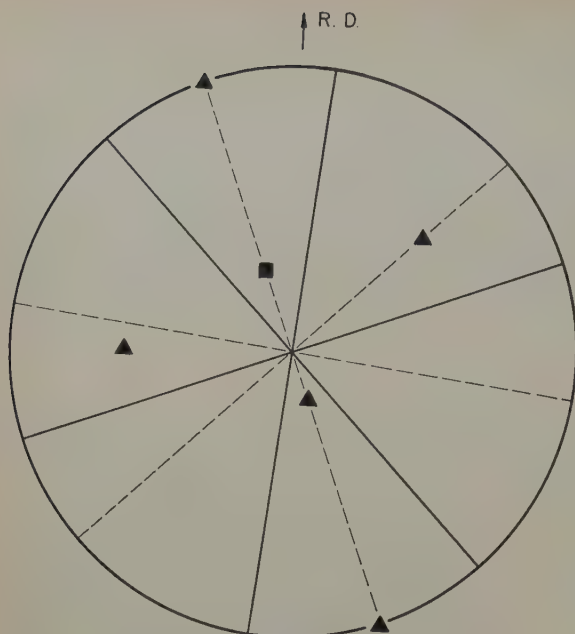


Fig. 23—Stereographic analysis of Fig. 22.

exist, are the result of the rotational reorientation or "recrystallization in situ."

As indicated by Table I, the temperature range used in this experiment covers the range of the recrystallization process. By comparing Figs. 4, 5, and 6, it is clearly seen that no significant change in the recrystallization texture has been produced by time during isothermal annealing. Also, in general the annealing temperature has a rather small effect on the orientation of the recrystallized grains, provided annealing has been carried out above 500°C.

Microscopically, the recrystallization process in the present specimen is entirely different from what has been reported previously for the polycrystalline copper strip. The specimen was very reluctant to recrystallize. No sign of recrystallization was observed after an anneal of 300 sec at 300°C. On increasing the annealing time to 1000 sec some recrystallization was observed. Annealed for a week at 200°C, the amount of recrystallization was estimated as less than 1 pct.

At a very early stage of recrystallization, a few large grains were found together with a small number of fine grains. In no case was a grain of circular outline observed. No attempt was made to measure the rates of nucleation and growth in the present investigation.

The characteristic feature of the microstructure of the recrystallized grains in the present specimens is the abundance of annealing twins. Figs. 14 to 18 show the typical structure of these specimens. It is interesting that the textures are not a twinned type in the usual sense (i.e., not twinned across planes perpendicular to the rolling plane and containing the rolling direction or the transverse direction), although they possess two-fold rotational symmetry.

Preferential growth of the recrystallized grains takes place during the recrystallization process. Figs. 19 and 20 show that the grain boundaries of the recrystallized grains are very jagged and extend finger-like into the deformed matrix. Even the microstructure of the specimen which has been annealed 300 sec at 900°C, Fig. 21, shows grain boundaries which clearly indicate that the equilibrium shape of grains has not yet been attained.

In testing the validity of the results obtained on the basis of the pole figure data, the orientation of certain grains could be determined by means of three twin families. It was expected that these orientations so independently determined should be among the eight orientations produced by the recrystallization rotations described above. All the measurements made both on the micrographs and under metallographic inspection conformed to this expectation. One of the micrographs, Fig. 22, is, therefore, reproduced here with the stereographic analysis.[†]

[†] In the stereographic analysis, the solid lines represent the traces of the twins in the corresponding micrograph, and the dotted lines represent the locus of octahedral poles corresponding in turn to these solid lines. The solid triangles represent the [111] poles of one of the eight equivalent orientations suggested by the recrystallization mechanism.

From both the pole figure and microstructure studies, it may be concluded that the recrystallization reorientations suggested in the present investigation are in good agreement with experimental observations.

Summary

1—A single-crystal specimen of cathode copper was cut with the (110) plane parallel to the rolling plane and was rolled in a [112] direction. After cold rolling, a pole figure showed that the final strip retained its original orientation with a spread of about 8° after a 99.5 pct reduction in thickness.

2—Specimens electrolytically cut from the cold-rolled strip were annealed at temperatures and times ranging from the initial stages of recrystallization to just below the melting point of copper.

3—Qualitatively, increasing the annealing temperature causes little change in the final recrystallization texture, provided the annealing temperature is above 500°C in the present specimen. Annealing time had no measurable effect on the orientations of the recrystallized grains.

4—The recrystallization reorientation found in the present investigation can be described as: 30° rotation clockwise and counterclockwise, about each of four [111] poles of the deformation texture at low annealing temperatures (up to 400°C) and only three at higher annealing temperatures (500°C and above).

5—The distribution of deformation stresses is considered an important factor which influences recrystallization reorientations.

Acknowledgment

The authors would like to express their gratitude to William Tragart of Yale University, Edmund C. Burke of the Dow Chemical Co., and Harold Margolin of the Research Div., New York University for their helpful reading of the manuscript. The copper was supplied by the Raritan Copper Works, Perth Amboy, N. J., through the courtesy of Stanislaus Skrowronski.

References

- 1 J. S. Bowles and W. Boas: The Effect of Crystal Arrangement on Secondary Recrystallization in Metals. *Journal Inst. Metals* (1948) **74**, p. 501.
- 2 M. L. Kronberg and F. H. Wilson: Secondary Recrystallization in Copper. *Trans. AIME* (1949) **185**, p. 501; *JOURNAL OF METALS* (August 1949).
- 3 G. W. Rathenau and J. F. H. Custers: Secondary Recrystallization of Face-Centered Nickel-Iron Alloys. *Philips Research Reports*. (1949) **4**, p. 241.
- 4 P. A. Beck and H. Hu: Recrystallization Texture and Coarsening Texture in High Purity Aluminum. *Trans. AIME* (1949) **185**, p. 627; *JOURNAL OF METALS* (September 1949).

⁵ P. A. Beck and H. Hu: Annealing Texture in Rolled Aluminum Strip. *JOURNAL OF METALS* (October 1950) p. 1215.

⁶ C. S. Barrett and F. W. Steadman: Structure of Copper after Rolling. With discussion. *Trans. AIME* (1942) **147**, p. 57.

⁷ P. W. Bridgman: Certain Properties of Single Crystals of Sb, Bi, Te, Cd, Zn and Sn. *Proc. Nat. Acad. Soc.* (1925) **60**, p. 305.

⁸ A. Taylor: *An Introduction of X-Ray Metallography*. (1945) New York. John Wiley and Sons.

⁹ B. F. Decker: Preferred Orientations in Rolled Metals. Construction of Pole Figures. *Trans. ASTM* (1943) **43**, p. 785.

¹⁰ M. K. Yen: A Study of Textures and Earing Behavior of Cold Rolled (87-89 pct) and Annealed Copper Strip. *Trans. AIME* (1949) **185**, p. 59; *JOURNAL OF METALS* (January 1949).

¹¹ F. H. Wilson and R. M. Brick: Textures, Anisotropy and Earing Behavior of Brass. *Trans. AIME* (1945) **161**, p. 173.

¹² Tentative Methods of Preparation of Metallographic Specimen. *Trans. ASTM Standards*, Part 2 (1949) p. 944.

¹³ J. E. Burke and C. S. Barrett: The Nature of Strain Markings in Alpha Brass. *Trans. AIME* (1948) **175**, p. 106; *METALS TECHNOLOGY* (February 1948).

¹⁴ B. L. Averbach and B. E. Warren: Atomic Displacement and Crystallite Orientations in the Deformation of Single Crystals. MIT. Unpublished.

¹⁵ C. S. Barrett: *Structure of Metals* (1943) New York. McGraw-Hill Book Co.

¹⁶ H. Hu and P. A. Beck: Rolling Texture in Aluminum. *JOURNAL OF METALS* (October 1950) p. 1214.

¹⁷ H. Hu, described by P. A. Beck in Chapter III of W. E. Kingston: *The Physics of Powder Metallurgy* (1951) p. 44.

¹⁸ R. Maddin, C. H. Mathewson, and W. R. Hibbard, Jr.: The Origin of Annealing Twins in Brass. *Trans. AIME* (1949) **185**, p. 655; *JOURNAL OF METALS* (September 1949).

¹⁹ N. K. Chen and C. H. Mathewson: Recrystallization of Aluminum Single Crystals after Plastic Extension. *Trans. AIME* (1952) **194**, p. 501; *JOURNAL OF METALS* (May 1952).

²⁰ J. A. Collins and C. H. Mathewson: Plastic Deformation and Recrystallization of Aluminum Single Crystals. *Trans. AIME* (1940) **137**, p. 150.

²¹ M. Kornfeld and W. Pavlov: *Phys. Z. Sowjet* (1934) **6**, p. 537; (1937) **12**, p. 658.

²² W. R. Hibbard, Jr. and M. K. Yen: Wire Textures of Copper and its Binary Alpha Solid Solution Alloys with Aluminum, Nickel and Zinc. *Trans. AIME* (1948) **175**, p. 126; *METALS TECHNOLOGY* (February 1948).

Technical Note

On the Distribution of Sodium in Modified Al-Si Alloys

by A. B. Michael and M. B. Bever

THE structure of cast Al-Si alloys is altered profoundly by modifying agents. Sodium, in particular, reduces the size of the silicon particles in the eutectic and tends to change their shapes from plates to nearly rounded grains. This refinement is accompanied by a shift of the eutectic to higher silicon concentrations and lower temperatures. Similar effects can be attained by rapid solidification.

Hypotheses advanced to explain modification have involved the formation of a ternary eutectic,¹ the removal of oxides by fluxing,² and even a presumed allotropic transformation of silicon. Other hypotheses assume that the modifying agent causes an envelopment of the silicon particles by the aluminum-rich solid solution, but attribute this envelopment to different mechanisms. According to various explanations, the growth of the silicon particles is obstructed by an immiscible sodium-rich liquid,³ an adsorbed layer of sodium,⁴ or a ternary compound;⁵ this obstruction has been conceived as purely mechanical or as a colloidal action.⁶ It has also been proposed that sodium reduces the surface tension on the Al-Si interface, thus permitting the aluminum-rich solid to grow faster and to envelop the silicon particles.⁷ Still other hypotheses stress undercooling and the attendant change in the rate of nucleation of silicon, but fail to ascribe any definite function to the sodium addition.⁸⁻¹⁰

Procedure

High-purity alloys of aluminum and 3 or 7 pct Si were treated with modifying agents containing radioactive sodium tracers. The experiments were intended to investigate the partition of sodium between the primary aluminum-rich solution and the

eutectic, and, if possible, to determine whether sodium is concentrated in or around the silicon particles in the eutectic. Radioactive sodium fluoride, alone or mixed with stable sodium chloride, was allowed to react with the alloy for 5 min immediately before solidification in the crucible. Modification could not be attained with additions of less than the equivalent of approximately 0.1 pct Na. Some alloys were not completely modified, but comparison of the structures of treated and untreated specimens indicated a very considerable reduction in particle size of the silicon in all of the former. A treated alloy is shown in Fig. 1.

Radioactive sodium fluoride was prepared by bombardment with deuterons having an energy of 14 mev. This bombardment (totaling, for example, 6 microampere-hours in one run) produced radioactive Na^{24} (half-life 14.8 hr) by the reaction $_{11}\text{Na}^{23}(\text{d}, \text{p})_{11}\text{Na}^{24}$. The radioisotopes of fluorine also produced have short half-lives and were not detected. A half-life determination by counting confirmed that the measured activity was due to Na^{24} .

The distribution of the sodium in the solidified alloys was determined by an autoradiographic technique by which a suitable stripping film is attached to a very thin metallographic specimen. After exposure and development, this emulsion remains superimposed on the specimen and may be examined microscopically or photographed by reflected light. The emulsion of the autoradiograph can be correlated directly with the underlying surface by simple adjustment in focus. The details of this technique have been described elsewhere.¹¹

Results

Fig. 2 is a micrograph of the autoradiographic emulsion ("autoradiograph") lying directly above the area of eutectic in Fig. 1. Fig. 3 shows a similar autoradiograph of a region consisting of primary solid solution. The small black dots (tracks) in these autoradiographs are developed grains in the emul-

A. B. MICHAEL, formerly Research Assistant at M.I.T., is now associated with the Research Dept., Allis-Chalmers Manufacturing Co., Milwaukee, Wis., and M. B. BEVER, Member AIME, is Associate Professor, Dept. of Metallurgy, Massachusetts Institute of Technology, Cambridge, Mass.

TN 157E. Manuscript, Dec. 29, 1952.

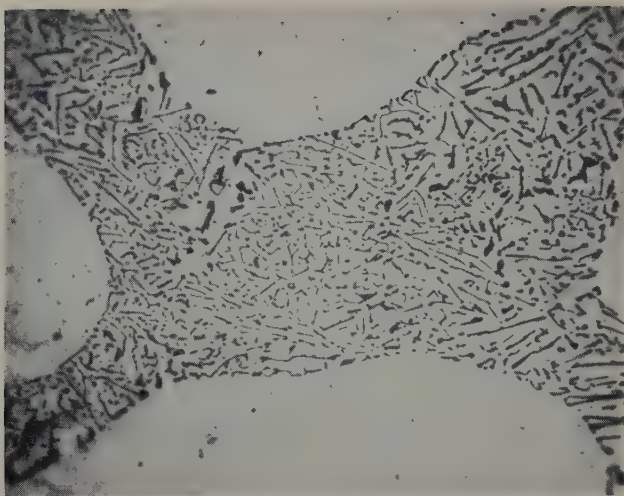


Fig. 1—Micrograph of metallographically prepared surface of alloy of aluminum and 7 pct Si, treated with modifying agent containing radioactive sodium. Etched with Keller's reagent. Photographed through autoradiographic emulsion. X500. Area reduced approximately 50 pct for reproduction.

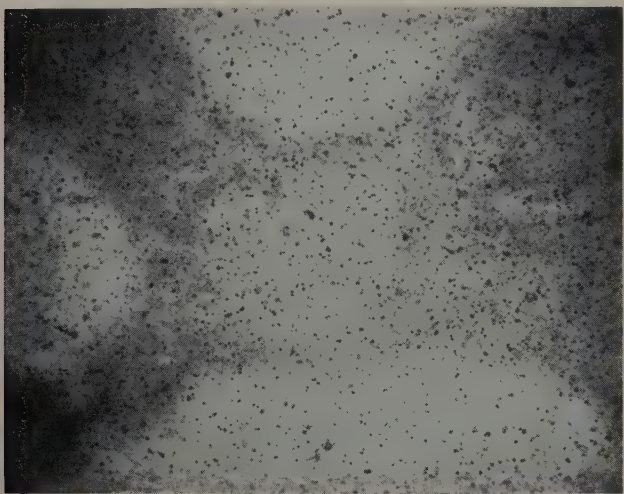


Fig. 2—Micrograph of autoradiograph corresponding to the area shown in Fig. 1. X500. Area reduced approximately 50 pct for reproduction.

sion due to radiations emitted by disintegrating sodium atoms. The uniform dark areas are eutectic in the underlying metal surface, which was not in focus when the micrographs of the emulsions were made. Blanks were processed simultaneously with the radioactive specimens. Their autoradiographs showed a negligible number of tracks.

The β tracks in the autoradiographs could not be traced to either of the two phases in the eutectic. The partition of sodium between the primary constituent and the eutectic, however, was determined by counting the number of developed grains in the emulsion above unit areas of these structures. These counts were made on ground glass images and on micrographs focused at a constant depth below the surface of the emulsion to eliminate possible variations with depth in the number of developed grains. Only the centers of large areas of eutectic or primary constituent were examined to avoid any effects due to cross radiation, which would occur near the boundaries between these structures. Since the thickness of the specimens was only about 20 microns, interference from subsurface layers was not appreciable.

In counts made on several specimens of the 3 and 7 pct Si alloys the number of developed grains was

found to be approximately equal above regions of eutectic and of primary solid solution. This observation shows that sodium was not concentrated preferentially in the eutectic. It can be inferred as probable that in the eutectic sodium was associated with the aluminum-rich solid solution rather than with the silicon particles. In that case, the ratio of sodium to aluminum was higher for the eutectic than for the primary constituent, but this may be attributed to the lower temperature at which the eutectic solidifies from the residual liquid.

The finding that sodium was approximately equally distributed between the eutectic and the primary constituent and the inference that it probably was associated with the secondary aluminum-rich solid solution in the eutectic does not directly lead to a choice between the various hypotheses of modification. In particular, it can be argued that only a small fraction of the total sodium present may be effective in inducing modification and that the location and action of this effective portion is still not known. On the other hand, the observations reported here invalidate any hypothesis of modification which im-

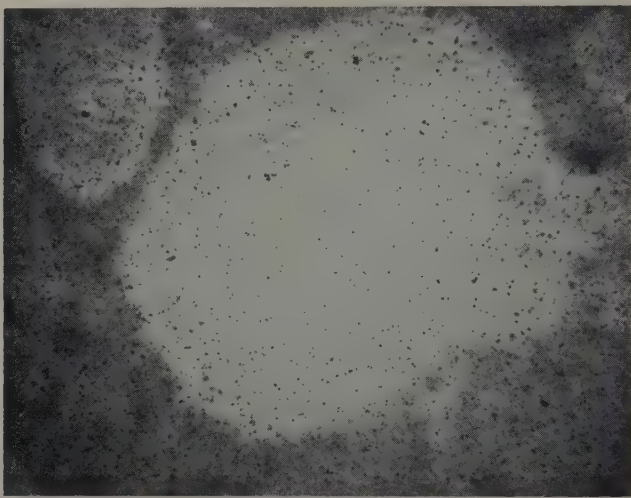


Fig. 3—Micrograph of autoradiograph of primary aluminum-rich solution. The area shown is adjacent to the area of Figs. 1 and 2. X500. Area reduced approximately 50 pct for reproduction.

plies a close association of the bulk of the sodium with the silicon.

Support of this work through a fellowship sponsored by the Aluminum Company of America is gratefully acknowledged.

References

- ¹ E. Schulz: *Ztsch. Metallkunde* (1948) **39**, p. 123.
- ² L. Guillet: *Revue de Métallurgie* (1922) **19**, p. 303.
- ³ B. Otani: *Journal Inst. Metals* (1926) **36**, p. 243.
- ⁴ A. G. C. Gwyer and H. W. L. Phillips: *Journal Inst. Metals* (1926) **36**, p. 283.
- ⁵ C. E. Ransley and H. Neufeld: *Journal Inst. Metals* (1950) **78**, p. 25.
- ⁶ J. D. Edwards and R. S. Archer: *Chemical and Metallurgical Engineering* (1924) **31**, p. 504.
- ⁷ B. M. Thall and B. Chalmers: *Journal Inst. Metals* (1950) **77**, p. 79.
- ⁸ M. L. V. Gayler: *Journal Inst. Metals* (1927) **38**, p. 157.
- ⁹ E. Scheil and R. Zimmermann: *Ztsch. Metallkunde* (1949) **40**, p. 24.
- ¹⁰ E. Scheuer: *Foundry Trade Journal* (1950) **90**, p. 569.
- ¹¹ A. B. Michael, W. Z. Leavitt, M. B. Bever, and H. R. Spedden: *Journal of Applied Physics* (1951) **22**, p. 1403.

Rate of Formation of Isothermal Martensite in Fe-Ni-Mn Alloy

by R. E. Cech and J. H. Hollomon

KURDJUMOV and Maksimova reported experiments with manganese steels and high carbon steels¹ and with an Fe-Ni-Mn alloy² in which martensite was formed isothermally over a range of temperatures. They found in some cases that martensite formation could be suppressed by rapid quenching to liquid nitrogen temperature. From their microstructural observations of martensite formed isothermally, they concluded that the rate controlling step is nucleation rather than growth.

Kulin and Cohen,³ in an attempt to reproduce these experiments, found that with a steel having the same composition as that reported by Kurdjumov and Maksimova, the transformation to martensite was essentially complete above the temperature range of Kurdjumov and Maksimova's isotherms. The possible reasons for this disagreement were not considered.

Recent papers by Das Gupta and Lement⁴ and Kulin and Speich⁵ report the formation of isothermal martensite in a high chromium steel and in an Fe-Cr-Ni alloy, but neither paper can be considered a verification of the original Kurdjumov and Maksimova results. Further, in neither case were the authors able to suppress the formation of martensite entirely.

Because of the important bearing the Kurdjumov and Maksimova results have to an understanding of the mechanism of martensite reactions it was felt that an experimental investigation directly concerned with checking the validity of their results was in order. This paper describes the results obtained on the isothermal transformation over the temperature range from -79° to -196°C of an alloy of iron, nickel, and manganese.

Experimental Apparatus

A 15 lb heat of an alloy containing 73.3 pct Fe, 23.0 pct Ni, and 3.7 pct Mn was melted by induction and cast under argon. The ingot was forged to 1-in. bar and a portion rolled to $1/16 \times 1\frac{1}{2}$ -in. strip. This strip was pack-homogenized 300 hr at 1100° in a helium-filled sealed iron tube. The composition after homogenization was 73.2 pct Fe, 22.94 pct Ni, 3.73 pct Mn, 0.05 pct C, and 0.015 pct N. The strips were cut to $\frac{1}{2}$ -in. width for dilatometer and metallographic specimens. Only the center portion of the $1\frac{1}{2}$ -in. strip was used in the present investigation.

The dilatometer employed was similar in design to one described by Flinn, Cook, and Fellows.⁶ A concentric fused quartz rod and tube assembly with hooks for holding the specimen was mounted so as to transmit the specimen dilation to a $1/10,000$ in.,

$1/10$ in. travel dial gage. The dilatometer proper was mounted by means of extension arms to a counterweighted sliding member on a vertical standard. This method of mounting permitted rapid transfer of the dilatometer from the austenitizing furnace to the quenching bath and low temperature chamber. A small electrical vibrator on the dilatometer kept frictional effects of the quartz members at a minimum.

The austenitizing unit was a vertical, molybdenum-wound, hydrogen atmosphere furnace maintained at a constant temperature $\pm 3^{\circ}\text{C}$ by means of constant power input. A 12-in. stainless steel jacketed copper liner having $\frac{1}{2}$ -in. wall thickness acted to equalize the temperature in the hot zone of the furnace. This liner, closed at the bottom end and open at the top to permit entrance of the dilatometer and specimen, was kept filled with dry nitrogen gas. A chromel-alumel thermocouple was placed inside the tube to determine the temperature. The 4-in. dilatometer specimens in the chamber varied less than $\frac{1}{2}^{\circ}$ across the specimen length except for a $1\frac{1}{2}^{\circ}$ drop at the end nearest the open end of the furnace.

The low temperature isothermal holding bath was a double Dewar arrangement similar to one described by Turnbull.⁷ The outer bath was filled with a refrigerant at a temperature lower than the desired holding temperature. The inner bath was filled with Freon "11" or "12" or a mixture of both, depending upon the holding temperature. This inner bath which tended to be cooled by the outer bath was kept at a constant temperature by introducing a small amount of heat with a manually controlled electric heater. Stirring was accomplished by bubbling dry air through the bath. A Leeds and Northrup type K potentiometer was used to measure the inner bath temperature as indicated by a five element copper-constantan thermopile. The bath temperature was maintained within $\pm 0.2^{\circ}\text{C}$ of the desired temperature by occasionally adjusting the heater current so as to keep the Leeds and Northrup galvanometer at zero deflection with a constant setting of the potentiometer. Isothermal tests were usually continued for 300 to 400 min and another reading made at approximately 1000 min if the bath, unattended overnight, had not deviated in temperature more than 5°C . Transformation curves are drawn dashed (Fig. 1) through the time region where temperature was not controlled precisely.

Experimental Procedure

Dilatometer specimens of $1/2 \times 1/16$ -in. strip were cut to $4\frac{1}{2}$ -in. length and holes were drilled for the quartz hooks with proper spacing to give a 4-in. measured length. A thermocouple consisting of 0.012-in. diameter chromel and alumel wires was spot welded to the specimen and threaded between the dilatometer rods to binding posts near the dial

R. E. CECH and J. H. HOLLOMON, Junior Members AIME, are associated with the Research Laboratory, General Electric Co., Schenectady.

Discussion on this paper, TP 3463E, may be sent, 2 copies, to AIME by July 1, 1953. Manuscript, April 8, 1952; revision, Sept. 10, 1952.

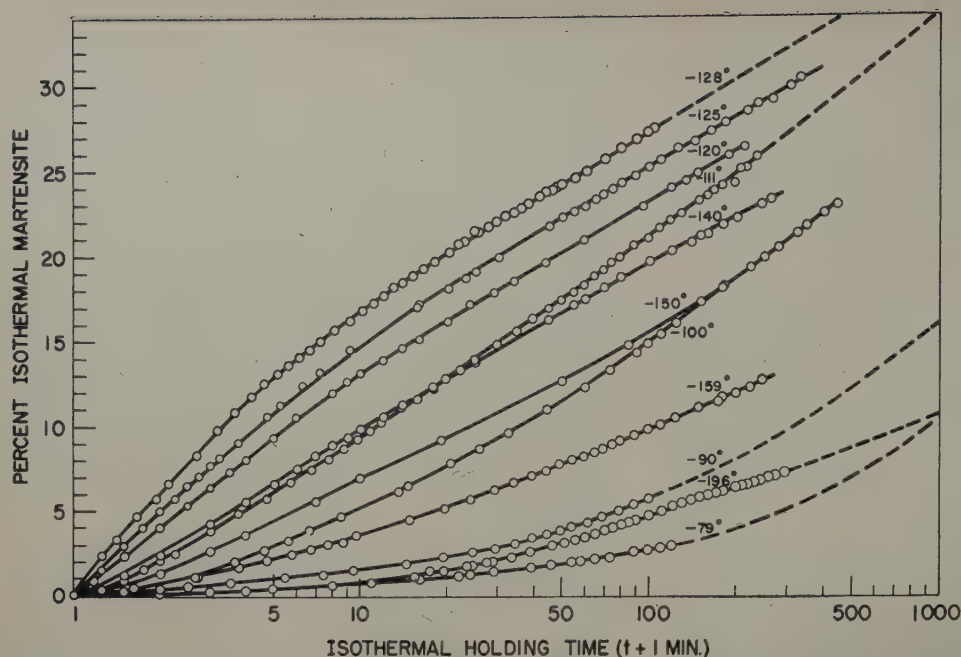


Fig. 1—Isotherms for martensite formation in Fe-Ni-Mn alloy.

gage. A new thermocouple was used for each specimen.

Specimens were austenitized 2 hr at 940°C, quenched into icewater and held 10 sec, rinsed in alcohol near 0°C for 20 sec, and quenched into the Freon holding vessel. A self-balancing photoelectric potentiometer connecting the specimen thermocouple produced a temperature time record of the quench. Dial gage readings of the specimen length were begun as the specimen approached the holding temperature and continued as a function of time of holding. The specimen length passed through a minimum as its temperature approached that of the bath and martensite forming isothermally caused a volume increase equal to that of thermal contraction. The time at which this minimum occurred was taken to be the initial time at transformation temperature, and the specimen length at this time to be the initial length. The martensite formed from isothermal-type transformation during the slow approach to the holding temperature was determined separately as is described later.

Isothermal transformation runs were made at -79°, -90°, -100°, -120°, -125°, -128°, -140°, -150°, -159°, and -196°C. Each isotherm was repeated three times, in some cases using three different specimens and in others with the same specimen re-austenitized. Isotherms were reproducible within 2 pct except at -79°, -90°, and -196°C, where reproducibility was 3 to 4 pct. The austenite mean grain diameter of 0.325 mm resulting from the high temperature homogenization did not change even after repeated transformation and re-austenitization of the specimen.

The amount of martensite present at the time the specimen had reached the holding temperature was determined by quenching separate specimens, in the same manner as the dilation specimens, up-quenching into warm water at the time corresponding to the initial dilation reading and examining metallographically. The amount of martensite formed on cooling a number of specimens in this manner is listed in Table I. The scatter was quite large both between specimens and in different areas of the same specimen. Specimens cooled to -196°C were entirely free of martensite with the exception of a few regions containing a fraction of 1 pct of mar-

tensite. However, a significant amount (2 to 5 pct) could be formed by warming slowly from -196°C in air instead of up-quenching.

The major factor influencing the amount of martensite in the specimens listed in Table I is believed to be the period of time in cooling and reheating during which the specimen temperature was in the region of rapid transformation. For specimens cooled to -100° to -159°C this time was about 15 to 30 sec depending upon bath composition, bath temperature, and surface condition of specimen. For specimens quenched in liquid nitrogen the time was 3 sec.

The data in terms of specimen length change as a function of time at constant temperature were converted to the percentage of martensite formed as a function of time by up-quenching a specimen at the end of the test and determining through metallographic lineal analysis the total amount of martensite present. Each specimen was sectioned at two points and the martensite determined on each section. The amount of martensite formed on cooling to the temperature of holding, Table I, was subtracted from the total to obtain the isothermal martensite percentage. The total isothermal length change of that specimen was divided into the isothermal martensite percentage in order to determine the percentage of martensite formed per unit length expansion. This calibration was applied to all dilatometer specimens having reproducible dilation curves. A distribution curve of the number of specimens vs martensite-length change calibration value

Table I: Martensite Formed During Approach to the Holding Temperature

Transformation Temperature, °C	Initial Martensite, Pct
-79	0
-90	0
-100	0.5-1.5
-111	1.0-2.0
-120	1.0-3.0
-125	1.0-3.0
-128	1.0-3.0
-140	1.0-3.0
-150	1.0-3.0
-159	1.0-3.0
-196	0 -0.5

was determined. The curve was normal indicating a randomness of errors. The value of the mean was found to be 7.4 pct martensite per 0.001 in. per in. linear isothermal expansion. The probable error of the mean was ± 0.1 pct martensite corresponding to an error in calibration of $1\frac{1}{3}$ pct. The change in calibration factor due to variation of specific volume change with temperature was calculated from the thermal expansion in the region of -70°C of a fully austenitic specimen and a specimen containing 45 pct martensite. It was found that the error introduced in the temperature region of the isotherms was much less than the $1\frac{1}{3}$ pct error of the mean. Further, it was found that the addition of this correction factor to the dilation calibration did not result in a reduction of the calculated error. Therefore, it was felt unnecessary to include this additional correction factor.

A surface layer of higher martensite content was formed to a depth of 0.002 to 0.005 in. during isothermal transformation. In making lineal analyses to determine martensite content of specimens, this surface layer was avoided. Visual observation of specimens that had been transformed different lengths of time indicated that the martensite content in the surface layer increased with holding time in about the same manner as the interior. It is believed that this surface effect results from depletion of manganese or carbon at the surface.

The isothermal transformation curves are plotted in Fig. 1. Time was plotted as $t + 1$ min to permit the inclusion of the first minute of isothermal transformation on a log plot. The curves were cross-plotted to obtain the TTT curve of Fig. 2.

Isothermal transformation rates were also determined for two temperatures, -111° and -159°C , by a metallographic method. Specimens were transformed for various lengths of time, quenched to room temperature, and prepared for metallographic examination. The quantity of martensite present in each specimen was determined by lineal analysis. Only one cross section per metallographic specimen was used in the lineal analysis determination of martensite in this case. The scatter of individual martensite determinations was about 1 to 2 pct which was within the estimated uncertainty of the lineal analysis measurements.

Micrographs from a number of specimens of one

series are shown in Fig. 3. The metallographically determined points are plotted in Fig. 4 along with the corresponding dilatometrically determined curves. In both cases, only the percentage of martensite formed isothermally is plotted. Though the agreement at -111°C is good, five of the eight metallographically determined points at -159°C are high, although only two are at greater variance with the dilatometric curve than the expected limit of error of a linear analysis measurement. Postulations regarding the discrepancy are of a speculative nature. One possibility is that the bath temperature was incorrectly adjusted for subzero treatment of metallographic specimens. Another is that, since metallographic specimens were taken from a different portion of the ingot, the composition may have varied slightly from that of the dilatometer specimens. At the time of the investigation it was felt that the deviation was not sufficiently greater than the expected errors to warrant repeating the experiment.

The effect of interruption of isothermal transformation at -111°C upon further transformation at -111°C was investigated. It was found that a small amount of martensite formed on heating from the holding temperature. After aging 5 min at room temperature and recooling, transformation continued at a much decreased rate. These results are in agreement with the findings of Das Gupta and Lement⁴ on a high chromium steel.

A preliminary experiment to determine if a delayed quench resulted in stabilization was performed by delaying the quench at 20°C for 2 and 30 sec before subcooling to a transformation temperature of -111°C . The results indicated that the magnitude of stabilization in these times is less than the scatter of individual isotherms. However, a similar quenching treatment resulted in stabilization of the isothermal transformation at -128°C . Specimens were held in a water bath at 20°C for 2 sec, for 30 sec, and for 24 hr before subcooling. The specimens given the 30-sec delay and the 24-hr delay in quenching transformed at a slower rate for the first few minutes of isothermal transformation than did the specimen given the 2-sec delay. Transformation rates were about equal after this time. The difference in initial transformation rates corresponded to 2 pct martensite for the specimen subjected to a

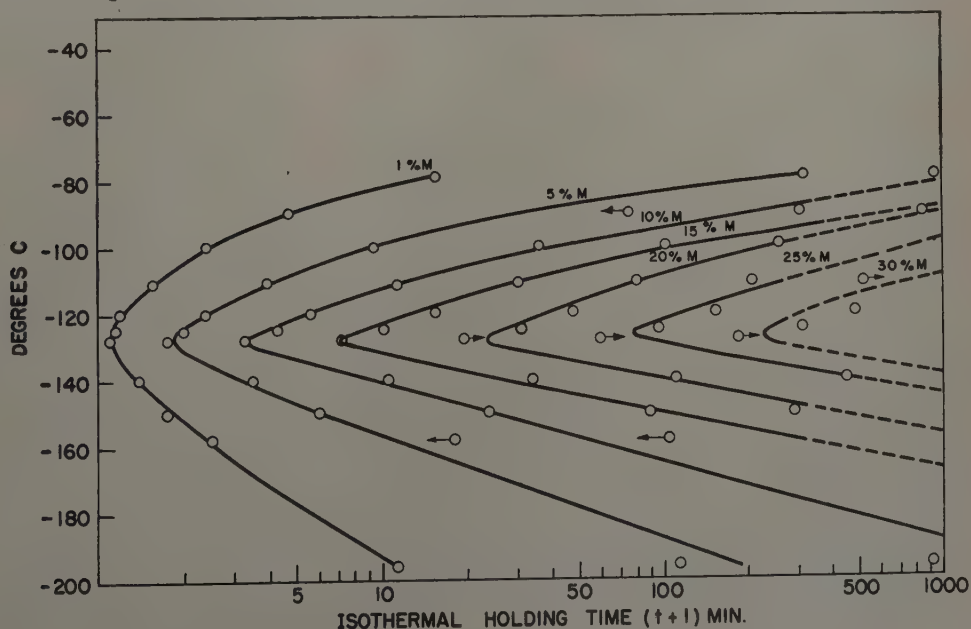


Fig. 2—TTT curves for martensite formation in Fe-Ni-Mn alloy.



Fig. 3—Isothermal martensite formation at -111°C . Picral etch followed by ferric chloride etch. X100.

a (upper left)—0 time 1.5 pct martensite.

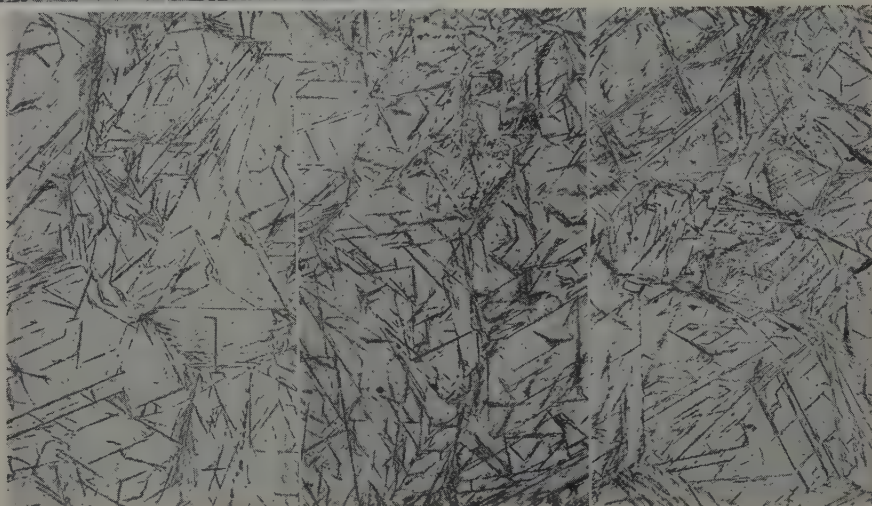
b (upper center)—1 min 4.9 pct martensite.

c (upper right)—4 min 6.5 pct martensite.

d (lower left)—16 min 12.5 pct martensite.

e (lower center)—64 min 19.1 pct martensite.

f (lower right)—128 min 23 pct martensite.



30-sec delay and 4 pct martensite for the specimen subjected to a 24-hr delay in quenching. The term "stabilization" refers, in this report, to the above mentioned slowing of isothermal transformation.

These experiments may indicate that stabilization occurs only below a certain critical temperature. However, it is felt that these data are not yet extensive enough to completely substantiate such a conclusion. A more thorough investigation of stabilization in this and other materials is in progress.

In the opinion of the authors the dilatometric data and room temperature observation of microstructures of transformed specimens provide insufficient evidence to resolve with certainty the question of whether isothermal martensite is produced by slow growth of pre-existing nuclei or by thermal nucleation followed by rapid growth to full size martensite platelets. To determine directly the speed of growth of martensite platelets a high-low temperature microscope stage was designed and built. The construction and operation of this stage are described elsewhere.⁸ It was possible to reproduce the time-temperature history of dilatometric specimens very closely in this stage.

Specimens were cut to size, metallographically polished, and austenitized in an evacuated quartz tube for 2 hr at 940°C . After cooling to room temperature, specimens were mounted in the microscope stage, austenitized 10 min at 940°C , quenched directly to a subzero temperature and held isothermally. The subzero holding temperatures elected for successive experiments were -125° and -190°C . The specimen surface was observed at these tem-

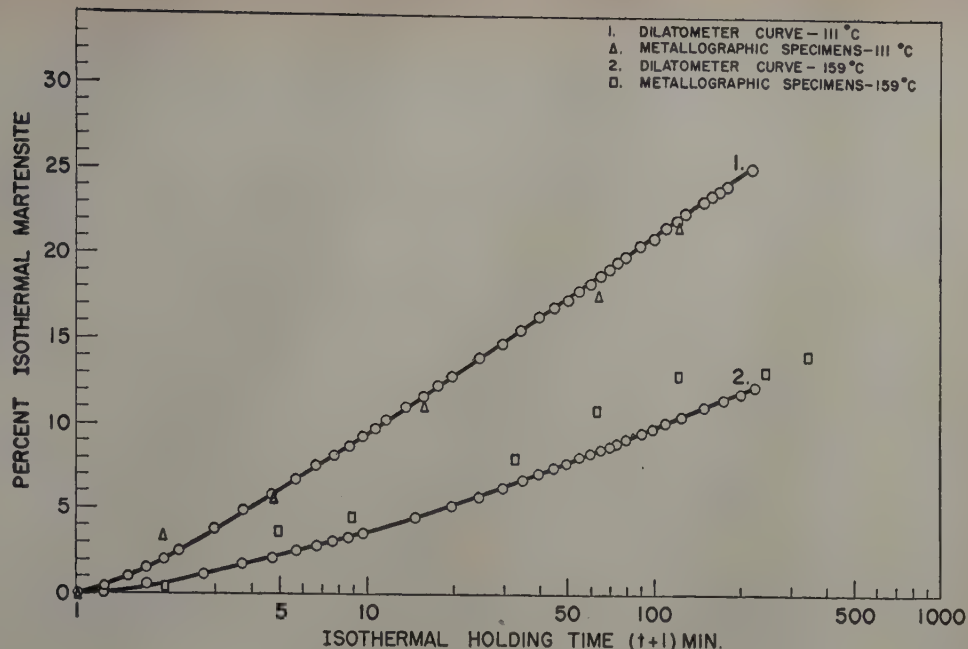
peratures for periods ranging from 10 to 30 min both visually and with the aid of a 16 mm motion picture camera set to a speed of 24 frames per sec.

It was found by visual observation, and examination of motion picture frames, that individual martensite platelets began growing at different times and grew to full size in less than $1/24$ sec. In some cases a martensite platelet would grow larger after initial growth by a series of discontinuous increments. These observations confirm the findings of Kurdjumov and Maksimova^{1,2} of Das Gupta and Lement,⁴ and of Machlin and Cohen⁶ based on the room temperature examination of microstructures of transformed specimens.

The results of this investigation support, at least qualitatively, the experimental findings of Kurdjumov and Maksimova on the isothermal transformation in a 23 pct Ni, 3.4 pct Mn alloy. There are significant differences, however. Kurdjumov and Maksimova's temperature of maximum transformation rate (-47°C) differs by 80°C from the temperature of maximum transformation rate (-128°C) found in this investigation. The greater manganese content, 0.3 pct, of the present alloy would be expected to lower the martensite formation temperature 10° to 20° at most (for athermal transformation). It seems unlikely that its effect on isothermal transformation would be great enough to account for the difference. It is more likely that the composition of Kurdjumov and Maksimova's alloy was at variance with that stated in his publication.

An error in the composition of the alloy used by Kurdjumov and Maksimova in a previous investiga-

Fig. 4—Comparison of dilatometrically and metallographically determined isotherms.



tion may also have been responsible for Kulin and Cohen's failure to reproduce the experiment on the 6.0 pct Mn, 0.6 pct C steel.

Kurdjumov and Maksimova report an M_s temperature (-17°C) for the Fe-Ni-Mn alloy, thereby inferring that athermal martensite forms to some extent. However, the cooling rate of 10°C per min used in its determination was sufficiently slow to allow detectable quantities of isothermal martensite to form at the reported M_s .

Kurdjumov and Maksimova do not state whether or not an athermal component was found on rapidly quenching to the lowest possible temperature. In the present investigation it was shown that the formation of martensite could be entirely suppressed by rapidly quenching small specimens in liquid nitrogen to temperatures as low as -196°C . It can then be concluded that athermal transformation is not a necessary prerequisite to subsequent isothermal transformation.

The stabilizing effect of an interruption of holding in the temperature region of isothermal transformation is believed to be due to the same factors causing partial stabilization by an interruption of quench prior to subcooling. In the latter case no martensite was present during the stabilizing treatment. It thus appears that the suggestion of Das Gupta and Lement (that stabilization is caused by the removal of an accelerating effect imposed on the steel by partial transformation) does not apply for the alloy used in this investigation. It is more likely that the diffusion of carbon plays a role in this stabilization phenomenon.

The isothermal transformation data reported in this investigation have been interpreted by Fisher¹⁰ as thermal nucleation of martensite followed by rapid growth.

Summary

The following characteristics of the austenite-martensite transformation have been observed in an Fe, 23 pct Ni, 3.7 pct Mn alloy:

1—Isothermal formation of martensite occurs in the temperature range from -79° to -196°C . The rate of formation increases with decreasing temperature to a maximum at -128°C and decreases with further lowering of temperature.

2—The formation of martensite can be suppressed

completely in this alloy by rapid quenching below room temperature.

3—Partial stabilization can be brought about by aging at room temperature, either prior to subcooling or after some isothermal transformation.

4—Isothermal transformation proceeds by delayed formation of martensite nuclei followed by rapid growth to full size martensite platelets.

Acknowledgments

The authors are pleased to acknowledge the assistance of D. Turnbull in many helpful discussions and criticism and of Mrs. LaVerne Danko for performing many of the lineal analyses required in the present investigation.

References

- ¹G. V. Kurdjumov and O. P. Maksimova: Kinetics of the Transformation of Austenite to Martensite at Low Temperatures. *Doklady Akademii Nauk, SSSR* (1948) 61, No. 1, p. 83.
- ²G. V. Kurdjumov and O. P. Maksimova: Work Required in the Formation of Martensite Nuclei. *Doklady Akademii Nauk, SSSR* (1950) 73, No. 1, p. 95.
- ³S. A. Kulin and M. Cohen: On the Martensitic Transformation at Temperatures Approaching Absolute Zero. *Trans. AIME* (1950) 188, p. 1139; *JOURNAL OF METALS* (September 1950).
- ⁴S. C. Das Gupta and B. S. Lement: Isothermal Formation of Martensite at Subzero Temperatures in a High Chromium Steel. *Trans. AIME* (1951) 191, p. 727; *JOURNAL OF METALS* (September 1951).
- ⁵S. A. Kulin and G. R. Speich: Isothermal Martensite Formation in an Iron-Chromium-Nickel Alloy. *Trans. AIME* (1952) 194, p. 258; *JOURNAL OF METALS* (March 1952).
- ⁶R. A. Flinn, E. Cook, and J. A. Fellows: A Quantitative Study of the Austenite Transformation. *Trans. ASM* (1941) 31, p. 41.
- ⁷D. Turnbull: Kinetics of Solidification of Supercooled Liquid Mercury Droplets. *Journal of Chemical Physics* (1952) 20, No. 3, pp. 411-424.
- ⁸R. E. Cech: A High Low Temperature Microscope Stage. *Review of Scientific Instruments* (1950) 21, No. 8, p. 747.
- ⁹E. S. Machlin and M. Cohen: Isothermal Mode of the Martensitic Transformation. *Trans. AIME* (1952) 194, p. 489; *JOURNAL OF METALS* (May 1952).
- ¹⁰J. C. Fisher: Application of Nucleation Theory to Isothermal Martensite. *Acta Metallurgica* (1953) 1, No. 1, p. 32.

Identification of the Precipitate Accompanying 885°F Embrittlement in Chromium Steels

by R. M. Fisher, E. J. Dulis, and K. G. Carroll

IT is well known that ferritic steels containing more than 15 pct Cr when subjected to temperatures in the range of 700° to 1000°F exhibit increasing hardness and decreasing ductility. The phenomenon has been widely termed the "885°F embrittlement," after the temperature of most marked effect.^{1,2} In view of the excellent review articles available in the literature³⁻⁸ only a brief account of experimentally established facts need be given here.

The extent of changes in physical characteristics during embrittlement depends on chromium concentration and time at temperature, higher alloy content and longer time both promoting more rapid and extensive changes. In a 27 pct Cr steel, changes in impact strength and in angle of fracture in bending can be detected after only a 1 hr exposure at 885°F; after 50 hr this steel becomes quite brittle. Hardness increases slowly with time during thousands of hours exposure and may attain a maximum hardness number twice as large as that of the unexposed steel.

Microstructural changes accompanying embrittlement have been described as an initial widening of grain boundaries followed by eventual darkening of ferrite grains. Embrittled steels etch more readily, e.g., the weight loss of a 27 pct Cr steel in acid solution may occur at a rate one hundred fold greater following exposure at 885°F. Marked changes which accompany embrittlement have been observed in electrical resistivity, specific gravity, and magnetic coercive force. Changes in physical properties may be readily removed by heating at temperatures above the embrittling range, such as a treatment at 1100°F for 1 hr.

It has frequently been noted that the 885°F embrittlement suggests precipitation on a submicroscopic scale of a chromium-rich constituent, the nature of which has not been revealed by X-ray diffraction. Progressive broadening of the body-centered cubic diffraction lines during embrittlement has been observed,⁶ and recent observations by Lena and Hawkes⁷ upon single crystals have shown early asterism in X-ray photographs, disappearing within an hour at 900°F. Many workers have ascribed⁸⁻¹³ the phenomenon to a precipitation of σ phase (FeCr), which is known to cause embrittling effects at temperatures much higher than 885°F. Two general observations, however, suggest that σ precipitation cannot be responsible for the 885°F phenomenon: 1—prior cold work greatly enhances σ formation, whereas it scarcely affects the 885°F embrittlement,

Table I. Chemical Composition of Steels Used

Sample	Aging Time at 900°F, Hr	Chemical Composition, Wt Pct							
		C	Mn	P	S	Si	Ni	Cr	N
A	10,000	0.032	3.13	0.016	0.010	0.35	0.08	28.14	0.084
B	10,000	0.12	0.63	0.014	0.010	0.06	0.10	27.48	0.071
C	0	0.24	0.89	0.020	0.003	0.55	0.48	26.45	0.222
D	10,000	0.24	0.89	0.020	0.003	0.55	0.48	26.45	0.222
E	34,000	0.24	0.89	0.020	0.003	0.55	0.48	26.45	0.222
F*	5,000	0.08	0.55	0.014	0.008	0.05	0.10	16.54	—
G*	10,000	0.08	0.55	0.008	0.027	0.43	0.16	15.80	—
H*	10,000	0.08	0.55	0.009	0.022	0.64	0.11	15.05	—
I*	10,000	0.07	0.55	0.010	0.024	0.56	0.12	14.14	—

* These samples, obtained from Heger¹² and Link and Marshall,¹³ were cold-reduced 95 pct before exposure.

and 2—the presence of an alloying element such as nickel or manganese may have an effect on the 885°F embrittlement which is opposed to its effect upon σ formation.

The slight enhancement of σ formation and 885°F embrittlement observed in the presence of elements with strong carbide and nitride forming tendencies² is probably a consequence of lessened chromium depletion of the matrix. The bar graph in Fig. 1 shows a typical example, taken from two 27 pct Cr steels used in this work, of the hardness after exposure for 10,000 hr at 900°, 1050°, and 1200°F. Steel A (0.03 pct C, 3.13 pct Mn) showed marked hardening at 900° and 1200°F, whereas steel B (0.12 pct C, 0.63 pct Mn) exhibited only the 900°F hardening. The σ phase was found in steel A at the higher temperatures but not in steel B. Presumably σ formation is enhanced by the low-carbon and high-manganese concentrations in A.¹⁴ Thus there are two distinctly different hardening phenomena present which cannot both be ascribed to σ precipitation without invoking a transition phase possessing remarkable properties.

Materials

A number of chromium steels exposed for long periods (5000 to 34,000 hr) at 900°F, as well as unexposed samples of one of the steels, were available for this investigation. Table I gives the chemical compositions and aging treatments of these steels. In addition to these steels exposed in the elevated temperature test furnaces of the National Tube Division, a number of high-chromium steels were heated for short periods in small laboratory air furnaces and lead baths. Supplementing these commercial steels, a sample of high-purity (0.018 pct C, 0.002 pct N) 28 pct Cr iron, exposed 1000 hr at 887°F, was furnished by the Union Carbide and Carbon Corp. In addition, an alloy of iron and chromium of high purity containing 46 pct Cr was used. This

R. M. FISHER, E. J. DULIS, and K. G. CARROLL are associated with the Research Laboratory, United States Steel Corp., Kearny, N. J.

Discussion on this paper, TP 3524E, may be sent, 2 copies, to AIME, by Dec. 1, 1953. Manuscript, Nov. 21, 1952. Cleveland Meeting, October 1953.

material, made by vacuum fusion, was obtained from the National Research Corp., Cambridge, Mass.

Optical Microscope Examination of Embrittled Steels

The micrographs of Fig. 2 illustrate the phenomenon of 885°F embrittlement in a 27 pct Cr steel. Ferrite grains in the unexposed steel (sample C) are clear, the outlined or dark etching constituents being chromium carbide and nitride. After an exposure of 34,000 hr at 900°F (sample E), the ferrite appears darkened by a precipitate which is too fine to be resolved by the optical microscope, and a veining or subgrain structure can be seen in the darkened ferrite. This precipitate dissolves rapidly in the ferrite matrix upon heating to 1200°F, as shown in Fig. 2c, leaving the microstructure much as it appeared in the unexposed steel of Fig. 2a.

These changes in microstructure are reflected in hardness of 198, 369, and 202 diamond pyramid hardness for the specimens of Figs. 2a, 2b, and 2c, respectively. These results indicate that a definite microstructural change accompanies the hardness increase during the long time exposure at 900°F, and that the embrittled steel quickly returns to its initial hardness and to a structure similar to the initial microstructure upon heating at 1200°F. The hardness of sample E (369 DPH) was not significantly different from that of sample D (373 DPH).

Electron Microscope Examination

Fig. 3 shows electron micrographs of the samples shown in Fig. 2. These are photographs of uranium-shadowcast plastic replicas stripped from the polished and etched surfaces of the steel before and after exposure at 34,000 hr at 900°F. This one-step plastic replica technique results in negative replicas, in that unetched projections on the original surface appear as depressions in the micrographs. The smooth, unetched regions in both figures correspond to the carbides and nitrides in the steel. The rough background in Fig. 3b indicates the presence of a precipitate in the ferrite matrix which is too fine to be resolved by this replica technique. This is analogous to the ferrite darkening shown in the optical micrograph of Fig. 2b; however, the vein structure was not observed.

A new "Extraction Replica" technique that is applicable to these samples has recently been devel-

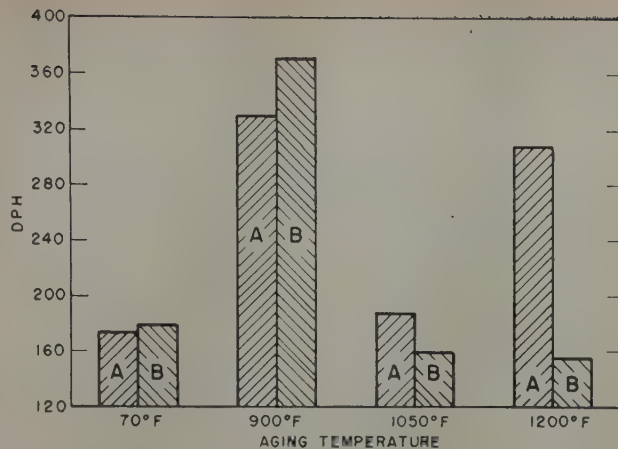


Fig. 1—Effect of aging temperature on hardness of two 27 pct Cr steels after 10,000 hr exposure.

oped at this Laboratory. This technique will soon be reported elsewhere and will be described here only briefly. It has been found possible to free from the metal matrix the precipitate particles that are partially embedded in the replica plastic by etching the sample a second time through the plastic. The replica contains the actual precipitate particles, thus avoiding the loss in resolution inherent in any replica technique. By suitable manipulation of the electron beam, it is possible to select areas of the replica containing separated particles for diffraction patterns by transmission. An alcoholic solution of picric and HCl acids (grain size reagent) has been found most effective for the stripping technique on chromium steels, although solutions of bromine or iodine in alcohol may also be used.

Fig. 4 shows particles of the precipitate which are responsible for the ferrite roughening of Fig. 3b. Fig. 4a is an extraction replica of sample D (10,000 hr, 900°F) and Fig. 4b shows the precipitate in sample E (34,000 hr, 900°F). The precipitate particles seem to be spherical as they always appear circular in the micrographs and never rodlike as would disks on edge. The particles are quite uniform in size, varying from about 150 to 300Å but averaging 200 in Fig. 4a and 230 in Fig. 4b. Resolution of the micrographs here limits accuracy to about $\pm 30\text{\AA}$.

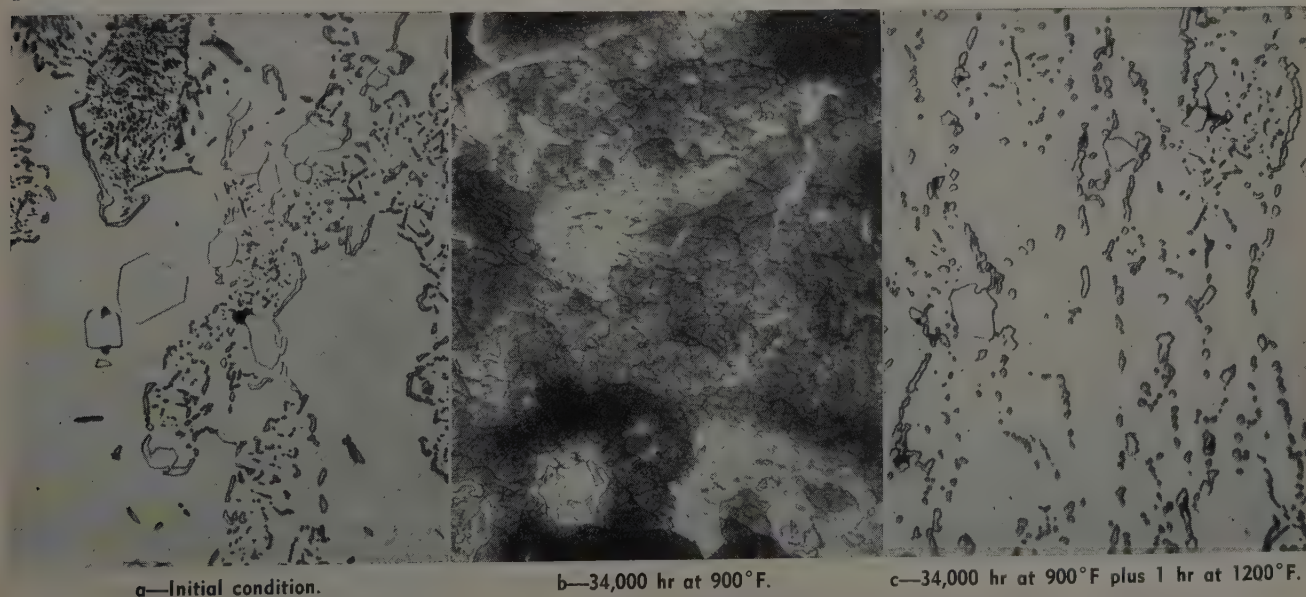


Fig. 2—Microstructures of steel C (27 pct Cr). Picric-HCl etch. X1000. Area reduced approximately 50 pct for reproduction.

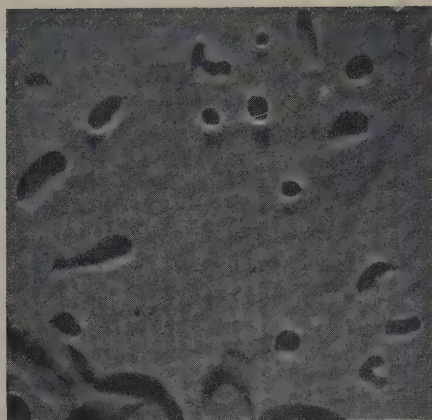


Fig. 3 — Uranium shadowed replicas of 27 pct Cr steel. HCl-picric etch. X15,000. Area reduced approximately 50 pct for reproduction.



a (upper) — Before exposure.

b (lower) — 34,000 hr at 900°F.

Fig. 4a and b also illustrates quantitatively the increase in numbers of particles from 10,000 to 34,000 hr exposure although there is little change in particle size. Some clustering of particles in Fig. 4b results from slightly over etching the second time so that some previously unexposed particles that are not fixed to the plastic are free to cluster together. This is difficult to avoid with such small precipitate particles.

Transmission electron diffraction from the same area of the replica shown in Fig. 4b gives the pattern, reproduced in Fig. 5, of a simple body-centered cubic phase of lattice parameter similar to that of iron or chromium. Because pure iron and pure chromium differ in lattice parameter by only 0.6 pct, it is not possible to distinguish between these two elements, or their solid solution, by means of electron diffraction alone. It is interesting to note the evidence of preferred orientation in the diffraction pattern of Fig. 5, which indicates that the replica technique removed the particles from the steel without disturbing their orientation. The six-fold symmetry in the inmost $\{110\}$ ring suggests that the precipitate formed with its $\{110\}$ planes coincident with the six $\{110\}$ planes of the ferrite matrix.

Electron diffraction examination by means of the same replica technique described above showed the presence of the body-centered cubic precipitate in sample F (17 pct Cr, 5000 hr, 900°F), sample G (16 pct Cr, 10,000 hr), and sample H (15 pct Cr, 10,000 hr). The patterns from these samples were considerably weaker than from the 27 pct Cr steels and the particle diameter of the precipitate was about 125Å in H to 175Å in F. No body-centered cubic pattern was obtained from sample I (14 pct Cr, 10,000 hr) and no precipitate particles were observed.

Weak patterns were obtained for the precipitate in samples of the 46 pct Cr alloy after 700 hr at 900°,

950°, and 1000°F. The strongest pattern was obtained from the 950°F sample and the $\{200\}$ diffraction line was unusually weak in all these cases.

The patterns from the high-purity Union Carbide and Carbon specimens (28 pct Cr, 1000 hr, 887°F, hardness 275 DPH) were rather weak and here also the $\{200\}$ line was relatively weaker than in the 10,000 hr samples. The particles were too small to be clearly resolved by the electron microscope and from this fact, and from measurements of line broadening effects, they are estimated to be less than 50Å in diameter.

No precipitate could be observed in extraction replicas of the sample of Fig. 2c (sample E reheated 1 hr at 1200°F) nor was a body-centered cubic electron diffraction pattern obtained from these replicas. A strong body-centered cubic pattern was obtained from an extraction replica of another small piece of sample E (27 pct Cr, 34,000 hr, 900°F) reheated ¼ hr at 1100°F. The precipitate particles were about 120Å in diameter and the hardness of this sample was 239 DPH.

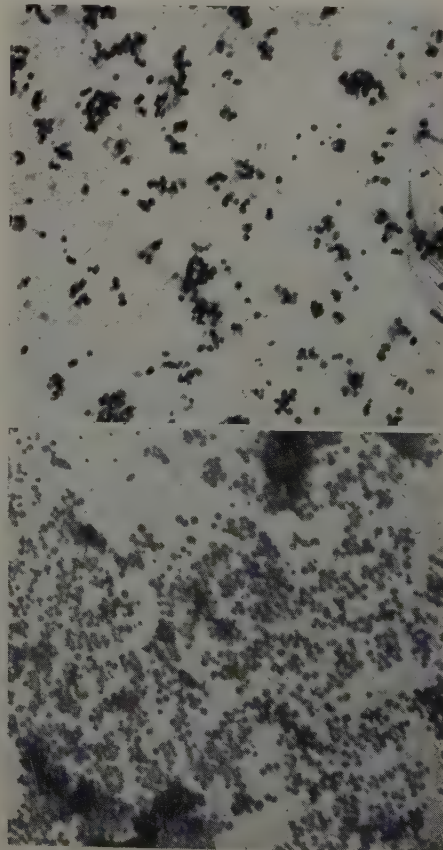
X-Ray Examination

X-ray examination of the etched surface of sample C (before) and samples D and E (after embrittlement) showed no new diffraction lines but only a slight broadening of the original body-centered cubic ferrite lines after exposure. Fig. 6 shows the diffraction pattern of the residue obtained by dissolving a small sample of embrittled steel (sample E, 34,000 hr, 900°F) in grain size reagent (HCl-picric acid in alcohol). This pattern was obtained on a Philips 90° spectrometer with filtered chromium radiation. It shows the presence of Cr_7N and Cr_{23}C_6 as minor constituents, along with strong $\{110\}$ diffraction from a body-centered cubic lattice. This material showed no evidence of ferromagnetism when tested with a small hand magnet and in a magnetic susceptibility balance. Similar patterns were obtained from the surface of the solid

Fig. 4 — Extraction replicas of 27 pct Cr steels. X60,000. Area reduced approximately 50 pct for reproduction.

a (upper) — 10,000 hr at 900°F.

b (lower) — 34,000 hr at 900°F.



steel specimen after it was etched deeply, except that the {110} diffraction line was masked by the ferrite {110} line.

X-ray fluorescence was used to measure the relative Fe-Cr composition of the extract from sample E. A copper target tube was used for excitation, and a sodium chloride crystal as monochromator. For calibration purposes a pure alloy of iron and chromium containing 46 pct Cr was used. Repeated observations on this and other similar extracted materials from samples D and E yielded a result of approximately 85 pct Cr-15 pct Fe. This, of course, includes the chromium in the carbide and nitride as well as the precipitate.

The lattice parameter of the body-centered cubic constituent was measured in the spectrometer modified for back reflection, by measuring the diffraction angle of the {211} reflection, under chromium radiation, in comparison with that from spectroscopically pure iron ($a = 2.8665\text{\AA}$). Values were obtained for extracts from steels D and E after 10,000 and 34,000 hr exposures at 900°F of 2.877 and 2.878 \AA , respectively. Precision of these measurements is limited by particle broadening which prevented accurate resolution of the α doublet. The lattice parameter measurements would imply a chromium content of about 70 pct;¹⁵ however, influence of residual elements as well as particle broadening prevents accurate estimates of composition from these measurements.

X-ray examination of the etched surfaces of samples F and G (heavily cold-worked before exposure at 900°F) showed the presence of σ phase (FeCr) as well as Cr_2N and Cr_{23}C_6 . The strength of the electron diffraction pattern for the precipitate from these samples indicated that extraction of it for X-ray examination was not feasible. The σ phase was found in sample A after aging at 1050° and 1200°F but not in steels B, D, or E after aging at these temperatures. X-ray observations of σ phase in these samples verifies previously reported identification by metallographic means.^{12, 13}

A small amount of residue extracted from the high-purity 28 pct Cr sample was examined by X-ray diffraction. No diffraction lines were obtained from the specimen due probably to the extremely small size of the particles. X-ray fluorescence analysis of the residue gave a chromium to iron ratio of about ten or twelve to one.

Chemical Composition of Extracted Materials

Table II lists the results of chemical analyses of the residues obtained by dissolving embrittled samples in the grain size reagent used previously as an etchant. Samples which were first investigated (D and E) were simply left in the etching solution until considerable residue had collected on the surfaces of the specimens and then removed from the solution and dried. After drying, the surfaces were carefully brushed and the residue collected. To obtain quantitative data on the amount of residue in an embrittled steel, samples A and B were crushed in a mortar, weighed, dissolved in grain size reagent, and the residue washed by decanting in alcohol. After washing, the residue was collected, dried, and weighed. The amount of residue available for analysis varied between 0.2 and 0.5 g. Rather more reliance is placed upon the chemical analysis of steels A and B because more extract was available for analysis and because of improved techniques in handling.

From Table II it is seen that the Cr-Fe ratio agrees



Fig. 5—Electron diffraction pattern of area shown in Fig. 4b.

moderately well with the ratio determined by X-ray fluorescence analysis. While the reported nitrogen contents of the extracted materials from samples A and B are quite consistent with the yield factors and the nitrogen contents of the initial steels (Table I), the carbon values are several times larger than would be expected from the yield factors and the carbon content of the steels. It is probable that these discrepancies are due to organic contamination both from the etchant and from etching products not removed during washing. The estimated carbon contents listed in Table II were obtained by multiplying the original carbon content of the steels by the concentration factor in the extraction. This assumes that all the carbon in the steels was combined as carbide and was recovered in the extraction.

Since the X-ray results showed that the extract consists only of Cr_{23}C_6 , Cr_2N , and the body-centered cubic precipitate, it is possible to compute the relative proportions of these three phases in the extract, and also the composition of the precipitate. Table III lists the results of these computations, using the nitrogen values from the analyses and the estimated

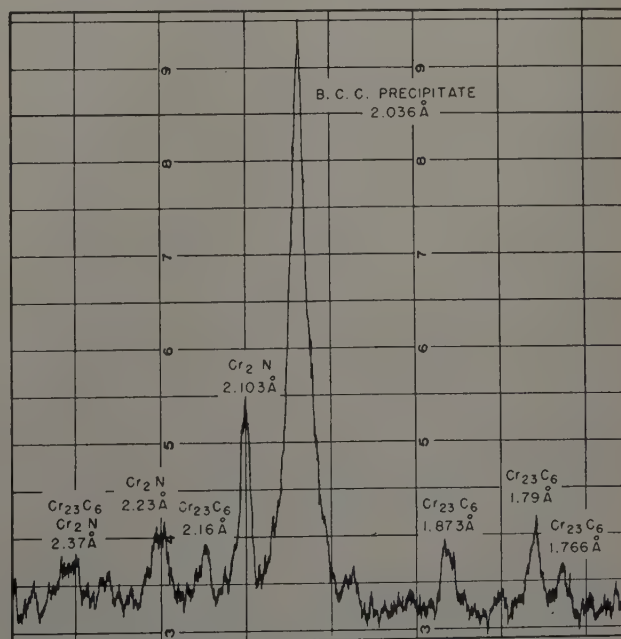


Fig. 6—X-ray diffraction pattern of residue extracted from 27 pct Cr steel exposed 10,000 hr at 900°F .

Table II. Composition of Extracted Material, Wt Pct

Specimen	Yield	Cr	Fe	N	C	Total	Estimated C
A	11.5	64.0	11.3	0.84	1.69	77.8	0.28
B	9.9	66.4	11.1	0.77	2.75	81.0	1.2
D	13.1*	61.5	12.2	1.7	—	75.4	1.8
E	18.5*	70.9	11.6	1.2	1.9	85.6	1.3

* Estimated from nitrogen values of steel and extract.

values for carbon. Agreement among the samples in the composition of the body-centered cubic precipitate is quite good except for sample D which was the smallest sample and yielded the bare minimum of residue that could be analyzed.

The proportions by weight of the constituents in the extracts can be converted into weight proportions in the embrittled steels by using the yield values of Table II. Table IV shows the results of calculating the composition of the steels in this way. Values in parentheses are the values for the carbide and nitride that would be expected from the carbon and nitrogen contents of the steels. The values computed from the analyses of the extract are all higher than the values computed from the steel analyses. This error, whatever its origin, tends to decrease both the apparent chromium content of the body-centered cubic precipitate and the apparent amount of precipitate formed. The chromium content of the remaining ferrite is computed by subtracting the chromium combined as nitride, carbide, and body-centered cubic precipitate from the original steel chromium analysis and calculating its weight percent in the remaining ferrite matrix.

Magnetic Measurements

Preliminary qualitative observations with a small Alnico permanent magnet revealed that the extractions from embrittled steels were either nonmagnetic, or only weakly magnetic. Quantitative measurements were made in a magnetic susceptibility balance. In this instrument a magnetizing field of about 400 oersteds was provided, and the tractive force in an inhomogeneous field was measured on a standard chemical balance. Extracts from specimens D and E revealed no detectable ferromagnetism; those from A and B gave tractive forces equal to about 10 pct of the specimen weights. For comparison, under identical conditions, steel C gave a tractive force equal to twice its weight. Electron diffraction examination of one of the magnetic residues indicated the presence of magnetite, which may account for the slight ferromagnetism.

Small pieces of embrittled steels D and E were investigated over a range of temperatures up to 670°C (1238°F) in the same instrument. No evidence was found for any Curie temperature, other than the principal one at 600° ± 5°C (1112° ± 9°F) which, according to Adcock,¹⁵ is appropriate to a 27 pct chromium ferrite. No hysteresis effects were found upon heating above and cooling below the Curie

temperature; hence no chromium depletion of the ferrite was evidenced. In view of other findings this may be ascribed to the rapidity of solution of the precipitate in the ferrite matrix above 475°C (887°F), because during the course of the measurements at least 30 min was spent in increasing the specimen temperature from 475° to 600°C. It would appear that direct observation of a chromium-depleted ferrite is impossible by magnetic means. The nonmagnetic residue of sample E was examined for a low-temperature Curie point down to -195°C (-319°F). A slight tractive force was observed at -195°C for this sample which might have been due to paramagnetism just above the Curie point. From the work of Adcock,¹⁵ a Curie point below -195°C indicates a chromium content in excess of 78 pct.

Experimental Results

The experimental results described in the preceding sections indicate the formation of a sub-microscopic precipitate during the embrittlement of ferritic chromium alloy steels at 885°F.

The electron and X-ray diffraction measurements show that the precipitate has the body-centered cubic structure with lattice parameter between that of iron and chromium. This lattice parameter of 2.878Å is equal to that of a pure alloy of 70 pct Cr-30 pct Fe. Chemical analyses of the residues extracted from embrittled steels indicate that the precipitate is between 78 to 82 pct Cr and that the precipitate can amount to as much as 10 pct by weight in a 27 pct Cr steel exposed for four years. X-ray fluorescence analysis of the extract from a high-purity 27 pct Cr iron aged 1000 hr at 900°F showed a chromium content of 92 to 94 pct Cr.

Magnetic measurements on the precipitate show that it is not ferromagnetic above -195°C, which is the Curie point for a 78 pct Cr-22 pct Fe alloy. Electron microscope observations reveal that the diameter of the precipitate particles depends both on time of exposure and on chromium content of the steel. In 27 pct Cr steels the precipitate diameter varied from less than 50Å after 1000 hr exposure to about 225Å after 34,000 hr exposure. For 10,000 hr exposure, diameter varied from about 125Å in a 15 pct Cr steel to about 200Å in a 27 pct Cr steel. The precipitate particles formed during 34,000 hr at 900°F completely dissolved during 1 hr reheating at 1200°F and shrank from 225 to 120Å in diameter during ¼ hr at 1100°F.

The precipitate was found in steels with chromium contents above 14 pct and was found to coexist with σ (FeCr) in steels which had been severely cold-worked before exposure at 885°F. In well annealed 27 pct Cr steels, σ phase was found after exposure at 1050° and 1200°F in samples that increased in hardness during aging and was not found in samples that did not harden at these temperatures. No precipitate was found to form above 1000°F.

Discussion

As stated in the introduction, changes in properties of ferritic chromium steels during embrittle-

Table III. Computed Composition of Extract, Wt Pct

Specimen	Cr ₂ N	Cr ₂₃ C ₆	Body-Centered Cubic Precipitate
A	9.3	6.5	84.2 (82.5% Cr, 17.5% Fe)
B	8.2	26.5	65.3 (78.6% Cr, 21.4% Fe)
D	18.6	41.0	40.4 (61.0% Cr, 39.0% Fe)
E	11.9	26.9	61.2 (77.5% Cr, 22.5% Fe)

Table IV. Computed Composition of Embrittled Steel, Wt Pct

Specimen	Cr ₂ N	Cr ₂₃ C ₆	Body-Centered Cubic	Cr Content of Ferrite
A	1.07 (0.7)	0.75 (0.56)	9.7	21
B	0.81 (0.69)	2.62 (2.1)	6.5	21
D	2.42 (1.85)	5.37 (4.2)	5.3	19
E	2.20 (1.85)	4.98 (4.2)	11.3	14

ment at 885°F are accompanied by precipitation of a chromium-rich phase. The small particles of the embrittling phase have the body-centered cubic structure of the matrix with a lattice parameter only 0.2 pct larger and are probably coherent with the matrix, thus greatly increasing its hardness due to internal strains. The formation of a fine precipitate also explains the increase in the coercive force of the steel. Chromium depletion of the matrix during embrittlement lowers the corrosion resistance of the steel and also lowers its electrical resistivity. Data in the literature³⁰ suggest that the rate of corrosion for embrittled steels is several times greater than for a steel of chromium content equal to the composition of the depleted matrix (as calculated in this report). This effect could well be due to the presence of the precipitate particles in the steel.

Formation of the precipitate is difficult to explain. The Fe-Cr phase diagram indicates that ferrite and σ phase should be the stable phases in an equilibrated 27 pct Cr alloy; nevertheless during exposure at 885°F the alloy seems to prefer to separate into iron-rich and chromium-rich ferrites. However, in severely cold-worked steels the precipitate can coexist with σ at 885°F. Rate of growth of the precipitate is unusually slow. From diffusion considerations, the precipitate particles could grow to the observed 200Å diameter in less than 2 hr or, alternatively, in 34,000 hr the diffusion-limited diameter is more than 5000Å. In the cold-worked samples aged at 900°F the largest σ particles were within 20 pct of the calculated diffusion-limited size.

The size and structure of the precipitate is reminiscent of the "clusters," "knots," or "complexes"¹⁷ proposed to account for the changes in properties during age-hardening of nonferrous metals that occur before any microstructural changes can be discerned. Various transitional structures preceding formation of the equilibrium precipitate have been observed^{18, 19} by X-ray scattering at small angles from nonferrous metals undergoing age-hardening. In most cases the data have been interpreted as scattering from a two dimensional platelet but occasionally as from a spherical precipitate. The theory of these coherent transitional precipitates, as developed so far,^{19, 20} implies that the thickness of the platelet depends on the mismatch between the atom-atom distances in the precipitate and in the matrix, and also on the relative rigidity of the precipitate and the matrix. According to this theory, the small amount of mismatch between the chromium-rich body-centered cubic precipitate and the matrix, and the greater rigidity of the precipitate, could result in very thick platelets or essentially spheres.

If 885°F embrittlement is an age-hardening phenomenon it should exhibit overaging. This has not been observed for 27 pct Cr steels even after four years of aging. However, it is possible that overaging will be observed after further exposure, since the matrix has been depleted in chromium almost to the threshold composition of embrittlement and little more precipitate can form. The fact that the hardness did not increase during heating from 10,000 to 34,000 hr, while the amount of precipitate more than doubled with no change in particle size, may mean that the particles formed first lost coherency at about the same rate as new coherent particles formed. This idea is supported by the observations that the precipitate size, in a fully embrittled sample held a short time in the softening temperature range, is much larger than in a sample embrittled for just

a short period although the reheated sample is considerably softer. The resolution treatment may cause the precipitate particles to lose coherence while dissolving and thus soften the steel.

Acknowledgments

The authors wish to thank J. J. Heger, H. S. Link, and P. W. Marshall, of the Research and Development Laboratory, United States Steel Corp., together with A. B. Wilder, of National Tube Div., United States Steel Corp., and W. O. Binder, of Union Carbide and Carbon Corp., for supplying samples used in this investigation.

It is also a pleasure to acknowledge the assistance of many members of the Research Laboratory, including D. S. Miller for assistance in the magnetic measurements and L. S. Darken and G. V. Smith for valuable suggestions.

References

- ¹ F. M. Becket: On the Allotropy of Stainless Steel. *Trans. AIME* (1938) **131**, p. 15.
- ² G. Riedrich and F. Loib: Embrittlement of High Chromium Steels Within Temperature Range of 570-1100°F. *Archiv. Eisenhüttenwesen* (October 1941) **15**, pp. 175-182.
- ³ G. Bandel and W. Tofaute: Brittleness of Chromium Rich Steels at Temperatures Around 930°F. *Archiv. Eisenhüttenwesen* (1942) **15**, No. 7, pp. 307-319.
- ⁴ W. Dannohl, W. Hessenbruck, and E. Hengler: Brittleness Phenomena of High Chromium Steels in Temperature Range of 930°F. *Archiv. Eisenhüttenwesen* (1942) **15**, No. 7, pp. 319-320 (discussion of refs. 2 and 3).
- ⁵ J. J. Heger: 885°F Embrittlement of the Ferritic Chromium-Iron Alloys. *Metal Progress* (August 1951) pp. 55-61.
- ⁶ H. D. Newell: Properties and Characteristics of 27% Chromium Iron. *Metal Progress* (May 1946) pp. 977-1028.
- ⁷ A. J. Lena and M. F. Hawkes: Embrittlement of High Chromium Ferritic Stainless Steels at 475°C. *JOURNAL OF METALS* (February 1952) p. 146.
- ⁸ E. Houdremont: *Einführung in die Sonderstahlkunde* (1935) p. 183. Berlin. Julius Springer.
- ⁹ V. N. Krivobok: Alloys of Iron and Chromium. *Trans. ASM* (1935) **23**, pp. 1-60.
- ¹⁰ E. C. Bain and R. H. Aborn: The Iron-Nickel-Chromium System. *Metals Handbook* (1939) pp. 418-422. Cleveland. ASM.
- ¹¹ G. V. Smith, W. B. Seens, H. S. Link, and P. R. Malenock: Microstructural Instability of Steels for Elevated Temperature Service. *Proc. ASTM* (1951) **51**, pp. 895-917.
- ¹² J. J. Heger: The Formation of Sigma Phase in 17 Per Cent Chromium Steels. *ASTM Special Technical Publication No. 110* (1950) pp. 75-81.
- ¹³ H. S. Link and P. W. Marshall: The Formation of Sigma Phase in 13-16% Chromium Steels. *Trans. ASM* (1952) **44**, p. 549.
- ¹⁴ C. O. Burgess and W. D. Forgeng: Constitution of Fe-Cr-Mn Alloys. *Trans. AIME* (1938) **131**, p. 272.
- ¹⁵ F. A. Adcock: The Cr-Fe Constitutional Diagram. *Journal ISI* (1931) **124**, pp. 99-146.
- ¹⁶ Owen K. Parmiter: Wrought Stainless Steels. *Metals Handbook* (1948) p. 553. Cleveland. ASM.
- ¹⁷ A. H. Geisler: Precipitation from Solid Solutions of Metals. *Phase Transformations in Solids*. (1951) pp. 493-496. New York. John Wiley and Sons.
- ¹⁸ J. Calvet, P. Jacquet, and A. Guinier: Age Hardening of a Copper-Aluminum Alloy. *Journal Inst. Metals* (1939) **65**, p. 121.
- ¹⁹ F. R. N. Nabarro: Diffusion and Precipitation in Alloys. *Symposium on Internal Stresses in Metals and Alloys*. (1948) pp. 237-249. Inst. of Metals.
- ²⁰ J. C. Fisher, J. H. Hollomon, and J. G. Leschen: Precipitation from Solid Solution. *Industrial and Engineering Chemistry* (June 1952) **44**, pp. 1324-1327.

Densification and Kinetics of Grain Growth During The Sintering of Chromium Carbide

by H. J. Hamjian and W. G. Lidman

THE fabrication of many materials from powders involves a sintering process. A mass of powder will sinter because of the excess free energy over the same mass in the densified state caused by the higher total surface area of the powder. An understanding of the kinetics and mechanism of sintering should assist in improving the properties of such materials. The present investigation conducted at the NACA Lewis laboratory deals with the sintering of chromium carbide.

Dry sintering (sintering at a temperature below the melting point) was divided into two stages by Shaler:¹ the first stage, during which the particles preserve much of their original shape and the voids are interconnected, and the second stage, during which densification occurs and the pores are isolated. The mechanism of forming interfaces between particles, or welding together of particles, has been investigated by Kuczynski² and may be described by any one or a combination of the following mechanisms: viscous flow, evaporation and condensation, volume diffusion, or surface diffusion. The mechanism by which pores are closed or eliminated (densification) during sintering, is of interest.

Grain growth observed during sintering may be attributed to the variation in the surface energies of individual grains, causing some grains to grow at the expense of others. Grain boundary migration occurs presumably by a diffusion process, therefore the rate of grain growth would be expected to increase exponentially with increasing time and temperature. Thus, for practical sintering times of less than 1 hr, a certain minimum temperature may exist at which major structural and property changes will occur.

Densification and kinetics of grain growth during sintering under pressure of chromium carbide were investigated to provide additional information which will aid in describing more accurately the sintering process and the mechanisms involved. This material was selected for this study because of the current interest in high strength, oxidation resistant refractory materials, such as carbides, which are sintered to produce solid, dense materials from powders. Sintering under pressure is a process where the heat and pressure are applied to the compact simultaneously, specimens for this work were prepared by

sintering under pressure at different temperatures and for various time periods.

Experimental Procedure

Preparation of Specimens: Chemical analysis of the commercial chromium carbide used in this investigation was as follows: Cr 86.19 pct, C 12.14 pct, and Fe 0.2 pct. X-ray diffraction powder patterns gave characteristic diffraction lines of Cr_3C_2 crystal structure.

Powder particle size was determined microscopically and the average initial particle size was 6 microns with 85 pct between 2 and 10 microns. Specimens sintered under pressure were formed in graphite dies³ heated by induction. Sintering temperatures were measured with an optical pyrometer by sighting into a $\frac{3}{8}$ -in. hole drilled 1 in. deep at the midsection of the graphite die. A load of approximately 1 ton per sq in. was applied to the powder. The die assembly was heated in 20 min to the highest temperature (2500°F) at which no increase in grain size could be observed, and less than 2.5 min were required to heat from this temperature to the maximum temperature (3000°F). Sintering temperatures and times for the specimens of this investigation are indicated in Table I.

Analysis of Specimens: Specimens polished with diamond abrasives were etched to reveal the grain boundaries with a 1:1 mixture of 20 pct potassium hydroxide and 20 pct potassium ferricyanide heated to 160°F. Representative areas of each sample were photographed at 1000 diameters. The largest diameters of all well-defined grains were measured, but only the measurements of 15 of the largest grains were averaged in order to determine an index of grain size on the assumption that they were among the first to begin growth.

Densities were determined from differential weighing of the samples in air and water. The reported density values are considered correct within ± 0.01 g per milliliter.

Results and Discussion

Metal compacts have exhibited grain growth when sintered at temperatures about two-thirds of the absolute temperature of their melting point.⁴ Grain growth also occurs during the sintering of chromium carbide and is illustrated by the micrographs shown in Fig. 1. These micrographs were prepared from specimens sintered for 90 min at temperatures ranging from 1371°C (2500°F) to 1648°C (3000°F). Average grain size and density measurements of specimens investigated are presented in Table I. The relationship between grain size and sintering tem-

H. J. HAMJIAN, Junior Member AIME, is Senior Research Metallurgist, Utica Drop Forge and Tool Corp., Utica, N. Y., and W. G. LIDMAN is Section Head, Atomic Energy Div., Sylvania Electric Products Inc., Bayside, N. Y.

Discussion on this paper, TP 3474E, may be sent, 2 copies, to AIME by Dec. 1, 1953. Manuscript, Sept. 8, 1952. Cleveland Meeting, October 1953.

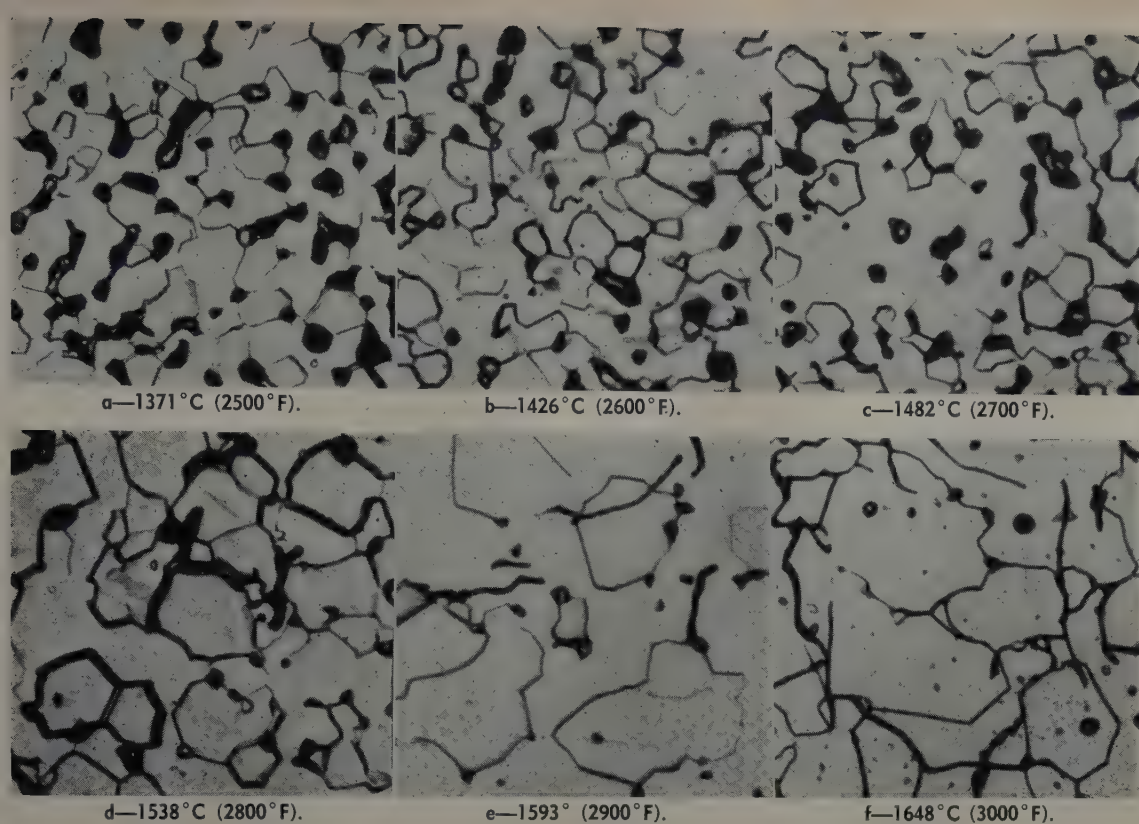


Fig. 1—Micrographs of specimens sintered at various temperatures for 90 min. X1000.

perature of samples shown in Fig. 1 is graphically represented in Fig. 2.

Grain growth in polycrystalline solids and in sintered bodies may occur by grain boundary migration which results in the gradual absorption of some grains by others. When sintering a mass of polycrystalline nonductile particles, grain growth probably occurs first within the particle boundaries. This internal grain growth (that is, within the particles) is assumed of little importance in the sintering process.⁵ Grain boundary migration across the particle boundaries begins after sintering has proceeded to a point at which substantial bonds are formed between particles which permit absorption of one grain by another. This welding or bonding of particles together has been investigated by Kuczynski.² Based on the results of the present investigation the bonding between particles may be classed as a first stage in the sintering process. A second and third stage become apparent when the density and grain size data are plotted as shown in Fig. 3. Sections of representative micrographs which show the size and position of the pores with different grain sizes have been included in this figure. This curve shows the

dependence of density on the change in grain size. The dashed portion of this curve shows that density increases with increasing grain size and may be designated as a second stage of sintering. A third stage is indicated by the solid portion, where grain size continues to increase with no appreciable increase in density. From the micrographs on this figure and those in Fig. 1 it can be seen that for specimens sintered at times and temperatures which fall in the second stage of sintering the pores are located in the grain boundaries. During the second stage, as the time and temperature conditions are increased, the pores decrease in number and size, and spheroidize while the grains grow. When specimens are sintered at conditions encountered in the third stage densification is complete, the pores have spheroidized and tend to be located within the grains and the grains continue to grow. The sintering process for chromium carbide may therefore be described by a first stage during which particles preserve much of their original shape and a substantial bond has formed between adjacent particles; a second stage during which densification occurs (pores reduce in number and size and spheroidize) accom-

Table I. Density and Grain Size Measurements of Chromium Carbide Specimens

Sintering Temperature		Sintering Time, Min													
		5		15		30		45		90		180		360	
°C	°F	Density, G per Ml	Grain Size, Microns	Density, G per Ml	Grain Size, Microns	Density, G per Ml	Grain Size, Microns	Density, G per Ml	Grain Size, Microns	Density, G per Ml	Grain Size, Microns	Density, G per Ml	Grain Size, Microns	Density, G per Ml	Grain Size, Microns
1260	2300									4.80					
1371	2500	5.38	6.50	5.66	7.30	5.88	7.70	5.94	8.20	6.03	8.50	6.12	9.4	6.43	9.9
1426	2600	5.54	8.05	5.98	8.95	6.04	9.75	6.12	10.05	6.30	10.60	6.59	11.4	6.64	11.8
1482	2700	5.99	8.65	6.11	9.95	6.12	10.75	6.37	11.10	6.42	11.50	6.66	13.2	6.65	15.0
1538	2800	6.04	9.10	6.34	10.80	6.57	12.35	6.57	13.20	6.61	14.90				
1593	2900	6.10	11.20	6.46	12.50	6.65	15.20	6.65	16.40	6.65	18.30				
1648	3000	6.62	12.75	6.61	15.90	6.64	18.60	6.64	19.10	6.65	21.40				

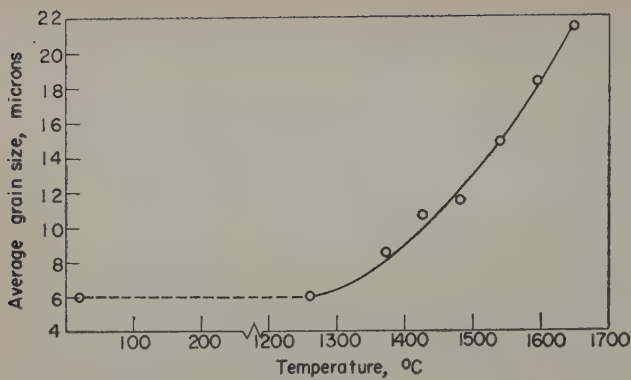


Fig. 2—Variation in average grain size of sintered chromium carbide with sintering temperature, time period of 90 min.

panied by grain growth, and a third stage during which there is no appreciable change in density, the few remaining pores tend to be located within the grains and grain growth is the predominant phenomena. In preparing compacts with maximum density and minimum grain size, sintering must be terminated in the early part of this third stage.

In order to determine whether grain growth during the sintering of chromium carbide could be expressed by an empirical equation, the average measured grain size was plotted against sintering time on logarithmic scales for constant sintering temperature (Fig. 4). Straight lines are apparent with two slopes which again demonstrates that there is a change in the sintering process. The relation-

ship between grain size and sintering time is expressed by the empirical equation

$$D^n = Kt \quad [1]$$

where D is the average grain size in microns; K , the rate constant (function of temperature and n); n , the reciprocal of the slope and constant for each sintering stage; and t , the sintering time in minutes.

The dashed lines which represent the data from specimens sintered for 360 min or less at 1371° and 1426°C (2500° and 2600°F) and for less than about 100 min at 1482°C (2700°F) are parallel and the reciprocal of the slope (n) is 10. A change in slope is observed for sintering times in excess of about 100 min at 1482°C (2700°F) and indicates the change in the sintering process. This change occurs in less than 5 min at 1538°C (2800°F) and above; all these solid lines are parallel and yield a value of n equal to 6. Examination of the structure of specimens sintered for conditions when n is 10 shows that the specimens are in the second stage as described earlier, that is, the pores are located in the grain boundaries and are decreasing in number, size and are spheroidizing while grain growth is occurring simultaneously. Micrographs of specimens sintered for conditions when n is 6 show the pores are spheroidized and tend to be located within the grains while the grains continue to grow; these specimens are in the third stage of sintering. There is no appreciable change in density during the third stage since the mechanism of eliminating the pores within

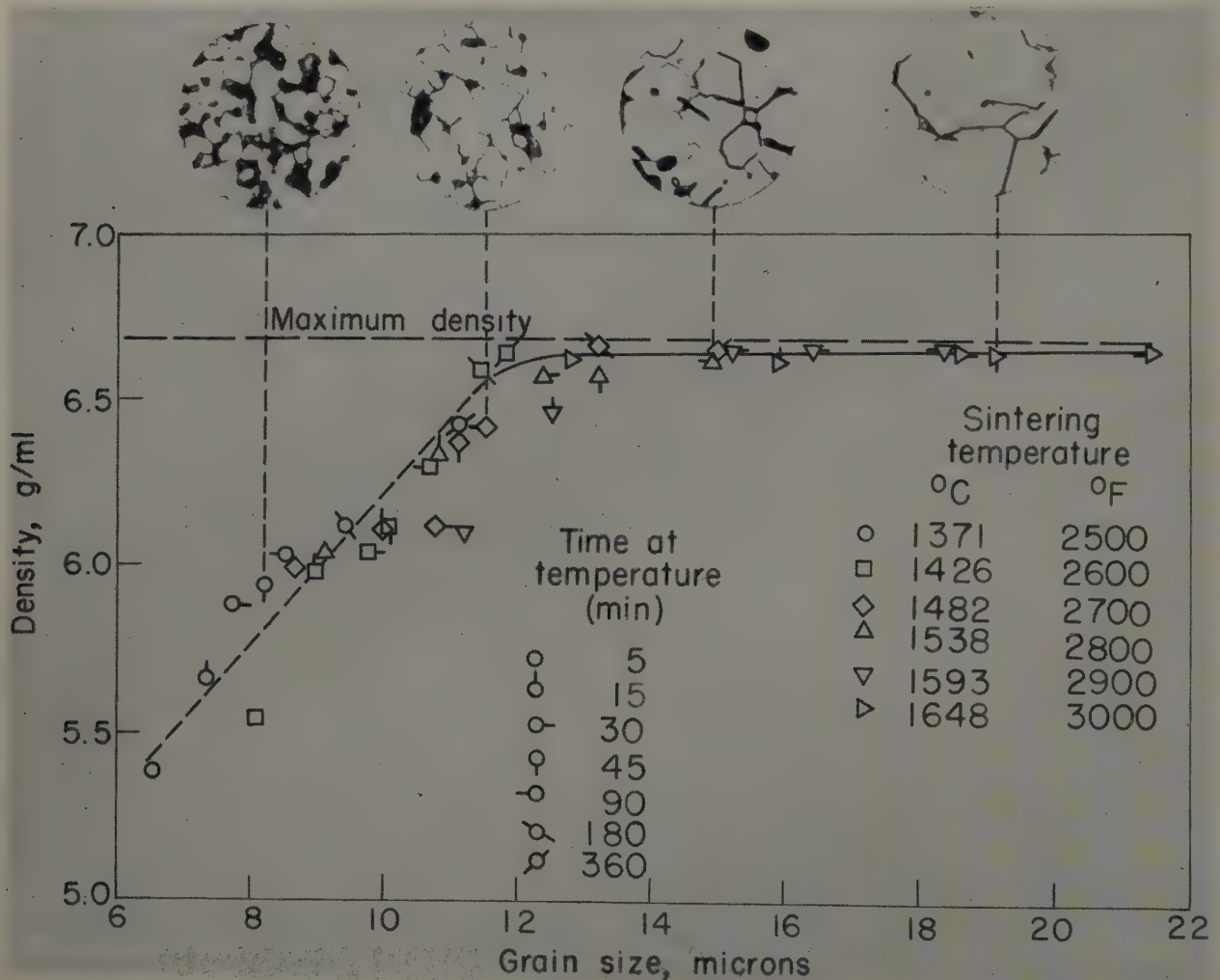


Fig. 3—Variation of density with grain size for specimens sintered at different temperatures and time periods.

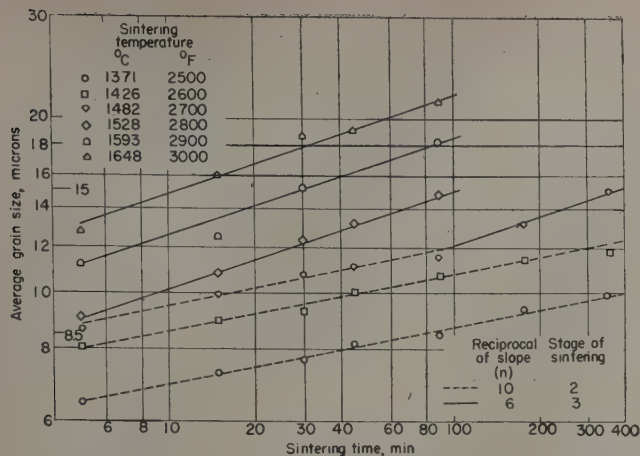


Fig. 4—Isothermal grain growth for sintered chromium carbide.

the grains is probably by self-diffusion which is a relatively slow process. The change in structure that is observed for each value of n corroborates the stage transition as shown in Fig. 3 and the value of n can therefore be associated with stages of sintering. The lower value of n (6) indicates that grain growth proceeds more rapidly during the third stage of sintering.

Grain growth during the sintering process appears to obey the Arrhenius type equation

$$K = Ae^{-Q/RT}$$

where K is a rate constant for sintering process (Eq. 1); A , a constant; Q , the molal energy of activation in cal per mol; R , the gas constant (1.99 cal per mol per °K); and T , the absolute temperature, °K. Thus

$$\ln K = n \ln D - \ln t = -\frac{Q}{RT} + \ln A$$

For a fixed grain size (D) and a given value n or stage, the plot of $\ln t$ against $1/T$ should give a straight line of slope Q/R . From Fig. 5 this relation appears to be valid for each stage of sintering (n is constant). Thus, in a certain time t_1 at an absolute temperature T_1 and in a time t_2 at a different absolute temperature T_2 (for a constant n), a given

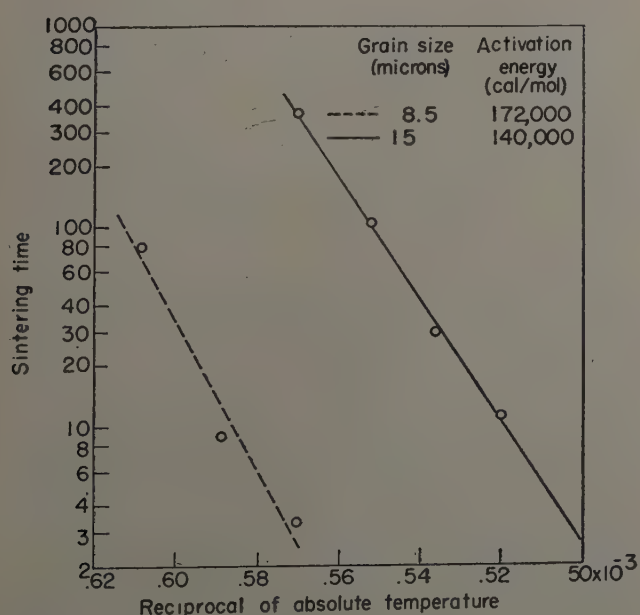


Fig. 5—Variation of sintering time to obtain average grain size of 8.5 and 15 microns with reciprocal of absolute sintering temperature.

Table II. Values of Energy of Activation

Sintering Stage	Reciprocal of Slope (n)	Grain Size, Micron (D)	Energy of Activation, Q, Cal per Mol
2	10	8.5	172,000
3	6	15.0	140,000

grain size can be obtained. The relation between these four quantities may be expressed as

$$\ln \frac{t_1}{t_2} = \frac{Q}{R} \left(\frac{1}{T_1} - \frac{1}{T_2} \right)$$

The values of Q obtained from Fig. 5 are shown in Table II.

During the second stage of sintering, the process consists of the complex mechanisms of densification as well as grain growth. The higher values of n (10) and activation energy (172,000 cal per mol) suggest that the pores in the grain boundaries during this stage act as barriers to grain growth. When n is 6 for the third stage, the pores are within the grains and no longer retard the grain growth process. In this stage there is no appreciable densification, grain growth proceeds more rapidly, and the resultant lower value of Q may be interpreted as the activation energy for grain growth.

Conclusions

The investigation of the densification and grain growth phenomena during the sintering of chromium carbide under pressure indicated that:

1—Densification (reduction in number, size, and spheroidization of pores) takes place during a second stage of the sintering process and grain growth occurs simultaneously.

2—After densification is nearly complete (when pores are located within the grains) grain growth continues; this may be considered as a third stage in the sintering process.

3—Grain growth during sintering follows the empirical equation $D^n = Kt$, where D is the grain diameter, K is a rate constant, and t is the sintering time. A change in n is associated with the second and third stages of sintering.

4—An activation energy for grain growth during the third stage of sintering chromium carbide can be computed.

Acknowledgments

The authors wish to express their appreciation to the National Advisory Committee for Aeronautics for permission to publish the results of this investigation. They also wish to acknowledge their indebtedness to the other members of Materials Research Section of the Lewis Laboratory for their assistance in various phases of work.

References

- A. J. Shaler: Seminar on Kinetics of Sintering. *Trans. AIME* (1949) 185, p. 798; *JOURNAL OF METALS* (November 1949).
- G. C. Kuczynski: Self-Diffusion in Sintering of Metallic Particles. *Trans. AIME* (1949) 185, pp. 169-178; *JOURNAL OF METALS* (February 1949).
- H. J. Hamjian and W. G. Lidman: Sintering Mechanism Between Zirconium, Carbide and Columbium. NACA TN 2198 (1950).
- W. D. Jones: *Principles of Powder Metallurgy*. (1941) p. 79. London. Edward Arnold and Co.
- P. E. Wretblad and John Wulff: *Powder Metallurgy*. (1942) p. 53. Cleveland. ASM.

Deformation of Ferrite Single Crystals

by F. L. Vogel, Jr. and R. M. Brick

THE elementary mechanism of deformation in the body-centered cubic metals has been a subject of dispute for many years. If the problem were merely that of designating the crystallographic plane or planes of slip, the solution would have appeared long ago. However, there must be greater differences in the deformation behaviors of the body-centered and face-centered types than the differences in their lattices would suggest. The lines of slip formed on the polished surface of a strained face-centered cubic metal conform to glide over a single plane of the crystal. Slip in body-centered cubic iron, however, is frequently observed as curved and forked lines which could not possibly define a single plane of atoms. This alone is sufficient reason to expect different modes of deformation to operate in the two lattice types.

The literature in this field now has generally accepted the proposition that {110}, {112}, or {123} planes will act as slip planes in iron. It is essential that the experimental evidence supposedly supporting this proposition be critically examined.

Taylor and Elam¹ in 1926, using relatively small single crystals, determined the operative slip systems by measurements of the distortion of a grid engraved on the specimens prior to deformation. Their results indicated that shearing had taken place in the close-packed direction on a plane adjacent to or coinciding with the plane of maximum shear which contained the slip direction. This led the authors to propose a theory of noncrystallographic

or banal slip. The authors considered an alternate rationalization of banal glide. Slip on two {110} planes or possibly two {112} planes containing the same $\langle 111 \rangle$ direction could produce the wavy slip lines. By employing plane segments of varying widths, the integrated plane could take any position in the $\langle 111 \rangle$ zone. They rejected this explanation, however, feeling that the preponderance of evidence was against it.

Taylor² continued the investigation of the plasticity of the body-centered cubic lattice on β brass. He reasoned that the resistance to shearing of a given plane in the zone of the slip direction was a function of the angle between the glide plane and the closest (110):

$$F = \frac{P}{A} \cos \xi \sin \xi \cos(\chi - \psi) \quad [1]$$

where F is the resistance to shear; P , the axial load at yielding; A , the cross sectional area; ξ , the angle between slip direction and load axis; χ , the angle between plane of maximum shear containing the slip direction and the (101) pole; and ψ , the angle between observed glide plane and the $(\bar{1}01)$ pole.

Differentiating Eq. 1 and rearranging,

$$\frac{dF}{F} = \tan(\chi - \psi) d\psi \quad [2]$$

which expresses the variation of the shear resistance with the angle ψ . Integrating this equation between the limits 0 and ψ yields

$$\ln F/F_0 = \int_0^\psi \tan(\chi - \psi) d\psi \quad [3]$$

Here, F_0 is the resistance to shear of the (110) plane and F is the resistance to shear of a plane ψ degrees from the (110). Thus, the variation of shear resistance with ψ can be calculated from an experimentally measured χ vs ψ relationship.

Fahrenhorst and Schmid³ used several methods, none of them involving direct observation, to determine the glide system in ferrite. They determined the variation of critical resolved shear stress with

F. L. VOGEL, JR., Junior Member AIME, formerly graduate student, University of Pennsylvania, is now Member of the Technical Staff, Bell Telephone Laboratories, Murray Hill, N. J., and R. M. BRICK, Member AIME, is Director, Metallurgical Engineering, Towne Scientific School, University of Pennsylvania, Philadelphia.

Discussion on this paper, TP 3523E, may be sent, 2 copies, to AIME by Dec. 1, 1953. Manuscript, Dec. 12, 1952; revision, Feb. 24, 1953. Cleveland Meeting, October 1953.

This paper is based on a dissertation by F. L. Vogel, Jr. submitted in partial fulfillment of requirements for the degree of Doctor of Philosophy to the Faculty of the Graduate School of the University of Pennsylvania.

orientation assuming that glide had occurred: 1—on planes of the type $\{110\}$, 2—on planes of the type $\{112\}$, 3—on planes of the type $\{123\}$, and 4—on the noncrystallographic plane of maximum shear stress. They state that the assumption that slip had occurred on a $\{123\}$ plane in the $\langle 111 \rangle$ direction best fitted the observed behavior. However, the differences in results between the alternative assumptions are slight and almost certainly less than the experimental error involved in obtaining the data. Equivalent results were obtained from analyses of axis migration or of shear stress-strain data and, although again the interpretation was in terms of $\{123\}$ slip, it appears certain that their tests were incapable of discriminating between the alternative assumptions.

In Barrett, Ansel, and Mehl's extensive study of slip in iron and silicon ferrite,⁶ no critical shear stress values were measured and the investigation was confined to a qualitative evaluation of the glide process. Deformation was induced in thin strip specimens over a wide range of temperatures extending from 500°C down to -195°C. Because of the specimen shapes, the authors were able to plot the traces of the glide markings in only one dimension, i.e., represented by lines on a stereographic projection. Planes of the types $\{110\}$, $\{112\}$, and $\{123\}$ were considered by this method and it was found that all of the 194 traces tabulated could be attributed to one of these three planes. The assumptions of this approach, however, exclude the possibility of determining a noncrystallographic plane of glide and should glide have occurred this way, an adjacent crystal plane would have been recorded as responsible for the marking. When as many different planes as this are under consideration, a trace normal placed at random in the projection has a relatively high probability of coming close to a crystal pole within the limits of error of the measurements. Therefore this investigation did not prove uniquely that slip in iron occurs on the crystal planes $\{110\}$, $\{112\}$, and $\{123\}$.

Andrade⁵ has concluded that in the body-centered cubic metals, all three of the planes $\{110\}$, $\{112\}$, and $\{123\}$ are possible slip planes and the temperature determines which shall operate. This viewpoint, while convenient, ignores significant facts which bear on the case of iron; viz., that at the same temperature, all three of the planes have been reported as planes of slip.

Chen and Maddin⁸ induced strain in molybdenum single crystals at room temperature and found that the glide ellipse could not be accounted for by the indices $\{112\}$ as predicted by Andrade. The glide ellipses which were observed in several specimens took various positions along the $\langle 111 \rangle$ zone. The authors analyzed the asterism which appeared on the Laue photographs of the deformed specimens and concluded that slip had taken place on $\{110\}$ planes regardless of the position of the glide ellipse. This theory had been proposed before by Greninger and by Taylor and Elam. It explains two of the common observations of the slip in iron: 1—that the glide plane may take any position between the $\{110\}$ and $\{112\}$ poles, and 2—that the glide plane will be irregular or wavy when viewed at the head of the ellipse and relatively straight when viewed at the side of the ellipse. The double $\{110\}$ shear hypothesis, however, fails to explain the observed behavior when the plane of glide actually coincides with a $\{110\}$ pole. Here, it would be predicted that in de-

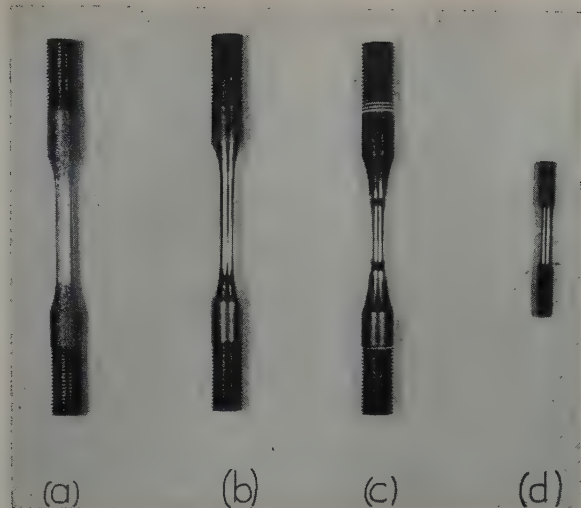


Fig. 1—Single-crystal tensile test specimens. a—Test bar macroetched to reveal single-crystal gage section and polycrystalline shoulders. b—Polished bar for tests at room temperature and above. c—Modification I for tests at -70°C. d—Modification II for tests at -105°C.

tail the glide ellipse should be composed of only one type of plane, a $\{110\}$, and therefore the slip line should be straight, regardless of where it is viewed with respect to the slip direction. This is not borne out by observations.

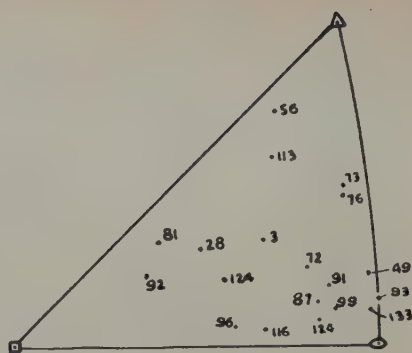
The analysis by Opinsky and Smoluchowski⁷ of slip in iron is similar to Taylor's in that the position of the glide plane is used to determine the relative resistances to shearing of planes along the zone of the slip direction. A cardinal point of difference between Taylor's approach and that of Opinsky and Smoluchowski is the implicit assumption of the latter that the glide which is observed and measured is on a crystallographic plane, $\{110\}$, $\{112\}$, or $\{123\}$. In a second paper,⁸ Opinsky and Smoluchowski measured the ratios of the critical shear strengths on these planes at various temperatures on compressed silicon ferrite crystals. The results show, as in ref. 4, that at low temperatures there is a preference for $\{110\}$ as the plane of glide in compression.

Experimental Work

Materials and Treatment: Tensile test bars with a $1 \times \frac{1}{4}$ in. diam gage section were machined from $\frac{1}{2}$ -in. rods of ingot iron. Single crystals were grown in the gage section by the strain anneal method described by Stone.⁹ The test bars were first annealed in helium to a ferritic grain size of ASTM 1. Each bar was given a uniform strain in tension of 3.7 pct reduction of area and returned to the helium tube furnace for program annealing. The temperature was rapidly brought to 450°C and then raised to 880°C at an average rate of 60°C per day. The specimens were held at 880°C for several days to absorb some of the small crystallites distributed throughout the single crystals. After furnace cooling, the specimens were etched deeply with 4 pct nital to determine which were single crystals. An average of about 50 pct of these trials resulted in the production of satisfactory single crystals. A large portion of the failures were bicrystals.

Electrolytic polishing of the ingot iron was not feasible because of pitting around oxide inclusions. Therefore, polishing of the single crystals was begun by abrading carefully through No. 600 grit Wet-or-Dry paper. Then, the roughly polished single crys-

Fig. 2—Standard projection of all crystals tested in this investigation.



tals were annealed in helium for four days at 880°C. This anneal gave a fairly good polish and minimized strains which may have resulted from the grinding. Laue photograms taken of all specimens after this polishing treatment had undistorted spots.

The crystals prepared in this manner were found to be satisfactory for the tests at room temperature and above. However, in preliminary tests at -70°C, the bars broke in the grain boundary between the single crystal gage section and the polycrystalline shoulders before yielding occurred in the single crystal. To eliminate this difficulty, the single-crystal bars were very carefully turned to a diameter of 0.200 in. and a length of 3/4 in., Fig. 1c. This modification reduced the load necessary for yielding of the gage section without reducing the load-bearing properties of the boundary and the tests at -70°C were performed successfully. The crystals so modified were helium anneal-polished at 880°C as before and examined by Laue back-reflection for distortion. Crystals which showed asterism or blurring of the spots were rejected.

Preliminary tests at -105°C indicated that the bars which were modified for use at -70°C were unsatisfactory at the lower temperature with brittle failure again occurring in the boundary at the shoulder. The gage length could be machined no more and therefore, a second modification was necessary. Fig. 1a shows that the single crystal extends out of the reduced section into the radius of the shoulder. New ends, 1/4 in. in diameter, were turned on the bars and threaded down to the 0.200 in. gage section. Now, two or more turns of threads extended onto the single crystal above the fillet and a considerable portion of the load was taken off of the boundary zone. This second modification was made without any working or loading the gage section in any way.

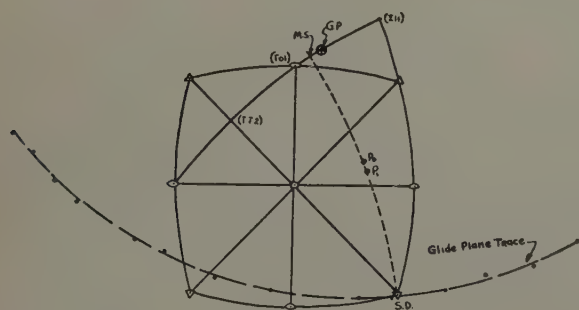


Fig. 3—Projection of crystal 104. P_0, P_1 specimen axis before and after deformation. M.S., pole of maximum shear plane containing [111]. G.P., pole of glide plane. S.D., slip direction.

It appeared desirable to ascertain whether the slip behavior of iron was the same in compression as in tension. For that purpose, compression specimens were prepared by scribing a fiducial mark running the length of the gage sections and up onto the shoulders on two test bars. These were then carefully cut into four single-crystal compression cylinders 1/4 in. in diam x 1/4 in. high. The compression faces of each specimen were polished to reduce lateral friction forces during testing.

Apparatus and Procedure: All tests were conducted using a universal testing machine equipped with an autographic load-extension recorder. The extension coordinate of the recorder was actuated by a microformer measuring the movement between the crossheads of the machine. While this device was unsatisfactory for measuring elastic strains in the gage length of the test bars, it was adequate for determining the load at which plastic flow was initiated. A constant reproducible strain rate of 0.01 per min was obtained by use of a strain pacer connected to the recording apparatus.

Provision was made for surrounding the tensile specimens with a suitable heat transfer medium for tests at other than room temperature. A double walled vessel with external insulation was suspended from the stationary crosshead support of the tensile machine. The lower specimen grip passed through the bottom of the vessel by means of a very flexible hose coupling which allowed slight misalignment of the vessel without subjecting the specimen to lateral loading. Axial loading was assured by the use of hardened chains as loading members.

At -105°C, Freon 12 was employed as the heat-transfer medium and was cooled by means of a pyrometrically controlled flow of liquid air through coils immersed in the test vessels. The temperature was maintained constant to $\pm 3^\circ\text{C}$. At -70°C, a mixture of dry ice and acetone was used and for 100°C, distilled water was maintained at its boiling point by an immersion heater. At 190°C, oil was used as the heat transfer medium with a controlled input of current through a Calrod immersion unit supplying the necessary heat.

Prior to testing, the orientation of each single crystal was determined by the Laue back-reflection method. In order uniquely to relate the orientation of the glide plane to the crystal, a line was scribed on the specimen as a fiducial mark of zero degrees azimuth to which rotations around the axis of the specimen could be referred.

For a series of tests at a given temperature, single crystals were selected with orientations distributed so that the maximum shear stress would fall at separated points along the zone of the slip direction. The crystals were extended to an elongation of 6 to 8 pct at the prescribed strain rate, removed, cleaned with alcohol, and dried in compressed air. A Laue photogram using the same convention as before was taken after each extension. In all cases, observations on the glide ellipses were referred to the Lauegram taken after deformation. These in general showed no asterism.

The angles which the traces of the glide or twinning planes made with respect to the crystal axis and the fiducial mark were measured with a goniometer mount on the rotating stage of a Zeiss Neophot microscope. The angle of inclination of a glide trace with the specimen axis was obtained at azimuthal positions of every 10° to 15° rotation of the specimen. Transferred to a stereographic projection,

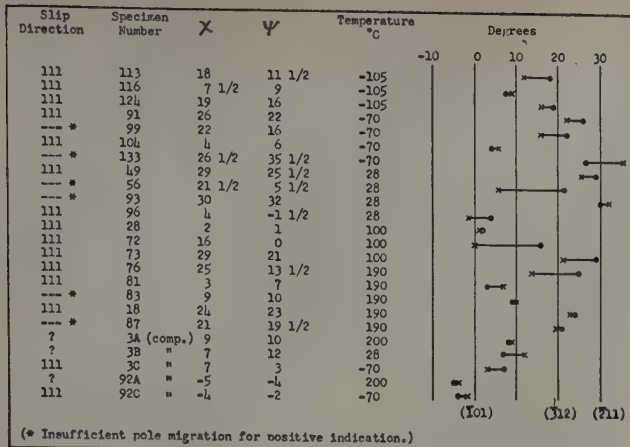


Fig. 4—Relative position of maximum shear stress poles (dots) and glide plane poles (crosses) along the zone [111].

this series of points plotted as a great circle and the pole of this circle located the position of the glide plane, Fig. 3. Many difficulties were involved in obtaining these measurements with a reasonable degree of accuracy. Preliminary tests showed that at least 4 pct strain was necessary to see any lines micrographically, i.e., at $\times 100$ to $\times 500$ magnification. With small amounts of shear, the lines appeared as a field of faint, blurred striations. When the lines were viewed on a plane perpendicular to the plane containing the slip direction and specimen axis, the waviness became severe and only a general direction was evident. It is estimated that the error in determinations of the glide plane position in this work is in the vicinity of $\pm 4^\circ$.

In the case of the compression tests, the sets of four specimens which had been cut from the same bar were cemented together with the fiducial mark aligned on each specimen and on the shoulders. In this way, each group of four specimens could be handled in the same manner as a tension specimen. Any slight misalignment would not cause errors because the microscopic observations were referred to the Laue photogram taken under the same set of conditions.

Determination of Plane of Glide: Fig. 2 shows the orientations of all crystals tested. Fig. 3 is a projection of crystal No. 104 which is shown here to illustrate the measurements which were made. The plane of maximum resolved shear stress containing the slip direction (M.S.) is the plane in the [111] zone having the minimum area. Its pole is located stereographically by projecting a great circle from the slip direction (S.D.) through the stress axis (P) onto the [111] zone. In the crystal of Fig. 3, the observed glide plane lies close to M.S. and on the same [111] zone. The locations of the glide planes with respect to the crystal planes and the M.S. plane are summarized in Fig. 4 for all cases where the information was obtainable. In Fig. 4, angular distances along the [111] zone are plotted on the abscissa. The location of the maximum shear plane is shown by a dot and the location of the microscopically observed glide plane by a cross. It is immediately evident that the glide plane frequently is not a usual crystallographic plane nor does it conform to the plane of maximum shear stress. However, in most of the tension tests, the glide plane is close to the M.S. plane but inclined away from it toward the $(\bar{1}01)$ plane. This deviation of the glide plane from

the plane of maximum shear is plotted in Fig. 5 as χ , the angle between the $(\bar{1}01)$ to the glide plane. Now, an order to the data becomes apparent. The values of χ vs ψ for a given temperature fall generally on one curve in tension and on another curve in compression, Fig. 6.

Examination of Fig. 4 shows that of the 24 crystals analyzed for slip the observed glide plane is:

- In 6 cases within 5° of (110)
- 3 cases within 5° of (112)
- 7 cases within 5° of (123)
- 9 cases within 5° of none of the above planes
- 10 cases within 5° of maximum shear stress plane in $\langle 111 \rangle$ zone.

Therefore it is concluded that slip in ferrite crystals does not necessarily occur either on a simple crystallographic plane or on the plane of maximum shear stress.

The selection of the glide plane in body-centered cubic ferrite apparently is more complicated than in the case of the close-packed lattices. Analyses of the plots of χ vs ψ of Figs. 5 and 6 using a graphical integration of Eq. 3 show the relative strengths of planes in the $\langle 111 \rangle$ zone for ingot iron at 28° and -70°C to be as given in Fig. 7. The reliability of these results depends on the error and scatter of data.

In obtaining the location of the glide ellipse of Fig. 3, for example, the angular data from the microscope were plotted on a blank sheet. After determining the location of the pole of the glide plane, this was superimposed on a projection of the crystal orientation. Taking care to eliminate conscious or unconscious influences on positioning of the glide plane, it was found that the pole of the glide plane was never more than $1\frac{1}{2}^\circ$ away from the $\{110\}$ to $\{112\}$ great circle. Therefore, assuming a maximum error of $\pm 4^\circ$ to 5° along this great circle would seem to be conservative.

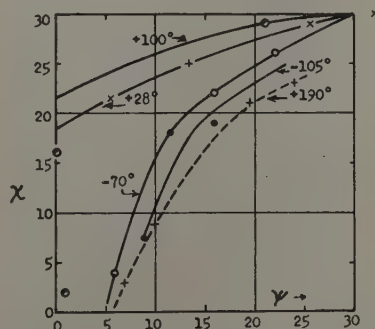


Fig. 5—Relation between χ , angle between $(\bar{1}01)$ and maximum shear stress plane, and ψ , angle between $(\bar{1}01)$ and glide plane, for single crystals strained in tension.

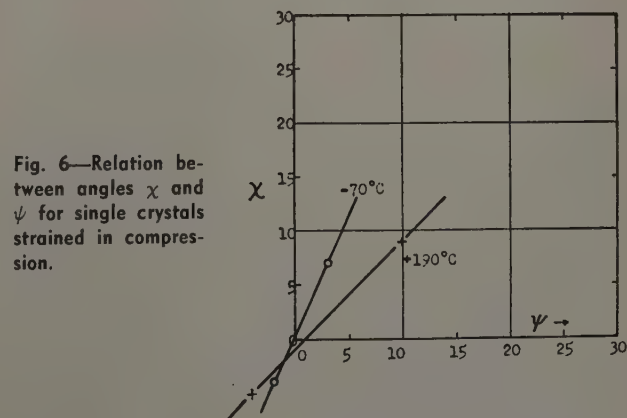


Fig. 6—Relation between angles χ and ψ for single crystals strained in compression.

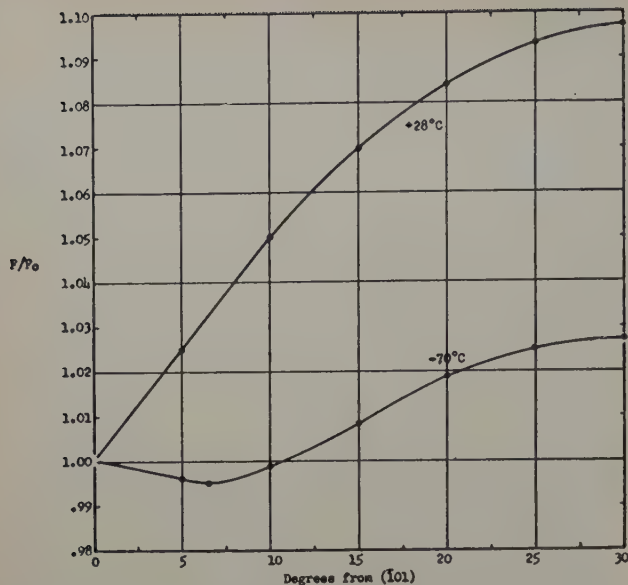


Fig. 7—Ratio of force required for initial shear on any plane in the [111] zone to force required for shear on the (101).

From +100° to -105°C, there is an evident tendency for the χ - ψ curves to lay below each other. Nevertheless, these χ vs ψ plots are not necessarily precisely defined lines and some points are appreciably off, particularly the 190°C data points which appear to be out of place. This may be a result of strain aging of ingot iron which at 190°C would be very rapid and could influence the glide plane selection.

The Taylor analysis is general and may be applied whenever deformation takes place in a specific crystallographic direction. The face-centered cubic metals are a special case where the slip can occur only on the planes of close packing because their resistance to shear is so very much lower than the resistance of adjacent planes.

The law of constant resolved shear stress which has been proven for the close-packed lattices does not hold in precisely the same way for the deformation of the body-centered cubic lattice. In the latter case, since deformation can occur on a variety of planes of differing shearing strengths, the critical shear stress on the glide plane is a function of orientation. However, the critical shear stress on any

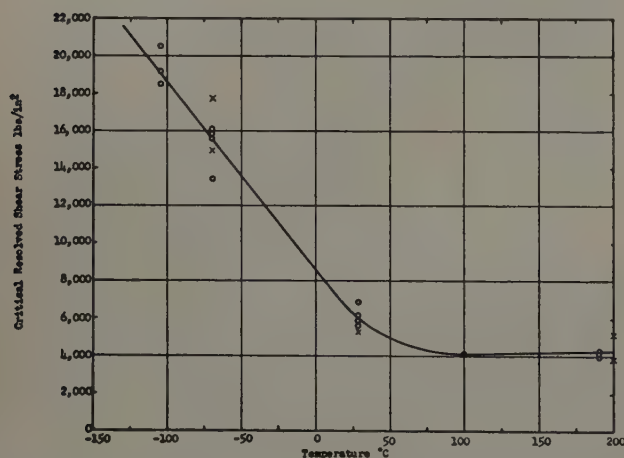


Fig. 8—Temperature dependence of critical resolved shear stress for ingot iron single crystals; circles represent tension tests, crosses represent compression tests.

plane can be calculated so that critical stress values can be put on a common basis for comparison. Except for the selection of the plane of glide, this variation of resistance to shearing is of minor importance because it is not great. For the case in tension at 28°C (Fig. 7), the maximum variation is about 9 pct from (101) to (211). Estimating the accuracy of critical stress measurements at 10 pct, this variation would not be detectable by direct methods. For this reason, the F over F_0 vs ψ curves which were obtained from the measurements of χ and ψ cannot be checked against the experimentally determined shear stress values.

The treatment of the results of this investigation differs from Taylor's² on at least one major item. Taylor drew two curves through his χ vs ψ points obtained in tension and compression, but the distinction between the two curves was on the basis of orientation of the specimen axis in the basic stereographic triangle and the direction of shearing. A great circle drawn from the $\langle 111 \rangle$ slip direction to the (101) pole divides the basic triangle into two areas. Taylor found that compression specimens falling in one area and tension specimens in the other had χ vs ψ values on one curve, and the situation was reversed for the other curve. Analysis shows

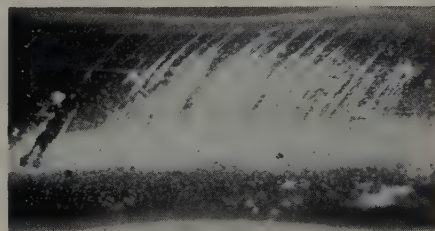
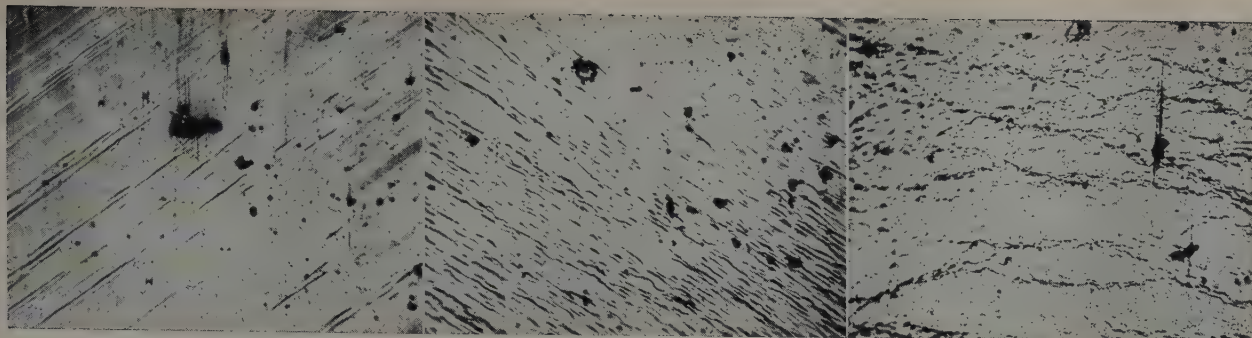


Fig. 9—Macrograph of surface markings on specimen No. 96 after deformation at room temperature. X3.

that Taylor's specimens could have been equally well distinguished on the sole basis of whether they were deformed in tension or compression.

A qualitative comparison can be made between the F/F_0 values obtained here and the shear stress ratios calculated by Opinsky and Smoluchowski. Their shear stress ratios are not the same in tension and compression at room temperature which agrees with this investigation. They found that in compression, an increase in temperature produces a decrease in the resistance to shearing of the (112) plane with respect to the shearing resistance of the (110) plane. This compares favorably with the relative slopes of the two F/F_0 curves of Fig. 7. While the numerical values should not check exactly because of the differences of the materials, it can be seen that the relative orders of magnitudes of the critical shearing stresses are the same. For instance, $S_{(112)}/S_{(110)} = 1.06$ from Opinsky at 190°C compared with $F/F_0 = 1.03$ from this research. That Opinsky's value is the higher is in agreement with the observation that silicon increases the tendency for glide to occur in the vicinity of the (110) pole.

Temperature Dependence of Resistance to Shear: The critical shear stress values calculated from the observed yield point values and the glide planes and directions are plotted against test temperature in Fig. 8. These critical shear values presumably should not be averaged at a given temperature because as the value of ψ varies, the shear strength of the plane



a—Viewed in plane almost parallel to slip direction. b—Viewed in plane 45° from slip direction. c—Viewed in plane perpendicular to plane of slip direction and specimen axis.

Fig. 10—Slip lines on specimen 3-c (compression). X150. Area reduced approximately 25 pct for reproduction.

may vary. In most cases, however, the change brought about by converting F values to F_0 values (Eq. 3) is less than the observed scatter in critical shear stress values. This is another manifestation of the fact that F over F_0 ratios cannot be determined with sufficient accuracy by stress measurements. The average value of the critical resolved shear stress at room temperature of 6140 psi from Fig. 8 compares well with Fahrenhorst and Schmid's value of 6340 psi for ingot iron.

The Yield Point: A striking correlation was obtained between the appearance of inhomogeneous yielding and macroscopic surface markings on these ingot iron crystal specimens. In tension, double yielding, or a drop in load at the start of plasticity was observed at room temperature and -70°C . As the temperature was increased, inhomogeneous yielding became less apparent and disappeared finally at 190°C , where a smooth transition existed between the elastic and plastic states of strain. Specimens which showed discontinuous yielding also showed large surface markings, akin to the glide ellipses, which could be seen by the naked eye, Fig. 9. None of the compression specimens showed inhomogeneous yielding even when the tensile specimens for the same temperature did. In addition, it was observed that the tensile specimen at -105°C did not show a double yield point despite the fact that it would otherwise be predicted for this low temperature. Further examination revealed a difference between the specimens which yielded inhomogeneously and those which did not. The bars which were used for tensile tests at -70°C and above had polycrystalline shoulders and therefore the load was applied to the single-crystal gage section through polycrystalline material. In the compression specimens, however, and also in the tensile bars for -105°C , the single-crystal sections were loaded directly because of their geometry, Fig. 1d. Apparently, grain boundary material must exist between the single crystal and the area on the ends where the load is applied for inhomogeneous yielding.

The homogeneous yield in the crystal without a grain boundary is in accord with modern theory.¹⁴ The grain boundary, when loaded, can trap and then later discharge to the crystal a sufficient number of dislocations to cause a yield point. The lower dislocation density of the crystal itself is insufficient for inhomogeneous yielding and therefore the presence of a grain boundary is required.

Observations on Luder's Lines and Slip Lines: The yield point phenomenon caused the formation of Luder's lines, as shown in Fig. 9, which after a strain of 1 or 2 pct were readily visible at low magnifications. At $\times 100$ or higher, however, no slip lines

at all were visible. The positions of the Luder's lines were determined at low magnifications and the plane of deformation was always in the $\langle 111 \rangle$ zone. Regular slip lines became observable at $\times 100$ when the crystal was re-strained to a total elongation of 4 pct or more. It was found in all cases where the two sets of lines were separately measured, that the slip lines which developed at greater strains were on the same plane, within the error of determination, as the Luder's lines.

The most striking characteristic of the slip lines in iron is the change in their nature as the plane of view is changed, i.e., they are straight when the plane of view is nearly parallel to the slip direction and they are wavy when the plane of view is perpendicular to the slip direction. This has received sufficient attention in previous papers and need not be amplified here. Fig. 10a, b, and c reproduces micrographs of the same set of slip lines taken at different azimuthal positions on a crystal deformed in tension. No change was apparent in the nature of the lines as either the identity of plane of slip or the temperature was varied. Even in the cases where the glide plane coincided with a crystal plane, e.g., the $(\bar{1}01)$, waviness in the slip direction was present to approximately the same degree.

There was no readily observable difference in the appearance of slip lines developed at different temperatures. The micrographs of Fig. 10 represent a specimen strained 6 pct in compression at -70°C . Specimens compressed or stretched an equivalent amount anywhere in the range -105° to $+190^\circ\text{C}$ showed slip lines whose spacing and degree of straightness were comparable to those of Fig. 10.

An anomalous effect was noticed in the deformation of several crystals. After extension, the colinear lines scribed on each of the shoulders of the test bars showed a relative rotation around the axis of the bar. In crystal No. 133, the top of the bar was rotated 8° with respect to the bottom in the clockwise sense as the bar was viewed from the top. It should be mentioned here that the chains loading the specimen were carefully aligned before testing and could not apply a torsional stress but would permit a torsional strain if the crystal chose to deform in this way.

Twinning: Table I gives an accounting of the occurrence of twinning. This means of deformation was observed in specimens deformed at -105° and -180°C . The twins were readily recognized and distinguished from slip lines by their width, regularity, and brightness or visibility. Table I shows that a $\{112\}$ type of plane was consistently the plane of twinning. Measurements of the inclination of the

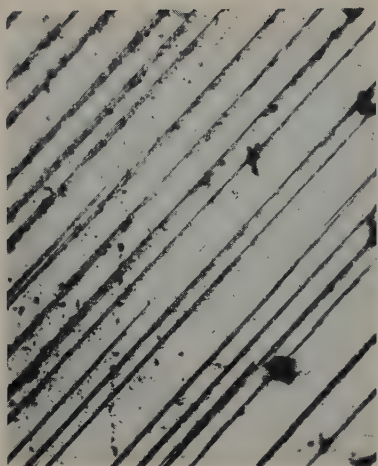


Fig. 11—Twins in specimen 3-D deformed at -180°C . Notice twin starting at lower left corner reduces in thickness to a thin line in the center of micrograph. X300.

twin planes were considerably easier to make than measurements of the glide ellipses and therefore the relative accuracy was improved.

It was observed frequently that, as a long twin was followed around a specimen, the width sometimes diminished gradually to a thin wavy line and then disappeared. There is a striking resemblance of the thin wavy line on a disappearing twin to the wavy slip lines although the connection is not obvious. This behavior can be observed in one of the twins in Fig. 11.

There were other manifestations of twinning besides the microscopic. Load-elongation curves of crystals deformed at low temperatures where twinning occurred show an irregularity in the elastic region. Concurrent with each of these instantaneous decreases of load shown in the curves there was a distinct "clicking" sound. Confirmation of the connection between the clicking sound, the drops in load, and the microscopic occurrence of twinning is afforded by specimen No. 113 which, while it was deformed at -105°C , showed none of these evidences of twinning.

Comparison of the three crystals loaded at -105°C provides information on the proposal that there exists a critical resolved stress for twinning. Crystals No. 116 and No. 124 twinned at widely different stresses. In addition, an eligible plane in crystal No. 113 was stressed beyond the value where the other two specimens twinned but no twin bands were to be found. If the critical shear stress on the (112) plane were the criterion for twinning, the critical stresses in No. 116 and No. 124 would have been the same

Table I. Occurrence of Twinning

Specimen Number		Temperature, $^{\circ}\text{C}$	Twin Plane	Resolved Stress on Twin Plane*
113	(Tension)	-105	No Twinning	16,400
116	(Tension)	-105	(112)	4,140
124	(Tension)	-105	(112)	12,700
3-D	(Compression)	-180	(211)	21,000
92-D	(Compression)	-180	(112) (121) (211)	—

* Resolved stress on twinning planes calculated assuming shear in a [111] type direction. In case of No. 116, where there were alternate choices of load values for plane, it was assumed that the most highly stressed plane sheared first. Resolved stresses could not be calculated for 92-D because of the multiplicity of operative planes. The resolved stress listed for No. 113 is the value for the most highly stressed (112) type plane at the yield point.

and No. 113 would have shown evidence of twinning, so it must be concluded that this is not the criterion.

Conclusions

From experiments on the deformation of ingot iron single crystals it may be concluded that:

1—Plastic deformation occurs by apparent glide in the $\langle 111 \rangle$ direction on a plane, not necessarily crystallographically significant, whose identity is determined by two factors:

- The orientation of the crystal with respect to the stress axis
- The variation of the resistance to shear of the planes containing the $\langle 111 \rangle$ glide direction. The interrelation of these two factors is a function of temperature and direction of stress application although the data here for ingot iron are not sufficient to delineate these factors with certainty.

2—The critical stress necessary to produce shear on the glide plane increases sharply below room temperature. From room temperature to 200°C the change is slight.

3—The junction of the single crystal and polycrystalline shoulders of these ingot iron specimens is a grain boundary region of pronounced brittleness at low temperatures.

4—Inhomogeneous yielding may occur at room temperature and below when an ingot iron single crystal is stressed through the grain boundary junction. Luder's lines appear in the single crystal concurrently with the inhomogeneous yield.

5—For static tensile strain rates, twin bands appear on planes of the type (112) for specimens deformed at -105°C or below. The criterion for twinning on the (112) plane is not a critical resolved shear stress.

Acknowledgment

The research reported in this paper was sponsored by the Flight Research Laboratory, United States Air Force under Contract AF 33(038)-15889.

References

- G. I. Taylor and C. F. Elam: *Proc. Royal Soc., London* (1926) **112A**, p. 337.
- G. I. Taylor: *Proc. Royal Soc., London* (1928) **118A**, p. 1.
- N. Fahrenhorst and E. Schmid: *Ztsch. Physik* (1932) **78**, p. 383.
- C. S. Barrett, G. Ansel, and R. F. Mehl: *Trans. ASM* (1937) **25**, p. 702.
- E. N. da C. Andrade: *Proc. Physical Soc.* (1940) **52**, p. 1.
- N. K. Chen and R. Maddin: *Trans. AIME* (1951) **191**, p. 937; *JOURNAL OF METALS* (October 1951).
- A. J. Opinsky and R. Smoluchowski: *Plastic Deformation of Crystalline Solids*. Mellon Institute (May 1950).
- A. J. Opinsky and R. Smoluchowski: *Journal of Applied Physics* (1951) **22**, p. 1488.
- F. G. Stone: *Trans. AIME* (1948) **175**, p. 908; *METALS TECHNOLOGY* (June 1948).
- J. R. Low and M. Gensamer: *Trans. AIME* (1944) **158**, p. 207; *METALS TECHNOLOGY* (December 1943).
- A. N. Holden and J. H. Hollomon: *Trans. AIME* (1949) **185**, p. 179; *JOURNAL OF METALS* (February 1949).
- A. H. Cottrell: *Report on a Conference of Strength of Solids*. Physical Soc., London (1948) p. 30.
- H. Schwartzbart and J. R. Low, Jr.: *Trans. AIME* (1949) **185**, p. 637; *JOURNAL OF METALS* (September 1949).
- A. N. Holden: *Trans. AIME* (1952) **194**, p. 182; *JOURNAL OF METALS* (February 1952).

Vapor Pressure of Silver

by C. Law McCabe and C. Ernest Birchenall

IN attempting to extend vapor pressure measurements of the type previously reported by Schadel and Birchenall¹ for silver and by Schadel, Derge, and Birchenall² for silver-silicon to other systems, it was observed that the materials melted at indicated temperatures 10° to 15° below their accepted melting points. Further investigation revealed that the thermocouple readings were in error due to appreciable conduction losses along the reference thermocouple wires. If the wire diameter of the reference couple inserted into the Knudsen cell was reduced, the correction for the indicating couple changed in a manner tending to explain the melting behavior. When extrapolated to zero wire diameter from measurements with several reference thermocouples of different wire thickness, the melting point of silver then agreed with the indicated temperature at which silver chips were observed to coalesce into a sphere. Approximately the same calibration was given by observing the melting of small wires of silver or gold in the Knudsen cell connected in series with an ammeter, where the leads into the cell were very fine in order to minimize heat conduction.

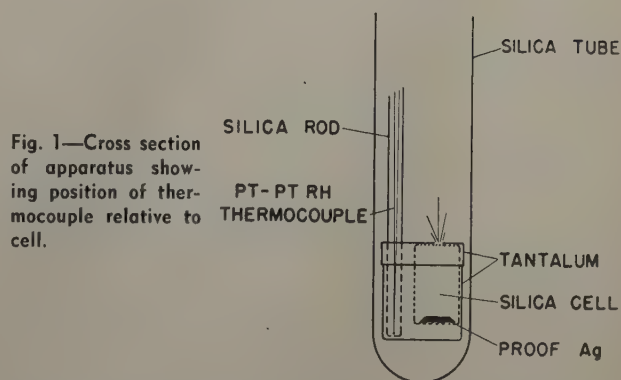
Unfortunately neither of these methods seemed to yield a sufficiently precise temperature calibration to match the apparent precision of the other aspects of the vapor pressure measurement. It was decided, therefore, to redetermine the vapor pressure of silver in another setup under conditions permitting precise temperature measurement. The vapor pressure of pure silver could then be used as an internal calibration of temperature in the older unit in making runs on alloys. This has been done; the present report is a correction to ref. 1.

Experimental Procedure

The apparatus, shown in Fig. 1, was very similar to that employed by Harteck,³ except that the orifice sizes were smaller and the residual pressure in the vacuum system was probably much lower. A small, sharp-edged hole, nearly circular in shape, was ground into the rounded end of a quartz tube. The orifice area was then measured by tracing the image at known magnification on graph paper and counting the squares enclosed. The silver specimen was sealed into the tube to make a Knudsen cell. A tantalum jacket surrounding the cell served to increase the uniformity of temperature. This assembly was placed in the bottom of a long quartz tube with an

C. L. McCABE is Member of the Staff, Metals Research Laboratory, Carnegie Institute of Technology, Pittsburgh, and C. E. BIRCHENALL, Junior Member AIME, formerly Member of the Staff, Metals Research Laboratory, Carnegie Institute of Technology, is now Associate Professor of Chemistry, The James Forrestal Research Center, Princeton University, Princeton, N. J.

Discussion on this paper, TP 3512E, may be sent, 2 copies, to AIME by Dec. 1, 1953. Manuscript, Sept. 17, 1952; revision, Dec. 18, 1952. Cleveland Meeting, October 1953.



inside diameter of about 1 in., which was connected to the vacuum system through a ground joint sealed with picein wax well removed from the furnace. A thermocouple tube inserted through the top of the vacuum line reached into the tantalum jacket so that the thermocouple junction was immediately adjacent to the Knudsen cell except for the protection tube wall. A resistance furnace could be raised to cover the end of the quartz tube containing the cell in such a way that the cell was in the uniform temperature zone 13 in. from the end of the furnace. An ionization gage was included in the vacuum system in the cold lines of wide diameter, immediately beyond the ground joint. The vacuum system consisted of a mercury one-stage diffusion pump, backed by a Welch duo-seal mechanical pump. The pumps were separated from the reactor chamber by a dry ice trap. The ionization gage always read less than 10^{-6} mm Hg after initial outgassing and before each run was started.

Each newly filled Knudsen cell was evacuated at high temperature overnight before the first weighing was made. The cell was returned to the system, heated for a measured time at constant temperature, cooled, and reweighed. The heating and cooling times were quite short since the hot furnace was raised to receive the reactor at the beginning of the run and removed again at the end. The tube heated or cooled quickly. The total mass loss was attributed entirely to effusion of silver vapor from the quartz cell, since empty quartz cells maintained constant mass through similar heating cycles. The vaporized silver condensed on the cold walls of the quartz tube extending above the furnace.

Earlier studies in the induction heated unit had shown that the same vapor pressure was found for silver, whether the silver was in contact with the tantalum metal cell or with porcelain or quartz liners.

The Pt-Pt-10 pct Rh thermocouple was calibrated against a secondary standard of the same material and found to agree with the published tables. Always operating in air at temperatures below 1000°C,

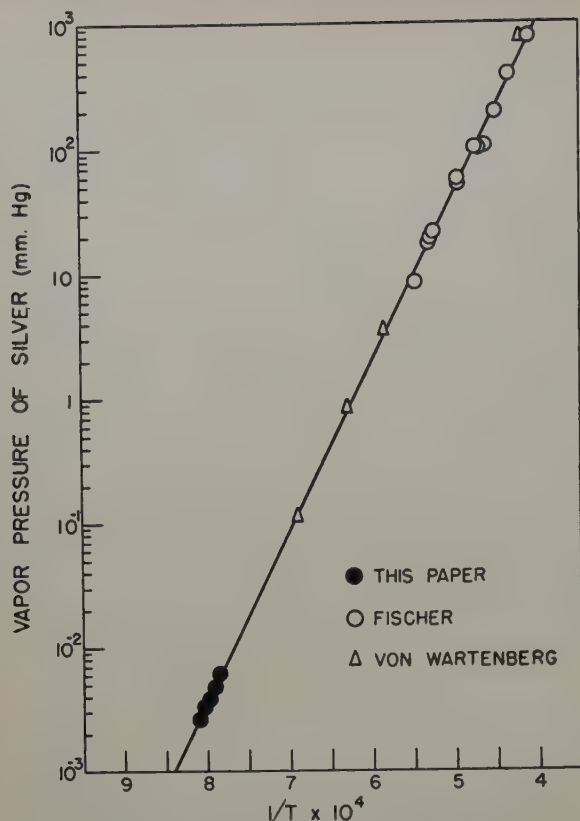


Fig. 2—Vapor pressure of silver vs $1/T$.

there was no evidence of couple deterioration. The calibration after the runs checked the initial calibration.

The silver metal was obtained from the U. S. Mint as proof silver, 99.99+ pct Ag. No further analyses were made.

Data and Calculations

Table I gives the pertinent experimental data—the orifice area, a , the temperature, T , the time, t , and the weight loss, G . From these data the pressure, p , may be calculated by the equation for effusion through an orifice

$$p = \frac{G\sqrt{2\pi RT}}{at\sqrt{M}}$$

where R is the gas constant and M is the molecular weight of the effusing vapor. Care was taken in these measurements to keep the orifice diameter

Table I. Vapor Pressure of Silver

Orifice, Area, Sq Cm	Temperature, °K	Time, Min	Wt Loss, Gram Ag	Pressure, Mm Hg
Solid Silver				
0.011725	1133	6020	0.0177	2.32×10^{-4}
0.011725	1143	4825	0.0186	3.06×10^{-4}
0.00643	1171	4390	0.0183	6.10×10^{-4}
0.00643	1183	6832	0.0382	8.22×10^{-4}
0.00643	1204	6850	0.0600	1.30×10^{-3}
0.00643	1213	4385	0.0477	1.62×10^{-3}
0.00643	1223	2540	0.0337	1.98×10^{-3}
0.00170	1224	8510	0.0304	2.05×10^{-3}
Liquid Silver				
0.00170	1235	5835	0.0268	2.60×10^{-3}
0.00170	1245	3980	0.0228	3.27×10^{-3}
0.00170	1253	4175	0.0278	3.83×10^{-3}
0.00170	1263.5	4090	0.0347	4.89×10^{-3}
0.00170	1273	2980	0.0310	6.01×10^{-3}

very small compared with the mean free path of the silver atoms.

Since the range of temperatures was not as great as in the previous study, it was felt that the vapor pressure curves might be established best in the following way. The liquid points reported here and those of von Wartenberg⁴ and Fisher⁵ were plotted as $\log p$ against the reciprocal of the absolute temperature, Fig. 2. The most satisfactory straight line was drawn through these points; there is no apparent systematic deviation. Using the Clapeyron-

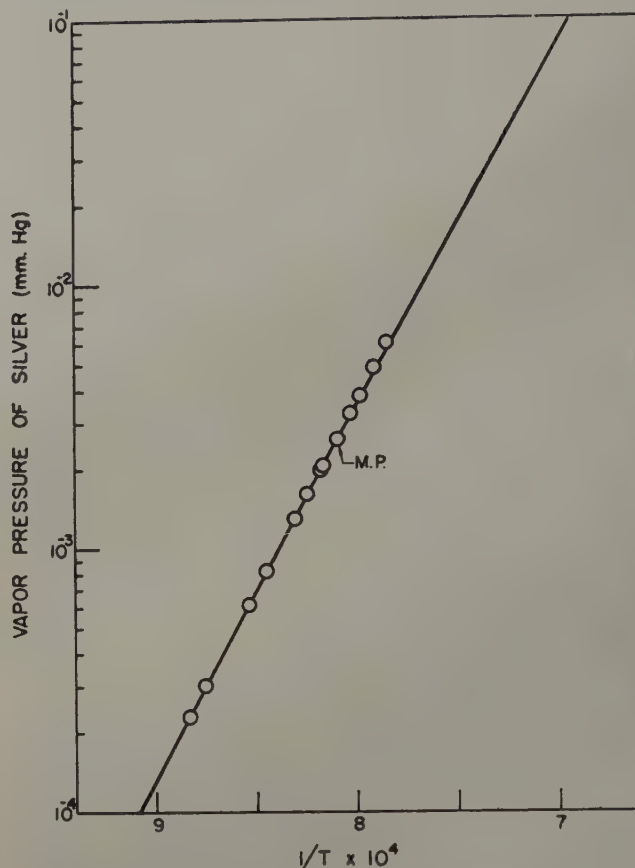


Fig. 3—Vapor pressure of silver vs $1/T$. See text for manner in which line was drawn.

Clausius equation, the heat of vaporization was calculated to be 62.60 kcal per gram atom. To find the slope of the vapor pressure line for solid silver, the latent heat of fusion, 2.86 kcal per gram atom given by Kelley,⁶ was added to the heat of vaporization. The heat of sublimation is then 65.46 kcal per gram atom. This value and the vapor pressure at the melting point, 2.51×10^{-3} mm of Hg, taken from the liquid curve, uniquely determine the vapor pressure line for the solid. This line was drawn in Fig. 3, and the experimental points were plotted on it for comparison. The agreement is seen to be excellent. The precision of these measurements seems to be somewhat better than that in the previous study.¹

The vapor pressure equations are for liquid silver

$$\log p = -\frac{62,600}{2.303 RT} + 8.496$$

and for solid silver

$$\log p = -\frac{65,460}{2.303 RT} + 9.003$$

where p is in mm of Hg and R is 1.986 cal per mol per degree.

When ΔH_v° , the heat of vaporization at absolute

zero, is calculated for the points in this study, a value of 67.87 ± 0.10 kcal per gram atom is obtained. The von Wartenberg and Fisher points only give 68.07 ± 0.44 , in good agreement. The average for all points is 68.02 ± 0.29 compared with a previously reported value of 67.71 ± 0.57 . Since the vapor pressures are about 40 pct lower than the earlier ones,¹ while ΔH° has changed little in value and apparent precision, it must be concluded that this is not a particularly sensitive test for vapor pressure data.

Harteck's³ points are still about 30 pct below the present data. However, this discrepancy is of the order to be expected from using too large an orifice and failure to obtain a good enough vacuum. The possibility of some other source exists, however, for a comparison of Harteck's values for gold in the same series of measurements with the recent work of Hall⁷ finds Harteck too low by a factor of almost 6. Since gold had a much lower vapor pressure than silver in Harteck's measurements, the mean free path condition was probably not violated by too

large an orifice. The only obvious source of this discrepancy lies in a very poor vacuum.

Acknowledgments

This work was supported by a contract with the Office of Naval Research. The authors are grateful for the assistance of Robert Miller in making the experimental measurements reported here.

References

- ¹H. M. Schadel, Jr. and C. E. Birchenall: *Trans. AIME* (1950) **188**, p. 1134; *JOURNAL OF METALS* (September 1950).
- ²H. M. Schadel, Jr., G. Derge and C. E. Birchenall: *Trans. AIME* (1950) **188**, p. 1282; *JOURNAL OF METALS* (October 1950).
- ³P. Harteck: *Ztsch. Physik. Chem.* (1928) **134**, p. 1.
- ⁴H. von Wartenberg: *Ztsch. anorg. allgem. Chem.* (1908) **56**, p. 320.
- ⁵J. Fischer: *Ztsch. anorg. allgem. Chem.* (1934) **219**, pp. 1 and 367.
- ⁶K. K. Kelley: Contributions to the Data on Theoretical Metallurgy. U. S. Bur. Mines Bull. (1949) **476**, p. 158.
- ⁷L. D. Hall: *Journal ACS* (1951) **73**, p. 757.

Vapor Pressure of Silver Over Silver-Gold Solid Solutions

by C. L. McCabe, H. M. Schadel, Jr., and C. E. Birchenall

Vapor pressure of silver over silver-gold alloys has been measured over a range of temperatures for four compositions. Orifice effusion has been compared with electromotive force measurement as a means for determining thermodynamic activities in these solid metallic alloys. Correlated activity coefficients are given for silver-gold alloys for the temperature range 200° to 1000°C.

SOUND development of a technique for the measurement of some property of matter requires a comparison with other recognized procedures which have been used to measure the same property. Such a check is especially useful if the assumptions on which the applications stand are basically different

C. L. McCABE is Member of the Staff, Metals Research Laboratory, Carnegie Institute of Technology, Pittsburgh, H. M. SCHADEL, JR., formerly Research Associate, Metals Research Laboratory, Carnegie Institute of Technology, is now associated with the Catalytic Construction Co., Philadelphia, and C. E. BIRCHENALL, Junior Member AIME, formerly Member of the Staff, Metals Research Laboratory, Carnegie Institute of Technology, is now Associate Professor of Chemistry, The James Forrestal Research Center, Princeton University, Princeton, N. J.

Discussion on this paper, TP 3467E, may be sent, 2 copies, to AIME by Dec. 1, 1953. Manuscript, Sept. 17, 1953. Cleveland Meeting, October 1953.

for the two methods. Agreement in the results tends to confirm both sets of assumptions.

The electromotive force method for determining thermodynamic activities depends upon the reversibility of the electrode processes and a knowledge of the valence states involved. The orifice effusion technique of determining vapor pressures requires that certain mean free path conditions be met, that the state of association of the vapor be known, and that efficient collection of vapors be maintained. Thus the requirements are quite different in nature. Although procedures often exist by which the fulfillment of these conditions may be tested internally, agreement of thermodynamic activities for a single system obtained by both methods constitutes a more severe test of the assumptions.

The binary alloy system silver-gold is excellent for this purpose for several series of emf measure-

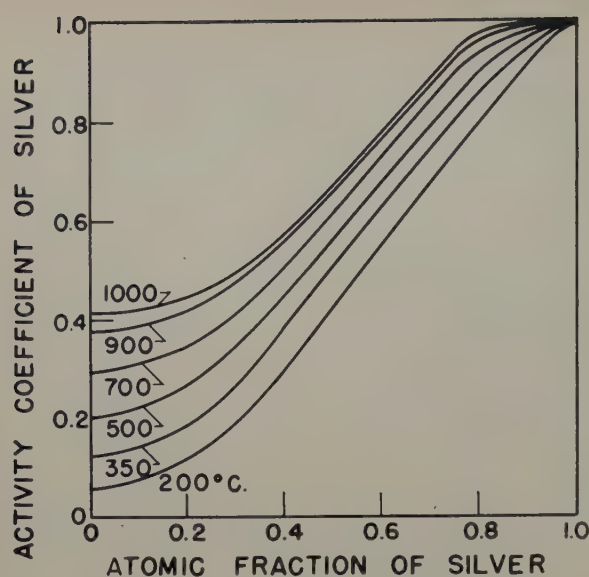


Fig. 1—Activity coefficient of silver in silver-gold alloys vs atomic fraction of silver based on emf measurements. 900° and 1000° values obtained by extrapolation.

ments have been made over wide temperature and composition ranges using various electrolytes.¹⁻⁴ Silver, the more electropositive component, has only the monovalent and neutral atom as likely states. Furthermore, silver is the more volatile component which makes it possible to determine silver activities directly by both emf and vapor pressure methods.

In principle, Hall's⁵ vapor pressure determinations for gold over gold-copper alloys could have been used for a similar comparison with the emf data^{1,6} for those alloys. However, the latter data gave copper activities while the former yielded gold activities. Neither set of data was consistent enough to make possible an integration of the Gibbs-Duhem equation. Consequently no quantitative comparison was made.

Lumsden⁷ has carried out several comparisons of emf and vapor pressure data (though the latter are not orifice effusion measurements) and finds that satisfactory correlations may be obtained.

Experimental

The apparatus employed was identical to that used in previous studies,^{8,9} while the procedure was similar to that used in the silver-silicon measurements except that a preliminary period of annealing *in situ* was required to homogenize the solid silver-gold beads, which was unnecessary for the liquid silver-silicon. Since much more silver than gold*

Gold in the vapor phase can interfere with the measurement of the silver vapor pressure in two ways: 1—change the mean free path for silver vapor, and 2—change the self-absorption of radioactivity significantly in the condensed sample on the target. To do the first, the gold vapor pressure in the chamber would have to be greater than the silver vapor pressure for the orifice sizes employed here. To do the second, the weight of gold on the target would have to be an appreciable fraction of the total sample weight. Since the vapor pressure of gold is less than that of silver, the effect of gold on the measurements may be safely neglected under these particular conditions.

was vaporized during the runs, the change in weight over a series of measurements was attributed entirely to silver loss in computing the concentration change. This range of concentration is given for each of the four series of alloy measurements in Table I. An assay for gold was made on a sample taken after each series. These analyses are the basis of the average compositions reported, although they are adjusted to the middle of the range derived from the

weight change. Since the alloy samples analyzed were quite small, 0.03 to 0.04 g, the average compositions may be in error by several tenths of a percent. At the present stage of development, this is probably not the only appreciable source of error.

Fine gold and proof silver from the U. S. Mint were used in making the alloys. The silver was mixed with active silver in aqueous nitrate solution. It was precipitated as the chloride and reduced to metal in hydrogen.

Pure silver was run at the start and between the second and third series to establish the temperature calibration. The apparent temperatures were adjusted to bring the silver vapor pressure curves into coincidence with those previously reported.¹⁰ These temperature corrections were then applied to the alloy measurements. The corrected data are given in Table I. The silver calibration runs are included

Table I. Vapor Pressures of Silver over Silver-Gold Alloys

Temperature, °K	P in Mm Hg	Temperature, °K	P in Mm Hg
Pure silver for temperature calibration for 19.5 and 38.0 pct alloy series			
(s) 1078	4.64×10^{-5}	(s) 1160	4.88×10^{-4}
1104	1.01×10^{-4}	1184	9.33×10^{-4}
1111	1.58×10^{-4}	1187	8.57×10^{-4}
1136	2.18×10^{-4}	1196	1.05×10^{-3}
1150	3.67×10^{-4}	1205	1.36×10^{-3}
1159	4.84×10^{-4}	1206	1.37×10^{-3}
1166	4.73×10^{-4}	1208	1.30×10^{-3}
1177	7.20×10^{-4}	1216	1.78×10^{-3}
1193	9.95×10^{-4}	1227	2.27×10^{-3}
1200	1.23×10^{-3}	1228	2.27×10^{-3}
1217	1.85×10^{-3}		
1225	2.00×10^{-3}	(1) 1238	2.82×10^{-3}
		1241	3.36×10^{-3}
(1) 1234	2.45×10^{-3}	1248	3.71×10^{-3}
1235	2.76×10^{-3}	1250	3.32×10^{-3}
1240	3.00×10^{-3}	1251	4.10×10^{-3}
1249	3.67×10^{-3}	1261	4.61×10^{-3}
1251	3.58×10^{-3}	1273	6.53×10^{-3}
1267	4.99×10^{-3}	1284	6.61×10^{-3}
1280	6.42×10^{-3}		
1287	6.27×10^{-3}		
1298	9.10×10^{-3}		
1310	1.19×10^{-2}		
1317	1.25×10^{-2}		
1336	2.03×10^{-2}		
19.5* atomic pct silver			
1195	8.00×10^{-5}		
1195	8.02×10^{-5}		
1215	1.46×10^{-4}		
1223	1.46×10^{-4}		
1233	2.12×10^{-4}		
1243	2.32×10^{-4}		
1252	3.19×10^{-4}		
1261	4.11×10^{-4}		
1270	5.36×10^{-4}		
1280	6.20×10^{-4}		
1298	8.16×10^{-4}		
1308	9.42×10^{-4}		
1317	1.17×10^{-3}		
1319	1.36×10^{-3}		
1327	1.60×10^{-3}		
1336	1.98×10^{-3}		
62.0† atomic pct silver			
1173	2.78×10^{-4}		
1179	3.89×10^{-4}		
1184	3.56×10^{-4}		
1195	4.11×10^{-4}		
1206	5.62×10^{-4}		
1206	6.68×10^{-4}		
1207	5.80×10^{-4}		
1216	7.75×10^{-4}		
1227	9.45×10^{-4}		
1238	1.16×10^{-3}		
1241	1.78×10^{-3}		
1242	1.42×10^{-3}		
1246	1.42×10^{-3}		
1248	1.55×10^{-3}		
1248	1.86×10^{-3}		
1251	1.58×10^{-3}		
1262	1.91×10^{-3}		
1272	2.27×10^{-3}		
1285	2.85×10^{-3}		
38.8‡ atomic pct silver			
		1127	3.91×10^{-5}
		1143	6.80×10^{-5}
		1156	8.77×10^{-5}
		1176	1.64×10^{-4}
		1176	1.96×10^{-4}
		1190	2.30×10^{-4}
		1204	3.20×10^{-4}
		1223	5.12×10^{-4}
		1233	6.05×10^{-4}
		1238	7.52×10^{-4}
		1243	6.22×10^{-4}
		1252	9.31×10^{-4}
		1271	1.46×10^{-3}
		1271	1.78×10^{-3}
		1284	2.04×10^{-3}
		1298	2.67×10^{-3}
		1307	3.47×10^{-3}
		1320	4.91×10^{-3}
		1327	4.78×10^{-3}
		1331	4.31×10^{-3}
		1339	5.95×10^{-3}
		1354	7.63×10^{-3}
77.5§ atomic pct silver			
		1141	2.19×10^{-4}
		1152	3.84×10^{-4}
		1155	4.30×10^{-4}
		1173	4.67×10^{-4}
		1195	6.76×10^{-4}
		1206	8.26×10^{-4}
		1214	9.82×10^{-4}
		1226	1.37×10^{-3}
		1237	2.08×10^{-3}
		1248	2.22×10^{-3}
		1259	2.78×10^{-3}
		1271	3.48×10^{-3}

* 20.3 to 18.7. † 41.8 to 35.8. ‡ 62.5 to 61.5. § 78.4 to 76.6.

so that the precision of temperature measurement by this method may be judged.

Discussion

Since the emf and vapor measurements cover different ranges of temperature, it was necessary to correlate one set of data or the other in order to make the extrapolation required. The emf data are more plentiful and from several sources, so these were chosen for the extrapolation.

Plotting $\log \gamma$ vs $1/T$ for the results of Wachter at 200°C, Wagner and Englehardt over the range 393° to 746°C, and Kubaschewski and Huchler over the range 304° to 629°C permits estimation of the lines corresponding to the average compositions used in the vapor pressure measurements. The lines chosen could not have been changed very much and still remained consistent with the pattern of experimental points as a consequence of the large number of points available rather than the precision of each point.

When the emf data were extrapolated by the method described in the preceding paragraph to the higher temperature range in which vapor pressures have been measured, activity coefficients were read off as a function of temperature. These extrapolated activity coefficients are represented in Fig. 1 by the 900° and 1000°C lines, while the lines for 350°, 500°, and 700°C are based on the results of Kubaschewski and Huchler and of Wagner and Englehardt, the 200°C line being that given by Wachter. They probably represent as good a set of internally consistent activity coefficients as the present data will yield.

Combining these activity coefficients with the known vapor pressures of pure solid silver¹⁰ (given in Fig. 2 as the 100 atomic pct Ag line), vapor pressure curves for 77.5, 62.0, 38.8, and 19.5 atomic pct Ag have been calculated. These lines are drawn in Fig. 2 and are derived from the emf data. The experimental vapor pressures determined here are plotted on the same diagram for comparison. It is evident that the agreement is as good as can be expected in view of the experimental uncertainties. Deviations occur in both directions to about the same extent.

It is difficult to compare the relative precision obtainable for a single measurement by the emf and vapor pressure methods as they have been employed for studies on silver-gold. In the several emf studies different compositions and temperatures have been used, although in a few cases both are close enough to warrant a direct comparison. For instance, at 404°C Wagner and Englehardt's measurements give an activity coefficient of 0.227 for an alloy of 0.240 atomic fraction silver. At 400°C Kubaschewski and Huchler's data yield activity coefficients of 0.262 for atomic fraction 0.234 and 0.253 for atomic fraction 0.2865. Except for very low atomic fractions of silver where the discrepancies are also very large, the values cited represent one of the largest deviations between the two sets, a difference of about 15 pct. Each of these emf activity coefficients is based upon a series of actual emf measurements for the same cell at a series of temperatures. Thus, although single vapor pressure points have given activity coefficients deviating from other measurements at the same composition and temperature by up to 40 pct, the precision of measuring a single vapor pressure or the emf of a cell cannot be very different.

While it is probable that the precision of the vapor pressure method can be improved considerably in subsequent studies, the extended application

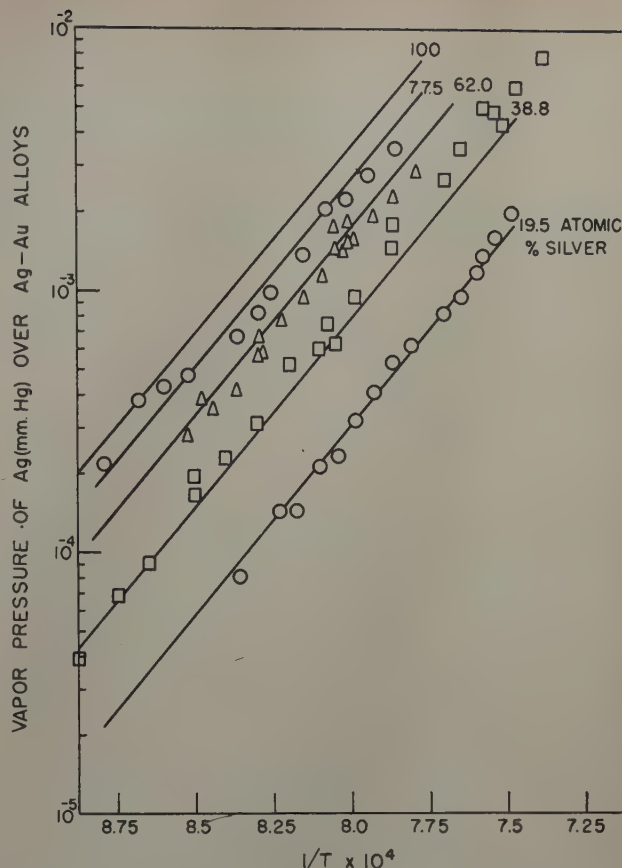


Fig. 2—Vapor pressure of silver over silver-gold alloys vs $1/T$. Solid lines calculated from vapor pressure of pure silver and activity coefficients from emf data. Experimental points from vapor pressure measurements reported here.

of the Knudsen orifice effusion technique would be justified even without improved precision, because it is applicable rigorously to cases in which the use of the emf method is doubtful or impossible. This study should demonstrate that both procedures yield the same thermodynamic information when the assumed limitations are not exceeded.

Acknowledgments

The authors are grateful to the Office of Naval Research for supporting this work. The alloy analyses were made by Audrey B. Kraus. The assistance of Robert Miller in carrying out the actual runs is gratefully acknowledged. The radioactive silver used in these measurements was obtained from the Isotopes Division of the Atomic Energy Commission.

References

- ¹ C. Wagner and G. Engelhardt: *Ztsch. Phys. Chem.* (1932) **A159**, p. 241.
- ² A. Ölander: *Journal ACS* (1931) **53**, p. 3577.
- ³ A. Wachter: *Journal ACS* (1932) **54**, p. 4609.
- ⁴ O. Kubaschewski and O. Huchler: *Ztsch. Elektrochem.* (1948) **52**, p. 170.
- ⁵ L. D. Hall: *Journal ACS* (1951) **73**, p. 757.
- ⁶ F. Weibke and U. von Quadt: *Ztsch. Elektrochem.* (1939) **45**, p. 715.
- ⁷ J. Lumsden: *Thermodynamics of Alloys* (1952) Inst. Metals, London.
- ⁸ H. M. Schadel, Jr. and C. E. Birchenall: *Trans. AIME* (1950) **188**, p. 1134; *JOURNAL OF METALS* (September 1950).
- ⁹ H. M. Schadel, Jr., G. Derge, and C. E. Birchenall: *Trans. AIME* (1950) **188**, p. 1282; *JOURNAL OF METALS* (October 1952).
- ¹⁰ C. L. McCabe and C. E. Birchenall: This issue, p. 707.

Metallographic Observations of the Deformation Of High-Purity Magnesium in Creep at 500°F

by A. R. Chaudhuri, N. J. Grant, and J. T. Norton

MOST of the recent work to establish the mechanism of creep in metals at high temperatures has utilized aluminum as the experimental material. It was thought desirable to initiate an investigation of a hexagonal close-packed metal, because of the relatively simple slip system, and compare the observed deformation characteristics with those that have been observed for the face-centered cubic metals. High-purity magnesium was chosen for this purpose, first, because its strength and other mechanical properties are similar to those of aluminum in the same temperature range, and second, because the existing equipment was ideally suited to observe magnesium during creep. It is proposed in this paper to present a pictorial and qualitative account of the changes that high-purity magnesium undergoes during creep at 500°F.

The characteristics of deformation of aluminum described below have been observed by various workers and accounts of these may be obtained from the papers of Chang and Grant.¹⁻³ These characteristics are: slip, subgrain formation, grain boundary sliding and migration, fold formation, deformation bands, and kink bands.

It is well known that in a flat magnesium specimen, slip on the basal plane (0001) in the $[11\bar{2}0]$ direction results in the formation of straight bands on the surface of the specimen. Schmid and co-workers⁴ have shown that this system is operative in the temperature range of -185° to 300°C (-300° to 572°F). They have also shown that a second system, slip on the pyramidal planes $\{10\bar{1}1\}$ or $\{10\bar{1}2\}$ in the $[11\bar{2}0]$ direction, is operative at temperatures higher than 225°C (437°F). Between 225° and 300°C (437° to 572°F), therefore, deformation by both these systems is expected. Bakarian and Mathewson⁵ confirmed the occurrence of pyramidal slip on the $\{10\bar{1}1\}$ plane and found that it resulted in irregular markings on the surfaces of their specimens. Burke and Hibbard⁶ obtained evidence of pyramidal slip in single crystals of magnesium deformed at room temperature. Bakarian and Mathewson⁵ suggested that the irregular appearance of these bands was due to slip on both of the pyramidal planes occurring simultaneously but in the same direction, the

close angular relationship between the planes making this process possible. Furthermore, since neither of these planes is close enough to the basal plane, slip on the latter does not exhibit the irregular appearance of slip bands resulting from pyramidal slip.

Experimental Procedure

High-purity magnesium, supplied by the Dow Chemical Co., was used in these experiments. The analysis was as follows: Al, 0.0002 pct; Mn, 0.0018; Fe, 0.0024; Cu, 0.0002; Sn, 0.001; Ca, 0.01; Ni, 0.0003; Zn, 0.01; Pb, 0.0005; Si, 0.001; and Mg, 99.972. The magnesium was supplied in the form of $\frac{1}{2}$ in. diam rods. The specimens had an overall length of $2\frac{1}{4}$ in., the round ends being threaded to fit the specimen holders. The previously round $3/16$ in. diam gage section of the specimen had two parallel flats machined on opposite sides for microscopic observation, yielding a test zone having the dimensions of $1 \times 3/16 \times 7/64$ in.

The specimens were electrolytically polished (without prior mechanical polishing of the machined flats), in a solution composed of 375 ml of orthophosphoric acid and 625 ml of ethyl alcohol.⁷ The cathode was a stainless steel sheet bent so that the specimen was completely surrounded. The voltage for successful polishing was 1.5 v at 100 to 300 milliamp current. Electropolishing for about 45 min sufficed to obtain a good metallographic surface on the specimens after they had been machined.

The creep tests were performed under constant load, and two types of equipment were used. In the first, designed by Servi and Grant,⁸ the specimens were beam-loaded, and a furnace could be lowered to surround the specimen. As the microstructural changes could not be observed during the course of the test, the tests had to be interrupted periodically by removing the specimen for microscopic examination. The second unit was a high temperature microscopy furnace designed by Chang and Grant.¹ The furnace was fitted with an optically flat quartz window having area dimensions 1.25×0.5 in., so that the whole test portion could be viewed through it at magnifications up to $\times 240$. The metallurgical microscope had three mutually perpendicular axes of motion, and, in addition, it was possible to measure angular displacements by rotation of the eyepiece. It was thus possible to make precise observations of the specimen during creep, and micrographs could be taken by attaching a camera to the eyepiece of the microscope.

The average grain size of the specimens that were tested was about 1 to 3 mm. This grain size could

A. R. CHAUDHURI is Research Associate, N. J. GRANT and J. T. NORTON, Members AIME, are Associate Professor and Professor, respectively, Dept. of Metallurgy, Massachusetts Institute of Technology, Cambridge, Mass.

Discussion on this paper, TP 3520E, may be sent, 2 copies, to AIME by Dec. 1, 1953. Manuscript, Dec. 3, 1952. Cleveland Meeting, October 1953.



Fig. 1—An example of the branching and forking of the pyramidal slip bands. Deformation by basal slip is also evident. Extension 10.6 pct. X50. Area reduced approximately 60 pct for reproduction.

be attained by annealing the specimens at 1100°F for about 15 hr. However, the grain size was never uniform throughout any one specimen, and even varied among specimens given the same treatment.

During annealing the specimens were enclosed in a magnesium capsule and the capsule placed in a steel cylinder closed at the two ends with screwed on caps. The high vapor pressure of magnesium resulted in a certain amount of pitting of the specimen. The surface could, however, be smoothed sufficiently by electropolishing after annealing so as to be suitable for metallographic examination. It was observed at 500°F, during creep testing, that very small shallow pits were formed on the surface. In addition to being distributed over the specimen surface, the pits tended to concentrate in the more highly deformed regions such as grain boundaries, slip bands, etc. It was suggested by Roberts⁹ that these pits were likely to be oxidation pits.

The micrographs shown were taken from the polished and deformed specimens, as the surface irregularities caused by creep deformation were sufficient to reveal the structure. The results given below are from tests made under constant load at a temperature of 500°F. The stress range varied from 570 to 690 psi. The tests were made in air. The micrographs presented are arranged so that the direction of tension runs from the top to the bottom.

Results and Discussion

Pyramidal Slip: Markings similar to those observed by Bakarian and Mathewson⁵ and caused, according to them, by pyramidal slip, have been found on deformed specimens in the present work. It must be emphasized that the terminology "pyramidal slip bands" given to these markings is based solely on the metallographic similarity they have to markings observed by Bakarian and Mathewson.⁵ They also determined the plane and direction of this type of pyramidal slip band which resulted in these

markings. Sometimes these markings are formed in grains in which basal plane slip bands may also be seen, as for example in Fig. 1. Bands resulting from pyramidal slip, in contrast to the sharp straight bands of basal plane slip are not straight, and consist of broad irregular bands, sometimes showing a considerable amount of branching and forking. In any one grain these bands have more or less the same direction, although the spacing between them varied and was greater than the basal plane slip spacing.

As a rule, these pyramidal slip bands in a grain tended to terminate at a grain boundary. At times, however, it appeared as if the bands in any one grain crossed a grain boundary and formed also in the neighboring grain, apparently without any change of direction. This is illustrated in Fig. 2. Since this type of slip band is rather wavy, it is difficult to determine whether the slip bands in any one grain are the continuation of the slip bands in the other, i.e., whether they obey the restrictions imposed by a change in orientation. Of course, if the orientation of the neighboring grains is nearly the same, it is possible that slip occurring in one grain will not stop at the boundary, but will initiate slip in the neighboring grain. In Fig. 2 it appears from the course of the basal slip bands that the grains are of similar orientation. A similar behavior of slip bands across grains of like orientation was found by Chang and Grant⁶ during the creep deformation of aluminum.

The progressive growth of pyramidal slip bands in a grain was followed microscopically throughout a test, with the final result in Fig. 3. These markings were noted to originate in the body of grain A at 1 and then advanced toward the grain boundary between grains A and B. On approaching the boundary, instead of crossing it, the individual bands split into many finer ones, resulting in extensive branching and localized nonhomogeneous deformation in this zone. Furthermore, the force exerted on the boundary by the impact of the slip bands was accommodated in grain B by subgrain formation near the boundaries of grains A and B, and in grain A by unusually heterogeneous branching of the slip bands.

Twinning: It is well known that twinning is one of the mechanisms by which magnesium and other hexagonal metals deform. In the creep experiments described it was found in some cases that a twin, after forming, appeared to be gradually disappearing. This process, unlike that of the first appearance of a twin, which in most cases is sudden, was a progressive one. A series of micrographs illustrating this are shown in Fig. 4. The traces of the original twin boundary were made more discernible because of pits which formed during the test and lay along these boundaries.

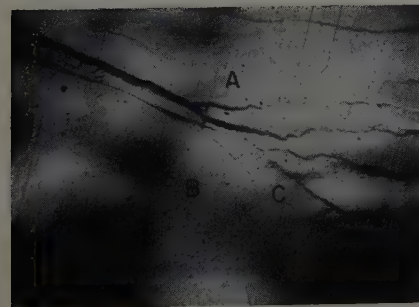
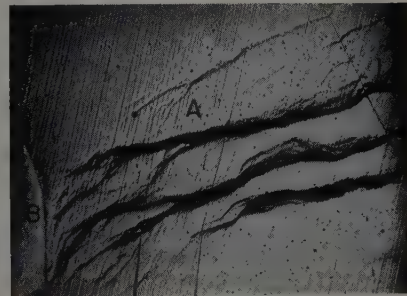
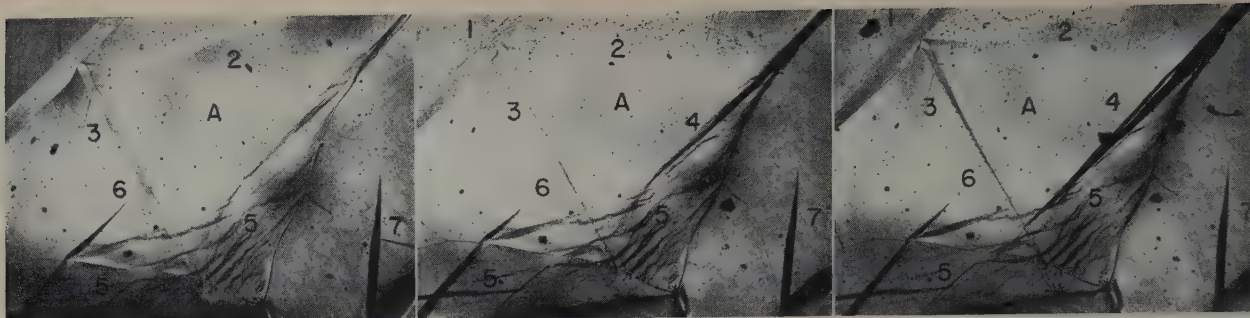


Fig. 2—(left) Shows three grains A, B and C with pyramidal slip bands running apparently continuously across the boundary between grains A and C. The course of the basal slip bands in the three grains indicates that the grains are of nearly similar orientations. Extension 4.7 pct. X75. Area reduced approximately 60 pct for reproduction.

Fig. 3 (right) The pyramidal slip bands started at 1 in grain A and advanced toward the grain boundary, branching into many slip bands, causing inhomogeneous deformation and the formation of subgrains in grain B. Extension 3.4 pct. X50. Area reduced approximately 60 pct for reproduction.



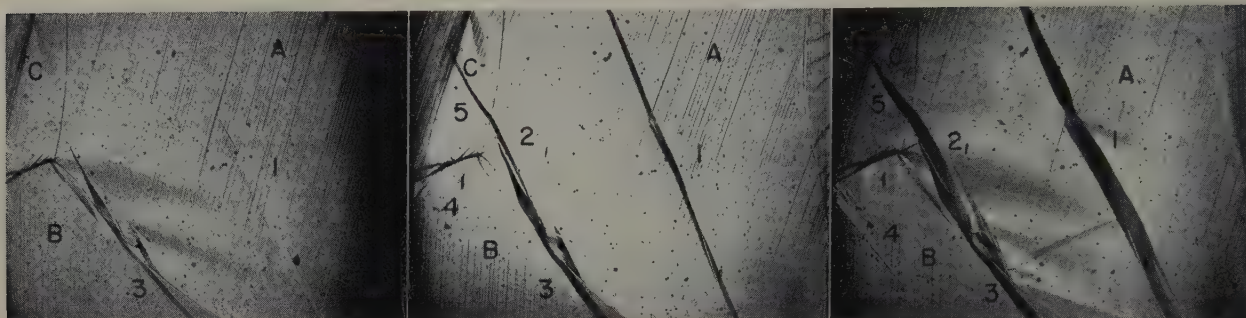


a—Extension 4.7 pct in 20 hr.

b—Extension 10.6 pct in 34 hr.

c—Extension 15.2 pct in 56.5 hr.

Fig. 4—Shows growth of twins and untwinning during creep. Twins 1, 2, and 3 grow thinner, 6 gets shorter and 7 disappears while over the same time interval twin 4 gets larger. Note pit demarcation of twins. Pyramidal slip bands (5) may also be noted. X75. Area reduced approximately 60 pct for reproduction.



a—Extension 4.7 pct in 20 hr.

b—Extension 10.6 pct in 34 hr.

c—Extension 15.2 pct in 56.5 hr.

Fig. 5—Shows growth of twins 1 and 2 (grain A), 3 and 4 (grain B), and 5 (grain C). Twin 5 is practically a continuation of 2, since basal slip bands in grains A and C suggest these grains are of nearly the same orientations. X50. Area reduced approximately 60 pct for reproduction.

Evidence of the growth of twins and of the untwinning of twins had previously been observed by Jillson¹⁰ during the compression of cleaved zinc single crystals, and the growth of twins was observed in continually deformed zinc by Burke.¹¹

Another feature observed in regard to twins formed during deformation is their growth both in length and in width after the initial appearance and, as may be seen from Fig. 5, this process of growth is also a progressive one. As a rule, the growth of twins and the untwinning of twins were observed individually in different grains. In some cases, however, as for example Fig. 4, both these mechanisms were observed to take place during the same time interval in the same grain. A further example of the appearance and growth of a twin is shown in Fig. 9.

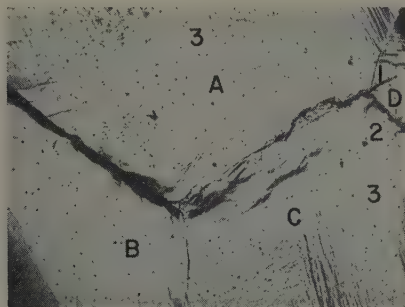


Fig. 6—Grain boundary migration may be seen along the boundaries of grains A and B, A and C, and C and D. The formation of folds 1 (grain D) and 2 (grain C) is shown. Subgrain boundaries (3) are also shown. Extension 8.6 pct. X75. Area reduced approximately 60 pct for reproduction.

Grain Boundary Migration: Considerable information has been accumulated by Servi and Grant¹² and by Chang and Grant,¹⁻³ during work on aluminum on the sliding and migration of grain boundaries during creep. These data were obtained at temperatures higher than those at which the present tests were run on magnesium; nevertheless, movements of portions of the grain boundaries have been detected during creep, an example of which is shown in Fig. 6.

Most of the cases where grain boundary migration was encountered took place near the points where three grains met. Fig. 7, however, shows an instance of the migration of the whole length of a boundary. It is presumed that at higher temperatures, when higher diffusion rates permit greater atomic mobility, the amounts of grain boundary migration observed will be greater.

In general, migration was observed along boundaries that were at 45° to the axis of tension; this is in agreement with the fact that the resolved component of the imposed stress is a maximum along a plane at 45° to the direction of the stress. In Fig. 7, migration may be seen to occur along three boundaries; two of which are at about 45° to the direction of tension and the third almost parallel to it. The migration of the third boundary could be explained on the basis that its migration was required in order to accommodate the strains due to the migration of the other two more favorably disposed boundaries. This picture also shows that grain A has deformed considerably by pyramidal slip.

After the creep-deformed specimens were electropolished, in those regions in which the above-mentioned shifting had occurred, the grain boundaries which were originally straight appeared wavy. The new boundaries followed the path formed as a



Fig. 7 (left) Boundary migration along the boundaries 1, 2, and 3. Considerable deformation in grain A due to extensive pyramidal slip is evident. Extension 3.7 pct. X75. Area reduced approximately 60 pct for reproduction.



Fig. 8—Shows a grain A with folds 1 and 2, stretching from the two triple points well into the grain. The white lines are subgrain boundaries formed in the body of the grain. Extension 8.6 pct. X150. Area reduced approximately 60 pct for reproduction.

result of shifting of the old boundary, but remained straight where there had been no movement.

A feature associated with grain boundary migration that has been observed in aluminum, namely, the formation of folds, was also observed in magnesium specimens during creep. As is shown in Figs. 6 and 8, fold formation takes place at triple points, taking the form of an extension of one or more of the slid grain boundaries into the opposite grains. Chang and Grant¹ have shown that fold formation is necessary to accommodate grain boundary sliding which occurs prior to the migration of the boundary. The length of these folds was small, as a rule, as for example the folds 1 and 2 in grains C and D in Fig. 6, suggesting that only small amounts of sliding took place. In some cases, however, the folds penetrated a fair distance into the grain, as shown in Fig. 8.

In this connection, it would be interesting to mention two types of zones formed within a grain dur-

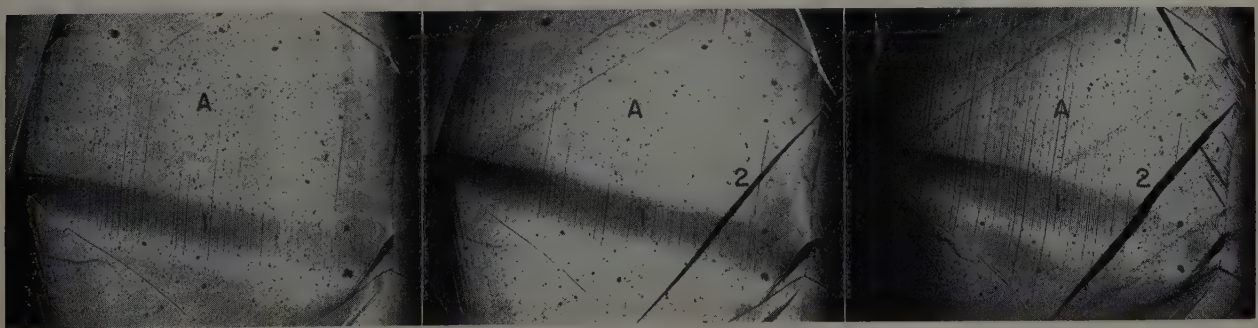
ing deformation. Fig. 9a, b, and c, shows one of these types; this deformation zone took the form of a fairly wide band stretching from a triple point across a grain. Slip bands deviated on crossing this region but returned to their original directions once they had crossed it. It shows also that with further deformation this band did not become any wider, nor did the slip bands crossing it tend to deviate by any greater amount, though this band appears wider in Fig. 9c due to a slight difference in the angle between the grain and the light beam while taking the picture.

The second feature observed was the formation of what appeared to be ridges in a grain, as if the surface had rippled, but not evenly; hence, parts of the grain between the ridges were left quite flat and undeformed. These ridges in each grain are more or less parallel, as may be seen from Fig. 10 which also shows localized grain boundary migration between grains A and D, and between grains A and C.

Subgrain Formation: One of the main changes observed in magnesium during creep was that of subgrain formation. The subgrain boundaries were extremely sharp and appeared as black or white lines running across grains. The appearance of the lines—black or white—depended on the microscopic focusing. That the surface of the grain was no longer level after the formation of these subgrains may be seen from the micrographs, for example, Fig. 11, in which in one grain some of the subgrains are bounded by white lines and some by black lines. This effect could be noted by rotating the specimen slightly about the long axis of the specimen, when viewed through a microscope. In contrast to subgrain formation in aluminum, the subgrain boundaries in magnesium were much sharper and much more clearly defined. It is interesting to note that observations by Ramsey¹⁸ on the creep deformation of zinc by subgrain formation showed that the same characteristics were exhibited by subgrains in this metal.

Subgrains were usually observed to have formed near the boundaries of the parent grains, as in Fig. 12; a certain amount of migration of the boundary between grains A and B may also be seen. These types of subgrains sometimes formed long boundaries running along the grain boundaries, and sometimes were more or less parallel to the slight bulges caused by the movements of the grain boundaries.

It will be seen that in grain A, Fig. 8, and grain E, Fig. 10, subgrains were sometimes formed in the body of the grains, their sizes, however, varied.



a—Extension 4.7 pct in 20 hr.

b—Extension 10.6 pct in 34 hr.

c—Extension 15.2 pct in 56.5 hr.

Fig. 9—Successive stages in the deformation of grain A. The region 1 results in the deviation of basal slip bands on crossing it, and does not get any wider with increasing deformation; nor does the direction of the slip bands alter as deformation progresses. The appearance and growth of twin 2 will be noted as also the formation of new twins in Fig. 9c. X50. Area reduced approximately 60 pct for reproduction.

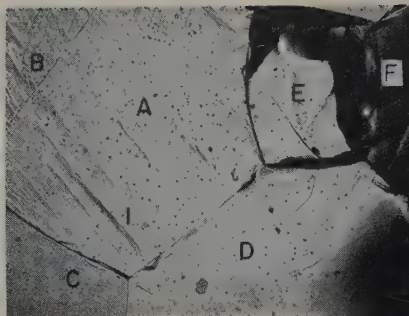


Fig. 10—Shows formation of "ripples" 1 (grain A). Localized migration may be seen along the boundaries of grains A and C, and A and D. Subgrains are evident in grain E, and in grain D near the triple point of grains D, E, and F. Extension 8.6 pct. X75. Area reduced approximately 60 pct for reproduction.



Fig. 11—Shows subgrain bounded by black or white lines. In some of the grains both these types of subgrain boundaries exist indicating the orientation difference between them. Extension 8.6 pct. X75. Area reduced approximately 60 pct for reproduction.

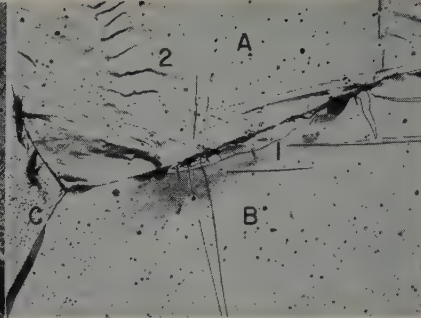


Fig. 12—Illustrates the migration of the boundary between grains A and B. Subgrains (1) may also be seen to have formed along this boundary, at times apparently parallel to the slight bulges caused by the migration of the boundary. Twin 2, formed by handling prior to a deformation, has pyramidal slip bands across it. Extension 5.6 pct. X150. Area reduced approximately 60 pct for reproduction.

Their formation in this manner could be attributed to bending caused by folds stretching from triple points well into the grain, or due to bending caused by ridges in the grain.

The subgrain boundaries were no longer perceptible on repolishing and etching (with a nital solution) after deformation, except those which exhibited a large difference in orientation as compared to the parent grain. However, the varying tilts of the subgrains with respect to the main grain, that is, changes in orientation, could be seen from the changes in the directions of the slip bands on crossing the subgrain boundaries, as for example, in Fig. 13. This picture not only shows the change in orientation of the subgrains with respect to the parent grain, but also with respect to each other.

Summary and Conclusions

The conclusions that may be drawn from the deformation of magnesium during constant load creep tests at 500°F and in the stress range of 570 to 690 psi (initial stress) are as follows:

The characteristics of creep deformation of magnesium are, 1—basal plane (0001) slip; 2—markings similar to those obtained by Bakarian and Mathewson⁶, and due, according to them, to slip along the pyramidal planes {10 $\bar{1}$ 1}; 3—twin formation, and sometimes their growth and untwinning; 4—boundary sliding and migration and fold formation; and 5—subgrain formation.

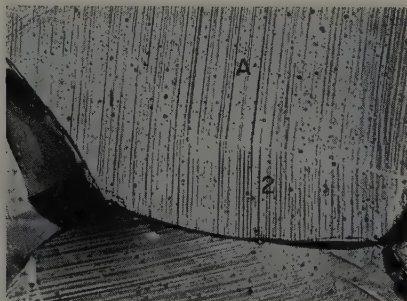


Fig. 13—1 and 2 are subgrains in grain A. The difference in orientation between these subgrains, and also between the grain and subgrains, is shown by the change in direction of the basal slip bands on crossing the subgrain boundaries. Extension 8.6 pct. X150. Area reduced approximately 60 pct for reproduction.

In general, these characteristics are similar to those met with in the deformation of aluminum, with the exception, of course, of twinning.

Acknowledgments

The authors wish to express their thanks to H. C. Chang and A. M. Gervais for taking part in many helpful discussions. Appreciation is expressed to the Dow Chemical Co. for supplying the high-purity magnesium, and to the Flight Research Laboratory, Wright Field, for sponsorship of the research.

References

- ¹ H. C. Chang and N. J. Grant: Observations of the Creep of the Grain Boundary in High Purity Aluminum. *Trans. AIME* (1952) **194**, p. 619; *JOURNAL OF METALS* (June 1952).
- ² H. C. Chang and N. J. Grant: Grain Boundary Sliding and Migration and Intercrystalline Failure Under Creep Conditions. *Trans. AIME* (1953) **197**, p. 305; *JOURNAL OF METALS* (February 1953).
- ³ H. C. Chang and N. J. Grant: Mechanism and Inhomogeneity of Deformation of Aluminum Under Creep Conditions. Unpublished.
- ⁴ E. Schmid and W. Boas: *Plasticity of Metal Crystals*. (1950) London. F. A. Hughes and Co., Ltd.
- ⁵ P. W. Bakarian and C. H. Mathewson: Slip and Twinning in Magnesium Single Crystals at Elevated Temperatures. *Trans. AIME* (1943) **152**, p. 226.
- ⁶ E. C. Burke and W. R. Hibbard, Jr.: Plastic Deformation of Magnesium Single Crystals. *Trans. AIME* (1952) **194**, p. 295; *JOURNAL OF METALS* (March 1952).
- ⁷ *Metals Handbook*. (1948) Cleveland. ASM.
- ⁸ I. S. Servi and N. J. Grant: Creep and Stress Rupture Behavior of Aluminum as a Function of Purity. *Trans. AIME* (1951) **191**, p. 909; *JOURNAL OF METALS* (October 1951).
- ⁹ C. S. Roberts: Dow Chemical Co., private communication.
- ¹⁰ D. C. Jillson: An Experimental Survey of the Deformation and Annealing Processes in Zinc. *Trans. AIME* (1950) **188**, p. 1009; *JOURNAL OF METALS* (August 1950).
- ¹¹ J. E. Burke: Quoted by C. S. Barrett in "The Crystallographic Mechanisms of Translation, Twinning and Banding." *Cold Working of Metals* (1949) Cleveland. ASM.
- ¹² I. S. Servi and N. J. Grant: Structure Observations of Aluminum Deformed in Creep at Elevated Temperatures. *Trans. AIME* (1951) **191**, p. 917; *JOURNAL OF METALS* (October 1951).
- ¹³ J. A. Ramsey: Some Observations on the Deformation of Polycrystalline Zinc. *Journal Inst. Metals* (1951-1952) **80**, p. 167.

Revealing the Subgrain Structure of Aluminum

by M. S. Hunter and D. L. Robinson

An extremely fine subgrain structure found in aluminum and aluminum alloys is shown and a method for revealing this structure is described. The appearance and some of the characteristics of this structure are described and the possible significance of subgrain structure in terms of chemical, electrochemical, and metallurgical processes is considered.

GRAINS and grain boundaries, which constitute the principal manifestations of the crystalline aggregates known as metals, play such an important part in determining the characteristics and properties of metals and alloys that their nature and behavior have long been of much concern to the metallographer. Many investigators have speculated on the possible existence of a finer structure within the usual grain structure and, through X-ray diffraction and metallographic techniques, have revealed evidence that such finer structures exist. Among these structures are the mosaic blocks and domains described by Burgers¹ and others in their contributions on crystalline structure and the dislocation theory, the small units associated with polygonization described by Cahn,² and the intragranular blocks revealed more recently by Lacombe and Beaujard.³ This paper describes some novel methods for clearly revealing a very fine granular substructure within the usual grains of pure aluminum and aluminum alloys. It also compares the characteristics and behavior of this subgrain structure with those of the ordinary grain structure and gives some examples of the manner in which this substructure may influence the characteristics of aluminum alloys.

Metallographic investigations of aluminum and its alloys have dealt extensively with the functions and behavior of grains and grain boundaries and have evolved a definite concept of the relation between grain structure, orientation and physical, mechanical, chemical, and electrochemical behavior. During the examination of etched samples, a roughening or mottling of the body of certain grains has occasionally been observed. Such roughening obviously represented differential attack by the etching solution, but its true significance was not at first realized. It is now known that this roughening probably represented a subgrain structure, although the particular etching treatments used were not capable of revealing this subgrain structure clearly. Also, in practically all cases, the subgrains were apparently far too small to be resolved by the light microscope.

Recently, a method has been developed for revealing clearly the subgrain structure of most aluminum alloys. This method is somewhat unique in that it eliminates much of the usual tedious mechanical polishing and the attendant danger of a surface layer of flowed metal and at the same time is simple, rapid, and effective. It involves the use of the Alcoa R5 Bright Dip, a patented chemical polishing treatment licensed by Aluminum Co. of America. This treatment produces a bright, highly polished surface at least the equal of any mechanical polish and also etches the subgrain boundaries as well as the ordinary grain boundaries to reveal both the grain and subgrain structure simultaneously.

Metallographic specimens to be examined are taken through the customary grinding and polishing operations used for aluminum alloys.⁴ The usual care required in the final polishing operation to prevent a flowed surface layer and to obtain a high polish is not necessary, however, because any flowed layer is eliminated and a high polish is produced by the final immersion in the Alcoa R5 Bright Dip. Depending on alloy type, this dip takes from a few seconds to about 3 min, after which the sample is rinsed well, blown dry, and is ready for examination.

The substructure can be revealed by some of the usual metallographic methods such as electropolishing or mechanical polishing and etching but no method has been found which is the equal of the new chemical polishing treatment. Mechanical polishing followed by the usual metallographic etching is not entirely satisfactory for revealing this substructure, probably because of the flowed surface layer resulting from the mechanical polish. If the usual etching methods are prolonged sufficiently to remove this layer, the specimen surface becomes quite rough and the substructure is not defined clearly.

M. S. HUNTER and D. L. ROBINSON are associated with the Metallography Div., Aluminum Research Laboratories, Aluminum Co. of America, New Kensington, Pa.

Discussion on this paper, TP 3509E, may be sent, 2 copies, to AIME by Dec. 1, 1953. Manuscript, Oct. 3, 1952. Cleveland Meeting, October 1953.

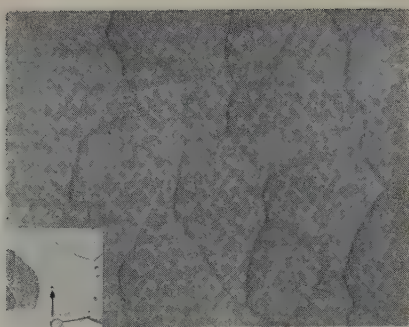


Fig. 1—Equiaxed subgrain structure of annealed 99.999 pct Al. Small dot in light micrograph at X100 (inset) indicates entire area of electron micrograph. Electron micrograph. Oxide film replica. X35,000. Area reduced approximately 60 pct for reproduction.

Some use of the light microscope may be made in examining the subgrain structure of aluminum and aluminum alloys, but the subgrain dimensions are generally so small that the substructure cannot be resolved by this instrument. Consequently, it is necessary to turn to the electron microscope with its higher magnification and greater resolving power to observe subgrain structure and to follow changes in subgrain size and shape and the various phenomena occurring at subgrain boundaries.

Inasmuch as the electron microscope develops an image only by differential transmission of electrons, examinations of the ordinary metallographic specimen cannot be made, and reproduction of the surface contour in an extremely thin, structureless film pervious to electrons is necessary.⁶ The choice of the optimum type of surface replica for the reproduction of subgrain structure is critical because of the extremely fine detail of such structures. While subgrain structures have been reproduced by several of the common replica methods, the anodic oxide replica method was selected for this work because it is the easiest to use, is capable of reproducing somewhat finer detail, and is the easiest to handle because of the inherent strength of the oxide film.

Replicas used in this work were prepared by first anodically coating the polished and etched specimen in a 3 pct tartaric acid solution adjusted with ammonium hydroxide of a pH of 5.5 using a potential of 17 v. In this type of electrolyte, a structureless barrier type of oxide coating is formed to a thickness of approximately 14Å for each volt of applied potential. Thus, the 17 v used produced an oxide film about 250Å thick, which was ideal from the transmission standpoint for the EMC-2A electron microscope. With other microscopes which use higher accelerating potentials, a greater thickness of replica could be used with some gain in contrast and ease of handling.

Removal of the oxide replicas is accomplished by amalgamation. The oxide coating on the surface of the specimen is first scribed into squares of a size convenient for handling on the small microscope specimen screens. Amalgamation is started by immersing the specimen in concentrated mercuric chloride solution until mercury is deposited along the scribed lines. The specimen is then transferred to distilled water and amalgamation is allowed to continue until the small squares of oxide separate from the metal. These squares are picked up on specimen screens, rinsed in distilled water, and allowed to dry on the screens.

When these replicas are examined in the electron microscope, it is found that the ordinary grain actually contains a finer structure which is not revealed clearly by the light microscope, Fig. 1. This fine structure is similar in appearance to the usual grain structure but, when the actual size of the subgrains is realized (Fig. 1, inset), it becomes apparent that each ordinary grain consists of millions of subgrains and subgrain boundaries. It is doubtful that this substructure represents the "blocks" or crystals formed during polygonization shown by other investigators because of differences in size and behavior which will be described later. It is possible that this substructure may actually be the domains or mosaic structure which have been used so widely in theoretical discussions of fundamental grain structure, but the descriptions of these structures are not sufficiently specific to warrant such a conclusion.

With the revelation of subgrain structure, the crystallographic concept of a grain becomes even more complex. The subgrain boundaries must represent regions with lattice vacancies resulting from slight disregistry, because they can be attacked selectively like grain boundaries by certain etching methods. This disregistry, however, cannot be as great as that existing at ordinary grain boundaries, because the subgrain boundaries are not revealed by many of the methods used to reveal the common grain boundary. Inasmuch as fairly sharp spots are obtained by X-ray diffraction from a single ordinary grain, it is evident that the orientation of each of the subgrains must be similar to that of the ordinary grain of which it is a part. Each subgrain, however, must have a slightly different orientation from its neighbor, although it is likely that this difference in orientation is small in comparison with the differences observed between ordinary grains. This is substantiated by the fact that subgrain boundaries do not etch as readily as ordinary grain boundaries, probably because the crystallographic planes are more nearly in registry and the resulting boundary vacancies are fewer and smaller.

Searching for additional information regarding the nature of this substructure, an investigation was made of the relation between the structure and size of ordinary grains and subgrains. It is known that ordinary grain size varies with metal purity and is generally finer in aluminum alloys than in the pure metal. In view of the similarity in character of subgrains and ordinary grains postulated above, it would be expected that subgrain size might vary in a similar manner. To follow this idea further, the structure and size of the subgrains were determined for several samples of annealed aluminum sheet of different purities and of two high purity base aluminum alloy sheet materials in the heat-treated and quenched temper. These were substantially homogeneous materials and had equiaxed grain structures as seen under the light microscope.

The subgrain structures of these materials (Figs. 1 to 5) at the magnification used had the appearance of ordinary grain structures, but the shape and size of the subgrains differed greatly from the shape and size of the ordinary grains of the same materials. While all materials had an equiaxed ordinary grain structure, a definite directionality of the subgrain pattern was apparent in the 99.8 pct Al (Fig. 2), the 99.3 pct Al (Fig. 3), and particularly the Al-Mn alloy (Fig. 4). It appears likely that this directionality is related in some manner either to crystal



Fig. 2 (left)—Elongated subgrain structure of annealed 99.8 pct Al. Electron micrograph. Oxide film replica. X35,000. Area reduced approximately 60 pct for reproduction.



Fig. 3 (right)—Subgrain pattern in three grains of annealed 99.3 pct Al. Electron micrograph. Oxide film replica. X35,000. Area reduced approximately 60 pct for reproduction.



Fig. 4 (left)—Highly elongated subgrain structure and "double boundaries" of Al-1 pct Mn alloy heat treated at 960°F and quenched. Electron micrograph. Oxide film replica. X35,000. Area reduced approximately 60 pct for reproduction.

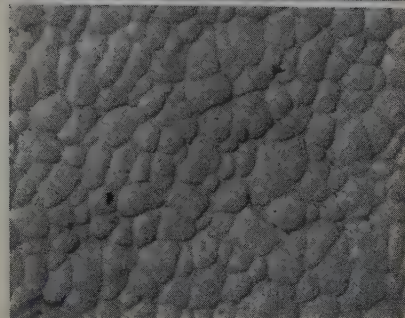


Fig. 5 (right)—Subgrain structure of aluminum-1 pct magnesium silicide alloy heat treated at 960°F and quenched. Electron micrograph. Oxide film replica. X35,000. Area reduced approximately 60 pct for reproduction.

orientation or working direction, even though no such indications were evident in the ordinary grain structure.

An additional feature of interest is the "double boundary" type of structure apparent in the Al-Mn alloy, Fig. 4. It is probable that this condition is related to a precipitation phenomenon, although no evidence of precipitate particles was present either in the ordinary grain or subgrain structure.

Some very interesting information is revealed by consideration of the actual size of the subgrains and the relation between subgrain size and ordinary grain size. In the case of the 99.999 pct Al, which had the largest subgrain size of the materials studied, the subgrain size was about one billion subgrains per cubic millimeter as compared to an ordinary grain size of about one grain per cubic millimeter. Thus, these subgrains are about 10,000Å in diameter, which is within the resolving power of the light microscope. In the case of the other materials, the subgrain size is appreciably finer and subgrain diameters range down to about 2000Å, which is below the resolving power of the light microscope. The ordinary grain size and subgrain size on the surface of the materials investigated are given in Table I.

With regard to the relationship between ordinary grain size and subgrain size, inspection of these data shows that ordinary grain size and subgrain size do not have any direct and consistent relationship although, with one exception, the materials having finer ordinary grain size also have finer subgrain size. A consistent trend is observed, however, in the ratio between the two types of grain size in

that the ratio becomes lower as the ordinary grain size becomes finer. This indicates that the subgrains may tend to be more nearly of the same size regardless of material and that variations in subgrain size may be much less than those encountered with ordinary grain size. This is supported by the fact that a variation of only 13 to 1 was observed in subgrain size among these samples, whereas the variation in ordinary grain size was about 12,500 to 1.

Having established the relation between ordinary grains and subgrains as far as structure and size was concerned, a comparison was made of the behavior of the ordinary grains and subgrains during cold rolling and subsequent annealing. It was expected, in view of the similarity of ordinary grain and subgrain structure, that the fragmentation on rolling and recrystallization during annealing, which is apparent in the ordinary grain structure, might also be observed in the subgrain structure. In this work, the subgrain structures of 99.995 pct Al sheet in the annealed condition and after reductions of 50, 70, and 90 pct by cold rolling were investigated.

Observations of these structures showed that, starting with an equiaxed subgrain structure of the type seen in Fig. 1, increasing amounts of reduction brought about elongation of the subgrains, higher degrees of fragmentation and increasing amounts of slip within the subgrains. These structural changes are the same as those that occur in the ordinary grains during cold working. At 90 pct reduction, most of the original subgrains have lost their identity by virtue of slip and fragmentation, although a few have been only slightly deformed, Fig. 6.

The behavior of subgrain fragments during annealing was investigated to determine whether structural changes in the substructure are similar to those observed in the ordinary structure. Starting with hard-rolled 99.999 pct Al sheet having highly fragmented substructure (Fig. 7), annealing treatments of 30 min at temperatures up to 600°F were applied. As recrystallization progressed with increasing temperature, the fragment boundaries disappeared and subgrains began to form in increasing numbers as atomic rearrangement occurred, Fig. 8. Finally, when recrystallization was complete, the structure showed no trace of the original elongated

Table I. Comparison of Ordinary Grain Size and Subgrain Size

Material	Temper	Grains per Sq Mm		Ratio of Subgrains to Ordinary Grains
		Ordinary Grains	Subgrains	
99.999% Al	Annealed	1	1,000,000	1,000,000
99.8% Al	Annealed	361	7,000,000	19,400
99.3% Al	Annealed	1122	13,000,000	11,600
99.95% Al+1.4% MgSi	Heat treated at 960°F and quenched	4	2,800,000	700,000
99.95% Al+1.0%Mn		0.09	7,000,000	77,800,000



Fig. 6—Fragmented subgrain structure of 99.995 pct Al sheet given 90 pct reduction by cold working. Electron micrograph. Oxide film replica. X35,000. Area reduced approximately 60 pct for reproduction.



Fig. 7—Highly fragmented substructure of hard-rolled 99.999 pct Al sheet. Electron micrograph. Oxide film replica. X35,000. Area reduced approximately 60 pct for reproduction.

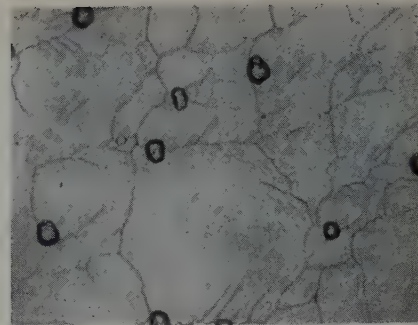


Fig. 8—Rearrangement of substructure resulting from partially annealing material seen in Fig. 7 (30 min at 475°). Electron micrograph. Oxide film replica. X35,000. Area reduced approximately 60 pct for reproduction.

fragmented structure and only equiaxed subgrains were apparent, Fig. 1. Thus, the rearrangement of the substructure during recrystallization is similar to that which occurs in the ordinary structure.

The growth tendencies of subgrains were investigated briefly to determine whether subgrains are separate units of a grain or whether they represent a transition stage in the formation of the ordinary grain. First, a sample of the annealed material from the recrystallization work was given an additional annealing treatment of 24 hr at 1000°F, which should produce grain growth if the subgrain was only a transition stage. This treatment, however, produced no noticeable change in subgrain size. Second, the subgrain structure of several artificially produced giant grains in 99.95 pct Al was observed. These grains had been produced by the strain-anneal method and had been subjected to many, long, high temperature annealing treatments. The subgrain size of these grains was of the same order as that of the other high purity material examined. Thus, the subgrain is apparently a fundamental unit in itself and is not merely a step in the transition from a fragmented to a recrystallized structure.

This investigation has shown that the subgrains are separate entities which have a structure similar in many respects to the usual grain structure and which behave similarly to ordinary grains during deformation and recrystallization. The most outstanding differences between the ordinary grain and the subgrain were in the matter of size and the directionality of the subgrain pattern in material having an equiaxed ordinary grain structure. Inasmuch as it was believed that this directionality of the subgrain pattern might be related to crystallographic orientation or rolling direction, the relation between these factors was investigated.

The orientation problem could not be approached directly, because it was not convenient to mark a grain in such a manner that the marking would appear in the field of view in the electron microscope. It was found, however, that the orientation of the replica could be determined accurately by indirect means from the shape and orientation of etch pits developed on the surface of the sample before formation of the replica. This approach has been used to good advantage by Lacombe and Beaujard.³

The particular samples used for investigating the relation between the directionality of the subgrain pattern, crystallographic orientation, and working direction were a group of tensile bars of 99.95 pct Al

in which large grains had been developed by the strain-anneal method. The working direction was considered to be along the length of these bars, inasmuch as the strain had been applied in this direction during the grain growth process. Metallographic samples were prepared from grains, the orientation of which had been determined by X-ray diffraction analyses. After the chemical polishing, the samples were given an etch of a few seconds' duration in a solution containing 10 cc of concentrated hydrochloric acid, 30 cc of concentrated nitric acid, and 20 cc of a 5 pct ferric chloride solution to develop etch pits. The faces of etch pits developed by this solution represent {100} planes.

In searching for appropriate grains it was found that the planes parallel to the surface of the available test bars fell into two principal orientations whereby the grain surfaces were approximately either a {100} or {110} type plane. Three grains were chosen for extensive investigation. The surfaces of two of those were almost parallel to the (001) plane, whereas the surface of the third approximated a {110} type plane. To establish the subgrain shape and orientation, it was necessary to section the grain along three faces at right angles to each other. For convenience, the three faces were chosen as planes parallel to the surface, edge, and end of the test bar. This terminology of surface, edge, and end will be used to describe corresponding surfaces of the samples removed from the various grains.

In the preparation of the specimens removed from the various grains, the routine of polish, Alcoa R5 Bright Dip and deep etch was employed, although it was found possible in some instances to develop the subgrain pattern on the faces of the etch pits by additional chemical polishing after the deep etch treatment, Fig. 12. Frequently, however, this tended to destroy many of the etch pits, so the additional treatment was not generally used.

The subgrain pattern on the three faces of the selected grains (Figs. 9 to 12) reveals the shape of the subgrains. While considerable variation naturally exists, the subgrain shape generally tends toward that of an ellipsoid, Fig. 10. In some cases, however, the subgrains have relatively flat surfaces and the subgrain shape approaches that of a rectangular prism, Fig. 9.

In the matter of orientation and subgrain directionality, a fairly definite correlation exists in that, in every case, the long dimension of the subgrain is parallel to a cube edge. The puzzling aspect of this relationship, however, is that if the long dimension

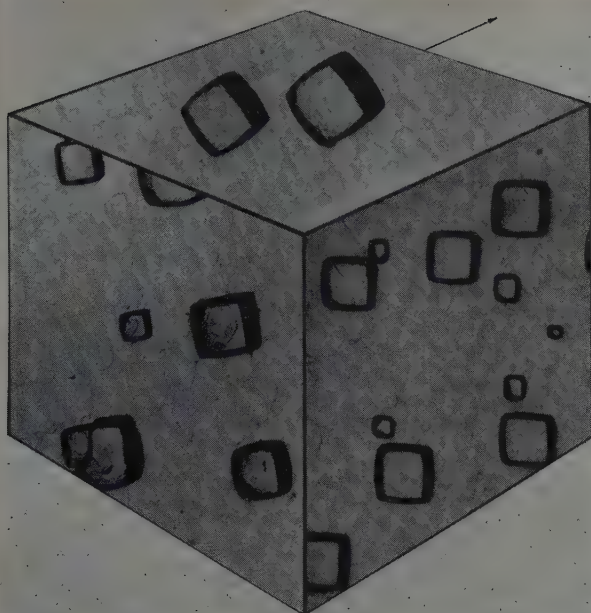


Fig. 9—Composite micrograph showing etch pits and subgrain shape on three faces of a single grain. Arrow indicates working direction. Electron micrograph. Oxide film replica. X35,000. Area reduced approximately 60 pct for reproduction.

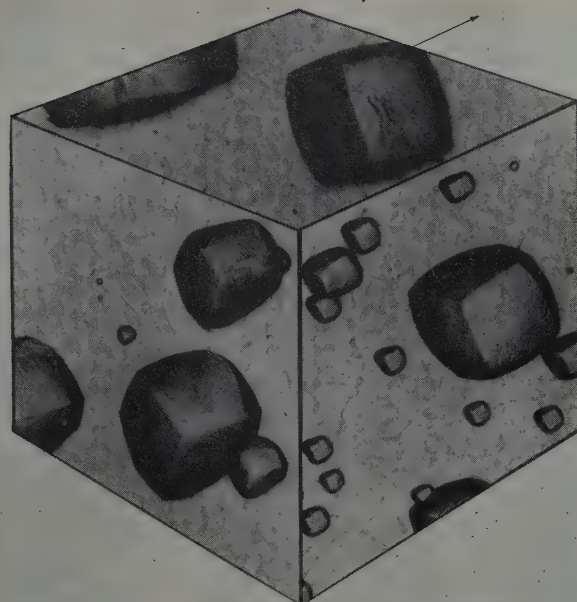


Fig. 10—Composite micrograph showing etch pits and subgrain shape on three faces of another single grain. Arrow indicates working direction. Electron micrograph. Oxide film replica. X35,000. Area reduced approximately 60 pct for reproduction.

of the subgrain is parallel to a cube edge, it is actually parallel to four edges but is at right angles to the other eight edges. The question then arises—why does the length of the subgrain lie parallel to one particular set of cube edges and not one of the other two?

It was believed that the answer to this question might lie in the relation between directionality and the working direction of the bar. Attempts to relate these factors, however, produce a complete lack of correlation. In the three grains, the long directions of the surface subgrain patterns are at angles of about 30° , 80° , and 100° to the rolling direction, Figs. 9 to 11. In two of these grains, little or no directionality is evident on the edge and end faces, whereas in the third a highly directional pattern is evident on the edge face, Fig. 12. This latter pattern extends at an angle of about 35° to a line perpendicular to the surface face, which means that the subgrains angle sharply down through the thickness of the piece.

This investigation of the directionality of the subgrain pattern and its relation to crystallographic orientation and working direction has shown that the long dimension of the subgrains lies parallel to $\{100\}$ poles of the lattice. An absolute lack of corre-

lation between directionality and working direction leaves unanswered the question as to why the long axis of the subgrain parallels one $[100]$ direction and not one of the others.

So far, the nature and behavior of subgrains, the relation between ordinary grains and subgrains, and the relationship between orientation and the directionality of the subgrain pattern have been shown. From the practical standpoint, the chemical, electrochemical, and metallurgical behavior of the subgrains, and particularly their boundaries, are of even greater importance.

In view of the similarities which have been shown to exist between the nature of the ordinary grain and that of the subgrain, it would be expected that the behavior of these units of structure might also be similar. Thus, like the ordinary grains and grain boundaries, the subgrain and its boundaries might play a very important role in chemical and electrolytic etching, anodic coating and in precipitation phenomena.

Before dealing specifically with these chemical, electrochemical, and metallurgical processes, a brief review of the nature of the subgrains and their boundaries in aluminum and its alloys is in order. Each subgrain appears to be a separate and distinct

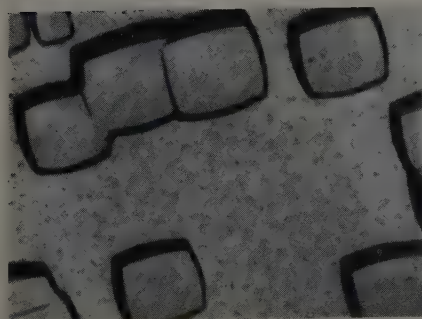
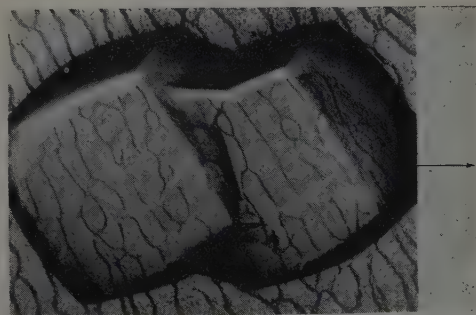


Fig. 11 (left)—Etch pits and subgrain shape on surface of a third single grain. Arrow indicates working direction. Electron micrograph. Oxide film replica. X35,000. Area reduced approximately 60 pct for reproduction.

Fig. 12 (right)—Etch pits and subgrain shape on edge of grain shown in Fig. 11. Arrow indicates working direction. Electron micrograph. Oxide film replica. X35,000. Area reduced approximately 60 pct for reproduction.



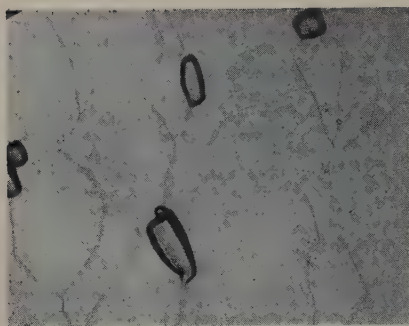


Fig. 13 (left)—Beginning of etch pit formation along subgrain boundaries and at subgrain junctions of 99.995 pct Al sheet reduced 50 pct by cold rolling. Electron micrograph. Oxide film replica. X35,000. Area reduced approximately 60 pct for reproduction.

Fig. 14 (right)—Start of electrolytic etching attack at subgrain boundaries of annealed 99.8 pct Al foil. Electron micrograph. Oxide film replica. X35,000. Area reduced approximately 60 pct for reproduction.

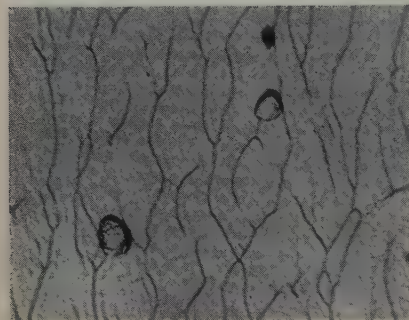
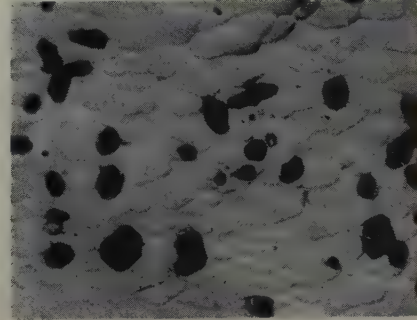
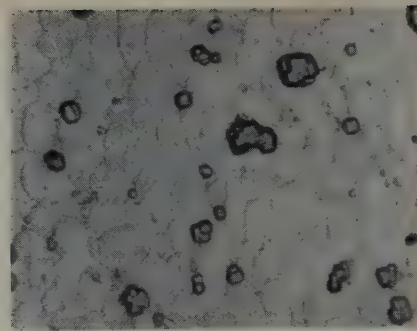


Fig. 15 (left)—Start of anodic oxide formation along subgrain boundaries of hard-rolled 99.999 pct Al sheet. Electron micrograph. Oxide film replica. X35,000. Area reduced approximately 60 pct for reproduction.

Fig. 16 (right)—Precipitation of magnesium silicide particles on subgrain boundaries of Al-1.4 pct Mg₂Si alloy heat treated, quenched and aged 2 hr at 650°F. Electron micrograph. Oxide film replica. X35,000. Area reduced approximately 60 pct for reproduction.



unit of structure and must necessarily have an orientation of its own which differs slightly from that of its neighbors. This results in disregistry with consequent vacancies at subgrain boundaries. Such regions would be expected to be ideal sites for precipitation, because less energy would be required for the formation of a particle in this place. Considering the ever-present natural oxide film on aluminum and its alloys, these vacancies in the metal might be reflected in a less dense oxide film at subgrain boundaries, with the result that these locations might be more susceptible to chemical or electrochemical action.

An outstanding example of the behavior of subgrain boundaries under chemical attack is the development of subgrain structure by the Alcoa R5 Bright Dip. In this acid solution, general attack takes place but the rate of attack is more rapid at the subgrain boundaries; these regions are dissolved out and the structure is revealed. Another example of the behavior of subgrain boundaries under chemical attack is found in the formation of etch pits of the type used in the orientation work already described. These etch pits were large compared to the size of the subgrains but, if only very light etching is employed, it is apparent that the first etch pits invariably start to form along subgrain boundaries, Fig. 13.

In the matter of subgrain behavior under electrochemical action, unusual but not unexpected behavior is evident at the start of electrolytic etching and anodic oxide coating formation. If aluminum foil is etched electrolytically in a chloride solution, cubic etch pits tend to form and the first pits start either at grain boundaries or subgrain boundaries, Fig. 14. Also, a predominance of pits is found at subgrain junctions, apparently because a greater number of vacancies exists at these locations.

At the beginning of the formation on aluminum of anodic oxide coatings, which are composed of close-packed columnar cells of aluminum oxide, the coating formation first starts along grain boundaries and subgrain boundaries. This is shown by Fig. 15, which illustrates the impression in the metal surface of the rounded ends of oxide cells that have just started to form. The cups along both sides of the subgrain boundaries are more clearly defined be-

cause they started to form first and are more fully developed.

With respect to precipitation, it would be expected that the larger number of vacancies along subgrain boundaries would permit precipitation in a manner similar to that encountered at ordinary grain boundaries. Such was found to be the case in an aluminum-magnesium silicide alloy, in which precipitate particles were observed primarily along subgrain boundaries and at subgrain junctions, Fig. 16. In this micrograph, the dark areas represent actual precipitate particles which were retained in the electron microscope replica.

These examples of the behavior of subgrain boundaries under chemical and electrochemical attack and during precipitation have shown a relationship between subgrain structure and behavior, although the full significance of this structure and the extent to which it controls the characteristics of aluminum and its alloys has yet to be established. It is highly possible that subgrain structure may play a part in corrosion, creep, fatigue and many other phenomena and may furnish an explanation for some of the puzzling peculiarities of behavior which have been encountered.

Acknowledgment

The authors wish to express their appreciation to F. Keller under whose direction this investigation was conducted.

References

- ¹ J. M. Burgers: Geometrical Considerations Concerning the Structural Irregularities to be Assumed in a Crystal. *Proc. Physical Soc., London* (1940) **52**, p. 23.
- ² R. W. Cahn: Slip and Polygonization in Aluminum. *Journal Inst. Metals* (May 1951) **79**, p. 129.
- ³ P. Lacombe and L. Beaujard: Application of Etch-Figures on Pure Aluminum to the Study of Some Micrographic Problems. *Journal Inst. Metals* (1947-1948) **74**, p. 1.
- ⁴ F. Keller and G. W. Wilcox: Aluminum Research Laboratories Technical Paper No. 7.
- ⁵ F. Keller and A. H. Geisler: Application of Electron Microscope to Study of Aluminum Alloys. *Trans. AIME* (1944) **156**, p. 82.

Alpha Solid-Solution Area of the Cu-Mn-Sn System

by C. W. Funk and J. A. Rowland

THIS investigation is a part of the United States Bureau of Mines work in conserving the Nation's resources. The isothermal sections presented were developed as a guide to a comprehensive investigation of the properties and fabricating characteristics of copper-base alloys containing manganese and tin. These alloys are being investigated as possible replacements for the commercial bronzes containing substantial quantities of tin. Development of the isothermal sections has, therefore, been limited to the area between 0 to 20 pct Mn and 0 to 25 pct Sn.

Since Heusler¹ reported the ferromagnetic properties of the Cu-Mn-Sn alloys in 1903, the system has been the subject of several investigations. These studies were largely concerned with correlation of magnetic properties and crystal structure.²⁻⁶ Vero,⁷ however, established the solidus surface of the system, between 20 pct Mn and 40 pct Sn, by thermal and microscopic methods. The α , β , and γ solid solutions were also observed by Vero and reported to extend into the interior of the ternary system.

For the present study, the annotated diagram of the Cu-Sn system prepared by Raynor⁸ and the Cu-Mn diagram by Dean and coworkers⁹ were used as the binary borders of the ternary system.

Procedure

The metals used in this investigation were electrolytic manganese, washed cathode copper, and three-star tin. The manganese, produced at the Boulder City pilot plant of the Bureau of Mines, had a purity of 99.9 pct; the copper contained less than 0.004 pct Bi and 0.001 pct S; the tin contained 0.070 pct Pb, 0.070 pct Sb, 0.050 pct Fe, and 0.065 pct Si.

Heats of 1 lb were melted in alundum crucibles with a 3-kw induction furnace. The heats were chill-cast in iron or copper molds to form 6-in. ingots $\frac{3}{4}$ in. in diameter. Molds were washed with graphite or zirconia, depending on the manganese content, and preheated to 150°C. The maximum impurity content of any alloy was 0.03 pct Fe, 0.02 pct Si, and 0.02 pct Al; in most cases, they contained less than half this quantity of any of these impurities.

Composition of the alloys and their treatment prior to homogenizing are shown in Fig. 1. Designations adjacent to each composition refer to the heat numbers. With a few exceptions, ingots containing 20 pct Sn or less were hot-swaged. These ingots were swaged, after a 24-hr preheat at 650°C, to obtain a total reduction of 70 pct in cross section. Intermittent reheating was necessary, and reductions were limited to either 0.025 or 0.050 in. in diameter per pass.

Selection of a 200-hr homogenizing treatment was based on extensive experiments which indicated that virtual equilibrium was reached after 150 hr.

C. W. FUNK, Junior Member AIME, formerly with the U. S. Bureau of Mines, is now associated with Aerojet-General Corp., Azusa, Calif., and J. A. ROWLAND, Member AIME, is Physical Metallurgist, Minerals Technology Div., Metallurgical Branch, U. S. Bureau of Mines, Rolla, Mo.

Discussion on this paper, TP 3455E, may be sent, 2 copies, to AIME by July 1, 1953. Manuscript, June 10, 1952.

Papers by authors on the U. S. Bureau of Mines staff are not subject to copyright.

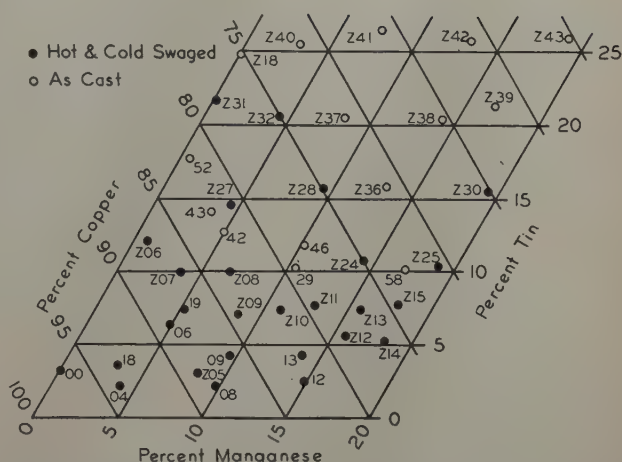


Fig. 1—Composition and condition of alloys prior to homogenization treatments.

Structures were retained by quenching in water. Grain sizes in the specimens homogenized at 350° and 450°C were generally small. These homogenizing treatments were preceded by a 50-hr anneal at 650°C to facilitate phase identification by increasing the grain size in these specimens. The specimens were furnace-cooled from this temperature to the homogenizing temperature, and the heat treatment was continued for the standard 200-hr period.

The homogenized samples were bisected to provide an internal section for metallographic examination. Optimum definition of the microstructure was obtained by successive polishing and etching. Quarter-strength ASTM copper reagent No. 13 gave the most satisfactory results.¹⁰

Filings from interior sections of the samples were used for diffraction studies. These filings were annealed in evacuated glass tubes at homogenizing temperatures for periods exceeding 50 hr and quenched in water. During this treatment the manganese content was reduced by significant amounts, probably by vaporization. This change in composition was considered in applying the diffraction data, which were used only as a means of identifying phases where the data were consistent with the metallographic evidence.

Phase Identification

The α solid solution is readily distinguished by the copper-colored, twinned, polyhedral grains, as shown in Fig. 2, and a face-centered cubic X-ray pattern. Tukon indentations, using a 25-g load, indicate a Knoop hardness of 155 for α quenched from 650°C.

Using white light developed by a Wratten 78 A filter, the β grains in etched specimens have a dark brown tint in contrast to the lighter copper-colored grains of the α phase. Knoop hardness values of 284 were obtained for the β structure in specimens quenched from 650°C. The β structure was also distinguished from the α phase by its body-centered cubic lattice.

The acicular structure appearing in Fig. 3 was evident in several alloys of higher tin content after quenching from either 750° or 650°C. Since a trans-



Fig. 2— α and retained β phases in heat Z28 quenched from 650°C. ASTM copper etch 13. X250. Area reduced approximately 55 pct for reproduction.

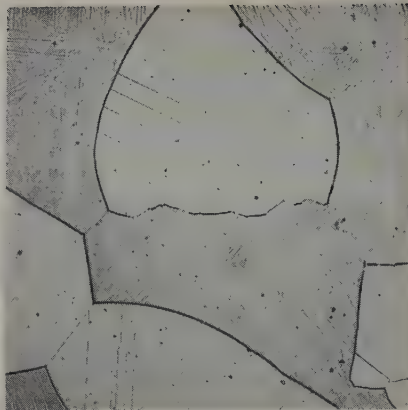


Fig. 3— α and transformed β phases in heat Z31 quenched from 650°C. ASTM copper etch 13. X250. Area reduced approximately 55 pct for reproduction.

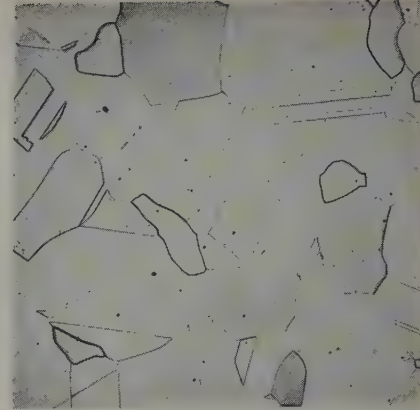


Fig. 4— α , γ , and θ phases in heat Z27 quenched from 550°C. ASTM copper etch 13. X250. Area reduced approximately 55 pct for reproduction.

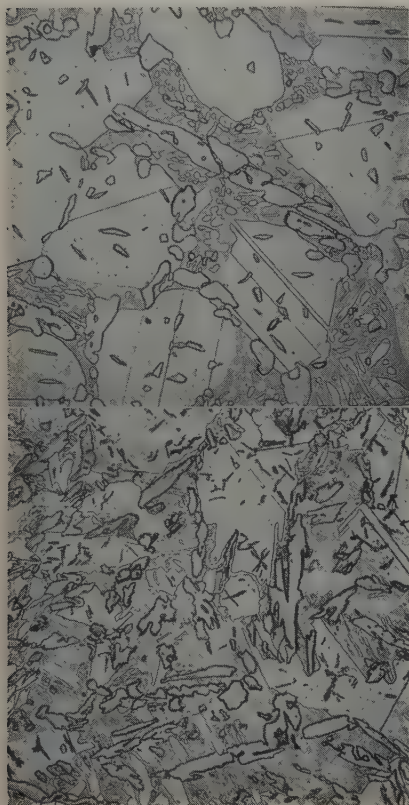


Fig. 5— α , δ , and θ phases in heat Z32 quenched from 450°C. ASTM copper etch 13. X250. Area reduced approximately 55 pct for reproduction.

formation is known to occur at a corresponding location in the Cu-Sn binary system, it seems probable that this structure represents a similar reaction in the ternary system. However, the Knoop hardness of 280 approximates the hardness of retained β .

The γ phase, shown in Fig. 4, replaces the β structure in alloys quenched from 550°C. Except for a lighter tint, the γ does not differ markedly in appearance from the β phase. The body-centered X-ray diffraction pattern is also similar to the β pattern. However, Knoop hardness values of 190 readily distinguished the γ phase in specimens quenched from 550°C from the softer α and the harder β phases.

An unidentified phase makes its appearance in alloys quenched from 550°C as shown in Figs. 4, 5, and 6. This phase is tentatively referred to as θ to conform with the terminology used by Eash¹¹ in describing the Cu-Ni-Sn system. Although the X-ray diffraction pattern resembles that of β manganese, positive agreement could not be obtained. However,

better agreement might be obtained with higher concentrations of θ . It is possible that θ is the compound Cu_3MnSn_2 predicted by Dehlinger¹² and later observed by Vero,⁷ but θ was not observed above 550°C and the Cu_3MnSn_2 was observed by Vero near the solidus. The θ phase exhibits a definite blue-white hue with reflected white light. Another characteristic particularly noticeable in the micrographs is a strongly defined grain boundary compared to the other phases in the system. Knoop hardness values of the phase were 539, 589, and 610 in specimens quenched from 550°, 450°, and 350°C, respectively, thus distinguishing this phase from any others encountered in these alloys.

The δ phase is identified by an X-ray pattern similar to the complex pattern of γ brass. A Knoop hardness of 420 was obtained for the δ phase.

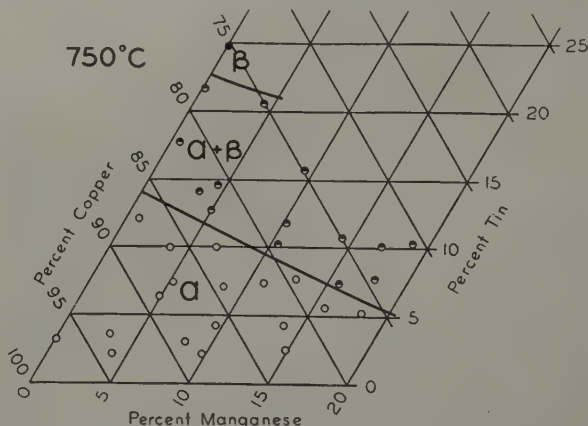


Fig. 7—Isothermal section of Cu-Mn-Sn system at 750°C.

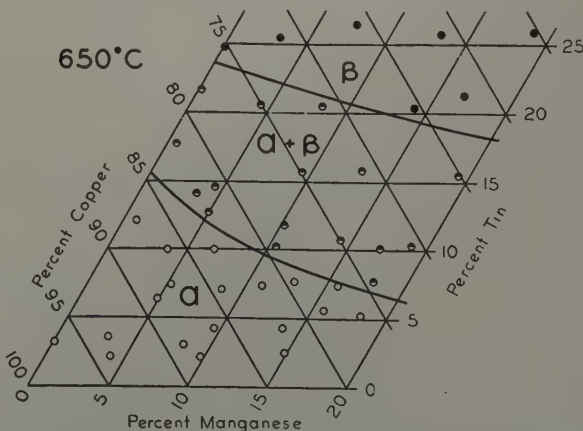


Fig. 8—Isothermal section of Cu-Mn-Sn system at 650°C.

The ϵ phase, which is encountered in alloys quenched from 350°C, is shown in Fig. 6. Although no metallographic distinction between δ and ϵ was apparent, the X-ray pattern of the orthorhombic ϵ is distinct from that of δ , and the Knoop hardness of ϵ is 388.

Isothermal Sections

Fig. 7 shows the isothermal section for 750°C. At this temperature the α solubility limit is slightly curved but shows an almost uniform decrease in the solubility of tin in copper with increasing manganese content. Conversion to atomic percent increases the curvature slightly with the deviation beginning near 10 atomic pct Mn. Using the 1.5 electron-atom ratio, as proposed by Hume-Rothery,¹⁸ this slope of the α solubility limit indicates an apparent manganese valence of 1.8. The α - β , β boundary extends into the ternary area along a line approximately parallel to the α solubility limit.

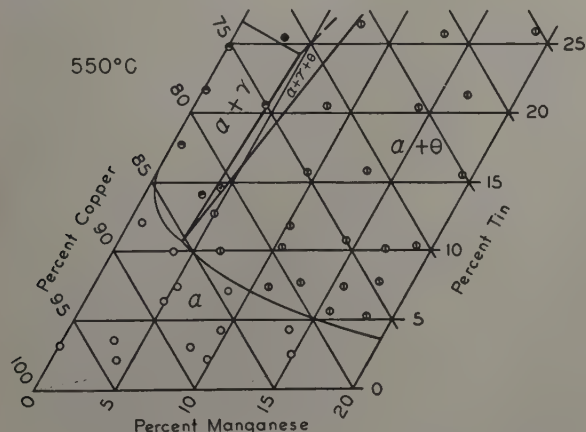


Fig. 9—Isothermal section of Cu-Mn-Sn system at 550°C.

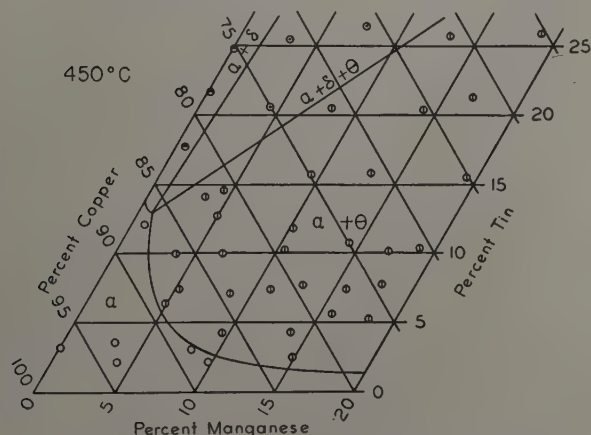


Fig. 10—Isothermal section of Cu-Mn-Sn system at 450°C.

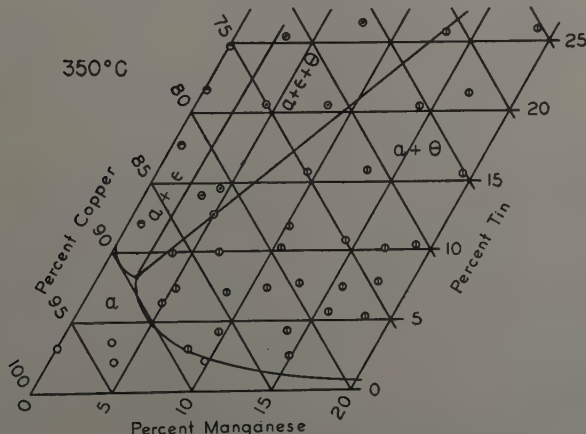


Fig. 11—Isothermal section of Cu-Mn-Sn system at 350°C.

At 650°C, Fig. 8, curvature of the α -solubility limit is more pronounced. The α - β , β boundary remains essentially parallel to the α boundary.

In the 550°C isothermal section, Fig. 9, β is replaced by the γ body-centered cubic phase and the tentatively identified phase referred to as θ . A three-phase field of α , γ , and θ is formed on the isothermal section, which limits the α - γ region to less than 5 wt pct Cu. At this temperature the α solubility limit begins to recede toward the Cu corner.

At 450°C, Fig. 10, the γ phase is replaced by the δ phase. An expanded three-phase field of α , δ , and θ compresses the α - δ area against the Cu-Sn binary in this isothermal section. The α solubility limit recedes, indicating a condition suitable for precipitation effects.

The 350°C isotherm, Fig. 11, shows that ϵ has replaced the δ phase. The expanded three-phase field of α , ϵ , and θ compresses the α - ϵ area to less than 3 wt pct Mn. Recession of the α solubility limit is at a maximum near 350°C.

Summary

The α solid solution area of the Cu-Mn-Sn system, up to 20 pct Mn and 25 pct Sn, has been established by a metallographic study. The evaluated results of the investigation are illustrated with isothermal diagrams for 100°C increments between 350° and 750°C. Additions of manganese, up to 20 pct, decrease the solubility of tin in copper. In general this effect is more pronounced as the temperature decreases. At the lower temperatures, particularly 350°C, the α solid solution area is greatly restricted, and only 5 pct Sn is soluble in alloys containing 5 pct Mn. As the manganese content is increased to 15 or 20 pct, the solubility of tin is further decreased to less than 2 pct.

Micrographs of typical microstructures of the ternary alloys containing the phases α , β , γ , δ , ϵ , and θ are presented.

References

- ¹ F. Heusler: *Verh. deut. phys. Gesell.* (1903) **5**, pp. 219-223.
- ² A. D. Ross and R. C. Gray: On the Magnetism of the Cu-Mn-Sn Alloys under Varying Thermal Treatment. *Proc. Royal Soc., Edinburgh* (1910) **31**, pp. 85-99.
- ³ E. Persson: X-ray Analysis of Cu-Mn Alloys. *Ztsch. Phys. Chem.* (1930) **9**, pp. 25-42.
- ⁴ A. J. Bradley and J. W. Rodgers: Crystal Structure of the Heusler Alloys. *Proc. Royal Soc., London* (1934) **A144**, pp. 340-359.
- ⁵ O. Heusler: Crystal Structure and Ferromagnetism of Cu-Mn-Al Alloys. *Ann. Physik* (1934) **19**, pp. 155-201.
- ⁶ L. A. Carapella and R. Hultgren: The Ferromagnetic Nature of the Beta Phase in the Cu-Mn-Sn System. *Trans. AIME* (1942) **147**, p. 232.
- ⁷ J. Vero: Equilibrium Conditions of Further Alloyed Bronzes, III Cu-Mn-Sn Alloys Rich in Cu. *Mitt. berg-huttenmann. Abt. ungar. Hochschule Berg-Forstw. Sopron* (1933) **5**, pp. 128-155.
- ⁸ G. V. Raynor: The Equilibrium Diagram of the System Cu-Sn. *Annotated Equilibrium Diagram Series No. 2*. Inst. Metals, London (1944).
- ⁹ R. S. Dean, J. R. Long, T. R. Graham, E. V. Potter, and E. T. Hayes: The Cu-Mn Equilibrium System. *Trans. ASM* (1945) **34**, p. 443.
- ¹⁰ ASTM Standards, Designation E3-46T (1946) p. 830.
- ¹¹ J. T. Eash and C. Upthegrove: The Cu-Rich Alloys of the Cu-Ni-Sn System. *Trans. AIME* (1933) **104**, p. 221.
- ¹² U. Dehlinger: Electronic Structure and Properties of Metals. *Ztsch. Electrochem.* (1932) **38**, p. 148.
- ¹³ W. Hume-Rothery: The Effect of Mn, Fe and Ni on the α/β Brass Equilibrium. *Philosophical Magazine* (February 1948) 7th Series, **39**, pp. 89-97.

Discussion — Institute of Metals Division*

Philadelphia Meeting, October 1952

Concentration Dependence of Diffusion Coefficients in Metallic Solid Solution (paper by D. E. Thomas and C. E. Birchenall. JOURNAL OF METALS, August 1952, p. 867).....	726
Thermodynamic Properties of Solid Nickel-Gold Alloys (paper by L. L. Siegle, M. Cohen, and B. L. Averbach. JOURNAL OF METALS, December 1952, p. 1320).....	728
Transformation in Cobalt-Nickel Alloys (paper by J. B. Hess and C. S. Barrett. JOURNAL OF METALS, June 1952, p. 645).....	729
Some Observations of Subgrain Formation During Creep in High Purity Aluminum (paper by I. S. Servi, J. T. Norton, and N. J. Grant. JOURNAL OF METALS, September 1952, p. 965).....	730
Observations of Creep of the Grain Boundary in High Purity Aluminum (paper by H. C. Chang and N. J. Grant. JOURNAL OF METALS, June 1952, p. 619).....	732
Mechanical Properties of Intermetallic Compounds at Elevated Temperatures (paper by R. Lowrie. JOURNAL OF METALS, October 1952, p. 1093).....	733
Dynamic Formation of Slip Bands in Aluminum (paper by N. K. Chen and R. B. Pond. JOURNAL OF METALS, October 1952, p. 1085).....	733
Surface Effects in the Slip and Twinning of Metal Monocrystals (paper by J. J. Gilman and T. A. Read. JOURNAL OF METALS, August 1952, p. 875).....	735
Kinking in Zinc Single-Crystal Tension Specimens (paper by J. Washburn and E. R. Parker. JOURNAL OF METALS, October 1952, p. 1076).....	737
Observations on Nodular Graphite (paper by H. M. Weld, R. L. Cunningham, and F. W. C. Boswell. JOURNAL OF METALS, July 1952, p. 738).....	738
Recrystallization Kinetics of Low Carbon Steel (paper by S. F. Reiter. JOURNAL OF METALS, September 1952, p. 972).....	739
Effect of Molybdenum and of Nickel on the Rate of Nucleation and the Rate of Growth of Pearlite (paper by R. W. Parcel and R. F. Mehl. JOURNAL OF METALS, July 1952, p. 771).....	740
A Study of Grain Shape in an Aluminum Alloy and Other Applications of Stereoscopic Microradiography (paper by W. M. Williams and C. S. Smith. JOURNAL OF METALS, July 1952, p. 755).....	741
Titanium-Chromium Phase Diagram (paper by F. B. Cuff, N. J. Grant, and C. F. Floe. JOURNAL OF METALS, August 1952, p. 848).....	743
Tungsten-Cobalt-Carbon System (paper by P. Rautala and J. T. Norton. JOURNAL OF METALS, October 1952, p. 1045).....	744
Role of the Binder Phase in Cemented Tungsten Carbide-Cobalt Alloys (paper by J. Gurland and J. T. Norton. JOURNAL OF METALS, October 1952, p. 1051).....	746
Solubility of Carbon and Oxygen in Molybdenum (paper by W. E. Few and G. K. Manning. JOURNAL OF METALS, March 1952, p. 271).....	746
System Molybdenum-Boron and Some Properties of the Molybdenum-Borides (paper by R. Steinitz, I. Binder, and D. Moskowitz. JOURNAL OF METALS, September 1952, p. 983).....	747
Systems Zirconium-Molybdenum and Zirconium-Wolfram (paper by R. F. Domagala, D. J. McPherson, and M. Hansen. JOURNAL OF METALS, January 1953, p. 73).....	747
Copper-Zinc Constitution Diagram, Redetermined in the Vicinity of the Beta Phase by Means of Quantitative Metallography (paper by L. H. Beck and C. S. Smith. JOURNAL OF METALS, October 1952, p. 1079).....	748

* TP 3521E

Concentration Dependence of Diffusion Coefficients in Metallic Solid Solution

by Donald E. Thomas and C. Ernest Birchenall

DISCUSSION, J. P. Nielsen presiding

R. W. Balluffi (Atomic Energy Div., Sylvania Electric Products Inc., Bayside, N. Y.)—Since porosity is known to form in the copper side of Cu-Ni couples during diffusion^{24,25} it is of importance to consider this factor in interpreting the large variations of chemical diffusivity with copper concentration reported for this system. The presence of porosity may affect the measurement of D in two ways: 1—density changes in the couple invalidate the usual solutions of the diffusion equation, and 2—the pores may act as short-circuiting paths when transport through the vapor or along internal surfaces is appreciable or else as open circuits when these effects are small.

The error produced by the first effect may be estimated by a graphical analysis. Fig. 8 shows the porosity generated in the copper side of the Kirkendall interface of a pure nickel vs pure copper couple after diffusion for 350 hr at 1040°C in hydrogen. In Fig. 9

the actual diffusion curve which would be obtained by the usual slicing technique is shown as a solid line drawn to the same scale (from the data of da Silva and Mehl²¹). The amounts of porosity (obtained by lineal analysis) and of nickel are graphically represented by the hatched areas.

The standard solutions of the diffusion equation are valid only when all volume elements of unit length and unit cross section contain equal numbers of atoms.²⁶ It is possible to correct the experimental curve to satisfy this condition by shrinking the couple in the direction of diffusion in such a way as to eliminate the porosity.* The corrected diffusion curve obtained after

* Experiments performed in this laboratory show that dimensional changes normal to the direction of diffusion in massive Cu-Ni couples are negligible for present purposes. Copper was diffused into both faces of a 3/16-in. thick 1-in. diam nickel disk from the vapor phase for 100 hr at 1070°C. The linear expansion normal to the direction of diffusion was found to be <0.2 pct.

this operation is shown dotted. When all mass move-

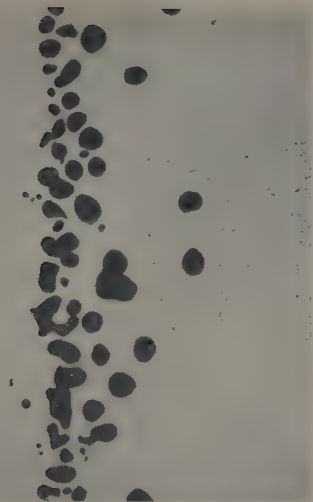


Fig. 8 (left)—Porosity generated in a Cu-Ni couple after diffusion for 350 hr at 1040°C in H₂. Unetched. X100. Area reduced approximately 50 pct for reproduction.

ment is referred to the nondiffused nickel end of the couple, the Matano interface of the corrected curve agrees, of course, with the initial position of the welded interface. However, the apparent Matano interface of the experimental curve appears displaced slightly toward the copper side of the original interface. Since appreciable porosity causes only a slight discrepancy between the apparent Matano interface and the original interface, it is interesting to note that an approximate agreement of the two interfaces is not a good criterion that no porosity exists as has been suggested by da Silva and Mehl.¹¹ By applying the Matano analysis to the two curves the variation of D with concentration was obtained in relative units, Fig. 10. The presence of porosity in the specimen is seen to cause a significantly higher apparent D in the porous region of the couple.

The quantitative effect of short or open-circuiting paths is more difficult to evaluate. Solutions of the analogous problem of heat conduction through a two-phase medium containing one phase in the form of isolated spheres²⁰ indicate roughly what effects may be expected. When the spheres act as short circuits the ratio of the apparent diffusivity in the two-phase medium to the diffusivity in the continuous phase increases with increased total volume of the spheres and attains a value of about 2.0 at 25 volume pct. When the spheres act as open circuits the ratio decreases and becomes equal to about 0.7 at 25 volume pct. At diffusion temperatures the vapor pressure of copper is appreciable and the pores may act as partial short circuits for copper atoms. The vapor pressure of nickel is lower by a factor of 10^6 and the pores probably act as open circuits for these atoms. Since the amounts of diffusion and porosity increase parabolically with time, the average effective porosity at any point during diffusion may be considered to be about one-half of the final observed amount.

On the basis of the above discussion it seems that the sum of errors produced by the porosity shown in Fig. 9 could not greatly exceed 100 pct of the true volume diffusion coefficient even in the most extreme case. The presence of porosity, therefore, cannot fully explain the rapid increase of diffusivity with copper concentration, but may still cause a significant error in the measurement of D . Experimental support for this argument is found by comparing the most recent and reliable data of da Silva and Mehl and of Thomas and Birchenall. At 947°C the variation of diffusivity with concentration found by both investigators agrees fairly well. This is expected since the amount of porosity in the couples from which these data were derived would be much less than that shown in Fig. 8. However, at 1054°C the diffusivities given by da Silva and Mehl in the 70 to 95 atomic pct Cu interval range up to 50 pct higher than the corresponding values of the present paper. This difference may be due to the presence of more porosity in the pure copper vs pure nickel

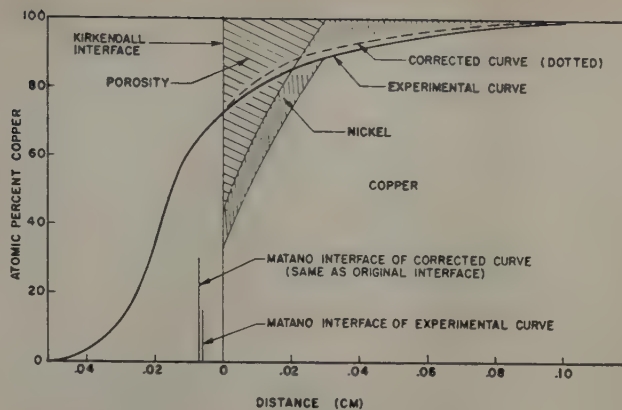


Fig. 9—Penetration curve after diffusion (from data of da Silva and Mehl¹¹).

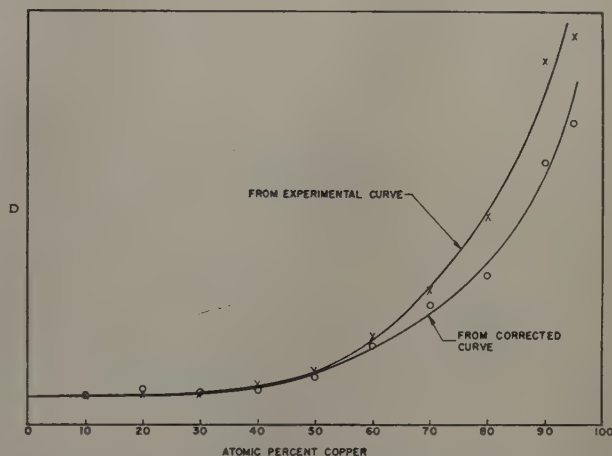


Fig. 10— D vs atomic percentage of copper obtained by Matano analysis from experimental and corrected curves.

couples used by da Silva and Mehl than in the incremental couples used by the present authors. These considerations indicate that accurate chemical diffusion coefficients are best obtained with such incremental type couples.

D. E. Thomas and C. E. Birchenall (authors' reply)—It has become increasingly clear during the past year, as a result of the excellent work by Balluffi and Alexander, Buckle and Blin, and Seith and Kottman, that a considerable amount of porosity may form in diffusion couples which have a large concentration difference. In addition, Seith and Kottman have shown that it is not always possible to neglect the area changes normal to the diffusion direction even in massive couples.

Although some of the couples reported in this paper were examined metallographically before and after diffusion to determine whether the welds were sound, small porosity might have been smeared over and overlooked. The only satisfactory answer can come from annealing similar specimens under similar conditions and making a careful search for porosity. Instead of doing just this, it may be more reasonable to open the wider question of how the generation of porosity depends upon the composition range of the couple. It seems likely that there is some composition range in a system at given temperature below which the vacancy supersaturation is too low to cause porosity to precipitate.

Dr. Balluffi has noted that his correction for porosity in the da Silva and Mehl 1054°C sample brings their result into closer agreement with our incremental values, indicating that the errors in the incremental case are less serious. He has been careful to point out that the correction is only that for the modification of the penetration curve and does not take into account the

open and short-circuit effects of the pores. An additional correction may be necessary in both cases.

The open and short-circuit effects must be more complicated than indicated. In a binary system a pore can hardly act as a short circuit for one component and completely open circuit for the other in the sense of preventing its transport by diffusion. Since the two components are thermodynamically interdependent, short-circuit transport would simply cause the pore to migrate. Thus, if surface and vapor diffusion are fast compared with volume diffusion around a pore of particular size and shape, porosity will accelerate diffu-

sion. If surface and vapor diffusion are slow compared with volume diffusion, diffusion will be inhibited. Translation of the pore produces greater average displacement of the component that is rich on the side of the couple toward which the pore is moving.

²⁴ R. W. Balluffi and B. H. Alexander: *JOURNAL OF METALS* (February 1952) p. 152.

²⁵ R. S. Barnes: *Proc. Physical Soc.* (1952) 65B, p. 512.

²⁶ G. S. Hartley and J. Crank: *Trans. Faraday Soc.* (1949) 45, p. 801.

²⁷ J. B. Austin: *Symposium on Thermal Insulating Materials* (1939) p. 3. ASTM.

Thermodynamic Properties of Solid Nickel-Gold Alloys

by L. L. Seigle, Morris Cohen, and B. L. Averbach

DISCUSSION, J. P. Nielsen presiding

H. K. Hardy (*Fulmer Research Institute, Stoke Poges, Bucks, England*)—It is very pleasing to have the results of such a full thermodynamic study of solid phase alloys as the authors have provided for the Ni-Au system. They also report unpublished calculations of the free energy from the phase diagram via the method of Borelius which is to fit the solubility data to an empirical equation of the form

$$\Delta F = ax^4y + bx^3y^2 + cx^2y^3 + dxy^4 + RT(x \ln x + y \ln y) \quad [8]$$

where x and y are the atomic fractions, a , b , c , and d are arbitrary constants. Eq. 8 can only predict the ideal entropy of solution. I have recently examined the thermodynamic properties of a "sub-regular" solution model in which²⁸

$$\Delta F = A_1x^2y + A_2xy^2 + RT(x \ln x + y \ln y) \quad [9]$$

where A_1 and A_2 can be solved from the solubility data at each temperature so that any temperature dependence can be examined. Using the solubility curve in *Metals Handbook*,²⁹ the Au-Ni system gives an additional apparent entropy term

$$\Delta S_{app} = -\frac{\partial \Delta F}{\partial T} = -x^2y \frac{\partial A_1}{\partial T} - xy^2 \frac{\partial A_2}{\partial T} \quad [10]$$

of 2.6 cal per degree per gram atom at the critical temperature and solubility when the positional entropy is 1.2 cal per degree per gram atom. The total calculated entropy is thus three times the positional entropy com-

pared with the authors' experimental value of twice the positional entropy.

The authors' results allow further checks on the sub-regular solution equation. Fig. 14 shows the calculated excess free energy of solution at 700° and 800°C and it will be noted that the values are more negative than in Fig. 7, particularly at the gold-rich side. This result is reflected in the activity composition curves calculated for 850° and 700°C in Figs. 15 and 16.

It seems fair to accept the "sub-regular" solution model as a useful alternative to the Borelius equation particularly when it is desired to allow for non-ideal entropies of solution. The authors' results would be met by an empirical equation with properties intermediate between Eqs. 8 and 9. It would be very difficult to provide a useful, simple empirical expression with such properties, and which could be solved at each temperature, because the solubility data fulfill not more than two independent thermodynamic conditions at any given temperature.

L. L. Seigle, M. Cohen, and B. L. Averbach (authors' reply)—The empirical equation of Borelius for the relative free energy of a solid solution, referred to by Dr. Hardy, may include other than the ideal entropy of mixing by allowing the coefficients a , b , c , and d to be temperature dependent. Dr. Hardy attempts to accomplish the same end in Eq. 9, using fewer parameters. However, a comparison of his calculated results in Fig. 14 with the experimental results in Fig. 7 of the paper discloses a substantial discrepancy. His derived free energies of mixing are in error by a factor of about three. The calculated activities (Fig. 15 of the discussion) are likewise deceptive (cf. Fig. 4 of the paper). On the other hand, the method of Borelius gives excel-

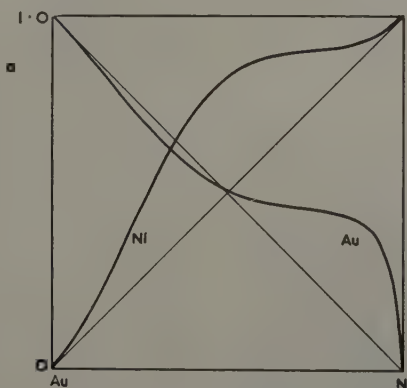
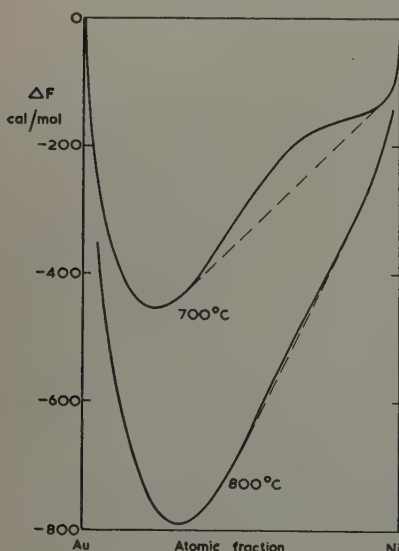


Fig. 14 (left)—Integral molar free energies of solution calculated from Eq. 9 solved at the solubility limits.

Fig. 15 (above)—Activity curves at 850°C for Ni-Au alloy calculated from the phase diagram using Eq. 9.

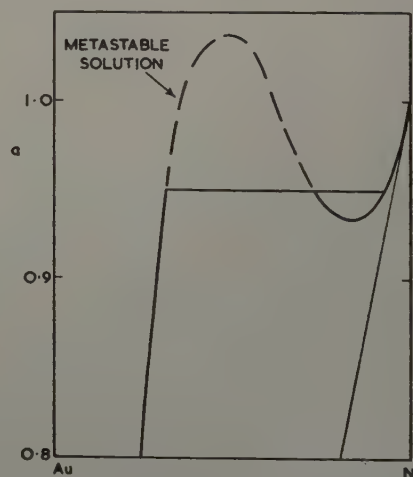


Fig. 16—Nickel activities in stable and metastable solid solutions of Ni-Au alloy at 700°C calculated from the phase diagram using Eq. 9.

lent agreement with the experimentally determined activities and free energies of mixing.

The situation becomes inherently worse in the computation of the entropy of mixing because the temperature coefficient of the free energy is undoubtedly very susceptible to experimental uncertainties in the phase diagram, even though the free energy itself may be considerably less sensitive. Hence, not much reliance can be placed on such entropy calculations. It would certainly be unwarranted to theorize on the cause of

an excess entropy unless the experimental data were on hand to verify its existence, and then the empirical calculations based on the phase diagram would lack real purpose.

It is hoped that the significance of Dr. Hardy's treatment will be discussed more fully in his forthcoming paper, which the authors await with interest.

²⁶ H. K. Hardy: To be published.

²⁷ L. A. Carapella: *Metals Handbook* (1948) p. 1172. Cleveland. ASM.

Transformation in Cobalt-Nickel Alloys

by J. B. Hess and C. S. Barrett

DISCUSSION, J. P. Nielsen presiding

T. R. Anantharaman and J. W. Christian (*The Inorganic Chemistry Laboratory, Oxford, England*)—We were very interested in the results obtained by the authors as we have similar work in progress. Our observations do not agree with the conclusion that complete strain-induced transformation to the hexagonal form is impossible in pure cobalt. Cobalt powder, after annealing and cooling to room temperature, contains as much as 40 to 50 pct cubic phase, but after 600 blows in a small agate mortar we could find no trace of the cubic lines. The authors' experiments in which they peened massive cobalt are not strictly comparable, but it would be interesting if they could give an estimate of the minimum intensity of the cubic {200} line, relative to the hexagonal {10 $\bar{1}$ 0} or {10 $\bar{1}$ 1} lines.

After strain-induced transformation, the intensities of the hexagonal (0002) and (0004) reflections in powder photographs were abnormally large. The (0002) line is overlapped by the cubic {111} line, but the magnitude of the effect precludes any explanation based on the presence of a remaining fraction of cubic phase. After severe cold working, the relative intensity of the (0002) line rose by nearly 200 pct. This phenomenon has been noted previously, e.g., by Doig and Schwartz⁹ in their discussion of the work of Troiano and Tokich. We believe it to be related to the presence of stacking faults on the close-packed planes. The theory developed by Wilson⁹ does indeed predict such an apparent rise in intensity, due to limitations in photometry, but of a much smaller order of magnitude. It seems more probable that the explanation arises from the destruction of primary or secondary extinction, as a result of stacking faults, increased density of dislocations, etc. In the same way, the intensity of the {111} line in face-centered cubic materials is often raised abnormally by cold working, especially in rhodium, α brass, and gold (see the work of Brindley and Ridley,¹⁰ Boas,¹¹ and Averbach and Warren¹²). We should be very interested to hear whether the authors have observed any similar intensity variations.

Most workers have reported that massive cobalt transforms completely to the hexagonal form on cooling to room temperature. In our work, oscillation photographs of large grained polycrystalline cobalt showed

traces of cubic reflections, though filings taken from this material gave only hexagonal Debye-Scherrer patterns. After dissolving away the surface layers of these filings in acid, and rephotographing them, faint cubic lines were visible. These disappeared again after cold working. We conclude that complete transformation to the hexagonal form never occurs spontaneously, except in single crystals, but complete transformation can be induced by straining, although this gives a very imperfect hexagonal structure.

A. G. Metcalfe (*Deloro Smelting and Refining Co., Deloro, Ont., Canada*)—The method used to detect spontaneous transformation by the examination of thermally etched specimens is interesting. This technique has recently been used¹³ to obtain supporting evidence for a high temperature transformation in cobalt of better than 99.9 pct purity, prepared by vacuum casting. The conditions used favored thermal etching, however, because the heating was done in a vacuum of 10^{-5} to 10^{-6} mm mercury for a total time of 1 hr. The structures shown in Figs. 3 and 4 were developed after 1 hr at 1090°C, and after 30 min at 1090°C and 30 min at 1135°C, respectively. It is believed that the structure developed at 1090°C was that characteristic of cubic cobalt whereas a structural change commencing at 1119°C caused the partial elimination of this structure on subsequent heating at 1135°C. The effect was even more marked when the second heating was at 1175°C.¹³

In view of the complex nature of the structure developed by these treatments it would be interesting if the authors would reproduce a typical micrograph for comparison. It was considered that the spots on the surface were the result of the low temperature transformation, although they were observed to be both in relief and depressed below the general surface. This was supported by a marked tendency of the elongated spots to bear some relation to the crystallography of the underlying structure. It is also noticeable that they have formed long lines of latent scratches.

It is noted that the nickel contained 0.61 pct C, which seems unduly high.

J. B. Hess and C. S. Barrett (authors' reply)—The sets of fine, roughly parallel striations which appear in Dr. Metcalfe's micrographs strongly resemble the striations which Chalmers, King, and Shuttlesworth¹⁴ produced on silver by thermal etching in the presence of

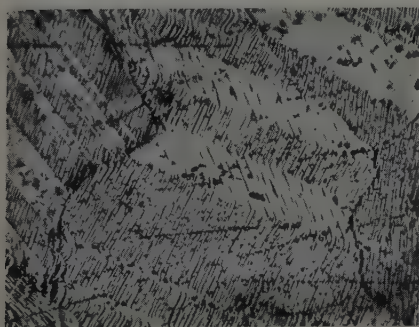
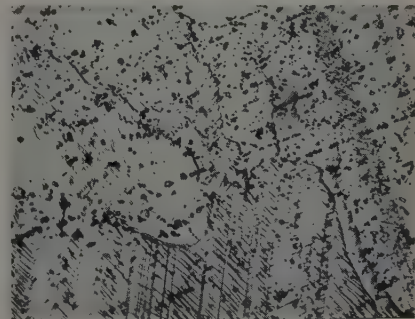


Fig. 3 (left)—Pure cobalt thermally etched at 1090°C.

Fig. 4 (right)—Pure cobalt with thermal etch at 1135°C superimposed on thermal etch at 1090°C.



oxygen. According to the interpretation of these authors, the striations are due to the formation of a "stepped-structure" composed of exposed crystallographic facets upon which the oxygen atoms are preferentially adsorbed. Because of this adsorption, the stepped structure yields a free surface having lower energy than could result from a flat minimum-area free surface composed of crystallographic planes of unspecific identities. We suggest that the discussor has mistaken the formation of an analogous stepped structure on his thermally etched cobalt specimens as evidence of a high temperature transformation. Similarly, the partial elimination of these markings on heating to high temperatures may be merely the result of grain boundary migration.

Some observations regarding the thermal etching of copper made by one of us (J.B.H.) also seem to be pertinent. Using a vacuum of 10^{-6} to 10^{-7} mm at 1000°C , the stepped structure on pure copper was frequently observed, except when special care was taken to insure that hydrogen was always present as the chief component of the residual atmosphere in the vacuum chamber. Small pits, similar to those which are so evident in Metcalfe's micrographs, were also observed. These developed chiefly, but not exclusively, in regions which had not been swept by the action of migrating grain boundaries during the course of the thermal etching treatment.

By employing a purified hydrogen atmosphere and allowing ample time for a large amount of grain boundary migration to occur, thermally etched specimens of cobalt and cobalt-nickel alloys could be produced which were substantially free of intragranular structure when cooled to room temperature, except insofar as relief striations were produced by the spontaneous cubic-to-hexagonal transformation in some of the alloys. Additional similar relief markings were produced whenever such specimens were lightly deformed by rolling, thus demonstrating that the strain-induced transformation results in the same habit as the spontaneous transformation, namely, as thin plates on (111) planes of the face-centered cubic matrix, a habit that was also deduced from another investigation.¹⁵ For the type of microstructure produced by such a transformation the reader may refer to published micrographs of copper-rich Cu-Si alloys.⁵

From the discussion of Anantharaman and Christian it appears that the resistance of our cobalt specimens against transforming completely at room temperature may have been due to our use of massive, fine-grained, polycrystalline specimens rather than filings. Filings may deform more homogeneously than polycrystalline massive specimens, so that our explanation for incomplete strain transformation may not apply in such cases. While we made no attempt at an accurate

determination of the relative intensities of the cubic and hexagonal lines, there could be no doubt as to the presence of a faint cubic (200) line in the peened massive cobalt specimens. With massive polycrystalline samples subjected to severe deformation, there would be many microscopic regions where residual stresses are of extreme intensity and where these, together with the tangled network of dislocations, would block the entrance of additional dislocations such as those required for the cubic to hexagonal transformation. It is not unreasonable that crystalline fragments of the cubic phase under these conditions can persist through very heavy deformation.

Regarding the high intensity of the (0002) plus (111) line in the cold-worked metal, it should be emphasized that the hexagonal component of the line would not be widened by faults, and two of the eight components of the cubic contribution would likewise not be widened by faults; thus there should be abnormally good contrast between the line and the nearby background which would make for a large apparent intensity on a photographic film compared with neighboring lines of the pattern, which are made up wholly of components that would be widened by faults. Paterson's recent analysis of fault widening discusses the nature of the widening and displacements of each face-centered cubic line in detail.¹⁶

The fact that fault streaks extend out large distances from the reciprocal lattice points makes the estimation of background intensities between the powder diffraction lines uncertain, and background estimation has probably been the major source of disagreement between different workers who have studied line intensities from cold-worked nontransforming metals. Without reliable background determination, the measurement of line intensities and the role of primary and secondary extinction becomes uncertain. In our work we did not attempt precise intensity determinations, since the Geiger counter spectrometers we tried on the problem failed to have a sensitivity in detecting weak, very broad lines equal to that of films from a small powder camera. We were working, also, with polycrystalline material, whereas for precise data on intensities in faulted material it might be best to use single crystals or pseudo-single crystals.

⁵ J. R. Doig and C. M. Schwartz: Discussion to ref. 1 of paper. *Trans. AIME* (1948) 175, p. 739; *METALS TECHNOLOGY* (August 1948).

⁹ A. J. C. Wilson: *Proc. Royal Soc.* (1942) 180A, p. 277.

¹⁰ G. W. Brindley and P. Ridley: *Proc. Physical Soc.* (1938) 50, p. 501 and (1939) 51, p. 432.

¹¹ W. Boas: *Ztsch. Kristall.* (1937) 96, p. 214.

¹² B. L. Averbach and B. E. Warren: *Journal of Applied Physics* (1939) 20, p. 1066.

¹³ A. G. Metcalfe: *Proc. World Metallurgical Congress*, Detroit, (1951) p. 717.

¹⁴ B. Chalmers, R. King, and R. Shuttleworth: *Proc. Royal Soc.* (1948) 193A, p. 465.

¹⁵ J. S. Bowles and C. S. Barrett: *Progress in Metal Physics* (1952) 3, p. 1.

¹⁶ M. S. Paterson: *Journal of Applied Physics* (1952) 23, p. 805.

Some Observations of Subgrain Formation During Creep in High Purity Aluminum

by Italo S. Servi, John T. Norton, and Nicholas J. Grant

DISCUSSION, L. A. Carapella presiding

P. L. Pratt (*Metallurgy Div., Ministry of Supply, A.E.R.E., Harwell, England*)—It is interesting to note that break down of the structure in the simplest cases represents an approximation to rotation about an axis in the slip plane and normal to the slip direction, and that this only occurs in large grains where well-developed and regular slip bands belonging to a single slip system are present. This may fairly be called polygonization in the sense originally used by Orowan and Cahn.²¹ The less regular patterns obtained from smaller grains which undergo a more complex type of deformation appear to originate from the grain boundaries, and this process cannot be called polygonization in the strict sense. Garrod, Suiter, and Wood²² have recently

concluded that there are three basic stages in the mechanism of deformation: slip at room temperature, cell formation, and boundary microflow. They could not detect slip with their electron microscope replica techniques in the second and third stages, although the work of McLean²³ makes it clear that fine slip does occur. Their conclusion "that the movements at the boundaries and sub-boundaries result from a concentration and irregular passage of dislocations in a manner determined by the conditions of deformation" is essentially the same as that of the present authors who say that "the formation of subgrains is indirectly related to the slip process in the grain." The terms "cell-formation" and "boundary microflow" perhaps give a clearer picture of the deformation than "a polygoniza-

tion process due to local bending caused by non-homogeneous grain boundary sliding and concurrent annealing," and both papers agree that the behavior of the grain boundary is all important in determining the nature of the deformation process.

The difference between polygonization and cell-formation can be seen from a consideration of their dislocation sources. For the former, in large-grained material, a single slip system is used with the most active sources grouped far apart, since they operate to give visible, coarse slip bands on the surface. Following Mott,²⁴ the generation of the elementary lines in the slip bands, 2000Å in length, is a rapid process, and half of the edge dislocations from each source are trapped within the crystal by impurities, growth defects, or, more important, deformation debris in the form of sessile dislocations or deformation bands. These dislocations are polygonized into walls during annealing, or deformation at high temperature, but if deformation takes place at room temperature the polygonization stage cannot occur and no cell structure is observed.

For smaller grained material a single slip system is insufficient to maintain grain boundary contact, and deformation must take place on many intersecting slip systems starting from the boundary. After a small total strain, the rapid generation of the elementary slip lines must be inhibited, since 2000Å slip lines are not produced, and the large number of active sources on many systems will produce slow-moving dislocations which can travel only a short distance before they are blocked. The effect of raising the temperature is then to permit these blocked dislocations to climb over their obstacles by vacancy diffusion, and to migrate into walls forming the three-dimensional cell-structure.

I. S. Servi, J. T. Norton, and N. J. Grant (authors' reply)—More recent work shows that subgrains can, in fact, be due to more than one process. Subgrains may form due to a process of kinking, in which event the boundary is sharply delineated and further deformation produces a larger difference in angle between the blocks. Subgrains may also form due to polygonization as a result of bending in the individual blocks on either side of the kink boundary. Subgrains may also form by local bending in the absence of kink bands. It does appear that finer grained structures would result in more kinking with a more irregular pattern, yielding the less regular patterns referred to by Mr. Pratt. However, the very coarse-grained specimens also show these same varieties of subgrains though in different proportions and of different distribution because grain boundaries play a large role in determining the strain distribution in the grains.

We are pleased to have Mr. Pratt's interpretation and differentiation of polygonization and cell-formation in which the source of the dislocations is the determining factor.

R. C. Gifkins and J. W. Kelly (*Baillieu Laboratory, University of Melbourne, Victoria, Australia*)—We wish to make some comments, mostly on metallographic matters, on this interesting paper. These comments arise from work we have been doing during the last 18 months, studying the formation of the cell substructure in aluminum and are quite apart from other more gen-

eral points which are relevant to the work published from this laboratory by Wood and his coworkers.²⁵

The results obtained with coarse-grained specimens differ from those with fine-grained ones in an important manner, namely, that the former are stated to show well developed slip at elevated temperatures. We have confirmed the electron microscope observations of Garrod, Suiter, and Wood,²² by using the phase-contrast microscope at a magnification of about $\times 500$, to show that slip is not visible on fine-grained specimens slowly strained at 300°C. We have not observed slip, using the ordinary microscope, on coarse-grained specimens (about 2 mm grain diameter) similarly strained. However, we have also confirmed McLean's²³ observation of very fine slip at low strains in specimens deformed at 200°C and further found that such slip can be "erased"²³ by annealing at 200°C for two or more days in the absence of applied stress. This might account for the failure to detect such slip at higher temperatures.

At 300°C, some grains show coarse, roughly parallel lines which are revealed as broad undulations by interference fringes. These may be related to the cells which occur in bands at temperatures up to about 200°C as shown by Hino, Shewmon and Beck²⁷ and McLean,²³ using the anodic film and polarized light technique, and by Rachinger²⁸ using deep etching. We have used the anodic film technique to follow the development of cells in fine and coarse-grained specimens and have found that the cells very often occur in bands of alternately similar orientation, even at 300°C in specimens strained at about 0.15 to 0.2 pct per hr. These would appear to be analogous to the bands detected by Servi et al. using X-ray methods, except that in our experiments no visible slip was present. Our experiments also confirm the suggestion that there is considerable variation in the cell size in any grain. Fig. 13 shows a typical area which illustrates this and the banded appearance. The micrograph was obtained using the anodic film and polarized light technique on a specimen of high purity aluminum, about 2 mm grain size, repolished and anodized after straining 17 pct in 98 hr at 300°C. No slip markings were seen on the surface.

We do not agree that the general size of cells is insensitive to change in temperature of deformation. Besides our own more recent observations with the anodic film technique, there is extensive X-ray evidence by Wood et al.,²⁵ and Rachinger²⁹ has found the cell-size to change with temperature by revealing the cells with deep etching in the normal aluminum reagent of 73 pct water, 25 pct concentrated nitric acid and 2 pct (48 pct strength) hydrofluoric acid. This latter technique shows subgrains very clearly. Ramsey³⁰ has used it to show very faint boundaries in recovery zones of deformed aluminum. We also feel that any attempt to correlate slip band width with cell size must be regarded very cautiously, because of the variation in cell size, unless the results are analyzed by statistical methods.

The metallographic techniques used by Servi et al. interested us greatly, particularly the use of Lacombe and Beaujard's pitting reagent. We have used this reagent repeatedly and have been unable either to show subboundaries convincingly or to obtain indications of subboundaries which coincide with those revealed by

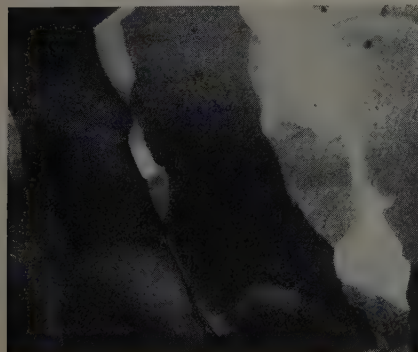
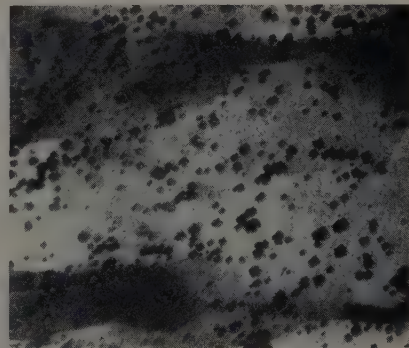


Fig. 13 (left)—High-purity aluminum. Deformed 17 pct at 300°C at 0.17 pct per hr. Repolished, anodized and photographed with polarized light. X150. Area reduced approximately 50 pct for reproduction.

Fig. 14 (right)—High-purity aluminum. Deformed 18.5 pct at 300°C at 0.17 pct per hr. Repolished, etched to produce pits, then anodized and photographed with polarized light. X150. Area reduced approximately 50 pct for reproduction.



the anodic technique. Fig. 14 shows this on a specimen deformed at 300°C to 18.5 pct in 109 hr, repolished and etched with the three-acid reagent to produce the pits and then anodized and photographed with polarized light.

With regard to the direct observation of cells by surface markings, we feel there are severe limitations to this method. We have commented on this elsewhere.²⁶ It appears from a comparison of the markings obtained with 1—narrow pencil illumination and slight de-focusing of the deformed surface, 2—multiple-beam interferograms, and 3—the repolished and anodically filmed condition, that cellular markings can correspond to a number of features other than subgrains. Moreover, as Betteridge and Franklin²¹ have pointed out, similar cellular markings can be obtained on unstrained and polished specimens. We believe this to be due to imperfect polishing. Another point to remember is that Rachinger²² has shown that grains on the surface extend, whereas those in the interior do not, although both show cell formation. The correspondence of surface markings to subboundaries revealed by other methods is good on specimens which have been strained several percent, then repolished and further deformed slightly under the same conditions. This has been illustrated elsewhere.²⁵ However, we do not believe that these surface markings are the result of flow at the subgrain boundaries as suggested by Servi et al. Our observations lead us to conclude that such flow is very small, but that migration of subboundaries under stress can be very marked at 300°C. It is probable that this could contribute to the formation of the observed markings. It may also be possible to explain them on the basis of a polygonization hypothesis.²³

We have used the anodic film technique to show that the configuration and orientation relationships of cells do not change greatly on successive removal of layers of about 0.002 in., thus confirming the results of Gervais quoted. There also appears to be some relation between cells of one grain and those of neighboring grains in regions close to the boundaries. This effect, incidentally, is very marked in zinc. We would therefore qualify the remark by Servi et al. regarding the unique configuration of cells in any grain.

We feel that it is very important, as Servi et al. point out, that X-ray results should be checked against metallographic observations and we would add that caution in interpreting the latter is also very necessary, particularly when relatively untried etching methods are used. Because it gives information about orientation differences as well as geometrical configurations, the anodic film and polarized light technique is of particular value in studying these effects of deformation.

I. S. Servi, J. T. Norton, and N. J. Grant—We very much appreciated the comments and interpretations advanced by Gifkins and Kelly. Several points probably merit comments on our part.

We have not yet made observations of the very fine slip at low strains in specimens tested in the temperature range of our work. The absence in our case may be due to the higher temperatures used as compared to the temperatures of 200° and 300°C in McLean's work and in the work of Gifkins and Kelly. More recently, work in our laboratory confirms the statement that the subgrains are definitely sensitive to changes in the

temperature of deformation. Working at temperatures above 550°C, we have, in fact, noted that the temperature is quite instrumental in determining the size of the resultant subgrains. We feel that it is difficult to differentiate the relative effects of stress and temperature, however by working at extremely high temperatures approaching the melting point, we have since been able to show a distinct coarsening in subgrain size with increasing temperature. We also agree that the cell size, which varies very markedly from one location in a grain to another, is a poor quantity to correlate with slip band spacing. However, in the research under discussion, the cell size was the cell size which existed in the vicinity of the slip bands, and this may correlate better than either the average cell size or the range of cell sizes which can exist in any one grain.

We believe that there is a very simple explanation to offer regarding the use of the Lacombe and Beaujard pitting reagent. Most of our work in which we were able to get fine delineation of subgrains by means of etch pits took place at temperatures higher than 550°C. At these high temperatures the subgrain size is extremely coarse, so coarse in fact that it is very much larger than the size of individual etch pits. Under such test conditions the etch pits readily delineate the substructure; however, at temperatures as low as 300°C, the subgrain size is so small that the etch pit technique does not work well at all. Direct observation of cells by surface markings as a primary mode of observation is, in fact, subject to severe limitations. We have on occasions, however, been able to utilize such markings to advantage in determining where to look more closely by means of X-rays or other etching techniques.

The average subgrain size or range of sizes on the surface and in the interior of specimens is about the same. We have determined this recently. The formation of folds, of sharp kink bands, and of slid grain boundaries which are readily noted on the surface of specimens must, of course, be compensated for in the interior of the specimen unless one wishes to suggest voids are forming below the surface to compensate for such surface changes. By intuition, therefore, it is necessary to believe that surface markings such as raised areas must be compensated for internally. Evidence of grain boundary migration on the inside of the specimen, however, cannot be checked by any method known to the authors. We have recently developed other etching techniques, including a very slow electrolytic etching method, which has thrown further light on the nature of the structures present, and has helped to correlate the results previously observed by means of X-rays and the etch pit techniques. These results should appear shortly.

²¹ R. W. Cahn: *Journal Inst. Metals* (1949-1950) 70, p. 161.

²² R. I. Garrod, J. W. Suiter, and W. A. Wood: *Philosophical Magazine* (June 1952) 43, p. 677.

²³ D. McLean: *Journal Inst. Metals* (1951-1952) 80, p. 507.

²⁴ N. F. Mott: *Philosophical Magazine* (November 1952) p. 1151.

²⁵ W. A. Wood, G. R. Wilms, and W. A. Rachinger: *Journal Inst. Metals* (1951) 79, p. 159.

²⁶ R. C. Gifkins and J. W. Kelly: Discussion of ref. 23. *Journal Inst. Metals*. To be published.

²⁷ J. Hino, P. G. Shewmon, and P. A. Beck: *Trans. AIME* (1952) 194, p. 373; *JOURNAL OF METALS* (August 1952).

²⁸ W. A. Rachinger: *Journal Inst. Metals* (1951-1952) 80, p. 415.

²⁹ W. A. Rachinger: Private communication.

³⁰ J. A. Ramsey: *Journal Inst. Metals* (1952-1953) 81.

³¹ W. Betteridge and A. W. Franklin: *Journal Inst. Metals* (1951-1952) 80, p. 147.

³² W. A. Rachinger: *Journal Inst. Metals* (1952-1953) 81, p. 33.

Observations of Creep of the Grain Boundary in High Purity Aluminum

by H. C. Chang and N. J. Grant

DISCUSSION, L. A. Carapella presiding

C. S. Roberts (*Metallurgical Laboratories, The Dow Chemical Co., Midland, Mich.*)—The authors' excellent metallography and clear analyses certainly yield valuable conclusions about grain boundary creep. In the

course of a fundamental research on the creep of magnesium-rare earth alloys, under sponsorship of Wright Air Development Center, I have conducted metallographic studies of unalloyed magnesium. The grain boundary deformation becomes more important with

increasing temperatures and decreasing secondary creep rate.

I should like to supplement the authors' conclusions by showing that under proper conditions with magnesium the process does appear to be restricted to a thin layer in the vicinity of the grain boundary. In these circumstances the polished grain surfaces remain relatively smooth. The micrographs in Fig. 12 show creep of rather fine-grained electrolytic magnesium at 600°F and 900 psi. The material was tested in the extruded condition. The electropolished surface was pro-

tected by a thin layer of silicone oil during creep. The cyclic nature of the process is nicely emphasized. Alternate boundary sliding and migration can even lead to complete consumption of grains, as is illustrated by a small grain in the top center of the field.

The boundary deformation is supplemented here by subgrain formation. At lower temperatures and higher creep rates where the migration probably cannot play its part fully enough, the roughening and breakup at the boundaries shown by the authors in Fig. 10a appears.

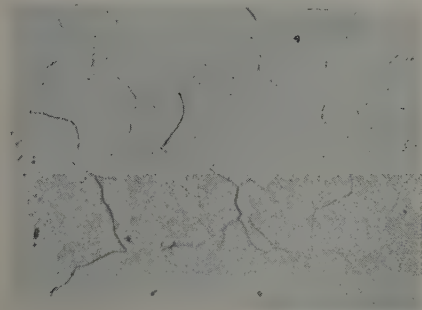
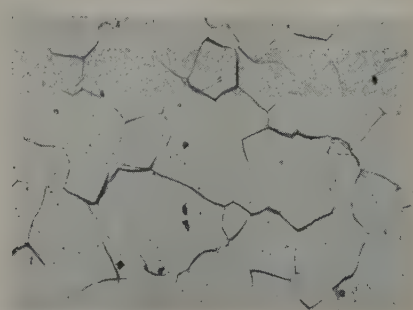


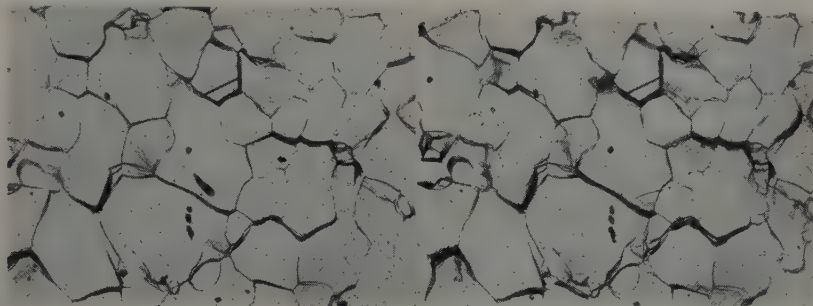
Fig. 12—Extruded electrolytic magnesium at 600°F and 900 psi. Stress axis vertical. X250. Area reduced approximately 50 pct for reproduction.

a (left)—Electropolished and etched.

b (right)—2 pct creep.



c (right)—4 pct creep.



d (left)—8 pct creep.

Mechanical Properties of Intermetallic Compounds at Elevated Temperatures

by Robert Lowrie

DISCUSSION, L. A. Carapella presiding

F. R. Morral (Div. of Metallurgical Research, Kaiser Aluminum and Chemical Corp., Spokane, Wash.)—The determination of mechanical properties of intermetallic compounds at elevated temperatures as well as at room temperature will permit a better understanding of the behavior of the materials in which they are present. Microhardness measurements of intermetallic phases have been made on occasion.*

* Al₇Cr microhardness 510 kg per sq mm.³¹

On p. 1099, it is stated that "... the structures of Al₇Cr, Al₃Cr, and Cu₃Si have not been solved and are presumably complex." It may be of interest to note here that Al₇Cr has been reported as monoclinic³² and orthorhombic.^{33,34} The diffraction pattern of Al₇Cr is similar to that of Al₇Cr.³⁵

The crystal structure of Cu₃Si is stated to have a hexagonal lattice³⁵ which comes close to having body-centered cubic atom arrangements; body-centered cubic with 19 Cu₃Si groups in the unit cell has also been suggested.³⁶

R. Lowrie (author's reply)—As Dr. Morral points out some work has been done on the structures of Al₇Cr, Al₃Cr, and Cu₃Si. The fact that in none of these investigations were the atomic coordinates in the unit cell determined forms the basis for my statement that the structure may be presumed to be complex.

³¹ Hanemann and Schrader: *Atlas Metallographicus* Bd III, p. 1.

³² W. Hofman and H. Wiehr: *Ztsch. Metallkunde* (1941) 33, p. 369.

³³ A. J. Bradley and S. S. Lu: *Journal Inst. Metals* (1937) 60, p. 319.

³⁴ K. Little: Unpublished work mentioned by J. N. Pratt and G. V. Raynor: *Journal Inst. Metals* (1951-1952) p. 456.

³⁵ S. Arrhenius and A. Westgren: *Ztsch. Phys. Chem.* (1931) 14, pp. 66-79.

³⁶ K. Sauter: Special report, M. Hansen: *Aufbau der Zweistofflegierungen* (1936) p. 628.

Dynamic Formation of Slip Bands in Aluminum

by N. K. Chen and R. B. Pond

DISCUSSION, T. E. Leontis presiding

P. Haasen and G. Leibfried (Institut für Theoretische Physik, Universität Göttingen, Göttingen, Germany)—Chen and Pond have measured the lengthening of slip bands (propagation of slip in the surface) on aluminum crystals. On the top surface they measured

velocities up to 7.6 mm per sec. They state that deepening of slip lines (propagation of slip in direction of glide) may be seen on their pictures.

By cinematographical research on the same metal (Al 99.99 pct) made recently¹ we can give some supplementary information on the work of Chen and

Pond. On the top surface we obtained velocities of lengthening up to 1/100 mm per sec. The difference between our measurements and those of Chen and Pond may be caused by the manner of loading and of preparing the surface. The authors applied the load continually with relatively high speed, we loaded by steps and observed the development of lines under constant load. The authors polished their crystals mechanically first, then electrolytically, we polished electrolytically only.¹²

Furthermore we measured the deepening of slip lines photometrically. Fig. 15 shows the development of a line (frequency 50 frames per sec; in the figure every fifth frame is shown, i.e., the frames are taken every 1/10 sec; just before the first picture the shear stress was raised from 320 g per sq mm to 360 g per sq mm). Fig. 16 shows the intensity measuring the increasing amount of shear in this line. It is seen that the intensity increases by steps (for other lines the structure is even more steplike).* The average depth of lines

* It is possible that one step corresponds to the formation of a new lamella in the slip band.

may be calculated by line-density and strain. The maximum velocity of deepening may then be shown to be 1/100 mm per sec.

We wish to emphasize that these velocities, measured in the experiments above, cannot be identified directly with velocities of dislocations without some care. In the following some possible explanations are discussed.

On the top surface deepening is caused by edge dislocations moving into the surface. These dislocations are generated by the source nearest to the surface. If the velocity of dislocations moving away from the

source is the process terminating the speed of deepening v_0 , then this velocity is given by $v_0 = v \cdot b/l$, where b is the length of Burgers vector, l the average distance, and v the velocity of edge dislocations moving to the surface. If $l/b \leq 10^4$ and v_0 equals the above-measured maximum value, v is smaller than 100 mm per sec (i.e., 10^{-4} · velocity of sound) in contrast to the interpretation of Chen and Pond.

Lengthening on the top surface may be caused either by moving screw dislocations along the surface or by the successive emerging of neighboring parts of edge dislocations on the surface. The second process can be terminated also by the velocity of screw dislocations in the interior if the neighboring edge dislocations belong to different sources separated by some obstacle. The screw dislocations of the first source are piled up at the obstacle and stimulate the second source by their stress field, etc. In this case the speed of lengthening would be of the order of the velocity of screw dislocations (i.e., 10^4 times smaller than the velocity of edge dislocations). Near the side surface the behavior is analogous to the roles of edge and screw dislocations being changed. On the side surface then the speed of lengthening might be equal to the velocity of edge dislocations, while the velocity of deepening is l/b times smaller than the velocity of screw dislocations. The possibilities discussed above show that the special model of plastic gliding plays an important role in calculating dislocation velocities from measurements of propagation of slip lines.

N. K. Chen and R. B. Pond (authors' reply)—It seems that the rate of loading is a predominating factor in determining the rate of slip propagation. If the step-wise loading used by Becker and Haasen¹¹ is compared with the continuous loading used in the present

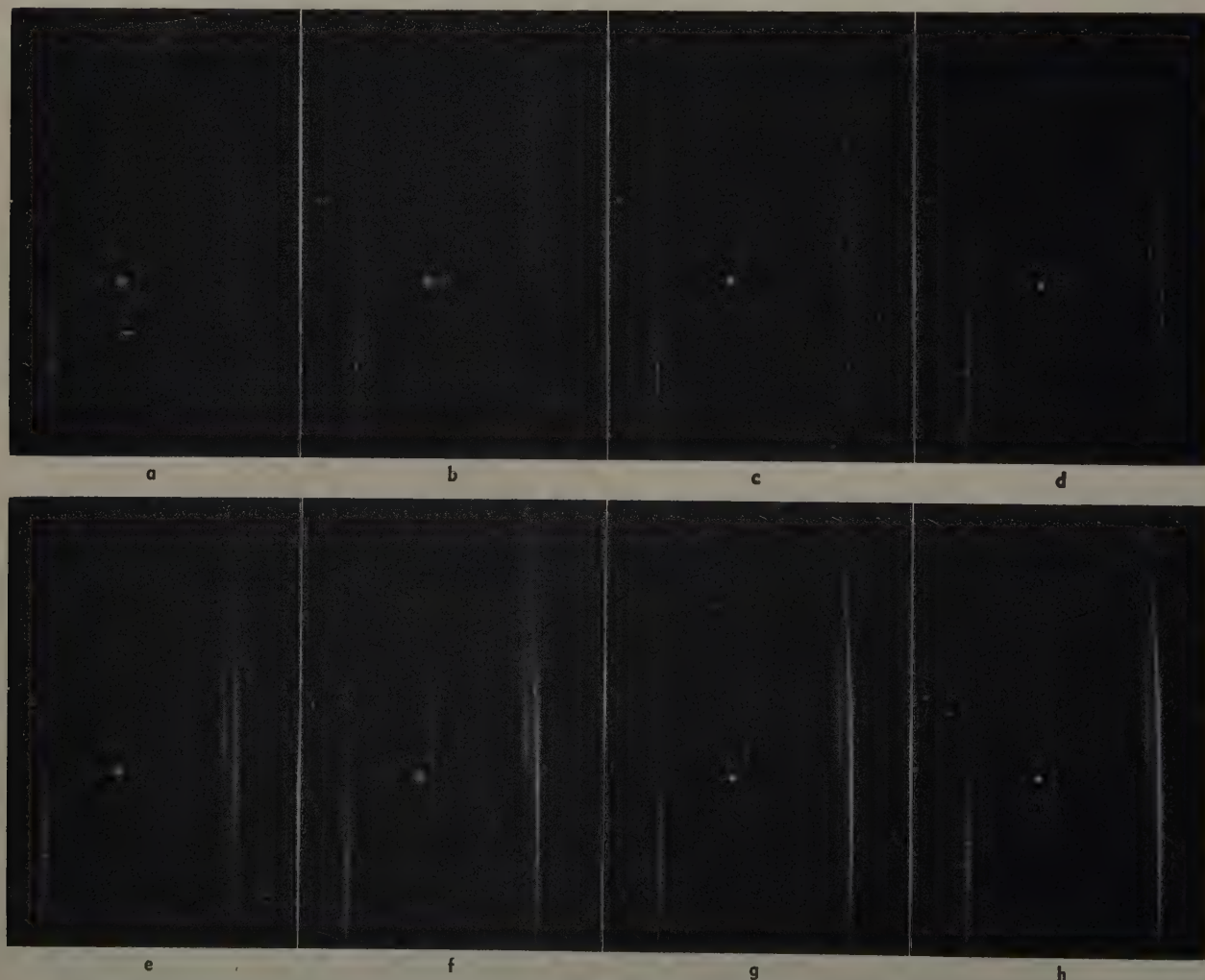


Fig. 15.—Deepening of a slip line on the top surface. X440. Area reduced approximately 60 pct for reproduction.

investigation, the average rate of loading (also the rate of elongation) in the former case is smaller by a factor of about 30 than the rate which we used. This would account for the slower rate of propagation perpendicular to the slip direction (10 microns per sec) which they observed as compared with a maximum rate of 7600 microns per sec in the present case.

It is interesting to see that Drs. Haasen and Leibfried were able to determine photometrically the rate of propagation in the slip direction. In this respect, we can point out that we have measured the increase in width of many slip bands from their appearance in the top surface (specimen A311). It seems a fair assumption that the increase in width of a slip band at this position should correspond to an increase of shear either by the formation of new lamellae in the slip zone or by additional slip in each lamella already formed. This is essentially based on the same principle which Drs. Haasen and Leibfried adopted in the measurement of slip lines by the photometric method. A typical curve is shown in Fig. 17 where the width of a slip band is plotted against time. It is noted that the width of the band increases in a step-like manner which is quite similar to the intensity-time plot reported by Drs. Haasen and Leibfried. It should be pointed out that great accuracy cannot be claimed from this type of measurement due to lack of sharpness of the slip band after enlargement. In general, however, three to five steps can be found in each curve and

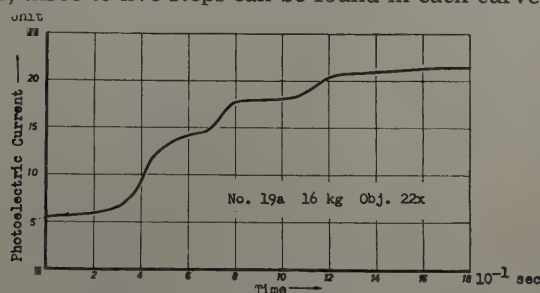


Fig. 16—Intensity-time plot for the slip line growing in Fig. 15, time in $1/10$ sec.

the shortest time interval for the step is $1/32$ sec, i.e., within the camera speed at 32 frames per sec. If it is true that each step represents the formation of a Heidenreich-Shockley lamella of 2000\AA thickness, then the maximum rate of its formation is calculated to be 0.64×10^{-2} mm per sec. While this rate is of the same order of magnitude as that reported by Becker and Haasen for maximum "deepening" of slip lines in their experiments, it may be merely coincidence in view of the difference in rate of loading used in both cases. On the other hand, if this rate were actually insensitive to the rate of loading, it would indicate that slip may build up under the surface and only break through in a finite time when enough has collected.

It is agreed that the observed rate of slip propagation on the specimen surface cannot be directly identified in terms of dislocation movements in the interior of the specimen. In the case of edge-type dislocations, this consideration is especially important since the movement of edge dislocations which is much faster than the screw-type dislocations has not been detected directly on the side surface. In order to assume that

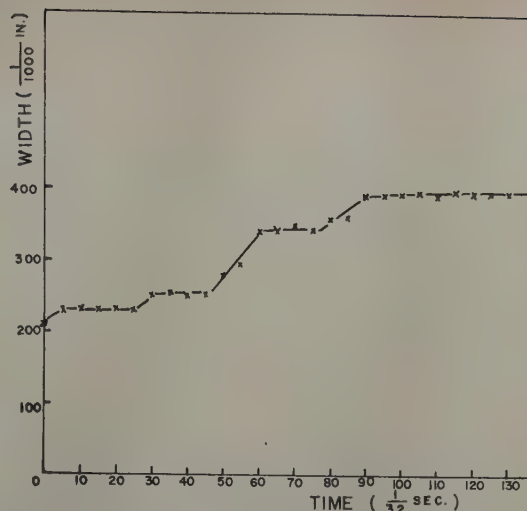


Fig. 17—Increase in width of a slip band during time of loading. Strain rate is 0.00053 per sec, specimen A311.

the increase in intensity or in width of a slip band on the top surface is caused by the edge dislocations entering into the surface, we must first postulate that these dislocations can pass through the surface within the time interval of measurement without first being trapped underneath the surface. If this is true, the factor l/b , as pointed out by Drs. Haasen and Leibfried, certainly should be multiplied to the observed rate to give the rate of moving edge dislocations (where l is the distance from a source which nucleates the particular slip band and b is the amount of the Burgers vector). It is understood that the degree of imperfections in the crystal would modify the factor l/b , and hence the calculated rate of edge dislocations.

Finally it is useful to cite one way which Dr. Cahn¹³ pointed out to account for the sudden appearance of slip bands on the side surface. Cahn suggested that since the screw dislocations move much more slowly than edge dislocations, the dislocation loops provided by Frank-Read source may take up an elongated rectangular shape instead of a circular one, with the edge components forming the shorter sides. Eventually the edge dislocations run out of the crystal while the screws form into two close bunches and move across the slip plane both ways. Judging from Fig. 1, the distance over which the slip line "fades out" (in frames 2234 and after) is about 70 microns. Most of the screw dislocations must be parked in this region, and when they have spilled over the edge of the crystal, the slip line will have appeared fully developed on the side surface. Assuming a velocity of the screw dislocations of 7000 microns per sec, then the whole bunch will spill over the edge in 0.01 sec, which is less than the time between successive film frames. This would be one way to account for the sudden appearance of slip lines on the side face, which in itself, however, does not give the rate of propagation of edge dislocations.

¹¹ R. Becker and P. Haasen: To be published.

¹² A. F. Brown and R. W. K. Honeycombe: *Philosophical Magazine* (1951) 42, p. 1046. These authors have shown that different surface preparation greatly influences the appearance of slip lines in the range of small deformation.

¹³ R. W. Cahn: Private communication.

Surface Effects in the Slip and Twinning of Metal Monocrystals

by John J. Gilman and T. A. Read

DISCUSSION, T. E. Leontis presiding

J. Takamura and H. Nishimura (Dept. of Metallurgy, Faculty of Engineering, Kyoto University, Kyoto, Japan)—The axial twisting described in this paper is of particular interest to us because of a similar investiga-

tion in face-centered cubic monocrystals being completed in our laboratory.³⁰ Axial twisting in simple tension was observed in all single crystals, without exception, of aluminum and copper whose lower ends were freely suspended. Crystals of shape B were used in our investigation and had the following dimensions:

1 to 2 mm thick, 5 to 20 mm wide, and 50 to 200 mm long. Fig. 10 gives an example of the reverse turn of twisting caused by deformation bands. The figure shows that the twisting in cubic crystals does not always increase progressively with increasing elongation as in the case of zinc crystals described in this paper, but it is sensitively affected by the secondary slip systems or such inhomogeneities as deformation bands or the clustering of slip bands.

We would like to ask the authors if they could give us any further information concerning the twisting of tin crystals which have many latent slip systems as cubic crystals. This paper described that tin crystals of shape A revealed the serrated corners as tensile kink bands. The fact is that the twisting was not uniform along the length of the crystals, and it is different from the twisting of zinc crystals. Did the twisting of tin crystals of shape A increase progressively with increasing deformation as in zinc crystals, or was the twisting affected by the inhomogeneities produced at the corner as in the twisting of cubic crystals? Since it is only natural that the axial twisting is caused by the heterogeneity, as pointed out by the authors, the twisting can be expected also in tin crystal AK of shape B which revealed the inhomogeneities at the corner. What can be the reason that the twisting did not occur in the tin crystal?

It is an important effect that zinc crystals of shape B did not exhibit the axial twisting; whereas in aluminum and copper monocrystals of shape B, the twisting was observed from the beginning of the plastic elongation where inhomogeneities were not yet revealed and only the single slip system was actually operative. Would the above-mentioned difference be attributable to that of the experimental procedure in both investigations, especially to the technique of gripping the specimen? If this is not the case, the difference in twisting between hexagonal and cubic crystals must be explained by a different process of deformation.

P. L. Pratt (*Metallurgy Div., Ministry of Supply, A.E.R.E., Harwell, England*)—The authors have shown strikingly in the first part of their paper that the shape of single crystals of zinc and tin may determine the details of their plastic deformation, and that, where the shape has an odd order of symmetry, rotational slip occurs owing to the preference of translational slip for the shortest path in the crystal. In the case of aluminum Wu and Smoluchowski²⁰ showed that the preference can only be found in thin plates with a cross-section ratio of about 10 to 1, whereas in sodium chloride under equivalent conditions it is found consistently even when the ratio is as high as 10 to 9. The essential difference between glide in aluminum and in sodium chloride is that in the former the individual elementary slip processes are not continuous across the crystal, whereas in sodium chloride they are continuous from one side to the other. This suggests that in the thin aluminum crystals the shortest path was

short enough not to contain any barrier to slip in the form of deformation bands or intersecting slip systems.

Zinc and tin behave like sodium chloride in that slip is continuous across the crystal, and the authors were perhaps fortunate in their choice of material for the discovery of this phenomenon. If this interpretation is correct, the effect should also occur in face-centered cubic crystals undergoing easy glide (small diameter, high purity, clean surfaces), where there is little hold-up of slip within the crystal.

The results of the work on metal surface films indicate in the authors' words, "that an important effect of a plated surface film is to impede the exit of dislocations from crystals." Have the authors any microscopical evidence of a difference in the amount of slip on each slip plane in plated and unplated crystals? It seems natural to account for the surface effects on plasticity in this way, and there should be a visible difference in the height of the slip steps on the surface. The effect of a ductile metallic film appears to be less harmful than the brittle oxide film which leads to cleavage.²¹

In sodium chloride the contracted surface layer acts in an analogous manner to these surface films on metals in that it retains slip within the crystal at room temperature if the surface is dry. The well known brittle fracture occurs after about 1 pct extension unless the surface layer is rendered harmless either by immersing in water, or by raising the temperature. Either frees the surface in such a way that the dislocations emerge in the form of visible slip bands, and the material becomes plastic and ductile.

J. J. Gilman and T. A. Read (authors' reply)—The authors were happy to learn of Dr. Pratt's very interesting work with rock salt and in particular that his data confirm the "slip distance" effect which was discovered by Smekal and his school. The role played by the "slip distance" is not clear to the authors because recent work by Makin on cadmium and one of the present authors on zinc indicates a preference in these materials for a long slip distance instead of a short slip distance as found by Dr. Pratt. The situation is complicated by the fact that the slip distance and the new surface area created by a unit slip process are nearly inversely proportional to one another. This makes it difficult to decide whether effects which are attributed to "slip distances" are really volume phenomena since surface phenomena may explain the data equally well. Furthermore, for the case of aluminum, it is known that deformation bands form more readily in thin specimens than in thick ones and this may be the reason for the "slip distance" effect in that material.

The authors have qualitative evidence that the distribution of slip step-heights is more uniform and the maximum slip step-heights smaller for plated crystals than for clean ones at constant strain. This has also been observed by E. Parker and his school.

Dr. Pratt's interpretation of the "wetting effect" for rock salt is in accord with the expectations of the authors and it is hoped that his point of view will be supported by his experimental evidence.

We were also interested in the work of Takamura and Nishimura. Unfortunately, we were not able to locate their reference so we cannot compare our work with theirs. We measured the twisting of our specimens along the gage length to avoid end effects. The results might be quite different if the rotation of grips relative to each other is measured. We did, in fact, observe grip rotation for rectangular crystals of zinc, but there was no twisting (approximate sensitivity was $\frac{1}{4}$ deg per in.) within the gage length.

Little work was done on the twisting of tin crystals, but the twisting did seem to increase progressively with increasing deformation. It was not uniform along the length because the deformation was nonuniform.

²⁰ H. Nishimura and J. Takamura: *Tech. Reports Eng. Inst., Kyoto University* (1952) 2, pp. 139-170.

²¹ J. J. Gilman: *Trans. AIME* (1951) 191, p. 1148; *JOURNAL OF METALS* (December 1951).

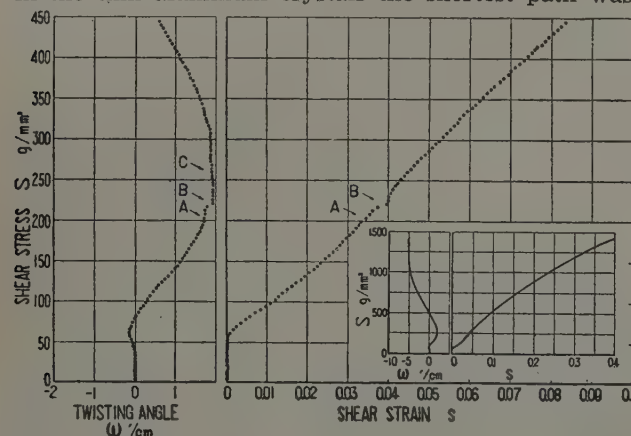


Fig. 10—Correlation between the axial twisting angle and the stress-strain curve in aluminum single crystal. The crystal was 1.5 mm thick and 15 mm wide. See ref. 30 for further details.

Kinking in Zinc Single-Crystal Tension Specimens

by Jack Washburn and Earl R. Parker

DISCUSSION, T. E. Leontis presiding

P. A. Beck (Dept. of Metallurgical Engineering, College of Engineering, University of Illinois, Urbana, Ill.)

—The experiments of Washburn and Parker demonstrate that the low energy boundaries formed in zinc crystals during deformation by the kinking mechanism can move quite freely under the influence of an externally applied stress. As the authors themselves point out, the kink boundaries studied by them are similar to the subboundaries found in plastically deformed polycrystalline material. The stress-induced movements of the kink boundaries are, therefore, undoubtedly related to the phenomenon of the acceleration of subgrain growth on annealing when the specimen is stressed.^{14,15} Apparently, ordinary grain boundaries are not subject to this effect.¹⁶

In the paper, the formation of kink boundaries or subboundaries is described as a result of simultaneous bending and polygonization. This may imply that the collection of the dislocations into sharp boundaries is greatly dependent on thermal activation. On the other hand, recent results obtained by Hirsch and his collaborators in England¹⁷ indicate that subgrain formation takes place even when high melting metals, such as iron and nickel, are cold-worked at room temperature. Also, Cohen found¹⁸ that subgrains are formed in zinc even when deformed at liquid nitrogen temperature. These results suggest that subgrain formation may take place with very little or no thermal activation. It now appears quite certain that the breaking up of the Laue asterism streaks into individual dots when bent single crystals are annealed, which was originally attributed to polygonization, is actually a result of the thermally activated growth of the very small subgrains, originally formed during plastic deformation. The low resolution X-ray techniques employed in the early work on polygonization were unable to detect the subgrains until after they have grown to fairly large sizes; the much higher resolution X-ray techniques now available show their presence directly after plastic deformation. It now seems very probable that the process originally designated as "polygonization," namely the thermally activated sectionwise straightening of bent crystals, does not actually occur.

The process of subgrain growth is, of course, thermally activated. The strong dependence of the size of mechanically formed subgrains upon the temperature of plastic deformation, as demonstrated by Wood and his collaborators,⁶ suggests that there may be some thermal effect involved also in the formation of the subgrains during deformation. It would be very desirable to study this question more fully by carrying out the plastic deformation at temperatures as near to absolute zero as possible and by using X-ray diffraction methods of the highest possible resolving power.

P. L. Pratt (Metallurgy Div., Ministry of Supply, A.E.R.E., Harwell, England)—The authors claim that "at -196°C when a thin wafer is cleaved from a large zinc crystal by introducing a wedge at one surface, a sharp boundary is formed which follows the base of the advancing cleavage crack." I should like to know what evidence they have for this claim since, in our

experience at Harwell, the continued advance of the cleavage crack under these conditions is only possible when this type of kinking does not occur. The tensile stress responsible for cleavage normal to the tip of the crack, Fig. 7, is created by the stiffness of the bent beam already cleaved; if the bending stresses are relaxed by such a kink, Fig. 8, the cleavage run is stopped. In fact a sharp boundary is formed at the base of the cleavage crack only when the cleavage has halted.

The occurrence of a series of kinks at high temperature and low strain rates in single crystals of zinc is most interesting, while the authors' discovery of the mobility of dislocation boundaries has taken its place in the history of metal physics. Recently Mr. Pugh and I¹⁹ have observed the mobility of more complicated boundaries on the cleavage face of zinc single crystals. Twin accommodation boundaries²⁰ will move at right angles to a slip direction on the basal plane under the shear stresses set up by widening of the twin; and these boundaries must contain dislocations with Burgers' vector alternately in the two directions at 60° to the kink. More generally, curved mosaic walls, stable at high temperature, will move in a direction inclined to the slip direction, but parallel to the applied shear stress. Curved walls, if they are to be stable in a fully annealed crystal, must consist of a complex array of dislocations. This array must involve some dislocations whose length does not lie in the basal plane, while all may be of mixed edge and screw type. Therefore, when such walls move, slip cannot be confined to the basal plane alone.

J. Washburn and E. R. Parker (authors' reply)—The authors wish to thank Professor Beck for his comments. The fact that dislocation boundaries do move under stress even at low temperatures is illustrated by the photographs of Fig. 9 showing two stages in the cleavage of a slab 1 in. thick from a spherical single crystal of zinc. A small angle boundary, revealed by the sharp change in brightness of reflected light, is seen to advance with the advance of the cleavage crack. Further work to be published soon has shown that the stress necessary to move a dislocation boundary increases with boundary angle. This means that when two boundaries join, the stress required to move the resulting combined boundary is considerably greater than that which was necessary to move either individually. Formation of subgrains during low temperature deformation probably involves this sort of

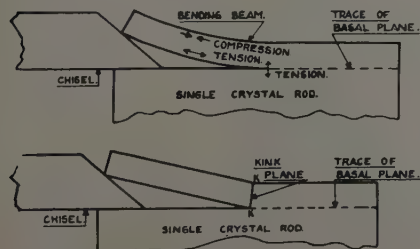


Fig. 7 (upper left) and Fig. 8 (lower left) — Cleavage of single-crystal rods of zinc.

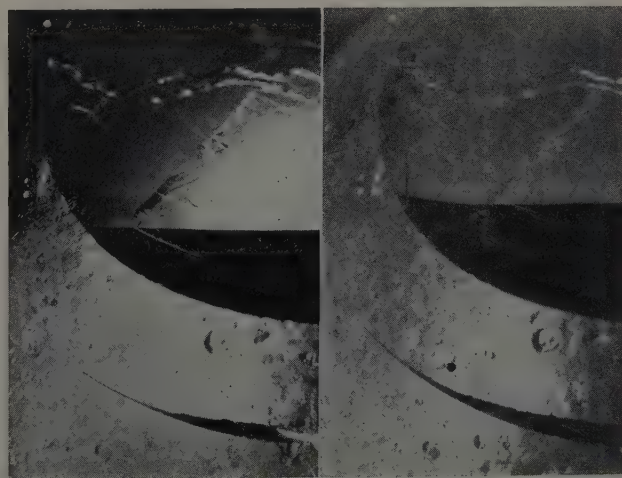


Fig. 9—Motion of a small angle boundary above the tip of an advancing cleavage crack. Pictures show two stages in the cleavage of a wafer $\frac{1}{8}$ in. thick from a spherical crystal of zinc.

collection of boundaries to form less mobile larger angle subgrain boundaries.

In answer to Dr. Pratt: it is hard to say why he was unable to observe the advance of a boundary with the growth of a cleavage crack. The fact that this does occur under some conditions is shown by Fig. 9. It should be pointed out that the boundary angle remains approximately constant during the motion and therefore its presence does not involve relaxation of the tensile stress normal to the cleavage plane at the base of the crack. The mobility of twin accommodation

boundaries and of curved boundaries has also been observed by the authors.

¹⁴ W. A. Wood and R. F. Scrutton: Mechanism of Primary Creep in Metals. *Journal Inst. Metals* (1950) 77, pp. 423-434.

¹⁵ J. Hino, P. G. Shewmon, and Paul A. Beck: Effect of Simultaneous Strain on Subgrain Growth. *Trans. AIME* (1952) 194, pp. 873-874; *JOURNAL OF METALS* (August 1952).

¹⁶ Paul A. Beck: Interface Migration in Recrystallization. *Symposium on Metal Interfaces* (1952) pp. 208-247. Cleveland. ASM.

¹⁷ P. B. Hirsch: Private communication.

¹⁸ Morris Cohen, MIT: Private communication.

¹⁹ P. L. Pratt and S. F. Pugh: A.E.R.E. Report M/R 1031.

²⁰ P. L. Pratt and S. F. Pugh: *Journal Inst. Metals* (1951-1952) 80, p. 653.

Observations on Nodular Graphite

by H. M. Weld, R. L. Cunningham, and F. W. C. Boswell

DISCUSSION, T. A. Read presiding

M. N. Parthasarathi and B. R. Nijhawan (*National Metallurgical Laboratory, Jamshedpur, India*)—We have noted with interest the explanation of the central white spot given by Weld and his coworkers. We are working on a similar subject and would like to take this opportunity to discuss some points in the light of our work.

It was felt that a systematic metallographic examination of one or more specific nodules across their different parallel sections would throw light not only on their structure but also on the tenability of different hypotheses so far proposed to explain the central white spot, "radial" structure, etc.

It has thus been possible to substantiate experimentally the observations of Weld and others regarding the central white spot. Fig. 7 shows the changes observed in the microstructure of graphite nodules at sections near and away from the center. The white spot was observed only in sections away from the center. It was not observed in sections through or near the vicinity of the center of the nodule. Regarding the relationship between the area of the nodule section and the size of the white spot at its center, the latter was observed to be large in sections near the periphery

of the nodule. The spot tended to shrink (Fig. 7) to a point as the plane of polish approached the center of the nodule. This tendency of the white spot to shrink or enlarge, depending upon the position of the plane of polish, was found to hold good in general, although minor deviations were observed in a few sections. These may be attributed to changes in shape and size of the central crystallites, since such factors determine the form and area of the central white spot. Sections of the same nodule with smaller cross-sectional areas (lying close to the periphery) show bigger white spots, while central sections with larger cross-sectional areas exhibit no white spot or merely a point.

Our study has shown that "radial"¹⁴ structures were observed only in sections taken near the center, while sections taken away from the center showed the "structureless" pattern. The schematic diagram presented by Weld and others (Fig. 4) can be used to explain the radial and structureless nodule. If a nodule is sectioned near its periphery, basal planes of the constituent crystallites would lie more or less parallel to the sectioning plane. Such a section shows the structureless pattern. In a section passing through the center of the nodule, the basal planes would meet this section at approximately 90°. Such a section exhibits a typically radial structure. This transition from the struc-

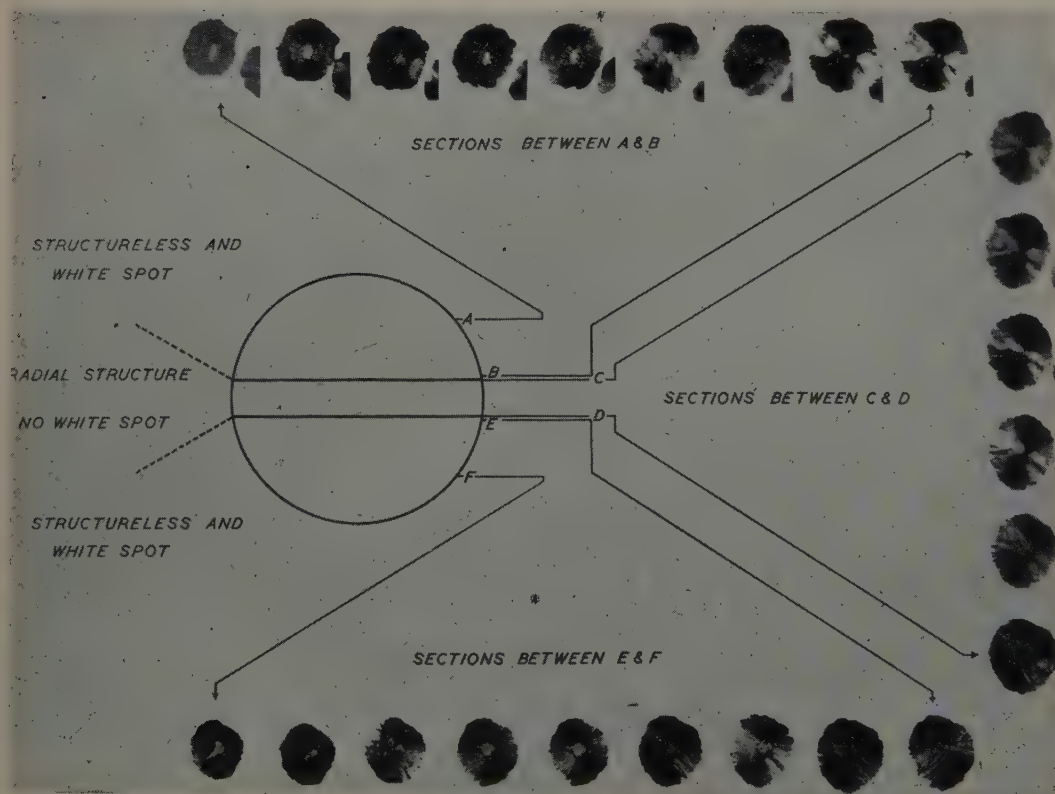


Fig. 7—Diagrammatic sketch depicting the changes observed at sections near the center and away from it. The photographs presented here belong to one of the nodules taken for study. The horizontal lines inside the circle represent approximately the thickness of the sections. Plane polarized light. X1570. Reduced to 1/25th.

tureless to the radial structure is gradual as anticipated from the diagram. Radial structure appearing first at the periphery of the sections tends to envelop the entire section as the plane of polish approaches the center of the nodule.

Further, structureless pattern was observed to be usually associated with the central white spot. This can be readily understood since the white spot is observed only in sections away from the center. It is also possible to come across a microsection of the nodule wherein both the central white spot and the radial structure are observed. Such a section is found to lie in a fortuitous position where the structureless pattern tends to merge into the radial structure.

The change in the smoothness of the area adjoining the white spot as shown in Fig. 6 was not observed by us.

H. M. Weld, R. L. Cunningham and F. W. C. Boswell

(authors' reply)—Messrs. Parthasarathi and Nijhawan are to be congratulated for their successful metallographic examination of a single graphite nodule in many sections. Their work provides visual evidence of the variation in size of the bright central spot in a succession of planes through the nodule and thereby forms a confirmation of the structural hypothesis supported in our paper.

It is understandable that the commentators would not observe the change in smoothness in the areas adjoining the central spot when using a light microscope. The fact that the structure of the graphite is well resolved in Figs. 3 and 5 is the result of the replica technique employed, together with the higher resolving power of the electron microscope.

¹⁴ A. I. Krynsky and H. Stern: *Foundry* (1952) 80, No. 3, p. 106; No. 4, p. 98.

Recrystallization Kinetics of Low Carbon Steel

by Stanley F. Reiter

DISCUSSION, T. A. Read presiding

C. R. Lillie and J. K. Stanley (*Engineering Research Dept., Standard Oil Co. (Indiana), Chicago*)—The author is to be congratulated on his presentation of further data on the process of recrystallization in metals. It is gratifying to the writers that these data substantiate the concept of nucleation and growth as a valid mechanism for recrystallization.

Eq. 2 in the paper was developed to be applied to recrystallization in which the diameter of the recrystallized grains is many times the specimen thickness, and is not valid for the case of three-dimensional recrystallization wherein the recrystallized grains are of a diameter less than the specimen thickness. Since the largest grain reported by Dr. Reiter is about 0.035 in. in diameter (Fig. 7), while the sheet thickness was 0.042 in., the experimental conditions were not truly two-dimensional in character, and the agreement of experimental and calculated curves shown in Fig. 8 may be considered to be fortuitous.

Data obtained by one of the writers for the recrystallization of low-carbon steel, in which all cementite was spheroidized, show activation energies for nucleation, growth, and overall recrystallization which are somewhat lower than those reported in this paper. While this difference may be related to Dr. Reiter's proposal that pearlite patches slow down recrystallization, it should not be overlooked that the results of three-dimensional recrystallization analysis may be expected to differ from those based on two-dimensional analysis.

S. F. Reiter (author's reply)—I would like to thank the discussers for their comments on this paper. The conditions for the use of the two-dimensional analysis originally stated by Johnson⁶ have been extended in the present case. The validity of this extension will be demonstrated by some further calculations.

First, an error was found in the values presented for a and b , the constants of the nucleation rate equation, Eq. 1. The corrected values are: $a = 4.55 \times 10^{-3}$ per sq cm per sec; and $b = 1.14 \times 10^{-3}$ per sec. This correction does not appreciably affect the calculated curve shown in Fig. 8, based on Eq. 2.

The values of N reported in the paper were determined by observing the rate of crystal formation on the surface. In order to convert this value to a three-dimensional nucleation rate,⁷ it is merely necessary to divide by the sheet thickness and multiply by two. The latter step is included to obtain a nucleation rate comparable with one determined at the mid section, where

Table VII. Comparison of Calculated Recrystallization Curves with the Data for 0.08 Pct C Steel, Elongated 8 Pct, 700°C

Time, Min	Pct Recrystallized		
	Two-Dimensional	Observed	Three-Dimensional
25	1.1	0.5	0.6
35	3.9	3.7	2.8
50	15.6	20.4	14.8
70	57.8	79.0	62.3
100	99.9	92.0	99.9

grains are observed which are nucleated both above and below the observation plane.

It is now possible to evaluate the nucleation constants a and b of Eq. 1 for three-dimensional nucleation. Using the data obtained for lot A steel recrystallized at 700°C after 8 pct elongation, $a = 85.3 \times 10^{-3}$ per cu cm per sec and b maintains the same value as above. Eq. 10 derived by Johnson and Mehl¹² may now be employed to calculate a three-dimensional recrystallization curve.

$$f(t) = 1 - e^{-\frac{8\pi G^3 a}{b^4} \left(e^{bt} - \frac{b^3 t^3}{6} - \frac{b^2 t^2}{2} - bt - 1 \right)} \quad [10]$$

In Table VII, values for the percent recrystallized are listed from the data and from the calculations using recrystallization Eqs. 2 and 10.

It is apparent that both methods of analysis agree equally well with the actual data. In the present investigation the use of the two-dimensional analysis is therefore held to be valid.

The experimentally determined curve, shown in Fig. 8, falls below the calculated curve after 85 pct recrystallization because the nucleation rate is decreasing rapidly. In the calculated curve, N is assumed to continue to increase exponentially. This assumption is shown by Fig. 7 to be incorrect.

It is to be expected that the activation energies for nucleation, growth, and overall recrystallization in low-carbon steel will be affected by both the carbon content and the condition of the carbide. The interference with grain boundary migration produced by carbide particles is an important subject, worthy of further study.

In the paper, on p. 976, Table III, the units for N are 10^{-3} per sq cm per sec.

Effect of Molybdenum and of Nickel on the Rate of Nucleation and the Rate Of Growth of Pearlite

by R. Wayne Parcel and Robert F. Mehl

DISCUSSION, T. A. Read presiding

E. E. Stansbury and J. H. Frye, Jr. (*University of Tennessee, Knoxville, Tenn., and Oak Ridge National Laboratory, Oak Ridge, Tenn., respectively*)—The discussers are pleased to see additional data on the austenite-pearlite reaction by Dr. Mehl and his coworkers. The contributions which their critical researches have made to an understanding of this complex process are indeed great and also serve to point out the amount of additional work necessary to explain the observed growth process. The data and discussions of the present paper are of particular interest to us, as it is related to work along similar lines now in progress in our laboratories.

In a recent review²⁴ of the eutectoid transformation, the factors involved in establishing theoretical growth rate expressions were analyzed with the conclusion that the most reasonable explanation of the large effect of alloying elements on the growth rate lies in the necessity for the diffusion of the alloying element and, perhaps, in the effect of the alloying element on the available free energy for the transformation. The authors have examined these points again in the present article. The discussers would like to call attention to a recent publication by Hultgren²⁵ and to some work which is soon to be presented. Hultgren has made a rather extensive experimental survey of the partitioning of several alloying elements when steels are transformed to pearlite, bainite, and spheroidized carbides resulting from tempering previously quenched martensite. Hultgren's data indicate that, in general, carbides separated from immediately formed bainite and from martensite tempered for short periods of time have approximately the same composition as the original austenite, indicating no preferential diffusion of the alloying elements. On continued heating, carbide-forming elements tend to concentrate in the carbide and noncarbide-forming elements, in the ferrite. In the case of partitioning between the lamellae of pearlite, the data are not quite so conclusive, although trends toward an absence of partitioning at least at the lower transformation temperatures are evident. Data are given indicating that at certain transformation temperatures no partitioning was observed in the case of manganese and nickel at the end of transformation. These results are in general agreement with recent data obtained by Picklesimer and McElroy²⁶ on manganese steels of eutectoid carbon concentration. They were able to show that in terms of the extracted carbides no partitioning had occurred if transformation had taken place at 620°C or lower. At progressively higher transformation temperatures, more manganese was observed in the carbide, from which it is safe to say that the pearlite undoubtedly transformed to unpartitioned pearlite at some temperature above 620°C—perhaps as high as 650°C. Hultgren's data on molybdenum indicate that some partitioning has occurred at the completion of the transformation. Undoubtedly, the degree of partitioning here is less at the actual interface—much of the partitioning having taken place behind the interface. The effect of such interdiffusion in the case of molybdenum is particularly important because of the relatively long times required for the transformation and the high temperature at which transformation occurs as a result of the raising of the critical temperature by this element. The results in general, however, indicate that the rate of transformation may be greatly decreased in the presence of alloying elements, but without the necessity of partitioning. Indeed, it may be that partitioning is a consequence of the slow rate rather than the cause.

The discussers have recently proposed the following expression for the rate of growth of the interface:²⁷

$$r = \frac{-\Delta E^* / RT}{C \Delta F \Delta T} e$$

where r is the rate of growth of the interface; C , a constant; ΔF , the free energy change per mol of austenite transforming; ΔT , the undercooling below the critical temperature, °C; ΔE^* , the activation energy; R , the gas constant; and T , the absolute temperature.

The expression is somewhat similar to that of Zener⁴ except that it has been derived on a more general basis and takes into consideration the actual change of the free energy with temperature rather than assume that it varies directly with the degree of undercooling. Measurements are in progress on the effect of alloying elements on ΔF ; but, in agreement with the present authors, it does not seem probable that the change in ΔF will be great enough to explain the decrease in rate. In the derivation of the above expression, no assumptions are made as to the nature of the energy barrier—the activation energy for which is ΔE^* . To investigate the applicability of the above expression for alloy steels, it will be necessary to obtain rates of growth over temperature ranges indicating no partitioning such that the same products will be forming. Appropriate thermodynamic data will also be needed. If, with these data available, the proposed equation appears to be correct and yields systematic changes of ΔE^* with alloy content, then the importance of ΔE^* is apparent and its meaning should be further investigated. Research along these lines is in progress.

The observation that poorly developed pearlite tends to form from the high-purity austenite containing molybdenum is interesting, for similar results have been observed in certain high-purity alloys in these laboratories. A recent article by Iwase and Homma²⁸ may be of interest in this regard. From a series of studies on the development of the abnormal structure in carburized steels, they conclude that for a given grain size, definite amounts of any given alloying element must be present to avoid the abnormal structure. It is interesting that small amounts of silicon are sufficient to produce the normal structure, and such additions have been made in the present investigation to produce well developed pearlite.

R. F. Mehl, R. W. Parcel, and W. C. Hagel (authors' reply)—It has been observed many times that alloy partition shows a downward trend as reaction temperature is lowered. This can be interpreted to mean that the carbide waits for less alloying element as the free energy of the transformation increases. However, partition data of all kinds are badly needed, and the results of Hultgren are admittedly too few to permit generalization.

Two phases at equilibrium in a three-component system at constant pressure and temperature have one degree of freedom. If the concentration of alloy in one phase is selected, that in the other phase is fixed. The ratio of the two may be determined quantitatively as follows: Since the chemical potential, or partial molar free energy, of the alloy in the two phases must be equal

$$\mu_f + RT \ln a_f = \mu_c + RT \ln a_c$$

where a_f and a_c are the activities of the alloying element in ferrite and carbide, respectively, and μ_f and μ_c are the molar free energies of the alloy in the pure

components and may be taken for the present purpose as two arbitrary constants. Then

$$RT \ln a_c - RT \ln a_f = \mu^{\circ}_f - \mu^{\circ}_c = \text{constant}$$

$$RT \ln \frac{a_c}{a_f} = \text{constant}$$

$$\left(\frac{a_c}{a_f} \right)_T = \text{constant}$$

Thus the distribution of alloy between two phases is proportional to its activity in the two phases. In ideal dilute solutions, the ratio of concentrations in the two phases may be considered a constant. The assumption of ideal behavior for metallic systems is risky, however, and it is very doubtful if the equilibrium activities would be obtained in a system which is not at equilibrium such as under consideration here.

The view has been taken by Zener that no partition takes place until after the pearlite reaction has been completed, and when with time full equilibrium conditions prevail. This would seem to be the other extreme, and is probably equally invalid.

If the laws which govern the pearlite reaction require that some partitioning must take place during growth in a striving toward equilibrium, or that only certain types of carbides may nucleate, it follows that alloying elements must diffuse prior to nucleation and that such diffusion must continue during growth. If the rates of diffusion of the alloying element are very much slower than that of carbon, then the movement of alloy would become the controlling factor in growth, assuming that transfer of atoms at the interface was rapid enough that it did not interfere. Since it is known that different types of pearlite carbides are formed at different alloy contents in several systems (as in the case of the molybdenum steels studied here), it seems likely that the various carbides are nucleated as such and grow as such. Otherwise the assumption would have to be made that the alloy did not have time to diffuse during pearlite formation, but that immediately after pearlite formation was complete, the alloy diffused to the carbide and changed its crystal structure. It seems much simpler and more logical

to assume that the crystal structure was the same from the first instant; the behavior of growth as a function of molybdenum content shows a discontinuity at compositions where a new carbide forms, indicating that partitioning takes place during growth. As noted in the paper and the cogent references, a simple assumption that the alloying element, e.g., molybdenum, simply diminishes the free energy change of the transformation, affecting the pearlite spacing proportionately, and the rate of growth similarly proportionately, cannot, at the most, be strictly true, for the proportionality between the spacing and the rate of growth does not exist. No such problem as this can be answered out of hand: unambiguous data on partitioning, values of interface energies, and determinations of the pertinent free energy changes are needed. Possibly the true circumstance lies somewhere between the two extremes noted at the outset of this reply. This question has now been discussed so often that pure logic seems exhausted (as are less pure logicians), and the rather subtle point should without more ado be referred to experiment. It has been claimed in the past that alloying elements did not affect the rate of growth of pearlite; the present paper is an experimental answer on this point.

Mr. W. C. Hagel and Dr. G. M. Pound of this laboratory have designed and constructed a calorimeter especially for a study of the formation of pearlite. By varying interlamellar spacing and applying the necessary thermodynamic treatment, they are able to determine interfacial energies from calorimetric measurements. Their apparatus permits very accurate measurement of the heat of transformation as affected by alloy content and is capable of resolving whether or not cobalt, in contrast to manganese, nickel, and molybdenum, does produce an anomalous effect upon the thermodynamics of the pearlite transformation as proposed.

²⁴ R. F. Mehl and A. Dube: *Phase Transformations in Solids* (1951) p. 545. New York. John Wiley and Sons.

²⁵ Axel Hultgren: *Jernkontorets Annaler* (1951) 135, p. 403.

²⁶ M. L. Picklesimer and D. L. McElroy: Unpublished research, Oak Ridge National Laboratory and University of Tennessee.

²⁷ J. H. Frye, Jr., E. E. Stansbury, and D. L. McElroy: Absolute Rate Theory Applied to the Rate of Growth of Pearlite. *Trans. AIME* (1953) 197, p. 219; *JOURNAL OF METALS* (February 1953).

²⁸ K. Iwase and M. Homma: *Science Reports Research Inst., Tohoku University* (1949) 1, p. 95.

A Study of Grain Shape in an Aluminum Alloy and Other Applications Of Stereoscopic Microradiography

by W. M. Williams and Cyril Stanley Smith

DISCUSSION, T. A. Read presiding

H. K. Hardy and T. J. Heal (*Fulmer Research Institute, Stoke Poges, Bucks, England*)—The authors are to be congratulated on having made a most stimulating use of stereoscopic microradiography to study the three-dimensional shapes of crystal grains in an Al-Sn alloy. A considerable amount of work on Al-Sn alloys as potential bearing materials has been carried out at the Fulmer Research Institute under the sponsorship of the Tin Research Institute and we are particularly interested in any method showing the distribution of the tin particles in the aluminum matrix. In the cast condition an Al-Sn alloy with, for example, 30 pct Sn, possesses the tin in the form of more or less continuous interdendritic films. A redistribution of the tin into relatively discrete particles can be brought about by cold working and recrystallization. We have found that the lower the temperature of recrystallization the finer the tin particles and the finer the grain size of the matrix.¹ On the other hand, Fig. 11 in the authors' paper stands in apparent contradiction to this statement since the size (and number) of the tin particles and grains changes only very slightly over the range 350° to 600°C. We have therefore carried out some experimental work on this point.

An aluminum-5.2 wt pct Sn alloy (super-purity aluminum) was chill-cast to 1 in. diam bar and cold-forged to ½ in. sq section. Short lengths were annealed for 16 hr at 350°C, 16 hr at 580°C, and a duplex treatment of 16 hr at 580°C followed by 16 hr at 350°C. Microspecimens were prepared by conventional methods and electrolytically etched in a 1 pct solution of ammonium persulphate in 50 cc of water and 50 cc of glycerine. Sections for microradiography of between 0.005 and 0.020 in. thick were obtained by grinding on emery papers. The sections were strapped to Kodak Maximum Resolution plates and exposed to cobalt radiation from a tube with a 1 mm focus. The focus-specimen distance was 12 in. and the stereoscopic shift was equivalent to 10°. Typical exposure times for the 0.005, 0.015, and 0.020 in. sections were 15 min, 1 hr, and 2 hr respectively. Kodak D178 developer was used and it was found desirable to over-expose and develop for only 2 min in order to reduce the graininess of the emulsion to its lowest level. It is believed that this technique will give an increased sharpness to the radiographs so that a larger magnification can be used than the authors'.

The results are illustrated by Figs. 13 to 15. The specimens annealed at 580° or at 580° plus 350°C were almost indistinguishable. The stereographic micro-

radiographs showed that nearly all the grain edges were penetrated by tin which sometimes spread into the grain interfaces where it was also present as isolated disks. The specimen annealed only at 350°C possessed a much smaller grain size with more finely dispersed tin particles and not all the grain edges were occupied by tin. These results are in agreement with our previous work on commercial purity alloys in which we found that the process of recrystallization and grain growth greatly facilitated the attainment of the minimum surface energy conditions. This has the important practical result that aluminum alloys containing high proportions of tin (30 pct and over) can be made substantially free from grain boundary films of tin and consequently with adequate strength and ductility at temperatures at which bearings operate, i.e., up to about 200°C. We would like to ask the authors whether the alloy shown in Fig. 11 had first been an-

nealed at a high temperature before annealing at 350°C or whether they can suggest other differences in experimental technique which could explain the discrepancy.

E. B. Matzke (*Dept. of Botany, Columbia University, New York*)—This investigation makes available data on metal grain shapes for comparison with results obtained by different techniques for cells in tissues. The range in kinds of faces is fairly similar in both. Like the grains, cells are not of uniform volume, but volume differences in the cells studied are not so great as in the alloy. This is reflected in the relatively wide range in total number of faces and in the variety of combinations of faces in the alloy. Abnormal vertices apparently occur in the grains more frequently than in the cells. However, the cells were examined for the most part under relatively high magnifications, up to 1500 diameters, and not uncommonly a four-rayed vertex, on a single cell, under low magnification, becomes two three-

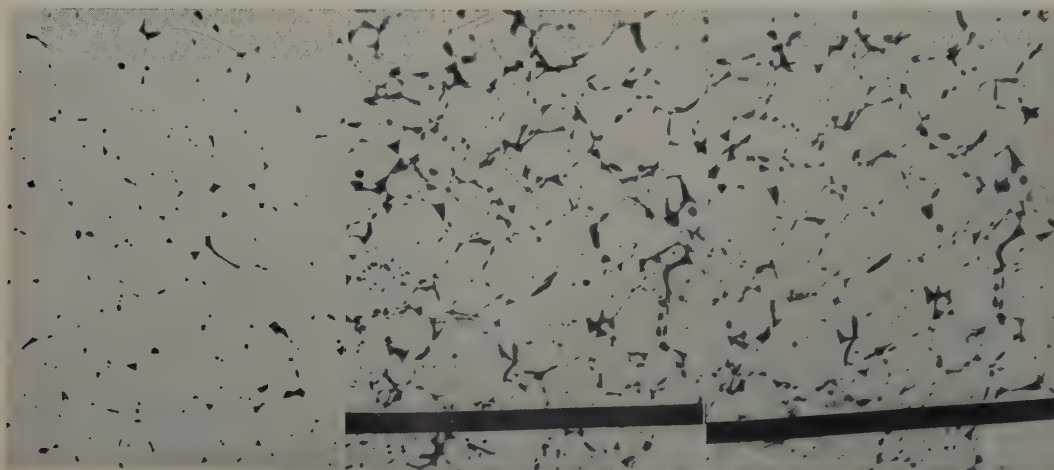


Fig. 13 (left)—Cold-worked and annealed at 350°C. A, left; b, center; c, right.

Fig. 14 (right)—Cold-worked and annealed at 580°C. A, right; b, center; c, far right.

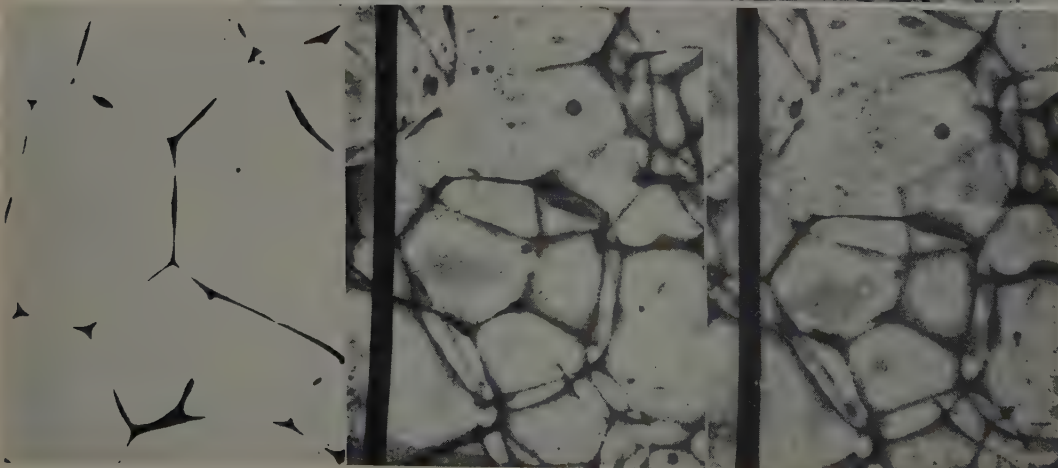
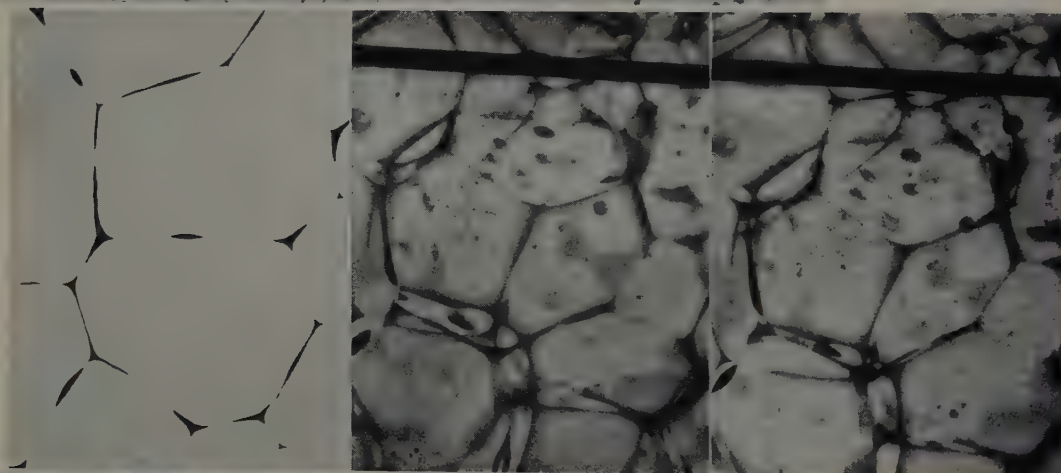


Fig. 15—Cold-worked and annealed at 580°C followed by 350°C. A, left; b, center; c, right.

Figs. 13-15—Structures of S. P. aluminum-5.2 wt pct Sn alloys. In each case, a is a micrograph, b and c are stereoscopic microradiographs (stereo angle 10°) and the tin particles are dark. X100. Area reduced approximately 50 pct for reproduction.

rayed vertices with a short edge between under high magnification.

The origin of cells by division introduces a factor different from those present in alloys and soap films. If these divisions are wholly or predominantly in one direction, a regularity, involving symmetry, results, and in isolated instances approximations to Kelvin's minimal tetrakaidecahedron are achieved.

Applications of the new technique developed by Dr. Williams and Dr. Smith to tissues should be carefully investigated.

Perhaps the most important contribution to biology of this scholarly presentation is a philosophical one. The authors conclude that in this alloy no one combination of faces constitutes a type. Plant and animal cells, like the grains, normally also do not achieve a type, although various configurations have been stoutly defended as such in the past. Cells in tissues, with walls, cytoplasm, nuclei, vacuoles, intercellular spaces, etc.,

are far more complex in organization than metal grains; still they show marked resemblances to metal grains, due to the operation of similar factors.

W. M. Williams and C. S. Smith (authors' reply)—Messrs. Hardy and Heal are, of course, right in suggesting that the grain size of a worked and annealed Al-Sn alloy would depend upon the maximum annealing temperature. One would expect, however, that the true dihedral angle would be unaffected by grain size and depend only on final annealing temperature. We therefore suppose that the similarity between Messrs. Hardy and Heal's Figs. 14 and 15 results from inadequate time to re-establish long-range equilibrium geometry at the lower temperature of anneal. If this is so, examination at a high magnification would show a higher angle at the extreme apex.

The authors appreciate Professor Matzke's comments on the relation between metallurgical and biological shape studies.

Titanium-Chromium Phase Diagram

by F. B. Cuff, N. J. Grant, and C. F. Floe

DISCUSSION, J. E. Burke presiding

M. K. McQuillan (Birmingham, England)—I am glad to see general experimental confirmation, in addition to that recently provided by Van Thyne, Kessler, and Hansen,⁵ of my work on the Cr-Ti system.⁴ I feel, however, that the work would have been of greater value from this point of view if the experimental evidence put forward could have been more detailed. When my own work on this subject was published last year, the word "provisional" was included in the title, not because I had any doubts concerning the results of my investigations or about the general nature of the system, but because, in covering a whole equilibrium diagram in a limited amount of time, I was unable to offer the extensive and refined evidence usually required before a new diagram is considered to be finally established. I had hoped that later work in the same field would remedy this deficiency, and locate the phase boundaries with greater precision than I was able to do.

There are one or two comments I would like to make on the paper, the first concerning the relationship between lattice parameter and composition for the continuous series of body-centered cubic solid solutions. I found that only almost instantaneous quenching from the temperature region 1360° to 1400°C was sufficient to retain completely the body-centered cubic solid solution in alloys containing about 40 to 70 pct Cr. Quenching times of a second or so were too long, and compound formation was invariably found to have begun in such cases. That this also occurred in the authors' experiments, as would be expected if their method of quenching is considered, may be seen from Fig. 8, in which the partial breakdown of the solution to form the compound is quite evident. I think that the authors might have seen this more clearly had they used a different etchant. I did not find hydrofluoric acid very suitable for chromium-rich alloys, and preferred an electrolytic etch in a solution containing 10 pct potassium hydroxide and 10 pct potassium ferricyanide, which brings out the compound very clearly. The fact that the breakdown of the β solution has begun in the quenched samples of intermediate composition examined by the authors may well explain some of the observed deviations from Vegard's law in this composition range. The precipitation of a chromium-rich compound would move the composition of the β solution toward the titanium end of the system, and thus move the lattice parameter/composition curve toward the negative side of the linear relationship.

A point on which my views differ appreciably from those of the authors is that of the solubility of titanium in chromium at lower temperatures, and I would be glad to have more details of the X-ray work on which the authors base their statement that the solubility of

titanium in chromium is in the neighborhood of 15 pct at 600°C. As may be seen from my paper, I obtained a fair amount of metallographic evidence indicating that the solubility of titanium and chromium is much less than this—in fact, only of the order of 5 pct at 1000°C. I feel, therefore, that the dotted line inserted in the present diagram, unsupported by any explicit evidence, is misleading.

A further point of difference between the present work and my own is in the form of the solidus in the region 50 to 80 pct Cr. In the case of highly reactive alloys such as these, it is not easy to obtain really reliable information on the solidus, but I did find fairly convincing evidence of a flattening of the curve in the composition region in question, tending to make it almost horizontal, which is not inconsistent with the rest of the diagram when free-energy relationships are considered. I notice that Van Thyne et al. support me in this. I would be glad if the authors could present in more detail any evidence they may have to the contrary.

The authors' dilatometric evidence on the eutectoid temperature is particularly welcome, as the eutectoid line has not hitherto been fixed with any accuracy. In this connection, I presume that the authors used iodide titanium in preparing the alloys for this work, since, when magnesium-reduced material is used, a three-phase region occurs where a eutectoid line would normally be expected, and no sudden transitions, such as those observed by the authors, would be observed.

I am interested also in the figure given by the authors for the lattice parameters of the compound described as TiCr_2 . When the paper by Duwez and Taylor⁶ on the crystal structure of TiCr_2 appeared, I examined such evidence as I had on the compound. I found that though the structure they proposed did not quite account for all the unidentified lines on my powder photographs, the greater part of the lines fitted the proposed structure, giving a cell size of 6.91Å, a value which is significantly different from that found by Duwez and Taylor (6.929Å), but which agrees with that of the present authors.

Finally I would like to mention two points of technique. The authors say that they observed some increase in hardness when they melted a specimen of iodide titanium in their arc furnace. Though appreciable scatter in hardness readings is quite usual in this material owing to the large grain size normally found, melting techniques using arc furnaces with water-cooled copper hearths have developed to such a stage now that no general increase in hardness of the material on melting is expected. The other point concerns the methods for heat treatment of specimens at 1350°C. It would be very interesting to know on what the speci-

Table III. Phases Present at Various Temperatures for Various Chromium Contents

Solution Temperature, °C	Composition, Pct Cr	Phases Present by X-ray
1400	70	β
1350	70	TiCr ₂ + β
1300	70	TiCr ₂ + β
1350	75	β
1300	75	β
1200	75	TiCr ₂ + β
1200	80	β
1100	80	TiCr ₂ + β
1100	85	β

mens were supported during heat treatment, and by what means quenching was carried out.

R. J. Van Thyne and **H. D. Kessler** (*Armour Research Foundation of Illinois Institute of Technology, Chicago*)—The diagram presented by the authors is in good agreement with that previously published by staff members of the Armour Research Foundation.⁶ As our publication was not in print at the time the authors submitted their paper, it would be desirable to compare certain features of the two investigations here. Our partial diagram was determined using high-purity titanium and chromium and covered a range from titanium to a composition of 75 pct Cr. The solidus curve at the high titanium end of the system agrees closely with that of the present paper. However, our solidus curve is very flat from 40 to 70 pct Cr at a temperature level of about 1400°C. Unfortunately, no data points are given in the present paper to allow more positive comparison.

Our metallographic observations indicated eutectoid decomposition of the β phase in alloys annealed at 675°C, whereas no eutectoid was seen in alloys annealed at 700°C. We, therefore, placed the eutectoid temperature at approximately 685°C. This agrees quite well with the authors' dilatometric determination of 670°C.

Regarding Fig. 15, the appearance of the Widmanstätten precipitate (which could not be identified by X-ray) closely resembles that of α coming out of β and the fact that the precipitate occurs largely within the grain could be attributed to coring.

In our diagram, the intermediate phase was placed at 67 to 68 pct Cr on the basis of metallographic observations of heat-treated samples. We originally reported the structure of TiCr₂ to be of the cubic C15

(MgCu₂) type. However, during other phase diagram studies now in progress⁷ a high temperature modification of TiCr₂ was found to exist above 1300°C. This high temperature polymorph has been identified as having a hexagonal C14 (MgZn₂) structure. X-ray patterns of the two forms of TiCr₂ are very similar; the pattern of the hexagonal modification having all the lines of the cubic plus a few additional ones. The allotropic transformation of TiCr₂ will necessitate some revision in the Ti-Cr diagrams published to date.

The authors found that alloys containing 10 pct Cr or less exhibited a martensitic structure when quenched from the β field. In our studies, the β phase was completely retained upon water-quenching alloys in which the composition of β was 7 pct Cr or greater.

The hardness peak shown at 10 pct Cr in Fig. 6 was attributed to supersaturated α titanium. On the basis of our work on this and other systems, it seems more reasonable that the hardness peak shown was a result of a complex decomposition of the metastable β phase rather than the presence of the relatively soft supersaturated α titanium. Isothermal transformation studies made at the Armour Research Foundation have shown that even after a few minutes of annealing at 600°C, all of the supersaturated α is decomposed.

F. B. Cuff, **N. J. Grant**, and **C. F. Floe** (authors' reply)—Regarding Mrs. McQuillan's questions and comments, for which we wish to express our thanks, the primary purpose of the lattice parameter measurements was to confirm the existence of the continuous series of solid solutions that had initially been found metallographically. The authors feel that this confirmation was provided by the general adherence to Vegard's law of the specimens through the critical range of composition. It was noted in passing that the deviations, i.e., positive for the solidus minimum and negative for the compound, were in accord with previous experimental and theoretical studies. The possibility of some compound formation during quenching is admitted but it is felt that the quantity formed was not sufficient to account for the total amount of deviation.

The data in Table III provide the basis for constructing the line representing the solubility of titanium in chromium. The data in Table IV provide the basis for constructing the line representing the solidus at chromium percentages higher than 55.

Specimens heat-treated at 1350°C were contained in tantalum cups in a horizontal global furnace. At the end of the heat treatment the contents of the furnace pushed rapidly into the quenching medium. The elapsed time was somewhat less than a second. In connection with Van Thyne's and Kessler's discussion, the data for the solidus determination are presented in the above discussion. It is now generally agreed that the β field can be retained in alloys containing 7 pct Cr or more.

Table IV. Phases Present at Various Temperatures for Various Chromium Contents

Solution Temperature, °C	Composition, Pct Cr	Condition of Sample
1450	60	Complete melting
1400	60	No melting
1500	65	Partial melting
1450	65	No melting
1550	70	Partial melting
1500	70	No melting
1550	75	No melting

⁶ R. J. van Thyne, H. D. Kessler, and M. Hansen: *Trans. ASM* (1952) 44, p. 974.

⁷ F. Duwez and J. L. Taylor: *Trans. ASM* (1952) 44, p. 495.

⁸ B. Levinger: A High Temperature Modification of TiCr₂. *Trans. AIME* (1953) 197, p. 196; *JOURNAL OF METALS* (February 1953).

In ref. 1, 2, and 4 in the paper the volume numbers and page numbers are transposed: ref. 1 should be 14, p. 279; ref. 2, 55, p. 366; and ref. 4, 18, p. 379.

Tungsten-Cobalt-Carbon System

by Pekka Rautala and John T. Norton

DISCUSSION, B. H. Alexander presiding

R. B. Fischer (*Battelle Memorial Institute, Columbus, Ohio*)—In a study which we hope to publish in the future, other experimental evidence has been obtained at Battelle to show that the η phase is stable. It is interesting that the methods used were quite different although the conclusions were identical.

The last paragraph of the paper contains statements which we believe need elucidation. It has been the

opinion of workers in the carbide field that cooling rates from the sintering temperature generally have little effect on the properties and some of our work seems to confirm this opinion.

A. G. Metcalfe (*Deloro Smelting and Refining Co., Deloro, Ont., Canada*)—It has been suggested at various times that η , W₂C, and now WC are metastable. I would like to ask the authors if they feel there may not be a possibility for all of these phases to be stable. Their

Table II. Comparison of η and θ

Positions in $Or_3 - Fd\ 3\ m$	η (Co_3W_3C)	θ (Co_2W_4C)
16 : (c)	16 C	16 C
16 : (d)	16 Co	16 W
32 : (e)	32 Co	32 Co
48 : (f)	48 W	48 W

evidence appears to depend on one melt of composition 81 pct Co-9 pct W-10 pct C, but no evidence was advanced to support their expectation that the melt was initially homogeneous. In view of the ease with which carbon floats to the surface of such high-carbon melts, it is often difficult to achieve uniformity. In any case, the failure to detect the ternary eutectic, $L \rightarrow \eta + \beta + C$ by thermal analysis, indicates that either the cooling rate was too rapid to maintain equilibrium or that the reaction does not occur. The cooling rate of the melt 81 pct Co-9 pct W-10 pct C was presumably faster than that in the thermal analysis, so that the equilibrium reaction is less likely to be found. It is significant that commercial alloys containing η phase as well as $\beta + WC$, gradually transform to $\beta + WC$ on prolonged soaking in a carburizing atmosphere at 1400°C, indicating that WC is not unstable at this temperature.

The phases η_1 and η_2 discovered by Kislyakova fall into the phase fields θ and η , respectively. In the work reported by Sandford and Trent it was shown that these two phases were in equilibrium at 1100°C, so that it would be impossible for them to be the limiting compositions of the η field, as suggested, unless they are conjugate solutions. This seemed likely as they both possessed the $Fd\ 3\ m$ space groups. The intensities of the lines recorded in Table I vary systematically from θ to η phase, but there are too few lines to determine if the space groups are the same. Perhaps the authors have more evidence on this point.

Roland Kiessling (Laboratory for Hard Metal Research, Söderfors, Sweden)—This work is of great interest, and I wish to congratulate the authors on their results. At Söderfors we recently investigated the same system and have some additional information on the θ phase, which may be of interest. A complete survey has been given at the Symposium on the Reactivity of Solids in Gotenburg, Sweden, June 9-13, 1952, and will be published among the transactions from this conference.

In agreement with the authors we found that θ (we used the notation η_2) is a different phase from η and that a two-phase range separated the phases. We found θ (η_2) had a slightly extended homogeneity range around the composition Co_2W_4C , being cubic and with a parameter of 11.210Å at this composition. A complete structure determination of θ has been carried out, and the results are consistent with Kislyakova's work. From our analyses as well as from the formula obtained from

Table III. Relative Differences Between η and θ in Intensities

hkl	d		I	
η and θ	η	θ	η	θ
111	6.403	6.472	0.12	0.01
220	5.545	5.605	0.08	0.05
311	3.344	3.380	—	0.05
222	3.202	3.236	—	0.10
400	2.773	2.803	0.37	0.09
331	2.544	2.572	0.37	0.57
422	2.264	2.288	0.61	0.48
511	2.134	2.157	1.00	1.00
333				
440	1.960	1.982	0.37	0.48
531	1.875	1.895	—	0.03
442	1.848	1.868	0.02	0.03
600				
620	1.753	1.772	0.01	0.04
533	1.691	1.710	—	—
622	1.672	1.690	0.04	0.16
444	1.601	1.618	—	0.04

the structure determination we consider that θ has the formula Co_2W_4C and not Co_3W_3C , η as well as θ belongs to space group $Fd\ 3\ m$, with 96 metal and 16 carbon atoms in the unit cell. The difference between η and θ is given in Table II, which shows that for η both 16: (d) and 32: (e) are occupied by cobalt atoms, whereas for θ , 16: (d) is occupied by tungsten atoms and 32: (e) by cobalt atoms. The difference between the X-ray photographs of η and θ is not only a slight variation in the relative intensities, as mentioned by the authors, but certain reflections appear for θ which have the intensity zero for η , e.g., 311, 222, 531, and 444, and for some reflections a considerable difference in relative intensities is noted, e.g., the pairs 111 and 220, 400 and 331, 442 and 620. The relative intensities for η and θ within the range given by Rautala and Norton are, however, in relatively good agreement with ours and the main differences between η and θ appear for lower and higher angles, Table III.

The slight difference in d -values for η is probably due to the fact that the compositions are slightly different but both within the homogeneity range for η .

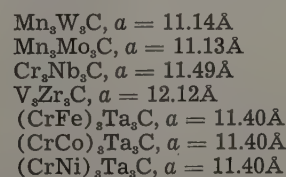
K. Kuo (Institute of Chemistry, University of Uppsala, Uppsala, Sweden)—The relationship between the equilibrium carbides and steel composition in molybdenum and tungsten steels has been found by the present writer^{8,9} to be as shown in Table IV. However, Fe_3W_3C

Table IV. Relationship Between Carbides and Steel Composition

Steel Composition	Equilibrium Carbides
Atomic Ratio Mo:C or WC	At 700°C
A.R. < 1	MoC (or WC) + Fe_3C
A.R. = 1	MoC (or WC)
2-3 > A.R. > 1	MoC (or WC) + Mo_5C (η)
4-5 > A.R. > 2-3	Mo_5C (η)
A.R. > 4-5	Mo_5C (η) + Fe_7Mo_6 (or Fe_7W_6 , δ)

appeared also temporarily on tempering as an intermediate product in steels with an atomic ratio W:C smaller than unity. The stability of the Fe_3Mo_3C and Fe_3W_3C carbide is, therefore, dependent upon the composition of the alloy under consideration. Thus Takeda's suggestion⁴ that the η carbide is always a metastable carbide seems to be incorrect. In this respect, this writer welcomes the conclusion concerning the stability of Co_3W_3C drawn by Drs. Rautala and Norton.

Besides the η carbides known to exist (Fe_3W_3C , Co_3W_3C , Ni_3W_3C , Fe_3Mo_3C , and Co_3Mo_3C), this writer has found the following new η carbides:



Among the above-mentioned η carbides the last three are triple carbides, since Ta did not form this carbide with Cr, Fe, Co, or Ni in the respective Ta-Me-C ternary systems. A hypothesis regarding the formation of η carbide, based upon the relative strength of the transition-metal-carbon bond, has been advanced and will be published shortly.

The κ carbide has also been found by this writer in the systems Ni-W-C and Mn-W-C and has been indexed on a hexagonal lattice with $a = c = 7.848$ and 7.756\AA , respectively. The intensity of the reflections agrees well with that given by the authors. An alloy of the composition Ni_3W_3C sintered at 1500°C for 10 min in a vacuum graphite resistance furnace showed only the existence of the η carbide. However, after 10 min at 1800°C κ began to appear together with η , and its amount increased with sintering time. This is probably due to the vaporization of cobalt and the carburization in the furnace, if we take Co_3W_3C as the composition of the κ carbide. However, attempts to prepare pure κ carbide have not been fruitful. Would the authors

kindly show how they have arrived at the composition of this carbide?

P. Rautala and J. T. Norton (authors' reply)—The question of the stability of the phase diagram presented here is of course, not definitely settled. Certain very limited evidence indicated the possibility of instability and the suggestion is made as to what form the "stable" diagram might have. Much more evidence is needed before a final conclusion can be reached.

The authors wish to thank Dr. Kiessling for his discussion of the θ phase which confirms the present results but gives considerably more information about the structure. This answers the question of Dr. Metcalfe in the matter of the space groups of the θ and η phases.

Dr. Kuo's comments on new members of the family of the η carbides are very interesting. It is pleasing to learn that he has confirmed the existence of the κ phase in the system Ni-W-C and that it is also to be found in Mn-W-C. In the present work, the κ phase was prepared by mixing the ingredients in the proper proportion and sintering at 1400°C. Chemical analyses showed that at this temperature the vaporization of the cobalt was not significant.

Again the authors wish to thank all those who have contributed to the discussion.

⁸ K. Kuo: *Jernk. Annaler* (1952) 136, p. 156.

⁹ K. Kuo: *Journal Iron and Steel Inst.* (1953).

Role of the Binder Phase in Cemented Tungsten Carbide-Cobalt Alloys

by Joseph Gurland and John T. Norton

DISCUSSION, B. H. Alexander presiding

R. B. Fischer (*Battelle Memorial Institute, Columbus, Ohio*)—Since we are very interested in cemented carbides, we would like to make the following comments about this paper:

In Fig. 1, a comparison is made of the effect of electrolytic leaching on 100 pct WC and on cobalt-bonded WC. Presuming that the 100 pct WC specimen was prepared without a binder, its particles would not be expected to be in the same physical state as the WC particles which have been subjected to the cobalt-binding reaction and, therefore, this difference should be considered in the interpretation of the leaching results. Perhaps this was considered by the authors, and they also used 100 pct WC prepared by the fugitive-binder technique but this was not mentioned specifically in the electrolytic experiments.

The authors' explanation of the dilatometric changes at the solidification temperature of the binder is very interesting.

It is stated that the evidence shows that the sintered compact is "one of tungsten carbide particles dispersed in a matrix of cobalt." We believe that the matrix is a

cobalt-rich alloy as is pointed out in the conclusion section of the paper.

In addition to the requirements for an effective binder as summarized by the authors, we believe that the binder should have low solid solubility of tungsten and carbon.

Whatever evidence has been presented pro and con on the skeleton theory, it should be noted that in the micrographs of low-cobalt cemented tungsten carbide, considerable carbide-to-carbide contact points exist as shown in Fig. 6 of the paper.

J. Gurland and J. T. Norton (authors' reply)—Mr. Fischer raises the interesting point of a "pure" WC specimen made by hot pressing as compared with one made by the fugitive binder technique and their reaction in the leaching experiment. This experiment was designed to show whether or not the leaching action would attack the carbide contact points in a skeleton and the hot-pressed specimens were made to only 64 pct of the theoretical density. A specimen made by the fugitive binder method would be much more dense and there would always be a question of remaining traces of cobalt and lack of possible penetration of the leaching solution.

Solubility of Carbon and Oxygen in Molybdenum

by W. E. Few and G. K. Manning

DISCUSSION, B. H. Alexander presiding

N. A. Gokcen (*Dept. of Metallurgical Engineering, Michigan College of Mining and Technology, Houghton, Mich.*)—The authors first remark that the oxygen pressure in Fig. 5 may not represent the equilibrium value and later state that the line of Fig. 6 represents the three-phase equilibrium between solid metal, solid oxide, and gaseous oxygen. These statements are not entirely in agreement because if Fig. 6 represents the equilibrium conditions in these experiments as such, then Fig. 5 should represent the equilibrium oxygen pressure of molybdenum oxide. Furthermore the pressure plotted in Fig. 5 cannot be that of oxygen entirely if the oxide of molybdenum is volatile as pointed out in the text. The thermodynamic calculations from the available data indicate that the oxygen pressure of molybdenum oxide is at least 200,000 smaller than those reported by the authors. Since the pressure of MoO_3 is 1 atm⁸ at 1424°K (2104°F) and its melting point 1068°K, then we may conclude that the only solid oxide observed in these experiments should be MoO_2 or a lower oxide. The oxide observed under very low oxygen pressures was MoO_2 in Tonosaki's⁹ experiments. It is, therefore, justifiable to assume the presence of the

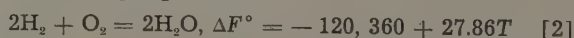
same oxide in these experiments and make the following calculations:

1—Tonosaki studied the equilibrium in reaction $\text{Mo(s)} + 2\text{H}_2\text{O(g)} = \text{MoO}_2\text{(s)} + 2\text{H}_2$ and expressed ΔF° as a function of temperature in five terms. We can express his results more simply as

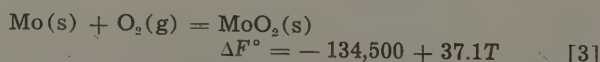
$$\Delta F^\circ = -14,100 + 9.2T \quad [1]$$

which is valid and sufficiently accurate in the range of 1200° to 2000°K in this simpler form.

2—Combining Eq. 1 with



we obtain



At 1700°K or 2600°F the oxygen pressure calculated from Eq. 3 is 6.7×10^{-10} atm or 5×10^{-4} micron of mercury pressure. The mixture of gas corresponding to this oxygen pressure is $\text{H}_2\text{O}/\text{H}_2 = 1.26$, meaning that the oxidation of Mo should take place in an atmosphere of $\text{H}_2 + \text{H}_2\text{O}$ containing more than 56 pct water vapor. This is in agreement with our experience, whereas the

Accordingly Fig. 5 does not represent the equilibrium state and Fig. 6 can only represent it between the two phases, i.e., dissolved oxygen and solid molybdenum oxide, as may possibly have been realized in experiments, provided that supersaturation in Mo-Oxide $\rightarrow \text{O}(\text{in Mo}) + \text{Mo}$ cannot take place under such high oxygen pressures.

W. E. Few and G. K. Manning (authors' reply)—In the last paragraph of Professor Gokcen's discussion, he draws substantially the same conclusions we emphasized in the paper. However, we do not believe that supersaturation of dissolved oxygen is a factor as he suggests. Had this occurred, we would have noted inconsistent results between specimens held for different times at temperature, i.e., some of the specimens shown in Table II treated for the longer times would have developed an oxide phase without an increase in oxygen content. Furthermore, in most cases, oxygen was added to the specimen during the isothermal treatment.

Addition of a solute during an isothermal treatment is not expected to cause supersaturation.

We are familiar with Tonosaki's values for the free energy of MoO_2 . Tonosaki's determinations were made in the temperature range of 918° to 1096°K , and with such a narrow temperature base, it is not at all surprising that his results cannot be satisfactorily extrapolated to 1700°K . Several years ago, we compared Tonosaki's values with the results of some welding and sintering studies. The indications were that the pressure of O_2 in equilibrium with MoO_2 was higher than that indicated by Tonosaki. If one must calculate the free energy of MoO_2 , then we believe the data in Fig. 5 will yield more satisfactory values than that given by Tonosaki, at least in the temperature range of 1400° to 2000°K . We recognize that because of the technique employed, the equilibrium pressures for oxygen must be somewhat lower than the values given by the ordinate in Fig. 5. However, it seems very unlikely that the ordinate in Fig. 5 could be in error by a factor of 200,000 as Professor Gokcen suggests.

⁹ K. Tonosaki: *Bull. Inst. Phys. Chem. Research, Tokyo* (1940) 19, p. 126.

System Molybdenum-Boron and Some Properties of the Molybdenum-Borides

by Robert Steinitz, Ira Binder, and David Moskowitz

DISCUSSION, B. H. Alexander presiding

Pekka Rautala (Dept. of Metallurgy, Massachusetts Institute of Technology, Cambridge, Mass.)—Fully appreciating the difficulties involved in this high temperature work, I would like to iron out a few mistakes. On page 985, the authors write: "The peritectic temperature of Mo_2B is 2000°C . The eutectic composition, determined by extrapolation, contains about 1 pct B." Such four phase equilibrium violates the phase theory. Fig. 7 gives one possible solution to this discrepancy.

Further down on page 985 it is stated: "This boride (Mo_2B_3) is formed by the peritectic decomposition of Mo_2B ." According to the diagram (Fig. 3) this reaction is eutectoid.

I also feel that Mo_2B_3 , despite its structure, should be called MoB_2 , or vice versa, because the same range of compositions is included in both cases.

R. Steinitz (authors' reply)—I thank Professor Rautala for his comments and, of course, agree with him that a four-phase equilibrium is not possible in the binary system. His suggestion of a correction of the diagram probably shows the conditions in the correct way. The peritectic temperature line for the Mo_2B decomposition is about 2000°C and the line for the eutectic temperature is probably less than 50°C lower.

The stoichiometric formulas which were attributed

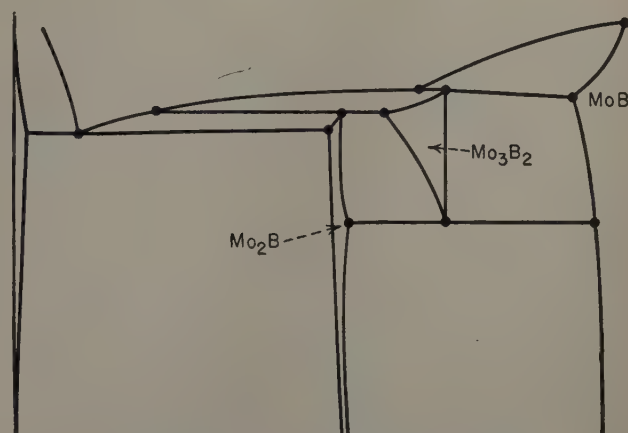


Fig. 7—Portion of Mo-B equilibrium diagram.

to the various compounds were selected according to the structure rather than to the chemical composition as MoB_2 is isomorphous with the diborides of all the other transition elements. This designation seems to be the most appropriate one. Neither MoB_2 nor Mo_2B_3 would represent the chemical composition correctly.

Systems Zirconium-Molybdenum and Zirconium-Wolfram

by R. F. Domagala, D. J. McPherson, and M. Hansen

DISCUSSION, B. H. Alexander presiding

G. A. Geach and G. F. Slattry (Research Laboratory, Associated Electric Industries Ltd., Aldermaston, Berks, England)—A study of the system Zr-W was completed in this Laboratory a few months before the paper by Domagala, McPherson, and Hansen appeared. Methods of investigation which we used were, for the most part, very similar to those described in the paper, but we also used dilatometry to determine the temperature of the $\alpha \leftrightarrow \beta$ transformation and made measurements of the liquidus temperatures of alloys in order to fix the eutectic point. Alloys were prepared from van Arkel zirconium and Johnson, Matthey &

Co's. H.S. tungsten rod by melting in nonconsumable tungsten electrode arc-furnaces.

The dilatometer used is similar to an extensometer employed by Bangham and Franklin⁷ for measuring the expansion of coal, but it is mounted in a silica tube evacuated to better than 10^{-5} mm pressure. The whole apparatus is of transparent fused silica. Cooling curves give the transformation less sharply than heating curves and at temperatures about 30°C lower. The values from heating runs with specimens containing 0, 10, 20, and 35 atomic pct W are $865 \pm 5^\circ$, $864 \pm 5^\circ$, $867 \pm 5^\circ$ and $865 \pm 5^\circ\text{C}$, respectively.

The method⁸ used to determine melting points in an arc-furnace is to so adjust the power in the arc that a

Table IX. Melting Points for Various Alloys

Composition (atomic pct W) "Melting point," °C	0	2.5	5.0	8.3	11.0	14.3	18.6	25.0	30.0
	1850	1830	1805	1790	1775	1830	1860	1955	2080

small specimen is held half molten and half solid, and then to measure with an optical pyrometer the temperature of the junction between the two states. Without opening the furnace, measurements can be made on several specimens in succession, and these may include

Table X. Comparison of Results

	Domagala, McPherson and Hansen	Geach and Slattery
Peritectic	2175°C 33.33 atomic pct W	2150°C c.33 atomic pct W
Eutectic	1650±15°C 10 atomic pct W	1700±50°C 10 atomic pct W
$\alpha \rightarrow \beta$ transformation	850±15°C	865±5°C
Solubility of Zr in W at peritectic temperature	c.10 atomic pct Zr	6± atomic pct Zr
		Metallography

certain pure metals of known melting points, so that the correction to be made to observed temperatures may be determined. The melting points of standard metals can be determined with an accuracy of $\pm 50^\circ\text{C}$, but values obtained with alloys may be rather less certain. Values obtained for this system, Table IX, make it difficult to place the eutectic temperature below 1700°C . These experiments also gave the form of the liquidus curve and so enabled us to fix the eutectic composition at 10.5 ± 1.5 atomic pct W.

Our results for the system are collected in Table X where they are compared with those published by Domagala, McPherson and Hansen. Agreement between the two investigations is excellent throughout.

R. F. Domagala, D. J. McPherson, and M. Hansen (authors' reply)—The authors were surprised and gratified to learn of the concurrent work on the Zr-W system by Geach and Slattery, particularly in view of the generally excellent agreement between the two independent studies. Within the admitted limits of accuracy, there is no single point of difference between the two sets of data. We accept without reservation the more accurate value of the discussers for the solubility of zirconium in wolfram at the peritectic temperature.

⁷ Bangham and Franklin: *Trans. Faraday Soc.* (1946) 42B, p. 289.

⁸ G. A. Geach and D. Summers-Smith: *Journal Inst. Metals* (1951) 80, p. 143.

Copper-Zinc Constitution Diagram, Redetermined in the Vicinity of the Beta Phase By Means of Quantitative Metallography

by Lilian Heikkinen Beck and Cyril Stanley Smith

DISCUSSION, B. H. Alexander presiding

R. Haynes (Dept. of Coal Gas and Fuel Industries with Metallurgy, The University, Leeds, England)—I am interested in the heat treatment given to the alloys in order to establish equilibrium at the various temperatures. The process, in the case of the α - β alloys, seems to be the tempering of the quenched β phase. An alternative method is to anneal the specimens at a high temperature, say 800°C , for a short time and to follow this by slowly cooling to the temperature at which it is desired to achieve equilibrium. The specimens can then be annealed at this temperature for a suitable length of time. This procedure would result in the formation of a large grain size and a coarse precipitate. If a sufficiently long traverse is made, extra sources of error are not introduced and errors due to the lack of sharpness of the grain boundaries are minimized. Perhaps the authors can express their opinion on the relative merits of the two approaches to equilibrium.

A short time ago I applied the point-counting method, described by Howard and Cohen⁸ to the study of isothermal transformations in eutectoid aluminum bronzes.¹⁰ The results showed that equilibrium between the proeutectoid constituents and the β phase was achieved in a few hours in the temperature range 450° to 560°C . There were indications that below this temperature range the time required to achieve equilibrium increased rapidly. The systems Cu-Al and Cu-Zn are analogous in many ways. It is probable that the rates of approach to equilibrium in both systems under similar conditions will be of the same order of magnitude. Have the authors decided upon the annealing times arbitrarily or has some measure of the rate of approach to equilibrium been made?

The authors give no measure of the accuracy of their metallographic results. A value for the standard deviation of the results (i.e., a measure of the variation

of the "count" in different fields of the specimen) would be of interest.

L. H. Beck and C. S. Smith (authors' reply)—The annealing conditions were arbitrarily selected on the basis of long experience with the behavior of the alloys in question. The quenching and reheating procedure was adopted in order to give relatively fine particles of the second phase within the β matrix so as to give small diffusion distances and a rapid approach to equilibrium. This has to be balanced against the conflicting requirement for larger particles on which greater accuracy of measurement is possible. That equilibrium was indeed achieved was shown by measurements on specimens annealed for half the times quoted which gave substantially the same results. Probably even shorter times would have been satisfactory, but the determination of this would have involved the expenditure of more personal effort in exchange for shorter furnace times.

No detailed statistical study was made. The measurements on the two halves of each specimen differed by an amount that rarely exceeded 1.5 pct of the total area, including all errors, and the average of the two was reported in the paper. Five successive measurements of the area of β phase in a single specimen of coarse anisotropic structure of the worst possible geometry were 13.7, 14.24, 14.51, 14.35, and 14.17 pct β , respectively. The individual traverses on such samples showed considerable differences, but the average of all 18 was fairly reproducible. On the above sample—the worst sample studied—the standard deviations for single traverses amounted to 2.7, 1.9, and 2.4 pct when measured by 18 traverses in each of three different directions. Much of this deviation results from segregation and anisotropy and is much less in uniform structures. It would be desirable to make more extensive statistical studies of the data.

¹⁰ R. Haynes: Ph.D. Thesis, University of Sheffield, England (September 1951).

The Influence of the Rate of Deformation on The Tensile Properties of Some Plain Carbon Sheet Steels

by Joseph Winlock

TO have been chosen by you to give the Howe Memorial Lecture is the greatest honor I have ever had and I should like to have you know that I appreciate it deeply.

Many years ago I had the privilege and the pleasure of working with Professor Howe in the private laboratory which he had established in his home at Bedford Hills, New York. Without doubt he was one of the world's greatest metallurgists and so you can imagine what a difficult task it has been for me to live up to his teachings.

Every morning Professor Howe would outline the work he wanted done and the recollections of those conferences are clear to me to this day. Sometimes he would ask me to ride in his automobile and the chauffeur had full instructions to go no more than fifteen miles an hour. If he did so, Professor Howe was sure to rap upon the man's shoulder with his cane. I assure you, however, Professor Howe's thinking was not at that rate. His homely advice, his patience and his perfect control of the English language still impress me. Many times I heard him dictate a complicated paper on metallurgy and never find it necessary to change a single word.

There are no better words to describe the character of Professor Howe, in my opinion, than those used by Professor Sauveur when he presented the John Fritz Medal to him in 1917:

"Lover of justice and humanity
Public servant and public benefactor,
Master of the English Language,
Loyal and devoted friend,
Untiring and unselfish worker in an
important field of science."

I hope you will bear with me with the same patience and understanding which he used to give to me.

The peculiar behavior of steel at the yield point has long been known and has been the subject of much research, both in this country and abroad.^{1,2} Many theories, including some of mine and my colleagues, have been suggested, but none of them, in our opinion, fully explains to our satisfaction why the phenomena occur. Of particular importance has

been the work of Nadai,³ Siebel and Pomp,⁴ Sachs and Fiek,⁵ Rawdon,⁶ Kenyon and Burns,⁷ Gensamer,⁸ Gensamer and Mehl,⁹ Davenport and Bain,¹⁰ Fell,¹¹ Deutler,¹² Brinkman,¹³ MacGregor,¹⁴ Hollomon,¹⁵ Cottrell,¹⁶ and Palm.¹⁷

The question of what is occurring during this singular behavior is not only of interest from an academic point of view, but is of great practical importance for at least two reasons: 1—The highly localized plastic flow which occurs during the deep drawing of light-gage steel gives rise to surface markings which seriously mar its appearance, Fig. 1. If the forces causing the deformation are primarily tensile forces, these surface markings occur as depressions in the surface. Whereas, if the forces causing the deformation are primarily compressive, irregular lines of elevations occur. These surface markings are known as Lüder's lines, Hartmann lines, the Piobert affect, and, in the shop, as "stretcher strains." 2—The steel is in the most suitable condition for deep drawing after the yield point phenomena have been removed. When this is done, the steel may be deep drawn more easily and to a greater extent.¹

It should be mentioned that steel is not the only metal which shows this peculiar behavior at the yield point. Stretcher strains occur, also, during the deformation of some copper-nickel-zinc alloys.¹⁸

The purpose of this paper is not an attempt to describe what *causes* the steel to behave in this peculiar manner, but an attempt: 1—to describe *what* is taking place at the yield point; and 2—to show the influence of the rate of deformation on the tensile properties of some plain carbon steels.

As is well-known, there are two methods of deforming a metal in tension: 1—by actually hanging an increasing amount of dead weight on the metal; or 2—by deforming the metal at some given rate or rates by means of oil pressure cylinders, screws, etc. With the first method, the load is always present and, clearly, no drop in load can ever occur while the steel is deforming. With the second method, the registered load is the resistance of the steel to the deformation being imposed upon it. The second method is the one most widely used, and is the one referred to throughout this paper.

In order to describe clearly what is occurring at the yield point in steel, it will help, I believe, if a description is first given of what occurs when alumi-

J. WINLOCK, Member AIME, is Chief Metallurgist, The Budd Co., Philadelphia.

TP 3539C. Manuscript, Feb. 18, 1953. Los Angeles Meeting, February 1953.

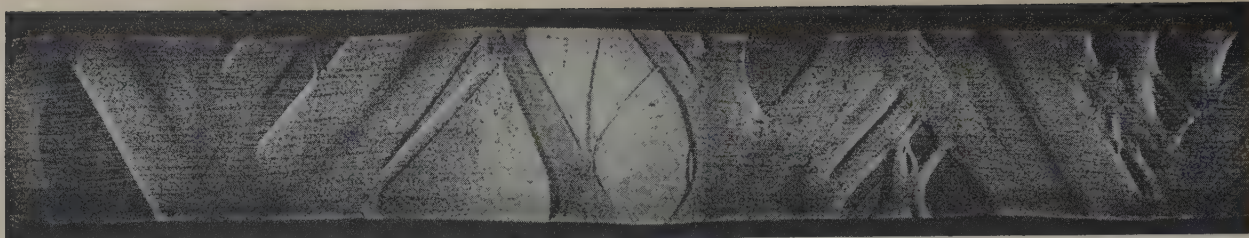


Fig. 1—Tensile specimen showing Luder's lines.

num and most other metals are elastically and plastically deformed in tension.

At the instant deformation begins, the aluminum begins to offer a resistance to deformation and for a certain distance the load-deformation curve rises as a substantially straight line. So long as the curve remains substantially straight, the deformation is substantially elastic. But, when the deformation becomes so great that the resistance of the metal to elastic deformation is overcome, plastic deformation takes place. This is shown in Fig. 2. It is to be noted, too, that the metal exhibits a continually increasing resistance to deformation until the maximum load is reached; and, of particular importance, is the fact that the curve is smooth from origin to fracture. That is, as the change from the substantially elastic state to the substantially plastic state takes place, the metal immediately offers a greater resistance to deformation and, consequently, increasingly higher loads are required for plastic deformation to continue.

When steel is deformed in a similar manner the metal behaves very differently. The steel appears to behave elastically in much the same manner, but a much greater load is required to initiate plastic deformation and when plastic deformation does occur, there is a lowering of the resistance to deformation and, consequently, the registered load is lower. This is shown by the solid line in Fig. 3. Our work has shown that substantial plastic deformation does not occur in a uniform manner as it does with aluminum, but occurs first at some point or points. This means

that parts of the specimen reach the yield point and begin to deform plastically before other parts. The stress at which plastic deformation first occurs, is, according to general testing practice, taken to be the yield point of the steel as a whole.

It is the differences in thickness produced by plastic flow occurring at different points which give rise to the surface markings. As the alternate local slipping and work-strengthening continues, and the extent and number of the depressions in the surface of the metal increase, the condition is reached where the entire test piece has been so affected. The differences in cross sectional area then become relatively minute. In effect, this is a return to the original even surface. The total elongation occurring during this peculiar process has been conveniently referred to as the "yield point elongation." When all of the grains have slipped in this manner, the load-deformation curve begins to rise again as a relatively smooth curve. Since the yield point elongation is of the order of 10 pct or less, stretcher strains occur in stampings or those parts of stampings in which the elongation of the steel is of this amount. Mathematical equations, it seems to us, cannot be established for this portion of the load-deformation curve on the basis of homogeneous or heterogeneous plastic deformation because neither uniform nor nonuniform plastic deformation is occurring! How can either of these be taking place when there are large portions of the metal which are not plastically deforming at all?

It appears that for steel to behave like aluminum,

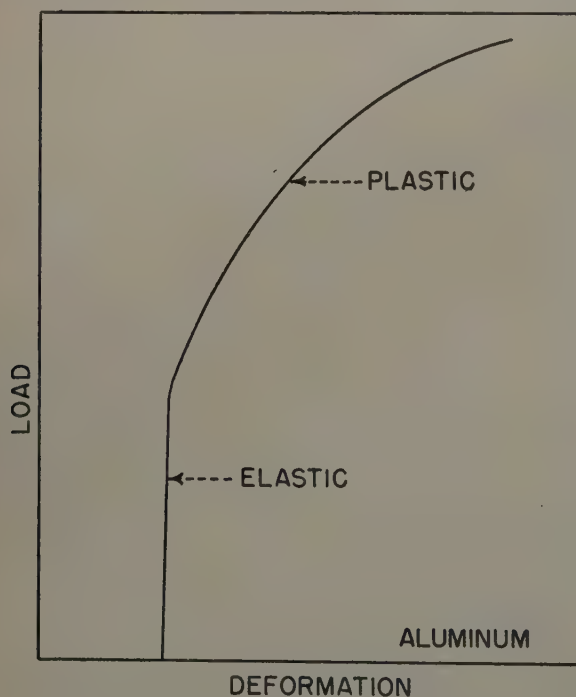


Fig. 2—Load-deformation curve of aluminum.

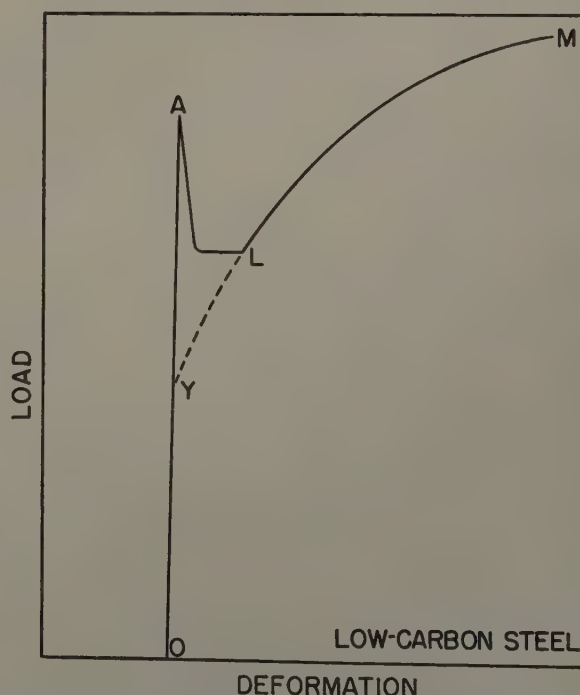


Fig. 3—Load-deformation curve of carbon steel containing free ferrite.

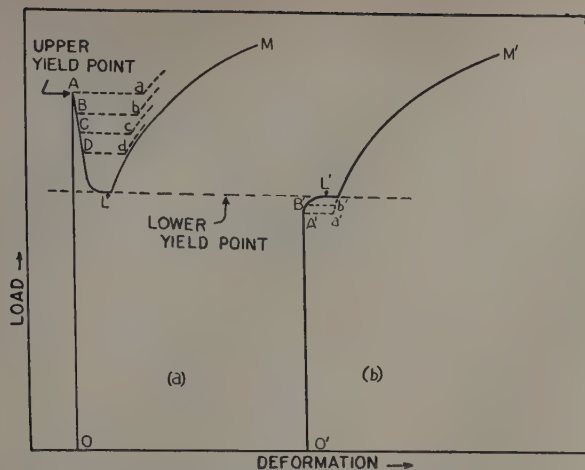


Fig. 4—Load-deformation curves of steels with and without upper yield points.

substantial plastic deformation should take place at the load Y in Fig. 3 and the load-deformation curve should be the curve OYLM. For some unexplained reason, however, the load Y is "overshot" and substantial plastic flow does not commence until the load A has been reached. This point has long been known as the "upper yield point." At the instant plastic deformation occurs, then, the steel finds itself overloaded, so to speak, with a resistance to further plastic deformation of only the load Y. The further behavior of the first increment of metal which has deformed plastically is dependent entirely upon its reaction to the precarious and unstable situation in which it finds itself. Because of the high load existing at the moment substantial plastic deformation occurs, the metal, because of its then lowered resistance to further plastic deformation, must deform at a very high speed, and it does so. The amount of metal forced to a great speed of deformation is partly governed by the amount of elasticity remaining in the other parts of the specimen and of the testing machine, and it is for these and other reasons that the downward path of the load-deformation curve veers away from the portion of the curve denoting elastic deformation. It should be emphasized that substantial plastic deformation may and often does occur at several isolated points instead of at just one point.

The following is a more detailed explanation of what we believe occurs: when the load A, Fig. 4a, is reached, the first increment of metal deforms plastically at the high load which it has built up for itself while in the elastic state. And, since it now has the resistance to further plastic deformation of only the load Y of Fig. 3, it does what it is forced to do, namely, travel at a high speed along the dotted line A-a. At the next instant, two other small increments, one on either side of the first, deform plastically at the load B an amount equal to B-b. The load on the specimen drops—first, because the metal has only the resistance to further plastic deformation of the load Y; second, because there is a concentration of stress at either end of the local constriction; third, there is now present some metal which has been cold-worked and this in itself throws a higher stress on the undeformed adjoining crystalline grains; and fourth, because the increment's speed of travel is greater than the head speed of the testing machine.

The total load registered by the specimen never drops to the load Y but only to the load L, known as the "lower" yield point, because a balance is reached

between 1—the increase in resistance of the metal undergoing plastic deformation, i.e., work-strengthening; 2—the increase in resistance of the metal to further deformation because of the high rate of deformation; and 3—the presence of metal in other parts of the gage length which has only been elastically deformed, and which must first be stressed to a value corresponding to the upper yield point before plastic deformation can occur.

The extremely important point to emphasize is that at the instant plastic deformation is initiated, it is not necessary to have present the load which the metal has built up for itself while in the elastic state, in order for plastic deformation to continue.

It should be emphasized, also, that whether or not an upper yield point is obtained in the load-deformation diagram, a yield point elongation cannot exist unless the steel possesses an upper yield point; and, further, that each increment of the steel must be stressed to the value of the upper yield point before plastic deformation can occur. In short, we believe that the true stress at the load A in Fig. 4a is the same as the true stress at the load B' in Fig. 4b.

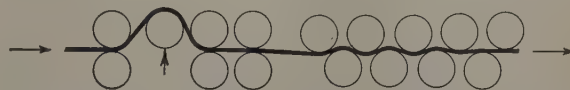


Fig. 5—Schematic drawing of the Budd-developed roller leveler.

In this connection it should be emphasized that the presence or the absence of an upper yield point depends to such a large extent upon the tensile specimen itself—that is, whether it is properly aligned in the testing machine, the presence of stress concentrations such as minute surface defects, etc.,—that often it cannot be obtained at all. As Dr. Mehl once so aptly said, "it would seem as though the load was increased so carefully (in especially prepared specimens) that the steel had hardly become aware of it,—much as the tax load may be increased on an unsuspecting body politic!"

It has long been known¹ that if the steel has been cold-worked a sufficient amount by cold rolling, or roller leveling, the load-deformation curve does take the shape of the curve OYLM in Fig. 3. In the deep drawing of sheet and strip steel we have, for many years, used a combination of cold rolling and roller leveling in a specially made roller leveler which we designed and built, Fig. 5. By this means we have prevented the irregular surface markings (stretcher strains) from occurring during the deep drawing operation, and we have found that after the yield point phenomena have been removed in this manner, the steel can be deep drawn more easily and at a faster rate of deformation. This is because if the rate of deformation is too rapid, and the yield point phenomena have not been removed, the steel may fracture where plastic deformation first occurs, that is, at the first stretcher strain.

In order to ascertain the influence of the rate of deformation on the load-deformation curve of low carbon steels, we performed a great many experiments some years ago.¹⁹ Briefly, it was found that the lower yield point, the yield point elongation, and the ultimate tensile strength increased as the grain size was made smaller and as the rate of deformation was increased. Due to limitations in our testing apparatus and methods of recording available at that time, rates of deformation of only 4.44 in. per in. per min were obtainable. This rate is some-

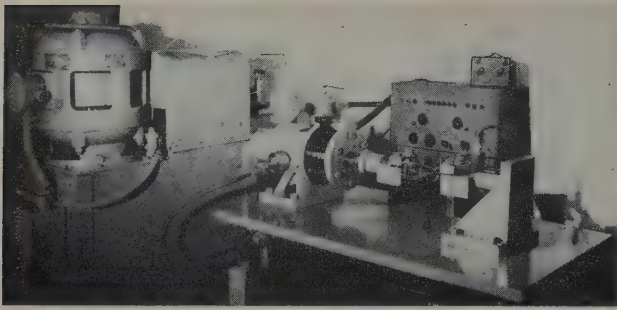


Fig. 6—High speed testing apparatus.

what below the average speed of most deep drawing operations which is of the order of 45 in. per in. per min. Therefore, in order to study the effects of much higher rates of deformation, we developed a testing apparatus shown in Fig. 6 which deforms and records the deformation of the steel at much higher speeds.

It consists of a hydraulic pump and ram system proportioned to allow a wide range of head speeds up to 450 in. per min and loads up to 3000 lb. The loads are recorded by means of a balanced bridge weighing system operating on a 1000 cycle carrier which transmits its signal to an oscillograph. Deformation is recorded with a microformer operating from the same carrier wave and feeding into the same oscillograph. Both load and deformation systems have positive integral calibrations that are activated with each run.

In this paper we have extended our experiments not only to include the influence of much faster rates of deformation on the load-deformation curve, but also to determine the effect of increasing the carbon in the steel.

We chose for our experiments five sheet steels

having carbon contents as follows: 0.06, 0.21, 0.34, 0.48, and 1.03 pct. The amount of the other elements was substantially the same in all of the steels.

The steels were all 0.035 in. in thickness and were carefully heat-treated to produce pearlite and ferrite,* that is, they were heated above the critical

* Professor Howe's definition of ferrite is pure iron, or rather carbonless iron. The word is now more commonly defined as a solid solution in which α iron is the solvent and which is characterized by a body-centered cubic crystal structure. In this paper the latter definition applies.

range and cooled in air. Micrographs were taken of each steel and these are shown in Figs. 7 to 11. Examination will show, as would be expected, that as the carbon is increased the amount of pearlite increases and the amount of free ferrite decreases.

Tensile specimens were made from each sheet and machined to the dimensions established by the ASTM for Standard Rectangular Tension Tests with a 2 in. gage length (E8-46).

The specimens were deformed at the following rates: 0.002, 0.018, 0.166, 1.500, 20.000, and 200.000 in. per in. per min.

It will be noted that the highest rate is some five times the average speed used in ordinary deep drawing operations and that these testing speeds represent a range of 100,000 to 1.

A series of load-deformation curves were made, Figs. 12 to 17, of the steels at different rates of deformation. The experimental data obtained from these curves were analyzed and are summarized in Table I and Figs. 18 to 22.

It may be seen in Fig. 18 that for any given steel the upper yield point increases as the rate of deformation increases. It may also be observed that the increase in the upper yield point for a given increase in the rate of deformation is independent of the

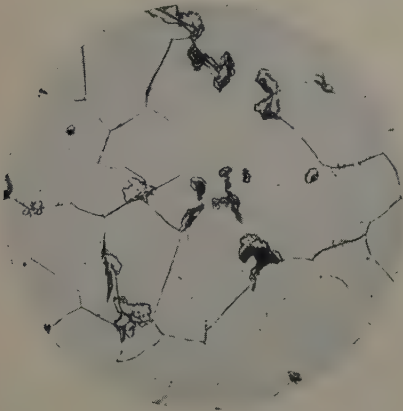


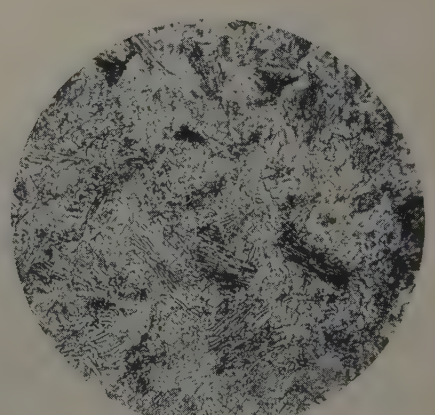
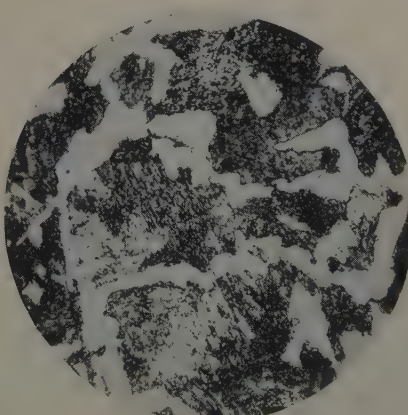
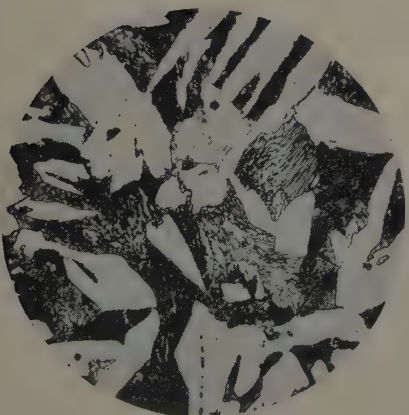
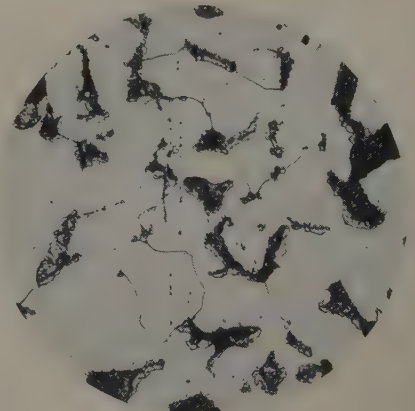
Fig. 7 (left)—Micrograph of 0.06 pct C steel. X500.

Fig. 8 (right)—Micrograph of 0.21 pct C steel. X500.

Fig. 9 (lower left)—Micrograph of 0.34 pct C steel. X500.

Fig. 10 (lower center)—Micrograph of 0.48 pct C steel. X500.

Fig. 11 (lower right)—Micrograph of 1.03 pct C steel. X500.



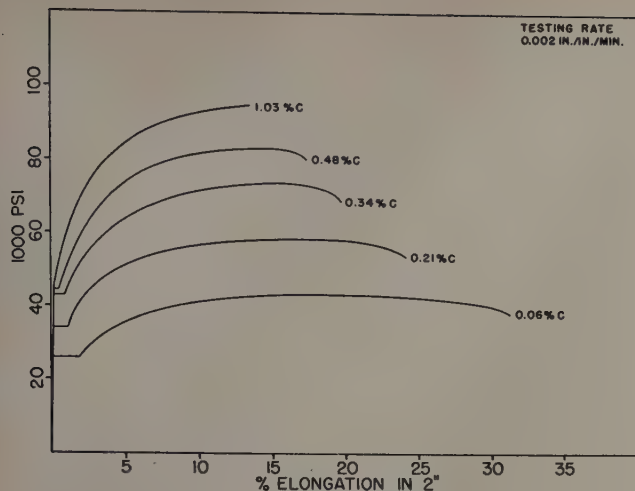


Fig. 12—Load-deformation curves of steels deformed at 0.002 in. per in. per min.

carbon content. However, when the carbon content is increased above the amount necessary to form the eutectoid, no upper yield point occurs, and, consequently, no lower yield point can exist. The apparently anomalous behavior of the hypereutectoid steel is not so much out of order, as it would seem, because we believe that all the upper and lower yield point phenomena are properties of free ferrite. For this reason, we have not included the curves of the "normally behaving" (if this term is permissible) hypereutectoid steels in Figs. 18, 19, and 20 which summarize the results of our experiments on the yield point phenomena of the hypoeutectoid steels containing free ferrite.

In this connection, some experiments were made with the hypereutectoid steel heat-treated so as to cause the carbon to be in the spheroidized condition,

Table I. Experimental Data Giving Tensile Properties of Steels of Different Carbon Content Deformed at Different Rates of Deformation

Speed of Test, In. per Min	Pct Carbon	Upper Yield Point	Lower Yield Point	Yield Point Elongation	Elongation, Pct in 2 In.	Ultimate Tensile Strength
0.002	0.06	25,000	26,000	1.75	31.50	43,500
0.018	0.06	28,000	28,000	2.50	32.25	44,000
0.166	0.06	31,000	29,500	3.00	33.25	45,000
1.500	0.06	34,000	31,500	4.00	34.50	46,500
20.000	0.06	37,500	33,500	5.25	36.50	46,500
200.000	0.06	40,500	35,500	6.75	39.00	47,500
0.002	0.21	33,000	34,000	1.25	24.25	59,000
0.018	0.21	36,500	36,000	1.50	24.75	60,000
0.166	0.21	40,000	38,000	2.00	25.50	61,000
1.500	0.21	43,000	41,000	2.50	26.00	62,500
20.000	0.21	47,000	44,000	4.50	26.75	63,500
200.000	0.21	51,000	46,500	4.75	27.25	65,000
0.002	0.34	38,500	43,000	1.00	20.00	74,000
0.018	0.34	41,500	45,000	1.10	20.25	77,000
0.166	0.34	45,000	48,000	1.25	20.50	80,500
1.500	0.34	48,500	50,500	1.75	20.75	82,000
20.000	0.34	52,000	53,500	2.25	21.00	86,000
200.000	0.34	56,000	56,000	3.25	21.25	88,500
0.002	0.48	44,000	44,500	0.50	17.5	83,500
0.018	0.48	47,500	47,000	0.60	17.5	86,500
0.166	0.48	50,500	50,000	0.75	17.5	89,000
1.500	0.48	53,500	53,000	1.00	17.5	91,500
20.000	0.48	57,000	56,000	1.25	17.5	94,500
200.000	0.48	60,500	59,500	1.50	17.5	97,000
0.002	1.03		45,500*		13.5	95,000
0.018	1.03		39,500*		13.5	98,000
0.166	1.03		45,000*		13.5	101,000
1.500	1.03		52,000*		13.5	104,000
20.000	1.03		60,000*		13.5	109,500
200.000	1.03		58,500*		13.5	114,500

* Yield strength—not lower yield point—that is, 0.5 pct extension under load.

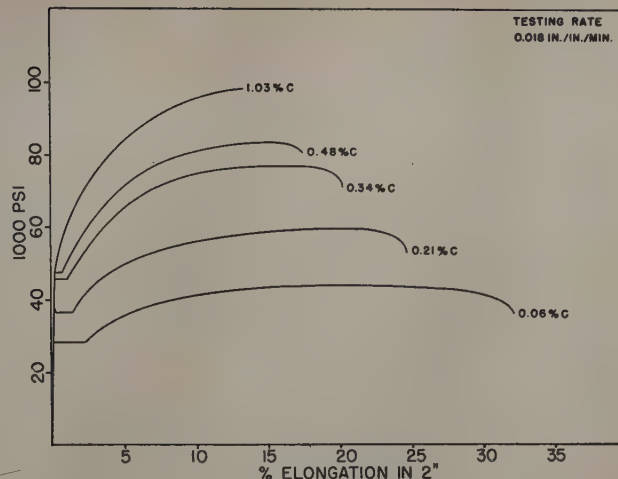


Fig. 13—Load-deformation curves of steels deformed at 0.018 in. per in. per min.

thus producing free ferrite. In these experiments we found that an upper and a lower yield point occurred at all rates of deformation.

In other words, when free ferrite is made to disappear by heat treatment, or when it is prestressed by cold working, or when it is cooled rapidly from just below the critical range, or when it is treated by heating in wet hydrogen,²⁰ the upper yield point

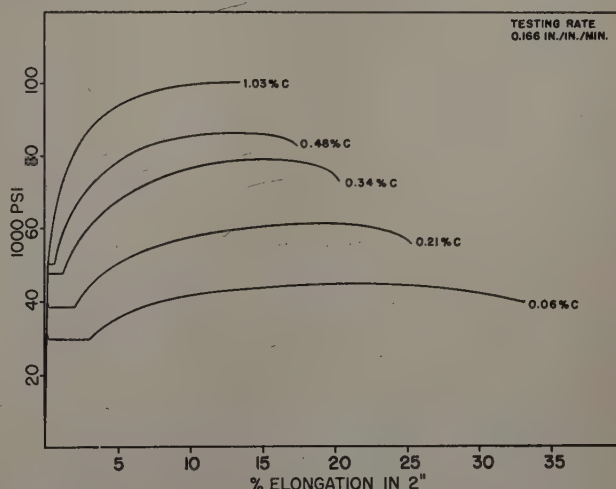


Fig. 14—Load-deformation curves of steels deformed at 0.166 in. per in. per min.

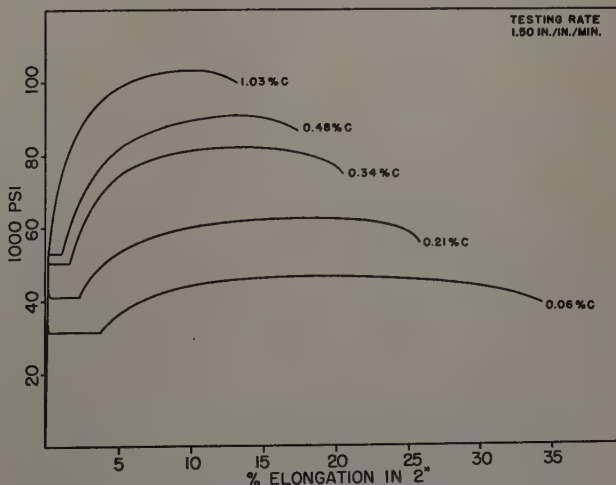


Fig. 15—Load-deformation curves of steels deformed at 1.50 in. per in. per min.

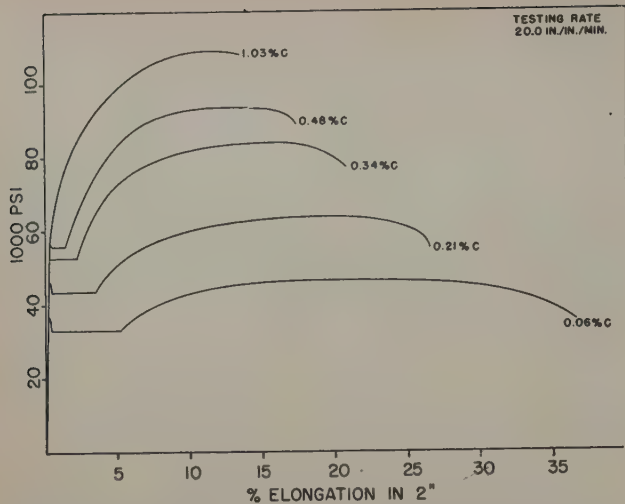


Fig. 16—Load-deformation curves of steels deformed at 20.00 in. per in. per min.

disappears from the load-deformation curve, and, consequently, the lower yield point disappears too.

As may be seen from the curves shown in Fig. 19, the lower yield point increases as the rate of deformation is increased and as the carbon is raised. And it may also be seen that as the carbon is raised, the lower yield point becomes more affected by an increase in the rate of deformation.

The lower yield point gives, we believe, a much more reliable indication of the end of substantial elastic behavior of the steel than the upper yield point because it is much less affected by those variables of testing which are difficult to control, as we have already mentioned.

It is of particular importance to note that the yield strength (0.5 pct extension under load) of the hypereutectoid steel containing no free ferrite is lower even at very high rates of deformation than some of the steels containing very much less carbon. In other words, the hypereutectoid steel, unencumbered by the yield point phenomena, deforms in much the same manner as does cold-worked low carbon steel, that is, the load-deformation curve is smooth from origin to fracture.

The amount of yield point elongation, Fig. 20, in-

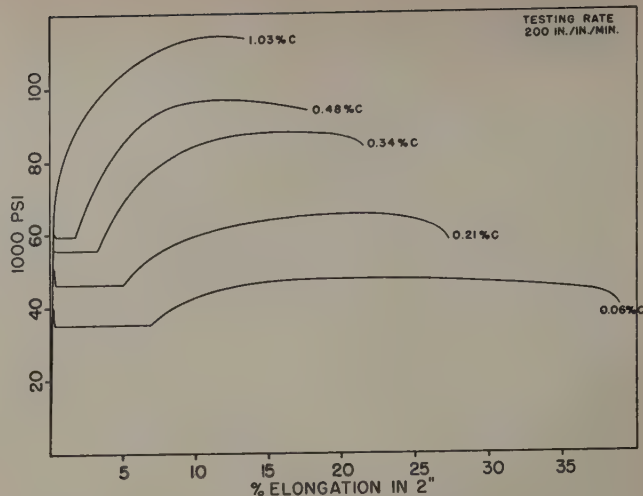


Fig. 17—Load-deformation curves of steels deformed at 200.00 in. per in. per min.

creases as the rate of deformation increases and decreases as the amount of carbon is raised. The amount of yield point elongation is less affected by an increase in the rate of deformation as the carbon is raised.

The total elongation, Fig. 21, either increases or does not change as the rate of deformation is increased, and decreases as the amount of carbon in the steel is increased. The amount of total elongation is less affected by an increase in the rate of deformation as the carbon is raised.

The ultimate tensile strength, Fig. 22, increases as the rate of deformation is increased, and increases as the carbon in the steel is increased. The ultimate tensile strength is more affected by an increase in the rate of deformation in the higher carbon steels than it is with the lower carbon steels. From the converging of the curves for the low carbon steels shown in Fig. 22, the very interesting and significant observation can be made that the ultimate strength of absolutely pure iron would be very little affected by high rates of deformation.

In summarizing the data, we can make the following statements regarding plain carbon steel:

1—All the load-sustaining properties increase

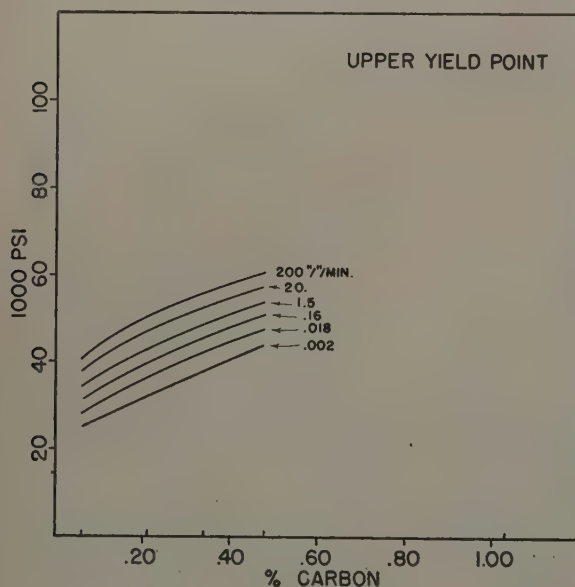


Fig. 18—Curves giving a summary of data of upper yield points of steels at different rates of deformation.

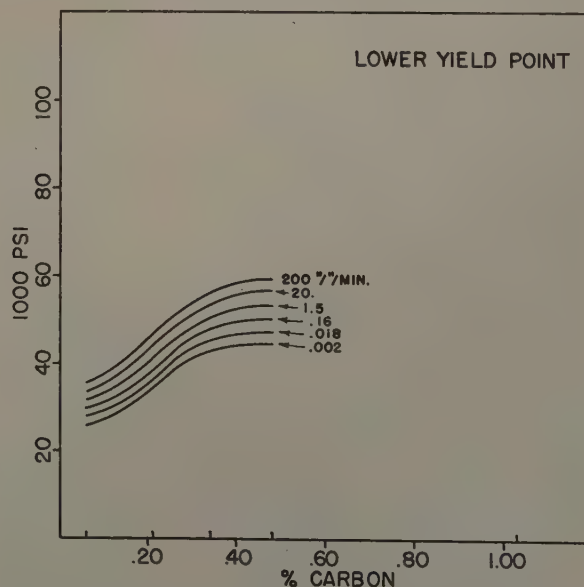


Fig. 19—Curves giving a summary of data of the lower yield points of steels at different rates of deformation.

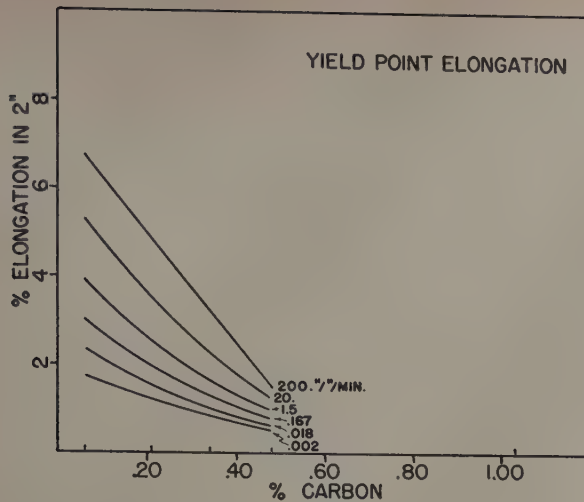


Fig. 20—Curves giving a summary of data of the yield point elongations of steels at different rates of deformation.

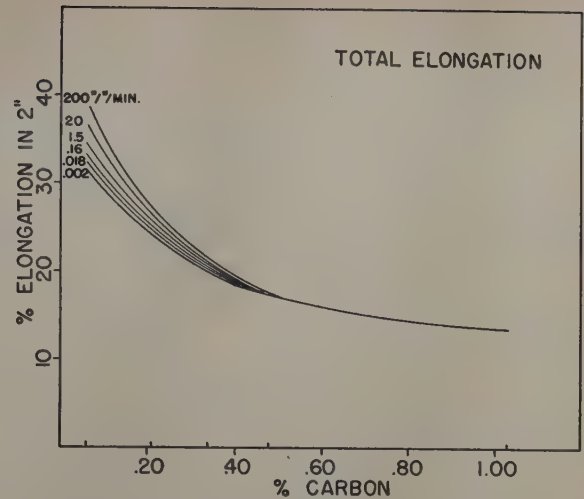


Fig. 21—Curves giving a summary of data of the total elongations of steels at different rates of deformation.

with increasing rates of deformation.

2—All percentage elongations either remain constant or increase with increasing rates of deformation.

3—All load-sustaining properties increase as the amount of free ferrite is decreased.

4—All percentage elongations decrease as the amount of free ferrite is decreased.

From a practical standpoint, these experiments, together with others which we have made, indicate that the plastic behavior of steel imposes no limitations on new methods of deep drawing involving much higher rates of deformation.

I should like to acknowledge to my colleagues, Dr. Ralph Leiter, Mr. Herbert Van Sciver, and Mr. Paul Nelson, my appreciation for their valuable assistance in the preparation of this paper. I should like, also, to express to Mr. Edward G. Budd, Jr. my gratitude for his interest and encouragement.

References

¹ G. L. Kelley and Joseph Winlock: U. S. Patent No. 1,649,704, Metal Working Machine. Filed Jan. 5, 1924 and issued Nov. 15, 1927. See also U. S. Patents Nos. 1,649,705 and 1,649,706. Filed May 29, 1925 and issued Nov. 1927, G. L. Kelley and C. L. Eksergian.

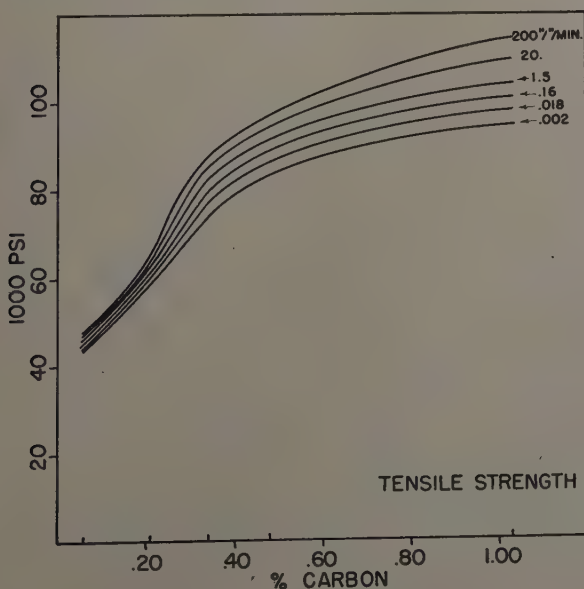


Fig. 22—Curves giving a summary of data of the tensile strengths of steels at different rates of deformation.

² W. Lüder: *Dinglers Polytechnisches Journal* (1860) 155, p. 18.

³ A. Nadai: *Plasticity*. (1931) New York. McGraw-Hill Book Co.

⁴ E. Siebel and A. Pomp: Einfluss der Formänderungsgeschwindigkeit auf den Verlauf der Fließkurve von Metallen. *Mitteilungen*, Kaiser-Wilhelm-Inst. für Eisenforschung (1928) 10, pp. 63-69.

⁵ G. Sachs and G. Fiek: *Der Zugversuch* (1926) Leipzig. Akademische Verlagsgesellschaft.

⁶ H. S. Rawdon: Strain Markings in Mild Steel Under Tension. U. S. Bur. of Standards, *Journal of Research* (September 1928) 1, No. 3, pp. 467-485.

⁷ R. L. Kenyon and R. S. Burns: Autographic Stress-Strain Curves of Deep Drawing Sheets. *Trans. ASM* (1933) 21, pp. 577-612.

⁸ M. Gensamer: The Yield Point in Metals. *Trans. AIME* (1938) 128, pp. 104-117.

⁹ M. Gensamer and R. F. Mehl: Yield Point of Single Crystals of Iron Under Static Loads. *Trans. AIME* (1938) 131, pp. 372-377.

¹⁰ E. S. Davenport and E. C. Bain: The Aging of Steel. *Trans. ASM* (1935) 23, pp. 1047-1096.

¹¹ E. W. Fell: Yielding Phenomena and Distortion in Iron, Steel, Aluminum Alloy and other Metals Under Stress. *Carnegie Scholarship Memoirs*, Iron and Steel Inst. of Great Britain (1937) 26, pp. 123-163.

¹² H. Deutler: Experimentelle Untersuchungen über die Abhängigkeit der Zuspännungen von der Verformungsgeschwindigkeit. *Physikalische Zeitschrift* (1932) 33, pp. 247-259.

¹³ H. Brinkman: Zerreißversuche mit hohen Geschwindigkeiten. Dissertation, Technische Hochschule, Hanover (1933).

¹⁴ C. W. MacGregor: Relations Between Stress and Reduction in Area for Tensile Tests of Metals. *Trans. AIME* (1937) 124, pp. 208-228.

¹⁵ John H. Hollomon: Tensile Deformation. *Trans. AIME* (1945) 162, pp. 268-288.

¹⁶ A. H. Cottrell: Effect of Solute Atoms on the Behavior of Dislocations. Report of Conference on Strength of Solids, Bristol, Physical Society, London (1948) p. 30.

¹⁷ J. H. Palm: Reflection on Yielding and Aging of Mild Steel. National Luchtvaartlaboratorium Report M. 1230 Prepared for Reports and Transactions, Vol. XV (1949).

¹⁸ R. Ergang: Stretcher Strains. *Metal Industry* (October 1952) 81, No. 14, pp. 261-264.

¹⁹ Joseph Winlock and Ralph W. E. Leiter: Some Factors Affecting the Plastic Deformation of Sheet and Strip Steel and Their Relation to the Deep Drawing Properties. *Trans. ASM* (1937) 25, pp. 163-205.

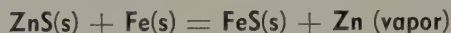
²⁰ J. R. Low, Jr. and M. Gensamer: Aging and the Yield Point in Steel. *Trans. AIME* (1944) 158, pp. 207-249.

Vapor Pressure of Zinc

In the Reduction of ZnS by Cu and Fe

by A. W. Bethune and L. M. Pidgeon

The equilibrium vapor pressure of zinc has been determined over the systems:



and



by reacting the components in an evacuated tube containing a thin copper fiber, and allowing equilibrium to be established with respect to the brass formed and the zinc in the vapor phase. The composition of the brass formed was determined and equilibrium vapor pressure values obtained from existing data. Between 850° and 1000°C, values for the first reaction ranged from 8 to 58 mm Hg; for the second reaction from 1.8 to 22 mm Hg.

THE direct reduction of metallic sulphides may be indicated by an equation of the form



where X is some suitable reducing agent.

In the case where M is a metal of relatively high volatility, the use of vacuum will displace the equilibrium to the right at comparatively low temperatures in the face of the usually unfavorable thermochemistry. For this technique to be feasible, MS, X, and XS, must of course be nonvolatile compared to M. In this regard, zinc becomes an obvious metal both from the point of view of its volatility and the fact that most commercial ore deposits of this metal occur as the sulphide, and its direct reduction would avoid the expensive roasting process necessary prior to present day reduction methods.

Two reducing agents are of interest, namely copper and iron, with the former having the added attraction of being relatively easily regenerated by oxidation in the copper converter.

The possibility of these reactions has been considered before. Imbert¹ patented a process whereby zinc sulphide was reduced by either copper or iron. The process as described took place at atmospheric pressure and, at the high temperatures required, the system was molten, resulting in the formation of a

matte with the consequent reduction in the activities of the reactants.

Peterson² did further experimental work on these reactions and, although promising results were obtained on a small scale, attempts to increase the size of the furnace led to excessive "blue powder" formation.

The early workers failed to realize the large reduction in temperature afforded by the use of vacuum and its desirable results.

More recently, the direct reduction of zinc sulphide by iron has been the subject of a thermodynamic investigation by Kelley,³ and Gross and Warrington⁴ have studied the kinetics of the reaction in the temperature range 900° to 1000°C, their experiments being conducted using vacuum and indicating that the reaction would proceed practically to completion in 1 to 3 hr, depending on the temperature.

A qualitative examination of the system ZnS-Cu carried out at this University indicated that 98 pct of the theoretical zinc in the charge could be recovered in 1 hr at 1000°C when operating under reduced pressure.

The purpose of this research program was to study the equilibrium of the two reactions. During the investigation, reference to the experimental work of Schenk⁵ was found but, due to lack of detail in the report, it was felt that it would be desirable to continue the equilibrium measurements.

Selection of Method

The measurement of vapor pressure of metals presents obvious problems resulting from the high temperatures which must be employed. In the present case, the production of the "reaction pressure" introduces a further difficulty since a chemical reaction must proceed before any metal vapor pressure is produced, resulting in depletion of the re-

A. W. BETHUNE is Graduate Student in Metallurgical Engineering, and L. M. PIDGEON, Member AIME, is Professor of Metallurgical Engineering, University of Toronto, Toronto, Ont., Canada.

Discussion on this paper, TP 3531D, may be sent, 2 copies, to AIME by Aug. 1, 1953. Manuscript, Nov. 21, 1953. Los Angeles Meeting, February 1953.

This paper is a contribution from the Metallurgical Engineering Laboratory and is based on a thesis by A. W. Bethune submitted in partial fulfillment of requirements for the degree of Doctor of Philosophy to the Graduate School of the University of Toronto.

actants. This reaction must proceed and approach an equilibrium pressure at which further reaction ceases. Experiments used first the entrainment method, as described by Pidgeon and King,⁶ and it was found that reaction rates were very slow near the equilibrium pressure, although experiments in vacuo had given rapid rates.

The advantages of a static method are obvious, and it was decided to measure the pressure of zinc by allowing the zinc vapor to come to equilibrium with copper and analyze the brass so produced. The vapor pressure of zinc over brasses has been measured by several workers and satisfactory results are available. As every brass of a particular composition has an equilibrium vapor pressure of zinc associated with it at each temperature, then the converse must hold true; that is, at equilibrium, a vapor pressure of zinc must create an equilibrium state with any copper with which it is in contact. The problem is, therefore, to achieve this equilibrium state.

Hargreaves⁶ modified a technique described by Eukens⁷ to obtain the vapor pressures of zinc above brasses in which the brass sample was held at an elevated temperature in an evacuated tube until equilibrium had been achieved and then the section of the tube remote from the brass sample cooled until condensation occurred from which the vapor pressure of zinc in the system was determined.

Experimental

Materials: Zinc sulphide used in the experimental work was in the form of clear amber sphalerite. Chemical analysis of this material indicated 66.5 pct Zn. Spectroscopic analysis showed the presence of trace quantities of copper, iron, sodium, and cadmium. This material was ground to pass a 200 mesh screen.

Chemically precipitated copper analyzing 99.9 pct Cu and passing 200 mesh was used as the reducing agent in studying the ZnS-Cu system, and was heated in a stream of hydrogen prior to each experiment to prevent any possibility of oxide contamination. The iron used in the subsequent experiments was also of reagent grade, total impurities being 0.02 pct. A fine electrolytic copper fiber, 3 mm wide and 0.04 mm thick, was used as a "gettering" agent for the zinc vapor.

Procedure: Reduction of Zinc Sulphide by Copper: A charge of 6 g was mixed in stoichiometric proportions and placed in one end of a transparent quartz reaction vessel, 10 mm ID and 10 cm long. This weight of charge was sufficient to produce 1.5 g of zinc. A copper fiber, carefully polished to remove oxide and grease coatings and accurately weighed, was inserted in the other end, the tube evacuated to a residual pressure of 5 microns and sealed off under vacuum. The system was placed in the furnace which was then sealed. The temperature was controlled to $\pm 2^\circ\text{C}$. Thermocouples were calibrated against a standardized Pt-Pt-Rh couple.

Curves were obtained from Herbenar's⁸ values for the vapor pressure of zinc above brasses at various temperatures. Isothermals were taken through these curves at appropriate temperatures yielding a plot of vapor pressure vs composition. These values were used in determining the pressure of zinc vapor within the system after analyzing the brass produced.

To obtain the time required to reach equilibrium, reaction vessels were left at temperature for periods

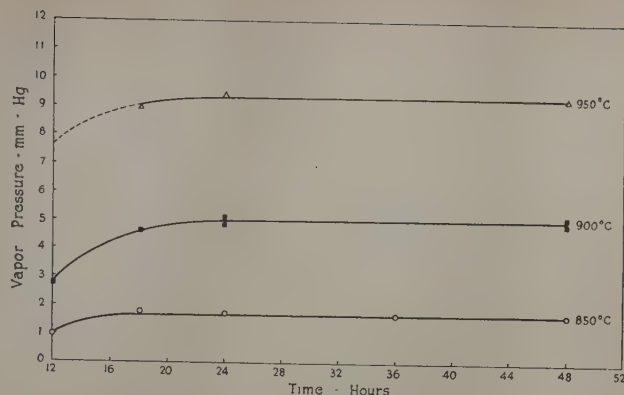


Fig. 1—Reaction pressure above the system $\text{ZnS} + 2\text{Cu}$ at 850° , 900° , and 950°C vs time at temperature.

of 12, 18, 24, and 48 hr. At the end of these four times, the tube would be removed and quickly cooled.

Three independent checks were obtained on the composition of the brass produced: 1—increase in weight over the copper fiber originally used, 2—electrolytic analysis of the brass for copper, and 3—gravimetric determination of the zinc by precipitation with di-ammonium hydrogen phosphate. All these methods agreed within 0.2 pct. This error corresponds to a maximum variation in zinc pressure of 0.5 mm. Although no analysis of sulphur was carried out, the deposit formed possessed a bright mirror finish and it is felt that the degree of contamination was negligible.

Fig. 1 shows in graphical form the results obtained for three temperatures. The graph shows that a constant condition is achieved in all cases by 24 hr. In spite of this, all subsequent experiments were maintained at temperatures for 48 hr as an additional safety factor.

Since the reaction mixture was depleted with respect to zinc as the brass was formed, a large excess of charge was essential. The initial experiments in this series were performed using 0.8 to 1.0 g of copper. These were conducted at 900°C and, on comparing with the values obtained using 0.2 g weights showed an apparently lower reaction pressure, although the weights of zinc absorbed were greater by a factor of three. Consequently, further experiments were conducted with decreasing weights of fiber. The results are plotted in Fig. 2. These experiments showed that constant composition was attained in this system using weights of

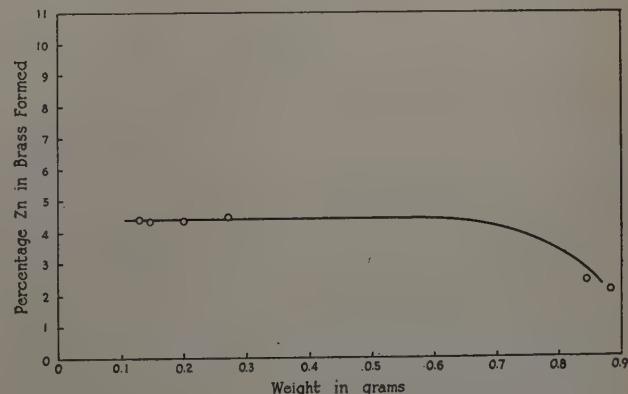


Fig. 2—Reduction of ZnS by copper. Effect of decreasing the weight of copper foil. Experiments, 24 hr at 900°C .

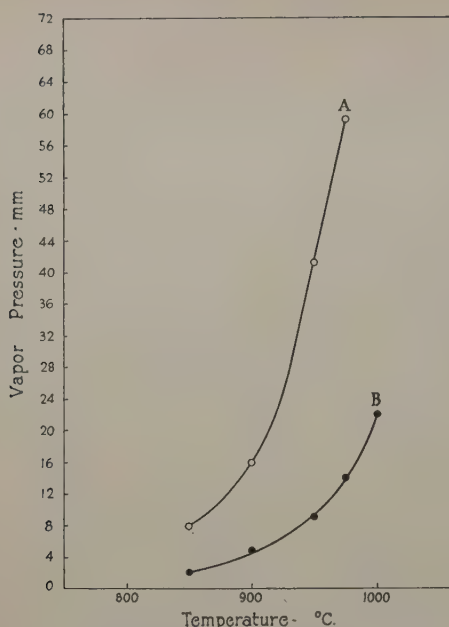


Fig. 3—Vapor pressure vs temperature for the systems.

Curve A (reaction 1)— $\text{ZnS(s)} + \text{Fe(s)} = \text{FeS(s)} + \text{Zn(vapor)}$.

Curve B (reaction 2)— $\text{ZnS(s)} + 2\text{Cu(s)} = \text{Cu}_2\text{S(s)} + \text{Zn(vapor)}$.

copper less than 0.3. The results shown in Fig. 3 were obtained using weights of copper fiber of 0.1 to 0.2 g.

Reduction of Zinc Sulphide by Iron: This reaction was studied using the technique already described. Stoichiometric charges of the material were heated in the evacuated tubes for 48 hr, and the copper fiber analyzed as before. The reaction pressures determined are shown in Fig. 3, curve A.

Alternate Method

The above results, obtained by an indirect method which depends upon the work of others, are also dependent on the attainment of equilibrium both over the reaction mixture and the brass. Corroborative results were obtained using the conventional entrainment method.⁹

In this method, a current of inert gas is passed through the sample until saturation is achieved. The metal vapors are condensed and weighed, and the volume of the inert gas also measured. From the known volume of the inert gas and the calculated volume of the metal, the partial pressure of the metal vapor may be obtained by application of the gas laws.

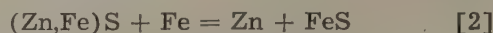
The ideal conditions inherent to accuracy are: 1—It is essential that complete saturation of the inert carrier gas must be established and the reactants must not be appreciably depleted. 2—Temperature, pressure, and rate of flow of the carrier gas must be constant and accurately measured. 3—Condensation of the zinc must be complete and the amount accurately determined. 4—The reacting charge should in effect be heated instantly to the reaction temperature and cooled instantly at the end of the measured period.

When these conditions had been met, results of the vapor pressure over ZnS-Cu were obtained agreeing within 5 pct with the values obtained using the previous method. The entrainment method, although apparently very simple, did not give consistent results at first. It was difficult to achieve

saturation of the gas stream. The method was tedious and cumbersome compared with that described above. Table I gives a comparison of the methods.

Vapor Pressure of Zinc Over System Marmatite-Iron

Most commercial zinc ores contain varying percentages of iron associated in some manner with the zinc sulphide. These ores are termed marmatites and are usually designated by the formula $(\text{Zn,Fe})\text{S}$. Little information is available on the actual method of association. An X-ray examination of marmatites containing varying percentages of iron¹⁰ showed a continuous increase in the lattice parameter which, in view of the similarity in the ionic radius of zinc and iron would suggest a substitutional solid solution. If this solid solution had any appreciable free energy of formation, this should be detectable by a decrease in the activity of the zinc sulphide with a consequent decrease in the vapor pressure of zinc over the system:



when compared with the ZnS-Fe system.

The above reaction was studied over the temperature range (850° to 1000°C) using marmatites of 7.6 and 8.6 pct Fe.

An insignificant decrease was noted at the lower temperatures. At 950°C, however, the reaction using marmatite containing 8.6 pct Fe indicated a reaction pressure 2.2 mm less than when pure sphalerite was used. This decrease was, however, of too low a magnitude to deduce any quantitative conclusions, although it does suggest a very low free energy of solution.

Discussion of Results

The equilibrium constants associated with reactions 2 and 1 are given by:

$$K_2 = \frac{p_{\text{Zn}} \cdot a_{\text{Cu}_2\text{S}}}{a_{\text{ZnS}} \cdot (a_{\text{Cu}})^2} \quad [3]$$

and

$$K_1 = \frac{p_{\text{Zn}} \cdot a_{\text{FeS}}}{a_{\text{ZnS}} \cdot a_{\text{Fe}}} \quad [4]$$

When it is possible to assign unit activity ($a = 1$) to the other reactants in the system, then the equilibrium constant may be identified with the partial pressure of zinc.

An examination of the Cu-S and Fe-S phase diagrams shows that, at the temperatures involved, all the reactants and products, with the exception of zinc, should remain solid and that the stable sulphides at these temperatures are Cu_2S and FeS with no solid solubility of copper or iron in their respective sulphides.

An X-ray examination of the products of the ZnS-Fe system showed no detectable distortion of the zinc sulphide lattice after 48 hr at 900°C. A comparison of the ionic radii ($\text{Zn} = 0.74\text{\AA}$, $\text{Fe} = 0.75\text{\AA}$, $\text{Cu} = 0.96\text{\AA}$) would indicate that iron would have a greater tendency to form a solid solution with zinc sulphide than would copper, and since no indication of solid solution was found in this case it is reasonable to assume that no solid solution should occur in the ZnS-Cu system. For these reasons, unit activities may be ascribed to zinc sulphide, copper sulphide, and iron sulphide.

In reaction 2 errors will be introduced in any thermodynamic calculation in which unit activity is assigned to copper. The Cu-Zn phase diagram shows

a solid solubility of zinc in copper up to 38 pct by weight. Although deviations in the activity of the copper should not vary too greatly from ideality in this region, the fact that in Eq. 3 its activity becomes a squared function makes its consideration necessary.

Birchenall and Mehl¹¹ using the Gibbs-Duhem equation have calculated the activities of copper in brasses from the experimental results of Hargreaves,⁹ Herbenar et al.,⁸ and Schneider and Schmid.¹²

In the case of iron, the limited solid solubility of zinc in iron at the temperatures concerned suggests that no appreciable decrease in the activity of the iron should be expected.

Assuming that ΔH , the calorimetric heat of reaction, does not vary appreciably over the temperature range involved, the integrated form of the Van't Hoff equation becomes

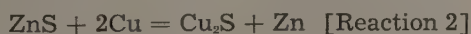
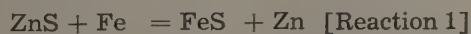
$$\ln K = \frac{-\Delta H}{RT} \quad [5]$$

and, if $\ln K$ is plotted against $1/T$ the result should be a straight line of slope $-\Delta H/R$. In the case of the ZnS-Fe system, the direct measurement of the slope should yield the true value of $-\Delta H/R$. In this case, the line corresponded to a calorimetric heat of reaction of +45,130 cal.

However, in the case of the ZnS-Cu system, the equilibrium to be considered is not between zinc sulphide and copper but between zinc sulphide and a brass of some composition related to the pressure existing over the system. It is impossible to determine this composition precisely. It appears reasonable to assume that the composition of the brass in equilibrium with unreacted zinc sulphide will be the same as the composition determined for the foil. With this assumption, the reduced activity of the copper may be determined and a calorimetric heat of 49,800 cal is calculated.

Summary

The vapor pressure of zinc over the reactions:



was determined experimentally. In reaction 1 (curve A, Fig. 3) it was found to vary from 1.8 to 22 mm Hg from 850° to 1000°C. In reaction 2 (curve B, Fig. 3) the pressure varied from 7.6 to 58.2 mm Hg over the temperature range 850° to 975°C.

Calculations based on these measurements indicated the calorimetric heat of reaction at a mean temperature of 1200°K to be:

Table I—Comparison of Alloy Formation and Entrainment Methods

Method	Temperature, °C	Vapor Pressure, Mm
Alloy formation	850	1.8
Entrainment	850	1.8
Alloy formation	900	5.2
Entrainment	900	4.9

Reaction 1

$$\Delta H = +49,800 \text{ cal}$$

Reaction 2

$$\Delta H = +45,100 \text{ cal}$$

Values of the heat of reaction calculated from existing data and from the experimental data determined in this investigation are listed as follows:

For the ZnS-Cu system

H_{1273} (calculated from existing data)	+54,100 cal
H_{1273} (from this investigation)	+49,800 cal
Difference	+4,300 cal

For the ZnS-Fe system

H_{1273} (calculated from existing data)	+48,400 cal
H_{1273} (from this investigation)	+45,100 cal
Difference	+3,300 cal

These differences agree within the degree of experimental error.

References

1. A. H. Imbert: U. S. Patents 807,271; 894,383 (1905, 1906).
2. P. E. Peterson: *Trans. Amer. Electrochem. Soc.* (1913) **24**, p. 215.
3. K. K. Kelley: Data on Theoretical Metallurgy VII. Thermodynamics Study of Sulphur. Bur. of Mines Bull. 406, pp. 137-146.
4. P. Gross and M. Warrington: Discussions of the Faraday Soc. (1948) pp. 215-217.
5. R. Schenk: Umsetzung von Sulphiden mit Metallen und Kohlenstoff. *Fiat Review of German Science* (1939-1946).
6. R. Hargreaves: *Journal Inst. Metals* (1939) **64**, p. 115.
7. A. Eucken: *Metallwirtschaft* (1936) **15**, p. 27.
8. A. W. Herbenar, C. A. Siebert, O. S. Duffendack: *Trans. AIME* (1950) **188**, p. 323; *JOURNAL OF METALS* (February 1950).
9. L. M. Pidgeon and J. A. King: Discussions of the Faraday Soc. (1948) pp. 197-206.
10. R. Thomson and G. Lattimer: B.A.Sc. Thesis, Dept. of Metallurgy, University of Toronto (unpublished).
11. C. E. Birchenall and R. F. Mehl: *Trans. AIME* (1947) **171**, p. 143; *METALS TECHNOLOGY* (June 1947).
12. A. Schneider and H. Schmid: *Ztch. Electrochem.* (1942) **48**, p. 627.

Technical Note

Kinetics of Galvanizing

by D. J. Blickwede

WHEN iron is dipped in molten zinc at temperatures in the range 840° to 930°F, the two metals react to form layers of Fe-Zn compounds which adhere to the iron. At the galvanizing tem-

perature, the successive layers are:¹ γ ($\text{Fe}_5\text{Zn}_{21}$), δ_1 (FeZn_7), and ζ (FeZn_{13}), in conformity with the Fe-Zn constitution diagram.

There is no quantitative information in the literature on the rates of growth of the individual alloy layers over the temperature range 840° to 930°F. Rather all the past experiments have studied the loss in weight of iron as a function of galvanizing

D. J. BLICKWEDE, Junior Member AIME, is associated with the Bethlehem Steel Co., Bethlehem, Pa.
TN 159E. Manuscript, Nov. 21, 1952.

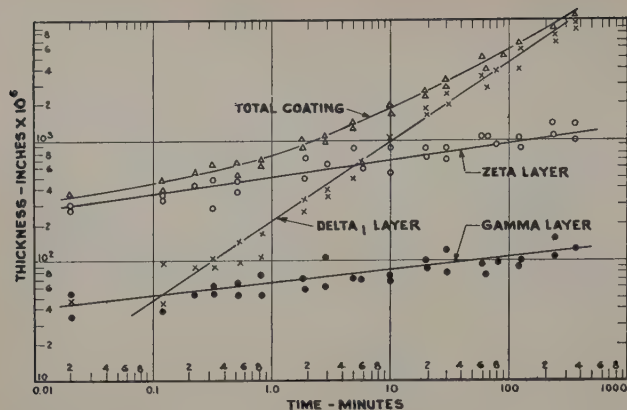


Fig. 1—Thickness of alloy layers after immersion in pure zinc at 840°F for various periods of time.

time and temperature. Generally, it has been found² that the weight loss-time curve is parabolic in form at 840°F, but with increasing temperature it begins to assume a more linear form until at 930°F it is a straight line. Above 930°F the curve again becomes parabolic. The rate of iron loss is also most rapid at 930°F, being less at temperatures below and above this point.

These and other published data have led to the commonly accepted assumption that the rate determining process of the galvanizing reaction at temperatures up to 900°F is diffusion of iron from the base metal and zinc from the spelter through the coating, where they form ζ and γ at the ζ -Zn and Fe- γ interfaces, respectively. However, this postulate has never been checked by actual thickness measurements of the alloy layers.

To obtain such information, suitably cleaned, pickled and fluxed specimens, 1½ in. square by 22 gage, of a 0.08 pct C sheet steel were dipped in pure

zinc for various periods of time at 840°, 870°, and 900°F. Transverse sections of the specimens were polished and etched using the techniques developed by Rowland.¹ The thickness of each alloy layer was measured with a microscope, and all values are the average of at least ten readings on a specimen. Typical of the results are the data for 840°F plotted on logarithmic coordinates in Fig. 1. The data at this temperature and at 870° and 900°F form straight lines on these coordinates, and hence may be described by an empirical equation of the form

$$y = kt^n \quad [1]$$

where y is the thickness in inches of the particular alloy layer at t minutes, and k and n are constants. Numerical values of the constants for each alloy layer at each temperature were evaluated by the method of least squares and are listed in Table I.

Table I. Values of Constants for Each Alloy Layer

Temperature, °F	γ Layer		δ_1 Layer		ζ Layer	
	k	n	k	n	k	n
840	8.29×10^{-5}	0.099	2.63×10^{-4}	0.60	5.37×10^{-4}	0.156
870	5.93×10^{-5}	0.109	3.11×10^{-4}	0.63	6.31×10^{-4}	0.28
900	1.39×10^{-5}	0.216	3.26×10^{-3}	0.64	y not measurable	

It may be shown that if the growth of the coating is solely controlled by diffusion of zinc and iron through the thickening layers, the constant n in Eq. 1 would be 0.50. In no case did the measured values of n approach this value. Hence, it appears that diffusion is not the rate determining process in galvanizing.

This conclusion is further substantiated by consideration of the temperature dependence of the constant, k , in Eq. 1. If diffusion were the rate determining process,

$$k = Ke^{-Q/RT} \quad [2]$$

where Q is the activation energy of the process, R the gas constant, and T the absolute temperature, and a graph of $\log k$ vs $1/T$ would be a straight line. As shown in Fig. 2, this is not the case for the present data.

It was mentioned that some of the literature indicates the weight-loss vs time curves give values of n in Eq. 1 of 0.5. However, the growth of the total coating ($\gamma + \delta_1 + \zeta$) for the present data, which might approximate the iron loss behavior, does not verify this, see Fig. 1. In fact, the empirical equation describing the growth of the total alloy coating must be quite complex, since it does not form a straight line on logarithmic coordinates.

The present data do not bring out any mechanism to account for the fact that the rate of growth of the alloy layers during galvanizing is not controlled by diffusion. It is probable that sloughing of the ζ layer into the zinc bath causes the slow apparent rate of growth of this layer. Also such features as slowness of the reactions at the alloy phase boundaries or cracks in the individual layers may be involved in the mechanism of growth.

References

- ¹D. H. Rowland: Metallography of Hot-dipped Galvanized Coatings. *Trans. ASM* (1948) **40**, p. 983.
- ²H. Grubitsch and F. Bruckner: The Reaction of Iron with Molten Zinc. *Stahl und Eisen* (1937) **57**, p. 819.
- ³H. Bablik: *Galvanizing*. 3rd Edition (1950) London. Spon.

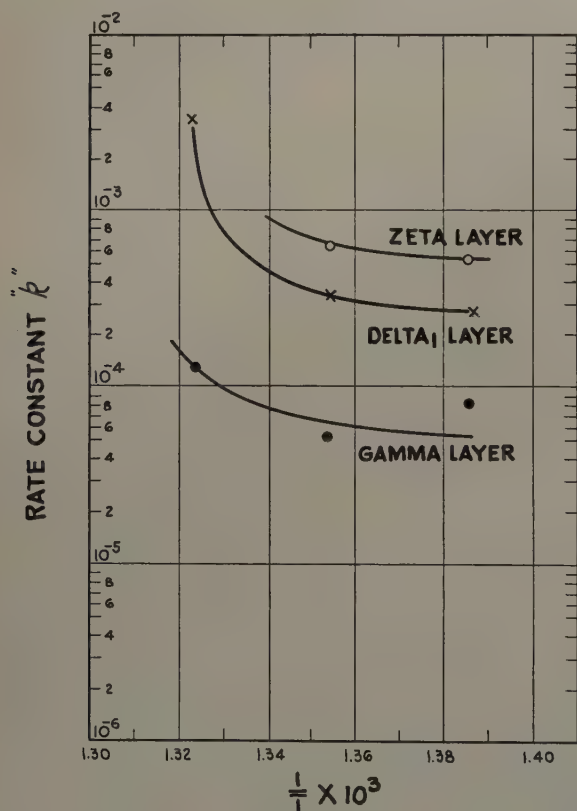


Fig. 2—Rate constant k in equation $y = kt^n$ vs the reciprocal of the absolute temperature.

Recrystallization and Stored Energy

by H. P. Leighly, H. L. Walker, and J. W. Marx

A relationship between recrystallized grain size and prior deformation is predicted from elementary statistical considerations, and reasonable agreement with experiment is obtained.

RECRYSTALLIZATION phenomena have received much theoretical and experimental attention, and very adequate discussions of the various mechanisms suggested have been given by Anderson and Mehl,¹ Cook and Richards,² and Burgers,³ and others. It suffices to note here that the initial concepts fitted one of two general hypotheses: 1—The new crystals are nucleated within microscopic regions at which there is a concentration of internal stress, i.e., volume elements of maximum strain energy. 2—The new crystals have their inception in volume elements of minimum strain energy.

In a comprehensive early review of the subject, van Arkel⁴ considered both possibilities and came to the conclusion that hypothesis 2 was inconsistent with the experimental fact that the number of nucleations increased with increasing deformation. He suggested that, if allowance was made for a preliminary atomic rearrangement at the points of large internal strain, hypothesis 1 provided the more reasonable concept.

Following the initial observations of Collins and Mathewson⁵ and Crussard,⁶ the systematic X-ray investigations of Cahn⁷ and Guinier and Tennevin⁸ established the existence of a polygonized structure in metals that had been cold-worked, and subsequently annealed, under conditions such that recrystallization did not occur. This new experimental evidence by no means disproved the first nucleation hypothesis, a fact recognized by both Beck⁹ and Cahn,¹⁰ who independently suggested nucleation

mechanisms based on the idea that regions of large strain might polygonize before the bulk of the less deformed material. These mechanisms, together with others recently proposed,³ are dependent upon the prior existence of some degree of polygonization in the deformed material.

On the other hand, a critical examination of the published data leads to the supposition that polygonization may not be the necessary precursor of recrystallization, but merely its favored energetic competitor. In regions where the lattice distortion is not too severe, the limited adjustment afforded by polygonization may permit the lattice to drop to a relatively stable low energy state in which the nucleation of a new crystal becomes improbable, even at elevated temperatures. Such structures, of course, might provide a fertile field for the growth of nuclei, if these could be introduced. In regions of concentrated lattice distortion, polygonization alone may not be able to accomplish an adequate strain reduction, and in these volume elements sufficient thermal activity permits the more drastic atomic rearrangement involved in nucleation.

Completely polygonized structures are known to withstand extended heating close to their melting points,¹¹ with no other effect than a slow enlargement of some of the subgrains at the expense of others. Once started, macroscopic recrystallization might be expected to go to completion in a matter of minutes under similar heat treatment. Crussard¹² and his coworkers have found that recrystallization may occur in single crystals of impure (about 99.7 pct) aluminum without any detectable prior polygonization. The indication here is that large Cottrell impurity atmospheres inhibit dislocation movement, thus suppressing polygonization to such an extent that the alternative process, recrystallization, dominates the lattice restoration.

Experimental studies relating recrystallization directly to stored energy have not, at the present time,

H. P. LEIGHLY, Junior Member AIME, formerly Olin Industries Fellow, University of Illinois, is now with the Research Laboratory, Bendix Aviation Corp., Detroit. H. L. WALKER, Member AIME, is Professor and Head, Dept. Mining and Metallurgical Engineering, and J. W. MARX is Research Assistant Professor, University of Illinois, Urbana, Ill.

Discussion on this paper, TP 3510E, may be sent, 2 copies, to AIME by July 1, 1953. Manuscript, Oct. 6, 1952; revision, Feb. 26, 1953.

been carried out on a comprehensive basis. The most extensive of the earlier measurements of stored energy have been summarized in a series of papers by Taylor and his associates.¹³⁻¹⁵ The ability of polycrystalline copper to store energy, for example, was found to approach saturation for reductions of more than 0.7 in compression. Below that deformation the ratio of stored energy to work energy expended was of the order of 10 pct. Both this work and the more recent initial results reported by Crussard¹² indicate that a portion of the stored energy is released in recovery processes prior to recrystallization, while the greater part of the balance is recovered early in the recrystallization itself.

No discussion of stored energy experiments would be complete without some mention of the remarkable results reported by Suzuki.¹⁶ The extraordinary feature of this work was the report that, after compressional reductions of polycrystalline copper ranging from about 0.05 to about 0.60, followed by heating at a rate of 2°C per min from room temperature to above 300°C, virtually all of the stored energy was recovered, yet recrystallization was noted in only one specimen.

In view of the fact that many investigators, among them Crussard,¹² find recrystallization proceeding with appreciable velocity below 200°C in cold-worked copper, the present writers attempted to verify Suzuki's work in this respect. Single crystals of spectrographically pure (99.999 pct) copper were deformed in compression and heated at 2°C per min. Some bending and "barreling" of the specimens occurred, but the deformation may still be presumed to be relatively homogeneous compared to that in a grain of polycrystalline material compressed by the same amount. In every case in which the compressional reduction exceeded 0.1, microscopic new crystals were formed on heating to 330°C, while for larger reductions, of the order of 0.5, a part of the recrystallized grains were macroscopic in size by the time the temperature reached 290°C, the lowest temperature at which any specimens were removed for observation.

Thus nucleation in single crystals may be said to occur below 300°C at the given heating rate. Presumably the process would be well advanced at even lower temperatures in polycrystals. In view of this observation, the second stage of energy release, which Suzuki observed above 200°C, may possibly be regarded as that associated at least with the nucleation, if not the extended growth, of new crystals. The fraction of recrystallized volume may easily have been too small to significantly lower the hardness, or be unambiguously distinguished from the rest of the polycrystalline matrix.

The first stage of energy release, which attained its maximum velocity between 150° and 200°C in Suzuki's experiments, may include some contributions from the coalescence of impurity atoms and edge-type dislocations. The number of available dislocation sites would, of course, depend upon the cold-working. Suzuki's copper contained more than 10¹⁹ impurity atoms per cubic centimeter, all of which could be accommodated for a reasonable cold-worked dislocation density of 10¹² per cu cm. Assuming a binding energy of 0.5 electron volt,¹⁷ in the limiting case in which all the impurities were condensed along dislocation lines, the exothermic reaction could produce between 0.1 and 0.2 cal per g, which is of the same order of magnitude as the observed effect. This very rough estimate, of course,

merely indicates that the impurity contribution should be carefully considered in calorimetric studies of stored energy.

On the basis of the hypothesis that nucleation occurs in volume elements of maximum strain energy, the postulates of elementary statistical mechanics may be applied to the problem of recrystallization after deformation. The task is one of predicting the number of successful nucleations, or new grains, that result when an annealed metallic solid is cold-worked and subsequently heated at a constant temperature for a time just sufficient to convert the deformed matrix essentially into new grains. The required idealizations are that the number of nucleations be large, and that the deformation be macroscopically homogeneous.

A first approach to the problem may be made by considering a quantity of stored energy W as distributed throughout n microscopic volume cells comprising one unit volume of material, subject to the condition that a lattice disorganization corresponding to a cell energy level Q is necessary before nucleation can occur in that cell. Even though some fraction of this energy may be recovered by other processes prior to recrystallization, the residual stored energy W' and the residual nucleation energy Q' may be presumed to be proportional to W and Q , and the initial distribution would then not be materially altered. The mean energy per cell is then simply W/n , which may be treated as a potential distribution modulus analogous to the well-known thermal distribution modulus kT . Following this analogy, taking the reasonable view that Q is large compared to W/n , the fraction of cells $\Delta n/n$ with strain energy greater than Q is given by

$$\frac{\Delta n}{n} = K \exp -nQ/W, K = 2(nQ/\pi W)^{1/2} \quad [1]$$

Since any changes in the coefficient K would be overwhelmed by the corresponding changes in the exponent, K may be regarded as a virtual constant. Q is not an activation energy.

The work of Taylor and Quinney^{13,14} shows that a metal's gross capacity to store energy saturates at large reductions in room temperature compression. It may be assumed that individual cells have a finite probability of becoming saturated for any deformation, and that the energy level Q lies close to the upper limit, if, indeed, it is not identical with it.

Up to this point each of the volume cells has been assigned an equal *a priori* probability of achieving the nucleation level Q . This assumption could only be justified for perfect single crystals. In polycrystalline materials, on which most investigations have been made, those cells encompassing a segment of a grain boundary appear to have a much greater probability of reaching the Q -level than similar volume elements in the grain interior. Two factors contribute to this statistical preference: 1—Grain boundary cells possess an initial strain energy, before deformation, by virtue of the lattice distortion in that region. 2—Slip propagation is inhibited at the grain boundaries, resulting in a concentration of residual strain in the adjacent volume elements.

For the simple case of a deformed single crystal, the number N_r of successful nucleations, or recrystallized grains per unit volume, should be proportional to the number Δn of cells which attain the near maximum energy level Q during deformation, or

$$N_r = \alpha \Delta n = \alpha K n \exp -nQ/W \quad [2]$$

where the proportionality coefficient α depends on both nucleation and growth rates of the new grains.¹ However, as Eastwood has pointed out,¹⁸ if the activation energies for nucleation and for growth are the same, or nearly the same, α will not vary much with temperature. No pertinent data have been obtained for single crystals, but the existing data on polycrystals, discussed below, indicates that α is substantially independent of the temperature, over the range investigated. Thus N_r would be simply proportional to Δn , the latter quantity corresponding to the potential nuclei in the Avrami theory.

In the polycrystalline case, because of the statistical weighting that must be given to the grain boundary cells, it would be expected that the recrystallized grain count would depend not only upon W_s , as for single crystals, but also upon the initial grain boundary area per unit volume. No exact solution could be attempted unless the ratio of energy stored in the grain boundary regions to energy stored in the grain interiors could be estimated. By making use of the experimental observation that a great majority of nucleations do occur at grain boundaries, a reasonable approximation may be tried.

Assuming that a fraction $W_s = CW$ of the total stored energy is distributed among the n_a cells comprising the total initial grain boundary area A_0 per unit volume, with the approximation that the probability of a successful nucleation at a grain boundary is overwhelmingly greater than that in a grain interior, Eq. 2 may be adapted to read, for a polycrystal

$$N_r = \alpha \Delta n_a = \alpha K_a n_a \exp -n_a Q/W_s \quad [3]$$

For geometrical simplicity, it is stipulated that there are N_0 cubic grains per unit volume before recrystallization, and N_r grains after. Using a more realistic space filling solid in place of the cube merely makes trivial changes in constants which are ultimately to be evaluated by experiment in any case. $N_0^{-1/3}$ then represents an average initial cube length, and may be taken as a convenient measure of the initial grain size G_0 . Similarly, $G_r = N_r^{-1/3}$. The average initial area per grain is $3/N_0^{2/3}$, and the total initial grain boundary area per unit volume becomes $A_0 = 3N_0^{1/3}$. This surface may then be divided into the n_a elements of area ΔA , so that $n_a = 3N_0^{1/3}/\Delta A$.

Taking the natural logarithms of both sides, Eq. 3 becomes

$$\ln G_r = (1/3) \ln MG_0 + (D/G_0) (1/W_s) \quad [4]$$

where $M = A/3\alpha K_a$ and $D = Q/\Delta A$ may be regarded as constants to be determined by experiment. An explicit dependence of the primary recrystallized grain size on the initial grain size, as well as on stored energy, is thus indicated. Since MG_0 is a number always less than one, the first term will be negative, while the second is always positive. Thus Eq. 4 predicts a decrease in grain size with increasing deformation, i.e., increasing W_s , which is consistent with experiment. The singularity at $W_s = 0$ is of trivial significance.

Eq. 4, as it stands, represents an approximate phenomenological solution to the problem. Unfortunately, in the relevant constant temperature recrystallization experiments to date, the stored energy is not a measured quantity. Instead, the more easily determined fractional change in length along some axis of compression has been generally employed. In order to compare calculation with ex-

periment, further approximations must be used to express W_s in terms of ν , the dimensional reduction as reported. It should be noted that these supplementary assumptions are the result of experimental, not theoretical, ambiguity, and do not prejudice the derived expressions in Eqs. 2 to 4.

Taylor and Quinney^{18,14} have shown that, up to about 70 pct reduction in compression, a rather definite fraction of the energy expended in deforming the material is retained as stored energy at room temperature. Granting that a considerable portion of this stored energy may be released upon heating, prior to recrystallization, the residual stored energy W_s might still be regarded as proportional to the work done in deforming the material.

Consider a unit cube compressed between frictionless parallel plates. The fractional reduction in L , the cube edge perpendicular to the plates, is denoted by ν , where $\nu = (L_0 - L_f)/L_0$. Hence $L_f = L_0(1 - \nu)$. If the area in contact with the plates is A , the assumption of constant density leads to the relation $A_0 L_0 = A_f L_f = 1$. For the unit volume cube, the average area \bar{A} in contact with the plates during the compression is then

$$\bar{A} = (A_0/2) \left\{ 1 + \left[\frac{L_0}{L_f} \right] \right\} = \frac{1}{2} A_0 \left[\frac{2 - \nu}{1 - \nu} \right]$$

Letting σ represent the unit stress that must be exerted by the plates in order to cause plastic flow in the specimen, an average value $\bar{\sigma}$ may be approximated by $\bar{\sigma} = \sigma_0 + \frac{1}{2} \epsilon \nu$. Here ϵ is regarded as an effective value of $d\sigma/d\nu$ over the measured interval.

The work done in deforming the specimen is then given by

$$W_s = \bar{\sigma} \bar{A} (L_0 - L_f)$$

Relating this quantity to W_s by the undetermined proportionality factor β , and substituting the values obtained above for the other factors, there results

$$W_s = \frac{\beta}{4(1 - \nu)} [4\sigma_0 \nu + 2(\epsilon - \sigma_0) \nu^2 - \epsilon \nu^3] \quad [5]$$

This expression could not be evaluated exactly without detailed information concerning ϵ , which is a measure of the work hardening, and which would depend upon the metal, the deformation temperature, and probably on the rate of deformation. Such detailed computation would hardly be warranted on the basis of the preceding assumptions, even if sufficient information were supplied for the experiments of present interest. Since ν is a quantity always less than unity, usually of order of magnitude 10^{-1} , it appears that a rough but sufficient approximation can be obtained by using only the first term of the polynomial in ν . This gives

$$W_s = \beta \sigma_0 \left[\frac{\nu}{1 - \nu} \right] \quad [5a]$$

Substituting this into Eq. 4, the following is obtained:

$$\ln G_r = B + P \left[\frac{1 - \nu}{\nu} \right] \quad [6]$$

For a constant initial grain size, as in the experiments discussed below, the quantities $B = (1/3) \ln MG_0$ and $P = D/G_0 \beta \sigma_0$ may be regarded as the experimentally determined constants, or fitting parameters.

Table I. Data on Values of $-\log G_r$

ν	Data	Eq. 6	Eq. 7
0.15	2.020	2.015	2.024
0.30	2.100	2.105	2.095
0.38	2.130	2.130	2.125
0.60	2.200	2.171	2.201

Eq. 6 is now in a form suitable for comparison with the empirical relationship first established by Walker¹⁹ for cartridge brass, and substantiated by the data of French²⁰ and Channon²¹ for brass, Wensch²² for commercial nickel, and Leighly²³ for commercial titanium. Walker's rule is normally written in the form

$$\log G_r = \log m + n(100\nu)^{1/2} \quad [7]$$

where $\log m$ and n are constants for a given initial grain size, and ν ranges between 0.1 and 0.7 for the measurements involved.

Since the two constants are found to be negative in Walker's equation, both theoretical (Eq. 6) and empirical (Eq. 7) expressions predict a decrease in recrystallized grain size with increasing ν . The general statistical approach, as well as the supplementary assumptions involved in the derivation of Eq. 6, makes the results invalid for $\nu = 0$ or $\nu = 1$, so comparison at these points is not significant.

When fitted to recent data on titanium, in which Leighly²³ has observed that the recrystallization follows Walker's rule, the two expressions yield approximately equivalent results at low strains, as shown in Table I.

Similar, or somewhat better, correspondence may be obtained by fitting the data of Walker, French, Channon, or Wensch. Because of the additional assumptions involved in converting the percentage of deformation into stored energy, some disagreement would certainly be expected, even if all the theoretical assumptions were valid. However, the procedure adopted appears to be the best that can be done with the evidence at hand.

Since $\log G_r$ is a rather insensitive function of ν , the comparison with existing data cannot be said to prove that the relationship developed is correct. The calculation does permit one to say that Walker's rule, which is well substantiated in the ν range between 0.1 and 0.7, yields results which are consistent with the phenomenological stored energy considerations employed above.

Where the materials used in recrystallization experiments undergo extensive mechanical twinning, it might be expected that the G_o referred to in Eq. 4 should be the grain size just after deformation, not the initial grain size. Both theoretical and empirical expressions should probably be limited in their application to specimens in which the initial and final grain sizes are less than the least dimension of the specimen. In addition, neither could be expected to hold for constant time recrystallization experiments, in which the primary recrystallized grain size is materially altered by competitive grain growth.

Polygonization, as the writers have discussed it above, is by no means the only fragmentation hypothesis now extant. As early as 1914, Darwin²⁴ suggested the well-known mosaic block model for the structure of an annealed metal, and, more recently, Wood and Rachinger²⁵ have proposed that plastic deformation directly breaks the lattice into very small crystallites. In support of this model are

the observations of Heidenreich,²⁶ who has noted structural segments of the order of 200Å on an edge in aluminum. Bragg²⁷ has employed this idea to calculate the mechanical strength of metals. Kellar, Hirsch, and Thorpe²⁸ also find small crystallites existing in deformed but unannealed aluminum.

Although mosaic blocks, polygonized segments, and Wood crystallites differ in the postulated formation mechanism, the ultimate structures seem to vary only in size and degree of orientation difference between fragments. This distinction may not be a fundamental one, i.e., the different nomenclature might very well describe different stages of the same phenomenon. It should be noted, however, that some time must elapse between the deformation of a metal and the taking of an X-ray picture. The fact that some crystallites are indicated by the X-ray evidence does not prove that these were formed simultaneously with the deformation.

References

- W. A. Anderson and R. F. Mehl: *Trans. AIME* (1945) **161**, p. 140.
- M. Cook and T. L. Richards: *Journal Inst. Metals* (1946) **73**, p. 1.
- W. G. Burgers: Article, *Solvay Conference on the Solid State*. (1952) p. 73. R. Stoop, Coudenberg, Bruxelles.
- A. E. van Arkel: *Ztsch. Metalle* (1930) **22**, p. 217.
- J. H. Collins and C. H. Mathewson: *Trans. AIME* (1940) **137**, p. 150.
- C. Crussard: *Revue Metallurgie* (1944) **41**, pp. 111, 133.
- R. W. Cahn: Report of Conference on Strength of Solids, Physical Soc. (1948) p. 136.
- A. Guinier and T. Tennevin: *Comptes Rendus Acad. Sci.*, Paris (1948) **226**, p. 1530.
- P. A. Beck: *Journal of Applied Physics* (1949) **20**, p. 633.
- R. W. Cahn: *Proc. Physical Soc.* (1950) **A63**, p. 323.
- A. Guinier: Article, *Imperfections in Nearly Perfect Single Crystals*. (1952) p. 402. New York. John Wiley and Sons.
- C. Crussard, F. Aubertin, B. Jaoul, and G. Wyon: Article, *Progress in Metal Physics*. (1950) p. 193. New York. Interscience Publishers, Inc.
- H. Quinney and G. I. Taylor: *Proc. Royal Soc.* (1937) **A163**, p. 157.
- G. I. Taylor and H. Quinney: *Proc. Royal Soc.* (1934) **A143**, p. 307.
- W. S. Farren and G. I. Taylor: *Proc. Royal Soc.* (1925) **107**, p. 422.
- T. Suzuki: Science Reports, Research Inst., Tohoku Univ. (1949) **1**, p. 193.
- N. F. Mott: Article, *Imperfections in Nearly Perfect Crystals*. (1952) p. 177. New York. John Wiley and Sons.
- L. W. Eastwood: Discussion to ref. 1, p. 168.
- H. L. Walker: Engineering Experiment Station Bull., Series 359, Univ. Illinois (1945).
- R. S. French: *Trans. AIME* (1944) **156**, p. 195.
- S. L. Channon and H. L. Walker: Preprint No. 8, ASM, Oct. 20, 1952.
- G. W. Wensch and H. L. Walker: *Trans. ASM* (1952) **44**, p. 1186.
- H. P. Leighly and H. L. Walker: To be published.
- C. G. Darwin: *Philosophical Magazine* (1914) **27**, p. 315.
- W. A. Wood and W. A. Rachinger: *Journal Inst. Metals* (1949) **75**, p. 571.
- R. D. Heidenreich: *Journal of Applied Physics* (1949) **20**, p. 993.
- W. L. Bragg: Symposium on Internal Stresses. Inst. Metals (1948) p. 221.
- J. N. Kellar, P. H. Hirsch, and J. S. Thorp: *Nature* (1950) **165**, p. 554.

Magnetic Annealing of a Co-Fe Alloy

by A. H. Geisler, J. P. Martin, Eberhard Both, and J. H. Crede

The investigation of a 50 pct Co alloy was undertaken to determine whether there was any direct correlation between the structure and properties of Co-Fe alloys which were given various magnetic heat treatments. The magnetic anisotropy and texture of the 0.002-in. cold-reduced 98 pct material tend to decrease and change in nature with increasing temperature of the recrystallization anneal. Annealing samples in a magnetic field had little effect on either the magnetic properties or texture. However, cooling them in a magnetic field greatly improved their magnetic properties.

THE beneficial influence of a magnetic field applied during the heat treatment of certain soft magnetic materials has been known for a long time. Early work showed that the presence of a magnetic field of a few oersteds during the heat treatment of Fe-Ni alloys will cause a large increase in maximum permeability. A pronounced increase in the residual induction which is produced by the magnetic anneal causes the hysteresis loop to approach the shape of a rectangle. Such results are beneficial since the desired properties are high permeability, high induction at maximum permeability, high residual induction, and low coercive force. More recently Libsch and coworkers¹ studied the effect of magnetic annealing on the hysteresis properties of a series of Co-Fe alloys prepared from powders. They observed good response for the 35 and 50 pct Co alloys but little response for the 42 pct Co alloy. They pointed out that this was somewhat surprising since the 42 pct alloy has a high linear magnetostriction and zero crystal anisotropy and similar conditions in Fe-Ni alloys give excellent response to magnetic annealing. They found optimum properties to be at the 50 pct composition with residual induction, $B_r = 19,000$

gauss and coercive force, $H_c = 0.68$ oersteds after the magnetic anneal. Before the magnetic anneal these values were $B_r = 12,600$ gauss and $H_c = 1.15$ oersteds. The optimum treatment consisted of cooling from above the γ - α transformation temperature to 900°C in a field of 20 oersteds, holding 1½ hr at 900°C, then cooling at a rate of 20° to 25°C per min in the field to below 230°C. Cooling rate mainly affected coercive force with the value decreasing from 1.09 to 0.88 oersteds as the rate was increased from 3° to 48°C per min. Cooling from 1020° to 900°C in a field followed by further cooling to 230°C without the field gave properties decidedly inferior to those for samples annealed with the field applied throughout the cooling. They concluded that to get the best properties the samples must be cooled in a field to a threshold temperature above which the alloy is plastic enough to be affected by magnetostriction. In this respect the holding temperature must be high enough so that the alloy exhibits good plasticity to permit the optimum orienting of magnetic domains by relaxation of magnetostriction. In contrast, the holding time was of less significance for there was little improvement when the time exceeded ½ hr.

The improvement in properties effected by magnetic annealing has usually been attributed to the establishment of a domain texture caused by the "freezing in" of magnetic strains. On the other hand, Smoluchowski and Turner^{2, 3} apparently found that a magnetic field applied during recrystallization could alter the crystal texture. If this effect is real, improved properties would also be expected when

A. H. GEISLER, Member AIME, is Research Associate, General Electric Co., Schenectady, J. P. MARTIN is Research Metallurgist, Research Laboratories, Allegheny Ludlum Steel Corp., Brackenridge, Pa., E. BOTH is Physicist, Signal Corps Engineering Laboratories, Fort Monmouth, N. J., and J. H. CREDE is Associate Director of Research, Allegheny Ludlum Steel Corp.

Discussion on this paper, TP 3513E, may be sent, 2 copies, to AIME by Aug. 1, 1953. Manuscript, July 23, 1952.

Table I. Analyses of Two Experimental Heats, Wt Pct

Samples	Co	C	Mn	P	S	Si
0.014 in.	50.59	0.023	0.51	0.008	0.020	0.052
All others	50.15	0.017	0.42	0.008	0.021	0.060

the applied field promoted the formation of a crystal texture with either an easy direction of magnetization or a direction of minimum magnetostriction in the field direction. Smoluchowski and Turner worked with a 35 pct Co alloy which they recrystallized at about 700°C. The normal recrystallization texture contained the following three main components:

R.D. = [110]	R.P. = (100)
R.D. = 15° from [110]	R.P. = (100)
R.D. = 15° from [110]	R.P. = (111)

where R.D. is the rolling direction and R.P. is the plane of rolling.

The influence of the magnetic field appeared to be a strong enhancement of the [110] (100) component of the recrystallized texture at the expense of the other two components. Their hypothesis for this behavior is based on anisotropy of magnetostriction. The available data showed that the [110] direction is one of low magnetostriction. Thus nuclei with this direction in the field direction would involve less strain energy and would be favored for growth during magnetic annealing, which apparently was confirmed by the texture studies. Subsequent work⁴ has shown that some of the previously published details need revision. When the influence of annealing temperature on the texture was considered it was found that the magnetic field suppressed the [110] (100) component to the contrary in favor of the other two previously mentioned components. Measurements on single crystals have shown that the magnetostriction in the [100] direction is low which conforms to the hypothesis of Smoluchowski and Turner based on anisotropy of magnetostriction. On the other hand, the more recent results thus do not exclude the alternate hypothesis that the texture is affected by virtue of a [100] direction of easy magnetization.

The present work was undertaken in order to achieve a direct correlation of the structure and properties of Co-Fe alloys. The work of Libsch,

et al. reported no permeability measurements or texture data; that of Smoluchowski and Turner contained no measurements of properties. It would be desirable to make property measurements and texture analyses on the same samples in order to appraise the influence of thermal history.

Experimental Procedure

The results reported here refer to an alloy of nominal 50 pct Co composition. This alloy is of special interest since Libsch, et al. found that the 50 pct alloy exhibited good response to magnetic annealing, also an order-disorder reaction occurs in this composition at about 732°C.

Two experimental heats of the analyses given in Table I were involved. The first analysis applies to the 0.014 in. thick samples listed in Table II, the second applies to all other samples including those which were used for preferred orientation studies. The alloys were hot-rolled to about 0.10 in. thick and then were cold-rolled to the final thicknesses of 0.014 in. and less. The hot-rolled strip, which is extremely brittle, was rendered sufficiently ductile for cold rolling by rapidly quenching in iced brine from above the order-disorder transformation temperature. Texture studies were made on the 0.002 in. strip only since this thickness was most suitable for the transmission X-ray diffraction technique.

The variables which were investigated included annealing temperature, presence or absence of a direct current field of 20 oersteds during annealing, the cooling rate, the presence or absence of a field during cooling, the thickness of the sheet, and the action of reannealing. All thermal treatments were conducted in an atmosphere of dry hydrogen.

The magnetic tests were made on three types of ring-shaped samples. These included stamped round rings and stamped square window laminations both made by punching flat sheet, and wound toroidal cores made by coiling long lengths of narrow strip about a mandrel. The field during heat treatment and subsequently during testing was applied by passing an electric current through a coil of copper wire which was wound through each ring sample. Direct current magnetization and hysteresis measurements were made on a ring tester employing a Fahy control board. The anisotropy resulting from annealing at various temperatures between 454°C* and 980°C was measured by a spinning

* The temperatures in this investigation were measured in Fahrenheit degrees and converted to centigrade degrees. The accuracy of measurement was $\pm 10^\circ\text{F}$.

Table II. Properties of the 0.014-In. Thick Strip*

Effect of Recrystallizing and Reannealing in Field

Entry No.	Annealing		Cooling		Residual Induction, $B_r \times 10^{-3}$	Coercive Force, H_c	Maximum Permeability, $\mu_{\text{Max.}} \times 10^{-3}$	Induction at $\mu_{\text{Max.}} \times 10^{-3}$
	Conditions	Field	Rate	Field				
1†	Recrystallized 2 hr 871°C	No	0.5°C per min	No	15.5	0.9	10	15
2†	Reannealed 2 hr 871°C	No	0.5°C per min	Yes	20.7	0.5	30	18
3	Recrystallized 2 hr 871°C	Yes	0.5°C per min	Yes	21.3	0.5	30	17.5
4	Reannealed 1½ hr 1260°C	No	0.5°C per min	No	17.1	1.6	6.8	15
5	Reannealed 18 hr 940°C	No	0.5°C per min	Yes	18.0	1.4	10	15.5
6	Recrystallized 18 hr 940°C	No	0.5°C per min	No	16.8	1.5	6.8	14
7	Recrystallized 5 hr 788°C	No	0.5°C per min	No	14.6	0.9	9	13
8	Reannealed 2 hr 788°C	No	Rapid	No	13.0	1.0	8.6	11
9	Recrystallized 1½ hr 871°C	Yes	Rapid	Yes	15.4	0.6	17	12.5
10	Reannealed ½ hr 593°C	Yes	0.5°C per min	Yes	19.8	0.5	26	16
11	Reannealed 1½ hr 704°C	Yes	0.5°C per min	Yes	20.9	0.5	30	17.5
12	Recrystallized 2 hr 871°C	Yes	Moderate	Yes	19.7	0.5	28	16.6
13	Reannealed 4 hr 593°C	Yes	0.5°C per min	Yes	21.1	0.45	34	19

* All data obtained on stamped ring specimens.

† See Fig. 1 for hysteresis loops.

disk test using 1.03 in. diam specimens of the 0.002 in. thick strip.

The preferred orientations of the as-rolled and recrystallized samples were determined with a General Electric XRD-3 X-ray diffraction spectrogoniometer by a previously described technique.⁵ Since the grain size of the recrystallized samples was only moderately fine, it was necessary to develop a new specimen goniometer in order to permit scanning of an area of the sample. The device which has been briefly described previously,^{6,8} reciprocates the sample through a 1 in. stroke past the X-ray beam so that an area of 1x0.3 in. (beam width) is covered in each stroke. At the same time the sample is rotated a fraction of a degree about an axis normal to its surface in synchronism with the movement of the chart recorder. Traces were made for increments of 5° about an axis in the surface of the sample from 0° to 60° starting from normal to the surface. This group of traces covers the major part of the pole figure. Corrections were made for the background of the traces and for the absorption of the samples. The results were plotted as pole figures with the contours of selected intensity levels in counts per second.

Results

Magnetic Properties: The results of the initial work which was conducted on 0.014 in. thick strip before texture studies were anticipated illustrate the influences of some of the annealing variables on the properties of the 50 pct Co alloy. A few of these results are listed in Table II. The first two entries illustrate the three-fold increase in maximum permeability obtained by cooling the sample in a magnetic field after it had been first recrystallized without an applied field. The hysteresis properties of these samples may be compared in Fig. 1. Comparison of the second and third entries shows that the properties for the sample recrystallized in the field (No. 3) are not superior to those of the sample which was recrystallized without the field (No. 2).

Table III. Effect of Thickness on Properties of Strip Recrystallized at 871°C*

Thick- ness, In.	Cold Reduc- tion, Pct	Residual In- duction, $B_r \times 10^{-3}$	Coercive Force, H_c	Maximum Perme- ability, $\mu_{Max} \times 10^{-3}$	Induction at $\mu_{Max} \times 10^{-3}$
0.014	86	20.0	0.33	39.0	14.6
0.006	94	19.2	0.45	28.0	15.2
0.002	98	16.9	0.62	16.7	12.0

* Recrystallized in field, cooled 0.5°C per min to 204°C in field, stamped ring samples.

These results indicate that any effect of an applied field during the initial recrystallization process is insignificant compared with the effect of cooling in the magnetic field. The fourth and fifth entries show that the good properties of entry 3 can be destroyed by heating to higher temperatures where grain size is increased and texture changed. In addition the results from entry 6 show that annealing at 940°C also gives poorer properties even though the material had not been annealed in the γ phase field. Entries 7 and 8 show that in the absence of an applied field two different cooling rates produce poorer properties, whereas entry 9 shows that when a field is applied even the rapid rate of cooling (about

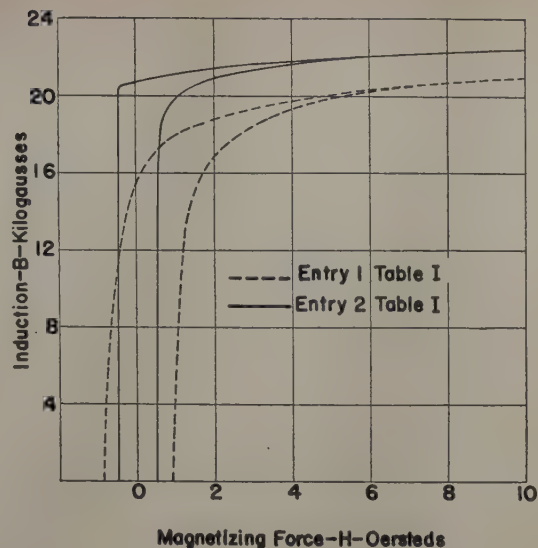


Fig. 1—Portions of hysteresis loops showing effect of magnetic anneal on 0.014-in. thick strip for peak magnetizing force of 100 oersteds. No field—Entry No. 1 in Table I. Field during cooling—Entry No. 2 in Table I.

33°C per min) gives better properties than slow cooling in the absence of the field. Comparison of the data for entries 10 and 11 with entry 9 illustrates that reannealing at lower temperatures followed by slow cooling in a field will provide good properties in material which initially had been cooled too fast. This is also shown by the data for entries 12 and 13 where the 4 hr anneal at 593°C promoted a well ordered structure according to superlattice lines in the X-ray diffraction pattern.

On the basis of these data it is apparent that the cooling conditions—rate and presence of a field—are of prime importance. The temperature at which the material is recrystallized is also important but the presence of a field during the recrystallization is not necessary to obtain optimum properties.

The optimum properties depend somewhat on the thickness of the strip according to the results in Table III. There seems to be a general trend toward poorer properties as the thickness of the strip is reduced below 0.014 in. While no attempt will be made to explain this trend which is related to the degree of final cold reduction, it should be realized that it exists and that the balance of the work to be reported was on 0.002 in. thick strip, the optimum thickness for X-ray diffraction studies.

In order to survey the effect of recrystallizing temperature and arrive at an optimum for the 0.002 in. thick strip, tests were made on samples that had been heat-treated at temperatures between 732° to

Table IV. Effect of Annealing Temperature on Properties of 0.002 in. Strip

Annealing Tempera- ture, °C*	Residual Induction, $B_r \times 10^{-3}$	Coercive Force, H_c	Maximum Permeability, $\mu_{Max} \times 10^{-3}$	Induction at $\mu_{Max} \times 10^{-3}$
732	19.6	0.78	16.5	16
760	20.5	0.64	25.5	17.6
788	19.7	0.59	21.6	16
816	20.2	0.55	27.6	16
871	19.9	0.68	18.7	15
927	19.5	0.53	27.4	16.4

* Held for 2 hr in field of 20 oersteds, cooled at about 0.5°C per min to 204°C in field. Wound toroidal samples.

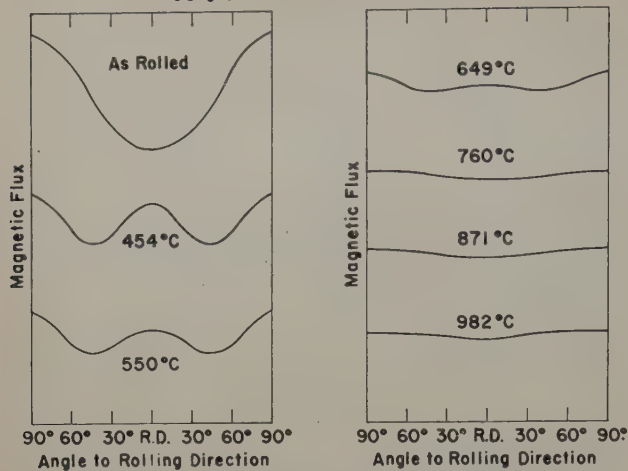


Fig. 2—Anisotropy of 0.002-in. thick strip annealed for 2 hr at indicated temperatures.

927°C. Properties are listed in Table IV. While there is some tendency for coercive force to decrease with increasing temperature, there is no clear trend in the properties for this range of temperatures. On the basis of the slightly higher residual induction value a temperature of 760°C was chosen for the subsequent studies of annealing treatments.

The variation of the anisotropy for various recrystallizing temperatures is shown by results from the spinning disk tests which are plotted in Fig. 2. The horizontal coordinate is the angular position around the disk starting from the transverse direction, moving to the rolling direction and then back to the transverse direction. The vertical coordinate is a relative value for the change of flux in the disks plotted on the same scale for all curves. Maxima and minima are related directly to the permeability. Thus, the best permeability direction is at 90° to the rolling direction in most cases but with minima in the rolling direction for the as-rolled sample and those recrystallized at 760° to 982°C and minima at

about 45° to the rolling direction for samples recrystallized at 454° to 649°C. Little anisotropy remains for the samples recrystallized at 760°C or above. The origin of the variation in anisotropy will be evident when the results of texture analyses are discussed later.

The properties of the samples used for texture studies are listed in Table V. Each group includes two or three types of specimens. The first entry in each group refers to a wound toroid of ¼ in. wide strip on which magnetic tests were made. The second entry refers to a core of 1 in. wide strip which was wound on a mandrel of square cross section and annealed with the first entry and used for texture studies. The texture specimens were cut from the 1½ in. long flat sides of the wound cores. Third and fourth entries refer to stamped square laminations with samples taken from two legs, one where the applied field was parallel (W) to the direction of rolling and the second where the field was across (X) the direction of rolling. While the texture components will be discussed later, the relationships between properties and thermal treatment can be compared with those for heavier gage. Again the improvement in properties afforded by cooling in a magnetic field is apparent. When the field was applied during cooling (groups 1 and 3) good properties were obtained and when no field was applied during cooling (groups 2 and 4) poorer properties were obtained regardless of whether or not a field was applied during recrystallization. In these respects the behavior was similar to that for heavier gage strip, Table II. On the other hand, holding at 593°C to promote a well ordered structure (group 5) did not increase the maximum permeability, while rapid cooling (group 6) did not have as detrimental an effect as with the heavier gage strip. The poorest properties were obtained with rapid cooling without an applied field (group 7).

Preferred Orientations: The texture of the original cold-rolled strip is of interest in explaining the recrystallization texture; it is the same as that of cold-rolled iron and is shown by Fig. 3. Various

Table V. Properties and Textures of 0.002 In. 50 Pct Co Strip Recrystallized 2 Hr at 760°C

Group	Recrystallization		Cooling		Residual Induction, $B_r \times 10^{-3}$	Coercive Force, H_c	Maximum Permeability, $\mu_{Max.} \times 10^{-3}$	Induction at $\mu_{Max.} \times 10^{-3}$	Texture Components*	
	Field	Direction	Field	Rate						
1	Yes	W	Yes	0.5°C per min	19.8	0.6	23	15.7	—	See Fig. 4a
	Yes	W	Yes	0.5°C per min	—	—	—	—	5 pct DE	
	Yes	W	Yes	0.5°C per min	—	—	—	—	10 pct A	
	Yes	X	Yes	0.5°C per min	—	—	—	—	15 pct A	
2	Yes	W	No	0.5°C per min	16.9	0.8	13	12.1	—	See Fig. 4b
	Yes	W	No	0.5°C per min	—	—	—	—	10 pct DE	
	Yes	W	No	0.5°C per min	—	—	—	—	20 pct A	
	Yes	X	No	0.5°C per min	—	—	—	—	20 pct A	
3	No	W	Yes	0.5°C per min	19.5	0.7	20	16.2	—	See Fig. 5a
	No	W	Yes	0.5°C per min	—	—	—	—	5 pct A—5 pct DE	
	No	X	Yes	0.5°C per min	—	—	—	—	10 pct A	
4	No	W	No	0.5°C per min	16.1	1.2	9	12.4	—	See Fig. 5b
	No	W	No	0.5°C per min	—	—	—	—	20 pct A—10 pct DE	
5	Yes	W	Yes	0.5°C per min†	20.6	0.9	18	16.5	—	See Fig. 7a
	Yes	W	Yes	0.5°C per min†	—	—	—	—	20 pct A—5 pct DE	
	Yes	X	Yes	0.5°C per min†	—	—	—	—	35 pct A—5 pct DE	
6	Yes	W	Yes	33°C per min	18.1	0.7	19.5	13.5	—	See Fig. 6a
	Yes	W	Yes	33°C per min	—	—	—	—	30 pct A—5 pct DE	
	Yes	X	Yes	33°C per min	—	—	—	—	25 pct A	
7	No	W	No	33°C per min	15.3	1.2	7.3	11	—	See Fig. 6b
	No	W	No	33°C per min	—	—	—	—	15 pct A—5 pct DE	

* In addition to the pure 760°C recrystallization texture which contains only components spread from H to K. The deformation texture corresponds to the spread from A to G.
† Held 4 hr at 593°C.

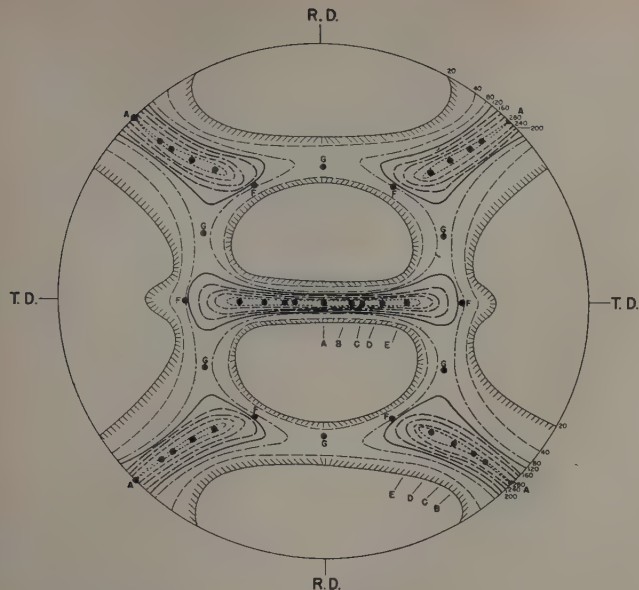


Fig. 3—Pole figure for cold-rolled 50 pct Co-Fe strip of 0.002-in. thickness showing distribution of (100) poles in stereographic projection.

components which contribute to the deformation texture are indicated by the letters A to G and are identified in Table VI. The main part of the texture can be defined as a continuous spread from (001) (A) to (111) (F) in the rolling plane about a [110]

Table VI. Components in Textures of Co-Fe Alloys

A. (001) [110]	H. (001) [120]
B. (117) [110]	J. 16° (001) 16° [120]
C. (115) [110]	K. (322) [315]
D. (113) [110]	L. (311) 2° [315]
E. (112) [110]	M. 4° (221) 6° [221]
F. (111) [110]	N. 3° (112) 9° [211]
G. (111) [112]	

direction in the rolling direction. There is almost an equal distribution from (001) to (112) (E) in the rolling plane. The component between F and G which has a [111] direction in the rolling direction is present in moderate amounts with an intensity above 80 counts per sec. Since the [111] direction is the direction of easy magnetization in this alloy,⁷ it might be expected that a possible effect of a field applied during recrystallization would be to intensify this component.

Pole figures for eight of the samples which had been recrystallized by annealing for 2 hr at 760°C are shown in Figs. 4 to 7. The main features of the texture are substantially different from those of the rolled texture. The components which spread from H to K and L in Fig. 4 are mostly complex as listed in Table VI. The main component, H, is the simplest because a (001) plane is in the rolling plane and a [120] direction is in the rolling direction. Under these conditions [100] directions are at 27° to the rolling direction and [110] directions are at 18° to the rolling direction. Evidently this is the component which was designated (100) 15° [110] by Smoluchowski and Turner.

On the whole there is little significant difference between the pole figures for samples recrystallized in a field, Fig. 4, and those recrystallized without an applied field, Fig. 5. There appears to be no concentration of intensity about the arcs which corre-

spond to [111] directions in the rolling direction which was also the field direction. The same is also true of rapidly cooled samples, Fig. 6. On the other hand, in addition to the main components there appear to be minor and spurious portions of the texture which are described by the components A to E in Figs. 4 to 7. These are components of the rolled texture, Fig. 3, and also dominant components of the recrystallization texture for annealing at temperatures below 760°C according to the summary in Table VII. Although the extent of these minor portions of texture in the pole figures for samples annealed at 760°C varies among the samples, there appears to be no clear correlation with the annealing variables. Semiquantitative measurements of the minor components relative to the major ones are listed on the right side of Table V for the various combinations of annealing variables. Comparison of results for groups 1 and 2 with 3 and 4 shows that when the annealing was performed either with or without an applied field the amounts of minor components were in both cases 5 to 20 pct A and 5 to 10 pct DE. The latter is a component between D and E as measured on a goniometer trace for an angle 20° to the normal of the strip surface. It is also noteworthy that samples with relatively good properties can have either large amounts of the minor components (groups 5 and 6) or small amounts (groups 1 and 3). There appears to be some variation in amounts between samples within the groups of Table V. This variation among samples having the same treatment is more evident from the results given in Table VIII. Some adjacent samples taken from two annealed cores were examined and an attempt was made to reduce or remove the minor components by additional annealing at about 760°C. The results show that while the DE component remains about the same in samples from each core the quantity of component A varies considerably from one sample to the next adjacent in the core. Also additional annealing of the same samples at a slightly higher temperature tended to reduce the amount of component A but had little effect on component DE. These uncontrollable variations would make questionable any attempted correlation with annealing variables.

Finally, comparison of the texture for rapidly cooled samples, Fig. 6, with that for samples held at intermediate temperatures for time periods longer than that permitted during the slow cool (0.5°C per min) shows that the new minor components M and N of Fig. 7 develop during holding. These have been attributed to a supplementary recrystallization reaction which is evident from the microstructure and which is promoted by strains accompanying the ordering process.⁸ The reaction occurs subsequent

Table VII. Occurrence of Various Components in Texture for Different Annealing Temperatures

Annealing Temperature, °C	Components	
	Predominant	Others
As-rolled	A,B,C,D,E	F,G
427	A,B,C,G	D,E,H
538	A,B,C,G	D,H
649	A,B,C,G,H	
760	H,J	K,L
871	J	H,L
982	L	G,K

See Table VI for descriptions of the components.

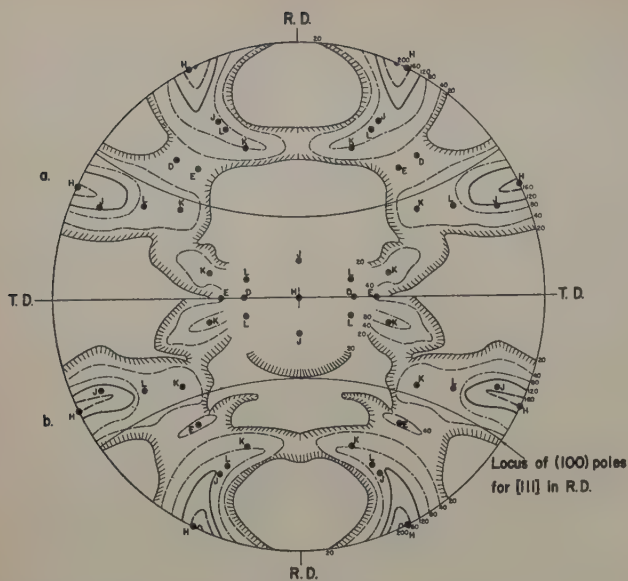


Fig. 4—Pole figures for samples recrystallized by annealing 2 hr at 760°C.

- a—Annealed in field and cooled 0.5°C per min in field.
b—Annealed in field and cooled 0.5°C per min without field.

to the ordering process since cooling at 0.5°C per min develops a well ordered structure without the appearance of components M and N.

Discussion

The type of crystal texture developed on recrystallizing the 50 pct Co alloy is very strongly dependent upon annealing temperature, Table VII. At temperatures of 649°C and less, components which were in the rolling texture (A to G) persist and some of these, notably G (111) [112], are strongly enhanced. Starting at 427°C or less the H component (001) [120] attains increasing prominence and at 760°C it is the main component while those similar to the rolling texture have essentially disappeared. At still higher temperatures other components gain prominence but at the same time the texture levels out. On annealing at 982°C detectable but not pronounced texture persists. The nature of the magnetic anisotropy as shown by the spinning disk curves, Fig. 2, can be directly correlated with the texture type and its variation with

temperature. Since [111] is the direction of easy magnetization in the 50 pct Co alloy, peaks corresponding to higher permeability will occur at peripheral positions around the disk where a [111] is in the rolling plane. The maxima in the as-rolled sample originate in component E which has a [111] in the transverse direction. This fact also accounts for the maxima in the transverse direction for samples annealed at 427° to 649°C. The maxima in the rolling direction for the latter samples are related to a component of the type (112) [111] which is near to the enhanced G component. With increasing annealing temperature the anisotropy diminishes as

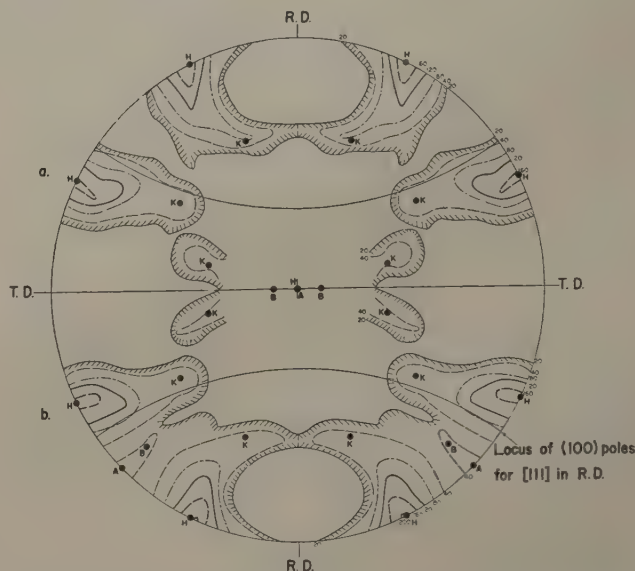


Fig. 5—Pole figures for samples recrystallized by annealing 2 hr at 760°C.

- a—Annealed without field and cooled 0.5°C per min in field.
b—Annealed without field and cooled 0.5°C per min without field.

the H component is enhanced and at 760°C and above little anisotropy remains because there are few crystals with a [111] in the rolling plane. The similarity of the disk test results for annealing at temperatures above 649°C probably accounts for the uniformity of the magnetic properties on annealing in the range 760° to 927°C in Table IV.

Both magnetic tests and texture studies failed to show any effect of an applied field on recrystallization during annealing of the 50 pct Co alloy at 760°C. This result is not surprising for there is no strong component in the rolled texture with the [111], the direction of easy magnetization, parallel to the field applied in the rolling direction. Thus, there could be little enhancement effected by the field if anisotropy of magnetization is the responsible factor. On the other hand single-crystal magnetostriction data are not yet available for the 50 pct Co alloy so the hypothesis of Smoluchowski and Turner which associates the effect in the 35 pct Co alloy with anisotropy of magnetostriction cannot be tested. On the other hand, there is a strong component E in the rolling texture with [111] in the transverse direction but tests failed to show that even this component was retained or enhanced by an applied field. First, a field would be operative in this direction on two sides of square laminations, but there was no increase in the DE component for cross (X) over with grain (W) sides of the squares according to Table V, and there was no improvement in the magnetic properties of square lamina-

Table VIII. Effect of Sampling and Repeated Annealing on Minor Texture Components

	Pct Component*	
	A	DE
Recrystallized 2 Hr at 760°C in Field, Cooled 0.5°C per Min, No Field		
Sample No. 1	0	10
Sample No. 2	20	10
Sample No. 3	15	10
Sample No. 3 reannealed 24 hr at 771°C	10	10
Sample No. 4 reannealed 24 hr at 754°C	15	10
Sample No. 5 reannealed 24 hr at 771°C	10	10
Recrystallized 2 Hr at 760°C in Field, Cooled 33°C per Min in Field		
Sample No. 6	30	5
Sample No. 7	10	5
Sample No. 7 reannealed 24 hr at 771°C	5	5
Sample No. 8 reannealed 24 hr at 754°C	10	5
Sample No. 9 reannealed 24 hr at 771°C	5	5
Above—repeated X-ray trace	5	5

* These are also components of recrystallization texture for lower annealing temperatures. Component A measured from 0° trace and DE from 20° trace.

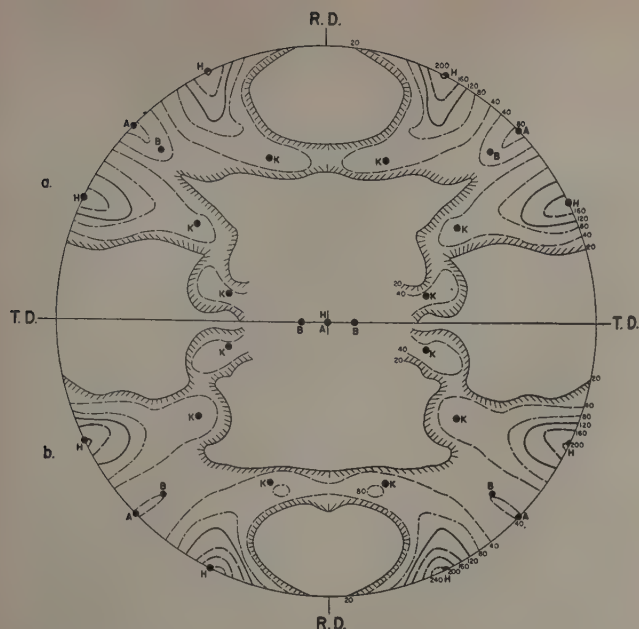


Fig. 6—Pole figures for samples recrystallized by annealing 2 hr at 760°C.

a—Annealed in field and cooled 33°C per min in field.

b—Annealed without field and cooled 33°C per min without field.

tions over wound cores. Second, there were no differences in the texture of simultaneously annealed disk samples in a series which was prepared so that the orientation of the field varied by increments of 5° from 0° to 90° to the rolling direction. Thus, the conclusion seems warranted that a field applied during the recrystallization of the 50 pct Co alloy at 760°C has no effect although cooling in a field after recrystallization does have a marked effect on properties.

The response of the 50 pct Co alloy to magnetic annealing at 760°C does not occur by virtue of a change in the overall crystal texture but by virtue of some change which occurs during cooling in the field subsequent to recrystallization. The nature of this change can only be postulated. At least two phenomena could be operative. First, the applied field could be promoting a preferred domain texture according to the older idea that the strains caused by the magnetic field are relieved by plastic flow in the alloy. In this way those [111] directions in the polycrystalline aggregate which are most nearly parallel to the applied field become directions of easiest magnetization. In each crystal the direction of spontaneous magnetization after a magnetic anneal will be the one preferred out of four $\langle 111 \rangle$ directions and in a sense a preferred domain texture exists in the aggregate. The other possibility is that the applied field causes preferential nucleation of certain orientations of particles of the ordered phase in the recrystallized, disordered matrix much the same as an applied field affects the transformation in the case of certain precipitation alloys such as Alnico 5. Perhaps it is not only coincidental that both Co-Fe and Ni-Fe alloys order at a sufficient rate in the temperature range where the applied field is effective so that consideration must also be given to the ordering reaction in these alloys. The discrepancy between the lattices of the ordered and disordered phases in both these alloys is very low, a condition which seems to be necessary for effective magnetic annealing of precipitation alloys. Nucleation of coherent particles of the ordered phase in the disordered matrix involves strains which would be

expected to lead to an intermediate tetragonal crystal structure and anisotropic shape for particles of the ordered phase. Preferential nucleation of a select orientation of the tetragonal axis and concurrent shape orientation from the several possible in each matrix crystal would arise by virtue of anisotropy energy decreasing the free energy required to nucleate the preferred orientation. If the prominent type of anisotropy energy is that of strain, then the process would embrace relaxation of magnetostriction by a permanent retention of the slight tetragonality imposed at the intermediate state by coherency much as outlined by the older interpretation.

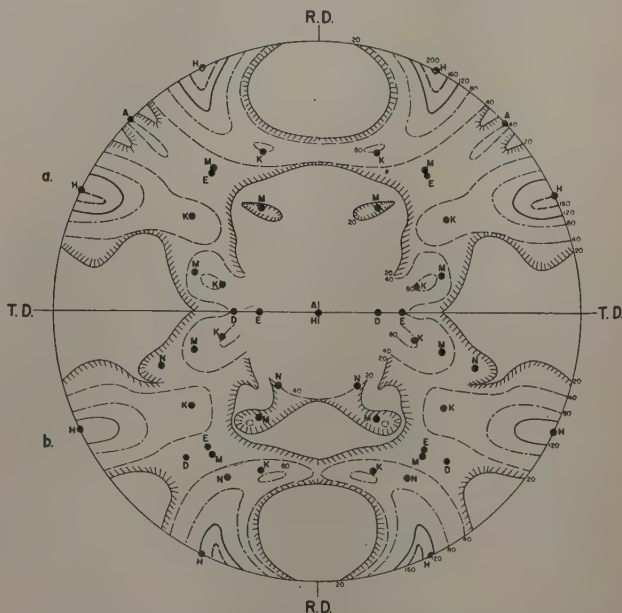


Fig. 7—Pole figures for samples held during cooling in field after recrystallizing for 2 hr at 760°C in field.

a—Held for 4 hr at 593°C.

b—Held for 10 hr at 600°C.

In either case whether the effects of magnetic annealing originate in domain texture or in the ordering process, if such a distinction can be made, even better properties would be expected if a preferred crystal orientation could be developed with a direction of easy magnetization in the applied field direction.

Summary

1—The presence of an applied magnetic field during recrystallization of a 50 pct Co-Fe alloy does not effect a significant change in either the magnetic characteristics or the recrystallized texture.

2—Improved magnetic properties, characterized by a rectangular hysteresis loop, result from cooling a recrystallized 50 pct Co-Fe alloy in the presence of an applied magnetic field from a temperature above 550°C.

3—The optimum temperature of recrystallization when followed by cooling in the presence of an applied magnetic field is dependent upon the thickness of the strip and thus is probably related to the degree of final cold reduction.

4—The magnetic anisotropy and texture of 0.002 in. thick strip cold-reduced 98 pct are strongly dependent upon the temperature of the recrystallizing anneal; they change and tend to decrease with increasing temperature until little magnetic anisotropy is apparent after a 760°C anneal although some preferred orientation is still present after a 982°C anneal.

5—Better magnetic characteristics are developed when an alloy of this composition is cooled slowly than when cooled rapidly regardless of whether or not a field is applied, but cooling at the faster rate of 33°C per min in an applied field gives better properties than cooling at 0.5°C per min without an applied field.

6—Optimum properties can be recovered by re-annealing and cooling slowly in an applied field provided that the prior recrystallization had been performed at a proper temperature but regardless of whether or not the initial cooling had been at a slow rate in a field.

7—Reannealing below the ordering temperature results in a supplementary recrystallization reaction subsequent to the ordering process which is believed to be promoted by strains accompanying the ordering process.

8—A possible role of ordering in promoting the domain texture is discussed.

Acknowledgment

A major portion of this work was done under contract W-36-039-SC-38243 with the Signal Corps Engineering Laboratories, Fort Monmouth, N. J. The authors wish to thank this agency for permission to publish the results of this investigation. We

also wish to thank C. G. Dunn of the General Electric Co., Pittsfield, Mass., for his cooperation in determining the anisotropy curves.

References

- ¹J. F. Libsch, E. Both, G. W. Beckman, D. Warren, and R. J. Franklin: Effect of Annealing in a Magnetic Field upon Iron-Cobalt and Iron-Cobalt-Nickel Alloys Prepared by Powder Metallurgy. *Trans. AIME* (1950) **188**, pp. 287-296; *JOURNAL OF METALS* (February 1950).
- ²R. Smoluchowski and R. W. Turner: Influence of Magnetic Field on Recrystallization. *Journal of Applied Physics* (1949) **20**, pp. 745-746.
- ³R. Smoluchowski and R. W. Turner: Continuous Pole Figure Study of Magnetic Recrystallization. *Physica* (1950) **16**, pp. 397-401.
- ⁴B. Sawyer: Dissertation, Carnegie Institute of Technology (1951).
- ⁵A. H. Geisler: Crystal Orientation and Pole Figure Determination. *Modern Research Techniques in Physical Metallurgy*. (1953) Cleveland. ASM.
- ⁶C. G. Suits: New Instruments from the Research Laboratory. *General Electric Review* (November 1951) **54**, pp. 32-33.
- ⁷J. W. Shih: Magnetic Properties of Single Crystals of Iron-Cobalt. *Physical Review* (1934) **46**, pp. 139-142.
- ⁸A. H. Geisler: Phase Transformations at Interfaces. *Interfaces* (1952) Cleveland. ASM.

Technical Note

Concentration Gradients Associated with Growing Pearlite

by Richard E. Grace

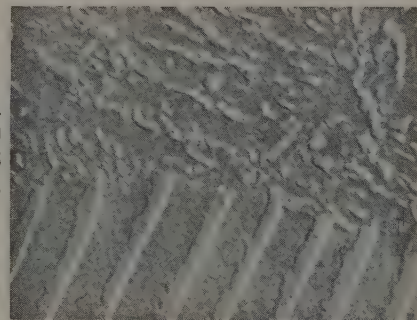
WHEN an Fe-C alloy, partially reacted to pearlite, is quenched rapidly enough to suddenly stop the growth process, it may be expected that any carbon concentration gradients will freeze *in situ* in the newly formed martensite. A short tempering treatment should precipitate finely dispersed iron carbide particles in approximately the same distribution in which carbon existed during the growth process. Examination with the electron microscope of areas of tempered martensite adjacent to the pearlite-martensite interface should reveal the existence of preferred areas of precipitation. Fig. 1 is an example of an electron micrograph used in this study.

Small sections of a commercial steel (0.9 pct C, 1.6 pct Mn, 0.25 pct Si) were austenitized at 945°C in air for 45 min, furnace-cooled to 697°C, isothermally reacted to pearlite for 30 min, and quenched into iced brine. Two samples were tempered 5 and 20 min, respectively, in air at 498°C and were subsequently quenched in water. The samples were mechanically polished and etched in 1 pct picral. Collodion replicas were made by the conventional technique; these were shadowed with chromium at about 650° from the horizontal, and electron micrographs were taken at a linear magnification of 14,200X. Prints were made at a magnification of 44,100X.

R. E. GRACE, Junior Member AIME, is Graduate Fellow, Dept. of Metallurgical Engineering, Carnegie Institute of Technology, Pittsburgh.

TN 160E. Manuscript, Feb. 19, 1953.

Fig. 1—Electron micrograph of pearlite and martensite tempered 5 min, 0.09 pct C steel. X20,000.



Lineal analysis of the prints was made as a function of the interlamellar spacing and volume percent of iron carbide. Straight lines were drawn into tempered martensite between adjacent lamellae at a distance $S/4$ or $S/6$ apart, where S is defined as the interlamellar spacing measured at the pearlite-martensite interface. The volume percent of iron carbide was measured along each of these traces with a "gage length" of $S/10$. The results of analyses of two samples are shown in Table I. The area included between the $S/2$ and S distance from the interface could be considered homogeneous within the sensitivity of the measuring technique. This value was used as a proportionality factor to evaluate an arbitrary carbon content of homogeneous austenite, and also as a parameter by which error in measurements could be evaluated. Results of the lineal analysis are shown in Figs. 2 and 3.

Fig. 4 shows the statistical nature of the interlamellar spacing for all lamellae measured in this

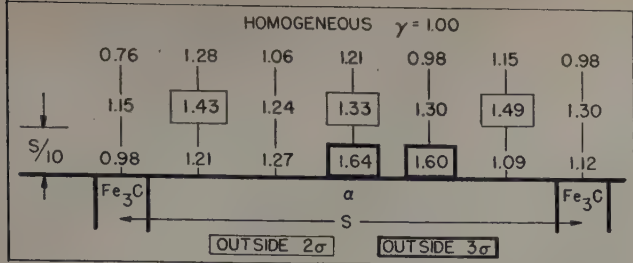


Fig. 2—No. 56b. Map of carbon concentrations preceding an advancing pearlite interface. OUTSIDE 2 σ OUTSIDE 3 σ

show statistically important areas in these measurements.

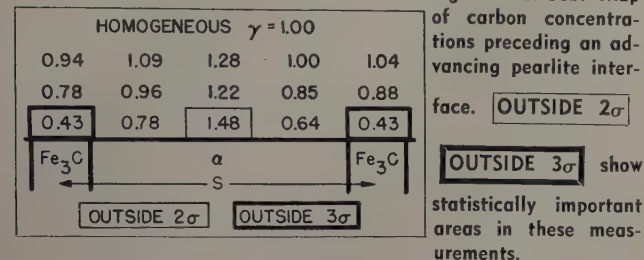


Fig. 3—No. 58b. Map of carbon concentrations preceding an advancing pearlite interface. OUTSIDE 2 σ OUTSIDE 3 σ

show statistically important areas in these measurements.

Table I. Analyses of Two Samples

Sample	
56b	Tempered 5 min, 498°C; 51 lamellae measured; Volume percent carbide measured within pearlite = 37 pct; Volume percent carbide measured within homogeneous tempered martensite, mean = 33 pct ($\sigma = 5.3$ v/o, $N = 35$)*
58b	Tempered 20 min, 498°C; 39 lamellae measured; Volume percent carbide measured within pearlite = 34 pct; Volume percent carbide measured within homogeneous tempered martensite, mean = 29.5 pct ($\sigma = 5.4$ v/o, $N = 25$)

* $\sigma = \left(\frac{\sum \Delta^2}{N} \right)^{1/2}$ where σ is the standard deviation from the arithmetic mean; Δ , the difference between volume percent measured and the arithmetic mean at each site between $S/2$ and S from the interface; and N , the number of sites between $S/2$ and S from the interface.

study. Center-to-center distances of adjacent carbide lamellae were measured at the interface of

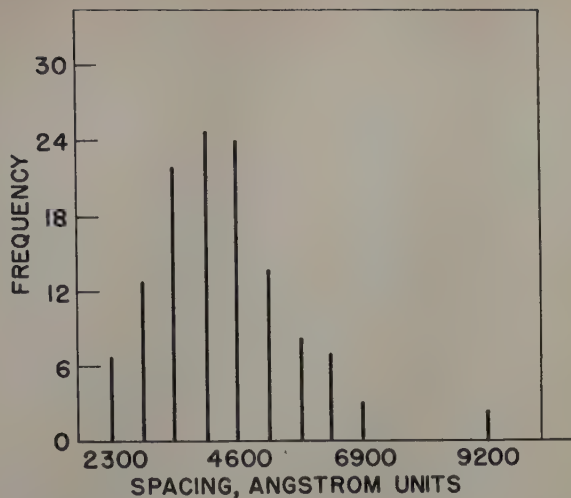


Fig. 4—Distribution of interlamellar spacings of No. 56b and No. 58b.

randomly selected pearlite colonies. The data are grouped about certain discrete points corresponding to 0.10-in. intervals in the measuring technique.

It does not appear that gross composition changes occur in austenite more than a fraction of an interlamellar spacing ahead of the growing pearlite colony. As tempering proceeds, the small carbides in front of the carbide lamellae will disappear in favor of the large lamellae. This may account for the very low carbon areas in Fig. 3. In general, this measuring technique is also applicable to the determination of the interlamellar spacing of pearlite. Etching and shadowing make carbide lamellae appear wider than their true width; but this should not affect careful lineal analysis, provided that the particle size distribution remains constant and only relative results are required.

Acknowledgment

The author wishes to thank A. L. Ellis for the use of the electron microscope at Manufacturing Research, International Harvester Co., Chicago; T. L. Thourson for taking the necessary electron micrographs; and Cyril Stanley Smith for his interest in this problem. This research was carried out at the Institute for the Study of Metals, University of Chicago under a grant from the Office of Ordnance Research, Contract No. DA-11-022-ORD-834.

Technical Note

Importance of the Iron Content of High-Purity Aluminum

by M. Metzger and J. Intrater

IN the large number of important studies on high-purity aluminum (e.g., recrystallization and grain growth, creep, internal friction), it does not seem to have been generally recognized that the iron content, despite its very low figure, has a strong influence on a number of properties. In part, its influence is due to the very low solubility of the Fe-Al θ phase. For aluminum of about 99.99 pct purity, the iron content may be 0.001 to 0.004 pct. For

values in this range, a second phase will be present below 410° to 480°C. This was determined by extrapolation of a log solubility vs inverse temperature plot of the solid solubility data of Edgar.¹ One consequence is the inhibition of grain coarsening below the solubility limit. This is shown in Table I, which gives, for three iron contents, the annealing temperature required for the absence of grains smaller than $\frac{1}{2}$ mm average diameter together with the minimum temperature for the presence of some grains larger than 2 mm diameter. The specimens were $\frac{1}{4} \times 1\frac{1}{2}$ -in. strips cut from hard-rolled 1/16-in. sheet supplied by the Aluminum Co. of America.

M. METZGER, Member AIME, and J. INTRATER are Members of Scientific Staff, Columbia University, New York.
TN 162E. Manuscript, March 9, 1953.

Table I. Effect of Annealing Temperature on Grains

Fe, wt pct	0.0004	0.004	0.023
Minimum temperature for absence of grains smaller than ½ mm, °C	450	500	600
Minimum temperature to produce some grains larger than 2 mm, °C	Less than 400	450	550
Solution temperature, °C	375	480	590

They were annealed at 50°C intervals starting at 300°C (no test at 350°C). The schedule of heating times follows that of Edgar, who used times of 24 hr at about 650°C and extended the annealing period by 24 hr for each 50°C below this temperature.

These tests were performed in connection with a study of the effect of iron on the intergranular corrosion of high-purity aluminum in hydrochloric acid. The experimental technique essentially consists of observing the rates of intergranular corrosion of aluminum of different iron contents after quenching from various temperatures within the solid solution range. It is found that aluminum of a given iron content treated at one temperature behaves like material of higher iron content at a higher temperature. The results indicate that the iron in solid solution has a strong tendency to segregate at the grain boundaries, probably because at sites in the boundary where the lattice is locally "compressed," stress can be relieved when the aluminum atoms are replaced by the smaller iron atoms. The reasoning follows that of Cottrell² and of McLean.⁸

Considering the simple model of solute atoms distributed among regions of different potential energy, the concentration, c , of solute atoms in the boundary (i.e., in the transition region several atomic spacings thick between adjacent grains) will depend on the average concentration, c_0 , according to the relation

$$c = c_0 \exp(-E/kT) \quad [1]$$

where E is the energy of interaction of the solute atom at the boundary site. For various sites, the value of E would be more negative for those at which the interaction is stronger. For iron in aluminum, the effective E determined by comparison of the results of corrosion experiments for different iron contents and temperatures is about -0.7 electron volt. This large energy is believed to indicate that the concentrations of iron in the boundary to which the corrosion test is sensitive are those which occur at the region in the center of the boundary where the lattice is highly distorted.

With an interaction energy of this magnitude for all grain boundary sites, Eq. 1 could hardly be valid, since it would indicate an excessive concentration of iron atoms at the boundary except at temperatures near the melting point. It is more likely that a progressive saturation of available boundary sites occurs as the temperature goes from just below the melting point, where only sites for which E is very large are occupied by iron atoms, to lower temperatures where sites of lower interaction energy can be occupied. Even with an iron content of order 0.001 pct, a large proportion of the boundary sites for which the interaction energy of an iron atom is comparatively high would be occupied at temperatures below 500°C. A saturation effect is also suggested by some of the experimental results.

Additional solute elements of smaller atomic diameter than aluminum would then be in competition with iron atoms for boundary sites. It is supposed

that the atoms of an element which has less tendency to concentrate in the boundaries than has iron will have a lower interaction energy at any given site. The atoms of such an element could then occupy relatively few sites not already taken by iron atoms even if the element were present in somewhat larger amounts. Thus, substantial modification of the properties of the grain boundaries by the segregation of other alloying elements in solid solution would be produced only by elements which either have effective atomic diameters less than that of aluminum, but have stronger segregation tendencies than iron, or which have larger effective atomic diameters than aluminum and thus can segregate to the "expanded" boundary positions which the smaller iron atoms would not occupy.

On this basis, it is possible to explain the results obtained by Starr, Vicars, Goldberg, and Dorn⁴ on the effects of alloying elements on the activation energy for grain boundary relaxation in aluminum as measured with the torsion pendulum. They found no significant effects for additions of zinc, silver, copper, and germanium, but there was an increase in the activation energy from 38,000 cal per mol in high-purity aluminum to 54,000 cal per mol for 1.617 atomic pct Mg. The alloys used contained 0.003 to 0.006 pct Fe and the temperatures of measurement ranged up to 500°C. It would therefore be expected, as indicated above, that the boundary sites most favorable for occupation by foreign elements of effective atomic diameter smaller than aluminum would have been taken up by iron atoms before any other elements were added. In the case of copper, relatively strong segregation would ordinarily be expected on the basis of its atomic diameter, which is considerably smaller than that of aluminum, but our corrosion experiments suggest that its tendency to segregate is slightly less than that of iron. Thus, only for additions of magnesium and (to a lesser extent) germanium, which have atoms larger than aluminum, would a considerable quota of grain boundary sites be available to the solute atoms.

Iron may produce an additional complication in experiments of this kind if the second phase exists as a precipitate in the grain boundaries and produces a restraining action on the relaxation of stress across the boundary.

The evidence of the authors and that of Starr et al. shows that, even in relatively pure aluminum, the behavior of the grain boundaries is strongly influenced by small amounts of other elements and that quantitative data obtained at temperatures considerably below the melting point should not be considered as good approximations to the values characteristic of the boundaries in the ideally pure metal.

The work out of which these observations grew was performed under contract Naw-6223 for the National Advisory Committee for Aeronautics to which the authors' thanks are due for permission to publish this note. An account of this work will be issued.

References

- ¹ J. K. Edgar: *Trans. AIME* (1949) **180**, p. 225; *METALS TECHNOLOGY* (June 1948).
- ² A. H. Cottrell: Report of a Conference on Strength of Solids. Physical Soc., London (1948) p. 30.
- ³ D. McLean: *Journal Inst. Metals* (1947) **73**, p. 791.
- ⁴ C. D. Starr, E. C. Vicars, A. Goldberg, and J. E. Dorn: Seventeenth Technical Report, Series 22, Issue 17 N7-onr-295, Task Order II, NR-031-048. January 1952.

Order-Disorder Transformation in Cu-Au Alloys

Near the Composition CuAu

by J. B. Newkirk

Results of a Debye-Scherrer X-ray investigation are given which show that the order-disorder transformation is a first-order or heterogeneous reaction in Cu-Au alloys with compositions near CuAu. Evidence was found for conventional tie-line segregation across a usual type of two-phase field separating the ordered and disordered fields in the Cu-Au equilibrium phase diagram. The horizontal and vertical widths of the two-phase fields are about 3 atomic pct and 20°C, respectively, at 43 and 54 atomic pct Au. No evidence for the existence of an ordered structure based on a stoichiometric composition of Cu_3Au_2 could be found.

ALTHOUGH the modern theories relating the degree of order of binary alloys to temperature and composition have met with considerable success, the nature of the transformation from the disordered state to the ordered state and vice versa has never been well understood. It has been assumed by some¹ that this is a second-order transformation, that is, a homogeneous change of state. Others² hold that the transformation is first-order and that the effects characteristic of heterogeneous phase transformation apply. Since this subject is discussed in detail in a recent paper,³ the arguments will not be repeated here.

The present paper summarizes an experiment which was designed to distinguish between these two viewpoints for the case of Cu-Au alloys near the composition CuAu. The Cu-Au system is an important one because it furnishes prototype alloys, the behavior of which has formed the basis of much of the present-day order-disorder theory. It has recently been shown³ that in alloys near Cu₃Au there is a temperature range within which the ordered and disordered states coexist in equilibrium and are distinguishable as separate phases. Therefore, the transformation must be first-order for these alloys.

A similar demonstration for alloys near CuAu, however, has been lacking.

Experimental Method

Essentially the experiment consisted of equilibrating Cu-Au samples at various temperatures, quenching them in water to retain the high temperature states, and then examining them at room temperature for the coexistence of the ordered and disordered structures. The thermal gradient method of heat treatment³ was used because it was important that all temperatures over the transformation range should be represented in the test. Briefly, this method consisted of holding a wire of the desired composition, sealed under vacuum in pyrex, in a known temperature gradient for a long enough time to allow each part of the wire to assume the crystal structure characteristic of the temperature at which it was held.

The temperature gradient was produced by inserting into an ordinary wire-wound cylindrical laboratory furnace, an 18 in. length of 1/8 in. ID ceramic tube which was heavily wrapped with asbestos. The furnace power was controlled by a Tagliabue Celestray controller and a chromel-alumel thermocouple with the junction located on the heating elements. During the equilibrating treatment the widest variation of temperature within the gradient tube was approximately 4°C at the highest temperature. The temperature at various places within the tube was determined, before inserting

J. B. NEWKIRK, Member AIME, is Research Associate, Research Laboratory, General Electric Co., Schenectady.

Discussion on this paper, TP 3537E, may be sent, 2 copies, to AIME by Dec. 1, 1953. Manuscript, Jan. 24, 1953. Cleveland Meeting, October 1953.

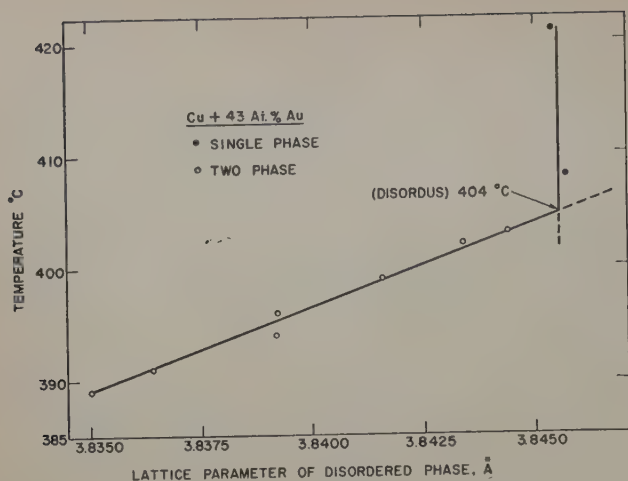
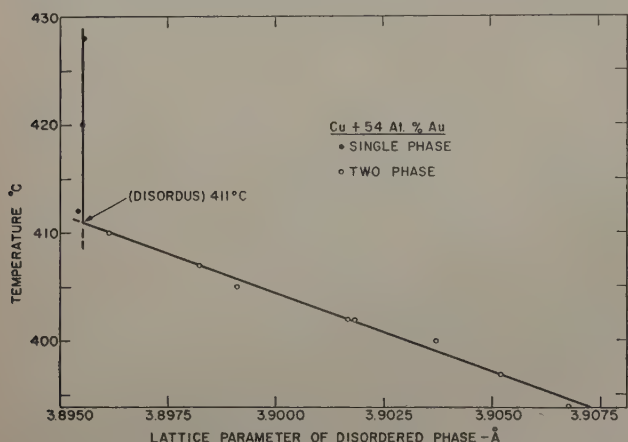


Fig. 1 (above) and 2 (below)—Relation between equilibrating temperature and lattice parameter of the disordered phase for two alloys on opposite sides of CuAu.



the specimen, by means of a small thermocouple probe which was introduced through a hole in the front of the furnace. By making tests with alloys having transformations at known temperatures (Cu₃Au, CuAu) it was found that the presence of the wire specimen does not significantly affect the measured temperature gradient if the wire is less than 0.020 in. in diameter.

The value of the thermal gradient method, as applied in these experiments, does not lie in the absolute accuracy with which transformation temperatures can be measured, but rather in the feature of continuous temperature variation along the length of a single specimen. When all sources of error were considered, it was estimated that the temperature of any point along the specimen was known to an accuracy of $\pm 10^\circ\text{C}$.

After equilibrium was reached, the wire was quenched and the phases present were identified by making room temperature Debye-Scherrer photographs at various points along the length of the wire. The time required to reach equilibrium was estimated on the basis of previous experiments^{2,4} in which electrical resistance of Cu-Au wires was measured as a function of time and temperature. In these resistance tests the specimen was held at constant temperature until no change in resistance, measured to a precision of 0.1 pct, was detected. The temperature was then altered slightly and the resistance was again allowed to become constant. Temperature-resistance curves, obtained in ascending steps of temperature, were superimposed upon corresponding curves made in descending steps. At

temperatures within the transformation range, a steady state was approached very slowly, frequently requiring several weeks. For the thermal gradient tests the equilibrating time was always in excess of one month. As a further test of equilibrium it became standard practice to seal two wires of the same composition in the same pyrex tube. One wire was in the as-drawn condition and the other had been previously ordered by cooling it slowly through the transformation range. After the wires had been equilibrated in the thermal gradient, they produced identical Debye-Scherrer patterns when photographed at corresponding points along their lengths. Whenever it was known that equilibrium was not reached, Debye-Scherrer lines were diffuse. In such cases longer heat treatment in the same gradient caused the lines to sharpen.

Three compositions were chosen for study: namely 40, 43, and 54 atomic pct Au. Results of incidental tests on two other Cu-Au alloys near CuAu are also given in the final summary of data. The alloys were made by melting electrolytic gold and oxygen-free electrolytic copper under a low pressure of argon in a quartz tube lined with graphite. The ingots were homogenized and worked into wires 0.017 in. in diameter. Chemical analyses, which were conducted by Lucius Pitkin, Inc., gave the results listed in Table I.

For each of the compositions listed in Table I, a 6 in. length of wire, in the as-drawn condition, was sealed in an individual evacuated glass tube and equilibrated in a temperature gradient of about 25°C per cm. The tube was then quenched into water and a stripe of high purity annealed copper powder in an amorphous binder was painted along one side of each wire. In this way, calibration lines of known diffraction angles were recorded on the photographic film along with the Debye-Scherrer pattern produced by the specimen wire. By using these calibration lines, the diffraction angles of the lines from the wire specimen could be measured with good accuracy. The photographs were made with a 10-cm diameter cylindrical camera, which was designed to accommodate the long wire specimen.⁸ Copper radiation ($K\alpha_1 = 1.5405\text{\AA}$) was used throughout.

Results: The diffraction patterns made at the high temperature end of all wires were characteristic of a disordered face-centered cubic structure with lattice parameters as listed in Table I. At the low temperature end the patterns were similar to those reported by Johansson and Linde⁶ for their CuAu II

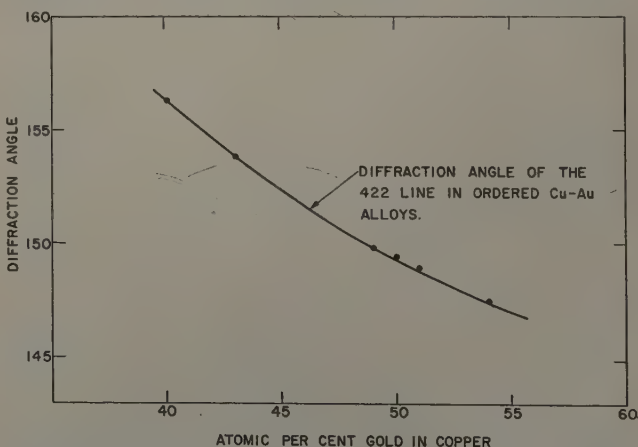


Fig. 3—Empirical curve showing the dependence of the diffraction angle of the 422 Debye-Scherrer line as a function of composition for ordered Cu-Au alloys.

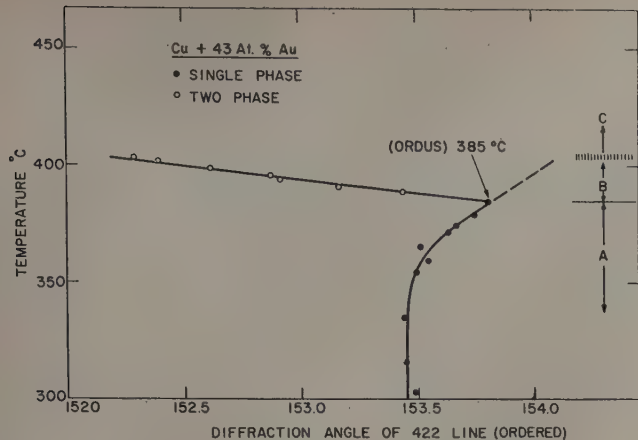
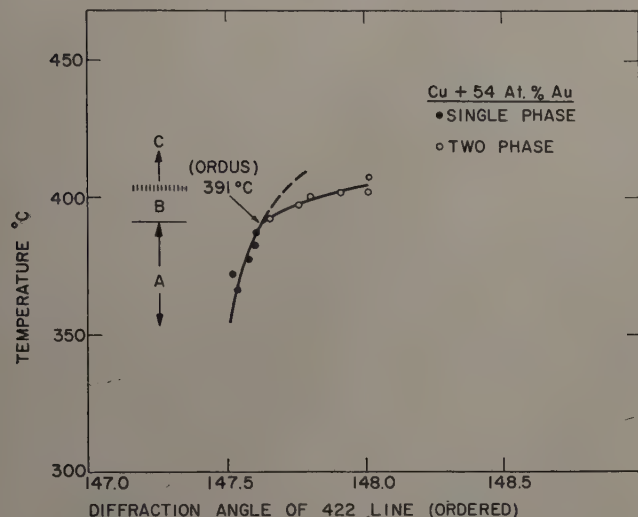


Fig. 4 (above) and 5 (below)—Relation between equilibrating temperature and the diffraction angle of the 422 Debye-Scherrer line of the ordered phase for two alloys on opposite sides of CuAu.



orthorhombic structure. A thorough study of the CuAu II structure was not made. Presumably, if the wires had extended to low enough temperatures and the annealing periods were sufficiently long, the tetragonal CuAu I structure would have been found at the low temperature end.

In each specimen there was a range of temperature over which patterns corresponding to the ordered CuAu II and the disordered structures were found on the same film. It was not assumed that equilibrium was reached unless all the lines of each pattern were sharp and back-reflection doublets were clearly resolved. To give such patterns, each of the diffracting particles must have been uniform in composition, relatively unstrained, and greater than 1000Å in minimum dimension. In the paragraphs that follow, the two patterns are discussed separately in terms of the manner in which they change with annealing temperature.

Disordered Cubic Structure

The lattice parameters corresponding to the disordered structure were calculated for various annealing temperatures. At temperatures where only the disordered pattern was visible on the film, the lattice parameter remained independent of temperature. Where both patterns were present, there was a decided temperature dependence, as shown in Figs. 1 and 2. This behavior can be interpreted in terms of changing composition of the disordered material with temperature, according to conventional tie-line

segregation across a two-phase region between the ordered and disordered fields. The two-phase region would be expected to ascend from both sides of the CuAu composition toward a maximum transformation temperature at 50 atomic pct. If this construction is correct, then the lattice parameter of the disordered phase in alloys on the copper-rich side of CuAu should increase with temperature because the disordered phase becomes richer in the component of larger atomic radius, i.e., gold, as the temperature increases. Conversely, in alloys on the gold-rich side of CuAu, the lattice parameter should decrease with increasing temperature because the disordered phase becomes leaner in gold. These effects were observed in all the Cu-Au alloys where a two-phase region was found.

If the data contained in Figs. 1 and 2 are used, the true disordus temperature can be found by extending the sloping lines to the lattice parameter of the alloy when it is all disordered. The intersection marks the disordus temperature for the composition in question. Knowing the dependence of a_o on composition, the portion of the disordus line which is associated with the overall composition of the specimen can be calculated. This is shown in Fig. 6, which is discussed in a later section.

Ordered Structure

The reflection angle of the 422 line in the ordered pattern varies with composition according to the experimentally determined curve in Fig. 3. These data were taken from Debye-Scherrer photographs made at points on the thermal gradient wires that had been equilibrated at least 25°C below the two-phase temperature range.

At temperatures well below those at which the last traces of the disordered pattern were seen, the diffraction angle of the 422 line was independent of temperature. As the two-phase region was approached the reflection shifted gradually to a higher angle. As soon as the two-phase region was entered, however, as indicated by the presence of the two patterns on the film, there was a marked dependence of the diffraction angle upon temperature. For the 43 pct Au alloy the shift was toward a lower angle with increasing temperature, and for the 54 pct alloy, the shift was toward a higher angle. This behavior is summarized in Figs. 4 and 5.

In the temperature range C, only the disordered pattern was observed; in range B both ordered and disordered patterns were seen, and in range A the disordered pattern was entirely replaced by the ordered. The ordus temperature can be located by the intersection of the lines in the A and B temperature ranges.

Evidently the shift to higher angle, as the two-phase region is approached, is a result of a lowering of the degree of long range order of the ordered

Table I. Chemical Analyses of Alloys

Nominal Composition, Atomic Pct Au	Composition by Analysis		Actual Atomic Pct Au	Disordered Phase a_o , Å
	Wt Pct Cu	Wt Pct Au		
40	32.61	67.35	39.97	3.832±0.001
43	29.88	70.08	43.06	3.845±0.001
50	24.39	75.58	49.99	3.876±0.001
51	23.59	76.38	51.16	3.882±0.001
54	21.58	78.40	53.95	3.895±0.001
Cu	Spectroscopically pure			3.615±0.001

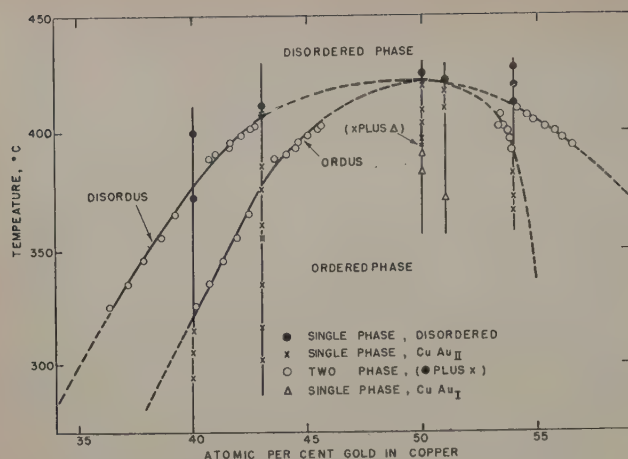


Fig. 6—Part of the Cu-Au equilibrium phase diagram.

phase. Within the two-phase region, the shift must have two components: 1—the effect of the changing composition of the ordered phase by tie-line segregation, and 2—the continuing shift to higher angles due to lowering long range order as the temperature is raised. The two components can be resolved and their magnitude estimated by extrapolating the line in region A into region B, as shown by the dashed line. The deviation of this line from its position at lower temperatures where θ is constant, represents the component due to the lowering long range order of the ordered phase. The horizontal distance between this extrapolated line and the experimentally determined line in range B would then represent the component of angular displacement due to composition change only. The magnitude of this change in composition can be estimated by referring the latter component of angular displacement to the experimentally determined curve of Fig. 3. This interpretation is consistent with a graphical scheme, described in an earlier paper,⁶ whereby the degree of long range order of the ordered phase is specified below and within the temperature range where both disordered and ordered phases coexist in equilibrium. It will be noticed that the angular shifts, in the temperature range B, are in opposite directions for alloys on opposite sides of the CuAu composition. Also, in each case the direction of the displacement is such that, when referred to Fig. 3, the composition of the ordered phase can be reasonably interpreted in terms of tie-line segregation, that is, the ordus lines slope toward a maximum at 50 atomic pct.

Discussion: The results described above can be summarized by means of the partial Cu-Au equilibrium diagram shown in Fig. 6. This diagram was constructed solely on the basis of the experimental data described above. By measuring the relative intensities of characteristic lines in the ordered and disordered patterns, it should be possible to make an independent determination of the relative amounts of the ordered and disordered phases through the two-phase region. This was not possible in the present study, however, because the necessarily long annealing times produced such large grains that Debye-Scherrer lines were too spotty to be measured accurately with the usual photometric equipment.

The diagram evidently contains two-phase regions which conform to the requirements of the Gibbs phase rule for heterogeneous equilibrium in a binary system. Therefore, in alloys near CuAu,

the ordered and disordered states should be treated as different phases.

By 1940, the sort of binary diagram found in this investigation had been proposed by at least four other investigators.⁷ Since then, however, due to a growing misconception that order-disorder transformations generally are homogeneous changes of state, the two-phase region separating the order and disorder fields has frequently been replaced by a single dashed line, which is supposed to show the temperature above which no long range order exists.⁸ Such a construction is not in accord with the experimental facts described here.

The present study shows a major deviation from the results of early workers who proposed phase diagrams containing an invariant maximum point at 40 atomic pct Au composition. In the present work no indication of congruent transformation was found at this composition. Since the experimental method used here is more direct than the methods used by others, such as measurements of the electrical resistivity or of the specific heat, it is reasonable to conclude that no superlattice exists which has a stoichiometric composition of Cu_3Au_2 .

Summary

1—X-ray evidence is given which shows that in Cu-Au alloys near CuAu in composition there is a finite temperature range within which the ordered and disordered states can coexist in equilibrium as conjugate phases. The transformation may therefore be regarded as heterogeneous or first-order.

2—Debye-Scherrer effects are interpreted in terms of normal tie-line segregation across two-phase regions separating the ordered and disordered fields near CuAu in the Cu-Au equilibrium phase diagram.

3—Part of the Cu-Au equilibrium phase diagram is plotted on the basis of observed Debye-Scherrer effects. The horizontal and vertical widths of the two-phase regions are about 3 atomic pct and 20°C , respectively, at both 43 and 54 atomic pct Au. In general, however, the two-phase regions are not symmetrical about the composition CuAu.

4—It is unlikely that an ordered structure exists which has a stoichiometric composition Cu_3Au_2 since the equilibrium transformation at this composition is divariant.

Acknowledgments

The author is indebted to R. A. Oriani, D. Turnbull, and A. H. Geisler for their helpful comments during the writing of this paper.

References

- ¹ S. Siegel: Order-Disorder Transitions in Metal Alloys. *Symposium on Phase Transformations in Solids* (1951) pp. 366-386. New York. John Wiley and Sons.
- ² F. N. Rhines and J. B. Newkirk: The Order-Disorder Transformation Viewed as a Classical Phase Change. *Trans. ASM* (1953) **45**, pp. 1029-1055.
- ³ J. B. Newkirk: A Thermal Gradient Method for the Study of Crystal Structure and its Application to Order-Disorder Research. To be published in *Review of Scientific Instruments*.
- ⁴ F. N. Rhines: Private communication.
- ⁵ C. H. Johansson and J. O. Linde: X-Ray Studies of Transformations in the CuAu Alloy. *Ztsch. Physik* (1928) **50**, p. 64ff.
- ⁶ J. B. Newkirk, A. H. Geisler, R. Smoluchowski, and D. L. Martin: Phase Equilibria in an Ordering Alloy System. *Journal of Applied Physics* (1951) **22**, p. 298.
- ⁷ M. Hansen: *Der Aufbau der Zweistofflegierungen*. (1936) pp. 216-223. Berlin. Julius Springer.
- ⁸ *Metals Handbook* (1948) Cleveland. ASM.

Self-Diffusion of Iron in Iron Oxides and The Wagner Theory of Oxidation

by L. Himmel, R. F. Mehl, and C. E. Birchenall

The rates of self-diffusion of iron in artificially prepared wüstites of various compositions have been determined using the decrease in surface activity technique. Similar measurements are reported for artificial magnetites of nearly stoichiometric composition and for natural hematite single crystals. These data, together with appropriate thermodynamic data derived from the present study or from the literature, are used to calculate the rates of oxidation of iron and its oxides, taking as a basis the theoretical rate equations developed by Wagner. The calculations are compared with experimental rate constant data for these same reactions and are shown to provide essential confirmation for the Wagner theory. For the most part, the results are also consistent with the previously proposed transport mechanisms in the oxides of iron.

WHEN a metal is exposed to an oxidizing atmosphere at elevated temperatures, a superficial oxide layer is formed which then thickens according to some characteristic rate law. Provided that the oxide layer is dense and continuous and does not present any paths for gaseous diffusion, continued growth must inevitably involve the migration of the reactants—either the metal or oxygen or both—through the lattice of the solid oxide. This is true whether the reaction rate is controlled by the diffusion process itself or by a slow step in a reaction at one of the interfaces. If the overall rate is limited by diffusion, and if the concentrations or thermodynamic activities of the reactants at the boundaries of the oxide layer are independent of time, the familiar parabolic rate law is observed.

Under these conditions, Wagner¹ has shown that the rate constant may be expressed in terms of the

mobilities of the reacting components and the appropriate concentration or activity gradients which are established across the growing oxide layer. In presenting the phenomenological basis for the theory, Wagner has emphasized the role played by lattice defects in diffusion processes in oxides. The essential validity of this theory has been confirmed by experiment for a number of simple systems including the growth of Cu_2O on copper.¹⁻⁴

One of the objectives of the present study has been to extend the Wagner approach to the more complex process of the oxidation of iron and its oxides, and particularly to wüstite, which is normally the major constituent of the oxide scales formed on iron at temperatures above approximately 570°C. For this purpose the rates of self-diffusion of iron in wüstite, magnetite, and hematite have been measured by tracer techniques and the necessary thermodynamic data have been obtained from equilibrium studies involving the oxides and their atmospheres. These data have subsequently been used to test the underlying assumptions of the Wagner theory as well as the detailed mechanism of the scaling of iron previously proposed by Davies, Simnad, and Birchenall.⁵

Lengthy treatments of diffusion and conduction phenomena in ionic crystals have been published.^{6,7} The latest, by Jost,⁸ also summarizes much of the existing experimental data. In general, however, the oxides of iron have not been considered specifically and hence a brief review of the available

L. HIMMEL, formerly Graduate Student, Carnegie Institute of Technology, is now Research Engineer, Westinghouse Research Laboratories, East Pittsburgh, Pa., R. F. MEHL, Member AIME, is Director, Metals Research Laboratory, and Head, Dept. of Metallurgical Engineering, Carnegie Institute of Technology, Pittsburgh, and C. E. BIRCHENALL, Junior Member AIME, is Associate Professor, Dept. of Chemistry, James Forrestal Research Center, Princeton University, Princeton, N. J.

Discussion on this paper, TP 3511E, may be sent, 2 copies, to AIME by Dec. 1, 1953. Manuscript, Oct. 20, 1952. Cleveland Meeting, October 1953.

This paper is based on a thesis by L. Himmel submitted in partial fulfillment of the requirements for the degree of Doctor of Science to the Faculty of Carnegie Institute of Technology.

structural and transport data for these materials will be pertinent.

Crystal Structures of the Oxides of Iron

Since the radius of the oxygen ion is approximately 1.4Å as compared to roughly 0.8Å for Fe^{++} and 0.7Å for Fe^{+++} , it is often convenient to regard all three oxides as relatively close-packed networks of oxygen ions with the smaller iron ions arranged in the interstices. The structures of the oxides of iron and the interrelations between them are discussed in considerable detail by Goldschmidt.⁹

Wüstite: In wüstite the oxygen ions and the cations occupy separate, interpenetrating, face-centered cubic lattices in the NaCl-type structure. This oxide is unstable, in bulk, below approximately 570°C, slowly decomposing into a eutectoid mixture of α -iron and magnetite. It is not observed as a stable constituent of the oxide layer on iron below this temperature.

Magnetite: According to Verwey and coworkers,¹⁰⁻¹² magnetite possesses the cubic, inverse spinel structure in which the oxygen ions have a cubic, close-packed arrangement. Among the sites available to the cations in the ideal unit cell of the spinel structure, eight are tetrahedral positions and sixteen octahedral positions. At the stoichiometric composition, the eight tetrahedral sites are occupied by Fe^{+++} ions, while the distribution of the remaining eight Fe^{+++} and eight Fe^{++} ions about the sixteen octahedral positions is random and fluctuating. This model satisfactorily accounts for the high electrical conductivity of magnetite at ordinary temperatures and may also be used to explain the unique structural transition observed in this oxide at low temperature.¹³

Hematite: Hematite or $\alpha\text{-Fe}_2\text{O}_3$ has the corundum structure, the symmetry being rhombohedral. The structure is best viewed as a slightly distorted, hexagonal close-packing of oxygen ions with the metal ions again residing in the interstices. A cubic, ferromagnetic variety of ferric oxide, designated as $\gamma\text{-Fe}_2\text{O}_3$ and having a structure very similar to that of magnetite has also been reported.¹⁴ Apparently this oxide is always metastable with respect to hematite;¹⁵ it is never observed in the oxide scales formed on iron at high temperatures.

Defect Structures and Transport Mechanisms in the Oxides of Iron

Diffusion and the related phenomenon of conductivity in oxides (and sulphides, halides, etc.) are commonly associated with the migration of ions and electrons rather than electrically neutral atoms or molecules. Although the cations, anions, and electrons all have some mobility in these materials, the transference number of one of the component particles generally far exceeds that of the others. Such marked differences in the mobilities of the various species can frequently be understood by a consideration of the structure of the crystal and the type of lattice defects which are present. In most oxides, for example, ionic transport can be attributed almost entirely to the metallic ions, either through the migration of cation vacancies as in Cu_2O , NiO , etc., or of interstitial ions as in ZnO , etc. In the alkali halides, where defects occur in both the cation and anion sites, the cations are often substantially more mobile because of their smaller size. Only a few examples are known in which the transport is due predominately to the migration of negatively charged anions or anion vacancies.^{1,8}

Wüstite: As shown by several investigators, notably Darken and Gurry,¹⁶ wüstite exists as a thermodynamically stable, single-phase structure over a relatively wide range of compositions, that does not seem to include the stoichiometric compound FeO . The maximum iron content found by Darken and Gurry corresponds to $\text{Fe}_{0.948}\text{O}$ and by Jette and Foote¹⁷ to $\text{Fe}_{0.958}\text{O}$. Recent claims by Benard¹⁸ that the stoichiometric compound is stable at temperatures above approximately 800°C have not been adequately substantiated.

Wüstite, like Cu_2O and NiO , is a cation-deficient structure. Jette and Foote have demonstrated by a comparison of X-ray lattice parameter and density measurements that an appreciable fraction of the lattice sites normally occupied by iron ions are vacant. Since the oxygen lattice is thought to be perfect, two Fe^{++} ions must be promoted to the ferric state for each vacant iron site, in order to maintain electrical neutrality. A recent correlation of the existing thermodynamic data for ferrous oxide by Kelley¹⁹ indicates that the vacancies themselves may be ordered instead of randomly distributed, as had previously been assumed.

Agreement on the transport mechanism in wüstite has been fairly universal since the work of Jette and Foote. The belief that ionic transport in wüstite occurs essentially by the interchange of vacancies with normal lattice sites is strongly supported by the observations of Wagner and Koch²⁰ on the electrical conductivity of wüstite as a function of oxygen pressure, and by marker movement studies of Davies, Simnad, and Birchenall.⁵ Wagner and Koch found, in fact, that the electrical conductivity of wüstite between 800° and 1000°C is roughly proportional to the 8th root of the oxygen pressure. Nevertheless, the early but rather crude marker experiments of Pfeil²¹ could have been interpreted to allow for considerable oxygen ion diffusion, while the more recent work of Dunnington, Beck, and Fontana²² places this contribution at approximately 10 pct.

Magnetite: Considerable disagreement exists in the literature regarding the stable range of the magnetite phase field. The most reliable evidence indicates that the deviations from stoichiometric ratio are in the direction of increased oxygen content. The homogeneity range is much narrower than that for wüstite, yet still of detectable magnitude. Verwey and Haayman¹¹ have shown by X-ray lattice parameter measurements that the deviations from stoichiometric composition are actually associated with the presence of vacancies in the cation sites rather than excess oxygen in interstitial positions. Defects are assumed to occur only in the octahedral sites, the Fe^{++} ions being replaced by Fe^{+++} and vacancies. It is also assumed that the vacant positions are statistically distributed over the available octahedral sites.

Although it would seem that the structure of magnetite is well established, studies of transport phenomena in this oxide appear to be contradictory. Thus Wagner and Koch found the electrical conductivity of magnetite to be essentially independent of the oxygen pressure. Furthermore, the marker movement experiments of Davies, Simnad, and Birchenall indicate a ratio of oxide ion mobility to iron ion mobility of almost four to one* in the

* It now appears that this conclusion is in error. A brief note correcting the original interpretation of the marker experiments will be published by Davies, Simnad, and Birchenall.

neighborhood of 900°C. The latter result, particularly, is difficult to reconcile with the structural model given by Verwey.

Hematite: The departure from stoichiometric composition in α -Fe₂O₃ is practically undetectable by analytical methods. Nevertheless, since the ferrous and ferric states of oxidation are the only ones readily available to iron, it would be expected that hematite is slightly oxygen deficient. Such a deficiency can be accounted for in either of two ways; i.e., the presence of oxide ion vacancies or interstitial iron ions. The existing information does not permit a clear-cut distinction between these two possibilities, although the former appears more likely.

Wagner and Koch were not able to observe any effect of oxygen pressure on the conductivity of α -Fe₂O₃, but Bevan, Shelton, and Anderson²⁸ have concluded, from similar studies, that conduction in this material most probably occurs by an oxide ion vacancy mechanism. Pryor and Evans²⁴ have employed the anion vacancy model to explain the dissolution behavior of hematite in acids. The interpretation of marker movement studies of Davies, Simnad, and Birchenall is somewhat uncertain but is also consistent with the vacancy picture. It should be pointed out, however, that the effect of oxygen pressure on the concentration of oxide ion vacancies cannot be distinguished from its effect on interstitial iron ions; the number of either kind of imperfection is decreased by an increase in oxygen pressure.

Self-diffusion data for iron in sintered hematite powder compacts have recently been reported by Lindner.²⁵ The significance of these measurements will be discussed in connection with the results obtained in the present investigation.

Experimental

The decrease in surface activity technique has been selected for the self-diffusion experiments. This choice was dictated largely by a consideration of the physical and chemical properties of the oxides themselves. Although preference is normally given to a sectioning method, the removal of uniformly thin layers of the bulk oxides for radiochemical analysis became prohibitively difficult. All of the wüstites and magnetites used in this work have been prepared by the direct oxidation of high-purity iron. Each specimen has been oxidized to completion at high temperature and then homogenized for prolonged periods in atmospheres of constant, known oxidizing potential. Not only did this technique permit close control over the composition and purity of the resulting oxides, but it invariably yielded dense products which were essentially free from cracks, voids, or other structural irregularities. Surprisingly enough, the hematites obtained in this manner were always rather porous and had very little mechanical stability. Natural single crystals of this oxide were employed instead of the artificially prepared material for this reason.

Materials: High-purity iron supplied by the National Research Corp. has been used as the starting material for the preparation of the oxides. This iron was received in the form of a 3-in. diam vacuum-melted and cast ingot. Insofar as chemical purity is concerned, it is very similar to the Westinghouse "Puron" employed in the kinetic studies of Davies, Simnad, and Birchenall. The maximum impurity contents, based on spectroscopic standards, are as follows: 0.02 pct O, 0.001 pct N, 0.005 pct H, 0.005

pct C, and 0.02 pct total metallic impurities. No attempt has been made to refine or further purify the as-received material.

The specimens were cut from blanks machined from the original ingot. They were in the form of disks approximately 2 cm in diameter and 1.5 to 2.5 mm thick, the thickness depending upon the temperature at which homogenization was to be effected. Each specimen contained a lip, integral with the disk, through which a small hole was drilled to facilitate suspension of the sample in the oxidation unit. After cutting to approximate shape and dimensions, both faces of the specimens were surface ground; the edges were also smoothed to reduce the tendency for subsequent cracking and spalling of the oxide layer.

Several large, natural, hematite crystals (α -Fe₂O₃) from Minas Geraes, Brazil, were obtained. The useful single crystals were selected primarily on the basis of their freedom from associated minerals or other structural faults. Even when finely pulverized, however, they were too slowly attacked by strong acids to obtain satisfactory analytical samples. Nearly all of the crystals selected possessed highly reflecting and remarkably well-developed crystal faces. The orientations of the most prominent faces of each crystal were determined by the back-reflection Laue technique. In general, these faces corresponded to the (00.1) or basal planes of the crystal. Rectangular parallelepipeds approximately $\frac{3}{4} \times 1\frac{1}{2} \times \frac{1}{4}$ in. were cut from the larger crystals using a water-cooled diamond cut-off wheel, the sectioning being accomplished so that the largest face of each crystal either contained or was perpendicular to the basal plane of the rhombohedral crystal.

The radioactive iron was obtained as an aqueous chloride solution from the Isotopes Div. of the United States Atomic Energy Commission. When originally received, this solution contained both Fe⁵⁵ and Fe⁵⁹ in roughly equivalent concentrations. The desired isotope is Fe⁵⁵ which decays by K-electron capture with the emission of soft X-rays (Mn K, $\lambda = 2.10\text{\AA}$). Since Fe⁵⁵ has a half-life of approximately 2.9 years as compared to roughly 46 days for Fe⁵⁹, the radioactive unit was allowed to decay for a period of more than a year before use in order to decrease the Fe⁵⁹ concentration to well below 0.5 pct. The active unit was then twice purified by continuous ether extraction from hydrochloric acid solution, after which the ether extract was evaporated to dryness and made up to the desired specific activity with distilled water. Absorption and decay measurements on samples taken from the ether extract served to establish its radiochemical purity.

Description of the Oxidation System: The wüstites were prepared and diffused in hydrogen-water vapor atmospheres in a dynamic system designed specifically to provide accurate control over the oxidizing potential of the furnace gases. This system consisted essentially of a fairly elaborate gas purification train, a saturator maintained at known constant temperatures for introducing controlled amounts of water vapor into the gases, and an electrically heated reaction chamber in which the specimens were suspended. The apparatus was of all-glass or silica construction and was operated under a slight positive pressure of 10 mm Hg. Hydrogen-water vapor mixtures generated in the saturator were preheated to the furnace temperature and then passed through the reactor at a vigorous rate to minimize the tendency for thermal segrega-

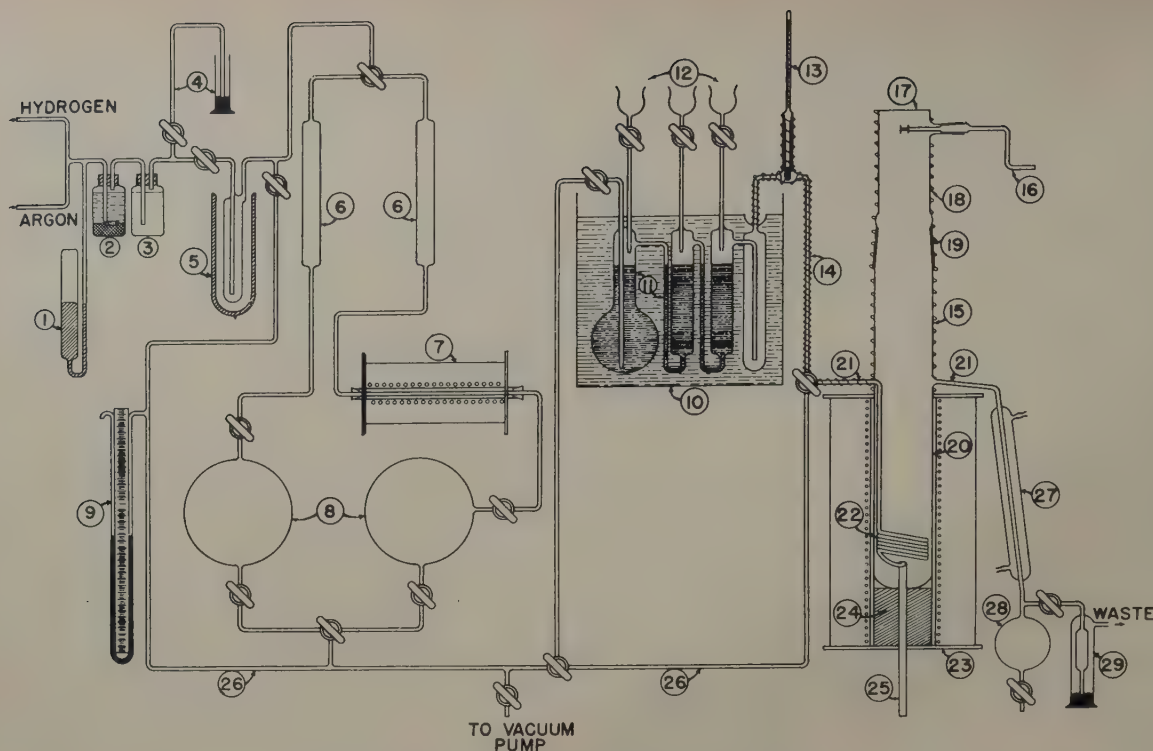


Fig. 1—Schematic diagram of the oxidation and diffusion unit.

- | | | |
|------------------------------------|-----------------------------------|--------------------------------------|
| 1—Safety trap. | 11—Saturator. | 21—Graded silica-to-pyrex seals. |
| 2—Vanadyl sulphate + Zn amalgam. | 12—Funnel tubes. | 22—Silica preheating spiral. |
| 3—Gas scrubbing tower. | 13—Mercury thermometer. | 23—Kanthal-wound resistance furnace. |
| 4—Vent line. | 14—Electrically heated line. | 24—Alundum support. |
| 5—Cold trap. | 15—Nichrome heating element. | 25—Silica thermocouple well. |
| 6—Auxiliary drying towers. | 16—Winch. | 26—Bypass line. |
| 7—Furnace containing Ti chips. | 17—Optical window. | 27—Water-jacketed condenser. |
| 8—Vacuum-flask storage reservoirs. | 18—Glass head. | 28—Collecting flask. |
| 9—Mercury manometer. | 19—Ground joint. | 29—Constant-head trap. |
| 10—Constant-temperature oil bath. | 20—Fused silica reaction chamber. | |

tion in the gas phase. The gases were not analyzed directly. Instead, the ratio P_{H_2O}/P_{H_2} of the atmosphere in the reaction chamber was calculated from the partial pressure of water vapor at the temperature of the saturator and the total pressure in the system. The apparatus is shown schematically in Fig. 1.

Gas Purification System: Commercial hydrogen or argon was led through the safety trap (1) into the scrubbing unit (2), (3) where traces of oxygen in the gas stream were removed. This unit contained 0.1 M vanadyl sulphate solution together with lightly amalgamated 20 to 30 mesh zinc powder; the principle of operation has been described by Meites and Meites.²⁰ Water vapor was effectively removed by condensation in the cold trap (5) and by absorption in the auxiliary drying towers (6) which were filled with "Ascarite" and activated alumina. The argon was further purified by allowing the gas to flow over titanium chips maintained at a temperature of 1000°C in a small resistance furnace (7). Vacuum-flask storage reservoirs (8) were provided for each of the pure gases. These reservoirs were by-passed (26) during the greater part of each run; they were useful, however, for rapid refilling of the system after it had been evacuated. The two reservoirs were joined through a three-way stopcock to a common line leading to the saturator.

The Saturator: This unit (11) comprised a pre-saturator flask, two saturating towers, and a mixing chamber joined together in that order. The first

three sections were partially filled with water while the mixing chamber was left empty. The overall capacity of the saturator was approximately 500 cc. Fritted glass disks were sealed into the base of the second and third towers to disperse the gases and insure complete saturating efficiency. Funnel tubes (12) with stopcocks attached permitted the individual compartments of the saturator to be refilled, during a run if necessary, without introducing air into the system. The entire unit was completely immersed in a well-insulated oil bath (10) whose temperature was maintained constant to within $\pm 0.01^\circ\text{C}$ by means of a mercury-toluene thermostat in conjunction with a sensitive thyatron tube relay circuit. A clear, low-viscosity mineral oil was used as the bath medium to allow continuous observation of the water level in the saturator. Temperatures were read on a mercury-in-glass thermometer with 0.1°C subdivisions which had been calibrated against a National Bureau of Standards thermometer. A Beckmann differential thermometer was also employed to indicate the normal temperature fluctuations in the bath.

The saturator was joined to the reaction chamber through an electrically heated line (14) which was kept at a temperature of roughly 10° to 15°C above that of the saturator in order to prevent condensation. The temperature was indicated on a mercury thermometer (13) with a standard taper joint inserted in a side-arm tube attached to the heated line. A bypass (26) was also provided so that hy-

drogen or argon could be admitted to the reaction chamber directly from the gas purification system.

Reaction Chamber: The reactor (20) was a gas-tight 22-in. long, 1 $\frac{3}{4}$ -in. diam fused silica tube fitted with a removable glass head (18), a silica preheater spiral (22), and a thermocouple well (25). It was mounted vertically with the lower half of the silica tube surrounded by a heavy Kanthal-wound resistance furnace (23). The protruding upper section was wrapped externally with nichrome wire (15) and suitably lagged with asbestos; this winding was actually continuous with that of the heated line from the saturator.

The glass head incorporated a winch (16) for manipulating and positioning the specimens in the reaction tube, and an optical window (17) through which the samples could be observed. By means of this arrangement, the specimens attached to the winch could be raised or lowered without reopening the system. Another highly important requirement was also fulfilled, namely, that the gas composition could be adjusted and the temperature stabilized before the specimens were introduced into the hot zone of the furnace. The removable head was connected to the silica tube through a standard taper ground joint which was sealed with Picein or Apiezon cement after the specimens had been inserted. This part of the system was also heated to prevent condensation.

The gas preheater (22) consisted of approximately six turns of 3/16-in. diam silica tubing wound into the form of a helix, having an inside diameter of roughly 1 $\frac{1}{4}$ in. It was supported concentrically inside the lower end of the chamber and joined to the heated line from the saturator through a graded silica-to-pyrex seal (21). The gases from the saturator passed downward through the preheater coil and entered the reaction chamber at a point very close to the thermal center of the furnace. Since the gas flow in the chamber was directed upward, and the specimens were suspended immediately above the gas inlet tube, the samples were continually bathed by fresh gases from the saturator. The linear flow rate of the gases in the reaction zone was of the order of 1 cm per sec at furnace temperature.

The gas-tight silica thermocouple well (25) was sealed into the bottom or closed end of the reaction chamber in such a way that the temperature of the entering gases could be determined. A Pt-Pt-Rh thermocouple calibrated against a secondary standard was employed for this purpose. The actual specimen temperature was measured both before and after each run by inserting another calibrated Pt-Pt-Rh thermocouple through the top of the reaction tube to the exact level at which the specimens were suspended. Temperatures determined in this fashion rarely differed from the inlet gas temperature by more than 1° or 2°C.

Except for a few minor details, the furnace design was fairly conventional. The Kanthal heating element was gradient wound on an alundum core into which the reaction chamber fitted rather snugly. A zone roughly 3 in. long was obtained within which the temperature did not vary by more than $\pm 1^\circ\text{C}$. The reaction tube was so positioned in the furnace by an alundum support (24) that the location of the constant-temperature zone and that of the preheater spiral practically coincided. It was precisely in this region that the specimens were suspended. Furnace temperatures were controlled to within $\pm 1^\circ\text{C}$ by a Leeds and Northrup Micromax recorder.

The gases which passed through the reaction chamber discharged into a water-jacketed condenser (27) where the residual water vapor was removed and collected in a receiving flask (28). From here the gases bubbled through a constant-head mercury trap (29) before being sent to waste.

An apparatus essentially similar to the one just described, but of much simpler construction, was used for the preparation of the magnetites. In this case, oxidation was performed in a flowing water vapor atmosphere using argon as the carrier gas.

Oxidation and Homogenization Procedure: Iron specimens of the approximate thickness employed here could be completely converted to the oxide in a relatively few hours at about 1000°C, provided the atmosphere was sufficiently oxidizing to maintain a large concentration gradient across the scale layer. In atmospheres of lower oxidizing potential, where the concentration gradients are shallow, and at lower temperatures where the diffusion rates are slower, the oxidation times may be of the order of several days. Since a long homogenization period is also required, every effort was made to reduce the oxidation times. Therefore, all specimens, regardless of subsequent homogenization treatment, were oxidized completely to wüstite in atmospheres of high oxidizing potential at temperatures of approximately 985°C.

The original iron specimens were polished through No. 3/0 emery paper, carefully degreased in benzene and in alcohol, and then weighed to within ± 0.1 mg on an analytical balance. They were then fastened to a silica hook with a heavy platinum wire and the hook in turn was suspended from the winch by a fully annealed 33-gage platinum wire. An alundum sleeve threaded through the hole in the lip of each specimen prevented direct contact between the platinum and the iron. Contamination by slow reaction with the alundum sleeve was confined to the lip of the specimen; this lip was removed following the oxidation and homogenization period. Two specimens were oxidized simultaneously in each run. The oxidation times varied between 14 and 18 hr depending upon the sample thickness, the product being an inhomogeneous wüstite of average composition either higher or lower than that desired.

Homogenization was effected without removing the specimens from the reaction zone. It was simply necessary to readjust the saturator temperature to obtain the appropriate water vapor to hydrogen ratio and then lower the furnace temperature. Four different homogenization temperatures were employed: 983°, 897°, 800°, and 699°C. By systematically varying the ratio $P_{\text{H}_2\text{O}}/P_{\text{H}_2}$ in the gas phase, and allowing sufficient time for equilibrium to be established in each case, a series of homogeneous wüstites covering the range of stability of this oxide were prepared at each of the first three temperatures.

In order to obtain an indication of the times required at each temperature, a series of step-wise homogenization experiments were performed in which samples were weighed at intervals until a constant weight was recorded. The progress of homogenization of one such sample at 983°C is shown in Fig. 2. Unfortunately, the thermal cycling to which the specimens were subjected eventually caused cracking and spalling of the oxides; hence, this technique had to be abandoned when the diffusion specimens were prepared. Based on these control runs, however, the homogenization times could

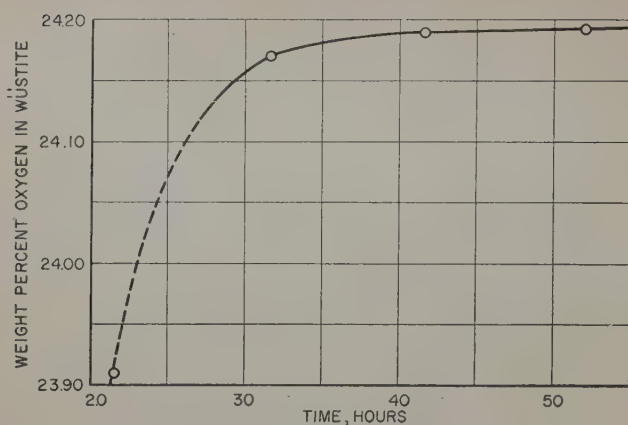


Fig. 2—Progress of homogenization of a wüstite specimen in a 20 pct H_2 -80 pct H_2O atmosphere at 983°C.

be estimated fairly accurately. The actual times employed ranged from 45 to 109 hr at 983°C, from 73 to more than 150 hr at 897°C, from 150 to 250 hr at 800°C, and were in excess of 300 hr at 699°C. The longer times at each temperature corresponded to the oxides of lower oxygen content since the diffusion rates in these oxides were somewhat slower.

In a further effort to achieve complete homogeneity, two-stage homogenization treatments were introduced at the lowest temperatures. The specimens were first annealed at 983°C and then subjected to a much lengthier homogenizing treatment at 800° or 699°C. The gas composition was adjusted in each part of the cycle so as to obtain an oxide of the same predetermined composition. These operations again were performed consecutively without an intervening quench to room temperature.

After the oxidation cycle was completed, the system was quickly evacuated and filled with pure dry argon. The specimens were then raised to the cold end of the reaction chamber and allowed to cool essentially to room temperature in argon, in order to prevent any change in surface composition. When cool, the specimens were reweighed and the average oxide composition was then calculated from the weight gain. One of the completed wüstite speci-

mens is illustrated in Fig. 3a; the same specimen after diffusion is shown in Fig. 3b.

It was found by microscopic examination that the gas quench was always sufficiently rapid to suppress completely the decomposition of the wüstite eutectoid. However, proeutectoid precipitation of magnetite was observed, and, in fact, could not be avoided, in the oxygen-rich wüstites. A rather extreme example of this type of precipitation is shown in Fig. 4. Faster quenching rates, such as would have been obtained, say, by dropping the oxides into mercury, could not be employed because of the danger of shattering the specimens. Gas-quenching in argon was about equivalent to an air cool and represented a compromise between the degree of precipitation on the one hand, and the tendency for cracking on the other. The effect of such precipitation on the magnitude of the observed self-diffusion coefficient in wüstite is discussed in more detail below.

The magnetites were prepared in essentially the same manner. Oxidizing temperatures varied between about 980° and 990°C while the time for complete conversion to magnetite in a flowing argon-water vapor atmosphere was approximately 150 hr at these temperatures. An additional 150 hr or so was allowed for homogenization, after which the specimens were again gas-quenched in argon. A deliberate attempt to vary the composition of the resulting oxides was not made because the extent of the magnetite phase field is very limited at temperatures below 1000°C.

Diffusion Technique: The standard procedure adopted for the diffusion runs was as follows: A flat surface was prepared on each specimen upon which a thin film of radioactive iron (Fe^{55}) was deposited by plating from aqueous solution. After counting to determine the initial surface activity, each specimen was diffused in its own equilibrium atmosphere so as to prevent any change in composition during the diffusion anneal. The specimen was then recounted to establish the fraction of the original surface activity remaining after diffusion. From this activity ratio and the previously determined absorption characteristics of the oxide, the self-diffusion coefficient was calculated.

Inasmuch as the raw oxides had rather rough surfaces (see Fig. 3), one face of each specimen was

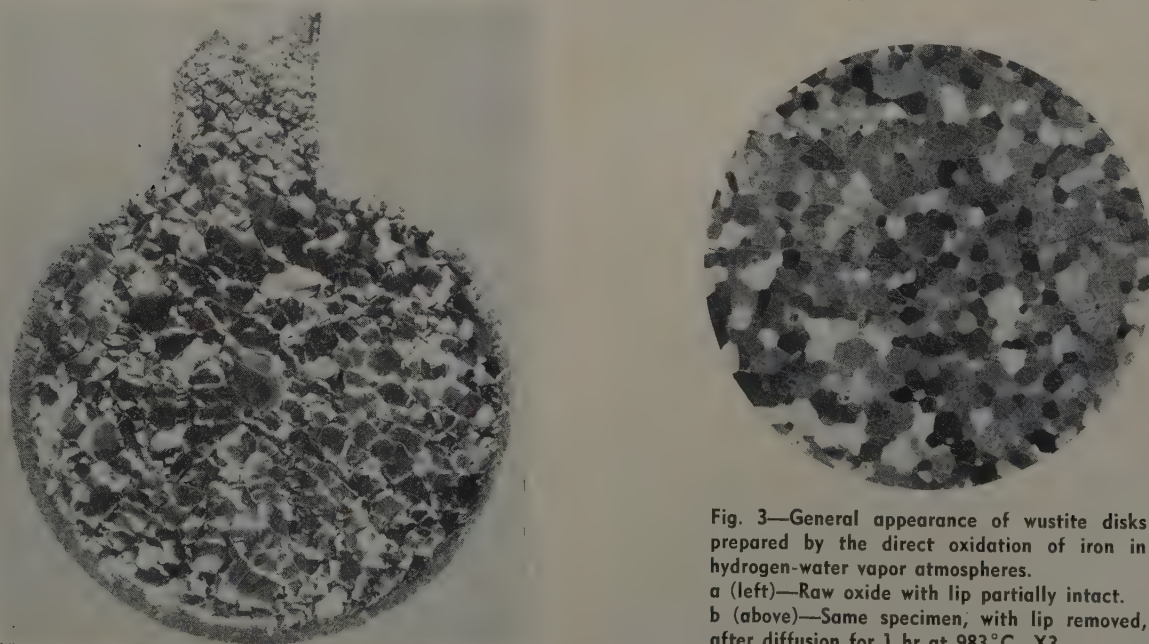


Fig. 3—General appearance of wüstite disks prepared by the direct oxidation of iron in hydrogen-water vapor atmospheres.
a (left)—Raw oxide with lip partially intact.
b (above)—Same specimen, with lip removed, after diffusion for 1 hr at 983°C. X3.

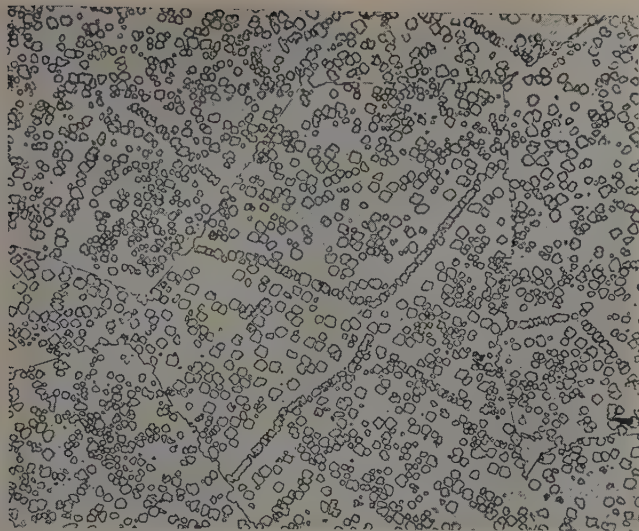


Fig. 4—Proeutectoid precipitation of magnetite from wustite having an average composition of 75.8 pct Fe. Specimen gas quenched in argon from 983°C. Etched in warm dilute HCl. X250. Area reduced approximately 75 pct for reproduction.

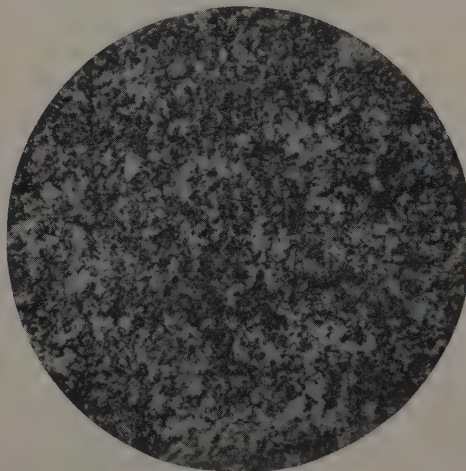
ground flat and then given a fine metallographic polish until the surface acquired a brilliant, almost metallic luster. This surface was freed from traces of polishing abrasive, degreased, and then electroplated with radioactive iron using a wet filter paper technique similar to that described by Birchenall and Mehl.²⁷ The aqueous ferric chloride plating solution contained approximately 4 mg of iron per ml. Roughly 2 to 3 min at a current density of 0.1 amp per sq cm were required to reach the desired activity. The uniformity of plating is indicated by the autoradiograph, Fig. 5a. Since the edges of the specimens were often somewhat porous, the activity was removed from these areas by swabbing with dilute HCl in alcohol and finally the entire specimen was cleaned in alcohol. Enough activity remained in the central area of about 1 sq cm to give a counting rate of between 8,000 and 12,000 counts per min. From the specific activity of the plating solution, the average thickness of the Fe^{55} film was calculated to be between 10^{-5} and 10^{-6} cm.

Counting was performed with a Tracerlab "Auto-scaler" using a mica end-window, X-ray sensitive Geiger-Müller tube. A total of 40,000 counts was taken on each specimen to reduce the statistical counting error to well below 1 pct. All counts were compared with an internal standard to eliminate normal day-to-day variations in counting efficiency and the usual corrections were made for background and coincidence errors. An individual wax mold, set in a metal cup, was prepared for each sample so that its counting geometry could be accurately reproduced after diffusion.

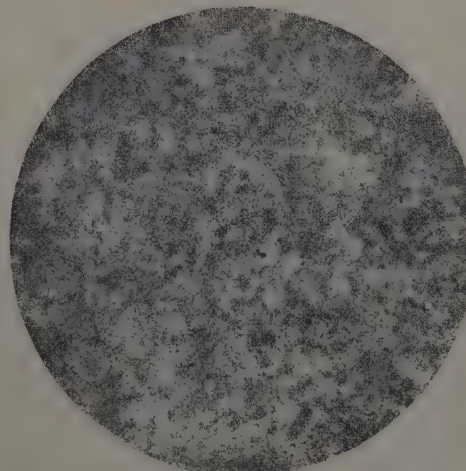
The diffusion anneal was rather critical, especially for the wüstites, since a change in the composition of the oxide could not be tolerated. For this reason, each wüstite specimen was diffused in the same atmosphere with which it was originally in equilibrium before being quenched from the homogenizing temperature. The specimens were hung in the cold portion of the system until the equilibrium conditions of temperature and atmosphere were established in the reaction tube. After flushing the system for at least 2 hr with the equilibrium gas mixture, the specimen was rapidly lowered into the constant temperature zone. The start of the run was taken as the time at which the specimen became indis-

tinguishable from its surroundings when viewed through the optical window. On the average, a total of about 90 sec was required for the specimen to reach the furnace temperature. The diffusion times for the wüstites were of the order of 1 to 2 hr depending upon the temperature. Longer times could not be employed because the radioactivity level then became too weak for practical use (see Fig. 5b); consequently, rapid heating and cooling were essential. At the end of the predetermined diffusion period, the specimen was quickly raised to the cold part of the system, which was then evacuated and filled with pure dry argon. With these precautions, it is doubtful if the errors introduced by the uncertainty in time measurement exceeded 1 or 2 pct.

Another method of specimen support was required, since the lip by which the sample was suspended during the oxidation and homogenization period had been removed. Each wüstite disk was placed active face up in a perforated platinum pan and covered with a platinum lid. The perforations allowed ready access to the atmosphere. Since the rough, under surface of the specimen made only point contact with the supporting pan, contamination by reaction with the platinum was probably very slight. The platinum lid was frequently checked for activity but no evidence of vaporization losses was ever detected, nor was any significant activity level found in the water condensed from the furnace



a—Before diffusion.



b—After diffusion for 1 hr at 897°C. Note that the original distribution of activity is not altered appreciably by lateral or surface diffusion. X4.
Fig. 5—Autoradiographs of the active or plated surface.

Table I. Calculated Linear Absorption Coefficients for Mn K α Radiation ($\lambda = 2.103\text{\AA}$) in the Oxides of Iron

Oxide	Wt Pct Fe	Density, G per Cu Cm	μ/ρ , Sq Cm per G	μ , Cm ⁻¹
Wüstite	75.60	5.56	76.5 ₇	425.7
	75.70	5.57	76.6 ₃	426.9
	75.80	5.58	76.6 ₉	427.9
	75.90	5.59	76.7 ₅	429.0
	76.00	5.60	76.8 ₁	430.1
	76.10	5.61	76.8 ₇	431.2
	76.20	5.62	76.9 ₃	432.3
	76.30	5.63	76.9 ₉	433.4
	76.40	5.64	77.0 ₅	434.5
	76.50	5.65	77.1 ₁	435.6
Magnetite	72.28	5.18	74.6 ₈	387
Hematite	69.94	5.26	73.2 ₆	385

gases. Furthermore, the walls of the reaction chamber remained inactive even after more than forty diffusion runs had been performed in the system.

The magnetites were diffused in much the same manner, for times of a few hours to several weeks at temperatures of 987° to 799°C, respectively. In each case the atmosphere contained approximately 90 pct water vapor and 10 pct argon by volume. A pair of hematite crystals of different orientation were diffused simultaneously. These were placed in an alundum boat with their active faces almost in contact to reduce the possibility of vaporization losses. The anneals were performed under essentially static conditions in a horizontal Globar-heated furnace at a pressure of 1 atm of oxygen.

Calculation of the Self-Diffusion Coefficient: Under the conditions of these experiments, the appropriate solution to the diffusion equation is that given by Steigman, Shockley, and Nix.²⁸ This solution has the form

$$F = e^z [1 - \phi(\sqrt{Z})] \quad [1]$$

where F is the fraction of the initial surface activity remaining after diffusion, $\phi(\sqrt{Z})$ is the Gaussian error integral, and Z is a parameter defined by

$$Z = \mu^2 Dt \quad [2]$$

μ being the linear absorption coefficient, cm⁻¹, D the self-diffusion coefficient, sq cm per sec, and t , the time in seconds. Only the calculation of the absorption coefficient requires further comment.

The absorption properties for the radiation emitted by Fe⁵⁵ were determined with aluminum, copper, and nickel absorbers. It was found that the measured absorption coefficients agreed within a few percent of the known X-ray mass absorption coefficients of these elements for Mn K α radiation ($\lambda = 2.103\text{\AA}$). The agreement was sufficiently good to justify the use of the X-ray values for iron and oxygen, namely 90.9 and 32.2 sq cm per g, respectively. Thus, for a homogeneous iron oxide, the linear absorption coefficient for Mn K α radiation is given by

$$\mu = \rho (90.9 f_{Fe} + 32.2 f_O) \quad [3]$$

where ρ is the density of the oxide, and f_{Fe} and f_O are the weight fractions of iron and oxygen respectively. Wüstite densities were taken from the work of Jette and Foote,¹⁶ the density of magnetite from Smiltens,²⁰ and that of hematite from Palache, Berman, and Frondel.³⁰ The values of μ calculated from Eq. 3 are recorded in Table I.

Results

The details of preparation of the lower oxides, wüstite and magnetite, are given in Table II. Only the oxidation and homogenization schedules which yielded massive oxides having the requisite density, purity, and chemical composition are recorded. The resulting oxides were always coarsely polycrystalline with a well-developed columnar grain structure. For the most part, the columnar grains appeared to be oriented so that the axis of preferred growth — very probably the (001) cube direction — was normal to the flat surface of the oxide disk. Although the homogenization times and temperatures varied widely, the average grain diameter was generally between 1 and 2 mm for the wüstites (see Fig. 3b) and of the order of 0.2 to 0.5 mm for the

Table II. Oxidation and Homogenization Treatments for Artificially Prepared Wüstites and Magnetites

Specimen No.	Oxidation Treatment			Homogenization Treatment			Final Composition, Wt Pct Fe
	Temperature, °C	Time, Hr	Atmosphere, Vol Pct H ₂ O	Temperature, °C	Time, Hr	Atmosphere, Vol Pct H ₂ O	
23,24	983	16*	85.0	983	45	85.0	75.65
25,26	981	18*	87.5	983	47	87.5	75.61
27,28	983	18*	80.6	983	52	80.6	75.81
29,30	982	16	84.7	983	48	79.5	75.91
31,32	983	16	84.4	983	60	75.4	76.11
35,36	983	17	82.3	983	84	69.6	76.20
37,38	982	18*	82.6	983	49	82.6	75.76
39,40	983	16*	87.2	983	49	87.2	75.63
41,42	983	17	81.9	983	109	60.2	76.45
43-47	984	150*	90†	984	191	90†	72.31
48-52	985	150*	90†	985	191	90†	72.26
53,54	983	16	84.0	983	73	75.7	76.07
55,56	983	17*	82.5	897	70	82.5	75.65
57,58	983	18	82.1	897	81	74.8	75.97
59,60	983	18	81.8	897	90	67.0	76.14
61,62	983	18	81.7	897	102	58.6	76.35
63,64	983	19	80.4	897	120	50.4	76.55
65,66	983	15	84.7	897	48	82.2	75.80
67,68	984	15	84.3	800	116	71.3	
				893	53	77.3	
69,70	983	15	85.0	800	130	61.8	76.00
				893	58	65.8	
				800	147	50.2	
71,72	981	15	84.6	893	62	58.0	76.34
				800	163	40.7	
				893	50	87.5	
73,74	983	14	84.4	699	241	55.2	76.02
				897	100	82.5	
				983	103	58.9	
75,76	983	18	84.8	897	62	58.1	76.53
77,78	983	17	84.7				
79,80	983	16	84.5				

* Estimated from the results of preliminary experiments.

† Argon-water vapor atmosphere. All other runs performed in hydrogen-water vapor atmospheres.

Table III. Self-Diffusion of Iron in Wüstite

Specimen No.	Number of Vacant Iron Sites per Cu Cm X 10 ⁻²¹	Diffusion Treatment		Corrected Surface Activity Ratio, After/Before	Linear Absorption Coefficient, μ , Cm ⁻¹	Diffusion Coefficient, D*, Sq Cm per Sec X 10 ⁻⁸
		Time, Sec	Atmosphere, Vol Pct H ₂ O			
Temperature, 983°C						
25	5.75	3600	87.5	0.0724	426	9.2
26	5.75	3600	87.5	0.0682	426	9.9
39	5.69	3600	87.2	0.0753	426	8.5
23	5.65	3600	85.0	0.0699	426	9.6
24	5.65	3600	85.0	0.0730	426	9.0
37	5.36	3600	82.6	0.0772	427	8.0
38	5.36	3600	82.6	0.0734	427	8.9
27	5.24	3600	80.6	0.0903	428	5.8
28	5.24	3600	80.6	0.0732	428	9.0
29	4.97	3600	79.5	0.0780	429	7.8
53	4.55	3600	75.7	0.0839	431	6.7
54	4.55	3600	75.7	0.0791	431	7.5
31	4.45	3600	75.4	0.0692	431	9.8
32	4.45	3600	75.4	0.0733	431	8.8
35	4.21	3600	69.6	0.0835	432	6.7
36	4.21	3600	69.6	0.0884	432	6.3
41	3.54	3600	60.2	0.1156	435	3.4
42	3.54	3600	60.2	0.1006	435	4.5
77	3.33	3600	58.9	0.1048	436	4.2
78	3.33	3600	58.9	0.0941	436	5.1
Temperature, 897°C						
75	5.80	3600	82.5	0.0989	425	4.9
76	5.80	3600	82.5	0.1079	425	4.0
55	5.65	3600	82.5	0.1325	426	2.7
56	5.65	5400	82.5	0.1112	426	2.5
57	4.81	3600	74.8	0.1102	430	3.8
58	4.81	5400	74.8	0.0928	430	3.6
59	4.37	3600	67.0	0.1163	432	3.4
60	4.37	3600	67.0	0.1198	432	3.3
61	3.81	4500	58.6	0.1217	434	2.5
62	3.81	4500	58.6	0.1290	434	2.2
63	3.27	4500	50.4	0.1213	436	2.4
79	3.11	3600	49.8	0.1259	438	2.8
Temperature, 800°C						
65	5.26	3600	71.3	0.2022	428	1.05
66	5.26	3600	71.3	0.2068	428	1.0
67	4.73	3600	61.8	0.2019	430	1.0
69	3.84	5400	50.2	0.1771	434	0.91
70	3.84	6300	50.2	0.1724	434	0.83
71	2.78	6300	40.7	0.1709	438	0.82
72	2.78	7200	40.7	0.1619	438	0.77
Temperature, 699°C						
73	4.68	3600	55.2	0.3660	430	0.24
74	4.68	7200	55.2	0.2666	430	0.27

magnetites, as determined on the polished diffusion surface.

It has been verified by microscopic examination that all of the specimens listed in Table II were originally single-phase oxides before quenching from the homogenizing temperature. However, proeutectoid precipitation of magnetite was not completely avoided during the quench, except in the wüstites containing greater than about 76.3 to 76.4 pct Fe. Most of the wüstites therefore appeared to be two-phase at room temperature (see Fig. 4), the percentage of magnetite increasing progressively with increasing oxygen content. Wüstite and magnetite were the only phases ever observed in these oxides. The pure magnetites did not undergo any structural changes on cooling.

As an added point of interest, no oxide which could definitely be considered a homogeneous single-phase structure was obtained having less than 76.73 pct Fe by weight; the stoichiometric compound FeO, if it existed, would correspond to 77.73 pct Fe.

Rates of Self-Diffusion of Iron in Wüstite: Results of the self-diffusion studies on artificially prepared wüstites are summarized in Table III, in which the diffusion conditions, i.e., time, temperature, and atmosphere are given, along with the surface activity and absorption data needed to calculate the self-diffusion coefficients. The fact that results of check runs normally agreed within 25 pct attests to the

uniformly high degree of reproducibility which has been achieved in these measurements. Also worthy of note is the observation that at lower temperatures, where diffusion times of greater than 1 hr were used, on occasion, close agreement has been obtained with the results of the shorter time experiments.

Before attempting to analyze the diffusion data for wüstite, it may be well to point out the various possible sources of error in these experiments. These errors are of several types: 1—random errors associated with the uncertainty in measuring the diffusion time or with the failure to duplicate exactly the equilibrium gas composition and temperature during the diffusion anneal; 2—statistical counting errors, as well as those associated with reproduction of the counting geometry and the calculation of the absorption coefficients; 3—errors due to the loss of radioactive iron by vaporization; 4—deviations of a more systematic nature introduced by residual concentration gradients which are not wholly eliminated during homogenization; and 5—completely systematic errors arising from the presence of microscopic inhomogeneities, such as precipitated magnetite particles, or grain boundaries. Since careful control has been exercised over the diffusion and counting procedures, the total error resulting from the first three causes is believed to be relatively small—probably of the order of 10 pct or less. The magnitude of the

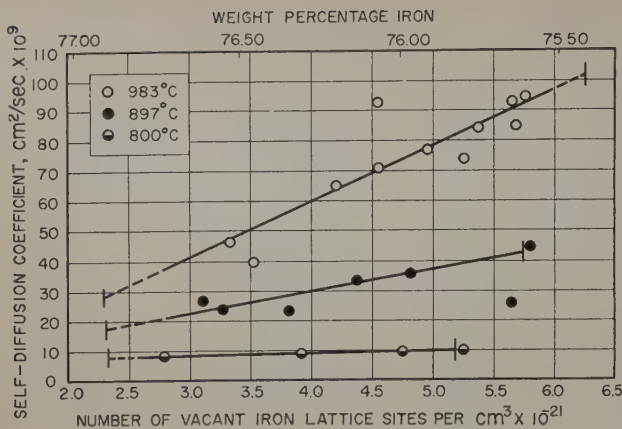


Fig. 6—Dependence of the self-diffusion coefficient of iron in wüstite on composition. The short vertical lines represent the limits of the wüstite phase field at each temperature, as taken from the work of Darken and Gurry¹⁶; the number of vacant iron lattice sites per unit volume has been calculated from the deviation from stoichiometric composition (77.73 pct Fe).

other errors is extremely difficult to assess, but a few qualitative remarks may be made.

A large concentration gradient exists at the completion of the oxidation period, the center of the wüstite specimen being richer in iron than the surface layers. If this gradient is not eliminated by homogenization, it will eventually act to retard the inward diffusion of radioactive iron ions and therefore lead to a low value of the self-diffusion coefficient. There is the possibility, however, that in some of the iron-rich wüstites, the residual iron gradient lies in the reverse direction. In any event, it can be assumed that the errors which accompany faulty homogenization are smaller the higher the homogenization temperature, all other factors being equal. The presence of magnetite as a second phase is responsible for systematically low results, as will be evident from the relative rates of diffusion of iron in magnetite and wüstite. Furthermore, the effect of such inhomogeneities is greater in the oxygen-rich wüstites, where the quantity of magnetite precipitated is a maximum, and at the lower diffusion temperatures, where a proportionately longer time is required before the magnetite particles redissolve and the matrix again becomes homogeneous. By taking all these factors into consideration, it has

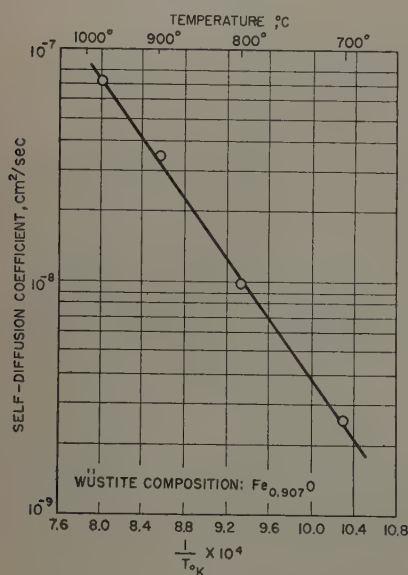


Fig. 7 — Temperature dependence of the self-diffusion coefficient of iron in wüstite for oxides having the composition $\text{Fe}_{0.907}\text{O}$ (76.02 pct Fe).

been concluded that the most reliable measurements are those obtained at the highest temperature, 983°C, at compositions lying near the approximate center of the stability range.

Variation with Composition: The concentration dependence of the self-diffusion coefficient at 983°, 897°, and 800°C is shown in Fig. 6, in which the average values of D^*_{FeO} for a given composition are plotted as a function of the calculated number of vacant iron sites per unit volume.[†] In addition to

[†] The number of vacant cation sites per cu cm, n_v , is given by $n_v = \frac{4\delta}{a_0^3}$, where δ is the deviation from stoichiometric composition,

expressed as the deficiency in the number of gram atoms of iron per gram atom of oxygen, and a_0 is the edge length of the unit cell in cm. If w_1 and w_2 are the weight fractions of iron and oxygen in the oxide and $M_1 (=55.85)$ and $M_2 (=16.00)$ are the gram atomic weights of iron and oxygen respectively, then $\delta = \left[1 - \left(\frac{w_1}{M_1} \right) / \left(\frac{w_2}{M_2} \right) \right]$ and $n_v = \frac{4}{a_0^3} \left[1 - \left(\frac{w_1}{w_2} \right) \left(\frac{16.00}{55.85} \right) \right]$.

The necessary values of a_0 as a function of composition are obtained from the work of Jette and Foote.¹⁷

being a sensitive measure of the deviation from stoichiometric composition, the vacancy concentration has fundamental significance with regard to the transport mechanism in wüstite. For added convenience, however, the corresponding weight percentages of iron in the oxides are also indicated. It is apparent that, over the range of compositions investigated at each temperature, the rate of self-diffusion of iron in wüstite increases continuously as the concentration of vacant iron sites increases. It further appears that this variation is essentially linear, within the precision of the measurements, and that the effect is noticeably greater at 983°C than at 897°C. The lines through the data in Fig. 6 are those given by least squares calculations, whereas the short vertical lines represent the stable limits of the wüstite phase field as taken from the work of Darken and Gurry.

There can be little doubt that the observed increase in the self-diffusion coefficient with vacancy concentration is real, even though the actual magnitudes involved may be rather uncertain. At 983°C, for example, the self-diffusion coefficient increases almost by a factor of four between the iron-rich and oxygen-rich boundaries of the wüstite field. A change of this order is well outside the expected limits of precision at this temperature. The relative change in the diffusion rate for a given change in vacancy concentration seems to be somewhat smaller at 897°C and even smaller still at 800°C. Whether or not this is significant cannot be definitely stated, especially in view of the previous discussion regarding the effect of inhomogeneities on the self-diffusion measurements.

Variation with Temperature: Since the self-diffusion coefficient is rather sensitive to changes in composition, the data accumulated at different temperatures are best compared at a given vacancy concentration. Only one value of the self-diffusion coefficient is available at 699°C and that corresponds to the composition $\text{Fe}_{0.907}\text{O}$ (=76.02 pct Fe). Accordingly, values of D^* at 983°, 897°, and 800°C have been read from Fig. 6 at this same composition. These are plotted on a logarithmic scale as a function of the reciprocal of the absolute temperature in Fig. 7. The data for this composition are well approximated by the equation

$$D^*_{\text{FeO}} = 0.118e^{-20,700/RT} \quad [4]$$

between 700°C (973°K) and 1000°C (1273°K). Although there are no data in the literature with which

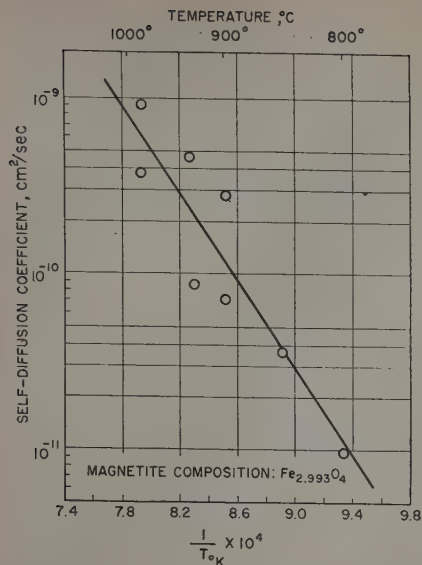
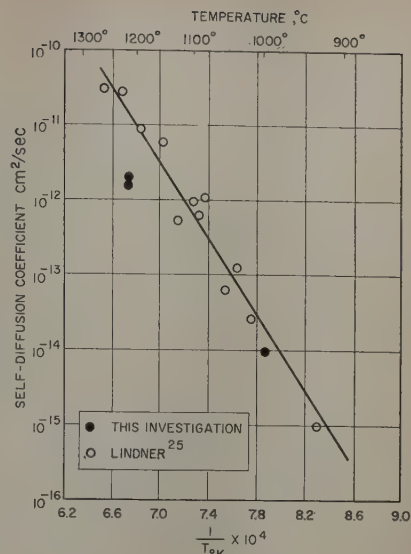


Fig. 8 (left)—The effect of temperature on the rate of self-diffusion of iron in artificially prepared magnetite polycrystals of average composition $\text{Fe}_{2.993}\text{O}_4$ (72.38 pct Fe).

Fig. 9 (right)—The self-diffusion coefficient of iron in hematite as a function of temperature; the present data refer to natural single crystals of $\alpha\text{-Fe}_2\text{O}_3$, Lindner's to pressed and sintered hematite powders.



the present results may be compared, it should be noted that the observed activation energy of 30 kcal per mol is very close to the value often quoted for the oxidation of iron (in air or oxygen).³¹ The latter, however, has little significance since it represents a composite quantity which also includes a contribution due to the expansion of the homogeneity range of the wüstite field with rising temperature.⁵

Activation energies for the self-diffusion of iron in wüstite have also been calculated at other compositions, but instead of an expected drop in activation energy at the higher vacancy concentration the opposite trend is observed. This is evident directly from Fig. 6. Such an inconsistency could well be associated with systematic errors of the type previously described.

Rates of Self-Diffusion of Iron in Magnetite and Hematite: The experimental data for artificial magnetite polycrystals and natural hematite crystals are given in Table IV. For the magnetites, the data refer to an average composition corresponding to the formula $\text{Fe}_{2.993}\text{O}_4$ (=72.38 pct Fe). The scatter in these measurements is fairly appreciable which may indicate that the magnetites were not in complete equilibrium with their atmospheres throughout the entire diffusion period. Nevertheless, if the data are plotted as in Fig. 8, the average values for the self-

diffusion coefficient of iron in magnetite can be approximated by

$$D_{\text{Fe}_2\text{O}_4}^* = 5.2e^{-55,000/RT} \quad [5]$$

over the range from 750° to 1000°C (1023° to 1273°K). The observed activation energy for self-diffusion appears to be substantially greater than the value of 45 kcal per mol found for the growth of magnetite upon iron at temperatures below 570°C.⁵ It also differs somewhat from the activation energy for the formation of magnetite on wüstite, as determined by Davies, Simnad, and Birchenall at temperatures between 850° and 950°C.

The self-diffusion data for the natural hematite crystals at 1000° and 1217°C are shown in Fig. 9 along with the more extensive determinations of Lindner²⁵ on pressed and sintered powder compacts. The present results seem to be somewhat lower; however, when allowance is made for the possibility that the measurements on sintered powders may involve slight contributions from grain boundary and surface diffusion effects, the agreement can be considered satisfactory. Between 950°C (1023°K) and 1300°C (1573°K), Lindner's data for the self-

† The constant, D_0 , given by Lindner is 4×10^4 but this is apparently in error by a factor of 10.

diffusion of iron in $\alpha\text{-Fe}_2\text{O}_3$ are represented empirically by the equation

$$D_{\alpha\text{-Fe}_2\text{O}_3}^* = 4 \times 10^5 e^{-112,000/RT} \quad [6]$$

The present experiments suggest a somewhat smaller activation energy, but since only two temperatures have been investigated, the unusually high value of 112 kcal per mol reported by Lindner must tentatively be accepted. According to Davies, Simnad, and Birchenall, the activation energy for the growth of hematite upon magnetite is only about 53 kcal in the neighborhood of 900°C. A strong indication is thus provided that the growth of the hematite layer depends but little on the diffusion of iron.

It is also interesting to note that, within the uncertainty of the present measurements, the rate of self-diffusion of iron in hematite is independent of the crystallographic direction.

Equilibria Between Wüstite Solid Solutions and $\text{H}_2\text{-H}_2\text{O}$ Atmospheres: The last two columns in Table II give the compositions of the oxides and their co-existing equilibrium atmospheres at the indicated

Table IV. Self-Diffusion of Iron in Magnetite and Hematite

Specimen No.	Temperature, °C	Time, Sec	Corrected Activity Ratio	μ , Cm ⁻¹	D^* , Sq Cm per Sec
Magnetites, Diffused in Water Vapor-Argon Atmosphere					
45	987	0.3354×10^5	0.2388	387	92×10^{-11}
48	987	0.2178×10^5	0.3978	387	38×10^{-11}
52	938	0.6120×10^5	0.2473	387	47×10^{-11}
51	933	0.5790×10^5	0.4636	387	8.8×10^{-11}
47	898	0.9543×10^5	0.2547	387	28×10^{-11}
44	897	1.523×10^5	0.3614	387	7.1×10^{-11}
49	848	4.281×10^5	0.3183	387	3.6×10^{-11}
50	799	17.28×10^5	0.3074	387	0.98×10^{-11}
Hematites, Diffused in Pure Oxygen at 1 Atm Pressure					
3*	1217	9.370×10^5	0.6120	385	2.0×10^{-12}
4†	1217	9.370×10^5	0.6388	385	1.6×10^{-12}
5*	1000	6.166×10^5	0.97	385	1×10^{-14}
6†	1000	6.166×10^5	0.97	385	1×10^{-14}

* Diffusion direction parallel to c-axis of rhombohedral crystal.

† Diffusion direction perpendicular to c-axis.

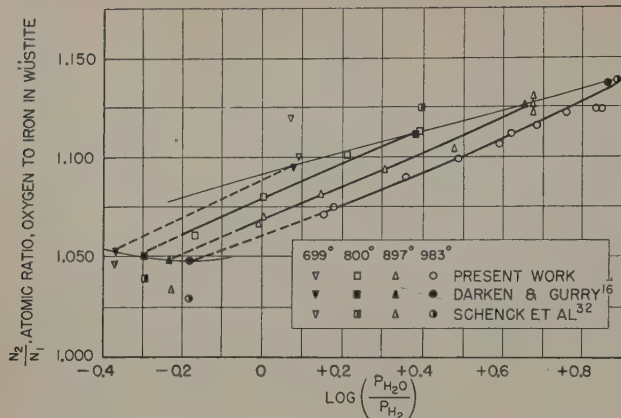


Fig. 10—Equilibria between wüstite solid solutions and hydrogen-water vapor atmospheres for compositions within the stable phase field for this oxide. The isotherms give the compositions of the oxides and their coexisting equilibrium gas compositions; included for comparison are data calculated from the work of Darken and Gurry¹⁶ and of Schenck et al.,³² for the iron-wüstite and wüstite-magnetite equilibria.

homogenization temperatures. Since it will be found convenient in subsequent calculations to express the oxide compositions in terms of the atomic ratios, N_2/N_1 , of oxygen to iron, and the gas compositions in the form P_{H_2O}/P_{H_2} or $\log (P_{H_2O}/P_{H_2})$, the pertinent equilibrium data have been recalculated and assembled in Table V. No corrections have been applied for the deviation from ideal gas behavior because at the temperatures and pressures employed, these corrections amount to considerably less than 1 pct and are probably within the limit of experimental error. Although neither the gases nor the oxides have been analyzed directly, it is believed that the probable error in the calculated water vapor to hydrogen ratios is of the order of ± 2 pct or less and that the average oxide compositions calculated from the weight gain are accurate to within ± 0.01 wt pct Fe.

Table V. Equilibria Between Wüstite Solid Solutions and H_2 - H_2O Atmospheres

Specimen No.	Wüstite Composition		Equilibrium Gas Composition		
	Wt Pct Fe	Atomic Ratio Oxygen to Iron, N_2/N_1	Vol Pct H_2O	P_{H_2O}/P_{H_2}	$\log P_{H_2O}/P_{H_2}$
Temperature = 983°C					
23,24	75.65	1.123	85.0	5.67	0.754
25,26	75.61	1.125	87.5	7.00	0.845
27,28	75.81	1.113	80.6	4.16	0.619
29,30	75.91	1.107	79.5	3.88	0.589
31,32	76.11	1.096	75.4	3.07	0.487
35,36	76.20	1.090	69.6	2.29	0.360
37,38	75.76	1.117	82.6	4.75	0.677
39,40	75.63	1.125	87.2	6.81	0.833
41,42	76.45	1.075	60.2	1.51	0.179
77,78	76.53	1.071	58.9	1.43	0.155
Temperature = 897°C					
55,56	75.65	1.123	82.5	4.71	0.673
57,58	75.97	1.104	74.8	2.97	0.473
59,60	76.14	1.094	67.0	2.03	0.308
61,62	76.35	1.081	58.6	1.42	0.152
63,64	76.55	1.069	50.4	1.02	0.008 ₆
75,76	75.59	1.127	82.5	4.71	0.673
79,80	76.61	1.066	49.8	0.992	-0.004
Temperature = 800°C					
65,66	75.80	1.114	71.3	2.48	0.395
67,68	76.00	1.102	61.8	1.62	0.209
69,70	76.34	1.082	50.2	1.01	0.004 ₃
71,72	76.73	1.059	40.7	0.686	-0.164
73,74	76.02	1.101	55.2	1.23	0.090

A series of roughly parallel isotherms are obtained when the appropriate values of N_2/N_1 are plotted against $\log (P_{H_2O}/P_{H_2})$ as in Fig. 10. Also included for comparison in Fig. 10 are the results of similar measurements by Darken and Gurry¹⁶ and by Schenck et al.,³² both of whom employed mixtures of CO and CO₂ to provide suitable oxidizing atmospheres. To convert the P_{CO_2}/P_{CO} ratios given by the latter investigators to the corresponding P_{H_2O}/P_{H_2} ratios, use is made of the equilibrium constant for the water gas reaction, i.e.,

$$K = \left(\frac{P_{CO}}{P_{CO_2}} \right) \left(\frac{P_{H_2O}}{P_{H_2}} \right) \quad [7]$$

The selected values of K , based on the data of Kassel³⁴ are: 1.62 at 983°C, 1.30 at 897°C, 0.949 at 800°C, and 0.635 at 699°C. The comparison points plotted in Fig. 10 refer only to the compositions at the extremes of the wüstite phase field.[§] It is evi-

[§] In making these calculations, it was necessary to interpolate the data of Darken and Gurry and of Schenck since these investigators worked at different temperatures than were employed here.

dent that the present results are in excellent agreement with the work of Darken and Gurry but that the data of Schenck are somewhat discordant.

Thermodynamic Calculations: Since wüstite can be regarded as an ionic solid solution, the thermodynamic activity of oxygen in wüstite is proportional to the square root of the equilibrium partial

Table VI. Standard States Used in Calculating the Activities of Oxygen and Iron in Wüstites at Various Temperatures

Temperature, °C	Iron - Wüstite Equilibrium			
	N_2/N_1^*	$P_{H_2O}/P_{H_2}^*$	P_{O_2} (Atm) [†]	k in Eq 8
983	1.048	0.658	8.74×10^{-16}	1.52
897	1.048	0.588	2.15×10^{-17}	1.70
800	1.049	0.505	1.61×10^{-19}	1.98
699	1.051	0.430	3.72×10^{-22}	2.34

* Interpolated from the data of Darken and Gurry.¹⁶

[†] Based upon equilibrium constants for the dissociation of water vapor obtained from free energy data compiled by Richardson and Jeffes.³³

pressure of oxygen in the gas phase. If the activity of oxygen in wüstite is designated as a_2 , then

$$a_2 = k \left(\frac{P_{H_2O}}{P_{H_2}} \right) \quad [8]$$

where the proportionality constant, k , depends upon the temperature and the choice of the standard state. The value of k will be fixed if the activity of oxygen is arbitrarily taken as unity for the wüstite in equilibrium with iron at the particular temperature in question. Adopting this procedure yields the values of k given in Table VI. Although other standard states might have been equally suitable, it was decided to follow the precedent of Darken and Gurry in this selection. The thermodynamic activities of iron in wüstite, a_1 , are obtained by the usual Gibbs-Duhem integration, choosing the same standard state as for oxygen. In Table VII the activities of both components are listed for various compositions covering the entire range of the wüstite field at 983°, 897°, and 800°C.

The partial molal heats of solution of oxygen and iron in wüstite and the heats of formation of wüstite at various fixed compositions have also been calcu-

lated from the equilibrium data. These data are omitted since they have no direct bearing on the future calculations. It should be mentioned, however, that the average value for the heat of formation of wüstite at 298°K obtained from the present study is -63.5 kcal per mol which is in good agreement with Darken and Gurry's value of -63.7 kcal and with the value $\Delta H_{298} = -63.8 \pm 0.2$ kcal recently quoted by Kelley et al.¹⁹ after a critical appraisal of the existing thermodynamic data for wüstite. This agreement offers some support for the contention that equilibrium has been closely approached in these experiments and that the various approximations involved in calculating the gas and oxide compositions have not introduced significant errors.

Analysis and Discussion

In contradiction to the work of Benard and Coquelle,²⁵ the kinetic studies of Davies, Simnad, and Birchenall have shown, rather conclusively, that the growth of each of the individual oxide layers is limited by diffusion and not by slow interface reactions. More recently Paidassi³⁰ has also demonstrated that all three oxide layers grow parabolically with time in the multi-layer scales. This being the case, it now becomes possible, with the aid of the data recorded in Tables III to VII to calculate the rates of growth of the three oxides and to compare these calculated rates with experiment. The basis for such calculations is the well-known theory of oxidation developed by Wagner. Three separate oxidation reactions are to be distinguished: 1—wüstite growing on iron, 2—magnetite growing on wüstite, and 3—hematite growing on magnetite. Since the Wagner theory has heretofore been applied only to systems in which the reaction layer is formed directly on the surface of the metal, an extreme test of its validity and general applicability is at hand. Moreover, if the theory is valid, then the extent to which the calculated growth rates agree with the experimental rate constant data may also furnish a qualitative indication of the relative mobilities of iron and oxygen in the oxides.

Under the assumption that the various component particles (iron = component 1, oxygen = component 2) migrate independently of one another, Wagner¹ has derived the following rate expression for the growth of a single oxide (or sulphide, halide, etc.) layer on a metal substrate:

$$K_r = |z_2|c_2 \int_{a'_2}^{a''_2} \left(\frac{z_1}{|z_2|} D^*_{*1} + D^*_{*2} \right) d \ln a_2 \quad [9]$$

$$= z_1 c_1 \int_{a'_1}^{a''_1} \left(D^*_{*1} + \frac{|z_2|}{z_1} D^*_{*2} \right) d \ln a_1$$

where K_r , the so-called rational rate constant, represents the number of chemical equivalents of oxide formed per second per square centimeter when the layer of reaction product is 1 cm thick; z_1 and z_2 are the chemical valences of iron and oxygen, c_1 and c_2 are the concentration of the two components in gram atoms per cu cm, D^*_{*1} and D^*_{*2} are the respective self-diffusion coefficients, and a_1 and a_2 denote the thermodynamic activities of iron and oxygen in the oxide, the primed and double-primed quantities referring to the conditions at the inner and outer surfaces of the growing oxide layer respectively. It should be noted that K_r , defined as in Eq. 9, does not depend on the choice of the standard state to which the oxygen or iron activities are referred. Of the

Table VII. Thermodynamic Activities of Oxygen and Iron in Wüstite

N_2/N_1	P_{H_2O}/P_{H_2}	P_{O_2} (Atm) [†]	$-\log a_1$	a_1	$\log a_2$	a_2
Temperature = 983°C						
1.048*	0.658	8.74x10 ⁻¹⁶	0	1	0	1
1.050	0.708	1.01x10 ⁻¹⁵	0.034	0.985	0.032	1.08
1.060	1.02	2.09x10 ⁻¹⁵	0.199	0.632	0.193	1.55
1.070	1.41	4.01x10 ⁻¹⁵	0.351	0.446	0.330	2.14
1.080	1.90	7.30x10 ⁻¹⁵	0.490	0.323	0.461	2.89
1.090	2.50	1.29x10 ⁻¹⁴	0.619	0.240	0.560	3.80
1.100	3.22	2.09x10 ⁻¹⁴	0.740	0.182	0.690	4.90
1.110	4.12	3.43x10 ⁻¹⁴	0.858	0.139	0.797	6.27
1.120	5.21	5.49x10 ⁻¹⁴	0.971	0.107	0.899	7.92
1.130	6.43	8.38x10 ⁻¹⁴	1.075	0.084	0.991	9.79
1.1375*	7.26	1.06x10 ⁻¹³	1.134	0.074	1.043	11.04
Temperature = 897°C						
1.048*	0.588	2.15x10 ⁻¹⁷	0	1	0	1
1.050	0.610	2.33x10 ⁻¹⁷	0.025	0.989	0.016	1.04
1.060	0.815	4.14x10 ⁻¹⁷	0.151	0.707	0.143	1.39
1.070	1.07	6.84x10 ⁻¹⁷	0.278	0.528	0.260	1.82
1.080	1.40	1.22x10 ⁻¹⁶	0.401	0.397	0.377	2.38
1.090	1.82	2.06x10 ⁻¹⁶	0.525	0.299	0.490	3.09
1.100	2.37	3.51x10 ⁻¹⁶	0.660	0.219	0.606	4.04
1.110	3.06	5.85x10 ⁻¹⁶	0.783	0.165	0.719	5.24
1.120	3.90	9.49x10 ⁻¹⁶	0.899	0.126	0.822	6.64
1.126*	4.46	1.24x10 ⁻¹⁵	0.957	0.110	0.880	7.59
Temperature = 800°C						
1.049*	0.505	1.61x10 ⁻¹⁹	0	1	0	1
1.050	0.514	1.67x10 ⁻¹⁹	0.021	0.991	0.008	1.02
1.060	0.630	2.51x10 ⁻¹⁹	0.101	0.792	0.097	1.25
1.070	0.776	3.81x10 ⁻¹⁹	0.198	0.634	0.188	1.54
1.080	0.968	5.93x10 ⁻¹⁹	0.301	0.500	0.283	1.92
1.090	1.22	9.42x10 ⁻¹⁹	0.410	0.389	0.384	2.42
1.100	1.61	1.64x10 ⁻¹⁸	0.542	0.287	0.504	3.19
1.110	2.17	2.99x10 ⁻¹⁸	0.686	0.206	0.635	4.31
1.112*	2.44	3.76x10 ⁻¹⁸	0.741	0.181	0.684	4.83

* Limits of the wüstite phase field as given by Darken and Gurry.¹⁶

† See dagger footnote, Table VI.

two equivalent forms of this equation, the first is the more practical since it eliminates the need for the Gibbs-Duhem integration and the errors associated therewith.

Some assumption must obviously be made regarding the relative magnitudes of D^*_{*1} and D^*_{*2} in order to evaluate K_r from Eq. 9. Although the relative mobilities of iron and oxygen in the three oxides are known approximately from marker movement studies, this information will be disregarded for the moment, and it will be assumed instead that iron is the only mobile component (besides electrons or electron holes) in each oxide layer. On the assumption that $D^*_{*1} \gg D^*_{*2}$, Eq. 9 can be simplified to

$$K_r = |z_2|c_2 \int_{a'_2}^{a''_2} \frac{z_1}{|z_2|} D^*_{*1} d \ln a_2 \quad [10]$$

The three oxidation reactions will now be considered individually with this equation as a basis.

Oxidation of Iron to Wüstite: If the diffusion of oxygen does not contribute to the growth of the wüstite layer, then since $\ln a_2$ is proportional to $2.303 \log P_{H_2O}/P_{H_2}$ (see Eq. 8), and $|z_2| = 2$, $z_1 = |z_2|N_2/N_1$, and c_2 is approximately 0.0832 gram atoms of oxygen per cu cm of oxide, Eq. 10 reduces to

$$K_r = 2.303 |z_2|c_2 \int_{a'_2}^{a''_2} D^*_{*1} \frac{N_2}{N_1} d \left(\log \frac{P_{H_2O}}{P_{H_2}} \right)$$

$$= 0.383 \int_{a'_2}^{a''_2} D^*_{*1} \frac{N_2}{N_1} d \left(\log \frac{P_{H_2O}}{P_{H_2}} \right) \quad [11]$$

The integration limits correspond to the boundaries of the wüstite phase field at the temperature in question; these are derived from the data of Darken and Gurry (see Table V). The value used for c_2 is based on an average oxide composition of 23.7 wt pct oxygen and an average density of 5.63 g per

Table VIII. Comparison Between the Experimental Scaling Rate Constants and Those Calculated from the Wagner Equation

Temperature, °C	Calculated Rational Rate Constant, K_r , Equivalents Per Cm Per Sec	Parabolic Scaling Constant, K_p , G-Cm ⁻² -Sec ^{-1/2}	
		Calculated	Experimental
A. Iron to Wüstite			
983	2.8×10^{-8}	7.7×10^{-4}	8.2×10^{-4}
897	1.1×10^{-8}	4.8×10^{-4}	5.0×10^{-4}
800	0.25×10^{-8}	2.3×10^{-4}	2.3×10^{-4}
B. Wüstite to Magnetite			
1100	9.2×10^{-9}	1.7×10^{-4}	1.8×10^{-4}
1050	4.1×10^{-9}	1.1×10^{-4}	1.3×10^{-4}
1000	1.4×10^{-9}	0.67×10^{-4}	0.90×10^{-4}
C. Magnetite to Hematite			
1100	1.7×10^{-12}	2.2×10^{-6}	1.0×10^{-4}
1000	2.1×10^{-14}	2.4×10^{-7}	4.8×10^{-5}

cu cm. Although the average composition of the wüstite layer does depend slightly on the temperature of oxidation, no significant error is introduced by assuming c_2 to be constant over the range from 800° to 1000°C. Eq. 11 is integrated graphically from plots of D^*N_2/N_1 vs $\log P_{H_2O}/P_{H_2}$ which are prepared from the data given in Fig. 6 and Table V. The resulting values of the rate constants for the growth of wüstite on iron at 983°, 897°, and 800°C are listed in Table VIIIA.

Oxidation of Wüstite to Magnetite: It is assumed that the self-diffusion coefficients reported here (Eq. 5) for iron in magnetite are sufficiently close to the effective averages that the variation with concentration may be neglected. Thus, with $z_1 = 8/3$ and $c_2 = 0.0897$ gram atoms of oxygen per cu cm of Fe_3O_4 , the rational rate constant for the growth of magnetite on wüstite becomes

$$K_r = 2.303 \times \frac{8}{3} \times 0.0897 D^* \int_{a'_2}^{a''_2} d \log a_2 = 0.551 D^* \log \left(\frac{a''_2}{a'_2} \right) \quad [12]$$

provided that the diffusion of iron in magnetite is rate-controlling and that there is no contribution due to oxide ion diffusion. An average magnetite composition of 27.72 wt pct oxygen and a density of 5.18 g Fe_3O_4 per cu cm have been used in computing c_2 . The oxygen activities corresponding to the limits of the magnetite field are obtained from the work of Darken and Gurry. A slight complication arises because of the fact that the available activity data refer to the temperature range from 1100° to 1400°C while self-diffusion coefficients are known only between 800° and 1000°C. The rate constants have therefore been calculated for the intermediate temperature range of 1000° to 1100°C so as to avoid excessively large extrapolations (see Table VIIIB).

Oxidation of Magnetite to Hematite: If this process takes place at a pressure of 1 atm of oxygen and if D^*_1 is again assumed independent of concentration, then since $z_1 = 3$ and $c_2 = 0.0983$ gram atoms of oxygen per cu cm of Fe_2O_3 , Eq. 10 becomes

$$K_r = 2.303 \times 3 \times 0.0983 D^* \int_{a'_2}^{a''_2} d \log a_2 = -0.679 D^* \log a'_2 \quad [13]$$

subject to the initial assumption that $D^*_1 \gg D^*_2$. The oxygen concentration in hematite has been cal-

culated for the stoichiometric composition (30.06 wt pct oxygen) using an oxide density of 5.24 g per cu cm. As in the previous example, the magnetite-hematite equilibrium given by Darken and Gurry requires extrapolation. The rate constants for the growth of hematite on magnetite have been calculated only at 1000° and 1100°C, at which temperatures $D^*_1 \approx 1 \times 10^{-14}$ sq cm per sec and 1×10^{-12} sq cm per sec respectively (see Fig. 9).

To test the various assumptions upon which the above calculations are based, a comparison will now be made with rate constant data obtained directly from kinetic studies. The recent measurements of Davies, Simnad, and Birchenall have been selected for this purpose. These investigators followed the course of oxidation of iron and of the lower oxides, wüstite and magnetite, by conventional weight gain techniques, finding in each case that the parabolic rate law was closely obeyed. The experimental rate constants reported by Davies, Simnad, and Birchenall are defined, accordingly, by the equation

$$\frac{W}{A} = K_p t^{1/2} \quad [14]$$

where W is the weight increase, i.e., the number of grams of oxygen added, A is the surface area of the specimen in square centimeters, t is the time in seconds, and K_p is the familiar parabolic scaling constant, having the dimensions g-cm⁻²-sec^{-1/2}. It can be shown¹ that K_p and K_r , defined as in Eq. 9, are related by the expression

$$K_p^2 = \frac{2M_2}{|z_2|} f_2 \rho K_r \quad [15]$$

M_2 being the weight of one gram atom of oxygen, and f_2 the weight fraction of oxygen in the growing oxide layer, the density of which is ρ ; hence with $M_2 = 16$ and $|z_2| = 2$

$$K_p^2 = 16 f_2 \rho K_r \quad [16]$$

Using this relationship, the calculated and experimental rate constants may be reduced to a common basis.

Although Eq. 16 holds for the reaction between oxygen and iron, it does not apply without qualification to the oxidation of the oxides themselves, because the parabolic scaling constant refers only to the oxygen which has been taken up by the specimen from the gas phase, whereas, by definition, the rational rate constant is a measure of the total quantity of oxygen in the growing oxide layer, regardless of its origin. When a metal is oxidized to form a single-layer scale, the weight gain and the amount of oxygen in the scale are identical, provided solubility in the underlying metal can be neglected. However, when one oxide is converted to a higher oxide only a fractional part of the oxygen in the product is actually derived from the gas phase. This fraction is calculable from the stoichiometric relations between the phases and represents a correction factor, α , which must be applied to K_r in Eq. 16, i.e.,

$$K_{p_{calc}}^2 = 16 f_2 \rho \alpha K_r \quad [17]$$

The value of α is unity for the growth of wüstite on iron; for the oxidation of wüstite to magnetite, α varies between approximately 1/5 and 1/7, depending on the composition of the starting material, while for magnetite being oxidized to hematite, α is very nearly 1/9.

The parabolic rate constants for the oxidation of iron to wüstite, calculated from K_p according to Eq. 17 are listed in Table VIIIA, along with the experimental values of K_p obtained from the data of Davies, Simnad, and Birchenall. The latter actually correspond to overall rate constants for the reaction between iron and oxygen gas at 1 atm pressure. Even in a pure oxygen atmosphere, however, the wüstite phase constitutes upwards of 95 pct of the growing scale layer.^{5, 30} Thus, despite the simultaneous formation of the higher oxides, the total or overall scaling rate is not significantly greater than the rate of growth of the wüstite layer alone, and a direct comparison is therefore permissible. It is evident from Table VIIIA that the rate constants calculated from the Wagner equation are in excellent agreement with the experimental rate constant data. Since it has been assumed that iron is the effective diffusing component in wüstite, and since the validity of this special assumption has been established by independent marker movement studies, the agreement between the calculated and observed rate constants may be taken as direct experimental confirmation for the Wagner theory.

One of the assumptions which has been made in the derivation of the Wagner equation is that the transference numbers of the ions are extremely small in comparison to the transport number for electrons. This is a perfectly valid assumption for most transition metal oxides, and particularly for the oxides of iron, which are known to be almost purely electronic conductors. The transference number of the cations in wüstite can be calculated, at least approximately, with the aid of the Nernst-Einstein relation,^{6, 8}

$$\sigma \tau = \frac{nz^2 e^2 D^*}{kT} \quad [18]$$

where σ represents the specific electrical conductivity of the oxide, τ is the transference number of the ion in question, n the number of cations per cubic centimeter, z the valence of the charge carrier, and D^* , its self-diffusion coefficient. At 1000°C (1273°K) and an oxygen pressure of approximately 4×10^{-15} atm, Wagner and Koch's³⁰ experimental value for σ is 107 ohm⁻¹-cm⁻¹; under these same conditions, $n \cong 4.88 \times 10^{22}$, while D^* , obtained from the present study, is roughly 6.4×10^{-7} sq cm per sec. Hence, with the appropriate values of the electronic charge, e , and the Boltzmann constant, k , the transference number of Fe⁺⁺ ions in wüstite is found to be approximately 2×10^{-4} . This may be compared, as to order of magnitude, with the experimental value of 5×10^{-4} obtained by Gundermann and Wagner³⁷ for the transport number of Cu⁺ ions in Cu₂O at 1000°C.

The Wagner treatment also assumes that the ions and electrons migrate independently of one another and that the Nernst-Einstein equation, relating the ionic mobilities and the respective self-diffusion coefficients, is satisfied. These fundamental assumptions imply virtually complete dissociation of the vacancies and electron holes, and the absence of large deviations from ideal solution behavior of the Debye-Hückel type. From their work on the oxidation of copper, Bardeen, Brattain, and Shockley³⁸ have inferred that only a small fraction of the defect centers in cuprous oxide are associated to form vacancy-hole pairs at temperatures near 1000°C. However, the agreement which has been obtained between the experimental rate constants for the oxidation of iron and those calculated from the self-diffusion and activity data, does not, in itself con-

stitute proof that diffusion in wüstite also occurs largely by the mechanism of dissociated vacant sites. In the oxygen-rich wüstites, for example, the concentration of vacancies and electron holes is so great that on the average, every Fe⁺⁺ ion must have at least one nearest-neighbor site which is vacant, and moreover, each vacancy must have at least two Fe⁺⁺ ions as nearest neighbors. In other words, virtually complete association, rather than dissociation, would be expected purely on geometrical grounds. There are of course additional factors to be considered, such as the electrostatic attraction between the positive electron holes and the cation vacancies, the latter having an effective negative charge; this attraction also promotes the formation of vacancy-hole complexes.

If these complexes were mobile to any appreciable extent, their motion would contribute to the measured self-diffusion coefficient but not to the conductivity, since the associated defect centers are electrically neutral.⁹ This would then lead, substantially, to a breakdown of the Einstein relationship.³⁹ Hence, in the absence of the necessary conductivity and transport number data with which to test the validity of the Einstein relationship directly, it cannot be established with certainty whether or not an appreciable fraction of the observed diffusion in wüstite occurs through electrically neutral "trapped" vacancies. On the other hand, the fact that the Einstein relationship leads to a reasonable value for the transference number of Fe⁺⁺ ions in wüstite may be taken as evidence that both diffusion and conductivity in this oxide are indeed due to the same mechanism, e.g., the migration of free or dissociated vacancies.

If this assumption is correct, and if at the same time there exists an appreciable fraction of neutral, associated centers, then the mobility of these complexes must be much smaller than that of the free vacancies. This means, in turn, that the effective number of vacant sites may be considerably less than the number calculated from the deviation from stoichiometric composition. Furthermore, since association is favored at the higher vacancy concentrations and at lower temperatures, the effective number of vacancies might be expected to vary in exactly the opposite sense. Arguments of this kind could conceivably be used to explain the observed changes in slope of the D^* vs vacancy concentration curves (Fig. 6) with temperature. As previously mentioned, however, the diffusion data are not considered precise enough to justify much speculation on this point. The subject is of sufficient general importance to warrant a more detailed study of the diffusion and conduction processes in wüstite, especially at lower temperatures than have been employed in this investigation. It might also prove helpful to examine Kelley's¹⁹ suggestion regarding the presence of an ordered arrangement of vacancies in wüstite; this should be amenable to direct experimental proof by X-ray techniques.

The basic assumption has also been made by Wagner that the oxide growing on the metal substrate has properties identical with those of the homogeneous bulk oxide of the same chemical composition. Wagner and his coworkers¹ showed this to be true for the growth of Ag₂S on silver. Supporting evidence has also been provided by the more recent work of Moore and Selikson,⁴⁰ who studied the self-diffusion of copper in bulk specimens of Cu₂O, obtaining essentially the same results as previously

reported by Castellan and Moore,⁴¹ and by Bardeen, Brattain, and Shockley, for self-diffusion in the cuprous oxide layer growing on the surface of the metal. It is probable that this assumption is fulfilled whenever the layer of reaction product reaches a thickness such that the substrate no longer exerts any appreciable influence on its properties.^{42, 43}

In the derivation of the rate equation (Eq. 9) Wagner also found it necessary to assume that the product oxide is nearly stoichiometric in composition. This was done in order that the sum of the equivalents of metal and nonmetal passing a given plane per unit time would be the same at any distance through the scale layer. If this condition is to be satisfied in wüstite, where the vacancy concentration and the self-diffusion coefficient increase rather rapidly in traversing the scale, there must be a corresponding decrease in the activity gradient between the inner and external surfaces of the wüstite layer. Experimental proof for this is lacking, but could be obtained fairly readily now that the activities are known as a function of composition. Attention should also be called to the fact that in carrying out the rate constant calculations for wüstite, z_1 has been allowed to vary with distance relative to $|z_2|$. This approximation does not seem to have introduced any serious error.

The interpretation of the rate constant calculations for the oxidation of wüstite (to magnetite) is complicated slightly by the apparent conflict which exists regarding the relative mobilities of iron and oxygen in Fe_3O_4 . Actually, however, close agreement has again been obtained between the calculated and experimental scaling rates for this reaction (see Table VIIIB). Such agreement seems to indicate that the diffusion of oxygen contributes only slightly to the growth of the magnetite layer, and if so, represents additional confirmation for the Wagner theory. This conclusion is consistent with the accepted structural model for Fe_3O_4 given by Verwey,¹⁰⁻¹² which provides a convenient mechanism for the diffusion of iron (through lattice vacancies), but not for oxygen. Still, an objection to this general picture seems to have been raised by the marker movement experiment of Davies, Simnad, and Birchenall. On the basis of the observed marker shift during the oxidation of wüstite to magnetite, these investigators originally concluded that the mobilities of oxygen and iron in Fe_3O_4 were of comparable magnitude at temperatures near 900°C. Since publication of this result, however, it was realized that the observed marker movements were misinterpreted (see asterisk footnote, p. 828), and it now appears that the marker measurements are also overwhelmingly in favor of iron ion diffusion as the controlling factor in the growth of the magnetite layer. Thus, within the uncertainty of the diffusion and rate constant measurements, the Wagner equation again gives acceptable agreement with experiment.

A few additional remarks concerning the temperature dependence of the rate constant for this reaction may be in order. Structural considerations alone make it probable that the activation energies for the self-diffusion of iron and oxygen in magnetite differ quite significantly. Nevertheless, a critical temperature range may exist within which the relative mobilities or diffusivities of the two components are approximately equal. Therefore, if iron is the dominant diffusing component above this critical temperature, oxygen must assume this role

at lower temperatures, and vice versa. In either case, a shift from one diffusion-controlled process to another requires that there be a corresponding change in the activation energy for the oxidation reaction on passing through this critical range. The experimental rate constant data⁵ for the oxidation of wüstite between 850° and 950°C do not indicate any such trend; however, in order to be conclusive, rate constant and mobility data are needed over a much wider temperature range.

As seen in Table VIIC, the assumption that iron is the only mobile component in $\alpha\text{-Fe}_2\text{O}_3$ leads to a discrepancy of approximately two orders of magnitude between the calculated and experimentally determined rate constants for the oxidation of magnetite. This lack of agreement is entirely consistent with expectation and strongly supports the earlier proposals of Bevan, Shelton, and Anderson,²⁸ and Davies, Simnad, and Birchenall with regard to transport predominately by oxygen ions or oxide ion vacancies. By taking oxygen as the effective diffusing component in hematite, and reversing the calculations, the average self-diffusion coefficient, D^*_{Fe} , can be evaluated from the experimental rate constant data. Thus D^*_{Fe} is found to be 3.6×10^{-9} sq cm per sec at 1100°C and 5.9×10^{-10} sq cm per sec at 1000°C; at these same temperatures the measured values of D^*_{O} are about 1×10^{-12} and 1×10^{-14} respectively. Nevertheless, no direct conclusions can be drawn regarding the validity of the Wagner approach. This must await the actual determination of the transference numbers or of the rates of self-diffusion of oxygen in hematite.

Summary

1—Techniques have been developed for the preparation of bulk, homogeneous wüstites and magnetites of controlled composition by the direct oxidation of high-purity iron in atmospheres of constant, known, oxidizing potential.

2—The rates of self-diffusion of iron in the large-grained, polycrystalline wüstites have been determined over a range of compositions and temperatures, using the decrease in surface activity method with Fe^{55} as the tracer isotope. Within the precision of the measurements at each temperature, the self-diffusion coefficient for iron in wüstite is found to increase in linear fashion with increasing deviation from stoichiometric composition. At 983°C, for example, a four-fold increase is observed between the iron-rich and oxygen-rich boundaries of the wüstite phase field. This observation essentially confirms the view that the diffusion mechanism in wüstite involves the exchange of cation vacancies with normal lattice ions. Between 699° and 983°C the activation energy for the diffusion process is approximately 30 kcal per mol for compositions lying near the middle of the stability range.

3—Similar measurements have also been made on artificially prepared magnetites at temperatures between 799° and 987°C and on natural hematite single crystals at 1000° and 1217°C. The self-diffusion data obtained for hematite compare favorably with the results of more extensive experiments by Lindner on sintered powder compacts. The activation energy for the self-diffusion of iron in magnetites of average composition $\text{Fe}_{2.998}\text{O}_3$ is approximately 55 kcal per mol; for $\alpha\text{-Fe}_2\text{O}_3$ the activation energy is at least 100 kcal per mol and probably greater.

4—At temperatures between 1000° and 1217°C the rate of self-diffusion of iron in single crystals of

α -Fe₂O₃ appears to be independent of the crystallographic direction.

5—The reactions between wüstite solid solutions and H₂-H₂O atmospheres have been investigated in the range from 699° to 983° in order to establish the compositions of the oxides and their coexisting equilibrium atmospheres.

6—From these data the thermodynamic activities of iron and oxygen in wüstite have been calculated at various round compositions within the wüstite phase field. The partial molal heats of solution of iron and oxygen in wüstite and the heats of formation of wüstite have also been evaluated. The observed value $\Delta H_{298^\circ\text{K}} = -63.5$ kcal per mol is in good agreement with existing thermodynamic data for this oxide.

7—Using the self-diffusion and thermodynamic data, and applying the theoretical rate equations developed by Wagner, rate constants have been calculated for the growth of wüstite on iron, magnetite on wüstite, and hematite on magnetite, under the assumption that iron is the only diffusing component (in addition to holes or electrons) in each of the growing oxide layers.

8—The calculated scaling constants are compared with experiment and it is shown that the applicability of the Wagner theory is perhaps even more general than previously suspected. Not only has acceptable agreement been obtained between the calculated and experimentally determined rate constants for the growth of an oxide layer on a metal substrate, e.g., wüstite on iron, but the same is true for the conversion of one oxide to another, e.g., wüstite to magnetite.

9—Except for some disagreement regarding the relative contributions of iron and oxygen diffusion to the growth of magnetite, the mechanism of the multi-layer scaling of iron proposed by Davies, Simnad, and Birchenall is also substantiated by these observations. This mechanism is now thought to involve the outward migration of iron in the wüstite and magnetite layers and the inward diffusion of oxygen in the hematite layer.

10—The transference number of Fe⁺⁺ ions in wüstite is estimated, from self-diffusion and electrical conductivity data, to be approximately 2×10^{-4} at 1000°C.

11—Previously reported effects of the α - γ transformation temperature on the kinetics of the oxidation of iron must be attributed to reactions occurring at the metal-scale interface since there are no structural changes, and therefore no discontinuities in the rates of self-diffusion in the oxides at this temperature.

Acknowledgments

This work was initiated under a graduate fellowship generously granted to one of us by the Westinghouse Electric Co., and completed under the sponsorship of the Office of Naval Research. The authors greatly appreciate the assistance offered by H. M. Schadel, Jr. in the construction of the apparatus, and by W. E. Bostrom and J. M. Ferrin who performed the radiochemical analyses.

References

- ¹ C. Wagner: Diffusion and High Temperature Oxidation of Metals. *Atom Movements* (1951) p. 153. ASM. See also *Ztsch. Physik. Chem.* (1933) **B21**, p. 25.
- ² K. Nagel and C. Wagner: *Ztsch. Physik. Chem.* (1934) **B25**, p. 71.
- ³ C. Wagner: *Ztsch. Physik. Chem.* (1936) **B32**, p. 447.

⁴ C. Wagner and K. Gruenewald: *Ztsch. Physik. Chem.* (1938) **B40**, p. 455.

⁵ M. H. Davies, M. T. Simnad, and C. E. Birchenall: *Trans. AIME* (1951) **191**, p. 889; *JOURNAL OF METALS* (October 1951).

⁶ N. F. Mott and R. W. Gurney: *Electronic Processes in Ionic Crystals* (1948) 2nd Ed. Oxford. Clarendon Press.

⁷ *Imperfections in Nearly Perfect Crystals* (1952) New York. John Wiley and Sons.

⁸ W. Jost: *Diffusion in Solids, Liquids and Gases* (1952) New York. Academic Press.

⁹ H. J. Goldschmidt: *Journal Iron and Steel Inst.* (1942) **146**, p. 157.

¹⁰ E. J. W. Verwey and J. H. de Boer: *Rec. trav. chim.* (1936) **55**, p. 531.

¹¹ E. J. W. Verwey and P. W. Haayman: *Physica* (1941) **8**, p. 979.

¹² E. J. W. Verwey, P. W. Haayman, and F. Romeijn: *Journal of Chemical Physics* (1947) **15**, p. 181.

¹³ C. A. Domenicali: *Physical Review* (1951) **78**, p. 458.

¹⁴ R. B. Sosman and E. Posnjak: *Journal Wash. Acad. Sci.* (1925) **15**, p. 329.

¹⁵ R. Fricke et al.: *Ztsch. Elektrochem.* (1934) **40**, p. 630; (1935) **41**, p. 617; (1937) **43**, p. 52.

¹⁶ L. S. Darken and R. W. Gurry: *Journal ACS* (1945) **67**, p. 1389; (1946) **68**, p. 798.

¹⁷ E. R. Jette and F. Foote: *Journal of Chemical Physics* (1933) **1**, p. 29; *Trans. AIME* (1933) **105**, p. 276.

¹⁸ J. Benard: *Bull. soc. chim. France* (1949) D109.

¹⁹ G. L. Humphrey, E. G. King, and K. K. Kelley: *Bur. Mines R.I.* 4870 (1952).

²⁰ C. Wagner and E. Koch: *Ztsch. Physik. Chem.* (1936) **B32**, p. 439.

²¹ L. B. Pfeil: *Journal Iron and Steel Inst.* (1929) **119**, p. 501; (1931) **123**, p. 123.

²² B. W. Dunnington, F. H. Beck, and M. G. Fontana: *Corrosion* (1952) **8**, p. 2.

²³ D. J. M. Bevan, J. P. Shelton, and J. S. Anderson: *Journal Chem. Soc., London* (1948) p. 1729.

²⁴ M. J. Pryor and U. R. Evans: *Journal Chem. Soc., London* (1949) p. 3330.

²⁵ R. Lindner: *Arkiv for Kemi* (1952) **5**, p. 1.

²⁶ L. Meites and T. Meites: *Analytical Chemistry* (1948) **20**, p. 984.

²⁷ C. E. Birchenall and R. F. Mehl: *Trans. AIME* (1950) **188**, p. 144; *JOURNAL OF METALS* (January 1950).

²⁸ J. Steigman, W. Shockley, and F. C. Nix: *Physical Review* (1939) **56**, p. 13.

²⁹ J. Smiltens: *Journal of Chemical Physics* (1952) **20**, p. 990.

³⁰ C. Palache, H. Berman, and C. Frondel: *Dana's System of Mineralogy* (1944) 7th Ed. Vol. 1. New York. John Wiley and Sons.

³¹ J. K. Stanley, J. von Hoene, and R. T. Huntoon: *Trans. ASM* (1951) **43**, p. 426.

³² R. Schenck et al.: *Ztsch. anorg. allgem. Chem.* (1929) **182**, p. 97.

³³ F. D. Richardson and J. H. E. Jeffes: *Journal Iron and Steel Inst.* (1948) **160**, p. 261.

³⁴ L. S. Kassel: *Journal ACS* (1934) **56**, p. 1838.

³⁵ J. Benard and O. Coquelle: *Review Metallurgie* (1946) **43**, p. 113.

³⁶ J. Paidassi: Discussion to ref. 5: *Trans. AIME* (1952) **191**, p. 536; *JOURNAL OF METALS* (May 1952). Also *Bol. soc. chilena quim.* (1951) **3**, p. 55.

³⁷ J. Gundermann and C. Wagner: *Ztsch. Physik. Chem.* (1937) **B37**, p. 155.

³⁸ J. Bardeen, W. H. Brattain, and W. Shockley: *Journal of Chemical Physics* (1946) **14**, p. 714.

³⁹ D. Mapother, H. N. Crooks, and R. Maurer: *Journal of Chemical Physics* (1950) **18**, p. 1231.

⁴⁰ W. J. Moore and B. Selikson: *Journal of Chemical Physics* (1951) **19**, p. 1539.

⁴¹ G. W. Castellan and W. J. Moore: *Journal of Chemical Physics* (1949) **17**, p. 41.

⁴² E. A. Gulbransen and J. W. Hickman: *Trans. AIME* (1947) **171**, p. 306; *METALS TECHNOLOGY* (October 1946).

⁴³ E. A. Gulbransen and R. Ruka: *Trans. AIME* (1950) **188**, p. 1500; *JOURNAL OF METALS* (December 1950).

High Temperature Corrosion in Nickel-Chromium Alloys

by Norman Spooner, John M. Thomas, and L. Thomassen

NI-CR and some Ni-Cr-Fe alloys, when used as electrical resistance heating elements in reducing atmospheres, at times suffer rapid breakdowns due to so-called "green rot." These reducing atmospheres are most frequently used in bright annealing and heat-treating furnaces which are kept for long periods of time at 1500° to 1800°F. The green rot is a preferential oxidation of the chromium in the alloy to such an extent that the remaining metal frequently becomes ferromagnetic. The Curie point (magnetic transition point) at room temperature for a pure Ni-Cr alloy is known to be at about 7 pct Cr.¹ This represents a severe loss in chromium for one popular grade of resistance alloy, which is nominally 80 pct Ni-20 pct Cr. The formation of oxides along the grain boundaries makes the ribbon brittle and gives the fracture a green, earthy appearance—hence the name.

The authors have studied this phenomenon, simulating the industrial conditions by heating resistance ribbons in various reducing atmospheres, such as moist hydrogen or the atmosphere specified in the ASTM test.² This atmosphere contains 16 pct H₂, 10 pct CO, 4 pct CO₂, 1 pct CH₄, 1.5 to 2.5 pct H₂O, balance N₂.

Little success was had in producing severe corrosion with the commercial 80 pct Ni-20 pct Cr alloys. It had been noticed, however, that 90 pct Ni-10 pct Cr alloy wires deteriorated very rapidly when placed in the bottom of narrow thermocouple protection tubes. The bottoms of the tubes with the wires were heated in air. This took place both in porcelain tubes and in Inconel* tubes either with

* Inconel is a heat and corrosion resistant alloy manufactured by the International Nickel Co. and has a nominal composition of 78 pct Ni, 14 pct Cr, balance Fe.

the cold end open or loosely stoppered with asbestos. On examination the wires showed microstructures which would be classified as green-rot corrosion.

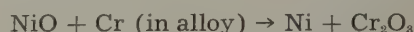
Subsequent investigations with various alloy wires confirmed the observation that corrosion occurred in some wires, including 80 pct Ni-20 pct Cr alloys, much more rapidly in such tubes than had occurred previously in test atmospheres mentioned above.

When 90 pct Ni-10 pct Cr alloys are oxidized with an abundant air supply, the oxide coat consists of both nickel and chromium oxides. In this case thermodynamic equilibrium between the oxides is not established.

N. SPOONER is Metallurgical Engineer, Hoskins Manufacturing Co., Detroit, J. M. THOMAS, Junior Member AIME, formerly with Hoskins Manufacturing Co., is now with Scientific Laboratory, Ford Motor Co., Dearborn, and L. THOMASSEN is Professor of Chemical and Metallurgical Engineering, University of Michigan, Ann Arbor, Mich.

TN 164E. Manuscript, June 27, 1952; revision, April 20, 1953.

However, when oxidized 90 pct Ni-10 pct Cr alloy specimens were heated to 1500° to 1800°F inside small diameter tubes, the oxide coat transformed to a bright metallic outer layer of nickel or nickel-rich alloy, beneath which appeared a green oxide, followed by intergranularly attacked metal. The obvious explanation is that in the narrow tubes, thermodynamic equilibrium is being established according to the equation



This reaction is favored due to the fact that the oxygen pressure over nickel oxide is more than 10¹⁰ times the oxygen pressure over the green chromium oxide. The initial oxygen in the tubes is depleted very rapidly by oxidation of the wire and of the tube, if it is metallic. A confirmation of the occurrence of the reaction, reduction of NiO by the chromium in the alloy, was obtained by putting oxidized nickel foil into an evacuated quartz tube along with a piece of bright 90 pct Ni-10 pct Cr alloy ribbon, and heating the tube at 1820°F for a number of hours. The nickel oxide on the foil was completely reduced to pure nickel, leaving a bright foil. The 90 pct Ni-10 pct Cr alloy became strongly magnetic and showed the typical green-rot structure. Weights of the samples before and after testing showed the weight loss of the foil to approximately equal the weight gain of the ribbon. Evidently the bottom of long, narrow protection tubes, stoppered or not, may under certain conditions act just as the sealed quartz tubes in respect to being a confined space in which oxygen is not freely replenished. This condition of oxygen depletion can be prevented by introducing a small amount of air into the bottom of the tube.

Many conditions becloud the green-rot phenomenon, such as carburization, sulphidization, and the presence of other corrosive agents. However, these experiments have shown that the basic reaction is a case of internal oxidation which can occur simply by adjusting the oxygen pressure to a low enough level so that the atmosphere will leave the nickel intact and oxidize the chromium. The action of the other agents in commercial atmospheres can then be taken up as individual cases.

From these and numerous other tests completed to date or still in progress, it is believed that a more critical evaluation of electrical resistance alloys for their resistance to green-rot corrosion can be made. A much better understanding of the mechanism for this type of corrosion should also result. A more complete report on these experiments will be published later.

References

- ¹ V. Marion: *Ann. Physik* (1937) 7, p. 502.
- ² ASTM Test for Effect of Controlled Atmospheres upon Alloys in Electric Furnaces. B181-43.

Correction

In the May 1953 issue: TP 3521E *Discussion: Solubility of Carbon and Oxygen in Molybdenum* by W. E. Few and G. K. Manning, discussion by N. A. Gokcen: p. 747, first column, the fifth, sixth, and seventh lines should be the first, second, and third lines, followed by the present first, second, third, fourth, eighth, ninth, and tenth lines.

Further Studies of the Tuyere Zone of the Blast Furnace

by J. B. Wagstaff

The raceway in front of the tuyere of the blast furnace has been studied quantitatively and a correlation obtained for the penetration of the blast. Some evidence is presented for the height and width of the raceway which suggests that all the raceways of a furnace overlap. The size of the coke in this zone has been measured photographically during normal operation and results are given for the various areas.

IN an earlier paper,¹ it was shown that a raceway exists opposite each tuyere of a blast furnace. This raceway is formed by the jet effect of the air emerging from the tuyere and consists essentially of a turbulence in which coke particles are recirculated at high speed.

Its presence was deduced originally from observations on movies taken with a high-speed camera through the tuyeres of various furnaces and was confirmed by experiments made on a model. In the model described,¹ this raceway was shown as operating in a vertical plane only, although there was a suggestion in the motion-picture film exhibited at that time that the raceway was three dimensional, unless artificially restricted. There was also some doubt then about the factors influencing its size.

This paper describes the next steps in the investigation. Since the size of the raceway is obviously of importance in the operation of the furnace, it seemed worth while to study the subject more carefully. It is probably in this region that about half the coke in the furnace is consumed, so that the movement of the stock column may well be controlled by raceway behavior. Furthermore, there is some evidence to suggest that the coke is packed densely in the center of the furnace to form the "dead man" and more loosely above the raceway. It is therefore probable that the bulk of the gases passing up the stack flow from the top surface of this raceway. Clearly then, a knowledge of this critical zone is of interest to the blast furnace operator, and the first half of this report is devoted to a quantitative discussion of the subject.

A further topic of interest among operators is the degree of breakdown of coke in the furnace, with

which is inseparably linked the importance of a strong coke. Indeed, the whole question of the optimum size and type of coke may be as dependent on the condition of the coke in the bottom of the blast furnace as at the top. Attempts have been made from time to time to obtain samples of coke from the tuyeres and other furnace openings but they all suffer from the fact that the coke is filled to a varying degree with metal and slag and is probably broken up by the very act of taking the sample. It has proved difficult to make any reliable studies of coke size by these methods.

However, it did seem possible to use the high-speed movies mentioned earlier¹ to estimate the size of the coke. These movies provide an accurate record of individual coke particles so that, in theory at least, it should be possible to measure the size of the particles one by one and to obtain, for the first time, information on the coke being blown around the raceway under actual operating conditions while the furnace is performing normally. Such a study has been made and is discussed in the second half of this paper. The results obtained enabled the blast furnace data to be correlated with the model results given in the first half.

Raceway Size

In order to make a quantitative study of the size of the raceway it was necessary to devise some apparatus of laboratory scale, which could be handled quickly and easily. This focused attention on models, which in turn means that the laws of similarity governing this particular process must be ascertained.

Method of Procedure: Since the work was to be carried out on a smaller scale than the blast furnace, the linear dimensions of the model became unimportant provided that the scale was known; it is only important to insure that the container does not affect the raceway being observed. The studies therefore were carried out in a glass-sided box, 11 in. high x 7 in. wide x 3 in. deep, using air jets ranging

J. B. WAGSTAFF, Member AIME, is associated with the Research Laboratory, United States Steel Corp., Kearny, N. J.

Discussion on this paper, TP 3577C, may be sent, 2 copies, to AIME by April 1, 1954. New York Meeting, February 1954; also presented at Blast Furnace, Coke Oven and Raw Materials Conference, Buffalo, April 1953.

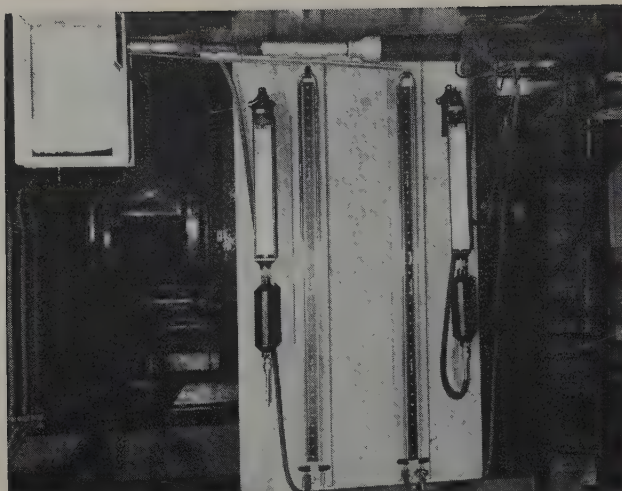


Fig. 1—Model apparatus.

from $\frac{1}{8}$ to $\frac{1}{2}$ in. in diameter. Fig. 1 shows the model box on the right-hand side filled with $\frac{1}{8}$ -in. wood particles, which served to study a single raceway. The air entered through the pipe that can be clearly seen at the bottom of the picture. Air flow was measured by readings of pressure drop across an orifice plate between the flanges shown. The orifice was calibrated against a Connersville-type positive displacement meter, proved and sealed by the Public Service Commission of New York State. The manometer used for pressure measurement is clearly shown in the photograph. The small pipe entering the box underneath the $\frac{1}{2}$ -in. air-supply pipe is the pressure offtake used in recording jet pressure. It was connected to the extreme end of the jet and great care was taken to insure that there was no roughness and that the pressure tap entered the jet at right angles to the jet axis.

The various types of granular materials used in the work are described in Table I. Most of the work was carried out on the wood blocks because the characteristics of the packing could then be determined with reasonable precision. The particle size was chosen so as to give the maximum practical range of size but with the limitation that it was not possible to get raceways if the particles were larger than the jet diameter, and there seemed to be a lower size limit beyond which regularly shaped particles could not be obtained. The sizes of the particles were obtained by direct measurement.

Crushed coke was used for checking the effect of particle shape. This was carefully screened to the sizes shown in Table I. The surface areas were calculated by assuming that the coke particles were all cubes and that length of the cube side was the mean of the screen sizes. This is an approximation but there does not seem to be any reliable and accepted technique of measuring with accuracy the particle surface of crushed coke. The particle sizes of the blast furnace cokes were determined by actual measurement by the method described in this paper. The particles were also assumed to be cubes.

It is realized that there may be other variables than those investigated that influence the raceway size. In particular, the packing of the particles may be important. It was found that if a raceway was blown in a freshly dumped bed by slowly increasing the air rate, there was a very sudden surge when the raceway first formed. This point was very marked but was not repeatable. If the raceway was slowly

collapsed and re-formed, it started smoothly the second time and formed at a much lower air flow than before. Visual observation suggested that the difference was due to the packing of the particles. By collapsing the raceway slowly, a very loose packing was formed around the jet, which enabled the particles to start moving more easily than in the freshly dumped bed. It also seemed that the particles outside the raceway moved slightly when the raceway expanded, so that the packing density of that part of the bed at which the jet was pointed seemed to increase; at the same time, the bed vertically above the jet seemed to loosen somewhat; however, in a bed 10 in. deep, a raceway of $2\frac{1}{2}$ -in. diameter could be formed before there was any movement of the top of the bed. The packing density or void fraction of the bed as a whole seems to have little importance. At the same time it is not easy to measure quantitatively the void fraction of a small part of a bed.

In view of this difficulty it was decided not to study the effect of void fraction at this stage. Instead, all runs were made on freshly dumped packings. This arrangement did not simulate blast furnace conditions, but it was hoped that it would provide a simple, reproducible condition that would serve at least for the initial studies.

A rather interesting incidental question arises from the difficulty of starting the raceway. It was found that, for the same flow conditions, the pressure at the jet is much greater before the raceway is formed than afterward. If more than one jet is fed from the same air line in the model work, the tendency is for one raceway to form first, then for the air to go in large quantity to that jet, and for the other raceways not to form. This possibility, which is being studied further at the present time, raises some interesting questions about the partition of flow between tuyeres in the blast furnace.

Preliminary model studies show that the raceway becomes approximately spherical in shape if it is free to expand in all directions except backward. The particles are blown by the jet and return either sideways or over the top and down above the jet. The jet seems to have a capacity for sucking in particles where the air emerges from the metal tube. In many cases, a small secondary recirculation occurs under the jet. This seemed to be quite minor in size and was treated as part of the main disturbance.

Since the main purpose of this work was to throw light on the penetration of the blast into a furnace, the most important measurement was the maximum "diameter" of the raceway measured in a direction parallel to the jet axis. If the raceway is free to expand in all directions, it must be surrounded by

Table I. Detail of Particles Used in Model Studies

Material	Size, In.		Particle Density
	Diameter	Height	
Wood cylinders	0.130	0.124	0.674
Wood cylinders	0.2535	0.2223	0.639
Wood cylinders	0.0770	0.1092	0.700
	Screen Opening, In.		
Crushed coke	0.0331	0.0788	1.0838*
Crushed coke	0.0788	0.157	0.9184*
Crushed coke	0.157	0.263	0.9281*

* Measured by the method proposed by Ergun.²

the particles being studied and cannot be examined visually, so that any estimates of its size must be made by probes. This is more difficult than visual observation. The box was fitted with a wire probe ending in a 1/4-in. disk, which could be pushed out above the jet until it hit the more solid bed. Sometimes it was easy to tell by feel when the probe hit the bed, but sometimes the probe would enter the bed comparatively easily, particularly when large particles and high air rates were used.

A series of measurements was therefore made to compare depth taken with the probe with those obtained visually with the jet close to the corner of the box blowing along the glass side. Thus the measurements taken with the probe could be "calibrated" against those taken visually. The jet was then moved to the center of the box side, so that the raceway could expand freely and be measured again. The results were somewhat erratic but seemed to show that the raceway was the same size whether it was restricted by the side of the box or not. Later measurements therefore were taken by visual observation. The raceway was always free to expand both upward and away from the glass at right angles to the jet.

An attempt was made to measure the size of the raceway in the horizontal direction at right angles to the jet axis by moving the jet away from the glass side until the raceway could just be detected. The method was not satisfactory because it was never certain whether the glass still interfered with the raceway formation. However, it was the only method available without cutting the raceway horizontally.

Results of Tests on Raceway Size: As this work was aimed at a study of raceway size, it is important to understand exactly what this size really is. The raceways are best pictured as roughly spherical in shape, so that they may be described in terms of three "diameters" at right angles. These three diameters are not quite the same size, so that it seems advisable to think of one as the main measurement and the other two as subsidiary. The one selected to be the main measurement was the horizontal diameter parallel to the jet axis; the other factors, such as air velocity, particle size, etc., were correlated with it.

The author was unable to find any work in the literature giving the effect of the different variables on raceway size. The work on jets, about which a great deal has been published, did not seem to apply and a theoretical approach seemed to be extremely complicated. As a result, purely empirical methods were used. However, it was found possible to group the variables into dimensionless ratios. It has been found that for many processes the grouping of variables into ratios that are independent of the units employed (as long as they are consistent) allows a wide range of conditions to be correlated. It was hoped that the same might apply in this case.

The ratios used here were

$$\frac{\rho V^2 D_r}{g \sqrt{S} P_j} \text{ and } \frac{D}{D_j}$$

where ρ is the density of air at the jet; V , the velocity of air at the jet; D , the diameter of the raceway; D_r , the diameter of the jet; g , the acceleration due to gravity; S , the surface area of an average particle; and P_j , the absolute pressure at the jet. Fig. 2 shows

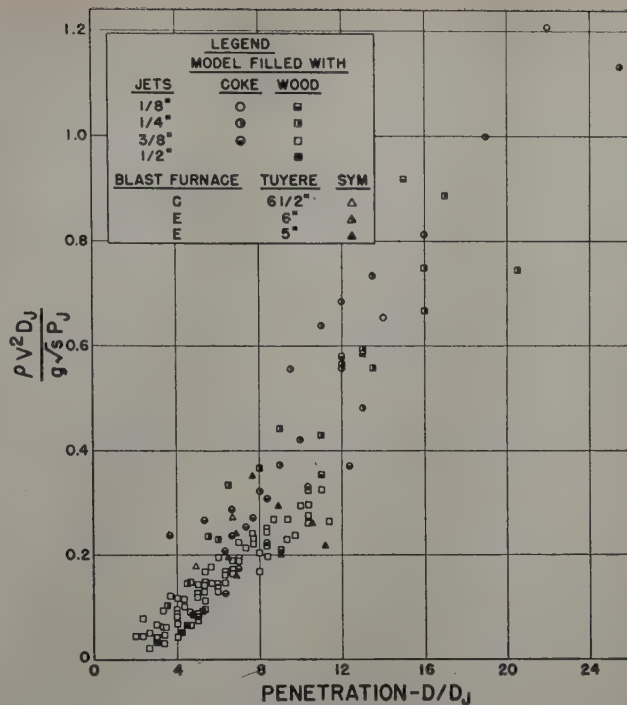


Fig. 2—Correlation of raceway diameter.

the relationship between these two ratios for the data available. This covers quite a wide range of variables because it has been found possible to include data taken on two different blast furnaces along with the data obtained from the model. The range of mean size of coke particles on the model was from 0.0560 to 0.210 in., or nearly 4 to 1, and up to 1.475 in. on the furnace, or a total range of 25 to 1. The range of wood-block size was 2.5 to 1 and the jet ratio 4 to 1 on the model, or 50 to 1 overall. All the points both from the model and the blast furnaces seem to fall fairly well in a band, as shown by Fig. 2.

In accepting the model technique as a method of studying raceway size, certain very definite disadvantages must be appreciated. The models are at uniform temperature and no chemical reaction takes place, conditions that do not occur in the blast furnace. Again, the models discussed in this paper do not involve movement of the main bulk of the bed but only of the gas. Also, there was no liquid in the models.

Despite these major differences, the correlation shown in Fig. 2 would appear to suggest that the main variables governing the raceway size are now understood. It does not seem probable that the agreement shown is a coincidence, as the correlation is reasonably complex and involves not only the flow conditions but particle and tuyere size as well as the overall pressure on the system.

It was mentioned earlier that no attempt was made to study the effect of the packing. It is almost certain that this is an important omission. Again, it can happen that the bed becomes aerated and therefore tends to expand, and the raceway size also increases. In any case, the model measurements are only approximate, as raceway diameter can be measured to the nearest particle at best and in some cases this represents a unit in the ratio of raceway-jet diameter, D/D_j . In a few cases with the 1/4-in. wood blocks, raceway movement seemed gradually

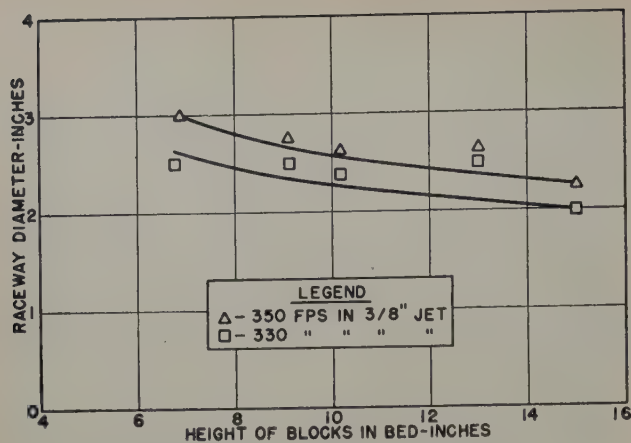


Fig. 3—Effect of bed height on raceway diameter.

to slow down into the bed and the dividing line between the rapidly moving particles and the stationary bed was indefinite. Undoubtedly this accounts for some of the spread observed in Fig. 2.

In an actual blast furnace, it can happen that the coke fails to feed smoothly into the raceway and then the void must increase, owing to combustion. This probably happened in blast furnace E and the smaller values of raceway-jet diameter, D/D_j , are therefore the more reliable.

Also the curve does not pass through the origin; but at zero flow there was a raceway of some two or three jet diameters, if extrapolation is permissible to this extent. This probably was due to the change in the packing density produced in the surrounding bed when the raceway was formed. When the air was turned off after a run, so that the raceway collapsed, the bulk volume of the bed as a whole decreased, despite the loose packing formed near the jet. That part of the bed subject to only slight movement must have compacted considerably. This observation compares with the commonly held view of a dense central zone or "dead man" in a blast furnace.

This discussion would not be complete without some reference to the many minor issues involved. For example, it was found that the height of the bed in the model affected raceway size slightly. This is shown in Fig. 3. The point was not followed in detail because somewhat different conditions exist in the blast furnace, in which there is some vertical movement of the bed. It was preferred to standardize on about 10 to 11 in. of particles, where the effect of changes of depth was slight.

While these measurements were being taken, a rather crude attempt was made to estimate the half-raceway width. The apparatus was not ideal for this purpose and the results should be accepted with caution. Fig. 4 shows the band produced by these measurements when half-raceway width is plotted against the penetration or main diameter of the raceway. It seems reasonable to draw the conclusion that the raceway is about as wide as it is long, or perhaps wider.

These measurements may be applied to the blast furnace with the precaution that there seems to be some slight change of shape as a raceway gets very big; that is, when the jet velocity is high, of the order of the velocity of sound. These velocities are not approached in the blast furnace. At high velocities, the raceway seems to become more pear shaped. Attempts have been made to sketch the probable

diameter of the raceways on scale drawings of actual furnaces. It seems that adjacent raceways touch each other, or nearly so. It is difficult to imagine a pillar of stationary coke a few inches wide between two streams of coke moving rapidly in the same direction. One is therefore forced to the conclusion that the raceways do "interlock" and that there is an annular ring in a blast furnace in which the coke particles are in rapid movement. From these measurements so far obtained, this ring would seem to be about 3 ft 6 in. to 4 ft wide at tuyere level in normal operation. However, with the present skimpy knowledge, these conclusions must be regarded as tentative.

The measurement of the vertical height of the raceway was complicated by the presence of a second raceway underneath the main one. The second one is much smaller but varies in size appreciably with the particular conditions of the experiment. In general, it seems to diminish in importance as the main

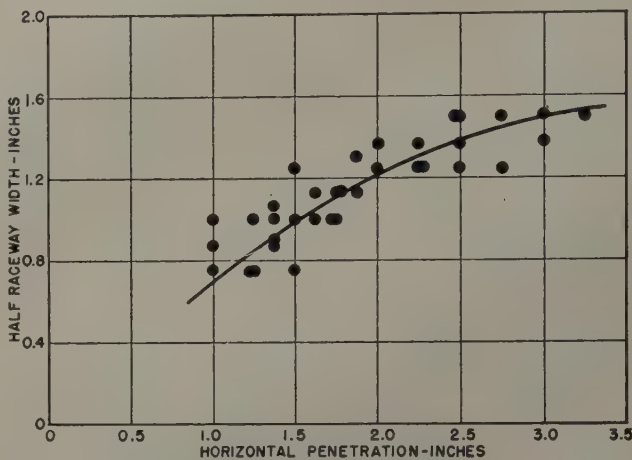


Fig. 4—Width of raceway.

raceway increases. Some evidence of this was found in all tests but so far the photographs of an actual blast furnace do not seem to show it. However, if it were there it would be difficult to detect. The second raceway could be eliminated by putting the air jet very close to the bottom of the box. It was not found in work on the narrow slice model.¹

As mentioned earlier, it seemed best to correlate the vertical height of the raceway against the penetration rather than attempt a new correlation in terms of the air flow and other conditions. Fig. 5a shows the results obtained with wood blocks. It seemed that the larger size of particles gave higher raceways. The height did not increase as rapidly as the penetration, since the curves seem to be concave downward. During the experiment, it became obvious that the vertical height was not as precise a measurement as the others and the edge of the raceway was often difficult to determine. This was particularly true with coke particles; Fig. 5b shows the erratic nature of the results obtained. Again it seemed that the larger particles gave higher raceways.

Since the height was apparently more sensitive than the penetration to small changes of conditions, it seemed likely that it would be different in the blast furnace and in the model because the solid particles are moving down and liquids are present in the furnace. Therefore, a detailed study of this

phenomenon was left until a more complex model could be made, which would more nearly resemble the blast furnace.

Coke Size

For many years, there has been controversy about the breakdown of coke in the blast furnace, which might be settled if a method were developed for measuring the size of coke at the bottom of the furnace. Also, the correlation of raceway size includes a term involving the size of the coke being recirculated. A technique has therefore been worked out to determine the coke size in the furnace raceway without disturbing the normal operation of the furnace.

Method of Procedure: The method of ascertaining coke size consists in photographing the raceway in a blast furnace with a high-speed camera at 2000 frames per second as described earlier.¹ The film is then projected in a specially built viewer, so that the particles appear about natural size on a frosted-glass plate. A transparent plastic sheet marked with rings of known diameter is then superimposed on each particle in turn and the size is thus estimated and recorded.

The magnification was determined by measurements on the end of the tuyere, which was given about 10 pct magnification over natural size. Since the particles were about 9 or 10 ft from the camera, and the tuyere nose 8 ft from the camera, the particles could reasonably be considered about natural size.

The particles in every two-hundredth frame were counted, so that 16 frames were examined in each film. This gave about 300 to 600 particles per film. It was difficult to distinguish the individual particles when the film was stationary, but if it was moved backward and forward the particles could be located, so that the plastic sheet could be superimposed. The total movement was about 25 frames either side of the one being counted.

It was found necessary for two observers to work together, one measuring and one recording. Furthermore, there was evidence of fatigue if an observer measured more than two frames in succession; the observers therefore took turns at measuring. Thus two results were obtained for each film, one from each observer. The two results were compared by the chi square test and in every case the differences were found to be within that expected from normal sampling errors. In all, five observers were employed in this work and their results were in satisfactory agreement.

Since this technique is new, it is necessary to discuss its accuracy, the more so since each observer believed at first that his results were unreliable. It has so far proved impossible to devise a method of direct calibration of this technique so that indirect reasoning is the only way of assessing the inherent errors.

First, since the film is shot in 100-ft lengths and requires about 1 1/3 sec to expose, the measure-

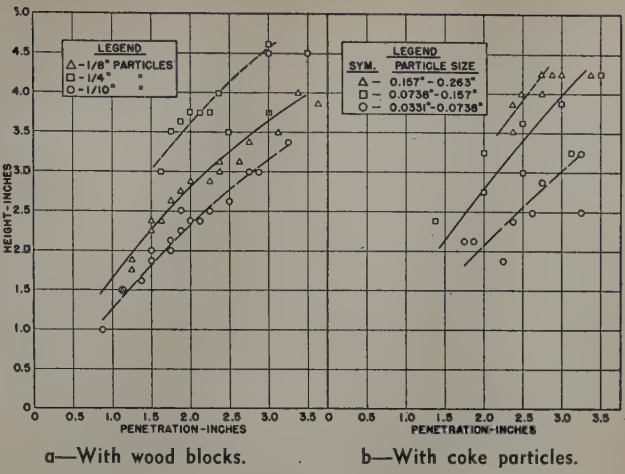


Fig. 5—Height of raceway.

ments on each film represent only a very short interval of time in the life of most blast furnace phenomena. There is then some question whether this instantaneous sample is representative of furnace conditions. This question is quite different from the other question as to whether or not the results obtained accurately describe furnace conditions at the instant of measurement. At this stage, only the measurement of the particular particles viewed by the camera will be discussed.

The optical system is basically simple and, except for the error introduced because the position of a particular particle is not known precisely, the method would seem satisfactory. This error is reasonably small as long as great precision is not required. The biggest source of error seemed to be the ability of the observer to isolate a representative sample of the particles recorded on the film and to estimate their size. In this estimation, an attempt was made to judge whether the area of the particle shadow was greater or less than the area of the various circles marked on the plastic sheet. Then the particle could be classified as within certain size limits.

The effect of this sampling problem is difficult to check but the fact that five different observers agreed among themselves, and that size counts were repeatable within themselves, led to greater and greater confidence in the results. For example the first film rated was measured a second time some two months after the first attempt. In the meanwhile many other films had been rated and the observers had gained much experience in this difficult technique. A comparison of the results is given in Table II, showing that the repeatability is good. It will never be exact because only every two-hundredth frame on the film is counted and, despite all precautions, precise repeatability is unlikely. Further, there is some doubt that an observer measures all the particles that could possibly be measured on a particular film, thus giving additional possibility of disagreement. The main question to be answered, however, is whether the results are a reasonable estimate of the particle size recorded on the film. The answer seems to be in the affirmative, judged by all the tests applied so far.

These results are not strictly comparable with normal sieve data, which are based in essence on the technique of picking up each particle and attempting to push it through the sieve. In the film

Table II. Repeat Count of First Film Rated

Size, In.	Number of Particles Observed						
	-0.25	0.25-0.5	0.5-1.0	1.0-1.5	1.5-2.0	2.0-2.5	+2.5
1st count	57	86	139	52	17	9	1
2nd count	63	89	149	69	23	9	0
Mean	60	88	144	61	20	9	1

Table III. Two Examples of the Comparison of Size Analysis on the Number Basis and the Weight Basis

Size In.	-0.25	0.25-0.5	0.5-1.0	1.0-1.5	1.5-2.0	2.0-2.5	+2.5
Furnace B							
Number, pct	1.9	10.8	42.8	28.0	11.1	4.6	0.8
Weight, pct	0.0	0.0	8.8	26.5	28.7	25.3	10.7
Furnace E							
Number, pct	40.4	23.8	25.2	7.3	2.2	0.7	0.4
Weight, pct	0.0	2.5	19.5	25.8	21.5	14.1	16.6

rating, this is obviously impossible, as the particles are observed as two dimensional shadows. However, the lack of agreement is not great enough to prevent all comparison of the two methods.

A more difficult problem to overcome arises from the way the results are recorded. The present method gives results in terms of the number of particles of a particular size present whereas the more conventional technique employs a weight basis. The two can be interconverted if it is assumed that all particles are of the same shape and density, but this is somewhat doubtful.

Another important objection to this conversion is the fact that much accuracy is lost in the process. Since one 2-in. particle weighs about the same as five hundred ¼-in. particles, a count which gives a reasonable percentage number of particles in the different categories from ¼ to 3 in. is going to show a negligibly small weight per cent of the smaller sizes. To be more specific, Table III has been drawn up to show two such comparisons. Such a conversion is obviously unsatisfactory. Thus, 40 pct by number of the smallest particles becomes a negligibly small percentage on a weight basis, whereas less than 0.5 pct of the material over 2½ in. becomes 16 pct when converted to the weight basis. The result is also sensitive to the size assumed for the over-size particles. As there seems to be no way out of this difficulty the results in this report are expressed on a number basis.

Results of Tests of Coke Sizes: As a first attempt to try out the method, a brief survey was made of the coke in the different areas of the United States. The conditions under which this series of films was taken are shown in Table IV. In most of the tests, the furnaces were on full wind. In the Southern practice, the films were shot with a 1-in. lens instead of the 4-in. lens used for the rest of this work, with the result that the magnification in the viewer was different and the appropriate correction had to be applied to the measurements taken.

The results of this survey are shown in Table V, in which it is possible to arrange the coke in order

of decreasing size, with Northern the largest and Western the smallest. The difference between Southern and Western coke is not very great. This order does not differ much from that which would be expected, except possibly that the Northern coke was appreciably larger than the Eastern.

It is not easy to assess the relative differences between these various cokes, since each size analysis involves so many numbers. A test has been devised, however, to show whether different analyses vary more than would be expected because of the chance factors of sampling. This test is known as the chi square test. When it is applied to the analyses given in Table V, it shows that, if the ¼-in. size is neglected, the analyses for furnaces C, D, and E are homogeneous within each furnace but that the differences between the furnaces are real and cannot be ascribed to sampling differences. This is remarkable in connection with furnace C, where film 54 was taken 18 months before the other two. It suggests that the coke size in the tuyere zone of a furnace may be a reasonably definite and permanent quantity. While this conclusion requires confirmation, such agreement is surprising. If true, this conclusion would seem to be of major importance.

The reason the ¼-in. data have been disregarded in this statement is that in some cases small objects, which seem to be "atomized" slag, are present and it is not possible to be certain that some of these were not counted with the small coke, despite the fact that reasonable precautions were taken to exclude them. This is particularly true of Western practice. In this, the slag droplets are sometimes so frequent as to appear like a rainstorm. This was so severe that out of nine films of Western practice only three were found clear enough to rate, owing either to excessive slag or to the presence of large pieces of agglomerate which were thought to disturb the raceway. This statement might be taken to imply that conditions are worse than in fact they are. The films were taken originally to study the different furnace conditions with particular emphasis on unusual occurrences. It has not yet been possible to take a second series of films on these furnaces, designed primarily for coke-size measurements.

The data in Table V show that there is much less uniformity in the coke in the Northern practice. The difference is striking because the films on each furnace were taken on the same day, yet tests show that the size analyses cannot reasonably have come from the same homogeneous batch of coke. This difference was so marked that it was investigated in some detail. However, before discussion of that study, attention should be directed to the compara-

Table IV. Furnace Conditions During Filming

Film No.	Date	Practice	Furnace	Wind, Cfm	Blast Pressure, Lb per Sq In.	Blast Temperature, °F	Time
133	6-4-51	Northern	A	85,000	19	700	Midway between casts
135	6-4-51	Northern	A	85,000	18	710	During cast
137	6-5-51	Northern	B	72,000	13.5	730	Midway between casts
138	6-5-51	Northern	B	72,000	15	730	Midway between casts
54	6-17-49	Eastern	C				½ hr after cast
126	1-11-51	Eastern	C	91,000	21.1	1060	1 hr 18 min after cast
127	1-11-51	Eastern	C	91,000	21.1	1095	1 hr 24 min after cast
17	3-24-49	Southern	D		24		2½ hr before cast
18	3-24-49	Southern	D		12		2½ hr before cast
151	9-14-51	Western	E	60,000	28	910	½ hr before cast
154	9-14-51	Western	E	61,000	22	900	Midway between casts
156	9-18-51	Western	F	48,000	21	1100	1 min after flush, 1 min before check

Table V. Size of Coke in Different Areas

Furnace	Film No.	Plant	Size, In.						
			-0.25	0.25-0.5	0.5-1.0	1.0-1.5	1.5-2.0	2.0-2.5	+2.5
A	133	Northern	15.7	22.1	37.1	17.2	5.7	2.2	0.0
A	135	Northern	2.9	10.0	42.8	22.2	13.0	5.6	3.5
B	137	Northern	1.9	10.8	42.8	28.0	11.1	4.6	0.8
B	138	Northern	0.0	3.6	47.4	28.3	12.3	5.1	3.3
C	54	Eastern	14.5	30.4	28.9	16.3	7.9	1.8	0.2
C	126	Eastern	34.0	21.7	26.4	9.7	5.0	2.0	1.2
C	127	Eastern	32.1	23.7	23.7	13.2	3.8	2.6	0.9
D	17	Southern	25.0	23.4	30.4	10.7	7.8	2.2	0.5
D	18	Southern	25.5	24.8	29.2	9.7	7.6	2.6	0.6
E	234	Western	29.1	24.5	29.1	13.0	4.1	0.0	0.2
E	237	Western	40.4	23.8	25.2	7.3	2.2	0.7	0.4
F	239	Western	34.7	28.7	27.2	6.3	2.2	0.6	0.3

tively small amount of fine material observed. When it is remembered that the results shown are based on the number of particles, it will be realized that in this practice there is a negligible quantity of coke under $\frac{1}{4}$ in. and very little under $\frac{1}{2}$ in. This is unexpected, in view of the fact that the coke is burning away in this zone. The presence of so much large coke also means that there cannot be much breakdown in the furnace except possibly of the largest material. There does not seem to be sufficient information in the literature to enable a calculation to be made of the amount of fine material to be expected at a particular time due to burning of larger lumps. The amount of fines seen, however, suggests that either the lumps break up suddenly to particles too small to be seen or that there is some

based on weight. The method of measurement is extremely cumbersome and tedious but seems the only one available. It may well prove to be of value, as so little is known of this important subject.

Detailed Studies of Coke Size in Northern Practice: In order to study the apparent irregularities of coke size in furnaces A and B operating on Northern practice, three films were taken at hourly intervals at the times shown in Table VI. During this test furnace A was supplied with $-3\frac{1}{2} + 1$ -in. coke and furnace B with $-5 + 1$ -in. material.

The results of the coke-size measurements are shown as histograms in Fig. 6. The sizes obtained on furnace B are larger apparently than those on furnace A, but there is considerable variation between the different ratings obtained at hourly intervals on the same furnace. Film 263 from furnace B shows an unusual size grading, as only one particle out of three hundred observed was less than $\frac{1}{2}$ in. In all cases, the quantity of small material was comparatively low, as was found before. The counts of all particles less than $\frac{1}{2}$ in. were grouped and no effort was made to separate the $-\frac{1}{4}$ in. from $-\frac{1}{2} + \frac{1}{4}$ in. It was realized from the earlier work that the

Table VI. Timing of Film Shots for Furnaces A and B

Day	Furnace A		Furnace B	
	Time	Film	Time	Film
1	10:00 a.m.	255	2:00 p.m.	258
	11:00 a.m.	256	3:00 p.m.	259
	12:00 noon	257	4:00 p.m.	260
2	2:00 p.m.	264	10:00 a.m.	261
	3:00 p.m.	265	11:00 a.m.	262
	4:00 p.m.	266	12:00 noon	263

segregation process involved, which automatically removes the small pieces. It is known that the gas velocities in this part of the furnace are high, so that it is reasonable to suppose that elutriation may take place, which would account for the phenomena observed.

On the model some runs were made with mixed $1/10$ -in. and $1/4$ -in. wood particles and it appeared that the $1/10$ -in. particles tended to flow out above the raceway, sometimes working back up the bed. On the coke runs, any fine dust formed by abrasion was blown up through the bed to the top. Often it looked as though the coke in the raceway was somewhat coarser than that in the rest of the bed; that is to say, it contained less fines. Although no measurements have so far been taken on this, all the evidence seems to support a theory of elutriation.

This preliminary survey has served to show that the size of coke in the furnace can be measured under actual operating conditions of temperature and pressure at least with sufficient accuracy to separate the cokes of the different parts of the country. These measurements are independent of the amount of slag or metal absorbed in the pores of the particles because the results are based on the number of particles. This is in contrast to any measurements

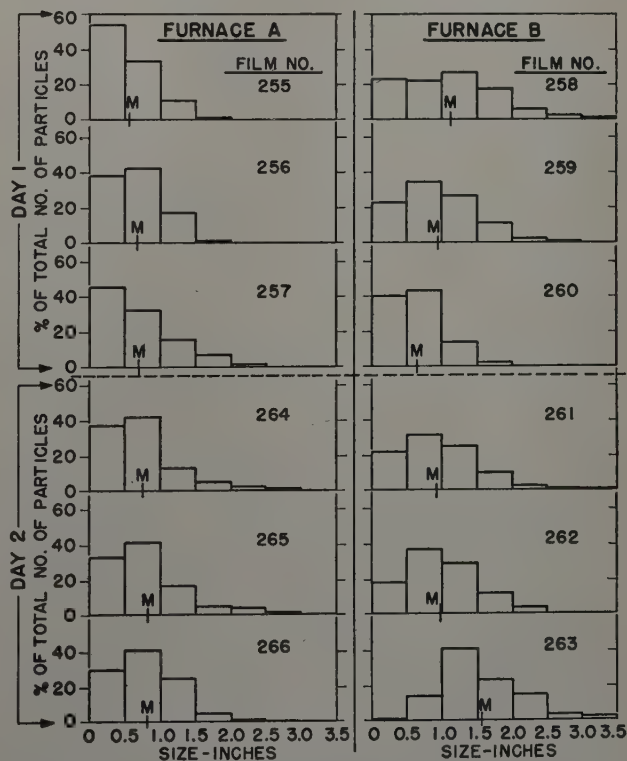


Fig. 6—Distribution of particle size on films. M indicates mean particle size.

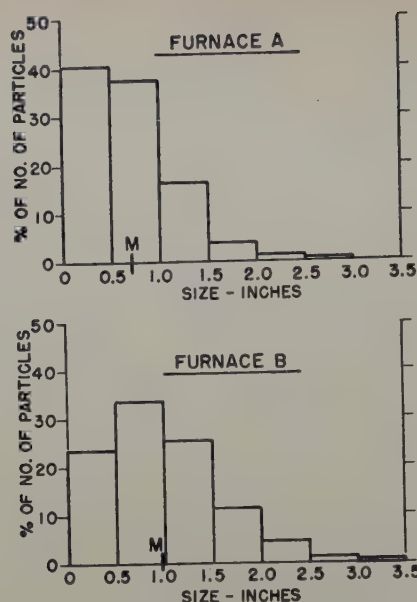


Fig. 7—Average size analyses of coke. M indicates mean particle size.

— $\frac{1}{4}$ -in. size was the least reliable count because of slag and other impurities.

An attempt was made to study statistically the differences in the size analyses obtained. First, the chi square test was applied to the three films taken in each of the four batches, to see whether they could be regarded as different samples from the same batch of coke. The results are shown in Table VII. The probability that the three films really described the same batch of coke is negligibly small in every case. This means that in these two furnaces the coke definitely changed from hour to hour, which did not seem to be true of the other furnaces observed. The cause of this change is unknown.

Owing to these changes between individual film counts, it is not sound to average the film analyses in each group. This greatly complicates the determination of the next problem, which is to decide whether the differences between furnaces, or between days on the same furnace, are greater than the differences between the hourly observations. Unfortunately, there is no simple statistical test to indicate whether the size gradings taken as a whole differed more between the four groups than within a particular group. It was therefore necessary to concentrate on the mean size of particles in each film.

Table VIII shows the mean size of coke in the various films. Disregarding the difference between morning and afternoon, a comparison can be made using the analysis of variance. Such a study showed that the difference between results on the different days is not larger than the difference found from hour to hour in one day. However, the difference between furnaces was real, since a difference as

Table VIII. Mean Coke Size

Day	Furnace A		Furnace B	
	Film	Mean Size, In.	Film	Mean Size, In.
1	255	0.555	258	1.115
	256	0.670	259	0.945
	257	0.694	260	0.653
2	264	0.739	261	0.926
	265	0.811	262	0.993
	266	0.809	263	1.551
Overall		0.699		0.978

large as that observed would have less than one chance in twenty of being observed if there actually were no differences between furnaces. The mean sizes were 0.699 and 0.978 in. for furnaces A and B, respectively. To show the relative differences more clearly, Fig. 7 has been drawn up giving average size analyses for the two furnaces. This more detailed study confirms the fact that the coke on furnaces A and B changed considerably over short times. However, as each film is shot in about 1 $\frac{1}{3}$ sec, it is an instantaneous sampling device for most purposes. Then again, the size of the coke sample is much smaller than that usually taken. This might be thought to have an influence on the lack of consistency but in fact it probably does not. The sample used for size analysis by conventional techniques must be large because the addition of one large piece that weighs the same as several hundred small ones may seriously disturb the results of a small sample. Here one piece more or less affects the size analysis to the same degree, no matter what its size. It is therefore possible to use much smaller samples, and two or three hundred particles are sufficient to give a reliable result. The method is impractical with very small particles.

The fact then remains that in furnaces A and B there is a considerable change in coke size from hour to hour, and possibly more frequently. The importance of this to the furnace operation cannot be accurately assessed without some information on the sensitivity of the furnace to frequent changes. Nevertheless, it would seem to be an unfortunate condition. At the present time there is no explanation of the difference between these two furnaces and the others.

Acknowledgment

The author wishes to thank the many people whose cooperation made this paper possible. In particular, R. A. Buchanan took all the high-speed movies on which the work is based. K. V. Smith and G. A. Welsch carried out much of the experimental work, R. Roeloffs gave much help and advice with the statistical work. The superintendents of the various steel plants not only cooperated by allowing measurements to be taken but also gave practical assistance and made many suggestions based on their wide experience with blast furnaces. Throughout the work B. M. Larsen gave continual encouragement and much helpful advice.

References

- ¹ J. F. Elliott, R. A. Buchanan, and J. B. Wagstaff: Physical Conditions in the Combustion and Smelting Zones of a Blast Furnace. *Trans. AIME* (1952) **194**, pp. 709-717; *JOURNAL OF METALS* (July 1952); *Blast Furnace, Coke Oven and Raw Materials Proc.* (1952) **11**, pp. 246-262.
- ² Sabri Ergun: *Analytical Chemistry* (February 1952) **24**, p. 388.

Table VII. Probability of Agreement of Size Analysis of Each Batch of Films

Furnace	Day	X ²	Degrees of Freedom	Probability of Difference Due to Chance Factors
A	1	65.5	6	0.001
A	2	20.5	8	0.01
B	1	211.8	8	0.001
B	2	185.7	8	0.001

Electrical Resistance of Titanium Metal

by James L. Wyatt

The electrical resistance of titanium as a function of purity and temperature was measured from -325° to 2800°F . Two points of inflection in the data plots were found, and an increase in resistance with increase in temperature above the transformation was observed.

IN 1948 Greiner and Ellis¹ reported on the thermal and electrical properties of titanium, including a study of the effect of temperature on the electrical resistance. The materials used in the research were obtained from the United States Bureau of Mines, where powder metallurgy techniques were being employed for consolidation purposes. These authors found a decreasing resistance with increasing temperature above 1625°F , and concluded that the latter temperature represented the point of transformation from hexagonal close-packed to body-centered cubic structure on heating. They reported a specific resistivity value of 55×10^{-6} ohm-cm, and showed that $d\rho/dt$ was positive, decreasing with increasing temperature above ambient.

In one of his early texts Hume-Rothery² mentioned that certain metals, including titanium, exhibited minima in plots of resistance vs temperature. He indicated that this occurred at 212°F .

Reporting many years ago on the effect of temperature on the electrical resistance of zirconium, de Boer and Fast³ showed that phase transformation in this sister metal occurred over a range of temperatures, the extent varying with its purity. Graphs

J. L. WYATT, Junior Member AIME, formerly Graduate Student at Massachusetts Institute of Technology, is now Assistant to the Technical Manager, Horizons Inc., Cleveland.

Discussion on this paper, TP 3550E, may be sent, 2 copies, to AIME by Sept. 1, 1953. Manuscript, Nov. 24, 1952.

This paper represents part of a thesis by J. L. Wyatt submitted in partial fulfillment of requirements for the degree of Doctor of Science to the Metallurgy Dept. of Massachusetts Institute of Technology, February 1953.

of resistance vs temperature, showing transformation effects over a range of several hundred degrees, were presented for relatively impure metal. In the latter case the resistance decreased with increasing temperature throughout the region of partial phase transformation, thereafter increasing as predicted for normal metals by modern theories of the solid state.

Since the quality of metal used in previous studies was substandard compared with iodide-type titanium, and in view of the fact that there seemed to be some rather unusual observations in the reported literature, it was decided to undertake a more extensive study of the thermal effects using high purity titanium, and to include temperature ranges beyond those which had been studied in order to ascertain whether or not the characteristics of zirconium would be duplicated.

Experimental Materials

Materials used in this investigation included commercial quality titanium (Ti-75A produced by the Titanium Metals Corp. of America) in the form of $\frac{1}{4}$ in. diam rods, and high purity iodide titanium (produced by the Foote Mineral Co.) in the form of crystal bar of irregular size. The latter was cold-swaged into rod form and machined to the desired size. Lead wires to all specimens consisted of 18 gage Ti-75A. Chemical analyses of the stock materials are given in Table I.

Experimental Procedures

Specimens $2\frac{1}{2}$ to 3 in. in length were prepared with diameters nominally 0.15 to 0.20 in. Two holes,

Table I. Chemical Analyses of Materials

Element	Pct	Element	Pct	Element	Pct
Iodide Titanium					
N	0.002	Al	0.012	Sn	0.003
Mn	0.01	Pb	0.007	Mg	0.001
Fe	0.004	Cu	0.001		
By difference, Ti—99.96 pct					
Commercial Titanium (Ti-75A)					
Cl	0.03	Sb	0.002	W	0.002
N	0.002	Sn	0.001	V	0.001
O	0.06	Mg	0.02	Cr	0.002
Si	0.08	Cu	0.001	Mo	0.001
Fe	0.03	Pb	0.002	Ni	0.002
Al	0.01	Mn	0.015		
By difference, Ti—99.74 pct					

sized to allow entry of the lead wires, were drilled transversely through both ends, approximately $\frac{1}{4}$ and $\frac{1}{2}$ in. from each end, respectively, and the leads passed through to extend about $\frac{1}{4}$ in. The specimen surface in the vicinity of the holes was then peened to form the best electrical contact possible. Current leads were inserted in the outermost holes, the inner ones accommodating the voltage leads.

Resistance measurements were made with a Kelvin double bridge. Readings could be taken with accuracy of ± 0.000001 ohm; data are therefore believed to be precise as tabulated.

Resistance values reported at temperatures below ambient were made with specimens immersed in liquid nitrogen, a dry ice-acetone mixture, or in an ice-water mixture. Temperatures below 75°F were measured with a copper-constantan thermocouple; Pt-Pt-10 pct Rh couples were employed for all other temperature determinations.

A platinum-wound alundum tube furnace with Variac control, equipped with suitable purification trains for removal of impurities from the helium atmosphere, was used for the high temperature portion of the investigation. A continuous flow of helium was maintained throughout each run. Temperatures were manually controlled, the resistance readings being taken after three consecutive temperature observations 2 min apart were found to coincide. Experience showed that this precaution probably was not necessary for the size of specimen employed, since the resistance was found to be ex-

tremely sensitive to temperature change. Readings were taken during the heating and the cooling cycles; data reported were all taken on the heating cycle, however. In every case it was observed that the readings taken during the cooling cycle were slightly higher than the corresponding readings taken on heating, with the exception that values between 1620° and 1700°F , i.e., in the range of partial transformation, lay to the left and below the values plotted.

Experimental Results

Table II is a tabulation of experimental data recorded during this investigation; in addition, the data of Greiner and Ellis, taken from a plot in their paper, are included for comparative purposes. In the table the first column lists the test temperature; the second shows the actual measured resistance for the particular specimen being used. The values listed in the third column are calculated, arbitrarily taking the value of 1.000 as the resistance of iodide titanium at 77°F . All data reduced in this manner correspond to a hypothetical specimen size which would give the value of unity to the resistance of the iodide titanium specimen; corresponding values were then adjusted for the other types of metal in accordance with the specific resistivity values of the specimen. Specific resistivity values were determined at 77°F by means of a special device incorporating two pin-point contactors spaced a precise distance apart. The accuracy is estimated to be ± 0.02 ohm-cm. The accuracy of the specific resistivity value reported by Greiner and Ellis is not known.

Discussion of Results

The experimental data, plotted in Fig. 1, do not substantiate Hume-Rothery's statement that there exists a minimum in the curve at 212°F . On the basis of these limited amounts of data there is no indication that with increasing impurity content a curve would be obtained which would exhibit a minimum. No explanation can be offered for this reported anomaly.

It seems obvious that the conclusions drawn by Greiner and Ellis were due entirely to a lack of experimental data above 1600°F . Undoubtedly had their work been continued to higher temperatures a curve of the general characteristics exhibited by the other two curves would have resulted. On the basis

Table II. Electrical Resistance Data for Titanium vs Temperature

Iodide Titanium			Commercial Titanium			Greiner and Ellis		
Temperature, °F	Resistance, Ohms x 10 ⁻³	Adjusted Resistance	Temperature, °F	Resistance, Ohms x 10 ⁻³	Adjusted Resistance	Temperature, °F	Resistance, Ohms	Adjusted Resistance
-323	0.124	0.140	-323	0.331	0.250	77	0.128	1.000
-118	0.490	0.554	-116	0.841	0.623	210	0.156	1.219
+32	0.787	0.890	+32	1.240	0.918	478	0.210	1.640
79	0.887	1.003	85	1.395	1.033	761	0.258	2.016
296	1.415	1.600	388	2.228	1.648	1013	0.292	2.280
518	1.862	2.106	715	2.970	2.198	1270	0.318	2.482
923	2.500	2.828	1020	3.541	2.621	1535	0.335	2.617
1343	2.943	3.328	1305	3.937	2.914	1644	0.338	2.641
1612	3.053	3.453	1500	4.095	3.031	1734	0.325	2.539
1644	2.777	3.141	1603	4.123	3.052	1832	0.320	2.500
1675	2.774	3.137	1660	3.963	2.933	R = 55 ohm-cm x 10 ⁻⁶		
1695	2.778	3.142	1708	3.831	2.836			
1722	2.780	3.144	1797	3.826	2.833			
1749	2.781	3.145	1900	3.852	2.851			
1786	2.783	3.148	2004	3.879	2.870			
1851	2.788	3.153	2111	3.908	2.893			
1925	2.792	3.158	2228	3.932	2.910			
2009	2.801	3.168	2420	3.972	2.940			
2090	2.816	3.185	2623	4.028	2.982			
2154	2.823	3.193	2735	4.073	3.015			
2240	2.841	3.213	R = 54.17 ohm-cm x 10 ⁻⁶					
2374	2.850	3.223						
2563	2.860	3.235						
R = 54.98 ohm-cm x 10 ⁻⁶								

of these data it can be stated that β titanium has the normal metal characteristic of increasing electrical resistance with increasing temperature.

In the transformation range this investigation has shown that the characteristics of titanium and zirconium are very similar. The apparent decrease in resistance with increasing temperature from 1625° to about 1700°F is due to the fact that in this region there exists not one phase but a mixture of two, probably due to small quantities of oxygen and nitrogen in the less pure varieties of titanium. The effect is almost entirely missing in the case of the iodide specimen, attesting to its purity. Both oxygen and nitrogen have the effect of raising the transformation temperature of titanium, so that the observed slope of the curve is as would be expected. Further, the relative slopes of the curves in the transformation region could be related directly to the amount of impurity present, a decreasing slope

vestigated in detail, so the exact temperature at which this reversal occurs was not uniquely determined.

It may be noted that at approximately 2200°F, indicated by arrows on the curves in Fig. 1, there occurs an irregularity in the plots. No readily apparent explanation of this is evident, since it occurs in the high purity metal as well as in the commercial variety. Existing phase diagrams for titanium and the known impurities are incapable of explaining these inflections. Since the curves were reproducible by alternate heating and cooling, any effect of precipitation or grain growth was eliminated.

Conclusions

The effects of temperature on the electrical resistance of high purity and commercial purity titanium from -325° to +2800°F have been determined. A plot of the data obtained, together with data reported in the literature, has shown the following:

1—From -325° to +1625°F the resistance of titanium increases continuously, without any evidence of a minimum within this temperature region.

2—Above the temperature of completion of phase transformation the resistance of titanium changes only slightly, but does increase with increasing temperature.

3—The temperature range of transformation is a function of the impurity content and is characterized by a decrease of resistance with increasing temperature. This is associated with the simultaneous presence of α and β titanium.

4—The resistance of titanium above about 100°F is apparently decreased by the addition of certain solutes, probably oxygen and nitrogen. This observation is contrary to laws governing metals in the solid state, but is observed in such materials as germanium. In this respect titanium acts somewhat as a semiconductor.

5—The curves of resistance vs temperature for different grades of titanium were observed to cross, intersecting near 100°F, these curves presumably representing different solute contents of a single family of alloys.

6—Discovery of an irregularity in the curves at approximately 2200°F is reported.

7—The relatively high degree of purity of iodide titanium is attested to by the observed transformation characteristics.

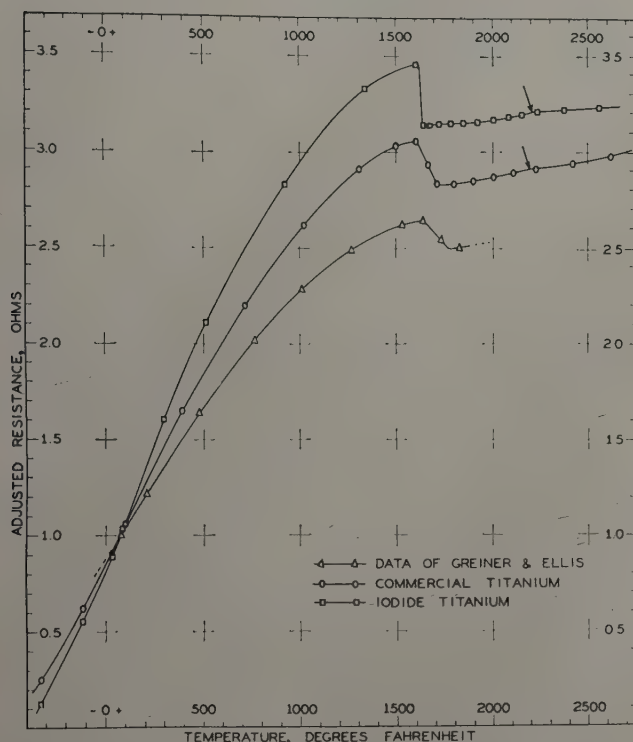


Fig. 1—Electrical resistance of titanium metal as a function of temperature.

corresponding to an increasing impurity content, qualitatively.

It is a characteristic of metals that the introduction of alloy additions increases their resistance. In this respect it would appear that titanium acts as a normal metal only at temperatures below approximately 100°F. Contrary to theory, the data indicate that the curves cross at about 100°F for various grades of titanium; the impurities are assumed to be of the same general type in each case. An additional observation shown by the data is that at the approximate point of crossing the curves undergo a point of inflection, reversing their directions of curvature. Such a phenomenon allows titanium to maintain a certain degree of respectability as a normal metal only above the point of intersection, as it is generally true that in a particular family of alloys the pure metal exhibits the maximum value of dp/dt at any particular temperature. Unfortunately the region between -100° and +300°F was not in-

Acknowledgments

The author would like to give special credit to Rolf Nordheim, through whose generosity the measuring equipment was made available, and to Charles Stein, who supplied the furnace for the tests. The project was under the supervision of N. J. Grant, Dept. of Metallurgy, Massachusetts Institute of Technology, and was made possible through the financial support of the Titanium Div. of the National Lead Co., Sayreville, N. J.

References

- 1 E. S. Greiner and W. C. Ellis: Thermal and Electrical Properties of Ductile Titanium. *Trans. AIME* (1949) **180**, p. 657; *METALS TECHNOLOGY* (September 1948).
- 2 W. Hume-Rothery: *The Metallic State*. Electrical Properties. (1931) p. 18. Oxford. The Clarendon Press.
- 3 J. H. de Boer and J. D. Fast: The Influence of Oxygen on the Alpha and Beta Transformation of Zirconium. *Rec. Trav. Chim. D. Pays. Bas* (1936) **55**, pp. 459-467.

Microscopical Examination of Tin Bronzes in the Alpha Range

by E. C. W. Perryman

On electropolishing, high-purity Cu-Sn and Cu-Sn-P alloys with more than 5 to 9 pct Sn were found to contain many grain boundaries with a ridge-and-furrow profile. The effect was not eliminated by solution treatment and was present at the new boundaries in recrystallized material. It could be produced by diffusing tin into the 3 pct Sn alloy and it is concluded that the effect is due to enrichment of certain boundaries in tin, or possibly in an impurity present in the tin, in solid solution.

IN the hot working of tin bronzes, especially those with moderately high tin contents, considerable difficulty is frequently encountered from intercrystalline weakness, which results in cracking at the edges in sheet on strip rolling and in the unsupported regions of the rod in rod rolling.¹ These difficulties are not at all pronounced with up to 3 pct Sn, but at 5 pct Sn impose serious limitations and at higher tin contents, especially if the phosphorus content is also high, they may become very severe. In some work carried out at the laboratories of The British Non-Ferrous Metals Research Association it was found that a notable lack of ductility in tension at elevated temperatures, associated with intercrystalline failure, was characteristic of tin bronzes even of relatively high purity. That the intercrystalline fracture is not due to a brittle or molten impurity phase at the grain boundaries was shown by the fact that the temperature at which intercrystalline fracture first occurred decreased with decrease of rate of straining. Tensile tests on some commercial tin bronzes, reported by Goetzel,² show a similar fall in ductility with increasing temperature.

As no visual evidence had been obtained showing that the grain boundaries of the tin bronzes were different from those in copper, a more detailed microscopical examination was carried out, and the results of this are given in the present report.

Several workers³⁻⁵ have observed that electrolytic polishing is a powerful tool for detecting small amounts of a second phase and in particular for detecting high solute concentrations, "equilibrium segregation," at grain boundaries. Since it had been found that the suggested solutions for electropolishing bronze and the standard solutions for brass and

E. C. W. PERRYMAN, formerly Investigator, British Non-Ferrous Metals Research Association, London, is now with Aluminium Laboratories Ltd., Kingston, Ont., Canada.

Discussion on this paper, TP 3535E, may be sent, 2 copies, to AIME by Dec. 1, 1953. Manuscript, Oct. 14, 1952. Cleveland Meeting, October 1953.

Table I. Spectrographic Analyses of Basis Materials

Element	In Copper, Pct	Limit of Detection, Pct	In Phosphor-Copper, Pct	Limit of Detection, Pct	In Chempur Tin, Pct	Limit of Detection, Pct
As	N.D.*	0.002	N.D.	0.002	N.D.	<0.004
Sb	N.D.	0.0001	N.D.	0.0002	N.D.	<0.001
Bi	N.D.	0.0001	0.0001	—	<0.0001	—
Sn	N.D.	0.0005	N.D.	0.0005	—	—
Pb	0.001	—	<0.0003	—	0.005	—
Te	N.D.	0.004	N.D.	0.004	—	—
Zn	N.D.	0.001	N.D.	0.001	<0.001	—
Cd	—	—	—	—	N.D.	0.001
Al	N.D.	—	—	—	<0.001	—
Si	<0.008	—	<0.008	—	—	—
Cu	—	—	—	—	0.0013	—
Ag	0.002	—	0.002	—	N.D.	—
Mn	0.001	—	N.D.	0.001	—	—
Fe	0.001	—	0.0002	—	0.001	—
Co	N.D.	0.0001	N.D.	0.0001	—	—
Ni	0.0003	—	0.001	—	<0.001	—

* N.D. = Not detected.

copper did not give satisfactory results it was first necessary to find a suitable electropolishing solution.⁶

Experimental Procedure

Materials Used: The cast and wrought materials used for this work were the same as those used for the mechanical tests referred to above. They comprised 3, 6, and 9 pct Sn alloys without phosphorus and the same three basic alloys with 0.03 and 0.4 pct P. A 5 pct Sn alloy without phosphorus, of similar purity, was also examined.

The basis materials were Chempur tin, high purity 15 pct phosphor-copper and cathode copper, and spectrographic analyses are given in Table I.

Treatment: The cathode copper was first melted under charcoal, degassed by plunging marble chips beneath the surface, and cast through a coal gas flame into sand molds to produce a number of small ingots which after machining were of a suitable size for subsequent vacuum melting. Chill cast bars of the alloys, approximately 1¼ in. in diameter, were then made by melting and casting in vacuo, the tem-



Fig. 1—As cast 6 pct tin bronze annealed at 625°C for 16 hr, water-quenched. Electropolished and electrolytically etched. X750.

Fig. 2—Wrought 3 pct tin bronze annealed at 625°C for 90 hr, water-quenched. Electropolished and electrolytically etched. X75.

Fig. 3—Wrought 6 pct tin bronze annealed at 625°C for 16 hr, water-quenched. Electropolished and electrolytically etched. X100.

perature and pressure just before casting being 1200° to 1225°C and less than 5 microns, respectively.

Analyses for nonmetallic impurities were made on typical ingots with the following results: Oxygen—0.0008 pct for bronzes without phosphorus and not more than 0.0001 pct for bronzes with phosphorus. Hydrogen— 5×10^{-6} pct. Sulphur—0.002 to 0.008 pct.

The wrought alloys were cold-rolled from these cast bars, after homogenizing for 7 hr at 625°C in oxygen-free nitrogen, to bars $\frac{3}{4} \times \frac{3}{8}$ in. The 3 pct Sn alloys without phosphorus and with 0.03 pct P were rolled directly to finished size, while the remainder were annealed at 600°C in hydrogen at approximately $\frac{7}{8}$ in. square.

All the materials, both wrought and cast, were finally given a heat treatment of 4 hr at 625°C in oxygen-free nitrogen after which the structures were all single phase.

Specimens containing phosphorus were annealed at 625°C for 90 hr in nitrogen and rapidly quenched in water at room temperature. This temperature was chosen because it is less than the eutectic temperature (637°C) of the Cu-Sn-P system.⁸ For the binary Cu-Sn alloys temperatures up to 850°C were used.

Specimen Preparation: Specimens were electrolytically polished as described by Perryman.⁹ Two electrolytes were used: 1—67 pct orthophosphoric acid, 10 pct concentrated sulphuric acid, and 23 pct distilled water for alloys up to 6 pct Sn, and 2—47 pct orthophosphoric acid, 20 pct concentrated sulphuric acid, and 33 pct distilled water for alloys with tin contents of 6 and 9 pct. The polishing conditions were the same with both solutions, namely, 1.8 to 2.2 v and a current density of 0.1 amp per sq cm.

The time of polishing depended upon the state of the initial surface but starting from a surface which has been ground on emery and rough polished with metal polish, 15 min was generally found to be sufficient. Because of the tendency of the second solution to cause pitting, the polishing time was generally restricted to a few minutes. To etch the specimen after polishing the voltage was reduced to 0.8 v for approximately 30 sec; the exact time of etching depended upon the metal or alloy being etched.

Taper sections of the electrolytically polished surfaces were prepared as follows: A thin layer of nickel was plated on to the polished surface followed by a thick layer of copper. The electroplated speci-

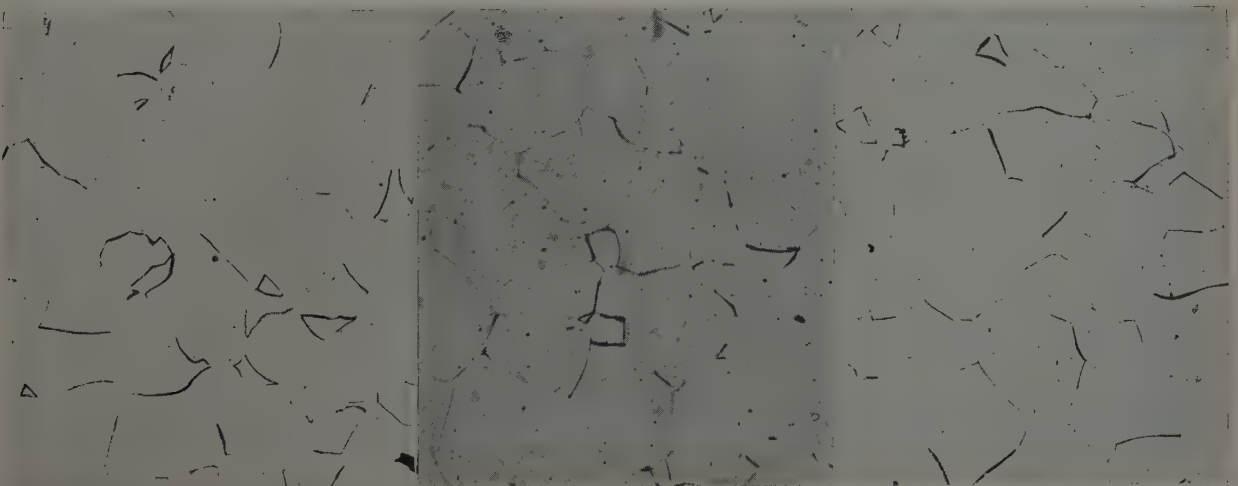


Fig. 4—Wrought 9 pct tin bronze annealed at 625°C for 16 hr, water-quenched. Electropolished and electrolytically etched. X75.

Fig. 5—Wrought 6 pct tin bronze containing 0.03 pct phosphorus annealed at 625°C for 90 hr, water-quenched. Electropolished and electrolytically etched. X100.

Fig. 6—Wrought 6 pct tin bronze containing 0.4 pct phosphorus annealed at 625°C for 90 hr, water-quenched. Electropolished and electrolytically etched. X75.



Fig. 7—3 pct tin bronze coated with tin and annealed at 625°C for 2 days. As electropolished. X1000.

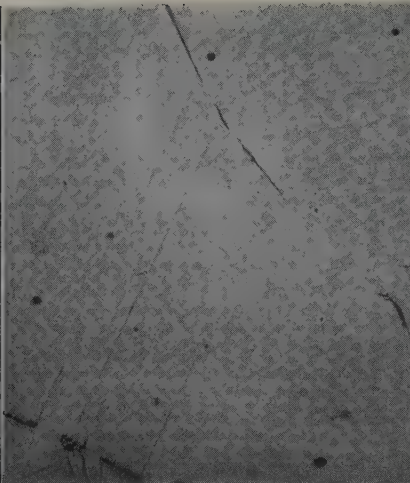


Fig. 8—Wrought 9 pct tin bronze annealed at 625°C for 90 hr, water-quenched. Electropolished and electrolytically etched. X750.

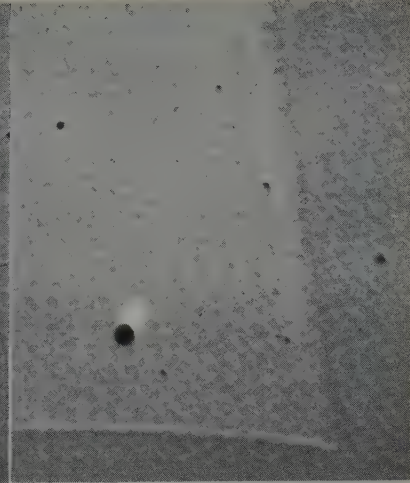


Fig. 9—Wrought 3 pct tin bronze annealed at 625°C for 90 hr, water-quenched. Electron micrograph of electropolished surface. Formvar replica Pd/Au shadowed. X10,300.

men was then placed on the inclined face of a special follower in the mounting press and the specimen mounted in bakelite in the usual way. The wedged-shape mount so obtained was then turned back in a lathe until the nickel-bronze interface was exposed. The specimen was then polished by the diamond dust technique.⁷ Specimens were taper-sectioned at angles of approximately 6° or 11½° to the original polished surface. By this means, the depth of irregularities in the original polished surface, such as ridges or grooves, are magnified 10 or 5 times, respectively, in the surface of the taper section.

Results

Examination of Cast Cu-Sn Alloys Annealed at 625°C for 16 hr and Water Quenched: Examination showed that the grain boundaries in the 3 pct Sn alloy were quite normal and were revealed by differences in level between grains. With the 6 and 9 pct Sn alloys, however, parts of some of the grain boundaries appeared darker and thicker, the number of grain boundaries showing this peculiarity being greater in the 9 pct than in the 6 pct Sn alloy. Fig. 1 shows this effect in an electrolytically polished 6 pct tin bronze. To determine whether these thick portions of the grain boundary were due to a second phase associated with the alloy system, specimens which had been annealed at 850°C for 16 hr and water-quenched were examined. No significant difference was observed, the thick grain boundaries being present as before. This result strongly suggests that the grain boundary effect observed is not due to a second phase associated with the alloy system. It should be pointed out that this grain boundary effect was present after electrolytic polishing alone without etching. In general specimens were lightly etched electrolytically in order to reveal those grain boundaries which were not apparent after polishing.

Examination of Wrought Alloys: After annealing at 625°C for 90 hr followed by water quenching the grain boundary effect which was observed in the cast and annealed 6 pct tin bronze was again seen at the grain boundaries of the worked and recrystallized materials. This effect was not apparent in pure copper, nor in the 3 pct tin bronzes containing 0,

0.03, and 0.4 pct P. It was first noticed in a 5 pct tin bronze and the number of grain boundaries showing this effect increased, 1—with tin content, and 2—for a given tin content with phosphorus content. Figs. 2 to 6 show how the grain boundary effect increases with tin and phosphorus content. Similar results were obtained on specimens which had been annealed at 850°C for 32 hr and water-quenched.

Further experimental evidence for the dependence of the grain boundary effect on tin content was obtained by hot dipping specimens of the 3 pct tin bronze in molten "Chempur" tin. After annealing these tinned specimens, at 625°C for two days, the grain boundary effect was present adjacent to the tin-bronze interface, see Fig. 7.

Besides varying with solute contents this grain boundary effect also appeared to be a function of the orientation of adjacent grains for, 1—it never appeared at all the grain boundaries, 2—it was never present on twin boundaries, Figs. 3 and 8, and 3—it occurred discontinuously where twins met the grain boundary, Fig. 8.

These results thus show that the grain boundary effect is not caused by insoluble impurities, for if it were the effect would not have appeared at the new grain boundaries formed during recrystallization. It is clear, however, that it increases with increasing tin and phosphorus content and depends also on the difference of orientation between grains.

Reproducibility of Etching Effect: To see if the observed differences between the 3, 6, and 9 pct Sn alloys were due to the different solutions used for electropolishing, specimens of the 3 and 6 pct Sn alloys were electropolished in the solution normally used for the 9 pct Sn alloy. The results obtained were the same as before. The 9 pct Sn alloy specimen after examination was mechanically polished with metal polish to remove the etch. On repolishing electrolytically followed by re-examination of the same fields, the effect occurred on the identical boundaries that it did on the first polishing. A further repolishing preceded by grinding on fine emery altered the plane of polish so that the grain pattern was changed somewhat but most grains were identifiable. Again the same boundaries as before showed the effect.



Fig. 10—Wrought 6 pct tin bronze annealed at 625°C for 90 hr, water-quenched. Electron micrograph of electro-polished surface. Formvar replica Pd/Au shadowed. X8000.



Fig. 11—Taper section of an electro-polished 3 pct tin bronze surface. Horizontal magnification X20,000, vertical X2000.

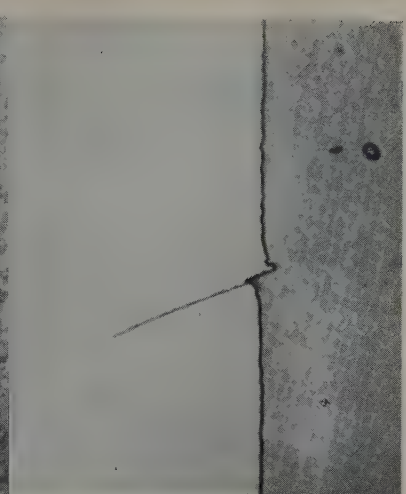


Fig. 12—Taper section of an electro-polished 6 pct tin bronze surface. Horizontal magnification X20,000, vertical X2000.

Effect of Slow Cooling: Specimens of the 3 and 6 pct Sn alloys were annealed at 625°C for 90 hr, furnace-cooled at 10°C per hr to 366°C, this being 60°C above the temperature at which the 6 pct Sn alloy crosses the α -phase solubility limit.⁹ After electropolishing, the 3 pct Sn alloy appeared the same as after quenching, i.e., no grain boundary effect was visible, while the 6 pct Sn alloy appeared to contain more grain boundaries showing the effect than it did after quenching from 625°C. In contrast to this a 6 pct tin bronze specimen, furnace-cooled from 850° to 450°C at 260°C per hr, appeared the same as specimens quenched from 850° or 625°C.

Electron Microscope Examination: To investigate further the nature of this grain boundary effect formvar replicas of the electropolished surfaces were prepared and examined before and after Pd-Au shadowing. Figs. 9 and 10 show typical electron micrographs from the 3 and 6 pct Sn alloys, respectively. The very black spots on these photographs are latex particles which have been used to show the direction of shadowing. Examination of the unshadowed replicas showed that there was a difference in level between the grains in the 3 pct Sn alloy, but that in the 6 pct Sn alloys, 1—there was no difference in level between grains, and 2—at some of the grain boundaries there was a raised portion. These observations together with those made on the shadowed replicas show that with the 3 pct Sn alloy there is a step at the grain boundary caused by a difference in level between the neighboring grains while with the 6 pct Sn alloy there is an elevated portion flanked by a groove, the general level of the adjacent grains being the same. Similar results were obtained with the 9 pct Sn alloy.

Taper-Section Examination: To confirm the finding of the electron microscope, 6° taper-sections of the electrolytically polished surface were prepared. Examination of the 3 pct tin bronze confirmed the electron microscope result that there was a difference in level between different grains, and moreover the angle of the step proved to be in general approximately the same as the angle between the grain boundary and the polished surface, Fig. 11. Examination of those alloys exhibiting the grain boundary effect showed that the contour across the affected

grain boundaries was a hill flanked by a valley, the grains on each side of the grain boundary having the same level, Fig. 12. Another interesting observation was that in all cases one side of the hill was a continuation of the grain boundary, as shown in Fig. 12. No such contours as this were seen at twin boundaries where in general there was a slight step between the two grains in twin orientation.

Discussion of Results

It is clear that there is a close correlation between the results of this microscopic examination and the mechanical behavior of the alloys, since the number of grain boundaries showing the grain boundary effect increases with tin content and for a given tin content with increasing phosphorus content in just the same way as does the incidence of grain boundary weakness at high temperatures.

There are obvious difficulties in explaining the metallographic observations in terms of a second phase of the Cu-Sn system or of an insoluble impurity because: 1—the grain boundary effect was observed in alloys quenched from temperatures far away from any two-phase region in the equilibrium diagram, 2—it occurred in alloys made from high purity materials, 3—the effect was still present at the grain boundaries after recrystallization, and 4—no coalescence took place after long annealing times or after very slow cooling.

On the other hand it is possible to explain the occurrence of this grain boundary effect by the theory of "equilibrium segregation"¹⁰ according to which solute atoms, differing considerably in size from the solvent atoms, tend to segregate to grain boundaries. The segregating solute is considered to be tin (see preceding section on Wrought Alloys and Fig. 7), although it could possibly be an impurity contained in the tin used. This possibility is remote as the main impurity, lead, was only present in the tin to 0.005 pct. The theory explains why the grain boundary effect is a function of the relative orientation of neighboring grains, for clearly the tin concentration at the grain boundaries will be dependent upon this orientation difference and in particular at a twin boundary where there is a perfect fit between the two crystal lattices there should be little or no

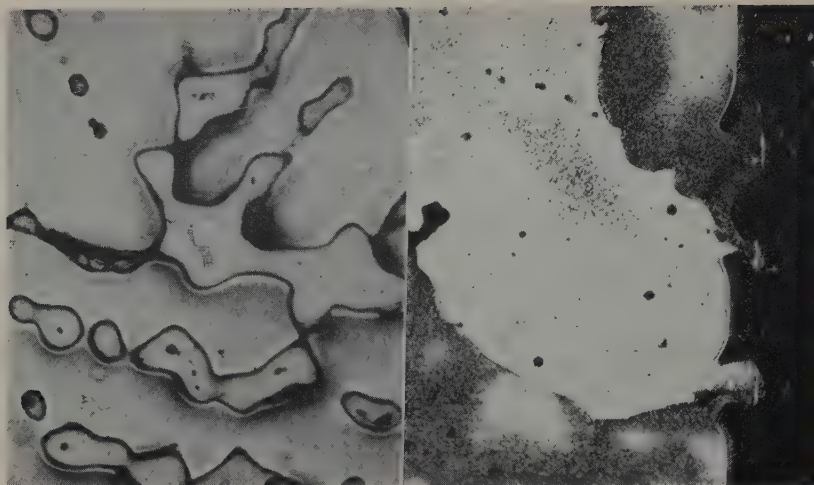


Fig. 13 (left)—As cast 6 pct tin bronze electropolished. X250.

Fig. 14 (right)—Taper section of an electropolished as cast 6 pct tin bronze surface. Etched with alcoholic ferric chloride. Horizontal magnification X1250, vertical X250.

tin concentration. Likewise the grain boundary concentration will increase with tin content, maximum concentration occurring when the grains are saturated. Similarly, in the absence of precipitation, the tin concentration at the grain boundaries should be greater at low temperatures than at high, thus explaining the increase in number of grain boundaries showing the grain boundary effect after very slow cooling. While it is clear from the results that the number of grain boundaries showing this grain boundary effect increases with increasing phosphorus content the reason for this is not certain. It may possibly be because of the effect of phosphorus in reducing the solid solubility of tin in copper, e.g., at 600°C the solid solubility of tin in copper is 15.5 pct and is reduced to 10 pct by the presence of 0.4 pct P.⁸

Similar grain boundary contours to that shown in Fig. 12 have been found by Samuels⁴ in Cu-Bi alloys and by McLean⁵ in Cu-Sb alloys, both authors attributing this etching effect to solute concentrations at grain boundaries. McLean held that if this contour were produced by a second phase at the grain boundaries it would be expected to be symmetrical about the grain boundary rather than asymmetrical. To show that this grain boundary contour could possibly be formed as a result of a tin concentration at the grain boundaries, a 6 pct tin bronze was examined as cast after electropolishing. It was found that while those areas poor in tin had polished, the tin-rich areas had not, the original polishing scratches still remaining, Fig. 13. An 11½° taper section of this electrolytically polished surface was prepared, and it was clearly seen that the tin-rich areas (dark areas in Fig. 14) were standing proud of the general surface level (Fig. 14), and furthermore that the rate of polishing was more rapid at parts adjacent to the tin-rich zones. Thus under the conditions of polishing used the tin-rich areas are cathodic and the tin-poor areas anodic. When two electrodes are immersed in direct contact the current density at a point on the anode will decrease with increasing distance from the cathode (see Evans¹¹). This effect is occurring during electropolishing since there is a shallow trough each side of the tin-rich zones. It is clear therefore that under the conditions of polishing used there are large electrochemical differences between the tin-poor and tin-rich zones in the cast tin bronze, and it is therefore to be expected that a tin concentration at a grain boundary will make the grain boundary cathodic to the grain during electropolishing leading to a valley as in Fig. 12. From these considerations

it might be supposed that owing to the cathodic nature of the grain boundary there would be a valley produced each side, resulting in a symmetrical notch rather than the asymmetrical contour shown in Fig. 12. The precise explanation of these contours is extremely difficult because: 1—the cathodic grain boundary zone is only supposed to be a few atoms thick, and 2—the electropolishing process is superimposed on the complicated system of local electrodes already present. In view of this no detailed explanation is offered. There are two features which are rather surprising: 1—the disappearance of the differences in level between adjacent grains when the effect shown in Fig. 12 occurs, and 2—the breadth of the peak on the left of the boundary in Fig. 12, bearing in mind that the postulated zone rich in tin, presumed cathodic to both adjacent grains, is only likely to be of the thickness of a few atoms. It is interesting to note that in Al-Fe alloys, which under certain conditions suffer grain boundary attack when immersed in 10 pct hydrochloric acid or 0.30N sodium hydroxide, there is the same tendency for the difference in level between grains to disappear as the grain boundary attack becomes more marked. Also in this case where there is no superimposed anodic attack, a symmetrical notch is formed at the grain boundaries.¹²

Acknowledgment

The author is indebted to the Director and Council of The British Non-Ferrous Metals Research Association for permission to publish this paper.

References

- ¹ D. W. D. Showell: *Journal Inst. Metals* (1950) **76**, p. 527.
- ² C. G. Goetzl: *Metals and Alloys* (1937) **8**, pp. 231, 245.
- ³ D. McLean and L. Northcott: *Journal Inst. Metals* (1946) **72**, p. 583.
- ⁴ L. E. Samuels: *Journal Inst. Metals* (1949) **76**, p. 91.
- ⁵ D. McLean: *Journal Inst. Metals* (1947) **73**, p. 791.
- ⁶ E. C. W. Perryman: *Metallurgia* (July 1952) **46** (273), pp. 55-57.
- ⁷ E. C. W. Perryman: *Journal Inst. Metals* (1950) **77**, p. 61.
- ⁸ J. Verö: *Ztsch. anorg. allgem. Chem.* (1933) **213**, p. 257.
- ⁹ G. V. Raynor: *Annotated Equilibrium Diagram No. 2*. Inst. Metals.
- ¹⁰ D. McLean and L. Northcott: *Journal Iron and Steel Inst.* (1948) **158**, p. 169.
- ¹¹ U. R. Evans: *Metallic Corrosion Passivity and Protection* (1946) p. 530. London. Edward Arnold & Co.
- ¹² E. C. W. Perryman: This issue, p. 911.

Grain Boundary Attack on Aluminum in Hydrochloric Acid And Sodium Hydroxide

by E. C. W. Perryman

The wide grooves formed at the grain boundaries when high purity aluminum is attacked by hydrochloric acid or sodium hydroxide have been attributed by earlier workers to the high energy of the grain boundary material. The effect has been investigated for high-purity Al-Fe alloys with up to 0.055 pct Fe as a function of iron content and heat treatment. It is shown that the explanation given above is untenable, but that the results can be explained on the assumption that iron segregates to the grain boundary in solid solution.

IN 1934, Rohrmann¹ showed that aluminum of 99.95 pct purity suffered intercrystalline corrosion when immersed in 10 to 20 pct hydrochloric acid, and that the susceptibility to intercrystalline corrosion depended upon the heat treatment given. The greatest susceptibility was found for specimens quenched from a high temperature (600°C) and the lowest susceptibility for specimens cooled slowly from that temperature. Lacombe and Yannaquis² have shown that super-pure aluminum (99.9986 pct) annealed at 600°C suffers intercrystalline attack in 10 pct hydrochloric acid and that this attack is intensified by anodic dissolution in the same solution at a current density of 10 milliamperes per sq dm. No difference in extent of intercrystalline attack was found between the 99.993 and 99.986 pct Al, which led the authors to suggest that impurities played only a secondary role in the mechanism of intercrystalline corrosion. It was found, however, that the attack at the grain boundaries depended upon the relative orientation of the grains, large differences in orientation favoring rapid attack. Boundaries where the two neighboring grains were similarly orientated showed high resistance to attack as did boundaries between grains which were in twin relationship. These observations led Lacombe and Yannaquis to suggest that the intercrystalline attack was due to lattice discontinuities present at grain boundaries. Assuming that the grain boundary is a layer three to five atoms thick and has a crystal structure which is a compromise between the two neighboring grains it is clear that the discontinuities will increase with increasing difference in orientation between the neighboring grains and hence the increasing tendency to intercrystalline attack. Roald and Streicher³ investigated the effect of heat treatment of aluminum alloys ranging in purity from 99.2 to 99.998 pct on the corrosion resistance in 20 pct hydrochloric acid and 0.30N sodium hydroxide. They found that in

hydrochloric acid the intercrystalline attack appeared to be determined by the type and quantity of impurities present and by the relative orientation of the grains. No difference in the susceptibility to intercrystalline attack was observed between specimens quenched and those furnace cooled, from 575°C. In 0.30N sodium hydroxide some materials exhibited intercrystalline attack, this taking the form of V-notches.

Rohrmann¹ offered no explanation for the greater susceptibility to corrosion of material quenched from 600°C. It seems possible that this difference is connected in some way with a different distribution of impurity elements in the quenched and slowly cooled specimens. The fact that Roald and Streicher³ observed no difference between quenched and slowly cooled specimens may possibly be due to differences in either rate of cooling or silicon content or possibly both. Both these would be expected to have an effect on the distribution of impurity elements.

Although the rate of cooling used by Rohrmann was slightly more rapid than that used by Roald and Streicher the position cannot be clarified because Rohrmann does not give the silicon content and Roald and Streicher give the silicon contents of only a few of their alloys.

That Lacombe and Yannaquis² found no difference in corrosion behavior attributable to impurities between the two materials they used may be because both were of high purity compared with the aluminum used by Rohrmann.¹ Although they found no difference in the corrosion behavior of their two materials it is possible that the results obtained by Lacombe and Yannaquis may, nevertheless, have been influenced by impurity distribution, since, on the transition lattice theory of grain boundary structure, it would be expected that sparingly soluble impurities would tend to segregate to boundaries where the orientation difference is such that there is a greater density of atomic sites of suitable size to contain them.

It was considered worth while, therefore, to examine the corrosion properties of a series of materials of differing impurity content with the objects of confirming the experimental observations made

E. C. W. PERRYMAN, formerly Investigator, British Non-Ferrous Metals Research Association, London, is now with Aluminium Laboratories Ltd., Kingston, Ont., Canada.

Discussion on this paper, TP 3514E, may be sent, 2 copies, to AIME by Dec. 1, 1953. Manuscript, Oct. 14, 1952. Cleveland Meeting, October 1953.

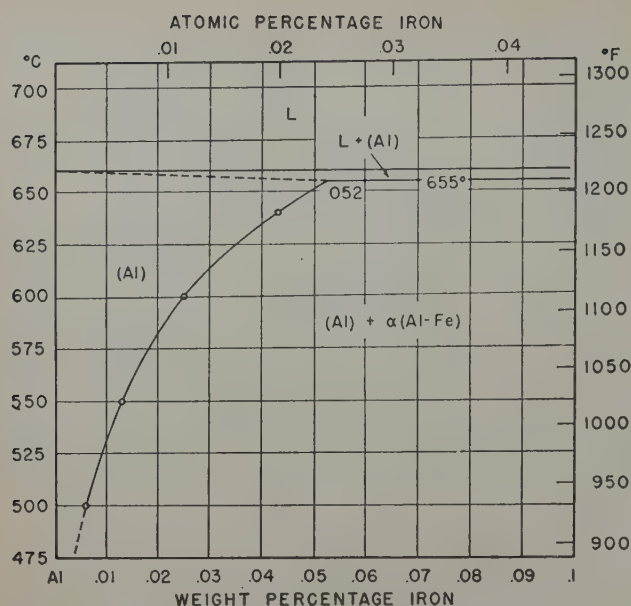


Fig. 1—Solvus curve at the aluminum end of the Al-Fe system. From J. K. Edgar.⁴

by Rohrmann, by Lacombe and Yannaquis, and by Roald and Streicher and determining whether it was possible to provide an explanation for them in terms of impurity distribution, special attention being paid to the role of iron.

In the papers referred to above it is clear that the attack at the grain boundaries occurs over a comparatively wide zone and this type of corrosion will be called "grain boundary attack" to distinguish it from the deep, penetrative intercrystalline attack found in alloys such as Al-Mg and Al-Cu.

In the Al-Fe equilibrium diagram at the aluminum-rich end, the eutectic composition has been reported to be at about 1.7 pct Fe, the phases in equilibrium with the liquid being α solid solution and FeAl₃. The solid solubility of iron is very small, various investigators giving the solubility as 0.028 to 0.052 pct at the eutectic temperature 655°C. The most recent investigation of this system has been carried out by Edgar⁴ who showed by electrical resistivity measurements that the solid solubility of iron at 655°C was 0.052 pct. This author stated that an alloy containing 0.025 pct Fe, annealed at 640°C for 24 hr

and water-quenched showed no second phase. The equilibrium diagram given by Edgar is shown in Fig. 1.

Experimental Procedure

The materials used were in the form of 0.064 in. sheet, and the analyses are given in Table I. All materials received a final cold reduction of 50 pct. It will be noted that the silicon contents are substantially the same (except for OOB1) and with the same exception the copper contents are low and all of the same order. The first five materials can therefore be regarded as essentially a series of dilute Al-Fe alloys of constant impurity.

Table I. Analyses of Materials

BNF Mark	Fe, Pct	Si, Pct	Cu, Pct
OCD	0.001	0.005	0.001
OCE	0.009	0.005	0.001
OCF	0.021	0.006	0.0005
OCG	0.037	0.007	0.001
OOB3	0.016	0.007	0.003*
OOB1	0.055	0.016	0.008*

* Determined by spectrographic analysis.

Specimen Preparation: Specimens 1 in. sq were emiered, polished with metal polish, and then annealed at 640°C for 72 hr. Some specimens were rapidly quenched in water at room temperature, some slowly cooled to room temperature in 17 hr, and others slowly cooled to room temperature in 70 hr, the approximate rate of cooling for the latter being 8½°C per hr. The specimens were then again polished on metal polish, electrolytically polished in a solution containing 1 part of 70 pct perchloric acid and 5 parts alcohol, washed in water and acetone, and dried. For the corrosion tests they were immersed vertically in 10 pct hydrochloric acid or 0.3N sodium hydroxide at room temperature.

Results

Examination of Electrolytically Polished Surfaces: The results of the microscopical examination of the various alloys are given in Table II. Typical structures of alloy OCG (0.037 pct Fe) after annealing at 640°C for 72 hr followed by quenching and by furnace-cooling are shown in Figs. 2 and 3, respectively.

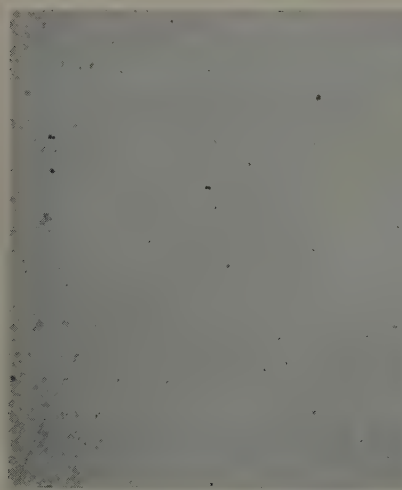


Fig. 2—Al-0.037 pct Fe (OCG). Three days at 640°C, water-quenched. Electrolytically polished. X75.



Fig. 3—Al-0.037 pct Fe (OCG). Three days at 640°C, furnace-cooled to room temperature in 70 hr. Electrolytically polished. X75.



Fig. 4—Al-0.001 pct Fe (OCD). Quenched from 640°C, corroded in 0.30N NaOH for 3 days. X8.

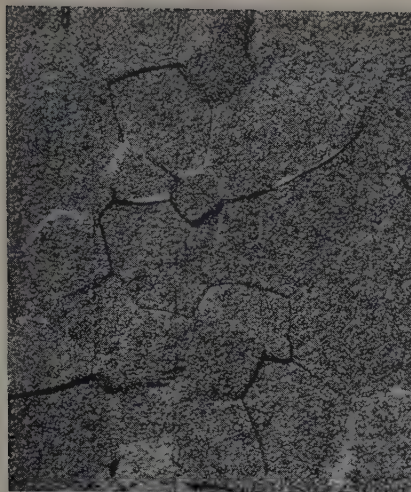


Fig. 5—Al-0.009 pct Fe (OCE). Quenched from 640°C, corroded in 0.30N NaOH for 3 days. X8.

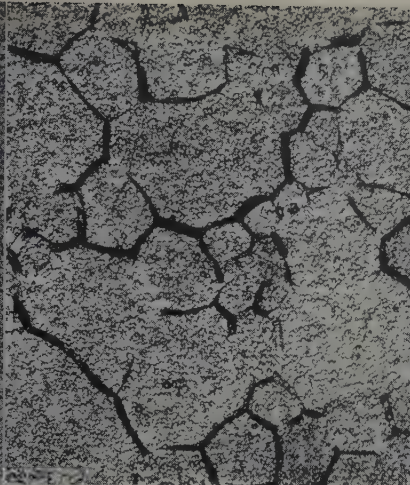


Fig. 6—Al-0.021 pct Fe (OCF). Quenched from 640°C, corroded in 0.30N NaOH for 3 days. X8.

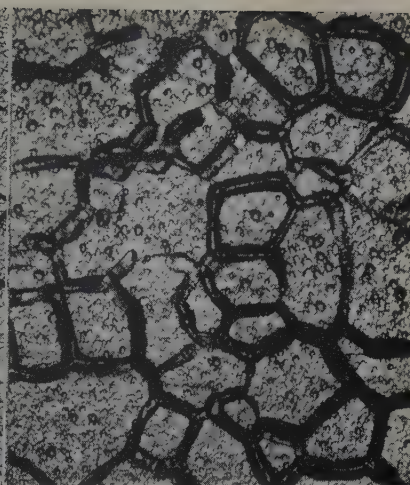


Fig. 7—Al-0.037 pct Fe (OCG). Quenched from 640°C, corroded in 0.30N NaOH for 3 days. X8.

These findings are apparently not in agreement with those of Edgar⁴ who found that the solubility of iron in aluminum at 655°C was 0.052 pct. This discrepancy may possibly be accounted for by the fact that the materials used by Edgar⁴ contained only 0.002 to 0.003 pct Si, while alloy OCG contains 0.007 pct Si, as well as 0.037 pct Fe. It may be that the second phase observed here is the ternary Al-Fe-Si phase and not FeAl₃.

Examination of Electrolytically Polished Surfaces after Immersion in 0.30N Sodium Hydroxide: Six specimens of each of the alloys marked OCD, OCE, OCF, and OCG in two conditions of heat treatment, 1—3 days at 640°C, water-quenched, and 2—3 days at 640°C, furnace-cooled to room temperature in 70 hr, were completely immersed in 0.30N sodium hydroxide for 3 days. During this time they suffered severe general corrosion, most of the specimens losing approximately 50 pct of their weight. Examination of the specimens showed that in those which had been water-quenched from 640°C the number of grain boundaries which suffered grain boundary attack and the depth of such attack increased with increasing iron content, Figs. 4 to 7. In the specimens of low iron content, which showed little or no grain boundary attack, the grain structure could be seen because of differences in level between the grains. This is presumably a result of the rate of corrosion being a function of crystallographic orientation. No such differences in level were observed with speci-

mens of higher iron content, which suffered severe grain boundary attack.

Specimens furnace-cooled from 640°C, except those of alloy OCD (0.001 pct Fe), showed very different corrosion behavior from those that had been water-quenched. Alloy OCD showed the differential grain attack mentioned above with no grain boundary attack, after furnace-cooling as after quenching. Alloy OCE (0.009 pct Fe) which showed only little grain boundary attack in the quenched condition, showed very heavy grain boundary attack after furnace-cooling, Figs. 5 and 8. On the other hand alloys OCF and OCG (0.021 and 0.037 pct Fe) showed a very marked decrease in grain boundary attack compared with those specimens which had been water-quenched, Figs. 7 and 9. These observations are summarized in Table III.

The grain boundary attack never occurred at all grain boundaries and, moreover, was not always continuous along a single grain boundary. To investigate this further, corroded specimens were electroplated with copper and sections were polished. Examination of these sections showed that the grain boundary attack on the quenched specimens increased in depth with increasing iron content and took the form of V-notches, these V-notches being symmetrical only when the grain boundary was perpendicular to the sectioned surface, Figs. 10 and 11. Sometimes, when two grain boundaries were close together, the grain boundary groove took the form

Table II. Microscopical Examination of Electrolytically Polished Surfaces

BNF Mark	Fe, Pct	Si, Pct	Heat Treatment		
			3 Days at 640°C, Water-quenched	3 Days at 640°C, Furnace-cooled to Room Temperature in 17 Hr	3 Days at 640°C, Furnace-cooled to Room Temperature in 70 Hr
OCD	0.001	0.005	α solid solution.	—	α solid solution.
OCE	0.009	0.005	α solid solution.	—	α solid solution.
OCF	0.021	0.006	α solid solution with very few particles of a second phase. No particles of second phase at grain boundaries.	—	α solid solution with particles of a second phase. Particles of second phase larger than in the quenched material and some precipitated at grain boundaries.
OCG	0.037	0.007	Same as for OCF except rather more second-phase particles.	—	Same as for OCF except rather more second-phase particles.
OOB3	0.016	0.007	α solid solution.	α solid solution with particles of a second phase.	—
OOB1	0.055	0.016	α solid solution with particles of a second phase. More particles of second phase than OCG.	α solid solution with second phase. Second-phase particles more numerous and larger than in quenched material.	α solid solution with second phase. Second-phase particles more numerous and larger than in material furnace-cooled in 17 hr.



Fig. 8—Al-0.009 pct Fe (OCE). Furnace-cooled (70 hr) from 640°C, corroded in 0.30N NaOH for 3 days. X8.

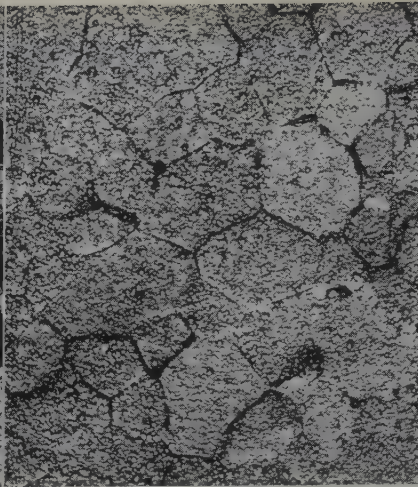


Fig. 9—Al-0.037 pct Fe (OCG). Furnace-cooled (70 hr) from 640°C, corroded in 0.30N NaOH for 3 days. X8.

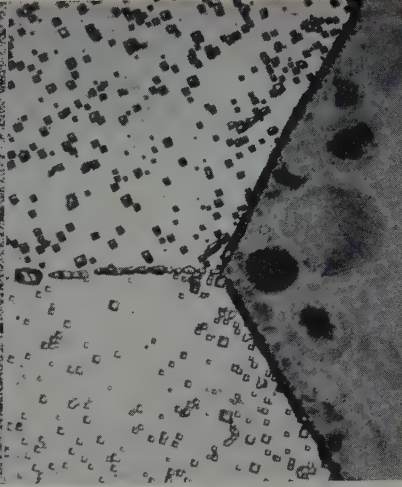


Fig. 10—Al-0.037 pct Fe (OCG). Quenched from 640°C. Normal section of surface corroded in 0.30N NaOH for 3 days. Etched in 1/3 HCl, 1/3 HNO₃, 1/3 H₂O, 2 pct HF. X200.

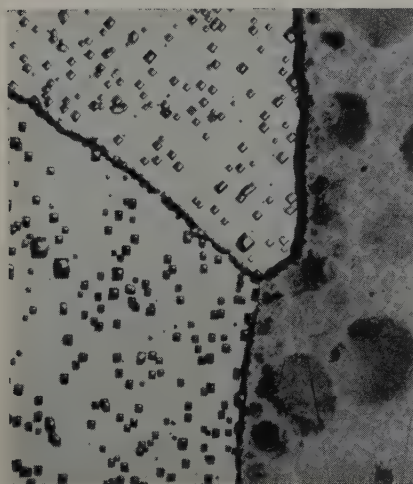


Fig. 11—Same as Fig. 10. Another field. X200.

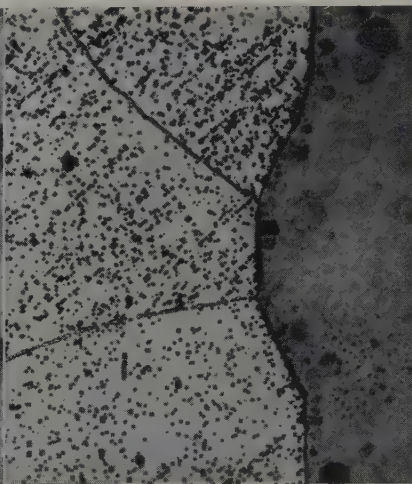


Fig. 12—Same as Figs. 10 and 11. Another field. X100.

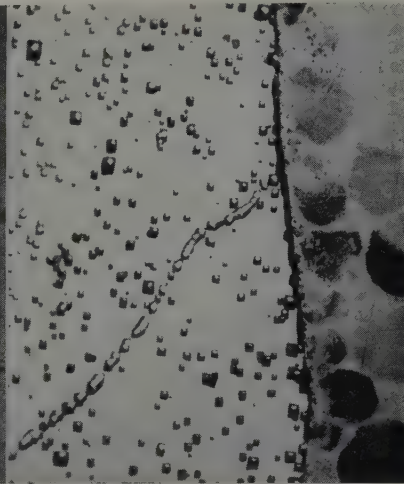


Fig. 13—Same as Figs. 10 to 12. Another field. X200.

shown in Fig. 12. It was also clear that the grain boundary attack was a function of the orientation of the neighboring grains. Figs. 10 to 13 show sections which have been polished and etched with a solution containing 1/3 hydrochloric acid, 1/3 nitric acid, 1/3 water, and 2 pct hydrofluoric acid, in order to develop etch pits. It is clear from these photographs that the grain boundary attack is dependent upon the orientation of the grains adjacent to the grain boundary.

Examination of Electrolytically Polished Surfaces after Immersion in 10 Pct Hydrochloric Acid: Alloys OCD, OCE, OCF, and OCG: Three specimens of each alloy marked OCD, OCE, OCF, and OCG in two conditions of heat treatment, 1—3 days at 640°C, water-quenched, and 2—3 days at 640°C, furnace-cooled to room temperature in 70 hr, were completely immersed in 10 pct hydrochloric acid for times varying from 5 to 40 days. As with the specimens immersed in sodium hydroxide the number of grain boundaries in the water-quenched specimens which showed grain boundary attack and the depth of such attack increased with increasing iron content, Figs. 14 and 15. The depth of grain boundary attack also increased with time of corrosion. The only differences between immersion in sodium hydroxide and hydrochloric acid appeared to be: 1—that alloy OCD (0.001 pct Fe) while showing no grain boundary attack in

sodium hydroxide showed a small amount in 10 pct hydrochloric acid, and 2—the width and depth of the grain boundary grooves were much greater after immersion in sodium hydroxide than in 10 pct hydrochloric acid.

Furnace cooling, instead of quenching, had little effect on alloys OCD (0.001 pct Fe) and OCE (0.009 pct Fe) but markedly reduced the grain boundary

Table III. Examination of Specimens Corroded 3 Days in 0.30N Sodium Hydroxide

BNF Mark	Fe, Pct	3 Days at 640°C, Water-quenched	3 Days at 640°C, Furnace-cooled to Room Temperature in 70 Hr
OCD	0.001	No grain boundary attack; differential attack from grain to grain.	No grain boundary attack; differential attack from grain to grain.
OCE	0.009	Some grain boundary attack; 5 pct of grain boundaries attacked. Differential attack from grain to grain.	Heavy grain boundary attack; 90 pct of grain boundaries attacked. No differential attack from grain to grain.
OCF	0.021	Grain boundary attack; 80 pct of grain boundaries attacked. No differential attack from grain to grain.	Some grain boundary attack; 30 pct of grain boundaries attacked. A little differential attack from grain to grain.
OCG	0.037	Heavy grain boundary attack; 90 pct of grain boundaries attacked. No differential attack from grain to grain.	A little grain boundary attack; 5 pct of grain boundaries attacked. Differential attack from grain to grain.

Table IV. Depth of Grain Boundary Attack after 34 Days in 10 Pct Hydrochloric Acid

Alloy	Depth of Attack at Various Grain Boundaries, Micron
Al-0.016 pct Fe (OOB3)	3.6, 2.0, 3.0, 3.4, 2.4.
Al-0.055 pct Fe (OOB1)	4.0, 7.4, 6.4, 4.2, 4.0, 7.4, 8.8, 6.2.

attack in alloys OCF and OCG (0.021 and 0.037 pct Fe), particularly in the latter, Figs. 15 and 16.

As with the specimens in sodium hydroxide the grain boundary attack seemed to be a function of the orientation difference between adjacent grains and also the intensity of attack varied along the length of some of the grain boundaries.

Alloys OOB3 and OOB1: After immersing quenched specimens of alloys containing 0.016 pct (OOB3) and 0.055 pct (OOB1) Fe in 10 pct hydrochloric acid for a few hours small isolated pits could be seen at some of the grain boundaries. This pitting appeared first in the less pure material, and is shown in Fig. 17. After longer times of immersion the grain boundary attack became more marked and at the same time general corrosion revealed the grain structure. As before the grain boundary attack took place mainly at those boundaries where orientation difference between the neighboring grains was large,

and the attack was not always continuous along one grain boundary. More grain boundaries suffered attack and the depth of attack was greater on the less pure OOB1 than on OOB3. Table IV gives a number of measurements of the depth of grain boundary attack made by focusing on the top and bottom of the grain boundary grooves. The depths varied considerably at different points on the same specimen.

To investigate the effect of furnace-cooling, specimens of alloy OOB1 were annealed at 640°C for 3 days, some were water-quenched, some furnace-cooled to room temperature in 17 hr, and some furnace-cooled to room temperature in 70 hr. These specimens were then totally immersed in 10 pct hydrochloric acid for 40 days. The quenched specimens suffered heavy grain boundary attack, approximately 95 pct of the grain boundaries being attacked. Specimens which had been furnace-cooled in 17 hr were similar to the quenched specimens except that slightly fewer grain boundaries had been attacked but specimens furnace-cooled in 70 hr were very different in that only about 10 pct of the grain boundaries were attacked. These results for the quenched and more slowly cooled material agree with those obtained with alloy OCF (0.021 pct Fe), described above.



Fig. 14—Al-0.001 pct Fe (OCD). Quenched from 640°C, corroded in 10 pct HCl for 40 days. X16.

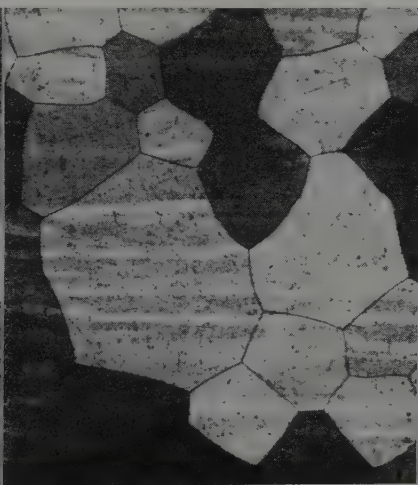


Fig. 15—Al-0.037 pct Fe (OCG). Quenched from 640°C, corroded in 10 pct HCl for 40 days. X16.



Fig. 16—Al-0.037 pct Fe (OCG). Furnace-cooled (70 hr) from 640°C, corroded in 10 pct HCl for 40 days. X16.



Fig. 17—Al-0.016 pct Fe (OOB3). Quenched from 640°C, corroded in 10 pct HCl for 21 hr. Dark field illumination. X250.

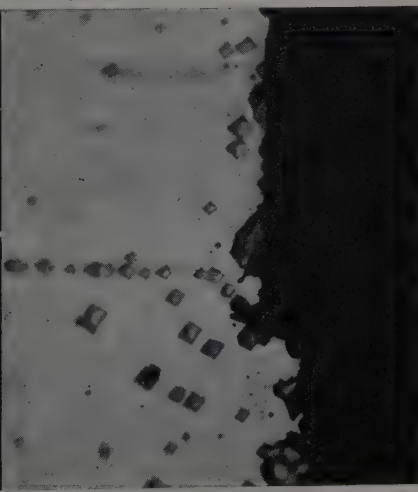


Fig. 18—Al-0.055 pct Fe (OOB1). Quenched from 640°C. Normal section of surface corroded in 10 pct HCl for 34 days. Etched in 1/3 HCl, 1/3 HNO₃, 1/3 H₂O, 2 pct HF. X1000.

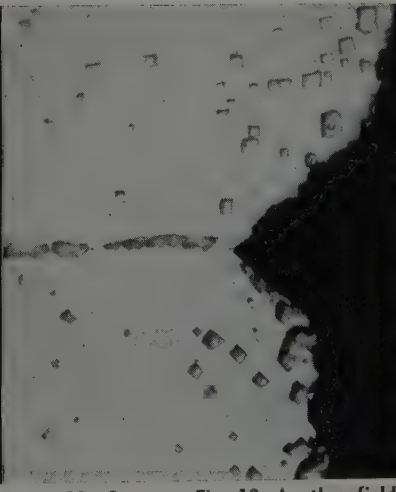


Fig. 19—Same as Fig. 18. Another field. X1000.

Examination of sections of the corroded surfaces confirmed that the depth of grain boundary attack depended upon the relative orientation of the neighboring grains, see Figs. 18 and 19. The shape of the grain boundary grooves was similar to those found in specimens corroded in sodium hydroxide. Comparison of Figs. 10, 11, and 19 shows clearly that not only is the attacked grain boundary region much wider in 0.30N sodium hydroxide than in 10 pct hydrochloric acid, but the ratio of the width to the depth is greater.

Discussion of Results

Properties of Grain Boundaries—Attribution of Observed Effects to "Equilibrium Segregation" of Iron in Solid Solution: Before considering the results in detail it will be worth while considering the properties of grain boundaries in a homogeneous metal or alloy. Owing to the distorted nature of the grain boundary it is clear that in a pure metal some atoms will be in compression while others will be in "holes" which are too large for them. For a solid solution the resulting local elastic stresses can be reduced if large atoms are placed in large holes and small atoms in small holes. On the other hand, a solute atom in the lattice of a grain, if much larger or smaller than the solvent, will cause elastic stresses around it. Thus the energy of the system as a whole should be reduced if some of the large solute atoms are transferred from the lattice of the grain to the large holes at the grain boundary, and some of the small atoms to small holes at the grain boundary. In the equilibrium state there should thus be a segregation of large or small solute atoms or both at the grain boundary, the degree of segregation depending upon the relative orientation of the neighboring grains. This will be referred to as "equilibrium segregation." Bragg and Nye⁵ have demonstrated this effect by means of a bubble model. The effect can also be deduced from Cottrell's theory⁶ of solute "atmospheres" around dislocations. Experimental evidence for "equilibrium segregation" has been given by McLean and Northcott⁷⁻⁹ for temper-brittle steels and antimony in copper and brass, Samuels¹⁰ for bismuth in copper, and Perryman^{11, 12} for aluminum in β brass and tin in α Cu-Sn alloys. The difficulties in obtaining direct evidence for these concentrations are considerable and the experimental evidence given by these authors is of an indirect nature. The most direct evidence for this type of segregation has been given by Chalmers and others,¹³ who showed, using radioactive tracers, that polonium, which is the decay product of Bi²¹⁰, segregated at the grain boundaries in Bi-Pb alloys. The difference in atomic size between solute and solvent necessary for "equilibrium segregation" to occur is not known but it is reasonable to suppose that a difference in apparent atomic diameter or Goldschmidt atomic diameter in excess of about 10 pct would cause a considerable effect. Bearing this in mind, it is probable that iron in aluminum will undergo "equilibrium segregation" (Al 2.85Å, Fe 2.52Å). Bearing in mind that the solid solubility of silicon in aluminum is considerable and that the apparent atomic diameter of silicon in aluminum is 2.73Å, "equilibrium segregation" of silicon is somewhat improbable.

In an alloy the grain boundary concentration of solute at a given temperature will increase with increasing concentration of solute within the grains. Maximum concentration will occur when the grains are saturated and any further addition of solute will result in precipitation of the next phase.

The effect of temperature on grain boundary seg-

regation can be assessed approximately from its effect on the solid solubility. In general, when a metal contains another metal of very different atomic diameter there is marked increase of solubility with temperature. This is especially so with Al-Fe alloys, see Fig. 1. This indicates that a given concentration in the crystals is accommodated much more readily at high temperatures, so that as the temperature increases there will be a lower concentration in the grain boundaries for a given concentration in the grains. Thus for an alloy of a given composition, which is initially a solid solution, the grain boundary concentration is likely to increase with a decrease in temperature until the solid solubility line is reached. Any further fall in temperature is likely to decrease the grain boundary concentration because of the general decrease in solubility.⁷ This decrease in grain boundary concentration will be accompanied by precipitation of a second phase. Thus by furnace-cooling an alloy in which grain boundary segregation is present, the grain boundary concentration will increase as the temperature falls until precipitation of the second phase starts, and with a further fall in temperature the grain boundary concentration will decrease. The extent to which these changes will take place will obviously depend upon the rate of cooling.

From the results of the corrosion tests in 0.30N sodium hydroxide and 10 pct hydrochloric acid it is clear that the rate of grain boundary attack is a function of: 1—the iron content, 2—the relative orientation of the neighboring grains and, 3—the rate of cooling from a high temperature.

The effect of iron content on the susceptibility to grain boundary attack can be simply explained by the theory mentioned above, for if the grain boundaries possess a higher iron concentration than the grains there is likely to be an electrochemical difference between them. That Lacombe and Yannaquis³ found no difference in susceptibility to grain boundary attack between aluminum of 99.993 and 99.9986 pct purity might be because the iron contents were not sufficiently different. It is interesting to note that Montariol et al.¹⁴ have recently found by autoradiography a segregation of impurities at the grain boundaries in aluminum of 99.998 pct purity.

The variation in degree of grain boundary attack with the orientation of the neighboring grains is also in keeping with the theory of "equilibrium segregation" because, as explained above, the amount of iron segregated at the grain boundaries will depend upon the relative orientation of the neighboring grains.

As already explained the effect of furnace cooling will be first to increase the iron concentration at the grain boundaries as the temperature falls and then when a second phase begins to appear to decrease the grain boundary concentration. Accordingly the following observations are all in keeping with the theory of "equilibrium segregation": 1—alloy OCE (0.009 pct Fe) was more susceptible to grain boundary attack after furnace-cooling than after quenching, and 2—alloys OCF and OCG (0.021 and 0.037 pct Fe) were more susceptible when quenched than after furnace-cooling when a second phase was precipitated and, 3—alloy OOB1 (0.055 pct Fe) decreased in susceptibility to grain boundary attack in the order water-quenched, furnace-cooled in 17 hr, furnace-cooled in 70 hr.

It is difficult to see how the results given here can be accounted for by the theory given by Lacombe and Yannaquis, for if the grain boundary attack is

due to lattice discontinuities at the grain boundaries: 1—there should be no difference between quenched and furnace-cooled material of very high purity, and 2—if the grain boundaries were anodic to the grains a more concentrated form of attack would be expected.

Mechanism of Corrosion: It has already been pointed out that the grain boundary corrosion observed here is very different from that observed in Al-Mg, Al-Cu, Al-Zn, and Al-Zn-Mg alloys after heat treatments conducive to such attack. It is now fairly well established that when these alloys are susceptible to intercrystalline corrosion there is a phase at the grain boundaries which is anodic to the grains. Under these conditions the corrosion at the grain boundaries penetrates deeply into the metal but is confined to a very narrow grain boundary zone, and this is in keeping with the presence of small anodes at the grain boundaries with large cathodes around them. In contrast to this, the attack observed here occurs in a relatively wide grain boundary zone; in 0.30N sodium hydroxide the width of the grain boundary groove is greater than the depth, while in 10 pct hydrochloric acid the width is approximately equal to the depth. Mears and Brown¹⁵ found that the grain boundaries of 99.986 pct Al water-queched from 620°C were anodic to the grains in 20 pct hydrochloric acid, while in slowly cooled specimens they were cathodic. It is difficult, however, to conceive of an anodic grain boundary leading to the shape of grain boundary grooves shown in Figs. 10 to 12 and 19. On the other hand such grooves are consistent with the grain boundary being cathodic to the grains, and indeed, if the iron concentration at the grain boundaries is greater than that within the grains, the grain boundaries would be expected to be cathodic in the corrodants used. As shown by Evans¹⁶ the current density will, under these conditions, decrease as one goes further away from the cathodic grain boundary, the distribution of corrosion being as shown diagrammatically in Fig. 20. From this it would be supposed that the contour of the grain boundary groove would not show any sharp discontinuity with the specimen surface as it does in Figs. 10 to 12 and 19.

A number of explanations could be devised to account for the shape of the grain boundary grooves, and the variation in the ratio of width to depth of these grooves. As none of these explanations can be put forward with assurance it would not be profitable to discuss the matter in detail. It should be mentioned, however, that Fig. 20 applies to a surface free from films, and Evans¹⁷ has pointed out that the presence of an oxide film may modify the distribution of corrosion, and possibly lead to the observed sharp discontinuity between the contour of the groove and the specimen surface. There is evidence that oxide films persist when the specimens are immersed in the acid solution (there being no visible hydrogen evolution except on scratching, a change of potential in the anodic direction on scratching, etc.). On the other hand there is little evidence that oxide films persist in alkaline solution (when there is continuous general evolution of hydrogen, little change of potential on scratching, etc.). Apart from these detailed considerations, however, the main point is clear—the grain boundary grooves produced are consistent with the presence of a cathodic zone at the boundary, i.e., with the presence of an increased concentration of iron.

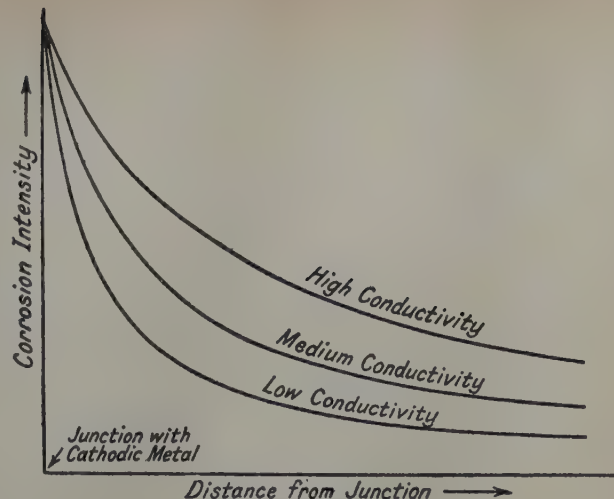


Fig. 20—Distribution of corrosion near a junction. From U. R. Evans, ref. 18, p. 530. Reprinted with permission of Edward Arnold & Co.

It was mentioned earlier (see Table III) that when only a few or none of the grain boundaries were attacked there were differences in rate of corrosion from grain to grain but that these differences were no longer present when a large proportion of the grain boundaries suffered attack. In all cases, however, it should be remembered that general corrosion was going on all the time. Presumably these differences in the rate of corrosion of different grains are due to potential differences set up because of differences in crystallographic orientation. When, however, a large proportion of the grain boundaries contain concentrations of iron, it must be presumed that the difference in electrochemical properties between these grain boundaries and grains are large enough to swamp the effect of smaller differences between the grains.

Acknowledgments

The author is indebted to the Director and Council of The British Non-Ferrous Metals Research Association for permission to publish this paper.

References

- ¹ F. Rohrmann: *Trans. Electrochem. Soc.* (1934) **66**, p. 229.
- ² P. Lacombe and N. Yannaquis: *Revue Métallurgie* (1948) **45**, p. 68.
- ³ B. Roald and M. A. Streicher: *Journal Electrochem. Soc.* (1950) **97**, p. 283.
- ⁴ J. K. Edgar: *Trans. AIME* (1949) **180**, p. 225; *METALS TECHNOLOGY* (June 1948).
- ⁵ W. L. Bragg and J. F. Nye: *Proc. Royal Soc.* (1947) **190A**, p. 474.
- ⁶ A. H. Cottrell: *Report of the 1947 Bristol Conference on the Strength of Solids* (1948) p. 30. *Phys. Soc.*
- ⁷ D. McLean and L. Northcott: *Journal Iron and Steel Inst.* (1948) **158**, p. 169.
- ⁸ D. McLean: *Journal Inst. Metals* (1947) **73**, p. 791.
- ⁹ D. McLean and L. Northcott: *Journal Inst. Metals* (1946) **72**, p. 583.
- ¹⁰ L. E. Samuels: *Journal Inst. Metals* (1949) **76**, p. 91.
- ¹¹ E. C. W. Perryman: B.N.F.M.R.A. Unpublished work.
- ¹² E. C. W. Perryman: This issue, p. 906.
- ¹³ M. T. Stewart, R. Thomas, K. Wanchope, W. C. Winegard, and B. Chalmers: *Physical Review* (1951) **83**, p. 657.
- ¹⁴ F. Montariol, P. Albert, and G. Chaudron: *Comptes Rendus* (1952) **235**, p. 477.
- ¹⁵ R. B. Mears and R. H. Brown: *Industrial and Engineering Chemistry* (1941) **33**, p. 1001.
- ¹⁶ U. R. Evans: *Metallic Corrosion Passivity and Protection* (1946) p. 530. London. Edward Arnold and Co.
- ¹⁷ U. R. Evans: Private communication.

Martensite Nucleation in Substitutional Iron Alloys

by John C. Fisher

Nucleation theory is applied to martensite nucleation in substitutional iron alloys. Composition fluctuations are neglected, and a steady rate of nucleation is predicted for any composition and temperature. The maximum rate of nucleation (as a function of temperature) is shown to be measurable only for an extremely narrow composition range, being too great or too small outside this range. A number of experimental observations, including completely isothermal transformation in some alloys and composition-dependence of M_s temperature in others, are compared with the calculated behavior.

IN a previous report,¹ nucleation theory was applied to the formation of isothermal martensite in an Fe-Ni-Mn alloy. The experimental observations of Cech and Hollomon² were accounted for quantitatively. It now is of interest to examine the predictions of nucleation theory with respect to martensite transformation in substitutional iron alloys of other compositions. Since Fe-Ni alloys have received considerable attention, both as to their transformation kinetics and their free energies, they will be treated in detail, although the results apply with equal validity to other substitutional alloys.

In substitutional alloys, where composition fluctuations can be neglected in volumes of critical nuclear size, the rate of nucleation of martensite in subcooled austenite is¹

$$\bar{n} = N\nu \exp(-W^*/kT) \quad [1]$$

where the free energy of formation of the critical size nucleus is

$$W^* = 8192 \pi (\theta^2 \sigma^3) / 27 \Delta f_v^4 \quad [2]$$

In the expressions for n and W^* , the symbols have the following meanings: N is the number of atoms per unit volume; ν , the atomic vibration frequency; θ , a function of the elastic constants of austenite and the shear angle of martensite; σ , the austenite/martensite interfacial free energy; and Δf_v , the free energy change per unit volume accompanying the transformation.

Jones and Pumphrey³ have determined the austenite to martensite free energy change as a function of nickel content and temperature for Fe-Ni alloys. Their expression is

$$\Delta F = 2500 C + 1.25 (1 - C) \Delta F_{Fe} \text{ cal per mol} \quad [3]$$

where C is the atom fraction of nickel, and ΔF_{Fe} is the free energy change per unit volume for pure iron as tabulated by Zener⁴ (or, equivalently, Fisher⁵).

From Eqs. 1 to 3, it is possible to calculate isothermal nucleation rates as a function of temperature and composition for Fe-Ni alloys. The only unknown parameter is $(\theta^2 \sigma^3)$. The best value of this

J. C. FISHER, Junior Member AIME, is associated with the Metallurgy Research Dept., Research Laboratory, General Electric Co., Schenectady.

Discussion on this paper, TP 3548E, may be sent, 2 copies, to AIME by Dec. 1, 1953. Manuscript, Nov. 13, 1952. Cleveland Meeting, October 1953.

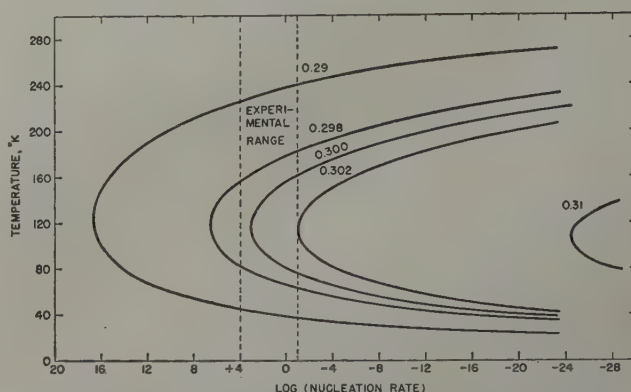


Fig. 1—Calculated isothermal nucleation rate as a function of temperature for Fe-Ni alloys in the composition range $0.29 \leq \text{atom fraction Ni} \leq 0.31$. Rates less than 10^{-1} and greater than 10^4 nuclei per cc per sec are difficult to measure experimentally.

parameter for Fe-Ni alloys, determined from M_s temperatures in a manner to be described shortly, is

$$(\theta^2 \sigma^3) = 9.92 (10)^{21} \text{ cgs units} \quad [4]$$

Taking this value of $(\theta^2 \sigma^3)$, C -curves for isothermal nucleation were calculated for Fe-Ni alloys of several compositions, and are plotted in Fig. 1.

It is evident from Fig. 1 that completely isothermal nucleation of martensite in Fe-Ni alloys can be observed experimentally for only a very narrow range of compositions. Cech and Hollomon find that a nucleation rate of about 10^4 nuclei per cc per sec is as fast as they can follow dilatometrically, and a rate of about 10^{-1} nucleus per cc per sec is about the slowest that can be measured conveniently. If the nucleation rate is to lie between the limits $10^{-1} \leq \bar{n} \leq 10^4$, the nickel content of an Fe-Ni alloy must fall in the atomic fraction range $0.299 \leq C \leq 0.302$. Nickel contents lower than 0.299 correspond to nucleation rates too great to follow, and those higher than 0.302 to nucleation rates too slow to measure in a reasonable time.* In view of the narrow com-

* The actual nickel composition corresponding to the middle of the range may differ by 0.01 or 0.02 from the calculated 0.300, owing to uncertainties in the calculation. However, these uncertainties have little influence on the calculated width of the range.

position range in which successful isothermal measurements can be made, it is not surprising that only one substitutional alloy has been described² that comes close to being in the proper range.

The alloy used by Cech and Hollomon had the approximate composition 23 pct Ni, 3.7 pct Mn, 0.05 pct C, 0.015 pct N, balance Fe, on a weight basis. This alloy is equivalent to about a 26 atomic pct Ni alloy, neglecting the carbon and nitrogen,¹ or about a 28 atomic pct Ni alloy including the carbon and nitrogen. It is close to the composition range for which isothermal nucleation should be observed, but not close enough according to Fig. 1. The fact that almost completely isothermal martensite was observed suggests that: 1—Fig. 1 is somewhat in error, or 2—the nickel-equivalent of manganese, carbon, and nitrogen has been underestimated, or 3—manganese alters the austenite/martensite interfacial free energy or the martensite shear angle. The third possibility is perhaps most likely, as the value of $(\theta^2 \sigma^3)$ deduced for Cech and Hollomon's alloy¹ was about six times larger than that in Eq. 4 deduced for Fe-Ni alloys.

The nucleation C-curves for nickel contents less than about 0.29 Ni suggest that, experimentally, a temperature very similar to an M_s should exist for these alloys. The nucleation rate changes from a negligibly small value to a very large one in a few degrees temperature drop. The temperature at which martensite would first be observed, then, in any experiment where the specimen temperature is steadily lowered, would be that for which the martensite nucleation rate became appreciable, say,

$$\bar{n} = 1 \text{ nucleus per cc per sec} \quad [5]$$

about 0.001 of the maximum rate observed by Cech and Hollomon (the results are very insensitive to the actual value selected for \bar{n} , as long as it is within a factor of a thousand or so of 1).

Taking Eq. 5 as the M_s criterion and taking N_v in Eq. 1 to be about 10^{26} , the M_s criterion becomes

$$W^*/kT = 82.9$$

or

$$\Delta F^* T = 6.55 (10)^{-11} (\theta^2 \sigma^3) \quad [6]$$

for ΔF in cal per mol. Taking the temperature for 10 pct transformation on continuous cooling at 10°C per min as the M_s temperature for Fe-Ni alloys, and using the data of Jones and Pumphrey,[†] M_s tem-

[†] The M_s temperature had to be placed at 10 pct transformation because Jones and Pumphrey reported temperatures for 10, 50, and 90 pct transformation only.

peratures are fairly well defined by the relationship

$$\Delta F^* T = 6.5 (10)^{-11} \quad [7]$$

The agreement is shown in Fig. 2. The value of $(\theta^2 \sigma^3)$ required is that given in Eq. 4.

Also shown in Fig. 2 is the curve for $\Delta F = 0$, which defines the temperature at which austenite and martensite are in metastable equilibrium. It is interesting to note that transformation in the temperature range $1000^\circ\text{K} \leq T \leq 1180^\circ\text{K}$ follows the curve $\Delta F = 0$, whereas transformation below 700°K follows Eq. 7.

The fact that transformation at high temperatures occurs at approximately the temperature where austenite and martensite are in equilibrium indicates one of two things: Either, 1—there is no appreciable nucleation barrier and no composition change during transformation, or 2—there is an appreciable nucleation barrier and a compensating composition change, giving a false significance to the curve $\Delta F = 0$. Assuming that the agreement with the curve $\Delta F = 0$ is not fortuitous, it appears that high temperature transformation is not impeded by strain energy,

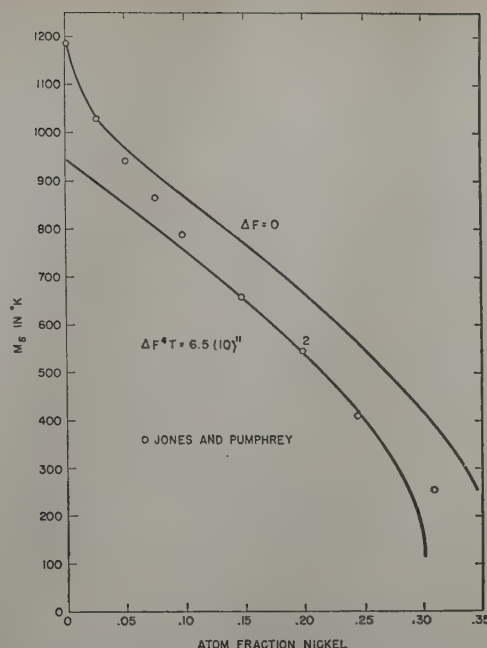


Fig. 2—Comparison of calculated and experimental temperatures for beginning of transformation in continuously cooled Fe-Ni alloys of varying nickel content. Experimental data taken from Jones and Pumphrey.³

either during nucleation or during growth. According to this view, the strain energy that normally accompanies martensite nucleation and growth is continuously relaxed at high temperatures. It might be, for example, that transformation proceeds by nucleation of ferrite at grain boundaries and edges, where stress relaxation and favorable interfacial free energy changes will allow easy nucleation, followed by noncoherent growth without composition change. In any event, whatever the interpretation at high temperatures, martensite appears to form in its characteristic fashion below 700°K .

Experimentally, the course of transformation on quenching an Fe-Ni alloy and holding it at constant temperature is as follows: In the first few seconds, while the specimen is coming to temperature, a considerable fraction of the volume is transformed to martensite. Subsequently, isothermal transformation is observed at a decreasing rate. At first glance it is not clear how the proposed isothermal nucleation description can apply to observations of this type. A clue to the answer lies in the fact that a constant rate of nucleation corresponds to an ever decreasing volume rate of transformation, owing to partition of the austenite by previously formed martensite plates. New plates are confined to smaller austenite volumes, and transform less material.

Two sorts of calculations can be made to check the idea that partitioning of the austenite can lead to the observed volume transformation effects. The first is a calculation of the volume transformed as a function of temperature for cooling at a constant rate, these data having been measured by Jones and Pumphrey.³ The nucleation rate is known as a function of temperature from Eq. 1 or Fig. 1, and the volume fraction transformed depends upon the total number of nuclei according to the relationship¹

$$V = 1 - [1 + (1 + f) n/n_0]^{-1/(1 + f)} \quad [8]$$

where V is the volume fraction transformed; n , the number of nuclei; n_0 , the number of austenite grains per cc; and f , the fraction of the austenite trans-

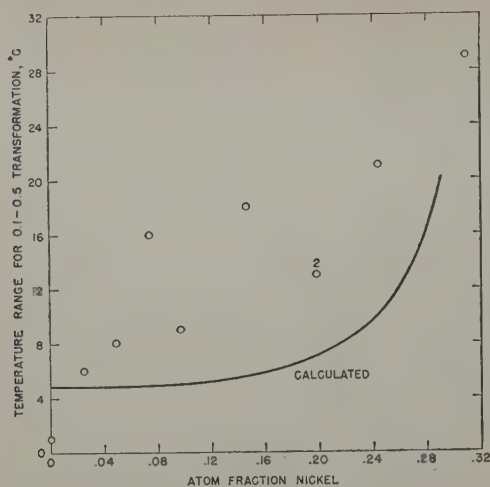


Fig. 3—Comparison of calculated and experimental widths of temperature ranges for 10 to 50 pct transformation on continuous cooling of Fe-Ni alloys. Data from Jones and Pumphrey.³

formed to martensite in the local volume where a typical plate forms. Taking $f \approx 0.05$, as suggested by analysis of Cech and Hollomon's data,¹ and n_0 as 10^5 grains per cc, the width of the temperature range for 10 to 50 pct transformation at a cooling rate of 10°C per min was calculated as a function of nickel content. It is compared in Fig. 3 with the range as determined by Jones and Pumphrey. The calculation cannot be extended to 90 pct transformation, for which experimental data are available, because Eq. 8 breaks down above about 50 pct transformation. There is agreement to within a factor of two, which may be considered as reasonable.

The second calculation of interest in clarifying the role played by partition in converting a constant nucleation rate into a sharply varying transformation rate is that of determining the fraction transformed as a function of time for a typical alloy. Selecting a 29 pct Ni alloy and temperatures in the neighborhood of 200°K , the calculated fraction transformed is plotted vs time in Fig. 4. The behavior illustrated in Fig. 4 is very similar to that reported by Das Gupta and Lement⁶ for the transformation of a high chromium steel containing about 15 pct Cr and 0.75 pct C, and by Kulin and Speich⁷ for a 14 pct Cr, 9 pct Ni steel. The results for both alloys were

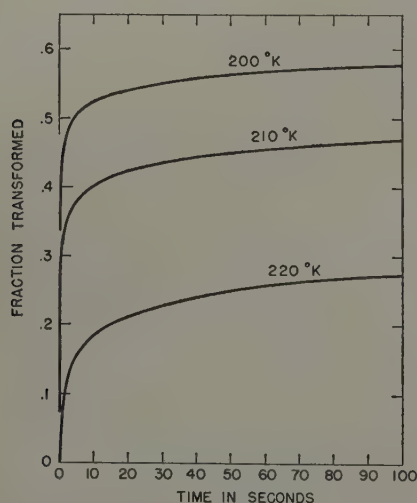


Fig. 4—Calculated isothermal transformation curves for an Fe-29 pct Ni alloy at three temperatures.

described in terms of two classes of martensite: that formed on cooling, and that formed isothermally. Actually, as suggested by Fig. 4, the martensite formed on cooling may have done so by thermal nucleation, in the same way as the subsequent isothermal martensite.

It should be pointed out that martensite that forms by rapid thermal nucleation, even though it forms during cooling, is not athermal martensite of the type described for steels containing significant amounts of carbon.⁸ In a carbon steel, the number of active nuclei is determined by frozen-in fluctuations of carbon concentration, and is a function only of the temperature. For Fe-Ni alloys, on the other hand, it is suggested here that there is no characteristic number of nuclei. Rather, there is a characteristic rate of thermal nucleation for each temperature, the rate increasing so rapidly with decreasing temperature that a fairly sharp "beginning of transformation" temperature is observed on continuous cooling. Experimentally, an isothermal run in the neighborhood of the M_s temperature should give an essentially constant number of nuclei in a carbon steel, and an essentially constant nucleation rate in a substitutional iron alloy.

It can be concluded that a kinetic description of martensite formation in Fe-Ni alloys, and therefore very probably for other substitutional iron alloys, can be made in terms of homogeneous thermal nucleation. This description is in agreement with the following experiments: 1—Completely isothermal transformation in alloys of a very limited composition range; 2—Absence of transformation in more highly alloyed austenite; 3— M_s temperature as it depends upon composition in less highly alloyed austenite; 4—Temperature range for transformation on continuous cooling; and 5—Subsequent isothermal transformation in alloys where a considerable volume fraction transforms during cooling.

A more accurate treatment of the martensite transformation in substitutional iron alloys would require that attention be given to its autocatalytic nature.⁹ Since the rate of thermal nucleation is increased by shear and tensile stresses, and in particular by stresses in the neighborhood of previously formed martensite plates, prior transformation can markedly increase the nucleation rate.¹⁰ Nevertheless, it appears that the characteristic features of the martensite transformation in substitutional iron alloys are the result of thermal nucleation that, as a first approximation, can be considered homogeneous.

References

- ¹ J. C. Fisher: *Acta Metallurgica* (1953) **1**, p. 32.
- ² R. E. Cech and J. H. Hollomon: *Trans. AIME* (1953) **197**, p. 685; *JOURNAL OF METALS* (May 1953).
- ³ F. W. Jones and W. I. Pumphrey: *Journal Iron and Steel Inst.* (1949) **163**, p. 121.
- ⁴ C. Zener: *Trans. AIME* (1946) **167**, p. 513; *METALS TECHNOLOGY* (January 1946).
- ⁵ J. C. Fisher: *Trans. AIME* (1949) **185**, p. 688; *JOURNAL OF METALS* (October 1949).
- ⁶ S. C. Das Gupta and B. S. Lement: *Trans. AIME* (1951) **191**, p. 727; *JOURNAL OF METALS* (September 1951).
- ⁷ S. A. Kulin and G. R. Speich: *Trans. AIME* (1952) **194**, p. 258; *JOURNAL OF METALS* (March 1952).
- ⁸ J. C. Fisher, J. H. Hollomon, and D. Turnbull: *Trans. AIME* (1949) **185**, p. 691; *JOURNAL OF METALS* (October 1949).
- ⁹ E. S. Machlin and M. Cohen: *Trans. AIME* (1951) **191**, p. 746; *JOURNAL OF METALS* (September 1951).
- ¹⁰ J. C. Fisher and D. Turnbull: *Acta Metallurgica* (1953) **1**.

Calculation of Martensite Nucleus Energy Using The Reaction-Path Model

by J. C. Fisher and D. Turnbull

ACCORDING to the "reaction-path" model^{1,2} of martensite nucleation, the shear angle of the embryonic martensite plate must be treated as a variable, and included in any calculation of nucleus critical size. Also, as can be deduced from this model, the interfacial free energy between austenite and martensite does not reach its final value until the shear is completed. It is zero for zero shear angle. However, in order to account for the kinetics of the martensite transformation, some sort of interfacial energy barrier appears to be necessary even with the reaction-path model, for otherwise the volume and the energy of formation of the critical size nucleus both collapse to zero.³ Cohen independently suggested that surface energy could be incorporated into the reaction-path model, with the overall free energy of a martensite embryo being a function of its volume and shear angle.⁴

It is possible to estimate the energy associated with the formation of a critical-size martensite nucleus starting with the reaction-path model and including a surface free-energy barrier. As the dependence of interfacial free energy upon shear angle is unknown, a simple type of dependence will be assumed, with the belief that the true dependence would not lead to appreciably different results.

Consider the work required to form a lenticular martensite plate with radius r , thickness t , and shear angle θ . There are three contributions; one being the interfacial free energy, one being the free energy change in the martensite plate, and one being the free energy increase in the surrounding austenite.

The interfacial free energy σ is assumed to depend upon the shear angle θ according to the relationship

$$\sigma = \sigma_0 (\theta/\theta_0)^n \quad [1]$$

where θ_0 is the equilibrium shear angle and n is an exponent that may lie in the range $0 \leq n \leq 2$. The work required to form the interfaces of a martensite plate then is

$$W_s = 2\pi r^2 \sigma_0 (\theta/\theta_0)^n \quad [2]$$

The free energy change per unit volume of martensite is composed of two parts, one the ordinary volume free energy Δf_v which is negative, and the other the elastic strain energy $G\gamma_m^2/2$, where G is the shear modulus and γ_m the shear strain relative to the martensite structure. This expression for the strain energy is valid only when the shear strain γ_m is sufficiently small that the martensite is within its linear elastic range. There is no doubt that γ_m lies beyond the linear elastic range for embryos that are considerably subcritical. However, for critical nuclei it will be shown that γ_m is 1.5 pct or less, within the linear elastic range of martensite. For embryos of nearly critical size, then, the strain energy of the

J. C. FISHER, Junior Member AIME, and D. TURNBULL, Associate Member AIME, are associated with the Metallurgy Research Dept., Research Laboratory, General Electric Co., Schenectady.

Discussion on this paper, TP 3533E, may be sent, 2 copies, to AIME by Dec. 1, 1953. Manuscript, Dec. 5, 1952. Cleveland Meeting, October 1953.

Table I. Values of $\theta_0 - \theta$, θ/θ_0 , and α as Functions of n

n	$\theta_0 - \theta$	θ/θ_0	α
0	0.0060	0.964	0.93
1	0.0105	0.937	0.80
2	0.0150	0.910	0.63

martensite is correctly given by $G\gamma_m^2/2$. The shear strain in the martensite is $\gamma_m = \theta_0 - \theta$, and the work required to form the strained martensite is

$$W_m = (\pi r^2 t/2) [\Delta f_v + G(\theta_0 - \theta)^2/2] \quad [3]$$

The free energy change in the austenite is entirely that due to elastic distortion. The elastic strain is not uniformly distributed in the austenite, being large near the martensite plate and small elsewhere. Approximately, however, the energy corresponds to a uniform shear strain

$$\gamma_a = (\theta t/2)/r \quad [4]$$

throughout the volume $4\pi r^3/3$ surrounding the plate. The work required to strain the surrounding austenite then is

$$W_a = (4\pi r^3/3) (G\gamma_a^2/2) = (G\theta^2/6) \pi r t^2 \quad [5]$$

For simplicity, the same shear modulus G is assumed for each structure.

The total free energy for forming a plate then is

$$W = W_s + W_m + W_a = 2\pi r^2 \sigma_0 (\theta/\theta_0)^n + (\pi r^2 t/2) [\Delta f_v + G(\theta_0 - \theta)^2/2] + (G\theta^2/6) \pi r t^2 \quad [6]$$

This expression is correct for nuclei and for embryos of nearly critical size, where, as will be shown, the strain energy in the martensite is correctly given by the expression $G(\theta_0 - \theta)^2/2$. Having W as a function of r , t , and θ , as in Eq. 6, there is a saddle-point where W has a stationary value, W subsequently decreasing indefinitely as the nucleus volume increases along the reaction path. The stationary value of W is the energy of the critical nucleus.

The critical nucleus has radius, thickness, and shear angle such that $\partial W/\partial r = \partial W/\partial t = \partial W/\partial \theta = 0$. Performing these differentiations and calculating the critical nucleus energy,

$$W^* = [8192\pi (G\theta_0^2/6)^2 \sigma_0^3/27 \Delta f_v^4] \alpha \quad [7]$$

where

$$\alpha = (\theta/\theta_0)^{3n+4}/[1 + G(\theta_0 - \theta)^2/2 \Delta f_v]^4 \quad [7a]$$

and where θ is to be determined from the equation

$$(1 + 3n/4) + G\theta(\theta_0 - \theta)/[\Delta f_v + G(\theta_0 - \theta)^2/2] = 0 \quad [8]$$

For Δf_v near -200 cal per mol or -10^9 ergs per cc, and θ_0 near $1/6$, as for iron-base alloys, Eq. 8 gives

$$\theta_0 - \theta \approx -(4 + 3n) \Delta f_v/4G\theta_0 \quad [9]$$

as the difference between the equilibrium shear angle and the actual shear angle for a critical nu-

cleus. Even for n as large as 2, the difference does not exceed $\theta_0 - \theta \approx 0.015$, an elastic shear strain in the martensite of about 1.5 pct. This strain is within the linear elastic range of martensite, as tentatively assumed above.

Values for $\theta_0 - \theta$ and θ/θ_0 can be calculated from Eq. 9 for various values of n . Throughout the calculation it is assumed that $\Delta f_v = -10^9$ ergs per cc, $G = 10^{12}$ dynes per sq cm, and $\theta_0 = 1/6$. The results are given in Table I.

Using the tabulated values of $\theta_0 - \theta$ and θ/θ_0 , the value of α in Eqs. 7 and 7a can be determined. The result is given in the final column of the table. It is evident that α is relatively insensitive to n , and is nearly unity. The quantity α is even more insensitive to Δf_v , increasing by 3 pct for $n = 0$ and by 10 pct for $n = 2$ when Δf_v is halved. In contrast, the term Δf_v^4 in Eq. 7 changes by 1600 pct at the same time, so that almost the entire temperature dependence of W^* lies in the bracketed coefficient of α .

In view of the above discussion, and of the other approximations involved in the nucleation calculation, α can be replaced by unity in Eq. 7 with little loss in rigor. Making this substitution,

$$W^* = 8192\pi(G\theta_0^2/6)\sigma_0^3/27\Delta f_v^4 \quad [10]$$

Eq. 10 is the expression derived earlier by Fisher,

Hollomon, and Turnbull⁵ for martensite nucleation. It has met with success in describing the athermal nucleation of martensite in Fe-C alloys, and the thermal nucleation of martensite in Fe-Ni-Mn⁶ and Fe-Ni⁷ alloys.

It now appears that the reaction-path model, with a surface free-energy barrier introduced, gives essentially the same magnitude for the critical frequency of martensite nucleus formation as the nucleation theory of Fisher, Hollomon, and Turnbull. According to either view, the nucleation of martensite requires that a free-energy barrier be surmounted. Its height, according to either view, is given by Eq. 10.

References

- ¹ M. Cohen, E. S. Machlin, and V. G. Paranjpe: *Thermodynamics in Physical Metallurgy*. (1950) p. 242. Cleveland. ASM.
- ² E. S. Machlin and M. Cohen: *Trans. AIME* (1952) **194**, p. 489; *JOURNAL OF METALS* (May 1952).
- ³ J. H. Hollomon and D. Turnbull: *Progress in Metal Physics* (1953) **4**, p. 333. London. Pergamon Press Ltd.
- ⁴ M. Cohen: Private communication.
- ⁵ J. C. Fisher, J. H. Hollomon, and D. Turnbull: *Trans. AIME* (1949) **185**, p. 691; *JOURNAL OF METALS* (October 1949).
- ⁶ J. C. Fisher: *Acta Metallurgica* (1953) **1**, p. 32.
- ⁷ J. C. Fisher: This issue, p. 918.

Technical Note

Effect of Nickel and Molybdenum on Stabilization Of the Austenite-Martensite Transformation

by D. J. Blickwede

PRESENT knowledge of the effects of time and temperature upon stabilization of the austenite-martensite reaction in steel is fairly complete,¹⁻³ but at the time the work described herein was initiated there was no information about the effects of alloy elements on the phenomenon. However, it has been assumed on theoretical grounds that alloy elements, particularly carbide formers, may have a significant effect on stabilization.⁴ The present work was undertaken to provide information about the effect of two common elements, nickel and molybdenum, on stabilization in hypereutectoid and hypoeutectoid steels.

Seven induction-furnace melted, 1.2 pct C steels with a variation of nickel from 0 to 6 pct and of molybdenum from 0 to 1.0 pct were used for most of the experiments. Along with these a series of 0.4 pct C steels containing 0 to 6 pct Ni were also studied. The chemical compositions of the steels are listed in Table I. Stabilization in these forged, hot-rolled, annealed, and centerless ground steels was measured by aging brine-quenched specimens (austenite temperature, 1800°F) at 95° and 150°F and then determining the change in specific volume produced by subsequent cooling from room temperature to -320°F.³

In presenting the results the decrease in the change in specific volume, $\delta\Delta V$, after various stabilization times is used. This is given by

$$\delta\Delta V = \Delta V_0 - \Delta V_t$$

where ΔV_0 is the change in specific volume on quenching directly to -320°F and ΔV_t is the change in specific volume on quenching to -320°F after stabilizing for time t . In other words, $\delta\Delta V$ is a direct measure of the amount of martensite that is lost to the subzero quench as a result of stabilization and hence is greater, the longer the aging time or the higher the aging temperature.

The results are shown in Fig. 1. The scatter of the data, which are not shown for clarity and brevity, was sufficient to make the relative location of the curves on the $\delta\Delta V$ axis inaccurate within $\pm 2 \times 10^{-5}$ cc per g. However, some generalities appear which are of interest.

Effect of Nickel

In the 0.4 pct C steels, up to 3 pct Ni has little, if any, effect on the rate or amount of austenite stabilized at 95°F, Fig. 1a. Increasing nickel from 3 to 6 pct almost doubles the amount of austenite stabilized in a given time.

In the 1.2 pct C steels aged at 95°F, increasing the nickel from 1 to 3 pct appears to decrease the amount of stabilization, and a further increase to 6 pct Ni completely eliminates stabilization as shown in Fig. 1b (M_s of 6 pct Ni steel was below room temperature). The same behavior was exhibited by these steels stabilized at 150°F, especially after aging for periods longer than 5 hr, Fig. 1c.

Thus it appears that up to 1 pct Ni has little effect on stabilization at low or high carbon levels. More than 1 pct Ni increases stabilization at low carbon contents and decreases it at high carbon contents. Ward, Jepson, and Rait⁵ have found that at inter-

D. J. BLICKWEDE, Junior Member AIME, is Research Engineer, Bethlehem Steel Co., Bethlehem, Pa.

TN 167E. Manuscript, Jan. 17, 1953; revision, April 24, 1953.

Table I. Composition of Steels

Steel No.	C	Mn	P	S	Si	Ni	Mo
1	0.40	0.33	0.030	0.013	0.30	0.03	—
2	0.40	0.33	0.030	0.014	0.34	0.50	—
3	0.41	0.30	0.032	0.013	0.32	1.02	—
4	0.40	0.33	0.030	0.013	0.32	2.99	—
5	0.40	0.32	0.026	0.014	0.32	6.02	—
6	1.23	0.35	0.018	0.023	0.28	—	—
7	1.16	0.34	0.015	0.024	0.40	0.50	—
8	1.20	0.35	0.010	0.019	0.33	1.03	—
9	1.22	0.28	0.015	0.020	0.32	3.20	—
10	1.22	0.29	0.015	0.021	0.42	6.02	—
11	1.22	0.35	0.021	0.022	0.36	—	0.28
12	1.25	0.33	0.024	0.026	0.34	—	1.00

mediate carbon contents (0.9 to 1.0 pct C) increasing nickel decreases the amount of austenite stabilized in a given time at 75°F.

It is possible to explain these diverging effects of nickel in high and low carbon steels on the basis of the reaction-path theory for the austenite-martensite transformation.^{2, 5} According to this theory nucleation of the martensite plate is considered to start in a strain embryo that comprises a state somewhere between austenite and martensite. The stabilization phenomenon is believed to be the relaxation of these strain centers. Since a large fraction of them are supplied by prior martensite formation, their number may be considered roughly proportional to the amount of martensite in the steel. Thus the number

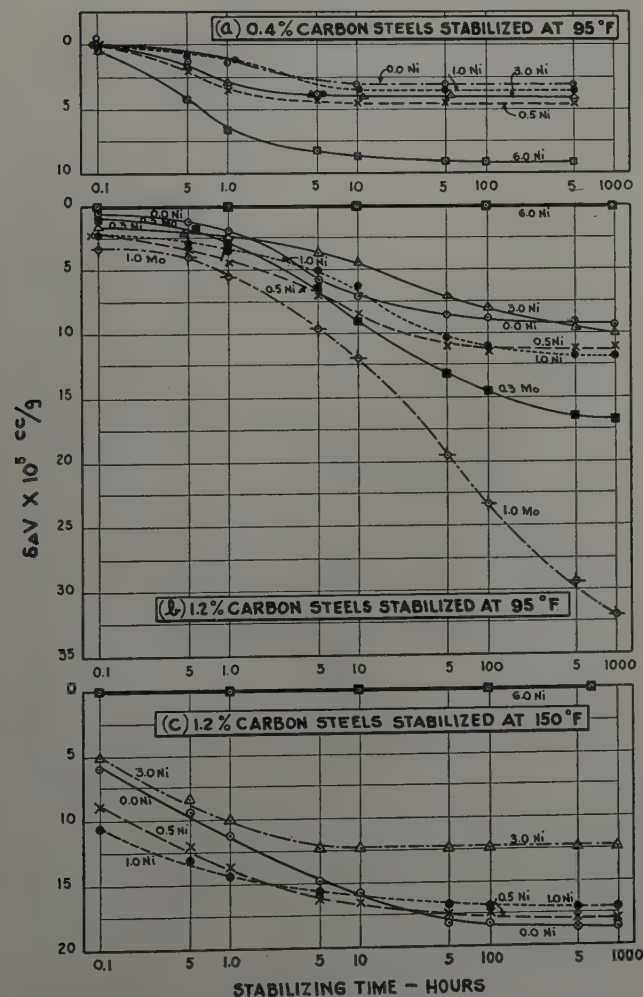
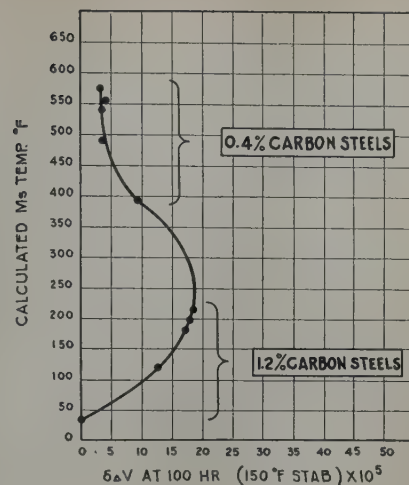


Fig. 1—Specific volume change on quenching to -320°F that is lost as a result of aging ($\delta\Delta V = \Delta V_0 - \Delta V_t$).

Fig. 2— M_s temperature vs decrease in change of specific volume ($\delta\Delta V$) due to stabilization of nickel steels at 150°F .



of strain centers capable of being stabilized would be larger, the greater the degree of undercooling below M_s . However, the amount of austenite available for stabilization becomes less as the steel is cooled further below M_s . The net result of these two opposing effects would cause stabilization at a given temperature to go through a maximum as the M_s temperature is decreased. This behavior seems to be exhibited by the low and high carbon nickel steels investigated here, as shown in Fig. 2. Thus in the 0.4 pct C steels the amount of austenite available for stabilization is low, but increases as the nickel content is raised; the result being an increase in stabilization. In the 1.2 pct C steels the number of strain embryos is low and decreases as the nickel content is raised, thereby decreasing stabilization. In other words, nickel appears to have little or no direct effect on stabilization, but influences the phenomenon indirectly through its effect on the amount of martensite in the as-quenched steel.

Ward, Jepson, and Rait⁵ have found a similar behavior in a series of 1.0 pct C steels with increasing manganese from 0.3 to 6.0 pct. Evidently, at 1.0 pct C such a variation of manganese includes the maximum in the stabilization vs M_s temperature curve.

Effect of Molybdenum

The influence of molybdenum on stabilization of 1.2 pct C steels at 95°F is shown in Fig. 1b. In contrast to nickel, molybdenum markedly increases stabilization at this carbon level. This is in accord with published results for chromium⁵ and theoretical considerations.⁴

References

- W. J. Harris, Jr. and M. Cohen: Stabilization of the Austenite-Martensite Transformation. *Trans. AIME* (1949) 180, p. 447; *METALS TECHNOLOGY* (September 1948).
- M. Cohen: Retained Austenite. *Trans. ASM* (1949) 41, p. 35.
- J. H. Hollomon, L. D. Jaffe, and D. C. Buffum: Stabilization, Tempering and Relaxation in the Austenite-Martensite Transformation. *Journal of Applied Physics* (1947) 18, p. 780.
- M. Cohen, E. S. Machlin, and V. G. Paranjpe: Thermodynamics of the Martensitic Transformation. *Thermodynamics in Physical Metallurgy*. (1950) p. 242. Cleveland. ASM.
- J. O. Ward, M. D. Jepson, and J. R. Rait: Effect of Alloying Elements on the Breakdown of Austenite at Sub-Zero Temperatures—Part I. *Journal Iron and Steel Inst.* (January 1952) p. 1.

Further Progress in the Development of Mg-Zr Alloys to Give Good Creep and Fatigue Properties Between 500° and 650°F

by C. J. P. Ball, A. C. Jessup, P. A. Fisher,

D. J. Whitehead, and J. B. Wilson

The properties of a new magnesium alloy ZT1 containing 3.0 pct Th, 2.5 pct Zn, 0.7 pct Zr are described. The alloy possesses good creep and fatigue resistance up to 650°F, is free from microporosity, and is readily sand-cast. ZT1 is shown to be superior to zinc-free Mg-Th-Zr alloys.

THE advent of the jet engine created a demand for a light sand-casting alloy capable of being cast into large complex shapes and capable of resisting creep at temperatures up to 500°F. This demand has been largely met by alloys of the magnesium-cerium mischmetal-zirconium types, containing about 3 pct Ce mischmetal and 0.7 pct Zr, typified by Elektron magnesium alloys MCZ and ZRE1, the latter alloy also having a zinc addition of 2.5 pct. These alloys utilize the valuable properties at elevated temperatures conferred by the addition of rare earth metals to magnesium, a fact which has been known for many years and discussed by several investigators.¹⁻⁷ Murphy and Payne⁸ showed that the addition of the powerful grain-refining element zirconium to Mg-Ce mischmetal alloys produced alloys

with attractive room temperature properties combined with good creep properties and castability.

With the increasing power of modern jet engines the temperatures to which some of the magnesium parts are subject are likely to exceed the safe working range of the cerium-mischmetal-containing alloys, and at the beginning of the research considerable interest had been shown by aeroplane engine designers in a magnesium sand-casting alloy suitable for service at higher temperatures, e.g., 600°F and above. At an early stage in the development of this type of alloy a check on the fatigue properties at elevated temperatures indicated that, since the fatigue limit even at 10⁸ reversals was appreciably higher than any permissible creep stress, the main emphasis of the research could be concentrated on creep behavior. The primary aim in developing the new alloy has therefore been to attain maximum creep resistance; but due consideration has also been given to other important properties such as castability, tensile strength, and cost.

It is by now well established that it is not possible to correlate creep strength with other short time mechanical properties such as are obtained in tensile

C. J. P. BALL, Member AIME, is Chairman and Managing Director, A. C. JESSUP is Chief Metallurgist, and P. A. FISHER, D. J. WHITEHEAD, and J. B. WILSON are Senior Metallurgists, Magnesium Elektron Ltd., Clifton Junction, near Manchester, England.

Discussion on this paper, TP 3546E, may be sent, 2 copies to AIME by Dec. 1, 1953. Manuscript, Nov. 18, 1952; revision, April 24, 1953. Cleveland Meeting, October 1953.

tests.* Creep testing is therefore essential in de-

* Such apparent correlations, at least for magnesium-base alloys, originated at a time when the number of alloys was considerably smaller than at present and when little information was available on creep strength at elevated temperatures. Thus the theory that ductility at operating temperatures adversely influences the creep resistance of an alloy, once widely held and even now occasionally expressed,⁹ may readily be proved false. For example, tensile tests at 400°F indicate that AZ91 alloy (in the as-cast condition) has an elongation of about 10 pct while Elektron ZRE1 has an elongation of about 30 pct. The creep resistance of ZRE1 is, however, well known to be many times better than that of AZ91 at 400°F.

veloping an alloy for high temperature service. Furthermore experience shows that it is very dangerous to attempt to predict long term creep behavior on the basis of short term tests.

The creep deformation of metals under constant load and at constant temperature is known to occur in three stages. In the first stage (primary creep) the rate of deformation is fairly rapid at the beginning, but soon decreases. In the second stage (secondary creep) the rate of deformation is constant. In the third stage (tertiary creep) the rate increases until the specimen fractures. The amount of deformation, and the time over which each stage persists, depends on the alloy, the temperature of the test, and the stress applied. For any given alloy an increase in temperature or stress usually results in increased deformation in the primary stage, an increase in the rate of deformation in the second stage, and a shorter period of secondary creep leading to earlier onset of tertiary creep and earlier fracture of the specimen. At very high temperatures or loads the secondary stage of creep may not be detectable, the specimen extending rapidly throughout the duration of test.

In developing a creep-resistant alloy the object is to obtain the minimum deformation in the first stage and the minimum rate of deformation, together with the maximum duration, in the second stage. It is very important to note that the onset of the third stage must be avoided in service since, at this point, fracture of the specimen may occur rapidly, the time being subject to wide and unpredictable variations. It is also very important to appreciate that the onset of the third stage of creep cannot be predicted without prior knowledge of the creep behavior of the material under examination. In other words, in examining a new material, the fact that a specimen has extended for a given time at a constant rate is no guarantee that it will continue to do so.

The evolution of a new high temperature alloy therefore necessitates the careful determination of its creep behavior over the whole range of its anticipated service life. Where this is not possible, for example in ground turbine installations designed for a life of 10 or 20 years, the only safe procedure is to use a sufficiently high safety factor which, however, almost inevitably means that the full properties of the alloy are not utilized. For aircraft the need to utilize material strength to the maximum, in order to avoid weight penalties, makes it imperative to examine the behavior of the material over the whole anticipated service life. Fortunately, the design life of aircraft engines is short enough to render such examination practicable. It is appreciated that where components are being designed for a short life—as in the case of certain engines for fighter aircraft—a choice of alloys may be made on the basis of 100 or 400 hr test results. In practice, creep results obtained from long term tests are perfectly satisfactory for short life evaluations; the converse unfortunately is not true.

In the development of this latest addition to the

ultra light, high temperature alloys a service life of 1000 hr has been anticipated and the creep tests have been carried out for at least this time. It is probable that, when the full potentialities of the gas turbine are developed for aircraft use, a test of 1000 hr duration will prove to be much too short and 5000 or 10,000 hr tests may become necessary.

Evaluation of Creep Data

The present authors are strongly of the opinion that if creep data are not to be misleading they should be presented in a form which illustrates plainly the interdependence of stress, strain, and time for a given temperature. The utilization of the conventional "creep limit" derivation,^{10, 11} does not fulfill the above requirement, and the information needed by the engineer is best presented as a family of curves relating stress to time at a given temperature for a series of values of strain, e.g., 0.001, 0.005, 0.01, and 0.05 pct. The maximum duration of time shown on the graph should be at least that expected as the maximum service life of components made from the material in question.

Where the time and available equipment have not been adequate for the completion of such a diagram, the present authors feel that in the absence of accurately drawn strain/time creep curves, full details of creep rates and strains should be given wherever possible. This method of presentation, although somewhat cumbersome to the reader, is the most informative and the least misleading, and has therefore been adopted in this paper.

During the work now recorded considerable thought was given to the possible utility of "time to rupture" tests, particularly in view of their wide use in the literature and for specification testing, particularly of turbine blade materials. A number of pilot tests convinced the authors that, owing to the large extension observed before rupture, the test was of very doubtful utility for the purpose of alloy development, since in every case component failure by extreme distortion would have preceded rupture. Provided that long term tests have been performed, there seems no reason why "time to rupture" tests should not be employed as acceptance tests whenever a satisfactory correlation with the longer tests can be obtained.

Previous Work on Mg-Th Alloys

The first indication that thorium has a beneficial effect on the creep resistance of magnesium was discovered by Sauerwald¹² who investigated both cast and wrought alloys. Leontis (whose work appears to have been carried out roughly in parallel with that described in the present paper) has published excellent surveys of the properties of Mg-Th and Mg-Th-Ce alloys¹⁰ and the effect of zirconium on such alloys.¹¹ Leontis concluded that a Mg-3 pct Th-Zr alloy represented the optimum composition.

Experimental Procedure

Tensile creep tests were performed on three types of machine, namely: 1—5-ton Denison machines made to a design of the National Physical Laboratory and fitted with modified Martens extensometers, 2—direct loading machines of the British Non-Ferrous Metals Research Association type, and 3—miniature creep test units of the type described by Harris¹³ and fitted with extensometers. The tests were carried out in accordance with British Standards Specifications 1686/1950 and 1687/1950.

The alloys examined in the present investigation were made by diluting Mg-Th hardener alloy with

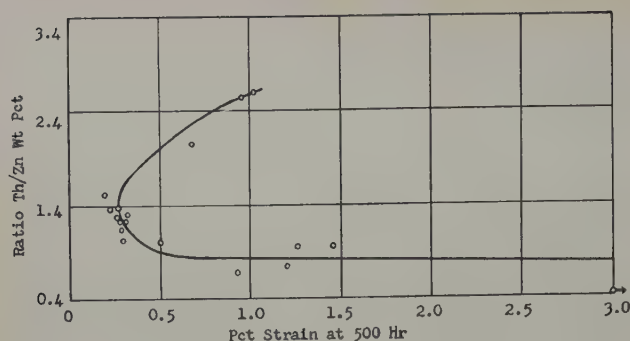


Fig. 1—Effect of Th-Zn ratio on creep resistance. Data plotted from results given in Table III.

pure magnesium and alloying with zirconium by reaction with a fused salt mixture ("Master Salt") containing a reducible zirconium halide. Test pieces were in all cases machined from green sand-cast DTD bars.¹⁴

Thorium occurs with, and must be separated from, rare earth metals of the cerium group. The purity of the alloying materials used in this work was such that the rare earth metal content of the alloy did not exceed 3 pct of the thorium content. Rare earth metals were added when required in the form of commercial cerium mischmetal, an alloy of 45 to 55 pct Ce, the balance being other rare earth metals with a small amount of iron and silicon as impurities.

Because of the wide scatter generally expected in results obtained on creep tests, much consideration was given to the advisability of carrying out duplicate experiments. In view of the time involved it was decided not to duplicate each test but rather to carry out further tests at the same temperature and different stresses since, in addition to providing more information, the departure of the results obtained from a smooth curve would give an adequate indication of the scatter within the results. In fact, experience has indicated that the scatter obtained on the alloys developed during the present work is remarkably small compared with that shown by many other alloys with which we have worked. In the judgment of the authors, the values quoted are suitable for use in the design of high duty components.

Experimental Results

Mg-Th-Zr Alloys: Tensile tests on Mg-Th binary alloys showed that the room temperature mechanical properties were very poor, the ultimate tensile strength being of the order of 10,000 psi in the as-cast state for a 3 pct Th alloy. Addition of zirconium to give a full zirconium content of approximately 0.7 pct raised the tensile strength to approximately 22,000 psi, the yield strength to about 11,000 psi, and the elongation on 2 in. to about 5 pct in the as-cast condition. In view of the superior mechanical properties of the ternary alloys, creep tests were commenced on them. Table I gives the results of a survey of the ternary alloys with thorium content varying from about 2 to 5 pct.

These exploratory tests show that an alloy containing 3 pct Th develops tertiary creep at a stress of 1680 psi at 600°F in the as-cast state. The microstructure of this alloy consists essentially of solid solution with a thorium-rich intergranular network. This intergranular phase is capable of solution treatment at temperatures of the order of 1050°F, the solution treatment being accompanied by only slight grain coarsening. The results of creep tests on solution-treated material show that although the creep properties are markedly improved by solution heat treatment, the alloy still develops tertiary creep at stresses of 3360, and 1120 psi at 600° and 662°F, respectively.

Extension of the duration of solution treatment from 2 to 16 hr appears to be of no benefit to the creep resistance in the case of the alloy containing 3 pct Th.

The room temperature tensile properties of these alloys can be improved by a low temperature aging treatment following the solution treatment. The following properties were obtained with the alloy containing 3 pct Th and 0.7 pct Zr after solution-treatment for 2 hr at 1050°F followed by aging for 16 hr at 400°F, British DTD bars being used: 0.2 pct proof stress, 15,750 psi; ultimate tensile strength, 31,500 psi; and elongation on 2 in., 6 pct. Slightly lower tensile values are obtained if the aging treatment is carried out at 600°F, the following being typical results: 0.2 pct proof stress, 14,750 psi; ulti-

Table I. Results of Creep Tests on Sand-Cast Mg-Th-Zr Alloys

Analysis, Pct		Temperature, °F	Stress, Psi	Plastic Strain, Pct					Creep Rate, In./In./Hr x10 ⁷	Initial Condition*
Th	Zr			100 Hr	300 Hr	500 Hr	700 Hr	1000 Hr		
3.0	0.71	600	1680	0.07	0.18	0.4	0.8	1.6	300(at 1000 hr)	As-cast
2.8	0.66	600	3360	0.55	9.0	21.8**			26,000(at 350 hr)	As-cast
2.8	0.63	600	1680	0.045	0.12	0.33	0.465	0.68	71(at 1000 hr)	Solution treated 2 hr at 1050°F
3.6	0.72	600	3360	0.3	1.1	3.75	9.2††		4,400(at 700 hr)	Solution treated 2hr at 1050°F
3.6	0.72	662	1120	0.08	0.30	0.60	1.03	1.78	280(at 1000 hr)	Solution treated 2 hr at 1050°F
3.0	0.71	600	3360	0.36	6.7	16.6**			19,000(at 350 hr)	Solution treated 16 hr at 1050°F
3.0	0.71	600	3360	0.38	4.6	17.4†			18,000(at 380 hr)	Solution treated 2 hr at 1050°F plus 16 hr at 400°F
1.9	0.65	600	3360	1.38	>20††				10,000(at 180 hr)	Solution treated 2 hr at 1050°F
4.7	0.66	600	3360	0.30	2.45	>24‡			19,000(at 420 hr)	Solution treated 16 hr at 1050°F

* All specimens were held for 16 hr at the temperature of test before applying the load.

** At 360 hr. Fractured.

† At 384 hr. Fractured.

†† At 240 hr.

‡ At 450 hr.

‡‡ Fractured at 700 hr.

Note. The work described in this report was carried out in accordance with British practice with temperature measured in degrees centigrade and load in long tons (2240 lb). For convenience these figures have been calculated back to degrees Fahrenheit and pounds.

Table II. Results of Creep Tests on Sand-Cast Mg-Th-RE*-Zr Alloys at 1680 Psi at 600°F

Analysis, Pct			Plastic Strain, Pct					Creep Rate at 1000 Hr, In./In./Hr x 10 ⁷	Initial Condition†
Th	RE*	Zr	100 Hr	300 Hr	500 Hr	700 Hr	1000 Hr		
3.4	1.4	0.7	0.24	0.91	1.71	2.35	3.37	332	As-cast
3.0	3.3	0.68	0.195	0.4	0.57	0.73	0.98	85	As-cast
3.0	4.0	0.7	0.13	0.275	0.415	0.56	0.85	81	As-cast
3.0	3.0	0.68	0.13	0.385	0.74	0.975	1.36	124	Solution treated 2 hr at 1050°F

* RE is cerium mischmetal.

† All specimens were held for 16 hr at the temperature of test before applying the load.

mate tensile strength, 30,000 psi; and elongation on 2 in., 6 pct.

It appears however that the creep resistance at 600°F of the alloy containing 3 pct Th may be adversely affected by the use of an aging treatment at 400°F. Comparison of the results obtained with and without the treatment at 400°F indicates that a considerably higher creep rate was obtained when this precipitation treatment was included, Table I. The results in Table I also indicate that the optimum thorium content is probably of the order of 3 pct.

It is evident that, for the ternary alloy containing 3 pct Th in the solution-treated state, the maximum feasible working stress at 600°F for a creep rate of less than 5×10^{-6} in. per in. per hr at 1000 hr is approximately 1680 psi. The alloy suffers from the serious drawback that a high temperature solution heat treatment is essential for the development of optimum creep resistance. Protective atmospheres are required for the heat treatment of magnesium alloys at 1050°F and large complex castings would require careful jiggling to avoid distortion.

Effect of Cerium Mischmetal Additions to Mg-Th-Zr Alloys: Results are given in Table II of an examination of the effect on creep resistance at 600°F of the addition of varying amounts of cerium mischmetal to the ternary Mg-Th-Zr alloy containing 3 pct Th.

The addition of up to 4 pct cerium mischmetal to this ternary alloy results in no improvement to the creep resistance obtainable in the solution-treated condition. Solution treatment of the ternary alloy to which 3 pct of cerium mischmetal has been added has no marked effect on the creep behavior at 600°F.

Effect of Zinc Additions to Mg-Th-Zr Alloys: Table III gives the results of creep tests carried out

at a common stress of 3360 psi at 600°F on 20 compositions in the Mg-Th-Zn-Zr series.

The results are given in order of increasing Th/Zn ratio and plotted in Fig. 1. It can be seen that, within the limits investigated, there is a clearly defined

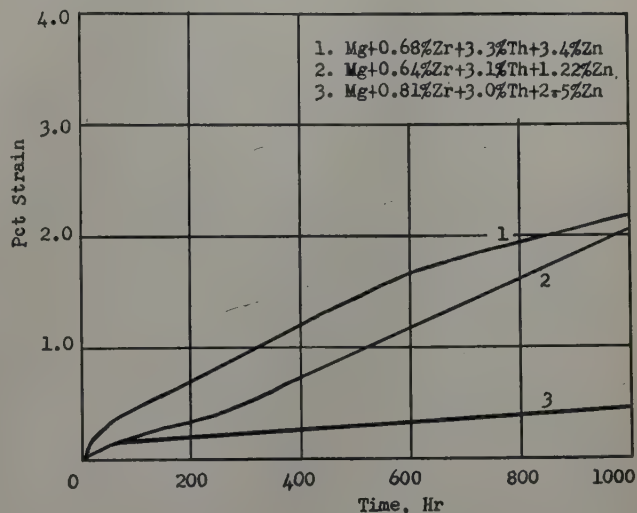


Fig. 2—Comparison of three alloys of equal thorium content with varying Th-Zn ratios. Tested at 3360 lb per sq in. at 600°F.

relationship between creep resistance (as defined by the strain at 500 hr) and composition. The optimum Th/Zn ratio for best creep resistance occurs at about 1.3, corresponding with a nominal composition of 3 pct Th, 2.5 pct Zn.† This composition has been

† From the curve plotted in Fig. 2, based on the results obtained to date, the following limits appear suitable for specification purposes: Th, 2.5 to 3.5 pct and Zn, 1.75 to 2.5 pct.

Table III. Results of Creep Tests on Sand-Cast Mg-Th-Zn-Zr Alloys at 3360 Psi at 600°F*

Analysis, Pct				Plastic Strain, Pct					Creep Rate at 1000 Hr, In./In./Hr x 10 ⁷
Th	Zn	Zr	Th/Zn	100 Hr	300 Hr	500 Hr	700 Hr	1000 Hr	
1.9	4.7	N.D.†	0.4	1.56	9 (fractured)	0.92	1.10	1.50	2800 (250 hr)
2.6	3.9	N.D.	0.67	0.45	0.77	1.2	2.1	—	75 (800 hr)
2.0	2.7	0.65	0.75	3.0	0.68	1.25	—	—	430 (800 hr)
3.85	4.1	0.74	0.94	0.32	0.78	1.45	1.82	2.16	240 (500 hr)
3.3	3.4	0.68	0.96	0.45	0.92	1.45	0.65	0.89	95
2.7	2.7	0.76	1.0	0.19	0.33	0.49	0.62	0.88	82
2.8	2.65	0.67	1.05	0.21	0.34	0.45	0.67	0.91	88
2.6	2.5	0.77	1.04	0.17	0.32	0.50	0.67	0.48	39
2.5	2.4	N.D.	1.04	0.10	0.19	0.29	0.26	0.49	42
5.1	4.4	0.44	1.16	0.116	0.10	0.29	0.368	0.355	15
3.1	2.5	0.67	1.24	0.13	0.225	0.28	0.315	0.45	31
3.0	2.5	0.81	1.24	0.15	0.23	0.31	0.36	0.63	87
2.0	1.5	0.65	1.30	0.095	0.18	0.26	0.37	0.80	110
2.6	2.0	0.88	1.30	0.15	0.23	0.32	0.47	—	30 (500 hr)
3.85	2.8	0.76	1.38	0.12	0.21	0.27	—	—	20
3.10	2.0	0.75	1.55	0.12	0.15	0.19	0.22	0.28	100
3.1	1.5	0.66	2.06	0.24	0.46	0.67	0.89	1.21	230
3.1	1.22	0.64	2.54	0.19	0.53	0.95	1.38	2.05	45
3.65	1.4	0.67	2.60	0.33	0.71	1.02	1.16	1.28	190 (500 hr)
1.9	0.7	0.70	2.7	0.2	0.6	0.90	—	—	—

* The initial condition was as-cast. All specimens were held for 16 hr at the temperature of test before applying the load.

† N.D., not determined.

Table IV. Results of Creep Tests on Sand-Cast Mg-Th-Zn-Zr Alloys at 2240 Psi at 600°F*

Analysis, Pct				Plastic Strain, Pct					Creep Rate at 1000 Hr, In./In./Hr × 10 ⁷
Th	Zn	Zr	Th/Zn	100 Hr	300 Hr	500 Hr	700 Hr	1000 Hr	
3.2	4.0	0.58	0.8	0.05	0.10	0.13	0.16	0.20	14
1.2	1.5	0.64	0.8	0.06	0.096	0.13	0.17	0.22	18
3.85	4.1	0.74	0.94	0.15	0.25	0.29	0.32	0.36	14
2.5	2.4	N.D.†	1.04	0.08	0.10	0.10	0.115	0.135	6
2.6	2.5	0.77	1.04	0.06	0.11	0.15	0.19	0.25	18
5.1	4.4	0.44	1.16	0.07	0.108	0.14	0.172	0.22	16
3.1	2.5	0.67	1.24	0.10	0.17	0.19	0.22	0.26	15
2.6	2.0	0.88	1.30	0.08	0.11	0.15	0.19	0.24	20
3.85	2.8	0.76	1.38	0.06	0.07	0.10	0.10	0.12	7
3.1	2.0	0.75	1.55	0.03	0.04	0.05	0.07	0.09	6
3.1	1.5	0.66	2.06	0.08	0.10	0.12	0.145	0.18	10
3.1	1.22	0.64	2.54	0.11	0.29	0.36	0.39	0.43	14
3.65	1.40	0.67	2.60	0.13	0.20	0.25	0.29	0.35	21

* The initial condition was as-cast. All specimens were held for 16 hr at temperatures of test before applying the load.

† N.D., not determined.

named Elektron magnesium alloy ZT1.‡ The marked

‡ The alloy composition (3.0 pct Th, 2.5 pct Zn, 0.7 pct Zr) is protected by U.S. Patent 2,604,396.

effect of Th/Zn ratio on creep resistance is further shown by Fig. 2 which gives strain/time curves for

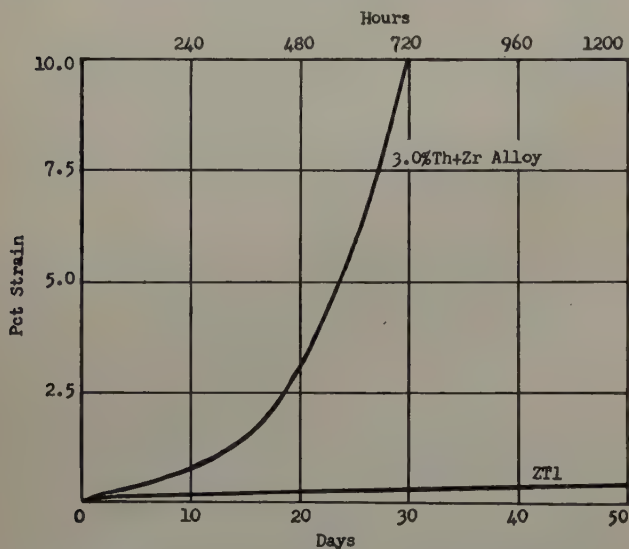


Fig. 3—Comparison of creep behavior of zinc-free thorium alloy with ZT1. Both alloys tested at 3360 lb per sq in. at 600°F.

tests at a stress of 3360 psi at 600°F on three alloys of sensibly equal thorium contents (3 pct) but with Th/Zn ratios of 0.96, 1.2, and 2.5. Tests on alloys containing 3.85 and 5.1 pct Th (Table III) indicate that under these conditions of test there is no advantage to be gained by increasing the thorium content over 3 pct while maintaining the Th/Zn ratio close to 1.3.

With thorium contents appreciably below 3 pct the results included in Table III indicate a tendency for the creep rate to increase toward the end of the

1000 hr test. It may be possible to produce an alloy having satisfactory creep resistance and containing as little as 2 pct Th, with the appropriate zinc content. It is evident, however, that the permissible variation in composition decreases as the thorium content is reduced and it remains for further investigation to determine whether an alloy containing as little as 2 pct Th can be safely employed in industrial practice. This point is now under investigation.

A number of tests on alloys of varying thorium and zinc contents have been carried out at a stress of 2240 psi at 600°F and the results are included in Table IV. It is evident that Th/Zn ratio is not so critical at the lower stress and a wide range of composition is capable of giving satisfactory creep rates. In fact all the alloys investigated, with Th/Zn ratios varying from 0.8 to 2.6, would be usable at a stress of 2240 psi at 600°F.

The very marked effect of zinc in improving the creep resistance of Mg-Th-Zr alloys is illustrated by Fig. 3 which shows the effect of a 2.5 pct Zn addition to a 3 pct Th, 0.7 pct Zr alloy when tested in creep at a stress of 3360 psi at 600°F. Although the zinc-free alloy is in the solution-treated condition it develops rapid tertiary creep after the 300 hr test, leading to ultimate fracture before the expiration of 1000 hr, whereas ZT1 alloy extends about 0.4 pct in 1000 hr.

Effect of Prior Heat Treatment on the Creep Resistance of ZT1: Results are given in Table V of creep tests carried out on ZT1 after heat treatment for 24 hr at temperatures from 750° to 930°F.

It is evident that the use of heat-treatment temperatures between about 700°F and about 930°F damages the creep resistance of ZT1. The solidus of this alloy is believed to be between 930° and 1025°F. The damaging effect on creep resistance apparently decreases as the solidus temperature is reached and this suggests that solution of a thorium-rich phase occurs at about 930°F. Below this temperature it is

Table V. Results of Creep Tests on ZT1 after Various Heat-Treatment Cycles. Tests at 3360 Psi at 600°F

Analysis, Pct			Plastic Strain, Pct					Creep Rate at 1000 Hr, In./In./Hr × 10 ⁷	Initial Condition*
Th	Zn	Zr	100 Hr	300 Hr	500 Hr	700 Hr	1000 Hr		
3.1	2.5	0.67	0.13	0.225	0.28	0.315	0.355	15	As-cast
3.3	2.6	0.78	0.22	0.39	0.49	0.60	1.01	180	H.T. 24 hr at 750°F
3.4	2.6	0.74	0.16	0.27	0.41	0.65	1.08	150	H.T. 24 hr at 880°F
3.4	2.6	0.74	0.22	0.35	0.47	0.59	0.76	58	H.T. 24 hr at 930°F

* All specimens were held for 16 hr at temperatures of test before applying the load.

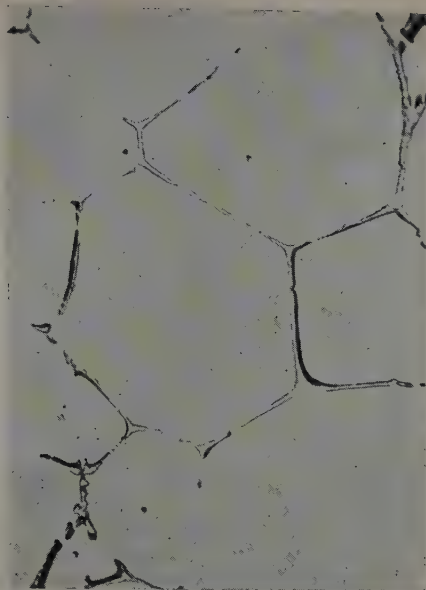


Fig. 4—Micrograph showing typical structure of Mg-Zn-Th-Zr alloy illustrating blue tortuous phase. X1000. Area reduced slightly for reproduction.

probable that precipitation of this phase occurs, the creep resistance being impaired by progressive coarsening of this precipitate as the heat-treatment temperature is increased, as suggested by Mellor and Ridley.⁶ In this respect ZT1 alloy appears to behave in a manner similar to that of Elektron ZRE1.

Microstructural Features of Mg-Th-Zn-Zr Alloys: The microstructure of Mg-Th-Zn-Zr alloys is generally similar to that of the Mg-Ce-Zn-Zr alloys, the grain boundaries being well delineated by free intermetallic compound resulting from breakdown of the eutectic. Two distinct forms of grain boundary phase have been observed in Mg-Th-Zn-Zr alloys, one blue in color and tortuous, and the other brown and more acicular in shape. The type of grain boundary phase is dependent on the Th/Zn ratio. With high zinc contents, at ratios below about 0.5, only the blue tortuous phase is present, and with low zinc contents, at ratios above about 1.4, only the brown acicular phase is present.

The optimum creep resistance appears to be associated with compositions at which the brown phase preponderates over the blue. Reduction of zinc content below this point, although completing the conversion to the brown phase, results in a decrease in creep resistance. Typical micrographs of the phases are shown in Figs. 4 and 5.

Effect of Cerium-Mischmetal Additions to Mg-Th-Zn-Zr Alloys: Partial Replacement of the Thorium Content of ZT1 with Cerium Mischmetal: In view of the relatively high cost of thorium as an alloying

constituent, tests were carried out to determine whether a proportion of the thorium content of ZT1 could be replaced by rare earth metals without impairment of the creep performance at 600°F.

The first two tests of Table VI show that although ZT1 alloy in which about 50 pct of the thorium has been replaced by cerium mischmetal behaves satisfactorily at a stress of 1680 psi at 600°F, the creep resistance at 3360 psi is seriously affected. It is evident that economies cannot be effected in this manner without some sacrifice of creep strength.

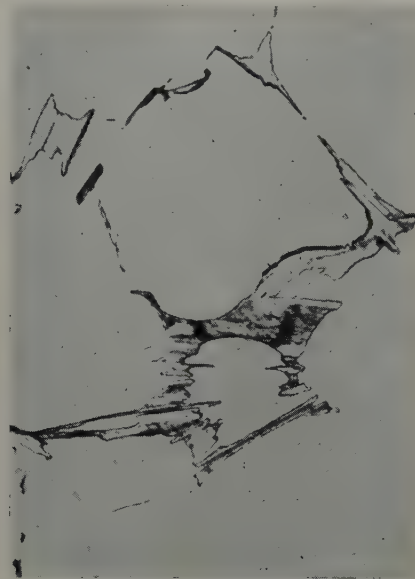


Fig. 5—Micrograph showing typical structure of Mg-Zn-Th-Zr alloy illustrating brown acicular phase. X1000. Area reduced slightly for reproduction.

Addition of Cerium Mischmetal to ZT1 Alloy: In view of the deleterious effect of cerium mischmetal on Mg-Th-Zn-Zr alloys, further tests were carried out to investigate the damaging effect in more detail. Table VI gives the results of tests on ZT1 alloy containing up to 1.2 pct Ce mischmetal at 3360 psi at 600°F. It is evident from these tests that a rare earth metal content of 0.2 pct or greater has an adverse effect on creep resistance. With a rare earth metal content of greater than 0.2 pct there is a tendency for the alloy to develop tertiary creep after 500 hr.

Properties of ZT1 Alloy

The essential properties required of a high temperature material have been summarized¹⁵ as follows: 1—creep resistance, i.e., resistance to deformation under the influence of a steady applied stress; 2—fatigue strength, i.e., resistance to cracking under the influence of a cyclic stress; 3—resistance to corrosion by the surrounding atmosphere (including

Table VI. Results of Creep Tests on Sand-Cast Mg-Th-RE-Zn-Zr Alloys at 600°F

Analysis, Pct				Stress, Psi	Plastic Strain, Pct					Creep Rate at 1000 Hr, In./In./Hr x 10 ⁷
Th	RE	Zn	Zr		100 Hr	300 Hr	500 Hr	700 Hr	1000 Hr	
3.1	<0.1	2.5	0.7	1,680	0.05	0.125	0.15	0.175	0.20	12
1.1	1.8	2.3	0.79	1,680	0.12	0.19	0.22	0.25	0.30	11
3.1	<0.1	2.5	0.7	3,360	0.13	0.225	0.28	0.315	0.355	15
1.57	1.52	2.5	0.65	3,360	1.1	1.92	—	—	—	980(150 hr)
3.1	0.2	2.6	0.72	3,360	0.08	0.15	0.24	0.39	0.72	130
3.1	0.5	2.5	0.72	3,360	0.17	0.32	0.46	0.63	1.24	250
3.1	0.8	2.6	0.73	3,360	0.22	0.43	0.64	0.90	1.63	250
3.0	1.2	2.6	0.69	3,360	0.40	—	—	—	—	400(250 hr)

* The initial condition was as-cast. All specimens were held for 16 hr at the temperature of test before applying the load.

oxidation and scaling at operating temperature); 4—resistance to thermal shock, i.e., resistance to cracking under the influence of stresses developed by rapid changes of temperature. In considering the specific requirements of a magnesium-base casting alloy for elevated temperature service, the following additional factors may be included: 5—satisfactory strength and ductility at room temperature; 6—ability to withstand high stresses of short duration at high temperature without excessive permanent set; 7—ease of casting; and 8—other factors of importance, including cost, weldability, pressure tightness, density and ease of machining.

It is of interest to see how ZT1 alloy meets these requirements.

Creep Resistance: Table VII gives the creep properties of ZT1 at 600° and 662°F. These properties are

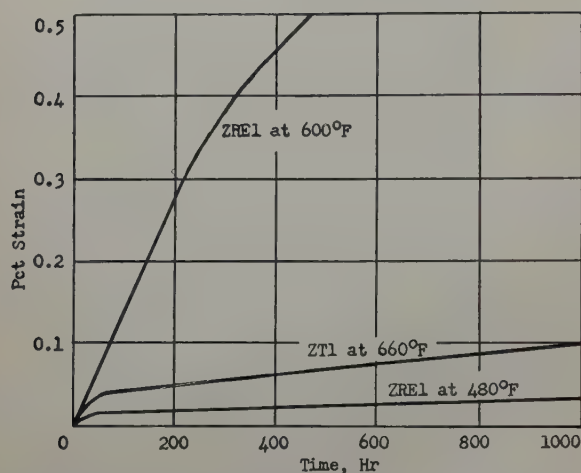


Fig. 6—Comparison of creep behavior of ZT1 and Elektron ZRE1 alloys. All tests at 1120 lb per sq in.

a considerable advance on the creep resistant magnesium alloys at present in use. For conditions of equal stress, ZT1 offers a permissible increase of about 120°F in service temperature over ZRE1 alloy. Fig. 6 illustrates the improved creep resistance of ZT1 as compared with ZRE1 alloy. Whereas ZRE1, although perfectly satisfactory at a stress of 1120 psi at 482°F, shows considerable deformation at 600°F, ZT1 is seen to display very satisfactory creep resistance at 1120 psi at 662°F.

Fatigue Strength: Table VIII gives the results of single point loading alternating bending fatigue tests on ZT1 alloy at room and elevated temperature.

Resistance to Corrosion and Oxidation: Corrosion tests on ZT1 alloy indicate that it has the same order of corrosion resistance as the existing high temperature magnesium alloys containing mischmetal, for example, a 28 day total immersion test in 3 pct salt solution saturated with $Mg(OH)_2$ gave for ZT1 (heat-treated 16 hr 600°F) a rate 1 mg per sq cm per day, and for ZRE1 (heat-treated 16 hr 350° to 400°F) a rate 1.5 to 2 mg per sq cm per day; and a 6 months sea water spray test gave for ZT1 (heat-treated 16 hr 600°F) a rate 0.4 mg per sq cm per day, and for ZRE1 (heat-treated 16 hr 350° to 400°F) a rate 0.3 to 0.5 mg per sq cm per day.

Although accurate determinations of the rate of oxidation at elevated temperatures have not been carried out on ZT1 alloy, it has been observed that exposure to normal atmosphere at temperatures up

Table VII. Creep Properties of ZT1 at Elevated Temperature

Temperature, °F	Stress, Psi	Plastic Strain, Pct					Creep Rate 1000 Hr, In./In./Hr x 10 ⁷
		100 Hr	300 Hr	500 Hr	700 Hr	1000 Hr	
600	1680	0.10	0.125	0.147	0.170	0.20	12
600	2240	0.10	0.17	0.19	0.22	0.26	15
600	3360	0.13	0.225	0.28	0.315	0.355	15
662	1120	0.035	0.05	0.07	0.08	0.105	9
662	1680	0.09	0.25	0.475	0.90	1.99	35
662	2240	0.12	0.30	0.60	1.15	2.59	430

to 662°F for periods of up to 1000 hr results in only superficial tarnishing. No serious exfoliation has been observed at temperatures up to 752°F.

Resistance to Thermal Shock: The ductility of ZT1 alloy at room and elevated temperatures is more than adequate to insure freedom from cracking under stresses developed by rapid changes in temperature.

Mechanical Properties at Room Temperature: These are of importance in view of the fact that the castings must be capable of being machined and fitted without danger of cracking or distortion. DTD type test bars in ZT1 alloy, stabilized 16 hr at 600°F and tested at room temperature, give the following properties: 0.2 pct proof stress, 12,500 to 15,000 psi; ultimate tensile strength, 27,000 to 31,000 psi; and elongation on 2 in., 5 to 10 pct. These properties are a considerable advance on those obtainable from the rare earth metal containing, creep resistant Mg-Zr alloys at present in use, particularly as regards ultimate tensile strength. The room temperature tensile properties of ZT1 may therefore be considered as adequate.

Tensile Properties at Elevated Temperature: Table IX lists the high temperature tensile properties of ZT1. It can be seen that ZT1 shows good retention of tensile properties over the temperature range 527° to 662°F. In particular, it is to be noted that the value for limit of proportionality shows no drop over this temperature range. The progressive reduction in values for elongation with increase in the temperature of test is an unusual feature in a magnesium casting alloy. The tensile elongation appears to reach a minimum value of about 35 pct over a temperature range of 650° to 700°F but above this range the elongation increases progressively, and at 750°F is about 40 pct. The values for elongation are, however, well above any minimum likely to arise as a service requirement and this progressive decrease in elongation is therefore more of a metallurgical novelty than of practical significance.

Table VIII. Results of Fatigue Tests on ZT1 Alloy

Temperature of Test, °F	Fatigue Limit for 5x10 ⁷ Reversals in Psi. Notched*	Fatigue Limit for Specified Reversals in Psi. Unnotched		
		10 ⁷	5x10 ⁷	10 ⁸
68	± 10,080		± 10,080	
392		± 7,170		± 7,170
482		± 6,050		± 6,050
600		± 4,700		± 3,360
662		± 3,470		± 2,350

* The notch used in this test had a stress concentration factor of 2.

Table IX. Elevated Temperature Tensile Properties of ZT1

Temperature of Test, °F	Limit of Proportionality, Psi	0.1 Pct Proof Stress, Psi	0.2 Pct Proof Stress, Psi	Ultimate Tensile Strength, Psi	Elongation, Pct on 2 In.
527	3300	7050	7900	12,100	50
572	3300	6800	7600	10,750	45
617	3300	6300	7100	10,080	40
662	3300	6100	6900	9,630	35

Castability of ZT1 Alloy: Several large castings of up to 200 lb in weight have been made in ZT1 alloy. The alloy is completely free from microporosity and can be handled in the foundry in the same manner as Elektron alloys ZRE1 and MCZ. A tendency to the formation of folds due to casting skins in thin sections has been observed in certain castings, but this can be overcome by the choice of suitable running techniques.

Other Factors: ZT1 alloy, being a magnesium alloy not subject to microporosity, can be cast into large thin walled shapes with the certainty that the resultant casting will be pressure tight provided it is free from cracks and hot tears. The casting characteristics of ZT1 are such that no trouble should be experienced with cracks or hot tears. Only a simple low temperature heat treatment is required.

Like Elektron magnesium alloys ZRE1 and MCZ, ZT1 is readily weldable using the techniques at present in use for magnesium alloys. This is an important factor in foundry economics and obviates the scrapping of castings for minor defects amenable to repair by welding.

ZT1 alloy possesses the same ease of machining as other magnesium alloys.

High Temperature Tensile Properties of Zinc-Free 3 pct Th Alloy

It was thought to be of interest to examine the high temperature tensile properties of the zinc-free 3 pct Th-Zr alloy under the same testing conditions as used for ZT1, and Table X gives the values obtained.

The two different temperatures for precipitation treatment were examined in order to provide a comparison with the values quoted by Leontis,¹¹ who used a precipitation temperature of 400°F, and to examine the effect of precipitation at 600°F in view of the apparent loss in creep strength when the lower temperature was used, see Table I.

The higher precipitation temperature results, as might be expected, in a decrease in values for limit of proportionality and proof stress but does not

Table X. Elevated Temperature Tensile Properties of 3 Pct Th, 0.7 Pct Zr Alloy

Temperature of Test, °F	Limit of Proportionality, Psi	0.1 Pct Proof Stress, Psi	0.2 Pct Proof Stress, Psi	Ultimate Tensile Strength, Psi	Elongation, Pct on 2 In.
Heat-Treated 2 Hr 1050°F, Plus 16 Hr 400°F					
572	5600	9400	10,700	17,500	24
662	2800	5500	6,400	13,200	30
Heat-Treated 2 Hr 1050°F, Plus 16 Hr 600°F					
572	4500	8000	9,200	17,000	18
662	2500	4900	5,800	15,000	25

affect the value for tensile strength appreciably. The value for proof stress at 572°F may be compared roughly with that quoted by Leontis at 600°F and is about 2000 psi lower than he obtained. This is very probably due to the use of a test bar of different types and possibly to differences in method of testing.

[§] Leontis appears to have used unmachined cast to shape bars, which give values for proof stress appreciably higher than those obtained from the British DTD bar.

In comparison with ZT1 it can be seen that the tensile properties of the 3 pct Th-0.7 pct Zr alloy are higher at 572°F but show a marked drop over the temperature range 572° to 662°F. The values for limit of proportionality and proof stress thus become lower than those for ZT1 at 662°F, the value for ultimate strength remaining above that for ZT1.

Conclusions

1—Mg-Th-Zn-Zr alloys are capable of showing a high level of creep resistance at temperatures of 600°F and above.

2—For optimum creep resistance, the zinc content must be closely controlled in relationship to the thorium content. A preferred composition of 3 pct Th, 2.5 pct Zn, 0.7 pct Zr has been determined: the composition has been termed ZT1.

3—ZT1 alloy possesses superior creep resistance to the equivalent zinc-free alloy.

4—The alloy possesses good fatigue properties at room and elevated temperatures combined with good tensile properties and corrosion resistance.

5—ZT1 alloy shows good retention of high temperature tensile properties over the range 527° to 662°F. In particular the value for the limit of proportionality shows no drop over this temperature range.

6—ZT1 alloy can be successfully cast in sand molds. The alloy is nonmicroporous and shows very good freedom from tendency to hot cracking.

7—Additions of cerium mischmetal are detrimental to the creep resistance of ZT1.

References

- ¹ A. Beck: *The Technology of Magnesium and Its Alloys* (1940) pp. 267-268. London. F. A. Hughes & Co.
- ² J. L. Haughton and W. E. Prytherch: *Magnesium and Its Alloys* (1937) London. H. M. Stationery Office.
- ³ P. A. Fisher: *Magnesium Review and Abstracts* (1944) 4, p. 65.
- ⁴ A. A. Moore and J. C. McDonald: *Symposium for Gas Turbines* (1946) p. 180. ASTM.
- ⁵ T. E. Leontis and J. P. Murphy: *Trans. AIME* (1946) 166, p. 295; *METALS TECHNOLOGY* (April 1946).
- ⁶ G. A. Mellor and R. W. Ridley: *Journal Inst. Metals* (1949) 75, p. 679.
- ⁷ R. F. Marande: *Materials and Methods* (1946) p. 23.
- ⁸ A. J. Murphy and R. J. M. Payne: *Journal Inst. Metals* (1947) 73, p. 105.
- ⁹ *Symposium on Materials and Design for Light Weight Construction* (February 1951) p. 34. Issued by Engineering Research and Development Laboratories, Fort Belvoir, Va.
- ¹⁰ T. E. Leontis: *Trans. AIME* (1952) 194, p. 287; *JOURNAL OF METALS* (March 1952).
- ¹¹ T. E. Leontis: *Trans. AIME* (1952) 194, p. 633; *JOURNAL OF METALS* (June 1952).
- ¹² F. Sauerwald: *Ztsch. anorg. allgem. Chem.* (1949) pp. 258, 296.
- ¹³ G. T. Harris: *Metallurgia* (1946) 34, p. 129.
- ¹⁴ British Standards Institution: Specification L.101. Fig. 1B.
- ¹⁵ L. B. Pfeil: *High Temperature Materials: Tests Used as Criteria of Service Behavior. Schweizer Archiv* (1952) pp. 88-97.

Textures of Rolled and Annealed Iodide Zirconium

by J. H. Keeler, W. R. Hibbard, Jr., and B. F. Decker

Textures of hot-rolled, of cold-rolled, and of cold-rolled and annealed zirconium sheets were determined by use of an X-ray spectrogoniometer. All textures showed a tilt of the basal planes $\pm 40^\circ$ from the rolling plane about the rolling direction. Deformation textures showed the [1010] direction to be approximately in the rolling direction. After recrystallization, the [1120] direction was approximately in the rolling direction. This texture was sharpened by annealing above the allotropic transformation. Textures of sheet produced by alternately cold rolling and then annealing were less strongly oriented than sheets that underwent severe deformation without intermediate anneals.

THIS study of the deformation and annealing textures of high purity zirconium was carried out to supplement an investigation of zirconium and zirconium-base alloys. The spectrogoniometer method of pole figure determination was used and yielded more detailed and precise information than the photographic techniques used by previous investigators.

Earlier investigations of the rolling textures of hexagonal metals titanium,^{1,2} beryllium,³ and zirconium^{4,5} having a c/a ratio slightly less than 1.6 disclosed a rotation of the basal planes from the rolling plane about the rolling direction so that the basal poles were inclined toward the transverse direction, and with one exception,⁴ the [10 $\bar{1}$ 0] direction was found parallel to the rolling direction. Similarly, hot rolling produced a spread of the basal poles in the transverse direction,^{2,3,5} with the [10 $\bar{1}$ 0] direction parallel to the rolling direction. The textures of these metals after recrystallization differ somewhat from each other although still exhibiting the transverse rotation of the basal poles about the rolling direction. Zirconium⁵ was found to have the [11 $\bar{2}$ 0] direction in the rolling direction, beryllium³ continued to have the [10 $\bar{1}$ 0] direction in the rolling direction, and titanium² was shown to have the [10 $\bar{1}$ 0] direction in the rolling direction (the cold-rolling texture) when annealed at 1000°F, changing to the [11 $\bar{2}$ 0] direction in the rolling direction when annealed at 1500°F. It was suggested² that the titanium retains the deformation texture after recrystallization, and preferred grain growth at higher temperatures produces the second texture. Annealing above the allotropic transformation temperature did not appreciably change the high temperature recrystallization texture for titanium.² Coarse-grained zirconium showed more spread⁵ in the transformation texture than in the recrystallization texture.

J. H. KEELER, W. R. HIBBARD, Jr., Members AIME, and B. F. DECKER are associated with the Metallurgy Research Dept., Research Laboratory, General Electric Co., Schenectady.

Discussion on this paper, TP 3549E, may be sent, 2 copies, to AIME by Dec. 1, 1953. Manuscript, Jan. 3, 1953. Cleveland Meeting, October 1953.

Table I. Composition of Crystal-Bar Zirconium

Element	Weight Pct
Hf	0.3 max.
Fe	0.02-0.1
Al	0.005-0.02
Cr	0.02-0.1
Cu	0.001-0.005
Ni	0.005-0.02
Mg	0.001-0.005
Mo	0.01
N ₂	0.007*

* Chemical analysis (oxygen and carbon are estimated at 0.02 pct).

Experimental Procedure

The material used in this investigation was crystal-bar zirconium prepared by the iodide process. The major impurity was hafnium which was less than 0.3 pct. The composition obtained by spectrographic analysis is given in Table I.

The hot-rolled specimen was prepared from a 50-g button of zirconium arc-melted in a water-cooled crucible under an argon atmosphere. This button was enclosed in a welded sheath of soft iron and the ensemble was rolled at 825°C. After each pass the sheath was put back into the furnace to allow it to return to the desired temperature. The zirconium ingot was reduced in this manner to a thickness of about 0.035 in., a reduction of approximately 90 pct. The sheet after removal from the sheath was alternately polished and etched to a thickness of 0.001 in.

Cold-rolled specimens were prepared from crystal bar by a series of reductions of approximately 0.010 in. until the sheet reached a thickness of 0.010 in. after which it was cold-rolled to 0.001 in. thickness between sheets of alloy steel. The total cold reduction amounted to about 99.8 pct. Specimens were annealed in an evacuated Vycor or quartz tube.

The transmission pole figures were obtained by the quantitative method of Decker, Asp, and Harker⁶ modified by Geisler⁷ using an X-ray spectrogoniometer with Cu K α radiation. Unless otherwise specified all four quadrants were examined with 5° increments along the radius of the pole figure. Absorption corrections were made for changes in length of the X-ray path through the sample as inclination of the

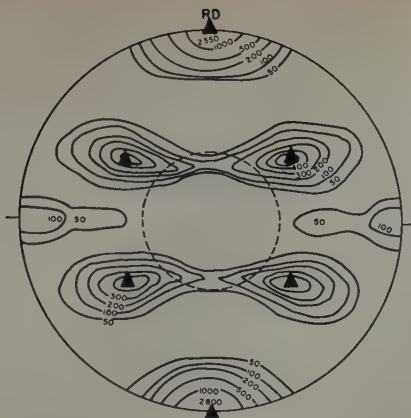


Fig. 1— $(10\bar{1}0)$ pole figure for 99.8 pct cold-rolled zirconium sheet. The orientations of $(10\bar{1}0)$ poles for the deformation texture $(0001) [10\bar{1}0]$ with a tilt of $\pm 40^\circ$ about the axis of the rolling direction are indicated by triangles.

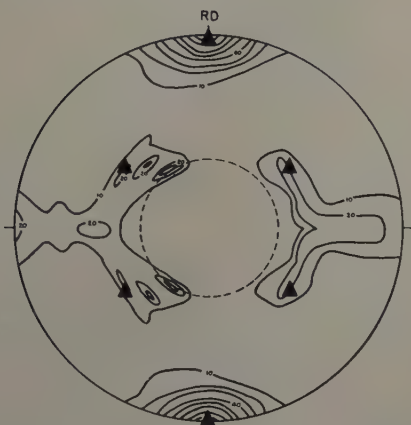


Fig. 2— $(10\bar{1}0)$ pole figure for zirconium sheet hot-rolled in a sheath at 825°C to a reduction of approximately 90 pct. Two quadrants examined. The orientations of $(10\bar{1}0)$ poles for the deformation texture $(0001) [10\bar{1}0]$ with a tilt of $\pm 40^\circ$ about the axis of the rolling direction are indicated by triangles.

sample to the beam changed. During examination, the specimen was translated back and forth in its plane through a $\frac{1}{2}$ -in. distance in order to increase the total number of grains contributing to the measured X-ray intensity.



Fig. 3—Micrograph of hot-rolled zirconium. Electropolished. Polarized light. X250.

Results and Discussion

The pole figures for the cold-rolled, Fig. 1,* and for the hot-rolled, Fig. 2, zirconium showed the

* The contour units are arbitrary and are relative for a given pole figure. Units should not be compared from different pole figures.

$[10\bar{1}0]$ direction to be parallel to the rolling direction in agreement with McGeary and Lustman⁵ and different from the findings of Burgers and Jacobs⁴ that the "digonal axis I," the $[11\bar{2}0]$ direction, was in the rolling direction in cold-rolled zirconium. It was also observed that the texture is characterized by a tilt of basal poles toward the transverse direction with an average orientation of the planes at $\pm 40^\circ$ from the rolling plane (indicating that the basal planes were tilted $\pm 40^\circ$ from the rolling plane about the rolling direction). This 40° tilt is to be compared with the 30° tilt found by McGeary and Lustman.⁵ Fig. 3 shows the microstructure of the hot-rolled zirconium.

Annealing at 300°C for 1 hr produced a texture

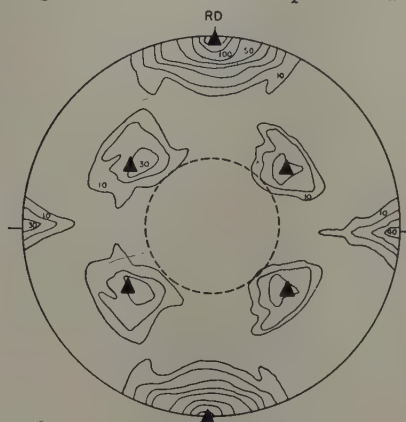


Fig. 4— $(10\bar{1}0)$ pole figure for 99.8 pct cold-reduced zirconium sheet annealed 1 hr at 400°C . Two quadrants examined. The orientations of $(10\bar{1}0)$ poles for the deformation texture $(0001) [10\bar{1}0]$ with a tilt of $\pm 40^\circ$ about the axis of the rolling direction are indicated by triangles.

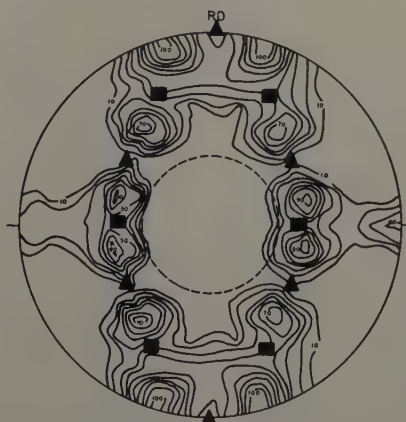


Fig. 5— $(10\bar{1}0)$ pole figure for 99.8 pct cold-reduced zirconium sheet annealed 1 hr at 500°C . Two quadrants examined. The orientations of $(10\bar{1}0)$ poles for the deformation texture $(0001) [10\bar{1}0]$ with a tilt of $\pm 40^\circ$ about the axis of the rolling direction are indicated by triangles. The orientations of $(10\bar{1}0)$ poles for the recrystallization texture $(0001) [11\bar{2}0]$ with a similar tilt are indicated by squares.



Fig. 6a—Micrograph of 97 pct cold-rolled zirconium sheet annealed 1 hr at 400°C. Longitudinal section. Bright field. Etched with $\text{HNO}_3\text{-H}_2\text{O-HF}$. X1000.

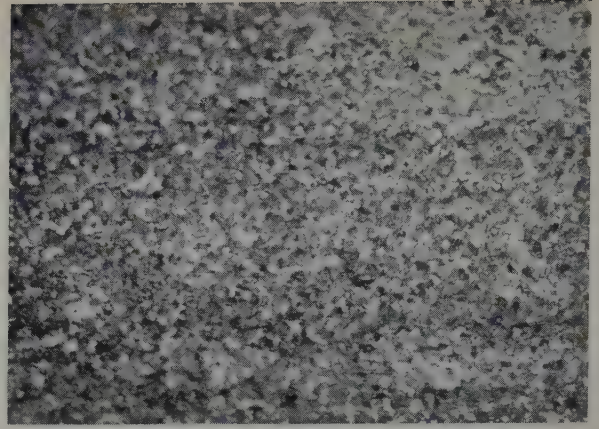


Fig. 6b—Micrograph of 97 pct cold-rolled zirconium sheet annealed at 500°C for 1 hr. Electropolished longitudinal section. Polarized light. X250.

which differed from the cold-rolled texture, Fig. 1, by having the four high-intensity regions near the center of the pole figure unconnected.

Annealing for 1 hr at 400°C produced a texture, Fig. 4, that was only slightly different† from that of

† The elongation of tensile samples annealed 1 hr at 400°C after a cold reduction of 97 pct was that of cold-rolled material although the yield strength has decreased slightly from that of the cold-rolled material.

the cold-rolled material. Metallographic examination disclosed the start of recrystallization as shown in the micrograph of Fig. 6a. It can be observed from the pole figure, Fig. 4, that the “fingers” extending from the high intensity areas are suggestive of the start of rotation which may be associated with the start of recrystallization. The change in texture from Fig. 1 to Fig. 4 is not necessarily a sharpening since, although the low intensity areas are smaller, the high intensity areas are not relatively more intense.

The texture of rolled crystal bar annealed 1 hr at 500°C, Fig. 5, disclosed a double rotation about the poles of the basal plane placing the $[11\bar{2}0]$ direction in the rolling direction.

The texture after annealing 1 hr at 500°, Fig. 5, can also be described as a rotation of the cold-rolling texture, Fig. 1, of roughly 20° in either direction about the normal of the rolling plane. However, if this stage of the annealing is considered intermediate between the cold-rolling texture, Fig. 1, and the

texture obtained at higher annealing temperatures, Fig. 7, rotation about the basal pole is more easily rationalized because the rotation about the normal of the rolling plane does not fit the textures obtained at higher annealing temperatures. Vestiges of the rolling texture remain as can be seen from the lower intensity $[10\bar{1}0]$ areas extending in both the rolling direction and in the transverse direction. This material‡ exhibited a very fine recrystallized grain

‡ Tensile samples annealed 1 hr at 500°C after a cold reduction of 97 pct also indicated that recrystallization was not quite complete since the percentage of elongation was slightly lower and the yield strength slightly higher than the values obtained for material annealed at 600° or 700°C.

size as shown in Fig. 6b.

The texture of zirconium annealed 30 min at 600°C also indicated a double rotation of the texture had occurred during recrystallization, Fig. 7. From

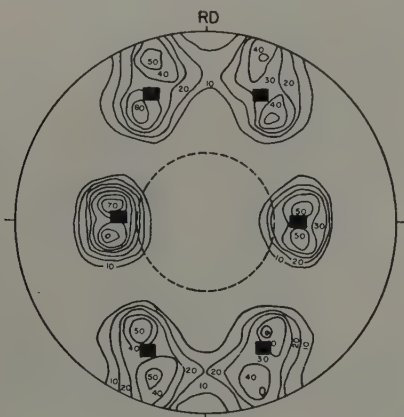


Fig. 7— $(10\bar{1}0)$ pole figure of 99.8 pct cold-reduced zirconium sheet annealed 30 min at 600°C. The orientations of $(10\bar{1}0)$ poles for the recrystallization texture $(0001) [11\bar{2}0]$ with a tilt of $\pm 40^\circ$ about the rolling direction are indicated by squares.

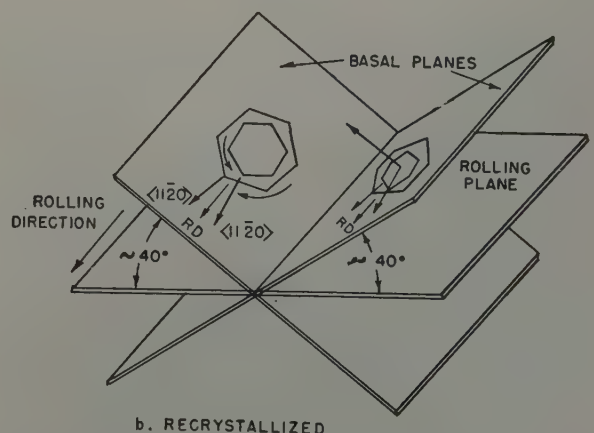
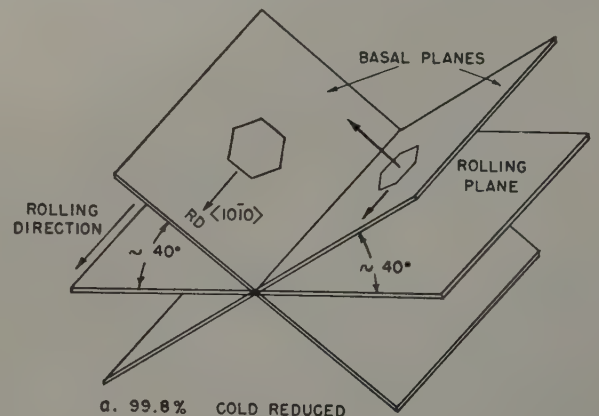


Fig. 8—Schematic representation of deformation and recrystallization textures found in zirconium sheet.

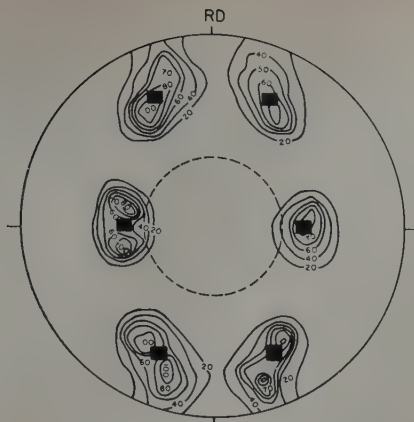


Fig. 9— $(10\bar{1}0)$ pole figure of 99.8 pct cold-reduced zirconium sheet annealed 30 min at 900°C . The orientations of $(10\bar{1}0)$ poles for the recrystallization texture $(0001) [11\bar{2}0]$ with a tilt of $\pm 40^{\circ}$ about the rolling direction are indicated by squares.

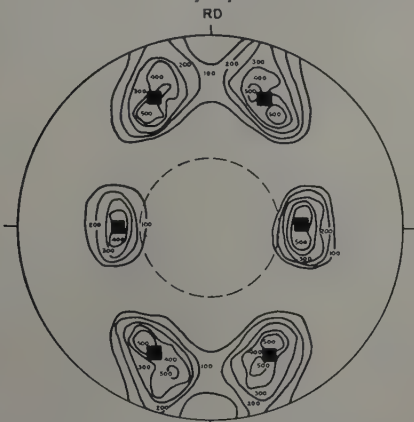


Fig. 10— $(10\bar{1}0)$ pole figure of 99.8 pct cold-reduced zirconium sheet annealed 30 min at 900°C and furnace-cooled. The orientations of $(10\bar{1}0)$ poles for recrystallization texture $(0001) [11\bar{2}0]$ with a tilt of $\pm 40^{\circ}$ about the rolling direction are indicated by squares.

the data obtained for cold-rolled sheet annealed at 400° , 500° , and 600°C it is apparent that the deformation texture disappears during recrystallization and that a new texture with the $[11\bar{2}0]$ direction in the rolling direction takes its place. This is different from the results reported for titanium² and beryllium³ where the recrystallization texture was similar to the rolling texture.

The rotational difference between the deformation orientation and the annealing orientation is nominally 30° in agreement with McGearry and Lustman,⁵ compare Figs. 1 and 7. However, measurement of the angle of rotation from the high intensity areas of the deformation texture to each of the double maxima in the annealing orientations showed that in detail the rotations appeared to be combinations of a small rotation of the range 16° to 24° and a larger rotation in the range 34° to 46° . The reasonable rotation combinations about the c -axis accounting for the change from the cold-rolled texture could be one or both of the following: 1— 34° to 46° rotation in opposite directions, 2— 16° to 24° rotation in opposite directions. From these rotations it follows that actually the $[11\bar{2}0]$ directions of the recrystallized texture are still not in the rolling plane but tilted about 10° from the rolling direction (and out of the rolling plane) since the planes

of rotation (tilt) are the basal planes that are about 40° from the rolling plane. Deformation and recrystallization textures are shown schematically in Fig. 8.

The transformation texture obtained, Fig. 9, by heating cold-rolled zirconium to 900°C , about 40°C above the allotropic transformation temperature, was found to be very similar to the recrystallization texture, in which the $[11\bar{2}0]$ direction was in the rolling direction. The principal texture was sharper than that obtained at 600°C and the spread of the secondary double texture was reduced. This sharpening differs from the finding of McGearry and Lustman that the transformation orientation showed more scatter than that for annealing below the transformation temperature. It is not certain whether or not any recrystallization had occurred below the transformation temperature in the case of the transformation texture.

Fig. 9 shows the texture of 99.8 pct cold-reduced zirconium sheet annealed 30 min at 900°C and cooled fairly rapidly in the evacuated quartz tube, and Fig. 10 is the texture of similarly rolled and annealed sheet cooled slowly in the furnace. The texture shown in Fig. 11 is that of the specimen annealed at 600°C (texture shown in Fig. 7) and later annealed again for 30 min at 900°C . In all three instances the transformation textures are similar to the recrystallization texture showing a symmetrical texture having $\pm 40^{\circ}$ tilts of the basal planes out of

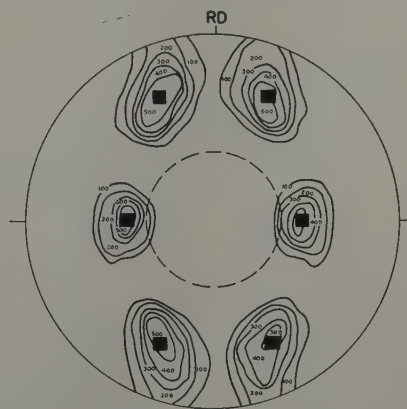


Fig. 11— $(10\bar{1}0)$ pole figure of 99.8 pct cold-reduced zirconium sheet annealed first at 600°C for 30 min (Fig. 8) and later at 900°C for 30 min. The orientations of $(10\bar{1}0)$ poles for the recrystallization texture $(0001) [11\bar{2}0]$ with a tilt of $\pm 40^{\circ}$ about the rolling direction are indicated by squares.

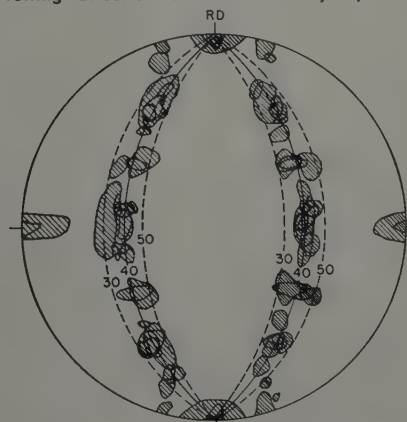


Fig. 12—Plot of locations of high intensity areas of $(10\bar{1}0)$ poles showing concentration along 40° meridian.

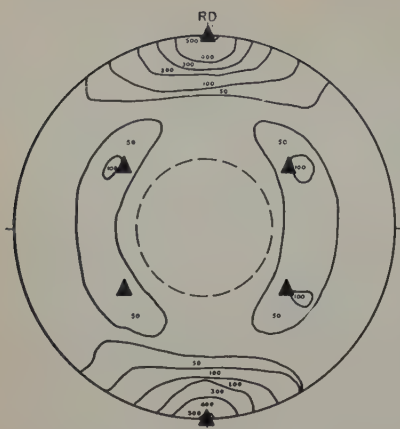
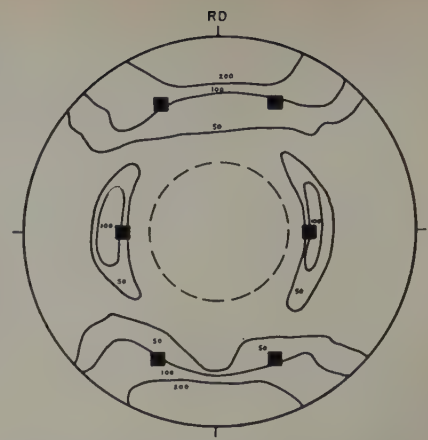


Fig. 13 (left)—(1010) pole figure for 50 pct cold-reduced zirconium sheet prepared by cold reduction in 50 pct increments with intervening anneals for 30 min at 600°C. The orientations of (1010) poles for the deformation texture (0001) [1010] with a tilt of $\pm 40^\circ$ about the axis of the rolling direction are indicated by triangles.

Fig. 14 (right)—(1010) pole figure for recrystallized zirconium sheet prepared by cold reduction in 50 pct increments with intervening anneals for 30 min at 600°C. As annealed. The orientations of (1010) poles for the recrystallization texture (0001) [1120] with a tilt of $\pm 40^\circ$ about the rolling direction are indicated by squares.



the rolling plane and with the [1120] direction approximately in the rolling direction.

It was observed that the texture of sheet zirconium that had been recrystallized and then annealed above the allotropic transformation temperature, Fig. 11, did not show the double maxima in the high-intensity areas exhibited by the other annealing textures.

The symmetrical texture at $\pm 40^\circ$ from the rolling plane continued to be present in the textures of annealed sheets, recrystallized and cycled through the allotropic transformation temperature. The location of high intensity areas of (1010) poles along the 40° meridians for various cold-rolled and annealed textures is shown in Fig. 12.

Burgers⁷ has pointed out that in the transformation of the β body-centered cubic zirconium to the α hexagonal close-packed form at approximately 860°C, the parallel planes for the transformation are the basal (0001) planes of the hexagonal close-packed form and the body diagonal (110) planes for the body-centered cubic modification. The parallel close-packed directions are the [1120] direction of the hexagonal close-packed phase and the [111] direction of the body-centered cubic structure. These relationships would indicate that during transformation from the body-centered cubic modification there are 12 possible orientations which could be obtained in the hexagonal close-packed structure being formed. It is difficult to explain the return to the original texture after a recrystallized specimen has been heated and cooled through the transformation temperature unless some nucleating sites remain to cause the return of the body-centered cubic material during cooling to its original hexagonal close-packed orientation.

A strong texture in a material is often undesirable particularly when forming operations are planned. To obtain zirconium sheet with a weaker texture, several samples of crystal bar were rolled into thin sheet, 0.001 in. in thickness, by alternately cold reducing by 50 pct, and then annealing in vacuo for 30 min at 600°C. Pole figures from these specimens in the cold-rolled and in the annealed conditions are shown in Figs. 13 and 14. The sheet obtained in each case was more weakly oriented than the corresponding material prepared by cold-reduction of 99.8 pct and then annealing. Although the cold-rolled and the annealed specimens have somewhat similar textures, it can be seen that the [1010] direction of the cold-rolled material and the [1120] direction of the annealed material are approximately in the rolling direction. It can also be observed that the symmetrical texture produced by the 40° tilts of the basal

plane out of the rolling plane is present in the material prepared by the cold-reduction and annealing cycle.

Summary

The deformation and annealing textures of iodide zirconium disclose a symmetrical orientation characterized by an average tilt of the basal planes $\pm 40^\circ$ out of the rolling plane toward the transverse direction and about the rolling direction.

The deformation orientations of cold-rolled and of hot-rolled material indicate the [1010] direction to be parallel to the rolling direction.

The recrystallization texture is related to the deformation by a rotation about the (0001) poles which can be rationalized as a combination of 16° to 24° and/or 34° to 46° rotations, so that the [1120] direction becomes approximately parallel to the rolling direction.

Working by alternately cold reducing and annealing produces a less highly oriented texture than does a single severe cold rolling and annealing.

Acknowledgment

The authors wish to thank Mrs. Ann S. Cooper who obtained the X-ray data and constructed the pole figures, and also other members of the Metallurgy Research Dept. who assisted in the experimental portions of this study. This work was supported by the U. S. Atomic Energy Commission under Contract No. W-31-109-Eng-52.

References

- ¹H. T. Clark, Jr.: The Textures of Cold-Rolled and Annealed Titanium. *Trans. AIME* (1950) **188**, pp. 1154-1156; *JOURNAL OF METALS* (September 1950).
- ²C. J. McHargue and J. P. Hammond: Preferred Orientations in Iodide Titanium. *Trans. AIME* (1953) **197**, pp. 57-61; *JOURNAL OF METALS* (January 1953).
- ³A. Smigelskas and C. S. Barrett: Preferred Orientation in Rolled and Recrystallized Beryllium. *Trans. AIME* (1949) **185**, pp. 145-148; *JOURNAL OF METALS* (February 1949).
- ⁴W. G. Burgers and F. M. Jacobs: *Metallwirtschaft* (1935) **14**, p. 285.
- ⁵R. K. McGeary and B. Lustman: Preferred Orientation in Zirconium. *Trans. AIME* (1951) **191**, pp. 994-1002; *JOURNAL OF METALS* (November 1951).
- ⁶B. F. Decker, E. T. Asp, and D. Harker: Preferred Orientation Determination Using a Geiger Counter X-ray Diffraction Goniometer. *Journal of Applied Physics* (April 1948) **19**, pp. 388-392.
- ⁷A. H. Geisler: Modern Techniques of Physical Metallurgy. ASM Seminar, 1952.
- ⁸W. G. Burgers: On the Process of Transition of the Cubic-Body-Centered Modification into the Hexagonal-Close-Packed Modification of Zirconium. *Physica* (1933-1934) **1**, pp. 561-586.

Anelastic Behavior of Pure Gold Wire

by Donald R. Mash and Lewis D. Hall

The paper presents the results of experiments on the anelastic behavior of gold, as manifested by grain boundary relaxation. Two grain boundary internal friction peaks are found for 99.9998 pct Au. It is found that the peaks are associated with primary and secondary recrystallization. However, the existence of two discrete peaks cannot be explained on the basis of grain size and shape alone. It is suggested that grain boundary stability, as determined by orientation, plays a role in the observed effects.

EVIDENCE for the viscous behavior of grain boundaries in metals has been presented in recent years by several investigators, based upon studies of various anelastic effects, especially internal friction. Kê¹ has contributed greatly to this field, having put forward a coherent body of evidence for stress relaxation by the viscous intercrystalline flow mechanism. In this connection, he has made extensive use of pure aluminum (99.991 pct) as the test material, although he has also studied other metals and alloys, including pure iron (Puron).² Rotherham, Smith, and Greenough³ have studied the internal friction of pure tin, interpreting their results in a manner similar to that of Kê. In view of the importance of such studies in shedding light upon the fundamental structure and behavior of the grain boundaries in pure metals, it appears that the use of a very pure test material which is inert to its environment should provide useful information on anelastic properties and the source of such behavior in pure metals.

The present work was carried out on spectrographically pure, 99.9998 pct Au, free of all impurities except for a trace of silver, estimated to be present to the extent of about 0.0002 pct. The term "pure gold" will hereafter refer to this very pure material. Gold of commercial purity, 99.98 pct, was also studied to observe the effects of small amounts of impurities. A pure gold "single crystal" specimen was also tested for comparison.

The variation of the internal friction and rigidity modulus as a function of temperature was determined by means of a torsion pendulum apparatus employing extremely low stress amplitudes and a frequency of vibration of the order of 1 cycle per sec. A 12 in. length of 0.031 in. (20 gage) gold wire formed the suspension element. The apparatus was similar to that described by Kê.¹ The test procedure and the basic requirements to be met for obtaining useful experimental data by this method have been given elsewhere.^{1,2} It should be made clear that in all of the experiments to be described, the internal friction and rigidity were independent of the amplitude of torsional vibration.

The semilog plot of amplitude of vibration vs ordinal number of vibration was a straight line. This was carefully verified for each internal friction

measurement. The linear variation shows that the internal friction was independent of stress; i.e., that the specimens were not being cold-worked during testing. The reproducibility of the internal friction curves, which were obtained by cyclic heating and cooling, indicates that the gold was unaffected by its environment during the tests.

The measure of internal friction adopted in the present study is the conventional "logarithmic decrement," defined as follows:

$$\log. \text{ dec.} = 1/n \ln A_0/A_n \quad [1]$$

where n is the number of cycles or vibrations; A_0 , the initial amplitude of vibration; and A_n , the amplitude after the n th cycle. When the logarithmic decrement is small, the shear modulus, G , of the wire is proportional to the square of the frequency of vibration provided the length and radius of the wire are kept constant. A plot of frequency squared vs temperature gives the following ratio:¹

$$\frac{G_R}{G_U} = \left(\frac{f_p}{f_s} \right)^2 \quad [2]$$

This expresses the fraction of the stress which has not been relaxed at a given temperature. G_R and G_U are the relaxed and unrelaxed moduli, respectively. The frequency of vibration in the polycrystalline specimen is f_p , and the frequency of vibration of a single crystal is f_s . This latter quantity is obtained simply by extrapolating the linear, low temperature portion of the curve of frequency squared vs temperature for the polycrystalline specimens.

The theory of viscous grain boundary stress relaxation as demonstrated by the anelastic behavior of metals has been discussed in detail by Zener⁴ and need not be reproduced here.

Experimental Results

Initial measurements of the internal friction of pure gold were carried out on specimens which had been drawn with no intermediate annealing, resulting in a material which had undergone approximately 99 pct reduction of area in final processing. Annealing was then carried out at successively higher temperatures starting at 400°F for 1 hr and proceeding in this manner to as high as 1600°F in 100°F intervals. After each annealing treatment an internal friction and rigidity vs temperature curve was obtained over the range from room temperature to the particular annealing temperature. The resulting internal friction curves did not exhibit well defined maxima (peaks), but rather several fairly flat

D. R. MASH, Junior Member AIME, formerly Graduate Student, School of Mineral Sciences, Stanford University, is now associated with the Livermore Research Laboratory, California Research and Development Corp., Livermore, Calif., and L. D. HALL is Assistant Professor of Metallurgy, Stanford University, Stanford, Calif.

Discussion on this paper, TP 3536E, may be sent, 2 copies, to AIME by Dec. 1, 1953. Manuscript, Jan. 13, 1953. Cleveland Meeting, October 1953.

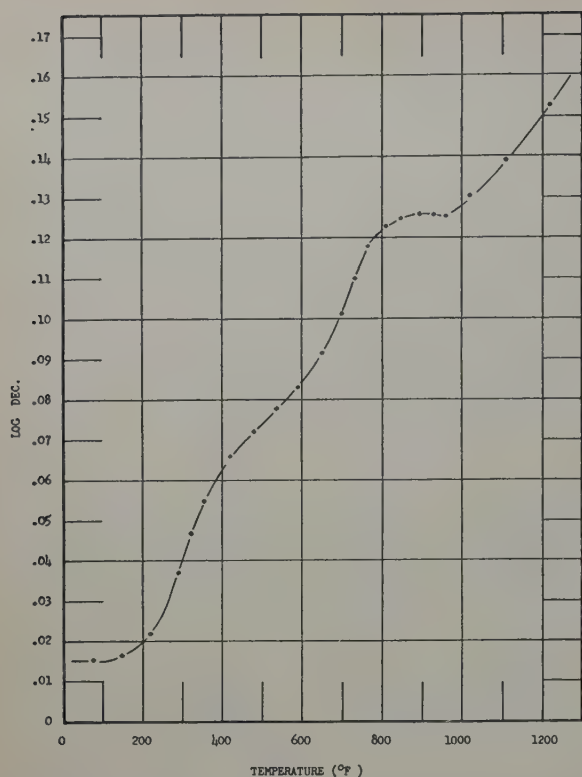


Fig. 1—Temperature variation of the internal friction of 99.9998 pct Au wire which had previously undergone 99 pct reduction of area. Specimen annealed 6.5 hr at 1600°F.

inflection points were obtained. For example, Fig. 1 shows that even after annealing for 6.5 hr at 1600°F no definite peaks were obtained in specimen No. 1, a result which is typical of heavily cold-worked material.

Tests on this material were, therefore, discontinued in favor of specimens which had undergone considerably less final cold working. Most of the work was performed on specimens which had been reduced in area about 36 pct in final drawing. Typical results for a series of annealing temperatures on the same test wire, No. 2, are shown in Figs. 2 and 3. In order to minimize confusion, the graphs contain only the results of anneals at 1000°, 1250°, and 1500°F. Curves were actually run for annealing temperatures at intervals of 100°F, from 400°F upward, as

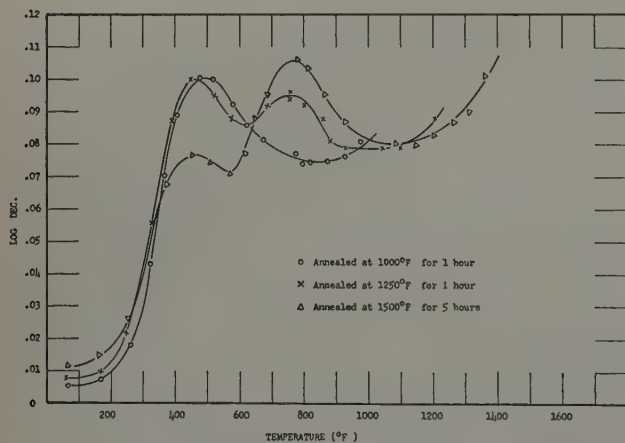


Fig. 2—The effect of annealing treatment upon the temperature variation of the internal friction of pure gold (specimen No. 2). Specimen had undergone 36 pct reduction of area prior to testing.

previously explained. A metallographic sample was taken after each anneal from specimens placed near the gold suspension wire in the furnace. This provided information concerning the microstructure associated with each annealing treatment and corresponding internal friction and rigidity curves. Fig. 4 shows some typical microstructures for specimen No. 2 after successive annealing treatments. These samples showed that after complete recrystallization had occurred at 600°F gradual grain growth continued until 800°F where an average grain diameter of about 0.105 mm obtained. This remained relatively constant up to 1000°F where "secondary" recrystallization was initiated; a few larger grains about 0.135 mm diam were observed. The curves shown in Figs. 2 and 3, after the 1000°F anneal are typical of the curves obtained at 800°F, also.

It can be observed that a single peak exists in the internal friction curve at about 500°F, while the point of inflection in the modulus curve⁵ occurs at the same temperature. The peak is broad, indicating that it represents a wide distribution of relaxation times. The modulus curve shows a tendency to approach a value of G_R/G_U of about 0.80. This does not correspond closely to the theoretical value of 0.684 obtained by using the relation¹

$$\frac{G_R}{G_U} = \frac{2(7 + 5\sigma)}{5(7 - 4\sigma)} \quad [3]$$

and a value of 0.42 for Poisson's ratio, σ , of pure gold. Kê, in his extensive and widely quoted experiments with aluminum,¹ obtained almost perfect agreement of his experimental G_R/G_U ratio with that predicted by theory. It should be emphasized, however, that the equation for G_R/G_U is based on the assumption of elastic isotropy,⁶ a condition which is closely approached in the case of aluminum but not in the case of gold. It is interesting to note that Rotherham, Smith, and Greenough,⁸ working with tin, which is also quite anisotropic, found a similar discrepancy between theory and experiment. These results indicate that in comparing the very regular and orderly results of Kê with the behavior of other materials, it should be remembered that in few if any other systems is there a comparable degree of elastic isotropy. The deviations of any actual material from "ideal" behavior as regards anelastic properties must clearly be influenced by its degree of anisotropy. It should also be pointed out that the values of Poisson's ratio used in Eq. 3 are usually those for room temperature, whereas the relaxation occurs at elevated temperature. Since Poisson's ratio varies with temperature, calculated values of G_R/G_U will be correspondingly affected.

Annealing at 1250°F produced considerable grain growth, resulting in a microstructure containing an average grain size of about 0.195 mm diam. Secondary recrystallization had apparently been completed, Fig. 4. The internal friction curve is then found to consist of two peaks, separated by about 300°F (167°C), a rather surprising result and one which does not appear to have been observed before. Also, the background internal friction appears to have increased slightly, indicating that some other source of energy loss has become active. The lower temperature peak has become centered about 460°F and appears to be somewhat narrower than that due to the 1000°F anneal, indicating a more restricted range of relaxation times. The second peak, centered about 760°F, possesses a somewhat lower maximum value of the decrement and is rather broad. Anneal-

ing at 1500°F for 5 hr produced a relatively uniform grain size of about 0.270 mm. It can be observed from Fig. 2 that an inversion of the two peaks has occurred. The lower peak has decreased to a decrement of about 0.077, while the upper peak has reached a value of almost 0.11. Study of Fig. 3 shows that this sudden occurrence, and final predominance, of the second peak corresponds to the gradual broadening of the relaxation band of the dynamic modulus curve at 1250° and at 1500°F. The relaxation in the modulus from G_v to G_R now requires a much wider temperature range for its completion. However, after its initial decrease to about 0.80, the ratio G_R/G_v changes little, as shown by Fig. 3. This indicates that the same relaxation mechanism continues to prevail. In the modulus curve for the 1500° anneal a second, though slight, point of inflection has appeared at about 775°F, while the principal point of inflection occurs at about 475°F. The extreme breadth of the two internal friction peaks should also be noted.

It was desired to compare the activation energy values associated with the two maxima. This was done by means of the following relation:²

$$Q = \frac{R \ln (f_2/f_1)}{1/T_1 - 1/T_2} \quad [4]$$

where Q is the activation energy, f_1 and f_2 are two different frequencies of vibration on the same test specimen, $(1/T_1 - 1/T_2)$ is the horizontal shift of one curve to superimpose it on the other when plotted against $1/^\circ\text{K}$ as abscissa, and R is the gas constant. Fig. 5 shows the curve for specimen No. 3, also subjected to 36 pct reduction of area prior to testing, annealed at 1000°F for 1 hr in order to obtain one peak only. The value of Q was found to be about 34,500 cal per mol, which is accurate to about 10 pct. This specimen was annealed at 1500°F for 5 hr in order to produce the double peaks. From Fig. 6, the activation energy for the high temperature peak was found to be 58,000 cal per mol. It should be pointed out here that if the two peaks, high and low temperature, of one curve possessed similar activation energies, this superposition should have brought them both into coincidence with the double peaks of the other curve. This is clearly not the case. Specimen No. 4, possessing only about 17 pct reduction of area, was run in a manner similar to No. 3, already described. Similar results were obtained.

In order to evaluate the effect of the grain boundaries, a 10 in. long "single crystal" pure gold wire,

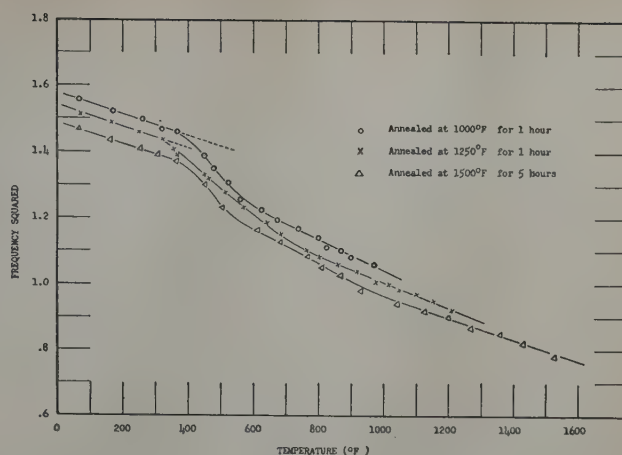


Fig. 3—The effect of annealing treatment upon the temperature variation of the "rigidity" of pure gold, specimen No. 2. Compare with Fig. 2.

approximately 0.040 in. diam, was produced. The entire specimen actually consisted of about three large crystals. The results of the test on this specimen are shown in Fig. 7. Unfortunately, in removing this specimen from the mold and subsequently placing it in the torsion pendulum apparatus, some cold working was unavoidable and is reflected in the curves of the internal friction and modulus vs temperature. The point of the sudden rise in internal friction in the specimen coincides rather closely with the position of the high temperature peak in the polycrystalline specimens. However, no peak is observed. Such behavior in single-crystal specimens which have undergone small amounts of cold work prior to testing has been observed by Kê⁷ in the case of aluminum.

The great purity of the test material was thought to be a factor in revealing the double peak in the polycrystalline metal. Therefore, for purposes of comparison, a sample, No. 5, of commercially pure gold, 99.98 pct, possessing a final reduction of area of 36 pct was tested. Fig. 8 shows that no double peak was obtained. Instead, a single peak occurs at about 635°F which is intermediate between the low and high temperature peaks of the pure material. Annealing at 1500°F is seen to produce no result other than the movement of the peak to a higher temperature and a lower maximum value of the internal friction. The grain structure of the specimen after the two annealing treatments is shown in Fig.

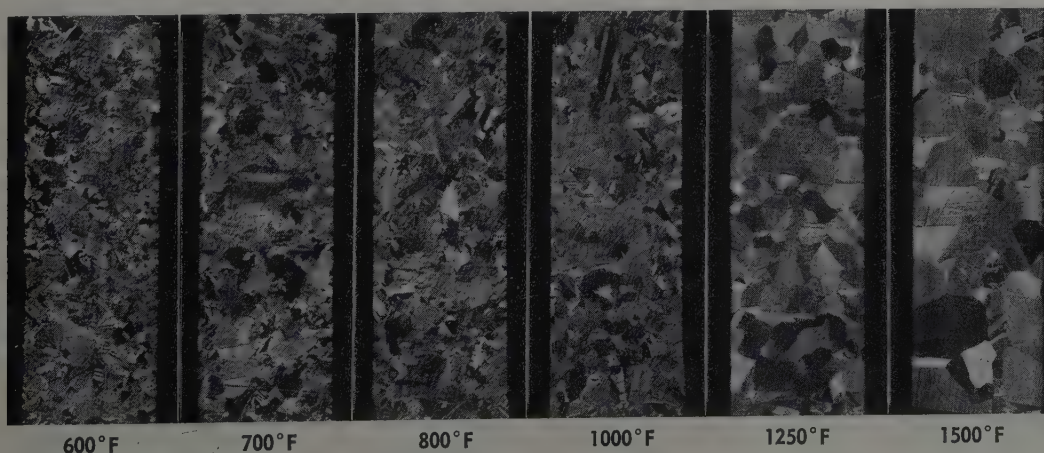


Fig. 4—Typical microstructures of pure gold specimens after treating at successively higher annealing temperatures. Compare with Figs. 2 and 3. X25.

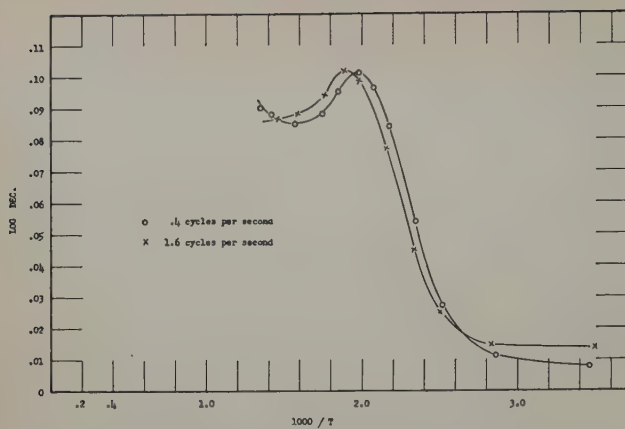


Fig. 5—Pure gold specimen No. 3 annealed for 1 hr at 1000°F to produce a single grain boundary peak. The activation energy is 34,500 cal per mol.

9. The 1000°F anneal produced a fairly uniform grain size of about 0.195 mm; the 1500°F treatment resulted in grains most of which were 0.360 mm in diam, although a few 0.270 grains were present. The value of G_R/G_U was found to be about 0.82, which closely corresponds to that of the purer material.

In an effort to throw some light on the source of this effect, the double peak, further experimental work was carried out. X-ray analyses by back-reflection and transmission techniques were carried out at different temperatures with pure polycrystalline specimens, treated comparably to No. 2. The transmission patterns, made with filtered $\text{CuK}\alpha$ radiation, on a specimen which was etched to 0.014 in. diam showed the existence of a recrystallization texture, approximately [211], in the interior of the wire, after annealing at 1000°F and below, which had almost disappeared after a 1600°F anneal. These patterns are shown in Figs. 10 and 11.

In considering possible sources of the anelastic effect which is manifested in the double peak, two possibilities may be eliminated at the outset. The stress-induced preferential orientation of foreign atoms cannot be a factor, since, as just pointed out, two peaks appear only in 99.9998 pct Au, while gold of 99.98 pct purity exhibits a single peak.

The possibility of a contribution to the internal friction by the motion of dislocations which have been introduced by cold work during the fabrication of the test wires is recognized. This, however, results in internal friction which increases continuously at high temperatures, with no tendency to form a peak. Further, the effect of prior cold work is to mask the grain-boundary peak or peaks, as shown by comparison of Figs. 1 and 2.

The behavior of both internal friction peaks in general, particularly the lower peak, corresponds to that which is predicted of the grain boundary as a relaxation center. They are found only in polycrystalline specimens, and not in the single-crystal specimen. With increasing grain size they move to higher temperatures, the lower peak being more strongly affected by this treatment than the upper. The curve of rigidity modulus vs temperature (Fig. 3) has its chief point of inflection at approximately the temperature of the lower peak, with a small, but perceptible second point of inflection at approximately the temperature of the upper peak. The broadness of the two peaks is reflected in the wide temperature range required for the complete

relaxation of the modulus from its unrelaxed value, G_U , to its relaxed value, G_R .

The evidence cited indicates clearly that the lower peak is connected with grain boundary movement. For the upper peak, there is additional evidence linking it to this same phenomenon. First, the fact that the fraction of stress relaxation observed increased little after its initial drop to about 0.80, Fig. 3, argues in favor of the operation of a single relaxation process. If further relaxation arose from within the grains, the fraction would not remain roughly constant, but would increase markedly, due to the new contribution to the overall amount of stress relaxation. Furthermore, examination of the microstructure resulting from the 1500°F annealing treatment reveals a grain size which is still considerably smaller than the diameter of the test wire. It is, therefore, reasonable to expect that such a large volume of grain boundaries should contribute considerably more to the internal friction than that represented by the relatively small lower peak under these conditions.

Further consideration leads to the conclusion that grain size and shape are not the only factors leading

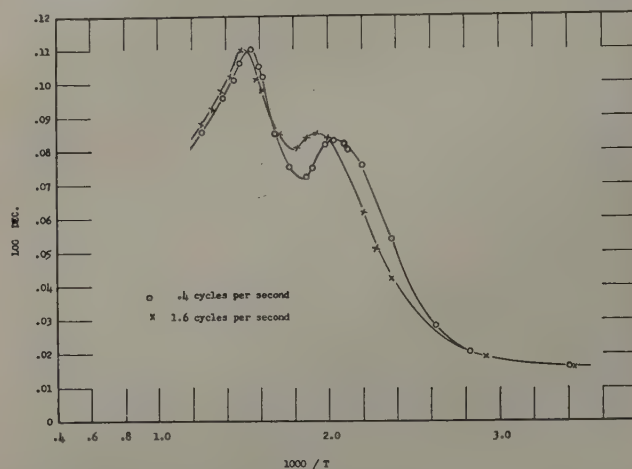


Fig. 6—Determination of the activation energy of the "upper" peak. Same specimen (No. 3) as Fig. 5, annealed for 5 hr at 1500°F to obtain the double peaks. A value of 58,000 cal per mol is obtained.

to a double grain boundary peak as opposed to a single peak. In fact, it is difficult to see a direct relation between cause and effect based only on grain size and shape. Careful scrutiny of the 1250° and 1500°F specimen in Fig. 4 does not disclose such an obvious degree of grain size contrast at either temperature as would account for a difference of some 300°F (167°C) between the low and high temperature peaks. This corresponds to a difference in relaxation time of about 0.01 sec, which is appreciable.

The explanation, on the basis of grain size, of the simultaneous existence of two peaks after annealing at intermediate temperatures, demands the existence of a marked duplex structure, with two widely different coexisting grain sizes. This is not observed. In the case of the 1500°F anneal, resulting in a uniform grain size, with almost no evidence of a duplex structure, only a single peak would be expected. However, the two peaks persist, although the lower peak has subsided considerably. The pronounced subsidence of the lower peak after annealing at 1500°F, and its further degeneration to a mere arrest in the curve after annealing at 1650°C, cannot be explained on the basis of grain size, since

the grain size of the specimen remains small in comparison with the specimen diameter.

The metallographic evidence shows that the lower peak is associated with primary recrystallization and the upper peak with secondary recrystallization. These latter phenomena are not yet well understood; therefore, only a qualitative explanation of the double peak effect in terms of them can be given. It is generally accepted that the driving force for secondary recrystallization is surface energy, i.e., the grains tend to adopt such configurations that the surface energy of their interfaces is a minimum. The change from primary to secondary structure thus entails an increase in boundary stability. The primary grains will thus have a certain grain boundary peak associated with them; a peak of lower activation energy because of the lower degree of boundary stability associated with this configuration. Upon secondary recrystallization, a structure with lower boundary free energy and greater boundary stability results. The grain boundary peak associated with this structure has a higher activation energy. Annealing at the highest temperatures results in almost complete disappearance of the primary structure and of the lower peak.

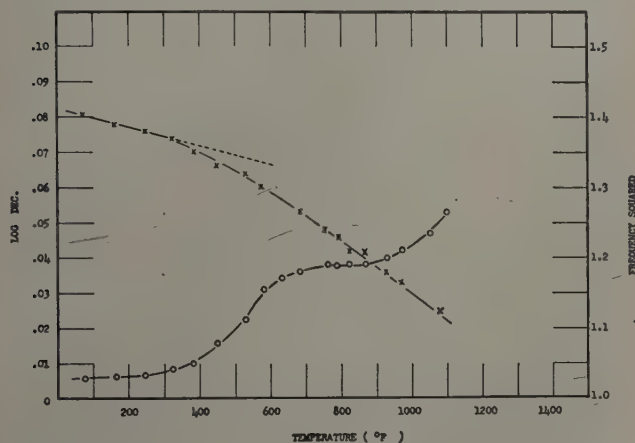


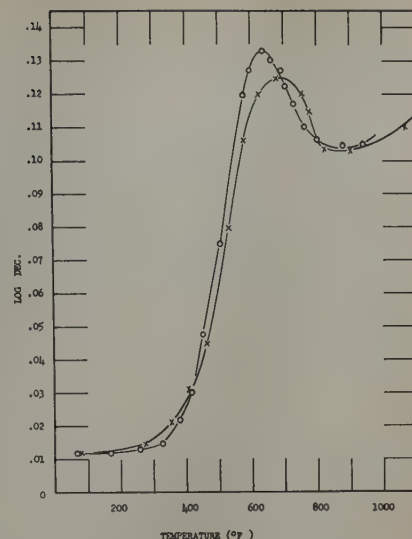
Fig. 7—Temperature variation of the internal friction and of the "rigidity" of a single-crystal specimen of pure gold.

These arguments are also confirmed by the X-ray evidence, which indicates the presence of a [211] recrystallization texture at 1000°F which has almost disappeared after annealing at 1600°F. Annealing at temperatures below 1000°F resulted in a single peak; annealing above 1000°F produced a second peak, the upper peak, and finally, annealing at about 1650°F (curve not shown) caused the lower peak to degenerate to an arrest in the curve, while the upper peak had decreased only slightly from its maximum height.

The upper peak was quite stable (resistant to further annealing treatments) but was also quite broad, indicating a wide range of relaxation times. This is rather remarkable in view of the fact that the grain size of such specimens was uniform, Fig. 4. On the basis of uniformity of grain size and shape alone, a narrow peak, such as was found in the commercially pure gold, would be expected. This lends additional support to the contention that other factors are of importance in grain boundary internal friction.

The question arises as to why no other investigators have reported a double grain boundary peak. This may be a result of: 1—degree of purity of materials used, and/or 2—maximum annealing

Fig. 8—Internal friction vs temperature for a commercially pure, 99.98 pct Au specimen, No. 5. Specimen had previously undergone 36 pct reduction of area. Circle annealed at 1000°F for 1 hr; cross annealed at 1500°F for 5 hr.



temperature employed in the course of measurements. As stated earlier, those impurities present in gold of 99.98 pct purity were sufficient to eliminate the double peak, which was intermediate in position between the two peaks of the 99.9998 pct Au. These results show the powerful effect which trace amounts of impurities can have in masking certain physical phenomena. They accent the desirability of working with materials of the highest possible purity and maximum resistance to contamination by their environment.

Kê⁸ reports work on 99.999 pct Cu in which only one peak was observed, which would seem to cast some doubt on the first reason mentioned above. However, his maximum annealing temperature was 600°C (1112°F) and it is not known whether annealing above that temperature would have produced a second peak. It should be remembered that the upper peak in 99.9998 pct Au did not appear until the specimen had been annealed at 1250°F. In the case of other investigators and other materials, the purity of the specimens used has been comparable to the 99.98 pct Au, which showed only a single, narrow peak.

The maximum annealing temperature has an influence in determining the orientations existing in the material and the presence or absence of secondary recrystallization. Usually, if not always, in the case of other investigators this temperature has not been high enough to alter the deformation texture appreciably. For example, Barrett⁹ states that the deformation texture of 99.996 pct Cu, which is [111], [100], is not altered by annealing at and below 500°C and retains the [111] component at 1000°C. He also states that the deformation texture of aluminum is not altered by annealing below 500°C. Kê, in his extensive experiments with aluminum, used a maximum annealing temperature of 450°C.

The failure of other investigators to detect a double peak lends support to the contention that orientation is a factor, since the grain sizes employed by them (e.g., see Kê¹) have been comparable to those used in the present work. It is interesting to note that no detailed studies have been reported to date on the effect of grain orientation on such processes as grain boundary relaxation, grain boundary diffusion, and similar grain boundary phenomena. In this connection, it would be interesting to investigate the difference in grain



Fig. 9—Microstructures associated with curves shown in Fig. 8 for commercially pure gold specimen. Compare also with Fig. 4. X25. Area reduced approximately 50 pct for reproduction. a (upper)—1000°F. b (lower)—1500°F.

boundary relaxation between specimens prepared in various ways so as to produce various types of preferred orientation.

Summary

The anelastic behavior of grain boundaries in pure (99.9998 pct) gold was investigated by studying the variation of the internal friction and shear modulus in torsional vibration, using frequencies of the order of 1 cps. For comparison, commercially pure (99.98 pct) gold was also investigated, as well as a pure gold single-crystal specimen.

After annealing at temperatures between about 1200° and 1600°F, the curves of internal friction vs temperature of measurement for polycrystalline pure gold specimens exhibit two discrete grain boundary peaks at 460° and 760°F, with activation energies of 34,500 and 58,000 cal per mol, respectively. This effect has not previously been reported in the literature for any material. Only one peak appears in pure gold after annealing at temperatures outside this range. Commercially pure (99.98 pct) gold showed only one peak regardless of annealing temperature.

It is suggested that grain boundary stability, as determined by orientation, plays a role in the observed effects, and that grain size and shape are not the only factors involved. This conclusion is based on the following observations: 1—the association of the peaks with primary and secondary recrystallization; 2—the absence of duplex grain structure; 3—the considerable difference in the temperatures

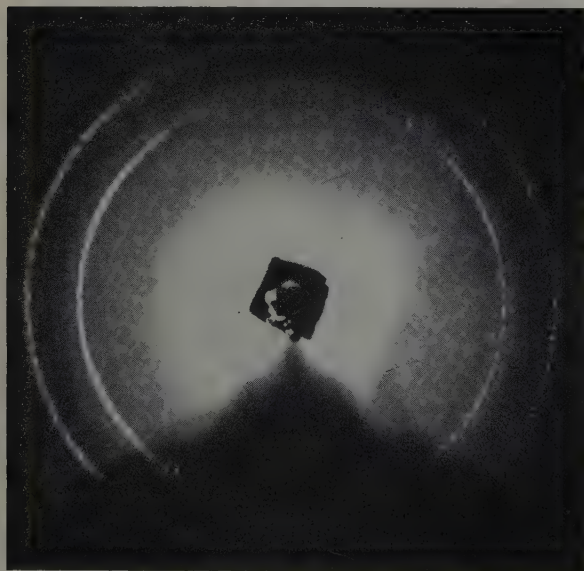


Fig. 10—Orientations after annealing at 1000°F. Texture: scatter about [211].

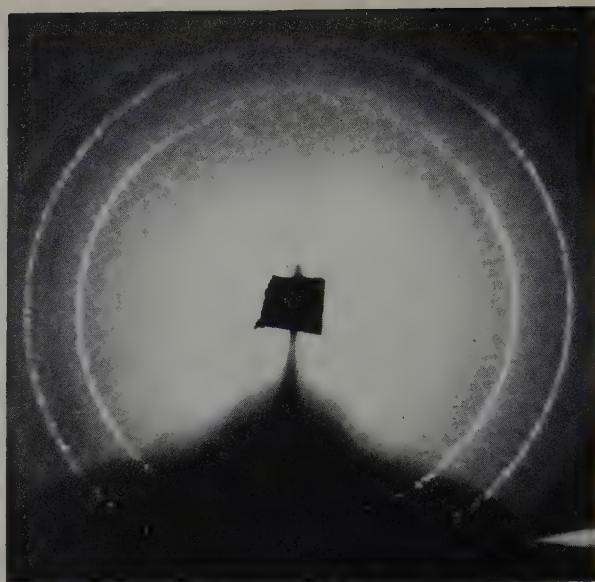


Fig. 11—Orientations after annealing at 1600°F. [211] texture has practically disappeared.

and activation energies of the two peaks; 4—the greater breadth of the peaks compared with the single peak in 99.98 pct Au of the same grain uniformity; 5—the marked subsidence of the lower peak after annealing at high temperatures, despite a grain size which is still small compared with the specimen diameter; 6—the correlation of the peaks with the presence and breakdown of a [211] wire texture.

Trace amounts of impurities have a remarkably strong influence in eliminating the double peak and reducing the width of the single peak that results. The impurities present in 99.98 pct Au as compared with 99.9998 pct Au (in which the double peak was observed) were sufficient to eliminate the double peak and to reduce greatly the width of the resulting single peak. This effect, in addition to the fact that high annealing temperatures are necessary to cause a second peak to appear in the pure material, probably accounts for the fact that other investigators have not observed the phenomenon.

The experimental results point up the advisability of considering the effect of grain orientation in processes which take place at grain boundaries, as well as the necessity of taking elastic anisotropy into account when comparing the anelastic behavior of different materials.

Acknowledgments

This investigation was sponsored by the Office of Naval Research, Contract N6-ori-154 Task V, Project N6-031-012.

References

- ¹T. S. Kê: *Physical Review* (1947) **71**, p. 533.
- ²T. S. Kê: *Trans. AIME* (1948) **176**, p. 448; *METALS TECHNOLOGY* (June 1948).
- ³L. Rotherham, A. D. N. Smith, and G. B. Greenough: *Journal Inst. Metals* (1951) **79**, p. 439.
- ⁴C. Zener: *Elasticity and Anelasticity of Metals* (1948) Chicago. University of Chicago Press.
- ⁵Ref. 4, p. 48.
- ⁶C. Zener: *Physical Review* (1941) **60**, p. 906.
- ⁷T. S. Kê: *Journal of Applied Physics* (1950) **21**, p. 414.
- ⁸T. S. Kê: *Journal of Applied Physics* (1949) **20**, p. 274.
- ⁹C. S. Barrett: *Structure of Metals*. 2nd Ed (1952) p. 486. New York. McGraw-Hill Book Co.

Vacuum Dezincing of Desilverized Lead Bullion

by T. R. A. Davey

THE possibilities of separating and purifying metals by high vacuum distillation were examined by Kroll.¹ He suggested vacuum treatment for the removal of zinc from the lead produced after Parkes desilverizing. The St. Joseph Lead Co. developed the first commercial vacuum dezincing process at their Herculaneum refinery, as described by Isbell.² The Broken Hill Associated Smelters at Port Pirie, Australia, has, after several years of pilot plant operations and fundamental investigations, developed a continuous process, which will be described briefly in a forthcoming publication.³

As the full-scale continuous vacuum dezincing plant at Port Pirie is still experimental, publication of full practical details of the plant will be deferred until the unit is operating as a normal part of the continuous refinery. This paper deals only with theoretical aspects of vacuum distillation processes, with particular reference to vacuum dezincing. The method of mathematical analysis is of general interest as it may be applicable to other metallurgical separations which have been investigated recently.⁴⁻⁶

Evaporation Processes

At about atmospheric pressure, or higher, most liquids possess a boiling point—a temperature at which any heat put into the liquid is absorbed only as latent heat, not as specific heat. If a steady heat input is supplied, the liquid's temperature rises to this value, then remains constant while bubbles of vapor form beneath the surface. The rate of evaporation is determined solely by the rate of heat transfer to the liquid; the temperature of boiling is determined by the partial pressures of the volatile constituents in the liquid, and the total pressure above the surface. If the rate of heat transfer to the liquid is increased, the temperature remains constant, and the rate of boiling increases.

When evaporating metals under vacuum, however, the partial pressures concerned are generally so small that boiling does not occur, because at even a fraction of a millimeter below the surface the hydrostatic pressure is usually too great to permit the formation of a pocket of vapor. In addition, the

high thermal conductivity of metals tends to prevent the local superheating which is necessary for bubble formation.¹ Although this effect is doubtless also exerted when boiling metals at higher pressures, the magnitude will be less because the degree of superheat required to form bubbles is very much less at the higher temperatures involved.

Under vacuum, therefore, evaporation of volatile constituents takes place only from the exposed surface, and the rate of evaporation depends upon the surface area, the surface concentration of volatile constituents, the surface temperature, and the partial pressures of volatile constituents immediately above the surface. If the heat input is raised above a certain level, the effect is not to increase the evaporation rate at constant temperature, but to raise the temperature of the liquid until at some higher level an increased rate of evaporation (and thus of latent heat absorption) again balances the heat input rate.⁷

Many substances (including metals) have a very large intrinsic evaporation rate at quite low temperatures—far below their normal boiling points. However, at atmospheric pressure, the large numbers of atoms evaporated are almost completely deflected back into the liquid (or solid) surface by air molecules. Thus the back condensation rate is practically equal to the gross evaporation rate, and the net evaporation rate is practically zero.

It can therefore be seen that an overall distillation rate depends not only upon the intrinsic evaporation rate, but also upon the ability of the volatile atoms to move away from the evaporating surface. This movement is facilitated by the provision of a condensing surface close by.

Vacuum Distillation: The function of the vacuum above the evaporating surface is to remove foreign molecules, so that the chances of deflection of an evaporated atom back into its source are reduced. When the residual gas pressure is reduced so far that the evaporated atoms have a high probability of reaching a nearby condensing surface without suffering collision with a foreign molecule, the state of affairs is termed "molecular distillation." This process is practiced commercially today for the purification of numerous organic chemical products of high unit value, but not, to the writer's knowledge, for any metallurgical separation.

When the degree of vacuum produced in a still is not sufficient to promote molecular distillation, then the evaporated molecules must diffuse through the

T. R. A. DAVEY is associated with the Research Dept., The Broken Hill Associated Smelters Pty. Ltd., Port Pirie, South Australia.

Discussion on this paper, TP 3538D, may be sent, 2 copies, to AIME by Oct. 1, 1953. Manuscript, Dec. 17, 1952. Los Angeles Meeting, February, 1953.

The word bullion as used in this paper refers to impure lead.

Table I. Values of Constants

Temperature, °C	DP	$10^2 \alpha a$	$10^5 \alpha b^*$	c^\dagger	r
580	0.89	1.62	2.76	0.171	0.381
600	0.93	1.60	2.82	0.173	0.279
620	0.96	1.58	2.86	0.175	0.209
650	1.02	1.55	2.94	0.178	0.138

* Assuming distillation space $L = 30$ cm.

† Assuming $T_c = 420^\circ\text{C}$; if $T_c < 300^\circ\text{C}$, $c < 0.002$.

distillation space, from evaporating to condensing surfaces. There will then be a partial pressure of volatile atoms above the evaporating surface, which produces some back condensation. A net evaporation rate results, smaller than the intrinsic or gross rate. Under steady state conditions this evaporation rate is equal to the rate of migration of atoms across the distillation space, and equal to the rate of condensation.

If the construction of the still is such that obstruction is offered to the flow of vapor by the vessel walls, pipe lines, or baffles, then of course mass flow is permitted, and the total pressure is different in different parts of the distillation space. If such obstructions do not exist, then obviously the total pressure must be uniform throughout the distillation space.

Vacuum Dezincing

It can be shown that in vacuum dezincing as practiced today the distillation proceeds by diffusion of zinc atoms from the bullion surface, through the stagnant atmosphere, to a nearby condensing surface. The designs of apparatus insure that there is no resistance to the flow of zinc vapor apart from that due to the residual gas pressure.

The bullion prior to treatment is just above its freezing point, and after dezincing will be refined at about 450° to 500°C . It is therefore conveniently treated in the liquid state. In order that the free surface exposed to vacuum shall not be mechanically obstructed, the metal surface should be clean, i.e., free from dross. Since distillation is much more rapid than diffusion of zinc through molten lead, vigorous agitation is required to prevent surface impoverishment in zinc, and also to prevent a fall of temperature at the surface due to radiation loss and provision of the latent heat of vaporization of zinc.

The St. Joseph batch operation employs a mechanical stirrer to produce agitation. The Port Pirie continuous operation utilizes a falling film* of bullion, which flows turbulently, and does not require mechanical agitation.

* The term "film" is not meant to be understood in the strict physical sense of lamellar flow, but simply in the sense of a thin flowing stream.

Nature of Distillate: In a batch process the distillate may conveniently be condensed in solid form. For a truly continuous process the distillate should be condensed either as a liquid, or else on to a liquid vehicle, so that in either case it may be removed from the still without breaking the vacuum. On the other hand, a continuous process may also be operated to produce solid distillate, if removal of the distillate is accomplished so rapidly that the vacuum is broken for a negligibly small period.

In order that a solid distillate shall not occupy too great a volume in the vacuum chamber, it should

be condensed in a compact (dense) form. The observations of St. Clair and Spendlove,⁷ on the condensation of zinc, and Betcherman and Pidgeon,⁴ on the condensation of magnesium, are in general agreement with our own, which may be summarized as follows:

Low rates of distillation and high residual gas pressures tend to produce loose clusters of dendritic crystals; with good vacuum (less than 100 microns) tightly packed columnar crystals are produced, the mass when fractured appearing very similar to a broken slab of cast zinc; with very high rates of distillation, with high lead content, or with high temperatures of condensation (as when the distillate layer is very thick) the edges of the crystals appear rounded, and show evidence of having been liquid—individual crystals tend to merge into a large mass, the surface of which may exhibit large crystals as on a slowly cooled cast bar.

Condensation phenomena will not be discussed further; for the practical operation it is necessary only to know that, at pressures less than about 150 to 200 microns, with a condensate surface less than about 6 in. from the water-cooled surface, the condensate consists of closely packed columnar crystals.

The amount of lead distilling over with the zinc increases with temperature, because the relative difference in vapor pressures becomes less as the temperature is raised. The best separation is obtained at the lowest temperatures, as Kroll has observed.¹ However, the zinc recovered from desilverized bullion is used again for desilverizing, so that contamination with lead is of no consequence. The amount which occurs in practice is less than 10 pct, which represents less than 0.05 pct of the lead treated, so is not a very great circulating load.

It is desirable that the condensate be as free as possible of oxygen. On melting the distillate for solution in lead, not only is any zinc oxide present wasted, but also its removal as dross incurs further loss of entangled metallic zinc and lead.

With an indicated vacuum of less than about 150 to 200 microns, very little zinc is oxidized, and the distillate is very shiny in appearance.

Rate of Distillation

The rate of distillation is of paramount importance, as it determines whether or not the process will be economic. By considering the three parts of the process—evaporation, migration, and condensation—the distillation rate may be determined. In the first analysis the presence of lead vapor may be neglected.

Consider unit area (1 sq cm) of evaporating surface, distillation space, and condensing surface, the temperature of evaporating surface and vapor being T ($^\circ\text{K}$) and of condensing surface T_c ($^\circ\text{K}$), the distillation space being L (cm) across, the pressure being P (mm Hg) throughout. Let the partial pressure of w pct Zn in the bullion at the evaporating surface be p' , in vapor above the evaporating surface be p_1 , in vapor above the condensing surface be p_2 , and in the condensing surface be p_c (all mm Hg).

Zinc diffuses through an atmosphere of nitrogen, since any oxygen present is quickly combined as zinc oxide, and removed from the atmosphere. If there are no air leaks in the system, and the vacuum line off-take is adjacent to the condensing surface, then the partial pressure of nitrogen immediately

above the condensing surface will be V (mm Hg), the recorded vacuum.

At any instant the total pressure at all points in the distillation space is constant, and equal to the sum of the partial pressures of zinc and nitrogen, then,

$$P = p_2 + V \quad [1]$$

From Langmuir's equation for absolute rates of evaporation,

$$E = a(p' - p_1) \quad [2]$$

$$C = ap_2 - kp_c \quad [3]$$

where $a = \frac{0.472}{\sqrt{T}}$ and $k = \frac{0.472}{\sqrt{T_s}}$ for zinc.

Using the methods of Lewis and Chang³ for isothermal diffusion of zinc vapor through nitrogen,

$$M = b \ln \frac{P - p_2}{P - p_1} \quad [4]$$

$$= b \ln \frac{V}{V + p_2 - p_1} \quad [4a]$$

where $b = \frac{0.796DP}{TL}$.

Values of DP —independent of all other terms except temperature—are given in Table I.

Placing $E = M = C$ in Eqs. 2, 3, and 4a, the following is obtained:

$$p' = V + c + \frac{2E}{a} - V \exp \left(-\frac{E}{b} \right) \quad [5]$$

where $c = \frac{kp_c}{a}$

This is the fundamental equation relating E , the net distillation rate, to p' , the partial pressure of

the volatile element in the distilland (the material to be distilled), with the constant terms V (measured vacuum), a (depending only on temperature and the distilling element's vapor pressure and molecular weight), b (depending on temperature, length of distillation path, and the diffusivity of distillate molecules through the inert atmosphere molecules), and c (depending on condensing temperature and the other factors influencing a).

If the ratio between w and p' be represented by r , then,

$$w = r \left[V + c + \frac{2E}{a} - V \exp \left(-\frac{E}{b} \right) \right] \quad [5a]$$

where $r = w/p'$.

In the process being considered the behavior of zinc atoms in diffusing is likely to be adiabatic rather than isothermal, as indeed previous writers have assumed.⁷ However, the expression then obtained is very complex, and tedious to manipulate mathematically. It has been evaluated and compared with Eq. 5 for sufficient values to indicate that in the region of practical interest the difference between isothermal and adiabatic diffusion does not introduce errors greater than about 10 pct.

An approximation to Eq. 5a may be made for the values of constants applying in practice, since the exponential term is then negligible—much less than 1 pct of the right-hand side of Eq. 5a,

$$E = \frac{a}{2r} (w - rV - rc) \quad [5b]$$

provided that $w > r \left(\frac{16b}{a} + V + c \right)$.

A further approximation may be made if the condensing temperature is less than 300°C, since then c may be neglected. Thus for conditions of cold condenser (designated "C.C." in the figures),

$$E = \frac{a}{2r} (w - rV) \quad [5c]$$

Practical Application

The equations just derived will be considered as they apply to the apparatus of the St. Joseph batch process, and also to the apparatus of the Port Pirie continuous process, although strictly speaking it is not applicable in the latter case because P is not constant throughout the distillation space. The limitations will be discussed more fully in a later publication.

Batch Process: If the rate of evaporation from the surface area A (sq cm) of B (g) of bullion is E (g cm⁻² sec⁻¹) at time t (sec) after the start, when the zinc concentration is w (wt pct) and the concentration of zinc changes by $-dw$ pct in time dt sec, then,

zinc evaporated = zinc lost from bullion,

$$\text{i.e., } EAdt = -\frac{Bdw}{100} \text{ g}$$

$$\text{or } t = \frac{B}{100A} \int_w^{w_i} \frac{dw}{E} \text{ sec} \quad [6]$$

$$= 13.2 \int_{0.05}^{0.50} \frac{dw}{E} \text{ sec} \quad [6a]$$

for the St. Joseph plant conditions.

Nomenclature

Although these units must be used in equations, in the text temperatures are given in degrees centigrade and pressures in microns.

Symbol	Dimensions	Explanation
A	Sq cm	Area of evaporating surface = 8.0×10^4 in St. Joseph plant
a	—	Constant in Eqs. 2, 3, 5, 7, 8, and 10 See Table I
B	Grams	Quantity of bullion = 1.055×10^8 in St. Joseph plant
b	—	Constant in Eqs. 4, 5, 7, and 10. See Table I
C	G cm ⁻² sec ⁻¹	Rate of condensation
c	—	Constant in Eqs. 5 and 10. See Table I
D	Cm ² sec ⁻¹	Maxwell's diffusivity
E	G cm ⁻² sec ⁻¹	Rate of evaporation or distillation
F	Tons per hr	Bullion flow rate
k	—	Constant in Eq. 3
L	Cm	Distance across distillation space
M	G cm ⁻² sec ⁻¹	Rate of migration of vapor
P	Mm Hg	Total pressure in distillation space
p'	Mm Hg	Partial pressure of zinc in evaporating surface of bullion
p_1	Mm Hg	Partial pressure of zinc above evaporating surface
p_2	Mm Hg	Partial pressure of zinc above condensing surface
p_c	Mm Hg	Partial pressure of zinc in condensing surface
r	—	Ratio w/p'
T	*K	Temperature of evaporating surface, and of vapor above evaporating surface
T_2	*K	Temperature of vapor above condensing surface
T_s	*K	Temperature of condensing surface
t	Sec	Time in seconds after start of a batch distillation process
u	—	E/b
V	Mm Hg	Vacuum, or residual gas pressure
w	—	Weight percent zinc in bullion
Subscript i	—	Initial
Subscript f	—	Final

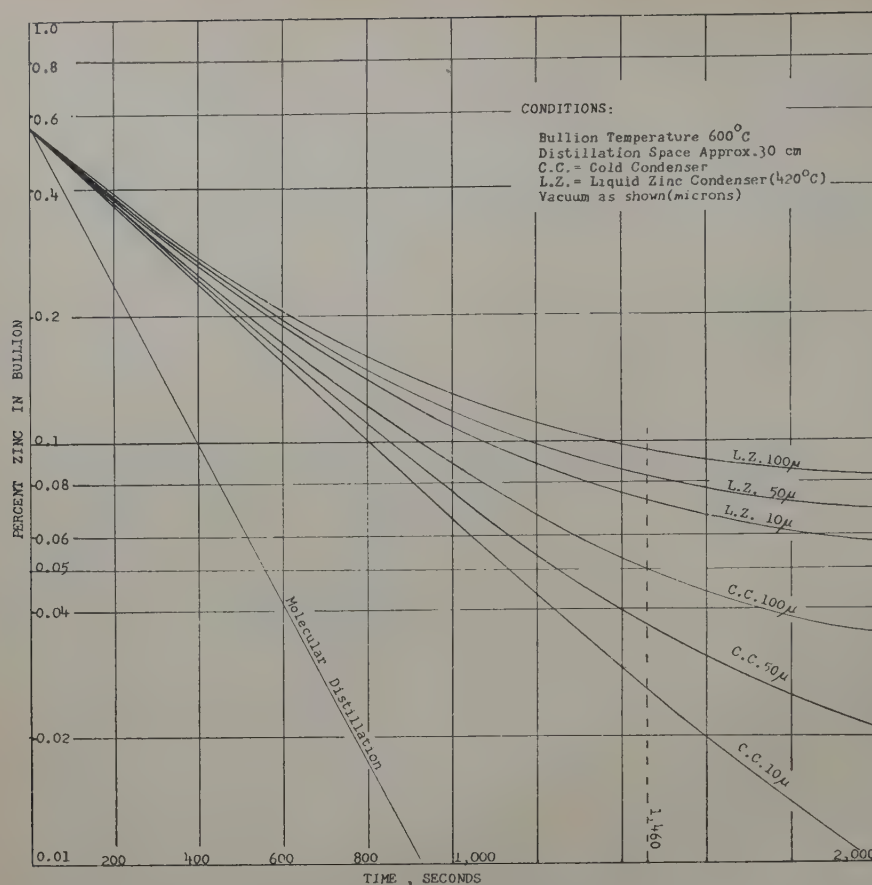


Fig. 1 — Time-elimination curves.

Substituting Eq. 5a or 5c in 6a, the following is obtained:

$$t = \frac{26.4r}{a} \ln \frac{E_i}{E_f} + \frac{13.2rV}{b} \int_{u_f}^{u_i} \frac{e^{-u}}{u} du \quad [7]$$

where $u = E/b$

$$\text{or } t = \frac{26.4r}{a} \ln \frac{w_i - rV}{w_f - rV} \quad [7a]$$

As a matter of interest, the corresponding equation for molecular distillation is

$$t = \frac{13.2r}{a} \ln \frac{w_i}{w_f} \quad [8]$$

Molecular distillation cannot occur unless the distillation space is reduced to approximately 0.2 cm with a vacuum of 100 microns, as compared with approximately 30 cm obtaining in practice; or the pressure is reduced to less than 0.7 microns with a distillation space of 30 cm.

It is of interest to consider Eq. 7a more closely: the time of treatment is shown to depend upon initial and final zinc content of bullion; residual gas pressure (or vacuum, V); and temperature of bullion, which enters the constant term a . It is, however, independent of the distillation space, L , which enters only into the term b and is not significant in the practical range (down to 0.05 pct Zn). L becomes significant only at values of w below 0.04 pct Zn. Eq. 7a is also independent of the condenser temperature provided it is below 300°C. If T_c exceeds 300°C then the full Eq. 7 must be used.

Some evaluations of Eq. 7 are presented in Fig. 1, for a bullion temperature of 600°C, and vacua of 10, 50, and 100 microns. For comparison, the rate of molecular distillation is also shown (Eq. 8) and

further evaluations of Eq. 7 on the assumption that the condenser is at the melting point of zinc, 420°C.

The value of r has been determined using Kelley's vapor pressure data for pure zinc,⁹ and Lumsden's expression¹⁰ for the free energy of mixing of zinc and lead, after checking its accuracy against the vapor pressure measurements of Jellinek and Wannow¹¹ together with the Zn-Pb phase diagram

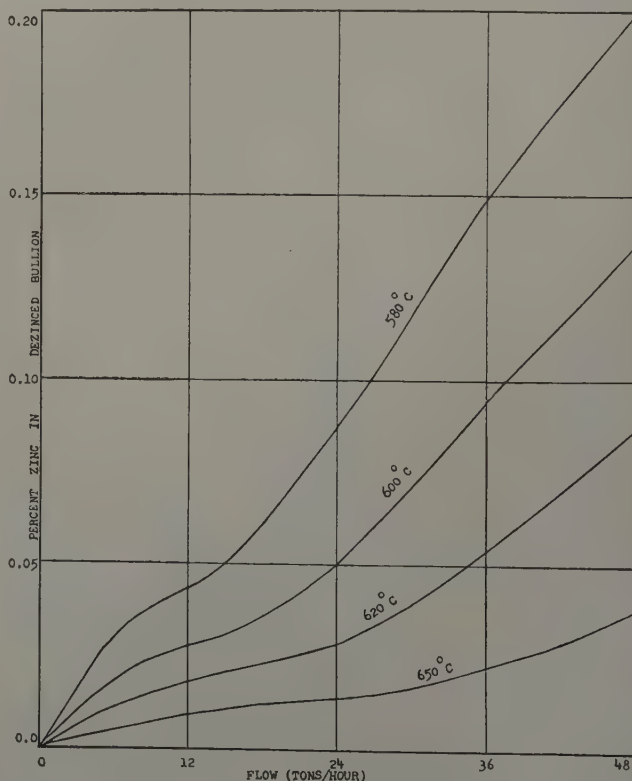


Fig. 2—Effect of bullion flow rate.

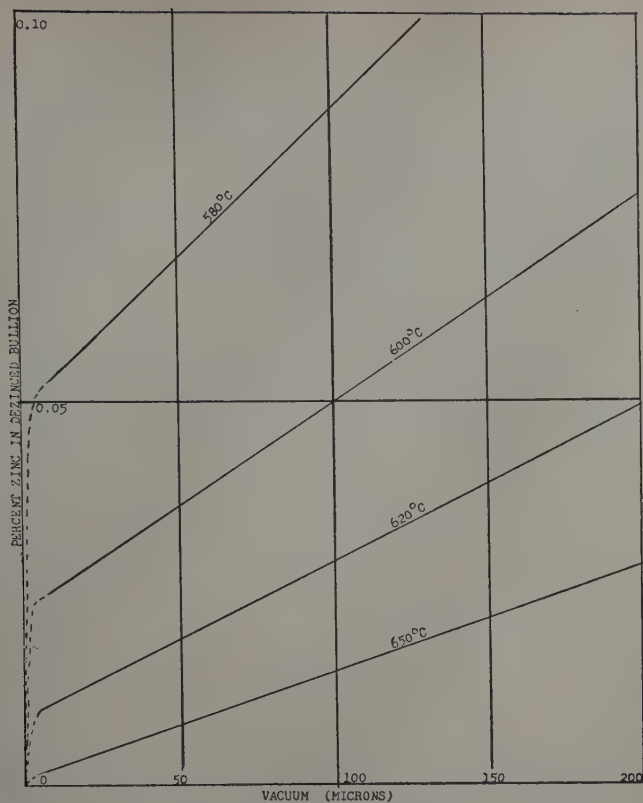


Fig. 3—Effect of vacuum.

of Waring et al.¹² Values of a , b , c , and r for a variety of bullion temperatures are given in Table I.

It is evident, from Fig. 1, that under the normal St. Joseph operating conditions, treatment time should be 1,460 sec, whereas in practice it is about 5 hr, or 18,000 sec. The discrepancy could be due to one of two causes: 1—concentration of zinc, or the temperature, may be lower at the bullion surface than in the bulk; and 2—some zinc vapor may condense before reaching the condensing surface, fall back into the bullion bath, and require re-evaporating. Although the first factor certainly operates to some extent, its effect is small compared with that of the second. This point will be discussed subsequently.

Continuous Process: In identical manner to the derivation of Eq. 6, it is found that:

$$\frac{1}{F} = \frac{2.82}{A} \int_{w_f}^{w_i} \frac{dw}{E} \text{ hr per ton} \quad [9]$$

or

$$\frac{1}{F} = \frac{5.64r}{Aa} \ln \frac{w_i - rV - rc}{w_f - rV - rc} + \frac{2.82rV}{Ab} \int_{u_f}^{u_i} \frac{e^{-u} du}{u} \quad [10]$$

The area A required to dezinc any flow of bullion (F ton per hr) may then be determined by insertion of appropriate values of the constants. At a bullion temperature of 600°C, a vacuum of 100 microns, and with a cold condenser, zinc is removed from 0.56 to 0.05 pct if approximately 0.34 sq ft of evaporating area is provided for each ton per hr of bullion flow.

Fig. 2 shows the manner in which variation in flow produces variation in dezincing bullion assay, assuming a constant 0.56 pct Zn in desilverized bullion. In this evaluation of Eq. 10, A has been taken as 8.1 sq ft (7,500 sq cm), when a bullion flow of 24 tons per hr is dezincing to 0.05 pct Zn at $T = 600^\circ\text{C}$, $V = 100$ microns.

Fig. 3 shows how the dezincing bullion assay varies with vacuum for a variety of bullion temperatures with a cold condenser.

Fig. 4 shows the variation in dezincing bullion assay with bullion temperature, for a variety of vacua, for liquid zinc condensation (at 420°C) as well as cold condenser. It is apparent that in order to obtain the same operating results with a liquid zinc condenser as with a cold condenser, in the same size of apparatus, the bullion temperature should be 30° to 35°C higher.

The theoretical limit of zinc removal shown in Fig. 4 is imposed by the fact that at the concentrations and temperatures shown the partial pressure of zinc in bullion equals the vapor pressure of zinc at its melting point—154 microns.⁹

The agreement between calculation and practice has been found to be reasonably good in the Port Pirie falling-film type of apparatus, both as to the absolute magnitude of the distillation rate and as to the dependence of results upon vacuum and temperature and independence of distillation space. The dependence on rate of bullion flowing through the unit is not demonstrated, however, because the area available for evaporation is automatically varied with the bullion flow.

It should be mentioned that Figs. 3 and 4 apply as well to a batch process as to a continuous process, provided that precondensation of zinc vapor does not falsify the results.

Comparison With Other Theoretical Work

Carman¹³ presented a mathematical description of vacuum distillation processes in 1948. As his work has been quoted recently^{14, 15} it will be of interest to compare his results with the presentation here.

Carman presents an equation for evaporation exactly as Eq. 2, but his analogue of Eq. 4 is:

$$M = b \ln \frac{P - p_c}{P - p_1} \quad [\text{Carman 1}]$$

It is seen that Carman assumes the partial pressure of zinc above the condensing surface p_2 to be equal to p_c , whereas it is quite evident that p_2 equals

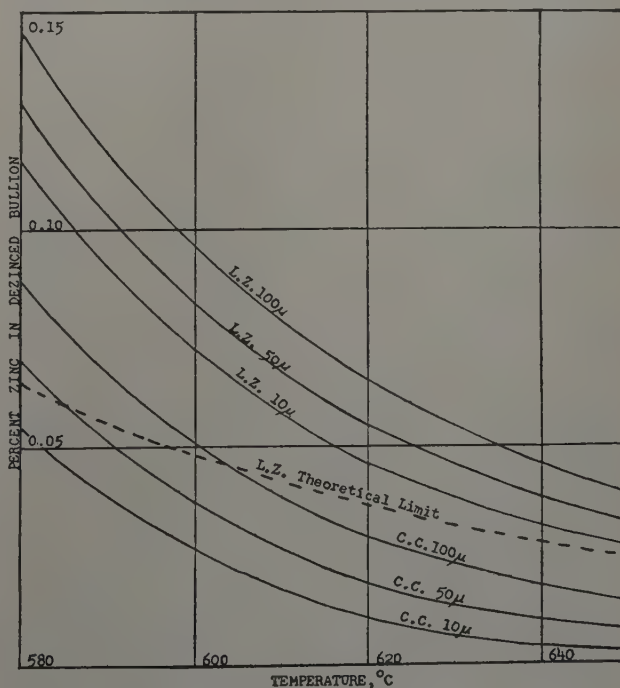


Fig. 4—Effect of temperature.

p_c only if the rate of condensation is zero. His expression for M is therefore much too high because in general p_2 is much greater than p_c .

Further errors of implication arise through confusion of P , the total pressure in the still, with V , the residual gas pressure. These will not be discussed here beyond stressing that P may be many times greater than V , and varies during a batch dezincing operation from roughly 1000 microns initially to about 130 microns finally, whereas V remains constant, after the initial pump-down period, at 50 to 100 microns.

Richardson¹⁰ makes the same confusion, in writing of the St. Joseph process: "In the actual process the pressure falls to 0.05 mm in the first two hours of distillation, corresponding to rapid removal of the zinc to 0.1 pct concentration in the liquid." It is clear that V is not affected in any way by p' , and hence bears no relation to w .

Precondensation

As Kroll has observed,¹ in metal distillation processes there frequently occurs condensation of vapor into liquid globules before the vapor reaches the condensing surface. In his original vacuum dezincing experiments he placed the condenser below the evaporating bullion, to prevent zinc droplets from falling back into the bullion.

When upward distillation is employed, as in the St. Joseph apparatus, precondensate forms and falls back into the bullion to such an extent that the treatment time is increased approximately twelve-fold. When sideways or horizontal distillation is employed, as in the Port Pirie continuous apparatus, precondensate forms to much the same extent, but the liquid globules continue to move away from the (vertical) bullion surface and toward the condenser, presumably in parabolic paths. The distillation rate under such conditions is approximately equal to the calculated rate, although formation of precondensate could be expected to alter the pressure relations assumed for the calculations.

The cause of this precondensation is by no means obvious, since it is not primarily due to fall of temperature of zinc vapor by adiabatic diffusion. The value of T_2 may be calculated on the assumption of adiabatic expansion from T_1 , p_1 , to T_2 , p_2 , and it is found that T_2 falls below the saturation temperature of zinc vapor only toward the end of the operating cycle.

There is a good deal of evidence that precondensation is connected with lead vapor, which is drawn into the zinc vapor streaming across the distillation space, in much larger quantities than would be the case if lead were distilling alone. The distillation space is therefore always supersaturated in lead vapor, and condensation of lead to liquid globules tends to occur even just above the evaporating surface, without any appreciable fall in temperature. As soon as a liquid phase of lead is formed, zinc can condense on to it, particularly if the globule loses temperature by radiation to the condenser.

Such precondensation amounts to a fractionation of the mixed vapor, and so it would be expected that the percentage lead in the distillate would be greater, the closer the condenser surface is to the bullion. This has been observed in practice. It would also be expected that the lead content of distillate produced by horizontal distillation would increase from the top to the bottom of the (vertical) condenser, since the lead globules tend to hit the condenser lower down. This also has been observed, the lead content

increasing from 0.1 to 0.3 pct at the top, to 5 to 10 pct at the bottom.

While not proving the suggested connection between lead vapor and the cause of precondensation, the facts stated above are in complete accord with theoretical expectations.

Calculation of Other Interesting Values

It is of interest to consider absolute evaporation rates, average velocity of zinc atoms, percentage lead in distillate, and the heat effects of vaporizing and condensing zinc.

Absolute Evaporation Rates: Inserting values from Table I in Eq. 5c, for the conditions: $T = 600^\circ\text{C}$, $V = 100$ microns, cold condenser, the following is obtained:

$$E = 0.0287 (w - 0.0279) \text{ g cm}^{-2} \text{ sec}^{-1}.$$

$$\text{At } w = 0.56 \text{ pct, } E = 0.0153 \text{ g cm}^{-2} \text{ sec}^{-1} = 113 \text{ lb ft}^{-2} \text{ hr}^{-1}.$$

$$\text{or } w = 0.05 \text{ pct, } E = 0.000634 \text{ g cm}^{-2} \text{ sec}^{-1} = 4.68 \text{ lb ft}^{-2} \text{ hr}^{-1}.$$

Mean Velocities of Zinc Vapor: At p mm Hg pressure, 1 g of zinc vapor occupies

$$\frac{22,400}{65.4} \times \frac{873}{273} \times \frac{760}{p} = \frac{7.76 \times 10^5}{p} \text{ cu cm at } 600^\circ\text{C}.$$

Now, at 0.56 pct Zn, $p' = 1.950$, $E = 0.0153$, thus $p_1 = 1.0$ approximately, hence $0.0153 \text{ g cm}^{-2} \text{ sec}^{-1} = 11,900 \text{ cm sec}^{-1}$ mean velocity.

Similarly, at 0.05 pct Zn, $p' = 0.186$, $E = 0.000634$, $p_1 = 0.146$, hence $0.000634 \text{ g cm}^{-2} \text{ sec}^{-1} = 3,400 \text{ cm sec}^{-1}$ mean velocity.

These compare with the molecular velocity of zinc vapor, at 600°C , of $54,700 \text{ cm sec}^{-1}$.

Percent Lead in Distillate: At 600°C the vapor pressure of pure lead is $3.8 \times 10^{-4} \text{ mm Hg}$. Assuming that lead enters the vapor to this extent, back condensation being equivalent to that of the zinc, the expected lead content of distillate would be

$$\frac{3.8 \times 10^{-4}}{1.950} \times \frac{207.2}{65.4} \times 100 = 0.062 \text{ pct from bullion containing } 0.56 \text{ pct Zn, and}$$

$$\frac{3.8 \times 10^{-4}}{0.186} \times \frac{207.2}{65.4} \times 100 = 0.65 \text{ pct from bullion containing } 0.05 \text{ pct Zn.}$$

The figures obtained in practice are somewhat higher than these.

Latent Heat of Vaporization of Zinc: Latent heat of vaporization of pure zinc, according to Kelley,⁹ is 28,400 cal per mol at 600°C , and 28,954 cal per mol at 420°C .

Lumsden's expression¹⁰ yields values for the heat of mixing of lead and zinc at 600°C , of 100.6 cal per mol of solution at 0.56 pct Zn, and 9.06 cal per mol of solution at 0.05 pct Zn. Hence the removal of zinc from a solution to reduce its composition from 0.56 to 0.05 pct consumes 5,700 cal per mol of zinc removed.

Thus, to evaporate 1 mol of zinc from lead bullion at 600°C , requires $28,400 + 5,700 = 34,100 \text{ cal}$. Although this figure applies strictly only to removal of zinc between the limits 0.56 to 0.05 pct the variation would not be great if other limits were taken.

The stated reduction of zinc in solution amounts to a molar fraction of 0.016, hence the heat requirement related to bullion is

$$0.016 \times 34,100 = 545 \text{ cal per mol of bullion}$$

= 2.65 cal per g
= 4.78 Btu per lb
= 10,500 Btu per ton

Taking the specific heat of lead as 6.8 cal per mol,^o the temperature fall of bullion, if heat were not supplied by an external agency while zinc is distilling, would be about 82°C.

If the zinc vapor cools from 600° to 420°C, then condenses to liquid at that temperature, the total heat liberated is $846 + 28,954 = 29,800$ cal per mol of zinc, equivalent to 2.325 cal per g of bullion, or 9,200 Btu per ton of bullion.

If the zinc vapor condenses to solid zinc at a temperature of 200°C on the condenser, the corresponding figures are 32,840 cal per mol of zinc, equivalent to 2.64 cal per g of bullion, or 10,400 Btu per ton of bullion. This is the quantity of heat which must be removed by the condenser coolant (in addition to the heat radiated by the bullion to the condenser).

Distillation Process

The following brief description applies not only to the distillation of zinc from lead, under a vacuum of about 10 to 100 microns, but to any similar process where the distilling element has a partial pressure of about 100 microns or greater, and the non-volatile constituents have a partial pressure of less than about 10 microns, provided that extensive evaporating and condensing surfaces are situated parallel to one another without obstructions to vapor flow in between, and with a vapor path short enough for the resistance of the vessel walls to be neglected.

Zinc atoms leave the evaporating surface to form vapor with a partial pressure roughly half that in the distilland. The nitrogen partial pressure there is negligibly small, thus the motion of zinc vapor away from the surface is extremely rapid, and a relatively large amount of lead vapor is drawn into the stream.

Only quite close to the condensing surface does the nitrogen partial pressure rise, quite steeply, to the measured degree of vacuum. The lead content of the vapor, which is at supersaturation values, tends to lower itself by condensation to liquid globules, which are formed in an atmosphere of nearly pure zinc vapor and thus are saturated with zinc.

If the flow of vapor is vertically upward, these droplets of precondensate tend to fall back into the distilland, and the distillate will be lower in lead content, the greater the distance between evaporating and condensing surfaces.

If the vapor flow is horizontal, then the precondensate globules tend to fall toward the lower part of the condenser.

The overall rate of distillation is more dependent upon the difference in partial pressure of zinc between distilland surface and vapor just above the surface than upon any other factors. Hence a rise in evaporating temperature, which raises the vapor pressure of zinc, increases this difference, and thus markedly increases the distillation rate.

A reduction of the residual gas pressure (the vacuum) lowers the pressure of zinc vapor above the distilland surface slightly, and thus slightly improves the distillation rate. If the residual gas pressure is lowered to the point where molecular distillation can occur, a great improvement in distillation rate should result.

If the condenser temperature is high enough for the partial pressure of zinc in the distillate to be appreciable, the effect on the overall distillation

rate, as compared with cold condensation, is roughly equivalent to raising the residual gas pressure by the same amount as the partial pressure of zinc in the distillate.

Alterations in the distance across the distillation space do not exert any appreciable influence on the rate of distillation, because the partial pressure of nitrogen is negligibly small over most of the space, and rises steeply only near the condensing surface.

Acknowledgments

The writer is indebted to D. R. Blaskett of the Broken Hill Associated Smelters Pty. Ltd. Research Department staff, and G. M. Willis of the Melbourne University School of Metallurgy, for many discussions which have been of great assistance in developing the concept of the distillation process which has been presented; and to K. C. Williams of the Broken Hill Associated Smelters Pty. Ltd. Research Department staff for performing the lengthy calculations of activity from Lumsden's data. The permission of the Management of Broken Hill Associated Smelters Pty. Ltd. to present this paper is also gratefully acknowledged.

References

- ¹ W. J. Kroll: The Vacuum Distillation of Metals. *Metal Industry* (1935) **47**, p. 155. Also, Melting and Evaporating Metals in a Vacuum. *Trans. Electrochem. Soc.* (1945) **87**, p. 571; and Vacuum Metallurgy. *Vacuum* (1951) **1**, p. 163.
- ² W. T. Isbell: Vacuum Dezincing in Lead Refining. *Trans. AIME* (1949) **182**, p. 186; *METALS TECHNOLOGY* (April 1947).
- ³ Extractive Metallurgy in Australia. (1953) Vol. 4b. Fifth Empire Mining and Metallurgical Congress Publication.
- ⁴ I. I. Betcherman and L. M. Pidgeon: The Distillation of Calcium and Magnesium. *Canadian Min. and Met. Bull.* (1951) **44**, pp. 253, 460.
- ⁵ R. R. Rogers and G. E. Viens: The Refining of Magnesium by Vaporization of Extremely Low Pressures. *Journal Electrochem. Soc.* (1950) **97**, p. 419.
- ⁶ R. R. Rogers and G. E. Viens: Refining Lithium by Vaporization at Low Pressure. *Canadian Min. and Met. Bull.* (1951) **44**, p. 15.
- ⁷ M. J. Spendlove and H. W. St. Clair: Low Pressure Distillation of Zinc from Al-Zn Alloy. *Trans. AIME* (1949) **185**, p. 553; *JOURNAL OF METALS* (September 1949). Also, Rate of Evaporation of Zinc at Low Pressures. U. S. Bur. Mines Report No. 4710 (1950).
- ⁸ W. K. Lewis and K. C. Chang: The Mechanism of Rectification. *Trans. A.I.Ch.E.* (1928) **21**, p. 127.
- ⁹ K. K. Kelley: Contributions to the Data on Theoretical Metallurgy, Pt. III. U. S. Bur. Mines Bull. 383 (1935).
- ¹⁰ J. Lumsden: Thermodynamics of Lead-Zinc Alloys. Discussion of Faraday Soc. (1948) No. 4, p. 60.
- ¹¹ K. Jellinek and A. Wannow: Vapor Pressures and Activities of Completely and Incompletely Miscible Metals in Liquid Binary and Ternary Alloys with One or Two Volatile Components. *Ztsch. Elektrochem.* (1935) **41**, p. 346.
- ¹² R. K. Waring, E. A. Anderson, R. D. Springer, and R. L. Wilcox: Equilibrium in the Lead Zinc System with Special Reference to Liquid Solubility. *Trans. AIME* (1934) **111**, p. 254.
- ¹³ P. C. Carman: Molecular Distillation and Sublimation. *Trans. Faraday Soc.* (1948) **44**, p. 529.
- ¹⁴ A. W. Schlechten: Discussion to ref. 5. *Journal Electrochem. Soc.* (1950) **98**, p. 257.
- ¹⁵ H. Kramers and S. Stemerding: *Applied Scientific Research* (1951) **A3**, p. 73. Abstract in *Vacuum* (1951) **1**, p. 339.
- ¹⁶ F. D. Richardson: Principles Underlying Refining Processes. P. 83. *Principles of Extraction and Refining of Metals.* (March 1951) Inst. of Metallurgists.

Isothermal Temper Embrittlement of SAE 3140 Steel

by F. L. Carr, M. Goldman, L. D. Jaffe, and D. C. Buffum

IN an earlier investigation by Jaffe and Buffum,¹ a time-temperature transformation diagram for isothermal temper embrittlement of an SAE 3140 steel showed some suggestion of two overlapping "noses." These authors mentioned, as a possible explanation, that their specimens embrittled at 525°C were slightly softer than expected, perhaps because of some slight unknown variation in tempering treatment. Because a double nose would be of considerable importance in elucidating the mechanism of the temper brittleness reaction,² it appeared worthwhile to redetermine the portion of the diagram near 525°C.

The same heat of SAE 3140 steel was used as in the previous work, and experimental procedures were the same.¹ Blanks were austenitized 1 hr at 900°C, water-quenched, tempered 1 hr at 675°C, and water-quenched. Groups were then embrittled isothermally at the temperatures and for the times

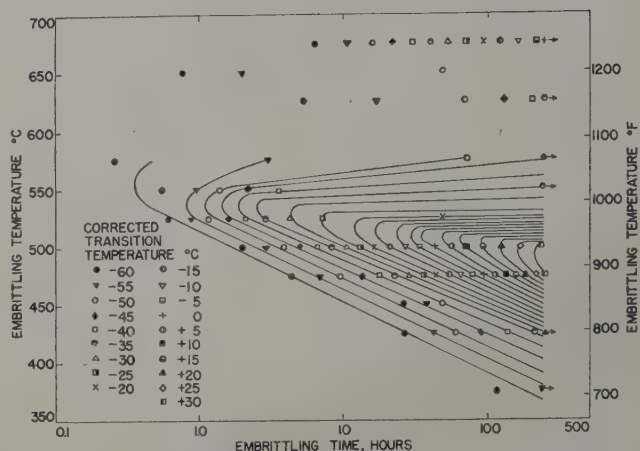


Fig. 1—Time-temperature diagram for temper embrittlement of SAE 3140 steel.

Table I. Transition Temperatures, °C. 100 Pct Fibrous Criterion

Em- brittling Tempera- ture, °C	Embrittling Time				
	5 Min	20 Min	1½ Hr*	8 Hr	48 Hr
450	-68	-70	-70	-69	-50
475	-70	-68	-68	-55	-20
500	-73	-74	-65	-38	+ 2
525	-65	-65	-46	-24	-18
550	-68	-63	-52	-38	-42
575	-71	-60	-59	-54	-54

Temper- ing Tempera- ture, °C	Tempering Time				
	1 Hr	4 Hr	16 Hr	48 Hr	240 Hr
675	-80	-68 (Rc 21)†	-57 (Rc 19½)	-42 (Rc 15½)	-20 (Rc 10)

* This time is the average of treatments of 1 hr 20 min and 1 hr 40 min.

† Rockwell C hardness.

shown in Table I, and water-quenched. For comparison, one series was tempered various times at 675°C, water-quenched, and given no further treatment. V-notched Charpy impact specimens machined from the blanks were tested over a range of temperatures. Energy absorption and percentage of fibrous fracture were plotted vs test temperature for each group, utilizing both the new data and those for the same treatment obtained in the earlier work,¹ except that the earlier data at 525°C were discarded.*

* One of the embrittling times used in this study was 1 hr 20 min; the corresponding time in the previous work was 1 hr 40 min. Both sets of data were plotted together. The time of "4 min" listed in the earlier paper should have read "5 min."

Hardnesses of all groups were between Rockwell C22 and C25, except where indicated in the table.

From the graphs mentioned, temperatures of transition from tough to brittle failure were read, and

F. L. CARR, associated with National Research Corp., Cambridge, Mass., and M. GOLDMAN, associated with Goodyear Aircraft Corp., Akron, Ohio, were formerly with Watertown Arsenal, and L. D. JAFFE and D. C. BUFFUM, Members AIME, are associated with Watertown Arsenal, Watertown, Mass.

TN 165E. Manuscript, April 3, 1953.

are given in Table I. After a small correction ($-0.28^{\circ}\text{C}/\text{BHN}$) for the variation of hardness³ from Rockwell C24, the transition temperatures were plotted against embrittling time for each embrittling temperature, using the data of Table I for the range of treatments covered there, and using previous data¹ for other treatments. By cross-plotting, Fig. 1 was finally obtained. It appears from this figure that if there are two noses to the time-temperature-transformation diagram for isothermal temper embrittlement of SAE 3140 steel, the upper nose must lie above 575°C.

As interest had been primarily in the region near 525°C, a thorough study of embrittlement above 575°C was not made. Fig. 1 shows that such a study is needed, especially since preliminary measurements at the tempering temperature of 675°C reveal much more rapid embrittlement than would be expected from the data at lower temperatures. The transition temperature increased, approximately, as the logarithm of the tempering time (about $8\frac{1}{2}^{\circ}\text{C}$, after correction for hardness, for each doubling of the time).⁴ Since three tensile specimens tempered 240 hr at 675°C and water-quenched had an average yield-tensile ratio of 0.844, with 70.7 pct reduction of area, it is assumed¹ that the tempering temperature is not above A_{e1} . The omission of a quench-and-reheat operation below A_{e1} for the groups tempered at 675°C, as compared to groups embrittled at lower temperatures, should not affect results.⁵

More detailed investigation of embrittlement above 575°C is now under way.

References

1. L. D. Jaffe and D. C. Buffum: Isothermal Temper Embrittlement. *Trans. ASM* (1950) 42, pp. 604-614.
2. M. Baeyerztz: Discussion to ref. 1. *Trans. ASM* (1950) 42, pp. 614-615.
3. D. C. Buffum and L. D. Jaffe: Effect of Hardness on Temper Brittleness. *Trans. AIME* (1951) 191, p. 540; *JOURNAL OF METALS* (July 1951).
4. L. D. Jaffe and D. C. Buffum: Retrogression of Temper Brittleness. *Revue de Metallurgie* (1951) 48, pp. 609-612.
5. L. D. Jaffe, D. C. Buffum, and F. L. Carr: Effect of Various Heat Treating Cycles upon Temper Brittleness. *Trans. ASM* (1953) 45, pp. 725-731.

Examination of a High Sulphur Free-Machining Ingot, Bloom and Billet Sections

by D. J. Carney and E. C. Rudolphy

IT has been demonstrated that inclusion size, distribution, and composition affect the machinability of resulphurized steels. Merchant and Zlatin¹ concluded that large sulphide inclusions aided machining by forming a (lubricating) coating on the tool face. Boulger et al.² and Van Vlack³ noted that the size, distribution, and composition of the inclusions in the steel affected the machinability. Steel specimens containing large globular sulphide inclusions usually exhibited excellent cutting properties, while machinability was adversely affected by the presence of numbers of oxide-type inclusions. Consequently a thorough knowledge of all the factors which affect the inclusions in the final product is desirable.

Since almost all the inclusions have their origin in liquid steel, it was necessary to begin a study of inclusions in free-machining steels by studying the inclusions and chemical segregation in the as-cast ingot. Very little information is available on the size, distribution, shape, and composition of inclusions in large, capped, free-machining steel ingots, particularly the B1113 grade. Gregory and Whiteley⁴ made a general study of the inclusions in a small, high sulphur, free-machining steel ingot. Also, numerous authors have described the solidification and segregation characteristics of the four basic types of steel ingots, namely, rimmed,⁵⁻⁷ capped,⁷ semikilled,^{7, 8} and killed^{7, 9, 10} ingots. Most of these studies were made with plain carbon or low alloy, low sulphur steel.

It was desirable to study not only the ingot but also the change in size, shape, and number of inclusions on rolling an ingot to a bloom and thence to a billet. This procedure was followed and it is hoped that this study may serve the dual purpose of adding to the general knowledge of ingot solidification as well as contributing to the knowledge of the size, shape, distribution, and composition of inclusions from the ingot to the billet in a high sulphur, free-machining steel.

Procedure

A 12,000-lb 23x35x75 in. slab ingot of the B1113 grade was cast, sectioned, and studied both macroscopically and microscopically. An adjacent ingot from the same heat and of the same size was rolled to a 7 $\frac{7}{8}$ x7 $\frac{7}{8}$ in. bloom and thence to a 2 $\frac{1}{2}$ x2 $\frac{1}{2}$ in. billet. These various bloom and billet sections were also sectioned and studied macroscopically and microscopically.

Sectioning the Ingot: The ingot herein described was obtained from the United States Steel Corp.'s South Works Bessemer Blow No. 0193, a B1113 mechanically capped heat. The 23x35 in. ingot (No.

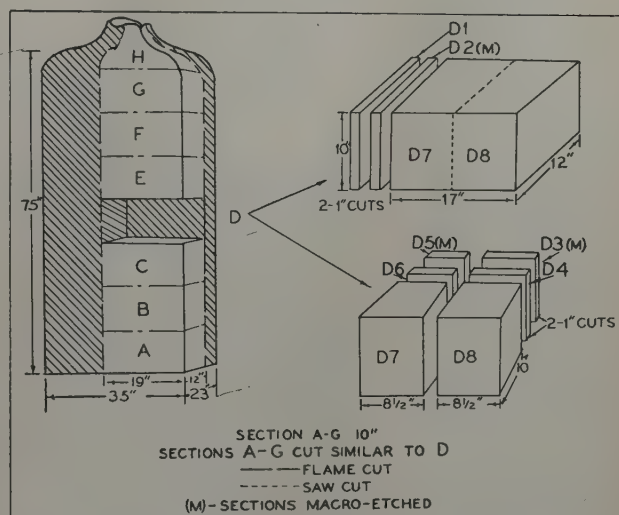


Fig. 1—Method of sectioning the B1113 ingot.

2) was teemed according to normal procedures and after stripping and transportation to the rolling mill was not placed in the soaking pit but allowed to air cool in an upright position. When completely solidified, the ingot was cut into sections by means of a powder scarfing torch and further sectioned by saw cutting as indicated in Fig. 1.

Cut No. 2 (1x10x12 in.) from sections A through H was cleaned thoroughly, macroetched in a solution of 50-50 water and hot muriatic acid and used to obtain a macrograph of a horizontal section from the surface to slightly beyond the center of the 23-in. ingot dimension. Cuts No. 5 and 3 (1x8 $\frac{1}{2}$ x10 in. each) from sections A through H were treated in a similar manner to obtain a macrograph of a horizontal section from the surface to slightly beyond the center of the 35-in. ingot dimension. The composite macrograph of these horizontal ingot sections, which shows a vertical section of the ingot from top to bottom, is shown in Fig. 2. It should be noted that sections No. 2 are normal to sections 5 and 3 in the composite.

Drillings for chemical analyses were obtained from selected positions within the above-mentioned ingot sections as noted in Fig. 3. The oxygen content was determined by the vacuum-fusion method. Samples for microscopic examination were cut from

D. J. CARNEY, Member AIME, is Chief Development Metallurgist, and E. C. RUDOLPHY, Junior Member AIME, is Petrographer, South Works, United States Steel Corp., Chicago.

Discussion on this paper, TP 3573C, may be sent, 2 copies, to AIME by April 1, 1954. Manuscript, Feb. 9, 1953. New York Meeting, February 1954.

these, as indicated in Fig. 4. The samples were taken from the indicated positions for microscopic examination on the basis of the results of the chemical analyses. They were chosen to obtain the best relationships between chemical segregation and inclusion studies, as well as to obtain the representative microstructure and inclusion data from center to surface and from top to bottom of the ingot.

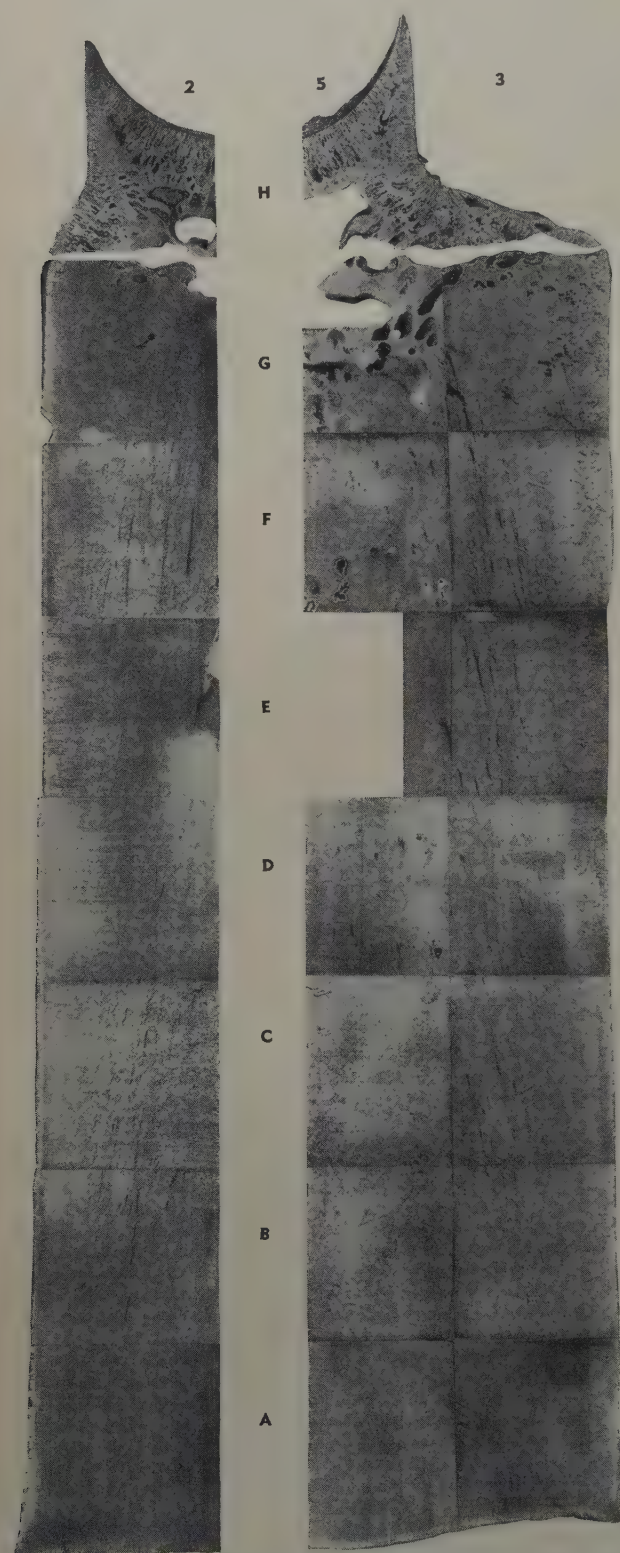


Fig. 2—Composite macrostructure of B1113 ingot. Sections 2 in a vertical plane normal to that of sections 5 and 3, see Fig. 1. 50 pct muriatic acid etch. X1/5. Area reduced approximately 75 pct for reproduction.

Sectioning of Bloom and Billet Samples: In addition to the as-cast samples obtained from ingot No. 2 samples were taken from each bloom and billet of the succeeding ingot (No. 3) of this heat. The ingot was rolled into four $7\frac{7}{8} \times 7\frac{7}{8}$ in. \times 14 ft bloom sections and thence into eighteen $2\frac{1}{2} \times 2\frac{1}{2}$ in. \times 30 ft billet sections. Cuts of 9 in. were obtained from the top of each bloom and a cut of the same size from the bottom of the bottom bloom. Cuts of 12 in. were taken from the top billet of each bloom and a 12-in. bottom cut was taken from the bottom billet of the bottom bloom. Further sectioning to sample size was done as indicated in Fig. 5.

The final bloom and billet sections were macroetched in a manner similar to the ingot sections and photographed, see Figs. 6 and 7. Samples for microscopic examination were then selected taking a full section from surface to center of each bloom and billet as shown in Fig. 5.

Microscopic Examination: All samples selected for microscopic examination were saw cut and rough finished on 0, 00, and 000 emery paper. They were then polished on a high speed polishing wheel using a polishing solution of iso-propyl alcohol and fine-grained alumina on a gammal cloth. Etching for structure and grain size was accomplished by alternate polishing and etching in a 2 pct nital solution until the proper depth of etch had been obtained.

The techniques used to measure the length-width ratios (L/W) and the number of inclusions in ingot, bloom, and billet samples were similar to those used by Van Vlack³ and therefore will not be described in detail here. Because of the use of a different microscopic lens combination than that used in the above-mentioned work, only those inclusions greater than 0.007 mm in length were counted. However, the relative size of inclusions was calculated by utilizing the length and width values of the inclusions measured, in the equation, $V = 1.08 LW^2$, for the determination of the relative inclusion volume (size). This method of determining relative inclusion size was developed by Van Vlack and the derivation of this equation will be found in the appendix to this text. At least 50 lengths and widths were measured at random locations within each microsection examined. The relative size of the average inclusion within the section was then calculated. For the purpose of direct comparison, the values for the size, number, and L/W ratios of the ingot inclusions were obtained from those ingot sections which would correspond with the bloom and billet samples.

Results and Discussion

Ingot—Macroscopic Examination: It can be noted in Fig. 2 that the capped B1113 steel ingot exhibits a structure similar to that of killed ingots rather than to that of normal low sulphur (0.04 pct maximum S) capped ingots.^{4,7,9} The presence of "V" segregation, "inverted V" segregation, positive and negative chemical segregation, pipe and blowhole location tends to support this statement, see Fig. 8. Apparently the high sulphur content of the liquid metal suppressed the formation and evolution of carbon monoxide. In a previous British study⁴ this same observation was made and considerable discussion of the finding was presented. It was stated that the sulphur probably deoxidized the steel. Recent work by Hilty¹¹ on a pure liquid iron system showed that sulphur is a poor deoxidizer. It is more reasonable to expect that sulphur suppresses the

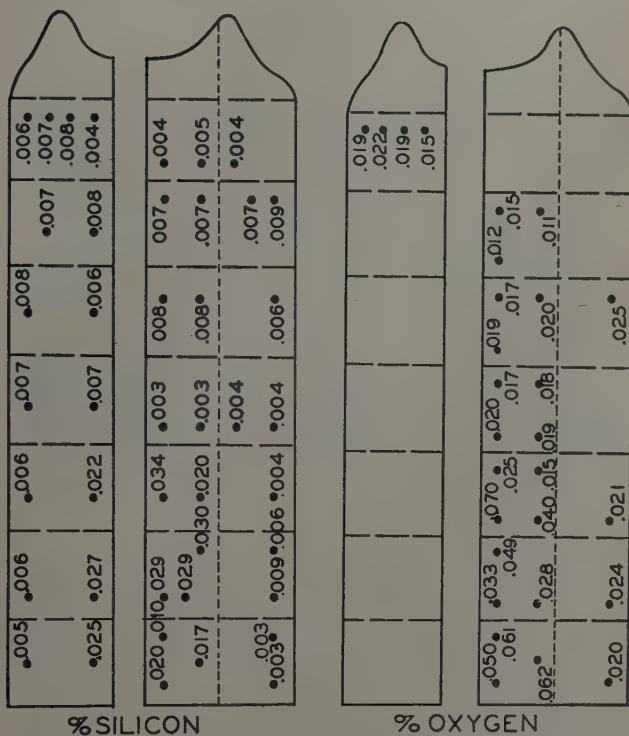
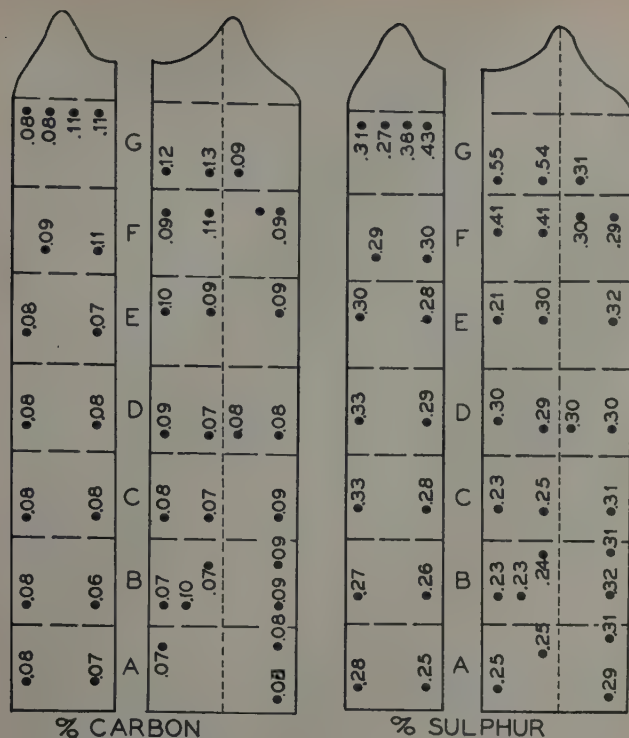


Fig. 3—Chemical analyses of samples selected from ingot sections. a, top. b, bottom.

carbon monoxide evolution by way of its affect on the chemical activity of carbon and/or oxygen.

The pipe and secondary blowholes were confined primarily to the topmost sections of the ingot, H and G. The V segregate was found in the top of section G, while the inverted-V segregate extended from section B near the bottom of the ingot to section G where it ended forming an inverted truncated cone. These features were noted also by Gregory and Whiteley in similar work with a 5000-lb ingot.⁴ The V segregate was occasioned by large sulphide inclusions which were segregated in this area. Small dot etch pits that can be noted lower in the ingot in

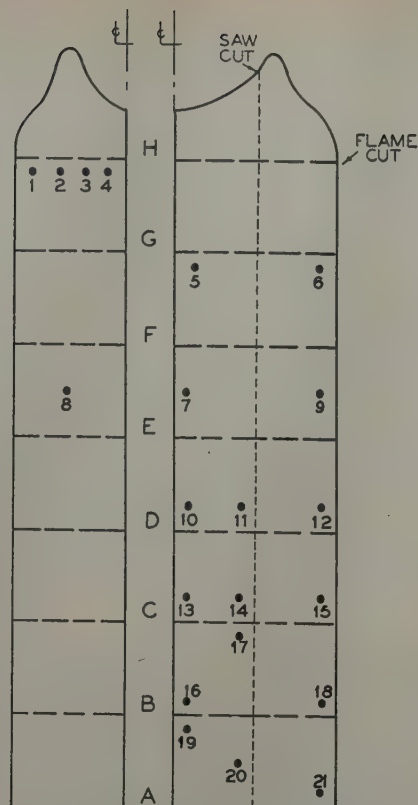


Fig. 4—Location of samples selected for microscopic examination.

sections B and C are caused by silicate inclusions. These observations are confirmed by examination of microsections and chemical analyses, see Fig. 9 and Table I.

The rate of solidification of the ingot from the bottom was rapid. Furthermore, no patches of sulphide or dot etch were evident in this section (A), so that the extreme bottom portion of the ingot was sound steel. At the surface of the bottom section where inclusions were noted in number, they were exceptionally fine, further evidence of rapid solidification along the mold wall.

Chemical Segregation: Chemical analyses are summarized in Table I and Fig. 3. Maximum positive chemical segregation was confined to the topmost sections of the ingot, G and F, in the case of carbon, sulphur, phosphorus, and manganese. Silicon and oxygen tended to segregate positively in the bottom third of the ingot in which the above-mentioned elements tended to reach maximum negative segregation.

Sulphur tended to segregate positively in the center of the top one third of the ingot while silicon

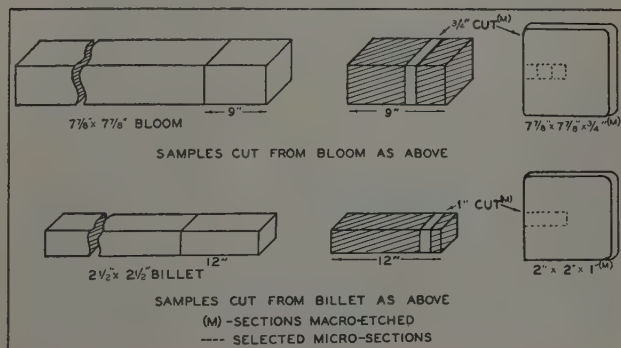
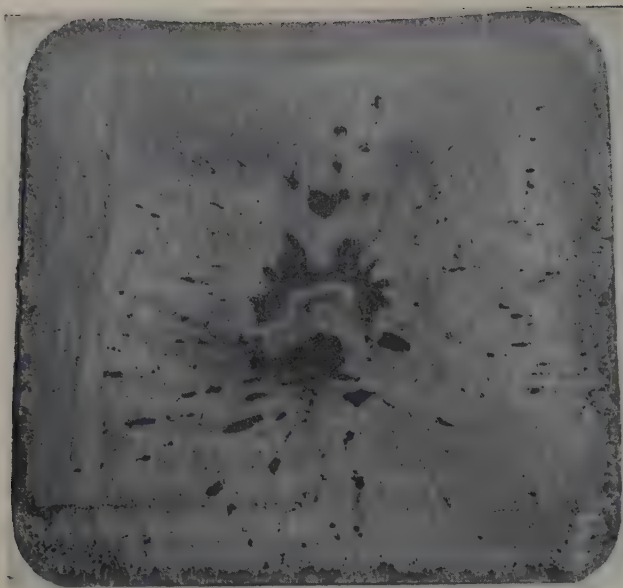
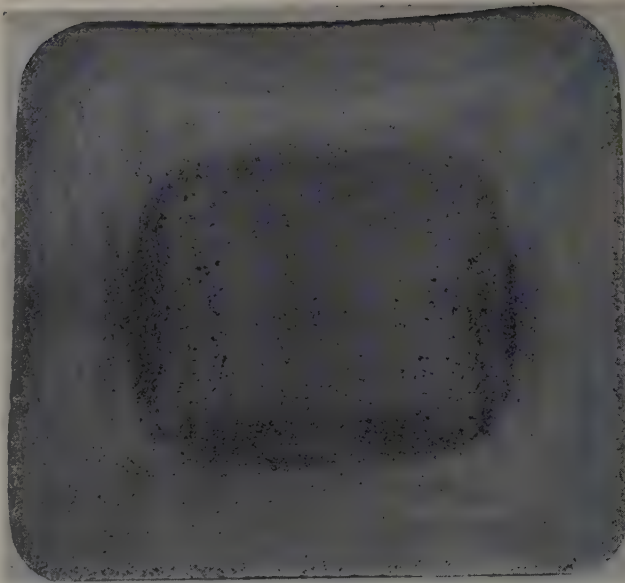


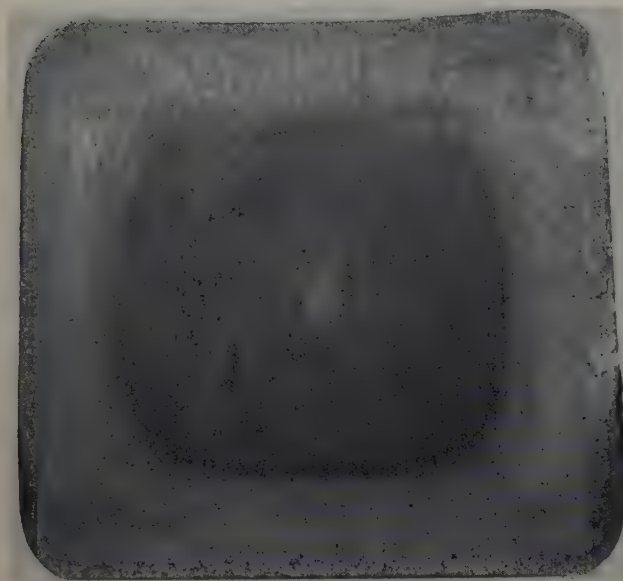
Fig. 5—Method of sectioning the bloom and billet samples.



a—Bloom 1—top.



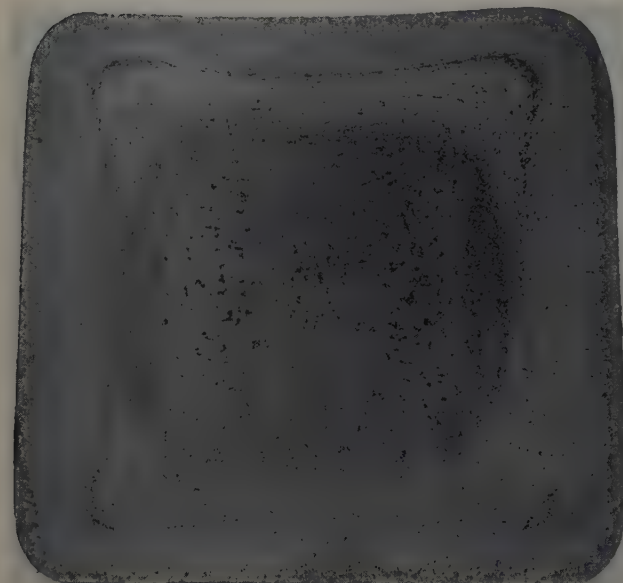
d—Bloom 4—top.



b—Bloom 2—top.



e—Bloom 4—bottom.



c—Bloom 3—top.

Fig. 6 a to e—Macrostructure of B1113 bloom sections. Locations given in Fig. 5. 50 pct muriatic acid etch. Area reduced approximately 75 pct for reproduction.

and oxygen showed positive segregation toward the center of the bottom of the ingot. Lower oxygen levels were observed in those sections with the higher sulphur content. The segregation of carbon, manganese, phosphorus, and nitrogen was very similar to that noted in capped ingots with lower sulphur contents. However, this segregation was not considered to be of any real significance in this study.

The presence of higher oxygen contents in the bottom cuts of ingots was suspected in earlier work and confirmed by oxygen analyses of B1112 and B1113 bar samples which had shown poor machining qualities.³ A similar segregation of oxygen has been noted in the examination of an ingot with approximately the same composition.⁴ Although the segregation of silicon and oxygen in the bottom of the ingot has never been explained satisfactorily, it was observed microscopically that the presence of high oxygen in these sections of the ingot is the re-

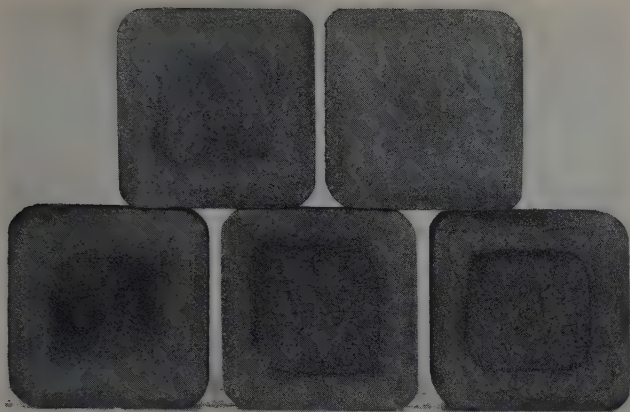


Fig. 7—Macrostructure of B1113 billet sections. Locations given in Fig. 5. 50 pct muriatic acid etch. Upper row: left, 15T; right, 18B. Lower row: left, 2T; center, 6T; right, 10T. Area reduced approximately 75 pct for reproduction.

sult of siliceous inclusions, Fig. 9. The analytical methods used in this report for analyses of steel for silicon and oxygen yield the total silicon and total oxygen contents, with no distinction as to the quantity of oxygen or silicon dissolved in the metal or in the inclusions. The explanation of the segregation of silicon and oxygen as silica in the bottom of the ingot and sulphur in the top of the ingot probably lies within the phase relationships of the liquidus surface of the Fe-Si-Mn-S-O system. Recent data on the Fe-S-O system¹¹ indicate the presence of two immiscible liquids. Possibly the segregation of silica and sulphur during the solidification of the ingot is related to immiscible silica and sulphide phases.

Microscopic Examination: Most of the inclusions in the ingot tended to be globular in shape regardless of location or apparent composition. This is shown by the proximity to unity of the length-width ratios (L/W), Table I and Fig. 9. Also, the inclusions tended to decrease in size but to increase in number from the center to the surface of the ingot. This was true in all sections from the top to the bottom of the ingot as shown in Fig. 10.

The predominant type of inclusions noted varied considerably, depending on ingot position, and this variation is shown pictorially in Fig. 9. In the top part of the ingot large single-phased MnS inclusions were most common, but numerous duplex (Fe,Mn) sulphides were found in sections G and F.¹² Several FeS inclusions, which as such are relatively uncommon in commercial steels, were also noted in sections G and F,* see Fig. 11. Occasional oxide-sul-

* MnS will dissolve up to about 50 pct FeS in solid solution. The exact amount is dependent upon the manganese and sulphur content of the steel. Likewise the sulphide phase will dissolve an undetermined amount of oxygen.

phide duplex inclusions were noted at the bottom of section E, as the study progressed from the top toward the bottom of the ingot. The constituents of these duplex inclusions are usually MnS and a glassy phase which is $\text{MnO} \cdot \text{SiO}_2$ glass,[†] although some FeO has been noted.

† The etching characteristics indicate that the siliceous glass is comparatively rich in MnO.

In section C from the center to midway to the surface, the majority of the inclusions were large and siliceous in type, although there were numbers of these inclusions containing small globules of manganese sulphide. In sections A, B, and C, where chemical analyses revealed high silicon and oxygen,

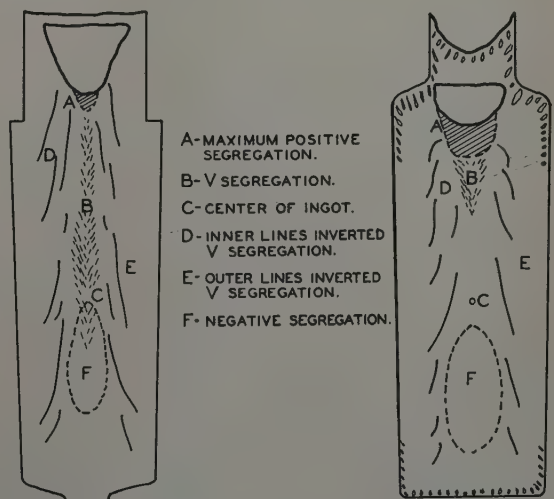
these siliceous inclusions were found, as well as the negative segregation of sulphur. The negative sulphur segregation was evidenced by fewer sulphide inclusions in the center of the ingot in sections A, B, and C than noted in the upper sections of the ingot. Sulphide inclusions were most prevalent in these sections from the center to the surface but the siliceous type of inclusion was more prominent from the ingot center to midway to the surface. In the ingot sections that were low in oxygen content the inclusions were primarily single-phase sulphide inclusions, whereas in sections that were high in oxygen the inclusions were of the duplex or single-phase siliceous type. It should again be mentioned that an earlier investigation⁸ showed that bottom cut bar samples showed poor machining properties which were attributed to these glassy oxide inclusions. Armour¹³ also observed that the presence of glassy oxide inclusions had an adverse effect on machinability by causing a reduction in tool life.

The explanation of the duplex nature of some of the inclusions is probably closely related to the aforementioned explanation of silica segregation. It is plausible that within this system the sulphide and silicate phases separate as a pair of liquids, and the manganese silicate may then devitrify from a glass.

The general crystal structure of the ingot from center to surface as determined by examination of the etched microsections is shown in Fig. 12. As can be seen in this figure, the chill zone consists of fine equiaxed grains of ferrite. Inside this surface zone, which was very thin, was a section of columnar dendritic ferrite crystals, almost normal to the ingot surface. Midway to the center of the ingot, the core of larger equiaxed ferrite grains was noted.

The process of solidification caused the entrapment of less pure liquid between the crystals in the columnar zone as indicated by pearlite in the grain boundaries. The slight segregation of carbon in the top center portion of the ingot was also indicated by an increased amount of pearlite, Fig. 12.

In general, the inclusions (regardless of composition) were found within the ferrite grains. In the midway position at the top of the ingot the iron sulphide inclusions and some manganese sulphide inclusions were observed at the ferrite grain boundaries.



TYPICAL SEGREGATION PATTERN OF A KILLED STEEL INGOT⁵

SEGREGATION PATTERN OF A MX-B1113 INGOT

Fig. 8—Schematic comparison of killed ingot structure with B1113 ingot.

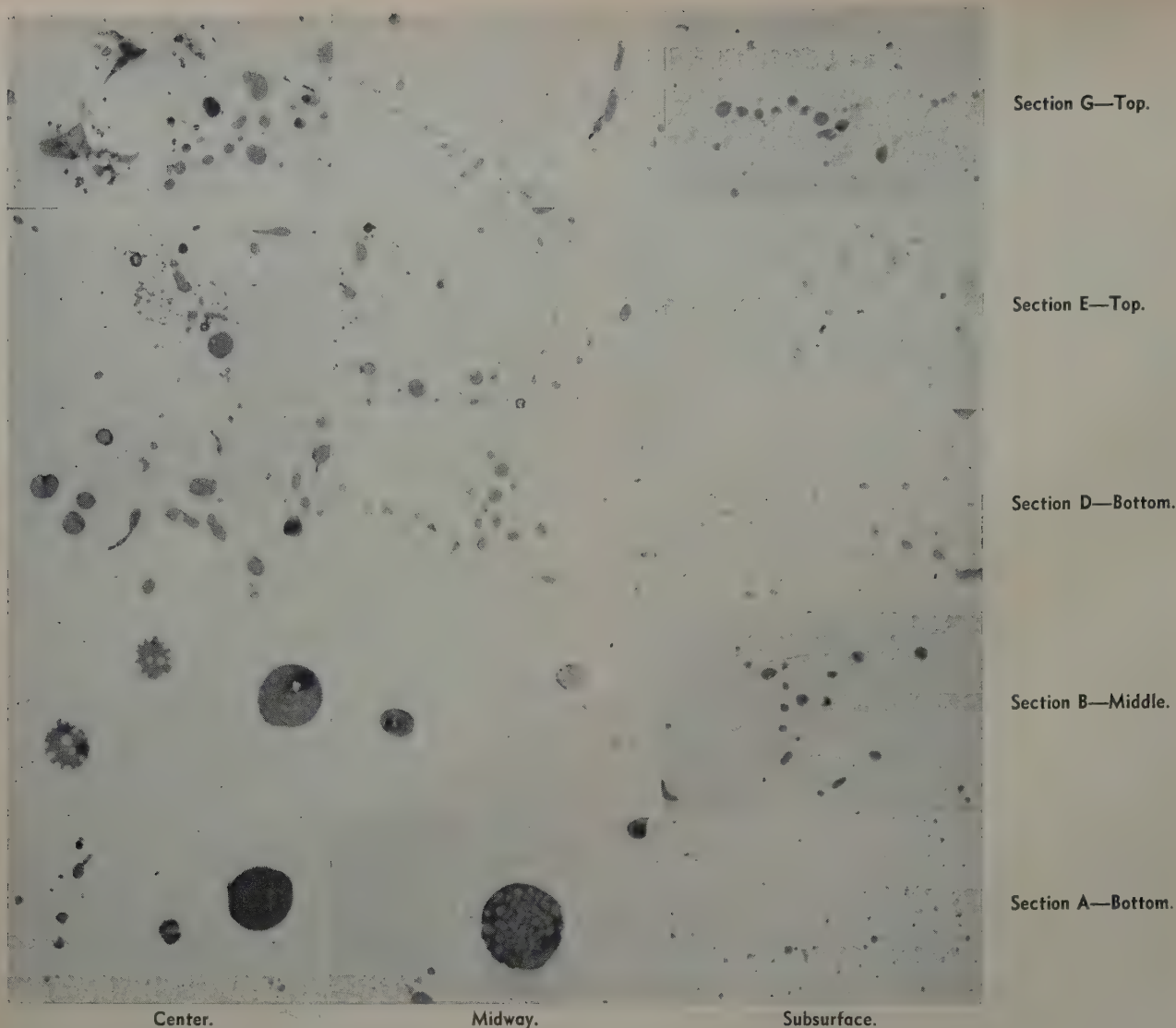


Fig. 9—Micrographs showing typical inclusions at ingot positions corresponding to the bloom and billet sections. Unetched. X100. Area reduced slightly for reproduction.

Bloom—The chemical analyses of the bloom sections are summarized in Table II and the macrographs of the etched bloom sections are shown in Fig. 6.

Chemical and Macroscopic Examination: In examining the macroetched topmost section of the bloom samples, a large blotchy area was noted in the central portion of this sample, Fig. 6a. Chemical analyses in this area in the bloom sample indicated a high sulphur content. Chemical analyses of ingot samples from the corresponding section, which was

very porous and contained large blowholes, showed approximately the same sulphur content. These blowhole cavities were closed on rolling and the larger ones appeared to have been filled with the lower melting, sulphur-rich metal in the top of the ingot. This can be further indicated by the sharp boundaries in this area of the top bloom section, Fig. 6a.

The double etch pattern, as shown in Fig. 6c and b, appeared to result from sulphide inclusions in the outer pattern and silicate inclusions in the inner pattern. It has been mentioned in the literature¹⁴ that this pattern effect is due to crystallization of the ingot, and is found in the part of the rolled product that was the columnar structure of the ingot. There was no evidence in this work that showed the concentration of either type of inclusion in a given crystal structure, although there were more sulphides noted toward the surface.

Microscopic Examination: Micrographs of typical bloom sections are shown in Figs. 13 and 15. The inclusion study data on the bloom sections are summarized in Table II and shown graphically in Figs. 14 and 16.

In rolling the ingot to $7\frac{7}{8} \times 7\frac{7}{8}$ in. blooms, the L/W ratio of the inclusions was increased as much as five times. This resulted in longer, thinner inclusions as compared to the essentially globular in-

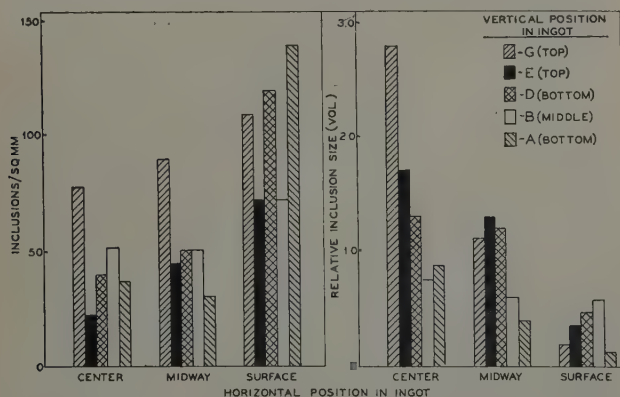


Fig. 10—Number and relative size of inclusions at ingot positions corresponding to the bloom and billet sections.

Table I. Chemical Composition and Inclusion Study Data of B1113 Ingot Heat No. 0193, Ingot No. 2

Ladle Analysis: C, 0.08 pct; Mn, 0.88; P, 0.11; S, 0.30; and Si, 0.007. Poured at 2885°F. Rolled at 2375°F.

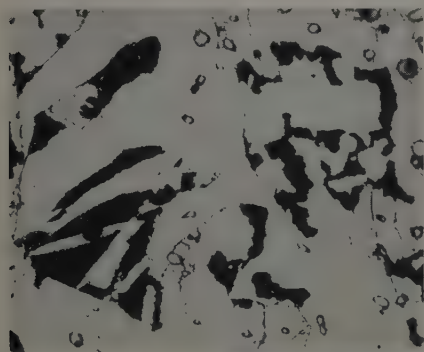
Ingot Section	Position*	Chemical Composition, Pct							Average Inclusions per Sq Mm	Average L/W	Average Relative Inclusion Size
		C	Mn	P	S	Si	O	N			
G2	c	0.11			0.43	0.004	0.015	0.009	103	1.0	
	m ₁	0.11		0.16	0.38	0.008	0.019	0.007	77	1.4	
	m ₂	0.08			0.27	0.007	0.022	0.008	111	1.2	1.30
	s	0.08	0.94	0.12	0.31	0.006	0.019	0.009	77	1.2	
G5 and 3	c	0.12		0.10	0.55	0.004					
	m ₁	0.13			0.54	0.005					
	m ₂	0.09			0.31	0.004					
F2	c	0.11			0.30	0.008					
	s	0.09			0.29	0.007					
F5 and 3	c	0.09	0.95	0.16	0.41	0.007	0.015	0.012	32	1.4	
	m ₁	0.11	0.96	0.15	0.41	0.007	0.011	0.015			
	m ₂	0.09	0.92	0.12	0.30	0.007					
	s	0.08	0.95	0.11	0.29	0.009			103	1.3	
E2	c	0.07	0.92	0.12	0.28	0.006			49	1.4	
	s	0.08			0.30	0.008					
E5 and 3	c	0.10			0.21	0.008	0.017	0.010	22	1.3	
	m	0.09			0.30	0.008	0.020	0.017			0.72
	s	0.09			0.32	0.006	0.025	0.010	74	1.3	
D2	c	0.08			0.29	0.007					
	s	0.08			0.31	0.007					
D5 and 3	c	0.09	0.87	0.11	0.30	0.003	0.020	0.010	40	1.1	
	m ₁	0.07	0.86	0.12	0.29	0.003	0.019	0.005	52	1.4	0.97
	m ₂	0.08			0.30	0.004					
	s	0.08	0.91	0.12	0.30	0.004			123	1.3	
C2	c	0.08			0.28	0.022					
	s	0.09			0.33	0.006					
	c	0.08			0.23	0.034	0.070	0.008	62	1.3	
C5 and 3	m	0.07			0.25	0.020	0.040	0.006	57	1.2	
	s	0.09			0.31	0.004	0.021	0.012	92	1.1	
B2	c	0.06			0.26	0.027					
	s	0.08	0.87		0.27	0.006					
B5 and 3	c ₁	0.07			0.23	0.029	0.033	0.010	57	1.0	
	c ₂	0.10	0.86	0.087	0.23	0.029	0.028	0.011			0.64
	m	0.07	0.95		0.24	0.030			52	1.1	
	s	0.09			0.32	0.009	0.024	0.011	72	1.2	
A2	c	0.07			0.25	0.025					
	s	0.08			0.28	0.005					
A5 and 3	c (top)	0.07			0.20	0.010	0.061	0.007	37	1.2	
	c (bot.)				0.25	0.010	0.050	0.007			
	m				0.25	0.017	0.062	0.009	33	1.1	0.47
	s (top)	0.08			0.31	0.003					
	s (bot.)	0.08			0.29	0.003	0.020	0.006	150	1.2	

* c, center; m, midway; s, surface.

got inclusions. This increase in L/W ratio is indicated in Fig. 13A, and is shown graphically in Fig. 16. The inclusions in the samples from blooms 1T and 2T tended to retain their globular shape, but as shown in Fig. 13A the inclusions in bloom samples 3T and 4T have rolled out into stringer-type inclusions. It was in the corresponding ingot locations that siliceous inclusions segregated and examination of these bloom inclusions showed that most

of these long stringers were of the siliceous inclusion type although some sulphide inclusions had also rolled out. In the 4B bloom sample, inclusions of both types were found, the sulphides tending to retain their globularity, and the silicates being strung out. This indicates that the inclusion composition had an important effect on inclusion plasticity.

In addition to the changes in L/W ratio, there was



a (left)—Carbon segregation in section G. 2 pct nital etch. X100.

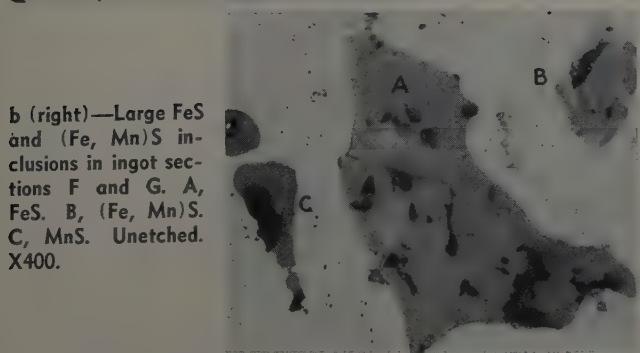


Fig. 11—Micrographs showing some effects of chemical segregation in the top sections of the B1113 ingot.

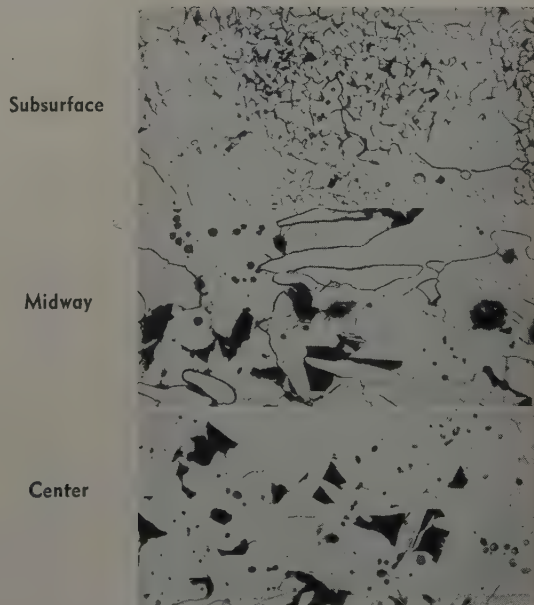


Fig. 12—Micrographs showing variation in microstructure from center to surface of ingot section D. Similar variations were noted at other levels. 2 pct nital etch. X100. Area reduced approximately 75 pct for reproduction.

Table II. Chemical Composition of B1113 Bloom Sections. Heat No. 0193, Ingot No. 3

Bloom	Position	C	Mn	P	S	Si	Average Inclusions per Sq Mm	Average L/W	Average Relative Inclusion Size
3-1-T	c-seg(A)				0.42	0.003	119	2.0	0.28
3-1-T	c-seg(B)				0.61	0.003			
3-2-T	c	0.08	0.92	0.12	0.30				
	m ₁	0.10			0.37	0.004	95	5.2	0.36
	m ₂	0.08			0.37	0.005			
	s	0.09			0.32	0.005			
3-3-T	c(A)				0.27	0.008			
	c(B)				0.27	0.004	95	5.6	0.35
	s(A)				0.30	0.006			
	s(B)				0.32	0.004			
3-4-T	c	0.07	0.92	0.10	0.25	0.006			
	m ₁				0.25	0.020	112	5.0	0.39
	m ₂	0.08			0.25	0.005			
	s(A)	0.09			0.30	0.006			
	s(B)				0.32	0.008			
3-4-B	c				0.25	0.011			
	m				0.27	0.010	119	2.3	0.36
	s				0.29	0.006			

an increase in the number of inclusions and a decrease in relative inclusion size, in rolling from ingot to bloom. Although the number of inclusions did increase, there was no major fracturing of the inclusions. The decrease in the relative size of the inclusions can be related to this increase in number, which in turn can be related to mechanical deformation and inclusion composition. This has been noted in previous work,^{2,3} that the number, size, and shape of the inclusions are influenced by the plasticity of

the inclusion which is affected by the composition and mechanical working.

The structural changes that took place during rolling from the ingot to bloom stage are shown in Figs. 12 and 15. The ferrite grain size of the ingot was predominantly No. 1 and larger.† The grain

† ASTM austenite grain size ratings at 100X.

size was reduced to No. 3 to No. 4 in the blooms.

Billets—Macroscopic Examination: A macrograph

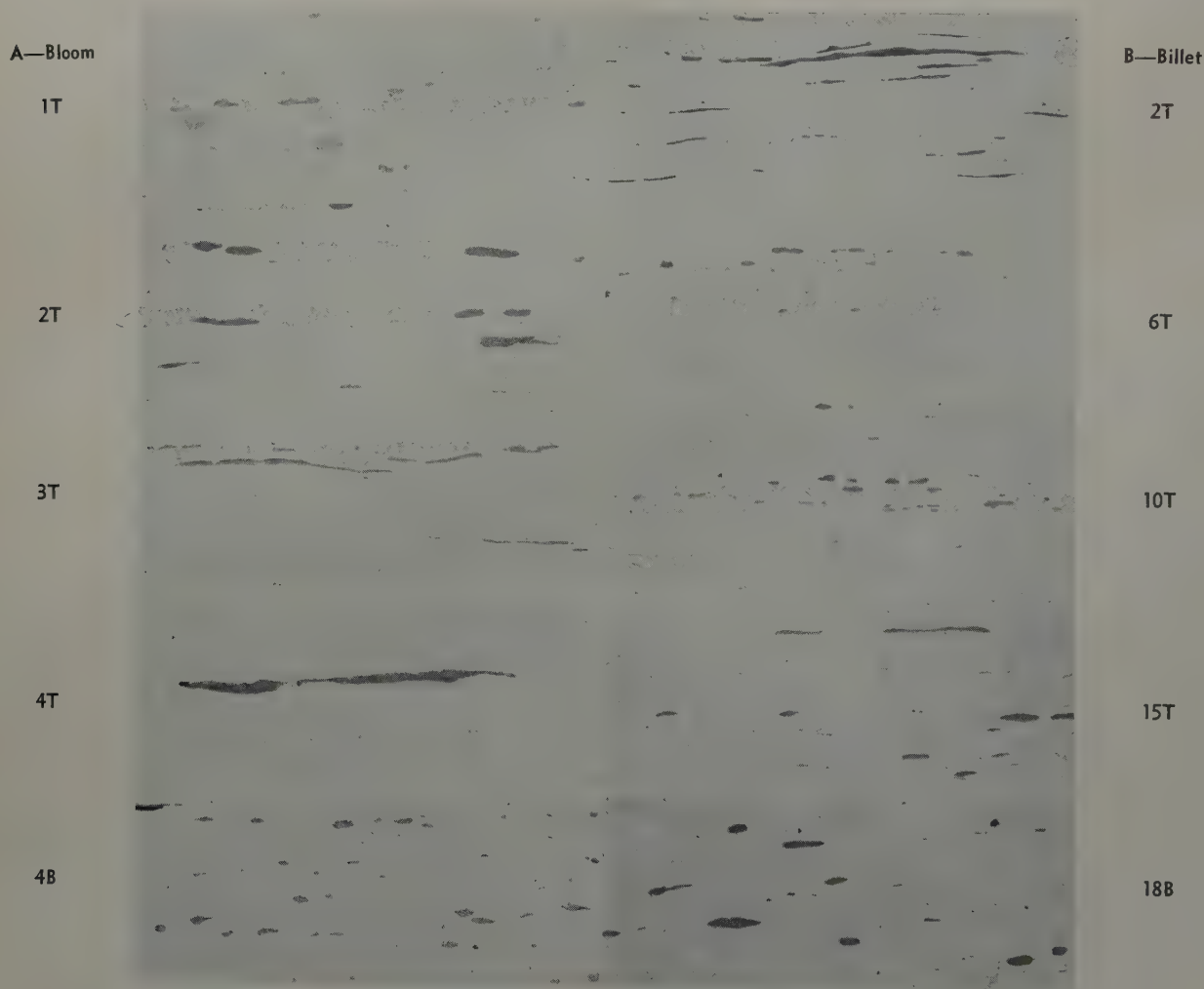


Fig. 13—Micrographs showing typical inclusions at corresponding positions in B1113 bloom and billets. These positions are also related to those in Fig. 9. Unetched. X100. Area reduced approximately 30 pct for reproduction.

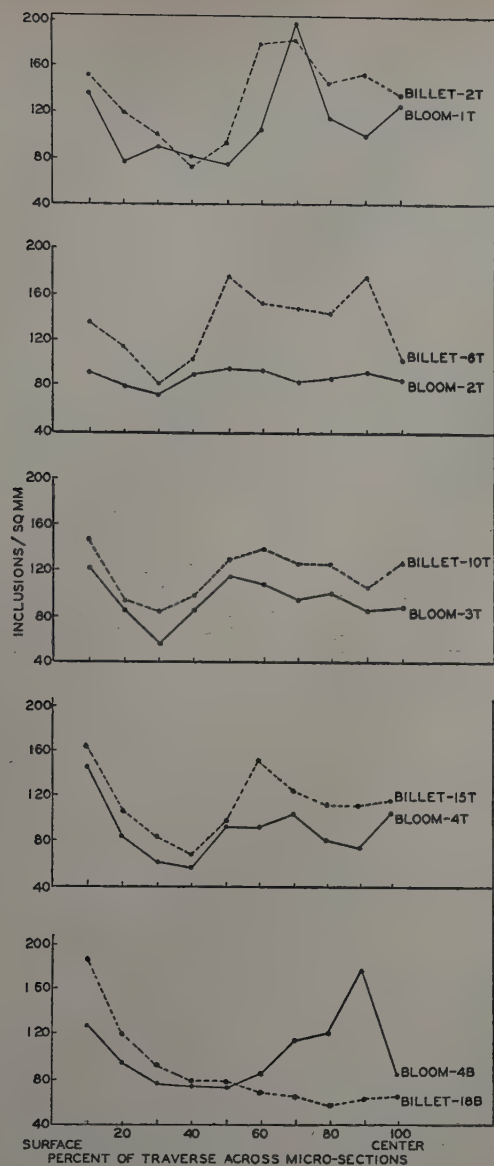


Fig. 14 (left)—Relationship between number of inclusions and percentage of traverse from surface to center of the same B1113 bloom and billet sections shown in Fig. 13.



Fig. 15 (upper right)—Micrographs showing typical microstructure of B1113 blooms and billets reduced from adjacent portion of the same bloom. Bloom reduced from same section of ingot shown in Fig. 12. 2 pct nital etch. X100. Area reduced approximately 75 pct for reproduction. Upper micrograph—Bloom 3T. Lower micrograph—Billet 10T.

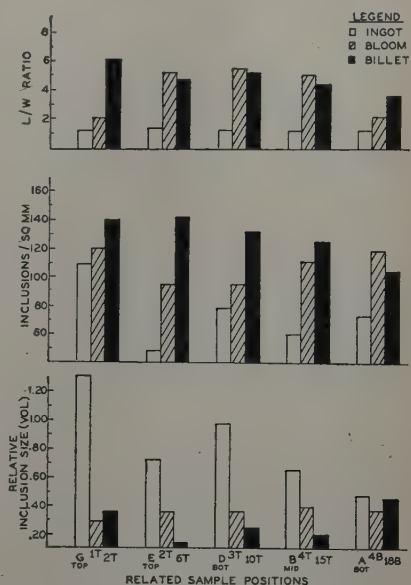


Fig. 16 (lower right)—Ingot to bloom to billet inclusion relationships.

of the etched billet sections is shown in Fig. 7. Examination of these sections indicated structures similar to those noted in the larger bloom sections. In the top billet of the top bloom the same blotchy high sulphur area as noted in the top bloom (Fig. 6a) was present. The double ingot pattern noted in blooms 3T and 4T was again present in the corresponding billet sections, 10T and 15T.

Microscopic Examination: Micrographs of typical billet sections are shown in Figs. 13 and 15 and the

related inclusion studies are summarized in Table III and shown graphically in Figs. 14 and 16.

Further rolling from the $7\frac{1}{8} \times 7\frac{1}{8}$ in. bloom size to $2\frac{1}{2} \times 2\frac{1}{2}$ in. billets produced the following changes in inclusion size, shape, and distribution. The number of inclusions increased approximately 20 pct on rolling from bloom to billet. There was some fracturing of inclusions but still not to any major extent. The inclusions in billets 2T, 6T, and 16T appear to have been rolled out and pinched off to a

Table III. Inclusion Study Data of B1113 Blooms and Billets

Bloom No.	Inclusions per Sq Mm										Billet No.
	(Surface)		Pct of Micro Traverse							(Center)	
	10	20	30	40	50	60	70	80	90	100	
I	160	74	91	83	77	100	203	115	100	138	2
	150	118	83	71	123	178	180	141	127	133	
II	96	87	78	102	98	93	86	90	93	81	6
	135	111	85	105	178	153	151	141	183	110	
III	123	87	63	84	116	108	93	96	83	87	10
	143	95	83	101	133	140	125	125	110	122	
IVT	143	80	60	59	93	91	109	82	77	145	15
	170	105	80	68	103	153	141	115	113	118	
IVB	130	93	75	73	97	100	130	120	187	90	18
	183	83	92	78	73	66	65	60	58	63	

degree, while those in billet 15T have been strung out and in the case of the siliceous-type inclusions some have been fractured. In Fig. 14 the relationship of the number of inclusions in the bloom to the number in the billets is shown graphically. In reference to bloom 4B and billet 18B there appears to be a relationship that does not occur in the top four blooms and billets. This is caused by the method of inclusion counting, as there is a minimum size (0.007 mm) to the inclusions counted as described earlier in the text.

The inclusion size decreased and the length-width ratio remained approximately the same or increased slightly. The changes in length-width ratio and inclusion size as well as the number again appear to have been affected by inclusion composition and mechanical deformation. The greatest number of inclusions are found at the surface in all the rolled sections. This can be explained by the fact that the inclusions near the surface of the ingot are smaller and in rolling this portion probably undergoes the greatest mechanical deformation. Further structural changes that took place during rolling from the bloom stage are shown in Fig. 15. The ferrite grain size reduced to No. 3 to No. 4 in the blooms, was further reduced to No. 6 to No. 8 in the billets. It is recognized that the grain size is dependent upon finishing temperature and the cooling rates associated with the different section sizes.

Conclusions

Ingot—1—The mechanically capped, high sulphur B1113 ingot solidified in a manner similar to that of a killed-steel ingot with very little apparent gas evolution.

2—The segregation of carbon, manganese, phosphorous, and nitrogen was similar to that noted in capped ingots with low sulphur contents.

3—Silicon and oxygen segregated positively in the center of the bottom one third of the ingot, while sulphur segregated positively in the center of the top of the ingot. This was the result of the segregation of silicate and sulphide inclusion phases.

4—The ingot inclusions tended to be globular regardless of composition.

5—The rate of solidification in from the bottom was so rapid that the extreme bottom section had relatively few inclusions of any size.

6—Inclusion size increased while the number of inclusions decreased moving from the surface to the center of the ingot.

Blooms and Billets—1—The length-width ratio (L/W) of the inclusions increased approximately four-fold on rolling the ingot to blooms.

2—In rolling from ingot to billet the inclusion size decreased approximately 60 pct.

3—The composition of the inclusion had the greatest effect on the reaction of the inclusions to mechanical deformation, with the more plastic siliceous inclusions having been elongated on rolling from the ingot to blooms and billets. The sulphide inclusions tended to retain a more globular shape.

4—Blowhole cavities in the top of the ingot, which were closed on rolling, were surrounded by a low melting, sulphur-rich metal, and the larger cavities appeared to have been filled with this low melting metal on rolling.

5—The ferrite grain size of the ingot was No. 1 and larger, and was reduced to No. 3 to No. 4 in the blooms and No. 6 to No. 8 in the billets.

Acknowledgments

The authors would like to express their appreciation for the encouragement to carry out this work and helpful advice of the late Marcus Grossmann and T. M. Garvey, of the Pittsburgh Research and Development Staff of The United States Steel Corp., and to acknowledge the helpful assistance in the mathematical calculations of L. H. Van Vlack, of the Pittsburgh Process Metallurgy Staff, and in the tedious microscopic work for this report of Mrs. Winnifred Oakes, of the South Works' Research Group.

Appendix—Volume of Inclusions

Assume an inclusion in rolled steel has the shape of a prolate spheroid, with the following dimension: length, $2a$; width, $2b$; volume, $4/3 \pi ab^2$. The average length L , and average width, W , of all planes through the spheroid, parallel to a and b respectively are:

$$L = \frac{\pi ab}{2b} \frac{dy}{dy} \quad W = \frac{\pi b^2}{2b} \frac{dz}{dz}$$

$$L = \frac{\pi}{2} a \quad W = \frac{\pi}{2} b$$

$$a = \frac{2}{\pi} L \quad b = \frac{2}{\pi} W$$

Therefore, the volume of the average spheroid is

$$V = \frac{4}{3} \pi \left(\frac{2}{\pi} L \right) \left(\frac{2}{\pi} W \right)^2$$

$$V = 1.08 LW^2$$

A statistical error in this calculation is enlarged by the W^2 .

References

- ¹ M. E. Merchant and N. Zlatin: Basic Reasons for Good Machinability of "Free Machining" Steels. *Trans. ASM* (1949) **41**, pp. 647-672.
- ² F. W. Boulger, H. A. Moorhead, and T. M. Garvey: Superior Machinability of MX Explained. *Iron Age* (May 17, 1951) **167**, pp. 90-95.
- ³ L. H. Van Vlack: Correlation of Machinability with Inclusion Characteristics in Resulphurized Bessemer Steels. ASM Preprint No. 16, 1952; Presented at the 34th Annual ASM Convention, Philadelphia (October 20-24, 1952).
- ⁴ E. Gregory and J. H. Whitely: Examination of a High-Sulphur, Free Cutting Steel Ingot. *Journal Iron and Steel Inst.* (1941) **144**, No. 2, pp. 9-32.
- ⁵ A. Hayes and J. Chipman: Mechanism of Solidification and Segregation in a Low Carbon Rimmed Steel Ingot. *Trans. AIME* (1939) **135**, pp. 85-125.
- ⁶ A. Hultgren and G. Phragmen: Solidification of Rimmed Steel Ingots. *Trans. AIME* (1939) **135**, p. 133.
- ⁷ B. R. Queneau: The Solidification of Steel Ingots. *The Solidification of Metals and Alloys* (1951) pp. 52-73. AIME.
- ⁸ M. Tenenbaum: Structure, Segregation and Solidification of Semi-Killed Steel Ingots. *Trans. AIME* (1948) **176**, pp. 108-162; *METALS TECHNOLOGY* (September 1947).
- ⁹ J. W. Spretnak: Macro-Segregation in Some Alloy Steel Ingots. *Trans. ASM* (1948) **40**, pp. 897-916.
- ¹⁰ B. M. Larsen: Review of Factors Underlying Segregation in Steel Ingots. *Trans. AIME* (1945) **162**, p. 414.
- ¹¹ D. C. Hilty and W. Crafts: The Liquidus Surface of the Iron-Sulphur-Oxygen System. Unpublished—private communication.
- ¹² C. E. Sims: Non-Metallic Inclusions. *Basic Open Hearth Steel Making*. (1944) p. 293. AIME.
- ¹³ J. D. Armour: Metallurgy and Machinability. *Machining—Theory and Practice* (1950) p. 142. ASM.
- ¹⁴ Macro-Etching of Iron and Steel. (1948) p. 393. Sub-Committee on Macro-Etching. *Metals Handbook*. ASM.

Reducing Period in Stainless Steel Melting

by H. P. Rassbach and E. R. Saunders

MUCH progress has been made in recent years in the theory and practice of making stainless steel. By effective utilization of oxygen for decarburization and more suitable alloying agents, it has been possible to attain consistent production of very low-carbon stainless steel. In order to facilitate economical production of stainless steels, the Electro Metallurgical Co. has carried out an extended experimental program that has clarified some of the complex interrelations of temperature and composition under decarburizing and reducing conditions. These results¹⁻³ have been founded in large part on small experimental heats, and in order to confirm their validity and significance under commercial conditions, a survey of stainless steel melting practice has been made with the cooperation of stainless steel producers.

Conditions required for decarburization and associated oxidation of chromium, manganese, and iron have been fairly well established in relation to the beneficial effect of the highest practicable temperature. The recovery of chromium and manganese from highly oxidized slags by reduction with silicon has been indicated with somewhat less precision and this study has shown significant deviation in large commercial heats from the small experimental heats. In spite of an unsatisfactory degree of accuracy in estimating the conditions affecting reduction of metallic values, it has been possible to calculate a slag weight in reasonably good agreement with the results observed in large heats. While there still is much to be learned about both the qualitative and quantitative aspects of stainless steel melting, this survey has indicated the manner by which the efficiency of the production process may be measured.

Oxidation Period

In order to establish practices for the recovery of chromium and manganese from the slag the amounts of these metals oxidized should be known. Moreover, since reduction of oxidized chromium and manganese must necessarily be accompanied by similar reduction of iron, knowledge of the total quantity of metallics oxidized is essential.

The relations between carbon, chromium, and temperature under oxidizing conditions were developed by Hilty in 1948.¹ While it had been realized previously that retention of chromium in the metal during carbon oxidation is favored by high temperatures, the Hilty relation provided quantitative information useful for evaluating melting procedures.

H. P. RASSBACH, Member AIME, is Metallurgical Engineer, and E. R. SAUNDERS is Metallurgist, Technical Service and Development Laboratory, Electro Metallurgical Co., a Division of Union Carbide and Carbon Corp., Niagara Falls, N. Y.

Discussion on this paper, TP 3574C, may be sent, 2 copies, to AIME by Oct. 1, 1953. Manuscript, Feb. 10, 1953. Los Angeles Meeting, February 1953.

For example, it was shown that decarburization to moderate carbon levels can be achieved while retaining substantial amounts of chromium. However, in decarburizing to the low-carbon level necessary for producing 0.03 pct maximum carbon stainless steel, very little chromium remains in the bath at the temperatures generally employed. For this reason, Hilty, Healy, and Crafts² later projected an extension of the chromium-carbon relation to the low-chromium region.

Although this chromium-carbon-temperature relation defined the composition of a chromium steel bath at the end of the oxidizing period, it did not provide a direct means for estimating the total amount of metallic oxidation occurring during decarburization of a stainless steel heat. This subject was investigated by Crafts and Rassbach³ and, later, by Hilty, Healy, and Crafts² who demonstrated that metallic oxidation is a function of the chromium content of the initial furnace charge, the minimum carbon content attained, and the temperature. It was further demonstrated from data on 1-ton heats that an empirical relationship exists between the ratio of chromium plus manganese to iron in the slag (*S*) to the corresponding ratio of these components present in the metal bath. The following expression was derived to permit the calculation of the amount of metallics oxidized during decarburization of a given charge:

$$W = 2000 \frac{(Cr_1 + Mn_1) - (Cr_2 + Mn_2)}{\frac{100S}{S + 1} - (Cr_2 + Mn_2)} \quad [1]$$

where *W* is the pounds of chromium, manganese, and iron oxidized per ton of charge; *Cr*₁, the percentage of chromium in the charge; *Mn*₁, the percentage of manganese in the charge; *Cr*₂, the percentage of chromium in the bath after oxidation; *Mn*₂, the percentage of manganese in the bath after

oxidation; and $S = \frac{\% Cr + \% Mn}{\% Fe}$ in the slag after oxidation.

In order to establish whether the slag ratios of commercial heats are consistent with those found in the experimental heats, the slag and metal analyses shown in Table I were evaluated. These data represent samples taken after the oxidation of two 1-ton and seven 15 to 25-ton heats of types 303, 304, and 304L stainless steel made in chromite, acid, and basic hearths.

Fig. 1 illustrates that the results for the commercial heats correlate reasonably well with the relationship originally established for experimental 1-ton heats. It will be noted that in the range of metal composition of these heats, the slag values generally lie above the line. As was suggested by

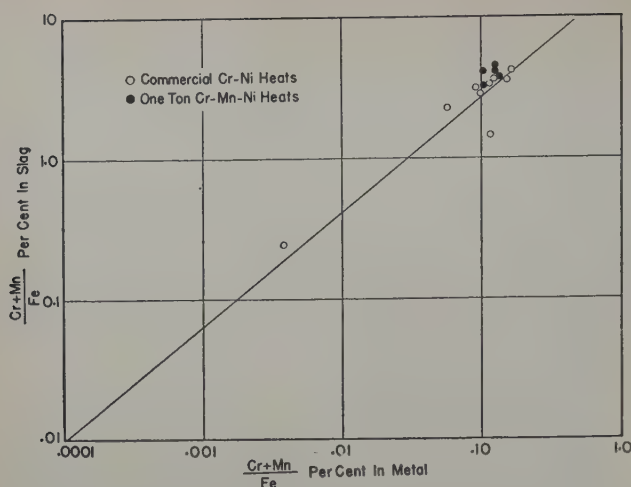


Fig. 1—Correlation of ratios of Cr+Mn/Fe in slag with relationship proposed by Hilty, Healy, and Crafts.²

Hilty, Healy, and Crafts the relationship may be better defined by two intersecting lines, but sufficient information is not available to justify such a representation. In view of the agreement shown, it is concluded that an estimated value of the slag may be used for the calculation of metallics oxidized in commercial heats.

This relation may also be expressed in terms of the total metallics oxidized. By use of Eq. 1, the total amount of metallics oxidized was calculated using both the actual *S* and the estimated *S* values for the commercial chromium-nickel heats, Fig. 2.

In order to determine the utility of this relationship for wider ranges of composition, data from five experimental 1-ton heats of high-manganese, chromium-nickel steels have been included in Figs. 1 and 2. These results also correlate reasonably well with the original curve indicating that manganese appears to be equivalent to chromium in this relationship.

Through the use of Fig. 1 for estimating *S* in Eq. 1 and by employing the published chromium-carbon-temperature relations for estimating the composition of the bath after oxidation, the amount of metallic oxidation occurring in heats oxidized to any given carbon level at any specified temperature can be predicted for charges containing various amounts of chromium, manganese, and nickel. On this basis, Fig. 3 has been prepared for a representative range of carbon contents and temperatures and an arbitrary assumption of 10 pct Ni in the bath after oxidation.

The metallics oxidized for the commercial chromium-nickel and experimental high-manganese, chromium-nickel heats, calculated on the basis of the actual slag analyses, are shown on these charts using temperatures estimated from the chromium-carbon relation. Assuming that the temperature at the end of oxidation is known from past performance or can be estimated from chromium and carbon analyses, the charts provide a reasonably accurate basis for estimating the total amount of chromium, manganese, and iron oxidized—the information necessary for establishing a reduction practice.

Slag Reduction Period—Review

It has long been known that the recovery of chromium in stainless steel melting is related to some extent to the refractory hearth employed, that is, the basic, chromite, and acid hearth process. In commercial experience better recovery of chromium is realized with the basic process than with the other processes, and the difficulties encountered in attempts to recover chromium from the slag in acid and chromite hearth heats have been described.^{4,5} A common feature of the acid and chromite hearth processes is that refractory erosion is less severe when acid or neutral slags are employed. It has been generally realized that basicity is a major factor controlling the chromium content of slags, but quantitative data have become available only recently.

In the reducing period, after completion of oxidation and for the purpose of recovering metal from the slag, it has been the practice to add silicon or aluminum or both. Silicon is the element most widely used for slag reduction, and the commonly used alloys are low in carbon and contain chromium and silicon in varying concentration. Under the conditions of the reducing period the reaction of silicon with the metallic oxides in the slag is exothermic, so that the progress of the reaction should be favored by lower temperatures. Data are not available to evaluate this tendency, but it has been noted in practice that excessive temperature in the reducing period may adversely influence chromium recovery.⁶ For this reason, addition agents of low-silicon concentrations are used to good effect as the massive addition lowers steel temperature. Apart from the problem of slag reduction, it is desirable and frequently imperative to lower the bath temperature rapidly at the end of the oxidizing period to prevent serious refractory deterioration. Experimental determination of the temperature changes resulting from the solution of different types of silicon-bearing

Table I. Metallic Oxidation Data

Heat No.	Type	Size, Tons	Lining	End of Oxidation																Cr+Mn/Fe Slag, Pct		Lb Cr+Mn+Fe Oxidized per Ton	
				Charge, Pct		Metal Analyses, Pct					Slag Analyses, Pct												
				Cr	Mn	C	Cr	Mn	Ni	Cr ₂ O ₃	Met. Cr	MnO	FeO	CaO	MgO	SiO ₂	Al ₂ O ₃	Actual (S ₁)	Est. (S ₂)	Actual (W ₁)	Est. (W ₂)		
1	303	15	Basic	16.00	0.64*	0.048	8.18	0.08	8.35	53.64	—	3.11	18.14	11.84	0.85	10.22	3.06	2.78	2.65	257	260		
2	303	15	Basic	14.70	0.71*	0.068	9.46	0.11	8.12	45.68	—	3.29	30.37	8.74	0.77	9.39	2.32	1.43	3.02	237	178		
3	304	15	Basic	15.00	0.70†	0.040	7.43	0.18	9.75	54.04	1.04	8.37	17.98	12.36	4.62	7.12	1.26	3.18	2.50	236	253		
4	304	15	Basic	14.84	0.70†	0.046	9.24	0.17	9.21	50.97	1.81	7.20	16.28	14.02	8.17	10.26	1.72	3.34	3.00	181	187		
5	304L	15	Basic	5.90	0.50†	0.010	0.32	0.01	14.53	11.63	—	1.22	46.84	22.24	4.23	7.08	1.28	0.245	0.191	627	773		
6	304	25	Chromite	15.85	0.32*	0.040	9.77	0.07	10.08	63.65	1.38	2.17	16.67	1.63	3.62	6.62	5.98	3.60	3.15	185	192		
7	304	25	Chromite	15.80	0.30*	0.073	11.57	0.22	10.44	21.23	1.35	0.43	5.82	26.02	28.72	12.28	1.40	3.59	3.74	130	128		
8	304	1	Acid	17.40	0.95*	0.072	12.27	0.16	12.30	35.60	6.52	5.31	10.73	3.70	—	38.02	1.54	4.19	4.04	173	175		
9	304L	1	Basic	12.02	0.68	0.014	4.51	0.03	14.95	31.69	0.97	12.07	18.07	5.94	13.51	18.24	7.58	2.28	1.68	251	281		
10	CrMnNi	1	Basic	10.45	3.48	0.08	9.14	1.18	6.46	25.39	—	14.80	8.91	8.46	13.52	23.00	—	4.17	3.18	103	110		
11	CrMnNi	1	Basic	10.90	2.94	0.07	7.92	0.81	6.22	15.15	—	7.49	6.47	13.35	37.32	19.36	0.60	3.21	2.73	151	158		
12	CrMnNi	1	Basic	10.95	3.00	0.06	9.86	1.44	6.37	12.80	—	8.81	5.39	16.82	19.02	32.14	2.62	3.72	3.46	78	80		
13	CrMnNi	1	Basic	10.71	3.11	0.08	9.02	1.45	6.31	15.05	—	11.51	5.42	20.41	21.69	19.94	2.52	4.56	3.24	94	102		
14	CrMnNi	1	Basic	10.55	9.73	0.05	6.74	2.45	1.20	25.21	—	30.78	12.79	8.92	13.01	10.80	3.40	4.14	2.73	311	346		

* Calculated from nickel balance.

† Estimated.

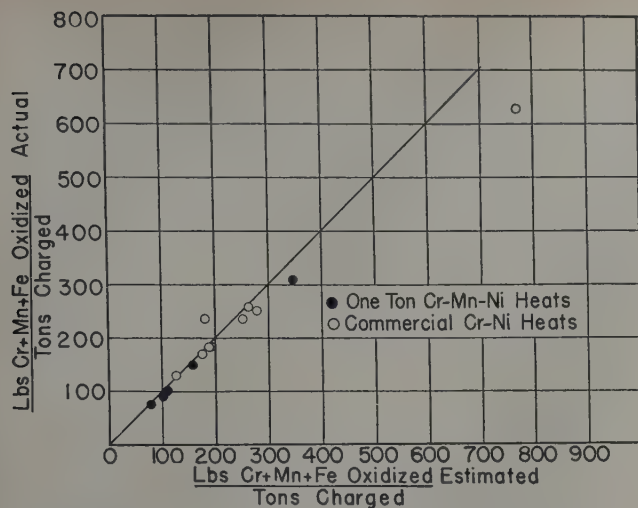


Fig. 2—Correlation of estimated and actual metalics oxidized.

ing alloys in the bath without chemical reaction is shown in Table II.

In 1950, Taylor⁷ indicated a relation between chromium oxide, the slag basicity, and silicon in the metal. The ratio of CaO to SiO₂ was used as the index of basicity, and it was shown that high basicity favored reduction of chromium from the slag. Crafts and Rassbach included a preliminary evaluation of basicity and other factors related to the control of chromium oxide in the slag. Because of refractory erosion, significant amounts of magnesia are often present in these slags, and, therefore, this constituent was included in the basicity ratio which was expressed as the ratio of the sum of pct CaO + pct MgO to pct SiO₂. Data from a number of experimental heats and some commercial heats were used to illustrate the relation between slag basicity and slag chromium content. The heats used to establish these relations contained approximately 18 pct Cr, and the silicon contents varied from 0.30 to 1.00 pct. It was

observed that the correlation of silicon content with slag chromium content for a given basicity was poor.

Shaw⁸ showed a relation observed in commercial practice between the percentage of chromium in the slag converted to Cr₂O₃ and the ratio of CaO to SiO₂. The shape of the curve was similar to that shown by Crafts and Rassbach, and a comparison of the two curves suggested that the incorporation of MgO in the basicity factor would result in good agreement between the two sets of data. Shaw's data showed a variation of bath silicon contents from 0.10 to 0.54 pct, and there was little correlation between bath

Table II. Effect of Silicon-Bearing Alloys on Temperature

Composition of Addition Agent, Pct			Loss in Bath Temperature, °F, with Addition of 1 Lb of Silicon per Ton
Si	Cr	Fe	
6	65	25	30
45	39	15	2

silicon content and chromium content of the slag for a given basicity.

It is evident from this review of some previous investigations that knowledge of the slag-reducing procedure is limited, and that a substantial portion of the data came from experimental heats. This new investigation includes some additional data from large commercial furnaces in an effort to extend further some of the basic relations in the slag-reduction period that are needed for closer process control.

Effect of Basicity on Recovery of Chromium

Additional information on the relation of unreduced metallic oxides to basicity was obtained from a number of heats representing a wide variety of operating conditions, as shown in Table III and illustrated in Figs. 4 and 5. Furnaces from which the

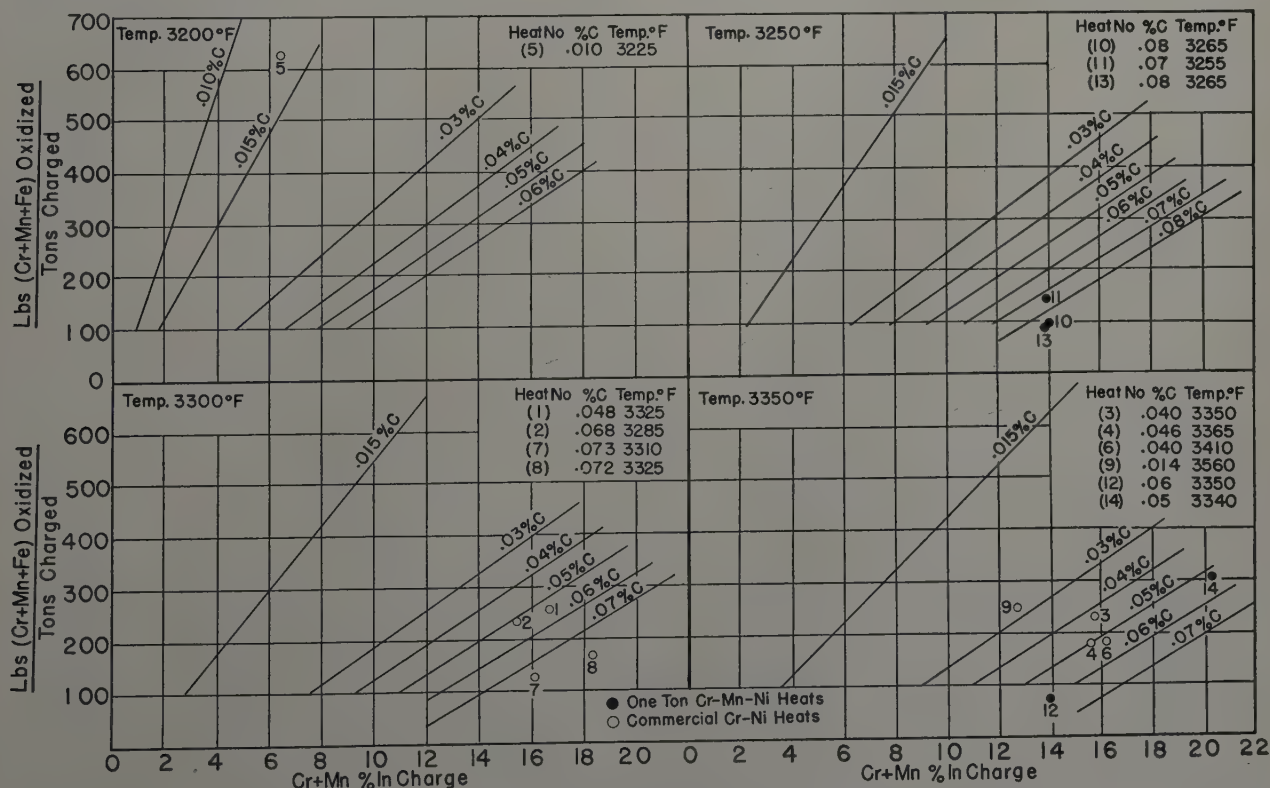


Fig. 3—Estimated metalics oxidized in decarburizing to various carbon contents.

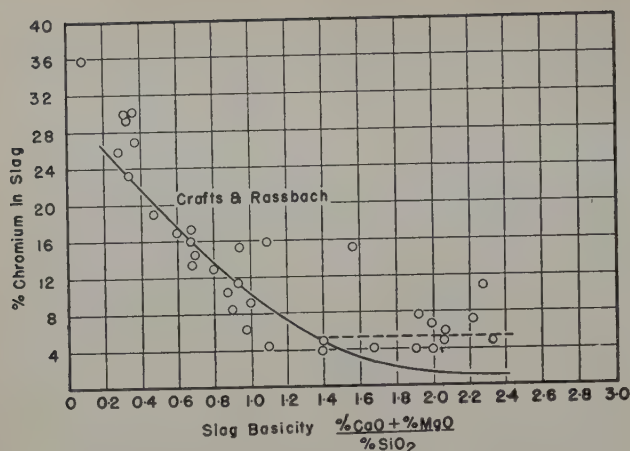


Fig. 4—Relation between chromium in slag and the basicity at end of reduction for commercial heats.

data were obtained varied in capacity from 7 to 75 tons, and the percentage of charged chromium ranged up to 15 pct. While most of the heats were from basic furnaces, some data from chromite hearth furnaces have been included and appear in the very low basicity range of the curves.

The solid lines in Figs. 4 and 5 are those established by Crafts and Rassbach based principally upon experimental data. While there is good general agreement of the new data with the old, it is significant that, in the basicity range of 1.4 to 2.2, slag chromium content and the sum of the metallic oxides in the slag remained constant instead of continuing to decrease as in the case of the experimental 1-ton heats. The new data, however, are consistent with those of Shaw when compared on a CaO-SiO_2 basicity ratio. It is, therefore, concluded that in large heats there is a significant deviation at high basicity from the experimental heats as indicated by the dotted lines in Figs. 4 and 5. While present knowledge of the chemistry of the process is too limited to provide an explanation of this behavior, it is a matter of observation that the small experimental furnace operates with less stratification in the bath and

with more fluid slags than large furnaces with similar metal and slag compositions. This observed difference in operation may be due in part to major differences in the physical proportions of the furnaces. For example, the ratio of hearth area to bath depth and the ratio of electrode arc area to total slag area may have significance. This trend toward incomplete reduction of chromium oxide in large furnaces suggests that further experimentation with methods of improving slag-metal contact and slag fluidity may be desirable.

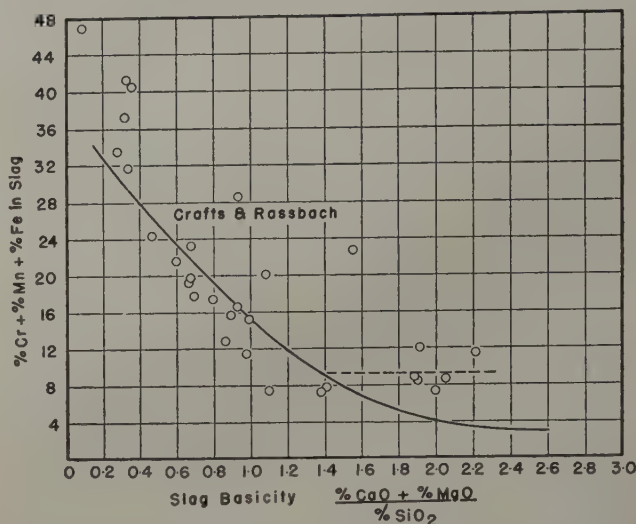


Fig. 5—Relation between Cr+Mn+Fe in slag and the basicity at end of reduction for commercial heats.

The previous studies of the influence of bath silicon concentration on slag chromium content for a given basicity showed poor correlation. Because it is believed that further investigation of this problem is warranted, data from a number of commercial heats covering a wide range of basicities, as shown in Table IV, have been plotted in Fig. 6. The heats used in this study contained from about 12 to 20 pct Cr and were in the range of 0.18 to 1.28 pct Si at the end of slag reduction. Fourteen of these heats con-

Table III. Slag Analyses at End of Reduction in Commercial Cr-Ni Heats

Heat No.	Lining	Size, Tons	Type	Si in Metal, Pct	Slag Analyses, Pct								$\text{CaO} + \text{MgO} / \text{SiO}_2$, Pct
					Cr_2O_3	Met. Cr	MnO	FeO	CaO	MgO	SiO_2	Al_2O_3	
15	Chromite	50	430	0.32	37.96	—	2.58	7.26	8.66	1.80	37.81	3.99	0.28
16	Chromite	50	430	0.07	52.50	—	2.66	11.69	1.14	1.24	26.04	5.01	0.09
17	Chromite	50	430	0.13	44.08	—	2.48	10.99	7.46	2.52	23.02	4.70	0.36
18	Chromite	50	430	0.51	39.32	—	2.42	4.38	9.94	2.88	24.50	6.80	0.37
19	Chromite	50	430	0.32	42.86	—	2.98	12.38	8.84	0.90	29.80	2.48	0.33
20	Chromite	50	430	0.16	43.85	—	2.83	11.99	8.00	1.42	29.14	2.58	0.32
21	Basic	75	430	0.34	25.57	—	4.42	2.82	18.81	7.60	38.94	1.45	0.68
22	Basic	75	430	0.07	22.20	—	2.14	7.22	24.57	13.05	25.32	3.46	1.56
23	Basic	75	18-6-4	0.33	22.36	—	11.48	5.26	23.72	5.36	30.76	1.18	0.94
24	Basic	75	18-6-4	0.27	23.27	—	1.80	3.43	26.32	9.90	33.10	2.53	1.09
25	Basic	75	302	0.38	13.43	—	5.29	2.47	24.32	12.91	37.10	4.12	1.00
26	Basic	75	302	—	19.51	—	3.99	4.41	21.41	6.66	41.30	2.52	0.68
27	Basic	7	302	0.18	7.19	—	—	—	34.57	11.20	22.30	—	2.05
28	Basic	7	347	0.40	6.21	—	—	—	32.20	11.62	26.00	—	1.68
29	Basic	7	316	0.19	15.95	—	—	—	32.63	11.72	19.49	—	2.27
30	Basic	7	316	0.39	7.25	—	—	—	37.80	15.69	23.06	—	2.32
5	Basic	15	304L	0.27	11.40	—	0.96	4.39	43.88	5.67	25.84	4.90	1.92
31	Basic	15	430	0.29	23.76	2.90	2.04	4.38	10.48	9.27	42.30	2.45	0.47
32	Basic	15	430	0.48	23.06	1.27	2.13	3.95	13.18	10.16	39.74	3.06	0.60
33	Basic	15	430	0.70	14.06	4.99	1.81	2.44	16.20	12.21	40.72	7.80	0.70
34	Basic	15	430	0.78	8.69	2.72	1.73	2.37	18.24	15.52	38.60	8.61	0.87
35	Basic	15	303	0.60	19.58	10.34	5.43	3.01	8.82	7.02	46.70	2.87	0.34
36	Basic	15	303	0.38	11.45	4.96	3.94	1.94	23.81	7.14	38.72	3.61	0.80
37	Basic	15	303	0.31	3.68	2.68	2.66	0.86	41.52	5.33	33.20	6.40	1.41
38	Basic	15	303	0.45	3.33	2.75	2.52	1.01	38.88	7.78	33.60	6.55	1.39
3	Basic	15	304	0.33	5.01	0.54	3.48	2.16	47.18	8.75	29.48	5.32	1.90
4	Basic	15	304	0.93	5.07	0.51	2.91	1.66	50.50	7.23	28.82	5.84	2.00
1	Basic	15	303	1.87	10.34	—	1.30	4.19	46.32	2.38	21.90	8.86	2.22
2	Basic	15	303	3.67	8.81	—	1.64	1.45	45.78	2.98	23.60	10.38	2.06
6	Chromite	25	304	1.25	6.58	11.35	2.05	2.66	22.20	4.55	39.58	7.82	0.67
7	Basic	25	304	1.74	7.75	1.19	0.67	1.94	39.26	16.21	29.36	3.04	1.89
39	Basic	65	304L	0.45	11.39	3.54	3.19	3.59	20.26	17.36	37.58	2.84	0.93
40	Basic	65	304L	0.70	6.53	1.71	4.13	2.73	22.12	14.80	40.30	2.50	0.98
41	Basic	75	304L	1.28	5.87	—	—	6.77	32.05	13.84	35.50	2.24	1.29
42	Basic	65	304L	0.66	10.80	1.01	2.40	6.89	30.77	3.33	38.04	3.82	0.90
43	Basic	65	304L	0.97	1.48	3.36	2.91	1.21	37.27	9.36	42.36	1.28	1.10

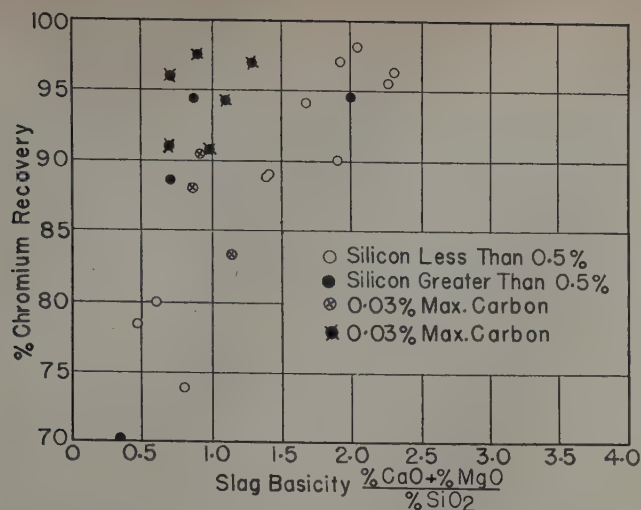


Fig. 6—Relation between chromium recovery and slag basicity at end of reduction for commercial heats.

tained a substantial amount of chromium in the initial charge, so that chromium was first oxidized and was then partially reduced by silicon. Ten of the heats were made for an 0.03 pct maximum carbon specification using chromium-free scrap charges. After the oxidation periods and in the presence of the iron oxide-rich slags, silicon-bearing ferrochromium was added. Loss of chromium resulted from partial oxidation and transfer of chromium into the slags in the presence of silicon. Equilibrium between the slag and metal with respect to chromium was, therefore, approached from both directions.

Although no close correlation was obtained with these data, several significant trends may be observed. It is notable that there was no appreciable difference between those heats in which chromium was present in the initial charge and those in which all the chromium was added after oxidation. This observation is of considerable interest, but its implications are not sufficiently well established to justify a conclusion that comparable chromium recoveries will be obtained under all conditions.

In heats with high-basicity slags, recovery was not greatly affected by silicon content. Heats made under the neutral slags, which minimize carbon pickup in melting low-carbon stainless steels, showed that high silicon aided chromium recovery. However, in the very low-basicity range, silicon

concentration had little influence on chromium recovery. The effect of silicon content is also illustrated by Fig. 7 where silicon content after slag reduction is plotted against chromium recovery. This relation is quite complex and a need for further investigation is indicated.

Recovery of Manganese from Cr-Mn Steel Slags

Data from the five experimental 1-ton heats of high-manganese stainless steel listed in Table V are shown in Fig. 8 to illustrate the influence of basicity on chromium and manganese in the slag at the end of reduction. It is evident that for a given basicity

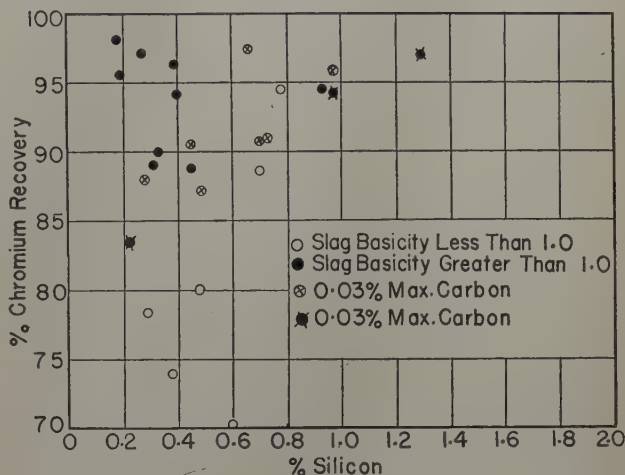


Fig. 7—Relation between chromium recovery and silicon content of the metal in commercial heats.

the manganese content of the slag was higher than that of chromium.

In the high-manganese heats the relation between chromium in the slag and basicity apparently followed closely that obtained on low-manganese heats, and, therefore, appeared to be unaffected by manganese in the slag. It may be inferred that good recovery of manganese from the slag depends upon a substantially higher basicity ratio than that required for chromium. For example, in the case of the heat, No. 14, having a basicity ratio of 1.75, the loss of chromium was 7.2 pct, whereas the loss of manganese in the slag was 29.5 pct. In the production of very high-manganese stainless steels, it appears that relatively high basicities are required to avoid excessive manganese losses.

Table IV. Data on Recovery of Chromium vs Pct Silicon and Slag Basicity

			Chromium Added, Lb			Cr Lost in Slag					Recovery of Cr		Si in	Slag Analysis, Pct				
Heat No.	Type	Size, Tons	Charge	FeCrSi	Simplex FeCr	Total	Slag Wt, Lb	Cr, Pct	Cr, Lb	Metal Wt, Lb	Cr, Pct	Lb	Pct	Metal, Pct	CaO	MgO	SiO ₂	"V"
44	304L	45	0			18,828				98,000	19.40	15,780	83.4	0.21	37.20	7.53	39.48	1.14
45	304L	45	0			21,905				98,200	19.40	19,050	87.0	0.48	18.00	11.20	33.40	0.87
46	304L	45	0			21,257				96,115	20.12	19,340	91.0	0.67	16.90	9.47	37.46	0.70
39	304L	65	236		22,167	22,403				113,850	17.81	20,276	90.5	0.45	20.26	14.80	37.58	0.93
47	304L	45	0			18,876				94,280	19.20	18,100	96.0	0.97	17.00	4.60	30.92	0.70
40	304L	65	173			22,752				110,650	18.78	20,780	90.8	0.70	22.12	17.36	40.30	0.98
41	304L	75	0			34,500				171,000	19.64	33,580	97.0	1.28	32.05	13.84	35.50	1.29
42	304L	65	0			25,441				125,420	19.76	24,783	97.4	0.66	30.77	3.33	38.04	0.90
43	304L	65	0			24,593				126,245	18.37	23,191	94.3	0.97	37.27	9.36	42.36	1.10
48	304L	25	0			9,539				48,300	17.59	8,500	88.1	0.27	20.00	11.98	37.20	0.87
31	430	15	4348			4,348				27,650	12.52	3,451	79.4	0.29	10.48	9.27	42.30	0.47
32	430	15	4348	655		5,003				28,250	14.18	4,006	80.0	0.48	13.18	10.16	39.74	0.60
33	430	15	4348	744		5,092				29,000	15.55	4,510	88.6	0.70	16.20	12.21	40.72	0.70
34	430	15	4348	886		5,234				31,100	15.91	4,948	94.5	0.78	18.24	15.52	38.60	0.87
35	303	15	4900	—		4,900				27,100	12.68	3,436	70.1	0.60	8.82	7.02	46.70	0.34
36	303	15	4868	655	—	5,523				27,550	14.81	4,080	73.9	0.38	23.81	7.14	38.72	0.80
37	303	15	4900	673	—	5,573				28,200	17.58	4,958	89.0	0.31	41.52	5.33	33.20	1.41
38	303	15	4895	709		5,604				28,600	17.61	5,036	88.8	0.45	38.88	7.78	33.60	1.39
3	304	15				5,096				27,300	16.81	4,589	90.0	0.33	47.18	8.75	29.48	1.90
4	304	15				6,056				29,800	19.22	5,727	94.6	0.93	50.50	7.23	28.82	2.00
49	302	7	2505	160		2,665	1000	4.92	49	—	—	2,616	98.2	0.18	38.47	11.20	22.30	2.05
50	347	7	2348	200		2,548	3500	4.25	149	—	—	2,399	94.2	0.40	32.20	11.62	26.00	1.68
51	316	7	2310	200		2,510	1005	10.92	110	—	—	2,400	95.6	0.19	32.63	11.72	19.49	2.27
52	316	7	2488	200		2,688	1955	4.96	97	—	—	2,591	96.4	0.39	37.80	15.69	23.06	2.32

Table V. Slag Analyses at End of Reduction of Cr-Mn-Ni in 1-Ton Heats

Heat No.	Composition, Pct			Si in Metal, Pct	Slag Analyses, Pct							CaO+MgO/SiO ₂ , Pct
	Cr	Mn	Ni		Cr ₂ O ₃	MnO	FeO	CaO	MgO	SiO ₂	Al ₂ O ₃	
1	18	5	5	0.37	2.31	3.83	2.87	29.33	31.57	25.24	3.06	2.41
2	18	5	5	0.57	2.81	5.52	3.16	39.82	20.46	27.40	0.60	2.20
3	18	5	5	0.71	0.58	1.06	2.12	51.76	15.90	23.96	2.52	2.83
4	18	5	5	0.44	0.58	1.41	1.15	50.47	13.68	24.52	3.28	2.61
5	16	16	0.6	0.09	4.93	18.70	2.59	33.37	8.80	24.00	2.00	1.75

Silicon Usage in Slag Reduction

The amount of chromium plus manganese plus iron reduced per pound of silicon oxidized must be known to establish the reduction practice. In the previous investigation⁸ the experimental heats showed an average of 3 lb of metal reduced per pound of silicon oxidized. The variation between individual heats was quite wide, a range of about 2.5 to 3.5 lb being observed.

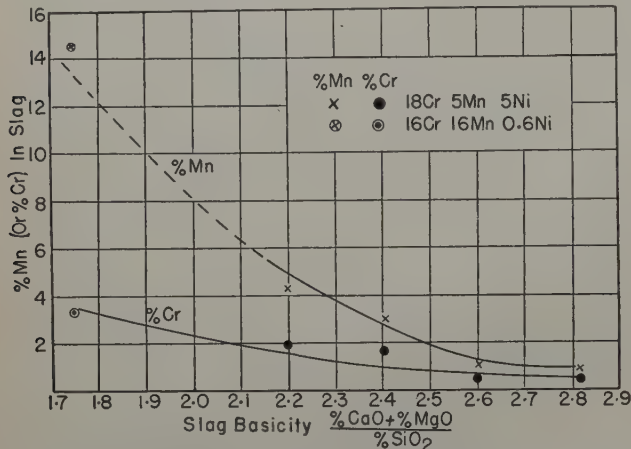


Fig. 8—Relation among manganese and chromium contents in the slag, and basicity at the end of reduction for experimental Cr-Mn-Ni heats.

An effort to develop information on commercial heats resulted in data from the four heats of 15 to 25 tons shown in Table VI. The chromium content of materials charged was known, and slag and metal analyses were obtained at the end of the oxidation period. Calculations on the basis of these data were made to determine the weight of metal oxidized. Information with respect to alloying additions, slag analyses and weights, final steel tapped weight, and composition made it possible to calculate the pounds of chromium plus manganese plus iron reduced per pound of silicon added. It was found that for these four heats the pounds of metal reduced per pound of silicon oxidized were 2.37, 2.53, 2.55, and 2.76. These

results are within the range of the experimentally determined values and do not permit further generalization.

Estimation of Slag Weight

Since the amount of chromium lost in a slag is dependent on both the chromium concentration and the weight of the slag, control of slag weight at the end of reduction is of primary importance in chromium recovery. As was observed in Fig. 4, the data from large furnaces indicated a constant level of about 6 pct Cr at the end of reduction. This trend suggests that increasing basicity above 1.4 tends to decrease chromium recovery due to an increase in slag weight while maintaining the same chromium concentration. It is recognized also that large slag volumes result in unfavorable operating conditions and severe erosion of refractories. Estimation of slag weight, therefore, is of real interest in establishing chromium steel melting practices.

As part of the previous investigation,⁸ Hilty described a technique for estimating slag weights. The assumptions made in those calculations were that 1 lb of silicon reduces 3 lb of chromium plus manganese plus iron (reduction factor) from the slag, and that 1 lb of these elements is equivalent to 1.29 lb of metallic oxides. Data from the four heats in Table VI were used to evaluate the accuracy of this method for calculating slag weights for commercial heats. Following the methods outlined by Hilty, a hypothetical table of the effects of graduated amounts of silicon oxidized upon the balance of the components of the slag was calculated for each heat. In each case the table was adapted to fit the actual conditions imposed by the heats. The quantities of slag components at the end of the oxidizing period were calculated from an estimation of metallic oxidation, as described earlier in this paper, and the known analysis of the slag. The remainder of the table was then calculated with the provision that the amounts of SiO₂, CaO, MgO, and Al₂O₃ ("non-reducible" oxides) should conform to the concentrations of these components in the actual slags after reduction. By interpolation from these tables it was

Table VI. Pounds Cr+Mn+Fe Reduced per Pound Silicon Oxidized

Heat No.	Cr+Mn+Fe Oxidized per Ton	Tons Charged	Total Cr+Mn+Fe Oxidized, Lb	Slag at End Reduction			Cr+Mn+Fe Reduced, Lb	Reducing Agent	Weight, Pct	Si Equiv., Pct*	Si Equiv., Lb*
				Weight, Lb	Cr+Mn+Fe, Pct	Cr+Fe+Mn, Lb					
3	236	13.8	3257	8,230	8.35	687	2570	FeCrSi#2	2500	44.0	1100
4	181	13.75	2489	7,330	7.51	550	1939	FeCrSi#2	2270	44.0	1000
								Simplex	1700	6.0	100
6	185	23.03	4260	7,415	19.66	1458	2802	FeCrSi	3000	45.2	1100
								50% FeSi	350	48.0	1356
								Al	68		168
											53
7	130	28.40	3692	11,015	8.69	957	2735	FeCrSi	3000	45.2	1577
								85% FeSi	300	85.0	1356
								Al	67		255
											52
										Total	1663

* Including the silicon stoichiometrically equivalent to the contained aluminum.

possible to estimate the amounts of silicon oxidized for each of the heats, and, by reference to the actual final slag compositions, to estimate the amounts of metallics reduced. The amounts of unreduced metal were then obtained by difference from the original amounts oxidized, and the slag weights were calculated from these quantities and the slag analyses. Comparison of these calculated weights with the actual weights are shown in Table VII. Although heats 3 and 4 were weighed quite accurately, the excellent agreement may be fortuitous since the reduction factor is known to vary considerably from heat to heat. Heat 7 had more than a normal amount of bottom erosion. The results suggest, however, that the technique described may be used to estimate slag volumes for commercial heats.

Summary

As part of a continuing program directed toward attaining improved production of stainless steel, a study was made to establish for commercial practice the validity of the relations previously derived from small, experimental heats. Primary emphasis was placed on data for the slag-reduction periods of commercial heats which were analyzed and compared with those from experimental heats in order to evaluate some of the factors which influence the recovery of chromium and manganese by silicon reduction of the oxidized slags resulting from decarburization.

Analytical data from the commercial heats of chromium-nickel steel confirmed the relationship, previously proposed from 1-ton heat data, which expressed the ratio of chromium plus manganese to iron in the slag as a function of the corresponding ratio of these elements in the metal after decarburization. The equivalence of manganese to chromium in this relationship was indicated by a similar correlation shown for data taken from 1-ton, Cr-Mn-Ni heats with high manganese (5 to 10 pct) in the charge. The calculated metallics oxidized, based upon actual slag analyses, were in excellent agreement with predicted values for both the commercial and the 1-ton heats used in this study.

The relation of basicity to chromium in the slag after reduction was compared with the previously developed relation which was based largely on data from experimental heats. The comparison showed a marked deviation in that chromium and the sum of metallic oxides remained constant in the range of 1.4 to 2.2 basicity suggesting that basicities above 1.4 have limited value for increasing recovery of chromium.

Table VI. Continued.

Heat No.	Bath Weight, Lb	Si, Pct	Si Al-loyed, Lb	Si Oxid., Lb	Cr+Mn+Fe Reduced/Si Oxid., Lb
3	27,300	0.33	91	1009	2.55
4	29,800	0.93	277	823	2.37
5					
6					
7	48,300	0.97	469	1108	2.53
	57,000	1.18	673	990	2.76
			Average		2.55

Table VII. Calculated Slag Weights

Heat No.	Type Hearth	Slag Weight After Reduction in Lb of Slag per Ton of Metal	
		Calculated	Actual
3	Basic	615	602
4	Basic	486	492
6	Chromite	279	305
7	Basic	470	387

Study of the influence of silicon in the metal on recovery of chromium at the end of the reduction period showed that unusually high concentration of silicon is not necessary for good recovery from high-basicity slags. At low basicities, however, relatively poor recovery of chromium was realized even at high-silicon contents. In the neutral range, which is desirable for controlling carbon pickup in melting the very low-carbon stainless steels, silicon in the metal after reduction had a strong influence on chromium recovery.

Comparison of slag-metal relations of commercial heats containing substantial amounts of chromium in the initial charge with those of heats in which no chromium was charged and in which the iron-rich slag was partially reduced with a silicon-bearing chromium alloy showed similar overall chromium recoveries with about the same conditions of basicity and silicon concentration. This observation provided an indication that equilibrium between slag and metal with respect to chromium is approached rapidly from both directions. A corollary to this conclusion is that in scrap heats in which part of the chromium is included in the charge and part is added while the slag is being reduced, the chromium from the initial charge remaining in the slag tends to be lowered as a result of furnace conditions, and, therefore, chromium from the late addition is not lost to the slag.

Experimental heats of high manganese-chromium-nickel steels showed that for a given slag basicity after reduction the manganese content of the slag was higher than that of chromium but that the general dependence of manganese concentration on basicity was similar to that observed for chromium. The presence of manganese in the slag had no appreciable influence on the reduction of chromium, so that a slag that is sufficiently basic to insure good chromium recovery may not be sufficiently basic to yield good manganese recovery.

Observations of the amount of metal reduced from the slag per pound of silicon oxidized for commercial heats were within the range of those previously made on experimental heats. There is need, however, for additional data to achieve better understanding of reasons for the wide variations in this reduction factor.

A method for calculating slag weight was demonstrated to be suitable for use in the appraisal of the practicability and economic aspects of a proposed melting practice. Since it is predicated upon a material balance with respect to slag-metal reactions, it provides a basis for checking the overall accuracy of the oxidation and reduction methods proposed.

Acknowledgments

The authors wish to express their appreciation to Walter Crafts, Associate Director of Research, and D. C. Hilty, Research Metallurgist, of the Union Carbide and Carbon Research Laboratories, Inc., for their very generous and valuable cooperation. It is evident that this study was made possible through

the aid of stainless steel producers in providing the necessary data. This assistance is acknowledged with grateful appreciation.

References

¹D. C. Hilty: Relation between Chromium and Carbon in Chromium Steel Refining. *Trans. AIME* (1949) **185**, pp. 91-95; *JOURNAL OF METALS* (February 1949).
²D. C. Hilty, G. W. Healy, and W. Crafts: Metallic Oxidation in Chromium Steel Melting. *Trans. AIME* (1953) **197**, pp. 649-653; *JOURNAL OF METALS* (May 1953). Abstracted by D. J. Girardi and D. C. Hilty: Oxygen in Steelmaking. *JOURNAL OF METALS* (July 1952) p. 705.
³W. Crafts and H. P. Rassbach: Melting Low-Carbon

Stainless Steel. *Electric Furnace Steel Proceedings*, AIME (1951) **9**, pp. 95-104.
⁴D. C. Hilty: High-chromium Steel in the Acid Arc Furnace. *Electric Furnace Steel Proceedings*, AIME (1949) **7**, pp. 95-104.
⁵J. E. Harrod: Discussion on ref. 3. *Electric Furnace Steel Proceedings*, AIME (1951) **9**, pp. 104-106.
⁶B. R. Queneau and A. C. Ogan: Stainless Steel Melting Practices Have Changed. *Iron Age* (Dec. 4, 1952) pp. 165-169.
⁷C. R. Taylor: Some Observations on the Metallurgy of Electric-furnace Melting. *Electric Furnace Steel Proceedings*, AIME (1950) **8**, pp. 91-97.
⁸R. B. Shaw: Discussion on ref. 3. *Electric Furnace Steel Proceedings*, AIME (1951) **9**, pp. 106-107.

Technical Note

Thermal Conductivity of Nodular Iron

by M. J. Sinnott

WITH the advent of nodular iron as an engineering material, considerable interest has been shown in developing this material for various applications. Generally the strength, hardness, or ductility are the more common properties used for design purposes but occasionally applications involving a knowledge of the thermal conductivity of the material is required. A search of the literature showed, rather surprisingly, that relatively little work has been done on this property for all types of cast iron. Insufficient data are available on thermal and electrical conductivities to develop the Weidemann-Franz ratio, or the Lorentz relationship, for estimation purposes. There are no data on nodular irons and the published data on malleable irons are quite sketchy. For these reasons the conductivity of the group of nodular irons listed in Table I were measured.

Table I. Chemical Composition of Nodular Irons

Iron	Total C	Si	Mn	S	P	Ni	Mg
I	3.57	1.12	0.33	0.004	0.035	1.33	0.06*
II	3.56	2.27	0.33	0.010	0.025	1.30*	0.06*
III	3.47	3.53	0.29	0.012	0.030	1.30*	0.06
IV	3.36	4.34	0.40	0.010	0.030	1.23	0.06
V	3.33	2.28	0.50	0.010	0.055	1.12	0.06

* Estimated.

Irons I to IV were made in such a fashion as to maintain the carbon and alloy content essentially the same while varying the silicon content. Test specimens were cut from the mid-section of 4-in. keel castings. Iron V is a commercial casting of nodular iron. The test specimen of this iron was cut from the center of a large cast billet 3x10x26 in. All alloys were tested in the as-cast condition. A microstructural examination showed that each iron had spheroidal graphite but the size and distribution varied with the silicon content of the iron. The spheroid size decreased while the number of graphite nodules increased as the silicon content of the iron was increased. The matrix structures of each iron consisted of pearlite and ferrite with the proportions varying from predominantly pearlite in the low-silicon iron to mostly ferrite in the high-silicon iron. The commercial heat, iron V, was predominantly pearlite probably because of its higher manganese and phosphorus content.

M. J. SINNOTT, Member AIME, is Associate Professor of Metallurgical Engineering, University of Michigan, Ann Arbor, Mich. TN 171E. Manuscript, May 5, 1953.

Two methods for measuring the thermal conductivity were used. The first was a modification of the techniques described by Powell and Hickman¹ and Van Dusen and Shelton,² the second method was a simpler technique described by Jakob and Hawkins.³ Since the agreement of both methods as tested on two sets of duplicate samples was excellent, the simpler experimental technique was used. The results of the measurements are given in Table II along with a summary of the microstructural constituents.

Table II. Thermal Conductivity and Microstructures of Nodular Irons

Iron	Thermal Conductivity, Btu/Hr-Ft ² -Ft/°F (210° to 160°F)	Pearlite, Pct	Ferrite, Pct	Graphite, Pct	Graphite Size, In. x 100
I	21.8	61	30	9	0.186
II	21.5	40	50	10	0.121
III	20.9	35	55	9	0.096
IV	20.3	5	85	10	0.081
V	20.6	85	5	10	0.175

These conductivity data indicate that as the percentage of silicon increases there is a corresponding decrease in the thermal conductivity even though the structure is changing from pearlitic to ferritic. Such a change in microstructure is usually accompanied by an increase in conductivity.⁴ A third factor involved in the behavior of these irons is the size and distribution of the graphite nodules. The relative amounts of graphite do not change greatly but the size and distribution do. Generally graphite improves the conductivity but in the present case such an effect is probably masked by the alloying effect from the silicon and its dispersion through the matrix.

The thermal conductivity of the nodular irons studied is less than that of regular foundry irons by some 10 to 30 pct and is less than that of regular malleable irons.⁴ The cause of the decreased conductivity is probably the more highly alloyed ferrites obtained in these irons and the changed mode of distribution of the graphite as compared to the regular foundry irons.

References

¹R. W. Powell and M. J. Hickman: *Journal Iron and Steel Inst.* (1946) **154**, No. 2, p. 99.
²M. S. Van Dusen and S. M. Shelton: U. S. Bur. Standards *Journal of Research*, RP668 (1934) **12**, p. 429.
³M. Jakob and G. A. Hawkins: *Elements of Heat Transfer and Insulation*. 2nd Ed. (1950) New York. John Wiley and Sons.
⁴J. W. Donaldson: *Journal Iron and Steel Inst.* (1933) **128**, No. 2, p. 255.

Silicon-Oxygen Equilibrium in Liquid Iron — A Revision

by John Chipman and Nev A. Gokcen

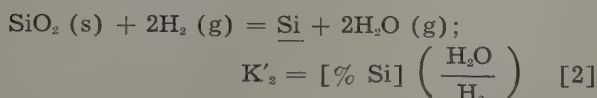
A revised treatment of the authors' published data eliminates the complex relation previously proposed between concentration of silicon and activity coefficient of oxygen in liquid iron. Revised values of the thermodynamic properties of the liquid solution are presented.

IN a recent experimental study of the reaction

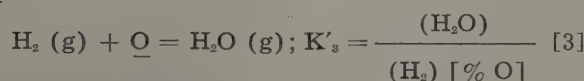


the authors¹ found a substantially constant equilibrium product in liquid iron at 1600°C of 2.8×10^{-5} .

They also reported extensive data on the reactions:



and



From the results on reaction 3 and earlier data of Dastur² on this same reaction in the absence of silicon, they determined the activity coefficient of oxygen, f_{O} , on the basis of the definition $K_3 = (\text{H}_2\text{O})/(\text{H}_2)f_{\text{O}} [\% \text{O}]$ where K_3 is the equilibrium constant and f_{O} is taken as unity in the pure Fe-O system. Similarly values of f_{Si} were deduced from results on reaction 2.

In a more recent study³ of analogous reactions in the system Fe-Al-O, it was found impossible to reconcile the results on reaction 3 with Dastur's data; accordingly the latter were ignored and the equilibrium results were extrapolated to find a value of K_3 at zero concentration of aluminum. This procedure failed to locate the cause of the discrepancy but it did yield reasonable values of activity coefficients. It also avoided introduction of the complex empirical relation between the oxygen activity coefficient and the concentration of the added element.

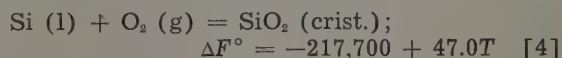
The same type of discrepancy exists for system Fe-Si-O.¹ In the earlier paper an attempt was made to fit both sets of data by a single curved line (Fig. 6 of ref. 1), the form of which is contrary to the theoretical requirement of a finite slope at infinite dilution. In the light of experience on the Fe-Al-O system the discrepancy must be recognized as one which can be resolved only by more refined measurements. Accordingly Figs. 6 and 10 are retracted. It is pointed out also that until the discrepancy is

resolved Figs. 7, 8, and 11 are subject to some uncertainty.

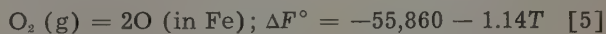
Qualitatively the following conclusions still appear valid: 1—The activity coefficient of oxygen is reduced by addition of silicon. 2—In dilute solutions the activity coefficient of silicon increases with its concentration. 3—With respect to equilibrium in reaction 1, the above effects are approximately compensating.

The discussion of K'_1 in the previous paper requires no revision. It was pointed out that the constancy of the product $[\% \text{Si}] [\% \text{O}]^2$ indicated a compensating effect of the activity coefficients of silicon and oxygen. Therefore, as a very good approximation, $K_1 = K'_1$ and the following average values are suggested both for K_1 and K'_1 at the temperatures 1550°, 1600°, and 1650°, respectively, 1.0×10^{-5} , 2.8×10^{-5} , and 5.5×10^{-5} .

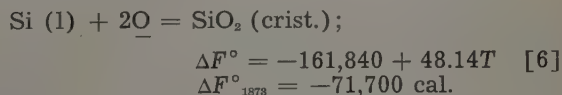
Revision of the thermodynamic treatment is necessitated by the recent appearance of new data, based on a combination of combustion and solution calorimetry,⁴ which yields for the heat of formation of low-cristobalite from the elements, the value $-209,330 \pm 250$ cal per mol at 25°C. This is about 4000 cal larger than the value previously accepted. The new value for cristobalite is used, together with Kelley's tables of high-temperature heat contents⁵ and entropies⁶ and with Körber and Oelsen's⁷ heat of fusion of silicon to obtain the following equation for the standard free energy of cristobalite in the temperature range 1700° to 2000°K:



The free energy of solution of O_2 in liquid iron is:⁸



and these two equations are combined to give:



From the experimental value of $K_1 = 2.8 \times 10^{-5}$,

$$\text{Si} + 2\text{O} = \text{SiO}_2(\text{crist.}); \Delta F^\circ_{1878} = -39,000 \text{ cal.} \quad [7]$$

The combination of Eqs. 6 and 7 yields the free energy change when liquid silicon dissolves in iron to form the dilute solution of unit activity (1 pct).



The heat effect in this process according to Körber and Oelsen⁷ is an evolution of 28,500 cal per gram

J. CHIPMAN, Member AIME, is Professor, Dept. of Metallurgy, Massachusetts Institute of Technology, Cambridge, Mass., and N. A. GOKCEN, Member AIME, is Associate Professor of Metallurgy, Michigan College of Mining and Technology, Houghton, Mich.

Discussion on this paper, TP 3575C, may be sent, 2 copies, to AIME by Oct. 1, 1953. Manuscript, March 6, 1953; revision, May 27, 1953.

atom. The difference falls into an entropy term to yield the equation:

$$\text{Si (l)} = \text{Si}; \Delta F^\circ = -28,500 - 2.23T \quad [9]$$

A similar but not identical result could be obtained from the observed value of K_2 and the free energy of water vapor. The above calculation, however, is probably more dependable and is consistent with all previous studies of oxygen in iron.

Combination of Eqs. 6 and 9 gives:

$$\begin{aligned} \text{Si} + 2\text{O} &= \text{SiO}_2 \text{ (crst.)}; \\ \Delta F^\circ &= -133,340 + 50.37T \quad [10] \\ \log K_1 &= -29,150/T + 11.01 \end{aligned}$$

According to this equation the values of K_1 at 1550°, 1600°, and 1650° are 1.05×10^{-5} , 2.8×10^{-5} , and 7×10^{-5} , respectively. This is in fair agreement with the average observed values.

Eq. 9 may be further used to obtain γ° for silicon in very dilute solution in liquid iron. This is the value which is approached by the ratio of activity to mol fraction when the latter approaches zero. From Eq. 16-10 of *Basic Open Hearth Steelmaking*:⁸

$$\text{Si (l)} = \text{Si}; \Delta F^\circ = +4.575T \log (0.5585 \gamma^\circ / 28.06)$$

From this and Eq. 9 it follows that:

$$\begin{aligned} \log \gamma^\circ &= -6230/T + 1.213 \quad [11] \\ \gamma_{1873}^\circ &= 0.0077 \end{aligned}$$

This is smaller than the value 0.017 previously reported.⁹ The difference results from the new higher heat of formation of cristobalite and the lower value of K_1 found in this study.

Summary

The authors' previously published results¹ on equilibrium in the Fe-Si-O system are reviewed. Previous conclusions regarding activity coefficients in the liquid solution now appear unjustified. Values of the deoxidation product [% Si] [% O]² in the earlier paper provide the best estimates of the true equilibrium constant.

A newly published value of the heat of formation of cristobalite is used with the equilibrium results to revise the thermodynamic data for the dilute solution. Referring to *Basic Open Hearth Steelmaking*,¹⁰ Eq. 16-11 should be replaced by Eq. 9; Eq. 16-27 by Eq. 4, and Eq. 16-29a by Eq. 10. Figs. 16-7, 16-20, and 16-29 are substantially unaffected by the revision.

References

- ¹ N. A. Gokcen and J. Chipman: *Trans. AIME* (1952) **194**, p. 171; *JOURNAL OF METALS* (February 1952).
- ² M. N. Dastur and J. Chipman: *Trans. AIME* (1949) **185**, p. 441; *JOURNAL OF METALS* (August 1949).
- ³ N. A. Gokcen and J. Chipman: *Trans. AIME* (1953) **197**, p. 173; *JOURNAL OF METALS* (February 1953).
- ⁴ G. L. Humphrey and E. G. King: *Journal ACS* (1952) **74**, p. 2041.
- ⁵ K. K. Kelley: *U. S. Bur. Mines Bull.* 476 (1949).
- ⁶ K. K. Kelley: *U. S. Bur. Mines Bull.* 477 (1950).
- ⁷ F. Körber and W. Oelsen: *Mitt. Kaiser Wilhelm Inst. Eisenforschung* (1936) **18**, p. 109.
- ⁸ *Basic Open Hearth Steelmaking*. 2nd Edition (1951) pp. 638-640. AIME.
- ⁹ J. Chipman: *Discussions, Faraday Soc.* No. 4 (1948) p. 23.
- ¹⁰ Ref. 8, p. 659.

Corrections

In the July 1953 issue, *Further Studies of the Tuyere Zone of the Blast Furnace* by J. B. Wagstaff, p. 896: Fig. 1 is printed upside down.

In the June 1953 issue, *Concentration Gradients Associated with Growing Pearlite* by Richard E. Grace: page 820, the caption for Fig. 1 should read: Electron micrograph of pearlite and martensite tempered 5 min, 0.9 pct C steel. X20,000. Page 820, first column, second paragraph, the eleventh line should read, in part: chromium at about 65° from the horizontal.

In the August 1952 issue, *Concentration Dependence of Diffusion Coefficients in Metallic Solid Solution* by Donald E. Thomas and C. Ernest Birchenall: page 870, Table I as printed below should be substituted for Table I in the paper. The authors are grateful to Dr. T. Heumann of the University of Münster for pointing out the error in Table I. Page 871, first column, the following paragraphs should be substituted for the two paragraphs preceding "Discussion":

Table I also includes the marker movements observed by da Silva and Mehl for pure nickel vs pure copper couples C4 and B38. In the former the marker was at 80.5 atomic pct Cu and in the latter at 71.0 atomic pct.

Following the method of Darken,¹⁴ the diffusion coefficients of the individual components were calculated at the average marker composition. Although there is no clear trend of the ratio of D_{Cu} to D_{Ni} with temperature, the decrease in the ratio with decreasing copper concentration may be real.

Table I. Marker Displacements and Diffusion Coefficients in Cu-Ni Alloys

Temperature, °C	Sample	x_m , Cm	$2t$, Sec	dN/dx , Cm ⁻¹	D_{Cu} , Cm ² per Sec	D_{Ni} , Cm ² per Sec	$D_{\text{Cu}}/D_{\text{Ni}}$
1049	2	0.0056	6.61x10 ⁵	6.4	1.6x10 ⁻⁹	3.7x10 ⁻¹⁰	4.3
1022	13	0.0079	1.16x10 ⁶	5.1	1.6x10 ⁻⁹	2.8x10 ⁻¹⁰	5.7
	20	0.0079	1.16x10 ⁶	4.5	1.9x10 ⁻⁹	3.4x10 ⁻¹⁰	5.6
975	17	0.0043	8.95x10 ⁵	7.9	8.0x10 ⁻¹⁰	1.8x10 ⁻¹⁰	4.4
924	3	0.0051	3.63x10 ⁶	6.0	3.0x10 ⁻¹⁰	6.8x10 ⁻¹¹	4.4
	11	0.0051	3.63x10 ⁶	5.9	3.0x10 ⁻¹⁰	6.2x10 ⁻¹¹	4.8
922	6	0.0058	5.83x10 ⁶	5.0	2.7x10 ⁻¹⁰	6.7x10 ⁻¹¹	4.0
	16	0.0071	5.83x10 ⁶	4.8	3.1x10 ⁻¹⁰	6.4x10 ⁻¹¹	4.8
1054	C4*	0.0140	2.25x10 ⁶	6.4	1.4x10 ⁻⁹	4.2x10 ⁻¹⁰	3.3
947	B38†	0.0039	2.60x10 ⁶	29.	1.1x10 ⁻¹⁰	5.5x10 ⁻¹¹	2.0

* Composition at marker interface — 80.5 atomic pct Cu.

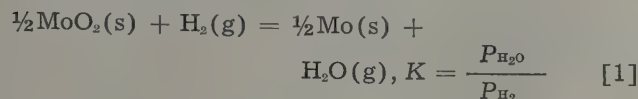
† Composition at marker interface — 71.0 atomic pct Cu.

All others—Composition at marker interface — 89.9 atomic pct Cu.

Thermodynamic Properties of Molybdenum Dioxide

by Nev A. Gokcen

THE data of Chaudron,¹ Tonosaki,² and Collins³ on the thermodynamic properties of MoO₂ disagree widely. These authors, by using essentially similar methods, studied the following reaction:



Tonosaki used a vacuum system consisting of a furnace containing MoO₂ and a water saturator whose temperature was kept at 25°C with a thermostat. After repeated evacuation, hydrogen was admitted slowly into the system. The experiments were based upon the fact that at a constant furnace temperature and constant partial pressure of water, the total pressure of gas mixture over MoO₂ + Mo is constant. Any attempt to vary the pressure by external forces would vary only the amounts of MoO₂ and Mo, after which the pressure should return to the equilibrium value in accordance with the equilibrium constant of reaction 1. The actual value of *K* was determined from the total equilibrium pressure (sum of *P*_{H₂O} + *P*_{H₂}) at each temperature. The total pressure of gas was varied within the range of 80.2 to 125.4 mm Hg, within a temperature range of 645° to 823°C. The results were summarized as log *K* = 0.9413 - 1444.6/*T* for reaction 1. The ratio of H₂O/H₂ was considered to be uniform in spite of the presence of a thermal gradient across the static gas phase. It was shown by Rosenqvist and Cox,⁴ however, that in somewhat similar circumstances the error resulting from thermal diffusion may be large.

Collins³ improved Tonosaki's method by attempting to avoid thermal diffusion errors. His equilibrium data were obtained at 700°, 800°, and 900°C, and the result for reaction 1 was expressed as log *K* = 1.258 - 1822/*T*.

The purpose of this investigation was to study reaction 1, avoiding the thermal diffusion errors, and to obtain equilibrium data in a considerably wide temperature range for the reliable extrapolation of the resulting thermodynamic functions.

Experimental Procedure

The diagram of the apparatus is shown in Fig. 1. Tank hydrogen was passed through a tube containing platinized asbestos at 425°C in order to convert a trace of oxygen into water vapor. The flow rate was carefully controlled with a capillary-type flowmeter *B* and a bubbling column *D*. The gas was then presaturated sufficiently at *P* and led into a condenser system immersed in a thermostat, controlled to within ±0.002°C. The temperature of the thermostat was measured with a thermometer calibrated against a certified standard. The temperature of *P* was adjusted to avoid the condensation of unduly large amounts of water as judged from the rate of flow out of the capillary tube *M*.

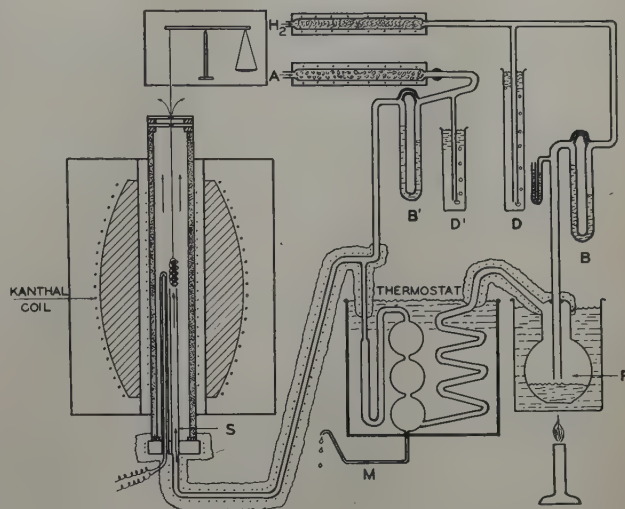


Fig. 1—Apparatus.

Argon was purified⁵ by passing it through magnesium chips kept at 630°C. After passing through the flowmeter *B'*, it was mixed with moist hydrogen emerging from the thermostat. The resulting gas mixture was then led into the hot zone of the furnace through the heated glass tubing and the silica tube *S*, thus insuring the same ratio of *P*_{H₂O}/*P*_{H₂} from the condenser to the reaction chamber, thus avoiding thermal diffusion. The entire gas system was of all-glass construction, except at the magnesium train.

The furnace comprised a glazed alumina tube over which a 15-in. platinum coil was wound. The lower end of the alumina tube was tightly closed with a brass bottom and a silicone rubber gasket, and the upper end with two glass disks, each with a hole of 1/16 in. in diameter, through which the gas mixture escaped into the atmosphere. A back-up coil of kanthal wire facilitated the temperature control of the furnace. A coil of annealed molybdenum strip of 99.99 pct purity, 0.005 in. thick and 0.050 in. wide, and weighing 17 g was hung in the furnace with a 0.010-in. platinum wire attached to one end of a sensitive analytical balance. The temperature of the furnace was measured with a Pt-Pt-10 pct Rh thermocouple checked against a standard.

The experimental procedure consisted of heating the gas purification trains, adjusting the gas flow rates, attaining a constant thermostatic temperature, flushing the entire system for 2 hr while heating the furnace to well above the expected equilibrium temperature and then cooling it at a rate of 0.3°C per min during which time the change in the weight of molybdenum was observed on the balance. For a given thermostatic temperature, i.e., a constant *P*_{H₂O}/*P*_{H₂}, molybdenum oxidized upon cooling slightly below the equilibrium temperature. The procedure was then repeated by heating the furnace and thus reaching a temperature slightly above the equilibrium value. The average of the two temperatures, differing by 2° to 3°C, was considered to be the true equilibrium temperature.

In order to determine the stoichiometric composition of the oxide phase present in this investigation,

N. A. GOKCEN, Member AIME, is Associate Professor of Metallurgy, Michigan College of Mining and Technology, Houghton, Mich.

Discussion on this paper, TP 3579D, may be sent, 2 copies, to AIME by Oct. 1, 1953. Manuscript, Nov. 1, 1952; revision, March 23, 1953. Los Angeles Meeting, February 1953.

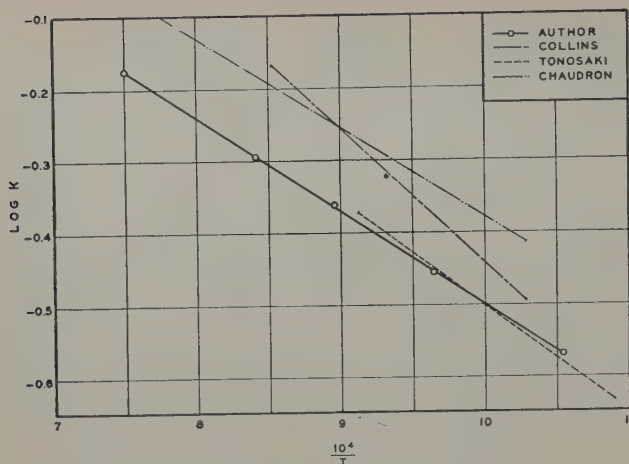


Fig. 2—Variation of the equilibrium constant $K = P_{H_2O}/P_{H_2}$ with temperature.

the loss of oxygen from a known amount of pure molybdenum trioxide (chemically pure MoO_3), contained in a suspended platinum crucible, was determined at $700^\circ C$ under the experimental conditions in which an oxide was the only stable phase. The loss of oxygen indicated that the composition of this phase was MoO_2 .

Results

The results are summarized in Table I. The value of P_{H_2O} corresponding to each thermostatic temperature was found from a recent steam table and corrected for a small deviation from ideality; the values of P_{H_2} were determined from the barometric pressure over the apparatus, minus P_{H_2O} , and the resulting ratios of P_{H_2O}/P_{H_2} are tabulated in the fourth column.

The data are plotted in Fig. 2 together with the lines of Chaudron, Tonosaki, and Collins. The results may be summarized by the following equation:

$$\log K = -\frac{1297}{T} + 0.798 \quad [2]$$

The experiments show that the addition of argon did not affect the results from the point of view of thermal diffusion.^{5, 6}

Thermodynamic Calculations

From Eq. 2, the standard free energy change is expressed as

$$\Delta F^\circ = 5935 - 3.65T, \text{ for } \quad [3]$$

$$\frac{1}{2}MoO_3(s) + H_2(g) = \frac{1}{2}Mo + H_2O$$

This expression is sufficiently accurate within the

Table I. Equilibrium Data for Reaction $\frac{1}{2}MoO_3 + H_2 = \frac{1}{2}Mo + H_2O$

Run No.	Hydrogen Flow Rate, Millimol per Min	Ratio, $H_2/Argon$	$K = P_{H_2O}/P_{H_2}$	Furnace Temperature, $^\circ C$	Equilibrium Temperature, $^\circ C$
2	7.50	2.20	0.5082	915*	916
3	7.50	1.97	0.4342	843* 845	844
4	7.50	2.20	0.3483	764* 767	765
5	6.70	3.35	0.2700	675* 677	676
6	3.10	0.94	0.6663	1060*	1061
	3.10	0.44		1061	

* Temperature at which oxidation began upon cooling; other refers to reduction.

range of temperatures not too far above or below the investigated limits of 949° and $1396^\circ K$. The extrapolation of ΔF° and ΔH° values of this equation to room temperature can be accomplished by the use of ΔC_p for reaction 1. Heat capacity of MoO_2 is not known, but it may be estimated as 17.6 in the range of 298° to $900^\circ K$ on the basis of comparison of the available C_p values for the dioxides of metals, i.e., UO_2 , MnO_2 , and PbO_2 , and by considering Kopp's rule. Heat capacity of other substances in reaction 1 are given by Kelley.⁷ Combination of C_p functions yields

$$\Delta C_p = -5.41 + 2.43 \times 10^{-3} T - 0.04 \times 10^{-5} T^{-2}$$

Contribution from the last term is very small, hence it may be disregarded. By using ΔC_p , and the values of ΔH° and ΔF° at $900^\circ K$ from Eq. 3, the following functions, valid from 900° to $298^\circ K$, are obtained:

$$\Delta H^\circ = 9824 - 5.41T + 1.21 \times 10^{-3} T^2 \quad [4]$$

$$\Delta H^\circ_{298} = 8320 \text{ cal}$$

$$\Delta F^\circ = 9824 + 12.44T \log T - 1.21 \times 10^{-3} T^2 - 43.63T \quad [5]$$

$$\Delta F^\circ = 5888 \text{ cal}$$

$$\Delta S^\circ_{298} = 8.16$$

The absolute entropy of MoO_2 at $298^\circ K$, $S^\circ_{298} = 18.3$ E.U., is calculated from $\Delta S^\circ_{298} = 8.16$ and the absolute entropies of $H_2(g)$, $H_2O(g)$, and $Mo(s)$ compiled by Rossini, et al.⁸

The ΔH° and ΔF° functions for $2H_2(g) + O_2(g) = 2H_2O(g)$, obtained from the recent references,^{7, 8} are combined with Eqs. 4 and 5 to express the standard free energy and heat of formation of MoO_2 in the range of 298° to $900^\circ K$:

$$Mo(s) + O_2(g) = MoO_2(s) \quad [6]$$

$$\Delta H^\circ_f = -133,504 + 4.96T - 1.14$$

$$\times 10^{-3} T^2 - 0.32 \times 10^5 T^{-1} \quad [7]$$

$$\Delta H^\circ_{f,298} = -132,234 \text{ cal}$$

$$\Delta F^\circ_f = -133,504 - 11.384T \log T + 1.14$$

$$\times 10^{-3} T^2 - 0.16 \times 10^5 T^{-1} + 69.806T \quad [8]$$

$$\Delta F^\circ_{f,298} = 121,050 \text{ cal}$$

The value of $\Delta H^\circ_{f,298}$ agrees very closely with the calorimetric value of $-130,000$ reported by Mixter.⁹

In the range of steelmaking temperatures, ΔF° for reaction 6 is obtained by combining Eq. 3 with

$$\Delta F^\circ = -120,380 + 27.80T \text{ for } 2H_2 + O_2 = 2H_2O:$$

$$\Delta F^\circ = -132,250 + 35.1T \quad [9]$$

Acknowledgments

The author wishes to express his appreciation for the encouragement received from Dr. Corbin T. Eddy. Professor Russell J. Smith and the members of staff of the Metallurgy Department extended their cooperation in the construction of the apparatus. This research was sponsored by the Michigan College of Mining and Technology.

References

- 1 Chaudron: *Ann. Chim.* (1921) **16**, p. 221.
- 2 Tonosaki: *Bull. Inst. Phys. Chem. Res.*, Tokyo (1940) **19**, p. 126.
- 3 Collins: Sc. D. Thesis, Massachusetts Institute of Technology (June 1949).
- 4 Rosenqvist and Cox: *Trans. AIME* (1950) **188**, p. 1389; *JOURNAL OF METALS* (November 1950).
- 5 Gokcen and Chipman: *Trans. AIME* (1952) **194**, p. 171; *JOURNAL OF METALS* (February 1952).
- 6 Dastur and Chipman: *Discussions, Faraday Soc.* (1948) No. 4, p. 100.
- 7 Kelley: U. S. Bur. Mines, *Bull.* 476 (1949).
- 8 Rossini, et al.: Circular 500, Nat. Bur. of Standards (1952).
- 9 Mixter: *American Journal of Science* (1910) **29**, p. 488.

Influence of Aluminum and Silicon Deoxidation on The Strain Aging of Low-Carbon Steels

by W. C. Leslie and R. L. Rickett

The influence of deoxidation practice, prior thermal history, and aging time and temperature on the strain-aging behavior of low-carbon open-hearth steels was investigated. The criterion of aging employed was the increase in yield strength in the tensile test, after straining and aging. Composition, prior heat treatment, and aging conditions were all found to be important in governing the strain-aging characteristics of these steels.

THAT deoxidation changes the strain-aging propensities of low-carbon steels has been known for a long time, but there has been little agreement, and even contradiction, between results obtained by different investigators and between results obtained in the laboratory and in the mill. This investigation was begun in the hope that some of the uncertainties connected with the strain aging of commercial steels could be eliminated.

In considering this problem, it was necessary to define strain aging and to examine the methods used to measure this property. Strain aging can be defined as the changes in properties of a metal or alloy with time, after cold working. The rate at which these changes occur increases as the temperature is raised above atmospheric. The requisite plastic strain is the principal distinction between strain aging and quench aging, the latter being due to precipitation from supersaturated solid solution. Strain aging is also characterized by rapid attainment of maximum hardness at high aging temperatures and lack of softening (overaging) at low aging temperatures.

Several possible criteria of strain aging have been

listed by Sachs¹ and by Davenport and Bain.² Because changes in mechanical properties are the most easily measured and the most commonly used, consideration of methods to be used in this investigation was confined to three tests: tensile, notch-impact, and hardness. Hardness tests are the most economical and easiest to perform, but produce only one measure of strain aging. Also, as pointed out by Felmly, Hartbower, and Pellini,³ hardness changes due to aging are not pronounced for steels containing more than 0.15 pct C. Notch-impact tests require careful preparation of large numbers of specimens. Above and below the transition temperature the test lacks sensitivity; furthermore, it is extremely difficult to impart a uniform strain to the specimens, followed quickly by aging and final testing; machining must generally take place after straining.

For these reasons, the tensile test was selected for use. Although this test requires a considerable expenditure of time, labor, and money in preparation of the specimens and performance of the test, more information can be gained than from any other single mechanical test, information which includes upper and lower yield points, yield-point elongation, tensile strength, strain-hardening exponent, reduction of area, and elongation. Low and Gensamer⁴ and Schwartzbart and Low⁵ also used the tensile test, taking the increase in flow stress after straining in tension and aging as a measure of strain aging. In our work, as in theirs, each specimen was strained an arbitrary amount, sufficient to pass through the

W. C. LESLIE, Junior Member AIME, formerly with the Research Laboratory, United States Steel Corp., is now associated with Thompson Products, Inc., Cleveland, and R. L. RICKETT, Member AIME, is associated with the Research Laboratory, United States Steel Corp., Kearny, N. J.

Discussion on this paper, TP 3572E, may be sent, 2 copies, to AIME by Dec. 1, 1953. Manuscript, Feb. 20, 1953. Cleveland Meeting, October 1953.

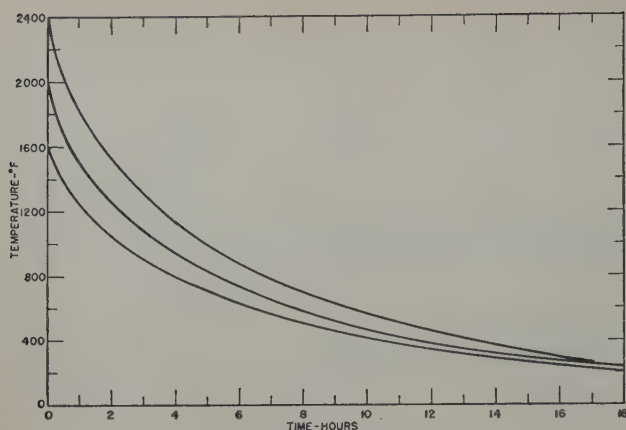


Fig. 1—Typical furnace cooling curves.

yield-point elongation and into the region of uniform plastic strain, then the load was removed and the specimen was given the appropriate aging treatment. The amount by which the yield strength was raised upon reloading was used as a measure of the amount of strain aging.

In using this method, the effect of relaxation must be considered, because this process may go on concurrently with strain aging. No method is known for separating the two phenomena. Low and Gensamer⁴ attempted to correct for the effect of relaxation by comparing the strain aging of a steel strained various amounts with the decrease in yield strength (relaxation) of the same steel given identical straining and aging treatments after annealing in wet hydrogen to eliminate strain aging. This method is open to the objection that the relaxation of steel containing carbon and nitrogen may not be the same as the relaxation of steel from which carbon and nitrogen have been removed by annealing in wet hydrogen. Low and Gensamer encountered no relaxation in steel treated in wet hydrogen, then strained 5.1 pct and aged 3 hr at 200°C (390°F). In the present investigation the amount of strain was generally less, the aging times were shorter, and the aging temperatures were lower; it is believed, therefore, that if any relaxation occurred the amount was insignificant.

Materials and Experimental Procedures

With two exceptions, the steels from which specimens were cut came from two basic open-hearth

heats, each with graded aluminum additions. One heat was made to rimming practice, then deoxidized by various aluminum additions to the molds. The other heat was killed with ferrosilicon in the furnace, then the same aluminum additions were made to the molds as in the case of the first heat. Identification and composition of all steels used are given in Table I.

Bars from the middle cut of the ingots were forged to 1-in. diameter. These bars were later forged to 5/8-in. diameter, then cut into 4 1/2 in. lengths. Over-size tensile test blanks machined from these short lengths were heat-treated, then finish machined. In an attempt to insure only tensile stresses in the 2-in. gage length, the 0.252-in. diameter reduced section was made 3 1/4 in. long. The diameter, between the 1/8-in. fillets, was held to 0.2520 ± 0.0005 in., with no taper.

All specimens were heat-treated. The specimen blanks were austenitized in a closed-end porcelain tube containing a small amount of carburizing compound. The furnace was brought to temperature, then the specimens were inserted. They were held for 5 min after a thermocouple, which was in a protection tube that touched the specimens, reached the desired temperature. When specimens were to be furnace-cooled or cooled at slower controlled rates, several were treated simultaneously, otherwise they were treated in duplicate. Since cooling rates were found to be of considerable importance, typical furnace cooling curves are presented in Fig. 1. Fig. 2 shows heating and cooling curves determined on two tensile test blanks austenitized at 1600°F, then air-cooled. Chromel-alumel couples (14 gage) were spot welded into center holes 1/4 in. deep drilled in the ends of these specimens. Temperatures were followed by means of a high-speed recording potentiometer. When specimens were held isothermally after austenitizing, they were quenched into the largest lead bath available in order that the comparatively large specimens would have the minimum effect on the temperature of the bath.

Tensile tests were performed on a Baldwin-Southwark machine. The specimens, after heat treatment and final machining, were strained 4 pct, or through the yield point elongation, whichever was greater. The maximum extension used on any specimen was 5 pct, with three exceptions which ranged up to 10 pct. The specimens were then unloaded, the wedge-type extensometer was removed,

Table I. Description of Steels

Steel	Deoxidation Practice	Chemical Analysis, Pct								Spectrographic Analysis, Pct					
		C	Mn	P	S	Si	Al ⁺	Al ₂ O ₃	N**	Cr	V	Ti	Mo	Zr	B
A	No Al added	0.10	0.41	0.011	0.024	0.01	0.001	0.001	0.004	0.03	N.D.*	N.D.*	0.02	N.D.*	N.D.*
D	1 lb Al per ton in mold	0.10	0.42	0.011	0.025	0.01	0.013	0.017	0.004						
E	2 lb Al per ton in mold	0.10	0.43	0.010	0.025	0.01	0.047	0.019	0.004	0.03	N.D.	N.D.	0.02	N.D.	N.D.
F	4 lb Al per ton in mold	0.10	0.44	0.012	0.023	0.01	0.144	0.015	0.004						
G	FeSi in furnace, no Al	0.20	0.83	0.011	0.018	0.18	0.004	0.001	0.007	0.03	N.D.	N.D.	0.004	N.D.	N.D.
J	FeSi in furnace, 1 lb Al per ton in mold	0.19	0.82	0.010	0.019	0.16	0.029	0.013	0.006						
K	FeSi in furnace, 2 lb Al per ton in mold	0.19	0.81	0.012	0.019	0.16	0.076	0.016	0.005	0.03	N.D.	N.D.	0.004	N.D.	N.D.
L	FeSi in furnace, 4 lb Al per ton in mold	0.19	0.81	0.011	0.020	0.17	0.158	0.016	0.006						
M	1.9 lb Al per ton in ladle	0.19	0.81	0.014	0.018	0.036	0.035	0.004	0.005	0.03	N.D.	N.D.	0.004	N.D.	N.D.
X	FeSi in furnace	0.25	0.50	0.013	0.027	0.23	0.005	—	0.006						

* V — N.D. — Less than 0.002 pct, if any.
 Ti — N.D. — Less than 0.001 pct, if any.
 Zr — N.D. — Less than 0.005 pct, if any.
 B — N.D. — Less than 0.0005 pct, if any.
 + — Acid-soluble aluminum.

** Total (acid soluble) nitrogen.

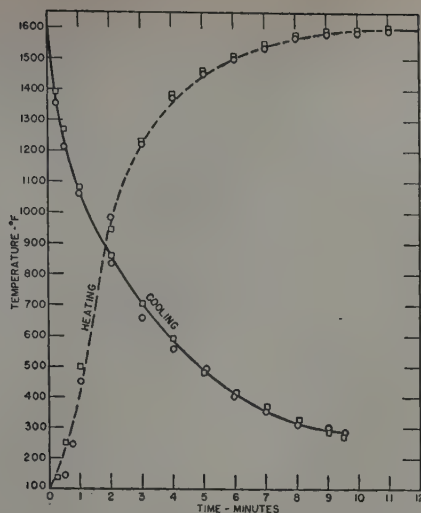


Fig. 2—Heating and cooling curves for tensile test blanks austenitized at 1600°F, then air cooled.

and the specimens were given the desired elevated-temperature aging treatment. At the end of the proper period, they were rapidly cooled by dipping into water at room temperature, dried, and replaced in the grips; the extensometer was replaced in the original gage marks and the test was continued. The time between initial and final straining of the specimens, aside from the time taken up by the aging treatment, was held to a minimum and actually varied between 2 and 7 min. Efforts were made to keep a constant strain rate, as measured between the gage points; it generally ranged between 0.020 and 0.030 in. per in. per min. An autographic load-elongation record was obtained from each specimen, using a 40X magnification and a 6000-lb load range on a 10-in. chart. Values for the upper and lower yield points, load at 4 pct elongation, upper and lower yield points after aging (if any), maximum load, and load at fracture were taken from the load

indicating dial of the testing machine. The lower yield point was taken as the lowest value of stress reached during the yield-point elongation. These values were checked against those indicated on the load-elongation record. From this record, values were obtained for initial yield-point elongation and for yield-point elongation after aging. Since there was no taper within the gage length, specimens often broke at, or outside, the gage marks and their elongation could not be measured. Elongation, expressed as percent in 2 in., of specimens that broke

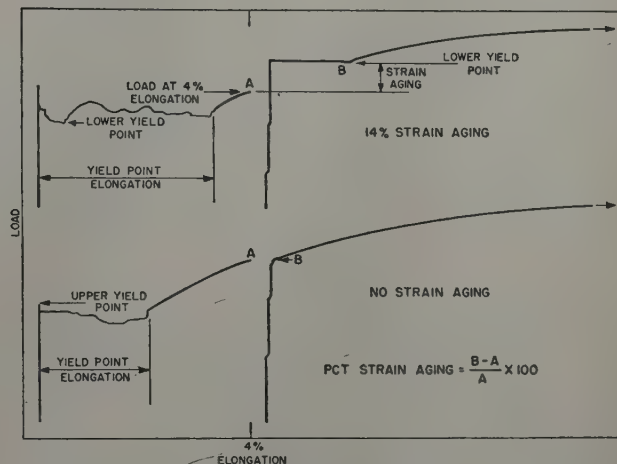


Fig. 3—Portions of load-elongation records showing occurrence and absence of strain aging.

within the gage length was recorded and reduction of area was measured on all specimens in the usual manner. Because of the rapidly changing load, load at fracture could only be estimated.

The extent of strain aging was determined by subtracting the stress at the point A (Fig. 3) at which the load was released (generally 4 pct elongation), from B, the lower yield point after aging,

Table II. Strain Aging of Specimens of Steels A and E Austenitized at 2000°F, Held Isothermally at 1650°F, Then Air Cooled

Time at 1650°F	Aging Treatment	Col. X		Col. Y		Y-X		(100) $\frac{Y-X}{X}$	
		Load at 4 Pct Strain Psi x 10 ⁻³		Lower Yield Point After Aging, Psi x 10 ⁻³		Psi		Pct Strain Aging	
		A	E	A	E	A	E	A	E
30 sec	4 hr, 300°F	54.2*	41.4	61.8	48.6	7600	7200	14	17
2 min	4 hr, 300°F	45.3	41.5	52.2	47.9	6900	6400	15	15
5 min	4 hr, 300°F	45.6	41.5	52.9	48.8	7300	7300	16	18
10 min	4 hr, 300°F	45.4	40.8	52.8	46.8	7400	6000	16	15
1 hr	4 hr, 300°F	45.6	42.0†	53.6	48.2	8000	6200	17	15
2 hr	4 hr, 300°F	46.4	40.1	54.0	45.9	7600	5800	16	15
30 sec	15 min, 300°F	45.5	41.3	52.3	47.4	6800	6100	15	15
2 min	15 min, 300°F	45.3	41.9	52.0	48.2	6700	6300	15	15
5 min	15 min, 300°F	45.6	41.1	52.8	47.1	7200	6000	16	15
10 min	15 min, 300°F	45.0	41.4	51.8	47.9	6800	6500	15	16
1 hr	15 min, 300°F	46.1	40.8	53.0	46.4	6900	5600	15	14
2 hr	15 min, 300°F	44.7	39.6	51.8	45.3	7100	5700	16	14
30 sec	1 min, 300°F	45.5	40.9	52.2	46.6	6700	5700	15	14
2 min	5 min, 200°F	45.8	41.4	50.9	46.5	5100	5100	11	12
5 min	30 sec, 200°F	44.9	41.6	45.8	42.6	900	1000	2	2
10 min	1 min, 153°F	45.2	40.8	45.9	41.0	700	200	2	1
1 hr	5 min, 153°F	45.6	40.2	47.0	41.4	1400	1200	3	3
2 hr	1 min, 300°F	45.5	40.0	52.3	44.8	6800	4800	15	12

* Strained 10 pct before aging.
† Strained 4.75 pct before aging.

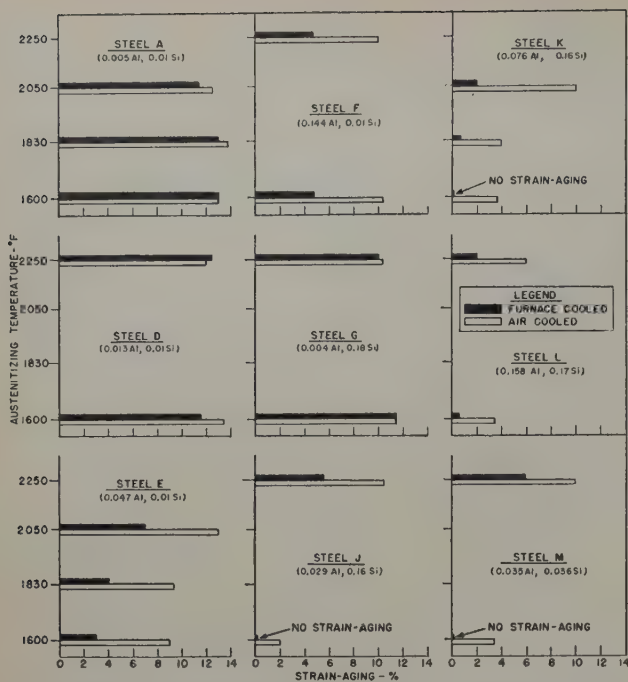


Fig. 4—Effect of austenitizing temperature and cooling rate on subsequent strain aging. Aged 5 min at 210°F.

dividing by A and expressing the result as a percentage, thus, after Schwartzbart and Low,⁵

$$\text{Percent strain aging} = \frac{B-A}{A} \times 100$$

Fig. 3 is a representation of load-elongation diagrams illustrating an example in which aging occurred and one in which it did not occur, with the points of interest marked. The amount of strain aging varied between 0 and 20 pct. A range of ± 1 pct strain aging is probably about the limit of accuracy of this method.

A majority of the specimens was aged in boiling water. Those aged 1 min at 300°F and various periods at 200° and 153°F were held in a polyalkylene glycol bath.* The remainder was aged in air in a

* "Ucon" grade 50-HB-280-X.

tempering furnace. Temperature variation in this furnace was held to about $\pm 4^\circ\text{F}$.

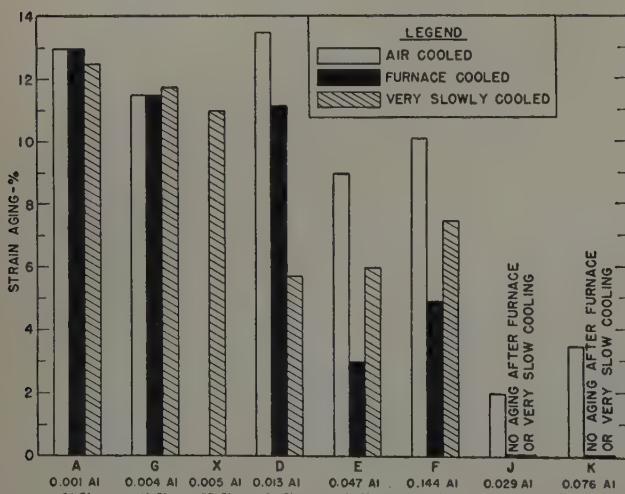


Fig. 5—Effect of rate of cooling from 1600°F on subsequent strain aging. Aged 5 min at 210°F.

Initial Tests: The specimens of the first group tested were austenitized at 2000°F, quenched into lead at 1650°F, held for from 30 sec to 2 hr and air-cooled. This procedure was adopted because of a desire to determine the effects of solution and subsequent precipitation of aluminum nitride on strain aging. Later on, better information on the "solution temperature"^{7,8} and time-temperature requirements for precipitation of aluminum nitride⁷ became available and the heat treatments were changed accordingly. Work was confined to two steels, A (rimmed) and E (aluminum-killed). Specimens were tensile tested in the base condition (unaged), also as-aged from 1 min at 153°F to 4 hr at 300°F. The results are presented in Table II.

In the range from 1 to 15 pct strain aging, there was no apparent difference in the strain-aging behavior of the two steels. The only observed difference between the two steels was the higher stress level of the load-elongation curve of the rimmed steel (A), which was 3000 to 4000 psi higher than

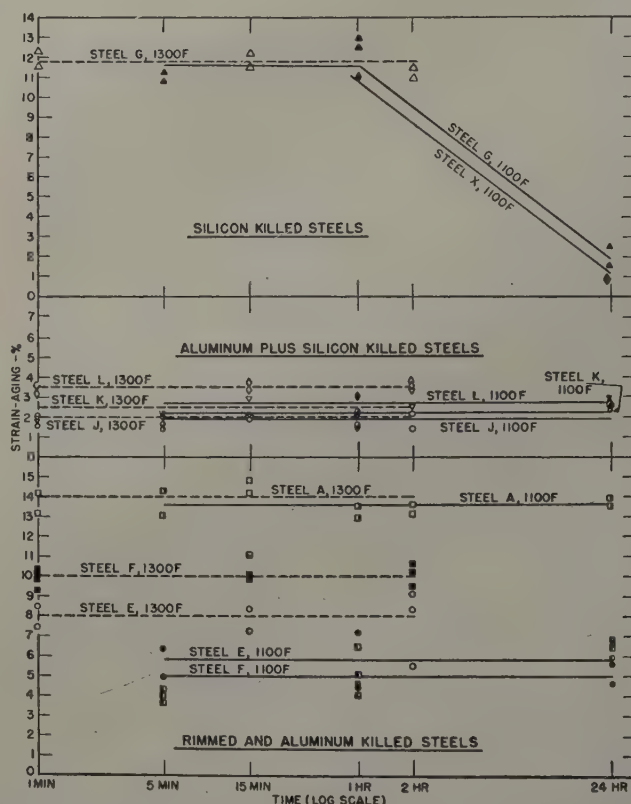


Fig. 6—Effect of time at 1100° and 1300°F on subsequent strain aging. Specimens austenitized at 1600°F.

that of the aluminum-killed steel (E). Time at 1650°F, when aging conditions were held constant, made no difference in the strain-aging results. Aging apparently reached completion within 1 min at 300°F but required more than 5 min (the longest time used) at 200°F and lower.

Variation of Austenitizing Temperature and Cooling Rate: Three steels, A, E, and K, the last containing 0.16 pct Si and 0.076 pct Al, were used in the second phase of the investigation. Since the results of the initial tests indicated no difference in the strain-aging behavior of rimmed and aluminum-killed steels austenitized at 2000°F, held isothermally at 1650°F, and then air-cooled, it was decided to study the effects of varying the austenitizing temperature and the cooling rate from those tem-

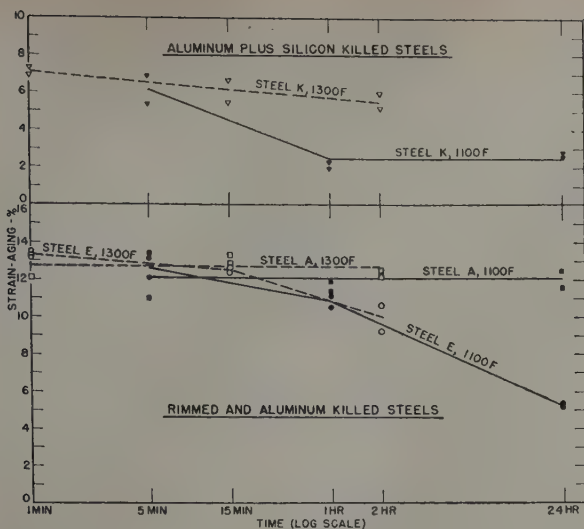


Fig. 7—Effect of time at 1100° and 1300°F on subsequent strain aging. Specimens austenitized at 2050°F.

peratures. The steels were austenitized at 1600°, 1830°, or 2050°F, held 5 min at temperature, then air-cooled, air-cooled and preaged 2 hr in boiling water, or furnace-cooled. The calculated "AlN solution temperature" of steel K containing the highest concentration of aluminum is about 2050°F,² and for steel E, about 1920°F. The preaging treatment was performed to determine whether quench aging would interfere with the strain-aging measurements. If the steel is susceptible to quench aging, 2 hr in boiling water is sufficient to cause maximum quench aging and perhaps some overaging,² and the effects of quench aging can be separated from those produced by subsequent strain aging. All specimens were aged 5 min in boiling water, after straining. These and all subsequent tests were performed in duplicate, at least.

Some results of this phase of the investigation are included in Figs. 4 and 5. These results indicate that high austenitizing temperatures and rapid cooling rates tend to increase the strain aging of killed steels, and low austenitizing temperatures and slow cooling rates tend to decrease strain aging of these steels. The strain aging of rimmed steel, however, is not affected by austenitizing temperature or cooling rate. Steel K, killed with silicon and aluminum, strain-aged less than steel E, killed with aluminum alone. The preaging treatment had no effect on the amount of strain aging, so this procedure was abandoned.

This work was then extended to include six more steels, D, F, G, J, L, and M (see Table I). Steel L contained the largest amount of aluminum, 0.158 pct, and 0.006 pct N; the calculated "AlN solution temperature" of this steel is about 2220°F, so an austenitizing temperature of 2250°F was used for this series rather than 2050°F. Specimens were air and furnace-cooled from 2250° and 1600°F. Results for this series are also presented in Figs. 4 and 5. Steel G, killed with silicon, was not affected by either the austenitizing temperature or cooling rate. The strain aging of this steel was equivalent to that of the rimmed steel, A. Use of aluminum alone as a deoxidizing agent reduces strain aging, particularly after furnace cooling, but strain aging is not completely eliminated (for aging 5 min in boiling water) even in a steel (F) containing 0.144 pct acid-soluble

aluminum. Strain aging was eliminated in steels J, K, L, and M, deoxidized with silicon plus aluminum, by austenitizing at 1600°F followed by furnace cooling. Steel M, containing 0.035 pct Al and 0.036 pct Si, showed no strain aging after furnace cooling from 1600°F, while steel F, containing 0.144 pct Al and 0.01 pct Si, strain-aged about 5 pct.

Effect of Very Slow Cooling: These results led to a determination of the effect of slow, controlled cooling from the austenitizing temperature. Eight steels were used, A, D, E, F, G, J, K, and X. They were cooled at either 13° or 15°F per hr from 1600°F. After heat treatment, the specimens were finish machined, strained 4 pct in tension, then aged 5 min in boiling water. Results are presented in Fig. 5. The strain aging of only one steel, D, was decreased from the strain aging obtained after furnace cooling from 1600°F. Results obtained fall into three groups; the rimmed steel, A, and the two silicon-killed steels G and X strain-aged from 11 to 12 pct, the three aluminum-killed steels, D, E, and F, from 5½ to 7½ pct, and the two silicon-aluminum-killed steels, J and K, did not strain age.

Isothermal Treatments: When steels killed with aluminum or silicon and aluminum are cooled slowly, some change occurs which decreases subsequent strain aging. It was believed, therefore, that the behavior of specimens quenched from the austenitizing temperature to a lower temperature and held isothermally, then air cooled, strained, and aged, might yield information which would aid in the identification of this process. Accordingly, specimens were austenitized at 1600°, 2050°, or 2250°F for 5 min, then quenched into lead at 1100° or 1300°F and held for the following periods: at 1100°F—5 min, 1 hr, or 24 hr, at 1300°F—1 min, 15 min, or 2 hr. Since the process by which strain aging was reduced was believed to be the removal of nitrogen

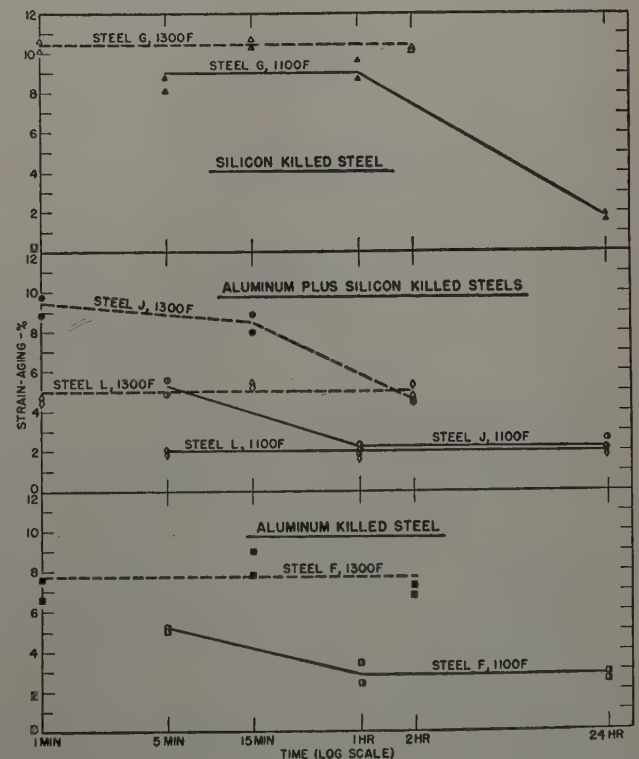


Fig. 8—Effect of time at 1100° and 1300°F on subsequent strain aging. Specimens austenitized at 2250°F.

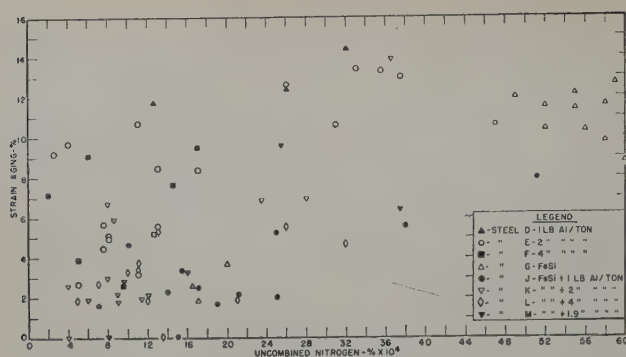


Fig. 9—Correlation between strain aging and uncombined nitrogen in low carbon steels.

from solid solution in ferrite as a result of formation of aluminum nitride, these times were chosen after consideration of the approximate time-temperature relations for complete formation of aluminum nitride in a low carbon steel.⁷ The austenitizing temperatures were the same as used in the study of the effect of continuous cooling.

Results are presented in Figs. 6 to 8 in which the percentage of strain aging is plotted against time at the isothermal holding temperature. An unexpected result is illustrated in Figs. 6 and 8. The strain aging of steel G (0.18 pct Si, 0.004 pct Al) had been found to be the same regardless of austenitizing temperature or cooling rate over the range investigated (see Figs. 4 and 5), from which it might be concluded that the strain aging of silicon-killed steels is not influenced by prior heat treatment; however, this conclusion would be incorrect. Although, as shown in Fig. 6, specimens austenitized at 1600°F, then held at 1100°F for 5 min or 1 hr, strain aged about 12 pct, after 24 hr at 1100°F the strain aging was reduced to about 2 pct. However, steel G displayed no change in strain aging after austenitizing at 1600°F, followed by holding at 1300°F for 1 min, 15 min, or 2 hr. The process which reduces strain aging in silicon-killed steels, presumably the formation of silicon nitride, proceeds very slowly. This result was checked by use of another steel, X, containing 0.23 pct Si and 0.005 pct Al. As shown in Fig. 6, the strain aging of this steel after 1 hr or 24 hr at 1100°F is identical with that of steel G. Much the same effect was obtained with steel G when the austenitizing temperature was increased to 2250°F, as shown in Fig. 8.

With the exception of the silicon-killed steels, three levels of strain aging are evident in Fig. 6, with the rimmed steel, A, showing the greatest amount, 13 to 15 pct, regardless of heat treatment, followed by the aluminum-killed steels, E and F, which strain aged 8 to 11 pct after isothermal treatment at 1300°F and 4 to 7 pct after holding at 1100°F. The results for steel F may indicate an increase in subsequent strain aging with increasing time at 1100°F. More data are needed before a definite conclusion can be made; pending this, a horizontal line was drawn in Fig. 6. The third level of strain aging included the steels killed with silicon and aluminum, which strain aged about 2 to 4 pct after being held at 1100° or 1300°F.

The strain-aging behavior of some of the same steels austenitized at 2050°F before isothermal treatment at 1100° and 1300°F is illustrated by Fig. 7. For the rimmed steel, A, the subsequent strain aging

is again independent of time at 1100° or 1300°F, and the amount of aging is the same as for this steel austenitized at 1600°F. With steels E (aluminum-killed) and K, (silicon-aluminum-killed) the strain-aging behavior when austenitized at 2050°F, then quenched to 1100° or 1300°F, is quite different from the behavior when the austenitizing temperature was 1600°F. The aluminum-killed steel has the same aging characteristics as the rimmed steel when held at 1300°F for 15 min or less, or when held 5 min at 1100°F. With longer holding times at 1100° or 1300°F, the subsequent strain aging is reduced. After quenching from 2050° to 1300°F and holding for 2 hr, the amount of strain aging is slightly greater than when the steel was austenitized at 1600°F, then held 2 hr at 1300°F. When held 24 hr at 1100°F, after austenitizing at 2050°F, the strain aging was the same as after austenitizing at 1600°F and holding 5 min to 24 hr at 1100°F.

The behavior of steel K (silicon-aluminum-killed) is similar in that subsequent strain aging was reduced after austenitizing at 2050°F and quenching to 1100° or 1300°F. An hour at 1100°F was sufficient to bring the amount of strain aging down to the same level (approximately 2 pct) reached when the steel was austenitized at 1600°F and held at 1100° or 1300°F. Two hours at 1300°F after quenching from 2050°F was not sufficient to bring the strain aging down to the level reached when the steel was quenched from 1600° to 1300°F and held 1 min to 2 hr.

The results obtained when killed steels were quenched from 2250°F to 1100° or 1300°F and held at these lower temperatures are illustrated in Fig. 8. Except for steel L, the extent of strain aging decreased with increasing times at 1100°F. Only steel J was affected by increasing the time at 1300°F, within the range investigated.

The subsequent strain aging of killed steels tended to decrease with time at 1100° or 1300°F, until an equilibrium level characteristic of each steel was reached. This level was independent of the austenitizing temperature, but raising the austenitizing temperature increased the time required at the lower temperatures for equilibrium to be reached. In the aluminum-killed or aluminum-silicon-killed steels, 5 min at 1600°F followed by 1 min at 1300°F and air cooling or 5 min at 1100°F and air cooling suffice for the attainment of equilibrium. In steels killed with silicon alone the reaction is very sluggish and 24 hr at 1100°F are required for reduction of strain aging to the equilibrium level. In the case of a rimmed steel, none of the prior heat treatments tested affected strain aging. The isothermal treatments at 1100° or 1300°F did not completely eliminate subsequent strain aging, even in steels killed with aluminum and silicon, although these steels showed no strain aging after furnace cooling from 1600°F. From an examination of Figs. 6 to 8, it appears that strain aging of killed steels is reduced by a process which bears the characteristics of precipitation from solid solution. These results support the conclusion that the strain aging of aluminum-killed or silicon-killed steels is reduced through the removal of nitrogen from solution in ferrite by formation of aluminum or silicon nitrides. Formation of these nitrides in steel is dependent on heat treatment.⁸⁻¹⁰ The solubility of these nitrides at 1100°F in the steels used evidently is sufficient to cause about 2 pct strain aging, which is a minor amount;

in order to eliminate the aging it is necessary to cool slowly below this temperature. The effect of raising the austenitizing temperature is to increase the solubility of the nitrides and to increase the time required for their precipitation at lower temperatures.

Determination of Aluminum Nitride: In an attempt to determine directly the influence of nitrogen in solution in ferrite on strain aging, a number of broken tensile test specimens of eight steels were analyzed for "AlN nitrogen" by the Beeghly method.⁹ The AlN nitrogen obtained by this procedure was subtracted from the total (acid soluble) nitrogen to give the concentration of nitrogen in solution in ferrite. The Beeghly method suffers from lack of any standards; also, aluminum nitride particles in the very early stages of growth cannot be separated from the ferrite matrix. During the course of the work it was found that the presence of silicon nitride, Si_3N_4 , interferes with the determination of AlN nitrogen.¹⁰ Except in steels containing more than about 0.5 pct Si, the total of Si_3N_4 plus AlN nitrogen will be obtained by the Beeghly method. Moreover, it is apparently necessary to determine the uncombined nitrogen to the fourth place to the right of the decimal point in order to measure its effect on strain aging and a method based on chemical separation of a precipitate is hardly likely to give this degree of accuracy. However, since no other method was available, it was decided to use this technique. Results are presented in Fig. 9. The most that can be said, from the evidence shown here, is that uncombined nitrogen must be reduced to a very small concentration before strain aging is eliminated. Fast¹² found that as little as 0.001 pct N caused maximum strain aging in high purity iron and 0.0004 pct N was sufficient to produce an easily measured amount. From his results, it seems that the uncombined nitrogen in low-carbon steels must be reduced to about 0.0001 pct or less to eliminate strain aging.

Variation of Aging Conditions: In most of the experiments described up to this point the specimens were aged 5 min in boiling water. To determine the effect of varying the aging conditions, particularly in the case of steels which could be rendered non-aging as measured after aging 5 min in boiling water, further tests were made on five steels, A, E, F, K, and L. Specimens were furnace-cooled from 1600°F, and in addition specimens of steel K were air-cooled from 2050°F, which is about 25°F above the calculated "AlN solution temperature" for this steel. Duplicate specimens were strained 4 pct, aged 5 min in boiling water (to check previous results), 1 hr in boiling water, 1 hr at 345°F or 1 hr at 480°F. Results are presented in Fig. 10a and b. The strain aging of rimmed steel, A, increased from about 14 pct when aged 5 min in boiling water to 16 or 17 pct when aged 1 hr in boiling water. The aging of this steel then remained constant even when the aging treatment was 1 hr at 480°F. Steel E (0.047 pct Al, 0.01 pct Si) strain aged 3 pct after 5 min in boiling water and about 9 pct after 1 hr at this temperature. It showed an increase to 12 or 13 pct after 1 hr at 480°F. The behavior of steel F (0.144 pct Al, 0.01 pct Si) was quite similar; thus, increasing the aluminum content of the steel from 0.047 to 0.144 pct did not influence the aging behavior. The behavior of steels K (0.76 pct Al, 0.16 pct Si) and L (0.158 pct Al, 0.17 pct Si), furnace-cooled from 1600°F, was identical. They showed no aging after 5 min or 1 hr at 212°F. After 1 hr at 345°F they aged about

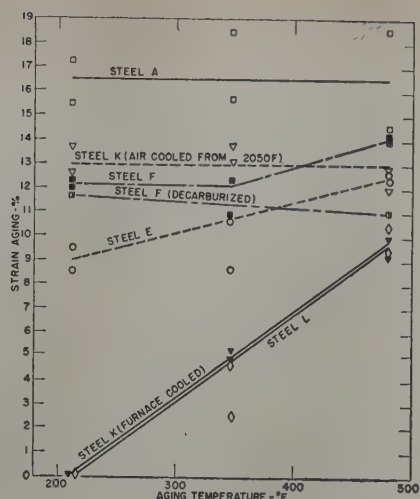


Fig. 10a—Strain aging of steels furnace-cooled from 1600°F (except as noted), strained 4 pct, and aged 1 hr at indicated temperatures.

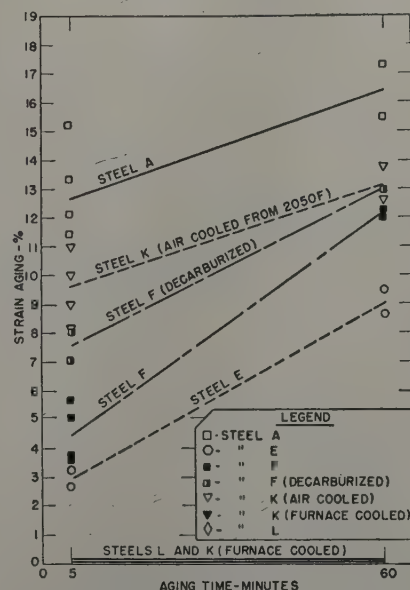


Fig. 10b—Influence of time at 210°F on strain aging of steels furnace-cooled from 1600°F (except as noted), then strained 4 pct, and aged.

5 pct, and about 10 pct after 1 hr at 480°F. Still more aging might have occurred had the aging temperature been higher or the time at 480°F been longer. This may be said also for steels F and E. In the case of steel K, air-cooled from 2050°F, the aging amounted to about 9 pct after 5 min in boiling water and 13 pct after 1 hr in boiling water. It remained constant at about 13 pct after 1 hr at 347°F and 1 hr at 480°F. Thus, a thoroughly killed steel, given different heat treatments, can show 0 or 13 pct strain aging after straining 4 pct and aging 1 hr in boiling water.

The results of these experiments indicate that composition, thermal history prior to straining, and aging conditions are all of importance in determining the strain-aging characteristics of low-carbon steel.

Discussion of Results

Mechanism of Strain Aging: A large amount of evidence^{4, 5, 11-14, 25} has accumulated which lends sup-

port to the conclusion that the strain aging of mild steel is due to carbon and nitrogen in solution in ferrite. The mechanism by which these interstitial solute atoms produce the effects of strain aging is not known; the most promising hypothesis is that advanced by Cottrell.^{12, 15-17} The region around a dislocation provides more favorable sites for interstitial solute atoms (carbon and nitrogen) than can be found in the undisturbed lattice, so these atoms tend to cluster around dislocations, forming "atmospheres." These atmospheres hinder the movement of the dislocations under applied external loads. When the external force on the dislocations exceeds the maximum force which can be exerted by their atmospheres, the metal exhibits a sharp yield point as the first dislocations break loose from their clouds of solute atoms. These moving dislocations interact with dislocations still anchored by their atmospheres, causing them to break loose, thus producing the yield point elongation. When strained iron is aged, the interstitial solute atoms again diffuse to regions around dislocations. The metal shows a return of the yield point (strain aging) when it is again subjected to external stress.

It is not possible to predict the concentration of solute atoms necessary to produce strain aging, since this will depend upon the number of solute atoms required to anchor a dislocation and also upon the density of dislocations; however, a rough estimate can be made. It was estimated by Seitz and Read¹⁸ that an annealed metal contains 10^8 dislocations per square centimeter and that a heavily cold-worked metal saturated with dislocations will contain 10^{12} dislocations per square centimeter. Annealed iron containing 0.0004 pct N by weight, for example, will have between 100 and 1000 nitrogen atoms per dislocation, which is certainly enough for formation of atmospheres. If this same iron is considered to contain 10^{10} dislocations per square centimeter after slight straining, there will be from 1 to 10 nitrogen atoms per dislocation. If the Cottrell mechanism is the one which operates, it is easy to see why the concentration of interstitial solute atoms must be brought to an extremely low level before strain aging can be eliminated.

As pointed out by Fast,¹¹ the rate of strain aging will depend upon the product of the solubility and diffusivity of the interstitial solute atoms carbon and nitrogen. Fast stated that nitrogen was the essential cause of the strain aging of iron at room temperature or slightly above because of its greater solubility in α iron in this temperature range as compared with carbon. Since the publication of his paper, more data on the diffusivity and solubility of carbon and nitrogen in α iron have become available. For the diffusivity of carbon in α iron between -35° and 700°C (-31° and 1292°F) Wert²⁰ gives the equation

$$D_C = 0.02e^{-\frac{20,100}{RT}}$$

This is only slightly different from that given by Stanley,²⁰ whose work was confined to temperatures above 514°C (957°F),

$$D_C = 0.0079e^{-\frac{18,100}{RT}}$$

The diffusivity of nitrogen in α iron, as given by Wert,²¹ is less certain, since determinations were made only between -30° and 40°C (-22° to 104°F) and since there is no other work against which the

Table III. Solubilities of Carbon and Nitrogen

Temperature	Solubility of Carbon, Wt Pct	Solubility of Nitrogen, Wt Pct
20°C (68°F)	0.15×10^{-6}	25×10^{-6}
100°C (212°F)	5.4×10^{-6}	350×10^{-6}
207°C (405°F)	100×10^{-6}	3000×10^{-6}
288°C (550°F)	500×10^{-6}	8700×10^{-6}

equation can be checked.

$$D_N = 0.003e^{-\frac{18,200}{RT}}$$

When the diffusivities of carbon and nitrogen at 100°C are calculated by these equations the following results are obtained:

$$D_C = 3 \times 10^{-14} \text{ sq cm per sec (Wert)}$$

$$D_C = 20 \times 10^{-14} \text{ sq cm per sec (Stanley)}$$

$$D_N = 7 \times 10^{-14} \text{ sq cm per sec}$$

The diffusivities of carbon and nitrogen in α iron at 100°C (212°F) appear to be nearly equal.

For the solid solubility of carbon in α iron between 150° and 700°C (302° and 1292°F) Wert²² gives the equation

$$C_C = 2.55e^{-\frac{9,700}{RT}}$$

This is in agreement with the results of Stanley,²⁰ Smith,²³ and Dijkstra.²⁴ In the case of nitrogen, the available data are not as reliable. From the work of Dijkstra,²⁴ in the temperature range 200° to 590°C (392° to 1094°F) Fast¹¹ gives the equation

$$C_N (\log \% \text{ N}) = -\frac{7100}{4.575 T} + 0.70$$

The solubilities at various temperatures calculated from these two equations are given in Table III. Thus, from an examination of the best data available, it seems likely that the greater effectiveness of nitrogen in producing strain aging as compared with carbon is due to its greater solubility. At low temperatures, the solubility of nitrogen in α iron is about 100 times that of carbon.

Apparently no one has succeeded in producing strain aging in iron at temperatures below 100°C that could definitely be traced to carbon alone. Fast¹¹ found that 40 hr at 50°C (122°F) produced no strain aging in a specimen of high purity iron to which 0.04 pct C had been added. Only very slight aging (increase in hardness of 3 VPN) was produced by 2 hr at 100°C . If our supposition is correct, a steel in which all the nitrogen is combined as nitrides will strain-age only if raised to a temperature at which the solubility of carbon is sufficient to cause aging. This temperature is probably close to 100°C .

Effect of Aging Conditions: Some of the apparently contradictory results reported in the literature can now be reconciled. Edwards, Jones, and Walters,²⁵ using commercial rimmed and silicon-killed steels with 0.08 pct C, conducted experiments to determine the effect of cooling rate on aging. They found aging to occur after both air and furnace cooling from 950°C (1742°F), and after air cooling from 950°C , reheating to 600°C (1112°F) and slow cooling. Specimens from a special heat containing 0.48 pct Al aged as much as rimmed steels. The aging treatment was 1 hr at 250° or 300°C (482° or 572°F).

Table IV. Strain Aging of a Decarburized, Aluminum-Killed Steel, Steel F

Specimen	Aging Treatment	A	B	B-A, Psl	Pct Strain Aging	Acid Soluble Al, Pct	Total (Acid Soluble) N, Pct	N Combined as AlN, Pct	C, Pct	S, Pct
		Load at 4 Pct Strain, Psl $\times 10^{-3}$	Lower Yield Point After Aging, Psl $\times 10^{-3}$							
1	5 min, 210°F	27.6	29.8	2200	8	0.105	0.0070	—	0.0068	—
2	5 min, 210°F	27.4	29.4	2000	7	—	0.0078	0.0074	0.0052	0.021
3	1 hr, 210°F	26.8	29.9	3100	12	—	0.0075	0.0067	0.0046	0.022
4	1 hr, 480°F	27.5	30.4	2900	11	—	0.0097	0.0085	0.0073	0.021

Edwards, Phillips, and Jones,²⁷ using a series of low-carbon steels containing from 0.02 to 3.39 pct Al, air-cooled and furnace-cooled from 950° and 1050°C (1742° and 1922°F), found these alloys to age after straining 6 pct in tension and aging 1 hr at 250°C (482°F). These results were puzzling in view of the fact that "nonaging" aluminum-killed steels were being produced commercially. The strain aging produced was almost certainly due to the relatively high aging temperature used. As shown in Fig. 10 of this paper steels thoroughly killed with silicon and aluminum that show no sign of strain-aging after being strained 4 pct and held 1 hr at 212°F, age much more when strained 4 pct and held 1 hr at 480°F. Presumably, the nitrogen in these steels was combined as aluminum or silicon nitride by furnace cooling from 1600°F, but the carbon was still free to cause strain aging if the aging temperature was sufficiently high. The effect is not likely to be due simply to changes in rate of aging, for the silicon-aluminum-killed steels showed no change in aging with variations in aging time (up to 1 hr) at 212°F.

Effectiveness of Deoxidizing Elements: One result of the present work which is difficult to rationalize on the basis of decrease of aging by combination of the nitrogen is the greater effectiveness of deoxidation with aluminum and silicon as compared with deoxidation by aluminum alone. As shown by Figs. 4 and 5, steels containing only 0.01 pct Si and from 0.013 to 0.144 pct Al strain-aged from 3 to 7 pct, even after furnace cooling or very slow cooling from 1600°F. Steels containing 0.036 pct Si and 0.035 pct Al or 0.16 pct Si with 0.029 to 0.158 pct Al showed no aging after furnace cooling or very slow cooling from 1600°F. Aging conditions were constant at 5 min in boiling water. If elimination of aging under these conditions is due to removal of nitrogen from solution by combination with the deoxidizing elements, it is difficult to see why strain aging was not eliminated in the steel containing 0.01 pct Si, 0.144 pct Al, and 0.004 pct N by formation of aluminum nitride. Very slow cooling from 1600°F favors complete formation of AlN.⁷ By use of the data of Darken, Smith, and Filer⁸ the solubility product of aluminum nitride, i.e., the product of the concentrations of aluminum and nitrogen in solution, can be calculated for any temperature in the austenitic range. The solubility product of aluminum nitride in ferrite can only be approximated. The ratio between the solubility product in ferrite and the solubility product in austenite will equal the ratio between the concentrations of nitrogen and aluminum in solution in ferrite and in austenite at equilibrium, or,

$$\frac{K_s(\alpha)}{K_s(\gamma)} = \frac{C_N(\alpha) C_{Al}(\alpha)}{C_N(\gamma) C_{Al}(\gamma)}$$

Reliable data for the nitrogen concentrations were

furnished by Darken, but the situation is not as satisfactory in the case of aluminum. The partition of aluminum between ferrite and austenite at equilibrium is not known,²⁸ but the ratio cannot be far from one. At 1400°F (760°C) the solubility product of aluminum nitride in ferrite for a steel containing 0.144 pct Al and 0.004 pct N will be, approximately,

$$\frac{K_s(\alpha)}{8 \times 10^{-6}} = \frac{0.0022}{0.028} \times 1$$

$$K_s(\alpha) = 8 \times 10^{-7}$$

This is the product of the concentrations of aluminum and nitrogen, so there will be about 6×10^{-6} pct N in solution in the ferrite. Since the solubility of nitrogen in ferrite decreases with temperature, the concentration of nitrogen in solution at 212°F will be even smaller than this extremely low figure and much less than required to produce strain aging. Nevertheless, when this steel was cooled at about 13°F per hr from 1600°F to allow equilibrium to be approached, then strained 4 pct and aged 5 min at 212°F, it strain aged 6 to 9 pct. A steel containing 0.029 pct Al, 0.16 pct Si, and 0.006 pct N, given the same treatment, showed no strain aging. An explanation of this behavior and of the greater effectiveness of deoxidation with aluminum and silicon as compared with deoxidation by aluminum alone may be that the aluminum cannot react with the nitrogen because of prior combination with some other element. This other element is almost certainly not oxygen; the Al_2O_3 content of the aluminum-killed steel is 0.015 pct and the "acid soluble" aluminum content is 0.144 pct. There is a possibility that aluminum was combined with sulphur and perhaps with carbon. Iron-aluminum carbides have been reported.^{29, 30} This hypothesis might be tested by examining the strain-aging behavior of an aluminum-killed steel from which carbon and sulphur had been removed but not nitrogen. Accordingly, four tensile test blanks of steel F (0.144 pct Al) were held in a flowing 94 pct H_2 -6 pct N_2 atmosphere at 2280°F for from 48 to 50 hr. The gas mixture was bubbled through water at room temperature before entering the furnace. The specimens were rapidly cooled to room temperature, placed in a furnace at 1600°F, held for 10 min, then cooled in the furnace to room temperature. After final machining the specimens were strained 4 pct, aged, and pulled to fracture. The broken specimens were then analyzed for aluminum, nitrogen, carbon, and sulphur. Results of the aging tests and analyses are shown in Table IV. The nitrogen content of the steel was close to the expected value, but the carbon content was greater than anticipated. The sulphur content remained unchanged. Removal of nearly all of the carbon from this steel did not alter its strain-aging characteristics (Fig. 10). The apparent reluctance of aluminum, even when present in consider-

able excess, to combine with the last traces of nitrogen probably is not due to prior combination with carbon and the sulphur present is sufficient to combine with less than a fifth of the aluminum. The cause of the slight strain aging of slowly cooled aluminum-killed steels remains a mystery.

Apparently, the function of silicon in a silicon-aluminum-killed steel is to combine with the last traces of nitrogen which are not removed by combination with aluminum. Deoxidation with silicon alone is not an efficient method for eliminating strain aging because of the very slow formation of silicon nitride, see Figs. 6 and 8.

Correlation with Previous Work

The conclusions reached in this study have sometimes been implied by other investigators, though seldom stated explicitly. Hayes and Griffis³¹ were aware of the importance of heat treatment in the production of "nonaging" steels. Their heat treatment consisted of heating below the A_3 , preferably below the A_1 , then slow cooling. Our evidence confirms the necessity for slow cooling, but does not confirm the need for the top heating temperature to be below the A_3 .

Altenburger³² stated many of the same conclusions reached in this paper. He believed the strain aging of mild steel to be due to nitrogen, and that nitrogen may be fixed by silicon, aluminum, zirconium, titanium, or vanadium. He also stated that the susceptibility of killed steels to strain aging depends upon their prior history, and that estimates of aging susceptibility in the hot-rolled condition are unreliable because of the great variation in cooling rates. The criterion of strain aging used in Altenburger's work was the difference in tensile strength of sheet specimens tested at 75° and 400°F. Annealing temperatures of 1150° or 1200°F seemed to be more favorable for reducing the strain aging of silicon-killed sheet than 1050° or 1300°F. Altenburger states that although silicon can be used to produce "nonaging" sheet, it is not used because of its hardening effect.

The effects on Charpy impact strength at room temperature produced by normalizing aluminum-killed and rimmed open-hearth steels at 1650°F in contrast to furnace cooling from 1650°F, each followed by straining and aging at temperatures ranging from 300° to 660°F, are presented by Enlund.³³ Both rimmed and killed steels remained ductile at room temperature after the normalizing treatment, but the rimmed steel was embrittled at room temperature after slow cooling while the aluminum-killed steel remained ductile. A determination of the shift in transition temperatures due to aging would have been more illuminating, but these results do illustrate the danger of comparing results obtained by use of different criteria of strain aging. Enlund concluded that aging properties of a steel are governed by the composition, prior heat treatment, and microstructure; slow cooling was detrimental to impact strength after aging. This author recommended that a quench-and-temper treatment be given to mild steels to prevent brittleness due to aging. The change in stress required to cause plastic flow, as used in the present investigation, is more suitable for determination of changes occurring within ferrite than is the impact test, which is very sensitive to changes in ferrite grain size and carbide distribution. Prior heat treatment may influence formation of nitrides, ferrite grain size, and carbide distribution, but in Enlund's work, effects produced

by combination of nitrogen may have been completely masked by gross microstructural changes.

Good qualitative correspondence between strain-aging effects as measured by the tensile test and the Charpy notch-impact test were reported by Felmley, Hartbower, and Pellini.³ These investigators used four steels; rimmed, silicon-killed, aluminum-silicon-killed, and titanium-vanadium-silicon-killed. Specimens were normalized at 1650°F, then reheated to 1200°F and either furnace-cooled or brine-quenched. Only the rimmed and silicon-killed steels strain aged when furnace cooled from 1200°F, as indicated by the tensile test data, and only these two steels showed marked increases in transition temperature. When the steels were brine quenched from 1200°F, all four showed pronounced strain aging by both the tensile and impact criteria. These results are in general agreement with results of this investigation. The experimental procedures of Felmley, et al., were less likely to produce large changes in microstructure, so their results are more nearly a measure of the strain-aging effects than are those of Enlund, who necessarily measured the effect of gross changes in the microstructure on the impact properties, as well as strain-aging effects.

Daniloff, Mehl, and Herty,³⁴ using impact data obtained on normalized steels, concluded that the more thorough the deoxidation of the steel, the less was the tendency to strain age.

Comstock and Lewis³⁵ reported that strain-aging embrittlement can be prevented by titanium deoxidation as well as by aluminum deoxidation, and that susceptibility to strain aging depended, in part, upon prior heat treatment.

Summary and Conclusions

The effect of composition, heat treatment, and aging conditions on strain aging were determined, using specimens taken from two low-carbon open-hearth heats, one of which was silicon-killed, the other made to rimming practice. A graded series of aluminum additions was made to ingots of both heats (Table I). Tensile test specimens from bars rolled from these ingots were heat-treated, machined, strained 4 pct, or through the yield point elongation, whichever was greater, then aged and pulled to fracture. The extent of strain aging was measured by the increase in yield strength after aging and expressed in percent. The conclusions reached are based upon use of this criterion and caution should be exercised in predicting results to be expected by use of other measures of strain aging, such as behavior in the notch-impact test. The results obtained are in agreement with those reported in recent investigations.

The conclusions are as follows:

1—Strain aging of commercial steels is primarily due to nitrogen in solution in ferrite; deoxidation with silicon and aluminum affects strain aging principally through formation of nitrides and removal of nitrogen from solution in ferrite. Carbon is a secondary cause of strain aging and for this reason, aluminum or silicon-killed steels cannot be completely "nonaging" under all conditions. When high aging temperatures are used, carbon will cause strain aging even in steels completely killed with aluminum and silicon. To produce a steel which will show no strain-aging effects would require the addition of elements which reduce the solubility of both carbon and nitrogen in ferrite to a very low level.

2—The strain aging of killed steels is governed by prior heat treatment. The heat treatments which reduce subsequent strain aging are those which promote complete precipitation of nitrides. For aluminum-killed or aluminum-silicon-killed steels, slow cooling from the hot rolling temperature is effective. For silicon-killed steels, extended treatment in the neighborhood of 1100°F is required, preferably followed by slow cooling. Conversely, killed steels can be made susceptible to strain aging by rapid cooling, which retains nitrogen and carbon in solution in ferrite. The usual types of rimmed steel strain age regardless of heat treatment because they do not contain elements which form stable carbides and nitrides.

3—To reduce strain aging of commercial steels to a low level, it is necessary to reduce nitrogen in solution in ferrite to a very low concentration, in the neighborhood of 0.0001 pct.

4—Nitrogen is more effective than carbon in producing strain aging because of its greater solubility in ferrite at low temperatures. When solubility of carbon in ferrite is increased by high aging temperatures, strain aging is produced even when nitrogen has been completely removed from solution.

5—Strain aging may be reduced by deoxidation with either aluminum or silicon, followed by the proper heat treatment. Because of the more rapid formation of aluminum nitride (AlN) and its greater range of stability as compared with silicon nitride (Si₃N₄), deoxidation with aluminum is more effective than deoxidation with silicon. For reasons which are not entirely clear, deoxidation with silicon and aluminum is much more effective in preventing strain aging than deoxidation with either alone.

Acknowledgments

The authors wish to thank W. B. Seens and W. L. Jensen for their aid in conducting the tensile tests. Chemical analyses were performed by G. W. Mommeyer and Mrs. Irene Christmas. Spectrographic analyses were done at Gary Steel Works. We are indebted to several members of the staff for helpful suggestions and discussion, in particular, to G. V. Smith, F. Garofalo, and L. S. Darken.

References

- ¹ G. Sachs: Strain Aging Criteria. *Iron Age* (May 13, 1948) **161**, p. 79.
- ² E. S. Davenport and E. C. Bain: The Aging of Steel. *Trans. ASM* (1935) **23**, p. 1047.
- ³ C. R. Felmley, C. E. Hartbower, and W. S. Pellini: Effect of Cooling Rate on the Aging Characteristics of Structural Steels. Advance Copy, A.W.S. (1951).
- ⁴ J. R. Low, Jr. and M. Gensamer: Aging and the Yield Point in Steel. *Trans. AIME* (1944) **158**, p. 207.
- ⁵ H. Schwartzbart and J. R. Low, Jr.: The Yielding and Strain-Aging of Carburized and Nitrided Single Crystals of Iron. *Trans. AIME* (1949) **185**, p. 637; *JOURNAL OF METALS* (September 1949).
- ⁶ L. S. Darken, R. P. Smith, and E. W. Filer: Solubility of Gaseous Nitrogen in Gamma Iron and the Effect of Alloying Constituents—Aluminum Nitride Precipitation. *Trans. AIME* (1951) **191**, p. 1174; *JOURNAL OF METALS* (December 1951).
- ⁷ W. C. Leslie, R. L. Rickett, C. L. Dotson, and C. S. Walton: Solution and Precipitation of Aluminum Nitride in Relation to the Structure of Aluminum-Killed Low-Carbon Steels. To be published.
- ⁸ W. C. Leslie, K. G. Carroll, and R. M. Fisher: Diffraction Patterns and Crystal Structure of Si₃N₄ and Ge₃N₄. *Trans. AIME* (1952) **194**, p. 204; *JOURNAL OF METALS* (February 1952).
- ⁹ H. F. Beeghly: Determination of Aluminum Nitride Nitrogen in Steel. *Analytical Chemistry* (1949) **21**, p. 1513.
- ¹⁰ H. F. Beeghly: Behavior of Nitrogen and some of its Compounds in Steel. *Analytical Chemistry* (1952) **24**, p. 1095.
- ¹¹ J. D. Fast: Ageing of Iron and Steel. *Iron and Coal Trades Review* (1950) **160**, p. 837.
- ¹² A. H. Cottrell and A. T. Churchman: The Change of Electrical Resistance During the Strain Ageing of Iron. *Journal Iron and Steel Inst.* (1949) **162**, p. 271.
- ¹³ S. Harper: Precipitation of C and N in Cold Worked Alpha Iron. *Physical Review* (1951) **83**, p. 708.
- ¹⁴ A. N. Holden: The Yielding Behavior of Iron Single Crystals. *Journal of Applied Physics* (1951) **22**, p. 1290.
- ¹⁵ A. H. Cottrell: Effect of Solute Atoms on the Behavior of Dislocations. *Report on Conference on Strength of Solids*. The Physical Society, London (1948).
- ¹⁶ A. H. Cottrell and B. A. Bilby: Dislocation Theory of Yielding and Strain Ageing of Iron. *Proc. Phys. Soc., London* (1949) **62A**, p. 49.
- ¹⁷ A. H. Cottrell: The Yield Point in Single Crystal and Polycrystalline Metals. *Symposium on Plastic Deformation of Crystalline Solids*. (May 1950) p. 60. Pittsburgh. Mellon Institute.
- ¹⁸ F. Seitz and T. A. Read: Theory of the Plastic Properties of Solids. II. *Journal of Applied Physics* (1941) **12**, p. 170.
- ¹⁹ C. A. Wert: Diffusion Coefficient of Carbon in Alpha Iron. *Physical Review* (1950) Series 2, **79**, p. 601.
- ²⁰ J. K. Stanley: The Diffusion and Solubility of Carbon in Alpha Iron. *Trans. AIME* (1949) **185**, p. 752; *JOURNAL OF METALS* (October 1949).
- ²¹ C. A. Wert: Measurements on the Diffusion of Interstitial Atoms in B.C.C. Lattices. *Journal of Applied Physics* (1950) **21**, p. 1196.
- ²² C. A. Wert: Solid Solubility of Cementite in Alpha Iron. *Trans. AIME* (1950) **188**, p. 1243.
- ²³ R. P. Smith: Equilibrium of Iron-Carbon Alloys with Mixtures of CO/CO₂ and CH₄/H₂. *Journal ACS* (1946) **68**, p. 1163.
- ²⁴ L. J. Dijkstra: Precipitation Phenomena in the Solid Solutions of Nitrogen and Carbon in Alpha Iron below the Eutectoid Temperature. *Trans. AIME* (1949) **185**, p. 252; *JOURNAL OF METALS* (March 1949).
- ²⁵ A. H. Cottrell and A. T. Churchman: Discussion on Homogeneous Yielding of Carburized and Nitrided Single Iron Crystals. *Trans. AIME* (1949) **185**, p. 877; *JOURNAL OF METALS* (November 1949).
- ²⁶ C. A. Edwards, H. N. Jones, and B. Walters: A Study of Strain-Age-Hardening of Mild Steel. *Journal Iron and Steel Inst.* (1939) **139**, p. 341.
- ²⁷ C. A. Edwards, D. L. Phillips, and H. N. Jones: The Influence of Some Special Elements Upon the Strain-Ageing and Yield Point Characteristics of Low-Carbon Steels. *Journal Iron and Steel Inst.* (1940) **142**, p. 199.
- ²⁸ *Metals Handbook*. (1948) p. 1161. Cleveland. ASM.
- ²⁹ F. R. Morral: The Constitution of Iron-Rich Fe-Al-C Alloys. *Journal Iron and Steel Inst.* (1934) **130**, p. 419.
- ³⁰ K. Löhberg and W. Schmidt: Die Eisenecke des Systems Eisen-Aluminium-Kohlenstoff. *Archiv. Eisenhüttenw.* (1938) **12**, p. 607.
- ³¹ A. Hayes and R. O. Griffis: U. S. Patent 2,069,758 (1937).
- ³² C. L. Altenburger: The Metallurgy of Cold Reduced Sheets. *Yearbook Amer. Iron and Steel Inst.* (1947) p. 459.
- ³³ B. D. Enlund: The Aging of Steel. *Jernkontorets Annaler* (1946) **130**, p. 553; *Engineering Digest* (1947) **4**, p. 61.
- ³⁴ B. N. Daniloff, R. F. Mehl, and C. H. Herty, Jr.: The Influence of Deoxidation on the Aging of Mild Steels. *Trans. ASM* (1936) **24**, p. 595.
- ³⁵ G. F. Comstock and J. R. Lewis: A Comparison of Aluminum and Titanium Deoxidation for Preventing Strain Aging Embrittlement in Low Carbon Steel. *Trans. ASM* (1945) **34**, p. 425.

Some Properties of Columbium Containing Nitrogen

by Choh-Yi Ang and C. Wert

Quench aging of supersaturated solid solutions of nitrogen in columbium takes place in reasonable times in the temperature range 300° to 500°C. Changes in internal friction, hardness, and electrical resistivity are found to accompany this change.

THERE is practically no detailed information in the literature concerning interstitial solid solutions in either columbium or tantalum. The fact that both of these metals are used extensively commercially in both pure and alloyed states makes studies of their properties of value. While the plan is to study both these metals and their alloys extensively, so far only a small number of measurements have been made. This paper presents data obtained in the initial investigations of columbium.

The principal interstitial impurities of columbium are likely to be hydrogen, carbon, oxygen, and nitrogen. The first of these, hydrogen, is outside the scope of internal friction measurements at present and nothing quantitative is known about the initial hydrogen content of the specimens. However, it is believed that it is completely absent after the preliminary heat treatments are carried out. The carbon content of the original samples is low and can be reduced still further during sample preparation. Oxygen is normally present to some extent in columbium and can also be added or removed easily. Nitrogen is also normally present in small amounts and can also be controlled within limits.

Since it is not possible yet to remove all the nitrogen from columbium and since it is possible to remove essentially all the oxygen and carbon, initial measurements were made on the alloy system nitrogen in columbium. In this sense then, the alloys are true binary alloys. Little is known about the effects of nitrogen on the physical and metallurgical properties of columbium, so it was necessary to perform some rather elementary measurements on the specimens. These measurements are described briefly in the next section and are discussed in detail in later sections.

Scope of the Work

That internal friction is associated with diffusion of nitrogen in columbium has been known for some time. It is similar in nature to that for carbon and nitrogen in α -iron. In these latter cases, the information obtained from internal friction has been useful metallurgically,¹ and it is not too much to expect useful information from similar studies on columbium containing nitrogen. The technique of internal friction measurements is adequately described by Kê.²

At a frequency of 1 cps the internal friction peak for nitrogen in columbium occurs at 300°C and that for oxygen at 160°C.³ So that all the measurements will be meaningful metallurgically, the internal friction has been calibrated by making a measurement of the damping at the two peaks and a measurement of oxygen and nitrogen content by chemical analysis. A comparison of the two gives the following calibration factor: To go from damping capacity expressed in terms of $1/Q$ to weight percent of oxygen and nitrogen in solid solution in columbium, multiply the peak values of internal friction by about 4 and 3 respectively.* Data from

* The gas analyses were made for us by the National Research Corp.

which these factors were calculated are presented in Table I.

The increase of electrical resistance of columbium caused by the addition of oxygen and nitrogen as interstitial impurities has been quantitatively determined. At room temperature the percentage increase is small for small additions of impurities (<0.1 wt pct); as the temperature is lowered it becomes an increasingly larger factor of the total resistance. An empirical relation has been established to express the resistivity at -195°C in terms of weight percent of oxygen and nitrogen in solid solution.

It is easy to make supersaturated solid solutions of nitrogen in columbium and to observe aging phenomena. The optimum aging temperature, as in the case for carbon and nitrogen in α -iron, occurs at the temperature for which the time necessary for a single place-change in diffusion is about 1 to 10 millisecc. This means for nitrogen in columbium that significant property changes should take place for this alloy at about 400° to 500°C in reasonable time intervals. Results of such aging experiments are

CHOH-YI ANG is Graduate Research Assistant, and C. WERT is Research Associate Professor, Dept. of Mining and Metallurgical Engineering, University of Illinois, Urbana, Ill.

Discussion on this paper, TP 3534E, may be sent, 2 copies, to AIME by Dec. 1, 1953. Manuscript, Nov. 21, 1952. Cleveland Meeting, October 1953.

This work was supported in part by the Office of Ordnance Research.

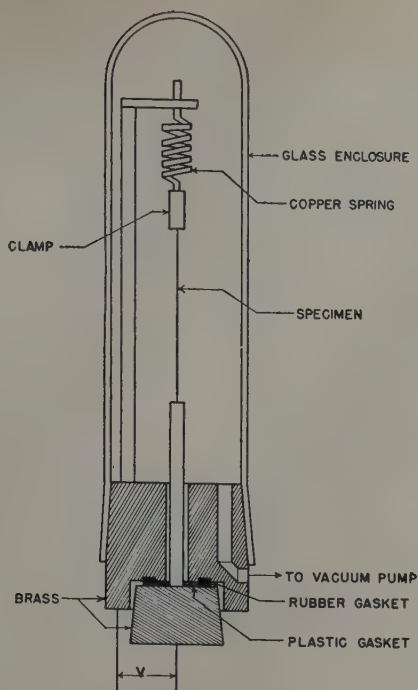


Fig. 1—Heat treatment apparatus.

presented. They show that: 1—The internal friction decreases with the time of aging. 2—The level to which the internal friction falls upon prolonged aging is a function of the temperature of aging. Utilization of this fact made it possible to calculate solid solubility as a function of temperature. 3—The electrical resistance at -195°C decreases during aging. 4—The hardness decreases during aging. This was at first somewhat unexpected, but has been verified by measurements on about eight samples aged at various temperatures.

Method of Purifying and Nitriding Columbium

For meaningful measurements to be made, it was necessary to have as nearly ideal binary alloys as possible. This meant that the interstitial impurities carbon and oxygen had to be eliminated. Furthermore, it was necessary to know that whatever nitrogen was introduced went into solid solution. A method of heat treatment was devised to do these things simultaneously. The method is a three-step process: 1—The sample is purified by heating it at

serves as a heating element. This apparatus is illustrated in Fig. 1. A pyrex glass envelope encloses a wire specimen and heavy current leads. A current of some 25 to 75 amp is passed through the wire. Expansion is allowed by use of a copper spring under light tension. An associated vacuum system and gas storage and transfer system completes the apparatus.

The first operation is that of freeing the original material from its initial charge of nitrogen, oxygen, and carbon (these impurities are present in a typical specimen to about 0.05 wt pct N_2 , 0.1 wt pct O_2 , and a smaller but unknown amount of carbon†).

† The carbon peak in columbium has so far been rather elusive. It is believed that it exists at about 140°C at 1 cps. Thus it can easily be masked by the oxygen peak at 160°C when both carbon and oxygen are present together. The difficulty of preparing a sample containing a small amount of carbon and no oxygen has prevented quantitative measurement of the carbon content.

This was done by heating a 30 mil wire specimen in vacuum at 2000°C or above for some 5 min. This operation cleans the surface of the wire, straightens it, and reduces the impurity content to less than 0.002 pct C, 0.002 pct O_2 , and 0.007 pct N_2 . (With the exception of Table I, all values of carbon, oxygen, and nitrogen content quoted in this paper were measured or estimated from internal friction measurements.)

At this time the specimen is nitrided in half an atmosphere of either NH_3 or N_2 at about 1500°C . The time necessary for this operation is from 5 to 30 min, depending somewhat on the amount of nitrogen desired in the sample. No attempt was made to observe any difference in the rate of nitriding with the two gases; nor was an attempt made to observe the rate of nitriding as a function of temperature or gas pressure. Because of the ease with which absorbed oxygen can be removed from columbium, no serious attention was paid at this time to keep the oxygen at a very low level. The oxygen was removed and any nitrogen which may have precipitated at 1500°C put into solid solution by heating the specimen to 2000°C or higher in a vacuum of 10^{-5} mm Hg for a few minutes.

The temperatures cited above were all measured with an optical pyrometer and were corrected for the emissivity of columbium. Since deviations of 100° or more from the ones finally used make little difference in the final product, systematic errors in temperature measurement are of no significance. Furthermore, because of conduction of heat from the wire to the grips, it was clear that the specimens were not heated uniformly. Since the largest part of the heat loss is by radiation, however, the central section of the wire was essentially uniform in temperature to within approximately 100° . The ex-

Table I. Data Used to Obtain Multiplying Factors to Go from Peak Value of Internal Friction to Wt Pct N_2 and O_2 in Solid Solution

Specimen	N_2 , Wt Pct	O_2 , Wt Pct	Q^{-1} Peak	Multiplying Factor
1	0.051	—	0.0180	2.8
2	0.063	—	0.0211	3.0
3	0.021	—	0.0068	3.1
4	—	0.037	0.0095	3.9
5	—	0.032	0.0072	4.4
6	—	0.030	0.0076	4.0
7	—	0.059	0.0143	4.1

2000°C in a vacuum of about 10^{-5} mm Hg. 2—Next it is nitrided at about 1500°C . 3—Finally the specimen is reheated to 2000°C or above in the high vacuum again for several minutes, then cooled rapidly.

Because of the high temperatures involved, a furnace was constructed in which the specimen itself

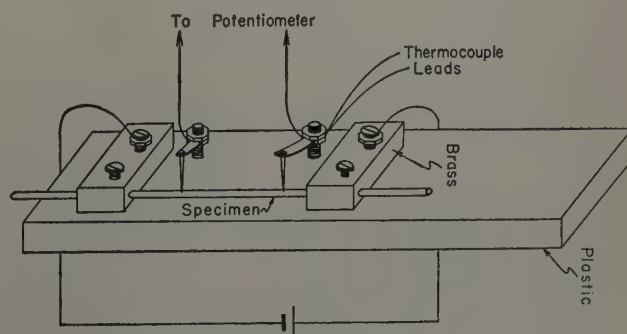


Fig. 2—Specimen holder for electrical resistance measurement.

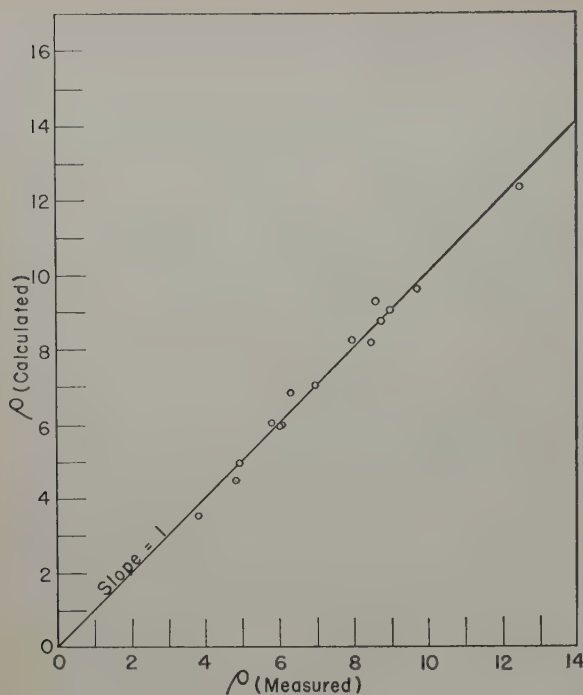


Fig. 3— ρ calculated vs ρ measured.

treme ends of the specimen, which were clearly much colder than the middle, were cut off before further measurements were made.

Electrical Resistance

The electrical resistance of a metal (except possibly in very special cases) increases upon the addition of impurities. This contribution to the resistance is virtually temperature independent. Accurate measurement of the impurity contribution at room temperature is difficult because superimposed upon it is the resistance due to thermal motion. For relatively small impurity additions, indeed, the thermal contribution may almost hide that caused by impurities. By making measurements at low temperature, however, the total resistance can be reduced while the impurity contribution is kept constant. For example, at room temperature, adding 0.05 pct N_2 in columbium causes a change in resistance of about 15 pct, whereas at -195°C , it causes a change in resistance of nearly 100 pct.

The effect on electrical resistivity of varying amounts of oxygen and nitrogen in solid solution

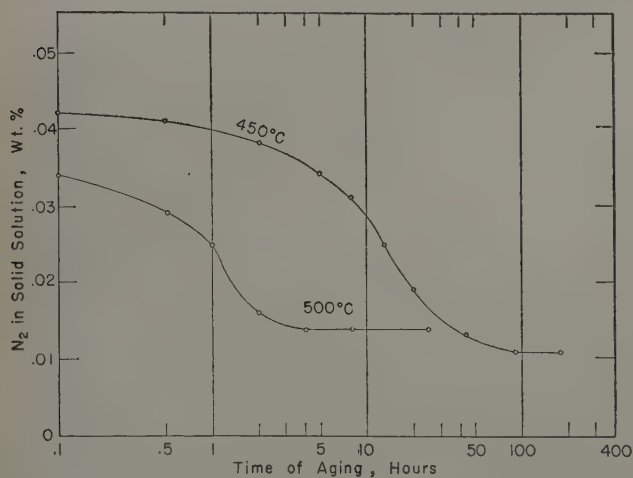


Fig. 4—Aging curves for nitrogen in solid solution in columbium.

has been measured quantitatively. Measurement by adding each of these elements in the absence of the other was attempted, but it was not possible to completely eliminate either. The total resistance of the specimen when both were present was then presumed to obey the linear equation

$$\rho_{\text{total}} = \rho_{\text{Cb}} + A \times (\text{wt pct } N_2) + B \times (\text{wt pct } O_2)$$

To find the constants A , B , and ρ_{Cb} it was necessary only to prepare three samples of varying oxygen and nitrogen content, measure their resistivities, and solve the three equations simultaneously for these constants. Additional samples served to check these calculations. The amount of nitrogen and oxygen present in each case was determined by internal friction measurements.

The resistance of a sample was measured by determining the potential drop across a sample when a known current is passed through it. The apparatus in which the specimen was mounted is shown in Fig. 2; it is immersed directly into liquid nitrogen for the measurement. Heavy current leads supply about 1 amp of current to the specimen; spring loaded potential leads are connected to a type K potentiometer. A second potentiometer measures the electromotive force across a standard resistor. From these two measurements of emf, together with knowledge of the resistance of the standard resistor, the resistance of the sample is readily calculated. Measurement of the wire cross section and specimen length complete the data necessary to calculate the resistivity.

The values of ρ_{Cb} , A , and B calculated from measurements on three selected samples give for ρ_{total} (in microhm cm) the equation

$$\rho_{(-195^\circ\text{C})} = 3 + 55 \times (\text{wt pct } N_2) + 47 \times (\text{wt pct } O_2) \quad [1]$$

A plot of ρ calculated using Eq. 1 against that value of ρ measured for all the samples is presented in Fig. 3.

At this time, these values of A and B cannot be interpreted in terms of the nature of the nitrogen or oxygen ion in columbium. When similar data are obtained for the effect of nitrogen and oxygen in other metals, it may then be possible to infer significant facts about these ions.

Aging Experiments and Solid Solubility

Many physical changes have been observed to take place in alloys upon aging, and the alloy nitro-

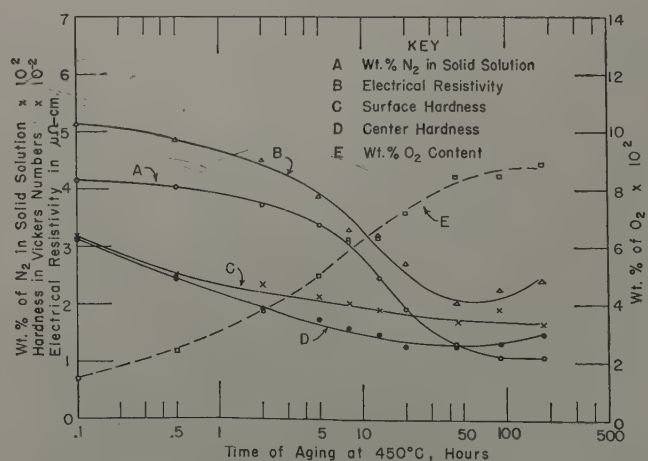


Fig. 5—Affect of aging in columbium containing nitrogen and oxygen.

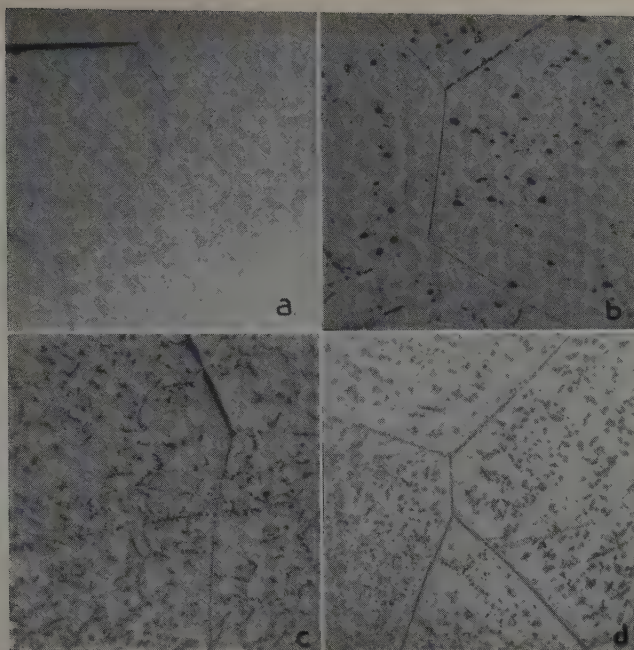


Fig. 6—Precipitation of nitrogen from solid solution in columbium during aging at 450°C. Swabbed 20 sec with 90 pct HNO₃ (70 pct) + 10 pct HF (50 pct) at 80°C. X250.

a—As quenched. c—Aged 44 hr.
b—Aged 5 hr. d—Aged 178 hr.

gen in columbium is no exception. A number of specimens of columbium were prepared containing about 0.04 pct N₂ in solid solution and aging experiments were carried out with them in the temperature range 300° to 500°C. Aging was carried out in a vacuum of about 10⁻⁴ mm Hg. Measurements were made of decrease in internal friction, decrease in electrical resistance, and change in hardness upon aging.

Serious attempts were made to keep the oxygen content low during the entire process. These efforts were not wholly successful. It was possible to produce specimens having fairly low oxygen content originally (<0.02 wt pct). During aging at elevated temperatures, however, it was not possible to prevent further oxygen pickup. The oxygen content of the specimens was estimated to have increased a few hundredths weight percent upon prolonged aging. The increased damping due to this oxygen in solid solution can be measured easily, but it is not easy to accurately express this increased damping in terms of weight percent oxygen. Fundamentally, this comes about because such absorbed oxygen will not be distributed uniformly radially. The calibration factor ($4 \times 1/Q = \text{wt pct O}_2$) is not directly applicable since it is based upon a uniform solid solution of oxygen in columbium. If this calibration factor of 4 is used for this nonuniform distribution of oxygen (as is done in the plot of Fig. 5), such calculation probably overestimates the average oxygen content by a factor of 2 or more.

The amount of nitrogen in solid solution at any time was determined by the height of the relaxation peak at that time. Since the internal friction was calibrated directly in terms of nitrogen content, the amount of nitrogen in solid solution can be plotted as a function of time of aging. This is shown for two aging temperatures in Fig. 4.

A certain amount of nitrogen in solid solution does not have the same effect on electrical resis-

tance as does that amount of nitrogen in the form of a nitride. Hence, a change in electrical resistance during aging might be expected. A change is observed and it is presented in Fig. 5. In this figure, curve A shows the nitrogen in solution as a function of time. Curve E is the approximate oxygen content vs time. B shows the change in electrical resistivity upon aging. These values are corrected point by point for the contribution to resistance due to oxygen content using curve E and the value 47 in Eq. 1. Because the oxygen content was measured only approximately, the corrections are not highly accurate. It should be emphasized, however, that even without any correction, the measured resistivity decreases steadily during aging and rises only at the end when the nitrogen has essentially reached an equilibrium division between solid solution and precipitate.

At intervals during aging small sections of the specimens were cut off. Hardness measurements were made on these sections. Surface hardness readings in Vickers numbers were taken on these sections mounted in bakelite before they were polished. After the samples were polished and etched the center hardness readings were made. These two sets of data plotted against aging time in Fig. 5 show that aging in this alloy is a softening process. It is worth noting that the surface and center hardness values are the same for the as-quenched samples and for the samples taken early in the aging process. This indicates that the method of heat treatment did result in an even distribution of nitrogen and oxygen radially in the sample. That curves C and D branch apart during aging is presumably caused by oxygen pickup at the surface of the specimen during aging. Diffusion of this new oxygen into the center is slow at this temperature, hence an oxygen-enriched case exists initially. This case extends gradually into the center of the sample so that near the end curves C and D approach each other. Although oxygen appears not to have too great an effect on the hardness† of columbium, brit-

† Several specimens, containing less than 0.01 pct N₂ and from 0.01 to 0.10 pct O₂, show an increase in hardness from 86 to 122 VHN.

tleness was evident in wire specimens which had been purposely highly oxidized.

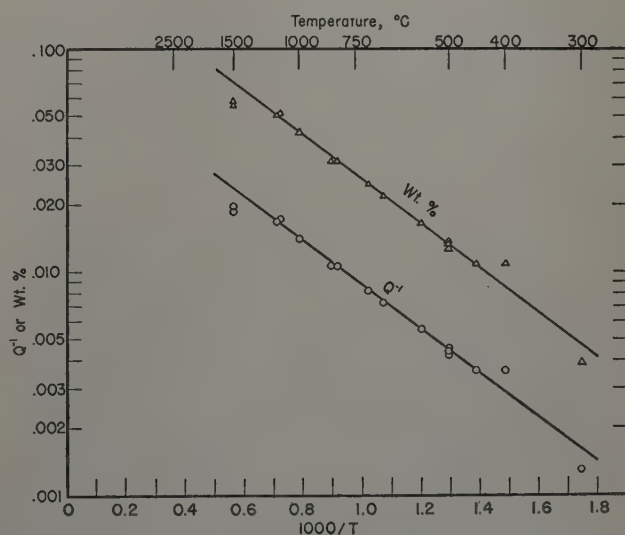


Fig. 7—Solid solubility of nitrogen in columbium as a function of temperature.

Metallographic examination of the specimen at various stages of aging at 450°C showed that the amount of precipitate increased as aging progressed. This finding substantiates the result of internal friction measurements, which show that the amount of nitrogen in solid solution decreased with time of aging. Fig. 6a shows the as-quenched specimen with practically no evidence of precipitation, whereas b, c, and d represent respectively the microstructures at the end of 5, 44, and 178 hr of aging and reveal the increasing amount of precipitate.

The final level of internal friction during prolonged aging is markedly dependent on the temperature of aging. This gives a method of finding the solid solubility in equilibrium with the nitride as a function of temperature. Fig. 7 shows the equilibrium value of internal friction at 300°C as a function of temperature of aging and the curve cal-

culated from these data using the multiplying factor of 3 quoted above. The heat of solution calculated from this curve is 4600 cal per mol. The equation for this curve over the temperature range 300° to 1200°C is

$$C = 1.7e^{-4600/RT} \quad [2]$$

where C is expressed in atomic pct N_2 . The factor 1.7 is only as accurate as the multiplying factor taken from Table I.

References

¹C. Wert: Phenomena Accompanying Precipitation from Solid Solutions of C and N in Alpha-Iron. *Thermodynamics in Physical Metallurgy* (1950) pp. 178-200. Cleveland. ASM.

²T. S. Kê: Experimental Evidence of the Viscous Behavior of Grain Boundaries in Metals. *Physical Review* (1947) **71**, p. 533.

³C. Ang: Diffusion of O_2 and N_2 in Nb and Ta. *Acta Metallurgica* (1953) **1**, p. 123.

Technical Note

Plastic Bending of Zinc Crystals

by G. P. Conard II, B. L. Averbach, and Morris Cohen

IT has been frequently observed that, when metal crystals are bent and annealed or when they are bent at elevated temperatures, the asterism of the Laue spots is split discontinuously into tiny intensity maxima. This finding indicates that segmented crystallites or subgrains are produced, which are relatively undistorted within themselves but which differ slightly in orientation from their neighbors.

The following viewpoints have been put forward concerning the nature of this segmentation process: 1—Crussard¹ has described the phenomenon as "recrystallization in situ." According to this mechanism, the deformed lattice recrystallizes on heating into an aggregate of comparatively strain-free subgrains separated from one another by low-angle boundaries and having nearly the same orientation as the original crystal. This process differs from the classical type of recrystallization in that the latter involves the formation of grains having quite different orientations from that of the mother crystal. 2—A similar but more detailed picture has been advanced by Cahn² who adopted the term "polygonization." In this interpretation, the plastic bending of lattice planes results in an excess of dislocations of one sign, but at suitable temperatures these dislocations migrate along slip planes and collect in localized

regions to form an array of low-angle boundaries. Concurrently, the lattice segments between the boundaries lose their curvature and elastic strain. 3—The "cell formation" concept of Wood and co-workers,³ unlike the two hypotheses cited, postulates that the segmentation of the lattice is basically a mode of deformation and is not an annealing phenomenon. Cell formation appears to compete more effectively with respect to the normal slip process as the deformation temperature is increased and as the strain rate is decreased.

The present work was performed on 3.2 mm diameter 99.99+ pct Zn single crystals, grown from the melt in a gradient furnace. The major impurity was 0.003 pct Fe. The crystal orientations ranged from those with basal plane parallel to the rod axis to those with the basal plane almost perpendicular to the rod axis. The specimens were bent on templates to effective radii varying from 14.2 to 1.3 cm at the temperatures from -196° to 100°C. In each case, the axis of bending was parallel to the basal plane. Subsequent annealing was carried out at temperatures from -196° to 400°C.

Back-reflection Laue pictures were taken on the convex surface of the bent specimens, before and after annealing. This procedure was found to yield better resolution of the detail in the diffraction spots than did the previously used Laue transmission technique. Some X-ray pictures of rods bent at -196° and -78°C were taken at these respective temperatures without intermediate warming to room temperature. In addition, bent crystals were acid cut⁴ parallel to the basal plane, and double-crystal spectrometer rocking-curves were obtained from the etched (0001) face before and after increment an-

G. P. CONARD II is associated with the Dept. of Metallurgical Engineering, Lehigh University, Bethlehem, Pa., and B. L. AVERBACH, Junior Member AIME, and M. COHEN, Member AIME, are Assistant Professor and Professor, respectively, Dept. of Metallurgy, Massachusetts Institute of Technology, Cambridge, Mass.

TN 163E. Manuscript, Feb. 25, 1953.

This paper is based on a thesis by G. P. Conard II submitted in partial fulfillment of the requirements for the degree of Doctor of Science to the Massachusetts Institute of Technology, June 1952.

neals up to 60 hr at 400°C, with the (0001) face of an undeformed zinc crystal serving as the analyzing crystal. Laue back-reflection pictures were also taken under these conditions.

The experiments clearly demonstrated that the bending deformation produced discontinuous asterism streaks in the Laue back-reflection pictures, thus denoting a segmentation of the lattice into units of slightly differing orientation. This phenomenon was observed most commonly in specimens bent to effective radii between 8.5 and 2.4 cm. For larger radii, the bending deformation was evidently too small to yield much segmentation, whereas for radii less than 2.4 cm the severe deformation probably resulted in segmentation on too fine a scale to be resolved by the Laue technique employed here.

The occurrence of segmentation due to bending was rather insensitive to the temperature of deformation within the range investigated. It could be detected in specimens bent and X-rayed at -196°C in addition to those bent at -78° and at 100°C. These findings suggest that the crystal segments form as a part of the deformation process and do not require thermal activation for their origin, although (as will be pointed out) annealing may make it easier to detect the fine structure in the Laue spots.

In cases where the crystal orientation was such that the bending could readily cause slip in the standard $[2\bar{1}10]$ direction on the (0001) plane, the intensity maxima in the asterism streaks showed that boundaries of the segmented units corresponded to $(2\bar{1}10)$ planes; that is, the boundaries lay perpendicular to the slip plane and slip direction. The angular difference between adjacent segments varied widely, but was roughly of the order of 10 to 30 min about the $[01\bar{1}0]$ direction lying closest to the bending axis. When the conditions of deformation became complicated so that identification of the active slip system was no longer possible (for example, if the specimen inadvertently spiraled during the bending), the segmentation behavior became complex and seemed to vary in an unpredictable manner. Evidence of cross segmentation was found.

The rocking-curve for an annealed, undeformed zinc crystal showed a sharp (0001) reflection of about 6 min in half-width; but after the specimen was bent to a 1.3 cm radius at room temperature, this reflection broadened into a multi-peaked curve of about 2° in overall half-width. The numerous intensity maxima disclosed the existence of segmentation even though it was not resolved by the Laue method in this case. After the bent crystal was annealed for 5 hr at 400°C, the peaks sharpened because of a reduction in background intensity, and the Laue streaks then revealed corresponding discontinuities in the asterism.

For a specimen bent to a 6.3 cm radius, the multiple peaks of the (0001) reflection in the rocking-curve occurred at angular intervals of about 10 min. During the first few hours of annealing at 400°C, these peaks became more clearly defined; they did not disappear or change in angular position. After annealing for more than 5 hr at 400°C, there was evidence that some minor peaks disappeared while others became sharper and more intense. However, even after 60 hr at 400°C, the structure remained highly segmented, while the sharpness of the individual peaks comprising the (0001) reflection and the intensity of the intervening background approached those of the original undeformed crystal.

More complete studies with the Laue method

showed that the sharpening of existing maxima in the asterism streaks on annealing increased with the annealing temperature and with the severity of the prior bending deformation. The bent crystals displayed little tendency to recrystallize in the conventional sense, except after rather complex bending followed by annealing at high temperatures.

The foregoing experiments demonstrate that zinc crystals do not undergo uniform bending, but deform in an heterogeneous manner on a fine scale to produce slightly disoriented lattice segments or subgrains, separated by boundaries in which most of the bending is concentrated. Such localized "buckling" has already been postulated by Jillson⁵ and by Hess and Barrett,⁶ and may turn out to be a basic mode of deformation. It provides the crystal lattice with a high degree of "plastic flexibility," and may be operative in a major way along the grain boundaries of polycrystalline aggregates where the deformation is quite complex. In any event, it must be emphasized that the segmentation occurs primarily during the deformation process. Possibly the moving dislocations of like sign tend to pile up at imperfections already present in the original crystal, thus tending to localize the bending deformation.

According to this picture, the subgrains themselves may be somewhat curved as a result of the deformation, but this lattice strain is minor compared to the concentrated bending at the subboundaries. During annealing, the lattice strain disappears as shown by the improved resolution of the maxima in the Laue spots due to the decrease in the background intensity between the maxima. It is visualized that this recovery process is achieved by the further concentration of dislocations at the subboundaries, in the manner suggested by Cahn,² although the main part of the "polygonization" (at least in zinc) now appears to take place during deformation prior to annealing.

With additional annealing, the subboundaries are capable of migration, thereby permitting subgrain growth to take place. These boundaries are particularly mobile under applied stress,⁷⁻⁹ and could readily lead to the cell formation observed by Wood³ and by Servi^{10, 11} under creep conditions.

Acknowledgments

The zinc used for the single crystals in this work was supplied by the Platt Brothers and Co. of Waterbury, Conn. D. C. Jillson, then of the New Jersey Zinc Co., furnished some of the zinc crystals that were used in the early stages of the program. This research is part of a program sponsored by the United States Atomic Energy Commission under Contract No. AT(30-1)-1002, Scope III.

References

- ¹ C. Crussard: Etude de Recuit de l'Aluminium. *Revue de Metallurgie* (1944) **41**, p. 111.
- ² R. W. Cahn: Internal Strains and Recrystallization. *Progress in Metal Physics* (1950) Vol. 2, Chapter 5, p. 151. London. Butterworths Scientific Publications.
- ³ W. A. Wood, G. R. Wilms, and W. A. Rachinger: Three Basic Stages in the Mechanism of Deformation of Metals at Different Temperatures and Strain Rates. *Journal Inst. Metals* (1951) **79**, p. 159.
- ⁴ R. Maddin and W. R. Asher: Apparatus for Cutting Metals Strain-Free. *Review of Scientific Instruments* (1950) **21**, p. 881.
- ⁵ D. C. Jillson: An Experimental Survey of Deformation and Annealing Processes in Zinc. *Trans. AIME* (1950) **188**, p. 1009; *JOURNAL OF METALS* (August 1950).

⁶ J. B. Hess and C. S. Barrett: Structure and Nature of Kink Bands in Zinc. *Trans. AIME* (1949) **185**, p. 599; *JOURNAL OF METALS* (September 1949).

⁷ W. A. Wood and R. F. Scrutton: Mechanism of Primary Creep in Metals. *Journal Inst. Metals* (1950) **77**, p. 423.

⁸ J. Hino, P. G. Shewmon, and P. A. Beck: Effect of Simultaneous Strain on Subgrain Growth. *Trans. AIME* (1952) **194**, p. 873; *JOURNAL OF METALS* (August 1952).

⁹ J. Washburn and E. R. Parker: Kinking in Zinc

Single-Crystal Tension Specimens. *Trans. AIME* (1952) **194**, p. 1076; *JOURNAL OF METALS* (October 1952).

¹⁰ I. S. Servi and N. J. Grant: Structure Observations of Aluminum Deformed in Creep at Elevated Temperatures. *Trans. AIME* (1951) **191**, p. 917; *JOURNAL OF METALS* (October 1951).

¹¹ I. S. Servi, J. T. Norton, and N. J. Grant: Some Observations of Subgrain Formation During Creep in High Purity Aluminum. *Trans. AIME* (1952) **197**, p. 965; *JOURNAL OF METALS* (September 1952).

Technical Note

Modifications of the Schulz Technique for The X-Ray Determination of Preferred Orientation in Rolled Metal

by M. L. Fuller and George Vaux

AN apparatus and procedure for the determination by X-ray reflection of preferred orientation of crystals in rolled metal with the Geiger counter X-ray spectrometer was described by Schulz.¹ This

¹ L. G. Schulz: *Journal of Applied Physics* (1949) **20**, pp. 1030-1033.

is an excellent procedure and we have used it continually for several years. In our use of the procedure, two modifications have been made and used during most of this period. One of these provides for automatic scanning and recording of the reflections, and the other makes possible the application of the procedure to coarse-grained specimens and permits measurement of almost all orientations without resort to the transmission technique.

The automatic scanning and recording are accomplished by a motor drive of the inner ring of the Schulz apparatus (see R_2 in Fig. 2 of his paper and R_2 in Fig. 1 of this note) in synchronism with the chart recorder of the North American Philips 90° X-ray spectrometer. A rate of 10° per min is used. A scan of 180° is obtained corresponding to poles on the stereographic projection whose locus is a great circle.

The modification for coarse-grained material is accomplished by allowing a larger area of the specimen to contribute to the X-ray diffraction. In the Schulz apparatus the incident X-ray beam is confined by a slit system to rays in the plane of the spectrometer. Schulz demonstrated that this restriction of the X-ray beam permits a survey of the X-ray reflections without correction up to about 80° on either side of that specimen position in which the specimen is perpendicular to the plane of the spectrometer. This is the angle ϕ of rotation of the inner ring R_2 . One of these slits is horizontal and extends across the X-ray source side of the specimen. In the modification this slit is removed, thus permitting greater divergence in the X-ray beam and the irradiation of a larger area of the specimen surface. Fig. 1 shows the apparatus with the motor drive and with the slit removed. Discontinuities in the recorded X-ray intensity plot due to the few

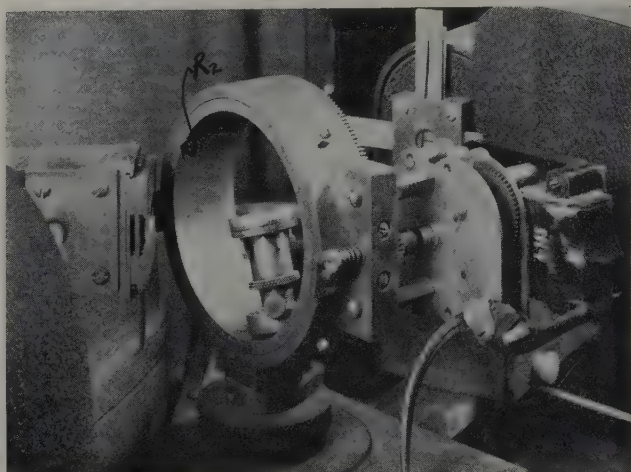


Fig. 1—Preferred orientation apparatus.

participating crystals in coarse-grained metal are much lessened. The increased divergence does not cause reflections from other crystal planes to enter the Geiger counter slit.

An important advantage of the original Schulz scheme is thus lost and a system for correction is required. To do this, a compact of atomized copper powder was prepared and tested by the original Schulz method for the absence of preferred orientation. The horizontal slit was then removed and a curve recorded showing the variation of intensity with angle ϕ . In our arrangement the intensity was uniform within the range ϕ equals $\pm 30^\circ$. Beyond this the intensity fell off rapidly reaching zero at $\pm 90^\circ$. The curve thus produced is then used to correct measurements made on preferred orientation specimens. In practice this is accomplished by constructing from this calibration curve a family of curves which, as a transparency, can be superimposed on the recorder chart to read corrected intensity directly. Not only does this method permit the handling of coarse-grained material but it also makes possible the plotting of intensities almost to the circumference of the stereographic pole figure projection. Thus, nearly the entire pole figure can be plotted without the necessity of using the transmission technique. Moreover, intensities are much greater, an advantage when surveying crystal planes of poor reflecting power.

M. L. FULLER, Member AIME, is associated with the Research Dept., The New Jersey Zinc Co. (of Pa.), Palmerton, Pa., and G. VAUX is at Bryn Mawr, Pa.
TN 170E. Manuscript, April 24, 1953.

Oxygen Activity in Iron Oxide Slags

by Hugo Larson and John Chipman

The ferrous and ferric oxide concentrations of slags, expressed as $j = \text{Fe}^{++}/(\text{Fe}^{+++} + \text{Fe}^{++})$, have been established through gas-slag equilibrium at 1550°C in a range of oxygen pressure of 10^{-1} to 10^{-9} atm. The value of j is increased by basic additions (BaO , CaO , MgO , MnO) and decreased by acidic oxides (SiO_2 and TiO_2). Oxygen pressure is shown graphically as a function of composition for slags which are analogous to those at the slag-gas interface of the open hearth furnace.

THE progress which has been made in recent years in understanding the chemistry of metallurgical slags has been based largely on studies of slag-metal and slag-gas equilibria. There is a considerable body of knowledge which is applicable to reactions occurring at the slag-metal interface in open hearth steelmaking. There is little information concerning reactions of the slag with the furnace atmosphere and hence little basis for an understanding of the transfer of oxygen, sulphur, or hydrogen between gas and slag.

The oxygen pressure of the open hearth atmosphere is normally of the order of 10^{-1} to 10^{-3} atm which differs by several orders of magnitude from that of about 10^{-9} atm at the slag-metal interface. The chemical properties of the slag, for example, the ratio of ferric to ferrous iron and the ability of the slag to hold sulphur in solution, are greatly affected by changes in oxygen pressure.

This investigation was undertaken to enlarge our knowledge of the effect of oxygen pressure on steel-making slags. Using air or controlled mixtures of CO and CO_2 a range of oxygen pressures from 10^{-1} to 10^{-7} was covered.

Review of the Literature

There are only a few references in the literature which pertain directly to this investigation. The most important is that of Darken and Gurry^{1, 2} on the system iron-oxygen. This work included the determination of the phase diagram of the system and also a study of the field of homogeneous melts and their oxygen pressures. Their apparatus and procedure were very similar to that used in this

study. Iron oxide was melted in a platinum crucible under an atmosphere of CO_2 :CO, CO_2 : H_2 , H_2O , CO_2 , air or O_2 depending upon the partial pressure of oxygen desired. After equilibrium was reached, the sample was quenched and analyzed for ferrous and ferric oxide. By appropriate calculations these authors were able to determine the oxygen and iron activities in the various slags, heats of formation of the oxides of iron, and heats of solution of iron and oxygen in the liquid slags.

In a subsequent paper³ the same authors made a less thorough investigation of the effects of additions of lime and manganese oxide on the composition of iron oxide melts. Only a few experiments were made and those in a narrower range of temperature and oxygen pressure.

Darken⁴ has investigated the fusion temperature of iron oxide in contact with silica under various atmospheres. He found that the temperature changes from 1120° to 1447°C as the gas composition changes from CO_2 /CO equal to 20.8 to pure oxygen.

A comprehensive paper by White⁵ predates the work of Darken and Gurry. The decomposition of ferric oxide into oxygen and lower oxides of iron was studied from 1000° to 1650°C and under oxygen pressures from 2 to 76 cm of mercury. The effect of

H. LARSON, Junior Member AIME, is Metallurgist, American Brake Shoe Co., Mahwah, N. J., and J. CHIPMAN, Member AIME, is Professor, Dept. of Metallurgy, Massachusetts Institute of Technology, Cambridge, Mass.

Discussion on this paper, TP 3586C, may be sent, 2 copies, to AIME by Nov. 1, 1953. Manuscript, April 11, 1953. Los Angeles Meeting, February 1953.

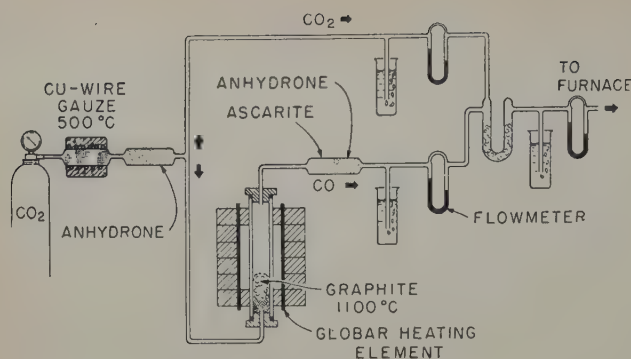


Fig. 1—Diagram of apparatus.

additions of lime and silica upon this reaction was also observed. The experimental procedure involved suspending a sample in a platinum crucible from one arm of an analytical balance. The proportions of ferrous and ferric oxides could be calculated by observing the weight loss caused by the reaction $\text{Fe}_2\text{O}_3 = 2\text{FeO} + \frac{1}{2}\text{O}_2$. Unfortunately iron dissolves in the crucible according to $\text{FeO} = \text{Fe (in Pt)} + \frac{1}{2}\text{O}_2$ which causes a permanent weight loss to the system. The method used to correct for this reaction appears rather unsatisfactory. The results seem consistent in themselves, but in the pure iron-oxygen system they do not agree very well with those of Darken and Gurry. Moreover, the effect of additions of lime and silica differs from the results of this investigation.

Krings and Schackmann⁶ have studied the same problem by a different procedure. They melted ferric oxide in an evacuated system and measured the oxygen pressure which resulted from its decomposition. Besides using pure ferric oxide they employed mixtures of lime and ferric oxide in the ratios 1:2, 1:1, and 2:1, and also silica and ferric oxide in a 1:1 ratio. The temperatures employed were 1550°, 1575°, and 1600°C. Their results for pure ferric oxide agree with those of Darken and Gurry better than do those of White. However, in the system lime:ferric oxide their results deviate considerably from those of both Darken and Gurry and of this investigation.

Analogous methods of slag-gas equilibria have been employed by Schuhmann and Ensio⁷ and by Michal and Schuhmann⁸ in studies of the thermodynamic properties of iron silicate slags.

The work of Feters and Chipman⁹ provided data at oxygen pressures corresponding to equilibrium with molten iron and served to fix the relation between slag composition and oxygen content of the metal. Their data, together with later studies of Taylor and Chipman¹⁰ and Winkler and Chipman¹¹ and earlier work of Körber and Oelsen¹² provide a fairly comprehensive picture of the oxygen activity in slags which are in equilibrium with molten iron.

Experimental Method

The experimental procedure followed in these experiments is very similar to that described by Darken and Gurry.² The method of controlling the oxygen pressures is also similar to that used by Schuhmann and Ensio.⁷

Control of Oxygen Pressure: Air provides a constant oxygen pressure of 0.2 atm. Lower oxygen pressures were obtained through the reaction $\text{CO} + \frac{1}{2}\text{O}_2 = \text{CO}_2$, $K = p_{\text{CO}_2}/p_{\text{CO}} \cdot p_{\text{O}_2}^{1/2}$. Since the value of K is known, the oxygen partial pressure can be calculated from the CO_2/CO ratio. The most recent

thermodynamic data for this reaction are available in tables published by the National Bureau of Standards¹³ which are adequately represented by

$$\text{the expression}^{14}: \log K = \frac{14.550}{T} - 4.405.$$

The carbon dioxide:carbon monoxide atmosphere was prepared by starting with tank carbon dioxide containing approximately 0.09 pct oxygen, 0.07 pct water vapor, and 0.34 pct nitrogen. The carbon dioxide first passed through copper gauze maintained at 500°C to remove oxygen (Fig. 1) and then through anhydron to remove water vapor. Since the gases were analyzed gravimetrically the presence of several tenths of a percent of nitrogen did not introduce any error in the measured CO_2/CO ratio. The gas stream then separated and one portion passed through a furnace containing graphite at 1100°C. The reaction $\text{CO}_2 + \text{C} = 2\text{CO}$ is virtually complete at this temperature; traces of carbon dioxide were absorbed in ascarite. Then both the carbon dioxide and the carbon monoxide passed through flowmeters, mixed, and passed on to the furnace containing the slag sample. The total flow amounted to between 200 and 300 cc per min.

The gas mixture was analyzed as follows: First the carbon dioxide was absorbed in a bulb containing ascarite and anhydron, then the carbon monoxide was oxidized to carbon dioxide in a furnace containing copper oxide at 500°C, and finally the carbon dioxide so formed was absorbed in another absorption bulb containing ascarite and anhydron. Assuming ideal behavior, the ratio of the partial pressures of carbon dioxide to carbon monoxide is equal to the ratio of the weight gains in the two absorption bulbs. The analytical train was flushed with purified nitrogen before and after taking a sample. Samples taken before and after passage through the furnace gave substantially identical results.

The gas from the graphite furnace was analyzed to determine if any hydrogen was being evolved either from hydrogen, hydrocarbons, or adsorbed water in the graphite. Less than one part of hydrogen was found per thousand parts of carbon monoxide.

Furnace: A schematic diagram of the furnace setup is shown in Fig. 2. The heating element was

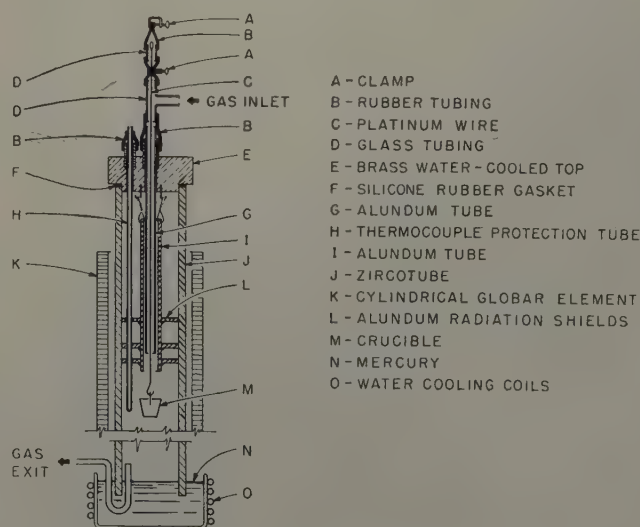


Fig. 2—Diagram of furnace.

a cylindrical global element supplied by a motor-generator set. Inside the global was a refractory zircotube whose dimensions were 1 5/8 in. ID, 1/8 in. wall thickness and 30 in. in length. This tube was sealed at the top by a brass water-cooled head with a silicone rubber gasket. The lower seal was formed by a pool of mercury, also water cooled, which served as a means of quenching the samples.

The temperature was measured by a thermocouple inserted in a protection tube. With this arrangement it was possible to remove the thermocouple between readings, a procedure which decreased the rate of deterioration of the Pt-Pt-Rh thermocouple. The furnace temperature was controlled by another thermocouple inserted through the side of the furnace and connected through compensating lead wire to a Celestray controller. Furnace temperature was controlled to $\pm 1^\circ\text{C}$. The temperature at the center of the furnace varied only 1°C over a length of 2 in. Since the platinum crucibles were only 1/2 in. in height, it was not difficult to position them properly.

The majority of these experiments were made with small platinum crucibles with a capacity of 1.3 cc. They held up very well as long as they were used in the more oxidizing atmospheres. In a reducing atmosphere the crucibles picked up appreciable amounts of iron which embrittled the platinum, and the crucibles broke when the sample was being removed. For these atmospheres smaller crucibles were made in a two-stage deep drawing process from 0.004 in. platinum foil. They were not as convenient, but they were more economical.

Procedure: The crucibles were suspended on a platinum wire, and when the slags had reached equilibrium they were quenched by being lowered rapidly until the crucible was floating in the mercury at the bottom of the refractory tube. The speed of cooling seemed important only for those slags which were melted in air. These have a tendency to pick up oxygen unless they are cooled with sufficient speed.

It was often possible to equilibrate several samples simultaneously. One advantage, of course, was that more data could be obtained in a given time. Second, since experimental conditions were the same for each sample, any discrepancies could be attributed to some factor which entered after the samples were removed from the furnace. Some of the more fluid slags could not be treated in this manner since some spilling inevitably occurred on quenching.

The sample weight varied with the type of crucible. In most of these experiments a 1 g sample was melted; in the smaller crucibles only 0.6 g was used.

In a number of preliminary experiments it was found that equilibrium was established within 1 hr. Nearly all runs were conducted for 1 1/2 to 2 hr. It was usually possible to predict the approximate amounts of ferric and ferrous oxide which would be present in the equilibrated slags, and the appropriate amounts of the two oxides were added to the charge. This, of course, reduced the time necessary to attain equilibrium. An effort was made to have some slags in each series approach equilibrium from the oxidizing side and some from the reducing side. The attainment of equilibrium was indicated by agreement between samples obtained in this manner, see Fig. 3.

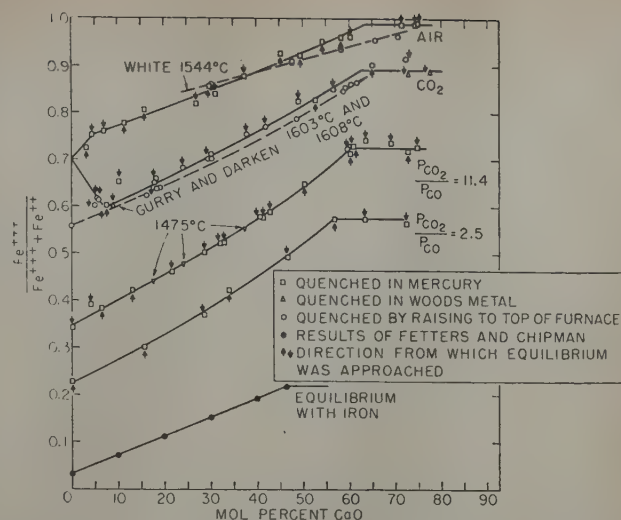


Fig. 3—Effect of atmosphere on lime-iron oxide slags at 1550°C .

Analytical Methods: Slag samples were dissolved in air-free hydrochloric acid saturated with CO_2 . Usually one portion of a sample was used to determine total iron, and a second portion was titrated for ferrous or ferric oxide using KMnO_4 or TiCl_3 , depending upon which oxide was present in smaller amount. At the outset, CaO was determined directly but this was done by difference in later experiments because the sum of the percentages of the iron oxides plus lime was in almost every case 100 ± 0.25 . Moreover in slags containing both lime and silica, the ratio of lime to silica was fixed by the composition of the three master slags, and both of these components could be determined by difference. In the iron oxide-magnesia slags, however, the magnesia content was seldom above 5 pct, and it was always determined directly.

The question arises as to whether the crushing or grinding of the slags prior to analysis oxidizes ferrous oxide to ferric oxide. Schuhmann and Ensio⁷ report this difficulty in connection with their work on the system $\text{FeO}-\text{Fe}_2\text{O}_3-\text{SiO}_2$. They finally adopted a procedure of grinding to only 20 mesh, a fairly coarse size. It may be that their slags, all of which were in equilibrium with metallic iron, were particularly sensitive in this respect. In these experiments a different technique was used. The sample was crushed in a Plattner's diamond mortar to pass a 60 or 100 mesh screen. In order to reduce the tendency for the fines to oxidize by repeated crushing, the sample was crushed by a few taps with pestle and then screened. The oversize was then crushed lightly and screened again. This process was repeated six to ten times in order to crush the sample completely.

Several samples were made large enough to furnish material for several analyses. Separate portions were crushed to pass 40, 60, and 100 mesh screens. No tendency toward a higher ferric oxide content was observed in the more finely divided samples. Most of the samples were ground to pass a 60 mesh screen.

Most of the slags dissolved satisfactorily in hydrochloric acid, but those with high silica contents required the addition of a small amount of hydrofluoric acid. Even so several of the slags did not dissolve completely. The undissolved residue was fused with sodium bisulphate and analyzed for total iron. This was calculated to magnetite and the ap-

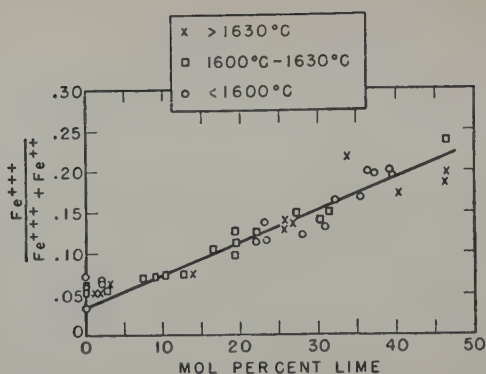


Fig. 4— $Fe^{+++}/(Fe^{+++} + Fe^{++})$ for lime-iron oxide slags in equilibrium with iron (Fetters and Chipman).

appropriate amount was added to the percentages of ferrous and ferric oxide.

Lime-Iron Oxide Slags

Experimental Results: The ternary system $CaO-FeO-Fe_2O_3$ was studied at $1550^{\circ}C$ under the following atmospheres: air, CO_2 , $CO_2/CO = 11.4$ and $CO_2/CO = 2.50$. The corresponding oxygen pressures are 2×10^{-1} , 2.6×10^{-3} , 9.1×10^{-6} , and 4.4×10^{-7} atm. For each atmosphere lime additions were made from zero percent to lime saturation. Three slags were equilibrated at $1475^{\circ}C$ under an atmosphere with a CO_2/CO ratio of 11.4. The slags were analyzed for FeO , Fe_2O_3 , and CaO .*

* The analyses are given according to atmosphere in Table I. However, since the experimental data are completely shown in the figures, Tables I to III have been omitted. Copies of the tables may be obtained on request addressed to Professor John Chipman, Dept. of Metallurgy, MIT, Cambridge, Mass.

The analytical results expressed in weight percent were converted to mol percent, and the ratio of ferric iron to total iron was obtained. This ratio, $Fe^{+++}/(Fe^{+++} + Fe^{++})$, will hereafter be referred to by the symbol j . It is convenient to remember that j is always within 10 pct of the weight ratio, $Fe_2O_3/(Fe_2O_3 + FeO)$.

For each slag the value of j is plotted against the mol percent lime in Fig. 3. The increase of j with mol percent of added lime is roughly linear.

The experiments in a CO_2 atmosphere were the first to be performed. Most of these slag samples were quenched by being lowered to the bottom of the furnace. However, difficulty was anticipated if samples equilibrated in air were quenched in this manner. Without a more rapid quench the latter will pick up oxygen as they cool. Molten Wood's metal was the next quenching medium to be tried. Three samples were run, and the results are indicated by triangular points on Fig. 3. However, the platinum crucibles were ruined, and this method was abandoned. Mercury was next used, and the results seemed satisfactory both with respect to quenching efficiency and absence of attack on the crucibles. Mercury quenching was used for all subsequent experiments.

The discontinuity in the curves for air and CO_2 at small amounts of lime can be explained by the formation of solid magnetite. If pure iron oxide is heated to $1550^{\circ}C$ in air or CO_2 , solid magnetite is formed rather than liquid iron oxide. The melting point in air is about $1595^{\circ}C$ and in CO_2 is about $1575^{\circ}C$. The composition of the solid magnetite was taken from Darken and Gurry.² In CO_2 magnetite has the stoichiometric composition Fe_3O_4 ; in air it has excess oxygen. A certain amount of lime must

be added in order to flux the magnetite, approximately 4 mol pct for slags heated in air and 7 pct for those in CO_2 . These phase relations can be understood more readily by referring to the ternary composition diagram in Fig. 7.

The discontinuities in the curves of Fig. 3 at high percentages of lime indicate saturation with CaO . After lime saturation is reached, further additions of lime do not change the composition of the liquid, and the j value of the liquid remains constant. The analyzed j value, i.e., j of material which was liquid at $1550^{\circ}C$ plus excess solid lime, also remains constant since the solubility of iron oxide in lime is negligible.

The arrow beside each point indicates the direction from which equilibrium was approached. The fact that charges which were originally above and below the line fall on the same line indicates that sufficient time was allowed for equilibrium to be reached.

It was often possible to equilibrate several samples simultaneously. No attempt was made to indicate this on Fig. 3 since several different designations were already being used to indicate the method of quenching.

Comparison with Other Data: The only data of White's which can be compared with this investigation are those at 1544° with an air atmosphere. As shown in Fig. 3, the agreement is unsatisfactory.

Gurry and Darken's data at 1603° and 1608° under a CO_2 atmosphere are also shown. The dis-

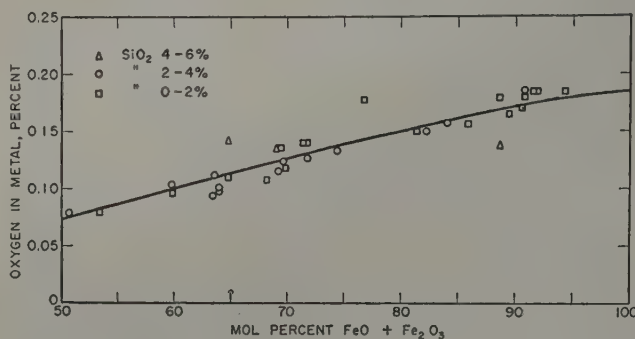


Fig. 5—Oxygen in liquid iron in equilibrium with $CaO-FeO-Fe_2O_3$ slags at $1550^{\circ}C$ (Fetters and Chipman).

tance between the two lines is expected from the temperature coefficient they found for pure iron oxide melts.

Darken and Gurry found almost no temperature effect between 1550° and 1475° for pure iron oxide melted under a gas with a CO_2/CO ratio of 11.4. As indicated on Fig. 3, the addition of lime did not alter this temperature relationship.

Slags in Equilibrium with Iron: It was impossible to use an atmosphere more reducing than a CO_2/CO ratio of approximately 2.50. Iron is absorbed into the platinum crucibles according to the reaction $FeO(\text{slag}) + CO = Fe(\text{Pt}) + CO_2$, and in the extreme case melting of the crucibles occurs. However, data are available for slag-metal equilibria, and by appropriate calculations the data can be expressed in terms which permit extension of the present data to oxygen pressures corresponding to iron saturation.

The data of Fetters and Chipman⁹ were used. They melted pure iron in an induction furnace and allowed the metal to come to equilibrium with various basic slags in the system $CaO-SiO_2-FeO$. Vari-

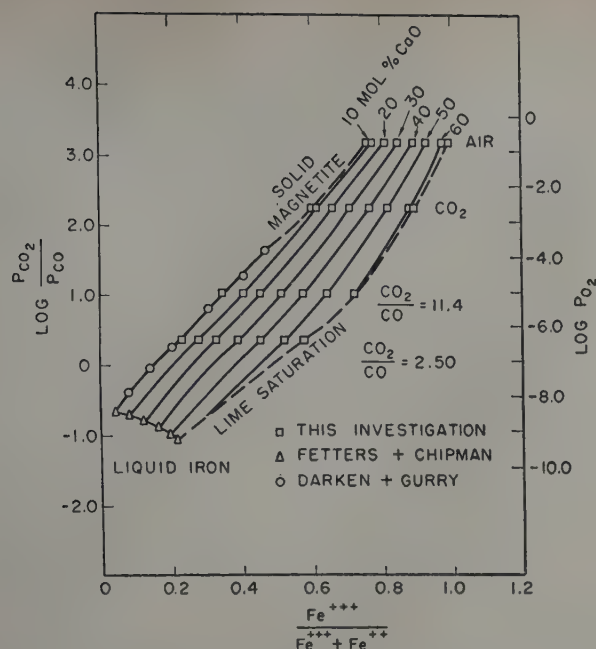


Fig. 6—Oxygen pressures in CaO-FeO-Fe₂O₃ slags at 1550°C.

ous amounts of magnesia were introduced from the magnesia crucible. From their data those slags were selected which had less than 6 pct SiO₂, the average being about 3 pct. The magnesia content varied from 5 to 12 pct with an average of about 7 pct. The *j* value of each slag was plotted against the mol percent of lime as shown in Fig. 4. Magnesia and silica, of course, exerted some effect, but no attempt was made to correct for them. The effect of magnesia is less than that of lime, and the magnesia and silica tend to neutralize each other. The temperature varied from 1550° to 1700°C, and the slags were divided into three groups according to temperature: less than 1600°C, 1600° to 1630°C, and greater than 1630°C. However, no temperature effect was observed; the points for the three groups are scattered at random. The *j* value for zero percent lime (0.034) was taken from Darken and Gurry.

The oxygen pressure or CO₂/CO ratio corresponding to each slag was calculated from the oxygen content of the metal in equilibrium with the slag. Since the data of Fetters and Chipman were obtained over a range of temperatures, it was necessary to convert their oxygen values to 1550°C. They found that the temperature coefficient of oxygen solubility in these slags was the same as under pure iron oxide slags. Therefore, it is possible to write

$$\frac{\% \text{ O (at } T)}{\% \text{ O (sat. at } T)} = \frac{\% \text{ O (at } 1550^\circ)}{\% \text{ O (sat. at } 1550^\circ)} \times \% \text{ O (sat. at } 1550^\circ)$$

After converting in this manner the data were plotted in Fig. 5 as % O vs $N_{\text{FeO}} + N_{\text{Fe}_2\text{O}_3}$.

The next problem is to determine what slag in the CaO-FeO-Fe₂O₃ will produce the same pct O as the impure slag for which data are available. As an example, suppose a slag has a composition of 20 pct CaO, 10 pct MgO + SiO₂, and 70 pct FeO + Fe₂O₃. There are three ways the impurities can be treated to convert this to a ternary system: 1—Ignore them and figure the composition on a silica and magnesia free basis; this gives 22 pct CaO + 78 pct FeO + Fe₂O₃. 2—Assume they act similarly to iron oxides; this gives 20 pct CaO and 80 pct FeO + Fe₂O₃. 3—Assume they act similarly to lime which gives 30 pct

CaO and 70 pct FeO + Fe₂O₃. Since the oxygen in the metal is determined primarily by the iron oxide content, it seems most satisfactory to use method 3 and this has been done in constructing Fig. 5. On the other hand, lime has a much greater effect on *j* than does magnesia, and therefore in preparing Fig. 4, method 2 was adopted and the actual mol fraction of CaO was used.

The CO₂/CO ratio in equilibrium with oxygen-saturated iron at 1550°C according to Darken and Gurry is 0.200. The solubility is 0.185 pct and the oxygen activity is proportional to its concentration. It follows that the equilibrium constant for the reaction $\text{O} + \text{CO} = \text{CO}_2$ is

$$K = \frac{p_{\text{CO}_2}}{p_{\text{CO}} \cdot [\% \text{ O}]} = \frac{0.200}{0.185} = 1.08$$

This permits reading values of $p_{\text{CO}_2}/p_{\text{CO}}$ from Fig. 5.

System CaO-FeO-Fe₂O₃: Oxygen pressures or CO₂/CO ratios throughout the liquid range of the ternary system may now be obtained by combining the data of Figs. 3, 4, and 5. The result is shown in Fig. 6 where $\log \{ \text{CO}_2/\text{CO} \}$ and $\log p_{\text{O}_2}$ are plotted against *j* for slags of 0, 10, 20, 30, 40, 50, and 60 mol pct lime. The point on the zero lime curve at which solid magnetite appears was taken from the data of Darken and Gurry.² The same data are shown as a ternary plot in Fig. 7 as lines of constant oxygen pressure and the phase boundaries of the system at 1550°C.

Magnesia-Iron Oxide Slags

Experimental Results: Magnesia-iron oxide slags were melted at 1550°C in platinum and magnesia crucibles.[†] The magnesia crucibles were of two

[†] Results are shown in Table II which also gives the analyses of the various slag layers referred to below. See footnote on p. 1092.

sizes, the larger 1½ in. high, ¾ in. OD, and slightly more than 1/16 in. in wall thickness; the smaller were ¾ in. high, 15/32 in. OD, and slightly less than 1/16 in. in wall thickness. Thermal shock characteristics were excellent and slag penetration was slight. During the course of a 3 or 4 hr experiment the slag would become saturated with magnesia, and iron oxide would penetrate the crucible wall to a depth of approximately 1/32 of an inch.

When the larger magnesia crucibles were used, several distinct layers could be seen in the sample.

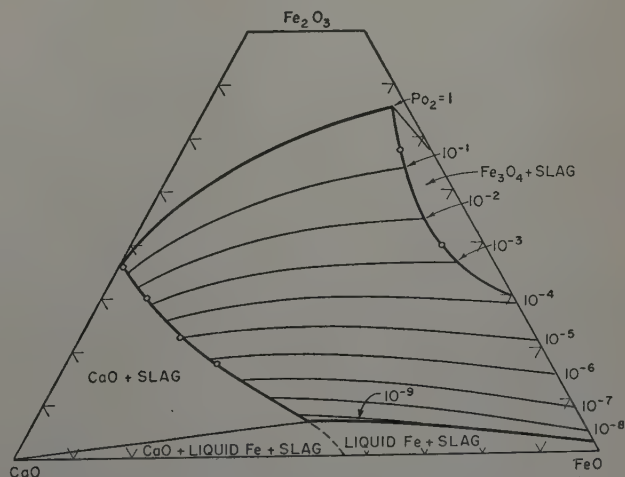


Fig. 7—Section of the ternary system at 1550°C showing oxygen pressures. Coordinates are mol fractions.

As shown in Fig. 8, they consisted of: 1—the portion of the crucible wall penetrated by iron oxide; 2—a layer which is probably a magnesia-wüstite solid solution; and 3—the portion of the sample which was liquid at temperature. The second and third layers broke away from the crucible wall quite easily. Portions of the crucible wall, which included zone 1, could be analyzed for the ratio of ferric to ferrous oxide. In several experiments it was possible to separate the two inner layers; either layer 3 could be ground away from layer 2 or vice versa.

As long as the solid solution layer (2) is completely removed from the slag layer (3), the latter sample will be representative of the material which

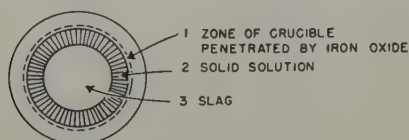


Fig. 8—Phases present after experiments in magnesia crucibles.

was liquid at 1550°C. However, the composition of the solid solution varies, and the composition of the sample taken from this layer depends upon how much of it was removed in the process of grinding away layer (2). Thus these values are only approximate averages.

The results of all experiments on magnesia slags are shown in Fig. 9 where the j value is plotted against mol percent MgO. The solubility of MgO is indicated by a vertical line at about 8.7 mol pct. This corresponds to the analyses of slags melted in the large magnesia crucibles; it is evident that slags from the smaller magnesia crucibles contained portions of zone 2. The solubility limit indicated also corresponds to intersections of the two branches of the series at CO_2/CO ratios 11.4 and 2.50.

Discussion: It is evident that MgO increases the value of j less strongly than does lime. This is in keeping with its generally weaker basic properties. At the high values of j associated with CO_2 atmospheres, the slags were solid or semisolid. It seems probable that magnetite occurred but the composition of this phase and its relation to other solid phases in the system remain unknown.

Referring again to Fig. 8, the conclusions regarding magnesia-iron oxide slags are summarized as follows: The liquid slag, zone 3, contains a maximum of about 8.7 mol pct MgO and its j value is higher than that of simple iron oxide slag. Zone 2 is a solid solution built up on the inner wall of the refractory; its j value is only slightly higher than that of the slag. Zone 1, the area of penetration, has a slightly lower j value.

Lime-Silica-Iron Oxide Slags

Experimental Results: Equilibrium in lime-silica-iron oxide slags was studied at 1550°C in a manner similar to that already described for lime-iron oxide slags. The same four atmospheres were used: air, CO_2 , $\text{CO}_2/\text{CO} = 11.4$, and $\text{CO}_2/\text{CO} = 2.50$. Three master slags were prepared which had molar lime:silica ratios of 0.540, 1.306, and 2.235. Iron oxide was added as a mixture of ferrous and ferric oxide in proportions approximating the expected equilibrium composition. This, of course, decreased the time necessary to attain equilibrium.

The slags were analyzed for ferrous and ferric oxides and lime-plus-silica was determined by subtracting the sum of the iron oxides from 100. Occasional slags were analyzed completely and the lime:silica ratios agreed adequately with those of the master slags.

The experimental results† are presented in Figs.

† Results are also listed in Table III. See footnote on p. 1092.

10 to 13 as the ratio j against the mol percent of lime-plus-silica, the sum of these two at constant ratio being treated as a single component.

1—Lime:Silica Ratio 0.540. This system was studied from pure iron oxide to 100 pct lime plus silica. The results at low amounts of lime plus silica appear rather precise, but with larger amounts they show considerably more scatter.

These slags were the most difficult to analyze of those investigated. In several samples part of the iron oxide remained undissolved even with the addition of hydrofluoric acid. This insoluble portion was fused and analyzed for iron which was calculated as magnetite.

In Figs. 10 to 13 similar symbols along any one curve, except open circles, designate slags which were equilibrated simultaneously; open circles designate single samples. If one sample of a group deviates from the curve more than the others, the reason must be in either crushing or analysis. Any error in temperature, atmosphere, or quenching should produce a consistent error in all the slags in the group.

2—Lime:Silica Ratio 1.306. This system could

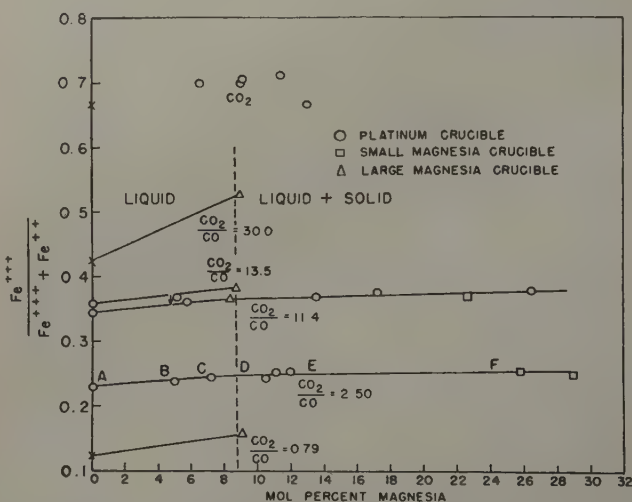


Fig. 9—Effect of atmosphere on magnesia-iron oxide slags at 1550°C.

also be studied from pure iron oxide to pure lime-plus-silica. Again the results at low concentrations of lime and silica are relatively consistent, while those at higher concentrations are not. The j value passes through a maximum, and the position of the maximum shifts toward pure iron oxide as the atmosphere becomes more reducing.

3—Lime:Silica Ratio 2.235. According to the FeO-CaO-SiO_2 phase diagram, the slags become saturated with dicalcium silicate when the lime-plus-silica is greater than approximately 50 pct. Charges were made to exceed this saturation value but there is no break in any of the curves. Samples

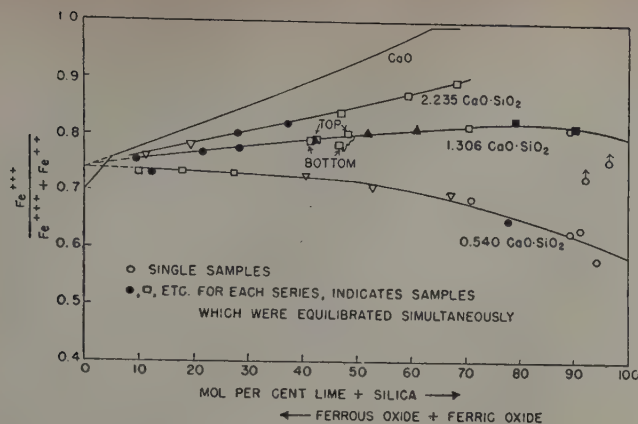


Fig. 10—Equilibria in lime-silica-iron oxide slags at 1550°C, air atmosphere.

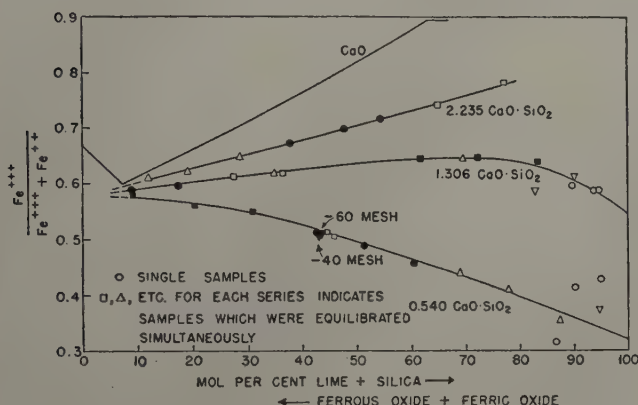


Fig. 11—Equilibria in lime-silica-iron oxide slags at 1550°C, CO₂ atmosphere.

286 and 287 are the top and bottom portions of a sample equilibrated under a CO₂/CO ratio of 2.50. If dicalcium silicate had precipitated, it should have segregated either at the top or the bottom of the crucible. Although some mixing probably occurred upon quenching, it was expected that the j ratio of the two layers would be the same even if the total amount of iron oxide differed. This is analogous to the situation which prevails when lime saturation is reached in lime-iron oxide slags. However, according to Fig. 13 neither the ratio nor the total amount of the two iron oxides were the same. Surprisingly both points fall equally well on the curve through the other points for that series. It seems likely that a solid phase is present which contains iron oxide in which the proportions of ferrous and ferric oxide are only slightly different from that in the liquid.

Bowen, Schairer, and Posnjak¹⁵ have determined the phase diagram for the system 2CaO·SiO₂-2FeO·SiO₂. At the dicalcium silicate end of the diagram solid solutions are present which contain up to 10 pct iron silicate. Although the effect of large amounts of ferric oxide is unknown, the possibility remains that some other solid phase than dicalcium silicate is present.

Under an air or CO₂ atmosphere at 1550°C pure iron oxide exists as solid magnetite. However, for each of the lime:silica ratios the addition of 10 mol pct lime plus silica was sufficient to produce a single liquid phase. No attempt was made to determine the actual boundary of the magnetite field.

The ability of a particular oxide or group of oxides to increase the ratio of ferric iron to total iron can be taken as a measure of the basicity of the ox-

ides. Lime is a strong base and increases this ratio. Silica is a strong acid and has an almost equal ability to decrease the ratio. As indicated by Figs. 10 to 13, various combinations of lime and silica have intermediate effects. Of the slags studied those with a lime:silica ratio of 1.306 are the closest to neutrality as far as this criterion is concerned.

The System CaO-SiO₂-FeO-Fe₂O₃: Data are available for slags in equilibrium with iron which have the same lime:silica ratios as those used in the present investigation. The data of Fetters and Chipman⁹ and of Taylor and Chipman¹⁰ were used respectively for the more basic and the more acid slags. Graphical interpolation was used to determine the oxygen contents of metal (hence p_{O_2}) and j values for the slags along lines of constant lime-silica ratio.

The experimental data of this investigation and the data for slags in equilibrium with iron were plotted on curves similar to that of Fig. 4. Compositions at various oxygen pressures were determined, and these are plotted on the ternary composition triangle of Fig. 14. By interpolating between these curves it is possible to determine the oxygen pressure of any slag in the lime-silica-iron oxide system with a lime:silica ratio of 0.540 to 2.235 up to lime saturation.

Iron Oxide Slags with Other Additions

Iron oxide slags with additions of barium oxide, silica, manganese oxide, alumina, and titania were equilibrated under an atmosphere of CO₂/CO = 11.4 at a temperature of 1550°C. The experimental

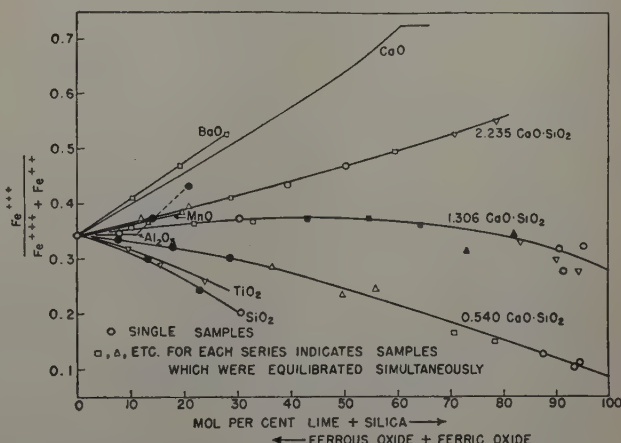


Fig. 12—Equilibria in iron oxide slags with various additions at 1550°C. CO₂/CO=11.4.

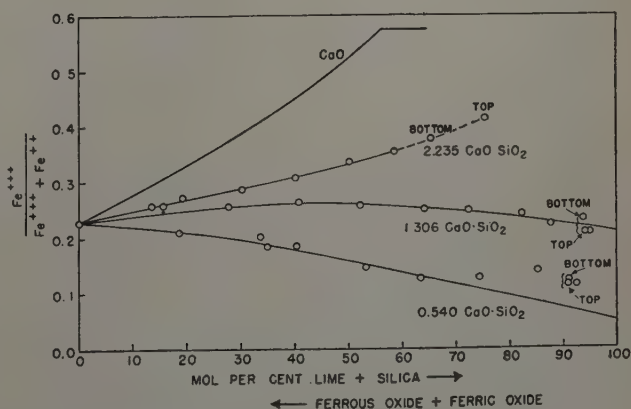


Fig. 13—Equilibria in lime-silica-iron oxide slags at 1550°C. CO₂/CO=2.50.

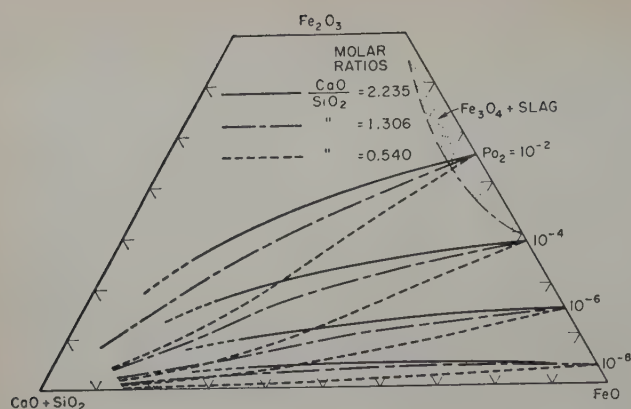


Fig. 14—Oxygen pressures in slags containing CaO, SiO₂, FeO, and Fe₂O₃.

results are plotted in Fig. 12 as j against mol per cent added oxide.

The results for barium oxide, silica, and titania additions are such as would be expected from their usual chemical behavior. Barium oxide is somewhat more basic than lime. Titania and silica are both acidic with silica being somewhat stronger.

The effect of manganese oxide additions, however, is rather surprising. Gurry and Darken³ report that manganese oxide is only slightly less basic than lime. This conclusion seems warranted from a comparison of their data for lime and manganese oxide additions at 1600°C under a CO₂ atmosphere. From the results of the present investigation, manganese oxide would be placed in a class with magnesia which has a much smaller effect than lime. Although only two samples with manganese oxide additions were obtained, their two points and the point for pure iron oxide lie on an easily defined curve. Also since these results were obtained immediately between the results for barium oxide and titania additions, both of which are apparently satisfactory, a major error in temperature or atmosphere control was improbable.

The results for alumina additions require some explanation. Since alumina is usually considered to have a weakly acidic effect, the first point at 8 mol pct Al₂O₃ appears reasonable. Actually it seems to be exactly neutral as far as its effect on the ratio of ferric to total iron is concerned. Moreover, this sample was equilibrated simultaneously with the sample containing 30 mol pct SiO₂, and the latter sample agrees with the others containing silica additions.

The other two alumina points define a line which deviates sharply from the line between the point for pure iron oxide and the first alumina point. This effect is not an analytical error. The samples having 8 and 14 mol pct Al₂O₃ were reanalyzed for total iron, and the figure obtained agrees very well with that from the first analysis. Also experiments before and after under the same atmosphere were satisfactory.

According to the phase diagram for the system FeO-Al₂O₃ determined by McIntosh, Rait, and Hay,¹⁰ saturation with pure alumina occurs at about 27 pct Al₂O₃. Therefore, all of the present slags should lie well within the liquid region. However, both experimental and circumstantial evidence support the conclusion that the two high alumina slags are in a liquid-plus-solid region. The 20 mol pct Al₂O₃ sample was porous, had a rough uneven surface and fell

out of the crucible in one piece. This might indicate that the sample had sintered rather than melted.

No diagram is available for the Fe₂O₃-Al₂O₃ system, but the two oxides are isomorphous in various naturally occurring minerals, particularly in spinels. Chromium trioxide, also similar in crystal structure and lattice constants, forms a continuous series of solid solutions with alumina. The compound hercynite, FeO · Al₂O₃, is formed in the FeO-Al₂O₃ system. Perhaps in the ternary system FeO-Fe₂O₃-Al₂O₃ this compound has a variable composition in which the ferric oxide replaces part of the alumina. The solid phase present may be either such a compound or a simple solid solution of Fe₂O₃ in Al₂O₃.

Summary

This paper covers a study of equilibrium between slags containing iron oxide and gases consisting of air or mixtures of CO₂ and CO. Together with earlier data on equilibrium between similar slags and molten iron, the results establish the value of $j = (\text{Fe}^{+++})/(\text{Fe}^{+++} + \text{Fe}^{++})$ over a range of oxygen pressures from 10⁻¹ to 10⁻⁹ atm.

The value of j is strongly increased by additions of CaO and to a lesser degree by MgO. In slags containing CaO + SiO₂ the value of j is increased by additions in which the molar ratio (CaO)/(SiO₂) is 2.2 or 1.3 and decreased when the ratio is 0.54. For other additions the effect of basic oxides, e.g., BaO, is to increase j while acid oxides such as SiO₂ and TiO₂ have the opposite effect.

Oxygen activities at 1550°C are shown graphically for the ternary system CaO-FeO-Fe₂O₃ and for three pseudo-ternaries (CaO + SiO₂)-FeO-Fe₂O₃. The data cover slag compositions which are more or less similar to those at the slag-gas interface in the open hearth furnace.

Acknowledgments

The authors wish to thank D. L. Guernsey and his associates for the analytical work, and the Republic Steel Corp. for a fellowship grant which made the research possible.

References

1. L. S. Darken and R. W. Gurry: *Journal ACS* (1945) **67**, p. 1398.
2. L. S. Darken and R. W. Gurry: *Journal ACS* (1946) **68**, p. 798.
3. R. W. Gurry and L. S. Darken: *Journal ACS* (1950) **72**, p. 3906.
4. L. S. Darken: *Journal ACS* (1948) **70**, p. 2046.
5. J. White: *Journal Iron and Steel Inst.*, London. *Carnegie Scholarship Memoirs* (1938) **27**, p. 1.
6. W. Krings and H. Schackmann: *Ztsch. Electrochemie* (1935) **41**, p. 479.
7. R. Schuhmann and P. J. Ensio: *Trans. AIME* (1951) **191**, p. 401; *JOURNAL OF METALS* (May 1951).
8. E. J. Michal and R. Schuhmann, Jr.: *Trans. AIME* (1952) **194**, p. 723; *JOURNAL OF METALS* (July 1952).
9. K. L. Fetters and J. Chipman: *Trans. AIME* (1940) **140**, p. 170.
10. C. R. Taylor and J. Chipman: *Trans. AIME* (1943) **154**, p. 228.
11. T. B. Winkler and J. Chipman: *Trans. AIME* (1946) **167**, p. 111; *METALS TECHNOLOGY* (April 1946).
12. F. Körber and W. Oelsen: *Mitt Kaiser Wilhelm Inst. Eisenforsch.* (1932) **14**, p. 181; (1933) **15**, p. 280.
13. *Selected Values of Chemical Thermodynamic Properties*. National Bureau of Standards (1947).
14. *Basic Open Hearth Steelmaking*. Revised Edition (1951) AIME.
15. N. L. Bowen, J. F. Schairer, and E. Posnjak: *American Journal of Science* (1933) Series 5, **25**, p. 273.
16. A. B. McIntosh, J. R. Rait, and R. Hay: *Journal Royal Technical College, Glasgow* (1937) **4**, p. 72.

Constitution of the $\text{FeO-Fe}_2\text{O}_3\text{-SiO}_2$ System

At Slagmaking Temperatures

by R. Schuhmann, Jr., R. G. Powell, and E. J. Michal

Liquidus surfaces in the ternary system $\text{FeO-Fe}_2\text{O}_3\text{-SiO}_2$ were determined from 1250° to 1450°C by the procedure of equilibrating small samples in platinum crucibles, quenching, and microscopic examination. The experimental results were combined with previously published information to construct a ternary diagram for the system showing the entire temperature-composition range of stability of iron silicate slags. Metallurgical applications of the diagram, especially in copper smelting, are discussed briefly.

IRON oxides are almost unique among the common oxide constituents of metallurgical slags in that the iron occurs in two different states of oxidation, ferrous and ferric. Moreover, in liquid slags the degree of oxidation of the iron is readily changed by reactions of the slags with oxidizing agents or reducing agents. This behavior of iron oxides in slags accounts, for example, for the effective transfer of large quantities of oxygen through slag layers in open hearth steelmaking. In this process, oxygen supplied by reactions at the gas-slag interface is dissolved in the slag with the oxidation of ferrous iron to ferric. Ferric oxide is transported across the slag layer by convection, and at the slag-metal interface the oxygen reacts with liquid metal while the ferric iron is reduced back to the ferrous state. Another group of processes in which variation in degree of oxidation of iron has great practical importance is in copper smelting. In matte smelting and converting, such large proportions of the iron are oxidized to the ferric state that problems are encountered in preventing or controlling the formation of solid magnetite. The ferrous-ferric relationship also affects the attack of iron oxides on high- SiO_2 refractories,

which appears to be most severe under reducing conditions for which ferrous iron predominates.

Darken and Gurry¹ determined the chemical properties and phase equilibria of pure iron oxide slags. Their data show that iron oxide melts can have compositions ranging almost all the way from FeO to Fe_2O_3 . The melts of lowest oxygen contents, which exist in equilibrium with metallic iron, approach ferrous oxide in composition but still have a small percentage of ferric oxide. The melts of highest oxygen contents, which have oxygen dissociation pressures of 1 atm, are above magnetite in oxygen content, with over two-thirds of the iron in the ferric state.

The previously established phase diagrams for silicate slag systems all show FeO as the iron oxide component. However, Bowen and Schairer,² who determined the FeO-SiO_2 diagram and many of the other diagrams used by slag chemists, have been careful to point out that their systems always contained both ferrous and ferric iron. Thus, their data are for limiting mixtures with minimum contents of ferric iron, obtained by melting and equilibration in iron crucibles. Under these conditions, the Fe_2O_3 percentages found by analysis were small enough to justify simplification of the published phase diagrams by calculating the Fe_2O_3 to equivalent FeO and ignoring Fe_2O_3 as an additional component.

On the basis of experimental measurements of melting points of iron oxides on silica in the presence of various gas mixtures, Darken³ worked out phase diagrams for the Fe-Si-O system which show the important phase equilibria in terms of temperature and gas composition. This study clarified many aspects of the application of the phase rule to the $\text{FeO-Fe}_2\text{O}_3\text{-SiO}_2$ system and was an important basing

R. SCHUHMAN, JR., Member AIME, is Associate Professor of Metallurgy, Massachusetts Institute of Technology, Cambridge, Mass., R. G. POWELL is a Staff Member of the Division of Industrial Cooperation, Massachusetts Institute of Technology, and E. J. MICHAL, Junior Member, AIME, is Research Metallurgist, National Lead Co., South Amboy, N. J.

Discussion on this paper, TP 3587D, may be sent, 2 copies, to AIME by Nov. 1, 1953. Manuscript, Jan. 13, 1953. New York Meeting, February 1952.

This paper is based on a thesis submitted by R. G. Powell in partial fulfillment of requirements for the degree of Master of Science to Massachusetts Institute of Technology.

point for the work described in the present paper.

The experimental work to be described in this paper consisted primarily in the determination of the liquidus surfaces in the $\text{FeO-Fe}_2\text{O}_3\text{-SiO}_2$ system, especially the three liquidus surfaces corresponding to equilibria with magnetite, wüstite, and silica (tridymite) respectively. By combining these new data with available data for other parts of the ternary system, a ternary diagram was developed which shows the entire temperature-composition range of stability of iron silicate slags containing both ferrous and ferric iron. Applications of this phase diagram are discussed briefly.

Experimental Methods

The experimental procedure was similar to that used by Bowen and Schairer² in studying the FeO-SiO_2 system and consisted in equilibration of known mixtures of FeO , Fe_2O_3 , and SiO_2 at constant temperature, quenching to room temperature, and microscopic study of the quenched specimens to determine the phases present.

Materials: The primary starting materials were ferric oxide (Baker's chemically pure reagent), hydrogen-reduced iron powder (Mallinckrodt), precipitated silica, and Armco iron crucibles. From these materials, secondary stocks were prepared of fayalite slag (approximately 2FeO:SiO_2 in composition), wüstite slag, and magnetite. These three secondary stocks with precipitated silica were mixed in appropriate quantities to obtain 10 to 20 g each of 76 experimental mixtures. Each of these experimental mixtures was homogenized by heating to 1450° to 1500°C in nitrogen in a platinum crucible, quenching, grinding to minus 65 mesh, and mixing. When complete fusion did not occur, this homogenization treatment was repeated two more times. The final mixtures were analyzed for FeO , Fe_2O_3 , and SiO_2 , and the subsequent equilibrations were conducted on small portions of these analyzed mixtures.

Apparatus: The equilibration experiments were made in a platinum-wound furnace provided with an automatic temperature controller. The furnace was of standard design, built around a vertical Alundum tube 24 in. long x 3 in. ID. Six closely spaced porcelain tubes, 42 in. long x $\frac{5}{8}$ in. OD, passed through this furnace and provided for simultaneous and independent equilibration of six different samples at a time. A mercury bath sealed the lower ends of these porcelain tubes. Rubber stoppers were used on the upper ends. During the runs a stream of over 10 ml N_2 per min flowed through each tube. A positive pressure of 2 to 3 mm Hg was maintained in each tube by discharging the exit nitrogen under glycerine. The nitrogen fed to the tubes was purified in a train including ascarite, drierite, and anhydrous absorption tubes and a deoxidizing furnace containing hot copper gauze.

The experimental mixtures were held in home-made platinum crucibles, $\frac{3}{8}$ in. high x $\frac{1}{4}$ in. in diameter and with a capacity of about 0.5 g of solids. Each crucible was suspended in a furnace tube by a fine platinum wire, brought out through a glass tube with a simple rubber-tubing and screw-clamp seal mounted in the rubber stopper at the upper end of the tube.

Temperatures were measured with a Pt, Pt-Rh thermocouple whose junction was located in one of the furnace tubes at the same level as the samples. Temperature explorations in the furnace tubes indicated that the reported temperatures represented

actual sample equilibration temperatures to within about 3°C .

Procedure: The plan of experimentation involved the determination of five isothermal sections of the $\text{FeO-Fe}_2\text{O}_3\text{-SiO}_2$ system, at 1250° , 1300° , 1350° , 1400° , and 1450°C , respectively. At each of these temperatures a number of the experimental mixtures were brought to equilibrium, quenched, and studied microscopically. The studies were continued systematically at each temperature until sufficient data were available to locate the boundary curves of the melt field and to locate the lines separating the two-phase and three-phase fields.

First the furnace was brought to the desired temperature and flushed with nitrogen gas. Then the platinum crucibles were quickly introduced and suspended in the lower cold ends of the furnace tubes for at least 15 min of flushing with nitrogen to insure elimination of oxygen. After this flushing, the samples were pulled up into place in the hot zone of the furnace. Most of the points were checked by repetition of the equilibrations for different lengths of time. When the mixture fused or formed a substantial quantity of a liquid phase, equilibrium was attained quite rapidly and the runs were made for periods of 30, 60, and 90 min. Longer periods were used when the mixtures yielded little liquid phase. At the end of the run, the sample was quenched in the upper cold end of the furnace tube. This type of cooling did not prevent crystallization of the melt phase, especially at high iron contents, but no difficulty was experienced in differentiating primary crystals from the finer crystals and dendrites formed during cooling. Originally the samples were folded in platinum foil and quenched in mercury, but this technique proved troublesome with the most fluid melts and was little better than the simple cooling procedure in preventing partial crystallization of the liquid phase.

The quenched samples were broken out of the crucibles and crushed lightly. The large grains thus obtained were mounted in bakelite, and polished sections were prepared for microscopic examination. The sections were examined by reflected light using a standard metallurgical microscope. For the mixtures investigated, the phases present at the equilibration temperatures included liquid, wüstite, magnetite, and silica (tridymite). Primary tridymite and primary magnetite were readily recognized in the quenched samples both from their well-developed crystalline habits and from their reflectivities. The identification of the primary silica phase as tridymite was checked by refractive index measurements on loose grains, using the immersion technique. Wüstite grains quenched to a light gray, usually heterogeneous-looking structure. Some wüstite grains were rimmed with magnetite, others were peppered with small crystals of secondary magnetite, apparently formed during cooling. The quenching behavior of the melt phase varied considerably with composition. In some instances a dark gray glass was observed, but more commonly some sort of fine structure developed in the glass during the cooling. Many of the quenched melts were penetrated by very fine dendrites of magnetite. Some of the more silicious melts showed tiny rosettes of silica. A few typical structures are shown in Fig. 1.

Iron Absorption by Platinum Crucibles: The mixture analyses eventually used in plotting the equilibrium diagrams were the chemical analyses of the

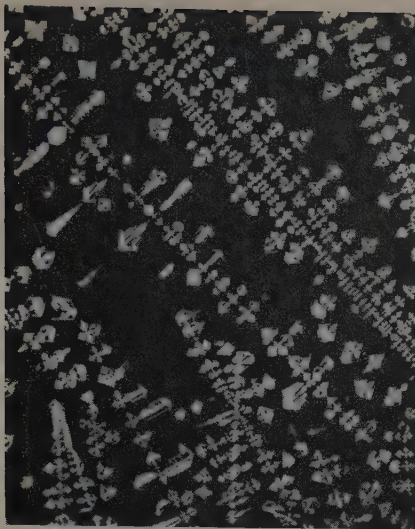


Fig. 1a—Quenched melt, showing magnetite dendrites formed in cooling. 47.0 pct FeO, 24.5 pct Fe_2O_3 , and 28.5 pct SiO_2 , equilibrated at 1350°C. X500. Area reduced approximately 50 pct for reproduction.

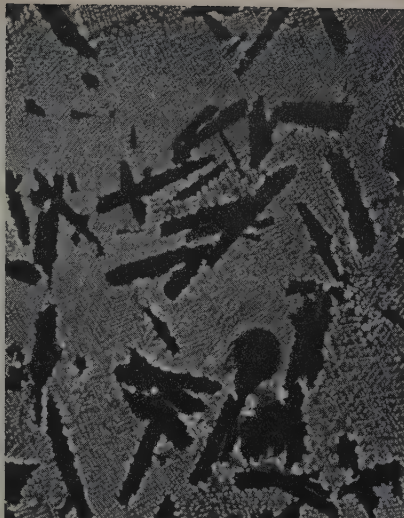


Fig. 1b—Primary tridymite plus melt, with dendrites formed during cooling. 45.0 pct FeO, 20.3 pct Fe_2O_3 , and 34.7 pct SiO_2 , equilibrated at 1350°C. X150. Area reduced approximately 50 pct for reproduction.

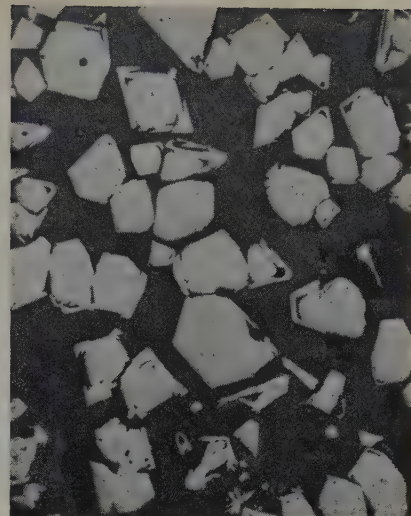


Fig. 1c—Primary magnetite and melt. 55.8 pct FeO, 29.1 pct Fe_2O_3 , and 15.1 pct SiO_2 , equilibrated at 1350°C. X150. Area reduced approximately 50 pct for reproduction.

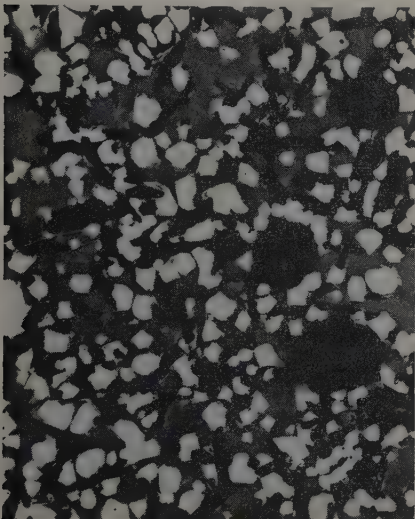


Fig. 1d (left)—Primary tridymite, primary magnetite, and melt. 44.1 pct FeO, 26.4 pct Fe_2O_3 , and 29.5 pct SiO_2 , equilibrated at 1350°C. X150. Area reduced approximately 50 pct for reproduction.

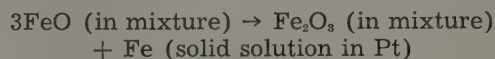
Fig. 1e (right)—Primary wustite (partly decomposed) and melt, with wustite dendrites formed during cooling. 70.0 pct FeO, 23.3 pct Fe_2O_3 , and 6.7 pct SiO_2 , equilibrated at 1350°C. X150. Area reduced approximately 50 pct for reproduction.



powdered experimental mixtures after the homogenization treatment but before equilibration. Accordingly, the principal sources of error in the final data were the changes in composition which occurred when the small samples were equilibrated in platinum crucibles. Analysis of the contents of each crucible after equilibration would have been desirable, of course, but this procedure was not adopted because it would have required a larger scale of experimentation with high platinum consumption and would have multiplied the analytical work.

The changes in composition during the equilibration runs were studied in a preliminary group of tests on five representative mixtures, and the results of these tests are summarized in Table I. Two series of tests were run for 1 hr at 1300° and 1400°C, respectively, with new platinum crucibles for each test. These crucibles and samples were weighed separately before use. After the equilibration tests, the crucibles were cleaned and reweighed. A third series of tests were then made with used crucibles, each crucible having been used once with the same mixture so that some opportunity was afforded for the crucibles to approach equilibrium with the various mixtures. In all cases, it can be seen that heat-

ing the mixtures in the nitrogen atmosphere and in the platinum crucible caused a decrease in the percentage of FeO, a comparable increase in the percentage of Fe_2O_3 , and little change in the percentage of SiO_2 . The increase in crucible weight is accounted for by transfer of iron from the mixture to the crucible in accordance with the reaction.



To confirm this interpretation, the analyses of the various mixtures after equilibration were calculated from the weights and analyses of the original mixtures assuming that the increase in crucible weight represented iron transferred to the crucible in accordance with the chemical equation given above. These calculated analyses are given in parentheses in Table I, and are seen to check the actual analyses reasonably well when the various experimental difficulties in analyzing small samples and in cleaning the crucibles are considered. To eliminate the possibility that the composition changes might also reflect pickup of oxygen, a number of tests were made with weighed, empty Armco iron crucibles and with weighed rolls of copper gauze. These showed negligible weight increases in expo-

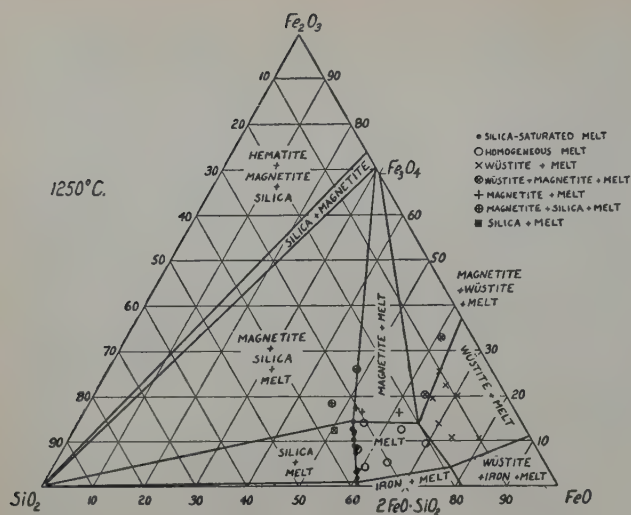


Fig. 2—1250°C isothermal section.

tures up to several hours.

On the basis of the results just discussed, it was decided to conduct all final equilibrations in crucibles which had been used at least once before with the same mixture. In the tests with once-used crucibles reported in Table I, the average change in composition was a decrease of about 2.2 pct FeO and a similar increase in the percentage of Fe_2O_3 , and the maximum change was a 3.3 pct decrease in FeO and corresponding increase in Fe_2O_3 . Accordingly, it is probable that the final results are subject to systematic errors of the order of +1 to +3 pct FeO and -1 to -3 pct Fe_2O_3 .

Silica Liquidus: Experimental work on equilibria of silica-saturated iron silicate slags was reported in an earlier paper by two of the authors.⁴ This earlier paper includes numerous analyses of iron silicate slags in equilibrium with solid silica at various temperatures, which afford determinations of points on the silica liquidus by a different and more refined technique than that of the work reported in the present paper. Also, in the work reported

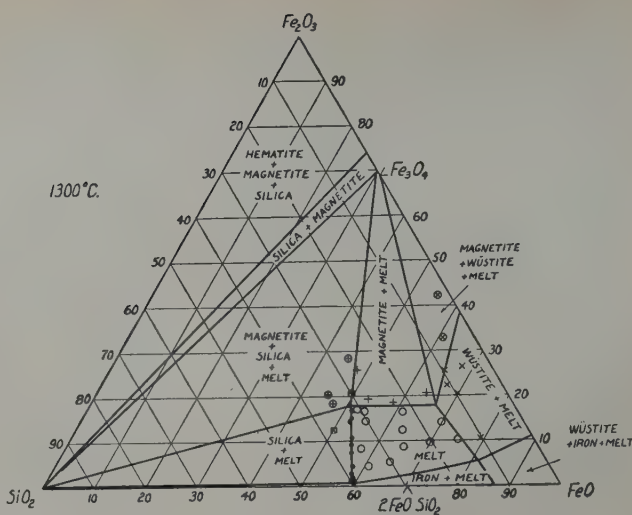


Fig. 3—1300°C isothermal section.

earlier, special pains were taken to determine the composition of slags saturated with respect to both solid silica and solid magnetite, and these data also were given major weighting in preparing the constitution diagrams to be discussed subsequently.

Results

The experimental results are plotted in the five isothermal sections, Figs. 2 to 6. For each composition studied by equilibration, quenching, and microscopic examination, the observed combination of phases is indicated by the different symbols as shown in the legend. In the 1250°, 1300°, and 1350°C isotherms, the compositions of silica-saturated liquids determined during gas-slag equilibrium studies in silica crucibles⁴ are also plotted, and in this temperature range it can be seen that results of the two very different experimental methods are quite consistent. No new data were obtained in this investigation on the liquids in equilibrium with solid iron, since these compositions have already been studied thoroughly and are well established except

Table I. Composition Changes During Equilibration Tests in Platinum Crucibles

Mixture No.	Description of Equilibration Test	Sample Weight, Grams	Increase in Crucible Weight, Mg	Analyses,* Wt Pct		
				FeO	Fe_2O_3	SiO_2
3						
		Original Analysis		63.60	12.59	23.81
	New crucible, 1 hr at 1300°C	0.502	8.1	58.29	17.68	24.03
	New crucible, 1 hr at 1400°C	0.572	10.7	(58.4)	(17.4)	(24.2)
4						
		Original Analysis		53.84	19.19	26.97
	New crucible, 1 hr at 1300°C	0.556	4.7	51.86	20.96	27.18
	New crucible, 1 hr at 1400°C	0.550	7.5	(51.0)	(21.8)	(27.2)
7						
		Original Analysis		50.70	22.18	27.12
	Used crucible,† 1 hr at 1400°C			(49.3)	(23.4)	(27.3)
				52.42	21.04	26.54
10						
		Original Analysis		55.81	29.11	15.08
	New crucible, 1 hr at 1300°C	0.605	6.6	52.67	31.77	15.46
	New crucible, 1 hr at 1400°C	0.637	7.9	(52.1)	(32.6)	(15.3)
11						
		Original Analysis		51.42	33.38	15.20
	Used crucible,† 1 hr at 1400°C			(51.7)	(33.0)	(15.3)
				54.70	30.22	15.08
11						
		Original Analysis		69.73	13.98	16.29
	New crucible, 1 hr at 1300°C	0.573	12.0	65.11	18.18	16.71
	New crucible, 1 hr at 1400°C	0.457	10.1	(63.0)	(20.4)	(16.6)
11						
		Original Analysis		61.45	22.04	16.51
	Used crucible,† 1 hr at 1400°C			(62.4)	(20.9)	(16.7)
				66.48	17.31	16.21
11						
		Original Analysis		57.54	8.35	34.11
	New crucible, 1 hr at 1300°C	0.504	5.7	54.30	11.29	34.41
	New crucible, 1 hr at 1400°C	0.401	6.9	(53.8)	(11.7)	(34.5)
11						
		Original Analysis		52.40	13.48	34.12
	Used crucible,† 1 hr at 1400°C			(51.8)	(13.5)	(34.7)
				55.16	10.70	34.14

* Analyses in parentheses were calculated from original mixture analysis, sample weight and weight increase of platinum assuming the reaction: $3\text{FeO (sample)} = \text{Fe}_2\text{O}_3 \text{ (sample)} + \text{Fe (crucible)}$.

† Used once with same experimental mixture.

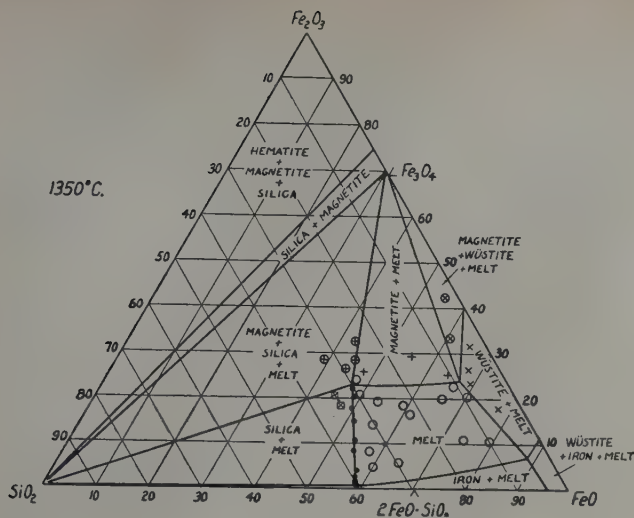


Fig. 4—1350°C isothermal section.

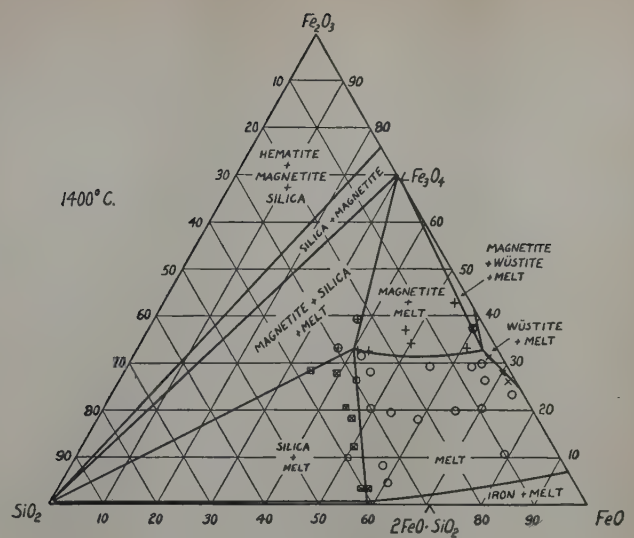


Fig. 5—1400°C isothermal section.

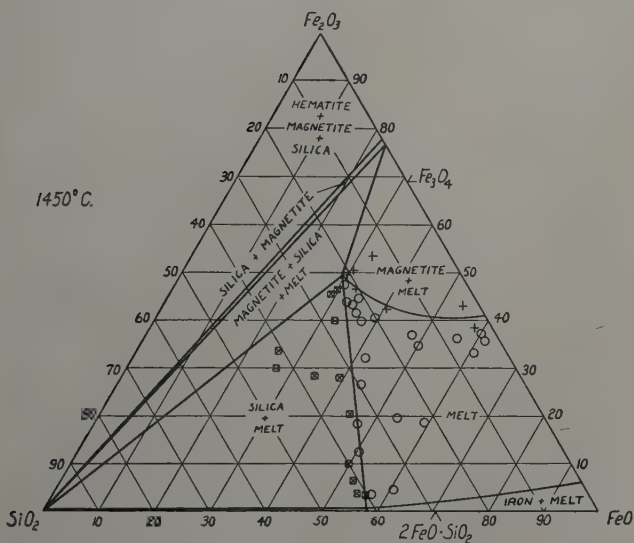


Fig. 6—1450°C isothermal section.

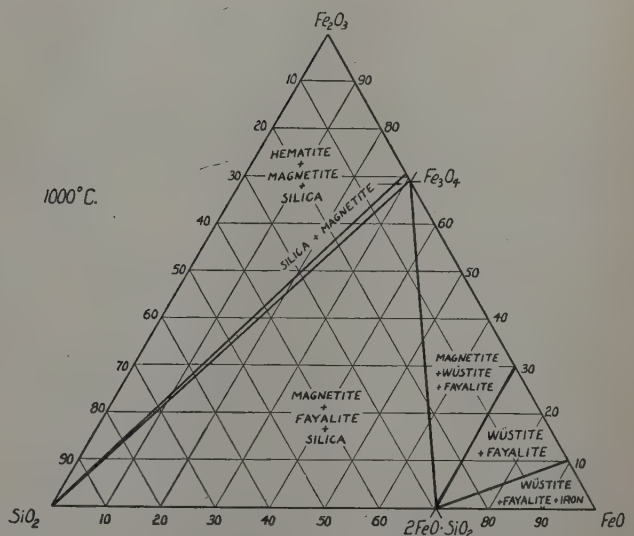


Fig. 7—1000°C isothermal section, based on binary systems.

for small uncertainties in Fe_2O_3 content.^{2, 5} The points along the $\text{FeO-Fe}_2\text{O}_3$ edges of the isothermal sections are taken from the Fe-O diagram of Darken and Gurry.¹

The final locations and shapes given to the melt field boundaries in Fig. 2 to 6 in some instances deviate a little from the curves of best fit with the experimental data. These deviations are the result of smoothing the data for the ternary system as a whole in accordance with the phase rule to eliminate minor discrepancies between the different sets of data on which diagrams are based.

In the figures and subsequent discussion, the solid silica phase is referred to simply as silica, although, strictly speaking, tridymite is the stable form of silica from 870° to 1470°C, and cristobalite is the stable form from 1470°C to the melting point. As pointed out by Darken,³ changes in the crystalline form of silica have very minor effects on the equilibrium data under consideration.

Lower Temperature Isotherms: No equilibrium studies below 1250°C were made in the present investigation so that no new data were obtained directly measuring the fayalite liquidus. However, it

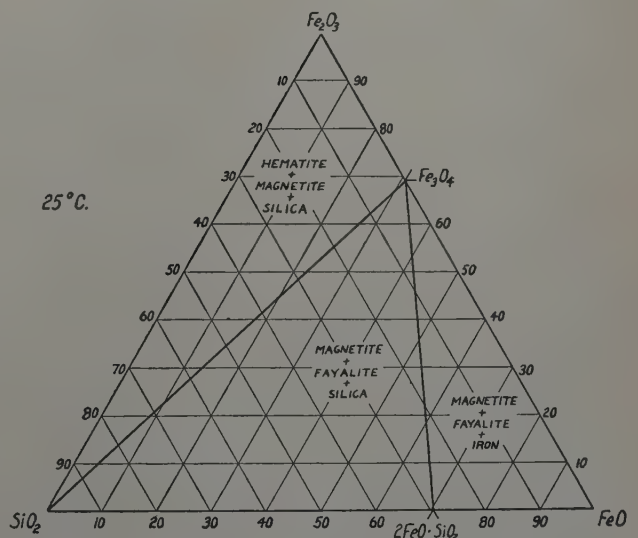


Fig. 8—25°C isothermal section, based on binary systems.

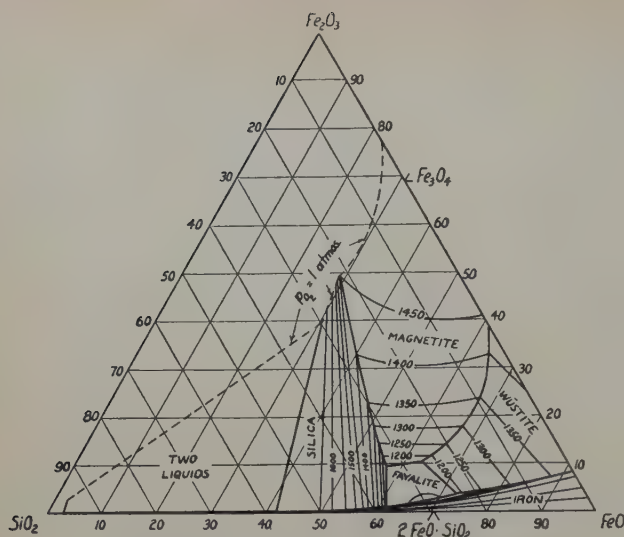


Fig. 9—Liquidus diagram for FeO-Fe₂O₃-SiO₂ system.

is now possible to locate the fayalite liquidus with reasonable confidence by combining the data of Bowen and Schairer on fayalite-iron-melt equilibria and Darken's determinations of invariant temperatures of the fayalite liquidus with extrapolations of composition data from the present investigation. The results of these constructions are shown in the complete liquidus diagram discussed later. Several successive isotherms would be necessary to describe the system completely in the temperature range of the fayalite liquidus (from 1208°C, the melting point of fayalite, down to 1118°C, the fayalite-magnetite-silica eutectic temperature).

Since no ternary compounds or ternary solid solutions have been found in the FeO-Fe₂O₃-SiO₂ system, the isothermal sections for temperatures below the ternary eutectic temperature are readily constructed from available knowledge of the binary systems. Between the invariant temperature 1118°C (magnetite, fayalite, silica, melt, and gas in equilibrium) and the invariant temperature 560°C (magnetite, wüstite, iron, gas in equilibrium), the system is represented by isotherms like Fig. 7. Fig. 8 shows the phases present in mixtures of various compositions below 560°C.

Liquidus Surfaces in FeO-Fe₂O₃-SiO₂ System: By combining the data of the present investigation with data published by various other investigators, the ternary diagram shown in Fig. 9 was constructed. This diagram shows all the liquidus surfaces in the FeO-Fe₂O₃-SiO₂ system and shows the complete temperature-composition field of stability of iron silicate slags at 1 atm. The basic data are outlined briefly below:

FeO-Fe₂O₃ edge: Complete data for the intersections of the iron, wüstite, and magnetite surfaces with the FeO-Fe₂O₃ edge were taken from the work of Darken and Gurry.¹

Region of immiscible liquids: The limits of liquid immiscibility were measured by Greig.⁶

Silica liquidus: The silica liquidus is determined primarily by 1—the univariant curve for silica-iron-melt completely measured by Bowen and Schairer² and checked by Schuhmann and Ensio,⁶ 2—the univariant curve for solid silica-liquid silica-liquid slag determined by Greig,⁶ and 3—data of the present investigation in the range 1250° to 1450°C. The univariant curve silica-magnetite-melt is ter-

minated at 1450°C where Darken found p_{O_2} equal to 1 atm.⁸ The same univariant curve is extrapolated down to 1118°C, the temperature determined by Darken for the invariant equilibrium silica-magnetite-fayalite-melt.

Magnetite liquidus: This surface was determined in the present investigation from 1250° to 1450°C. The two terminal points of the bounding curve for p_{O_2} equal to 1 atm have been determined as already discussed, but the shape of this curve was estimated. The univariant curve magnetite-wüstite-melt was extrapolated to 1150°C, the temperature estimated by Darken for the invariant point magnetite-wüstite-fayalite-melt.

Iron liquidus: Bowen and Schairer's data on the "FeO-SiO₂" system, confirmed by Schuhmann and Ensio, locate the iron liquidus. However, to avoid an apparent violation of the phase rule, the Fe₂O₃ percentages given by Bowen and Schairer were lowered to be consistent with Darken and Gurry's measurement of the Fe₂O₃ content of molten iron oxide in contact with metallic iron at 1371°C.

Wüstite liquidus: Curves of intersection of the wüstite liquidus with the FeO-Fe₂O₃ edge and the iron liquidus were located as described above, and the rest of the surface was determined in the present investigation.

Fayalite liquidus: This surface is drawn to pass through the appropriate univariant curves and invariant points for which the methods of location were described above.

Table II summarizes temperatures and compositions for important fixed points in the ternary liquidus diagram.

Discussion

The liquidus diagram for the FeO-Fe₂O₃-SiO₂ system shows a number of relationships which are of practical importance in slagmaking and fluxing. All the iron silicate slags of lowest freezing points (e.g., 1200°C and below) have compositions close to that of the mineral fayalite (ferrous orthosilicate: 2FeO·SiO₂ or Fe₂SiO₄). The lowest temperature at which a stable iron silicate melt can exist is 1118°C, and the slag with this minimum freezing point has approximately the composition: 57 pct

Table II. Data on Fixed Points in FeO-Fe₂O₃-SiO₂ Liquidus at 1 Atmosphere

Phases in Equilibrium	Temperature, °C	Analysis of Liquid Phase, Wt Pct		
		FeO	Fe ₂ O ₃	SiO ₂
Magnetite, iron oxide melt, and O ₂ at 1 atm	1583	22.6	77.4	0.0
Magnetite, silica, melt, and O ₂ at 1 atm	1447	29	49	22
Magnetite, congruent melting point	1597	31.1	68.9	0.0
Magnetite, wüstite, and iron oxide melt	1424	61.0	39.0	0.0
Magnetite, wüstite, fayalite, and melt	1150	63.0	10.5	26.5
Magnetite, silica, fayalite, and melt	1118	57.0	9.5	33.5
Wüstite, γ-iron, and iron oxide melt	1371	91.8	8.2	0.0
Wüstite, fayalite, γ-iron, and melt	1180	72.8	3.8	23.4
Fayalite, incongruent melting point	1208	68.4	2.3	29.3
Fayalite, silica, γ-iron, and melt	1180	61.0	1.0	38.0
Solid silica, liquid silica, liquid iron, and liquid slag	1690	42	—	58
		3	—	97
Solid silica, liquid silica, liquid slag, and air ($p_{O_2} = 0.21$ atm)	1665	31.7	36.7	31.6
		2.4	2.0	95.6

FeO, 9.5 pct Fe₂O₃, and 33.5 pct SiO₂. Ferric oxide in amounts up to 10 to 12 pct has little effect on the freezing point of fayalite slags, but increasing amounts of Fe₂O₃ beyond this point progressively raise the freezing point. When slags high in ferric iron are cooled from high temperatures, a substantial part of the ferric iron will have frozen out as magnetite by the time the temperature reaches about 1200°C. If the slag is then frozen and cooled slowly to room temperature, the remainder of the ferric iron also will appear finally as magnetite.

Stating the observations of the preceding paragraph in a different way, FeO is a good flux for SiO₂ whereas Fe₂O₃ and more particularly Fe₂O are very poor fluxes for SiO₂. Thus, the higher iron oxides form silicate slags only if reducing agents are available to yield ferrous iron. In Fig. 9 the isotherms in the silica liquidus are substantially straight lines, and the extensions of all these lines come very close to the Fe₂O₃ corner of the diagram. That is, for slags saturated with silica, the ratio of SiO₂ to FeO is nearly independent of the Fe₂O₃ content of the slag. For example, at 1500°C, 57 parts by weight of FeO will flux a maximum of 43 parts of SiO₂ regardless of the amount of Fe₂O₃ present in addition. The relationship of the state of oxidation of iron to the fluxing of SiO₂ is also of obvious importance in understanding the behavior of silicious refractories in steelmaking, and has been discussed elsewhere by one of the authors.⁷

The magnetite liquidus surface covers a relatively large and centrally located portion of the composition triangle in Fig. 9, and thus it is not surprising that the nonferrous smelterman encounters problems which appear to be related to magnetite precipitation. Copper converting is conducted under relatively oxidizing conditions and with limited additions of silicious flux. A typical converter slag might analyze 45 to 50 pct total Fe, 25 pct SiO₂, and 15 to 20 pct Fe₂O₃. Recasting this analysis into terms of the percentages of FeO, Fe₂O₃, and SiO₂ and ignoring other slag constituents by adjusting (% FeO + % Fe₂O₃ + % SiO₂) to 100 pct, the composition is found to be equivalent to about 10 to 15 pct Fe₂O₃, 55 to 60 pct FeO, 25 to 30 pct SiO₂. On the ternary diagram (Fig. 9), such a composition falls in the region of the magnetite liquidus surface and in fact corresponds to saturation with magnetite at temperatures around 1200°C. Although the idea that copper converter slags are often saturated with magnetite is not new, it is significant that this apparent approach to saturation is confirmed quantitatively as an equilibrium condition in the phase diagram. In reverberatory slags, in general, lower contents of Fe₂O₃ and higher contents of SiO₂ are found than in converter slags, so that reverberatory slag compositions are represented in Fig. 9 by points below and to the left of the points representing compositions of converter slags. That is, reverberatory slag compositions apparently approach the conditions of silica saturation along the silica liquidus surface. Comparisons of published slag analyses with the phase diagram do not show clearly how closely silica saturation is actually approached in practice since no satisfactory basis is available for allowing for the effects of the CaO, Al₂O₃, MgO, and other minor slag constituents on the SiO₂ solubility.

Reference is sometimes made to the solubility of magnetite in slags. From the data summarized in Fig. 9 it is possible to evaluate at any given temperature the quantity of magnetite which can be

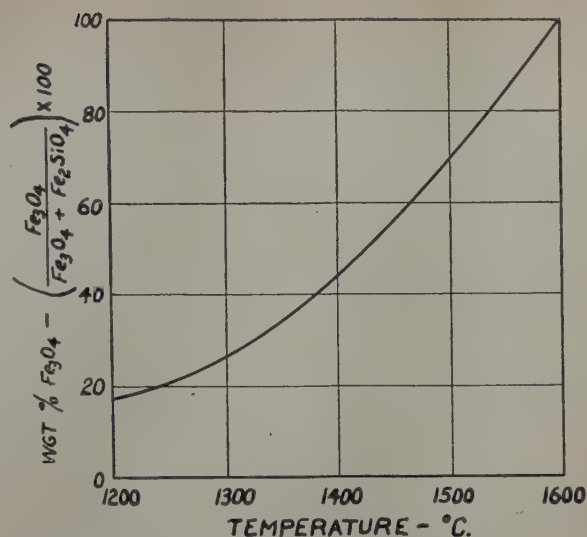
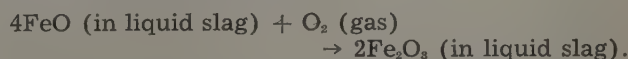


Fig. 10—Effect of temperature on magnetite solubility in fayalite slags.

dissolved in an iron silicate slag of given initial composition. To illustrate the variation of magnetite solubility with temperature, the ideal stoichiometric composition of fayalite, 2FeO·SiO₂, may be taken as a starting point. Fig. 10, based on the data of the magnetite liquidus in Fig. 9, shows the solubility of magnetite in fayalite slags as a function of temperature. The variations in Fe₂O₃ solubility with FeO-SiO₂ ratio in the initial slag are relatively small, so this plot probably is a good approximation of the magnetite solubility vs temperature relation for all types of iron silicate slags including copper converter slags. This graph shows that magnetite solubility increases rather rapidly with increasing temperature up to 1597°C, the melting point of Fe₃O₄ in the absence of silica. For example, from 1300° to 1250°C the solubility of magnetite drops from 25 pct down to 20 pct so that a slag saturated with magnetite at 1300°C would have to precipitate about 5 pct Fe₂O₃ in cooling only 50°C (90°F). To be even more specific, a ladle containing 10 tons of homogeneous magnetite-saturated slag at 1300°C would yield on cooling to 1250°C a mixture of 9.5 tons slag with 0.5 ton precipitated magnetite.

In some metallurgical processes, one of the important functions of the slag is to act as a carrier for oxygen. Oxygen dissolution in the slag involves oxidation of ferrous iron to ferric, and the reverse reaction occurs when the oxygen is given up. The dissolution of oxygen gas (e.g., in exposure of slag to air) may be written



The solubility of oxygen in the slag at a given temperature might be defined as the maximum quantity of oxygen which can be dissolved without precipitating a new phase. Since oxidation by the above reaction not only increases the Fe₂O₃ content, but also reduces the FeO-SiO₂ ratio in the slag, the result of oxidation is that the point representing slag composition will move both upward and to the left on the composition triangle in Fig. 9. Thus, for some slags, the maximum oxygen dissolution is achieved when magnetite starts to form as a separate phase while in other slags the maximum oxygen dissolution is achieved when solid silica starts to form. Using the data in the ternary diagram, the sequence

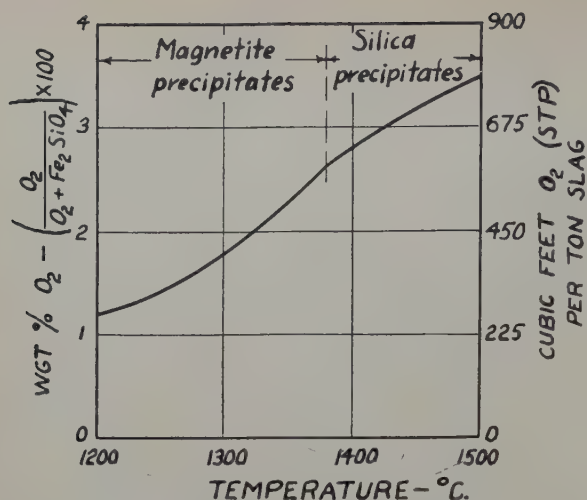


Fig. 11—Oxygen solubility in fayalite slags.

of changes during oxidation for any given initial slag composition can be easily followed. If the ideal stoichiometric composition $2\text{FeO} \cdot \text{SiO}_2$ is taken as a starting point, as was done previously in considering magnetite solubility, the oxygen solubility is given by Fig. 11. For this slag, the limit of oxygen dissolution at any temperature below 1380°C is reached when magnetite starts to precipitate. Above 1380°C , precipitation of silica limits the oxygen solubility.

The shape and location of the wüstite liquidus surface suggest the possibility that wüstite rather than magnetite might be the iron oxide phase forming in contact with iron silicate slags, especially for slags low in SiO_2 (less than 25 pct SiO_2) and at the same time low in Fe_2O_3 . However, for the specific

conditions of copper converting, thermodynamic calculations show that if conditions are sufficiently oxidizing to oxidize the sulphur of the matte to SO_2 , magnetite will form automatically in preference to wüstite. This is another way of saying that the primary converting reaction will not proceed without formation of a high- Fe_2O_3 or high-magnetite slag.

Acknowledgment

The authors wish to express their appreciation to the American Iron and Steel Institute for their financial support of this work.

References

- ¹L. S. Darken and R. W. Gurry: The System Iron-Oxygen. *Journal ACS* (1945) **67**, pp. 1398-1412; (1946) **68**, pp. 798-816.
- ²N. L. Bowen and J. F. Schairer: The System $\text{FeO}-\text{SiO}_2$. *American Journal of Science* (1932) **24**, pp. 177-213.
- ³L. S. Darken: Melting Points of Iron Oxides on Silica; Phase Relations in the System $\text{Fe}-\text{Si}-\text{O}$ as a Function of Gas Composition and Temperature. *Journal ACS* (1948) **70**, pp. 2046-2053.
- ⁴E. J. Michal and R. Schuhmann, Jr.: Thermodynamics of Iron Silicate Slags: Slags Saturated with Solid Silica. *Trans. AIME* (1952) **194**, pp. 723-728; *JOURNAL OF METALS* (July 1952).
- ⁵R. Schuhmann, Jr. and P. J. Ensio: Thermodynamics of Iron Silicate Slags: Slags Saturated with Gamma Iron. *Trans. AIME* (1951) **191**, pp. 401-411; *JOURNAL OF METALS* (May 1951).
- ⁶J. W. Greig: On Liquid Immiscibility in the System $\text{FeO}-\text{Fe}_2\text{O}_3-\text{Al}_2\text{O}_3-\text{SiO}_2$. *American Journal of Science* (1927) **14**, pp. 473-484.
- ⁷R. Schuhmann, Jr.: Silica-Iron Oxide Systems. *Amer. Iron and Steel Inst., Chicago Regional Meeting* (1951).

Technical Note

Some Low Temperature Properties of Titanium Alloy RC-130-B And Stainless Steel

by W. W. Tyler, L. B. Nesbitt, and A. C. Wilson, Jr.

INVESTIGATIONS of thermal conductivity and impact strength of the titanium alloy RC-130-B and 316 stainless steel were undertaken because of interest in strong, nonmagnetic, commercially available alloys of low thermal conductivity for use in low temperature experiments. Measurements of electrical resistivity and thermoelectric power were also made for some of the samples studied.

The titanium alloy designated as RC-130-B is manufactured by Rem Cru Titanium Inc. It contains 0.14 pct C, 3.99 pct Al, and 4.7 pct Mn. A general discussion of properties of the two phase Ti-4Mn-

4Al alloys is given by Finlay and Vordahl.¹ The alloy is machinable and has a yield strength greater than 130,000 lb per sq in. at 0.2 pct offset. The 316 stainless steel sample used for both conductivity and impact strength measurements was obtained from the Allegheny-Ludlum Steel Corp. and is designated as Allegheny metal 18-8M, Type 316, Grade 316. The sample had received 25 pct minimum final cold reduction and had a Brinell hardness rating of 255. Several impact tests were made on a sample of 316 stainless which had not received the 25 pct cold reduction. Also several data points are reported giving thermal conductivity and electrical resistivity for a sample of 304 stainless steel taken from stock.

Figs. 1 and 2 give thermal conductivity and electrical resistivity data for the titanium alloy and for

W. W. TYLER, L. B. NESBITT, and A. C. WILSON, Jr., formerly with Knolls Atomic Power Laboratory, are now associated with the Research Laboratory, General Electric Co., Schenectady, TN 168E. Manuscript, March 25, 1953.

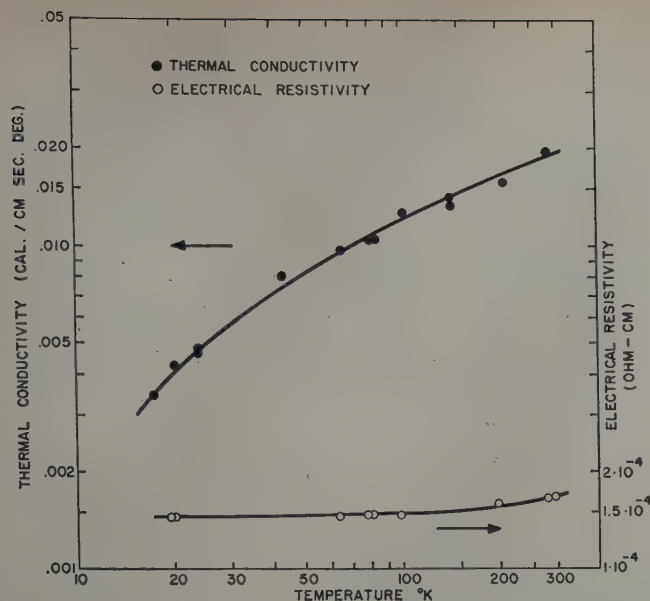


Fig. 1—Thermal conductivity and electrical resistivity of titanium alloy RC-130-B.

the stainless steel samples. Conductivity values for the stainless steel types 304 and 316 agree within our experimental error with the more extensive data on stainless steels obtained by Powers² and by Estermann and Zimmerman.³ Fig. 3 shows the absolute thermoelectric power of the titanium alloy. This was derived from the thermoelectric power of a couple consisting of the titanium alloy and copper, using values of the absolute thermoelectric power of copper given by Borelius.⁴ The absolute thermoelectric power for both the 316 and 304 stainless steels is of the order of a microvolt per degree or less throughout the temperature range and is consequently not given in detail.

The equipment and experimental techniques used in making the conductivity measurements have been reported in some detail⁵ and will not be described here. The uncertainty in the magnitude of the thermal conductivity data estimated from knowledge of errors resulting from lead losses, thermal drift, and radiation losses is at most ± 10 pct for the titanium alloy and less for the stainless steel. Values of electrical resistivity are correct within ± 2 pct. Thermoelectric power data are probably accurate to within ± 0.5 microvolt per degree.

As a measure of the behavior of the alloys under shock loading, Charpy impact tests were made on

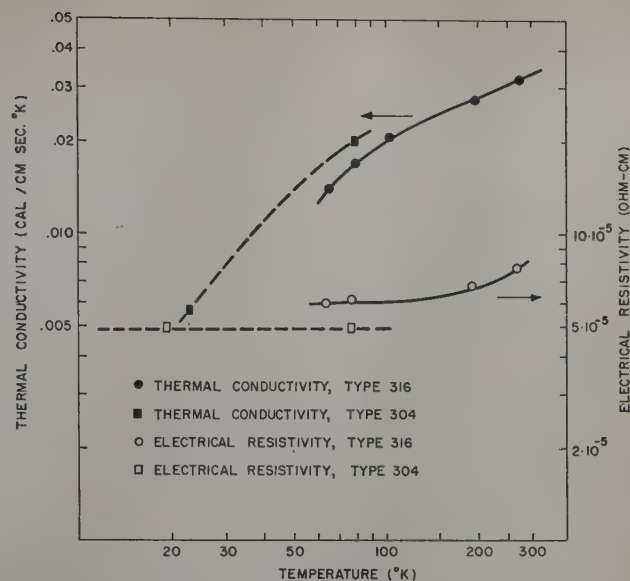


Fig. 2—Thermal conductivity and electrical resistivity of stainless steel.

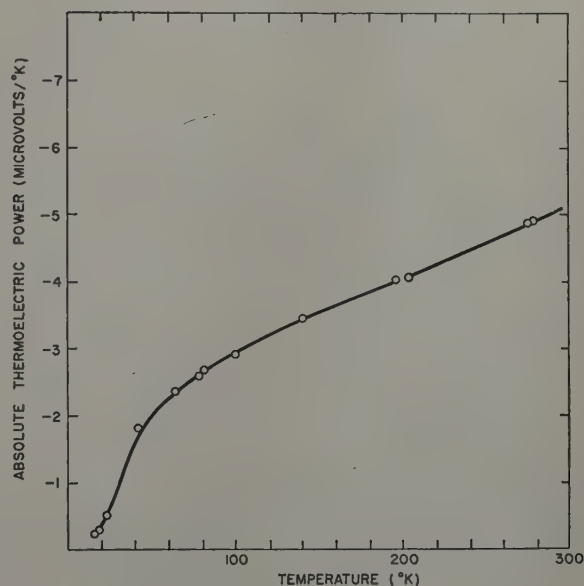


Fig. 3—Absolute thermoelectric power for the titanium alloy RC-130-B.

RC-130-B, cold drawn 316 stainless steel, and normal 316 stainless steel samples. The results are given in Table I. Tests were made at room temperature, liquid nitrogen temperature, and liquid hydrogen temperature. N_2 and H_2 temperatures were maintained for the 4 to 6 sec necessary to make the test by a reservoir of the liquid in a paper box surrounding the sample. The presence of the paper box introduced no appreciable error in the measurement.

References

- W. L. Finlay and M. B. Vordahl: *Metal Progress* (1952) **61**, p. 73.
- R. W. Powers: To be published.
- I. Estermann and J. E. Zimmerman: *Journal of Applied Physics* (1952) **23**, p. 578.
- G. Borelius: *Handbuch der Metallphysik* (1935) Vol. 1, pp. 181-485. Leipzig. Akad. Verlags Gesellschaft.
- W. W. Tyler and A. C. Wilson, Jr.: *Physical Review* (1953) **89**, p. 870.

Table I. Results of Charpy Impact Tests*

Sample	Room Temperature	N_2 Temperature	H_2 Temperature
RC-130-B 1/2 size		6-7	6-7
Full size	12-18†		
316SS (25 pct reduction)			
1/2 size	41	42-44	42
Full size	101	87-100	91-89
316SS (Normal)			
1/2 size	66	84-85	76-74
Full size	189	159-175	178-179

* The numbers indicate energy absorbed during fracture of the sample in units of ft lb. For some of the materials, several tests were made and a range of values is indicated.

† Data provided by Rem Cru Titanium Inc.

Solutions of Metals in Fused Salts

by Daniel Cubicciotti

Measurements have been made of the solubilities of a number of metals in their fused halides and the effect of added salts on these solubilities. A structural model for the solution of metal in salt is presented to account for the experimental data.

IT has long been known that some metals are capable of being dispersed or dissolved in certain of their fused salts.¹ Davy² and Bunsen³ were among the first to observe that in some fused salt electrolyses, a highly colored, strongly reducing salt phase appeared in the neighborhood of the cathode. Later workers found that the current efficiency of the electrolysis was markedly reduced when such a phase appeared. It was also found that the strongly reducing salt could be made by melting the metal and normal salt together. Chemical analysis showed that in such salts the metal ion to anion ratio was always larger than in the normal salt.

From such observations arose two different explanations of the nature of metal in salt solutions. When a solution of this type is quenched, it is possible to find small globules of metal in the salt. From this and other observations, Lorenz⁴ and co-workers assumed the metal in salt solution to be a colloidal dispersion of metal in the fused salt and called it "metallnebel" or metal fog formation. They made a number of experiments to substantiate this point of view. Another school felt that when the metal dissolved it reduced the salt partially to a mixture or solution of normal salt and subsalt. Both of these ideas could explain the strong reducing character of the salt formed and the low current efficiency of the electrolysis. If either a metal colloid or a subsalt were formed at the cathode and diffused to the anode, it would be oxidized to the normal salt. Thus a cyclic process of oxidation and reduction could be set up conducting the current without giving rise to a net change in the system.

These facts led the author to investigate some of the properties of metal in salt solutions with the

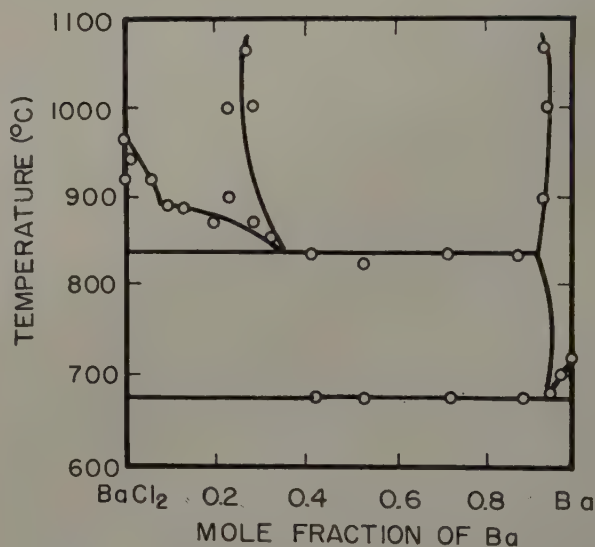


Fig. 1—The temperature-composition diagram for the barium-barium chloride system (from ref. 5).

hope of elucidating their nature further. Among the metal-salt systems that form metal in salt solutions most markedly are the alkaline earth metal-halide systems and cerium, bismuth, and cadmium halides. Other systems of halides, oxides and sulphides form such solutions to a lesser degree. The first work undertaken was a study of the temperature-composition diagrams of some of the systems.⁵ From such diagrams it would be possible to distinguish between a subhalide formation or a colloid. A subhalide should give rise to characteristic changes in the phase diagram, while a colloidal dispersion of metal in salt would not alter the freezing point of the salt.

The results obtained on a number of alkaline earth metal-halide systems were all quite similar. Fig. 1 shows the barium-barium chloride system. The other

D. CUBICCIOTTI is associated with the Atomic Energy Research Laboratory, North American Aviation, Inc., Downey, Calif.

Discussion on this paper, TP 3589D, may be sent, 2 copies, to AIME by Nov. 1, 1953. Manuscript, Feb. 24, 1953. Los Angeles Meeting, February 1953.

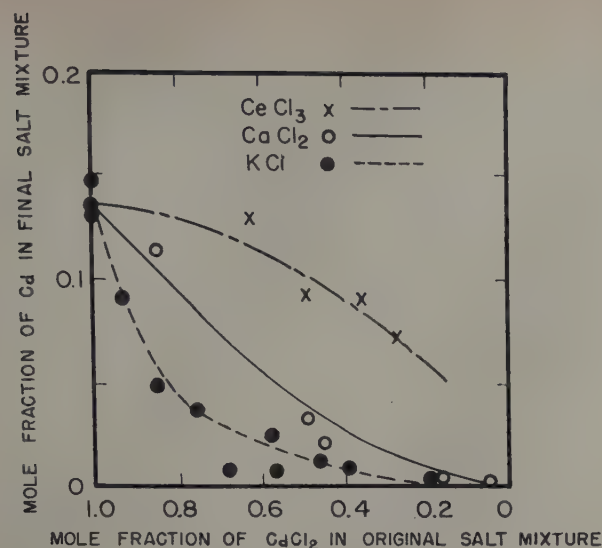


Fig. 2—The solubility of cadmium in mixtures of cadmium chloride with the chlorides of monovalent, divalent, and trivalent electropositive metals at 740° (from ref. 7).

systems were all of this type—a simple eutectic system with a region of liquid immiscibility. The phase diagrams of these systems show that no high temperature stable subhalide was formed. In addition, they show that the solution cannot be colloidal in nature because the freezing point of the salts were depressed as the metals were added. Thus the metal in salt solutions are simply true solutions in the normal sense.

From a comparison of the solubilities of the alkaline earth metals in their fused chlorides an interesting correlation can be made. Going down the periodic table from magnesium to barium, including the subgroup elements zinc and cadmium, it is seen that the solubility of the metal in the salt increases. In Table I these solubilities are compared with the reducing power of the metal (i.e., the free energy of formation of the normal salt) and the ionic radius of the metal ion. There is no correlation between the solubility and the reducing power of the metal; however, as the cationic radius of the metal increases so does its solubility in the fused chloride—for this group of the periodic table.⁵ Another correlation can be made between the solubility and valence of cation or better cation to anion ratio in the normal salt. In Table II are given the solubilities of potassium, strontium, and cerium in their chlorides.⁶ For these metals the cationic radii are essentially the same but the solubility increases as the ratio of number of cations to anions decreases.

The effect of added foreign salt on the solubility of

Table I. Solubilities of the Metals of Group II in Their Molten Chlorides. From Ref. 5

Metal	Solubility* in Chloride, Mol Pct	Tempera- ture, °C	Radius of +2 Ion, Å	-ΔF ₂₉₈ for Forma- tion of Salt, Kcal per Mol
Mg	1.2	900	0.65	141.2
Ca	16	900	0.99	180.1
Sr	20	900	1.13	186.0
Ba	30	900	1.35	193.2
Zn	10 ⁻⁴	500	0.74	88.5
Cd	16	650	0.97	82.7

* The solubilities for zinc and cadmium are not known above 500° and 650°C, respectively.

Table II. Solubilities of Metals in Their Salts at About 800°C. From Ref. 6

Metal	Solubility, Mol Pct	Cation Radius, Å
K	1	1.33
Sr	20	1.13
Ce	33	1.15

a metal in its halide was another variable that could easily be investigated.⁷ For this investigation the cadmium-chloride and bismuth-chloride systems were chosen because these metals would have little tendency to reduce the added salts. In Fig. 2 is shown the effect of several foreign chlorides on the solubility of cadmium in its chloride. It may be seen that any added salt reduced the solubility of the cadmium and further the larger the cation to anion ratio the more effective the added salt in reducing the solubility. The effect of different salts with the same cation to anion ratio is seen in Fig. 3. There it can be seen that the more electropositive the metal of the cation of the added salt, the more the solubility of the cadmium was reduced. The electropositive character of the metal of the added salt is given in Table III. The smaller the equilibrium constant the more electropositive the metal of the salt.

Table III. Equilibrium Constants for the Reactions of Salts with Cadmium at 740°C. From Ref. 7

Salt	Equilibrium Constant for Reaction
	$Cd + \frac{2}{n} \times Cl_n =$ $CdCl_2 + \frac{2}{n} X$
CaCl ₂	10 ^{-23.4}
MgCl ₂	10 ^{-11.9}
MnCl ₂	10 ^{-4.4}
ZnCl ₂	10 ^{-1.9}

Similar results were obtained in the bismuth-chloride system.⁸ These are shown in Fig. 4. The solubility of the bismuth was decreased by the addition of any salt. The smaller the cation to anion ratio of the added salt, the less the solubility was depressed. For the same cation to anion ratio the

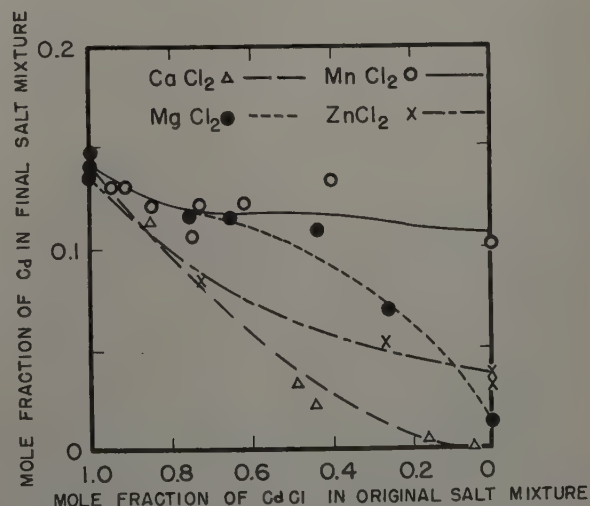


Fig. 3—The solubility of cadmium in mixtures of cadmium chloride with several divalent chlorides at 740° (from ref. 7).

more electropositive the metal of the added salt, the greater the decrease of the bismuth solubility.

The data so far obtained on the solubilities of metals in their fused chlorides can be summarized as follows: 1—For the metals of group II of the periodic table the solubility of the metals in their chlorides increases as the cation radius increases. 2—The solubility increases as the ratio of number of anions to cations increases (shown in the case of potassium, strontium, and cerium). 3—The solubility is decreased (for cadmium in cadmium chloride) on the addition of the chloride of an electropositive metal; the smaller the anion to cation ratio of the added salt, the more the solubility is decreased. 4—On the addition of chlorides (divalent chlorides to cadmium chloride) the solubility is decreased, and the more electropositive the metal of the added chloride, the greater the decrease in the solubility.

These experimental facts are in accord with the following picture of metal in salt solutions.* The

* From the model presented above little or no solubility of sodium in molten sodium chloride would be expected because the octahedral holes are all occupied in the normal salt. However, Dr. M. Bredig of the Oak Ridge National Laboratory has found this solubility to be about 11 mol pct. He has suggested to the author that the sodium ions may be small enough to fit into the unoccupied tetrahedral holes that occur in the close-packed structure.

chloride ions of the molten salt may be considered to be arranged approximately in a close-packed structure. They are packed in that way and determine the general structure of the system because they are the larger ions. The positive ions are situated in the

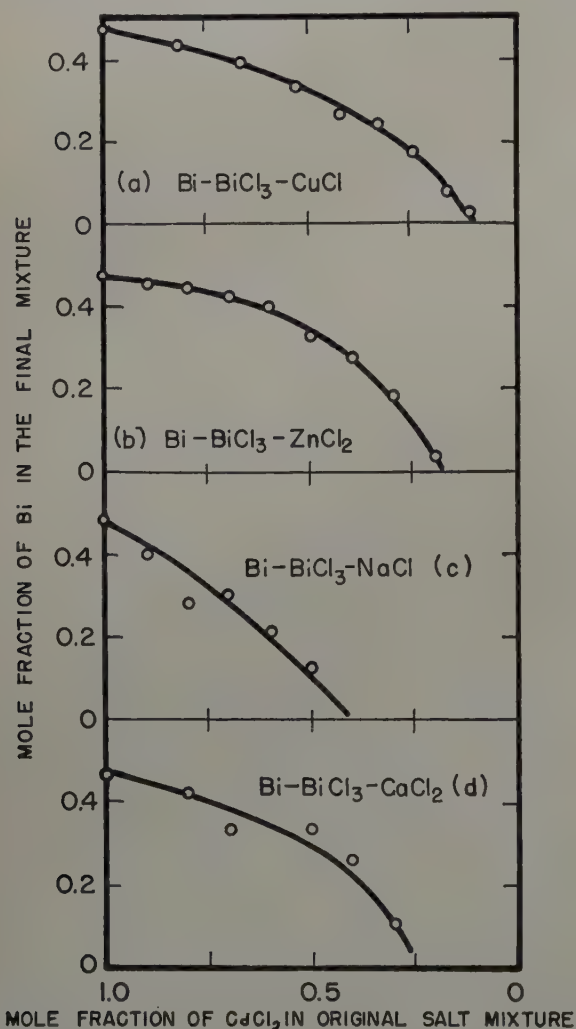


Fig. 4—Influence of added salt on the solubility of bismuth in its trichloride at 450° (from ref. 8).

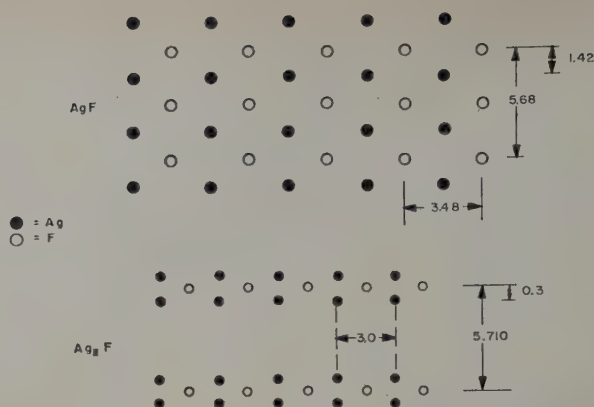


Fig. 5—Comparison of the structures of AgF and Ag₂F. Distances are in Angstrom (from refs. 9 and 10).

octahedral holes left among the chloride ions. The cations of the dissolved metal go into any such unoccupied holes.

In a 1-1 salt there are as many cations as holes and so in the pure salt the holes are all filled. In a 2-1 or a 3-1 salt, one-half and two-thirds of the holes are empty. Therefore, the greater solubility of metal in a salt of large anion to cation ratio (item 2 above) is plausible since the concentration of holes in the salt depends upon the anion to cation ratio. The larger the cation the further the anions surrounding the hole are separated. Thus the metals with larger cations are more soluble (items 1 and 3 above).

The electrons transferred to the salt by the dissolved metal are in bands or zones of energy states belonging to the salt system as a whole. As the salt of a more electropositive metal is added the energy levels would be raised, making it more difficult for an electron from the metal to be transferred to the salt and in effect reducing the solubility of the metal (item 4 above).

In the silver-fluoride system in addition to the compound AgF there exists a substance of empirical formula Ag₂F in the solid. The structures of these two phases have been determined.^{9,10} It is interesting to note that the two structures are very similar except that a series of fluoride vacancies exist in the Ag₂F structure. The two structures are shown schematically in Fig. 5. It can be seen that a layer of fluoride ions is missing in the Ag₂F structure. The addition of the fluoride ions to Ag₂F would be comparable to the addition of Ca to CaCl₂. This similarity to the picture proposed for metal in salt solutions may be entirely coincidental and not a confirmation of the proposal.

References

- ¹ A collection of references in this field was made by Cubicciotti, USAEC declassified document MDDC-1058, June 1946.
- ² H. Davy: *Trans. Royal Soc., London* (1807) **97**, p. 1.
- ³ R. Bunsen and G. Kirchhoff: *Pogg. Ann.* (1861) **113**, p. 364.
- ⁴ R. Lorenz and W. Eitel: *Pyrosole*, Leipzig. (1926).
- ⁵ D. Cubicciotti and C. Thurmond: *Journal ACS* (1949) **71**, p. 2149.
- ⁶ D. Cubicciotti: *Journal ACS* (1949) **71**, p. 4119.
- ⁷ D. Cubicciotti: *Journal ACS* (1952) **74**, p. 1198.
- ⁸ G. Cleary and D. Cubicciotti: *Journal ACS* (1952) **74**, p. 557.
- ⁹ A. F. Wells: *Structural Inorganic Chemistry*. (1945) London. Oxford Press.
- ¹⁰ Terrey and Diamond: *Journal Chem. Soc., London* (1928) **131**, p. 2829.

Reaction of Silver With Aqueous Solutions of Cyanide and Oxygen

by G. A. Deitz and J. Halpern

The kinetics of dissolution of silver in cyanide solutions under oxygen pressure have been investigated over a wide range of conditions with a view to establishing the reactions involved and the factors which influence the rate. The results indicate that the rate is determined principally by the transport of reactants in solution to the silver surface. The thermodynamic features of the reaction with particular reference to the influence of pH and CN^- are also discussed and summarized in the form of potential-pH diagrams.

METALLIC silver is readily attacked and dissolved by cyanide solutions in the presence of oxygen. This reaction has long been recognized and extensively applied¹ in the well-known cyanide process for the extraction of silver from its ores. While this process has been subjected in the past to a number of investigations^{2,3} both of a practical and fundamental nature, some features relating to the chemistry of the reactions involved, the role of oxygen, the nature of the rate-controlling step, and the effects of pH and certain reagents such as lime, are still not fully understood. It was felt that this situation justified a further investigation of the reaction, made with a view to obtaining a better understanding of its kinetics and mechanism.

In the present investigation rate curves for the dissolution of silver were determined over an extensive range of carefully controlled reaction conditions. By carrying out the reactions in a pressure vessel, the partial pressure of oxygen, and hence its concentration, could be varied widely. The influence on the reaction of other variables including temperature, pH, and the concentrations of cyanide, peroxide, and other salts was also examined.

The results of these kinetic studies are presented and discussed in this paper, together with a summary of available thermodynamic information relating to the possible reactions which can accompany the attack on silver by aqueous solutions of cyanide and oxygen.

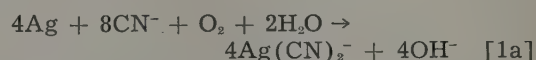
Chemistry and Thermodynamics of the Reaction

The chemistry of the reactions of gold and silver with aqueous cyanide solutions has been the subject

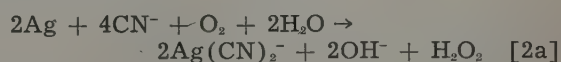
G. A. DEITZ is associated with Kaiser Aluminum and Chemical Corp., Trentwood Plant, Spokane, Wash., and J. HALPERN is Assistant Professor of Metallurgy, University of British Columbia, Vancouver, Canada.

Discussion on this paper, TP 3590D, may be sent, 2 copies, to AIME by Nov. 1, 1953. Manuscript, Feb. 13, 1953; revision, June 18, 1953. Los Angeles Meeting, February 1953.

of several recent reviews.^{2,3} It has been proposed² that the following reaction occurs when silver dissolves in cyanide solutions in the presence of oxygen:



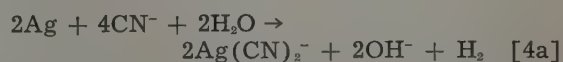
An equation of this form, for the corresponding dissolution of gold, was first suggested by Elsner.⁴ Bodlaender⁵ proposed a similar overall reaction, but suggested that it took place in two steps,



followed by



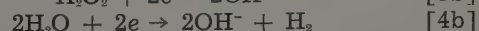
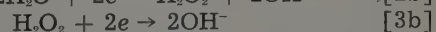
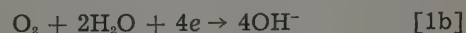
On the other hand, Janin⁶ suggested that the dissolution of gold can occur with the liberation of hydrogen, rather than by reduction of oxygen. The corresponding equation for the dissolution of silver is



All these reactions represent oxidation-reduction processes and may be resolved into the corresponding separate oxidation and reduction components. The oxidation step involves the formation of the argentocyanide ion and is the same for all the reactions, i.e.,



However, reactions 1a, 2a, 3a, and 4a differ in the nature of the reduction steps which are, respectively,



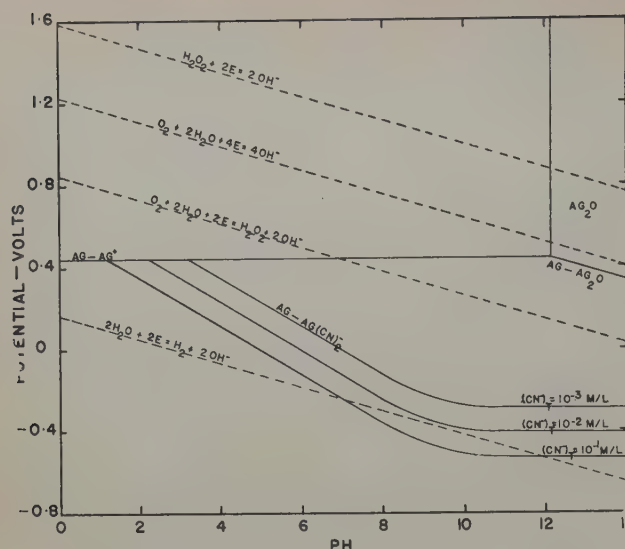


Fig. 1—Potential-pH diagrams for Ag-H₂O and Ag-H₂O-CN⁻. Temperature, 25°C.

The potentials corresponding to these reactions are shown in Fig. 1 as functions of the pH and total CN⁻ concentration of the solution. The calculations were made and the results plotted according to the method of Pourbaix⁷ whose diagram for the system Ag-H₂O,⁸ has been extended to include the effect of CN⁻. Only silver and its monovalent compounds have been considered. The potentials shown for the reduction of O₂ and H₂O correspond to pressures of 1 atm of O₂ and 10⁻⁶ atm of H₂, respectively, and to a concentration of H₂O₂ of 10⁻⁶ mol per liter. The potentials for the oxidation of Ag and the equilibrium between Ag⁺ and Ag₂O correspond to dilute silver solutions, the total concentration of dissolved silver (including Ag⁺ and Ag(CN)₂⁻) being arbitrarily taken as 10⁻⁶ mol per liter in accordance with the convention of Pourbaix. Details of the calculations which are based on data of Latimer⁹ are given in an appendix to this paper.

The diagram shows that in the absence of cyanide, the solubility of Ag⁺ exceeds 10⁻⁶ mol per liter at pH values below 12.3. At higher pH an insoluble

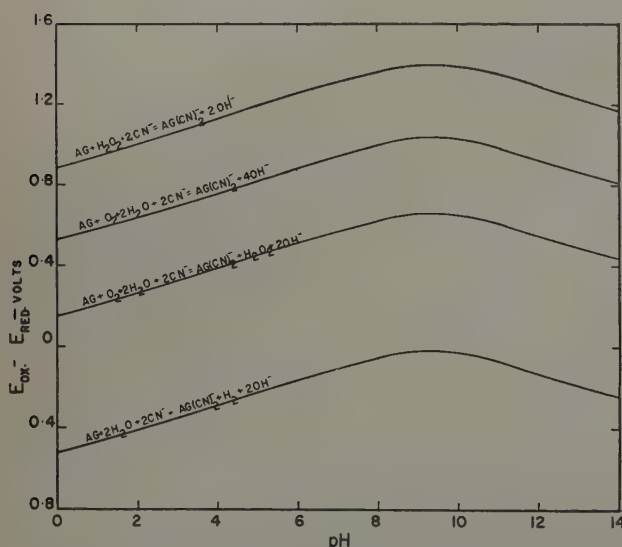


Fig. 2—Potentials for various dissolution reactions of silver in aqueous cyanide. Temperature, 25°C. (CN⁻)_T, 10⁻² mol per liter.

Ag₂O phase is formed. The equilibrium potential between Ag and Ag⁺ is 0.446 v. Cyanide lowers the concentration of free Ag⁺ ion (corresponding to a given total silver concentration of 10⁻⁶ mol per liter through formation of the argentocyanide complex



This results in the disappearance of the Ag₂O phase and in the lowering of the Ag-Ag⁺ potential.

These results are further summarized in Fig. 2, where the differences between the potentials for the various reduction and oxidation reactions are plotted as functions of pH, under the conditions noted above for a total cyanide concentration (including CN⁻ and HCN) of 10⁻² mol per liter. These plots show that Eqs. 1a, 2a, and 3a all correspond to positive potentials (i.e., to a decrease in the free energy, ΔF) and are therefore thermodynamically feasible. Reaction 4a corresponds to a negative potential and is therefore thermodynamically improbable under these conditions. A similar conclusion was reached by Barsky, Swainson, and Hedley² who determined the equilibrium constants for these re-

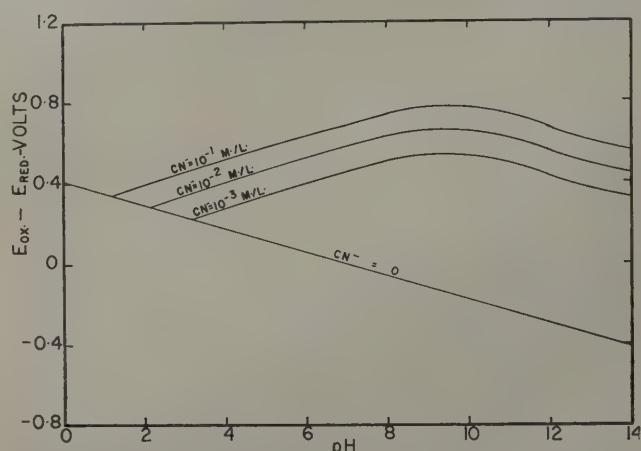
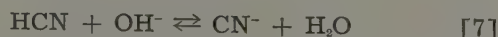


Fig. 3—Effect of pH and total cyanide concentration on the potential for the dissolution of silver with reduction of O₂ to H₂O₂. Temperature, 25°C. (Ag⁺)_T, 10⁻⁶ mol.

actions. Experimental confirmation was obtained by McLaurin,¹¹ Christy,¹² and other investigators who have found that gold and silver do not dissolve in cyanide solutions in the absence of oxygen. Bodlaender⁶ has shown that reaction 2a occurs by observing the formation of H₂O₂ in the solution. It has also been suggested^{2,3} that reactions 1a and 3a participate in the dissolution process although the evidence for this is less conclusive.

Fig. 3 shows the plots of the potential for reaction 2a against pH for various cyanide concentrations, the total silver ion concentration remaining constant at 10⁻⁶ mol per liter. The potential is seen to increase with the total cyanide concentration, due to increased formation of Ag(CN)₂⁻ ion in accordance with Eq 6. This also accounts for the rise in potential with pH, for any given total cyanide concentration, since there is a corresponding increase in the amount of free CN⁻ due to the ionization of HCN which is a weak acid, i.e.,



This equilibrium lies effectively to the left at pH values below 4, and in this region cyanide (which exists largely as HCN) is without appreciable effect on the potential. On the other hand at pH values

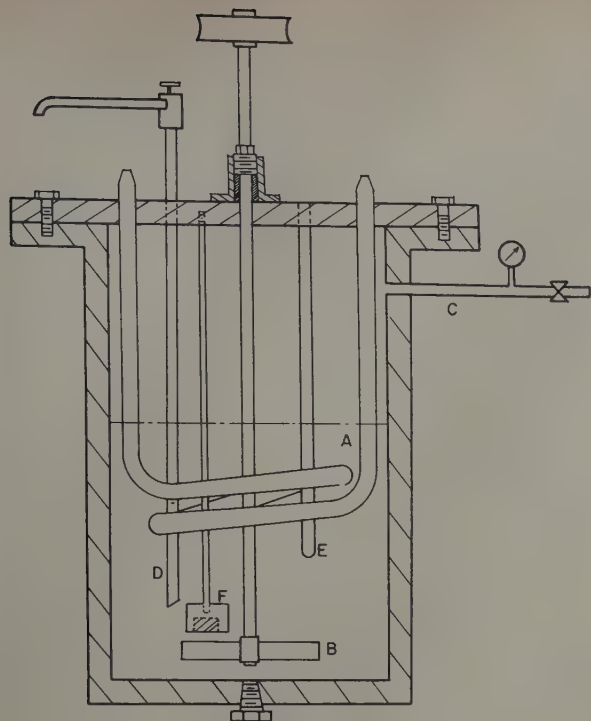


Fig. 4—Schematic diagram of stainless steel pressure vessel. A—Cooling coil. B—Stirrer. C—Gas inlet tube. D—Sampling tube. E—Thermometer well. F—Silver specimen in bakelite mount.

above 10, the equilibrium lies far to the right and increasing pH does not result in any further substantial increase in the amount of free CN^- . The decrease in overall potential for reaction 2a in this region, shown in Fig. 3, is due to a lowering in the potential for the reduction of oxygen.

Experimental

Materials: Reagent grade sodium cyanide and other chemicals used in making up the solutions, were supplied by Nichols Chemical Co. Oxygen was supplied in cylinders by Canadian Liquid Air Co. and used without further purification. Pure silver (99.99 pct) was melted in an induction furnace under an argon atmosphere and cast into ingots of 2 cm diameter. The ingots were cold-worked into rectangular bars, and sections of 2 cm length were annealed above the recrystallization temperature for 24 hr. The annealed sections were mounted in bakelite to insulate them electrically and to leave exposed only a desired surface cross section. The exposed surface of the silver was polished and etched prior to measurement of the dissolution rate.

Apparatus: The apparatus used in this study is described in Fig. 4, and was constructed entirely of stainless steel which was inert to the solutions used. The vessel measured 7 in. ID x 11 in. in height and

was designed for pressures up to 10 atm. The bakelite mount containing the insulated silver specimen was held by a stainless steel rod, so that the silver surface was exposed to the solution about 5 mm above the stirrer which was 2 in. in diameter and rotated at 895 rpm. The autoclave was heated externally by a gas burner, and the temperature of the solution maintained to within $\pm 0.5^\circ\text{C}$ by a Wheelco controller coupled to a platinum resistance thermometer. A desired pressure of oxygen was maintained above the solution by means of a standard two-stage gas regulator mounted on the oxygen regulator. A 2.5 liter volume of solution was generally used.

Procedure: The course of the reaction was followed by withdrawing samples of the solution through the tube D, at measured time intervals and determining the concentration of dissolved silver by the mixed-color dithizone method¹⁰ using a Beckman DU spectrophotometer. The samples were first rendered free of cyanide, which interferes with the colorimetric determination, by acidifying with HNO_3 and evaporating to dryness.

Cyanide concentrations were determined by titra-

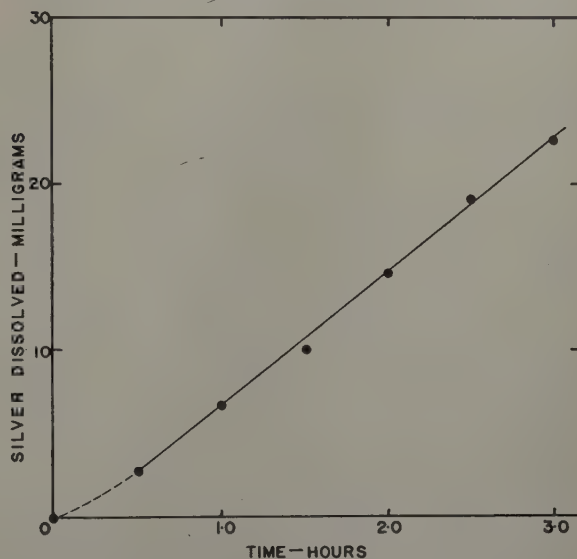


Fig. 5—Typical rate curve for the dissolution of silver. NaCN , 0.0096 mol. Temperature, 24°C . O_2 , 3.4 atm.

tion with standard AgNO_3 using KI as indicator. The pH measurements were made with a Beckman H-2 pH meter. Other determinations were made by standard analytical procedures.

Results

Rate Curves for the Reaction: A typical rate curve for the dissolution of silver is shown in Fig. 5. A short induction period, of the order of 15 min, was generally observed and is believed to be due to the slow dissolution of an oxide film initially present on the silver surface. Following this induction period, the rate plots were always linear, indicating a zero order reaction rate. Rates were calculated from the slope of this linear region.

The reproducibility of the rate measurements is illustrated in Table I. In a series of five experiments made under similar conditions, the measured rates ranged from 4.50 to 5.15 mg Ag per sq cm per hr. The average deviation of the rates from the mean value was ± 4.6 pct. The maximum deviation was 8 pct.

KCN solutions were found to give dissolution

Table I. Reproducibility of Rate Measurements

(NaCN)_T, 0.0096 mol per liter. Temperature, 24°C . O_2 pressure, 3.4 atm.

Experiment No.	Dissolution Rate, Mg Ag per Sq Cm per Hr	Deviation from Mean Rate, Pct
1	4.50	-5.6
2	4.94	+3.6
3	4.66	-2.3
4	4.61	-3.4
5	5.15	+8.0
Mean	4.77	± 4.6

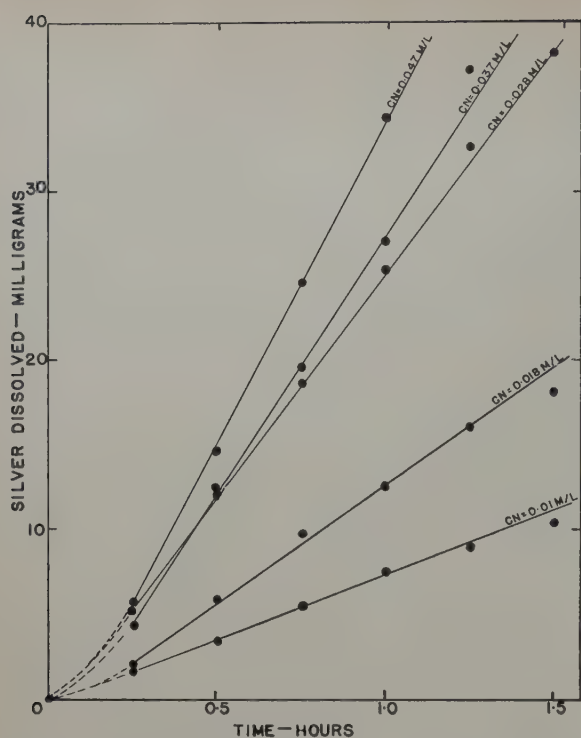


Fig. 6—Rate curves for the dissolution of silver at different NaCN concentrations. Temperature, 24°C. O_2 , 7.5 atm.

rates identical with those for NaCN solutions of the same molar cyanide concentration.

Micrographic examination of the silver surface at the end of the experiments indicated that dissolution occurred uniformly on the surface. There was no evidence of etch pits or preferential grain boundary corrosion. The linearity of the rate curves indicates that the surface area of the silver remains effectively constant during the dissolution experiment, and that the dissolved silver is without effect on the reaction.

Effect of Cyanide and Oxygen Concentrations: Measurements of the rate of dissolution were made using solutions with NaCN concentrations ranging from zero to 0.065 mol per liter* at oxygen pres-

* The initial pH of the solutions varied with the concentration of NaCN due to hydrolysis of CN^- according to the following reaction: $CN^- + HOH \rightarrow HCN + OH^-$. The pH for any solution of given NaCN concentration can readily be calculated from the known ionization constant of HCN (Eq. 23, Appendix), which leads to the following approximate relation: $pH = 11.699 + \frac{1}{2} \log [NaCN]$.

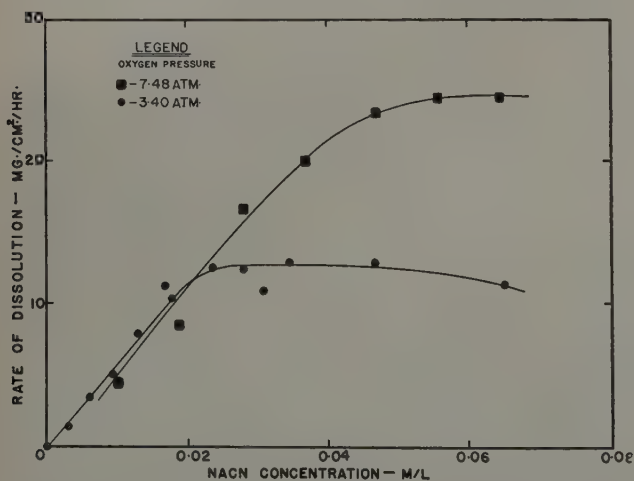


Fig. 7—Effect of cyanide concentration on the rate of dissolution of silver. Temperature, 24°C.

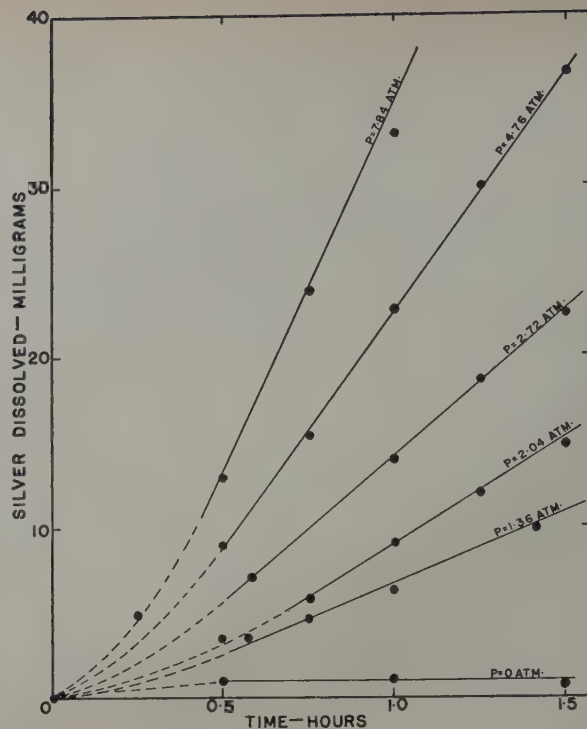


Fig. 8—Rate curves for the dissolution of silver at different O_2 pressures. Temperature, 24°C. NaCN, 0.055 mol.

ures of 3.40 and 7.48 atm. Some typical rate curves are shown in Fig. 6 and the rates of dissolution, at both oxygen pressures, are plotted against cyanide concentration in Fig. 7.

It is seen that at low NaCN concentrations the rate is proportional to the concentration of NaCN and is independent of the oxygen pressure. As the cyanide concentration is increased a point is reached where the rate levels off to a limiting value. The NaCN concentration at which this occurs is proportional to the oxygen pressure. The limiting rate also depends on the oxygen pressure.

To establish this dependence a series of experiments was made in which the limiting rate was measured at various oxygen partial pressures, ranging from 0 to 8 atm. The NaCN concentration was maintained constant at 0.055 mol per liter (i.e., corresponding to the limiting rate region). The rate curves are shown in Fig. 8 and the results summarized in Fig. 9 where the rate is plotted against

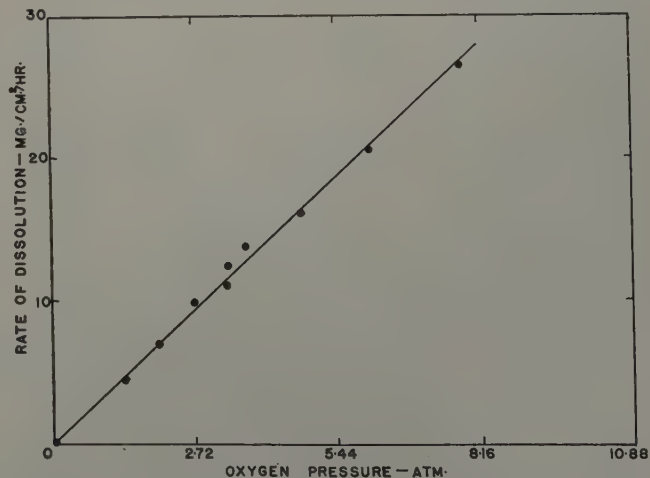


Fig. 9—Effect of oxygen on the rate of dissolution of silver. Temperature, 24°C. NaCN, 0.055 mol.

the oxygen pressure. It is seen that the limiting rate is directly proportional to the oxygen pressure. No appreciable dissolution occurs in the absence of oxygen.

These results suggest that at low NaCN concentrations, when oxygen is present in excess, the diffusion or transport of CN^- to the silver surface controls the rate of the reaction. This corresponds to the region in which the rate is independent of oxygen concentration but proportional to the concentration of cyanide. At higher cyanide concentrations the CN^- ions are transported to the surface more rapidly than the oxygen, and the diffusion of oxygen becomes rate controlling. This corresponds to the limiting region where the rate is independent of cyanide concentration but proportional to the concentration of oxygen. The small decrease in rate with further increase in the NaCN concentration in this region, evident in Fig. 7, may be attributed to a lowering of the solubility of oxygen.¹⁷

Similar conclusions regarding the existence of two regions corresponding to rate control by the transfer of oxygen and cyanide, respectively, have been reached by White¹³ who studied the dissolution of gold in cyanide solutions.

The concentration of oxygen in air-saturated cyanide solutions has been determined,⁹ and found to have a value close to 8.5 mg O_2 per liter. Assuming that this concentration is proportional to the partial pressure of oxygen above the solution, over the range of pressures investigated, it can be seen from the results in Figs. 7 and 9, that the transition from the region of rate control by cyanide transport to that by oxygen transport always occurs at a concentration ratio in the solution of 6.7 g of NaCN per g of O_2 , or 4.4 mol NaCN per mol of O_2 .

Effect of Temperature: Measurements of the rate of dissolution of silver in 0.037 mol NaCN solutions under 3.4 atm of O_2 were made at temperatures ranging from 24° to 110°C. The rate curves were all of the same linear form as described earlier. An Arrhenius plot showing the effect of temperature on the rate is given in Fig. 10. The activation energy for the dissolution process, calculated from the slope of this plot which is exactly linear over the entire temperature range, is 2400 cal per mol. Low activation energies of this order are generally considered to indicate a rate controlled by a diffusion process. This supports the conclusions noted earlier. Accurate measurements could not be made at temperatures exceeding 110°C because of excessive decomposition of the cyanide.

Effect of H_2O_2 : Qualitative tests showed that peroxide was formed in the solution, and that its concentration increased with the amount of silver dissolved. This suggests that oxygen is reduced in accordance with Eq 2a and is in agreement with the results of Bodlaender,⁵ who was able to account for about 70 pct of the theoretical amount of peroxide

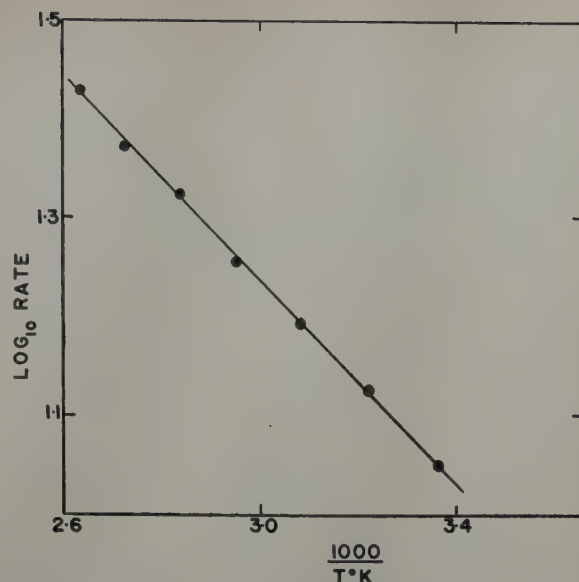


Fig. 10—Arrhenius plot showing the effect of temperature on the rate of dissolution of silver. NaCN, 0.037 mol. O_2 , 3.4 atm.

that should be formed according to this equation. No attempt was made to determine quantitatively the amount of H_2O_2 formed in the present study.

However, experiments were conducted to determine the effect of peroxide on the rate of dissolution of silver, by adding different amounts of H_2O_2 to the solution. The results of these experiments are summarized in Table II.

It can be seen that small amounts of peroxide are entirely without effect on the rate. These results, together with the evidence for the build-up of H_2O_2 in the solutions, suggest that the predominant reaction in the dissolution of silver is that represented by Eq. 2a, involving the reduction of O_2 to H_2O_2 , and that the further reduction of H_2O_2 to OH^- , represented by Eq. 3a, occurs only to a minor extent.

Effect of pH and Added Salts: Barsky, Swainson, and Hedley² found that the rate of dissolution of gold in cyanide solutions fell off with increasing pH and that this effect was particularly marked, when $\text{Ca}(\text{OH})_2$ was used to raise the pH. Neutral calcium salts such as CaSO_4 and CaCl_2 were without effect. They were unable to provide an explanation for these results.

An investigation was undertaken to determine whether the dissolution of silver was similarly influenced by pH and salts. Varying amounts of KOH, $\text{Ca}(\text{OH})_2$, and $\text{Ba}(\text{OH})_2$ were added to standard NaCN solutions (0.057 mol per liter) and the rate of dissolution of silver in these solutions was measured. Rate curves for the KOH and $\text{Ca}(\text{OH})_2$ series are shown in Figs. 11 and 12, and the results are summarized in Table III and Fig. 13. Addition of KOH, $\text{Ca}(\text{OH})_2$, and $\text{Ba}(\text{OH})_2$ all resulted in a falling off in the rate of dissolution. The effects of KOH and $\text{Ca}(\text{OH})_2$ were similar to those observed by Barsky, Swainson, and Hedley² for the dissolution of gold. The effect of $\text{Ba}(\text{OH})_2$ was intermediate between that of KOH and $\text{Ca}(\text{OH})_2$.

It was observed that a white coating was formed on the surface of the silver specimens which had been exposed to reaction with the solutions containing $\text{Ca}(\text{OH})_2$. The amount of material on the surface increased with the lime content of the solution. X-ray analysis showed that the coating consisted of calcium peroxide, CaO_2 .¹⁴

Table II. Effect of H_2O_2 on the Rate of Dissolution of Silver

(NaCN)_T, 0.057 mol per liter. Temperature, 24°C.
 O_2 pressure, 4.8 atm.

(H_2O_2), Mol per Liter	Rate of Dissolution, Mg Ag per Sq Cm per Hr
0	16.04
1.8×10^{-4}	15.85
3.5×10^{-4}	16.30

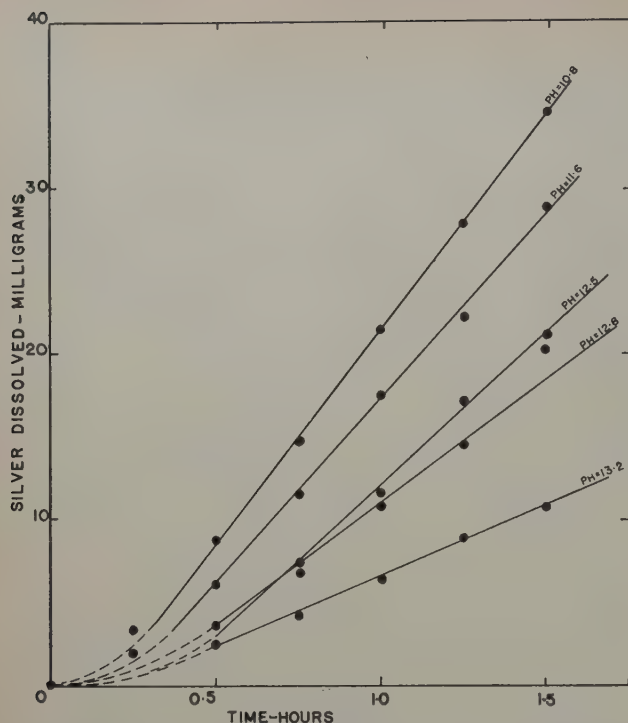
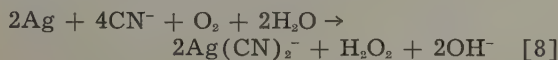


Fig. 11—Rate curves for the dissolution of silver in solutions containing different amounts of KOH. Temperature, 24°C. NaCN, 0.057 mol. O_2 , 4.8 atm.

It is known that this salt, which is very slightly soluble, is formed when H_2O_2 is added to solutions of $Ca(OH)_2$. In these experiments the H_2O_2 arises from the reduction of O_2 , as discussed earlier. The following reactions are involved:



The oxygen is reduced at the silver surface and the CaO_2 which is then formed appears to deposit on the surface. The resulting coating impedes the reaction and accounts for the observed lowering of the rate. This explanation receives further support from the fact that at high $Ca(OH)_2$ concentrations, the rate curve for the dissolution of silver was no longer linear, but showed a tendency to flatten out as the reaction proceeded. This is characteristic of rates which are determined by diffusion through a solid film whose thickness increases as the reaction proceeds.¹⁵

Eq. 9 shows that both Ca^{++} and OH^- ions are required for the formation of CaO_2 . In agreement with the results of Barsky et al.,² neutral calcium salts, such as calcium acetate, were found to be without appreciable effect on the rate.

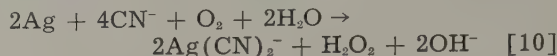
The formation of a similar surface coating was observed when the solutions contained $Ba(OH)_2$. In this case the coating was presumably BaO_2 , although the data necessary for its identification by X-ray diffraction measurements were not available. The relative magnitude of the retarding effects of $Ca(OH)_2$ and $Ba(OH)_2$ on the rate is to be expected, since the solubility of BaO_2 exceeds that of CaO_2 .¹⁵

The effect of KOH on the rate which is less marked than that of $Ca(OH)_2$ and $Ba(OH)_2$ cannot be similarly explained, since potassium peroxide is quite soluble. It appears more likely that the effect of KOH in retarding the reaction at high pH values

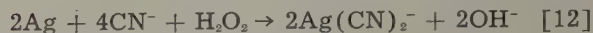
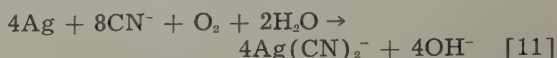
is due to a lowered solubility of oxygen¹⁷ and to a lowered potential for its reduction. (See Figs. 1 to 3.)

Discussion

Nature of the Reaction: The results obtained in this investigation indicate that the predominant reaction responsible for the dissolution of silver in aqueous solutions of cyanide and oxygen is



The following reactions do not appear to participate to any appreciable extent, although they would appear to be more probable on the basis of their thermodynamic properties which have been summarized earlier in this paper in the form of potential-pH- CN^- relations.



The following evidence supports these conclusions:

1— H_2O_2 was observed to accumulate in the solution as the reaction proceeded. This has also been confirmed quantitatively by Bodlaender.⁵ When the solutions contained $Ca(OH)_2$ or $Ba(OH)_2$, the formation of a deposit of CaO_2 or BaO_2 , respectively, on the silver surface was observed. These results suggest that the reduction of oxygen results in the formation of H_2O_2 , in accordance with Eq. 10, and that the H_2O_2 thus formed is relatively stable with respect to further reduction.

2—Addition of H_2O_2 to the solution did not affect the rate. This suggests that reaction 12 does not occur to an appreciable extent.

3—The transition from the region where the rate is controlled by transport of CN^- to the region of control by transport of O_2 , occurs at a ratio of con-

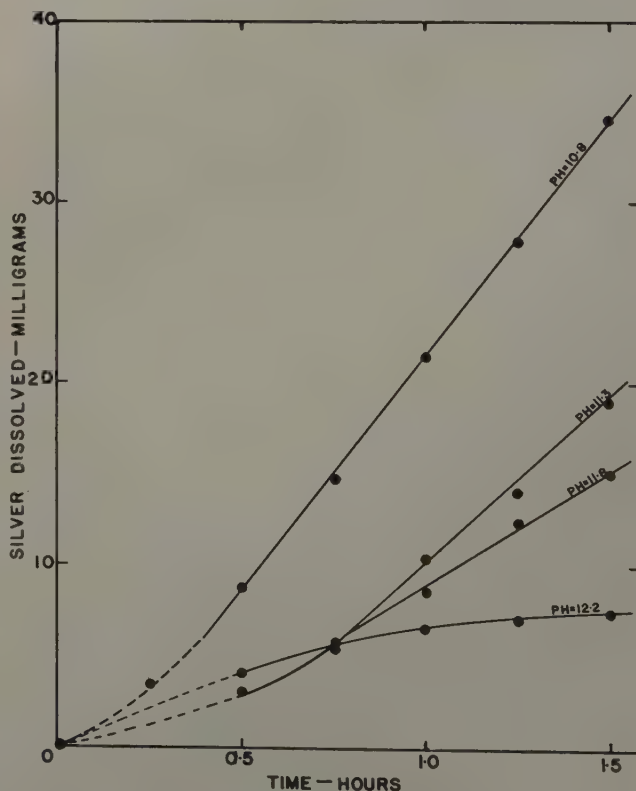


Fig. 12—Rate curves for the dissolution of silver in solutions containing different amounts of $Ca(OH)_2$. Temperature, 24°C. NaCN, 0.057 mol. O_2 , 4.8 atm.

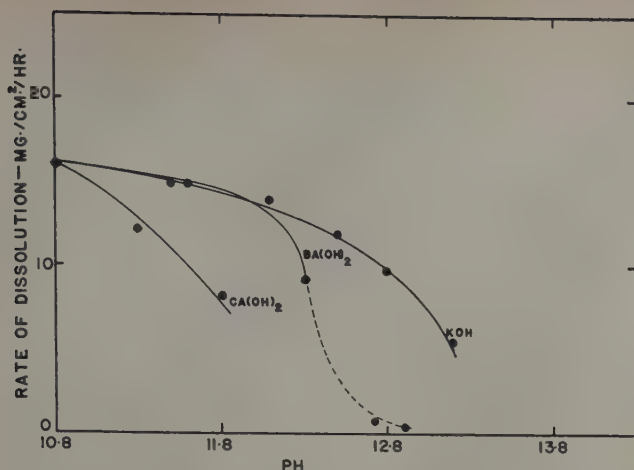
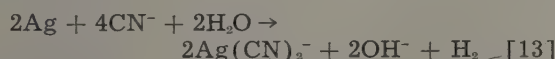


Fig. 13—Effect of KOH, Ca(OH)₂, and Ba(OH)₂ on the rate of dissolution of silver. Temperature, 24°C. NaCN, 0.057 mol. O₂, 4.8 atm.

centrations (NaCN): (O₂) of 4.4 mol per mol. This is close to the value of 4.0 which would be expected on the basis of Eq. 10 assuming that the diffusion coefficient of O₂ and NaCN are equal. The difference between the two values could be due to incomplete ionization of the cyanide, or to a slight difference between the two diffusion coefficients.

Eqs. 11 and 12 would correspond to a value of 8.0 for this ratio. Values of this order have been observed in similar studies on the dissolution of gold^{3, 18} and it is possible that these reactions participate in the dissolution of gold, but not in the corresponding dissolution of silver.

The oxidation of silver by water, with liberation of hydrogen,



has been shown to be thermodynamically unfavorable at 25°C. Julian and Smart¹⁸ suggested that this reaction became important at higher temperatures, but measurements of the rate of dissolution up to 110°C failed to support this conclusion. The Arrhenius plot was exactly linear over the entire temperature range indicating that nature of the reaction did not change with temperature. Participation in the dissolution process, of a reaction such as 13, which does not involve oxygen would be expected to result in a change in slopes of the Arrhenius plot. This was not observed.

Rate Control: Over the range of conditions investigated, the rate of dissolution was found to be controlled by the transport of the reactants to the silver surface. The results indicated that at low NaCN concentrations, when oxygen is present in excess, the transport of CN⁻ controls the rate. This corresponds to a region where the rate is independent of the oxygen concentration but is proportional to the cyanide concentration. At higher cyanide concentrations, when CN⁻ is transported to the surface more rapidly than oxygen, the transport of oxygen becomes rate determining. In this region the rate is essentially independent of cyanide concentration but is proportional to the concentration or pressure of oxygen.

Rate control by diffusion of oxygen persisted up to oxygen partial pressures of 8 atm. This is consistent with the conclusions of Salzberg et al.,¹⁹ that metal dissolution reactions with a large potential difference between the metal and oxidant (as is the

case for this reaction) are generally diffusion controlled.

In view of the fact that the rates of dissolution of silver, measured in this study, were controlled by a physical process (i.e., diffusion) the kinetic results obtained provide little information about the detailed mechanism of the chemical reaction itself.

Effect of Ca(OH)₂: The marked effect of Ca(OH)₂ in lowering the rate of dissolution of silver has been shown to result from the formation of a deposit of calcium peroxide, CaO₂, on the silver surface. Ba(OH)₂ was found to have a similar effect.

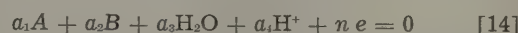
Acknowledgment

This research was supported by funds provided by the Atomic Energy Control Board and administered by the National Research Council of Canada.

Appendix

Calculation of Potential-pH Relations

General Procedure: Potential-pH relations were calculated according to the method of Pourbaix.⁷ The equation for an oxidation-reduction reaction can be written in the general form



where A and B are the oxidized and reduced forms of the reactant, respectively.

The potential, *E*, for this reaction at 25°C is then given by the following relation:

$$E(\text{volts}) = -\frac{1}{23060n} \sum a_i F^\circ_i + \frac{0.0591}{n} \sum a_i \log(i) \quad [15]$$

where *a_i* is the number of mols of each species, *i*, in Eq. 14; (*i*) is the corresponding activity (assumed to be the same as the concentration); and *F[°]_i* is the corresponding standard free energy of formation.

The subsequent calculations are based on this relation, the data being taken in all instances from Latimer.⁹ Since the systems considered involve dilute solutions, the activity coefficients of the dissolved species have been taken as unity.

Potential-pH Relations for O₂ and H₂O Reduction Reactions:

(i) O₂ + 2H₂O + 2e = H₂O₂ + 2OH⁻ (sample calculation)

<i>i</i>	<i>a_i</i>	(<i>i</i>)	<i>F[°]_i</i>
O ₂ (g)	1	1 atm	0 cal per mol
H ₂ O (l)	2	1	56,690
H ₂ O ₂ (aq)	1	10 ⁻⁸ mol per liter	31,470
OH ⁻ (aq)	2	variable	37,595

Table III. Effect of pH and Added Salts on the Rate of Dissolution of Silver

(NaCN)_T, 0.057 mol per liter. Temperature, 24°C. O₂ pressure, 4.8 atm.

Added Salt, Mol per Liter	pH	Rate of Dissolution, Mg Ag per Sq Cm per Hr
None	10.8	16.0
KOH—0.0004	11.6	14.8
0.084	12.5	11.9
0.164	12.8	9.8
0.222	13.2	5.4
Ba(OH) ₂ —0.003	11.5	14.8
0.018	12.1	13.9
0.034	12.3	9.2
0.160	12.9	0.0
Ca(OH) ₂ —0.0029	11.3	12.2
0.0064	11.8	8.2
0.0210	12.2	Rate fell off with time
Ca (C ₂ H ₃ O ₂) ₂ —0.063	10.8	15.8
0.126	10.8	15.6

Eq. 15 takes the form

$$E = \frac{-1}{23060n} (F^\circ_{O_2} + 2F^\circ_{H_2O} - F^\circ_{H_2O_2} - 2F^\circ_{OH^-})$$

$$+ \frac{0.0591}{n} \log \frac{(O_2)(H_2O)^2}{(H_2O_2)(OH^-)^2} \quad [16]$$

$$= +0.679 - 0.0591 \text{ pH} - \frac{0.0591}{2} \log (H_2O_2)$$

$$+ \frac{0.0591}{2} \log (O_2)$$

$$= 0.856 - 0.0591 \text{ pH, when } (O_2) = 1 \text{ atm and } (H_2O_2) = 10^{-6} \text{ mol per liter.}$$

Similarly for:

$$(ii) \quad O_2 + 2H_2O + 4e = 4OH^-; E = 1.229$$

$$- 0.0591 \text{ pH} + \frac{0.0591}{4} \log (O_2)$$

$$\text{when } (O_2) = 1 \text{ atm, } E = 1.229 - 0.0591 \text{ pH} \quad [17]$$

$$(iii) \quad H_2O_2 + 2e = 2OH^-; E = 1.77 + \frac{0.0591}{2}$$

$$\log (H_2O_2) - 0.0591 \text{ pH}$$

$$\text{when } (H_2O_2) = 10^{-6} \text{ mol per liter, } E =$$

$$1.59 - 0.0591 \text{ pH} \quad [18]$$

$$(iv) \quad 2H_2O + 2e = H_2 + 2OH^-; E = 0 - \frac{0.0591}{2}$$

$$\log (H_2) - 0.0591 \text{ pH}$$

$$\text{when } (H_2) = 10^{-6} \text{ atm, } E = 0.174 - 0.0591 \text{ pH} \quad [19]$$

Potential-pH Relations for the System, Ag-H₂O:

$$(i) \quad Ag^+ + e = Ag; E = 0.800 + 0.0591 \log (Ag^+)$$

$$\text{when } (Ag^+) = 10^{-6} \text{ mol per liter, } E = 0.446 \quad [20]$$

$$(ii) \quad Ag_2O + 2H^+ + 2e = 2Ag + H_2O;$$

$$E = 1.173 - 0.0591 \text{ pH} \quad [21]$$

$$(iii) \quad Ag_2O + 2H^+ = 2Ag^+ + H_2O$$

$$\log (Ag^+) = 6.32 - \text{pH}$$

$$\text{when } (Ag^+) = 10^{-6} \text{ mol per liter, pH} = 12.32$$

Relation Between Total Cyanide, CN⁻ and pH: In an aqueous solution of a cyanide salt, such as NaCN, the cyanide is present in two forms, as HCN and as free CN⁻. Neglecting the cyanide tied up in complex ions, (i.e. as Ag(CN)₂⁻),

$$(NaCN)_{\text{Total}} = (HCN) + (CN^-) \quad [22]$$

The following equilibrium relation applies in all aqueous solutions at 25°C:

$$\frac{(H^+)(CN^-)}{(HCN)} = 4 \times 10^{-10} = \frac{(H^+)(CN^-)}{(NaCN)_T - (CN^-)} \quad [23]$$

This equation can be reduced to the form:

$$\log (CN^-) = \log (NaCN)_T + \text{pH} - 9.397$$

$$- \log (1 + 10^{\text{pH}-9.397}) \quad [24]$$

Relation Between (Ag⁺), (CN⁻), and (Ag(CN)₂⁻): The equilibrium



is governed by the relation

$$\frac{(Ag^+)(CN^-)^2}{(Ag(CN)_2^-)} = 1.8 \times 10^{-10} \quad [26]$$

$$\text{or } \log (Ag^+) = \log (Ag(CN)_2^-) -$$

$$\frac{2 \log (CN^-) - 18.745}{2} \quad [27]$$

According to this, when (CN⁻) < 4.3 × 10⁻¹⁰ mol per liter, (Ag⁺) > (Ag(CN)₂⁻). In the construction of the potential-pH diagrams it has been assumed that in this region (i.e., at (CN⁻) < 4.3 × 10⁻¹⁰) the silver ions are predominantly in the form, Ag⁺, and the small amount of Ag(CN)₂⁻ has been neglected. This assumption introduces negligible error.

Similarly, when (CN⁻) > 4.3 × 10⁻¹⁰ mol per liter, Eq. 27 shows that (Ag(CN)₂⁻) > (Ag⁺). In this region of cyanide concentrations, the dissolved silver is predominantly in the form of Ag(CN)₂⁻ and the concentration of free Ag⁺ ion has been neglected by comparison.

Potential-pH Relation for the System, Ag-Ag(CN)₂⁻: Combining Eqs. 20 and 27 gives:

$$E = -0.308 + 0.0591 \log (Ag(CN)_2^-)$$

$$- 0.118 \log (CN^-) \quad [28]$$

Assuming that (Ag)_T = (Ag(CN)₂⁻) = 10⁻⁶ mol per liter, this becomes

$$E = -0.663 - 0.118 \log (CN^-) \quad [29]$$

or substituting for (CN⁻) from Eq. 24

$$E = -0.663 + 0.118 \{ \log (NaCN)_T +$$

$$\text{pH} - 9.397 - \log (1 + 10^{\text{pH}-9.397}) \} \quad [30]$$

As indicated above, this relation applies when (CN⁻) > 4.3 × 10⁻¹⁰ mol per liter.

References

- ¹J. V. Dorr and F. L. Bosqui: *Cyanidation and Concentration of Gold and Silver Ores*. (1950) New York. McGraw-Hill Book Co.
- ²G. Barsky, S. J. Swainson, and N. Hedley: *Trans. AIME* (1934) **112**, pp. 660-667.
- ³*Chemistry of Cyanidation*. American Cyanamid Co., Mineral Dressing Notes, No. 17 (February 1950).
- ⁴L. Elsner: *Journal Prakt. Chem.* (1846) **37**, pp. 441-446.
- ⁵G. Bodlaender: *Ztsch. Angew. Chem.* (1896) pp. 583-587.
- ⁶Janin: *Mineral Industries* (1892) **1**, p. 239.
- ⁷M. Pourbaix: *Thermodynamics of Dilute Aqueous Solutions*. (1949) London. Edward Arnold and Co.
- ⁸P. Delahay, M. Pourbaix, and P. Van Rysselberghe: *Journal Electrochem. Soc.* (1951) **98**, pp. 65-67.
- ⁹W. M. Latimer: *The Oxidation States of the Elements and Their Potentials in Aqueous Solutions*. (1952) New York. Prentice-Hall.
- ¹⁰J. S. McLaurin: *Trans. Chem. Soc.* (1893) **63**, pp. 724-727.
- ¹¹S. B. Christy: *Trans. AIME* (1896) **26**, p. 735; (1900) **30**, p. 864.
- ¹²E. B. Sandell: *Colorimetric Determination of Traces of Metals*. (1950) New York. Interscience Publishers.
- ¹³H. A. White: *Journal Chem. Met. Min. S. Africa* (1934) **35**, pp. 1-11.
- ¹⁴V. Katov and S. Raikhshtein: *Journal Phys. Chem. USSR* (1941) **15**, pp. 1057-1058.
- ¹⁵N. F. Mott: *Trans. Faraday Soc.* (1939) **35**, p. 1175; (1940) **36**, p. 472.
- ¹⁶N. V. Sidgwick: *The Chemical Elements and Their Compounds* (1950) Vol. I, p. 249. Oxford University Press.
- ¹⁷A. Seidell: *Solubilities of Inorganic and Metal Organic Compounds* (1940) New York. D. Van Nostrand Co.
- ¹⁸H. J. Julian and E. Smart: *Cyaniding Gold and Silver Ores* (1921) London. Griffin.
- ¹⁹H. W. Salzberg, H. Knoetgen, and A. M. Molless: *Journal Electrochem. Soc.* (1951) **98**, pp. 31-35.

System Zirconium-Boron

by Frank W. Glaser and Benjamin Post

Three borides of zirconium have been reported: ZrB ,¹ ZrB_2 ,^{2,3} and ZrB_{12} .⁴ The phase relationships, ranges of stability, and some physical properties of these compounds are described.

THE zirconium borides differ considerably from one another, particularly with respect to their relative stabilities at high temperatures in the presence of carbon.^{4,5} ZrB_2 is extremely stable at all temperatures (to the melting point) in contact with carbon. Both ZrB and ZrB_{12} tend to decompose at elevated temperatures when carbon is present in excess of about 0.5 pct. ZrB forms ZrB_2 and ZrC , and ZrB_{12} decomposes to form ZrB_2 and a boron-carbide phase. In the ZrB_{12} preparation, boron present in excess of that needed to form ZrB_2 reacts with carbon, if present, to form carbides, in preference to forming the higher boride. Similar instability of borides, other than diborides of the transition metals of the 4th and 5th groups of the periodic table, has been reported.^{6,7} Special precautions had, therefore, to be taken to minimize carbon contamination in the preparation of ZrB and ZrB_{12} .

Reactions below 1400°C were carried out by heating powdered mixtures of zirconium hydride and boron in quartz tubes in a hydrogen atmosphere. For temperatures above 1400°C , reactions were carried out in graphite molds. Carbon contamination from the molds was minimized by employing extremely rapid heating rates to reduce carbon diffusion into the body of the specimen, and by subsequent "shaving" of sample surfaces that had been in contact with the graphite dies. A heating rate of about 2000°C per min was obtained by heating the dies (by direct conduction), using a current of

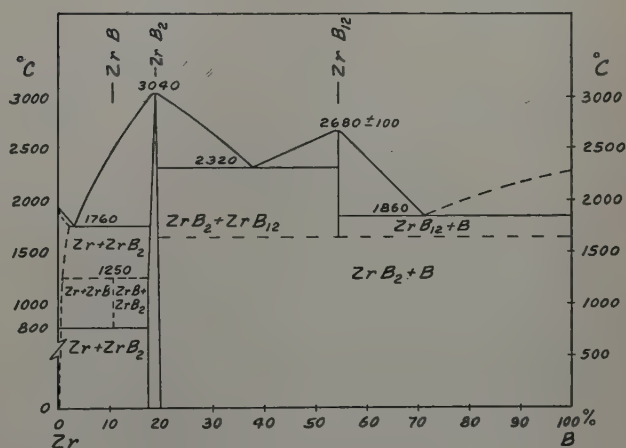


Fig. 1—Zr-B phase diagram.

40,000 amp. Although this type of heating cycle apparently allowed little time for "homogenization," close approximations to equilibrium conditions were usually obtained as a result of the very strongly exothermic reactions between zirconium hydride and boron at elevated temperatures. Reproducibility of results in repeated runs under varying conditions was taken as a reasonable indication that equilibrium conditions had been effectively achieved.

Quenching was accomplished by rapidly immersing the entire die, containing the reaction products, in water. Specimens could also be cooled at controlled rates by adjustment of the rate of flow of water through the water-cooled copper electrodes in contact with the graphite dies.

F. W. GLASER, Member AIME, is associated with the American Electro Metal Corp., Yonkers, N. Y., and B. POST is associated with Polytechnic Institute of Brooklyn, Brooklyn.

Discussion on this paper, TP 3569E, may be sent, 2 copies, to AIME by Nov. 1, 1953. Manuscript, Jan. 3, 1953.

Table I. Description of Various Zr-B Compounds

Phase	Structure	Density Calculated	Density Measured	Electrical Resistivity, Microhm-cm at 20°C	Hardness, Rockwell A	Appearance
ZrB	Face-centered cubic (NaCl type). $a_0 = 4.65 \pm 0.03 \text{ \AA}$	6.7	5.7	30-35	69-72	Gray to silvery-metallic luster and shows some ductility
ZrB ₂	Primitive hexagonal alternating layers of Zr and B atoms. $a_0 = 3.170 \pm 0.003 \text{ \AA}$ $c_0 = 3.533 \pm 0.003 \text{ \AA}$	6.09	6.10	9.2	87-89	Gray to silvery-metallic luster
ZrB ₁₂	Face-centered cubic. $a_0 = 7.408 \pm 0.002 \text{ \AA}$ Zr atoms in face-centered positions and at centers of boron polyhedra consisting of 24 B-atoms	3.6	3.7	60-100	92-92.5	Black—no metallic luster

Analysis of the zirconium hydride starting material showed 98.2 pct Zr and 1.4 to 1.6 pct H. The boron powder was about 96.7 pct pure and contained, in addition, about 0.3 pct Fe and 0.08 pct C.

A series of mixtures of zirconium hydride and boron was prepared ranging in 2 pct steps, from 98 to 25 pct total zirconium content. For each composition several samples were used. In the regions of interest, samples were heated to temperatures differing by 50°C increments. Smaller intervals were employed in some critical regions. At low temperatures, 20° to 1400°C, temperature measurements were carried out with thermocouples. Above 1400°C, temperatures were measured using optical pyrometers that had been calibrated by melting metals or alloys of known melting points. Visual examination of cooled specimens indicated when specimens had melted.

Specimens were analyzed chemically after preparation. Phases present in the reaction mixtures were identified by X-ray diffraction methods supplemented by metallographic inspection. A Norelco Geiger counter spectrometer, using Cu K α radiation, was used in the X-ray investigation.

Results and Discussion

The results of this investigation are summarized in Fig. 1. Details of the α/β transformation of zirconium have been omitted for lack of experimental evidence. The melting points shown for zirconium⁸ and boron⁹ were taken from the literature. ZrB₂ was found to melt at 3040°C; this value is in good agreement with melting points previously reported.^{7,9} X-ray evidence and chemical analyses indicated a narrow range of homogeneity for this compound. The dimensions of the unit cell are listed in Table I. These refer to the dimensions at stoichiometric composition; variation of parameters over the narrow range of composition was within the range of experimental error.

Pure ZrB₁₂ samples could not be isolated; all specimens contained, at room temperature, 10 pct or more of ZrB₂ even after rapid quenching. There is, therefore, an uncertainty of approximately 100°C in the melting point reported for ZrB₁₂ (2680°C). Estimates of the electrical resistivity of this phase were computed by extrapolating experimental values to 100 pct dense and essentially pure ZrB₁₂. The interesting crystal structure of ZrB₁₂ has been described elsewhere.⁴

The ZrB phase has an extremely narrow range of stability and very rapid quenching is necessary in order to retain it at room temperature. There

are indications that traces of carbon help to stabilize this phase somewhat.

The X-ray spectra of ZrN, ZrC, and ZrB are almost identical; in particular, the lattice constants of the latter two compounds are the same within experimental error. The X-ray data could, therefore, only indicate that one or more of these compounds was present; chemical analysis was necessary to exclude the possibility that the face-centered cubic phase was the carbide or nitride or some solid solution containing these compounds. Thus, specimens whose spectra indicated the presence of a considerable amount of the face-centered cubic phase, were found, on careful chemical analysis, to contain no detectable nitrogen and less than 0.3 pct C. Considerations of this sort, together with the zirconium and boron analyses, proved that the phase was ZrB.

In Table I a summary of some physical properties and structural data of ZrB, ZrB₂, and ZrB₁₂ is given.

Summary

The phase diagram of the Zr-B system has been prepared. The phase relations among the three zirconium borides are shown. Only one of the three, namely, ZrB₂, exhibits good thermal and chemical stability. The preparation of the two other phases, ZrB and ZrB₁₂, is rather difficult, as has been described.

Acknowledgment

This work was supported by the Office of Naval Research and the authors would like to thank that agency for permission to publish this data.

References

- ¹ B. Post and F. W. Glaser: *Journal of Chemical Physics* (June 1952) **20**, p. 1050.
- ² J. T. Norton, H. Blumenthal, and S. J. Sindeband: *Trans. AIME* (1949) **185**, pp. 749-751; *JOURNAL OF METALS* (October 1949).
- ³ R. Kiessling: *Acta Chem. Scand.* (1949) **3**, p. 90.
- ⁴ B. Post and F. W. Glaser: *Trans. AIME* (1952) **194**, p. 631; *JOURNAL OF METALS* (June 1952).
- ⁵ F. W. Glaser: *Trans. AIME* (1952) **194**, p. 391; *JOURNAL OF METALS* (April 1952).
- ⁶ R. Steinitz: *Powder Met. Bull.* (1951) **6**, No. 1, pp. 54-56.
- ⁷ F. W. Glaser: *Powder Met. Bull.* (1951) **6**, No. 1, pp. 51-54.
- ⁸ R. F. Domagala, D. J. McPherson, and M. Hansen: *Trans. AIME* (1953) **197**, p. 279; *JOURNAL OF METALS* (February 1953).
- ⁹ K. Moers: *Ztsch. anorg. allgem. Chem.* (1931) **198**, pp. 262-275.

A Study of Some Binary Hafnium Compounds

by Frank W. Glaser, David Moskowitz, and Benjamin Post

Lattice parameters of various hafnium compounds, two borides, a carbide and a nitride were determined. Some physical properties were measured and comparisons with the properties of the corresponding zirconium compounds were drawn.

ALTHOUGH borides of transition metals have been extensively investigated in recent years, there are few references in the literature to borides of hafnium. This is not surprising, in view of the extreme scarcity and great cost of the purified metal. Becker¹ reported the existence of a boride, carbide, and nitride of hafnium; he listed the formulas as HfB, HfC, and HfN. However, in his work no mention was made of chemical analyses of the reaction products. In this paper results of a study of various hafnium compounds, including borides, carbides, and nitrides, are reported. It was expected, of course, that these compounds would closely resemble their zirconium analogues, which have previously been extensively investigated.

Three borides of zirconium are known: ZrB_2 ,² ZrB_3 ,³ and ZrB_{12} .⁴ In addition, one carbide, ZrC ,⁵ and one nitride, ZrN ,⁶ have been reported. It should be noted that ZrB and ZrB_{12} are stable phases only in relatively high-temperature regions, unlike ZrB_2 , which is stable from room temperature to its melting point.⁶ It was felt that hafnium would yield corresponding borides, carbides, and nitrides with similar stability ranges.

Experimental Procedures and Results

A quantity of hafnium metal that was better than 97 pct pure, with zirconium as its major impurity, was furnished by the Argonne National Laboratories. The boron powder used was approximately 96.5 pct pure. In general, the procedure involved

F. W. GLASER, Junior Member AIME, and D. MOSKOWITZ are associated with the American Electro Metal Corp., Yonkers, N. Y., and B. POST is associated with Polytechnic Institute of Brooklyn, Brooklyn.

Discussion on this paper, TP 3570E, may be sent, 2 copies, to AIME by Nov. 1, 1953. Manuscript, Jan. 3, 1953.

Table I. Lattice Constants of HfB_2 and ZrB_2 , Å

Lattice	HfB_2	ZrB_2 ³
<i>a</i>	3.141 ± 0.002	3.170 ± 0.002
<i>c</i>	3.470 ± 0.002	3.533 ± 0.002
<i>c/a</i>	1.105	1.114

mixing the metal and boron powders in the desired proportions, and subsequently hot pressing them. The resulting specimens were analyzed chemically and phases present were identified by X-ray diffraction methods. A Philips Norelco Geiger counter spectrometer was used for identification of components and for measurement of lattice constants. Filtered copper radiation was used for all X-ray work.

Electrical resistivity and density measurements were carried out at room temperature.

The stable diboride, HfB_2 , will be described first. Stoichiometric quantities of boron and metal were heated to approximately 2000°C during hot pressing. The reaction product was shown by X-ray diffraction methods to be isomorphous with ZrB_2 (space group D_{6h}^{14} ; $P \frac{6}{m} \frac{6}{m} \frac{6}{m}$). Values of lattice constants of HfB_2 compared with those of ZrB_2 are shown in Table I.

The calculated density of HfB_2 is 11.2 g per cc, compared with a measured (pycnometric) value of 10.5 g per cc. HfB_2 specimens prepared under a wide variety of conditions (including variations in initial Hf-B ratios) showed only insignificant variations in lattice constants, indicating a very narrow range of homogeneity. Like ZrB_2 ,⁷ HfB_2 is an excellent electrical conductor. The resistivity at room temperature of hot-pressed samples, approximately 85 pct dense, is 12 microhm-cm. This compares favorably with the electrical resistivity of 10 mi-

crohm-cm reported by Becker,¹ indicating that his "hafnium boride" was probably HfB₂. The melting point of HfB₂ was measured with an optical pyrometer and found to be 3250° ± 100°C. The average coefficient of thermal expansion of HfB₂ from room temperature to 1000°C as measured under inert atmosphere was 5.3x10⁻⁶ per °C. Some physical properties of HfB₂ and ZrB₂ are listed for comparison in Table II.

When the starting mixture contained less than 66.7 atomic pct B, X-ray diffraction diagrams of the reaction products showed, in addition to the HfB₂ pattern, the pattern of a face-centered cubic phase. By analogy with similar zirconium and titanium phases,² this was identified as HfB. Strong patterns, due to this face-centered cubic phase, were obtained even in instances where chemical analysis showed the reaction products to contain less than 0.4 pct C and 0.15 pct N, precluding the possibility that the pattern was due either to HfC or HfN. Measurements of the lattice constant of this cubic phase showed $a_0 = 4.62 \pm 0.02\text{\AA}$; the range of homogeneity could not be exactly established, but the variation in lattice dimensions of different samples indicated the possibility that it was rather wide.

A sample of HfC was prepared by hot-pressing a mixture of the elements at 2150°C. It was then

Table II. Some Physical Properties of HfB₂ and ZrB₂

	HfB ₂	ZrB ₂
Calculated density, g per cc	11.2	6.10
Measured density, g per cc	10.5	5.82
Melting point, °C	3250 ± 100	3040 ± 100
Resistivity, microhm-cm (85 pct dense samples)	12	13 to 15
Coefficient of thermal expansion per °C (20°-1000°C)	5.3x10 ⁻⁶	5.5x10 ⁻⁶

checked for structure and composition by X-ray and chemical analysis. In addition, HfN was prepared by heating hafnium powder under a nitrogen atmosphere at 2000°C. Both these phases are cubic and isomorphous with the monoboride.

Values of a_0 of HfB, HfC, and HfN, as determined in this investigation, are listed in Table III. Values of a_0 of the corresponding zirconium compounds are listed for comparison. It is interesting, and perhaps surprising, to note that the lattice constants of the monoborides are smaller than those of the corresponding carbides, although the boron atom is larger than the carbon atom. McKenna³ reported a_0 for HfC as $4.4578 \pm 0.0003\text{\AA}$. That value appears to be much too low, and has, in fact, been criticized as "certainly incorrect."

Efforts were also made to prepare the dodecaboride of hafnium. The conditions under which ZrB₂ was prepared were duplicated,⁴ but the only boride detectable in the X-ray diffraction pattern of the product was HfB₂. A wide variety of starting mixtures, reaction temperatures, and quenching procedures was tried, without yielding detectable amounts of HfB₁₂. It is evident that HfB₁₂, if it exists,

Table III. Lattice Constants of Various Hafnium and Zirconium Compounds, Å

HfB	4.62 ± 0.02	ZrB ₂	4.65 ± 0.03
HfC	4.64 ± 0.02	ZrC ⁵	4.685
HfN	4.52 ± 0.02	ZrN ⁵	4.567

Table IV. Lattice Constants of Hafnium and Zirconium, Å*

	This Investigation	Hafnium		Zirconium	
		Nothling and Tolksdorf ¹⁰	Van Arkel ¹¹	Van Arkel ¹¹	
a	3.193 ± 0.002	3.33	3.206 ± 0.002	3.229 ± 0.002	
c	5.052 ± 0.003	5.47	5.087 ± 0.005	5.133 ± 0.003	
c/a	1.581	1.64	1.586	1.589	

* While this paper was being prepared for publication, a redetermination of the lattice constants of hafnium by Duwez¹² came to our attention. He reported $a = 3.1952\text{\AA}$ and $c = 5.0569\text{\AA}$, in very good agreement with the values obtained in this investigation.

has a surprisingly narrower range of stability than does the analogous zirconium compound.

Because of its purity compared with samples hitherto available, the hafnium metal used in this investigation was also subjected to X-ray diffraction analysis. Precision determinations of the lattice constants of the close-packed hexagonal unit cell revealed significant differences from the currently accepted values.^{10,11} These values, together with corresponding values for zirconium, are listed in Table IV. It is interesting to note that the presence of zirconium in hafnium would lead to an increase in the hafnium lattice parameter and might account for the larger unit cells reported by previous investigations.

Summary

A variety of hafnium compounds, including HfB, HfB₂, HfC, and HfN, have been investigated, using powder metallurgy techniques. X-ray diffraction methods were used to identify individual phases. Lattice parameters were determined and comparisons were made with the corresponding zirconium compounds. Measurements of some physical properties of HfB₂ were made. In addition, a redetermination of the lattice constants of hafnium metal has been made.

Acknowledgment

Thanks are due to the Office of Naval Research, under whose sponsorship this work was carried out, for permission to publish this data.

References

1. I. K. Becker: *Hochschmelzende Hartstoffe und ihre Technische Anwendung*. (1933) Berlin. Verlag Chemie.
2. B. Post and F. W. Glaser: *Journal of Chemical Physics* (1952) **20**, p. 1050.
3. F. Norton, H. Blumenthal, and S. Sindeband: *Trans. AIME* (1949) **185**, p. 749; *JOURNAL OF METALS* (October 1949).
4. B. Post and F. W. Glaser: *Trans. AIME* (1952) **194**, p. 631; *JOURNAL OF METALS* (June 1952).
5. P. Duwez and F. Odell: *Journal Electrochem. Soc.* (1950) **97**, p. 299.
6. F. W. Glaser and B. Post: The System Zr-B. This issue, p. 1117.
7. K. Moers: *Ztsch. anorg. allgem. Chem.* (1931) **198**, p. 262.
8. P. M. McKenna: *Industrial and Engineering Chemistry* (1936) **28**, p. 767.
9. R. E. Rundle: *Acta Cryst.* (1948) **1**, p. 180.
10. W. Nothling and S. Tolksdorf: *Ztsch. Krist.* (1925) **62**, p. 255.
11. A. E. Van Arkel: *Ztsch. Physik Chem.* (1927) **130**, p. 100.
12. P. Duwez: The Allotropic Transformation of Hafnium. *Journal of Applied Physics* (1951) **22**, p. 1174.

Creep Behavior of Extruded Electrolytic Magnesium

by C. S. Roberts

The creep mechanism and kinetics of fine-grained magnesium have been studied over the temperature range 200° to 600°F. As a result of a photographic study of microstructural changes, transient and steady-state creep components have been correlated with slip, subgrain formation, and cyclic deformation at the grain boundaries.

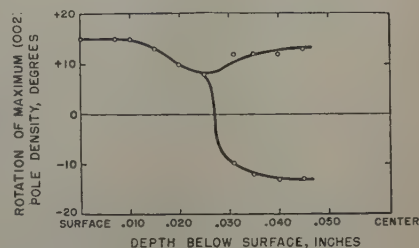
THE approach of this research has been the blend of a quantitative study of the creep strain of polycrystalline magnesium as a function of time, stress, and temperature with direct microstructural observations of the operative deformation processes. The validity of the conclusions is dependent on the condition that the microstructural changes seen on the polished surface qualitatively represent those occurring in the bulk of the metal. The work was intended as much to lay a background to a study of highly creep-resistant magnesium alloys as to provide a description of the behavior of the base metal itself.

The spectroscopic analysis of the electrolytic magnesium used in this study is as follows: Al, 0.009 pct; Ca, <0.01; Cu, 0.0011; Fe, 0.021; Mn, 0.012; Ni, 0.0004; Pb, 0.0012; Si, <0.001; Sn, <0.001; and Zn, <0.01. The impurity level is approximately that of commercial magnesium alloys. The original ingot was melted under Dow type 310 flux and cast as a 3 in. diam billet. It was extruded into 1½x½ in. flat stock under the conditions: billet preheat 800°F (1 hr), container and die temperature 800°F, speed 3 ft per min, and area reduction ratio 45:1. The extrusion process was chosen in preference to rolling and recrystallization because it allowed easier grain size control from specimen to specimen.

The grains of the extruded metal were fairly equiaxial and uniform in the size range of 4 to 6 thousandths of an inch. The preferred orientation of basal planes about the transverse direction was determined by an X-ray diffraction surface reflection method. A beam of filtered copper radiation was directed at an angle of 17° to both the transverse direction and the surface yet perpendicular to the extrusion axis. Analysis of the (002) diffraction arcs in the resulting photographic patterns gave an approximate intensity distribution along the great circle which extends through the center of the basal plane pole figure and to the extrusion axis poles. Successive layers of metal were removed by macro-etching between exposures.

The extruded texture is relatively sharp, but the most significant point is the position of the maximum basal plane pole density and its variation with depth below the surface. Fig. 1 shows that this maximum is rotated 15° from the normal at the surface toward the extrusion direction. Such an inclination has been reported for extruded 1 pct Mn and 8 pct Al-0.5 pct Zn

Fig. 1—Preferred orientation of extruded electrolytic magnesium. Positive angles toward extrusion direction.



alloys.¹ The inclination decreases until the maximum splits at about 0.025 in. depth into two elements of equal and opposite rotations from the ideal. The double texture persists to as great a depth as was experimentally convenient to examine. It probably continues to the very center of the extrusion. There is no great change in the sharpness of the individual elements of the texture with depth.

A plate of metal about 0.015 in. thick at the surface of the extruded stock was produced by etching. A transmission diffraction pattern was made for the purpose of determining any preferred orientation of a direction in the basal planes. Relatively uniform {100} and {101} rings were produced. There is little tendency for parallelism of a given direction in the plane with the projection of the extrusion axis on it.

The creep specimens were machined from 6¼ in. lengths of the extruded stock. Creep was measured on the reduced section, ½x½x2¼ in. long. This section was electropolished on one side for the studies of microstructural changes during creep. An orthophosphoric acid-ethyl alcohol electrolyte was used under the conditions recommended by Jacquet.² Hand polishing was used for previous mechanical preparation. Electropolishing was continued until all mechanical twins had been removed. The electropolished surface was protected from oxidation during creep testing by a thin layer of silicone oil. All micrographs were taken at room temperature on conventional metallographic equipment and after removal of the oil film.

The creep tests were performed with machines which have been described in detail by Moore and McDonald.³ Five testing temperatures, 200°, 300°, 400°, 500°, and 600° ±3°F were used. Difference in temperature between the two ends of the specimen reduced section was 2°F or less. The testing was done at constant load. Strain readings were taken as frequently as necessary to develop usable creep curves.

Tensile Creep vs Time, Stress, and Temperature

A definition of terms is necessary. Whenever successive sections of a creep strain-time curve show decreasing, constant, and increasing slope with time they will be termed primary, secondary, and tertiary

C. S. ROBERTS, Junior Member AIME, is associated with The Dow Chemical Co., Midland, Mich.

Discussion on this paper, TP 3596E, may be sent, 2 copies, to AIME by Dec. 1, 1953. Manuscript, March 16, 1953. Cleveland Meeting, October 1953.

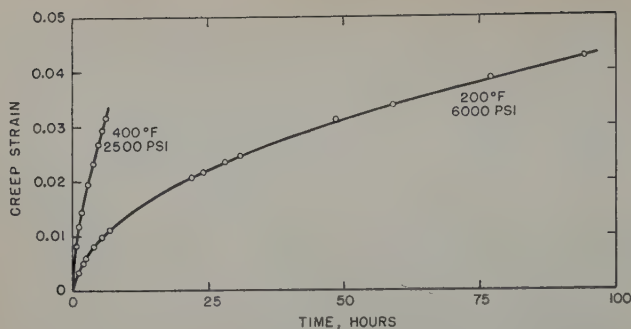


Fig. 2 (above)—Creep curves for extruded electrolytic magnesium when transient creep is the major process.

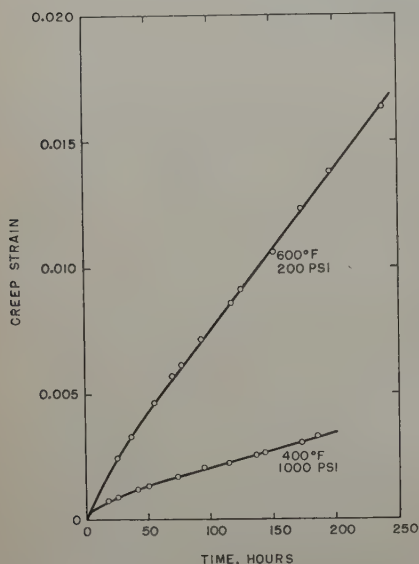


Fig. 3 (left)—Creep curves for extruded electrolytic magnesium when steady-state creep is the major process.

creep, respectively. The terms transient and steady-state creep will be applied in the conventional manner to the two separable elements which show finite decreasing and constant strain rates, respectively, from the beginning of the test. Primary creep may be used for a quantitative analysis of the transient component only when the steady-state creep is negligible. Secondary creep may be analyzed as steady-state creep only when the transient element is negligible.

Quantitative analyses of the linear coordinate plots of creep strain vs time for magnesium proved the existence of both transient and steady-state components. Transient creep was predominant for all stresses tested at the lowest temperature of test, 200°F. Steady-state creep becomes more predominant as the temperature increased and to a lesser extent as the stress decreased. There is negligible transient creep at the limit of low stresses at 600°F. The representative creep curves shown in Figs. 2 and 3 illustrate the change of curve shape over the experimental range of stress and temperature. Transient creep is predominant in the curves of Fig. 2. Fig. 3 illustrates the predominance of steady-state creep. Tertiary creep was never observed, although many tests were carried to a creep strain of 0.10.

In the first phase of this investigation creep curves were obtained from tests at the temperatures of 300°, 400°, 500°, and 600°F. Each test was continued until rectilinearity of the plot had demonstrated the existence of secondary creep. Secondary creep was never generated within the measurable strain range in the tests at 200°F. The first kinetic analyses were made with secondary creep rate, stress, and temperature as the variables. Attempts were made to fit isothermal rate data to the exponential, power, and hyperbolic sine functions of stress. With the use of tables constructed for the purpose⁴ it was found

that the latter function gave a poor fit of the data. Curvature of the semilog plot of stress vs secondary creep rate shown in Fig. 4 constitutes proof of the invalidity of the exponential relation. The plot of the data on log-log coordinates in Fig. 5 is a test of the power relation between stress and secondary creep rate. The rectilinearity of the isotherms proves the validity of the power function. A relatively sharp transition between two straight line segments in each isotherm is required to fit the data. Such transitions have been reported and discussed by Servi and Grant.^{5, 6}

Transient Creep: The creep strain-time data for the higher stresses at 200°, 300°, 400°, and 500°F, where transient creep is very predominant, were plotted on log-log coordinates. Straight lines were obtained in agreement with the equation

$$\epsilon_1 = \beta t^n$$

where ϵ_1 is transient creep strain; β , a function of temperature and stress; t , the time in hours; and n , a constant.

Values of β and n , which are equal to the intercept at 1 hr and slopes of the straight line, respectively, are given in Table I. A remarkable constancy of n with an average value of 0.53 was found. The dependence of β on stress and temperature is shown in Fig. 6. Straight and reasonably parallel lines prove that β is of the form $B(T)\sigma^m$ where m , the average slope in Fig. 6, is 4.0. A straight line in the plot of β at 3000 psi vs the reciprocal of the absolute temperature, Fig. 7, shows $B(T)$ to be of the form $Ae^{-Q/RT}$. The β values plotted are the intercepts of the lines in Fig. 6, using extrapolation of the 500°F data. The temperature coefficient Q , is equal to 15,500 cal per gram atom. In the experimental range, the average slope in Fig. 6, is 4.0. A straight line in the the range of 200° to 500°F and 1250 to 10,000 psi may be represented by

$$\epsilon_1 = 4.5 \times 10^{-9} e^{\frac{-15,500}{RT}} \sigma^{4.0} t^{0.53}$$

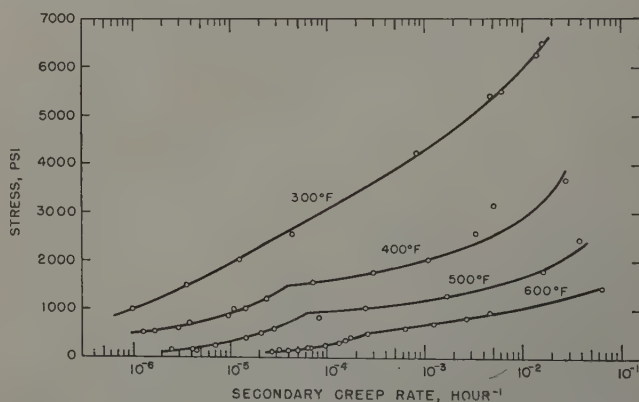


Fig. 4—Semilog plot of stress vs secondary creep rate for extruded electrolytic magnesium.

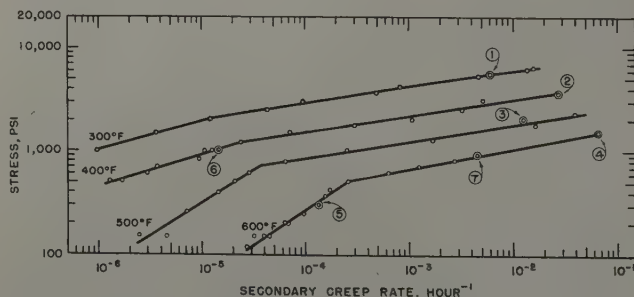


Fig. 5—Log-log plot of stress vs secondary creep rate for extruded electrolytic magnesium.

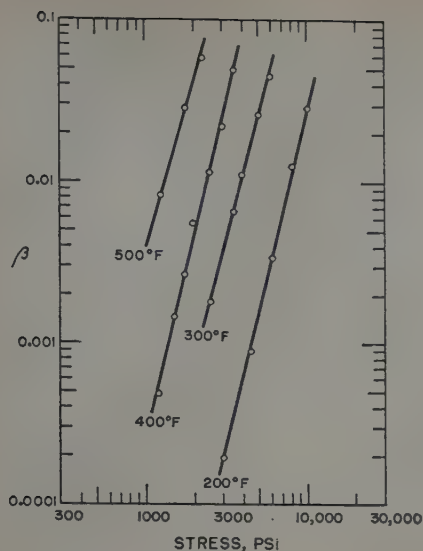


Fig. 6 (left)—Stress and temperature dependence of transient creep.

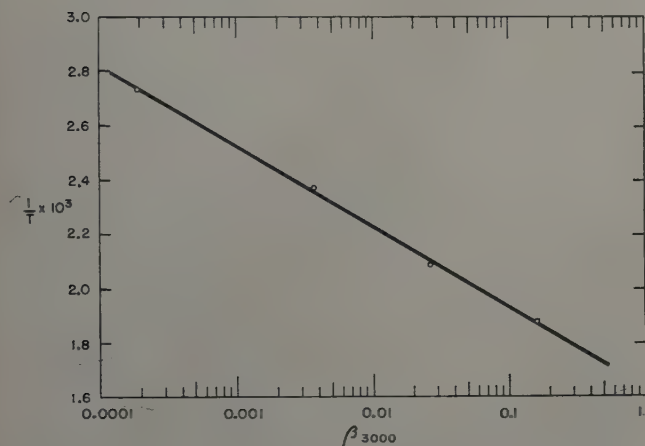


Fig. 7 (below)—Plot for determination of temperature coefficient Q , of transient creep.

Steady-State Creep: Calculations were made of the transient creep rate $d\epsilon_1/dt$ which was occurring at the strain level of individual curves where the secondary creep rate was measured for the general kinetic analysis. Comparison of these rates with the measured secondary rates led to an understanding of the transitions shown in Fig. 5. The measured rates are predominantly the steady-state creep element on the high temperature-low stress side of a transition. Under conditions represented by the low temperature-high stress side of a transition, the measured rates are predominantly the transient creep element. Because of the markedly different stress dependence of the two rates, only in the near vicinity of the transition on the log-log plot are they of the same order of magnitude at the strain levels where the secondary rates were measured.

An analysis of the stress and temperature dependence of the steady-state creep element alone was made on the low stress segments of the isotherms of Fig. 5. The only conclusion that could be drawn was that the steady-state creep coefficient, k , was a power function of stress with the exponent b a function of temperature. The separable element of temperature dependence showed no simple form. That is, steady-state creep in polycrystalline electrolytic magnesium may be represented by

$$\epsilon_2 = k (\sigma^{b(T)}, T) t.$$

Deformation Processes in Creep

Low-Temperature Type Deformation: Several electropolished specimens were deformed at high creep rates. Fig. 8 presents the microstructure of a specimen deformed at 200°F. The microstructures

shown in Figs. 9 to 12 correspond to the test conditions labeled by the encircled numerals 1 to 4 in Fig. 5. With the exception of the one produced at 400°F, the structures may be directly compared at a total creep strain of about 0.04.

The slip lines are straight with a fineness and uniformity of spacing which decrease with increasing temperature. The formation of sharp subgrains is common to all temperatures. The sharpness of the subboundaries is clearly shown with vertical illumination in Fig. 10. At the lower strain level, oblique illumination is valuable in revealing their sharpness as in Fig. 11b. In general, however, oblique illumination was avoided because of the excessive shadows produced at the grain boundaries. The slight deviation of slip lines which pass through the subboundaries and the results of a few X-ray back-reflection studies showed that neighboring subgrains were only slightly disoriented with respect to each other. In all of these structures deformation at the grain boundaries is much less than that within the grains. However, the boundary deformation increases in magnitude and changes from a rough and broken-up to a smooth appearance as the temperature increases.

High-Temperature Type Deformation: The smooth variety of grain boundary deformation is a cyclic process of sliding and migration which is best studied under conditions when it is predominant. Figs. 13 to 14 which correspond to points 5 and 6 on the low-stress high-temperature segments in Fig. 5 present microstructures obtained when primary creep was nearly absent. The mechanical twins and vertical polishing scratches which unfortunately appear in Fig. 13 were present before testing because of insufficient electropolishing of this specimen only. All other specimens used in the research were free of twins and scratches after electropolishing. Subgrain formation has disappeared and slip lines are few in number. The ribbing of the displaced regions was the first clue to the cyclic nature of the process. Inspection of many grain boundaries revealed the following characteristics:

1—In almost all cases grain boundary sliding is such that the grain having the convex surface boundary contour subsides.

2—In all cases grain boundary migration is "down-hill," i.e., into the subsided grain. Thus it is almost

Table I. Stress and Temperature Dependence of β , n , and m

Temperature, °F	Stress Psi	n	β	m
200	3,000	0.58	0.00019	4.2
	4,500	0.58	0.00088	
	6,000	0.56	0.0034	
	8,000	0.50	0.0124	
	10,000	0.53	0.0285	
	Average	0.55		
300	2,500	0.49	0.0018	3.9
	3,500	0.50	0.0066	
	4,000	0.50	0.0110	
	5,000	0.54	0.0260	
	6,000	0.55	0.0450	
	Average	0.53		
400	1,200	0.53	0.00048	4.2
	1,500	0.49	0.00145	
	1,750	0.49	0.00265	
	2,000	0.51	0.0055	
	2,500	0.51	0.0113	
	3,000	0.49	0.0220	
	3,500	0.53	0.0500	
	Average	0.51		
500	1,250	0.54	0.0082	3.5
	1,750	0.54	0.0285	
	2,250	0.53	0.0580	
	Average	0.54		
	Average	0.53		4.0

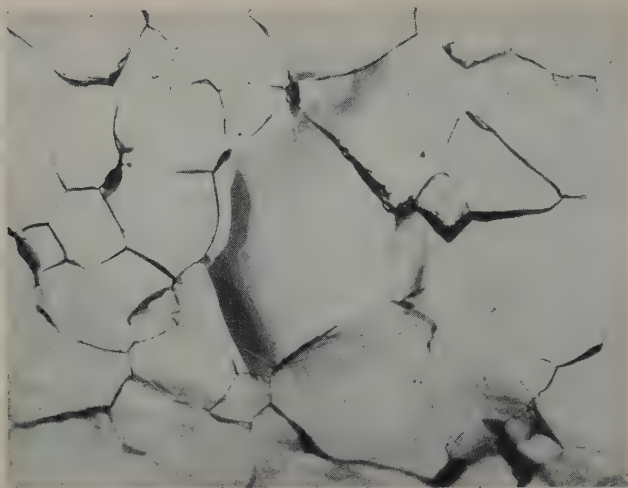


Fig. 8—Electrolytic magnesium after 0.04 creep strain at 200°F and 6000 psi. Stress axis vertical. X250.

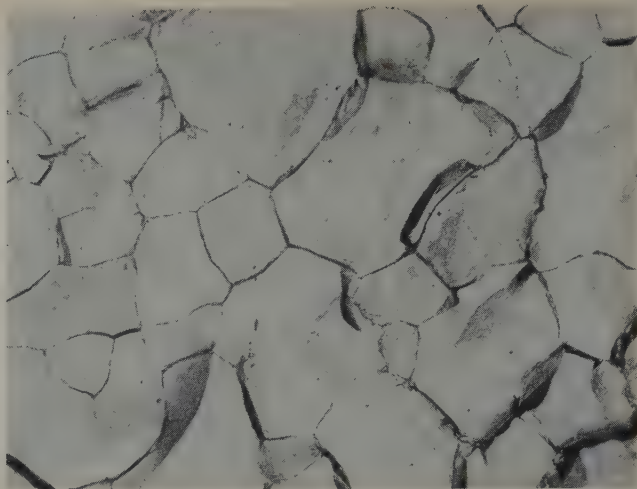


Fig. 9—Electrolytic magnesium after 0.04 creep strain at 300°F and 5500 psi, conditions of point 1 in Fig. 5. Stress axis vertical. X250.

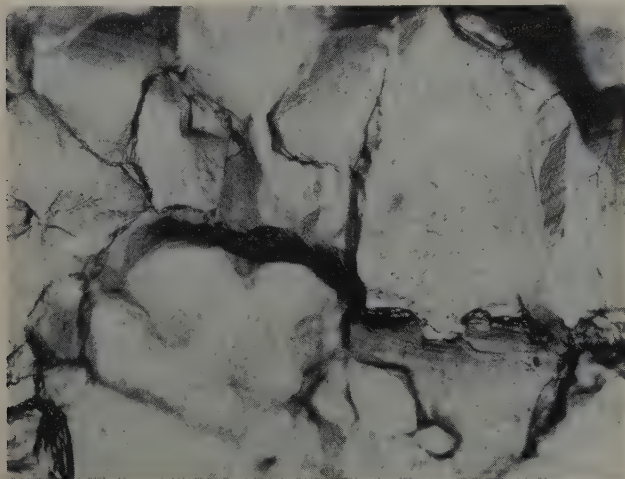


Fig. 10—Electrolytic magnesium after 0.08 creep strain at 400°F and 3675 psi, conditions of point 2 in Fig. 5. Stress axis vertical. X250.

always in the normal direction for grain growth (grain boundary energy induced process).

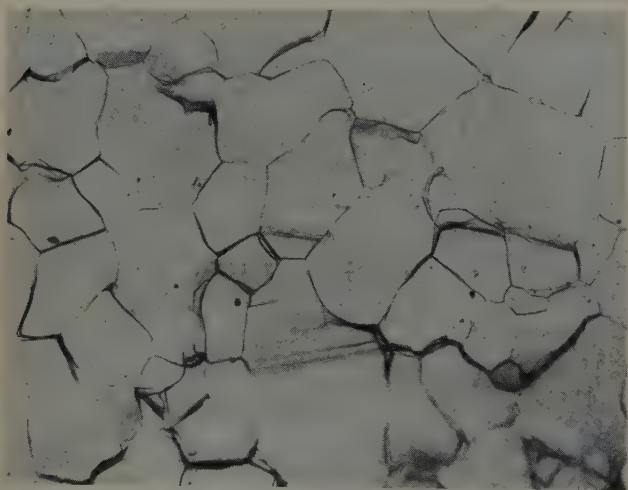
Grain growth is negligible if specimens are annealed at temperatures and for times equal to those necessary to produce boundary migration in the cyclic deformation process. It is reasonable to regard the process as one of accelerated grain growth accompanied by the generation of strain. The process

can lead to the ultimate consumption of grains as is shown in Figs. 12 and 13. A series of photographs which also illustrates this point and which corresponds to point 7 in Fig. 5 has been presented.⁷

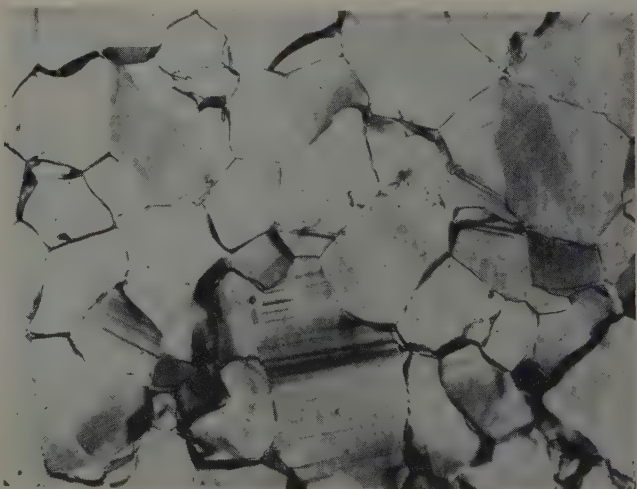
Discussion of Results

The cyclic grain boundary deformation process is perhaps the most striking one observed in this research. It has been observed and analyzed in the creep of polycrystalline aluminum by Servi and Grant^{5, 6} and Chang and Grant.^{8, 9} The latter investigators employed precise measurements of creep across the boundaries to obtain cyclic creep curves which correlated with the alternate elements of sliding and migration. The structure resulting from this process appears in the micrographs of aluminum by Hanson and Wheeler,¹⁰ Wilms and Wood,¹¹ and McLean,¹² iron alloys by Jenkins and Mellor,¹³ zinc by Cottrell and Aytekin¹⁴ and Ramsey,¹⁴ tin-antimony alloy by Betteridge and Franklin,¹⁵ lead-thallium alloy by Gifkins,¹⁶ magnesium by Suiter and Wood,¹⁷ and tin by Puttick and King.¹⁷

Sliding appears to occur on boundaries nearest to 45° to the stress axis until stopped by the local interference at edges and vertices. The strain energy localized at the grain boundary regions then accelerates the activation of boundary migration. The migration evidently lowers the strain energy (local stress relief) and allows more sliding at the bound-



a—Vertical illumination. X250.



b—Oblique illumination. X250.

Fig. 11—Electrolytic magnesium after 0.04 creep strain at 500°F and 2000 psi, conditions of point 3 in Fig. 5. Stress axis vertical.

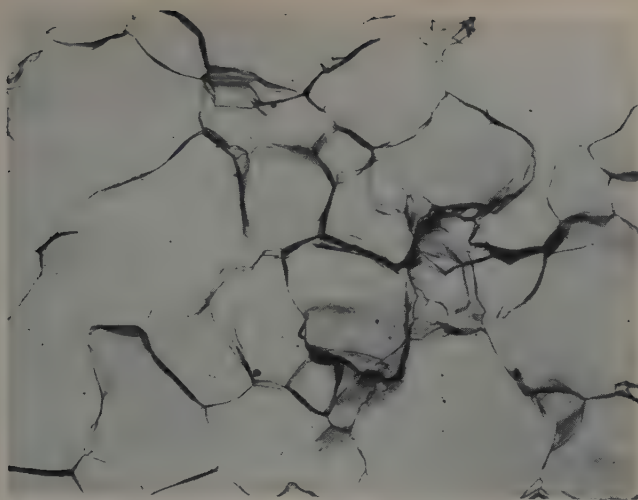


Fig. 12—Electrolytic magnesium after 0.041 creep strain at 600°F and 1500 psi, conditions of point 4 in Fig. 5. Stress axis vertical. X250.

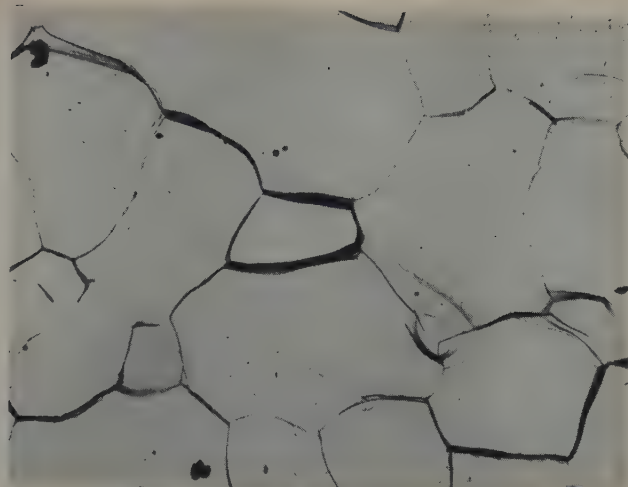


Fig. 13—Electrolytic magnesium after 0.02 creep strain at 600°F and 300 psi, conditions of point 5 in Fig. 5. Stress axis vertical. X250.

ary. In other words, the process is guided by the tendency to lower both strain energy and surface energy. This was a conclusion reached in a previous study of aluminum.⁹ The sparseness of slip lines in Figs. 13 and 14 indicates that in the limiting case of high temperature and low stress this process may be the sole mechanism of creep. The change of mass of the grain adds another degree of freedom not possessed by the deformation processes which lead only to change of grain shape.

The predominance of grain boundary deformation correlates with the predominance of steady-state creep. Perhaps the constancy of creep rate results from the existence of the cyclic self-recovery which boundary migration provides. The whole picture developed from these studies of creep rate and microstructural changes supports the concept of transient creep resulting from deformation within the grains and steady-state creep from grain boundary deformation. This viewpoint was first presented by Andrade^{18, 19} and has since been supported by many investigators.^{20, 11, 12, 15, 5, 6}

Although transient creep in magnesium obeys the power function of time, the exponent, 0.53, differs from the classical value 1/3. This is in contrast with the work on zinc by Cottrell and Aytakin¹⁸ and that on aluminum by Servi and Grant⁵ where agreement was found. This difference may be due to the testing conditions of constant load rather than constant stress. If this were the cause, it would hardly seem possible to obtain such consistent results, however. The exponential relation between transient creep and temperature has been found to hold over a range of 300°F (167°C) for extruded electrolytic magnesium. It has been proven for nickel over a 75°C range by Hazlett and Parker²¹ and for zinc, aluminum, and magnesium over a 100°C range by Crussard.²² The latter investigator reported Q for magnesium as ranging from 16,000 to 18,000 cal per gram atom, a good agreement with the result of this research. There is no evidence that Q can be identified as the activation energy of any simple rate-controlling process.

The occurrence of twinning was not found in any of the microstructural studies of extruded magnesium. This can be understood after an examination of the preferred orientation, Fig. 1. When basal planes lie at small angles to the tension axis, twinning is not to be expected. However, recent work

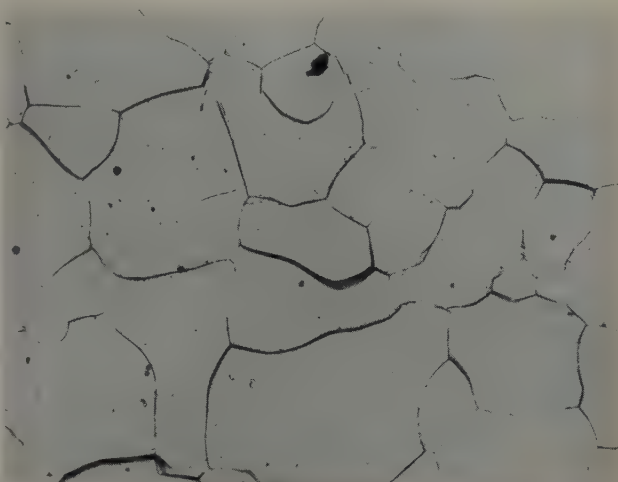


Fig. 14—Electrolytic magnesium after 0.01 creep strain at 400°F and 1000 psi, conditions of point 6 in Fig. 5. Stress axis vertical. X250.

on very coarse grained magnesium by Chaudhuri et al.²³ and the studies of zinc by Cottrell and Aytakin¹⁸ and magnesium by Suiter and Wood¹⁷ have shown that when orientation conditions allow it twinning plays an important part in creep behavior. Recent work on the rare-earth alloys of magnesium in this laboratory has elucidated the roles of twinning and also of non-basal slip in creep deformation. The results will be reported elsewhere.

The significance of subgrain formation in the creep deformation of aluminum, zinc and magnesium has been well established.^{9, 11, 12-15, 17, 20, 24, 25} The similarity of this polycrystalline deformation process to kinking and polygonization phenomena in single crystals has been discussed by Washburn and Parker.³⁰ They illustrate how continuity at grain boundaries may be aided by the occurrence of subgrain formation. It has been concluded in some of the past investigations that the process is of importance only at high temperatures and low creep rates and further that there is an appreciable increase of subgrain size with increasing temperature. The present results show that subgrain formation in magnesium is most pronounced at high creep rates at all temperatures. As the creep rate decreases at a given temperature, it disappears before slip does. The cyclic boundary deformation serves as its successor. The microstruc-

tural studies show no appreciable change in subgrain size over the entire experimental range of temperature and creep rate.

The results show that with increasing temperature and decreasing stress, predominance in creep changes from the processes of slip and subgrain formation to that of grain boundary deformation. It seems possible that at very low stresses and at temperatures approaching the melting point, the viscous self-diffusion process postulated by Nabarro²⁵ and Herring²⁶ may become predominant. All these processes must overlap each other in operation. Nevertheless, transitions may be expected from one to the other as the major creep rate-controlling process.

Fortunately it is becoming more and more apparent as time passes that there is more similarity than difference in the creep mechanism and kinetics of polycrystalline metals. The agreement between studies of magnesium, aluminum, and zinc points out that although minor differences may be of technical importance, they can generally be integrated into a coherent picture of the fundamentals.

Conclusions

1—The creep strain of extruded polycrystalline electrolytic magnesium over the temperature range 200° to 600°F consists of both transient and steady-state elements. The two elements of creep strain may be represented as a function of time, stress and temperature by

$$\epsilon = 4.5 \times 10^{-9} e^{-\frac{15,800}{RT}} \sigma^{4.0} t^{0.53} + k(\sigma^{b(T)}, T) t.$$

2—A rather sharp transition occurs between two straight line segments of the isotherms in the log-log plot of stress vs observed secondary creep rate. This results from the markedly different stress and temperature dependence of the two creep components.

3—The transient component of creep results from the intragranular processes of basal slip and subgrain formation. It is of major importance at low temperatures and/or high stresses.

4—The steady-state element of creep results from a cyclic process of sliding and migration of the grain boundaries. It is predominant at high temperatures and/or low stresses.

5—Slip lines become coarser and less uniformly spaced as the creep temperature increases.

6—The size of subgrains formed in creep is independent of creep rate and temperature over the experimental range studied.

Acknowledgment

This work was sponsored by the Flight Research Laboratory, Wright Air Development Center, under Contract No. AF 33(038)-16655.

References

- ¹ R. L. Dietrich: Surface Orientation and Rolling of Magnesium Sheet. *Trans. AIME* (1949) **185**, p. 621; *JOURNAL OF METALS* (September 1949).
- ² P. A. Jacquet: *Electrolytic Polishing of Metallic Surfaces and Its Applications* (1948) p. 64. Saint-Germain-En-Laye. Editions Metaux.
- ³ A. A. Moore and J. C. McDonald: Tensile and Creep Strengths of Some Magnesium-Base Alloys at Elevated Temperature. *Proc. ASTM* (1946) **46**, p. 970.
- ⁴ P. G. McVetty: Creep of Metals at Elevated Temperatures. The Hyperbolic-Sine Relation Between Stress and Creep Rate. *Trans. ASME* (1943) **65**, p. 761.
- ⁵ I. S. Servi and N. J. Grant: Creep and Stress Rupture Behavior of Aluminum As a Function of Purity.

Trans. AIME (1951) **191**, p. 909; *JOURNAL OF METALS* (October 1951).

⁶ I. S. Servi and N. J. Grant: Structure Observations of Aluminum Deformed in Creep at Elevated Temperatures. *Trans. AIME* (1951) **191**, p. 917; *JOURNAL OF METALS* (October 1951).

⁷ C. S. Roberts: Discussion on ref. 8; *Trans. AIME* (1953) **197**, p. 732; *JOURNAL OF METALS* (May 1953).

⁸ H. C. Chang and N. J. Grant: Observations of Creep of the Grain Boundary in High Purity Aluminum. *Trans. AIME* (1952) **194**, p. 619; *JOURNAL OF METALS* (June 1952).

⁹ H. C. Chang and N. J. Grant: Grain Boundary Sliding and Migration and Intercrystalline Failure Under Creep Conditions. *Trans. AIME* (1953) **197**, p. 305; *JOURNAL OF METALS* (February 1953).

¹⁰ D. Hanson and M. A. Wheeler: The Deformation of Metals Under Prolonged Loading. Part I—The Flow and Fracture of Aluminum. *Journal Inst. Metals* (1931) **45**, p. 229.

¹¹ G. R. Wilms and W. A. Wood: Mechanism of Creep in Metals. *Journal Inst. Metals* (1949) **75**, p. 693.

¹² C. H. M. Jenkins and G. A. Mellor: Investigation of the Behavior of Metals Under Deformation at High Temperatures. Part I—Structural Changes in Mild Steel and Commercial Irons During Creep. *Journal Iron and Steel Inst.* (1935) **132**, p. 179.

¹³ A. H. Cottrell and V. Aytakin: The Flow of Zinc Under Constant Stress. *Journal Inst. Metals* (1950) **77**, p. 389.

¹⁴ J. A. Ramsey: Some Observations on the Deformation of Polycrystalline Zinc. *Journal Inst. Metals* (1951) **80**, p. 167.

¹⁵ W. Betteridge and A. W. Franklin: An Investigation of the Structural Changes Accompanying Creep in a Tin-Antimony Alloy. *Journal Inst. Metals* (1951) **80**, p. 147.

¹⁶ R. C. Gifkins: Grain Movements During Creep. *Nature* (1952) **169**, p. 238.

¹⁷ J. W. Suiter and W. A. Wood: Deformation of Magnesium at Various Rates and Temperatures. *Journal Inst. Metals* (1952) **81**, p. 181.

¹⁸ E. N. daC. Andrade: On the Viscous Flow in Metals, and Allied Phenomena. *Proc. Royal Soc.* (1911) **84**, p. 1.

¹⁹ E. N. daC. Andrade: The Flow in Metals Under Large Constant Stresses. *Proc. Royal Soc.* (1914) **90**, p. 329.

²⁰ E. Orowan: Creep of Metals. *Journal West Scotland Iron and Steel Inst.* (1947) **54**, p. 45.

²¹ T. H. Hazlett and E. R. Parker: Nature of the Creep Curve. *Trans. AIME* (1953) **197**, p. 318; *JOURNAL OF METALS* (February 1953).

²² C. Crussard: The Role of Grain Boundaries in the Deformation of Metals. Application to Creep and Fatigue. *Revue Metallurgie* (1946) **43**, p. 307.

²³ A. R. Chaudhuri, N. J. Grant, and J. T. Norton: Metallographic Observations of the Deformation of High-Purity Magnesium in Creep at 500°F. *Trans. AIME* (1953) **197**, p. 712; *JOURNAL OF METALS* (May 1953).

²⁴ J. A. Ramsey: The Subgrain Structure In Aluminum Deformed at Elevated Temperatures. *Journal Inst. Metals* (1952) **81**, p. 215.

²⁵ F. R. N. Nabarro: *Report of Conference on the Strength of Solids* (1948) p. 75. London. Physical Society.

²⁶ C. Herring: Diffusional Viscosity of a Polycrystalline Solid. *Journal of Applied Physics* (1950) **21**, p. 437.

²⁷ K. E. Puttick and R. King: Boundary Slip in Bicrystals of Tin. *Journal Inst. Metals* (1951-1952) **80**, p. 537.

²⁸ D. McLean: Crystal Fragmentation in Aluminum During Creep. *Journal Inst. Metals* (1952-1953) **81**, p. 287.

²⁹ D. McLean: Grain-Boundary Slip During Creep of Aluminum. *Journal Inst. Metals* (1952-1953) **81**, p. 293.

³⁰ J. Washburn and E. R. Parker: Kinking in Zinc Single-Crystal Tension Specimens. *Trans. AIME* (1952) **194**, p. 1076; *JOURNAL OF METALS* (October 1952).

High Pressure Oxidation Rate of Metals—Copper in Oxygen

by William McKewan and W. Martin Fassell, Jr.

The oxidation rates of copper have been determined at temperatures from 600° to 900°C in oxygen from 14.7 to 400 psi total oxygen pressure. The oxidation rate of copper is unchanged by oxygen pressures within the range studied. The observed data extend Feitknecht's conclusion concerning the pressure independence of copper from atmospheric pressure to 400 psi. All samples studied in the above-mentioned temperature and pressure range have both Cu_2O and CuO present in the oxide film.

NUMEROUS papers have been published on the oxidation of copper, some of which have noted the effect of oxygen pressure on the oxidation rate of copper. It must be noted, however, that no data on the oxidation rates of copper at pressure in excess of 1 atm have been reported in the literature. (Le Chatelier¹ reported that a black oxide of silver was formed at 300°C and 15 atm pressure.) This is likewise true for the other metals.

This investigation was initiated to obtain experimental oxidation rate constants for pure metals at elevated temperatures and high oxygen pressure. Copper was selected as the first metal since probably more reliable data are available on its oxidation rates and related physical and chemical properties than for any other metal or alloy.

As a general summary, the following conclusions appear well established for the oxidation of copper:

1—The oxide coating consists of Cu_2O with a superficial coating of CuO providing the ambient oxygen pressure exceeds the equilibrium pressure for the coexistence of Cu_2O and CuO .² The following sequence of phases is then $\text{Cu}/\text{Cu}_2\text{O}/\text{CuO}/\text{O}_2$ (gas). The Cu_2O consists of large crystals that have no relation to the orientation of the metal crystals, except for a very thin layer adjacent to the metal.³ The CuO consists of very fine crystals randomly oriented. If the oxygen pressure is below the equilibrium pressure for the coexistence of Cu_2O and CuO , the coating consists of Cu_2O only.^{2,4,5}

W. M. McKEWAN, Junior Member AIME, formerly graduate student in Metallurgy, University of Utah, is now with the New Jersey Zinc Co. (of Pa.), Palmerton, Pa., and W. M. FASSELL, Jr., Member AIME, is Assistant Professor, Dept. of Metallurgy, University of Utah, Salt Lake City.

Discussion on this paper, TP3595E, may be sent, 2 copies, to AIME by Dec. 1, 1953. Manuscript, Dec. 31, 1951; revision, Jan. 2, 1953. Cleveland Meeting, October 1953.

This paper is a report of work done under contract with the Atomic Energy Commission.

2—The rate-determining factor in the parabolic oxidation of copper is the diffusion of Cu^+ ions through the Cu_2O layer.^{4,6,7} The Cu^+ ions are accompanied by electrons to maintain electrical neutrality. The mechanism of the reaction at the $\text{Cu}_2\text{O}/\text{CuO}$ interface and the method of growth of the CuO is in some doubt.

3—On copper, there are three reported pressure effects: (a) At pressures below 0.3 mm Hg oxygen pressure, the oxidation rate increases directly with pressure.^{2,4,5} Oxygen starvation at the surface may account for this effect. (b) At oxygen pressures from 0.3 to 63 mm, the oxidation rate increases as the 7th root of the oxygen pressure providing the temperature is such that only Cu_2O is present in the film. (c) At pressures from above the equilibrium pressure for the coexistence of Cu_2O and CuO (varies with temperature) to atmospheric pressure, the oxidation rate is independent of the oxygen pressure.²

Equipment

In order to determine the oxidation rates of metals in an oxidizing atmosphere at pressures up to 400 psi, the equipment is somewhat different than for low pressure work as is shown in Figs. 1 and 2. A Leeds and Northrup Micromax recording controller (A) is used to control the temperature of the Nichrome furnace winding in conjunction with a Micromax electric drive unit. The drive unit adjusts a 20 amp Variac (variable transformer) to control the power input into the Nichrome furnace winding.

Due to the "self heating" of the sample by oxidation, frequently encountered in oxidation rate studies, it is essential that the sample temperature be measured independently. This is done by means of a series of six chromel-alumel calibrated thermocouples located spirally around the oxidizing metal sample. Each thermocouple is partially shielded from the direct radiation of the furnace wall by

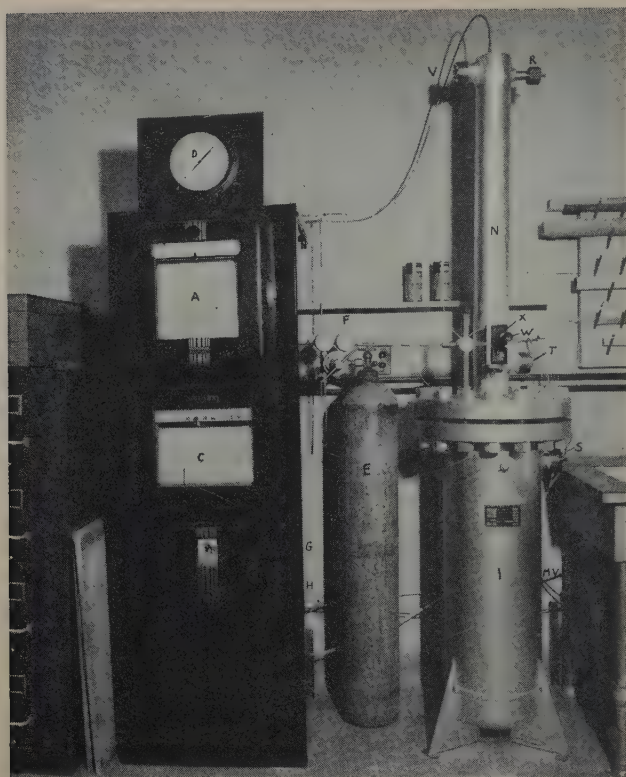


Fig. 1—Equipment for high pressure oxidation rate studies. See caption of Fig. 2 for explanation of letters.

means of an alundum shield (J). This arrangement gives apparent sample temperatures that are near the true temperature. The six sample thermocouples are connected to a Brown Electronic 12 point recorder (C).

The pressure in the furnace is measured by means of gage (D) (Master Gage Type 101, 0 to 600 psi, 3 pct accuracy with recalibration). For pressure measurements from 0 to 28 psi, a mercury absolute pressure gage is used for higher precision, not shown in Fig. 1. The oxygen from cylinder (E) is delivered via a high pressure reduction valve (F) (0 to 1000 psi) to the drying unit. The drying unit, not shown in Fig. 1, consists of an 18 in. length of 2 in. heavy wall pipe capped on the ends and packed with 2 lb of activated alumina (4-s mesh grade F-1, Alcoa). The dry oxygen is delivered from the drier to the furnace and pressure gage.

In order to remove the air in the furnace prior to the introduction of the oxidizing atmosphere, a Megavac vacuum pump (MV) is connected to the system. Valves (G) and (H) are used to release the pressure and connect the vacuum pump to the system, respectively.

The furnace shell consists of two sections. The lower section (I) contains the No. 18 Nichrome 7 heating element wound on a 2 in. ID x 36 in. alundum tube (Norton No. 12310), the alundum shielding tube 1 in. ID x 24 in. (Norton RA 98), the furnace insulation (L) (MgO, calcined chemical precipitate) and the thermocouple and power leads (M). The upper section (N) contains the quartz spring balance (O) (0 to 5 g capacity 12 mm diam x 65 mm length [Type B Houston Technical Laboratories]), and the gold suspension chain (P), wound around an 18-8 stainless steel drum (Q) used to lower the sample into the furnace. A No. 30 B and S Pt-20 pct Rh wire suspends the sample from the quartz spring.

In order to keep the sample centered with respect to the cathetometer, the furnace tube, and the measuring thermocouples, the pitch of the threads on the drum is the same as that in the bonnet of the packing gland (R) so that there is no relative horizontal motion of the chain, quartz spring, and sample (Z).

The access opening (T), in the top section, is used for the placement and removal of samples on the Pt-Rh suspension wire. The sample is suspended on a small platinum hook coated with a thin layer of alundum cement, fired in situ. Access opening (V) is used for the initial placement and adjustment of the weighing and suspension components.

The microscope (W) and cathetometer (X), used to measure the rate of elongation of the quartz spring through the observation window (Y), are mounted rigidly to the furnace shell.

All power and thermocouple leads enter the lower section of the furnace through the multiple pressure packing gland (S).

Procedure

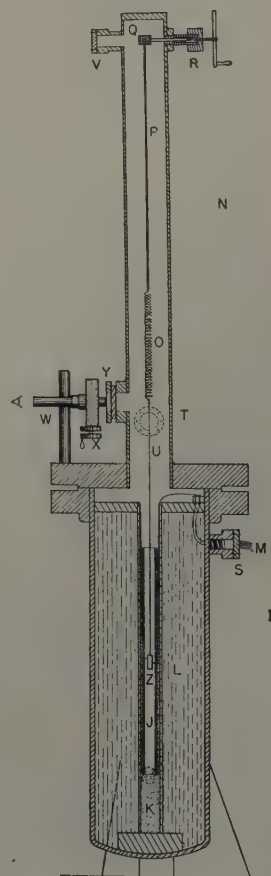
The copper metal samples used in this investigation are annealed commercial electrolytic sheet 0.018 in. thick x 1/2 in. x 1 1/2 in.

The geometric surface area of each sample is calculated from micrometer measurements of the dimensions. A 0.125 in. hole is drilled near the top end for the suspension hook. Prior to oxidation, the sample is etched 5 min in 10 pct ammonium persulphate to remove any oxide film present, washed with distilled water and dried. After cleaning, the sample is weighed and placed on the hook through access opening (T).

With the sample in place, the cover plate is bolted on and the furnace evacuated. After the air is removed, oxygen is allowed to enter the furnace slowly to the desired pressure. The furnace is

Fig. 2—High pressure oxidation furnace.

- A—Recording controller
- B—Electric control unit
- C—12 point recorder
- D—Pressure gage
- E—Oxygen cylinder
- F—High pressure reduction valve
- G—Pressure valve
- H—Vacuum pump valve
- I—Lower section of furnace shell
- J—Alundum shield
- K—Grain alundum
- L—Furnace insulation
- M—Thermocouple and power leads
- MV—Vacuum pump
- N—Upper section of furnace
- O—Spring balance
- P—Suspension chain
- Q—Stainless steel drum
- R—Packing gland
- S—Packing gland
- T—Access opening
- U—Pt-20 pct Rh suspension wire
- V—Access opening
- W—Microscope
- X—Cathetometer
- Y—Observation window
- Z—Sample



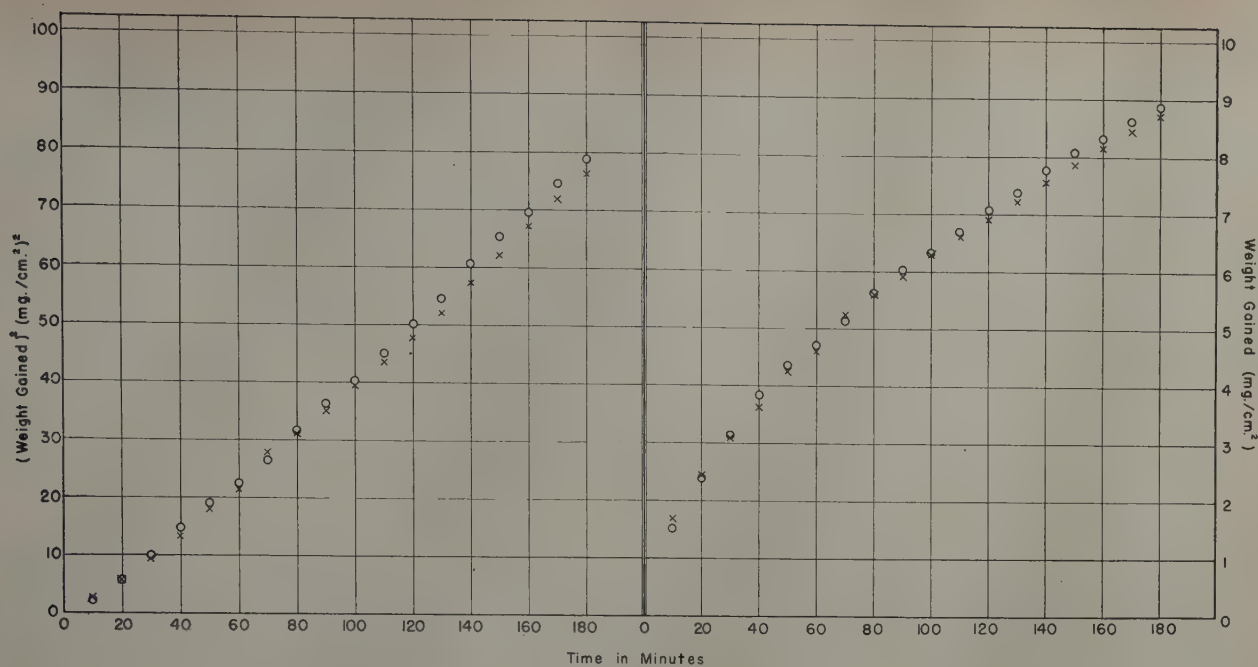


Fig. 3—Typical oxidation rate curves of pure copper. o No. 48 copper at 400 psi oxygen at 800°C. x No. 29 copper at 14.7 psi oxygen at 800°C.

brought to temperature and when thermal equilibrium is attained, usually in about 20 to 30 min, the sample is lowered into the hot section of the furnace and weighings are started immediately at 10 min intervals. The present equipment is capable of detecting weight changes of 0.04 mg.

Experimental Results

The results to be described are based upon the experimental observations of the oxidation of 63 copper samples in oxygen at 600°, 800°, and 900°C. The absolute oxygen pressure was varied from 14.7 to 400 psi. Typical curves showing the increase of weight with time for pure copper at 800°C are shown in Fig. 3. The direct plot of the weight gain vs time is satisfied approximately by the general equation of the parabolic law

$$w^2 = Kt + c.$$

The entire series of rate constants at 800°C obtained from the rate curves are plotted vs oxygen pressure in Fig. 4. The theoretical curve calculated from Wagner-Grunewald pressure dependence equation is included for comparison. Of course, it does not apply directly to the system investigated since Cu_2O and CuO are present. Fig. 4 indicates that the oxidation rate of pure copper in oxygen is independent of pressure above 1 atm total pressure. The rate constants obtained for each sample are listed in Table I.

Discussion of Results

The values of the rate constants obtained for copper agree reasonably well with those reported by Pilling and Bedworth.⁵ They found the rate constants in oxygen at 1 atm pressure for copper at 600°, 800°, and 900°C to be 3.24 , 86.9 , and $349 \times 10^{-10} \text{ g}^2 \text{ cm}^{-4} \text{ sec}^{-1}$, respectively, while the present work shows values of 3.28 , 76 , and $301 \times 10^{-10} \text{ g}^2 \text{ cm}^{-4} \text{ sec}^{-1}$ at the same temperatures and pressures.

These results clearly demonstrate that the conclusions reached by Feitknecht in 1929 and confirmed by Fröhlich⁸ in 1936 on the pressure independence of oxygen on copper (maximum of 1 atm

pressure) can be extended to 27.2 atm total pressure.

Aside from the experimental results previously mentioned, a few miscellaneous observations are worthy of note. In a run of 900°C, 14.7 psi O_2 , oxidation rate measurements were continued for some time after the copper metal was completely oxidized. At the disappearance of copper, a sharp change in slope occurred on the w^2 vs t plot. The value of K for the gain in weight with copper metal present was $252 \times 10^{-10} \text{ g}^2 \text{ cm}^{-4} \text{ sec}^{-1}$ and for the oxidation of Cu_2O to CuO , $K = 0.775 \times 10^{-10} \text{ g}^2 \text{ cm}^{-4} \text{ sec}^{-1}$. The calculated value of $K = 22.2 \times 10^{-10} \text{ g}^2 \text{ cm}^{-4} \text{ sec}^{-1}$ from Valensi's equation⁹ does not agree with the experimental value.

The question of the mechanism at the $\text{Cu}_2\text{O}/\text{CuO}$ interface and the method of growth of the CuO is of interest in the problem of oxidation of copper under conditions wherein both oxides coexist. Wagner⁴ has shown experimentally that the rate is affected by oxygen pressure when only Cu_2O is present. In the present work and in that of Feitknecht and Fröhlich, CuO was present on the exterior of the sample. Hence, the CuO must be relatively impervious to oxygen and the effective concentration of oxygen at the $\text{Cu}_2\text{O}/\text{CuO}$ interface remains unchanged at 27 atm oxygen pressure. Czerski¹⁰ reported that CuO is nontransparent to oxygen and Seitz¹¹ states that the vapor pressure of oxygen has no effect on CuO as a semiconductor. It has been

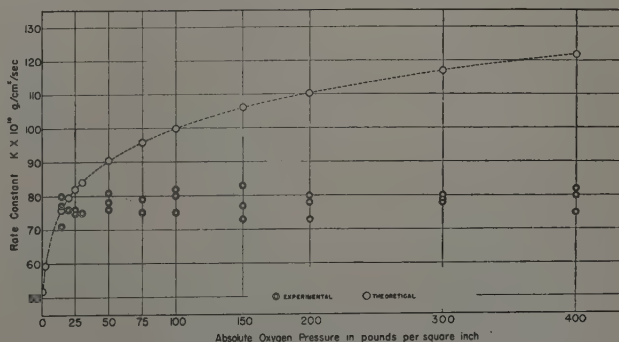


Fig. 4—Oxidation rate of copper vs oxygen pressure at 800°C.

shown experimentally^{4,6,7} that the migration of Cu⁺ ions alone is responsible for the growth of the Cu₂O film. The growth of CuO must occur by a similar process, since the CuO is apparently impervious to oxygen. The following mechanism of growth of the system Cu/Cu₂O/CuO/O₂ is proposed:

1. Formation of Cu⁺ ions and electrons at the Cu/Cu₂O interface.
 $(\text{Cu}^+ + \epsilon)_{\text{Metal}} \rightarrow \text{Cu}^+_{\text{Film}} + \epsilon.$
2. Migration of Cu⁺ ions and electrons through the Cu₂O film.
3. Reaction of Cu⁺ ions and electrons with CuO to form Cu₂O at the Cu₂O/CuO interface.
 $\text{Cu}^+ + \epsilon + \text{CuO} \rightarrow \text{Cu}_2\text{O}.$
4. Migration of unreacted Cu⁺ ions and electrons through the CuO film.*

* An alternate possibility may exist for steps 4 and 5. Since the CuO is a transition-type semiconductor,¹² an equilibrium concentration of oxygen vacancies could exist near the Cu₂O/CuO interface. The vacancies could then diffuse to the CuO/O₂ interface and be filled with oxygen. Then concentrations will be independent of the oxygen pressure at the CuO/O₂ interface. The net result would be essentially equivalent to steps 4 and 5.

5. Reaction of Cu⁺ ions and electrons to form CuO.



It is not reasonable to expect the CuO to decompose to form Cu₂O and Cu since the CuO is thermodynamically stable. The oxidation process is a kinetic process and there is always a supply of Cu⁺

Table I. Oxidation Rate Constants for Copper at 600°, 800°, and 900°C, at Various Total Oxygen Pressures

Run No.	Temperature, °C	Oxygen Pressure, Psi	$K \times 10^{10} \frac{\text{G}^2}{\text{Cm}^{-4} \text{Sec}^{-1}}$	Average K
51	600	14.7	3.42	3.28
52			2.93	
53			3.48	
54	600	300	3.34	3.17
55			3.05	
56			3.11	
27	800	14.7	79.8	76.0
28			71.4	
29			76.9	
25	800	20	75.8	75.3
22	800	25	74.8	
24			75.4	
47			75.8	
26	800	30	75.1	
16	800	50	76.3	78.3
31			77.5	
46			81.1	
15	800	75	74.8	77.4
30			78.7	
45			78.7	
17	800	100	79.8	78.4
33			82.2	
44			75.3	
18	800	150	77.4	78.0
37			83.7	
42			72.8	
19	800	200	73.0	77.3
38			80.3	
41			78.5	
20	800	300	79.5	79.2
39			78.2	
40			79.9	
48	800	400	74.7	78.7
49			79.7	
50			81.7	
85	900	14.7	315	301
86			295	
87			293	
88	900	300	279	275
89			258	
90			261	
91			301	

ions and electrons as long as any metal remains which can easily react with the CuO. It is implied that there is a temperature dependent distribution of copper ions between steps three and four. Such a distribution of Cu⁺ leads to a constant ratio of the thickness of the Cu₂O and CuO films at constant temperature and pressure. This is in agreement with the reported results of Valensi.¹³

When the metal is consumed, a different system is present. The following mechanism is proposed for the system Cu₂O/CuO/O₂:

1. Decomposition of Cu₂O at the Cu₂O/CuO interface to form CuO and Cu⁺ ions and electrons.
 $\text{Cu}_2\text{O} \rightarrow \text{CuO} + \text{Cu}^+ + \epsilon.$
2. Migration of Cu⁺ ions and electrons through the CuO film.
3. Reaction of Cu⁺ ions and electrons with oxygen to form CuO.



A gradient of Cu⁺ ions and electrons will be established in the CuO film by the decomposition of the Cu₂O that will control the rate of oxidation. This process has been shown to be parabolic by Valensi¹⁸ and in the present paper. However, this second process without metal present cannot be used to make predictions on the first process with metal present for the following reasons: The first process has metal present that stabilizes the Cu₂O in the presence of CuO. In the second process the metal is no longer present, and the Cu₂O is not stable in the presence of CuO and will decompose.

The CuO is disappearing at the Cu₂O/CuO interface and forming at the CuO/O₂ interface for the system Cu/Cu₂O/CuO/O₂. For the system Cu₂O/CuO/O₂, however, the CuO film is growing at both the Cu₂O/CuO interface and the CuO/O₂ interface.

In summary, the following pseudo equilibrium reaction at the Cu₂O/CuO interface can be considered:



In the presence of copper metal the reaction goes to the right. When the metal is gone, the reaction goes to the left. Therefore, the rate of formation of CuO, in the absence of the copper metal, cannot determine the rate of formation of CuO when metal is present.

References

- ¹ H. Le Chatelier: *Ztsch. Physik Chem.* (1887) **1**, p. 516.
- ² W. Feitknecht: *Ztsch. Electrochemie* (1929) **35**, p. 142.
- ³ R. F. Mehl, E. L. McCandless, and F. N. Rhines: *Nature* (1934) **134**, p. 1009.
- ⁴ C. Wagner and K. Grunewald: *Ztsch. Physik Chem.* (1938) **B40**, p. 455.
- ⁵ N. B. Pilling and R. E. Bedworth: *Journal Inst. Metals* (1923) **29**, p. 259.
- ⁶ C. Wagner: *Ztsch. Physik Chem.* (1933) **B21**, p. 25; (1936) **B32**, p. 447.
- ⁷ J. Bardeen, W. H. Bratten, and W. Shockley: *Journal of Chemical Physics* (1946) **14**, p. 714.
- ⁸ K. W. Fröhlich: *Ztsch. Metallkunde* (1936) **28**, p. 368.
- ⁹ G. Valensi: *Revue Metallurgie* (1948) **45**, No. 7, p. 205.
- ¹⁰ L. Czerski: *Rozniki Chem.* (1937) **17**, p. 436.
- ¹¹ F. Seitz: *Modern Theory of Solids* (1940) p. 70. New York. McGraw-Hill Book Co.
- ¹² O. Kubaschewski and B. E. Hopkins: *Oxidation of Metals and Alloys* (1953) pp. 34-36. Academic Press.
- ¹³ G. Valensi: *Comptes Rendus* (1936) **203**, p. 1354-1356.

Plasticity of Columbium Single Crystals

by R. Maddin and N. K. Chen

Columbium single crystals were deformed in tension and compression. Reorientation by X-rays and stereographic projections of slip traces indicate that plane of slip may be considered as $\{110\}$. The plastic behavior is shown to be quite similar to the deformation of molybdenum single crystals.

STUDIES on the crystallography of the deformation process in body-centered cubic metals have been renewed recently with investigations of α iron single crystals¹⁻³ and molybdenum single crystals.⁴ It is now apparent that too many exceptions to the rationalization based upon the ratio of absolute testing temperature to absolute melting point by Andrade⁵ exist to permit more serious discussion of this type of analysis. The considerations of resolved shear stress utilizing only planes of the type $\{110\}$, $\{112\}$, and $\{123\}$ ⁶ permit analysis of the deformation only on the basis of those three types of planes.

The suggestions made by Elam⁷ and by Greninger⁸ in which the slip process is envisioned as a composite slip on two nonparallel $\{110\}$ planes can be illustrated schematically in Fig. 1. It may be seen that an unresolved trace on any plane containing a $\langle 111 \rangle$ direction may be accomplished by varying the number of atoms participating in the composite process. By further varying the number of atoms in each plane but keeping the ratio of participating atoms constant, jogs could be obtained in the traces and hence wavy slip lines could be produced.

Vogel and Brick¹ studied the behavior of α iron single crystals in which they suggest that the plane of glide is "non-crystallographic" and may be predicted from the intersection between the great circle joining the slip direction and specimen axis with the great circle whose zone axis is the slip direction. In a more recent investigation on iron single crystals, Steijn and Brick⁹ suggest that the slip mechanism may be considered as made up of a type of composite slip occurring on $\{110\}$ and $\{112\}$ planes.

Evidence for a possible composite nature of the

slip process has been presented for the case of molybdenum in the form of analysis of asterism and specimen axis rotation.⁴ Definite proof of a composite slip process must, however, await good electron microscopic resolution of the individual traces making up the unresolved optical trace used in determining the acting slip plane.

The present investigation was undertaken to study the behavior of columbium single crystals not only in tension but also in compression since the specimen axis migration should indicate the plane or planes of glide in the same manner that the specimen axis migration in tension indicates the direction of glide.

The orientations of eleven crystals investigated are shown in Fig. 2. Specific orientations are missing (those in the vicinity of $[111]$ and $[001]$) and consequently the effect of orientation on the crystallography of deformation could not be considered.

Experimental Procedure

The $\frac{1}{8}$ -in. rods (7 in. long) were subjected to an axial tension in vacuo while at temperatures in the vicinity of 2000°C for 2 to 4 hr. This treatment resulted in large cylindrical grains (about $\frac{1}{2}$ in. long) occupying the entire cross section. A number of these rods were used for the tension studies by observing the behavior of the individual grains. For the compression studies, single crystals approximately $\frac{1}{4}$ in. long by $\frac{1}{8}$ in. in diameter were cut from the rods; the ends were ground parallel. All specimens were polished electrolytically in a solution of 15 cc HF (48 pct) and 85 cc H₂SO₄ (concentrated) using a platinum cathode, a current density of 0.04 amp per sq cm and a temperature between 25° and 60°C.¹⁰ Orientations were obtained using a Laue back-reflection method (3 cm film to specimen distance) with a $\frac{1}{2}$ mm collimator 9 cm long. For the compression specimens, a reference mark was scratched on one of the compression sur-

R. MADDIN, Member AIME, is Associate Professor of Metallurgy, and N. K. CHEN, Junior Member AIME, is Assistant Professor of Metallurgy, The Johns Hopkins University, Baltimore.

Discussion on this paper, TP 3606E, may be sent, 2 copies, to AIME by Dec. 1, 1953. Manuscript, Jan. 2, 1953; revision, April 20, 1953. Cleveland Meeting, October 1953.

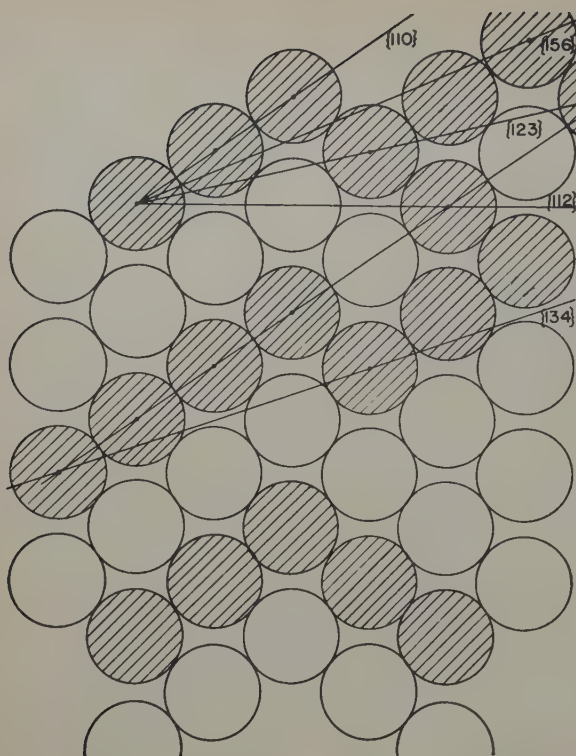


Fig. 1—Illustration showing the integrated trace produced by using different numbers of atoms in nonparallel {110} planes.

faces on each of the crystals. This reference scratch was aligned with a scratch on a specially constructed crystal holder which contained a steel indicator in line with the reference scratch on the surface of the holder. The assembly was used for all X-ray analysis and also for metallographic observations. The tensile specimens contained a reference mark on the surface just below one of the grip ends. All X-ray exposures were made with careful regard to the position of the reference marks so that subsequent metallographic observations (always made with respect to the reoriented specimen) could be coordinated with the photograms.

Compression was performed in a specially constructed apparatus operated by a hydraulic compression machine. A clip gage made of phosphor bronze to which were glued two SR-4 type A-1 strain gages was calibrated and used to measure strain. The compression plates were liberally greased. The same hydraulic machine was used for the tension studies.

Results

Tension: The specimen axis migrations for all crystals investigated in tension are shown in Figs. 3 to 5. Since all the tension specimens were rods

composed of large grains, it is not known with certainty that the stress was simple tension. Nevertheless, analysis was referred to specimen axis rotation (stress axis) assuming a simple tension. Whenever surface conditions were satisfactory, i.e., no mistake could be made in differentiating slip traces from spurious markings, stereographic analysis of the traces was used.

The pole rotations for specimens Cb-2, 4, and 11 are shown in Fig. 3. Stereographic analysis of the traces on Cb-2 indicated a "noncrystallographic" glide plane deviating about 5° from the predicted plane (Fig. 3) using the method of Vogel and Brick.¹ Although the axis migration for 2 and 11 are too small for accurate interpretation, there is indication that these crystals behaved in an expected manner, i.e., the axis rotated toward the direction of slip, D . A lack of pronounced asterism prevented analysis by this method.⁴ The larger amount of asterism shown in Fig. 6a for specimen Cb-4 after a greater amount of extension permitted analysis. The participation of more than one slip system is evident

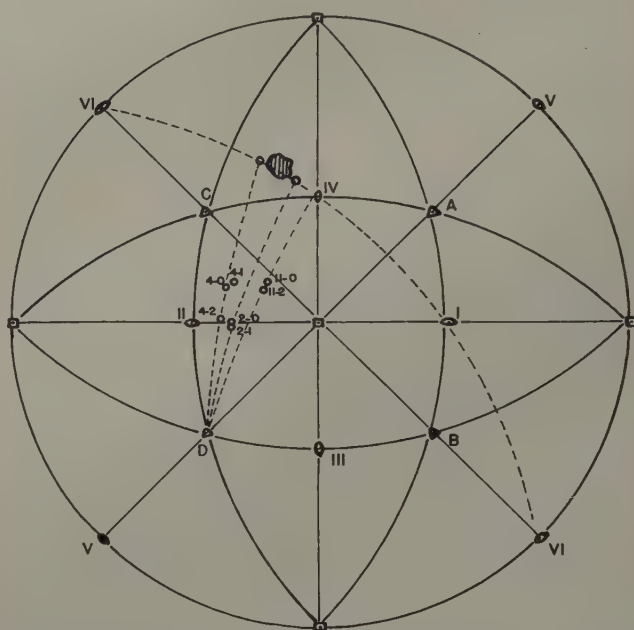


Fig. 3—Specimen axis migration for crystals Cb-2, 4, and 11 (tension). Stereographic determination of slip plane (Cb-2) from traces is shown as hatched area. Predicted planes are shown at intersection of the two dotted great circles.

from the splitting of the Laue reflections shown in Fig. 6a, if it is assumed that the asterism is crystallographic in origin. The ends of the major asterism were plotted on the same projection and indicated an axis shift from position 4-0 to 4-1. In an effort to determine more accurately the axis about which the asterism occurred, Laue back-reflection photograms were made every 2° about the specimen axis in the vicinity of the critical position. The photogram (Fig. 6b) demonstrates a [112] axis as that about which the asterism occurred. The determination of the plane by the slip trace method indicated a noncrystallographic plane. A further extension until necking produced an axis shift to position 4-2. Based upon axis shift and asterism analysis, it would appear that slip systems IVD and IIA have operated in the deformation of Cb-4.

The behavior of crystals Cb-6 and 7 is shown in Fig. 4. The extension of Cb-7 (about 5 pct) produced an axis shift along a great circle towards

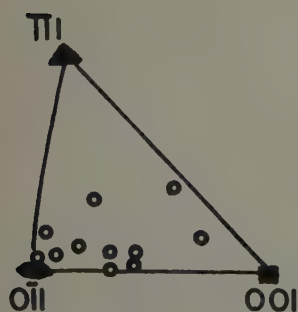


Fig. 2—Initial orientations of all crystals investigated.

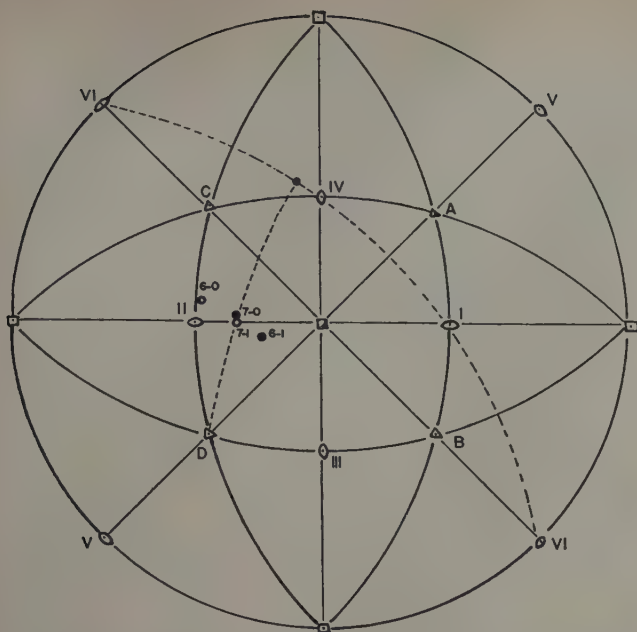


Fig. 4—Specimen axis migration of crystals Cb-6 and 7 (tension). The predicted plane for crystal Cb-7 is shown as the intersection of the two dotted great circles.

direction *D* and analysis of the traces showed plane IV as the plane of glide. The predicted plane based upon resolved shear stress is shown as the intersection of the two dotted great circles. Asterism was complex but not enough developed to permit accurate analysis.

Crystal Cb-6 was pulled until necking occurred. The pole rotation was determined by plotting only the points of maximum intensity on very extensively blurred streaks. The unexpected behavior cannot be explained on the basis of slip on only one plane of high resolved shear stress since the initial orientation is at a position where the resolved shear stress is almost the same on four different $\{110\}$ planes (III, IV, V, VI). The behavior of Cb-6 should be compared with the behavior of Cb-9 which has a similar orientation.

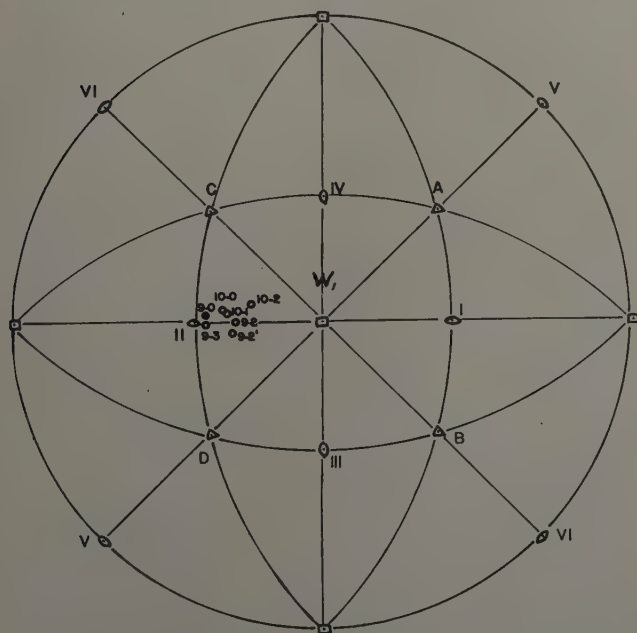


Fig. 5—Specimen axis migration of crystals Cb-9 and 10 (tension).

Since the orientation of crystal Cb-9 was quite close to that of Cb-6, a more careful technique was adopted. Two flat surfaces at 90° angles were polished on the specimen held in sealing wax. After etching in concentrated HF, the specimen was electropolished. Laue back-reflection photograms were made of each surface to indicate the removal of material affected by the polishing.

The specimen was extended about 2 pct and examined with microscope and X-ray. No slip lines and little or no axis shift were observed. The specimen was extended again to a total elongation of about 6 pct. Although slip lines were visible, great difficulty was encountered in attempting analysis from the traces. X-ray photograms made at different positions around the specimen axis testified to the complex behavior of this crystal. Referring to

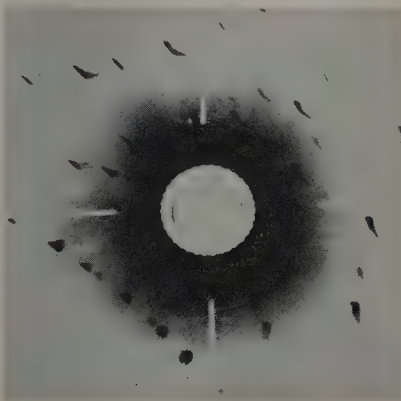
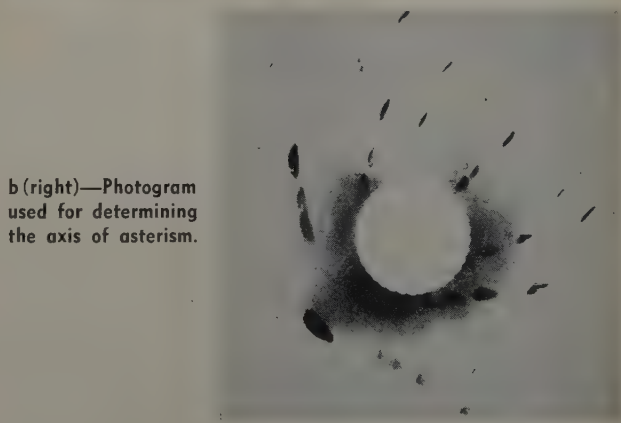


Fig. 6—X-ray photograms of crystal Cb-4.

a (left)—This shows two asterisms. The larger of the two is plotted as positions 4-0 and 4-1.



b (right)—Photogram used for determining the axis of asterism.

Fig. 5, the initial orientation of the crystal is plotted as 9-0 and the position of the axis after 6 pct elongation by 9-2. (Note the similarity to Cb-7.) The axis shift indicates a rotation towards B, a possible slip direction. The system II-B, however, is one of very low shear stress. Consequently, it is believed that the action may be of a composite nature involving the planes III, IV, V, and VI. After extension again to about 16 pct, the position of the axis was at 9-3. The slip lines were extremely complex showing not only a very wavy nature but also the pronounced development of markings similar to deformation bands or rumpling.

The behavior of Cb-10 with an initial orientation almost the same as Cb-9 but farther along the symmetry curve II- W_1 , was not quite so complex. After about 6 pct elongation, the axis shift, 10-0 to 10-1 in Fig. 5, might likewise be explained on the participation of planes IV, V, and VI. However, after 16 pct elongation the axis shift indicated a possible

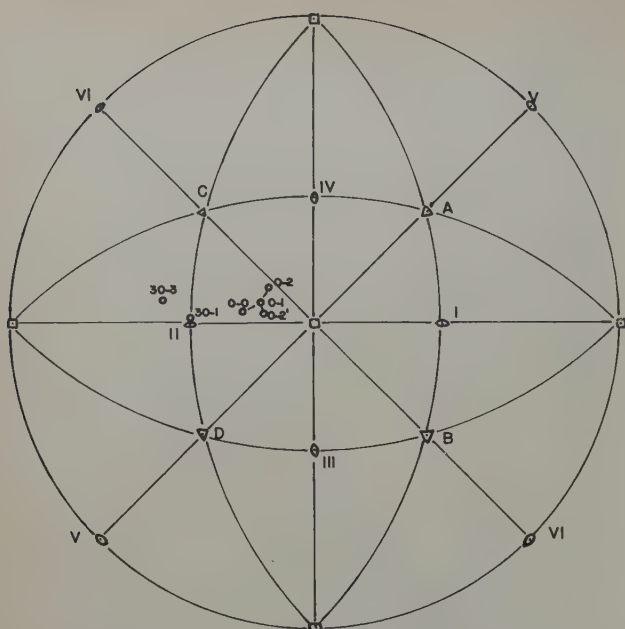


Fig. 7—Specimen axis migration for crystals Cb-0 and Cb-30 (compression).

participation of (II-A). The small deviation along the great circle to (B) may perhaps be attributed to the continual participation of IV and V in direction B, but on a small scale. However, the position of 10-2, being at the outer limit of the accuracy of orientation determination, cannot be classed as rigorously indicating the later activity of (II-A).

Compression: The axis migration of the specimens studied in compression are shown in Figs. 7 and 8. Crystal Cb-30 whose initial orientation is very close to II showed complex behavior similar to specimens Cb-6, 9, and 10 in tension. It appears very likely that more than one and perhaps all the planes concerned (III, IV, V, and VI) contributed to the deformation of Cb-30.

Crystal Cb-0 was compressed 5.97 pct. Analysis of the traces indicated IV as a plane of glide. From the axis migration to position 0-1 (Fig. 7), it appears more than likely that another plane contributed to the deformation since enough rotation was observed to show a decided deviation from the "prescribed" course toward IV. After compression to 11 pct, asterism was pronounced and showed indication

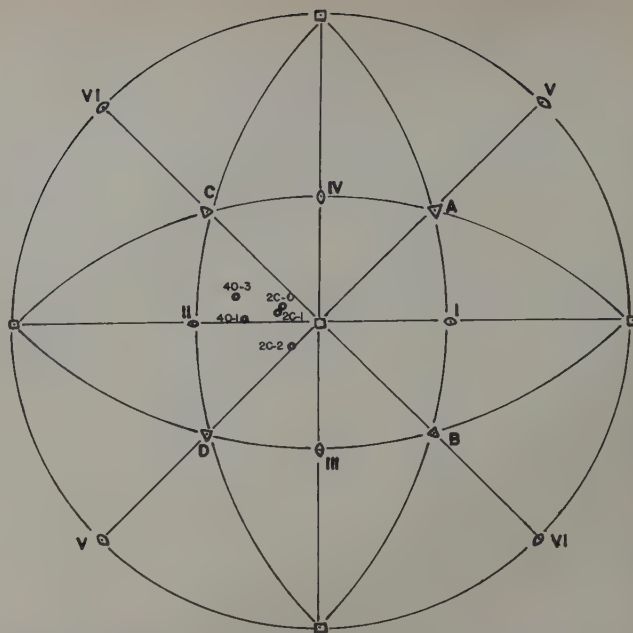


Fig. 8—Specimen axis migration for crystals Cb-2c and Cb-40 (compression).

of a dual nature (Fig. 9). The tails of both the asterisms shown in Fig. 9 were plotted stereographically as positions 0-2 and 0-2' in Fig. 7. It is believed here that planes IV and III have participated in the plastic deformation of Cb-0.

The appearance of slip traces on Cb-0 after the first compression is shown in Fig. 10a to d. The traces are, for the most part, straight and prove to be caused by the $(\bar{1}01)$ plane, (IV). The forked bands are presumably deformation bands whose boundaries agree with no low indices, high atomic density plane. In certain cases, the bands are seen to consist of small but straight lines reminiscent of bands of secondary slip in aluminum.

The behavior of crystals Cb-2c and 40 are shown in Fig. 8. Specimen Cb-2c was treated in the same manner as Cb-0. It was compressed 2.91 pct and observed by microscope. Analysis of the traces indicated three glide planes to have been operative; these were VI, II, and III. A micrograph of three sets of traces is shown in Fig. 11. It is possible that the slip direction is the same for all three of these planes. If the amount of glide on each of these planes in the same slip direction is the same, the movement of the axis along a great circle to II would be expected. However, as may be seen in Fig. 8, the pole movement 2c-0 to 2c-1 is not exactly along this great circle indicating an uneven amount of glide on the $\{110\}$ planes concerned. After 14.5 pct compression, however, it is apparent that the glide on plane III predominates as shown by the movement of 2c-1 to 2c-2.

Crystal Cb-40 behaved in a somewhat complex manner, probably owing to its initial orientation on a symmetry curve. Nevertheless, the pole movement from 40-1 to 40-3 (Fig. 8) indicates a participation of both IV and VI (the resolved shear stress on both these planes are somewhat similar).

Stress-Strain Curves: A stress-strain curve for crystal Cb-30 is shown in Fig. 12. No attempt has been made to calculate a critical resolved shear stress since it is not known with certainty on what plane to resolve the stress.

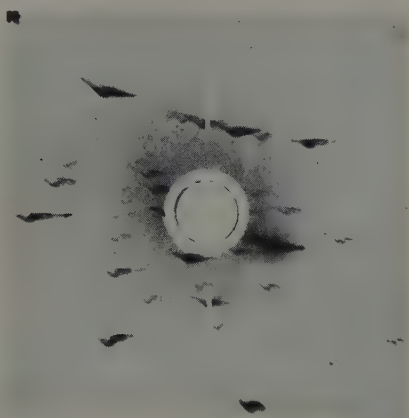
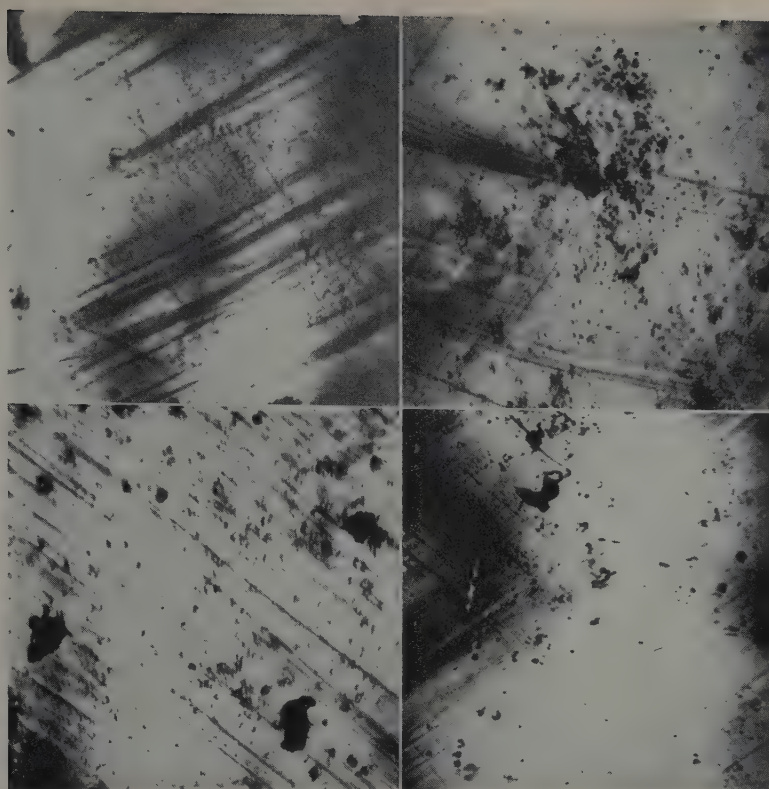


Fig. 9—X-ray photograph showing two asterisms. The ends of the asterisms are plotted in Fig. 7 as positions 0-1, 0-2, 0-2'.

a—Position at the reference mark.



b—Rotated 58 degrees from position (a)

c—Rotated 160 degrees from position (a)

d—Rotated 20 degrees from position (a)

Fig. 10—Slip lines and deformation bands in crystal Cb-0 (compression). X500.



Fig. 11—Three sets of slip lines in specimen Cb-2c (compression). X500.

Results from Berg-Barrett Method: In an attempt to consider more carefully the extent of disorientation existing in the surface layers of the specimen after deformation, the Berg-Barrett microscopy^{11,12} was used. Cu $K\alpha$ radiation, 30kv, was reflected from a bent quartz crystal monochromator and focused on the specimen supported on a two circle goniometer. Reflections were obtained for certain specimen positions and recorded on spectroscopic VO plate held parallel to the focused beam almost tangent to the specimen surface yielding the reflection. Exposures of from 30 min to 4 hr were necessary to obtain suitable records. In Fig. 13a and b there is shown the striated and banded structure observed by this technique. The amount of disorientation as a result of 5.47 and 11 pct compression (Cb-2c) can be seen, at least qualitatively in these X-ray micrograms.

Throughout these compression studies, the amount of distortion (asterism) produced per amount of deformation was far greater in the case

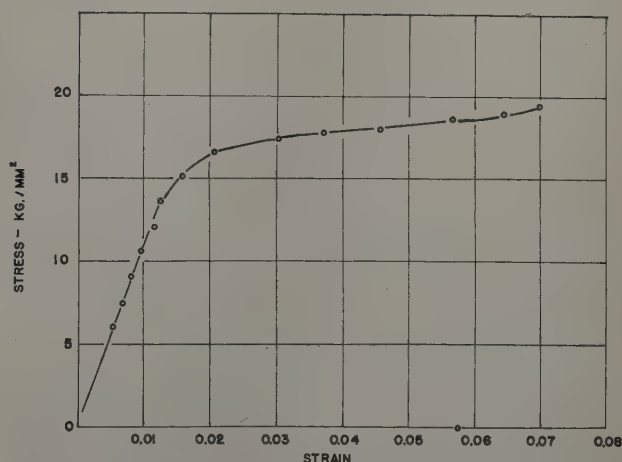
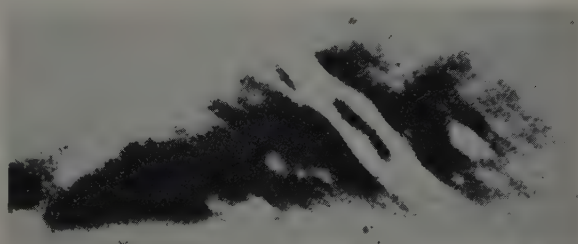


Fig. 12—Stress-strain curve for crystal Cb-30 (compression).

a—Cb-0 after first compression. X70.



b—Cb-0 after second compression. X110.

Fig. 13—Berg-Barrett micrograms of crystal Cb-0 made using a bent quartz crystal monochromator; 30 Kv, Cu $K\alpha$ radiation, V-O plate.

of compression than in tension. For example, after 16 pct compression, the asterism is so great as not to permit orientation determinations whereas the same amount of extension produces much less disorientation.

Discussion of Results

Determination of glide planes from observation of the traces on the surface might be questionable when these traces are wavy, branched, and forked. Such is normally the case with traces observed on plastically deformed body-centered cubic crystals. Nevertheless, a direction is generally assigned to a wavy trace and with many such observations, a determination of the apparent glide plane is made.

With compression of columbium, however, the deformation markings are of a different character. Two types can be noted: those lines which are straight and narrow wherever observed and those bands of relatively large width which are branched, forked, and wavy. Stereographic plots of the straight narrow lines show $\{110\}$ to be the glide plane whereas similar plots of the bands yield no confirmation of any low indices plane. However, it is sometimes possible to observe very small straight, narrow segments composing the bands; these, too, apparently are caused by $\{110\}$ planes.

Perhaps a more sensitive indication of the glide plane would be found in analysis of the asterism resulting from deformation. As in the case of molybdenum,⁴ a $\langle 112 \rangle$ axis is shown to be the axis about which asterism occurs. In the case here reported (Fig. 6b), it is readily seen that this axis is $[121]$ in which case the plane of glide is $(\bar{1}01)$ (IV) and the direction $[1\bar{1}1]$ if it can be assumed that plastic deformation in the body-centered cubic crystals produces a Taylor type rotation, i.e., rotation of the plane of glide about an axis in the plane and normal to the direction of glide. There appears to be sufficient observations to support this assumption in the body-centered cubic crystals.^{13,14} Had other types of planes acted as glide planes, other axes should be observed as the axes about which rotation occurs, e.g., for a $\{112\}$ a $\langle 110 \rangle$ would operate. However, these have not been observed to date.

The optical analogy between diffraction of X-rays by bent atomic planes and the reflection of light by curved mirrors provides the basis of a method for interpreting asterism from deformed single crystals at least qualitatively in terms of the direction of rotation of the atomic planes.¹⁵ Thus, if the ends of the asterism are plotted stereographically, the direction of displacement of these asterisms interpreted as positions of the longitudinal axis of the specimen indicates the direction of glide in tension and the plane of glide in compression. For example, the extent of asterism for Cb-4 in Fig. 3 indicates the participation of slip plane II in the first extension. Later rotation, however, shows the operation of plane IV. It would appear that the correct interpretation might be that both planes operated. In the compression case, Cb-0 (Fig. 7), a more apparent activity presents itself. Here, the rotation independent of asterism is not directly conclusive of any particular plane of glide, whereas the extent of asterism clearly demonstrates the collateral operation of IV and its conjugate III.

The use of X-ray microscopy lends further support to the idea that slip in the body-centered cubic crystals occurs in a complex manner. Although the resolution derived by this method is not greater

than what is generally attainable with light microscopy, effects of surface conditions can be eliminated. Thus if there existed a sudden change in direction of slip traces which could not readily be observed because of surface conditions, X-ray microscopy might be expected to show this. Examples of this effect have been found in extended molybdenum single crystals.¹⁶ Examples in Fig. 13 show relatively straight striae and bands where optical microscopy reveals branched and wavy bands.

The problem of resolving the traces into their possible composite nature would best be solved with aid of the electron microscope provided the actual number of atoms participating in the process is sufficiently large (the ratio remaining constant). Attempts are now being made using extended molybdenum single crystals.

A second possibility of presenting good evidence in favor of composite slip would be to develop a sensitive load measuring device in order to distinguish the small differences in load resolved along actual and "pseudo" planes. Careful resolved shear stress measurements would indicate the plane or planes along which glide has occurred. These experiments are now being contemplated using single crystals of various body-centered cubic metals.

Acknowledgment

The authors wish to acknowledge with appreciation the many helpful discussions of Dr. C. H. Mathewson and for application of the idea of composite slip to the present analysis. This work was supported by the Office of Naval Research under Contract No. Nonr 248(14).

References

- ¹ F. L. Vogel and R. M. Brick: Deformation of Ferrite Single Crystals. Technical Report No. 1; July 1, 1952, Contract AF 33-(038)15889, Univ. of Pa., Philadelphia.
- ² A. J. Opinsky and R. Smoluchowski: Crystallographic Aspect of Slip in Body-Centered Cubic Crystals. *Symposium*. Carnegie Inst. Tech., May 1950.
- ³ A. J. Opinsky and R. Smoluchowski: The Crystallographic Aspect of Slip in Body-Centered Cubic Single Crystals. *Journal of Applied Physics* (1950) **22**, p. 1488.
- ⁴ N. K. Chen and R. Maddin: Plasticity of Molybdenum Single Crystals. *Trans. AIME* (1951) **191**, p. 937; *JOURNAL OF METALS* (October 1951).
- ⁵ E. N. daC. Andrade: Report of a Conference on Internal Strains in Solids. *Proc. Physical Soc., London* (1940) **52**, p. 1.
- ⁶ N. Farhenhorst and E. Schmid: *Ztsch. Physik* (1932) **78**, p. 383.
- ⁷ C. F. Elam: *The Distortion of Metals* (1935) Oxford. Clarendon Press.
- ⁸ A. B. Greninger: Discussion to C. S. Barrett, G. Ansel, and R. F. Mehl: Slip, Twinning and Cleavage in Iron and Silicon Ferrite. *Trans. ASM* (1937) **25**, p. 702.
- ⁹ R. P. Steijn and R. M. Brick: Flow and Fracture of Single Crystals of High Purity Ferrites. Technical Report No. 2; January 1, 1953, Contract No. AF 33 (038)15889, Univ. of Pa., Philadelphia.
- ¹⁰ G. W. Wensch: Private communication.
- ¹¹ W. Berg: Load History of Deformed Crystals. *Ztsch. Krst.* (1934) **89**, p. 286.
- ¹² C. S. Barrett: A New Microscopy and its Potentialities. *Trans. AIME* (1945) **161**, p. 15.
- ¹³ E. N. daC. Andrade and L. C. Tsien: Glide of Single Crystals of Sodium and Potassium. *Proc. Royal Soc., London* (1937) **A163**, p. 1.
- ¹⁴ C. S. Barrett: *Structure of Metals*. 2nd Edition (1952) p. 375. New York. McGraw-Hill Book Co.
- ¹⁵ *Ibid.*: pp. 414-420.
- ¹⁶ N. K. Chen and R. Maddin: Glide in Extended Molybdenum Single Crystals. Unpublished.

Electrical Resistivity of Liquid Metals and of Dilute Liquid Metallic Solutions

by E. Scala and W. D. Robertson

Electrical resistivity of a number of pure liquid metals and alloys has been measured as a function of temperature and composition. The data show a close correspondence between the liquid and solid states with respect to thermal, structural, and compositional relationships.

STUDY of diffuse scattering of X-rays by liquid metals¹ has demonstrated that some degree of order persists above the melting point and that the atomic constitution of liquids is more analogous to the solid state than to a gas. Consideration of the change in various thermodynamic properties that accompanies transformation from solid to liquid leads to the same general conclusion.² Nevertheless, specific knowledge of the constitution of the liquid state is limited when compared with that of the solid and gaseous states owing, in part, to the difficulty of interpreting the X-ray data and in part to the indirect character of deductions based on thermodynamic data.

Of the structure-sensitive physical properties, electrical resistivity of liquid metals is perhaps the most easily interpretable, particularly when comparison is made with the solid state. According to the available data, most of which was obtained prior to 1914, cubic metals exhibit a normal linear and positive temperature dependence in the liquid

state and the data have been accepted without question. The divalent metals, zinc and cadmium, are apparently exceptional in that resistivity is not linear with temperature and it passes through a minimum. Mercury also exhibits a nonlinear temperature dependence but the slope is always positive. Important comparisons with magnesium could not be made at the time the following work was undertaken because the necessary experimental data were not available.

Data on liquid solutions are very limited and are largely from a single source.³⁻⁶ Based on Bornemann's work, Norbury⁷ pointed out that the resistivity of liquid copper alloys appeared to be dependent on the valence of the solute and that the increase due to the solute was of the same order as in the solid state. However, large extrapolations were involved and no quantitative relationship was developed.

Therefore, before proceeding with additional deductions regarding the resistivity of liquid metals and interpretation in terms of structure, it appeared necessary to verify and extend the previous work with particular emphasis on divalent metals and the effect of alloying elements of different valence in dilute liquid solutions.

The present work includes: 1—A determination of the resistivity of high purity liquid magnesium, tin, indium, copper, zinc, and cadmium as a function of temperature. 2—The effect of 1 atom pct of copper, cadmium, aluminum, tin, antimony, and

E. SCALA, Junior Member AIME, is associated with Chase Brass and Copper Co., Waterbury, Conn., and W. D. ROBERTSON, Member AIME, is associated with Hammond Metallurgical Laboratory, Yale University, New Haven, Conn.

Discussion on this paper, TP3598E, may be sent, 2 copies, to AIME by Dec. 1, 1953. Manuscript, March 27, 1953. Cleveland Meeting, October 1953.

This paper is based on a thesis by E. Scala submitted in partial fulfillment of requirements for the degree of Doctor of Engineering to the School of Engineering, Yale University.

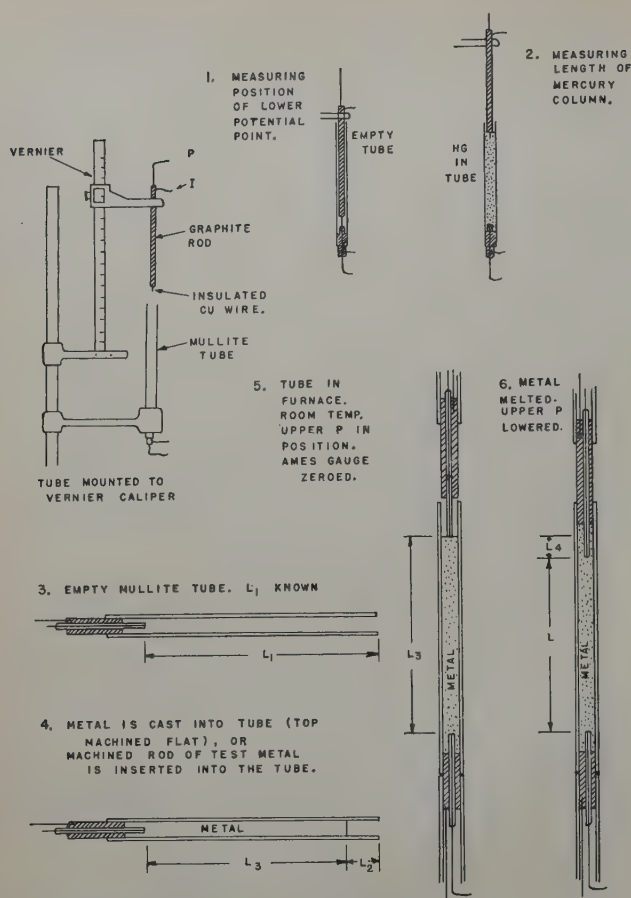


Fig. 1—Determination of the cross-sectional area of the liquid metal container and the distance between potential points.

bismuth on the resistivity of liquid zinc. 3—The effect of 1 atom pct of zinc, aluminum, indium, tin, and phosphorus on the resistivity of liquid copper.

Experimental Procedure

The principle employed in all determinations was to pass a measured current through a known cross section of liquid metal and measure the potential difference between two points at an accurately known distance from each other.

Except in the case of magnesium, the liquid metal was contained in a refractory insulating tube, approximately 0.6 cm ID by 13 cm long. The effective cross section of the tube was determined before each experiment by measuring the electrical resistance of triple distilled mercury at room temperature over a known length determined to 0.001 in. This was done by attaching one of two potential contacts to a vernier caliper as illustrated in Fig. 1.

Potential contacts were made of molybdenum wire cemented in small refractory insulating tubes which passed through graphite (spectrographic carbon) plugs carrying the current leads. Current and potential contacts were separated by about 1 cm from each other, as detailed in Fig. 3a.

After determining the geometry of the container and locating the lower potential contact with respect to the top of the ceramic tube, Fig. 1, the tube was filled by either of two methods: 1—Melting and casting metal in argon after previous evacuation in the unit illustrated in Fig. 2. A flat face was subsequently machined on the top surface of the solidified metal which then served to define the position of the lower potential contact. This method was used for the low melting point metals and the

zinc alloys. 2—The copper alloys were poured under argon into graphite molds and then swaged and machined to fit the refractory tubes.

The tube containing the metal and lower contacts was cemented to a long refractory supporting tube. When placed inside the temperature equalizing graphite block mounted in the furnace, shown in Fig. 3, the supporting tube rested on the alundum blocks at the base of the furnace. The upper potential and current leads were placed in position and the height adjusted with respect to the machined face of the specimen by means of an ammeter indicator to determine contact, and a dial gage. Subsequent changes in length accompanying thermal expansion and fusion were followed with the dial gage acting as a dilatometer. The distance between the potential points was thereby known at all times. Correction for the linear thermal expansion of the entire unit was obtained by calibration with pure solid nickel. Calculated corrections were made for the increase in cross-sectional area of the refractory tube at elevated temperatures.

The uniformity of temperature over the length of the specimen was determined with three thermocouples at top, middle, and bottom, touching the ceramic tube. Temperature differences were generally less than 1°C and were determined together with each measurement of resistance.

Potential measurements were made with a precision potentiometer and current was determined by potential drop across a calibrated resistance. The current density employed was 1.7 amp per sq cm. An atmosphere of dried argon gas was maintained at all times. Measurements were made at constant temperature after equilibrium was obtained in both heating and cooling cycles.

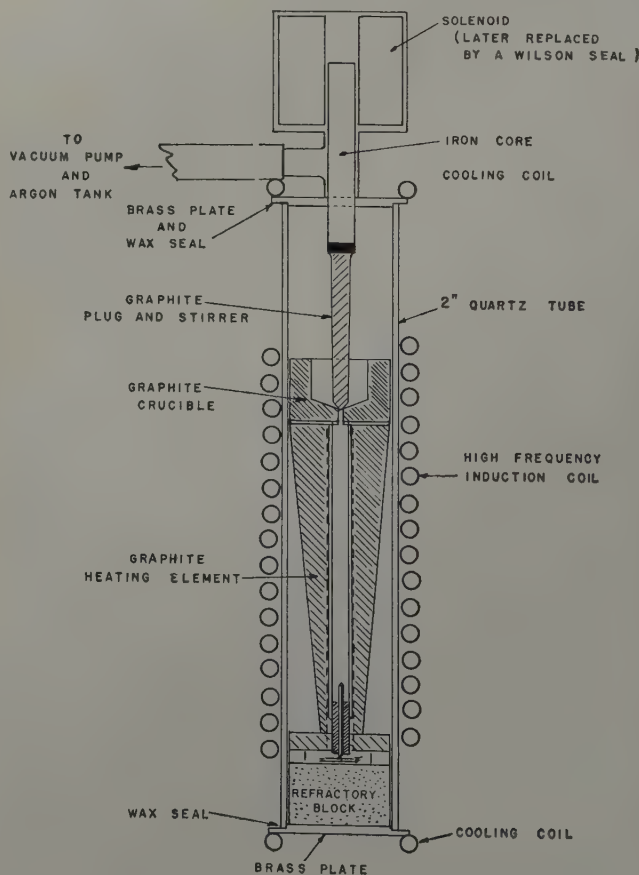


Fig. 2—The casting unit for low temperature metals and alloys.

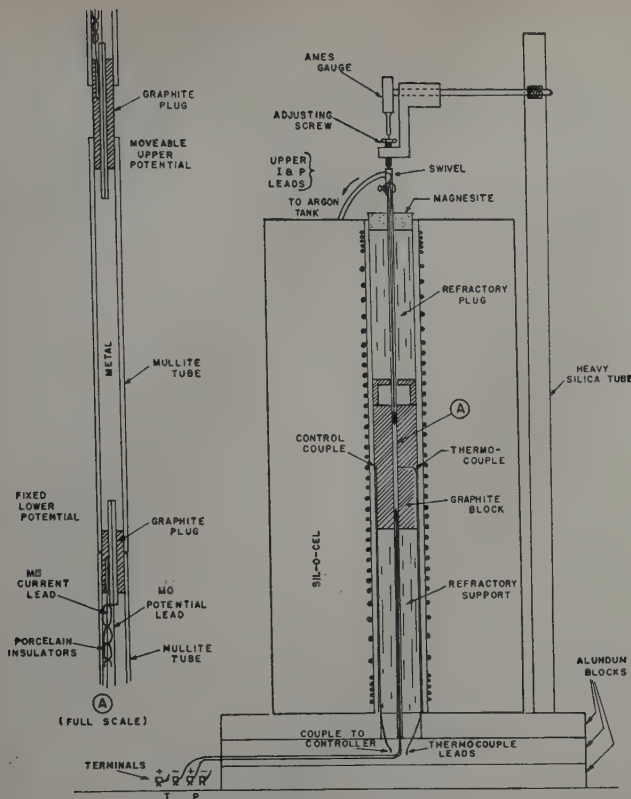


Fig. 3—The testing furnace and assembly of the testing unit. Right-hand drawing one quarter scale, entire figure reduced one half for reproduction.

Except for magnesium, the molten metals did not attack the refractory tubes. In the case of magnesium the procedure was modified by the use of a graphite container in place of ceramic tubes, avoiding contamination of the metal and change of dimensions. Machined graphite tubes were employed and their inside diameters were determined by weighing the mercury required to fill the tubes. The cell constant required for the conducting container was determined over the entire temperature

Table I. Chemical Analysis of Metals and Alloys

Metal	Source	Purity, Wt Pct	Major Impurities, Wt Pct
Tin	Commercial	99.96+	0.01% Fe, In, Sb
Tin	Vulcan Detinning	99.9957	0.0015% Fe, 0.0005% Pb
Cadmium	A. S. & R.	99.9976	0.0015% Cu, 0.0009% Pb
Zinc	A. S. & R.	99.9978	0.0006% Cd, 0.0007% Pb
Indium	Indium Corp.	99.98+	0.01% Pb
Magnesium	Dominion Mag. Ltd.	99.975	0.01% Cd, 0.004% Al, 0.003% Si, Pb
Copper	A. S. & R.	99.999	0.0002% As, Te; 0.0001% Pb, Sn, Ni, Se and S

	Chemical Analysis, Atomic Pct	Major Impurities, Wt Pct
Zinc Alloys, Nominal		
1 at. % Cu in Zn	0.996% Cu	Pb, Si <0.001%
1 at. % Cd in Zn	0.89 % Cd	Pb, Si <0.001%
1 at. % Al in Zn	1.13 % Al	Pb, Si <0.001%
1 at. % Sn in Zn	1.03 % Sn	Pb, Si <0.001%
1 at. % Bi in Zn	1 % Bi	
1 at. % Sb in Zn	1 % Sb	
Copper Alloys, Nominal		
1 at. % Zn in Cu	1.25 % Zn	<0.001% Si, Mg, Fe
1 at. % In in Cu	1.00 % In	<0.001% Si, Mg, Pb, Fe
1 at. % Al in Cu	0.95 % Al	<0.001% Si, Mg, Sn, Fe
1 at. % Sn in Cu	1.03 % Sn	<0.001% Si, Mg, Fe
1 at. % P in Cu	0.94 % P	<0.001% Si, Pb, Bi, Fe

range to be covered by measuring the resistance of high purity tin in identical graphite tubes. This procedure eliminated any assumption regarding a difference in temperature coefficient between magnesium and tin and because the resistivity of both metals is of the same order, the current distribution could be assumed to be similar.

At an early stage in the work it was found that with all possible precautions there was an internal source of electromotive force in the liquid metal container. The magnitude of this effect was independent of current (polarization) and temperature difference across the cell within the experimental limits. It was, however, dependent on the temperature level as shown in Fig. 4, obtained with cadmium at zero current. It was found that one half the difference in potential across the cell with current passing in opposite directions ($\Delta E/2$, Fig. 4) was exactly equal to the internal electromotive force measured in the absence of any outside source of current. Consequently, all data are the arithmetic average of sets of readings obtained with reversed current, which effectively eliminates the internal electromotive force. Similar procedures have been adopted in previous work^{8-6, 11} but the magnitude of the effect observed was not reported.

All metals and alloys were analyzed chemically and spectrographically before and after determinations. There was no significant accumulation of impurities or detectable solution of molybdenum contacts. The data are summarized in Table I.

Experimental Results

High Purity Metals: The results for tin, indium, magnesium, cadmium, and zinc are shown in Figs. 5 and 6, as a function of temperature. The data interpolated from the smooth curves are sum-

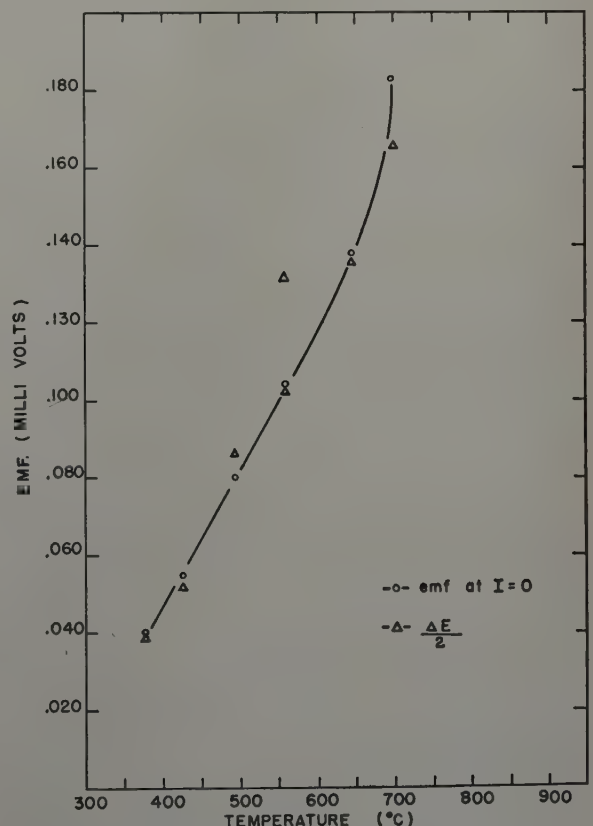


Fig. 4—Electromotive force in liquid cadmium as a function of temperature.

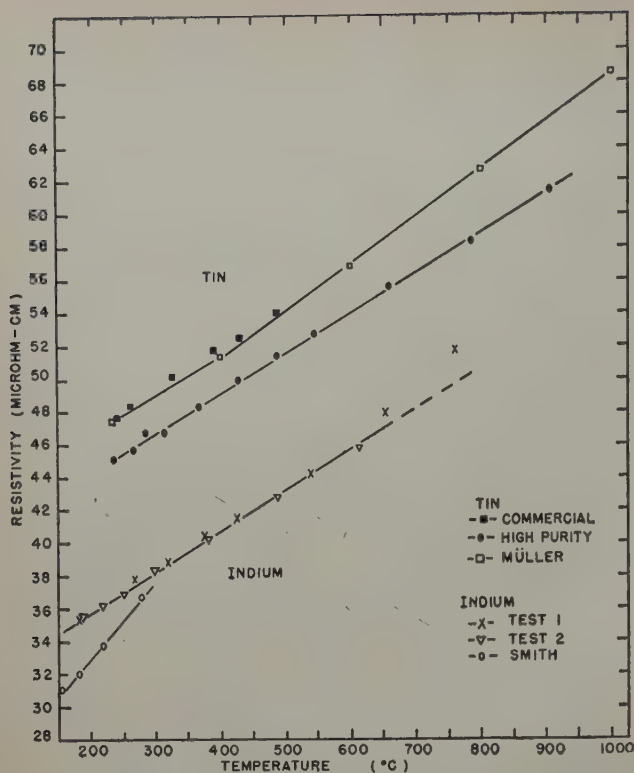


Fig. 5—Resistivity of liquid tin (commercial and high purity) and indium.

marized in Table II at integral values of temperature.

With regard to tin, essentially identical results were obtained with 99.96 pct Sn, containing antimony and iron as principal impurities, as were reported by Müller,^{3,4} and Northrup and Suydam.⁸ In view of the relative simplicity of experiments with tin and the availability of two previous determinations, the agreement obtained was taken as an indication of the general adequacy of the present technique which differed from both of the previous experiments. However, with higher purity tin (99.996 pct Sn), the values fall definitely below those for tin of commercial grade and the temperature coefficient is accurately linear from the melting point.

The only available data for indium¹⁰ appear to be considerably in error, both in magnitude and temperature coefficient. As shown in Fig. 5, two independent determinations gave similar results except at the highest temperatures where two points are evidently anomalous.

At the time this investigation was in progress, no resistivity data were available for liquid magnesium. Values have since been published by Horn¹¹ which are essentially in agreement with those reported here, Fig. 6. In view of the different methods employed (ceramic cell and graphite cell) the agreement may be taken as a verification of procedure and results. The only point of difference is that the present work indicates a small but significant negative temperature dependence, constant over the range investigated.

Previous work with zinc indicated some disagreement between Northrup and Suydam⁸ and Müller.⁴ The present redetermination confirms the results of Northrup and Suydam in all respects except at the highest temperatures where the resistivity appears to be slightly higher than re-

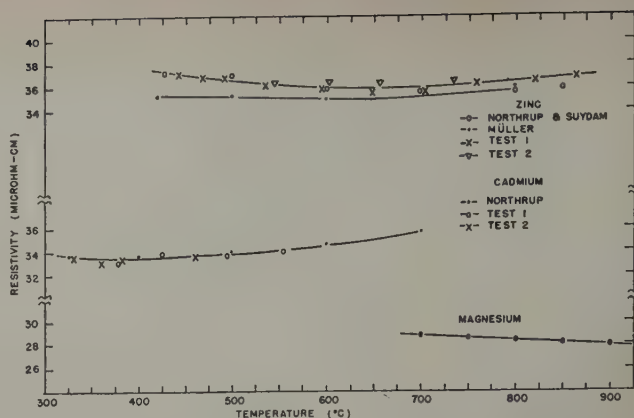


Fig. 6—Resistivity of liquid zinc, cadmium, and magnesium.

ported. The temperature dependence at the melting point is negative and changes to positive at a temperature about 230°C above the melting point.

The results for cadmium are also in exact agreement with those of Northrup and Suydam.⁸ The temperature coefficient at the melting point is small and negative, increasing to zero at about 50°C above the melting point and becoming increasingly positive with rising temperature.

In summary, the unusual dependence of resistivity on temperature for cadmium and zinc is confirmed, as is the magnitude of the values previously reported by Northrup and Suydam. The remaining close-packed hexagonal metal, magnesium, has a small negative temperature dependence which is constant to 200°C above the melting point. Indium has a higher resistivity and smaller linear temperature coefficient than was previously reported. Finally, the resistivity of high purity liquid tin appears to be about 5 pct lower at all temperatures than the previously available values.

Copper Alloys: The results for dilute liquid solutions of zinc, indium, aluminum, tin, and phosphorus in copper are shown in Fig. 7 as a function of temperature, together with experimental data for pure copper.

The high temperatures at which the measurements are necessarily made increase the experimental difficulties and produce some scatter in

Table II. The Resistivity of High Purity Liquid Metals

Temperature, °C	Microhm — Cm						
	Sn*	Sn	Zn	Cd	In	Mg	Cu
200					33.8		
250	48.3	45.4			35.0		
300	49.6	46.7			36.2		
350	50.8	47.8		33.6	37.4		
400	52.0	49.1		33.5†	38.7		
450	53.2	50.3	37.1	33.6	39.9		
500	54.5	51.5	36.5	33.8	41.2		
550	55.7	52.7	36.2	34.0	42.4		
600		54.0	36.0	34.4	43.7		
650		55.2	35.9		44.9		
700		56.4	36.1‡			28.8	
750		57.7	36.2			28.6	
800		58.9	36.4			28.4	
850		60.1	36.7			28.2	
900		61.3				28.0	
1100							22.9
1150							24.0
1200							25.1
1250							26.2
1300							27.3

* Commercial Tin, 99.96 pct.

† Minimum on curve at about 375°C.

‡ Minimum on curve at about 670°C.

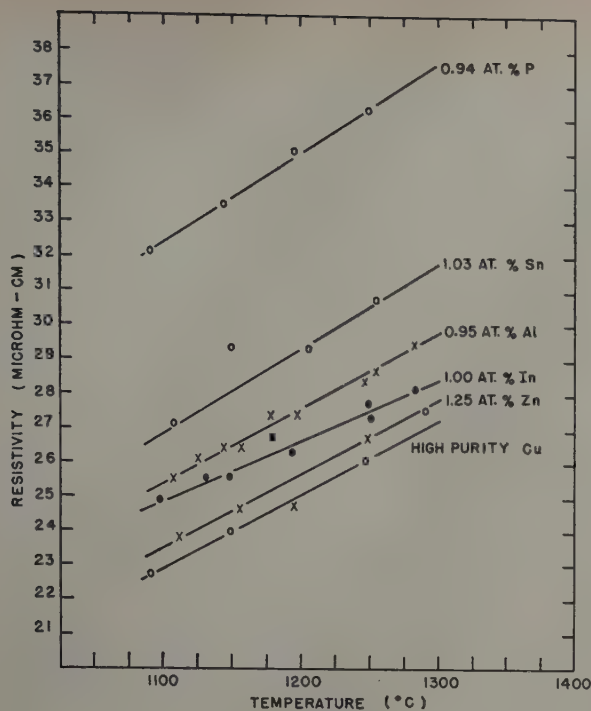


Fig. 7—Resistivity of liquid copper alloys (one atom pct solute).

values. The resistivity of copper determined in these experiments is about 5 pct higher than reported by Northrup⁹ as it is for copper alloys when compared to values computed at 1 atomic pct from Bornemann's data on more concentrated solutions. In summary: 1—The introduction of a small number of solute atoms increases the resistivity to the same degree as in the solid state. 2—The change in resistivity is dependent on the valence of the solute, specifically on the square of the difference in valence of solute and solvent as in the solid state. 3—The rate of change of resistance with respect to temperature for all dilute copper alloys is the same, with the possible exception of indium. This temperature dependence is in accordance with Matthiessen's rule which was formulated for the solid state.

Zinc Alloys: Fig. 8 shows the results for liquid zinc solutions containing 1 atomic pct copper, cadmium, aluminum, tin, antimony, and bismuth compared with pure zinc as a function of temperature.

In alloys of zinc containing copper and tin, some difficulty was experienced at high temperatures due to an unexplained increase in resistivity that occurred on heating as compared with the corresponding resistivity-temperature curve followed when cooling, indicated by the dotted lines in Fig. 8. Duplicate runs with cadmium and aluminum did not show this effect whereas the effect was always present in the case of copper and tin. In drawing the curves greater weight was given to the points obtained on cooling that are in accord with those for high purity zinc, in which this effect was never observed.

Unlike copper alloys, the addition of 1 atomic pct copper, cadmium, aluminum, or bismuth to liquid zinc does not significantly affect the resistivity at any temperature. The addition of tin or antimony, however, increases the resistivity and to about the same extent in both cases. Tin and antimony apparently also increase the negative temperature coefficient at the melting point and

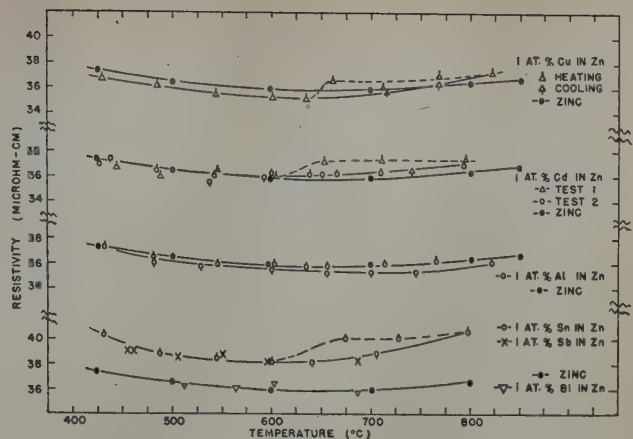


Fig. 8—Resistivity of liquid zinc alloys (one atom pct solute).

correspondingly lower the temperature of the minimum in the resistivity curve by about 50°C.

Discussion

The preceding data indicate that there is a one-to-one correspondence between solid and liquid copper solutions with respect to resistivity-temperature and compositional relationships. It appears, therefore, that insofar as the conduction of electricity is concerned the atomic constitution of the liquid state is very similar to that of the solid state. The differences between the two states appear to be a matter of degree rather than the result of any unique property peculiar to the liquid state.

Mott¹² has shown that it is possible to represent quantitatively the ratio of conductivity in the solid and liquid states at the melting point by the expression

$$\frac{\sigma_L}{\sigma_S} = \left(\frac{V_L}{V_S} \right)^2 = e^{-\frac{80L}{T_M}}$$

where V_L and V_S are vibrational frequencies of atoms in the liquid and solid states respectively; L is the heat of fusion in kilo-joules per gram atom, and T_M °K is the melting point. The essential agreement between observed and calculated values for a variety of close-packed metals indicates that the principal assumption is probably correct; namely, that the atoms in the liquid state vibrate about mean positions with a frequency V_L and that the positions, while moving in time, do so with velocities slow compared with the velocity associated with the vibration of the atoms. Implicit in this assumption is the idea that the resistivity in the liquid state is not primarily a function of disorder, relative to the solid state, but of thermal vibration amplitude and, therefore, the dependence of resistivity in the liquid state on temperature and composition should be similar to that in the solid state. The data in Fig. 7 on copper alloys appear to provide a critical test and confirmation of this hypothesis.

Thus, the increase in resistivity of liquid copper resulting from the addition of 1 atomic pct of various solutes is essentially the same as that for copper solid solutions as reported by Linde.¹³ Furthermore, Linde showed that the increase in resistivity per atomic percent solute is proportional to the square of the difference in charge between solute and solvent. Fig. 9 demonstrates that this relationship holds for liquid solutions as well as for

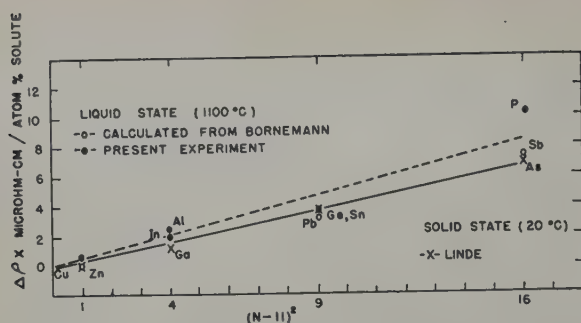


Fig. 9—The application of Linde's rule to dilute copper alloys in the liquid state compared with the solid state.

the substitutional solid solutions with which it is compared. The magnitude of the change in resistivity is similar in both cases, and is independent of temperature.

The introduction of small concentrations of atoms of different size and charge results in the same increase in resistivity and dependence on scattering charge as applies to the solid state. Apparently, then, the disorder in the liquid state, relative to the solid state, cannot be large. Otherwise, it would seem that the effect of one foreign atom in one hundred would be lost in comparison with the effect of extensive disorder.

In this connection, the linear temperature dependence of liquid metals and alloys, except zinc, cadmium, and mercury, appears to indicate that the same type of thermal dependence applies in the liquid state as in the solid state. Furthermore, in the case of both copper and silver, the resistivity in the liquid state extrapolates to zero at 0°K, within the limits of accuracy of the data from the present work on copper and that of Northrup¹⁵ for liquid silver. While the present data do not permit definitive conclusions, it may be inferred that at least a part of the change in resistance associated with lattice expansion and melting can be accounted for by a change in Debye temperature.

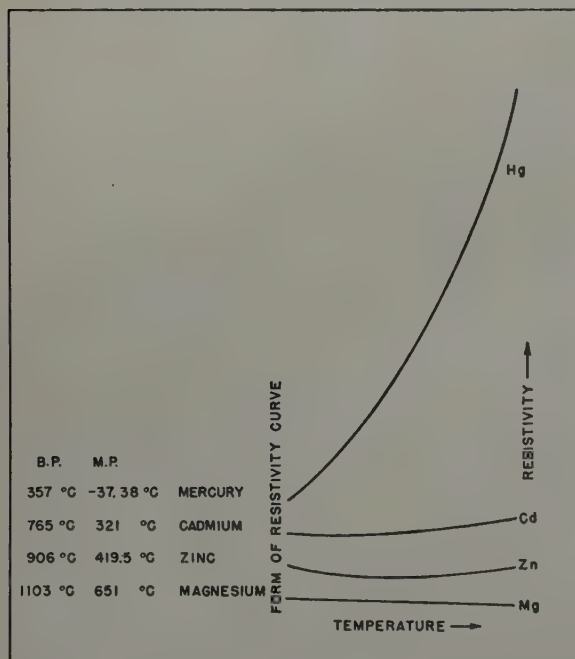


Fig. 10—A schematic drawing of the form of the resistivity temperature curves of liquid magnesium, zinc, cadmium, and mercury.

The resistivity of polyvalent liquid tin and indium, while linear with temperature, do not extrapolate to zero at 0°K, indicating some significant difference between the monovalent and polyvalent metals in the liquid state.

On the other hand, the resistivity of the divalent metals, cadmium, zinc, and magnesium (and mercury), behaves quite differently with respect to temperature. The increase in resistivity on melting, except for mercury, is again of the magnitude indicated by considerations based on the amplitude of displacement about a mean position. However, in the solid state the number of electrons that are available for conduction in these divalent metals is limited and conduction is crystallographically anisotropic owing to scattering at the surfaces of energy discontinuity, the Brillouin zone boundaries. Thus, in addition to the component of resistivity arising from thermal vibration, there is also a structural component in divalent metals.

The negative temperature coefficient at the melting point of the three hexagonal metals and alloys may be accounted for by assuming that the limitation on conduction, imposed by zone boundary overlap, is relaxed in the liquid state.¹² In the case of cadmium and zinc, the change in slope from negative to positive at 50° and 230°C above the melting point, respectively, may be interpreted as a superposition of structural and thermal effects with the latter predominating at temperatures above the minimum.

In this connection, a comparison may be made between the four divalent metals, mercury, cadmium, zinc, and magnesium, Fig. 10. Assuming that the minimum represents a balance of structural and thermal scattering, the thermal component appears to take over in the four metals at a temperature relative to the melting point that increases in the same order as the melting and boiling points, or, in other words, with bond strength. This hypothesis implies that there is not only a degree of order in the liquid state but also a significant degree of order in the crystallographic sense, over short distances and effective in scattering electron waves. The effective order persists above the melting point and disappears with rising temperature in accordance with the respective bond strengths of the four metals. In the case of magnesium, the temperature of the minimum was evidently not attained.

Further evidence that structural factors are controlling resistivity of divalent metals may be derived from the effect of alloying elements added to zinc. It has already been observed, Fig. 8, that unlike copper there appears to be no systematic change in resistance with the valence of the solute; tin and antimony increasing resistance to the same degree, bismuth and aluminum leaving it unchanged as do copper and cadmium. If the effective number of electrons alone were involved, independent of structure, it might be anticipated that the addition of at least some of these solutes would decrease the resistance, as they do in mercury,¹⁴ instead of either increasing it without respect to scattering charge, or leaving it unchanged. Unfortunately, comparison with zinc solid solutions appears to be excluded by the limited solubility of most metals in zinc and, therefore, the effect of solutes on the resistivity of the hexagonal close-packed zinc lattice is unknown.

In the preceding discussion it may appear that

there is some conflict of interpretation with respect to the structure of the liquid state as deduced from electrical measurements and that provided by X-ray evidence which indicates a close-packed aggregate without long range order. It may be concluded that in the liquid state the two methods of observation are not recording precisely the same thing. This is best illustrated by the fact that the radial distribution functions obtained from X-ray data for the cubic and hexagonal metals are exactly similar in form while the properties as observed by resistivity are entirely different. To avoid misunderstanding, all preceding statements regarding structure have been qualified by reference to resistivity.

Conclusions

Redetermination of the resistivity of pure liquid tin, zinc, and cadmium shows that the available data is essentially correct except that the present work indicates that the resistivity of pure tin is about 5 pct lower than has been reported. A new set of values is proposed for the resistivity of pure indium as a function of temperature. The resistivity of pure magnesium has been determined and is in essential agreement with recently published data.

Investigation of dilute liquid solutions of copper shows that the effect of alloying elements on the resistivity of simple metallic liquid solutions is identical with that of similar solid solutions; specifically, 1—the increase in resistivity due to the addition of solutes is proportional to the square of the difference in valence of solute and solvent; 2—the increase in resistivity due to the solute is independent of temperature; and 3—the magnitude of the increase is the same in both solid and liquid states.

The resistivity of liquid zinc, cadmium, and magnesium appears to be dependent on structure and, except for tin and antimony which increase resistivity equally, the resistivity of zinc is unaffected by the addition of 1 atomic pct of copper, cadmium, aluminum, or bismuth.

It is suggested that temperature dependence of resistivity of the divalent metals may be explained by a superposition of structural dependence associated with bond strength, and thermal vibration.

Insofar as electrical conduction is concerned, it may be concluded that there is essentially complete correspondence between the liquid and solid states of metals including thermal, structural, and compositional relationships.

Acknowledgments

We wish to thank Dr. D. K. Crampton, whose cooperation enabled us to undertake this project, and to acknowledge the help and assistance of many people at Chase Brass and Copper Co. We are also grateful to the Indium Corp. of America for supplying the indium used in the experiments and to Dominion Magnesium, Ltd., for the high purity magnesium.

References

- ¹N. S. Gingrich: *Revue of Modern Physics* (1943) **15**, p. 90.
- ²O. Kubaschewski: *Trans. Faraday Soc.* (1949) **45**, p. 931.
- ³K. Bornemann and P. Müller: *Metallurgie* (1910) **7**, p. 396.
- ⁴P. Müller: *Metallurgie* (1910) **7**, pp. 730, 755.
- ⁵K. Bornemann and G. Von Rauschenplat: *Metallurgie* (1912) **9**, p. 473.
- ⁶K. Bornemann and G. Wagenmann: *Ferrum* (1913-1914) **11**, pp. 276, 289.
- ⁷A. L. Norbury: *Trans. Faraday Soc.* (1920-1921) **16**, p. 570.
- ⁸E. F. Northrup and V. A. Suydam: *Journal Franklin Inst.* (1913) **175**, p. 153.
- ⁹E. F. Northrup: *Journal Franklin Inst.* (1914) **177**, p. 1.
- ¹⁰A. W. Smith: *Ohio Journal of Science* (1916) **16**, p. 244.
- ¹¹F. H. Horn: *Physical Review* (1951) **84** (2), p. 855.
- ¹²N. F. Mott: *Proc. Royal Soc.* (1934) **146A**, p. 465.
- ¹³J. O. Linde: *Ann. Physik* (1932) **15**, p. 219.
- ¹⁴H. Feninger: *Handbuch der Metallphysik* (1935) Vol. 1, Part I, p. 344. Leipzig.
- ¹⁵E. F. Northrup: *Journal Franklin Inst.* (1914) **178**, p. 85.

Technical Note

Effect of Grain Size Upon Temper Brittleness

by L. D. Jaffe, F. L. Carr, and D. C. Buffum

SINCE the temper brittleness of steels is generally considered to be a grain-boundary phenomenon^{1, 2} it would be expected that austenitic grain size would affect temper brittleness. Several investigators³⁻⁶ reported that temper brittleness, as measured by room-temperature impact tests, increased as the austenitizing temperature was raised. It was subsequently pointed out that conclusions as to temper brittleness

based upon room-temperature impact tests are likely to be misleading.^{1, 6} Hurlich⁷ used a range of testing

L. D. JAFFE and D. C. BUFFUM, Members AIME, are associated with Watertown Arsenal, Watertown, Mass., and F. L. CARR, formerly with Watertown Arsenal, is now with National Research Corp., Cambridge, Mass.

TN 174E. Manuscript, April 20, 1953.

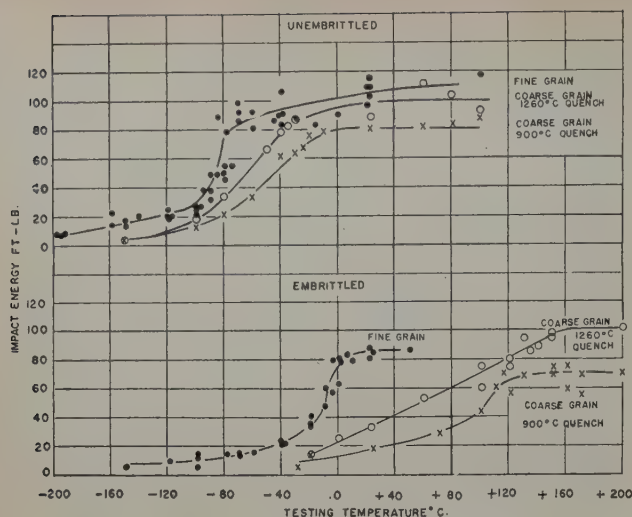


Fig. 1—Impact energy vs testing temperature.

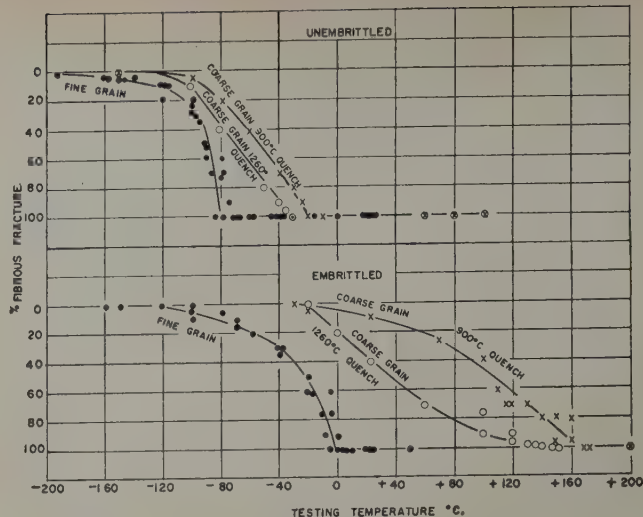


Fig. 2—Percentage of fibrous fracture vs testing temperature.

temperatures which was unfortunately too narrow to permit evaluation of his data on the basis of any single criterion of transition from tough to brittle failure. Craig⁹ pointed out that quenching from different austenitizing temperatures might introduce differences in respects other than grain size; for example, in stresses resulting from quenching. Accordingly, experimental work was planned in which the austenitizing treatment would be varied with and without changing the temperature from which the steel was quenched.

The steel used was SAE 3140, 5/8 in. round hot-rolled bar stock from a heat previously studied.¹⁰ About 100 blanks 2 3/16 in. long were austenitized for 1 hr at 900°C, then water-quenched, giving an austenite grain size of ASTM 8. Another 100 blanks were austenitized for 4 hr at 1260°C. Half of these were water-quenched. The other half were quenched into salt at 900°C and held 1 hr and 40 min, then water-quenched. The austenite grain size resulting from both of these treatments was predominantly ASTM 0, with some larger grains. In all cases the structure was 100 pct martensite with no visible carbides.

All blanks were tempered 1 hr at 675°C, then water-quenched to room temperature. Half of the tempered blanks from each of the three austenitizing treatments were next isothermally embrittled in salt at 500°C for 48 hr, then water-quenched. The blanks were machined into standard V-notched Charpy bars which were broken at various temperatures on a 217 ft-lb impact machine (16.8 ft per sec striking velocity). The data, presented in Figs. 1 and 2, show that an increase in austenite grain size results in an increase in transition temperature. This confirms earlier work.^{7,11}

It is likewise evident that the shift in transition temperature due to temper embrittlement is greater for large grain size than for small grain size. This is in agreement with the view of Herres and Lorig⁸ that temper brittleness should become more apparent the larger the grain size. Lowering the quenching temperature did not reduce the transition temperature of the coarse-grained specimens but rather raised it slightly, at least on the basis of fracture behavior, Fig. 2. This is contrary to the theory of temper brittleness suggested by Spretnak and Speiser,¹² as previously pointed out.¹³

The impact energy level of the unstabilized coarse-grain specimens quenched from 1260°C was higher than that of the coarse-grained specimens quenched from 900°C. The fracture of all coarse-grained specimens at temperatures producing 0 pct fibrous fracture was predominantly transcrystalline in the unembrittled state and intercrystalline in the embrittled state. Microscopic examination revealed some intercrystalline fracture with the transcrystalline and vice versa.

It is concluded that an increase in austenitic grain size increased the shift in transition temperature associated with temper brittleness. At fixed grain size, lowering the quenching temperature had little effect upon the transition temperature, perhaps raising it slightly.

The authors acknowledge with thanks the metallographic work performed by M. R. Norton for this investigation.

References

- 1 J. H. Hollomon: Temper Brittleness. *Trans. ASM* (1946) **36**, pp. 473-542.
- 2 L. D. Jaffe: What to do about Temper Brittleness of Steels. *Steel* (Nov. 29, 1949) **125**, No. 21, pp. 86-89, 114.
- 3 R. H. Greaves and J. A. Jones: Temper-Brittleness of Nickel-Chromium Steels. *Journal Iron and Steel Inst.* (1920) **102**, pp. 171-222.
- 4 W. Bischof: Contribution to the Question of Temper Brittleness. *Arch. Eisenhüttenw.* (1935) **8**, pp. 293-301.
- 5 E. Maurer, O. H. Wilms, and H. Kiessler: Influence of Phosphorus and of Various Alloying Elements on the Temper Brittleness of Structural Steel. *Stahl u. Eisen* (1942) **62**, pp. 81-89, 115-121.
- 6 H. Jolivet and G. Vidal: The Temper Brittleness of Steel. *Comptes Rendus* (1943) **216**, pp. 664-666.
- 7 A. Hurlich: Discussion on ref. 8. *Trans. ASM* (1948) **40**, pp. 805-809.
- 8 S. A. Herres and C. H. Lorig: Influence of Metallurgical Factors on the Mechanical Properties of Steel. *Trans. ASM* (1948) **40**, pp. 775-805.
- 9 W. F. Craig, Jr.: Private communication, 1949.
- 10 L. D. Jaffe, D. C. Buffum, and F. L. Carr: Effect of Various Heat Treating Cycles upon Temper Brittleness. *Trans. ASM* (1953) **45**, pp. 725-731.
- 11 L. D. Jaffe and J. F. Wallace: Discussion on ref. 8. *Trans. ASM* (1948) **40**, p. 809.
- 12 J. W. Spretnak and R. Speiser: *Trans. ASM* (1951) **43**, pp. 734-758.
- 13 D. C. Buffum: Discussion on ref. 12. *Trans. ASM* (1951) **43**, pp. 748-750.

A Rationalization of Measured High Temperature Properties Of Fe-Cr-Co-Ni Alloys

by J. D. Nisbet and W. R. Hibbard, Jr.

The high temperature properties of Fe-Cr-Co-Ni base alloys and the effects of hardening element additions on these properties are rationalized on the basis of general principles of alloying.

DURING the past few years the base elements in high temperature austenitic alloys have gradually been changed from iron-rich materials to nickel-rich, then to cobalt-rich and more recently to various iron, cobalt, and nickel combinations, all with an approximately constant chromium content of 20 pct. Concurrently, the hardening additions of the incongruous* elements, have been shifted from small

* Elements having a relatively low solubility in Fe-Ni-Cr-Co solid solutions.

amounts of a single element to various ratios of molybdenum, tungsten, columbium, carbon, titanium, and aluminum with the percentages of these constituents continually increasing.

It has been known that the typical soft high temperature alloy (such as Inconel) consisted of face-centered cubic austenite, but the effect of varying the composition of the base elements, iron, chromium, nickel, and cobalt, has not been broadly analyzed. Therefore, it was reasoned that the first major problem in the understanding of the properties or the further development of high temperature alloys was to study systematically the effect of composition upon the mechanical properties of face-centered cubic Fe-Ni-Co-Cr austenitic solid solutions.

The matrix of the strong high temperature alloys

J. D. NISBET, Associate Member AIME, formerly with General Electric Co., is now associated with Universal Cyclops Steel Co., Bridgeville, Pa., and W. R. HIBBARD, Jr., Member AIME, is associated with the Metallurgy Research Dept., Research Lab., General Electric Co., Schenectady.

Discussion on this paper, TP 3618E, may be sent, 2 copies, to AIME by Dec. 1, 1953. Manuscript, Sept. 16, 1952; revision, April 16, 1953. Cleveland Meeting, October, 1953.

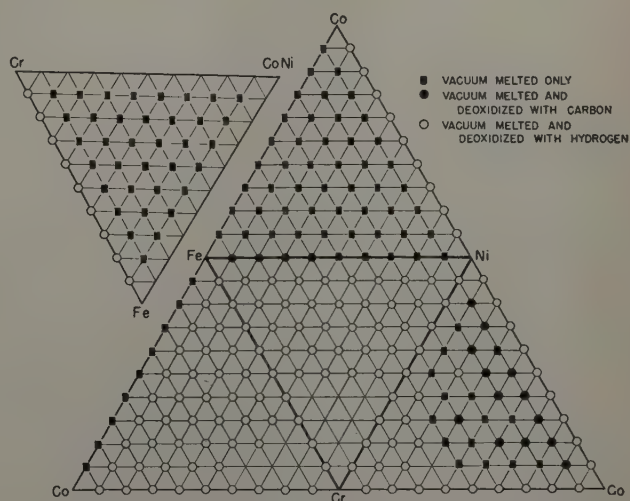


Fig. 1—Nominal compositions in atomic percent and melting practices of the base alloys investigated. CoNi indicates alloys in which the CoNi content is 50 pct Co and 50 pct Ni.

(such as Inconel X) is usually also a face-centered cubic solid solution of iron, nickel, chromium, and cobalt but with additional phases which can be generally classified as intermetallic compounds and carbides. It is usually observed that combinations of the hardening elements, tungsten, molybdenum, columbium, tantalum, titanium, aluminum, carbon, and others have been used in these strong high temperature alloys. Thus, it was reasoned that a second major problem in studying these alloys was to understand the effect on mechanical properties of adding

Table I. Chemical Compositions of Incongruous Elements Added to Different Base Alloys

Nominal Base Analysis	Base Classification	Incongr. Alloy	Nominal and Analyzed (in Parentheses) Atomic Percentages of Incongruous Element Added									
20%Cr-80%Ni	Unsaturated	Ta	1	(1.2)	5	(3.9)	8	(7.2)	10	(9.7)		
		Cb	1	(0.76)	5	(3.5)	8	(6.1)	10	(7.9)		
		W	1	(1.3)	5	(4.5)	8	(7.0)	10	(7.9)		
		Mo	2	(2.4)	4	(3.3)	8	(6.4)	12	(9.6)		
		Zr	1	(0.39)	3	(1.6)	6	(3.2)	9	(7.4)		
		Ti	1	(0.50)	4	(2.8)	8	(6.3)				
		Al	1	(0.34)	3	(1.2)	6	(4.1)				
		Be	1	(0.45)	2	(0.77)	4	(1.9)	8	(3.2)		
		C	0.5	(0.19)	1	(0.25)	2	(1.4)	3	(1.8)		
									4	(2.9)		
		O	1 min.	(0.086)	5 min.	(0.079)						
		N	10 min.	(0.136)	5 min.	(0.621)						
			1 min.	(0.734)								
			10 min.	(0.509)								
30%Cr-30%Co-40%Ni	Saturated	Ta	2	(1.6)	4	(3.4)	8	(6.7)				
		Zr	1	(0.11)	2	(1.0)	4	(2.1)				
40%Cr-20%Co-40%Ni	Supersaturated	Mo	2	(1.8)	4	(3.4)						
		V	2	(1.3)	4	(3.4)	8	(6.6)				
20%Fe-30%Cr-25%Co-25%Ni	Saturated	Cb	2	(1.3)	4	(2.9)	8	(5.8)	10	(7.2)		
		Mo	2	(1.8)	4	(3.9)	8	(7.2)	10	(8.9)		
									12	(11)		
		Zr	6	(2.7)	8	(3.5)	10	(6.6)				
		Ti			2	(0.30)	4	(1.84)	6	(2.8)		
					8	(3.5)	10	(5.2)				
		C	0.2	(0.14)	0.4	(0.10)	0.8	(0.42)	1.5	(0.46)*		
							2	(0.75)	1	(1.3)*		
		Ta	10	(7.91)								
		V	10	(9.16)	12	(11.13)						
20%Fe-40%Cr-20%Co-20%Ni	Supersaturated	Be	1	(0.2)	2	(0.3)	4	(0.6)				
		W	2	(1.9)	4	(4.0)	8	(6.8)				
		Al	2	(0.39)	4	(3.5)	8	(5.6)				
20%Fe-20%Cr-60%Ni	Unsaturated	C	5	(0.19)	10	(0.24)						
		Al	2	(0.36)	4	(1.2)	6	(2.2)				
		Ti	2	(1.04)	4	(2.3)	6	(3.3)				
30%Fe-20%Cr-50%Ni	Unsaturated	Al	6	(4.9)	8	(6.8)	10	(8.2)	12	(10.1)		
50%Fe-20%Cr-30%Ni	Saturated	C	5	(0.23)	10	(0.23)						
		Al	2	(0.66)	4	(1.5)	6	(2.2)				
		Ti	2	(2.4)	4	(2.5)	6	(4.1)				
80%Fe-20%Cr	Unsaturated	C	5	(0.45)	10	(0.69)						
60%Fe-40%Ni	Unsaturated	Al			5	(4.10)	10	(6.78)	15	(11.11)		
		Cb	1	(0.56)	5	(4.00)	10	(8.33)	15	(12.02)		
		Ti	1	(0.60)	5	(3.48)	10	(6.44)	15	(10.27)		

All alloys vacuum melted and hydrogen treated except two (*) carbon alloys which were vacuum melted only.

various compounds of different composition and characteristics to various face-centered cubic solid solutions. Therefore, a systematic exploratory research was started in 1946 to study the metallurgy of alloys at high temperatures from these viewpoints. Certain principles have been deduced from this research. It is the purpose of this paper to present data leading to these principles.

Experimental Procedure

More than two hundred alloys consisting of binary, ternary, and quaternary combinations of iron, chromium, cobalt, and nickel were made to evaluate and compare the properties of the base alloys. The elements varied in steps of 10 atomic pct** as illustrated schematically in Fig. 1. More

** Compositions are expressed in atomic percent throughout the paper.

than a hundred supplementary alloys with incongruous additions listed in Table I were tested in the second part of the work. Typical of analysis of the four starting materials used in the base alloys are those listed in Table II. The hardening elements were added in the purest form available, as follows:

Al, 99.996 pct; Be, 99.8; Mo, 99.9; Cb, 99.4; Ta, 99.9+; titanium hydride, 94.0; W, 99.9; Va, 99.7; and zirconium hydride 96.0. Since these elements were added in amounts no larger than 12 pct, it is believed that the impurities are not significant.

All alloys were produced by a vacuum-melting technique^{1,2} to reduce the amounts of extraneous impurities. Certain alloys were deoxidized with carbon or hydrogen as indicated symbolically in Fig. 1, or as noted in Table I. All alloys were centrifugally cast, in vacuum, into a permanent molybdenum or copper segmented mold to yield castings of the form shown in Fig. 2. Each casting was homogenized at 2100°F for 15 hr in hydrogen and water quenched. Mechanical tests were performed with the material in this initial condition. Hardness tests were made on quenched specimens aged 2 hr at 400°, 800°, 1200°, 1400°, 1600°, 1800°, and 2000°F, respectively. This type of data is shown plotted in Fig. 3a. All heat-treating and testing temperatures were maintained within 5°F.

Both tensile and rupture tests were made on button-head cylindrical specimens machined to a gage length of 1½ in. and a gage diameter of 0.160

Table II. Analysis of Base Components

	C	S	Si	Mn	P	O	H	N	Fe	Cr	Pb	Ni	Cr	Co
Electrolytic nickel	0.02	0.006	Nil	None	Trace	0.006	0.0003	0.0000	ND	ND	—	Rem.	—	—
Electrolytic chromium	0.01	0.019	—	—	—	0.41	0.034	0.007	0.054	0.01	0.001	—	Rem.	—
Electrolytic iron	0.03	0.004	Trace	Trace	0.02	0.061	0.0004	0.0018	Rem.	Trace	—	Nil	Trace	Nil
Rondell's cobalt	0.02	0.003	0.22	Trace	—	0.119	0.0001	0.0000	Nil	Nil	—	Trace	Nil	Rem.

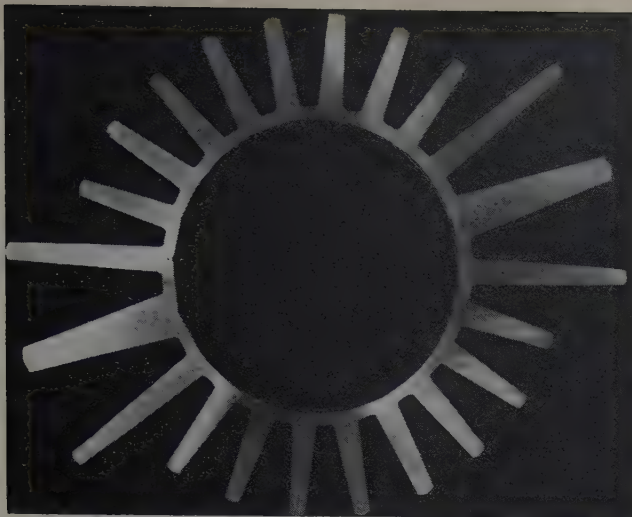


Fig. 2—Cross section of permanent mold centrifugally cast specimen. X0.6. Area reduced approximately 80 pct for reproduction.

± 0.0005 . Tensile tests were made on a Baldwin-Southwark testing machine adapted for elevated temperature testing. Tests were run at a rate of 0.050 in. per min at room temperature, 600°, 1200°, 1400°, 1600°, 1800°, and 2000°F in air. An example of the tensile data is shown plotted in Fig. 3b. The time of tensile testing varied with the elongation to fracture. For this paper, however, an average value of 0.1 hr is used. This value is typical of that obtained for tests at temperatures near 1500°F.

Two types of rupture apparatus were used: a large 48-bar unit³ and a single-bar apparatus of a common design. Constant-load rupture tests were carried out at 1000°, 1200°, and 1500°F. Three to five samples were tested at each temperature and loaded so that the fracture time was between 1 and 1000 hr. An example of the type of data obtained is shown in Fig. 3c.[†]

[†] In this paper, since the results of both tensile and rupture tests are plotted together, the term "breaking strength" is used to indicate the maximum load divided by the initial cross-section area. This value for tensile tests is the conventional ultimate strength, and for rupture tests is the initial stress.

Metallographic samples of each alloy were examined to evaluate cleanliness in the vacuum melting and casting process, and to determine the microstructure. Typical micrographs are shown in Fig. 4a, b, and c. The grain size varied from about ASTM No. 1 for solid solution alloys to about No. 7 for multiphase alloys, usually in typical progression, as shown in Fig. 4a. Since grain size is a dependent variable, the effects of composition reported in this paper include the effects of grain size. The significance of grain size in elevated temperature tests has never been clearly and undisputably evaluated, since the heat treatment and changes in procedure required to control grain size also change other factors which affect the strength. The types of microstructures encountered in this investigation are illustrated in Fig. 4b and c, including solid solution alloys and alloys undergoing allotropic transformation during quenching (Fig. 4b, left), mixed-phase alloys of approximately equal proportions (Fig. 4b, center and right), and the effects of incongruous additions where a second phase is formed in a massive condition (Fig. 4c, first three micrographs), or where the second phase appears interdendritically (Fig. 4c, last three micrographs).

A chemical analysis of the principal elements was made on approximately every tenth alloy,

except for those containing incongruous additions as noted below. The melting practice was developed to a high degree of reproducibility; therefore, deviations from the nominal compositions were minor. Variations of as much as 1 or 2 pct in the composition of any one of the four elements iron, chromium, cobalt, and nickel were found to produce only small differences in mechanical properties. The analyses made indicated that variations were usually less than this amount. Chemical analyses of impurities were made frequently to establish the effectiveness of the purifying treatments carried out during vacuum melting. An analysis typical of alloys prepared is 0.0006 atomic pct H, 0.021 O, 0.005 N, and 0.08 to 0.13 C. Since all the alloys were prepared in a similar manner and checked wherever practicable, it is believed that in all alloys the impurity contents are under control. Chemical analyses were run on all incongruous addition elements. The nominal and actual compositions are listed in Table I.

The base compositions used in the investigation of incongruous elements are listed in Fig. 5, together with the 1500°F phase boundaries. All alloys are face-centered cubic solid solutions except 80 pct Fe-20 pct Cr, which is body-centered cubic as-quenched from 2100°F. They include base alloys which are unsaturated solid solutions such as 80 pct Ni-20 pct Cr, nearly saturated solutions such as 30 pct Cr-30 pct Co-40 pct Ni and supersaturated solid solu-

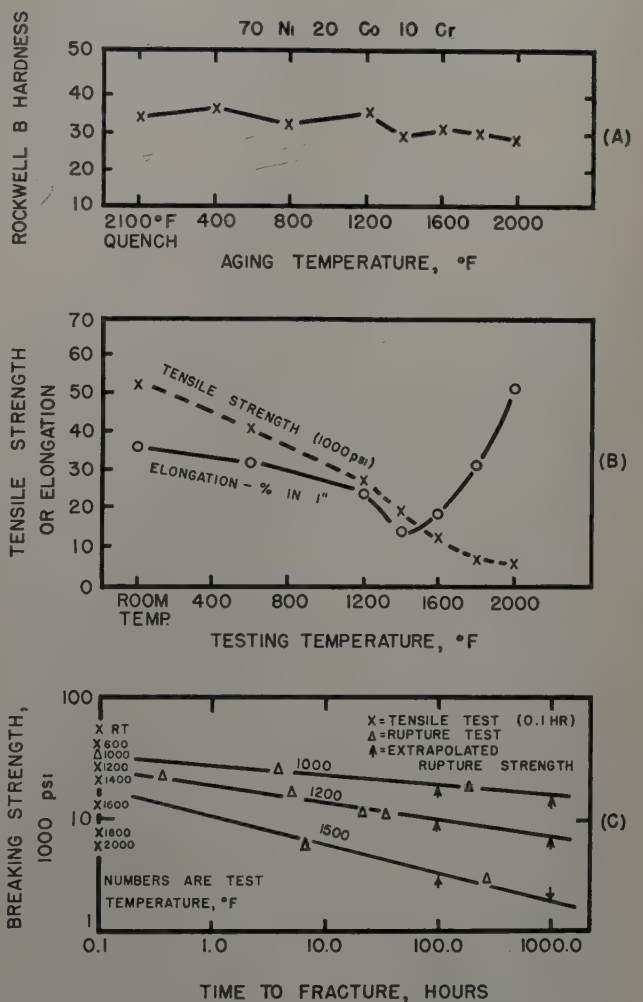


Fig. 3—Hardness, tensile, and rupture data for 70 pct Ni-20 pct Co-10 pct Cr base alloy plotted conventionally. Breaking strength is defined as the maximum load divided by the original cross-section area.

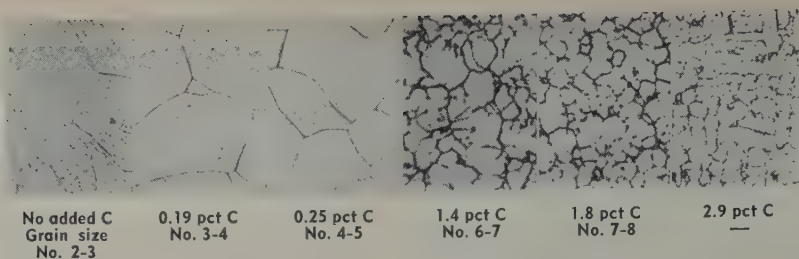


Fig. 4a—80 pct Ni-20 pct Cr base alloy. Effect of carbon additions on microstructure. Electrolytic (oxalic acid) etch. X100.

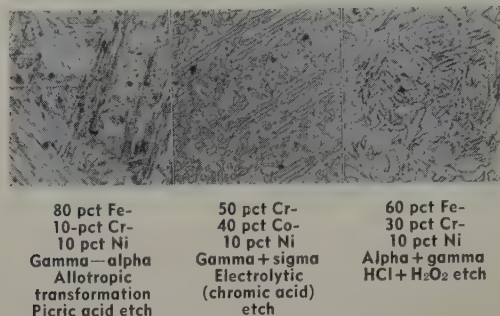


Fig. 4b—Multiphase base alloys. Etchants as indicated. X100.

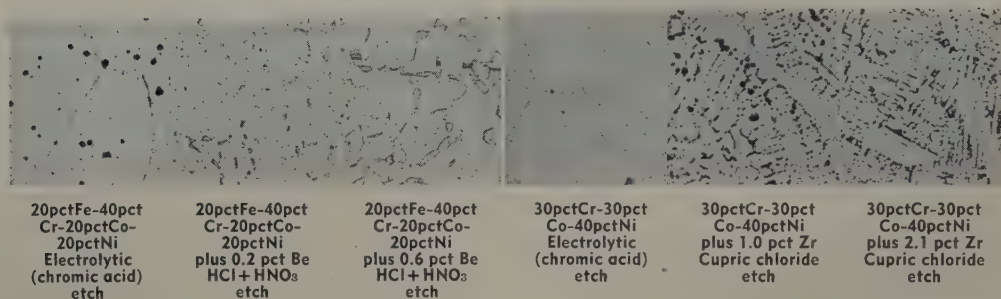


Fig. 4c—Effects of incongruous additions on microstructure. Etchants as indicated. X100.

tions such as 40 pct Cr-20 pct Co-40 pct Ni as indicated in Table I. Although several of the alloys are supersaturated solid solutions as-quenched from 2100°F, there was no indication of age hardening in terms of hardness tests on specimens subsequently aged at various temperatures. These base compositions cover the range of high temperature strength found for the Fe-Cr-Co-Ni solid solution alloys.

Incongruous elements having a variety of melting points, atomic diameters, compressibilities, and crystal structures, as listed in Table III, were chosen for alloying with the selected base materials. A series of compositions with increasing amounts of incongruous additions was prepared in an attempt to include unsaturated, supersaturated, and multiphase alloys.

Technique of Plotting: Time Temperature Parameter

The customary procedure for presenting time-temperature breaking strength data consists of plotting the logarithm of the breaking strength as a function of the logarithm of the time to failure at each testing temperature. This method of plotting, Fig. 3c, is clumsy to use for comparing the effects of wide varieties of time and temperature upon the fracture strength of alloys. A more useful method in which time and temperature are interrelated as a single-valued function of breaking strength has been found to facilitate the comparison of the properties of different alloys.^{4,5} This time-temperature function which will be referred to as a parameter

may be expressed as follows:

$$T (C + \log t)$$

where T is temperature in degrees Rankine,†† t is

†† °F plus 459.4.

time in hours, and C is a constant equal to 11 in the present work.‡ When the logarithm of the breaking

‡ The constant was determined by trial and error. By plotting \log time against $1/T \times K$ for various constant strengths and extrapolating to a convergence point at $1/T = 0$, a value of C may be determined graphically. Since data at any given strength level are limited by the nature of the alloys and the difficulties of running very short and very long-time tests, the extrapolation is so long as to preclude any accurate determination of C . A single average value of the constant was used. For further discussion, see ref. 4.

strength is plotted against this parameter, a single line as shown in Fig. 6 replaces the customary sets of curves and can include both short-time tensile strengths at different temperatures and stress-rupture strengths at different times and temperatures. For parameter numbers above about 19,000, this line is straight for data such as those shown in Fig. 6 (19,000 corresponds to a tensile test—0.1 hr—at 1340°F, or a 1000-hr rupture test at about 900°F). The 1000-hr rupture strength at 1500°F (a parameter number of 27,400) is more accurately defined in Fig. 6 than in Fig. 3c, primarily because more data points are used in the parameter plot. This strength is used as a basis of comparison of different alloys in this paper. For purposes of evaluating the parametric method, interpolated and extrapolated rupture values from conventional log stress-log

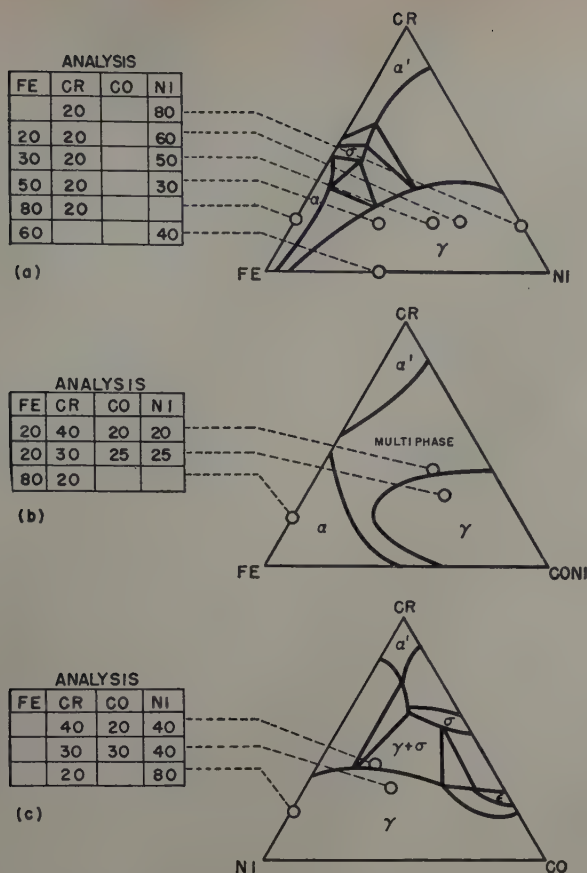


Fig. 5—Composition and 1500°F phase boundaries for base alloys selected for alloying with incongruous additions.

time plots are included on the parametric plots to illustrate the similarities of the values obtained by the two methods. These values are labeled "extrapolated rupture strength" for purposes of brevity, but were not used in fitting lines to the data points. An important advantage of the parametric method is that all types of data are included on the same plot. Other advantages and disadvantages of the parametric method of plotting are discussed in subsequent sections.

Results of Tests

Parametric plots were constructed from tensile and rupture strength data determined from specimens of all alloys considered. A few examples will be discussed in detail to illustrate the correlation

Table III. Some Characteristics of Alloying Elements

Element	Melting Point, °F	Atomic Diam., Å	Compress. $10^4 \text{ Cm}^2/\text{Kg}$	Valence	Crystal Structure
W	6170	2.82	0.293	*	BCC
Ta	5425	2.95	0.479	*	BCC
Mo	4760	2.80	0.347	*	BCC
Cb	4380	2.94	0.570	*	BCC
Cr	3430	2.57	0.600	*	BCC
Ti	3300	2.93	0.797	*	CPH-BCC
Zr	3200	3.19	1.097	*	CPH-BCC
V	3150	2.71	0.609	*	BCC
Fe	2802	2.52	0.587	*	FCC-BCC
Co	2723	2.50	0.539	*	CPH-FCC
Ni	2651	2.49	0.529	*	FCC
Be	2340	2.25	0.855	2	CPH
Al	1220	2.80	1.34	3	FCC
C	6700			4	Hex.
O	-362			6	Orth.
N	-346			5	Cubic

* Transition.

between the parametric plots and different types of alloys.

Solid Solutions: An important experimental generalization^{††} is that the high temperature data for

^{††} Lines were independently fitted to experimental data points for a large number of alloys. Subsequent inspection of these plots lead to the recognition of the common slopes.

all single-phase cobalt-containing alloys of the Fe-Cr-Co-Ni type can be represented on parametric plots by a straight line having a slope of -0.117 (illustrated in Fig. 6) and that the high temperature data for single-phase Fe-Cr-Ni or cobalt-free austenitic alloys (except alloys having allotropic phase changes) can be represented by a straight line with a slope of -0.133 (illustrated in Figs. 7 and 8). This finding is empirical and not understood, but is convenient for the analysis of data. It is interesting to note that, since the slope is empirically defined by the composition, the straight-line portions of the parametric plots used in this investigation may be reconstructed from the 1000-hr 1500°F rupture strengths (parameter No. 27,400) in Fig. 17 by the point-slope method. In addition, because of the similarities of slopes, similar composition-strength contours will result from any constant parameter number (condition of testing time and temperature), provided it lies on the straight-line portion of the plot.

Supersaturated Solid Solutions: When metallurgical changes which affect properties occur as functions of time and temperature different from the $T (C + \log t)$ parameter, the strength is not a single-valued function of the parameter. Under these conditions, several strength values can occur at a

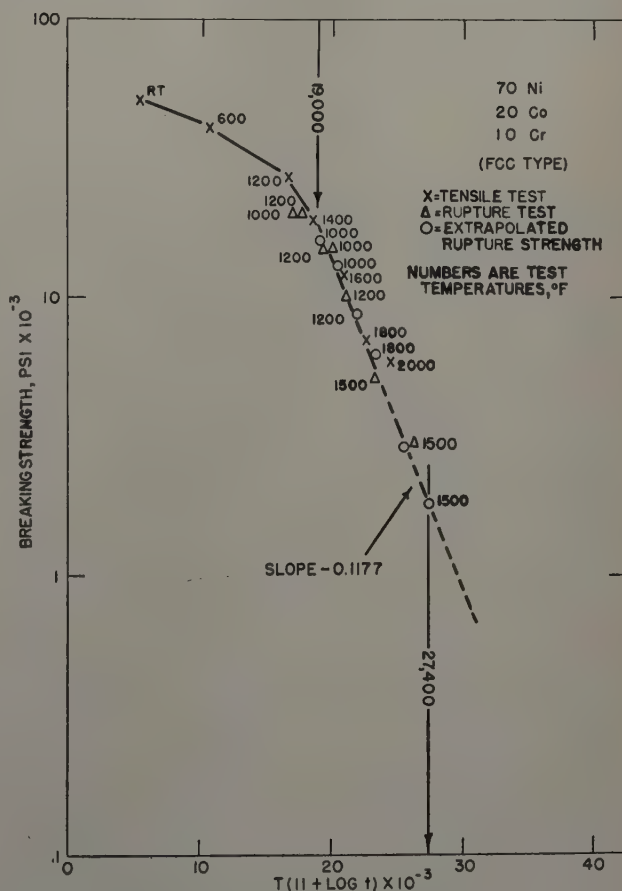


Fig. 6—Parametric plot of the tensile and rupture data of Fig. 3 for 70 pct Ni-20 pct Co-10 pct Cr base alloy, illustrating the characteristic slope for cobalt-containing alloys.

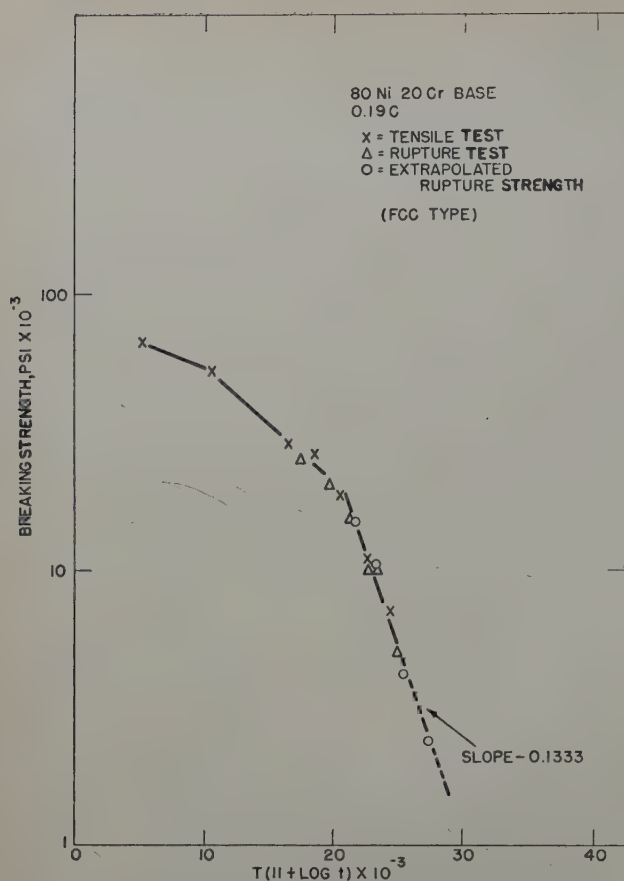


Fig. 7—Parametric plot of data for the 80 pct Ni-20 pct Cr base alloy of the face-centered cubic solid solution type, illustrating the characteristic slope for cobalt-free alloys.

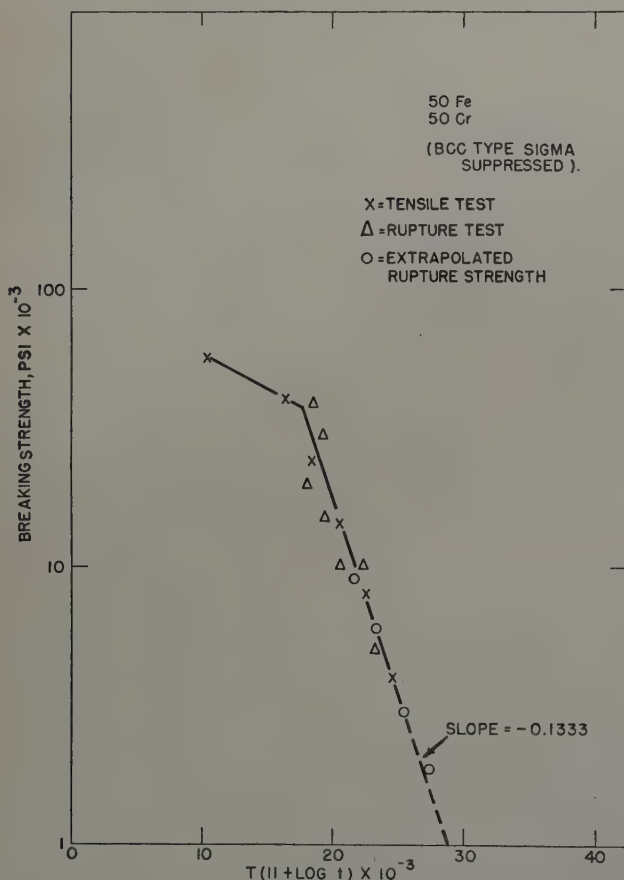


Fig. 8—Parametric plot of data for the 50 pct Fe-50 pct Cr base alloy of the body-centered cubic supersaturated solid solution type.

single parameter number which includes different combinations of time and temperature causing varied properties.

Thus, the parametric plots for supersaturated solid solutions of age-hardening alloys varied from a well-defined single line to a band of strength values. For specimens which fractured at values of the parameter at times and temperatures such that no measurable age-hardening occurred, a single-line parametric plot resulted. If the times and temperatures of tests were such that significant age-hardening occurred, a band of strength values was found, depending upon the amount of hardening. Data from different types of alloys exhibited certain characteristic behaviors.

The binary 50 pct Fe-50 pct Cr body-centered cubic alloy represents one type of behavior. In this alloy σ phase exists up to 1500°F under equilibrium conditions, but there was no evidence of σ phase

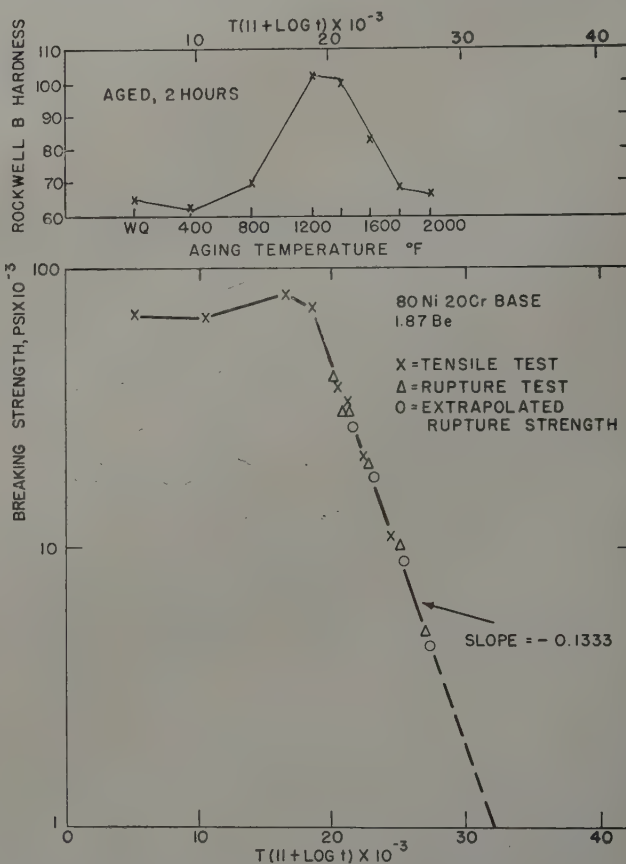


Fig. 9—Hardness data and parametric plot of data for the 1.87 pct Be addition to the 80 pct Ni-20 pct Cr base alloy, illustrating the results for an alloy which age hardens to a maximum at temperatures below 1500°F.

revealed by metallographic examination of specimens in the cast or quenched condition or in stress-rupture specimens after 1000 hr at either 1200° or 1500°F. Thus, this supersaturated solid solution alloy did not transform during the tests and the parametric plot of test data shown in Fig. 8 is a single-line characteristic of solid solutions, although there is some spread of data. In other experiments it was found that σ did occur in the samples of this alloy cold-worked 60 to 70 pct at room temperature and heat-treated to cause age hardening. Since it is known that age-hardened materials are stronger than the supersaturated solutions at temperatures where the precipitated phase is stable, an even

wider spread of data than that shown in Fig. 8 would be expected for results of tests of this alloy under all possible structural conditions.

For some age-hardenable alloys such as shown in Fig. 9, data from both long and short-time tests at high temperatures could be represented by a single line at high parameter values. Based on the hardness-temperature curves in Fig. 9, this Ni-Cr-Be alloy did age-harden in the temperature range of 1200° to 1400°F. Data points from stress-rupture tests and tensile tests, however, showed no measurable deviations from a single line, probably because none of these tests were carried out under conditions of time and temperature associated with measurable age hardening. When tested under conditions promoting maximum age hardening below the straight-line part of the curve, a wide band could be obtained, as was experimentally determined for several alloys of this type.

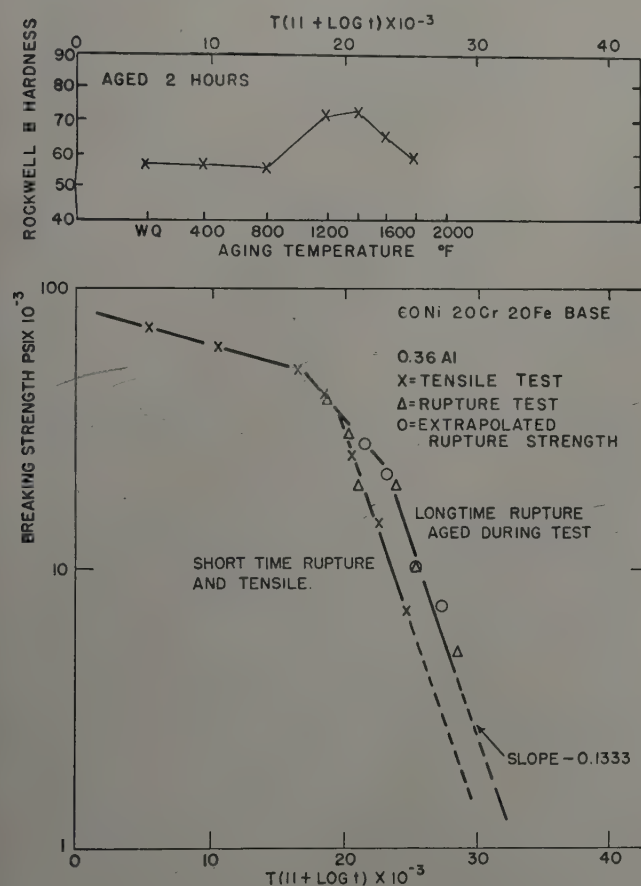


Fig. 10—Hardness data and parametric plot for the 0.36 pct Al addition to the 60 pct Ni-20 pct Cr-20 pct Fe base alloy, illustrating the band formed for an alloy which age hardens to a maximum near 1500°F.

For other age-hardenable alloys for which maximum hardening occurred near 1500°F, data from long-time tests causing age hardening did not conform to the straight line which fitted data from short-time tests at high parameter values. Data for a Ni-Cr-Fe alloy of this type is shown in the parametric plot in Fig. 10. For this alloy, the long-time (>100 hr) rupture values for 1200° and 1500°F fall along a single line of characteristic slope, while the tensile test data and short-time rupture data at 1200° and 1500°F form a single parallel line at a lower strength level.

These results indicate that data for age-hardening

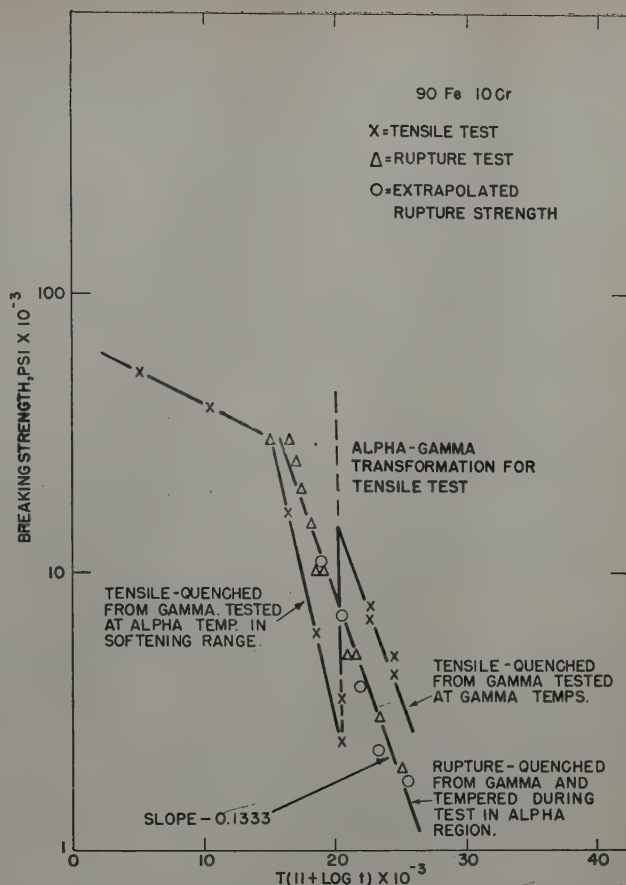


Fig. 11—Parametric plot of data for the 90 pct Fe-10 pct Cr base alloy, illustrating the effects of an allotropic transformation.

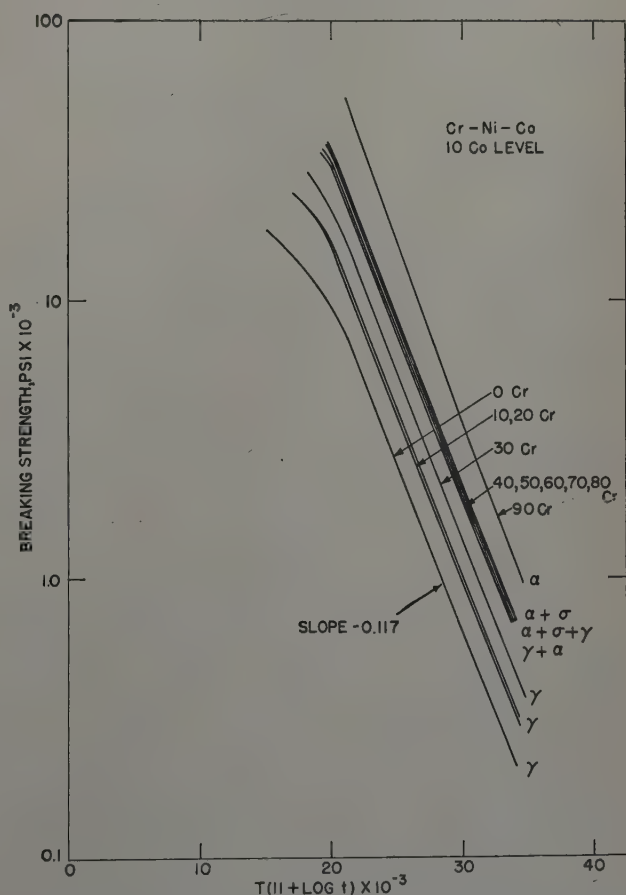


Fig. 12—Parametric plots of data for Cr-Ni-Co alloys with 10 pct Co constant, illustrating the effects of stable multiple-phase alloys.

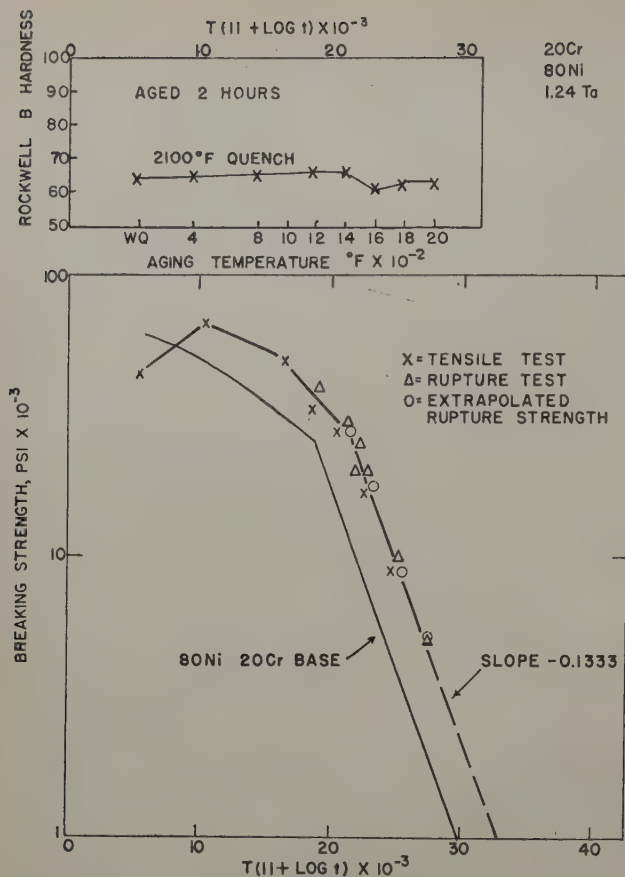


Fig. 13—Hardness data and parametric plot for data from alloy with 1.24 pct Ta addition to 80 pct Ni-20 pct Cr base.

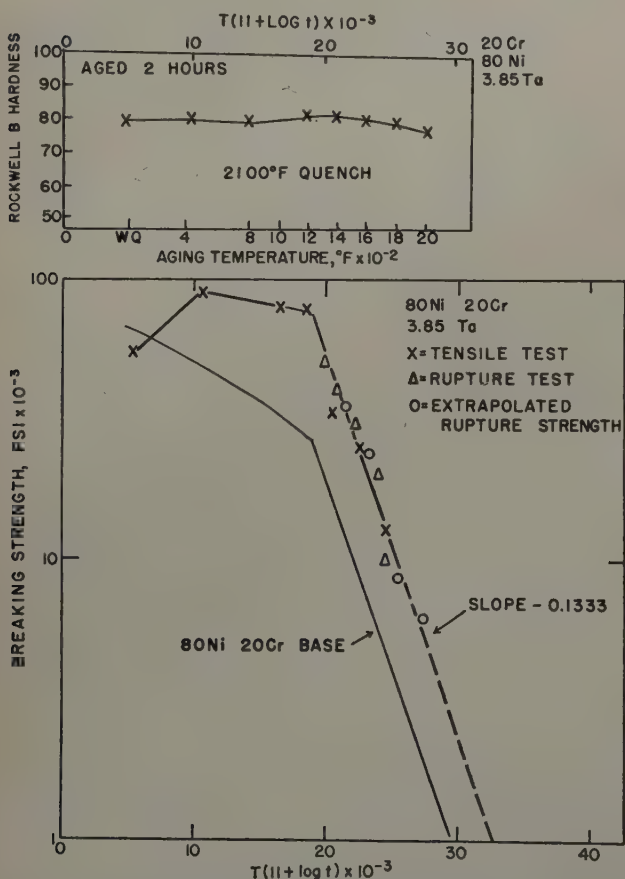


Fig. 14—Hardness data and parametric plot for data from alloy with 3.85 pct Ta addition to 80 pct Ni-20 pct Cr base.

alloys may form a band of strength values for each of the parameter values depending upon the prior metallurgical history and the effect of time and strain upon the strength at the testing temperature. The possible ramifications are extensive. The exact pattern of the data for various temperatures within the parameter band is not definite. It is believed that more complete strength data for different testing temperatures might form families of curves with the extremes of strength values falling on parallel lines. It is significant, however, that two parallel straight lines of characteristic slopes can be

± 0.117 for cobalt-containing alloys; -0.133 for cobalt-free alloys.

used to approximate the limiting strengths for the times, temperatures, and, in turn, the parameter numbers used in this analysis. This convenience will be used for determining the range of strengths of the alloys studied.

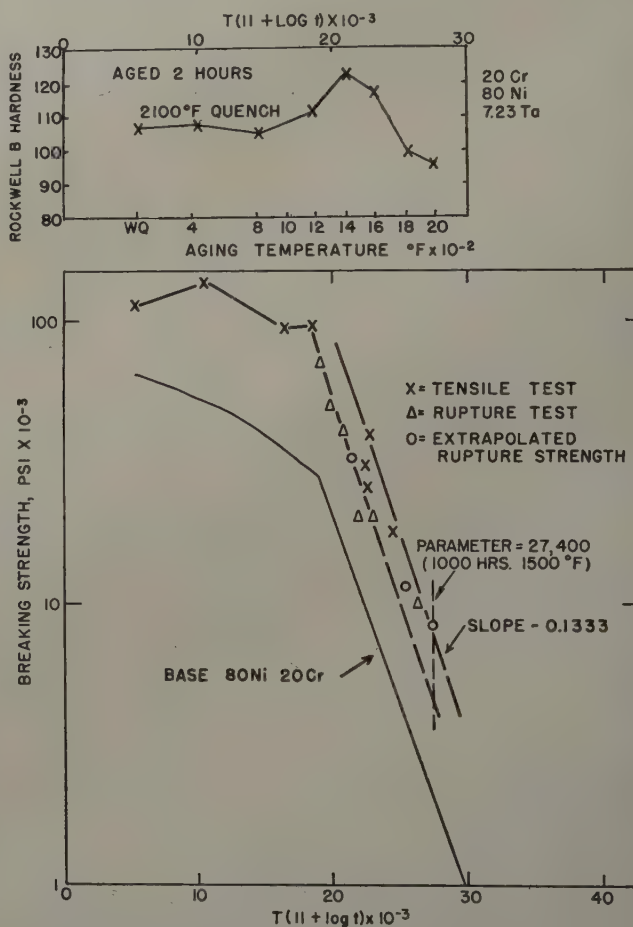


Fig. 15—Hardness data parametric plot for data from alloy with 7.23 pct Ta addition to 80 pct Ni-20 pct Cr base.

Allotropic Transformations: Iron-rich and cobalt-rich alloys of the Fe-Cr-Co-Ni system undergo allotropic changes on heating. For alloys where a single parameter number covers a range of temperature and time including both allotropic modifications, the parametric plot may consist of a broad band rather than a single line, depending upon the relative properties and amounts of the phases. A 1000-hr test at 755°F of a specimen of ferritic iron would result in a strength different from that of a tensile test (0.1 hr) of austenitic iron at 1800°F, although both tests correspond to a parameter number of 22,600. Data from specimens of an Fe-Cr alloy

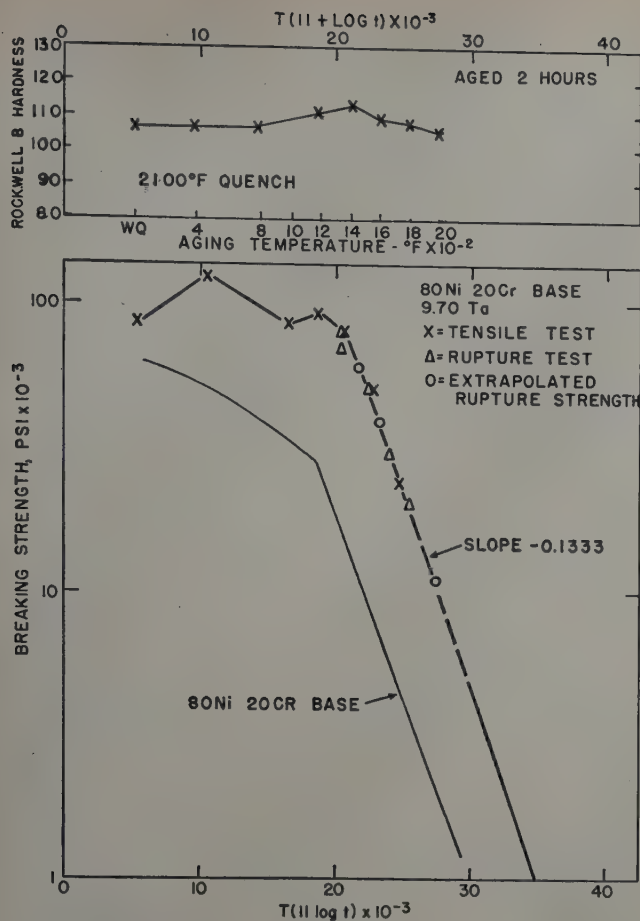


Fig. 16—Hardness data and parametric plot for data from alloy with 9.70 pct Ta addition to 80 pct Ni-20 pct Cr base.

which undergoes an allotropic transformation within the range of testing temperatures are plotted in Fig. 11. The line for points corresponding to the high temperature phase is at a higher strength than the line for points corresponding to the low temperature phase. When allotropic transformation of a martensitic type occurs, the parametric plot can be further complicated by nonequilibrium conditions. This alloy was quenched from 2100°F and was subsequently tempered during testing at elevated temperatures. Under these conditions it became stronger, which is the expected behavior.⁹

Multiple Phases and Crystal Structure: Single-line parametric plots were obtained for data from stable multiple-phase alloys. In Fig. 12, single-line parametric plots are reconstructed in composite for the purpose of comparing the strengths of alloys in the Cr-Co-Ni system consisting of α , γ , α - γ , and α - γ - σ phases with 10 pct Co and varying chromium contents. The strength of these alloys increases with increasing chromium contents and the appearance of a second phase. The γ solid solution alloys with less than 40 pct Cr are relatively weak. The stronger alloys with 40 pct Cr or more (Fig. 12) contain the more complex σ or α chromium phases and are brittle at low temperatures.

Single Additions of Incongruous Elements: With progressively increasing amounts of additions of a single incongruous element to a given solid-solution alloy, the following three characteristic types of alloys were recognized by relating microstructure, parametric plots and age-hardening data: 1—single-phase alloys, 2—supersaturated solid solutions

which age hardened, and 3—multiphase alloys at all testing temperatures. This behavior is shown in Figs. 13 through 16 for tantalum additions to 80 pct Ni-20 pct Cr and can be rationalized as follows:

1—For small tantalum additions, the hardness of the base was increased, but no large change in hardness occurred during aging tests. The data for this type of alloy will form a single line on the parametric plots as shown in Figs. 13 and 14.

2—When the amount of incongruous addition was increased and maximum age hardening occurred near 1500°F, the corresponding strength data on a parametric plot developed a band characteristic of age-hardening alloys which age at high temperatures as shown in Fig. 15.

3—As the amount of incongruous addition was increased further beyond the optimum addition so that the age-hardening peak in the hardness-temperature plot became smaller, or disappeared, the corresponding strength data on parametric plots formed a single line in the high temperature range, as shown in Fig. 16, similar to Fig. 13.

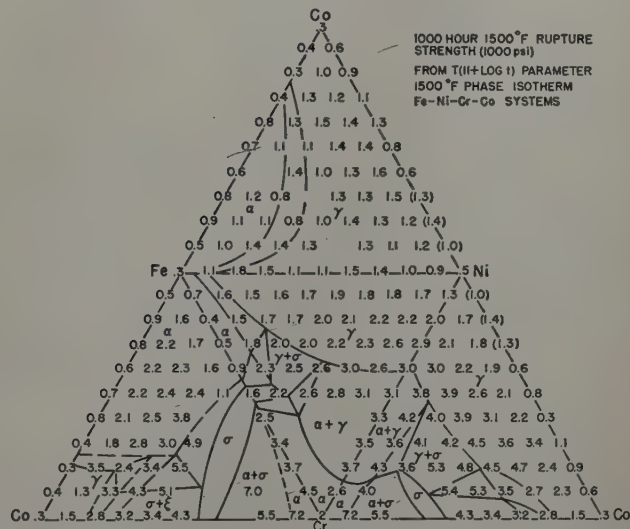


Fig. 17—1000 hr, 1500°F rupture strengths (1000 psi) of Fe-Ni-Cr-Co base alloys determined from parametric plots. 1500°F phase boundaries superimposed.

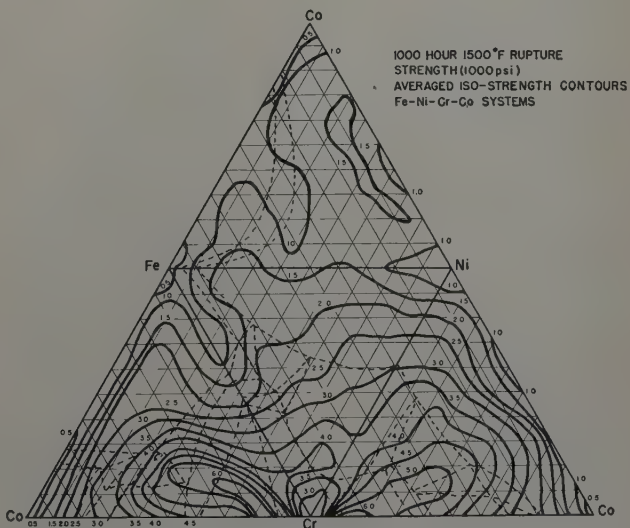


Fig. 18—Iso-strength contours for Fe-Ni-Cr-Co ternary systems indicating 1000 hr, 1500°F rupture strength (1000 psi).

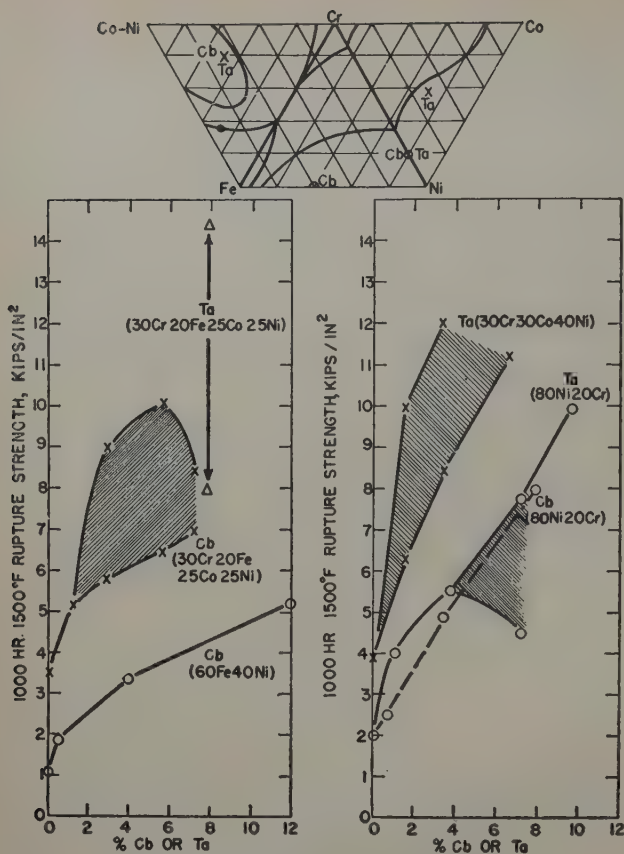


Fig. 19—Effect of single additions of columbium or tantalum on the 1000 hr, 1500°F rupture strength of selected base alloys. Location of base alloys with respect to 1500°F solubility limits indicated on phase isotherms at top.

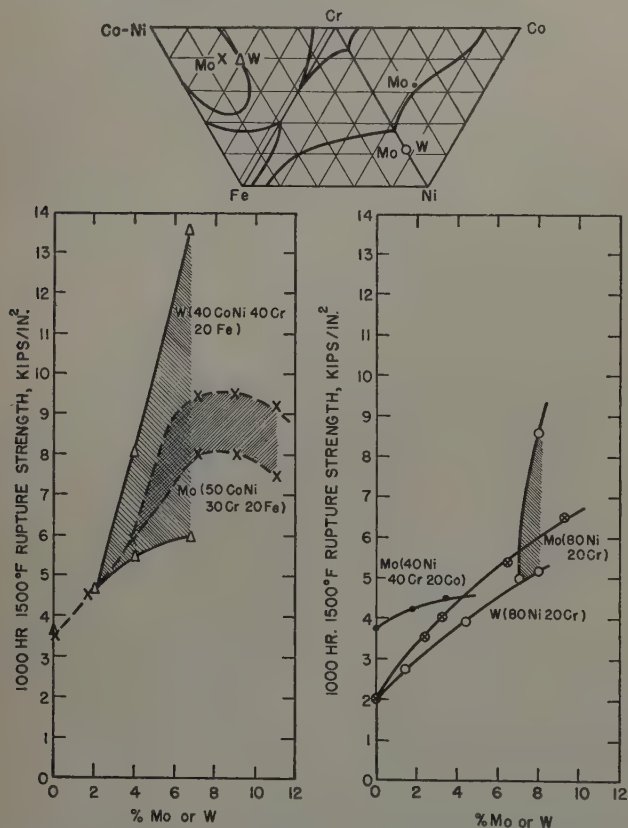


Fig. 20—Effect of single additions of molybdenum or tungsten on the 1000 hr, 1500°F rupture strength of selected base alloys. Location of base alloys with respect to 1500°F solubility limits indicated on phase isotherms at top.

Comparative Rupture Strength

From the parametric plots, a value of 1000 hr, 1500°F rupture strength ($P = 27,400$) was determined for each alloy. These values of strength are used throughout as a basis for comparing the high temperature properties of the alloys, in order to develop some principles of alloy design and not merely to report property data.

Fe-Ni-Cr-Co Alloy Bases: Data for the strength of alloy bases determined from parametric plots are shown in Fig. 17 on ternary plots of the Ni-Cr-Fe, Ni-Cr-Co, and Fe-Ni-Co systems. Where available, 1500°F equilibrium phase boundaries are indicated based on refs. 7 through 13. Fig. 18 is an iso-strength plot based on the averaged values from three intersecting plots of strength as a function of the percentages of two of the elements for a constant amount of the third element. Similar data for quaternary alloys are not included since the data for the ternary alloys adequately illustrates the principles involved. The strongest alloys in Fig. 17 could not be investigated in detail because alloys with large amounts of σ are too brittle to test accurately.

Incongruous Additions: For alloys containing incongruous additions which resulted in parametric plots having a band of strength values, two parallel lines, as shown in Fig. 15, were drawn to approximate the range of available strength from the unaged to the fully-hardened conditions. From these plots, two values of strength were obtained at the single parameter number of 27,400. It should be emphasized that these two values do not represent scatter but do represent the variability of strength resulting from heat treatment or changes in structure.

The 1000-hr, 1500°F strengths obtained from additions of tantalum and columbium are plotted in Fig. 19 as a function of composition, together with the ternary diagrams indicating the base alloy compositions. Where a single-strength value is indicated for a given composition, a single-line parametric plot was obtained. For alloys where a range of strength values is indicated by shading, a parametric plot with a band of strength values was obtained. In each case, the data represent lines fitted to the experimental points, and not experimental scatter. It should also be noted that a given addition element has very different effects on different base alloys, as illustrated in Fig. 19 by comparing the columbium curves for 60 pct Fe-40 pct Ni and 30 pct Cr-20 pct Fe-25 pct Co-25 pct Ni. These observations suggest an advantage of using a supersaturated alloy base as compared with an unsaturated alloy base. It should be noted also that there is a question as to whether these alloys were solution treated to obtain maximum solubility.

The range of strength obtained from the parametric plots are plotted against the percentage of molybdenum or tungsten additions in Fig. 20, together with ternary diagrams showing the location of the base alloys. Three characteristic types of plots are shown as follows:

- 1—For all molybdenum additions to the 80 pct Ni-20 pct Cr base, single strength values were obtained.
- 2—In the case of tungsten additions to the 80 pct Ni-20 pct Cr base, it was evidently soluble in the base up to about 7 atomic pct, forming a single strength-composition line. Near the solubility limit, the plot branches into a band indicative of age hardening.

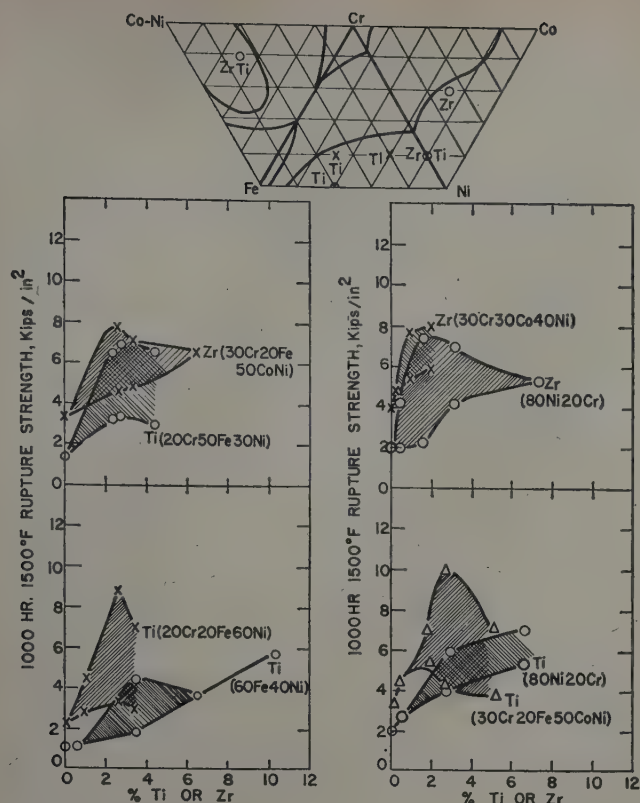


Fig. 21—Effect of single additions of titanium or zirconium on the 1000 hr, 1500°F rupture strength of selected base alloys. Location of base alloys with respect to 1500°F solubility limits indicated on phase isotherms at top.

3—For molybdenum additions to the 40 pct Ni-40 pct Cr-20 pct Co base the alloy is probably a stable two-phase structure, but the data did not

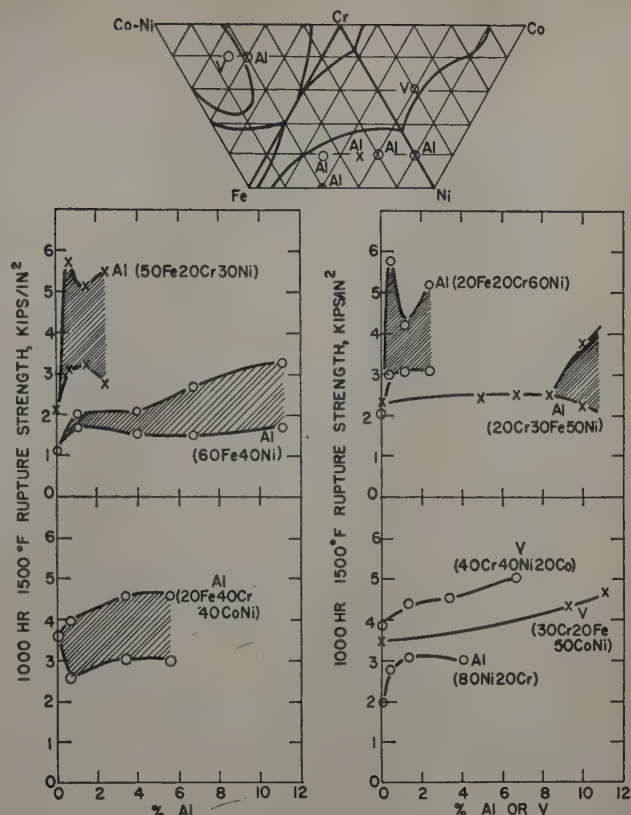


Fig. 22—Effect of single additions of aluminum or vanadium on the 1000 hr, 1500°F rupture strength of selected base alloys. Location of base alloys with respect to 1500°F solubility limits indicated on phase isotherms at top.

produce any measurable deviations from single strength values characteristic of age hardening. There is a question as to whether or not these alloys

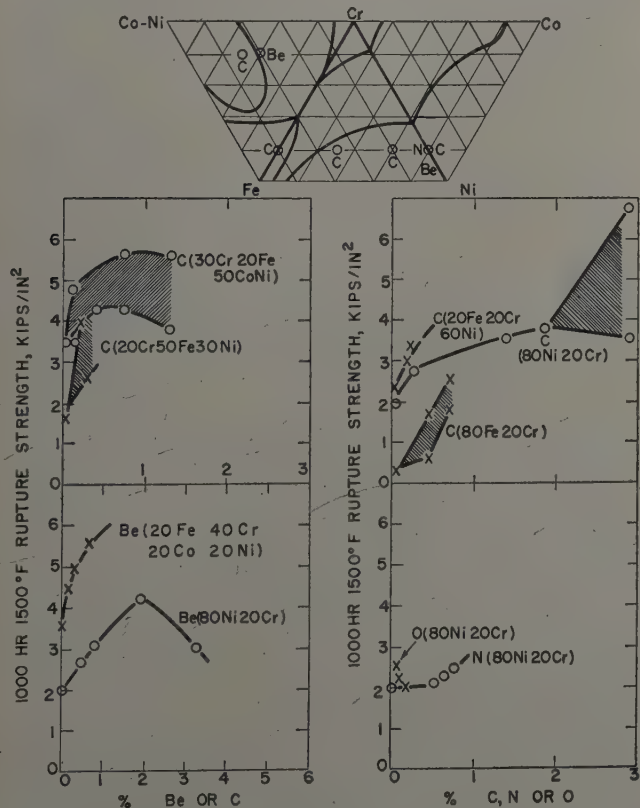


Fig. 23—Effect of single additions of beryllium, carbon, nitrogen, or oxygen on the 1000 hr, 1500°F rupture strength of selected base alloys. Location of base alloys with respect to 1500°F solubility limits indicated on phase isotherms at top.

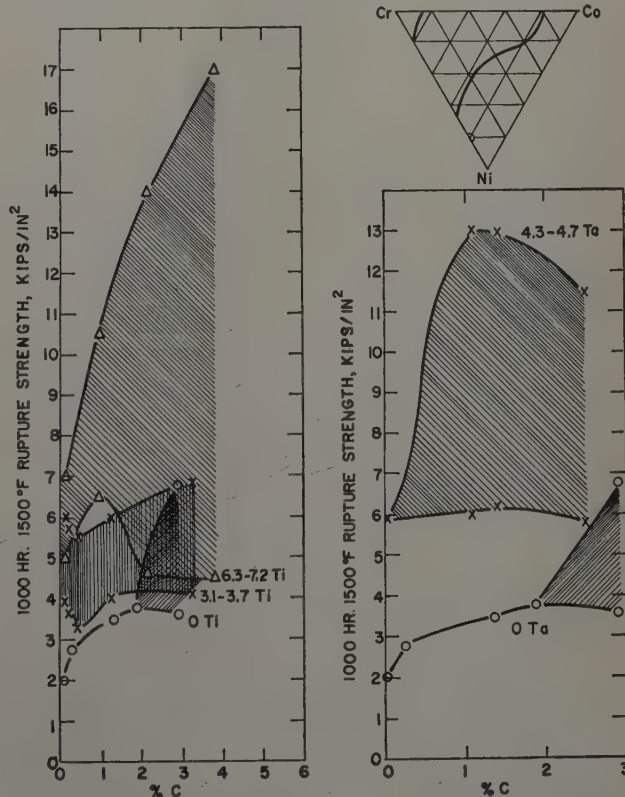


Fig. 24—Effect of additions of carbon and tantalum or titanium on the 1000 hr, 1500°F rupture strength of 80 pct Ni-20 pct Cr base alloy. Location of base alloy with respect to 1500°F solubility limit indicated on phase isotherm at top.

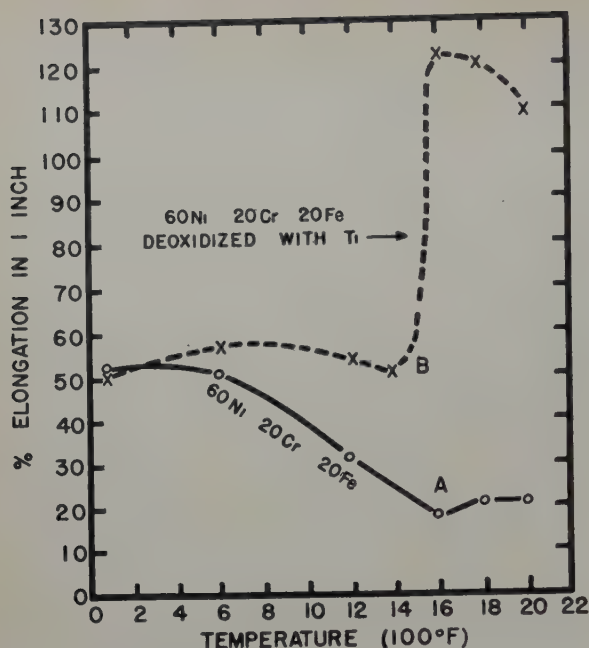


Fig. 25—Elongation data from tensile tests of the 60 pct Ni-20 pct Cr-20 pct Fe base alloy as a function of temperature, illustrating the improved ductility obtained from deoxidation with titanium.

were properly solution treated—2100°F is not sufficiently high a temperature to obtain maximum solution for all these alloys. Both of these elements, molybdenum and tungsten, are similar, but are different in atomic characteristics from the base elements.

The strengths resulting from titanium or zirconium additions to various base alloys are shown in Fig. 21 and again with reference ternary diagrams. These alloys age hardened and the extent is indicated by the spread in parametric plots. It is somewhat less than for tantalum, tungsten, or molybdenum.

The effect of aluminum or vanadium on the 1000-hr 1500°F rupture strength of selected bases is plotted in Fig. 22. For the limited amount of data available for vanadium, the effect of this element is very small as might be expected because of its similarity to chromium (Table III). In the case of aluminum there is a pronounced age-hardening effect for two of the base alloys, 50 pct Fe-20 pct Cr-30 pct Ni and 20 pct Fe-20 pct Cr-60 pct Ni, but in both cases the alloy contained small amounts of carbon. Three other aluminum additions produced small age-hardening effects. In the case of the 20 pct Fe-40 pct Cr-20 pct Co-20 pct Ni base, the minimum strength obtained from the age-hardening alloys was lower than that for the alloy base. This decrease suggests that aluminum had a purifying effect on the base material which caused the strength of the alloy to be lower than that of the base. Apparently, this effect is similar to that reported by Lacy and Gensamer for chromium added to iron.¹⁴

The effects of single additions of beryllium, carbon, nitrogen, or oxygen on various bases are shown in Fig. 23. The data for alloys of oxygen and nitrogen are somewhat limited; however, for nitrogen additions the strength obtained for various compositions extrapolated to a lower base value than that obtained for the base itself. Oxygen appears to have a large strengthening effect in very

small amounts which then decreases with increasing additions. The difficulty of accurately analyzing for gases in metals should be recognized in considering these results.

Fig. 24 shows the effects of simultaneous additions of carbon with titanium or tantalum on the strength of the 80 pct Ni-20 pct Cr base. Carbon, in this case, is combined with strong carbide formers, titanium or tantalum, which produces large age-hardening effects due to the precipitation of these carbides. The strong interaction effects resulting from this carbide formation would suggest that the effects of these simultaneous additions would be considerably different from the sum of the effects of each element independently.

Ductility: The percentage of elongation at fracture in tensile tests is plotted in Fig. 25 (curve A) as a function of temperature for an Fe-Ni-Cr alloy. This plot is typical of those found in the Fe-Cr-Co-Ni face-centered cubic alloys with a minimum elongation in the high temperature range related to the transition from transgranular to intergranular fracture. The minimum does not occur in data from alloys thoroughly deoxidized with hydrogen and 2 pct Ti¹⁵ as illustrated in curve B of Fig. 25. Above 1200°F, where fracture even in short-time tests was intergranular, the ductility of these alloys becomes low except at very high testing temperatures. For certain alloys, such as Ni-Cr binary alloys and the Fe-Ni-Cr alloys, the minimum point in the elongation curve moves toward lower ductility levels and higher temperature levels with increasing chromium composition, and it is believed to follow approximately with the recrystallization temperature. In comparison, for alloys such as 90 pct Fe-10 pct Cr which undergo allotropic changes, the highest elongation occurred at temperatures corresponding to the allotropic transformation region. Likewise, at temperatures below the minimum where the fracture is transgranular the ductility of Fe-Cr-Co-Ni face-centered cubic solutions tended to be very high near the saturation limit in chromium-rich alloys. Precipitation hardening alloys showed low ductility at a temperature causing rapid precipitation near the transgranular-to-intergranular transition and below the recrystallization temperature.

Discussion of Results

The variation in strength of alloys is believed to be related to the melting temperature, the crystal structure, and other alloying characteristics. For solid solutions relative atomic size, relative valency, and relative compressibility are important. For multiple-phase alloys, phase interaction (for example, coherency), together with the relative strengths, size, shape, and distribution of the phases should be considered. These factors, known to affect the strength of alloys, are used to rationalize the strengths of the materials studied.

Melting Point: The greater the difference between the testing temperature and the melting temperature (where the interatomic bond of the solid crystal is thermally broken) the stronger an alloy should be.¹⁶

By considering the relative strengths of the Fe-Cr-Co-Ni alloys at a constant fraction of the absolute melting temperature (a homologous temperature), differences in melting temperature (the melting point effect) are equalized to a first approximation.

From a plot of the liquidus temperature for these systems shown in Fig. 26, the temperatures cor-

responding to 0.6 of the absolute melting temperature were calculated for each alloy, and the 1000-hr rupture strength at these temperatures determined from its parameter plot. The resulting averaged iso-strength contours are shown in Fig. 27. The contours of Fig. 27 can now be considered on the basis of the other factors affecting strength.

Crystal Structure: This factor is probably related to the ease of deformation and can be considered on the basis of the number of possible slip systems (a stable function of the slip direction, since the slip plane may vary). On the basis of the number of possible slip directions, increasing hardness should occur in the order given in Table IV, assuming equality of all other factors.

Westbrook¹⁶ has shown that, based on extrapolated hardness at 0°K within experimental error, the differences in strength between pure nickel, iron, chromium, and cobalt due to crystal structure should be small, with the complex σ phase having a strength possibly several times greater. Experimentally, from Fig. 27, cobalt, iron, nickel, and chromium have similar strengths ranging from about 500 to 1300 psi. The complex Cr-Co σ structure is associated with two peaks at strengths of 8000 to 9000 psi.

Solid Solution Strengthening: Fundamental alloying characteristics of solid solutions are believed to be related to:

1—Relative Atomic Size of Constituents: Qualitatively, at least, larger differences in atom size, or more specifically, larger percentage of changes in lattice parameter per atomic percentage of solute addition, cause larger strengthening effects.^{14, 17-19} Solutes which decrease the lattice parameter appear to be more effective strengtheners than those which increase it.²⁰

2—Relative Compressibility of the Atoms: The smaller the compressibility of the solute atom with respect to the solvent atom, the greater the strain introduced in the lattice by solution and the strengthening is greater. The effect is probably a function of whether the change in lattice parameter is positive or negative. A large negative change in lattice parameter and a large negative difference in compressibility between the solvent and solute would have greatest effects.^{21, 22}

Each of the factors (atomic size and compressibility) vary periodically when plotted against the atomic number of the pure element. It is interesting to note that the solution-hardening effect can also be related periodically to the atomic number of the solute element.²³

In the Fe-Ni-Co system in Fig. 27, except for a small region near iron and extending toward cobalt, the alloys are entirely γ with the existing α near its maximum temperature (i.e., by raising the homologous fraction to 0.7 α would disappear), and for all other factors listed in Table II, the elements are very similar. Thus, a flat strength plateau is reasonable in this system.

Table IV. Order of Increasing Hardness

No.	Structure	No. of Slip Directions
1.	Face-centered cubic	6
2.	Body-centered cubic	4
3.	Hexagonal close-packed, c/a 1.6	3
4.	Hexagonal close-packed, c/a 1.9	3
5.	Other complex	3

The reason for the lack of a high peak in the equilibrium σ region of the Fe-Cr system in Fig. 27 is believed to be a result of the fact that iron and chromium form a nearly complete solid solution at this temperature (except for a small region of σ under equilibrium conditions at 50/50 ratio of Fe-Cr which was suppressed) and thus approach Fe-Ni-Co in character.

The Cr-Co maximum in Fig. 27 is associated with the σ phase existing at very high temperatures and, also, because chromium and cobalt are different with respect to the factors affecting solution hardening listed in Table III. Chromium is also an active element and combines readily with oxygen and nitrogen to form stable compounds which are difficult to reduce and, thus, impurities remain. Therefore, some hardening would be expected from impurities which represent an unisolated alloying factor.

The maximum strength in the Cr-Ni system in Fig. 27 is believed to be due to the alloying effect, since nickel and chromium are the most different of the metals considered in Table III, with limited mutual solubility.

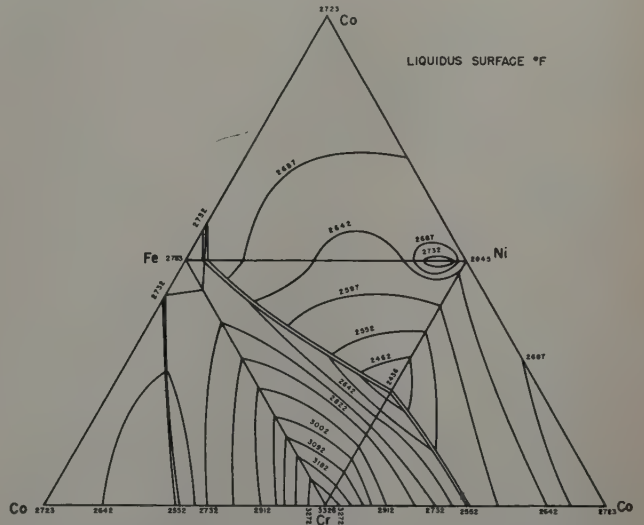


Fig. 26—Isothermal contours of liquid surface for ternary Fe-Ni-Cr-Co systems based on data of Kase,⁹ Pugh and Nisbet,¹¹ and Koster.¹² Eutectic troughs indicated by double lines.

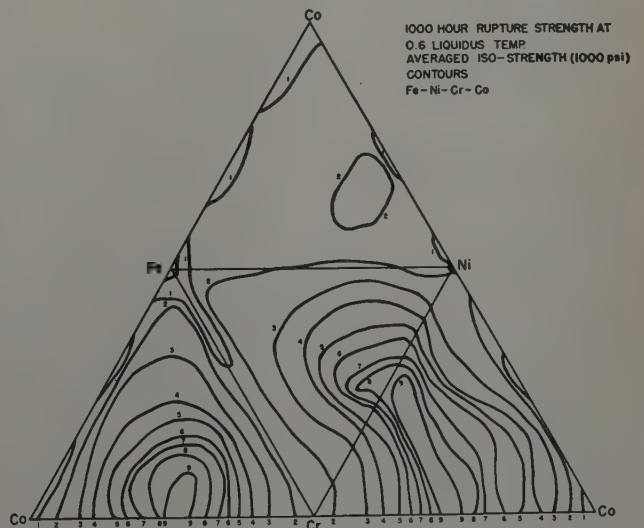


Fig. 27—Iso-strength contours for Fe-Ni-Cr-Co ternary systems indicating 1000 hr rupture strength at 0.6 liquidus temperature (°K) from parametric plots.

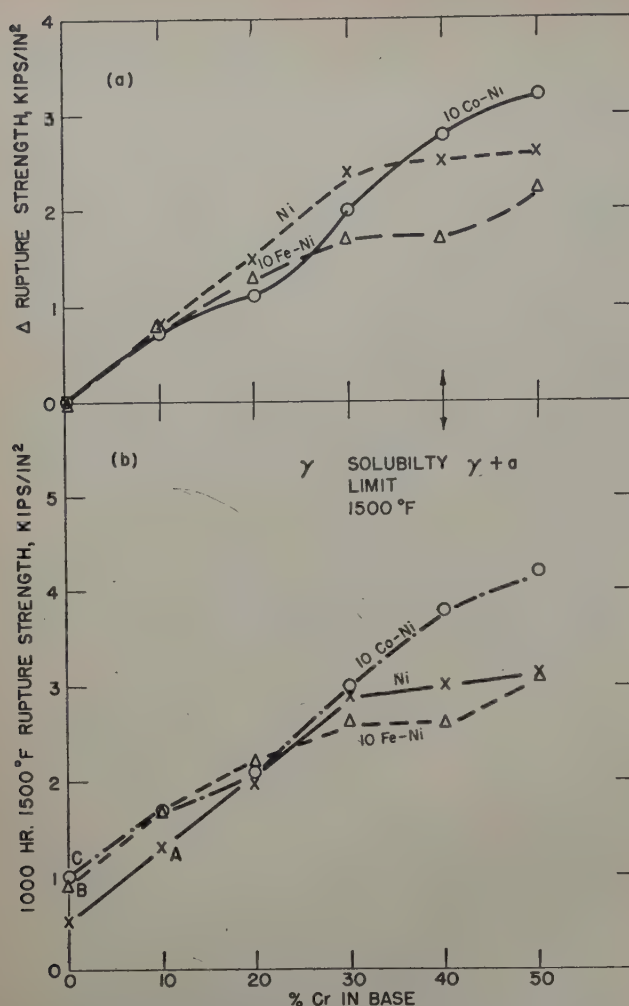


Fig. 28—Effect of chromium additions on the 1000 hr, 1500°F rupture strength of nickel with and without 10 pct Fe or 10 pct Co.

The factors controlling solution hardening also may be those which affect the limit of solid solubility. Solubility limits at 1500°F are approximately as follows:

- Ni-Co, Complete face-centered cubic
- Ni-Fe, Nearly complete face-centered cubic, small amount body-centered cubic Fe
- Ni-Cr, 35 pct Cr face-centered cubic
- Co-Cr, 18 pct Cr face-centered cubic
- Cr-Fe, Nearly complete body-centered cubic, small amount of σ
- Co-Fe, 22 pct Fe face-centered cubic.

According to these data, chromium is the element least soluble in nickel and consequently should be the most effective binary hardener. The solubility of chromium in cobalt is half of the solubility of chromium in nickel. Consistent with the concept that more limited solubility leads to more extensive solution hardening, in the presence of cobalt the strengthening of nickel due to chromium should increase. Iron, however, is extensively soluble in chromium, nickel, and cobalt at 1500°F. Larger amounts of more potent hardeners such as chromium or cobalt should be required in nickel to reach a given strength level with iron present than when iron is absent. This concept is consistent with the findings that alloy additions are not independent of one another, but that there are interactions between solutes as well as between the solvent and solute, as

illustrated in Fig. 28. Chromium is the most effective hardener of nickel (compare point A with points B and C). The strengths of the ternary Ni-Cr-Fe alloys with 10 pct Fe fall below the strengths of the binary Ni-Cr alloys of comparable alloy content. The strengths of the Ni-Cr-Co alloys with 10 pct Co reach values one-third higher than the Ni-Cr or Ni-Cr-Fe alloys. The strengths of these base alloys are least different from each other at the 20 pct Cr level found in many commercial alloys. This interaction effect indicates that when iron is used in large amounts compensatory additions of chromium and/or cobalt are necessary to maintain a given strength.

The interaction effects are more significant for the most effective addition elements and will be discussed in subsequent sections.

Relative Strengthening Effects of Incongruous Additions: For multiphase alloys, all of the above factors for solid solutions will apply to determine the inherent strength of each phase. Relative strengths, amounts, and distribution and condition of the phases will determine the strength of the alloy and will be modified by temperature and strain history, as they control the several factors such as strain aging, strain hardening, allotropic transformation, precipitation hardening, recovery, recrystallization and grain size.^{17, 24-26}

The strengthening of the various incongruous additions was obtained by subtracting the base strength from the strengths of the alloys containing incongruous elements. These results reflect the general relative strengthening effects of the various additions.[†]

[†] It is clear that the experimental work did not include a sufficiently wide composition range of all incongruous alloys for their maximum effects to be considered comparable. In addition, the order of strengthening when compared on the basis of the maximum effects (regardless of amount) is not the same as that when the comparative strength is considered at low concentrations and at constant amounts. It is also believed that the strengthening effect reaches a maximum and usually falls off at higher concentrations of incongruous elements.

From these data on the basis of comparing maximum effects the decreasing order of effectiveness appears to be as follows: 1—tantalum and tungsten, 2—columbium and molybdenum, 3—zirconium and titanium, 4—carbon, 5—aluminum which has been treated with carbon, 6—beryllium and aluminum, 7—vanadium, and 8—oxygen and nitrogen. The greatest strengthening effects come from the *high melting* incongruous additions, tungsten, tantalum, columbium, and molybdenum. Among these four, the element with the *largest atomic diameter*, tantalum, is most effective. The next most effective additions are titanium and zirconium which are widely different from the base alloy in terms of atomic diameter, but similar in terms of melting point. This order suggests that the most important characteristic, aside from *melting point*, is a difference in *atomic diameter*. Beryllium which has a lower melting point than the base elements is the next in order of effectiveness and aluminum which has the lowest melting point and vanadium which has the smallest difference in atomic diameter are least effective. The effects of carbon, nitrogen, and oxygen are somewhat uncertain because deoxidizing effects partly mask the true strengthening and the data are limited. Also, they are probably interstitial and exhibit characteristics different from the substitutional incongruous elements. The results on simultaneous additions of carbon with titanium or tantalum clearly emphasize the complex effects

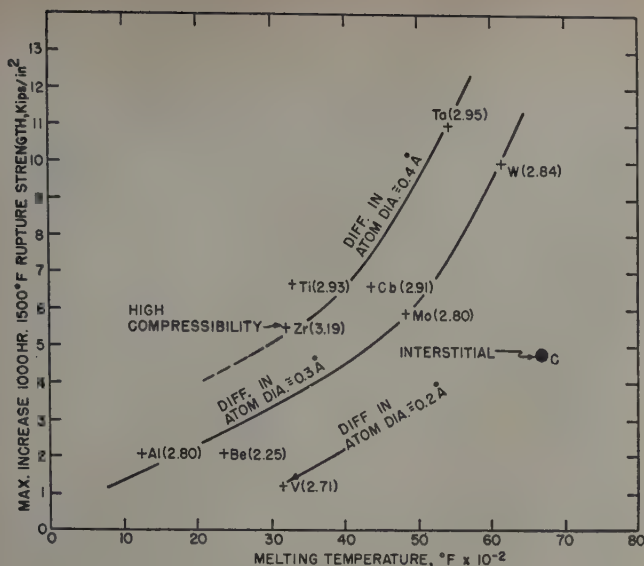


Fig. 29—Correlation between the maximum increase in 1000 hr, 1500°F rupture strength due to single addition of incongruous elements to selected base alloys with the melting temperature and atomic diameter of the incongruous element.

possible from multiple alloy additions found in commercial alloys. They also suggest that the best commercial alloys may be those where the interaction effects are most pronounced. The multiple incongruous elements added should have high melting points, high compound forming tendencies and low solubility in each other as well as low solubilities in the base elements, and the compounds formed should be very stable.

In Fig. 29, the maximum strengthening effect of each incongruous element obtained in these tests is plotted against its melting point. The data points are connected according to the difference in atomic diameter between the incongruous element and the base (except for the interstitial element carbon, for which the atomic diameter is not certain). This family of curves clearly indicates the strengthening effects of high melting elements with large differences in atomic size. Zirconium has a somewhat lower strengthening effect than would be predicted from its melting point or atomic diameter, probably because of its high compressibility. The effect of valence is not apparent, probably because most of these elements are transitions or because valence difference for these elements is a less important factor in hardening.

The significance of the relationship in Fig. 29 may be further clarified by reference to studies of magnesium alloy systems, where the phase diagrams are well documented. Fig. 30 is based on magnesium alloy binary systems in which the terminal magnesium-rich solid solution is in equilibrium with intermetallic compounds forming directly from the liquid. For these systems, the melting temperature of the intermetallic compound is related directly to the melting temperature of the addition element (with the exceptions Mg_2Sn and Mg_2Cu). It has been shown²⁸ that the higher melting point compounds (and from Fig. 30 high melting point alloying elements) are associated with high eutectic temperatures, low eutectic compositions, and low maximum solubility limits. Thus, the results in Fig. 29 suggest that the addition of higher melting point elements results in the formation of higher melting point compounds which are more effective

hardeners at 1500°F than lower melting point elements which form lower melting point compounds.

Alloying Principles

The complex alloys used at high temperatures may be considered as consisting of a solid solution matrix or base alloy to which incongruous elements are added to saturate and strengthen the solution and to form second phases.

In this paper, the strength of the base alloys has been explained in terms of the relative solution-hardening effects of solute elements on the strength of the solvent element. It has been shown that the largest strengthening effect is obtained by the addition of solute elements which are least soluble in the solvent element and most unlike it with respect to atomic diameter, compressibility, and crystal structure. Supplementary strengthening results from interaction effects due to combinations of solute elements which are unlike each other and emphasize these mutual differences with the solvent element. Addition elements, on the other hand, which are completely soluble with all other constituent elements at high temperatures and are intermediate among them in atomic characteristics, tend to decrease the strengthening characteristics of more potent hardeners.

The crystal structure is an important factor associated with the differences in strength of alloys as it is related to the ease of deformation and to allotropic transformations. Strong alloys result from complex crystal structures which are stable at operating temperatures.

Other things being equal, the strength of an alloy is significantly influenced by the testing temperature in terms of the fraction of the absolute melting point. A careful compromise in composition is usually necessary since alloy additions usually lower the melting temperature.

The largest strengthening effects were obtained from incongruous elements with high melting points and large differences from the base elements with respect to atomic diameter. These elements have low compressibility and tend to form compound-

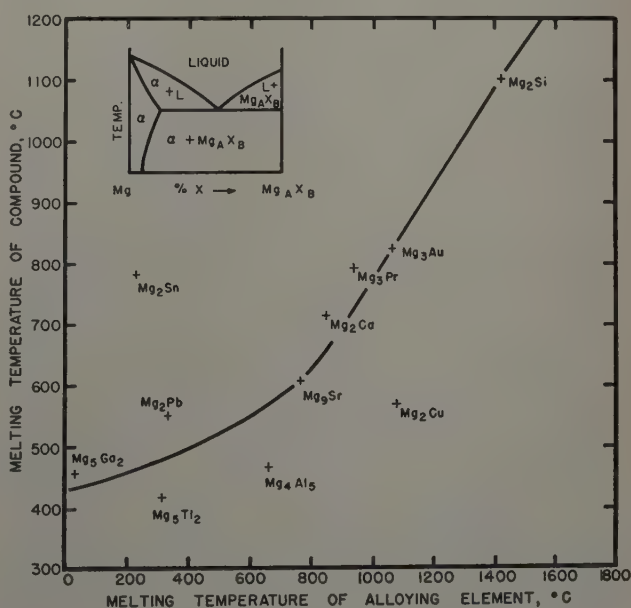


Fig. 30—Correlation between the melting temperature of magnesium compounds of the type indicated in the phase diagram and the melting temperature of the alloying elements.

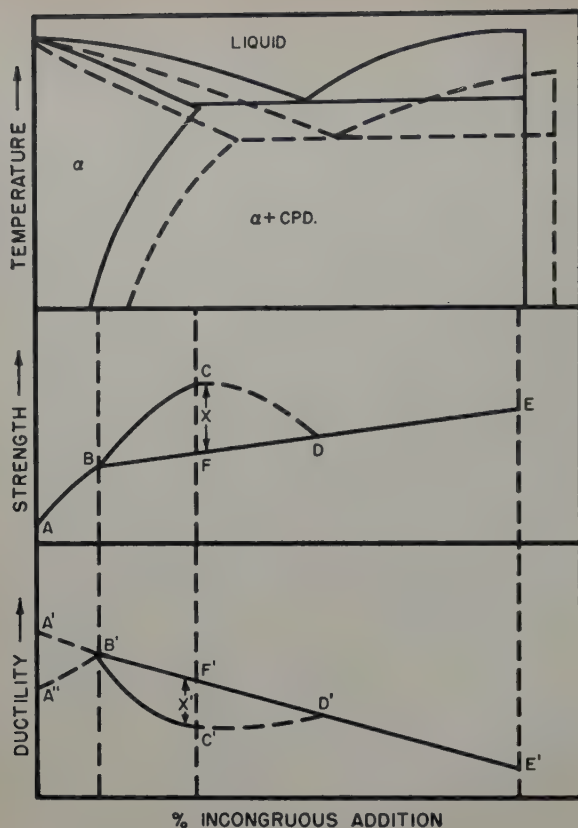


Fig. 31—Schematic relationships between the phase diagrams, strength, and ductility of base alloys with incongruous additions.

type phases with the base metals. Although pertinent phase diagrams are not available for discussion, it appears that the effective incongruous elements are relatively insoluble in the base alloys and small additions serve to complete the saturation of the matrix phase with a more prominent solution-hardening effect than that associated with any of the base elements at saturation compositions. In addition, these elements form supplementary phases which produce age hardening. The most effective age-hardening temperatures were higher for alloys having higher melting incongruous elements which maintained their hardening effects at the test temperature as compared to lower melting incongruous elements whose structures usually overaged and softened at the test temperature. Alloys which age harden at temperatures well above the test temperature exhibit improved ductility as compared to those which age harden at the test temperature. The strengthening effect of some incongruous elements passed through a maximum as a function of composition in a manner which suggests that the presence of insoluble stable second phases is not necessarily desirable for age-hardening-type alloys. (The ductility of these "overalloyed" materials is very low and this brittleness may result in an apparent low strength.) Maximum strength may occur near the maximum limit of solubility and this suggests the advantages of strengthening by age hardening as compared to the strengthening associated with equilibrium multiple phases. The phenomenon emphasizes the apparent effectiveness of small optimum amounts of incongruous elements within the maximum solid solubility limit as compared to large additions producing massive second phases. The latter may be considered as overalloy-

ing. These considerations lead to generalizations relating strength, ductility, and composition presented in Fig. 31.

In Fig. 31a, the solid line represents the constitution diagram formed with a high melting element as compared to the dashed lines which represent the diagram formed with a low melting element. Fig. 31b is based on the ideal relationships of Mehl and Jetter²⁰ for age hardening of alloys from the phase diagram in Fig. 31a (solid lines). AB represents solution hardening, BDE represents the overaged or equilibrium strengthening excluding the possible effect of particle size. BCD represents the age-hardening effect, and X is the maximum strengthening due to age hardening. It is possible, therefore, to obtain strengths within the range BD to BCD, depending upon the treatment used or the stability at high temperatures. The corresponding changes in ductility are indicated in Fig. 31c. In the range of solid solubility, sometimes the ductility is increased with increasing additions (A'B') and in some systems it is decreased (A'B'). In any case, the optimum combinations of strength and ductility probably occur in alloys near the maximum solubility limit.

These schematic diagrams are substantiated by the findings of this research that high melting incongruous addition elements are associated with low maximum solubilities occurring at high temperature, which are related to pronounced solution-hardening and age-hardening effects. The age-hardening peak in the strength plot is also related to the maximum limit of solubility and for high melting additions should occur at a high aging temperature and thus be stable at a high service temperature. The schematic ductility plot suggests that little strength is gained and considerable ductility is lost beyond the composition of the maximum solubility limit. In addition, forging difficulties might be more pronounced with alloys which are multiple phase at forging temperatures. These effects can be derived with some consistency from the effects of single incongruous additions considered in this paper. The application of these principles to complex multiple-component commercial high temperature alloys with uncertain phase diagrams and interactions with respect to strengthening and embrittling effects are as yet obscure and require considerably more fundamental data than are now available.

Summary

1—The high temperature properties of binary ternary, and quaternary Ni-Cr-Co-Fe alloys and the effects of single additions of incongruous elements have been analyzed using the $T(C + \log t)$ parameter, (a) to determine the 1000 hr, 1500°F rupture strength from tensile and rupture tests from room temperature to 2000°F, (b) to characterize the variety of alloys as follows: (1) solid solution alloys, (2) allotropic transformation alloys, (3) precipitation hardening alloys, and (4) multiple phase alloys, and (c) to emphasize the importance of such factors as relative melting points, relative atom sizes, recrystallization and recovery, and their interactions.

2—The strength of these alloys can be rationalized on the basis of strengthening effects related to fundamental characteristics of the components and their possible phase relationships.

3—Nickel-rich solid solutions are hardened more

effectively by chromium than by cobalt or iron. Solute additions are not mutually independent, but interaction effects, generally positive for cobalt and negative for iron, indicate that variations in base composition require quantitative compensation to maintain a given strength.

4—Several factors influence ductility, including: alloy content, crystal structure, temperature at which fracture changes, temperature dependence of precipitation hardening, temperature of allotropic transformation, deoxidation practice, recovery, and recrystallization.

5—In the design of alloys for high temperature applications, it appears that the characteristics of the base alloy should include: (a) Solid solutions as nearly as possible saturated at the temperatures of maximum solubility with the most potent solution-hardening elements (i.e., large differences in atom diameter, valency, compressibility, and minimum solubilities). (b) The most complex structures consistent with acceptable ductility. (c) The highest melting alloys, preferably for service at temperatures < 0.5 melting temperature. (d) Since solution-hardened alloys are usually lower melting unless they form peritectics and since complex structures are not readily fabricated, the optimum compromise between all of these factors should be sought. In seeking this compromise, it should be remembered that solution-hardening elements in addition to raising the base strength also increase the amount of strain hardening and raise the recrystallization temperature. These factors in part counteract the lowering of the melting point.

6—The relative strengthening effects of various incongruous additions appear to be related to the melting point of the incongruous addition, to the difference in atom diameter between the incongruous addition and the base and probably to the compressibility. The high melting point of the incongruous addition probably reflects itself in the melting point of the compound formed during age hardening. This effect was particularly apparent in the simultaneous additions of carbon and titanium or tantalum which formed high melting carbides and produced the largest amount of strengthening found.

7—A limited amount of data on simultaneous additions of carbon and titanium or tantalum suggests that when the incongruous elements have large interaction effects their strengthening effect upon a base will be considerably different from that obtained from individual elements.

8—It was found that several of the alloy additions had purifying effects on the base as indicated by a lowering of the base strengths.

Acknowledgment

The authors wish to express their appreciation to members of the Metallurgy Research Dept. of the General Electric Research Laboratory and particularly to the many laboratory assistants who performed most of the tests and compiled a great deal of the data reported. The advice of W. E. Ruder, A. H. Geisler, and J. H. Westbrook is particularly appreciated.

References

- ¹ J. D. Nisbet: Producing High Purity Metals with Vacuum. *Iron Age* (June 19, 1947) p. 56.
- ² J. D. Nisbet: Vacuum Melting Techniques. *Iron Age* (March 18, 1948) p. 79.
- ³ J. D. Nisbet: Rupture Testing in a 48-Bar Furnace. *Iron Age* (February 12, 1948) p. 81.

⁴ F. R. Larson and J. Miller: A Time-Temperature Relationship for Rupture and Creep Stresses. *Trans. ASME* (1952) **74** (5) p. 765.

⁵ J. H. Hollomon and L. D. Jaffe: Time-Temperature Relations in Tempering Steel. *Trans. AIME* (1945) **162**, p. 223.

⁶ P. Grün: Creep of Steels as a Function of Alloy Content and Heat Treatment. *Arch. Eisenhutt.* (1934) **8**, p. 205.

⁷ A. R. Elsea and C. C. McBride: The Effects of Nitrogen, Iron or Nickel Upon the Alpha-Beta Transformation and Gamma Precipitation in Cobalt-Chromium Alloys. *Trans. AIME* (1950) **188**, p. 154; *JOURNAL OF METALS* (January 1950).

⁸ *Metals Handbook*. Sections on constitution diagrams. (1948) Cleveland, ASM.

⁹ T. Kasé: On the Equilibrium Diagram of the Iron-Nickel-Cobalt System. *Sci. Rpt. Tohoku Univ.* (1927) **16**, p. 496.

¹⁰ W. D. Manley and P. A. Beck: The Sigma Phase in Ternary Cr-Co-Fe and Cr-Co-Ni Alloys. *Trans. AIME* (1949) **185**, p. 354; *JOURNAL OF METALS* (June 1949).

¹¹ J. W. Pugh and J. D. Nisbet: A Study of the Iron-Chromium-Nickel System. *Trans. AIME* (1950) **188**, p. 268; *JOURNAL OF METALS* (February 1950).

¹² W. Köster: The System Iron-Cobalt-Chromium. *Arch. Eisenhutt.* (1932) **6**, p. 113.

¹³ S. Rideout, W. D. Manley, E. L. Kamen, B. S. Lement, and P. A. Beck: Intermediate Phases in Ternary Alloy Systems of Transition Elements. *Trans. AIME* (1951) **191**, p. 872; *JOURNAL OF METALS* (October 1951).

¹⁴ C. Lacy and M. Gensamer: The Tensile Properties of Alloyed Ferrites. *Trans. ASM* (1944) **32**, p. 88.

¹⁵ U. S. Patent 2,564,498.

¹⁶ J. H. Westbrook: Temperature Dependence of the Strength of Pure Metals. *Trans. ASM* (1953) **45**, p. 221.

¹⁷ O. D. Sherby, R. A. Anderson, and J. E. Dorn: Effect of Alloying Elements on the Elevated Temperature Plastic Properties of Alpha Solid Solutions of Aluminum. *Trans. AIME* (1951) **191**, p. 643; *JOURNAL OF METALS* (August 1951).

¹⁸ R. M. Brick, D. L. Martin, and R. P. Angier: Effects of Various Solute Elements on the Hardness and Rolling Textures of Copper. *Trans. ASM* (1943) **31**, p. 675.

¹⁹ J. E. Dorn, P. Pietrowsky, and T. E. Tietz: The Effect of Alloying Elements on the Plastic Properties of Aluminum Alloys. *Trans. AIME* (1950) **188**, p. 933; *JOURNAL OF METALS* (July 1950).

²⁰ A. P. Gulyeav and E. F. Trusova: Relationship in the Variations of the Properties of Solid Solutions. *Zhur, Tekhn, Fiziki* (1950) **20** (1) p. 66.

²¹ R. F. Mehl: Interatomic Forces in Metals and Alloys. *Trans. AIME* (1928) **78**, p. 405.

²² J. H. Frye, J. W. Caum, and R. M. Treco: Hardness and Lattice Stress in Solid Solutions. *Trans. AIME* (1943) **152**, p. 83.

²³ A. P. Gulyeav: Periodicity of the Influence of Alloys on the Mechanical Properties of Metals. *Doklady Akad. Nauk. SSSR* (1950) **75**, p. 25 (cf. *Chemical Abstracts* (1950) **44**, 8710f).

²⁴ J. D. Lubahn: Strain Aging Effects. *Trans. ASM* (1952) **44**, p. 643.

²⁵ J. D. Lubahn: Simultaneous Aging and Deformation in Metals. *Trans. AIME* (1949) **185**, p. 702; *JOURNAL OF METALS* (October 1949).

²⁶ B. L. Averbach: The Effect of Plastic Deformation on Solid Reactions. Part I Diffusion Reactions. *Trans. ASM* (1949) **41A**, p. 262.

²⁷ A. Beck: *Magnesium and Its Alloys*. (1940) London. R. A. Hughes and Co.

²⁸ L. A. Carapella: Fundamental Alloying Nature of Magnesium. *Metals Progress* (August 1945) p. 297. (A review of investigations primarily by W. Hume-Rothery and G. V. Raynor.)

²⁹ R. F. Mehl and L. K. Jetter: The Mechanism of Precipitation from Solid Solution. The Theory of Age Hardening. *Symposium of Age Hardening* (1940) Cleveland. ASM.

Subgrain Formation in High-Purity Aluminum During Creep At High Temperatures

by Andre M. Gervais, John T. Norton, and Nicholas J. Grant

An investigation of the creep deformation of coarse-grained high-purity aluminum at temperatures approaching the melting point permitted the formulation of a theory of subgrain formation. Subgrain boundaries were found to be formed by two different processes: kinking and polygonization. Polygonization is considered as the main factor in subgrain formation.

SINCE "slipless flow" was first discussed in detail by Hanson and Wheeler,¹ many studies have been undertaken to determine how metals deform at high temperatures. Several types of observations have been reported. Jenkins and Mellor,² working on the creep of mild steels and various grades of commercial irons, found metallographic evidence of a kind of substructure within the grains after deformation at high temperatures. Homes³ observed after creep deformation of steel at high temperatures that the original X-ray spots were sharply divided into several small ones. The same phenomenon was reported by Hirst⁴ from his studies on lead and later by Crussard⁵ from his work on aluminum.

The works of these investigators demonstrated beyond any doubt that the splitting of the X-ray spots was due to the fact that the grains underwent a division into subgrains during deformation at high temperatures.

Since then, numerous experiments have been undertaken on aluminum in order to determine the mechanism of formation of subgrains. Research workers can be divided, for the purpose of discussion, into two different groups as regards thinking on subgrain formation.

On one hand, based on the work on polygonization by Cahn,⁶ Guinier and Lacombe,⁷ Greenough and Smith,^{8,9} Crussard,^{10,11} and Servi, Norton, and Grant,¹² it was concluded that subgrain formation was a consequence of the simultaneous effects, first, of inhomogeneous deformation which produced bending of the lattice, and second, polygonization.

On the other hand, Wood and coworkers¹³⁻¹⁶ based their work on the results of an earlier report¹⁷ which dealt with crystallite size and a fragmentation theory. It is interesting to note that while Greenough and Smith⁸ and Wood et al. performed similar experiments, their conclusions were quite different. Wood et al. did not recognize polygonization as a fundamental mechanism and said that aluminum, at the beginning of the deformation, fragmented immedi-

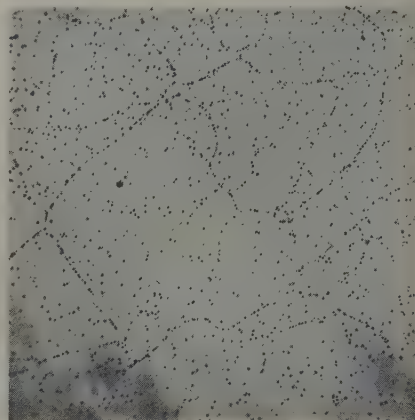


Fig. 1—Region in a grain of specimen 2 deformed by creep at 1150°F and at a stress of 45 psi. Total elongation 4.7 pct. Surface as revealed by etch pit technique after electrolytic polishing. The etch pit network represents the subgrain boundaries. X50. Area reduced approximately 50 pct for reproduction.

ately into subgrains in order to permit deformation of the metal, the number of these subgrains being a function of strain rate and temperature. They concluded that deformation of grains occurred by flow along the subgrain boundaries.

In view of the contradictory conclusions, it would appear that the data were not explicit enough to provide an unambiguous conclusion. It appears that the techniques by which most of the results were obtained, namely, X-ray work, were not enough by themselves to solve the problem.

Another approach was needed. In the present research, therefore, an extensive metallographic study was planned to supplement the X-ray work. The importance of revealing the subgrain boundaries metallographically was realized, and this will explain the extensive development and use of etching techniques. In order that subgrains would be considerably larger and therefore more readily visible under a microscope, the creep experiments were performed at very high temperatures approaching the melting point of aluminum.

Development of Experimental Technique

Creep tests were run at constant load on high purity (99.995 pct) aluminum specimens having a very coarse grain size. None of the specimens was run to fracture. The specimens were originally round (diameter, 0.187 in.; gage length, 1 in.) and had parallel flats milled in the gage section to permit

A. M. GERVAIS, Student Associate AIME, formerly Research Assistant MIT, is now with the Societe Commentry-Fourchambault et Decazeville, Imphy (Nievre), France, and J. T. NORTON and N. J. GRANT, Members AIME, are Professor and Associate Professor, respectively, Dept. of Metallurgy, Massachusetts Institute of Technology, Cambridge, Mass.

Discussion on this paper, TP 3620E, may be sent, 2 copies, to AIME by Dec. 1, 1953. Manuscript, April 14, 1953. Cleveland Meeting, October 1953.

This paper is based on a thesis by A. M. Gervais submitted in partial fulfillment of the requirements for the degree of Doctor of Science in Metallurgy to the Massachusetts Institute of Technology, February 1953.



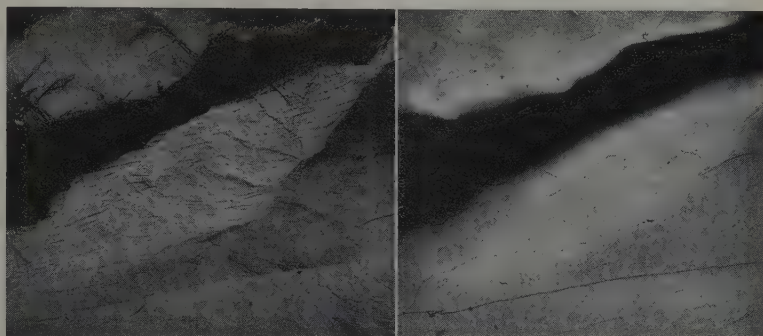
a—Film to specimen distance was 3 cm. b—Film to specimen distance was 15 cm.

Fig. 2—Laue back-reflection photographs with X-ray beam located in the region indicated by Fig. 1. No division of spots is observed, only marked asterism in Fig. b.

Fig. 3—Region of specimen 11 deformed by creep at 1150°F and at a stress of 90 psi. Total elongation 4.2 pct. Agreement between patterns is seen in both pictures (the black band, shadow, is due to grain boundary sliding and migration). X50. Area reduced approximately 50 pct for reproduction.

a (left)—Surface after deformation (very fine black markings are cracks in the oxide skin).

b (right)—Same location after careful electrolytic polishing and electrolytic etching.



easier metallographic and X-ray observations. The final thickness between the milled flats was 0.120 in. and the final gage length 0.85 in.

The specimens were annealed at 1150°F for at least 15 hr to obtain a coarse grain size. This coarse grain size was obtained by direct grain growth and not by strain-annealing, to avoid the introduction of any deformation which would affect the results. In order to prevent bending of the gage length during annealing, the specimens were placed flat on a bed of alumina powder contained in a boat.

Extensive grain boundary migration during creep at high temperatures was minimized by using such coarse grained specimens. Due to the limited amount of grain boundary migration with respect to the size of the grains, metallographic and X-ray observations were easily performed on the same grain during a series of several experiments.

Many tests were run but only the typical cases are reported. Among the several hundreds of micrographs and X-ray patterns taken during this research only those related to the typical cases are presented.

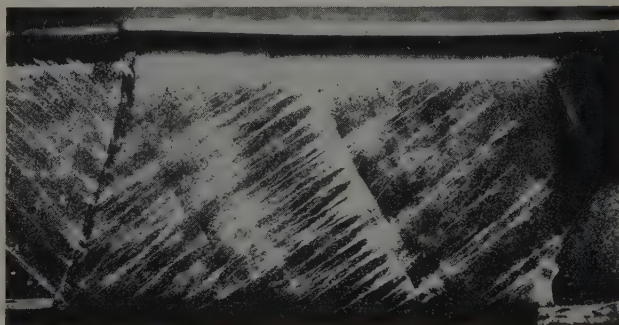
At the beginning of this research some effort was devoted toward improving X-ray techniques. Monochromatic radiation was not suitable for very refined work on this subject. In agreement with Bragg's law, spots produced by some elements could appear or disappear with a slight change in orientation of these elements during deformation. Consequently, it was not possible to follow step by step the evolution of a spot, that is to say, of the element of the structure that produced this spot. Therefore, the Laue technique using white radiation was adopted in these investigations. The grains were considerably larger than the X-ray beam itself, which permitted

the beam to be located entirely within a single grain, if desired.

Guinier and Tennevin¹⁸ refined the X-ray technique by using a focusing Laue transmission technique so that neighboring elements differing in orientation by even 10 sec of arc could be resolved. In the present work the above technique could not be used because it requires very thin specimens having thicknesses of the order of less than 0.5 mm. Such thin specimens were not adequate for creep work because the specimen surface was too large with respect to its volume and consequently the influence of the surface would be too great. Furthermore, the handling of such thin specimens during creep testing could result too easily in bending and thus modify and color the results.

Therefore, the Laue back-reflection technique had to be used, but in such a case no focusing was possible. The ordinary method was improved for some of the determinations by increasing the film to specimen distance from 3 to 15 cm. The collimator length

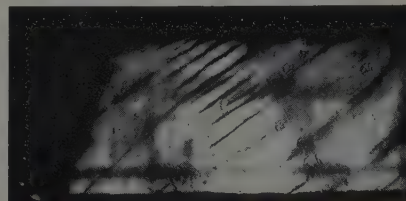
was also increased to decrease the divergence of the X-ray beam. The first problem with this apparatus was the very long exposure time (about 10 hr) which was required. The second was that the resolving power was not high enough in all cases to reveal the subgrains. A clear example of this is shown in Figs. 1 and 2. Fig. 1 shows the microstructure of a typical test specimen, the subgrains being revealed by an etch pit technique which will be described later. Fig. 2a is a Laue back-reflection



a—Surface after deformation (oblique illumination).

Fig. 4—Kink band in a grain of specimen 10 deformed by creep at 1150°F and at a stress of 90 psi. Total elongation 4.3 pct. X11. Area reduced approximately 50 pct for reproduction.

b—Surface after careful electrolytic polishing and electrolytic etching (direct illumination). Kink band boundaries are clearly revealed by electrolytic etching.



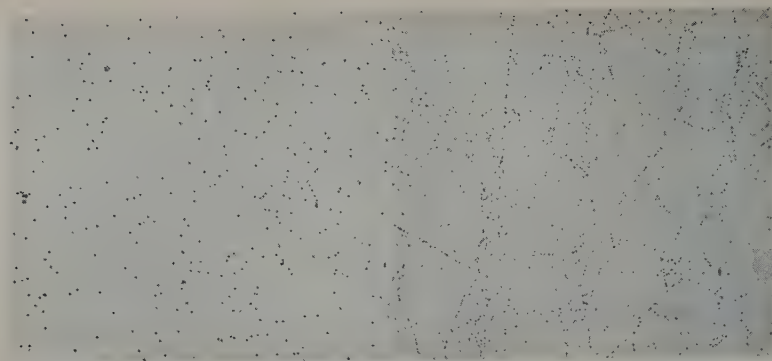


Fig. 5—Region of a grain of specimen 13 as revealed by etch pit technique after electrolytic polishing. X50. Area reduced approximately 50 pct for reproduction.

a (left)—After annealing at 1150°F, before deformation.

b (right)—After deformation by creep at 1150°F and at a stress of 70 psi. Total elongation 5.1 pct. Note the etch pit network.

photograph (film to specimen distance of 3 cm) with the X-ray beam located in the same region shown in Fig. 1. Fig. 2b is a Laue back-reflection photograph (film to specimen distance of 15 cm) with the X-ray beam located at the same spot. The asterism is marked in the second case, but still no subgrains are indicated by this refined technique in spite of the fact that subgrains are quite evident (Fig. 1). From this it can be concluded that the Laue back-reflection technique alone is inadequate to measure or detect all the changes taking place. An X-ray

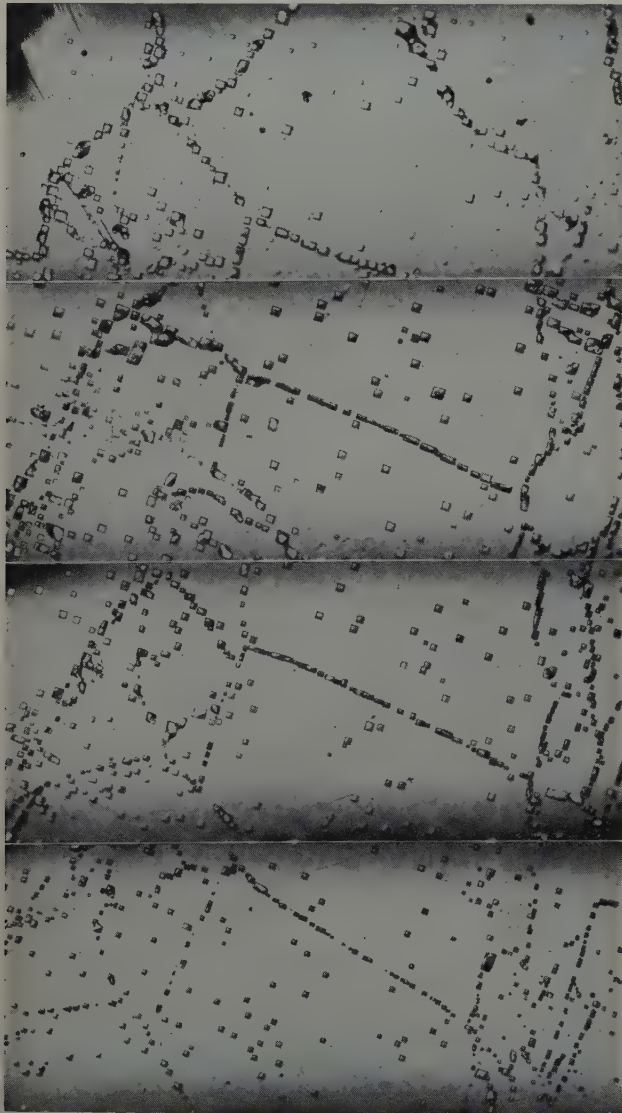


Fig. 6—Gradual change in substructure as 0.001 inch of metal is removed successively from the surface after each repolish and etch. HCl, HF, HNO₃, in alcohol. a—top. b—second from top. c—second from bottom. d—bottom. X100. Area reduced approximately 50 pct for reproduction

microbeam technique²⁰ was not used because its resolving power does not seem to be superior to that of the other techniques.

Polarized light,^{20, 21} used for similar research, was not utilized here because it appeared that the results obtained with this very delicate technique were approximately identical to those obtained by electrolytic etching, a very simple technique. After electrolytic polishing of the specimens in the Jacquet solution²² (2/3 acetic anhydride + 1/3 perchloric acid) at a voltage of about 30 v, the specimens were kept in the same solution at a temperature of about 20°C and at a very low voltage of about 2 v for 1 hr or more.

After deformation, the untouched surface of the specimen revealed boundaries as shown in Fig. 3a. These boundaries are revealed more precisely by the electrolytic etching as seen in Fig. 3b, but do not have the same intensities indicated in Fig. 3a. This is due to the fact that there is a selective appearance of these boundaries which is related to the difference in angle between the blocks. The greater the difference, the more distinct do the boundaries appear. Electrolytic etching, when applied similarly to grains containing kink bands,²³ revealed that the kink band boundaries were sharp and that rather important differences in orientation were present as shown in Fig. 4. This relationship between sharp bending and kinking will be discussed later.

The etch pit technique was a modification of the one devised by Lacombe and Beaujard²⁴ to show subgrain boundaries in the case of polygonization.²⁵ The specimens were etched after careful electrolytic polishing. The chemical composition of the etching reagent was as follows: methyl alcohol, 50 cc; hydrochloric acid, 32 cc; nitric acid, 50 cc; and hydrofluoric acid, 2 cc.

The reagent was cooled in an ice bath during preparation and a fresh solution was made each time. The etching was performed at a temperature of about 10°C. As established before²⁴ the rate of growth of the etch pits varied with the orientation of the surface of the grain; very fast for a surface parallel to (111), slow for a surface parallel to (100). Consequently, no specific etching time could be defined, every grain having its own optimum etching time. Therefore, this method was sometimes tedious.

A reproducible network was not revealed by the etch pits on a specimen after annealing at 1150°F and before deformation (Fig. 5a) but after creep deformation at the same temperature of 1150°F a very clear reproducible network is apparent (Fig. 5b). Consequently the relation between deformation and the etch pit network is very evident.

The main question was whether etching with this reagent revealed the existing structure accurately. Fig. 6 shows a region of a specimen deformed at 1200°F and then polished and etched four times so

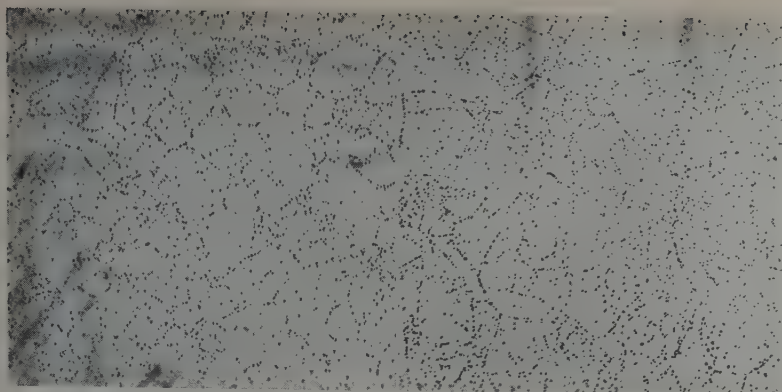


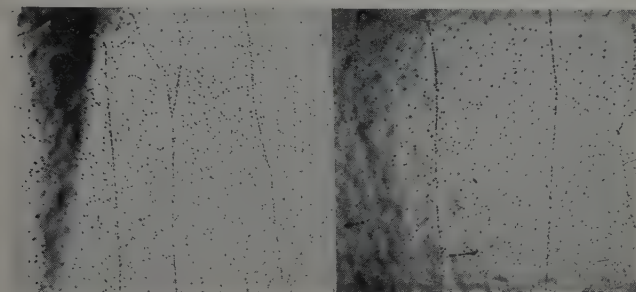
Fig. 7—Specimen 1 deformed by creep at 1150°F and at a stress of 50 psi. Total elongation 6 pct. Etch pit technique after electrolytic polishing. X50. Area reduced approximately 50 pct for reproduction.

a—Region of a grain on the surface of the specimen.

b—Region of the same grain in cross section. Note similarity of subgrain size in both directions.

that after each electrolytic polishing, about 1/1000 in. was removed. The four pictures show the substructure of the same area located by a small prior identification scratch. It is easy to recognize the same etch pit subgrain network and to follow the progressive changes in depth. Fig. 7a shows the front surface of a creep deformed specimen after being etched by the etch pit technique and Fig. 7b shows the surface of the cross section at right angles to this area. This shows that subgrains are formed through the whole thickness of the specimen, and are on the average about the same size.

Another example of the nature and utility of this network of etch pits is given by the following ex-



a—Convex side.

b—Concave side.

Fig. 8—Grain of specimen slightly bent by sagging during annealing at 1150°F, polished and etched. The etch pit boundaries are perpendicular to the axis of the specimen. X25. Area reduced approximately 50 pct for reproduction.

periment. A very coarse-grained specimen was slightly bent under its own weight during annealing at 1150°F, the axis of bending being parallel to the flat milled surface of the specimen and perpendicular to the axis of the specimen. Fig. 8 shows the two opposite surfaces of one of the grains of the specimen after polishing and etching, Fig. 8a showing the convex side and Fig. 8b the concave side. The lines of etch pits are perpendicular to the axis of the specimen, that is, parallel to the bending axis.

X-ray diffraction confirmed that the etch pits in Fig. 8 were located at the boundaries of two blocks which had a slight difference in orientation caused by the curvature of the specimen due to bending. Every spot of the Laue back-reflection photograph (Fig. 9a) taken on the convex side was sharply divided into two parts and this separation line was perpendicular to the specimen axis, that is to say, parallel to the etch pit lines. A schematic explanation of the division of the X-ray spots is given in Fig. 9b. In such an experiment no errors were introduced because the X-ray beam could not hit more than two subgrains delineated by the etch pits.

This illustrates very well the process of polygonization as described by Cahn⁸ where dislocations move to surfaces (walls of dislocations) in order

to occupy a state of lower energy.²⁶ Ramsey²⁷ was opposed to polygonization because he did not believe that dislocations of the same sign could move in opposite directions toward these surfaces. Actually the dislocations can move in any direction since their final state would be one of lower energy.

Because etch pits have a certain size, or range of sizes, the minimum subgrain size that could readily be detected under a microscope after etching with the reagent had to be much larger than the etch pit size. In the present work, therefore, the range of deformation temperatures for which subgrains could be easily observed and studied was rather limited; that is, it was only above a certain minimum temperature that the subgrain size was large enough to be revealed distinctly by the etch pit technique.

It must be pointed out that, at first, it was quite difficult to see any relation between the results of the two different etching techniques (etch pit and electrolytic) because of the high density of subgrain boundaries shown by the etch pit technique with respect to that indicated by electrolytic etching.



Fig. 9a—Laue back-reflection photograph of the convex side of the grain in Fig. 8a. Spots are sharply divided in their middle.

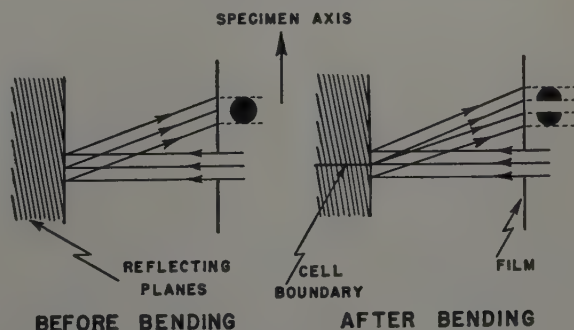


Fig. 9b—Schematic representation of the division of the X-ray spots of Fig. 9a.



Fig. 10—Region of a grain of specimen 10 deformed by creep at 1150°F and at a stress of 35 psi. Total elongation 6.9 pct. Boundary network in Fig. a is confirmed in Fig. b (indicated by arrows in several more prominent locations). X50. Area reduced approximately 50 pct for reproduction.

a (left)—Electrolytic etching after careful electrolytic polishing.

b (right)—Etched with the etch pit reagent after careful electrolytic polishing.



However, a relation was found between these two types of networks, as shown in Fig. 10. It is possible, as indicated by the arrows, to identify the pattern of subgrain boundaries revealed by electrolytic etching within the pattern of subgrain boundaries revealed by using the etch pit technique.

Fig. 11 shows three micrographs of an area after deformation, after polishing and electrolytic etching, and after polishing and etching with the etch pit technique. In this case it was not as easy to match the patterns obtained by the two etching techniques as it was for the case presented in Fig. 10, where the subgrain size was much larger (i.e., the number of subgrain boundaries and hence the number of etch pits were less).

Since it had been indicated before that the boundaries revealed by electrolytic etching were related to the boundaries seen on the surface after deformation, it is, consequently, possible to correlate these boundaries with those revealed by the etch pit technique.

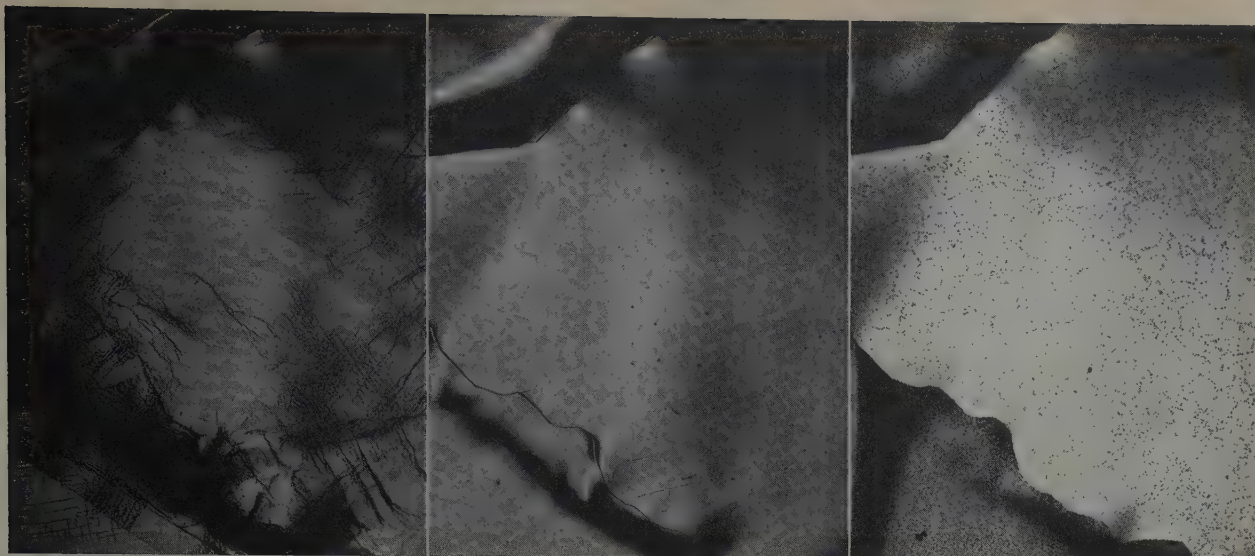
Mechanism of Subgrain Formation

After deformation, when one looks at a region in a grain, the boundaries appear to separate dark regions from light regions, this difference in illumination being due to the sudden change in orientation across these boundaries. This type of boundary is somewhat similar in appearance to the ideal kink band boundaries previously described,²³ but is different in that the boundaries of the ideal kink bands cross the entire width of the specimen, the cross section being occupied by only one grain. In the case where a smaller grain size is involved, the quantity of grain boundary with respect to the volume of the grain is greater; therefore, the bending moments are not so homogeneously distributed in the smaller grains during heavy grain boundary

sliding.²³ On the other hand, there is a unique bending moment in a large grain with kink bands crossing the width of the specimen. In the case of smaller grain size the kinking process is not regular and results in the formation of blocks (as contrasted to bands). The boundaries produced by the process of kinking are the locations of sharp changes in orientation of the lattice, but the bending in this case was sharp from the very beginning of the deformation. This initial difference in orientation then increased with a progressive tilt of the neighboring block (rotation as in the case of kink bands).^{23, 29}

These metallographic observations are in contradiction to the theory of Wood and coworkers on the flow between subgrains to permit deformation of the grain.^{13, 14, 16} Fig. 12 shows schematically why Wood's idea cannot be accepted in the case of such boundaries. In case II of Fig. 12, flow along subgrain boundaries, as suggested by Wood et al., would produce the same effect as that along grain boundaries (see for example, Figs. 3 and 11); that is to say, dark bands would be observed to separate two neighboring blocks which would have about the same intensity. On the contrary, case I of Fig. 12 would be observed with a sharp change in orientation at the boundary, that is, kinking with no movement of the boundary during the process of rotation of one block with respect to the other. It may be seen from a study of the micrographs in Figs. 3a and 11a that case II is not applicable to the observations.

Boundaries revealed by electrolytic etching correspond to the kinks observed on the surface after deformation due to selective etching based on the difference in angle between the blocks on each side of the boundary. As these kinking boundaries present a greater difference in orientation they were



a—Surface after deformation (boundaries inside the grain separate regions of completely different illumination). Forked black markings are cracks in the oxide.

b—Electrolytic etching after careful electrolytic polishing.

c—Etched with the etch pit technique after careful electrolytic polishing (small subgrain size).

Fig. 11—The same region of a grain of specimen 11 deformed by creep at 1150°F and at a stress of 90 psi. Total elongation 4.2 pct. X50. Area reduced approximately 50 pct for reproduction.

revealed first by electrolytic etching. In Fig. 11b the subgrain boundaries revealed by electrolytic etching are apparently only those boundaries of higher difference in orientation of the lattice because frequently they join the grain boundaries at points where the grain boundaries change their orientation. This is due to their higher energy with increasing difference in orientation of the lattice.^{30, 31}

On the other hand, the magnitude of the difference in orientation of the lattice on each side of the subgrain boundaries, as revealed by the etch pit technique, does not seem to have an influence on the appearance of the boundary. Opposite results are found when boundaries are revealed by electrolytic etching (Fig. 10). The result of etching with the etch pit technique is that boundaries separating subgrains having only a small difference in orientation are virtually identical in appearance to boundaries separating blocks which have a larger difference in orientation.

It appears, therefore, that the etch pit technique is a more sensitive method of detecting the first appearance of subgrains but does not differentiate on the basis of the angular difference between subgrains. Electrolytic etching, on the other hand, does not detect subgrain boundaries with small angular difference between subgrains, but is capable of delineating orientation differences at fairly large angles, for example due to kinking. Consequently, electrolytic etching can quite easily give erroneous information on the number of subgrains and on the real subgrain size, as for example, in Rachinger's work.³²

In the work on kink band formation,²³ it was shown that in addition to sharp bending along the kink band boundaries, X-rays revealed a smooth bending in the bands themselves or in regions outside the kink bands. These results were observable primarily because of the large size of the kink bands,²³ but this phenomenon remains the same in the case of smaller blocks formed by kinking in the present work on subgrain formation, namely, that in addition to the sharp bending produced by kinking, a smooth bending occurred inside the blocks formed by kinking.

In observations of the formation of kink bands,²³ as compared with observations of general substructures revealed by etching methods and by observations of the microstructures after deformation, it is possible to distinguish two processes of subgrain boundary formation: 1—By kinking, which forms sharp boundaries from the very beginning of the deformation process; 2—By polygonization of the smoothly bent regions within the zones formed by prior kinking.

In opposition to the case of ideal smooth bending about a single axis, the boundaries formed by polygonization, as revealed by etch pits inside the zones formed by kinking, are not parallel to each other because the amount of bending and the axes of bending vary from one spot to another due to the

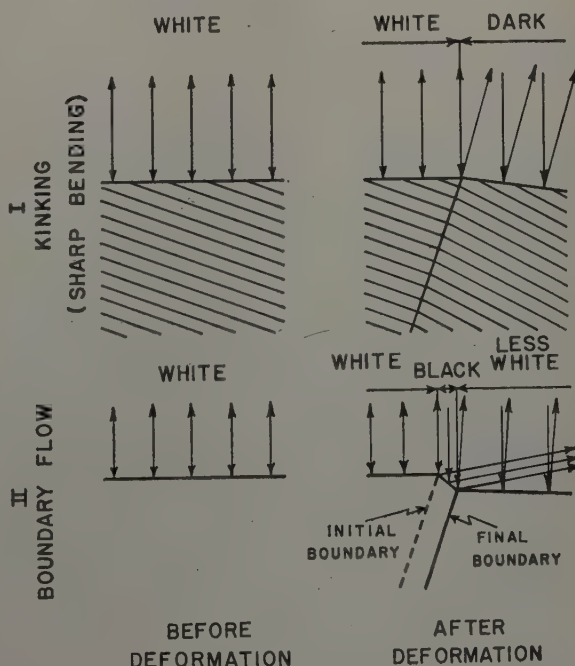


Fig. 12—Schematic representation of the appearance of boundaries in microscopic observations as produced by kinking or fragmentation and boundary flow.

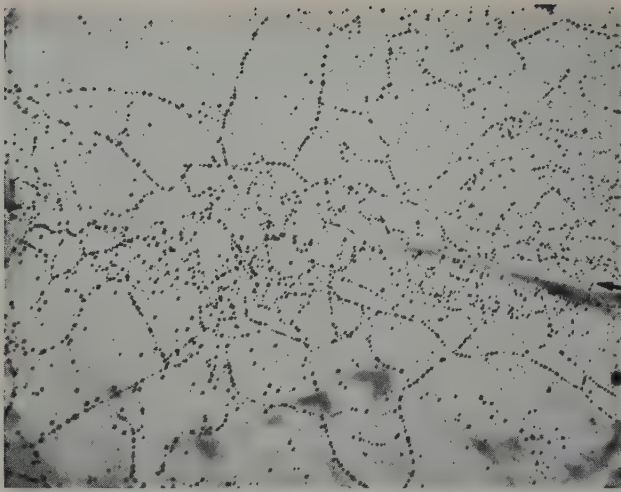


Fig. 13—Subgrains near a grain boundary of specimen 2 deformed by creep at 1150°F and a stress of 45 psi. (Grain boundary indicated by arrows). Electrolytically polished and etched (etch pit technique). Note greater density of subgrains near the grain boundary. X50. Area reduced approximately 50 pct for reproduction.

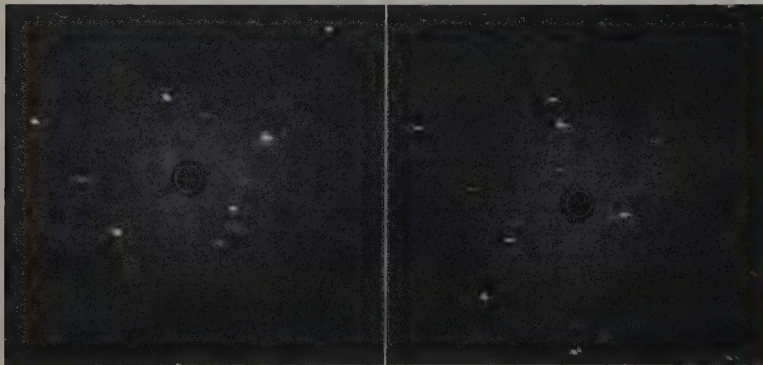


Fig. 14a (left)—Laue back-reflection photograph with X-ray beam at a point removed from the grain boundary indicated in Fig. 13.

Fig. 14b (right)—Laue back-reflection photograph with X-ray beam located just along the grain boundary indicated in Fig. 13. Higher bending of the lattice is noticeable near the grain boundary.

extensive inhomogeneity of deformation in creep testing.

Fig. 11 shows that the number of subboundaries as revealed by the etch pit technique was much greater than the number of subboundaries which could be seen on the unetched surface either after deformation or after electrolytic etching. Such observations indicate that the number of subboundaries formed by polygonization is much higher than that which is formed by kinking. Consequently, polygonization appears to be the main factor responsible

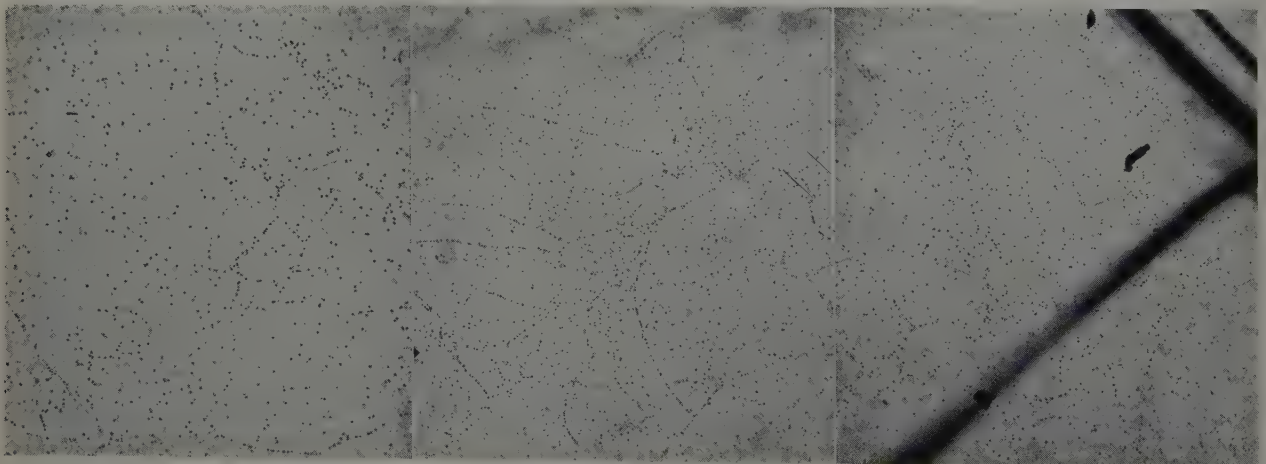
for subgrain formation.

In the present work which was performed at high temperatures not far from the melting point, diffusion rates are high and dislocations can move easily and reach stable positions very rapidly. Hence, if polygonization is really the main factor in subgrain formation, it is reasonable to believe that the subgrain size would be primarily a function of the total amount of bending and of temperature, namely, smaller subgrain size with higher bending and lower temperature.³³ Results found in the present investigation agree with this theory, and the typical cases are presented below.

It is known that at high temperatures, because of heavy sliding along grain boundaries, deformation initially is greater along grain boundaries than inside the grains.^{28, 34} Fig. 13 shows such a grain boundary (indicated by arrows) and the neighboring regions. The subgrains are considerably finer adjacent to the grain boundary. Fig. 14a is a Laue back-reflection photograph of a region far from the grain boundary shown in Fig. 13, and Fig. 14b is

a Laue back-reflection photograph of a region just along the grain boundary. Fig. 14b clearly supports the etch pit evidence in Fig. 13 of higher bending of the lattice adjacent to the grain boundary.

In another test specimen 5 was successively elongated by 1, 3, and 12 pct in a creep test at the same initial stress and temperature. Fig. 15 indicates that the subgrain size decreased with increasing elongation. In the third step of the creep test heavy duplex slip took place during increased deformation in the grain (Fig. 15c). Increasing deformation re-



a—After 1 pct elongation.

b—After 3 pct elongation.

c—After 12 pct elongation. (Slip and conjugate slip occurred inside the grain for such a total elongation).

Fig. 15—Same region of specimen 5 deformed by creep at 1150°F and at a stress of 50 psi, electrolytically polished and etched (etch pits). Note the decrease in subgrain size with the greater deformation of the grain. X50. Area reduced approximately 50 pct for reproduction.

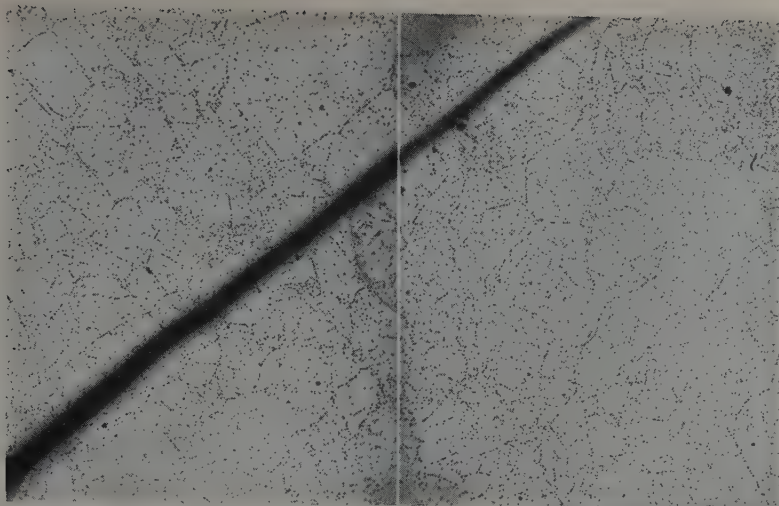
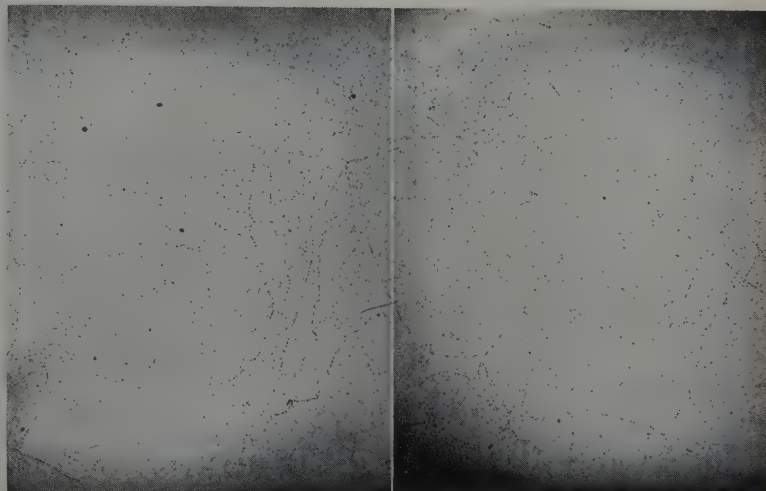


Fig. 16—Same region of a grain of specimen 10 deformed by creep at 1150°F, electrolytically polished and etched (etch pits). X50. Area reduced approximately 50 pct for reproduction.

a (left)—Deformed at a stress of 90 psi. Strain rate: $3.2 \times 10^{-3} \text{ hr}^{-1}$. Total elongation from 0 to 4.3 pct.

b (right)—Further deformed at a stress of 35 psi. Strain rate: $4 \times 10^{-4} \text{ hr}^{-1}$. Total elongation from 4.3 to 6.9 pct.

No distinct change in subgrain size. Subgrain size varies markedly within the grain.

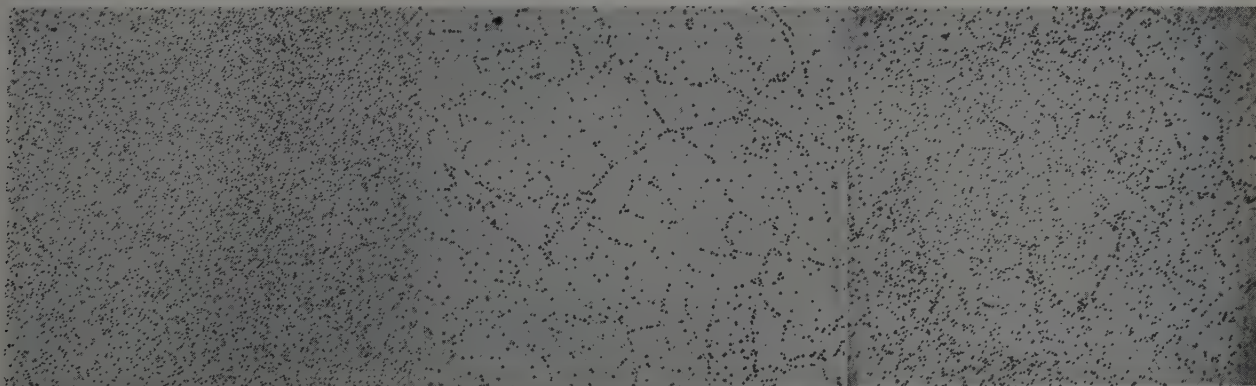


sulted in greater bending and consequently in diminishing the subgrain size.

In a test to evaluate the role of strain rate, specimen 10 was first deformed by creep at 1150°F at a stress of 90 psi; later a small additional increase in strain was obtained by creep at 1150°F and at a decreased stress of 35 psi. In the second portion of the test the strain rate was 800 times smaller than in the first. The metallographic results are shown in Fig. 16, and an important change in subgrain size is not evident. This result does not agree with the assumption that the subgrain size largely determines the mechanical strength exhibited by the metal during deformation.^{14, 16} Furthermore, it must be pointed

out that in the micrographs of Fig. 16 the subgrain size is not the same all over the grain, and this fact is not in agreement with the theory of strength as a function of the subgrain size. On the contrary, bending can vary in different parts of a grain and the explanation of subgrain size as a function of local bending seems more feasible.

Finally, the influence of temperature on subgrain size was very striking, as shown in Fig. 17. In this case the tests were run on the same specimen at the same initial stress but at three different temperatures. It will be noted that the subgrain size increased markedly with temperature at these high temperatures.



a—Deformed at 1075°F. Strain rate: 1.1×10^{-1} . Total elongation from 0 to 5.2 pct. b—Deformed at 1150°F. Strain rate: 3.8×10^{-1} . Total elongation from 5.2 to 10.8 pct. c—Deformed at 1100°F. Strain rate: 1.02×10^{-1} . Total elongation from 10 to 17.3 pct.

Fig. 17—Same region of specimen 15 deformed by creep under a stress of 90 psi, electrolytically polished and etched (etch pits). Note the change in subgrain size as a function of temperature in spite of the fact that the specimen was deformed at the same stress. X50. Area reduced approximately 50 pct for reproduction.

Conclusions

A theory of subgrain formation has been proposed. The striking fact is that this theory bridges the gap between the theory based on fragmentation on the one hand and that based on polygonization on the other.

Wood and coworkers were not entirely wrong in saying that fragmentation was taking place if fragmentation is synonymous with kinking. Due to kinking, a small number of boundaries are formed which are sharp from the very beginning of the deformation process. Contrary to Wood et al.'s argument, however, significant sliding has not been noted to occur along this type of boundary but primarily rotation.

In addition, the idea that polygonization was the only process of subgrain formation, while subject to some modification, is essentially correct since most of the subgrain boundaries are formed by polygonization of the smoothly bent regions delineated by kinking.

X-ray and metallographic evidence indicate that polygonization was the main factor in subgrain formation. The subgrain size was found to be a function of the extent of bending and of temperature. The experiments, which had to be performed at high temperatures where diffusion rates were very high, showed temperature to be a very important factor. Since polygonization is indicated to be chiefly responsible for subgrain formation, subgrains must form as a consequence of deformation and are not a main cause of deformation.

Acknowledgments

The authors wish to express appreciation to H. C. Chang and A. R. Chaudhuri for frequent helpful discussions. Thanks are also extended to the Flight Research Laboratory (WCRRL) Wright Air Development Center, for sponsoring this research under Contract AF 33 (038) -23281.

References

- ¹ D. Hanson and M. A. Wheeler: The Deformation of Metals Under Prolonged Loading. Part I: The Flow and Fracture of Aluminum. *Journal Inst. Metals* (1931) **45**, p. 229.
- ² C. H. M. Jenkins and G. A. Mellor: Part I: Structural Changes in Mild Steels and Commercial Irons During Creep. *Journal Iron and Steel Inst.* (1935) **132**, p. 179.
- ³ G. A. Homes: Recherches sur le Mechanisme structurale du Comportement Mecanique des Metaux aux Temperatures elevees. *Revue de Metallurgie* (1939) **36**, p. 373.
- ⁴ H. Hirst: Deformation of Single Crystals of Lead by Creep. Part IV: Process of Deformation During Creep. *Proc. Australasian Inst. of Mining and Metallurgy* (1941) **121**, p. 11.
- ⁵ C. Crussard: Le Role des Joints Intergranulaires dans la Deformation des Metaux. Application au Fluage et a la Fatigue. *Revue de Metallurgie* (1946) **43**, p. 307.
- ⁶ R. W. Cahn: Recrystallization of Single Crystals after Plastic Bending. *Journal Inst. Metals* (1949) **76**, p. 121.
- ⁷ A. Guinier and P. Lacombe: L'etat "polygonise" du Cristal Metallique. *Metaux et Corrosion* (1949) **23**, p. 212.
- ⁸ G. B. Greenough and E. M. Smith: The Mechanism of Creep as Revealed by X-ray Methods. *Journal Inst. Metals* (1950) **77**, p. 435.
- ⁹ G. B. Greenough, C. M. Bateman, and E. M. Smith: X-ray Diffraction Studies in Relation to Creep. *Journal Inst. Metals* (1952) **80**, p. 545.
- ¹⁰ C. Crussard: Discussion on Ref. 13. *Journal Inst. Metals* (1949) **75**, p. 1125.
- ¹¹ G. Wyon and C. Crussard: Modifications de Structure de l'Aluminium au cours du Fluage. *Revue de Metallurgie* (1951) **48**, p. 121.
- ¹² I. S. Servi, J. T. Norton, and N. J. Grant: Some Observations of Subgrain Formation During Creep in High Purity Aluminum. *Trans. AIME* (1952) **194**, p. 965; *JOURNAL OF METALS* (September 1952).
- ¹³ G. R. Wilms and W. A. Wood: Mechanism of Creep in Metals. *Journal Inst. Metals* (1949) **75**, p. 693.
- ¹⁴ W. A. Wood and W. A. Rachinger: The Mechanism of Deformation in Metals with Special Reference to Creep. *Journal Inst. Metals* (1949) **76**, p. 237.
- ¹⁵ W. A. Wood and R. F. Scrutton: Mechanism of Primary Creep in Metals. *Journal Inst. Metals* (1950) **77**, p. 423.
- ¹⁶ W. A. Wood, G. R. Wilms, and W. A. Rachinger: Three Basic Stages in the Mechanism of Deformation of Metals at Different Temperatures and Strain Rates. *Journal Inst. Metals* (1951) **79**, p. 159.
- ¹⁷ W. A. Wood: The Lower Limiting Crystallite Size and Internal Strains in Some Cold-worked Metals. *Proc. Royal Soc., London* (1939) **172A**, p. 231.
- ¹⁸ A. Guinier and J. Tennevin: Sur deux Variantes de la Methode de Laue et leurs Applications. *Acta Crystallographica* (1949) **2**, p. 133.
- ¹⁹ P. Gay and P. B. Hirsch: An X-ray Technique for the Study of Substructures in Materials. *Acta Crystallographica* (1951) **4**, p. 284.
- ²⁰ D. McLean: Creep Processes in Coarse-grained Aluminum. *Journal Inst. Metals* (1952) **80**, p. 507.
- ²¹ J. Hino, P. G. Shewmon, and P. A. Beck: Effect of Simultaneous Strain on Subgrain Growth. *Trans. AIME* (1952) **194**, p. 873; *JOURNAL OF METALS* (August 1952).
- ²² P. Jacquet: Sur une Nouvelle Technique de Polissage Electrolytique de l'Aluminium et de ses Alliages. *Metaux et Corrosion* (1943) **18**, p. 198.
- ²³ A. M. Gervais, J. T. Norton, and N. J. Grant: Kink Band Formation in High Purity Aluminum During Creep at High Temperatures. Unpublished.
- ²⁴ P. Lacombe and L. Beaujard: The Application of Etch-Figures on Pure Aluminum (99.99%) to the Study of Some Micrographic Problems. *Journal Inst. Metals* (1947) **74**, p. 1.
- ²⁵ P. Lacombe: "Sub-boundary" and Boundary Structures in High Purity Aluminum. *Report of a Conference on Strength of Solids*. University of Bristol, July 7-9, 1947. Published by the Physical Society, 1948.
- ²⁶ F. R. Nabarro: The Mathematical Theory of Stationary Dislocations. *Advances in Physics* (July 1952) **1**, p. 315.
- ²⁷ J. A. Ramsey: The Recovery of Polycrystalline Aluminum. *Journal Inst. Metals* (1952) **81**, p. 61.
- ²⁸ H. C. Chang and N. J. Grant: Observations of Creep of the Grain Boundary in High Purity Aluminum. *Trans. AIME* (1952) **194**, p. 619; *JOURNAL OF METALS* (June 1952).
- ²⁹ H. C. Chang and N. J. Grant: Inhomogeneity in Creep Deformation of Coarse Grained High Purity Aluminum. This issue, p. 1175.
- ³⁰ K. T. Aust and B. Chalmers: Surface Energy and Structure of Crystal Boundaries in Metals. *Proc. Royal Soc., London* (1950) **204A**, p. 359.
- ³¹ C. G. Dunn, F. W. Daniels, and M. J. Bolton: Relative Energies of Grain Boundaries in Silicon Iron. *Trans. AIME* (1950) **188**, p. 1245; *JOURNAL OF METALS* (October 1950).
- ³² W. A. Rachinger: The Effect of Grain Size on the Structural Changes Produced in Aluminum by Slow Deformation. *Journal Inst. Metals* (1952) **80**, p. 415.
- ³³ C. G. Dunn and F. W. Daniels: Formation and Behavior of Subboundaries in Silicon Iron Crystals. *Trans. AIME* (1951) **191**, p. 147; *JOURNAL OF METALS* (February 1951).
- ³⁴ E. A. Calnan and B. D. Burns: Some X-ray Observations on the Nature of Creep Deformation in Polycrystalline Aluminum. *Journal Inst. Metals* (1950) **77**, p. 445.

Inhomogeneity in Creep Deformation of Coarse Grained High Purity Aluminum

by H. C. Chang and N. J. Grant

Creep of very coarse grained high purity aluminum was studied at 400°, 700°, and 1100°F at initial stresses of 50 to 1200 psi. Local strain measurements were made across the grain boundaries and in different regions of various grains during creep, thereby permitting the drawing of component creep curves. The relative amounts of elongation as measured across a grain boundary and in the grains adjacent to the boundary depend on the temperature of testing. The significance of creep curve equations and activation energies is discussed.

THIS paper presents some of the results of a research program devoted to the study of the mechanism of creep in high purity aluminum. Previous publications have dealt with the cyclic processes of alternating grain boundary sliding and migration, and the deformation in the grains caused by these processes;¹ the direction and the driving force of grain boundary sliding and migration;² the deformation in the grains and the restricting effects of the grain boundaries on this deformation.³ These previous papers were based mainly on either microscopic observations or X-ray data, or both. Sometimes creep curves across two closely spaced reference marks (about 0.6 to 0.7 mm apart) were also presented with a view to correlating the elongation values with the optical observations in general, and with certain deformation processes in particular. These curves shall henceforth be referred to as component creep curves. No attempts were made, however, to compare either the component creep curves which were obtained in different regions of a specimen, or those obtained from different specimens subjected to different creep test conditions.

It is the purpose of this paper to present these component creep curves. Among the factors influencing the behaviors of these curves, those studied were stress, temperature, and grain arrangements in the specimens. It is proposed to show how greatly the deformation can vary from grain to grain and within an individual grain in a coarse grained specimen.

H. C. CHANG, Associate Member AIME, is associated with the DIC Staff, and N. J. GRANT, Member AIME, is Associate Professor, Dept. of Metallurgy, Massachusetts Institute of Technology, Cambridge, Mass.

Discussion on this paper, TP3629E, may be sent, 2 copies, to AIME by Dec. 1, 1953. Manuscript, Sept. 15, 1952; revision, June 19, 1953. Cleveland Meeting, October 1953.

The experimental technique and procedure have been presented.¹ It remains necessary to emphasize that the reference marks were produced by pressing a thin sewing needle into the surface of the specimen before the final annealing at 900°F for 24 hr and at 1150°F for 12 hr. The cold work around the needle indentations was therefore removed. The depth of these holes after electropolishing the annealed specimens was about 0.01 mm. This depth and area were negligible in comparison with the thickness of the specimens, 2.3 mm, and hence would not affect the creep behavior.

Results

Fig. 1 shows a development diagram of specimen P-8. The dots on the surface locate the needle point reference marks used to obtain the component creep curves. A curve obtained between two dots across a grain boundary measures not only the boundary deformation but also the deformation associated with boundary sliding occurring in the grains in the region between these indents. The original distance between two reference marks was about 0.6 to 0.7 mm. The maximum error of measurement was 0.01 mm, or in terms of percentage elongation, of the order of ± 1.5 pct.

Whereas the component creep curves shown in the figures to follow were drawn as a gross average of the points, in view of the fineness of some of the steps of grain boundary sliding and migration, as shown in the previous publications,^{1,2} it appears logical to expect that some of the finer cycles of movement have not been delineated for the strain sensitivity of the measuring system. It seems justifiable to say that the curves are not as smooth as shown.

700°F Tests: Fig. 2 shows component creep curves across four of the grain boundaries in specimen P-8, tested at 700°F and 85 psi. These curves clearly show alternate cycles of increasing and decreasing

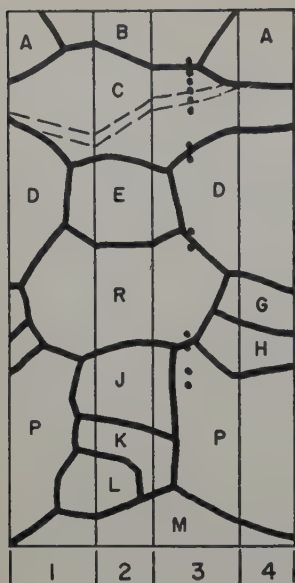


Fig. 1—Structural development drawing of specimen P-8, tested at 700°F and 85 psi. Dashed line indicates the course of heavy slip bands. The black dots indicate reference marks for component creep curves. 1—Back surface. 2—Left edge. 3—Front surface. 4—Right edge.

creep rates. It has been shown¹ that these cycles are associated with the consecutive processes of grain boundary sliding and migration.

It can be seen from Fig. 1 that the boundary between grains B and C lies about 75° to the direction of applied stress. This boundary was not too favorably oriented for sliding; the component creep curve obtained across this boundary is shown as curve IV in Fig. 2. After one cycle of increasing and decreasing creep rates in the early stages of the test, the creep rate settled down to a low fairly constant value in the later stages of creep. The elongation across this boundary at the time when the test was stopped was only 7.5 pct which is low compared to the values for the other three boundaries.

As shown in Fig. 1, the boundary between grains C and D at the reference marks was favorably oriented for sliding; however, the balance of the boundary was curved at the start of the creep test. After an initial period of about 15 hr, during which time creep deformation was small, this grain boundary became relatively straight as a result of boundary migration. As this boundary straightened out, the blocking effect at the triple point of grains C, D, and E, Fig. 1, on the front surface was overcome, and rapid deformation occurred as shown by creep curve III, Fig. 2, the elongation increasing sharply for the next 20 to 25 hr. A period of recovery followed

before another period of increasing creep rate could occur after about 65 hr.

The grain boundary between grains D and R, with two small grains E and G (Fig. 1) at its ends offering relatively small resistance, was favorably oriented for sliding. Extensive deformation occurred from the very beginning, showing a fairly continuous increase in elongation, curve II, Fig. 2.

Curve I, Fig. 2, shows the component creep curve across the boundary between grains R and P. This boundary at the reference marks, Fig. 1, is a short straight boundary close to 45° to the stress axis. Furthermore, this region of the specimen contains more grains (finer grain size) than the rest of the specimen. It was shown previously² that the extent of grain boundary sliding and migration increases with decreasing grain size at high temperatures. The large initial creep deformation and the final large deformations are the result of this particular grain arrangement. After about 80 hr, at a time

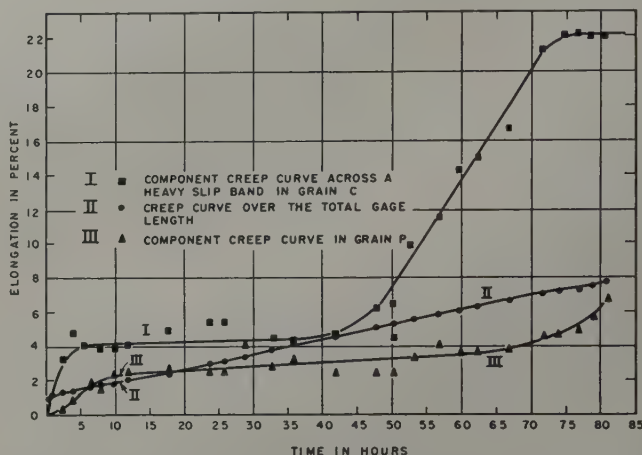


Fig. 3—Specimen P-8, 700°F, 85 psi. Component creep curves in the grains and a creep curve over the total gage length. See also Fig. 1.

when the total deformation for the specimen was about 8 pct, this was 18 pct elongation across boundary RP and as little as 7.5 pct across boundary BC.

It is interesting to note from the curves in Fig. 2, curves I and II in particular, that the periodicity of decreasing and increasing rates gets smaller as the amount of creep increases.

Many component creep curves were also obtained in the grains of specimen P-8. Two typical examples of these are shown in Fig. 3, curves I and III.

Curve I was obtained across a heavy slip band in grain C. The nature of a component creep curve across such a band has been discussed.⁶ It is shown here for the purpose of comparison with curve III, which was obtained in a region of grain P where subgrains, instead of heavy slip bands, were formed. The amount of extension in a region in which subgrains were formed, as curve III demonstrates, is very much less than that in a region in which heavy slip bands were formed. However, they are qualitatively similar in that they show a cyclic behavior.

In Fig. 3 is also shown the creep curve over the entire gage length of the specimen, curve II. Regardless of the step-wise nature of component creep curves obtained from this specimen, P-8, curve II is not only similar to the conventional creep curve but is also surprisingly smooth.

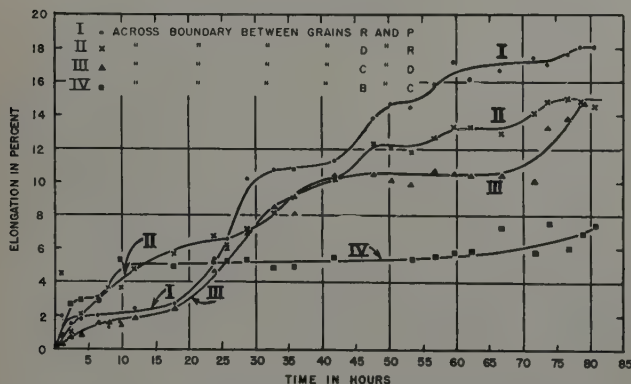


Fig. 2—Specimen P-8, 700°F, 85 psi. Component creep curves across grain boundaries of various orientations with respect to the specimen axis. See Fig. 1 for location of markers.

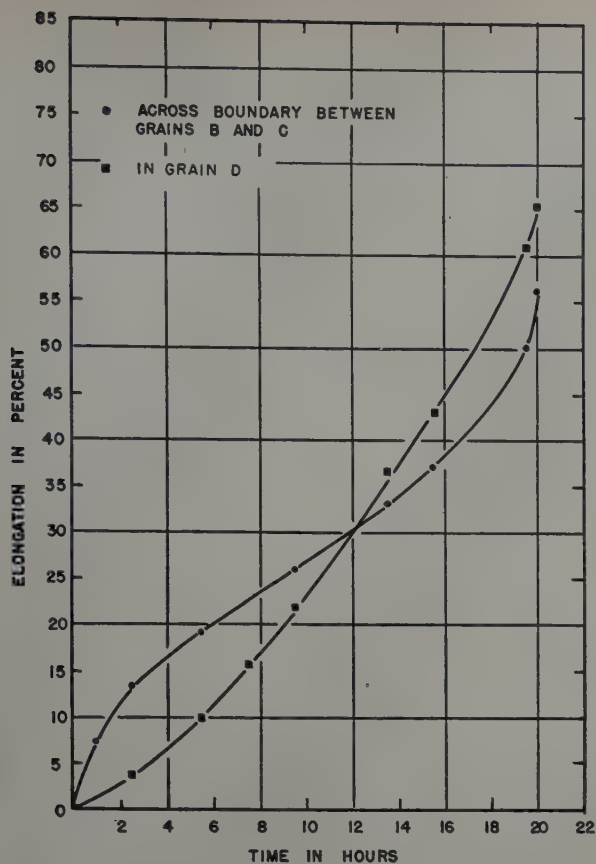


Fig. 4—Specimen P-6, 700°F, 200 psi. Component creep curves. See Fig. 6.

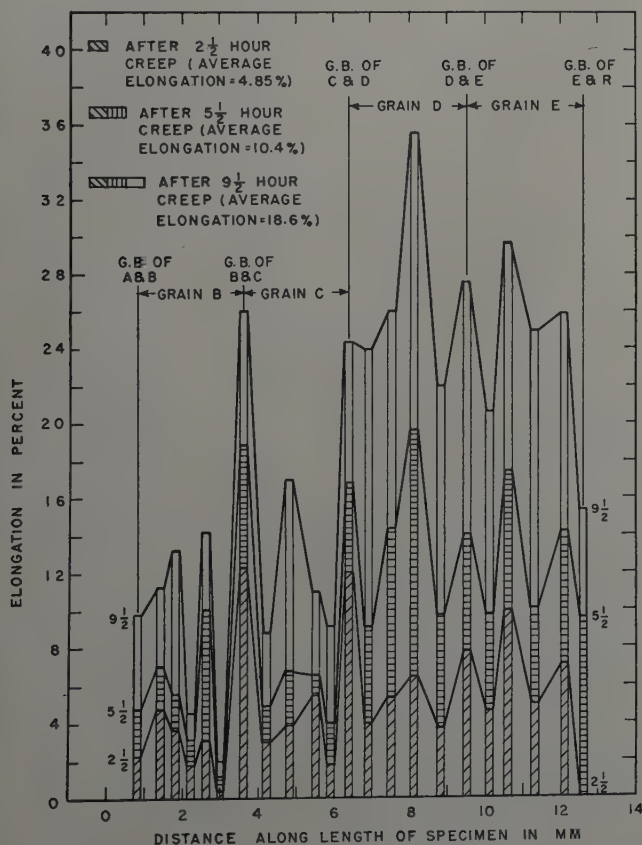


Fig. 5—Specimen P-6, 700°F, 200 psi. Deformation along the gage length of specimen P-6 (see Fig. 6) after fixed intervals of time, comparing relative creep across grain boundaries and within grains.

In order to show the effect of higher stresses on the form of component creep curves, two typical component creep curves, one across a grain boundary and the other for a grain, obtained from specimen P-6, are shown in Fig. 4. The development diagram of this specimen is shown in Fig. 5. Specimen P-6 was subjected to creep at 700°F and 200 psi (fractured in about 22 hr), whereas P-8 was at 700°F and 85 psi. The initial period of rather rapid increase of creep strain across a grain boundary, curve I, was in accord with the optical observations during the test which showed that boundary sliding and migration were primarily responsible for the deformation in the early period at 700°F. Comparison of curves I and II, Fig. 4, shows that deformation in the grains can overtake the deformation across the grain boundaries, in the later stages of creep.

It appears that the step-wise nature of component creep curves at high stresses, Fig. 4, is less distinct than at low stresses, Figs. 2 and 3; however, the infrequency of measurements relative to the creep rate of this specimen is very probably one of the reasons.

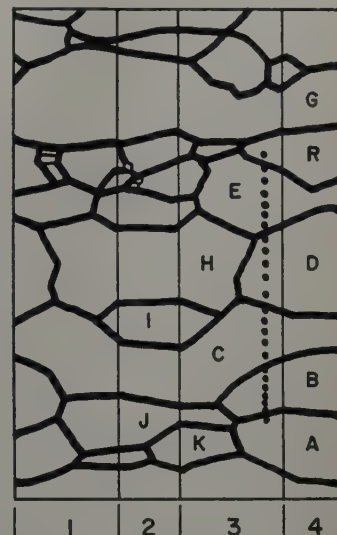


Fig. 6—Structural development drawing of specimen P-6, tested at 700°F and 200 psi. Black dots indicate reference marks for component creep curves. 1—Back surface. 2—Left edge. 3—Front surface. 4—Right edge.

Fig. 5 shows a plot taken from specimen P-6 of percentage elongation, represented by blocks between consecutive markers along the gage length of the specimen (see Fig. 6) at three different time intervals during the course of the creep test. Each column along the abscissa is at the midpoint between two reference markers, the distances being taken with respect to grain boundary AB as a reference. The areas between the various time levels show the deformation which has occurred in that time interval. The elongation at a grain boundary was arbitrarily considered as the elongation between two reference marks across the grain boundary. Fig. 5 also shows that boundaries, oriented favorably for the application of shear stress, such as the boundaries of grains B and C, and D and E, show greater deformation than less favorably oriented ones. That the elongation across the boundary between grains E and R is relatively small in comparison with the other three equally favorably oriented boundaries may be the result of a slight orientation difference across this grain boundary in addition to the complicated arrangement of the grains in that part of the specimen.

The point mentioned above in connection with Fig. 4, that the amount of deformation in the grains

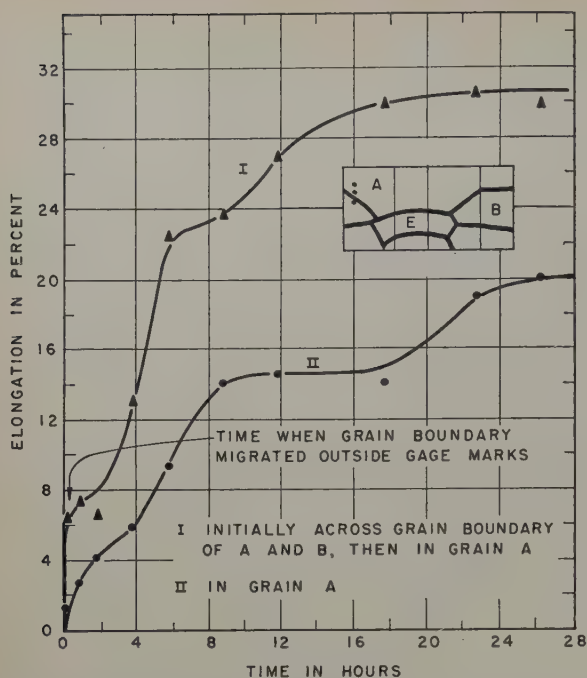


Fig. 7—Specimen P-10, 1100°F, 50 psi. Component creep curves showing large initial deformation due to grain boundary sliding and migration. Insert shows a portion of the development diagram of specimen P-10.

overtakes that across the grain boundary in the later stages of creep, is more clearly illustrated in the case of grain D, Fig. 5. It can be seen from this figure that after 2½ hr of creep, the largest elongation in grain D was about 7 pct whereas the elongation across the boundary between grains C and D was 12.5 pct. However, after the specimen was subjected to creep for 9½ hr, the largest elongation in grain D increased to 36 pct whereas that across the boundary between grains C and D increased only to 24.5 pct.

Another point of interest in connection with Fig. 5 is that the elongation in that part of the grain which is close to a grain boundary favorably oriented for sliding is often less than the deformation close to the center of the grains, or across the grain boundaries. It is interesting to compare these results with those obtained by Boas and Hargreaves who measured the local strains of tensile deformed



Fig. 8—Specimen P-11, 400°F, 400 to 750 psi. Illustration of restriction of deformation due to orientation and geometry effects. Note especially grain J. X100. Area reduced approximately 50 pct for reproduction.

specimens (at room temperatures) of coarse grained commercially pure aluminum.⁴ They found that the deformation tends to be continuous across the grain boundaries, and that the grain boundaries, in general, restrict the deformation in the grains. This restricting effect of the boundaries on the deformation in the grains still exists under creep conditions of testing both at high and low temperatures, and results in an elongation, measured in the neighborhood of the grain boundaries, which is often smaller than that in the center of the grains, depending on geometry.

1100°F Test: As shown in a previous publication,² a grain boundary in a specimen subjected to creep at 1100°F, migrated quickly in a step-wise manner to a position almost perpendicular to the specimen axis during the early stage of the test, each step of migration being accompanied with small amounts of sliding. Fig. 7 shows two component creep curves obtained on this specimen

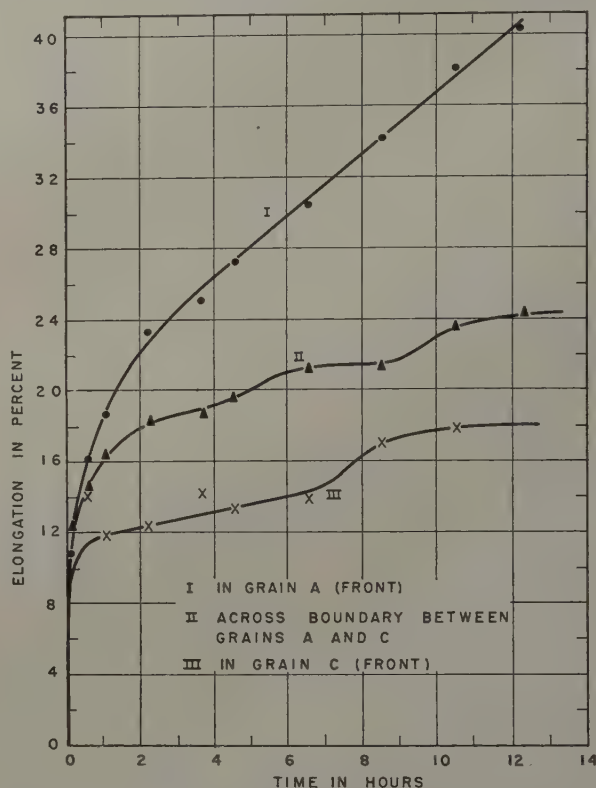


Fig. 9—Specimen P-7, 400°F, 1200 psi. Component creep curves across and adjacent to grain boundary of grains A and C, Fig. 10, representing the case where slip can be transmitted across the grain boundary.

(P-10, tested at 1100°F, 50 psi). Curve I represents a component creep curve obtained across the original boundary between grains A and B (represented by the two lower reference marks in the insert of Fig. 7). Curve I shows that an elongation of about 7 pct occurred in the first ½ hr period. During this time the grain boundary between grains A and B slid and migrated down and out of the field covered by the two noted reference marks. In comparison with the upper curve, the balance of which was actually obtained in grain A, curve II (the two upper dots are reference marks) shows a relatively small amount of creep in the first ½ hr period. Thereafter, both curves represent the deformation in grain A by slip and subgrain formation. Both curves show a cyclic behavior as did those obtained from specimen P-8 tested at 700°F.

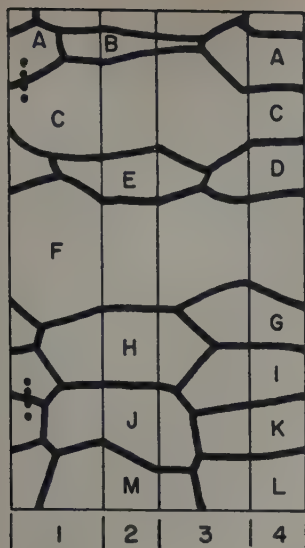


Fig. 10—Structural development drawing of specimen P-7, tested at 400°F and 1200 psi. Black dots indicate the reference marks for component creep curves. 1—Front surface. 2—Right edge. 3—Back surface. 4—Left edge.

As in the previous instances the deformation throughout the specimen, as measured by component creep curves, is severely inhomogeneous.

400°F Test: It has been shown⁸ that creep deformation at 400°F, in contrast to that at 700° to 1100°F, is characterized by slip band formation in the early stages of creep and by slip and subgrain formation in the later stages of creep. Grain boundaries slid slightly only in the late stages of creep. Clear steps of boundary migration were not observed at this temperature. Thus the characteristics of deformation at this temperature are more similar to those of room temperature deformation.

The behavior of the grain boundaries at 400°F can be divided into two types based on grain and grain boundary orientation relationships. The first depends on whether the orientation difference across the grain boundary is small, so that deformation in one grain can be easily transmitted to the other grain; the second type depends on whether the adjacent grains are of such orientation that the deformation in both grains is restricted, see grains L and J, Fig. 8.

The nature of the creep curve for the case where deformation can continue across the grain bound-

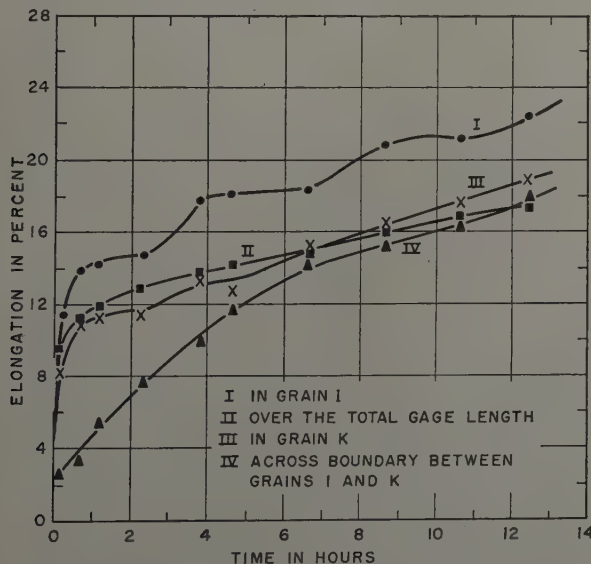


Fig. 11—Specimen P-7, 400°F, 1200 psi. Component creep curves across and adjacent to grain boundary of grains I and K, Fig. 10, representing the case where orientation difference across the grain boundary is large.

ary is shown in Fig. 9 for specimen P-7, tested at 400°F and 1200 psi. Curve II shows the elongation across the boundary between grains A and C, Fig. 10. The elongation values shown in curve II lie in between those of curves I and III. Curves I and III represent the creep in grains A and C, respectively, in the vicinity of the boundary. The case wherein the deformation in both grains is restricted, is shown in Fig. 11. The extent of deformation across the grain boundary is smaller than that in either grains. A creep curve over the whole gage length is also shown in Fig. 11 for specimen P-7, and again a smooth creep curve was obtained.

Fig. 12 was prepared in the same way as Fig. 5. It can be seen that the deformation in the grains follows the same general trend at two different times. The peaks and valleys appeared to correspond respectively to regions between reference marks which included heavily slipped bands and

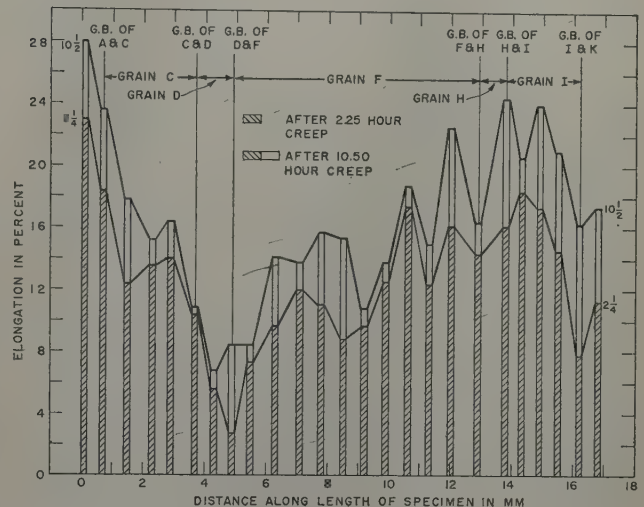


Fig. 12—Specimen P-7, 400°F, 1200 psi. Deformation along the gage length of specimen P-7 (see Fig. 10) after fixed intervals of time, comparing relative creep across grain boundaries and within grains.

regions between markers where deformation was less noticeable. While the initial deformation across grain boundaries was relatively small, the amount of deformation became more significant in the later stages of creep, as for example across the boundaries between grains D and F and between grains H and I, Fig. 12. This corresponds to the optical observation that at 400°F boundary sliding occurs in the later stages of creep with the initial deformation occurring primarily in the grains.

Fig. 12, for the 400°F, 1200 psi creep test, when compared with the same kind of plot for specimen P-6 tested at 700°F, Fig. 5, shows that in general the grain boundary regions show more restricted deformation than regions removed from the grain boundary. The phenomena which have been described above in connection with Figs. 9 and 11 are also clearly revealed in Fig. 12.

Thus, at 400°F, although the relative contributions of the grains and grain boundaries are significantly different from 700° and 1100°F, it is still to be noted that the component creep curves still show extreme inhomogeneity of creep deformation in the various portions of the specimen.

Discussion

It has been shown that when a specimen is subjected to creep at 700°F, the deformation in the

grains may eventually overtake the deformation across the grain boundaries, Fig. 4. It is thought that this phenomenon is associated with the nature of the grain boundaries in the later stages of creep. As shown previously,¹ heavy boundary sliding causes the grain boundary to become strongly irregular and angular after boundary migration. Consequently, the angular nature of the grain boundary might be expected to make further sliding difficult or at least to occur in shorter cycles. Whereas it could be expected that the angular grain boundary might decrease the creep rate, the angularities could also initiate slip bands or deformation bands at those places where sharp changes of curvature of the boundary had taken place. This is shown in Fig. 13

The observation that the periodicity of the cyclic processes of boundary creep increases with increasing deformation, Fig. 2, may also be ex-



Fig. 13—Specimen P-6, 700°F, 200 psi, front surface. Deformation bands started from that part of the grain boundary where sharp curvature occurred as a result of uneven boundary sliding and migration. X100. Area reduced approximately 25 pct for reproduction.

plained by the development of the angular grain boundaries as creep progresses. It is obvious that the more angular the grain boundary becomes the shorter the distance the grain boundary can slide, and therefore the more frequently the cycles of grain boundary migration, i.e., recovery needed for further boundary sliding.

It must be evident from the data that creep is a complex process, even in high purity materials. The component creep curves show that while the deformation in the grains and across grain boundaries must balance, the relative amounts are a function of the strain, of temperature, of time, and of orientation relationship among the grains and grain boundaries. At 400°F the initial deformations appear to be greater in the grains than in the grain boundaries, whereas at 700° and 1100°F the initial deformation is generally greater along the grain boundary regions. But, equally important, the deformation after a given time varies vastly from one grain boundary to another and from one grain to another. On the other hand, even for these coarse grained test specimens, the overall creep curves have been surprisingly smooth and conventionally shaped to encourage the seeking of equations to describe them.

Thus, while it is admitted that processes of an activation type take place during creep, the cyclic nature of the component creep curves and the large variations in creep rates between adjacent zones in any one specimen make it difficult, if not impossible, to believe that either a single activation process can describe creep behavior or that a single activation process exists. Certainly a different value of activation energy must exist for grain and for grain boundary creep.

It has been suggested by many that such a single activation energy can be determined for creep, however the activation energy is probably a statistical summation of a number of activation processes.

Since the total creep is made up of many dissimilar component creep curves, the creep curve exists only in a statistical sense. The applicability of certain equations to the creep curve must therefore depend on the material tested, time, temperature, etc. No one equation could ever be expected to apply in all instances. The assignment of physical significance⁶ to constants in such equations is without basis since the creep curve equation is a statistical equation.

Conclusions

Based on many component creep curves measured between closely spaced consecutive gage marks, in tests run at 400°, 700°, and 1100°F, the following conclusions are drawn:

1—A cyclic behavior is exhibited both across grain boundaries and in the grains. The periodicity of these cycles obtained across grain boundaries appears to increase as creep progresses, but the deformation per cycle decreases.

2—Boundary deformation is very significant in creep from the start of the test for specimens tested at 700° and 1100°F. At 400°F, boundary sliding becomes noticeable only in the later stages of creep.

3—In view of the inhomogeneity of high temperature creep, as exemplified by component creep curves along the length of a test bar, it is unlikely that a single activation process can be considered for creep.

4—Any equation intended to define a conventional creep curve must be considered to be a statistical summation of equations describing the various component processes of creep.

Acknowledgments

The authors wish to express appreciation to A. R. Chaudhuri who contributed significantly to this research. Thanks are also due to the Bureau of Ships for sponsoring this research.

References

- ¹H. C. Chang and N. J. Grant: Observations of Creep of the Grain Boundary in High Purity Aluminum. *Trans. AIME* (1952) **194**, p. 619; *JOURNAL OF METALS* (June 1952).
- ²H. C. Chang and N. J. Grant: Grain Boundary Sliding and Migration and Intercrystalline Failure Under Creep Conditions. *Trans. AIME* (1953) **197**, p. 305; *JOURNAL OF METALS* (February 1953).
- ³H. C. Chang and N. J. Grant: Mechanism of Creep in Coarse Grained High Purity Aluminum. Unpublished.
- ⁴W. Boas and M. E. Hargreaves: On the Inhomogeneity of Plastic Deformation in the Crystals of an Aggregate. *Proc. Royal Soc.* (1948) **A193**, p. 89.
- ⁵T. H. Hazlett and E. R. Parker: Nature of the Creep Curve. *Trans. AIME* (1953) **197**, p. 323; *JOURNAL OF METALS* (February 1953).

Plastic Stress-Strain Relations for Aluminum Alloy 14S-T6 Subjected to Combined Tension and Torsion

by Joseph Marin and H. A. B. Wiseman

This paper presents results of an experimental study dealing with the plastic stress-strain relations of aluminum alloy 14S-T6 subjected to combined biaxial tension and compression stresses. Plastic stress-strain relations for both constant and various types of variable stress ratios were determined and a comparison made with the simple flow theory of plasticity.

THIS investigation was undertaken for two main purposes: 1—to obtain plastic stress-strain relations for Alcoa 14S-T6 when subjected to various combinations of biaxial stresses, and 2—to determine the validity of the flow theory in predicting plastic stress-strain relations for combined stresses. The biaxial stresses used were tension combined with compression. These stresses were produced by subjecting a thin-walled tube to axial tension and torsion.

Various types of combined stress conditions were investigated. To provide control test data and information on the influence of biaxial stresses on the strength, the usual constant stress ratio type tests were made. These tests showed that the biaxial yield strength agrees approximately with the distortion energy theory. However, the Prager semi-empirical theory agrees best with the test results. For these constant stress ratio tests the plastic stress-strain relations were found to agree approximately with the flow theory. (For constant stress ratio the flow and deformation type theories are identical.)

In view of the fact that the constant stress ratio tests cannot distinguish between the flow and deformation theories, a number of variable and special biaxial stress tests were made. These tests showed that the flow theory is inadequate, since large differences exist between the experimental and theoretical results.

Special tests were also conducted to check the validity of the isotropic yielding assumption. This assumption is made in the linear-type flow theory. In these tests specimens were loaded in tension to predetermined values beyond the proportional limit stress. The tension load was removed from the specimen and the specimen was subsequently loaded in torsion to fracture. Other tests were applied with the order of torque and tension loading reversed.

J. MARIN and H. A. B. WISEMAN are associated with the Dept. of Engineering Mechanics, The Pennsylvania State College, State College, Pa.

Discussion on this paper, TP 3605E, may be sent, 2 copies, to AIME by Dec. 1, 1953. Manuscript, Sept. 10, 1952; revision, March 17, 1953. Cleveland Meeting, October 1953.

The nominal stress-strain curves for these two tests approximately coincide indicating that the assumption of isotropic yielding is valid. In addition, these tests verified the requirement by the slip theory of plasticity that prestraining below 140 pct of the proportioned limit stress in either torsion or tension did not influence the subsequent plastic stress-strain relations in tension or torsion.

Another type of test was conducted to check the assumption that the axes of principal stress and strain coincide during plastic flow and variable stress conditions. These tests were conducted by applying combinations of axial tension, internal pressure, and torsional loads such that the axes of maximum principal stress could be rotated through 90° during the loading path. The results of those tests showed that the angle between the axes of principal stress and strain varied greatly and that the assumption of coincidence between axes of principal stress and strain is not valid.

Introduction

In various metal processes including forming of sheets, rolling of bars, and extrusion of rods, metals are subjected to stresses beyond the yield strength of the material. Often these stresses are not simple stresses acting in one direction, but are combined stresses acting in more than one direction. Structural and machine members are often subjected to combined stresses. To adequately determine the factors of safety for these members, it is necessary to know the plastic stress-strain relations of the material used for various combined stress conditions.

Various theories have been proposed for predicting the plastic stress-strain relations for combined stress in terms of the simple tension plastic stress-strain relation for the material. To determine which theory might be adequate, test results must be obtained for various combined stress conditions, in order to compare the actual with the assumed theoretical behavior. Although there is considerable test data available for combined stress conditions in which the principal stress ratios are constant, relatively little test information is available for vari-

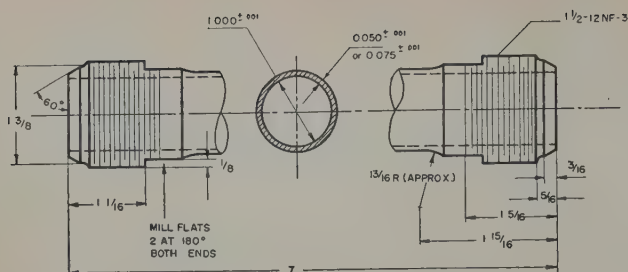


Fig. 1—Tubular specimen tension diagram.

able stress conditions. In order to determine the adequacy of the flow theory,* constant stress ratio

* When reference is made to the flow theory the simple isotropic theory based on the octahedral or significant stress and strain is intended.

tests are inadequate since for the case of constant stress ratios the flow and deformation theories coincide. This paper gives the results of an investigation for both constant and variable combined stress conditions. Special tests are also reported in which the validity of basic assumptions made in flow theory are checked.

Test Procedure

Material Tested and Specimens: The material tested was an aluminum alloy designated as 14S-T6. The material was supplied in the form of hot-rolled machined cylinders $7\frac{1}{4}$ in. long with a $1\frac{1}{8}$ in. OD and a $11/16$ bore. The normal composition in addition to aluminum and normal impurities, consists of 4.4 pct Cu, 0.8 pct Si, 0.8 pct Mn, and 0.4 pct Mg. The Research Laboratories of the Aluminum Co. of America supplied control data on the yield strength, tensile strength, and ductility. These data were obtained primarily to provide information on the degree of anisotropy of the specimens. For this purpose, specimens taken from the cylinders were tested in the axial, lateral, and diagonal directions. The average values of the properties were: yield strength 62,400 psi ± 3 pct, tensile strength 69,100 psi ± 4 pct, elongation in 4 diameters 6.5 to 12 pct. The data supplied showed that only about one-half the percentage variations in strength was due to anisotropy, the remaining differences being due to normal variations in the material.

The dimensions of the machined specimen are given in Fig. 1. Both the inside and outside surfaces of the specimens were machined. The wall thicknesses of the tubular specimens were measured using the apparatus previously described.¹ The ratio of the wall thickness to diameter was selected so as to delay buckling as much as possible and at the same time to yield an essentially uniform stress distribution throughout the wall of the specimen.

Testing Machine: The special tension-torsion machine as shown in Fig. 2 was designed to conduct the tests described in this report. The axial tensile load is applied to the tubular specimen (S) by means of the hydraulic jack (H) through the pulling rod (R). The axial load is measured by the SR-4 dynamometer (D_e). The twisting moment is applied by a $\frac{3}{4}$ hp dc motor (M) and speed reducer (SR). Variation in rate of application of torque load is provided by rheostat (RH) and a motor generator set. A disk (D) is attached to the lower part of the specimen to which cables are connected passing over frictionless pulleys to the bar (B). The torque is measured by the calibrated bar (B) using SR-4

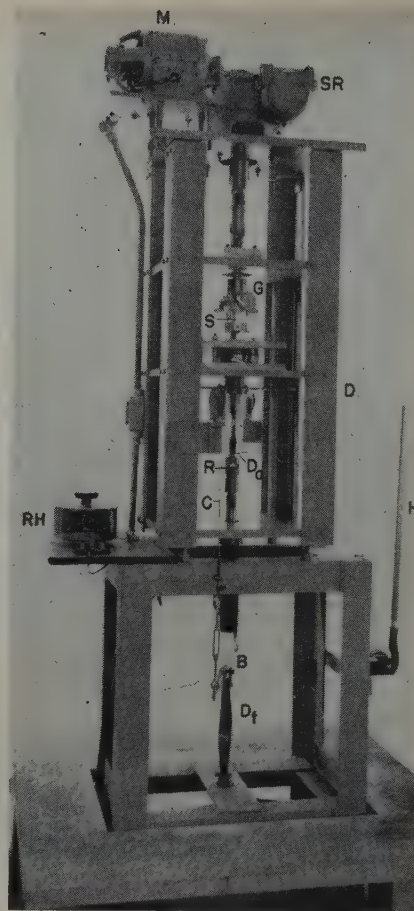


Fig. 2—Tension-torsion testing machine.

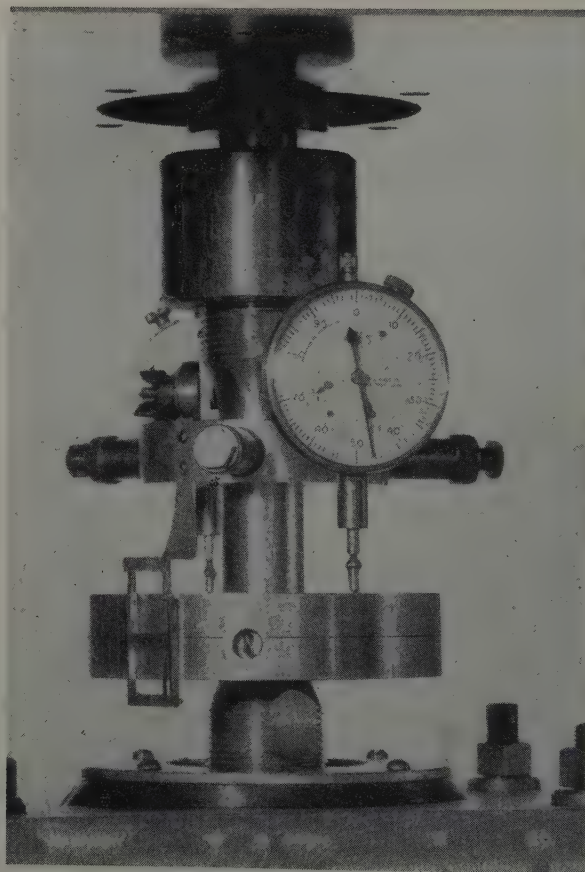


Fig. 3—Tension-torsion strain gage.

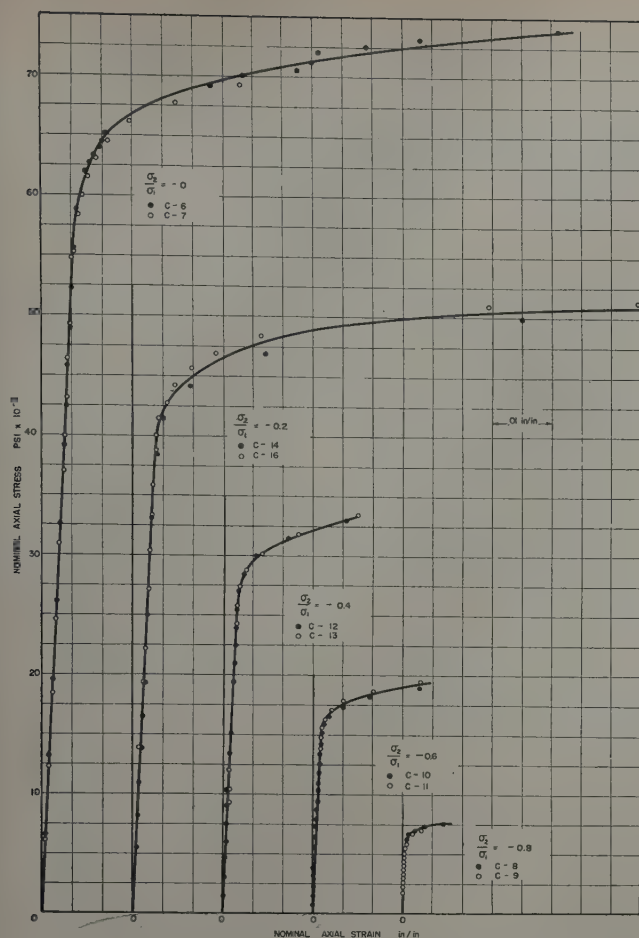
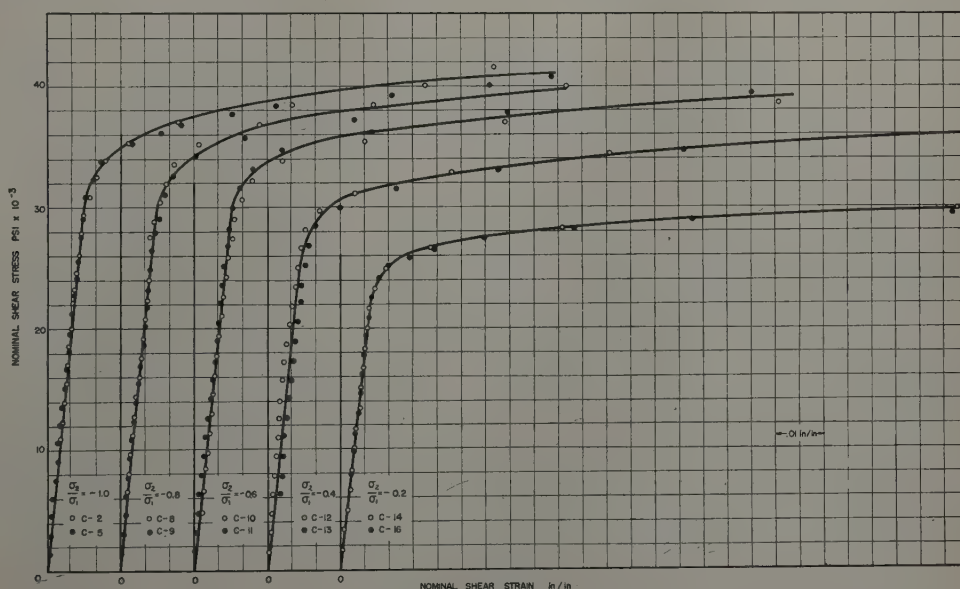


Fig. 4a (above)—Stress-strain relations for constant stress ratio tests, nominal axial stress and strain.

Fig. 4b (right)—Stress-strain relations for constant stress ratio tests, nominal shear stress and strain.



strain readings to indicate the load. A 2000 lb dial-type dynamometer (D_b) is attached to the bar (B) to check the foregoing torque value. In some tests in addition to axial tension and torsion, internal pressure was applied by a specially built pump unit not shown in the Fig. 2.

Method of Measuring Strains: A special mechanical-type strain gage was designed for the measurements of plastic angles of twist and axial strains as shown in Fig. 3. By this mechanical gage, axial strains were measured for a 2 in. gage length by two 0.0001 in. dials placed 180° apart. The angles of twist were measured for a 2 in. gage length by the twistmeter part of the gage. Attachment of the

strain gage to the specimen during plastic flow was maintained by rods which bear on the specimen at one end and are connected by preloaded springs to the strain gage at the other end. By adequate initial spring pressure, the gage remained attached to the specimen without slipping even in cases where the specimen had considerable reduction in diameter.

Method of Testing: The specimen is first assembled in the testing machine with the elastic SR-4 gages and the special mechanical gage as shown in Fig. 3. Increments of axial tensile load and torque are then applied as prescribed by the particular test. For each load increment applied, axial strain and angle of twist readings are recorded.

Constant Stress Ratio Tests

Plastic stress-strain relations for various constant values of the biaxial stress ratios were obtained to provide information on the influence of biaxial stresses on the plastic stress-strain relations and on the yield strength.

Conventional Stress-Strain Results: The average conventional stress-strain curves for various principal stress ratios and for the axial and shear stress components are shown in Fig. 4a and b. The values of the nominal axial and average shear stresses used in Fig. 4 were determined respectively from the approximate relations.

$$\sigma_a^1 = \frac{P}{\pi t(d+t)} \quad [1]$$

and

$$\tau_{xy}^1 = \frac{2M_t}{\pi t(d+t)^2} \approx \frac{2M_t}{\pi dt(d+2t)} \quad [2]$$

where P is the axial load; M_t , the twisting moment; d , the internal diameter of the specimen; and t , the wall thickness.

The nominal axial and shear strains for the above stresses in terms of the measured strains are, respectively,

$$e_a = \frac{\delta_{1a} + \delta_{2a}}{2L_o} \quad [3]$$

$$\gamma_{xy}^1 = \frac{\pi}{360} \frac{(d+t)}{L_o} \rho \quad [4]$$

where δ_{1a} , δ_{2a} are the measured axial strains on op-

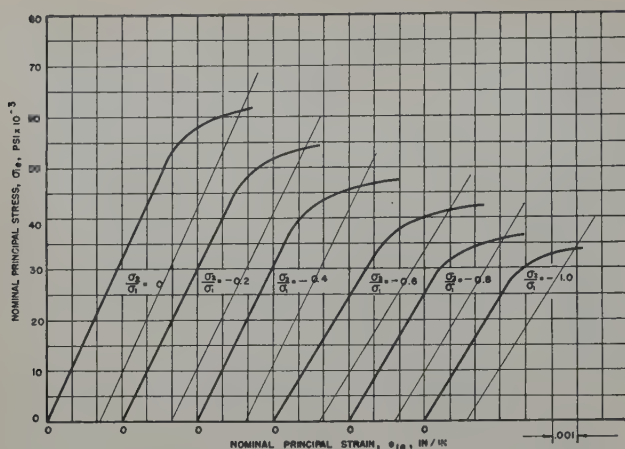


Fig. 5a—Elastic stress-strain relations for constant stress ratio tests for maximum principal yield stress.

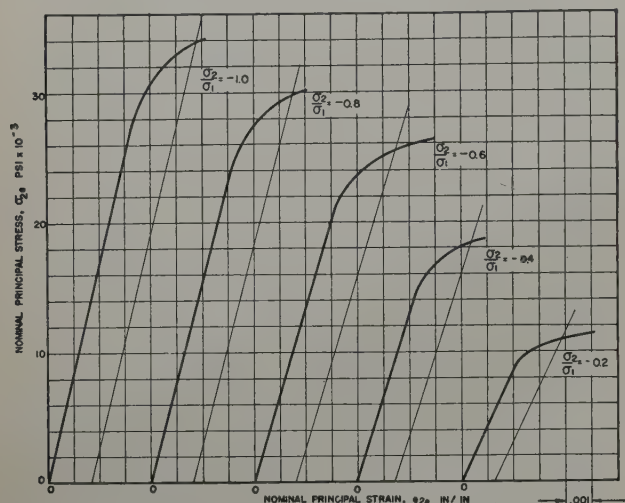


Fig. 5b—Elastic stress-strain relations for constant stress ratio tests for minimum principal yield stress.

posite sides of the specimens; L_0 is the gage length; and ρ , the angle of twist in degrees.

The initial elastic part of the nominal stress-strain diagrams are shown in Fig. 5a and b for the maximum and minimum nominal principal stress values. The values of the nominal principal stresses and strains used for plotting Fig. 5a and b have been shown to be, respectively,

$$\left. \begin{matrix} \sigma_{1e} \\ \sigma_{2e} \end{matrix} \right\} = \frac{\sigma_x^1}{2} \pm \sqrt{\left(\frac{\sigma_x^1}{2}\right)^2 + (\tau_{xy}^1)^2} \quad [5]$$

$$\left. \begin{matrix} e_{1e} \\ e_{2e} \end{matrix} \right\} = \frac{e_x + e_y}{2} \pm \frac{1}{2} \sqrt{(e_x - e_y)^2 + (\gamma_{xy}^1)^2} \quad [6]$$

To define elastic failure or yielding, the yield strength in simple tension will be determined based on an offset strain of 0.002 in. per in., as shown in Fig. 5. For combined stresses an equivalent offset strain value was used to determine yielding.⁷

Plastic Stress-Strain Results: To determine the plastic stress-strain relations, the changes in the dimensions of the specimens must be considered and the true stresses and strains calculated. Fig. 6a and b gives the average true plastic stress-strain relations considering the change in gage length and dimensions in the plastic range. The values of the true stress components in terms of the nominal stresses can be shown to be,² respectively,

$$\sigma_x = \sigma_x^1 (1 + e_x) \quad [7]$$

$$\tau_{xy} = \tau_{xy}^1 (1 + e_x)^{3/2} \quad [8]$$

Ref. 2 also shows that the true strain components are in terms of the nominal strains

$$\epsilon_x = \ln (1 + e_x) \quad [9]$$

$$\gamma_{xy} = \frac{\gamma_{xy}^1}{(1 + 1.5e_x)} \quad [10]$$

The true stresses and strains used in plotting Fig. 6 are those defined in Eqs. 7 to 10.

Analysis and Discussion: A comparison of the experimental and theoretical values of the yield strength for various biaxial stress ratios is given in Fig. 7. The theories shown in Fig. 7 include the distortion energy, and shear theories and a semi-empirical theory by Prager⁸ based on the second and third stress invariants. A comparison of the theoretical values and the test results shows that the yield strengths can best be defined by the Prager theory.

A comparison of the flow theory and experimental results was made by plotting the significant stress-strain relations,⁴ where the significant stress and strain are, respectively,

$$\bar{\sigma} = \sqrt{\sigma_x^2 + 3\tau_{xy}^2} \quad [11]$$

$$\bar{\epsilon} = \sqrt{(\epsilon_x)_p^2 + \frac{1}{3}(\gamma_{xy})_p^2} \quad [12]$$

The total strains and not the increments are considered in the interpretation of these tests, since for constant stress ratio tests the flow theory reduces to the deformation theory. Values of the stress components used in calculating the significant strain are the plastic strains or the total strains less the elastic strains. Fig. 8 gives the significant stress-strain relations for various principal stress ratios. By the flow theory all these relations should coincide with the simple tension plastic stress-strain relation. An examination of Fig. 8 shows that the relations agree approximately and that the flow theory is therefore a good approximation.

In Fig. 6 the plastic stress-strain relations are compared with the values predicted by the flow theory. These results show that the theory gives a reasonable approximation to the test results.

In plotting the theoretical stress and strain values in Fig. 6, the following procedure is used. It is first noted that for constant stress ratios, the deformation and flow theories coincide and the strain components can be shown to be⁴

$$(\epsilon_x)_p = \frac{1}{D} \left[\sigma_x - \frac{1}{2} \sigma_y - \frac{1}{2} \sigma_z \right] = \frac{\sigma_x}{D} \quad [13]$$

$$(\gamma_{xy})_p = \frac{3}{D} \tau_{xy} \quad [14]$$

where D is the plasticity modulus.

The total strains in terms of the stress components then become

$$\epsilon_x = \frac{\sigma_x}{E} + \frac{\sigma_x}{D} \quad [15]$$

$$\gamma_{xy} = \frac{2(1 + \nu)}{E} \tau_{xy} + \frac{3}{D} \tau_{xy} \quad [16]$$

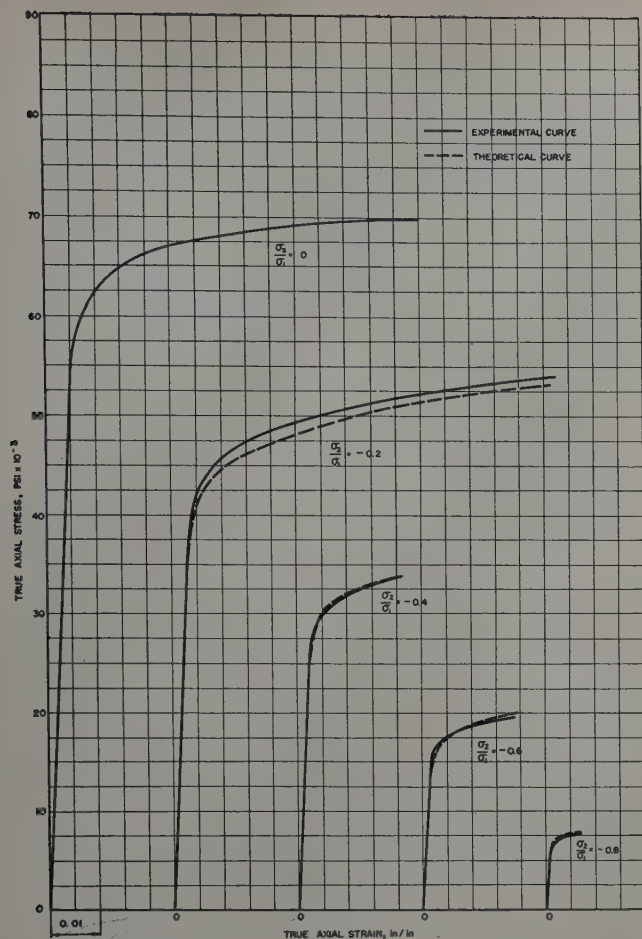


Fig. 6—Comparison of true plastic stress-strain relations with deformation theory for constant stress ratios.
a (above)—True axial stress and strain.
b (right)—True shear stress and strain.

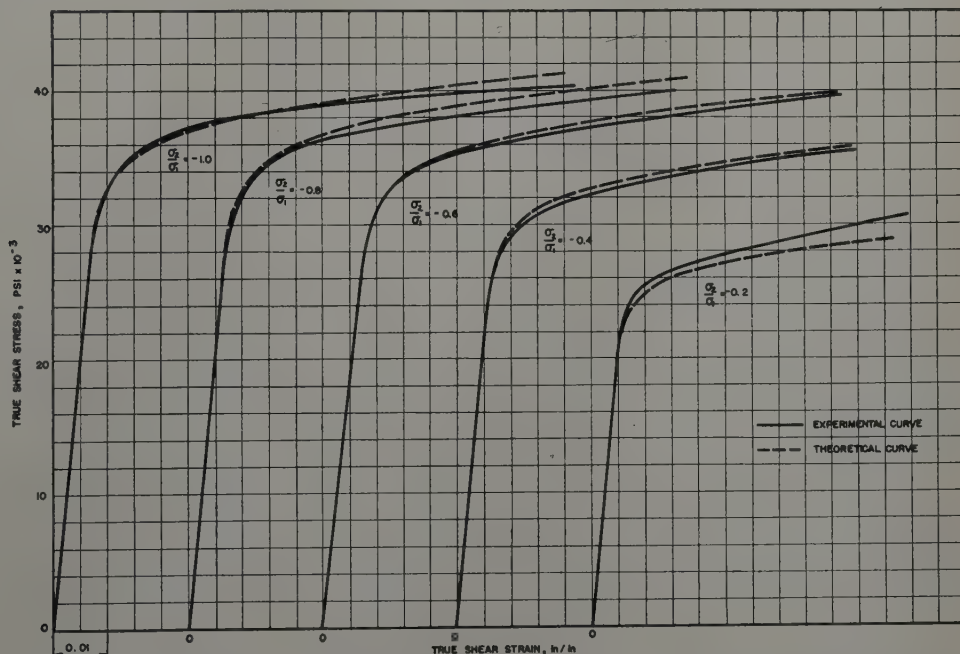
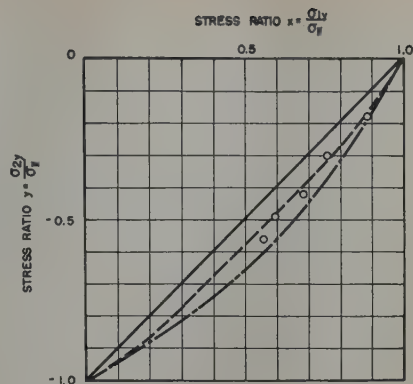


Fig. 7—Comparison of yield strengths with theories of failure. Solid line, shear theory; dashed line, Prager's theory; dash-dot line, deformation theory; circles, test points.



the theoretical strains can be calculated by Eqs. 13 and 14 and the theoretical stress and strain components may then be plotted as shown in Fig. 6.

Variable Stress Ratio Tests Without Unloading—Type A

The foregoing constant stress ratio tests cannot determine the validity of the flow theory, since for constant stress ratios the flow and deformation theories coincide. For this reason, variable stress ratio tests were conducted by applying a stress in one direction followed by stressing in the other direction. Two sets of variable stress ratio tests were made—Set A, in which an axial tensile stress was applied followed by twisting moment and Set B, in which a twisting moment was applied followed by axial tension. In both series of tests various initial amounts of straining in the plastic range were used. Sample nominal stress-strain diagrams for

From Eqs. 11 and 12, for simple tension, $\bar{\sigma}/\bar{\epsilon} = \sigma/\epsilon_p$ and by Eq. 13 for simple tension $\sigma/\epsilon_p = D$ or

$$\frac{\bar{\sigma}}{\bar{\epsilon}} = D \quad [17]$$

Eqs. 11, 13, 14, and 17 can now be used to find the theoretical stress-strain relations. For given values of σ_x and τ_{xy} , $\bar{\sigma}$ can be found by Eq. 11. Using the simple tension plastic stress-strain relations in Fig. 8, for a given stress $\bar{\sigma}$ the strain $\bar{\epsilon}$ can be found from the curve and $D = \bar{\sigma}/\bar{\epsilon}$ determined. With D known,

both the axial and torsional stresses are shown in Figs. 9 and 10. The manner of loading and the amount of initial uniaxial stress and strain are also shown in Figs. 9 and 10. The stage of loading is also indicated by points labeled P_0 , P_1 , and P_2 .

Analysis and Discussion: A comparison of the actual true plastic stress-strain relations with the theoretical relations as given by the flow theory for both Set A and B tests are shown in Figs. 11 and 12 for the sample tests. The determination of the theoretical values for the deformations based on the uniaxial tension test results is described in the fore-

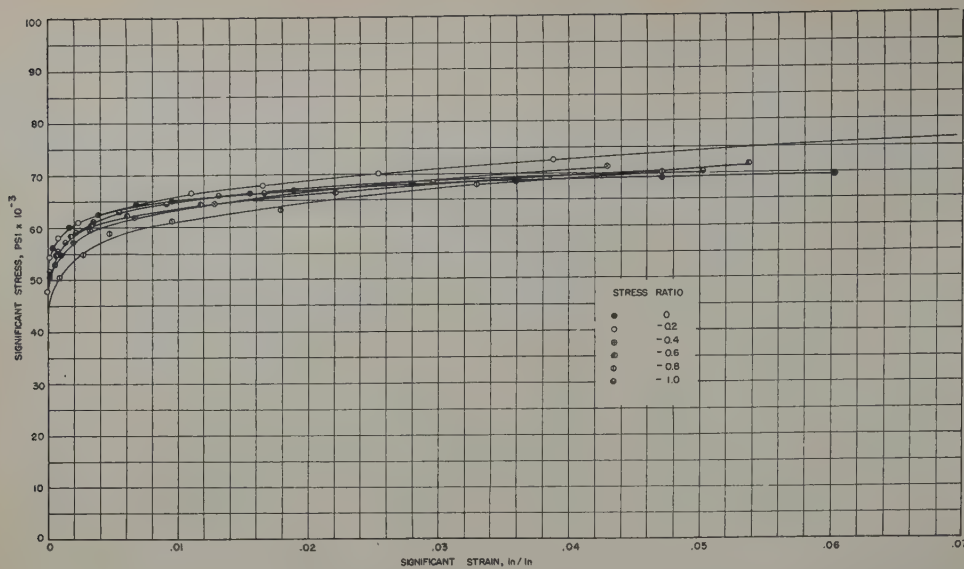


Fig. 8—Comparison of significant stress-strain relations with uniaxial stress-strain values for constant stress ratio tests.

Fig. 9—Nominal stress-strain relations for variable stress ratio tests. Set A.

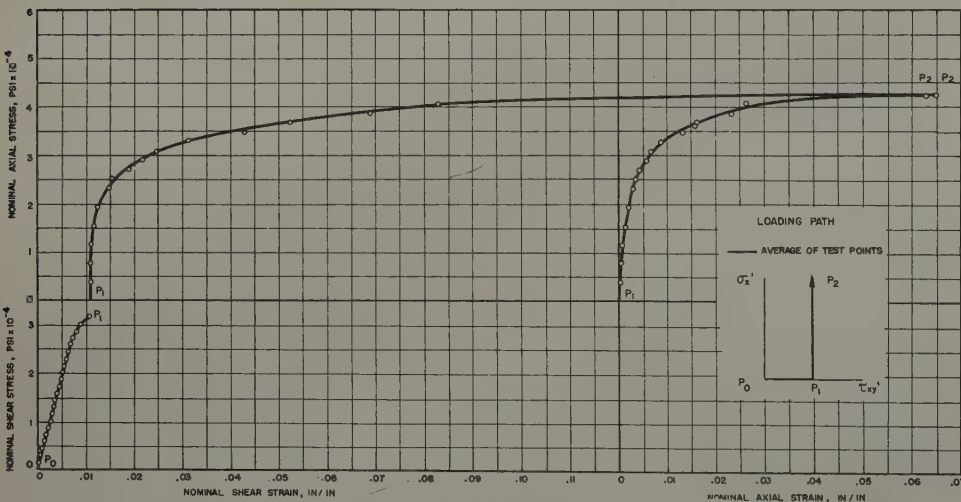
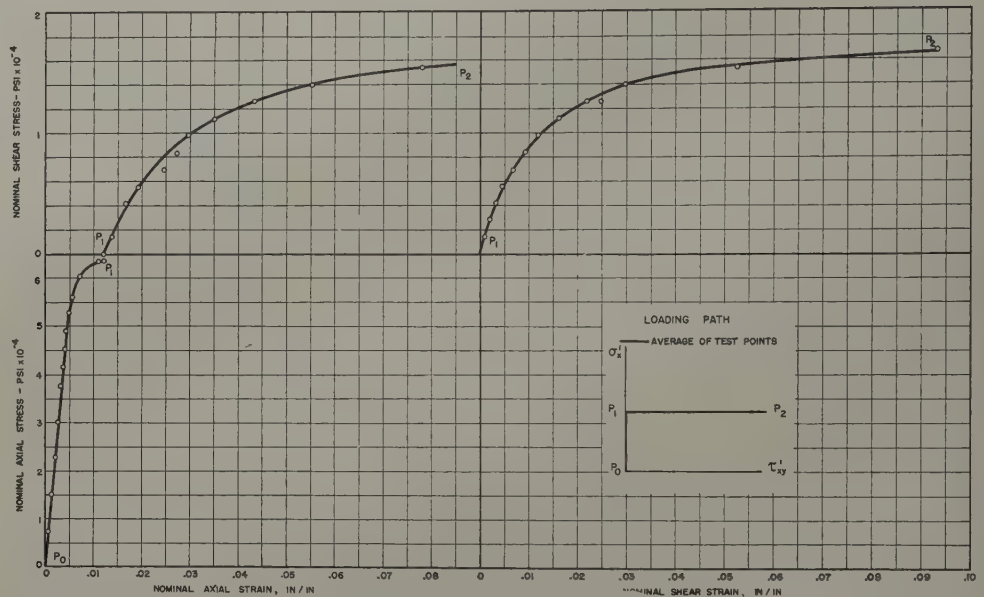


Fig. 10—Nominal stress-strain relations for variable stress ratio tests. Set B.

going section. The theoretical values based on the flow theory were computed as discussed in the appendix. From Figs. 11 and 12 it is seen that the flow theory is in poor agreement with the test results. An empirical relation is also shown in Figs. 11 and 12 based upon the equation

$$\bar{\sigma}^2 = \sigma_x^2 + 3\tau_{xy}^2 + e^{-k\alpha} \sigma_x \tau_{xy} \quad [18]$$

where e is the Naperian base and k and α are ex-

perimental constants. Although this empirical relation proposed has no theoretical basis, it appears to agree well with the test results. The foregoing conclusion was also noted for three other sets of data not included herein because of space limitations. The deformation theory is mathematically inconsistent for variable stress ratios and Figs. 11 and 12 show that this theory is in poor agreement with the test results.

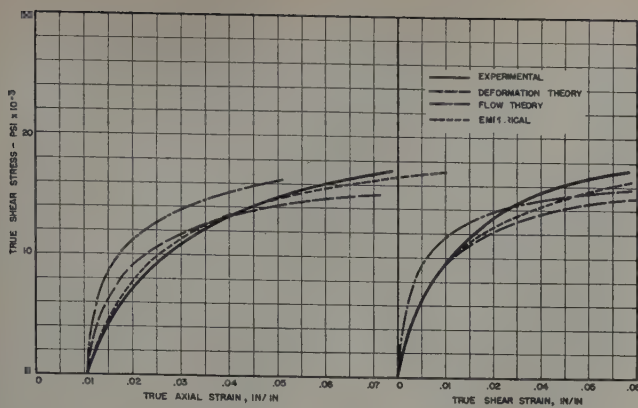


Fig. 11—Comparison of true stress-strain diagrams with plasticity theories for variable stress ratio tests. Set A.

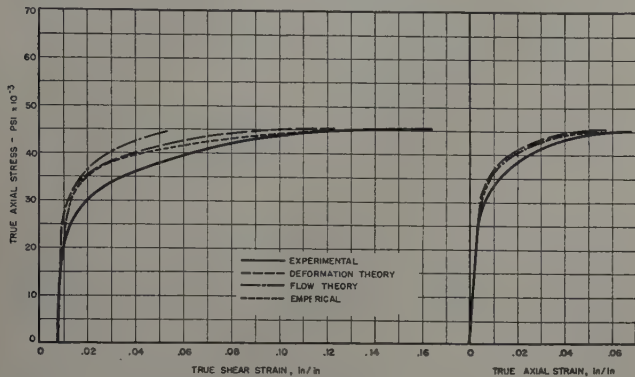


Fig. 12—Comparison of true stress-strain diagrams with plasticity theories for variable stress ratio tests. Set B.

Variable Stress Ratio Tests Without Unloading— Type B

Another type of variable stress ratio test conducted in this study consisted in loading first in tension then torsion followed by tension as indicated in Fig. 13. Four different tests were made in which true initial axial stresses were 54,250, 56,000, 57,100, and 58,100 psi, followed by a shear stress of 14,400 psi in each test prior to final stressing to failure in tension. Another group of four tests illustrated in Fig. 14, consists of loading in the order torsion, tension, and torsion. In these tests initial torsional stresses were selected equal to one-half

the initial tensile values and the subsequent tensile stresses were taken as twice the torsional stress used above or 28,800 psi. The nominal stress-strain relations for one sample of each of these tests are illustrated in Figs. 13 and 14. Figs. 15 and 16 give the true stress-strain relations corresponding to Figs. 13 and 14. The theoretical plastic stress-strain results based on the flow theory are also shown in Figs. 15

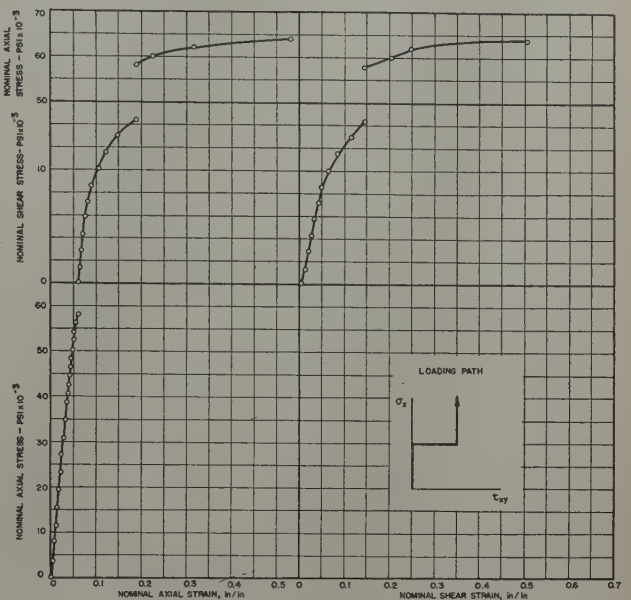


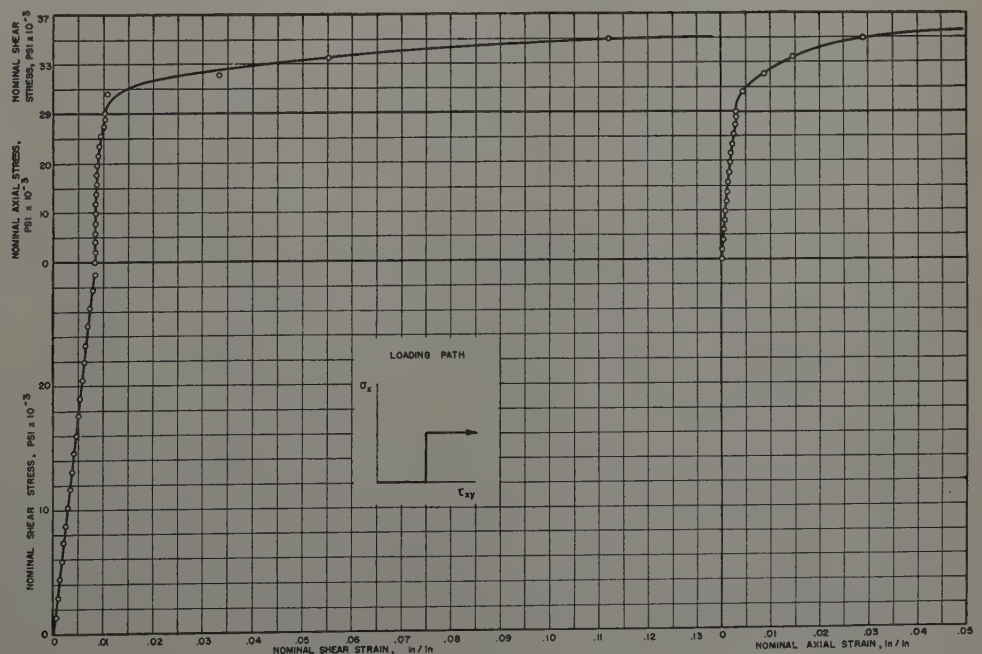
Fig. 13—Nominal stress-strain relations for variable stress ratio tests. Set C.

and 16. All four sets of test results show poor agreement with the flow theory. However, an empirical relation based upon Eq. 18 gives, as indicated in Figs. 15 and 16, a good representation of the test results.

Special Unloading Tests

It is assumed in the isotropic linear flow theories that initial prestrains will not produce anisotropy. In other words, it is assumed that isotropic yielding occurs. To determine the accuracy of this assumption a test was made in which a specimen was stressed first in the axial tension direction to a specified strain value. This axial stress was removed

Fig. 14—Nominal stress-strain relations for variable stress ratio tests. Set D.



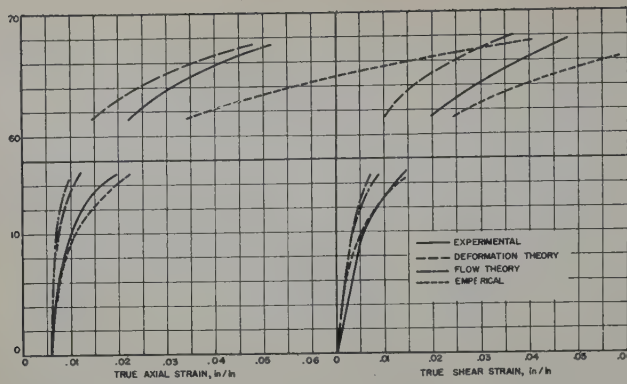


Fig. 15—Comparison of true stress-strain diagrams with plasticity theories for variable stress ratio tests. Set C.

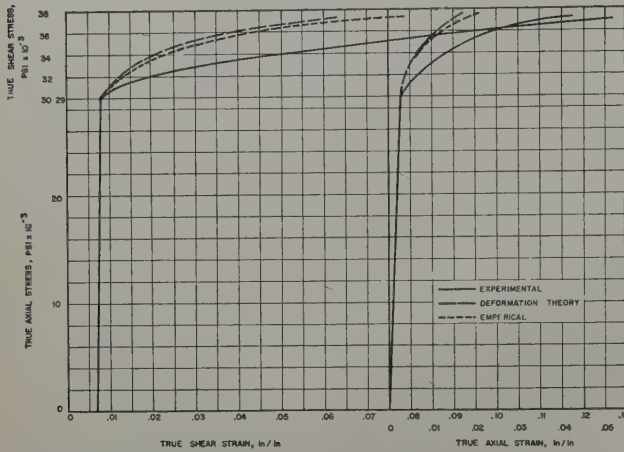


Fig. 16—Comparison of true stress-strain diagrams with plasticity theories for variable stress ratio tests. Set D.

and the specimen was stressed in torsion until failure occurred. Another specimen was initially stressed in torsion to an equivalent initial strain value as used in the first specimen. The torsional stress was then removed and axial tension stress was applied to failure. For the assumption of isotropic yielding to be valid, the nominal stress-strain curves for each of the foregoing tests should coincide.

Two sets of tests were made as described for initial stresses in tension and torsion equal to 120 and 140 pct of the proportional limit stress. A comparison of the stress-strain relations with the nominal stress-strain relations based on pure torsion and simple tension respectively are shown in Figs. 17 and 18. Since these stress-strain relations are in approximate agreement it may be assumed that the assumption of isotropic yielding is verified by these tests.

Variable Stress Ratio Tests

Tests were conducted to determine if the directions of the principal stresses and strains coincide during plastic flow under conditions where the principal stress ratio is variable. For this purpose four tests were conducted in which the significant stress was maintained constant throughout the combined stress loading, but the maximum principal stress direction was varied from 0° to 90° by changing the relative magnitudes of the axial tension, internal pressure, and torque applied. The four tests conducted were for significant stress values of 55,000, 57,500, 59,000, and 60,000 psi. For each load increment the strain components were measured and the directions of the maximum principal strain were computed. The differences between the directions of the maximum principal stress and principal strain

are represented as a function of the principal stress direction in Fig. 19. An examination of these results shows a variation between about 2° and 18° , indicating that the direction of the principal stresses and strains cannot be assumed to coincide.

Conclusions

For the Alcoa 14S-T6 tested and for biaxial stresses obtained in combined tension and torsion the main conclusions that can be made based on the results obtained are:

1—The plastic stress-strain relations for combined stresses and constant stress ratios can be approximately defined by the flow theory.

2—Two types of variable stress ratio tests indicate that the flow theory is inadequate for defining the plastic stress-strain relations.

3—Special unloading tests confirm the assumption of isotropic yielding made in the linear flow theories.

4—The assumption that the direction of the principal stresses and strains coincide is disproved by the test results obtained.

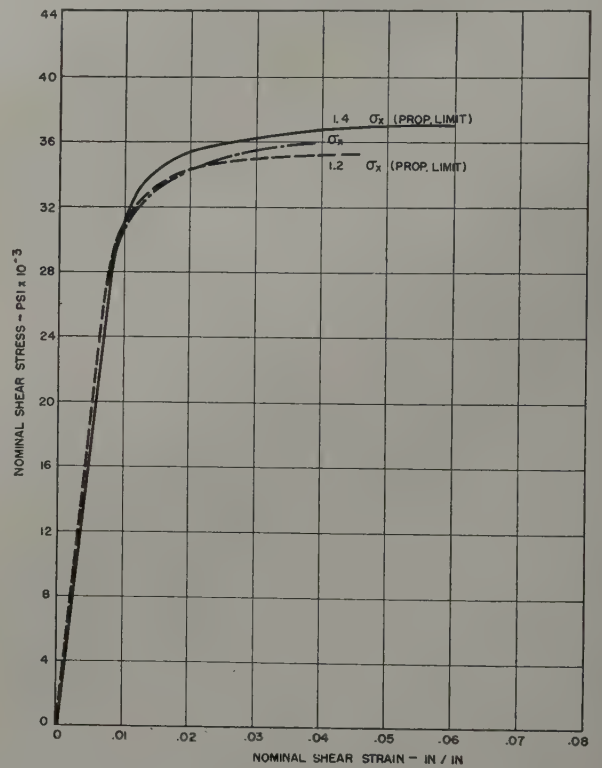


Fig. 17—Comparison of stress-strain relations for special tests with pure torsion.

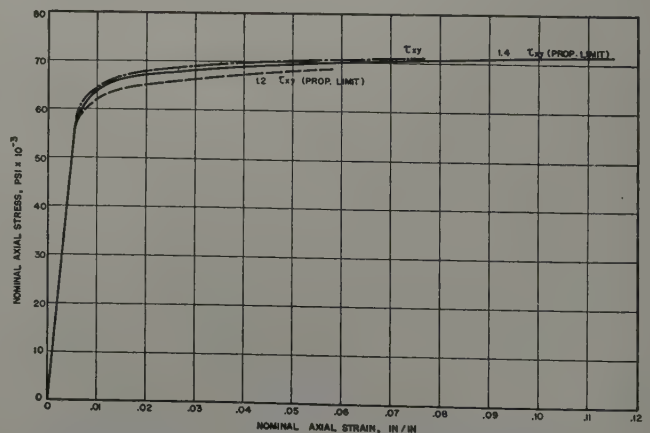
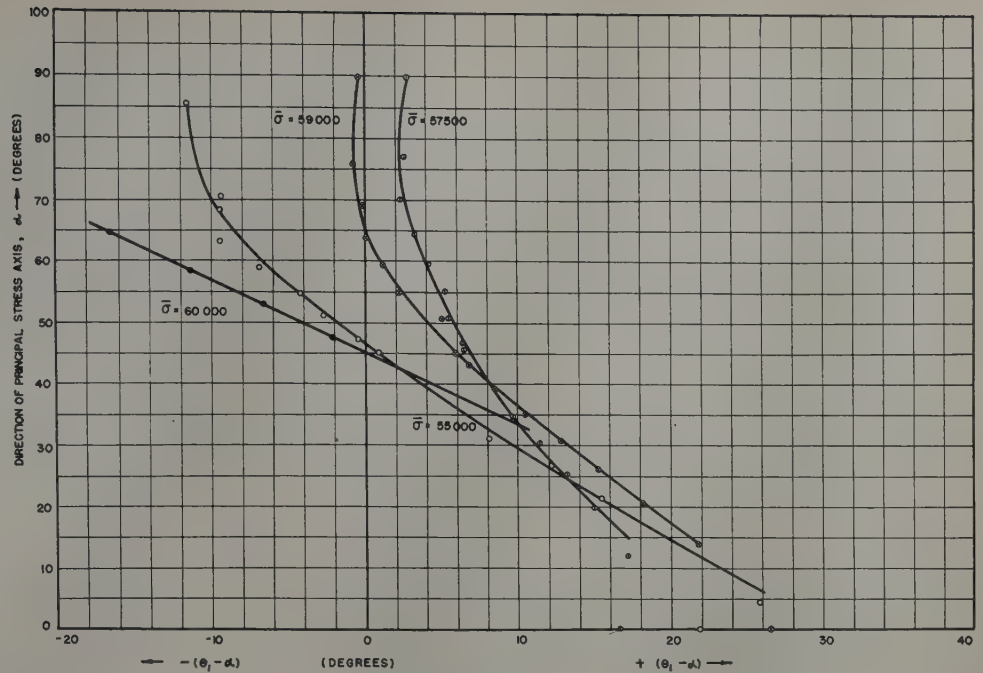


Fig. 18—Comparison of stress-strain relations for special tests with simple tension.

Fig. 19—Comparison of the direction of the principal stress axis with the difference between the direction of the principal strain axis and the direction of the principal stress axis.



Acknowledgments

The research described in this paper was performed in the Plasticity Laboratory of The Pennsylvania State College under the sponsorship and with the financial assistance of the Office of Ordnance Research of the Army Department. H. A. B. Wiseman, L. W. Hu, and J. Hamburg of the Plasticity Laboratory staff conducted the tests. H. A. B. Wiseman also made the necessary calculations for the interpretation of the test results. The testing machine and test specimens were made by S. S. Eckley and L. H. Johnson of the Engineering Mechanics Dept. The assistance given by Office of Ordnance Research and the foregoing individuals in making possible this investigation is greatly appreciated.

Appendix

Determination of Plastic Strain Components by the Flow Theory for Variable Stress Ratios

For an element subjected to normal stresses σ_x , σ_y and σ_z , and shear stress τ_{xy} , τ_{yz} and τ_{zx} , it has been shown⁵ that for the simple type isotropic flow theory the increments of strain are defined as

$$\left. \begin{aligned} \delta \epsilon_x &= \left(\frac{\delta \bar{\epsilon}}{\bar{\sigma}} \right) \left[\sigma_x - \frac{1}{2} (\sigma_y + \sigma_z) \right] \\ \delta \epsilon_y &= \left(\frac{\delta \bar{\epsilon}}{\bar{\sigma}} \right) \left[\sigma_y - \frac{1}{2} (\sigma_z + \sigma_x) \right] \\ \delta \epsilon_z &= \left(\frac{\delta \bar{\epsilon}}{\bar{\sigma}} \right) \left[\sigma_z - \frac{1}{2} (\sigma_x + \sigma_y) \right] \end{aligned} \right\} \quad [19]$$

where

$$\bar{\sigma} = \sqrt{\frac{1}{2} \{ (\sigma_x - \sigma_y)^2 + (\sigma_y - \sigma_z)^2 + (\sigma_z - \sigma_x)^2 \} + 6[\tau_{xy}^2 + \tau_{yz}^2 + \tau_{zx}^2]} \quad [20]$$

and

$$\delta \bar{\epsilon} = \sqrt{(\delta \epsilon_x)^2 + (\delta \epsilon_y)^2 + (\delta \epsilon_z)^2} \quad [21]$$

For many engineering materials, including the alloy reported herein, the simple tensile plastic stress-strain relation can be approximately defined by $\epsilon = K\sigma^n$ where ϵ is the plastic strain; σ , the stress; and K and n are experimental constants. For simple tension and by

$$\text{Eqs. 20 and 21, } \bar{\sigma} = \sigma \text{ and } \bar{\epsilon} = \epsilon, \text{ and since } \epsilon = K\sigma^n \quad [22]$$

Placing the value of $\bar{\epsilon}$ from Eq. 22 in Eqs. 19

$$\left. \begin{aligned} \delta \epsilon_x &= Kn\bar{\sigma}^{n-2} \left[\sigma_x - \frac{1}{2} (\sigma_y + \sigma_z) \right] \delta \bar{\sigma} \\ \delta \epsilon_y &= Kn\bar{\sigma}^{n-2} \left[\sigma_y - \frac{1}{2} (\sigma_z + \sigma_x) \right] \delta \bar{\sigma} \\ \delta \epsilon_z &= Kn\bar{\sigma}^{n-2} \left[\sigma_z - \frac{1}{2} (\sigma_x + \sigma_y) \right] \delta \bar{\sigma} \end{aligned} \right\} \quad [23]$$

For the stress state considered in this investigation

$\sigma_y = \sigma_z = \tau_{yz} = \tau_{zx} = 0$ and then by Eq. 20

$$\bar{\sigma} = \sqrt{\sigma_x^2 + 3\tau_{xy}^2} = \sigma_x \sqrt{1 + 3\alpha^2} \quad [24]$$

where $\alpha = \tau_{xy}/\sigma_x$.

From Eqs. 23 and 24

$$\epsilon_x = \int \delta \epsilon_x = Kn \int_{\alpha_1}^{\alpha_2} \sigma_x^n (1 + 3\alpha^2)^{\frac{n-2}{2}} \delta (1 + 3\alpha^2)^{\frac{1}{2}} \quad [25]$$

Similarly it can be shown that

$$\gamma_{xy} = 3Kn \int_{\alpha_1}^{\alpha_2} \sigma_x^n (1 + 3\alpha^2)^{\frac{n-2}{2}} \alpha \delta (1 + 3\alpha^2)^{\frac{1}{2}} \quad [26]$$

For the case in which σ_x is constant and the stress ratio α is variable Eqs. 25 and 26 become

$$\epsilon_x = \frac{Kn}{n-1} \sigma_x^n [(1 + 3\alpha^2)^{\frac{n-1}{2}}]_{\alpha_1}^{\alpha_2} \quad [27]$$

and

$$\gamma_{xy} = \frac{3Kn}{n-1} \sigma_x^n [\alpha (1 + 3\alpha^2)^{\frac{n-1}{2}} - \int_{\alpha_1}^{\alpha_2} (1 + 3\alpha^2)^{\frac{n-1}{2}} d\alpha] \quad [28]$$

The integral in Eq. 28 can be evaluated by expansion into a Taylor's series. Then for known values of α_1 and α_2 the strains ϵ_x and γ_{xy} can be evaluated.

For the case in which τ_{xy} is constant and the stress ratio α is variable Eqs. 25 and 26 become

$$\epsilon_x = \frac{Kn}{n-1} \tau_{xy}^n [\beta (\beta^2 + 3)^{\frac{n-1}{2}} - \int_{\beta_1}^{\beta_2} (\beta^2 + 3)^{\frac{n-1}{2}} d\beta] \quad [29]$$

$$\gamma_{xy} = \frac{3Kn}{n-1} \tau_{xy}^n [(\beta^2 + 3)^{\frac{n-1}{2}}]_{\beta_1}^{\beta_2} \quad [30]$$

where $\beta = \sigma_x/\tau_{xy} = 1/\alpha$

The integral in Eq. 29 can be evaluated by use of Taylor's series expansion. Then for specific values of β_1 and β_2 , the strains ϵ_x and γ_{xy} can be determined using Eqs. 29 and 30.

References

¹J. Marin, J. H. Faupel, V. L. Dutton, and M. W. Brossman: Biaxial Plastic Stress-Strain Relations for 24S-T Aluminum Alloy: N.A.C.A. T.N. 1536 (1948).
²J. Marin, D. H. Ulrich, and W. P. Hughes: Plastic Stress-Strain Relations for 75S-T6 Aluminum Alloy Subjected to Biaxial Tensile Stresses. N.A.C.A. T.N. 2425 (1951).

³J. Marin: Stress-Strain Relations in the Plastic Range for Biaxial Stresses. *Journal Franklin Inst.* (September 1949) **248**, No. 3, pp. 231-249.
⁴W. Prager: Strain Hardening Under Combined Stresses. *Journal of Applied Physics* (December 1945) **166**, No. 12, pp. 837-840.
⁵A. Nadai: *Theory of Flow and Fracture of Solids*. Vol. 1, Second Edition (1950) New York. McGraw Hill Book Co.
⁶L. W. Hu and J. Marin: Determination of Theoretical Plastic Stress-Strain Relations for Variable Combined Stress Ratios. *Journal of Applied Mechanics* (December 1952) **19**, No. 4, pp. 485-488.

Technical Note

Crystallographic Angles for Orthorhombic (Alpha) Uranium

by R. B. Russell

SINCE Cahn's¹ paper on plastic deformation in orthorhombic (α) uranium an increasing amount of work is to be expected on orientation of single crystals and preferred orientation in this metal. It would seem desirable to have a table of angles (ϕ) between crystallographic planes (hkl) and (HKL). Table I shows these angles as distances from (100),

Table I. Angles Between Crystallographic Planes in Orthorhombic (α) Uranium Calculated from the Data in Ref. 3

hkl	HKL			hkl	HKL		
	(100)	(010)	(001)		(100)	(010)	(001)
h00	0°	90°	90°	130	55.6°	34.4°	90°
0k0	90	0	90	131	57.5	38.4	71.9
00l	90	90	0	132	61.7	46.3	56.9
hk0	—	—	90	133	66.2	53.9	45.6
h0l	—	90	—	134	69.9	55.9	37.5
0kl	90	—	—	135	72.8	64.5	31.5
101	30.0	90	60.0	150	67.6	22.4	90
102	49.1	90	40.9	151	68.2	25.4	77.6
				152	69.6	32.1	66.3
310	9.2	80.8	90	153	71.5	39.4	56.7
311	14.1	81.0	79.3	154	73.4	46.0	48.7
312	29.5	81.9	69.2				
313	30.9	82.0	60.4	172*	74.5	24.2	72.0
110	25.9	64.1	90	061	90	11.2	78.8
331	27.6	64.5	80.2	041	90	16.5	73.5
221	29.5	65.0	75.5	031	90	21.6	68.4
111	37.0	67.2	62.6	021	90	30.7	59.3
223	44.8	69.8	52.1	043	90	41.7	48.3
112	51.4	72.3	44.0	011	90	49.9	40.1
113	60.9	76.3	32.7	045	90	56.0	34.0
114	67.0	79.1	25.8	023	90	60.7	29.3
115	71.1	81.0	21.1	012	90	67.1	22.9
				025	90	71.4	18.6
120	44.2	45.8	90				
241	45.4	46.9	78.3				
121	52.2	49.9	67.5				
243	52.5	53.8	58.2				

* Does not appear with Cu $K\alpha$ x-radiation.

(010), and (001), and in Fig. 1 as a standard (001) stereographic projection. Only the locations of poles whose diffracting planes produce Cu $K\alpha$ reflections up to $\theta = 70.5^\circ$ (i.e. (154)) are given.* The relative

* (172) which does not appear with Cu $K\alpha$ radiation is also shown (ref. 1).

powder diffraction intensities from the lowest order

R. B. RUSSELL is associated with the Division of Industrial Cooperation, Massachusetts Institute of Technology, Cambridge, Mass. TN 179E. Manuscript, June 19, 1953.

Work performed as MIT Metallurgical Project under Contract No. At(30-1)-981 with the United States Atomic Energy Commission.

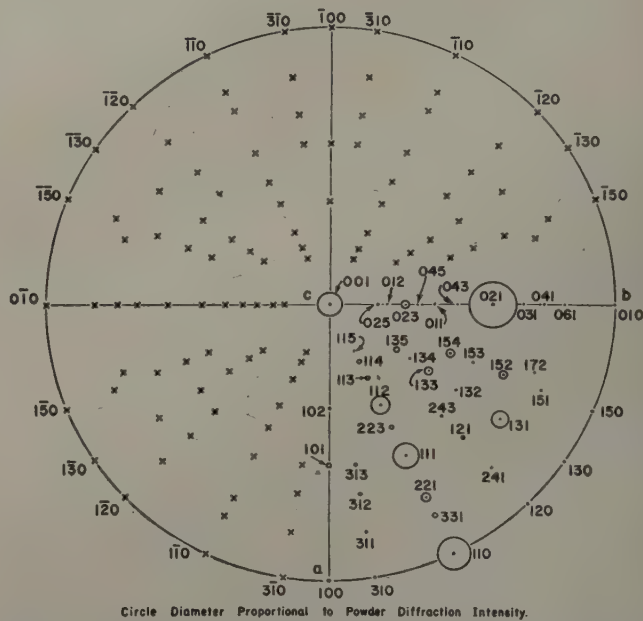


Fig. 1—Standard (001) projection for uranium based on parameters and Cu $K\alpha$ intensities given by Jacob and Warren.³

reflection of these planes are represented by circle diameters. It is hoped that the projection may also be used in making inverse pole figures, originally suggested by Harris.²

Values of ϕ were calculated from the expression

$$\cos \phi = d_{hkl} d_{HKL} \left(\frac{hH}{a^2} + \frac{kK}{b^2} + \frac{LL}{c^2} \right)$$

where the lattice parameters a , b , c , and the spacings d were taken from the work of Jacob and Warren.³ (They report $a = 2.852$ kX (2.8578 Å), $b = 5.865$ kX (5.8768 Å), $c = 4.945$ kX (4.9550 Å).) The parameters reported by them may be subject to revision,^{4,5} accordingly the interplanar angles are listed to only the nearest tenth of a degree.

References

¹R. W. Cahn: *Acta Metallurgica* (1953) **1**, p. 49.
²G. B. Harris: *Philosophical Magazine* (1952) **43**, p. 113.
³C. W. Jacob and B. E. Warren: *Journal ACS* (1937) **59**, p. 2588.
⁴J. S. Lukesh: *Acta Crystallographica* (1949) **2**, p. 420.
⁵J. Thewlis: *Nature* (1951) **168**, p. 198.

Deformation Mechanisms in Alpha Titanium

by E. A. Anderson, D. C. Jillson, and S. R. Dunbar

THE present work was undertaken to furnish information, lacking in the literature, on the deformation mechanisms active in pure titanium at room temperature. Since it was started, Rosi, Dube, and Alexander¹ have indicated that slip can occur in coarse-grained (2 to 6 mm diameter) titanium on the {1010} and {1011} planes and twinning can take place on the {1012}, {1122} and {1121} planes. Liu and Steinberg,² working with titanium flakes produced by fused salt electrolysis, found evidence of twinning on the {1012}, {1121}, {1122}, {1123}, and {1124} planes.

The crystals used in the present work were substantially longer (up to nearly 2 in. in length) and possibly purer.

Production of Large Crystals

It was the purpose of this part of the work to provide single crystal or large grain specimens for use in the deformation studies rather than to study the mechanism of crystal growth. Accordingly, all further exploratory studies on methods were abandoned when it was found that cold-rolled bars sealed in vacuo in individual Vycor tubes and given three or more cycles of 4 hr at 1200°C and three to five days at 850°C, gave large grains. Eighteen specimens about 0.2 in. square x 2 in. long yielded 33 useful grains, ranging from ¼ in. to nearly 2 in. in length, with an agreeably wide range of orientations, Fig. 1.

The 0.25 in. thick strip from which the starting specimens were cut had been reduced 67 pct on 18 in. diameter rolls from a scalped, hot-forged (950° to 1000°C), arc-melted, iodide titanium ingot. The bar was at room temperature, but the rolls were at 200°C. Reductions of about 0.03 in. per pass were used. The bar was cut into four segments, each of which was rolled in a somewhat different manner. No effect on the growth of large grains was noted.

E. A. ANDERSON, Member AIME, and S. R. DUNBAR, Associate Member AIME, are associated with the Research Dept., The New Jersey Zinc Co. (of Pa.), Palmerton, Pa., and D. C. JILLSON, Member AIME, formerly with The New Jersey Zinc Co. (of Pa.), is now with General Electric Co., Syracuse, N. Y.

Discussion on this paper, TP 3594E, may be sent, 2 copies, to AIME by Dec. 1, 1953. Manuscript, April 1, 1953. Cleveland Meeting, October 1953.

Table I. Analysis of Titanium Ingot

Element	Pct	Element	Pct
Oxygen	0.027	Molybdenum	Not detected
Nitrogen	0.002	Lead	0.006
Hydrogen	0.0076	Nickel	Not detected
Carbon	0.05	Copper	0.015
Manganese	0.02	Tin	0.008
Iron	0.02	Magnesium	0.006
Aluminum	0.03	Tungsten	Not detected

Note: Metallic elements determined spectrographically; nitrogen by modified Kjeldahl method; oxygen and hydrogen by vacuum fusion on piece of machined, forged bar; carbon by combustion.

The composition of the titanium, determined on turnings from the ingot scalping operations, is given in Table I. The Rockwell A hardness of the ingot was 26.

The standard starting specimens, about ¼x¼x2 in., were milled on all four sides, hand polished on 280 and 400 mesh emery papers, etched for 3 min in a 50 HF-50 glycerine solution, rinsed, and dried in alcohol and ether just before sealing them in Vycor tubes. The average specimen weight was 7.5 g, and the tube volume was 6.5 cc. A vacuum of less than 1 micron pressure was applied.

The specimen tubes were placed in an evacuated Inconel muffle to minimize the danger of collapse of the glass tubes at temperature. In practice the specimens were first heated to 1200°C for 4 hr and then transferred fairly quickly to an 850°C furnace where they were held for three to five days. This cycle was repeated at least three times before the specimens were cooled, removed from the tubes, lightly polished and etched on one surface for examination. Those in which large grains had not developed were resealed in Vycor and returned to the cycling.

Satisfactory specimens (about one out of every four cycled) were polished with emery paper on all four sides, then metallographically polished using etching between wheels to remove distorted metal and, finally, given a very light etch to reveal the grain boundaries. This was necessary because the surface was roughened by the sublimation of titanium under high temperature vacuum conditions.

Specimens were identified by TiXl numbers using supplementary letters to designate specific grains.

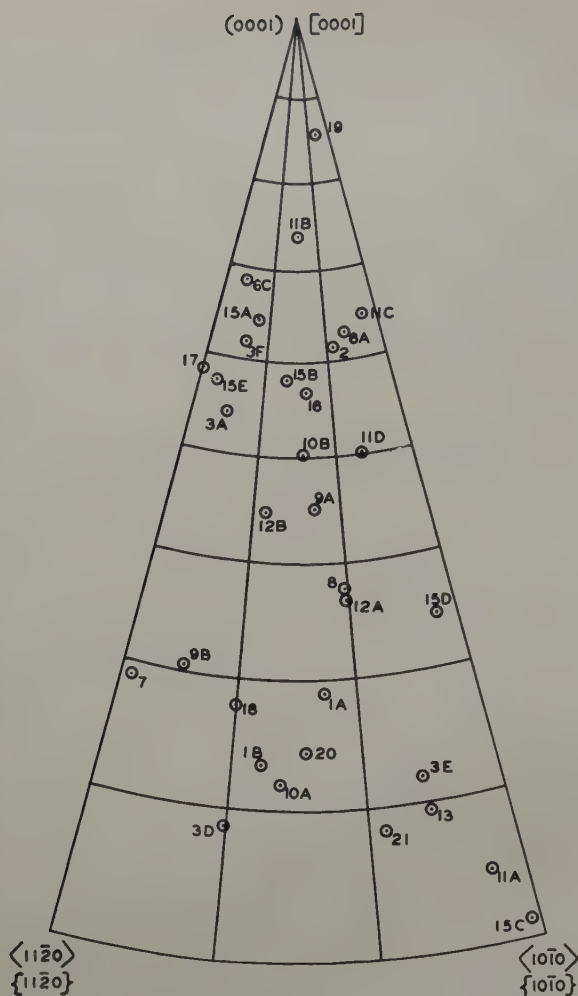


Fig. 1—Orientations of useful large crystals of titanium. Points indicate stereographic projections of specimen axes.

The orientations of the crystals relative to the specimen axis as determined by standard Laue X-ray back-reflection methods are shown stereographically in Fig. 1.

Table III. Effect of Glass Contact on Oxygen Contamination

Specimen No.	Treat-ment	Sample Location	Oxygen, Pct
Ti-138-1	As forged	—	0.04
Ti-138-2, 3, 4	(a)	Middle	0.036(d)
Ti-138-5, 6, 7	(b)	Middle	1.08(d)
Ti-138-8, 9	(c)	Middle	0.068(e)

- (a) Cycled once in 1/5 atm of argon out of contact with glass tube.
 (b) Cycled once in 1/5 atm of argon — specimen immersed in soft glass beads.
 (c) Cycled once in 1/5 atm of argon — specimen in contact with glass tube.
 (d) Average of three runs.
 (e) Average of two runs.

Cycling in vacuo had the disadvantage that the specimen surfaces became roughened and the section thickness reduced by the sublimation of titanium. It had the advantage, however, that the β grain size and shape were revealed by selective evaporation. When the sublimation was suppressed by admitting 1/5 atm of pure argon to the tubes no large grains were obtained.

All of the specimens were contaminated with oxygen, as shown in Table II, which also contains information on the crystal lengths obtained. The specimen ends consistently showed higher oxygen contents than the centers. That the source of the oxygen contamination was the glass containers is indicated by the data in Table III.

The reason for the failure of large grains to develop in the presence of argon is not clear. The fact, however, that the specimen surfaces were not detectably altered in the argon treatment while significant amounts of metal were removed in the vacuum cycling suggests that an effect associated with the surface is involved. The presence of unremoved thin distorted layers from the machining operation or of an oxygen gradient are possibilities. Either source would be minimized by the evaporation of the surface layers in vacuo.

No detailed study of the internal perfection of the crystals was made. Visual inspection of the Laue spots on the back-reflection photograms revealed no recognizable evidence of imperfections but such

Table II. Identification, Length and Analysis of Large Titanium Crystals

Specimen No.	Cycled In	Sample Location	Analysis, Pct			Crystal Length, In.
			O	H	N	
TiX1-2	Vacuum	—	(a)	(a)	(a)	2A $\frac{3}{8}$
TiX1-3	Vacuum	X1-3A	0.11	0.012	(a)	3A 1
TiX1-3	Vacuum	X1-3D	0.058	0.015	(a)	3D $\frac{1}{8}$ – $\frac{1}{2}$ *
TiX1-6	Vacuum	X1-6A	0.14	0.016	(a)	6A $1\frac{3}{4}$
TiX1-6	Vacuum	Spec. end	0.39	(a)	(a)	—
TiX1-6	Vacuum	Adjacent to spec. end	0.18	(a)	(a)	—
TiX1-8	Vacuum	X1-8A	0.18	0.008	(a)	8A $1\frac{1}{4}$
TiX1-9	Vacuum	X1-9A	0.093	0.012	(a)	9A $1\frac{5}{8}$
TiX1-9	Vacuum	—	—	—	—	9B $5/16$
TiX1-9	Vacuum	Spec. end	0.32	0.012	(a)	—
TiX1-10	Vacuum	X1-10A	0.098	0.011	(a)	10A $1\frac{3}{8}$
TiX1-10	Vacuum	—	—	—	—	10B $\frac{5}{8}$
TiX1-11	Vacuum	Spec. end	0.26	0.012	(a)	—
TiX1-11	Vacuum	—	—	—	—	11A $\frac{1}{8}$ – $\frac{5}{8}$ *
TiX1-11	Vacuum	—	—	—	—	11B $\frac{3}{4}$
TiX1-12	Vacuum	X1-12A	0.16	0.008	(a)	12A $1\frac{1}{4}$
TiX1-12	Vacuum	—	—	—	—	12B $\frac{5}{8}$
TiX1-12	Vacuum	Near end	0.24	0.010	(a)	—
TiX1-17	Vacuum	Adjacent to X1-17A	0.039	0.010	(a)	17A $\frac{5}{8}$
TiX1-19	Vacuum	X1-19A	0.17	0.015	(a)	19A $1\frac{1}{2}$
Run 23-1	Argon	Center	0.15	0.011	(a)	—
Run 23-2	Argon	Center	0.13	0.011	(a)	—
Run 22-1	Argon	Center	0.30	0.028	0.002	—
Run 22-2	Argon	Center	0.29	0.019	0.002	—
TiX1-15	Argon	Spec. end	0.16	0.013	(a)	—
TiX1-15	Argon	Other end	0.42	0.007	0.002	—

(a) Not determined.

* Irregular shape.

Table IV. Deformation Mechanisms Observed in Large Titanium Crystals

Crystal No.	Length, In.	Analysis, Pct		Slip Plane	Slip Direction	Critical Resolved Shear Stress, G Per Sq Mm	Twinning Plane	Stress Direction
		O	H					
TiX1-3D	1/8-1/2	0.058	0.015	{1010}	<1120>	5,000	None	Tension
TiX1-9A	1 3/8	0.093	0.012 ^a	{1010}	<1120>	4,500	None	Tension
TiX1-9B	5/16	(a)	(a)	{1010}	<1120>	5,500	None	Tension
TiX1-10A	1 3/8	0.098	0.011	{1010}	<1120>	5,000	None	Tension
TiX1-11A	1/8-3/8	(b)	—	{1010}	(c)	6,700	None	Tension
TiX1-12A	1 1/4	0.16	0.008	{1010}	<1120>	11,700	None	Tension
TiX1-8A	1 1/4	0.18	0.008	{1010}	(d)	6,500	None	Compression
TiX1-1A(e)	1/4	(a)	(a)	{1010}	(d)	(a)	{1012} (f)	Compression
TiX1-1B(e)	1/4	(a)	(a)	{1010}	(d)	(a)	None	Compression
TiX1-2A	3/8	(a)	(a)	{0002}	(g)	(a)	{1121}	Tension
TiX1-3A	1	0.058	0.015	{0002}	<1120>	10,900	{1121}	Tension
TiX1-6A	1 3/4	0.14	0.016	{0002}	<1120>	13,100	(h)	Tension
TiX1-11B	3/4	0.17	0.004	{0002}	<1120>	13,500	(i)	Tension
TiX1-19A	1 1/2	0.17	0.015	(j)	—	—	{1012}	Tension
TiX1-17A	3/8	0.039	0.010	{0002}	(d)	(a)	{1122}	Compression

(a) Not determined.

(b) 0.26 at end of specimen — possibly less in test area.

(c) Probably <1120> but not determined.

(d) Not determined but probably <1120> in opposite sense to tension slip.

(e) From preliminary tests on another iodide titanium bar.

(f) {1012} twinning at crystal boundary.

(g) Not determined but probably <1120>.

(h) {1121} twinning in later stages of deformation.

(i) {1121} and {1012} twinning in later stages of deformation.

(j) No slip detected.

could have been present undetected by this simple test. Where more than one X-ray examination was made on the same grain, the orientations agreed within experimental error. It was judged that the specimens were reasonably perfect and suitable for use in the deformation studies.

Plastic Deformation Studies

Test Procedures: All deformations were made at room temperature in a 20,000-lb capacity hydraulic testing machine at 0.1 in. per min free head speed. Tension specimens were gripped for a length of about 1/4 in. at each end in Templin self-aligning grips. Axiality of loading was judged visually. Gage marks were produced by very fine scratching. Elongations, with load released, were measured at 18X by comparison with a machine-ruled scale graduated in hundredths from which thousandths could be estimated.

For compression testing, the crystals were machined to produce plane, parallel ends on test pieces 1/2 in. in length, giving a length to width ratio of about 3. Compression was carried out between lubricated polished steel plates. In all testing the load was removed periodically to permit measurement of change in length, identification and study of deformation markings and, where desired, X-ray identification of change in orientation.

While no attempt was made to obtain data from which to construct precise stress-strain curves, the yield points usually were determined with sufficient accuracy to permit the calculation of approximate critical resolved shear stresses.

Initial orientations and changes in orientation due to deformation were determined by standard Laue X-ray techniques using a North American Philips Unicam to line up the specimen surface normal to the X-ray beam to within 1/2°. Unfiltered copper radiation was used with a specimen-to-film distance of 1 in. and an exposure time of about 1 hr.

A semitransparent zinc sulphide mirror affixed to the specimen surface provided a reflecting surface for the optical setting-up procedure. This was necessary when the surfaces became too distorted for good light reflection. The mirror was left in place during the X-ray exposure. It caused no difficulty and may have produced some improvement in photograph quality.

Examinations of deformation markings were made with the aid of binocular and metallographic microscopes at magnifications up to 1000X. The angles between the markings and an edge were measured with the revolving stage of the latter. Identification of the operating plane was based on measurements on at least two, and frequently all four, surfaces. Many markings could be traced over an edge but in other cases the numbers and fineness of the markings made definite pairings impossible. In these cases, markings, on two or more surfaces, defining a single low-index type plane were considered definite pairs.

Experimental Results: The deformation mechanisms observed are assembled in Table IV together with the calculated critical resolved shear stresses for slip. The observed and probable slip rotations in tension are plotted stereographically in Figs. 2 and 3. Fig. 4 shows probable directions of slip and slip rotation in compression. Characteristic slip and twin markings are shown in Figs. 5 through 10.

Discussion: It is evident from Figs. 2 to 4 that the crystals may be divided into two groups to facilitate the discussion. In Group 1 are those in which the {0002} plane made angles of from about 5° to about 40° with the specimen axis. Group 2 contains those in which this angle exceeded about 40°.

Group 1: The deformation mechanism operating in this group of crystals was slip on the most highly stressed {1010} plane in the <1120> close-packed direction. While the slip direction in compression was not determined, there seems little doubt that

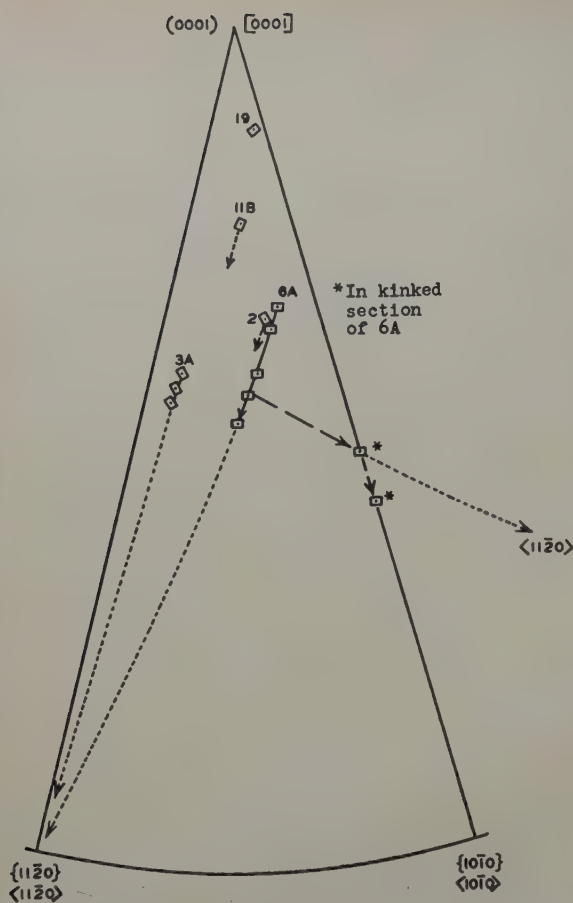


Fig. 2—Rotation due to $\{0002\}$ slip in $\langle 11\bar{2}0 \rangle$ direction in tension. (Also probably $\{10\bar{1}0\}$ slip in another $\langle 11\bar{2}0 \rangle$ direction in part of TiXl-6A.)

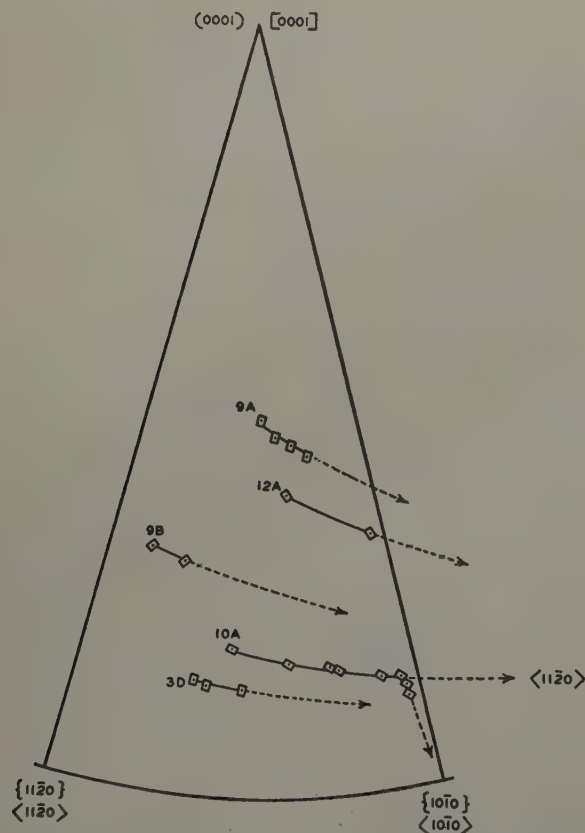


Fig. 3—Rotation due to $\{10\bar{1}0\}$ slip in $\langle 11\bar{2}0 \rangle$ direction in tension.

it was the $\langle 11\bar{2}0 \rangle$ direction in the opposite sense to the tensile slip. The only twinning observed in this series was that incident to local restraints.

The experience of TiXl-10A is worthy of comment. As can be seen in Fig. 3, this crystal was subjected to a very large total extension which was sufficient to rotate it to the point where a second $\{10\bar{1}0\}$ plane should become active. Consequent double slip evidently rotated the specimen axis toward the $\langle 10\bar{1}0 \rangle$ direction. At this time, a kink of the unusual configuration shown in Fig. 11 developed. The Laue X-ray back-reflection patterns establishing the rotation were taken $\frac{1}{8}$ to $\frac{1}{4}$ in. from the kink. No satisfactory patterns were ob-

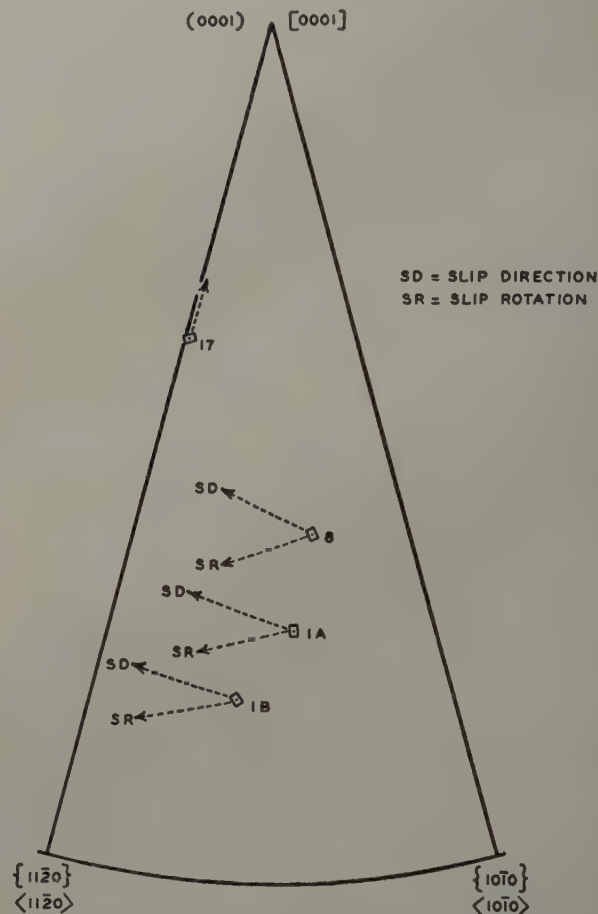


Fig. 4—Probable directions of slip (SD) and slip rotation (SR) due to $\{0002\}$ and $\{10\bar{1}0\}$ slip in compression.

tained in the kink nor were the markings informative.

The critical resolved shear stress for $\{10\bar{1}0\}$ slip in the $\langle 11\bar{2}0 \rangle$ direction was of the order of 5000 g per sq mm. The higher values noted for TiXl-11A, 12A, and 8A probably reflect the influence of higher gas impurity contents.

Group 2: The deformation behavior of this group (Fig. 2) was somewhat complex, requiring more detailed discussion of the tests on the individual crystals. TiXl-2A, 3A, and 6A constitute a group rather similarly oriented but varying in crystal length. Slip on $\{0002\}$ was observed in all three crystals and slip in the most highly stressed $\langle 11\bar{2}0 \rangle$ direction was proved for TiXl-3A and 6A. However, $\{11\bar{2}1\}$ twinning also was observed at extensions which varied with the crystal length. These twins

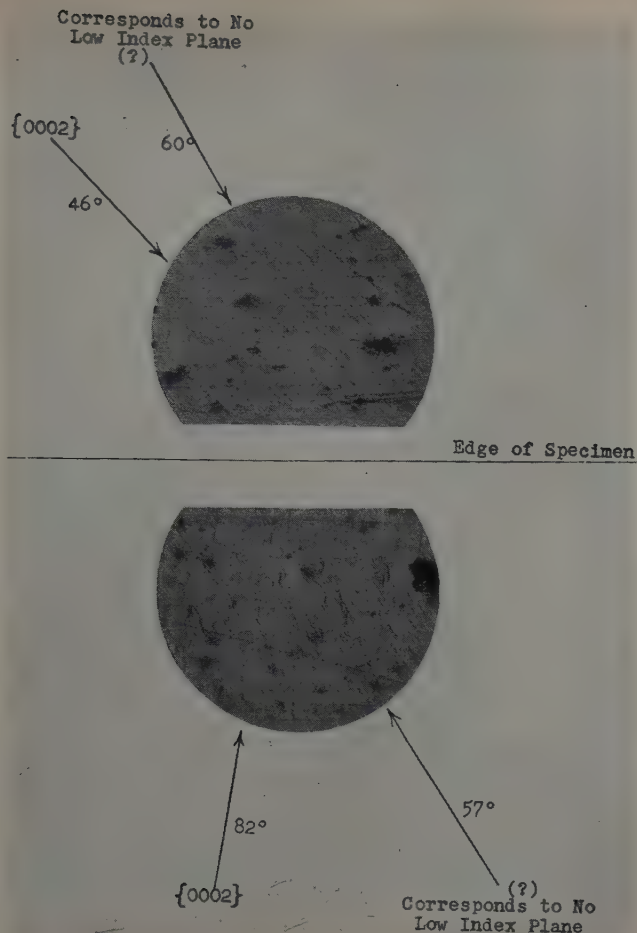


Fig. 5—Micrographs of two adjacent surfaces of TiXl-6A pulled to 10 pct elongation. Note $\{0002\}$ slip and cross markings. X250. Area reduced approximately 60 pct for reproduction.

developed first near the grip or grain boundary restraints, moving toward the crystal center as the extension was increased and possibly largely replacing the basal slip mechanism as the preferred deformation process. Thus TiXl-2A ($\frac{3}{8}$ in. long)

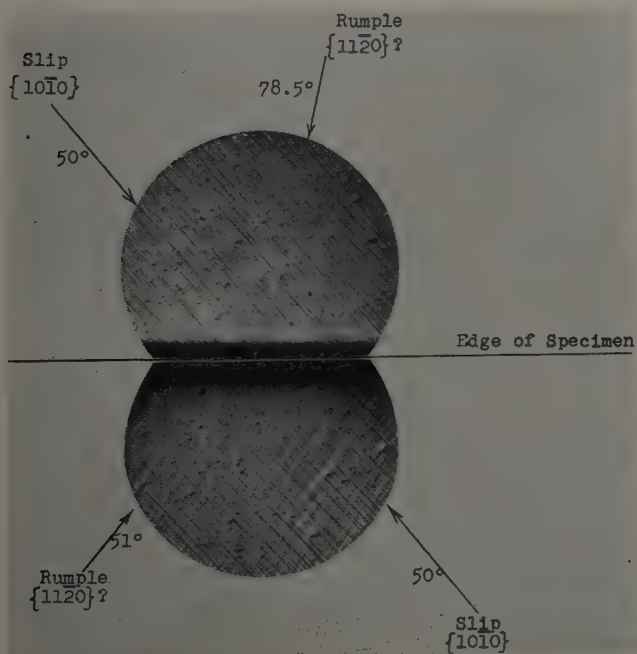


Fig. 6—Micrographs of two adjacent surfaces of TiXl-10A pulled to 12.5 pct elongation. Note $\{1010\}$ slip and $\{1120\}$? rumple marks. X25. Area reduced approximately 60 pct for reproduction.

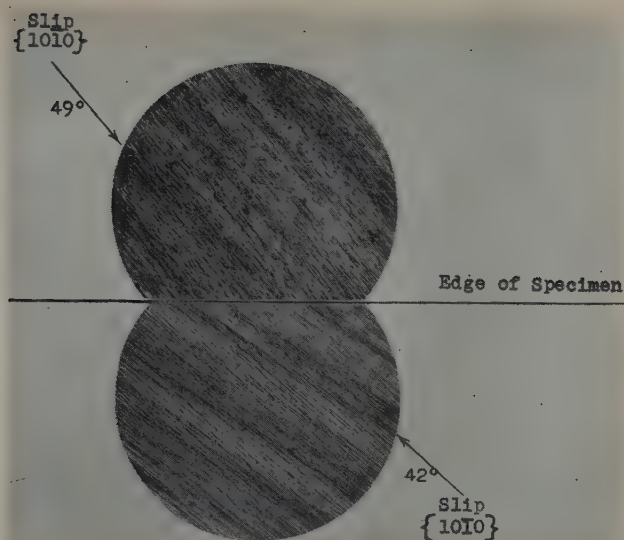


Fig. 7—TiXl-10A pulled to 49.3 pct elongation. Note irregularities in markings. X250. Area reduced approximately 60 pct for reproduction.

showed abundant $\{11\bar{2}1\}$ twinning after small extensions; TiXl-3A (1 in. long) required 9.2 pct extension before twinning at the crystal center was observed; and TiXl-6A ($1\frac{3}{4}$ in. long), while twinned for a distance from each grip, had no twins at the center after 28.2 pct extension.

It seems evident that basal slip is unlikely to be an important mode of deformation in polycrystalline titanium of normal grain size. Perhaps the failure of Rosi, Dube, and Alexander¹ to detect evidence of $\{0002\}$ slip was due to their use of comparatively small crystals of commercial purity titanium.

The considerable length and desirable orientation of TiXl-6A made it of special interest. It was obvious that the rotation due to $\{0002\}$ slip would ultimately reorient the crystal sufficiently to bring the stress on a $\{10\bar{1}0\}$ plane to the critical resolved shear

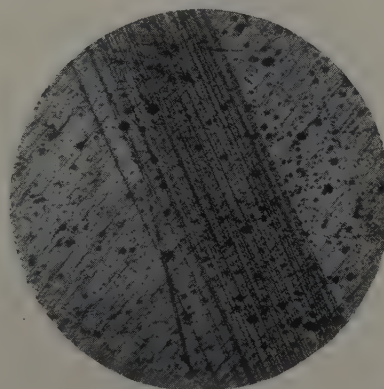
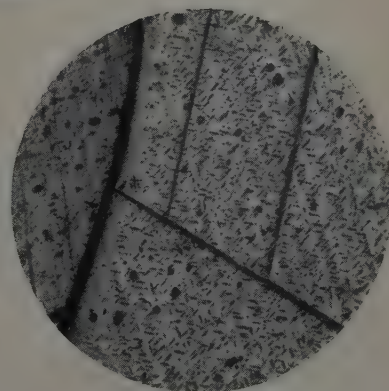


Fig. 8 (left)—TiXl-3A $\{0002\}$ and $\{11\bar{2}1\}$ twinning. Note slight change in slip direction in twinned area. X75. Area reduced slightly for reproduction.

Fig. 9 (right)—TiXl-3E (crystal at right). 2 sets of $\{1122\}$ twins. Crystal at left is 3D showing $\{10\bar{1}0\}$ slip. X75. Area reduced slightly for reproduction.



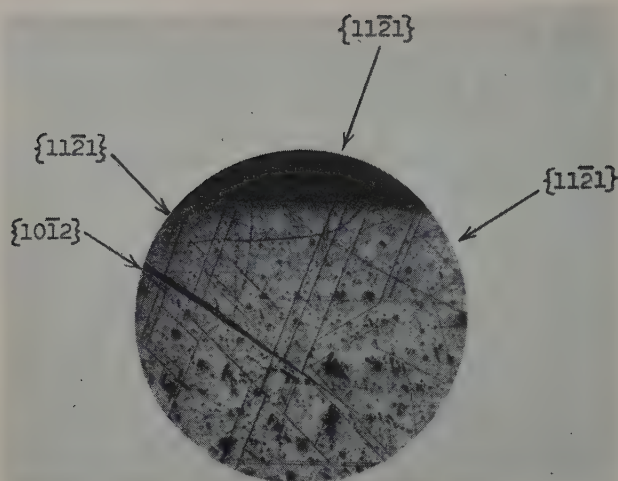


Fig. 10—TiX1-3A showing $\{10\bar{1}2\}$ twin and 3 sets of $\{11\bar{2}1\}$ twins. X75. Area reduced approximately 50 pct for reproduction.

value required to initiate prismatic slip. This apparently happened since a kink developed at the third extension which, from its orientation, seems to have resulted from $\{10\bar{1}0\}$ slip in the $\langle 11\bar{2}0 \rangle$ direction in a limited volume of the crystal.

After the fourth extension, the main crystal showed only a continuation of the basal glide rotation while the orientation of the metal in the kink indicated double slip with rotation toward the $\langle 10\bar{1}0 \rangle$ pole. Due, possibly, to the considerable extension applied to the crystal, the deformation markings in the kink were indeterminate.

The critical resolved shear stress for $\{0002\}$ slip in the $\langle 11\bar{2}0 \rangle$ direction was calculated to be about 10,900 to 13,500 g per sq mm. The lower value was obtained on the purest crystal and is probably the more nearly correct one.

TiX1-11B represents a crystal with a somewhat steeper angle between the basal plane and the specimen axis. While only a single small extension (0.8 pct) was applied, markings consistent with $\{0002\}$ slip and $\{11\bar{2}1\}$ and $\{10\bar{1}2\}$ twinning were found.

TiX1-19A had the steepest angle of any of the crystals at hand. Extension to the extent of 14.5 pct

resulted in abundant $\{10\bar{1}2\}$ twinning. While final inspection of the crystal was made difficult by the roughening effect of the extensive $\{10\bar{1}2\}$ twinning, no evidence of any other deformation mechanism was observed at this stage or earlier.

TiX1-17A (Fig. 4), tested in compression, showed evidence of $\{11\bar{2}2\}$ twinning and $\{0002\}$ slip. The twinning was noted at an earlier stage in the deformation than was the basal slip. This is in contrast with the tension experience with TiX1-2A, 3A, and 6A in which basal slip preceded the $\{11\bar{2}1\}$ twinning.

Slip Markings: While the identification of the slip planes and directions is conclusive, the markings themselves had some peculiarities. Seldom had they the clear-cut appearance of similar markings in zinc. The basal plane slip markings characteristically showed cross linkages, the angles of which with an edge corresponded to no plane of low index (Fig. 5). It is the writers' suggestion that these might represent an unresolved (at 1000X) com-

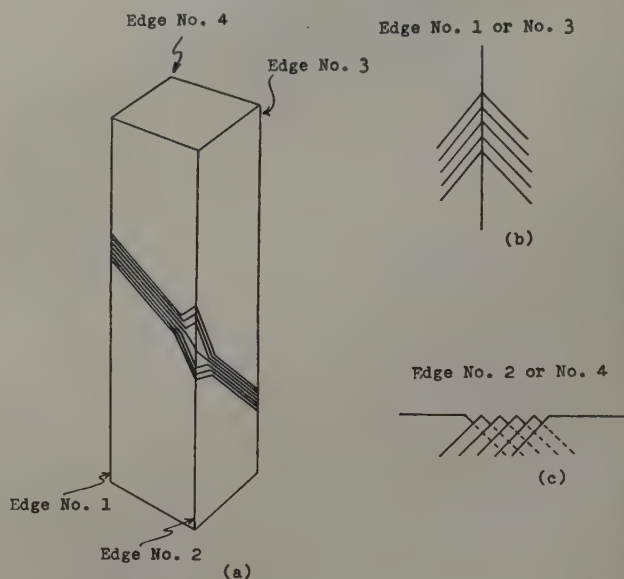


Fig. 12—Effect of edges on $\{11\bar{2}1\}$ twinning.

posite slip between the basal plane and some other, probably pyramidal, plane having a close-packed direction in common.

$\{10\bar{1}0\}$ slip lines appear simple in nature at low extensions but become irregular at greater extensions. This results (Fig. 7) in a light and dark banding of a hill-and-valley type at a small angle to the slip markings. These are quite similar in appearance to the striae observed by Calnan⁸ in stretched single crystal aluminum specimens and attributed to areas of complex slip, possibly including rotational (polar) slip. Rumpling or kinking about an $\langle 0001 \rangle$ axis giving approximate $\{11\bar{2}0\}$ markings is apparent at the lower elongations (Fig. 6). The latter bands differ in appearance and probable origin from the former and can be rationalized without assuming complex slips (ref. 4).

Twin Markings: The three twinning planes found in this work have characteristic appearances. $\{10\bar{1}2\}$ twins in titanium resemble those in zinc and magnesium. They are broad and lenticular and appear to increase in width with increase in stress. $\{11\bar{2}1\}$ twins, on the other hand, are narrow and straight. They appear to traverse the entire width of a crys-

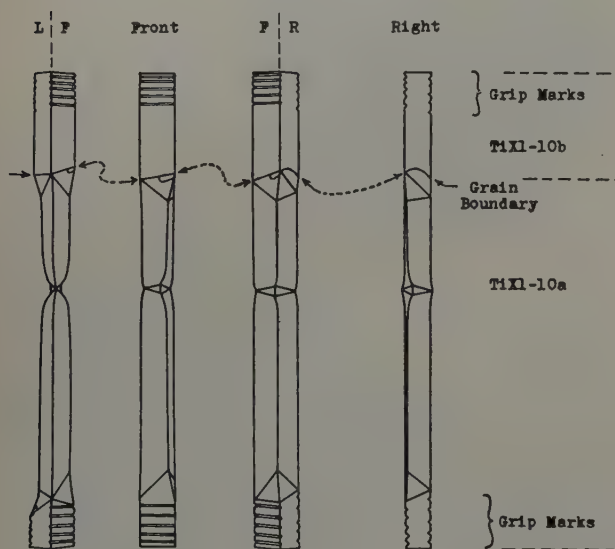


Fig. 11—Appearance of TiX1-10A after final extension. Note kink at center and bend plane adjustments to grips and grain boundary restraints.

Table V. Identification of Deformation Planes

Mechanism	Plane	Rosi, Dube, Alex- ander	Liu, Stein- berg	Pres- ent Work
Slip	{10 $\bar{1}$ 0}	X	(a)	X
Slip	{10 $\bar{1}$ 1}	X	(a)	(b)
Slip	{0002}	(b)	(a)	X
Twinning	{10 $\bar{1}$ 2}	X	X	X
Twinning	{11 $\bar{2}$ 1}	X	X	X
Twinning	{11 $\bar{2}$ 2}	X	X	X
Twinning	{11 $\bar{2}$ 3}	(b)	X	(b)
Twinning	{11 $\bar{2}$ 4}	(b)	X	(b)

(a) Not reported — apparently not looked for.

(b) Did not find.

tal. A branching habit near alternate crystal edges appear common. This is shown diagrammatically in Fig. 12. Twinning leaves exposed corners at edges Nos. 2 and 4 (Fig. 12c) but not at edges Nos. 1 and 3 (Fig. 12b). The specimen tends to avoid the high energy condition of Fig. 12c by twinning on an alternative {11 $\bar{2}$ 1} plane that produces the form of Fig. 12b; or perhaps it should be said that the formation of an initial twin changes the stress distribution along the edge sufficiently to change the active plane. {11 $\bar{2}$ 1} twins do not appear to grow with increased specimen stressing; instead new twins appear. {11 $\bar{2}$ 2} twins are intermediate in appearance between the {11 $\bar{2}$ 1} and {10 $\bar{1}$ 2} twins.

Twinning directions and shears were not given close attention, but observations on TiX1-3A suggested that the twinning direction for {11 $\bar{2}$ 1} twinning was perpendicular to the trace of that plane in the basal plane.

Comparison with Other Work: The deformation planes identified by Rosi, Dube, and Alexander, Liu and Steinberg, and the present writers are set forth in Table V.

There is agreement on the identification of {10 $\bar{1}$ 0} slip and {10 $\bar{1}$ 2}, {11 $\bar{2}$ 1} and {11 $\bar{2}$ 2} twinning. Rosi et al. detected {10 $\bar{1}$ 1} slip while the present workers did not. The present workers established the reality of basal slip which Rosi et al., for reasons

discussed earlier, did not find. Liu and Steinberg report {11 $\bar{2}$ 3} and {11 $\bar{2}$ 4} twinning which were not observed by Rosi et al. or the present writers at room temperature.

The best conclusion at present seems to be that α titanium is capable of deforming by slip on the {10 $\bar{1}$ 0} and {0002} planes and by twinning on the {10 $\bar{1}$ 2}, {11 $\bar{2}$ 1}, and {11 $\bar{2}$ 2} planes. In view of this unexpectedly large number of operating planes, it should not be surprising to find that additional planes can be active.

Summary

Large grains of α titanium can be grown by cycling several times between 4 hr at 1200°C and three to five days at 850°C in vacuo.

Alpha titanium can deform at room temperature by slip in the $\langle 11\bar{2}0 \rangle$ direction on the {10 $\bar{1}$ 0} plane at a critical resolved shear stress of about 5000 g per sq mm or on the {0002} plane in the $\langle 11\bar{2}0 \rangle$ direction at a critical resolved shear stress of about 11,000 g per sq mm.

Alpha titanium can deform at room temperature by twinning on the {10 $\bar{1}$ 2}, {11 $\bar{2}$ 1}, and {11 $\bar{2}$ 2} planes. The choice of deformation mechanism was dependent largely upon the crystal orientation and the direction of stressing but in the case of {0002} slip was also related to crystal size.

Acknowledgments

This work was carried out under contract with the Watertown Arsenal to whom the writers are indebted for permission to publish. They are deeply grateful to C. H. Mathewson for his advice and counsel during the work and to C. B. Tennant for his careful X-ray examinations.

References

- ¹ F. D. Rosi, C. A. Dube, and B. H. Alexander: *Trans. AIME* (1952) **194**, p. 189; *JOURNAL OF METALS* (February 1952).
- ² T. S. Liu and M. A. Steinberg: *JOURNAL OF METALS* (October 1952) p. 1043.
- ³ E. A. Calnan: *Acta Crystallographica* (1952) **5**, p. 557; *Trans. AIME* (1952) **191**, p. 526; *JOURNAL OF METALS* (May 1952).
- ⁴ N. K. Chen and C. H. Mathewson: *Trans. AIME* (1951) **191**, p. 653; *JOURNAL OF METALS* (August 1951).

Technical Note

Filler Material for the Brazing of Titanium

by N. A. DeCecco and H. M. Meyer

IN the early stages of a titanium brazing investigation, binary titanium systems partially or completely known and fundamental metallurgical data were surveyed to select the pure metal most likely to be satisfactory for producing a ductile high strength joint.

The phase diagrams for the purpose of this survey were classified into two groups: 1—systems with

large solubility in β titanium, but negligible solubility in α titanium, and 2—systems with large solubility in α titanium.

Those metals with melting points believed to be too high or too low for titanium brazing ($T_m = 1730^\circ\text{C}$) were eliminated from consideration. The melting points of vanadium, tungsten, tantalum, hafnium, zirconium, and the platinum group are too high and those of zinc, lead, cadmium, and tin are too low.

The remaining metals were grouped as follows:

1—large β solubility: Cr,¹ Mn,² Fe,³ Co,⁴ Ni,⁵ Cu,⁶ Be,⁷ Si.⁸ 2—large α solubility: Al.⁹

N. A. DeCECCO and H. M. MEYER, Member AIME, are associated with the Welding Section, Armour Research Foundation of Illinois Institute of Technology, Chicago.

TN 177E. Manuscript, Feb. 19, 1953; revision, May 18, 1953.

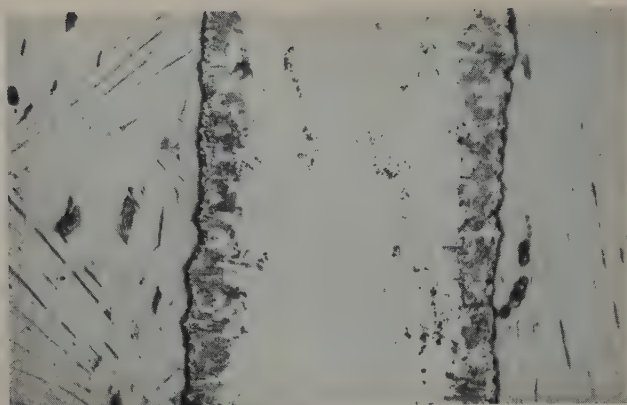


Fig. 1—Silver brazed joint of titanium. Note the columnar grains of the compound growing from the interfaces into the silver. Etchant: 60 cc $C_2H_5O_2$, 20 cc HNO_3 , 20 cc HF. X500. Area reduced approximately 50 pct for reproduction.

It was noted that the sequence of elements from chromium through copper follow titanium in the first long period of elements. The corresponding metals in the second and third long period, zirconium through palladium and hafnium through platinum, as well as vanadium, the immediate neighbor, were eliminated because of their melting points. Therefore, only the metals of subgroup I-b, silver and gold, remain from the second and third long periods for consideration as filler materials.

Gold¹⁰⁻¹² and the metals listed in groups 1 and 2 form intermetallic compounds with titanium (Table I) which are known to be brittle. This brittleness is undesirable for a brazing material because the compound formation imparts brittle physical properties to the joint.

The metal remaining is silver. Silver and titanium were either believed to be immiscible in both the liquid and solid states^{10, 11} or to have a solubility of at least 2 pct Ag in Ti.¹³ Metals of subgroup I-b are known to show frequent similarities in their metallurgical behavior. Furthermore interatomic spacing of silver and titanium differs by only 2 pct and both have close-packed structures; a circumstance which is considered favorable for formation of solid solutions. Therefore the brazing of titanium with fine silver was tried.

Experiments in a helium atmosphere furnace were conducted to determine the wetting properties of molten silver on a heated titanium surface. It was found that silver wet and flowed; metallographic examination of the specimens indicated alloying of the two metals. Subsequently, brazed joints were made with fine silver as the filler metal. The joints were made of 1x $\frac{1}{8}$ in. strips of commercially pure titanium clamped vertically in a fixture with a $\frac{1}{8}$ in.

overlap. A length of fine silver wire was placed across the end of one titanium specimen and covered with dry powdered flux composed of 10 pct AgCl, 36 pct KCl, 9 pct LiF, and 45 pct NaCl. The joint was then heated with an oxyacetylene torch, until the fine silver fused and flowed into the capillary space.

The ultimate shear strengths of the joints have a mean value of 31,500 lb per sq in. with a standard deviation of 5400 lb per sq in. All the specimens break with a ductile shear fracture.

Metallographic studies of the Ti-Ag brazed joints indicate the presence of an intermetallic compound which exhibits considerable ductility. This experimental observation contradicts the consideration that an extended solid solubility can be expected. Instead an equiatomic compound forms which is not brittle. It is an open question why this is so. This compound seems to serve as a kind of bridge between the two metal structures because of their structural and geometric similarities. Fig. 1 is a micrograph of a joint cross-section. The black lines at the titanium-brazed metal interface are caused by metallographic etching relief. Adjacent to the black line is the columnar structured compound which formed on the titanium surface and extends into the brazed metal.

It was believed that an investigation to determine the composition and confirm the ductility of the compound was warranted. The details and results of the subsequent study are reported elsewhere.¹⁴

Acknowledgments

This work was sponsored by Watertown Arsenal, whose permission to publish this paper is gratefully acknowledged. The authors also wish to express their appreciation to C. A. Johnson for the metallographic work.

References

- ¹ P. Duwez and J. L. Taylor: *Trans. ASM* (1952) **44**, p. 495.
- ² D. J. Maykuth, H. R. Ogden, and R. I. Jaffee: *Trans. AIME* (1953) **197**, p. 225; *JOURNAL OF METALS* (February 1953).
- ³ R. J. Van Thyne, H. D. Kessler, and M. Hansen: *Trans. ASM* (1952) **44**, p. 974.
- ⁴ B. Egeberg: *Abh. Inst. Metallk. Elektromet.*; T. H. Aachen (1915) **1**, No. 1, p. 37.
- ⁵ J. R. Long et al.: U. S. Bur. Mines Publ. R. I. 4463 (1949).
- ⁶ A. Joukainen, N. J. Grant, and C. F. Floe: *Trans. AIME* (1952) **194**, p. 766; *JOURNAL OF METALS* (July 1952).
- ⁷ P. Ehrlich: *Ztsch. anorg. allgem. Chem.* (1949) **259**, p. 1.
- ⁸ M. Hansen, H. D. Kessler, and D. J. McPherson: *Trans. ASM* (1952) **44**, p. 518.
- ⁹ E. S. Bumps, H. D. Kessler, and M. Hansen: *Trans. AIME* (1952) **194**, p. 609; *JOURNAL OF METALS* (June 1952).
- ¹⁰ F. Laves and H. J. Wallbaum: *Naturwissensch.* (1939) **27**, p. 674.
- ¹¹ E. Raub, P. Walter, and M. Engel: *Ztsch. Metallk.* (1952) **43**, p. 112.
- ¹² P. Duwez and C. B. Jordan: *Acta Cryst.* (1952) **5**, p. 213.
- ¹³ C. M. Craighead, O. W. Simmons, and L. W. Eastwood: *Trans. AIME* (1950) **188**, p. 485; *JOURNAL OF METALS* (March 1950).
- ¹⁴ R. J. Van Thyne, W. Rostoker, and H. D. Kessler: *Trans. AIME* (1953) **197**, p. 670; *JOURNAL OF METALS* (May 1953).

Table I. Intermetallic Compounds Known to Form in Binary Titanium Systems

Metal	Compounds	References
Cr	TiCr ₂	1
Mn	TiMn; TiMn ₂	2, 10
Fe	TiFe; TiFe ₂	3, 10
Co	Ti ₃ Co(?) ; TiCo; TiCo ₂	10
Ni	Ti ₃ Ni; TiNi; TiNi ₃	10
Cu	Ti ₃ Cu; TiCu; Ti ₂ Cu ₃ ; TiCu ₃	6, 10
Be	TiBe; TiBe ₂	7
Si	Ti ₃ Si ₂ ; TiSi; TiSi ₂	8
Al	TiAl; TiAl ₃	10
Au	Au ₃ Ti; Au ₃ Ti ₂ ; AuTi ₃	10, 11, 12

Effects of Solid Solution Alloying on The Cold-Rolled Texture of Titanium

by Carl J. McHargue, Sam E. Adair, Jr., and Joseph P. Hammond

Cold-rolled sheet textures have been determined for binary solid solutions of aluminum, columbium, tantalum, and zirconium in titanium. An alloy containing 3.8 pct Al had a (0002) [10 $\bar{1}$ 0] texture, whereas alloys with the other elements had rotated (0002) [10 $\bar{1}$ 0] textures similar to that of iodide titanium.

THERE have been relatively few studies of the effect of alloying on deformation textures. A second element may be present in the base metal in solid solution and/or as a second phase. The literature offers no satisfactory explanation for the effects of solid solution alloying on textures noted thus far. For example, there is no satisfactory explanation of the difference in the textures of copper and α brass.

The most complete study of the effects of solid solution alloying on deformation textures has been that of Brick, Martin, and Angier.¹ These investigators reported that the copper texture was retained by alloys of copper with up to 30 pct Ni, less than 5 pct Zn, less than 2 pct Al or Co up to the limit of solubility. Copper containing more than 5 pct Zn, more than 2 pct Al, or the maximum soluble concentration of tin, silicon, or manganese showed the deformation texture of α brass.

Bakarian² reported that additions of 0.20 pct Ca to 99.98 pct Mg or 2.0 pct Mn plus 0.15 pct Ca to magnesium resulted in entirely different textures than for the pure magnesium. The texture obtained for high-purity magnesium sheet showed the basal plane to be concentrated parallel to the rolling plane. The texture obtained for the alloy containing 0.20 pct Ca had the basal planes concentrated in elliptical areas whose centers were tilted 15° from the center of the pole figure toward the rolling

direction. This split basal orientation was even more pronounced in the alloy containing 2.0 pct Mn and 0.15 pct Ca.

Fuller and Edmunds³ studied the rolled sheet textures in a zinc alloy containing 1 pct Cu and 0.01 pct Mn. The basal pole figure of this alloy contained a region of strong concentration not found in the pole figure for pure zinc.⁴

In the above cases, results were discussed in terms of possible changes in slip and/or twinning systems and critical shear stresses. However, there were no experimental data to relate these speculations with the observed textures.

It has been suggested that the deformation textures of titanium, zirconium, and beryllium could be directly ascribed to their low c/a ratios. The complex deformation mechanisms of titanium⁵ also have been suggested to be characteristic of hexagonal close-packed metals with low c/a ratios. The purpose of this investigation was to study the cold-rolled sheet textures in binary titanium-base α alloys in which the c/a ratios were greater than, less than, and about the same as the c/a for iodide titanium. The annealed textures of these alloys will be reported in a subsequent article.

Materials and Methods

The chemical analyses of the metals used in this investigation are given in Table I.

The alloys were prepared as 15 g buttons on a water-cooled copper block in a vacuum arc-furnace. The furnace was evacuated to pressures of the order of 10^{-5} mm Hg, flushed with 99.98 pct pure argon, and melting was carried out in 0.2 atm pressure argon. Each button was remelted until radiographs and chemical analyses indicated complete solution of the solute elements.

All buttons were forged and homogenized 72 hr at 500°C. The buttons to be rolled were ground and etched to sizes and shapes suitable for the rolling

C. J. McHargue, Junior Member AIME, formerly Research Metallurgist, Dept. of Metallurgical Engineering, University of Kentucky, is now Metallurgist, Oak Ridge National Laboratory, Oak Ridge, Tenn.; S. E. ADAIR, JR., Student Associate AIME, formerly Research Associate, Dept. of Metallurgical Engineering, University of Kentucky, is now Engineer, Linde Air Products, Indianapolis, Indiana, and J. P. HAMMOND is Associate Professor of Metallurgical Engineering, University of Kentucky, Lexington, Ky.

Discussion on this paper, TP 3607E, may be sent, 2 copies, to AIME by Dec. 1, 1953. Manuscript, April 15, 1953. Cleveland Meeting, October 1953.

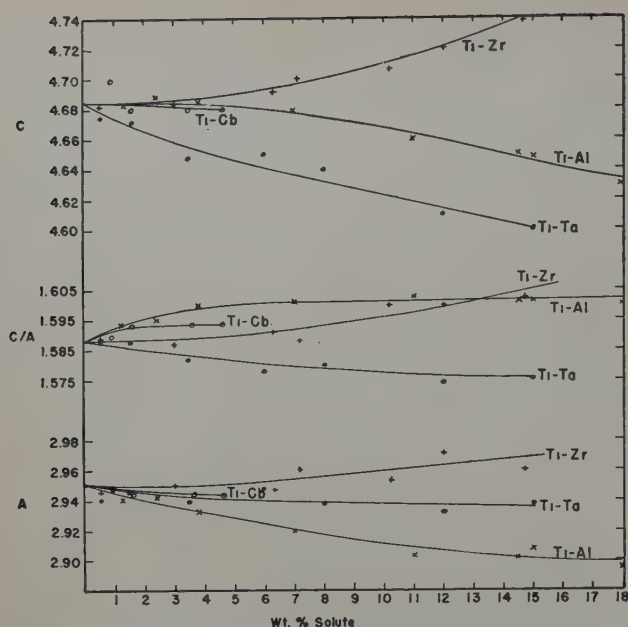


Fig. 1—Variation of lattice parameters with composition of titanium-base alloys.

schedule and vacuum annealed at 700°C. Filings for the parameter studies were annealed at 500°C in titanium capsules which were in turn sealed in evacuated quartz tubes.

The alloyed buttons were cold-reduced 93 pct to 0.007 in. using a 2-high rolling mill with 4 in. diam rolls. A reduction of approximately 10 pct per pass was used, and the rolling direction was changed 180° between passes.

Strips of the rolled sheet were made into small rods for use as the X-ray specimens. A flat strip was placed in a jig, and the edges were ground, polished, and etched away until a rod-shaped specimen was obtained. Transmission X-ray photograms were made with a Laue-type camera using molybdenum radiation (45 kv, 18 ma). It was necessary to insert a zirconium filter between the specimen and film because of the fluorescent radiation. Preliminary exposures were made with the beam perpendicular to the rolling direction at rotations of 0, 11°, 26°, 41°, 56°, 71°, and 79°, and with the beam perpendicular to the cross direction at rotations of 11°, 26°, 56°, 71°, and 79°. Additional exposures were then made where necessary to determine boundaries of intensity regions accurately. The variations in intensity were estimated visually with the aid of an exposure chart.

Films for the α -lattice parameter determinations of the alloys were obtained with a 114.59 mm powder camera with the film mounted according to the method of Straumanis. Nickel filtered copper radiation was used, and a 0.001 in. aluminum foil was placed inside the camera to reduce the high background encountered with titanium. The parameters were calculated by a least squares solution of the

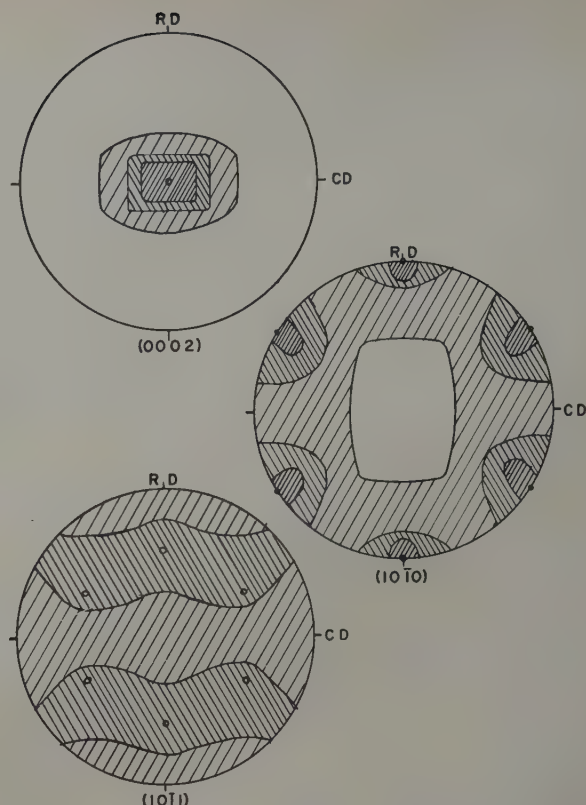


Fig. 2—Cold-rolled sheet texture of alloy containing 3.8 pct Al. O = (0002) [1010]

five strongest high angle lines and provided an accuracy of $\pm 0.005\text{\AA}$ or better.

Experimental Results

Titanium-Aluminum: The effect of alloying on the lattice parameters of the Ti-Al alloys is shown in Fig. 1. These results are similar to those published by Rostoker,⁸ differing mainly in rapidity of the rise of the c/a curve for low aluminum concentrations. It was desired to determine the texture for an alloy with the greatest possible c/a ratio, but alloys containing more than approximately 5 wt pct Al could not be cold-reduced the desired amount (90 pct or better.) The material selected for study contained 3.8 pct Al and had a c/a ratio of 1.600.

The cold-rolled sheet textures of this alloy are shown in Fig. 2. These pole figures show an "ideal" texture differing from that of iodide titanium (Fig. 3). Fig. 2a and b indicates that the basal planes are concentrated parallel to the rolling plane and that the digonal axis [1010] is parallel to the rolling direction, or that the "ideal" texture is (0002) [1010]. The major spread is in the cross direction.

Titanium-Columbium: It is seen from Fig. 1 that there are only slight changes in the parameters of the Ti-Cb alloys. The c/a ratio at 4.5 pct Cb has shifted only to 1.592 from 1.588.

Table I. Compositions of Materials Used

	Mn	Fe	Al	Pb	Cu	Sn	Mg	C	W	Cb	N ₂
Iodide Ti	0.004	0.0065	0.0065	0.0025	0.01	0.002	—	—	—	—	0.002
Al	—	—	99.983	—	—	—	—	—	—	—	—
Cb	—	Tr.	—	—	—	Tr.	—	0.05	—	—	—
Ta	—	0.02	—	—	—	—	—	0.01	0.04	0.05	—
Zr	0.001	0.04	0.01	0.001	0.01	0.001	0.003	0.001	0.001	—	0.01

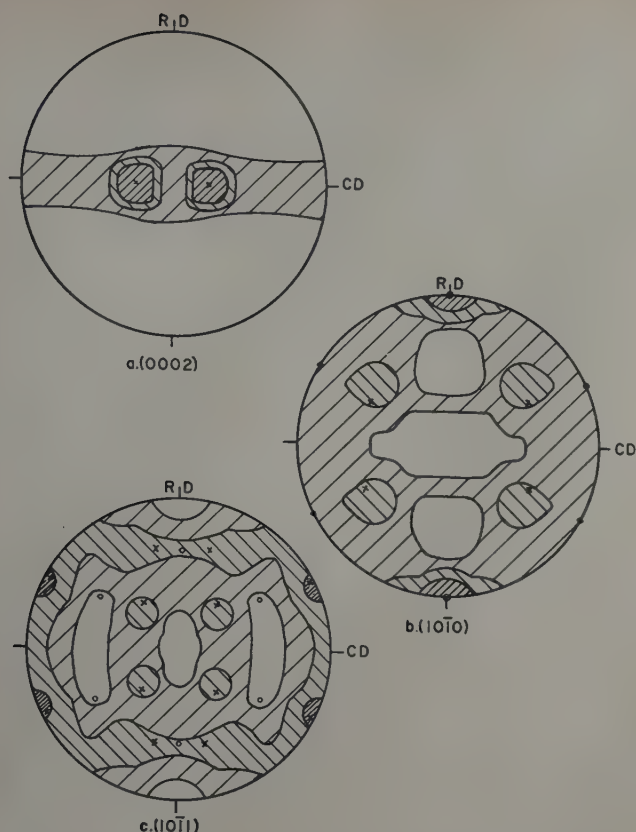


Fig. 3—Cold-rolled sheet texture of iodide titanium. O = (0002) $[10\bar{1}0]$; x = (0002) rotated 27° about rolling direction, $[10\bar{1}0]$

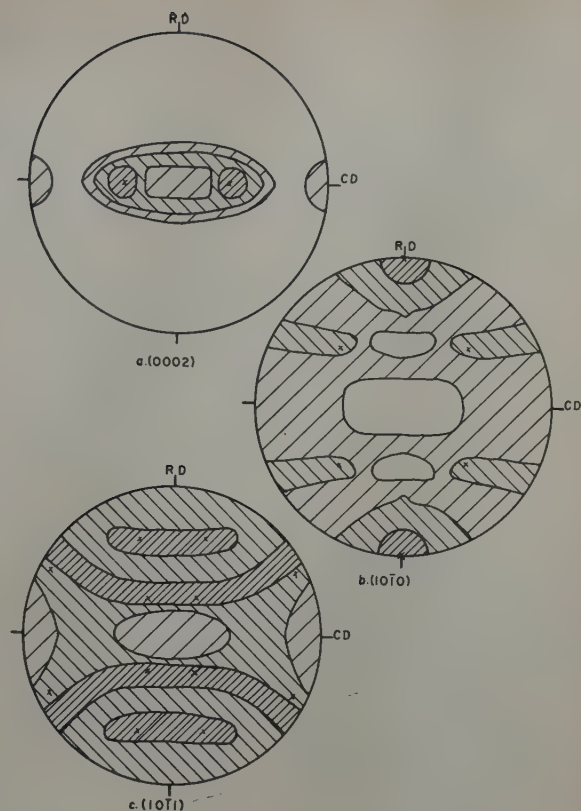


Fig. 4—Cold-rolled sheet texture of alloy containing 3.6 pct Cb. x = (0002) rotated 40° about rolling direction, $[10\bar{1}0]$

The cold-rolled sheet pole figures for an alloy containing 3.6 pct Cb and having $c/a = 1.592$ are shown in Fig. 4. These are similar in form to those of titanium; however, the maxima in the (0002) pole figure are centered approximately 40° from the center of the pole figure instead of 27° as for titanium. There is a region of second high intensity in the (0002) pole figure approximately 15° to 20° from the center in the rolling direction which did not appear for unalloyed titanium. The lowest intensity region of the (0002) pole figure of the Ti-Cb alloy shows a break near the basic circle, whereas that region for the iodide titanium extended all the way across the figure. The figures for the $(10\bar{1}0)$ and $(10\bar{1}1)$ planes are consistent with the rotated basal, $[10\bar{1}0]$ texture and show very much spread in the cross direction.

Titanium-Tantalum: It was observed that the c/a ratio of the α solid solution decreased with increasing concentrations of tantalum, Fig. 1. Textures were determined for two alloys of titanium with tantalum. One alloy contained 3.6 pct Ta and had a c/a ratio of 1.584 while the other contained 15.4 pct Ta and had a c/a ratio of 1.575.

The pole figures for the 3.6 pct Ta alloy cold-reduced 93.6 pct in thickness are illustrated in Fig. 5 and show the rotated basal, $[10\bar{1}0]$ texture. The only differences in the basal pole figures for this alloy and iodide titanium are the absence of (0002) poles near the basic circle and the presence of the region of second high intensity near the center of the figure in the rolling direction. In other respects

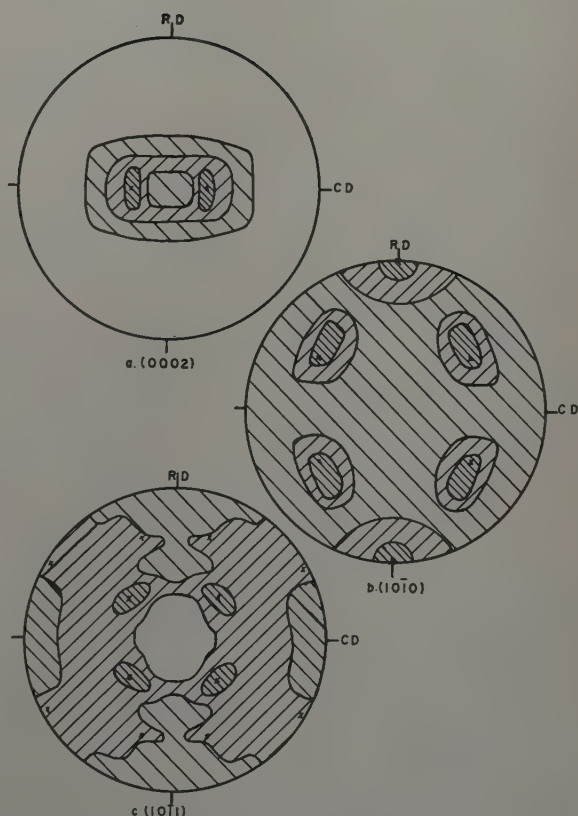


Fig. 5—Cold-rolled sheet texture of alloy containing 3.6 pct Ta. x = (0002) rotated 27° about rolling direction, $[10\bar{1}0]$

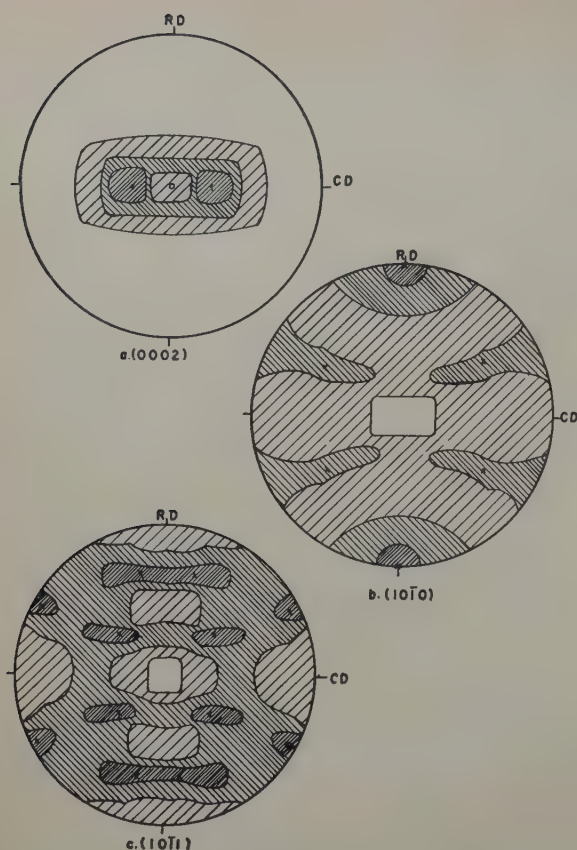


Fig. 6—Cold-rolled sheet texture of alloy containing 7.1 pct Zr. $x = (0002)$ rotated 30° about rolling direction, $[10\bar{1}0]$

the alloyed texture was essentially the same as the unalloyed.

The texture for the 15.4 pct Ta alloy cold-rolled 93.6 pct showed no significant differences from Fig. 5. The regions of maximum intensity in the (0002) pole figure were approximately 25° to 27° from the center in the transverse direction as for iodide titanium and the alloy of 3.6 pct Ta.

Titanium-Zirconium: Titanium and zirconium show complete solid solubility in both crystal forms, and the α lattice parameters have a negative deviation from Vegard's law.⁷ The composition parameter results of the present study are shown in Fig. 1.

Textures were studied for alloys containing 7.1 pct Zr ($c/a = 1.590$) and 14.75 pct Zr ($c/a = 1.602$) which were cold-reduced 93.6 pct in thickness. Fig. 6 contains the pole figures for the 7.1 pct Zr alloy. The figures for both alloys were similar and differ from those for iodide titanium only in those respects discussed for the Ti-Ta textures. These alloys showed the rotated basal, $[10\bar{1}0]$ texture.

Discussion of Results

While a complete explanation of the effects of solid solution alloying on deformation textures cannot be given at this time, some observations can be made as a result of this investigation. Although limited data are available, it appears that the c/a ratio is an equivocal factor in the establishment of deformation textures.

It has been suggested that the deformation mechanisms and deformation textures of hexagonal close-packed metals were peculiar to the deviation of their c/a ratios from the ideal packing. On this basis, it was suggested that the textures of metals

or alloys having the same c/a ratio would be similar. However, as can be seen in Table II, the results of this investigation do not justify this belief.

In the cases of the titanium-base alloys containing 3.8 pct Al and 14.75 pct Zr, having c/a ratios of 1.600 and 1.602, respectively, there were entirely different textures. The Ti-Al alloy possessed a cold-rolled texture described as (0002) $[10\bar{1}0]$ and the Ti-Zr alloy possessed a rotated (0002) $[10\bar{1}0]$ texture similar to that of iodide titanium ($c/a = 1.588$).

It has been observed that the cold-rolled texture of beryllium,⁸ (0002) $[10\bar{1}0]$, resembles that of magnesium. However the scatter from this mean orientation is toward the cross direction, whereas that for magnesium is toward the rolling direction. This texture of beryllium is inconsistent with any relationship between c/a and texture since the texture is that which has been associated with higher c/a ratios (near 1.63). Furthermore, an alloy was investigated during this study which has a c/a ratio close to that of beryllium (1.575 and 1.57 respectively). The Ti-Ta alloy had the rotated (0002) $[10\bar{1}0]$ texture in contrast to the (0002) $[10\bar{1}0]$ texture of beryllium.

The textures of titanium alloyed with columbium ($c/a = 1.592$), tantalum ($c/a = 1.584$ and 1.575) and zirconium ($c/a = 1.590$ and 1.602) have the same basic textures and differ from the texture of iodide titanium only by having areas of second high intensity 15° to 20° from the center of the (0002) pole figure in the rolling direction, shifts in the positions of the basal maxima along the cross direction, and in general, more scatter. In addition to these differences, the basal pole figures of the alloys containing zirconium, columbium, and tantalum did not show the low intensity region extending completely across the figure.

An interesting observation may be made from consideration of the phase diagrams of the systems studied. As indicated in Table II, the Ti-Al system shows a wide α solid solution range and two intermediate phases. The Ti-Cb and Ti-Ta systems show more restricted α regions, and the β phase is stabilized to room temperature for higher concentrations of the solute. The Ti-Zr system shows complete solid solubility. At least in this investigation, the system showing intermediate phases has a deformation texture different from that of the pure solvent, whereas those systems with no intermediate phases retained the texture of the solvent. Eventu-

Table II. Summary of Textures Listing c/a Ratios and Type of Phase Diagrams

	c/a	Texture	Type of Phase Diagram
Ti	1.588	(0002) tilted 27° , $[10\bar{1}0]$	
Zr	1.589	(0002) tilted 40° , $[10\bar{1}0]^8$	
Be	1.57	(0002) $[10\bar{1}0]^9$	
Ti—3.8% Al	1.600	(0002) $[10\bar{1}0]$	Wide α range, intermediate phases
Ti—3.6% Cb	1.592	(0002) tilted 40° , $[10\bar{1}0]$	Narrow α range, β stabilized
Ti—3.6% Ta	1.584	(0002) tilted 27° , $[10\bar{1}0]$	Moderate α range, β stabilized
Ti—15.4% Ta	1.575	(0002) tilted 27° , $[10\bar{1}0]$	Moderate α range, β stabilized
Ti—7.1% Zr	1.590	(0002) tilted 30° , $[10\bar{1}0]$	Complete solid solubility
Ti—14.75% Zr	1.602	(0002) tilted 30° , $[10\bar{1}0]$	Complete solid solubility

ally it may be possible to relate the factors determining the nature of the phase diagram with the choice of deformation mechanisms and deformation textures.

Most rationalizations of textures have been based on considerations of the crystal structure, deformation mechanisms, and relative ease of deformation on various systems. Before a complete analysis of the effect of alloying on textures can be carried out along these lines, it will be necessary to determine the effect of alloying on the deformation characteristics.

Summary

1—The deformation texture of a titanium alloy containing 3.8 pct Al and having c/a equal to 1.600 is very different from that of iodide titanium. The texture of the alloy can be described as (0002) $[10\bar{1}0]$.

2—The cold-rolled textures of a titanium alloy containing 3.6 pct Cb ($c/a = 1.592$), alloys containing 3.6 and 15.4 pct Ta ($c/a = 1.584$ and 1.575, respectively), and alloys containing 7.1 and 14.75 pct Zr ($c/a = 1.590$ and 1.602, respectively) were essentially the same as the cold-rolled texture of iodide titanium.

3—The deformation textures of hexagonal close-

packed materials cannot be predicted entirely from a knowledge of the c/a ratios.

Acknowledgment

This work is part of a study of the preferred orientations in titanium and titanium-base alloys sponsored by the Flight Research Laboratory, Wright-Patterson Air Force Base under Contract No. AF 33(038)-19574.

References

- ¹R. M. Brick, D. L. Martin, and R. P. Angier: *Trans. ASM* (1943) **31**, p. 675.
- ²P. W. Bakarian: *Trans. AIME* (1942) **147**, p. 266.
- ³M. L. Fuller and G. Edmunds: *Trans. AIME* (1934) **111**, p. 146.
- ⁴V. Caglioti and G. Sachs: *Metallwirtschaft* (1932) **11**, p. 1.
- ⁵F. D. Rosi, C. A. Dube, B. H. Alexander: *Trans. AIME* (1953) **197**, p. 257; *JOURNAL OF METALS* (February 1953).
- ⁶W. Rostoker: *Trans. AIME* (1952) **194**, p. 212; *JOURNAL OF METALS* (February 1952).
- ⁷E. T. Hayes, A. H. Roberson, and O. G. Paasche: *Bur. Mines R.I. No. 4826* (1951).
- ⁸R. K. McGeary and B. Lustman: *Trans. AIME* (1951) **191**, p. 994; *JOURNAL OF METALS* (November 1951).
- ⁹C. S. Barrett and A. Smigelskas: *Trans. AIME* (1949) **185**, p. 145; *JOURNAL OF METALS* (February 1949).

Technical Note

Structure of the Phase TiMn and the Indexing of Powder Patterns Of Sigma-Type Phases

by R. P. Elliott and W. Rostoker

TWO intermediate phases enter into equilibrium with the primary solid solutions of titanium.¹ The TiMn₂ phase was identified by Wallbaum² as of the C14 type isomorphous with MgZn₂. Contrary to Maykuth, et al.,¹ the phase occurring at about the 50-50 atomic proportion has been shown to derive from a peritectoid reaction.³ A 30 day anneal at 900°C of an alloy containing 52 wt pct Mn developed sufficient of the new phase to give a clear and predominant diffraction pattern. The powder pattern was taken in a 14 cm diameter powder camera using filtered Cu K α radiation. In all, 75 lines were recognized and measured. Interplanar spacing and observed intensities for the first 26 of these are given in Table I.

R. P. ELLIOTT and W. ROSTOKER are Assistant Metallurgist and Senior Metallurgist, respectively, Metals Research Dept., Armour Research Foundation of Illinois Institute of Technology, Chicago.
TN 172E. Manuscript, May 14, 1953.

Table I. Observed Interplanar Spacings of σ -TiMn

d , kX	Intensity*
1. 2.358	vft
2. 2.301	vft
3. 2.272	vw
4. 2.247	vft
5. 2.215	w
6. 2.191	vft
7. 2.156	vw
8. 2.109	diffuse vft
9. 2.001	ft
10. 1.967	vft
11. 1.945	vft
12. 1.893	diffuse vw
13. 1.819	vft
14. 1.778	vft
15. 1.728	vft
16. 1.685	vft
17. 1.667	vft
18. 1.492	vft
19. 1.433	ft
20. 1.407	vft
21. 1.345	vft
22. 1.331	vft
23. 1.314	vw
24. 1.302	vw
25. 1.290	vw
26. 1.255	vft

* w, weak; vw, very weak; ft, faint; vft, very faint.

Table II. Powder Pattern Lines of Sigma Phases Indexed According to the True Unit Cell (kX Units)

(hkl)	σ -FeCr, ⁸	σ -CrCo, ⁸	σ -FeV, ⁸	σ -CoV, ⁸	σ -NiV, ⁸	σ -TiMn	
	d, Observed	d, Observed	d, Observed	d, Observed	d, Observed	d, Observed	d, Calculated
101		4.00	4.01	4.07	4.10		
111		3.68	3.72	3.68	3.71		
201*			3.22	3.20	3.22		
220				3.10	3.12		
211				3.01			
300			2.97	2.94			
310			2.84	2.79			
221		2.61					
301	2.50						
311	2.36	2.36		2.35		2.358	2.383
002	2.27	2.26	2.31	2.28	2.31	2.272	2.266
102	2.215	2.20				2.191	2.196
400	2.22					2.215	2.215
321	2.16	2.15				2.156	2.161
410		2.124	2.155	2.140	2.160		
112						2.109	2.131
330	2.065	2.062	2.110	2.081	2.087		
202	2.019	2.010	2.050	2.032	2.052	2.001	2.018
212†	1.967	1.958	1.998	1.978	1.997	1.967	1.967
420							
411	1.925	1.922	1.961	1.940	1.959	1.945	1.942
331	1.879	1.878	1.914	1.895	1.911	1.893	1.897
222	1.833	1.827	1.864	1.846	1.859		
421						1.819	1.816
302				1.805			
312	1.757	1.752	1.788	1.769	1.785	1.778	1.772
500-430							
322	1.663	1.655	1.685	1.676	1.687	1.667	1.666
501-431	1.637	1.633	1.665	1.650	1.662		
511	1.608	1.607	1.636	1.621	1.640		

* (201) line does not belong to $D_{\frac{14}{4h}}$ or $C_{\frac{4}{4v}}$ space groups.

† Bracket indicates indistinguishable indices.

Note: The (100), (110), (200), (210), (320), (510), and (520) planes also should reflect in the sigma lattice, but have not been detected.

By inspection, a close resemblance was noted to powder patterns of σ -type phases. Although single-crystal studies by Shoemaker and Bergman,^{4, 5} Dickens and Douglas,⁶ and Christian and Pearson⁷ have shown σ -type phases to be tetragonal (space

group $D_{\frac{14}{4h}}$ or $C_{\frac{4}{4v}}$) with an axial ratio of about 0.5,

published powder patterns⁸ have been indexed on the basis of a tetragonal unit cell of axial ratio $\cong 1.46$. For the proper identification of the structure of the new intermediate phase in the system Ti-Mn, it was considered necessary to re-index the powder patterns of Duwez and Baen⁸ according to the correct unit cell.

For this purpose, a large Hull-Davey chart was constructed for the tetragonal lattice in the axial ratio range of 0.4 to 0.6. A log d scale of 50 in. per log cycle was used. From the lattice constants for σ -FeCr^{4, 5} as derived from the single-crystal studies, it was apparent that the (002) planes possessed an interplanar spacing of 2.27 kX. Duwez and Baen⁸ report lines of relatively high intensity at about this spacing for the powder patterns of σ -FeCr, σ -CrCo, σ -FeV, σ -CoV, and σ -NiV. With the use of the Hull-Davey chart and by locating the appropriate line at the (002) position, it was possible to index the rest of the patterns in every case. Calculations of lattice parameters from indices and spacings agreed well with results reported on single crystals. A summary of line spacings and indices is given in Table II.

Using the same procedure, the pattern for the new intermediate phase of the Ti-Mn system was successfully indexed. The results are compiled in Table II to provide a comparison with other members of the σ -phase family. Four very faint lines of the pattern could not be indexed. The lattice parameters

of σ -TiMn were calculated by a least squares solution of best fitting lines as follows:

$$c = 4.533 \text{ kX}; a = 8.862 \text{ kX}; c/a = 0.512$$

Using these lattice parameters, interplanar spacings were calculated for comparison with observed values (see Table II). The agreement was quite satisfactory. It is to be noted that the indices determined for lines of all of the σ -phase patterns obey the sys-

tematic extinction requirements for the $D_{\frac{14}{4h}}$ and

$C_{\frac{4}{4v}}$ namely, for lines of type $(h0l)$ reflections will

not occur unless $(h + l)$ is even.

Acknowledgment

The authors wish to express appreciation for the sponsorships of this work by Ordnance Corps, U. S. Army, Watertown Arsenal, Watertown, Massachusetts, and for permission to publish. The work was performed under Contract DA-11-022-ORD-272.

References

- ¹ D. J. Maykuth, H. R. Ogden, and R. I. Jaffee: *Trans. AIME* (1953) **197**, pp. 225-230; *JOURNAL OF METALS* (February 1953).
- ² H. J. Wallbaum: *Ztsch. Metallkunde* (1941) **103**, p. 391.
- ³ W. Rostoker, R. P. Elliott, and D. J. McPherson: Discussion on Ref. 1. To be published.
- ⁴ D. P. Shoemaker and B. G. Bergman: *Journal ACS* (1950) **72**, p. 5793.
- ⁵ B. G. Bergman and D. P. Shoemaker: *Journal of Chemical Physics* (1951) **19**, p. 515.
- ⁶ G. I. Dickens and A. M. B. Douglas: *Journal Iron and Steel Inst.* (1951) **167**, p. 27.
- ⁷ J. W. Christian and W. B. Pearson: *Nature* (1952) **169**, p. 70.
- ⁸ P. Duwez and S. R. Baen: *ASTM Tech. Pub. No. 110* (1951) pp. 48-60.

The Ternary System Ti-Ta-C

by John G. McMullin and John T. Norton

An 1820°C isothermal cross section of the Ti-Ta-C ternary diagram was prepared from X-ray diffraction and metallographic data. No phases other than those appearing in the three binary diagrams were observed. At temperatures above the titanium transition temperature titanium and tantalum form a complete series of solid solutions containing up to 2 atomic pct C. The phases TiC and TaC also form a continuous series of solid solutions extending across the diagram.

PREVIOUS work on this alloy system was very limited. Of the three binary constitution diagrams involved, only one, the Ta-C system was available in the literature. Preliminary data on the other two systems was received from the investigators during the course of the investigation and both have been published in recent months. It had been shown that TiC and TaC formed a continuous series of solid solutions, but the range of carbon content in this phase was not known. While Ta₂C had been described, its solubility for or reactions with other carbides had not been reported. It was not known whether or not any ternary compounds occurred in the system.

The present program was undertaken to determine experimentally the general form of the ternary diagram. It is hoped that the results will be of value in furthering the development of sintered carbide cutting materials and high temperature ceramets, many of which contain combinations of TiC and TaC.

The Binary Systems

Of the three binary diagrams involved only that of Ta-C was available at the time this project was started. The diagram of Ellinger¹ redrawn in Fig. 1, shows a hexagonal phase Ta₂C having a very small composition range and a cubic TaC phase having a composition range of from 40 to 50 atomic pct C.

J. G. McMULLIN, Junior Member AIME, is associated with the General Electric Research Laboratory, Schenectady, and J. T. NORTON, Member AIME, is Professor of Metallurgy, Massachusetts Institute of Technology, Cambridge, Mass.

Discussion on this paper, TP 3602E, may be sent, 2 copies, to AIME by Dec. 1, 1953. Manuscript, April 15, 1953. Cleveland Meeting, October 1953.

This paper is based on a thesis by J. G. McMullin submitted in partial fulfillment of requirements for the degree of Doctor of Science in Metallurgy to the Massachusetts Institute of Technology, May 1952.

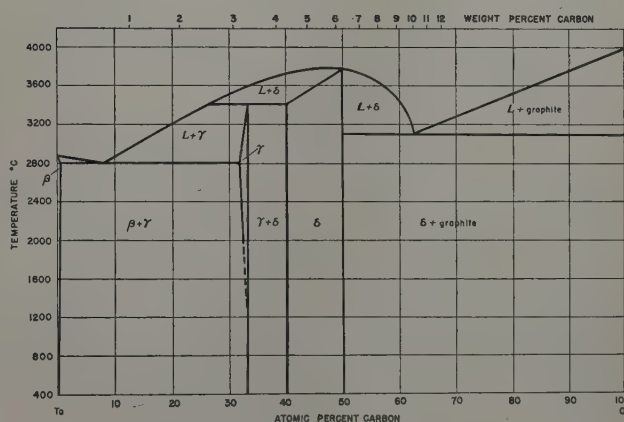


Fig. 1—Ta-C system after Ellinger.¹

The authors made a separate determination of the composition range of TaC using lattice constant values and found the range to extend from 40 to 49.7 atomic pct C in good agreement with Ellinger's diagram.

Two determinations of the Ti-Ta system have appeared recently.^{2,3} These two diagrams are in good agreement and show that β titanium and tantalum form a complete series of solid solutions.

The Ti-C diagram by Cadoff and Nielsen⁴ shows a very limited solubility of carbon in both α and β titanium. The single carbide formed persists over a wide range of carbon contents. Several values for the upper limit of carbon content of this phase have been reported.⁵⁻⁸ The highest value obtained in the M.I.T. Laboratory was 47.5 atomic pct C with a lattice constant of 4.328 Å.⁵ Fettinger⁷ describes a gas carburization method which he claims produces stoichiometric TiC although he does not present any data showing that he actually had 50 atomic pct combined carbon. Several complete analyses on

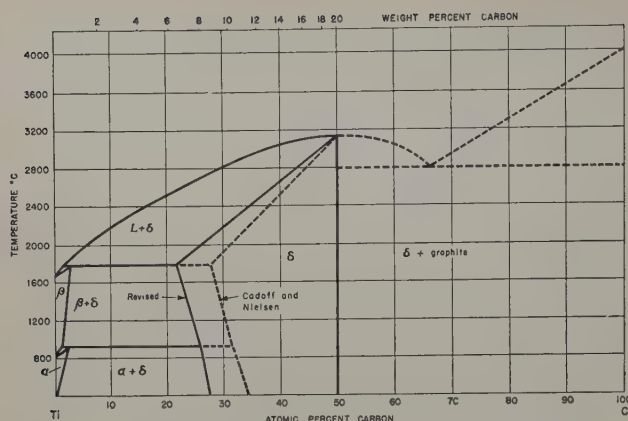


Fig. 2—Ti-C system tentative constitution diagram after Cadoff and Nielsen.⁴

commercially prepared titanium carbides have been made recently which have shown as high as 49.8 atomic pct combined carbon, and there seems to be no reason to doubt that the true upper limit of the phase is at 50 atomic pct. Cadoff and Nielsen⁴ show the lower carbon limit of the δ phase to be about 27 atomic pct C at 1750°C. This is not in good agreement with the value of 22 atomic pct found by Ehrlich,⁸ Rengstorff,⁹ and Ragone.⁵ The latter value was used in constructing the isothermal section shown in Fig. 3. No published data were available concerning reactions between TiC and graphite, but Stover¹⁰ has observed a eutectic microstructure in melted alloys containing over 50 atomic pct C. Accordingly a eutectic is indicated in Fig. 2 although its temperature is not known.

Experimental Procedure

Alloy Preparation: All the alloys used in this program were prepared by powder metallurgy methods. The titanium and tantalum were added in the form of powdered metal hydrides, while carbon was added in the form of lampblack. The titanium hydride and tantalum hydride were carefully weighed out on an analytical balance in amounts calculated to give the desired atomic ratio of the two metals and the necessary amount of carbon was

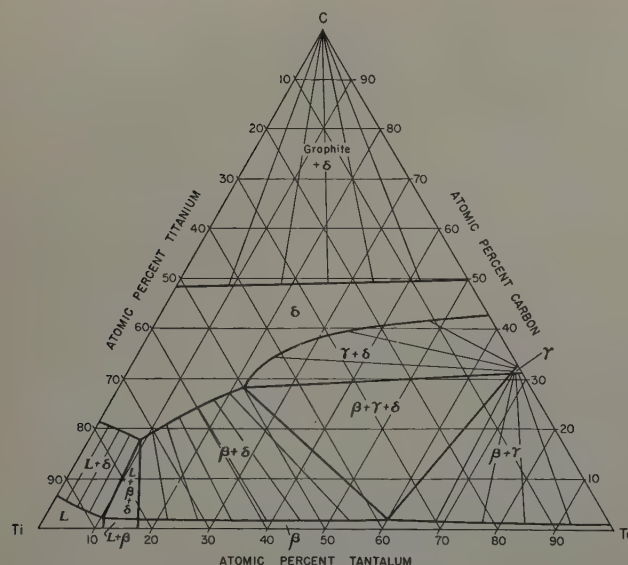


Fig. 3—Constitution of Ti-Ta-C alloys at 1820°C in atomic pct.

added. The powders were thoroughly mixed and cold-pressed into compacts about 25x6x6 mm.

The compacts were sintered 3 hr at 1820°C in a vacuum Arsem furnace with a vacuum better than one micron. The furnace cooled about 400°C in the first minute and was below 1000°C in 4 min. The cooling rate below the visible temperature range was slow because of the excellent vacuum in the furnace. A few specimens were cooled faster by filling the furnace with helium as soon as the power was shut off.

X-Ray Diffraction Methods: All specimens for X-ray examination were crushed and ground to -200 mesh. A suitable amount of the -200 mesh specimen was mounted on a glass microscope slide using collodion thinned with amyl acetate.

The X-ray diffraction patterns were made using a high angle X-ray spectrometer with copper radi-

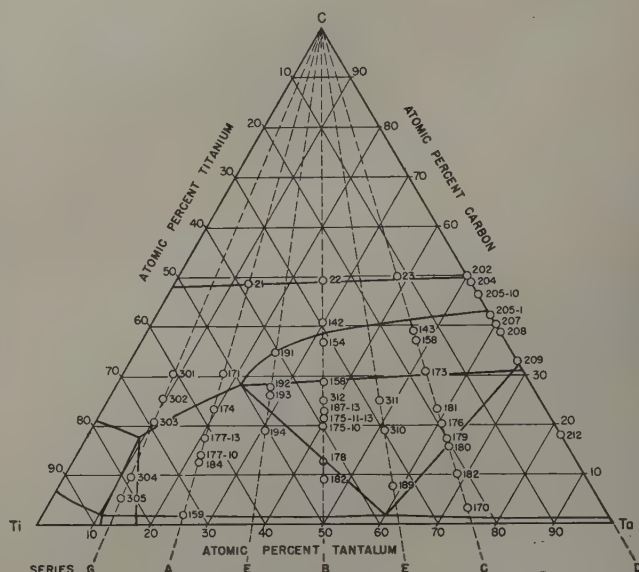


Fig. 4—Alloy compositions in atomic pct.

tion and a nickel filter. All lattice constant calculations were made using a value of 1.5405Å for the wavelength of the Cu K α 1 line.

Chemical Analysis Methods: A carbon analysis was made on all samples. Total carbon analysis was made by combustion of the powdered carbide in a conventional carbon train.

Free carbon was determined by dissolving the carbide in a mixture of HF and HNO₃ and filtering. The residue on the filter was washed first with KOH, then with HCl and finally water. The residue was then ignited in the carbon train.

Combined carbon was determined by subtracting the free carbon from the total carbon analysis. A few analyses were made for titanium and tantalum and it was found that this ratio remained unchanged during the sintering. Fig. 4 shows the compositions of the alloys investigated.

The 1820°C Isothermal Section

The 1820°C isothermal section of the ternary diagram was chosen for extensive investigation for several reasons. It was desired to select a temperature which was below the solidus over most of the section but which was high enough to insure equi-

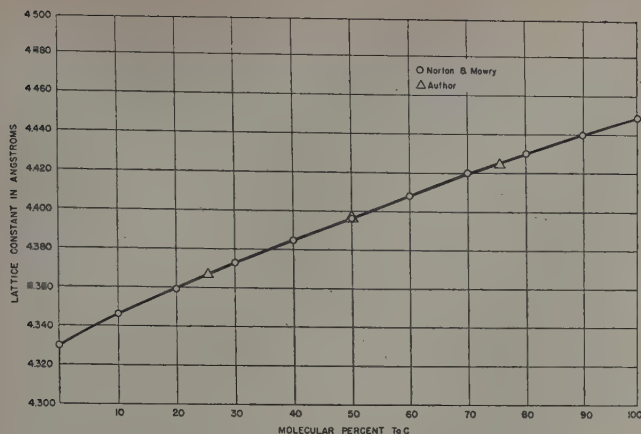


Fig. 5—Lattice constants of carbon-saturated δ phase.

librium in only a few hours at temperature. From the three binary diagrams it appeared that 1800°C would be an appropriate temperature. The particular temperature of 1820°C was chosen because the sintering furnace maintained this temperature very well but was difficult to control at 1800°C.

From the three binary diagrams it is apparent that five phases, liquid, β , γ , δ , and graphite (see Figs. 1 and 2) must be present at 1820°C. No other phases were observed at this temperature. With the δ phase extending across the diagram from TiC to TaC as shown by Norton and Mowry¹¹ and the boundary conditions imposed by the binary diagrams, it was evident that two three-phase fields must be present in the isothermal section. One of these, the liquid- β - δ field was not extensively investigated although its presence was definitely established. The β - γ - δ field was more thoroughly investigated and its boundaries located. Fig. 3 shows the 1820°C isothermal section as it was determined.

The β phase has a body-centered cubic structure with a comparatively narrow range of lattice constants.³ In alloys containing less than 25 pct Ta the β phase transforms during cooling in a manner dependent on the rate. The small solubility of carbon in the β phase was not determined.

The δ phase has a face-centered cubic structure of the NaCl type. Fig. 5 shows the variation of lattice constant in carbon-saturated δ phase compositions between TiC and TaC. As the carbon content of the δ phase decreases, there is a marked decrease in the lattice constant.

The γ or Ta₂C phase was observed to have a hexagonal close-packed structure ($a = 3.097\text{\AA}$, $c/a = 1.595$) as previously reported.¹² Since a pure Ta-C alloy (No. 209) containing 32 atomic pct C showed a trace of δ phase, it is apparent that the γ phase contains slightly less carbon than the stoichiometric Ta₂C. Its behavior is therefore exactly parallel to that of W₂C, with which it is isomorphous.¹³ No shift in the high angle diffraction lines was observed in any specimen containing γ phase. This invariance of the lattice constants indicates that the composition range of γ phase is very small with respect to both carbon and titanium.

Because of this very small composition range of the γ phase the tie lines in the β - γ and β - δ fields can

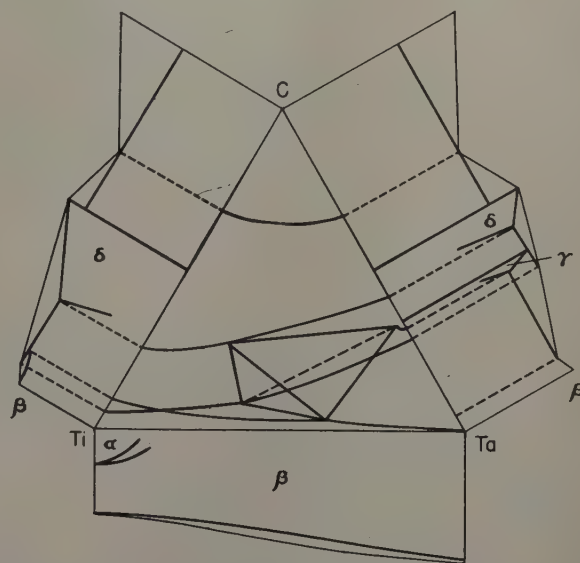


Fig. 7—Saturation lines in the Ti-Ta-C ternary constitution diagram.

be drawn in as shown. The δ phase lattice constants were used to locate the tie lines in the β - δ two-phase field.

Ternary Reactions

In the three binary diagrams there are six isothermal lines of two-fold saturation which must be considered in the ternary diagram.

The β Ti- α Ti-TiC peritectoid line probably moves in to the ternary as shown in Fig. 6 to form an α - β - δ three-phase field although this low temperature portion of the diagram was not investigated.

Two of these lines, the TiC-liquid-graphite eutectic and the TaC-liquid-graphite eutectic lines very probably join along a warped surface leaving a eutectic valley across the liquidus surface as indicated in Fig. 7.

The other three lines, the TiC- β Ti-liquid peritectic, the TaC-Ta₂C-liquid peritectic, and the Ta₂C-liquid-Ta eutectic could theoretically be joined on a four-phase invariant plane having either the eutectic or peritectic arrangement. A ternary eutectic plane would necessarily be at a temperature below the lowest binary reaction which in this case is the TiC- β Ti-liquid peritectic at about 1750°C. It is

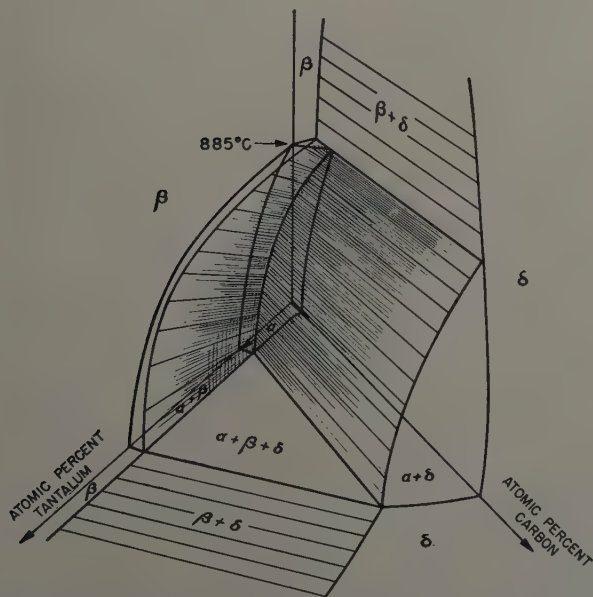


Fig. 6—Titanium-rich corner of the Ti-Ta-C ternary constitution diagram.

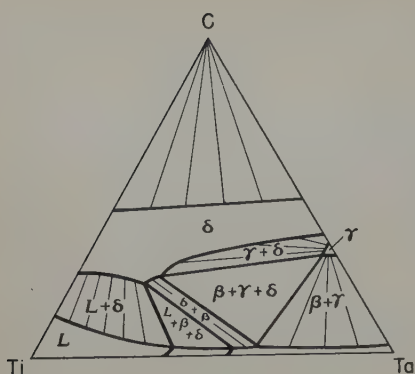


Fig. 8 (left)—Isothermal section at temperature below invariant plane.

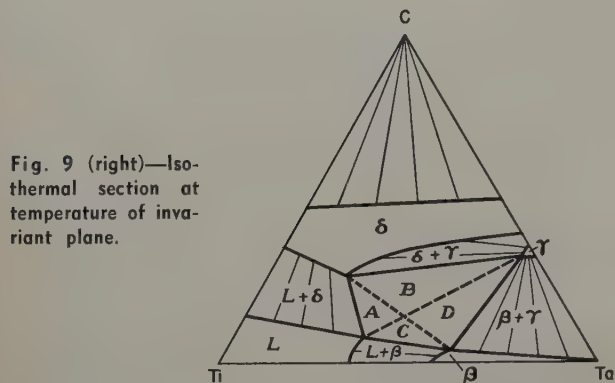


Fig. 9 (right)—Isothermal section at temperature of invariant plane.

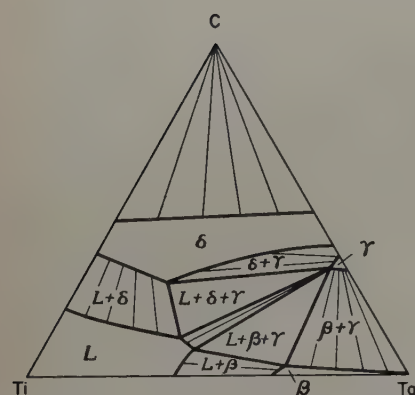


Fig. 10 (left)—Isothermal section at temperature above invariant plane.

evident from the 1820°C isothermal section shown in Fig. 3 that the ternary eutectic does not occur. With this possible arrangement eliminated, it was safe to assume that a ternary peritectic reaction occurred at some temperature above 1820°C and below the Ta_2C -liquid-Ta eutectic temperature of 2800°C.

To locate this temperature and the same time verify the assumed type of reaction, the following experiments were conducted. Several specimens of alloy No. 178 (43.1 pct Ti, 43.1 pct Ta, and 13.8 pct C) were prepared and sintered at 1820°C. After sintering, the specimens contained approximately equal amounts of β and δ phases in accordance with Fig. 3. Each of these specimens was given a short time anneal at successively higher temperatures above 1820°C and rapidly cooled with helium. Specimens annealed at temperatures up to and including 2020°C gave no evidence of melting. The X-ray pattern of the specimen annealed at 2020°C contained only β and δ X-ray lines. Specimen No. 178-17, heated to 2030°C and rapidly cooled showed physical evidence of partial melting by its rounded corners. The X-ray diffraction pattern of this specimen contained a substantial amount of γ phase as well as β and δ . Its microstructure gave definite evidence of melting. The appearance of γ phase and

liquid was proof that the invariant temperature had been exceeded. Allowing for temperature measurement error, the temperature of the invariant plane is thus fixed at $2025^\circ \pm 15^\circ C$. On heating through this plane the so-called, "two over two" reaction of $\beta + \delta \rightarrow \gamma + \text{liquid}$ occurred. On rapid cooling some of the γ phase remained while the liquid decomposed to $\delta + \beta$.

As shown in Fig. 9, the invariant plane is divided into four quadrants; A, B, C, and D. The same reaction of $\beta + \delta \rightarrow \gamma + \text{liquid}$ occurs during the melting of alloys in all four quadrants although the phases present just above and below the invariant plane are different for each quadrant as shown by Figs. 8 and 10.

Summary

An isothermal cross section of the Ti-Ta-C alloy constitution diagram was determined. An invariant plane of four-fold saturation was found to occur at 2025°C. The reaction occurring at this temperature was $\beta + \delta \rightleftharpoons \gamma + \text{liquid}$.

No compounds or phases other than those occurring in the three binary constitution diagrams were observed.

The Ta_2C or γ phase was shown to be deficient in carbon containing only 31.5 atomic pct C instead of 33.3 pct. This carbon content appeared to be fixed and no solubility of titanium in Ta_2C was detected.

Titanium carbide and tantalum carbide formed a continuous series of solid solutions.

Acknowledgments

The authors wish to express their appreciation to Donald Guernsey for supervising the chemical analysis and to Kenneth Carlson for assistance in the experimental work. This project was sponsored by the Office of Naval Research under Contract No. N5ori-07817.

References

- ¹ F. H. Ellinger: The Tantalum-Carbon System. *Trans. ASM* (March 1943) **31**, p. 89.
- ² D. J. Maykuth, H. R. Ogden, and R. I. Jaffee: Ti-W and Ti-Ta Systems. *Trans. AIME* (1953) **197**, p. 231; *JOURNAL OF METALS* (February 1953).
- ³ D. Summers-Smith: The Constitution of Ta-Ti Alloys. *Journal Inst. Metals* (October 1952) **81**, pp. 73-76.
- ⁴ I. Cadoff and J. P. Nielsen: Ti-C Phase Diagram. *Trans. AIME* (1953) **197**, p. 248; *JOURNAL OF METALS* (February 1953).
- ⁵ D. V. Ragone: Masters Thesis, Dept. of Metallurgy, Massachusetts Institute of Technology, 1951.
- ⁶ G. A. Meerson and Ya. M. Lipkes: Study of Conditions of Carburization-Titanium. *Zhurnal Prikladnoi Khimii* (1941) **14**, No. 3, p. 291. (Brutcher translation 2099).
- ⁷ V. Fattinger: Experimental Production of Pure TiC Powder by Means of Carburizing Gases. In *Physics of Powder Metallurgy* (1951) New York: McGraw-Hill Book Co.
- ⁸ Ehrlich: On the Binary Systems of Titanium with the Elements Nitrogen, Carbon, Boron, and Beryllium. *Ztsch. anorg. allgem. Chemie* (1949) **259**, No. 1-4, pp. 1-21.
- ⁹ G. P. W. Rengstorff: Masters Thesis, Dept. of Metallurgy, Massachusetts Institute of Technology, 1947.
- ¹⁰ E. Stover: Personal communication.
- ¹¹ J. T. Norton and A. L. Mowry: Solubility Relationships of the Refractory Monocarbides. *Trans. AIME* (1949) **185**, p. 133; *JOURNAL OF METALS* (February 1949).
- ¹² H. J. Goldschmidt: The Structure of Carbides in Alloy Steels. *Journal Iron and Steel Inst.* (December 1948) p. 345.
- ¹³ P. Rautala: Personal communication.

System Titanium-Chromium-Iron

by R. J. Van Thyne, H. D. Kessler, and M. Hansen

The phase diagram of the titanium-rich portion of the system Ti-Cr-Fe to 70 pct Ti was established by means of isothermal sections at 900°, 800°, 750°, 700°, 650°, 600°, and 550°C, using arc-cast alloys. An isotherm at 800°C was determined for the section bounded by Ti, TiFe₂, and TiCr₂. Micrographic analysis was employed as the principal method of investigation, supplemented by X-ray diffraction and incipient melting studies. A ternary eutectoid, $\beta \rightleftharpoons \alpha + \text{TiCr}_2 + \text{TiFe}$, occurs at approximately 8 wt pct Cr, 13 wt pct Fe, and about 540°C.

AMONG the first titanium-base alloys in commercial production were the Ti-Cr-Fe alloys. For this reason, the Materials Laboratory, Wright Air Development Center, sponsored an investigation of the system. No information on the constitution of the titanium-rich corner was available. Vogel and Wenderott studied titanium-poor ternary alloys.¹

As part of this program, the binary systems Ti-Cr and Ti-Fe have been determined previously by the authors.² Other investigators have also studied the binary systems Ti-Cr,³⁻⁷ Ti-Fe,⁸⁻¹⁰ Both of the binary systems are characterized by the eutectoid decomposition of the β phase.

Most of the effort of the present work has been concentrated on the titanium-rich corner with compositions of less than 30 pct total chromium and iron content. The determination of isothermal sections was the experimental approach used to obtain the ternary phase diagram. Vertical sections were used to check the consistency of the isothermal sections.

While this investigation was in progress, a study of the Ti-Mo-Cr system at Armour Research Foundation disclosed the existence of a high temperature modification of TiCr₂ above 1300°C.¹¹ This allotrope has a hexagonal structure of the MgZn₂ type, isomorphous with TiFe₂, whereas the low temperature modification of TiCr₂ is cubic,⁶ of the MgCu₂ type. The existence of allotropy in TiCr₂ of course means

R. J. VAN THYNE is Associate Metallurgist, H. D. KESSLER, Junior Member AIME, is Supervisor, Nonferrous Metals Research, and M. HANSEN, Member AIME, is Chairman, Metals Research Dept., Armour Research Foundation of Illinois Institute of Technology, Chicago.

Discussion on this paper, TP 3603E, may be sent, 2 copies, to AIME by Dec. 1, 1953. Manuscript, April 20, 1953. Cleveland Meeting, October 1953.

Table I. Analyses of Impurities in Materials Used

Iron		Chromium	
Si	0.0093%	C	0.015%
Ni	0.012	O	0.066
P	0.0023	N	0.0022
S	0.013		
C	0.011		

a more complicated set of phase relationships in this general region than if the phase were monomorphic, as was first assumed.

Additional studies were made late in the investigation in order to clarify the part that the hexagonal TiCr₂ phase plays in the ternary phase relationships. These will be discussed in a separate section. Because they are of greatest practical significance, the phase relationships in the titanium-rich corner will be presented first, omitting the equilibria involving the hexagonal modification of TiCr₂ in an effort to simplify the presentation somewhat.

Experimental Procedure

Materials: The titanium used in the preparation of the alloys was iodide crystal bar (99.9 pct pure) produced by the New Jersey Zinc Co. High purity chromium and iron were obtained from the National Research Corp. Table I gives the analyses of these materials.

Melting Practice: Over 100 alloy ingots weighing 10 to 20 g were melted in a nonconsumable electrode arc-melting furnace. As the techniques are identical to those reported previously,^{12, 13} they will not be detailed here. The ingots were melted in the cavity of a copper melting block insert under a slight positive pressure of helium. No measurable hardness

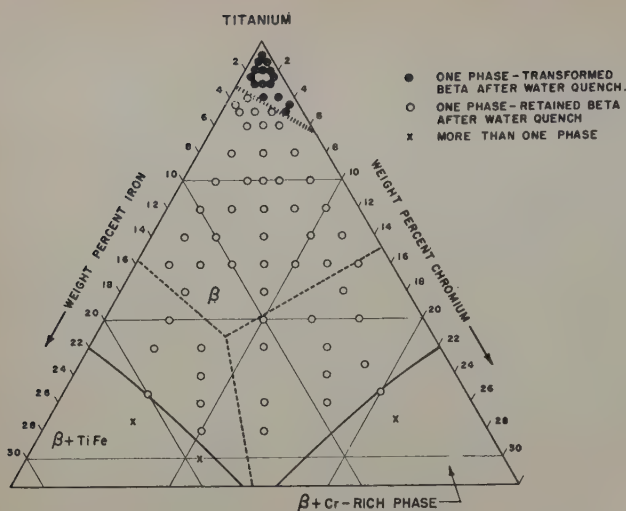


Fig. 1—Partial isothermal section at 900°C of the Ti-Cr-Fe system.

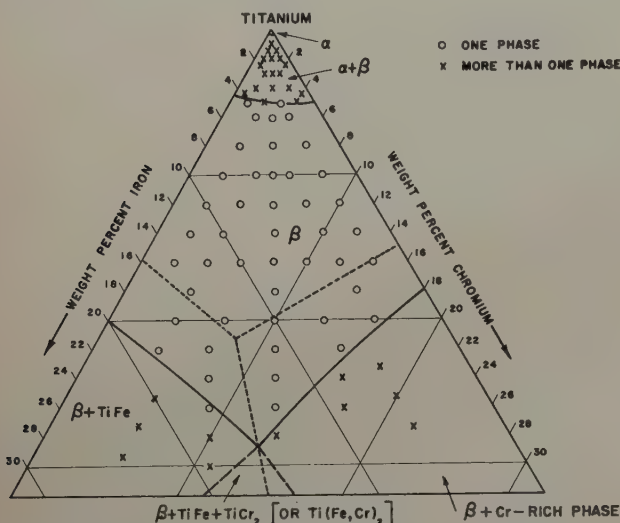


Fig. 2—Partial isothermal section at 800°C of the Ti-Cr-Fe system.

increase was found on remelting small control ingots of iodide titanium. To insure homogeneity of composition, each ingot was turned over and remelted four times without opening the furnace.

The alloy charges and resultant ingots were weighed to the nearest milligram. As the average weight losses on melting were small, the actual compositions were judged to be very close to the nominal compositions. Many check analyses, particularly for the binary alloys, substantiated the general use of nominal compositions.

Annealing Treatments: Annealing treatments of as-cast specimens were carried out in Vycor (to 1100°C) and quartz bulbs. The bulbs were sealed under vacuum for temperatures up to 1000°C; but for higher temperatures a partial pressure of argon was necessary to prevent their collapse. Information

Table II. Annealing Conditions for Ti-Cr-Fe Alloys

Temperature, °C	Time, Hr	Temperature, °C	Time, Hr
1300	1/2	750	192-288
1200	1/2-15	700	192-288
1100	1-30	650	432
1050	24	600	576-600
1000	2-40	550	744
900	22-72	500	720
800	144		

on the annealing times used for various temperatures is given in Table II. All samples heat-treated below 800°C were first annealed at 900°C for 2 to 8 hr and then slowly cooled to the temperature of final annealing. The furnace temperature control was within $\pm 3^\circ\text{C}$ of the reported temperatures below 1100°C, and about $\pm 10^\circ\text{C}$ for higher temperatures.

Coring was observed in some alloys containing over 5 pct total alloy content of chromium and iron. Therefore, these alloys were homogenization annealed at 1050°C for 24 hr prior to the regular isothermal anneals.

Melting Range Determinations: Metallographic analysis after isothermal annealing was used to outline the solidus surface. The annealing temperatures were selected by first determining the temperature of visible melting upon heating as described earlier.^{12, 13} The samples for micrographic analysis were separated with molybdenum sheet during annealing to prevent contact in case of melting. The accuracy of these data is estimated to be $\pm 10^\circ\text{C}$.

Results and Discussion

The Phase Diagram: The constitution of the titanium corner of the Ti-Cr-Fe system is of the ternary eutectoid type. Curves of double saturation ($\beta \rightleftharpoons \alpha + \text{TiCr}_2$ and $\beta \rightleftharpoons \alpha + \text{TiFe}$) descend into the space

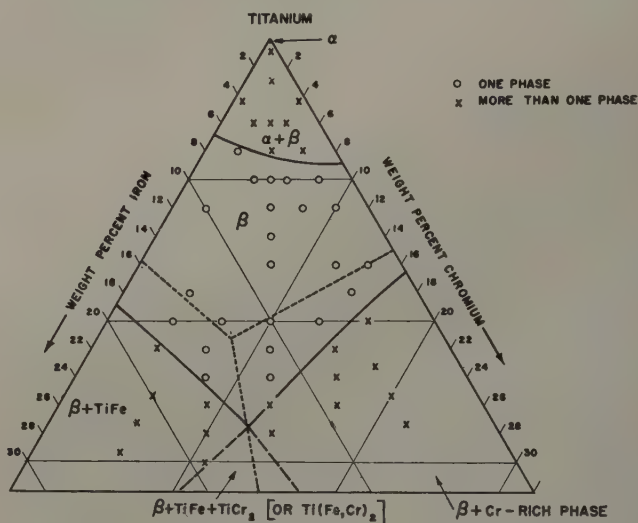


Fig. 3—Partial isothermal section at 750°C of the Ti-Cr-Fe system.

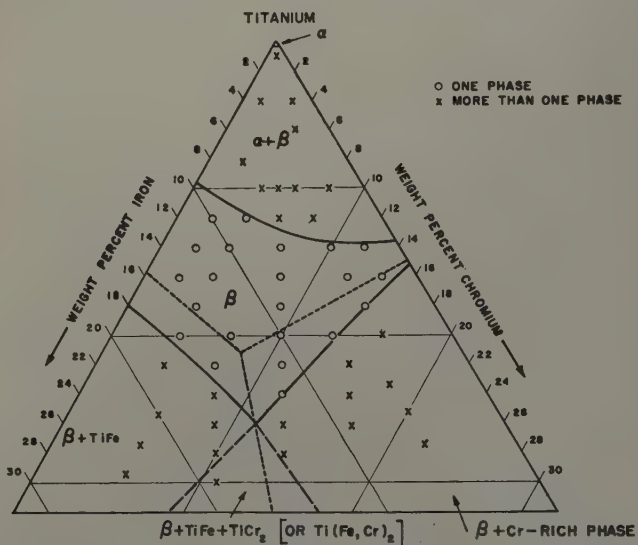


Fig. 4—Partial isothermal section at 700°C of the Ti-Cr-Fe system.

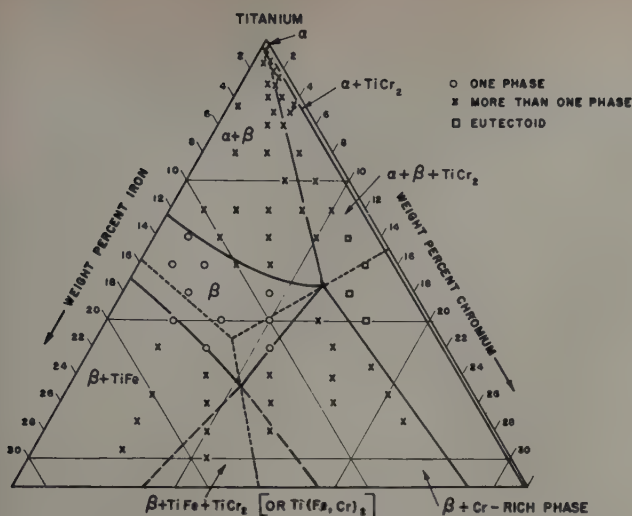


Fig. 5—Partial isothermal section at 650°C of the Ti-Cr-Fe system.

model from the two binary eutectoid points at 15 pct Cr, 685°C and 16 pct Fe, 585°C, respectively, along with that expressing saturation of the two compounds ($\beta \rightleftharpoons \text{TiCr}_2 + \text{TiFe}$). These three space curves meet to form a ternary eutectoid point ($\beta \rightleftharpoons \alpha + \text{TiCr}_2 + \text{TiFe}$) at approximately 8 pct Cr, 13 pct Fe and 540°C.

Isothermal Sections: Isothermal sections at temperatures between 900° and 550°C are presented in Figs. 1 to 7. At 900°C, Fig. 1, the β field extends over almost the entire composition area shown. The transition from transformed to retained β after water quenching these alloys from the β state is shown as a shaded band. This appears to be a straight line joining the similar transition compositions in the binary systems; that is, between 3 and 4 pct Fe, and 6 and 7 pct Cr. The samples of lower alloy content transformed to an acicular product (α') partially or completely during water quenching, and those of higher alloy content consisted entirely of retained β . The position of the three space curves of double saturation have been shown as dotted lines on all of the isotherms.

Sections through the space model at 800°, 750°, and 700°C (Figs. 2 to 4) show the enlargement of the $\alpha + \beta$ and $\beta + \text{compound}$ fields. In general, the limits of the β field in the isothermal sections were not determined by the data points obtained at a particular temperature alone. After the data had been obtained for all temperature levels (900° to 550°C), graphical interpolation, using the isothermal and vertical sections, was done, placing emphasis on the binary intercepts. Therefore, the isotherms shown are an integration of all the data.

The exact location of the sectional phase boundaries at 650°C and below (Figs. 5 to 7) was greatly impeded by the fact that the rate of diffusion at these temperatures is extremely low. As a consequence, the ternary β phase remains in a metastable state, and only in the alloys rich in chromium was microscopic evidence found of the reaction, $\beta \rightleftharpoons \alpha + \text{TiCr}_2$.

The isothermal section for 650°C is presented in Fig. 5. With the eutectoid decomposition in the Ti-Cr system occurring at 685°C, the eutectoid decomposition of the ternary β phase ($\beta \rightleftharpoons \alpha + \text{TiCr}_2$) would take place within a certain range of compositions along the entire Ti-Cr side of the system. However, as shown in Fig. 5, most of the hypo-

eutectoid alloys in the $\alpha + \beta + \text{TiCr}_2$ field were actually found to be only two-phase ($\alpha + \beta$), even after 18 days of annealing. The fact that the eutectoid decomposition did not occur in the hypoeutectoid alloys of low alloy content at annealing temperatures fairly close to the eutectoid temperature, was also observed in the binary systems.²

Because of the reluctance of the eutectoid to develop, alloys with less than 12 pct Cr could not be used in positioning the boundary between the $\alpha + \beta$ and $\alpha + \beta + \text{TiCr}_2$ fields at 650°C. However, as alloys of compositions near the space curve of double saturation showed eutectoid decomposition and the boundaries of the adjacent β field have to meet at the vertex of the $\alpha + \beta + \text{TiCr}_2$ triangle, this point could be located at approximately 13 pct Cr and 5 pct Fe.

The isothermal section at 600°C (Fig. 6) is similar to that at 650°C, with changes only in the extent of the phase fields. Eutectoid decomposition was observed in a greater number of alloys on the chromium-rich side with falling temperature, although the β phase in samples of low alloy content continued to be metastable. As at 650°C, the vertex point of the $\alpha + \beta + \text{TiCr}_2$ triangle was positioned using the intersection of the sectional phase boundaries

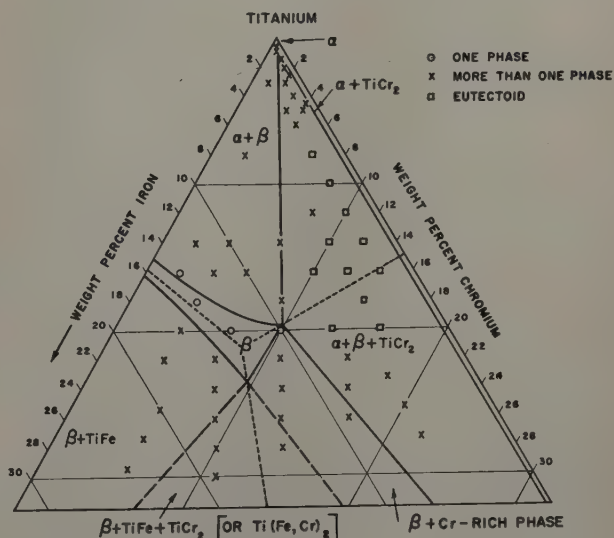


Fig. 6—Partial isothermal section at 600°C of the Ti-Cr-Fe system.

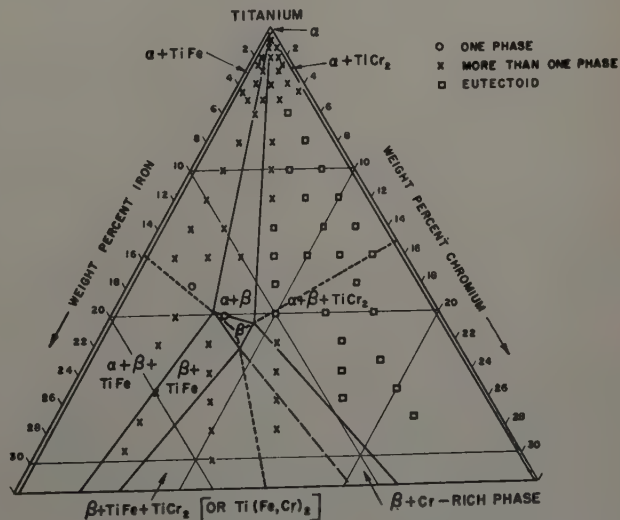


Fig. 7—Partial isothermal section at 550°C of the Ti-Cr-Fe system.

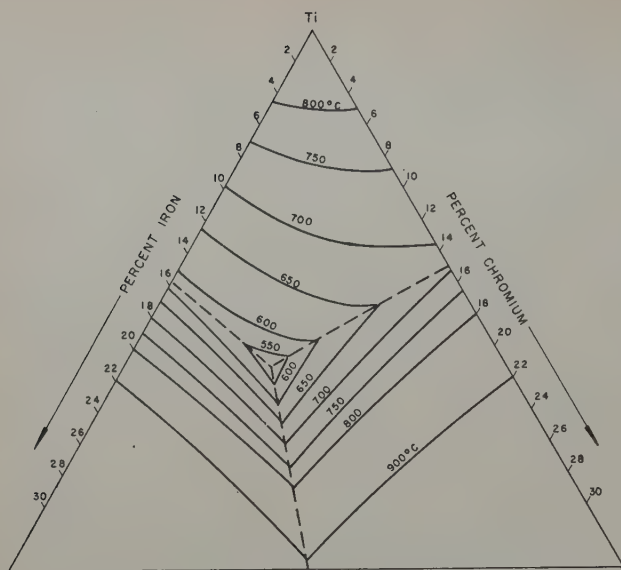


Fig. 8—Isotherms of the lower surfaces of the β phase space in the Ti-Cr-Fe system.

$\beta/\alpha + \beta$ and $\beta/\beta + \text{Cr-rich phase}$ in addition to the projection of the space curve of double saturation.

The section at 550°C (Fig. 7) is below the binary Ti-Fe eutectoid level, 585°C; therefore, the $\beta + \text{TiFe}$ and $\alpha + \beta + \text{TiFe}$ fields should now be evident. It can be seen from the data points that no eutectoid structures were observed in ternary alloys on the iron side annealed at 550°C for 31 days although under similar annealing conditions the β phase of the binary Ti-Fe system started to decompose eutectoidally.² In the iron-rich ternary alloys, the eutectoid decomposition $\beta \rightarrow \alpha + \text{TiFe}$ will start below the eutectoid temperature of the Ti-Fe system. It is not surprising, therefore, that at these low temperatures, equilibrium is approached only at a very low rate and that a definite indication of eutectoid was not observed.

The two curves of double saturation extending from the binary eutectoid points were positioned by the identification of either α or compound constituents in the microstructures of alloys lying on either side of the line. For example, at 550°C (Fig. 7), the microstructures of the 2 pct Cr-14 pct Fe and the 4 pct Cr-16 pct Fe samples consist of $\alpha + \beta$ and $\beta + \text{TiFe}$, respectively. The 4 pct Cr-14 pct Fe alloy is single-phase (β), although the alloy is located in the $\alpha + \beta + \text{TiFe}$ phase field. The apparent anomaly is explained on the basis that the composition lies very close to the space curve of double saturation. Thus, no proeutectoid constituents would be expected in the microstructure, and the indicated β is metastable.

At 650° and 600°C, the β field is extensive enough

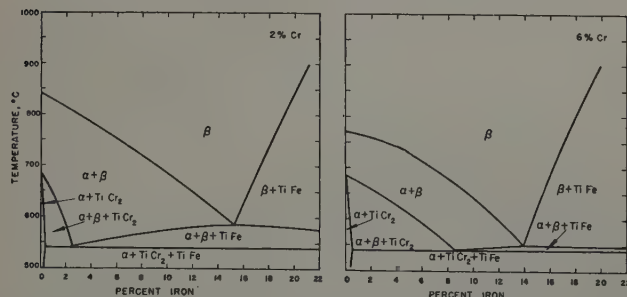


Fig. 9—Vertical sections of the Ti-Cr-Fe system at constant chromium contents.

that data points are available to accurately locate the limits of the β field and hence the other phase fields. However, at 550°C, the β field is very small and the data points on the isotherm alone did not permit the accurate placement of phase boundaries. A number of vertical sections were drawn, some of which will be presented later. From the extrapolation of data from higher temperatures, it was apparent that the β field was very restricted at 550°C and that the ternary eutectoid temperature occurs at approximately 540°C. Therefore, the β field has been constructed as very small with the limits located at points on the space curves of double saturation. The lines expressing double saturation intersect at the ternary eutectoid point; approximately 8 pct Cr and 13 pct Fe.

Although the data are not presented, alloys were annealed at 500°C for 30 days. In general, the microstructures were very fine and conclusive evidence of the binary Ti-Fe or ternary eutectoid decomposition was not observed in the ternary alloys. Several other techniques were tried to obtain the ternary eutectoid decomposition. A powder sample and a specimen that had been cold pressed were prepared. As slight amounts of contamination are known to greatly accelerate the reaction, an 8 pct Cr-13 pct Fe alloy was prepared using sponge titanium. These samples were annealed at 525°C

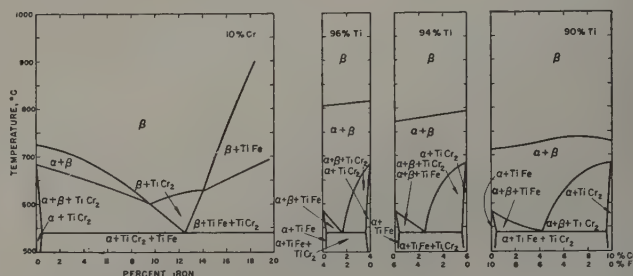


Fig. 10—Vertical sections of the Ti-Cr-Fe system at constant chromium and titanium contents.

for 12 days but no definite evidence of the ternary eutectoid decomposition either metallographically or by X-ray diffraction was found.

The solubility of chromium and iron in α titanium is less than 1 pct total alloy content. The curve of maximum solubility has been arbitrarily drawn at equal iron and chromium contents. Only a very narrow duplex phase space exists between α and TiCr_2 , because of the restricted solubility of chromium and iron in α titanium. At equilibrium, the eutectoid reaction would be complete in this region, and β is consumed. No attempt was made to locate the extent of the $\alpha + \text{TiCr}_2$ or $\alpha + \text{TiFe}$ fields at high alloy contents because they apparently are very restricted.

Fig. 8, which is a composite of isotherms of the lower surfaces of the β phase space, illustrates the good correlation obtained on combining the results. Although not shown, additional alloys were prepared and annealed to more accurately locate the ternary eutectoid point. However, because of the very small size and small amounts of phases present in these microstructures, they could not be identified.

Vertical Sections: Vertical sections at constant chromium and titanium contents are illustrated in Figs. 9 and 10. The data used in preparing these curves were taken from the isothermal sections presented earlier. Excellent correlation of data was

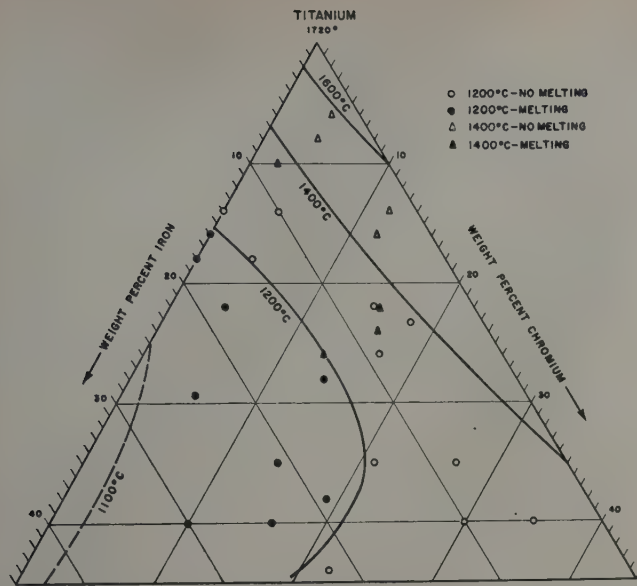


Fig. 11—Isotherms of the solidus surface of the Ti-Cr-Fe system.

obtained when plotting these sections and others that have been omitted due to space considerations.

Melting Range Determinations: The results of the solidus determinations are presented in Fig. 11; the data points shown were determined by metallographic examination of samples that were isothermally annealed and water quenched. The isotherms were drawn using previously determined solidus temperatures for the binary systems.³ Incipient melting data were obtained for a number of alloys by visible sign of melting on heating and, in general, substantiated the isotherms illustrated. Annealing at 1100°C showed that only the binary Ti-Fe alloys were melted. Therefore, chromium additions raise the temperature of the binary Ti-Fe eutectic (1080°C).

Alloys Rich in Chromium and Iron: With the discovery of the hexagonal modification of TiCr_2 , it became evident that at high temperatures a continu-

Table III. X-Ray Diffraction Data for Alloys Lying on the Section TiCr_2 - TiFe_2

Composition, Wt Pct			Annealing Treatment		Phases Observed	Lattice Parameters of Ti(Fe,Cr)_2		
Ti	Cr	Fe	°C	Hr		c(kX)	a(kX)	c/a
34	66	0	1300	1/2	TiCr_2 (Hex.)	7.987	4.919	1.624
			1200	1/2	TiCr_2 (Hex.)			
			1200	15	TiCr_2 (Hex.)			
			1100	1	TiCr_2 (Hex.)			
			1100	30	TiCr_2 (Hex.)			
			1000	2	TiCr_2 (Hex.) + TiCr_2 (Cubic)			
34	63	3	1000	40	TiCr_2 (Cubic)	7.976	4.899	1.628
			900	22	TiCr_2 (Cubic)			
			800	144	Ti(Fe,Cr)_2 + TiCr_2			
34	61	5	700	288	Ti(Fe,Cr)_2	7.976	4.900	1.628
			800	144	Ti(Fe,Cr)_2 + TiCr_2			
			600	576	Ti(Fe,Cr)_2 + TiCr_2			
34	58	8	500	696	Ti(Fe,Cr)_2	7.985	4.898	1.630
			1000	30	Ti(Fe,Cr)_2			
			800	170	Ti(Fe,Cr)_2			
33	47	20	700	288	Ti(Fe,Cr)_2	7.967	4.894	1.628
			600	576	Ti(Fe,Cr)_2			
			1000	30	Ti(Fe,Cr)_2			
32	36	32	800	170	Ti(Fe,Cr)_2	7.963	4.861	1.638
			600	144	Ti(Fe,Cr)_2			
			1000	30	Ti(Fe,Cr)_2			
31	22	47	7.925	4.839	Ti(Fe,Cr)_2	7.928	4.838	1.639
			800	144	Ti(Fe,Cr)_2			
			600	144	Ti(Fe,Cr)_2			
30	10	60	7.869	4.812	Ti(Fe,Cr)_2	7.869	4.812	1.635
			600	144	Ti(Fe,Cr)_2			
			1000	30	TiFe_2			
30	0	70	7.806	4.780	TiFe_2	7.806	4.780	1.633
			600	144	TiFe_2			

ous series of solid solutions may exist between TiCr_2 and TiFe_2 , which are isomorphous. At lower temperatures the cubic modification of TiCr_2 is stable. If a continuous single-phase field exists between TiCr_2 and TiFe_2 at high temperatures, it must continuously retreat away from TiCr_2 with falling temperature. This by itself would not necessarily affect the titanium-rich portion of the diagram that had been investigated. However, if the hexagonal phase extends into the ternary system and enters into equilibrium with β phase, the isothermal sections would then necessarily contain additional two and three phase regions.

To decide if the phase relationships mentioned above do exist, an X-ray pattern was obtained for a

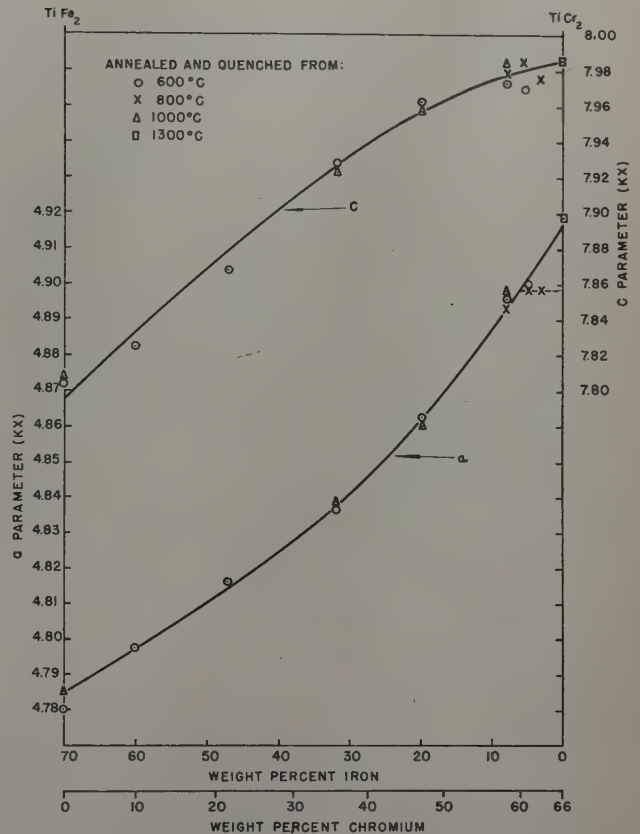


Fig. 12—Lattice parameters of the hexagonal Ti(Fe,Cr)_2 phase.

22 pct Cr-22 pct Fe alloy annealed at 800°C. This sample was found to contain β , TiFe , and the hexagonal modification of TiCr_2 . Therefore, the hexagonal modification does enter into equilibrium with β . For this reason, the phase relationships concerning Ti(Fe,Cr)_2 (the designation Ti(Fe,Cr)_2 will be used to describe the ternary phase of hexagonal structure) were studied.

Over 20 samples of high alloy content, the compositions of which are shown as data points in Fig. 14, were annealed at several temperature levels between 1000° and 500°C. However, the 800°C isotherm will serve to illustrate the equilibria involved. As there are no metallographic differences between TiCr_2 or Ti(Fe,Cr)_2 , X-ray diffraction was the principal method used to identify the phases. Micrographic analysis was used where it was helpful, such as for the identification of samples in the β + TiFe + Ti(Fe,Cr)_2 field.

X-ray diffraction data for the group of alloys with compositions spaced along a tie line between

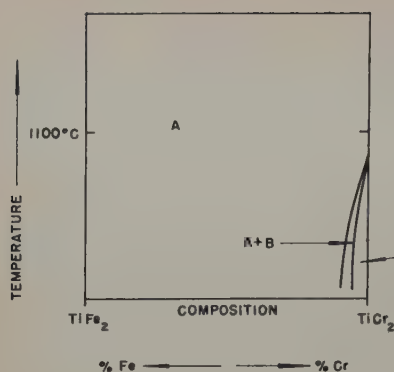


Fig. 13—Vertical section of the Ti-Cr-Fe system through TiFe_2 and TiCr_2 . A— $\text{Ti}(\text{Fe}, \text{Cr})_2$, hexagonal high temperature. B— TiCr_2 , chromium-rich cubic phase.

TiFe_2 (70 wt pct Fe) and TiCr_2 (66 wt pct Cr) were obtained. Samples were annealed at temperatures between 1300° and 500°C for 30 min to 29 days. All alloys treated were found to consist of only the hexagonal phase, $\text{Ti}(\text{Fe}, \text{Cr})_2$ at elevated temperatures. A summary of the lattice parameter measurements is shown in Table III. The polymorphic transformation of TiCr_2 was found to occur between 1000° and 1100°C.

The data shown in Table III are plotted in Fig. 12; smooth curves were obtained for both lattice parameter values at elevated temperatures. This proves the existence of a continuous series of solid solutions between TiFe_2 and hexagonal TiCr_2 . Parameter values for a given alloy in the one-phase field at different temperature levels were in close agreement. A break occurs in the lattice parameter curves (particularly curve *a*) at the chromium-rich side with lowered temperature. This is due to the appearance of the two-phase field $\text{TiCr}_2 + \text{Ti}(\text{Fe}, \text{Cr})_2$, and hence the composition of the hexagonal phase in equilibrium with the cubic phase remains the same. Fig. 13 schematically illustrates the vertical section through the two compounds.

The 800°C isotherm, given in Fig. 14, is based on X-ray data (Table IV) and metallographic observations. It is evident that the phase relationships are more complex than those shown in Fig. 2. They indicate that the β phase is in equilibrium with both TiCr_2 and $\text{Ti}(\text{Fe}, \text{Cr})_2$ at 800°C. However, the location of the α , $\alpha + \beta$, and β spaces, on which most of the effort has been concentrated, is not affected by these findings.

The corners of the phase field $\beta + \text{TiFe} + \text{Ti}(\text{Fe}, \text{Cr})_2$ are located at the saturated β phase, TiFe , and approximately 58 pct Cr-8 pct Fe, representing the $\text{Ti}(\text{Fe}, \text{Cr})_2$ phase. The latter value was

obtained by comparing the lattice parameters of the $\text{Ti}(\text{Fe}, \text{Cr})_2$ phase of alloys in the three-phase field with those of the section TiFe_2 - TiCr_2 (Fig. 12). The other three-phase field, $\beta + \text{TiCr}_2 + \text{Ti}(\text{Fe}, \text{Cr})_2$, was located as shown, as the structure of the 35 pct Cr-5 pct Fe alloy was found by X-ray diffraction to consist of three phases.

Upon examination of the 800°C isotherm, it is recognized that additional phase relationships will occur below this temperature. No attempt was made to study these. For simplicity, it was assumed that the eutectoid decomposition of the ternary β phase involves the phases, α , TiFe , and TiCr_2 . This would be true if a four-phase reaction, $\beta + \text{Ti}(\text{Fe}, \text{Cr})_2 \rightleftharpoons \text{TiFe} + \text{TiCr}_2$, takes place, eliminating equilibria involving $\text{Ti}(\text{Fe}, \text{Cr})_2$ in alloys lying on the high titanium side of a tie line extending between TiFe and TiCr_2 . However, it is realized that an alternate reaction, $\beta + \text{TiCr}_2 \rightleftharpoons \alpha + \text{Ti}(\text{Fe}, \text{Cr})_2$, could proceed at a temperature between that of binary Ti-Cr eutectoid (685°C) and the ternary eutectoid (540°C). If this reaction should occur, the ternary eutectoid would consist of $\alpha + \text{TiFe} + \text{Ti}(\text{Fe}, \text{Cr})_2$.

Microstructures: Only a limited number of micrographs are presented as, in general, the microstructures

Table IV. X-Ray Diffraction Identification of Phases Present in Ti-Cr-Fe Alloys Annealed at 800°C

Composition, Wt Pct				Annealing Time, Hr	Phases Observed	Lattice Parameters of $\text{Ti}(\text{Fe}, \text{Cr})_2$		
Ti	Cr	Fe				<i>c</i> (kX)	<i>a</i> (kX)	<i>c/a</i>
34	63	3		144	$\text{Ti}(\text{Fe}, \text{Cr})_2 + \text{TiCr}_2$	7.976	4.899	1.628
34	61	5		144	$\text{Ti}(\text{Fe}, \text{Cr})_2 + \text{TiCr}_2$	7.983	4.899	1.630
60	35	5		144	$\beta + \text{TiCr}_2 + \text{Ti}(\text{Fe}, \text{Cr})_2$			
34	58	8		170	$\text{Ti}(\text{Fe}, \text{Cr})_2$	7.976	4.896	1.629
60	30	10		144	$\beta + \text{Ti}(\text{Fe}, \text{Cr})_2$			
60	24	16		144	$\beta + \text{Ti}(\text{Fe}, \text{Cr})_2$			
68	16	16		144	$\beta + \text{Ti}(\text{Fe}, \text{Cr})_2$			
43	39	18		170	$\text{Ti}(\text{Fe}, \text{Cr})_2$	7.999	4.893	1.635
33	47	20		170	$\text{Ti}(\text{Fe}, \text{Cr})_2$			
65	14	21		144	$\beta + \text{TiFe}$			
56	22	22		144	$\beta + \text{TiFe} + \text{Ti}(\text{Fe}, \text{Cr})_2$	7.988	4.905	1.630
32	36	32		170	$\text{Ti}(\text{Fe}, \text{Cr})_2$			
37	21	42		144	$\text{TiFe} + \text{Ti}(\text{Fe}, \text{Cr})_2$	7.904	4.849	1.631
30	0	70		170	TiFe_2			

tures observed were similar to those for the alloys of the binary systems. For typical microstructures representative of the various phase fields, the reader is referred to the binary systems.²

The low solubility of chromium and iron in α titanium is shown by the duplex structure of Fig. 15. Fig. 16 illustrates the $\alpha + \text{TiCr}_2$ eutectoid structure of the $\alpha + \beta + \text{TiCr}_2$ space. As previously discussed in another section, no microstructural evidence of eutectoid decomposition in the $\alpha + \beta + \text{TiFe}$ space was observed. Also, no ternary eutectoid decomposition was noted at 500°C, although this temperature is below the ternary eutectoid plane. The $\text{Ti}(\text{Fe}, \text{Cr})_2$ phase is illustrated in Fig. 17.

Fig. 18 shows the microstructure of an alloy annealed at 800°C in the $\beta + \text{TiFe} + \text{Ti}(\text{Fe}, \text{Cr})_2$ space. An X-ray diffraction pattern of this sample confirmed the metallographic evidence of the two intermediate phases. To differentiate between the coexisting intermediate phases, staining etchants were tested. A 10 pct aqueous solution of various etchants was used. Of the many etchants tried, electrolytic etching with a $\text{K}_3\text{Fe}(\text{CN})_6 + \text{NaOH}$ solution was the most useful. The polished samples were etched first with a $\text{HNO}_3 + \text{HF} + \text{glycerine}$

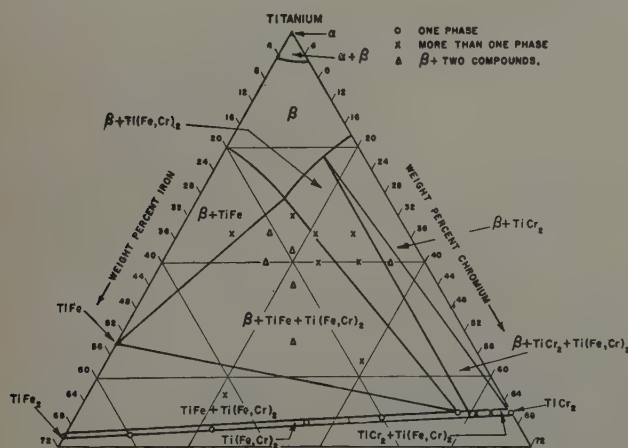


Fig. 14—Partial isothermal section at 800°C of the Ti-Cr-Fe system.

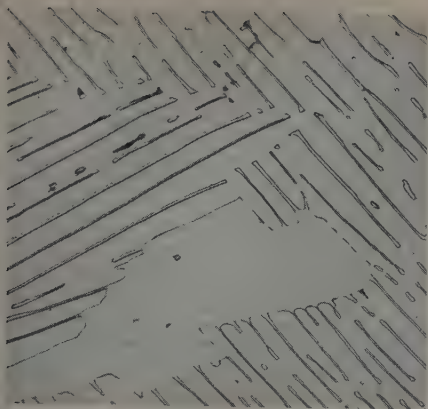


Fig. 15—A 0.5 pct Cr, 0.5 pct Fe alloy, water-quenched after annealing at 650°C for 432 hr. α + retained β (smaller amount). Etchant: HNO_3 + HF + glycerine. X500. Area reduced approximately 30 pct for reproduction.

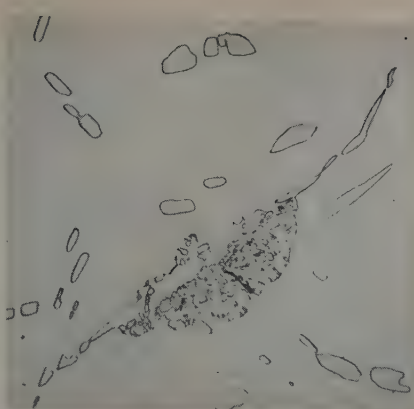


Fig. 16—A 12 pct Cr, 2 pct Fe alloy annealed at 650°C for 432 hr. Eutectoid (α + TiCr_2) and α in a matrix of retained β . Etchant: HNO_3 + HF + glycerine. X500. Area reduced approximately 30 pct for reproduction.



Fig. 17—A 47 pct Cr, 20 pct Fe alloy, water-quenched after annealing at 800°C for 144 hr. Nearly single phase, Ti(Fe,Cr)_2 . Etchant: HNO_3 + HF + glycerine. X500. Area reduced approximately 30 pct for reproduction.

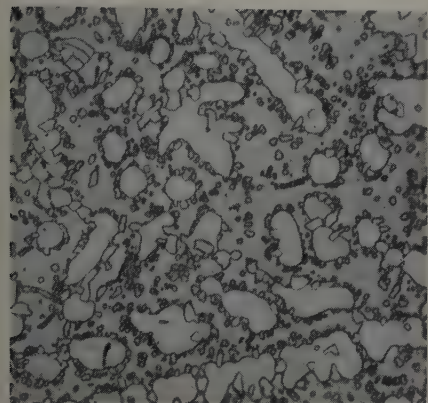


Fig. 18—A 22 pct Cr, 22 pct Fe alloy annealed at 800°C for 144 hr and water-quenched. Ti(Fe,Cr)_2 (larger crystals) and TiFe in a matrix of β . Etchant: HNO_3 + HF + glycerine. X750. Area reduced approximately 30 pct for reproduction.

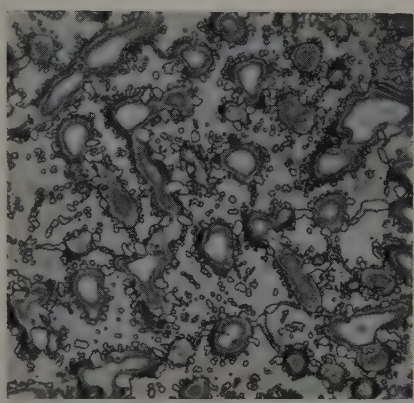


Fig. 19—The same microstructure as Fig. 18. Ti(Fe,Cr)_2 is now stained although TiFe is not. Etchant: electrolytic $\text{K}_3\text{Fe(CN)}_6$ + NaOH + H_2O superimposed upon the structure etched with HNO_3 + HF + glycerine. X750. Area reduced approximately 30 pct for reproduction.

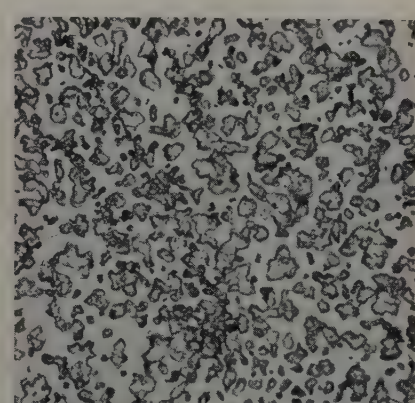


Fig. 20—A 50 pct Cr alloy, water-quenched after 24 hr at 1000°C. β and stained TiCr_2 . Etchant: same as Fig. 19. X250. Area reduced approximately 30 pct for reproduction.

solution (Fig. 18) and were then electrolytically etched with the $\text{K}_3\text{Fe(CN)}_6$ + NaOH solution, preferentially staining Ti(Fe,Cr)_2 (Fig. 19).

A size difference may be noted in Fig. 18; Ti(Fe,Cr)_2 is larger with the smaller TiFe crystals surrounding it. In order to prove that the differential staining in Fig. 19 is due to the different phases present and not just size variations, binary alloys containing either TiCr_2 or TiFe were stain-etched. Both alloys were polished and etched under conditions identical to those used in the preparation of Fig. 19. Figs. 20 and 21 conclusively show that TiCr_2 is heavily stained whereas the TiFe is unaffected by the $\text{K}_3\text{Fe(CN)}_6$ + NaOH + H_2O etchant.

As another technique of differentiating between the two compounds, heat tinting was tried. With this method a sample previously polished is placed in a preheated furnace with an air atmosphere. At 700°C, the only temperature investigated, 40 sec appears to be the best time. Shorter times result in little tinting, whereas longer times produce deeper tints that mask the true structure.

Hardness: Vickers hardness data of Ti-Cr-Fe alloys annealed at and quenched from temperatures between 1000° and 650°C are presented graphically in Fig. 22. The alloys used are on the vertical section through the ternary system at the Cr:Fe ratio

of 1:1. These alloys exhibit the same trends observed in the binary systems Ti-Cr and Ti-Fe.² The hardness curves for samples water-quenched from above 800°C reach a peak at about 5 pct total alloy content, which corresponds to the composition at which β is retained upon water quenching. Hardness peaks at 7 pct Cr and 4 pct Fe were obtained on quenching from the β field.

Annealing the ternary alloys at 650° or 700°C resulted in a linear increase in hardness with alloy composition up to 10 pct. Such alloys have α + β

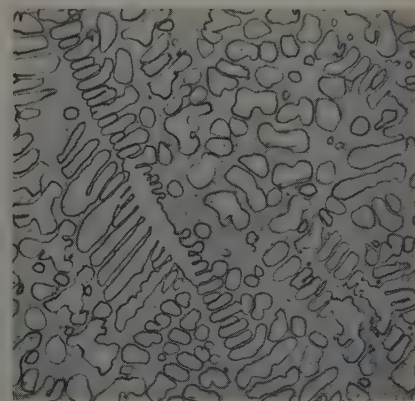


Fig. 21—A 40 pct Fe alloy annealed the same as Fig. 20. β and unstained TiFe . Etchant: same as Fig. 19. X250. Area reduced approximately 30 pct for reproduction.

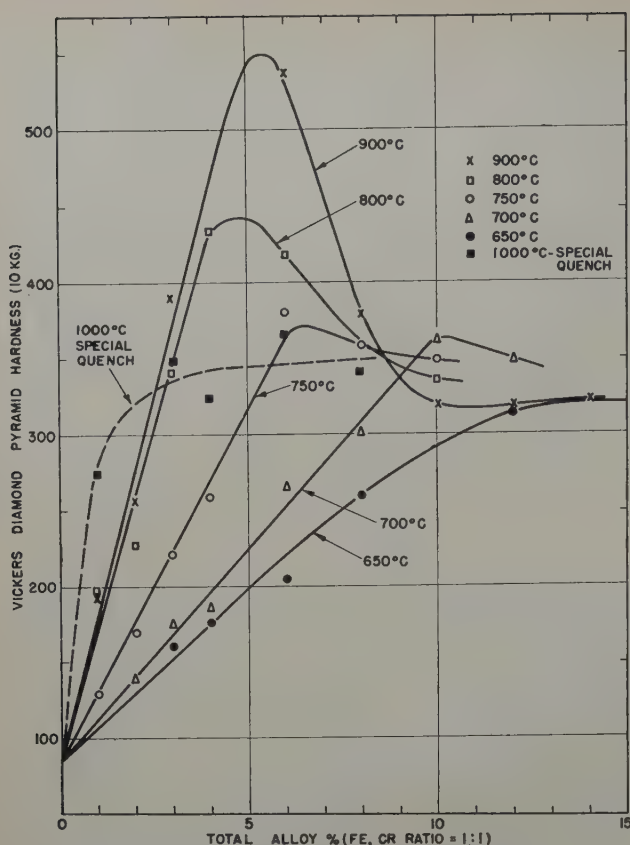


Fig. 22—Vickers hardness of Ti-Cr-Fe alloys (Fe, Cr ratio = 1:1).

structures, and are much softer than the product (β') obtained by quenching from above the transformation temperature. It can be seen from Fig. 22 that the hardness of alloys in the lower composition range, i.e., those in the commercial alloy region, may be very greatly changed by heat treatment. The hardness of the 5 pct alloy annealed at 650°C is 200 DPH, but quenching the same alloy from 900°C resulted in a hardness of over 500 DPH.

With very rapid quenching from the β field, the high hardness peak is eliminated. Samples were annealed at 1000°C for 15 min and rapidly quenched into an iced 10 pct NaOH solution. The specimen size was approximately 1/8x1/8x1/16 in. Temperatures as low as 100°C will age these metastable structures to much higher hardness.¹⁴ Therefore, the hardness readings were obtained on unmounted samples. Similar results were obtained with binary Ti-Cr alloys. As the hardness peak obtained on quenching from the β field cannot be suppressed in samples a little larger than those described above, probably no commercial usage will be made of the phenomenon.

Summary

There is a continuous space of ternary β solid solution ranging from the Ti-Fe to the Ti-Cr system. Under equilibrium conditions, the following phase changes will occur with fall in temperature: According to the composition of the alloy, the ternary β phase starts to decompose by primary rejection of either one of the three phases, α , TiFe, or TiCr₂. This is followed by the eutectoid decomposition into α + TiCr₂, α + TiFe, or TiFe + TiCr₂, respectively, taking place within a temperature interval. The phase changes are terminated by the formation of the ternary eutectoid α + TiFe + TiCr₂

at about 540°C. The ternary eutectoid is located at approximately 8 pct Cr-13 pct Fe. Whereas the precipitation of α , TiFe, and TiCr₂, respectively, takes place at a high rate, the "binary" and especially the ternary eutectoid decompositions, due to their low temperature of initiation, are extremely sluggish and can be enforced only by very long annealing times. Therefore, under ordinary conditions of heat treatment, the β phase remains metastable, similar to the conditions in the binary systems Ti-Fe and Ti-Cr.

A continuous series of solid solutions exists above 1100°C between TiFe₂ and the high temperature modification of TiCr₂. Solidus data are presented and show that chromium raises the binary Ti-Fe eutectic temperature (1080°C). Hardness data are presented and illustrate the pronounced effect of heat treatment.

Acknowledgments

The authors wish to thank the Materials Laboratory, Wright Air Development Center, who sponsored the work under Contract AF 33 (038)-8708 for permission to publish this paper. The help of the many associates at Armour Research Foundation is appreciated. Special thanks are due to R. F. Domagala who was responsible for the heat treatment of the alloys; W. Rostoker, for the X-ray diffraction data; and C. A. Johnson, for the metallographic work.

References

- ¹ R. Vogel and B. Wenderott: The Constitution Diagram Iron-Chromium-Titanium. *Archiv Eisenhüttenwesen* (1940) **14**, p. 279.
- ² R. J. Van Thyne, H. D. Kessler, and M. Hansen: *Trans. ASM* (1952) **44**, pp. 974-989.
- ³ C. M. Craighead, O. W. Simmons, and L. W. Eastwood: Titanium Binary Alloys. *Trans. AIME* (1950) **188**, pp. 485-513; *JOURNAL OF METALS* (March 1950).
- ⁴ D. J. McPherson and M. G. Fontana: Preparation and Properties of Titanium-Chromium Binary Alloys. *Trans. ASM* (1951) **43**, pp. 1098-1125.
- ⁵ M. K. McQuillan: A Provisional Constitutional Diagram of the Chromium-Titanium System. *Journal Inst. Metals* (1951) **79**, pp. 379-390.
- ⁶ P. Duwez and J. L. Taylor: A Partial Titanium-Chromium Phase Diagram and the Crystal Structure of TiCr₂. *Trans. ASM* (1952) **44**, p. 495.
- ⁷ F. B. Cuff, N. J. Grant, and C. F. Floe: Titanium-Chromium Phase Diagram. *Trans. AIME* (1952) **194**, pp. 848-853; *JOURNAL OF METALS* (August 1952).
- ⁸ H. W. Worner: The Constitution of Titanium-Rich Alloys of Iron and Titanium. *Journal Inst. Metals* (1951) **79**, pp. 173-188.
- ⁹ W. J. Fretague, C. S. Barker, and A. E. Peretti: Air Force Technical Report 6597, Parts 1 and 2 (November 1951-March 1952).
- ¹⁰ A. D. McQuillan: The Application of Hydrogen Equilibrium-Pressure Measurements to the Investigation of Titanium Alloy Systems. *Journal Inst. Metals* (1951) **79**, pp. 73-88.
- ¹¹ B. W. Levinger: High Temperature Modification of TiCr₂. *Trans. AIME* (1953) **197**, p. 196; *JOURNAL OF METALS* (February 1953).
- ¹² M. Hansen, E. L. Kamen, H. D. Kessler and D. J. McPherson: The Systems Titanium-Molybdenum and Titanium-Columbium. *Trans. AIME* (1951) **191**, pp. 881-888; *JOURNAL OF METALS* (October 1951).
- ¹³ M. Hansen, H. D. Kessler, and D. J. McPherson: The System Titanium-Silicon. *Trans. ASM* (1952) **44**, p. 518.
- ¹⁴ W. M. Parris, L. L. Hirsch, and P. D. Frost: Low Temperature Aging in Titanium Alloys. *Trans. AIME* (1953) **197**, pp. 178-179; *JOURNAL OF METALS* (February 1953).

Plastic Deformation of Rectangular Zinc Monocrystals

by John J. Gilman

The data presented indicate that the critical shear stress and strain-hardening rate of a zinc monocrystal depend on the orientation of its slip direction with respect to its external boundaries. The tendency of a crystal to form deformation bands also depends on its shape.

THE plastic behavior of pairs of zinc monocrystals in which both members of the respective pairs had the same orientation with respect to the longitudinal axis, but each had different orientations with respect to their rectangular external shapes, were compared in this investigation. The purpose of the investigation was to see what influence the shape or surface of a zinc crystal has on its mechanical properties. In a previous investigation of triangular zinc monocrystals,¹ anomalous axial twisting was observed which seemed to be related to the triangular shape of the crystals.

Wolff,² in 400°C tensile tests of rectangular rock-salt crystals bounded by cubic cleavage planes, found that, of the four equivalent slip systems, the two with the "shorter" slip directions yielded and produced slip lines at lower stresses than the other two. This observation and the work of Dommerich³ was formulated by Smekal⁴ as a "new slip condition" for rock-salt: "among two or more slip systems permitted by the shear stress law, with reference to the formation of visible slip lines by large individual glides, that slip system is preferred which has the shortest effective slip direction."

More recently, Wu and Smoluchowski⁵ reported essentially the same effect for ribbon-like (20x2x0.2 mm) aluminum crystals at room temperature.

Experimental

Chemically pure zinc (99.999 pct Zn), purchased from the New Jersey Zinc Co., was the raw material. Glass envelopes, containing graphite molds and zinc, were evacuated while hot enough to outgas the graphite but not melt the zinc. At a vacuum of about 0.2 micron the envelopes were sealed off and then lowered through a furnace at 1 in. per hr so as to melt and resolidify the zinc and produce monocrystals.

One-half of one of the molds is shown in Fig. 1a. Each mold consisted of four pieces from a cylindrical graphite rod that was split longitudinally and transversely at its midpoints. Rectangular milled grooves 0.050 in. deep and $\frac{3}{8}$ in. wide formed the mold cavity when the split halves were assembled with twisted wires. Fig. 1b shows the specimen shape obtained when the top and bottom mold-halves were rotated 90° with respect to each other. Good fits prevented leakage and excess zinc was necessary

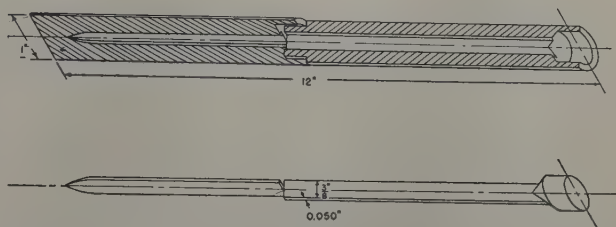


Fig. 1a (top)—Schematic drawing of one-half of the split graphite mold.

Fig. 1b (bottom)—Shape of monocrystalline specimens produced in molds like Fig. 1a.

to provide enough liquid head to fill the mold completely.

In removing soft crystals from the molds it was impossible to avoid small amounts of bending. However, manipulations were carried out whenever possible with the crystals protected by grooved brass blocks. All specimens were annealed prior to testing.

From the top and bottom sections of each crystal, X-ray specimens and tensile specimens 7 to 8 cm long were sawed. The tensile specimens were annealed inside evacuated tubes for 1 hr at 375°C. Next the crystals were cleaned and polished by 2-min dips in a solution of 22 pct chromic acid, 74 pct water, 2.5 pct sulphuric acid, and 1.5 pct glacial acetic acid.⁶ Cleaning was followed by a 10-sec dip in a 10 pct caustic solution, then washed in water and alcohol, and dried. This treatment results in a bright surface covered by an invisible oxide film.

The testing grips were a slotted type with set screws and were supported in a V-block during the mounting operations in order to avoid bending the crystals. A schematic diagram of the recording tensile-testing machine is shown in Fig. 2. The machine has been described elsewhere.⁷ The head speed was 0.3 mm per sec for all tests.

The crystal orientations were determined by the Geringer X-ray back-reflection method with an estimated accuracy of $\pm 1^\circ$.

Description of Crystal Geometry

A schematic picture of a rectangular zinc monocrystal is shown in Fig. 3. ABD designates the front edge of a basal plane (0001) of the crystal, the only active slip plane for zinc at room temperature. Of the three possible ($2\bar{1}\bar{1}0$) slip directions, the active one is indicated by an arrow. Cartesian coordinates are taken parallel to the specimen edges. The normal, n , to the basal plane (n is parallel to the hexagonal axis) has the direction cosines α , β , and γ . $\chi_0 = 90^\circ - \gamma$ is the angle between the longitudinal axis and

J. J. GILMAN, Junior Member AIME, formerly with Columbia University, is now associated with Metallurgy Research Dept., Research Laboratory, General Electric Co., Schenectady.

Discussion on this paper, TP 3571E, may be sent, 2 copies, to AIME by Dec. 1, 1953. Manuscript, Sept. 16, 1952; revision, Feb. 28, 1953. Cleveland Meeting, October 1953.

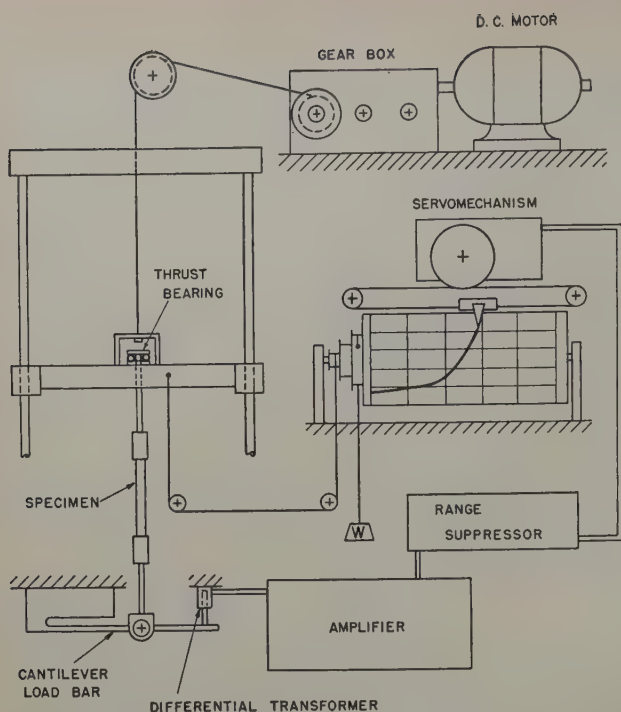


Fig. 2—Schematic drawing of the automatic recording tensile machine used for testing the specimens.

the basal plane, and λ_0 is the angle between the longitudinal axis and the slip direction. The breadth and thickness of the specimen are b and t , respectively. θ is the angle between the projection of the slip direction into the cross-sectional plane and the normal to the wide side of the crystal. ξ and η are the angles between the surface traces of the slip plane and the x and y axes, respectively. ω is the angle between the slip direction and a line lying in the slip plane and perpendicular to \overline{AB} , its intersection with the side. δ is the angle between \overline{AB} and \overline{BD} . s is the "length" of the slip direction and is the length of a unit slip (equal to the distance between atoms in the slip direction).

If α , ρ , γ , and λ_0 are known, the other angular parameters, δ , θ , ω , ξ , λ , and η , may be calculated. However, they may be quickly measured on a stereographic plot of the specimen, so this was the method used here; a few calculations were made as checks.

The "length" of the slip direction, s , is found as follows:

$$s = \frac{GH}{\sin \lambda_0} = \frac{t}{\cos \theta \sin \lambda_0} \text{ or } \frac{b}{\sin \theta \sin \lambda_0} \quad [1]$$

whichever is smaller. The area of the slip plane is:

$$a_0 = \overline{AB} (\overline{BD} \sin \delta)$$

Since d_0 is very small compared with b and t , the

increase in surface area of the crystal per unit slip is

$$\begin{aligned} a' &= 2c \overline{AB} + 2e \overline{BD} \\ &= 2 \left(\frac{cb}{\cos \xi} + \frac{et}{\cos \eta} \right) \\ &= 2d_0 \left(b \frac{\cos \omega}{\cos \xi} + t \frac{\sin \omega}{\cos \eta} \right) \end{aligned} \quad [2]$$

The perimeter of the slip plane is just

$$P = 2(\overline{AB} + \overline{BD}) = 2 \left(\frac{b}{\cos \xi} + \frac{t}{\cos \eta} \right) \quad [3]$$

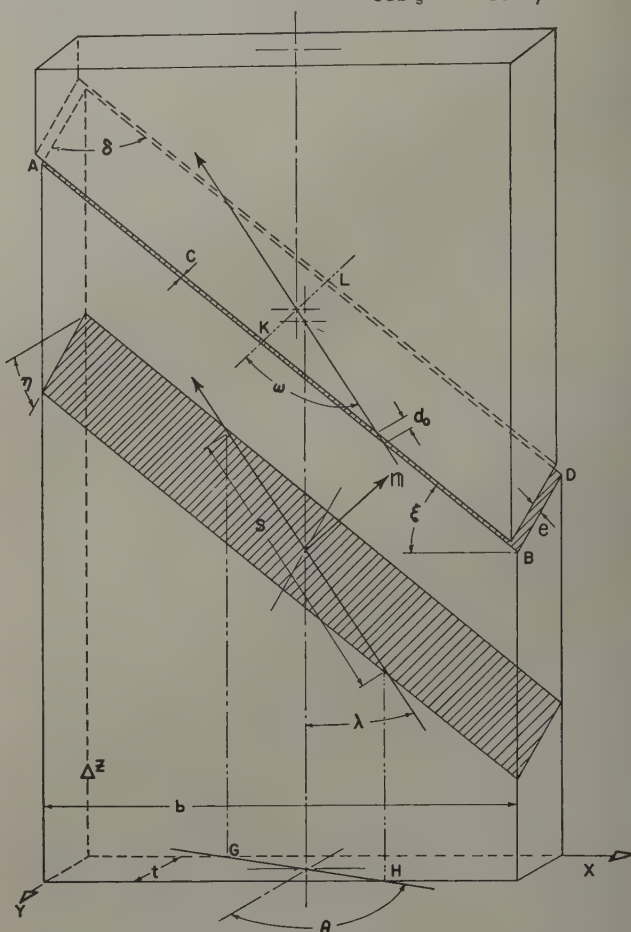


Fig. 3—Schematic geometry of a rectangular zinc monocystal.

and the component of the perimeter perpendicular to the slip direction is twice the quantity in the brackets of Eq. 2. The quantities in Eq. 3 will be used in the discussion of the results.

Results

About thirty-five pairs of crystals were grown and tested. The growth technique yielded a majority

Table I. Reproducibility of the Stress-Strain Data for Pairs of Rectangular Zinc Monocrystals, with Zero Mold Rotation

Crystal Pair	Orientation Angles						Thickness, Mm	Gage Length, Cm	Resolved Shear Stresses, Elongation, Pct			Twinning	
	χ_0	λ_0	ξ	η	θ	ω			1/10	1	10	Stress, Kg per Sq Mm	Elongation, Pct
15T	9	11	74	79	3	69	1.25	8.3	36.3	58.6		1.12	5.7
B									36.5	59.5		1.16	5.8
16T	64	66	15	20	59	60	1.25	7.8	34.8	45.2	86.8		
B							1.04		34.0	42.1	80.0		
18T	12	12	52	78	16	54	1.25	7.7	38.7	54.1	156	0.91	1.6
B							1.04		38.3	51.5	154	0.97	1.7
20T	4	26	—	—	—	—	0.99	8.3	—	—	—	1.07	<0.1
B							1.02					1.03	

of crystals with low χ_0 values, however, which slipped very little before they began to twin. For crystals which deformed by slip, it was considered that χ_0 must be about 14° to 15° , if the orientation effects were not to be obscured by end effects. Crystals for which χ_0 was less than 5° were considered to have deformed entirely by twinning. Crystals of intermediate orientations were not considered.

Slip: A major difficulty in experiments on the mechanical properties of monocrystals is that of obtaining reproducible results. In order to see how much reproducibility might be expected of the present crystals, four pairs were grown for which the top and bottom halves of the mold were given zero rotation. Data for these pairs are presented in Table I. For both slip and twinning the reproducibility was good. On the basis of Table I, the experimental error in stress-strain data is estimated to be 5 pct between two *crystals* of any pair. However, the differences between *pairs* of crystals were considerably larger, amounting to as much as 15 pct.

Table II lists data for pairs of crystals that were rotated 30° and 90° relative to each other in the mold. In most cases the θ values differ by just about this amount, but in some cases the difference is less than this because symmetry makes ($\theta = 90$) the same as θ . The resolved shear stresses are given at various percentages of elongations. These were calculated from the usual expression,

$$T = \sigma \sin \chi \cos \lambda$$

where σ is the tensile stress; χ , the instantaneous angle between axis and slip plane; and λ , the instantaneous angle between axis and slip direction.

The resolved shear stresses at 0.1 and 1.0 pct elongation are given as indices of the yield behaviors of the crystals. The difference between the shear stresses at 10 and 1 pct elongation, $T_{10} - T_1$, divided by the difference in corresponding shear strains, $\gamma_{10} - \gamma_1$, is a measure of the strain-hardening rate of a crystal. These values are listed in Table II after the critical shear stresses. Table II also lists the geometric parameters, s and a' .

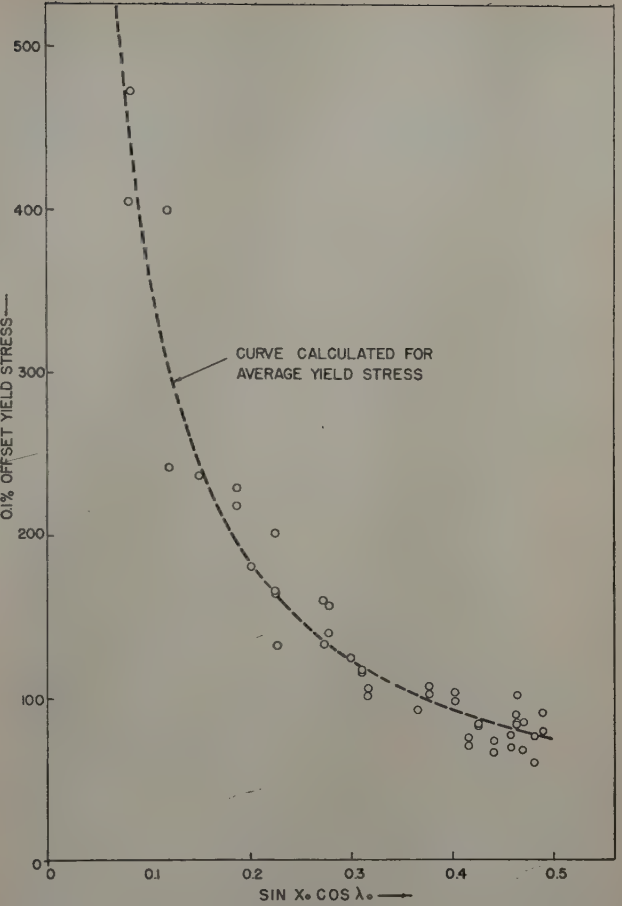


Fig. 4—Plot of 0.1 pct offset yield stress data listed in Table II.

The values of the resolved shear stresses differ considerably among crystals and pairs. This is shown graphically in Fig. 4 where the data are scattered about the curve calculated for the average resolved shear stress at 0.1 pct elongation; 37.0 g per sq mm. The reason for the scatter between castings is not known. Part of the cause was the

Table II. Tensile Test Data for Slip of Zinc Crystal Pairs

Crystal Pair	Orientation Angles						Gage Length, Cm	Resolved Shear Stress (G per Sq Mm) Elongation, Pct			Strain-Hardening $T_{10}-T_1$ $\gamma_{10}-\gamma_1$	Geometric Parameters	
	χ_0	λ_0	ξ	η	θ	ω		0.1	1.0	10		s , Mm	a' Sq Mm $\times 10^{-7}$
2T	37	37	12	53	13	18	7.0	36.7	47.3	93.7	209	2.03	52.5
B			37	56	48	58		28.6	39.0	73.3	152	3.15	43.8
4T	34	34	54	24	62	74	2.9	38.3	51.8	—	—	4.83	30.9
B			48	49	32	55		42.9	53.8	—	—	2.36	50.8
7T	31	31	25	58	26	35	8.7	31.2	38.8	75.8	151	2.74	53.1
B			52	51	58	70		29.5	35.9	70.4	143	4.43	37.8
10T	35	42	32	52	70	69	7.4	34.7	43.7	87.5	176	5.46	31.4
B			3	56	38	22		35.1	45.1	104	242	2.03	50.9
11T	20	22	0	71	36	14	8.7	33.6	45.3	98.6	158	3.93	53.7
B			50	67	3	43		32.0	41.0	90.9	148	3.23	68.6
14T	29	31	13	60	32	28	8.9	29.4	36.6	76.6	156	2.77	52.0
B			48	54	62	71		31.3	39.5	71.9	122	5.25	35.5
17T	45	49	42	27	87	88	8.3	39.4	48.7	101	234	11.6	9.84
B			44	8	57	66		47.2	57.1	112	245	3.09	35.0
21T	34	34	12	56	2	9	3.2	39.9	53.1	109	—	2.17	53.0
B			26	56	38	42		41.2	52.4	109	—	7.36	48.5
23T	34	35	54	32	81	84	7.5	—	42.6	81.3	161	13.5	16.6
B			42	49	52	62		—	43.4	80.1	152	2.88	39.3
25T	63	65	22	14	37	42	3.6	40.2	53.2	106	—	1.73	45.3
B			13	16	2	7		38.4	52.3	119	—	1.34	52.5
27T	18	26	71	8	40	70	4.6	38.8	57.3	168	—	3.60	59.1
B			70	62	8	60		43.8	61.2	143	—	2.28	84.1
29T	14	21	73	56	68	82	8.2	31.6	45.6	113	145	9.03	35.5
B			65	74	79	83		37.6	50.9	119	144	18.3	38.5
32T	22	34	54	67	27	38	8.4	36.5	52.8	146	281	2.37	80.3
B			62	51	74	80		35.7	48.3	124	227	8.25	29.4
35T	22	37	20	66	64	52	5.5	37.1	50.9	133	242	4.73	46.0
B			68	34	46	64		37.7	55.3	147	271	3.04	66.5
37T	19	33	64	62	6	48	4.9	43.5	56.8	144	—	2.34	88.3
B			56	65	86	86		36.4	51.3	140	—	17.5	22.6
38T	55	55	18	32	18	24	4.2	40.0	48.6	89.7	—	1.53	51.7
B			32	21	73	76		32.0	42.0	73.8	—	4.14	19.9
39T	51	51	23	36	42	46	8.3	—	49.3	83.5	157	2.10	43.8
B			28	28	50	56		—	51.0	82.3	141	2.50	38.4



Fig. 5—Pair of rectangular zinc monocrystals which deformed by slip. $\chi_0 = 31^\circ$, $\lambda_0 = 31^\circ$.
a (top)— $\theta = 58^\circ$. b (bottom)— $\theta = 26^\circ$.

variable average θ values among the castings, but some of the scatter seems to have originated in the casting process.

The average value, 37.0 g per sq mm, of the critical resolved shear stress is not inconsistent with the value found by Jillson,⁸ 18.4 g per sq mm. Jillson made his measurements at constant load-rate instead of constant elongation-rate so no direct comparison is possible, but, since his rate of resolved stress increase was 0.1 g per sq mm per min, the strain-rate must have been much lower than it was in the present tests. Furthermore, if the present data is extrapolated to 0 pct elongation, the extrapolated value falls between 15 and 20 g per sq mm in approximate agreement with Jillson's data.

There are several instances among the data of Table II where the shear stress values for a crystal pair differ by more than the 5 pct experimental error. Therefore, a shape or surface effect seems to exist for these crystals. Study of the data has indicated the following:

1—The harder crystal of a pair came from the top half of the mold about 50 pct of the time and from the bottom half about 50 pct of the time. Thus, the observed differences cannot be attributed to mold conditions.

2—Relatively large differences in the critical stresses for a pair of crystals were always associated with marked differences in the cross-sectional shape changes upon deformation. The shape changes are closely related to the θ values for the crystals. The relations may be simply expressed for the case of $\chi_0 = \lambda_0$ as follows:

$$b' = b \left(1 + \frac{\Delta l}{l} \sin \theta \right), \quad t' = t \left(1 + \frac{\Delta l}{l} \cos \theta \right)$$

where b' and t' are the breadth and thickness after deformation. Thus, if $\theta = 0$ a crystal thins without changing in breadth and if $\theta = 90^\circ$ it narrows without changing in thickness. For all other θ values, the rectangular crystal becomes parallelepiped. A typical case is shown in Fig. 5 which is a photograph of pair 7. The top part (the right side in the figure) of this crystal pair thinned without changing much in breadth, while the bottom crystal (the left side in the figure) narrowed and thinned to form a parallelepiped.

Crystals which thinned more than they narrowed were harder than those which narrowed more than they thinned. Thus, the crystal in Fig. 5b was harder than the one in Fig. 5a.

3—For crystals free of end effects, the strain-hardening rate was greater for the crystal of a pair which was initially the hardest. The difference in strain-hardening rate was not great for any of the crystals. Short crystals (3 to 4 cm) did not adhere to this rule because more material is constrained at the ends of a crystal if θ is large than if θ is small. For a short crystal, this results in rapid apparent hardening.

4—The geometric parameters, s (slip length) and

a' (slip plane area exposed) correlate fairly well with the tensile test data. The correlation with the slip plane perimeter is not as good. In general, it is found that the crystal of a pair which has the highest yield strength has a "shorter" slip direction, s , and forms more new surface area per unit slip, a' , than the softer crystal. This is true for 13 out of 17 crystals of Table II (76 pct). In the exceptional cases, (crystals No. 11, 14, 25, 39), it is found that: first, all of the differences in the various quantities are small so that they may be attributed to experimental error; second, the crystal with small s and large a' strain-hardens more than its partner. This is significant because the strain-hardening rates are found from relative data and hence are subject to much smaller accidental errors than the shear stresses.

Although the data show too much scatter to allow a determination of the functional relations between the geometric parameters and the tensile data, large critical stress differences are associated qualitatively with large differences in s and a' .

Thus, for these zinc monocrystals at room temperature, crystals with small s and large a' had higher critical shear stresses and strain-hardened more rapidly than crystals of the same orientation but large s and small a' .

5—Examination of the deformed crystals has shown that those which have small θ values, and therefore tend to thin during deformation, have a

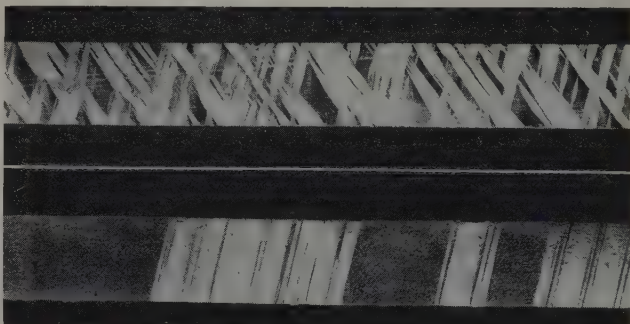


Fig. 6—Crystal pair No. 8 after deformation by twinning. ($\chi_0 = 2^\circ$, $\lambda_0 = 17^\circ$) X15. Area reduced approximately 60 pct for reproduction.

a (top)— $\theta = 28^\circ$, twinning stress = 1.19 kg per sq mm.
b (bottom)— $\theta = 1^\circ$, twinning stress = 1.45 kg per sq mm.

greater tendency to form tensile kink bands than their opposites. In fact, crystals with θ near 90° often deform without forming any tensile kink bands, but those with θ near 0° seem never to deform without the formation of some kink bands. This may be one reason why the latter strain-harden more rapidly than the former. The crystals in Fig. 5 illustrate this point. Fig. 5b has a wavy surface because it contains many kink bands while the surface of the softer one, Fig. 5a, is smooth except for slip bands.

Twinning: Nine specimens were grown for which χ_0 was 5° or less. These deformed primarily by twinning. The crystal orientations and twinning stresses are listed in Table III and Fig. 6 shows the appearance of one of the crystal pairs after deformation. It may be seen in Fig. 6a that twinning sometimes (and in fact, usually) occurred on two sets of planes almost simultaneously. Therefore the value of calculations of resolved shear stresses is doubtful and these are not reported; rather, the tensile stress at first twinning is reported.

Twinning seems to be influenced by specimen

shape according to the data of Table III. Both halves of crystal-pair No. 20, which was grown in an unrotated mold, had nearly the same twinning stress, whereas marked differences are shown for most of the other pairs. These differences seem to correlate with the directions of twinning with respect to the external sides. When the twinning directions lay in a plane roughly perpendicular to the flat face of a crystal (as in Fig. 6b), the crystal showed a higher twinning stress than its mate with twinning directions lying more nearly parallel to its flat faces (as in Fig. 6a). This held true in six out of eight cases. In the exceptional cases (pairs No. 19 and 28) both crystals of each pair had nearly the same appearance after deformation so it could not be determined whether the above correlation is valid for them. However, the fact that no contradictions to the correlation were found tends to support its validity.

Although the crystal in Fig. 6b appears to have only one set of twin bands, actually it has two as shown by the appearance of its edges.

Discussion

It must be noted that the conclusions stated in paragraph 5 above appear to be in direct contradiction with the results of previous work on rock salt² at 400°C and aluminum at room temperature.⁶ In these earlier studies it was found that "short" slip directions favored easy slip. In this investigation it was found that "long" slip directions favored easy slip. The reason for this contradiction is not known at present, but perhaps it is only apparent. Rock salt, aluminum, and zinc can hardly be called similar materials and there are other marked differences in their plastic behaviors.

On the other hand, the present results agree with what would be expected for a surface effect: That is, the crystals of each pair which led to larger increases in surface area during deformation, hence larger increases in surface energy, were more difficult to deform than their partners. The effect may not have been intrinsic, but the result of a surface film. From this point of view, the present results are complementary to the results of Roscoe,⁹ Lichtmann and Rehbindler,¹⁰ Ono,¹¹ and Makin and Andrade.¹² The last named authors found a marked increase in the strength of cadmium crystals with decreasing specimen diameters for diameters below about 0.5 mm. Ono found the same effect, but less marked, for aluminum crystals with diameters in the range 3 to 8 mm. The results of these authors contradict the observations on rock salt by Smekal and on alumi-

num by Wu and Smoluchowski, but they agree with the present results.

The interpretation of all of the known size or shape effects is difficult because they may either be bulk effects which depend on s or surface effects which depend on a' or some other surface parameter. Since s and a' are almost inversely proportional to each other it has not yet been possible to make an unambiguous distinction. Surface effect studies similar to those of Pfutzenreuter and Masing¹³ may help to resolve the dilemma. They found that both anodic and cathodic polarization of metals in electrolytes may increase the flow rates. They interpret their results in terms of a' .

The observation that zinc crystals with small s tend more to form tensile kink bands than do those of the same orientation but large s is of some interest. Perhaps this means that aluminum crystals, which seem to form kink bands spontaneously, would not do so if they were tested in large sections.

Summary

By means of a special casting technique, it has been shown that zinc monocrystals, which have the same orientation with respect to the tension axis but different orientations with respect to their external sides, differ significantly in their plastic properties.

Rectangular monocrystals, having orientations such that they thin during a tensile test without changing in breadth, have higher critical shear stresses at room temperature and strain-harden more rapidly than crystals which become narrow during deformation without changing in thickness.

The geometric parameters, s , the "length" of the slip direction, and a' , the ideal increase in surface area per unit slip, seem to correlate with the stress-strain data. Crystals with small s and large a' are harder initially and strain-harden more rapidly than crystals of the same orientation with respect to the tension axis but large s and small a' .

Zinc monocrystals with small s values tend to form tensile kink bands more rapidly than those with larger s values.

Crystals of twinning orientation twin at lower stresses when the twinning direction is roughly parallel to the flat faces of a rectangular crystal than when it is nearly perpendicular to the flat faces.

Acknowledgments

The author was assisted by A. Greene in the growth and preparation of the crystals. He is grateful to the General Electric Research Laboratory for aid in preparing the manuscript which J. C. Fisher kindly reviewed. This work was sponsored by the Office of Naval Research under Contract N6-onr-27128.

References

- 1 J. J. Gilman and T. A. Read: Surface Effects in the Slip and Twinning of Monocrystals. *Trans. AIME* (1952) **194**, p. 875; *JOURNAL OF METALS* (August 1952).
- 2 H. Wolff: Directional Dependence of the Slip Mechanism in Rock Salt Crystals at High Temperatures. *Ztsch. Phys.* (1934) **93**, p. 147.
- 3 S. Dommerich: Directional Dependence of the Yield Point of Homogeneous, Cleaned Rock Salt Rods. *Ztsch. Phys.* (1934) **90**, p. 189.
- 4 A. Smekal: A New Slip Condition. *Ztsch. Phys.* (1934) **93**, p. 166.
- 5 T. Wu and R. Smoluchowski: A New Criterion for the Occurrence of Slip in Thin Single Crystals. *Physical Review* (1950) **78**, p. 468.

Table III. Twinning of Pairs of Zinc Monocrystals

Crystal Pair	χ_0	λ_0	θ	Gage Length, Cm	Twinning Stress, Kg per Sq Mm
8T	2	17	20	8.8	1.19
B			1		1.45
13T	2	22	78	8.7	1.09
B			44		1.40
19T	1	25	57	7.6	1.20
B			80		1.42
20T	4	26	72	8.3	1.07
B					1.03
28T	4	4	72	8.1	1.45
B			40		1.25
30T	1	12	33	7.5	1.72
B			4		2.12
31T	5	15	32	6.6	1.00
B			1		1.30
33T	4	25	54	5.8	1.15
B			33		1.31
36T	2	20	28	6.9	1.30
B			58		1.27

⁶J. Rodda: Private communication through M. Metzger.

⁷J. Gilman: A Simple Recording Tensile Machine for Metal Monocrystals. *Review of Scientific Instruments* (December 1952).

⁸D. C. Jillson: Quantitative Stress-Strain Studies on Zinc Single Crystals in Tension. *Trans. AIME* (1950) **188**, p. 1129; *JOURNAL OF METALS* (September 1950).

⁹R. Roscoe: The Plastic Deformation of Cadmium Single Crystals. *Philosophical Magazine* (1936) **21**, p. 399.

¹⁰V. I. Lichtman and E. K. Venstrom: Effect of Dimensions of Metal Single Crystals on the Shape of the Stress-Strain Diagram and on the Strength Lowering

Effect of Adsorption. *Dokl. Akad. Nauk. SSSR* (1949) **66**, p. 881.

¹¹A. Ono: On the Glide-Resistance of Aluminum. *Proc. Third International Congress on Applied Mechanics* (1930) **2**, p. 230.

¹²E. N. daC. Andrade: The Effect of Surface Conditions on the Mechanical Properties of Metals, Mainly Single Crystals. *Monograph No. 13* (1952) London. Inst. Metals.

¹³A. Pfutzenreuter and G. Masing: Increase of the Velocity of Plastic Flow of Metals in Electrolytes upon Electrochemical Polarization. *Ztsch. Metall.* (1951) **42**, p. 361.

Technical Note

Detection of Microcracks in Steel

by W. L. Jensen and R. F. Campbell

IT is not uncommon for martensitic high carbon steels having a coarse austenite grain size to exhibit microcracks when polished and etched and examined with a microscope, as described by Davenport, Roff, and Bain.¹ Whether such cracks exist before etching or are the result of acid attack during etching has been debated from time to time. Fig. 1 illustrates the effect of electrolytic polishing, mechanical polishing and etching subsequent to each polish on microcracks produced by oil quenching from 1800°F a steel containing 1.14 pct C, 0.23 pct Mn, 0.33 pct Si, and 0.45 pct Mo. The austenite grain size was 3-4 on the ASTM scale.

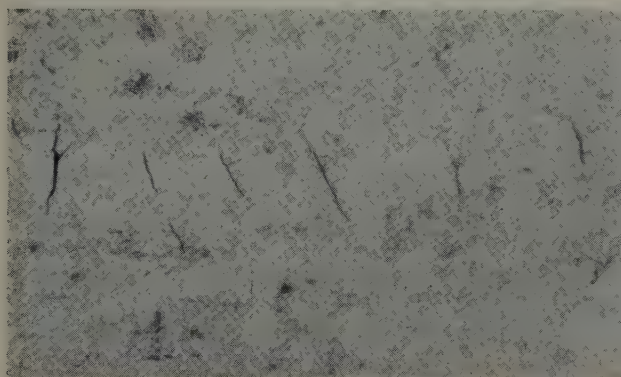
Grinding on lead laps followed by either electrolytic polishing with acetic anhydride-perchloric acid

solution² or mechanical polishing with Linde "B" alumina on "microcloth" (sometimes referred to as Gamal cloth) revealed microcracks without conventional etching, as shown in Fig. 1a and b, respectively. These same fields, after subsequent etching with saturated picral, are shown in Fig. 1c and d, and the cracks are seen to be typical microcracks; moreover, the cracks appear to be broader and longer than before etching. Although the microcracks were revealed by electrolytic polishing alone, the possibility of acid attack was present; however, the mechanical polish was accomplished without any intermediate etching to remove disturbed metal, hence this is regarded as definite evidence that microcracks are present before etching.

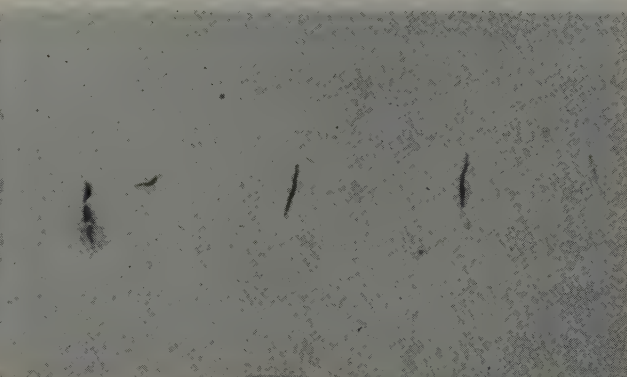
W. L. JENSEN and R. F. CAMPBELL are associated with the Research Laboratory, United States Steel Corp., Kearny, N. J. TN 178E. Manuscript, June 24, 1953.

¹E. S. Davenport, E. L. Roff, and E. C. Bain: Microscopic Cracks in Hardened Steel, Their Effects and Elimination. *Trans. ASM* (1934) **22**, pp. 289-310.

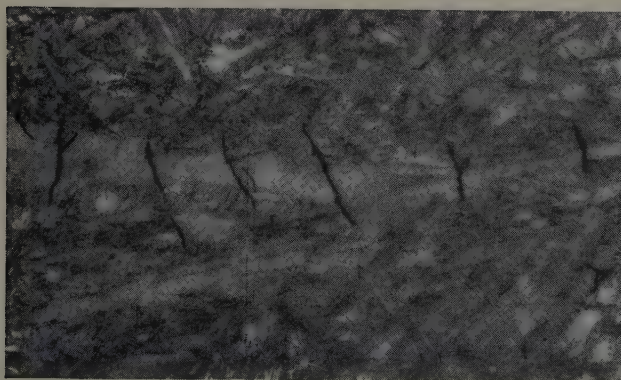
²G. F. Meyer, G. D. Rahrer, and J. R. Vilella: Electrolytic Polishing of Steel Specimens. *Metals and Alloys* (1941) **13**, pp. 424-430.



a—Electrolytic polish. Unetched.



b—Mechanical polish. Unetched.



c—Same field as Fig. 1a. Picral etch.



d—Same field as Fig. 1b. Picral etch.

Fig. 1—Microcracks as revealed by electrolytic and mechanical polishing and by subsequent etching. X750.

Variation of Plastic Properties with Annealing Procedure In Zinc Single Crystals

by Choh Hsien Li, J. Washburn, and Earl R. Parker

Yield stress in single crystals of zinc was shown to be dependent on prior annealing temperature and rate of cooling after annealing. Rate of strain hardening beyond the yield was not sensitive to annealing procedure. A tentative mechanism for the effect was discussed.

COMPARATIVE mechanical tests of metal single crystals generally show a large scatter of results. Many factors may contribute to this variation. The present investigation was undertaken to evaluate the influence of two factors not ordinarily considered of major importance—annealing temperature and cooling rate after annealing.

Since plastic properties of crystals are thought to depend on the presence of lattice imperfections, it follows that a variation in properties should result from differences in the distribution and density of these imperfections. Furthermore, in the light of current theories of interaction between edge dislocations and lattice vacancies,¹ it seems possible that annealing temperature and subsequent rate of cooling might play a part in this distribution. Analysis of the effect of these variables on plastic properties may lead to a better understanding of the annealed state.

Single crystals of zinc which have been strained in simple shear undergo complete recovery of mechanical properties upon subsequent annealing. This behavior is useful because a single specimen can be used repeatedly, thus eliminating the uncontrollable variables introduced by the use of many crystals. The test section of the crystals used for these experiments was a cylinder $\frac{1}{8}$ in. thick with a cross-sectional area of about $\frac{1}{3}$ sq in. The specimens were acid-machined from spherical single crystals 1 in. in diameter in such a way that the slip plane (0001) was at right angles to the axis of the cylinder. In testing, a shear stress was applied along one of the slip directions, $[2\bar{1}10]$ in the (0001) plane.² All crystals, unless otherwise noted, were grown in a helium atmosphere from molten 99.99 pct pure Horse Head Special Zinc.

Fig. 1 is a family of curves obtained from one

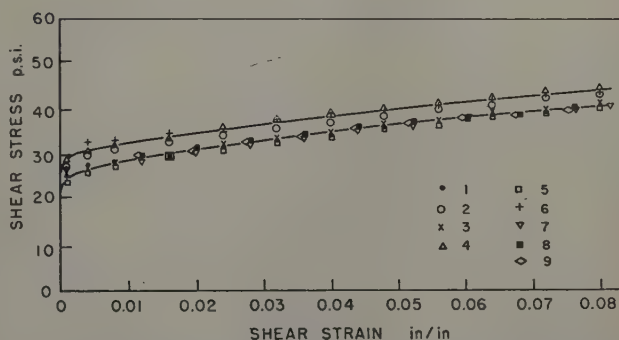


Fig. 1—Nine successive stress-strain curves from the same specimen showing complete recovery of mechanical properties—annealed 1 hr at 260°C before each test.

crystal. Each curve was obtained by deforming the crystal to 10 pct strain at a rate of 3 pct per min, following an anneal of 1 hr at 260°C. The strain direction was reversed every other time so that no progressive change in shape of the specimen took place during the series of tests. Since the stress-strain curve was reproducible within a fairly narrow range under the same conditions of annealing, it was then possible to determine the effect of changes in annealing conditions. A crystal was tested repeatedly as previously described but the annealing temperature and rate of cooling preceding each test were varied (Fig. 2). Two cooling rates were used, approximately 30°C per min and 3°C per min. Annealing was conducted at three temperatures, 200°, 300°, and 400°C. For a given annealing time and rate of cooling the room temperature flow stress was higher the higher the annealing temperature. The increase in flow stress was small as the annealing temperature was increased from 200° to 300°C but rose rapidly when the annealing temperature was raised from 300° to 400°C. Faster cooling from the high temperature produced an even greater strengthening of the crystal. The curves were obtained in the order indicated by the numbers. The stress level associated with a certain annealing treatment was, within the limits of scatter, always the same regardless of the

C. H. LI is Research Engineer, Institute of Engineering Research, and J. WASHBURN and E. R. PARKER, Member AIME, are Instructor and Professor in Metallurgy, respectively, University of California, Berkeley, Calif.

Discussion on this paper, TP 3600E, may be sent, 2 copies, to AIME by Dec. 1, 1953. Manuscript, April 16, 1953. Cleveland Meeting, October 1953.

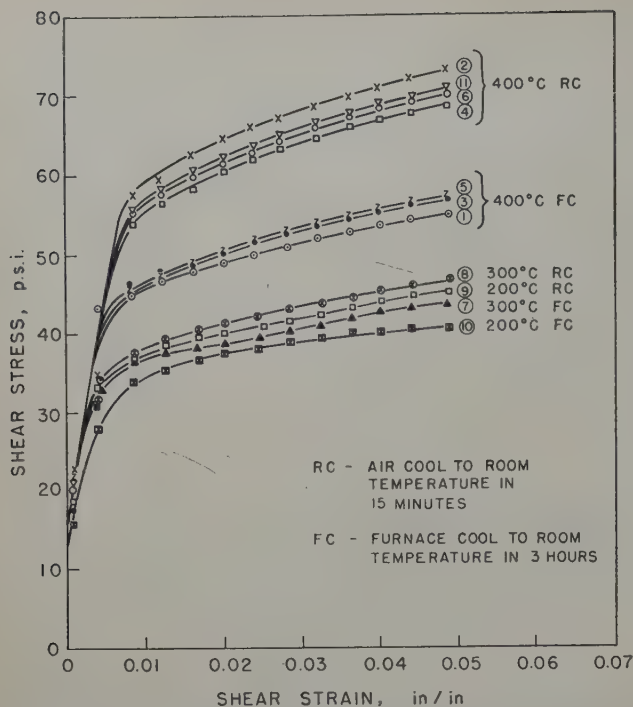


Fig. 2—Effect of annealing temperature and cooling rate on the initial part of the stress-strain curve of a zinc single crystal. Numbers indicate order of test.

penultimate treatment. This indicated that no continuous change in state of the crystal had occurred during the series of tests. Apparently the state at room temperature was characteristic of the annealing procedure. The two important differences observed in the stress-strain curve were: 1—change in the “yield stress” (or break in the stress strain curve), and 2—a change in amount of plastic flow prior to the break.

It seemed possible that these effects might be associated with the presence of impurities. This was a difficult question to settle because the effect might have been caused by a specific impurity.

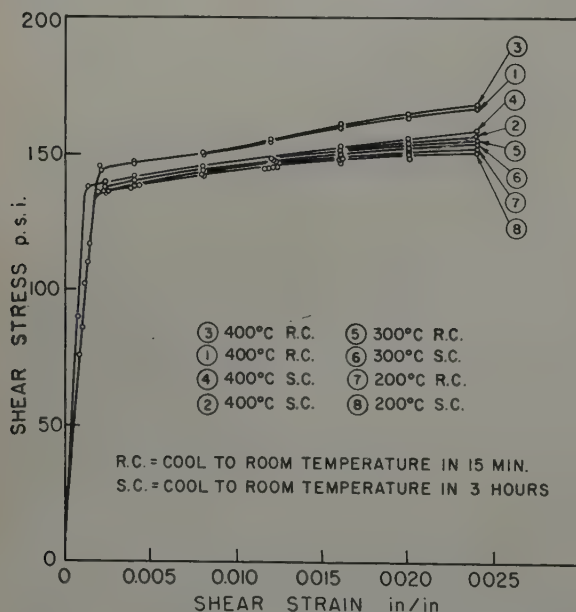


Fig. 3—Stress-strain curves after various annealing treatments of a zinc crystal containing 0.02 pct Cu in solid solution. Note change in shear stress scale for comparison with other figures.

Nevertheless, as a partial check on this possibility, some crystals were prepared containing a small amount of copper in solid solution while others were grown in a nitrogen atmosphere to introduce dissolved nitrogen. Results from one of the copper alloy crystals are shown in Fig. 3. The presence of copper in solid solution increased the “yield point” and the slope of the strain-hardening curve after the yield point by a factor of five, but the effect due to annealing temperature and cooling rate was no greater than for high purity crystals. Results from one of the crystals grown in nitrogen are shown in Fig. 4. The stress-strain curves for all annealing treatments were about the same as those for crystals grown in helium. Strain-aging characteristics

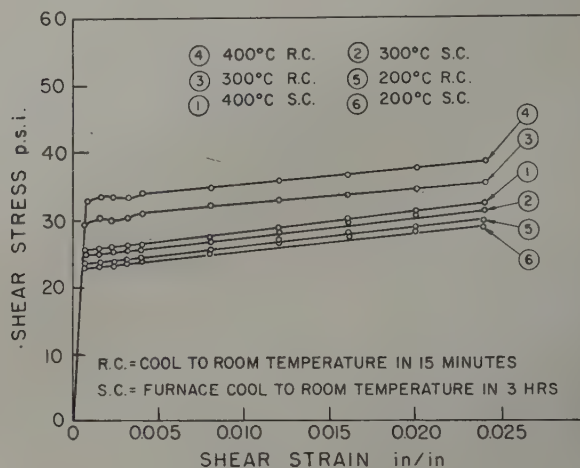


Fig. 4—Stress-strain curves after various annealing treatments of a zinc crystal grown in nitrogen atmosphere.

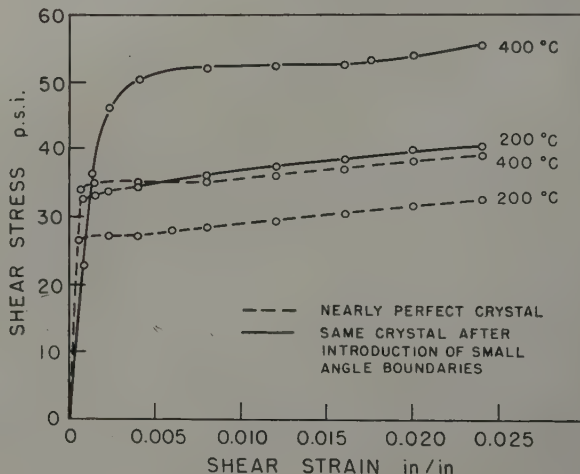


Fig. 5—Stress-strain curves of a 99.99 pct pure zinc crystal showing the effect of introducing a substructure of small angle boundaries. Specimen was cooled to room temperature in 15 min after each anneal.

were observed for the nitrogen-bearing crystals, as previously reported by Cottrell.⁸ However, no increase in the annealing temperature effect was produced by the presence of nitrogen.

Thermal stresses as a possible cause of the annealing effect were excluded from consideration because no significant temperature gradients were found during furnace cooling.

The magnitude of the annealing temperature effect was found to vary considerably for different crystals. The first crystal (Fig. 2) showed a larger effect than any subsequently tested. It seemed

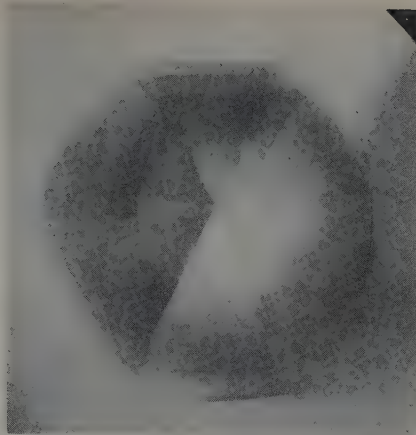


Fig. 6—Photograph of cleavage face showing system of small angle boundaries introduced during experiment of Fig. 5.

possible that this specimen might have been accidentally damaged in such a way as to produce polygonized regions in the test section. Therefore, a substructure of small angle boundaries was intentionally introduced in a test specimen to investigate its influence on annealing characteristics. A series of curves was obtained from a single specimen both before and after introducing a substructure. The results are shown in Fig. 5. The system of small angle boundaries was made by applying a concentrated load acting in a direction parallel to the *C* axis. The specimen was at 350°C during this operation. After the subsequent anneals and tests, the specimen was cleaved through the gage section. Fig. 6 is a photograph of this cleavage face showing the network of boundaries introduced by the concentrated load. The presence of this substructure raised the yield stress of the crystal under all conditions of heat treatment and furthermore, greatly exaggerated the effect produced by the high temperature anneal. It caused little if any change in the rate of work hardening beyond the yield point.

Discussion

All crystals contain to a greater or lesser degree, regions of relatively perfect lattice which are slightly disoriented relative to one another. Substructures of macroscopic, microscopic, and submicroscopic proportions may be present. The nature of the boundaries between disoriented regions may be the same regardless of the scale of the substructure. Arrays of dislocations satisfy the geometrical conditions of the transition across boundaries. Furthermore, there is now direct evidence that small angle boundaries consist of arrays of dislocations.^{4,5}

If most of the dislocations in an annealed crystal exist in the substructure boundaries, then the experiments described above suggest that the nature of these boundary regions between volumes of relatively perfect crystal may be extremely important in determining the stress at which slip is able to propagate entirely across the specimen. As shown in Fig. 5, the introduction of a network of dislocation boundaries of macroscopic proportions raised the stress at which the "yield-point" or break in the stress-strain curve occurred and also increased the amount of plastic strain which took place before the break. The rate of hardening or slope of the curve remained approximately the same both be-

fore and after the "yield-point" for the two conditions. In a recent photoelastic study of slip in sodium chloride crystals,⁶ it was shown that plastic flow before the break in the stress-strain curve is associated with local slip processes which are not able to cross substructure boundaries. Thus it becomes evident that substructure boundaries play an important role in governing plastic properties of metals. Furthermore, the fact that annealing temperature and cooling rate become more important when a pronounced substructure is introduced suggests that the annealing effect is associated with subboundaries.

The results reported herein might be interpreted to mean that fairly rapid cooling from a high annealing temperature causes the boundaries to become more effective as barriers to slip. Just how this happens is not known but the following is a tentative suggestion: Huntington and Seitz have estimated that the equilibrium concentration of vacancies (in copper) at the melting point is of the order of 10^{-3} atomic pct.⁷ The following possible disposition of these vacancies on cooling has been discussed by Seitz:¹ 1—condensation of vacancies on existing dislocations, and 2—condensation of vacancies to form new dislocation loops. The choice between these two alternatives was considered to depend on the density of existing dislocations.

If, near the melting point the equilibrium concentration of vacancies is as high as estimated, then on cooling, a large number of vacancies recombine with edge dislocations. It is conceivable that fairly rapid cooling may not allow time for recombination of vacancies in such a way that long segments of straight dislocation lines in the slip planes are retained. Rapid cooling may result in freezing in of numerous steps in the dislocation lines. Dislocation lines containing many segments which do not lie in the slip plane would be harder to move under stress than those which are wholly contained in a single slip plane. Therefore, a small angle boundary composed of such wavy dislocations might form a more effective barrier to the passage of other dislocations.

Acknowledgment

Support of this work by the Office of Naval Research and in particular, the interest and encouragement of Dr. O. Marzke and Dr. Julius Harwood is gratefully acknowledged.

References

- ¹ Frederick Seitz: On the Formation of Dislocations From Vacancies. *Physical Review* (1950) **79**, No. 5, p. 890.
- ² J. Washburn and Earl R. Parker: Deformation of Single Crystals. *Modern Research Techniques in Physical Metallurgy* (1952) ASM.
- ³ H. L. Wain and A. H. Cottrell: Yield Points in Zinc Single Crystals. *Proc. Physical Soc., London* (May 1950) **63**, Sec. B, p. 339.
- ⁴ J. Washburn and E. R. Parker: Kinking in Zinc Single-Crystal Tension Specimens. *Trans. AIME* (1952) **194**, p. 1076; *JOURNAL OF METALS* (October 1952).
- ⁵ Choh Hsien Li, E. H. Edwards, J. Washburn, and Earl R. Parker: Stress Induced Movement of Crystal Boundaries. *Acta Metallurgica* (1953) **1**, No. 2, p. 223.
- ⁶ P. L. Pratt: Strain Hardening of Single Crystals. A. E. R. E. Report M/R 883, Ministry of Supply, Harwell, Berks. (1952).
- ⁷ H. B. Huntington and F. Seitz: Mechanism for Self-Diffusion in Metallic Copper. *Physical Review* (1942) **61**, p. 315.

Recovery in Single Crystals of Zinc

by R. Drouard, J. Washburn, and Earl R. Parker

Temperature dependence of the rate of recovery in zinc single crystals after a simple shear deformation at low temperature was investigated. Some tentative suggestions regarding the annealed and strain-hardened states of a crystal are discussed.

RECOVERY may be defined as the gradual return of the mechanical and physical properties of strain-hardened metal to those characteristic of the annealed material; an increase in temperature increases the rate of recovery. The annealing process in strain-hardened polycrystalline metals is complicated by the inhomogeneity of strain which always exists in aggregates. Polygonization in bent regions of the crystals and growth of new almost strain-free grains starting at points of severe local distortion¹⁻³ make it almost impossible to isolate and study the recovery process. Homogeneously strained single crystals, however, do not polygonize or recrystallize and hence they can be used advantageously to study recovery. In such crystals strain hardening is completely removed by recovery alone.

Since recovery is a process whereby certain lattice disturbances introduced by plastic flow are gradually reduced, a knowledge of the rate and temperature dependence of this process for various conditions of prestrain might be helpful in formulating a model of the strain-hardened state. For simplicity it seemed desirable to limit the type of prestrain to the simplest obtainable, i.e., simple shear strain.

In the experiments to be described, recovery was studied by observing changes in the stress-strain curve of prestrained zinc single crystals held for various times at temperatures above that employed for straining. Single crystals were grown from the melt by a modified Bridgman technique from Horse Head Special zinc 99.99 pct pure, and from spectrographically pure zinc 99.999 pct pure. They were grown as 1 in. diameter spheres and acid-machined⁴ to the final specimen contour. The test section was a cylinder about $\frac{1}{8}$ in. high and $\frac{3}{4}$ in. in diameter. The conical sections adjacent to the test section were cemented into the grips so the load could be transmitted to the crystal as uniformly as possible. The specimens were oriented so

that in testing the maximum shear stress was applied along one of the slip directions, $[2\bar{1}10]$, in the (0001) plane. Details of the production and testing of such specimens have been presented.⁴

Each test was carried out according to the following schedule:

1—The crystal was strained at -50°C until it reached a maximum shear stress, σ_m . The strain rate was approximately 5 pct per min in all cases.

2—After straining, the crystal was unloaded before the temperature was changed. Unloading required about 3 min.

3—The temperature of the specimen was then increased from -50°C to the temperature, T , of recovery. This change in temperature was completed in a time of less than 2 min. The specimen remained at temperature, T , for a time, t , which differed for the various specimens.

4—Thereafter the temperature was again reduced to -50°C in approximately 3 min.

5—While at -50°C , the stress-strain curve after recovery was obtained.

6—The specimen was then unloaded and annealed for 1 hr at 375°C in a helium atmosphere to bring about complete recovery. Cooling to room temperature after anneal required 90 min.

7—The same crystal could be re-used for another test because the plastic properties after annealing closely duplicated those of the original crystal.

The specimen was immersed during the test in a bath of methyl alcohol which, through a system of tubes, could be pumped through either of two heat exchangers to regulate the temperature; this was accomplished by circulating the liquid through coils immersed in a bath of acetone and dry ice for cooling or in a bath of warm water for heating. Test temperatures were thus maintained constant within $\pm 1^{\circ}\text{C}$. The -50°C temperature was low enough so that no measurable recovery occurred during unloading and reloading.

The stress-strain curve continued after recovery along a path below, but approximately parallel to, the path of a curve obtained in an uninterrupted test. Fig. 1 shows some of the results from a specimen of 99.999 pct Zn. The amount of downward displacement of the curve due to recovery was a

R. DROUARD, formerly Graduate Student, is now in Paris, France, and J. WASHBURN and E. R. PARKER, Member AIME, are Instructor and Professor of Metallurgy, respectively, University of California, Berkeley, Calif.

Discussion on this paper, TP 3591E, may be sent, 2 copies, to AIME by Dec. 1, 1953. Manuscript, April 14, 1953. Cleveland Meeting, October 1953.

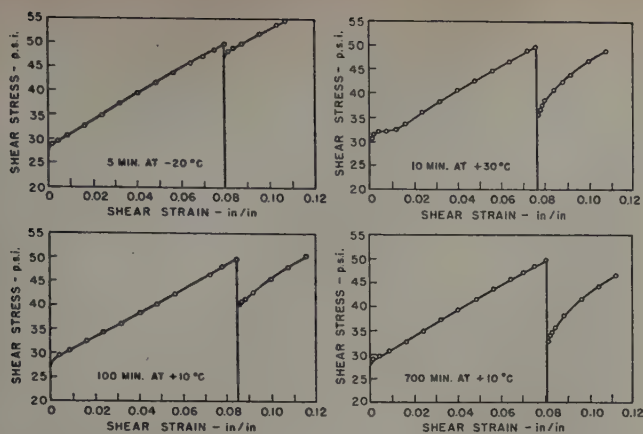


Fig. 1—Stress strain-curves at -50°C for a 99.999 pct Zn crystal showing drop in flow stress due to recovery for various times at higher temperatures.

function of both time and temperature. The quantitative measure of recovery which was adopted for comparison is illustrated in Fig. 2. $R = \frac{\sigma_m - \sigma}{\sigma_m - \sigma_0}$ is

the ratio of the reduction in flow stress due to recovery to the total increase in flow stress due to strain hardening. The values of σ and σ_0 were obtained by extrapolation of the linear part of the curve to the corresponding value of the stress for zero strain. This extrapolation avoided some secondary effects which caused changes in the shape of the initial portion of the curve. The sharpness of the yield after recovery varied considerably, being fairly sharp for the short times and low temperatures and somewhat rounded for high temperatures and long recovery times. Since this transient recovery effect became pronounced only at large values of R , it differed from the meta-recovery observed by Dorn et al.² in their studies of polycrystalline aluminum.

An attempt was made to reproduce exactly the prestrain portion of the stress-strain curve so that the recovery process could always be started with the crystal in the same state. However, small variations in the yield stress after annealing did occur. This made necessary the use of the above definition of recovery as a fraction of the amount of strain hardening. In addition to correcting for variations in stress, this definition was found to have validity

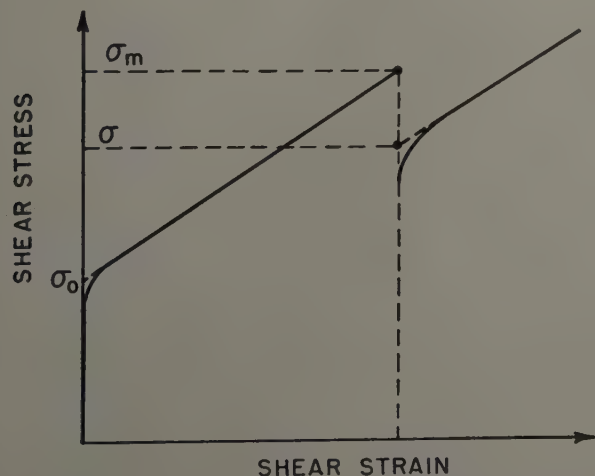


Fig. 2—Definition of recovery: $R = \frac{\sigma_m - \sigma}{\sigma_m - \sigma_0}$.

over a large range of prestrains, and for both 99.99 and 99.999 pct pure zinc. Most of the tests were made with a prestrain of about 8 pct but a few tests were made with 4 pct prestrain and others with 25 pct prestrain. The recovery as defined by R was apparently independent of the amount of prestrain because the points obtained in these tests were consistent with the data obtained for 8 pct prestrain. Large variations in yield stress σ_0 were also produced by changing the temperature at which the crystal was annealed prior to some of the tests. The effect of annealing temperature on the stress-strain curve of zinc shear specimens is a complicated phe-

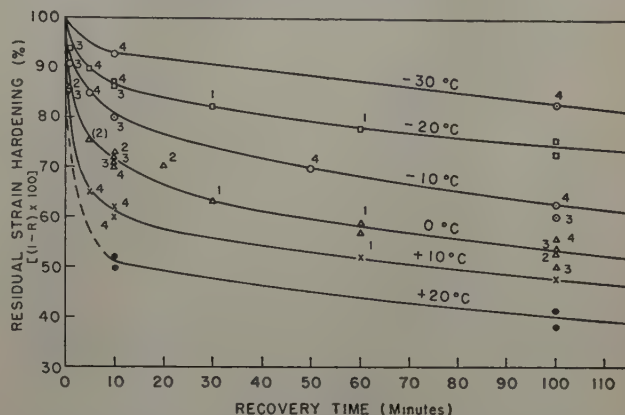


Fig. 3—Recovery of strain hardening as a function of time at various temperatures. Figures opposite experimental points indicate different specimens.

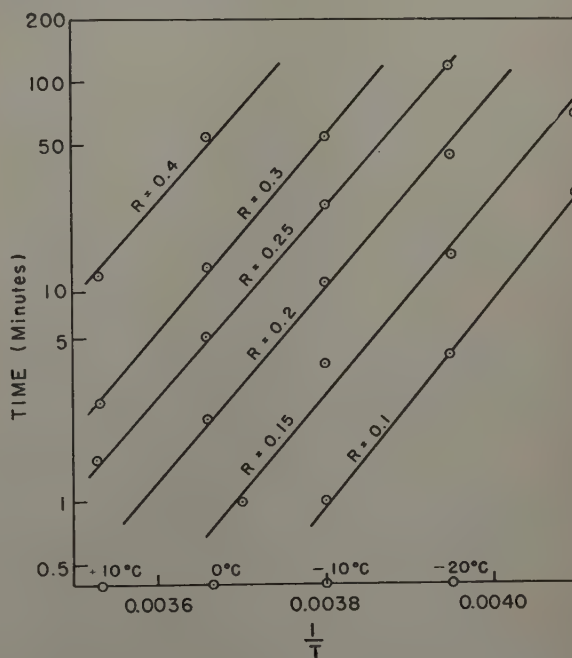


Fig. 4—Temperature dependence of the time required for various amounts of recovery.

nomena and will be discussed in detail in a separate publication.⁶ Briefly, raising the annealing temperature above 200°C resulted in a raising of the yield point for the annealed crystal. However, the slope of the strain-hardening curve was not appreciably altered by change in annealing temperature. Recovery was found to be independent of stress level produced by these changes in annealing treatment. It seems, therefore, that recovery defined by

$R = \frac{\sigma_m - \sigma}{\sigma_m - \sigma_0}$ is dependent only upon time and tem-

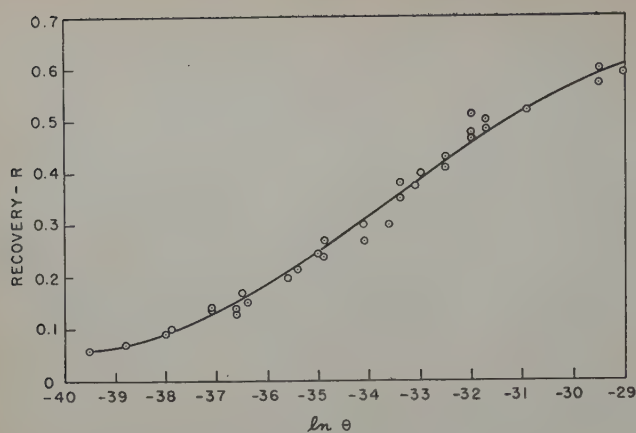


Fig. 5—Recovery — R vs $\ln t - Q/RT$.

perature and is independent of σ_m and σ_o . Results of tests for six different recovery temperatures are given in Fig. 3, where $(1-R)$ is plotted against recovery time.

Fig. 4 shows the temperature dependence of the time required to reach a given percentage of recovery. By plotting the natural logarithm of the recovery time against the reciprocal of the absolute temperature a series of straight lines was obtained corresponding to different fixed values of R . No consistent change in slope of the lines was detected with change in R from 10 to 40 pct. The average value of the slope or activation energy for the process was 20,000 cal per mol. The equivalence of temperature and time is further illustrated by Fig. 5 where recovery, R , for all the experimental points, including those tests where yield stress or prestrain was varied, is plotted as a function of temperature compensated time ($\ln t - Q/RT$). (Note: the R at the end of the preceding sentence and the last R in the caption for Fig. 5 refer to the gas constant rather than recovery as otherwise used in this paper.) By using the value of 20,000 cal per mol for Q all the points scatter fairly closely about a single curve.

Discussion

Since the activation energy for recovery after a simple shear deformation corresponds closely to that found by Miller and Banks⁷ for self-diffusion in the C -axis direction in zinc ($[20.4 \pm 0.9] \times 10^3$ cal per mol) the results suggest that motion of lattice vacancies in the C -axis direction may be the rate-controlling factor during recovery.

The fact that recovery was independent of the yield strength apparently means that only those imperfections introduced by the strain are removed during this low temperature recovery. Although none of the tests were carried beyond 80 pct recovery, in most cases the crystal appeared to be approaching it immediately preceding the strain. Since both the initial yield strength of a crystal and the increase in strength attending strain are probably due to the presence of dislocations, it becomes important to consider the possible ways in which dislocations may be distributed.

Stress-strain curves for zinc single crystals deformed in simple shear (easy glide) show nearly the same rate of strain hardening beyond the yield regardless of the stress level at which yielding occurs.⁸ The yield stress on the other hand is greatly affected by temperature of testing, prior annealing conditions, and geometrical perfection of the crystal. Therefore the shear strength of a crystal appears to

be governed by two factors. 1—the initial structure of the crystal, and 2—the strain. The yield strength is characteristic of the annealed crystal. It is a reproducible value, determined for a given crystal largely by the annealing temperature. There seems to be little doubt that yielding depends to a great extent upon the nature of the substructure in the crystal,⁴ whether it be macroscopic dislocation boundaries or submicroscopic mosaic blocks. Slip presumably increases the free energy of the structure by increasing the elastic strain energy in the system. Thus the altered structure is thermally less stable and tends to return to the lower energy state. The extent to which such strain-induced structural changes can be removed by recovery depends upon the test conditions, complete recovery at low temperatures being possible for simple shear but not for bending or for multiple slip such as usually occurs in cubic metals.

When a shear stress is applied to a crystal by a gradually increasing load, the process of slip is thought to begin by local shear displacements at many points throughout the crystal. When the yield stress is reached, the structural barriers provided by dislocation boundaries are penetrated. Slip on some of the slip planes then traverses the entire specimen and observable slip steps are formed at the surface. The growth of each elementary slip line presumably takes place in a short time and over a very narrow range of applied stress.⁸ Once flow has ceased on a given slip plane it does not again become active in spite of considerable increase in applied stress. The reason for cessation of slip in an active slip line after a fairly definite amount of shear is still not clear. The most likely explanation seems to be that large numbers of lattice vacancies are produced by moving dislocations which, along with interactions between

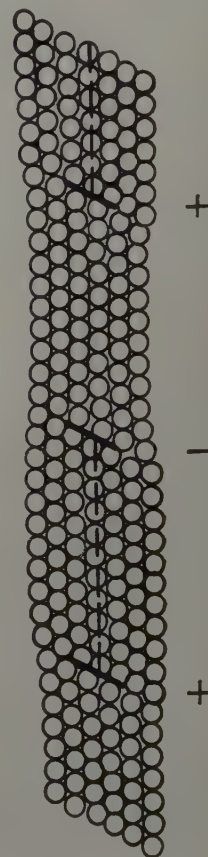


Fig. 6—Annihilation of edge dislocations. Condensation of lattice vacancies on the three dislocations shown would cause the central negative dislocation and the lower positive dislocation to move together by elimination of the extra partial plane of atoms between them. Escape of vacancies would cause the negative dislocation and the upper positive dislocation to annihilate each other in a similar way.

dislocations, bring slip to a halt.⁹ The measured strain hardening should not be confused with this local hardening occurring in the immediate neighborhood of a slip line. Macroscopic strain hardening must be interpreted to mean that growth of each group of slip lines (slip band) across the crystal makes the next increment of slip a little more difficult. Therefore, measured strain hardening and the capacity of the strain-hardened crystal for recovery would seem to be greatly affected by the distribution of dislocations which became stuck primarily within the previously formed slip bands.

In the case where the shear stress acting in a crystal is uniform, i.e., where there are no shear stress gradients, it is to be expected that equal numbers of positive and negative dislocations would become trapped in each small volume of crystal. Elastic strain energy in the material between bands would be small and rate of strain hardening would be a minimum. On the other hand, when the stress system is such that local bending moments develop during deformation, positive dislocations tend to group themselves in some regions of the slip bands whereas negative dislocations collect in other parts. Groups of dislocations of like sign on neighboring slip bands tend to align themselves in an array at right angles to the active slip direction, thus forming small angle boundaries. The difference between simple shear deformation and other more complex deformations (for which the rate of strain hardening is greater) may be that in the former there is less tendency for groups of like dislocations to form.

The recovery characteristics are quite different for the two cases. If it is assumed that recovery is a return of the crystal to the structure it possessed before the deformation, then it involves a removal of lattice vacancies and bound dislocations introduced by the strain. Since it is not reasonable to suppose for the times and temperatures of these experiments that migration of vacancies over long distances can occur, then the changes taking place must be due to short range diffusion. For example, segments of edge dislocation lines having opposite signs, but existing on different parallel slip planes, can, by interaction with lattice vacancies, move onto the same slip plane and annihilate each other as illustrated in Fig. 6. Where each small volume of crystal within a slip band contains an equal number of positive and negative dislocations, this process for elimination of stuck dislocations during recovery seems reasonable. However, if dislocations are segregated into groups of like sign, low temperature recovery might be expected to cause some rearrangements (polygonization) but could

not be expected to eliminate the dislocations introduced by the inhomogeneous strain.

The annealed or fully recovered state of a crystal then, is one in which all the existing dislocations are segregated into fairly widely spaced arrays of dislocations of like sign. Simple shear strain introduces equal numbers of positive and negative dislocations which may also concentrate at the existing substructure boundaries. Recovery returns the crystal toward its initial state by recombination of nearby positive and negative dislocation segments. Recovery after a nonhomogeneous strain, such as that occurring during deformation of a polycrystalline aggregate, would not be expected to return the crystal to its initial state since new widely separated arrays of dislocations of like sign are introduced by the strain.

The fact that zinc crystals subjected to simple shear do not show asterism even after large strains and that they recover completely at low temperatures suggests that both positive and negative dislocations are introduced by strain and that they are not concentrated into large widely separated groups of like sign.

Acknowledgment

Support of this work by the Office of Naval Research and in particular the interest and encouragement of Dr. O. Marzke and Dr. Julius Harwood is gratefully acknowledged.

References

- ¹ Von G. Tammann: The Result of Cold Working and Recovery of Metals from This State on Heating. *Ztsch. Metallkunde* (1936) **28**, pp. 6-17.
- ² T. V. Cherian, P. Pietrowsky, and J. E. Dorn: Some Observations on the Recovery of Cold Worked Aluminum. *Trans. AIME* (1949) **185**, pp. 948-956; *JOURNAL OF METALS* (December 1949).
- ³ N. Thorley: The Calculation of the Activation Energy of Recovery and Recrystallization from Hardness Measurements on Copper. *Journal Inst. Metals* (1950) **77**, p. 141.
- ⁴ E. R. Parker and J. Washburn: Deformation of Single Crystals. *Modern Research Techniques in Physical Metallurgy* (1953) Cleveland. ASM.
- ⁵ G. I. Taylor: The Mechanism of Plastic Deformation of Crystals. *Proc. Royal Soc.* (1934) **145A**, p. 362.
- ⁶ Choh Hsien Li, J. Washburn, and Earl R. Parker: Variation of Plastic Properties with Annealing Procedure in Zinc Single Crystals. This issue, p. 1223.
- ⁷ P. H. Miller and R. F. Banks: Self Diffusion in Zinc. *Physical Review* (1942) **61**, p. 648.
- ⁸ A. F. Brown: Surface Effects in Plastic Deformation of Metals. *Advances in Physics* (October 1952) **1**, No. 4, pp. 427-479.
- ⁹ N. F. Mott: A Theory of Work Hardening of Metal Crystals. *Philosophical Magazine* (1952) **43**, pp. 1151-1178.

Technical Note

Relation Between Initial Creep Rate and Resolved Shear Stress In Zinc Single Crystals

by N. Brown, J. Washburn, and Earl R. Parker

MOST previous quantitative work on creep of single crystals has been concerned primarily with developing empirical equations for the creep curve. Although the equations used by Cottrell and

Aytekin¹ and Tyndall² represented the data quite well, it was often necessary to use different values of the constants for different specimens even though they were apparently tested under identical conditions. In the course of previous work on the effect of surface coatings on creep of zinc single crystals,³ it was found that equal resolved shear stress frequently did not produce equal creep rates in different specimens. The work of Chalmers⁴ in the very

N. BROWN is Assistant Professor, University of Pennsylvania, Philadelphia, J. WASHBURN is Instructor, and E. R. PARKER, Member AIME, is Professor, Dept. of Metallurgy, University of California, Berkeley, Calif.

TN 180E. Manuscript June 18, 1953.

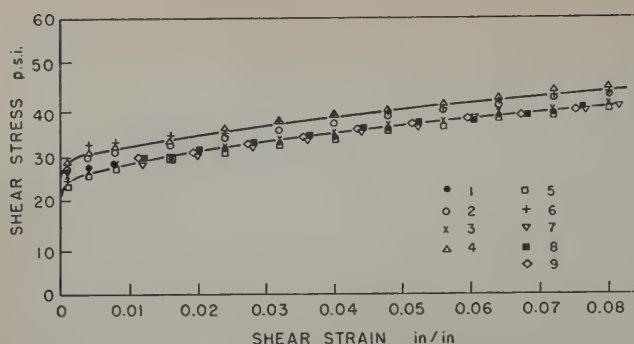


Fig. 1—Nine successive stress-strain curves from the same specimen showing complete recovery of mechanical properties. Annealed 1 hr at 260°C before each test.

low stress range appears to be the only data which shows a definite relation between initial creep rate and stress. In the microcreep range, where the creep process apparently consists only of a transient stage, initial creep rate was found to be directly proportional to stress.

The present work was undertaken in an attempt to establish some reproducible relation between initial creep rate and resolved shear stress at higher stress levels where the total creep strain is not limited. Many of the difficulties encountered when testing single crystals in tension^{5,6} were avoided by the use of shear specimens. The production, mounting, and testing techniques used for achieving an essentially pure shear strain in these crystals have been discussed.⁷ The purity of the zinc was 99.999. Fig. 1 shows a series of nine stress-strain curves from a single shear specimen. An anneal of 1 hr at 260°C prior to each deformation resulted in complete recovery of mechanical properties. No upward trend in the level of the curves was found since the ninth test was among the lowest of the series. The curves were essentially parallel, all the scatter being in the yield stress. From the results of another investigation,⁸ the variation in yield stress has been found to be due to variations in annealing procedure. Even though reasonable care was taken in this case to keep the annealing conditions constant, a significant amount of scatter occurred.

Since single crystals creep at appreciable rates only for stresses above the yield stress, it seemed possible that the creep rate might correlate better

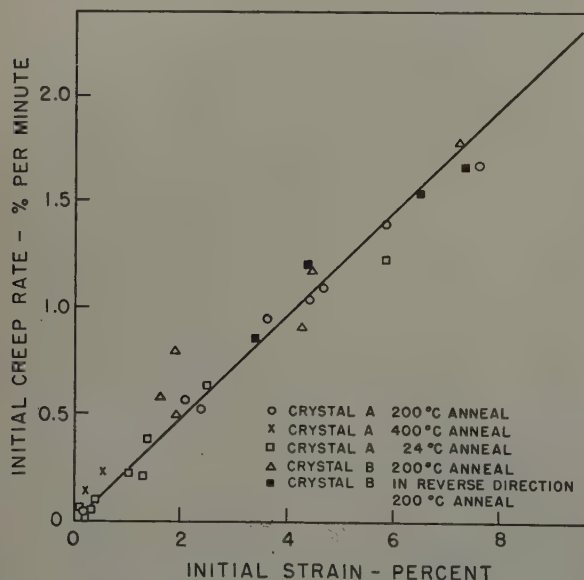


Fig. 2—Initial creep rate vs initial strain.

with the increment of stress above the yield stress than with the total stress.

$$\dot{\gamma}_0 = f(\sigma - \sigma_0) \quad [1]$$

where $\dot{\gamma}_0$ is initial creep rate, σ is total stress, and σ_0 is the yield stress. Consequently a method of applying the creep load was adopted which permitted recording of the stress-strain curve during loading. σ_0 was difficult to establish experimentally, because of the curvature of the initial portion of the stress-strain curve. However, as shown in Fig. 1, the increment of stress above the yield stress is approximately proportional to the total strain,

$$\gamma \sim (\sigma - \sigma_0).$$

Thus it follows that a criterion nearly equivalent to that of Eq. 1 is

$$\dot{\gamma}_0 = f(\gamma) \quad [2]$$

where $\dot{\gamma}_0$ is initial creep rate and γ is the strain at the instant loading is completed.

The results of a number of tests on two different specimens are shown in Fig. 2, where initial creep rate is plotted as a function of initial strain, γ_0 . Although large variations in σ_0 resulted from annealing at widely different temperatures prior to testing, all of the experimental points fell along the same curve. Initial creep rate was found to increase linearly with initial strain and consequently with the increment of stress above the yield stress.

The yield stress σ_0 may be the stress at which dislocations are able to break through substructure boundaries in a manner analogous to that recently observed for sodium chloride crystals.⁹ This picture also seems to be consistent with the rather sharp transition from microcreep to macrocreep which occurred when a critical stress level was reached in Chalmers experiments.⁴

Acknowledgment

Support of this work by the Office of Naval Research and in particular the interest and encouragement of Dr. O. Marzke and Dr. Julius Harwood is gratefully acknowledged.

References

- ¹ A. H. Cottrell and V. Aytakin: Andrade's Creep Law and the Flow of Zinc Crystals. *Nature* (1947) **160**, pp. 328-329.
- ² E. P. T. Tyndall: Creep of Zinc Crystals. A Symposium on the Plastic Deformation of Crystalline Solids. Mellon Inst., Pittsburgh, May 1950. Under the Joint Sponsorship of the Carnegie Institute of Technology and the Department of the Navy, Office of Naval Research. p. 49.
- ³ M. R. Pickus and Earl R. Parker: Creep Behavior of Zinc Modified by Copper in the Surface Layer. *Trans. AIME* (1951) **191**, p. 792; *JOURNAL OF METALS* (September 1951).
- ⁴ B. Chalmers: Precision Extensometer Measurements in Tin. *Journal Inst. Metals* (1937) **61**, p. 103.
- ⁵ J. Washburn and Earl R. Parker: Kinking in Zinc Single-Crystal Tension Specimens. *Trans. AIME* (1952) **194**, p. 1076; *JOURNAL OF METALS* (October 1952).
- ⁶ R. W. K. Honeycomb: Inhomogeneities in the Plastic Deformation of Metal Crystals. *Journal Inst. Metals* (1951) **80**, p. 45.
- ⁷ Earl R. Parker and Jack Washburn: Deformation of Single Crystals. *Modern Research Techniques in Physical Metallurgy* (1952) Cleveland. ASM.
- ⁸ Choh Hsien Li, J. Washburn, and Earl R. Parker: Variation of Plastic Properties with Annealing Procedure in Zinc Single Crystals. This issue, p. 1223.
- ⁹ P. L. Pratt: Strain Hardening of Single Crystals. A.E.R.E. Report, Harwell, Berks., M/R 883.

Plastic Deformation of Single Crystals of Copper

by J. J. Becker and J. N. Hobstetter

Slip lines in deformed copper single crystals exhibit very pronounced cross-slip and clustering if the stress axes are not too far from $\langle 100 \rangle$. This orientation dependence seems to persist whether or not attempts are made to reduce the bending constraints of ordinary mechanical tests.

THE purpose of this paper is to report some microscopic features of the plastic deformation of copper single crystals.

The material used was OFHC copper obtained from the American Brass Co. Single crystals about 3 in. long and 5/16 in. in diameter were made by lowering graphite crucibles containing this copper out of the hot zone of a vertical tubular furnace at a rate of 1 1/4 in. per hr. The furnace atmosphere was nitrogen. The orientations of the crystals were determined by the back-reflection Laue technique.¹ The X-ray spots usually indicated a slight lineage structure of not more than a degree or two.

The crystallography of slip is discussed in Schmid and Boas.² The terms classical slip, cross-slip, and conjugate slip are used here with the same meanings as in ref. 3.

Compression

Specimen 17 (Fig. 1) was selected because the resolved shearing stresses on eight slip systems dif-

J. J. BECKER, Junior Member AIME, formerly Teaching Fellow, Dept. of Engineering Sciences and Applied Physics, Harvard University, is now associated with General Electric Research Laboratory, Schenectady, and J. N. HOBSTETTER, formerly Assistant Professor, Dept. of Engineering and Applied Physics, Harvard University, is now associated with Bell Telephone Laboratories, Murray Hill, N. J.

Discussion on this paper, TP 3592E, may be sent, 2 copies, to AIME by Dec. 1, 1953. Manuscript, April 15, 1953; revision, June 15, 1953. Cleveland Meeting, October 1953.

This paper is based on a thesis by J. J. Becker submitted in partial fulfillment of requirements for the degree of Doctor of Philosophy in the field of engineering sciences and applied physics to the Faculty of Arts and Sciences, Harvard University, January 1951.

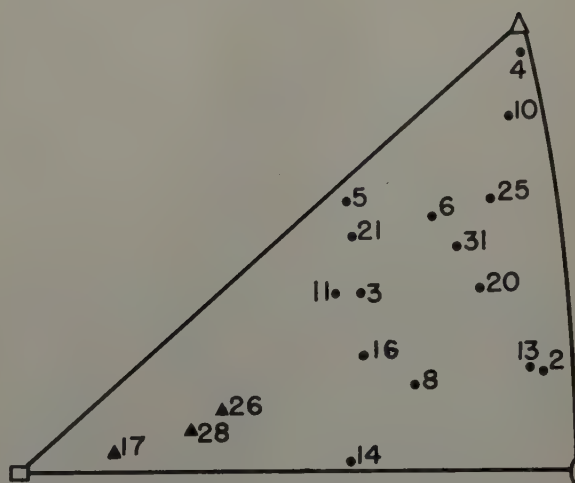


Fig. 1—Orientations of all specimens deformed. Triangles, specimens showing pronounced cross-slip.

fered at most by a factor of 1.2. It was hoped that in this situation such effects as cross-slip might be made more prominent.

Two intersecting planes parallel to the stress axis were ground on the crystal, using optical abrasive on a lead lap. The large plane was approximately perpendicular to the plane of the axis and the primary slip direction. Its exact orientation was determined by X-ray. The smaller made an angle of 49° with the larger, measured by reflecting a small light source. The specimen was etched with nitric acid until its diameter had been reduced 0.010 in., and then was given a metallographic polish and very

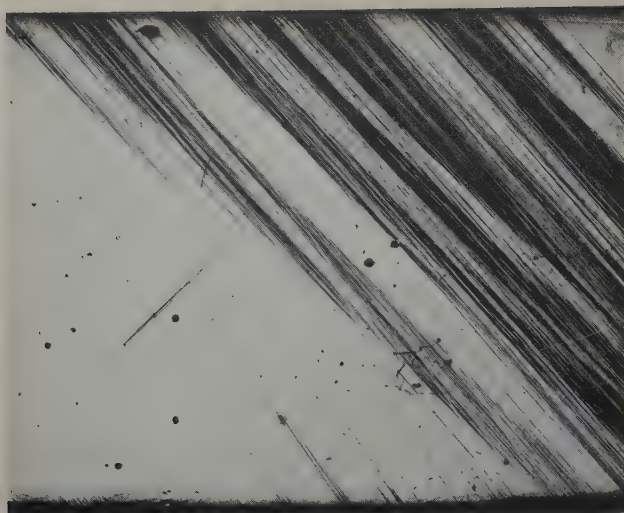


Fig. 2—Slip and cross-slip on specimen 17-A. Compressed 1 pct. Stress axis horizontal. X21. Area reduced approximately 50 pct for reproduction.

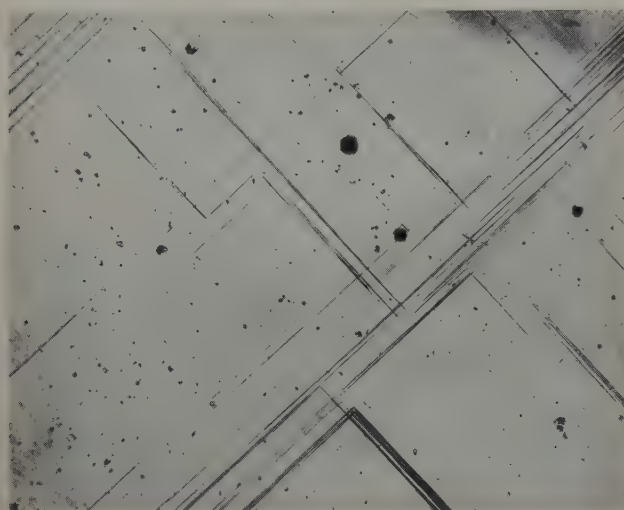


Fig. 3—Cross-slip on specimen 17-A. Compressed 1 pct. Stress axis horizontal. X75. Area reduced approximately 50 pct for reproduction.

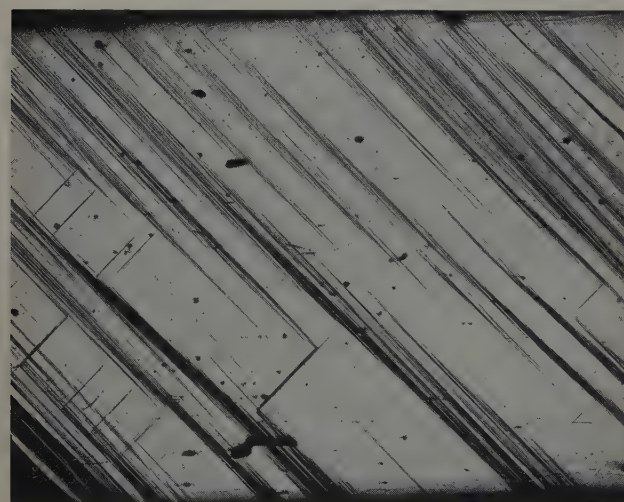


Fig. 4—Specimen 17-C after 1 pct compression. Stress axis horizontal. X21. Area reduced approximately 50 pct for reproduction.

heavily etched. The crystal was cut in thirds with a jeweler's saw and the ends faced on a lathe to the same length, 0.909 in. The flat surfaces were again

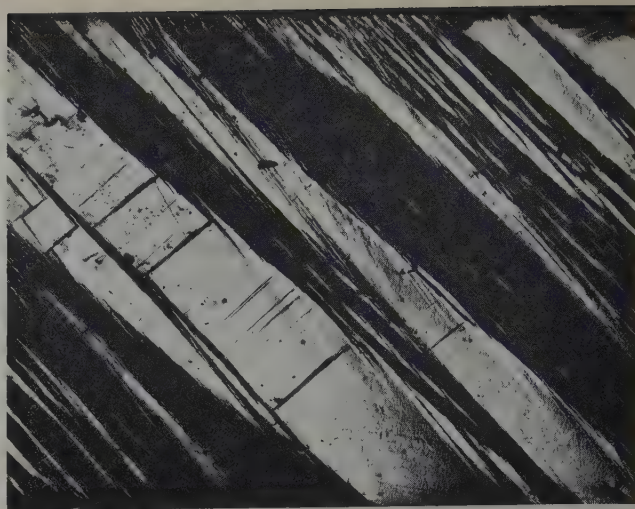


Fig. 5—Specimen 17-C after 5 pct compression. Stress axis horizontal. X21. Area reduced approximately 50 pct for reproduction.

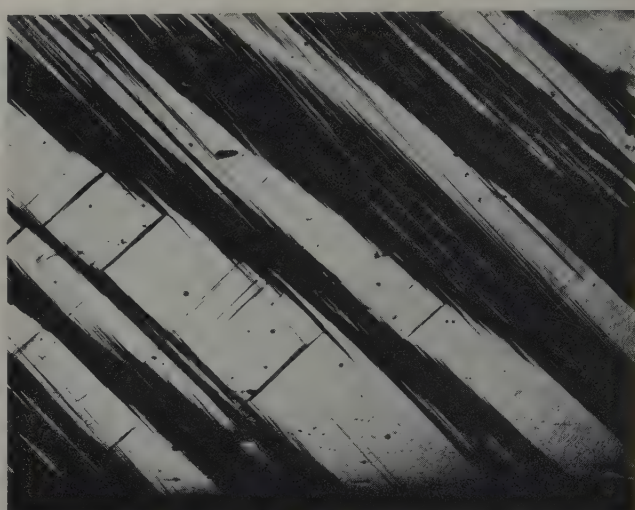


Fig. 6—Specimen 17-C after 10 pct compression. Stress axis horizontal. X21. Area reduced approximately 50 pct for reproduction.

polished and etched, the faced ends being protected from the etchant by paraffin which was then removed with xylol. This entire procedure did not change the nature of the X-ray diffraction spots.

The three specimens, 17-A, 17-B, and 17-C, were compressed 0.009 in., or 1 pct. 17-B and 17-C were then compressed to a total of 5 pct, and 17-C to a total of 10 pct. The strain rate was approximately constant and equal to about 0.001 in. per in. per min.

All three specimens showed very similar patterns of slip lines. A representative area from one of them is shown in Fig. 2, which shows about one quarter of the polished surface. Here, as in all the illustrations, the observation plane is perpendicular to the plane of the specimen axis and primary slip direction. A portion of this specimen, Fig. 3, shows many examples of the joining of slip and cross-slip lines at a corner. The cross-slip shown in these specimens is on an extremely large scale, compared with previous illustrations of the phenomenon.

Figs. 4 to 6 show the same region after 1, 5, and 10 pct compression. The most striking feature of these pictures is the accuracy with which the pattern of slip lines of the smaller deformation is pre-



Fig. 7—Slip on specimen 20. Deformed in shearing machine. Shear 0.5. Elongation, 27 pct. Stress axis horizontal. X75. Area reduced approximately 50 pct for reproduction.

served. Increasing the deformation by a factor of 10 results in the formation of heavy clusters of slip and cross-slip lines at the original slip and cross-slip lines. Regions which were practically free from slip lines remain conspicuously so. These figures also illustrate the very characteristic avalanching of slip lines, and avalanching of cross-slip lines as well. The boundaries of the clusters of slip lines go off at a slight angle to the lines themselves. Many examples could be seen of two slip lines which over-

lap for a considerable distance but are not connected by cross-slip. Deformations of single crystals are often specified in terms of "amount of shear" computed from geometry or from reorientation measured by X-ray. This computation assumes uniform shear on only one slip system, and is thus hardly applicable to complex cases such as specimen 17.

Attempts to Produce Slip on a Single System

The bending constraints imposed in the simple tensile test of a single crystal make such a test difficult to interpret. Attempts to eliminate these constraints were made by two methods, both of which have subsequently been described in the literature. One was to deform the specimen in a shearing machine essentially like that devised by Röhm.⁴ The other was to use a tensile machine in which knife-edges at the grips provided a rotation axis through the midpoint of the first completely free glide ellipse at each end, the specimen being appropriately oriented about its own axis, precisely as described by Diehl and Kochendorfer.⁵ Rosi⁶ has also built a rotating-grip machine which provides two rotation axes instead of one.

Specimen 20 (Fig. 1) was tested in the shearing machine. It was given a deformation corresponding to an extension of 27 pct. This gives a geometrically computed overall shear of 0.5. The shear computed from the change in orientation of the center part of the crystal measured by X-ray was less than this. Since the specimen showed some bending at the ends, the reorientation of the center portion was

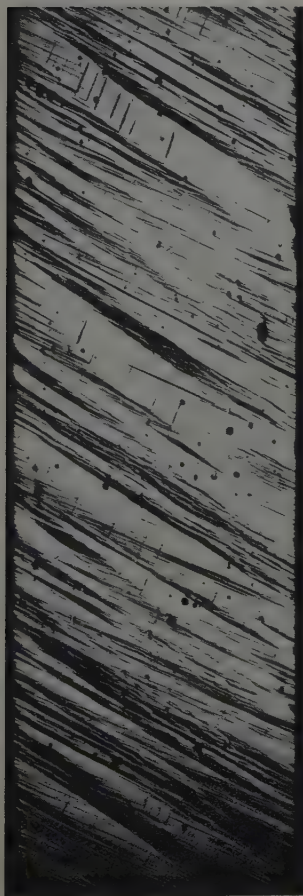


Fig. 8 (left)—Specimen 28 after 8 pct extension in rotating-grip machine. Stress axis vertical. X7.3.

Fig. 9 (right)—Specimen 31 after 11.8 pct extension in rotating-grip machine. Stress axis vertical. X7.3.





Fig. 10—Slip in specimen 31 after 11.8 pct extension in rotating-grip machine. Stress axis vertical. The faint vertical striations were present before deformation. X75. Area reduced approximately 50 pct for reproduction.

less than that deduced from simply measuring the angle from the new specimen axis to the original. Incidentally, since measurement of this angle was the method used by Röhms to find his shear strains, it is possible that the lowering of the shear stress-strain curves reported by him is due to the same cause.

Classical primary slip lines appeared very even and uniform during the process of deformation. None of the clustering, cross-slip, or other irregularities that specimen 17 showed could be seen in the center portion of the specimen. Premature conjugate slip was absent.

Fig. 7 shows the microscopic appearance of a typical portion of the center of the specimen. At the very ends of the specimen, where the bending was greatest, a little cross-slip could be seen. X-ray pictures showed no change in the nature of the diffraction spots.

Although the rotating-grip machine appears to accomplish the same results as the shearing machine, they are not entirely equivalent. The load applied

by the rotating-grip machine is always axial. There is no externally applied bending moment. In principle, then, it might appear to be superior to the shearing machine. In practice, it was found difficult to use. Axiality of the knife edges was of the utmost importance. Although the machine was built with considerable care, the alignment of the specimens was not easy. After a number of trials, two tests were made which will be described here.

In the first test specimen 28 (Fig. 1) was used. It was given an extension in the machine of 8 pct. The grips rotated in the predicted direction, although one grip rotated somewhat more than the other. The unexpected appearance of the slip lines is shown in Fig. 8. The similarity of this to the specimen deformed in compression is striking. It shows exactly the same clustering of primary slip lines and cross-slip lines, and is the very opposite of what the machine was intended to do. An X-ray picture taken after the deformation showed a distinct spot structure but no asterism.

Another test was conducted on specimen 31 (Fig. 1). It was extended 11.8 pct, with quite different results. The overall appearance of its slip lines is shown in Fig. 9. Fig. 10 shows a region practically free from cross-slip at higher magnification. In general, there was very little cross-slip to be seen.

The completely different behavior of these two specimens led to a re-examination of all the specimens deformed during the course of this work. Their orientations are given in Fig. 1. A brief description of their deformation is given in Table I. Specimens 17, 26, and 28 showed similar patterns of very conspicuous cross-slip and clustering, and all have orientations near [100]. For the most part, specimens with orientations far from [100] did not show cross-slip, or showed it on a smaller scale. It seems as though the detailed nature of plastic deformation might depend more strongly on the orientation of the specimen than on the exact means of deforming it.

Conclusions

1—Plastic deformation in copper single crystals is complicated far beyond the naive idea of a "glide ellipse" on the classical slip plane. Clustering and avalanching are prevalent. Cross-slip and other unpredicted slips are frequent.

2—The occurrence of large-scale cross-slip seems to be favored by an orientation near [100] regardless of the way in which the crystals are deformed.

3—Large-scale cross-slip and severe clustering seem to be associated with each other.

References

- ¹A. B. Greninger: Determination of Orientation of Metallic Crystals by Means of Back-Reflection Laue Photographs. *Trans. AIME* (1935) **117**, p. 61.
- ²E. Schmid and W. Boas: *Kristallplastizität* (1935) Berlin. Julius Springer.
- ³R. Maddin, C. H. Mathewson, and W. R. Hibbard, Jr.: The Active Slip Systems in the Simple Axial Extension of Single Crystalline Alpha Brass. *Trans. AIME* (1949) **185**, p. 527; *JOURNAL OF METALS* (August 1949).
- ⁴U. Dehlinger: The Experimental and Theoretical Results of Plasticity at Normal Speeds of Strain. *Symposium on Plastic Deformation of Crystalline Solids*. (May 1950) pp. 19-20. Mellon Institute.
- ⁵J. Diehl and A. Kochendörfer: Zugverformung an Einkristallen mit Drehbaren Fassungen. *Ztsch. Angew. Phys.* (1952) **4**, p. 241.
- ⁶F. D. Rosi: Homogeneous Deformation of Single Crystals. *Review of Scientific Instruments* (1951) **22**, p. 708.

Table I. Deformation and General Appearance of Specimens

Specimen No.	Description
2	Slightly compressed. No cross-slip.
3	Slightly compressed. No cross-slip.
4	Heavily compressed. Two intersecting slip systems, heavy clustering but no cross-slip.
5	Sheared perpendicular to specimen axis. Three intersecting systems but no cross-slip as such.
6	Compressed. No cross-slip.
8	Compressed. No cross-slip.
10	Compressed, one end free to move transversely. Much overlapping of primary slip lines, but no cross-slip.
11	Deformed in shearing machine. Slipped out of lower grip. Overlapping primary slip lines but no cross-slip.
13	Deformed in shearing machine. Slipped out of upper grip. No cross-slip.
14	Rough tensile test. No cross-slip.
16	Sheared nearly perpendicular to axis. Three intersecting slip systems but no cross-slip.
17	Compressed (Section 3.2). Very pronounced cross-slip and clustering.
20	Deformed in shearing machine. No cross-slip.
21	Deformed in rotating-grip machine. Slight cross-slip.
25	Deformed in earlier model of rotating-grip machine. Some cross-slip.
26	Deformed in rotating-grip machine. Very prominent cross-slip.
28	Deformed in rotating-grip machine. Very prominent cross-slip.
31	Deformed in rotating-grip machine. Very slight cross-slip.

Orientation Relationships in the Recrystallization Of Deformed Copper Single Crystals

by J. J. Becker and J. N. Hobstetter

Deformed copper single crystals exhibited, upon annealing, a recrystallized twinned grain with a twin plane parallel to an active deformation plane, rotated approximately 22° about its pole, or else did not recrystallize at all. If extraneous deformation was not carefully removed, no simple orientation relationship was found.

RECRYSTALLIZATION textures have been a subject of practical interest for many years, but any real understanding of their formation will have to start with a study of the recrystallization of carefully deformed single crystals. Some efforts have been made in this direction,¹⁻⁴ but much more experimental information is needed before a satisfactory picture of the crystallography of recrystallization can be formed. This paper reports a few results in copper single crystals.

The crystals studied in this investigation were grown by the Bridgman method,⁵ and their orientations determined by the back-reflection Laue technique.⁶ Some specimens were simply deformed in compression, others were sheared, and still others tested in a rotating-grip device, in attempts to remove end constraints. The details of their deformation behavior are described elsewhere.⁷ The deformed specimens were annealed and the orientations of the recrystallized grains were determined optically, as described by Barrett and Levenson.⁸

Compressed Specimens

Specimen 17-A, whose orientation is given in Fig. 1, was compressed to a total of 19 pct. As observed before,⁷ increasing deformation took place by increasing density of slip lines in initially formed clusters, with little if any formation of new slip clusters in unslipped areas. The specimen was then etched in nitric acid until its length had been reduced from 0.766 to 0.735 in. It was annealed at 1000°C , in increments of a few minutes. After 63 min, two small grains had appeared in the center, Fig. 2. They were found to be twinned with respect to each other (AB, Fig. 4). After 30 min more, the specimen was completely recrystallized. A typical

J. J. BECKER, Junior Member AIME, formerly Teaching Fellow, Dept. of Engineering Sciences and Applied Physics, Harvard University, is now associated with General Electric Research Laboratory, Schenectady, and J. N. HOBSTETTER, formerly Assistant Professor, Dept. of Engineering and Applied Physics, Harvard University, is now associated with Bell Telephone Laboratories, Murray Hill, N. J.

Discussion on this paper, TP 3593E, may be sent, 2 copies, to AIME by Dec. 1, 1953. Manuscript, April 15, 1953. Cleveland Meeting, October 1953.

This paper is based on a thesis by J. J. Becker submitted in partial fulfillment of requirements for the degree of Doctor of Philosophy in the field of engineering sciences and applied physics to the Faculty of Arts and Sciences, Harvard University, January 1951.

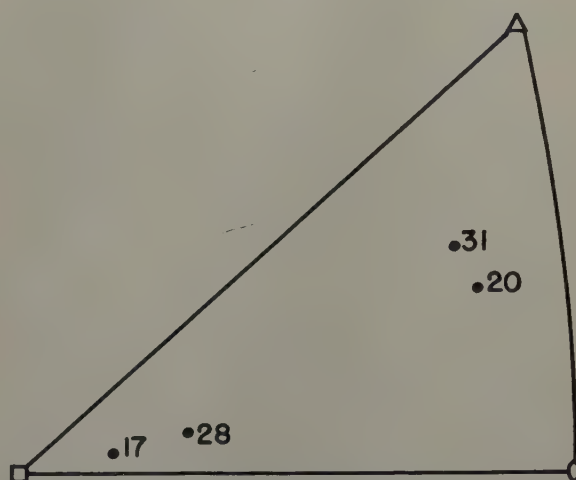


Fig. 1—Orientations of single crystals.

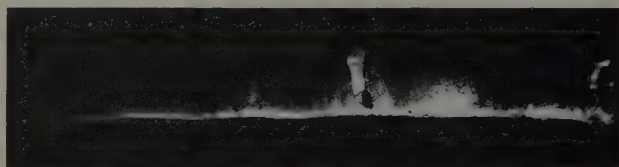


Fig. 2—Recrystallized grains beginning to form in specimen 17-A. X7.3. Area reduced slightly for reproduction.



Fig. 3—Specimen 17-A after complete recrystallization. X7.3. Area reduced approximately 50 pct for reproduction.

view of it is given in Fig. 3. A summary of all orientations found is given in Fig. 4, in which the prominent grain G is in (001) standard projection, and the poles of the active slip planes after deformation are indicated by SP (primary slip plane), CrSP (cross-slip plane), and CnSP (conjugate slip plane). All the orientations found were related through seven orders of twinning. A "family tree" of these twins is given in Fig. 5. Furthermore, the BG twin composition plane lies close to the cross-slip plane

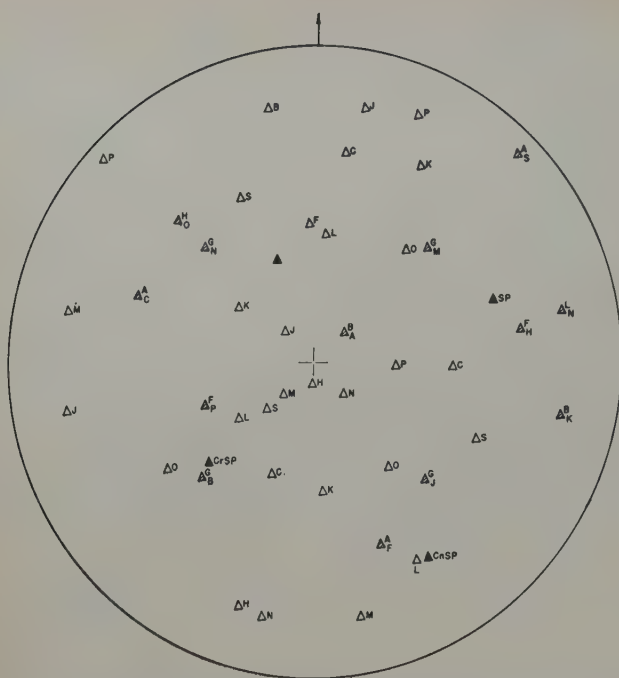


Fig. 4—Orientations of recrystallized grains in specimen 17-A.

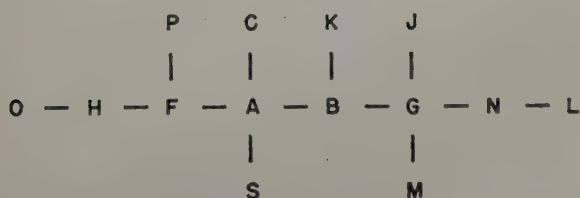


Fig. 5—Twin relationships of recrystallized grains in specimen 17-A.

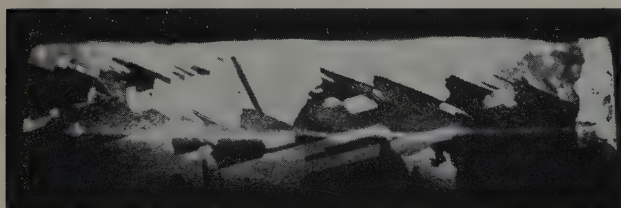


Fig. 6—BG twins in specimen 17-A. X4.8. Area reduced slightly for reproduction.

and the orientation of grain G is rotated approximately 24° in this plane. Fig. 6 was taken to show BG twins prominently. The dark grains are B, and the twins along the bottom of the picture are G.

Specimen Deformed in Shearing Machine

Specimen 20 (Fig. 1) was deformed 27 pct in a device designed to shear the specimen in such a way as to minimize the end constraints. It showed relatively uniform classical slip lines only. A piece about $\frac{1}{2}$ in. long was removed from the center of this specimen with a jeweler's saw. This piece was etched until its thickness had been reduced 0.007 in. After 6 min at 1020°C, it showed no sign of recrystallizing. After another 15 min, it was entirely recrystallized. Figs. 7 and 8 show its appearance on opposite sides. Note that the orientations *X* and *D*, which are twins, occupy roughly the center two-thirds of the specimen. The orientations of these various grains are given in Fig. 9, in which the deformed crystal is in (001) standard projection. The *XD* composition plane is very close to the primary slip plane of the crystal.

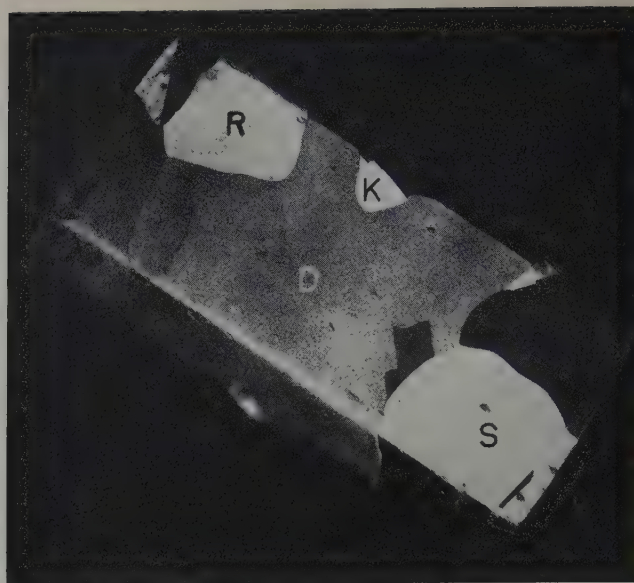


Fig. 7—Specimen 20 after recrystallization. X7.3. Area reduced slightly for reproduction.

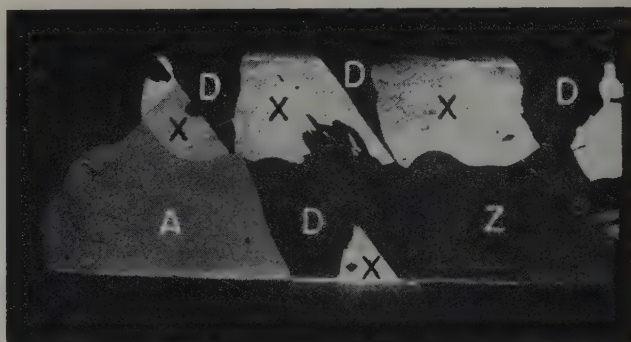


Fig. 8—Specimen 20 after recrystallization. X7.3. Area reduced slightly for reproduction.



Fig. 9—Orientations of recrystallized grains in specimen 20.



Fig. 10 (left)—Recrystallized grains at end of specimen 31. X11.9. Area reduced slightly for reproduction.



Fig. 11 (right)—Recrystallized grains at end of specimen 31. X11.9. Area reduced slightly for reproduction.

No other close correlation appears. Furthermore, the orientation of X is related to the deformed crystal by a rotation of 22° about the pole of the classical slip plane.

Specimens Deformed in Rotating-Grip Machine

Specimen 28 was extended 8 pct in the rotating-grip machine, and specimen 31 was extended 11.8 pct. Their orientations are given in Fig. 1. Pieces about 1/2 in. long were cut from their centers with a jeweler's saw. The ends of these center pieces were ground with optical abrasive on a lead lap until their length had been reduced 0.050 in. They were etched in nitric acid until their lengths had been reduced another 0.016 in. The center of specimen 28 did not recrystallize after 75 min at 1000°C.

The center portion of specimen 31 was carefully placed in a copper foil capsule and annealed a total of 80 min at 1000°C plus 70 min at 1020°C. It did not recrystallize.

Gross recrystallization did not occur in either of the specimens deformed in the rotating-grip machine, even though one of them showed cross-slip and clustering and the other did not.

Effects of Random Nuclei

In all the instances that have been described here, in which distinctive orientation relationships were observed or recrystallization did not take place at all, the specimens had been considerably etched down after deformation and before annealing. This was done to remove the nuclei which might have been produced by saw cuts or by grips. A number of other specimens were annealed without this preliminary etch.

Specimen 17-C, with the same orientation as 17-A, was compressed 10 pct and recrystallized. The orientations of the recrystallized grains bore no obvious relationship to that of the deformed matrix. The end pieces of specimens 20 (deformed in the shearing machine) and 28 (deformed in the rotating-grip machine) were recrystallized as cut. In all cases recrystallization started under the grips and at the saw cut. No simple orientation relationship was found.

The ends of specimen 31 (deformed in the rotating-grip machine) were recrystallized without further treatment for 3 min at 1000°C. Both partially recrystallized. Two views of one of the recrystallized ends are given in Figs. 10 and 11. It would be expected that cutting a crystal with a saw would pro-

vide a multitude of nuclei in many orientations, among which those of certain orientations would grow most rapidly.⁹ The large twinned grain in Fig. 11 corresponds to the conspicuous twinned grain at the bottom of Fig. 10, and illustrates this preferential growth. However, this does not result in a $\langle 111 \rangle$ rotation, or any other simple relationship. The orientations of these twins and of the deformed grain are given in Fig. 12. Selective growth, in this instance, does not lead to recognizable relationships.

Summary and Conclusions

Experiments are still needed in which geometrically simple deformation can be directly related to recrystallized orientations. The experiments reported here illustrate the following phenomena:

1—Whenever extraneous deformation was removed from the ends of deformed copper single crystal specimens, either they did not recrystallize at all, or else they exhibited a recrystallized twin plane parallel to one of the active deformation planes, with a rotation of about 22° about its pole. This same rotational relationship was found by Kronberg and Wilson¹⁰ in the secondary recrystallization of copper. The identity of the twin plane

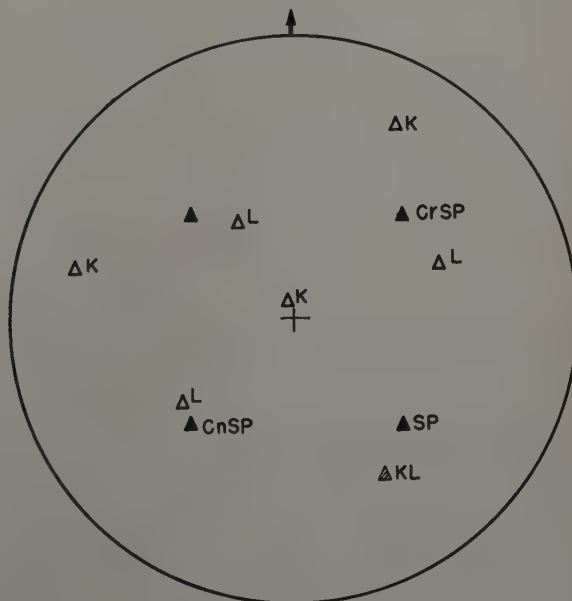


Fig. 12—Orientation of large grain in Figs. 10 and 11.

and the active slip planes was also found by Maddin, Mathewson, and Hibbard in the primary recrystallization of single crystals of α brass.⁴

2—When extraneous deformation was left in the specimens, and they recrystallized from grip marks or saw cuts, oriented growth could be observed, but it never resulted in a simple orientation relationship to the matrix.

References

¹W. G. Burgers and P. C. Louwerse: *Über die Zusammenhang Zwischen Deformationsvorgang und Rekristallisationstextur bei Aluminium*. *Ztsch. Phys.* (1931) **67**, p. 605.

²J. A. Collins and C. H. Mathewson: Plastic Deformation and Recrystallization of Aluminum Single Crystals. *Trans. AIME* (1940) **137**, p. 150.

³C. S. Barrett: Recrystallization Texture of Aluminum after Compression. *Trans. AIME* (1940) **137**, p. 128.

⁴R. Maddin, C. H. Mathewson, and W. R. Hibbard, Jr.: The Origin of Annealing Twins in Brass. *Trans. AIME* (1949) **185**, p. 655; *JOURNAL OF METALS* (September 1949).

⁵P. W. Bridgman: Certain Physical Properties of Single Crystals of Tungsten, Antimony, Bismuth, Tellurium, Cadmium, Zinc, and Tin. *Proc. Amer. Acad. Arts and Sci.* (1925) **60**, p. 305.

⁶A. B. Greninger: Determination of Orientation of Metallic Crystals by Means of Back-Reflection Laue Photographs. *Trans. AIME* (1935) **117**, p. 61.

⁷J. J. Becker and J. N. Hobstetter: This issue, p. 1231.

⁸C. S. Barrett and L. H. Levenson: Determination of Orientations by Etch Pits. *Trans. AIME* (1940) **137**, p. 76.

⁹P. A. Beck, P. R. Sperry, and H. Hu: The Orientation Dependence of the Rate of Grain Boundary Migration. *Journal of Applied Physics* (1950) **21**, p. 420.

¹⁰M. L. Kronberg and F. H. Wilson: Secondary Recrystallization in Copper. *Trans. AIME* (1949) **185**, p. 501; *JOURNAL OF METALS* (August 1949).

Technical Note

Thermal Conductivity, Electrical Resistivity, And Thermoelectric Power of Uranium

by W. W. Tyler, A. C. Wilson, Jr., and G. J. Wolga

THE physical properties of uranium have been reviewed by Katz and Rabinowitch.¹ Their review includes thermal conductivity data for temperatures above 375°K. Recently, Mendelssohn and Rosenberg² have published data on the thermal conductivity of uranium from 2° to 20°K. Our measurements indicate the temperature dependence of the thermal conductivity in the temperature interval from 20° to 300°K. Electrical resistivity and thermoelectric power were measured on the same sample.

The material studied was normal uranium which had been heated at 700°C in a lead bath for 10 min and then quenched in a water bath held at 50°C. From this material a rod $\frac{1}{2}$ in. in diameter and $2\frac{1}{2}$ in. long was machined. Two 0.040 in. holes were drilled into the rod $1\frac{3}{4}$ in. apart. Copper-constantan thermocouples for temperature and potential measurements were soldered to copper pins which were pressed tightly into these holes. Details of the equipment and experimental techniques used in making the measurements have been described elsewhere.³

Fig. 1 shows micrographs of a section of the sample studied. Fig. 1a was taken with unpolarized light and shows impurity inclusions, probably uranium carbide. Fig. 1b, showing the same field, was taken with polarized light and gives some indication of the grain size and twinning within the grains.

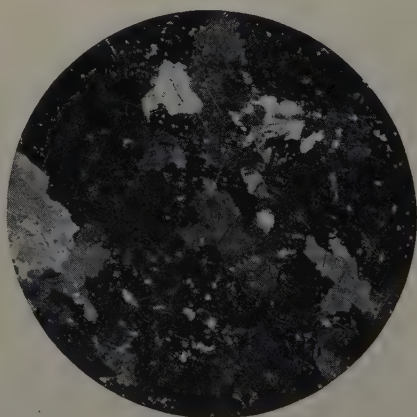
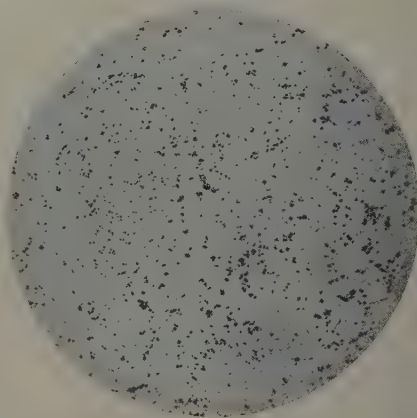
Experimental Results

Thermal conductivity and electrical resistivity data are shown in Fig. 2. Table I shows values of

W. W. TYLER and A. C. WILSON, Jr., associated with the Research Laboratory, General Electric Co., Schenectady, and G. J. WOLGA, associated with Cornell University, Ithaca, N. Y., were all formerly with Knolls Atomic Power Laboratory.

TN 169E. Manuscript, March 25, 1953.

a (right)—Bright field illumination showing impurity inclusions. X100. Area reduced approximately 50 pct for reproduction.



b (left)—Same field as in Fig. 1a but illuminated with polarized light showing microstructure. X100. Area reduced approximately 50 pct for reproduction.

Fig. 1—Micrographs of uranium.

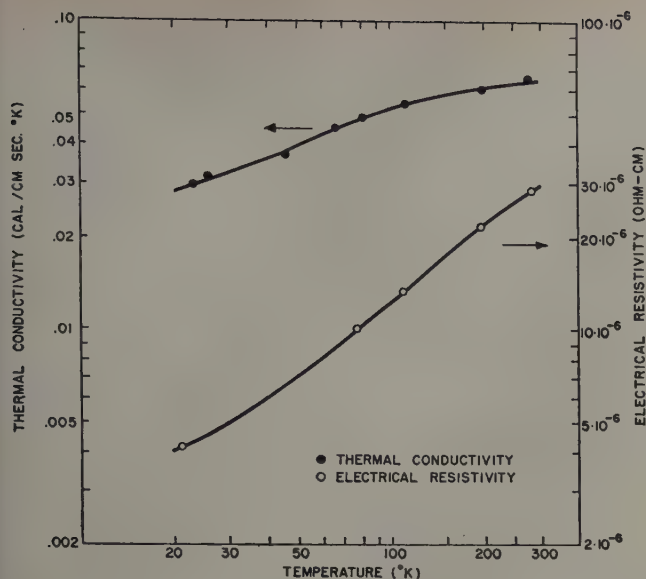


Fig. 2—Thermal conductivity and electrical resistivity of uranium.

the Wiedemann-Franz ratio calculated from the smoothed curves of Fig. 2. Fig. 3 shows values of the absolute thermoelectric power of uranium obtained from measurements of thermoelectric power of a uranium-copper couple using data of Borelius⁴ for the absolute thermoelectric power of copper.

The uncertainty in the magnitude of thermal conductivity data is estimated to be ± 5 pct. Heat loss by heater and thermocouple leads was at the most 2 pct of the heat conducted by the specimen. Correction for this loss was made in a manner which has been described.⁸ Errors due to thermal drift and radiation losses were at most 1 pct. A temperature-independent geometric error of about 2 pct resulted from the finite dimensions of the thermocouple contacts.

The accuracy of the electrical resistivity measurements was limited by the geometry of the sample. Due to the low values of the potential measured, the relative values of the resistivity data are uncertain by several percent in addition to the temperature-independent error due to form factor. Data points for electrical resistivity shown in Fig. 2 are averages of several points taken at approximately the same temperature. Assuming that the data of Borelius are applicable to the copper used in our couples, the thermoelectric power data are accurate to within 0.5 microvolts.

Discussion of Results

The values of the observed Wiedemann-Franz ratio vary from slightly below the free electron theoretical value of 2.45×10^{-8} (volts per degree)² at 20°K to slightly above the theoretical value at 300°K. The lattice does not contribute appreciably to ther-

Table I. Calculated Values

Temperature, °K	Wiedemann Franz Ratio (Volts/Degree) ²
20	2.34×10^{-8}
60	2.46×10^{-8}
100	2.75×10^{-8}
140	2.88×10^{-8}
180	2.88×10^{-8}
220	2.82×10^{-8}
260	2.73×10^{-8}
300	2.67×10^{-8}

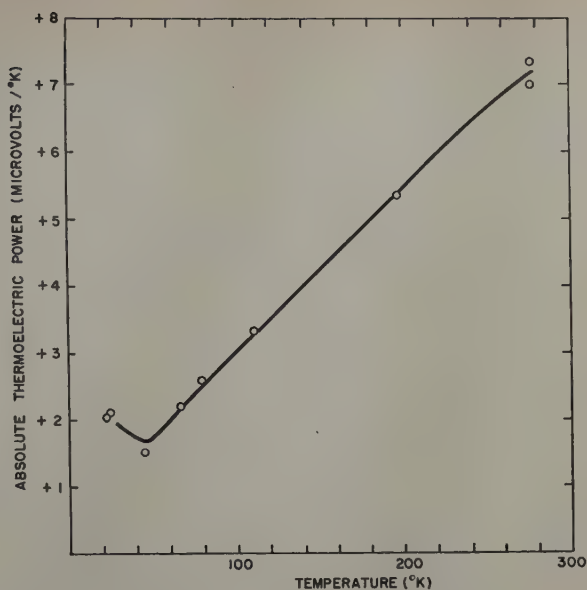


Fig. 3—Absolute thermoelectric power of uranium.

mal conductivity. This is in agreement with observations of Mendelssohn and Rosenberg² in the lower temperature range.

No maximum in the thermal conductivity characteristic of good electronic conductors⁵ is observed for uranium. Extrapolation of our data gives somewhat higher conductivity at 350°K than indicated by data reported by Katz and Rabinowitch.¹ At 20°K, the conductivity of our sample is about 70 pct of that reported by Mendelssohn and Rosenberg. These differences, somewhat greater than experimental uncertainties, are probably due to differences in purity. The chemical purity of our sample is not accurately known and is not quoted for the other samples. Electrical resistivity data for our sample agree well with data quoted by Katz and Rabinowitch.¹ Their survey of available data indicates that the resistivity values depend upon purity and previous heat treatment.

Our value of absolute thermoelectric power at room temperature is in approximate agreement with values deduced from the data on thermoelectric power of uranium against copper and against platinum given by Ebert and Schulze.⁶ The positive sign of the absolute thermoelectric power implies that conduction is predominantly due to holes.

The measurements reported were made at the General Electric Low Temperature Laboratory. We are indebted to J. E. Burke for his suggestion of this study and for his helpful discussion related to the interpretation of the micrographs.

References

- ¹J. J. Katz and E. Rabinowitch: *The Chemistry of Uranium*. National Nuclear Energy Series (1951) Div. VIII, Vol. 5. New York. McGraw-Hill Book Co.
- ²K. Mendelssohn and H. M. Rosenberg: *Proc. Phys. Soc.* (1952) **65**, 390A, p. 388.
- ³W. W. Tyler and A. C. Wilson, Jr.: *Physical Review* (1953) **89**, p. 870.
- ⁴G. Borelius: *Handbuch der Metallphysik* (1935) Vol. 1, pp. 181-485. Leipzig. Akad. Verlags. Gesellschaft.
- ⁵R. E. B. Makinson: *Proc. Cambridge Philosophical Soc.* (1938) **34**, p. 474.
- ⁶H. Ebert and A. Schulze: *Ztsch. Metallkunde* (1947) **38**, p. 46.

Age Softening of Beta Brass

by Harry Green and Norman Brown

The effect of quenching temperature and of aging temperature and time on compression stress-strain curves of β brass was investigated. Age softening occurs at a rate which decreases with decrease of quenching temperature below the critical temperature for ordering. The activation energy for softening is 15,400 cal per mol.

NO matter how rapidly β brass is quenched or what the temperature from which it is quenched, practically complete order is obtained at room temperature. It has been demonstrated that with respect to the specific heat,^{1,2} electrical resistivity,³ X-ray diffraction,⁴ and microstructure, the slowly cooled and rapidly quenched specimens are the same and that complete long range order exists in both cases. However, Smith⁵ showed that the hardness of β brass depended upon the cooling rate and the temperature from which β brass is quenched. Smith showed that the hardness was a maximum for specimens quenched from about 445°C and that the as-quenched structure softened at room temperature at a rate depending upon the temperature prior to quenching. This softening after quenching is in this paper referred to as age softening.

The results of this investigation are qualitatively the same as the findings of Smith. However, a more detailed analysis of these phenomena has been possible since the stress-strain curve offers a more sensitive index of the state of the metal than hardness. It is the purpose of this paper to show how the mechanical properties are related to the ordering of β brass.

A 200-lb ingot made from electrolytic copper and electrolytic zinc was extruded to ½-in. rod. Chemical analyses at frequent intervals along the rod showed that the alloy contained 51.5 pct Cu with

H. GREEN is Metallurgist, Horizons Inc., Cleveland, and N. BROWN is Assistant Professor of Metallurgy, Towne Scientific School, University of Pennsylvania, Philadelphia.

Discussion on this paper, TP 3627E, may be sent, 2 copies, to AIME by Dec. 1, 1953. Manuscript, April 15, 1953. Cleveland Meeting, October 1953.

This paper is based on a thesis by H. Green submitted in partial fulfillment of requirements for a M. S. degree to the Graduate School, University of Pennsylvania.

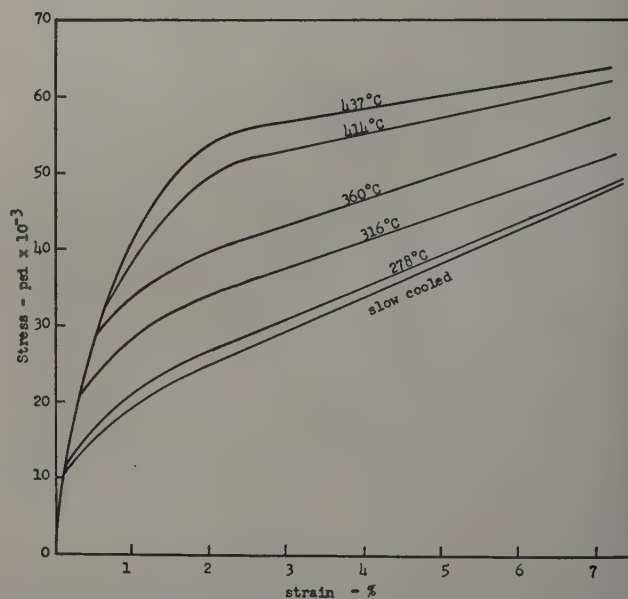


Fig. 1—Typical stress-strain curves showing effect of quenching temperature.

the greatest impurity being iron, at 0.01 to 0.001 pct. To obtain a constant test material, the ½-in. extruded rod was warm-rolled to ⅜ in. diameter at 200°C and then recrystallized to a grain size of 2.0 mm.

The specimens for the compression test were ⅜ in. high and ⅜ in. in diameter. The specimen ends were polished on 600 metallographic paper and coated with Molykote for a lubricant. The compression rig consisted of an anvil resting on the machined table of the Baldwin Southwark testing machine and a plunger fixed to the movable cross

head. For strains up to 7 pct, practically no barreling was observed.

The rate of strain for all tests was about 0.01 in. per in. per min. The change in length of the specimen was recorded automatically with the load upon a drum recorder. The change in length was indicated by a microformer unit placed along side the specimen under the cross head.

Experimental Results

All specimens were originally slowly cooled from 500°C to room temperature, putting them in a standard state of complete order. They were then reheated to various temperatures up to 500°C, and held 15 min at temperature prior to quenching in water. In order to determine whether equilibrium was achieved prior to quenching, a series of specimens were reheated to 500°C, rapidly cooled to a lower temperature, and then after 15 min water-quenched to room temperature. These different methods of approaching the quenching temperature had no effect upon the resulting mechanical properties.

Typical stress-strain curves for the states immediately after quenching are given in Fig. 1. Those states that exhibited higher flow stresses at low strains also work hardened at a slower rate so that all flow curves tend to converge at large strains.

The way in which the flow stress and the rate of work hardening depend on the quenching temperature is given in Fig. 2. The structure prior to quenching was shown to be at equilibrium with

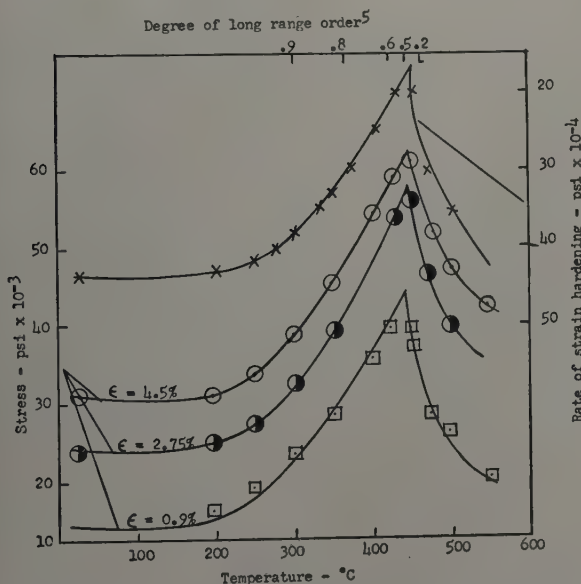


Fig. 2—Flow stress and rate of strain hardening vs quenching temperature.

respect to the resulting mechanical properties. Thus, the prequenched structure as represented by the degree of long range order prior to quenching has also been plotted along with the quenching temperature, Fig. 2. The data for the degree of order as a function of temperature was taken from the X-ray investigation by Warren and Chipman.⁴ The maximum in the flow stress occurs when about 0.5 order existed prior to quenching. When the rate of work hardening as measured by the linear portion of the stress-strain curve is plotted against quenching temperature, the curve has a minimum at the same degree of order that the flow stress is at a maxi-

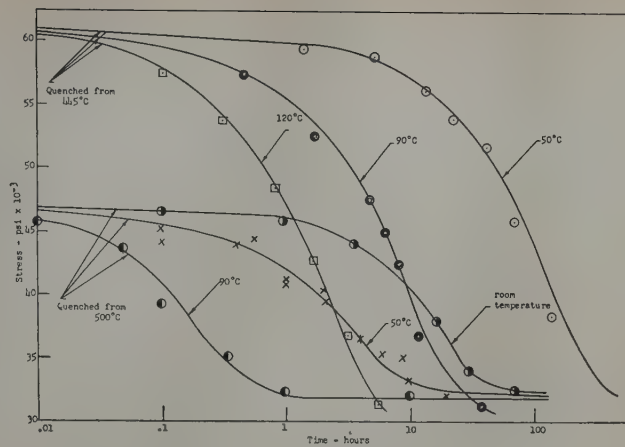
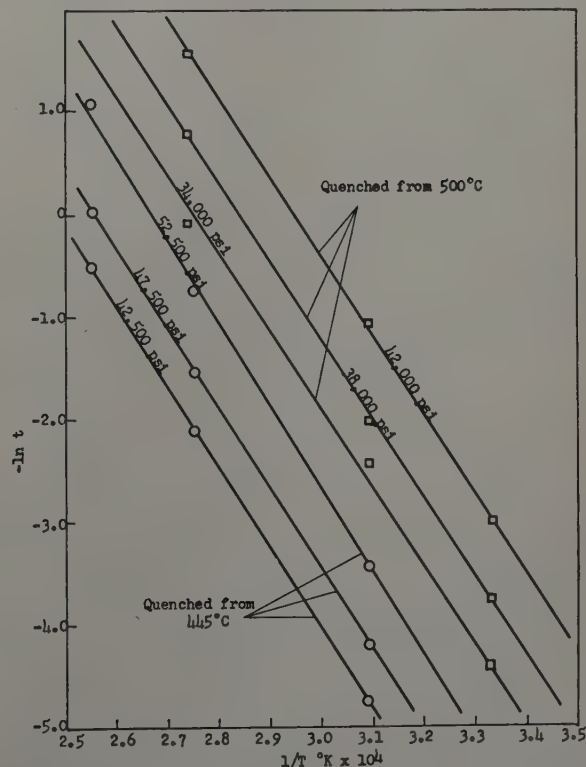


Fig. 3—Flow stress at 4.5 pct strain as a function of time at various aging temperatures for indicated quenching temperatures.

mum, Fig. 2. This behavior correlates with the rates of recovery to be presented later.

The as-quenched structure is unstable in the vicinity of room temperature and changes with time. The strength of all states decreases to the value characteristic of specimens slowly cooled to room temperature. This phenomenon will be called age softening. The way in which the age softening depends on time, aging temperature, and the temperature prior to quenching is shown in Fig. 3. The rate of softening as a function of the aging temperature was investigated by plotting the logarithm of the time against the reciprocal of the absolute temperature at which a given degree of softening was produced, Fig. 4. The slope of the resulting straight line was independent of the degree of softening and indicates that the age-softening phenomenon is a thermally activated process. An activation energy of 15,400 cal per mol is indicated by the slope of the straight line. This activation energy was found to be independent of



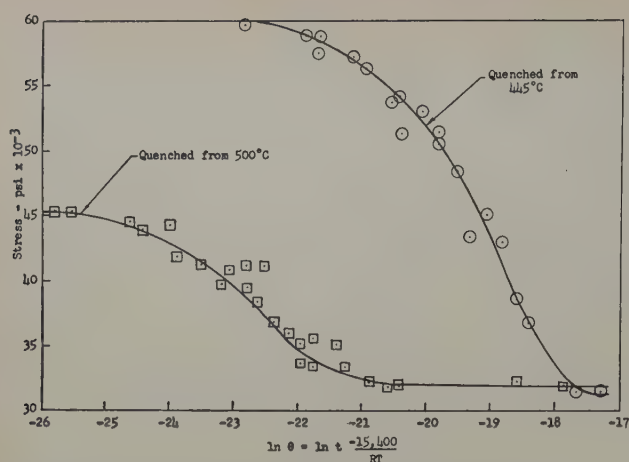


Fig. 5—Composite effect of time in hours and temperature in °K on aging of β brass quenched from indicated temperatures.

the temperature prior to quenching. The softening process is better described by using a temperature-modified time as shown in Fig. 5.

It was observed that the softening process following quenching displayed the following general characteristics:

1—The equilibrium value of the stress was the same for all quenching temperatures.

2—All curves had a delay time or incubation period before the softening was measurable.

3—The greater the delay time, the slower the rate of softening.

4—The softening curves were identical for specimens quenched from varied temperatures above the critical temperature of ordering.

5—For quenching temperatures below the critical temperature the rate of softening decreased as the quenching temperature decreased. These observations are based on Fig. 6, representing quenching temperatures ranging from 500° to 300°C. The aging temperatures ranged from 25° to 120°C and were chosen so that the aging times could be accurately measured and were not inconveniently long. Because it appeared to be more significant, the percentage of change in stress between the as-quenched and equilibrium state was plotted against the temperature-modified time.

It is to be noted that for quenching temperatures above 464°C, the critical temperature, the softening curves are identical. For a quenching temperature of 460°C, the rate of softening decreases abruptly and at the same time there is a pronounced scatter in the data. This scatter is significant because it means that in the range of temperature immediately below the critical it is difficult to reproduce the

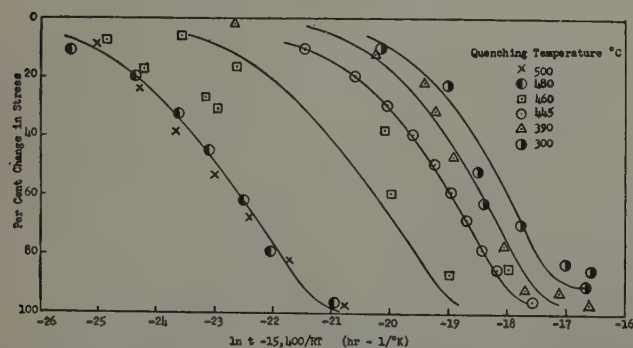


Fig. 6—The effect of quenching temperature on the age softening process. The aging temperatures ranged from 25° to 120°C.

same structure. This is attributed to the fact that the degree of long range order changes very rapidly just below the critical temperature, and thus, very small differences in temperature produce very large differences in the degree of order. Similarly, since the critical temperature depends on composition, small differences in composition will produce large differences in the degree of order even if the difference between the quenching temperature was exceedingly small.

As the quenching temperature is further decreased below the critical, the excessive scatter disappears, and the rate of softening decreases uniformly. Within the limits of the experimental error, all the curves in Fig. 6 have the same shape and the essential difference is based on their relative displacements along the time axis. This means that all the curves may be represented by a single empirical equation of the form

$$\frac{\sigma_1 - \sigma_t}{\sigma_1 - \sigma_E} = F(\ln t - 15,400/RT + \ln K) \quad [1]$$

where σ_1 is the initial stress; σ_E , equilibrium stress; σ_t , the instantaneous stress; t , the time; T , the ab-

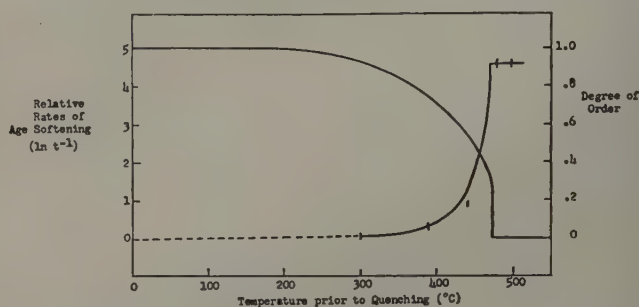


Fig. 7—Rate of age softening and degree of order prior to quenching as related to the quenching temperature.

solute temperature; R , the gas constant; $\ln K$ = the relative displacement of the curves along the time axis in Fig. 6; and F is a function describing the shape of the curve. The value of K is a measure of the relative rates of age softening and is also a measure of the relative lengths of the delay times before any softening is measurable.

The relationship between K and the quenching temperature is given in Fig. 7 where it is demon-

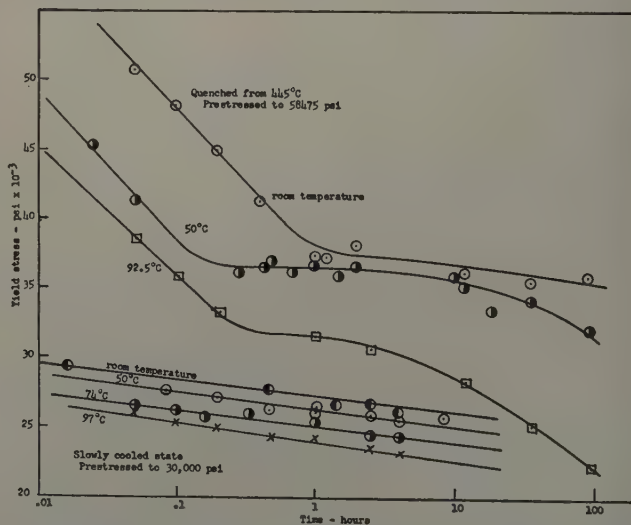


Fig. 8—Change in yield stress with time after prestraining. The recovery temperatures are indicated.

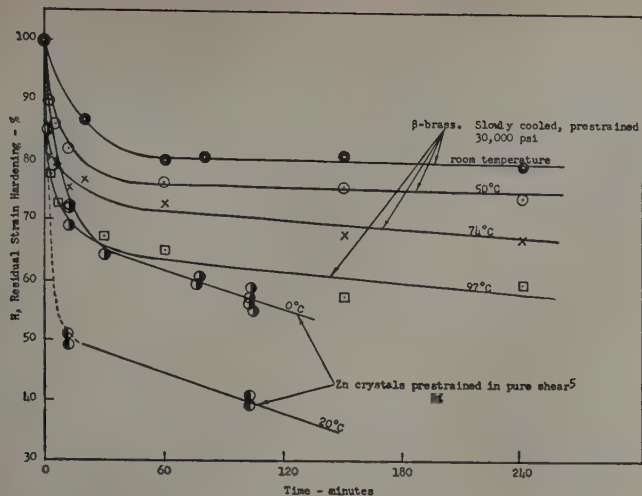


Fig. 9—Recovery of strain hardening as a function of time at various temperatures for slowly cooled β brass and for zinc crystals.⁵

strated that the rate of softening is constant down to the critical temperature, decreases sharply just below the critical temperature, and then appears to approach an equilibrium value. The functional relationship between the rate of age softening and the quenching temperature bears a strong resemblance to the functional relationship between the degree of long range order* prior to quenching and the

* The degree of order as a function of temperature was measured by Warren and Chipman⁴ by means of a high temperature X-ray method.

quenching temperature, Fig. 7. The scatter in the data for the 460° quench is readily appreciated in the light of Fig. 7. The K values are such that a specimen quenched from above the critical softens about 200 times faster than one quenched from 300°C where the degree of order prior to quenching is about 0.92.

The age-softening process was further investigated by giving the specimens a deformation prior to age softening. In order to determine the recovery effect without the presence of age softening, slowly cooled specimens were also used. The rate of softening after prior deformation is shown in Fig. 8. The recovery curves for the slowly cooled specimens have a different shape than those obtained from specimens quenched from 445°C. The slowly cooled

specimens exhibit a recovery curve which is similar to the recovery of zinc⁵ as shown in Fig. 9. In the case of the slowly cooled specimens, an activation energy of the recovery process was determined by plotting $\ln t$ against the reciprocal of the recovery temperature for a given degree of recovery. The slope of the straight line obtained in Fig. 10 corresponds to an activation of about 20,000 cal per mol for the recovery process. It should be pointed out that recovery of the strained β brass presumably involves a reordering of the lattice disordered by strain as well as the phenomena ordinarily associated with "recovery."

When the same procedure was used to obtain an activation energy for the recovery of specimens quenched from 445°C, a linear relationship was not obtained between $\ln t$ and the reciprocal of the recovery temperature as shown in Fig. 11. This is attributed to the age-softening process having a delay time whereas the maximum rate of recovery occurs at zero time. Thus age softening and recovery presumably are different processes.

Discussion

Although studies of the specific heat,^{1,2} microstructure,³ electrical resistivity, and X-ray diffraction showed no difference among specimens in the different mechanical states, some type of boundaries or crystal imperfections must be responsible for the variations in the mechanical properties. In accordance with current views by Barrett,⁶ Smith,³ and Cottrell⁷ it is postulated that the difference in mechanical properties is caused by various configurations of the out-of-phase domains.

Warren and Chipman⁴ attempted to determine whether there was any difference between a slowly cooled specimen and one quenched from 500°C. They decided that there was no difference with respect to out-of-phase domains, but their results are not conclusive because they polished and etched the specimen after quenching and they do not state what time elapsed between the quench and the X-ray examination. From the age-softening curves of Fig. 3, it is readily apparent that after such a history the specimen could have age-softened almost completely before the X-ray examination was made.

During the quench, the centers of short range

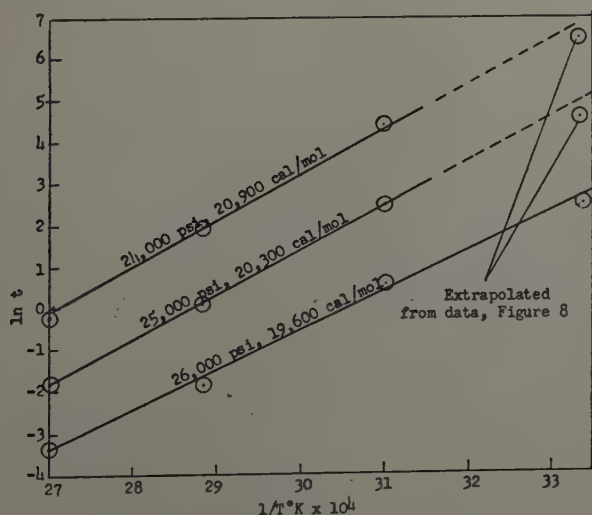


Fig. 10—Determination of activation energy for recovery after prestraining slowly cooled β brass.

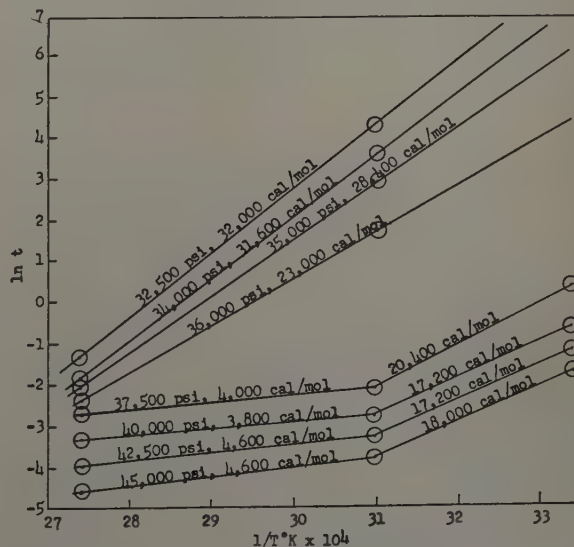


Fig. 11—Same as Fig. 10 except specimens were quenched from 445°C.

order nucleate the domains of long range order. If these domains are nucleated independently, then the superlattice sites occupied by the copper atoms in one domain will not always be the same sites occupied by copper atoms in the adjoining domains. This gives rise to out-of-phase domains in each of which complete long range order exists. During the age-softening process, these domains grow to a size limited by the grain boundaries. In the light of the low activation energy for age softening it is not surprising that β brass orders so rapidly. The observed value for age softening agrees closely with the activation energy for diffusion of 17,600 cal per mol.⁸

If the age-softening process is one of out-of-phase domain growth then some relationship must exist between the size of the domain and the percentage of change in stress. Although this relationship is not known, a general function may be assumed. Thus, Eq. 1 transforms to

$$\frac{dD}{dt} = g(D) K e^{-Q/RT} \quad [2]$$

where D is the domain size; g , the function of domain size; and Q , the activation energy. In general a growth process such as grain growth may be represented by

$$\frac{dD}{dt} = N \times M \quad [3]$$

where N is a function related to the number of domains and M is a function of the rate of boundary migration. If the interfacial energy of the boundaries do not vary with domain size, then it may be assumed that M is independent of the quenching temperature. The differences in the rates of growth are attributed to differences in N . Therefore Eqs. 2 and 3 give the result that

$$K = N \quad [4]$$

In Fig. 7 it is indicated that K depends upon the degree of order prior to quenching. This means that the degree of order prior to quenching determines the number of out-of-phase domains formed immediately after quenching. The relationship between K and the degree of order prior to quenching is given by the empirical equation

$$\ln K = 5.6(1 - S) \quad [5]$$

where S is the degree of order prior to quenching. For all states the rate of age softening may be described by

$$\frac{d\left(\frac{\sigma_1 - \sigma}{\sigma_1 - \sigma_B}\right)}{dt} = H\left(\frac{\sigma_1 - \sigma}{\sigma_1 - \sigma_B}\right) e^{-15,400/RT} e^{5.6(1-S)} \quad [6]$$

where H is a function related to the shape of the age-softening curve.

The nature of the interaction between the out-of-phase domain boundaries and dislocations is not certain. This effect is quite large as evidenced by the flow stress at 0.9 pct strain in the specimen quenched from 445°C, which is about three times the flow stress for the slowly cooled specimens. It is proposed that the density of trapped vacant lattice sites may be the cause. The aging process would then consist of the migration of vacancies to dislocations. This process would increase the length of dislocations and at the same time tend to remove jogs in the dislocations loop. It would be expected

that such a process would produce a decrease in density during age softening. Since such a change in density is expected to be very small, the change in density is difficult to measure. A method has been devised using an electrical strain gage which detects changes in density on the order of 10^{-5} . An SR-4 strain gage was cemented on a specimen quenched from 445°C and the compensating gage was cemented in identical fashion on a slowly cooled specimen. The gages were balanced with an SR-4 type K strain indicator. After aging for two weeks at room temperature about a 10^{-4} change in strain was measured. Any drift in the indicator was minimized by using it only for the short time necessary to take a reading. The correlation between this density change and the change in mechanical properties is not definite because the rates are not the same. The change in density is slower and extends over a somewhat longer period of time. Further studies are being made of this density change. The presence of a large concentration of vacancies is consistent with the observation of a large Kirkendall effect in β brass.

Conclusions

1—The stress-strain curve of β brass depends on the temperature from which it is quenched. The greater the flow stress observed, the less is the rate of work hardening.

2—When about 50 pct order exists prior to quenching, a maximum in flow stress is obtained in the as-quenched state.

3—The as-quenched state is unstable and age-softens by a thermally activated process governed by an activation energy of 15,400 cal per mol.

4—The rate of age softening varies inversely with the degree of long range order existing prior to the quench.

5—Slowly cooled specimens of β brass recover after prior deformation with an activation energy of about 20,000 cal per mol.

Acknowledgment

The authors acknowledge the assistance of Marvin Herman throughout the work. The research was initiated by R. M. Brick who contributed greatly by his continued interest and discussions. The original ingot was made at Frankford Arsenal. The extrusion was done through the courtesy of the Bridgeport Brass Co. The research was supported by the Office of Ordnance Research, U. S. Army, under contract DA-36-034-ORD491.

References

- ¹ C. Sykes and H. Wilkinson: The Transformation in the Beta Brasses. *Journal Inst. Metals* (1937) **61**, p. 223.
- ² C. S. Smith: A Simple Method of Thermal Analysis. *Trans. AIME* (1940) **137**, p. 236.
- ³ C. S. Smith: Hardness Changes Accompanying Ordering of Beta Brass. *Trans. AIME* (1943) **152**, p. 144.
- ⁴ D. Chipman and C. Warren: X-ray Measurements of Long Range Order in Beta Brass. *Journal of Applied Physics* (1950) **21**, p. 696.
- ⁵ R. Drouard, J. Washburn, and E. Parker: Recovery in Single Crystals of Zinc. This issue, p. 1226.
- ⁶ C. S. Barrett: *Structure of Metals*. Second Edition (1952) p. 292. New York, McGraw-Hill Book Co.
- ⁷ A. H. Cottrell: *Theoretical Structural Metallurgy* (1948) p. 222. London, Longmans, Green and Co.
- ⁸ U. S. Lendergren and R. F. Mehl: Rates of Diffusion and Marker Movements in Beta Brass. *JOURNAL OF METALS* (February 1953) p. 153.

Plastic Deformation of Iron Between 300° and 77.2°K

by Donald F. Gibbons

THIS investigation was undertaken in order to gain further information on the mechanism of plastic deformation of iron at temperatures between room temperature and 77.2°K, and also to contribute to our understanding of the low temperature brittleness phenomenon that occurs in both the tensile and impact tests. It was decided to study as pure an iron as possible and to use the tensile test in order to simplify the problem as much as possible.

Two series of iron were used throughout the investigation: iron A, obtained from the National Research Corp. and supplied as gas-free, high purity iron; and iron B, obtained from Fast¹ and produced by melting iron under purified hydrogen. Typical analyses of samples of both irons, after fabrication, are given in Table I.

The main difference in composition of these irons is in their nickel and oxygen contents. Nickel has a very large solid solubility in iron. However, oxygen has an extremely small solid solubility. An attempt was made to reduce the oxygen content still further by remelting under purified hydrogen. This was successful in reducing the oxygen content to ~0.0006 pct. However, no results on tests of this iron are included, since difficulty was encountered in fabricating the ingot.

Wire specimens 1 mm in diameter were used for the investigation. The wires were produced from the ingots, as supplied, by cold rolling and swaging, with intermediate vacuum anneals at 700°C. Care was taken to reduce preferred orientation in the wires to a minimum by keeping the percentage of reduction in area between anneals of 30 to 40 pct. X-ray transmission photographs showed no indication of preferred orientation. The final grain size of iron A was 20 to 24 grains per linear mm and of iron B, 16 to 18 grains per linear mm.

All specimens were tested in the decarburized and denitrided condition unless otherwise stated. The procedure was to pass hydrogen, saturated with water vapor at 26°C, over the specimens at 730°C for 2 hr. The specimens were quenched in iced water and then annealed in a vacuum of $\sim 5 \times 10^{-6}$ mm Hg for one day at 560°C to remove hydrogen. Higher temperatures were used for the vacuum anneal but this temperature was found to be quite satisfactory in removing hydrogen. The specimens were slow-cooled after the vacuum anneal. Where it is stated that the specimens were carburized, the specimens were given an identical decarburizing treatment and then carburized by passing hydrogen, saturated

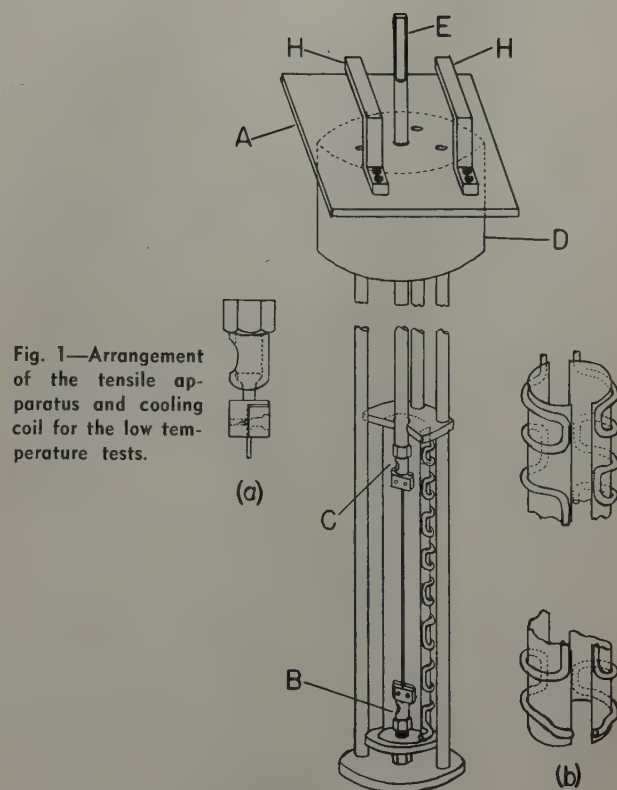


Fig. 1—Arrangement of the tensile apparatus and cooling coil for the low temperature tests.

with pure n-heptane vapor at 0°C, over the specimens at 730°C. The specimens were then homogenized at 730°C for 2 hr in dry hydrogen. After the carburizing treatment the specimens were given the same vacuum anneal as for the decarburized specimens. The carbon content was determined from the maximum value of the internal friction carbon peak.²

Apparatus

Fig. 1 shows a diagram of the tensile apparatus, with half the cooling coil removed. The cooling coil enabled temperatures from 200° to 77.2°K to be obtained. The apparatus was designed to fit a standard Tinius Olsen Universal tensile machine.

The apparatus consisted of the rigid plate A which carried two carefully machined hooks H. These hooks attached the plate firmly to the moving crosshead of the tensile machine. The lower grip B was rigidly suspended from the plate A by three stainless steel rods. The upper grip C was joined to the upper grip of the tensile machine by the stainless steel rod E. The lower part of the apparatus was surrounded by a Dewar vessel, which was made a sliding fit inside the brass collar D. The specimen was held in a clamp which fitted into the grip, forming a ball and socket joint (see inset a). This was to attain as nearly pure

D. F. GIBBONS, Junior Member AIME, formerly the University of Chicago, is now Research Associate, Physics Dept., Royal Military College, Kingston, Ont., Canada.

Discussion on this paper, TP 3585E, may be sent, 2 copies, to AIME by Dec. 1, 1953. Manuscript, March 2, 1953; revision, May 19, 1953. Cleveland Meeting, October 1953.

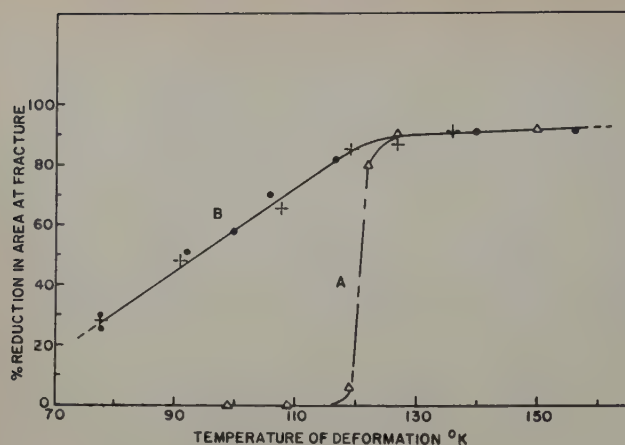


Fig. 2—Variation of the percentage of reduction in area at fracture with temperature of test.

Curve A—For specimens of iron A. Curve B—For specimens of iron B.

tension in the specimen as possible. The stress was applied to the specimen by lowering the crosshead, and so the lower grip B, at a constant speed of 0.05 in. per min.

The temperature of the specimen was controlled by the coil assembly shown in inset b. This was a split brass cylinder onto which $\frac{1}{8}$ in. ID copper tube was soldered as shown. Cold evaporated nitrogen gas was passed through the assembly by immersing one end of the tube (this section of the tube was lagged) in liquid nitrogen. The other end of the coil was joined to the laboratory vacuum line by a Hooke valve. By setting this valve, the rate of gas flow and therefore the temperature could be controlled manually to within $\pm \frac{1}{2}^{\circ}\text{K}$ with ease.

The temperature gradient along the specimen was checked by placing a dummy specimen in position, which had copper-constantan thermocouples soldered to it at 1-in. intervals. The gradient along the specimen was found to be 3°K with a maximum deviation from the mean of 1.75°K . This was regarded as being satisfactory for this investigation.

Experimental Results

Ductility: As the testing temperature of iron A specimens was decreased, the ductility, as measured by the percentage of reduction in area of fracture, remained nearly constant, until between 127° and 119°K it suddenly dropped to zero. Curve A, Fig. 2 shows the plot of the percentage of reduction of area vs testing temperature in this temperature range. Direct observation of the fractured surface on a specimen deformed below 124°K showed apparently a wholly cleavage type of fracture. However, if a longitudinal section was taken through the fracture, grain boundary failure as well as the cleavage failure could be seen. Fig. 3a shows the region adjoining a

fractured surface in which fracture also started, it can be seen to follow the grain boundary. Fig. 3b shows a section through a fracture, which was nickel plated before sectioning, the intercrystalline as well as cleavage nature of the fracture can be seen clearly. This sudden onset of brittleness also occurred if the specimens were quenched from 700°C after the vacuum anneal instead of being slowly cooled.

As the testing temperature of iron B specimens was decreased there was no sudden loss in ductility corresponding to that in specimens of iron A. However, at approximately the same temperature the ductility started to decrease steadily. Curve B, Fig. 2 shows a plot of the percentage of reduction in area vs temperature of deformation for iron B.

Neumann Lamellae: Below 125°K the stress-strain curve became serrated and the deformation in this serrated region was accompanied by a series of characteristic "sharp" sounds, similar to a sharp rifle "crack." Curves a, b, and c of Fig. 4 show typical stress-strain curves in this temperature region. Metallographic examination of specimens after deformation revealed that below 125°K decreasing the temperature of deformation increased the number of Neumann lamellae. The end of the serrated region of the stress-strain curve was found to coincide with the cessation of the characteristic sound of deformation and there was no discernible increase in the number of Neumann lamellae present in the specimen after the end of the serrated region of the stress-strain curve.

The rate of work hardening of a specimen was affected quite markedly by the temperature of deformation below 125°K . Fig. 4, curves a, b, and c, shows stress-strain curves for specimens deformed at 77.2° , 96.5° , and 124°K , respectively. It can be seen that the lower the deformation temperature, and so the greater the amount of deformation occurring by the formation of Neumann lamellae, the greater is the rate of work hardening. It can also be seen from these curves that there is a change in the rate of work hardening coincident with the end of the serrated region. This change is more marked the lower the deformation temperature.

Fig. 5 shows a plot of yield stress, as defined by a 0.1 pct proof stress, vs temperature of deformation. The curve shows a definite approach to a constant value of the yield stress below 120°K .

If iron A was carburized to a value as little as 0.004 pct C, it no longer exhibited the sudden loss of ductility at 125°K . The curve of the percentage of reduction in area vs temperature of deformation followed that for iron B (curve B, Fig. 2). The curve for lower yield stress vs temperature of deformation was of the same form as for iron B. However, the curve was displaced along the stress axis toward higher stress due to the carbon content. The

Table I. Analyses of Iron Used

Iron	Analysis, Wt Pct											
	Al	Cu	Mg	Ni	Si	Ag	Mn	Co	Be	C	N	O
A	0.001	0.001	—	0.05*	0.008	—	0.001	—	—	0.005	0.0005†	0.021†
B	0.005	0.0008	0.0005	0.002	0.005	N.D.	N.D.	N.D.	N.D.	0.002	0.0005†	0.0034†

* Wet analysis.

† Vacuum fusion analysis. All other determinations spectrographic.

N.D. Not determined.

These analyses were made on specimens as tested, after all heat treatments were carried out.



Fig. 3a—Area near fracture in specimen of iron A tested at 105°K. X60. Area reduced approximately 60 pct for reproduction.

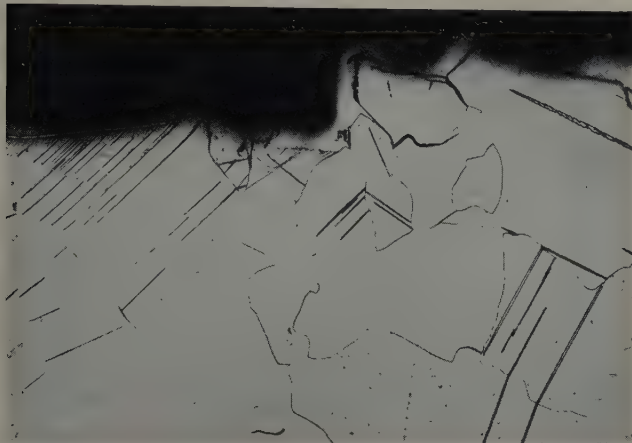


Fig. 3b—Section through fracture in specimen of iron A tested at 109°K. X200. Area reduced approximately 60 pct for reproduction.

removal of the sudden loss in ductility by carburizing occurred whether the carbon was retained in solid solution by quenching from 730°C, or precipitated as carbide, as determined by the disappearance of the carbon internal friction peak.

Lüders Bands: After complete decarburization a small yield point and yield point elongation could still be observed in specimens of both iron A and B tested at temperatures above 125°K, see Fig. 4 curve d for iron B. However, the yield point elongation was small, only ~ 1 pct, as compared with the carburized specimens which had a yield point elongation of 7 to 8 pct in this temperature range. This small yield point is attributed to oxygen in solid solution and confirms the observations of Boulanger.⁸ Boulanger⁴ has since shown the existence of an internal friction peak in iron due to oxygen which would also indicate that this yield point is due to oxygen in solid solution. No Lüders bands were detected in these specimens.

In specimens of iron A carburized to 0.006 pct C, the Lüders bands were very pronounced. Examination of specimens deformed above 125°K showed that a Lüders band was always initiated at each grip, the boundary between the deformed and undeformed regions being propagated toward the center of the specimen. However, during deformation below 125°K (the temperature for the onset of Neumann lamellae formation) the number of Lüders bands formed increased. Many Lüders bands were formed along the length of the specimen, in addition to those initiating at each grip. The stress-strain curve during the yield point elongation was also serrated, as was the case in the initial part of the stress-strain curves of iron B tested in this temperature range.

All the Neumann lamellae were found to be pro-

duced during the yield point elongation; there was no change in the number of Neumann lamellae present in specimens whose deformation was stopped at the end of the yield point elongation and those which were deformed until fracture occurred. Secondary evidence to support this conclusion is that the characteristic sound accompanying Neumann lamellae formation also ceased at the end of the yield point elongation.

Below 125°K the magnitude of the yield point elongation of carburized wires was found to decrease with decreasing temperature of deformation. The percentage of yield point elongation vs temperature of deformation is shown in Fig. 6. The form of this curve is similar to that of Fig. 2 (curve B) where the percentage of reduction in area vs temperature of deformation is plotted.

The yield point and yield point elongation occurring in decarburized specimens of iron B when tested above 125°K was completely removed when the specimens were tested below this temperature. This is illustrated by the stress-strain curves of Fig. 4.

Deformation of Single Crystals: A number of single crystals, 3 to 4 cm long, were grown in specimens of iron A by the strain-anneal method. The specimens tested, therefore, consisted of a number of single crystals in a "bamboo" type structure. In some cases the single crystals were separated by a large grained polycrystalline region approximately ½ cm in length.

After a standard decarburizing treatment the single crystals were found to be quite ductile down

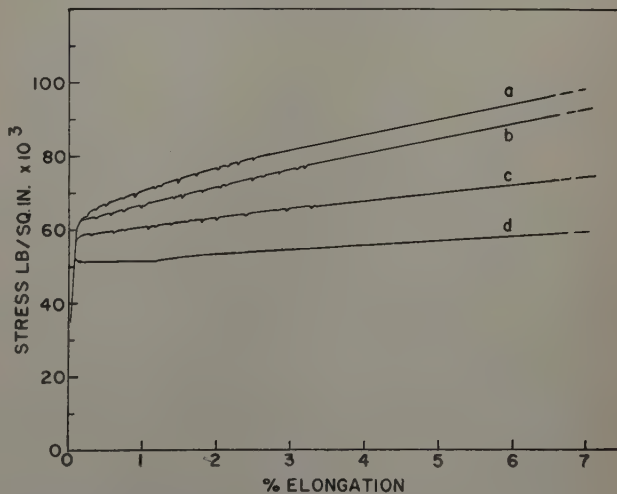


Fig. 4—True stress-strain curves for specimens of iron B tested as follows: a—77.2°K, b—96.5°K, c—124°K, d—150°K.

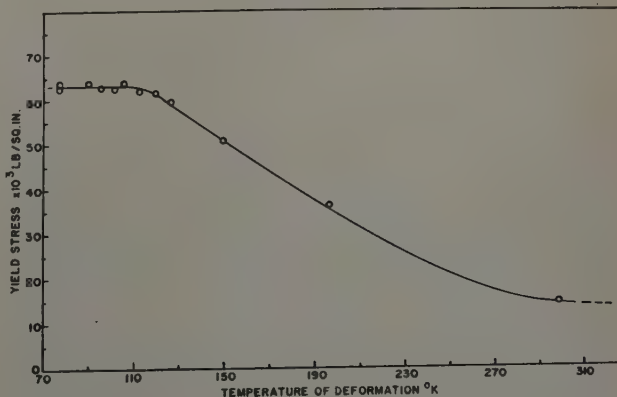


Fig. 5—Variation of yield stress with temperature of deformation for iron B.

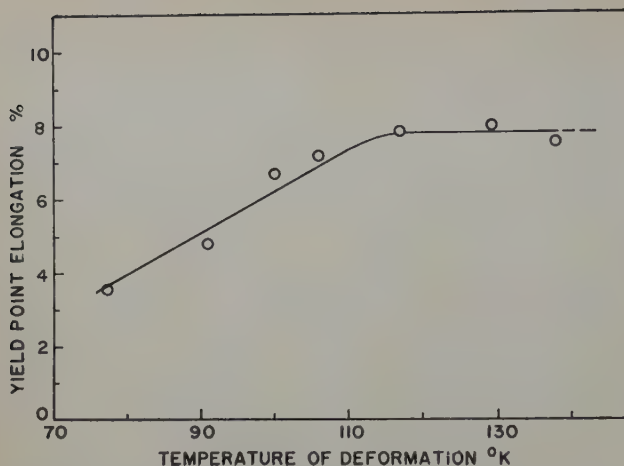


Fig. 6—Variation of percentage of yield point elongation with temperature of deformation for carburized specimens of iron A.

to 77.2°K and the stress-strain curve showed no evidence of a yield point. The fracture was a typical, single-crystal wedge-type fracture, the percentage of reduction in area at the fracture being ~ 95 pct. The stress-strain curve was serrated and the characteristic sound was emitted during the early stages of the deformation, as was the case in the polycrystalline specimens of iron B. Fig. 7 is a longitudinal section through a single crystal after deformation showing the Neumann lamellae.

Crystallographic Relations of the Neumann Lamellae: The orientation and crystallographic relationship of Neumann lamellae has been studied in silicon ferrite by Harnecker and Rassow⁵ and Mathewson and Edmunds⁶ by microscopic and X-ray reflection methods, respectively. However, it was felt that their evidence was inconclusive.

The crystallographic plane and direction of shear of the lamellae was determined from single-crystal wires and found to be the $\{112\} \pm \frac{1}{2}^\circ$ and $\langle 111 \rangle \pm 4^\circ$, respectively. A technique similar to that used by Bowles,⁷ to determine the crystallographic relationship of martensite, was used to determine the angle of shear and decide if the lamellae were twins. The angle was found to coincide within $\pm 3^\circ$, the angle predicted by twinning theory.*

* After this work was completed, Paxton⁸ reported on a similar analysis which agrees with results given here.

Effect of Prior Deformation at Room Temperature: A specimen of iron B was elongated by 4 pct at 300°K and then tested immediately at 109°K. The stress-strain curve was quite smooth with no serrations and the noise during deformation was absent. A micrograph of such a specimen showed complete absence of Neumann lamellae. This phenomenon has been observed previously by Pfeil.⁹ After annealing such a specimen for several days at room

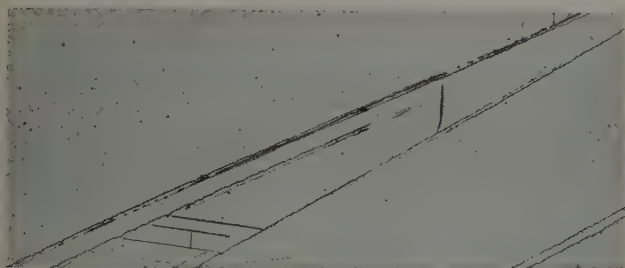


Fig. 7—Micrograph of Neumann lamellae in a single crystal of iron A tested at 77.2°K. X60. Area reduced approximately 60 pct for reproduction.

temperature, no Neumann lamellae were produced on deformation below 125°K. However, if the specimen was annealed at 100°C for 14 hr, after 4 pct elongation at 300°K, and then tested below 125°K, the Neumann lamellae formation partially returned. The serrations on the stress-strain curve and noise during deformation also returned.

A specimen of iron A was deformed at 300°K prior to testing at 109°K and the specimen exhibited some ductility ~ 45 pct, as measured by the percentage of reduction in area at the fracture. As in the case of iron B there was no evidence of Neumann lamellae formation.

Discussion

In iron A, which exhibits the sudden onset of brittleness, fracture occurs by rupture, at least in part, along the grain boundaries. It has also been shown that a single crystal is completely ductile. It is evident, therefore, that the brittleness is intimately associated with the grain boundaries. As the two series of iron used only differ in their oxygen content, it seems justifiable to correlate the removal of this low temperature brittleness, in iron B, with the decrease in oxygen content. This agrees with the recent work of Rees and Hopkins¹⁰ who found that intercrystalline failure started to occur if the oxygen concentration was greater than ~0.003 pct. This leads to the conclusion that the oxygen must be associated with the grain boundaries and in some manner cause failure along these boundaries. One question to be decided, therefore, is whether the oxygen at the grain boundary is in solid solution or present as a second phase.

The most recent value for the solid solubility of oxygen in α iron at 700°C is given as ~ 0.01 pct by Ziegler.¹¹ This value may be expected to be an over estimate, however, because it was near the limit of accuracy of his experimental procedure. This value for the oxygen solubility indicates that the oxygen concentration in iron B is below and that in iron A above the solubility limit. Oxygen may be expected to be present at the grain boundary as an oxide phase, therefore, in iron A.

Examination of metallographic specimens by the light or electron microscope showed no evidence of the existence of a second phase at the grain boundary. This, however, cannot be regarded as positive evidence that it was not present. An examination under the microscope of the fractured surfaces with polarized light, showed regions, on exposed grain boundaries, which exhibited bi-refringence. These regions showed extinction at 90° intervals, which would correspond to Fe_2O_3 .¹² However, since it was impossible to view a relatively large flat field, this extinction could have been spurious and due to geometric factors.

Positive evidence of a difference in the grain boundary behavior between the two irons was, however, given by internal friction measurements. The internal friction of the wires was determined using the torsion pendulum developed by Kê.¹³ Curve A, Fig. 8 shows the grain boundary peak for a specimen of iron A which had been quenched from the decarburizing treatment. Curve B, Fig. 8 shows the peak obtained for iron B after an identical treatment. The temperature at which the maximum of the peak occurs has been shifted from 580°C in iron A to 460°C in iron B, and the magnitude of the peak lowered in the case of iron B. Due to the difference in grain size of the two irons, a small difference

in the temperature at which the maximum of the peak occurs would be expected.¹⁴ However, this change should only be $\sim 20^\circ$ to 30°C and in the opposite direction to that in which it occurred.

The shift in the temperature at which the peak maximum occurs means that the time of relaxation for a shear stress across the grain boundary has been markedly altered. There is no way of calculating whether the shear stress relaxation time for an oxide-iron interface would be greater or less than that for an iron-iron interface; therefore, no quantitative deductions can be made from these internal friction measurements.

If the oxygen is present as an oxide at the grain boundary, there is no reason why the oxide alone should be responsible for the brittleness, because at temperatures down to 125°K the grain boundary has deformed "normally." The sudden onset of brittleness is, however, coincident with the beginning of deformation by twinning. It is suggested, therefore, that the combination of an oxide at the grain boundary and deformation by twinning may be necessary for the brittleness. A possible reason for this may be the rapid rate of formation of the twins, which would involve a rapid rate of deformation at the oxide-iron interface and so permit the formation of "microcracks." Whereas, when deformation occurs by glide there may be sufficient time for the stresses at the interface to be accommodated in the iron matrix. There is some indication that this may be the case, since when twin formation is suppressed by prior deformation at room temperature, specimens of iron A do exhibit some ductility below 120°K .

The mechanism by which carburizing iron A removes the brittleness is uncertain. If an oxide is either directly or indirectly, the cause of brittleness, there would have to be a solid state reaction between carbon and oxygen at the grain boundary at 730°C , the carburizing temperature. Whatever the mechanism, however, it must be reversible, since decarburizing the specimen makes it brittle again.

It has been suggested^{15,16} that, because of the similarity between the atom movements in slip and twinning, it is logical to expect twinning during deformation to occur by a dislocation mechanism also, for the same reasons that they were proposed for slip. Cottrell and Bilby¹⁷ have postulated a dislocation mechanism for the growth of twins during deformation which involves the dissociation of a unit dislocation into two partial dislocations. This mechanism predicts that there should be a constant stress for the onset of twinning, being that stress required to form the initial interface. This has been shown to be the case, see Fig. 5, which shows that below the temperature at which twinning starts the yield stress becomes constant. In the case of one single crystal, which after deformation of about 1 pct exhibited only one active twinning system, it was possible to calculate the lower resolved critical shear stress for twinning, which was 37×10^8 lb per sq in.

The mechanism of Cottrell and Bilby also shows that twins could form in the order of microseconds, which has been shown to be the case experimentally for tin.¹⁸ The serrations on the stress-strain curve and the "sound" during deformation are considered to be caused by bursts of twins forming rapidly within the specimen.

The dislocation mechanism also gives an explanation for prior deformation at room temperature suppressing the formation of twins. During plastic deformation at room temperature many dislocation

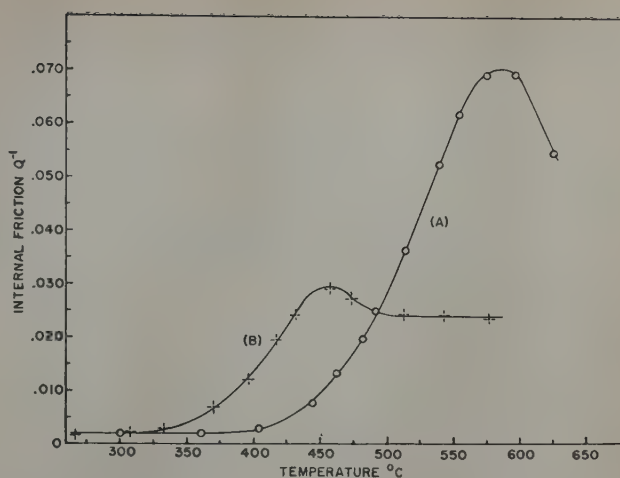


Fig. 8—Variation of internal friction with temperature. Curve A—For specimen of iron A. Curve B—For specimen of iron B.

lines will intersect each other, forming "jogs" in the dislocation line.¹⁹ Also, as is evident from the wavy nature of visible slip lines, dislocations move out of one glide plane into a neighboring plane. Both of these factors inhibit the dissociation of a unit dislocation into partial dislocations. Therefore, the formation of twins, which requires this dissociation into partial dislocations, would be stopped. Annealing for 14 hr at 100°C would allow some recovery to occur and so permit the dislocations to dissociate once more. Since an anneal at 100°C for 14 hr only allows a partial return of twin formation it indicates that the activation energy for the process is much greater than would be expected by an interstitial atom diffusion, such as carbon.

Summary

A study was made of the tensile deformation, between 300° and 77.2°K , of two samples of iron, containing 0.0034 and 0.021 pct O, respectively.

Iron containing 0.021 pct O becomes completely brittle below 120°K , the fracture being a combined intercrystalline and cleavage type. Ductility can be restored by carburizing to 0.006 pct C.

Iron containing 0.0034 pct O remained ductile down to 77.2°K ; however, the ductility slowly decreases between 125° and 77.2°K . At 125°K deformation starts to occur by the formation of Neumann lamellae, the number of lamellae produced increases with decreasing temperature.

Single crystals of iron containing 0.021 pct O are completely ductile down to 77.2°K .

Internal friction measurements on the grain boundary peak indicate a marked difference between iron containing 0.021 pct O and that containing 0.0034 pct O.

Deformation at 300°K prior to deformation below 125°K suppresses the formation of Neumann lamellae and restores ductility to iron containing 0.021 pct O.

The Neumann lamellae produced by deformation below 125°K are shown to be deformation twins.

It is considered that the brittle failure of iron containing 0.021 pct O is caused by a combination of the grain boundary oxide phase and deformation by twinning. The removal of twin formation by prior deformation can be explained by considering Cottrell and Bilby's mechanism for growth of deformation twins.

Acknowledgments

The author wishes to thank K. K. Ikeuye for pre-

paring the micrographs, E. D. Selmanoff for preparing the wire specimens, and A. Moskowitz for making the vacuum analyses.

References

- ¹ J. D. Fast: *Philips Research Reports* (1949) **4**, p. 370.
- ² L. J. Dijkstra: *Philips Research Reports* (1947) **2**, p. 357.
- ³ C. Boulanger: *Revue de Metallurgie* (1950) **47**, p. 547.
- ⁴ C. Boulanger: Private communication.
- ⁵ K. Harnecker and E. Rassow: *Ztsch. Metallkunde* (1924) **16**, p. 312.
- ⁶ C. H. Mathewson and G. H. Edmunds: *Trans. AIME* (1928) **80**, p. 311.
- ⁷ J. S. Bowles: *Acta Crystallographica* (1951) **4**, p. 162.
- ⁸ H. W. Paxton: *Acta Metallurgica* (1953) **1**, p. 141.
- ⁹ L. B. Pfeil: *Journal Iron and Steel Inst.* (1926) **15**, p. 319.

- ¹⁰ W. P. Rees and B. E. Hopkins: *Journal Iron and Steel Inst.* (1952) **172**, p. 403.
- ¹¹ N. A. Ziegler: *Trans. Amer. Soc. Steel Treatment* (1932) **20**, p. 73.
- ¹² *Metals Handbook* (1948) p. 449. Cleveland. ASM.
- ¹³ T. S. Kê: *Physical Review* (1947) **71**, p. 533.
- ¹⁴ T. S. Kê: *Physical Review* (1947) **72**, p. 41.
- ¹⁵ J. Frenkel and T. Kontorova: *Journal of Physical Chemistry* (1939) **1**, p. 137.
- ¹⁶ F. Seitz and T. A. Read: *Journal of Applied Physics* (1941) **12**, p. 470.
- ¹⁷ A. H. Cottrell and B. A. Bilby: *Philosophical Magazine* (1951) **42**, p. 573.
- ¹⁸ W. P. Mason, H. J. McSkimin, and W. Shockley: *Physical Review* (1948) **73**, p. 1213.
- ¹⁹ F. Seitz: *Advances in Physics. Quarterly Supp. Philosophical Magazine* (1952) **1**, No. 1.

Technical Note

A Corrected Interpretation of the Mechanism of Growth Of Magnetite During Oxidation

by M. H. Davies, M. T. Simnad, and C. E. Birchenall

THE marker movements observed by Davies, Simnad, and Birchenall¹ during the growth of magnetite on wüstite have been misinterpreted. It is the purpose of this note to correct the original interpretation.

In that investigation wüstite specimens were prepared by oxidizing pure iron disks in water vapor until the iron was consumed. Argon was used as a carrier gas for the water vapor and on the complete conversion of the metal to its oxides ('FeO' plus a small amount (10 pct) of surface Fe₃O₄) the water supply was bypassed and the specimens were annealed in argon alone in order to equilibrate the wüstite with the overlying magnetite.

After cooling, the magnetite was ground off, a crude magnetic test being employed to determine its complete removal. Radioactive silver streaks were then applied to the surface and the specimen was oxidized completely in water vapor to prevent hematite formation. After complete oxidation the markers were found to enclose about 80 pct of the magnetite with the other 20 pct lying outside the markers. This observation was interpreted to mean that oxygen transport was four times as great as iron transport during the growth of the magnetite. The conclusion would have been correct if, as in the case of wüstite growing on iron, all the iron had started from one side of the marker and all the oxygen from the other side initially.

Actually a material balance is required. For simplicity, take wüstite to be exactly FeO, and magnetite to be Fe₃O₄. Then at the start of the reaction

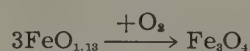


All of the iron and three-fourths of the oxygen of the final product will be within the marker inter-

faces. The other fourth of the oxygen is in the gas phase outside the marker.

From the experimentally determined final position of the markers simple calculation shows that one-fifth of the total iron has crossed the marker interface, while one-twentieth of the total oxygen has crossed in the reverse direction. The simplified result favors iron transport in the ratio four to one.

However wüstite is not stoichiometric FeO. At 900°C, the temperature of the measurement, the composition is about FeO_{1.13}. When the material balance for the same experimental result is repeated, assuming the product will be 1 mol of Fe₃O₄, it is found that 0.6 gram atoms of iron and 0.19 gram atoms of oxygen must have passed the marker in the same direction. (This is readily apparent from the reaction to form 1 mol of Fe₃O₄.



The total oxygen supplied from the atmosphere is 0.61 gram atoms, but the iron which passes the marker interface, i.e., 0.6 gram atoms, requires 0.8 gram atoms of oxygen to convert it to Fe₃O₄.)

If all the transport during magnetite growth is due to iron ion diffusion, then the marker would enclose about 85 pct of the final magnetite and the original measurement is in error by about 5 pct. This error is probably less than the uncertainty in locating the markers by autoradiography. The possibility also exists that the starting wüstite was not quite saturated with oxygen and underwent further enrichment with consequent envelopment of the marker before magnetite caught up with the marker interface.

In any case it appears that these measurements actually favor iron ion diffusion in magnetite overwhelmingly as the factor controlling its growth, although further experimental measurements are needed to eliminate the error in material balance described. Such studies are planned.

M. H. DAVIES is Physical Metallurgist, Fulmer Research Inst. Ltd., Stoke Poges, Bucks, England, M. T. SIMNAD, Junior Member AIME, is a Member of Staff, Metals Research Lab., Carnegie Institute of Technology, Pittsburgh, and C. E. BIRCHENALL, Junior Member AIME, is associated with the James Forrestal Research Center, Princeton University, Princeton, N. J.

TN 175E. Manuscript, June 8, 1953.

¹ M. H. Davies, M. T. Simnad, and C. E. Birchenall: *Trans. AIME* (1951) **191**, p. 889; *JOURNAL OF METALS* (October 1951).

Rate of Propagation of Martensite

by R. F. Bunshah and R. F. Mehl

A fast amplifier technique has been developed for the measurement of the rate of propagation of martensite in an Fe-29.5 pct Ni alloy. The time of formation of one plate of martensite is 3×10^{-7} sec and the rate of propagation is 3300 ft per sec approximately.

IT has been known for some time that the plate-like structural unit of martensite forms from austenite with great rapidity. Wiester¹ and Hanemann, Hofmann, and Wiester² took motion-pictures of the transformation as it occurs in a 1.65 pct C steel; they demonstrated that a single plate formed fully in the time interval between successive frames, viz., 1/20 sec, thus setting an upper limit. Förster and Scheil,³ using an Fe-Ni alloy with 29 pct Ni, recorded the sonic characteristics of the process electrically, upon an oscillograph, setting the upper time limit at 0.002 sec. Förster and Scheil,⁴ measuring the change in electrical resistance in the same alloy upon a cardiograph, set a limit of 0.02 sec. Förster and Scheil⁵ later, employing the same alloy, improved their technique, reporting an upper limit of $7 \cdot 10^{-5}$ sec. In studying signals of such short duration, it is an important question whether the frequency response of the electrical system used is high enough compared to frequency of the pulse measured, or, put differently, whether the system is able to reproduce without distortion the signal arising, in this case, from the formation of a single martensite plate. Förster and Scheil (referring only to their last paper) obtained signals of a frequency of 30 kilocycles (hereinafter kc); this was about the frequency response of the equipment used; thus, if the signal had a frequency higher than 30 kc, it would still appear as a signal of frequency 30 kc. All of these results thus provided upper limits only.

Recent developments in electronics have made available equipment with very high frequency response, very high sweep-speeds, high gain, etc. The electrical characteristics of such equipment, used in the present study, are given in Table I. Such equipment offers obvious attraction in the study of

the rate of propagation of a martensite structural unit—and perhaps of other structural alterations proceeding at a very high rate.

This paper reports an attempt to develop a technique employing such equipment to measure the time of propagation of a martensite structural unit and the variation of this with temperature, with the mode of formation—athermal and isothermal—in both polycrystalline and single-crystal samples; and from such measurements to obtain the rate of propagation. As will be seen, the results obtained are useful theoretically.

Materials

All data presented here are for an Fe-Ni alloy of the following analysis: 29.5 pct Ni, 0.027 pct C, 0.135 pct Mn, 0.094 pct Si, balance Fe. There were several reasons for choosing this alloy: 1—it is substantially the one used by previous investigators; 2—it exhibits both the athermal⁶ and the isothermal⁷ mode of formation of martensite, both studied in detail by Machlin and Cohen; 3—the subzero temperatures of transformation in this alloy are experimentally very convenient; 4—it exhibits the “burst phenomenon”;⁸ 5—the change in electrical resistance upon the formation of martensite, a decrease, is great, approximately 50 pct.⁹

The polycrystalline specimens were in the form of wires of 0.025 in. diameter; the single crystals were $1 \times \frac{1}{4} \times \frac{1}{4}$ in.

Experimental Methods

Electrical Apparatus: Fig. 1 is a schematic drawing of the electrical circuit used. The principle used in these measurements is the same as that used by Förster and Scheil.⁵ A small direct current, about 1 to 2 amp, is passed through the sample. When a martensite plate forms, the resistance of the sample changes and a high frequency signal is generated. This signal is picked up by the probes attached to the sample, fed into the bank of amplifiers and thence to the vertical deflection plates of a cathode-ray oscilloscope. The signal itself triggers the oscilloscope trace which flashes across the tube face and is photographed by means of a 35 mm movie camera at the end of a light-tight hood. The camera has no shutter. As soon as the signal flashes

R. F. BUNSHAH, Junior Member AIME, is Research Associate, Metals Research Laboratory, and R. F. MEHL, Member AIME, is Head of Dept. of Metallurgical Engineering and Director, Metals Research Laboratory, Carnegie Institute of Technology, Pittsburgh.

Discussion on this paper, TP 3604E, may be sent, 2 copies, to AIME by Dec. 1, 1953. Manuscript, April 13, 1953. Cleveland Meeting, October 1953.

This paper is based on a thesis by R. F. Bunshah submitted in partial fulfillment of requirements for the degree of Doctor of Science to Carnegie Institute of Technology, June 1952.

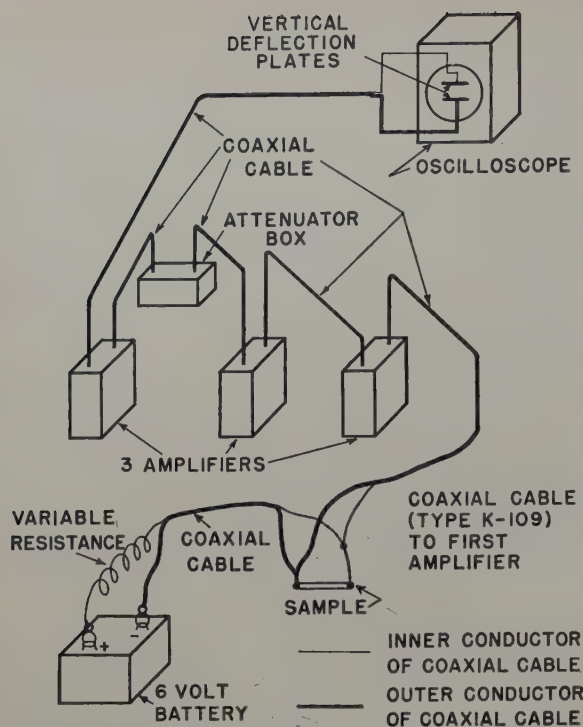


Fig. 1—Schematic representation of the electrical circuit.

across the screen, it is photographically recorded, and the film is moved one frame forward by the experimenter, so that the set-up is ready for recording the next signal. The movie camera used in this single-shot fashion is very convenient for the purpose of recording transient signals occurring in very rapid succession. Appendix I deals with the electrical apparatus and its workings in greater detail.

Metallurgical Apparatus and Procedure: The temperature range for the formation of martensite in this alloy is -20° to -200°C . Athermal martensite was formed in the apparatus shown in Fig. 2. The sample resting in one of the lucite holders was lowered gradually toward liquid nitrogen in the bottom of a Dewar flask. The temperature of this sample could not be measured directly, since a thermocouple circuit attached to the sample would completely upset the electrical circuit; accordingly, an identical dummy sample, resting in the twin lucite holder, positioned similarly with respect to the bath served this purpose, with the temperature

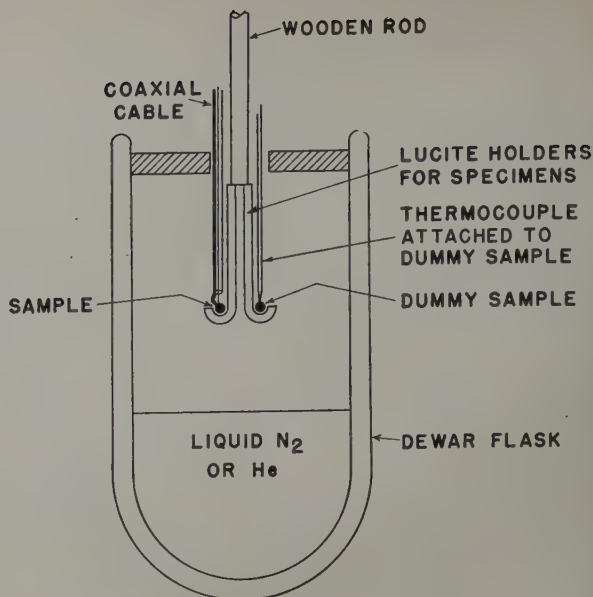


Fig. 2—Apparatus for subzero temperature experiments.

measured by a copper-constantan thermocouple; a check experiment showed the temperatures of the two samples to differ by no more than 3°C . The apparatus used to study the formation of isothermal martensite was similar to that employed by Das

Table II. Austenitizing Treatments and Resulting Grain Diameters in an Fe-30 Pct Ni Alloy

	Austenitizing Time, $^{\circ}\text{C}$	Austenitizing Time, Hr	Resultant Average Grain Diameters, In.
A	1300	18	0.01
B	1100	2	0.005-0.007
C	900	$\frac{1}{2}$	0.001

Gupta and Lement;⁹ it is essentially a nichrome-wound furnace with liquid nitrogen on the outside, maintaining the outside temperature at -196°C ; the specimen was inserted in an inner tube containing iso-pentane (melting point -155°C); the generation of heat by the nichrome winding is thus set against the loss of heat to the liquid nitrogen; the temperature can be raised, or lowered, or maintained constant.

Table I. Electrical Characteristics of the Equipment Used

	Chain Pulse Amplifier Type 202	Chain Pulse Amplifier Type 214	Oscilloscope Type 517
Manufacturer	Spencer-Kennedy Labs. Cambridge, Mass.	Spencer-Kennedy Labs. Cambridge, Mass.	Tektronix, Inc. Portland, Oregon
Band-width (frequency response)	40 kc to 80 mc	100 kc to 200 mc	200 cycles — 75 mc
Gain	30 db \pm 215 db	20 db \pm 1 db	
Sweep speeds			20 microseconds per cm to 10 millimicroseconds per cm
Accelerating potential			24,000 v

Definitions of Symbols:

kc = kilocycle; mc = megacycle = 10^6 cycles = 1000 cycles
db = decibels
1 microsecond = 10^{-6} second; 1 millimicrosecond = 10^{-9} second

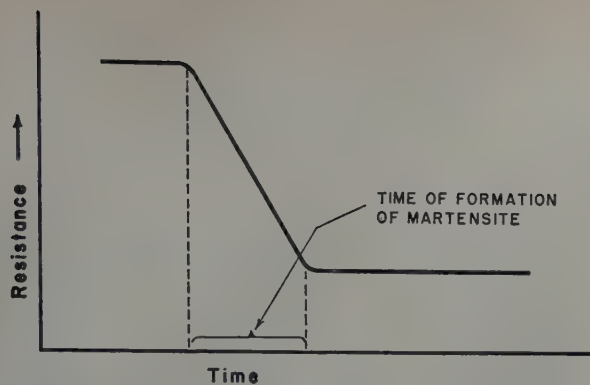


Fig. 3—Idealized picture of an oscilloscope trace during the martensite transformation.

Samples of the alloy wire were cut into 2-in. lengths and sealed in Vycor tubes in purified argon. These samples were austenitized at the temperatures and at the times shown in Table II; they were then water-quenched, and were found to be completely austenitic. The diameters of the austenite grains were measured, and are recorded in Table II.

Experimental Results

General Observations: The resistance of the martensite is lower than that of the austenite in an Fe-30 pct Ni alloy. The signal resulting from the unit martensitic transformation should thus be negative, as shown in Fig. 3, i.e., the resistance decreases with time. Strangely enough, this was never observed. Fig. 4 shows a photograph of the signal resulting with the sweep-speed set at 50 millimicroseconds per cm and the trigger on "positive signal." It is seen that the resistance of the sample first increases to a maximum and then decreases to a value lower than the initial ambient level. In order to determine whether this initial increase in resistance during the transformation is actually a part of the process of formation of a structural unit of martensite or is some other effect not connected with the martensitic transformation,

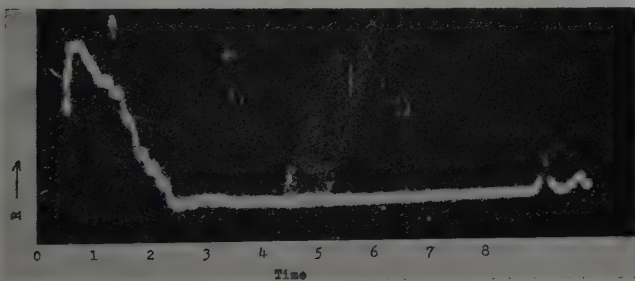


Fig. 4—Photograph of the oscilloscope screen during the martensite transformation. Each division corresponds to 50 millimicroseconds. Positive signal trigger.

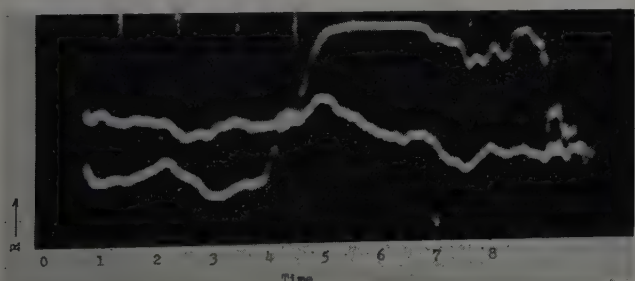


Fig. 5—Photograph of the oscilloscope screen during the martensite transformation. Each division corresponds to 100 millimicroseconds. Negative signal trigger.

the following experiment was performed: The oscilloscope was set to trigger on "negative signal" and the signals resulting from the martensitic transformation photographed, an example of which is shown in Fig. 5, which shows two consecutive traces on one frame of the film. It may be noted that the initial part of the signal consisting of the increase to the maximum and the subsequent decrease to the initial ambient level is missing. The signal triggered the sweep only on going negative. Thus the initial increase is not a characteristic of the apparatus *per se*.

It may be concluded that the signal resulting from the formation of a martensite plate in an Fe-30 pct Ni alloy consists of an initial increase in resistance of the sample up to a maximum value and a subsequent decrease to a value below its initial ambient level. Hereinafter, the term "pulse cycle" will refer to the complex signal described above.

The time of formation of a plate of martensite corresponding to one pulse cycle is 1.10^{-7} sec from Fig. 4.

Figs. 6, 7, and 8 show signals resulting from the martensitic transformation with sweep speeds varying from 50 to 200 millimicroseconds per cm and "positive signal" trigger setting. These figures show a large number of pulse cycles following each other;

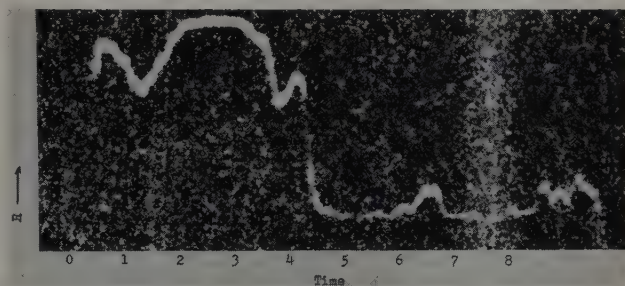


Fig. 6—Photograph of the oscilloscope screen during the martensite transformation. Each division corresponds to 50 millimicroseconds. Positive signal trigger.

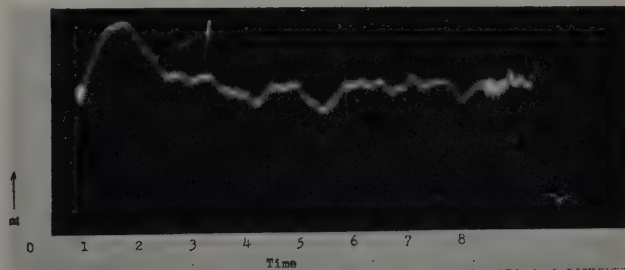


Fig. 7—Photograph of the oscilloscope screen during the martensite transformation. Each division corresponds to 100 millimicroseconds. Positive signal trigger.

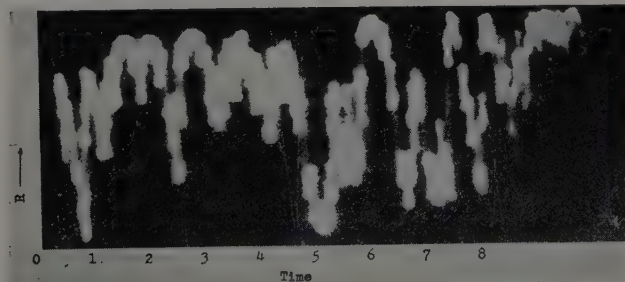


Fig. 8—Photograph of the oscilloscope screen during the martensite transformation. Each division corresponds to 200 millimicroseconds. Positive signal trigger.

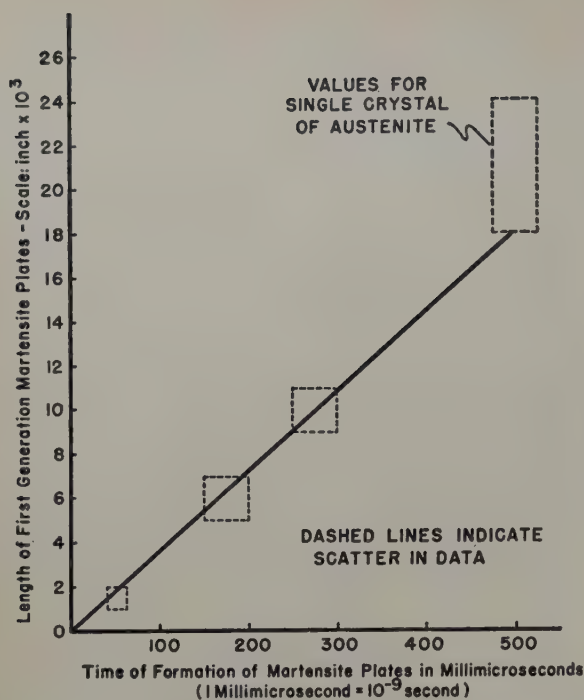


Fig. 9—Plot of first generation martensite plates vs their time of formation.

in most cases, the pulse cycle due to one martensite plate is superimposed in time on the one from the previously formed plate. The error due to this superposition is about $\pm 0.3 \times 10^{-7}$ sec, as can be seen from the fairly steep slopes of the traces. From an analysis of about 200 such oscilloscope traces, the time of formation of a plate of martensite varies from 5.0×10^{-7} to 0.5×10^{-7} sec depending on the size of the martensite plate formed, as will be seen.

These signals correspond to a frequency of 10 megacycles. From Table I, it can be seen that the system responds to frequencies up to 75 megacycles. Thus, the signals resulting from the martensitic transformation are well within the frequency response of the apparatus used and represent an undistorted or true value for the time of formation of martensite, i.e., this is the first measurement of the lower limit in time. The experimental error in measurement due to the electrical measuring system is ± 5 pct.

Thus far, it has been tacitly assumed that each pulse cycle corresponds to the formation of one structural unit of martensite. The large number of pulse cycles observed and their superposition in time may be considered as indirect evidence of this. The following type of critical experiment was performed to check the validity of this assumption. The martensite transformation in a large-grained austenitic sample was allowed to proceed until only a very small amount of martensite had formed, with further transformation prevented by "up-quenching" to room temperature. The entire sample (1 in. long and 0.025 in. in diameter) was polished across the medial longitudinal section and etched and the number of martensite plates counted. A count of the number of pulse cycles in the oscilloscope photographs taken was also made. The two counts differed by about 3 to 4 in a total of about 20. This appears to be fairly satisfactory evidence that each pulse cycle corresponds to a single martensite plate. More direct proof though possible would be unwarrantedly laborious.

Interrelationship Between Size of Martensite Plates, Their Time of Formation, and Signal Strength: As is well known, the first generation of martensite plates traverse the entire austenite grain (provided it is not large) until their growth is stopped at discontinuities of the lattice-like grain boundaries, twin interfaces, and inclusions, etc.

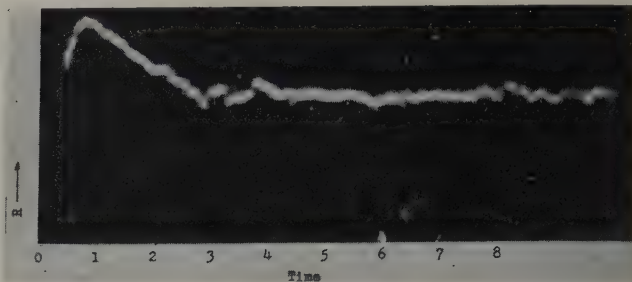


Fig. 10—Photograph of the oscilloscope screen during the martensite transformation. Each division corresponds to 100 millimicroseconds. Positive signal trigger. Isothermal run at -90°C .

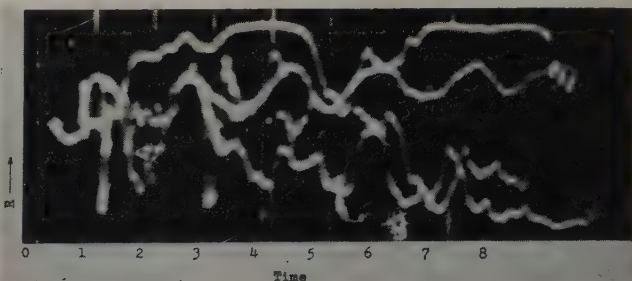


Fig. 11—Photograph of the oscilloscope screen during a "burst" in polycrystalline and single crystal specimens. Each division corresponds to 100 millimicroseconds. Positive signal trigger.

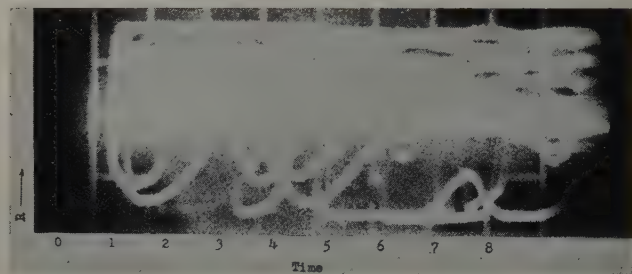


Fig. 12—Photograph of the oscilloscope screen during a "burst" in polycrystalline and single crystal specimens. Each division corresponds to 200 millimicroseconds. Positive signal trigger.

Thus, it may be assumed that the length of the martensite plate is approximately the same as the diameter of the austenite grain for the first generation of martensite plates. Austenitic samples of this alloy with grain diameters varying from 0.001 to 0.01 in. were prepared by the heat-treatments given in Table II. They were transformed to martensite and the time of formation of the first generation martensite plates measured. Single-crystal austenite specimens were also transformed and the time of formation of first generation plates measured. (It may be noted that there appears to be a limiting size to the martensite plates formed in a single crystal of austenite, as has been also observed by Kurdjumov¹⁵ and Machlin and Cohen.⁶ Fig. 9 shows a plot of length of first generation martensite plates vs their time of formation. It may be noted that the plot is linear, thus indicating that the overall process of the propagation of martensite is a constant velocity process. The experi-

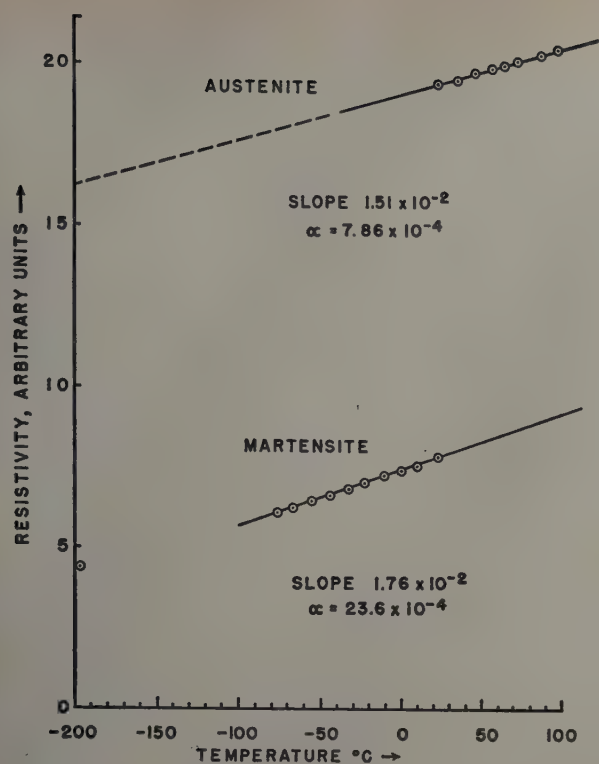


Fig. 13—Resistivity of a 71 pct Fe-29 pct Ni alloy as a function of temperature.

mental scatter is $\pm 0.25 \times 10^{-7}$ sec on the time scale and 1.10^{-8} in. on the length scale, as may be seen from Fig. 9.

The average slope of the straight line drawn through the data which is a measure of the rate of propagation of martensite is 3300 ft per sec or 100,000 cm per sec, approximately. The maximum error in the rate of propagation due to the scatter in data is about ± 20 pct.

It was also observed that the signal strength resulting from the martensite transformation varies directly with the size of the martensite plate formed.

Influence of Temperature on the Athermal Transformation: The time of formation of a martensite structural unit was measured from -20° to -195°C and was found to be of the order of 10^{-7} sec throughout this temperature range. The variation was from about 3.10^{-7} sec at -20°C to 0.5×10^{-7} sec at about -195°C for specimens with initial austenite grain size 0.01 in. This does not represent a change in the velocity of propagation however. It may be seen from Fig. 9 that this decrease in the time of formation at lower temperatures can be accounted for by the decrease in size of the martensite structural units with decrease in temperature as a result of the partitioning of the parent austenite by the prior formation of martensite. Thus the velocity of martensite propagation is independent of the temperature of transformation within the temperature range -20° to -195°C ; the maximum error due to the scatter in experimental data is ± 20 pct.

Isothermal Transformation: The time of formation of isothermal martensite at four different reaction temperatures, -60° , -90° , -105° , and -195°C was measured, and found to be of the order of 10^{-7} sec. About 10 runs were made at each temperature. Fig. 10 shows a photograph of the oscillo-

scope trace during an isothermal run at -90°C . The pulse cycle has identical characteristics with those occurring during the athermal transformation.

The Burst Phenomenon: Machlin and Cohen⁶ define the burst phenomenon as a large amount of martensite ($> \frac{1}{2}$ pct) forming in the time interval of an audible click. This phenomenon was observed and photographs of the oscilloscope screen taken during a "burst" are shown in Figs. 11 and 12. The very large number of pulse cycles on one frame of the movie film show very graphically that the "burst" consists of a large number of martensite structural units forming in a very small period of time, the reaction occurring in a cataclysmic or autocatalytic fashion; presumably the stresses caused by the formation of one plate nucleate the succeeding ones.

Discussion

On the Nature of the Pulse Cycle: The pulse cycle corresponding to the formation of a plate of martensite consists of an initial increase of the resistance to a maximum followed by a subsequent decrease to below the initial level. The initial increase is new. The overall decrease in resistivity is in accord with expectations for this alloy. Several explanations may be advanced for the initial anomalous increase:

1—The austenite-martensite transformation is accompanied by the evolution of heat. The resistance of a metal characteristically increases with

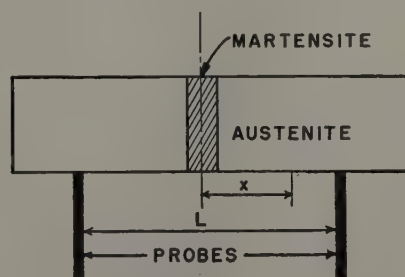


Fig. 14—Representation of boundary conditions for problem considered in Appendix II.

increasing temperature; thus, the sudden release of the latent heat in the localized region of the specimen transformed to martensite might account for this initial increase in the resistance of the sample.

This argument would be valid only if the amount of heat liberated would be sufficient to cause the observed increase in resistance, and if the flow of heat from the localized region was rapid enough to account for the subsequent decrease in resistivity.

Smithells¹⁰ gives the latent heat of transformation of austenite to martensite in a 0.9 pct C steel as 500 cal per gram-atom, and that of the transformation of $\gamma \rightarrow \alpha$ iron at 720 cal per gram-atom. For an Fe-30 pct Ni alloy, it will be assumed that the latent heat of transformation is 720 cal per gram-atom or 13 cal per gram as an upper limiting value. The specific heat of this alloy is 0.119 cal per gram per $^\circ\text{C}$.¹¹ Thus, the temperature rise corresponding to the liberation of 13 cal per gram-atom is $13/0.119$, or roughly 110°C .

Fig. 13 shows the resistivity vs temperature curves for samples of Fe-30 pct Ni alloys in the 100 pct austenitic and martensitic (about 90 pct

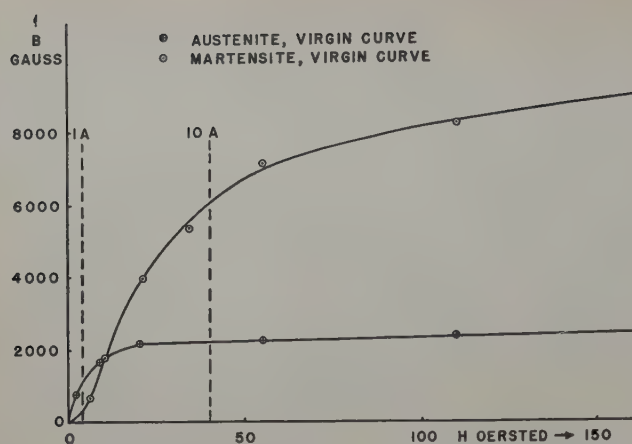


Fig. 15—Magnetization curves for a 71 pct Fe-29 pct Ni alloy.

martensite) states.¹² It will be assumed that a martensite plate forms completely across the cross section of the wire as shown in Fig. 14. This assumption is obviously biased to favor the argument. From Fig. 13, it may be seen that the increment in resistance of the newly formed martensite structural unit on being raised in temperature by 110°C would not even increase its resistance to a value corresponding to that of the same volume of the austenite, whereas an overall increase in resistivity is observed. A rough calculation based on the slope of the plots in Fig. 13 and the pulse cycle shows that a heating of about 1500°C would be required to validate the argument. Thus, the localized liberation of latent heat of transformation to the martensite unit alone cannot account for the initial increment of resistance observed.

It may be argued that the flow of heat from martensite to austenite would account for the subsequent decrease observed in the pulse cycle, since the temperature coefficient of resistance of austenite is one-third that of martensite. However, as the slopes of the resistivity vs temperature plots for austenite and martensite and their relative specific heats are almost the same, the decrement in the resistance of the sample due to a fraction of the heat flowing from the martensite to the austenite would approximately balance the increment of the resistance of the austenite caused by this heat transfer. Thus, the decrease in resistance observed in the pulse cycle cannot be explained as due to the flow of heat from martensite to austenite, even in the very small time observed for this decrease, viz., 10^{-7} sec. The calculation illustrated in Appendix II shows that the decay time, τ , for one-half of the initial quantity of heat to flow past the probes is 41 sec which is much too long for the time observed for the decrease in resistance, viz., 10^{-7} sec.

Thus the localized heating of the martensite structural unit formed cannot account for the pulse cycle observed for the formation of this structural unit of martensite.

2—Stresses increase the electrical resistance of metals and alloys. Wheeler and Jaswon¹³ have estimated an average value of 93 tons per sq in. for the microstresses in a structure consisting of martensite and retained austenite in Fe-C alloys. It might be argued that the very high microstresses occurring during the formation of martensite cause the initial "anomalous" increase in resistance of the sample, and that these stresses are subsequently

relieved by the plastic flow of the matrix thus permitting the resistance to decrease to the level for martensite.

From Fig. 13, it is seen that the resistance of austenite is 2 to 3 times greater than that of martensite, the variation depending upon the temperature. From the pulse cycle, it may be observed that the initial increment in resistance is roughly of the same order of magnitude. Thus it appears rather unlikely that the stresses due to the formation of one structural unit of martensite could increase the resistance of the sample by 4 to 6 times the value of the resistance of martensite.

3—It has been suggested, on the basis of rough calculations, that this initial increase may be due to a part of the sample going from a very low ferromagnetic state (austenite) to one which is highly ferromagnetic (martensite). As this transformation occurs in a very short time interval, the sudden change in the distribution of the magnetic lines of force causes a temporary apparent increase in the resistance of the sample, which may account for the initial increase in resistance observed in the pulse cycle. The following critical experiments led to the abandonment of this possibility:

Fig. 15 shows the B-H curves of fully austenitic and fully martensitic (90 pct martensite approximately) for an Fe-30 pct Ni alloy as obtained in this laboratory by the use of a Koepsal permeameter.¹² It may be noted that the curves cross each other, i.e., below a field strength of about 15 oersteds austenite has a greater permeability ($\mu = B/H$) than martensite and above 15 oersteds the reverse is true. Thus, the conditions necessary for the effect postulated would exist in the latter situation (above 15 oersteds) and not for the former. The field strength within the sample can be varied by varying the current passing through the sample. Thus, for wire specimens (diameter of 0.025 in.) a current of 1 amp produces a field strength of 4 oersteds and a current of 10 amp produces a field strength of 40 oersteds. The pulse cycles resulting from the martensite transformation at field strengths 4 and 40 oersteds in the samples show identical characteristics. Pulse cycles observed at intermediate values of field strengths also showed the same characteristics. Thus this possibility is excluded.

4—Of the many publications on the crystallographic nature of the transformation of the face-centered cubic (austenite) lattice to the body-centered cubic (or body-centered tetragonal martensite) lattice, all have found it necessary to assume the process to occur as a result of two shearing or distortion processes. Since other possibilities seem excluded above, it appears that the form of the pulse cycle observed is experimental confirmation of such a two-stage distortion process. The form of the pulse cycle cannot be taken as evidence for a complete separation in time of the two distortions; though the two distortions are sequential in time, there is doubtless overlap; indeed the roundness of the maximum suggests overlap; the absence of a truly horizontal plateau at the maximum would appear to demonstrate that the two stages are not separated in time; Machlin and Cohen¹⁴ have speculated on the sequence and the overlap of two distortions.*

* It may be possible to explain the nature of the pulse cycle on the basis of a shear-like distortion and subsequent stress-relieving slip or twinning mechanism proposed by Geisler (*Acta Metallurgica* (1953) Vol. 1, No. 3); whether this mechanism can account for the very small times observed awaits further consideration.

Correlation of the Velocity of Martensite Propagation and Elastic Wave Propagation: The slope of the plot in Fig. 12 gives the velocity of martensite propagation, estimated to be 3300 ft per sec. The velocity of elastic wave propagation in a solid is given by

$$v = \sqrt{\frac{G}{d}}$$

where v is the velocity of elastic wave propagation in the solid; G , the modulus of rigidity; and, d , the density of solid. The values of G and d for an Fe-30 pct Ni alloy are¹¹

$$G = 8,600,000 \text{ psi}$$

$$d = 510 \text{ lb per cu ft.}$$

This gives a value of 9925 ft per sec as the velocity of propagation of elastic waves in an Fe-30 pct Ni alloy.

McReynolds⁸ has shown that for an Fe-30 pct Ni the value of G and d are invariant with temperature at subzero temperatures. Thus the velocity of elastic wave propagation in this alloy should also be invariant with temperature below room temperature. The results of this investigation show that the velocity of martensite propagation is constant in the temperature range -20° to -195°C .

Thus, it may be concluded that the martensite transformation is an elastic-wave-like propagation in the solid. The apparent discrepancy between the velocity of martensite propagation (3300 ft per sec) and that of elastic wave propagation (9925 ft per sec) may be reconciled if it is considered that the martensite transformation consists of two stages sequential in time, but each proceeding possibly with the velocity of elastic waves, thus decreasing the overall velocity of martensite propagation from 9925 to 3300 ft per sec. This is in good accord with the strain-wave model of martensite propagation.

Concerning Theories on the Martensite Transformation: During the past five years, two theories have been proposed for the martensite transformation. Kurdjumov and coworkers^{15,16,17} and Fisher, Hollomon, and Turnbull¹⁸ have applied a modified version of regular nucleation and growth† kinetics

† In this discussion, the term "growth" refers exclusively to the conventional atom-by-atom growth process across the interface.

to the martensite transformation. Scheil¹⁹ in 1929 proposed that the transformation occurs by nucleation and a subsequent very rapid propagation of the martensite phase into the parent austenite in the manner of a strain-wave, to form a fully grown martensite plate. Machlin and Cohen⁷ have put this theory on a more quantitative footing. The two theories essentially differ in one important respect; i.e., the rate equation for the nucleation and growth theory contains a term

$$e^{-Q/RT}$$

where Q is the activation energy for growth, which is absent from the rate equation of the propagation theory. This difference has fundamental significance however. The term Q represents the activation energy for the growth of a nucleus to the final martensite plate by a process of atom-by-atom transfer across the austenite-martensite interface. For transformation propagated as a strain-wave, the activation energy for growth should be virtually zero.⁷ Machlin and Cohen⁷ in an elegant critical experiment showed that martensite formed with its

characteristic high velocity of propagation even at 4°K on deforming a specimen of an Fe-29 pct Ni alloy, as evidenced by the audible clicks. This would be impossible according to the nucleation and growth theories, as, even if new nuclei are formed as a result of the deformation, their growth rate would be inappreciable. On the other hand, the strain-wave propagation theory would predict that as soon as the nuclei are formed by the applied stress, they grow to full-size plates.

According to the nucleation and growth theories, the activation energy for growth of martensite is 500 to 2000 cal per mol. For an activation energy of 500 cal per mol,¹⁷ the ratio of the velocity of propagation at 250°K to that at 80°K is calculated to be about 8. For an activation energy of 2000 cal per mol this ratio is 3000.¹⁸

The results of this investigation demonstrate that this ratio is unity with the maximum possible deviation due to experimental scatter raising this ratio to about 2. Thus the activation energy for the propagation of martensite is very small, virtually zero, neglecting frictional effects.

The strain-wave propagation theory does not distinguish between the athermal and isothermal modes of the martensite propagation. The results of this investigation show that the characteristics of the pulse cycle are identical for both modes of transformation.

In general, this investigation has yielded results which are in excellent agreement with the strain-wave propagation theory and differ with the concept of growth of martensite plates by an atom-by-atom transfer across the moving interface.

Summary

1—An experimental technique has been established capable of measuring accurately phenomena of very short duration occurring in metals and alloys.

2—The time of formation of a plate of martensite 0.01 in. long in an Fe-30 pct Ni alloy is 3.10^{-7} sec; this represents perhaps the most accurate value reported for the propagation of martensite.

3—The rate of propagation of martensite is 3300 ft per sec or 100,000 cm per sec approximately, and is independent of temperature in the range -20° to -195°C in this alloy.

4—Thus, the "activation energy" for the propagation of martensite is virtually zero.

5—It may be concluded from 3 and 4 that the concept of martensite formation by a process of atom-by-atom growth is incorrect. On the other hand, these results are in very good accord with the strain-wave propagation theory proposed for the martensite transformation.

6—The characteristics of the transformation, viz., the time of formation of martensite units, and the general nature of the pulse cycle resulting from the martensite transformation are independent of whether the transformation occurs athermally or isothermally.

7—The time of formation and the signal strength vary directly with the size of the plate formed.

8—The velocity of martensite propagation is of the same order of magnitude as the velocity of elastic wave propagation in the solid.

9—From considerations on the nature of the pulse cycle, it may be concluded that the martensite propagation consists of two stages proceeding with the velocity of elastic wave propagation in the solid.

10—This technique is ideally suited for the study of rapidly occurring phenomena in metals and alloys such as slip, twinning, cleavage, etc. Such investigations are underway in this laboratory.

Acknowledgments

This research work was sponsored by the Office of Air Research and carried out under Contracts AF 18 (600) — 161 and AF 33 (038) — 10218. Our thanks are also due to Professor E. M. Williams and coworkers of the Department of Electrical Engineering for their extended assistance with the complex electronics equipment. Our appreciation is also extended to Eliel Lahtenkorva for his able assistance in the laboratory.

Appendix I

The following major pieces of electrical equipment were used in this investigation: Two of Type 202P Spencer-Kennedy Chain-Pulse amplifiers; one of Type 214 Spencer-Kennedy Chain-Pulse amplifier; and a Cathode Ray Oscilloscope, Tektronix, Type 517. Some of the characteristics of these apparatus are given in Table I. A 160-ohm impedance cable, No. K 109 of the Federal Telephone and Radio Corp. is used to connect the various parts of the circuit, excluding the battery loop.

The following special characteristics of the cathode-ray oscilloscope should be noted:

1—Accelerating potential of 24,000 v. In making a photographic record of very fast transient signals flashing across the face of a cathode-ray tube (of the order of 0.1 microsecond), it is obvious that there is no control over the exposure time of the film. Thus the intensity of the light emanating from the face of the tube must be very high. This is accomplished by having a very high accelerating potential of 24,000 v on the cathode-ray beam, since the intensity of the light varies better than linearly as the velocity of the electron beam or the accelerating potential on the tube. A metallized 5XP cathode-ray tube with a P11 phosphor (which emits blue light) in conjunction with Eastman Linagraph Pan 35 mm Film developed in Developer SD 19 (a) (Ref. Kodak Formulary) permits a satisfactory photographic record of the oscilloscope trace.

2—The oscilloscope can be set to trigger on either a positive or negative signal.

Appendix II

The problem under consideration is the time necessary for the latent heat liberated in a martensite plate to flow out of the entire sample past the probes, see Fig. 14.

The specific resistivity of a homogeneous sample is linear with temperature. Moreover, at the temperatures under consideration the specific heat is nearly independent of temperature. Therefore, if a quantity of heat is suddenly generated within the sample, the decay time of the voltage signal due to this heating is determined by the time needed for the heat to flow out of the sample.

It is assumed that at time $t = 0$, an amount of heat ν is generated instantaneously in a thin cross section of a long cylindrical wire and is distributed uniformly in that cross section. Neglecting radial heat transfer, the problem reduces to a simple one-dimensional case, whose solution is

$$T = \frac{1}{\sqrt{4\pi\alpha t}} e^{-x^2/4\alpha t}$$

where T is the absolute temperature at time t and position x , α is the thermal diffusivity of the material; x is measured from the cross section at which ν was

generated. The integral

$$\int_{-x'}^{x'} T dx = \frac{2}{\sqrt{\pi}} \int_0^{x'} \frac{2}{\sqrt{\pi}} e^{-\left(\frac{x}{\sqrt{4\alpha t}}\right)^2} d\left(\frac{x}{\sqrt{4\alpha t}}\right) = \operatorname{erf}\left(\frac{x'}{\sqrt{4\alpha t}}\right)$$

is proportional to the heat remaining between points $-x'$ and x' at any given instant t . Since $\operatorname{erf}(\infty) = 1$, the interval τ during which $\nu/2$ flows beyond $-x'$ and x' is determined by the condition

$$\operatorname{erf}\left(\frac{x'}{\sqrt{4\alpha\tau}}\right) = \frac{1}{2}$$

From tables of the error function, this is the case when

$$\frac{x'}{\sqrt{4\alpha\tau}} = 0.477$$

If the leads of the signal circuit are attached symmetrically at $x = -L/2$ and $x = L/2$, (see Fig. 14), the decay time is

$$= 0.477^2 \frac{L^2}{16\alpha}$$

For $\alpha = 0.027$ sq cm sec⁻¹ and $L = 2$ cm

$$\tau = 41 \text{ sec}$$

It is thus seen that decay times of this order of magnitude are very much longer than the observed time interval corresponding to the decrease, viz., 10^{-7} sec.

References

- ¹ H. J. Wiester: *Ztsch. Metallkunde* (1932) **24**, p. 276.
- ² H. Hannemann, W. Hofmann, and H. J. Wiester: *Archiv. Eisenhuttewesen* (1932-1933) **6**, p. 199.
- ³ F. Förster and E. Scheil: *Ztsch. Metallkunde* (1936) **28**, p. 295.
- ⁴ F. Förster and E. Scheil: *Naturwissenschaften* (1937) **25**, p. 439.
- ⁵ F. Förster and E. Scheil: *Ztsch. Metallkunde* (1940) **32**, p. 165.
- ⁶ E. S. Machlin and M. Cohen: *Trans. AIME* (1951) **191**, p. 746; *JOURNAL OF METALS* (September 1951).
- ⁷ E. S. Machlin and M. Cohen: *Trans. AIME* (1952) **194**, p. 489; *JOURNAL OF METALS* (May 1952).
- ⁸ A. W. McReynolds: *Journal of Applied Physics* (1949) **20**, p. 896.
- ⁹ S. C. Das Gupta and B. S. Lement: *Trans. AIME* (1951) **191**, p. 727; *JOURNAL OF METALS* (September 1951).
- ¹⁰ C. J. Smithells: *Metals Reference Book* (1949) pp. 418-421.
- ¹¹ J. S. Marsh: *Alloys of Iron and Nickel* (1938) McGraw-Hill Book Co.
- ¹² E. E. Lahtenkorva, R. F. Bunshah, and R. F. Mehl: Unpublished research, Carnegie Institute of Technology, 1952.
- ¹³ J. A. Wheeler and M. A. Jaswon: *Journal Iron and Steel Inst.* (1947) **157**, p. 161.
- ¹⁴ E. S. Machlin and M. Cohen: *Trans. AIME* (1951) **191**, p. 1019; *JOURNAL OF METALS* (November 1951).
- ¹⁵ G. V. Kurdjumov: *Journal of Technical Physics U.S.S.R.* (1948) **18**, No. 8, p. 999.
- ¹⁶ G. V. Kurdjumov and O. P. Maksimova: *U.S.S.R. Academy of Sciences Report* (1948) **61**, p. 53.
- ¹⁷ G. V. Kurdjumov and O. P. Maksimova: *Ibid.* (1950) **73**, No. 2, p. 95.
- ¹⁸ J. C. Fisher, J. H. Hollomon, and D. Turnbull: *Trans. AIME* (1949) **185**, p. 691; *JOURNAL OF METALS* (October 1949).
- ¹⁹ E. Scheil: *Ztsch. anorg. allgem. Chem.* (1929) **183**, p. 98.

Decay of Lattice Defects Frozen into an Alloy by Quenching

by A. E. Roswell and A. S. Nowick

Anelastic measurements of atomic mobility in an Ag-Zn substitutional solid solution, make possible a study of the rate of decay of lattice defects frozen into the alloy by quenching.

A WIDE variety of experimental evidence has accumulated recently in support of the belief that atomic mobility or diffusion in face-centered cubic lattices occurs principally through the movement of lattice defects, as contrasted to a mechanism by which two or more atoms directly exchange lattice positions. The most direct evidence, summarized in a recent review,¹ includes the Kirkendall-effect measurements and anelastic measurements on quenched alloys. Theoretical calculations² have focused attention on the lattice vacancy as the defect probably responsible for diffusion in the common metals. Later calculations³ have also shown the possible importance of combined pairs of vacancies in producing diffusion. The only defect that has been considered seriously, in addition to the vacancy and combination of vacancies, is the "interstitialcy" (an

atom which has left its normal lattice position and entered an interstitial position); the calculated energy of formation of an interstitialcy in a close-packed lattice is too large to permit a reasonable probability for the occurrence of this defect.² In view of these calculations it may be tentatively concluded that the defects producing atomic movements are single or multiple vacancies.

Anelastic measurements of atomic mobility in substitutional solid solutions provide a valuable method for the study of lattice defects. By means of this method it was first demonstrated⁴ that defects may be frozen into a lattice by rapid quenching from high temperatures. (It was subsequently shown⁵ that resistivity measurements may also be capable of detecting the presence of frozen-in defects.) A summary of the principles involved in these anelastic measurements will now be presented.

The anelastic method is based on a relaxation phenomenon in substitutional solid solutions, first discovered by Zener⁶ in α brass and subsequently investigated extensively in a series of Ag-Zn solid solutions.⁷ This relaxation effect may be observed in the usual way⁸ either dynamically, as a peak in

A. E. ROSWELL, Student Associate AIME, and A. S. NOWICK, Junior Member AIME, are Graduate Student and Assistant Professor, respectively, Dept. of Metallurgy, Yale University, New Haven, Conn.

Discussion on this paper, TP 3619E, may be sent, 2 copies, to AIME by Dec. 1, 1953. Manuscripts April 13, 1953. Cleveland Meeting, October 1953.

the curve of internal friction vs temperature, or statically as a stress relaxation or elastic after-effect phenomenon. A simple interpretation of these anelastic effects is suggested by Zener,⁸ who focuses attention on pairs of solute atoms in the substitutional solid solution. Thus, suppose that the solute atoms have a larger atomic diameter than the solvent atoms. The application of a tensile stress to the solid solution will then result in a preferential alignment of pairs of solute atoms along those crystallographic directions that lie nearest to the tensile axis, since such redistribution of atoms acts to relieve the stress. Since the rate of this reorientation of solute atom pairs depends on the rate of atomic diffusion, the application of stress will produce typical anelastic behavior with a relaxation time closely related to the mean atomic jump time in the solid solution.

It is pointed out by one of the authors^{7,9} that Zener's pair reorientation mechanism is a special example of stress-induced ordering, where the application of stress to an initially random solid solution produces preferential atomic rearrangements accompanied by anelastic strain. Furthermore, it is argued that since a large solute concentration (usually greater than 15 pct) is required in order that the effects be observable experimentally, most solute atoms will have at least two nearest neighbors that are solute atoms. The concept that isolated solute atom pairs are the unit which undergoes ordering therefore seems to be an oversimplification. Investigation of the orientation dependence of the anelastic effects in single crystals, which are now under way, should lead to a more accurate picture of the relaxation process. It is important to note, however, that regardless of the relaxation mechanism, the experimentally measured relaxation time, τ , represents the time for atomic redistribution under an applied stress and is therefore of the same order of magnitude as the mean jump time of an atom in the lattice. (Because diffusion takes place through the movement of defects, the rate of movement of solute and solvent atoms is not generally the same; under these conditions the mean jump time of the slower atomic species should determine the measured relaxation time.^{7,9}) It is therefore possible, by the use of relaxation measurements in appropriate substitutional solid solutions, to measure atomic mobility at temperatures far below those at which ordinary diffusion experiments can be carried out. Such measurements make possible a demonstration^{4,10} that an excess of defects may be frozen into the lattice of an alloy by quenching to produce abnormally short relaxation times at low temperatures. (Evidence is presented¹⁰ to rule out the possibility that the observed effects can be attributed to quenching stresses.)

The earlier investigation¹⁰ of the freezing-in of lattice defects utilized almost entirely an Ag-Zn solid solution containing 30 atomic pct Zn. Decay curves, which show the variation of the relaxation rate (i.e., of atomic mobility) with time after quenching, were obtained at different temperatures. The precise form of the decay curves could not be obtained because of the rapidity of the rate of decay. During these measurements on the 30 atomic pct Ag-Zn alloy, preliminary experiments were also conducted on a solid solution containing 33.5 atomic pct Zn. These experiments showed that the decay rates for the latter alloy were considerably slower than for the 30 pct alloy and that, consequently, more precise

decay curves could be obtained. The present paper describes detailed experiments of this type carried out with the 33.5 pct solid solution. Inasmuch as equilibrium measurements of atomic mobility for this solid solution had not been carried out previously, such measurements are also included.

The theory required for the interpretation of the measurements has been presented in the earlier papers.^{7,10} For the sake of completeness, the basic equations are briefly outlined below.

Theory

The rate of relaxation, τ^{-1} , is determined by the product of the concentration of defects, c , (expressed as an atom fraction) and the rate of jump of defects, or

$$\tau^{-1} = Ace^{-\Delta H_f/RT} \quad [1]$$

where ΔH_f is the heat of activation for movement of a defect and A is a frequency factor. The defects may be considered to be vacancies, in order to be specific. If the two component atoms of the binary solid solution do not jump into a vacancy at the same rate, then, as mentioned in the previous section, the quantity ΔH_f should correspond to the slower moving component, i.e., ΔH_f is the larger of the two heats of activation for vacancy jump. Under conditions of thermal equilibrium, the vacancy concentration is given by \bar{c} , where

$$\bar{c} = Be^{-\Delta H_f/RT} \quad [2]$$

The dimensionless quantity B is related¹⁰ to the entropy of formation of a defect, while ΔH_f is its heat of formation. Thus, the equilibrium value of τ may be written

$$\bar{\tau} = \bar{\tau}_0 e^{H_r/RT} \quad [3]$$

where H_r is the composite "activation energy" for relaxation, given by

$$H_r = \Delta H_f + \Delta H_i \quad [4]$$

The value of H_r may not be precisely the same as the "activation energy" obtained from a diffusion experiment if the two component atoms diffuse at different rates. The quantity $\bar{\tau}_0$ is equal to $(AB)^{-1}$.

In a quenched specimen, the concentration of defects, c , to be inserted in Eq. 1 is much greater than the equilibrium value, and decays in time toward \bar{c} . In general, the function is written $c = c(t)$, with $c(0)$ for the concentration frozen in by quenching. From equilibrium measurements of $\bar{\tau}$ as a function of temperature, and from measurements of $\tau(0)$, the value obtained immediately after quenching, as a function of temperature, the quantity $c(0)$ may be estimated. The freezing-in temperature, T_f , defined as the temperature at which $c = c(0)$, is then given by

$$c(0) = Be^{-\Delta H_f/RT_f} \quad [5]$$

The freezing-in temperature can be less than or equal to the quenching temperature. The decay curve, which shows the variation of τ^{-1} with time after quenching at constant temperature, is also a measure of the time variation of the concentration of defects at the temperature of measurement, since from Eq. 1

$$\frac{\tau^{-1}(t)}{\tau^{-1}(0)} = \frac{c(t)}{c(0)} \quad [6]$$

Eq. 6 is only valid as long as one type of defect is operative.

Specimens and Procedure

The Ag-Zn specimens used in this investigation were prepared by melting electrolytic silver and high purity zinc in a graphite crucible under charcoal. The casting was homogenized at 650°C, after which it was reduced in diameter by rolling and swaging. Finally, it was cold drawn to a diameter of 0.032 in. In order to grow coarse grains (to avoid complications due to grain boundary relaxation¹¹) the drawn wire was sealed under vacuum in a quartz tube and heated to 650°C where it was held for five days. The final specimens contained 33.5 atomic pct Zn.

The relaxation time is obtained either from the position of an internal friction peak (when $\tau < 1$ sec) or from measurements of elastic after-effect (when τ is in the range between 10 and 10,000 sec). For the internal friction measurements, if T_m is the temperature of maximum damping, the relaxation time, $\tau(T_m)$ at this temperature, is obtained⁸ from the equation

$$\tau(T_m) = (2\pi f)^{-1} \quad [7]$$

where f is the vibration frequency. For an elastic after-effect measurement, the wire specimen is twisted through a desired angle for an appropriate length of time, then, upon release of the applied torque, the residual (anelastic) strain is measured as a function of time. A plot of the anelastic strain against the logarithm of the time shows an inflection point at a time τ_i , called the "time to inflection." Under equilibrium conditions, when the relaxation time τ is not changing with time, this quantity τ_i is equal to τ . For the quenching experiments, on the other hand, where τ is a function of time, a correction is required to relate the measured time to inflection to the appropriate relaxation time.¹⁰ This correction was important in the earlier experiments, where the decay rates were so rapid that the change in relaxation time between successive measurements was large. In the present experiments the decay rates are much slower, so that τ_i is equal to τ without significant correction, and the use of the symbol τ_i is therefore superfluous.

In the quenching experiments, the specimen, supported against a heavier wire, is held at 400°C in a nitrogen atmosphere for 4 min, then allowed to fall freely into a tube containing water at room temperature. (It has been shown¹⁰ that the results ob-

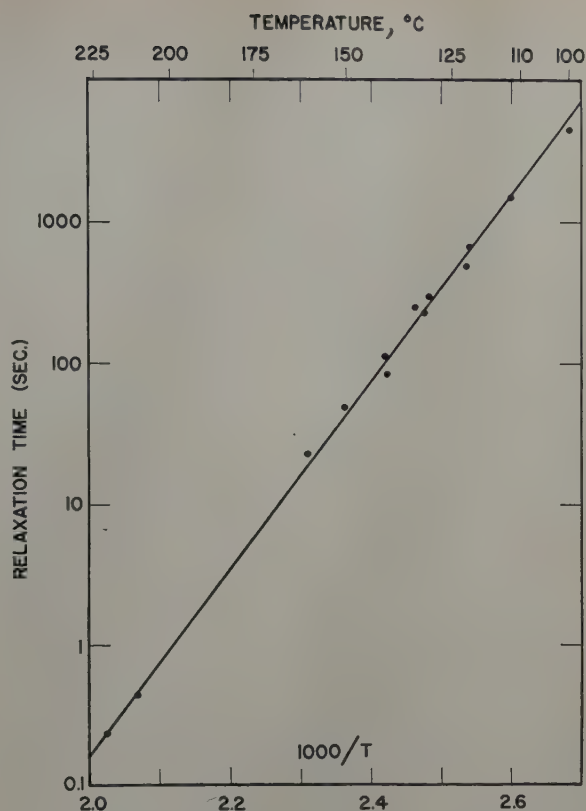


Fig. 1—Variation of the equilibrium time of relaxation with temperature, corresponding to a composite "activation energy" of 30.5 kcal per mol.

tained are independent of the annealing time at the quenching temperature.) After this quenching operation, the specimen is mounted in the measuring furnace which is at the desired temperature. The time of relaxation is determined as a function of the total time at temperature from a series of elastic after-effect measurements. Inasmuch as the decay at room temperature is negligible over a period of several hours, the total time may be measured from the time of insertion of the specimen into the measuring furnace. The error due to the time required for the wire to reach temperature and to the time for the furnace temperature to become stabilized, means that the first relaxation measurement is often less reliable than the rest. Except for this initial instability, the temperature is held to $\pm \frac{1}{2}^\circ\text{C}$ by means of an electronic proportioning temperature controller.

Equilibrium Measurements

The relaxation time under equilibrium conditions, for the 33.5 pct Ag-Zn alloy, is shown as a function of temperature in Fig. 1. The two points at the high temperature end of the curve are obtained from internal friction peaks at two different frequencies; the remaining points are obtained from the elastic after-effect measurements. Although a straight line is obtained in Fig. 1, previous measurements⁷ on Ag-Zn alloys of lower zinc concentration have shown that when the data are extended to higher temperatures by the use of high frequency internal friction measurements, the plots of $\log \tau$ against T^{-1} show a small but definite curvature. This result implies that the quantity H_r (Eq. 3) is a

Table I. Principal Numerical Results of Measurements and Calculations

Measured Quantities	
H_r , kcal per mol	30.5 (± 0.5)
$\log \tau_0$ (sec)	-14.1 (± 0.3)
ΔH_f , kcal per mol	18.6 (± 0.8)
$\log A_c(0)$ (sec ⁻¹)	10.0 (± 0.5)
Deduced Quantities	
ΔH_f , kcal per mol	11.9
$c(0)$	2.5×10^{-4}
\bar{c} (m.p.)	7×10^{-3}
T_F	360°C
N	10^6

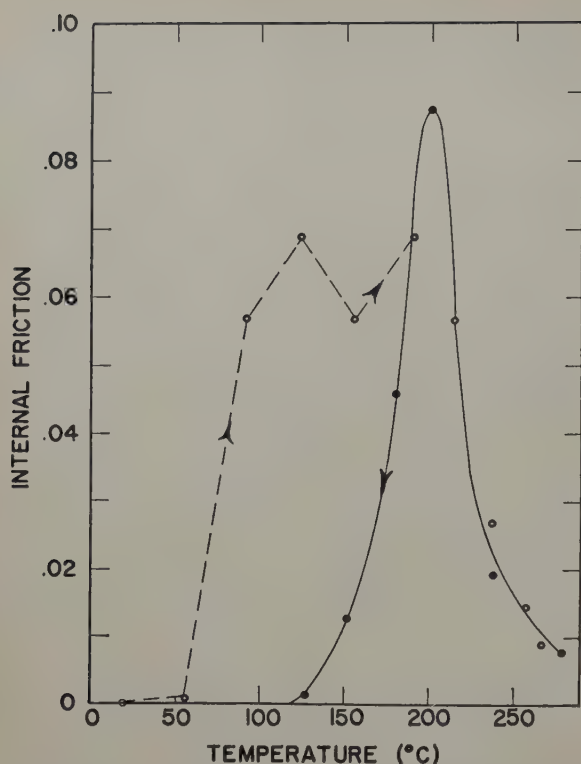


Fig. 2—Internal friction (Q^{-1}) during rapid heating (open circles) and cooling (solid circles) of the quenched Ag-Zn alloy. The solid curve represents the equilibrium internal friction peak. Frequency of vibration is 0.18 sec^{-1} .

slowly-varying increasing function of temperature. In the range of Fig. 1, however, appreciable deviation from a straight line is not detectable. The best values of the parameters in Eq. 3, obtained from Fig. 1, are $H_r = 30.5 \text{ kcal per mol}$ and $\log \bar{\tau}_0 = -14.1$. These values, together with their estimated reliability, are listed in Table I.

Nonequilibrium Measurements

As in the earlier experiments, quenching a specimen from 400°C into water at room temperature results in abnormally short relaxation times at low temperatures. A specimen slowly cooled or dropped out of the furnace into still air shows no such effects, and is therefore assumed to be more nearly in equilibrium than the water-quenched specimen. The effect of varying the quenching temperature has already been observed;¹⁰ in the present experiments the quenching temperature is always 400°C .

Static measurements (e.g., elastic after-effect measurements) are better suited to the study of quenched specimens than internal friction measurements because the latter must be measured at higher temperatures where the rate of decay of the quenching effects becomes very large. It was felt, however, that internal friction measurements on a quenched specimen might be very illustrative, qualitatively, of the effects of quenching. According to the interpretation given to these measurements, the atomic jump time, and therefore the relaxation time, is decreased by quenching because of the abnormally high defect concentration. For a given vibration frequency, it follows from Eq. 7 and the temperature dependence of τ that the effect of quenching is to shift the peak to lower temperatures. Due to the rapid decay of the effects of quenching at temperatures near the internal friction peak, it is expected

that the peak will be moving toward higher temperatures during attempts to measure it. Accordingly, the quenched specimen was heated as quickly as possible while measurements of internal friction and temperature were taken in rapid succession. When the temperature reached 280°C , the furnace power was shut off and cooling data taken in a similar fashion. The results are shown in Fig. 2, where each measured value of internal friction is plotted against the average temperature during the measurement. The results show that the peak was constantly moving to the right during the course of the measurements, so rapidly in fact, that it was not possible to climb over the peak until a temperature of 190°C had been reached. Beyond this point, the data follow the solid curve, which represents the equilibrium internal friction peak, both on heating and cooling. When the same experiment was carried out with a slower rate of heating of a quenched specimen, similar results were obtained, but the values of internal friction attained in the vicinity of 100° to 150°C were not as high as in Fig. 2 and equilibrium was attained at a lower temperature. Thus, nonequilibrium internal friction effects must be measured very rapidly, with a resulting loss in ability to follow the approach to equilibrium. Such experiments, however, are of qualitative value in demonstrating that the relaxation peak is moved to a lower temperature by quenching, and therefore that the atomic mobility is increased.

By means of static measurements, it becomes possible to study the approach to equilibrium quantitatively. Fig. 3 shows the variation of τ with time after quenching, obtained by means of elastic after-effect measurements at 69°C . This figure is essentially a decay curve, as defined earlier, except that the ordinate is τ in place of τ^{-1} . Extrapolation of Fig. 1 shows that the equilibrium value of the relaxation time at 69°C is about $2 \times 10^5 \text{ sec}$. The initial relaxation time after quenching, $\tau(0)$, obtained by extrapolating the data of Fig. 3 to zero time, is about 75 sec. The data of Fig. 3 are represented closely by two straight lines, with a sharp break at about $\tau = 800 \text{ sec}$. Beyond this break, data are observed to fall along the second straight line out to 5000 min (i.e., well beyond the range shown in Fig. 3). The

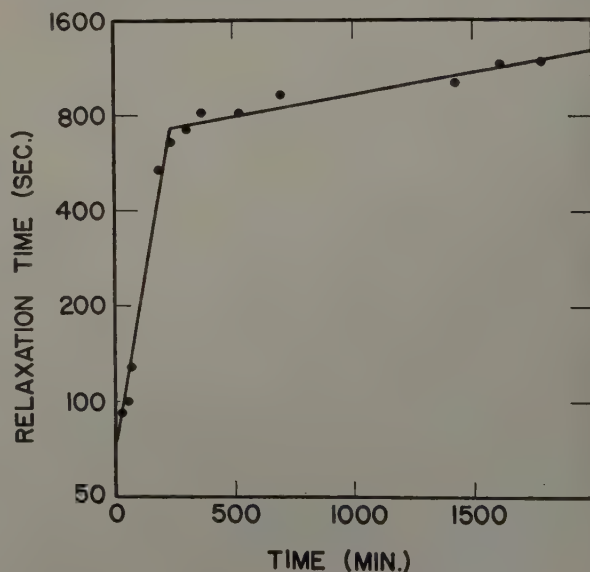


Fig. 3—Variation of the relaxation time with total time at 69°C for a quenched specimen. Equilibrium relaxation time equals $2 \times 10^5 \text{ sec}$.

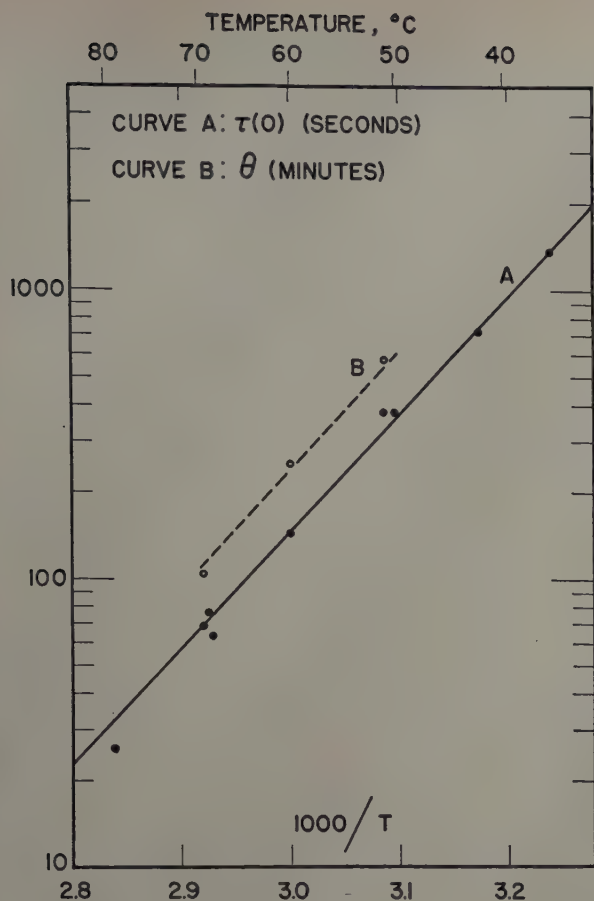


Fig. 4—Curve A: Initial relaxation time after quenching as a function of temperature of measurement. Curve B: Variation of the decay time with temperature for stage I.

occurrence of such breaks will be discussed further below. It should be noted here, however, that the abrupt decrease in the rate of decay cannot be attributed to the fact that the relaxation time is approaching its equilibrium value, since the break occurs when the relaxation time is still about 250 times smaller than the value of $\bar{\tau}$ for this temperature.

From a series of decay curves at different temperatures, similar to that of Fig. 3, values of the initial relaxation time, $\tau(0)$, may be obtained as a function of temperature; the results are given in Fig. 4, curve A. The higher the temperature, the less accurate the extrapolation to zero time; the 80°C point is therefore considered the least reliable. Below 50°C the rate of attainment of equilibrium is too slow to permit the measurement of decay curves. However, additional points are obtainable below 50°C, since the initially measured relaxation time at these temperatures may be taken equal to $\tau(0)$ with negligible correction. From Eq. 1 with $c(0)$, the initial concentration of defects directly after quenching, substituted for c , it is clear that the slope of the straight line of Fig. 4A yields the quantity ΔH_i , while the product $Ac(0)$ is obtained from the intercept. The values obtained and their estimated reliability are listed in Table I. From H_r and ΔH_i , the quantity ΔH_f may be obtained,[†] Eq. 4. It is also

[†] As noted in the previous paper,¹⁰ the quantities H_r and ΔH_i are measured in different temperature ranges. Since H_r is known to be a function of temperature, this calculation of ΔH_f is not strictly valid. The error resulting from the failure to take this temperature dependence into account is probably small, and such as to yield a value for ΔH_f smaller than that calculated here.

possible to obtain $c(0)$ as follows. The quantities

$Ac(0)$ and $AB(=\tau_0^{-1})$ are already known experimentally, while B can be estimated from theoretical considerations¹⁰ to have a value of 3.0 (probably to within a factor of 2). The concentration of imperfections trapped by quenching, $c(0)$, is therefore estimated to be 2.5×10^{-4} . This value is probably reliable to within a factor of 5, in view of the uncertainties in the quantities from which it is calculated. The value of the equilibrium concentration of vacancies at the melting point (the solidus temperature) of the alloy is readily obtained from Eq. 2, to be

$$\bar{c}(\text{m.p.}) = 7 \times 10^{-8}$$

to within a factor of about 2.5. In the calculation of this quantity, no account is taken of the possible dependence of ΔH_f on temperature. If such a correction were required, however, a still larger value would be obtained for $\bar{c}(\text{m.p.})$. The above value is larger than the equivalent quantity for pure copper calculated theoretically.²

The freezing-in temperature, T_f , defined by Eq. 5 may also be calculated from the results reported thus far. The value obtained is 360°C, and is probably reliable to about $\pm 40^\circ\text{C}$. This result is therefore consistent with the fact that the quenching temperature is 400°C. There is no reason to require that T_f be equal to the quenching temperature, i.e., that all defects present at the quenching temperature be frozen in. On the contrary, the earlier experiments,¹⁰ which determined the dependence of initial relaxation time at a given temperature of measurement on the quenching temperature, show that defects present at the quenching temperature are not completely frozen in. These various deduced quantities, $c(0)$, $\bar{c}(\text{m.p.})$, and T_f , are listed in Table I.

The most significant results obtained from these experiments are the decay curves. In view of Eq. 6, the ratio $\tau(0)/\tau(t)$ represents the concentration of defects at any time t relative to the value $c(0)$ frozen in by quenching. When this ratio is plotted on a logarithmic scale against the time, the curves obtained may be represented by two intersecting straight lines, as shown in Fig. 5. (In some of the runs, however, a slight negative curvature is indicated at the start of the decay curves.) The occurrence of a sharp break was already noted in the case of the 69°C measurements given in Fig. 3.

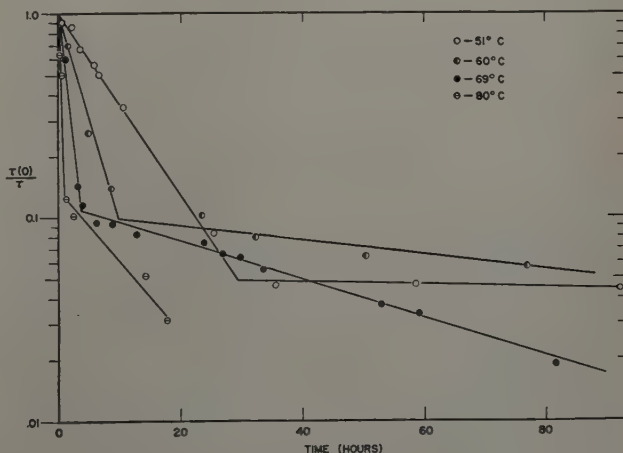


Fig. 5—Decay curves showing the variation of the reciprocal of the relaxation time (relative to its initial value) with total time at four different temperatures of measurement.

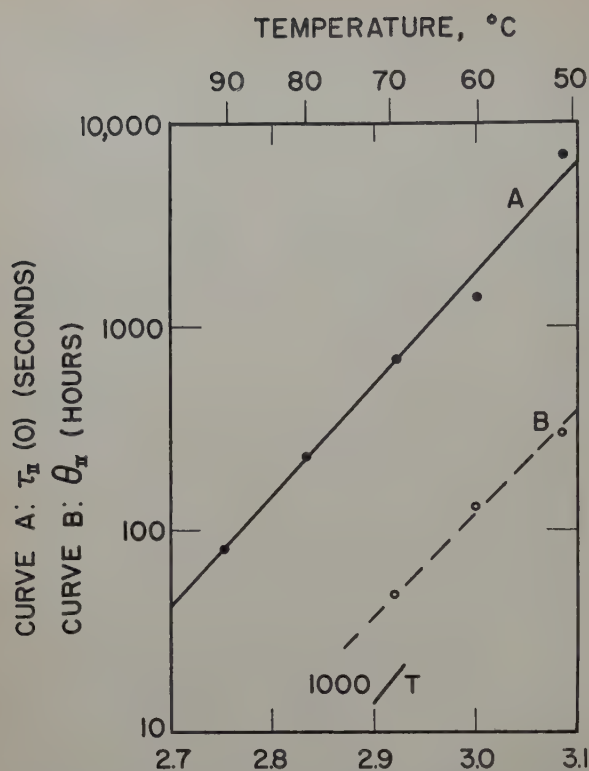


Fig. 6—Dependence of the parameters of stage II of the decay curves on the temperature. Curve A: Initial relaxation time, $\tau_{II}(0)$ Curve B: Decay time, θ_{II} .

The decay curves of Fig. 5 are suggestive of the occurrence of two stages in which there is a distinct difference, either in the manner by which relaxation is produced or in the mechanism of the decay of imperfections. The early portion of the decay curve, before the sharp break, will be designated "stage I," and the later portion, "stage II," for convenience in future reference. The slope of the decay curve in stage I may now be obtained as a function of temperature. Since the curve is approximately a straight line, it may be represented as

$$\tau(0)/\tau = e^{-t/\theta} \quad [8]$$

where θ may be termed the decay time. The temperature dependence of θ should be of the form

$$\theta = \theta_0 e^{\Delta H'/RT} \quad [9]$$

The quantity $\Delta H'$, which is an effective heat of activation for the decay of defects in stage I, may not be the same as the quantity ΔH_j , derived from the variation of $\tau(0)$ with temperature. A difference may be expected, first because the rate of relaxation is controlled by the slower moving atomic species of the binary solid solution, as already mentioned in the theory section, while the rate of migration of defects is controlled by the faster moving component. This factor acts to make $\Delta H'$ smaller than ΔH_j . On the other hand, the rate of atomic mobility has been shown⁷ to be strongly concentration dependent; it is therefore to be expected that defects, in moving through local variations in concentration in the alloy, will be held up for relatively long periods in certain regions, i.e., where the heat of activation for jump is larger than the average value. The decay rate is controlled by the rate of jump in these special regions. This factor acts to make $\Delta H'$ larger than ΔH_j . In view of these two opposing factors, it is not clear as to whether $\Delta H'$ should be smaller or larger than ΔH_j .

Experimental values of θ as a function of temperature are given in Fig. 4B. It is difficult to obtain a precise value of $\Delta H'$, since measurements are limited to a narrow temperature range. In addition, as already shown in the previous work,¹⁰ the decay rate is structure sensitive; a small amount of cold working changes this rate appreciably. In the present experiments the wire specimen, used for the series of runs of Fig. 5, was accidentally dropped and bent before the 80°C run, but after measurements had already been obtained at 51°, 60°, and 69°C. It is found that the slope of the 80°C decay curve does not fall into agreement with the corresponding values at 50° to 70°C given by Fig. 4B, but instead, the 80°C value of θ is about a factor of 1.9 too small. Correspondingly, repetition of runs at 50° and 70°C shows that the value of θ at these temperatures subsequent to the accidental bending, is lower by about the same factor.† Annealing at 400°C for 15 min

† The authors are not completely certain that the bending of the specimen was entirely responsible for the subsequent change in decay rates. Other changes in the specimen, not as clearly defined, may have occurred at about the same time.

does not seem to produce recovery of the original decay rate. The three determinations of θ before the 80°C run are plotted in Fig. 4B; they indicate a value of $\Delta H'$, possibly slightly larger than the quantity ΔH_j obtained from Fig. 4A. Since any difference in slope of the two lines is within experimental error, it seems that, pending further measurements, $\Delta H'$ may be considered to be equal to ΔH_j for this solid solution. It should be noted that in the earlier measurements on the 30 pct alloy,¹⁰ it appeared that $\Delta H'$ may be about 2 to 3 kcal per mol less than ΔH_j (just outside of experimental error).

Under the assumption that the two straight lines of Fig. 4 are parallel, the value of $\theta_0 = 10^{-8}$ sec is obtained for the temperature independent factor of Eq. 9. The value of θ at the freezing-in temperature (360°C) is then found to be 0.03 sec. This decay time is in good agreement, in order of magnitude, with the anticipated time of quenching, and therefore serves as a check on the self-consistency of the results of these experiments.

It is useful to estimate the mean number of jumps, N , of a defect (for stage I) before it is rendered inactive. For this purpose, the ratio of the decay time, θ , to mean jump time of a defect must be obtained. The mean jump time will be assumed to vary with temperature with the same heat of activation, $\Delta H'_j$, as the decay time (Eq. 9). Since the temperature-independent factor of the decay time is $\theta_0 = 10^{-8}$ sec, and the corresponding temperature-independent factor for the mean jump time is of the order of magnitude 10^{-14} sec (see ref. 10), the estimated value of N , obtained from the ratio of these two quantities is 10^6 jumps.

For the interpretation of the sharp break in the decay curves, it is important to know the value of the activation energy associated with stage II. A heat of activation may be obtained both from the dependence of the intercept and of the slope (decay time) of the straight line of stage II on the temperature of measurement, in a way analogous to Fig. 4. The results are given in Fig. 6. Besides the points derived from the decay curves of Fig. 5, an additional run at 90°C is included; this run was not included in Fig 4 because at this temperature the decay rate in stage I is too rapid to allow a precise determination of $\tau(0)$. From the data for the intercept of the straight lines of stage II, a heat of activation to 25 kcal per mol is obtained. This result is

greater than the value of ΔH_i obtained from stage I by an amount which seems to be well outside of experimental error. The decay times in stage II (Fig. 6B) give a heat of activation of 23.5 kcal per mol, but the uncertainty in this value is large.

Although the heats of activation associated with stages I and II differ, the magnitude of the relaxation effects are not detectably different in the two stages. This result is significant, since it indicates that the nature of the atomic rearrangement produced by the application of stress to this alloy is the same in both stages.

Comparison with Previous Results

The previous experiments¹⁰ on the freezing-in of defects were conducted on an Ag-Zn alloy containing 30 atomic pct Zn, as contrasted to the present 33.5 atomic pct solid solution. A comparison of the principal results of the two sets of experiments seems desirable at this point.

The equilibrium measurements on the two alloys show that relaxation takes place more rapidly for the 33.5 pct alloy. This difference is attributed to the fact that H_i is 1.0 kcal per mol larger for the 30 pct alloy. This small but experimentally significant change of H_i with zinc concentration is in keeping with earlier equilibrium measurements on a series of Ag-Zn alloys.⁷ The nonequilibrium measurements for the 30 pct alloy seem to show that this difference in H_i enters entirely into the term ΔH_i , and that the values of ΔH_i are the same for the two alloys. In view of the uncertainties in the determinations of ΔH_i , however, it is probably more likely that the 1 kcal per mol difference in H_i is taken up by both ΔH_i and ΔH_f . The value of ΔH_i obtained in the present experiments is more reliable than that obtained for the 30 pct alloy because of the wider range of measurement and the greater precision in the determination of $\tau(0)$. The estimated values of $c(0)$, $\bar{c}(\text{m.p.})$, and T_f are consequently more reliable in the present experiments, although their values are in agreement within experimental error with the same values for the 30 pct alloy.

The most important difference in the nonequilibrium behavior of the two alloys is in the decay rates. The value of θ (for stage I) for the present alloy at 60°C is 250 min, while the equivalent value observed for the 30 pct alloy at the same temperature is about 58 min. The decay rate is, therefore, more than four times greater in the 30 pct alloy, in spite of the fact that the equilibrium atomic mobility is actually lower in this alloy. Thus the ratio $\theta/\tau(0)$ is about 100 in the present case, and only 14 in the earlier work. There are two possible explanations for this large difference: First, the structure sensitivity of the rate of decay, as illustrated¹⁰ by the fact that a small amount of cold working results in a change in decay rate of almost a factor of two, suggests a possible difference in dislocation density in the two alloys. Second, the measurements on the 30 pct alloy indicate that the heat of activation, $\Delta H'_i$, which controls the decay rate, may be somewhat lower than ΔH_i . In the present experiments, however, Fig. 4 shows that $\Delta H'_i$ is at least as large as ΔH_i , if not larger. Thus, in spite of the more rapid equilibrium relaxation in the 33.5 pct alloy, the value of $\Delta H'_i$ may be larger in this case than in the 30 pct alloy. In order to determine which of these two explanations best explains the large differences in the rate of decay of defects in the two alloys, further experiments are necessary.

Discussion

The self consistency in the interpretation given to these experiments is indicated by the reasonable values obtained for three of the quantities deduced from the experimental results: the freezing-in temperature T_f , the value of θ at T_f , and the equilibrium defect concentration at the melting point $\bar{c}(\text{m.p.})$.

The most striking result is the form of the decay curves; the remainder of this discussion will therefore be devoted to this subject. It is noteworthy that the decay curves in both stages I and II obey a simple exponential of the form of Eq. 8 within experimental error (except for a slight curvature at the start of some of the curves, as reported above). The linearity of the decay curves indicates that the process of decay is similar to a first-order reaction, i.e., that the defects are annihilated or rendered ineffective at fixed points in the crystal. An alternative possibility, that the defects combine to form pairs, would result in a curve that corresponds to a second-order reaction, the decay rate then decreasing proportionately to the time. The present data are not in agreement with this latter possibility.

From the number of jumps, N , made by a defect in stage I before it becomes inactive, it is possible to test the hypothesis that vacancies and similar lattice defects are brought to equilibrium principally at edge dislocations^{12,13} in this stage. If it is assumed that the dislocation density has the reasonable value of 10^6 cm^{-2} , then one lattice site in 10^6 lies on a dislocation line, in agreement with the calculated value of N (Table I). The fact that the decay is a first-order reaction is consistent with the belief that the defects terminate at dislocations. Finally, the previous demonstration,¹⁰ that cold working produces an increase in the decay rate in the early stage, is also in accordance with this belief. In view of the calculated result that $c(0)$ is of the order of 10^{-4} , it becomes difficult to understand why annihilation of defects is not accomplished by their combination to form pairs (in the form of a second-order reaction), which would require, at the outset, only 10^4 jumps instead of the 10^6 required to reach a dislocation trap. If combination to form defect pairs results in a lowering of the energy of the system (as indicated³ at least for the combination of single vacancies to form divacancies) this implies an attractive force between individual defects at close range. It does not follow, however, that there may not be a long-range repulsion between defects which would greatly lower the probability of their combination. This question deserves further theoretical investigation.

The tendency for the decay rate to decrease sharply, when the relaxation time reaches about ten times its initial value, $\tau(0)$, is reported¹⁰ on the basis of the earlier quenching experiments on the 30 pct Ag-Zn alloy. In view of the slower decay rates in the present 33.5 pct alloy, and consequently the higher precision attainable, it is shown that the decay curves break more sharply than had been suspected from the earlier measurements; in fact, the curves reported in this paper can usually be represented as two intersecting straight lines, within experimental error. The authors have considered several possible explanations for this sharp break and will outline these below.

One possible explanation, proposed earlier,¹⁰ is the exhaustion of the dislocation sites or other sinks at which defects are absorbed, i.e., it is assumed that these sites have only a limited capacity for the

absorption of defects and that once these sites are filled the decay rate of defects will be greatly decreased. If this hypothesis were correct, a gradual rather than an abrupt decrease in decay rate would be anticipated. Furthermore, the activation energy associated with stage II should then be the same as that of stage I, in contradiction to the present experimental results.

A second explanation is based on the existence of local regions in which the mobility of a defect is considerably slower than in the bulk of the lattice. Such regions are referred to here as *S*-regions. Since it has already been shown⁷ that the average mobility in a series of Ag-Zn alloys depends strikingly on the composition, it is clear that within a solid solution both the probability of finding a defect and the mobility of a defect will fluctuate considerably from one lattice position to another. *S*-regions may therefore exist due to these fluctuations in composition. Another possibility is that lattice positions near dislocations may serve as *S*-regions. It then seems reasonable that in stage I the defects present in the bulk of the lattice directly after quenching control the rate of atomic movement, while in stage II relaxation is controlled by those defects released from *S*-regions. The higher activation energy in stage II is thus readily explained. In order to account for the sharpness of the break in the decay curve, it is necessary to assume a high degree of similarity in the various *S*-regions throughout the lattice. It is also necessary that the capacity of these *S*-regions for defects be very large, to account for the continuance of the straight line of stage II out to long times, as observed experimentally.

The final explanation, proposed to account for the sharp breaks in the decay curves, is the existence of two types of defect present in nonequilibrium quantities upon quenching, each capable of producing atomic mobility independently of the other. The decay curve may be described as due to the predominance of one defect in producing relaxation in stage I, and to the predominance of the second defect when the concentration of the first is greatly decreased, in stage II. The sharpness of the break is then a consequence of the logarithmic scale, in much the same way as the sharp break obtained in the plot of $\log D$ (diffusion coefficient) against T^{-1} when both volume and grain-boundary diffusion occur simultaneously.¹⁴ This hypothesis also provides a natural explanation for the different activation energies associated with the two stages. In accordance with this hypothesis, an equation analogous to Eq. 1 may be written for the defect responsible for stage II. The results of Fig. 6A then indicate that the quantity $Ac(0)$ for stage II is about 10^{13} (or 100 times larger than the corresponding quantity for stage I). This means that either A or $c(0)$ for stage II defects is much larger than the same quantity for stage I. It is not reasonable to expect much more than a concentration of 10^{-4} for stage II defects, but it is possible that the frequency factor A is 100 times larger than for stage I if a large positive entropy of activation were associated with the movement of the stage II defect.

In view of the above discussion, it seems that only the first of the three proposed explanations for the break in the decay curve is inconsistent with the present experimental results.

Summary

A study is made of atomic mobility, in an Ag-Zn

solid solution containing 33.5 atomic pct Zn, by means of anelastic methods. Measurements are made both under conditions where lattice defects are in equilibrium and in the presence of a large excess of defects frozen into the lattice by quenching. The quenching experiments make possible the separation of the composite "activation energy" for atomic mobility under equilibrium conditions into a heat of activation for movement of a defect, equal to 18.6 kcal per mol, and the heat of formation of a defect, equal to 11.9 kcal per mol. It is estimated that about 0.03 atomic pct of defects are frozen in by quenching from 400°C into water.

The decay curve, which is essentially a plot of the logarithm of the atomic mobility as a function of time after quenching (at constant temperature), is closely represented by two intersecting straight lines; the sharp break occurs when the mobility reaches about one-tenth its initial value after quenching. Various possible explanations are given for the existence of two distinct stages in the decay process.

Acknowledgments

The authors wish to express their appreciation to W. Heller for stimulating discussions and criticism, to the Higgins Fund which financed the basic equipment used in these experiments, and to the Office of Ordnance Research for their sponsorship of this work.

References

- ¹ A. D. LeClaire: Diffusion in Metals. *Progress in Metal Physics* (1953) **4**, p. 265. London. Pergamon Press Ltd.
- ² F. Seitz: Fundamental Aspects of Diffusion in Solids. *Phase Transformations in Solids* (1951) p. 77. New York. John Wiley and Sons. See also the original calculations by H. B. Huntington and F. Seitz: *Physical Review* (1942) **61**, pp. 315, 325.
- ³ J. H. Bartlett and G. J. Dienes: Combined Pairs of Vacancies in Copper. *Physical Review* (1953) **89**, p. 848.
- ⁴ A. S. Nowick: The Production and Detection of a Non-Equilibrium Number of Vacancies in a Metal. *Physical Review* (1951) **82**, p. 551.
- ⁵ J. W. Kauffman and J. S. Koehler: Quenching in of Lattice Vacancies in Pure Gold. *Physical Review* (1952) **88**, p. 149.
- ⁶ C. Zener: Internal Friction of an Alpha Brass Crystal. *Trans. AIME* (1943) **152**, p. 122.
- ⁷ A. S. Nowick: Anelastic Measurements of Atomic Mobility in Substitutional Solid Solutions. *Physical Review* (1952) **88**, p. 925.
- ⁸ C. Zener: *Elasticity and Anelasticity of Metals* (1948). Chicago, Univ. Chicago Press; Stress Induced Preferential Orientation of Pairs of Solute Atoms in Metallic Solid Solution. *Physical Review* (1947) **71**, p. 34.
- ⁹ A. S. Nowick: Internal Friction in Metals. *Progress in Metal Physics* (1953) **4**, p. 1. London. Pergamon Press Ltd.
- ¹⁰ A. S. Nowick and R. J. Sladek: Anelastic Measurement of Atomic Mobility Under Non-Equilibrium Conditions. *Acta Metallurgica* (1953) **1**, p. 131.
- ¹¹ T. S. Kê: Experimental Evidence of the Viscous Behavior of Grain Boundaries in Metals. *Physical Review* (1947) **71**, p. 533.
- ¹² F. R. N. Nabarro: Deformation of Crystals by the Motion of Single Ions. *Report on a Conference on Strength of Solids* (1948) p. 75. London. The Physical Society.
- ¹³ F. Seitz: On the Formation of Dislocations from Vacancies. *Physical Review* (1950) **79**, p. 890.
- ¹⁴ D. Turnbull: Grain Boundary and Surface Diffusion. *Atom Movements* (1951) p. 129. Cleveland. ASM.

Measurement of Approximately Cylindrical Particles In Opaque Samples

by Robert L. Fullman

Relationships are derived between average dimensions measured on a polished cross section and the spatial dimensions of particles dispersed as uniform cylinders. The equations are applicable to the measurement of rods or plates without the stipulation that they be extremely thin.

QUANTITATIVE analysis of the elements of microstructures has been limited by a lack of knowledge concerning the relationships between observations on plane surfaces and the spatial nature of the structure. This paper is an extension of previous efforts to establish equations suitable for the quantitative investigation of microstructures. The equations derived fill two gaps in the range of particle shapes for which measurements may be required, namely those shapes lying between extremely thin plates and equiaxed particles (approximately spherical), and those intermediate between equiaxed particles and extremely thin rods or needles.

In a previous paper¹ equations were developed relating dimensions measured on a polished cross section to the average spatial dimensions of particles in the form of spheres, extremely thin plates, and extremely thin rods. For extremely thin rods the dimensions measured on a polished cross section were found to depend on the radius only, so that no information concerning the rod lengths or number of rods per unit volume could be obtained from observations on a cross section. In this paper equations are derived relating dimensions measured on a polished cross section to the spatial dimensions of particles in the form of identical cylinders. These equations may be used to evaluate the dimensions of rods, as well as the dimensions of plates, without the stipulation that the plates or rods be extremely thin. The impossibility of evaluating the length of extremely thin rods from planar measurements appears as an increase in the amount of data required for a given precision, as the length-radius ratio increases.

Consider a sample containing particles of a phase in the form of cylinders of uniform radius r and height t . If the cylinders are randomly oriented, as in a sufficiently large sample of a fine grained polycrystalline material, area and lineal analysis may be

R. L. FULLMAN, Junior Member AIME, is associated with the Research Laboratory, General Electric Co., Schenectady.

Discussion on this paper, TP 3597E, may be sent, 2 copies, to AIME by Dec. 1, 1953. Manuscript, April 15, 1953. Cleveland Meeting, October 1953.

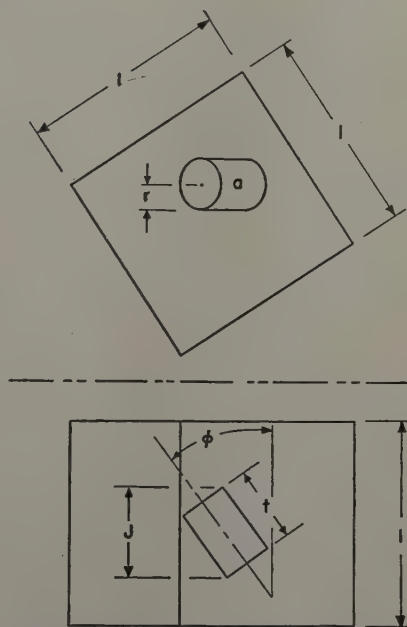


Fig. 1—Diagram of a cylindrical particle in a unit cube.

carried out with parallel cross-sectional planes and lineal traverses. If the cylinders are not randomly oriented, it is necessary to randomize the orientations of the cross-sectional planes and traverse lines. Let a unit cube be cut from the sample, and a cross-section plane be passed through the cube parallel to one of the cube faces. The number of particles N , cut by the cross-sectional plane per unit area is equal to the number of particles N_v per unit volume times the probability p_1 of a plane intersecting a single randomly positioned and randomly oriented cylinder in the cube. Let J be the maximum cylinder dimension in the direction normal to the cross-section planes, as shown in Fig. 1. Since, of the various possible positions for the cross-sectional plane over the unit length from top to bottom of the cube, only those positions existing over the length J

would lead to the plane intersecting the cylinder, the probability of intersecting a single cylinder is equal to \bar{J} , the mean value of J for all possible orientations of the cylinder.

Let ϕ be the angle between the cylinder axis and the normal to the cross-sectional planes, and let $p_\phi d\phi$ be the probability that a cylinder orientation is described by an angle between ϕ and $\phi + d\phi$. Then for randomly oriented cylinders $p_\phi = \sin \phi$. Let $p_J dJ$ be the probability that a given particle has a maximum dimension between J and $J + dJ$ in the direction perpendicular to the cross-section planes. Referring to Fig. 1,

$$p_J = p_\phi \left| \frac{d\phi}{dJ} \right| = \frac{\sin \phi}{2r \cos \phi - t \sin \phi} \cdot J = 2r \sin \phi + t \cos \phi.$$

The average value of J is equal to the integral, over all possible orientations, of the product of J and its probability.

$$\bar{J} = \int_0^{2\pi} J p_J dJ = \int_0^{\pi/2} (2r \sin \phi + t \cos \phi) \sin \phi d\phi = \frac{1}{2} (\pi r + t).$$

$$N_s = N_v p_1 = N_v \bar{J} = \frac{N_v}{2} (\pi r + t). \quad [1]$$

Combining Eq. 1 and the equality of volume and area fractions f , a relationship is obtained between the average area \bar{s} of particles intersected by a random cross section and the particle dimensions.

$$f = N_v V = N_v \pi r^2 t = N_s \bar{s} = \frac{N_v}{2} (\pi r + t) \bar{s}.$$

$$\bar{s} = \frac{2\pi r^2 t}{\pi r + t}. \quad [2]$$

Eq. 2 may be compared with the equations derived previously, Eq. 1, for extremely thin plates and rods. If $r \gg t$, Eq. 2 reduces to $\bar{s} = 2rt$, as was found for very thin plates. If $r \ll t$, Eq. 2 reduces to $\bar{s} = 2\pi r^2$, as was found for very thin rods.

If randomly placed lines are passed through the unit cube parallel to an edge, the number N_L of particles per unit length intersected by the lines is equal to the number of particles per unit volume times the probability p_2 that a line will intersect a single randomly positioned and randomly oriented cylinder in the cube. Let a be the area of the projection of a cylinder on the plane perpendicular to the traverse lines, as shown in Fig. 1. Since, of the various positions for the traverse line over the unit area of the cube top, only those positions within the area a would lead to the line intersecting the cylinder, the probability of intersecting a single cylinder is equal to \bar{a} , the mean value of a for all possible orientations of the cylinder.

Cauchy^{2,3} has shown that the average projected area of a convex particle* is equal to one-fourth

* A convex body, in the sense used here, is one whose surface cannot be pierced in more than two places by any straight line.

the particle's surface area. Therefore, $p_2 = \bar{a} = \pi(r^2 + rt)/2$.

$$N_L = p_2 N_v = \frac{\pi}{2} N_v (r^2 + rt). \quad [3]$$

Combining Eq. 3 with the equality of volume and lineal fractions f , a relationship is found between the average traverse length \bar{l} and the particle dimensions.

$$f = N_v V = N_v \pi r^2 t = N_L \bar{l} = \frac{\pi}{2} N_v (r^2 + rt) \bar{l}.$$

$$\bar{l} = \frac{2rt}{r + t}. \quad [4]$$

Eq. 4 may be compared with the equations previously derived for extremely thin plates and rods. If $r \gg t$, Eq. 4 reduces to $\bar{l} = 2t$, as was found for very thin plates. If $r \ll t$, Eq. 4 reduces to $\bar{l} = 2r$, as was found for very thin rods. Before applying Eqs. 2 and 4 to the analysis of moderately thick plates or rods, it is desirable to estimate the degree to which the equations are sensitive to the precise shape assumed, i.e., circular cylinders. If, for approximately equiaxed cylinders, the equations correspond to those previously found for spheres,¹ they may be applied with confidence to plates and rods that depart significantly from extreme thinness. Eq. 2 corresponds to that for a sphere ($\bar{s} = 2\pi r^2/3$) for $t = \pi r/2$, and Eq. 4 corresponds to that for a sphere ($\bar{l} = 4r/3$) for $t = 2r$. Both of these relationships correspond to roughly equiaxed cylinders.

In order to find the particle dimensions in terms of the average particle area \bar{s} and average traverse length \bar{l} , or in terms of the volume, area, lineal, or point fraction f of the phase and the area and lineal counts N_s and N_L , Eqs. 2 and 4 or 1 and 3 may be combined.

$$r = \frac{\pi \bar{s} \pm \sqrt{\pi^2 \bar{s}^2 - 2\pi(\pi - 1) \bar{l}^2 \bar{s}}}{2\pi \bar{l}}. \quad [5]$$

$$t = \frac{\bar{l}(\pi \bar{s} \pm \sqrt{\pi^2 \bar{s}^2 - 2\pi(\pi - 1) \bar{l}^2 \bar{s}})}{2(\pi \bar{s} \pm \sqrt{\pi^2 \bar{s}^2 - 2\pi(\pi - 1) \bar{l}^2 \bar{s}} - \pi \bar{l}^2)}. \quad [6]$$

$$r = \frac{\pi N_L \pm \sqrt{\pi^2 N_L^2 - 2\pi(\pi - 1) f N_s}}{2\pi N_s}. \quad [7]$$

$$t = \frac{f(\pi N_L \pm \sqrt{\pi^2 N_L^2 - 2\pi(\pi - 1) f N_s})}{2N_L(\pi N_L \pm \sqrt{\pi^2 N_L^2 - 2\pi(\pi - 1) f N_s} - \pi f N_s)}. \quad [8]$$

In Eqs. 5 to 8, the positive sign is used before the radical for particles in the form of plates, and the negative sign for particles in the form of rods.

Conclusions

Equations have been derived permitting the evaluation, from measurements on polished cross sections, of the dimensions of particles dispersed as uniform cylindrical plates or rods. The validity of the equations is not limited to extremely thin plates or rods nor to particles of exactly cylindrical shape. The relationships do not appear sufficiently simple to encourage their extension to the analysis of non-uniform particles.

References

- ¹ R. L. Fullman: Measurement of Particle Sizes in Opaque Bodies. *Trans. AIME* (1953) **197**, p. 447; *JOURNAL OF METALS* (March 1953).
- ² A. Cauchy: *Memoires sur la rectification des courbes et la quadrature des surfaces courbes*. (1832) Paris.
- ³ V. Vouk: Projected Areas of Convex Bodies. *Nature* (1948) **162**, p. 330.

System $\text{Ag}_2\text{O}-\text{B}_2\text{O}_3$; Its Thermodynamic Properties as a Slag Model

by G. M. Willis and F. L. Hennessy

The oxygen pressure in equilibrium with silver and $\text{Ag}_2\text{O}-\text{B}_2\text{O}_3$ melts has been measured between 800° and 900°C, to obtain the thermodynamic properties of the liquid. The compound $\text{Ag}_2\text{O} \cdot 4\text{B}_2\text{O}_3$ appears to exist in the liquid, which shows marked heat content and entropy effects.

A KNOWLEDGE of the thermodynamic properties of binary liquid silicates, borates, and phosphates would be of considerable assistance in the interpretation of the behavior of multi-component metallurgical slags. However, the literature contains comparatively few studies of the thermodynamics of binary slags.

The system $\text{Ag}_2\text{O}-\text{B}_2\text{O}_3$ attracted our attention as it was known to give a single liquid phase,^{1,2} in which high contents of silver could be obtained (up to 61 pct Ag according to Foëx³). Further, it would be expected that the partial pressure of oxygen over melts in equilibrium with metallic silver could be used to determine the activity of Ag_2O in the $\text{Ag}_2\text{O}-\text{B}_2\text{O}_3$ system. In many respects, it may be expected that the reaction of a basic oxide with boric oxide would be analogous to its reaction with silica. Liquid immiscibility frequently occurs in both borate and silicate systems. With B_2O_3 and SiO_2 reaction with a basic oxide presumably involves a breakdown of the three-dimensional network of the acid oxide by reaction with oxygen atoms common to more than one silicon or boron atom. $\text{Ag}_2\text{O}-\text{B}_2\text{O}_3$ was therefore investigated as a model of a slag system in the hope that its thermodynamic properties would assist in understanding those of other systems.

Several methods for determining the activity of a component in a slag have been described in the literature. Chang and Derge⁴ used high temperature electromotive force measurements to obtain the activity of SiO_2 in $\text{CaO}-\text{SiO}_2$ and $\text{CaO}-\text{Al}_2\text{O}_3-\text{SiO}_2$ slags, but the cell reaction in their work is not clear.⁴ Calow has used rate of volatilization and vapor pressure measurements combined with phase diagrams to obtain activities in the systems $\text{K}_2\text{O}-\text{SiO}_2$, $\text{Na}_2\text{O}-\text{SiO}_2$, and $\text{Li}_2\text{O}-\text{SiO}_2$ ⁵ and $\text{PbO}-\text{SiO}_2$.⁶ Taylor and Chipman⁷ extrapolated their results for the distribution of FeO between liquid iron and $\text{CaO} (+\text{MgO})-\text{FeO}-\text{SiO}_2$ slags to obtain the activity of FeO in the binary $\text{FeO}-\text{SiO}_2$ system.

G. M. WILLIS is Senior Lecturer in Chemical Metallurgy in the University of Melbourne, Australia, and F. L. HENNESSY is now with Mt. Morgan Ltd., Mt. Morgan, Queensland, Australia.

Discussion on this paper TP 3588D, may be sent, 2 copies, to AIME by April 1, 1954. Manuscript, Jan. 23, 1953. New York Meeting, February 1954.

In principle, one of the most direct methods for obtaining the activity of a metallic oxide in a phase is by comparison of the equilibrium oxygen pressure for the system metal-pure oxide with that of metal oxide-containing phase. Schenck and others⁸ have studied the stabilization of Ag_2O on combination with other oxides (MO_x) in the solid state by measurements of the oxygen pressure in systems of the type $\text{Ag}-\text{Ag}_2\text{O} \cdot x\text{MO}_x-\text{MO}_x-\text{O}_2$ (gas). Schuhmann and Ensio⁹ have determined the activity of FeO in iron silicate slags in equilibrium with solid iron, using CO/CO_2 mixtures to establish known partial pressure of oxygen. Although the method gives the activity of FeO without ambiguity, the slag is not a binary system, and interpretation of the results in terms of the hypothetical binary system $\text{FeO}-\text{SiO}_2$ is not possible.

If a metal is solid at temperatures at which the properties of the slag containing its oxide are to be studied, this method has the considerable experimental advantage that the metal can be used as the container for the slag, and contamination by contact with refractories is avoided. In this work, crucibles for $\text{Ag}_2\text{O}-\text{B}_2\text{O}_3$ melts were made from silver, and the liquid brought to equilibrium with definite pressures of oxygen gas. The oxygen pressure P_{O_2} thus fixes the activity of Ag_2O in the liquid silver borate. For the reaction

$2\text{Ag}_{(\text{c})} + \frac{1}{2}\text{O}_{2(\text{gas})} = \text{Ag}_2\text{O} \text{ (in slag)}$
at a given temperature.

$$K = \frac{a_{\text{Ag}}^2 \cdot P_{\text{O}_2}^{1/2}}{a_{\text{Ag}_2\text{O}}} \quad [1]$$

and since a_{Ag} is substantially constant, $a_{\text{Ag}_2\text{O}}$ is directly proportional to the square root of the equilibrium oxygen pressure. Varying the oxygen pressure changed the silver oxide content of the liquid and it was possible to obtain the activity of Ag_2O over a range of composition.

Experimental Procedure

In principle, the method consisted of bringing melts in silver crucibles or boats to equilibrium at a fixed temperature under a definite pressure of oxygen and analyzing the glass after solidification.

Materials: B_2O_3 glass was prepared from A.R. quality boric acid by fusion in platinum. The silver

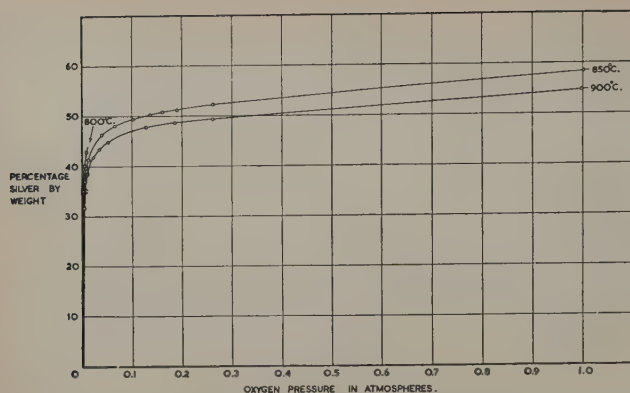


Fig. 1—The composition of $\text{Ag}_2\text{O-B}_2\text{O}_3$ melts as a function of the oxygen pressure. For clarity, the experimental points at very low pressures are not shown.

used was the purest available, and contained less than 0.002 pct Cu as the largest impurity followed by lead at less than 0.0005 pct. No contamination of the melts by these elements could be detected. Cylinder oxygen was purified by passage over CaCl_2 , ascarite, and P_2O_5 . Regular determinations of the oxygen content of the gas were made, and corrections applied to the measured pressure. The same purification train was used in some experiments which were run using air, and one with cylinder nitrogen which contained 0.411 pct O_2 , determined by the method of Powell and Joy.¹⁰ A.R. quality AgNO_3 was used to prepare silver-rich glasses by melting it with B_2O_3 glass in silver.

Temperature Control and Measurement: Care was taken to insure uniformity of temperature over a considerable distance within the furnaces; this was facilitated by lining them with silver sheet. Temperatures were controlled by Cambridge controllers, actuated by thermocouples placed near the furnace windings. These controlled a small fraction of the total furnace current, in order to minimize fluctuations in temperature. Temperatures were measured by calibrated thermocouples and potentiometer, and the temperatures are believed to be accurate within $\pm 1^\circ\text{C}$.

Pressure Measurement and Control: Here, the experimental methods varied considerably depending on the range of pressure in use. For high pressures, a mercury manometer was used; for lower pressures, a butyl phthalate manometer, and to extend the measurements to liquids comparatively low in the Ag_2O a McLeod gage was required. Except for runs with a total gas pressure of substantially 1 atm, gas pressures had to be controlled. In the higher pressures, this was done by using the manostat described by Spadero, Vix, and Gastrock.¹² For the lowest pressures, a needle-diaphragm valve provided a controlled and sensibly constant leak of oxygen into the furnace system.

For experiments at high pressures, it was necessary to use silver crucibles suspended by silver wire in a vertical tube furnace, as the silver borate crept rapidly up the walls of boats, and only at low oxygen pressures was it possible to keep the melt in a silver boat in a horizontal furnace. Even with relatively high crucibles "creeping" of the liquid was a continuous difficulty; it was often necessary to collect (in a silver tray beneath the crucible) the liquid which had crept over the edge and finally dripped off the bottom, and return this to the crucible to have sufficient liquid on hand.

In all cases, a continuous flow of oxygen was maintained through the system. Pressures below atmospheric were maintained by a small vacuum pump on the outgoing end of the system. Before commencing a run, the whole train was tested to insure that it was gas tight.

Preliminary experiments were run approaching equilibrium by bubbling oxygen from a silver tube through liquid B_2O_3 in silver crucibles. (The bubbling stopped as the liquid crept up the walls of the crucible.) About five days were required for the liquid to attain constant composition. Equilibrium could be reached much more rapidly (one to two days) from the silver-rich side, and so most of the results were obtained by the decomposition of melts initially richer in Ag_2O than the equilibrium value. These melts were prepared from B_2O_3 and metallic Ag, or by fusing AgNO_3 with B_2O_3 in silver. Liquids equilibrated at high P_{O_2} could be used as starting materials for lower P_{O_2} runs.

Sampling: Upon withdrawal from the furnace, the crucible or boat and its contents were rapidly cooled in a jet of air. The resulting glass was crushed and a sample for analysis taken and stored in a weighing bottle in a desiccator. Experiment showed no effect of different rates of cooling; there was no sign of gas evolution from the liquid, and the sluggishness of the reactions makes it unlikely that any appreciable change in composition took place during cooling. Samples taken from the top and the bottom of a crucible were identical in composition. After taking a sample, the container was returned to the furnace to continue the run.

Analysis: Prolonged heating of the silver container resulted in grain growth and the melt penetrated along the grain boundaries of the metal, and occasionally a large crystal of silver would become detached, and sink to the bottom of the liquid. To insure that no such crystals were present, the sample was examined under a binocular microscope. As a further check, both silver and B_2O_3 were determined.

For the determination of silver, the weighed sample of glass was dissolved in dilute HNO_3 and the solution titrated with standardized NH_4CNS . B_2O_3 was determined by dissolving the sample in water, precipitating the silver as AgCNS , boiling gently to remove CO_2 taking care not to drive off boric acid, and adjusting to neutrality to methyl orange if required. Mannitol was then added and the B_2O_3 titrated in the usual way with CO_2 -free NaOH . Check

Table I. Silver Content in $\text{Ag}_2\text{O-B}_2\text{O}_3$ Melts in Equilibrium with Solid Silver and Oxygen

$t = 900^\circ\text{C}$		$t = 850^\circ\text{C}$		$t = 800^\circ\text{C}$	
Wt Pct Ag	$10^3 \times P_{\text{O}_2}$ (Atm)	Wt Pct Ag	$10^3 \times P_{\text{O}_2}$ (Atm)	Wt Pct Ag	(Atm) $10^3 \times P_{\text{O}_2}$
54.4	998	58.40	1.000	42.79	8.7
49.27	260.7	52.19	261.2	40.04	4.9
48.88	184.7	51.04	191.5	34.95	2.2
48.81	185.2	51.00	190.5	28.31	0.99
47.93	128.9	50.84	160.7	23.01	0.59
44.96	52.1	50.18	137.0	15.88	0.22
43.44	34.2	49.46	104.8	9.73	0.06
41.82	22.1	48.11	65.5		
38.57	10.1	46.27	38.9		
35.14	4.8	46.19	38.7		
31.65	2.82	41.22	11.7		
24.20	1.38	39.94	8.0		
17.26	0.57	37.12	4.2		
12.15	0.30	29.37	1.6		
6.08	0.09	19.36	0.5		
		14.8	0.26		
		8.51	0.09		

analyses on known samples of $\text{AgNO}_3 + \text{B}_2\text{O}_3$ showed these methods to be reliable.

Experimental Results

The composition of the liquid was well-defined for any given P_{O_2} and good agreement was obtained between the occasional duplicates. For example, at 850°C silver contents of 58.4 pct and 58.3 pct were obtained in two runs with oxygen pressures of 1.00, and 0.99, atm, respectively. Similar agreement was found between melts prepared by synthesis and decomposition. At 850°C and $P_{\text{O}_2} = 0.0042$ synthesis gave 37.12 pct Ag while decomposition gave 37.24 pct. As a rule, runs were continued until the composition had remained constant over 48 hr.

Fig. 1 shows the composition of the liquid at 800° , 850° , and 900°C as a function of the partial pressure of oxygen; the experimental data are summarized in Table I. At 800°C equilibrium could not be attained at higher oxygen pressures and the glass was found to contain a small amount of a second phase, which was not identified. The silver content of the glass is clearly determined by the oxygen pressure and the temperature, and there is little doubt that the silver is present in an oxidized form, and not as dispersed metal. The glasses were a clear lemon-yellow color, and showed no sign of colloidal metal on examination with the ultra-microscope. The well-defined silver content would not be expected if the metal were present in colloidal form.

If the silver content is calculated as Ag_2O then the sum of Ag_2O and B_2O_3 has been found to be 100.0 pct to within the analytical error of about 0.1 pct on the total. Furthermore, determination of the oxygen content by loss in weight on decomposition, showed the oxygen to be equivalent to the silver calculated as Ag_2O .

The melts may therefore be regarded as containing Ag_2O and B_2O_3 and any departure from stoichiometry of the system, or silver present in the atomic state as suggested by Weyl,¹³ is less than the analytical errors.

These results are in agreement with the observations of Bogitch,¹³ Kubachewski,¹⁴ and Stookey,¹⁵ all of whom found the silver content of silicate glasses to be increased by increasing the oxygen pressure and therefore consider it to be present as oxide.

Fig. 2 shows the activity of Ag_2O as a function of composition at 850°C . Since the activity of the dissolved Ag_2O is proportional to $P_{\text{O}_2}^{1/2}$, it is convenient to define the standard state of unit activity of Ag_2O as that for which $P_{\text{O}_2} = 1$ atm in equilibrium with pure solid silver. Then, the activity of the Ag_2O (a_2) is simply given by $P_{\text{O}_2}^{1/2}$ when P_{O_2} is in atmospheres. The activity of the B_2O_3 (a_1) is obtained from the Gibbs-Duhem equation, and shows strong negative deviations from Raoult's law. For dilute solutions the Ag_2O appears to obey Henry's law, as shown in Fig. 3. In view of the experimental errors at the low O_2 pressures involved not much weight was at first given to the linear relation. However, as will be shown below, the partial molar heat of solution of Ag_2O in the dilute solution is constant, as it should be, and it is thought that the results are significant.

Discussion of Results

Nature of the Dissolved Silver Oxide: The proportionality between activity and mol fraction for Ag_2O in dilute solution implies that it is present as an entity of the type $\text{Ag}_2\text{O} \cdot n\text{B}_2\text{O}_3$ rather than $\frac{1}{2}\text{Ag}_2\text{O} \cdot n\text{B}_2\text{O}_3$, where " $n\text{B}_2\text{O}_3$ " indicates that por-

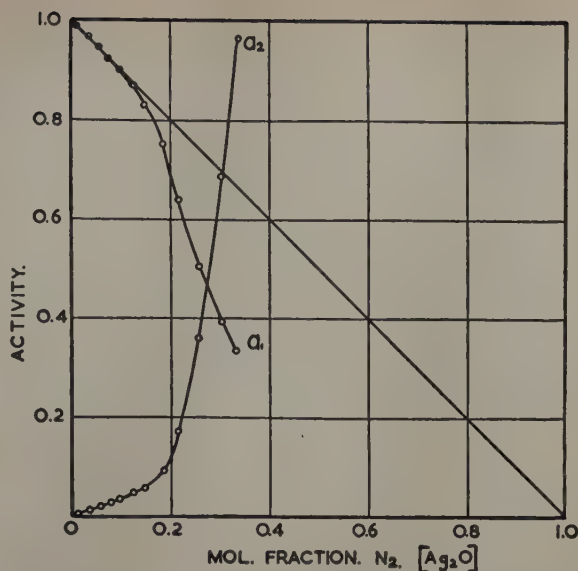


Fig. 2—Activities of Ag_2O and B_2O_3 at 850°C . The standard state for Ag_2O is the melt in equilibrium with silver and oxygen at 1 atm; that for B_2O_3 is the pure liquid.

tion of the B_2O_3 which has been affected by the Ag_2O . The solution may therefore be regarded as containing Ag_2O solvated by B_2O_3 rather than one in which Ag^+ ions are dispersed throughout the liquid as independent species. "Dissociation" of Ag_2O apparently does not occur.

The reason for this behavior is probably that when Ag_2O is introduced into the B_2O_3 the O^- ion, whether it changes the coordination number of B from 3 to 4, or breaks a B-O-B bond, produces "unsaturated" oxygens in the network, and the Ag^+ ions remain in the immediate neighborhood of these oxygens. This tendency for the cations to remain together to make the maximum use of what "unsaturated" oxygens are present in dilute solutions of oxides was recognized by Warren,¹⁶ and the results are consistent with his picture of the structure of glasses.

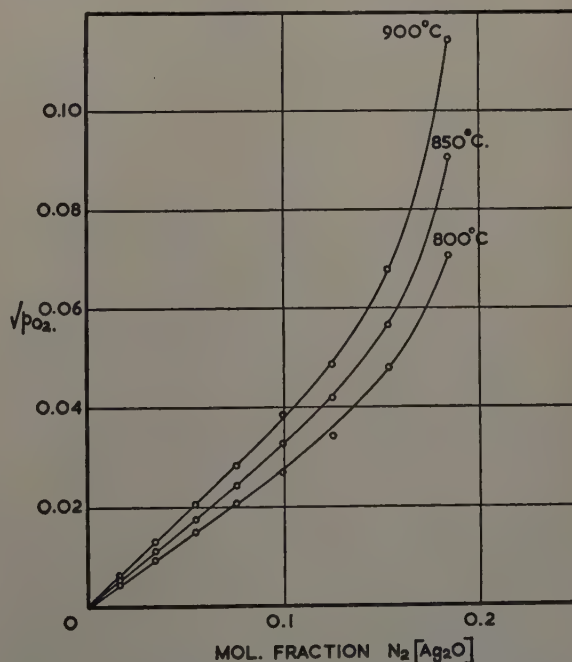


Fig. 3—The activity $a_2 (= P_{\text{O}_2}^{1/2})$ of Ag_2O in dilute solutions in B_2O_3 .

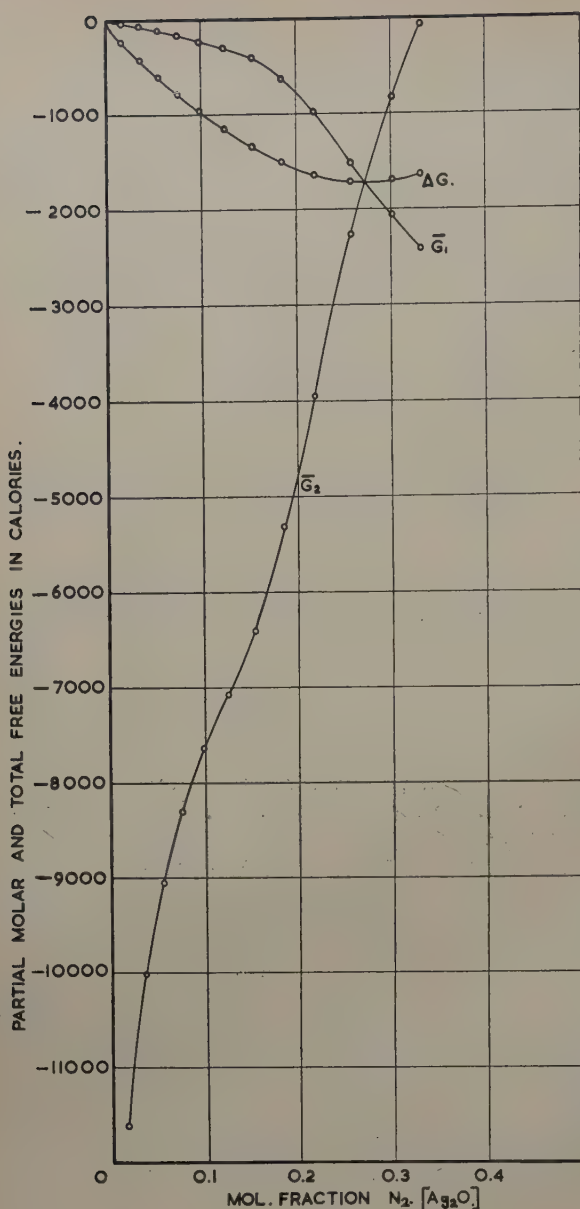


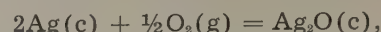
Fig. 4—Partial molar free energies of Ag_2O (\bar{G}_2) and B_2O_3 (\bar{G}_1) in Ag_2O - B_2O_3 melts; integral free energy of formation of 1 mol $\text{Ag}_2\text{O} + \text{B}_2\text{O}_3$ (ΔG). Standard state for Ag_2O : silver and oxygen at 1 atm.

For the SiO_2 liquidus in the alkali oxide-silica systems, Kracek¹⁷ showed that a plot of $\log N \text{ SiO}_2$ vs $1/T$ gave a straight line for very dilute solutions, indicating that Henry's law is obeyed by the alkali oxides in SiO_2 . The same considerations appear to apply to dilute solutions in both SiO_2 and B_2O_3 . It is to be expected that as the proportion of basic oxide in a melt increases, and an ample supply of "unsaturated" oxygens is available, "dissociation" of oxides should occur giving more or less independent cations.

Compound Formation in Ag_2O - B_2O_3 : Although the standard state for Ag_2O used above is convenient, it is of interest to use solid Ag_2O as the standard state. This of course requires a considerable extrapolation of the experimental results on which the thermodynamic data for Ag_2O are based. For the purposes of illustration, exact numerical values are not required. The use of solid Ag_2O as the standard state for Ag_2O then makes it possible to express the

activity of Ag_2O in the melt relative to that of a more common single phase, viz., the oxide.

For the reaction



Thompson¹⁸ gives the standard free energy change $\Delta G^\circ = -6690 + 14.61 T$. At 850°C , the dissociation pressure of O_2 is 6000 atm or the numerical value of K in Eq. 1 is $(6000)^{1/2} = 77$. To convert the activities of Ag_2O to the new standard state, the values in Fig. 2 have to be multiplied by $1/77 = 0.013$. It is clear that Ag_2O shows marked negative deviations from Raoult's law, and even if it were possible to use liquid Ag_2O as a standard state, the general trend would not be greatly altered, as no great difference in thermodynamic properties between solid and liquid oxide would be expected.

The classical explanation of pronounced negative deviations from Raoult's law is to ascribe them to compound formation. In the dilute solutions, combination between Ag_2O and B_2O_3 undoubtedly occurs, but the fact that the solution obeys Henry's law implies that the greater part of the B_2O_3 is unaffected by the presence of the Ag_2O .

Fig. 4 shows the partial molar free energy \bar{G}_2 of Ag_2O at 850°C . This is equal to $R T \ln a_2$; the curve shown refers to $P_{\text{O}_2} = 1$ atm as the standard state for Ag_2O . The curve shows a weak inflection at about $N_2 = 0.2$. Such an inflection is analogous to that found at the end-point of potentiometric titrations. Comparison of the activity and the partial molar free energy curves for Ag_2O shows that the latter function is more suitable for the recognition of compound formation, if it is assumed that an inflection does in fact correspond to a compound at the particular composition. This is certainly true for Na_2O - SiO_2 melts, for which the \bar{G} vs mol fraction curves show marked inflections at the metasilicate composition.¹⁹ (For compositions near the metasilicate calculations can be made by the method of Haufler and Wagner.²⁰) It is suggested that partial molar free energy curves are worth further attention as a means for recognizing "end-points" in the reaction between acid and basic oxides in the liquid state.

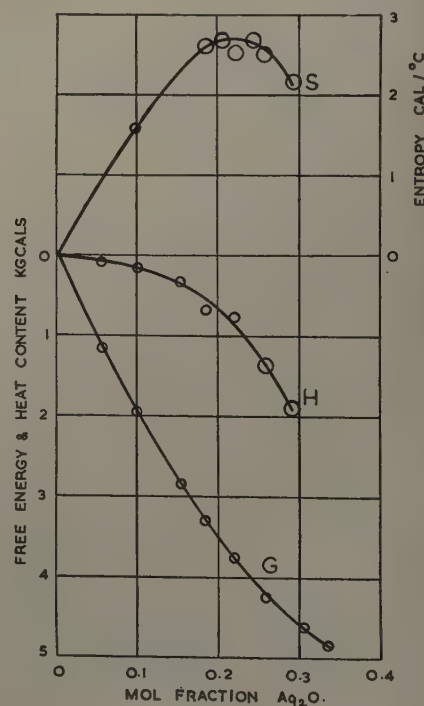


Fig. 5—Free energy (G), heat content (H) and entropy (S) of Ag_2O - B_2O_3 melts, relative to $\text{Ag}_2\text{O}(c)$ and $\text{B}_2\text{O}_3(l)$.

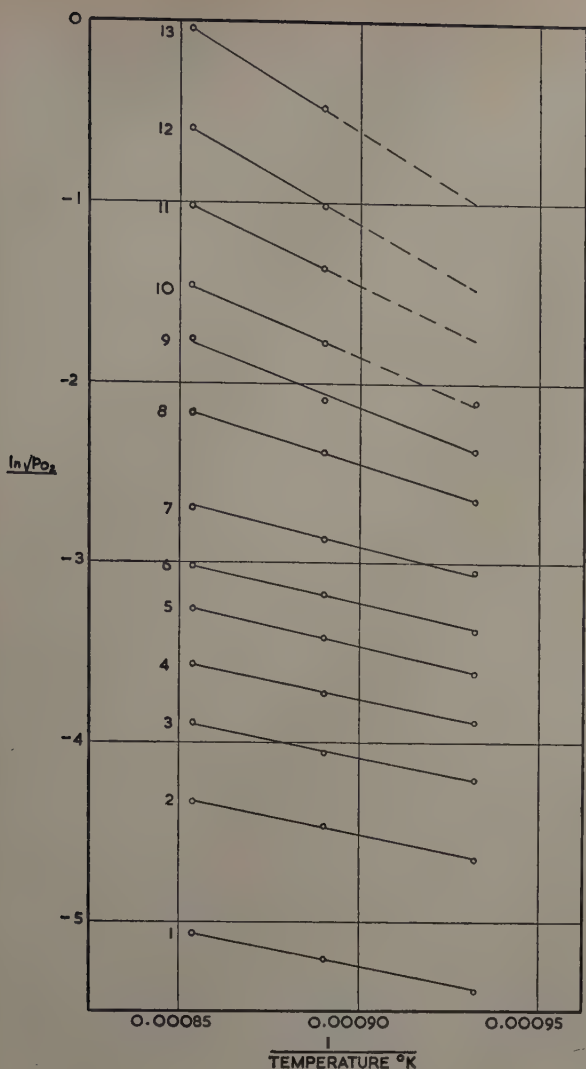
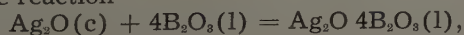


Fig. 6— $\ln a_2$ ($\ln P^{1/2}O_2$) vs $1/T$ plots at constant composition; the curves 1, 2 . . . 13 refer respectively to mol fractions of Ag_2O of 0.0168, 0.0349, 0.0545, 0.0760, 0.099, 0.124, 0.153, 0.184, 0.205, 0.219, 0.242, 0.258, 0.293.

In the Ag_2O - B_2O_3 system, the inflection is not sufficiently definite to fix precisely the composition of the compound. In alkali oxide- B_2O_3 systems, compounds of the type $M_2O \cdot 4B_2O_3$ are well-known, and to judge from their melting points, comparatively stable. $Ag_2O \cdot 4B_2O_3$ has been described by de Carli²¹ as a solid compound, with a melting point of $570^\circ C$, and apparently is the only compound recognized by thermal analysis of melts in the range of composition studied (3 to 5 mol B_2O_3 per mol Ag_2O). This additional evidence makes it possible to ascribe the inflection to the formation of the compound $Ag_2O \cdot 4B_2O_3$ in the melt. The slight inflection shows that the compound formed in the melt is comparatively weak.

The partial molar free energy curve for Ag_2O in Fig. 4 may be converted to that for solid Ag_2O as the standard state by subtracting 9680 cal throughout (Thompson's equation gives the standard free energy of Ag_2O as + 9680 cal at $850^\circ C$). Combining this with the data for B_2O_3 , the integral free energy may be calculated for $Ag_2O \cdot 4B_2O_3$ at $850^\circ C$. For a total of one mol $Ag_2O + B_2O_3$, the value is -3500 cal.

For the reaction



the free energy change is -17,500 cal at $850^\circ C$.

The integral free energy of the liquid relative to $Ag_2O(c)$ and $B_2O_3(l)$ is shown in Fig. 5. If continued, there are two possibilities for the curve. If $850^\circ C$ is below the (unknown) melting point of Ag_2O , it must become tangential to a line from $N_2 = 1$, $G = 0$ corresponding to saturation with solid Ag_2O . If $850^\circ C$ is above the melting point of Ag_2O , the curve must conclude at $N_2 = 1$ at the value of the free energy of the liquid oxide. The regions to the right of the diagram of course are unstable except at very high oxygen pressures. It is probable that there is a minimum in the free-energy curve at some higher concentration of Ag_2O indicating some more basic compound may exist. The precipitation of $Ag_2O \cdot B_2O_3$ from aqueous solutions would indicate that it is comparatively stable at room temperature but at elevated temperatures it would not

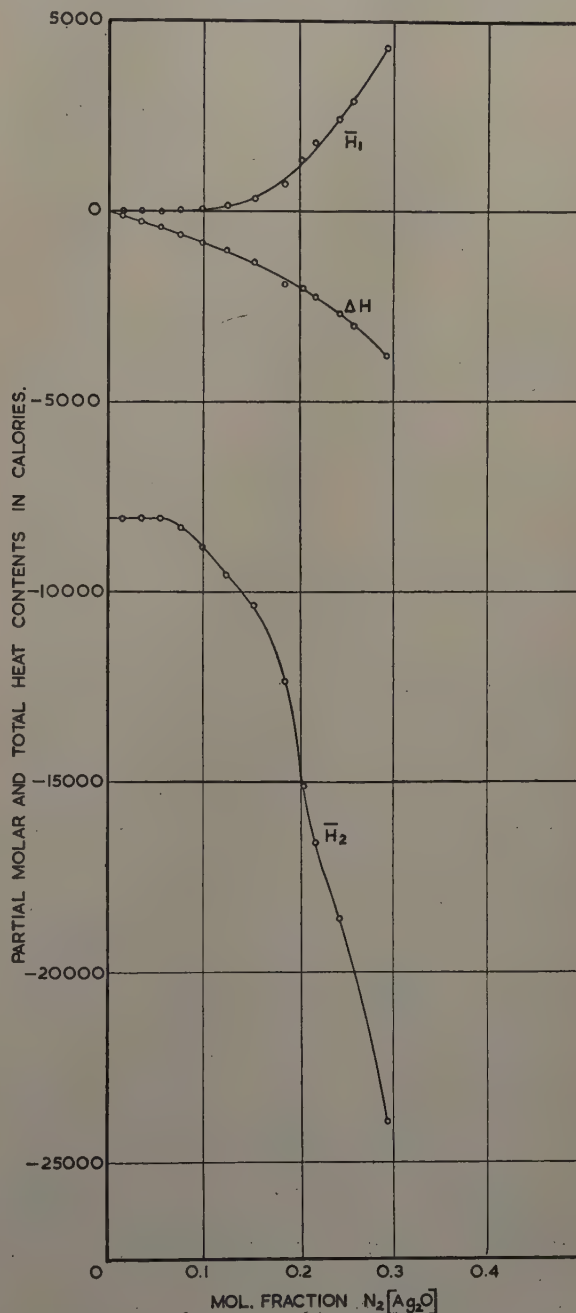


Fig. 7—Partial molar heat content changes for $Ag_2O(H_2)$ and $B_2O_3(H_2)$ in Ag_2O - B_2O_3 melts; integral change in heat content for 1 mol $Ag_2O + B_2O_3$ (ΔH). Standard state for Ag_2O : silver and oxygen at 1 atm.

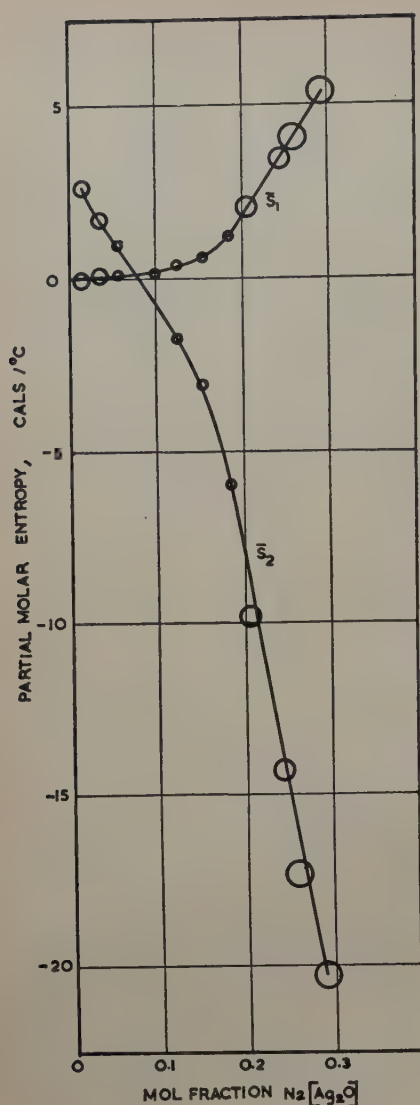


Fig. 8—Partial molar entropies of $Ag_2O(\bar{S}_2)$ and $B_2O_3(\bar{S}_1)$ in $Ag_2O-B_2O_3$ melts; standard state for Ag_2O : silver and oxygen at 1 atm.

be stable except under high oxygen pressures. An approximate calculation²² of the free energy of formation at room temperature of $Ag_2O \cdot B_2O_3$ from $Ag_2O(c)$ and $B_2O_3(glass)$ gives $-14,000$ cal, which is not inconsistent with the possibility of its existence in melts at elevated temperatures.

Heats of Solution: From curves of $P^{1/2}O_2$ vs N_2 at each temperature, values of $P^{1/2}O_2$ were read at a series of constant compositions of the liquid. From plots of $\log P^{1/2}O_2$ against $1/T$ at constant composition (Fig. 6) the partial molar heat content change was obtained for the reaction



The change in partial molar heat content for Ag_2O (\bar{H}_2) is given in Fig. 7 along with that for B_2O_3 which is obtained by the Gibbs-Duhem equation. For dilute solutions, \bar{H}_2 is constant, as it should be for solutions in Henry's law region.

With increasing Ag_2O content, \bar{H}_2 decreases, indicating that Ag_2O is bound in sites of lower energy as the proportion of oxide increases. A possible inflection occurs at $N_2 = 0.2$ followed by a further drop in \bar{H}_2 .

The inflection in \bar{H}_2 may be expected when compound formation occurs in a liquid. Marked changes in \bar{H} should occur on passing through the stoichiometric composition as the structure of the melt changes.

The general decrease in \bar{H}_2 here as the Ag_2O content increases shows that the structure of the melt changes so as to provide on the average sites of lower energy for the Ag_2O . In general, sites of lower energy would be those in which some appropriate co-ordination of oxygen around silver is attained. The form of the curve suggests that after the composition $Ag_2O \cdot 4B_2O_3$ is passed, a further change in structure of the liquid occurs, and another inflection may be expected at higher Ag_2O concentrations. Up to $N_2 = 0.2$, the liquid may be visualized as having steadily increasing proportions of the arrangement more or less characteristic of the compound; for higher Ag_2O contents, it is possible that the structure gradually changes to one associated with a higher compound.

Integral heat content curves are given in Fig. 7 for $2Ag + \frac{1}{2}O_2$ and in Fig. 5 for Ag_2O . The shapes of the curves are unusual; somewhat similar behavior may be recognized in liquid Cd-Sb alloys, which have been studied by Elliott and Chipman.²³ The ΔH curve also suggests the existence of another silver borate, as peaks in integral heat content curves are generally associated with compound formation, and the curves must have minima at high Ag_2O concentrations.

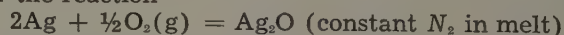
To account for the miscibility gap in some silicate systems, Warren^{16, 24} suggested that the energy would be a minimum when the cations were able to surround themselves with a sufficient number of co-ordinated oxygens, i.e., when sufficient basic oxide was present. The results here are consistent with this viewpoint, but of course cannot give any information as to the constitution of the liquid.

The partial molar heat of solution of liquid FeO in iron silicate slags was found by Schuhmann and Ensio¹⁹ to be independent of composition. This result is in marked contrast to the observations here; the reason for the disparity must be decided by further work on suitable systems.

Entropy Changes: From plots of \bar{G}_2 at constant composition against T , it is possible to obtain \bar{S}_2 , the partial molar entropy of the Ag_2O in the melt, since $\frac{\partial \bar{G}}{\partial T} = -\bar{S}$. This can also be obtained from the relation

$$\bar{S} = (\bar{H} - \bar{G}) / T.$$

The use of the two methods provides a useful check on the errors in interpolation and in graphical integrations. The partial molar entropy of solution of B_2O_3 was obtained by using the "entropy fractions" suggested by Kleppa²⁵ to make use of the Gibbs-Duhem equation. Fig. 8 shows the entropy change for the reaction



while the integral entropy of the liquid is shown in Fig. 5 where the components are solid Ag_2O and liquid B_2O_3 . Thompson's equation was used to obtain a mean value of the entropy of formation of Ag_2O .

The curves show no resemblance to those for the ideal entropy of mixing. For the dilute solutions, \bar{S}_2 is equal to constant $-R \ln N_2$, as it should be for solutions obeying Henry's law. As N_2 increases, \bar{S}_2 decreases rapidly as the composition $Ag_2O \cdot 4B_2O_3$ is approached, and presumably indicates the development of some ordered arrangement in the liquid. At the stoichiometric composition of a compound, the liquid structure will resemble that of the crystalline solid, without the long-range order of the solid, but

with the same cations occupying similar sites, with average co-ordination numbers much the same, and the anionic network consisting of substantially the particular poly-anion characteristic of the crystal. For compositions of the liquid other than the stoichiometric, more than one type of ion may be present, and a variety of sites for the cations may be imagined, depending on the types of anions, or the extent to which the network of the acid oxide has been broken down in the vicinity of the cations. Considerations of this sort suggest that the stoichiometric liquid is "ordered" compared with liquid of different composition.

In liquid alloys, entropy effects associated with compound formation exist in the systems Cd-Sb²³ and Au-Sn.²⁸

In the present example, the effect due to ordering may explain the behavior for N_2 less than 0.2, but an increase in the total entropy would be expected again at higher Ag₂O concentrations. The liquid Ag₂O·4B₂O₃ should, on the picture outlined above, have a lower entropy than liquids whose compositions lie on either side of it. The observed behavior is probably associated with the increased strength of bonding of Ag₂O (shown by the changes in \bar{H}_2) as the concentration increases. There is a rough correlation between the changes in \bar{H}_2 and \bar{S}_2 , except for Henry's law region. If this is significant, it indicates a decrease in entropy as the Ag₂O becomes more firmly held in the liquid. Tentatively, the decrease in entropy for N_2 greater than 0.2 may be identified with the loss in "vibrational" entropy which must be assumed to mask the expected increase in configurational entropy. Tightly bound Ag⁺ ions of course have less freedom than loosely held ones, so the entropy change will be of the correct sign.

Conclusions

The observations in general confirm Warren's views on the nature of the interaction between basic oxides and the network-forming oxides. The use of the partial molar free energy and heat content curves appear to offer a suitable criterion for the recognition of compounds in the liquid state. In Ag₂O·B₂O₃ melts Ag₂O·4B₂O₃ appears to be just recognizable as a compound, and there are indications of another compound richer in Ag₂O outside the region studied here.

As the proportion of Ag₂O in the liquid increases, the Ag₂O becomes more firmly held; at the same time, marked changes in entropy occur, the signifi-

cance of which is not clear. Conclusions of general validity must await more work on the thermodynamic properties of slag systems, but most of the effects observed here may be expected in other borate and silicate systems.

Acknowledgment

One of us (F. L. Hennessy) was in receipt of a Melvin Scholarship in the University of Melbourne when this work was performed.

References

- ¹ W. Guertler: *Ztsch. anorg. allgem. Chem.* (1904) **40**, p. 225.
- ² M. Foëx: *Comptes Rendus* (1938) **206**, p. 349.
- ³ Lo Ching Chang and G. Derge: *Trans. AIME* (1947) **172**, p. 90; *METALS TECHNOLOGY* (October 1946).
- ⁴ L. S. Darken: *Trans. AIME* (1947) **172**, p. 116.
- ⁵ R. J. Callow: *Trans. Faraday Soc.* (1950) **46**, p. 663.
- ⁶ R. J. Callow: *Trans. Faraday Soc.* (1951) **47**, p. 370.
- ⁷ C. R. Taylor and J. Chipman: *Trans. AIME* (1943) **154**, p. 228.
- ⁸ R. Schenck, A. Bathe, H. Keuth, and S. Süß: *Ztsch. anorg. allgem. Chem.* (1942) **249**, p. 88.
- ⁹ R. Schuhmann and J. Ensio: *Trans. AIME* (1951) **191**, p. 401; *JOURNAL OF METALS* (May 1951).
- ¹⁰ J. S. Powell and P. C. Joy: *Analytical Chemistry* (1949) **21**, p. 297.
- ¹¹ J. J. Spadaro, H. L. E. Vix, and E. A. Gastrock: *Industrial and Engineering Chemistry. Anal. Ed.* (1946) **18**, p. 214.
- ¹² W. A. Weyl, J. H. Schulman, R. J. Ginther, and L. W. Evans: *Trans. Electrochem. Soc.* (1949) **95**, p. 70.
- ¹³ B. Bogitch: *Comptes Rendus* (1934) **198**, p. 1928.
- ¹⁴ O. Kubachewski: *Ztsch. Elektrochem.* (1936) **42**, p. 5.
- ¹⁵ S. D. Stookey: *Journal Amer. Cer. Soc.* (1949) **32**, p. 246.
- ¹⁶ J. Biscoe and B. E. Warren: *Journal Amer. Cer. Soc.* (1938) **21**, p. 287. B. E. Warren: *Journal of Applied Physics* (1942) **13**, p. 602.
- ¹⁷ F. C. Kracek: *Journal ACS* (1930) **52**, p. 1436.
- ¹⁸ M. deK. Thompson: *The Total and Free Energies of Formation of the Oxides of Thirty-two Metals*. (1942) New York. The Electrochem. Soc.
- ¹⁹ G. M. Willis and F. L. Hennessy: *Proc. Aust. Inst. Min. & Met. N. S.* (1950) No. 158-159, p. 265.
- ²⁰ K. Hauffe and C. Wagner: *Ztsch. Elektrochem.* (1940) **46**, p. 160.
- ²¹ F. de Carli: *Atti accad. Lincei* (1927) **5** (6) p. 41. Cited from *Chem. Abs.* (1927) **21**, p. 1771.
- ²² G. M. Willis: Unpublished.
- ²³ J. F. Elliott and J. Chipman: *Trans. Faraday Soc.* (1951) **47**, p. 138.
- ²⁴ A. G. Pincus and B. E. Warren: *Journal Amer. Cer. Soc.* (1940) **23**, p. 301.
- ²⁵ O. J. Kleppa: *Journal ACS* (1949) **71**, p. 3275.
- ²⁶ O. J. Kleppa: *Journal ACS* (1950) **72**, p. 3346.

Technical Note

Some Effects of Microstructure Upon Temper Brittleness

by D. C. Buffum and L. D. Jaffe

EARLY papers¹⁻⁴ reported that temper brittleness is influenced by microstructure. This conclusion was based on room temperature impact tests, the inadequacy of which has been pointed out.⁵⁻⁶ Pellini and Queneau⁷ measured impact energy absorption at -80° to +25°C for several microstructures. On the basis of the shift, associated with temper brittleness, in the energy vs testing temperature curve they concluded that tempered martensite is somewhat more susceptible to temper brittleness

than is tempered pearlite. The range of temperatures was insufficient to give complete curves covering the transition from tough to brittle behavior, so it is difficult to evaluate quantitatively the shift for the different microstructures. Also, the smaller shift of pearlite might be attributed to its already being temper embrittled at its temperature of formation.^{8,9}

Accordingly, blanks 2 3/16 in. long were cut from a heat of SAE 3140 hot rolled steel barstock, 5/8 in. diameter, on which other work has been reported.⁹ A set of blanks was austenitized 1 hr at 900°C, water-quenched, tempered 16 hr at 675°C, and water-quenched, giving a microstructure of 100 pct

D. C. BUFFUM and L. D. JAFFE, Members AIME, are associated with Watertown Arsenal, Watertown, Mass.
TN 182E. Manuscript, June 24, 1953.

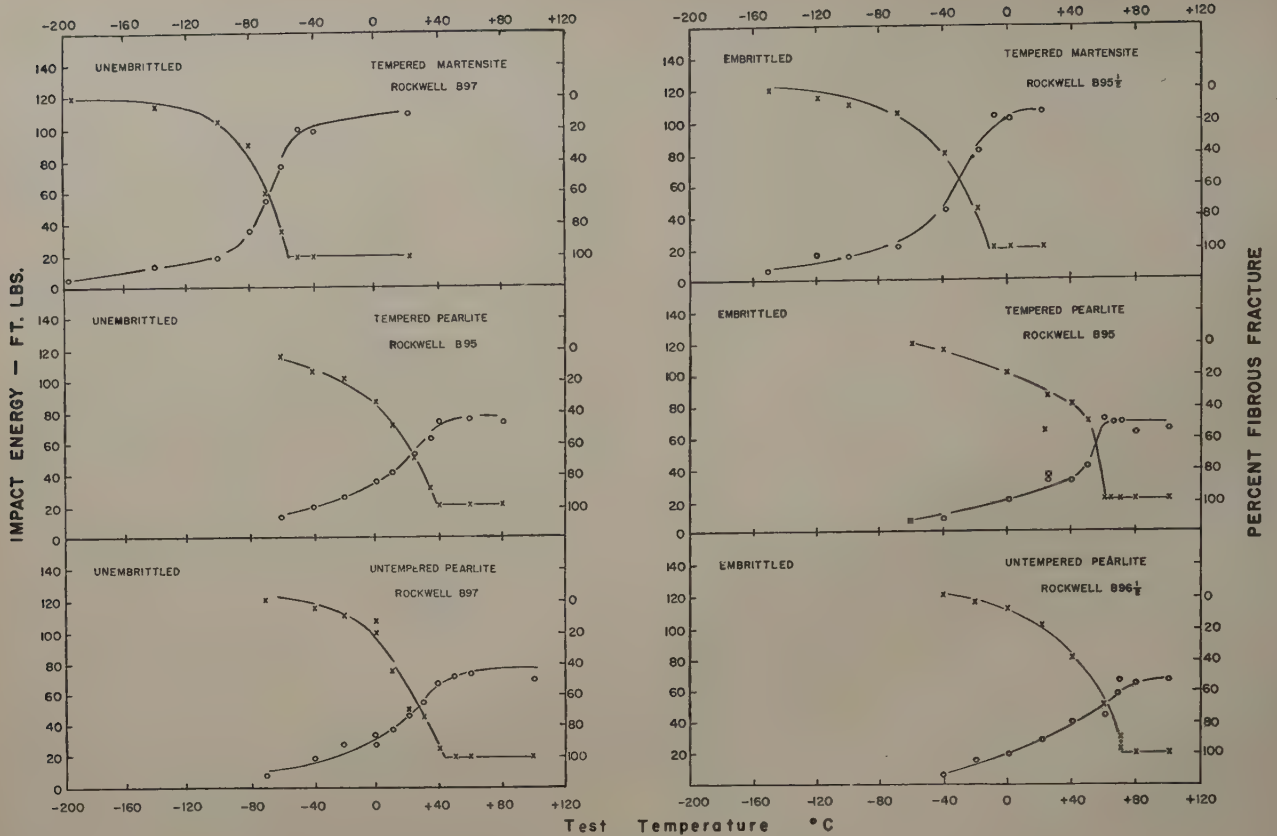


Fig. 1—Impact energy and fracture appearance vs temperature of test.

tempered martensite. A second set of blanks was austenitized 1 hr at 900°C, quenched in salt at 625°C, held 8 min, and water-quenched. The microstructure was approximately 50 pct pearlite and 50 pct proeutectoid ferrite. A third set was transformed to pearlite plus ferrite in the same way, then tempered 1 hr at 675°C, and water-quenched. Half of each set was embrittled by holding 48 hr at 500°C and water-quenched. The heat-treated bars were machined into standard V-notched Charpy specimens, which were tested over a range of temperatures on a standard 217 ft-lb Charpy machine (striking velocity 16.8 ft per sec) with the results shown in Fig. 1.

The temperature of transition from tough to brittle failure (100 pct fibrous fracture criterion) was raised by the embrittling treatment 45°C in the tempered martensite and 20° to 30°C in the pearlite-ferrite structures. It cannot be assumed that the embrittlement is directly proportional to the transition temperature increase, but it would appear that a given amount of embrittlement would produce, roughly, a certain number of degrees increase in transition temperature, a certain percentage increase in transition temperature, or¹⁰ a certain decrease in the reciprocal of the transition temperature. On any of these bases, the observed embrittlement was greatest for the tempered martensitic steel. Also, without intentional embrittlement, the transition temperature of the tempered pearlite plus ferrite (+40°C) was the same, within experimental error, as that of the untempered pearlite plus ferrite (+45°C). If the pearlite and proeutectoid ferrite had been significantly temper embrittled at their temperature of formation, it would be expected that the subsequent tempering treat-

ment would have removed this embrittlement and significantly lowered the transition temperature.¹¹

Thus, in the experiment conducted, pearlite and ferrite formed isothermally did not become significantly temper brittle during their formation. For a fixed embrittling treatment, less temper brittleness developed in pearlite and proeutectoid ferrite than in tempered martensite of the same composition.

Acknowledgment

The authors would like to thank M. R. Norton and W. P. Clancy for the metallographic work and F. L. Carr and I. L. Preble for their cooperation in the experimental program.

References

- ¹ J. H. S. Dickenson: West of Scotland Iron and Steel Inst. (April 1919).
- ² L. Grenet: *Bull. de L'Industrie Minerale* (1919) **15**, p. 339.
- ³ R. H. Greaves and J. J. A. Jones: *Journal Iron and Steel Inst.* (1920) **102**, p. 171.
- ⁴ E. Maurer, O. H. Wilms, and H. Kiessler: *Stahl und Eisen* (1942) **62**, pp. 81, 115.
- ⁵ H. Jolivet and G. Vidal: *Comptes Rendus* (1943) **216**, p. 664.
- ⁶ J. H. Hollomon: *Trans. ASM* (1946) **36**, p. 473.
- ⁷ W. S. Pellini and B. R. Queneau: *Trans. ASM* (1947) **39**, p. 139.
- ⁸ L. D. Jaffe: *Steel* (Nov. 21, 1949) **125**, No. 21, pp. 86, 114.
- ⁹ L. D. Jaffe, D. C. Buffum, and F. L. Carr: *Trans. ASM* (1952) **45**, p. 725.
- ¹⁰ N. Brown: Unpublished research, University of California, 1952.
- ¹¹ L. D. Jaffe and D. C. Buffum: *Revue de Metallurgie* (1951) **48**, p. 609.

Effect of Chloride on the Deposition of Copper, in the Presence Of Arsenic, Antimony, and Bismuth

by V. Hospadaruk and C. A. Winkler

PREVIOUS papers from this laboratory have discussed the effect of chloride ion on the cathode polarization during electrodeposition of copper from copper sulphate-sulphuric acid electrolytes, in the presence and absence of gelatin.¹⁻³ The steady state polarization^{4,5} was found to decrease sharply and pass through a minimum with increasing chloride ion concentration in the presence of gelatin. The minimum shifted to higher chloride ion concentrations and to higher polarization values with increase in current density or gelatin concentration, while an increase of temperature shifted the minimum toward lower halide concentrations and lower polarizations.

Since these observations were made in acid-copper sulphate electrolytes that contained no other addend than gelatin, there was obviously the possibility that they were not applicable to deposition of copper from commercial electrolytes that contain a variety of other substances in relatively small amounts. In particular, it was of interest to determine whether the presence of arsenic, antimony, or bismuth in the electrolyte would materially alter the behavior. Experiments have now been made under a variety of conditions with systems containing these cations, and the results are summarized in the present paper.

Experimental

Polarization measurements were made at 24.5°C in a Haring cell in the manner described previously.² Electrolytes were made with doubly-distilled water, and contained 125 g per liter of copper sulphate and 100 g per liter sulphuric acid, both of reagent grade Eimer and Amend gelatin from a single stock was used throughout. Chloride ion was introduced as reagent grade sodium chloride, and arsenic, antimony, and bismuth by dissolving the chemically pure metal in hot concentrated sulphuric acid and adding appropriate amounts of the solutions to the electrolyte.

Each cathode, of 1/16-in. thick rolled copper, was first etched in 40 pct nitric acid and washed thoroughly with distilled water. The surface was then brought to a standard condition^{4,5} by electrodeposition from an acid-copper sulphate electrolyte containing no gelatin, at a current density of 3 amp per sq dm for 30 min, followed by deposition at a current density of 2 amp per sq dm for 1 hr.

As in previous studies, the cathode polarization eventually attained a steady-state value (15 to 75

min) such that further change in polarization did not exceed 0.2 mv per min. The polarization values recorded are those for the steady states.

"Excess weights" were determined with arsenic and antimony present in the electrolyte, as the difference between the weights of the deposits obtained in the presence of these cations and those obtained in their absence, with the two cells connected in series. When gelatin was present along with the arsenic or antimony, it was also added to the electrolyte in the cell in series.

Results and Discussion

The results of the study are summarized in Figs. 1 to 6. From Fig. 1, top, it is evident that the presence of arsenic or antimony alone results in an increase of polarization, while bismuth alone causes a decrease. The presence of gelatin (25 mg per liter) rather drastically modifies all three cation effects, as indicated in the lower panels of the same figure. The addition of chloride ion, when no gelatin is present, causes comparable decreases in polarization in the presence of antimony and bismuth, but a relatively larger decrease when the electrolyte contains arsenic. It is interesting to note that the decrease in polarization brought about by addition of chloride when both arsenic and antimony are present parallels the behavior with arsenic alone, while the polarization in the electrolyte containing the cation mixture, without chloride added, corresponds to that for an electrolyte containing only the antimony cation. Similarly, the polarization at zero concentration of chloride in electrolyte containing arsenic and bismuth is that corresponding to an electrolyte containing arsenic alone.

From Figs. 3a, 4a and 4b, it is clear that, in the presence of gelatin at a level of 25 mg per liter, the effect of chloride in the presence of arsenic and antimony, or a mixture of the two, becomes quite analogous to that observed in the absence of added cations. When both bismuth and gelatin are present (Fig. 5), the decrease in polarization with increased chloride concentration is virtually absent. This is perhaps a reflection of the large decrease in polarization brought about by the bismuth itself in the presence of gelatin.

The shifts of the minimum in the polarization-chloride concentration curves brought about by changes of temperature (Fig. 3b), gelatin concentration (Figs. 3c and 4c) and current density (Fig. 3d) when the metal cations were present are all similar to the corresponding shifts observed in their absence.²

The approximately linear "excess weight"-antimony concentration relation recorded in Fig. 6 would seem to indicate that antimony is codeposited with copper to a considerable extent. On the other hand, only very limited amounts of arsenic appear to be adsorbed or codeposited.

V. HOSPADARUK and C. A. WINKLER are associated with the Physical Chemistry Laboratory, McGill University, Montreal, Que., Canada.

Discussion on this paper, TP 3547D, may be sent, 2 copies, to AIME by Dec. 1, 1953. Manuscript, Nov. 28, 1952. Los Angeles Meeting, February 1953.

This paper is a contribution from the Physical Chemistry Laboratory, McGill University with financial assistance from the National Research Council of Canada.

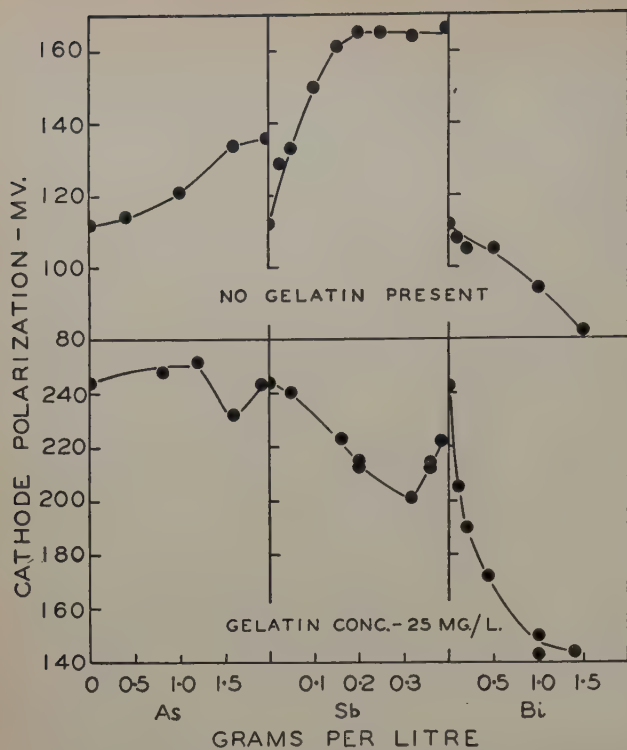
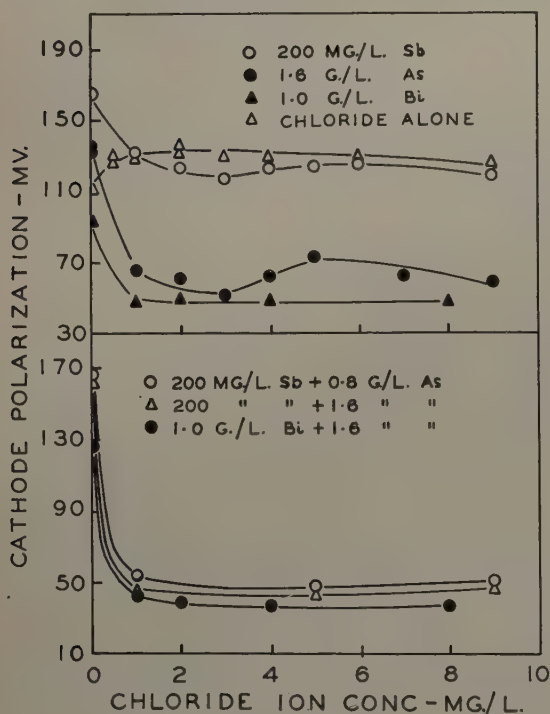


Fig. 1 (above)—Effect of arsenic, antimony, and bismuth on cathode polarization in the absence of chloride. a (top)—In the absence of gelatin. b (bottom)—In the presence of 25 mg per liter gelatin.

Fig. 2 (below)—Effect of chloride on cathode polarization. a (top)—In the presence and absence of antimony, arsenic, and bismuth where gelatin is absent. b (bottom)—In the presence of antimony-arsenic and bismuth-arsenic mixtures.



Several cathodes were analyzed for their antimony contents, with the results given in Table I. It would appear that the presence of gelatin in the electrolyte encouraged inclusion of antimony in the deposits.

While much more information about the factors responsible for metal polarization is obviously necessary for an adequate explanation of the observed behavior, some tentative suggestions may be

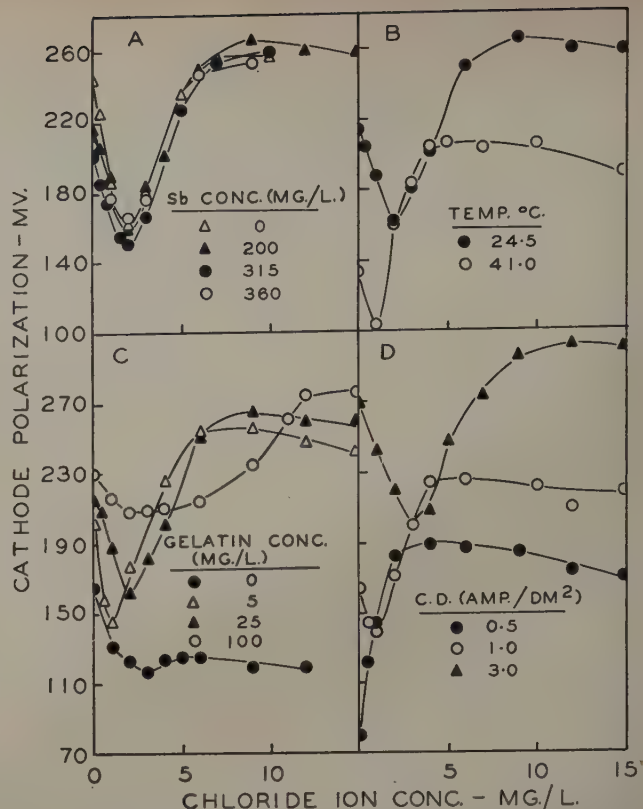
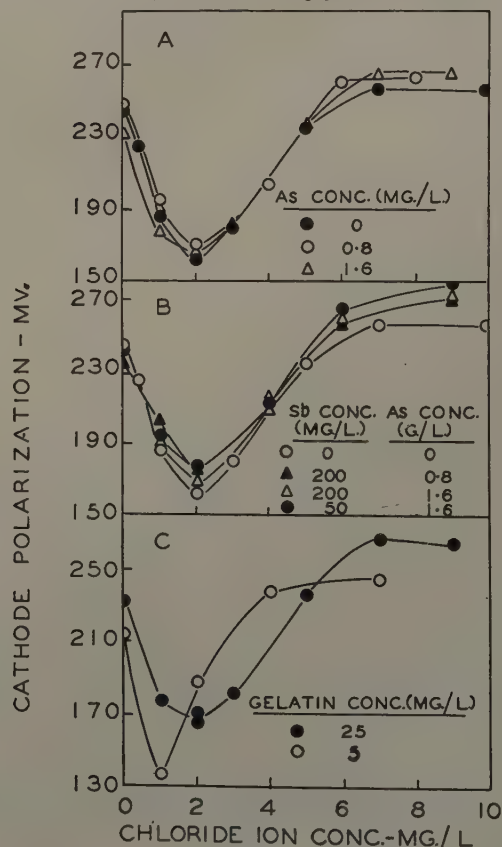


Fig. 3 (above)—Effect of chloride ion on cathode polarization. A—At different antimony concentrations, in the presence of 25 mg per liter gelatin. B—At different temperatures, in the presence of 200 mg per liter antimony and 25 mg per liter gelatin. C—At different gelatin concentrations, in the presence of 200 mg per liter antimony. D—At different current densities, in the presence of 200 mg per liter antimony and 25 mg per liter gelatin.

Fig. 4 (below)—Effect of chloride ion on cathode polarization. A—At different arsenic concentrations, in the presence of 25 mg per liter gelatin. B—At different antimony and arsenic concentrations, in the presence of 25 mg per liter gelatin. C—At different gelatin concentrations, in the presence of 1.6 g per liter arsenic.



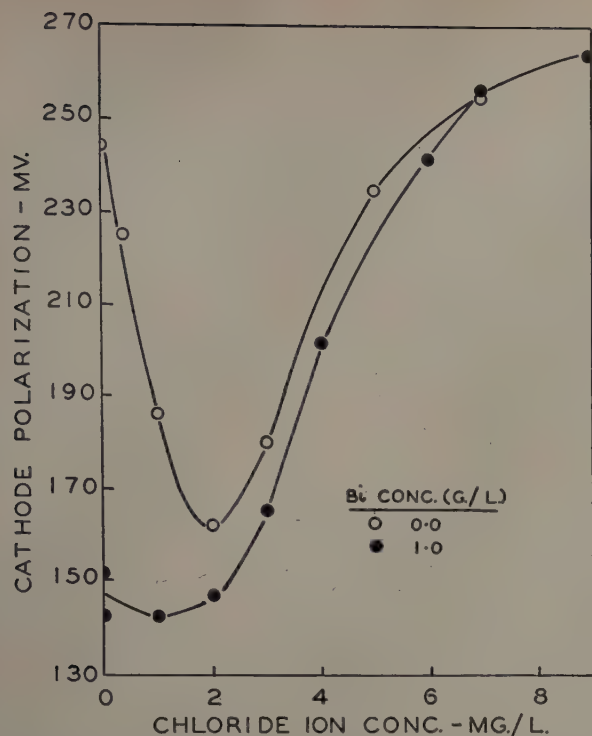


Fig. 5—Effect of bismuth and chloride ion on cathode polarization in the presence of 25 mg per liter gelatin.

made, following a line of thought that has been outlined in earlier papers from this laboratory. Briefly, it has been proposed that if the active area of the cathode (as opposed to its apparent area) is increased from any cause the true current density, and concomitantly the polarization, are decreased; a decrease of active area is assumed to have the reverse effects. On this basis, the increase of polarization occasioned by the presence of gelatin in the electrolyte has been attributed to a decrease in active area on which deposition might occur.

The decrease in polarization brought about by chloride ion in the presence of gelatin has been ascribed to an increase of active area as a result of attack by the ion at those portions of the surface not covered by gelatin. Similarly, the presence of arsenic, antimony, or bismuth on the cathode surface might induce corrosion, hence an increase of active area, as a result of local cell action. With arsenic and antimony in particular, the tendency for increase in active area from this cause would, perhaps, be partially offset by adsorption of oxides or oxyacids of these substances. Such oxy-compounds may be formed, to some extent at least, by the local cell action responsible for the corrosion. In the absence

of gelatin, the decrease in active area from adsorption of oxy-compounds may be predominant over the increase in active area by corrosion. In the presence of gelatin, which may be assumed to cover existing active centers very effectively, there would probably be a predominant tendency for an increase in active area by corrosion at the relatively inactive portions of the surface. Without attempting a detailed analysis of all the features recorded in Figs. 1 to 6, it does seem that the main features of the study may be tentatively accounted for by appro-

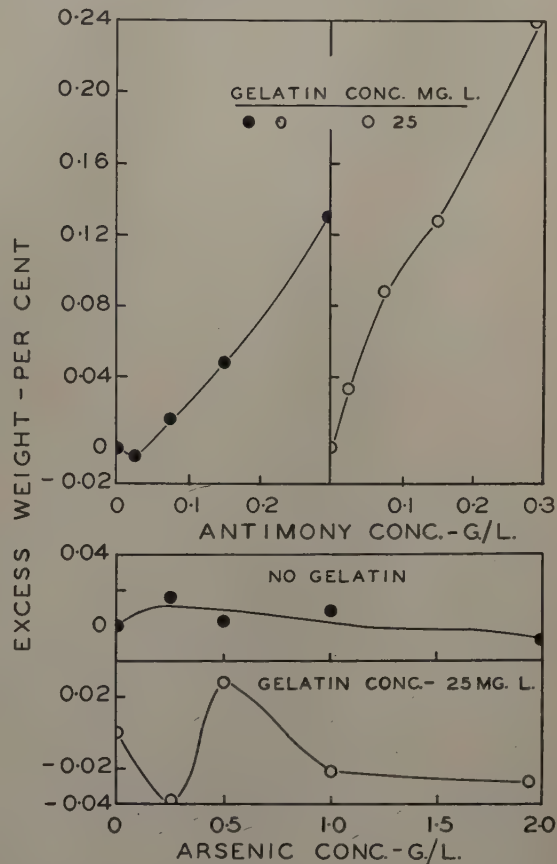


Fig. 6—The excess weight of copper deposited from acid copper sulphate electrolyte containing various amounts of antimony and arsenic in the presence and absence of gelatin. Current density: 2 amp per sq dm.

appropriate assumptions about the relative extents to which active area may be decreased (by gelatin or oxy-compounds) or increased (by chloride ion attack or local cell action). Studies of the initial polarization pattern with a recording potentiometer, in the manner described recently,⁶ might materially assist in interpretation of the effect of metal cations on the polarization.

References

- ¹ W. Gauvin and C. A. Winkler: *Journal Electrochem. Soc.* (1952) **99**, p. 71.
- ² L. Mandelcorn, W. B. McConnell, W. Gauvin, and C. A. Winkler: *Journal Electrochem. Soc.* (1952) **99**, p. 84.
- ³ R. C. Turner and C. A. Winkler: *Canadian Journal of Chemistry* (1952) **30**, p. 507.
- ⁴ W. Gauvin and C. A. Winkler: *Canadian Journal of Research* (1943) **A21**, p. 37.
- ⁵ W. Gauvin and C. A. Winkler: *Canadian Journal of Research* (1943) **B21**, p. 81.
- ⁶ B. I. Parsons and C. A. Winkler: Paper presented at the 102nd meeting of the Electrochemical Society, Montreal, Oct. 27, 1952.

Table I. Analyses* of Cathodes

Antimony in Electrolyte, Mg per Liter	Antimony in Deposit, Pct	
	No Gelatin Present	Gelatin Present, 25 Mg per Liter†
0	0.012	0.020
25	0.052	0.028
75	0.028	0.076
150	0.068	0.161
288	—	0.161
300	0.036	—

* The analyses were made by the Analytical Laboratory, Canadian Copper Refineries, Montreal East.

† Average of duplicate determinations.

The Cold Rolled Texture of Titanium

by D. N. Williams and D. S. Eppelsheimer

The cold rolled textures of iodide titanium and of three samples of commercial titanium were examined using the Schulz-Decker Geiger counter technique. The iodide titanium and two of the three samples of commercial titanium showed a (0001) $[10\bar{1}0]$ texture rotated 30° toward the transverse direction about an axis in the rolling direction. The third sample of commercial titanium showed a double texture.

THE metals of the hexagonal system tend to deform similarly if the c/a ratios are similar. Thus titanium, zirconium, and beryllium, with c/a ratios of 1.601, 1.590, and 1.570, respectively,¹ should have similar cold rolled textures. The cold rolled texture of high purity iodide titanium has been described as (0001) $[10\bar{1}0]$ rotated 30° toward the transverse direction about an axis in the rolling direction.² The texture of zirconium has also been reported as (0001) $[10\bar{1}0]$ with a transverse rotation from the ideal position of approximately 30° about an axis in the rolling direction.³ This texture differs from that reported for titanium however since a continuous spread of (0001) poles toward the transverse direction was reported rather than distinct (0001) maxima 30° from the rolling plane normal. Beryllium has a texture similar to that of zirconium although the angle of transverse rotation of the (0001) poles is much less.⁴ These three metals thus show a common type of cold rolled texture, as yet unexplained, which can be described as (0001) $[10\bar{1}0]$ with various degrees of rotation toward the transverse direction about an axis in the rolling direction.

Since titanium showed the greatest degree of rotation from the (0001) $[10\bar{1}0]$ position, the cold rolled texture of titanium was re-examined using a semiquantitative Geiger counter X-ray technique to obtain more accurate experimental data from which a theoretical interpretation of this new type of hex-

Table I. Analyses of Titanium Samples Used

Sample	H	N	O	C	Metallic Im-purities	Tl (Diff.)
Iodide titanium	*	0.001	*	*	0.102	99.90
Comm. grade No. 1	0.014	0.024	0.109	0.02	0.411	99.42
Comm. grade No. 2	0.013	0.027	0.141	0.03	0.186	99.60
Comm. grade No. 3	0.021	0.021	0.119	0.10	0.453	99.29

* Not determined.

agonal rolling texture could be developed. The cold rolled textures of iodide titanium and of three samples of commercial titanium were determined. Table I gives the analyses of the titanium samples.

Experimental Procedure

Preparation of Samples: Prior to the final rolling operation each of the samples was given an initial reduction of approximately 50 pct and annealed to remove the gross effects of any previous treatments. Samples were annealed in vacuum, high purity helium, and air to determine whether annealing atmosphere had any effect on the cold rolled textures developed. All samples were annealed 1 hr at 800°C .

Grain size determinations were made using the formula,

$$D \text{ (in mm)} = \frac{1.075}{M} \sqrt{\frac{A}{n}}$$

in which n is the number of grains counted in an area A (in sq mm) and M is the magnification of the area counted.⁵ This formula gives the diameter between opposite flats assuming hexagonal grains. At least three areas containing more than sixty grains each were counted in each grain size determination. Rockwell B hardness readings were made on the annealed samples. The results of the measurements of

D. N. WILLIAMS, Junior Member AIME, formerly National Lead Research Fellow, Missouri School of Mines and Metallurgy, is now Research Engineer, Kaiser Aluminum and Chemical Corp., Spokane, Wash., and D. S. EPPELSHEIMER, Member AIME, is Professor of Metallurgical Engineering, Missouri School of Mines and Metallurgy, Rolla, Mo.

Discussion on this paper, TP 3648E, may be sent, 2 copies, to AIME by Jan. 1, 1954. Manuscript, Sept. 9, 1952; revision; March 19, 1953. Cleveland Meeting, October 1953.

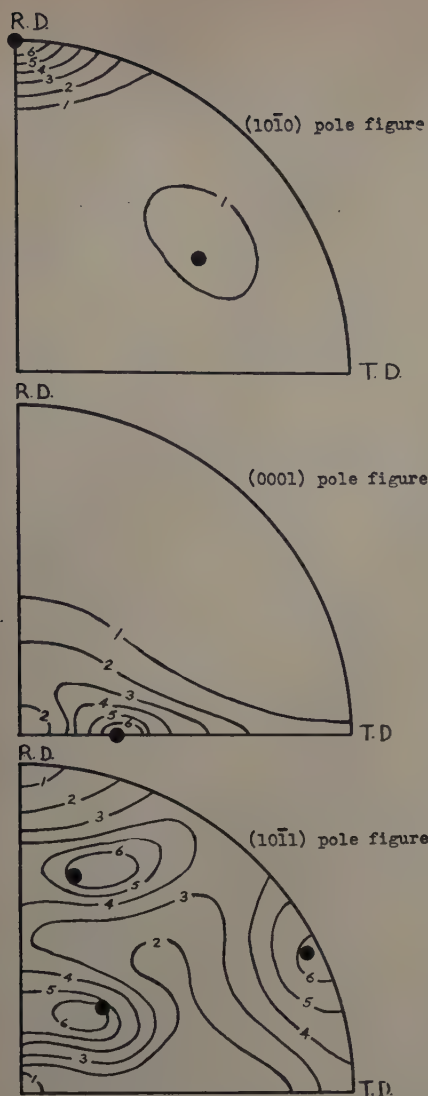


Fig. 1—Cold rolled iodide titanium. •—(0001) $[10\bar{1}0]$ rotated 30° toward the TD about an axis in the RD.

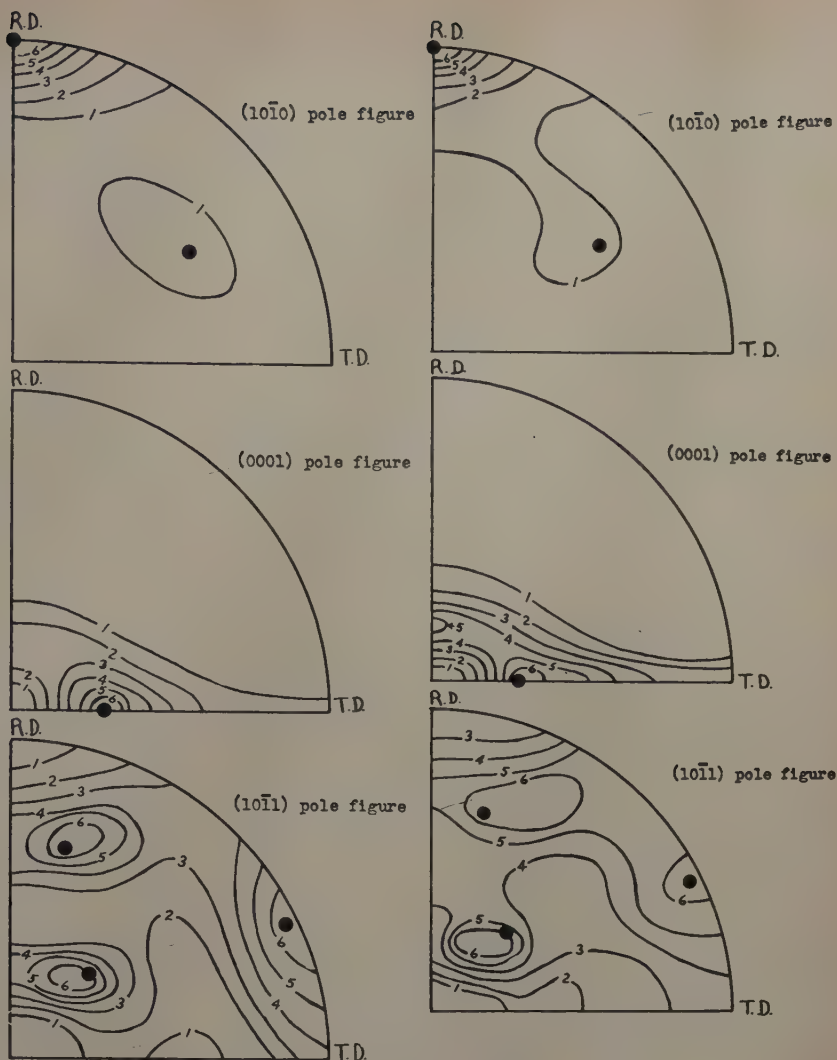


Fig. 2—Cold rolled commercial titanium sample number one. •—(0001) $[10\bar{1}0]$ rotated 30° toward the TD about an axis in the RD.

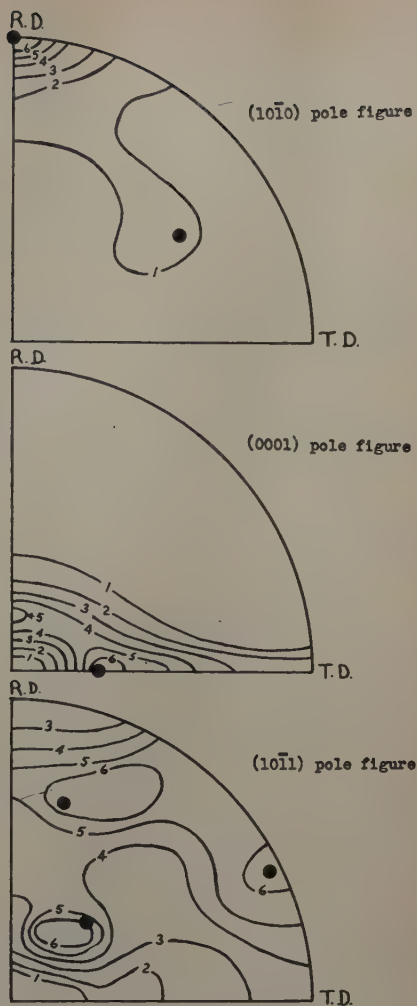


Fig. 3—Cold rolled commercial titanium sample number three. •—(0001) $[10\bar{1}0]$ rotated 30° toward the TD about an axis in the RD.

annealed grain size and hardness are given in Table II, as well as the final cold rolled reductions given each sample.

The three commercial samples of titanium are not distinguished from one another other than by number. All three were obtained from different sources and had different work histories. Although the commercial samples designated Nos. 1 and 2 were similar except for the annealed grain size, sample No. 3 had a second phase in the grain boundary region which is reflected in the hardness data. The origin of this grain boundary phase was not apparent from the analysis. The hardness varied considerably between samples but was evidently almost independent of grain size and annealing atmosphere.

Cold Rolling Procedure: The annealed samples, approximately 1.5 cm wide and 0.33 cm thick, were rolled with small reductions per pass in a set of 2 in. laboratory rolls to a final thickness of approximately 0.010 cm. About 80 passes were used to bring each sample to its final thickness. Sufficient time was allowed between passes to prevent temperature effects. Edge cracking was noticed in all of the commercial grades of titanium beyond 60 pct reduction in area. No edge cracking was apparent in the iodide titanium. Considerable increase in width during rolling

was noticed in all of the samples. An example of the rolling procedure is given in Table III.

X-ray Examination: Pole figures were constructed for the $(10\bar{1}0)$, (0001) , and $(10\bar{1}1)$ planes using the Schulz-Decker Geiger counter technique.⁶ This technique requires two samples for complete pole figure determination, one for use in making reflection patterns and one for use in making transmission patterns. Laminated reflection samples were prepared from two pieces of the cold rolled material which had been etched after rolling in a HF, HNO₃, H₂O solution (1:2:5 by volume) to 0.009 cm. Transmission samples were made by etching a third piece of the cold rolled material to approximately 0.001

Table II. Grain Size, Hardness, and Final Reduction of Samples Examined

Sample	Annealed In	Annealed Grain Size, Mm	Rockwell B Hardness	Final Reduction, Pct
Iodide titanium	Vacuum	0.102	<0	93.2
Comm. Ti No. 1	Vacuum	0.045	83	95.8
Comm. Ti No. 1	Air	0.045	83	94.9
Comm. Ti No. 2	Vacuum	0.011	84	95.7
Comm. Ti No. 2	Vacuum	0.010	102	94.0
Comm. Ti No. 3	Helium	0.008	107	78.3
Comm. Ti No. 3	Helium	0.008	107	95.8

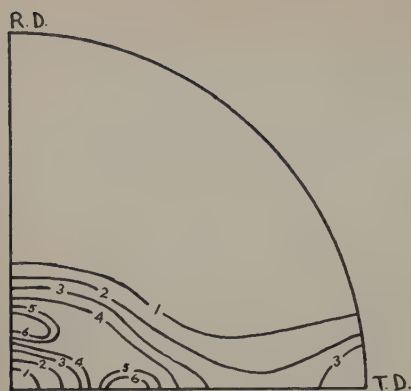
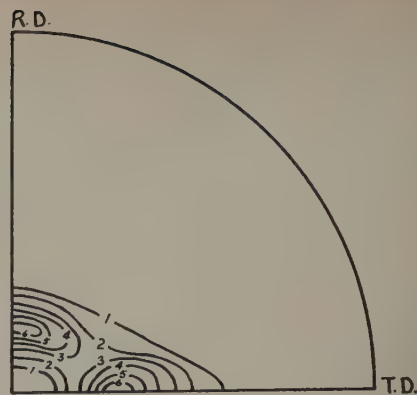


Fig. 4—(0001) pole figures of cold rolled commercial titanium sample number three.

a—78.3 pct reduction in area.

b—95.8 pct reduction in area.



cm. Transmission intensity readings were obtained with angles of revolution from 0° to 50° and reflection readings made from 50° to 90° . Readings were made at 10° intervals of latitude and longitude on a polar stereographic net except in regions near the various maxima where more accurate information was necessary.

After correcting the transmission data for the error due to absorption, using the formula developed by Decker, Asp, and Harker,⁷ and adjusting the reflection data so that it would correspond with the corrected transmission data in the region of overlap, the maximum intensity was reduced to 70 intensity units and all other readings reduced proportionally for convenience of plotting. The intensity contour system of plotting was used with the contours for intensities of 60, 50, etc., shown on the pole figures by the numbers 6, 5, etc.

Experimental Results

The pole figures of iodide titanium reduced 93.2 pct are shown in Fig. 1. The texture was found to be (0001) $[10\bar{1}0]$ rotated 30° or more in the transverse direction about an axis in the rolling direction.

The most noticeable feature of the pole figures was the high degree of preferred orientation which occurred in the rolling direction of the $(10\bar{1}0)$ pole figure. The (0001) pole figure showed a considerable spread of orientations along the transverse axis with a maximum of about 30° from the rolling plane normal. The low intensity of the (0001) pole figure at the rolling plane normal was particularly interesting. This minimum indicated that the ideal (0001) $[10\bar{1}0]$ cold rolling texture common to several of the hexagonal metals was completely absent in titanium. Although the $(10\bar{1}1)$ pole figure showed a less distinct preferred orientation, the positions of the $(10\bar{1}1)$ maxima confirmed the texture indicated by the $(10\bar{1}0)$ and (0001) pole figures.

The commercial titanium samples Nos. 1 and 2 showed a cold rolled texture almost identical with that of iodide titanium. The pole figures of the commercial titanium sample No. 1, annealed in vacuum before cold rolling, are shown in Fig. 2. The pole figures of the commercial titanium sample No. 1,

annealed in air before cold rolling, and No. 2, annealed in vacuum before cold rolling, were practically identical with Fig. 2 and are not included.

The pole figures of the commercial titanium sample No. 3, annealed in vacuum before cold rolling, are shown in Fig. 3. A noticeable difference in the (0001) pole figure was seen in comparing Fig. 3 with Figs. 1 and 2. In this sample a second (0001) maximum was apparent in the rolling direction 20° from the rolling plane normal superimposed on the normal (0001) rotated texture.

In the $(10\bar{1}0)$ pole figure the only noticeable change was a slight increase in the intensity between the two $(10\bar{1}0)$ maxima causing them to be joined by the lowest intensity contour. The absence of definite maxima in the $(10\bar{1}0)$ pole figure corresponding to the second maximum in the (0001) pole figure does not indicate an error in the results. Because of the extremely high $(10\bar{1}0)$ maximum in the rolling direction, all other maxima are effectively masked by the method of plotting used. Thus the second maximum in the $(10\bar{1}0)$ pole figure of Fig. 1, for example, is only about 10 intensity units. This orientation has an intensity of 70 intensity units in the (0001) pole figure.

The $(10\bar{1}1)$ pole figure showed a more random orientation in Fig. 3 than in Figs. 1 and 2 with an increase in $(10\bar{1}1)$ intensity near the rolling direction. This is probably due to the second texture present.

The (0001) pole figures of the commercial titanium sample No. 3, annealed in air before cold rolling, are shown in Fig. 4. These pole figures show the variation in texture with increased reduction in area. The double maxima noticed in Fig. 3 were apparent in both pole figures. An (0001) maximum was apparent in the transverse direction in the specimen reduced 78.3 pct. A small increase in the (0001) intensity was noticed in all of the pole figures near the transverse direction but in the case of higher reductions it was usually too slight to appear with the method of plotting used.

Discussion of Results

From the pole figures of two of the commercial samples of titanium and from the iodide titanium it is apparent that the ideal cold rolled texture can be described as (0001) $[10\bar{1}0]$ rotated 30° in the transverse direction about an axis in the rolling direction as reported by Clark.² These pole figures indicate however that the principal orientation tendency of cold rolled titanium is the location of a $\langle 10\bar{1}0 \rangle$ direction in the rolling direction. The (0001) maximum 30° from the rolling plane normal is a secondary tendency.

Table III. Rolling Procedure for Commercial Titanium Sample No. 2

Specimen	Condition	Reduction in Area, Pct	Increase in Width, Pct	Number of Passes
a	Ann.	0	0	0
b	C.R.	64.3	1.7	40
c	C.R.	82.0	7.9	54
d	C.R.	91.4	12.2	72
e	C.R.	95.7	18.8	90

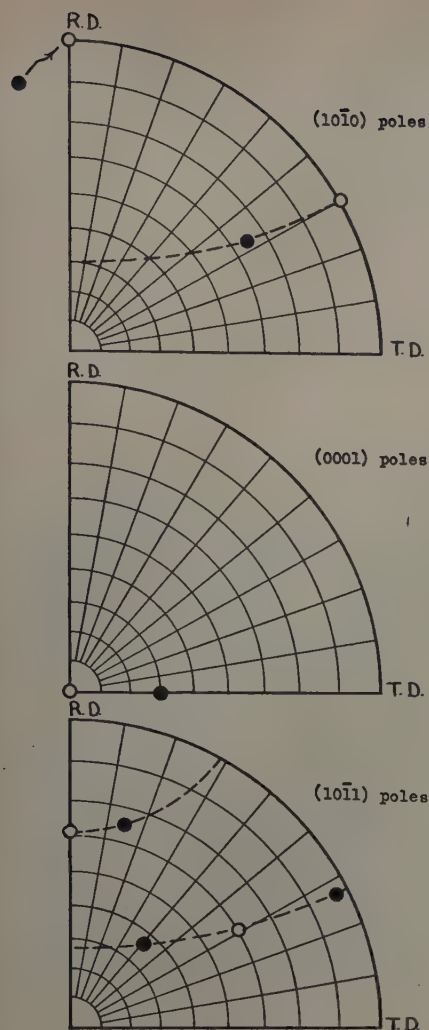


Fig. 5—Position of the ideal textures.
 ○—(0001) $[10\bar{1}0]$.
 ●—(0001) $[10\bar{1}0]$ rotated 30° toward TD about an axis in the RD.

In Fig. 5 the positions of the $(10\bar{1}0)$, (0001) , and $(10\bar{1}1)$ poles of the $(0001) [10\bar{1}0]$ texture before rotation (white circles) and after rotating 30° toward the transverse direction about an axis in the rolling direction (black circles) are plotted over a polar stereographic net. As the $(0001) [10\bar{1}0]$ texture is rotated toward the transverse direction the poles move along the dashed lines in Fig. 5. By consideration of these movements the experimentally determined texture can be rationalized.

As the (0001) pole moves from the rolling plane normal to the transverse direction in Fig. 5, the $(10\bar{1}0)$ pole in the rolling direction stays fixed and acts as a rotation axis. The second $(10\bar{1}0)$ pole however rotates from the position of the white circle to the intersection of the dashed line with the rolling axis. Thus the measured intensities of the two positions will vary considerably. The $(10\bar{1}0)$ pole not in the rolling direction will have maximum intensity at the black circle to correspond to the maximum intensity in the (0001) pole figure. The intensity from the white circle to the rolling axis of the $(10\bar{1}0)$ pole figure will vary proportionally with the intensity in the (0001) pole figure from the rolling plane normal to the transverse direction. The $(10\bar{1}0)$ pole in the rolling direction remains in one position for all of these orientations, however, and thus its intensity is proportional to the sum of all of the (0001) intensities from the rolling plane normal to the transverse direction.

The $(10\bar{1}1)$ rotations and the resulting $(10\bar{1}1)$

pole figure can be developed in the same manner. In this case it should be noticed that a rotation of the $(0001) [10\bar{1}0]$ orientation to the right about an axis in the rolling direction produces the black circles nearest the rolling direction and the transverse direction while a rotation to the left is necessary to produce the black circle nearest the rolling plane normal in the $(10\bar{1}1)$ pole figure.

The positions of the maxima of the rotated ideal texture have been indicated in Figs. 1, 2, and 3 by black circles.

The origin of the second (0001) maximum in the commercial titanium sample No. 3 is not apparent. The appearance of a visible grain boundary phase in this sample suggests, even though no large difference in composition was apparent in the analyses given in Table I, that the second maximum is due to a difference in composition.

The pole figures of cold rolled titanium are seen to be influenced by two main factors. The first is a very strong tendency for one of the $\langle 10\bar{1}0 \rangle$ directions to be in the rolling direction. The second is a tendency for the (0001) plane to be 30° or more away from the rolling plane.

The appearance of a pronounced minimum at the rolling plane normal in the (0001) pole figure of titanium suggests that zirconium and beryllium may also show a similar, but less noticeable, minimum which was not apparent when using the photographic pole figure technique.

A theoretical investigation of the texture of titanium has shown that the texture can be explained assuming $\{0001\} \langle 11\bar{2}0 \rangle$ and $\{10\bar{1}1\} \langle 11\bar{2}0 \rangle$ slip and $\{11\bar{2}2\}$ and $\{10\bar{1}2\}$ twinning.⁸ The disappearance of the (0001) maximum in the transverse direction of the (0001) pole figure indicates that $\{10\bar{1}0\} \langle 11\bar{2}0 \rangle$ slip is relatively unimportant at higher reductions.

Summary

1—The $(10\bar{1}0)$, (0001) , and $(10\bar{1}1)$ pole figures of iodide titanium and of three samples of commercial titanium were determined after cold rolling using a semiquantitative Geiger counter technique.

2—The iodide titanium sample and two of the three samples of commercial titanium showed a $(0001) [10\bar{1}0]$ texture rotated 30° toward the transverse direction about an axis in the rolling direction.

3—A third sample of commercial titanium, having a much higher annealed hardness, showed a second maximum in the (0001) pole figure 20° toward the rolling direction from the rolling plane normal.

4—The main tendency of titanium in cold rolling was to have a $\langle 10\bar{1}0 \rangle$ direction in the rolling direction. A secondary tendency for the (0001) planes to be at least 30° from the rolling plane was also apparent.

Acknowledgment

The authors wish to thank the Titanium Alloy Manufacturing Div. of the National Lead Co. for the support of the fellowship under which this work was conducted.

References

- ¹ S. S. Sidhu: Private communication.
- ² H. T. Clark, Jr.: The Textures of Cold-Rolled and Annealed Titanium. *Trans. AIME* (1950) 188, p. 1154; *JOURNAL OF METALS* (September 1950).
- ³ R. K. McGeary and B. Lustman: Preferred Orientation in Zirconium. AECD-2951, USAEC (1950).
- ⁴ A. Smigelskas and C. S. Barrett: Preferred Orientation in Rolled and Recrystallized Beryllium. *Trans.*

AIME (1949) 185, p. 145; JOURNAL OF METALS (February 1949).

⁵F. J. Dunkerley, F. Pledger, V. Damiano, and J. Fulton: Grain-Growth and Recrystallization Characteristics of Zirconium. *Trans. AIME* (1951) 191, p. 1003; JOURNAL OF METALS (November 1951).

⁶D. N. Williams and D. S. Eppelsheimer: Universal Specimen Mount for Pole Figure Determination Using the Schulz-Decker Technique. *Bull. Univ. of Mo.*

School of Mines and Met., Tech. Series No. 79, 1952; *Review of Scientific Instruments* (1952) 23, p. 229.

⁷B. F. Decker, E. T. Asp, and D. Harker: Preferred Orientation Determination Using a Geiger Counter X-ray Diffraction Goniometer. *Journal of Applied Physics* (1948) 19, p. 388.

⁸D. N. Williams and D. S. Eppelsheimer: A Theoretical Investigation of the Deformation Textures of Titanium. *Journal Inst. Met.* (1952-1953) 81, p. 553.

Technical Note

Notes on a Molybdenum-Rhenium Alloy

by Carl J. McHargue and Hal W. Maynor, Jr.

DURING the course of an investigation of materials suitable for use as thermocouples at elevated temperatures by one of the authors, several molybdenum-rhenium alloys were prepared. Micrographs of an annealed alloy containing 25 pct Re (intended concentration; analysis not obtained) showed a number of twins, Fig. 1, suggesting a face-centered cubic structure. This note reports the structure and recrystallized wire texture of an alloy containing 25 wt pct Re.

Alloys were prepared from 99.9 pct Mo (Fansteel Metallurgical Corp.) and rhenium obtained from the University of Tennessee (purity unreported). Powders were combined and briquetted at 56,000 psi and sintering was carried out at 2400°C for 5 hr

Table I. X-Ray Data for 75 Pct Mo-25 Pct Re Alloy

Hkl	d(Obs.)	d(Cal)*	I(Obs.)
111	2.180	2.190	ms
200	1.846	1.852	s
220	1.306	1.309	s
311	1.115	1.117	m
222	1.065	1.069	m
400	0.9250	0.9259	mw
331	α_1 0.8479	0.8496	m
331	α_2 0.8492		mw
420	α_1 0.8278	0.8281	ms
420	α_2 0.8279		m

A_0 (extrapolated to $\theta=90^\circ$) 3.703 \AA .

* Calculated from value of A_0 .

m, medium; ms, medium strong; s, strong; mw, medium weak.

in vacuum. Ingots so prepared were swaged at 982.2° to 1037.8°C into wires 0.036 in. diameter, a reduction in diameter of 85.6 pct. These wires were vacuum-annealed 1 hr at 2000°C.

A North American Philips 114.59 mm powder camera and nickel-filtered copper radiation were used for structure determination. For the texture determination a Laue-type camera was used with zirconium-filtered molybdenum radiation and, because of the high background, aluminum foil was mounted next to the film. Exposures were taken with the wire perpendicular to the X-ray beam and tilted by 10°.

C. J. MCHARGUE, Junior Member AIME, formerly Research Metallurgist, University of Kentucky, is now Metallurgist, Oak Ridge National Laboratory, Oak Ridge, Tenn., and H. W. MAYNOR, Jr., Junior Member AIME, formerly Associate Engineer, Institute for Atomic Research, Iowa State College, is now Research Associate, University of Kentucky, Lexington, Ky.

TN 183E. Manuscript, June 25, 1953.

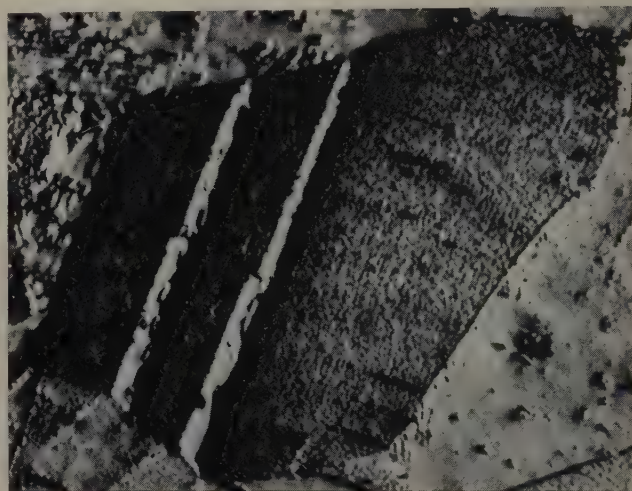


Fig. 1—Annealing twins in 75 pct Mo-25 pct Re alloy annealed 1 hr at 2000°C. Etch: 1 part HNO₃; 2 parts H₂O; 3 parts HCl. X2000. Area reduced approximately 85 pct for reproduction.

It was found that the X-ray pattern could be indexed on the basis of a face-centered cubic structure. Because of difficulties associated with obtaining a good X-ray pattern for this material, accurate parameter determinations were not made. An indicated parameter value of 3.70 \AA was obtained. The X-ray data are given in Table I.

The annealed wire texture was observed to be a sharp [111] texture. The spread about this fiber axis was $\pm 8^\circ$ at the surface of the 0.036 in. wire. The annealed wire textures of aluminum have been reported as retention of the [111] deformation texture for anneals below 500°C and a new [112] texture for anneals above 600°C.¹ In copper wires, with a [111] plus [100] deformation texture, results indicate a retention of this texture for annealing at lower temperatures and new components or the disappearance of components for annealing at higher temperatures.¹ The presence of the strong [111] texture in the molybdenum-rhenium alloy after a 2000°C anneal suggests that the deformation texture was the same.

Acknowledgment

The wires used in this study were prepared and heat-treated at the Institute for Atomic Research, and Ames Laboratory, Iowa State College, and the authors wish to express their thanks to the Institute for allowing the use of the material and permission to publish the results.

¹C. S. Barrett: *Structure of Metals*. (1952) New York. McGraw-Hill Book Co.

Hurley Furnace and Boiler Description and Design

by E. A. Slover

THE usual reverberatory system of smelting copper concentrate or calcine has for its component parts a furnace and one or two waste heat boilers. These parts are operated on a basis of compromise, since the furnace can send gas to the boilers at too high a temperature and the boilers by plugging, due to dust or slag, can place a definite limit on the amount of fuel the furnace can burn.

Over the years the copper concentrate smelting furnace has had few advances in design. The simple rules of design such as the flame should wipe the bath and the speed of the gases should be reasonably low for dust carrying purposes seem to cover the main features.

In the construction of the individual furnaces some innovations are always being introduced. Among these are charging so that the work of smelting is a complete bath process, the use of suspended brick arches in place of sprung arches, the use of basic brick, not only in the crucible, but also in roof and sidewalls, the use of various means to feed the charge, the use of magnetite or other heavy material to construct the hearth, water cooling of bridgewall and slag skimming bay, the smelting of raw charge instead of calcine, the use of preheated air, and possibly the use of oxygen-enriched air for combustion. But the general outlines of the furnaces have not changed much except as to size.

Furnaces at Hurley

As shown on Fig. 1, the furnace at Hurley is 126 ft long between the longitudinal buckstays and 32 ft wide at the skewback plates.

The foundation is a concrete retaining wall with piers at intervals that go deeper into the earth. Purposely the wall at the burner end of the furnace is not backed-up as tightly as the other parts of the foundation so that movement due to expansion may take place here rather than into the boiler foundations. Within these foundation retaining walls of concrete, the earth has been removed to allow the placement of the crucible brick base inside of which a silica hearth is laid 4 ft 6 in. in depth. No expansion is left in the brick base and crucible where they are in contact with the hearth.

E. A. SLOVER, Member AIME, is Assistant General Manager, Chino Mines Div., Kennecott Copper Corp., Hurley, New Mexico.

Discussion on this paper, TP 3580D, may be sent, 2 copies, to AIME by Jan. 1, 1954. Manuscript, Jan. 5, 1953. Los Angeles Meeting, February 1953.

The hearth itself is of quartzite crushed to 1 in. size with fines left in the product. An 8 in. layer is laid and tamped with paving tampers to about 6 in. in thickness. Then a layer of silica flour is spread and vibrated into the hearth. This operation is repeated until a depth of 4 ft 6 in. is occupied by the silica mass onion-skinned in layers of approximately 6 in. Before firing the entire hearth is covered with broken slag to a depth of 4 in. so that a seal may be formed on the hearth.

The crucible is completely faced with magnesite chemically bonded brick while the outside, against the foundation, is made of silica brick. The sidewalls are carried up with silica brick in which expansion joints are left at intervals. Above the crucible the sidewall is corbelled to form a shelf on which the charge may build up along the sidewalls, see Fig. 2.

The arch of the furnace is sprung 20 in. silica brick, with the longitudinal centerline horizontal the length of the furnace, and some 9 ft in the center above the bath. Both straight and wedge brick are used in the construction and a thin silica mortar is troweled for joints. After the arch under heat has assumed its permanent shape, a silica slurry is spread over the arch to fill any cracks that have formed, thus giving bearing surface to the brick and preventing dust from entering the body of the arch to act as a future fluxing agent.

The uptake of the furnace slopes up to the boiler entrance where a brick pilaster divides the gas stream for the two boilers. Over this flared uptake is a suspended flat arch of firebrick. The pilaster and sidewalls are constructed of firebrick but the bottom of the uptake is lined with silica brick and fettled through holes in the roof with siliceous fettling. Close to the entrance of each boiler is a brick covered slot through which water-cooled dampers may be lowered in event of boiler trouble.

These water-cooled dampers are hung permanently in position ready to be lowered when needed. Flexible hoses to follow the dampers as they are lowered are connected at all times and individual chain blocks are used to lower the dampers. A pump supplying water is started before the dampers enter the heat.

Charging of the furnace along the sidewalls for some 80 ft from the bridgewall is accomplished by electric vibrating conveyors fed by belt from charge storage bins above the furnace. These conveyors

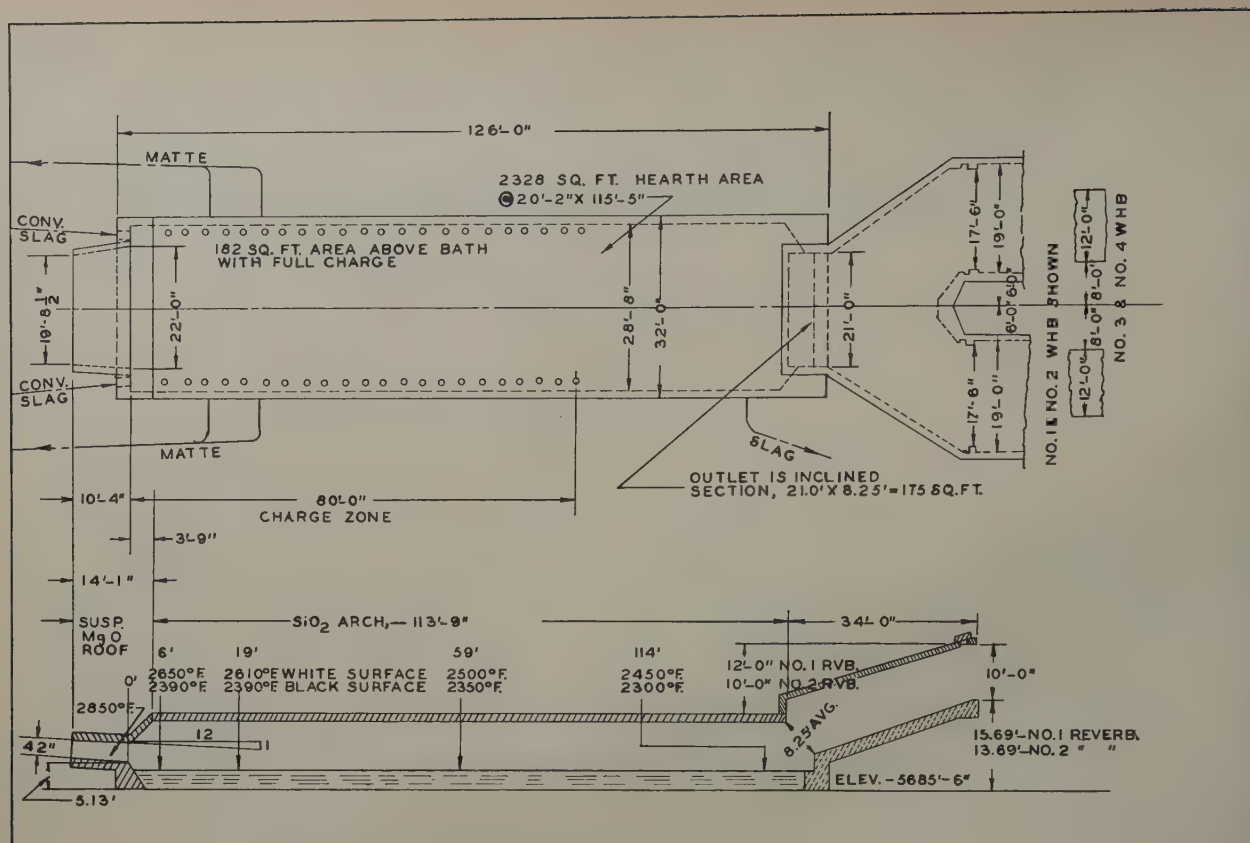


Fig. 1—General arrangement of reverberatory furnace.

are carried on steelwork separate from the building and furnace steelwork so that vibration is not transmitted. There is no trackage or flooring over the furnace except for a walkway along each vibrating conveyor. In the feeder trough are 24 door-covered slots at 40 in. centers through which charge is dropped into the furnace along the sidewalls.

The furnace was originally equipped with multi-jet air inspiration type of burners set in a panel above the bridgewall. These were low pressure gas burners and the tubes through which air was inspired to mix with the gas were rather short. Fireclay was used in the construction of these tubes.

Return converter slag is poured into the reverberatory furnace through launders on each side of the burner panel in the firing end of the furnace. Matte is tapped into ladles in the converter aisle through launders on each side of the furnace with two tap-holes available for each launder.

Once the dimensions of a furnace are fixed there has to be an overwhelming reason to change them. These reasons have their inception around the main function of the furnace, namely the transfer of heat.

The furnace as constructed never smelted much tonnage, 600 tons of concentrate being a good day's run. Magnetite soon filled the hearth so that the bath was of small proportions. With gas fuel the furnace never was hot enough to do rapid smelting. The temperature drop of the entire furnace was some 200°F from 2600°F in the combustion zone to 2400°F at the outlet.

Some minor changes were made in the multi-jet gas burners to obtain better air-gas mixing with the object of obtaining a higher temperature in the combustion zone but no pronounced success was observed.

To get this desired higher temperature in the combustion zone forced draft of pre-heated air

burned with gas in a "Dutch Oven" was introduced. The thought here was to obtain as hot a flame as possible before turning the flame into the working zone of the furnace. Temperatures between 2800° and 2900°F can easily be maintained in the Dutch Oven. Two temperature gradients are given in Fig. 1. The first when the surface of the bath is covered with a white scum from the more refractory charges shows a gradual temperature drop of 400°. The other is when the bath is clean, or appears black, for less refractory charges. Here there is a very sharp drop of 460° in 6 ft, with an overall drop of 550°F. Results of this larger heat release have been a furnace without severe magnetite build-up and an increase in tonnage smelted. The furnace has not produced something for nothing but has been able to burn more gas than previously. Fuel ratio's have gone down from 6.635 to 5.627 million Btu gross and from 2.873 to 2.636 million Btu net per ton of new metal bearing material over the period 1942 to 1951.

A second reverberatory smelting furnace has been constructed at Hurley with dimensions about the same as the No. 1 furnace. This second furnace was built with the horizontal arch some 18 in. closer to the bath in order to be able to wipe the bath with the flame when burning a reduced amount of gas. A lower fuel ratio was achieved but other difficulties arose in respect to the restricted space for the charge. The furnace is being returned to an arch height similar to the original furnace.

Heat data are given in Table I. The days covered by this tabulation are not maximum smelting days but are days on which test work was done.

The changes over the years have been minor on the Hurley furnaces and when the heat transfer

It was when an attempt was made to reach a much greater tonnage smelted that the boilers became a very definite limiting factor.

Waste Heat Boilers at Hurley

There are two sets of waste heat boilers with two boilers in each set corresponding to the two furnaces. The newer boilers will be described first. They were designed and made by Babcock & Wilcox and erected by Stearns-Roger Mfg. Co.

These boilers were designed for waste heat boiler use and incorporate ideas in regard to temperature, draft, and dust control. The smelter staff desired to obtain boilers that would allow for increased fuel burning in the furnace and at the same time would not need constant manual attention to keep them functioning.

The boilers are 12 ft in width and 35 ft in length, independently suspended from a separate structure of steel so that boiler and hopper move as a unit with expansion. They are not of great height in order to minimize the pressure in the upper parts of the boiler due to the buoyancy of the hot gases. With the setting under draft, should manual attention be necessary, the boiler can be approached by men to do the work. As the hot gases from the furnace go through the boilers the sequence of chambers is as follows: a cooling radiation chamber, a platten filled chamber where radiation in a cavity can take place, a superheater chamber, and a cross-flow two-drum boiler unit, see Fig. 3.

Table 1. No. 2 Reverberatory. Averages for Tests of March 15, 16, and 17, 1951

1. Tons smelted in reverb per day	813
2. Cu ft natural gas burned in reverb per hour	153,000
3. Cu ft natural gas burned in preheater per hour	19,000
4. Cu ft natural gas charged to reverb per hour	172,000
5. Cu ft natural gas charged to reverb per day	4,128,000
6. Btu per cu ft natural gas	1,107
7. Btu per day from natural gas charged to reverb	4,570,000,000
8. Btu per ton natural gas charged to reverb	5,620,000
No. 7 + No. 1	
9. Cu ft preheated air per min, 60°F, 24.45 in. Hg	21,000
10. Temperature, °F, preheated air	650
11. Lb preheated air per day	1,814,400
12. Btu per lb preheated air, sp ht = 0.24 Btu/lb/°F	141.6
13. Btu in preheated air per day	257,000,000
14. Btu from sulphur, per cu ft natural gas burned in the reverb	287
15. Btu from S per day	1,054,000,000
No. 14 x (No. 2 x 24 hr)	
16. Subtotal Btu to reverb per day, natural gas + S	5,624,000,000
No. 7 + No. 15	
17. Total heat into reverb per day, natural gas burned + S + preheated air (No. 2 x 24 hr) x No. 6 + No. 15 + No. 13	5,376,000,000
18. Reverb draft, H ₂ O	-0.04
19. Pct CO ₂ + SO ₂ by volume in reverb offtake gases	11.8
20. Pct O ₂ by volume in reverb offtake gases	1.1
21. Pct CO by volume in reverb offtake gases	0.6
22. Pct excess air at reverb offtake	3.96
23. Highest flame temperature °F in reverb + Dutch Oven	2,890
24. Gas temperature reverb offtake, °F	2,320
25. Btu sensible heat per lb reverb offtake gas, + 60°F (No. 24 - 60°F) x sp ht 0.284	642
26. Lb reverb gases per day, at offtake	5,038,940
27. Btu sensible heat reverb gases per day	3,235,000,000
28. Btu potential heat reverb gases per day	207,000,000
29. Btu latent heat volatilization in H ₂ O charge + natural gas per day	512,000,000

The first cooling chamber has tubes on each side and the roof in order to reduce gas temperatures rapidly. From the boiler makers view this was desirable because the rate of steam generation of the

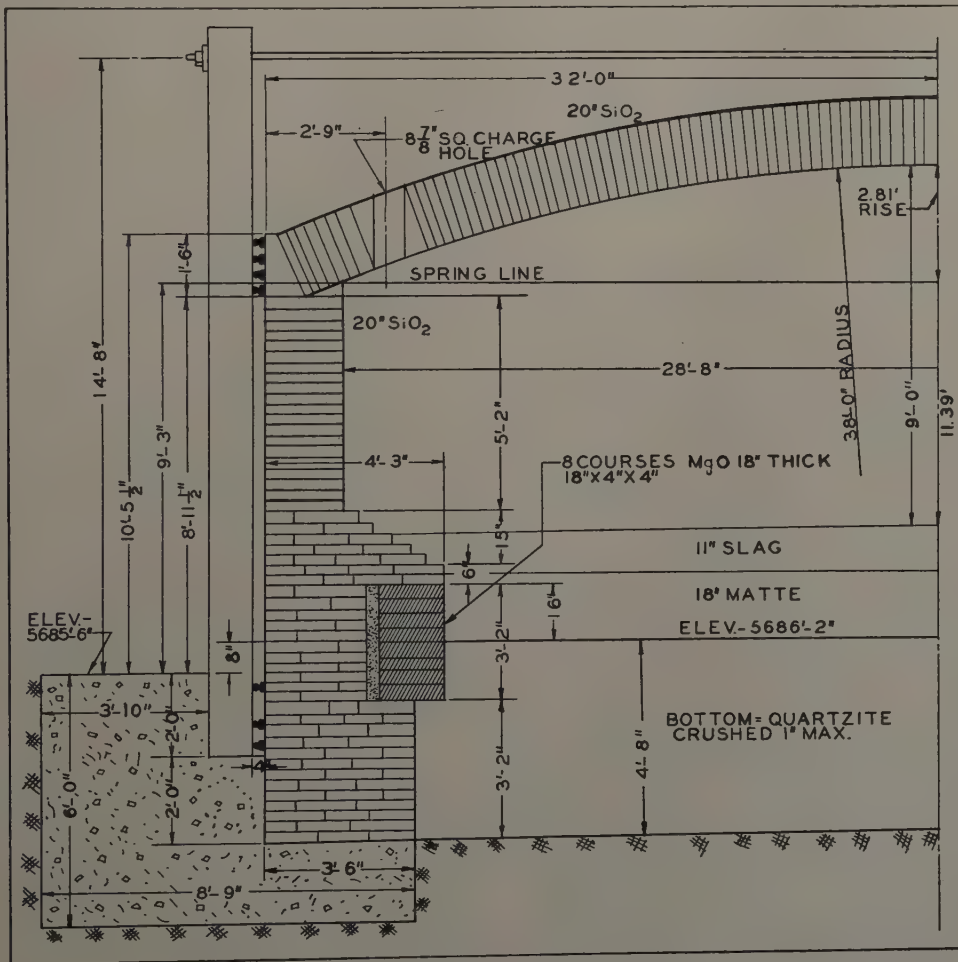


Fig. 2—Half-section of reverberatory furnace.

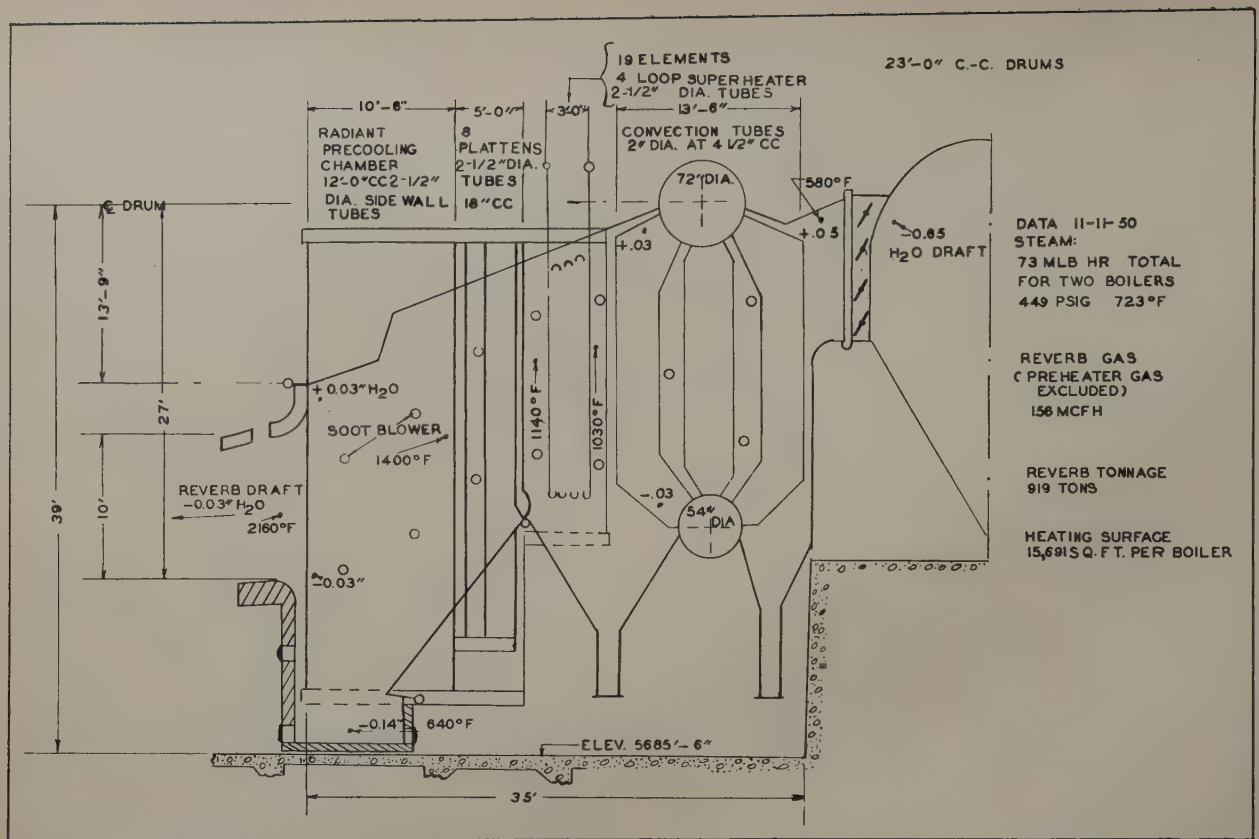


Fig. 3—No. 3 and No. 4 waste heat boilers.

first tubes of the plattens might be too high for natural circulation were the gases initially to impinge directly on these leading tubes. From the smelter point of view it was desirable to reduce the temperature of the sulphide dust before it met the leading tubes of the plattens so that sticking and corrosion would be avoided.

The platten chamber is 5 ft long, and has seven rows of plattens made up of 2½ in. tubes. There are eight passages 15½ in. wide between tubes. In this chamber the temperature of the gases is still further reduced before passing to the superheater tubes.

There are 19 superheater elements of four tubes each. Originally there were 24 superheater elements but 930°F superheater temperature was obtained. In order to reduce this temperature, five elements were removed so that now the superheat temperature follows a flat curve at 730°F.

From the superheater chamber the gases pass through a two drum special boiler. Cross flow of the tubes by the gases has been obtained.

In the entire boiler there is not a baffle to separate dust from the gas or to add draft loss to the system. The tubes are as simple in design as possible in order to make replacements easy.

In the design of these boilers it was considered necessary to have the drums at 23 ft 0 in. centers, in order to get enough height to insure proper water circulation. It was thought that the hot gas stream might go all the way through the boiler only as deep as the height of the boiler entrance (10 ft 0 in.) with the chance that about 7.5 ft of the net 17.5 ft tube height might not be touched by the hot gas. And in the calculation of the heating surface on this basis, a compromise was made between a somewhat higher offtake temperature than ordinary, and a larger amount of tubing. However, in actual operation, the bottom of the gas stream, with about 160

Table II. Waste Heat Boilers No. 3 and No. 4. Averages for Tests of March 15, 16 and 17, 1951

Heat Data		
30. Lb steam per hour, total of the two boilers		91,000
31. Lb steam per day, total of the two boilers		2,184,000
32. Temperature of feedwater at WHB, °F		325
33. Pressure of steam, psi, gage		468
34. Pressure of steam, psi, gage		480
35. Temperature of steam, °F		765
36. Btu put into steam per lb, in WHB		1,066
37. Btu put into steam per day		2,328,000,000
38. Pct CO ₂ + SO ₂ by volume at WHB exits		10.6
39. Pct O ₂ by volume at WHB exits		2.7
40. Pct CO by volume at WHB exits		0.4
41. Pct excess air by volume at WHB exits		13.5
42. Pct air infiltration, reverb offtake to WHB exits, by volume		8.8
43. Pct H ₂ O draft, boiler side WHB exit dampers		+ 0.05
44. Pct H ₂ O draft, stack side WHB exit dampers		- 0.52
45. Lb gases per day from WHB exits		5,501,000
46. Lb gases per hour to each boiler, reverb offtake basis		105,000
47. Lb gases per hour to each boiler, WHB exit basis		115,000
48. Temperature of gases entering WHB, °F		2,120
49. Temperature of gases leaving WHB, °F		580
50. Btu sensible heat per lb WHB exit gases, + 60°F, sp ht 0.261		135.7
51. Btu sensible heat per day, leaving WHB exits		746,000,000
Input to Waste Heat Boilers		
52. Sensible heat in reverb offtake gases, Btu/day—pct	3,235,000,000—	81.9 %
53. Potential heat in reverb offtake gases	207,000,000—	5.2
54. Latent heat vol H ₂ O, charge + fuel, per day	512,000,000—	12.9
55. Total input to waste heat boilers	3,954,000,000—	100.0
Output from Waste Heat Boilers		
56. Btu put into steam per day	2,328,000,000—	58.9 %
57. Btu sensible heat exit gases per day	746,000,000—	18.9
58. Latent heat volume H ₂ O, charge + fuel, per day	512,000,000—	12.9
59. Btu unaccounted for per day	368,000,000—	9.3
60. Total output from waste heat boilers, Btu per day	3,954,000,000—	100.0
Miscellaneous		
61. Pct of heat in fuel charged to reverb recovered in steam (No. 37 + No. 7) x 100		50.9
62. Pct total heat put into reverb present at WHB entrances		73.5
63. Thermal efficiency of reverb, pct 100.0 pct — No. 62		26.5
64. Efficiency of WHB, total heat basis, pct (No. 56 + No. 55) x 100		58.9
65. Efficiency of WHB, sensible heat basis, pct (No. 56 + No. 52) x 100		72.0

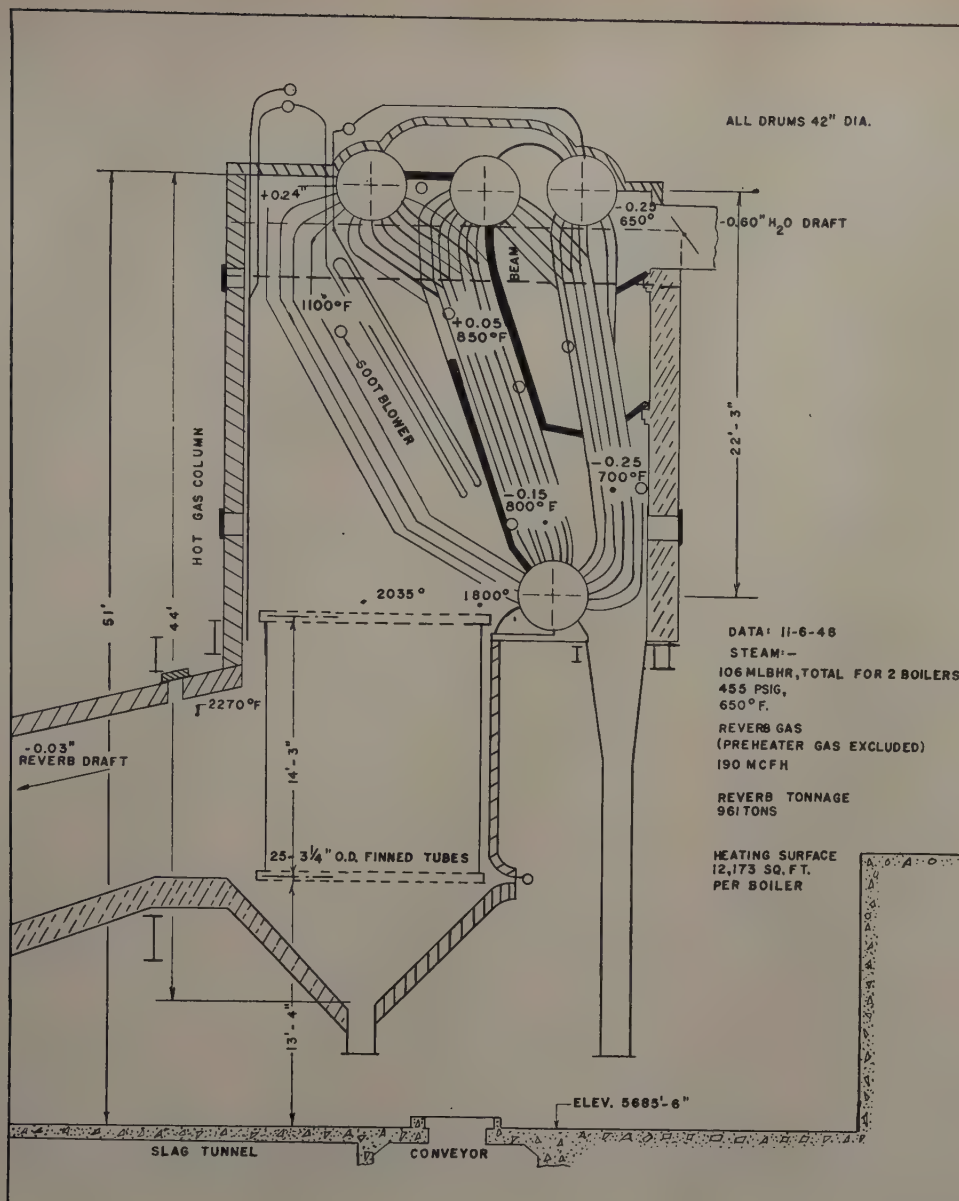


Fig. 4—No. 1 and No. 2 waste heat boilers as originally installed in 1939.

M cu ft per hr natural gas burned in the reverberatory, comes down to the top of the lower drum, with the result that the exit gas temperature is substantially lower than predicted. This dropping down of the gas stream's lower boundary may be due to the fact that there is a slight build-up of pressure in the boiler, from front to back, so the gas is forced and to some extent packed or stuffed into the boiler, causing it to spread.

The setting is attached to the tubes by Nelson studs. For the side surfaces there is a layer 1½ in. thick of B & W K2 cement, then a foam glass block of 3½ in., and finally an air-sealing layer of Air-Tight cement about ¼ in. thick. Wire attached to the studs holds the foam glass blocks in place. On the top of the boiler an additional layer of firebrick is placed between the K2 cement and the foam glass blocks and at the rear where the tubes are separated, tile is used to span the space between the tubes.

Considerable attention was given to the hopper beneath the radiation chambers of the boiler since most dust would accumulate here. Floor tubes form the steeply sloping rear wall of the hopper while the sidewalls are partly made of sidewall tubes

from the radiation chamber and partly of Detrick suspended tile. The front wall is stationary and constructed of Detrick tile. Dust knocked into the hopper by the soot blowers does not slag and is removed manually by rabbles. It was thought afterward that this dust could be removed easily and continuously by a stoker arrangement working through an air seal. Since the only part of the entire boiler that does not move as a unit is the front wall of the hopper and all the vertical movement is downward it is important that the hopper bottom does not hit the floor. Both units at Hurley stop moving ½ in. from the floor.

Soot blowers are depended on to keep the boilers clean but hand lancing doors have been provided as a safety matter. To date little hand lancing has been done. In the radiation chamber, four soot blowers of the Diamond IR or surface type are used on each side of the 12 ft wide chamber. Then there are 9 IK type which travel across the entire boiler for the platten chamber and the balance of the boiler. Both types are retractive. The platten chamber has left in each platten a 15 in. vertical slot through which two soot blowers operate. The IR soot blowers use

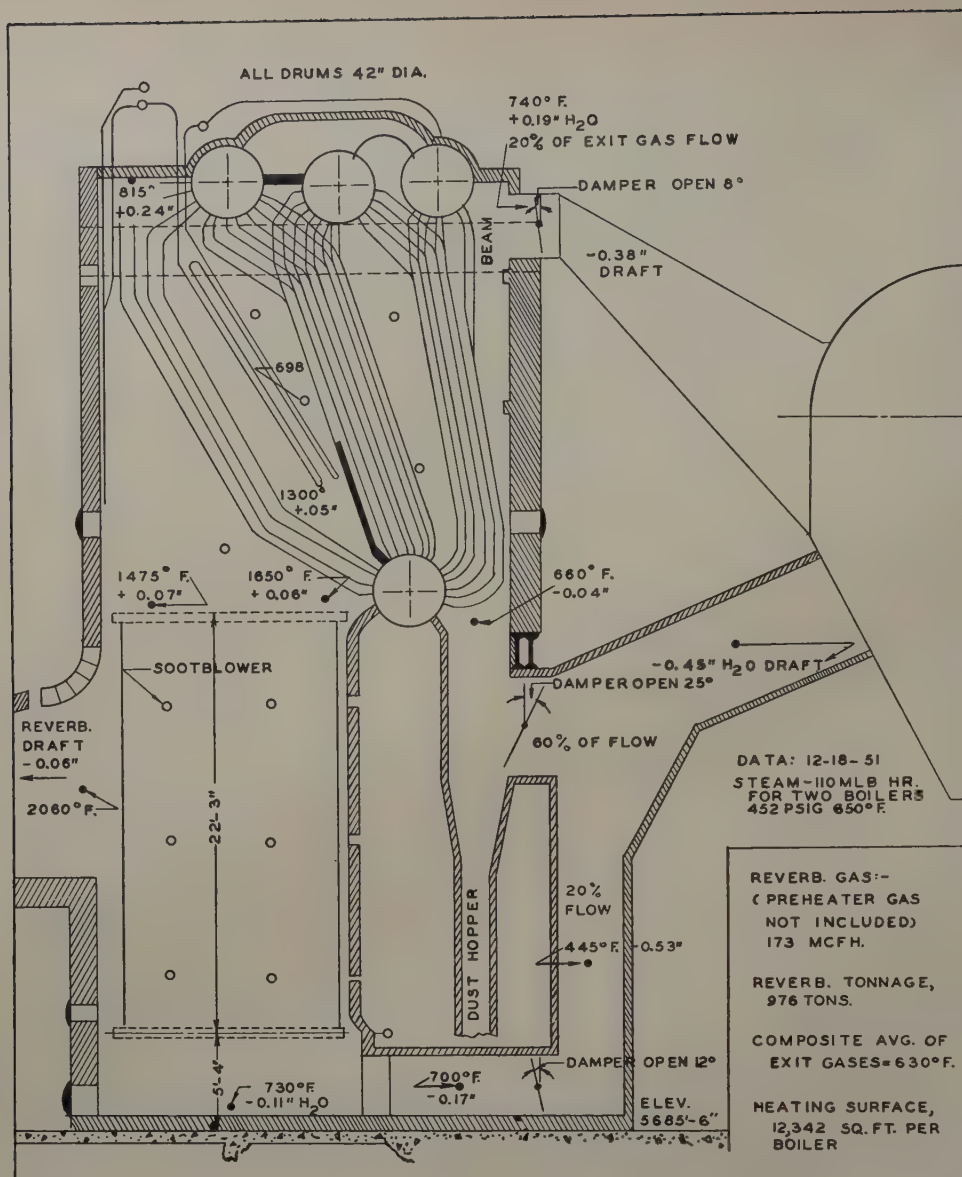


Fig. 5—No. 1 and No. 2 waste heat boilers as revised in 1951.

steam at 250 lb and IK soot blowers at 210 lb pressure. Ingersol-Rand air motors which revolve and advance the blowers and purge air at 3 lb pressure are used when the soot blowers are not in operation. The soot blowers may be operated automatically in sequence from a panel board or each may be operated individually in any sequence.

To date no tubes have been replaced or welded and there has been no trouble with this set of boilers. Also no slag has been formed in the boilers or in the hoppers. It was demonstrated that one boiler could carry the furnace with normal firing when the water-cooled dampers had the other boiler cut out for superheater tube reduction. Draft is automatically regulated using a Hagan control. Some data on this set of boilers is listed in Table II.

The two boilers of the second set which are behind the original furnace are Combustion Engineering Company's fin furnace boilers, see Fig. 4.

As far as the gas flow and baffling are concerned, these are Sterling type boilers with three passes. But the water circulation is different from a Sterling boiler. As shown in Fig. 4, the tubes are cross connected in the two back passes, with alternate rows of tubes going to different top drums. That makes what amounts to Sterling type water circulation in the

front of the boiler, and an economizer in the back, with the two mixed up in the middle.

These boilers are 19 ft wide inside and have a large combustion chamber, three sides of which are composed of tubes with fins. Above this radiation chamber is the boiler with three steam drums and one mud drum suspended from I-beams below the steam drums.

There is no object in describing these boilers as originally installed other than to call attention to the troublesome features when used as waste heat boilers in a copper smelter.

First, there was a constant dust problem since the height of the boilers allowed the buoyancy of the hot gases to exert itself and the upward velocity attained drew the gases from the radiation chamber very rapidly. Except toward the bottom of the entering gas stream, the gas stream did not extend far across the chamber. The velocity of the ascending gas stream carried dust that deposited on the front bank of tubes in the boiler where, because of the lack of heat transfer in the radiation chamber, the heat baked the dust on the tubes.

Second, the pressure generated in the boilers made it impossible to lance the tubes properly to keep the dust from building up and plugging the

boiler. No increase in firing rate was possible under these conditions.

Third, the setting of both boilers had disintegrated from sulphur impregnation and finally the boilers in expanding while heating after a repair invariably sprung leaks where the tubes were rolled into the mud drum due to mud drum space restriction.

In the redesign, shown in Fig. 5, the third and fourth objections were taken care of by using foam glass, tile, and air tight cement, but no studs attached the setting to the boiler tubes. The setting is supported by steel beams and does not move with the boiler. The mud drum has been freed to move without hindrance.

The other problems were approached from the standpoint of cooling the gases in the chamber made for that purpose and removing baffles that served to hold dust.

A model of the boiler was constructed and from applied suction it was determined that one-sixth the draft of the boiler exit was needed as a vertical component applied at the bottom of the boiler to cause the hot furnace gases to penetrate well into the radiation chamber and give up a greatly increased quantity of heat. The cooler gases would not bake the dust on the lower part of the tubes in the first pass. Then, to prevent dust deposition in a narrow second pass the baffle was greatly shortened between the first and second passes and removed between the second and third passes. The reason the baffle was not completely removed before the second pass was that no short circuiting of the superheater was contemplated. In effect much additional cross flow was obtained, but to be certain of this a new central duct was constructed that forced cross flow in the boiler proper. The original

outlet to the flue was also maintained. Each outlet was dampered so adjustments can be made. The water wall tubes on three sides of the radiation chamber were extended downward an additional 8 ft 0 in. into a square-shaped, flat bottomed dust collecting hopper to be certain no slag was formed from the dust knocked down.

In operation the boiler has caused no trouble but the top flue has had to be opened at times to reduce excessive pressure near the top at high firing rates on the furnace. Apparently no close approach has been made to the firing rate on the furnace that will cause the boiler to be a limiting factor.

Soot blowers have been installed on these boilers, the same in type as on the new set of boilers: the IR type, of which there are 18 on the radiation chamber, and the IK type of which there are four on each side of one boiler and four extra long ones on but one side of the other boiler. There is one G 9B blower, which is non-retractable and rotates through a whole circle. This arrangement was necessary because of the narrow space between boilers.

The boilers are well cleaned by the soot blowers but some accretion has built up at the back of the radiation chamber where dust that has been given a direction by the splitting pilaster accumulates. It is not serious.

Automatic draft control has been applied to the center flue exit, the top and bottom exit being fixed when once set.

Acknowledgment

Thanks are due by the writer to the Smelter Staff, and to H. W. Mossman and C. L. Lockart, of the Smelter Metallurgical Dept., for assistance in preparing data for this paper.

Technical Note

Change in Ingot Shape During Zone Melting

by W. G. Pfann

WHEN a molten zone traverses a long, solid ingot in a level, open boat the ingot becomes tapered. While the taper may be slight after one zone pass, it can be appreciable after repeated zone passes, even to the extent of causing an overflow of matter at the end of the boat. It will be shown here that such *matter transport* by a molten zone arises from the volume change on melting and that it corresponds in magnitude and direction to the magnitude and sign of the volume change. It will be shown also that the mechanism of matter transport is basically similar to that of solute transport by a molten zone, which has been discussed elsewhere,^{1,2} and that the two processes can be described by similar equations. Finally it will be shown that matter transport can be prevented by inclining the ingot at a critical angle.

Contraction on melting results in forward transport, that is, transport in the direction of zone

travel; expansion on melting results in reverse transport. The way in which forward transport arises from the contraction on melting may be seen as follows:

At the starting end of a solid horizontal ingot of uniform rectangular cross section of height h_0 , form a molten zone of length l , as shown in Fig. 1. The height h of the liquid will be αh_0 , where α is the ratio of density of solid to that of liquid. Advance the molten zone, at constant length, a distance dx . The volume of solid melted will be $h_0 dx$; the volume of solid frozen will be $h dx$, because the height of the freezing solid will tend to be equal to that of the liquid. The resultant change, dv , in liquid volume will be the difference in these quantities multiplied by the density ratio. Hence the following equation may be used for a zone at any distance x from the origin:

$$dv = l dh = \alpha (h_0 - h) dx. \quad [1]$$

Solving Eq. 1 for h gives

$$h/h_0 = 1 - (1 - \alpha)e^{-\alpha x/l} \quad [2]$$

which is valid in all but the last zone length in the

W. G. PFANN, Member AIME, is associated with the Chemical and Metallurgical Research Dept., Bell Telephone Laboratories, Murray Hill, N. J.

TN 186E. Manuscript, July 2, 1953.

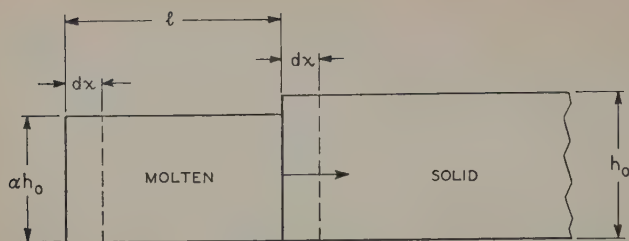


Fig. 1—Formation and advance of a molten zone in a level, uniform ingot. A transport of matter arises from the height difference between melting and freezing solids.

ingot. Eq. 2 is identical in form to Eq. 2 of ref. 1,

$$C/C_0 = 1 - (1 - k)e^{-kx/l} \quad [3]$$

for the solute concentration C after passage of a molten zone of length l through an ingot of uniform solute concentration C_0 , where k is the ratio of solute concentration in the freezing solid to that in the liquid.

Eq. 2 shows that the zone accumulates height as it travels, which process continues, if the ingot is long enough, until h becomes substantially equal to h_0 . No further increase in h occurs until the zone reaches the end of the ingot, whereupon it solidifies by normal freezing. This results in further increase in height and it is readily shown that

$$h/h_0 = (1 - g)^{a-1} \quad [4]$$

where h_0 is the height of the liquid at the start of

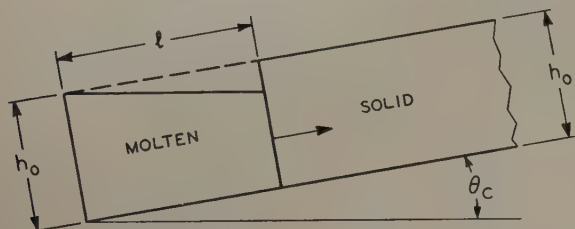


Fig. 2—Molten zone at beginning of its travel in an ingot inclined at the critical angle for zero transport.

normal freezing and g is the fraction of the zone length which has solidified. Eq. 4 is identical in form to the equation for solute concentration in normal freezing.

Likewise the ultimate distribution of height, which cannot be altered by further zone passes, is seen by analogy with solute transport to be

$$h/h_0 = A'e^{Bx} \quad [5]$$

where

$$\alpha = \frac{Bl}{e^{Bd}-1} \text{ and } A' = \frac{Bd}{e^{Bd}-1}$$

d being the ingot length. Eq. 5 shows that a large

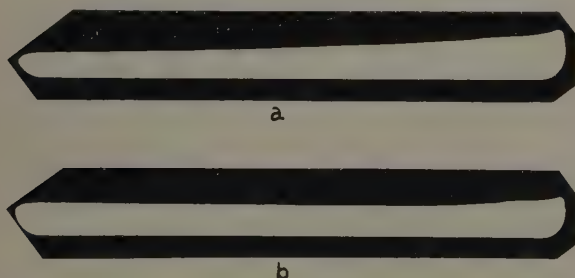


Fig. 3—Silhouettes of originally uniform germanium ingots after passage of 12 molten zones from left to right: a—ingot horizontal, b—ingot inclined at 2° from horizontal. Ingot length, 12 in.; mean zone length, 2 in.

change in ingot height can be produced, even for a rather small α . For example, if $\alpha = 0.95$, $l = 1$, $d = 10$, then h/h_0 is 0.58 at $x = 0$ and 1.4 at $x = 9$, which represents a variation of about 2½ to 1 in ingot height.

The transport process can be modified by inclining the ingot, which act in effect changes the value of α in Eq. 2. A case of particular interest, that of zero transport, for which $\alpha = 1$, is illustrated in Fig. 2. The critical inclination θ_c for zero transport is that for which the height of the freezing solid is h_0 , where θ_c is given by

$$\theta_c = \tan^{-1} 2h_0(1-\alpha)/l \quad [6]$$

The effect of passing 12 molten zones through a uniform germanium ingot is shown in Fig. 3 for a horizontal ingot and for an ingot inclined at the critical angle, which was 2°, determined experimentally. Germanium contracts on melting, the volume change being rather large, about 5 pct or more.* Inclination of the ingot can minimize, but

* Matter transport in the zone melting of germanium has also been observed by Alexander³ and was attributed by him to the contraction on melting. A summary of this note was given by the writer during the same discussion. Change in ingot shape during normal freezing of germanium was discussed in a paper by Bradshaw⁴ and some discussion of zone freezing was given orally. A value of 11.5 pct for the contraction on melting was given by Bradshaw.

cannot completely prevent, matter transport in normal freezing.

Matter transport can also be prevented, except in the last zone, by altering the height of solid in the molten zone at the beginning of the ingot so that, on melting, the liquid height equals h_0 . This method corresponds, in solute transport, to using a starting charge of concentration C_0/k in an ingot of uniform concentration C_0 . It is useful for one pass only.

A consequence of matter transport is that the equations for solute distribution in ref. 1 are strictly accurate only if the ingot is inclined at the critical angle, although the error involved would be negligible in general.

Eq. 6 provides a means for estimating the volume change on freezing. However, surface tension effects have not been considered and more experimental data will be required before Eq. 6 can be used for this purpose.

The similarity of the equations which govern matter transport and solute transport suggests that these phenomena are basically the same. It appears that their common feature lies in the concept of concentration. In solute transport the concentration of solute freezing out of a molten zone is k times that in the zone. In matter transport the concentration of matter freezing out of a zone is α times that in the zone. The similarity of k to α lies in the fact that a density ratio is really a concentration ratio, when concentrations are expressed on a volume basis, as they have been throughout this work.

The writer is indebted to F. Monforte for performing the experiments of Fig. 3.

References

- W. G. Pfann: Principles of Zone-Melting: *Trans. AIME* (1952) **194**, p. 747; *JOURNAL OF METALS* (July 1952).
- W. G. Pfann and K. M. Olsen: Purification and Prevention of Segregation in Single Crystals of Germanium. *Physical Review* (1953) **89**, p. 322.
- B. H. Alexander: Unrecorded discussion on ref. 1 at the Philadelphia Meeting, AIME, October 20, 1952.
- S. E. Bradshaw: Phenomena Observed in the Melting and Solidification of Germanium. *Journal Electrochemical Soc.* To be published.

Preparation of Metallic Iron of High Purity

by George A. Moore

A brief review is given of methods designed to produce metallic iron of high purity, and typical results are listed. A recent method, utilized at the National Bureau of Standards, consists of the extraction of ferric chloride by ether, reduction of this ferric chloride to ferrous chloride, further purification of this chloride, and the subsequent electrolytic deposition of metallic iron. Iron produced by this procedure apparently is softer than, and otherwise different in properties from, any iron previously prepared and contains appreciably smaller amounts of impurities.

THE history of attempts to produce "pure" iron reaches to antiquity and it may be presumed that each ancient armorer who succeeded in making a better steel concluded, correctly, that he had done a better job of removing the "base metals," and incorrectly, that he now at last had a "pure" metal. Early metallurgical papers mentioned use of "pure iron" in making alloys—this "pure" iron in most cases being inferior to some commercial stocks of the present time. Improvement has been continuous, and usually at a sufficient rate to convince each succeeding group of workers that they, at last, were using the really pure metal (until the analysts also improved their techniques to again discover the impurities). These adventures were reviewed in some detail by Cleaves and Thompson.¹

Although the ores of a metal may be abundant, difficulties in extracting it may make the pure metal very rare. When impurities are restricted to a total of a few parts per million, nearly all pure metals become rarities. Lead, copper, gold, mercury, silver, zinc, aluminum, bismuth, and the six platinum metals are claimed to be available with total impurities ranging from 2 to 50 ppm. The present small and scattered world supply of so-called "pure" iron holds an unimpressive place in another group of 16 metals having approximately 100 ppm of foreign material. Of about 20 less rare metals, only the platinum metals are more costly to prepare.

While the production of such rare varieties of iron may appear insignificant in the presence of thousand-ton operations with 95 to 99 pct metal, it must be emphasized that all researches on commercially interesting irons and steels are in fact studies of the modifications of the properties of iron by additional

materials. Until the properties of high purity iron are directly measured, all ferrous research must operate without known base values.

Traces of impurities may affect the properties of a metal in many ways. Infinitesimal traces of solutes, by disturbing the electronic configuration, greatly change the electrical properties of transistors and semiconductors²⁻³ and slightly larger traces might alter these quantities in iron. Soluble impurities which disturb the perfection of lattice arrangement not only may alter the magnetic constants and electric properties, but by their close association with dislocation phenomena probably control the very existence of the "yield point"; determine the value of yield stress; and perhaps control the selection of slip and cleavage planes. It has been speculated that impurities might even cause the allotropic transformation in iron, but in any case their rearrangement must contribute to the unreliability of heat capacity and other thermodynamic measurements.

Impurities which do not remain in solution may cause even greater effects on the properties. Microscopically visible amounts of phases other than ferrite can be found in all high purity irons which have come to my attention. It can be calculated that from 50 to as little as 2 ppm of an insoluble material might be sufficient to completely film all grain boundaries in irons having grain sizes from ASTM Nos. 10 to 1. Should this occur, such films, even though invisible, may be very important in fracture problems, especially at extremes of temperature.⁴ Studies of grain growth and diffusion normally imply consideration of a single-phase system, hence, in the presence of insoluble impurities they can be expected to give ambiguous data.⁵

High purity iron is also in demand for use as chemical and spectro-chemical standards; for work in classifying the lines of the iron spectrum; for biological work in nutrition; and for work in nuclear physics where the presence of some sensitive

G. A. MOORE, Member AIME, is Metallurgist, National Bureau of Standards, Washington, D. C.

Discussion on this paper, TP 3626D, may be sent, 2 copies, to AIME by Jan. 1, 1954. Manuscript, Feb. 18, 1953. Los Angeles Meeting, February 1953.

impurity as dilute as one part per hundred million may disrupt the experiment.

Considering the vital importance of all these factors it becomes evident that new means of producing iron of progressively higher purity must be developed.

Extensive interest in high purity iron at the National Bureau of Standards began about 1914 with the electrolytic preparation of some iron of about 99.95 pct purity, according to the analytical procedures then available. Intensive study from about 1930 until 1942, resulted in the monograph mentioned¹ and papers by Cleaves, Thompson, and Hiegel⁷⁻¹⁰ dealing with iron of about 99.99 pct purity prepared by the nitrate crystallization process. Some larger ingots of similar iron were prepared by Cleaves and Lindberg between 1947 and 1950.

Processes Available

Numerous processes are available for purification of iron and it is frequently difficult to judge which is best. These processes can be basically classified as pyrometallurgical, electrochemical, and chemical. Some typical results obtained are listed in Table I. Basic open hearth ingot iron has represented the practical commercial limit of strictly pyrometallurgical process for at least 25 years and is represented by the various National Bureau of Standards samples No. 55 through 55B. Irons of 99.75 to 99.85 pct purity appear to represent the practical limit of

this process. Some further removal of nonmetals can be accomplished by vacuum melting or hydrogen annealing.

The purity of electrolytic iron depends both on the purity of the anode metal and of the iron salt used for electrolyte. Both are normally comparable with ingot iron. Comparatively noble metals, for example copper, and active metals such as chromium, may be removed, but nickel, cobalt, manganese, and other metals similar to iron are usually unaffected. Electrolytic iron as deposited usually contains appreciable amounts of oxygen, and iron from sulphate baths usually contains considerable sulphur. The total impurities in electrolytic iron, as deposited, are comparable with ingot iron. Manganese and sulphur may be reduced by remelting in air, and oxygen by vacuum melting with a suitable slag, or by hydrogen treatment of hot sheet, or the melt. Such reworked electrolytic iron has been reported to be 99.95 to 99.97 pct Fe.

The carbonyl process is by no means a certain method of purification. Apparently nickel (and probably cobalt) is carried over with the iron, together with some copper and chromium. Carbon and oxygen are important nonmetallic impurities in the powder. Aluminum, magnesium, silicon, etc., may be introduced during remelting of the carbonyl powder.

The pyrometallurgical and electrochemical processes therefore seem to be incapable, at present, of producing iron of appreciably better than 99.95 pct

Table I. Typical Analysis of Iron by Various Processes, Expressed in Parts per Million Parts of Iron

Material	BOH Ingot Iron	Ingot, Hydrogen Purified	Carbonyl, Hydrogen Purified	Swedish, Vacuum Remelt	Electro- lytic	Electro- lytic, Vacuum Remelt	Electro- lytic, Vacuum Remelt	Nitrate, Ingots 1-19	Nitrate, Ingots 21-26	Chloride, Electro- deposited Lot 7
Producer (Date)	Armco		C.I.T. ('35)	NPL ('51)	Various	NER ('50)	Univ. Pa. ('50)	NBS ('39)	NBS ('49)	NBS ('52)
References	(a, b, c)	(a)	(a, d)	(e)	(a, f)	(c, f)	(g)	(f)	(f)	(f)
Impurity										
Al	20-30		20	10-40	<20-80	50-60	—	1	0.5	<0.1
B			Tr*							Nil*
Be							7-50	2	16	0.5
Ca								Nil†	8	<0.01
Co	60-80		[~50]	[~20]	80-100	90	[~5]			2.1
Cr	20-80		120	10-20	<20-100	<20-50	4	Nil†	4	Nil*
Cu	400-460		170	40-70	8-10	<20-50	[~10]	<20	4.1	4.1
Ga										Nil*
Ge										Nil†
Mg	Nil*		Tr*			Tr*		Nil†	4	1.1
Mn	160-600	280	50	40	~100	<100	5-30			<0.1
Mo	20-40				~20	<20-50	[~5]			Nil†
Ni	160-200		130	50-70	<50-220	140-400	3-8	Nil†	0.8	0.8
Pb	Tr*					Tr*				<0.05
Sb	20									
Si	10	12	300	20-30	5-50	300	10-50	<0.01	12	3.7
Sn	60-90				~10	<<30	[~10]	Nil†	Nil*	<0.05
Ti	Nil*					80				0.4
V	5-10				<30	<<50	[~5]			Nil*
Zr	Nil*					Tr*				Nil†
Total Metals	~1280	[~1280]	~840	~250	~500	~980	~125	<32	49	<13
As	60-120	[~20]				Tr*				Nil*
C	100-150	50	2-7	20-40	20-60	60-100	[~10]	10	19.7	
H ₂	[~3]	[~5]	2	<0.05		1.7	0-2	2	0.3	
N ₂	30-40	1	<10	10-20		1-10	3-16	2	6.2	
O ₂	660-700	30	<20-100	10-20	~2000	26-80	3-14	27	9.0	
P	30-50	40	<10	<10	10-50	10-20	50-60	<5	<5	
S	170-250	30	<20	40-60	0-40	20	10-40	19	7.5	
Total Nonmetals	~1180	~175	~100	~120	~2100	~175	~110	<65	<48	
Total Impurities	~2460	~1450	~940	~370	~2600	~1150	~235	<98	<97	

[~] Order estimated from value for source material or subsequent product.

* Quantitative meaning of nil and trace not given by analyst.

† Nil represents less than about 1 ppm.

* Nil represents less than about 0.1 or 0.2 ppm.

(a,b,c) Total range of composition covered by following sources:

(a) *Metals Handbook*, (1948) p. 424, Cleveland. ASM.

(b) N.B.S. certificates Nos. 55, 55A, 55B.

(c) Keeler and Davis.¹⁴

(d) Moore and Smith.¹⁵

(e) Rees et al.⁴

(f) N.B.S. files.

(g) Smith, Fostini, and Brick.¹²

purity. For greater purity, processes utilizing chemical purification of iron salts can be regarded as hopeful, and in these, major efforts should be directed to the removal of nickel, cobalt, copper, manganese, and chromium. Other elements which may be present in the starting material may usually be controlled in later processing of the metal produced. Some basic chemical processes which may be considered are as follows:

Recrystallization: Since the iron salt should not contain acid radicals yielding harmful impurities on reduction, nitrates or chlorides should be used. Recrystallization of ferric nitrate from strong nitric acid was used by Cleaves and Thompson⁸ and recrystallization of ferrous chloride from dilute HCl was tried by them and earlier by investigators at the National Physical Laboratory.¹¹ Both procedures work efficiently provided a large part of the iron is discarded, since impurities concentrate in the mother liquids and only the primary crystals are of high purity. It is also, by the very nature of the process, difficult to maintain clean conditions when recrystallization is conducted on a large scale.

Precipitation Reactions: No reaction is known by which insoluble iron salt can be precipitated and recovered free from the impurities in the solution, giving a product which is convertible to high purity metal.⁸

The precipitation of impurities from an iron solution is possible, provided, first, that a sufficiently insoluble salt is found, and, second, that the very small volume of insoluble material can be effectively separated from solution. The precipitation of copper sulphide may meet these requirements. Many other suggested precipitation reactions have been eliminated as unsuitable either because they require the addition of undesirable reagents; or they do not operate in the acid condition necessary to prevent solution of the glass containers.

Solvent Extractions: Of all available processes, the transfer of a solute from one liquid to another probably offers the greatest number of possibilities for metal purification. These have the great advantage that they may be operated in a semi-automatic manner in closed, and therefore dust proof, systems. The number of possible liquid pairs which might be utilized is practically unlimited. It is desirable, but not necessary, that either the desired salt, or the impurities, be insoluble in one liquid, but in the absence of this requirement, it may still be found that the partition of a salt between two liquids may be almost entirely one way. For example the use of ether extraction is a familiar technique in the analysis of iron.

Proposed Method of Iron Production

At the beginning of the present campaign it was decided that the nitrate crystallization as used by Cleaves and Thompson, while a good method, was too laborious. A process giving a greater reduction of impurities might be hoped for, and a simpler method of attaining the same purity would be considered a success.

From the experience of numerous analysts, ether extraction was selected as the basic purification step. Additional purification has, however, proved necessary, and the process must also include reduction to metal, conversion of the reduced metal to solid useful form, and the elimination, as completely as possible, of oxygen and other nonmetals. The several steps considered or investigated for the proposed

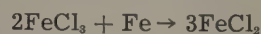
process, with commercially available ferric chloride of reagent grade as a starting material, are as follows:

I—*Ether Extraction of FeCl₃ complex from solution in 6 N-HCl, with regeneration of aqueous solution and ether recovery.*

A—In batch operation.

B—In countercurrent column operation.

II—*Reduction of FeCl₃ to FeCl₂ with high purity iron*



III—*Additional Purification of FeCl₂*

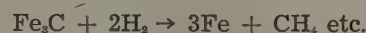
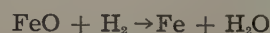
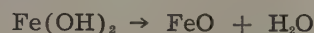
A—By recrystallization

B—By sulphide precipitation

C—By ether extraction of impurities from solution of ether-insoluble FeCl₂.

IV—*Electro-deposition of metal from FeCl₂ solution.*

V—*Hydrogen anneal of pellets*



VI—*Production of massive metal*

A—Ordinary vacuum melting

B—Drip casting

C—Melting in magnetic field support

D—Compacting and sintering

The apparatus used in step I for both batch and countercurrent column operations is shown diagrammatically in Figs. 1 and 2. About 25 lb of FeCl₃·6H₂O, AR grade, containing up to 150 ppm Cu and Zn (on Fe basis) and considerable arsenic, phosphate, sulphate and "insoluble matter," is dissolved in 2.5 liters of concentrated HCl plus 1.25 liters of redistilled water. The resulting saturated solution (about 9 liters) is fed to either extractor one liter at a time. About 90 pct of the iron content may be extracted by contact with 5 to 6 volumes of ether in the column extractor, but up to 30 volumes of ether may be required in the batch apparatus. The same volume of ether is used repeatedly in either case, and is recirculated at a rate of approximately 1 liter per hr.

Contrary to the implications of the standard analytical use of ether extraction in iron analysis, very appreciable amounts of cations other than Fe⁺⁺⁺ appear to be carried over in the ether-HCl extract. Excepting molybdenum and tungsten, all of the metals listed in Table I have been found in the extract in at least trace amounts. In the best results so far obtained, a purification ratio as high as 30 to 1 has been observed for Cu+Zn, but the average purification efficiency is certainly much lower.

It is believed that the amount of impurity carried into the extract is closely proportional to the total amount of ether that comes in contact with the solution. Hence the column extractor, which continually treats a saturated solution, is preferred to the batch extractor on grounds of both purity and speed.

At the end of the run, most of the ether is removed from the extract by heating gradually to about 100°C. At this stage the extract contains about 2 lb of FeCl₃·6H₂O per liter, and around 200 cc of ether per liter. Running a second extraction of this stock has not appeared feasible for a number of reasons, including the possible fire hazard associated with the further concentration of this ether-

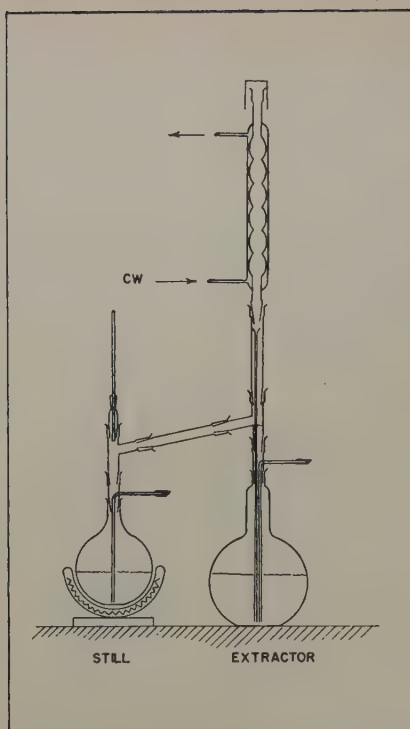


Fig. 1—Apparatus used for ether extraction of FeCl_3 in batch operation and for extraction of impurities from FeCl_2 .

containing solution. The extract is instead diluted with 1 to $1\frac{1}{2}$ times its volume of redistilled water, and the ether thus freed is distilled off, leaving FeCl_3 solution in a condition for further processing.

Step II, reduction to the ferrous state, is introduced both to bring the iron solution into convenient form for electrolysis and to prepare for additional purification reactions. A 2.5 liter batch of diluted FeCl_3 extract, containing about 0.5 lb of iron metal, is poured over about 0.5 lb of intermediate grade iron.

The intermediate iron used for reduction may be: Scraps of high purity iron from previous operations, or iron electrodeposited from the tailings of a batch of FeCl_3 solution, or directly from FeCl_3 solution after the first purification. The latter procedure, using about twice the current used in electrolyzing FeCl_3 , is preferred in the absence of available scrap.

The reaction



will run to completion in a few hours at room temperature, or may be hurried by warming. Some iron metal reacts with excess HCl in the extract



so that the final solution contains almost as much iron from solution of the intermediate reducing metal as from the fresh extract. The FeCl_2 solution normally is boiled to drive off arsenic, germanium, or other metals having volatile chlorides, but no general overall reduction of impurity metals has been demonstrated.

Further purification (step III) is required since the ferric chloride extract (and therefore the FeCl_3 solution) contains anywhere from 5 to 20 parts of copper per million parts of iron.

Recrystallization (step IIIA) was used to produce some $\text{FeCl}_2 \cdot 4\text{H}_2\text{O}$ which contained only 0.9 ppm total of copper, zinc, and lead, but only the first crop

representing about one-fourth of the iron in solution was of this degree of purity. The process is laborious, inefficient, and it is difficult to avoid oxidation of the FeCl_2 .

Step IIIB, sulphide precipitation, was tried in two ways. Immediately after reduction to FeCl_2 was completed, about 150 mg of FeS chips (chemically pure grade) were added to each liter of the acid (5 pct HCl) solution. After allowing 20 min for solution of the FeS , the solution was boiled 20 min to drive off excess H_2S . A small amount of insoluble precipitate was caught in a fine glass frit funnel. Electrolysis of solutions of this type gave irons whose copper contents varied from 1.8 to 7.8 ppm, indicating that the efficiency either of precipitation or of filtering was somewhat variable.

In a subsequent experiment, a reagent consisting of activated charcoal containing 20 pct of absorbed FeS was added at a rate of 1 to 2 grams per liter to moderately cool FeCl_2 solution containing about 1 pct HCl . This was intended to act as an ion exchange absorbent; very little free H_2S was released. The used reagent was filtered out cleanly on fine glass frit, and was found to have increased in copper content. Preliminary indications are that better elimination of copper is obtained by this procedure than with FeS chips, but final analytical results are not yet available.

Step IIIC was tried on the assumption that ether-soluble impurities, that accompanied FeCl_3 in the first ether extraction, would still be soluble in ether and could thereby be separated from ether-insoluble FeCl_2 . To investigate this possibility about 6 volumes of redistilled ether were percolated through a FeCl_2 solution which contained 5 pct free HCl . No detectable amount of ferrous iron was removed, but about 0.1 pct of the total iron in the solution was extracted as FeCl_3 . Organic wax (probably polymerized ether) and the metals, aluminum, boron, beryllium, calcium, chromium, copper, gallium, germanium, magnesium, molybdenum, nickel, silicon, tin, and zinc were identified in the concentrated extract after the ether had been boiled off. It has not been possible to date to establish the extent to which the FeCl_2 solution is improved by the extraction of these impurities, which were identified only in highly concentrated form. From available evidence it does not appear that this operation was in all respects as good as step IIIB, hence it is possible that some impurities are soluble in ether only when combined with FeCl_3 in complex ions, and that some impurities may undergo valence changes that affect their solubility in ether. At any rate the process is worth while to remove the wax, pending establishment of its other merits.

Step IV, electrodeposition of iron from acidified FeCl_2 solution, is an efficient and convenient method of recovering metallic iron. There is little probability of picking up impurities, and active impurities such as tin and zinc appear to be completely eliminated.

The process is operated in closed 2-liter cells, Fig. 3, using a high purity iron rod as the cathode and a high purity graphite rod as anode. Graphite powder is retained in a porous alundum cup which rests in a glass cylinder closed at the bottom by an extra coarse glass frit plate. A little colloidal graphite sometimes finds its way into the main chamber, but this normally settles between the glass beads at the bottom so that little or none migrates to the cathode. The possibility of contamination by

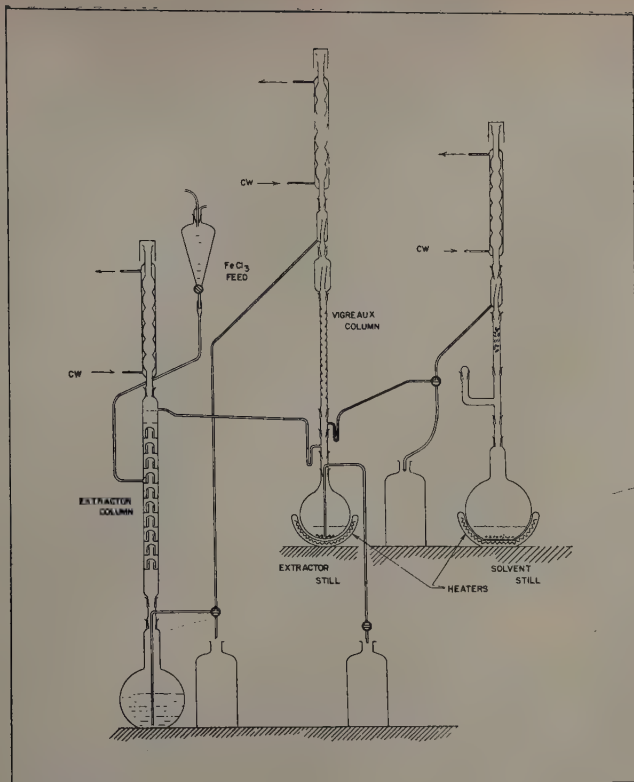


Fig. 2—Apparatus used for ether extraction of FeCl_3 in column operation.

graphite could be eliminated if an iridium anode were available for use. Ferric ions produced at the anode remain in the anode cylinder and do not interfere with the deposition.

The cell is normally operated at 4 amp and 16 ± 3 v, under which condition water evaporates nearly as fast as iron is deposited from solution, so that the concentration of the solution remains fairly constant. The volume is maintained by addition of fresh portions of electrolyte. Each cell can produce 1 lb of iron metal in about 300 hr of operation at the current stated. The iron cathodes contain about 0.25 pct of oxygen (as FeO or $\text{Fe}(\text{OH})_2$), together with some other gases and possible traces of carbon.

Step V, annealing in hydrogen, has been used to remove oxygen and possible carbon. The cathode iron is slowly heated in undried hydrogen and held at 400° to 500°C for 8 to 16 hr to remove any carbon which may be present on the surface of the iron. The undried hydrogen is then replaced by dried hydrogen and the temperature raised to 1100°C and held at that point for about three days to remove oxygen.

The efficiency of the high temperature hydrogen anneal is very largely controlled by the purity and dryness of the hydrogen atmosphere. Early trials with a commercial alumina drier following a "De-Oxo" purifier allowed some tarnishing during cooling, and reduced the oxygen only to 70 ppm. Recent anneals with hydrogen from specially built driers, with cobalt indicator sight gages to observe the efficiency of drying, have given completely bright metal. It must be appreciated that no statement of oxygen analysis is pertinent except that made with respect to a finished specimen after final treatment.

Step VI, production of massive metal—Previous investigators of high purity iron and its alloys have recognized the probability of contamination of the purified metal by the refractory crucibles in which

the melting was done. The extent of this contamination varies in the different reports and is influenced by the nature and purity of the refractory used and particularly by the temperature at which the refractory is fired. Small ingots of nitrate iron prepared at National Bureau of Standards (Table I, col. 8) contained traces of impurities that presumably came from the small high-fired beryllia crucibles, but larger ingots subsequently prepared in crucibles differently fabricated (Table I, col. 9) were more seriously contaminated. From this and other evidence it is doubtful that iron approaching 99.999 pct purity could survive melting in any available refractory.

Three alternative procedures offer possibilities. First, and perhaps most desirable, the possibility of melting a charge suspended in vacuum in a magnetic field¹⁸ appears close to realization, although no practical results are yet available. Second, drip melting of a compacted bar is feasible. Both methods reduce the possibilities of contamination of the metal by refractories. The third and most convenient method of obtaining massive metal without refractory contamination is the use of powder metallurgy procedures. Encouraging possibilities of this procedure have been encountered in experiments where pellets of the iron of lot 7 (see Table I) have been compressed to bars which were subsequently squeezed, rolled, and swaged to $\frac{1}{4}$ and $\frac{1}{8}$ in. rods, resintering as appeared to be necessary. Hardness values encountered during this series of operations remained surprisingly low. The $\frac{1}{8}$ in. rods have been used as cell cathodes, while $\frac{1}{4}$ in. rods appear usable for property determinations when their composition has been established.

Results

To date, ten lots of iron have been prepared, ranging in size from one to a few pounds each. The majority of these runs were of an experimental nature, designed to indicate qualitatively the merits

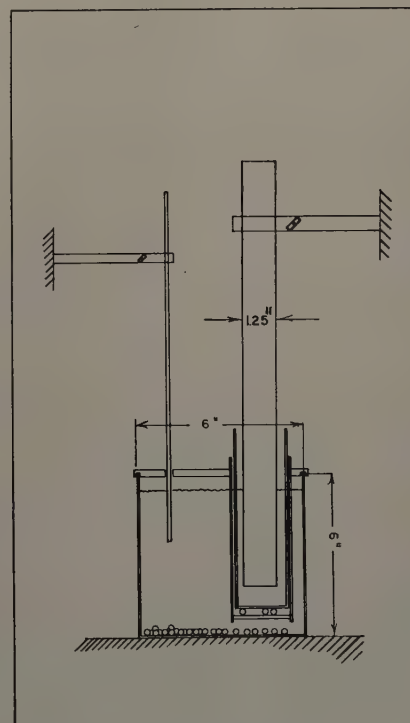


Fig. 3—Cell used for electrodeposition of iron from acidified FeCl_2 solution.

of variations of the steps in the purification process, and much of the metal produced has been consumed in subsequent runs, chiefly in the reduction of FeCl_3 to FeCl_2 .

Procurement of verified quantitative data for all of the impurities that may be present constitutes a major research by the analytical department because the degree of precision desired is frequently far beyond that of established analytical procedures. Determination of a number of elements each of which is present in amounts of one part per million, or a small fraction of a part per million, and the determination of the absence of these or other elements with an equal degree of precision and certainty, are at best difficult and laborious processes that are not yet completely established.

Complete and verified analyses have been reported to date only for the product of the following sequence of operations:

$\text{FeCl}_3 \cdot 6\text{H}_2\text{O}$ was processed in the batch extractor and the purified ferric chloride was reduced to FeCl_2 with metal from previous runs. The ferrous chloride solution was treated with FeS chips and, after filtering, was electrolyzed. Pellets of the cathode iron were annealed in wet and dry hydrogen, using the commercial drier. Two batches of 25 lb each of $\text{FeCl}_3 \cdot 6\text{H}_2\text{O}$ were put through this combination of steps IA, II, IIIB, IV, and V, to produce lots 6 and 7 of iron. The analytical data for lot 7, recorded in the final column of Table I, show that very high purity iron was obtained. Practically identical results were obtained in the analysis of lot 6.

Further experimental runs indicated possible improvements in the sequence of steps used in the production of lot 7 and the final production run to date was made as follows: 75 lb of $\text{FeCl}_3 \cdot 6\text{H}_2\text{O}$ were processed in the column extractor. One-half of the processed FeCl_3 was electrolyzed directly to supply metallic iron for reduction of the remaining FeCl_3 . The FeCl_2 solution was treated with the ion exchange sulphide reagent and, subsequently, with ether. As in other runs, iron was recovered from the purified FeCl_2 solution by electrodeposition. Analysis of this lot 10 is not yet complete but there are indications that the total of metallic impurities in lot 10 is less than it was in lot 7.

A few interesting observations of the behavior of iron of lot 7 have been made. The metal appears to be unusually resistant to corrosion as indicated by the resistance of pellets to tarnish in the laboratory atmosphere and by the difficulties encountered in dissolving pellets in warm HCl , for purposes of analysis. Conversion of the cathode metal to more useful forms by powder metallurgy and forming techniques, with sintering or annealing in dried hydrogen, appears to be practical. Rods $\frac{1}{4}$ and $\frac{1}{2}$ in. in diameter have been produced and will be used for property determinations. The indentation hardness of some of these compacted specimens, after sintering at 1100°C , approximates the values usually associated with commercially pure aluminum.

Summary

The current attempt, to produce iron of higher established purity than has been attained previously, employs the following principles: purification of ferric chloride solution by ether extraction; conversion of the purified ferric chloride to ferrous chloride with subsequent purification of the ferrous chloride solution; recovery of metallic iron by electrolysis of the purified ferrous chloride with subse-

quent removal, from the cathode iron, of carbon and oxygen by annealing in hydrogen.

A small amount of iron containing less than 13 parts per million total of metallic impurities has been prepared and some of its properties, e.g., indentation hardness and corrosion resistance, confirm the analytical evidence that this is iron of unusually high purity. However, it is not certain that the ideal process has been achieved; subsequent modification of some of the details of the production process has produced iron which, according to incomplete analyses, contains even less metallic impurities.

One of the major difficulties encountered in this investigation has been the determination of impurities, in high purity iron, with the desired accuracy and precision.

This process for the production of high purity iron is still in the stages of experimental development, and it will be some time before enough stock can be accumulated to comply with any requests for iron of established super purity.

Acknowledgment

The writer wishes to express grateful appreciation to J. G. Thompson, Chief, Metallurgy Div., and to H. E. Cleaves, formerly Chief, Chemical Metallurgy Section, for much helpful advice, to W. S. Clabaugh and R. Gilchrist for advice on the chemistry of iron, to B. F. Scribner and Mrs. M. M. Darr for spectrographic analyses, and to the Chief of Ordnance, U.S. Army, for sponsoring the present phase of this work. The writer has been capably assisted in the laboratory by R. J. Sherman.

References

- ¹ H. E. Cleaves and J. G. Thompson: *The Metal-Iron* (1935) New York. McGraw-Hill Book Co.
- ² C. Wagner: The Electrochemistry of Ionic Crystals. *Journal Electrochem. Soc.* (1952) **99**, 346 C—354 C.
- ³ W. Shockley: Solid State Physics in Electronics and in Metallurgy. *Trans. AIME* (1952) **194**, pp. 829-842; *JOURNAL OF METALS* (August 1952).
- ⁴ W. P. Rees, B. E. Hopkins, and H. R. Tipler: Tensile and Impact Properties of Iron and Some Iron Alloys of High Purity. *Journal Iron and Steel Inst.* (1951) **169**, pp. 157-168. (See p. 161, proposition that impurity concentration need not be sufficient to form a second phase.)
- ⁵ W. P. Rees and B. E. Hopkins: Intergranular Brittleness in Iron-Oxygen Alloys. *Journal Iron and Steel Inst.* (1952) **174**, pp. 403-409. For production of this iron, see *Journal Iron and Steel Inst.* (1951) **168**, pp. 377-383.
- ⁶ G. Wiener: Grain Growth in High Purity Iron. *Trans. ASM* (1952) **44**, pp. 1169-1185. See discussion by G. A. Moore, p. 1184, of Wiener's statement of a "limiting grain size."
- ⁷ J. G. Thompson and H. E. Cleaves: A Summary of Information on the Preparation and Properties of Pure Iron. *Journal of Research, National Bur. Standards* (1936) **16**, pp. 105-130.
- ⁸ H. E. Cleaves and J. G. Thompson: Preparation of Iron Oxide as a Source of High-Purity Iron. *Journal of Research, National Bur. Standards* (1937) **18**, pp. 595-607.
- ⁹ J. G. Thompson and H. E. Cleaves: Preparation of High Purity Iron. *Journal of Research, National Bur. Standards* (1939) **23**, pp. 163-177.
- ¹⁰ H. E. Cleaves and J. M. Hiegel: Properties of High Purity Iron. *Journal of Research, National Bur. Standards* (1942) **28**, pp. 643-667.
- ¹¹ C. H. Desch: The Work of the Alloys of Iron. Research Committee. *Proc. Inst. Mech. Eng.* (1934) **127**, pp. 277-298.

¹² R. L. Smith, R. V. Fostini, and R. M. Brick: The Low Temperature Properties of Relatively High Purity Iron-Carbon Alloys. 1st Progress Report Project SR-109 to Committee on Ship Steel (SSC-52): National Acad. of Science, N.R.C. Washington, Aug. 29, 1952.

¹³ D. M. Wroughton, E. C. Okress, P. H. Brace, G. Comenetz, and J. C. R. Kelly: A Technique for Eliminating Crucibles in Heating and Melting of Metals. *Journal Electrochem. Soc.* (1952) **99**, pp. 205-211 (also *Journal of Applied Physics*, May 1952).

¹⁴ J. H. Keeler and H. M. Davis: Density and Hydrogen Occlusion of Some Ferrous Metals. *Trans. AIME* (1953) **197**, pp. 44-48; *JOURNAL OF METALS* (January 1953).

¹⁵ G. A. Moore and D. P. Smith: Occlusion and Evolution of Hydrogen by Pure Iron. *Trans. AIME* (1939) **135**, pp. 255-295.

DISCUSSION, N. C. Fick and B. W. Gonser presiding

H. B. Goodwin (Battelle Memorial Institute, Columbus, Ohio)—Dr. Moore's work appears to be a real advance toward the achievement of ultimate purity in iron. Having been engaged for several years in attempting to prepare large batches (300 lb) of high purity iron (although not nearly as pure as Dr. Moore's) I can appreciate how painstaking his work was.

I would like to see more details on the method of forming the pellets and of consolidating the iron into bars or rods, as apparently was done in some cases. I would also like more detail on the analytical procedures, which, in themselves, must be real advances.

In the present paper the actual sequence of steps for the various lots of iron produced is somewhat confused. This could possibly be clarified by a flowsheet-type diagram with lines showing processing of various lots.

G. A. Moore (Author's reply)—Charges of about ¼ lb have been compressed in a double action side pressure bar die. These have been coined by alternate use of concave and flat face plungers operating at 100,000 psi. About eight strokes are used, the compact rotated 90° and the process repeated. The bars have then been sintered in hydrogen and the process repeated. The coined bars can be rolled and swaged without difficulty. At this writing, a density of 99.5 pct of the theoretical value has been obtained on the coined compacts.

The development of the analytical methods has been under the direction of B. F. Scribner, Chief, Spectrochemistry Section, Chemistry Div., National Bureau of Standards, who has kindly supplied the following statement:

Spectrographic analyses of the iron were made by three methods which are identified and described as follows:

1—*Direct Arc Method*: This method involves preparation of the metal in the form of rods, approximately ¼ in. diameter, shaped by turning and filing. The rods serve as electrodes for direct-current arc excitation under optimum conditions for detecting the impurity elements. The method is useful for detecting certain elements such as molybdenum, germanium, or tin, for which the detectability by the other methods is poor. For most of the elements the method is not as sensitive as the remaining two methods and is subject to error if the impurities are segregated in the sample. The method was applied to preliminary surveys of samples, to studies of portions of samples for segregation, and to analyses in the early part of the program on pure iron.

2—*Chloride Solution Method*: This method involves preparation of a concentrated solution of a representative portion of the iron in hydrochloric acid. The solution is added to high purity graphite electrodes, which are dried in an oven and then subjected to arc excitation. Standard samples are prepared from ferric chloride specially purified by the ether extraction technique, and to which known amounts of the impurities are added. This method has proved to be about ten times more sensitive than the first method. It also has the advantages of simplicity in handling the sample, of ease in preparation of standard samples, and of sampling a large portion of metal.

3—*Ether Concentration Method*: This method involves a careful and painstaking separation of most of the impurities by extraction of the sample as iron chloride with diethyl ether. The concentrated solution containing the impurities is evaporated to dryness on a weighed portion of pure zinc oxide which serves as a carrier. The mixture is analyzed with the dc arc relative to standard samples of zinc oxide containing added amounts of impurities. Depending on the size of the iron sample used for the extraction process, this method results in a 10 to 100 fold increase in sensitivity of detection over the chloride method. However, care must be observed in the procedure; the acid is redistilled in an all-quartz apparatus, the ether is extracted with the pure acid before it is used, and extreme cleanliness is observed. The accuracy of the procedure was checked with standards of ether extracted iron to which known amounts of impurities were added.

Various sequences of steps were used on various lots and the paper makes no claim to have found the ultimate combination. We feel that a flowsheet in the paper might imply that a best process had been decided upon, and prefer to reserve this for an occasion when we can be more certain of its validity.

Technical Note

The Habit Plane of Beta in Alpha Titanium

by Paul A. Albert

THE β to α transformation has been investigated by Newkirk¹ in sponge titanium alloys which had been relatively slow-cooled so that several α grains formed in a former β grain.

P. A. ALBERT, Student Associate AIME, is Research Assistant, Engineering Research Div., New York University, New York.

TN 181E. Manuscript, June 15, 1953.

This paper is based on a thesis by P. A. Albert submitted in partial fulfillment of requirements for the degree of Master of Science in Metallurgy to the Graduate Div., College of Engineering, New York University.

For α nucleated from β , Newkirk assumed the following relationships and found them consistent with his experimental results:

$$\begin{array}{l} (00.1)_{\alpha} \parallel (110)_{\beta} \\ [11.0]_{\alpha} \parallel [111]_{\beta} \end{array}$$

Liu and Margolin,² in their investigation, found that the habit planes of martensitic α in β titanium consisted of planes of the families $\{334\}_{\beta}$ and $\{344\}_{\beta}$. Using Newkirk's orientation relationship, the $\{334\}_{\beta}$ habit plane is found to correspond to the $\{1450\}$ plane of α .

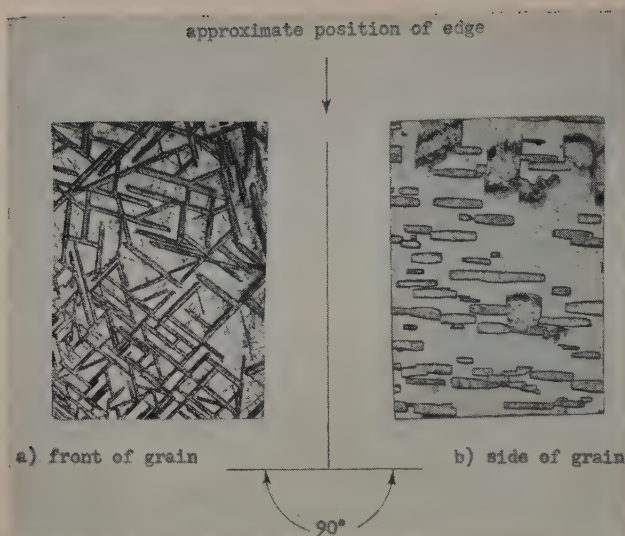


Fig. 1—Micrographs showing areas from two adjacent normal surfaces of an α grain. $\alpha + \beta$ transformed β platelets. X75. Area reduced approximately 60 pct for reproduction.

The purpose of the present investigation was to determine the habit plane of β isothermally grown in α titanium.

Experimental Procedure

Binary alloys with alloying compositions of up to 1.25 pct N and up to 1.5 pct O were prepared using TiO_2 and TiN powders supplied by Watertown Arsenal Laboratory. The specimen preparation and melting procedures have been described.³

Large grains of β were obtained in the specimens by annealing at 1400°C in helium atmospheres.

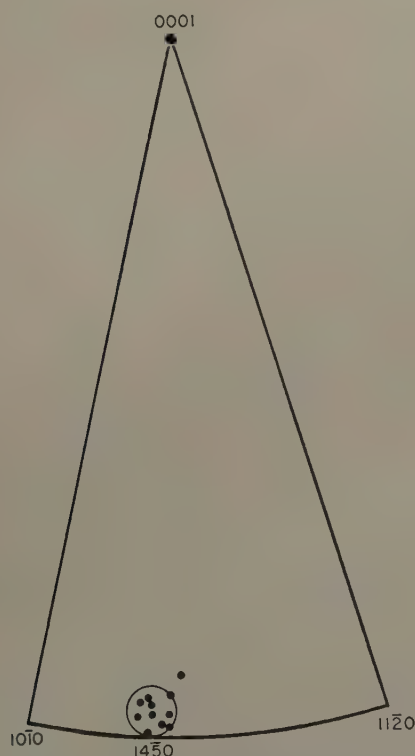


Fig. 2—Unit stereographic triangle for α titanium showing results of single-surface analysis (large circle) and points from two-surface analysis.

Suitable α grains were then obtained from the β grains by hot rolling 5 pct at 800°C , and subsequently annealing for 48 hr at temperatures slightly below the α transus.

The large-grained specimens were then annealed at temperatures in the $\alpha + \beta$ region, and subsequently water-quenched and examined.

Analysis

The Laue back-reflection method was used to determine specimen orientations. The habit plane determinations were made by single-surface analysis and checked by two-surface analysis.²

The transformed β platelets were short, so that one trace did not appear on two surfaces. However, in one of the grains analyzed, a single trace direction in one surface was found to be responsible for six traces in the second surface and consequently two-surface analysis was possible.

Fig. 1a and b, micrographs of these surfaces, shows that the traces in the side surface (Fig. 1b) vary in thickness depending on the angles between the traces in the front surface (Fig. 1a) and the edge of the specimen. The habit plane determination made on this grain agreed with the results of single-surface analysis. These results were corroborated by a similar analysis of five traces in a second grain.

Results

Determination of the habit plane by single-surface analysis resulted in a group of points with a scatter of $\pm 2^\circ$, at a position 2° from the $\{1450\}$ pole. The results of single-surface analysis lie within the region designated by the circle in Fig. 2. The two-surface determinations are indicated as small filled circles in Fig. 2, and it can be seen that all but one of the poles lie within the area of scatter of the single-surface points.

The habit plane of isothermal α in β has been determined in the Ti-Fe system to be $\{334\}_\beta$.⁴ Since the $\{1450\}_\alpha$ habit of β can be converted to $\{334\}_\beta$ according to Newkirk's results,¹ it appears that whether α or martensite forms from β , or β forms from α , the same pair of planes of each lattice is involved, i.e., $\{334\}_\beta$ and $\{1450\}_\alpha$.

Acknowledgments

The author wishes to thank Y. C. Liu, H. Margolin, and the staff of the Metallurgy Laboratory at New York University for their assistance in this research. He also wishes to thank the U. S. Army Ordnance Corps, Watertown Arsenal, Watertown, Mass., for permission to publish this work, which was performed under Ordnance Corps Contract No. DA-30-069-ORD-935.

References

- ¹J. B. Newkirk: Private communication. Also Minutes of Conference on "Crystallography of Titanium and its Alloys," New York University, June 27, 1952, under the auspices of the Ordnance Metallurgical Advisory Committee on Titanium.
- ²Y. C. Liu and H. Margolin: Martensite Habit Planes in Quenched Titanium-Manganese Alloys. *Trans. AIME* (1953) **197**, p. 667; *JOURNAL OF METALS* (May 1953).
- ³I. Cadoff and J. P. Nielsen: Titanium-Carbon Phase Diagram. *Trans. AIME* (1953) **197**, p. 248; *JOURNAL OF METALS* (February 1953).
- ⁴G. Hahn: The Habit Plane of Isothermal Alpha in Beta of Ti-Fe Alloys. Senior Thesis, New York University, June 1952.

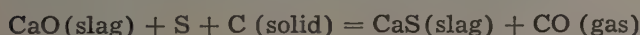
Manganese as an Indicator of Blast Furnace Slag Oxidation and Desulphurizing Power

by Nicholas J. Grant, John W. Dowding, and Robert J. Murphy

A large number of blast furnace slag-metal tests were examined to determine if the manganese reduction could be used as a primary indicator of the degree of oxidation or reduction of the slag and of its desulphurizing power. Slag basicity and temperature were also evaluated. Two laboratory heats were made and sampled prior to reaching equilibrium to check blast furnace data.

IN a recent investigation of the factors affecting desulphurization in the blast furnace, it was evident that manganese reduction appeared to parallel the course of desulphurization. Grant, Kalling, and Chipman¹ pointed this out in a series of time studies utilizing closely controlled laboratory melts. Fig. 1 is a composite plot of sulphur removal and manganese reduction as a function of time under two slags of different basicity. Manganese reduction appears to approach equilibrium at approximately the same rate as does sulphur. It was also demonstrated that the addition of oxygen to the slag, as manganese oxide, caused a sharp reversal of sulphur from the slag to the metal.¹

It has been shown that "Excess CaO" was a primary factor in measuring the degree of desulphurization under ideal reducing conditions,^{1,2} the following reaction being representative of the process:



It was also evident that a second reaction could drive the sulphur from the slag into the metal. A suggested reaction was¹



Any change in the oxidizing power of the system would thus affect both the sulphur and the manganese without causing any change in the calculated basicity of the slag. "Excess CaO," "Excess Base," and other similar basicity values, under such oxidizing conditions, would therefore not be the best measure

N. J. GRANT, Member AIME, is Associate Professor of Metallurgy, Massachusetts Institute of Technology, Cambridge, Mass., and J. W. DOWDING and R. J. MURPHY, Junior Member AIME, formerly students of Metallurgy, MIT, are now associated with Latrobe Steel Co., Latrobe, Pa., and U. S. Steel Corp., Duquesne Works, Duquesne, Pa., respectively.

Discussion on this paper, TP 3643C, may be sent, 2 copies, to AIME by April 1, 1954. Manuscript, May 29, 1953. New York Meeting, February 1954.

This paper is based on a thesis by J. W. Dowding and R. J. Murphy submitted in partial fulfillment of the requirement for the Bachelor of Science degree to Massachusetts Institute of Technology.

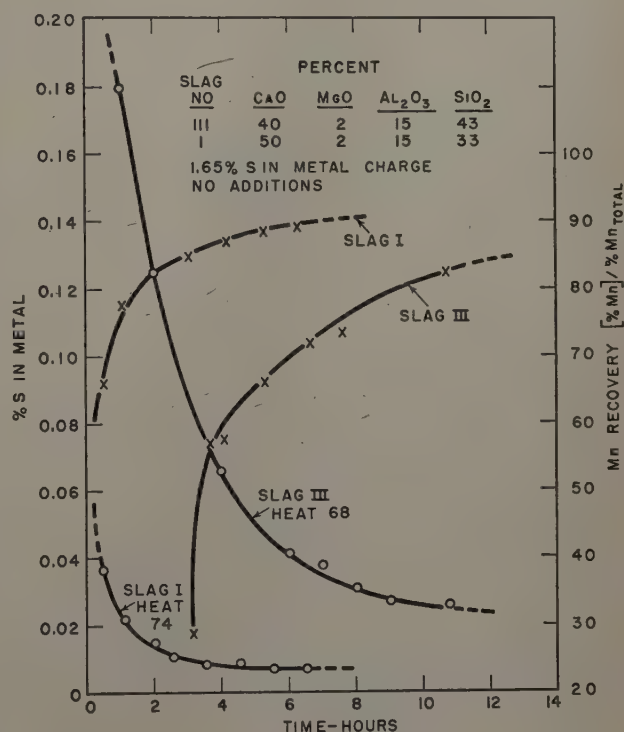


Fig. 1—Sulphur removal and manganese reduction as a function of time for two slags at 1525°C, from work of Grant, Kalling, and Chipman.¹

of desulphurizing power; instead, as was shown by Rocca, Grant, and Chipman³ the oxygen content of the slag at low oxygen levels would be the controlling factor. Unfortunately, the extent to which FeO is reduced in the blast furnace makes it difficult to utilize slag FeO as an accurate indicator of the degree of oxidation. By comparison, manganese reduction in the blast furnace proceeds more slowly and is generally only about 40 to 70 pct complete. Thus manganese, which is present in significant amounts and is readily analyzed, offers an opportu-

Table I. Desulphurizing Index of Lime and Manganese

Fig. No.	Variable	Slope of Line	Spread in Desulphurization Ratio At	
			50 Pct Confidence Interval	95 Pct Confidence Interval (2σ)
2	Excess CaO	1350	$\pm 32(S)/[S]$	$\pm 100(S)/[S]$
3	Mn reduction	59	$\pm 16(S)/[S]$	$\pm 37(S)/[S]$

ity to use it as an indicator, not only of the degree of oxidation or reduction of the slag, but also of the desulphurizing power. The similar use of manganese as an indicator also was suggested recently by Oelsen and Maetz⁴ and by Weilandt, Maetz, and Oelsen.⁵

Results from Blast Furnace Tests

A series of 66 acceptable tests were obtained from a blast furnace campaign (heats 5202 to 5308 furnished by Republic Steel Corp.) at a time when relatively good cast temperatures and slag-metal analyses were available. In general, three tests were taken of temperature and of the manganese, silicon, and sulphur contents of the metal. Where large variations in analysis for any of the three elements occurred, the cast was not used for this study. It is to be realized, however, that sampling cannot be perfect under operating conditions and accordingly some scatter of data was to be expected.

Fig. 2 shows the relationship between Excess CaO³ and desulphurizing power, the latter defined in the usual manner by the ratio

$$\frac{(\%S)_{\text{slag}}}{[\%S]_{\text{metal}}}$$

It will be noted that whereas desulphurization improves with increasing basicity, the sulphur ratio is rather insensitive to Excess CaO between 0.16 and 0.24 Excess CaO. Without exception, the desulphurization ratios are far below those which are predicted from equilibrium studies as indicated by the upper solid curve in Fig. 2.¹ Whereas the blast furnace data show a desulphurization ratio of 30 to 100 (average of about 60) at an Excess CaO value of 0.20, the equilibrium data indicate that the ratio should be 200, or from 2 to 6 times as good.

Attempts to use Excess Base^{1, 2, 6} and other basicity ratios gave even poorer relationships, as was expected, and the plots are omitted for the sake of brevity.

In Fig. 3 the same test data are shown, now plotted as desulphurizing ratio vs manganese ratio. The manganese ratio was arbitrarily chosen as "per cent manganese in the metal" over "per cent manganese in the slag." It is immediately evident that a more sensitive measure of desulphurization is attained by using manganese as the indicator.

As a comparison of the relative merits of the various plotting methods, the best curve was calculated

Table II. Initial Slag Compositions

Slag No.	Source	CaO	SiO ₂	Al ₂ O ₃	MgO
A	Present work	50	35	15	—
I	Grant, Kalling, and Chipman ¹	50	33	15	2
B	Present work	40	45	15	—
III	Grant, Kalling, and Chipman	40	43	15	2

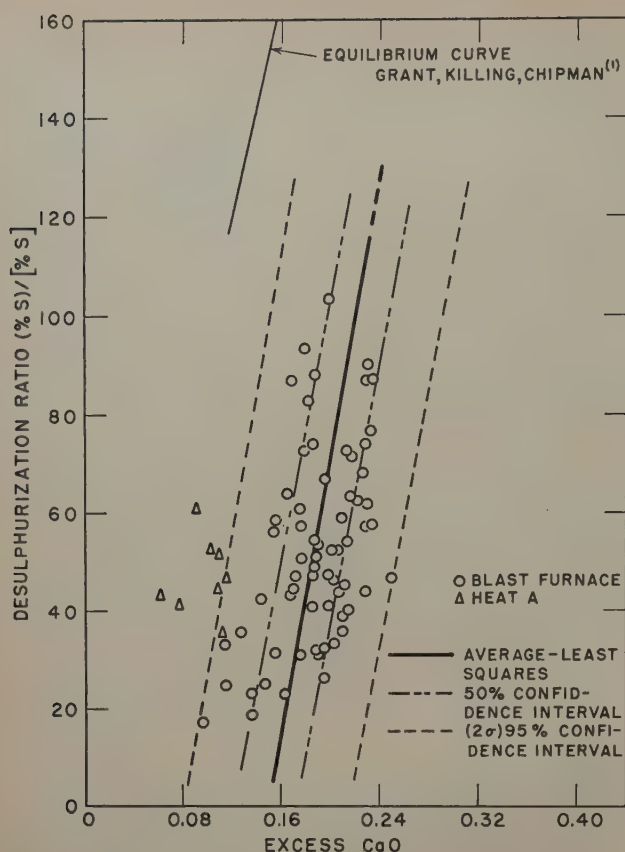


Fig. 2—Desulphurization ratio vs Excess CaO from blast furnace data, showing 50 and 95 pct (2σ) confidence intervals. Note position of experimental nonequilibrium points and equilibrium curve from Grant, Kalling, and Chipman.¹

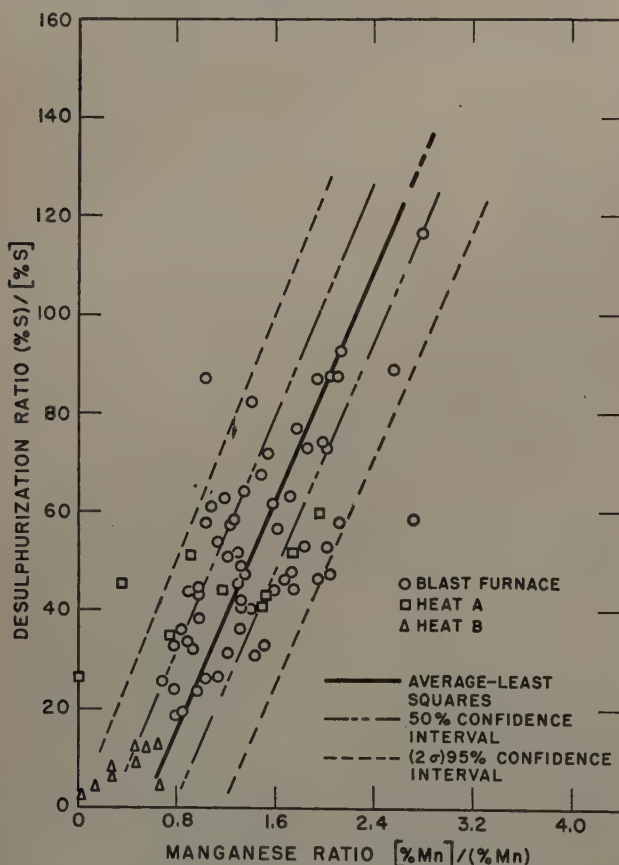


Fig. 3—Same blast furnace data as in Fig. 2 but plotting desulphurization ratio vs manganese ratio. Note position of experimental nonequilibrium points.

by the method of least squares and is shown by the solid line in Figs. 2 and 3. Parallel lines were drawn to show the 50 and 95 pct (2σ limits) confidence intervals and Table I shows the spread in sulphur ratio between these two sets of curves.

Efforts to measure the effect of temperature on the distribution of points in both Figs. 2 and 3 met with complete lack of success, even though the range of temperatures noted for the casts was from about 2500° to 2750°F. It is to be recalled that equilibrium studies showed only a small beneficial result of increasing temperature on desulphurization.^{1, 2, 6} These two sets of results lead to the speculation that data presented in the past on the improvements in desulphurization with increasing temperature might not be entirely due to any physical-chemical effects of higher temperatures on the sulphur distribution; instead, the higher temperatures have an indirect result on desulphurization in that the rate and degree of manganese and silicon reduction improve materially and the fluidity of the slag increases.

Laboratory Heats

To extend the results given above, the same equipment which was described previously by Grant, Kalling, and Chipman¹ was used to make two heats in which two slag compositions utilized by the former authors were selected for additional tests. One slag was considerably more acid and was selected because of its slower desulphurizing ability. The more basic slag was selected as being more typical of the blast furnace, and therefore permitting comparison with the data from blast-furnace casts shown in Figs. 2 and 3.

Table II lists the two heats A and B both made at 1525°C and compares them with slags No. 1 and III of Grant, Kalling, and Chipman. Table III lists the slag and metal analyses of the current heats A and B as a function of sampling time.

During the course of both of these heats, a number of additions of manganese oxide were made to the

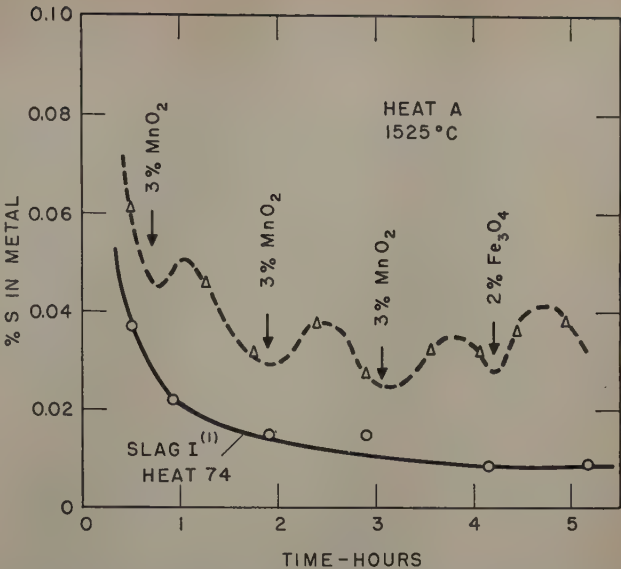


Fig. 4—Effect of additions of MnO₂ and Fe₃O₄ on sulphur removal for heat A, compared to desulphurization in a heat in the absence of oxygen additions.¹

slag in quantities of about 3 pct (by weight) of MnO₂. Before equilibrium could be achieved, further additions were made, followed by sampling of the slag and metal. In the case of heat A, the reoxidation of the system maintained a sulphur content of the metal about comparable to that found in regular blast furnace operation, but considerably higher than the equilibrium value as indicated in Fig. 4 by reference to a slag with no additions; and it might be inferred that the degree of oxidation was also comparable to that existing in the blast furnace since the manganese recovery values ranged from about 40 to 67 pct (compared to 40 to 70 pct found in the blast furnace).

Heat B was similarly kept oxidized, with the sulphur level at a higher value than that normally

Table III. Composition of Slag and Metal Samples

Heat No.	Sample No.	Time, Hr	Metal, Wt Pct			Slag, Wt Pct					
			S	Mn	Other	S	CaO	SiO ₂	Al ₂ O ₃	MnO	FeO
A	1	0.50	0.061	0.000	13.9 g MnO ₂ added	1.640	49.26	34.66	15.47	0.00	0.020
		0.75									
	2	1.25	0.045	0.581	13.0 g MnO ₂ added	1.585	48.56	34.12	15.29	1.03	0.014
	3	1.75	0.031	0.821		1.610	49.68	33.82	16.71	0.6	0.014
		1.92									
	4	2.42	0.037	1.345	12.5 g MnO ₂ added	1.590	48.00	34.04	14.87	1.16	0.010
	5	2.92	0.027	1.466		1.640	47.94	34.04	15.95	0.95	0.015
		3.07									
	6	3.57	0.032	1.848	6.4 g Fe ₃ O ₄ added	1.485	48.80	32.08	16.15	6.44	0.081
	7	4.07	0.031	2.205		1.585	47.36	33.02	15.83	3.19	0.160
		4.22									
B	8	4.47	0.036	2.180	14 g MnO ₂ added	1.610	48.52	32.94	16.18	2.40	0.035
	9	4.97	0.038	2.360		1.560	48.26	33.50	16.55	2.02	0.017
	1	0.50	0.551	0.000	13.3 g MnO ₂ added	1.110	39.64	43.62	16.02	0.00	0.027
		0.80									
	2	1.30	0.311	0.167		1.360	38.21	42.80	16.75	1.64	0.003
	3	1.80	0.212	0.276	12.3 g MnO ₂ added	1.435	39.32	42.98	16.01	1.30	0.043
		2.00									
	4	2.50	0.178	0.688		1.435	38.58	41.86	15.94	3.96	0.012
	5	3.00	0.164	0.881	6.3 g Fe ₃ O ₄	1.510	38.80	42.30	15.80	2.56	0.058
		3.13									
	6	3.64	0.111	1.401		1.460	37.96	41.02	16.38	3.79	0.055
	7	4.14	0.107	1.548		1.460	38.00	41.88	15.64	3.79	0.075
		4.3									
	8	4.5	0.243	1.660		1.535	36.32	41.90	15.92	3.20	0.058
	9	5.05	0.115	1.500		1.560	38.32	41.74	16.42	3.25	0.054

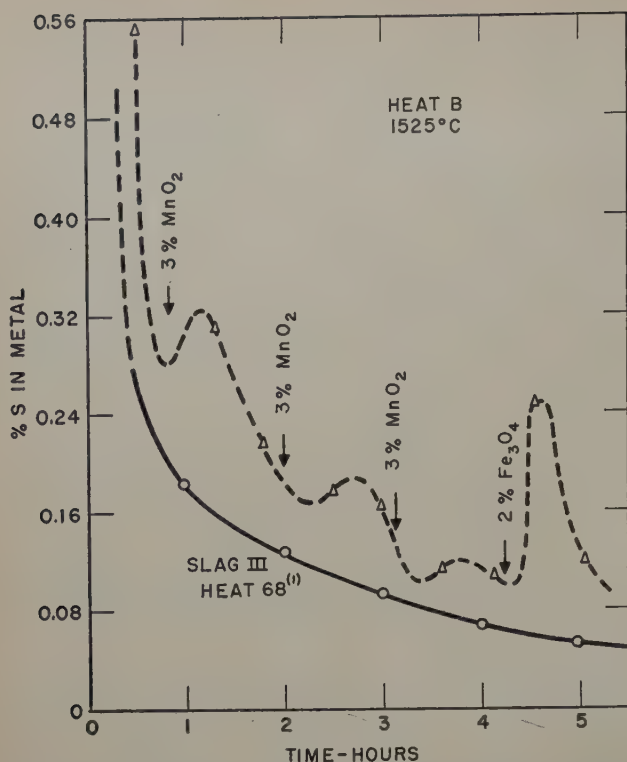


Fig. 5—Effect of additions of MnO_2 and Fe_3O_4 on sulphur removal for heat B, compared to desulphurization in a heat in the absence of oxygen additions.¹

found in the blast furnace. The manganese recovery values were lower than in heat A, ranging from 20 to 40 pct.

At the end of each of these two heats, an addition of 2 pct (by weight) of Fe_3O_4 was added to the slag to see how it would affect desulphurization compared to additions of MnO_2 . The addition of 3 pct by weight of MnO_2 results in an addition of about 1.1 pct by weight of oxygen, whereas an addition of 2 pct of Fe_3O_4 adds only about half as much oxygen or 0.55 pct. The effects of these two additives on desulphurization should be compared on the basis of their oxygen contributions and the stability of the oxides.

Fig. 4 shows the course of sulphur removal from the metal as a function of time for heat A, with the times of addition noted by arrows. While sufficient test samples were not taken to draw an exact curve in this figure, sulphur reversion is readily evident. For comparison the desulphurization curve for a similar slag from the work of Grant, Kalling, and Chipman (slag No. I, heat 74) is also shown. The sulphur reversion noted by the former authors is confirmed. Fig. 5 similarly compares the course of desulphurization for heat B, which is compared to slag III, heat 68, from the same reference.¹

Discussion

The data presented clearly show that the blast furnace is not desulphurizing as efficiently as the slag basicity would permit. The probable reason for this is that the slag is not reduced sufficiently at any time between casts to permit higher desulphurizing power. In part this is due to the lack of time for silicon and manganese equilibrium to be approached more closely. Also, there is a continuous input of manganese oxide into the slag which provides a source of oxygen to decrease desulphurization.

The evidence of the large effect of oxygen is clearly seen in Figs. 2 and 3 where the nonequilibrium points from the experimental heats A and B are plotted along with the actual blast furnace data. These points are from tests in which manganese recoveries of 40 to 67 pct for heat A and 20 to 40 pct for heat B were recorded. These are comparable in the case of heat A with the manganese recoveries attainable in the iron blast furnace. Note that these nonequilibrium points match the grouping of Fig. 3 better than they do Fig. 2, confirming the assumptions that manganese is the better indicator of the overall blast furnace chemistry. By comparison the manganese recoveries measured for similar slags which were appreciably closer to equilibrium ranged from 80 to 94 pct¹ depending on basicity of the slag and distance from equilibrium.

The role of temperature in the blast furnace with respect to desulphurization must be an indirect one. The small effect of temperature on the equilibrium desulphurization ratio and its lack of effect in the blast furnace data which were utilized here, confirm this. The beneficial temperature effect of desulphurization must be interpreted in terms of viscosity effects on the slag and on the greater rate and extent of reduction of manganese (decreased oxygen potential).

Conclusions

1—The reversion of sulphur from slag to metal due to additions of oxygen to the system (derived from MnO_2 or Fe_3O_4) has been confirmed.

2—Manganese reduction is a better indicator of the desulphurizing power of the blast furnace than is any common measure of slag basicity.

3—The blast furnace does not desulphurize to its maximum ability because of the oxidation potential in the system. This oxidation potential is probably due primarily to the presence of considerable amounts of MnO in the slag.

4—Temperature benefits in desulphurization are probably due to indirect effects on the rest of the system.

Acknowledgments

The authors wish to express their appreciation to Charles W. Sherman and James Fulton for considerable assistance throughout this research and to John Chipman for his guidance. The work was supported by the American Iron and Steel Institute.

References

- ¹ N. J. Grant, U. Kalling, and J. Chipman: The Effects of Manganese and Its Oxide on Blast Furnace Desulphurization. *Trans. AIME* (1951) **191**, p. 666; *JOURNAL OF METALS* (August 1951).
- ² C. W. Sherman and N. J. Grant: Evaluation of pH Measurements with Regard to the Basicity of Metallurgical Slags. *Trans. AIME* (1949) **185**, p. 898; *JOURNAL OF METALS* (November 1949).
- ³ R. Rocca, N. J. Grant, and J. Chipman: Distribution of Sulphur Between Molten Iron and Slags at Low Iron Oxide Concentrations. *Trans. AIME* (1951) **191**, p. 319; *JOURNAL OF METALS* (April 1951).
- ⁴ W. Oelsen and H. Maetz: Contribution to Blast Furnace Metallurgy. *Stahl und Eisen* (1949) **69**, p. 147.
- ⁵ B. Weilandt, H. Maetz, and W. Oelsen: Effects of Basic Oxides Upon Desulphurization in the Blast Furnace. *Arch. Eisenhüttenwesen* (1952) **23**, p. 163.
- ⁶ G. Hatch and J. Chipman: Sulphur Equilibria Between Iron Blast Furnace Slags and Metal. *Trans. AIME* (1949) **185**, p. 274; *JOURNAL OF METALS* (April 1949).

Diffusion of Calcium Ion in Liquid Slag

by Helen Towers, Michel Paris, and John Chipman

A simple radioactive tracer technique is used to measure the diffusion coefficient of calcium ion in molten slags. In a slag of 40 pct CaO-40 pct SiO₂-20 pct Al₂O₃, $D_{Ca^{++}}$ at 1450°C is 1.3×10^{-6} cm² sec⁻¹.

THE application of the principles of thermodynamics to steel and iron making problems has proved so fruitful that the kinetic approach has tended to be neglected. It seems probable that in some reactions the rate-determining step is the diffusivity of the reactants or of the products. But knowledge of the diffusion coefficients of the constituents of liquid slag and metal is singularly lacking. The present work was undertaken as a first step toward supplying such data for slags. Furthermore, any additional information on the physical properties of liquid slags might be expected to help in elucidating their structure. It is essentially a preliminary investigation, the course of which was determined more by the necessity of establishing a method than by the immediate intrinsic interest of the results.

For example, the selection of calcium ion to be studied was dictated by the suitability of the isotope Ca⁴⁵ in that it is a simple β emitter with a long half-life. Of the other ions commonly encountered in slags, the isotopes of iron and manganese have relatively complex radiations as well as the normal disadvantage of requiring control of the oxygen potential of the atmosphere; Mg²⁷ and Al²⁸ have half-lives measured only in minutes; Si³¹ has a simple decay process but its half-life of 2.8 hr is too short for preliminary studies; the only useful oxygen isotope is the stable O¹⁸; and there remain only sulphur and phosphorus both of which have suitable isotopes but were rejected as being of less fundamental interest than calcium. Similarly a lime-alumina-

silica slag was used in preference to calcium silicate primarily because of its low melting point and its capacity to form a glass on fairly rapid cooling.

Literature Review

Very few studies of diffusion in liquid silicate systems have been reported. In order to determine the origin of diopside inclusions in felspathic rocks, Bowen¹ investigated the diffusion between diopside and various mixtures of albite and anorthite. Platinum crucibles were used with diopside, the heavier of the two liquids, forming the lower half of the cell and diffusion taking place against gravity. Change in concentration along the diffusion path was found by measuring the refractive index of the quenched glass.

Nearly thirty years later McCallum and Barrett² used essentially the same method to determine the diffusion coefficient of lime in lime-alumina-silica slags. In this case the interest was to find the rate-determining step in the process of slag attack on refractory materials.

In an investigation of the kinetics of the sulphur reaction, Derge, Philbrook, and Goldman³ determined the diffusion coefficient of sulphur in a typical blast furnace slag by the simple procedure of melting a slag containing 2 pct S over an identical slag sulphur-free. They make no claim to a high degree of accuracy but suggest that D_s is of the order of 10^{-6} cm² sec⁻¹.

Other high temperature liquid diffusion studies have been concerned with metals. Holbrook, Furnas, and Joseph⁴ determined the diffusion coefficients of silicon, phosphorus, sulphur, manganese, and carbon in liquid iron by immersing a small carbon crucible containing pure iron-carbon alloy in a large vessel containing iron with a high concentration of the particular element. Their results were confirmed by Paschke and Haultmann⁵ using a similar method.

Diffusion coefficients in silicates in the glassy state have been studied by Johnson, Bristow, and Blau.⁶ Both Na²⁴ and Ca⁴⁵ were used as tracers but only the

H. TOWERS is Lecturer in Metallurgy, Royal Technical College, Glasgow, Scotland, M. PARIS, formerly Graduate Student at Massachusetts Institute of Technology, is now in Paris, France, and J. CHIPMAN, Member AIME, is Professor, Dept. of Metallurgy, Massachusetts Institute of Technology, Cambridge, Mass.

Discussion on this paper, TP 3625C, may be sent, 2 copies, to AIME by Jan. 1, 1954. Manuscript, April 16, 1953. Los Angeles Meeting, February 1953.

This paper is based on a thesis by M. Paris submitted in partial fulfillment of requirements for the degree of Master of Science to Massachusetts Institute of Technology.

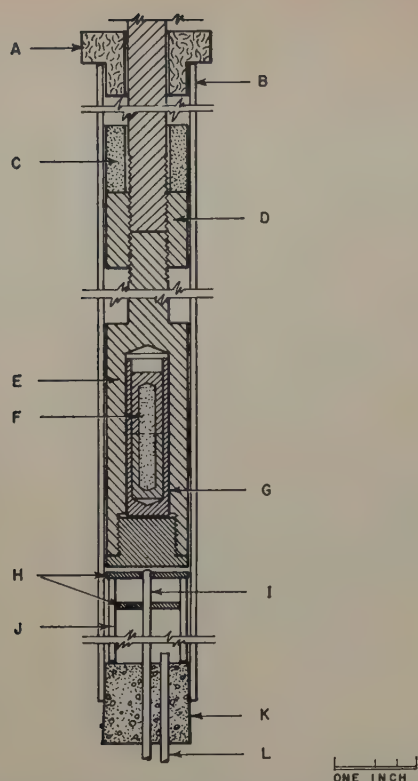


Fig. 1—Section along zirco tube containing the diffusion cell. This was heated by a globar furnace not shown in figure. A—Refractory stopper. B—Zirco tube. C—Carbo-cell insulating block. D—Graphite block. E—Graphite container. F—Diffusion cell. G—Graphite crucible. H—Radiation shields. I—Thermocouple sheath. J—Supporting tube. K—Rubber stopper. L—Argon inlet.

sodium results were reported. From these the authors were able to reach conclusions concerning the structure of the glass.

Experimental Method

The principle was similar to that used by Bowen.¹ Two slags of essentially the composition, 40 pct CaO-40 pct SiO₂-20 pct Al₂O₃, were brought into contact in a graphite diffusion vessel. One of the slags contained the radioactive tracer Ca⁴⁵ but was otherwise identical in composition with the other. The assembly was held at a temperature above the melting point for a predetermined time, quenched, and sectioned longitudinally. The distribution of the tracer was determined by its action on a photographic film and from this the diffusion coefficient was calculated.

Preparation of Slags: A master slag was melted in graphite, ground to a fine powder, and analyzed. The composition was 40.32 pct CaO, 19.15 pct Al₂O₃, 40.06 pct SiO₂. A graphite crucible 3/16 in. ID and about 1 in. long was charged with this slag, held at 1400°C for 15 min, quenched, and radiographed to insure absence of bubbles. To prepare the active slag, 0.8x10⁻⁶ g Ca⁴⁵ was added in the form of Ca⁴⁵Cl₂ solution to 0.6 g of the fine powder. This was equivalent to 2.7 microcuries. After evaporation to dryness the powder was thoroughly mixed and then heated in a second graphite crucible to 1400°C for 3 hr to insure homogeneity.

Diffusion Apparatus: The two crucibles were cut transversely to 1/2 in. lengths, then placed inside a larger graphite block as shown in Fig. 1, the two

cut faces being in contact. The assembly was then inserted into the furnace in which an argon atmosphere was maintained. The temperature was measured by two Pt-10 pct Rh-Pt thermocouples, one directly below the graphite block and the other outside the zirco tube, level with the cell. An exploring standard couple was used to find the relationship between the temperatures recorded by the two permanent couples and that obtaining in the diffusion cell. The temperature variation along the length of the diffusion specimen is shown in Fig. 2. When the furnace had reached thermal equilibrium, the graphite container was lowered into position. This method did not allow the diffusion time to be known exactly but the accuracy of estimation was about ±2 pct. At the end of the experiment the container was withdrawn rapidly so that the slag solidified as a glass.

Measurement of Ca⁴⁵ Concentration: The slag cylinder was approximately 1 in. long contained in carbon. This was ground and polished longitudinally under kerosene to give an exact semi-cylinder which was placed in contact with an Ilford G X-ray film for 1 3/4 hr. The film was calibrated by exposures of varying times to one of the active slags; the intensity of darkening was found to be a linear function of the logarithm of exposure time, or for a fixed time, of the logarithm of the concentration of Ca⁴⁵. A typical microdensitometer record of a film made from a diffusion specimen is shown in Fig. 3.

Calculation of the Diffusion Coefficient D: The particular solution of the diffusion equation for the given conditions is

$$\frac{2C}{C_0} - 1 = -\left(\operatorname{erf} \frac{x}{2\sqrt{Dt}} \right)$$

where C₀ is the initial concentration of Ca⁴⁵ in the active slag, and C its concentration at distance x from the interface after time t. A concentration-penetration curve, (C/x) was obtained from the microdensitometer record and the interface (x = 0) fixed at the point where C/C₀ = 0.5. Values of C/C₀ were then plotted against x on arithmetic probability paper and D calculated from the slope of the straight line thus obtained.

Results

Diffusion runs were made at three temperatures, 1350°, 1400°, and 1450°C; the corresponding diffusion times were of the order of 8, 6, and 4 hr respectively. Attempted measurements at 1500°C failed due to reaction involving gas evolution.

Two main difficulties were encountered during the work. The first, not unexpected, was due to convection. Fortunately, it was at least very easy to detect from the photograph when convection had

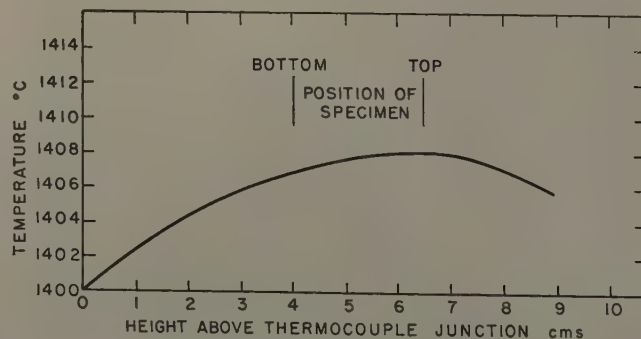


Fig. 2—Temperature variation within diffusion cell.

taken place and the results from such runs were discarded. Approximately 50 pct had to be jettisoned in this way.

The second trouble which arose was unforeseen. In almost every case the interface between the active and inactive slags was not plane but strongly curved. The effect was greater the higher the temperature. The cause of this phenomenon was not appreciated early enough for it to be avoided and indeed is as yet imperfectly understood. Apparently the interfacial tension between the active slag and graphite is less than that between the inactive slag and graphite. The curvature is simply the result of a higher energy surface being replaced by a lower. The active slag creeps along the wall and this surface layer drags with it liquid from the interior.

There were two differences in the method of preparation of the two slags which could contribute to this effect. The first lay in the length of time for which the slags were held molten. It is now known that the contact angle and therefore the interfacial tension between this slag and graphite decreases with time above a certain critical temperature. This difference in preparation was eliminated for some of the later runs but neither short nor long melting times had any effect on the shape of the interface.

The second difference was caused by the addition of $\text{Ca}^{45}\text{Cl}_2$ solution. Chloride ion is known to be surface active in glasses but the concentration in this slag was only 3.45×10^{-6} g Cl^-/g . Two runs in which the inactive slag contained the same concentration of ordinary CaCl_2 were unfortunately among the convection discards.

While the interfacial tension effect is obviously undesirable it is considered that the results are not thereby invalidated. If a narrow cylindrical element of liquid along the central axis were completely free to move in the direction of its length, diffusion along this cylinder should take place with but little effect from the translatory movement of the whole. After long diffusion times however there is the probability of additional Ca^{45} ions penetrating this central element from that part of the active slag which has crept along the wall.

The results are given in Fig. 4 where $\log D$ is plotted against $1/T$. Average values of D at 1350° , 1400° , and 1450°C , respectively, are 3.3×10^{-7} , 6.8×10^{-7} and 1.3×10^{-6} $\text{cm}^2 \text{sec}^{-1}$. Although these results are somewhat lacking in precision they serve to illustrate the applicability of a very simple tracer technic to diffusion studies in slags.

The slope of the line corresponds to 73 kcal for the energy of activation. This can be regarded only as an approximation which is best rounded off to 70 ± 20 kcal.

Comparison with Other Work

The diffusion coefficient of sodium in glasses at a temperature of about 1000°C was found by Johnson, Bristow, and Blau⁶ to be between 10^{-6} and 10^{-7} cm^2 per sec. Their results for calcium are not reported. The slags used by McCallum and Barrett² were higher in SiO_2 and lower in Al_2O_3 than that used here. For a slag containing 37.5 pct CaO , 10 pct Al_2O_3 , 52.5 pct SiO_2 , D_{CaO} was found to be 9.6×10^{-6} $\text{cm}^2 \text{sec}^{-1}$ at 1450°C and 12.15×10^{-6} cm^2 per sec at 1500°C giving an activation energy of 29 kcal.

It is perhaps of greater interest to compare the present result for the diffusion coefficient with that obtained for electrical conductivity by Martin and Derge.⁷

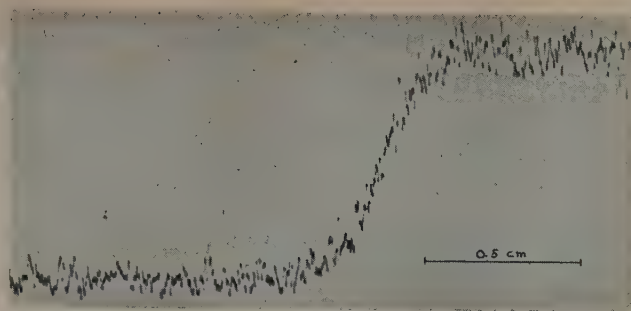


Fig. 3—Microdensitometer record along center of film exposed to slag after diffusion.

The authors are indebted to Professor C. Wagner for the following derivation of the relation between conductance and diffusion constant of an ion.

Let κ be the specific ionic conductance, C the concentration in mols cm^{-3} , and z the valence of the ion. Then

$$\kappa = 96,500 zCu$$

where u is the mobility in cm sec^{-1} per volt cm^{-1} . The Nernst-Einstein relation is

$$D = BkT$$

where D is the diffusion coefficient, B the absolute mobility in cm sec^{-1} dyne $^{-1}$, k is the Boltzmann constant, and T the absolute temperature. The mobility u is given by the following expression in which e is the electronic charge:

$$u = \frac{ze}{300} \quad B = \frac{ze}{300} \frac{D}{kT}$$

Substitution of this in the above equation for κ yields the desired relation:

$$\kappa = \frac{96,500}{300} \frac{z^2 e}{kT} DC$$

Appropriate values of the constants are $e = 4.80 \times 10^{-10}$ esu and $k = 1.380 \times 10^{-16}$ ergs per degree molecule, hence

$$\kappa = 1.12 \times 10^9 z^2 DC/T$$

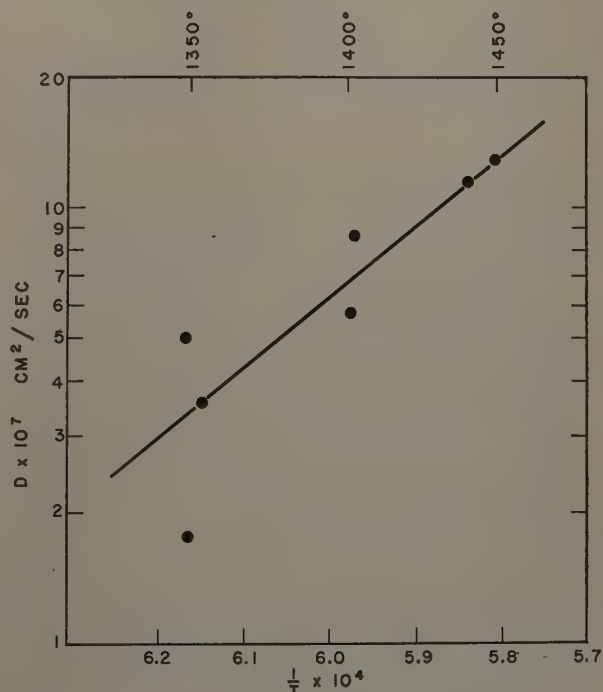


Fig. 4—Relationship between $\log D$ and $1/T$.

Taking the density of the slag as 2.8 g cm^{-3} the concentration of Ca^{++} is $0.40 \times 2.8 / 56 = 0.020 \text{ mols cm}^{-3}$.

The diffusion coefficient found at 1450°C was $1.3 \times 10^{-6} \text{ cm}^2 \text{ sec}^{-1}$. The calculated specific conductance due to Ca^{++} is therefore

$$\kappa = 0.067 \text{ ohm}^{-1} \text{ cm}^{-1}$$

For their very similar slag No. 13 at 1450° Martin and Derge found a specific conductance of $0.098 \text{ ohm}^{-1} \text{ cm}^{-1}$.

Our results are not sufficiently accurate to warrant a conclusion that Ca^{++} is responsible for 70 pct of the conductivity. In the light of the evidence presented by Bockris and coworkers⁸ that the conductance of silicate slags is wholly cationic, it seems preferable to regard the agreement between calculated and observed conductance as evidence for the validity of the method used in these diffusion experiments.

Summary

The possibilities of using radioactive isotopes to measure diffusion coefficients of the components in liquid slags have been explored and the basis of a technique established.

The diffusion of calcium ion in a slag containing 40 pct CaO , 20 pct Al_2O_3 , and 40 pct SiO_2 has been measured over a temperature range of 1350° to

1450°C . The values of D are approximately 3.3×10^{-7} and $1.3 \times 10^{-6} \text{ cm}^2 \text{ sec}^{-1}$ at these temperatures and the energy of activation is approximately $70 \pm 20 \text{ kcal}$. The value of D is of the order of magnitude of that calculated from the electrical conductivity of similar slags.

Acknowledgments

The authors wish to record their indebtedness, for fellowships, to the International Federation of University Women and the Department of State (Smith-Mundt Fellowships); also to the French Government.

References

- ¹ N. L. Bowen: *Journal of Geology* (1921) **29**, p. 295.
- ² N. McCallum and L. R. Barrett: *Trans. Brit. Ceram. Soc.* (1952) **51**, p. 523.
- ³ G. Derge, W. O. Philbrook, and K. M. Goldman: *Trans. AIME* (1950) **188**, p. 1111; *JOURNAL OF METALS* (September 1950).
- ⁴ W. E. Holbrook, C. C. Furnas, and T. L. Joseph: *Industrial and Engineering Chemistry* (1932) **24**, p. 993.
- ⁵ M. Paschke and A. Hautmann: *Archiv. Eisenhüttenwesen* (1935) **9**, p. 305.
- ⁶ J. R. Johnson, R. H. Bristow, and H. H. Blau: *Journal Amer. Ceram. Soc.* (1951) **34** (6) p. 165.
- ⁷ A. E. Martin and G. Derge: *Trans. AIME* (1943) **154**, p. 104.
- ⁸ J. O'M Bockris, J. A. Kitchener, S. Ignatowicz, and J. W. Tomlinson: *Trans. Faraday Soc.* (1952) **48**, p. 75; Bockris, Kitchener and A. E. Davies, *ibid*, p. 536.

Technical Note

The Silver-Cadmium Beta and Zeta Phases

by L. Muldawer, M. Amsterdam, and F. Rothwarf

SILVER-cadmium near the composition AgCd shows three equilibrium phases. As with β brass, the high temperature phase is disordered body-centered cubic (β) and the low temperature phase has the ordered CsCl structure (β'). However, there is an intermediate temperature phase which is hexagonal close-packed (ζ).

In a recent paper, Speich and Mack¹ report on a study of the Ag-Cd eutectoid near the AgCd composition. Unfortunately, the phase diagram upon which they base some of their conclusions is incorrect. That diagram is taken from the *Metals Handbook*² and the error is that the β' and ζ phases have been interchanged. The Handbook gives the low temperature phase as hexagonal (designated ζ) and the intermediate temperature phase as cubic ordered

(designated β'). The error may be typographical or it may be one of confusion resulting from the use of ζ , β , and β' for the intermediate phase in various papers.

A careful search of the literature reveals that a number of authors have indicated the correct relative positions of the β , ζ , and β' phases. The comprehensive work of Fraenkel and Wolf³ clearly stated that the high and the low temperature phases are either identical or are very similar. Ölander,⁴ on the basis of electrochemical measurements, showed that the β phase is disordered and the β' phase (designated β'' in his paper and in refs. 3 and 5) is ordered. Further work by Durrant⁵ using thermal and metallographic analyses provided a more precise phase diagram. A summary of these works was given by Hansen⁶ and shows the correct relative positions of the phases. Owen, Rogers, and Guthrie⁷ located correctly the upper two phases by X-ray diffraction. Their failure to find the low tem-

L. MULDAWER, Junior Member AIME, is Assistant Professor of Physics, and M. AMSTERDAM and F. ROTHWARF are Graduate Students, Temple University, Philadelphia.

TN 189E. Manuscript, Aug. 12, 1953.

perature β' phase is incomprehensible. Köster⁸ made measurements of the elastic modulus of AgCd as a function of temperature and again showed the true relative positions of the phases. Differences between the various workers are reported in the transformation temperatures. This is presumably because different techniques and different compositions were used. The centers of the existence regions of the three phases are found at quite different compositions.

We have investigated this region of the Ag-Cd phase diagram using X-ray diffraction on quenched samples and on samples at temperature and by measurement of electrical resistance as a function of temperature. The specimen used for X-ray diffraction contained 51.7 pct Ag by weight, while that used for resistance measurements contained 49.9 pct Ag. The relative positions of the three phases were confirmed. The transformation temperatures obtained by these three methods differed from one another. It should be noted that the β and β' phases cannot be distinguished by means of X-ray diffraction because of the almost identical scattering factors of the silver and cadmium atoms. However, in this note the low temperature phase will be indicated by β' .

High temperature diffraction patterns showed the following main phases: β at 500° and 488°C; ζ at 361°, 229°, and 204°C; and β' at 192°C. No attempt was made to determine the exact transformation temperatures since the purpose was to determine equilibrium phases. However, a lower transformation temperature around 200°C is indicated. This is subject to the error inherent in the temperature calibration of the high temperature camera.

Studies with quenched filings gave similar results except that the lower transformation temperature is indicated as being between 250° and 280°C. Durrant⁵ stated that this transformation occurred between 230° and 240°C. The difficulties of quenching AgCd alloys have been observed by several workers^{3, 5, 7} and the rapidity of the ζ to β' transformation may have caused the 251°C specimen to transform before quenching could be effective. The experimental technique may have played a part in this. Filings were sealed in evacuated Vycor containers, annealed at temperature for at least two days, and then quenched in ice water without, however, breaking the container. Thus, there must have been some time between the removal from the furnace and the cooling action of the ice water on the filings. A summary of these results is given in Table I. Quenching from temperatures above the upper

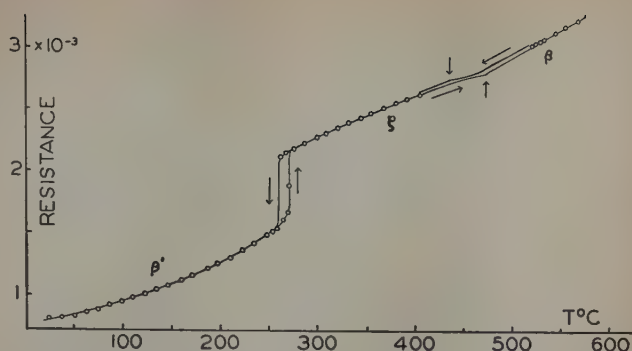


Fig. 1—AgCd resistance in ohms as a function of temperature. The ζ to β transformation points are indicated by vertical arrows. Experimental points in the neighborhood of this transformation were too close to permit inclusion in the figure.

transformation temperature invariably showed ζ as one of the predominant phases. This was due to the nature of the quench. The presence of β' phase in the intermediate region is explained similarly. The upper transformation temperature is seen to be around 450°C; this result is in accord with previous research. The presence of a good deal of α in the intermediate region is in accord with Durrant's phase diagram.

Electrical resistance measurements were made on a Ag-Cd rod about $\frac{1}{8} \times 4$ in. A Kelvin bridge was used for the measurement of resistance and a thermocouple attached to the center of the rod gave the temperature. The results are shown in Fig. 1. Specific resistivity at room temperature is about 10 microhm-cm. Fraenkel and Wolf³ measured electrical resistance but it is clear from the extremely wide hysteresis loops that their rate of change of temperature was much too fast. We investigated the hysteresis loop around 265°C very carefully; most of the points indicated were taken after the specimen had been at temperature for at least a day. The upper transformation temperature, centered around 455°C, was not obtained as carefully. The 10°C hysteresis loop observed for the lower transformation seems to be a real phenomenon and indicates a displacive transformation. The curvature in the β' region indicates the beginning of disordering. Further studies on these phenomena are being carried out.

We should like to acknowledge financial aid from the Office of Ordnance Research and a grant-in-aid from Temple University.

References

- ¹G. R. Speich and D. J. Mack: Silver-Cadmium Eutectoid. *Trans. AIME* (1953) **197**, p. 549; *JOURNAL OF METALS* (April 1953).
- ²*Metals Handbook* (1948) Cleveland. ASM.
- ³W. Fraenkel and A. Wolf: Die Umwandlungen im festen Zustande bei Silber-Cadmiumlegierungen. *Ztsch. anorg. allgem. Chem.* (1930) **189**, p. 145.
- ⁴A. Ölander: Eine elektrochemische Untersuchung von Cadmium-Silber-Legierungen. *Ztsch. physikalische Chem.* (1933) **163**, p. 107.
- ⁵P. J. Durrant: The ϵ , γ , and β Phases of the System Cadmium-Silver. *Journal Inst. Metals* (1935) **56**, p. 155.
- ⁶M. Hansen: *Aufbau der Zweistofflegierungen* (1936) Berlin. J. Springer.
- ⁷E. A. Owen, J. Rogers and J. C. Guthrie: X-ray Study of Ag-Cd Alloys. *Journal Inst. Metals* (1939) **65**, p. 457.
- ⁸W. Köster: Elastizitätsmodul und Dämpfung der intermediären Phasen in den Systemen Kupfer-, Silber-, Gold-Zink und Silber-Kadmium. *Ztsch. Metallkunde* (1940) **32**, p. 151.

Table I. Phases Present in Quenched Alloys*

Annealing Temperature, °C	Strong	Medium	Weak
202	β'		α
251	β'		α
280	β'		β'
303		α	β'
354		α	β'
401		α	β'
428		α	β'
446		α, β	
476	β, β'		α
501	β, β'		α
552	β, ζ		α

* Relative amounts indicated by the intensity of the diffraction lines.

Neptunium-Aluminum Intermetallic Compounds

by O. J. C. Runnalls

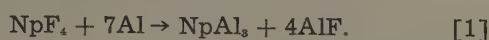
The intermetallic compounds NpAl_2 , NpAl_3 , and NpAl_4 have been prepared, and examined by X-ray diffraction methods. The compounds are isostructural with the corresponding U-Al compounds. NpAl_2 is face-centered cubic with $a = 7.785\text{\AA}$ and has the MgCu_2 structure. NpAl_3 is simple cubic with $a = 4.262\text{\AA}$ and has the AuCu_3 structure. NpAl_4 is body-centered orthorhombic with $a = 4.42\text{\AA}$, $b = 6.26\text{\AA}$, and $c = 13.71\text{\AA}$. The published description for the atomic positions in UAl_4 applies also to NpAl_4 .

THE U-Al system has been examined by Gordon and Kaufmann.¹ They identified the following intermetallic compounds: UAl_2 , UAl_3 , and a third, tentatively identified as UAl_5 . A structure analysis of the latter compound by Borie² proved that the formula UAl_4 was more consistent with the X-ray data. The crystal structures of UAl_2 and UAl_3 have been reported by Rundle and Wilson.³ UAl_2 was found to be isostructural with MgCu_2 . The atomic positions in the simple cubic UAl_3 cell were found similar to those in the AuCu_3 structure. Three analogous compounds exist in the binary system Np-Al. X-ray data for the compounds NpAl_2 , NpAl_3 , and NpAl_4 are reported below.

The neptunium used in the investigation was supplied through the courtesy of the Argonne National Laboratory as neptunium (V) nitrate. It was stated to have a radioactive content of 99.25 pct Np^{237} . The impurity limits had been established by a spectrographic analysis given in Table I. Any titanium, boron, or bismuth impurity should be effectively removed during the fluorination of NpO_2 to NpF_4 , and sodium, lithium, magnesium or strontium during the alloying procedure.

The oxalate ignition technique, described by Westrum⁴ for the preparation of finely-divided reactive PuO_2 , was used. The neptunium (V) nitrate solution, containing 100 mg Np, was evaporated to dryness on oxalic acid crystals. The resulting oxalate was calcined to NpO_2 by heating in platinum at 650°C for 2 hr. An equimolar mixture of anhydrous hydrogen fluoride and purified hydrogen was passed over the NpO_2 for 2 hr at 500°C . According to Fried and Davidson⁵ the above fluorination conditions should produce the purple-black fluoride, NpF_3 . However, the light-green product showed only NpF_4 lines on an X-ray diffraction pattern and contained only an estimated 5 pct of finely dispersed black NpF_3 particles on microscopic examination.

NpAl_3 : An intimate mixture of 50 mg of neptunium fluoride and aluminum powder (99.99 pct pure, -28 to +60 mesh) was heated to 900°C in a BeO crucible in vacuum by a tungsten coil for 2 hr, to allow the following reaction to proceed:



The formation and sublimation of aluminum monofluoride in this system was verified from an X-ray

O. J. C. RUNNALLS is associated with the Chemistry Branch, Atomic Energy of Canada Limited, Chalk River, Ont., Canada.

Discussion on this paper, TP 3654E, may be sent, 2 copies, to AIME by April 1, 1954. Manuscript, July 3, 1953. New York Meeting, February 1954.

Table I. Spectrographic Analysis

Element	Impurity, Pct	Element	Impurity, Pct
Fe	<0.1	Na	<2.0
Al	<0.2	Li	<0.0004
Ti	<1.0	Mg	<0.07
B	<0.3	Sr	<0.002
Bi	<0.5		

diffraction analysis of the sublimate. The diffraction pattern was similar to one obtained in the aluminum reduction of UF_4 to UF_3 ,⁶ showing both Al and AlF_3 lines.

The resulting alloy was sintered at 1100°C for 1 hr. A powdered specimen of the crystalline product was sealed in a thin-walled quartz capillary for X-ray examination. The photograph was taken on a 14.32 cm General Electric powder diffraction camera, using filtered copper radiation. The films were calibrated in terms of a NaCl standard pattern. The wavelengths used in the calculations were 1.5418\AA for $\text{Cu K}\alpha$ and 1.5405\AA for $\text{Cu K}\alpha_1$.

The powder diffraction pattern showed that NpAl_3 is simple cubic with $a = 4.262 \pm 0.005\text{\AA}$, and is isostructural with UAl_3 where $a = 4.27\text{\AA}$ or $a =$

Table II. Comparison of the NpAl_3 and UAl_3 X-Ray Powder Diffraction Patterns

hkl	$\text{Sin}^2\theta\text{-NpAl}_3$	Observed Intensities*	
		NpAl_3	UAl_3^1
100	0.0329	s	s
110	0.0657	s	s
111	0.0982	s	s
200	0.1310	s—	s
210	0.1638	s	s
211	0.1965	s—	s
220	0.2618	m	m-s
221,300	0.2944	m+	m-s
310	0.3267	m—	m
311	0.3596	s	s
222	0.3925	w+	w-m
320	0.4248	m—	m
321	0.4574	m+	m-s
400	0.5231	w	w
410,322	0.5549†	m+	m-s
411,330	0.5871†	m	m
331	0.6200†	m+	m
420	0.6536†	m	m
421	0.6861†	m+	m
332	0.7187†	w+	w-m
422	0.7839†	m+	m-s
500,430	0.8170†	w+	w-m
501,431	0.8495†	s—	m-s
511,333	0.8818†	m+	w-m
520,432	0.9474†	s—	Not reported
521	0.9801†	m+	Not reported

* w, weak; m, medium; and s, strong.
† Obtained with $\text{Cu K}\alpha_1$ radiation.

Table III. Unit Cell Dimensions for NpAl_4 and UAl_4

	NpAl_4	UAl_4 ²
a	$4.42 \pm 0.01 \text{ \AA}$	$4.41 \pm 0.02 \text{ \AA}$
b	$6.26 \pm 0.01 \text{ \AA}$	$6.27 \pm 0.02 \text{ \AA}$
c	$13.71 \pm 0.03 \text{ \AA}$	$13.71 \pm 0.03 \text{ \AA}$

4.287 \AA ³ (see Table II). The calculated density is $6.82 \text{ gram cm}^{-3}$, assuming one NpAl_3 formula weight per unit cell. The atomic positions in the structure are:

1 Np at $0,0,0$.

3 Al at $0, \frac{1}{2}, \frac{1}{2}$; $\frac{1}{2}, 0, \frac{1}{2}$; $\frac{1}{2}, \frac{1}{2}, 0$.

The unit cell is illustrated in Fig. 1.

NpAl_4 : A 50 mg sample of NpAl_3 was diluted with aluminum to form a mixture containing 30 wt pct Np. The mixture was heated to 1100°C in the vacuum furnace, and the resulting alloy was cooled at 100°C per hr to 600°C , then cooled to room temperature. The small ingot was reacted with 3N NaOH to dissolve the free aluminum present. Several single crystals were obtained from the crystal-line residue, Fig. 2. An X-ray diffraction pattern on a powdered crystal showed a close similarity to the UAl_4 pattern, suggesting that the compound was NpAl_4 .

Small single crystals, mounted in thin-walled quartz capillaries, were used as X-ray specimens. A series of three rotation photographs about each crystallographic axis was made using filtered copper radiation in a 5 cm radius General Electric rotation camera. An orthorhombic cell with dimensions similar to UAl_4 was revealed, Table III.

The calculated density of NpAl_4 is $6.04 \text{ gram cm}^{-3}$, assuming four formula weights per unit cell. The spectra found missing by Borie² in the UAl_4 analysis also were missing in the NpAl_4 pattern, i.e., the reflections present were:

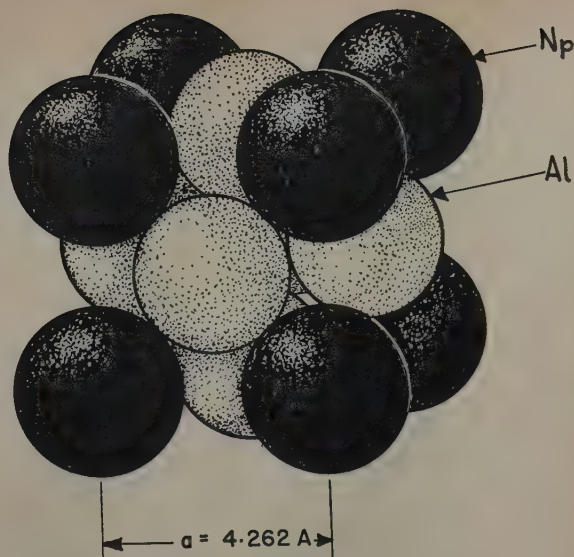
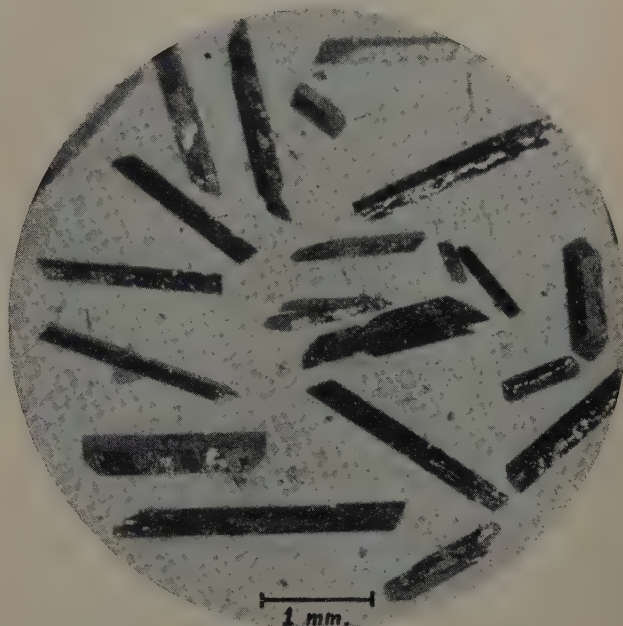
- (a) hkl — only for $h + k + l = 2n$
- (b) $hk0$ — only for $h = 2n$ and $k = 2n$
- (c) $h0l$ — only for $h + l = 2n$
- (d) $0kl$ — only for $k + l = 2n$.

These data indicate that the cell is body-centered with an $00l$ glide plane and may be described by either the space group Ima or $Imma$.

A visual comparison of the intensities of NpAl_4 and UAl_4 showed the two to be identical. Hence,

Table IV. Interatomic Distances in NpAl_4

Atom	No. of Neighbors	Kind of Neighbors	Distance, \AA
Np (4e)	3	Al (4e)	3.13
	4	Al (4b)	3.11
	4	Al (8h)	3.01
	2	Al (8h)	3.30
Al (4e)	3	Np (4e)	3.13
	4	Al (4b)	3.11
	4	Al (8h)	2.79
	2	Al (8h)	3.10
Al (4b)	4	Np (4e)	3.11
	4	Al (4e)	3.11
	2	Al (4b)	3.13
	2	Al (8h)	2.56
Al (8h)	2	Np (4e)	3.01
	1	Np (4e)	3.30
	2	Al (4e)	2.79
	1	Al (4e)	3.10
	1	Al (4b)	2.56
	2	Al (8h)	2.82
	1	Al (8h)	3.54
	1	Al (8h)	2.72

Fig. 1— NpAl_4 unit cell.Fig. 2—Single crystals of NpAl_4 .

Borie's description² for UAl_4 has been applied here for the atomic positions in space group $Imma$.

$(0,0,0; \frac{1}{2}, \frac{1}{2}, \frac{1}{2}) +$

4 Np in (e) $0, \frac{1}{4}, z; 0, \frac{3}{4}, z; z = 0.111$

4 Al in (e) $0, \frac{1}{4}, z; 0, \frac{3}{4}, z; z = -0.111$

4 Al in (b) $0, 0, \frac{1}{2}; 0, \frac{1}{2}, \frac{1}{2}$

8 Al in (h) $0, y, z; 0, \bar{y}, z; 0, \frac{1}{2} + y, z; 0, \frac{1}{2} - y, z; y = -0.033; z = 0.314$.

The interatomic distances are tabulated in Table IV and the unit cell is illustrated in Fig. 3.

NpAl_4 : A 16 mg powdered sample of NpAl_4 was heated in a BeO crucible for 1 hr at 1150°C in a high vacuum furnace. The product was identified as NpAl_3 from its powder diffraction pattern. A further treatment for 15 min at 1375°C produced a crystalline residue with an X-ray diffraction pattern similar to UAl_3 . Several weak lines not due to NpAl_3 were present also. The latter fitted the published description for NpO_2 .

The powder diffraction pattern showed that NpAl_4 is face-centered cubic with $a = 7.785 \pm 0.005 \text{ \AA}$. The

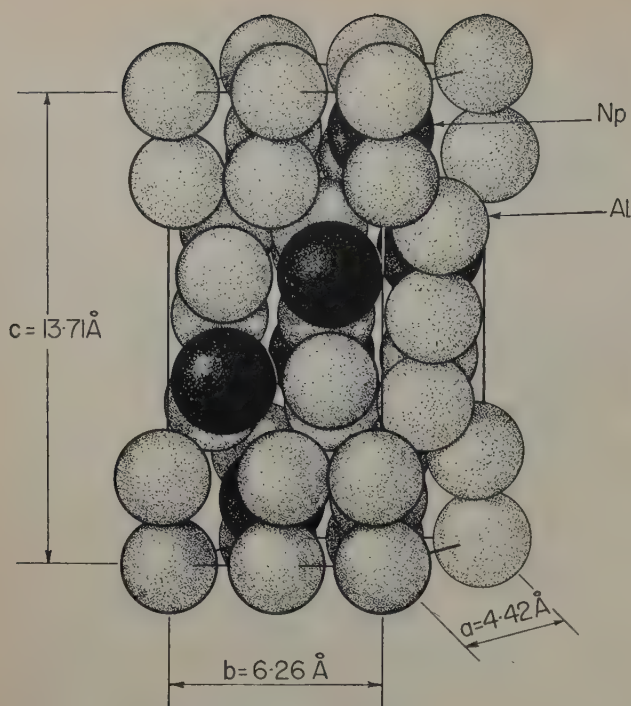


Fig. 3—NpAl unit cell.

compound is isostructural with UAl_2 where $a = 7.74\text{\AA}$ or $a = 7.811\text{\AA}$ (see Table V). The calculated density is 8.19 gram cm^{-3} , assuming eight NpAl_2 formula weights per unit cell. The atomic positions in the structure are:

$(0,0,0; 0, \frac{1}{2}, \frac{1}{2}; \frac{1}{2}, 0, \frac{1}{2}; \frac{1}{2}, \frac{1}{2}, 0) +$
 8 Np in $0,0,0; \frac{1}{4}, \frac{1}{4}, \frac{1}{4}$
 16 Al in $\frac{5}{8}, \frac{5}{8}, \frac{5}{8}; \frac{5}{8}, \frac{7}{8}, \frac{7}{8}; \frac{7}{8}, \frac{5}{8}, \frac{7}{8}; \frac{7}{8}, \frac{7}{8}, \frac{5}{8}$.

The interatomic distances are tabulated in Table VI and the unit cell is illustrated in Fig. 4.

Discussion

The presence of NpO lines in the NpAl_2 powder diffraction pattern suggests that no other compound

Table V. Comparison of the NpAl_2 and UAl_2 Powder Diffraction Patterns

hkl	Sin $^2\theta$ NpAl_2	Observed Intensities*	
		NpAl_2	UAl_2 ¹
111	0.0301	m—	w-m
220	0.0801	s	s
311	0.1094	s	s
400	0.1584	w	w
331	0.1882	m	m
422	0.2374	s	s
333,511	0.2671	s—	s
440	0.3158	m	m
531	0.3452	m	m
620	0.3941	m+	m
533	0.4233	m—	m-w
622	0.4331	vw	Not reported
444	0.4722	w	w
551,711	0.5019	w+	w-m
642	0.5509	s	s
553,731	0.5804	s	s
800	0.6290	w	vw
733	0.6585	w	vw
660,822	0.7061†	m+	m-s
555,751	0.7356†	m+	m-s
840	0.7840†	m—	m
753,911	0.8133†	m	m
664	0.8614†	m	m
931	0.8908†	m+	m
844	0.9398†	m+	Not reported
933	0.9694†	m	Not reported

* vw, very weak; w, weak; m, medium; and s, strong.
 † Obtained with Cu $K_{\alpha 1}$ radiation.

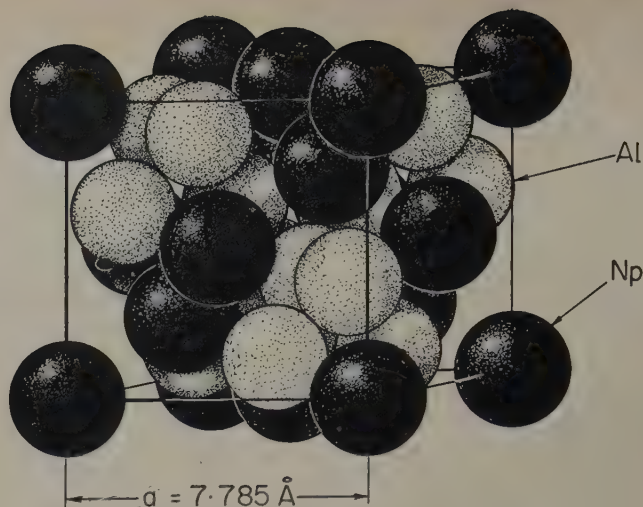


Fig. 4— NpAl_2 unit cell.

exists between the composition range NpAl_2 and Np. The Np in a mechanical mixture of Np and NpAl_2 would oxidize in air to NpO during the preparation of a powdered X-ray sample. On the Al-rich side, no compound exists between Al and NpAl , according to X-ray evidence, i.e., a powder diffraction pattern of a 30 pct Np in Al alloy showed only Al and NpAl lines. Further, the observed decomposition of NpAl , on heating parallels that for UAl . The Np-Al system is, therefore, closely analogous to the U-Al binary system, with three intermetallic compounds characterized as follows:

1— NpAl_2 face-centered cubic with $a = 7.785\text{\AA}$ and the MgCu_2 structure.

2— NpAl_3 simple cubic with $a = 4.262\text{\AA}$ and the AuCu_3 structure.

Table VI. Interatomic Distances in NpAl_2

About each Np	4 Np at 3.37Å	12 Al at 3.23Å
About each Al	6 Al at 2.75Å	6 Np at 3.23Å

3— NpAl , body-centered orthorhombic with $a = 4.42\text{\AA}$, $b = 6.26\text{\AA}$, and $c = 13.71\text{\AA}$ and the UAl structure.

Acknowledgment

The author is grateful to R. R. Boucher for technical assistance in the preparation of the compounds. The unit cell models were drawn by W. A. Cobbett. The neptunium was kindly supplied by the Argonne National Laboratory, Lemont, Ill.

References

- ¹P. Gordon and A. R. Kaufmann: *Trans. AIME* (1950) **188**, p. 182; *JOURNAL OF METALS* (January 1950).
- ²B. S. Borie: *Trans. AIME* (1951) **191**, p. 800; *JOURNAL OF METALS* (September 1951).
- ³R. E. Rundle and A. S. Wilson: *Acta Crystallographica* (1949) **2**, p. 148.
- ⁴E. F. Westrum: Paper in "The Transuranium Elements." Edited by G. T. Seaborg, J. J. Katz, and W. M. Manning. (1949) p. 938. New York. McGraw-Hill Book Co.
- ⁵S. Fried and N. Davidson: *Journal ACS* (1948) **70**, p. 3539.
- ⁶O. J. C. Runnalls: *Canadian Journal of Chemistry* (1953) **31**, p. 694.
- ⁷W. H. Zachariasen: Paper in "The Transuranium Elements." Edited by G. T. Seaborg, J. J. Katz, and W. M. Manning. (1949) p. 1490. New York. McGraw-Hill Book Co.

Diffusion and Solubility of Boron in Iron and Steel

by Paul E. Busby, Mary E. Warga, and Cyril Wells

Fundamental data on the rate of diffusion of boron in austenite and solubility of boron in the α and γ phases of iron and steel have been obtained from deboronizing experiments and provide partial explanations for some of the phenomena observed in boron steels. The rate of diffusion of boron is about the same as carbon in austenite. The solubility of boron in austenite at normal heat-treating temperatures is less than 0.001 pct. A partial tentative Fe-B phase diagram in the important low boron concentration ranges and an equation representing the diffusion of boron in austenite are presented.

ALTHOUGH a search of the literature revealed that boron diffusion had not been studied quantitatively and systematically prior to 1948, a few qualitative observations which were made by following the diffusion of boron into iron packed in ferro-boron¹⁻³ suggest that boron obeys normal diffusion laws and that the rate of diffusion increases with increasing temperature. The claim of Cornelius and Bollenrath¹ that boron does not appear to influence the rate of carbon diffusion has recently been substantiated by Wells, Batz, and Mehl.⁴ Calculations based on data from the paper by Campbell and Fay² indicated that the diffusion coefficient (D) for boron in iron at 900°C is approximately 3×10^{-7} sq cm per sec; a value of 2×10^{-7} sq cm per sec at 1038°C has been reported by Digges et al⁵ in connection with decarburizing experiments on a commercial boron steel containing 0.43 pct C.

During the period 1948 to 1950 several diffusivity constant (D) values for the diffusion of boron in the γ phase of iron and steel and a number of solubility values for boron in both α and γ phases were reported. It was concluded tentatively as a result of Metals Research Laboratory studies that D values for boron in γ and α phases are about the same as for carbon in the comparable phases⁶ and that carbon up to 0.4 pct did not affect the rate of diffusion of boron in γ iron above 1000°C within the limits of experimental error. Whether saturation of the γ or α phases with carbon would significantly affect

rates of diffusion of boron through them was then and still remains in doubt. The best estimate of Q (activation energy) was reported to be about 25,000 cal, somewhat lower than that for carbon in γ iron. The solubility of boron in γ iron at 1000°C was thought to be higher than 0.004 pct B but not as high as a more recent analysis of available data shows it to be. The solubility of boron in α iron at 700°C was reported to be 0.0004 pct B, but it would not have surprised the authors if the true solubility value is actually lower than this. Breaks in diffusion curves which were not understood when first obtained prior to 1950 have now been recognized as indicating solubility limits, and these are included in the present paper.

Experimental Procedure

Two methods were employed in an effort to determine diffusion coefficients (D) for boron in austenite. Early experiments involved the use of welded couples prepared in accordance with the procedure of Wells and Mehl,⁷ but when the results of these experiments proved to be unsatisfactory for calculating D values, studies were continued by means of deboronizing experiments. In both cases, boron analyses following the diffusion anneal were carried out spectrographically and all D values were computed using the Grube solution of Fick's law. The precision of the spectrographic method used proved to be about equal to that reported by Corliss and Scribner⁸—average deviation from the mean about 5 pct of the amount present when the boron content is 0.003 pct.

Concentration-penetration curves obtained from spectrographic analyses of welded couples generally indicated that practically no boron was transported across the weld interface during the diffusion anneal. Furthermore the concentration-penetration

P. E. BUSBY is Research Metallurgical Engineer, C. WELLS, Member AIME, is Principal Research Metallurgical Engineer, Metals Research Laboratory, Carnegie Institute of Technology, Pittsburgh, and M. E. WARGA is Director, Spectroscopy Laboratory, University of Pittsburgh, Pittsburgh.

Discussion on this paper, TP 3633E, may be sent, 2 copies, to AIME by April 1, 1954. Manuscript, April 15, 1953; revision, July 10, 1953. New York Meeting, February 1954.

Table I. Chemical Composition of Materials

Material No.	Element, Pct								
	C	Mn	P	S	Si	Ni	Cr	Mo	B
1	0.43	1.64	0.020	0.019	0.37	0.01	0.04	0.01	0.0038
2*	<0.005	0.001	<0.001	<0.001	<0.001	<0.00015	<0.00005	<0.0001	0.015
3*	0.28	0.001	<0.001	<0.001	<0.001	<0.00015	<0.00005	<0.0001	0.0014
4	0.025	0.26	0.006	0.031	0.008	0.03	0.02	0.01	0.040
5	0.41	0.45	0.010	0.023	0.16	0.12	0.19	0.08	0.030
6	0.032	0.30	0.010	0.024	0.19	0.06	0.03	0.03	0.025
7	0.036	0.25	0.007	0.025	0.12	0.05	0.03	0.02	0.03

* Spectrographic traces of other elements, except for aluminum which is about 0.05 pct.

curves for duplicate experiments (same steels and heat treatment) and the D values calculated therefrom were not reproducible. Diffusion coefficients determined from couple experiments were as much as 100 times lower than those obtained from later deboronizing experiments. Since results of welded couple experiments are not included in this paper, subsequent sections will be limited to data pertaining to deboronizing experiments.

Composition of Materials: The compositions of the materials used for deboronizing experiments are given in Table I. Steel 1 was obtained from the Bureau of Standards and is one of the commercial steels (C-18) described by Digges and Reinhart.⁹ Materials 2 and 3 are high purity heats produced from electrolytic iron and excess aluminum together with ferro-boron (material 2) and ferro-boron plus graphite (material 3); the charge was heated to near the melting point under vacuum after which purified argon was admitted as an atmosphere and the crucible was lowered slowly from the heating zone. Materials 4 through 7 consist of laboratory heats of plain C-B steels similar in purity to high quality commercial steels. Aluminum was added to all materials prior to the addition of boron.

Boron additions were made with bortam (steel 1), ferro-boron (2 and 3), and Grainal No. 79 (all others). The wide variations in the boron contents among the various alloys were necessitated by the lack of available information on the solubility of boron in the α and γ phases of iron.¹⁰ Materials 2 and 3 were heat-treated in the as-solidified form (1 in. rounds) and all other materials were forged to 1 or 1½ in. diameter rounds prior to the diffusion anneal.

Diffusion Anneal: Samples for deboronizing experiments consisted of cylinders 1 to 1½ in. in diameter and about 2 in. long; both ends of the specimens were faced perpendicular to the axis of the cylinder prior to the deboronizing (and decarburizing) heat treatment in an atmosphere of wet hydrogen. Times and temperatures of the various

treatments which yielded diffusion and solubility data are recorded in Tables II and III. Temperatures are probably correct within 5°C and errors in the reported times are negligible.

Specimens were heat-treated in a wire-wound resistance tube furnace using a McDanel tube as an atmosphere chamber. Temperatures were measured by means of a calibrated Pt-Pt-10 pct Rh thermocouple wired to the diffusion specimen. The hydrogen atmosphere was obtained by passing tank hydrogen through water at room temperature prior to admission to the furnace; the flow of wet hydrogen was maintained for the duration of the diffusion anneal. When the heat treatment was completed, specimens were removed from the furnace and cooled rapidly in air or water-quenched.

Determination of Boron: Following the diffusion anneal, specimens were machined to ½ in. diameter cylinders to avoid radial diffusion effects. Boron determinations were made on surfaces prepared by removing successive layers of the sample perpendicular to the cylindrical axis with a boron free wheel on a surface grinder. Depending on the location with respect to the original surface, the layers varied from 0.003 to 0.020 in. in thickness. The distance measurements which are subsequently utilized in plotting concentration-penetration curves are believed to be accurate to about 0.0005 in. (0.001 cm).

Calculation of D : In order to calculate diffusion coefficients from concentration-penetration data, the Grube solution of Fick's law was applied. The procedure used has already been described¹¹ and involves the use of the equation

$$1 - \frac{2C}{C_0} = \phi\left(\frac{x}{2\sqrt{Dt}}\right)$$

where: C_0 is twice the maximum boron content of the deboronized specimen, pct; C , $C_0/2$ plus the boron content at a discrete value of x , pct; x , the distance from the surface, cm; D , the diffusion coefficient, sq cm per sec; t , the diffusion time, sec; and ϕ , the Gauss error function or probability integral.

After boron analyses were obtained, values of C/C_0 were plotted on probability paper as a function of x and the line of best fit was determined by the method of least squares. Data obtained from this line, together with the time of diffusion, permit the equation above to be solved for D .

In order to obtain the proper gradient for the calculation of D , values of C and $C_0/2$ were corrected for the surface concentration (C_s) of boron in solution. This concentration was calculated for each experiment by substituting the value of the

Table II. Summary of Experiments Which Provided Diffusion Coefficients in Austenite

Test No.	Material	Time, Hr	Temperature, °C	$D \times 10^{-7}$ Sq Cm per Sec
1	1	29.0	950	2.6
2	3	11.5	992	3.6
3	1	11.0	998	4.1
4	1	11.1	1000	4.5
5	1	11.1	1000	5.8
6	1	6.0	1072	8.3
7	1	6.0	1072	9.0
8	1	5.0	1203	10.9
9	1	4.0	1299	23.3

intercept, C/C_0 , obtained from the probability plot, in the equation $C = C_0/2 - C_s$ and solving for C_s . The proper values for substitution in the Grube expression then become $C_0/2 - C_s$ and $C - C_s$.

Although D values cannot be calculated from results of experiments in which the initial boron content is above the solubility at the temperature of diffusion, such data are useful for estimating the solubility of boron since the gradient of boron in solution must vary from near zero at the surface to the limit of solid solubility at the deboronizing temperature. Stanley¹² has already demonstrated that the values for the solubility of carbon in ferrite determined by this method are in agreement with those obtained by the Van Ostrand-Dewey method.

Results

Diffusion in Austenite: The results of deboronizing (and decarburizing) experiments which were conducted on steel 1 at temperatures ranging from 950° to 1300°C are summarized in Table II. In addition, data obtained on a pure Fe-C-B alloy (steel 3) are included for comparison. A typical concentration-penetration curve for boron, and the associated curve for carbon are presented in Fig. 1.* The

* Chips for carbon analyses were obtained from successive circumferential layers taken from portions of the cylinder not used for spectrographic analysis. It may be noted that the boron curve apparently approaches a maximum concentration of approximately 0.003 pct B whereas Table I indicates that this steel should contain 0.0038 pct B. This result is believed to be due to segregation of boron from specimen to specimen rather than a consequence of radial diffusion, since the maximum boron concentration obtained in various specimens appears to be unrelated to the time and temperature of heat treatment.

boron curve is similar to the carbon curve wherein the concentration of carbon follows a Gaussian curve from the original composition to zero at the surface except that boron diffuses to the surface where it forms an insoluble oxide and accumulates to the high concentration shown. However if the high concentration of insoluble boron at the surface is disregarded, diffusion coefficients may be calculated. The obvious objection to these deboronizing experiments is the fact that both carbon and boron atoms are diffusing to the surface simultaneously.

Results of deboronizing experiments carried out on steel 1 are plotted in Fig. 2 as $\log D$ vs the reciprocal of temperature. The line of best fit shown was computed using the method of least squares. The activation energy, Q , determined from the slope of this line is about 21,000 cal per mol or roughly half that reported for the diffusion of carbon in austenite.⁴ The data may be represented approximately by the equation: $D = 2 \times 10^{-3} e^{-21,000/RT}$. Based on a standard statistical analysis† it appears that within

† Procedures for estimating the limits of accuracy of a set of data are given in many standard texts^{13,14,15} and technical papers.¹⁶

the range 8.2 to 6.2 (abscissa, Fig. 2) the odds are about 20 to 1 in favor of true values of D falling between limits represented by the upper and lower (dashed) curves. The odds are also estimated to be 20 to 1 that the true value of Q falls between limits of 21,000 + 7000 cal and 21,000 - 7000 cal.

Solubility: Data on the solubility of boron in austenite were obtained from the results of deboronizing experiments in the range 800° to 1100°C. Estimates of solubility limits from diffusion experiments are based on the knowledge that a change of phase in a system is accompanied by a sudden change in the concentration of the solute element. In order to determine the solubility of boron in austenite above 1000°C, materials containing more than 0.003 pct B were selected because the smooth curves obtained

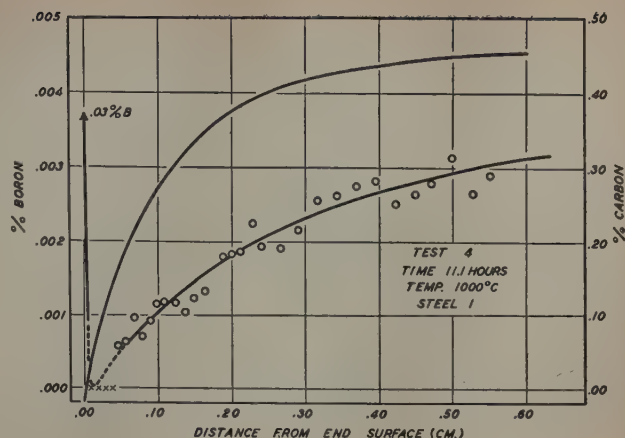


Fig. 1—Concentration-penetration curves for boron and carbon from test 4 after deboronization and decarburization in wet hydrogen. The symbol "x" denotes that no boron line was observed on the spectrographic plate.

from deboronizing experiments, Fig. 1, indicated that at least 0.003 pct B is in solid solution at these temperatures. Experiments on these high boron materials at temperatures between 1000° and 1100°C produced curves of the type shown in Fig. 3. From this curve, the solubility of boron in austenite at 1002°C is estimated to be about 0.009 pct B, i.e., the concentration of boron about 0.07 cm from the surface where the "break" in the penetration curve indicates that austenite was in equilibrium with austenite plus boride.

The curves of Fig. 4 were obtained from results of spectrographic analyses of two individual specimens which were annealed at approximately 800°C. The intercepts indicated by the horizontal arrows are considered to represent the solubility of boron in austenite, and the similarities in the curves demonstrate the reproducibility of the method. From

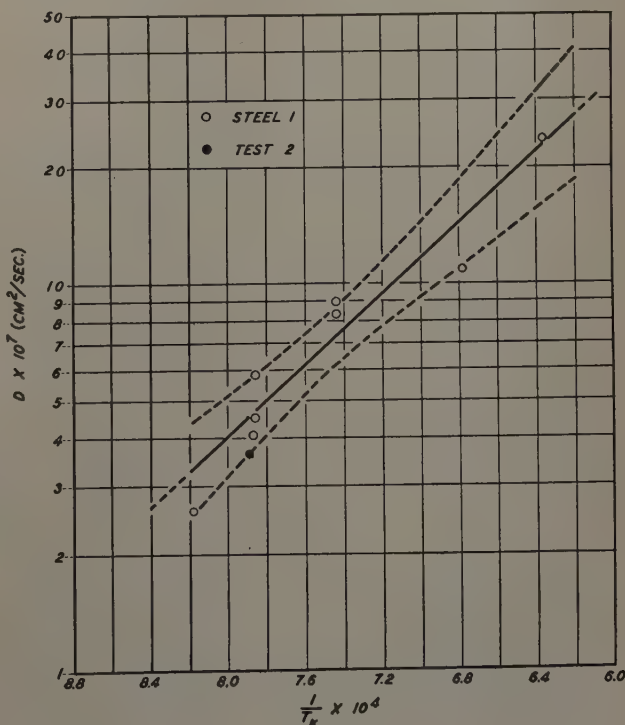


Fig. 2—Effect of temperature on the diffusion coefficient for boron in austenite. All tests made on steel 1, except test 2 which was a high purity Fe-C-B alloy.

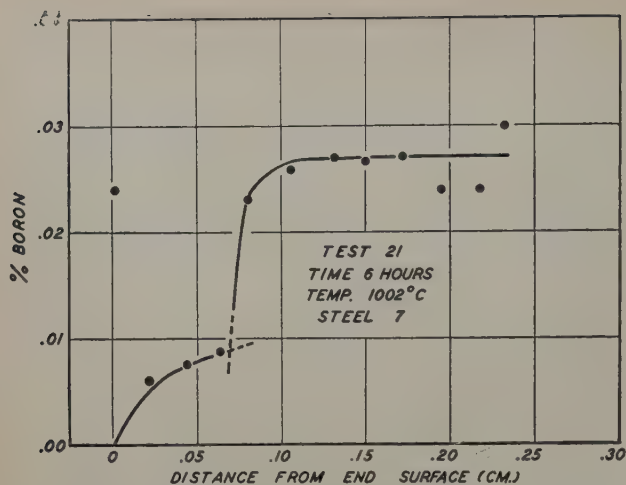


Fig. 3—Concentration-penetration curve for test 21, indicating the solubility limit of boron in austenite to be about 0.009 pct B at the diffusion temperature.

these curves, the solubility of boron in austenite at 800°C is estimated to be about 0.0006 pct B.

The curve of Fig. 4A is associated with the microstructure of Fig. 5a which reveals that carbon was removed preferentially from the surface of the specimen during the diffusion run, so that the banding which existed in this commercial steel prior to heat treatment is accentuated. As a result of segregation, the α and γ phases coexisted at the temperature of diffusion, and because of the differences in the rate of diffusion of carbon in the separate phases, carbon was removed more rapidly from the α regions; subsequent cooling produced the structure of conspicuous ferrite and pearlite bands.

The distance from the surface represented by the right side of the micrograph, Fig. 5a, is about 0.10 cm so that the "break" in the boron penetration curve occurs at a position where the structure has evidently not been affected by the circumstances just described, i.e., a position where the steel was essentially all austenite at temperature.† Chemical

† As a result of the high manganese content, the A_3 in this steel at a position where decarburization has not been extensive is considerably less than 910°C.

analyses indicate that the carbon content at the boron interface is about 0.25 pct and the D value based on carbon penetration data for this specimen shows that diffusion in austenite controlled the rate of removal of carbon. The microstructure of this steel after diffusion at 930°C shows, as expected,

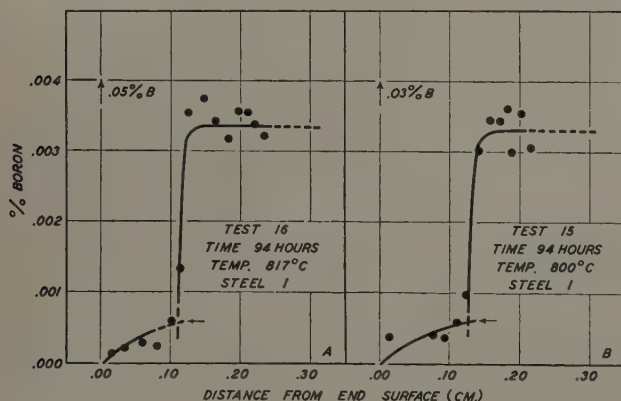


Fig. 4—Concentration-penetration curves for tests 16 and 15 showing the reproducibility of the deboronizing method for estimating solubility limits.

much less evidence of banding as indicated in Fig. 5b.

Information on the solubility of boron in the α phase was obtained from the results of deboronizing experiments conducted on alloys containing Fe+B and Fe+C+B at temperatures between 700° and 850°C. Curves similar to those just described were obtained, and the solubility limits were similarly estimated.

Results of tests which provided data on the solubility of boron in α and γ are listed in Table III. In some cases, the solubility values are given as less than or greater than a given amount when the

Table III. Summary of Experiments Which Provided Solubility Data

Test No.	Material	Time, Hr	Temperature, °C	Solubility, Pct B in α	Solubility, Pct B in γ
11	1	94	700	0.0003	
12	1	97.8	751	0.0006	
13	2	17	835	0.0018	
14	4	17.1	850	<0.0035	
15	1	94	800		0.0006
16	1	94	817		0.0006
17	1	94	817		0.0006
18	1	35.5	900		0.0012
19	1	29	930		0.0010
20	1	29	950		>0.003
21	7	6	1002		0.008
22	5	6	1002		0.009
23	6	6	1072		0.016
23	6	6	1086		0.016

numerical values are known to be in error. For example, the table includes results of a deboronizing experiment (test 1) which yielded a smooth concentration penetration curve from which a D value was calculated; such data indicate that all boron in the sample was in solid solution at the diffusion temperature and it may be concluded that the solubility is greater than this amount. In test 14 the interface movement resulting from the diffusion treatment was only about 0.035 cm as determined by metallographic examination of the specimen and the "break" in the concentration-penetration curve. The only boron determination available between the surface and the interface gave a value less than 0.0002 pct B after which the boron content rose sharply from 0.0035 to 0.031 pct. Thus, these data suggest that the solubility of boron in α at 850°C is somewhat less than 0.0035 pct B. In the case of tests 16 and 17 a small amount of α existed in the samples at the position of the interface so that the determined value is an average of the solubilities in both α and γ . Since other data demonstrate that the solubility of boron in α at 800°C is higher than that in γ , the solubility value for γ is believed to be slightly less than the determined value; by similar reasoning, the value obtained for the solubility of boron in ferrite at 751°C (test 12) is probably too low. However, it must be emphasized that in the last three mentioned experiments, the magnitude of error introduced by accepting the determined values is probably less than the limit of analysis.

Data listed in Table III are plotted in Fig. 6 together with previously published information²⁰ on the Fe-B system and suggest a peritectoid reaction at about 915°C.

Although D values calculated from welded couple experiments show considerable lack of reproducibility, solubility values do not. Results from three couples gave solubility limits (based on the Van Ostrand-Dewey method) of 0.0035 pct B in austenite at 982°C, 0.002 pct B in α at 842°C, and 0.002 pct B in α at 825°C, which are in fair agreement with

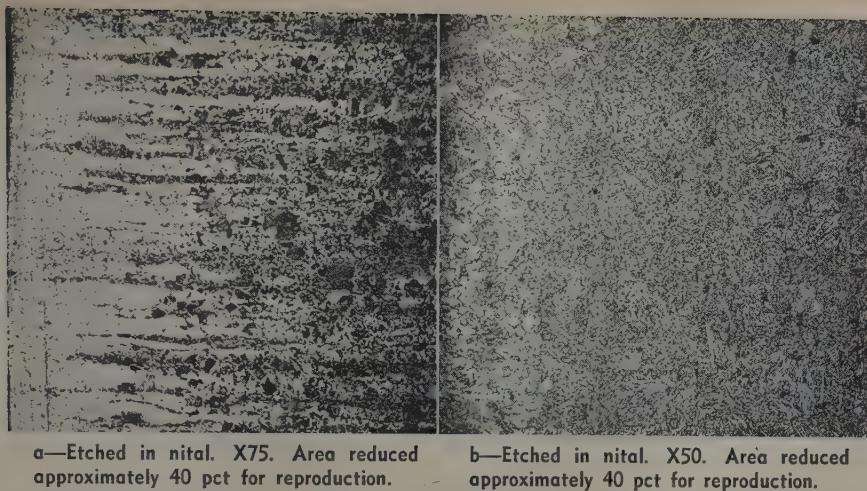


Fig. 5—Micrographs of steel 1 after decarburization at (a) 817°C, test 16, showing the preferential removal of carbon and (b) 930°C, test 19.

the data plotted in Fig. 6. The value for austenite was obtained from a couple consisting of two commercial steels containing 1.7 pct C and 0.04 and 0 pct B, respectively; the values for α were obtained from specimens of material 6 (Table I) welded to a boron-free steel of otherwise similar composition.

Discussion

Much of the information included in this paper has already been discussed in the foregoing sections. However, a few additional comments regarding some of the solubility and diffusion data, as well as their relation to hardenability, appear to be justified.

It has already been shown⁴ that boron up to 0.009 pct does not significantly affect the rate of diffusion of carbon; the authors stated that "while it is suspected that boron . . . lowers D slightly, the evidence is not conclusive." In the present study, the observation that the boron concentration data from deboronizing experiments fit a straight line on the probability plot of C/C_0 vs x within the wide limits of experimental error, is accepted as evidence that the rate of diffusion of boron in austenite does not vary with, 1—boron concentration, at least, up to about 0.003 pct B or 2—carbon concentration up to 0.43 pct. The latter conclusion is substantiated by the similarity of results obtained from decarburized 0.43 and 0.28 pct C steels; in connection with the former conclusion it may be stated that some of the concentration-penetration curves suggest a slight departure from linearity on the probability plot. At some future time more and better data may show this curvature to be real, thus indicating an increase of D with concentration.

The solubility of boron in the α phase and in the γ phase up to 0.43 pct C is apparently independent of carbon content although the result of one welded couple experiment suggests that the solubility of boron in austenite may be lowered when the austenite is saturated with carbon. It appears reasonable therefore, to accept the Fe-B diagram of Fig. 6 as a first approximation despite the fact that many of the solubility values on which the diagram is based were obtained from commercial materials containing up to 0.43 pct C as well as alloying elements.

The present investigation was initiated on the basis that a knowledge of diffusion rate and solubility of boron in the α and γ phases of iron and steel might provide needed basic data for understanding the mechanism by which boron improves the hard-

enability of steels. It is generally accepted that boron increases hardenability of hypoeutectoid steels by suppressing the rate of nucleation of proeutectoid ferrite. Among the intriguing aspects of the influence of boron however is the fact that published data^{9, 17} with one exception²² indicate that the relative increase in hardenability resulting from the addition of boron appears to be practically independent of the amount of boron present as determined by chemical or spectrographic analysis. The hardenability effect is known to be a function of carbon content.¹⁷⁻²⁰ There is also evidence that the effect of boron may be affected by heat-treating temperature^{6, 18} and, in some steels the hardenability effect can be completely destroyed by high temperature homogenization and cannot be recovered by subsequent heat treatments.¹⁸

Data presented in Table III show that the solubility of boron in austenite is about 0.0006 pct at normal heat-treating temperatures. This may account in part for the often observed fact^{9, 17, 18} that the effect of boron on hardenability appears to be independent of the amount of boron present. Since boron in quantities over the solubility limit would probably not affect hardenability, the relationship between boron content and improved hardenability could be expected only when the former lies between 0 and 0.0006 pct; the amount of boron added

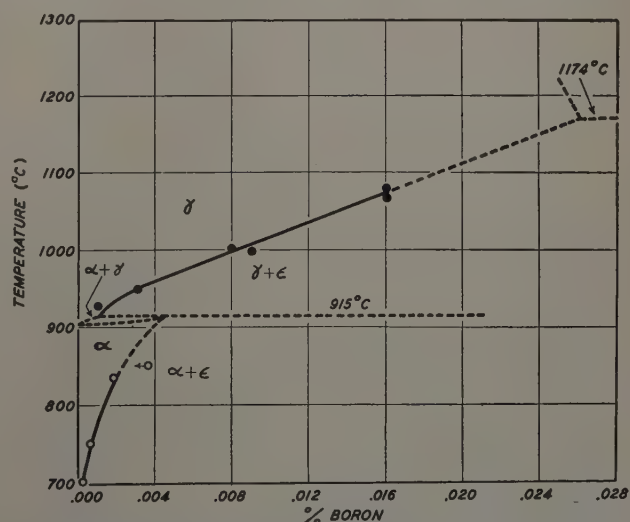


Fig. 6—Tentative partial Fe-B diagram based on deboronizing (decarburizing) experiments. Isotherms from Metals Handbook.¹⁰

to steels is usually greater than this amount. Another condition which has led to difficulty in this connection is the high affinity of boron for oxygen⁵ and nitrogen^{2, 5, 9} which leads to the ready formation of compounds and renders the boron ineffective; in some steels, improved hardenability is not obtained even when analysis indicates the presence of relatively large amounts of boron. It is therefore not surprising that the anticipated relationship between boron content and improved hardenability has not yet been determined experimentally with adequate precision.

Before other observations concerning the influence of boron on the hardenability of steels can be understood, the new data provided in this paper must be substantially augmented. The increase in solubility with increasing temperature is probably an important part of the required explanation of the effect of austenitizing temperature. In fact, solubility theory alone might reasonably be used to explain this effect if it were not for the disturbing observations which have been reported regarding the so called "boron constituent."^{15, 18} Spretnak and Speiser²¹ have explained some of the characteristics of the boron constituent on the basis of positive adsorption theory which should not be overlooked in the search for the full understanding of the effect of boron additions on the hardenability of hypoeutectoid steels. Before this objective can be attained however, further studies appear to be required to determine the causes for the lack of consistent behavior among boron-treated steels.

Summary

1—A spectrographic method was developed for determining boron in the range 0.0006 to 0.02 pct. The precision of the method is about the same as that developed by the Bureau of Standards⁸ and the sensitivity is of the order of 0.0002 pct.

2—Diffusion coefficients for boron in austenite were determined by the Grube method from the results of welded couple and deboronizing experiments. Reasonable D values were obtained from the latter experiments carried out on a commercial 0.43 pct C steel in the range 950° to 1300°C, but results from the welded couples are not in good agreement nor reproducible.

3—The diffusion of boron in austenite is comparable with that of carbon and may be represented by the equation

$$D_{\gamma} = 2 \times 10^{-5} e^{-21,000/RT}$$

Within the limits of experimental error, D_{γ} appears to be independent of carbon and boron up to 0.43 and 0.003 pct, respectively.

4—The solubility of boron in austenite at normal heat-treating temperatures is less than 0.001 pct B, but increases rapidly with temperature above 925°C. The solubility of boron in α at 835°C is about 0.002 pct, i.e., considerably higher than that in austenite at the same temperature, suggesting a peritectoid reaction. Solubility in both α and γ phases appears to be unaffected by carbon content, unless the austenite is saturated with carbon, in which case the solubility limit may be somewhat lowered.

5—The low solubility of boron in austenite explains some of the unusual effects of boron on the hardenability of steel but additional experimental data are required before the mechanism can be fully understood.

Acknowledgment

Part of this work was carried out under contracts with the Ordnance Department, Department of the

Army and the Office of Naval Research, Department of the Navy. The authors are indebted to T. G. Digges, H. A. Bright, and C. H. Corliss of the National Bureau of Standards for providing some of the steels and spectrographic determinations, to the Metallurgical Department of the Central Alloy District of the Republic Steel Corp. for supplying many of the alloys, and to G. Cressman, D. P. Hart, A. M. Hanna, L. R. Redmerski, M. Conrad, M. A. Redmerski, and J. Vojtecky of the Metals Research Laboratory for conducting the heat treatments and spectrographic analyses.

References

- ¹ H. Cornelius and F. Bollenrath: Einfluss von Kohlenstoff auf die Diffusion einiger Elements in Stahl. *Archiv. Eisenhüttenwesen* (September 1941) **15**, p. 145.
- ² T. D. Campbell and H. Fay: The Case Hardening of Steel by Boron and Nitrogen. *Industrial and Engineering Chemistry* (1924) **16**, p. 719.
- ³ T. Kase: Cementation of Boron on Some Metals. Abstracted in *Metals and Alloys* (1938) **9**, p. M.A. 661.
- ⁴ Cyril Wells, Walter Batz, and Robert F. Mehl: Diffusion Coefficient of Carbon in Austenite. *Trans. AIME* (1950) **188**, p. 553; *JOURNAL OF METALS* (March 1950).
- ⁵ T. G. Digges, Carolyn R. Irish, and Nesbit L. Carwile: Effect of Boron on the Hardenability of High Purity Alloys and Commercial Steels. *Journal of Research. National Bur. Standards* (1948) **41**, R.P. 1938, p. 545.
- ⁶ C. E. Birchenall: Volume Diffusion—An Empirical Survey. *Atom Movements*. (1951) p. 112. Cleveland. ASM.
- ⁷ C. Wells and R. F. Mehl: Rate of Diffusion of Carbon in Austenite. *Trans. AIME* (1940) **140**, p. 279.
- ⁸ C. H. Corliss and B. F. Scribner: Spectrographic Determination of Boron in Steel. *Journal of Research. National Bur. Standards* (1946) **36**, R.P. 1705, p. 351.
- ⁹ T. G. Digges and F. M. Reinhart: Influence of Boron on Some Properties of Experimental and Commercial Steels. *Journal of Research. National Bur. Standards*. (1947) **39**, R.P. 1815, p. 67.
- ¹⁰ R. M. Parke: Boron-Iron Constitution Diagram. *Metals Handbook* (1948) p. 1175. Cleveland. ASM.
- ¹¹ C. Wells: Chemical Techniques and Analysis of Diffusion Data. *Atom Movements* (1951) p. 26. Cleveland. ASM.
- ¹² J. K. Stanley: The Diffusion and Solubility of Carbon in Alpha Iron. *Trans. AIME* (1949) **185**, p. 752; *JOURNAL OF METALS* (October 1949).
- ¹³ M. Ezekial: *Methods of Correlation Analysis* (1941) Second Edition. New York. John Wiley and Sons.
- ¹⁴ G. W. Snedecor: *Statistical Methods* (1946) Fourth Edition. Ames, Iowa. The Iowa State College Press.
- ¹⁵ H. Arkin and R. R. Colton: *An Outline of Statistical Methods* (1939) Fourth Edition. New York. Barnes and Noble.
- ¹⁶ E. G. Olds and C. Wells: Statistical Methods for Evaluating the Quality of Certain Wrought Steel Products. *Trans. ASM* (1950) **42**, p. 845.
- ¹⁷ M. C. Udy and P. C. Rosenthal: Boron in Certain Alloy Steels. *Trans. AIME* (1947) **172**, p. 273; *METALS TECHNOLOGY* (October 1946).
- ¹⁸ R. A. Grange and T. M. Garvey: Factors Affecting the Hardenability of Boron-Treated Steels. *Trans. ASM* (1946) **37**, p. 136.
- ¹⁹ G. D. Rahrer and C. D. Armstrong: The Effect of Carbon Content on the Hardenability of Boron Steels. *Trans. ASM* (1948) **40**, p. 1099.
- ²⁰ W. Crafts and J. L. Lamont: Effect of Some Elements on Hardenability. *Trans. AIME* (1944) **158**, p. 157.
- ²¹ J. W. Spretnak and Rudolph Speiser: Grain and Grain-Boundary Compositions: Mechanism of Temper Brittleness. *Trans. ASM* (1951) **43**, p. 734.
- ²² Yūnoshin Imai and Hikotarō Imai: The Research Inst. for Iron, Steel and Other Metals. *Sci. Repts. Research Inst. Tōhoku Univ.* (April 1950) Series A, Vol. 2, No. 2 (in English). Sendai, Japan.

Effects of Temperature on the Flow and Fracture Characteristics of Molybdenum

by J. H. Bechtold

Tensile properties of annealed molybdenum were investigated from 1000° to -200°C. In the vicinity of room temperature a well-defined transition in tensile properties occurs. Reduction in area decreases from over 80 pct to 0 pct and, simultaneously, the yield strength increases about 60,000 psi.

MOLYBDENUM, tungsten, iron, and many other metals and alloys with the body-centered cubic and hexagonal close-packed crystal structures change from ductile to brittle behavior over some relatively narrow temperature range. The temperature at which this transition in ductility occurs depends on chemical composition, microstructure, and method of testing. When fine grained, completely recrystallized molybdenum of commercial purity is tested in uniaxial tension at a slow strain rate, the transition occurs at slightly below room temperature.¹ Iron² and tungsten³ tested under similar conditions become brittle at temperatures close to the boiling point of nitrogen, -195°C and at about 200°C, respectively. A sharp change in ductility is uncommon in metals with the face-centered cubic crystal structure, however, a relatively sharp transi-

tion in notched bar impact properties has been observed below room temperature in a face-centered cubic copper-antimony alloy.⁴

A transition from ductile to brittle behavior is usually explained by the concepts originally developed by Ludwik,⁵ and discussed and elaborated on by others including Orowan,⁶ Hollomon and Jaffe,⁷ and Gensamer.⁸ In brief, there are two aspects to strength, first the resistance to flow and second the resistance to fracture. Both are functions of temperature, strain, strain rate, stress system, composition, and microstructure. With decreased test temperature the flow stress required to initiate plastic deformation increases more rapidly than the fracture strength and brittle fracture occurs at that temperature where the yield strength equals or exceeds a brittle fracture strength.

This investigation was conducted to determine the effects of temperature, strain, and rate of straining on the flow and fracture strengths of molybdenum above, through, and below the ductile-to-brittle transition. Other variables were held constant during testing. This information is believed to show

J. H. BECHTOLD, Junior Member AIME, is associated with the Research Laboratories, Westinghouse Electric Corp., East Pittsburgh, Pa.

Discussion on this paper, TP 3644E, may be sent, 2 copies, to AIME by April 1, 1954. Manuscript, March 10, 1953; revision, July 1, 1953. New York Meeting, February 1954.

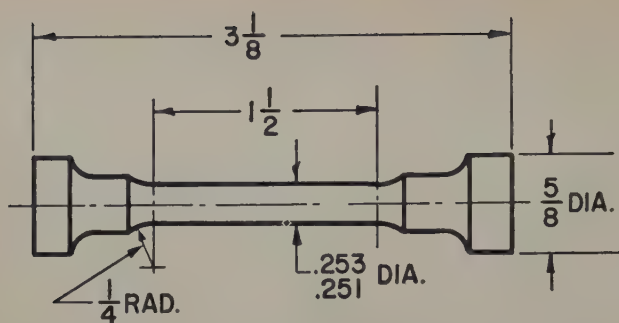


Fig. 1—Tensile specimen.

clearly the characteristics that lead to the brittleness in molybdenum at low temperatures and probably in other metals with a body-centered cubic crystal structure as well.

Material and Test Procedures

High purity molybdenum powder reduced from ammonium molybdate was hydrostatically pressed into a compact about 3x3x24 in. and sintered by a modification of the Hall-Ramage⁹ process to a density equivalent to 97 to 98 pct of the theoretical density of molybdenum. It was rolled to 5/8 in. diameter by a process designed to give a uniform, fine grain structure after a final recrystallization anneal.¹⁰ The chemical composition of this molybdenum sample, WNS-5000S, was as follows: 0.014 pct C, 0.0017 pct O₂, 0.0056 pct N₂, 0.001 to 0.10 pct Fe,* 0.0005 to 0.05 pct Si,* trace of Cu,* and trace of Mg.*

* Probable concentration range estimated from spectrographic analysis.

Tensile specimens with the dimensions shown in Fig. 1 were machined from the as-rolled bars and annealed after machining for 1 hr at 1150°C. This annealing treatment produced a uniform recrystallized grain structure of approximately 900 grains per sq mm (ASTM grain size No. 6 to 7). The tensile testing machine combined the features of a constant rate of extension and an autographically recorded load-elongation curve. For the low temperature tests the specimens were cooled in gaseous nitrogen by the method of Wessel and Olleman.¹¹ Above 400°C the specimens were protected from oxidation by a nitrogen atmosphere.

Room Temperature Tensile Properties of Annealed Molybdenum

The relation between stress and plastic strain for a number of metals is expressed by the following empirical equation:

$$\sigma = K\delta^n \quad [1]$$

where σ is the true stress, i.e., load divided by instantaneous area; δ , the natural strain, $\ln A_0/A$; K , a constant, the true stress at unit natural strain; and n , a second constant usually referred to as the work-hardening exponent. Preliminary tensile tests revealed that, with certain limitations, plastic flow in molybdenum follows this relation. The form of Eq. 1 indicates that a straight line of slope n should be obtained when true stress is plotted as a function of natural strain on logarithmic coordinates. The curve obtained by plotting true stress vs natural

strain on logarithmic coordinates is referred to here as the flow curve and Eq. 1 as the flow equation.

The room temperature (18°C) flow curve of molybdenum extended at a constant rate of 2.8×10^{-4} sec⁻¹ is shown in Fig. 2. At room temperature, annealed molybdenum has an upper and lower yield point and is in the low temperature portion of the ductile-to-brittle transition zone, but it still has considerable ductility and necks locally prior to fracture. All deviations from the flow equation observed over the entire temperature range studied are present at this temperature.

The initial, approximately horizontal, portion of the flow curve is due to the yield point phenomenon. At most temperatures the flow curve is a single straight line from the limit of the yield point elongation to the strain at which necking occurs. However, at room temperature and at other temperatures in the low temperature portion of the ductile-to-brittle transition zone the slope of the flow curve changes after about 0.04 strain. The reason for this

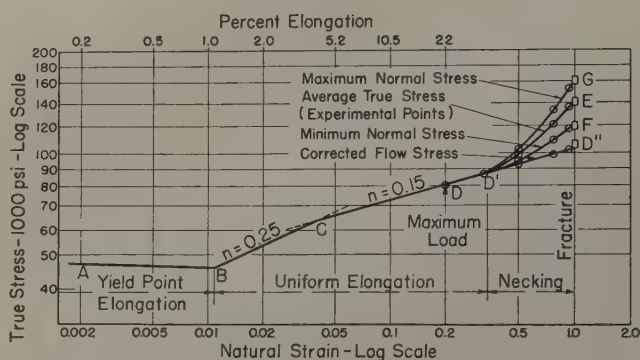


Fig. 2—Flow curve of annealed molybdenum at 17° to 18°C. Grain size, 900 grains per sq mm. Rate of extension, 2.8×10^{-4} sec⁻¹.

change in slope is unknown, but it has been observed for a large number of samples with different compositions and microstructures.

Once necking occurs, the flow curve diverges upward sharply as shown by the average stress in Fig. 2. To ascertain if this divergence in the flow curve is due to radial constraint from necking or to the basic flow characteristics of molybdenum, the distribution of stress over the cross section under the root of the neck of several specimens strained beyond the maximum load point was analyzed. The distribution of stress calculated by the equations of Davidenkov¹² for one specimen which was strained almost to fracture ($\delta = 1.0$) is shown in Fig. 3. The minimum normal stress is the real flow stress because the metal would deform at this stress and not the average normal stress in the absence of the neck. However, when the minimum normal stress is plotted as a function of strain, Fig. 2, it still diverges upward from the flow curve extrapolated from lower strains.

When a tensile specimen necks down, plastic deformation is restricted to the necked region, and the effective gage length decreases. Consequently, the strain rate increases if the rate of extension is held constant, as it was in these tests. If the radius of curvature of the contour of the neck is taken as the approximate gage length of the necked specimens, the actual rate of strain at the root of the neck can be estimated. Using data reported later in this

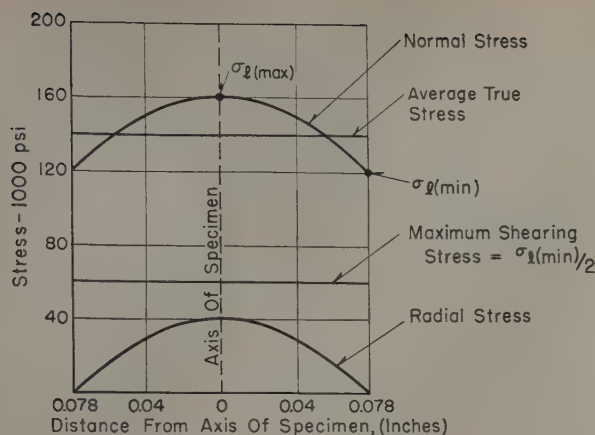


Fig. 3—Distribution of stress over the cross section under the root of the neck of a specimen strained to about $\delta=1.0$ at 17° to 18°C . Distribution of stress calculated by equations of Davidenkov.¹²

paper on the effects of strain rate on the yield strength of molybdenum, the minimum normal stresses were corrected to a strain rate of $2.8 \times 10^{-4} \text{ sec}^{-1}$. The corrected flow stresses fall quite well on an extrapolation of the flow curve before necking, indicating that molybdenum obeys the flow equation after necking and the divergence of the experimental points after necking is due to radial constraint and increased strain rate resulting from the formation of the neck.

As a result of these observations the flow curves at higher and lower temperatures were determined experimentally only to the strain at which necking occurred. The flow stresses at higher strains or at fracture were estimated by extrapolating the experimentally determined portion of the flow curve to the desired strain.

Effects of Temperature on Tensile Properties

Tensile specimens were pulled to fracture at several temperatures between -195°C and $+970^\circ\text{C}$ at a constant rate of extension of $2.8 \times 10^{-4} \text{ sec}^{-1}$. Test results are plotted as a function of test temperature in Fig. 4. To facilitate discussion, Fig. 4 is divided into four zones based in part on yield strength,[†]

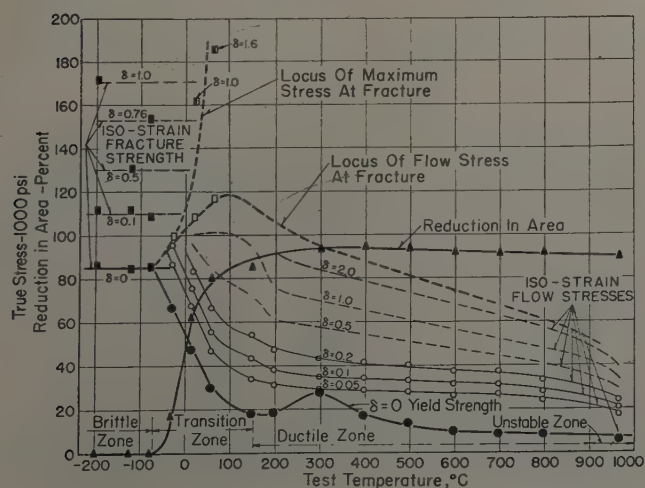


Fig. 4—Effects of temperature on the flow and fracture characteristics of annealed molybdenum. Grain size, 900 grains per sq mm. Rate of extension, $2.8 \times 10^{-4} \text{ sec}^{-1}$. Flow stresses above $\delta=0.20$ and flow stress at fracture above 60°C estimated from flow curves in Fig. 5.

ductility[‡] and fracture characteristics. The first, or

[†] The yield strength is defined herein as the stress at which the engineering load-elongation curve deviates from linearity, i.e., the proportional limit.

[‡] The reduction in area at fracture is taken as the measure of ductility.

"brittle zone," extends from the lowest test temperature to about -75°C and is characterized by the absence of measurable ductility and bright transgranular fractures. The second, or "transition zone," extends from -75°C to about $+150^\circ\text{C}$ and is characterized by a rapid increase in ductility and a correspondingly rapid decrease in the yield strength with increased test temperature. In this zone there is a change from bright, brittle, transgranular fractures at the lower temperatures to dull fibrous fractures at the higher temperatures. The third or "ductile zone" extends from about 150° to about 900°C and is characterized by excellent ductility, a yield strength essentially independent of temperature, except when affected by yield point phenomena, and a dull fibrous fracture. The fourth, or "unstable zone" occurs above about 900°C and is due to thermal instability, probably recovery, or partial recrystallization during testing.¹⁰

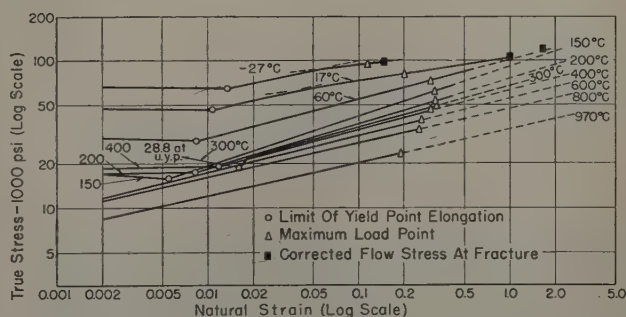


Fig. 5—Flow curves of annealed molybdenum at several test temperatures. Grain size, 900 grains per sq mm. Rate of extension, $2.8 \times 10^{-4} \text{ sec}^{-1}$.

Yielding; The most pronounced effect of temperature on yield strength occurs in the transition zone. The increase of about 65,000 psi between $+150^\circ\text{C}$ and -75°C is exceedingly large for a metal with a melting point of 2620°C . Presumably the yield strength would continue to increase at lower temperatures but fracture precedes yielding. The intersection of the yield strength curve with the brittle fracture strength curve divides the transition and brittle zones. In the ductile zone, the yield strength decreases gradually with increasing test temperature, except between 200° and 400°C where a maximum associated with a very pronounced upper and lower yield point occurs.

Flow curves for several test temperatures are shown in Fig. 5. These curves show that the yield point phenomenon occurs at temperatures below about 600°C and is most prominent at about 300°C . The curves are linear from the limit of the yield point elongation to the maximum load point except at the two lowest test temperatures where the slope changes after a strain of about 0.04.

Flow stresses at several strains are replotted as a function of temperature as iso-strain flow curves in Fig. 4. At small strains the iso-strain flow curves roughly parallel the yield strength curve. However, the maximum in the yield stress curve at about 300°C is not observed once the yield point strain is exceeded. The slope of the iso-strain flow curves

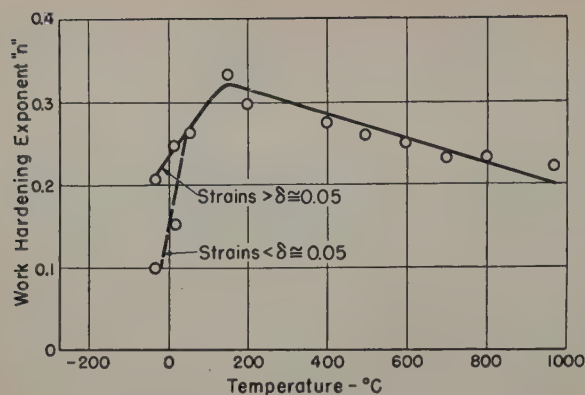


Fig. 6—Effect of temperature on the work hardening exponent of molybdenum.

is greater at higher strains due to an increase in the rate of work hardening with decreased test temperature. The iso-strain flow curves for large strains decrease quite rapidly above 800° to 900°C due to thermal softening or partial recrystallization during test.

Strain Hardening: The slopes of the flow curves in Fig. 5, which are the work hardening exponent n in Eq. 1 are plotted as a function of test temperature in Fig. 6 and are a maximum at 150°C. The rate of work hardening, i.e., the rate of change of stress with strain, obtained by differentiating the flow equation is as follows:

$$d\sigma/d\delta = n\sigma/\delta. \quad [2]$$



Fig. 8—Microstructure normal to the fracture in specimen tested at -196°C. No measurable ductility. Electrolytic polish. Etched in alkaline $K_3Fe(CN)_6$ solution. X100. Area reduced approximately 75 pct for reproduction.

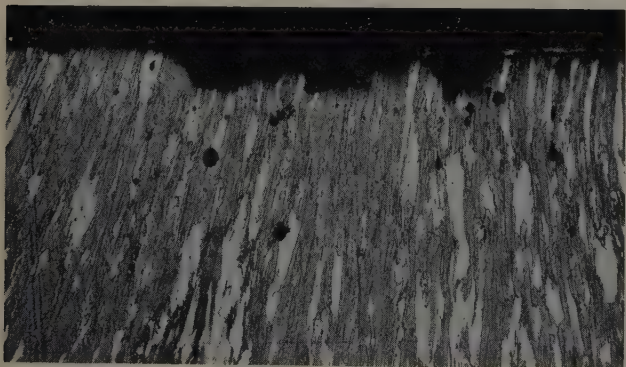


Fig. 10—Microstructure normal to the fracture in specimen tested at 60°C. 80 pct reduction in area at fracture. Electrolytic polish. Etched in alkaline $K_3Fe(CN)_6$ solution. X100. Area reduced approximately 75 pct for reproduction.

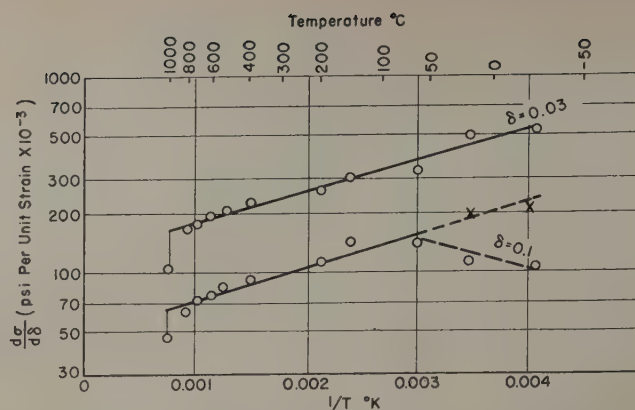


Fig. 7—Effect of temperature on the rate of work hardening of molybdenum at strains of $\delta = 0.03$ and $\delta = 0.10$.

When the logarithm of the rate of work hardening is plotted as a function of the reciprocal of the absolute temperature, Fig. 7, straight lines are obtained at a strain of 0.03 and above 60°C at a strain of 0.1, indicating that there probably is a unique relation between temperature and rate of work hardening. Below 60°C the experimental points for 0.1 strain do not fall on the 0.1 strain curve because of the change in slope in the flow curves at low temperatures as discussed previously. These results are interpreted to mean that there is no significant difference in the mechanism of strain hardening in the ductile and transition zones at small strains.

Fracture: In the brittle zone and in the lower temperature portion of the transition zone, the frac-

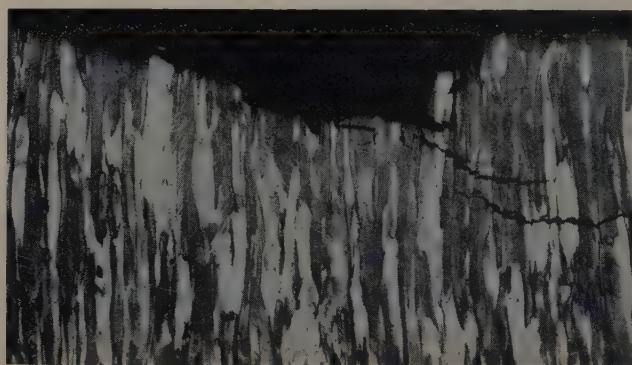


Fig. 9—Microstructure normal to the fracture in specimen tested at 17°C. 62 pct reduction in area at fracture. Electrolytic polish. Etched in alkaline $K_3Fe(CN)_6$ solution. X100. Area reduced approximately 75 pct for reproduction.

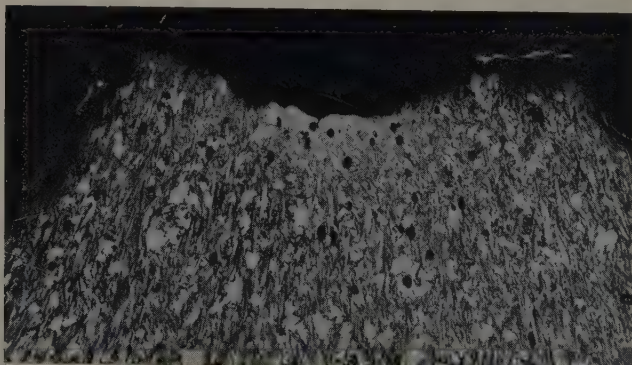


Fig. 11—Microstructure normal to the fracture in specimen tested at 400°C. 94 pct reduction in area at fracture. Electrolytic polish. Etched in alkaline $K_3Fe(CN)_6$ solution. X100. Area reduced approximately 75 pct for reproduction.

tures have a bright crystalline appearance, although fracture in the transition zone may be preceded by considerable plastic deformation. In the high temperature portion of the transition zone and in the ductile zone the fracture surfaces are dull and fibrous. Photographs of the microstructure normal to the fracture in specimens tested at -195°C (brittle zone), at 17° and 60°C (transition zone), and at 400°C (ductile zone), are shown in Figs. 8, 9, 10, and 11, respectively. At -195°C and $+17^{\circ}\text{C}$ the fractures are entirely of the bright brittle type. The fracture occurs suddenly and the actual break is surrounded by numerous cracks. The fracture at 60°C is intermediate between the brittle and ductile types, the fracture at the center being of the dull fibrous type and nearer the surface the bright brittle type. Above 60°C the fracture is entirely of the dull fibrous type. The dull fibrous type of fracture appears to proceed slowly, starting at the center of the specimen, and it was impossible to determine when fracture first started. Both the bright brittle and dull fibrous types of fracture are transgranular; however, the bright brittle type can be better classified as a cleavage type of fracture whereas the dull fibrous fracture is probably more adequately described as a shearing type of fracture.

The stress at fracture in the brittle zone was about 85,000 psi and essentially independent of test temperature as shown in Fig. 4. The effect of strain on the fracture strength in the brittle zone cannot be determined directly, since fracture precedes plastic strain. However, an estimate was obtained by prestraining specimens at room temperature and then fracturing in the brittle zone. The brittle fracture strength after various amounts of prestrain is shown by the iso-strain brittle fracture curves in Fig. 4. The curves indicate that the brittle fracture strength of molybdenum increases with strain. Only the 0 and the 0.1 strain brittle fracture curves were determined by more than one test and the curves at higher strain levels may be inaccurate. Also necking occurred during prestraining to the higher strain levels and the distribution of stress at the fracture was probably not uniform. It has been shown previously¹ that notched tensile specimens tested in the brittle zone fracture when the maximum normal stress calculated from elasticity theory equals the brittle fracture strength of unnotched specimens. It was assumed that the necks act as notches and the maximum normal stress was calculated by the method of Neuber,¹³ and taken as the correct brittle fracture strength. The correction is quite small and the qualitative picture of the effect of strain on the brittle fracture strength is the same whether the correction is used or not.

The brittle fracture strength in the brittle zone and the maximum normal stress at fracture in the lower portion of the transition zone are about the same when compared after equivalent amounts of strain. Apparently, the Ludwik hypothesis, that fracture occurs when the maximum normal stress exceeds a brittle fracture strength, holds in these regions. However, at higher temperatures where the fracture is of the dull fibrous instead of the bright crystalline type, it is unlikely that fracture is governed by a normal stress fracture strength. At least it is not the same fracture strength as that measured in the brittle zone.

In the brittle zone strain markings are always found in a few grains in the vicinity of the fracture although fracture occurs before measurable elonga-



Fig. 12—Deformation markings resembling "Neumann bands" in the vicinity of the fracture in specimen fractured at -196°C . Electrolytic polish. Etched in alkaline $\text{K}_3\text{Fe}(\text{CN})_6$ solution. X500. Area reduced approximately 50 pct for reproduction.

tion. An example of these strain markings in a specimen tested at -195°C is shown in Fig. 12. The markings are different from slip markings observed at higher temperatures and are quite reminiscent of the mechanical twins (Neumann bands) found in ingot iron deformed at low temperatures. Bruckner¹¹ has postulated that brittle fracture in ingot iron may be nucleated by mechanical twinning. However, it was impossible to ascertain if the strain markings in molybdenum are mechanical twins and, if they are, whether they are the cause or the result of fracture. It is possible that twinning provides the microstress concentrations (Griffith cracks) necessary for brittle fracture at a stress well below the theoretical cleavage strength of molybdenum.

Effects of Strain Rate: The temperature of the ductile-to-brittle transition is not a characteristic temperature but depends on the method of testing, e.g., the strain rate and the contour of the specimen. The effect of strain rate was studied to illustrate how this variable affects the ductile to brittle transi-

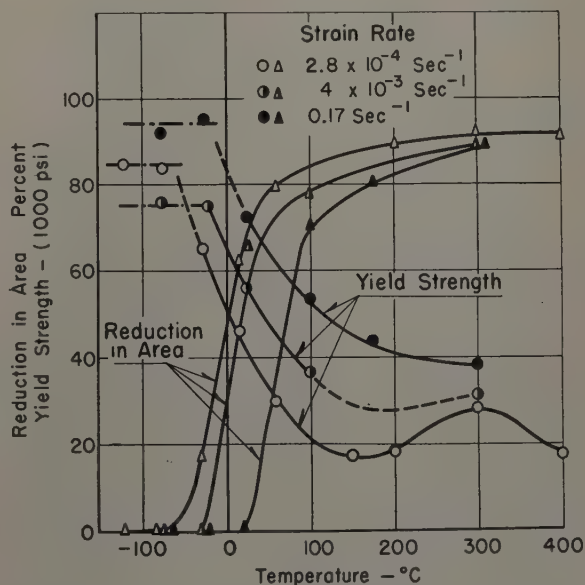


Fig. 13—Effects of temperature and strain rate on the ductility, yield strength, and brittle fracture strength of annealed molybdenum. Grain size, 900 grains per sq mm.

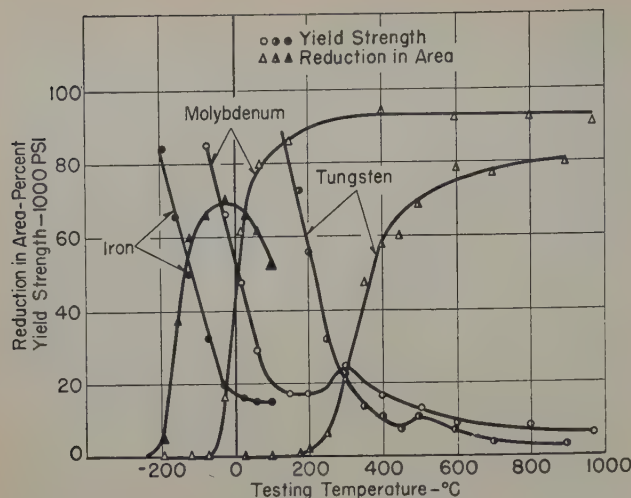


Fig. 14—Effect of temperature on tensile properties of annealed ingot iron,² molybdenum, and tungsten.³

tion temperature and the flow characteristics in the transition zone. Reduction in area at fracture, yield strength, and brittle fracture strength are plotted as a function of temperature for three different strain rates in Fig. 13. An increase in the strain rate raises the transition temperature zone primarily through an increase in the yield strength.

Discussion

The usefulness of molybdenum for applications where mechanical properties are important is fairly well restricted to the ductile zone since at lower temperatures the metal is brittle, or approaching brittle behavior, and at higher temperatures it is structurally unstable. The exact temperature limits of the ductile zone are not completely defined by any one type of test but depend on the conditions under which the metal is loaded. To increase the utility of molybdenum as a structural material, it is desirable to extend the ductile zone to higher and lower temperatures. It is not too difficult to raise the high temperature limit of the ductile zone since this merely requires raising the recrystallization temperature, which can be done quite readily by solid solution alloying.¹⁵ To shift the low temperature limit of the ductile zone to a lower temperature, presents a more formidable problem.

The conditions which lead to brittle behavior in molybdenum are believed to be exactly the same as those which cause low temperature brittleness in iron, steel, and other metals with the body-centered cubic crystal structure. The striking similarity in the effect of temperature on the tensile properties of iron, molybdenum, and tungsten is shown in Fig. 14. Not only does each of these metals exhibit a sharp transition in ductility but each exhibits a rapid increase in yield strength in the transition zone. The fracture strength below the transition zone and the yield strength above the transition zone are about the same when the impurities and microstructures are similar. It should be possible to apply, qualitatively at least, the extensive knowledge of the effects of composition, microstructure, and testing method on the ductile-to-brittle transition of iron and ferritic iron alloys to predict the effects of these variables on the behavior of molybdenum.

From the literature on the low temperature brittleness of iron and ferritic alloys two things are evident. First, although numerous theories have been advanced to explain the ductile-to-brittle transition, the basic reason for the phenomenon has not been determined. Second, although it is possible to lower the temperature of the transition temperature somewhat by removal of impurities and by alloying, low temperature brittleness has never been overcome except by the addition of enough alloying element to change the crystal structure from body-centered cubic to face-centered cubic. Since molybdenum, unlike iron, is body-centered cubic at all temperatures, it is very unlikely that this method of lowering the ductile-to-brittle transition temperature is possible.

Basically, the problem is not one of ductility but of resistance to deformation, specifically the rapid increase in the yield strength with decreasing testing temperature and brittle fracture at a low stress relative to the theoretical strength of the crystal lattice. Particularly important is whether this increase in yield strength is caused by traces of interstitial solute atoms or is a basic characteristic of crystallographic slip in molybdenum. If the increase in yield strength in the transition zone is related to impurities, it is reasonable to expect that the activation energy associated with yielding would be re-

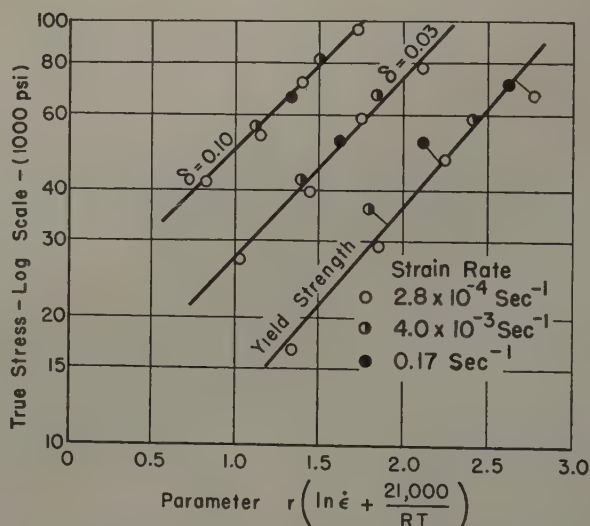


Fig. 15—Demonstration of equivalence of temperature and strain rate for molybdenum tested in the transition range.

lated to the activation energy for diffusion of the element causing the increase in yield strength.

Zener and Hollomon¹⁶ have shown for steel tested at low temperatures that stress is related to temperature T and strain rate $\dot{\epsilon}$ as follows:

$$\sigma = \sigma_0 [(\dot{\epsilon} e^{Q/RT})^r, \delta'] \quad [3]$$

where δ' is a function representing the condition of the metal, i.e., the amount of strain hardening, grain size, etc.; Q , a heat of activation; σ_0 , a constant; and r another constant. At a constant strain rate and condition of the metal, Eq. 3 implies the following relation between stress and temperature:

$$\sigma = \sigma_0' e^{q/RT} \quad [4]$$

where

$$q = Qr. \quad [5]$$

Table I. Activation Energy for Flow in Ductile-to-Brittle Transition Zone

Condition of Metal, Natural Strain	q , Cal per Gram Mol	τ	Heat of Activation Q , Cal per Gram Mol
0.0	1700	0.08	21,000
0.03	1300	0.06	21,000
0.10	1100	0.05	22,000

At constant temperature and condition of the metal, Eq. 3 implies the following relation between stress and strain rate:

$$\sigma = \sigma_0 \epsilon^{\tau} \quad [6]$$

These equations apply for molybdenum in the transition zone, -75° to $+150^{\circ}\text{C}$, and values of q associated with the yield strength and the 0.03 and 0.10 strain flow stresses are recorded in Table I. The exponent τ was determined from strain rate data at 24°C and also recorded in Table I. The heat of activation Q determined by Eq. 5 is about 21,000 cal per mol.

Originally it was hoped that the activation energy calculated in this manner could be correlated with the activation energy for the diffusion of some interstitial impurity such as carbon, nitrogen, or hydrogen, and thereby predict if the rapid increase in strength in the transition zone might be related to one of these impurity elements. Unfortunately, there are no data available in the literature on the activation energy for the diffusion of these impurities in molybdenum. However, the activation energy is of the magnitude of that expected for diffusion of interstitial impurities in molybdenum. The activation energy associated with flow in molybdenum is somewhat higher than the value of 10,000 to 14,000 cal per gram mol obtained by Zener and Hollomon for steel.¹⁶ However, it is considerably lower than the 37,800 cal per gram mol obtained by Sherby and Dorn¹⁷ for slip in aluminum in the temperature range 150° to 250°C .

The equivalence of temperature and strain rate on the flow strength of molybdenum is demonstrated in Fig. 15 where the logarithm of the yield strength and the flow stresses at 0.03 and 0.10 strain are plotted vs the parameter, $\tau[\ln \dot{\epsilon} + 21,000/RT]$ for all tests made in the transition zone.

Summary

The flow and fracture characteristics of a sample of annealed molybdenum were studied between -195°C and $+970^{\circ}\text{C}$ by tension tests at a constant rate of extension of $2.8 \times 10^{-4} \text{ sec}^{-1}$. This temperature range can be divided into four zones; a brittle zone, a transition zone, a ductile zone, and an unstable zone.

The "brittle zone" occurs below -75°C and is characterized by the lack of measurable ductility and bright transgranular cleavage type fractures.

The "transition zone" extends from about -75°C to $+150^{\circ}\text{C}$ and is characterized by a rapid increase in yield strength and a simultaneous decrease in ductility with decreased test temperature and a change from bright transgranular fracture to a dull fibrous fracture.

The "ductile zone" extends from about 150°C to about 900°C and is characterized by low yield strength, excellent ductility and a dull, fibrous fracture.

The "unstable zone" extends above 900°C and is due to thermal instability of the microstructure developed during test.

The ductile-to-brittle transition in molybdenum is caused by a rapid increase of the yield strength with decreased test temperature through the transition zone and a brittle fracture at a stress well below the theoretical strength of the crystal lattice. The activation energy associated with the increase in yield strength is about 21,000 cal per gram mol.

Strain markings resembling mechanical twins were observed in the brittle zone and they may be related to the brittle fracture strength.

The equivalence of temperature and strain rate in the transition zone through the Zener-Hollomon parameter, $(\ln \dot{\epsilon} + Q/RT)$, is demonstrated.

Acknowledgments

The author wishes to acknowledge his indebtedness to the members of the Metallurgical and Ceramic Dept. of the Westinghouse Research Laboratories and particularly to Howard Scott for many helpful comments and criticisms. Special appreciation is due J. W. Marden, retired, formerly manager, Molybdenum Development Div., Bloomfield Plant, Westinghouse Electric Corp.

References

- ¹ J. H. Bechtold and Howard Scott: Some Mechanical Properties of Arc-Cast and Powder Metallurgy Molybdenum. *Journal Electrochemical Soc.* (1951) **98**, No. 12, p. 495.
- ² G. W. Geil and N. L. Carwile: Tensile Properties of Ingot Iron at Low Temperatures. *Journal of Research, National Bur. of Standards* (1950) **45**, pp. 129-137.
- ³ P. Shewmon and J. H. Bechtold: Effects of Temperature on the Flow and Fracture Characteristics of Tungsten. To be published in *Trans. ASM* (1954).
- ⁴ D. McLean: The Embrittlement of Copper-Antimony Alloys at Low Temperatures. *Journal Inst. Metals* (1952) **81**, pp. 121-123.
- ⁵ P. Ludwik: *Elements der Technologischen Mechanik*. (1909) Berlin. J. Springer.
- ⁶ E. Orowan: Fracture and Strength of Solids. *Reports on Progress in Physics* (1948-1949) **12**, pp. 185-230.
- ⁷ J. H. Hollomon and L. D. Jaffe: *Ferrous Metallurgical Design*. (1947) pp. 76-121. New York. John Wiley and Sons.
- ⁸ M. Gensamer: Strength and Ductility. *Trans. ASM* (1946) **36**, pp. 36-60.
- ⁹ R. D. Hall and J. H. Ramage: Metal Powder Consolidation. U. S. Patent 2,431,690, December 2, 1947.
- ¹⁰ J. H. Bechtold: Recrystallization Data Applied to Control of the Mechanical Properties of Molybdenum. To be published in *Trans. ASM* (1954).
- ¹¹ E. T. Wessel and R. D. Olleman: Apparatus for Tensile Testing at Sub-Atmospheric Temperature. *ASTM Bull. No. 187* (January 1953) pp. 56-60.
- ¹² N. N. Davidenkov and N. I. Spiridonova: Mechanical Methods of Testing. *ASTM* (1946) **49**, pp. 1147-1156.
- ¹³ H. Neuber: Theory of Notch Stresses. (1946) Ann Arbor, Mich. J. W. Edwards.
- ¹⁴ W. H. Brucker: Micromechanism of Fracture in the Tension Impact Test. *Welding Journal* (1950) **29**, pp. 467-S-476-S.
- ¹⁵ J. L. Ham, F. P. Bens, and G. A. Timmons: Arc-Cast Molybdenum Base Alloys. Quarterly Report to ONR covering period May 1 to July 31, 1951, Contract N8onr-787000, Climax Molybdenum Co.
- ¹⁶ C. Zener and J. H. Hollomon: Effect of Strain Rate on the Plastic Flow of Steels. *Journal of Applied Physics* (1944) **15**, pp. 22-32.
- ¹⁷ O. D. Sherby and J. E. Dorn: Creep Correlations in Alpha-Solid Solutions of Aluminum. *Trans. AIME* (1952) **194**, p. 959; *JOURNAL OF METALS* (September 1952).

Formation of Sigma Phase in the Mn-Mo System

by B. F. Decker, R. M. Waterstrat, and J. S. Kasper

THE existence of σ phase in the Mn-Mo system was discovered in this laboratory several years ago,¹ but neither the conditions of its formation nor its composition were known, and preliminary attempts to reproduce the phase were unsuccessful. We wish now to specify the information appropriate to σ phase formation on the basis of experiments performed since that time.

The starting materials were in every case electrolytic manganese and high purity molybdenum. Two methods of preparation were employed: 1—arc-melting varying combinations of the elements in an inert atmosphere and subsequent heat treating, and 2—sintering compressed mixtures of finely divided powders of the elements. In the latter method, the powders were first passed through 200 mesh screen and then compressed into cylinders of $\frac{3}{8}$ in. diameter and $\frac{1}{2}$ in. length, which were sintered at elevated temperatures in an atmosphere of dry hydrogen. For some samples, the sintering temperature was 1200°C (for 1 hr), and these were then heat-

Table I. Results Obtained from Samples Produced by Sintering Compressed Mixtures

Sam- ple	Treatment	Wt Pct Mn	Wt Pct Mo	At. Pct Mn	X-Ray Pattern
1	Sintered 1125°C 3 hr	53.0	46.7	66.5	σ + some α -Mn
2	Sintered 1125°C 3 hr	49.8	49.6	63.7	σ + trace α -Mn†
3	Sintered 1125°C 3 hr	43.4	56.5	57.3	σ + some Mo
4	Sintered 1125°C 3 hr	33.1	66.8	46.4	σ + some Mo
5	Sintered 1200°C 1 hr				
	+ 1125°C 24 hr	80*	20*	87.5*	α -Mn + trace σ
6	Sintered 1200°C 1 hr				
	+ 1125°C 24 hr	90*	10*	94.0*	α -Mn

* Nominal starting composition.

† Only evidence for α -Mn is one very weak line.

treated at lower temperatures for times up to 24 hr. Eventually it was found, for the proper composition, that essentially pure σ phase could be produced by sintering at 1125°C for 3 hr. Quenching to room temperature was effected by means of a stream of cold, dry hydrogen in a water-cooled chamber.

The arc-melting procedure was found to be unsatisfactory after an investigation of many samples at different compositions and temperatures. Large quantities of manganese were vaporized during melting and none of the products were homogeneous or contained extended regions of pure σ phase. Nonetheless, these experiments established that no σ formation occurs in the Mn-Mo system below 1115°C, and indicated, at least roughly, the composition range of interest for further exploration.

The more definite results obtained from samples produced by the second method are given in Table I.

B. F. DECKER, R. M. WATERSTRAT, and J. S. KASPER are associated with the Metallurgy Research Dept., Research Laboratory, General Electric Co., Schenectady.

TN 196E. Manuscript, Aug. 24, 1953.

Table II. X-ray Powder Pattern for Mn-Mo Sigma (64 Atomic Pct Mn). Crystal system, tetragonal $a_0 = 9.10$, $c_0 = 4.74\text{\AA}$. Cr K α radiation.

Mn-Mo σ			Fe-Mo σ^3	
hkl	d	I^*	d	I^*
311	2.463	m	2.46	w
002	2.368	m	2.35	mw
410	2.205	s	2.21	s
330	2.144	ms	2.13	m
202	2.097	ms	2.08	m
212	2.045	s	2.04	ms
411	2.000	vs	1.99	s
331	1.952	s	1.93	m
222	1.907	mw	1.90	w
312	1.829	mw+	1.82	w
431, 501	1.697	vvw		
511	1.672	vvw		
432	1.444	mw	1.44	vw
611, 512	1.426	mw	1.43	mw
313	1.385	vw		
621, 522	1.377	ms	1.37	m
541	1.362	vvw		
532, 631	1.304	s	1.30	ms
413, 550, 710	1.286	vs		
602	1.279	m		
333	1.272	ms	1.28	s
612	1.267	m		
701, 720	1.253	s		
551, 711	1.244	m	1.246	mw
622	1.232	mw		
542, 641	1.221	mw	1.220	m
721	1.211	ms		
433, 503	1.195	vvw	1.205	w
004	1.187	s	1.177	m

* w, weak; mw, medium weak; vw, very weak; vvw, very, very weak; m, medium; ms, medium strong; s, strong; vs, very strong.

A portion of sample 2 heated for 16 hr at 1000°C in a Vycor tube transformed to molybdenum plus unidentified phases of complex X-ray pattern.

From these few results it appears that the region of σ phase is quite narrow in composition. It is of interest that the composition is such as to make for difficulties in correlating this structure on an electron atom basis with other σ structures of iron, cobalt, and nickel. In that respect Mn-Mo shows the same anomaly as Mn-Cr and Mn-V systems.² A second feature is that in common with the two other known molybdenum σ 's (Fe-Mo and Co-Mo), Mn-Mo σ exists only at elevated temperatures.

The X-ray powder pattern of the pure σ phase of Mn-Mo is given in Table II. It agrees well with the patterns established for other σ structures, especially with that for Fe-Mo σ as given by Goldschmidt.³ An attempt is being made to establish whether an ordering of the respective atoms occurs and such information will be reported in a future publication.

Acknowledgment

The authors acknowledge gratefully the assistance of Mrs. J. R. Belanger in some portions of this work.

References

- 1 J. S. Kasper, B. F. Decker, and J. R. Belanger: *Journal of Applied Physics* (1951) **22**, p. 361.
- 2 A. H. Sully: *Journal Inst. Metals* (1951) **80**, p. 173.
- 3 H. J. Goldschmidt: *Research* (1949) **2**, p. 343.

Bending of Molybdenum Single Crystals

by K. T. Aust, R. Maddin, and N. K. Chen

Lattice rotations occurring on the tension and compression sides during the bending of molybdenum single crystals at room temperature were followed in detail. Observations were also made concerning crystallite rotations and slip traces. The results indicated the participation of $\{110\}$ as slip planes and the $\langle 111 \rangle$ as slip directions. Crystallite fragmentation during bending was also noted.

SEVERAL investigations have been conducted on pure bending of face-centered cubic metals.¹⁻³ Structural changes as a result of "bend-gliding," and the importance of bending and constraints during conditions of axial stressing, have been noted.^{4,5} It was evident that the mechanism by which the bending deformation occurs is more complex than the case of simple shear. Studies of the bending of body-centered cubic metals from the aspect of the crystallographic mechanism appear to be lacking. Molybdenum single crystals therefore were subjected to deformation by bending in order to determine the reaction of the body-centered cubic lattice to bending stresses.

It might be expected for the bending of single crystals that lattice rotation as represented by the axis of compression would proceed toward the pole of the active slip plane and that rotation of the tensile stress axis should indicate the slip direction.¹ It was believed therefore that a study of the tension and compression sides of bent molybdenum single crystals should give data concerning the operative slip system. Specific problems which are pertinent to the overall picture of plastic deformation were also investigated, e.g., whether the constraints offered by pure bending give rise to the deformation band, and also the nature of the asterism occurring on the tension and compression sides during the stages of deformation.

Experimental Procedure

Eight single crystal specimens were grown from sintered molybdenum rods $\frac{1}{8}$ in. diameter using the method described previously.⁶ The purity of this material was reported as 99.9 pct as described elsewhere.⁷ The specimens were $\frac{1}{8}$ to $1/10$ in. in diameter x 7 in. long, with single crystals approximately 1 to 2 in. in length occupying the entire center sections of each specimen. The specimens were electrolytically polished using an electrolyte of 300 cc



Fig. 1—Bending apparatus assembled at X-ray machine. A, B—Stationary bearings. C—Single crystal specimen. D—Movable steel plate. E—Load cell. F—Deflection cell.

methyl alcohol, 60 cc H_2SO_4 , 130 cc HCl , and a current density of 4 amp per sq in.

Each specimen was then loaded in a bending apparatus similar to that used by Yen and Hibbard,¹ as shown in Fig. 1. The load was applied by means of a spring and screw arrangement through four ball-bearing surfaces set 1.5 in. apart. Either the inner two bearings or the outer two (A, B, Fig. 1) were attached to a movable steel plate (D) through which the load was transmitted. Since the apparatus was mounted on a track of the X-ray apparatus, the tension or compression side of the specimen could

K. T. AUST, Junior Member AIME, is Research Associate, Metallurgy Section, R. MADDIN, Member AIME, is Associate Professor, and N. K. CHEN, Junior Member AIME, is Assistant Professor, Dept. of Metallurgy, The Johns Hopkins University, Baltimore.

Discussion on this paper, TP 3623E, may be sent, 2 copies, to AIME by April 1, 1954. Manuscript, May 13, 1953. New York Meeting, February 1954.

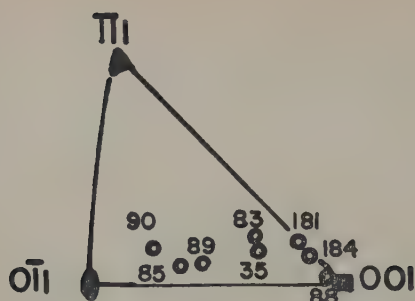


Fig. 2—Orientations of crystals investigated.

arrangement, since it was only necessary to keep the film to specimen distance constant without any realignment of the specimen. However, determination of the lattice rotations in the opposite sides of the specimens could not be obtained with the same accuracy, particularly where the total rotation was small, since only the initial and final orientations were determined and realignment of the specimen was required after unloading. The nature of the asterism occurring on the tension and compression sides of the bent specimens was noted from the X-ray photographs.

The eight specimens, M-35, M-83, M-85, M-88, M-89, M-90, M-181, and M-184 were bent through

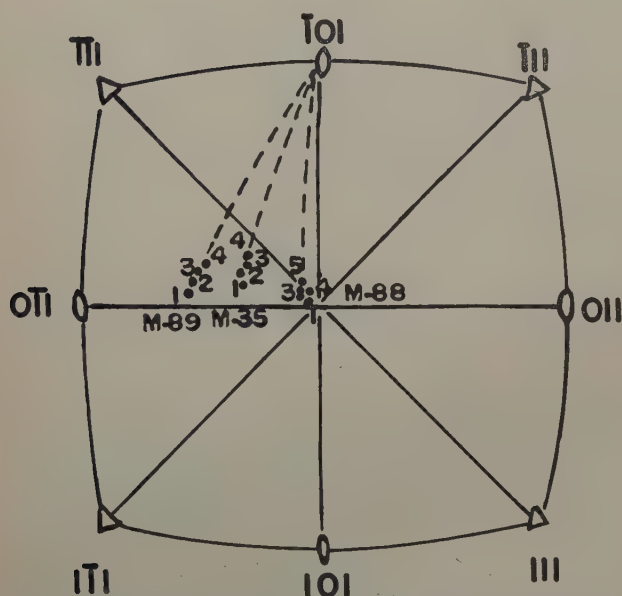


Fig. 3—Projection of M-35, M-88, and M-89 showing specimen axis rotations on the compression side.

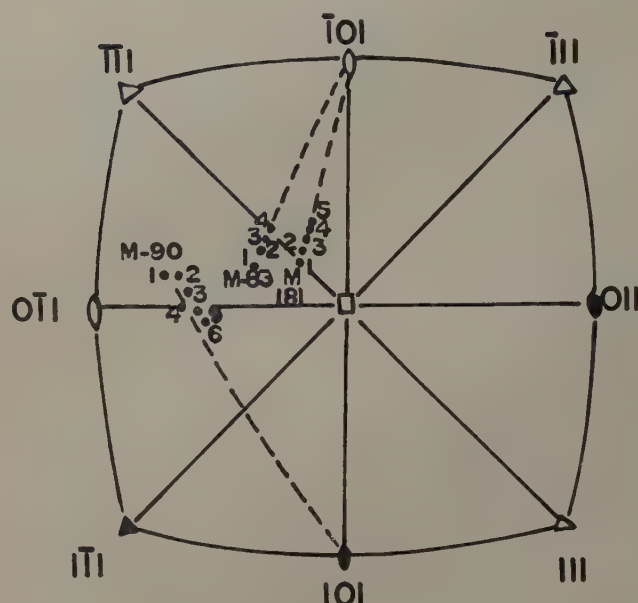


Fig. 4—Projection of M-83, M-90, and M-181 showing specimen axis rotations on the compression side.

be set up for exposure by interchanging the bearings. For example, when the inner two bearings were attached to the movable plate, the specimen was set up for exposure on the tension side, and when the outer two bearings were attached to the movable plate the specimen was exposed to the X-rays on the compression side.

The load was measured by a calibrated clip gage (*E* in Fig. 1), using SR-4 type A-1 strain gages; the deflection was measured similarly using a calibrated clip gage (*F*). Load and deflection were measured by employing strain indicators. The load could be measured to a minimum of 0.0005 lb and the deflection to 0.0001 in.

X-ray back-reflection Laue photographs of the same position on each specimen were taken before bending, and at successive stages during the bending with the load applied but not increasing. The lattice rotations were then plotted in a standard stereographic projection from the photographs. The entire course of deformation was followed in detail on the compression side for specimens M-35, M-83, M-88, M-90, and M-181, and on the tension side for specimens M-85, M-89, and M-184. Considerable accuracy could be attained in the determination of these lattice rotations with the present experimental

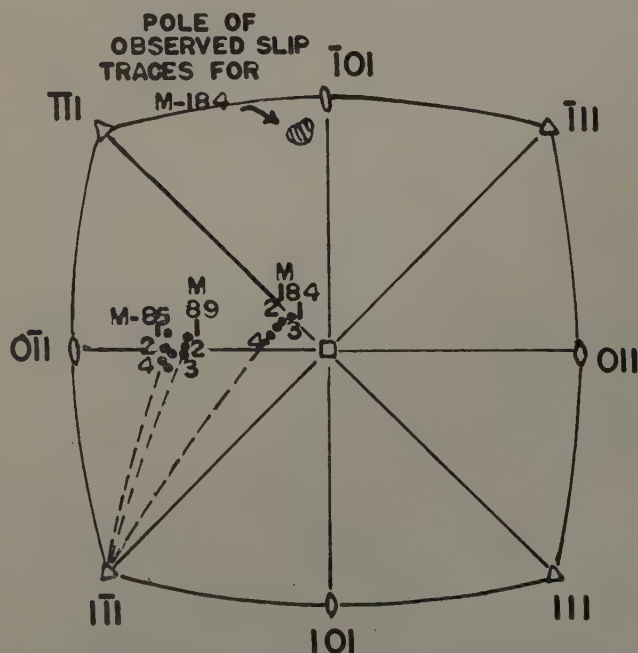


Fig. 5—Projection of M-85, M-89, and M-184 showing specimen axis rotation on the tension side and pole of observed slip traces for M-184.

Results and Discussion

Lattice Rotation: The specimen axis orientations for the initially unstrained crystals are shown in Fig. 2 in a standard cubic stereographic projection. The specimen axis or lattice rotations which occurred on the compression side during the bending tests are shown in Figs. 3 and 4. It is evident from Fig. 3 that specimens M-35 and M-89 showed a definite rotation toward the $(\bar{1}01)$ pole although the evidence for specimen M-88 is only slight. In Fig. 4 the specimen axis rotation for specimens M-83 and M-181 was again clearly toward the $(\bar{1}01)$ pole. However, some scatter in the rotations was obtained for specimen M-90, although there is an apparent rotation toward the (101) pole.

The specimen axis shift for the tension side of specimens M-85, M-89, and M-184 after increased amounts of bending are shown in Fig. 5. The rotations were clearly toward the $[1\bar{1}1]$ direction for each of these three specimens. It should be noted that the $[1\bar{1}1]$ direction is contained in the $(\bar{1}01)$ plane.

The results presented in Figs. 3 and 4 have shown that the lattice rotations on the compression side of bent single crystals of molybdenum were always toward a $\{110\}$ pole. Also, rotations on the tension side, as illustrated in Fig. 5, were toward the $[1\bar{1}1]$ direction. It is well established that for a single crystal loaded in compression, the lattice rotation takes place in such a manner that the slip plane approaches the compression plane; for tensile loading the slip direction approaches the stress or tension axis.⁸ It would also be expected from the bending work of Yen and Hibbard¹ that rotation of the lattice on the compression side would proceed toward the pole of the active slip plane and that rotation on the tension side should indicate the direction of glide. The present results, therefore, appear to indicate that the slip planes are of the type $\{110\}$ and the slip direction $\langle 111 \rangle$ for molybdenum single

Fig. 6—Laue photograms of compression side of M-181 (left) and tension side of M-85 (right) after increasing amounts of deflection from 0° to 12° and 16° , respectively.

the following final angles: 13° , 10° , 16° , 10° , 16° , 11° , 12° , and 15° , respectively. Micrographic examination was carried out to determine the characteristics of the deformation markings appearing on the surface of the electropolished specimens after bending, and also to determine the pole of the slip plane. Measurements on those specimens where the slip lines could be observed satisfactorily were made at each 15° for several positions around the specimen axis on the metallograph. An indicator was attached to the specimen along a reference mark that was also used for the X-ray determination of the orientation. The angle of rotation was measured on a protractor attached to the metallograph stage as noted by the indicator. The angle between the specimen axis and the slip marking was then determined at a magnification of X400. The orientation of the specimens after deformation was always used in correlating slip traces measured on the metallograph with the orientation determined from X-ray.

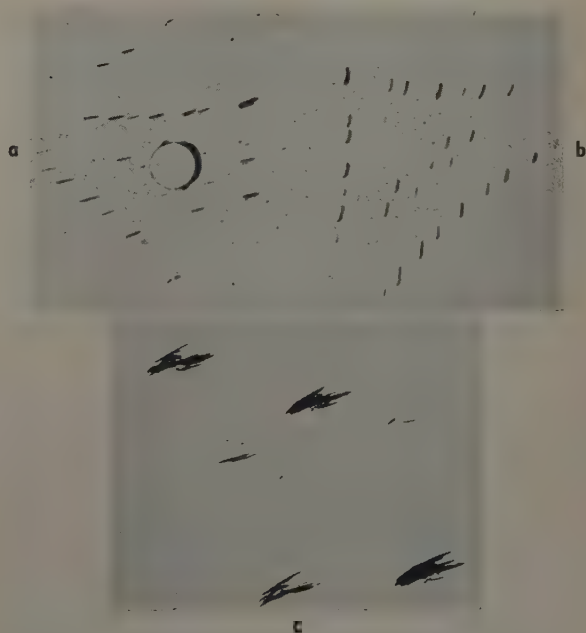


Fig. 7—Laue photograms of M-35 after bending through 13° . a (upper left)—Tension side. b (upper right)—Compression side. Note change in direction of asterism. Film to specimen distance 3 cm. c (lower center)—Same Laue reflections as in Fig. 7a, but with film to specimen distance equal to 12 cm.

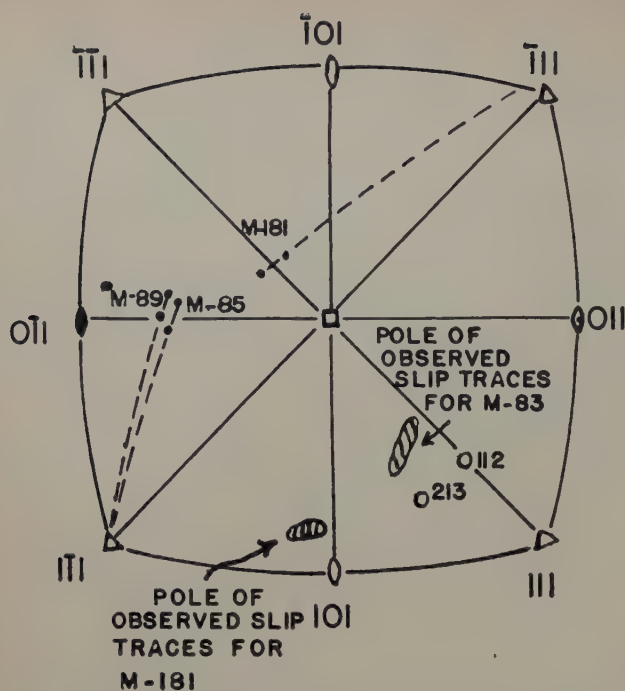


Fig. 8—Projection of M-181, M-85, and another grain in specimen M-89 showing crystallite rotations obtained from asterism on the tension side and pole of observed slip traces for M-83 and M-181.

crystals deformed at room temperature. These results for lattice rotation in bending also support earlier findings of Chen and Maddin⁷ on the plastic behavior of molybdenum single crystals. It is also worthy of note that the change of orientation on the compression and tension sides of a molybdenum single crystal (e.g., M-89) appears to resemble that of two separate crystals deforming under compression and tension loading, respectively. Yen and Hibbard¹ also reached a similar conclusion for the transverse bending of single crystals of aluminum.

Asterism: X-ray back-reflection patterns, in conjunction with the load-deflection tests, revealed that the distortion of the Laue spots appeared when the specimen was subjected to loading beyond the yield. A progressive increase in the amount of asterism on the tension or compression sides was also noted with increasing plastic deformation due to bending, Fig. 6. The extent of asterism was usually somewhat larger on the tension side than on the compression side, although about equal amounts of asterism were obtained on the tension and compression sides of M-35. X-ray photographs of the neutral region, i.e., 90° from the tension or compression sides where the stress, theoretically, should be zero, indicated very little asterism even after considerable bending.

It was observed that the Laue spots from the tension side appeared to be elongated in the direction approximately parallel to the specimen axis, whereas those on the compression side were elongated in the direction 90° to the former one, Fig. 7a and b. However, the asterism characteristic of the compression side was slightly curved, thus indicating that crystallite rotation may have occurred about two or more axes. The asterism from the tension side was generally a line-type streak for the usual film to specimen distance of 3 cm. However, when the Laue reflection from the tension side is enlarged by increasing the film to specimen distance to 12 cm, a very complex type of asterism is revealed, Fig. 7c.

It is evident, however, that the present observations concerning the type and extent of asterism suggest that the tension and compression sides of a bent molybdenum single crystal may be deforming as two different crystals.

Evidence was presented by Chen and Maddin⁷ for molybdenum single crystals deformed in tension that asterism is crystallographic in nature and represents a true account of plasticity in the specimen. It appears possible, therefore, to obtain information on the slip elements by plotting stereographically the crystallite rotations from the end points of Laue spots showing asterism. This was done in Fig. 8 for the tension side of those specimens which showed considerable asterism of the line-type streak. The crystallite rotations on the compression side were not determined due to the curvature of the Laue spots. Two of the specimens, M-85 and M-89, indicated a possible rotation toward the $[1\bar{1}1]$ direction, while specimen M-181 gave slight evidence for rotation toward $[1\bar{1}1]$. It is interesting to note that the crystallite rotations as determined from the

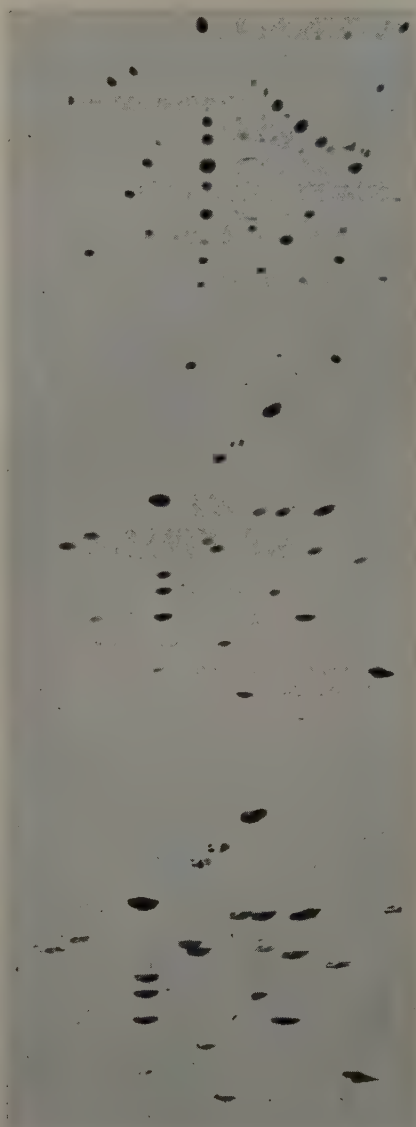
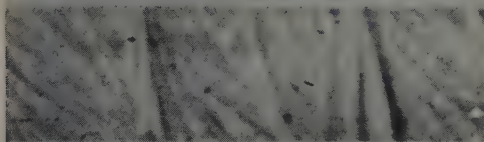


Fig. 9—Laue photographs of tension side of M-184 after increasing amounts of deflection from 0° to 15° showing a break-up of the Laue reflections into high intensity regions connected by diffuse areas.

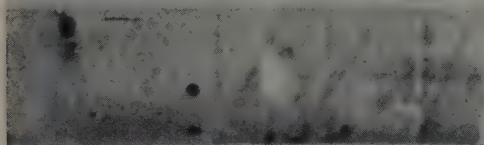
a— $\phi = 25^\circ$.



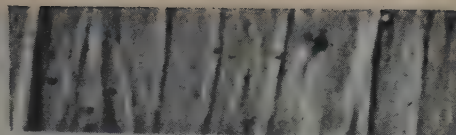
b— $\phi = 45^\circ$.



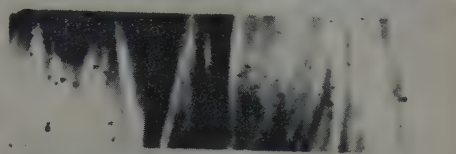
c— $\phi = 90^\circ$.



d— $\phi = -30^\circ$.



e— $\phi = -60^\circ$.



f— $\phi = -10^\circ$.



Fig. 10—Deformation bands and slip lines of tension side, a, b, and c, and compression side, d, e, and f, of specimen M-89. Specimen axis is horizontal. Bend axis is rotated in a plane perpendicular to the plane of the paper an amount shown by ϕ . $\phi = 0$ refers to position where bend axis is vertical and in the plane of the paper. X200.

extent of asterism were the same as the lattice or specimen axis rotations for specimens M-85 and M-89. The lattice rotation on the tension side of M-181 gave a slight indication of movement toward $[\bar{1}11]$ and the crystallite rotation was toward $[\bar{1}11]$. The pole of the observed slip traces on the tension side of M-181 (Fig. 8) appeared to indicate the operation of the slip plane (101), which contains both of these directions. The present results of stereographic analysis of asterism indicate that in the determination of slip elements, it appears of value to consider the alterations in the structure as shown by the formation of asterism.

Yen and Hibbard⁷ have observed a splitting of the Laue reflections into discrete spots after bending in two of their ten single-crystal specimens of aluminum. They attributed this split-up of Laue spots to crystallite fragmentation. A break-up of Laue spots into individual areas was also observed in a single crystal of molybdenum bent through an angle of 15° at 2400°C ⁸ which was attributed to polygonization. In the present studies, division of the Laue reflections into high intensity areas was observed in all of the crystals bent, Fig. 9. However, these high intensity regions were always connected by diffuse areas. Consequently, it seems reasonable to interpret this phenomenon in terms of crystallite fragmentation where the individual crystallites are connected by high strain regions which may account for the diffuseness existing between the fragments producing the high intensity reflections.

Metallographic Observations: Microscopic examination of both the tension and compression sides of M-89 were made at low and high magnifications. Fig. 10 shows representative micrographs of the markings at different positions around the periphery on the tension and compression sides. No marked difference was observable in the microscopic appearance of the markings on the tension and compression sides. Two distinct types of markings can be noted—deformation bands and slip lines. Whenever the slip lines could be clearly observed in the specimens examined, they were always straight. The deformation band, however, became wavy as it was followed around the specimen. At the position represented by Fig. 10c, the deformation band can be seen to split into two bands. The appearance of the bands illustrated in Fig. 10a, b, d, and e, is some-

what similar to the "slip lines" observed in extended sodium, potassium,¹⁰ and mercury single crystals¹¹ at low magnifications. Stereographic analyses of the lines on more than one surface of M-89 appeared to indicate that the lines correspond to the (101) plane. This result is in agreement with the X-ray data for the rotation on the compression side of M-89 (Fig. 3), i.e., toward the (101) pole.

Stereographic analyses of the slip lines on the tension side of specimens M-184, M-181, and M-83 gave the following results: The pole of the observed slip traces for M-184 was in the vicinity of (101), i.e., within 5° to 10° , as illustrated in Fig. 5. The lattice rotation on the tension side of this same crystal, M-184, gave a definite movement toward the $[\bar{1}11]$ direction which is contained in the (101) plane. The slip plane on the tension side of M-181, as determined from slip traces, was near the (101) pole, Fig. 8. The (101) plane might account for the lattice or crystallite rotations on the tension side of M-181. Although the pole of the slip traces for the tension side of M-83 was not located at any plane of low indices, it was closer to the (112) or (213) planes than to any of the {110} planes, Fig. 8. This is in agreement with previous observations of the extension of molybdenum single crystals with this initial orientation.⁷

It can be concluded from the present data that in three of the four cases where slip lines could be clearly observed, the pole of the slip traces was located near the {110} planes.

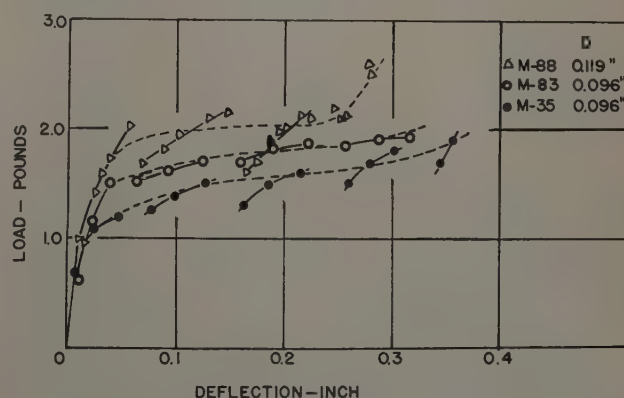


Fig. 11—Load-deflection curves of specimens M-35, M-83, and M-88.

Load-Deflection Data: Typical load-deflection curves for molybdenum crystals under bending are shown in Fig. 11. These curves indicate a normal type of stress-strain behavior with relaxation during loading. This relaxation occurred during the time when the X-ray patterns were obtained, with the load applied but not increased for intervals of approximately 1 hr. It is believed that the load-relaxation shown here may be characteristic of the specimen rather than due to relaxation of the spring, since the spring was rated at 50 lb and the loads were never above 3 lb when these relaxations were observed.* The various load-deflection curves did

* This belief is also supported by bending tests on 1/8 in. diam steel rods in which no relaxation effect was observed using the same bending apparatus with loads up to 5 lb and times up to 15 hr.

not appear to vary greatly for different orientations if the cross-sectional areas of the crystals are considered.

The maximum normal stress S_n for round specimens is given by the simple beam formula

$$S_n = \frac{2PL}{3\pi r^3} \quad [1]$$

where P is the load in grams, L is the lever arm in mm (115 mm in the present work), and r is the radius of the specimen. The maximum normal stress for the onset of plastic deformation was of the order of $7\frac{1}{2}$ kg per sq mm for the various crystals tested. Since no definite yield points were observed, the value of P was arbitrarily taken as the intersection of the best straight lines through the curve where the load-deflection initially showed a steep rise and the curve where the load-deflection is gradually flattened. If it is assumed that slip takes place under the same conditions as uniaxial loading, the resolved shear stress, S_s , along the operative slip plane may be calculated by multiplying Eq. 1 by $\sin \chi \cos \lambda$, where χ is the angle between the specimen axis and the major axis of the glide ellipse and λ is the angle between the specimen axis and the slip direction. For those specimens where the results appeared to indicate that the plane acting was $(\bar{1}01)$ $[\bar{1}\bar{1}1]$, the resolved shear stress in bending is calculated to be approximately $3\frac{1}{2}$ kg per sq mm (5000 psi). Kochendorfer³ has reported that the critical shear stress observed in bending may be 1.7 times greater than that in uniaxial loading for round specimens. This might indicate a resolved shear stress of the order of 2 kg per sq mm for molybdenum single crystals

subjected to uniaxial loading. However, the values of resolved shear stress reported here can only be regarded as approximate because of the arbitrary value of P in Eq. 1 and because of the assumptions made in the calculations.

Summary

A summary of the slip elements determined in this investigation is shown in Table I.

1—Lattice rotation during bending of molybdenum single crystals was found to occur toward the $\{110\}$ pole on the compression side and toward the $\langle 111 \rangle$ direction on the tension side.

2—Crystallite rotation determined from asterism and observations of slip traces appeared to indicate the participation of the $\{110\}$ planes and the $\langle 111 \rangle$ directions.

3—The results in 1 and 2 above support the suggestions of Chen and Maddin that the slip planes are of the type $\{110\}$ and the slip direction $\langle 111 \rangle$ for molybdenum single crystals deformed at room temperature.

4—The orientation change on the compression and tension sides of a molybdenum single crystal during bending are similar to that of two separate crystals deforming under compression and tension loading, respectively.

5—A relaxation in load up to 0.5 lb was obtained in the bending of molybdenum single crystals.

6—Laue reflections generally revealed a break-up which is interpreted as crystallite fragmentation.

Acknowledgments

The authors would like to thank Professor R. B. Pond for his help in the construction of the apparatus and the Office of Naval Research for support of their work under Project NR034-403. The assistance of Mrs. Dorothy Schaeffer in the growth of the molybdenum single crystals is gratefully acknowledged.

References

- ¹ M. K. Yen and W. R. Hibbard, Jr.: The Transverse Bending of Single Crystals of Aluminum. *Trans. AIME* (1949) **185**, p. 710; *JOURNAL OF METALS* (October 1949).
- ² R. W. Cahn: Recrystallization of Single Crystals After Plastic Bending. *Journal Inst. Metals* (1949) **76**, p. 121.
- ³ A. Kochendorfer: *Plastische Eigenschaften von Kristallen und Metallischen Werkstoffen* (1941) J. Springer.
- ⁴ R. Maddin, C. H. Mathewson, and W. R. Hibbard, Jr.: The Active Slip Systems in the Simple Axial Extension of Single Crystalline Alpha Brass. *Trans. AIME* (1949) **185**, p. 527; *JOURNAL OF METALS* (August 1949).
- ⁵ N. K. Chen and C. H. Mathewson: Structural Studies of Plastic Deformation in Aluminum Single Crystals. *Trans. AIME* (1951) **191**, p. 653; *JOURNAL OF METALS* (August 1951).
- ⁶ N. K. Chen, R. Maddin, and R. B. Pond: The Growth of Molybdenum Single Crystals. *Trans. AIME* (1951) **191**, p. 461; *JOURNAL OF METALS* (June 1951).
- ⁷ N. K. Chen and R. Maddin: Plasticity of Molybdenum Single Crystals. *Trans. AIME* (1951) **191**, p. 937; *JOURNAL OF METALS* (October 1951).
- ⁸ C. S. Barrett: *Structure of Metals* (1952) New York. McGraw Hill Book Co.
- ⁹ N. K. Chen and R. Maddin: Observations on Cleavage and Polygonization of Molybdenum Single Crystals. *Trans. AIME* (1951) **191**, p. 531; *JOURNAL OF METALS* (July 1951).
- ¹⁰ E. N. DaC Andrade and L. C. Tsien: Glide of Single Crystals of Sodium and Potassium. *Proc. Royal Soc.* (1937) **163**, p. 1.
- ¹¹ K. M. Greenland: Slip Bands on Mercury Single Crystals. *Proc. Royal Soc.* (1937) **163**, p. 28.

Table I. Summary of Slip Elements

Specimen No.	Slip Elements	
	Compression Side	Tension Side
M-35	$(\bar{1}01)^1$	—*
M-83	$(\bar{1}01)^1$	$\sim (112)$ or $(213)^3$
M-85	—*	$[\bar{1}\bar{1}1]^{1,2}$
M-88	$(\bar{1}01)^1$ and s	$(\bar{1}01)^3$
M-89	$(\bar{1}01)^1$	$[\bar{1}\bar{1}1]^{1,2}$
M-90	$\sim (\bar{1}01)^1$	—*
M-181	$(\bar{1}01)^1$	$[\bar{1}\bar{1}1]^{1,2}$ $[\bar{1}\bar{1}1]^{1,2}$ $(101)^3$
M-184	—*	$[\bar{1}\bar{1}1]^1$ $(\bar{1}01)^3$

1—Lattice rotation.

2—Asterism analysis.

3—Slip traces.

* Insufficient rotation for positive indication.

Kink Band Formation in High Purity Aluminum During Creep at High Temperatures

by Andre M. Gervais, John T. Norton, and Nicholas J. Grant

An investigation of the creep deformation of coarse grained specimens of high purity aluminum in the temperature range 800° to 1150°F, permitted the formulation of a theory explaining the formation of kink bands. The X-ray Laue back-reflection technique was used in conjunction with metallographic studies to determine the crystallographic elements involved in kinking and to measure the rotations of the bands.

THAT metals deform by the formation of kink bands was first shown by Orowan¹ in 1942. He manually compressed cadmium single-crystal wires, the basal planes of which were parallel to the wire axis and to the direction of compression. He found that kink bands formed quite suddenly. Similar experiments were performed by Hess and Barrett² on zinc with a hydraulic testing machine to permit slower more careful compression. They observed that kink bands formed progressively with increasing compression. Recently Washburn and Parker³ observed the formation of kink bands in zinc single-crystal specimens during tension creep experiments. Each of these authors observed the formation of kink bands but did not make a complete analyses of the crystallographic relationships.

In addition to these studies on hexagonal metals, extensive investigations of kink bands formed during deformation of aluminum in tension at room temperature have been reported.⁴⁻⁹ Two types of deformation bands have been observed during the deformation of aluminum at room temperature. These are: 1—kink bands: these exhibit a sharp curvature of the lattice along certain surfaces, and 2—bands formed by secondary slip along certain regions.

As has already been shown by Honeycombe,⁴ it is important to point out the difference characterizing the two types of deformation bands. In the first case, for moderate deformation, only one system of slip planes normally is active; in the second case, however, two slip systems are active in the deformation bands. The latter have a rumpled surface because of the action of the two slip systems. In the present

work only the first type of band was studied and to avoid any confusion the term *kink band* will be used exclusively in the discussion which follows.

Honeycombe⁴ observed that very narrow kink bands (width, 0.01 mm) formed along the (110) planes during the deformation of high purity aluminum at room temperature. He observed narrower ones in commercially pure aluminum and found also that their width decreased with decreasing temperatures. Chen and Mathewson⁵ reported the formation of kink bands during tensile testing of single crystals of high purity aluminum at room temperature and pointed out that some rotation occurred about a [211] direction.

The influence of the bending moment on the formation of kink bands was illustrated by the experiments of Röhm and Kochendörfer¹⁰ who used a Polanyi apparatus to obtain pure shear during tensile testing of high purity aluminum single crystals. Under such conditions only one slip system was active and no kink bands were observed; consequently, no noticeable asterism was detected after deformation. The influence of the bending moment will be discussed later.

Calnan⁶ gave a detailed account of the work performed on kink bands obtained during deformation of aluminum at room temperature.

Because no explanation of the process of kink band formation in creep was given in the previous investigations and because some of the above observations are vital to the following discussion the brief review of the literature has been given. It is proposed in the present work to provide an explanation of kink band formation during creep deformation at elevated temperatures.

Results and Discussion

Kink bands were observed to form during tensile creep testing of high purity (99.995 pct) aluminum specimens, having a very large grain size, in the temperature range 800° to 1150°F. These observations were made in grains which occupied the whole cross section of the specimen. The specimens were originally round (diameter, 0.187 in.; gage length, 1 in.) and had parallel flats milled to permit easier metallographic and X-ray observations. The final

A. M. GERVAIS, Student Associate AIME, formerly Research Assistant MIT, is now associated with the Societe Commeny-Fourchambault et Decazeville, Imphy (Nievre), France, and J. T. NORTON and N. J. GRANT, Members AIME, are Professor, and Associate Professor, respectively, Metallurgy Dept., Massachusetts Institute of Technology, Cambridge, Mass.

Discussion on this paper, TP 3647E, may be sent, 2 copies, to AIME by Jan. 1, 1954. Manuscript, Feb. 27, 1953; revision, June 16, 1953. Cleveland Meeting, October 1953.

This paper is based on a thesis submitted by A. M. Gervais in partial fulfillment of the requirements for the degree of Doctor of Science in Metallurgy to the Massachusetts Institute of Technology, February, 1953.



Fig. 1—Kink bands in a grain of specimen 6 deformed in creep at 800°F and at a stress of 150 psi. Oblique illumination. X1.5. Area reduced approximately 25 pct for reproduction.

thickness was 0.120 in. and the final gage length 0.85 in.

In contrast with results obtained at room temperature, the observation of kink bands in the high temperature range was easy, and conclusions could be drawn clearly on the mode of deformation of the metal by kinking. Kink bands were not found to form in every specimen, thus possibly indicating that specific orientation of the grain is required for their formation. The distinct appearance of these kink bands at low magnification may be seen in Fig. 1. X-ray work was performed rather easily on these kink bands because of their comparatively large width with respect to the width of kink bands at room temperature (of the order of 0.01 mm).

It is well known that the formation of a second active slip system is due to the fact that in the conventional tensile testing of single crystals pure shear is not obtained. Fig. 2 (steps 1 and 2) gives a schematic representation of the phenomenon showing that after the first slip system has been operative a transverse force takes place and the second set of slip planes becomes active. Under the action of this second slip system the transverse force is relieved and the specimen continues to elongate. That is the classical case of duplex slip.

Now, in those cases where kink bands are formed, Fig. 2, steps 1 and 3, the first slip system operates as above and a bending moment is produced by the transverse force. This bending moment is relieved by the formation of a kink band which permits continued elongation of the specimen. The result of

such a process, namely, the relief of the bending moment (transverse force) and the elongation of the specimen, is identical to that obtained by duplex slip.

Kink band deformation is illustrated by Fig. 3 taken on a rounded side surface of a specimen. Such a process of deformation is feasible because it does not require a change in volume of the kink band for moderate deformation. In Fig. 2 the parallelogram *ABCD* always maintains the same area during kinking since the kink boundary always bisects the angle between the slip planes within and without the band. In the process of the formation of kink bands as explained in Fig. 2, the width of the kink band



Fig. 3—Kink bands in a grain of specimen 16 deformed by creep at 1075°F and at a stress of 90 psi. Note the change in orientation at the right side of the specimen as schematically shown in Fig. 2 and the smaller slip band spacing inside the kink bands. Oblique illumination. X7.

does not increase with increasing deformation of the grain. However, the angular difference of the two blocks about the kink band boundary does increase as deformation continues.

Cahn⁸ had suggested that the kink band boundaries move in a direction perpendicular to the kink boundary but always parallel to themselves during deformation. Because a very thin oxide layer is formed on the specimen surface at these high temperatures, the movement of such kinking planes would produce cracks in this oxide which would be clearly visible under a microscope. No traces of such movement were observed as is indicated by Fig. 12a. Consequently, Cahn's idea is not supported by these results.

The progressive change in orientation of the kink band with respect to the remaining part of the grain was clearly pointed out by Chang and Grant¹¹ who continuously observed the deformation of a specimen microscopically during the actual creep test. By taking successive photographs of a region, kink bands appeared increasingly darker, that is to say, the amount of light which was reflected back to the microscope became progressively smaller. This could only be explained by the continued increase in the tilt of the kink bands. Furthermore, sliding along the kink boundaries was not observed by Chang and Grant¹¹ nor in the present research.

The sharp change in orientation at the kink band boundaries was large enough to be seen without a

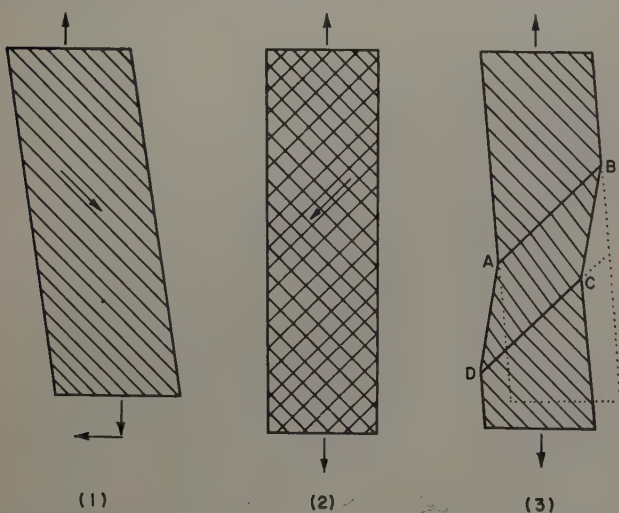


Fig. 2—Steps 1 and 2—Process of deformation in tensile testing with two active slip systems. Slip planes are perpendicular to the plane of the paper.

Steps 1 and 3—Process of deformation in tensile testing with only one active slip system and kink bands. The slip plane and the bending planes are perpendicular to the plane of the paper. (1) The first active slip system produces a transverse force. (2) The second active slip system is under the action of the transverse force, allowing elongation of the specimen. (3) A kink band forms under the influence of the bending moment (1) and allows elongation of the specimen.

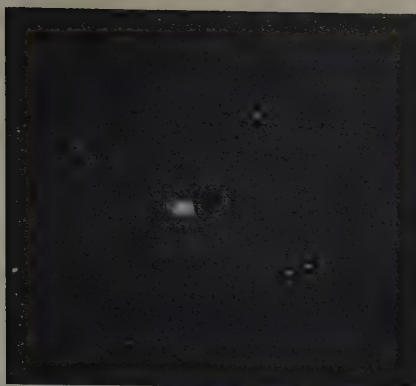


Fig. 4—X-ray Laue back-reflection photograph. The X-ray beam was located on a kink band boundary of specimen 6. Note the sharp division of each spot indicating a sharp change in orientation at the kink band boundary. Rotation of 4° .

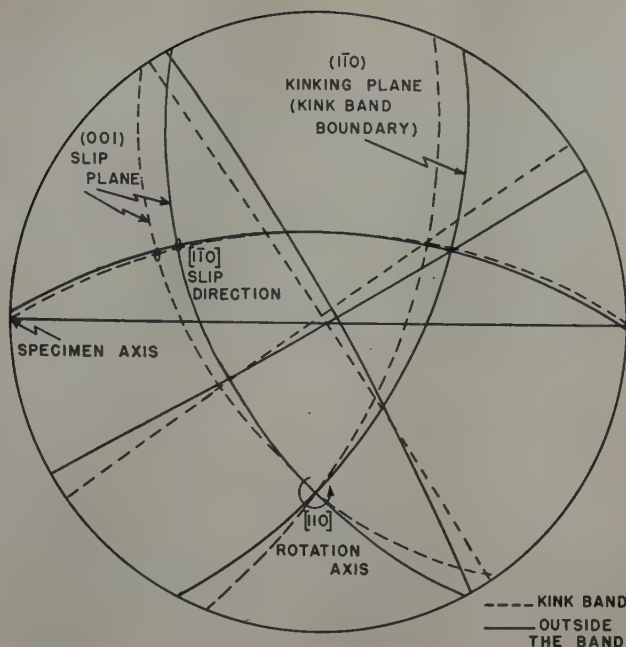


Fig. 7—Stereographic projection deduced from a Laue back-reflection photograph with X-ray beam located on a kink band boundary of specimen 16. Note the rotation about the $[110]$ axis. Rotation of 6° . Case II.

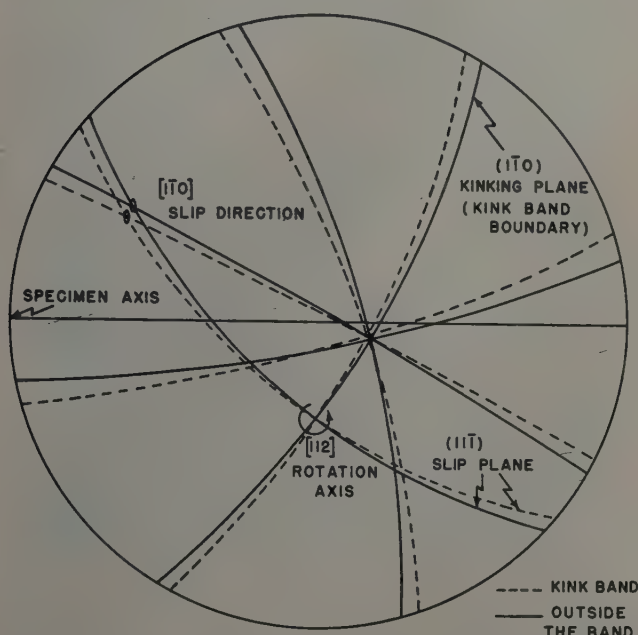


Fig. 5—Stereographic projection deduced from a Laue back-reflection photograph with X-ray beam located on a kink band boundary of specimen 6. Note the rotation about the $[112]$ axis. Rotation of 4° . Case I.



Fig. 8—X-ray Laue back-reflection photograph. The X-ray beam was located on a kink band boundary of specimen 16. The specimen was oriented so that the $[110]$ spot was recorded. Note the rotation about the $[110]$ axis. Rotation of 6° . Case II.



Fig. 6—X-ray Laue back-reflection photograph. The X-ray beam was located on a kink band boundary of specimen 10. The specimen was oriented so that the $[211]$ spot was recorded. Note the rotation about the $[211]$ axis. Rotation of 2° . Case I.

microscope. This orientation difference was confirmed by X-ray work, using a Laue back-reflection camera.

A series of Laue back-reflection photographs were taken along the length of the creep deformed specimen which was moved longitudinally by a calibrated screw. When a completely different orientation was seen between two successive photographs it was concluded that a grain boundary had been crossed. This was confirmed by metallographic work. This grain boundary then was used as a reference mark for taking Laue patterns over the full length of the grain and the distances were checked from micrographs. It was seen from the micrographs that the width of the kink bands was much larger in these specimens than the diameter of the X-ray beam. Consequently, it was possible to fix the X-ray beam exactly on a kink band boundary or inside a band.

Fig. 4 shows a Laue back-reflection photograph obtained when the X-ray beam was located on a

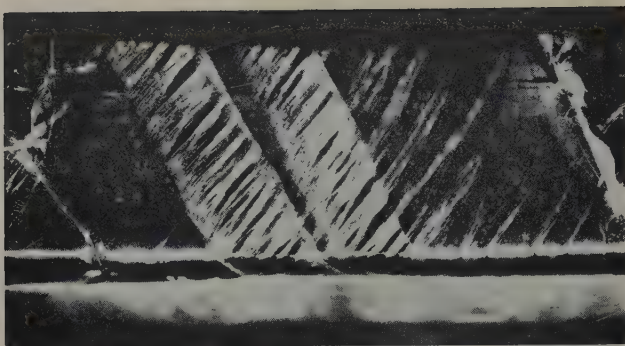


Fig. 9—Kink bands in a grain of specimen 16 deformed by creep at 1075° and at a stress of 90 psi. Note the slip bands which stop at the plane of sharp bending on the left side of the kink bands. Oblique illumination. X11. Area reduced approximately 60 pct for reproduction.

kink band boundary. It is clearly evident that each spot is sharply divided into two parts and this could only indicate that there is a sharp change in orientation about the boundary. The crystallographic relationship of the process of deformation was obtained from the change in orientation so noted.

Stereographic projections showing the orientations of grains and the rotation of the kink bands were built up from the Laue back-reflection photographs with the use of a Geringer chart.²²

The determination of the planes of kinking and slip was made by measuring the angle of their traces on the specimen surfaces with a goniometer set-up on a microscope. Later, these data were assembled on the stereographic projections.

As a result of these investigations two different cases were found:

Case I: Slip took place along a (111) plane. Kinking occurred along a (110) plane perpendicular to the (111) slip plane and to the [110] slip direction. The two planes [(111) slip plane and (110) kinking plane] intersected along a [211] direction which was the axis about which the kink band rotated. Fig. 5 is a stereographic projection which shows the rotation about the [211] direction. For the pattern

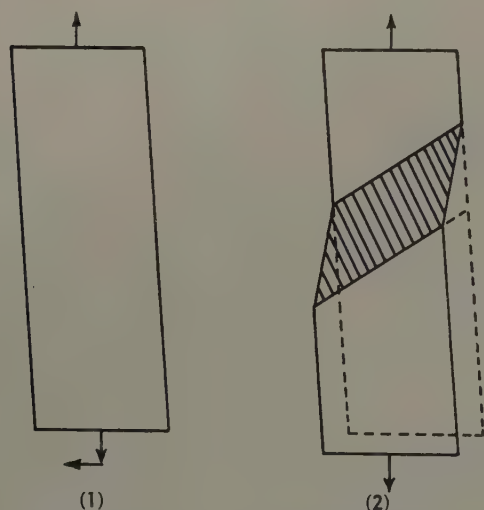


Fig. 10—Schematic representation of the formation of kink bands without previous slip and with slip in the kink band only.

(1)—Bending moment produced on a grain by slip in other places or grain boundary sliding.

(2)—Kink band formed to accommodate the bending moment. Slip occurs in the band only to allow the deformation of this band.

shown in Fig. 6, the specimen was set in such a way that the spot corresponding to the rotation axis could be located in the Laue back-reflection photographs. The rotation about this [211] axis is clearly evident.

Case II: In the second case, slip took place along a (100) plane. At elevated temperatures, slip has frequently been observed on the (100) plane and definitely confirmed by X-ray analysis. It appears to be one of the regular modes of deformation in aluminum. Kinking occurred along a (110) plane perpendicular to the (100) slip plane and to the [110] slip direction. The two planes [(100) slip plane and (110) kinking plane] intersected along a [110] direction which was the axis about which the kink band rotated. Fig. 7 is a stereographic projection which shows the rotation about the [110] direction. For the pattern shown in Fig. 8 the specimen was set in such a way that the spot corresponding to the rotation axis could be located in the Laue

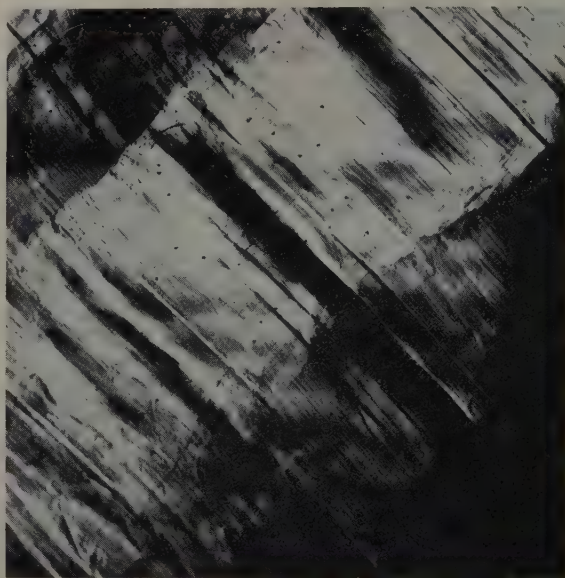


Fig. 11—Kink bands in a grain of specimen 9 deformed by creep at 800°F and at a stress of 150 psi. Note forked appearance of the kink band boundaries due to high rotation of the bands (10°). Oblique illumination. X50.

back-reflection photograph. The rotation about this [110] axis is evident.

The same process of kinking takes place in the two cases described above, the difference being that two sets of crystallographic elements are involved.

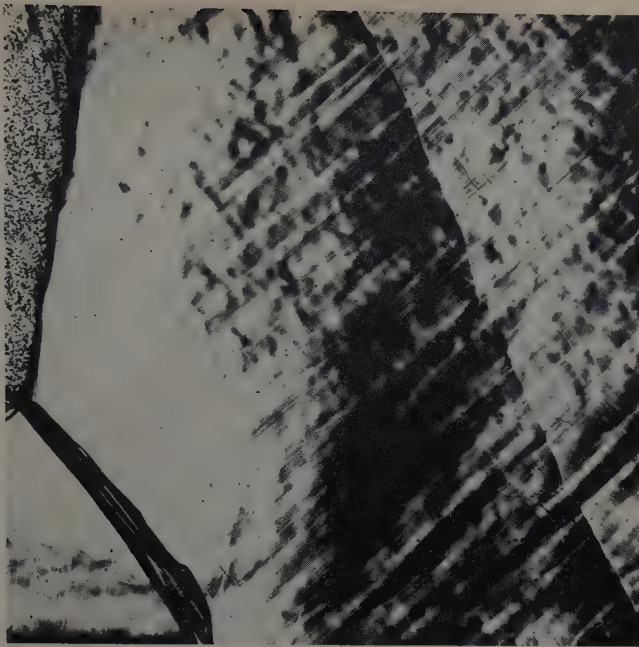
The process of kinking can be summarized as follows:

1—The plane of kinking bisects the angle between the slip planes on the two sides of the kink boundary. The line of intersection between the kink plane and both sets of slip planes is perpendicular to both slip directions.

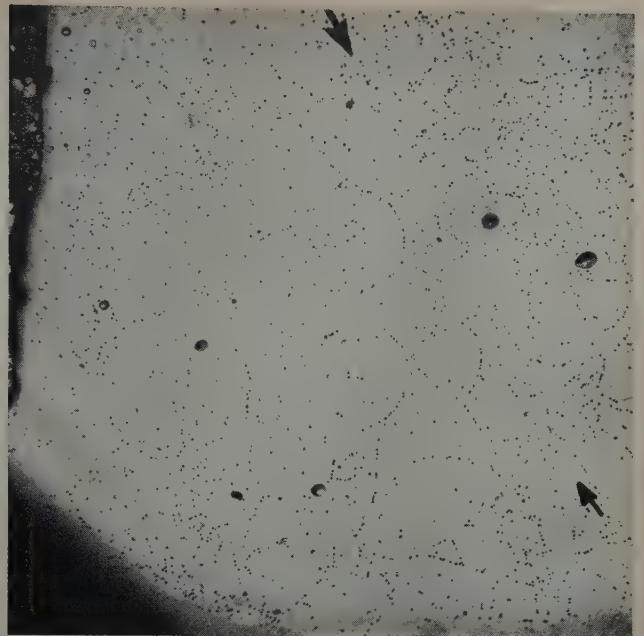
2—The progressive rotation of the regions located between the slip bands within the kink band occurs about an axis which is the intersection of the slip planes with the bending plane.

It should be mentioned that in the above explanation of the formation of kink bands (see Fig. 2), the kink bands always formed in regions which had been deformed by prior slip.

Examination of Fig. 9, however, shows that slip bands in each kink band stopped sharply at the kink band boundaries, particularly on the left side of the band. The reason for such a phenomenon is ex-



a—Before polishing. Oblique illumination shows the sharp ridge of a kink band boundary.



b—After annealing at 1150°F for 1 hr and polishing and etching. Sharp bend location indicated by arrows. Note the difference in subgrain size on each side of the position of the kink.

Fig. 12—Spot in a grain of specimen 6 where kink bands occurred during creep at 800°F and at a stress of 150 psi. X50.

plained schematically in Fig. 10. Prior to the formation of the kink band, the grain is under the influence of a bending moment caused by deformation in other parts of the specimen and by sliding along grain boundaries. The extent of such grain boundary sliding is heavy at these high temperatures.¹³ Therefore slip must operate to form the kink band itself and accommodate the deformation; but in such a case, slip effectively takes place simultaneously with kink band formation.

This illustrates very well that kinking could be considered to be a process of deformation of itself, and also that it obeys specific crystallographic laws. It does not seem adequate therefore to use the expression "deformation bands"^{12,5} for such a process of deformation.

An interesting observation was made regarding slip band spacing. Fig. 3 shows that the slip spacing inside the kink bands is much smaller than the slip spacing outside of them (upper part of the picture). Outside the kink bands the slip spacing corresponds to that indicated by Servi and Grant¹⁴ (order of magnitude of 0.75 mm). Smaller slip spacing in the kink bands is a consequence of the higher strain in the bands because of rotation during kinking.

Kink band boundaries are not always as straight as is shown in Fig. 12a; instead they have, in the case of heavy deformation (Fig. 11) a forked appearance which is due to the great difference in strain on each side of the boundaries.

It must be pointed out, as shown by Laue back-reflection photographs, that asterism was sometimes quite marked inside or outside the kink bands. Asterism within the kink band was readily detected because the kink bands were much wider than the diameter of the X-ray beam. Back-reflection photographs show that in addition to the sharp bending along the kink band boundaries there is also a smooth curvature within the kink band itself.

Fig. 12a is a photograph of a kink band boundary. In Fig. 13 the X-ray patterns show that the amount of smooth bending is different on each side of the kink. The marked asterism in Fig. 13b compared to Fig. 13a shows considerably greater bending to the right of the kink band boundary in Fig. 12a. After annealing the specimen for 1 hr at 1150°F, it was electrolytically polished and etched with an etch pit reagent used for revealing the subgrain boundaries.¹⁵ The appearance of the same region is shown in Fig.

a (right)—X-ray beam was located in the grain on the left side of the kinking plane (small bending).



b (left)—X-ray beam was located in the grain on the right side of the kinking plane (high bending).

Fig. 13—X-ray Laue back-reflection photographs of the location shown in Fig. 12a.

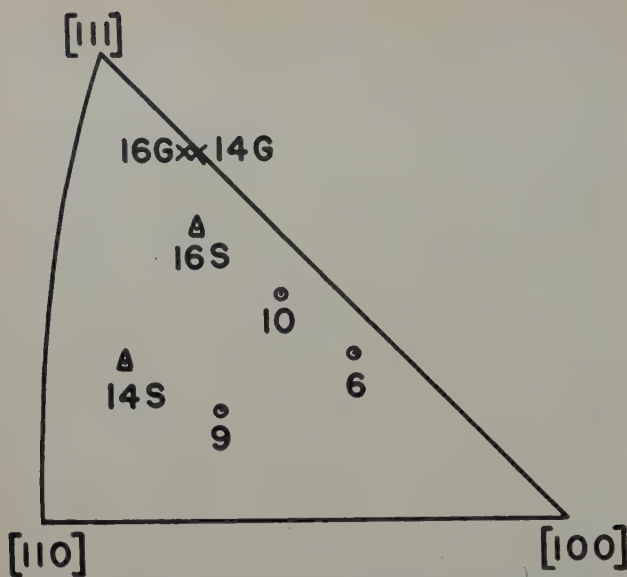


Fig. 14—Dependence of kink band formation on initial grain orientation. The stereographic projection shows orientation of various grains from various specimens where kink bands were observed in relation to the specimen axis (axis of tension). Numbers are specimen numbers, G and S are used when two different grains presented kink bands.

○—Slip bands along a (111) system.

×—Slip bands along a (100) system.

△—Grain too small for accurate determination of the slip system.

12b. Two different sizes of subgrains can be observed on each side of the original boundary. The smaller subgrain size on the right side of the kink band boundary is due to a greater bending.¹⁰ This result points out, once more, how inhomogeneous the deformation can be in different parts of a grain.

Finally, the orientations of all the grains which had shown distinct kink bands were plotted and are shown in Fig. 14. Data on these specimens are given in Table I. No clear result was brought out by this diagram. However, it seems reasonable to believe that a certain crystallographic orientation of a grain with respect to the axis of the specimen is required since kinking occurred only in a few grains of the specimen tested. Furthermore, only well-determined planes are kinking planes. At room temperature too, a marked spreading of the results in the fundamental triangle was reported.^{5,7}

Summary

1—A mode of formation of kink bands was described indicating the need of a bending moment during the deformation in tension of a specimen.

2—The kinking plane bisects the angle between the slip planes on the two sides of the kink boundary. The line of intersection between the kink plane and both sets of slip planes is perpendicular to both slip directions. The regions located between the slip bands within the kink band rotated progres-

sively about axes defined by the intersection of the kinking plane with the slip planes. Two different slip systems were observed: (111) and (100).

In contrast to the usual case, kink bands were observed to form in regions not previously crossed by a slip system. Kink bands occurred under the influence of a bending moment, and slip took place simultaneously.

3—The kink bands were observed to keep the same width during the deformation process for moderate deformations.

4—In addition to the sharp bending about the kinking planes, a smooth bending was observed in the bands themselves and also in regions outside them.

Acknowledgments

The authors wish to express their appreciation to H. C. Chang and A. R. Chaudhuri for frequent helpful discussions. Thanks are also extended to the Flight Research Laboratory (WCRRL), Wright Air Development Center, for sponsoring this research under Contract No. AF33 (038) -23281.

References

- 1 E. Orowan: A Type of Deformation New in Metals. *Nature* (1942) **149**, p. 643.
- 2 J. B. Hess and C. S. Barrett: Structure and Nature of Kink Bands in Zinc. *Trans. AIME* (1949) **185**, p. 599; *JOURNAL OF METALS* (September 1949).
- 3 J. Washburn and E. R. Parker: Kinking in Zinc Single-Crystal Tension Specimens. *Trans. AIME* (1952) **194**, p. 1076; *JOURNAL OF METALS* (October 1952).
- 4 R. W. K. Honeycombe: Inhomogeneities in the Plastic Deformation of Metal Crystal. *Journal Inst. Metals* (1951) **80**, p. 45.
- 5 N. K. Chen and C. H. Mathewson: Structural Studies of Plastic Deformation in Aluminum Single Crystals. *Trans. AIME* (1951) **191**, p. 653; *JOURNAL OF METALS* (August 1951).
- 6 A. Laloeuf and C. Crussard: Relation entre la Déformation et la Recristallisation de Monocristaux d'Aluminium. *Revue de Métallurgie* (1951) **48**, p. 462.
- 7 K. Lücke and H. Lange: Über die Form der Verfestigungskurve von Reinstaluminiumkristallen und die Bildung von Deformationbändern. *Ztsch. Metallkunde* (1952) **43**, p. 55.
- 8 E. A. Calnan: Laue Asterism and Deformation Bands. *Acta Crystallographica* (1952) **5**, p. 557.
- 9 R. W. Cahn: Slip and Polygonization in Aluminum. *Journal Inst. Metals* (1951) **79**, p. 129.
- 10 F. Röhm and A. Kochendörfer: Neue Ergebnisse über Verfestigung bei der plastischen Verformung von Kristallen. *Ztsch. Metallkunde* (1950) **41**, p. 265.
- 11 H. C. Chang and N. J. Grant: Inhomogeneity in Creep Deformation of Coarse Grained High Purity Aluminum. *Trans. AIME* (1953) **197**, p. 1175; *JOURNAL OF METALS* (September 1953).
- 12 A. B. Greninger: Determination of Orientations of Metallic Crystals by Means of Back-Reflection Laue Photographs. *Trans. AIME* (1935) **117**, p. 61.
- 13 H. C. Chang and N. J. Grant: Observations of Creep of the Grain Boundary in High-Purity Aluminum. *Trans. AIME* (1952) **194**, p. 619; *JOURNAL OF METALS* (June 1952).
- 14 I. S. Servi and N. J. Grant: Structure Observations of Aluminum Deformed in Creep at Elevated Temperatures. *Trans. AIME* (1951) **191**, p. 917; *JOURNAL OF METALS* (October 1951).
- 15 A. M. Gervais, J. T. Norton, and N. J. Grant: Subgrain Formation in High Purity Aluminum During Creep at High Temperatures. *Trans. AIME* (1953) **197**, p. 1166; *JOURNAL OF METALS* (September 1953).
- 16 C. G. Dunn and F. W. Daniels: Formation and Behavior of Subboundaries in Silicon Iron Crystals. *Trans. AIME* (1951) **191**, p. 147; *JOURNAL OF METALS* (February 1951).

Table I. Data From the Specimens Which Showed Kink Bands

Specimen No.	Temperature, °F	Initial Stress, Psi	Specimen Total Elongation, Pct	Rotation at the Kink Band Boundaries
6	800	150	5.5	4°
9	800	150	10.0	10°
10	1150	90	4.3	2°
14	1000	90	5.5	10° (grain 14G)
16	1075	90	5.9	6° (grain 16G)

The Properties of Sand Cast Mg-Th-Zn-Zr Alloys

by K. E. Nelson

The effect of thorium and zinc variations on the strength and 100-hr creep characteristics of Mg-Th-Zn-Zr alloys was investigated. Optimum resistance to creep at 650° and 700°F are attainable within a certain range of thorium and zinc contents. This range does not conform to that which develops maximum tensile properties.

RAPID advances have been made during the last few years in the development of magnesium alloys for elevated temperature applications demanding high resistance to creep. The beneficial effect of rare-earth metals on the creep resistance of magnesium alloys has been emphasized by a number of publications¹⁻¹³ and such alloys are now in commercial production.

The use of thorium as an alloying ingredient in magnesium was mentioned by McDonald^{14, 15} and also in two Alien Property Custodian patent applications.^{16, 17} The initial observation of Sauerwald¹⁸ that thorium contributes still higher creep resistance to magnesium than is attainable with rare-earth metals has recently been substantiated.¹⁹⁻²¹ In fact, it has been demonstrated that the useful temperature range of magnesium alloys is appreciably extended by the use of thorium. In all cases, it was observed that zirconium must be included in the alloys in order to render them fine grained and more readily castable. Several recent publications²²⁻²⁵ indicate that a still further improvement in creep resistance and a further extension of the useful temperature range can be realized by the addition of zinc to Mg-Th-Zr alloys.

The primary purpose of this paper is to present the results of a comprehensive study of the effect of zinc on the strength and creep characteristics of Mg-Th-Zr alloys. Compositions covering the range of thorium content from ½ to 6 pct and zinc content from 0 to 5 pct have been investigated. The creep characteristics at 650° and 700°F reported in this paper are based on results of tests of 100-hr duration. It is appreciated that creep tests of 100-hr duration might not yield adequate data for design purposes for parts with much longer expected life. However, for the purposes of the present discussion, it is felt that the combination of stresses and temperatures used in the 100-hr creep tests have yielded a clear representation of the compositional

variation of creep resistance at the temperatures investigated. Creep tests of 1000-hr duration are now in progress on a few of the most promising alloys.

Preparation and Testing of Alloys

The alloys studied in this intensive investigation were prepared in 25 lb capacity mild steel crucibles. The thorium, zinc, and zirconium were alloyed and poured as described in earlier publications.^{21, 25} The thorium was introduced into the melt in the form of a Mg-Th hardener,²⁵ the zinc added in the metallic form, and the zirconium alloyed in the form of the commercial hardener containing magnesium and 30 to 50 pct Zr.^{19, 26} Fluxing practices for melting and refining were the same as for magnesium-rare-earth metal-zirconium alloys.^{7, 10}

The melts were sampled for analytical determinations and poured into separately cast ½ in. diameter standard tensile bars. The test bars were given a precipitation treatment of 16 hr at 600°F in laboratory furnaces. It has been shown by other tests that a high temperature solution treatment followed by an aging treatment is unnecessary for the development of optimum properties in Mg-Th-Zn-Zr alloys. The selection of 600°F as the aging temperature was based on an attempt to achieve metallurgical stability without coalescence of the undissolved phases and the attendant loss in strength.

The thorium, zinc, and zirconium contents of each melt were determined chemically. The zirconium contents are reported in two parts, "soluble" and "insoluble," referring, respectively, to the portions present in the alloy which are soluble and insoluble in dilute HCl acid. Distinction is being made between these two components of the zirconium content in the alloys because it has been found that only that portion of the zirconium content which is soluble in dilute inorganic acids affects the structure and properties of the alloys. The usual impurities consisting of copper, iron, manganese, and nickel were determined spectroscopically. The analysis for each melt is listed in Table I.

A description of the methods of tension and creep testing has been detailed in earlier papers.^{1, 27} The tests were performed with the cast skin re-

K. E. NELSON is associated with the Metallurgical Laboratories, Magnesium Dept., The Dow Chemical Co., Midland, Mich.

Discussion on this paper, TP 3624E, may be sent, 2 copies, to AIME by Jan. 1, 1954. Manuscript, April 15, 1953. Cleveland Meeting, October 1953.

Table I. Analyses and Grain Size Measurements

Th	Zn	Analyses, Pct						Average Grain Size, In.
		Sol. Zr	Insol. Zr	Fe	Mn	Ni	Cu	
0.50	0.55	0.58	0.02	0.002	0.053	<0.001	<0.001	0.003
0.53	1.52	0.67	0.01	<0.001	0.050	<0.001	<0.001	0.002
1.07	0.98	0.64	0.02	0.002	0.038	<0.001	0.002	0.002
1.15	1.95	0.68	0.02	0.002	0.036	<0.001	0.004	0.002
1.09	3.01	0.71	0.03	0.002	0.043	<0.001	<0.001	0.003
0.86	4.00	0.73	0.03	0.001	0.030	<0.001	<0.001	0.003
1.02	4.93	0.72	0.04	0.006	0.043	<0.001	0.002	0.0035
1.46	0.56	0.64	0.02	0.002	0.052	<0.001	0.001	0.002
1.91	1.01	0.73	0.03	0.002	0.037	<0.001	0.001	0.002
1.92	1.96	0.77	0.02	0.002	0.037	<0.001	0.001	0.002
1.84	2.96	0.79	0.03	0.002	0.037	<0.001	0.001	0.002
1.81	3.99	0.73	0.03	0.001	0.038	<0.001	0.002	0.0015
1.82	4.98	0.79	0.03	0.001	0.041	<0.001	0.001	0.0015
2.99	1.04	0.71	0.03	0.002	0.040	<0.001	0.002	0.002
3.01	1.99	0.78	0.03	0.001	0.039	<0.001	0.002	0.002
2.92	2.94	0.81	0.03	0.001	0.040	<0.001	0.002	0.002
2.91	3.94	0.80	0.04	0.002	0.039	<0.001	0.002	0.0015
2.87	4.91	0.86	0.06	0.001	0.041	<0.001	0.002	0.002
4.00	1.04	0.74	0.06	0.002	0.034	<0.001	0.004	0.0012
4.00	1.99	0.74	0.04	0.002	0.043	<0.001	0.003	0.0015
4.17	2.93	0.87	0.07	0.002	0.042	<0.001	0.004	0.002
3.93	4.00	0.87	0.05	0.001	0.042	<0.001	0.004	0.0015
3.93	4.91	0.88	0.03	0.001	0.042	<0.001	0.004	0.002
5.12	1.04	0.69	0.03	0.002	0.037	<0.001	0.004	0.0012
5.14	1.99	0.71	0.05	0.001	0.036	<0.001	0.004	0.0012
5.01	2.93	0.84	0.03	0.001	0.036	<0.001	0.003	0.002
5.11	3.61	0.70	0.05	0.002	0.043	<0.001	0.003	0.002
5.92	1.00	0.65	0.02	0.003	0.033	<0.001	0.002	0.001
6.00	1.99	0.69	0.03	0.003	0.037	<0.001	0.002	0.001
6.28	2.99	0.78	0.04	0.001	0.039	<0.001	0.003	0.002
6.12	4.02	0.84	0.05	0.001	0.033	<0.001	0.002	0.0025

* Average of two to four samples.

maining on the bars. Two parameters are used to describe the creep characteristics of each alloy as obtained by interpolation of log stress vs log-extension plots of the original data. These parameters are: 1—creep limit based on 0.2 pct total extension in 100 hr, and 2—creep limit based on 0.5 pct total extension in 100 hr. The creep extension as well as the initial extension resulting from application of the load are combined to give the total extension values.

Grain size determinations were obtained on samples from the reduced section of the test bars using the comparison method reported by George.²⁸

Tensile and Creep Properties

The room and elevated temperature tensile properties are shown in Table II. The values for the ternary Mg-Th-Zr alloys are the optimum values obtainable and are in the solution-treated and aged condition. These were obtained from earlier publications.^{21, 25} The maximum room temperature results are developed by the 5 pct Zn-1 pct Th, 5 pct Zn-2 pct Th, and 5 pct Zn-3 pct Th alloys. In general, the higher thorium-higher zinc alloys have lower elongation values at room temperature than do the other compositions. In the zinc-containing quaternary alloys, for a given thorium content through 4 pct, the room temperature yield and tensile strengths increase with increasing zinc contents.

The best combination of tensile properties at 650° and 700°F are obtained with the magnesium plus 3.56 pct Th plus 0.72 pct Zr and magnesium plus 6.05 pct Th plus 0.97 pct Zr alloys. No one composition in the Mg-Th-Zn-Zr group of alloys can be pointed out as superior to others although the higher thorium-higher zinc alloys appear somewhat

better, though in no case equivalent to the zinc-free alloys.

Average grain size determinations made on the compositions tested are recorded in Table I. Within the grain size range exhibited by these alloys (0.001 to 0.0035 in.), there appears to be no correlation between grain size and the strength properties or ductilities listed in Table II. This grain refinement was effected by the addition of zirconium as indicated earlier. The amount of zirconium that can be introduced into the magnesium and retained in an "acid-soluble" form appears to increase both with the zinc and thorium contents of the alloy.

A graphical presentation showing the 100-hr creep limits obtained at 650° and 700°F for the various Th-Zn combinations are shown in Figs. 1 through 4 where the two parameters of creep are plotted. Iso-strength lines have been drawn to define more clearly the differences in creep strength existing among the alloys.

As shown in Figs. 1 and 2 there appears to be a ridge indicating compositions of optimum creep resistance starting with the 0.5 pct Th-0.5 pct Zn composition and extending through 3 pct Th-2.5 pct Zn, 4.5 pct Th-2.5 pct Zn, and on up to the 6 pct Th-3 pct Zn alloy. The optimum composition is around 5 pct Th-3 pct Zn. Although alloys containing more than 6 pct Th have not been studied, the results indicate that the creep resistance may be reaching its maximum at this level of thorium content. Many interesting phenomena can be seen

Table II. Room and Elevated Temperature Tensile Properties of Sand Cast Mg-Th-Zn-Zr Alloys. Separately Cast Test Bars*

Composition, Pct			Tensile Properties†								
			Room Temperature			650°F			700°F		
Th	Zn	Sol. Zr	%E	TYS	TS	%E	TYS	TS	%E	TYS	TS
0.50	0.55	0.58	18.5	10.6	27.9	30.5	4.5	7.7	29.0	4.0	7.5
0.53	1.52	0.67	15.0	15.0	31.8	28.8	6.0	8.0	24.8	5.6	7.8
0.93	—	0.68	12.0	11.7	30.3	44.2	5.5	11.5	35.8	4.0	8.8
1.07	0.98	0.64	19.2	12.4	29.8	31.2	5.0	8.4	27.5	4.8	8.4
1.15	1.95	0.68	10.2	15.2	30.8	35.2	6.8	9.4	27.5	6.1	8.6
1.09	3.01	0.71	13.8	17.8	34.9	34.2	6.8	9.1	34.2	6.1	8.1
0.86	4.00	0.73	14.2	19.8	38.0	33.8	6.3	8.6	32.5	5.6	7.4
1.02	4.93	0.72	11.5	20.9	39.4	28.0	6.8	8.4	31.2	6.0	7.2
1.46	0.56	0.64	11.0	12.8	27.5	29.2	5.6	10.6	29.0	4.6	9.8
1.84	—	0.67	10.8	14.6	35.0	36.0	8.0	14.0	40.0	5.8	10.5
1.91	1.01	0.73	14.2	12.1	27.5	29.5	5.7	9.8	27.2	5.4	10.0
1.92	1.96	0.77	14.8	13.9	31.0	30.2	6.6	9.8	26.5	6.2	9.3
1.84	2.96	0.79	5.2	18.8	31.0	28.2	8.2	11.0	25.2	7.3	9.8
1.81	3.99	0.73	8.2	21.6	36.4	27.2	8.6	11.0	28.0	7.4	9.7
1.82	4.98	0.79	12.0	22.4	39.4	34.2	8.2	10.2	33.0	7.3	9.0
2.99	1.04	0.71	12.5	13.0	29.2	27.0	6.2	11.6	28.5	5.8	11.4
3.01	1.99	0.78	10.5	14.2	30.8	29.5	6.5	10.4	27.0	6.8	10.4
2.92	2.94	0.81	4.8	15.9	28.8	29.2	7.8	11.2	26.0	7.2	10.4
2.91	3.94	0.80	4.2	19.8	31.3	22.5	9.2	11.9	24.2	8.0	10.6
2.87	4.91	0.86	2.8	22.3	32.6	27.0	8.8	11.7	26.0	7.8	10.0
3.56	—	0.72	8.0	18.2	37.4	21.7	10.2	17.0	25.8	8.6	13.8
4.00	1.04	0.74	7.0	14.6	27.2	25.5	6.6	13.0	28.5	6.0	12.0
4.00	1.99	0.74	12.0	14.4	31.6	27.5	6.8	11.2	28.8	6.5	11.3
4.17	2.93	0.87	7.2	15.3	30.8	27.2	7.6	11.6	27.2	7.2	10.9
3.93	4.00	0.87	3.0	18.4	28.1	25.2	8.6	11.8	24.2	7.9	11.0
3.93	4.91	0.88	2.8	20.8	30.4	23.8	9.1	12.7	24.8	8.7	11.3
5.12	1.04	0.69	3.0	16.0	23.8	22.8	7.2	14.2	26.0	6.1	13.1
5.14	1.99	0.71	12.0	14.8	32.2	28.0	6.8	12.1	30.0	6.6	12.2
5.01	2.93	0.84	7.8	15.8	31.6	26.5	7.8	12.2	26.8	7.8	11.7
5.11	3.61	0.70	3.8	16.4	26.8	27.0	8.0	12.2	26.5	7.6	11.3
6.05	—	0.97	3.8	18.7	30.2	8.3	11.2	16.8	8.3	8.8	13.6
5.92	1.00	0.65	4.2	17.3	26.2	23.0	7.9	15.2	27.8	6.4	13.6
6.00	1.99	0.69	7.2	16.1	30.3	28.8	7.2	13.3	31.0	6.6	13.0
6.28	2.99	0.69	8.2	17.2	33.9	28.0	8.2	13.0	27.2	7.8	12.6
6.12	4.02	0.84	4.0	17.2	29.4	27.0	8.8	13.2	26.2	7.9	12.3

* Heat Treatment = 16 hr at 600°F.

† Results are averages of 2 test bars.

%E = Elongation in 2 in.

TYS = Tensile yield strength, 1000 psi.

TS = Tensile strength, 1000 psi.

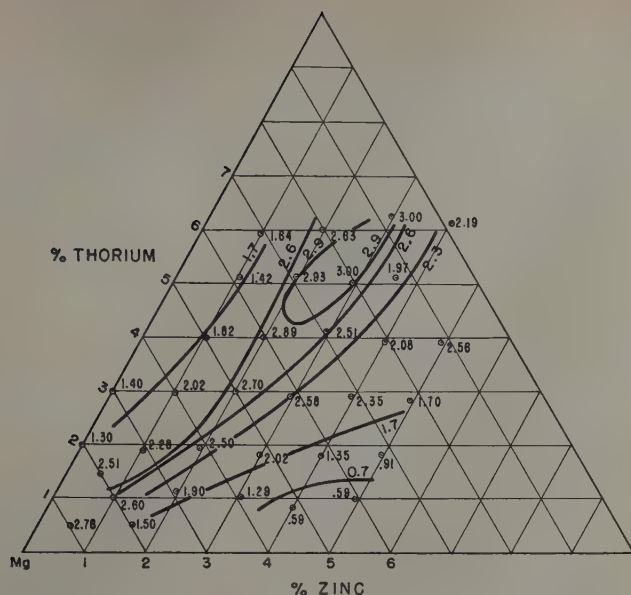


Fig. 1—Stress in 1000 psi necessary to give 0.2 pct total extension in 100 hr at 650°F. Mg-Th-Zn-Zr alloys.

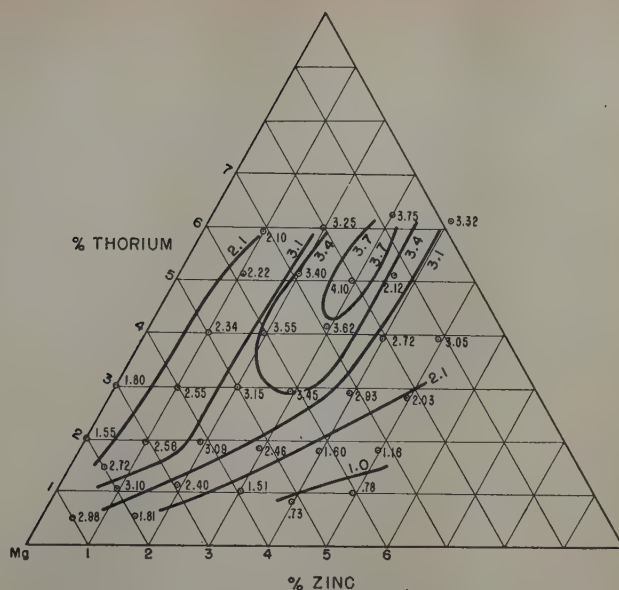


Fig. 2—Stress in 1000 psi necessary to give 0.5 pct total extension in 100 hr at 650°F. Mg-Th-Zn-Zr alloys.

in these figures. Particular attention is called to the very narrow ridge and the steepness of it, specifically with small increases or decreases in zinc content. The values for the ternary Mg-Th-Zr alloys are the mean values of a range in creep resistance obtained on bars sectioned from castings as reported earlier.²⁵ Experience has shown that the mean value obtained from a number of creep tests performed on such bars falls reasonably close to results obtained on separately cast test bars. The good creep resistance retained by the low thorium-low zinc alloys is very interesting and warrants further investigation both as to sand cast and wrought alloys. Possibly more effort should be expended to investigate magnesium "metallurgy behind the decimal point."

The composition of the ridge depicting maximum creep resistance follows quite closely the range in composition covered by a recent patent.²² The superiority of the commercial alloy 3 pct Th-2.5 pct Zn-

0.7 pct Zr, designated as HZ32XA or ZT1,²²⁻²⁴ over the 3 pct Th-0.7 pct Zr alloy, designated as HK31XA, as shown in these 100-hr creep comparisons has been substantiated on 1000-hr tests at temperatures of 550°, 600°, and 662°F.²⁵ It was also shown²⁵ that at 400°F the ternary alloy is superior in creep resistance to the quaternary Mg-Th-Zn-Zr alloy for testing times through 1000 hr, whereas at 500°F, the superiority of the ternary alloy decreases with increasing testing time up to 1000 hr. It is expected that the differences in creep resistance seen in the 100-hr tests on the Mg-Th-Zn-Zr alloys at 650° and 700°F will prevail after 1000 hr testing at 600° and 650°F, respectively.

Figs. 3 and 4 show that at 700°F there is an indication of a ridge following similar Th-Zn compositions as observed in the 650°F data. The form appears to be much flatter at 700°F, however, and the crest of the hill is in the range of 5.5 pct Th-4 pct Zn. Thorium levels about 6 pct again have

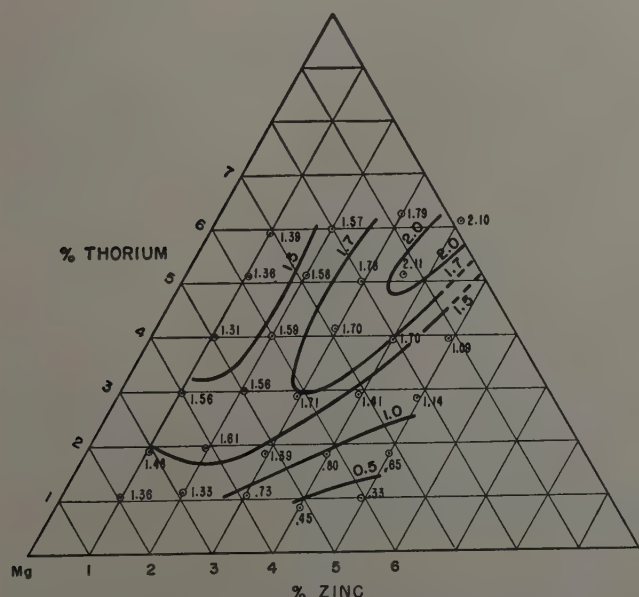


Fig. 3—Stress in 1000 psi necessary to give 0.2 pct total extension in 100 hr at 700°F. Mg-Th-Zn-Zr alloys.

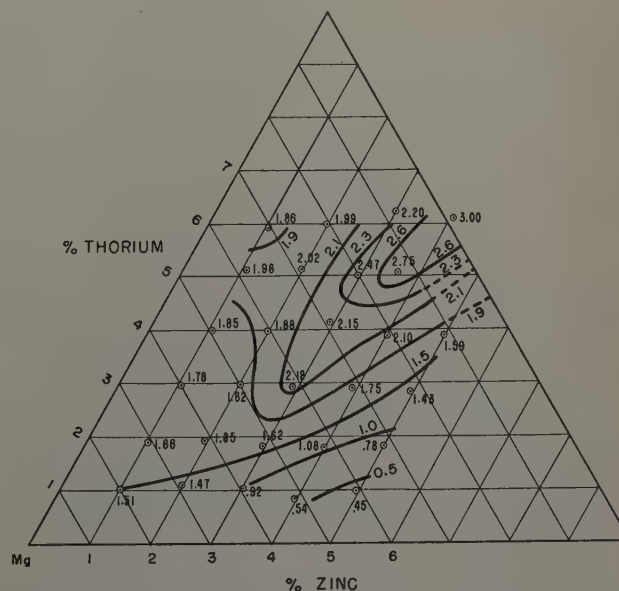
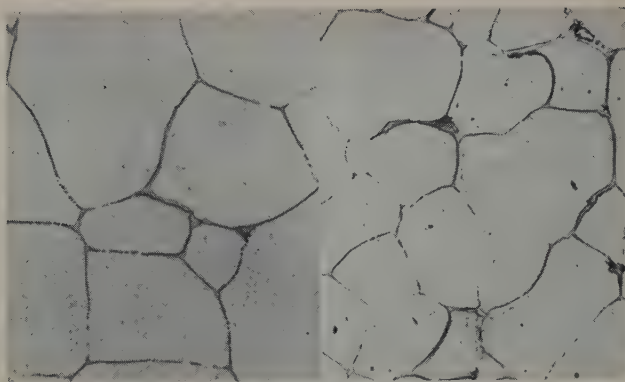


Fig. 4—Stress in 1000 psi necessary to give 0.5 pct total extension in 100 hr at 700°F. Mg-Th-Zn-Zr alloys.



a—Mg + 1.46 pct Th + 0.56 pct Zn + 0.64 pct Zr. Glycol. b—Mg + 5.92 pct Th + 1.00 pct Zn + 0.65 pct Zr. Glycol.

Fig. 5—Structure of sand cast Mg-Th-Zn-Zr alloys falling to the left of the crest of creep resistant alloys shown in Figs. 1 through 4. X500. Area reduced approximately 40 pct for reproduction.

not been explored, and therefore, the iso-strength lines are not connected. The good creep resistance observed on the low thorium-low zinc alloys at 650°F does not hold at 700°F. It is interesting to observe that at 650°F creep resistance on the 1 pct Zn alloy decreases when the thorium content is increased from 0.5 to 6 pct, while at 700°F increasing thorium tends to increase the resistance of the alloy to creep. The fact that the decrease in creep resistance of the 6 pct Th-4 pct Zn alloy with increasing temperature (650° to 700°F) is so little might indicate that this or a similar composition will prove to be superior to the other compositions after long exposure times. For some reason the 0.2 pct extension value for the 5 pct Th-4 pct Zn alloy at 650° is lower than at 700°F.

Microstructure

Microstructural differences can be seen within the group of alloys studied. Figs. 5 through 7

depict some of the types of structure observed. These structures might be listed as follows:

1—Magnesium solid solution matrix with an intermetallic compound resulting from divorcement of the eutectic similar to that observed in ternary Mg-Th-Zr alloys²¹ (Figs. 5a, 7a and b). In some alloys partial divorcement of the eutectic resulted in structures consisting of Mg₂, intermetallic compound, and patches of eutectic (Fig. 7d).

2—Magnesium solid solution matrix with two phases having irregular jagged plate-like shapes at the grain boundaries (Fig. 6).

No identification of the composition of these phases has been made to date.

The structure described in item 2, above, and particularly exemplified in Fig. 6b, c, and d by the 3 pct Th-2 pct Zn, 4 pct Th-2 pct Zn, and the 6 pct Th-4 pct Zn alloys appears to correlate with maximum creep resistance. The compounds in the 0.5 pct Th-0.5 pct Zn alloy (Fig. 6a) exhibit the same tendency to form a jagged structure but, of course, are present in much smaller amounts because of the low alloy content. In spite of the low alloy content this composition still exhibits good creep resistance as might be expected if this property is a result of this type of structure.

Alloys whose structures are shown in Figs. 5 and 7 exhibit lower resistance to creep than the optimum attainable in this alloy system. Figs. 5a, 7b and d show structures as described in item 1, above. Figs. 5b and 7a are similar with an indication of the presence of two phases at the grain boundaries. Fig. 7c also is representative of an alloy having two phases at the grain boundaries. One of the compounds has a thin needle-like appearance and is quite irregular in the direction in which it lies at the grain boundaries. In general, alloys having a high Zn-Th ratio such as those whose structures are shown in Fig. 7a and c when etched more drastically reveal also copious precipitation within the solid solution matrix as often found in magnesium



a (left)—Mg + 0.50 pct Th + 0.55 pct Zn + 0.58 pct Zr. Electrolytic polish. 10 pct HCl in methyl cellosolve.

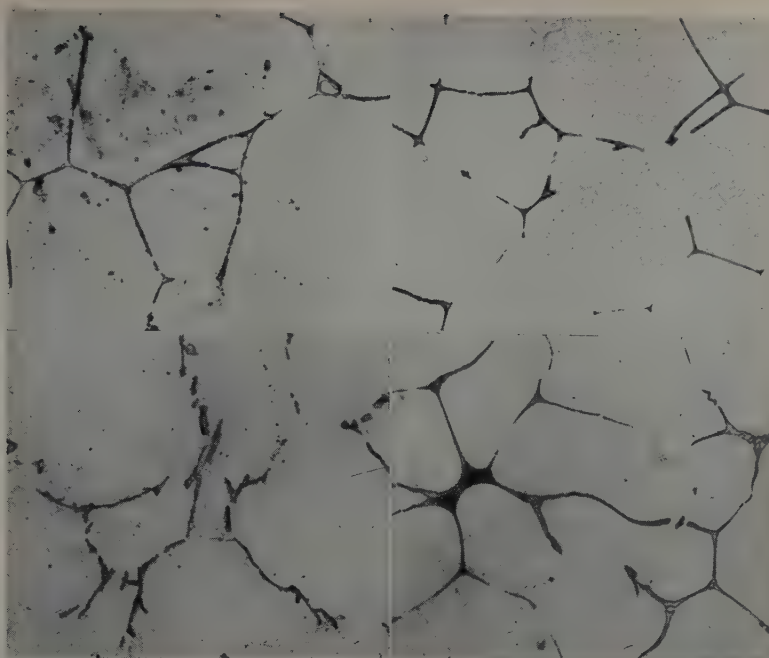
b (right)—Mg + 3.01 pct Th + 1.99 pct Zn + 0.78 pct Zr. Electrolytic polish. 10 pct HCl in methyl cellosolve.

c (left)—Mg + 4.00 pct Th + 1.99 pct Zn + 0.74 pct Zr. Electrolytic polish. 10 pct HCl in methyl cellosolve.

d (right)—Mg + 6.12 pct Th + 4.02 pct Zn + 0.84 pct Zr. Electrolytic polish. 10 pct HCl in methyl cellosolve.

Fig. 6—Structure of sand cast Mg-Th-Zn-Zr alloys following the crest of creep resistant alloys shown in Figs. 1 through 4. X500. Area reduced approximately 40 pct for reproduction.

a (left)—Mg + 0.53
pct Th + 1.52 pct Zn
+ 0.67 pct Zr. Glycol.



b (right)—Mg + 1.15
pct Th + 1.95 pct Zn
+ 0.68 pct Zr. Glycol.

c (left)—Mg + 1.02
pct Th + 4.93 pct Zn
+ 0.72 pct Zr. Glycol.

d (right)—Mg + 3.93
pct Th + 4.91 pct Zn
+ 0.88 pct Zr. Glycol.

Fig. 7—Structure of sand cast Mg-Th-Zn-Zr alloys falling to the right of the crest of creep resistant alloys shown in Figs. 1 through 4. X500. Area reduced approximately 40 pct for reproduction.

alloys containing zirconium. However, this feature is not shown in the micrographs included herein because such etching would obscure the characteristic compound formations. The alloys exhibiting these structural phenomena are usually associated with the lowest creep resistance in the system.

Summary

The results of this comprehensive investigation on the effect of varying thorium and zinc contents on the strength and 100-hr creep characteristics of Mg-Th-Zn-Zr alloys may be summarized as follows:

1—Good combinations of strength and ductility at room and elevated temperatures may be developed over a wide range of thorium and zinc contents.

2—Exceptionally high creep resistance at 650° and 700°F can be developed within a certain range of thorium and zinc contents which conforms to neither the range giving maximum room temperature strength nor that exhibiting optimum static properties at the elevated temperatures.

3—The commercial alloy containing magnesium plus 3 pct Th plus 2.5 pct Zn plus 0.7 pct Zr is a good overall choice for elevated temperature applications based upon its combination of tensile and creep properties as well as conservation of costly and critical materials. However, for specific applications there are alloys in the Mg-Th-Zn-Zr system having better creep resistance.

4—Alloys of magnesium plus zirconium containing as little as 0.5 pct Th and 0.5 pct Zn may have useful applications in stressed parts operating as high as 650°F.

5—High creep resistance in this alloy system is generally associated with a microstructure in which the intermetallic constituent has a jagged plate-like shape.

References

- ¹ T. E. Leontis and J. P. Murphy: *Trans. AIME* (1946) **166**, p. 295; *METALS TECHNOLOGY* (April 1946).
- ² A. J. Murphy and R. J. M. Payne: *Journal Inst. Metals* (1946) **73**, p. 105.
- ³ C. J. P. Ball: *Metal Industry* (1949) **75**, p. 152.
- ⁴ T. E. Leontis: *Trans. AIME* (1949) **185**, p. 968; *JOURNAL OF METALS* (December 1949).

⁵ G. A. Mellor and R. W. Ridley: *Journal Inst. Metals* (1949) **75**, p. 679.

⁶ J. W. Meier and M. M. Martinson: *Trans. Canadian Inst. Min. Met.* (1950).

⁷ K. E. Nelson and F. P. Strieter: *Trans. Amer. Foundrymen's Soc.* (1950) **58**, p. 400.

⁸ K. Grube and L. W. Eastwood: *Proc. ASTM* (1950) **50**, p. 989.

⁹ T. E. Leontis: *Trans. AIME* (1951) **191**, p. 987; *JOURNAL OF METALS* (November 1951).

¹⁰ K. E. Nelson and F. P. Strieter: *Trans. Amer. Foundrymen's Soc.* (1951) **59**, p. 532.

¹¹ H. J. Millward: *American Foundryman* (1951) **20** (3), p. 44.

¹² G. A. Mellor and R. W. Ridley: *Journal Inst. Metals* (1953) **81**, p. 245.

¹³ T. E. Leontis: Unpublished.

¹⁴ J. C. McDonald: *Trans. AIME* (1941) **143**, p. 179.

¹⁵ J. C. McDonald: U. S. Patent No. 2,371,531 (March 13, 1945).

¹⁶ U. S. Patent Application No. 369,749; Sauerwald et al.; published by Alien Property Custodian (June 15, 1943).

¹⁷ U. S. Patent Application No. 369,824; Sauerwald et al.; published by Alien Property Custodian (June 15, 1943).

¹⁸ F. Sauerwald: *Ztsch. anorg. allgem. Chem.* (1949) **257**, p. 296.

¹⁹ J. C. McDonald: *Light Metal Age* (December 1951) **9**, Nos. 11, 12, p. 13.

²⁰ T. E. Leontis: *Trans. AIME* (1952) **194**, p. 287; *JOURNAL OF METALS* (March 1952).

²¹ T. E. Leontis: *Trans. AIME* (1952) **194**, p. 633; *JOURNAL OF METALS* (June 1952).

²² A. C. Jessup: U. S. Patent No. 2,604,396 (July, 1952).

²³ Anonymous: *Metal Industry* (1952) **81**, p. 169.

²⁴ C. J. P. Ball: Presented before the 8th Annual Meeting of the Magnesium Association, November 1952.

²⁵ K. E. Nelson: *Trans. Amer. Foundrymen's Soc.* (1953) **61**.

²⁶ W. P. Saunders and F. P. Strieter: *Trans. Amer. Foundrymen's Soc.* (1952) **60**, p. 581.

²⁷ A. A. Moore and J. C. McDonald: *Proc. ASTM* (1946) **46**, p. 970.

²⁸ P. F. George: *Trans. Amer. Foundrymen's Soc.* (1949) **57**, p. 133.

Titanium-Rich Regions of the Ti-C-N, Ti-C-O, And Ti-N-O Phase Diagrams

by L. Stone and H. Margolin

The Ti-C-N and Ti-C-O systems were investigated in the temperature range from 500° to 1400°C and in the composition range up to 2 pct C and 5 pct N or O. Characteristic isothermal sections at 800°, 900°, 1000°, and 1300°C are presented. The Ti-N-O system was studied in the temperature range from 900° to 1400°C with alloys containing up to 6 pct total alloying content. Characteristic isothermal sections at 1000° and 1400°C are presented. Melting-point data for all three systems are also included.

THIS paper reports on one of a series of investigations which have been conducted on the phase diagrams resulting from interstitial alloying with iodide titanium. The other investigations involved delineation of the binary systems with carbon,¹ nitrogen and boron,² and oxygen.³ The Ti-O binary system has also been investigated by Bumps et al.⁴ In varying degrees, each of these interstitial elements has been shown to stabilize the low temperature α modification of titanium¹⁻⁵ and each forms a face-centered cubic TiX compound (henceforth designated δ). In addition, the Ti-N and Ti-O systems reveal a low temperature tetragonal phase (ϵ) formed by a peritectoid reaction between α and TiX.²⁻⁴

Experimental Procedure

The development of experimental techniques for the study of titanium alloy systems has, to a large extent, become standardized. In this investigation, the equipment and procedures described in detail by Cadoff and Nielsen¹ have been used.

Arc Melting: In general, binary alloys with carbon, nitrogen, and oxygen, prepared in the composition range of interest in this investigation, show negligible composition changes during arc melting.¹⁻⁴ However, the possibility of the formation of some gaseous combination of alloying elements such as CO, CN, or NO during the preparation of these ternary alloys was considered. Calculations showed that the evolution of only 0.05 gram of such a gas would be detectable as a pressure change in the closed system used during preparation of these alloys. Such pressure changes were not observed. Consequently, nominal compositions have been used in plotting the data.

The compositions of the materials used in the preparation of the alloys are shown in Table I. After melting for 3 to 5 min at 275 to 350 amp, the

L. STONE and H. MARGOLIN, Junior Members AIME, are Research Assistant and Research Associate, respectively, Research Div., New York University, New York.

Discussion on this paper, TP 3630E, may be sent, 2 copies, to AIME by Jan. 1, 1954. Manuscript, April 17, 1953. Cleveland Meeting, October 1953.

This paper is based on a thesis by L. Stone submitted in partial fulfillment of requirements for the degree of Master of Engineering Science to the Graduate Div., College of Engineering, New York University.

Table I. Composition of Materials Used in Preparation of the Alloys

Material	Purity	Source
Titanium	(Iodide) 99.96 pct	New Jersey Zinc Co.
Carbon	Spectroscopic grade	National Carbon Co.
Oxygen (as TiO ₂)	99.98 pct	Baker Chemical Co.
Nitrogen (as TiN)	97 to 99 pct	Watertown Arsenal Laboratory

alloys were checked for homogeneity by microstructural examination. Alloys containing up to 1 pct C were homogeneous in the presence of less than 3 pct N or O. At higher alloying contents, some inhomogeneities in the carbon distribution became evident. Alteration of the melting procedure toward longer times and higher currents did not improve the homogeneity of these alloys. Ti-N-O alloys were homogeneous in the range to about 3 or 4 pct total alloying addition. Beyond this, almost all of the specimens showed as-cast microstructures consisting only of the α phase. Consequently, inhomogeneities could not be detected by examination of microstructures.

Ten alloys from each of the systems were analyzed for two of the elements present (oxygen being omitted in all cases and titanium being omitted in the Ti-C-N alloys). In all cases the analyses were found not to be sufficiently precise to serve as criteria for the total composition of these alloys. On the basis of phase distribution in heat-treated alloys, however, it appears that carbon is distributed throughout the alloys most uniformly, with oxygen and nitrogen following in that order.

Heat Treatment: Specimens for heat treatment were wrapped in titanium sheet before sealing in the argon-filled quartz capsules. Heat-treatment times varied from 100 hr at 800°C to 0.5 hr at 1400°C. After heat treatment the specimens were quenched by breaking the capsule in water. With the exception of alloys in the low composition region, heat treatment did not have an appreciable effect on the as-cast microstructures.

Metallography: Following heat treatment, the specimens were prepared for metallographic examination by grinding on emery paper and electrolytic polishing. For the majority of the specimens a 10-sec etch with Remington "A" agent (25 pct HNO₃, 25 pct HF, and 50 pct glycerin) adequately

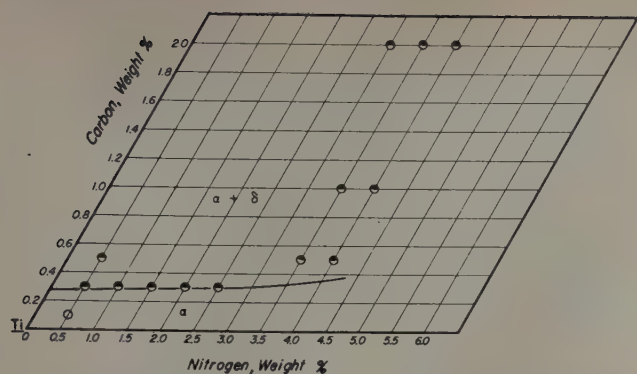


Fig. 1—Isothermal section at 800°C in the Ti-C-N system.

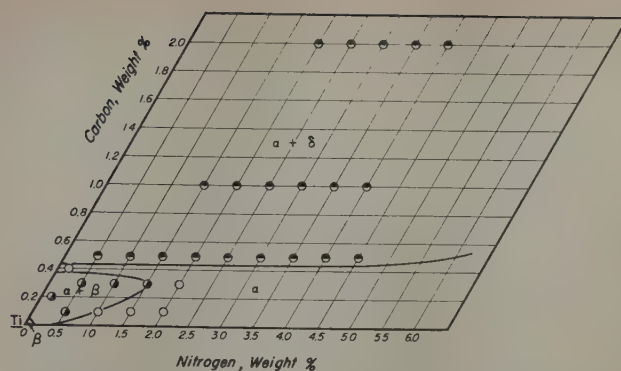


Fig. 2—Isothermal section at 900°C in the Ti-C-N system.

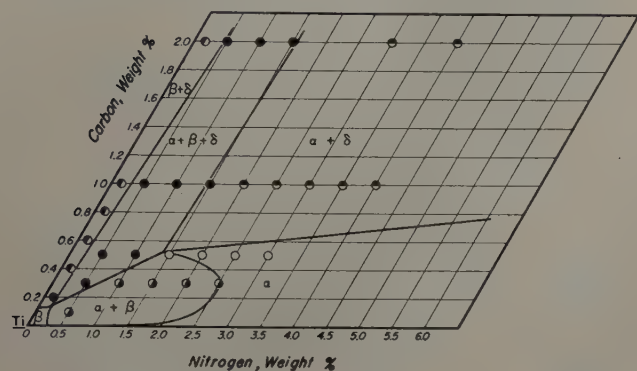


Fig. 3—Isothermal section at 1000°C in the Ti-C-N system.

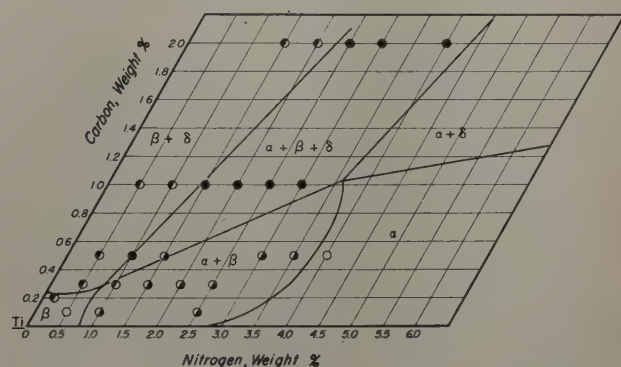


Fig. 4—Isothermal section at 1300°C in the Ti-C-N system.

revealed the microstructure. This reagent does not, however, differentiate between α and carbide in microstructures where one or both constituents are present in small amounts. In this case, the use of an electrolytic 10 pct NaCN etch⁶ produced excellent results by staining the carbides orange and the α blue.

Precision: In general, the phase diagrams have been delineated on the basis of microstructural examination of heat-treated specimens.

Table II is included to indicate the estimated order of precision which the authors feel may be attributed to the phase boundaries of the isothermal sections. The column entitled "Precision" is to be interpreted as the width of the lines which have been drawn as phase boundaries. On this basis the Ti-C-O system is probably delineated with the greatest precision, with the Ti-C-N and the Ti-N-O systems following in that order.

Ti-C-N System

Isothermal sections were delineated in the temperature range from 500° to 1400°C at 100° intervals and in the composition range up to 2 pct C and 5 pct N.⁷ The sections at 800°, 900°, 1000°, and 1300°C are shown in Figs. 1 to 4.

Table II. Estimated Order of Precision of Phase Boundaries of Isothermal Sections

Element	Precision of Delineation	
	Range	Precision
Carbon	0 to 0.5 pct C	0.05 pct
	0.6 to 1.0 pct C	0.10 pct
	1.1 to 2.0 pct C	0.20 pct
Oxygen	0 to 2.0 pct O	0.2 pct
	2 to 3 pct O	0.3 pct
	More than 3 pct O	0.4 pct
Nitrogen	0 to 1.5 pct N	0.25 pct
	1.5 to 3 pct N	0.35 pct
	More than 3 pct N	0.5 pct

In addition, the following melting-point results were obtained:

1—The addition of nitrogen to alloys containing 2.0 pct C results in a rise in the liquidus temperature from 1935°C at 0 pct N^{1,2} to approximately 2510°C at 3.0 pct N, and a rise in the temperature of the solidus surface* to approximately 2070°C at 2.5 pct N.

* It is not possible, with the experimental apparatus used, to distinguish between the solidus surfaces of primary and secondary separation.

2—The addition of from 1 to 2.5 pct N to alloys containing 0.5 pct C has little effect on the incipient melting temperature, which is approximately 1735°C. Beyond this point the solidus temperature rises with increasing nitrogen content.

On the basis of the incipient melting points and the presence of peritectically formed α in as-cast microstructures (see Fig. 5), it would seem reason-

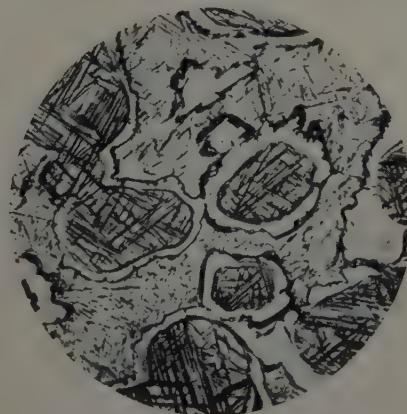


Fig. 5—2.0 pct C, 3.0 pct N, as-cast structure. Carbide containing precipitated α , surrounded by peritectically formed α , in a transformed β matrix. Remington "A" etch. X700. Area reduced approximately 30 pct for reproduction.

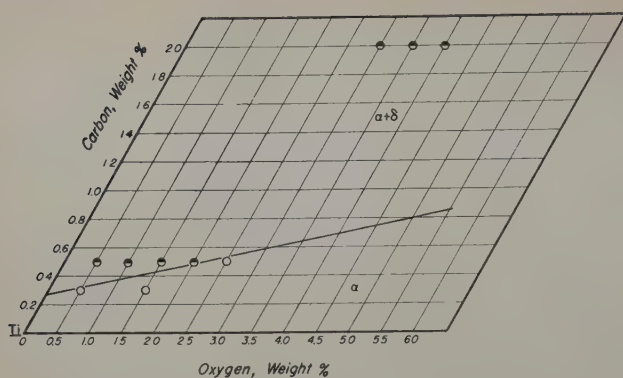


Fig. 6—Isothermal section at 800°C in the Ti-C-O system.

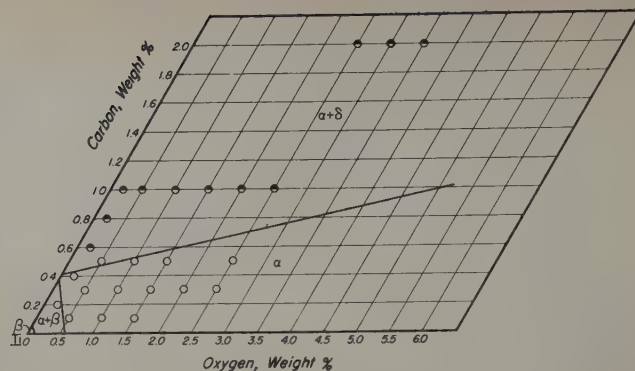


Fig. 7—Isothermal section at 900°C in the Ti-C-O system.

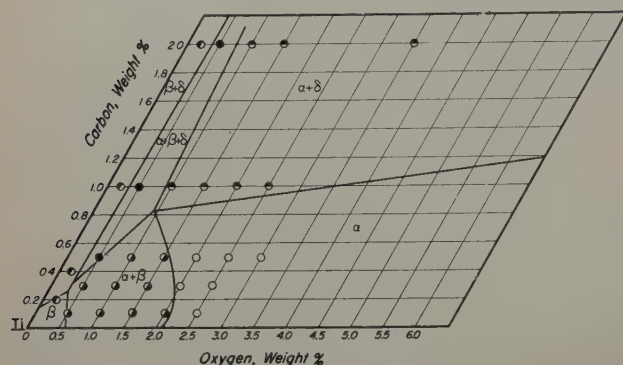


Fig. 8—Isothermal section at 1000°C in the Ti-C-O system.

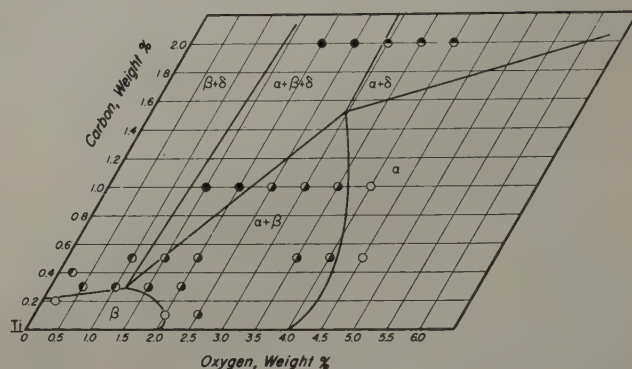


Fig. 9—Isothermal section at 1300°C in the Ti-C-O system.

able to postulate that the reaction $L + \alpha \rightleftharpoons \beta + \delta$ occurs in this system near 1735°C. The three-phase fields, $\alpha + \beta + L$ and $\alpha + \delta + L$, which exist above the ternary peritectic temperature, are generated respectively by the reactions $L + \alpha \rightleftharpoons \beta$ and $L + \delta \rightleftharpoons \alpha$ in the binary Ti-N system. Below the ternary peritectic temperature the three-phase fields which exist are $\beta + L + \delta$ and $\alpha + \beta + \delta$, which disappear, respectively, into the binary Ti-C peritectic, $L + \delta \rightleftharpoons \beta$, and peritectoid, $\beta + \delta \rightleftharpoons \alpha$, reactions.

This development requires complete solid solubility between TiC and TiN. Excellent evidence for such solubility has been obtained by Beattie and Ver Snyder,⁸ who have reported lattice parameters for Ti(C,N) microconstituents containing varying amounts of carbon and nitrogen. In addition, it is necessary that the temperature of the ternary reaction be above the carbon peritectic reaction temperature ($1750^\circ \pm 20^\circ\text{C}$). While the ternary reaction temperature observed is at 1735°C, the discrepancy is of the order of the precision of the apparatus.

Ti-C-O System

Isothermal sections were delineated in the temperature range from 500° to 1400°C at 100° intervals and in the composition range up to 2 pct C and 5 pct O.⁷ The sections at 800°, 900°, 1000°, and 1300°C are shown in Figs. 6 to 9.

In addition, the following melting-point data were obtained:

1—Alloys containing 0.5 pct C and from 1 to 3 pct O all melted at approximately 1690°C. In the absence of microstructural evidence of eutectic solidification, it was concluded that measurements were being made along the $\beta/\beta + L$ surface of primary separation. The temperature of 1690°C is within experimental error of the 1700°C melting point reported for titanium by Adenstedt et al.⁹ and probably reflects the small increase in melting point

due to oxygen addition.

2—Alloys containing 0.5 pct C with from 3.5 to 5.0 pct O, and 2 pct C with from 0.5 to 2.5 pct O, showed incipient melting at 1770°C.

Since the only primary dendrites observed in the as-cast structures were carbides and since, in the high alloy region, α formed as a peritectic wall around the carbides, it would appear reasonable to postulate a development in this system paralleling that described in the Ti-C-N system. This identifies the constant incipient melting range at 1770°C as a ternary peritectic reaction $\alpha + L \rightleftharpoons \beta + \delta$ and imposes the following restrictions on the binary diagrams: the oxygen binary reaction involving L, α , and β and the reaction involving α , L, and δ must occur at temperatures higher than 1770°C; also the binary carbon peritectic must occur lower than 1770°C. These relative values for the binary reaction temperatures all agree, within experimental error, with values obtained by Bumps et al.⁴ and New York University.¹⁻³

For the reaction $\alpha + L \rightleftharpoons \beta + \delta$, the phases TiC and TiO must be isomorphous. The isothermal section at 1300°C (Fig. 9) suggests that oxygen and carbon are interchangeable in TiC, since the δ corner of the three-phase field ($\alpha + \beta + \delta$) extends into the ternary section.

Ti-N-O System

On the basis of microstructural examination of heat-treated alloys, isothermal sections have been drawn in the temperature range from 900° to 1400°C,⁷ and sections at 1000° and 1400°C are shown in Figs. 10 and 11.

The simplicity of the phase relations in this system is apparent from the isothermal sections. It has been observed⁷ that as the β and $\alpha + \beta$ fields expand with increasing temperature, the rate of expansion decreases. This is characteristic of both the Ti-N and Ti-O binary systems.

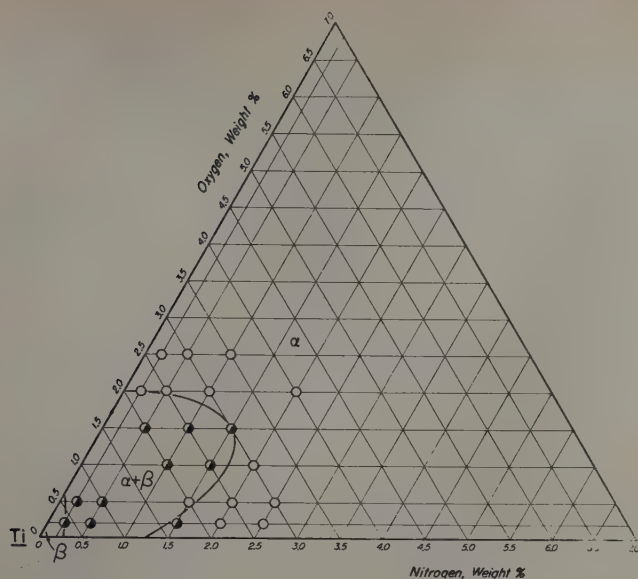


Fig. 10—Isothermal section at 1000°C in the Ti-N-O system.

Very little information on the liquidus region could be obtained from microstructural examination of the as-cast alloys. Only β , $\alpha + \beta$, and α structures were observed. Coring in the α was not marked, which would indicate the absence of any extensive liquid-plus-solid regions in the composition range investigated.

Data obtained with the melting-point apparatus indicated that nitrogen generally raises the temperature for incipient and complete melting considerably more rapidly than oxygen, in agreement with the binary diagrams. The effect of oxygen additions to low nitrogen alloys was so slight as to be approximately on the order of the precision of the apparatus. A similar effect was noted with the addition of oxygen to low carbon alloys. No clear indications were obtained of any ternary reactions in the range investigated.

Microstructures

In general, the α , β , $\alpha + \beta$, and $\alpha + \delta$ microstructures observed were identical to those which have been noted in the binary systems containing carbon, nitrogen, and oxygen. In addition, microstructures for the Ti-C-N and Ti-C-O systems were quite similar and consequently, except as specifically noted, no attempt will be made to differentiate between these two systems in discussing microstructures.

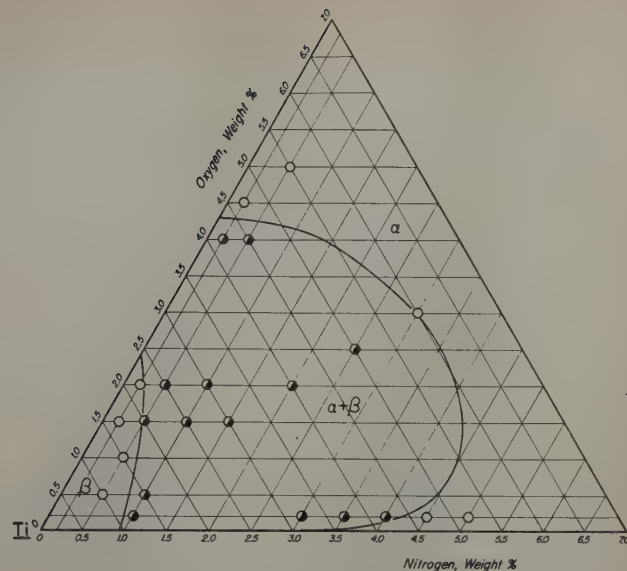


Fig. 11—Isothermal section at 1400°C in the Ti-N-O system.

Two types of three-phase ($\alpha + \beta + \text{carbide}$) microstructures were observed. The first is shown in Fig. 12 and is typical of three-phase alloys with low alloying content. In the higher alloy region the as-cast dendritic distribution of the carbides is not removed by heat treatment, and a typical three-phase structure appears as shown in Fig. 13. Here the α which solidified adjacent to the carbide is richer in oxygen than that which solidified last. Consequently, on quenching, the transformation of α to β occurs earliest in the regions not immediately adjacent to the carbides.

A structure quite similar to the $\alpha + \delta$ structures seen in the Ti-N and Ti-O systems was encountered in Ti-C-N and Ti-C-O alloys. In Ti-C-N alloys the structure is common to all alloys containing at least 0.5 pct C and 1.5 pct or more N. For Ti-C-O alloys, higher contents of carbon and oxygen are required. A typical structure is shown in Fig. 5 for the as-cast condition, and in Fig. 14 for a heat-treated specimen. Heat treatment has coarsened the line structure and it can be seen that the precipitate is α , since it is continuous with the α matrix.

X-Ray Diffraction

To check the metallographic observation that the line structure in Figs. 5 and 14 was α , X-ray diffraction patterns were obtained for the 2.0 pct C, 3.0 pct

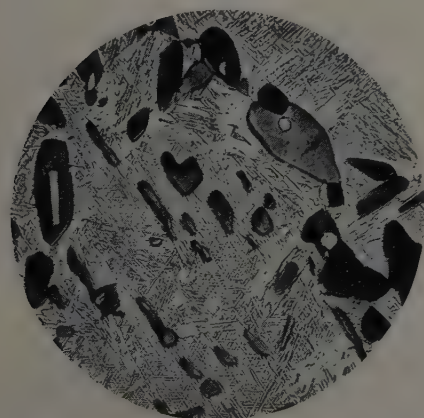


Fig. 12—0.3 pct C, 0.5 pct N, 48 hr at 1000°C, water-quenched. Isothermal α (dark) and carbide (white) in a transformed β matrix. Remington "A" etch and NaCN electrolytic etch. X300. Area reduced approximately 30 pct for reproduction.



Fig. 13—2.0 pct C, 1.5 pct O, 24 hr at 1100°C, water-quenched. Dendritic carbide and α plus transformed β . Remington "A" etch. X200. Area reduced approximately 30 pct for reproduction.

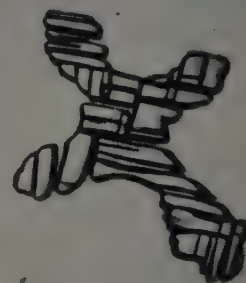


Fig. 14—2.0 pct C, 3.0 pct O, 24 hr at 1100°C, water-quenched. Carbide with precipitated α , α matrix out of focus. Remington "A" etch. X1000. Area reduced approximately 30 pct for reproduction.

N specimen in both the as-cast state and after heat treatment at 1400°C. In both cases two sets of α lines, corresponding to the different composition of α and transformed β , in addition to carbide lines, were observed. Indications of other phases were absent.

When a Ti-C-N alloy showing the line structure of Fig. 5 was heated at 800°C for 100 hr, a weak diffraction pattern of the nitrogen tetragonal phase, ϵ , was obtained. The reaction to form ϵ must occur by the reaction $\alpha + \delta \rightleftharpoons \epsilon$ (in agreement with results obtained in the investigations of the binary systems)^{2,4} and consequently occurs at α - δ interfaces, see for example, Fig. 9 in ref. 2.

If it is considered that the interfaces available for this reaction exist only at the junction of carbide and peritectoidally formed α (see Fig. 5), then because of the sluggishness of formation, a detectable amount of ϵ would not form. If the precipitate in the carbide is α , then a sufficient interfacial area would be available to form appreciable amounts of ϵ . This is indirect proof that the precipitate within the carbide is α .

The ϵ phase is not indicated in any of the isothermal sections because no information was available on the composition of this phase and the composition of α and δ which react to form it. The ϵ phase was not observed in the diffraction patterns of Ti-C-O alloys.

Discussion

As has been indicated,^{2,3} the presence of small amounts of oxygen in sponge may be responsible for the shift of the α -transus in Ti-N alloys to higher nitrogen contents. This shift may be explained by reference to Figs. 10 and 11. The trace of the $\alpha/\alpha + \beta$ phase surface in this isothermal section is seen to move to higher nitrogen contents with additions of oxygen. In a vertical section parallel to the Ti-N binary diagram this movement would appear as a shift of the α -transus to higher nitrogen contents.

A similar shift in the $\alpha/\alpha + \beta$ phase surface for Ti-N alloys on addition of carbon is also observed, see for example Fig. 2. The addition of carbon and oxygen to alloys containing nitrogen thus appears to reduce the effectiveness of nitrogen as an α stabilizer.

The fact that small amounts of oxygen may markedly affect the Ti-N diagram suggests that Ehrlich's¹⁰ reported solubility for carbon in α titanium may be due to incidental pickup of oxygen and nitrogen. Ehrlich obtained his alloys by sintering at 1800°C in a vacuum and furnace cooling. He estimated that the resulting structures were characteristic of heat treatment at 700° and 800°C, and determined solubility by measurement of lattice parameters. The values obtained by Ehrlich for the maximum solubility of carbon in α titanium compare as follows with recently reported results: Ehrlich's value for TiC was 1.96 wt pct, while Cadoff and Nielsen¹ found the value of 0.48 wt pct.

In the Ti-C-N and Ti-C-O systems, it can be seen that the addition of nitrogen or oxygen to carbon-containing alloys increases the solubility of carbon in α titanium. The addition, for example, of 3.5 pct O to titanium at 1400°C raises the solubility of carbon in α titanium to 1.5 pct C¹ and would indicate: 1—that total nitrogen and oxygen contamination of the order of 3 or 4 wt pct was present in Ehrlich's alloys, and 2—that the alloys were representative of specimens which had been heat-treated above 1400°C.

Finally, in reference to the increase of carbon solubility in α titanium by additions of nitrogen and oxygen, it can be seen from Figs. 1, 4, 6, and 9 that oxygen is more effective in increasing carbon solubility than is nitrogen.

Summary

1—In overall characteristics, the Ti-C-N and Ti-C-O phase diagrams are very similar, with a ternary $\alpha + \beta +$ carbide phase field dominating the diagram in the temperature interval from 1000° to 1400°C.

2—The Ti-N-O system is characterized by α , $\alpha + \beta$, and β phase fields, all of which expand to higher alloying contents with increasing temperature.

3—Indications were obtained that the Ti-C-N and Ti-C-O systems contain a ternary peritectic reaction at approximately 1735° and 1770°C, respectively.

4—The addition of carbon or oxygen to Ti-N alloys reduces the effectiveness of nitrogen as an α stabilizer.

5—Nitrogen and oxygen increase the solubility of carbon in α titanium, with oxygen as the more effective of the two.

Acknowledgments

The authors wish to thank the members of the staff of the Metallurgy Laboratory of New York University for assistance in this research and to express their appreciation to Professor John P. Nielsen for his keen interest and encouragement. The authors also wish to thank the Ordnance Corps, Watertown Arsenal for permission to publish the results of this investigation. The work was carried out for the U. S. Army, Ordnance Corps, Watertown Arsenal Laboratory, Watertown, Mass., under Contract No. DA-30-069-ORD-208.

References

1. I. Cadoff and J. P. Nielsen: Titanium-Carbon Phase Diagram. *Trans. AIME* (1953) **197**, pp. 248-252; *JOURNAL OF METALS* (February 1953).
2. A. E. Palty, H. Margolin, and J. P. Nielsen: Titanium-Nitrogen and Titanium-Boron Systems. To be published in *Trans. ASM*, Vol. 46.
3. New York University, Engineering Research Div.: Binary Alloys of Titanium with Carbon, Nitrogen, Oxygen and Boron. Final Report to Watertown Arsenal Laboratory on Contract No. DA-30-069-ORD-76, October 31, 1952.
4. E. S. Bumps, H. D. Kessler, and M. Hansen: The Titanium-Oxygen System. *Trans. ASM* (1953) **45**, pp. 1008-1025.
5. R. I. Jaffee, H. R. Ogden, and D. J. Maykuth: Alloys of Titanium with Carbon, Oxygen and Nitrogen. *Trans. AIME* (1950) **188**, pp. 1261-1266; *JOURNAL OF METALS* (October 1950).
6. New York University, Engineering Research Div.: Titanium-Aluminum-Chromium Alloys. Final Report to Bureau of Aeronautics, Navy Dept., on Contract No. N0a(s) 51-331-C (1952).
7. New York University, Engineering Research Div.: Titanium-Rich Ternary Alloys of Titanium with Carbon and Nitrogen, Carbon and Oxygen, and Nitrogen and Oxygen. Final Report to Watertown Arsenal Laboratory on Contract No. DA-30-069-ORD-208, April 15, 1953.
8. H. J. Beattie, Jr. and F. L. Ver Snyder: Microconstituents in High Temperature Alloys. *Trans. ASM* (1953) **45**, pp. 397-423.
9. H. K. Adenstedt, J. R. Pequignot and J. M. Raymer: The Titanium-Vanadium System. *Trans. ASM* (1952) **44**, pp. 990-1003.
10. P. Ehrlich: About the Binary Systems of Titanium with the Elements Nitrogen, Carbon, Boron and Beryllium. *Ztsch. anorg. allgem. Chem.* (1949) **259**, pp. 1-41.

On the Theory of the Formation of Martensite

by M. S. Wechsler, D. S. Lieberman, and T. A. Read

A theoretical analysis of the austenite-martensite transformation is presented which predicts the habit plane, orientation relationships, and macroscopic distortions from a knowledge only of the crystal structures of the initial and final phases.

THIS paper presents a new theory of the formation of martensite. This theory makes possible the calculation of the austenite planes on which the martensite plates form, the orientation relationship between the austenite and martensite crystal axes, and the macroscopic distortions which are observed. The only input data needed are the crystal structures and lattice parameters of the austenite and martensite.

Considerable effort has been devoted over the past thirty years to the development of an understanding of the crystallographic features of martensite reactions. Much of this work has been done on steels and iron-nickel alloys, for which a great deal of data has been accumulated concerning the shape and orientation of the martensite plates, the relative orientations of the austenite and martensite crystal axes, and the observable distortions which result from transformation. These observations are reviewed in refs. 1, 2, and 3.

The first major step toward an understanding of these phenomena was made in 1924 by Bain,⁴ who showed that the α body-centered cubic structure can be produced from the γ face-centered cubic structure by a contraction of about 17 pct in the direction of one of the austenite cube axes and an expansion of 12 pct in all directions perpendicular to it. Since that time, most of the efforts at further interpretation have been made by investigators who have worked from the phenomenological data, incorporating some of the information from the lattice properties, and have sought an analysis into likely deformations which would produce the observed results.⁵⁻⁹ All but the three most recent papers on the subject have already been reviewed in some detail.³ Machlin and Cohen¹⁰ measured the components of the distortion matrix and verified that the habit plane is a plane of zero distortion and rotation for the (259) case. They showed that the measured distortion matrix, when applied to the parent lattice, does not yield the product lattice and hence some inhomogeneous distortion must occur. Frank,¹¹ working from the lattice properties and taking some clues from the observations, considered the correspondence of close-packed rows and planes in the

austenite and martensite. He predicted substantially the observed lattice relationship and habit plane for certain steels which have a (225) habit. Geisler¹² suggested that there is a natural tendency for the habit plane to be a (111) and postulated certain slip processes to account for the fact that the experimentally observed habit plane is irrational and deviates from the assumed one.

The present work differs from previous treatments of martensite formation in that it permits calculation of all the major manifestations of the process. Habit plane indices, orientation relationships, and observable distortions are all calculated from a knowledge of the crystal structures of the initial and final phases alone. The calculations contain no adjustable parameters. The agreement found between calculated results and the observations reported in the literature constitutes powerful evidence in favor of the mechanism of martensite formation proposed. The theory is applicable to systems other than steel (as is discussed later in this paper) which exhibit a diffusionless phase change but because of the wide-spread interest in the austenite-martensite transformation, particular attention will be given to the iron-base alloys. For other systems which undergo a similar face-centered cubic to face-centered tetragonal transformation, the mathematical treatment is identical with that presented here. Hence the theory successfully describes the transformation in the indium-thallium alloy.¹³

Homogeneous Transformation to Martensite

The distortion which any homogeneously transforming volume of austenite undergoes in order to become martensite is shown in Fig. 1, as was first suggested by Bain.⁴ (This distortion will hereafter be referred to as the "Bain distortion.") This specification of a contraction along one cube axis combined with an expansion in all directions perpendicular to this axis describes what is properly called the "pure" distortion associated with this transformation.

The distinction between a "pure" and an "impure" distortion plays an important part in the discussion which follows. A "pure" distortion is characterized by the existence of at least one set of orthogonal axes fixed in the body which are not rotated by the distortion. (These are called the "principal axes" of the distortion.) No such set of axes exists in the case of an "impure" distortion. On the other hand, an impure distortion can always be represented as the result of a pure distortion combined with the rotation of the specimen as a rigid body. For a given impure distortion the corresponding pure distortion

M. S. WECHSLER, D. S. LIEBERMAN, and T. A. READ, Member AIME, are associated with the Dept. of Metallurgy, School of Mines, Columbia University, New York.

Discussion on this paper, TP 3632E, may be sent, 2 copies, to AIME by Jan. 1, 1954. Manuscript, April 20, 1953. Cleveland Meeting, October 1953.

This paper is based on a thesis by M. S. Wechsler submitted in partial fulfillment of the requirements for the degree of Doctor of Philosophy to the Faculty of Pure Science, Columbia University.

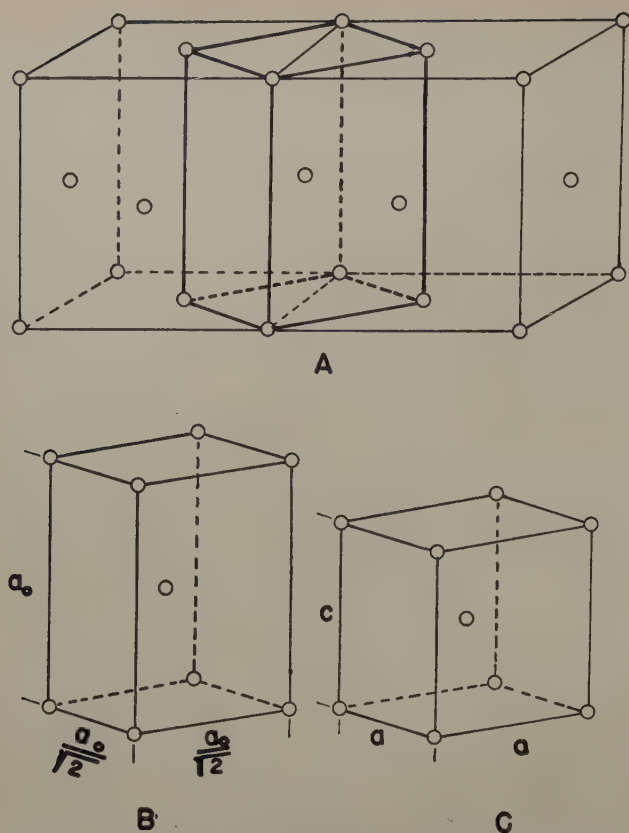


Fig. 1—(A) Body-centered tetragonal cell delineated in face-centered cubic structure. The Bain distortion takes (B) into (C).

and rigid body rotation are unique.* It is to be par-

* More precisely, there are two combinations of pure distortion and rotation, one of which corresponds to a distortion followed by a rotation and the other to a rotation followed by a distortion. In this discussion it is simpler to use the formulation where the distortion is considered to occur first.

ticularly noted that these statements are not restricted in validity to the small distortions and rotations dealt with by elasticity theory.

The distortion which occurs during the complete transformation of an austenite single crystal to martensite is both impure and inhomogeneous. But if the transformation of sufficiently small volumes of austenite, still large compared with the unit cell, is considered, the distortion of these, while still impure, will be homogeneous (otherwise X-ray diffraction patterns could not reveal the martensite structure). The distortion specified by Bain gives this homogeneous pure distortion of a small volume of material, without saying anything about the rigid body rotation which accompanies it.

It is particularly to be noted that while many distortions will generate a body-centered cubic (or body-centered tetragonal) structure from a face-centered cubic one, the Bain distortion involves considerably less distortion than any of the others. Any distortion which converts a face-centered cubic lattice into a body-centered cubic one can be represented as the Bain distortion followed by a distortion which carries the body-centered cubic lattice into another body-centered cubic lattice with the same lattice parameter. The smallest of these additional distortions is the one involved in the familiar mechanical twinning of the body-centered cubic lattice. In this case, the maximum extension is in the direction of one of the cube axes of the body-centered cubic structure. If the cube axis which is

stretched is the one which had come from one of the original face-centered cubic cube axes, then the combination of Bain distortion followed by twinning simply gives the Bain distortion over again, with a different choice of axes. If, however, the body-centered cubic cube axis which is stretched during twinning is one which before transformation was a face-centered cubic face diagonal direction, then the total increase in length in this direction produced by the Bain distortion followed by twinning is 59 pct. This is to be compared with a maximum extension of 12 pct which is produced by the Bain distortion alone.

The discussion above brings out the fact that the Bain distortion produces a body-centered cubic structure from a face-centered cubic one by means of much less drastic changes in interatomic distances than any other distortion which accomplishes the same change in structure. Another illuminating way of comparing alternate distortions is by considering nearest neighbor relationships for the atoms in the two crystal structures. In the face-centered cubic structure each atom has twelve nearest neighbors, whereas in the body-centered cubic structure it has only eight. After the Bain distortion, each atom's eight nearest neighbors are eight of the twelve it had previously had when the crystal structure was face-centered cubic. In contrast with this, the next simplest distortion leads to the result that two of the nearest neighbors of each atom in the body-centered cubic crystal had been only next-nearest neighbors before transformation. There are, therefore, strong physical grounds for concluding that the Bain distortion is the pure distortion which describes what actually happens in any small region which transforms homogeneously from austenite to martensite. A complete description requires in addition, of course, a specification of the rigid body rotation of the region.

Mechanism of Martensite Formation

Several investigators have shown that the distortion which occurs as martensite is formed is inhomogeneous even within a single martensite plate. The most complete study of this aspect of martensite formation was carried out by Machlin and Cohen,¹⁰ who demonstrated this inhomogeneity in a convincing manner. It is then clear that any proposed mechanism of martensite formation must provide for inhomogeneous distortion during transformation.

In the present paper two particularly simple types of inhomogeneity will be considered. The striking result is obtained that the predicted habit planes and macroscopically observable distortions are the same for the two types of inhomogeneity. They differ only in that in the one case it is predicted that a single martensite plate is a single crystal and in the other case the single plate contains two twin-related martensite crystal orientations. It has been shown experimentally^{13, 14} for the cubic-tetragonal transformation of indium-thallium alloys, to which the present analysis also applies, that the immediate result of transformation is the twinned product. But it has not yet been determined experimentally which of these predictions is the correct one for martensite. Therefore in the present paper both types of inhomogeneity will be considered.

Consider first the type of transformation inhomogeneity which leads to the twinned product. In this case no atom acquires any new nearest neighbors as a result of transformation, or, in other words, no

slip occurs. The inhomogeneity simply involves the pure transformation distortion being different in adjacent parts of a martensite plate. The only difference possible, in terms of Bain's transformation distortion, is that different cube axes of the face-centered cubic structure become the principal distortion axes along which contraction occurs.

If this inhomogeneity of transformation occurred in a random way from one part of the martensite plate to another, very large misfit strains would be produced. There is, in fact, only one way in which this type of inhomogeneity can occur and still have the differently transforming regions fit together without difficulty. This pattern of inhomogeneity consists of the transformation of parallel-sided slabs of austenite crystal which differ in the cube axis which is compressed. The planes separating these regions are parallel to one of the two austenite face diagonal planes which bisect the angle between the two cube axes which are compressed. This type of inhomogeneous transformation yields an array of twin-related martensite single crystals.

It will be shown below that if the ratio of the thicknesses of the twins has a certain critical value, then *there exists a plane in the austenite which undergoes no net distortion as a result of the transformation.* The physical significance of a pattern of inhomogeneity which results in a plane of zero net distortion is that it permits the strain energy of misfit between the martensite and austenite to be much smaller than in the case of homogeneous distortion. By "net" distortion is meant here the distortion-averaged over many of the twins, which are presumed to be very thin. The indices of this plane of zero net distortion are irrational and depend upon the lattice parameters of the austenite and martensite.

The second type of transformation inhomogeneity considered can be described most simply as a homogeneous Bain distortion occurring simultaneously with a certain amount of slip. The slip plane is one which is initially an austenite face-diagonal plane and becomes a martensite (112) plane. The slip direction is one which becomes a martensite [11 $\bar{1}$] direction. The slip is presumed to be distributed in a uniform way throughout the martensite plate and hence appears macroscopically as a homogeneous shear. It will be shown that if the amount of slip has a certain critical value, then there also exists in this case a plane in the austenite which undergoes no net distortion as a result of transformation. (By "net" distortion is meant here the distortion averaged over a region that contains many planes on which slip has occurred.) Hence as in the case of twins, the misfit strain energy will be small for this pattern of inhomogeneity.

The requirements that a plane of zero net distortion exist and that this plane must be the interface plane between the martensite and the as yet untransformed austenite serve to define a mathematical problem which has a unique answer. In the next section of this paper the solution of this problem is obtained by the use of matrix algebra. This solution contains a specification of: 1—the direction cosines of the normal to the habit plane (i.e., the interface plane between the austenite and martensite) with respect to the austenite crystal axes; 2—the relative thicknesses of the twin-related martensite regions, or the amount of slip; 3—the observed distortions which accompany transformation; and 4—the rela-

tive orientations of the austenite and martensite crystal axes.

Mathematical Theory of Austenite-Martensite Transformation

Mathematical Preliminaries

In the mathematical analysis of transformations in solids it is convenient to utilize the methods of matrix algebra, as was pointed out by Jaswon and Wheeler.⁷ Matrices are useful in this connection because they can be employed to express concisely linear transformations in space. In this section, the notations to be used are given as well as some of the characteristics of the matrices to be employed. The reader who is unfamiliar with matrix methods and vector analysis is referred to standard texts on the subject.^{15, 16}

In matrix notation $\mathbf{M} \cdot \mathbf{r}$ means that a vector

$$\mathbf{r} = \begin{bmatrix} x \\ y \\ z \end{bmatrix}$$

(a vector may be written as a column matrix) when operated on by a matrix,

$$\mathbf{M} = \begin{bmatrix} m_{11} & m_{12} & m_{13} \\ m_{21} & m_{22} & m_{23} \\ m_{31} & m_{32} & m_{33} \end{bmatrix}$$

is transformed to the vector

$$\mathbf{r}' = \begin{bmatrix} x' \\ y' \\ z' \end{bmatrix}$$

where

$$x' = m_{11}x + m_{12}y + m_{13}z, \text{ etc.}$$

\mathbf{r} denotes the vector, and r or $|\mathbf{r}|$ its scalar magnitude. The matrices used here are of three types: rotation matrices, pure distortion matrices, and impure distortion matrices. A rotation matrix characterizes rigid body rotations (Greek letters will be used; Φ indicates the matrix and ϕ the angle of rotation) hence if $\Phi \cdot \mathbf{r} = \mathbf{r}'$, then

$$|\mathbf{r}| = |\mathbf{r}'|.$$

The distortion matrices do not, in general, leave the length of a vector unchanged, but rotate the vector and alter its magnitude. (Distortion matrices will be denoted by bold face upper case English letters, e.g., \mathbf{M} .) If the components of a vector or a matrix are given with respect to an axis system (x, y, z) , it is frequently convenient to express the components with respect to another axis system (x_0, y_0, z_0) . A subscript on the symbol for the vector or the matrix indicates the axis system to which the components are referred. If the two systems of axes are related by the rotation Φ , then

$$\mathbf{r}_0 = \Phi \cdot \mathbf{r}$$

and

$$\mathbf{M}_0 = \Phi \cdot \mathbf{M} \cdot \Phi^* \quad [1]$$

Eq. 1 expresses the similarity transformation of \mathbf{M} to \mathbf{M}_0 and Φ^* , the "conjugate of Φ ," is obtained by interchanging the rows and columns of Φ . Rotation matrices have the property that

$$\Phi^* \Phi = 1 \text{ and } \det \Phi = 1.$$

A pure distortion matrix is symmetric ($m_{ij} = m_{ji}$) and can be diagonalized, i.e., written in a form in which $m_{ij} = 0$ for $i \neq j$, by a similarity transformation so chosen that the new set of axes coin-

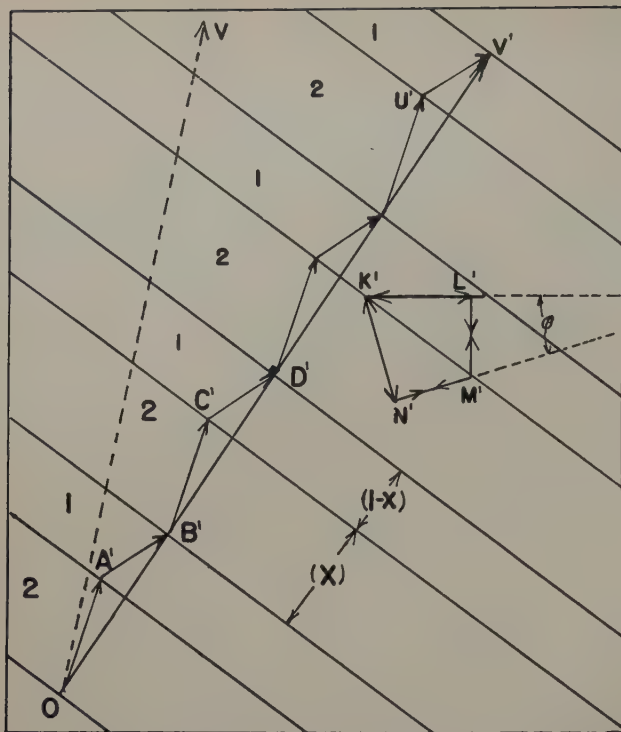


Fig. 2—Section through a martensite plate, showing the banded structure of relative amounts x of twin 2 and $(1-x)$ of twin 1. The broken line $OA'B'C'D'E' \dots U'V'$ was the straight line OV on the original austenite single crystal. The principal axes of the Bain distortion after transformation are indicated for each twin. The plane of the paper is that containing the axis of compression for each twin. It is perpendicular to the twin plane.

cides with the principal axes of distortion. An impure distortion is expressed by a nonsymmetric matrix. In general, a nonsymmetric matrix, \mathbf{M} , can be decomposed into the product of a rotation matrix, Ψ , and a pure distortion (symmetric) matrix, \mathbf{M}_d . Then if the rotation matrix Γ in the similarity transformation which diagonalizes \mathbf{M}_d is used, \mathbf{M} can be written as

$$\mathbf{M} = \Psi \mathbf{M}_d = \Psi \Gamma \mathbf{M}_d \Gamma^*.$$

\mathbf{M}_d is of the form $\begin{pmatrix} \lambda_1 & 0 & 0 \\ 0 & \lambda_2 & 0 \\ 0 & 0 & \lambda_3 \end{pmatrix}$ where the λ 's are

the principal distortions.

Transformation by Twin-Related Bain Distortions

As mentioned above, the transformation is first considered to be one in which a single crystal of face-centered cubic austenite is transformed to a banded structure of twin-related body-centered cubic or face-centered tetragonal domains. It will be shown that if the ratio of the thicknesses of the twins has a certain critical value, then there exists a plane in the austenite such that no line in the plane changes in length when averaged over many bands of the martensite twins. This plane is then determined and postulated to be the habit plane. Then since this plane forms an interface between the austenite and martensite, the property that this plane does not rotate permits the determination of the total distortion. This means, in effect, that the net effect of the transformation is to produce a simple shear on the habit plane plus an extension perpendicular to the habit plane to account for the

change in volume. Once the total distortion is determined in this way, the magnitude and direction of the shear and the orientation relationships are determined. The concept that the interface between the two phases be one of zero average distortion over a twin-related banded martensite structure is the foundation upon which this analysis is based.

A section through a martensite plate, Fig. 2, shows a volume of austenite that has transformed to a banded, twin-related structure of martensite of relative amounts, x of twin 2 and $(1-x)$ of twin 1. A scratch $\mathbf{r} = \mathbf{OV}$ that was originally a straight line in the austenite single crystal becomes the broken line $OA'B'C'D'E' \dots U'V'$. Initially, observable effects of the transformation are of interest and therefore the straight line vector sum, $\mathbf{r}' = \mathbf{OA}' + \mathbf{A'B}' + \mathbf{B'C}' + \dots \mathbf{U'V}'$, is considered rather than the broken line segments. If \mathbf{M}_1 and \mathbf{M}_2 are the matrices which describe what happens to vectors in the two regions as a result of transformation, \mathbf{OV}' can be written as

$$\mathbf{OV}' = \mathbf{r}' = (1-x)\mathbf{M}_1 \cdot \mathbf{r} + x\mathbf{M}_2 \cdot \mathbf{r} = [(1-x)\mathbf{M}_1 + x\mathbf{M}_2] \cdot \mathbf{r}. \quad [2]$$

Hence

$$\mathbf{r}' = \mathbf{E} \cdot \mathbf{r} \quad [3]$$

where

$$\mathbf{E} = (1-x)\mathbf{M}_1 + x\mathbf{M}_2. \quad [4]$$

\mathbf{E} will be referred to as the "total distortion matrix." Eq. 3 states that if \mathbf{r} is a vector in the austenite, then as a result of the transformation \mathbf{r} goes to $\mathbf{r}' = \mathbf{E} \cdot \mathbf{r}$ where both \mathbf{r} and \mathbf{r}' are expressed with respect to the cube edge directions in the as yet untransformed austenite.

The Bain distortions which produce the body-centered tetragonal domains are such that contraction occurs along one of the austenite cube directions for one of the twins and along another cube edge for the other twin (see Fig. 1). In what follows, twins 1 and 2 are considered to be produced by contraction along the y and x axes respectively†

† There are six choices of pairs of twins, each choice corresponding to a different but crystallographically equivalent solution. Other choices similar to the choice of twins enter the analysis; these will be pointed out at appropriate points in the development. When all possibilities are considered, we are left with a multiplicity of 24, i.e., 24 solutions for the habit plane. This matter is considered in more detail in the section on multiplicity of solutions.

and isotropic expansion in the plane perpendicular to the contraction axis in each case. In Fig. 2 are drawn the principal axes of the Bain distortion after transformation (the principal axes rotate during the distortion) with the expansions and contractions indicated for each twin. The expansion perpendicular to the plane of the paper is the same for each twin.

The Bain distortions for the two twins can be written as

$$\mathbf{T}_1 = \begin{pmatrix} \eta_1 & 0 & 0 \\ 0 & \eta_2 & 0 \\ 0 & 0 & \eta_1 \end{pmatrix} \text{ and } \mathbf{T}_2 = \begin{pmatrix} \eta_2 & 0 & 0 \\ 0 & \eta_1 & 0 \\ 0 & 0 & \eta_1 \end{pmatrix} \quad [5]$$

where

$$\eta_1 = \frac{\sqrt{2}a}{a_0}, \quad \eta_2 = c/a_0.$$

a_0 is the austenite cube edge and c and a are the martensite lattice parameters. In general, the principal axes of distortion in each region will rotate relative to the austenite axes during transformation.

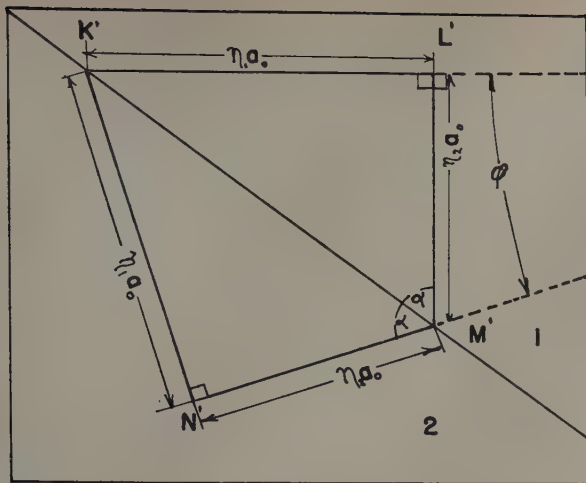


Fig. 3—The principal Bain distortions in the two twins after transformation. For region 1, the principal distortions are $K'L' = \eta_1 a_0$ and $L'M' = \eta_2 a_0$ and for region 2, $K'N' = \eta_1 a_0$ and $N'M' = \eta_2 a_0$. Since $N'M'$ and $K'L'$ were parallel directions before transformation, the relative rigid body rotation which has occurred during transformation to insure coherent twins is ϕ .

If the rotations for regions 1 and 2 are Φ_1 and Φ_2 respectively,

$$\mathbf{M}_1 = \Phi_1 \mathbf{T}_1 \text{ and } \mathbf{M}_2 = \Phi_2 \mathbf{T}_2 \quad [6]$$

and Eq. 4 becomes

$$\mathbf{E} = (1-x) \Phi_1 \mathbf{T}_1 + x \Phi_2 \mathbf{T}_2. \quad [7]$$

From the development thus far, Φ_1 and Φ_2 cannot be determined, but their relative rigid body rotation can be obtained. The angle of rotation ϕ of one region relative to the other is determined by the condition that regions 1 and 2 be coherent twins. From consideration of Fig. 3, the relative rotation matrix Φ is seen to be

$$\Phi = \begin{bmatrix} \cos \phi & -\sin \phi & 0 \\ \sin \phi & \cos \phi & 0 \\ 0 & 0 & 1 \end{bmatrix} \quad [8]$$

where $\cos \phi = \sin 2\alpha = \frac{2\eta_1 \eta_2}{\eta_1^2 + \eta_2^2}$

$$\sin \phi = \frac{\eta_1^2 - \eta_2^2}{\eta_1^2 + \eta_2^2}.$$

Region 2 undergoes rotation Φ relative to region 1. But region 1 is rotated by Φ_1 relative to the austenite axis system. Therefore relative to the austenite axes, region 2 undergoes rotation $\Phi_1 \Phi$. Thus

$$\Phi_2 = \Phi_1 \Phi$$

and Eq. 7 may be written as

$$\mathbf{E} = \Phi_1 [(1-x) \mathbf{T}_1 + x \Phi \mathbf{T}_2] = \Phi_1 \mathbf{F} \quad [9]$$

where

$$\mathbf{F} = (1-x) \mathbf{T}_1 + x \Phi \mathbf{T}_2.$$

From Eqs. 5 and 8

$$\mathbf{F} = \begin{bmatrix} \eta_1 \left(1 - \frac{\eta_1^2 - \eta_2^2}{\eta_1^2 + \eta_2^2} x \right) & -\eta_1 \frac{\eta_1^2 - \eta_2^2}{\eta_1^2 + \eta_2^2} x & 0 \\ \eta_2 \frac{\eta_1^2 - \eta_2^2}{\eta_1^2 + \eta_2^2} x & \eta_2 \left(1 + \frac{\eta_1^2 - \eta_2^2}{\eta_1^2 + \eta_2^2} x \right) & 0 \\ 0 & 0 & \eta_1 \end{bmatrix} \quad [10]$$

Eq. 10 shows that \mathbf{F} is nonsymmetric and therefore represents an impure distortion. But \mathbf{F} can be expressed as the product of its rotation matrix Ψ and pure distortion matrix \mathbf{F}_d . Furthermore, by means of a similarity transformation on \mathbf{F}_d , the rotation matrix Γ can be found such that

$$\mathbf{F}_d = \Gamma \mathbf{F}_d \Gamma^* \quad [11]$$

where \mathbf{F}_d is diagonal, i.e.,

$$\mathbf{F}_d = \begin{bmatrix} \lambda_2 & 0 & 0 \\ 0 & \lambda_3 & 0 \\ 0 & 0 & \lambda_1 \end{bmatrix}. \quad [12]$$

Thereby

$$\mathbf{F} = \Psi \mathbf{F}_d = \Psi \Gamma \mathbf{F}_d \Gamma^* \quad [13]$$

and

$$\mathbf{E} = \Phi_1 \Psi \Gamma \mathbf{F}_d \Gamma^*. \quad [14]$$

The form of \mathbf{F} in Eq. 10 shows that the rotations Ψ and Γ are about the z axis and hence \mathbf{F} can be written

$$\mathbf{F} = \begin{bmatrix} \cos \psi & -\sin \psi & 0 \\ \sin \psi & \cos \psi & 0 \\ 0 & 0 & 1 \end{bmatrix} \begin{bmatrix} \cos \gamma & -\sin \gamma & 0 \\ \sin \gamma & \cos \gamma & 0 \\ 0 & 0 & 1 \end{bmatrix} \begin{bmatrix} \lambda_2 & 0 & 0 \\ 0 & \lambda_3 & 0 \\ 0 & 0 & \lambda_1 \end{bmatrix} \begin{bmatrix} \cos \gamma & \sin \gamma & 0 \\ -\sin \gamma & \cos \gamma & 0 \\ 0 & 0 & 1 \end{bmatrix} \quad [15]$$

where the λ 's are the principal distortions.

By inspection of the form of \mathbf{F} in Eq. 10 and the component matrices of \mathbf{F} in Eq. 15, it is seen immediately that $\lambda_1 = \eta_1$. Another relation for the λ 's in terms of η_1 and η_2 is obtained by a consideration of the volume ratio, V , of the transformed and original volumes. In general the volume ratio for any distortion is given by the determinant of the distortion matrix. Therefore the volume ratio for region 1 is

$$V_1 = \det \mathbf{M}_1 = \det \Phi_1 \mathbf{T}_1 = \det \Phi_1 \det \mathbf{T}_1.$$

But the determinant of a rotation matrix is unity since a rigid body rotation involves no change in volume. From Eq. 5 then

$$V_1 = \det \mathbf{T}_1 = \eta_1^2 \eta_2.$$

In a similar way V_2 is also found to be equal to $\eta_1^2 \eta_2$. It follows then that the volume ratio brought about by the total distortion \mathbf{E} must also be $\eta_1^2 \eta_2$. Hence from Eq. 14,

$$\begin{aligned} \det \mathbf{E} &= \eta_1^2 \eta_2 \\ \det \Phi_1 \Psi \Gamma \mathbf{F}_d \Gamma^* &= \eta_1^2 \eta_2 \\ \det \mathbf{F}_d &= \eta_1^2 \eta_2 \end{aligned}$$

whereby, since $\lambda_1 = \eta_1$

$$\lambda_2 \lambda_3 = \eta_1 \eta_2. \quad [16]$$

Further evaluation of the principal distortions depends on the criterion for the habit plane. This is described in the next section.

Derivation of the Direction of the Habit Plane Normal: The derivation of the indices of the habit plane depends upon the following important theorem for which the proof is here presented: The necessary and sufficient condition that a plane of zero distortion exist is that one of the principal distortions be unity, i.e., one of the principal strains vanish. First consider all vectors \mathbf{r} such that

$$r^2 = r'^2 = |\mathbf{E} \cdot \mathbf{r}|^2. \quad [17]$$

All vectors \mathbf{r} which satisfy Eq. 17 suffer no change

in length during transformation. From Eq. 9

$$|\mathbf{E} \cdot \mathbf{r}|^2 = |\Phi_1 \mathbf{F} \cdot \mathbf{r}|^2 = [\Phi_1 (\mathbf{F} \cdot \mathbf{r})]^2 = \mathbf{r}^* \cdot \mathbf{F}^* \Phi_1^* \Phi_1 \mathbf{F} \cdot \mathbf{r} = |\mathbf{F} \cdot \mathbf{r}|^2 \quad [18]$$

since Φ_1 is a rotation matrix.

From Eq. 17 then,

$$|\mathbf{F} \cdot \mathbf{r}|^2 = r^2. \quad [19]$$

From Eq. 13 and the fact that Γ is the rotation between the (x, y, z) and (x_d, y_d, z_d) systems:

$$\mathbf{F} = \Psi \Gamma \mathbf{F}_d \Gamma^*$$

and

$$\mathbf{r} = \Gamma \cdot \mathbf{r}_d.$$

Then

$$\begin{aligned} |\mathbf{F} \cdot \mathbf{r}|^2 &= |\Psi \Gamma \mathbf{F}_d \Gamma^* \cdot \Gamma \cdot \mathbf{r}_d|^2 = |\Psi \Gamma \mathbf{F}_d \cdot \mathbf{r}_d|^2 \\ &= \mathbf{r}_d^* \cdot \mathbf{F}_d^* \Gamma^* \Psi^* \Psi \Gamma \mathbf{F}_d \cdot \mathbf{r}_d \\ &= \mathbf{r}_d^* \cdot \mathbf{F}_d^* \mathbf{F}_d \cdot \mathbf{r}_d = |\mathbf{F}_d \cdot \mathbf{r}_d|^2. \end{aligned}$$

Also the magnitude of a vector is independent of the reference system to which it is referred, so that $r^2 = r_d^2$. Therefore Eq. 19 becomes

$$|\mathbf{F}_d \cdot \mathbf{r}_d|^2 = r_d^2. \quad [20]$$

From Eq. 12:

$$\begin{aligned} \lambda_2^2 x_d^2 + \lambda_3^2 y_d^2 + \lambda_1^2 z_d^2 &= x_d^2 + y_d^2 + z_d^2 \\ (\lambda_2^2 - 1)x_d^2 + (\lambda_3^2 - 1)y_d^2 + (\lambda_1^2 - 1)z_d^2 &= 0. \end{aligned} \quad [21]$$

x_d^2, y_d^2 , and z_d^2 are always positive; therefore a sufficient condition for Eq. 21 to be satisfied is that one of the λ 's be unity, say $\lambda_3 = 1$, since Eq. 21 is satisfied with

$$\frac{\lambda_2^2 - 1}{\lambda_1^2 - 1} = -\frac{z_d^2}{x_d^2}$$

which is the equation for a plane.

To prove the necessary condition of the theorem, consider the intersection of the surface, Eq. 21, with the planes $x_d = 0, y_d = 0, z_d = 0$ in turn. This shows that each $(\lambda_i^2 - 1)$ must differ in sign from each of the others. This is impossible unless one of the $(\lambda_i^2 - 1)$ equals zero. Therefore it is necessary that one of the λ 's be unity for a plane of zero distortion to exist. Hence the theorem is proved.

In the previous section it was found that

$$\lambda_1 = \eta_1$$

and

$$\lambda_2 \lambda_3 = \eta_1 \eta_2.$$

If we set

$$\lambda_3 = 1$$

(if $\lambda_3 = 1$ is chosen a crystallographically equivalent habit plane is obtained), it follows that

$$\lambda_1 = \eta_1, \lambda_2 = \eta_1 \eta_2, \lambda_3 = 1$$

and Eq. 12 becomes

$$\mathbf{F}_d = \begin{bmatrix} \eta_1 \eta_2 & 0 & 0 \\ 0 & 1 & 0 \\ 0 & 0 & \eta_1 \end{bmatrix}. \quad [22]$$

From Eq. 21 then, vectors (x_d, y_d, z_d) which satisfy

$$\frac{z_d}{x_d} = -K \quad [23]$$

where

$$K = \sqrt{\frac{1 - \eta_1^2 \eta_2^2}{\eta_1^2 - 1}}$$

determine the plane of zero distortion, i.e., the habit plane. (The negative square root in Eq. 23 has been chosen arbitrarily; the positive square root yields a crystallographically equivalent habit plane.) Two vectors in the habit plane are then $(x_1, 0, -Kx_1)$ and $(x_2, y_2, -Kx_2)$ and their vector cross-product gives the direction of the normal to the habit plane. In this way it is seen that in a system of axes (x_d, y_d, z_d) aligned along the principal directions of the distortion, the habit plane normal is given by

$$\mathbf{n}_d = \frac{1}{\sqrt{1 + K^2}} \begin{bmatrix} K \\ 0 \\ 1 \end{bmatrix} \quad [24]$$

and since Γ is the rotation which transforms austenite axes to (x_d, y_d, z_d)

$$\mathbf{n} = \Gamma \cdot \mathbf{n}_d \quad [25]$$

where \mathbf{n} is the normal to the habit plane in the austenite system. Therefore the rotation matrix Γ must first be determined in order to express the habit plane normal with respect to the austenite axes.

In order to determine Γ , however, an expression for the line of intersection of the twin and habit planes will first be derived. From the nature of the distortions to which regions 1 and 2 are subjected and the requirement that coherent twins be formed as a result of transformation, it follows that vectors which lie in the (110) plane in the austenite must lie in the twin plane after transformation. In particular this is true for vectors which are to lie in the intersection of the twin and habit planes. Therefore a vector along this line of intersection as a result of the transformation must have had the direction of \mathbf{d} in the austenite, where

$$\mathbf{d} = \begin{bmatrix} b \\ -b \\ a \end{bmatrix} \text{ and } a^2 + 2b^2 = 1.$$

[The $(1\bar{1}0)$ plane could equally well have been chosen as the plane in the austenite which becomes the twin plane after transformation. In this case the vector \mathbf{d} would have components (b, b, a) . This choice gives a crystallographically equivalent solution.] Now a point on the twin plane can be associated either with region 1 or region 2 and therefore the vector \mathbf{d} goes into the same vector \mathbf{d}' as a result of distortion \mathbf{M}_1 applied to region 1 or distortion \mathbf{M}_2 applied to region 2. This fact and the requirement that \mathbf{d} shall lie in the habit plane allows a and b to be evaluated since the vector \mathbf{d} must remain unchanged in magnitude when subjected to either of the distortions \mathbf{M}_1 or \mathbf{M}_2 . The distortion applied to region 1 is $\mathbf{M}_1 = \Phi_1 \mathbf{T}_1$. Therefore

$$\mathbf{d}' = \mathbf{M}_1 \cdot \mathbf{d} = \Phi_1 \mathbf{T}_1 \cdot \mathbf{d}$$

and

$$\begin{aligned} \mathbf{d}'^2 &= (\Phi_1 \mathbf{T}_1 \cdot \mathbf{d})^2 = [\Phi_1 (\mathbf{T}_1 \cdot \mathbf{d})]^2 = (\mathbf{T}_1 \cdot \mathbf{d})^* \Phi_1^* \\ &\quad \Phi_1 (\mathbf{T}_1 \cdot \mathbf{d}) = (\mathbf{T}_1 \cdot \mathbf{d})^2. \end{aligned}$$

Now

$$\mathbf{T}_1 = \begin{bmatrix} \eta_1 & 0 & 0 \\ 0 & \eta_2 & 0 \\ 0 & 0 & \eta_1 \end{bmatrix}.$$

Therefore

$$\mathbf{T}_1 \cdot \mathbf{d} = \begin{bmatrix} \eta_1 b \\ -\eta_2 b \\ \eta_1 a \end{bmatrix}$$

and

$$d'^2 = \eta_1^2 b^2 + \eta_2^2 b^2 + \eta_1^2 a^2.$$

Then, since \mathbf{d}' lies in the habit plane,

$$d'^2 = d^2$$

$$\eta_1^2 b^2 + \eta_2^2 b^2 + \eta_1^2 a^2 = 2b^2 + a^2.$$

This equation and the normalization condition $a^2 + 2b^2 = 1$ determine a and b to be

$$a = \sqrt{\frac{2 - \eta_1^2 - \eta_2^2}{\eta_1^2 - \eta_2^2}}$$

$$b = \sqrt{\frac{\eta_1^2 - 1}{\eta_1^2 - \eta_2^2}}$$

and thus the intersection of the twin and habit planes is given by

$$\mathbf{d} = \begin{bmatrix} \sqrt{\frac{\eta_1^2 - 1}{\eta_1^2 - \eta_2^2}} \\ -\sqrt{\frac{\eta_1^2 - 1}{\eta_1^2 - \eta_2^2}} \\ \sqrt{\frac{2 - \eta_1^2 - \eta_2^2}{\eta_1^2 - \eta_2^2}} \end{bmatrix} \quad [26]$$

Since this vector lies in the habit plane, it must remain unchanged in magnitude as a result of the total distortion \mathbf{E} , i.e.,

$$d'^2 = d^2$$

where

$$\mathbf{d}' = \mathbf{E} \cdot \mathbf{d}.$$

From Eq. 14

$$\mathbf{E} = \Phi_1 \Psi \Gamma \mathbf{F}_d \Gamma^*$$

and

$$(\mathbf{E} \cdot \mathbf{d})^2 = (\Phi_1 \Psi \Gamma \mathbf{F}_d \Gamma^* \cdot \mathbf{d})^2 = \mathbf{d}^* \cdot \Gamma \mathbf{F}_d^* \Gamma^* \Psi^* \Phi_1^* \Phi_1 \Psi \Gamma \mathbf{F}_d \Gamma^* \cdot \mathbf{d}$$

$$= \mathbf{d}^* \cdot \Gamma \mathbf{F}_d^2 \Gamma^* \cdot \mathbf{d}.$$

Therefore

$$\mathbf{d}^* \cdot \Gamma \mathbf{F}_d^2 \Gamma^* \cdot \mathbf{d} = d^2$$

and substitution from Eqs. 22 and 26 yields

$$\begin{bmatrix} \sqrt{\frac{\eta_1^2 - 1}{\eta_1^2 - \eta_2^2}} \\ -\sqrt{\frac{\eta_1^2 - 1}{\eta_1^2 - \eta_2^2}} \\ \sqrt{\frac{2 - \eta_1^2 - \eta_2^2}{\eta_1^2 - \eta_2^2}} \end{bmatrix} \begin{bmatrix} \cos \gamma & -\sin \gamma & 0 \\ \sin \gamma & \cos \gamma & 0 \\ 0 & 0 & 1 \end{bmatrix} \begin{bmatrix} \eta_1^2 \eta_2^2 & 0 & 0 \\ 0 & 1 & 0 \\ 0 & 0 & \eta_1^2 \end{bmatrix}$$

$$\begin{bmatrix} \cos \gamma & \sin \gamma & 0 \\ -\sin \gamma & \cos \gamma & 0 \\ 0 & 0 & 1 \end{bmatrix} \begin{bmatrix} \sqrt{\frac{\eta_1^2 - 1}{\eta_1^2 - \eta_2^2}} \\ -\sqrt{\frac{\eta_1^2 - 1}{\eta_1^2 - \eta_2^2}} \\ \sqrt{\frac{2 - \eta_1^2 - \eta_2^2}{\eta_1^2 - \eta_2^2}} \end{bmatrix} = 1.$$

This equation yields the result that

$$2 \sin \gamma \cos \gamma = A \quad [27]$$

$$\text{where } A = \frac{(\eta_1^2 - 1)(1 - \eta_2^2)}{1 - \eta_1^2 \eta_2^2} \quad [28]$$

whereby

$$\cos^2 \gamma = \frac{1}{2} (1 + \sqrt{1 - A^2}) \quad [29]$$

$$\sin^2 \gamma = \frac{1}{2} (1 - \sqrt{1 - A^2}). \quad [30]$$

The habit plane normal is then given by

$$\mathbf{n} = \Gamma \cdot \mathbf{n}_d = \begin{bmatrix} \cos \gamma & -\sin \gamma & 0 \\ \sin \gamma & \cos \gamma & 0 \\ 0 & 0 & 1 \end{bmatrix} \frac{1}{\sqrt{1 + K^2}} \begin{bmatrix} K \\ 0 \\ 1 \end{bmatrix}$$

$$= \frac{1}{\sqrt{1 + K^2}} \begin{bmatrix} K \cos \gamma \\ K \sin \gamma \\ 1 \end{bmatrix} \quad [31]$$

where

$$K = \sqrt{\frac{1 - \eta_1^2 \eta_2^2}{\eta_1^2 - 1}}.$$

If h, k, l ($|h| < |k| < |l|$) are the direction cosines of the habit plane normal, then by substitution in Eq. 31 the direction cosines relative to austenite axes are expressed explicitly in terms of η_1 and η_2 . Then

$$\mathbf{n} = \begin{bmatrix} k \\ h \\ l \end{bmatrix}$$

where

$$h = \frac{1}{2\eta_1} \left\{ \sqrt{\frac{\eta_1^2 + \eta_2^2 - 2\eta_1^2 \eta_2^2}{1 - \eta_2^2}} - \sqrt{\frac{2 - \eta_1^2 - \eta_2^2}{1 - \eta_2^2}} \right\} \quad [32]$$

$$k = \frac{1}{2\eta_1} \left\{ \sqrt{\frac{\eta_1^2 + \eta_2^2 - 2\eta_1^2 \eta_2^2}{1 - \eta_2^2}} + \sqrt{\frac{2 - \eta_1^2 - \eta_2^2}{1 - \eta_2^2}} \right\} \quad [33]$$

$$l = \frac{1}{\eta_1} \sqrt{\frac{\eta_1^2 - 1}{1 - \eta_2^2}} \quad [34]$$

$$\eta_1 = \frac{\sqrt{2}a}{a_0}, \quad \eta_2 = \frac{c}{a_0}.$$

Thus the criterion that the habit plane is a plane of zero net distortion in a banded twin-related martensite structure has permitted the habit plane direction cosines to be expressed as an explicit function of the austenite and martensite lattice parameters. This treatment gives the result that the habit plane is irrational.

Evaluation of the Relative Amounts of the Twins: In the previous section, the rotation matrix Γ which diagonalizes \mathbf{F} , was determined as a function of η_1 and η_2 . \mathbf{F} , can now be determined. From Eqs. 11 and 22

$$\mathbf{F}_s = \Gamma \mathbf{F}_d \Gamma^*$$

$$= \begin{bmatrix} \cos \gamma & -\sin \gamma & 0 \\ \sin \gamma & \cos \gamma & 0 \\ 0 & 0 & 1 \end{bmatrix} \begin{bmatrix} \eta_1 \eta_2 & 0 & 0 \\ 0 & 1 & 0 \\ 0 & 0 & \eta_1 \end{bmatrix}$$

$$\begin{bmatrix} \cos \gamma & \sin \gamma & 0 \\ -\sin \gamma & \cos \gamma & 0 \\ 0 & 0 & 1 \end{bmatrix}$$

$$= \begin{bmatrix} \eta_1 \eta_2 \cos^2 \gamma + \sin^2 \gamma & -\sin \gamma \cos \gamma (1 - \eta_1 \eta_2) & 0 \\ -\sin \gamma \cos \gamma (1 - \eta_1 \eta_2) & \eta_1 \eta_2 \sin^2 \gamma + \cos^2 \gamma & 0 \\ 0 & 0 & \eta_1 \end{bmatrix} \quad [35]$$

The rotation matrix Ψ was defined as one such that

$$\mathbf{F} = \Psi \mathbf{F}_s.$$

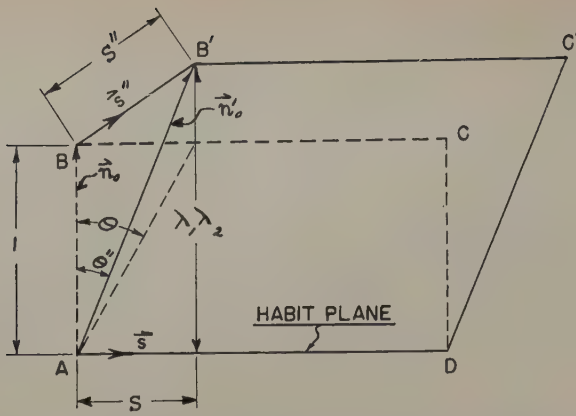


Fig. 4—Simple shear on the habit plane plus an extension, $\lambda_1 \lambda_2 = \eta_1 \eta_2$, equal to the volume change, in the direction of the habit plane normal. $ABCD$ is transformed to $AB'C'D$.

Inspection of \mathbf{F} (Eq. 10) and \mathbf{F}_d (Eq. 35) indicates that Ψ must be of the form

$$\Psi = \begin{bmatrix} \cos \psi & -\sin \psi & 0 \\ \sin \psi & \cos \psi & 0 \\ 0 & 0 & 1 \end{bmatrix} \quad [37]$$

The substitution of Eqs. 10, 35, and 37 in Eq. 36 yields four equations (not all independent) from which the angle of rotation Ψ and x may be evaluated. In this way it is found that

$$\begin{aligned} \cos \psi &= \frac{\eta_1 + \eta_2}{1 + \eta_1 \eta_2} \left[1 - \frac{(\eta_1 - \eta_2)^2}{\eta_1^2 + \eta_2^2} x \right] \\ \sin \psi &= \frac{\eta_1 + \eta_2}{1 + \eta_1 \eta_2} \frac{\eta_1^2 - \eta_2^2}{\eta_1^2 + \eta_2^2} x \\ x &= \frac{1}{2} \pm \frac{1}{2} \frac{(1 - \eta_1^2 \eta_2^2)}{\eta_1^2 - \eta_2^2} \sqrt{1 - A^2} \quad [38] \\ \text{where } A &= \frac{(\eta_1^2 - 1)(1 - \eta_2^2)}{1 - \eta_1^2 \eta_2^2} \end{aligned}$$

Eq. 38 shows that there are two solutions for the relative amounts of the two twins: one solution giving x of twin 1 and $(1-x)$ of twin 2 and vice versa for the other solution. These two possibilities yield two crystallographically equivalent solutions. In what follows, let x take on the larger of the two values given by Eq. 38. This means (from Eq. 4) that the variant chosen specifies a larger amount of twin 2 than twin 1.

Determination of Magnitude and Direction of the Average Shear: A fundamental point in this analysis is that as a result of the transformation, there is one plane (the habit plane) which has the property that, 1—it does not rotate, and 2—no line in the plane undergoes extension or contraction. This means that the habit plane is one on which simple shear occurs plus extension in a direction perpendicular to the habit plane to account for the observed increase in volume. Because of this extension, the direction of motion is not in the undistorted plane.

It follows then that the total distortion matrix, expressed with respect to a system of axes, x_0, y_0, z_0 , with x_0 in the direction of shear and z_0 along the habit plane normal, will take the form

$$\mathbf{E}_0 = \begin{bmatrix} 1 & 0 & -S \\ 0 & 1 & 0 \\ 0 & 0 & \lambda_1 \lambda_2 \end{bmatrix}$$

where S is the projection of the displacement S'' (see Fig. 4) on the habit plane, and $\lambda_1 \lambda_2$ is the ratio of the volumes. The matrix \mathbf{E}_0 is related to \mathbf{E} by a similarity transformation.

S is easily evaluated by consideration of Fig. 4 which indicates the result of the transformation on a unit normal to the habit plane \mathbf{n}_0 . From the figure,

$$|\mathbf{n}_0'|^2 = (\lambda_1 \lambda_2)^2 + S^2 \quad [39]$$

where $\mathbf{n}_0' = \mathbf{E}_0 \cdot \mathbf{n}_0$. The magnitude of a vector is the same no matter what system of axes it is referred to. Therefore

$$|\mathbf{n}_0'|^2 = |\mathbf{n}'|^2 = |\mathbf{E} \cdot \mathbf{n}|^2$$

But from Eq. 14

$$\begin{aligned} \mathbf{E} \cdot \mathbf{n} &= \Phi_1 \Psi \Gamma \mathbf{F}_d \Gamma^* \cdot \mathbf{n} \\ |\mathbf{E} \cdot \mathbf{n}|^2 &= \mathbf{n}^* \cdot \Gamma \mathbf{F}_d^* \Gamma^* \Psi^* \Phi_1^* \Phi_1 \Psi \Gamma \mathbf{F}_d \Gamma^* \cdot \mathbf{n} \\ &= \mathbf{n}^* \cdot \Gamma \mathbf{F}_d^* \mathbf{F}_d \Gamma^* \cdot \mathbf{n} \\ &= (\Gamma^* \cdot \mathbf{n})^* \mathbf{F}_d^* \mathbf{F}_d (\Gamma \cdot \mathbf{n}) \\ &= \mathbf{n}_d^* \cdot \mathbf{F}_d^* \mathbf{F}_d \cdot \mathbf{n}_d \\ &= (\mathbf{F}_d \cdot \mathbf{n}_d)^2. \end{aligned}$$

Then

$$|\mathbf{n}_0'|^2 = |\mathbf{F}_d \cdot \mathbf{n}_d|^2$$

which gives (from Eqs. 22 and 24)

$$|\mathbf{n}_0'|^2 = \frac{1}{1 + K^2} (\lambda_1^2 + K^2 \lambda_2^2)$$

$$\text{where } K = \sqrt{\frac{1 - \lambda_2^2}{\lambda_1^2 - 1}}$$

Substitution in Eq. 39 yields

$$S = \sqrt{(\lambda_1^2 - 1)(1 - \lambda_2^2)} \quad [40]$$

The direction of \mathbf{s} can be calculated by considering the pure distortion, \mathbf{F}_d , and the habit plane normal, \mathbf{n}_d , both expressed in the x_d, y_d, z_d system (Eqs. 22 and 24). The form of \mathbf{F}_d shows that a line in the y_d direction remains undistorted as a result of this pure distortion and an inspection of \mathbf{n}_d indicates that the y_d axis lies in the habit plane and is therefore not rotated by the transformation. It follows then that the y_d axis is perpendicular to the shear direction and that the shear direction in the x_d, y_d, z_d system is given by

$$\mathbf{s}_d = \mathbf{n}_d \times \mathbf{y}_d = \frac{1}{\sqrt{1 + K^2}} \begin{bmatrix} -1 \\ 0 \\ K \end{bmatrix}$$

With respect to the austenite axes, the shear direction \mathbf{s} is

$$\mathbf{s} = \Gamma \cdot \mathbf{s}_d = \frac{1}{\sqrt{1 + K^2}} \begin{bmatrix} -\cos \gamma \\ -\sin \gamma \\ K \end{bmatrix} \quad [41]$$

and the corresponding shear angle is given by

$$\tan \theta = S.$$

Also from Fig. 4 and Eqs. 40 and 41,

$$S'' = \sqrt{S^2 + (\lambda_1 \lambda_2 - 1)^2} = \lambda_1 - \lambda_2 \quad [42]$$

$$\mathbf{s}'' = \frac{1}{S''} [S\mathbf{s} + (\lambda_1 \lambda_2 - 1)\mathbf{n}] \quad [43]$$

which becomes when normalized,

$$s'' = \frac{1}{N} \begin{bmatrix} -[S - K(\lambda_1\lambda_2 - 1)] \cos\gamma \\ -[S - K(\lambda_1\lambda_2 - 1)] \sin\gamma \\ (\lambda_1\lambda_2 - 1) + SK \end{bmatrix}$$

where

$$N^2 = \frac{(\lambda_1 - \lambda_2)^2 (\lambda_1^2 - \lambda_2^2)}{\lambda_1^2 - 1}$$

$$K = \sqrt{\frac{1 - \lambda_2^2}{\lambda_1^2 - 1}}$$

$$S = \sqrt{(\lambda_1^2 - 1)(1 - \lambda_2^2)}.$$

Also

$$\tan \theta'' = \frac{S}{\lambda_1\lambda_2} = \frac{\sqrt{(\lambda_1^2 - 1)(1 - \lambda_2^2)}}{\lambda_1\lambda_2}. \quad [44]$$

Orientation Relationships: The orientation relationships between the austenite and each of the martensite twins depend upon the distortions to which each twin region is subjected separately, i.e.,

$$\mathbf{M}_1 = \Phi_1 \mathbf{T}_1 \quad [45]$$

and

$$\mathbf{M}_2 = \Phi_2 \mathbf{T}_2 = \Phi_1 \Phi \mathbf{T}_2. \quad [46]$$

The only matrix as yet undetermined here is Φ_1 , and Φ_1 can be evaluated by applying the condition that a vector, \mathbf{v} , in the habit plane remains unchanged as a result of the total distortion, \mathbf{E} . For such vectors then

$$\mathbf{E} \cdot \mathbf{v} = \Phi_1 \mathbf{F} \cdot \mathbf{v} = \mathbf{v}$$

or

$$\mathbf{F} \cdot \mathbf{v} = \Phi_1^* \mathbf{v}. \quad [47]$$

Three vectors in the habit plane can easily be obtained by taking the cross-products of \mathbf{n} and unit vectors along the x , y , and z axes. These become

$$\mathbf{v}_1 = \begin{bmatrix} 0 \\ -l \\ h \end{bmatrix} \quad \mathbf{v}_2 = \begin{bmatrix} l \\ 0 \\ -k \end{bmatrix} \quad \text{and} \quad \mathbf{v}_3 = \begin{bmatrix} -h \\ k \\ 0 \end{bmatrix}.$$

By substitution of \mathbf{v}_1 , \mathbf{v}_2 , and \mathbf{v}_3 in Eq. 47, nine equations (only six of which are independent) are obtained for the nine elements of Φ_1 ; however three additional relations are supplied by the normalization conditions, e.g.,

$$(\Phi_1)_{11}^2 + (\Phi_1)_{12}^2 + (\Phi_1)_{13}^2 = 1$$

so that the nine elements of Φ_1 can be determined.

The separate distortions \mathbf{M}_1 and \mathbf{M}_2 of twins 1 and 2 can then be evaluated by substitution of Φ_1 , Φ , \mathbf{T}_1 , and \mathbf{T}_2 in Eqs. 45 and 46. The directions of the martensite axes for each twin are determined by applying \mathbf{M}_1 and \mathbf{M}_2 to the appropriate cube edge and face diagonal directions in the austenite. These six equations are:

$$\mathbf{x}_{M_1} = \mathbf{M}_1 \cdot \begin{bmatrix} \frac{a_0}{2} \\ 2 \\ 0 \\ \frac{a_0}{2} \\ 2 \end{bmatrix} = a \begin{bmatrix} \alpha_{11} \\ \alpha_{12} \\ \alpha_{13} \end{bmatrix}$$

$$\mathbf{x}_{M_2} = \mathbf{M}_2 \cdot \begin{bmatrix} 0 \\ -\frac{a_0}{2} \\ -\frac{a_0}{2} \\ \frac{a_0}{2} \end{bmatrix} = a \begin{bmatrix} \beta_{11} \\ \beta_{12} \\ \beta_{13} \end{bmatrix}$$

$$\mathbf{y}_{M_1} = \mathbf{M}_1 \cdot \begin{bmatrix} \frac{a_0}{2} \\ 2 \\ 0 \\ -\frac{a_0}{2} \end{bmatrix} = a \begin{bmatrix} \alpha_{21} \\ \alpha_{22} \\ \alpha_{23} \end{bmatrix}$$

$$\mathbf{y}_{M_2} = \mathbf{M}_2 \cdot \begin{bmatrix} 0 \\ -\frac{a_0}{2} \\ \frac{a_0}{2} \\ 2 \end{bmatrix} = a \begin{bmatrix} \beta_{21} \\ \beta_{22} \\ \beta_{23} \end{bmatrix}$$

$$\mathbf{z}_{M_1} = \mathbf{M}_1 \cdot \begin{bmatrix} 0 \\ a_0 \\ 0 \end{bmatrix} = c \begin{bmatrix} \alpha_{31} \\ \alpha_{32} \\ \alpha_{33} \end{bmatrix}$$

$$\mathbf{z}_{M_2} = \mathbf{M}_2 \cdot \begin{bmatrix} -a_0 \\ 0 \\ 0 \end{bmatrix} = c \begin{bmatrix} \beta_{31} \\ \beta_{32} \\ \beta_{33} \end{bmatrix}$$

where α 's and β 's are direction cosines. Thus, given a vector \mathbf{r}_A expressed with respect to austenite axes, this same vector expressed with respect to martensite axes in the two twin regions is given by

$$\mathbf{r}_{M_1} = \mathbf{A} \cdot \mathbf{r}_A = \begin{bmatrix} \alpha_{11} & \alpha_{12} & \alpha_{13} \\ \alpha_{21} & \alpha_{22} & \alpha_{23} \\ \alpha_{31} & \alpha_{32} & \alpha_{33} \end{bmatrix} \cdot \mathbf{r}_A$$

$$\text{and } \mathbf{r}_{M_2} = \mathbf{B} \cdot \mathbf{r}_A = \begin{bmatrix} \beta_{11} & \beta_{12} & \beta_{13} \\ \beta_{21} & \beta_{22} & \beta_{23} \\ \beta_{31} & \beta_{32} & \beta_{33} \end{bmatrix} \cdot \mathbf{r}_A.$$

The matrices \mathbf{A} and \mathbf{B} then serve to define the orientation relationships.

Multiplicity of the Solutions: This analysis yields 24 crystallographically equivalent solutions for the direction of the habit plane normal relative to austenite axes and for the orientation relationship between the austenite axes and each of the twin martensite axes. For the case under consideration, this is the number of crystallographically equivalent planes for a plane whose indices are unequal and non-zero. In terms of the above development the multiplicity of 24 can be seen in the following way: Assume at the outset that the two twin martensite regions are distinguished by specifying that a smaller amount of twin 1 be formed than twin 2. There are three ways of specifying the Bain distortion for twin 1, i.e., the contraction axis may be any one of the three austenite cube edge directions, which leaves either of two contraction axes for the Bain distortion of twin 2. Thus there are six choices of pairs of twins. For each of these cases, either of the two perpendicular face diagonal planes which bisect the two contraction axes [e.g., (110) or (1 $\bar{1}$ 0) for contraction axes x and y] can be chosen as the plane in the austenite which becomes the twin plane separating the martensite twins. There are thus 12 choices. Another choice is between the two solutions of Eq. 21 ($\lambda_3 = 1$)

$$\frac{z_d}{x_d} = \pm K$$

which determine the habit plane. Each of the choices considered above leads to a different habit plane and orientation relationship and thus the solution has a multiplicity of 24.

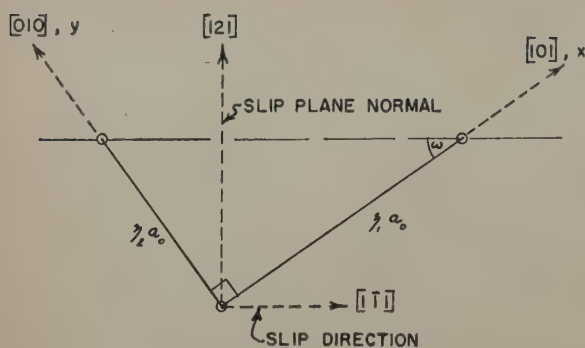


Fig. 5—View on the $(\bar{1}01)$ martensite plane. Directions are with respect to martensite axes. x and y refer to the austenite axes from which the indicated directions are derived.

In the detailed mathematical analysis, alternate forms of certain of the matrices may be used. (For example, Eq. 27 is equally well satisfied when the values of $\sin^2 \gamma$ and $\cos^2 \gamma$ in Eqs. 29 and 30 are interchanged.) However this type of change yields the same solution as one of those already considered. The particular variant used in this development was chosen so that the orientation relationship between the austenite axes and martensite axes for one of the twins corresponds to that which has been most frequently treated in the literature.^{7,9}

Existence of the Solutions: The proof of the existence of a plane of zero average distortion in the martensite, for a critical value of relative twin thickness x , can now be stated simply. A solution of the sort that has been derived above will always exist providing η_1 and η_2 , the components of the pure homogeneous transformation distortion matrix, have values such that the relative twin thickness x given by Eq. 38 has a real, positive value between zero and one. This requires that one of the η 's be less than unity and the other greater than unity, and that if η_1 is greater than unity the sum of their squares be less than two (if η_1 is less than unity, as in the case of indium-thallium, the sum of the squares of η_1 and η_2 must be greater than two). This condition is certain to be satisfied by all iron-base alloys which undergo austenite-martensite reactions.

Transformation by Single Bain Distortion Coupled with Slip

In this section it will be demonstrated that, as far as macroscopic distortions are concerned, transformation by twin-related Bain distortions is equivalent to transformation based upon a single Bain distortion coupled with slip. This equivalence can be seen qualitatively by a consideration of a fact mentioned earlier; namely, that a Bain distortion followed by the body-centered cubic or body-centered tetragonal mechanical twinning shear (shear on a (121) plane in $[\bar{1}\bar{1}1]$ direction) can give another Bain distortion with a different (twin-related) choice of axes. Imagine region 2 of the previous section to be subjected to two distortions which produce equal and opposite macroscopic changes in shape. The first of these is a "detwinning" shear on the (121) plane in the $[\bar{1}\bar{1}1]$ direction which converts the martensite to a single crystal and the second is slip on the same plane, the macroscopic effect of which is to produce a shear with the same elements but of opposite sign. In this way the system

of distortions in which regions 1 and 2 undergo twin-related Bain distortions may be replaced by one in which regions 1 and 2 are subjected to the same Bain distortion coupled with slip in region 2. In this case, it makes no macroscopic difference if only a fraction x of the material undergoes slip (in analogy to the analysis of the previous section) or if the slip is distributed over the whole martensite region with a correspondingly larger average distance between slip lines. This latter alternative describes a transformation by a single Bain distortion coupled with slip and thus demonstrates the macroscopic equivalence stated above.

A quantitative description of this equivalence is obtained from a consideration of the matrices which describe the slip-product distortion. Consider the austenite to undergo the Bain distortion

$$\mathbf{T}_1 = \begin{bmatrix} \eta_1 & 0 & 0 \\ 0 & \eta_2 & 0 \\ 0 & 0 & \eta_1 \end{bmatrix} \quad [48]$$

and a slip shear \mathbf{G} of amount g on the $(121)_M$ plane in the $[\bar{1}\bar{1}1]_M$ direction. It is seen from Fig. 5 that the matrix \mathbf{G} with respect to austenite axes is given by

$$\mathbf{G} = \Omega \begin{bmatrix} 1 & -g & 0 \\ 0 & 1 & 0 \\ 0 & 0 & 1 \end{bmatrix} \Omega^*$$

where

$$\Omega = \begin{bmatrix} \cos \omega & \sin \omega & 0 \\ -\sin \omega & \cos \omega & 0 \\ 0 & 0 & 1 \end{bmatrix}$$

$$\text{and } \cos \omega = \frac{\eta_1}{\sqrt{\eta_1^2 + \eta_2^2}} \quad \text{and } \sin \omega = \frac{\eta_2}{\sqrt{\eta_1^2 + \eta_2^2}}.$$

This gives

$$\mathbf{G} = \begin{bmatrix} 1 - \frac{\eta_1 \eta_2}{\eta_1^2 + \eta_2^2} g & -\frac{\eta_1^2}{\eta_1^2 + \eta_2^2} g & 0 \\ \frac{\eta_2^2}{\eta_1^2 + \eta_2^2} g & 1 + \frac{\eta_1 \eta_2}{\eta_1^2 + \eta_2^2} g & 0 \\ 0 & 0 & 1 \end{bmatrix} \quad [49]$$

The quantity analogous to \mathbf{F} of the previous section is

Table I. Calculation of Habit Plane

$r = \frac{c}{a}$	$V = \frac{2a^2c}{a_0^3}$	$\eta_1 = \frac{\sqrt{2} a}{a_0}$	$\eta_2 = \frac{c}{a_0}$	Direction Cosines of Habit Plane Normal
1.00	1.03	1.1336	0.8016	0.1891 0.5864 0.7876
1.08	1.03	1.1049	0.8438	0.1531 0.5907 0.7923
1.00	1.04	1.1372	0.8041	0.2012 0.5637 0.8011
1.08	1.04	1.1084	0.8465	0.1654 0.5623 0.8102
1.00	1.05	1.1409	0.8067	0.2150 0.5388 0.8146
1.08	1.05	1.1120	0.8492	0.1801 0.5308 0.8281

$$\mathbf{F} = \mathbf{G}\mathbf{T}_1$$

which becomes upon substitution of Eqs. 48 and 49

$$\mathbf{F} = \begin{bmatrix} \eta_1 \left(1 - \frac{\eta_1 \eta_2}{\eta_1^2 + \eta_2^2} g \right) & -\frac{\eta_1^2 \eta_2}{\eta_1^2 + \eta_2^2} g & 0 \\ \frac{\eta_1 \eta_2^2}{\eta_1^2 + \eta_2^2} g & \eta_2 \left(1 + \frac{\eta_1 \eta_2}{\eta_1^2 + \eta_2^2} g \right) & 0 \\ 0 & 0 & \eta_1 \end{bmatrix} \quad [50]$$

Now for closer comparison with the previous analysis, g may be replaced by the parameter f where

$$f = \frac{\eta_1 \eta_2}{\eta_1^2 - \eta_2^2} g. \quad [51]$$

Eq. 50 then becomes

$$\mathbf{F} = \begin{bmatrix} \eta_1 \left(1 - \frac{\eta_1^2 - \eta_2^2}{\eta_1^2 + \eta_2^2} f \right) & -\eta_1 \frac{\eta_1^2 - \eta_2^2}{\eta_1^2 + \eta_2^2} f & 0 \\ \eta_2 \frac{\eta_1^2 - \eta_2^2}{\eta_1^2 + \eta_2^2} f & \eta_2 \left(1 + \frac{\eta_1^2 - \eta_2^2}{\eta_1^2 + \eta_2^2} f \right) & 0 \\ 0 & 0 & \eta_1 \end{bmatrix} \quad [52]$$

Upon identifying f with the parameter x of the previous analysis, Eq. 52 is seen to be identical with Eq. 10. The total distortion is then given by $\Phi_1 \mathbf{F}$, where \mathbf{F} is the same as in the twin-product analysis.

From this equality it follows that the mathematical problem in this case is identical with that of the twin-product analysis and that there is a marked parallelism in the physical interpretation of the results. In particular Eqs. 32, 33, and 34 give the direction cosines of the habit plane normal. It follows from Eqs. 38 and 51 that the amount of slip shear g necessary for a plane of zero distortion is given by

$$g = \frac{\eta_1^2 - \eta_2^2}{\eta_1 \eta_2} \left\{ \frac{1}{2} \pm \frac{1}{2} \frac{(1 - \eta_1^2 \eta_2^2)}{\eta_1^2 - \eta_2^2} \sqrt{1 - A^2} \right\} \quad [53]$$

where

$$A = \frac{(\eta_1^2 - 1)(1 - \eta_2^2)}{1 - \eta_1^2 \eta_2^2}.$$

The expressions given in the section on determination of magnitude and direction of the average shear are equally valid for this analysis. As regards the orientation relationship, for each of the 24 variants of the habit plane there are two possible orientation relationships between the austenite and the single crystal martensite. Since the slip distortion does not rotate crystallographic planes and directions, the orientation relationship is obtained by determining the relation between the austenite axis directions and the directions to which these transform as a result of the distortion $\Phi_1 \mathbf{T}_1$. By way of comparison, it should be pointed out that the two orientation relationships for each habit plane are identical with the orientation relationships which the two twin regions of the previous analysis bear to the parent austenite for the same habit plane.

Comparison with Experimental Results

In this section predictions of the proposed theory are compared with the experimental observations that have been made by other investigators.^{8,17} Theoretical calculations of the habit plane were made

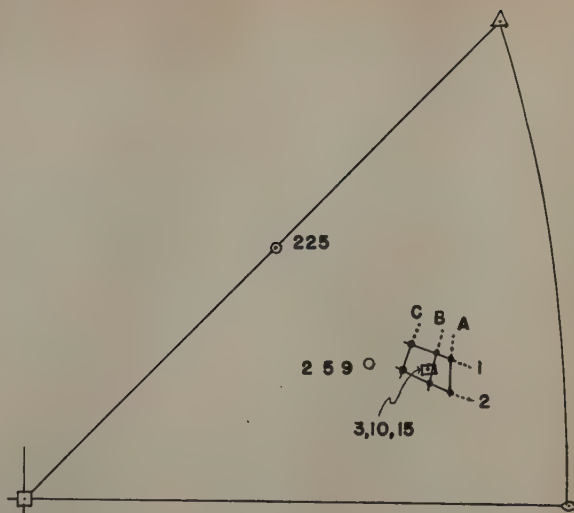


Fig. 6—Stereographic plot of the habit planes listed in Table I. Lines of constant volume ratio: A-1.03, B-1.04, C-1.05; lines of constant axial ratio: 1-1.00, 2-1.08.

for a range of volume ratios, V , from 1.03 to 1.05 and for a range of c/a ratios, r , from 1.00 to 1.08. This range of values includes those appropriate for all the iron-base nickel and carbon alloys that have been investigated in connection with the austenite-martensite transformation. It is seen that the habit plane is relatively insensitive to the particular values of V and r (and hence of the lattice parameters) that are used. The habit planes listed in the last column of Table I are plotted on the stereographic triangle of Fig. 6. The region in which the theoretically calculated habit planes fall is delineated by the grid of lines of constant volume ratio and c/a ratio. This grid is reproduced in Fig. 7 for comparison with the experimental results of Greninger and Troiano¹⁷ on iron-nickel alloys with 32.5 pct Ni. In this case the agreement between the calculated and observed habit plane orientations is excellent. The scatter in the experimental data is in fact appreciably greater than the total range of calculated values for all the axial ratios and volume ratios considered, which cluster about the austenite plane (3, 10, 15). For some other alloys the observed habit planes correspond more nearly to the

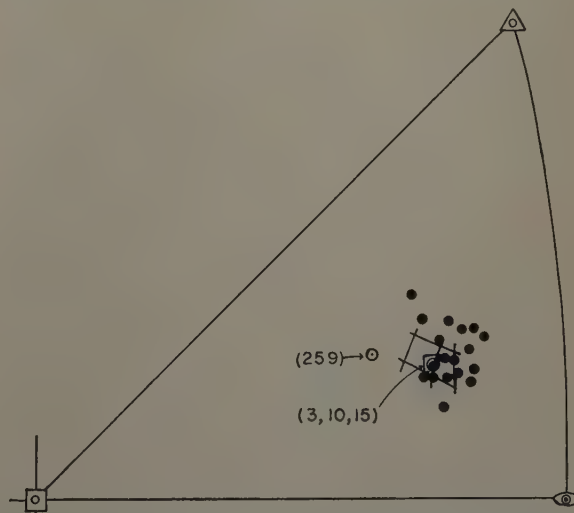


Fig. 7—Stereographic plot of habit planes. Grid delineates planes predicted by the theory. Solid dots are the observed planes of Greninger and Troiano (Fe-Ni, 32.5 pct Ni, ref. 8).

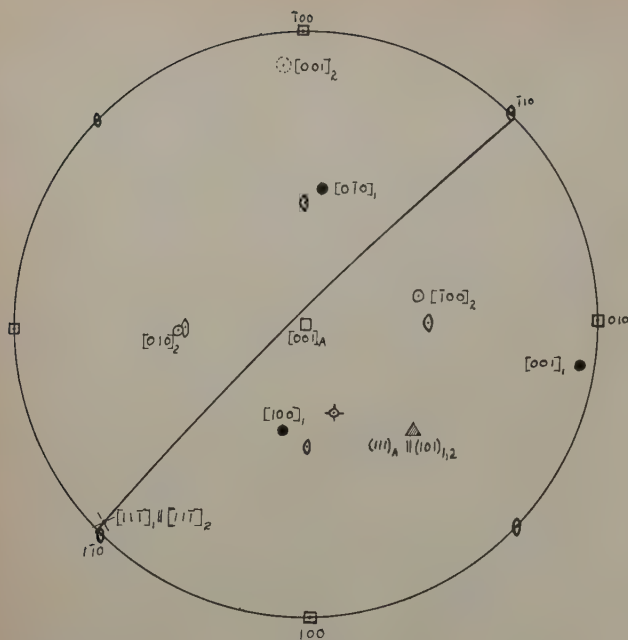


Fig. 8—Stereographic plot of the calculated orientation relationship. • martensite axes for twin 1, ○ martensite axes for twin 2, ⊗ habit plane. Diagonal line is the trace of the twin plane. For the slip-product analysis, • and ○ are the two single crystal martensite orientations corresponding to the indicated habit plane. Plane of projection is the austenite (001).

plane (259), which differs by almost 5° in orientation from the (3, 10, 15). A possible reason for this discrepancy may lie in the fact that the actual martensite plates are imbedded in the austenite crystal and therefore are subject to two constraints which have not been taken into account in these theoretical calculations. These additional constraints are, 1—the interference with the volume expansion of the martensite plate, which is about 5 pct less dense than austenite, and 2—the interference with the macroscopic average shear of the plate. Both of these are second-order effects compared with the effect which has been taken into account, which is the “fitting” of the martensite plate to the austenite at the interface parallel to the plane of the plate. To the approximation that the plate is negligibly thin compared with its lateral dimensions these two additional constraints vanish, whereas the one considered does not. Nonetheless, since actual martensite plates do have a finite thickness, it is not unexpected that small systematic discrepancies between calculations and observations are found. An understanding of why the discrepancies are larger for some steels than for others must await an analysis of the effects of these additional constraints.

In some steels, notably the low alloy steels which contain less than 1.4 pct C, the martensite habit plane has been established experimentally as being approximately (225). In these cases it may be that the volume and shear restraints lead to a drastic change in the apparent habit because they favor the formation of martensite plates with a more complex structure than those considered above. Such structures might consist, for example, of two or more of the 24 variants that have been calculated, which form in some interlocking manner and lead to an apparent habit plane which is some sort of an average of those appropriate for the individual plates. Possibly the fact that the normal to the (225) plane

very nearly bisects the angle between the normals to the (259) and (529) planes is related to a phenomenon of this kind.

A second important basis for comparison with experiment is the orientation relationship between axes in the austenite and martensite. Two orientation relationships, the Kurdjumov-Sachs⁵ and the Nishiyama,⁶ represent extremes of the relationships which have been observed. These can be described respectively by:

$$\begin{aligned} (111)_A \parallel (101)_M & \quad (111)_A \parallel (101)_M \\ & \text{and} \\ [1\bar{1}0]_A \parallel [11\bar{1}]_M & \quad [1\bar{1}2]_A \parallel [10\bar{1}]_M. \end{aligned}$$

Greninger and Troiano⁸ made precision measurements on a Fe-Ni-C (22 pct Ni, 0.8 pct C) alloy in order to determine the habit plane, the orientation relationships, and the magnitude and direction of shear. A summary of their experimental results is found in Table II. The theoretical values listed in Table II were calculated using the values ($a_0 = 3.592\text{\AA}$, $a = 2.845\text{\AA}$, $c/a = 1.045$) of the lattice parameters given in Greninger and Troiano's paper.

The calculated orientation relationship is also presented in the stereographic plot of Fig. 8. It is found that the (101) martensite plane in both twins makes an angle of 15 minutes of arc with (111)_A. Furthermore, the [11 $\bar{1}$] direction in both twins is 3° from [1 $\bar{1}$ 0] in the austenite. Thus the orientation relationship between each of the martensite twin regions and the austenite may be said to be approximately that of Kurdjumov and Sachs. The comparison in Table II between the theoretically determined orientation relationship and that observed by Greninger and Troiano is seen to be quite good.

The calculations yield a different sort of result for the Nishiyama relation. Here it is found that [101]_{M1} is 7°37' from [1 $\bar{1}$ 2]_A and [10 $\bar{1}$]_{M2} is 1°43' from [2 $\bar{1}$ 1]_A. Since here the orientation relationship involves two different austenite directions and since the sum of the angular discrepancies is somewhat larger in the

Table II. Comparison of Experimental and Theoretical Results

	Experimental	Theoretical, This Analysis
Habit plane	$\begin{pmatrix} 10 \\ 3 \\ 15 \end{pmatrix} \approx \begin{pmatrix} 0.5472 \\ 0.1642 \\ 0.8208 \end{pmatrix}$	$\begin{pmatrix} 0.5691 \\ 0.1783 \\ 0.8027 \end{pmatrix}^*$
Orientation relationship	$(111)_A \parallel (101)_M$ to within 1°	$(111)_A$ 15' from $(101)_{M1, M2}$
	$[1\bar{1}0]_A$ 2½° from $[11\bar{1}]_M$	$[1\bar{1}0]$ 3° from $[11\bar{1}]_{M1, M2}$
Shear angle†	$\gamma = 10.66^\circ$	$\theta'' = 10.33^\circ$ $\theta = 10.71^\circ$
Shear direction‡	$\begin{pmatrix} -0.7315 \\ -0.3828 \\ 0.5642 \end{pmatrix}$	$\begin{pmatrix} -0.7660 \\ -0.2400 \\ 0.5964 \end{pmatrix}$

* $\begin{pmatrix} 0.5691 \\ 0.1783 \\ 0.8027 \end{pmatrix}$ is 1°49' from $\begin{pmatrix} 10 \\ 3 \\ 15 \end{pmatrix}$.

† In ref. 8, the average of 12 measurements of shear angle (each $\pm 2^\circ$) is given as $\gamma_0 = 10.75^\circ$. The angle γ , where $\tan \gamma = \frac{2}{2 \tan \frac{\gamma_0}{2}}$ (see Fig. 9, ref. 8), corresponds more closely to our angles θ or θ'' . Both θ and θ'' are given above because, although the input data for the calculation of the shear angle in ref. 8 was the martensite relief which involves an expansion perpendicular to the plane of shear, this expansion was not included in the first shear in the analysis of experimental results.

‡ The angle between the experimental and observed shear directions is 8.6°. The accuracy of an individual measurement of shear direction is $\pm 10^\circ$, although the spread in observed directions is about 30° (see ref. 8).

Nishiyama case, it seems advisable to use the Kurdjumov-Sachs relation as a rational approximation to the actual irrational orientation relation. Furthermore the Kurdjumov-Sachs relation has the proper multiplicity of 24, whereas the Nishiyama relation has a multiplicity of only 12.

Table II also includes a comparison of the angles and directions of shear obtained experimentally⁸ with those calculated from this analysis. Greninger and Troiano analyzed observed relief effects from the point of view of a two stage process, the first being a homogeneous shear on the habit plane and the second a macroscopically heterogeneous shear required to give the final structure. Their first shear does not quite correspond to our total distortion because of the fact that, in computing the elements of their first shear, they did not include the expansion perpendicular to the habit plane that accounts for the change in volume. For this reason, both θ and θ'' (Fig. 4) are included in Table II. The effect of this expansion on the angle of shear is small and the agreement is seen to be excellent. The experimental direction of shear in Table II was computed from Fig. 6 of ref. 8, using a direction in the center of those indicated on the stereographic projection. Because of the experimental difficulties involved in the measurement of shear direction, each measured shear is accurate to only $\pm 10^\circ$ and there is considerable scatter in the observed directions. The directions (Fig. 4) is used for comparison with Greninger and Troiano's direction of shear and the agreement is within experimental error.

On the basis of the experimental information available at present, it is impossible to decide with certainty whether it is the twinned product or the slipped product that forms in the austenite-martensite transformation of iron-base alloys. Desch¹⁸ has made the observation that the fine lines which have appeared on high magnification micrographs of martensite plates may be evidence of twins. The possibility that martensite is twinned has also been suggested by Geisler.¹⁹ However the final answer to this question awaits further metallographic and X-ray investigation of the martensite product.

Application to Other Systems

The ideas upon which this theory is based were first conceived during recent studies on the indium-thallium system, then developed for the gold-cadmium system and the austenite-martensite transformation. The theory successfully describes the face-centered cubic to twinned face-centered tetragonal transformation in the alloy indium-thallium (18 to 23 atomic pct Tl) in which the habit plane was found to be $< 1^\circ$ from the observed (110).¹⁸ The AuCd alloy (47½ atomic pct Cd) undergoes a diffusionless phase change from body-centered cubic to twinned orthorhombic^{19, 20} and although the analysis is more complex, the theory adequately describes the mechanism. The calculated habit plane was found to be $< 1^\circ$ from the observed (331) and well within experimental error.²¹

Conclusions

A theory of the formation of martensite is proposed which permits calculation of the observed crystallographic features of the transformation. The calculations are based on the knowledge that the transformation distortion is inhomogeneous and two types of inhomogeneity are considered. The habit plane, the orientation relationships, and the shear are derived as functions only of the lattice para-

meters of the two phases and calculated values agree well with the results of experiment. The predicted habit plane and orientation relationship are both irrational as has been observed.

Acknowledgment

The work was sponsored in part by the Atomic Energy Commission, contract No. AT(30-1)-904. The authors wish to thank Dr. E. S. Machlin for helpful conversations and Mr. Richard Winter and Mr. Richard H. Dudley for their assistance in the preparation of the manuscript and the calculation of numerical results.

References

- ¹ M. Cohen: The Martensite Transformation. *Phase Transformations in Solids*. Chap. 17. Edited by Smoluchowski, Mayer, and Wehl. (1951) New York. John Wiley and Son.
- ² C. S. Barrett: *Structure of Metals*. (1952) New York. McGraw-Hill Book Co.
- ³ J. S. Bowles and C. S. Barrett: Crystallography of Transformations. *Progress in Metal Physics*. Vol. 3, Chap. 1. Edited by B. Chalmers. (1952) New York. Interscience Publishers.
- ⁴ E. C. Bain: Nature of Martensite. *Trans. AIME* (1924) **70**, p. 25.
- ⁵ G. Kurdjumov and G. Sachs: Über den Mechanismus der Stahlhartung. *Ztsch. Phys.* (1930) **64**, pp. 325-343.
- ⁶ Z. Nishiyama: X-Ray Investigation of the Mechanism of the Transformation from Face-Centered Cubic Lattice to Body-Centered Cubic. *Sci. Rpts. Tohoku Imp. Univ.* (1934) **23**, pp. 637-664.
- ⁷ M. A. Jaswon and J. A. Wheeler: Atomic Displacements in the Austenite-Martensite Transformation. *Acta Crystallographica* (1948) **1**, p. 216.
- ⁸ A. B. Greninger and A. R. Troiano: The Mechanism of Martensite Formation. *Trans. AIME* (1949) **185**, p. 591; *JOURNAL OF METALS* (September 1949).
- ⁹ J. S. Bowles: The Crystallographic Mechanism of the Martensite Reaction in Iron-Carbon Alloys. *Acta Crystallographica* (1951) **4**, p. 162.
- ¹⁰ E. S. Machlin and M. Cohen: Habit Phenomenon in the Martensitic Transformation. *Trans. AIME* (1951) **191**, p. 1019; *JOURNAL OF METALS* (November 1951).
- ¹¹ F. C. Frank: Martensite. *Acta Metallurgica* (1953) **1**, p. 15.
- ¹² A. H. Geisler: Crystallography of Phase Transformations. *Acta Metallurgica* (1953) **1**, p. 260; Gordon Conference (1952). Unpublished.
- ¹³ M. W. Burkart and T. A. Read: This issue, p. 1516.
- ¹⁴ J. S. Bowles, C. S. Barrett and L. Guttman: Crystallography of Cubic-Tetragonal Transformation in the Indium-Thallium System. *Trans. AIME* (1950) **188**, p. 1478; *JOURNAL OF METALS* (December 1950).
- ¹⁵ Margenau and Murphy: *The Mathematics of Physics and Chemistry*. (1943) New York. D. Van Nostrand Co.
- ¹⁶ Gibbs and Wilson: *Vector Analysis*. (1901) Second Edition. New Haven. Yale University Press.
- ¹⁷ A. B. Greninger and A. R. Troiano: Crystallography of Austenite Decomposition. *Trans. AIME* (1940) **140**, pp. 307-336.
- ¹⁸ C. H. Desch: Discussion to ref. 17. *Trans. AIME* (1940) **140**, p. 331.
- ¹⁹ L. C. Chang and T. A. Read: Plastic Deformation and Diffusionless Phase Changes in Metals—The Gold-Cadmium Beta Phase. *Trans. AIME* (1951) **191**, p. 47; *JOURNAL OF METALS* (January 1951).
- ²⁰ L. C. Chang: Atomic Displacements and Crystallographic Mechanism in Diffusionless Transformation of Gold-Cadmium Single Crystals containing 47.5 atomic percent Cadmium. *Acta Crystallographica* (1951) **4**, p. 320.
- ²¹ D. S. Lieberman, M. S. Wechsler and T. A. Read: To be published.

Diffusionless Phase Change in the Indium-Thallium System

by M. W. Burkart and T. A. Read

The crystal geometry of the cubic-tetragonal interface after partial transformation of an indium-thallium alloy single crystal is described and a general theory is presented. The effects of applied stresses on this transformation are interpreted and the latent heat of transformation is obtained from observations of transformation under stress.

A DIFFUSIONLESS phase transformation between face-centered cubic and face-centered tetragonal structures has been reported for the indium-thallium system by Bowles, Barrett, and Guttman.^{1, 2} The transformation takes place at approximately 105°C at 18 atomic pct Tl and 25°C at 23 pct Tl. In their study, Bowles, Barrett, and Guttman used polycrystalline samples whereas in the present study single crystals were used to eliminate the transformation constraints imposed by adjoining grains. The use of single crystals made possible a comprehensive study of the effect of stress on the transformation. In the course of the work, it was possible to formulate a new method of analyzing diffusionless transformations (presented in this paper) which permits calculation of the geometry of the interphase interface from a knowledge of the crystal structures of the initial and final phases.

The specimens were prepared from chemically pure thallium and 99.97 pct In which were weighed out to produce 3 to 4 grams of alloy of the desired concentration. The metal was placed in clean fused silica tubing, then melted, degassed and sealed under vacuum. (To obtain single crystals, it was found that both degassing and extreme cleanliness were essential.) Single-crystal specimens were grown by a modified Bridgman technique.³ Specimens were removed from the tube by dissolving the quartz in concentrated hydrofluoric acid which attacks the specimen very slowly. The specimen then was polished mechanically to produce four flat surfaces, electropolished, and annealed at 140°C for 48 hr.

M. W. BURKART, Junior Member AIME, is associated with the Dept. of Metallurgy, and T. A. READ, Member AIME, is Associate Professor of Metallurgy, School of Mines, Columbia University, New York.

Discussion on this paper, TP 3631E, may be sent, 2 copies, to AIME by Jan. 1, 1954. Manuscript, April 20, 1953. Cleveland Meeting, October 1953.

This paper represents part of a thesis by M. W. Burkart submitted in partial fulfillment of the requirements for the degree of Doctor of Philosophy to the Faculty of Pure Science, Columbia University.

The electropolishing solution used was that described by Bowles, Barrett, and Guttman and the polishing was carried out on both the high and low temperature phases of the alloy. The high temperature polishing was done at 110°C with a stainless steel cathode.

Visual Observation of the Transformation in Single Crystals

A visual study of the transformation was made on specimens which had been electropolished in the high temperature phase. The specimens were supported on the stage of a metallograph by an electrically heated holder which contained an opening for observing the specimen. Visual evidence of transformation was found in the presence of an interface which separated the two phases. The interface plane defines the boundary of the phase undergoing transformation and manifests itself by the sharp change in angle between the surface of the specimen and the incident light at the juncture of the two phases. On slow cooling, well-annealed specimens transformed from the face-centered cubic structure to the face-centered tetragonal structure by the motion of a single plane interface which traversed the specimen from one end to the other. Upon heating, the interface moved back in the reverse direction.

The interface could be started, stopped, or reversed at will. A temperature hysteresis of about 3½°C was observed in the reversal of the interface. Holding an interface stationary caused it to disappear completely in most cases, whereas in other instances the interface became less distinct depending upon its orientation. The interface could be made to reappear by changing the temperature of the specimen. The low temperature tetragonal structure exhibits only the fine markings or subbands reported by Bowles, Barrett, and Guttman and is illustrated in Fig. 1. These subbands are twin-related. Back-reflection Laue patterns show the breakup of the cubic spots into pairs of spots corresponding to the twin orientations of the tetragonal phase.

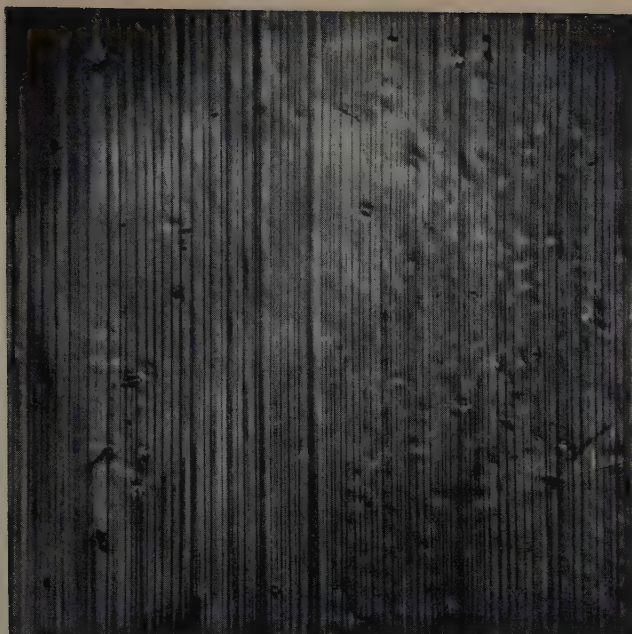


Fig. 1—Twinned structure after single interface transformation of an In-Tl alloy. X200. Area reduced approximately 50 pct for reproduction.

The plane of the interface was determined from its traces on two sides of the specimen and the specimen's orientation. In all cases the interface plane was approximately a $\{110\}$ plane of the cubic phase; that is, the pole of the interface plane was within 1° of the $\{110\}$ pole. It was found that a specimen could transform by any one of the six different $\{110\}$ interfaces. The selection of the interface is determined by the temperature gradient and stress distribution within the specimen. Once the specimen has transformed by a given interface it will tend to undergo all subsequent transformations by the same interface. A change from one interface to another could be achieved by heating the specimen in such a manner as to cause rapid and violent motion of the interface. In all cases back-reflection Laue patterns obtained at a 3 cm specimen to film distance showed the high temperature cubic phase to be a single crystal.

The specimens were also observed to transform by the motion of two interfaces, usually intersecting in the form of an X as shown in Fig. 2. In the case of multiple interface transformation both interfaces cannot simultaneously represent a boundary between the cubic and tetragonal phases. Portions of each interface may simultaneously define the boundary or only one of the interfaces may do so, while the other interface represents the boundary between variously oriented tetragonal structures.

The two interfaces may traverse the specimen with motions independent of each other. Transformation by crossed interfaces seems to occur when the specimen is bent, mishandled, or subjected to violent transformation upon heating. After the specimen has transformed a few times by means of an X interface, it is somewhat difficult to make the transformation revert to the single interface type, although it is relatively easy to change the planes making up the crossed interface. As with the single interface, the specimen can transform on cooling from the face-centered cubic to the face-centered tetragonal structure by means of a given set of crossed interfaces; and then, on heating, transform back to the cubic by a crossed interface which may

contain none, one, or both of the interfaces observed on cooling. The specimen can also transform by a single interface in one direction and a double interface in the reverse direction. In all cases the planes defining the crossed interfaces are approximately of the form $\{110\}$. Furthermore, any combination of these planes can form an X interface, regardless of whether they were at 60° or 90° to each other. Back-reflection Laue patterns of the low temperature phase show that as a result of X transformation the pairs of spots characteristic of single interface transformation are broken up into clusters of spots denoting a variety of orientations. After subsequent single interface transformation it was not possible to return to a diffraction pattern yielding spot pairs, although the number of spots in a cluster was reduced. This could be achieved, however, by annealing for a few hours at 130°C .

Analysis of Transformation

When a single crystal of the cubic phase was transformed by cooling without the application of stress, the low temperature tetragonal phase always consisted of a banded twin aggregate. This observation can be rationalized on the basis of a consideration of the structural difference between the two phases. It is not possible to have a coherent interface between two single crystals of these phases without severe elastic strain over appreciable distances from the interface between them. The misfit strain between the two phases can be minimized, however, if the tetragonal phase is twinned so that the sign of the strain changes from twin to twin. It will be shown that there exists a unique interface plane between the cubic crystal and the array of tetragonal twins such that, for an appropriate ratio of twin thicknesses, the average misfit strain is zero.

An experiment was performed to determine whether the requirement of minimum interfacial strain was a necessary condition to be fulfilled by the resulting microstructure. A single crystal of the low temperature tetragonal phase was obtained by straining the specimen to eliminate one of the twin

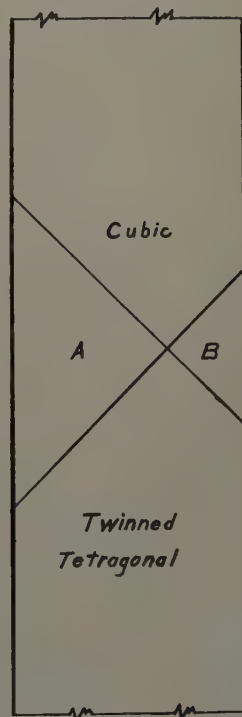


Fig. 2—Sketch illustrating crossed interface transformation. A and B represent differently twinned tetragonal regions.

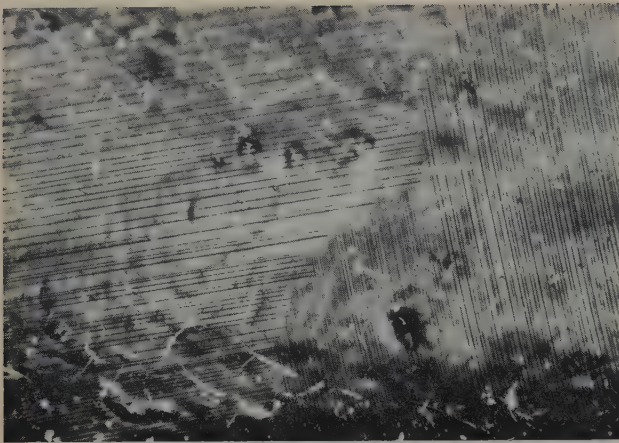


Fig. 3—Structure after partly transforming tetragonal crystal to the cubic phase followed by cooling. X200. Area reduced approximately 50 pct for reproduction.

orientations. This was done by first annealing the specimen in the cubic phase to obliterate the previous transformation history, and then cooling the specimen through the transformation under stress. After this treatment the specimen remains a low temperature phase single crystal even when the stress is removed. The crystal then was heated until it had partly transformed to the cubic structure and then was cooled back to the tetragonal. If the requirement of minimum interfacial strain was not necessary, no markings or twinning would be expected in the single-crystal tetragonal region which had not undergone transformation. It was observed, however, that this region was no longer a single crystal but consisted of a banded twin structure. Fig. 3 illustrates the microstructure observed. The region to the left of the interface had been single-crystal tetragonal and the region to the right cubic before cooling.

On the basis of the preceding observations, it is seen that the specimen transforms heterogeneously in order to minimize the strain at the interface between the two phases. Each twin, however, represents a region homogeneously transformed from the cubic phase. It has been found^{1,2} that after transformation one of the cube edges is increased in length by 2ϵ and the other two decreased by ϵ . Thus within each twin crystal the net effect of transformation is an increase in length along one of the crystallographic axes and a decrease in length along the other two. The maximum displacement of an atom relative to its nearest neighbor is approximately 1 pct of the interatomic spacing. Thus throughout the twin crystal, nearest neighbor relationships are maintained and there is a one-to-one correspondence between the positions of the atoms in the face-centered cubic and face-centered tetragonal lattices after transformation. There are then only three possible choices for the tetragonal axis depending upon which cube axis becomes a c axis of the tetragonal structure. Within each twin, the transformation may then be described in terms of a pure distortion of the cubic structure.

According to the analysis of transformation presented in this paper, the habit plane is a plane of zero average strain. It should then be possible to calculate both the habit plane and the relative amounts of the variously oriented structures from the lattice parameters of the two phases. When the transformation occurs by the motion of a single interface separating the two phases, a single crystal

of the transformation product is never produced from a single crystal of the parent phase. In the case of indium-thallium a twinned tetragonal structure is formed in which each tetragonal twin results from an extension of one of the cube axes by an amount 2ϵ and a contraction of ϵ along the other two.

The transformation strain to produce one of the twins resulting from contractions along the x and y axes and expansion along the z axis, that is,

$$\epsilon_{xx} = -\epsilon, \epsilon_{yy} = -\epsilon, \epsilon_{zz} = 2\epsilon,$$

may be written in matrix notation as

$$\begin{pmatrix} -\epsilon & 0 & 0 \\ 0 & -\epsilon & 0 \\ 0 & 0 & 2\epsilon \end{pmatrix}.$$

Similarly, the strain matrix representing transformation to the other twinned orientation is

$$\begin{pmatrix} -\epsilon & 0 & 0 \\ 0 & 2\epsilon & 0 \\ 0 & 0 & -\epsilon \end{pmatrix}.$$

The average strain for the transformation to the twinned structure is then

$$x \begin{pmatrix} -\epsilon & 0 & 0 \\ 0 & -\epsilon & 0 \\ 0 & 0 & 2\epsilon \end{pmatrix} + (1-x) \begin{pmatrix} -\epsilon & 0 & 0 \\ 0 & 2\epsilon & 0 \\ 0 & 0 & -\epsilon \end{pmatrix}$$

where x is the volume fraction of one of the twin orientations. These expressions are only approximate, since the relative rotation necessary to insure coherent twins has been neglected. The exact expression is derived in ref. 4. In the indium-thallium case, the difference between the exact and approximate treatments is negligible and hence the simplified expression will be used. In order to find a plane of zero average strain one of the average principal strains must be made to vanish. This can be accomplished by selecting the proper proportions of the two orientations. The average strain may be written

$$\begin{pmatrix} -\epsilon & 0 & 0 \\ 0 & 2\epsilon - 3\epsilon x & 0 \\ 0 & 0 & -\epsilon + 3\epsilon x \end{pmatrix}.$$

The value of the determinant of this matrix is equal to the product of its diagonal elements, which must be zero if one of the principal strains is zero. The values of x which will make the determinant zero are $1/3$ and $2/3$. Taking $x = 1/3$, the resulting average strain matrix is

$$\begin{pmatrix} -\epsilon & 0 & 0 \\ 0 & \epsilon & 0 \\ 0 & 0 & 0 \end{pmatrix}.$$

The plane of zero average strain would then be parallel to the z direction and bisect the angle between the x and y axes. This is the $(\bar{1}10)$ plane and is the habit plane for the transformation. The habit plane and resulting transformation products are shown in Fig. 4. The increase in length along a $[\bar{1}\bar{1}0]$ diagonal in going from a cube to a tetragonal twin with a c - a diagonal is $2a\epsilon$ which is one-half the decrease in length going to an a - a diagonal. The average strain along the $[\bar{1}\bar{1}0]$ direction can then be made equal to zero if there are twice as many c - a diagonals parallel to it as there are a - a diagonals.

Furthermore, with the particular twinning plane chosen, the average strain in the [001] direction 90° to the $(\bar{1}10)$ is also zero since in this direction there are twice as many tetragonal axes parallel to it that have undergone a contraction of ϵ as there are axes which have extended 2ϵ .

The structural arrangement presented above was verified dilatometrically. The change in length on transformation was measured using a dilatometer with the specimen loaded in tension. The effect of the tensile loading is to favor the orientation of the twins having their c axes most nearly parallel to the axis of tension, thus giving the maximum change in length of the specimen. The transformation strain in a specimen having a [100] direction 5° from the axis of tension was observed to be one-half that required to extend one of the cube axes to a c axis. This is exactly the transformation strain expected on the basis of zero average strain at the interface such that the volume of twins with c axes parallel to the axis of tension is twice the volume with a axes parallel to it.

As mentioned previously the strain matrices used were those to produce twins having parallel axes. The effect of including the small relative rotation of the twins would yield an irrational habit plane whose orientation is slightly different from the $(\bar{1}10)$. This exact calculation, which has been published,⁴ yields the following expressions for the habit plane indices (hkl) :

$$h = \frac{1}{2\eta_1} \left\{ \sqrt{\frac{2\eta_1^2\eta_2^2 - \eta_1^2 - \eta_2^2}{\eta_2^2 - 1}} - \sqrt{\frac{\eta_1^2 + \eta_2^2 - 2}{\eta_2^2 - 1}} \right\}$$

$$k = \frac{1}{2\eta_1} \left\{ \sqrt{\frac{2\eta_1^2\eta_2^2 - \eta_1^2 - \eta_2^2}{\eta_2^2 - 1}} + \sqrt{\frac{\eta_1^2 + \eta_2^2 - 2}{\eta_2^2 - 1}} \right\}$$

$$l = \frac{1}{\eta_1} \sqrt{\frac{1 - \eta_1^2}{\eta_2^2 - 1}}$$

where

$$\eta_1 = \frac{a}{a_0} \text{ and } \eta_2 = \frac{c}{a_0}$$

and a_0 is the cubic lattice parameter and a and c are the tetragonal parameters. Values of these are given in ref. 1, which on substitution yield for the calculated irrational habit plane indices (0.013, 0.993, 1). This plane differs from the reported (011) habit plane by 26 minutes of arc.

After transformation from a single crystal of the high temperature phase in the indium-thallium and gold-cadmium systems, the polycrystalline product reverts to the single-crystal parent when the transformation is reversed. Those transformations resulting in a single crystal will be termed unique and those which may result in a polycrystalline structure non-unique.

A reason for this behavior may be found in the consideration of the symmetry properties of the structures. If a crystal is transformed from one structure to another, the symmetry about any direction in the structure may increase, decrease, or remain unchanged. The symmetry about a direction may be determined by considering a row of atoms parallel to the direction in question. If, after transformation, the symmetry of lattice sites about the row of atoms is altered, the symmetry about this direction is changed. Thus in the austenite-martensite reaction, for example, a cube edge of the austenite having four-fold symmetry becomes a

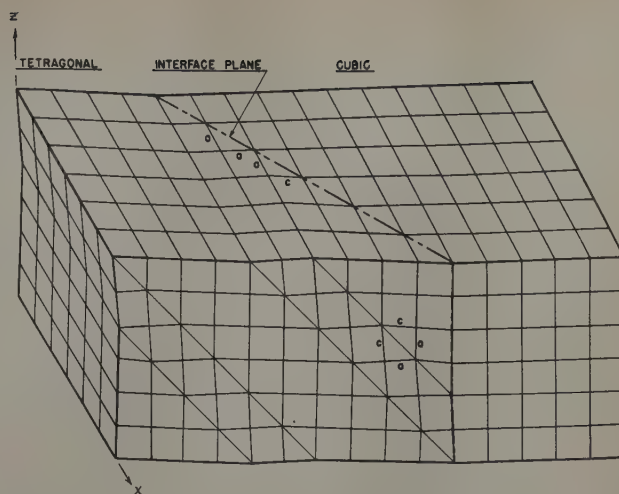


Fig. 4—Schematic representation of the structure at the interface between the high and low temperature phases.

martensite face diagonal with two-fold symmetry and two austenite face diagonals of two-fold symmetry become martensite cube edges having four-fold symmetry. If the symmetry decreases, more than one crystal may be produced, the maximum number dependent upon the loss of symmetry involved. If, however, the symmetry remains unchanged or is increased, no multiplicity of structures exists and a single-crystal transformation product will result. Thus in the indium-thallium alloys, for example, two of the cube axes having four-fold symmetry become, after transformation, tetragonal axes possessing two-fold symmetry. The third cube axis remains a four-fold axis of symmetry after transformation. As a result of the decrease in symmetry, a multiplicity of tetragonal structures is possible. If the transformation is reversed, the polycrystalline tetragonal structure will revert to a single crystal. In this case there is no loss in symmetry and thus no multiplicity in the transformation.

In the transformation concept presented thus far no indication has been given of the thickness of the tetragonal twins. For the total strain energy at the interface to be a minimum, the width of the twins would be expected to be of atomic dimensions. According to Fig. 1, however, the lamellar spacing is approximately 5×10^{-4} cm. The observed spacing can be rationalized if the interfacial energy between the twins is taken into account. The total energy may then be written as the sum of the strain energy at the interface and the twin surface energy. If the depth of the strained area on each side of the interface is considered equal to the thickness of the twins according to St. Venant's principle, the energy at the interface is approximately

$$W = \epsilon^2 Y \bar{h} t I \sin \theta + \frac{\gamma}{t} \bar{l} \bar{h} I \sin \theta$$

where t is the thickness of the lamellae, \bar{h} their average height and \bar{l} their average length. Furthermore, ϵ is the strain, Y the modulus of elasticity, γ the twin boundary surface energy, and θ the angle between the lamellae and the interface of length I . Taking the derivative of W with respect to t , the total energy will be a minimum when the strain energy is equal to the twin interface energy. Using a strain of 1×10^{-2} and a modulus of 1×10^{11} dynes per sq cm the twin interface energy $\gamma = (t^2 \epsilon^2 Y) / \bar{l}$ is

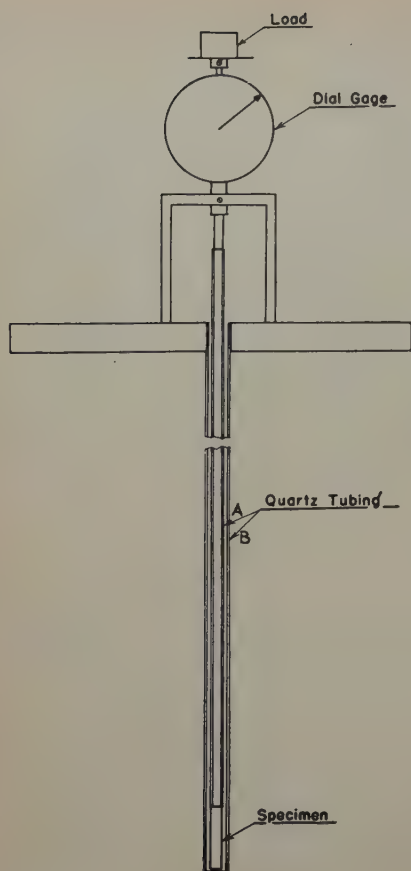


Fig. 5—Dilatometer used for studying transformations.

found to be 2.5 ergs per sq cm. This compares with a value of 24 ergs per sq cm reported for the coherent twin boundaries in copper.⁵

Effect of Stress

As a result of their work, Bowles, Barrett, and Guttman^{1,2} concluded that the phase change is of the second order. This was based on their finding that the deviation of the volume from additivity with the addition of thallium was a continuous function, at room temperature, over the region in which the phase change occurred. The conclusion however is subject to doubt. There was considerable scatter in the points defining the volume additivity curve and the change in volume on transformation is less than 0.1 pct and probably less than 0.03 pct.^{1,2} In addition, plots of the lattice parameter vs composition and temperature revealed a discontinuity at the transformation.

It was found that the transformation could be easily followed by dilatometric means. The specimen was cemented to a quartz tube (A) in contact with a thermocouple contained therein. This was then inserted into another quartz tube (B) of the same length, one end of which was sealed off and the other end fastened to a brass plate. The other end of the tube (A), which was fastened to the specimen, was in contact with an indicating dial gage mounted on the brass plate. The dilatometer is shown in Fig. 5. A curve of length vs temperature typical of the transformation is shown in Fig. 6. According to the figure a discontinuity in the length of the specimen occurs at the transformation temperature. The elongation at this point is 0.37 pct and the hysteresis between the transformation temperatures on heating and cooling is 3.7°C for a specimen whose [100] direction is 5° from the specimen axis.

By definition, a first-order phase change is one in which a first derivative of the Gibbs free energy is discontinuous over the phase change. Since the specimen length may be written as

$$L = \left(\frac{\partial G}{\partial F} \right)_T$$

where F is the load on the specimen,* the face-cen-

* This is the uniaxial compression analog of the familiar thermodynamic relation $V = \left(\frac{\partial G}{\partial P} \right)_T$, as discussed in ref. 6.

tered cubic to face-centered tetragonal transformation in the indium-thallium alloys conforms to the definition of a first-order phase change. In Fig. 6 it may be seen that when the specimen is made to transform under load the transformation temperature is increased both on heating and cooling. The specimens were transformed under compressive loading, the load being applied to the top of the shaft running through the dial indicator in contact with the quartz rod to which the specimen was cemented. The transformation was observed over a range of compressive loads and the transformation temperatures determined. These results are plotted in Fig. 7 showing the effect of load on transformation temperature. The line on the right corresponds to the transformation temperature on heating and on the left to the transformation on cooling. As can be seen, the relationship between transformation temperature and applied load is linear and furthermore, the lines are parallel. The two lines may be considered to bracket the equilibrium temperature of the transformation. Since they are parallel the effect of load upon the equilibrium temperature is assumed to be the same as on the transformation temperatures plotted. On this basis a latent heat of the transformation was calculated using the Clausius-Clapeyron equation

$$\lambda = \frac{1}{\rho} T \frac{d\sigma}{dT} \epsilon$$

where σ is the applied stress, ϵ the transformation strain, ρ the density of the alloy, and T the temperature of transformation in °K. The value for the latent heat obtained by this method is 2.66×10^{-3} cal per gram.

The strain ϵ , and the slope $d\sigma/dT$ of the transformation temperature vs stress curve are functions of the orientation of the specimen with respect to the

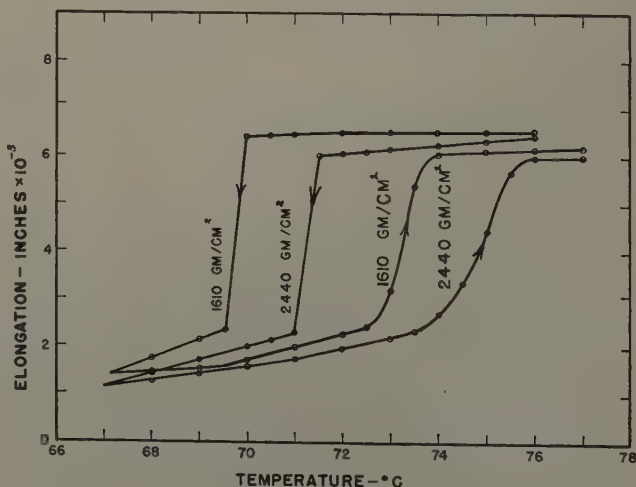


Fig. 6—Typical curve illustrating change in length during transformation. Composition of specimen 20.7 pct Tl.

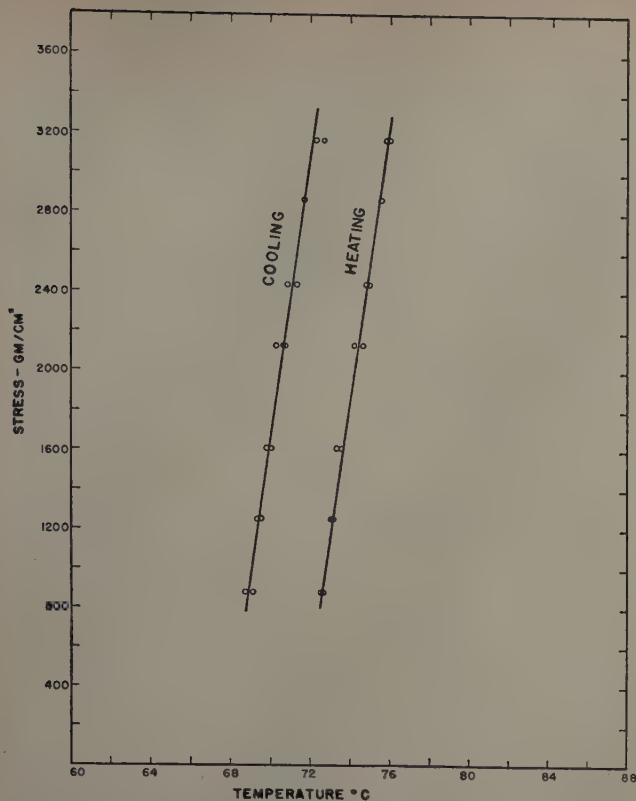


Fig. 7—Effect of compressive loading on transformation temperature for both heating and cooling. Composition of specimen 20.7 pct Tl.

applied load. In addition, according to the Clausius-Clapeyron equation it would not be expected that the slope would be the same in both compression and in tension since the strain should be different in the two cases. In tension the transformation should be such that the twin orientations having their c axes most nearly parallel to the axis of tension will be favored, whereas in compression the a axes would be favored. If this did not occur, an elongation of the specimen would take place when transforming from the cubic to the tetragonal phase under compressive loading, which is contrary to observation.

The transformations under load were repeated with a specimen of the same orientation held in tension. Fig. 8 illustrates the effect of tensile loading upon transformation temperature. The slope $d\sigma/dT$ was 323 gram per sq cm per °C in tension compared to 680 gram per sq cm per °C in compression. Within the accuracy of measurement, the value of the latent heat was the same in both cases.

Since the application of stress to the specimen is found to increase the transformation temperature it may be possible, according to Figs. 6 through 8, to increase the load sufficiently so that the transformation temperature, on cooling of the stressed specimen, is above that of the transformation temperature on heating of the unstressed specimen. Accordingly then it should be possible to transform the specimen isothermally from the face-centered cubic to the face-centered tetragonal phase and back again merely by the application and removal of a sufficient load. This was found to be the case in the indium-thallium system as shown in the load-elongation curves of Fig. 9. The transformation begins at the deviation from linearity in the curves and was carried out at $73^\circ \pm 0.2^\circ\text{C}$. That the transformation had gone to completion was determined

by transforming the specimen under full load from the high temperature phase to the low temperature phase. The load was then removed and the specimen reverted to the high temperature phase. Further heating produced no additional transformation. The same result was obtained when the procedure was carried out in the opposite direction. Subsequent to these findings Reynolds and Bever⁷ published a paper reporting a similar experiment in which they were able to induce a partial martensitic transformation in either direction in a brass alloy by the isothermal application of stress. It is believed that the results reported herein, on indium-thallium, constitute the only case known where it has been possible to induce complete transformation in either direction by the application and release of stress.

Rubber-Like Behavior

The application of stress to the low temperature tetragonal phase of the indium-thallium alloys was also studied. When the specimen is pulled in tension clicks can be heard; it is also possible to hear the typical twinning cry on bending the specimen. Under favorable surface and orientation conditions at room temperature, an interface may be seen which traverses the specimen upon the application and reversal of stress. Furthermore, the specimen yields readily when bent until a certain strain is reached at which it becomes rigid. With the aid of the microscope the surface of the specimen is seen to consist of the twinned bands as shown in Fig. 1. If the specimen is stressed while under microscopic examination, one of the twin orientations is seen to disappear at the expense of the other. This change is evidenced by the motion of the twin boundaries between the alternate light and dark bands. Thus, for example, when the specimen is bent in a given direction the light bands increase in width until the entire surface is uniformly light. Reversing the

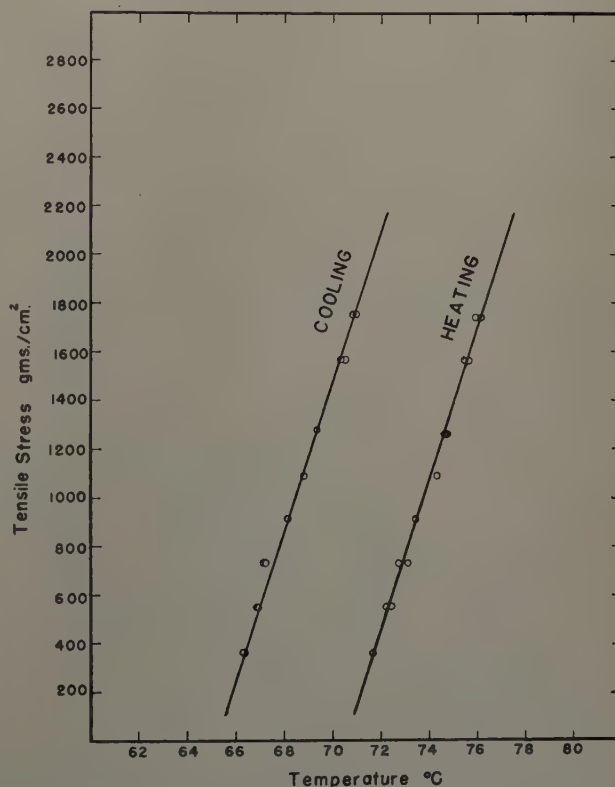


Fig. 8—Effect of tensile loading on transformation temperature for both heating and cooling. Composition of specimen 20.7 pct Tl.

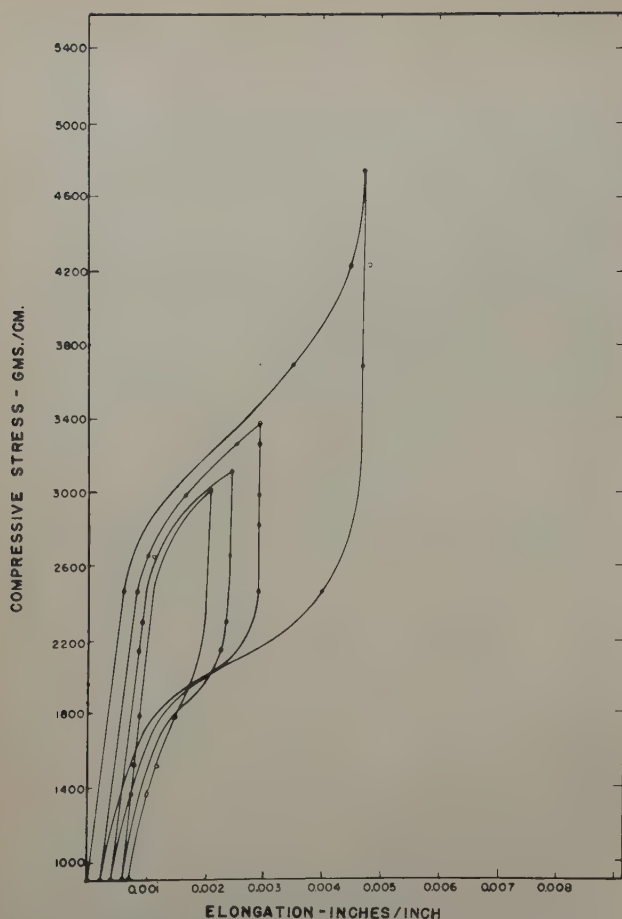


Fig. 9—Diffusionless phase transformation produced by the application and release of stress at 73°C. Composition of specimen 20.7 pct TI.

bend causes the reappearance of the dark twins and further bending will result in a surface uniformly dark. Back-reflection Laue patterns taken from a specimen before and after the application of a tensile load are presented in Fig. 10 and show that the multiple spots corresponding to the twin orientations become single spots when the specimen is stressed.

When the specimen is dipped into a bath of dry ice and acetone it becomes rubber-like in behavior compared to its room temperature properties. After bending, it straightens itself immediately when released; when pulled in tension and then released, it

snaps back like a piece of rubber. As at room temperature, it can be bent easily only so far, at which point it becomes rigid. When allowed to heat to room temperature the specimen loses its rubbery behavior. Furthermore, if the specimen is bent within the rubbery range and this configuration forcibly maintained while the specimen is heated to room temperature, it will retain the new configuration even when cooled down again to the dry ice and acetone temperature. In fact if it is straightened at this temperature it will spring back to the bent configuration. Experiments were conducted over a range of compositions to determine whether there was any relationship between the temperature for the onset of rubber-like behavior and alloy composition or transformation temperature. The onset of rubber-like behavior occurs between -5° and -10°C and no relationship could be found.

From the various observations noted above it is possible to suggest a mechanism for the rubber-like behavior. From metallographic observation and X-ray diffraction study, it is seen that the effect of an applied stress at room temperature is to move the twin boundaries. Zener⁸ has shown that a shear stress across a twin interface can induce movement of the twin boundary. The anelasticity resulting from such movement has been measured in copper-manganese alloys by Worrell.⁹ It has been stated¹⁰ that copper-manganese alloys undergo the same type of transformation studied in this paper; the quenched alloy is face-centered tetragonal and exhibits the same structure of main bands and sub-bands as polycrystalline indium-thallium. In both alloys the atomic displacements to produce a movement of the twin boundaries are very small, requiring a shear strain of only a few percent. Thus it should be relatively easy to strain the indium-thallium alloys in tension at room temperature thereby causing a displacement of the twin boundaries until only one of the orientations remains. Resistance to additional strain would then be increased to a value consistent with the elastic modulus of the alloys.

When the temperature of the specimen is lowered sufficiently the configuration of twin interfaces becomes stabilized, and if this configuration is altered by means of an applied stress it will return to the stabilized one when the stress is removed. Similarly if a new configuration is given the sample in the rubber-like region and forcibly retained while heating to room temperature, it will become the stabilized form at low temperatures. Two of the pos-

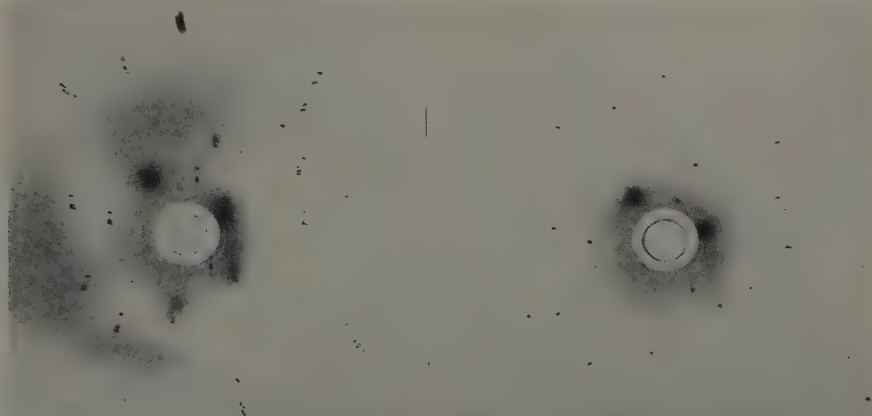


Fig. 10—Application of tensile stress to specimen having Laue pattern at left yields single crystal pattern at right.

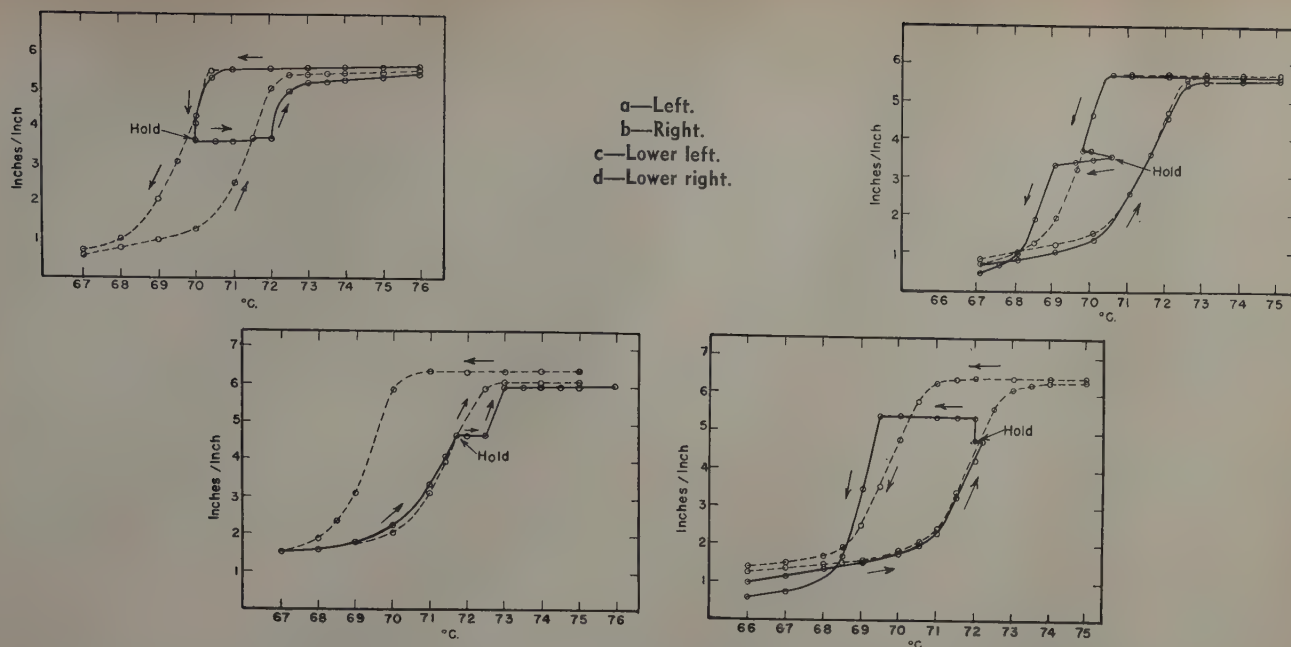


Fig. 11—Effect of interrupting the transformation and holding the specimen at constant temperature for six hours. The dashed curves show the transformation behavior with constant heating and cooling rates. In all cases the subsequent transformation behavior is affected if the specimen temperature is held constant at temperature indicated.

sible methods by which stabilization could be achieved will be mentioned.

The stabilization of the twin boundaries may be achieved by relaxation processes occurring at the twin interfaces. Thus at room temperature, relaxation proceeds at such a rate that the twin boundaries displaced by the applied stress are immediately stabilized and the new configuration retained. At lower temperatures, however, where relaxation is much slower or does not occur at all, another configuration of twin interfaces would become unstable relative to the unstrained state where relaxation had taken place. The specimen would then be expected to exhibit rubber-like properties at these temperatures.

Rubber-like behavior might also be expected if there existed a preferential distribution of interstitially dissolved impurities in the tetragonal lattice. Upon displacement of the twin boundary those interstitial atoms swept over by the moving boundary would be located in unfavorable positions. At high enough temperatures the atoms can diffuse to the new preferred sites whereas at temperatures limiting diffusion, the interfaces would be unstable relative to their original configuration.

Rubber-like behavior has been observed in only one other alloy system,¹¹ namely in the gold-cadmium alloys between 47 and 50 atomic pct Cd. The suggested mechanism predicts, however, that it should also be present in those alloys producing twinned structures, analogous to the indium-thallium alloys, as a result of diffusionless transformation. Thus at small ratios of c/a and at favorable temperatures the rubber-like behavior might be found in the copper-manganese,⁹ chromium-manganese,¹² and indium-cadmium¹³ alloys and in barium titanate.¹⁴

Relaxation Effects

The presence of relaxation processes other than that associated with the rubber-like behavior of the alloys, as mentioned above, is indicated by the disappearance of the interfaces upon holding and the

tendency of the crystal to undergo succeeding transformations by the same interface. Also if the specimen is partly transformed and then held at constant temperature for a short period of time the interface becomes stabilized. In the case of gold-cadmium¹⁵ alloys the specimen must be heated an additional 1° to 3°C in order to make the interface move further. Measurements on indium-thallium indicate that a change in temperature of a degree or less is required. If after the holding and subsequent completion of the reaction, the transformation is immediately reversed, the specimen will "remember" the position at which the interface was held and it will resist further motion until sufficient change in temperature is achieved. Furthermore, a short distance before the interface reaches the position of previous holding an increase in velocity is observed. These observations, readily obtained with gold-cadmium but barely perceptible in indium-thallium alloys, indicate the existence of a relaxation process whose effects are retained through subsequent transformation.

The effect of holding on the indium-thallium transformation as determined dilatometrically is shown in Fig. 11. In all cases the specimen was held at temperature for 6 hr within $\pm 0.2^\circ\text{C}$. The stabilizing effect of holding is clearly seen although it is not possible to determine from these results whether the transformation temperature has actually been shifted.

An experiment was conducted to investigate further the relaxation properties of the alloy. In this instance the specimen was annealed for 12 hr at 120°C to remove any effects of previous history and then cooled slowly through the transformation under tensile loading. It was next held in tension for 48 hr just below the transformation temperature. An X-ray diffraction pattern obtained from the cooled specimen after the load had been removed showed it to be a single crystal. The crystal was then dipped into a water bath 2°C above the transformation temperature for periods as short as 3 sec, and then cooled. In no instance did this procedure

yield a single crystal after complete transformation. The relaxation which took place during the 48-hr hold was incapable of stabilizing the single-crystal configuration through a subsequent transformation cycle. The experiment was repeated with a gold-cadmium alloy whose interfacial relaxation time for rubber-like behavior was long compared to the time of the no-load transformation cycle. It was also impossible to get a single crystal in this alloy. However, when an indium-thallium single crystal of the low temperature tetragonal phase was partly transformed to cubic and then cooled, a single crystal of the tetragonal structure was obtained in one case but the result was not reproducible.

Discussion

The experiments and observations that have been described provide ample support for the mechanism of the diffusionless phase transformation as presented in this paper. This mechanism differs from that of a previous study,^{1,2} of the indium-thallium transformation, where it was concluded that the transformation occurred by a double shear. Other investigators have used shear mechanisms to describe diffusionless phase transformations in general. The double shear mechanism has been resorted to in order to explain the observed relief effects on the specimen after transformation. In the case of the indium-thallium alloys the observed {110} habit plane was interpreted as the plane of first shear. A second shear on another {110} plane 60° to the plane of the first shear had to be postulated in order to produce the observed tetragonal structure. Actually the resulting structure was triclinic and could be made tetragonal after slight adjustments of the atom positions.

If, instead of occurring on {110} planes, the two shears were to take place on irrational planes within 1° of the {110}, as determined by an exact calculation of the type presented in this paper, a tetragonal structure would result. Both mechanisms would describe the change in atomic configuration. The first shear of the double shear mechanism is then equivalent to the average strain obtained by the present treatment. The heterogeneous second shears produce no macroscopic distortion of the habit plane.

Although a second heterogeneous shear is necessary to produce the final structure, its use implies the presence of an intermediate structure before the second shear occurs. In addition, the failure of the rational shear planes to produce a tetragonal structure for the indium-thallium alloys calls attention to the fact that the transformation geometry must first be determined by observation in order to formulate a double shear mechanism. But using the criterion of zero average strain, it is possible to calculate the habit plane, the orientation relationship, and the relative amounts of the variously oriented transformation products solely from the lattice parameters of the two phases. The transformation geometry is uniquely determined, independent of any observation of the phase change. There is then no need to postulate a double shear mechanism.

Similarly, the change in axial ratio with temperature has been expressed as an anisotropic thermal expansion or contraction and in terms of a double shear. In the former the change in axial ratio can be described in terms of pure strains and rigid body rotations. In comparison, there appears to be little merit in expressing this change in terms of additional shears in the polycrystalline aggregate.

The nature of the transformation mechanism involved in X-interface motion, as shown in Fig. 2, has not as yet been established in detail. A possible explanation is that the portions of the interfaces leading their point of intersection each represent a transformation producing a set of twins. The segments of the interfaces behind the point of intersection may then be considered as an extension of the leading segments which removes one of the twinned orientations. Thus those portions of the interfaces would represent moving twin boundaries. In order to gain further understanding of the mechanism it is necessary to obtain the orientation relationships of the material on each side of the point of intersection between the interfaces and of the structures on each side of the interface. In the case of indium-thallium this has not been possible because the crossed interfaces disappear on holding. However, the orientation relationships can be obtained in the gold-cadmium system, and an analysis thereof may prove fruitful.

Summary

An analysis of the diffusionless transformation has been presented in terms of a concept of zero average strain at the interface between the phases. This analysis permits the complete determination of the transformation geometry from a knowledge of the lattice parameters of the phases involved. The application of stress to the specimen raised the transformation temperature on both heating and cooling. Using sufficient stress it was possible to induce complete transformation in either direction at constant temperature by the application and release of load. With the aid of dilatometer measurements the phase change was found to be of the first order, having a latent heat of transformation of 0.0025 cal per gram. Rubber-like behavior was found in the alloy system and is believed to result from the stress-induced displacement of twin boundaries and their stabilization at low temperatures.

Acknowledgment

This work was supported by the Atomic Energy Commission under Contract No. AT-(30-1)-904.

References

- ¹ L. Guttman: *Trans. AIME* (1950) **188**, p. 1472; *JOURNAL OF METALS* (December 1950).
- ² J. S. Bowles, C. S. Barrett, and L. Guttman: *Trans. AIME* (1950) **188**, p. 1478; *JOURNAL OF METALS* (December 1950).
- ³ M. W. Burkart and T. A. Read: To be published.
- ⁴ M. S. Wechsler, D. S. Lieberman, and T. A. Read: This issue, p. 1503.
- ⁵ R. L. Fullman: *Journal of Applied Physics* (1951) **22**, p. 448.
- ⁶ M. Zemansky: *Heat and Thermodynamics*. (1943) 2nd Edition. New York. McGraw-Hill Book Co.
- ⁷ J. E. Reynolds, Jr. and M. B. Bever: *Trans. AIME* (1952) **194**, p. 1065; *JOURNAL OF METALS* (October 1952).
- ⁸ C. Zener: *Elasticity and Anelasticity of Metals*. (1948) Chicago. University of Chicago Press.
- ⁹ F. T. Worrell: *Journal of Applied Physics* (1948) **19**, p. 929.
- ¹⁰ Z. S. Basinski and J. W. Christian: *Journal Inst. Metals* (1952) **80**, p. 659.
- ¹¹ A. Olander: *Ztsch. Krist.* (1932) **83A**, p. 145.
- ¹² S. J. Carlile, J. W. Christian, and W. Humelroth: *Journal Inst. Metals* (1949) **77**, p. 169.
- ¹³ W. Betteridge: *Proc. Physical Soc.* (1938) **50**, p. 519.
- ¹⁴ B. Mathias and A. von Hippel: *Physical Review* (1945) **73**, p. 1378.
- ¹⁵ L. C. Chang: *Journal of Applied Physics* (1952) **23**, p. 727.

Some Observations on the Work Hardening of Metals

by E. H. Edwards, Jack Washburn, and Earl R. Parker

The mechanism of strain hardening was discussed in connection with some recent observations on the stress-induced motion of dislocation boundaries and on the simple shear deformation of zinc, cadmium, and copper crystals.

THE nature of work hardening accompanying plastic deformation of metals has long been the subject of speculation. As early as 1925, Becker¹ suggested a thermodynamic process to explain slip based on the statistical probability for the occurrence of local glide steps. The theory that plastic glide was due to the presence of lattice defects known as dislocations was first introduced in 1934 by Taylor,² and Orowan,³ and Polanyi.⁴ Taylor presented a rather complete analysis of the behavior and interaction of dislocations. He assumed a certain type of stress field to be associated with a single dislocation, and postulated that work hardening would result from plastic flow in two ways. First, dislocations following one another across a slip plane might encounter a barrier which would impede their movement, thereby gradually diminishing and eventually stopping plastic flow on that plane. The second mechanism involved the concept of dislocations traveling in opposite directions on nearby planes attracting one another to form a metastable lattice. The interaction of dislocations in such an array was shown to be large enough to require an increase in stress before plastic flow would continue.

Kochendörfer^{5, 6} extended the concept of work hardening involving a back stress due to an accumulation of like dislocations on a slip plane. He suggested that the formation of a new dislocation is hindered by those dislocations already present. The hardening resulting from the interaction of newly forming dislocations with bound dislocations was designated as "formative hardening," and indicated to be the only type of hardening necessarily

connected with the slip process. In another detailed picture of work hardening, Mott and Nabarro⁷ assumed that sufficient dislocations are primarily present in the crystal as a consequence of growth irregularities (mosaic structure) to initiate slip. Work hardening resulted from the interaction of migrating dislocations with localized internal stresses produced during deformation. More recently, however, Mott⁸ has modified his treatment to include the generation of dislocations at Frank-Read sources and he accounts for the hardening by the formation of sessile dislocations.

It has been widely accepted that metals of hexagonal structure, usually possessing only one set of glide planes, exhibit mechanical behavior markedly different from those having cubic structures. However, the differences in behavior of the two classes may be less fundamental than suggested. Rohm and Kochendörfer⁹ have shown that a single crystal of aluminum subjected to approximately simple shear gives the type of stress-strain curve associated with the hexagonal metals. Similar behavior has been demonstrated for gold and silver crystals by Andrade and Henderson.¹⁰ Thus when glide in cubic metals is restricted to one plane, the strain hardening characteristics closely resemble those of the hexagonal metals. It would appear, therefore, that an investigation of some of the strain hardening properties of single crystals sheared in simple glide might provide a more complete understanding of the phenomenon of work hardening. This report relates a number of recent observations made on single crystals of copper, zinc, and cadmium tested in simple shear. In addition, pertinent observations of effects accompanying stress-induced movement of dislocation boundaries are reported.

Experimental Procedure and Results

Details of the production and advantages of the type of single-crystal shear specimen employed for the following tests have been presented in a previous publication.¹¹ The method of testing makes

E. H. EDWARDS, J. WASHBURN, and E. R. PARKER, Member AIME, are Research Metallurgist, Instructor of Metallurgy, and Professor of Metallurgy, respectively, University of California, Berkeley, Calif.

Discussion on this paper, TP 3645E, may be sent, 2 copies, to AIME by Jan. 1, 1954. Manuscript, April 16, 1953. Cleveland Meeting, October 1953.

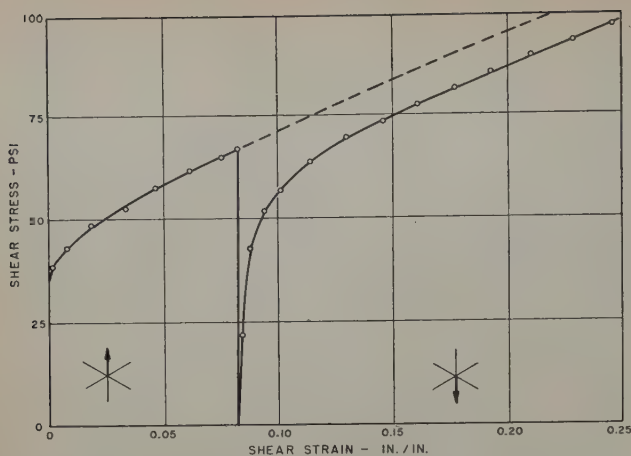


Fig. 1—Effect of reversing the strain direction during testing on the stress-strain curve in simple shear for a zinc crystal. Test temperature was -196°C . Dashed line shows normal course of curve had strain been continued in the original direction.

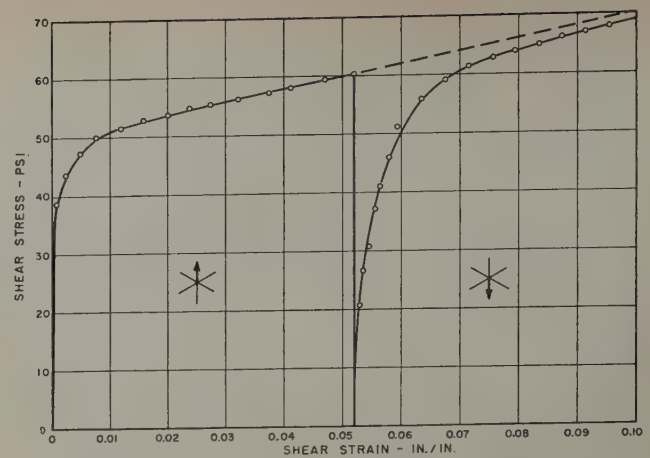


Fig. 2—Effect of reversing the strain direction during testing in simple shear on the stress-strain curve of a cadmium crystal. Test temperature was -196°C . Dashed line shows normal course of curve had strain been continued in the original direction.

possible the application of a shear stress accurately aligned with a crystallographic slip plane and direction and results in an unusually uniform shear strain. Spherical crystals were grown in a helium atmosphere by a modified Bridgeman technique and acid-machined to final specimen contour. The gage section of the crystals used in these experiments was a cylinder $\frac{1}{8}$ in. high and having a cross-sectional area of approximately $\frac{1}{3}$ sq in.

Stress-induced motion of small angle boundaries represents one of the simplest kinds of plastic deformation. The techniques previously described for forming and moving the boundaries in zinc crystals were utilized.¹² Whereas the dynamic behavior of single dislocations may never be observed directly, these small angle boundaries apparently consist of an array of edge dislocations of like sign whose movement through a crystal may be observed and controlled. The experimental observations of this localized plastic deformation so far have been consistent with the plastic behavior of crystals deformed in simple shear. For example, the shear stress necessary to cause boundary motion is the same as the yield stress in single crystals. Results of other boundary motion experiments will be compared with results obtained from simple shear deformations.

Strain hardening in simple shear is directional. Fig. 1 represents the strain hardening curve for a zinc crystal of 99.99 pct purity sheared in simple glide at -196°C . At a strain of 0.08, the direction of straining was reversed. Two effects on the path of the curve may be discerned. First, plastic flow begins at a stress much lower than that accompanying the onset of slip in the original direction. Second, although the crystal was held continuously at a temperature of -196°C , the level of the stress-strain curve was appreciably lowered by the strain reversal ("strain softening"). The identical behavior demonstrated by a high purity cadmium crystal under the same experimental conditions is shown in Fig. 2. A similar situation was encountered when the direction of the stress-induced movement of a dislocation boundary was reversed. Fig. 3 shows a load-displacement curve for a boundary of this type in a zinc crystal. In both directions of movement, the rate of motion was held approximately constant. The critical load for a constant rate of movement was decreased when the direction of movement was reversed.

Macroscopic substructure in a crystal has a marked effect on plastic properties.¹⁸ Fig. 4 shows stress-strain curves for a crystal with and without such a network of small angle boundaries. The presence of these subboundaries affects the stress-strain curve in two ways. First, the sharp break in the curve at the yield point characteristic of the nearly perfect crystal is replaced by a more gradual bending over of the curve. Second, the stress level of the curve is raised noticeably. At larger strains, the rates of strain hardening for the two cases are almost identical.

Simultaneous slip in two directions on the same plane (Fig. 4) results in a much higher rate of strain hardening. The yield point was about the same as for a crystal sheared along a single slip direction. In agreement with this result is the observation that hardening in a latent slip system may exceed that in the active system. Fig. 5 shows the effects on the stress-strain curve of a zinc crystal

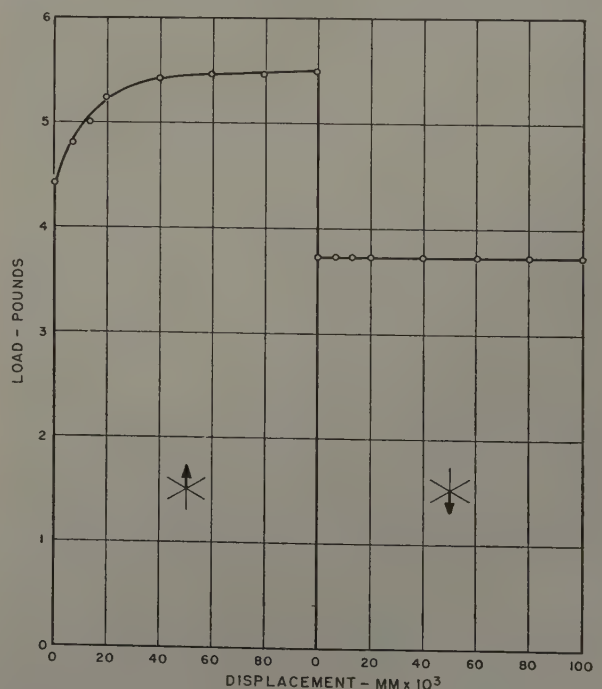


Fig. 3—Load-displacement curve for a moving dislocation boundary showing decrease in load when direction of motion was reversed. Rate of boundary motion held approximately constant. Temperature, 25°C .

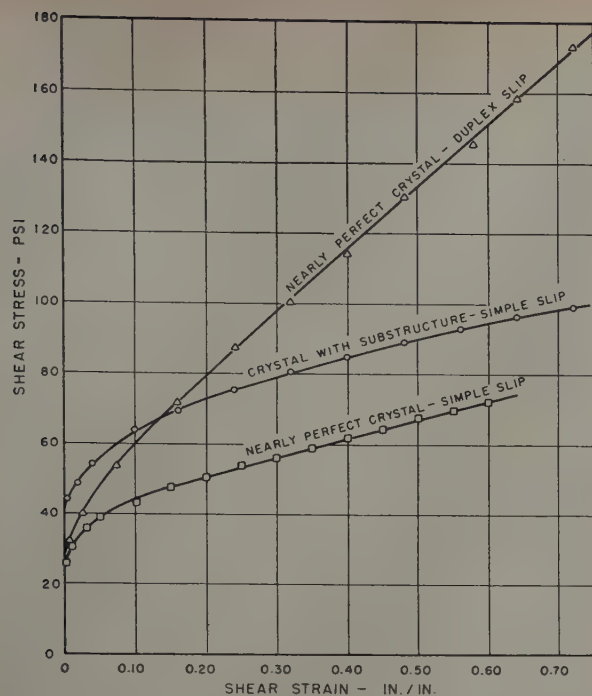


Fig. 4—Stress-strain curves for zinc crystals showing that the shape of the strain hardening curve for simple shear is influenced by substructure and by the number of slip systems operating. Test temperature was 25°C.

tem exceeded hardening in all latent systems. However, his experimental techniques were much more complex than those employed for zinc.

The presence of subboundaries in copper crystals tested in simple shear alters the strain hardening characteristics in a manner consistent with that observed for zinc crystals. Stress-strain curves for copper crystals with varying degrees of internal perfection are presented in Fig. 6. The subboundaries of the extensively polygonized crystal were formed by subjecting the crystal to a bending moment and subsequently annealing at 900°C. That polygonization had occurred was verified by the

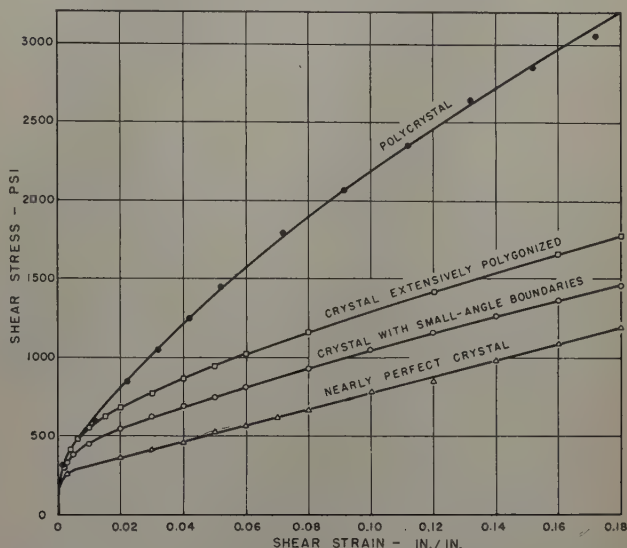


Fig. 6—Stress-strain curves for copper specimens tested in simple shear. The stress at which yielding occurs is influenced by the presence of mosaic boundaries. The rate of strain hardening in single crystals subjected to simple shear is substantially independent of substructure except in the small strain range.

splitting of reflection spots in back-reflection Laue photographs. The stress-strain curves for the three crystals form a homologous series, with the level of the curves rising as the extent of the internal boundaries increase. The results of a shear test of a polycrystalline copper specimen are presented for purposes of comparison.

Discussion of Results

Work hardening of zinc crystals subjected to simple shear on a single glide system can be completely removed upon annealing.¹¹ An additional feature of easy glide is that it does not involve local distortions of a type which give rise to asterism. A theory proposed by Seitz¹⁴ advances the possibility that hardening may be caused by production of large numbers of lattice vacancies by moving dislocations, thus impeding the further motion of dislocations. All current theories require the trapping of dislocations within the crystal in one way or another during plastic flow.

Direct experimental support for the concept that dislocations are obstructed in their movement across a slip plane is provided by observations accompanying the stress-induced movement of a dislocation boundary through a zinc crystal at room temperature. Careful measurement of the magnitude of the boundary angle shows that there is a significant decrease in the angle as the boundary moves through the crystal. The implication is that some of the edge dislocations of which the boundary is composed are trapped locally by internal imper-

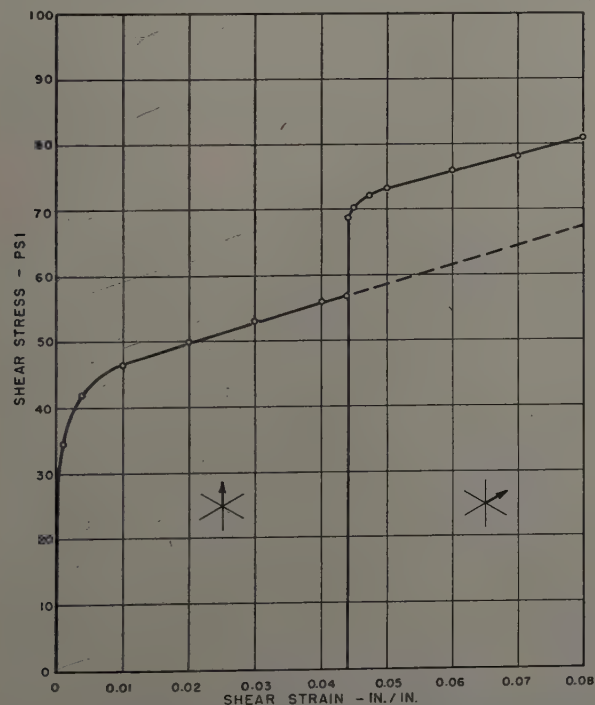


Fig. 5—Stress-strain curve for a zinc crystal showing effect of shifting the strain direction during testing to a new direction 60° from the original direction of slip. Test temperature was -196°C.

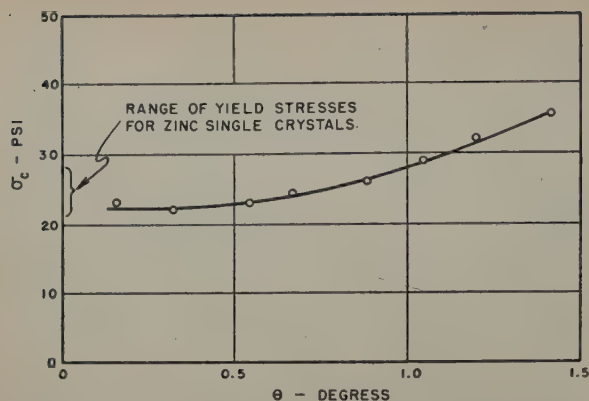


Fig. 7—Curve showing that the minimum stress required to move a dislocation boundary increases with increasing boundary angle. Temperature, 25°C.

fections and prevented from continuing freely with the boundary.

Further experimental evidence for the idea that some of the dislocations moving through a crystal during slip become piled up against barriers is afforded by the tests in which strain direction was reversed. Dislocations piled up against a barrier produce a back stress which is proportional to the number of piled up dislocations. The externally applied stress necessary to start slip in the reverse direction should be reduced in proportion to the magnitude of the back stress.

There seems to be good evidence for the trapping of dislocations at internal barriers during plastic straining of a crystal, and for the existence of back stresses associated with such bound dislocations. However, the view of Kochendörfer that this back stress is the primary cause of strain hardening may not be justified, particularly in view of the fact that latent slip directions are hardened more than the active system in zinc.

Any discussion of strain hardening is incomplete which ignores the lamellar nature of slip. The macroscopic strain hardening measured when a test section of ordinary size is employed must be interpreted to mean that formation of each elementary

slip line across the crystal makes growth of the next line a little more difficult. Ruling out the possibility of exhaustion hardening, this implies that the stress concentrations produced by pile-up of dislocations at barriers are sufficiently long range to account for hardening when the spacing of slip lines is many thousands of interatomic distances. For this to be possible the slip lines must contain clusters of dislocations of like sign. Such clusters would tend to align themselves to form dislocation boundaries.

The scale of the clustering is probably influenced by the conditions of deformation. For simple shear strain in hexagonal metals the clustering must be on a small scale because of the lack of asterism. With less uniform strain large scale dislocation boundaries may build up during the strain as a result of macroscopic or microscopic inhomogeneities in applied stress.¹⁵ In these cases strain hardening is more rapid than during simple glide due to an increase in the number and effectiveness of barriers.

Recently, Kellar, Hirsch, and Thorpe¹⁶ have found that cold working of polycrystalline metals resulted directly in the formation of subboundaries within the grains. These subboundaries apparently result from the tendency of edge dislocations to align themselves in stable arrays. Since it was indicated by these investigators that the average size of the subgrains decreased as work hardening increased, the progressive nature of work hardening seems to be due to the more effective trapping of moving dislocations by the progressively developing subboundaries.

The stress-induced movement of dislocation boundaries may provide an additional mechanism for increasing the effectiveness of barriers during straining. From Fig. 7, it may be seen that the critical stress required to move a dislocation boundary at a constant rate through a zinc crystal increases as the magnitude of the boundary angle increases. Furthermore, when two such moving boundaries unite, the load required to move the newly formed boundary is sharply increased, Fig. 8. Thus the stress-induced merger of subboundaries, creating boundaries of larger angular magnitude, increases the effectiveness of the barriers in blocking dislocation movement.

Conclusions

A study of single metal crystals tested in simple shear and of stress-induced movement of dislocation boundaries, has lead to the following conclusions on the nature of work hardening:

1—The movement of dislocations through a crystal is impeded by internal barriers, even during simple shear.

2—Duplex slip in single crystals and the more complex deformation in polycrystalline specimens are accompanied by a progressive formation of dislocation boundaries. These subboundaries act as barriers in the path of moving dislocations.

3—Stress-induced movement of dislocation boundaries leads to union of adjacent boundaries and increased effectiveness in blocking movement of active dislocations.

Acknowledgments

This investigation was sponsored by the Office of Naval Research, and the continued interest of Julius Harwood and O. T. Marzke is gratefully acknowledged. The authors wish to thank Choh Hsien Li and

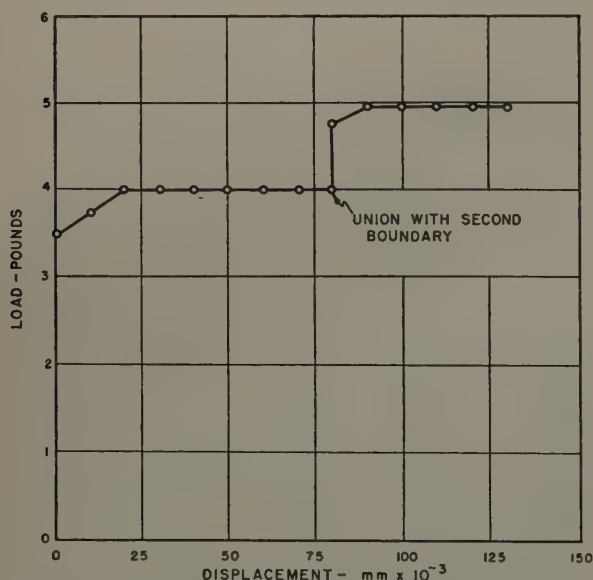


Fig. 8—Load-displacement curve showing that when two boundaries unite the load required for continued movement is increased. Rate of motion held approximately constant. Temperature, 25°C.

Douglas W. Bainbridge, who carried out different phases of the experimental work, and L. O. Seaborn and W. R. Arneson for their assistance in the construction of apparatus.

References

¹R. Becker: Über die Plastizität amorpher und Kristalliner fester Körper. *Ztsch. Physik* (1925) **26**, pp. 919-925.

²G. I. Taylor: The Mechanism of Plastic Deformation of Metals. *Proc. Royal Soc. London* (1934) **A145**, pp. 362-387 and 388-404.

³E. Orowan: Zur Kristallplastizität; I. Tieftemperatur-plastizität und Beckersche Formel; II. Die dynamische Auffassung der Kristallplastizität; III. Über den Mechanismus des Gleitvorganges. *Ztsch. Physik* (1934) **89**, pp. 605-613, 614-633, 634-659.

⁴M. Polanyi: Über eine Art Gitterstörung die einen Kristall plastisch machen könnte. *Ztsch. Physik* (1934) **89**, pp. 660-664.

⁵A. Kochendörfer: Theorie der Kristallplastizität. *Ztsch. Physik* (1937-38) **108**, pp. 244-264.

⁶A. Kochendörfer: Neue Ergebnisse über die Verfestigung bei der plastischen Verformung von Kristallen. *Ztsch. Metal.* (1950) **41**, pp. 265-272.

⁷N. F. Mott and F. R. N. Nabarro: *Proc. Physical Soc.* (1940) **52**, p. 86.

⁸N. F. Mott: A Theory of Work-hardening of Metal Crystals. *Philosophical Magazine* (1952) **43**, pp. 1151-1177.

⁹F. Röhm and A. Kochendörfer: *Ztsch. Metal.* (1950) **41**, p. 265.

¹⁰E. N. daC. Andrade and C. Henderson: *Phil. Trans. Royal Soc.* (1951) **A244**, p. 177.

¹¹Earl R. Parker and Jack Washburn: Deformation of Single Crystals. *Seminar on Modern Research Techniques in Physical Metallurgy*. ASM (1952) pp. 186-204.

¹²C. H. Li, E. H. Edwards, Jack Washburn, and Earl R. Parker: Stress-Induced Movement of Crystal Boundaries. *Acta Metallurgica* (1953) **1**, No. 2, p. 223.

¹³C. H. Li, Jack Washburn, and Earl R. Parker: Variations of Plastic Properties with Annealing Procedure with Zinc Single Crystals. *Trans. AIME* (1953) **197**, p. 1223; *JOURNAL OF METALS* (September 1953).

¹⁴Frederick Seitz: On the Generation of Vacancies by Moving Dislocations. *Philosophical Magazine Supplement* (1952) **1**, pp. 43-90.

¹⁵F. C. Frank: The Origin of Dislocations. Pittsburgh Conference on Plastic Deformation of Crystalline Solids. (1951) pp. 89-102.

¹⁶Jack Washburn and Earl R. Parker: Kinking in Zinc Single-Crystal Tension Specimens. *Trans. AIME* (1952) **194**, pp. 1076-1078; *JOURNAL OF METALS* (October 1952).

¹⁷P. Gay and A. Kelly: X-Ray Studies of Polycrystalline Metals Deformed by Rolling. I. The Examination of the Harder Metals, Copper, Nickel, and Iron. II. Examination of the Softer Metals, Tin, Zinc, Lead and Cadmium. *Acta Crystallographica* (1953) **6**, pp. 165-177.

Technical Note

Effects of Sample Surface and X-Ray Diffraction Camera Geometry On the Determination of Retained Austenite in Hardened Steels

by Karl E. Beu and Donald P. Koistinen

THE application of the integrated intensity X-ray diffraction method to the measurement of retained austenite concentrations in hardened steels has been fully described.¹⁻⁵ In developing this particular method, the assumption was made that the samples used would have flat surfaces which were free from voids and in which austenite was homogeneously distributed. The original calculation procedure¹ was modified to include the constant factor G which relates the intensity of a given diffraction line to the concentration of the component giving rise to that line. In order to include $A(\theta)$ in the constant factor G , it was further assumed that the geometrical conditions relating the X-ray beam, camera cylinder, and sample surface were precisely met.⁶ It has been demonstrated that these geometrical conditions can be met experimentally without

difficulty in many cases;⁵ however, for those samples which have irregular surfaces or where it is impossible to locate the sample in the proper position with respect to the X-ray beam and film cylinder, it is desirable to evaluate experimentally what effect these nonideal conditions have on the reliability of the austenite determination. This note describes the results of such experiments.

SAE 1095 bar stock was used throughout and all samples were heat-treated as follows: 1600°F for 1 hr in a neutral atmosphere, brine quench, and 300°F temper for 30 min. To control heat-treatment conditions as closely as possible, all samples were plated with 0.002 in. copper to protect the immediate surface from the heat-treating atmosphere. After heat treating, the samples were deplated electrolytically so that only the copper was removed. The heat-treated surfaces thus obtained were nearly as bright and polished as the original surfaces before copper plating although no mechanical work was done on the samples after heat treating.

K. E. BEU and D. P. KOISTINEN are associated with Research Laboratories Div., General Motors Corp., Detroit.
TN 188E. Manuscript, Aug. 3, 1953.

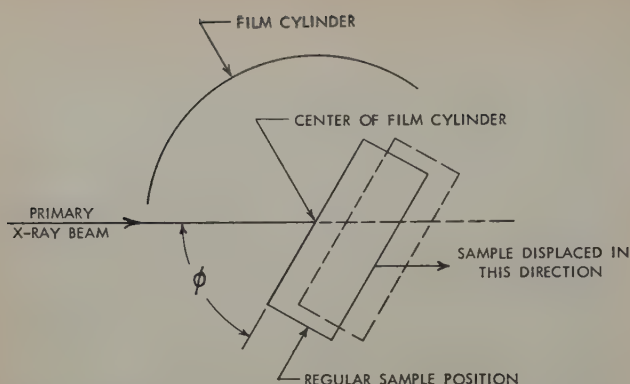


Fig. 1—Geometrical relationship of sample surface, X-ray beam, and film cylinder.

Before carrying out the sample surface and camera geometry experiments, it seemed worth-while to determine the reproducibility of the heat-treatment procedure with respect to the retained austenite content. To accomplish this, a series of six disks each 4.8 mm thick, were metallographically polished, copper plated, simultaneously heat treated, and deplated. The retained austenite contents of these six samples are given in Table I. The best estimate⁶ of the standard deviation for the austenite content of these six samples is ± 0.6 pct of the total sample. This deviation is a measure of the reproducibility of the determination of the austenite content which includes both the errors inherent in the X-ray determination and in the simultaneous heat treatment of a given set of samples. Any consistently greater deviation than this can be ascribed to the variable being studied,* providing the austenite is

* This applies only to a given set of samples heat-treated simultaneously. Because of the slight variations in the heat treatment from one set to the next, the average austenite content may vary slightly from set to set. This, however, causes no difficulty in interpretation since a flat, polished sample is included as a standard for each set.

homogeneously distributed throughout the sample surface.

The homogeneity of the austenite content of the disk-shaped samples used for this was tested by examining areas varying from 0.4×7.0 mm to 4.1×7.0 mm on one sample (M-276). It was found that variations in the austenite measurement for the several areas examined on this one sample were all within the standard deviation of ± 0.6 pct; hence, the surface inhomogeneities are apparently less than the experimental errors involved in making the measurements.

Table I. Reproducibility of Austenite Content Obtainable in Heat Treating Identical Samples Simultaneously

Sample No.	Sample Description	Austenite, Pct
M-276	4.8 mm thick disk of 1095 plated with 0.002 in. acid copper, austenitized 1 hr at 1600°F in neutral gas atmosphere, brine quenched, tempered 30 min at 300°F, deplated.	12.9
M-277	Prepared identically and heat-treated simultaneously with M-276.	14.6
M-278	Prepared identically and heat-treated simultaneously with M-276.	14.1
M-279	Prepared identically and heat-treated simultaneously with M-276.	13.7
M-280	Prepared identically and heat-treated simultaneously with M-276.	13.8
M-281	Prepared identically and heat-treated simultaneously with M-276.	13.6
Average percent austenite for six samples		13.8 pct
Best estimate ⁶ of standard deviation, σ		± 0.6 pct

The types of sample surfaces studied included, 1—flat, smooth surfaces (as standards of comparison), 2—flat surfaces with various degrees of roughness, 3—concave cylindrical surfaces, and 4—convex cylindrical surfaces with various radii of curvature. The effect of a given variable such as roughness could be studied by preparing a series of samples of various degrees of roughness (plus a standard flat and polished sample) and heat treating such a set simultaneously as described above. The geometrical conditions studied included, 1—varying ϕ , the angle the X-ray beam makes with the sample surface (see Fig. 1) in the range of 40° to 70° where $\phi = 60^\circ$ is the angle normally used,¹⁻³ and 2—varying the sample surface position along the X-ray beam axis for a constant value of $\phi = 60^\circ$.

Using four sets of samples with four or five samples per set it was found that the following variations in sample surface and camera geometry had no significant effect† on the retained austenite de-

†All austenite results for a given set of samples fell within a range of three times the absolute value of the standard deviation σ , while all except one set fell within a range of less than 2σ . On these experiments, $\sigma = 0.6$ pct, $2\sigma = 1.2$ pct, and $3\sigma = 1.8$ pct (see Table I). If it is remembered that, for the Gaussian error function, σ means that 68 pct of the results of an infinite number of samples fall within a range of $\pm\sigma$, that 95 pct fall within $\pm 2\sigma$, and that 99.7 pct fall within $\pm 3\sigma$, the meaning of the words "no significant effect" becomes clear.

termination: 1—varying the surface roughness in the range of 3 to 250 microinches,⁷ 2—varying the surface curvature from 21.0 mm convex radius through infinite radius to 6.4 mm concave radius, 3—varying the angle ϕ in the range of 40° to 70° , and 4—displacing the sample along the X-ray beam axis up to 2.9 mm from the center of a 45 mm radius camera (see Fig. 1). Further experimental details are available upon request.

In conclusion it can be said that the reliability of the austenite determination as described previously¹⁻⁵ does not depend rigorously on sample surface and camera geometry conditions. In fact, the austenite determination has been found to be reliable within the reproducibility limitations of the method itself over the wide range of experimental conditions indicated.

Acknowledgment

The authors would like to express their thanks to Daniel N. Callahan for carrying out the extensive calculations required to obtain these results.

References

1. B. L. Averbach and M. Cohen: X-ray Determination of Retained Austenite by Integrated Intensities. *Trans. AIME* (1948) **176**, p. 401; *METALS TECHNOLOGY* (September 1947).
2. B. L. Averbach, L. S. Castleman, and M. Cohen: Measurement of Retained Austenite in Carbon Steels. *Trans. ASM* (1950) **42**, p. 112.
3. K. E. Beu: Modifications of an X-ray Method for the Measurement of Retained Austenite Concentrations in Hardened Steels. *Trans. AIME* (1952) **194**, p. 1327; *JOURNAL OF METALS* (December 1952).
4. B. L. Averbach: Retained Austenite Determinations by X-ray Methods. *Trans. AIME* (1953) **197**, p. 87; *JOURNAL OF METALS* (January 1953).
5. K. E. Beu: Notes on the Determination of Retained Austenite by X-ray Methods. This issue, p. 1539.
6. C. H. Goulden: *Methods of Statistical Analysis* (1939) p. 12. New York. John Wiley and Sons.
7. A. F. Underwood, J. B. Bidwell, and J. H. Brems: The Surfagage, An Instrument for Roughness Measurement. 20th Annual Meeting of ASTE, Chicago, March 19, 1952.

Analysis of Molten-Zone Refining

by Norman W. Lord

The process of molten-zone refining is analyzed for long ingots and many zone passages. Formulas are derived which give the resultant impurity distribution in terms of finite series. A comparison with the approximate procedure of Hamming is given.

THE physical principles and applications of an extremely efficient form of metallurgical refinement has been described by Pfann.¹ The purpose of the present paper is to describe a method of analyzing exactly the particular program used which enables the segregation effect to be predicted for any number of molten-zone passages in a long ingot. The method is applied to the particular case of refinement of an ingot whose impurity initially is uniformly distributed throughout its length. A number of molten zones of equal length are passed through the ingot effecting a radical redistribution of impurity. Pfann has indicated an approximate method, due to R. W. Hamming, of calculating the resultant concentration after each successive zone pass for a particular value of the segregation constant defined in his paper. Here a solution will be presented in terms of the number of zone passes and the segregation constant. The expression, though cumbersome, is exact and susceptible to ordinary numerical computation procedures. The results of a similar computation using the procedure of Hamming are presented in a table together with the exact results of the present method. The discrepancy in terms of absolute concentrations is tabulated for the first eight zone-lengths.

To establish the notation (which follows that of Pfann¹ as closely as possible) and physical basis of the analytical equations, the physical model and principal assumptions may be reviewed. An alloy of two elements, where there is formed a continuous range of solid solutions, usually does not melt as a simple compound. Rather, a temperature is reached where the solid solution is in heterogeneous phase equilibrium with a liquid solution of different composition. The temperature dependence of these equilibrium compositions forms part of the phase diagram. For very small concentrations of a solute B in a solvent A , this usually takes the form of Fig. 1. Sometimes the solidus and liquidus slope upward. This corresponds to a segregation constant (defined below) which is greater than unity. The segregation constant is now defined as

$$k = C_n(x) / C_{nL}(x) \quad [1]$$

where $C_n(x)$ is the impurity concentration in the solid ingot at distance x during the n th passing of a molten zone and $C_{nL}(x)$ is the impurity concentration of the liquid zone from which the solid at dis-

tance x is formed (see Fig. 4 of ref. 1.) $C_n(x)$ remains the same after passage of the zone. The constant k may be either greater or less than unity in general. Purification in the former case is effected only in a finite ingot and in the portion that is melted last. For k less than unity purification is effected even in an infinite ingot. The method which follows gives, in the former case, the successive increases in impurity concentration and, in the latter case, the successive decreases in concentration. The general case of impurity redistribution will be considered first, and purification will be discussed later on. The analysis rests on the following assumption:

The movement of the zone is too rapid to allow appreciable atomic rearrangement in the solid sections and too slow to disturb the uniform impurity distribution in the liquid zone characteristic of equilibrium.

Hence, the composition in the solid at the left solidifying interface will be determined by Eq. 1 while the impurity concentration of the liquid zone will be uniform throughout its length. The reasoning which follows closely parallels that of Appendix II in Pfann's paper. It is reviewed here for the case of the n th zone pass in order to make clear the meaning of an operator essential to the present method. Fig. 4 of ref. 1 shows the movement of a molten zone of length l in an ingot of total length d .

Each $C_n(x)$ can be determined from the condition that the amount of solute added to the zone during an incremental advance, dx , is due to the melting in of a solid portion $C_{n-1}(x)dx$ and the freezing out of $kC_{nL}(x)$, that is

$$l \frac{d}{dx} C_{nL}(x) dx = C_{n-1}(x + l) - kC_{nL}(x)$$

or, in terms of $C_n(x)$

$$\frac{d}{dx} C_n(x) + \frac{k}{l} C_n(x) = \frac{k}{l} C_{n-1}(x + l). \quad [2]$$

This, of course, is derived from the main assumption, the fact that l is constant, and that the total impurity content previously present up to $x + l$ is constant. A correction has to be made for the region $(d - nl) < x < d$. This is due to the zone length changing during the passage of the solidifying interface beyond $x = d - l$. Since the general solution would be too complicated otherwise, only the region $0 < x < d - nl$ is considered. The general solution of Eq. 2 is

$$C_n(x) = \left[\int^x \frac{k}{l} C_{n-1}(x + l) e^{kx/l} dx + \text{constant} \right] e^{-kx/l}. \quad [3]$$

N. W. LORD is associated with the Research Div., Raytheon Manufacturing Co., Waltham, Mass.

Discussion on this paper, TP3635E, may be sent, 2 copies, to AIME by Jan. 1, 1954. Manuscript, Oct. 3, 1952, revision, July 17, 1953. Cleveland Meeting, October 1953.

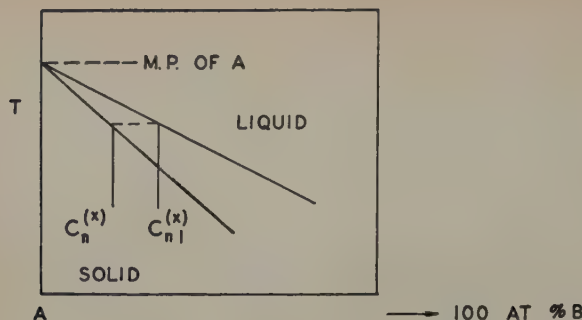


Fig. 1—Typical phase diagram of a dilute solution in the neighborhood of the melting point of the solvent.

The constant is determined by the condition, at the starting zone, that total impurity content is constant.

$$C_n(0)/k = C_{nL}(0) = \frac{1}{l} \int_0^l C_{n-1}(x) dx.$$

This condition, substituted into Eq. 3, yields the particular solution

$$C_n(x) = \frac{k}{l} e^{-kx/l} \left[\int_0^x C_{n-1}(x+l) e^{kx/l} dx + \int_0^l C_{n-1}(x) dx \right]. \quad [4]$$

It is convenient to change the variable x to a , the displacement measured in zone-lengths, under the relation $x = al$. Eq. 4 then becomes

$$C_n(a) = k e^{-ka} \left[\int_0^a C_{n-1}(a+1) e^{ka} da + \int_0^1 C_{n-1}(a) da \right]. \quad [4a]$$

Eq. 4a, clearly, is the analytic form for an operation on any previously existing impurity concentration. It corresponds to the passage of a molten zone of unit length (measured in units of a) and the result is the concentration existing after the passage of the zone. In the following, such a single operation is symbolized as θ in the equation equivalent to Eq. 4a:

$$C_n(a) = \theta C_{n-1}(a) \quad [5]$$

and repeated operations as $\theta^{(r)}$ in

$$C_n(a) = \theta^{(r)} C_{n-r}(a). \quad [5a]$$

In this form the meaning of $\theta^{(o)}$ is plainly multiplication by 1.

It is now easily shown that after n repeated passages of a molten zone the concentration may be represented in terms of the repeated operation θ on the simple expression e^{-ka} . This latter, $\theta^{(r)} e^{-ka}$, is then expressed as a finite sum of terms involving only a , k , and the index of the summation. To see this consider the effect of the first zone-pass on a uniform concentration, C_0 .

$$C_1(a) = \theta C_0 = k e^{-ka} \left[\int_0^a C_0 e^{ka} da + \int_0^1 C_0 da \right] \quad [6]$$

$$= C_0 [1 - (1-k) e^{-ka}] = C_0 [1 - (1-k) \theta^{(o)} e^{-ka}].$$

This leads with repeated operation θ to

$$C_n(a) = C_{n-1}(a) - (1-k) C_0 \theta^{(n-1)} e^{-ka} \quad [7]$$

or, in terms of differences in concentration

$$\frac{C_n(a) - C_{n+1}(a)}{C_{n-1}(a) - C_n(a)} = \frac{\theta^{(n)} e^{-ka}}{\theta^{(n-1)} e^{-ka}}. \quad [7a]$$

Calculations of $\theta^{(n)} e^{-ka}$ to $n = 7$, the results appearing in Table I, indicate the general relation

$$\frac{\theta^{(n)} e^{-ka}}{e^{-ka}} = \frac{\theta^{(n-1)} e^{-ka}}{e^{-ka}} - k^{(n-1)} e^{-nk} \left[\sum_{r=0}^{n-1} f_r^{(n)} a^r (r+1-ka) \right] \quad [8]$$

$$\text{where: } f_r^{(n)} = \frac{n^{n-r-2}}{(n-r-1)! r!}.$$

This formula can be proved correct by inductive reasoning (see ref. 2.) With some algebraic manipulation, the following convenient relations are obtained:

$$\theta^{(1)} e^{-ka} = e^{-ka}$$

$$\left\{ 1 - \sum_{s=1}^t \left[k^{s-1} e^{-ka} \sum_{r=0}^{s-1} f_r^{(s)} a^r (r+1-ka) \right] \right\}. \quad [9]$$

Table I. Calculated Results of the Iterated Operation θ on the Quantity e^{-ka}

$\frac{\theta e^{-ka}}{e^{-ka}} = 1 - e^{-k} (1-ka)$
$\frac{\theta^2 e^{-ka}}{e^{-ka}} = \frac{\theta e^{-ka}}{e^{-ka}} - k e^{-2k} \left[(1-ka) + \frac{a}{2} (2-ka) \right]$
$\frac{\theta^3 e^{-ka}}{e^{-ka}} = \frac{\theta^2 e^{-ka}}{e^{-ka}} - k^2 e^{-3k} \left[\frac{(3)^1}{2!} (1-ka) + \frac{1}{1!} a (2-ka) + \frac{a^2}{2!3} (3-ka) \right]$
$\frac{\theta^4 e^{-ka}}{e^{-ka}} = \frac{\theta^3 e^{-ka}}{e^{-ka}} - k^3 e^{-4k} \left[\frac{(4)^2}{3!} (1-ka) + \frac{4}{2!} a (2-ka) + \frac{1}{2!} a^2 (3-ka) + \frac{1}{3!4} a^3 (4-ka) \right]$
$\frac{\theta^5 e^{-ka}}{e^{-ka}} = \frac{\theta^4 e^{-ka}}{e^{-ka}} - k^4 e^{-5k} \left[\frac{(5)^3}{4!} (1-ka) + \frac{(5)^2}{3!} a (2-ka) + \frac{5a^2}{2!2!} (3-ka) + \frac{a^3}{3!} (4-ka) + \frac{a^4}{4!5} (5-ka) \right]$
$\frac{\theta^6 e^{-ka}}{e^{-ka}} = \frac{\theta^5 e^{-ka}}{e^{-ka}} - k^5 e^{-6k} \left[\frac{(6)^4}{5!} (1-ka) + \frac{(6)^3 a}{4!} (2-ka) + \frac{(6)^2 a^2}{3!2!} (3-ka) + \frac{6a^3}{2!3!} (4-ka) + \frac{a^4}{4!} (5-ka) + \frac{a^5}{5!6} (6-ka) \right]$
$\frac{\theta^7 e^{-ka}}{e^{-ka}} = \frac{\theta^6 e^{-ka}}{e^{-ka}} - k^6 e^{-7k} \left[\frac{(7)^5}{6!} (1-ka) + \frac{(7)^4}{5!} a (2-ka) + \frac{7^3 a^2}{4!2!} (3-ka) + \frac{7^2 a^3}{3!3!} (4-ka) + \frac{7}{2!4!} a^4 (5-ka) + \frac{a^5}{5!} (6-ka) + \frac{a^6}{6!7} (7-ka) \right]$

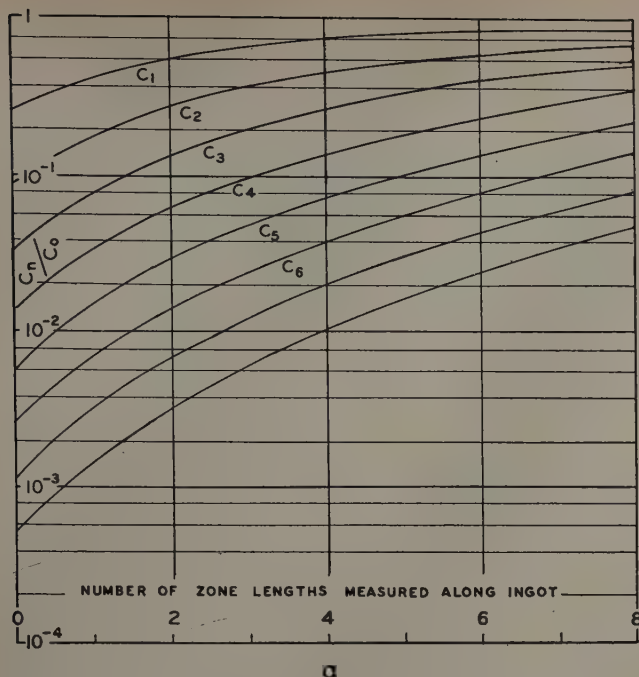


Fig. 2—Residual impurity concentrations after molten zone passages for $k = 0.25$.

For $t \geq 1$; $\theta^{(n)} e^{-ka} = e^{-ka}$

$$C_n(a) = C_0 \left\{ 1 - (1-k) e^{-ka} \right\}$$

$$\left[n - \sum_{t=1}^{n-1} \sum_{s=1}^t k^{s-1} e^{-sk} \sum_{r=0}^{s-1} f_r^{(s)} a^r (r+1-ka) \right] \cdot [10]$$

Using Eq. 10, the concentrations resulting after each of eight successive zone-passes are calculated for two cases ($k = 0.25, 0.1$), the results being shown in Figs. 2 and 3. This required only the terms already presented in Table I for $\theta^{(1)}$ to $\theta^{(7)}$. The total number of zone-lengths in the ingot is assumed greater than 16. These are practical values encountered in zone-refining procedures at Raytheon. For ready comparison, the results of Hamming's procedure for $k = 0.1$ are presented in Table II together with similar results from Eq. 10. Plotted on a logarithmic scale as in Fig. 3, there is no appreciable difference. However, from the table it can be seen that the error involved in using Hamming's procedure would increase with further zone passages. The computational labor using discrete half-zone-length steps is comparable to that involved in Eq. 10. Moreover, the parallelism between the

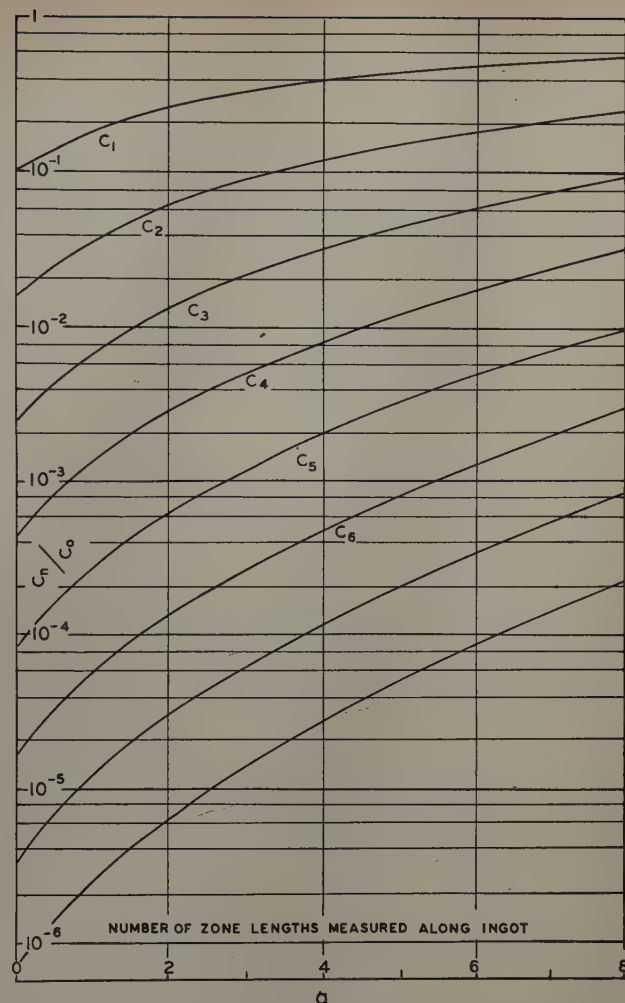


Fig. 3—Residual impurity concentrations after molten zone passages for $k = 0.1$.

above procedure and that of Appendix II in ref. 1 is exemplified in the formal similarity of Eq. 10 and Eq. 2 of the former work. As it stands, Eq. 10 is directly useful for cases where k is less than unity. For k greater than unity, it can be used in the form,

$$C_n(a) = C_0 \left\{ 1 + (k-1) e^{-ka} \right\}$$

$$\left[n - \sum_{t=1}^{n-1} \sum_{s=1}^t k^{s-1} e^{-sk} \sum_{r=0}^{s-1} f_r^{(s)} a^r (r+1-ka) \right] \cdot [10a]$$

to calculate the increase in impurity content for the ingot section $0 < x < d - nl$. The resultant average purification in the remaining section follows arithmetically.

Acknowledgment

The writer wishes to acknowledge the able assistance of Margaret Sturm and Joan Sullivan, who checked all derivations and performed most of the computations. The work was performed under the Navy Bureau of Ships Contract NObsr-57323.

References

- W. G. Pfann; *Trans. AIME* (1952) **194**, p. 747; *JOURNAL OF METALS* (July 1952).
- Raytheon Research Div., Second Quarterly Report, Study of Semiconductor Materials and Devices. Contract No. NObsr-57323, p. 31.

Table II. Comparison Between Hamming's Procedure and the Exact Formula (Eq. 10) for the Seventh and Eighth Zone Passages with $k = 0.1$

a	$C_7(a)/C_0$			$C_8(a)/C_0$		
	Exact Method	Hamming's Procedure	Difference, Pct	Exact Method	Hamming's Procedure	Difference, Pct
0	3.348x10 ⁻⁶	3.455x10 ⁻⁶	-3.1	6.94x10 ⁻⁷	7.285x10 ⁻⁷	-4.7
1	1.179x10 ⁻⁵	1.200x10 ⁻⁵	-1.8	2.525x10 ⁻⁶	2.602x10 ⁻⁶	-3.0
2	2.980x10 ⁻⁵	3.012x10 ⁻⁵	-1.1	6.602x10 ⁻⁶	6.737x10 ⁻⁶	-2.0
3	6.365x10 ⁻⁵	6.400x10 ⁻⁵	-0.5	1.461x10 ⁻⁵	1.480x10 ⁻⁵	-1.3
4	1.218x10 ⁻⁴	1.200x10 ⁻⁴	+0.2	2.900x10 ⁻⁵	2.923x10 ⁻⁵	-0.8
5	2.151x10 ⁻⁴	2.147x10 ⁻⁴	+0.2	5.314x10 ⁻⁵	5.336x10 ⁻⁵	-0.4
6	3.572x10 ⁻⁴	3.559x10 ⁻⁴	+0.4	9.149x10 ⁻⁵	9.159x10 ⁻⁵	-0.1
7	5.640x10 ⁻⁴	5.602x10 ⁻⁴	+0.7	1.498x10 ⁻⁴	1.495x10 ⁻⁴	+0.2
8	8.545x10 ⁻⁴	8.486x10 ⁻⁴	+0.7	2.351x10 ⁻⁴	2.342x10 ⁻⁴	+0.4

Calculation of Interdiffusion Coefficients When Volume Changes Occur

by Morris Cohen, Carl Wagner, and J. E. Reynolds

If the total volume of a diffusion couple changes during the diffusion, the measurement of distance becomes ambiguous. Use of distance parameters as suggested by Hartley and Crank is discussed. For small concentration differences, the standard form of Fick's second law is retained with conventional length units and the interdiffusion coefficient \tilde{D} . It is shown how \tilde{D} can be calculated from experiments involving large concentration differences and analyzed in terms of distance parameters. The merits of incremental diffusion couples involving small concentration differences are emphasized.

THE conventional form of Fick's second law for one-dimensional diffusion of component B in a binary solution of A and B is

$$\frac{\partial c_B}{\partial t} = \frac{\partial}{\partial x} \left(\tilde{D} \frac{\partial c_B}{\partial x} \right) \quad [1]$$

where c_B is the concentration of component B; x , the distance; t , the time; and \tilde{D} , the interdiffusion coefficient which may depend on c_B .

Hartley and Crank¹ have pointed out that Eq. 1 applies only if the total volume of the diffusion couple does not change during the diffusion process; otherwise, the definition of x becomes ambiguous. No change in total volume takes place if the specific volume of the solution is a linear function of the weight fraction W_B , or if the molar volume is a linear function of the mol fraction N_B . In some alloys, however, these relationships do not hold, and then it is necessary to introduce a modified measure of distance, ξ , in order to retain the general form of Eq. 1. The application of Hartley and Crank's suggestions to diffusion in alloys has been discussed by Wagner.²

Relation Between Measure of Distance and Units of Concentration

The definition of ξ depends on the choice of units for the concentration c_B as follows:

1—If the concentration c_B is measured as the

M. COHEN, C. WAGNER, Members AIME, and J. E. REYNOLDS, Junior Member AIME, are associated with the Dept. of Metallurgy, Massachusetts Institute of Technology, Cambridge, Mass.

Discussion on this paper, TP 3646E, may be sent, 2 copies, to AIME by Jan. 1, 1954. Manuscript, July 9, 1953.

weight fraction W_B (or weight percent), $\xi = \xi_w$ has to be defined so that equal increments of ξ_w contain equal increments of mass m of the solution, e.g.,

$$dm = \rho S dx = S d\xi_w \quad [2]$$

where ρ is the local density of the solution, and S is the cross-sectional area in sq cm which is taken to be constant in this problem of one-dimensional diffusion.*

* da Silva and Mehl³ have demonstrated the constancy of the cross-sectional area in the usual type of diffusion couple. However, experiments involving diffusion into thin wires^{4,5} may exhibit changes in cross-sectional area, and therefore are excluded from the present treatment.

Thus

$$d\xi_w = \rho dx \quad [3]$$

and the unit of ξ_w is gram per sq cm instead of cm.

2—If the concentration c_B is the mol fraction N_B , $\xi = \xi_N$ must be defined so that equal increments of ξ_N contain equal numbers of mols of solution, e.g.,

$$dn = (S/V) dx = S d\xi_N \quad [4]$$

where V is the local molar volume of the solution. Thus

$$d\xi_N = dx/V \quad [5]$$

and the unit of ξ_N is mols per sq cm.

3—If, as may be advisable in the case of interstitial solutions, the concentration c_B is measured in terms of the molar ratio of components B and A ($c_B = Y_B = n_B/n_A$, where n_B and n_A are numbers of mols of B and A), $\xi = \xi_Y$ has to be defined so that equal increments of ξ_Y contain equal numbers of mols of A, e.g.,

$$dn_A = (N_A S/V) dx = S d\xi_Y \quad [6]$$

where N_A is the local mol fraction of A in the solution. Thus

$$d\xi_r = (N_A/V) dx \quad [7]$$

and the unit of ξ_r is mols of A per sq cm. It may be noted that V/N_A is simply the volume of solution containing one gram-atom of A .

4—Concentrations in terms of mols (or grams) of B per unit volume of solution are not recommended in these considerations because the volume of solution is not conserved, and undue complications result.

In the following, a diffusion couple with uniform initial concentrations, N_{B_1} and N_{B_2} , on the left-hand side and the right-hand side of the welding plane is considered. In view of the subsequent use of the Boltzmann-Matano analysis,^{6,7} the excess of B in the region $x < 0$ compared to the initial state must be equal to the deficit of B in the region $x > 0$ compared to the initial state. Thus,

$$\int_{-\infty}^0 [(N_B - N_{B_1})/V] dx = \int_0^{\infty} [(N_{B_2} - N_B)/V] dx \quad [8]$$

as follows from Eq. 14.

Eq. 8 defines the plane $x = 0$. Analogous equations may be formulated for concentrations in terms of weight fraction or molar ratio, but the same location of the plane $x = 0$ is obtained.

The value of ξ is expressed by the corresponding integral of Eqs. 3, 5, or 7, with $x = 0$ as one limit of integration. For example, Eq. 5 gives

$$\xi_N = \int_0^x V^{-1} dx \quad [9]$$

Definitions of ξ in Eqs. 3, 5, and 7 may be modified by using the density or the molar volume of a reference alloy as a constant factor or divisor on the right-hand side of these equations in order to obtain the distance parameter ξ in cm, as has been suggested by Hartley and Crank¹ and Wagner.² It can be shown, however, that in the final calculation of the diffusion coefficient \tilde{D} , the values of such constant factors drop out, and, therefore, their introduction is not recommended.

Application of the Boltzmann-Matano Analysis

With mol fraction N_B as a measure of concentration and ξ_N as a measure of distance, Fick's second law becomes

$$\frac{\partial N_B}{\partial t} = \frac{\partial}{\partial \xi_N} \left(D_{\xi_N} \frac{\partial N_B}{\partial \xi_N} \right) \quad [10]$$

where D_{ξ_N} is the diffusion coefficient corresponding to the above measures of concentration and distance. The dimensions of D_{ξ_N} are sq mols per cm⁴ sec instead of the more familiar sq cm per sec.

For a diffusion couple with uniform initial concentrations on the left-hand and the right-hand side of the welding plane, Boltzmann⁶ and Matano⁷ have demonstrated that the concentration is a single-valued function of the auxiliary variable

$$\lambda = \xi_N/t^{1/2} \quad [11]$$

provided that the plane $x = 0$ or $\xi_N = 0$ is chosen so that^{7,8}

$$\int_{N_{B_1}}^{N_{B_2}} \xi_N dN_B = 0 \quad [12]$$

which is a necessary condition in order to conform with the given boundary conditions.

Substitution of Eq. 11 in Eq. 10 gives

$$-2\lambda \frac{dN_B}{d\lambda} = \frac{d}{d\lambda} \left(D \frac{dN_B}{d\lambda} \right) \quad [13]$$

Upon integrating Eq. 13 between $\lambda = -\infty$ and $\lambda = +\infty$, noting that $dN_B/d\lambda = 0$ at $\lambda = +\infty$ and $\lambda = -\infty$, and resubstituting $\lambda = \xi_N/t^{1/2}$, Eq. 12 results as a necessary condition for the supposition that N_B is a single-valued function of $\lambda = \xi_N/t^{1/2}$. Integration of Eq. 12 by parts yields

$$\int_{-\infty}^0 (N_B - N_{B_1}) d\xi_N = \int_0^{\infty} (N_{B_2} - N_B) d\xi_N \quad [14]$$

from which Eq. 8 is obtained by using Eq. 5.

Upon integrating Eq. 13 between $\lambda = -\infty$ corresponding to $N_B = N_{B_1}$ as the lower limit and an arbitrary upper limit, it follows that

$$\begin{aligned} D_{\xi_N}(N_B) &= -\frac{1}{2(dN_B/d\lambda)} \int_{N_{B_1}}^{N_B} \lambda_N dN_B \\ &= -\frac{1}{2t(dN_B/d\xi_N)} \int_{N_{B_1}}^{N_B} \xi_N dN_B \end{aligned} \quad [15]$$

and D_{ξ_N} can be evaluated as a function of concentration from a $N_B - \xi_N$ curve.

The foregoing procedure is completely consistent if there is a change in the overall volume of the sample due to a non-linear relation between molar volume and mol fraction. Since, however, data for most alloys are expressed in terms of the interdiffusion coefficient \tilde{D} as used in Eq. 1, it seems desirable to reconvert values of D_{ξ_N} to \tilde{D} , the latter being in sq cm per sec.

Relation Between the Modified Diffusion Coefficient D_{ξ_N} and the Standard Diffusion Coefficient \tilde{D}

Upon substituting $d\xi_N = V^{-1}dx$ from Eq. 5 in Eq. 10, the latter becomes

$$\frac{\partial N_B}{\partial t} = V \frac{\partial}{\partial x} \left(D_{\xi_N} V \frac{\partial N_B}{\partial x} \right) \quad [16]$$

Since the diffusion coefficient D_{ξ_N} and the molar volume V depend on N_B and hence on x , Eq. 16 may be rewritten as

$$\begin{aligned} \frac{\partial N_B}{\partial t} &= V \frac{\partial N_B}{\partial x} \frac{\partial}{\partial x} (D_{\xi_N} V) + V^2 D_{\xi_N} \frac{\partial^2 N_B}{\partial x^2} \\ &= V \left(\frac{\partial N_B}{\partial x} \right)^2 \frac{\partial}{\partial N_B} (D_{\xi_N} V) + V^2 D_{\xi_N} \frac{\partial^2 N_B}{\partial x^2} \end{aligned} \quad [17]$$

If the initial concentration difference in the diffusion couple is sufficiently small, $(\partial N_B/\partial x)^2$ becomes negligible compared to $(\partial^2 N_B/\partial x^2)$ and the first term on the right side of Eq. 17 may be neglected. Thus, the conventional form of Fick's second law is obtained:

$$\frac{\partial N_B}{\partial t} = V^2 D_{\xi_N} \frac{\partial^2 N_B}{\partial x^2} = \tilde{D} \frac{\partial^2 N_B}{\partial x^2}, \text{ if } N_{B_1} \cong N_{B_2} \quad [18]$$

where

$$\tilde{D} \text{ (cm}^2\text{/sec)} = V^2 \text{ (cm}^6\text{/mol}^2) \times D_{\xi_N} \text{ (mols}^2\text{/cm}^4\text{ sec)} \quad [19]$$

Thus, according to Eq. 19, \tilde{D} can be calculated by multiplying each D_{ξ_N} value by the square of the molar volume at the corresponding concentration.

\tilde{D} is not only in the standard units of sq cm per sec, but according to Eq. 18 it is identical with the conventional interdiffusion coefficient obtained with incremental couples having small concentration differences.

If W_B is the measure of concentration and ξ_w is the measure of distance, Fick's second law may be written

$$\frac{\partial W_B}{\partial t} = \frac{\partial}{\partial \xi_w} \left(D_{\xi_w} \frac{\partial W_B}{\partial \xi_w} \right) \quad [20]$$

Similarly, when Y_B and ξ_Y are the concentration and distance parameters, Fick's second law becomes

$$\frac{\partial Y_B}{\partial t} = \frac{\partial}{\partial \xi_Y} \left(D_{\xi_Y} \frac{\partial Y_B}{\partial \xi_Y} \right) \quad [21]$$

D_{ξ_w} and D_{ξ_Y} defined by Eqs. 20 and 21 can be evaluated by using corresponding forms of Eq. 15.

It can then be shown that

$$\tilde{D} \text{ (cm}^2\text{/sec)} = (1/\rho^2) \text{ (cm}^6\text{/gm}^2) \times D_{\xi_w} \text{ (gm}^2\text{/cm}^4\text{ sec)} \quad [22]$$

and

$$\tilde{D} \text{ (cm}^2\text{/sec)} = (V^2/N_A^2) \text{ (cm}^6\text{/mols of A)}^2 \times D_{\xi_Y} \text{ (mols of A)}^2\text{/cm}^4\text{ sec)} \quad [23]$$

All three equations, 19, 22, and 23, lead to the same value of \tilde{D} , which is the desired result.

It may be recalled that V and ρ are readily computed from the lattice parameters of the solution and the number of atoms per unit cell. For example, in a face-centered cubic substitutional solid solution, $V = a^3 N_o / 4$ and $\rho = 4(N_A M_A + N_B M_B) / N_o a^3$, where a is the lattice parameter in cm, N_o is Avogadro's number, and M_A and M_B are the atomic weights of A and B.

Discussion

Results obtained with diffusion couples consisting initially of pure metals A and B give, in principle, the interdiffusion coefficient \tilde{D} as a function of composition from a single run. This procedure seems very attractive and is certainly valuable for survey information, but some limitations should be kept in mind.

The foregoing treatment implies that a diffusion coefficient can be defined which depends only on temperature and concentration. In substitutional solid solutions, however, the concentration of vacancies (or interstitial atoms) by which diffusion takes place may differ from the equilibrium value corresponding to the local composition, if the rate of formation or disappearance of vacancies (or interstitial atoms) is not sufficiently high in comparison with the transport rate of the diffusing atoms.⁹ This may confine the validity of Fick's second law to relatively low concentration gradients. Such deviations

can be minimized by employing incremental diffusion couples with small initial concentration differences.

Further uncertainties are introduced by the formation of voids due to differences in the intrinsic diffusion coefficients of the two components. These voids change the effective volume of the solution, and their influence cannot be taken into account rigorously without a complete knowledge of their distribution as a function of distance and time. In addition, it must be ascertained whether the voids act as "open circuits" which decrease the diffusion cross section or as "short circuits" which accelerate diffusion by providing fast transport along internal surfaces or through the vapor phase. To reduce this source of error, it is desirable to use a series of incremental couples rather than overall couples comprising large composition ranges.

Moreover, the inherent accuracy of diffusion measurements is greater with incremental couples, e.g., involving concentration differences of about 10 to 20 atomic pct, than with wide range couples. At the same time, potential volume changes in the diffusion zone are reduced by using couples with small initial differences in composition; and use of the modified distance parameter, as discussed in this paper, then becomes purely academic.

Thus incremental couples are advantageous in many ways, and are to be recommended.

Conclusions

When a volume change occurs during diffusion, it is necessary to introduce a modified measure of distance in order for the diffusion equation to retain its usual form. Three cases are presented in which the concentration is given in terms of weight fraction, mol fraction, and molar ratio, respectively. It is shown that each case leads to the same values of the interdiffusion coefficient in sq cm per sec as a function of concentration, when the Boltzmann-Matano analysis is applied.

The above treatment becomes unnecessary when incremental couples are employed with sufficiently small initial differences in concentration. This procedure also minimizes possible errors due to the formation of voids and to deviations from the local equilibrium concentration of vacancies (or interstitial atoms).

Acknowledgment

This paper is based on a research program sponsored by the Wright Air Development Center (Contract No. AF 33(038)-23281, Scope 1) at the Massachusetts Institute of Technology.

References

- ¹G. S. Hartley and J. Crank: *Trans. Faraday Soc.* (1949) **45**, p. 801.
- ²C. Wagner: *Trans. AIME* (1952) **194**, p. 91; *JOURNAL OF METALS* (January 1952).
- ³L. C. Correa da Silva and R. F. Mehl: *Trans. AIME* (1951) **191**, p. 155; *JOURNAL OF METALS* (February 1951).
- ⁴W. Seith and A. Kottmann: *Naturwissenschaften* (1952) **39**, p. 40; *Angewandte Chemie* (1952) **64**, p. 379.
- ⁵R. W. Balluffi and B. H. Alexander: *Journal of Applied Physics* (1952) **23**, p. 953.
- ⁶L. Boltzmann: *Wiedem. Ann. Physik* (1894) **53**, p. 959.
- ⁷C. Matano: *Japanese Journal of Physics* (1933) **8**, p. 109.
- ⁸L. S. Darken: *Trans. AIME* (1948) **175**, p. 184; *METALS TECHNOLOGY* (January 1948).
- ⁹F. Seitz: *Acta Metallurgica* (1953) **1**, p. 355.

The Molybdenum-Boron System

by Paul W. Gilles and Bernard D. Pollock

THE pioneering work of Steinitz¹ and Steinitz, Binder, and Moskowitz² has shown conclusively the existence at high temperature of two additional phases in the molybdenum-boron system and thus brings to a total of six the number of structures appearing in this system. To the structures Mo_2B , MoB , and Mo_3B_5 they have added Mo_3B_2 , a new β - MoB form, and have shown that MoB_2 , which has the same range of composition as Mo_3B_5 , is only a high temperature structure of the latter. This solid solution, interestingly enough, includes neither of the compositions corresponding to the stoichiometric compounds, MoB_2 or Mo_3B_5 , but rather at all temperatures has intermediate values of composition.

These workers have also, in the course of their work, measured melting points, transition temperatures, eutectic and peritectic points in the system and have shown that Mo_3B_2 , because of its disproportionation at low temperature to Mo_2B and MoB , is stable only in a limited high temperature range.

During the course of the present work on the vaporization properties of the molybdenum-boron compounds, a few transition temperatures were observed. When the report of the other workers appeared, it was decided to repeat, in part, their study of the system. As a result, considerable evidence has been obtained that substantiates the specific kinds of melting processes they report as well as the general features of their diagram.

However, a marked difference was found between the temperatures they report and the ones observed in this study, with the latter being higher. The purposes of this paper are to present the evidence obtained in this laboratory that verifies their diagram of the system, to give some important temperatures in the system, to compare them with those previously published, and to seek an explanation of the difference.

Samples

The metal starting material was 400 mesh molybdenum powder with a purity stated by the manufacturer to be 99.9 pct. The initial treatment, designed to remove volatile contamination, consisted of heating in a vacuum for 10 min to a temperature of from 800° to 1000°C during which a loss of 0.3 to 0.4 pct occurred. An assay following this treatment showed it to be 99.4 pct pure, with the principal impurity probably being oxygen.

The boron starting material was obtained from the Cooper Metallurgical Laboratories and the Fairmount Chemical Co. as 325 mesh powder with manufacturers' analyses of 99 pct or better. Initial treatment consisted of heating in molybdenum in

a vacuum at about 1700°C for 10 min. During this time a loss of 3.5 pct occurred. An assay following this treatment showed the different samples to have purities ranging from 95.5 to 99.0 pct with iron and carbon as the principal impurities.

Following the initial treatment, the elements were combined to form stocks of Mo_2B and MoB by heating pressed mixtures in a vacuum to 1100° to 1200°C to accomplish reaction and to 1500° to 1900°C for a few minutes to evaporate the more volatile impurities. Analysis of the two compounds for boron by a modification of the method of Blumenthal³ and for molybdenum by the lead-molybdate method indicated them to have purities greater than 99 pct.

The individual samples to be studied had compositions in the Mo_2B - MoB range and consisted of mixtures of the stock compounds.

Procedure

As is usually the case in high temperature work the selection of containers for the samples posed some problems. For vapor pressure studies tantalum crucibles, allowing little contact with the pressed samples, were used and some of the observations made during these experiments are pertinent to the study of the phase diagram. Most of the experiments, however, were performed in graphite containers, as were those of the previous authors.

Two kinds of spectroscopic grade graphite crucibles were used. One was a $\frac{7}{8}$ in. cylinder, $\frac{3}{4}$ in. high, containing seven $\frac{3}{16}$ in. holes drilled $\frac{1}{2}$ in. deep into which were packed samples of the different mixtures weighing 250 to 500 milligrams. The other, consisting of separate crucibles, was prepared by drilling $\frac{3}{16}$ in. holes, $\frac{1}{2}$ in. deep into $\frac{1}{4}$ in. graphite rods $\frac{5}{8}$ in. long. The $\frac{7}{8}$ in. cylinder was heated directly by induction while the small crucibles were packed in a tantalum heating element for induction heating.

All heating was done in a high vacuum system in which the pressure was generally less than 1×10^{-6} mm and never rose above 2×10^{-6} mm when the samples were hot. The general pattern of the heating in graphite was to heat rapidly to a temperature somewhat below the desired one, then to raise the temperature slowly. The samples were held for 2 to 5 min at the maximum temperature, which in all cases was far higher than that needed to produce reaction. The short time was employed to reduce possible contamination by the crucible material and to reduce composition changes that would occur because of vaporization. After examination following the heating, the samples were reheated to a higher temperature.

Temperatures were measured with a Leeds and Northrup disappearing filament optical pyrometer, certified by the National Bureau of Standards, by sighting through a window at the top of the vacuum

P. W. GILLES is Associate Professor and B. D. POLLOCK is Research Assistant, Dept. of Chemistry, University of Kansas, Lawrence, Kansas.

Discussion on this paper, TP 3634E, may be sent, 2 copies, to AIME by Jan. 1, 1954. Manuscript, April 17, 1953.

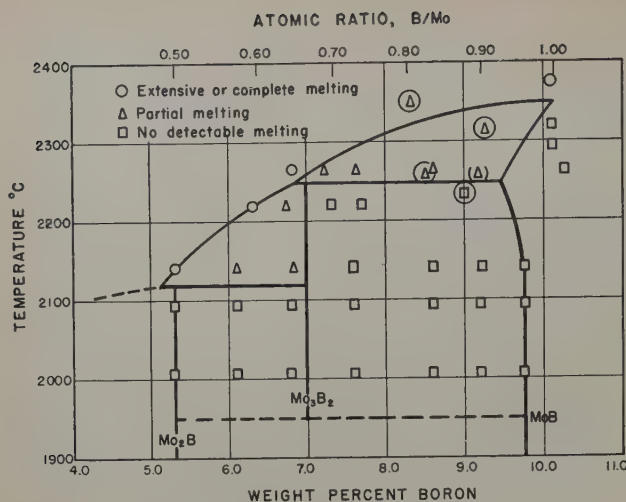


Fig. 1—Partial phase diagram of Mo-B.

system into the central hole in experiments with the graphite cylinder; into one of the graphite crucibles in experiments with those in the tantalum heating element; and through a hole in the lid acting as an effusion orifice in experiments with the tantalum crucible. The reproducibility in the settings of the temperature was about $\pm 5^\circ$. Numerous comparisons of pyrometer readings showing agreement among several workers in this laboratory have been made in the past. To the observed reading the certification correction and the window correction have been applied in the usual way. The absolute uncertainty of the temperature measurements is of the order of 20° .

After being heated and cooled the samples were examined visually for melting. Changes from a dull to a bright metallic surface, rounding of sharp edges, and partial or complete collapse of the sample were used to make rough estimates of the degree of melting. X-ray diffraction patterns showed that no reaction with graphite had occurred unless there had been extensive melting. Metallographic examinations were not made.

Results

Several samples were heated in graphite at 2008° , 2097° , 2142° , 2221° , and 2266°C . The results of the observations are shown in Fig. 1 in a manner similar to that of the previous authors in which the squares represent samples showing no melting, the triangles represent samples showing partial melting, and the circles represent samples showing extensive or complete melting. The four large circles containing squares or triangles indicate experiments carried out in tantalum crucibles. The triangle in the parentheses indicates an observation made on an annular ring of boride acting as its own heating element in the induction field. This point masks one of the points obtained in graphite at 2266°C .

The four points from observations in tantalum crucibles appear to lie on two diagonal lines sloping

upward to the left. These points occur at different compositions because they were taken from experiments designed to measure evaporation processes and since boron is lost preferentially from these samples the composition of the residue changes during experiments sufficiently long to give appreciable vaporization. The compositions of these samples have been calculated from incomplete vaporization results.

The three points at compositions of 10.1 pct B, corresponding to $\text{MoB}_{1.00}$, resulted from separate experiments designed to establish the melting point of MoB.

Except for the one point at about 8.3 pct B and 2350°C , obtained from experiments in a tantalum crucible, all the data on the diagram are consistent with the general features of the system as proposed by the previous workers and as drawn here. This one discrepancy is not considered serious in view of the fact that the composition of this sample was not well known because of uncertainties in the initial composition and in the changes of composition arising from vaporization.

At the temperatures 2142° and 2221°C the appearance of partially melted samples lying to the left of the Mo_3B_2 composition and the appearance of unmelted samples lying to the right of this composition clearly indicate the presence of the compound earlier reported. Rough estimates were made of the extent of melting of the different samples after the experiment at 2266°C and they showed for the points in the neighborhood of 7 pct B that the extent of melting decreased with increasing boron content, thus indicating that the proposed diagram is correct and excluding the possibility of a congruently melting compound at Mo_3B_2 . There seems, then, to be little doubt concerning the general features of the diagram.

It is apparent from Fig. 1 that the peritectic temperatures for Mo_2B and Mo_3B_2 and the melting point of MoB may be set within reasonably narrow limits. It is in these temperatures that the present work differs considerably from the previous work. The temperatures as reported by the earlier workers and as determined in this investigation are summarized in Table I.

Table I shows that the temperatures observed in this study are some 100° to 200° higher than the ones previously reported. Generally speaking, in temperature measurements with an optical pyrometer, errors other than those resulting from gross mismatching of brightnesses of the filament and the object tend to make the observed temperatures too low. Such is the case, for example, if the object is not a black body, if the pyrometer lenses are dirty, or if absorbing or scattering substances are in the light path.

It is possible that if the temperatures recorded by the previous workers are low they may be so for the following reasons. First, sighting through a gas, as apparently the previous workers have done, leads to uncertainties if any convection currents in the gas exist or if any particles remain suspended in the gas. Convection currents may lead to refraction effects and particles screen out light, both tending to make the observed temperature too low. Second, although it would appear as if in the experiments of the previous workers that the bottom of their black body tube into which they sighted to get a temperature observation should be at the same temperature as that of their sample

Table I. Temperatures ($^\circ\text{C}$) in the Molybdenum-Boron System

Substance	Phase Change	Previous Work ²	Present Work
Mo_2B	Incongruent melting	2000°	2097° - 2142°
	Complete melting	2060°	$<2142^\circ$
Mo_3B_2	Incongruent melting	2070°	2221° - 2266°
	Disproportionation	1850°	—
MoB	Melting	2180°	2325° - 2374°
	Melting	2100°	—

resting in the crucible adjacent to it, some doubt is raised concerning the appropriateness of the observations because neither the sample itself nor a hole drilled in it was actually observed.

Acknowledgment

The authors are pleased to acknowledge support of the Atomic Energy Commission in this work, and the conversations with and communications from Frank W. Glaser, Leo Brewer, and Alan Searcy.

Technical Note

Notes on the Determination of Retained Austenite by X-Ray Methods

by Karl E. Beu

IN the measurement of retained austenite concentrations in steels using the integrated intensity method,¹ Averbach has pointed out² that the absorption factor $A(\theta)$ for a flat sample making a glancing angle ϕ with the incident X-ray beam can be combined with his constant factor R to obtain our constant factor³ G provided that "1—There is no preferred orientation in the sample, and 2—The geometric requirements [for the sample, film, and X-ray beam] have been met precisely."² If $A(\theta)$ can be combined with R to give G according to the equation

$$G = R \cdot A(\theta) \quad [1]$$

then the possibility for making non-compensating errors in the austenite determination has been eliminated. This has been described previously in a technical note.³

Because of the brevity of the previous note,³ it was impossible to emphasize the fact that the two conditions on preferred orientation and geometry can be easily met experimentally, contrary to Averbach's statement that: "... the necessary conditions must be tested experimentally for each determination, and this is done most easily by observing whether the apparent absorption has the form of Eq. 2 [the theoretical equation for $A(\theta)$]."² The way in which these two conditions can be met experimentally will be discussed briefly to help clear up this point. In addition to these two conditions, other factors such as sample shape, homogeneity, and grain size which also affect $A(\theta)$ will be included in this discussion.

$A(\theta)$ depends on sample shape. The theoretical function for $A(\theta)$ was derived originally for a flat surface.¹ In general we have found that a flat sample surface is readily obtainable.* If such a surface can

* The effect of surfaces which are not flat on the measurement of retained austenite will be discussed later.

be obtained, it has the following advantages: 1—it is easily reproducible from sample to sample, 2—it is the form required for metallurgical examination—this type of examination being frequently desirable for this work, and 3—it is an efficient shape for diffraction purposes. Perhaps the most important of these features is that a flat sample surface is easily reproducible; hence, this requirement on the reproducibility of $A(\theta)$ from sample to sample is met for all such samples.

K. E. BEU is associated with the Physics-Instrumentation Dept., Research Laboratories Div., General Motors Corp., Detroit.
TN 190E. Manuscript, April 24, 1953.

References

- ¹ R. Steinitz: JOURNAL OF METALS (February 1952) 4, p. 148.
- ² R. Steinitz, I. Binder, and D. Moskowitz: Trans. AIME (1952) 194, p. 983; JOURNAL OF METALS (September 1952). P. Rautala: Discussion on ref. 2. Trans. AIME (1953) 197, p. 747; JOURNAL OF METALS (May 1953).
- ³ H. Blumenthal: Analytical Chemistry (1951) 23, p. 992.

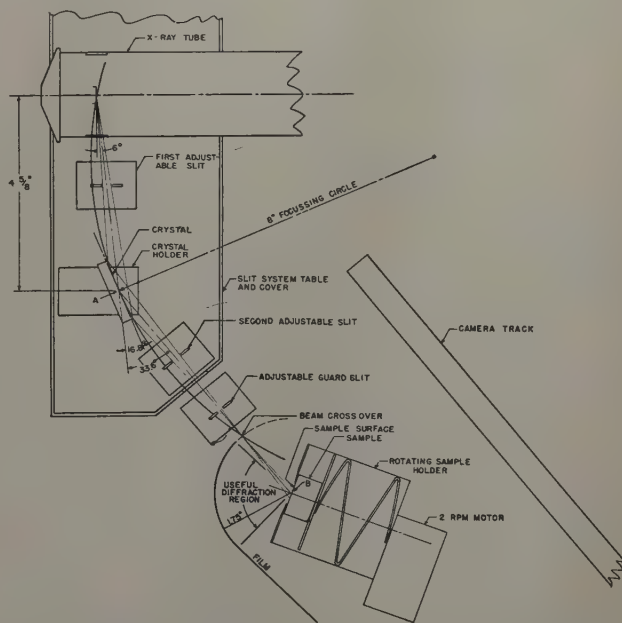


Fig. 1—Schematic diagram of the quartz crystal monochromator diffraction unit. The centerline of the main beam is at 6° to the target face. The tangent to the crystal face is at 16.8° to the main beam. The centerline of the monochromatic beam is at 33.6° to the main beam. The sample surface can be rotated in its own plane. The angle of the sample surface and the monochromatic beam can be adjusted by rotating about the vertical axis, B . The film holder can also be rotated about B so that the film can be exposed over the desired angular range. For Fe $K\alpha$, $\lambda = 1.932\text{\AA}$. $10\bar{1}1$ planes of quartz have $d = 3.35\text{\AA}$.

$A(\theta)$ depends on homogeneity and grain size. If the sample is badly segregated or the grain size is large, the effect of micro-absorption and primary extinction^{1, 4} must be considered. It has been shown, however, that for most plain carbon or low alloy hardened steels, neither micro-absorption nor primary extinction effects are present.¹

$A(\theta)$ depends on camera geometry. For a given angle θ , $A(\theta)$ remains theoretically constant from a geometrical viewpoint only if the following factors are kept constant: 1—the angle of inclination ϕ of the sample to the X-ray beam, and 2—the centering of the sample with respect to the film cylinder. These are mechanical problems which can be solved readily if the facilities of a good machine shop are available. The arrangement used to insure that the angle ϕ remains constant and the centering of the sample is reproducible is indicated schematically in Fig. 1. The sample is clamped against a thin plate with a hole in it by means of a spring-loaded pres-

sure plate. The focused monochromatic X-ray beam strikes the sample after passing through the hole in the thin plate without touching the edges of the hole. In this manner the sample surface can be precisely and reproducibly located with respect to the X-ray beam and film cylinder. The sample holder can accommodate samples of various shapes and sizes and the proper angular and centering relationships can be maintained as long as the surface to be examined is flat.

$A(\theta)$ is affected by preferred orientation. This effect can be minimized by rotating the flat sample surface in its own plane. This is accomplished by rotating the entire sample holder by means of small 2 rpm motor as indicated in Fig. 1. Such rotation does not disturb the angular relationships of the sample, X-ray beam, and film, but it does minimize preferred orientation, as well as grain size, effects. This has been borne out by the fact that, of the approximately 1500 austenite analyses made to date, no misleading results were obtained because of preferred orientation or grain size.

The factors discussed in the four preceding paragraphs are the significant factors which may affect the constancy of the $A(\theta)$ function from sample to sample for this problem. It has been demonstrated that either these factors have a negligible effect on $A(\theta)$ or they can be controlled so that $A(\theta)$ can be maintained constant from sample to sample. Hence, there are no valid reasons for excluding $A(\theta)$ from the constant factor R to give the new constant factor G , according to Eq. 1.

After having ascertained that the theoretical requirements on $A(\theta)$ could be met experimentally, we were interested in determining to what extent it was possible to depart from these requirements and still not affect the reliability of the austenite determination. We have investigated the effect of 1—sample surface roughness and curvature, 2—varying the angle ϕ over a range of 30° , and 3—displacing the sample from the film cylinder axis in the direction of the primary monochromatic X-ray beam. As a result of these investigations, it has been concluded that any or all of the factors can be varied over a wide range without affecting the austenite determination significantly; i.e., the results all fall within the range of the standard deviation of our measurements.[†] A conclusion that can be drawn

[†] These results will be reported elsewhere in detail.

from these observations is that it makes no significant difference in the final result of austenite percentage whether or not the sample or geometry conditions are closely maintained and reproduced. Thus, Averbach's statement that: "If these conditions are not met [precisely], the validity of the determination is questionable"² is not borne out by experimental observations.

Averbach also discusses the use of a Geiger counter diffraction technique for measuring austenite concentrations. He suggests the following procedure: "A series of readings are taken in the vicinity of the diffraction peak. The highest reading includes the diffraction peak plus background. The background is obtained from the average of several readings on each side of the peak."² It is worth-while to point out that this technique is susceptible to two types of errors which can be serious especially for low austenite concentrations (less than 2 or 3 pct). The difficulty in making peak intensity measurements as just described is related to the fact that the

shapes of the austenite and martensite diffraction peaks are affected, among other things, by the nature of the microstresses in the austenite and martensite grains. We have found that peak height measurements are not a reliable criterion of the austenite content of a given sample and it is for this reason that we have continued to use integrated intensity measurements. A study was made on a group of 38 miscellaneous samples to see if peak height and integrated intensity measurements could be correlated. It was found that errors as large as 75 pct of the amount of austenite present could be made if peak height measurements were used. Thus, integrated intensity measurements must be used where a high degree of accuracy is required.

Even if there were no difficulties encountered in making peak intensity measurements, there would be the problem of determining where to measure the true background. Referring to Fig. 1 of a previous note,² it can be seen from the microphotometer record of this figure that there are relatively strong cementite peaks in the vicinity of the austenite (220) and (311) peaks. If background measurements were made on or near the cementite peaks in the vicinity of the austenite (220) or (311) peaks, the austenite results could be seriously in error if the cementite concentration is on the order of 5 to 10 pct. This amount of cementite is normal in many hardenable steels including ball bearing and gage block steels.

Another statement² which may lead to some confusion is: "The absorption correction [$A(\theta)$] in ref. 1 [the original reference by Averbach and Cohen¹ to $A(\theta)$ is Z. Wilchinsky; *Journal of Applied Physics*, (1944) 15, p. 812] erroneously contained an extra $\sin \phi$ in the numerator." Whether or not this $\sin \phi$ term appears in $A(\theta)$ depends on the definition of the area term a used in $A(\theta)$. Wilchinsky states that

$$A(\theta) = \frac{a_w}{\mu} \frac{\sin \phi \sin (2\theta - \phi)}{\sin (2\theta - \phi) + \sin \phi}$$

where a_w is the area of the sample illuminated by the X-ray beam. Another form of this equation is

$$A(\theta) = \frac{a_A}{\mu} \frac{\sin (2\theta - \phi)}{\sin (2\theta - \phi) + \sin \phi}$$

where a_A is the cross-sectional area of the collimated X-ray beam.¹ It should be noted that these equations are related by the following equation:

$$a_A = a_w \sin \phi.$$

In his note,² Averbach let $a_A = 1$ so that his Eq. 2 was written as

$$A(\theta) = \frac{1}{\mu} \frac{\sin (2\theta - \phi)}{\sin (2\theta - \phi) + \sin \phi}.$$

The conclusion to be drawn from this discussion is that all three equations for $A(\theta)$ are identical, the differences being due only to the way in which the area term a is defined.

References

- ¹ B. L. Averbach and M. Cohen: *Trans. AIME* (1948) 176, pp. 401-415; *METALS TECHNOLOGY* (September 1947).
- ² B. L. Averbach: *Trans. AIME* (1953) 197, pp. 87-88; *JOURNAL OF METALS* (January 1953).
- ³ K. E. Beu: *Trans. AIME* (1952) 194, pp. 1327-1328; *JOURNAL OF METALS* (December 1952).
- ⁴ A. Taylor: *X-Ray Metallography*, (1949) pp. 89, 90, 350, 351. New York. John Wiley and Sons.

The Partition of Some Alloying Elements Between Carbide and Ferrite in Steels

by D. A. Scott and G. S. Farnham

Partition of certain elements, particularly nickel, was determined for slowly cooled steels, the greater number containing from 0.30 to 0.35 pct C. Approximately 3 pct of the nickel, 18 pct of the manganese, 33 pct of the molybdenum, and 35 pct of the chromium occur in the carbide phase. Partition of one element is not much affected by the presence of another.

THE object of this investigation was: 1—to determine the partition of nickel between cementite and ferrite in a medium and high carbon series of annealed steels; 2—to evaluate the effect of chromium and/or molybdenum or both on the partition of nickel in medium carbon annealed steels; 3—to determine the partition of chromium between ferrite and carbide in a series of medium carbon annealed steels; and 4—to study the chemistry of the carbides formed in an AISI 2330 steel during both isothermal transformation, and quench and draw experiments at 1150°F (620°C).

The partition of alloying elements between cementite and ferrite in annealed steels has been the subject of many investigations, a summary of which has been given by Austin¹. However, there is no satisfactory data available concerning the partition of nickel. It has generally been assumed that virtu-

D. A. SCOTT and G. S. FARNHAM, Member AIME, are associated with Canadian Development and Research, The International Nickel Co. of Canada Ltd., Toronto, Ont., Canada.

Discussion on this paper, TP 3650E, may be sent, 2 copies, to AIME by Jan. 1, 1954. Manuscript, Feb. 24, 1953; revision, June 4, 1953. Paper presented as a Research in Progress report at the Los Angeles Meeting, February 1953.

Table I. Analyses of Steels

Steel Type	Range of Composition, Pct					
	C	Si	Mn	Ni	Cr	Mo
Med. C, Ni	0.29-0.35	0.15-0.25	0.25-0.65	0.10-3.77	—	—
High C, Ni	0.82-0.85	0.23-0.28	0.27-0.29	0.10-3.35	—	—
Chromium	0.34-0.35	0.16-0.18	0.24-0.31	—	0.45-1.42	—
Ni-Cr	0.31-0.33	0.26-0.32	0.35-0.39	0.73-3.30	0.80-0.83	—
Ni-Mo	0.33-0.34	0.16-0.20	0.34-0.36	0.00-3.36	—	0.21-0.23
Ni-Cr-Mo	0.31-0.34	0.16-0.22	0.30-0.35	0.00-3.43	0.83-0.88	0.22-0.25

ally all of the nickel concentrates in the ferrite phase in annealed steels. Two investigators^{2,3} have reported the finding of nickel in extracted carbide residues. Recently, it has been shown⁴ that nickel substitutes up to 40 pct for iron in the lattice of cementite produced by the low temperature carburization of iron-nickel powders. In addition to the lack of data on nickel partition, the literature also fails to make reference to the effect of other elements on the nickel content of the carbide in nickel-bearing steels.

The partition of molybdenum between ferrite and carbide has been reported⁵⁻⁷ for hypoeutectoid steels, isothermally transformed at 1300°F (705°C) and

Table II. Composition of Steels

Alloy No.	Steel Analysis, Pct					
	C	Si	Mn	Ni	Cr	Mo
N1	0.33	0.15	0.25	0.10	—	—
N2	0.30	0.18	0.29	0.75	—	—
N3	0.35	0.16	0.26	1.56	—	—
N5	0.31	0.18	0.28	2.22	—	—
N6	0.29	0.25	0.65	3.39	—	—
N7	0.30	0.16	0.28	3.77	—	—
NC1	0.85	0.23	0.28	0.10	—	—
NC2	0.84	0.26	0.29	0.74	—	—
NC3	0.83	0.24	0.26	1.46	—	—
NC4	0.84	0.28	0.28	2.45	—	—
NC5	0.82	0.26	0.27	3.35	—	—
CR1	0.34	0.16	0.24	—	0.45	—
CR2	0.34	0.18	0.29	—	0.86	—
CR4	0.35	0.18	0.31	—	1.42	—
NCR1	0.33	0.26	0.39	0.73	0.83	—
NCR2	0.33	0.28	0.36	1.47	0.81	—
NCR3	0.32	0.32	0.38	2.42	0.81	—
NCR4	0.31	0.28	0.35	3.30	0.80	—
NM1	0.34	0.16	0.36	—	—	0.23
NM2	0.34	0.14	0.34	0.74	—	0.23
NM3	0.33	0.18	0.33	1.49	—	0.22
NM4	0.34	0.20	0.36	2.40	—	0.22
NM5	0.34	0.16	0.36	3.36	—	0.21
NCRM1	0.34	0.20	0.34	—	0.88	0.25
NCRM2	0.34	0.18	0.33	0.78	0.86	0.23
NCRM3	0.32	0.22	0.35	1.51	0.87	0.24
NCRM4	0.33	0.16	0.31	2.56	0.84	0.23
NCRM5	0.31	0.19	0.30	3.43	0.83	0.22

1200°F (650°C) and also quenched and drawn at these temperatures. As for the higher carbon steels, the data for molybdenum is somewhat complicated by the appearance of more than one carbide. For molybdenum contents below 0.5 pct in general, cementite was found to be stable, while at higher molybdenum values $(Fe,Mo)_{23}C_6$ occurred. With cementite dominant, the weight percentage of molybdenum in the carbide was four times the weight percentage of molybdenum in the steel. With the complex carbide dominant this ratio varied from (4.5 to 7):1. There was also an indication that the concentration of molybdenum in the carbide was somewhat greater when the isothermal transforma-

Table III. Partition Data for Annealed Steels

Alloy No.	Carbide Analysis, Pct						
	Carbide,* Wt Pct	C	Mn	Ni	Cr	Mo	Fe
N1	4.93	6.80	1.03	0.05	—	—	—
N2	4.47	6.68	1.08	0.41	—	—	91.40
N3	5.22	6.75	1.25	1.03	—	—	—
N5	4.63	6.78	1.16	1.54	—	—	—
N6	4.33	6.70	2.85	1.89	—	—	—
N7	4.47	6.72	1.11	2.05	—	—	—
NC1	12.7	6.68	0.98	0.05	—	—	92.45
NC2	12.5	6.71	0.95	0.47	—	—	91.69
NC3	12.4	6.70	0.93	0.96	—	—	91.68
NC4	12.5	6.72	1.12	1.59	—	—	90.80
NC5	12.3	6.70	0.96	2.07	—	—	90.21
CR1	5.07	6.64	1.08	—	2.90	—	—
CR2	5.07	6.66	1.20	—	5.95	—	—
CR4	5.22	6.65	1.01	—	8.96	—	—
NCR1	4.93	6.65	1.25	0.40	6.20	—	85.53
NCR2	4.93	6.67	1.28	0.98	6.31	—	84.76
NCR3	4.78	6.69	1.31	1.49	6.36	—	84.25
NCR4	4.63	6.65	1.18	2.03	6.43	—	83.82
NM1	5.07	6.65	1.28	—	—	1.39	90.82
NM2	5.07	6.66	1.35	0.42	—	1.48	90.16
NM3	4.93	6.68	1.28	0.88	—	1.53	89.63
NM4	5.07	6.66	1.38	1.37	—	1.42	89.21
NM5	5.07	6.65	1.29	1.96	—	1.45	88.81
NCRM1	5.07	6.68	1.18	—	5.86	1.40	84.62
NCRM2	5.07	6.64	1.14	0.30	5.92	1.55	84.43
NCRM3	4.78	6.70	1.21	0.70	5.96	1.57	83.98
NCRM4	4.93	6.68	0.96	1.15	5.84	1.49	83.52
NCRM5	4.63	6.70	0.98	1.69	5.81	1.56	83.00

* Calculated from carbon content of steel and theoretical carbon content of cementite.

tion temperature was raised from 1200°F (650°C) to 1300°F (705°C).

Experimental Work

Using a method proposed by R. W. Gurry, of the U.S. Steel Corp. Research Laboratory, Kearney, N. J., carbides were isolated electrolytically from the series of steels listed in Table I.

Compositions of the individual steels used are given in Table II. All steels except steel N6, a commercial heat which was used for isothermal transformation and quench and draw studies, were melted in a 50 lb induction furnace and cast in dry sand molds as 1 in. diameter bars weighing about 6 lb. All melts were deoxidized in the mold with approximately 1.5 lb of aluminum per ton. The bars were homogenized in vacuo at 2500°F (1370°C) after which they were annealed 2 hr at 1550°F (840°C) and finally furnace-cooled at a rate of 100°F per hr, measured at 1300°F (704°C).

Carbides were separated from 5/8 in. diameter x 3 1/4 in. long samples suspended vertically as the anode in an electrolytic cell, copper gauze forming the cathode. A solution containing 75 grams cadmium bromide per 200 ml of water was used, cad-

Table IV. Typical Partition Data for Annealed Steels

Alloy No.	Ferrite Analysis,* Pct				Ferrite Analysis,† Pct		
	Fe	Ni	Cr	Mo	Ni	Cr	Mo
N3	98.3	1.60	—	—	1.59	—	—
N7	95.8	3.80	—	—	3.85	—	—
CR4	97.9	—	1.10	—	—	1.00	—
NCR4	95.1	3.40	0.52	—	3.37	0.53	—
NM5	95.0	3.40	—	0.15	3.44	—	0.14
NCRM5	95.6	3.50	0.60	0.15	3.52	0.58	0.15

* From electrolyte analyses.

† From carbide weights and compositions.

mium being plated out at an anodic current density of about 0.08 amp per sq in. Carbides falling from the anode were caught in a paper extraction thimble. Nitrogen bubbling through the electrolyte prevented the oxidation of the iron and also acted as a stirring mechanism.

After electrolysis the carbides were collected and then washed successively with water, alcohol, and ether, and then dried. This was followed by weighing and chemical analyses. The electrolytes were analyzed for iron, and in some cases for the other elements, in order to check on the effectiveness of the carbide separation and the accuracy of the carbide analyses. The fact that the carbon content of the carbides corresponds to that of cementite shows that the carbides did not break down on separation. The methods followed appeared to be quantitative, since the electrolyte analyses checked those calculated from the compositions and amounts of carbides.

The results of the carbide analyses and the weight percentage of the carbide are listed in Table III. There has been no adjustment made to bring the total carbide composition to 100 pct, figures listed being those actually obtained. Divergence from the 100 pct figure, which is evenly divided on a plus and minus basis, indicates the inevitable minor analyses errors. Some corroborative ferrite compositions obtained from solution analyses are shown in Table IV,

Table V. Partition of Individual Elements in Annealed Steels

Alloy No.	Total Alloy Elements in Carbide, Pct			
	Mn	Ni	Cr	Mo
N2	17.0	2.40	—	—
N5	19.0	3.20	—	—
N7	18.0	2.40	—	—
NC2	35.0	8.00	—	—
NC3	44.5	8.20	—	—
NC5	43.5	7.60	—	—
CR1	23.0	—	33.0	—
CR2	21.0	—	35.0	—
CR4	17.0	—	33.0	—
NCR1	16.0	2.60	37.0	—
NCR2	17.5	3.40	38.5	—
NCR4	15.5	2.90	37.5	—
NM2	20.0	2.90	—	33.0
NM3	19.0	2.90	—	34.0
NM5	18.5	3.00	—	35.0
NCRM2	17.5	1.95	35.0	34.0
NCRM3	16.5	2.20	35.0	34.0
NCRM5	15.0	2.30	32.5	34.0
*Average	18.3	2.70	35.0	33.4

* For all medium carbon steels investigated.

which also lists for comparison ferrite compositions calculated from carbide weights and analyses. The partition of various elements in the carbide are shown for selected steels in Table V. The average figure listed for each element is for all of the medium carbon steels investigated. The analyses of carbides separated from the commercial steel N6 after both isothermal transformation and quenching and drawing are given in Table VI.

Discussion

The investigation shows that carbides of annealed nickel-bearing steel contain significant percentages of nickel, although the greater part of the nickel is contained in the ferrite phase; the weight percentage of nickel in the carbide was found to be directly related to the weight percentage of nickel in the steel. Previous investigators had found this to be the case for manganese, chromium, and molybdenum. For a given nickel content, increasing the carbon level did not affect the weight percentage of nickel in the carbide. It did, of course, by increasing the amount of carbide, increase the percentage of total nickel held by that phase, increasing this value from 2.8 pct for the medium carbon N series steel to 8.1 pct for the high carbon NC steel group.

For the same nickel content there is apparently less nickel in the carbide of the triple alloy NCRM series steel than in the carbide of the other nickel alloy steels tested. If this is a real effect, a possible explanation is that the increased total amount of carbide-forming elements present limits the amount of nickel that can be held by the carbide. However, the weight percentage of manganese, chromium, and

molybdenum in the carbide is relatively unaffected by the presence of other alloy elements.

It is not suggested that the findings of this investigation hold for steels of widely diverging compositions and heat treatments, for it is probable that an increase of the total alloy content of the carbide will affect the amount of any given element that can be held by the carbide. However, this investigation does show that there was no such effect for manganese, chromium, and molybdenum over a wide range of nickel contents.

Results reported in Table VI are for the analyses of carbides separated from the one steel examined that had been both isothermally transformed and drawn. They indicate that manganese gradually replaces nickel in carbide as the time of holding at subcritical temperatures is increased. This process apparently eventually slows down as the replacement at 100 hr was less than expected.

Summary

In variously alloyed annealed 0.30 to 0.35 pct carbon steels examined, the alloying element in the carbide as a percentage of the total amount of alloying element was found to be approximately 2.7 pct for nickel, 18.3 pct for manganese, 35.0 pct for chromium, and 33.4 pct for molybdenum. Increasing the nickel content of the steels was not found to affect these percentage values for the other elements present, nor did the addition of chromium or molybdenum affect the weight percentage of nickel in the carbide. However, the combined addition of these two elements lowered the nickel content of the carbide.

The weight percentage of nickel is the same in 0.30 to 0.35 pct carbon steels and 0.80 to 0.85 pct carbon steels having the same nickel content. However, the percentage of the total available nickel that is present in the carbide increases from 2.8 to 8.1 pct.

Increasing the holding time at 1150°F (621°C) of a 3.4 pct nickel steel, containing 0.65 pct manganese, led to a replacement of nickel in the carbide by manganese from the ferrite.

Acknowledgment

The authors wish to express their thanks to the various members of the Canadian Bureau of Mines staff for the very considerable assistance in this investigation. We are also grateful to T. N. Armstrong, of the International Nickel Co. Inc., for his helpful suggestions and criticisms.

References

- ¹J. B. Austin: The Effect of Changes in Conditions of Carbides on Some Properties of Steel. *Trans. ASM* (1947) 38, p. 28.
- ²F. L. Garrison: Carbides of Iron. *Journal Franklin Inst.* (1895) 140, p. 464.
- ³G. B. Waterhouse: The Influence of Nickel and Carbon on Iron. *Journal Iron and Steel Inst.* (1905) 68, p. 376.
- ⁴R. Bernier: Thermomagnetic Study of the Carbides of Iron and Nickel. *Ann. Chim.* (1951) 6, p. 104.
- ⁵F. E. Bowman: The Partition of Molybdenum in Steel and Its Relation to Hardenability. *Trans. ASM* (1945) 35, p. 112.
- ⁶F. E. Bowman and R. M. Parke: The Partition of Molybdenum in Iron-Carbon-Molybdenum Alloys at 1300°F and the Nature of the Carbides Formed. *Trans. ASM* (1944) 33, p. 481.
- ⁷F. E. Bowman: Partition of Molybdenum in Hypoeutectoid Iron-Carbon-Molybdenum Alloys. *Trans. ASM* (1946) 36, p. 61.

Table VI. Analysis of Carbides Separated from AISI 2330 Steel

Isothermally Transformed at 1150°F					Oil Quenched from 1450°F (790°C) and Drawn at 1150°F (620°C)				
Hr at 1150°F	C, Pct	Ni, Pct	Mn, Pct	Fe, Pct	Hr at 1150°F	C, Pct	Ni, Pct	Mn, Pct	Fe, Pct
1	6.75	1.95	2.35	88.62	4	6.70	2.06	2.05	89.05
2	6.73	1.85	2.45	88.75	7	6.68	2.02	2.26	88.81
4	6.70	1.85	2.48	88.73	25	6.69	1.88	2.46	88.87
8	6.69	1.80	2.53	88.61	50	6.69	1.79	2.66	88.78
100	6.68	1.68	2.95	88.83	100	6.70	1.73	2.89	88.86

System Titanium-Chromium-Molybdenum

by R. P. Elliott, B. W. Levinger, and W. Rostoker

Phase equilibria in the Ti-Cr-Mo system have been investigated for alloys containing 100 to 40 pct Ti in the temperature range 550° to 1300°C. Five experimental isothermal sections and a surface of incipient melting are presented in addition to a summary projection of the β space. Seven vertical sections have been constructed from the isothermal sections.

A STUDY of the system Ti-Cr-Mo was undertaken as part of a program sponsored by Watertown Arsenal toward the development of titanium-base phase equilibrium diagrams of potential technical importance to alloy development. The scope of the investigation included the composition range contained by the titanium corner and the line of 64 pct Ti (all compositions are by weight) and the temperature range 550° to 1100°C. A surface of incipient melting was constructed from measurements on a large number of alloys.

The system Ti-Cr has been established.¹⁻⁷ The phase diagram is characterized by a wide miscibility field of the β solid solution at elevated temperatures and a eutectoid reaction of the type: β (15 pct Cr) $\rightarrow \alpha + \text{TiCr}_2$ (685°C). The α solid solution has a very limited capacity for solution of chromium (< 0.5 pct Cr). The intermediate phase TiCr_2 has at best a very narrow composition range. It has been shown that two allotropic modifications of this phase exist.⁸ However, this behavior does not appear to be

perceptibly reflected in the form of phase boundaries of the type $\beta/\beta + \text{TiCr}_2$. In the system Ti-Mo,⁹⁻¹⁰ the β phase is stabilized to successively lower temperatures with increasing molybdenum content. There are no known intermediate phases. The α solid solution is limited to less than 0.5 pct Mo.

Because of the very extensive range of the β phase, the ternary system was ideally suited to the determination of the phase boundaries by the parametric method of Andersen and Jette.¹¹ A parametric surface was constructed to provide the necessary basis for the application of this method.

Preparation and Treatment of Alloys

More than 60 alloy compositions were prepared for the study of this system. Alloy buttons of 10 grams were arc-melted in a nonconsumable electrode furnace using inert atmosphere protection and a water-cooled copper crucible. The construction and operation of this type of melting unit have been adequately described elsewhere.¹² To insure complete solution of alloy additions, the buttons were remelted alternately on top or bottom as many as five times. This was accomplished by a suitable mechanism for "flipping" over the ingots.

Iodide titanium (99.97 pct Ti) was used as the alloy base. An especially high quality chromium (99.9 pct Cr) was obtained from the National Research Corp. Molybdenum sheet (0.005 in.) of 99.9 pct purity was used.

R. P. ELLIOTT is Assistant Metallurgist, and W. ROSTOKER is Senior Metallurgist, Metals Research Dept., Armour Research Foundation of Illinois Institute of Technology, Chicago, and B. W. LEVINGER, Junior Member AIME, is Research Metallurgist, Tung-Sol Electric Inc., Bloomfield, N. J.

Discussion on this paper, TP 3649E, may be sent, 2 copies, to AIME by April 1, 1954. Manuscript, June 5, 1953. New York Meeting, February 1954.

Table I. Summary of Annealing Schedules for Attainment of Equilibrium

Temperature, °C	Time, Hr
550	720
650	260
750	110
850	56
950	33
1050	19
1150	13
1200	9
1300	7

Charges were weighed to the nearest milligram and the resultant ingot reweighed to the same accuracy. Average weight losses for iodide titanium melts were of the order of 0.02 gram. It was assumed that the weight losses, less the 0.02 gram for titanium, represented volatilized chromium. Nominal compositions were corrected on this basis. The validity of this method of correction was checked frequently by chemical analysis. The alloy compositions in Fig. 1 are believed to be accurate to at least ± 1 pct.

Specimens heat treated below 1100°C were enclosed in Vycor bulbs. For temperatures in excess of 1100°C, quartz bulbs were used. Partial pressures of argon prevented collapse of the bulbs at temperatures above 950°C. Bulbs were simply evacuated at lower temperatures. Heat treatments were conducted in resistance element tube furnaces with temperature control of $\pm 3^\circ\text{C}$.

All as-melted alloys were given a preliminary homogenization anneal at 1000°C for 24 hr. Homogenized buttons were broken or cut to provide sufficient specimens for subsequent equilibrium anneals. Time schedules for the equilibrium anneals are given in Table I.

Examination of Alloys and Analysis of Data

Lattice parameters of the β phase were obtained from back-reflection patterns using filtered Cu K α radiation (Cu K $\alpha_1 = 1.5374$ kX units). Suitable powder specimens were prepared by filing or crushing annealed alloys and screening through 200 mesh. Annealing was performed by sealing in small Vycor tubes and heat treating for about 10 min at the temperature at which the original specimen was annealed. The powder capsule was then vigorously quenched but not broken. It was found by experiment that this method of quenching was sufficiently rapid to prevent detectable anisothermal transformation.

In principle, the precision measurement of the lattice parameter of a phase may be used in conjunction with the elementary rules governing the phase boundaries of isothermal sections to identify the composition of the saturated condition in two and three-phase fields. On any isothermal section, a two-phase field is made up of a family of tie-lines along which the compositions of the two phases are invariant but the proportions vary. Provided that, for any given isothermal section, the direction of the tie-line passing through a given alloy composition lying in the two-phase field is known, then the lattice parameters of the phases may be used to locate the extremities of the tie-lines. Obviously, the loci of such tie-line extremities are phase boundaries between single and two-phase fields. A preliminary necessity, therefore, is a knowledge of the variation of the lattice parameters with composition. In a

three component system, this relationship is represented by a parametric surface involving two independent composition coordinates and an independent parameter coordinate. Since a three-dimensional surface is awkward to use, it is common practice to develop a two-dimensional plot of isoparametric contours on the composition triangle. The family of isoparametric contours for the β phase is shown in Fig. 2.

The parametric method in three-component systems is most easily applied when the miscibility range of one of the phases of a two-phase field is very small. Then, essentially, the tie-lines converge to a point (within the accuracy of experiment) and the direction of any tie-line is defined by the alloy composition and the common point of tie-line intersections. This is the condition both for the ($\alpha + \beta$) and ($\beta + \text{TiCr}_2$) fields.

The three-phase field ($\alpha + \beta + \text{TiCr}_2$) was also located with the aid of lattice parameters. In this instance, two corners of the triangular-shaped field are substantially fixed at the same positions for all isothermal sections. The single variable is the corner identifying the composition of the β phase. Since

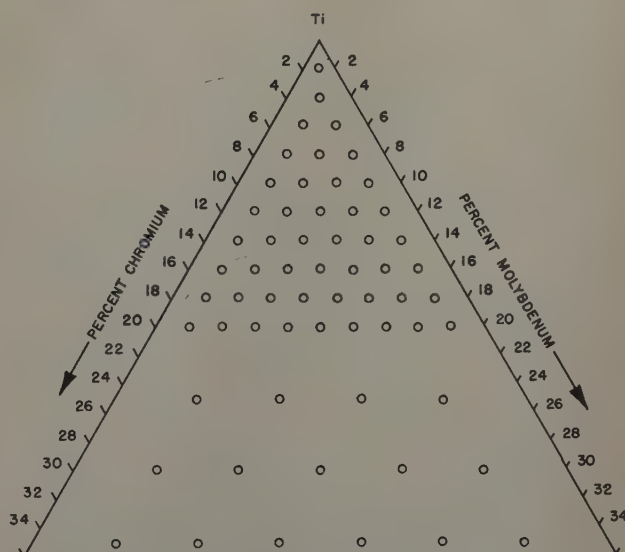


Fig. 1—Compositions of alloys melted.

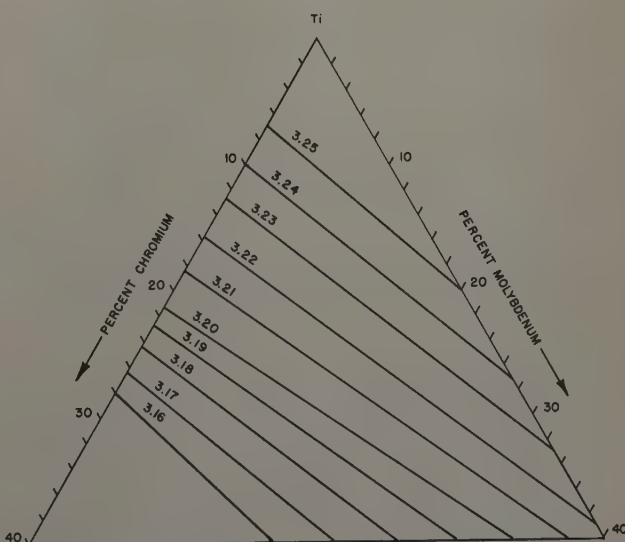


Fig. 2—Isoparametric contours of the β parametric surface.

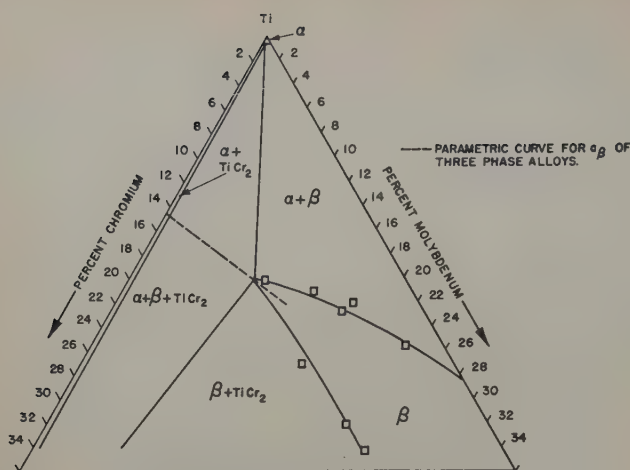


Fig. 3—Isothermal section at 600°C.

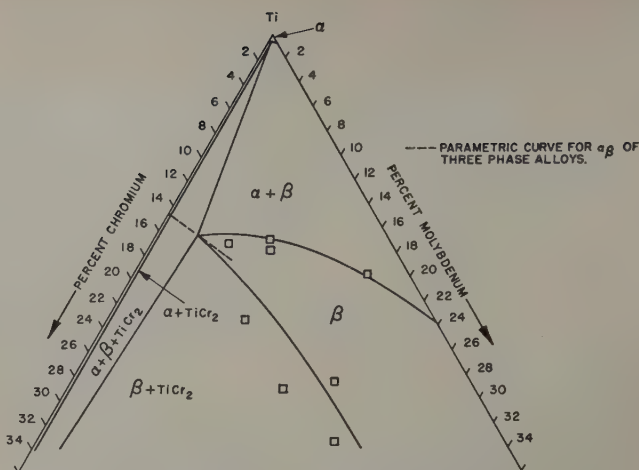


Fig. 4—Isothermal section at 650°C.

the composition of the β phase is invariant within the three-phase field, a number of alloys located within this field provide a best average value of the lattice parameter. Furthermore, since the three-phase field is the result of a eutectoid transformation, there is no vital necessity to approach complete equilibrium but only to insure complete rejection of proeutectoid phases. This is a considerable advantage because of the difficulty of recognizing the occurrence of three phases metallographically and because of the great sluggishness of the eutectoid transformation. The β corner of the three-phase field on any isothermal section is given by the intersection of the two boundaries $\beta/\beta + \text{TiCr}_2$ and $\beta/\alpha + \beta$ with the isoparametric line dictated by the best average lattice parameter for β in the three-phase field. These intersections are illustrated on the isothermal sections presented in the paper.

It is generally very difficult to measure the liquidus and solidus temperatures of refractory metal systems by thermal arrest methods. An approximation of the solidus temperature is achieved by the use of incipient melting techniques. In principle, sharp corners of small specimens are observed to round or collapse on heating to a temperature above the solidus at which sufficient liquid has formed to destroy the ability of the specimen to retain its external shape. When this observation is made with an optical pyrometer, the temperature at which incipient melting occurs can be measured concurrently. Specimens are suspended on a tungsten wire in a high temperature vacuum induction furnace. The design and operation of this unit have been described.¹² The incipient melting procedure was calibrated against a selection of pure metals with sufficiently diverse melting points that the correction curve covered the whole range encountered in the alloys under study. Thus, all corrections were based on interpolations.

Discussion of Phase Equilibria

As might be expected, the main points of question on the ternary equilibria are the rate of depression of the eutectoid ($\beta \rightarrow \alpha + \text{TiCr}_2$) temperature and the extent of the ($\beta + \text{TiCr}_2$) field.

Isothermal sections were constructed at 50°C intervals between 550° and 900°C, inclusive, and at

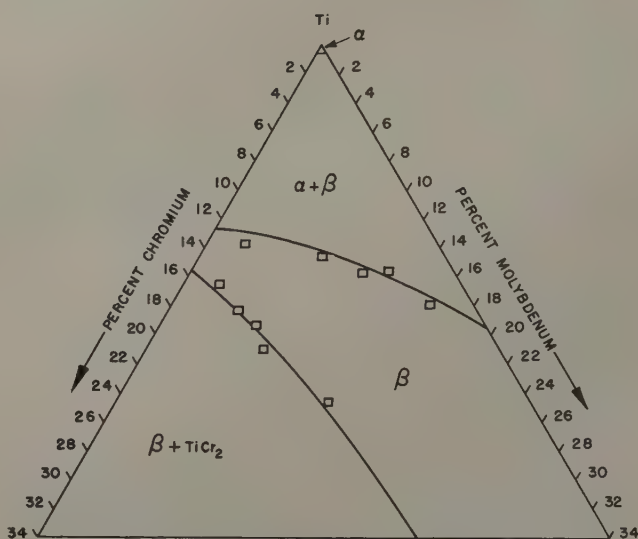


Fig. 5—Isothermal section at 700°C.

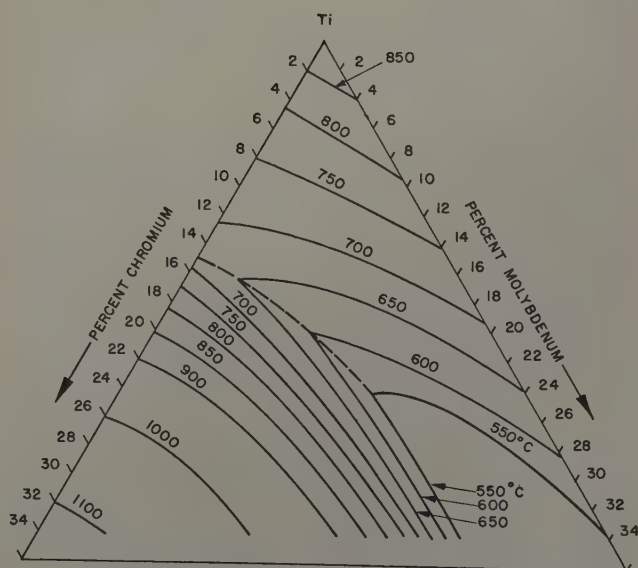


Fig. 6—Summary of β surface isotherms.

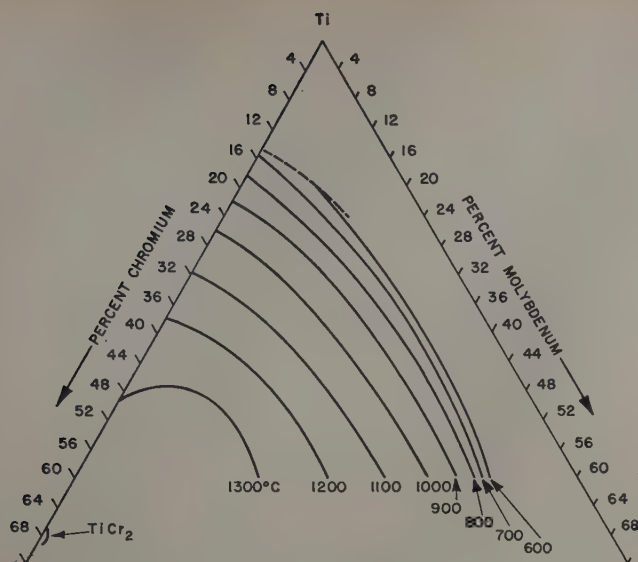


Fig. 7—Summary of $\beta/\beta + \text{TiCr}_2$ surface isotherms.

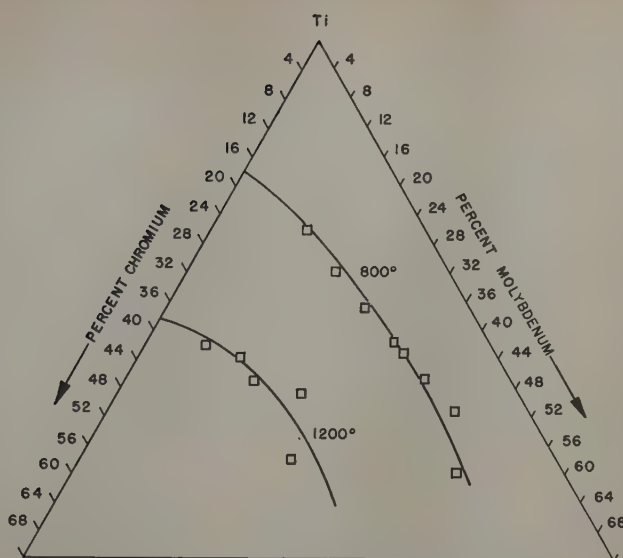


Fig. 8— $\beta/\beta + \text{TiCr}_2$ boundaries at 800° and 1200°C.

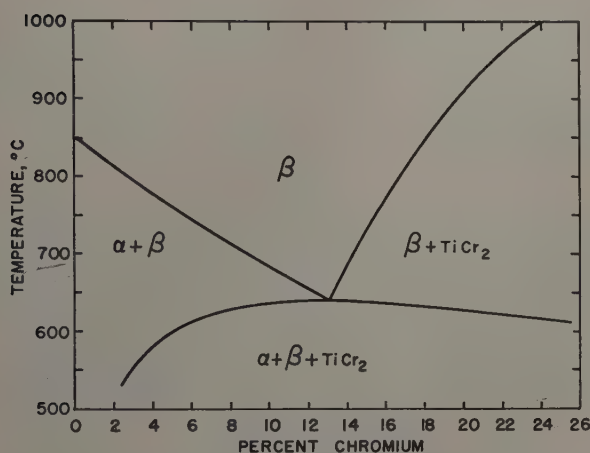


Fig. 9—Vertical section at 4 pct Mo.

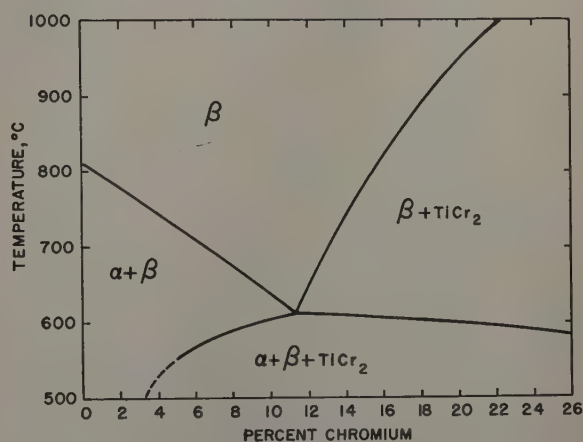


Fig. 10—Vertical section at 8 pct Mo.

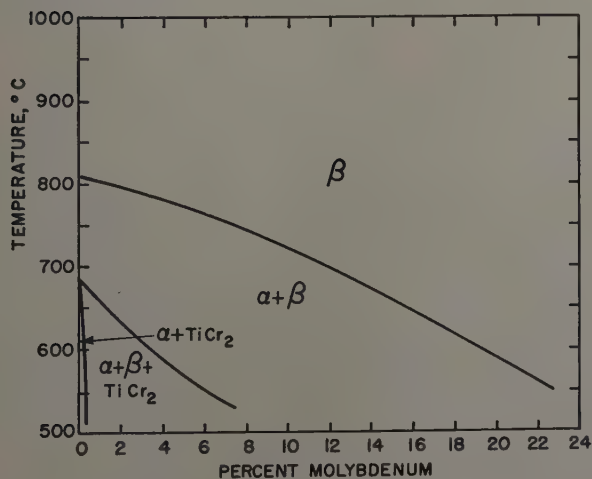


Fig. 11—Vertical section at 4 pct Cr.

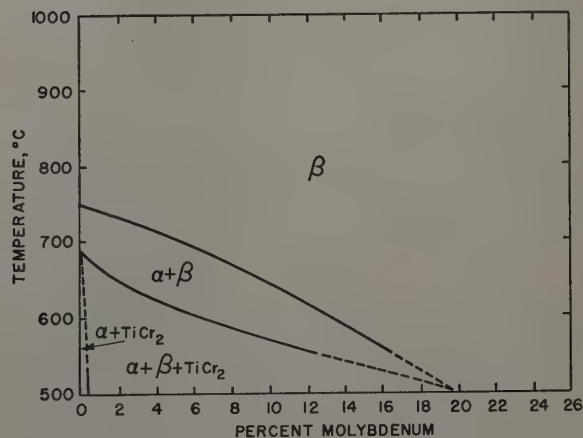


Fig. 12—Vertical section at 8 pct Cr.

100°C intervals between 900° and 1300°C, inclusive. Because of the insuppressible transformation $\beta \rightarrow \alpha'$ on quenching alloys of low chromium and molybdenum content, it was necessary to determine $\beta/\alpha + \beta$ boundaries at 800° and 850°C by metallographic means. Isothermal sections with the supporting data for the 600°, 650°, and 700°C levels

are shown in Figs. 3, 4, and 5. Fig. 6 presents a contour plan of the $\beta/\alpha + \beta$ and $\beta/\beta + \text{TiCr}_2$ surfaces and a projection of the course of depression of the eutectoid composition.

The ($\beta + \text{TiCr}_2$) field sweeps far into the composition triangle at lower temperatures. A compressed scale contour plan of the $\beta/\beta + \text{TiCr}_2$ surface is

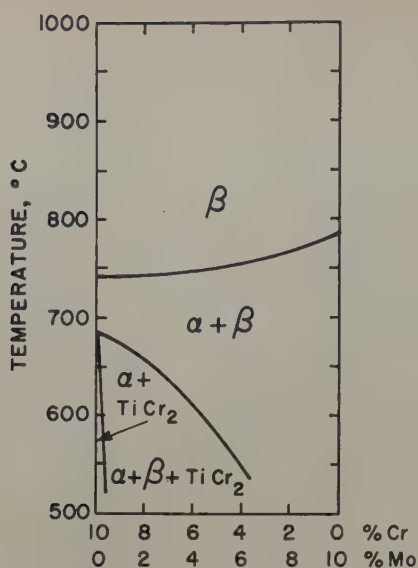


Fig. 13—Vertical section at 90 pct Ti.

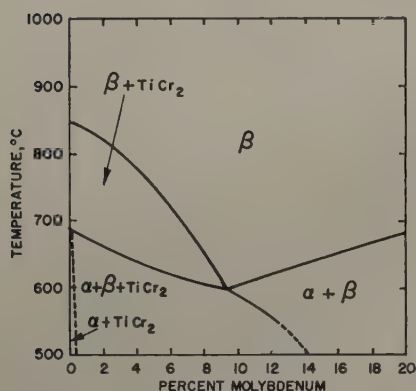


Fig. 14—Vertical section at 80 pct Ti.

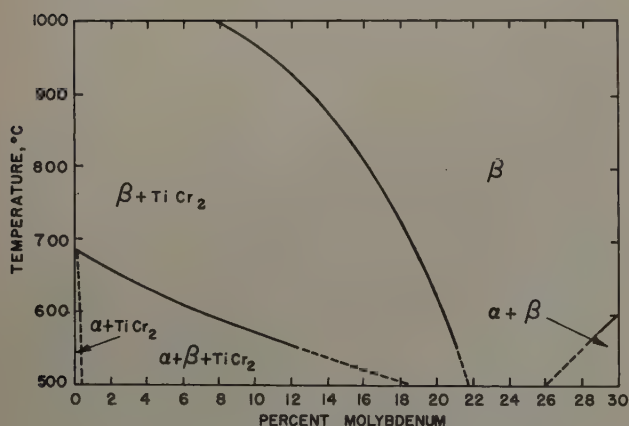


Fig. 15—Vertical section at 70 pct Ti.

given in Fig. 7. Data for the 800° and 1200°C boundaries are shown in Fig. 8.

The isothermal sections have been used to construct vertical sections along selected directions in the composition triangle. Vertical sections at 4 pct Mo, 8 pct Mo, 4 pct Cr, 8 pct Cr, 90 pct Ti, 80 pct Ti, and 70 pct Ti are shown in Figs. 9 to 15, respectively.

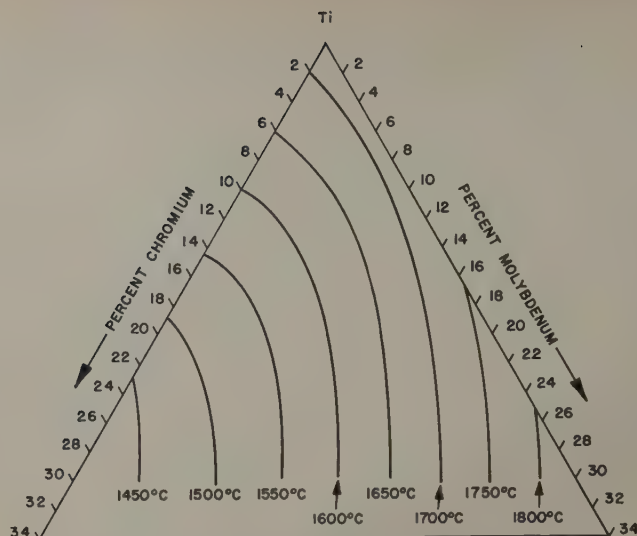


Fig. 16—Surface of incipient melting.

The incipient melting measurements for 23 alloys were used to construct the surface of incipient melting shown in Fig. 16. The method used was essentially the same as that used to construct a parameter surface.

Summary

1—The ternary equilibria of the Ti-Cr-Mo system has been investigated in the composition range .100 to 40 pct Ti and over the temperature range 550° to 1300°C.

2—The main features of the system are the depression of the binary eutectoid reaction ($\beta \rightarrow \alpha + \text{TiCr}_2$) and the extent of the ($\beta + \text{TiCr}_2$) space.

Acknowledgments

The authors wish to express their appreciation of the sponsorship of this work by the Ordnance Corps, U. S. Army, Watertown Arsenal, Watertown, Mass., and for their permission to publish this paper which is based on work on Contract DA-11-022-ORD-272.

References

- ¹R. Vogel and B. Wenderott: *Arch. Eisenhüttenwesen* (1940) **14**, p. 279.
- ²C. M. Craighead, O. W. Simmons, and L. W. Eastwood: *Trans. AIME* (1950) **188**, pp. 485-513; *JOURNAL OF METALS* (March 1950).
- ³M. K. McQuillan; *Journal Inst. Metals* (1951) **79**, pp. 379-390.
- ⁴P. Duwez and J. L. Taylor: *Trans. ASM* (1952) **44**, pp. 495-513.
- ⁵R. J. Van Thyne, H. D. Kessler, and M. Hansen: *Trans. ASM* (1952) **44**, pp. 974-989.
- ⁶F. B. Cuff, N. J. Grant, and C. F. Floe: *Trans. AIME* (1952) **194**, pp. 848-853; *JOURNAL OF METALS* (August 1952).
- ⁷A. D. McQuillan: *Journal Inst. Metals* (1951-1952) **80**, pp. 363-368.
- ⁸B. W. Levinger: *Trans. AIME* (1953) **197**, p. 196; *JOURNAL OF METALS* (February 1953).
- ⁹M. Hansen, E. L. Kamen, H. D. Kessler, and D. J. McPherson: *Trans. AIME* (1951) **191**, pp. 881-888; *JOURNAL OF METALS* (October 1951).
- ¹⁰P. Duwez: *Trans. AIME* (1951) **191**, pp. 765-771; *JOURNAL OF METALS* (September 1951).
- ¹¹A. G. H. Andersen and E. R. Jette: *Trans. ASM* (1936) **24**, pp. 375, 519.
- ¹²M. Hansen, H. D. Kessler, D. J. McPherson: *Trans. ASM* (1952) **44**, p. 518.

Discussion — Iron and Steel Division*

St. Louis Meeting, February 1951

Effect of Manganese on the Activity of Sulphur in Liquid Iron and Iron-Carbon Alloys (paper by J. P. Morris. JOURNAL OF METALS, September 1952, p. 939)	1549
New York Meeting, February 1952	
Liquidus Surface of the Fe-S-O System (paper by D. C. Hilty and Walter Crafts. JOURNAL OF METALS, December 1952, p. 1307)	1549
Los Angeles Meeting, February 1953	
Attainment of Equilibrium in Gas-Metal Reactions (paper by N. A. Gokcen. JOURNAL OF METALS, February 1953, p. 191)	1550
Thermal Conductivity Method for Analysis of Hydrogen in Steel (paper by B. M. Shields, J. Chipman, and N. J. Grant. JOURNAL OF METALS, February 1953, p. 180)	1551
Use of Oxygen in the Bessemer Converter (paper by W. T. Rogers and L. T. Sanchez. JOURNAL OF METALS, September 1952, p. 933)	1551
Evaluation of the pH and Conductivity Methods of Slag Control (paper by P. D. S. St. Pierre. JOURNAL OF METALS, January 1953, p. 41)	1552
Accelerated Solidification in Ingots: Its Influence on Ingot Soundness (paper by E. Marburg. JOURNAL OF METALS, February 1953, p. 157)	1553

* TP 3655C.

Effect of Manganese on the Activity of Sulphur in Liquid Iron And Iron-Carbon Alloys

by J. P. Morris

DISCUSSION, W. O. Philbrook and John Pollock
presiding

N. A. Gokcen (Michigan College of Mining and Technology, Houghton, Mich.)—The author should be congratulated for this and other careful investigations^{1,2} on the activity of sulphur in liquid iron alloys.

The activity coefficient of sulphur, represented by γ' for the system Fe-S, is very close to unity for the range of sulphur covered in this investigation. The overall coefficient γ in Fe-S-C-Mn can be calculated from the data on simpler systems Fe-S-C and Fe-S-Mn by using the following relation:^{6,7}

$$\gamma = \gamma_c \cdot \gamma_{Mn}$$

where γ_c and γ_{Mn} are the coefficients due to the effects of carbon and manganese in Fe-S-C and Fe-S-Mn, respectively. γ_c is given in the last column of Table I; γ_{Mn} is determined experimentally for test No. 134, and for the other tests, it can be calculated for a small variation of manganese from 1.8 to 2.8 pct by using either a straight line plot of $\log \gamma_{Mn}$ vs pct Mn, or the equation $\gamma_{Mn} = 1 - 0.10 (\text{Mn}\%/2)$, where -0.10 is the decrease in γ_{Mn} from 1.00 to 0.90 for an increase of Mn from 0.0 to 2.0 pct.

Table II gives the calculated values of γ_{Mn} and γ , and shows that the agreement between the calculated and reported values of γ is very good.

It is reported that manganese evaporates rapidly from the melt, though the data on the rate of vaporization is not given. Calculations from the available thermodynamic data⁸ give a vapor pressure of 1.06×10^{-8} atm at 1600°C for manganese in iron at a concentration of 2.0 pct if it is assumed, in view of the atomic

Table II. Calculated Values of γ_{Mn} and γ

Test No.	γ_c	γ_{Mn}	γ in Fe-S-C-Mn	
			Calculated	Reported
134	1.00	0.90	0.90	0.90
127	1.95	0.91	1.77	1.77
126	3.71	0.86	3.20	3.32
125	6.51	0.86	5.60	5.55

similarities of these metals, that iron and manganese form an ideal solution. If the rate of bubbling helium was 1 liter per min, then the maximum rate of loss should be 0.31 pct Mn per hr from the melt. It would be interesting to know how this calculation compares with the author's observations.

J. P. Morris (author's reply)—In test 134, the rate of manganese loss from the melt by volatilization was 0.20 grams per hr, as compared with the theoretical rate of 0.14 grams per hr, assuming ideal solution behavior. The closeness of agreement between these two values suggests that the bubbling technique used in the experiments may be a very satisfactory method for determining vapor pressures and activities of certain alloying elements in liquid iron.

It is also of interest to note that with melts containing carbon, manganese was volatilized at a slower rate. At carbon saturation the rate was roughly one-third that for the carbon-free metal.

⁶ J. Chipman: Discussions of the Faraday Soc. (1948) No. 4, p. 23.
⁷ N. A. Gokcen and J. Chipman: Trans. AIME (1952) 194, p. 171; JOURNAL OF METALS (February 1952).

⁸ National Bureau of Standards, Circular 500 (1952).

Liquidus Surface of the Fe-S-O System

by D. C. Hilty and Walter Crafts

DISCUSSION, G. Derge and D. J. Girardi presiding

N. A. Gokcen (Michigan College of Mining and Technology, Houghton, Mich.)—While the authors present very interesting results on the effect of sulphur

upon the solubility of oxygen, they have not established convincingly the lines of two-fold saturation (the valleys in Fig. 2) and the ternary eutectic point. Their contention that sample S-7, upon melting at

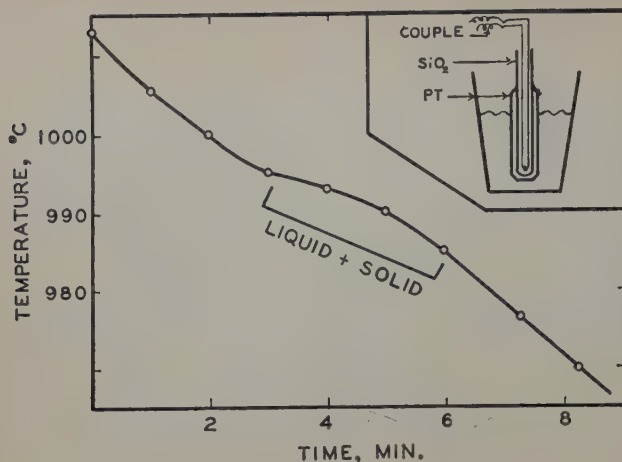
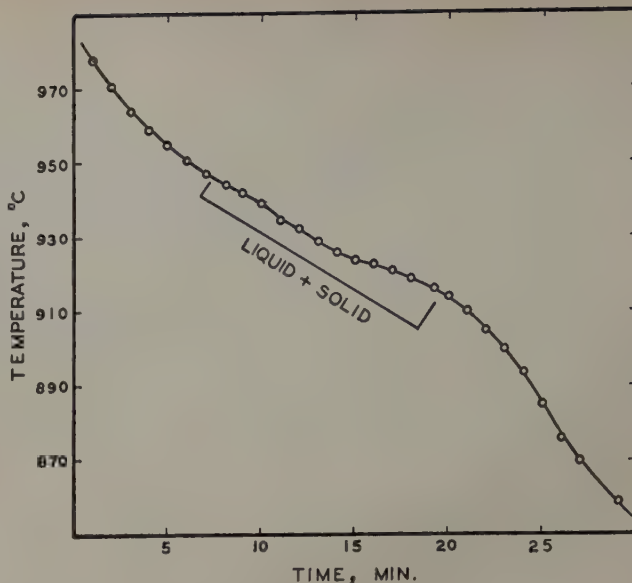


Fig. 7 (above)—Cooling curve, run A. Insert shows the crucible assembly.

Fig. 8 (right)—Cooling curve, run B.

925°C, contained only the ternary eutectic cannot be conclusive on the sole basis of microscopic examination. Further evidence such as the cooling curves of various mixtures are necessary in order to establish the ternary eutectic point.

The two runs, presented in this discussion, were made under the conditions outlined by the authors in order to obtain the cooling curves shown in Figs. 7 and 8. Run A consisted of 25 grams of the initial charge analyzing as mixture S-7, but melted in a platinum crucible. The thermocouple protection tube, inserted in a tightly fitting platinum protection tube, was used to stir the charge. Platinum was slightly attacked by the molten charge. Fig. 7 shows that the mixture did not indicate the presence of a measurable amount of ternary eutectic which should freeze at a constant temperature. Run B, Fig. 8, analyzing the same as the eutectic point *E* (67.3 pct Fe, 23.7 pct S, and 9.0 pct O) also failed to establish the eutectic point. Thus it is questionable that the two-fold saturation lines, hence the eutectic point, presented in this



paper are an improvement over those of Vogel and Fulling.⁵

D. C. Hilty and Walter Crafts (authors' reply)—The authors appreciate Dr. Gokcen's interest in this work. It is apparent, however, that taken at their face value his results are as inconsistent with those of Vogel and Fulling as with those of the present paper. Evaluation of Gokcen's results without analyses, microstructures, and better description of his samples is rather difficult. When mixtures of iron oxide and iron sulphide are melted in the absence of a considerable excess of metallic iron, as, for example, in a platinum crucible, extensive oxidation of the sulphide occurs unless very high SO_2 pressures are maintained, so that the ultimate composition of the melt may be at rather wide variance with the starting composition. It seems probable, therefore, that Gokcen's samples deviated significantly from compositions that would contain substantial amounts of the ternary eutectic. It appears that additional work and review of Gokcen's procedure are required before critical comment is possible.

Attainment of Equilibrium in Gas-Metal Reactions

by Nev A. Gokcen

DISCUSSION, G. Derge presiding

J. P. Morris (Pyrometallurgical Branch, U. S. Bureau of Mines, Pittsburgh)—The discussion in this paper calls attention to the effectiveness of the bubbling technique as a means of attaining the maximum rate of approach to equilibrium in studies of gas-metal reactions. To anyone who may be interested in using this method, I would like to point out that only a very shallow immersion of the tip of the bubbling tube is necessary. In our experiments, the depth of immersion was adjusted to the point where there was good agitation of the metal but little or no splashing. When immersion was too deep, violent splashing of the metal resulted. To use a deeper immersion, it would be necessary to cover the crucible and to maintain crucible, lid, and metal at a uniform temperature.

W. O. Philbrook (Carnegie Institute of Technology, Pittsburgh)—Dr. Gokcen's paper should be very helpful in planning experiments to obtain equilibrium data for certain reactions in which one of the reactants is added or removed from the system continuously and where the rate of supply of this reagent effectively limits the overall process in the manner of a pseudo-first-order reaction. In oral discussion of the paper,

Dr. Gokcen stated that this was not a "kinetic" approach but a "thermodynamic" one; a better word might have been "stoichiometric." Regardless of the viewpoint, the treatment is based on the kinetic relationships for first-order chemical reactions, and its use is therefore valid only for reactions which follow such behavior. The applications shown all involved gaseous reagents where presumably only one atom from a molecule of the gas participated in the reaction. For any new reaction, Dr. Gokcen's equations should be used with caution, for qualitative predictions only, until their validity has been established for the particular reaction in question. Subject to these precautions, Dr. Gokcen's equations should be useful in estimating the time required to attain equilibrium or the possibility of shortening the time of experiment by changing some of the conditions.

N. A. Gokcen (author's reply)—The author is indebted to the discussers for their valuable remarks.

It will be reported in a forthcoming paper that, in complete agreement with Mr. Morris' observations, the bubbling tube should be immersed approximately 2 to 3 mm as measured indirectly with a manometer indicating the pressure of gas.

Professor Philbrook's discussion, stressing the limitations of the derived equations, is very important in avoiding overdrawn conclusions regarding reaction rates at steelmaking temperatures. These limitations are the natural consequence of the fact that the calculated time is the minimum time, which appears to have been realized under certain conditions described in this paper.

In order to calculate the minimum time, it is necessary to assume that the outlet gas reaches equilibrium with respect to concentration of dissolved element at any time. The treatment is therefore based upon thermodynamic and stoichiometric limitations expressed in Eq. 6, and not on the order of reaction with respect to the gas phase or the dissolved elements in liquid iron.

Thermal Conductivity Method for Analysis of Hydrogen in Steel

by Bruce M. Shields, John Chipman, and Nicholas J. Grant

DISCUSSION, G. Derge presiding

R. L. Bohon and Scott Anderson (*The Anderson Physical Laboratory, Champaign, Ill.*)—The thermal conductivity method of hydrogen analysis in metals has been used in this laboratory with excellent success for almost a year. The apparatus and procedure are based on the M.I.T. design, but a few modifications have been made which simplify construction and eliminate some of the disadvantages of a single-station thermal conductivity cell.

A two station Pirani gage (type P G-1A, Distillation Products, Inc.) was utilized for thermal conductivity measurements. This unit consists of two identical tubes, one under permanent high vacuum and the other attached to the system. The two tubes are mounted side by side to reduce the chance of temperature differences. In operation one merely adjusts the voltage drop across the system tube to a constant value (3.0 v) and reads an ammeter which is calibrated directly in units of air pressure. The gage must be calibrated before analysis with pure N_2 and H_2 and the ammeter readings used merely as an index of gas thermal conductivity.

This type of gage has the advantage of being independent of room temperature fluctuations and therefore eliminates the necessity of using a constant temperature bath on the conductivity cell itself. This in turn eliminates the annoying mercury condensation mentioned by Shields et al. on the chilled walls of the cell and permits one to do away with the cold trap just preceding the cell. The difficulty of maintaining precisely constant volumes of the trap and cell at constant temperature throughout a day's operation can be readily eliminated by this simple substitution of thermal conductivity measuring device.

Another advantage of the Pirani gage is that sudden evacuation of the system does not cause great changes in filament temperature and there is little or no chance of overheating the wire such as is the case with the single filament gage described by Shields et al. Even a break in the system and consequent subjection to an

atmosphere of air can be tolerated for a short time without damaging the Pirani gage.

When using a commercial Pirani gage one must take into account that the upper limit of the ammeter scale usually corresponds to about 0.25 mm hydrogen and therefore the McLeod gage must be capable of reading low pressures quite accurately. Our gage covers the range from 10^{-6} to 2.0 mm Hg in two stages (10^{-6} to 0.12 mm and 0.12 to 2.0 mm). The volume of our system is somewhat larger than that of the M.I.T. apparatus to compensate for the lower maximum pressures which can be tolerated ($V_1 = 1346$ ml, $V_2 = 1701$ ml). On the other hand this low pressure sensitivity is quite advantageous when analyzing specimens of low hydrogen content.

A liquid nitrogen or dry ice-acetone trap has been added just prior to pump H_2 in order to freeze out any water vapor evolved during analyses. The trap is not cooled during the baking-out period. The use of this trap has materially reduced and stabilized blanks. Since it is not in the analytical portion of the system, its maintenance is not critical.

B. M. Shields, J. Chipman, and N. J. Grant (authors' reply)—Elimination of the cold trap preceding the thermal conductivity gage and operation of the gage itself at room temperature instead of at 0°C are quite possibly worthwhile advantages. However, it would appear that restriction of the hydrogen pressure to values less than 0.25 mm of helium is rather disadvantageous. At such low pressures, the thermal conductivity is extremely sensitive to pressure thus requiring extremely accurate pressure readings. We would prefer to work at considerably higher pressures, on the order of 1 to 2 mm of helium, and are redesigning our equipment to work in this range. The advantage of higher pressure operation is that less sensitive pressure readings are necessary due to the facts that pressure influences the thermal conductivity to a lesser extent and the difference between the thermal conductivity of hydrogen and nitrogen is substantially increased.

Use of Oxygen in the Bessemer Converter

by W. T. Rogers and L. T. Sanchez

DISCUSSION, H. P. Rassbach presiding

J. F. Elliott (*Inland Steel Co., East Chicago, Ind.*)—The authors are to be commended on the work reported here. They have utilized oxygen in their production efforts in a very intelligent manner in order to solve their problem of a variable supply of hot metal.

Fundamentally the addition of oxygen to the blast should have two major effects: 1—to increase the rate of oxidation because of the higher partial pressure of oxygen in the system, and 2—with a given system to

increase the amount of heat available either to raise the temperature of the bath or to melt cold materials. This latter effect results because proportionally less nitrogen passes through the vessel. It must be recognized, however, that in an operation of this type many factors may come into play which tend to obscure the direct observation of these basic effects.

It is of considerable interest to note that the time for the introduction of oxygen during the heat influences the ability to melt scrap. Oxygen added early in

the blow when silicon is being removed is not as efficient as is the same addition when carbon is being removed. Can this be interpreted to mean that oxygen carried through the bath and into the atmosphere of the vessel oxidizes CO to CO₂ during the carbon blow and thereby develops more heat in the upper part of the vessel?

There are some metallurgical questions which arise from the statistical treatment. The authors state "... the total heat produced is dependent on the composition of the iron rather than on increased amount of oxygen in the blast." This is true but the factor of significance is the available heat for melting scrap which is both a function of metal composition and the actual amount of nitrogen passing through the vessel. Nitrogen acts as a coolant and the amount is directly influenced by the oxygen concentration in the blast. Metallurgically one may expect the following factors to be interrelated: 1—metal composition; 2—concentration of oxygen in the blast, and actual total oxygen in the blast; 3—blowing time; 4—scrap melting ability; 5—tapping temperature; 6—charge weight; 7—vessel temperature; 8—metal temperature; and 9—miscellaneous factors. For example statistically it has been shown that an increased scrap charge shortens blowing time. The effects are rather complex. With a fixed tapping weight and with an increased proportion of scrap added, there will be less metalloids to be oxidized. Thus scrap acts as a diluent. Greater additions of oxygen should decrease the time for the removal of a given amount of metalloids. A faster refining time will reduce proportionately the heat losses so that more scrap can be melted because of the greater amount of available heat.

The point being made here is to repeat that old axiom that a statistical study of this type must be based on sound metallurgical principles and the results

must be interpretable by reasonable metallurgical thinking.

Do the authors have data on how this practice influences the nitrogen level in the steel?

This paper is of considerable interest and the authors are to be congratulated on making such a practical application of this relatively new raw material, commercially pure oxygen.

W. T. Rogers and L. T. Sanchez (authors' reply)—We wish to thank Mr. Elliott for his interesting comment on our paper. In general, it can be stated that the object of the paper was to show what happens with respect to scrap melting capabilities of the process when oxygen is introduced into the bessemer blast rather than why it happens. The reactions of oxidation, reduction, heat transfer, and combustion zones within the vessel were recognized as being too complex to lend themselves to explanation by a production experiment such as the one presented.

With respect to the efficiency of oxygen during the blow, it has been found on a previous experiment that the waste gases at the converter nose have a larger proportion of free oxygen present during the period of silicon removal than during the carbon removal period. It is therefore highly probable that CO is further oxidized to CO₂ in the vessel thus developing more heat during this phase of the process.

The statement that "the total heat produced is dependent more on the composition of the iron than on increased amount of oxygen in the blast" was made as a generally accepted theory. In this discussion, however, it may be interpreted as indicating that for a given practice with respect to oxygen and scrap charged the final teeming temperature is dependent on iron chemistry, particularly the silicon content.

With respect to the nitrogen level in the steel, Table IV in the paper shows no significant difference between the regular practice and the oxygen practice at the oxygen level used.

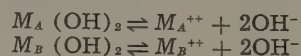
Evaluation of the pH and Conductivity Methods of Slag Control

by P. D. S. St. Pierre

DISCUSSION, C. M. Squarcy presiding

C. E. A. Shanahan (*British Iron and Steel Research Association, Sheffield, England*)—In view of the general increased metallurgical load to basic open hearth furnaces it is now essential more than ever to perform the necessary refining operations in the bath with a minimum of slag bulk. Consequently, attention has been drawn to methods of slag control and thus the subject of the author's paper is of great topical interest. The use of a pH or electrical conductivity measurement on the aqueous extract of a powdered slag sample as a measure of basicity is very attractive because its determination is rapid; it may be used to give data on the composition of slags before they have had time to change significantly in composition in the furnace. In this way a valuable guide is provided to further bath additions. The errors involved with this technique, such as those arising from the method of taking the slag sample, the compounds present, the specific surface area of the sample, time of extraction, etc., have often been superficially discussed but never examined in such detail as that given by the author. He shows that the equilibrium pH depends on the most easily hydrolyzable compound present, and is not a function of the amount. In this connection it is of interest to consider theoretically the equilibrium pH obtained from the presence of two pure oxides M_AO and M_BO . The action of water is presumably to convert the exposed parts of these oxides to hydroxides; the hydroxyl

ion concentration (and hence the pH) is then controlled by the equilibria.



If S_A and S_B are the solubility products of the two hydroxides

$$\begin{aligned}[M_A^{++}][OH^-]^2 &= S_A \\[M_B^{++}][OH^-]^2 &= S_B\end{aligned}$$

$$\text{i.e., } \{[M_A^{++}] + [M_B^{++}]\} [OH^-]^2 = S_A + S_B \quad [1]$$

It is reasonable to assume that any dissolved hydroxide is completely dissociated. Thus any M_A^{++} or M_B^{++} ion will contribute $2[OH^-]$, neglecting OH ions produced by $H_2O \rightleftharpoons H^+ + OH^-$ the total OH concentration will be $2\{[M_A^{++}] + [M_B^{++}]\}$

$$\text{i.e., } \{[M_A^{++}] + [M_B^{++}]\} = \left[\frac{OH^-}{2} \right]$$

Hence, Eq. 1 becomes

$$[OH^-]^3 = 2(S_A + S_B)$$

also

$$[H^+][OH^-] = 10^{-14} \text{ (ionic product for water)}$$

Hence

$$\frac{10^{-14}}{[H^+]^3} = 2(S_A + S_B)$$

$$\text{giving pH} = 14.1 + \frac{1}{3} \log_{10} (S_A + S_B) \quad [2]$$

If only one hydroxide (say, $M_A(\text{OH})_2$) is present a similar treatment yields

$$\text{pH} = 14.1 + \frac{1}{3} \log_{10} S_A \quad [3]$$

Eqs. 3 and 2 show the effect on the pH value of increasing the number of hydroxides in the system from one to two. If S_A is the greater solubility product (i.e., of the more soluble of the two hydroxides), then providing S_B is small by comparison, $S_A + S_B \sim S_A$ and the pH of the two hydroxide solutions is equal to that with $M_A(\text{OH})_2$ alone. The maximum divergence between the pH values of the two solutions occurs when S_B approaches the value of S_A . This corresponds to a

difference of approximately 0.10 in pH value, i.e., the pH value of the aqueous extract from the two hydroxides together is 0.10 higher than those of the separate hydroxide solutions. In the case of three hydroxides of approximately equal solubility products, the pH of the aqueous extract obtained from a mixture of the three hydroxides together is approximately 0.16 greater than that from one of the hydroxides separately, i.e., the difference in pH becomes larger as the number of hydroxide species is increased. Similar results can be obtained when hydroxides of metals of different valencies are considered. In general, of course, the solubility product of one of the hydroxide species will be greater than those of the others and any effects of the latter on the over-riding pH of the most soluble hydroxide will be well within experimental error, a conclusion compatible with the experimental findings.

Accelerated Solidification in Ingots: Its Influence on Ingot Soundness

by Edgar Marburg

DISCUSSION, C. M. Squarcy presiding

E. A. Loria (*The Carborundum Co., Niagara Falls, N. Y.*) and **R. L. Keller** (*Vanadium-Alloys Steel Co., Detroit*)—The author is to be congratulated for this outstanding paper which has been long awaited and which is a truly significant contribution to the subject. It is indeed difficult to find any real point of contention with the interpretation of the data. The only alternative is to ask questions which will amplify the scope of the paper and thus obtain the benefit of the author's thoughts and experience.

Mr. Marburg has described and shown that a major defect in killed steel ingots is center porosity revealed as a series of shrinkage voids at the axis of the ingot and extending from within a foot of the hot-top junction to within a foot of the bottom. Some investigators have called it a "chevron" or "herringbone" structure and believe that the series of V-shaped cavities appear to indicate some periodicity in the freezing process. Fig. 27 is a severe case of this defect which occurs in ingots of intermediate size, 15 to 25 in. width.

What practical suggestions can be offered to avoid axial porosity in the present, conventional ingot designs of this size? Would the author go along with the thinking that V segregate and axial porosity may be decreased to a minimum while keeping the transverse cooling rate the same by, 1—increasing the vertical cooling rate, 2—increasing mold wall taper, or 3—decreasing height of ingot with respect to width? The second and third factors would involve decreased ingot yield, greater mold costs per ton of ingots produced, and awkward ingot handling (soaking pit hogs) which would tend to discourage their consideration. The first factor would be produced by using water-cooled stools, better contact between mold and stool, increased stool size, and heavier bottoms on molds.

The exaggerated axial porosity in the alloy steel (AISI 4340) ingot shown in Fig. 27 can be compared with the completely sound plain carbon steel (AISI 1020) ingot shown in Fig. 9. Would the author attribute the difference to the effect of the alloy content in stiffening the dendrites or crystals which bridge across the unsolidified center portion of, and prevent the feeding of, hot-top metal into the interior of the ingot? In this regard, it would have been valuable to have had the complete longitudinal section for the 32 in. ingot of 2.08 pct Ni steel for which the dumping tests were made. Also, would the author comment on the effect of undercooling for the formation of columnar crystals and the undercoolability of the steel itself on the incidence of axial porosity?

By increasing the vertical freezing rate with respect

to the transverse, one would expect to obtain better feed from the hot top and hence a sound center in the ingot. However, in cases where the center of the ingot is to be bored in a subsequent processing operation, it would be advantageous to concentrate the V segregate in that area. Shrinkage due to long feeding distance and segregation is most pronounced in the long, narrow ingots shown in Fig. 22. In the more appropriate ingot sizes, 18 to 25 in. by 72 to 80 in. high, would not the pouring of cold metal from the furnace contribute to the formation of center porosity? Indeed, the author's conclusion on the ineffectiveness of the mold-wall taper is somewhat surprising. Usually, the V segregate has been shown to be minimized by increasing the taper on the ingot body to allow better shrinkage conditions. In certain forging ingot designs, an increase in the taper from top to bottom of the mold from 0.3 to 0.5 in. per ft has resulted in a considerable reduction in the frequency of occurrence and seriousness of center porosity.

From Marburg's calculations, it can be shown that complete solidification occurs vertically rather than transversely at a height of 65 in. for big-end-up ingots over 18 in. wide and in big-end-down ingots over 21 in. wide. The zone of negative segregation is believed to be the result of the vertical solidification of purer metal in the lower part of the vertical core. If the center of the ingot remains at nearly a constant temperature and if the liquid ahead of the transverse liquid-solid interface is of average or less pure composition, how can this be explained? Does the author believe that convection currents in the liquid metal may play a part in the formation of this zone? Also, it is noteworthy that inferior mechanical properties are obtained from transverse test specimens taken from the bottom third of forging ingots. These may not be so much related to the amount of inclusions as to the distribution of the inclusions.

The outer layers of inverted-V segregate are formed prior to acceleration of transverse solidification and therefore cannot be caused by the same mechanism found to cause the inner segregated streaks. Marburg accounts for these outer layers by postulating that segregation could rise readily from the upper side, but not from the lower side of a penetrating dendrite. The penetration of the long columnar crystals affords a preferred path for heat flow permitting solidification to occur upwardly in advance of the segregated layers and thus entrap them. On the basis of work done on gases in steel, could not these inverted-V streaks possibly be the result of gas evolution in the ingot?

Would the author comment on the effect of modifying the air gap between ingot chill skin and the mold wall,

brought about by the contraction of the solid skin and the expansion of the mold itself, on ingot structure based on relative rate of solidification? This change in the wall of the ingot, from being in contact with a surface which is conducting heat away rapidly, to contact with gases which are relatively nonconducting, alters the temperature gradient between the center of the ingot and the outside so that reheating of the outside of the ingot takes place by conduction from the hotter molten metal in the center causing a further tendency to expansion. This occurrence has produced corner weakness or tearing along segregate lines and some producers of forging ingots have considered heating molds locally on the outside, at the position where they occur, in order to expand the mold prior to teeming. Also progressively filling the mold wall-ingot skin with molten lead in order to give some support to the ingot chill skin and eliminate the nonconducting gaseous layer has even been suggested.

Elis Helin (*Elektriska Svetsningsaktiebolaget, Göteborg, Sweden*)—In his very interesting contribution to our hitherto limited knowledge on the solidification of steel ingots, Mr. Marburg reproduces a number of sulphur prints and macroetch figures, valid for fairly large ingots. Particularly the sulphur prints give good information on the lamellar segregation, while the macroetch figures reproduced do not reveal much about the details of the etching results of the ingots they represent.

The etch picture reproduced in Fig. 17 is, as far as I can understand, intended to show the freezing or the primary structure of a 29x66 in. large ingot of semi-killed steel with a carbon content of 0.24 pct. However, certain features of this figure make it doubtful that Fig. 17 really shows a primary structure. Rather it appears to show a transformation structure, a type which is usually called a secondary structure, the lowest part of the figure giving the impression that the macroetch contains longish crystals, which in the inner part of the ingot are continuously sloping upward. This fact is the reason for doubting that Fig. 17 shows a primary structure.

According to Hultgren¹⁵ longish crystals are not always primary crystals, but can be the result of a transformation in the solid state. In steel, freezing as δ iron and thereafter transforming into γ iron, a structure can arise which can be confused with a freezing structure. This transformation structure is distinguished by continuously bent crystals, and the bending is caused by the growing crystal accommodating to the form of the existing isotherm of the transformation. A primary crystal on the contrary continues to grow in the direction started and grows until it is stopped by other crystals. Thus a primary crystal, contrary to a secondary one, does not change its direction of growth through any alteration of the shape of the solidification isotherm. In the corners of the ingots the primary crystals grow rectilinearly until they meet crystals from the other side of the diagonal plane. Therefore the patterns of the two types of structure generally do not coincide.

On p. 163, Mr. Marburg says: "Above line *ada* vertical columnar crystals slope inwardly, which indicates that transverse components of heat extraction became effective along this line." Just this slope inwardly proves that Fig. 17 most probably shows a transformation structure. A steel containing 0.24 pct C starts its solidification with the precipitation of δ iron, this phase later being transformed to γ iron and forming secondary crystals. Despite lack of knowledge of the etching solution used, one cannot avoid the impression that Mr. Marburg transfers conditions that are valid for the solid state to the transformation of the liquid-solid. Since it is not plainly stated that Fig. 17 really reproduces the primary structure, statements regarding a bottom base cone have no reality.

When ingots of the sizes discussed by Mr. Marburg solidify in a normal way one first gets a thin layer of

columnar crystals and thereafter a thicker layer of columnar crystals. Inside this layer of columnar crystals we have the equiaxed crystals. Under normal pouring conditions the thickness of the layer of the columnar crystals probably will not exceed, let us say, 30 pct of the thickness of the ingot width. In large ingots the layer probably is thinner. The existence of a bottom base cone, built up by columnar crystals, therefore seems to be improbable. If on etching one cannot reveal a bottom base cone, the heat extraction seems to follow such rules as if a cone did exist. Mr. Marburg's investigation reveals evidently that, since a certain time has elapsed, the rate of solidification is accelerated not only in the vertical direction but also in the transverse one. The start of this acceleration must not be associated with a change in the type of crystallization. Here the statement from p. 163 seems to be sufficient. Very important both from theoretical and practical points of view is his conclusion that certain ingots can complete the solidification vertically, instead of the old assumption that solidification in normal ingots always is completed transversely, and also his statement that this depends on the ratio w/h .

As an explanation of the origin of the outer lines of inverse-V segregation the following can be suggested: According to the statement on p. 167 that the lines of inverse-V segregation start at the same depth and the fact that the solidified layer in the ingots investigated according to Figs. 6, 7, and 15 has a uniform thickness up to about 80 min after pouring, one is inclined to assume that these outer lines of inverse-V segregation originate from the transition from columnar crystallization to the formation of equiaxed crystals.

Adjacent to the columnar crystals one has through the selective freezing a liquid segregated layer, separating columnar crystals and the purer inner liquid, and in this segregated liquid layer the temperature for the formation of nuclears is much lower than in the liquid steel where equiaxed crystals are formed. If nuclears for equiaxed crystals have been formed and they have started to grow, diffusion from the segregated liquid layer is stopped. This impure liquid material therefore solidifies later than the inner liquid steel and will appear in the solidified ingot in the shape of lamellar segregations.

Edgar Marburg (author's reply)—The kind remarks of Messrs. Loria and Keller are greatly appreciated. I have attempted to answer their questions in tabulated form below.

Effects of Various Factors on Axial Porosity in Ingots:

1—Increase of vertical cooling rate—The effect of heat extracted by the stool on vertical solidification above the base cone is almost negligible. Hence it seems doubtful that thicker stools, copper or water-cooled stools would effectively reduce axial porosity in ingots.

2—Increase of mold-wall taper—For reasons given in the paper, I do not believe that increase of mold-wall taper beyond those now used would effect any significant improvement of internal soundness.

3—Increase of ingot taper—Increase of ingot taper from 0.3 to 0.5 in. per ft, as mentioned by the discussers, could quite possibly improve the internal soundness of killed carbon-steel ingots. Neither taper is extreme. Sykes,¹⁸ however, found no improvement in the internal soundness of alloy-steel ingots cast in molds of exaggerated internal tapers. It seems doubtful that increase of present ingot tapers would effect sufficient improvement in ingot internal quality to offset the practical disadvantages of extreme tapers.

4—Decrease of height of ingot with respect to width—The discussers have answered this question. Practical considerations govern.

5—Pouring metal cold—I have no data as to the effect of the pouring temperature on axial porosity. There is evidence, however, that the tendency of decrease of casting temperature would be to increase central unsoundness, at least in low-alloy-steel ingots. In the Second Report on the Heterogeneity of Steel

Ingots¹⁸ appear reproductions of the crystal structures of two 18x18 in. low-alloy-steel ingots cast at 2894° and 2822°F, respectively.* Although both ingots are quite

* The nozzle sizes used in casting these ingots varied slightly. A ¾ in. nozzle was used in casting the hotter steel, a 1 in. nozzle for the other. Any effect of this difference, however, should reduce the effect of the casting temperature difference on the crystal structures of the ingots.

sound, the one cast at the lower temperature reveals a vertical core that is definitely narrower than that in the ingot cast at the higher temperature.

Cause of Axial Porosity in Low-Alloy-Steel Ingots:

1—Effect of alloy content in stiffening dendrites—The theory that dendrites must break off to allow free feeding of steel in the ingot interior has never appealed to me. The difference in pressure between the top and bottom of a single dendrite is negligible.

2—Effect of undercooling.

a—On columnar crystals—The experiments of Siegel^{5,17} and others show that crystal structure is dependent on undercooling. Steels of low undercoolability (e.g., stainless steel) have predominantly long columnar crystals and large crystal size. Steels of deep undercoolability (e.g., low-alloy steels) comprise principally small, free (equiaxed) crystals, with only short columnar crystals.

b—On axial porosity—The experiments of Spretnak¹⁹ show that rates of ingot solidification vary with crystal structure. The solid section just below the hot-top junction in low-alloy-steel ingots (Fig. 27) indicates that such ingots solidify faster transversely relative to vertically than do carbon steel ingots. The vertical cores of low-alloy-steel ingots normally comprise fine equiaxed crystals. The density of nucleation in this core may hamper free downward flow of liquid metal in the core, so that excessive porosity develops.

Cause of Negative Segregation:

The basis for this question is not clear. If segregates may rise freely from the face solidifying in a vertical direction, but cannot escape from the faces solidifying transversely, it seems that conditions are such that very pure metal may be solidified vertically in the lower middle zone, whereas layers of inverted-V segregation may be entrapped transversely by the mechanism described in the paper.

1—Convection currents in the liquid metal—Granat and Bezdenezhnikh¹⁸ determined that the liquid steel in a 32 in. octagonal ingot attains the liquidus temperature in a matter of minutes after pouring. With no temperature gradients in the liquid metal, they conclude that convection currents are out of the question during the solidification of an ingot. It seems difficult to disagree with this conclusion.

2—Inclusions in the lower third of an ingot—The well-known prevalence of inclusions in the lower portion of an ingot indicates that inclusions do not escape upwardly during solidification, as do segregates.

Inverted-V Segregation:

1—Effects of gases in steel—The discussers do not specify the experimental work which, they say, indicates that gases in steel might be related to inverted-V segregation.

The fracture of an ingot at Homestead Works, Fig. 28, to which reference was made in the paper, reveals a network of fine dendrites in layers of inverted-V segregation. This structure seems to indicate that low-melting liquid layers were entrapped.

Inverted-V segregation is generally less pronounced in semikilled (gas evolving) ingots than in killed ingots. In some split ingots of the former type appear faint inner lines of inverted-V segregation with fainter traces of segregation directed inwardly and upwardly in paths that gas would be expected to follow. It seems probable, therefore, that gas escaping inwardly and upwardly carries with it a certain amount of the seg-



Fig. 28—6½x9 in. section from upper middle portion of 34 in. width of fractured 34x60x90 in. high, hot topped, big-end-up ingot, split at Homestead District Works, United States Steel Corp. Arrows designate inverted-V layers or streaks, which comprise fine dendrites. The ladle analysis was: C, 0.33 pct; Mn, 0.32, P, 0.026; S, 0.023; Si, 0.07; Ni, 3.62; and Cr, 1.89. Area reduced approximately 75 pct from natural size for reproduction.

regation from the liquid segregated layer, and thereby reduces the intensity of the latter.

Effect of Air Gap Between Ingot and Mold Wall on Ingot Structure:

I know of no evidence that the formation of an air gap between the ingot and the mold wall causes any retardation or reduction of the ingot-solidification rate. The dumping experiments of Chipman and Fonder-Smith¹⁰ reveal an apparent delay in the start of solidification of about 1 sec, but no delay beyond this. Contrary, perhaps, to what might be expected, heat seems to be conveyed across the widened air gap as effectively as it is across the narrow air gap always present between ingot and mold. As the widening of the air gap seems to have no significant effect on ingot-solidification rate, so it seems to have no effect on ingot crystal structure. Preheating of molds would probably have the same effect on ingot crystal structure as increased pouring temperature, namely, to increase columnar crystallization.

Dr. Helin questions whether the structure of the 29x66 in. ingot (Fig. 17) is not a secondary rather than a primary one, citing the bending of crystals as evidence. It is not quite clear, however, what significance he attaches to the question with regard to the findings.

The ingot in question was etched in hot 10 pct sulphuric acid in a mill pickling tank, which etching should, we believe, develop primary structure. Since metallographers¹⁹ tell us that it is not possible to develop exclusively one type of structure, however, it

seems quite likely that secondary structure may have been revealed also. One finds very little in the literature concerning the differences between primary and secondary structures, in particular as to whether any difference in length of columnar crystallization occurs between the two. Although Hultgren¹⁵ discusses in detail the bending of columnar crystals, in the only ingot in which he shows both primary and secondary structure, the columnar crystals are of equal length and slope. Hultgren comments, "It is seen that the direction of secondary crystals in the outer zone is governed by the existing primary crystals." Leitner²⁰ however, presents an example of a 16 in. diameter low-carbon-steel ingot in which the primary columnar crystals, as developed by Oberhoffer's reagent, are much shorter than the secondary columnar crystals revealed by an ammonium persulphate etch. When and to what extent, then, do primary and secondary columnar crystals differ in length?

Dr. Helin questions whether columnar crystals grow to the full height of the base cone of the 29x66 in. ingot. He says that columnar crystallization normally extends to not over 30 pct depth in an ingot. This generalization is probably true with respect to killed carbon-steel ingots, but we do not believe that it applies to semikilled ingots, the type in question. All the several semikilled ingots that, over the years, have been split at Homestead and Gary Works, reveal long columnar crystals. In some, the inner lines of inverted-V segregation mark the extent of columnar crystallization. That is, transition coincides with acceleration of heat extraction. In others, as in the 29x66 in. ingot, transverse columnar crystals extend to the vertical core. The vertical columnar crystals extend to the full height of the base cone in the latter, but not quite to this height in the former ingots.

As to the significance of the type of crystal structure of the 29x66 in. ingot upon the findings, the boundaries of the solidification zones of this ingot do not seem to hinge on this question. The vertical core and the base cone are clearly outlined by definite crystal structure

differences. There remain only the outer boundaries of the zones of accelerated transverse and accelerated vertical solidification, which boundary lines coincide with bending of columnar crystals growing from the sides and from the base, respectively. But the outer boundaries of the zones of accelerated transverse solidification were located coincidentally with inner lines of inverted-V segregation, which lines are loci of acceleration. This establishes that the bending of crystals does coincide with acceleration of solidification rates. In addition, line *ada*, the locus of bending of vertical columnar crystals, crosses the vertical axis at a height equal to one fourth the base width, the same relative depth at which acceleration from side corners reaches the middle axis, according to Nelson's data. Thus, even if the bending of the columnar crystals did occur after solidification, the loci of acceleration, transversely and vertically, are not changed, and the bending of the crystals correctly designates these loci.

Based on his belief that transition of crystal structure normally occurs at a fixed depth, Dr. Helin proposes that the depth of transition coincides with that of the origin of outer lines of inverted-V segregation. Although, as mentioned above, transition sometimes coincides with inner lines of inverted-V segregation, it does so because these lines are loci of acceleration of heat extraction, which acceleration favors transition. I have not seen any ingot in which coincidence as proposed by Dr. Helin occurs. It certainly could do so in killed carbon-steel ingots, but such coincidence would, I believe, be purely fortuitous.

¹⁵ A. Hultgren: *Jernk. Ann.* (1930) pp. 95-158.

¹⁶ Second Report on the Heterogeneity of Steel Ingots. Section IV "A Study of Nickel, Nickel-Chromium-Molybdenum Steel Ingots." Iron and Steel Inst., London (1928) 117, No. 1, pp. 437-476.

¹⁷ H. Siegel: Formation of Dendrite Structure in Stainless Chromium Steels. *Stahl und Eisen* (1938) 58.

¹⁸ I. Granat and A. Bezdenezhnikh: Influence of Mold-Wall Thickness on Solidification and Quality of Steel Ingots. *Metallurg* (1938) 13, No. 10, pp. 19-33.

¹⁹ T. Berglund: *Metallographers' Handbook of Etching*. (1931) London, Sir Isaac Pitman and Sons, Ltd.

²⁰ F. Leitner: Influence of Cooling Conditions on Macrostructure of Ingots. *Stahl und Eisen* (1930) 50, pp. 1081-1086.

Discussion — Extractive Metallurgy Division*

Spokane Regional Meeting, May 1952

Kinetics of the Oxidation of Galena in Sodium Hydroxide Solutions Under Oxygen Pressure (paper by J. E. Andersen, J. Halpern, and C. S. Samis. *JOURNAL OF METALS*, April 1953, p. 554) 1556

Los Angeles Meeting, February 1953

Vapor Pressure of Zinc in the Reduction of ZnS by Cu and Fe (paper by A. W. Bethune and L. M. Pidgeon. *JOURNAL OF METALS*, June 1953, p. 804) 1558

Preparation of Metallic Iron of High Purity (paper by G. A. Moore. This issue, p. 1449).

* TP 3656D.

Kinetics of the Oxidation of Galena in Sodium Hydroxide Solutions Under Oxygen Pressure

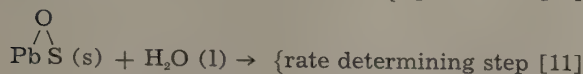
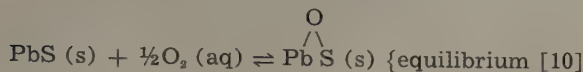
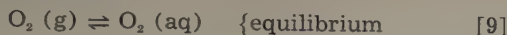
by J. E. Andersen, J. Halpern, and C. S. Samis

DISCUSSION, A. Y. Bethune presiding

M. E. Wadsworth and W. M. Fassell (*University of Utah, Salt Lake City*)—The authors of this paper should be complimented on the experimental techniques they have employed to investigate the rate of solution of galena in sodium hydroxide solution. Studies of this type are important not only as a practical means of leaching normally non-leachable substances, but also to determine the mechanism of solution at the solid-aqueous solution interface.

There is some question, however, as to the conclusions which have been drawn by these authors concerning their proposed mechanism. Unfortunately, the contribution of OH⁻ was not definitely established in their work, and concentrations less than 0.5 N NaOH evidently were not investigated. The pressure data at 123°C and 0.5 N NaOH were used to determine pressure dependency and the subsequent model proposed was taken as correct on the basis of the three points presented in Fig. 5 of the paper. In developing the

proposed mechanism the authors did not include the surface mass balance which should enter into the development as follows:



From Eq. 9 and considering activity coefficients as unity,

$$K_1 = \frac{[\text{O}_2] \text{aq}}{P_{\text{O}_2}} \text{ or } [\text{O}_2]^{1/2} \text{aq} = K_1^{1/2} P_{\text{O}_2}^{1/2} \quad [12]$$

and from Eq. 10

$$K_2 = \frac{C_{\text{Pb-S}}}{C_{\text{Pb-S}} (\text{s}) [\text{O}_2]^{1/2} \text{aq}} = \frac{\theta_x}{\theta_y} \frac{1}{[\text{O}_2]^{1/2} \text{aq}} \quad [13]$$

where θ_x represents the fraction of the total available surface sites which are covered by adsorbed oxygen, and θ_y , the fraction of uncovered sites. The surface mass balance equation,

$$\theta_x + \theta_y = 1 \quad [14]$$

and Eq. 12 combined with Eq. 13 result in the relationship,

$$\theta_x = \frac{K_2 K_1^{1/2} P_{\text{O}_2}^{1/2}}{1 + K_2 K_1^{1/2} P_{\text{O}_2}^{1/2}} \quad [15]$$

The fraction of the surface covered, θ_x , may be related to the true surface concentration by the constant, k_o . Accordingly, the rate determining step as represented by Eq. 11 becomes,

$$\begin{aligned} \text{Rate} &= k_o K \frac{kT}{h} \theta_x [\text{H}_2\text{O}] e^{-\Delta F^\ddagger / RT} \\ &= k_o K \frac{kT}{h} \frac{K_2 K_1^{1/2} P_{\text{O}_2}^{1/2}}{1 + K_2 K_1^{1/2} P_{\text{O}_2}^{1/2}} [\text{H}_2\text{O}] e^{-\Delta F^\ddagger / RT} \quad [16] \end{aligned}$$

At constant temperature Eq. 16 becomes,

$$\text{Rate} = K_o \left[\frac{K_2 K_1^{1/2} P_{\text{O}_2}^{1/2}}{1 + K_2 K_1^{1/2} P_{\text{O}_2}^{1/2}} \right] \quad [17]$$

If the rate of reaction over the range reported is proportional to $P_{\text{O}_2}^{1/2}$, the quantity $K_2 K_1^{1/2} P_{\text{O}_2}^{1/2}$ must be very much less than one. Using the mean deviation of ± 2 pct as reported in Table III and the mid range of the data reported, $K_2 K_1^{1/2} P_{\text{O}_2}^{1/2}$ must be equal to or less than approximately 0.1 in order to be negligible. A knowledge of the concentration of $[\text{O}_2] \text{aq}$ will therefore lead to a maximum value of K_2 since $[\text{O}_2] \text{aq} = K_1 P_{\text{O}_2}$. Complete solubility data for O_2 at elevated temperatures and pressures are not available for all conditions represented in the work, particularly in solutions containing NaOH. However, extrapolated values may be used from data which are available. Even if these are within 10 pct of correct the maximum value of K_2 may be determined within narrow limits. The data of Geffcken¹⁰ at low temperature and a partial pressure of 1 atm and the data of Bykow¹¹ at 100 kg per sq cm pressure and a wide temperature range indicate that the solubility of O_2 decreases approximately 18 to 22

Table III. Experimental Data and Calculated Oxygen Solubility in 0.5 N NaOH at 123°C

P_{O_2} , Atm	Rate Mols per Sq Cm per Sec	H_o^* Extra- polated	$[\text{O}_2] \text{aq}$ Mols per Liter	$0.80 \times [\text{O}_2] \text{aq}$ for 0.5 N NaOH Solution
2.2	5.8	7.08×10^4	1.73×10^{-3}	1.38×10^{-3}
5.6	10.0	7.16×10^4	4.34×10^{-3}	3.47×10^{-3}
10.3	12.8	7.38×10^4	7.72×10^{-3}	6.17×10^{-3}

* Henry constant.

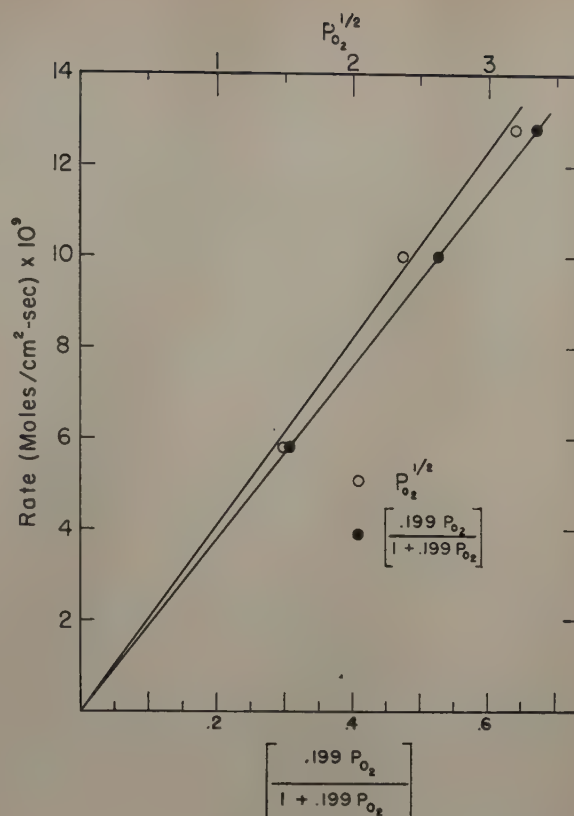


Fig. 8—Measured rate of reaction vs $P_{\text{O}_2}^{1/2}$ and $f(P_{\text{O}_2})$ of the Langmuir form.

pct in solutions containing 0.5 N NaOH. This is quite consistent even over this wide range of temperature and pressure. It seems logical therefore to correct the solubility of O_2 in pure water under the conditions of this experiment approximately 20 pct for the 0.5 N NaOH solution. Using extrapolated values for the solubility of O_2 in water at variable pressures and temperatures^{12,13} and the authors' data from Fig. 5 of their paper, Table III was prepared.

For the O_2 partial pressure of 10.3, it is found that the K_2 is equal to or less than approximately 1.3. This is equivalent to an adsorption potential of -208 cal. This value seems unusually small to explain an adsorption process capable of splitting an O_2 molecule at the surface as proposed.

An alternate mechanism may be proposed which also explains the experimental data. It is not intended here that this is suggested as the true mechanism since there is insufficient data available to support it. However, on the basis of the above data, the following may occur:

- (1) $\text{O}_2 (\text{g}) \rightleftharpoons \text{O}_2 (\text{aq})$ {equilibrium
- (2) $\text{PbS} + \text{O}_2 (\text{aq}) \rightleftharpoons \text{Pb} \overset{\text{O-O}}{\text{S}} (\text{s})$ {equilibrium
- (3) $\text{Pb} \overset{\text{O-O}}{\text{S}} + \text{OH}^- \rightarrow \text{HPbO}_2^- + \text{SO}$ {rate determining step
- (4) $\text{SO} + \text{O}_2 + \text{H}_2\text{O} \rightleftharpoons 2\text{H}^+ + \text{SO}_4^{2-}$ {fast

From these equations, using a similar development as before,

$$\begin{aligned} \text{Rate} &= k_o K \frac{kT}{h} \frac{K_2 K_1 P_{\text{O}_2}}{1 + K_2 K_1 P_{\text{O}_2}} [\text{OH}^-] e^{-\Delta F^\ddagger / RT} = k_o K \\ &\quad \frac{kT}{h} \frac{k_2 [\text{O}_2] \text{aq}}{1 + k_2 [\text{O}_2] \text{aq}} [\text{OH}^-] e^{-\Delta F^\ddagger / RT} \quad [18] \end{aligned}$$

It is not necessary to assume that $k_2 [\text{O}_2] \text{aq}$ is small compared to unity to fit the experimental data. At constant temperature and constant NaOH concentra-

tion, Eq. 18 becomes,

$$\text{Rate} = K_o \frac{k_2[\text{O}_2] \text{ aq}}{1 + k_2[\text{O}_2] \text{ aq}} \quad [19]$$

and k_2 is found to be 2.47×10^3 and the adsorption potential under these conditions is -4350 cal. This value, although small, can account for the adsorption of an O_2 molecule on the surface. The results of both proposed mechanisms are plotted in Fig. 8. These are plotted using P_{O_2} values instead of $[\text{O}_2] \text{ aq}$, and the value of the product $k_1 k_2$ of Eq. 18 was found to be 0.199.

J. Halpern (authors' reply): We are grateful to Drs. Wadsworth and Fassell for their detailed and valuable

discussion pointing out that an alternative mechanism to the one suggested by us is also consistent with our experimental results. It would appear that further experimental data are required to resolve the nature of the pressure dependence and establish the mechanism of the oxygen adsorption step. With regard to the sequence of reaction steps suggested by Drs. Wadsworth and Fassell, we doubt that Step 3 could be rate controlling since it implies that the reaction rate should increase with the concentration of OH^- . Our results on this point suggest an inverse dependence.

¹⁰ G. Geffcken: *Ztsch. Phys. Chemie* (1904) 49, p. 327.

¹¹ M. Bykow: *Acta Universitatis Vorohegiensis*. (1937) 9, p. 29.

¹² *International Critical Tables*, Vol. 3.

¹³ *Chemical Engineers' Handbook* (1941) p. 1128. Second Edition.

Vapor Pressure of Zinc in the Reduction of ZnS by Cu and Fe

by A. W. Bethune and L. M. Pidgeon

DISCUSSION, O. C. Ralston presiding

N. A. Gokcen (*Michigan College of Mining and Technology, Houghton, Mich.*)—Recent references,^{13, 14} superseding earlier work of Kelley,³ were overlooked by the authors in the calculation of the heats of reactions from existing data. In addition, the integration constant $\Delta S^\circ/R$ was omitted from Eq. 5, and the experimental values of ΔS° were not calculated and compared with the available data.

In order to complete these calculations, and present a comparison, the values of $\log K_2$ and $\log K_3$ are plotted vs $1/T$ in Fig. 4. On the basis of the assump-

Table II. Results at 1273°K

	For the ZnS-Cu System	For the ZnS-Fe System
ΔH°_{1273} (calculated)	+ 61,780 cal	+ 55,460 cal
ΔH°_{1273} (experimental)	+ 49,800 cal	+ 45,100 cal
Difference	+ 11,980 cal	+ 10,360 cal
ΔS°_{1273} (calculated)	+ 41.50 E.U.	+ 34.55 E.U.
ΔS°_{1273} (experimental)	+ 32.3 E.U.	+ 31.0 E.U.
Difference	9.20 E.U.	3.55 E.U.

tions presented in this paper, $K = (P_{\text{Zn}})/(a_{\text{Cu}}^2)$ and $K_3 = P_{\text{Zn}}$, where P_{Zn} is expressed in atmospheres.

The results at 1273°K are compared in Table II. It is obvious that, contrary to the authors' contention,

¹³ K. K. Kelley: *Bulletin* 476 (1949).

¹⁴ F. D. Rossini, et al.: *Selected Values of Chemical Thermodynamic Properties*. Bur. Standards, Circular 500 (February 1952).

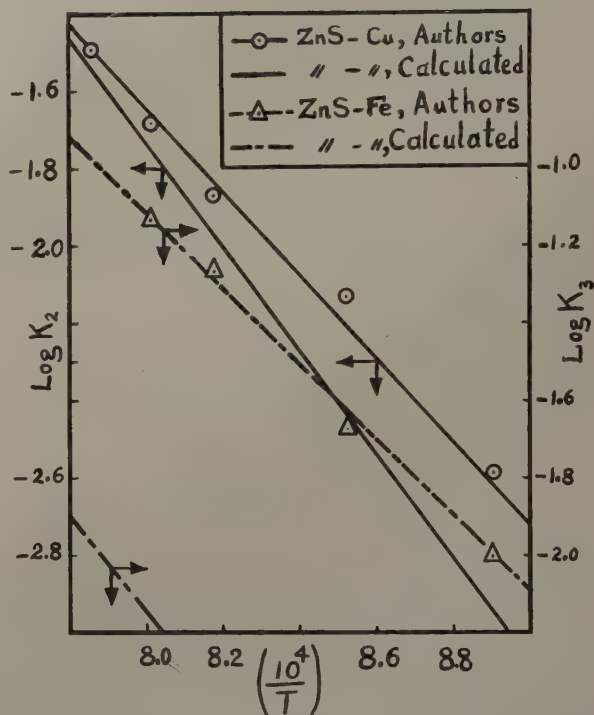


Fig. 4—Values of $\log K_2$ and $\log K_3$ plotted vs $1/T$.

these differences do not agree within the experimental errors.

Technical Note

The Energy State of Fatigued Copper

by B. Welber and R. Webeler

ACCORDING to accepted theory, fatigue in metals is connected with the occurrence of local strain hardening even at applied stresses below the yield point as a consequence of stress concentrations created by the presence of structural

inhomogeneities.¹ It seemed possible, therefore, that

B. WELBER and R. WEBELER are associated with the Radiation Physics Section, NACA Lewis Flight Propulsion Laboratory, Cleveland. TN 187E. Manuscript, Aug. 3, 1953.

a metal which had been subjected to cyclic stresses for a sufficiently large number of times, might possess a measurable stored energy in the same sense as a metal which had been cold-worked. Accordingly, using a calorimetric method, it was undertaken to determine whether the process of fatigue is connected with the storage of such a measurable amount of energy. For this purpose three specimens of OFHC copper were machined to a shape suitable for fatiguing in a Krouse machine, so as to have a cylindrical, narrower central portion measuring about $\frac{1}{2}$ in. in diameter by 3 in. in length, and annealed at a temperature of 450°C for 1 hr. They were then subjected to an alternating tensile stress for a total of about four million cycles, at a rate of 2000 cycles per min with the highest and lowest stress in each cycle being 20,000 and 1,000 psi, respectively, i.e., fatigued nearly to failure. The end portions of each test specimen were then cut off leaving the narrow central portion through which an axial hole about $\frac{1}{8}$ in. in diameter was drilled to accommodate a heating element. (In order to avoid premature annealing, all this machining was done at slow speeds and the sample was cooled so that its temperature never exceeded room temperature.) Finally, the sample was polished and cleaned immediately before being mounted in a vacuum calorimeter.

The calorimeter used in this investigation was the same as had previously been employed in the determination of the energy stored in copper by cold work.² A significant improvement of the technique of measurement was made, however, in that the heater power rather than the heater current was kept constant during the experiment. To achieve this, power from an electronically regulated constant voltage dc source was supplied to a heater connected in a series with a 700 ohm oil-cooled manganin resistor, this value being the average resistance of the heater during the course of a run. This arrangement assured a more uniform rate of heating of the specimen and thus greatly simplified the computations. It was found that during the course of a single "run" of approximately 45 min duration the power supplied to the heater would vary less than 7 parts in 10,000 although the resistance of the nichrome heater changed by as much as 5 pct.

In the course of a measurement, each sample was heated from 20° to 450°C and the temperature was recorded as a function of time of heating, i.e., of energy supplied. Two more runs were made without removing the sample from the calorimeter taking care that sufficient time elapsed between runs for the sample and the components of the calorimeter to return to room temperature.

The difference in heat content between the second and third run on each sample was substantially zero for all temperatures, T , up to the highest temperature attained, thus indicating that upon completion of the first heating the sample could be considered as "annealed" in the sense that another heating through the same temperature range led to no measurable energy release or absorption. Fig. 1

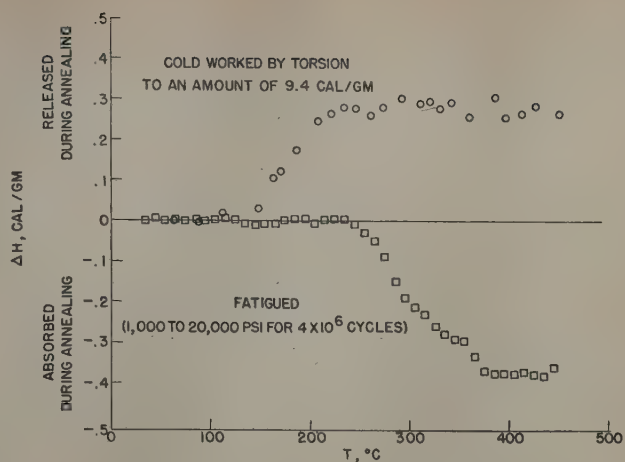


Fig. 1—Deviation in heat content ΔH of cold-worked copper and of fatigued copper relative to that of the "annealed" metal. The total work done in twisting the cold-worked sample was 9.4 cal per gram.

shows the quantity $\Delta H(T)$, the difference in heat content in calories per gram of the sample, between the first two runs, as a function of the temperature T , as well as the value of $\Delta H(T)$ found for the first two runs of a copper sample cold-worked by torsion to an amount of 9.4 cal per gram.* In con-

* These latter results were taken from the previous investigation.²

trast to the case of the cold-worked sample (where a certain amount of stored energy was released in the temperature range from 150° to 250°C on subsequent heating) there is no evidence of any energy release in this temperature range for the fatigued sample. Moreover, a greater amount of heat had to be supplied to bring the fatigued sample from about 250° to 400°C than was necessary in the same temperature range for the same sample in the "annealed" state, so that a fatigued sample of copper shows a tendency to absorb energy during the first heating in this temperature range. It may be remarked that all three specimens investigated showed a similar behavior. The asymptotic values ΔH_{\max} for the three samples are given in Table I, the errors being estimated by the random differences in ΔH between the second and third runs. Grain size measurements were made on the samples before and after they were fatigued and after they were removed from the calorimeter. There was no evidence of any recrystallization, the maximum, average, and minimum grain size remaining unchanged at about 2, 32, 128 grains per sq in., respectively, at 100X (ASTM grain sizes 2, 6, and 8).

In view of the fact that strain hardening is supposed to accompany the process of fatigue in metals, the results of these measurements, indicating the absence of any stored energy, are somewhat surprising. Moreover, the apparent absorption of energy in the higher temperature range is totally unexpected and at present there is no explanation of the phenomenon.

Acknowledgment

The authors are indebted to G. Groetzinger under whose guidance this work was pursued for his advice and encouragement, and to P. Schwed for several helpful discussions. In addition, they wish to thank G. M. Ault for supplying the fatigued samples.

¹ E. Orowan: *Proc. Royal Soc. (1939)* 171, p. 79.

² B. Welber: *Journal of Applied Physics* (1952) 23, p. 876.

Table I. Increase in Heat Content of Fatigued Copper Specimens

Sample	ΔH_{\max} , Cal per Gram
1	0.36 ± 0.04
2	0.42 ± 0.04
3	0.51 ± 0.04

Discussion — Institute of Metals Division*

No Meeting

Effect of Alloying Elements on the Behavior of Nitrogen in Alpha Iron (paper by L. J. Dijkstra and R. J. Sladek. JOURNAL OF METALS, January 1953, p. 69)	1560
Measurement of Internal Boundaries in Three-Dimensional Structures by Random Sectioning (paper by C. S. Smith and L. Guttman. JOURNAL OF METALS, January 1953, p. 81)	1561
<i>Los Angeles Meeting, February 1953</i>	
Mechanical Properties of High Purity Ti-Al Alloys (paper by H. R. Ogden, D. J. Maykuth, W. L. Finlay, and R. I. Jaffee. JOURNAL OF METALS, February 1953, p. 267)	1561
Microstructure and Mechanical Properties of Iodide Titanium (paper by F. C. Holden, H. R. Ogden, and R. I. Jaffee. JOURNAL OF METALS, February 1953, p. 238)	1562
Preferred Orientations in Iodide Titanium (paper by C. J. McHargue and J. P. Hammond. JOURNAL OF METALS, January 1953, p. 57)	1563
Titanium-Carbon Phase Diagram (paper by I. Cadoff and J. P. Nielsen. JOURNAL OF METALS, February 1953, p. 248)	1564
Constitution of Titanium-Rich Ti-Cr-Al Alloys at 1800° and 1400°F (paper by J. L. Taylor and P. Duwez. JOURNAL OF METALS, February 1953, p. 253)	1565
Titanium-Manganese System (paper by D. J. Maykuth, H. R. Ogden, and R. I. Jaffee. JOURNAL OF METALS, February 1953, p. 225)	1566
Recrystallization of a Cold-Rolled Copper Single Crystal (paper by Y. C. Liu and W. R. Hibbard, Jr. JOURNAL OF METALS, May 1953, p. 672)	1568
Cold-Rolling and Annealing Textures of Molybdenum Single Crystals (paper by N. K. Chen and R. Maddin. JOURNAL OF METALS, February 1953, p. 300)	1569
Statistical Grain Structure Studies: Plane Distribution Curves of Regular Polyhedrons (paper by F. C. Hull and W. J. Houk. JOURNAL OF METALS, April 1953, p. 565)	1570
Observations on Scaling of Iron (paper by W. J. Wrazej. JOURNAL OF METALS, February 1953, p. 265)	1570
Kinetics of Thermal Reorientations in Cold Rolled Zirconium (paper by R. K. McGeary and B. Lustman. JOURNAL OF METALS, February 1953, p. 284)	1573
Nature of the Creep Curve (paper by T. H. Hazlett and E. R. Parker. JOURNAL OF METALS, February 1953, p. 318)	1577
Grain Boundary Sliding and Migration and Intercrystalline Failure under Creep Conditions (paper by H. C. Chang and N. J. Grant. JOURNAL OF METALS, February 1953, p. 305)	1579
Absolute Rate Theory Applied to Rate of Growth of Pearlite (paper by J. H. Frye, Jr., E. E. Stansbury, and D. L. McElroy. JOURNAL OF METALS, February 1953, p. 219)	1581

* TP 3657E.

Effect of Alloying Elements on the Behavior of Nitrogen in Alpha Iron

by L. J. Dijkstra and R. J. Sladek

DISCUSSION

J. D. Fast and J. L. Meijering (*Philips Research Laboratories, N. V. Philips' Gloeilampenfabrieken, Eindhoven, Netherlands*)—After the departure of our friend Dijkstra to the United States, investigations on the effect of alloying elements on the behavior of nitrogen in α iron were continued in Eindhoven. We too found internal friction curves with two separate peaks for iron containing nitrogen in addition to 0.5 atomic pct V or 0.5 atomic pct Mo. Our first publication on these investigations¹⁰ appeared almost simultaneously with the paper now under discussion. At first sight our experimental results seem to be in harmony with their conclusions, but a closer examination reveals that in the case of the Fe-V-N alloy the abnormal peak is not controlled by one time of relaxation only.

Whereas iron containing 0.5 atomic pct Mn or Mo absorbs an amount of nitrogen of about the same magnitude as that absorbed by pure iron under identical conditions, iron containing vanadium absorbs in addition one nitrogen atom for every vanadium atom.

This last amount, far exceeding the first amount in the case under consideration, combines chemically with the vanadium and causes no internal friction. The "free" nitrogen in the vanadium alloy gives rise not only to a damping peak corresponding to that in pure iron but—due to the presence of VN particles in the metal—also to the abnormal peak at higher temperatures. The VN particles create interstitial sites around themselves where the free nitrogen atoms are bound much tighter than in the normal interstices. These abnormal interstices, therefore, will capture free nitrogen atoms rapidly, whereupon these give rise to the abnormal damping. The binding energy in the abnormal interstices is not the same for all, and with coarsening of the VN precipitate the distribution of these energies is displaced toward the side of stronger binding. This is deduced from a shift of the summit of the second peak toward higher temperatures (from 80° to 88°C in our experiments) caused by prolonged heating at 950°C. From the intermediate state where they cause the abnormal damping, the nitrogen atoms pass over rather rapidly into the fully precipitated state (iron

nitride) where they cause no damping. Consequently, the VN precipitate exerts a strongly accelerating influence on the precipitation of dissolved nitrogen.

For the Fe-Mo-N alloy our experimental results do not differ essentially from those of Dijkstra and Sladek.

The only difference is that the temperature of the maximum of the abnormal peak is found by us at a somewhat lower temperature (62°C instead of 75°C).

¹⁰ J. D. Fast and J. L. Meijering: *Philips Research Reports* (1953) 8, No. 1.

Measurement of Internal Boundaries in Three-Dimensional Structures by Random Sectioning

by Cyril Stanley Smith and Lester Guttman

DISCUSSION

S. M. Purdy (*The Carpenter Steel Co., Reading, Pa.*)

—The authors have presented a very able and worthwhile paper that should provide a stimulus to metallurgical research. One field that could make great use of the mathematical tools provided is investigation into the transformation of phases. However, in following these reactions, primarily those involving two or more phases, it may be of greater value to know the total surface area of the phases involved per unit volume of the alloy rather than the surface to volume ratio of each phase.

The following derivation, extending the authors' work, should provide a method of determining the total surface area of a phase in a structure of two or more phases. The same terms and notations as the authors' are used except for the few new terms introduced.

Notations in addition to authors: S_α , surface area of α phase; V_α , volume of α phase; v_α , volume fraction of α phase; and V , volume of specimen.

$$v_\alpha = \frac{V_\alpha}{V} \quad (1) \text{ By definition}$$

$$v_\alpha = \frac{V_\alpha}{1} = V_\alpha \quad (2) \text{ Taking unit volumes}$$

$$v_\alpha = \frac{L_\alpha}{L} = V_\alpha \quad (3) \text{ Table II, item 6, col. 2}$$

$$\frac{S_\alpha}{V_\alpha} = \frac{2N_\alpha}{L_\alpha} \quad (4) \text{ Table II, item 3, col. 2}$$

$$S_\alpha = \frac{2N_\alpha}{L_\alpha} \times V_\alpha \quad (5) \text{ Solving for } S_\alpha$$

$$S_\alpha = \frac{2N_\alpha}{L_\alpha} \times \frac{L_\alpha}{L} \quad (6) \text{ Substituting Eq. 3 in Eq. 5}$$

$$S_\alpha = \frac{2N_\alpha}{L} \quad (7) \text{ Surface area of } \alpha \text{ phase in terms of square units/unit volume of alloy}$$

This derivation is simply a combination of item 3, col. 2, Table II and item 6, col. 2, Table II, after first establishing the identity of the volume term (V_α) in the surface to volume ratio and the volume fraction (v_α) by taking unit volumes. The term S_α in Eq. 5 and following then is in terms area per unit volume.

This method can be used without any equipment other than a metallograph. The only measurements needed are the number of intersections of the phase concerned and the total length of the line. Both of these can be determined without using integrating stages.

Mechanical Properties of High Purity Ti-Al Alloys

by H. R. Ogden, D. J. Maykuth, W. L. Finlay, and R. I. Jaffee

DISCUSSION, J. E. Wilson presiding

C. W. Funk (*Aerojet-General Corp., Azusa, Calif.*)—Metallurgists in the aircraft industry are very much interested in the high strength, weldability, and higher operating temperature characteristics of all-alpha titanium alloys containing aluminum. Since this paper describes properties of high purity materials, it would be expected that improved strength properties could be obtained from the commercial grade material reportedly to be made available in the near future. We would like to know if the authors could elaborate on this from their experience.

H. R. Ogden, D. J. Maykuth, W. L. Finlay, and R. I.

Jaffee (authors' reply)—Mr. Funk's point that higher strength values would be obtained in Ti-Al alloys made from the commercial grade of titanium is well taken. As is well known, the difference in strength between high purity titanium and commercial purity titanium is caused by the presence of impurities in the base metal, the most influential being the interstitials, oxygen, nitrogen, and carbon. These impurities would also affect the properties of binary Ti-Al alloys such that the strength of a given alloy would be increased to about the extent that the impurities present would increase the strength of pure titanium. Also, since the quantity of impurities in the commercial grades of

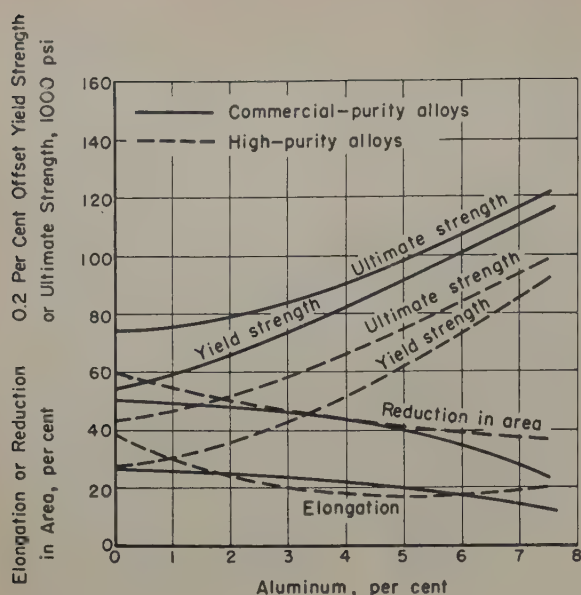


Fig. 13 (left)—Comparison of mechanical properties of α annealed high purity and commercial purity Ti-Al alloys.

titanium will vary from lot to lot, it is difficult to assign specific properties to a given titanium-base alloy unless the properties of the base metal used are known.

One example of the differences in properties obtained between high purity alloys and commercial purity alloys is shown in Fig. 13. The commercial purity alloys were made from titanium sponge having a yield strength of about 55,000 psi. The difference in strength between high purity titanium and this lot of sponge is carried through to the alloys. It should be noted that there is very little loss in tensile ductility when going from the high purity base to the commercial purity base at aluminum contents as high as 7.5 pct, indicating that the contaminants do not impair ductility. It should be pointed out, however, that the fabricability of the commercial purity alloys is not so good as the high purity alloys and that the maximum aluminum content permissible to avoid cracking during rolling is somewhat less than the 7.5 pct reported in this paper for high purity alloys.

Microstructure and Mechanical Properties of Iodide Titanium

by F. C. Holden, H. R. Ogden, and R. I. Jaffee

DISCUSSION, J. E. Wilson presiding

G. W. Geil (National Bureau of Standards, Washington, D. C.)—A true stress-true strain relationship of the type $\sigma = B\delta^n$ is linear when the values are plotted on logarithmic coordinates. The curves presented by the authors in Fig. 7 are of general sigmoidal shape, not straight lines. These data, therefore, cannot be closely represented by the above relationship. Thus, the values for the so-called "flow coefficient (B)" and the "flow exponent (n)" as determined by the straight line extrapolation are questionable. What physical significance can be given to the coefficient B in this case?

Sigmoidal true stress-true strain graphs on logarithmic coordinates were also obtained at the National Bureau of Standards for ingot iron,⁷ for copper, nickel, and copper-nickel alloys⁸ and for other materials, tested in tension at temperatures ranging from -196° to $+100^\circ\text{C}$. It was pointed out in the papers presenting these results that the slopes of the logarithmic true stress-true strain curves at the positions of maximum load and the upper and lower yield points are equal to the respective true strains at these positions. Moreover, this relationship holds true for any assumed general relation between the true stress and true strain and it is not restricted to a parabolic relationship such as $\sigma = B\delta^n$. Thus if the extrapolated straight lines in Fig. 7 were constructed as tangents to the curves at the maximum load points then the recorded values of n theoretically should be the same as the values of δ_{\max} . The data recorded in Table II, however, show considerable variation in these two values for the tests reported. Moreover, the values of δ_{\max} for the α annealed titanium do not indicate any significant trend of an increase in δ_{\max} with increase in the grain size such as that indicated by the values of n in Fig. 6 of the paper.

A question also arises in connection with data presented in Fig. 7. The extrapolated straight line portions of the curves are designated as belonging to different specimens than those portions of the curves

for which data are plotted. For example, the upper curve and its extrapolated portion are designated as TM1-15 and TM1-1, respectively. Should any special significance be given to this factor?

F. C. Holden, H. R. Ogden, and R. I. Jaffee (authors' reply)—The authors wish to thank Mr. Geil for his interesting discussion. The values for flow constants reported were determined by extending the straight-line portion of the flow curves from the point of maximum load up to unit strain. However, because the portions of the curves at low strains were of sigmoidal form, rather than straight lines, the actual curves were included in the paper.

Values for true strain were obtained using the relation $\delta = \log_e L/L_0$, which assumes constant volume, and readings were taken up to the point of maximum load. Accordingly, the values for δ_{\max} should theoretically correspond to the slope of the flow curve at maximum load, as pointed out by Mr. Geil. It is thought that the lack of correspondence here is caused principally by the difficulty of determining the point of maximum load exactly. In almost all tests, precise determination of the strain at maximum load was difficult because the load remained constant over a range of strain readings. Therefore, it was thought that the values of n would be more descriptive of the flow characteristics of the samples, and the variation of n rather than δ_{\max} with respect to grain size was plotted and given in Fig. 6.

With regard to the question concerning the marking of the flow curves of Fig. 7, there was an error in preparing the curves. The specimen designations on the left should be changed by deleting the numeral 5 in each case.

⁷ G. W. Geil and N. L. Carwile: Tensile Properties of Ingot Iron at Low Temperatures. Nat. Bur. Standards Journal of Research (1950) 48, p. 129. (RP2119).

⁸ G. W. Geil and N. L. Carwile: Tensile Properties of Copper, Nickel, and Some Copper-Nickel Alloys at Low Temperatures. Nat. Bur. Standards Circular 520—Mechanical Properties of Metals at Low Temperatures. (May 1952) p. 67.

Preferred Orientations in Iodide Titanium

by Carl J. McHargue and Joseph P. Hammond

DISCUSSION, J. E. Wilson presiding

R. K. McGeary and B. Lustman (*Westinghouse Electric Corp., Pittsburgh*)—The carefully determined pole figures of the authors are of particular value when interpreted in light of recent work on the annealing kinetics of zirconium.¹⁴ The pole figures for titanium are so similar to those obtained for zirconium¹⁴ that such an interpretation appears to be legitimate.

The authors interpret their various pole figures by assuming that the cold-rolled texture is retained and sharpened on primary recrystallization and that a new texture forms when grain growth and secondary recrystallization occur. However by analogy with the work on zirconium,¹⁴ we believe that the results may be explained by a different mechanism. It has been found that in the case of zirconium "recrystallization in situ," evidenced by the microscopic appearance of complete recrystallization and sharpening of the cold-rolled texture, occurs during the initial stages of annealing. That recrystallization in the usual sense is not complete at this stage is evidenced by the fact that a major portion of the deformation hardening is still retained. As annealing progresses a new texture gradually appears and eventually completely consumes the "recrystallization in situ" texture and eventually results in complete softening. Thus, by this interpretation, the authors' Figs. 3 and 4 would be regarded as intermediate stages between the initial (Fig. 2) and final (Fig. 5) textures and are not uniquely characteristic of the temperature of annealing.

Certain characteristic differences between zirconium and titanium are apparent: 1—the thermal reorientations in titanium occur presumably at higher temperatures than is the case for zirconium; the time of annealing is of importance and since no times are given by the authors this effect cannot be evaluated, 2—domain sizes in titanium must be larger than the 2 microns average domain diameter reported for zirconium since the authors state that the diffraction rings for all annealed specimens showed spottiness.

The textures for 1050°F (566°C) and 1450°F (788°C) rolling indicate what we believe to be the competition of deformation and "recrystallization in situ" on the one hand and annealing texture formation on the other. At the lower temperature, the $\langle 10\bar{1}0 \rangle$ direction is predominantly in the rolling direction indicating that the former mechanism prevails while at the higher rolling temperature neither the $\langle 10\bar{1}0 \rangle$ nor the $\langle 11\bar{2}0 \rangle$ directions are predominant, indicating that in this case both of the above mechanisms are operative.

In the case of zirconium,^{4, 15} application of more sensitive X-ray spectrometer techniques to the determination of the texture of fully annealed material revealed a splitting of the intensity maxima. It appears possible therefore that a similar effect would be revealed in the case of the textures shown in Fig. 5 by a more sensitive technique.

Under suitable conditions we have found that heating oriented titanium or zirconium through the allotropic phase transformation can produce either 1—the same texture as is produced by annealing just below the transformation, or 2—Burgers' mechanism: $\{110\}_\beta || \{0001\}_\alpha$, $\langle 111 \rangle_\beta || \langle 11\bar{2}0 \rangle_\alpha$. Very slow cooling is a factor that seems to favor the former mechanism, which may account for the fact that the authors detected only the annealing type of transformation texture.

J. P. Hammond and C. J. McHargue (authors' reply)

—Although the authors did not mean to imply the mechanisms involved in the annealing of titanium by the general terminology employed, the discussion of Messrs. McGeary and Lustman serves to focus attention on this important subject. Additional light will be thrown on the texture formation in titanium in papers to appear soon by the authors on the effects of alloying on cold-rolled and annealing textures in titanium. In the future questionable features of textures are to be re-evaluated with a Geiger counter spectrometer and supporting and/or definitive data obtained on the annealing mechanisms. Nevertheless comment will be offered on the questions brought up at this time.

First, it should be pointed out that the period of annealing at 1000°, 1300°, and 1500°F (resulting in Figs. 3, 4, and 5, respectively) was inadvertently omitted. This period was 1 hr for each temperature.

Since all evidence has revealed reorientation with primary nucleation, the mere fact that the low annealing texture (Fig. 3) has basically the orientation of the cold-rolled texture (Fig. 2) with some sharpening, suggests that the mechanisms responsible for this initial stage of annealing are polygonization and recrystallization in situ. Further, it is obvious that pronounced lattice bending, which is conducive to the polygonization process, accompanies the fragmentation and lattice rotations which bring the preferredness into focus during the cold rolling.

The latter stage of annealing represented in texture by Fig. 5, we tentatively suggest, is a result of preferred growth of existing grains rather than a process of nucleation and growth within them. Whereas for zirconium, McGeary and Lustman failed to observe an enlargement of grain size on going from a state where the low annealing texture existed to one where the fully annealed texture was 40 pct formed; and, further, found meager evidence of very large grains growing at the expense of small grains during this period of transition,¹ we hope in the future to cite more convincing evidence for the "preferred growth" in titanium.

We agree, as do McGeary and Lustman, that reorientation with annealing is a function of both time and temperature; also, that the reorientation, for the same annealing time, occurs at a higher temperature in titanium than in zirconium. In addition, it is apparent that the domain size for what appears to be the recrystallization in situ stage, is larger in titanium than it is in zirconium.

The suggestion that textures for 1050° and 1450°F rolling may result from a competition of deformation and recrystallization in situ on one hand and full annealing texture formation on the other is reasonable. This explanation is being examined for various alloys of titanium.

While it may appear that more accurate examination should reveal a fully annealed texture (Fig. 5) related to the low annealed texture (Fig. 3) by 20° and 40° rotations about basal normals as was the case for zirconium,¹⁴ we are inclined to believe that the observed 30° rotation may be correct for titanium. Jillson and Anderson's work on titanium using a Geiger counter spectrometer confirms our results in this connection.¹⁶

¹⁴ R. K. McGeary and B. Lustman: Kinetics of Thermal Reorientation in Cold-Rolled Zirconium. *Trans. AIME* (1953) 197, p. 284; *JOURNAL OF METALS* (February 1953).

¹⁵ J. H. Keeler, W. R. Hibbard, Jr., and B. F. Decker: Development of Zirconium Base Alloys. General Electric Research Lab. Report RL 767, October 1952.

¹⁶ Private communication from E. A. Anderson, The New Jersey Zinc Co., July 29, 1953.

Titanium-Carbon Phase Diagram

by Irving Cadoff and John P. Nielsen

DISCUSSION, J. P. Nielsen presiding

R. I. Jaffee and H. R. Ogden (*Battelle Memorial Institute, Columbus, Ohio*)—We have previously investigated the peritectoid region in the Ti-C system.² Although our investigation was not detailed and served chiefly to rough out the nature of the system, there are differences between our results and the results reported in the paper. These differences are: 1—The peritectoid reaction was above 900°C and below 920°C, whereas the paper gives 920°C on insufficient evidence as will be discussed later; 2—the solubility of carbon in β was less than 0.1 pct C, whereas the paper gives 0.15 pct C. The peritectoid reaction temperature was placed at 920°C, because, in the author's words, "... a three-phase structure, Fig. 6, was obtained which confirmed this temperature at 920° \pm 3°C." The existence of a three-phase structure is indicative of contamination by oxygen and/or nitrogen, and three-phase structures cannot be taken as giving the peritectoid temperature. To illustrate this, a commercially pure Ti-C alloy, containing 0.14 pct C by analysis, heated for 1 hr at 925°, 950°, and 975°C, and quenched into water, is shown in Figs. 14 to 16. These structures have been stain-etched with 0.5 pct HF to clearly distinguish between α , which stains dark, and TiC which remains white. Because of the content of approximately 0.1 pct oxygen and 0.02 pct nitrogen, this alloy shows the three-phase structure at 950°C, and would exhibit this structure over a considerable temperature range. Therefore, clearly, 920°C is too high for the peritectoid temperature on the basis of the authors' own results. In further confirmation of the bracketing of the peritectoid reaction between 900° and 920°C, we have recently been studying the effect of structure on the properties of high purity Ti-C alloys and have again found the β carbide field at 920°C and the α - β field at 900°C.

Concerning the solubility of carbon in β titanium,

Fig. 16 clearly shows carbides present at 0.14 pct C, which is about the same composition as the authors find as the terminal solubility of carbon in β . Carbon segregation does occur in arc melting, and it is probable that this is the cause for variations in results found thus far. The carbon content for the material shown in Figs. 14 to 16 was obtained by analyzing the microspecimens themselves. As another point, the hardness of the transformed β phase in high purity Ti-C alloys corresponds to only about 120 Vickers, or 20 to 30 Vickers points above the unalloyed base. This amount of solid-solution hardening is equivalent to about 0.1 pct C at the most.

It is our belief that more work should be done in this important region of the peritectoid to define the phase limits more positively than can be done using all data available at the present time.

Irving Cadoff and J. P. Nielsen (authors' reply)—Before answering the questions raised by Messrs. Jaffee and Ogden we should like to present the data on hardness given in Fig. 17. This comparison of hardnesses obtained by the present authors with those of Jaffee et al. in their earlier investigation² shows that in the 0 to 0.3 pct C range our hardness values are 25 to 40 Vickers hardness numbers lower. Since hardness is commonly used as a criterion of contamination we therefore assume that the contamination present in our alloys was less than that present in the alloys used for the earlier investigation. We introduce this data now since the major objection to our data was based on the assumption that oxygen and nitrogen were present. To date no one has claimed zero contamination in titanium alloys but, based on the hardness data available from earlier investigations, we conclude that the data presented in the present investigation could not have been distorted by the presence of contamination to a greater extent than the data previously reported.

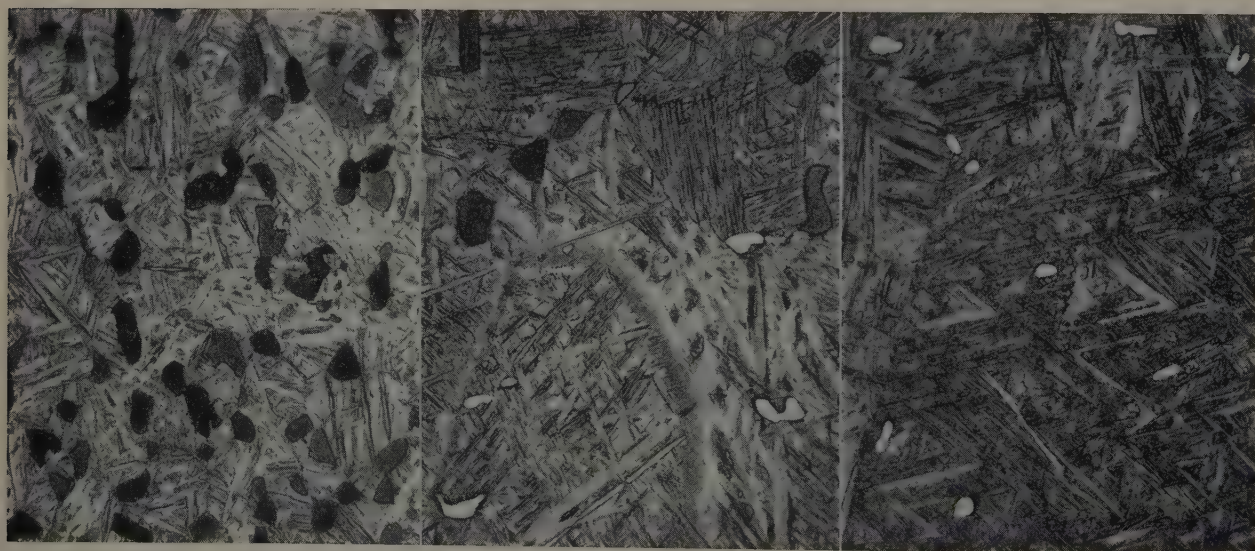


Fig. 14—Commercial Ti-0.14 pct alloy quenched from 925°C. Specimen held 1 hr at 925°C. X500. Area reduced approximately 50 pct for reproduction.

Fig. 15—Same alloy as Fig. 14 quenched from 950°C. Specimen held 1 hr at 950°C. X500. Area reduced approximately 50 pct for reproduction.

Fig. 16—Same alloy as Fig. 14 quenched from 975°C. Specimen held 1 hr at 975°C. X500. Area reduced approximately 50 pct for reproduction.

Contamination may either raise or lower the titanium transformation temperature but it always seems to increase the hardness. In the case of the peritectoid temperature, the arguments presented can work both ways. Jaffee and Ogden claim that 920°C is too high and attribute it to oxygen and/or nitrogen. It is just as plausible to assume that β stabilizers such as tungsten, copper, iron, and manganese may have been present in their alloys causing a lowering of the transformation temperature. Oxygen and nitrogen are not the only elements that will cause a three-phase field to appear. The three-phase $\alpha + \beta + \delta$ field should appear in any three component, Ti-C-X, system. If the 900° to 920°C were explored, a three-phase band should be present somewhere in that range, the exact location and width of the band dependent upon the nature and extent of the contamination. We support our data with the lower hardness values. The hardness values were obtained from the specimens used for metallographic study. It may be that the three-phase region which we observed was due to oxygen and/or nitrogen contamination, but this three-phase region was not encountered at 915°C nor at 925°C, which led us to conclude that the peritectoid reaction occurred between 917° to 923°C, the temperature being corrected for \pm control. It may also be that the reaction occurs in a temperature range representing the existence of an $\alpha + \beta + \delta$ field, but this field still can only exist between 917° to 923°C.

The example of a commercial titanium alloy cited by Jaffee and Ogden is misleading since other elements are present in addition to oxygen and nitrogen and if they had annealed a little below 920°C they would have encountered the three-phase structure, this effect also being due to the presence of the β stabilizers.

In the argument of the solubility of carbon in β titanium, the use of a commercial alloy to illustrate a point is again misleading since the many impurities present in this alloy do not enable one to rationalize their individual effect on carbon. In support of our contention that β stabilizers were present in Jaffee's alloys it has been reported that the presence of manganese lowers the solubility of carbon in β titanium¹⁴ and indications are that copper, tungsten, and iron have the same effect. We have been referring to manganese, iron, copper and tungsten since they are elements which either are present in iodide titanium or

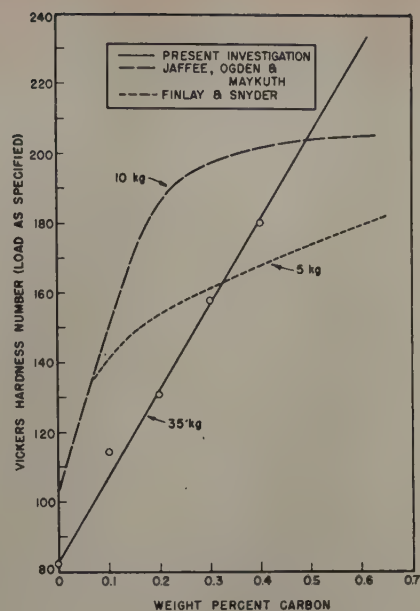


Fig. 17—Vickers hardness of α -phase Ti-C alloys. Also shown are hardness data reported by other investigators.

may be picked up during arc melting and processing. Chromium, also a β stabilizer, reduces the solubility of carbon in β titanium.¹⁴ Carbon segregation is not likely in the 0 to 0.2 pct C range since this amount of carbon is soluble in titanium at the liquidus, no carbide stringers being observed. Furthermore, alloys in this composition range were first annealed at 875°C, the single-phase α field, for 24 to 48 hr to homogenize the structure before annealing at investigation temperatures.

In all cases the chemical analysis was carried out on specimens which had been used for the metallographic examination.

¹⁴ E. Ence, W. Kirk, H. Margolin, and J. P. Nielsen: New York University, Reports on Contract No. DA-30-069-ORD-200 (Part III) to Watertown Arsenal.

Constitution of Titanium-Rich Ti-Cr-Al Alloys at 1800° and 1400°F

by Jack L. Taylor and Pol Duwez

DISCUSSION, J. P. Nielsen presiding

Harold Margolin (New York University, New York)
—We have been studying sponge-base Ti-Al-Cr alloys with and without carbon additions under sponsorship of the Bureau of Aeronautics.¹⁸ In regard to the phase diagram, it has been found that at 750°C aluminum additions do not increase the solubility of chromium in α titanium which is below 1 pct.^{6, 8} For example, alloys containing approximately 2.5 and 4.0 pct Al with somewhat more than 0.25 pct Cr show $\alpha + \beta$ structures. Additions of carbon have been found to shift the aluminum compositions at which TiCr_2 is observed from approximately 14.5 pct at 760°C (1400°F), as the authors have indicated, to 3 pct Al at 750°C.

In regard to M_s temperatures, we have obtained results which are considerably lower than those reported by the authors. Dr. Polykarp Herasymenko of our laboratory has been investigating temperature regions in which different microstructures develop in the commercial 3 to 5 pct Cr alloy on quenching from 1000°C in lead and Wood's metal bath. For isothermal transformation of small specimens (1/16 to 1/8 in. thick) in the interval from 600° to 200°C, he finds structures which can be described as β' . (The β' structure is the product of submicroscopic precipitation of α from the original β .) Martensite developed in 1/16 in. thick specimens only below about 200°C.

¹⁸ Investigations sponsored under Contracts NO(as) 51-331-C and NO(as) 53-018-C.

When bars of larger diameter ($\frac{1}{2}$ to $1\frac{1}{4}$ in. rounds) are first quenched in a lead bath at 350°C , held there for from 5 to 20 min and subsequently quenched in water, the outer zone of the bar has the β' structure and the central part is martensitic. If the bar is held longer, the transformation to β' proceeds from the outer regions in toward the center. A complete transformation to β' at 350°C requires 50 min for $\frac{1}{2}$ in. rounds and more than 100 min for 1 in. rounds.

As in the case of small specimens, it is necessary to quench below 200°C in order to obtain martensite. This is shown by the following tests: A $\frac{1}{2}$ in. round first quenched at 350°C , held there for 20 min, transferred to another metal bath at 225°C , held for 20 min and finally water quenched, shows the β' structure in the whole cross section. A bar of the same size held 40 min at 350°C and rapidly quenched to room temperature shows martensite at the center.

It does not appear possible to ascribe the lower M_s temperatures reported by Dr. Herasymenko to differences introduced by impurities in his alloys, since the major impurities here would tend to raise rather than lower β transformation temperatures. It is not known whether the difference in M_s temperature is due to stabilization effects or whether the breaks in the cooling curves obtained by the authors are due to some other reaction than the formation of martensite.

J. L. Taylor and Pol Duwez (authors' reply)—The authors thank Dr. Margolin for his interesting comments. The extent of the α solid solution with chromium content may very well be sensitive to small amounts of impurities and the lack of agreement between the two investigators might be due to the fact that sponge titanium instead of iodide titanium was used by Dr. Margolin.

In regard to the M_s temperature, we recognize that there might be some difference between the M_s temperature determined from microstructure and what was called, for simplicity, the M_s temperature in the present study. The significance of the temperature reported in the paper is that it is a temperature at which pronounced exothermic reaction takes place during cooling within the range of cooling rates from about 200° to 600°C per sec. This temperature has also been shown to be essentially independent of the rate of cooling for rates as high as 5000°C per sec. What exactly is the relation between this exothermic reaction and the M_s temperature as deduced from microstructure studies after a rather complicated thermal treatment is not clear at this time. Studies such as those made by Dr. Margolin will certainly lead to a better understanding of the transformation mechanism in titanium alloys.

Titanium-Manganese System

by D. J. Maykuth, H. R. Ogden, and R. I. Jaffee

DISCUSSION, J. P. Nielsen presiding

W. Rostoker, R. P. Elliott and D. J. McPherson (*Armour Research Foundation of Illinois Institute of Technology, Chicago*)—The writers have followed the development of the Ti-Mn phase diagram through interim technical reports to the sponsor and are pleased to note its appearance in final form.

The authors appear to have delineated the phase boundaries in this experimentally difficult system with accuracy in the region between titanium and the eutectic composition (42.5 pct Mn). The evidence from which they have suggested a peritectic generation of the γ intermediate phase seems, however, to be inconsistent and open to alternative interpretation in some cases.

If the γ phase were not generated by a peritectic reaction, the appearance of $\beta + \delta$ (TiMn₂) eutectic structures, always found by the authors, would be normal. If γ is peritectically formed, even by a sluggish reaction, the existence of such a "nonequilibrium eutectic of δ in β " has no parallel in the writers' knowledge.

To examine specifically the micrographs presented: Fig. 7a and b is said to contain γ phase as "large white crystals." If γ must form by the reaction $\text{Melt} + \delta \rightarrow \gamma$, this would infer regions of completed peritectic reaction, even though rims (the invariable mode of formation of a peritectic phase) are not to be seen around the other primary crystals of δ . These structures are not typically peritectic and could certainly be interpreted as two-phase, $\beta + \delta$. Fig. 8 shows light gray rims called γ , around dark gray primaries (δ), and a matrix of "nonequilibrium" $\beta + \delta$ eutectic. Here again, in the upper right corner, are large crystals of " γ " with no δ -core, indicating completion of the presumably sluggish peritectic in certain areas. The unorthodox manner of etching here is suspect. Heat tinting after etching can cause illusory effects. The

writers have seen apparent two-phase structures developed from single-phase alloys in this manner. Fig. 9a, for example, is labeled two-phase ($\beta + \gamma$) by the authors, but shows three distinct color tones after this treatment and might equally well be thought to consist of three phases.

The identity of phases in Figs. 9b and 10 is questioned. As compared with Fig. 8, γ and δ have reversed colors according to the authors' identification, δ now being light and γ dark. In addition, if the peritectic equilibrium did exist, δ should not be expected to be the matrix (continuous) phase at these compositions, but rather would maintain the primary configuration of its as-cast state, even after the annealing treatment employed. The dark and light areas of Fig. 9b are regarded by the writers as the same phase with individual grain differentiation due to the etching-heat tinting treatment, similar to Fig. 9a. The structures of Figs. 9a, b, and 10 are all regarded as δ (dark) in β (light).

Reflection will show that a very sluggish peritectic formation of γ (at 1200°C) suggested by the authors may not be compatible with the advanced states of equilibrium claimed for Figs. 9a, b, and 10 (at 1100°C). If the β present in the cast alloy of Fig. 10 has all been consumed on annealing, then the peritectic reaction is complete and the alloy should consist of 80 to 90 pct γ .

To assist in the development of certain ternary phase diagrams¹¹ independent investigations on the binary

¹¹ Contract No. DA-11-022-ORD-272 to Watertown Arsenal.

Ti-Mn system were conducted at Armour Research Foundation. Alloys were prepared by arc melting at 2 pct intervals in the range 37 to 70 pct Mn. Portions of the ingots were annealed at 1150° , 1100° , 1000° , 900° , 800° , and 700°C , respectively. Other specimens were annealed just below the eutectic temperature and

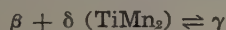
then subsequently at lower temperatures. Annealed and as-cast structures were studied by both metallographic and X-ray diffraction methods.

The as-cast structures, although similar to those presented in the paper, could not be interpreted as showing a peritectic reaction. The structures showed primary β or δ (TiMn_2), with interdendritic eutectic of ($\beta + \delta$). Diffraction patterns on the whole range of alloys annealed at 1100°C for 24 hr showed the presence only of δ and β . The microstructures of the annealed samples were clearly two-phase. Furthermore, the eutectic structure was completely erased by coagulation in this time period indicating a fairly high atomic mobility. A suppressed peritectic reaction might reasonably be expected to have begun under these conditions of anneal.

Table VI. Analysis of X-Ray Diffraction Patterns of a 50 Pct Mn Alloy

Anneal	Phases Identified
1150°C — 1 day	$\beta + \delta$
1000°C — 5 days	$\beta + \delta$
900°C — 30 days	$\beta + \gamma$
800°C — 10 days	$\beta + \gamma$
700°C — 15 days	$\beta + \gamma$

Below 1000°C, diffraction patterns gave evidence of new lines. Microstructures confirmed the presence of three phases. Fig. 18 shows a typical two-phase structure of a 48 pct Mn alloy as obtained at 1150°C. Fig. 19 shows the three-phase structure developed at 900°C. Table VI summarizes the analyses of the X-ray diffraction patterns of a 50 pct Mn alloy annealed at various temperatures. The anneal at 900°C was prolonged intentionally to permit sufficient γ to form to give a clear and predominant pattern. The evidence presented seems to the writers clearly to indicate that γ forms by means of the peritectoid reaction



at some temperature between 900° and 1000°C. A list of the observed diffraction lines of the phase γ is given in Table VII. If the viewpoint of a peritectoid generation of γ phase is adopted, the authors' evidence can be re-examined in the manner discussed earlier. The lack of peritectic rims in cast alloys (such as Fig. 7a and b) becomes normal, and if the inconsistent colorations imparted by the etching-heat tinting treatment are discounted, the configuration and relative

Table VII. Observed Powder Pattern Lines of the Gamma Phase

I^*	d, kX	I^*	d, kX
vft	2.358	vft	1.967
vw	2.272	vw	1.893
vft	2.247	vft	1.819
w	2.215	vft	1.778
vft	2.191	vft	1.728
vw	2.156	vft	1.667
vft	2.109	vft	1.492
w	2.073	vft	1.433
ft	2.001		

* w, weak; vw, very weak; ft, faint; vft, very faint.

amounts of phases in Figs. 9a, b, and 10 fit better a β - δ equilibrium at 1100°C. With these alternative interpretations, only the thermal analysis arrests are directly rejected, and it is perhaps possible that spurious effects were obtained between the relatively close eutectic and liquidus levels.

Attention should be called to two probable typographical errors in the manuscript. Wallbaum's correct TiMn_2 parameter is $a = 4.81\text{\AA}$, and Duwez and Taylor's TiX compound lattice type is CsCl.

D. J. Maykuth, H. R. Ogden, and R. I. Jaffee (authors' reply)—We appreciate the discussion of Rostoker, Elliott, and McPherson concerning the origin of the γ phase. We too have considered a peritectoid origin, but have rejected it for reasons brought out here.

Because of their metallographic similarity, distinction between and the identification of the β , γ , and δ phases in Ti-Mn alloys containing them is uncertain with conventional etching procedures. Nevertheless, by use of the usual HF-containing etchants, the cast structures of ingots containing 45.4 through 66.7 pct Mn showed that, contrary to the suggestion advanced by Rostoker et al., three separate phases were present in each of these alloys. Truly, the arc-cast structures are not typically peritectic in that γ , the phase which ordinarily should originate in a peritectic reaction between melt and δ at 1200°C, does not assume the usual reaction-rim structure about the primary δ crystals. However, as shown clearly in Fig. 7 of the paper, these cast structures do not fit the simple category of eutectic phase mixtures. Rather, the γ and β phases coexist with δ in a complex nonequilibrium-eutectic mixture interdendritic to the primary δ . This unusual behavior results from the combination of, 1—the proximity of the peritectic to the eutectic reaction temperature, and 2—the extremely rapid cooling rates en-

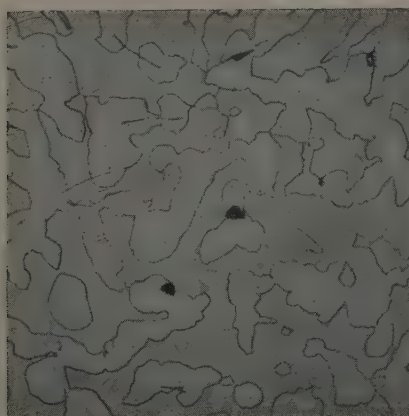


Fig. 18—48 pct Mn alloy annealed at 1150°C for 24 hr. Structure shows $\beta + \delta$. Etchant: 60 pct glycerine, 20 pct HF, and 20 pct HNO_3 . X300. Area reduced approximately 50 pct for reproduction.

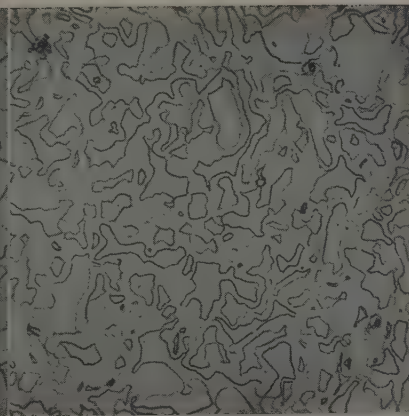


Fig. 19—48 pct Mn alloy annealed at 1100°C for 24 hr and then at 900°C for 16 hr. Structure shows β , δ , and γ in a peritectoid configuration. Etchant: 60 pct glycerine, 20 pct HF, and 20 pct HNO_3 . X300. Area reduced approximately 50 pct for reproduction.

countered in arc melting the 15 gram ingots used in this study.

By the use of slower cooling rates, the usual peritectic ring formation is observed as is illustrated in Fig. 9. In their criticism of this structure, Rostoker et al. imply that the γ phase should, in every instance, occur as a rim structure surrounding the primary δ . However, it appears entirely feasible that, under the conditions which maintain even with the slower cooling rates, isolated γ crystals could be nucleated directly from the melt. It is also apparent that additional precipitation of the γ phase from the β matrix will result because of the sharply decreasing solubility of manganese in β with decreasing temperature. Also, the fact that reproducible thermal arrests supporting the peritectic reaction were obtained on three separate alloys can hardly be ascribed to spurious effects.

Equilibrating treatments of 100 hr at 1100°C on samples containing 45.4 through 54.7 pct Mn produced structures which were similar to that shown in Fig. 18 after etching chemically. This photograph, according to the interpretation of Rostoker et al., consists of light-colored δ crystals in a β matrix. The differences in delineation of the δ crystals from the β matrix are apparently ascribed to orientation differences of this phase. We observed, however, that these "orientation differences" in the chemically etched structures were definitely related to alloy composition, thus suggesting that, in reality, three phases were present in this range of alloy composition. Accordingly, the structure of Fig. 18 best fits the interpretation of a three-phase structure consisting of γ crystals (sharply delineated) in a β matrix which also contains a small number of residual nonequilibrium δ particles (faintly delineated). As shown in Figs. 9 and 10 of the paper, heat tinting of the chemically etched structures amplifies, but does not otherwise alter, the phase differences. This procedure was of direct assistance in establishing the metallographic identity of the β phase which was not discolored nor oxidized by the treatment used. Both

the γ and δ phases, on the other hand, become covered with a superficial oxide film upon exposure to warm air. Since the coloration of these phases was due to the formation of thin, interference-color films, their final colors did occasionally vary from one sample to the next.

X-ray diffraction data on a 53.6 pct Mn alloy quenched from 1175°C confirmed the coexistence of the three phases in this structure. Other diffraction data on samples containing 60.4 to 67 pct Mn and equilibrated at 1175°C showed that no β lines were observed in any of these samples. It should be noted further that X-ray identification of the γ compound was carried out by means of a diffusion couple prepared at 1000°C, a temperature at which Rostoker et al. claim that the γ phase does not exist.

During the initial metallographic exploration of alloys within the β - γ field, it was observed that reheating samples to temperatures on the order of 50° to 100°C below the equilibrating temperature produced reaction-rim structures, similar to that shown by Rostoker et al., in Fig. 19, which appeared indicative of a peritectoid reaction. However, in a series of treatments designed to pin down the "peritectoid reaction," it was found that the formation of the reaction rims was inconsistent and depended primarily on the difference between the temperature used for the initial equilibration treatment and the subsequent, low temperature treatment. These rims were therefore interpreted as diffusion rings of γ representing additional growth of the original γ crystals as a result of treatment at lower temperature. It was also noted that the lower temperature treatments resulted in the precipitation of γ particles directly from the β matrix with no apparent core of δ as would be called for by a peritectoid reaction. Moreover, no such reaction-rim structures were observed in any of the equilibrated alloy structures containing 56.4 through 67 pct Mn during subsequent treatment at temperatures down through 750°C.

Recrystallization of a Cold-Rolled Copper Single Crystal

by Y. C. Liu and W. R. Hibbard, Jr.

DISCUSSION, E. R. Parker presiding

P. A. Beck (University of Illinois, Urbana, Ill.)—This paper represents excellent data on the reorientation upon recrystallization. These data are interesting since they bear directly on certain questions in dispute. Early work by Burgers and Louwerse²³ suggested that the reorientation upon recrystallization of deformed single crystals of aluminum takes place according to rotations around [112] axes lying in the active slip plane and perpendicular to the active slip direction. In later work by Dr. Hsun Hu and myself on aluminum⁴ and copper²⁴ it was found that this reorientation (including the data of Burgers and Louwerse) can be much better expressed in terms of rotations around [111] axes. In a recent review, Burgers indicated²⁵ that he considered the question still undecided. The careful work of Liu and Hibbard with a critically oriented copper crystal confirms the interpretation of this reorientation in terms of [111] rotations, without leaving any room for further doubt.

Another disputed point concerns the angle of rotation around the [111] axis. Kronberg and Wilson²

found the angles of rotation for copper to be 22° and 38°, in contrast to the 30° angle reported for coarsening in polycrystalline copper by Bowles and Boas¹ and for recrystallization in a rolled single crystal by Hu and Beck.²⁴ The recrystallization texture found by Liu and Hibbard can be best described by 30° rotations around [111] axes, in accordance with the results of Hu and Beck.

According to the oriented growth theory of recrystallization textures, one may expect a single orientation deformation texture of a face-centered cubic metal to recrystallize into eight texture components, corresponding to 30° rotations in two directions around each of the four [111] axes.² Burke pointed out²⁶ that in many recrystallization textures most of the expected eight components are missing. However, it is significant that in all cases cited by Burke the matrix texture is described by more than one "ideal" orientation. In the case of complex matrix textures, the oriented growth theory does not predict the development of recrystallization texture components except in such orientations as are favorable for growth with respect to all of the major and minor texture components and the

important orientation scatter ranges of the matrix texture. This requirement may exclude several or most of the eight "theoretical" orientations corresponding to each texture component of a complex matrix. But on the basis of the oriented growth theory, one may expect that all eight recrystallization texture components do occur when the matrix consists of a single orientation texture. The findings of Liu and Hibbard indicate that this is indeed the case. Accordingly, their results contribute an important additional piece of evidence in favor of the oriented growth theory of recrystallization textures.

The authors attempt to explain the disappearance on annealing at 500°C of two of the eight recrystallization texture components by assuming an effect of internal stresses, remaining in the rolled copper crystal at least in the early stages of annealing at that temperature. This explanation is not at all convincing. It is difficult to see how such residual stresses could remain effective at the temperatures in question and, particularly, how they could be more effective at 500° than at 400°C. It is certainly much more reasonable to expect that the grains of the missing orientations are absorbed by other grains, when grain boundary migration in the already recrystallized material is encouraged by the higher annealing temperature. On this view, the situation would be somewhat similar to that obtaining in the high temperature reorientation in rolled and recrystallized brass discovered by Wilson and Brick.¹¹ The question could be investigated by means of a simple experiment. It would have to be determined whether or not the incomplete texture is formed at 500°C, even after a previous 400°C anneal already produced in the specimen all of the eight recrystallization texture components. If the two orientations in question were found to disappear on subsequent 500°C annealing, the growth theory would have to be accepted. In the reverse event, the growth theory would be much less attractive, since it could be upheld only by making certain ad hoc assumptions; also, in

this case, the stress theory would certainly not be ruled out.

Y. C. Liu and W. R. Hibbard, Jr. (authors' reply)—Referring to Professor Beck's suggestion that the appearance of eight recrystallization texture components serves as another support for the "oriented growth" hypothesis, we feel that our investigation is not a critical experiment to evaluate one recrystallization hypothesis above the other. The "oriented nucleation" hypothesis can also be applied to explain this phenomenon without any modification of its basic concept.

Specimens are being prepared to evaluate Professor Beck's suggestion that the recrystallized grains related to octahedral pole IV in the text are likely to be absorbed by other grains at higher annealing temperatures. In the text, we did not propose that the internal stresses are more effective at 500° than at 400°C. From the theoretical analysis of the mode of deformation of our specimens during cold rolling, we concluded that the octahedral plane IV is probably stressed the least in comparison with the other three octahedral planes and therefore stored less strain energy. If it is assumed that the strain energy released during recovery is proportional to the magnitude of residual stresses existing in the individual slip plane, and also that it is proportional to the annealing temperature, the low-stressed octahedral plane IV would participate during the nucleation process at low annealing temperatures and become latent at high annealing temperatures owing to the very fact that the strain energy stored at this octahedral plane has been dissipated during recovery.

²³ W. G. Burgers and P. C. Louwerse: *Über den Zusammenhang zwischen Deformationsvorgang und Rekristallisationstextur bei Aluminium*. *Ztsch. Phys.* (1931) 67, p. 605.

²⁴ Paul A. Beck: *Orientation in Recrystallization and Grain Growth*. *The Physics of Powder Metallurgy*. (1951) pp. 40-51. New York, McGraw-Hill Book Co.

²⁵ W. G. Burgers: *Recrystallization and Grain Growth in Solid Metals*, *L'Etat Solide*. (1952) p. 431. Bruxelles, R. Stoops.

²⁶ J. E. Burke: *Origin of Recrystallization Textures*. *Trans. AIME* (1952) 194, p. 263; *JOURNAL OF METALS* (March 1952).

Cold-Rolling and Annealing Textures of Molybdenum Single Crystals

by N. K. Chen and R. Maddin

DISCUSSION, E. R. Parker presiding

P. A. Beck (University of Illinois, Urbana, Ill.)—Since the (001) [100] deformation textures show an unusually large spread around the normal direction, it would be interesting to recheck these textures by means of the quantitative methods now available. Quantitative texture determination methods often reveal much sharper textures than previously found for the same material by the photographic method. The question of texture retainment on annealing could be answered much more positively by checking also the annealing texture by the quantitative method. If a single orientation texture is actually retained on annealing, clearly no ordinary grain boundary migration ("recrystallization") could have taken place in the course of annealing. It seems preferable to consider the annealing mechanism in such a case as subgrain growth, that is, the migration of low angle boundaries, which do not involve noticeable reorientation. As suggested already by the earlier work of Semchyshen and Timmons² for polycrystalline material, it would appear

that in the case of molybdenum this annealing mechanism is a very important one.

N. K. Chen and R. Maddin (authors' reply)—There is no doubt that a quantitative determination of both the deformation and the annealing textures, as pointed out by Professor Beck, would be much more desirable and might have led to a separation of the intensities of the spread around the normal direction. Unfortunately, however, this equipment was not available at the time this work was performed. Additional research with a greater number of combinations of starting orientations is in progress.

It was pointed out in the paper that certain deformation textures were retained, while others had undergone a rotation during annealing. At the present time it seems difficult to differentiate the mechanism operating in the retention of one texture and the change in others. In the case where no noticeable reorientation was observed, the annealing mechanism might very well be a subgrain growth process as pointed out by Professor Beck.

Statistical Grain Structure Studies: Plane Distribution Curves Of Regular Polyhedrons

by F. C. Hull and W. J. Houk

DISCUSSION, Leo Shapiro presiding

P. K. Koh (*Allegheny Ludlum Steel Corp., Brackenridge, Pa.*)—I wish to compliment the authors for refining the thinking of the quantitative counting method. The discrepancy between the prevailing assumed spherical and actual polyhedral shape of grains in various phases becomes very significant as the size of the grains increases.

Most commercial sheet materials possess some degree of elongation of grains along the rolling direction. In order to evaluate the statistical grain structure of metallic sheets by the plane or line intercept method in light of the authors' finding, the introduction of some modifying factor to compensate for grain elongation seems to be desirable.

On p. 556, second paragraph, the authors stated that "although the form with plane faces and straight edges does not fulfill the surface-tension requirements, the difference in the figures, insofar as the plane distribution curve is concerned, is negligible." One wonders whether this approximation holds true in instances of secondary grain growth, when the secondary grains are much larger in size than the primary grains and also have concave edges to a pronounced degree.

Most materials exhibit mixed grain sizes in the heat-treated condition. For this reason it is probably of importance to consider size distribution of polyhedrons as well as their shape. This consideration would introduce another factor in the application of the authors' derivation to engineering materials.

We feel that it would be helpful if the authors gave the Miller indices for the planes with the maximum frequency in the distribution curves, since the planes may be related to slip planes.

F. C. Hull and W. J. Houk (authors' reply)—Contrary to the implication in the first paragraph of Dr. Koh's discussion, the relative shape of the plane distribution curve is independent of the absolute size of

the metal grains. There is a discrepancy between assuming spheres instead of the actual polyhedral shape of metal grains, but the percentage error is not a function of grain size.

It would be a simple but tedious matter to determine the plane distribution curve of an elongated polyhedral grain. The unfortunate fact is that a different distribution curve would have to be determined for each degree of eccentricity. As yet there is no adequate method to compensate for grain elongation.

On p. 556 the authors substituted the orthic tetrakaidecahedron for the tetrakaidecahedron of minimum area, to determine the distribution curve, because of the greater ease of measuring the areas of intersection of the plane-sided polyhedron. A reference to the drawings of these figures in Desch's paper will show how little difference there is between them. The distribution curve for this regular fourteen sided polyhedron would naturally differ from that of the special shapes developed by secondary grain growth. A single large grain in a matrix of small grains would have hundreds of concave faces. After the secondary grains have completely replaced the primary ones, conditions could return more nearly to normal.

The technique for calculating the distribution of grain sizes in space has been described by Scheil. It is necessary that the plane distribution curve of the average metal grain be known. One of the purposes of our paper was to show in what respects Scheil's plane distribution curve should be modified to correspond more closely to the case of polyhedral grains.

In the case of a cube, for example, the frequency curve rises abruptly at an area equal to that of one of the faces. To assign Miller indices to this group of planes would be incorrect, however, because the crystallographic planes of the metal grain bear no relation to its external shape which is determined by impingement with neighboring grains.

Observation on Scaling of Iron

by W. J. Wrazej

DISCUSSION, Leo Shapiro presiding

J. Paidassi (*University of Concepcion, Concepcion, Chile*)—It is evident that for an exact determination by micrographic methods of the kinetics of the oxidation of metals (the oxidizing phenomenon being observed at the purest state possible), two conditions must be fulfilled: 1—The experiments must be carried out under conditions such as to reduce complementary factors to a minimum (presence of chemical films on the surface, of tensions and residual gases in the metal lattice, etc.) so that the scales (and their different

layers) obtained may have as uniform a thickness as possible and be as reproducible as possible; and 2—The several scale layers must be measured exactly, which presupposes a sufficiently refined method of mounting and polishing. In this measurement the greatest error may be incurred in the determination of the thickness of the external layer of Fe_2O_3 , which is usually very thin and may even escape notice if the polishing technique is insufficient.

Seldom, so far, have these conditions been realized simultaneously in the study of the growth of scale

layers of microscopic thicknesses in the oxidation of iron. However, it seems evident that only a table of the complete data of the kinetics of the growth of the layers between 450°C (and even perhaps 400°C) and 1050° to 1100°C could provide a valid basis for the understanding of the intimate mechanism of the oxidation of iron, in its pure state.

The experiments of Mr. Wrazej do at any rate fulfill the second set of conditions, and he must be congratulated for the beautiful micrographs he has published. One may, however, ask whether the first conditions have been met satisfactorily.

From our experience, indeed, if a refined technique of physical-chemical preparation of the specimens of iron (such as the technique of Gulbransen and coworkers or Birchenall and coworkers) does not seem necessary for temperatures over 650°C, a minimum of preparation prior to the oxidation remains indispensable.

We have found in our experiments that to obtain, even at temperatures higher than 650°, scales perfectly uniform as to total thickness as well as to the proportion of the different layers, it is necessary to submit Armco iron, prior to oxidation, to treatment by hydrogen for several hours at temperatures ranging between 850° and 1000°C. (Other researchers like J. Benard and coworkers have made use of previous annealing at high temperatures in high vacuum.) Otherwise, there is a risk that the scales may be irregular and partially divorced from the metal and even that real blisters may develop.

This phenomenon becomes fundamental at high temperatures, particularly above 900°C, and it is owing to its not having been sufficiently considered that all researchers, up to Birchenall and coworkers¹ as well as the present writer,^{2,4} have been led to results which in our view are mistaken, both with regard to the total thickness and the proportion of Fe_2O_3 and Fe_3O_4 oxides in the scales, for temperatures exceeding 900°C.

It is possible that materials purer than Armco iron, such as Puron, may not require previous annealing in hydrogen for temperatures between 700° and 800°C (this seems to be the case with Puron, since Stanley and coworkers⁵ have obtained scales and layers of thicknesses close enough to ours in the time limit that they have studied and for temperatures of 700° and 800°C). In this regard we should like to ask Mr. Wrazej as to whether the Hilger iron he used yielded the same irregularities in the proportions of the Fe_2O_3 and Fe_3O_4 layers?

Mr. Wrazej has verified the presence of blisters in the scales he obtained and even places where the layer of Fe_2O_3 had disappeared entirely through peeling. Could not the fluctuations in temperature tolerated in the furnace ($\pm 5^\circ\text{C}$) be responsible for the cracking and peeling of the external parts of the films which occurred in spite of the precautions taken by the author to protect the surface of the samples tested from excessive thermal shocks?

If it were not hazardous to interpret isolated micrographs (without having actual samples), we should discern cracks concentric to the surface separating the metal and the scale (for example in the micrograph in Fig. 2) and this not only in the layer of FeO (these cracks accounting for the excessive growth of the layers of higher oxides with regard to FeO), but also in Fe_3O_4 (these cracks likewise explaining the exaggerated value found for the proportion of the thicknesses $\text{Fe}_2\text{O}_3:\text{Fe}_3\text{O}_4$). In the micrograph in Fig. 4 also a series of solutions of continuity is to be remarked in the layer of Fe_3O_4 .

These cracks and these zones in the scale with an exaggerated proportion of higher oxides are apparent in nearly all our samples of oxidized sheet iron at corners and edges, where evidently the growth of thickness is disturbed by partial separation caused by a concentration of tensions. (Such partial separation we have been unable to suppress completely at temperatures of 700°C and over in spite of our precaution

of carefully rounding the edges in the course of polishing the samples.)

It is essential to remember that since there is a separation, even though partial, between the iron and the scale, or a formation of longitudinal cracks in the scale, the proportion of higher oxides increases. We have verified this fact repeatedly, and the micrographic study we are making of the oxidation of the oxides FeO and Fe_3O_4 entirely confirms this assertion, so that it is essential to accept as sure measures only those results obtained from scale which adheres well to its support during the experiments of oxidation. As a criterion of adherence we have made up a whole list of conditions that must be simultaneously fulfilled; in particular numerous verifications have made it clear that within the range of temperatures of 450° to 750°C, we must discard scales with brownish red surface, partially divorced from the metal: such surface is really covered with fine needles of Fe_2O_3 presumably originating under conditions of tension (at least momentary) in the scale and of relatively slow growth. (We have not observed the needles and reddish tint beyond 750°C.) Figs. 5 and 6 show the aspect presented by the needles according to the conditions of their formation.

In our opinion, then, the high proportions of $\text{Fe}_2\text{O}_3 + \text{Fe}_3\text{O}_4/\text{FeO}$ given by the author correspond to a phenomenon of oxidation in which complementary factors intervene. The proportion of 20 pct given was, in addition, the same obtained by Tesche⁶ whose experiments should be viewed with similar reservations (particularly as we have verified that with very small gage wire it became excessively difficult to avoid partial separation of the scale from the metal and irregularities of the thickness).

Our final curves of the growth of Fe_2O_3 and Fe_3O_4 in the scales of Armco iron oxidized in air are already complete in the 450° to 1000°C range and we have no correction to make in the diagram of synthesis of Fig. 12 which has been published² (and this in spite of several additional control series, particularly that of 700°C). However we add our new experimental values at the temperatures of 750°, 920°, and 1000°C and find that they fall perfectly into the published curves.

As to the importance of the micrographic technique, that is to say, the second set of conditions, Mr. Wrazej is perfectly right in insisting on it. Nevertheless, we cannot agree that the pressure is indispensable to obtain correct results. The mountings with Bioplastic or Turtox in accordance with the procedure recommended by the manufacturers themselves yield, in our experience, excellent results. A rather important condition is evidently the hardness of the mounting (which renders unacceptable the use of fusible alloys of the Wood type). It happens, however, that, even with relatively hard mounting material like the plastics mentioned, a small valley is produced along the edge of the scale's section, resulting during the polishing in a given relief of the same. This, as we have verified, does not imply in all cases a tearing away of the outer layer. In any case, a direct control on the fractured scales must be made whenever possible. As an instance we are including the micrographs of the following scales mounted in Bioplastic: 625°C for 24 hr (Fig. 7) and 500°C for 24 hr (Fig. 8) where the perfect regularity of the layers is noticeable. The first micrograph shows, besides, that for high oxidation times, closer to conditions of equilibrium, the proportions of Fe_2O_3 , Fe_3O_4 layers are clearly weaker than the ones generally admitted.^{1,5,7} Fig. 8 shows that the layer of Fe_2O_3 is found in scales of incomplete oxidation from temperatures as low as 500°C. (We have had micrographic evidence of these layers in scales made at 500°C after 90 min oxidation and in those made at 450°C after 6 hr oxidation.)⁸ Regarding the micrographs included in the above quoted discussion² they on the contrary were made from samples previously mounted in bakelite under pressure. Nevertheless, the control series at 700°C was completed with a Bioplastic mounting and the results were identical. We have noticed also that mounting under pressure becomes

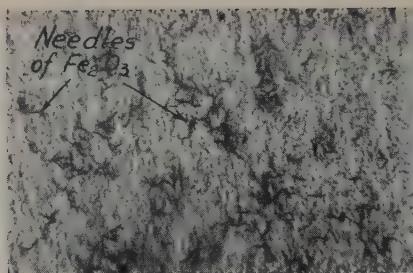


Fig. 5—Micrograph taken perpendicular to the exterior surface of a scale of incomplete oxidation of Armco iron in air, 500° for 12 hr. The needles of Fe_2O_3 are lying on the exterior surface of the scale.

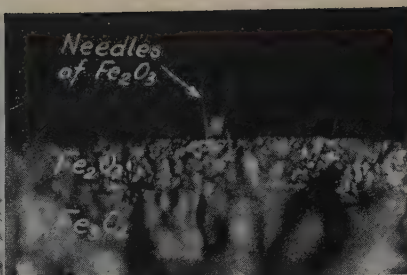
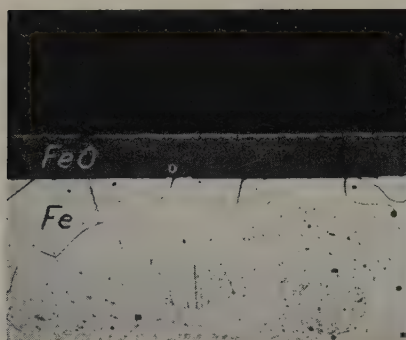
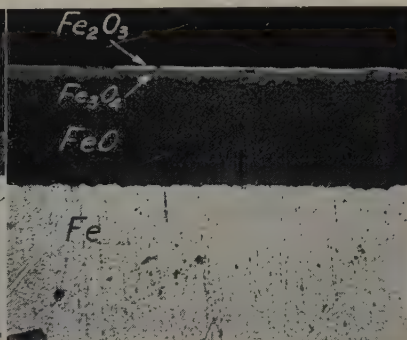


Fig. 6—Exterior edge of the fracture of a scale of incomplete oxidation of iron separated from its iron support and re-oxidized in the air during 48 hr at 700°C. Note the needles of Fe_2O_3 .



a—X150. Area reduced approximately 50 pct for reproduction.



b—X400. Area reduced approximately 50 pct for reproduction.

Fig. 7—Scale of incomplete oxidation of Armco iron in air, 625° for 24 hr.

impracticable for scales of iron corresponding to experiments made at temperatures over 900°C because

under such conditions these films are more fragile and become partially pulverized under pressure.

W. J. Wrazej (author's reply)—I agree with Professor Paidassi that the application of certain precautions is important when performing the scaling experiments. Of primary importance is the annealing which must be performed at temperatures about 900°C to remove any traces of cold work introduced into the sample during straightening, cutting, abrading, polishing, etc. Even polishing on 3-0 emery paper is not without any practical effect for the layer of metal as little as a few hundred atoms thick. To my mind, the prerequisites in this research appear to be annealing in vacuum and subsequently lightly etching to remove the recrystallized, but not always uniform, metal layer with traces of scale accidentally produced during annealing. However, annealing in hydrogen would not be without effect upon this capricious experiment.

Soft irons, whether Armco or Hilger electrolytic, are prone to surface damage. Cold work as well as carbon content favors the splitting and the loss of the layer

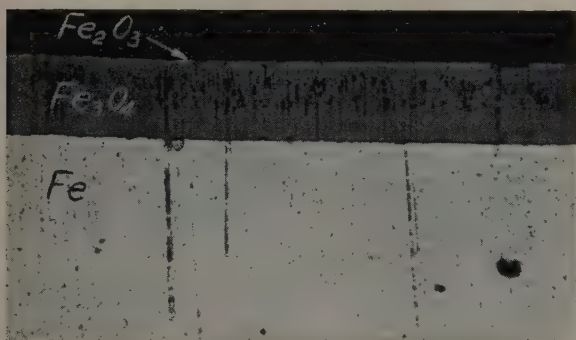
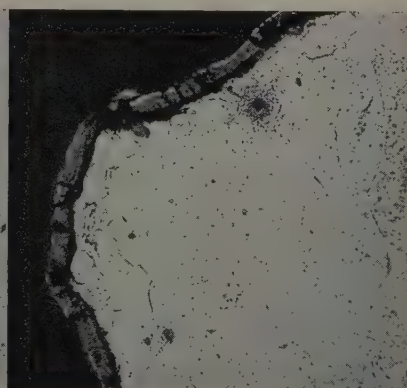


Fig. 8—Scale of incomplete oxidation of Armco iron in air, 500°C for 24 hr. X750. Area reduced approximately 50 pct for reproduction.



a—Smooth surface.



b—Corner and rough surfaces owing to a coarse emery paper abrading.

Fig. 9—Sample of Armco iron scaled in air at 500°C for 24 hr. 4 pct picral etch. X600. Area reduced approximately 50 pct for reproduction.

of scale. The use of the most carbon-free iron is essential. Soft iron with small quantities of copper or nickel will behave differently from pure iron, as those alloying elements make the scale adhere better.

The influence of the surface preparation can be seen from the following.

The sample of Armco iron ($\frac{1}{4}$ in. diameter, in the unannealed condition) was suspended from nichrome wire and heated in an open muffle furnace at 500° for 24 hr. The sample, together with the wire, was mounted cold in a dental plastic (Moldpac, repair acrylic) without any pressure. The difference in scaling between a smooth surface of the sample when carefully prepared (Fig. 9a) and that normally abraded after being cold cut and polished on coarse emery paper (Fig. 9b) is characteristic. The smoothed part of the surface (Fig. 9a) is similar to that shown by Professor Paidassi's Fig. 8 except that the outer layer is hardly discernible. Its existence appears rather doubtful. It would be very important to consider this question in further experiments. On the contrary the part of the surface normally abraded (Fig. 9b) shows a thinner layer of scale in which two phases are distinctly visible. Thus in microscale a distorted layer of metal can distinctly change the results. It has been stated that the relative diffusion ratio depends very appreciably upon the initial surface condition of the metal.⁹

A corner which in Professor Paidassi's opinion is prone to show a thicker layer of scale does not differ

in this particular case either in thickness or in the ratio of the two kinds of oxides from that shown on the sides of the sample. In this particular case the sample was taken out of the furnace and cooled in the air. For the very smooth surface this sudden change in temperature appears to be of no importance in the peeling off of the scale, whereas it is assumed that for the rough surface slow cooling would not have prevented scale loss. To what condition Professor Paidassi's layer (Fig. 8) can be ascribed, I do not know.

The question of surface preparation must still be studied and there may not be any general rules that are applicable to the whole range of temperature.

In my opinion a separate and a very important problem would be the extension of Professor Paidassi's research up to the melting point of iron.

⁴ J. Paidassi: Contribucion al estudio del mecanismo de la oxidación del hierro puro. Paper read at Fifth South American Congress of Chemistry, Lima Peru, May 4-11, 1951, in press. Published in part in *Ingeniería Química*. Univ. Concepción, Chile (1951) 10, No. 10.

⁵ J. K. Stanley, J. von Hoene, and R. T. Huntoon: *Trans. ASM* (1951) 43, p. 426.

⁶ O. A. Tesche: *Trans. ASM* (1950) 42, p. 641.

⁷ J. Benard and O. Coquelle: *Revue Metallurgie, Mémoires* (1946) 43, p. 113.

⁸ The partial results reported in this discussion are relative to the research corresponding to Contract No. 3 between the author and the "Consejo de Investigación Científica" de la Universidad de Concepción. This research further is carried on in conjunction with Professor J. Benard.

⁹ U. R. Evans: Oxidation of Iron in the Range 100° to 400°C. *Nature* (1949) 164, p. 909.

Kinetics of Thermal Reorientations in Cold Rolled Zirconium

by R. K. McGeary and B. Lustman

DISCUSSION, W. P. Wallace presiding

P. A. Beck (*University of Illinois, Urbana, Ill.*)—The authors' plan of attack, correlating the kinetics of reorientation with the kinetics of hardness change, and both with the microstructure, is an admirable one. From Fig. 10 it can be seen that 200 min annealing at 400°C produces a loss of approximately 50 pct of the work hardening which resulted from 97 pct cold rolling. It is interesting that, as Fig. 12 shows, the same annealing treatment results in no orientation change, within the limits of accuracy of such measurements. This means that very substantial softening can be attained without reorientation, i.e., without recrystallization involving the migration of high angle boundaries. This observation is related to that of Chen and Maddin²⁸ and of Semchyshen and Timmons,²⁹ who found that in work-hardened molybdenum in many cases complete softening may be produced on annealing, essentially without reorientation. It is now quite clear that this phenomenon, which was found by Crussard³⁰ in slightly deformed aluminum single crystals and named by him "recrystallization in situ," occurs very generally even in highly deformed polycrystalline metals. (Note: the authors' definition of "recrystallization in situ" is different, since they consider this process completed at a point in the annealing process where softening, without reorientation, is still progressing.)

Undoubtedly, a part of the softening effect may be due to recovery (without subboundary migration). However, as seen in Fig. 7, the substructure is already fully developed in less than 24 min of annealing at 395°C, where the hardness drop amounts only to about 25 pct. It is very likely that at least the subsequent half (but probably more) of the hardness drop attained

on annealing without recrystallization is a result of subgrain growth. The authors state that they were unable to detect microscopically any subgrain growth even up to much longer periods of annealing than 200 min at 400°C, in fact, even after substantial reorientation occurred. It may well be that the resolving power of the optical microscope is not quite sufficient to detect the changes involved here. It is hoped that eventually the results obtained by electron transmission microscopy will settle this question definitely. The suggestion of reorientation without boundary migration certainly appears unattractive. It is difficult to conceive of a reasonable mechanism to accomplish this.

I wonder how the authors can support their conclusion (p. 289) that, for instance, after 25 min of annealing at 400°C the domains are highly strained and that the strain energy is relieved only during a period of major change in crystal orientation; the paper presents no evidence as to the amount of lattice strain or strain energy. It is apparently assumed that the work hardening still present, for instance, after 25 min of annealing at 400°C, is due to lattice strain. But even if this assumption were true, the approximately 50 pct loss of work hardening obtained at 400°C without reorientation would seem to indicate considerable relief of strain prior to the period of major orientation change.

As the authors point out (p. 290), their results with 60° cross-rolled zirconium, which has a single orientation deformation texture, clearly show that the reorientation on annealing corresponds to a 30° rotation around the hexagonal axis. Since the reorientation in the straight rolled material, which has a double texture, is somewhat different, it appears logical to correlate the difference in reorientation behavior with the difference in the complexity of the deformation tex-

tures. It seems reasonable to conclude that the rate of growth of the new grains in a double texture matrix depends on their orientation relationship with both matrix texture components, and that, therefore, the orientation most favorable for growth will, in general, not be the same as in the case of a single orientation matrix.

W. E. Seymour and J. E. Burke (*General Electric Co., Schenectady*)—The authors of this paper have contributed some new and interesting thoughts to the theories of recrystallization which should stimulate much worthwhile discussion. They refer to papers by Decker, Harker, and Seymour^{13, 14} and state that in these papers reoriented material in copper and an iron-nickel alloy is accounted for by a nucleation and growth process and that in each case a single activation energy was found to express the total reorientation. While it is true that for the iron-nickel alloy the temperature dependence of the rate of recrystallization followed an Arrhenius type equation and a numerical value for the constant in the numerator of the exponent was determined and called the activation energy for recrystallization, the authors of that paper did not account for the reoriented material in the alloy by nucleation and growth of grains in the new orientation. In fact, from subsequent work on the iron-nickel alloy it was concluded that the reorientation as a result of recrystallization occurred principally from growth of oriented crystallites existing in the cold-worked material.

In any case, there is no fundamental requirement that a single activation energy be found if a process is to be described in terms of a rate of nucleation and a rate of growth. The temperature dependence of the rate of the combined processes of nucleation and growth will follow a simple Arrhenius relationship with a single activation energy only if the activation energies for nucleation and for growth are identical. However there are numerous examples where the activation energy for nucleation has been found to differ from the activation energy for growth. (See for example Anderson and Mehl.²¹)

Therefore there does not seem to be a valid experimental or theoretical basis from which to conclude that a simple nucleation and growth process should be characterized by a single activation energy.

A. H. Geisler, J. H. Keeler, and W. R. Hibbard, Jr. (*General Electric Research Laboratory, Schenectady*)—The authors have assumed that there is only one annealing texture for zirconium and that the development of this one texture completely characterizes the annealing process. This conclusion is a consequence of the authors' assumption that the rate of change of annealed material in an orientation corresponding to that at point C is the same as that at every other point of the pole figure. Such an assumption is contrary to the authors' earlier findings of six rather than twelve intensity maxima for some annealed samples. It is also contrary to the authors' data in Figs. 12 and 13 where the intensity at $\beta = 0^\circ$ first increased then decreased compared with the intensity for the cold-rolled sample, while at $\beta = 20^\circ$ the intensity first decreased then increased. The authors' assumption is further in discord with the data in Fig. 6 which compares the disappearance of the cold-rolled texture and appearance of the annealed texture and shows that not every volume of material leaving the old (cold-rolled) texture is immediately accounted for in the annealing texture, or else the two curves for a given temperature would superimpose rather than show variations of as much as 35 pct of annealing texture.

The behavior for zirconium is markedly different from the development of cube texture in copper¹³ and nickel-iron¹⁴ where only one, sharply defined component appears at the investigated temperature and disappearance of the rolled texture can be completely accounted for by the appearance of the cube texture. This comparison suggests that the appearance of the texture at point C does not represent the whole an-

nealing process but that several components must be operative in the case of zirconium. It seems to us that there are at least three discrete types of annealing textures depending on temperature and that a general interpretation based solely on one type may account for the misleading conclusions derived by the authors from the consideration of "activation energy" or temperature dependence of rate. We would regard the three types of annealing textures appearing in order of increasing temperature as, 1—an enhanced rolling texture characteristic of materials which recrystallize into the same texture as the rolling texture (referred to as "recrystallization by situ" by the authors) which we will refer to as the $[10\bar{1}0]$ texture, 2—the annealing texture considered here by the authors where the $[11\bar{2}0]$ direction is about 10° to the rolling direction which we will refer to as the $10^\circ [11\bar{2}0]$ texture, and 3—the unsplit-type texture with $[11\bar{2}0]$ in the rolling direction previously reported by the authors and found by us to dominate at the higher annealing temperatures well above 600°C . Each of these three basic types would have a characteristic "activation energy" which could be determined by studies of the rate of change of diffracting intensity at various points (C for type 2 above only) in the pole figure. Thus, the disappearance of intensity at points corresponding to the rolling texture could represent merely some complex function of appearance of intensity at any or all other points in the pole figure for the various types of annealing textures. Any "activation energies" such as the authors have determined in Fig. 14 based on disappearance of rolling texture of zirconium represents not a single nucleation process but a collection of processes, the development of the different annealing texture components each with a characteristic "activation energy" and each exhibiting varying degrees of dominance depending on temperature. The case is similar to precipitation from solid solution where various property measurements give a range of values for "activation energy," each depending upon the sensitivity of the particular property to the various concurrent factors such as localized precipitation, general precipitation, solid solution depletion, etc.²² This analogy illustrates that the presence of a range of values for "activation energy" alone is not a valid basis on which to conclude that a simple mechanism, such as nucleation and growth, does not govern the reorientation.

Instead of basing the determinations of "activation energy" on the disappearance of the rolling texture as in Fig. 14, the authors should have considered their data for the appearance of the components of the annealing textures. Fig. 15 represents the authors' data for the two components, 1—the $[10\bar{1}0]$ annealing texture, and 2—the reoriented $10^\circ [11\bar{2}0]$ texture analyzed by point C. Most of the lines have one of two slopes corresponding to the two processes, each with rather constant "activation energies." The higher "activation energy" is in the range 93,000 to 100,000 and presumably is characteristic of the development of the reoriented component only. The lines of low slope correspond to an "activation energy" in the range 36,000 to 44,000 and should be associated with the appearance of the $[10\bar{1}0]$ annealed texture component oriented like the rolled texture. Data from Fig. 5 were used to plot some of the lines of low slope in Fig. 15 which are identified in terms of percentages of the maximum increase of the intensity in the rolling direction over that for the cold-rolled sample. It seems to us that this procedure is of somewhat less questionable validity than the procedure used by the authors whereby the intensity of the $[10\bar{1}0]$ annealing texture provided by annealing at 295°C was used for the basis of calculating the disappearance of the original rolled texture at and above 500°C where such an increase was not reported.

On the basis of similarity of "activation energy," evidently the data for "10 pct" and "25 pct" of the an-

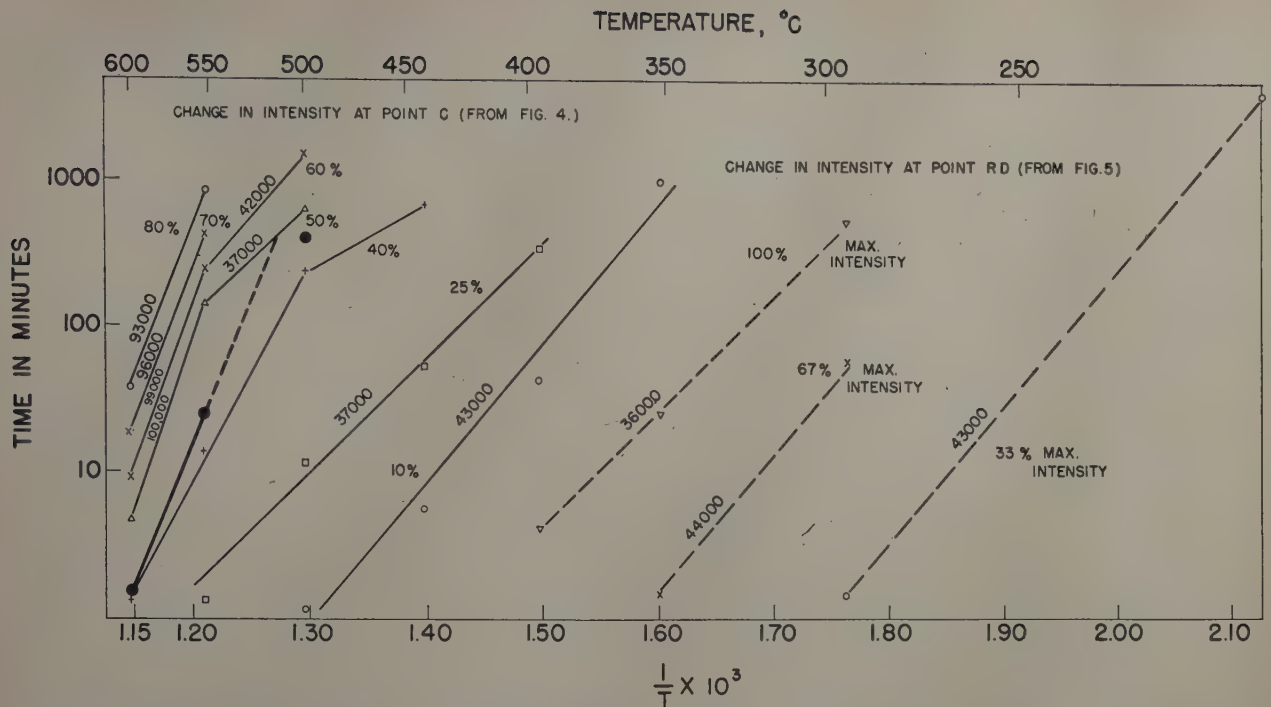


Fig. 15—Time-temperature dependence for increase in intensity at points in the pole figure corresponding to $[10\bar{1}0]$ and $10^\circ [11\bar{2}0]$ annealing textures from X-ray diffraction data. Solid circles at left for start of change in grain size apparent in microstructure.

nealing texture at point C represent the development of the component which has the same ideal orientation as the rolled texture but spread somewhat away from the optimum location. In order to explain this implication the data illustrated by Fig. 16 have been plotted, assuming that the intensity at our point D, which is the maximum in the $[10\bar{1}0]$ texture near point C in the $10^\circ [11\bar{2}0]$ reoriented texture, changes at the same rate as the maximum in the rolling direction of the cold-rolled texture studied by the authors. A similar spreading of the $[10\bar{1}0]$ annealing texture is apparent in Fig. 12 for the sample annealed 1839 min at 400°C . The authors interpret the spreading as development of the $10^\circ [11\bar{2}0]$ reoriented annealed texture on the basis of the exaggerated representation in Fig. 13 showing a prominent peak at $\beta = 20^\circ$ which is not present in the original data, Fig. 12. Thus, we are suggesting that the authors should have considered the possibility that the initial increase in the intensity at point C is associated with changes in intensity at the nearby point D in the $[10\bar{1}0]$ texture suggested in our Fig. 16. If such an interpretation is correct, then both the initial increase in intensity in the rolling direction (Fig. 5) and the initial increase at point C (Fig. 4) with the same "activation energy" are from the $[10\bar{1}0]$ annealing texture. The authors might have verified this suggestion if they had determined full pole figures for samples annealed long periods at 395° or 443°C . Judging from the traverse in Fig. 12 for 1839 min annealing at 400°C , the pole figure is essentially that for the $[10\bar{1}0]$ annealed texture rather than the $10^\circ [11\bar{2}0]$ annealed texture which the misleading ordinates on Figs. 4 or 5 indicate is present to the extent of 35 or 60 pct. One must conclude that the percentages listed on our Fig. 15 and assumed by the authors to represent volume of material with the annealed texture have no real significance since point C evidently is not sufficiently spaced from a peak in the $[10\bar{1}0]$ annealing texture to permit separation of the two components. A further consequence of our interpretation is that completion of the $[10\bar{1}0]$ annealing texture does not occur at the upper broken line in Fig. 10 but near

the lower broken line where the development of the reoriented texture starts and the polygonal grain structure in Fig. 8 typical of a 100 pct recrystallized metal is observed rather than the ill-defined structure of Fig. 7. This interpretation is consistent with the observation that the curves for hardness change seem to fall into one of two families, one below about 500°C with a final hardness near 100 and one above about 550°C , respectively, in agreement with the breakoff point of the rate curves from X-ray diffraction data in our Fig. 15. On this basis the grain growth curves in Fig. 9 refer to the development of the $10^\circ [11\bar{2}0]$ reoriented texture which follows the $[10\bar{1}0]$ annealing texture and proceeds along the second sigmoid in Fig. 4 at 500° to 600°C , starting at 0 pct reoriented texture rather than at 40 or 75 pct of the annealing texture (depending upon whether one refers to Fig. 4 or Fig. 5 in the paper). The time for the apparent start of the change in grain size in Fig. 9 is plotted as the solid

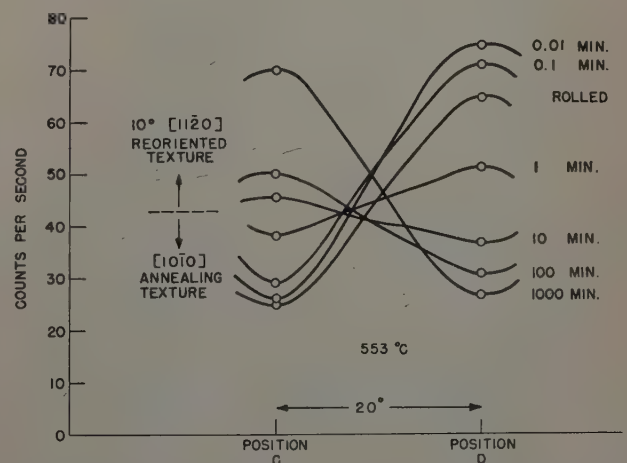


Fig. 16—Change in intensity of diffracted x-radiation at two points in the pole figure illustrating that the initial changes at position C might be associated with spreading of the $[10\bar{1}0]$ component which is centered at position D.

circles on the left side of Fig. 15. The "activation energy" is in the same range as that for the 10° $[11\bar{2}0]$ annealing texture and according to our interpretation of the X-ray diffraction data the process which the authors have referred to as "domain growth" is synonymous with the entire process for the development of the 10° $[11\bar{2}0]$ annealed texture with a peak at point C in the pole figure.

The kinetics of the third principal type of annealing texture for zirconium in which $[11\bar{2}0]$ is in the rolling direction with six intensity maxima instead of twelve awaits an analysis of samples annealed at temperatures above 600°C .

It should be remembered that if "time" is to be used instead of "rate," plots of the type of Fig. 14 in the paper and Fig. 15 in this discussion are valid if the shape of the property vs log time curves is independent of temperature. If several competing processes are occurring it is probable that the curves are not independent of temperature. This limitation is probably responsible for the peculiar slopes of the branches of the curve in Fig. 15 for "40 pct" since the equivalent intensity corresponds to the top of the first sigmoid for 443°C , to the junction for 500° and 553°C , and to part way along the second sigmoid for 600°C .

In the preceding discussion the kinetics of the development of the annealing textures were considered without the necessity of associating the various textures with polygonization, recrystallization, or grain growth. We have a number of questions concerning the associations which have been attempted by the authors. If the grains in the structure of the material annealed 24 min at 395°C were not clearly delineated, how can it be determined that the material had completely "recrystallized in situ" as indicated in Fig. 11 and how was the polygonization and "recrystallization in situ" distinguished from normal recovery? Without sufficient resolution of the microstructure one cannot be certain that recrystallization has occurred before reorientation has taken place. Presumably the grains seen "after reorientation" are not the same as those present before reorientation, otherwise by what mechanism does reorientation occur? Fig. 9 appears to be a normal growth portion of a recrystallization curve. Were there any specimens in which the grains were metallographically resolvable as recrystallized, and did not show the reoriented annealing texture?

Under Experimental Procedure, in the first and third sentences in the first paragraph concerning the X-ray

Diffraction Methods the deformation texture is described as the orientation "... in which prism poles, $\{10\bar{1}0\}$, are perpendicular to the rolling direction." The term "parallel" rather than "perpendicular" would be proper here, or the term "planes" rather than "poles" could be substituted.

With regard to pole figure asymmetry, can it be shown that each of the twelve double maxima in the high intensity regions of the $[10\bar{1}0]$ poles of the pole figure for annealed material has the same maximum intensity value? This does not appear to be so from Fig. 2. Were any pole figures determined in detail for all four quadrants?

R. K. McGeary and B. Lustman (authors' reply)—The authors wish to thank the discussers for their thoughtful and illuminating contributions.

In answer to Professor Beck's discussion, we disagree that no orientation change is observed after 200 min annealing at 400°C . It will be noted from Fig. 4 that an appreciable percentage of the annealing orientation (about 23 pct) results from this treatment. Likewise, in the case of the data represented in Fig. 12 it must be remembered that the deformation type of texture first increased in intensity, corresponding to the upper curve for 5 min annealing, before decreasing to the values shown for 200 min; this 30 pct decrease in maximum intensity value (represented in Fig. 5) indicates that appreciable reorientation had occurred. We found, in fact, that only about 30 pct of the cold working hardness increase is recovered at the end of the period we chose to call "recrystallization in situ." Close examination of Fig. 10 will reveal definite discontinuities in the curves of hardness vs time corresponding to this stage of annealing. The amount of recovery of a particular property will, of course, depend on the property being measured; thus, Bostrom and Kulin²⁸ found that about 40 pct of the electrical resistivity increase is recovered at this stage.

In Fig. 17 is shown a transmission electron micrograph (prepared by T. R. Padden) of a sample of zirconium annealed 500 min at 400°C . It will be noted that the grain size so revealed corresponds to that detected by the optical microscope. Grains were found to be metallographically resolvable from the point corresponding to decrease in intensity of the deformation texture onward. It is therefore believed that the optical microscope is fully capable of revealing grain structures of the 2 micron dimensions reported in the paper.

We agree with Drs. Seymour and Burke that there appears to be no requirement that a single activation energy describe a recrystallization process characterized by nucleation and growth. The comparison with the experiments of Decker, Harker, and Seymour was made to show that an essential difference exists between the behavior of zirconium on the one hand and that of copper and an iron-nickel alloy on the other in that the isothermal annealing characteristics of the latter can be described in terms of nucleation and growth parameters, and a single activation energy serves to describe the temperature variation, whereas neither of these characteristics apply in the former case.

The principal point raised in the discussion by Drs. Geisler, Keeler, and Hibbard is that the several annealing stages are not consecutive but are competitive and are characterized by different textures and activation energies. They further attach no significance to the maximizing of the $\{10\bar{1}0\}$ orientation, which condition we have called "recrystallization in situ," but prefer to consider this stage of optimum perfection of the deformation texture and the subsequent approach to a more random orientation as a single process, namely, an "enhanced" rolling texture produced by recrystallization into the $\{10\bar{1}0\}$ texture.

Concerning the latter point, it is difficult for the authors to visualize a single recrystallization mech-

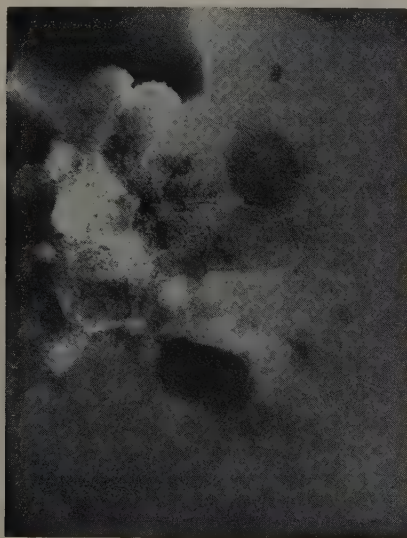


Fig. 17—Transmission electron micrograph of 97 pct cold-rolled zirconium annealed 500 min at 400°C . Hole appears at upper corners. X6000. Area reduced approximately 40 pct for reproduction.

anism which leads first to a sharpening of the deformation texture and then to its randomization. Furthermore, as pointed out above, a definite arrest is found in the curve of hardness change vs annealing time corresponding to the time of attainment of the maximum intensity of the deformation texture. This is a characteristic feature of the annealing of zirconium and is essentially different from the later annealing stages.

The discussers' Fig. 15 is, we believe, based on entirely inadequate data. A plot of the more closely spaced electrical resistivity data of Bostrom and Kulin³³ again indicates a continuous increase in activation energy as annealing progresses even during stages when, by the discussers' interpretation, only a single reorientation mechanism operates. In this connection, Bowen, Eggleston, and Kropschot³⁴ found by residual electrical resistivity measurements of pulse-annealed copper essentially the same activation energy for the recrystallization of copper as was reported by Decker and Harker. Furthermore, if the zirconium is completely recrystallized into the "diffuse" $\{10\bar{1}0\}$ texture at the start of the final sigmoid of Fig. 6, it would be expected that at this stage essentially all and not just 75 pct of the hardness increase would be lost. By the discussers' interpretation the final 25 pct loss of hardness induced by the cold working must be attributed to reoriented texture formation; i.e., the stage where simple grain growth was observed (Fig. 9). In the literature for other pure metals large changes in hardness have never been associated with grain coarsening or secondary recrystallization so that the discussers' interpretation of our data would yield a unique mechanism for the softening of zirconium.

In the pole figure for annealed material (Fig. 2) the intensity maxima of the type represented by *B* in Fig. 3 reach a maximum intensity of about 90 counts per sec while the type represented by *C* reach a maximum of about 80 counts per sec. Incidentally, this indicates rather good symmetry for all twelve maxima of the pole figure although as described in the paper only six maxima were actually measured. Thus, in considering our Fig. 12 the maximum intensity to be expected at *B* even in the fully annealed condition would only be about 90 counts per sec. Since the representation in Fig. 13 of the 1839 min annealing curve shows a definite grouping around *B*, the shape of the corresponding curve in Fig. 12 is believed to be attributable to comparatively small scatter of the reoriented texture about *B* rather than to the large scale scatter associated with recrystallization into a "diffuse" $\{10\bar{1}0\}$ texture.

We thank Dr. Geisler and codiscussers for pointing out our error in using the term perpendicular instead of parallel.

³³ N. K. Chen and R. Maddin: Cold Rolling and Annealing Textures of Molybdenum Single Crystals. *Trans. AIME* (1953) 197, p. 300; *JOURNAL OF METALS* (February 1953).

³² M. Semchyshen and G. A. Timmons: Preferred Orientation of Arc Cast Molybdenum Sheet. *Trans. AIME* (1952) 194, p. 279; *JOURNAL OF METALS* (March 1952).

³⁰ C. Crussard: Etude de Recruit de L'Aluminium. *Revue de Metallurgie* (1944) 41, p. 118.

³¹ W. A. Anderson and R. F. Mehl: *Trans. AIME* (1945) 161, p. 140.

³² A. H. Geisler: Metal Interfaces. *ASM* (1952) pp. 269-295.

³³ W. A. Bostrom and S. A. Kulin: Zirconium and Zirconium Alloys. *ASM* (1953) pp. 186-195.

³⁴ D. Bowen, R. R. Eggleston, and R. H. Kropschot: A Study of the Annealing Kinetics of Cold-Worked Copper. *NAA-SR-143*. October 1951.

Nature of the Creep Curve

by Thomas H. Hazlett and Earl R. Parker

DISCUSSION, O. C. Shepard presiding

C. S. Roberts (*The Dow Chemical Co., Midland, Mich.*)—I heartily support the worthy aims, the careful experimentation, and the painstaking quantitative analyses of the authors. However, I cannot accept their first conclusion as having been proven by their work or by any of the workers to whom they refer. Ever since the pioneer work of Andrade was completed, investigators have found that steady-state creep is very small compared with transient creep at high stresses and low temperatures relative to the melting point. These are evidently the conditions of the authors' tests. They base their conclusions mainly on tests of nickel and its alloys over a 75°C range which lies at less than 2/3 of the melting point on the absolute temperature scale. In addition, the stresses are relatively high. In order to observe steady-state creep with negligible interference from the transient component, the experimental range must be extended to higher temperatures and low stresses, thus low strain rates. Incidentally this is also the region where present-day designers are usually forced to operate.

The fact remains that steady-state creep has been observed in constant stress tests. The evidence of Cottrell and Aytakin⁹ for zinc is very clear on this point. Servi and Grant¹⁰ observed long stages of linear creep rate for aluminum. In a study of polycrystalline magnesium which I have recently completed, long stages of steady-state creep have been obtained at

400° to 600°F and at low stresses which were constant during the test to less than 1 pct. When the linear region represents a reasonably large portion of the creep curve, i.e., when steady-state creep is predominant, the test of expanded scales will not result in a change of creep rate. When the stress and temperature are such that steady-state creep is small compared with the transient component, the situation illustrated by the authors in Figs. 2 and 3 will result. On the other hand, if a steady-state region clearly exists it may well be concealed in the log-log type of plot. Professor Cottrell made this point in his discussion to ref. 5. I predict that if the authors lower their stresses and/or extend their temperature range upward sufficiently, they will find that nickel will also exhibit steady-state creep of detectable magnitude.

N. J. Grant (*Massachusetts Institute of Technology, Cambridge, Mass.*)—I wish to express my congratulations to the authors for tackling a tough problem, which has been knocking about for a long time, though without complete success. In the course of having run on the order of 1000 or more creep-rupture tests, and in trying to apply the equations suggested by the authors, as well as those suggested by Andrade and others, we have never succeeded in finding any one particular creep curve equation which was able to satisfy a large number of materials for the usual range of testing conditions. We have always found too many exceptions to any particular equation to make us con-

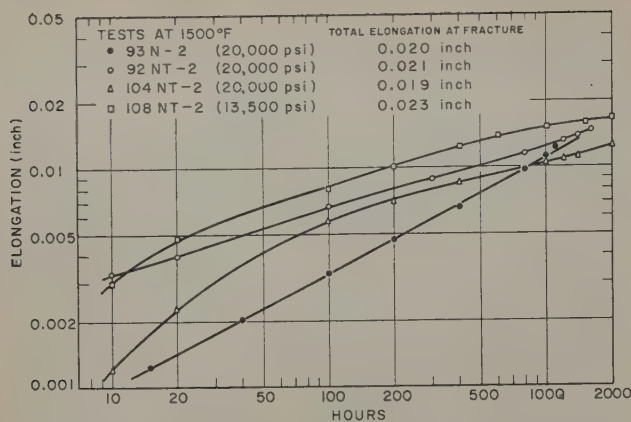


Fig. 21—Log-log plot of elongation vs time for cast high carbon N-155 alloys, Eq. 2.

fidant in applying it. Accordingly, I would appreciate it if the authors would consider the following comments and questions.

1—It is puzzling that Eq. 1 fits the creep curves for some of the nickel tests, for certain steels, platinum, and copper, but requires a modification of Eq. 1 to Eq. 2 to fit the creep curves of other nickel tests, lead, and aluminum. Since the value ϵ_0 is fixed and does not vary with time, it is difficult to see how the application of Eq. 1 results in a straight line log-log plot for certain of the materials, and Eq. 2 for others. Certainly these equations are not interchangeable for the different sets of data, and a correction of Eq. 1 which yields a straight line without the ϵ_0 term should become a curve when the correction ϵ_0 is applied unless ϵ_0 is zero, which it cannot be. This variability is in line with our experience noted above that some equations fit some materials and some do not.

2—In re-examining the constant-stress creep curves for aluminum, which we sent to the authors, as well as additional curves which were not sent to them, we found it extremely difficult to determine ϵ_0 , and frequently selected values which did not yield straight lines by either Eqs. 1 or 2. To see where some of the difficulty came from, it was decided to see how exact a so-called constant stress creep test really is. An aluminum creep test bar of the same stock as was used for the tests described in the authors' paper was extremely carefully machined and tested as a constant stress creep test at 500°F and 700 psi. While the creep curve was still following a straight line in the secondary portion of the curve and had definitely not begun to enter third stage creep, the test was stopped and the specimen was carefully examined. Since the constant stress creep test depends on a constancy of volume relationship for determining the unloading rate on the specimen, the elongation and change in cross section must be in agreement. Our measurements on this test bar showed that a significant deviation occurred due to the inhomogeneity of the deformation. There was a difference in average diameter along the length of the gage section of 3.64 pct which would result in a stress increase from the original value of 700 psi to 725 psi on that cross section. Furthermore, the specimen showed a maximum out of round variation of 1.6 pct at this same time. It is very difficult to see how such large dimensional deviations can exist and still not be detected by the plotting method used to evaluate Eq. 2, unless this method is rather insensitive to appreciable changes in total creep or creep rate, and it appears that it is insensitive.

3—In some recent creep-rupture tests wherein micro-creep measurements were made on high purity aluminum specimens, it was noted that at points within one grain separated by no more than 0.03 in. the elongation values between two adjacent points would be 5 and 50 pct, respectively. Across grain boundaries as

compared to centers of grains this variation was even greater. Again, it is difficult to see how any one equation is capable of correcting for such inhomogeneities. Certainly it would be difficult to visualize how any constant such as ϵ_0 , for example, could be termed a physical constant for a material in which strain variations of such large magnitude can occur and where both grain and grain boundary deformation processes are occurring at different rates.

4—It was thought that Eqs. 1 and 2 could be checked in a different way and probably very much more rigorously. From some old creep tests we examined four creep curves which were obtained on high carbon cast N-155 alloys. These tests were run in very high sensitivity creep equipment where temperature variations were less than 1°F at 1500°F and where elongations were measured with a sensitivity of two parts per 100,000 using a microscope sighted on gage markers attached to the specimen. The resulting creep curves which failed after about 2000 hr were composed of a secondary portion (minimum creep rate zone) which constituted about 90 pct of the total creep curve. The total elongation was only about 2 pct and reduction of area was less than 1 pct. It appeared relatively easy to determine ϵ_0 for these creep curves. In spite of the fact that these were constant load tests, they, in fact, fulfilled the requirements of a constant stress test very much better than did our constant stress creep tests on high purity aluminum and the authors' nickel tests. Also by contrast the second stage portion of these high carbon N-155 alloys was very much more extensive than that in the case of aluminum and nickel, permitting an examination of the curve over a greater portion of the log-log plot.

Fig. 21 shows the results of these tests using Eq. 2 for purposes of plotting. It will be noted that two of the curves yield almost straight lines, although they are definitely not straight, and two deviate quite markedly. Incidentally, the aluminum curve in the authors' Fig. 15 shows the same type of deviation from linearity if one draws the curve through the actual points rather than averaging them with a straight line, as the authors have done. These high carbon N-155 alloys were all pre-aged prior to testing and in our estimation are extremely stable alloys.

The authors are probably correct in claiming the absence of a true constant creep rate in the secondary portion of creep curves. There are few of us, however, who believe in an absolute minimum creep rate. If one were making creep tests to establish absolute values in each creep test, this would be important, but most of the concern with creep testing is to determine a relationship between the secondary creep rate and the stress and temperature. On this basis, it makes little difference whether the secondary portion of the creep curve is a true constant creep rate portion or not, since deviations from true constant rates will be averaged out by obtaining several values. As such, the minimum creep rate values commonly used in both research and engineering will continue to be extremely useful quantities.

T. H. Hazlett and E. R. Parker (authors' reply)—The authors wish to thank both discussers for their interest in this paper as evidenced by their comments. The limitation of narrow test temperature range referred to by Dr. Roberts is well taken, but we cannot accept his statement regarding the existence of a steady creep range, even at high temperatures. The authors believe that the conclusion reached by Lubahn⁴ is valid and the curvature is strictly a matter of degree. A creep curve produced by testing pure nickel at 900°C and 2000 psi is shown in Fig. 22 and it may be noted that the curve is continuously decreasing until the initiation of the "tertiary" stage. Although there is necessarily an inflection point, no extended region of constant creep rate is revealed. This test temperature is above the value of 2/3 of the melting point on the absolute scale which is referred to as the critical temperature. This absence of a true constant

creep rate in the secondary portion of creep curves is also confirmed by Dr. Grant in his final paragraph of discussion.

In reference to the work of Cottrell and Aytakin, it should be pointed out that they merely computed the constant rate portion of the creep curves from Andre's equation. The "transient" portion of the curves was not used. None of their published data show creep curves with extended constant rate portions.

The question raised by Dr. Grant as to why some of the data may be fitted to Eq. 1 while Eq. 2 is required for other curves, is best answered by referring to Figs. 11 and 12 of the paper. As has been pointed out already, the matter of best fit is one of degree only. It has been found in all cases studied in this laboratory that if the initial portion of the creep curve taken at very short times after loading is used, the ϵ_0 term must be included. This same equation has been tested independently by Bhattacharya, Congreve, and Thompson¹¹ with their data on many additional materials and found to be valid.

The point concerning inhomogeneous flow described under items 2 and 3 of Dr. Grant's discussion is well taken. However, many measurements of the nickel specimens after testing (but before the initiation of the accelerated creep rate stage) failed to reveal such dimensional changes as are described for the coarse grained aluminum. Plastic deformation was very uniform for all of the nickel specimens measured.

The creep curves for N-155 alloys presented in the discussion do not appear to be fitted with the correct value of ϵ_0 , so that the data do not represent a test of the equation. In the case of specimens 104 NT-2 and 108 NT-2 particularly, the values of ϵ_0 selected by the discussor are much too large, or the test bars were undergoing structural changes during the creep test. It has been the experience of the authors that when a logarithmic plot of total strain vs time results in a curve which is convex upward, grain growth, precipitation, or structural changes other than the develop-

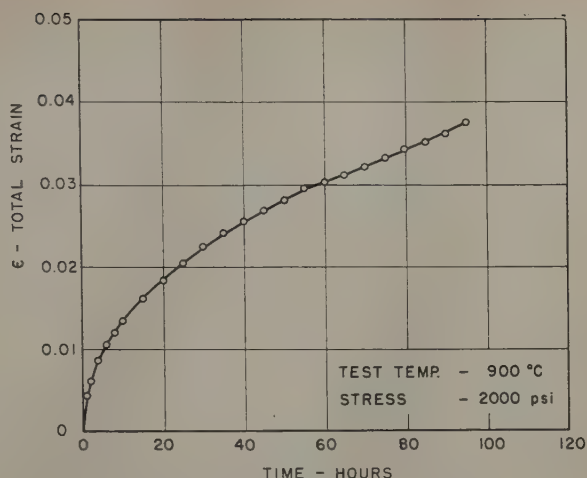


Fig. 22—Creep curve for pure nickel.

ment of substructure occurred during the test. So far as we know, all simple, structurally stable materials yield curves which are concave when plotted in this manner if gages of sufficient sensitivity are used and the early portion of the time scale is explored.

Although the authors do not feel that any data brought forth in the discussion justifies altering our original conclusions, it must be kept in mind that the proposed relationship is empirical only and subsequent work may reveal the necessity for a change in this position. Such data has not been brought to the attention of the authors to date.

⁹ A. H. Cottrell and V. Aytakin: The Flow of Zinc Under Constant Stress. *Journal Inst. Metals* (1950) 77, p. 389.

¹⁰ I. S. Servi and N. J. Grant: Creep and Stress Rupture Behavior of Aluminum as a Function of Purity. *Trans. AIME* (1951) 191, p. 909; *JOURNAL OF METALS* (October 1951).

¹¹ S. Bhattacharya, W. K. A. Congreve, and F. C. Thompson: Creep Time Relationship Under Constant Tensile Stress. *Journal Inst. Metals* (October 1952).

Grain Boundary Sliding and Migration and Intercrystalline Failure Under Creep Conditions

by Hsing C. Chang and Nicholas J. Grant

DISCUSSION, O. C. Shepard presiding

O. C. Shepard (*Stanford University, Stanford, Calif.*)

—In the paper the statement is made that grain boundary mobility prevents intercrystalline fracture in high purity aluminum. This statement surprises me because in tests at Stanford with very pure gold intercrystalline fractures are encountered with low stresses, so that the time to fail is 1000 hr or more. I should like to know the maximum times involved in the tests with pure aluminum.

H. H. Bleakney (*Dept. of Mines and Technical Surveys, Ottawa, Ont., Canada*)—The authors have performed a most meritorious service in presenting evidence to show that the motion of one grain past another may occur by plastic deformation of metal immediately adjacent to the grain boundary and that this deformation is followed by boundary migration. This evidence should help to dissipate some of the confusion arising from the rather widely disseminated concept

that creep is considerably influenced by viscous flow among the atoms lying in the transition zone between contiguous grains. McLean⁸ has already disposed of that concept, fairly thoroughly, but the additional evidence is welcome. Plastic deformation near the grain boundaries, or grain boundary migration or both can adequately account for the "quasi-viscous" phenomena in creep, including Kê's⁹ evidence.

In a recently published paper,¹⁰ evidence has been presented which indicates that the intercrystalline embrittlement noted in creep-rupture tests of many metals is attributable to a tendency for impurities to concentrate at grain boundaries in the course of a test. The evidence presented in Chang and Grant's paper confirms the contention that impurities are at the root of the trouble, but their explanation for the mechanism by which the impurities act is not consistent with all the evidence. According to the explanation suggested by Chang and Grant, higher temperatures, which increase the velocity of grain boundary motion, should

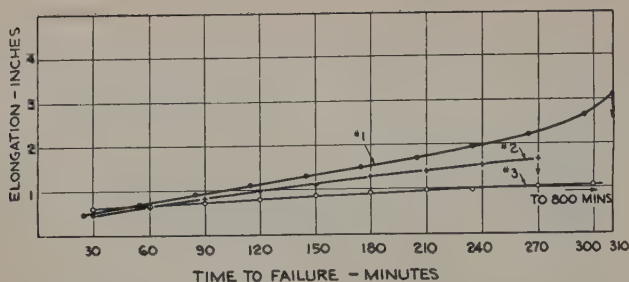


Fig. 21—Creep curves for three different high purity silver samples.

decrease the tendency for intercrystalline fissuring. The opposite is the case, and higher temperatures promote embrittlement. More direct evidence, however, is available. The mechanism proposed by the authors specifically postulates that embrittlement and strengthening of the metal both spring from the same origin, the inhibition of grain boundary migration by impurities at the grain boundaries. Therefore, for any given metal, a more brittle sample should have greater creep resistance than a less brittle sample. Fig. 21 shows creep curves of three samples of highly purified silver (99.99+). All samples were cold-reduced more than 95 pct and annealed for 1 hr at 350°C before testing under a stress of 5000 psi at the annealing temperature. Particulars of the three samples are as follows:

Curve No. 1—This curve was obtained from "proof" silver, purified at the Royal Canadian Mint for use as an analytical standard. The sample had a reduction in area of 95 pct after failure.

Curve No. 2—This curve was obtained from silver purified at the Mines Branch, Dept. of Mines and Technical Surveys, by the method used at the Mint, but which had been accidentally contaminated by about 0.003 pct S. The sample had a reduction in area of 30 pct after failure.

Curve No. 3—This curve was obtained from a sample of the purest silver available from commercial sources. The test sample had a reduction in area of 49 pct after failure.

The slightly higher creep rate of sample 1 as compared with sample 2 is quite inadequate to explain the great difference in ductility; and the higher ductility of sample 3 than sample 2 is completely inconsistent with its lower creep rate, on the basis of the proposed explanation. There does not appear to be any general law correlating the creep strength and the ductility of metals in creep-rupture tests.

The evidence is consistent with the hypothesis that impurities at grain boundaries lower the ductility of the metal by destroying the cohesion between the grains; it is inconsistent with other hypotheses.

W. R. Hibbard, Jr. and R. W. Guard (*General Electric Research Laboratory, Schenectady*)—The series of papers by Dr. Grant and his coworkers on the boundary sliding in aluminum are interesting and important. The evidence that boundary sliding is the cause of deformation within the grains (rather than deformation within the grains causing boundary sliding) is not clear. From Figs. 5a, 8, and 12a it appears that more slip occurs within the grain than at the boundary. This occurrence suggests that slip may have first occurred within the grain, but was blocked near the boundary and thus set up the stress distribution which caused sliding. Can the authors cite clear-cut evidence that boundary sliding occurs prior to deformation within grains?

Are subgrain formation, folding, and grain boundary sliding alternative mechanisms of creep deformation not involving dislocation motion along slip planes, or are they surface evidence of readjustments occurring with unresolvable slip?

The authors mention tests done at 400°F, but give no results. Do they find that same absence of slip at

the lower temperature as at 700°F and higher? McLean¹¹ gives data for tests at 200°C (392°F) which show that grain boundary displacement accounts for less than 20 pct of the total deformation.

The implication on p. 306 that boundary migration is attributable only to the applied stress is misleading. It appears that boundary migration of the type normally encountered in grain growth occurs as a result of the unstable boundary shape produced by boundary sliding. In this connection, there are many clear examples of boundary migration, but it is not clear from the illustration that all of this migration is activated by boundary sliding. It is quite possible that boundary migration could result from normal slip within the grains at or near the boundary. From the geometry of Fig. 3, one should be able to calculate the extension resulting from the grain boundary sliding of grain G. Is this extension a large percentage of the total extension recorded, or must other mechanisms be utilized to account for the amount of strain in the specimen?

H. C. Chang and N. J. Grant (authors' reply)—In reply to Dr. Shepard's question, we did not run our tests for long periods in the tests described here; but using exactly the same material, tests were run for 100 hr at 900°F without getting intercrystalline fracture, as described by Servi and Grant.⁷ The answer must be associated in some way with the types of impurities present in the aluminum and in the gold. In the above reference, it was noted that above 900°F there was a tendency for intercrystalline fracture to occur, as evidenced by a decrease in the ductility, nevertheless the fractures were transcrystalline for the 99.995 pct aluminum, the fracture being a sharp knife edge in most instances.

We are pleased to have Mr. Bleakney's support on the nature of the grain boundary deformation in creep and for his interesting discussion.

1—If there is "a tendency for impurities to concentrate at grain boundaries in the course of a test," active grain boundary migration would annul the effects of such concentration (which must be very slight), in which case intercrystalline fractures should not occur anyhow.

2—Grain boundaries must be fixed, essentially, for intercrystalline fracture to occur. Such grain boundary fixation is most readily achieved by alloying especially when a second phase occurs. It is only when grain boundaries stay in position that the intercrystalline fractures become evident.

3—Strengthening and relative embrittlement do, in fact, go hand in hand in most instances provided that the same alloying element is the basis of comparison. Some alloying elements will embrittle without strengthening if such elements tend to segregate into a weak zone, such as at a grain boundary. Such would be the case of sulphur in pure iron or of bismuth in gold. Some other alloying elements result in greater embrittlement for a given strengthening effect than do other elements. As yet there is insufficient evidence to classify the effects since this is a field in which much more work is needed.

Nevertheless, even on the basis of this loose generalization, it becomes difficult, if not impossible, to properly explain the effects shown in Mr. Bleakney's creep curves for silver. The quantities of specific alloying (impurity) elements must be known, as must their effects in silver, before the necessary explanation can be offered. It is insufficient to say simply that No. 3 is the purest, for undoubtedly, an element such as sulphur, even in minute quantities, will be much more embrittling and less effective in strengthening than would nickel.

4—We agree that alloying elements and impurities are of great importance in strengthening and in embrittlement in creep testing, but we doubt that the impurities have to be at the grain boundaries to get embrittlement. If it were necessary for impurities to get to the grain boundaries for embrittlement to occur, much larger differences in the ductility of fine and

coarse grained test bars would result than has been observed.

Regarding the discussion of Hibbard and Guard, adequate evidence of much larger initial deformation across grain boundaries than in grains has been obtained.¹² At 700°F and higher, extensive grain boundary sliding and migration have been observed to take place in the early stages of creep by optical means. Component creep curves, based on gage length of 0.6 to 0.7 mm between consecutive fine markers along the length of a regular coarse grained creep test bar, definitely show that the grain boundary region, through sliding, undergoes very marked creep at a time when the interior of the grain may barely have started to creep. At 400°F the opposite is true. In connection with the slip bands appearing on Figs. 5a, 8, and 12a, it should be pointed out that they were produced on putting this specimen into the creep furnace. They were not produced during creep. The slip bands produced during creep at 700°F are very much coarser than those appearing in these figures.

It is logical to think that any sort of deformation in a crystalline material, no matter what form the deformation may appear to take, must be associated with slip, resolvable or unresolvable. We think that Hibbard and Guard would agree that the last word on the mechanism of subgrain formation during creep has not been said, but subgrains do form as a result of inhomogeneous deformation as has been shown by several investigators as well as by us during the past year or two. Fold formation is even more poorly understood and the crystallographic relationships are to be examined in later work. Grain boundary sliding un-

doubtedly causes slip along the boundary regions. Kinking may also occur in this region. It is hoped that further work along this line may improve the understanding of those modes of deformation. As of now, however, the evidence does not support the idea that various deformation patterns are simply readjustments based on unresolvable slip.

It is clearly stated in the text that the driving force for boundary migration during creep is a combination of strain energy and surface energy. The applied stress serves to upset the equilibrium of forces along grain boundaries and at the triple point established as a result of long time high temperature annealing. Once this equilibrium of forces is upset, the surface energy then comes into play. Many additional observations have been made since reporting the above results. These observations indicate (more work will be done) that frequently the boundary migrates in a direction toward the center of curvature as noted by C. S. Smith in grain growth. Even more frequently, however, the boundary migrates away from its center of curvature, indicating the large effect of the applied stress.

⁸ D. McLean: Creep Processes in Coarse-Grained Aluminum. *Journal Inst. Metals* (May 1952) 80, Part 9, pp. 507-519.

⁹ Ting Sui Ké: Experimental Evidence of the Viscous Behavior of Grain Boundaries in Metals. *Physical Review* (1947) 71, pp. 533-546.

¹⁰ H. H. Bleakney: The Ductility of Metals in Creep-Rupture Tests. *Canadian Journal of Technology* (December 1952) 30, pp. 340-351.

¹¹ D. McLean: Grain Boundary Slip During Creep of Aluminum. *Journal Inst. Metals* (1953) 81, pp. 293-300.

¹² H. C. Chang and N. J. Grant: Inhomogeneity in Creep Deformation of Coarse Grained High Purity Aluminum. *Trans. AIME* (1953) 197, p. 1175; *JOURNAL OF METALS* (September 1953).

Absolute Rate Theory Applied to Rate of Growth of Pearlite

by J. H. Frye, Jr., E. E. Stansbury, and D. L. McElroy

DISCUSSION, O. C. Shepard presiding

J. F. Kahles (*Metcut Research Associates, Cincinnati, Ohio*)—Though the authors have quantitatively considered the rate of growth of pearlite from austenite in high purity iron-carbon alloys, they have only qualitatively indicated some of the problems associated with applying such theory to alloy steel.

A recent article by Phillips and Phillips²⁰ has indicated that small amounts of solute elements in copper greatly decrease the rate of growth of the recrystallizing interface. Since these effects may be similar to the effects of alloys on rate of growth of the pearlite interface, discussion by the authors of the general effects of solute elements on rates of growth of an interface would be of interest.

W. C. Hagel, G. M. Pound, and R. F. Mehl (*Carnegie Institute of Technology, Pittsburgh*)—Without assuming a specific mechanism, the authors have derived an expression for the rate of growth of pearlite which is very similar to an equation derived by Zener on the assumption that diffusion of carbon controls the rate of the process. Yet, in order to do this, the authors must make an assumption that can be explained only in terms of the Zener treatment, namely that supercooling *per se* enters the growth rate equation linearly. Actually, there is no experimental proof for this assumption which the authors arbitrarily introduce in their Eq. 2. It would seem invalid to draw any such conclusion about the kinetics of pearlite formation based on the work of Roberts and Mehl upon the kinetics of austenite formation.

Zener's basic rate equation may be written as:

$$r = \frac{D\Delta F}{4\alpha S_0} \quad [13]$$

where r is the rate of growth of pearlite; D , the diffusivity of carbon in austenite, $C'' \exp(-\Delta E^*/RT)$; ΔF , the bulk free energy change accompanying pearlite formation; S_0 , one half interlamellar spacing (minimum spacing realizable in a completely reversible process); and α , a constant.

Also, it is found that

$$S_0 = \frac{2v\gamma T_0}{\Delta H(T_0 - T)} = \frac{C'}{T_0 - T} = \frac{C'}{\Delta T} \quad [14]$$

where v is the specific volume of pearlite; γ , the cementite-ferrite interfacial free energy; ΔH , the bulk enthalpy change accompanying formation of pearlite; and T_0 , the bulk equilibrium temperature for austenite, ferrite, and cementite.

Substituting Eq. 14 into Eq. 13 and rearranging:

$$r = C\Delta T\Delta F \exp(-\Delta E^*/RT). \quad [15]$$

Thus, the Zener treatment leads to essentially the same result as the author's Eq. 9 without an arbitrary assumption about the relationship between rate and supercooling. Therefore, on the basis of existing knowledge, the Zener treatment would appear to be the more self-consistent.

Prigogine²¹ has shown that if ΔF and deviation from equilibrium are relatively small in a physicochemical

process as they are for pearlite growth, the rate of the process is roughly proportional to ΔF in form similar to that derived by the authors. However, as recently pointed out by Machlin²² the rate of growth of pearlite may not be simply proportional to the bulk free energy dissipated per unit advance of interface, owing to additional dependence upon the cementite-ferrite interfacial energy and the mobilities for other accompanying irreversible processes.

One of the present discussers also outlined the same general approach to the pearlite problem taken by the authors,²³ and for the past year we have been engaged in calorimetric measurements to determine the validity of Zener's theory. By comparing our free energy relationships for pearlites of different spacings to those of bulk ferrite and iron carbide, we have found that the interfacial energy involved is somewhat less than that predicted by Zener's theory but still quite appreciable.

Some mention should be made of the difficulties encountered when absolute rate theory is applied to solid-phase reactions. Little question remains as to the usefulness of absolute rate theory as developed for gaseous reactions which possess a definable activated complex. However, what is the activated complex in the case of pearlite growth? Further, without knowing the partition functions for solid-phase reactions from statistical mechanics, it is impossible to determine whether kT/h , as developed for gas-phase reactions, is the correct frequency factor for this reaction.

Assuming the correctness of kT/h , it may be possible to avoid evaluating partition functions and determining the nature of the activated complex by using the pseudo-thermodynamic approach of Eq. 1 and then resolving growth rate into a relationship containing $e^{(\Delta S^\ddagger)/R}$, as was done in Eq. 8. However, the uncertainty then lies in the entropy term which the authors assume does not vary with temperature and avoid computing by grouping into their constant C . This modified entropy term differs from that determined from equilibrium theory by a small amount owing to the removal of a degree of freedom for complex decomposition. Owing to the many uncertainties which exist with the application of absolute rate theory to any solid-phase reaction, one wonders if the resolution of this problem cannot better be accomplished by other theoretical means.

J. H. Frye, Jr., E. E. Stansbury, and D. L. McElroy (authors' reply)—Subsequent to the completion of the manuscript of the present paper, Phillips and Phillips²⁰ published the results of their investigation of the effect of certain solute elements on the recrystallization of copper. Their results tend to support the proposition examined by the present authors that the effects of alloying elements on the growth of pearlite may be due to interference by the solute element with actual interface mechanisms and that the diffusion of the alloying element, in the sense of atomic movements involving concentration differences, may not be the rate-limiting factor. There is no reason to suppose that such diffusion of solute atoms takes place during recrystallization, although considerable movements of both solute and solvent atoms presumably take place during the rearrangements accompanying recrystallization. Consequently, it is noteworthy that at 215.8°C, 0.0271 atomic pct Ag in copper reduces the growth rate of recrystallized grains from 2×10^{-2} mm per sec to 3.13×10^{-3} mm per sec without any appreciable effect on preferred orientation.²⁰ Thus, a tremendous effect may be exhibited by a solute element on the growth rate of an interface without diffusion of the kind which leads to concentration differences.

During creep, there must be atomic movements within a metal; and it is possible that there are similar movements at a growing interface and in bulk metal during recrystallization and during transformation of austenite to pearlite. If these movements are rate-controlling, one might expect to find some rough correlation between the effects of solutes on these three processes in iron. It is, therefore, interesting to observe that

chromium, manganese, and molybdenum strongly increase creep resistance, recrystallization temperature, and hardenability; whereas cobalt, nickel, and silicon only slightly affect any of the three.²⁴

The authors propose the following hypothesis: Solute elements decrease the rate of creep and the rate of grain growth during recrystallization of metals and decrease the rate of growth of pearlite from austenite, not primarily by decreasing the rates of diffusion,* but

* Defined as atomic movements involving concentration differences.

by decreasing the rates of atomic rearrangements at interfaces† or in the bulk of the metal. The latter is

† This idea was presented in the Bethlehem Steel Co. report referred to in the acknowledgments and independent of a somewhat similar proposal by Bowman discussed in the authors' reply to Messrs. Hagel, Pound, and Mehl.

apt to be important in processes involving large volume changes.

The authors appreciate the discussion of Messrs. Hagel, Pound, and Mehl. The discussers have a number of specific objections to the derivation of Eq. 9. Although the authors are in qualitative agreement with the criticisms, it seems pertinent to review certain points. Reference is made to the similarity of Zener's equations to Eq. 9. The authors have commented on this similarity and feel that emphasis should be placed on the essential differences in the basic assumptions upon which the two equations are based, namely, that Zener assumes that the diffusion of carbon is controlling. It would seem that evidence is accumulating which indicates that this may not be the case. The evidence is: 1—activation energies derived from fitting either equation to growth data do not agree with the activation energies for the normal diffusion of carbon in austenite; 2—alloying elements may decrease growth rate without necessity for diffusion of the alloy; and 3—the effects of alloying elements on the diffusion of carbon or interlamellar spacing are not great enough to account for the changes.

The authors wish to acknowledge the very excellent paper by Mehl on the austenite transformation,²⁵ in which he has discussed the above points at length and, in addition, has indicated the need for free energy data on alloy steels to test Zener's theory and that consideration should be given to the suggestion of Bowman²⁶ that the effect of alloying elements in controlling the growth rate of pearlite could be interference with the actual interface mechanism. The authors appreciate having the latter point brought to their attention, for it is in line with the proposal in the present paper that even in pure iron-carbon eutectoid alloys, the rate-determining step involves the interface mechanism. Bowman proposes that the alloying element has additional influence in slowing this step.

The discussers have also questioned the validity of the use of data on growth of austenite from pearlite as an argument for inclusion of the term ΔT . Since a rate equation of the form derived should be applicable to the reaction in either direction, and since the discussers give no reason for their objection, the authors can only repeat the argument given in the paper.

The application of the thermodynamic theory of irreversible processes by Machlin²² deserves careful consideration. There is certainly merit to an approach which includes all aspects of the interface mechanism.

It remains evident that much more theoretical and experimental work must be done to explain the growth characteristics of the austenite decomposition products. The authors look forward to the results being obtained in Dr. Mehl's laboratories.

²⁰ V. A. Phillips and Arthur Phillips: *Journal Inst. Metals* (1952) 81, p. 185.

²¹ T. Prigogine: *Etude Thermodynamique des Phenomenes Irreversibles*. (1947) Liege. DeSoer.

²² E. S. Machlin: *Trans. AIME* (1953) 197, p. 437; *JOURNAL OF METALS* (March 1953).

²³ R. F. Mehl: *Journal Iron and Steel Inst.* (1948) 159, p. 113.

²⁴ C. Austin, C. St. John, and R. Lindsay: *Trans. AIME* (1945) 162, p. 84.

²⁵ F. E. Bowman: *Trans. ASM* (1946) 36, p. 61.

Sintering Zinc Concentrates on the Blackwell 12 by 168 Ft Machine

by A. E. Lee, Jr.

THE Blackwell Zinc Co., Inc., a subsidiary of the American Metal Co., Ltd., operates a horizontal retort zinc smelter at Blackwell, Okla. The plant has 14 furnace blocks of 800 retorts each, fired with natural gas on a 48 hr cycle. Over 13,000 tons of zinc-bearing material, chiefly sulphide flotation concentrates, are treated monthly to produce slab zinc and high lead-cadmium fume.

In 1942 a program of rebuilding and modernizing the smelter was started. By 1947 furnace smelting capacity had been increased to a point where roasting and sintering facilities were inadequate, and it was necessary to purchase oxidized materials to supplement sinter production. The seven 210 ft Ropp roasters and three 42 in. x 44 ft Dwight-Lloyd machines then in use had been in service at least 20 years and were in need of major rebuilding. Thus it was entirely practical to consider all new equipment and a change of method rather than rebuilding and repairing obsolete units. A study of the problem indicated that roasting as such could be eliminated and roasting and sintering accomplished in one step by a modification of the Robson process,¹ which had been used since the early 1930's by the National Smelting Co., Ltd., at their plants at Avonmouth, England, and Swansea Vale, South Wales.

Francis P. Sinn, General Manager, Zinc Smelting Operations, The American Metal Co., Ltd., who was familiar with the practice in England, suggested the use of one large machine for the entire operation from concentrate to sinter. One step sintering appeared to best meet Blackwell's plant requirements and indicated substantial savings in labor, gas, coal, and repair costs.

Choice of Machine Size

The sinter machine size was set at 12x168 ft for a rated capacity of 540 tons per day. This tonnage, produced on a five day week, would meet the seven day requirements of the 14 furnace blocks. The one large machine was quoted at a lower cost than two or more 6 ft wide machines of similar total capacity. Further, the larger machine could be housed in a smaller structure and only one set of equipment for charge preparation and delivery and for disposal of sinter cake was needed. One machine on a five day week made possible a concentration of the skilled operating personnel and required less men than a plant including two or more machines and related equipment circuits. Fewer units of equipment meant less maintenance, and the two down days weekly allowed ample time to repair and, if necessary, to make up lost production.

Experience had indicated better sintering quality and rates with larger masses of material, not only

on wider machines, but also in deeper beds. The ratio of windbox perimeter to area for the 12x168 ft machine is 0.179, compared to 0.353 for a 6x102 ft machine and 0.617 for a 42 in. x 44 ft machine. This meant less air leakage with resulting fan power savings and less spoilage of charge along the pallet sides.

Performance

Initial operation of the new sinter plant was made in November 1951 and regular production attained late in December. The average product sinter output during 1952 and the first half of 1953 has been 18.2 tons per hr. The average for one month has been as high as 22.4 tons per hr. Considerable experimenting with varied operating conditions accounts in part for the below capacity — 24 tons per hr — average output, and work to further improve production rate continues.

A typical sinter analyses is 66.0 pct Zn, 0.3 pct Pb, 0.1 pct Cd, 0.3 pct S, 8.0 pct Fe, 2.0 pct SiO₂, 0.8 pct CaO, and 0.2 pct MgO. Use of this material has made possible increases in furnace burden and improved furnace operation over the former practice using sinter made from Ropp roasted concentrates. Better lead and cadmium elimination in sintering has permitted the furnace production of slab zinc lower in lead and cadmium.

Anticipated economies of operation have largely been gained. The sinter plant is operated by seven men per 8 hr shift — one head operator, three equipment operators and three sweepers — plus one oiler on day shift only. While it has been necessary at times to operate seven days a week to produce the required sinter tonnage, the five day work week usually has been adequate. Consumption of natural gas for sinter bed ignition is 200,000 to 300,000 cu ft per day.

Green Ore Sintering Practice

The 30 to 31 pct sulphur content of the -200 mesh zinc concentrates is the fuel used to sinter the charge, no coal addition being required. In the feed to the machine, sufficient concentrates are added to crushed return sinter fines containing 0.3 to 0.5 pct sulphur to produce a charge averaging 5.0 to 6.5 pct sulphur. Since the return sinter used in Blackwell's practice is varied from -1/2 to -1/8 in., the actual sintering mixture of fine sinter and concentrates is somewhat higher in sulphur. The coarser sinter particles are too large to resinter and merely aid porosity in the sinter bed. The ratio of concentrates to return sinter in the charge ranges from about 1:4 to 1:5.5. Variations are based on the appearance of pried up bed sections, bed exit gas temperature trends, windbox suction, and return sinter size. Sufficient sulphur must be used to obtain fritting of the charge into a soft sinter cake and to aid in the elimination of lead and cadmium. Excessive feed sulphur will result in partial slagging of the cake impairing porosity and prolonging sintering time.

A. E. LEE, JR., Member AIME, is Superintendent, Blackwell Zinc Co., Inc., Blackwell, Okla.

Discussion on this paper, TP 3668D, may be sent, 2 copies, to AIME by Feb. 1, 1954. Manuscript, Dec. 15, 1952; revision, Sept. 8, 1953. Los Angeles Meeting, February 1953.

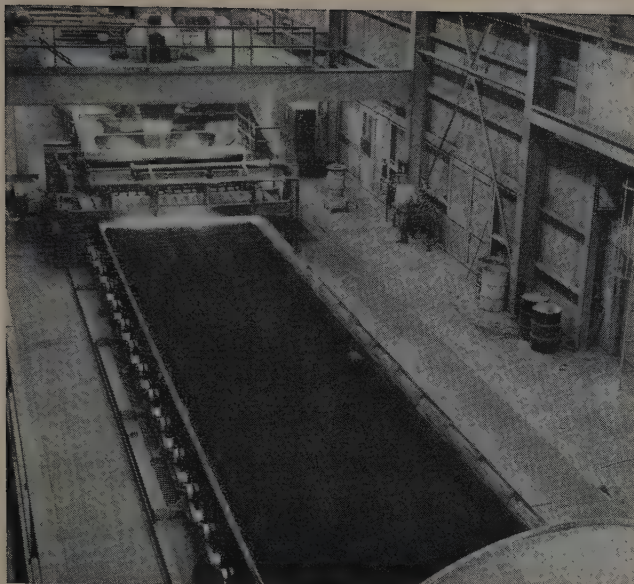


Fig. 2—View of 12x168 ft sinter machine, looking toward the feed end.

drawn through the grate openings into rectangular downcomers outside the machine frame. The downcomers discharge to large balloon flues below the machine where the gas velocity is only 1000 to 1500 ft per min, allowing most of the windbox drippings to settle out. Bottoms of the balloon flues consist of steep sided hoppers, discharging through flap-trap valves to the clean-up conveyor system.

Sinter Cake Crushing and Screening

From the discharge end of the sinter machine the cake falls to a sloping dead-plate and is broken to -9 in. by a special sinter breaker. A series of 4 ft diameter, $1\frac{3}{4}$ in. thick steel claws clearing the dead-plate about 4 in. and mounted on a slowly rotating shaft make up the breaker. From the dead-plate the sinter falls to a 32x42 in. jaw crusher, is broken to -5 in., and carried on a 42 in. wide apron conveyor to a pair of 5x10 ft double-deck shaker screens. The $+1$ in. top deck material is closed-circuited through a gyratory crusher back to the screens.

Sinter on the bottom $\frac{1}{2}$ in. opening screen flows to a pair of hoppers arranged for spill one to the other. One side delivers to a conveyor system supplying hearth layer to the sinter machine but is only used when a very large part of the return sinter is crushed to $-\frac{1}{8}$ in. The other side delivers usually to the product sinter circuit but may be sent back to the return sinter bins through a closed-circuited 16x42 in. roll crusher and $\frac{1}{8}$ in. screen when resintering is desired. Sinter in the product circuit is crushed to approximately $-\frac{1}{4}$ in. and delivered by conveyor to the furnace charge mixing plant.

The $-\frac{1}{2}$ in. sinter fines fall to a second pair of hoppers also arranged for spill one to the other. Discharge from these two hoppers is controlled by separate variable speed and reversible feeders. When one or both feeders operate in one direction, that sinter passes to the return sinter bins as is; i.e., $-\frac{1}{2}$ in. When one or both feeders operate in the reverse direction, that sinter delivers either to the product sinter circuit or back to the return sinter bins through the $\frac{1}{8}$ in. sizing circuit. This arrangement enables the operator to vary the ruling size of the return sinter in any proportion from all $-\frac{1}{2}$ in. to all $-\frac{1}{8}$ in.

Machine Exit Gas System

Gases from the collector main balloon flues servicing the six windboxes nearest the discharge end of the sinter machine pass through cyclones to a pair of draft fans connected in parallel. Each of these fans is designed to handle 117,000 cfm of 235°F gas at -20 in. water. Exit gases are piped to a baghouse for lead-cadmium fume collection.

Gases from the collector main balloon flues servicing the ten windboxes at the feed end of the machine pass through other cyclones to a second pair of fans in parallel. Each of these fans is designed to handle 103,000 cfm of 215°F gas at -28 in. water. Exit gases are piped either to the baghouse or to a recirculation hood over the last nine windboxes at the discharge end. Purpose of the recirculation system is to reduce by nearly half the gas volumes filtered by the baghouse. Since most of the lead and cadmium eliminated leaves the bed near the discharge end, the gases recirculating from the first ten windboxes contain relatively little fume. An automatic damper in the flue to the baghouse is controlled by the hood pressure to prevent gases from blowing out around the hood.

Baghouse

Collection of the lead-cadmium fume is made in ten Norblo No. 936-A automatic dust arresters, totaling 9360 bags, each 6 in. in diameter x 8 ft 3 in. long. The ten units are arranged in pairs over double width hoppers and serviced by five double inlet fans. Each fan is rated at 50,000 cfm of 200°F gas at -8 in. water. The dust is removed from the hoppers by a system of screw conveyors and elevator to a large storage bin from which shipment is made.

Filter bag cloth is unnapped, 4.2 oz, continuous filament orlon. Useful life of an orlon bag under normal operating conditions is about one year, the fabric porosity at that time having reduced to about 10 pct of original value. Patching of a continuous filament orlon bag for wear in a year's time is unusual.

The interval between bag shakings has been varied from 15 to 45 min, the latter time now regular practice. Inlet gas temperature to the baghouse is controlled at 240°F by automatic bleed-in of outside air. Lime additions to the inlet gases are used to maintain a relative alkalinity of at least 11 pct in the dust collected in a manner similar to that described by Shinkoskey.³

Acknowledgment

The basic metallurgical conceptions and practice embodied in the new sinter plant were developed by Francis P. Sinn, of The American Metal Company, Ltd. Complete design of the plant was made, under the direction of W. J. Urban, by the American Ore Reclamation Co., Chicago. The assistance and advice of Chester Skinner and Douglas Stafford at Blackwell in the preparation of this paper are gratefully acknowledged.

References

- ¹T. B. Gyles: Horizontal Retort Practice of the National Smelting Co., Ltd., Avonmouth, England. *Trans. AIME* (1936) **121**, pp. 418-426.
- ²W. J. Urban: The World's Largest Sintering Machine. *Blast Furnace and Steel Plant* (1951) **39**, pp. 339-342.
- ³R. E. Shinkoskey: Conditioning Dwight-Lloyd Gases to Increase Bag Life. *Trans. AIME* (1950) **188**, pp. 608-609; *JOURNAL OF METALS* (March 1950).

Some Observations of Slag-Metal Relations In the Acid Open Hearth Steel Furnace

by G. R. Fitterer

Trends in slag composition in acid open hearth practice, particularly the variation in iron and manganese oxides during refining, are reviewed. A procedure which is currently being used to control the refining reactions is described and partially explained through slag phase diagram considerations. In addition, the ionic nature of these slags is considered and it is proposed that silica combines with the oxide ion and forms a series of complex silicate ions. The effect of basic oxides such as FeO, MnO, and CaO is apparently additive in furnishing the oxide ion for this purpose.

IT is now possible to control^{1,2} the refining of steel in an acid open hearth furnace to a surprising degree. This control has been brought about through the knowledge and use of several facts and tests. These are: 1—A planned charge analysis based on a knowledge of the type of fuel, the bath depth, etc. 2—Knowledge and control of rate of fuel input as well as its method of atomization, if any. 3—Determination of the slag fluidity. 4—Bath temperatures (use of the Pt-Pt-Rh thermocouple). 5—Periodic determination of carbon content (use of the Carb-analyzer or Carbometer).

Through the use of these control methods, a heat may be made to "melt-in" with or without residual manganese and silicon. The rate of refining or carbon elimination may be controlled accurately, and the desired tapping (or "go-ahead") carbon may be approached at a rapid or slow rate according to preference and type of steel being made. Thus operating time may be predetermined and greatly reduced. Further, all of the refining can be done without any ore or other oxidizing additions, and the heat may be brought to the desired tapping temperature simultaneously with the attainment of the desired carbon analysis.

This control procedure is being used in most acid plants in the United States today and has been de-

scribed.^{1,2} Although the slag metal relations are sufficiently well known to control the heat as stated, yet it is possible to account for only about two-thirds² of the O₂ which must have been used for the elimination of the carbon and other metalloids. Phase diagram studies² of the slags, slag weights, the metal particle theory,² ore additions, limestone additions, etc., may all be taken into consideration; yet, the mechanism of oxidation and source of all the oxygen remain to be explained. This paper reviews some of the principles upon which the control methods were based and proposes other possibilities regarding the unexplained phenomena.

Old and New Acid Open Hearth Practice

Some of the recent statements in the literature regarding acid open hearth operation are based on old heat data which are not typical of modern American practice. These old heat logs have been responsible for many misconceptions regarding the acid hearth practice and represent heats which do not coincide with modern methods. In recent years, American practice has been altered materially and these changes will be briefly described.

Modern American Practice: A typical log of a modern American acid open hearth heat¹ is shown in Fig. 1 which indicates that the refining time was only two hours, during which the carbon was eliminated rapidly and the bath temperature increased at a fast rate. The manganese and silicon contents of the metal were essentially eliminated and their oxides had become constituent parts of the slag at the "melt-down" period. During the course of the heat, the MnO content of the slag remained practi-

G. R. FITTERER, Member AIME, is Dean, Schools of Engineering and Mines, University of Pittsburgh, Pittsburgh, and Director of Research, Acid Open Hearth Research Association, Inc.

Discussion on this paper, TP 3671C, may be sent, 2 copies, to AIME by Feb. 1, 1954. Manuscript, Feb. 16, 1953; revision, Sept. 18, 1953. Los Angeles Meeting, February 1953.

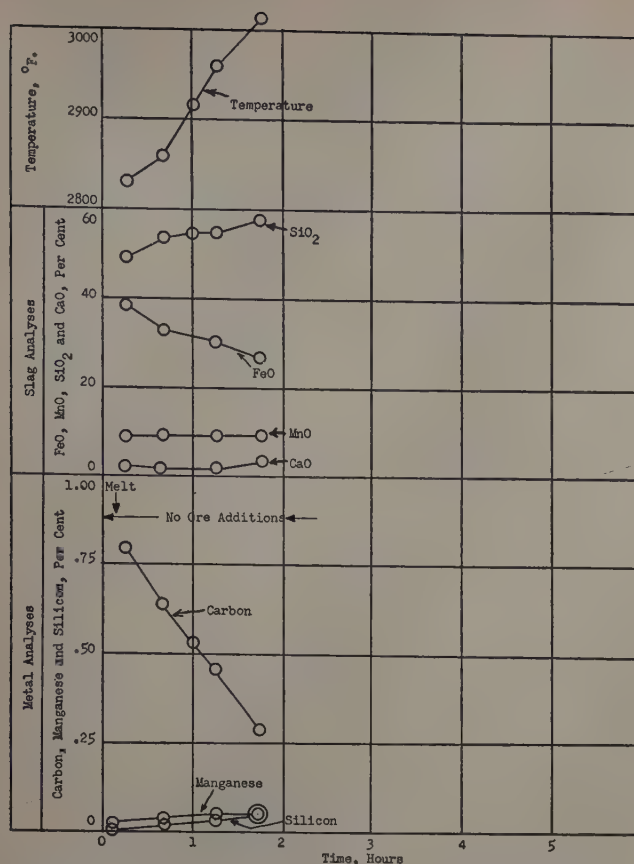


Fig. 1—Log of an acid open hearth heat.¹ American practice, low manganese charge.

cally constant; whereas, the FeO decreased and the SiO₂ increased.

Older European Practice: The acid open hearth practice which was in vogue in this country and in Europe about thirty years ago is illustrated² in Fig. 2. The rate of carbon elimination was only about one-half that of the heat in Fig. 1 and the rate of temperature increase was much slower. Throughout most of the second heat, the FeO content remained fairly constant; whereas, the MnO content decreased throughout the heat in direct contrast to modern practice. The SiO₂ content, however, increased as before. The manganese and silicon contents of the metal bath increased throughout the heat.

During the last two hours of this heat, practically no change in any of the slag or metal constituents occurred, but it was the practice to hold heats in the furnace for a long time in the early days in order to give the laboratory time to report analytical results prior to making the final additions.

The older practice resulted in high MnO slags; whereas, the modern slags contain much smaller quantities of this constituent. The differences in the behavior of FeO and MnO in the low and high MnO slags are worth consideration and raise certain important questions regarding slag-metal relations which have not hitherto been answered.

Behavior of FeO and MnO in the Acid Open Hearth

Heats with Low Manganese Charges: In modern American heats, the MnO content of the slags rarely exceeds 20 pct and the average is probably about 12 pct. Furthermore, the MnO content remains essentially constant throughout heats of this type and the percentage merely depends on the quantity of manganese charged. However, as the refining progresses, four main changes occur: 1—The carbon content of

the metal decreases. 2—The FeO of the slag decreases and the oxygen content of the metal increases. 3—The temperature of the bath increases. 4—The SiO₂ content of the slag increases.

The trends of carbon, MnO, and FeO in several modern American heats are shown in Fig. 3. The lower MnO points represented samples from heats with higher FeO, respectively, etc. Fig. 4 represents these trends for the single heat which was illustrated in Fig. 1. Obviously, as the heat progressed, the carbon of the metal and FeO of the slag decreased; whereas, the MnO remained constant. This situation is encountered in heats with as much as 20 pct MnO as shown in Fig. 5.

Heats with Intermediate Manganese Charges: If the manganese in the charge is increased so that the ultimate MnO content of the slag increases to about 25 pct, the relative behavior of FeO and MnO begin to change. With this amount of MnO, both the FeO and MnO in the slag decrease as the heat progresses as shown in Fig. 6. It appears that both oxides furnish oxygen for the carbon reaction in this case.

Heats with High Manganese Charges: If the manganese content of the charge is increased so that the ultimate MnO content of the slag exceeds 30 pct, the roles of MnO and FeO in the slag apparently become reversed. In this case the FeO appears to remain practically constant while the MnO decreases throughout the heat, Fig. 7. The trend of MnO in the heat, the log of which was shown in Fig. 2, indicates a decrease in MnO with essentially constant FeO, see Fig. 8. All of the data shown in Figs. 3 to 8 inclusive include heats with and without ore additions which seem to have little or no effect on the relative behavior of FeO and MnO outlined above.

Trend of FeO in the Metal: It is interesting to

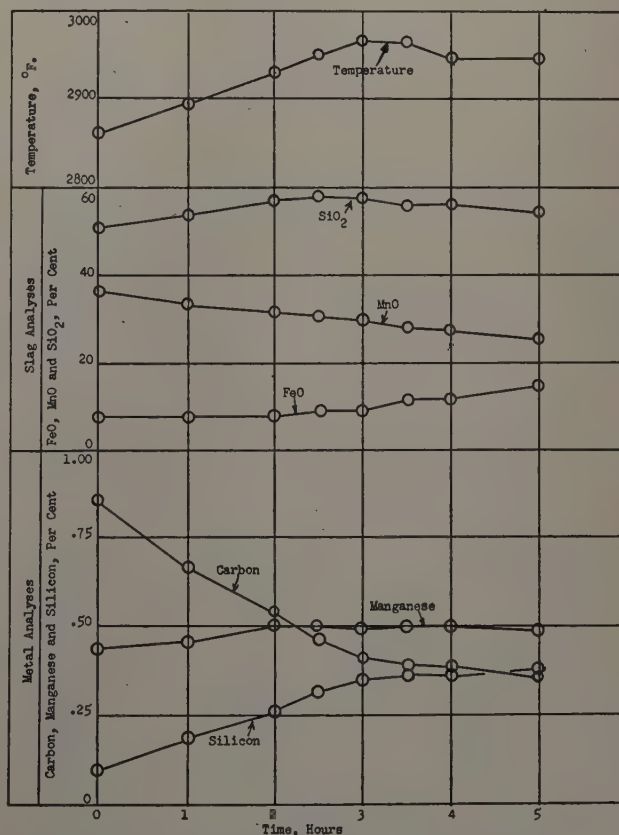


Fig. 2—Log of an acid open hearth heat.² Czechoslovakian practice, high manganese charge.

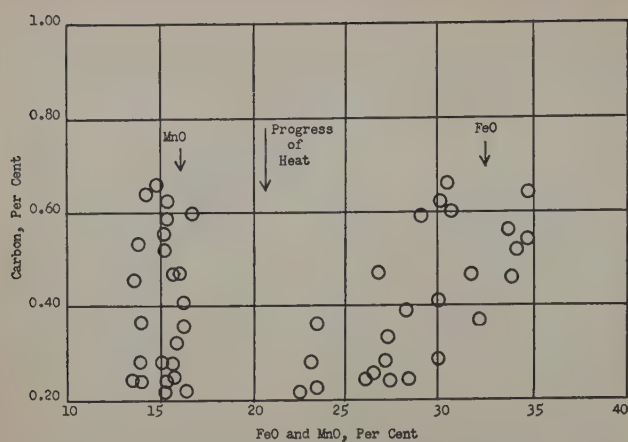


Fig. 3—Usual variation of FeO (and MnO) with the carbon content of the metal. American practice, intermediate manganese charge.

note that the FeO content of the metal increases with decreasing carbon content in the acid open hearth furnace as in the basic. However, the increase in the FeO content of the metal is coincident with a decrease in FeO content of the slag in low MnO slags. In high MnO slags, the FeO content of the metal increases with a decrease in MnO content of the slag. The FeO content of the slag remains constant during these changes as described previously. These relationships between the FeO (and MnO) contents of the slag with the FeO (or oxygen) content of the metal are inverse to those of the basic open hearth process.

Role of Silica and Changes in Slag Weight

The key to the behavior of FeO and MnO discussed above is undoubtedly to be explained through a knowledge of the role of SiO_2 and its relation to the other oxides in such slags together with slag weight studies. For example, in Fig. 9 the trend of SiO_2 with the progress of the heats is illustrated. As the carbon content decreases, the SiO_2 content of the slags increase in a regular manner as shown in Figs. 1 and 2. This occurs whether the FeO or the MnO is changing with the progress of the heat. Both types of heats are plotted in Fig. 9.

A study of the trends⁴ in slag weights throughout various heats indicated that the slag weight may decrease, increase, or remain essentially constant depending upon the refining rate and a few other factors. With extremely rapid carbon elimination in

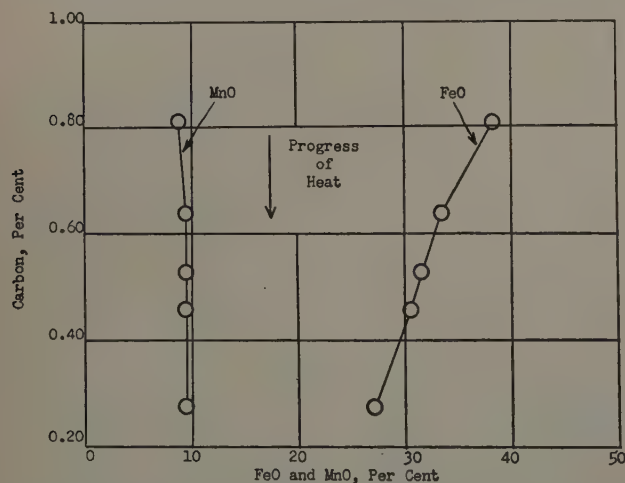


Fig. 4—Variation of FeO and MnO in an acid open hearth slag. American practice, low manganese charge.

which the refining time is less than an hour, for example, the slag weight will decrease somewhat. In this case, the FeO content is rapidly decreased without any time for diffusion of SiO_2 from the furnace walls. In such heats there are few, if any, ore additions and the rate of temperature increase is very rapid. Occasionally, however, with excessive boiling action and bottom repair sand which has not properly set, sufficient mechanical erosion takes place to cause the SiO_2 content to increase abnormally.

Usually in a heat requiring from two to three hours to refine, the loss in FeO content will be balanced by some diffusion of SiO_2 from the banks. However, such heats also require some small ore additions. These factors usually balance to keep the

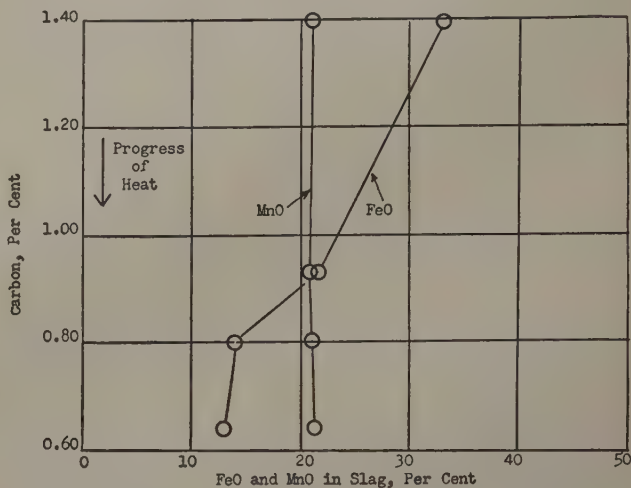


Fig. 5—Variation of FeO and MnO in an acid open hearth slag. American practice, high manganese charge.

slag weight about constant. Such heats also have a moderate rate of temperature increase, but not as rapid as in the first case above.

In very sluggish heats with a very slow temperature rise, many additions of ore are made and considerable erosion of the banks occurs. Such heats will indicate an appreciable increase in slag weight.

In all cases, however, the SiO_2 content of the slag tends toward the same percentage at a given temperature, presumably because of the phase diagram relationships which are about to be described.

Automatic Refining Phenomenon

It has been shown¹ that the acid hearth exhibits an automatic refining phenomenon which is not duplicated in any of the basic processes. Although this phenomenon has been utilized for the past several years by the member companies of the Acid Open Hearth Research Association, the scientific reasons for its occurrence have not yet been explained.

Oxidation and Temperature Changes: As stated previously, as the heat progresses in American practice, the percentage of FeO in the slag decreases while the MnO remains constant. Part of this decrease can be accounted for by the increase in SiO_2 and thus dilution. Some of the decrease can also be accounted for by the transfer of oxygen from the slag to the metal and the elimination of carbon as CO. However, these quantities of oxygen which can be accounted for through the loss of FeO in the slag, taking slag weights into consideration, are much less than the total weight of oxygen actually used for the elimination of carbon. This additional oxygen must originate in the gases above the slag and be

transferred to the metal bath by some process not yet described.

Another factor which is involved in the phenomenon under discussion is the temperature or rate of temperature increase. Through proper adjustment of the charge and the rate of temperature rise, many acid open hearth heats are made without any ore or other intentional oxidizing additions. If the manganese and silicon contents of the charge are properly adjusted according to the fuel in use,¹ the heat may be made to melt-down without residual manganese or silicon. Hence, it melts on a carbon boil.

Under these conditions, the only requirement for oxidation and carbon elimination is an increase in the temperature. If the rate of fuel input is low, the

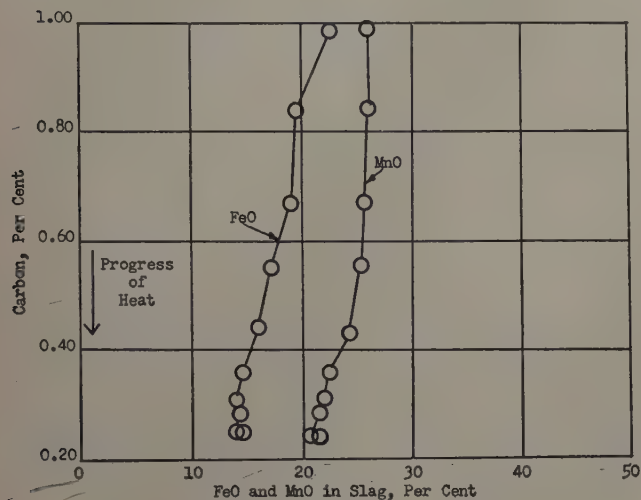


Fig. 6—Variation of FeO and MnO in an acid open hearth slag. American practice, high manganese charge.

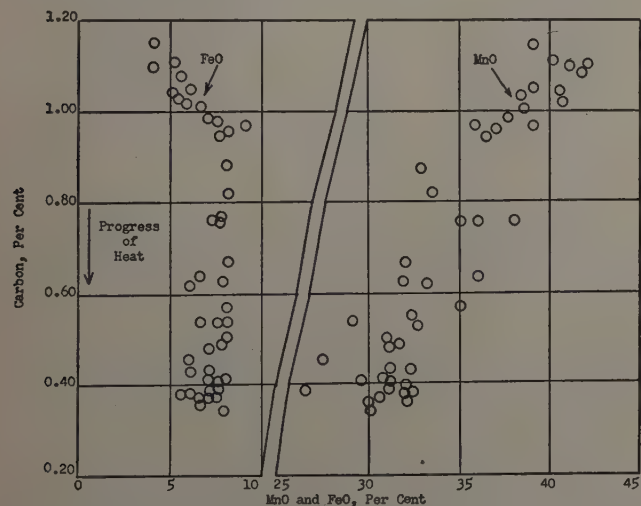


Fig. 7—Variation of MnO (and FeO) with carbon content of the metal. Czechoslovakian practice, high MnO slags.

rate of temperature increase will be correspondingly low, and only a small amount of carbon will be eliminated per unit of time. If, on the other hand, the fuel input and the rate of temperature increase is high, the rate of carbon elimination will be correspondingly high. If the fuel input is high for a while and then suddenly reduced, the carbon elimination will be rapid for a while and then slow up proportionally or stop.

Prior Explanation of the Phenomenon: Previously² this phenomenon was explained by the use of phase diagrams as shown in Fig. 10. For example,

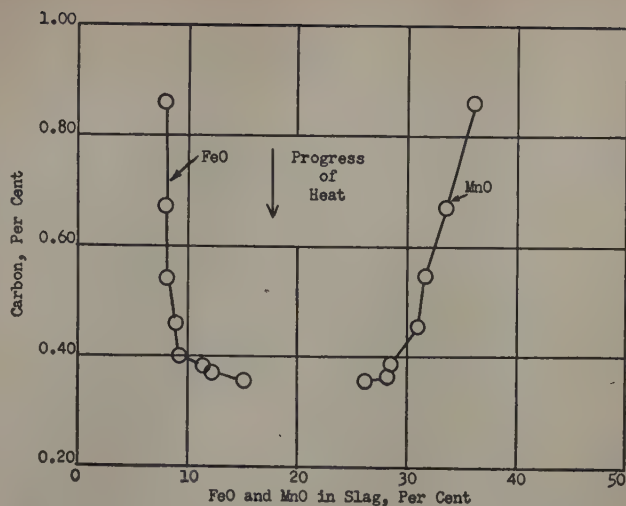


Fig. 8—Variation of FeO and MnO in an acid open hearth slag. Czechoslovakian heat, high manganese charge.

if an FeO-SiO₂ slag is held at some temperature as at point A of the figure, it was suggested that it would be saturated with SiO₂ and be essentially inactive. If, however, the temperature is increased rapidly through a high fuel input, the slag temperature might be raised to point B. Under this condition, the slag would be unsaturated with respect to SiO₂ and would be active in carbon elimination. If the temperature were held at this point (i.e., 3000°F), the slag would tend to approach point C through the loss of FeO to the metal and the oxidation of carbon. At this point, it would again become saturated and essentially inactive. In fact, the carbon content may be held constant under these conditions.

To carry this sequence still further, if the slag at point C is cooled to D, it would become entirely inactive since solid SiO₂ would be precipitated throughout the slag. By alternately increasing the fuel input and then cutting it back, these steps may be repeated many times. With a medium rate of fuel input, the slag composition might conceivably traverse a line just to the left of line AC in a series of small increments as the temperature is increased. The continuous increase in temperature would cause the slag analysis to tend toward an unsaturated condition with respect to solid silica, thus continuously releasing iron oxide for diffusion to the metal bath and reaction with carbon. The continuous loss of FeO from the slag as the temperature is increased

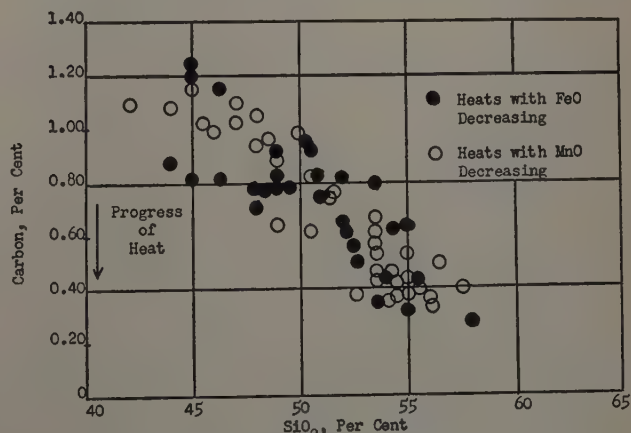


Fig. 9—Usual variation of SiO₂ in the slag during carbon elimination in the acid open hearth furnace.

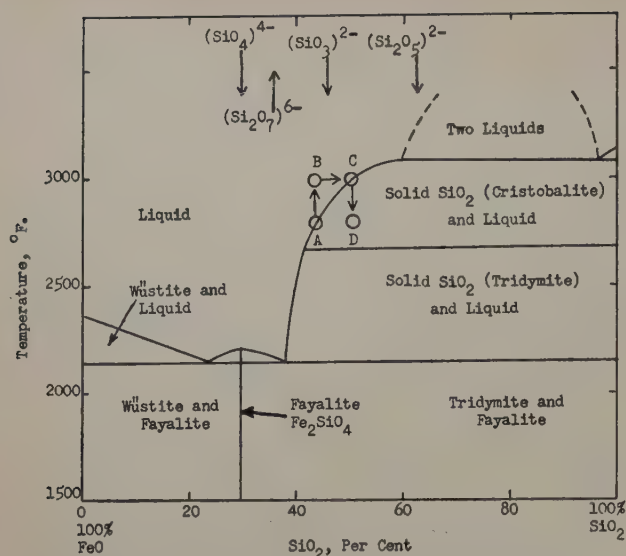


Fig. 10—System FeO-SiO₂ and its role in acid steel refining.

would cause the slag composition to follow a line just above AC.

If a greater rate of carbon elimination is desired, a greater rate of fuel input or increased rate of temperature rise will suffice to supply the required FeO (or oxygen) through this mechanism. If the desired tapping temperature is being approached in a given heat and the carbon elimination is to be retarded, a cut-back in fuel input will cause the boil to subside. It can also be seen that if the manganese and silicon contents of the charge are held at a minimum and if the carbon is not overcharged, the entire heat may be refined without any oxidizing additions such as ore. Many heats are currently being made with these factors and the above principles in mind. It might also be stated that the same principles have been applied to the acid electric process⁵ with similar results.

This is an overly simplified concept of the mechanism of oxidation and would not be complete without some consideration of the other oxides which normally exist in acid slags. Besides FeO and SiO₂, other oxides such as MnO, CaO, Al₂O₃, and Cr₂O₃ also must be considered as regular constituents, al-

though the latter three rarely exceed two or three per cent.

As shown previously, MnO exists in all acid open hearth slags and is inactive under 25 pct, but apparently furnishes oxygen to the bath for carbon elimination, if its content exceeds this amount. For this reason either the ternary system FeO-MnO-SiO₂ or the two binary phase diagrams FeO-SiO₂ and MnO-SiO₂ should be studied with these refining principles in mind.

Because of the uncertainty of the ternary system and for simplification the high silica portion of the two binary systems have been plotted in Fig. 11. Also the SiO₂ contents of slags from three typical heats have been plotted against their respective temperatures in this figure and it is obvious that the compositions of the slags fall between the two liquidus or saturation lines. The trends of the heats from the low to the high temperature indicate a tendency to follow the SiO₂ saturation plane existing between these two binary systems. Hence, it is not improbable that the phase diagram principle described for the simple FeO-SiO₂ system may be applied to the ternary system.

As stated previously, this principle is satisfactory for use in refining but it leaves many questions unanswered. For example, why does FeO apparently furnish the oxygen in a slag containing less than 25 pct MnO and why does MnO become the oxidizing medium above that percentage?

Even small additions of limestone (i.e., 1 or 2 pct CaO in the slag) will release an almost exact pound-mol equivalent of FeO to the metal bath. Obviously, it is more basic but no clue to this degree of basicity is to be found in the phase diagram relationships except that SiO₂ is apparently saturated with much less CaO than with the other two oxides.

Further information should be obtained regarding the behavior of Al₂O₃ and particularly Cr₂O₃ in the acid slags before complete understanding of the process is available.

Ionic Theory of Slags

Because of these and other unanswered questions regarding acid open hearth phenomena, the ionic as well as other theories must be considered for fundamental explanations. The following discussion is admittedly speculative and is presented for the purpose of provoking thought along new lines and with the hope of ultimately linking established acid open hearth slag-metal relationships with a more satisfactory and complete scientific theory.

Possibilities of Compound Formation in Slags: Mineralogists have reported the existence of both the mono (meta) and di (ortho) silicates of FeO, MnO, and CaO, yet particularly in the FeO-SiO₂ phase diagram only (FeO)₂SiO₂ or fayalite has been indicated.^{6,7}

Many acid open hearth slags have been studied by petrographic⁸ and X-ray⁹ diffraction methods in the "as-cast," slowly-cooled, and heat-treated conditions, yet no crystalline form of any of the silicates has been observed. This statement should not be taken to indicate that no such molecular associations or embryonal crystals are possible in either the solid or liquid states, but merely that the SiO₂ contents of acid open hearth slags are so great even at "melt-down" that the tendency to crystallize into any inter-oxide compound form is retarded through the tendency of SiO₂ to form amorphous glasses.

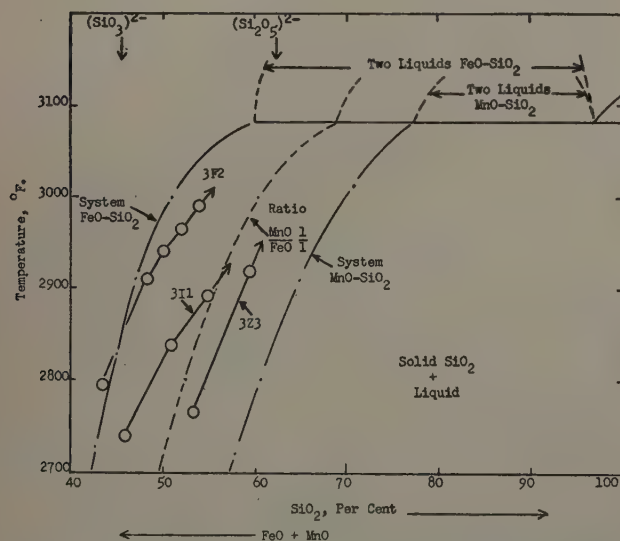


Fig. 11—Systems FeO-SiO₂ and MnO-SiO₂ and acid open hearth slags.

Only one type of crystalline species has been identified⁸ in recent acid open hearth slags. This is of the spinel family and can be observed when the Al_2O_3 or Cr_2O_3 contents of the slags exceed about 4 pct. The $(\text{FeO})_2\text{Al}_2\text{O}_3$ and $(\text{FeO})_2\text{Cr}_2\text{O}_3$ compounds apparently have a strong tendency to form and crystallize even in the presence of the high silica contents of acid slags.

Ionic Theories: As early as 1907 Doelter¹⁰ suggested that the molten iron silicates indicated high electrical conductivity and many other investigators since have checked this observation and concluded also that the conductance is of an ionic nature. In his studies of acid open hearth slags, Herasymenko¹¹ concluded that they were completely ionized in the molten state. This has much basis of fact.

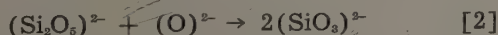
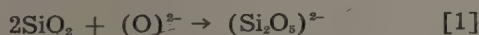
One of the best reviews of the ionic nature of slags was made recently by Chipman and Chang,¹² wherein it was shown that a new trend of thought was initiated by Lewis¹³ who suggested certain revised definitions of acids and bases. He proposed that a basic material such as the oxygen ion $(\text{O})^{2-}$ possesses electrons which are available to enter the electron shell of an atom of various molecular species to form a resulting bonded molecule. A molecular species containing an atom which can receive electrons in its valence electron shell was conversely defined as an acid.

Following this newly defined system, several investigators have developed a series of ideas regarding glasses and other silicates upon which most of the following is based. For example, Sun and Silverman¹⁴ and Sun¹⁵ suggested that the oxides could be arranged in the order of their increasing basicity according to this definition. The normal oxides present in acid open hearth slags may be arranged according to their increasing basicity as SiO_2 , Al_2O_3 , MnO , FeO , and CaO .

According to the Lewis theory, the more basic oxides such as those of iron, manganese, and lime would furnish the oxide ion $(\text{O})^{2-}$ concentration of a slag thereby making available an electron pair to any acidic molecular species.

Huggins and Sun¹⁶ suggested that the addition of the oxide ion to silica would change its acidity in progressive steps as shown in Table I.

According to this progressive series of silicate ions, the function of the basic oxides such as FeO , MnO , and CaO is to furnish the oxygen ion and its available electrons for bonding with the silicon to make a more basic molecular species. With more iron oxide (or MnO and CaO) more of the oxide ion $(\text{O})^{2-}$ would be made available to the slag in increasing steps as follows:



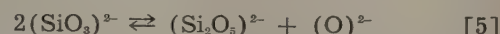
Ionic Theories and Acid Open Hearth Refining

In Fig. 9 it was shown that the SiO_2 contents of acid open hearth slags normally vary from 43 to 58 pct. Assuming that the remaining constituents were only FeO and MnO , then the molecular ratios of $(\text{FeO} + \text{MnO})/\text{SiO}_2$ vary from 0.60 to 1.11. Such a range in composition might suggest that the predominant silicate ions which normally exist in such slags would be $(\text{Si}_2\text{O}_5)^{2-}$ and $(\text{SiO}_3)^{2-}$ according to the progressive series of ions suggested by Huggins

Table I. Types of Silicate Ions as Determined by Presence of Basic Oxides

	Acid	Decreasing Acidity			Basic
Acidity Atoms of O per atoms of Si Molecule basic oxide to molecule SiO_2	SiO_2	$(\text{Si}_2\text{O}_5)^{2-}$	$(\text{SiO}_3)^{2-}$	$(\text{Si}_2\text{O}_7)^{6-}$	$(\text{SiO}_4)^{4-}$
	2	2.5	3	3.5	4
	0	0.5	1	1.5	2.0

and Sun.¹⁶ For the purposes of the discussion which follows, it will be suggested that both these and the oxygen ion exist simultaneously, together with the positively charged metallic ions. Possibly even a balance is assumed in the relationships of these ions according to the relation



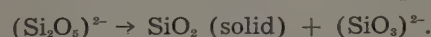
or the reverse of Eq. 2, with the understanding that the Fe^{2+} and Mn^{2+} ions are always present.

Oxidation of the Metal Due to a Temperature Increase: It was shown in the discussion of the phase diagram in Fig. 10 that apparently oxygen is released to the metal bath simply by means of a rapid increase in temperature. Inasmuch as less of the basic oxide is needed to saturate silica with increasing temperature, it might be assumed that the $(\text{Si}_2\text{O}_5)^{2-}$ ion is favored over the $(\text{SiO}_3)^{2-}$ ion at higher temperatures. Thus, the tendency would be for some of the $(\text{SiO}_3)^{2-}$ ion to release some of its oxygen as the temperature is increased and in accordance with the trend of Eq. 5.

Both excess oxygen and iron (or manganese) ions would be available for distribution to the metal bath. The oxygen would be furnished for carbon elimination and the iron simply becomes a part of the metal bath.

The chief advance in thought to be obtained from the ionic theory is that all of the basic oxides FeO , MnO , and CaO apparently serve the same function in furnishing the basic oxide ion $(\text{O})^{2-}$ to the SiO_2 to form the silicate ions, $(\text{Si}_2\text{O}_5)^{2-}$ and $(\text{SiO}_3)^{2-}$. Because FeO and MnO have nearly the same relative bond or basic strength according to Sun,¹⁵ the iron furnishes the additional oxygen if it is in excess of the MnO and the reverse becomes true in high MnO slags. That this is true is possibly indicated by the fact that in the latter slags the manganese content of the bath increases during the carbon boil.

SiO_2 Precipitation Due to a Temperature Decrease: The carbon reaction in an acid open hearth furnace may be caused to cease by either holding the temperature constant or permitting it to reduce slightly. According to the phase diagram concept holding the temperature would cause the slag to approach saturation with respect to SiO_2 (line BC) and to precipitate SiO_2 with a reduction in temperature (line CD). If it is assumed again that the $(\text{Si}_2\text{O}_5)^{2-}$ ion is favored by an increased temperature, then it might conceivably be less stable with a reduction in temperature so that some solid silica would precipitate.



This would conform with the phase diagram concept because on cooling the newly formed silica would tend to be in equilibrium with a liquid containing more oxygen at the lower temperature. However, this oxygen is not available for reaction in the metal phase. Instead, it is associated with the silicon in the higher oxygen complex, i.e., $(\text{SiO}_3)^{2-}$.

Transfer of Oxygen from the Flame to the Metal Bath: The acid slag is, of course, in direct contact with iron, but in addition some metal particles are forced through the slag and in direct contact with the flame because of the carbon boil. As described previously² the metal particles might be responsible for much of the transfer of oxygen from the flame to the metal because the slag contains as much as one or two per cent of metal particles during the boil. The oxidation of these particles and their subsequent contact with the slag and/or metal cause the continued elimination of the carbon.

As far as the slag phase is concerned, the oxidation of these particles would result in the formation of more oxide ion (O^{2-}) and the formation of the higher oxygen silicate ion just as would an ore addition.

Role of Cr_2O_3 and/or Al_2O_3 : The presence of several per cent of Cr_2O_3 or Al_2O_3 in the slag is apparent to the open hearth operator. If either oxide is present in quantities up to 5 pct or above, a noticeable decrease in oxidizing power of the slag results. As stated previously, these are the only oxides which can be detected in acid open hearth slags by either petrographic or X-ray methods. A strong tendency exists for these oxides to form spinels, i.e., $(FeO)_2 \cdot Al_2O_3$ or $(FeO)_2 \cdot Cr_2O_3$. The effect of such spinel formations on the oxidizing power of the slags is obvious. Further, it is likely that some ions are formed by the amphoteric oxides and that these might be $(Al_2O_3)^+$ and $(Cr_2O_3)^+$. However, because of their weak acidic nature but their strong tendency to form the high melting spinels, the latter crystallize readily and remove some of the oxide ion from its combination with the silicate ions or for oxidation of the metal bath.

It is known that high temperatures tend to break up these spinels and in the case of the chromium, it is reduced into the metal bath under such conditions. Thus, the ionic theory also aids in understanding the effects of spinels in acid slags.

Summary

Some operational phenomena that have been observed to occur in the refining of steels in the acid open hearth furnace have been described. It has been indicated that the refining process may be controlled within practical limits through the use of certain phase diagram considerations involving the slag constituents.

Some additional information was given to show that iron oxide and manganese oxide apparently reverse their respective trends depending upon the concentration of each present in the slag. If the percentage of manganese oxide is less than 25 pct (as in American practice), the concentration of manganese oxide will remain essentially constant throughout the heat. In this case, the iron oxide will decrease in concentration and apparently is responsible for the elimination of carbon under these conditions.

If, on the other hand, the manganese oxide content is increased to as much as 30 to 35 pct in the slag, the iron and manganese oxides reverse their trends. In this case the iron oxide content remains constant and the manganese oxide apparently furnishes the oxygen for the carbon removal. Simultaneously, a manganese increase in the metal bath is to be observed.

The phase diagram concept mentioned above does not adequately answer all the questions which arise in view of these phenomena and certain ionic

theories of slags were considered in the hope of answering some of the questions.

It was concluded that acid open hearth slags probably contain at least two silicate ions, i.e., $(Si_2O_5)^{2-}$ and $(SiO_3)^{2-}$. The oxygen (or oxide) ion (O^{2-}) as well as the positive ions of iron and manganese also probably exist in these slags at all times.

The addition of manganese and lime oxides to such a slag merely increases the oxide ion because these oxides apparently ionize and furnish more oxide ion, either for reaction with the constituents in the metal bath, or for the formation of a silicate ion containing more oxygen. The basic oxides are, therefore, additive in their supply of the oxygen ion and this additive nature was not previously explained by the phase diagram considerations.

If the MnO content exceeds 25 pct, it apparently furnishes the excess oxide ion for carbon elimination instead of the iron oxide which in this case is much lower in concentration. This is shown by the fact that such slags furnish oxygen for the metal bath simultaneously while a manganese reversion takes place.

It has been suggested that the $(Si_2O_5)^{2-}$ ion is benefited by an increase in temperature so that merely raising the temperature will cause the $(SiO_3)^{2-}$ ion to furnish the free oxide ion (O^{2-}) and some $(Si_2O_5)^{2-}$, thus increasing carbon elimination. This is in line with the phase diagram concept.

The presence of appreciable amounts of Al_2O_3 and/or Cr_2O_3 apparently will reduce the oxidizing characteristic of acid slags by combining with the oxide ion to form a complex ion such as $(Cr_2O_3)^+$ and ultimately stable solid compounds, i.e., the spinels.

In general, the ionic theories strengthen the phase diagram explanations and add to the science, particularly in suggesting the idea that basic oxides furnish the oxide ion (O^{2-}) to acid slags and that their effects are additive.

References

- ¹ G. R. Fitterer et al.: Acid Open Hearth Slag Fluidity and Its Significance. *Bulletin No. 1*, Acid Open Hearth Research Association, Inc., Pittsburgh (1945).
- ² G. R. Fitterer: *Trans. ASM* (1945) **34**, p. 1.
- ³ P. Herasymenko: *Journal Iron and Steel Inst.* (1947) **157**, p. 515.
- ⁴ C. A. Bruch: Oxidizing Characteristics of Acid Open Hearth Slags. Ph.D. Thesis, 1952. Univ. of Pittsburgh.
- ⁵ G. R. Fitterer: *Proc. Electric Furnace Steel Committee, AIME* (1946) **4**, pp. 185-198.
- ⁶ C. H. Herty, Jr. and G. R. Fitterer: *Industrial and Engineering Chemistry* (1929) **21**, No. 1, p. 51.
- ⁷ N. L. Bowen and J. F. Schairer: *American Journal of Science* (1932) 5th Ser., **24**, p. 200.
- ⁸ Charles R. Funk and Kenneth Midlam: *Proc. National Open Hearth Conference, AIME* (1950) **33**, p. 292.
- ⁹ J. W. Linhart and Nezh Rona: The System $(FeO)_2SiO_3$ -(MnO) $_2SiO_3$. M.S. Thesis, Metallurgical Engineering, Univ. Pittsburgh, 1945.
- ¹⁰ C. Doelter: *Sitzungsbir Wien Akad. Wissensch.* (1907) **116**, p. 1249.
- ¹¹ P. Herasymenko: *Trans. Faraday Soc.* (1938) **34**, p. 1245.
- ¹² J. Chipman and Lo-Chang Chang: *Trans. AIME* (1949) **185**, p. 191; *JOURNAL OF METALS* (February 1949).
- ¹³ G. N. Lewis: *Journal Franklin Inst.* (1938) **226**, p. 293.
- ¹⁴ K. H. Sun and A. Silverman: *Journal Amer. Ceramic Soc.* (1945) **28**, p. 8.
- ¹⁵ K. H. Sun: *The Glass Industry* (1948) **29**, p. 73.
- ¹⁶ M. L. Huggins and K. H. Sun: *Journal of Physical Chemistry* (1946) **50**, p. 319; (1947) **51**, p. 438.

Solid Phase Identification in Partially Reduced Iron Ore

by Gust Bitsianes and T. L. Joseph

THE reduction of a lump of iron ore is a complicated sequence of up to three reactions proceeding simultaneously in a gas-solid system. As the ore moves down the blast furnace into zones of higher temperature and higher reducing power, it is successively reduced through the three oxides of iron into metallic iron. The reduction process involves much more than chemical problems. Physical factors add to the complexity of the overall process.

Under optimum conditions, reduction of the ore is completed at a level about one-half way down the blast furnace stock column. At this point, the ore undergoing reduction has attained a temperature of about 1000°C and has been in the furnace for about 6 hr. On the practical side, the behavior of the ore during smelting has been of great interest to operators. Unsatisfactory blast furnace operation on burdens containing magnetite ore or badly slagged sinter has often been attributed to poor reducibility. The question of reducibility has also been raised in formulating quality standards for agglomerates such as nodules, briquettes, and pellets. In the present investigation, the solid phases formed during reduction were studied as a step toward a better understanding of the overall process.

Equilibrium Studies

The iron-oxygen equilibrium diagram shown in Fig. 1 reveals a number of facts pertinent to the gaseous reduction of iron ores. This diagram is from the work of Darken and Gurry^{1,2} and represents a correlation of the best available data. Four solid phases may exist during the complete reduction of hematite to metallic iron. These are hematite (Fe_2O_3), magnetite (Fe_3O_4), wüstite (FeO_x), and iron (Fe). The wüstite phase is a solid solution which is not stable below 570°C. At this temperature the solid solution undergoes a eutectoid-type of decomposition into the phases, magnetite and iron. Thus above 570°C, the diagram dictates that a hematitic ore should pass through a four-phase sequence on reduction to metallic iron. Below 570°C, only hematite, magnetite, and iron should appear.

Information on the iron-oxygen system has been derived largely from CO and H_2 reduction equilibria. The Fe-C-O relationships have been studied extensively by R. Schenck and his coworkers and well summarized by H. Schenck.³ More recent studies have been made by Darken and Gurry.^{1,2} Data from these sources have been combined and plotted in Fig. 2. With respect to the Fe-H-O system, the works of Emmett and Schultz⁴ seem the most reliable, and these data have also been included in Fig. 2.

G. BITSIANES and T. L. JOSEPH, Members AIME, are Assistant Professor and Professor of Metallurgy, respectively, Minnesota School of Mines and Metallurgy, Minneapolis.

Discussion on this paper, TP 3659C, may be sent, two copies, to AIME by April 1, 1954. Manuscript, July 2, 1953. New York Meeting, February 1954.

This paper is based on a thesis by G. Bitsianes submitted in partial fulfillment of requirements for the degree of Doctor of Philosophy to the University of Minnesota, August 1951.

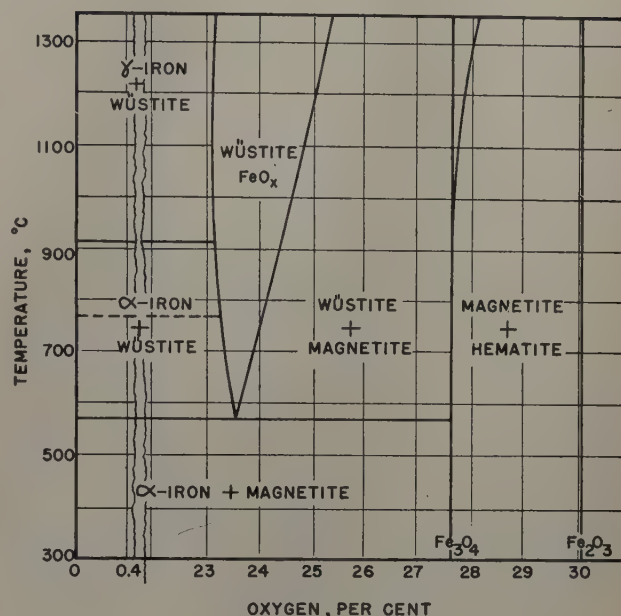
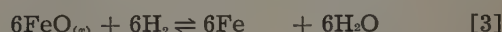
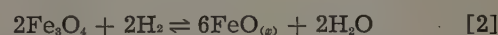
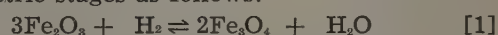


Fig. 1—Iron-oxygen equilibrium diagram.

Certain physical properties of the solid phases of the iron-oxygen system are summarized in Table I. The crystallographic information is of special interest as much of the present work has been concerned with the X-ray analysis of the products of reduction.

Reduction with Hydrogen

The reduction of ore with hydrogen is the net result of two or more gas-solid reactions. Above 570°C, the reaction sequence may be represented by stoichiometric stages as follows:



These reduction reactions follow the general form:



This type of gas-solid reaction has been investigated by Langmuir¹¹ who has shown that such reactions can occur only at the boundary between the two solid phases. Furthermore, a nucleus of the second phase must initiate the reaction. Once such an interface exists, the reaction proceeds through a layer of the solid reaction product (C). The specific mechanisms involved will depend a great deal on the properties and condition of this particular layer. A number of heterogeneous reactions such as the dehydration of single crystals of copper pentahydrate and the calcination of limestone follow this type of process. It should be noted that the interfacial type of reaction also occurs even in dense polycrystalline material which simulates a monocrystalline behavior.

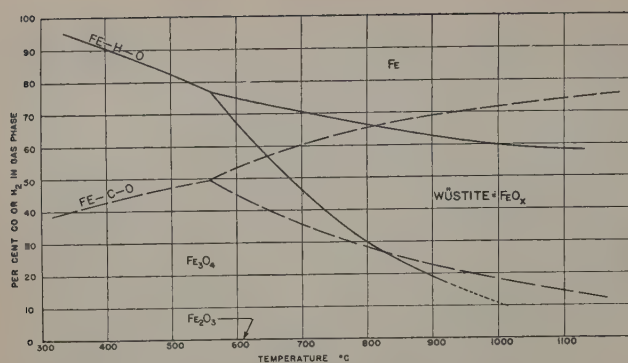


Fig. 2—Fe-C-O and Fe-H-O reduction equilibria.

Of further interest is the propagation of many of these reactions in such a way that the interface maintains a position parallel to the crystal face from which it originated. Advance of the interface is governed by rate-controlling factors and the geometry of the crystal. Sectioning of such a partially reacted specimen will often reveal an unaltered center which follows the contour of the original crystal. This behavior is especially characteristic of many heterogeneous reactions involving a gaseous phase. Solid state reactions which follow this behavior are a special type of what Kohlschütter¹² called "topochemical" reactions a long time ago. This designation will be used hereafter whenever a description of the basic process is necessary.

It has often been surmised that a lump of hematite is reduced successively through the oxides of iron in such a fashion that the phases are formed in a definite layered pattern. Of the many authors who have investigated this aspect of reduction, whether intentionally or not, only a few will be mentioned. Kalling and Lilljequist,¹³ Wienert,¹⁴ Baukloh and Froeschmann,¹⁵ Kalina and Joseph,¹⁶ and Chufarov and Tatievskaya¹⁷ have shown that reduction reactions tend to follow a topochemical path.

The reduction process is not a simple case of topochemistry but involves a series of such reactions. Multilayered structures in partially reduced products have been observed by many investigators so that this concept is not new. The clearest idea of the overall behavior may be gained by considering that the reduction of each oxide layer proceeds in a topochemical fashion of its own so that the spacing of the various interfaces is mainly a function of specific rate factors. The number of such interfaces is in turn a function of the number of phases involved in the overall process. There has been, however, a difference of opinion as to the number of phases that

may exist. The simplest approach is to assume that the number of phases and their relationships are fixed by the equilibrium requirements of the iron-oxygen system. Whether the equilibrium relationships, determined for specific conditions, dictate the manner in which a lump of iron ore is dynamically reduced, has been questioned.

Hofmann¹⁸ has claimed that the wüstite phase can form at any temperature above or below the quadruple point of 570°C and that in the same range of temperature, magnetite need not be a primary reduction product. Wienert¹⁴ reported wüstite or a "ferrophase" in products at 540°C. After using special kinetic measurements, Olmer^{19, 20} concluded that hematite is reduced directly to metallic iron above 325°C. Taylor and Starkweather²¹ reported a similar conclusion but at a temperature of 450°C. Most of these controversial results have been derived from simple rate measurements which are not sufficient to analyze the reduction process. A number of investigators^{17, 22-24} have attempted to identify the solid phases of reduction by means of metallographic or X-ray methods of analysis. Their results have been largely inconclusive because of the experimental difficulties encountered. Wiberg's work²² is an exceptional case. He obtained excellent micrographs of partially reduced Kiruna magnetite which showed the layered structure that would be expected from reduction equilibria.

Experimental Procedure

In early work the authors, like many previous investigators, attempted a study of the reduction process by an evaluation of rate data obtained under a variety of conditions. It soon became apparent, however, that a more direct approach was needed. The method finally adopted was that of quenching the specimen to "freeze" it at a certain reaction point, sectioning it to reveal its inner strata, and then investigating the section with all the available means. This method proved to be highly effective.

Carbon monoxide is the major reductant of industrial operations but it undergoes certain side reactions which complicate the reduction process and the identification of solid phases in partially reduced specimens. Purified cylinder hydrogen is convenient to use and is stable over the temperature range of interest. There are undoubtedly some differences in the behavior of hydrogen and carbon monoxide molecules during the reduction sequence but the general type of reaction should be much the same.

Selection of Iron Ore: Iron ores behave very differently during reduction. Some ores crack under

Table I. Physical Properties of Iron and Its Oxides at 20°C.⁵⁻¹⁰

Name and Formula	Molecular or Atomic Weight	Fe, Pct	Density, Gram per Cc	System and Structure	Crystallographic Data				Mols per Unit Cell
					Space Group: Schoenflies	a, Å	c, Å	Axial Angle	
Iron									
α Fe	55.85	100.0	7.874	bcc, W	O _h ⁸	2.8664			2
γ Fe	55.85	100.0	8.145 cal.	fcc, Cu	O _h ⁵	3.571			4
Wüstite,* FeO	73.07	76.43	5.645	fcc, NaCl type	O _h ⁵	extrap. 4.300			4
Magnetite, Fe ₃ O ₄	231.55	72.36	5.175	cubic, MgAl ₂ O ₄ type	O _h ⁷	8.391			8
Hematite									
α Fe ₂ O ₃	159.70	69.94	5.260	hexag. or rhomb.	D _{3d} ⁶	5.039	13.76		6
γ Fe ₂ O ₃	159.70	69.94	4.898 cal.	cubic, MgAl ₂ O ₄ type	O _h ⁷	5.426		55°17'	2
						8.33			10 2/3

* As wüstite is a solid solution, the physical properties for the phase are given only for the eutectoid composition at 76.43 pct Fe.

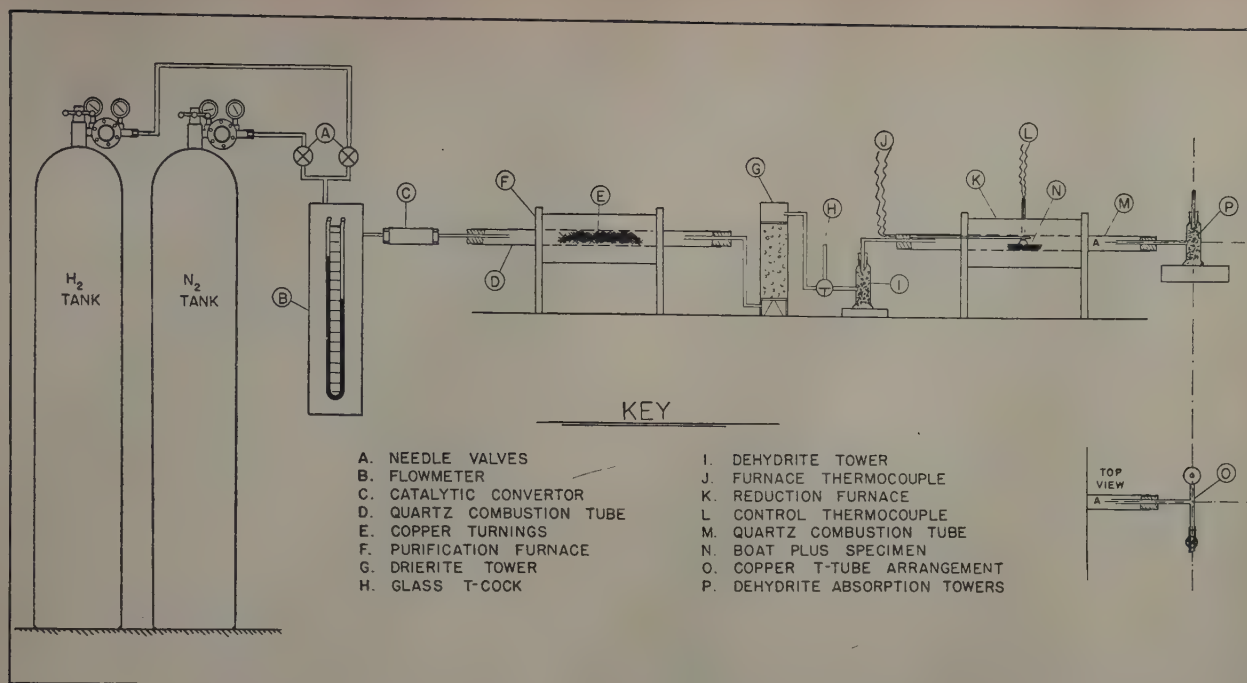


Fig. 3—Schematic representation of reduction apparatus.

the influence of heat alone. Others crack at various stages of reduction. Physical or chemical discontinuities tend to obscure phase relationships in partially reduced specimens. For the best results in studying the solid phases formed during reduction, an ore should possess the following properties: 1—The ore must be a hematite. Magnetites are too individualistic in their behavior. 2—The ore must be dense with a porosity of 10 pct or less. 3—The ore must be homogeneous with an even dispersion of pores and finely divided impurities. 4—The ore must be relatively pure to avoid cracking and the effect of complicated side reactions.

In view of these requirements, a dense ore from the Vermillion Range in Minnesota designated as 8B was chosen for much of the work. It contained 65 pct iron, about 7 pct silica, and was physically homogeneous with an even distribution of the 3 pct of pore space. Pieces of the ore resisted thermal spalling and reduced without excessive shrinkage or cracking.

Compacts of finely divided pure hematite offer certain advantages in a study of the reduction process. Moreover, work on such compacts affords an insight into some of the problems associated with the agglomeration of fine concentrates or fine iron ore. This aspect of the reduction field was extensively studied and the results will be reported later.

Reduction Apparatus: The apparatus used in the preparation of partially reduced specimens is shown schematically in Fig. 3. By automatic control of the electrical resistance furnace, the temperature of the specimen could be held to within $\pm 1^\circ\text{C}$. The reduction reactions were carried out in a quartz combustion tube of 1 in. ID. All specimens were held in a nichrome-screen boat which could be immediately withdrawn into a water-cooled "quenching" chamber attached to the end of the reaction tube. The remaining part of the apparatus was needed to supply and purify tank hydrogen and nitrogen at controlled rates.

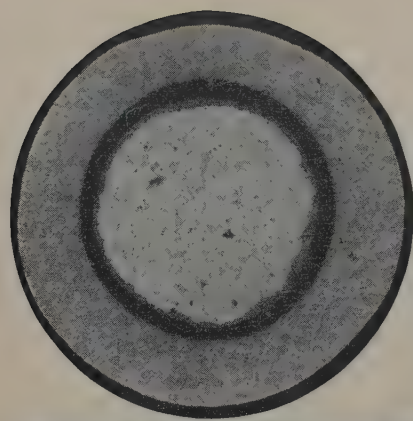
Nitrogen was passed over the specimen for 15 min while it was slowly brought up to the desired temperature. With the system in an isothermal state, hydrogen was passed over the specimen at the rate

of 1200 ml (standard temperature and pressure) per min. At the end of a run, the specimen was withdrawn into the quenching chamber where it cooled rapidly in an atmosphere of hydrogen. This moderate cooling rate was found to be fast enough to "quench" the reduction reactions without any cracking effects which could be detrimental to the later operations.

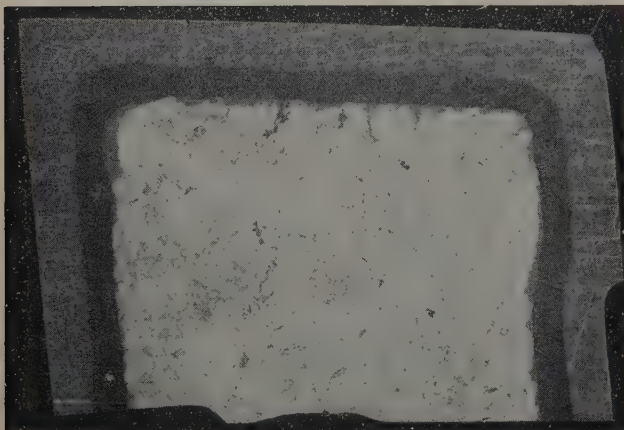
Examination of Partially Reduced Specimens: Most of the partially reduced specimens were too friable to be handled freely. It was not only necessary to strengthen the structure but also to fill in the cracks and pores characteristic of reduced material. After unsatisfactory results with many agents and techniques, impregnation with liquid organic monomers afforded a satisfactory solution to the problem. These liquids could be readily set by the simple process of polymerization. Either methyl methacrylate monomer, which polymerizes into Lucite, or styrene monomer, which polymerizes into polystyrene, was found to be satisfactory. Specimens were covered and impregnated with the prepared monomer using a conventional vacuum technique. Polymerization was then induced under a definite time-temperature schedule which required about three days at 45°C for the methyl methacrylate monomer. After cooling, the mass of polymer could be sectioned at will to reveal the strata of the partially reduced ore.

Macroexamination: Impregnated half-sections were mounted in bakelite and then ground on a glass plate with wetted carborundum powders. This rough surfacing was followed by a wet finish on special grades of abrasive paper (Wetordry). The latter had been found to give the clearest resolution of the reduction strata in macro form. In many cases the reduction strata were clearly visible to the eye and could be macrophotographed at magnifications of 3 to 5 diameters. These macrophotographs were valuable in directing the more searching techniques which were to follow.

Microexamination: The preparation of a highly polished surface on partially reduced iron ore was not a simple operation. A typical cross section in this work contained as many as four different



a (left)—Synthetic ore pellet. Partially reduced in hydrogen at 750°C for 40 min. Etched.



b (below)—Natural dense ore 8A. Half section of rectangular prism. Partially reduced in hydrogen at 850°C for 35 min. Etched.

Fig. 4—Topochemical aspects of dense ore reduction. X4.5. Area reduced approximately 30 pct for reproduction.

phases. The outer layer was normally one of soft metallic iron which surrounded an inner cored structure of up to three oxide phases of a varying mineralogical nature. Water-suspended abrasives held on a cloth or fabric of suitable texture were not satisfactory in polishing this type of material. When working with minerals, it is well known that the best polishing action is obtained with specialized techniques which involve the use of abrasives embedded on laps of relatively soft material. The Graton-Vanderwilt polishing machine which is based on this principle was used throughout this investigation. A special procedure was developed for the handling of partially reduced ore structures.

The specimens were polished on a sequence of cast iron and lead laps, each of which was charged with a diminishing size of emery abrasive. A lubricant of kerosene and oil was used and the best polishing action occurred when the laps were running in the relatively "dry" state. After attaining a suitable polish, the specimens were microexamined using conventional metallographic techniques. Micrographs were taken and the magnifications required for the proper resolution of detail were on the order of 500 diameters. It was found that there was normally enough phase contrast in the polished sections so that the various phases could be clearly differentiated. The one exception was that of the wüstite-magnetite combination in which no such differentiation existed. It was necessary to darken the wüstite with a 2 pct acidified solution of stannous chloride to produce a clear-cut boundary between the two phases.

X-Ray Analysis: Positive identification of some of the phases in partly reduced iron ore demanded a method more precise and reliable than microscopic examination. For these requirements the powder

method of X-ray analysis seemed most logical. After cutting a thin slice from the center of the impregnated block specimen, its corners were removed so that the strata were exposed in true layer fashion. Starting at the exterior surface, successive layers were filed off to yield representative powder samples for each 0.5 mm of file penetration. A typical sampling operation is shown in Fig. 5. Each series of samples was then X-rayed on a Picker's diffraction unit using unfiltered radiation from an iron target tube.

For the actual powder analyses a Picker's camera, 214.86 mm in diameter, was used and the powdered samples were held in collodion tubes 0.4 mm in diameter. The large patterns thus obtained were valuable in calculating accurate lattice parameters as well as in resolving structures containing two or more phases. During a run the X-ray tube was operated at 35 kv and with a filament current of 10 milliamperes. Under these conditions 5 hr were necessary to produce acceptable patterns.

It was necessary to have proper phase standards in order to use the X-ray data for solid phase identification. Electrolytic iron was chosen for iron, and material prepared from ore 8B was used in producing a standard X-ray pattern for wüstite. Crystalline magnetite from New York and crystalline hematite from Elba were used to obtain standards for these two oxides. The resulting patterns were measured and the crystallographic constants calculated from Bragg's law. A comparison of these values with those from the literature is given in Table II.

The selection of a standard reference for the wüstite phase presented some difficulties as this material does not exist in nature. As only a few milligrams were required, a rather simple method for its preparation was devised. When a dense hematite ore (8B) was partially reduced at above 570°C, a definite layered structure was formed. On X-raying the separate layers, it was found that the second of these gave a diffraction pattern different from that of iron, magnetite, or hematite. The diffraction lines of this unidentified phase were broad and diffuse and the doublets in the high θ region were entirely obscured. This condition could be attributed to the variable composition of the wüstite layer resulting from partial reduction. After annealing and homogenizing for 20 hr at 700°C, an excellent pattern was produced for standardization purposes. The pattern as evidenced in Fig. 6 had sharp lines throughout and its doublets were clearly resolvable. The agreement of d_o values and unit parameter with standard values reported in the literature positively identified the material as the wüstite phase.

Experimental Results

Topochemical Aspects of Dense Ore Reduction: The tendency of reduction to follow a topochemical path was observed early in this investigation. That is, under normal conditions, the phases were orientated in a definite layered pattern with the interfaces following the original contour of the specimen.

Table II. Parameter Data for the X-Ray Standards

Phase	System	Accepted Values		Experimental Values	
		a_o (Å)	Alpha	a_o (Å)	Alpha
Iron	Cubic	2.8664		2.866(9)	
Wüstite	Cubic	4.300 (eut.)		4.303(2)	(Layer average)
Magnetite	Cubic	8.391		8.396(3)	
Hematite	Rhomb.	5.426	55°17'	5.42(6)	55°16'

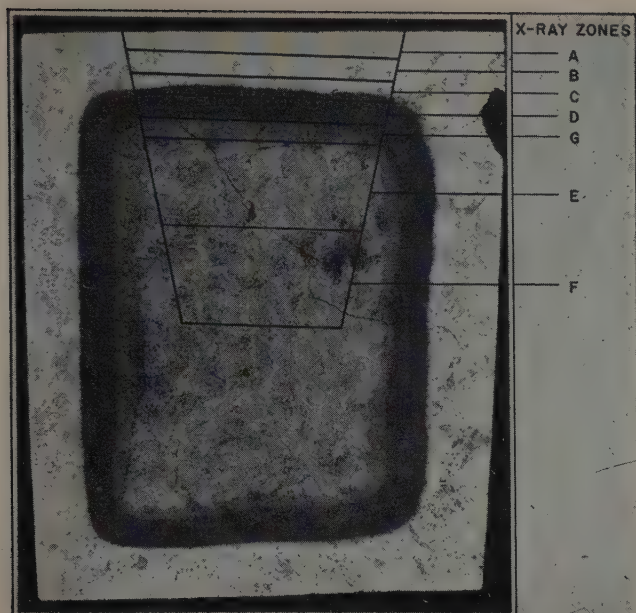


Fig. 5—Macrostructure of natural dense hematite, ore 8B. Partially reduced in hydrogen at 850°C for 35 min. Etched. X7. Area reduced approximately 70 pct for reproduction.

These interfaces were more apparent for certain types of ore and particularly at temperatures above 570°C. The topochemical behavior of dense hematitic ore is shown in Fig. 4. Two sections are illustrated; one for the standard dense hematite and one for a synthetic pellet. Close inspection of the macrographs reveals that the ore structures had apparently gone through the same fundamental mechanisms. A layered arrangement of four solid phases was evident and these were differentiated clearly by three reduction interfaces. The reacting interfaces were evenly spaced in topochemical fashion with respect to the boundaries of the original specimens.

Reduction of Dense Hematite Ore Above 570°C: The topochemical behavior of dense hematite ore was studied more extensively. For this study, a block specimen of ore 8B was partially reduced at 850°C and the resulting cross section is shown in Fig. 5. Some information about the four reduction phases may be gained from a simple macroexamination. For instance, it was immediately apparent that the center was unreduced and therefore representative of the starting material. The outer layer contained grinding scratches and presented a brilliant metallic luster, both typical of metallic iron. Identification of the two intermediate phases was less positive. The outer one of these two layers tended to darken perceptibly on etching with the stannous chloride reagent. This behavior suggested that the material was wüstite as magnetite is notably inert to such mild etching treatment. In later operations the inner layer tended to polish more readily. This action suggested that the material was magnetite as that particular phase has a good polishing reputation in the iron oxide family. The macroexamination technique was thus instrumental in providing a rough identification of the phases of reduction.

A more positive means of identification is that of X-ray analysis. Accordingly, seven separate layers were filed from the surface to the center of the specimen as indicated in Fig. 5. The X-ray patterns from the series of powder samples are presented in Fig. 6. To facilitate identification, the standard patterns for iron and its oxides have been inserted in the series at the appropriate positions for a com-

parative type of analysis. It is immediately apparent that the outermost layers A and B were metallic iron. The patterns obtained were broad-lined and diffuse because of the cold-worked nature of the iron particles. No attempt was made to anneal the powders of this particular series as the identification was positive enough without this treatment.

As shown by the X-ray evidence, layer C, which was located at the first reaction interface, contained both iron and wüstite. Proceeding deeper into the specimen, layer D was found to be composed entirely of the wüstite phase. The phase was a soft, black and easily powdered material of variable composition as indicated by the diffuseness of its X-ray pattern. Actually this same material had been used earlier in the preparation and study of the wüstite phase standard.

The next layer G was composed almost entirely of magnetite. As this layer was less than 0.5 mm thick, it was difficult not to include some of the wüstite phase in the sample. Beyond layer G, the material was not susceptible to filing. Block specimens were cut out and pulverized to obtain powdered samples from the unreduced core. The X-ray patterns of layers E and F correlate well with the macrograph in showing that the core was unreduced hematite corresponding with the original ore.

A microscopic study of the polished specimen revealed some additional information on the conditions at each of the reduction interfaces. Fig. 7a shows the iron-wüstite interface at 500 diameters. The iron was white and had a brilliant metallic luster. It had the typical appearance of newly formed sponge iron of relatively small grain size, and there was evidence that only a small amount of sintering had taken place. The wüstite phase in this particular section contained a large amount of interlocked silica from the original ore and had been etched to the color shown. It appears that the silica had no profound effect on the reduction of the wüstite phase. At this magnification the actual reduction interface was not a narrow one but represented a reaction zone on the order of 25 to 30 microns in width. This width was found to vary in general with the porosity of the phases undergoing reduction. The series of micrographs substantiates this finding by showing that the succeeding interfaces

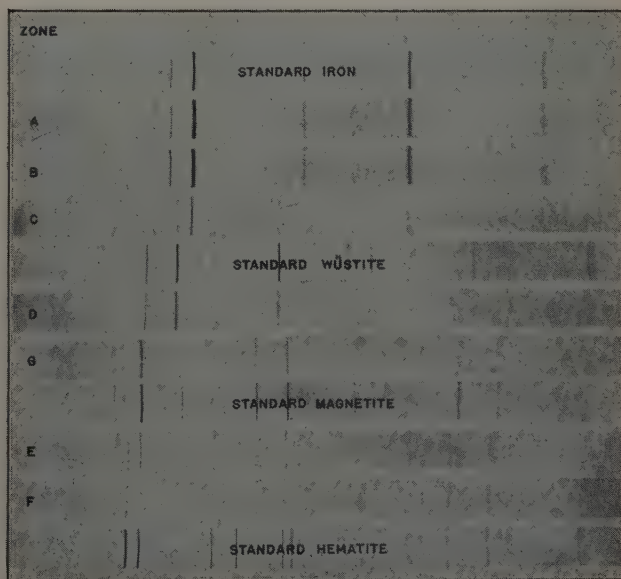
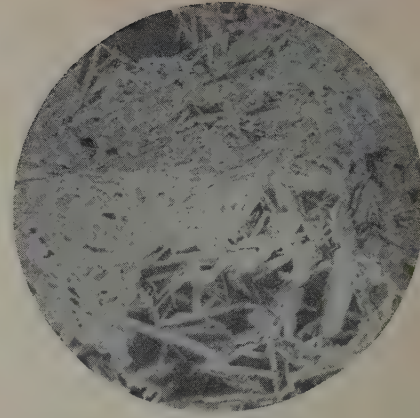
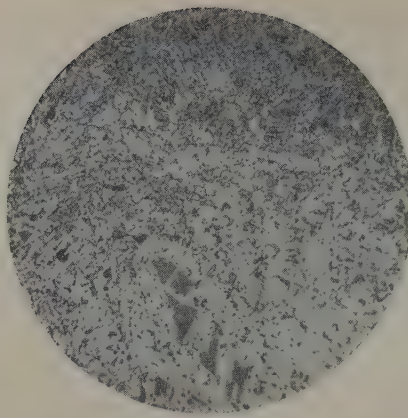
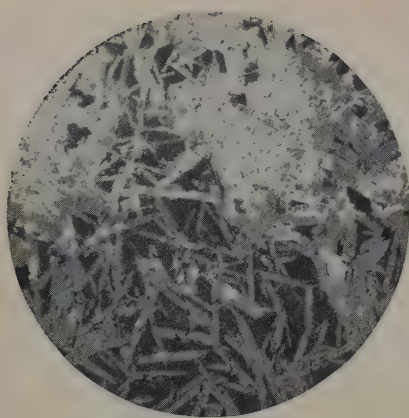


Fig. 6—X-ray study of specimen 8BX-1. X0.5. Area reduced approximately 75 pct for reproduction.



a—Iron-wüstite interface. White phase, iron; dark gray phase, wüstite; black inclusions, silica.

b—Wüstite-magnetite interface. Dark gray phase, wüstite; light gray phase, magnetite.

c—Magnetite-hematite interface. Light gray phase, magnetite; light phase, hematite; black inclusions, silica.

Fig. 7—Reduction interfaces of natural ore 8B. Reduced in hydrogen at 850°C for 35 min. Etched. X500. Area reduced approximately 30 pct for reproduction.

were progressively narrower than the one under discussion. The idea that the reaction zone may have a definite width can be explained on the basis of variations in physical structure or in chemical activity of the phases concerned. Due to unevenness in porosity, the hydrogen has a greater access to certain crystalline aggregates. From the chemical point of view, some of the wüstite grains may be more reactive than others thus giving width to the reaction zone.

The wüstite-magnetite interface shown in Fig. 7b could not be differentiated in the polished condition without the proper etching to darken the wüstite layer. Again the interface had a finite width for the reasons given. There was little evidence of any proeutectoid precipitation of magnetite from the wüstite phase. Finally the magnetite-hematite interface is shown in Fig. 7c. This interface had narrowed considerably and followed a jagged contour

in keeping with the acicular nature of the hematite undergoing attack.

Only the interfacial relations have been discussed here. A careful study across the polished layers confirmed the belief that these were generally homogeneous and of a single-phase constitution.

Reduction of Dense Hematite Below 570°C: For a study of the phases formed during reduction below 570°C, a 1 cm cube of hematite ore (8B) was partially reduced at 500°C and quenched in the manner previously described. As shown by the macrograph in Fig. 8a, the course of reduction differed from that followed at 850°C. The white outer layer had all the characteristics of sponge iron and appeared to have formed in a rough topochemical fashion. The reduction of the interior, however, was accompanied by a great deal of cracking despite the low temperature employed. Cracking promoted the formation of magnetite along paths of least resistance into the

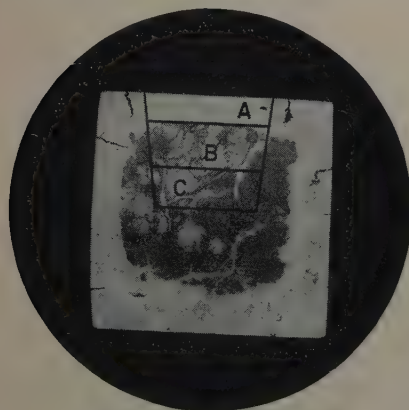
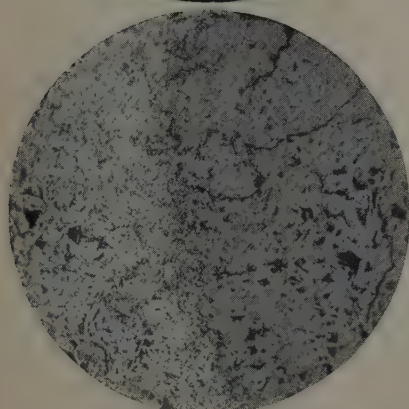
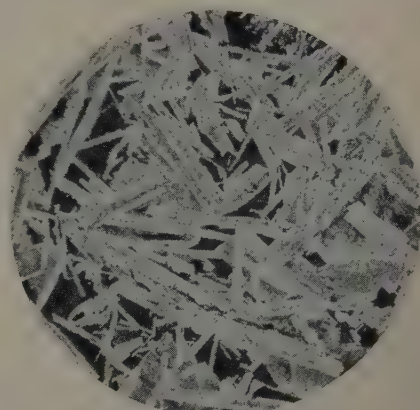


Fig. 8—Reduction phases and interfaces of ore 8B. Reduced in hydrogen at 500°C for 360 min. Etched.

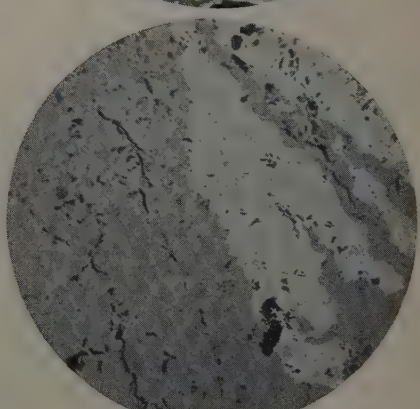
a (left)—Macrostructure of partially reduced ore cube. X4.5. Area reduced approximately 30 pct for reproduction.

b (right)—Microstructure of the iron layer. Heavily etched. X500. Area reduced approximately 30 pct for reproduction.



c (left)—Iron-magnetite interface. Light phase, iron; gray phase, magnetite. X500. Area reduced approximately 30 pct for reproduction.

d (right)—Magnetite-hematite interface. Gray phase, magnetite; white phase, hematite. X500. Area reduced approximately 30 pct for reproduction.



light gray areas of unreduced hematite. These conclusions were verified by X-ray analysis of samples removed from positions as shown on the macrograph. The results obtained were as follows: layer A—iron (very strong pattern); layer B—iron (medium), magnetite (very strong); and layer C—magnetite (very strong), hematite (medium).

The X-ray studies were supplemented with micrographs also shown in Fig. 8. A section of the iron layer which had been heavily etched to bring out a peculiar grain structure is shown in Fig. 8b. This needle-like structure was strongly pseudomorphic after certain areas of the original hematite. It was not characteristic of the entire layer of iron but only of those sections carrying a high concentration of interlocked silica inclusions.

The iron-magnetite interface is visible in Fig. 8c. The iron was fine-grained and made a narrow, sharply defined interface with the magnetite phase. This condition was in direct contrast with the wider interfaces formed with wüstite at temperatures above 570°C. A careful inspection of the magnetite phase revealed a continuous structure over to the magnetite-hematite boundary shown in Fig. 8d. The latter interface was narrow and followed an irregular contour due to cracking. Stringers of magnetite followed certain cracks which projected into the hematite.

It was concluded from all the studies made on the specimen partially reduced at 500°C that only the three phases, iron, magnetite, and hematite, were present. No wüstite had formed. Discontinuities due to excessive cracking prevented the formation of the well-defined, successive layers observed in specimens partially reduced at 850°C.

The entire sequence of observations was repeated on a cube of the same ore after partial reduction at 650°C. The specimen contained many cracks typical of low temperature reduction and accordingly deviated greatly from an ideal topochemical pattern. However, the number of phases and the phase sequence were exactly the same as in specimens reduced at 850°C.

Summary and Conclusions

An integrated technique was developed for identifying the solid phases in partially reduced iron ore. The procedure followed a coordinated sequence of macro-, micro-, and X-ray examinations.

The reduction of dense iron ore was found to take place at distinct interfaces between well-defined layers of the participating solid phases. The interfaces normally penetrated the ore body in topochemical fashion and remained parallel to the original contour of the specimen.

Four phases, iron, wüstite, magnetite, and hematite, were identified in dense iron ore partially reduced in hydrogen at 850°C. These phases were formed simultaneously as well-defined layers between three reacting interfaces. The same four phases were found on reduction at 650°C. Only three phases, iron, magnetite, and hematite, were found on reduction at 500°C. No wüstite could be identified in any part of the specimen. The phases were orientated in all cases in the order of increasing oxygen content with depth of penetration.

There was a distinct cracking effect which took place during the hydrogen reduction of dense iron ore in the temperature range of 500° to 700°C. This cracking disrupted the topochemical advance of the reduction interfaces and interfered with the formation of well-defined layers.

The reduction interfaces possessed a finite width.

This width was a function of temperature and the physical structure and chemical activity of the phases concerned.

The wüstite layer formed during the reduction of dense ore gave a diffuse and broad-lined X-ray pattern. This condition was indicative of a variation in oxygen content across the layer.

References

- ¹ L. S. Darken and R. W. Gurry: The System: Iron-Oxygen. I. The Wüstite Field and Related Equilibria. *Journal ACS* (1945) **67**, pp. 1398-1412.
- ² L. S. Darken and R. W. Gurry: The System: Iron-Oxygen. II. Equilibria and Thermodynamics of Liquid Oxide and Other Phases. *Journal ACS* (1946) **68**, pp. 798-816.
- ³ H. Schenck: *The Physical Chemistry of Steel-making*. (1945) English Translation. The British Iron and Steel Research Association. London.
- ⁴ P. H. Emmett and J. F. Schultz: Gaseous Thermal Diffusion—the Principle Cause of Discrepancies among Equilibrium Measurements on the Systems: $\text{Fe}_3\text{O}_4\text{-H}_2$, $\text{Fe-H}_2\text{O}$, $\text{Fe}_3\text{O}_4\text{-H}_2\text{-FeO-H}_2\text{O}$, and $\text{FeO-H}_2\text{-Fe-H}_2\text{O}$. *Journal ACS* (1933) **55**, pp. 1376-1389.
- ⁵ E. R. Jette and F. Foote: A Study of the Homogeneity Limits of Wüstite (FeO) by X-Ray Methods. *Trans. AIME* (1933) **105**, pp. 276-289.
- ⁶ E. R. Jette and F. Foote: An X-Ray Study of the Wüstite (FeO) Solid Solutions. *Journal of Chemical Physics* (1933) **1**, pp. 29-36.
- ⁷ *Handbook of Chemistry and Physics*. 33d Edition (1952) Cleveland. Chemical Rubber Publishing Co.
- ⁸ *Metals Handbook* (1948) Cleveland. ASM.
- ⁹ C. Palache, H. Berman, and C. Frondel: *Dana's System of Mineralogy*. 7th Edition (1944) Vol. 1. New York. John Wiley and Sons.
- ¹⁰ C. S. Barrett: *Structure of Metals*. 2nd Edition (1952) New York. McGraw-Hill Book Co.
- ¹¹ I. Langmuir: The Constitution and Fundamental Properties of Solids and Liquids. Part I. Solids. *Journal ACS* (1916) pp. 2263-2267.
- ¹² C. H. Desch: *The Chemistry of Solids*. (1934) Ithaca, N. Y. Cornell University Press.
- ¹³ B. Kalling and G. Lilljequist: Theoretical Considerations on the Reduction Process, Iron Ore-Iron Sponge. *Teknisk. Tids. (Bergsv. afd.)*. (1926) **56**, pp. 1-14.
- ¹⁴ F. Wienert: The Reduction of Iron Ores with Hydrogen and Carbon Monoxide. *Arch. Eisenhüttenwesen* (1933) **7**, pp. 275-279.
- ¹⁵ W. Baukloh and K. Froeschmann: Reduction Experiments on Iron Ore Cubes in Flowing Hydrogen. *Stahl und Eisen* (1934) **54**, pp. 415-416.
- ¹⁶ M. H. Kalina and T. L. Joseph: Reducing Iron Ore with Hydrogen. *Iron Age* (1941) **148**, pp. 39-43.
- ¹⁷ G. I. Chufarov and E. Tatievskaya: The Reaction Zones in the Reduction of Magnetite and Hematite with Hydrogen. *Acta Physicochim. U.R.S.S.* (1935) **3**, pp. 957-974.
- ¹⁸ K. Hofmann: The Reduction Mechanism of Iron Oxides in Flowing Cases, II. *Ztsch. angew. Chem.* (1925) **38**, pp. 715-721.
- ¹⁹ F. Olmer: A Method of Study of the Kinetics of Chemical Reaction. *Journal Physical Chemistry* (1943) **47**, pp. 313-317.
- ²⁰ F. Olmer: Reduction of Ferric Oxide by Hydrogen. *Journal of Physical Chemistry* (1943) **47**, pp. 317-325.
- ²¹ G. B. Taylor and H. W. Starkweather: Reduction of Metal Oxides by Hydrogen. *Journal ACS* (1930) **52**, p. 2314.
- ²² M. Wiberg: The Reduction of Iron Ores with Carbon Monoxide, Hydrogen, and Methane. *Jernkon-torets Ann.* (1940) **124**, pp. 179-212.
- ²³ G. I. Chufarov and B. D. Averbukh: Effect of the Form of Intermediate Phases on the Velocity of Reduction of Iron Oxide by Hydrogen. *Acta Physicochim. U.R.S.S.* (1936) **4**, pp. 617-634.
- ²⁴ N. Buinov, A. Komar, M. Zhuravleva, and G. Chufarov: Orientation of the Phases Formed during the Reduction of Magnetite by Hydrogen. *Acta Physicochim. U.R.S.S.* (1939) **11**, pp. 571-584.

Exchange of Iron Between Liquid Metal and Iron Silicate Slag

by G. Derge and C. E. Birchenall

IN studying the kinetics of slag-metal reactions,^{1, 2} it has become increasingly apparent that a complete knowledge of all aspects of interface phenomena will be required to clarify these processes adequately. A part of the data required for all oxidizing slags used in the refining of impure iron to steel is the rate of exchange of iron between the slag and metal phases. The simplest equilibrium of this type is that between liquid iron and iron silicate slag when both phases are equilibrated with the silica crucible containing them. In this study, the exchange of iron between the two liquid phases has been measured by using radioactive Fe^{55} as tracer. The observed high exchange rate indicates the ease with which such interfaces may be crossed in refining processes.

The experiments required for this study involved relatively minor and normal modifications of well established techniques. Melting was accomplished by induction heating in heavy walled, fused silica, rotating crucibles.³ Rotation was used to minimize dilution of the slag by crucible erosion. The melting stock was ingot iron. Slags were prefused in iron crucibles using chemically pure grade oxide reagents. The special conditions applying to the active iron additions will be described for individual experiments. Suitable precautions were observed with regard to protection against radiation hazards.⁴

Identification of Activity

This particular study was initiated several years ago, but held in abeyance because the radioactive iron available at that time contained a foreign activity which concentrated in the slag so as to

mask the iron activity and render the results uninterpretable. With the benefit of experiences from other studies, radioiron of suitable purity can now be prepared. As received from the Isotope Div. of A.E.C., the unit appears to contain $\text{Fe}^{55} + \text{Fe}^{59}$ and a high activity cobalt. The cobalt and iron are separated by repeated ether extractions, and the purified iron stored for sufficient time for the Fe^{59} (44 day half-life) to decay to negligible activity, leaving only Fe^{55} as the active isotope. This was confirmed by the absorption curves for slag and metal samples from heat No. 1. In Fig. 1 the experimentally measured points for the absorption curves of slag and metal are fitted by the calculated slope of 5.8 mg per sq cm in aluminum, which corresponds to the Mn $K\alpha$ doublet emission resulting from the capture of an orbital electron of Fe^{55} by the nucleus. This shows that the radioactive species are the same in both slag and metal and identifies it as Fe^{55} .

Description of Individual Heats

For the first heat, the radioactive iron was contained in the prefused slag. The active Fe^{55} had been precipitated with carrier and was added as Fe_2O_3 during fusion in the iron crucible.

The charge of 500 grams of ingot iron was melted, the protective iron sleeve added, rotation started, and a prefused, inactive slag was added to allow the system to approach equilibrium. After about 5 min at temperature, the wash slag was skimmed and the active slag added. Initial slag and metal samples were taken as soon as the slag was molten. Additional samples were taken at indicated intervals thereafter.

Slag samples were dipped with a small iron spoon and metal samples were sucked into $\frac{1}{4}$ in. ID silica tubes. The slag and metal samples were pulverized and mounted for radioactive counting. The slag samples were analyzed chemically for FeO .

Temperature was read after the last slag sample by immersion of a Pt-Pt-Rh thermocouple protected by a fused silica sheath. Since no significant variation of rate with temperature was observed

G. DERGE, Member AIME, is associated with Metals Research Laboratory, Carnegie Institute of Technology, Pittsburgh, and C. E. BIRCHENALL, Junior Member AIME, formerly with Metals Research Laboratory, Carnegie Institute of Technology, is now associated with the James Forrestal Research Center, Princeton University, Princeton, N. J.

Discussion on this paper, TP 3576C, may be sent, 2 copies, to AIME by April 1, 1954. Manuscript, March 16, 1953. New York Meeting, February 1954.

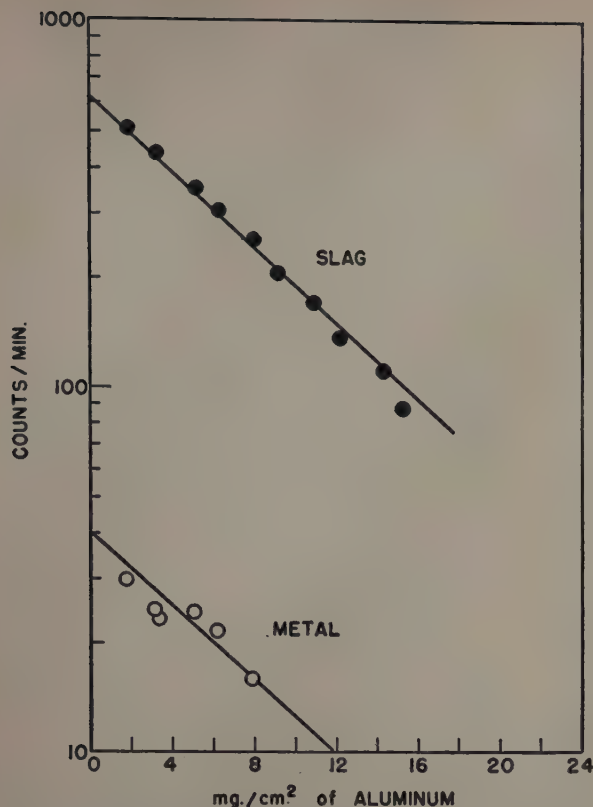


Fig. 1—Absorption curve for radioisotope (Fe^{55}) in slag (upper curve) and metal (lower curve) for heat No. 1.

for three heats ranging from 1530° to 1613°C , the data can be taken as representative of typical steel-making operations and will be referred to as 1600° hereafter.

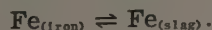
The data from this heat indicated the desirability of sampling over a longer time period and using slags of a higher specific activity.

The second heat differed in that the wash slag was not skimmed. This insured equilibrium at the initiation of sampling. The active iron, as oxide mixed with one gram of prefused slag, was contained in a capsule of iron foil and dropped into the already equilibrated "wash" slag. The specific activity was much greater than that of heat No. 1. This procedure was not entirely satisfactory as melting of the capsule was not as rapid or definite as had been anticipated. It was also necessary to terminate sampling prematurely as the third sample caused the slag cover to break.

The third heat was planned to give better data on the final stages of the reaction, since the first two heats showed the initial stages clearly but were interrupted before equilibrium was reached. In this heat, the entire residual slag from second heat was added after the bath had been equilibrated with the slag formed during melting. Samples were taken at longer time intervals to avoid breaking the slag cover before equilibrium was reached. This ran according to plan and was considered the most satisfactory of the group. The plot of activity vs time for both slag and metal from this heat is shown in Fig. 2.

Interpretation of Data

The exact reaction mechanism for the exchange of iron between the two liquid phases of this experiment is not known, and it is only possible to represent the process schematically as



In reality the iron may be associated with oxygen or involved in other complexes in both phases, and it is not intended to exclude these possibilities in the above representation. However, in view of the uncertainties indicated, only the simplest possible kinetic treatment is justified. It is not unreasonable to expect first-order behavior, and it will be seen that the data conform well with this assumption.

A standard method⁵ of treating first-order kinetic data is the relation

$$k = \frac{2.303}{t} \log \frac{a}{a-x},$$

which may be put in the form

$$t = \frac{2.303}{k} \log a - \frac{2.303}{k} \log (a-x),$$

where t is time, in sec; a , the initial concentration, counts per min; $(a-x)$, the concentration at time, t , counts per min; and k , the first order rate constant. Since $(2.303/k) \log a$ is constant, the plot of t vs $\log (a-x)$ should be linear and the slope of the line is $-2.303/k$, allowing an evaluation of the rate constant. It is also characteristic of this relation that the numerical value of k is independent of the units used to express concentration. Thus, in the present case, counts per minute may be substituted directly in the above expressions. Fig. 3 shows the plot of

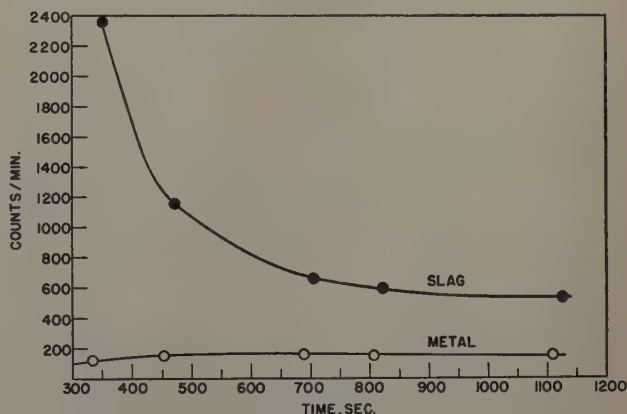


Fig. 2—Rate of transfer of iron between slag and metal, heat No. 3.

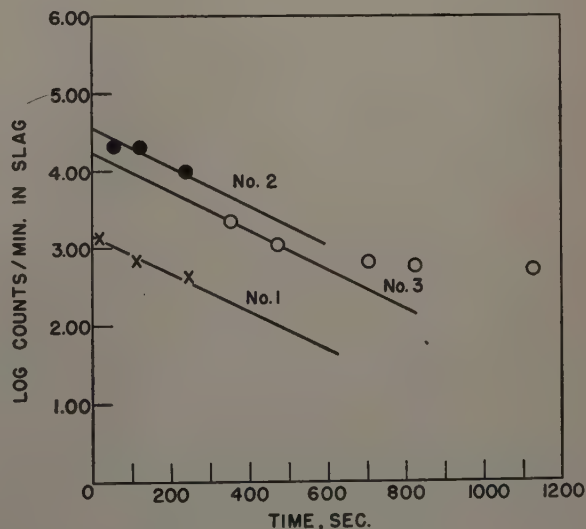


Fig. 3—Kinetic data for rate of transfer of iron between slag and metal.

the logarithm of counts per min vs time for all three heats. It is evident here that in heat No. 3 the reaction had proceeded so far toward equilibrium after 500 sec that the assumptions involved in the rate constant derivation are no longer valid. However, if the data are weighted so as to eliminate the disturbing features of the initial and final stages of the reaction, parallel lines represent all three heats and they all have the same rate constant, $k = 0.006$. In view of the experimental variations described for these heats, this would seem to establish the first-order kinetics of the process.

Another useful characterization of a first-order process is the half-life or time required to reduce the concentration of a reactant by one half. This will be the same at any time during the reaction and is given by

$$t_{1/2} = \frac{2.303}{k} \log 2,$$

where $t_{1/2}$ is the half life of the reaction. In the present case, $t_{1/2}$ equals 115 sec.

These values indicate a relatively rapid exchange of iron across the slag-metal interface, and in order to visualize its significance in metallurgical processes, it is useful to make some simple calculations which permit an estimate of the actual amounts of iron crossing a unit area of the interface. This will be based on the assumption that convection and stirring have been adequate to maintain a uniform composition in the slag and that the slag layer averaged 1 cm thick. Taking a density of 3.57 grams per cu cm³ for a silica-saturated slag analyzing 57 pct FeO, each cubic centimeter of slag contains 1.58 grams of iron. Thus, under the conditions of this experiment, one half of this amount, 0.79 gram or 0.014 mol, of iron cross the interface from slag to metal every 115 sec, the half-life period. Since the slag and metal are in equilibrium, a like amount

must pass in the reverse direction from metal to slag in the same period. On this basis, an interfacial area of 71.5 sq cm is adequate to transfer a gram-mol of iron in each direction every 115 sec. Although many simplifying assumptions have been made in arriving at these figures, it is apparent that the iron-slag interface is a very active site at 1600°C.

Such rates are sufficient to account for observed refining reactions and will help to explain the entire reaction mechanism when other kinetic data are determined.

Conclusions

Using radioactive Fe⁵⁵ as tracer, it has been determined that the equilibrium exchange of iron between silica-saturated iron silicate slag and liquid iron in a silica crucible follows first-order kinetics with a rate constant, k equals 0.006 at 1600°C.

Acknowledgments

This research was done in the Metals Research Laboratory, Carnegie Institute of Technology, with the support of the Office of Naval Research and the American Iron and Steel Institute. The purification of the iron unit and analyses of active slags were carried out by E. E. Duncan. Experimental work was carried out by J. R. Shegog and K. M. Goldman.

References

- ¹L. C. Chang and K. M. Goldman: *Trans. AIME* (1948) **176**, pp. 309-329; *METALS TECHNOLOGY* (June 1948).
- ²G. Derge, W. O. Philbrook, and K. M. Goldman: *Trans. AIME* (1950) **188**, pp. 1111-1119; *JOURNAL OF METALS* (September 1950).
- ³G. Derge: *Yearbook AISI* (1949) pp. 368-388.
- ⁴C. E. Birchenall and W. O. Philbrook: *The Iron Age* (Nov. 10, 1949) **164**, pp. 77-82.
- ⁵S. Glasstone: *Textbook of Physical Chemistry*. (1940) p. 1027. New York. D. Van Nostrand Co.
- ⁶F. Körber and W. Oelsen: *Mitt. Kaiser-Wilhelm Inst. f. Eisenforschung* (1933) **15**, p. 291.

Technical Note

A Crystallographic Analysis of the Ductile-Brittle Transition In Body-Centered Cubic Single Crystals

by A. J. Opinsky

MANY investigators, in their discussions, have reasoned that the ductile-brittle transition in iron could be explained by the intrusion of cleavage into the normal slip process. The purpose of this note is to apply the laws of critical normal stress for cleavage and critical shear stress for slip

A. J. OPINSKY, Junior Member AIME, is associated with the Atomic Energy Div., Sylvania Electric Products Inc., Bayside, N. Y. TN 202E. Manuscript, Oct. 5, 1953.

to explain the orientation and temperature dependence of the ductile-brittle transition in body-centered cubic metals. It will be found that within a certain temperature range, single crystals tested in tension will cleave or slip, depending on their orientation. Some data recently appearing in the literature will be analyzed from this standpoint.

For a single crystal with $[uvw]$ parallel to the tensile axis, the resolved shear stress on the slip

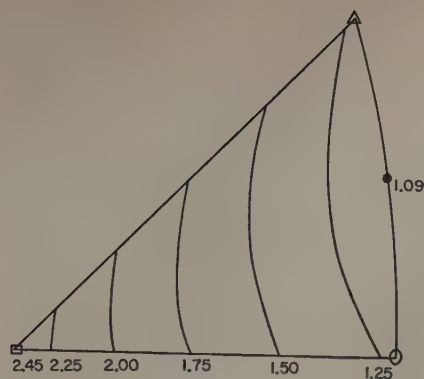


Fig. 1— C/S_{110} contours.

plane in the slip direction can be represented^{1,2} by

$$\tau_{101}^{111} = \frac{F}{A} \frac{(u+v+w)(-u+w)}{\sqrt{6}(u^2+v^2+w^2)} \quad [1]$$

$$\tau_{211}^{111} = \frac{F}{A} \frac{(u+v+w)(-2u+v+w)}{\sqrt{18}(u^2+v^2+w^2)} \quad [2]$$

$$\tau_{112}^{111} = \frac{F}{A} \frac{(-u+v+w)(u-v+2w)}{\sqrt{18}(u^2+v^2+w^2)} \quad [3]$$

and the largest normal stress in this unit stereographic triangle by

$$N_{001} = \frac{F}{A} \frac{w^2}{(u^2+v^2+w^2)} \quad [4]$$

For the beginning of slip $\tau_i = S_i$ (critical shear stress) and for the beginning of cleavage $N = C$ (cleavage stress). Considering first $\{110\}$ slip, the conventional stress (F/A) at which both slip and cleavage could occur simultaneously leads to the equation

$$\frac{F}{A} = \frac{S_{110} \sqrt{6}(u^2+v^2+w^2)}{(u+v+w)(-u+w)} = \frac{C(u^2+v^2+w^2)}{w^2}$$

$$\text{or } C/S_{110} = \frac{\sqrt{6}w^2}{(u+v+w)(-u+w)} \quad [5]$$

Similar expressions can be developed when $\{112\}$ slip is considered, except now two systems operate in the chosen unit stereographic triangle, and around $[001]$

$$C/S_{112} = \frac{\sqrt{18}w^2}{(-u+v+w)(u-v+2w)} \quad [6]$$

and near the great circle $[011] - [\bar{1}11]$

$$C/S_{112} = \frac{\sqrt{18}w^2}{(u+v+w)(-2u+v+w)} \quad [7]$$

If various values of C/S_i are chosen, the $[uvw]$ can be calculated, and contours can be drawn, Figs. 1 and 2. From Fig. 1, all crystals will be ductile if $C/S_{110} > 2.45$; all crystals will cleave if $C/S_{110} < 1.09$; if $1.09 \leq C/S_{110} \leq 2.45$, the orientation dependence will be as shown. All crystals with tensile axes to the left of the contour will cleave and those with axes to the right of it will slip. A similar argument can be given for Fig. 2. Cleavage with more complicated slip behavior than $\{110\}$ or $\{112\}$ can be inferred by using Figs. 1 and 2 as limits. In addition, the temperature dependence can be illustrated by assuming C constant. To make crystals of all orientations brittle, S_{110} would have to rise to more than double its value when cleavage was first noted; this

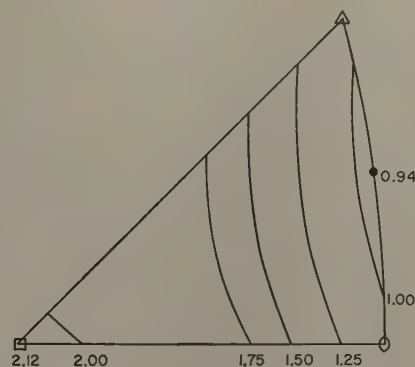


Fig. 2— C/S_{112} contours.

could be accomplished over a rather wide temperature range.

A major objection to the calculation is that twinning is not considered. However, since the criterion for twinning is still disputed, such a calculation would not rest on a firm basis.

The inverse problem, that of determining the C/S_i ratio for a given irrational orientation, can be handled easily by transforming Eqs. 5 or 6 and 7 into spherical polar coordinates. Some recent data³ showing a temperature dependence of ductile-brittle behavior in high purity ferrites can be thus treated, assuming $\{110\}$ slip. The pertinent results are that at -108°C , $20,200 < C < 28,600$ psi; at -118°C , $24,800 < C < 30,200$ psi; and at -185°C , $C < 37,800$ psi. The first two limits are in qualitative agreement with a value of 32,000 psi which can be obtained by extrapolating a curve³ of reduction of area vs cleavage stress to zero. The last value is considerably lower than the extrapolated value of 46,000 psi, but this could be due to the assumption of a low value of S_{110} at -185°C . The actual calculations are given in Table I.

References

¹ A. Opinsky and R. Smoluchowski: The Crystallographic Aspect of Slip in Body-Centered Cubic Single Crystals. A Symposium on the Plastic Deformation of Crystalline Solids. Mellon Institute, Pittsburgh. (May 19 and 20, 1950) p. 216.

² A. J. Opinsky and R. Smoluchowski: The Crystallographic Aspect of Slip in Body-Centered Cubic Single Crystals. I. Theoretical Considerations. *Journal of Applied Physics* (November 1951) 22, p. 1380.

³ R. P. Steijn and R. M. Brick: Flow and Fracture of Single Crystals of High Purity Ferrite. ASM Preprint No. 36 (1953).

Table I. Calculation of Cleavage Stress from Data of Ref. 3

Specimen No.	Temperature	C/S_{110}	Fracture*	S_{110} , [†] Psi	C, Psi
314	-108	1.26	D	16,000	20,200
342	-108	1.79	B	16,000	28,600
330	-118	1.38	D	18,000	24,800
332	-118	1.68	B	18,000	30,200
349	-118	1.88	B	18,000	33,800
207	-185	1.35	B	28,000	37,800
210	-185	1.37	B	28,000	38,400
224	-185	Not calculated because heavy twinning had occurred			

* Ductile or brittle.

[†] Read from curve in ref. 3.

After-Effects in Polycrystalline Cadmium

by Charles S. Barrett

The torsional after-effect in polycrystalline cadmium is interrupted by an abnormal twisting when the film is removed by etching. This is accounted for by the pile-up of dislocations beneath anodic or other oxide films during the original twisting, and the relief of the residual stresses from these by elastic and plastic processes during etching.

WHEN an iron or zinc wire coated with oxide is plastically twisted and then released, it untwists according to a law of equal increments in equal intervals of log time, but if the oxide is suddenly removed by etching this normal after-effect is interrupted by a transient, and thereafter the untwisting is slower.¹ Etching may even reverse the strain temporarily.

Related effects caused by hydrated oxide films on cadmium in creep tests have been observed by Phillips and Thompson;² definite transient strains caused by the removal of the film from single crystals of cadmium were observed; however, negligible effects were obtained with *polycrystalline* wires. Pronounced effects of both transient and steady nature were observed by Phillips and Thompson when anodic films 10^{-4} cm thick were etched off, and weak effects, transient only, occurred with hydrated oxide films 3×10^{-6} cm thick such as were formed by standing in water for 10 min. It was estimated that 10^{-7} cm films, formed in water in 1 or 2 min, could be detected in the apparatus of Phillips and Thompson.

Since abnormal after-effects were observed by the torsion method equally well with polycrystalline and monocrystalline iron and zinc wires,¹ it was anticipated that the torsion method would also disclose them in polycrystalline cadmium, in spite of the fact that analogous effects had not been observed in tensile creep tests on polycrystalline zinc

by Pickus and Parker³ or on polycrystalline cadmium in tensile studies by Andrade and Randall.⁴

Because of its high sensitivity, particularly its sensitivity to surface conditions, the torsion method was thought to merit further study as a method of investigating thin films of various types and the action of various reagents on these films.

Materials and Methods

Cadmium wires were cold-drawn to a diameter of 0.039 in. from a stock that was determined spectroscopically to contain 0.05 pct Bi, 0.005 pct Cu, 0.008 pct Pb, and 0.007 pct Si. The wires were cut to about $1\frac{7}{8}$ in. lengths and were annealed 1 hr in air at 290°C, after which the grain size was such that there were 5 to 7 grains across a diameter. The wires were then mounted as indicated in the insert in Fig. 1, one end being fastened with laboratory wax into a small diameter brass tube and the other end being waxed to a thin glass fiber which supported, on its upper end, a small galvanometer mirror. The wires were waxed with care to avoid straining or annealing, for it was found that the after-effect rate was sensitive to prior cold work in a wire. The assembly was then clamped above a beaker into which the reagent could be poured. The lower end of the wire was held in the hand while the wire was twisted 180°; it was then released immediately. Since precision timing of these manipulations was not attempted, the different wires cannot be compared as to exact rates of untwisting. The length subjected to plastic strain was $1\frac{5}{8}$ in.

The surface coatings studied were those produced by the annealing in air, by anodic treatment of

C. S. BARRETT, Member AIME, is associated with the Institute for the Study of Metals, University of Chicago, Chicago.

Discussion on this paper, TP 3675E, may be sent, 2 copies, to AIME by Feb. 1, 1954. Manuscript April 24, 1953; revision, July 27, 1953.

etched wires in a potassium hydroxide bath, and by immersion in distilled water.

Results

The principal results are summarized in Fig. 1, where the strain during the untwisting period is plotted vs log time, a plot that has been found¹ to give straight lines for the normal after-effect in most cases. In Fig. 1 the specimens were immersed in water, beginning at the times marked *W* and immersed in the etching solution at the times marked *E*. The rate of untwisting may be seen from the scale of degrees given, which has been displaced an arbitrary amount vertically for each curve, i.e., the zero position on this scale is without significance.

In curve *A*, which applies to a wire that had been oxidized at 290°C in air for 1 hr, the untwisting that occurred at 26°C after a twist of 180° in a length of 1½ in. was altered at point *E* by immersion in 0.25 pct H_2SO_4 at the same temperature. An abnormal after-effect resulted, the untwisting changing to a twisting. At time 19 min the etchant was replaced by water (distilled water was used throughout these tests) and an after-effect that was in the normal direction, but slower, was resumed. When this experiment was repeated on another wire with water at 2.5°C and with an etchant of 2 pct H_2SO_4 at 2.5°C, the initial slope was the same but the transient in the curve after applying the acid showed a downward trend—with a strain rate less than the original rate of untwisting—rather than an upward trend.

Curve *B* also applies to a specimen that had been annealed in air at 290°C for 1 hr and that was given two successive etches during untwisting and was maintained in water before and after the etchings. The first etching was for ½ min in 0.25 pct H_2SO_4 beginning 9 min after twisting (point *E*); this changed the untwisting rate markedly. The second etching was done similarly, 19 min after twisting (point *E'*); there was almost no change in the untwisting rate as a result of this. The same specimen, 35 min after twisting, was twisted again 180° and the subsequent after-effect is plotted as curve *C*; when 0.25 pct H_2SO_4 replaced the water at *E* on this curve, there was no change in slope. Thus twisting the freshly etched wire does not lead to transients and rate change upon etching, and once an untwisting wire has been cleaned of its oxide by etching, subsequent etching produces no further rate changes.

Curves *D* and *F* show the large transients that occur upon removal of anodic films. For curve *D*, 2 pct H_2SO_4 was applied at the time indicated by *E*, and for curve *F* the etchant was 0.1 pct H_2SO_4 ; the experiments were run at 27°C. It is seen that the stronger acid caused a shorter transient, as would be expected if it more quickly destroyed the anodic coating. It should be remarked regarding the shortness of the transient in curve *D* that visual evidence of the anodic coating disappeared in a few seconds with this etchant. No conclusions should be drawn from the greater magnitude of the transient in *D* compared with that in *F*, since the initial structure and the strain history of the wires was not controlled with sufficient accuracy for these slopes to be closely matched.

If the sensitivity of the method is judged by the rate changes caused by the removal of hydrated oxide films formed in water, the experiments covered by curves *B* and *C* and another, not reproduced, sug-

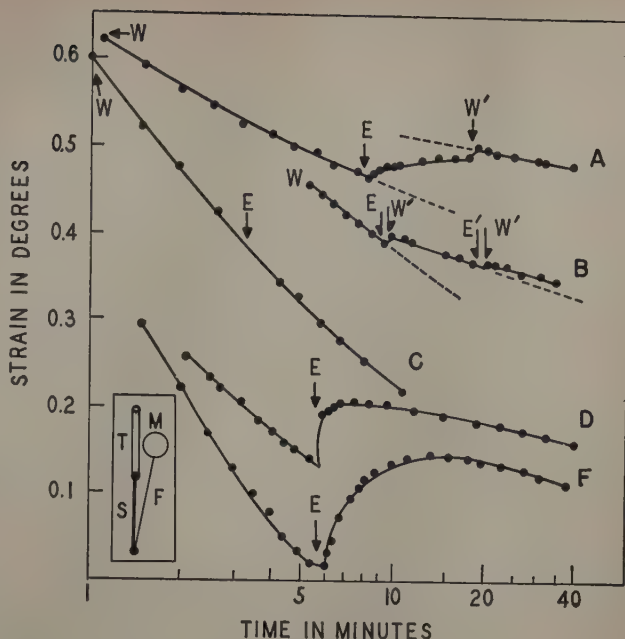


Fig. 1—Insert shows method of mounting specimens for the torsion experiments. Specimen *S* is waxed at one end to a glass fiber *F* supporting galvanometer mirror *M* and at the other end is waxed to tube *T*. Curves are for untwisting in water at *W* and *W'*, and in etchant at *E* and *E'*.

A—Oxidized 1 hr at 290°C, 0.25 pct H_2SO_4 applied at *E*.

B—Oxidized 1 hr at 290°C, 0.25 pct H_2SO_4 applied at *E* and *E'*.

C—Previously etched, 0.25 pct H_2SO_4 applied at *E*.

D—Anodic film. 2 pct H_2SO_4 applied at *E*.

F—Anodic film. 0.1 pct H_2SO_4 applied at *E*.

gest that films must form for longer times than 10 min in distilled water if they are to yield clearly discernible effects. The work of Phillips and Thompson² shows that such a film is about 3×10^{-6} cm thick and by their method this could be detected on single crystals. The present sensitivity, at least for polycrystals, is apparently less, but nevertheless it is very high, for an obvious change of slope, from 0.33 to 0.29 degrees per decade of log time, was observed when 2 pct H_2SO_4 was applied to an etched wire on which an oxide had been forming during 40 min in air at 25°C.

The strong influence of the oxide film is not removed by moderate plastic deformation of the wire. A specimen containing an oxide formed in air at 290°C was bent around a 5/16 in. mandrel, straightened, bent oppositely around the mandrel, straightened, and then twisted in the usual way. The subsequent untwisting was at an unusually high rate, 0.71 degrees per cycle of log time. Nevertheless, the effect of etching with 0.25 pct H_2SO_4 at time 6 min was definite, changing the rate to 0.63.

When a wire that had been oxidized at 290°C was allowed to untwist in air and then was suddenly immersed in water, it was found that no change of slope occurred, although the galvanometer mirror was subject to an abrupt displacement due to buoyancy effects. It was also found that results with wires that were twisted while immersed in water did not differ essentially from results obtained after twisting in air. These experiments did not reveal any important altering of properties of the surface film by water—at least in a matter of minutes.

Discussion

Every explanation that appears capable of explaining the abnormal after-effect involves the same

fundamental mechanism, namely, release by one means or another of residual stresses that have been built up when a surface layer has acted as a barrier to the escape of dislocation loops generated within the metal, and has resisted plastic flow more than the underlying layers. The residual stresses result directly from the piling up of dislocations beneath the surface, as suggested by Cottrell before the effect was discovered. Three methods of relief of these stresses are discussed below.

1—The stresses may be released by the escape of the piled-up dislocations through the surface. Since their motion in escaping is in the same direction as it was during the original twisting, the transient strains accompanying their escape are in the direction of twisting rather than untwisting.¹ Dislocations leaving the metal subsequently counterbalance in part those lying deeper within the metal that are returning toward their source in the normal after-effect, so that the rate of untwisting after the transient is completed is always less. With weaker acids, the surface film is destroyed more gradually and the escaping is initiated more slowly (curve *F* vs curve *D*). If a wire lacks a surface film at the time of twisting, no pile-up occurs. (Curve *C* is an example.)

2—The stresses may also be released by a twist that is elastic rather than plastic, as in a stress-analysis experiment, when the surface film is etched away. The transient strain thus introduced will be in the observed direction if at the time of twisting the surface film had a higher yield strength than the underlying metal.

While such elastic strain may well play a part in the stress readjustment, there is good reason to believe it cannot be the whole effect. Dislocation theory indicates that the spearhead of the dislocation pile must approach to within a distance that is only of the order of 10^{-7} cm from the barrier created by such a film, and since the following dislocations force the leading ones toward the surface, it is to be expected that some will move the remaining distance to the surface when the barrier is removed, being repelled by the local stress fields of the pile—just as the innermost dislocations of the pile are being forced back toward their source by the stress field of the pile, producing the normal after-effect.

3—A third possible mechanism for stress relief⁵⁻⁸ is the springing into operation of dislocation generators, located at the metal surface, that have been kept inactive by the presence of the oxide. If the direction of the shear stresses on the surface is examined, it will be found that there is one direction for stresses within a set of piled-up dislocation loops and the opposite direction for those outside of the pile (in other words, one direction in the areas along the side of a slip line, the opposite direction in the areas beyond the ends of a slip line). On this basis it was suggested¹ that if there were dislocation generators at the surface suddenly becoming active, they would have opposing signs in the two areas and could not therefore explain the abnormal after-effect. This implies the doubtful assumption, however, that the local shear stresses in the surface are in balance in such a way that their effects on surface sources would cancel. It is reasonable to expect, on the contrary, that the net rotational moment from residual stresses in the surface is not zero, and is balanced by that in underlying layers. Therefore suddenly activated surface generators could add to mechanisms 1 and 2 above in relieving the residual stresses. Surface generators may also be active in tensile stressing.

Coffin and Weiman propose that a thermal transient occurs when etching removes a surface film and that this accounts for the increased creep rate in tensile creep tests.⁶ While this may apply when the action of an etchant on a surface film is vigorous, it can be progressively reduced by diluting the etchant. Since the effects discussed in this paper and the preceding one¹ are found with very dilute acids and are not removed by further dilution, it is concluded that this theory does not apply.

Coffin and Weiman⁶ propose, also, that a thermal transient would occur and increase the creep rate even when no oxide film is present, and, finding such an effect with a "clean" surface, they conclude that a thermal transient does occur. In our previous after-effect tests, however, transients were not observed with clean metal,¹ and this is confirmed in the present tests. The Coffin-Weiman strain transients may have been caused by invisible oxide layers formed inadvertently at room temperature.

It is concluded that experiments of this type provide a sensitive and unusually simple method of obtaining information on surface conditions that influence mechanical properties of metals, particularly creep resistance at low loads.³ It is felt that a more detailed study of the method is merited, and in current investigations the method is being applied in more quantitative fashion to a study of various oxide films on high purity aluminum.

Summary

1—Torsion tests on polycrystalline cadmium wires disclosed abnormal after-effects when anodic or other oxide films on the wires were etched, as has been observed with iron and zinc wires.

2—The sensitivity of the test was sufficient to detect the films formed in air at room temperature in fractions of an hour.

3—The oxide films retained their influence after the wire had been subjected to moderate plastic deformation.

4—Prior cold work increased the rate of untwisting in the normal after-effect; the transient abnormal effect was slower when the etchant was more dilute.

5—The results are accounted for by the theory that the oxide-metal interface is a barrier to dislocations and that the residual stresses from dislocations piled up beneath the interface are relieved by elastic and plastic processes during etching. Control tests indicated that thermal transients were not involved.

Acknowledgment

This work was supported in part by Contract N6ori-02004, U. S. Office of Naval Research.

References

- ¹ C. S. Barrett: *Acta Metallurgica* (1953) **1**, p. 2.
- ² D. J. Phillips and N. Thompson: *Proc. Physical Soc.*, London (1950) **B63**, p. 839.
- ³ M. R. Pickus and E. R. Parker: *Trans. AIME* (1951) **191**, p. 792; *JOURNAL OF METALS* (September 1951).
- ⁴ E. N. da C. Andrade and R. F. Y. Randall: *Nature* (1948) **162**, p. 890; *Proc. Physical Soc.*, London (1952) **B65**, p. 445.
- ⁵ John J. Gilman and T. A. Read: *Trans. AIME* (1952) **194**, p. 875; *JOURNAL OF METALS* (August 1952).
- ⁶ F. D. Coffin and A. L. Weiman: *Journal of Applied Physics* (1953) **24**, p. 282.
- ⁷ T. A. Read: Private communication.
- ⁸ J. E. Fisher: Discussion on ref. 3. *Trans. AIME* (1952) **194**, p. 531; *JOURNAL OF METALS* (May 1952).

Torsional After-Effect Measurement and Applications To Aluminum

by C. S. Barrett, P. M. Aziz, and I. Markson

The abnormal after-effect in twisted wires that occurs when untwisting is interrupted by etching can be brought under control and used to study the mechanical properties of thin surface films and how they are effected by reagents and heat treatment. Results are given of studies of oxide films on high purity aluminum.

IF a wire is subjected to plastic deformation by torsion and then released, it untwists in the normal after-effect, but under certain circumstances the untwisting is abruptly lessened or reversed by the application of an etchant to the wire.^{1, 2} This abnormal after-effect may occur, for example, if there is a coherent oxide film on the surface of the wire which is removed by the etchant.

Following a suggestion of A. H. Cottrell that predicted this effect, it is attributed to dislocations that had piled up beneath the oxide layer and represents the rapid release of residual stresses caused by these dislocations. When the layer is removed, the stress relief may be by escape of piled-up dislocations from the metal, or by an activation of latent sources of dislocations located at the surface, together with rebalancing of elastic stresses to compensate for the loss of stressed material, as in a residual stress analysis determination, these mechanisms acting singly or in combination.² The slower the attack of the reagent, the more gradual is the stress relief and the smaller the change in strain rate when the reagent is applied.

A study has been made of the factors that influence the magnitude of the normal and abnormal after-effects with the object of developing techniques suitable for a quantitative investigation of the influence of various surface films on dislocations in wires, and of the rate and extent of the attack on the films by different reagents. It was found that reasonable sensitivity and reproducibility could be

achieved if a suitable choice of variables was made and if these variables were held constant through a series of experiments. The method was then applied to a study of oxide films produced and treated in different ways on the surface of high purity aluminum wires, and to a study of the damage to these films caused by various reagents.

Experimental Procedure

The material used throughout this work was prepared from 99.9968 pct Al. This high purity aluminum was melted, cast into ½ in. diameter ingots, and then swaged and drawn without intermediate annealing to 0.040 in. diameter wire. A sketch of the apparatus employed for twisting is shown in Fig. 1. The test wires were mounted into the apparatus by cementing one end of the wire to the beaker and the other to the tube with laboratory wax of high melting point. The length of the wire between the waxed joints was 4.2 ± 0.2 cm. Extreme care was taken during mounting to avoid cold-working the wire.

The wire was twisted through 335° in 2 to 4 sec by rotating the pinion on the gear box until the vertical post on the rotating table, which was initially touching the horizontal stop, was arrested by the stop. All the tests were conducted with apparatus and reagents at the same temperature (about 25°C). In all tests, except those where the duration of the initial torque was investigated, the torque was applied for a period of 2 min. At the end of this time the table was rotated back a few degrees away from contact with the stop and the wire allowed to untwist. The after-effects were measured by reflecting a beam of light from the mirror shown on the apparatus. After the wire had untwisted for 6 min, a reagent was carefully poured into the beaker and thereby applied to the surface of the wire. In some tests the liquid in the beaker was removed after a few minutes and replaced by an-

C. S. BARRETT, Member AIME, is associated with the Institute for the Study of Metals, University of Chicago, Chicago, and P. M. AZIZ, with Aluminium Laboratories Ltd., Kingston, Ont., Canada, and I. MARKSON, Glasgow, Scotland, were at the University of Chicago during these experiments, the latter as Mutual Security Agency Fellow.

Discussion on this paper, TP 3667E, may be sent, 2 copies, to AIME by April 1, 1954. Manuscript, Aug. 7, 1953. New York Meeting, February 1954.

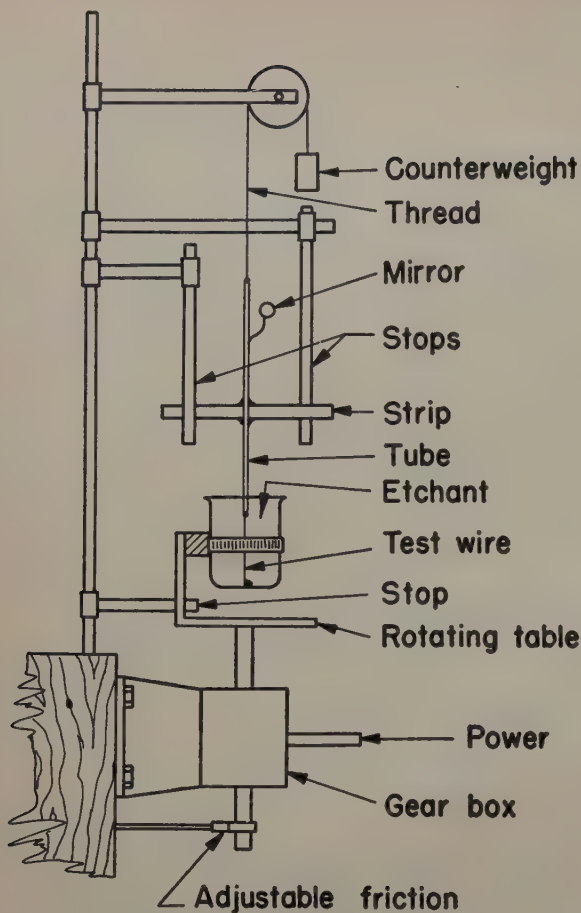


Fig. 1—Sketch of experimental apparatus.

other liquid. In these cases of replacement the second liquid would contain traces of the first reagent, to the extent of about 1 pct.

The data obtained were plotted as curves of strain vs log time and, as anticipated from previous work, linear curves were obtained for the normal after-effects, and frequently, also, for the abnormal ones. The curves were extrapolated and their slopes denoted by the strain in degrees between 10^0 and 10^{+1} min, a "cycle" of the log time plot. This was found to be a convenient method of comparing after-effects in different tests.

Very erratic results were obtained in the preliminary tests that were carried out on wires covered with the original oxide film that formed during casting and swaging. This film, crushed into the metal and cracked during the process of drawing, could not be expected to have a high degree of uniformity. It was therefore removed, either after drawing or, if a wire was annealed, after annealing, and replaced by a film formed in air, water, or a furnace, or by an anodic film. Apart from one early test (curve D, Fig. 4) in which the original film was removed by etching for 2 min in 85 pct H_3PO_4 at $70^\circ C$, the original films in all other tests were removed by chemically polishing, using the "R-5 Bright Dip" process (under a license from the Aluminum Co. of America and according to the technique suggested by F. Keller of that company). The wire when rinsed in water or acetone and dried in an air blast had a brightly polished surface covered with an extremely thin invisible oxide film.

The possibility must be considered that the abnormal after-effect may be due to the direct attack

of the reagent on the aluminum itself instead of the oxide. In the present work this is believed to be very unlikely. During the course of each run the surface of the wire was examined while immersed in the reagent, and visible gas evolution, which would indicate attack of the metal, was never observed. Furthermore, when wires carrying anodic films were twisted, very fine cracks appeared in the film. Microscopic examinations of these cracks after immersion in the reagent showed no widening or undercutting of the crack, indicating that attack of the metal had not taken place.

Results and Discussion

To obtain quantitative and reproducible results in tests of this nature it is obviously necessary to maintain control of geometrical variables such as the diameter and length of the wires and the angle through which the wires are initially twisted. Control of certain other somewhat less obvious variables is also necessary. These are the amount of cold work received by the wire previous to twisting, the amount of recovery or recrystallization that has taken place subsequent to the cold working, the grain size of the wire, the duration of the initial application of torque, and the thickness and nature of the oxide film covering the wire. These effects were investigated and the results are presented in Figs. 2 to 4, inclusive; a detailed discussion of these and subsequent figures appears in the sections to follow.

One of the variables that alters the abnormal after-effect rate is the time that elapses before the reagent is applied. In all tests reported here this was held constant at 6 min.

It has been suggested that when the medium at the surface of the wire is changed, the change of surface energy at the interface between metal and solution might allow slip to occur more easily and therefore contribute to the abnormal after-effect. Several tests were therefore carried out to determine the effects of changing surface tension, Fig. 5.

In addition to studying the factors affecting the magnitude and reproducibility of the abnormal after-effect, a series of experiments dealing with the attack of the oxide film by etchants was carried out. This was done by subjecting both anodic and high temperature oxide films to a series of organic and mineral acids and to different pretreatments such as annealing, treating with distilled water (a process known as sealing) at various temperatures, and pre-etching for different times, Figs. 6 to 11.

The presentation and discussion of the results are given in two parts, corresponding to 1—the study of the variables influencing both the normal and abnormal effect, and 2—the use of the abnormal after-effect in studying various films on aluminum and their attack by reagents.

Variables Affecting the Normal and Abnormal After-Effects

Fig. 2 shows the effect of the duration of the applied strain (time of holding) on the initial rate of untwisting in the normal after-effect. The wires used for these tests were annealed for $1\frac{1}{2}$ hr at $285^\circ C$ and chemically polished. All of the wires were twisted in the standard fashion and, after being held for various times at this strain, were released and the rate of untwisting measured. The time of holding was measured as the time from the commencement of twisting until the load was final-

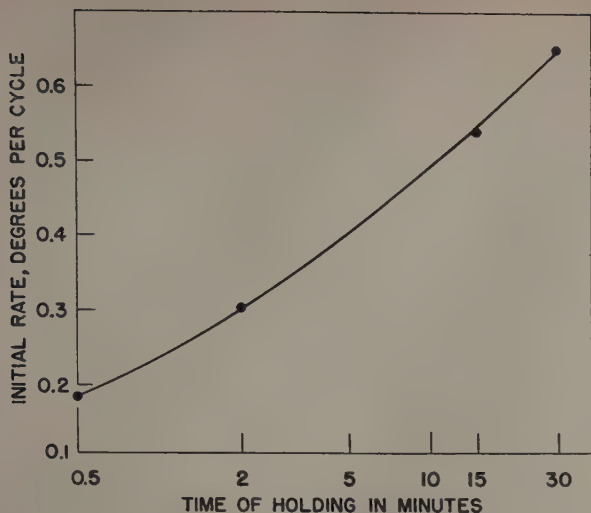


Fig. 2—Influence of time of holding at constant strain on the initial strain rate in air, in degrees per cycle of log time in minutes.

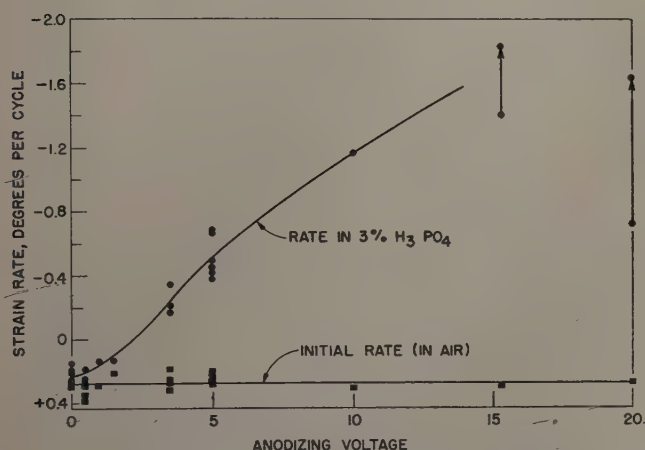


Fig. 3—Influence of anodic oxide film thickness measured in terms of the anodizing voltage on the initial strain rate in air and in 3 pct H_3PO_4 .

ly released. The initial rate of untwisting is seen to depend quite strongly on the time of holding and this variable was therefore controlled, at an arbitrary value of 2 min, in the remainder of the tests on aluminum discussed below.

The influence of film thickness was studied by forming oxide films anodically in a 3 pct chromic acid bath at $70^\circ C$ on wires annealed $1\frac{1}{2}$ hr at $285^\circ C$. As it is known that increasing the anodizing voltage increases the film thickness, a range of anodizing voltages was used giving a range of thicknesses. The measured strain rates in air and 3 pct phosphoric acid as a function of anodizing voltage are shown in Fig. 3. For the thinner coatings, produced at voltages less than 15 v, the change in strain rate when 3 pct phosphoric acid is applied increases with the anodizing voltage and hence with the film thickness. This is interpreted as indicating that the thicker coatings provide more effective barriers for stopping dislocations. For coatings thicker than these, the initial effect of etching was less pronounced, and the strain rate increased after a few minutes in acid (this is indicated by the vertical arrows in Fig. 3). Assuming a uniform rate of attack of the acid, this would indicate lower stresses in the outer layers of the oxide than in the layers near the interface. An unexpected result in Fig. 3

is that the strain rate in the normal after-effect, i.e., before etching, is virtually independent of the anodizing voltage that had been used in preparing the wire.

Although the variation of strain rates in 3 pct phosphoric acid for a given thickness of film on different wires is considerable (-0.38 to -0.69 degrees per cycle for a 5 v film), the curve might be used as a rough indication of the thickness of a film (in terms of anodizing voltage) produced in a chromic acid bath, or as a test of the effect of various treatments on a standard type of film. For further tests on the effect of different treatments on anodic films, 5 v chromic acid films were employed.

The effect of cold work and annealing on the initial rate is shown in Fig. 4. The rapid untwisting of cold-drawn wire illustrated by curve A is attributed to the many residual dislocations and local stresses within the cold-worked metal that act as barriers to the growth of the dislocation rings formed during twisting. The abnormally large number of these barriers compared with the number in annealed wires results in shorter average distances between barriers and dislocation generators, therefore in more tightly packed arrays of dislocations piled up against the barriers, and in more rapid return of the dislocations toward their source during the untwisting period. Annealing the wire before twisting reduced the barriers and lowered the untwisting rate, as seen in curve B for wire recovered and partially recrystallized by a 1 hr anneal at $250^\circ C$. Additional annealing still further reduced the rate, curves C and D.

Comparison of curves C and D shows the effect of grain size in fully recrystallized wire on the initial rate of untwisting. Here again the rate is doubtless governed by the number of barriers that block or impede the motion of dislocations, the obvious bar-

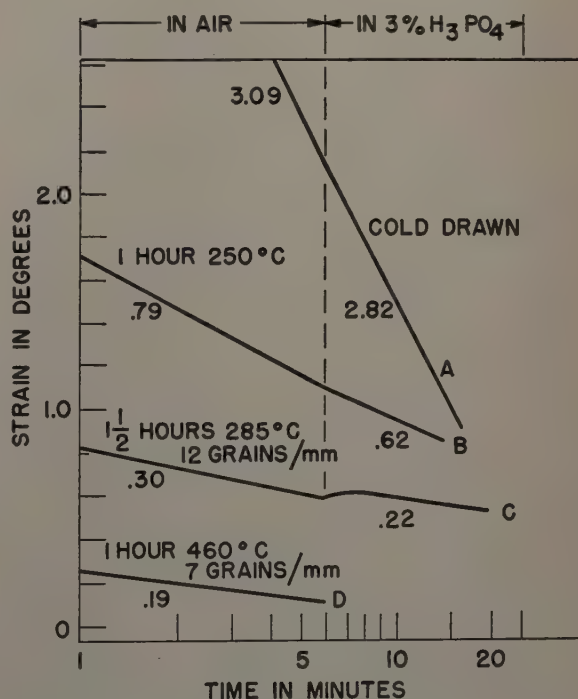


Fig. 4—Effect on the initial strain rate in air of cold working and of annealing chemically polished wires with air-formed oxide. Heat treatment, grain sizes, and strain rates are given. The zero positions on all scales of strain here and in the figures that follow are arbitrary.

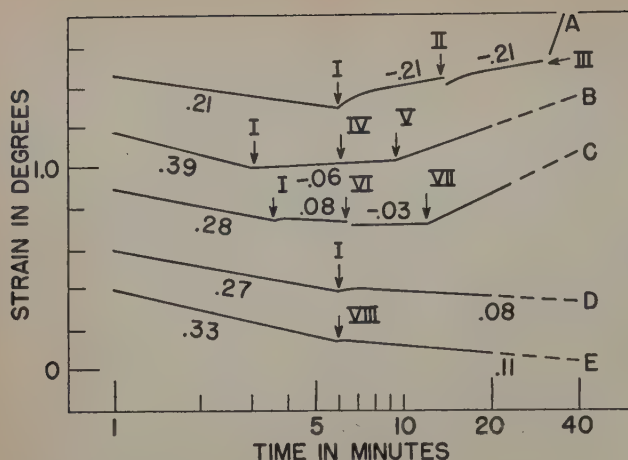


Fig. 5—Effect of surface tension on strain rates. Surface conditions employed: A,B—Annealed 2 hr at 460°C, anodized in 3 pct chromic acid at 50 v. C—Annealed 2 hr at 460°C, anodized in 3 pct chromic acid at 25 v. D,E—Annealed 1½ hr at 285°C, anodized in 3 pct chromic acid at 5 v. Numerical values of strain rates given in figure. At I, wire immersed in distilled water; at II, ½ volume of technical methyl alcohol added; and at III, ½ volume of 3 pct H_3PO_4 added. At IV and V, respectively, 1 ml of aerosol and 10 ml 3 pct H_3PO_4 added. At VI, wire immersed in 50 pct ethyl alcohol, and at VII, ¼ volume of 3 pct H_2SO_4 added. At VIII, wire immersed in a 50 pct solution of ethyl alcohol in distilled water.

riers in this case being the grain boundaries, though less obvious ones, perhaps subboundaries, may also play a part.

With larger grain sizes a larger statistical fluctuation in the number of grain boundaries and less reproducibility in initial rate was anticipated. The greater part of further work was therefore carried out on wires annealed 1½ hr at 285°C, the minimum annealing treatment that was judged adequate to insure complete recrystallization, as estimated from Laue photographs of the annealed wires. Reproducibility might be increased, also, by increasing the length and diameter of the wires, although this was not tried. Ten to twenty scale readings were taken in determining each untwisting curve; the

individual points are not reproduced but are represented to width-of-line accuracy by the lines shown in the figures. All deficiency in reproducibility lay in manipulations and in the specimen itself rather than in taking scale readings.

Several tests were carried out in order to determine whether surface tension changes contribute appreciably to the abnormal after-effect. The results are presented in Fig. 5. Curves A, B, and C show that practically no change in the after-effect rate occurs when the surface tension of distilled water surrounding a wire is altered by the addition of methyl alcohol, aerosol, or ethyl alcohol. When a reagent such as phosphoric acid is added, however, which is known to attack the oxide layer, there is a sudden change in the strain rate.

Since it could be argued that the reagents added for the purpose of altering surface tension might not have sufficient time to diffuse through water into fissures or pores in the oxide and alter surface energy of the underlying metal, a further test was carried out in which the different liquids were mixed together before application to the surface of the wire. This test is recorded in curve E. Comparison of curve E with curve D shows again that the change in surface tension due to the ethyl alcohol has had a negligible influence on the abnormal after-effect.

Study of Various Films on Aluminum and Their Attack by Reagents

The effect of different reagents on the surface oxide film on aluminum is not fully understood and while the terms "solvent action" and "dissolving" are used they are not to be construed in the sense of a complete solution of the oxide in the reagent. The reaction of aluminum with water is attended with a very large free energy decrease and it is only the presence of a surface oxide film that restrains this reaction from taking place with almost explosive violence. As has already been stated, no gas evolution was observed to take place from the surface of the wire during the course of these experiments and hence it must be assumed that some sort of surface film is retained on the wire even when immersed in the reagent. It is felt that while some direct superficial solution of the film takes place, the preponderant effect of the reagent is to penetrate and peptize the film, thus reducing its mechanical strength. These two effects will act simultaneously and it is their total effect that is observed, therefore the terms mentioned will be used to denote the general effect of the reagent on the film.

The alteration of strain rate on changing from air to a reagent was measured, for a series of reagents, on a set of wires that had been annealed 1½ hr at 285°C, chemically polished, and anodized (3 pct chromic acid, 5 v). The results are given in Fig. 6.

The solvent action of a 2 pct boric acid, 0.25 pct ammonium hydroxide solution on anodic films is known to be very small and this fact is confirmed by the small change in strain rate when that reagent is used, as the results given in curve A show. The changes in strain rate produced by 2 pct sulphuric acid, distilled water, 3 pct acetic acid, 3 pct oxalic acid, and 3 pct formic acid as shown in curves B to F, inclusive, suggest that all these reagents have an approximately equal effect on the film. In practice, commercial aluminum alloys are only very slightly corroded by these reagents although to somewhat

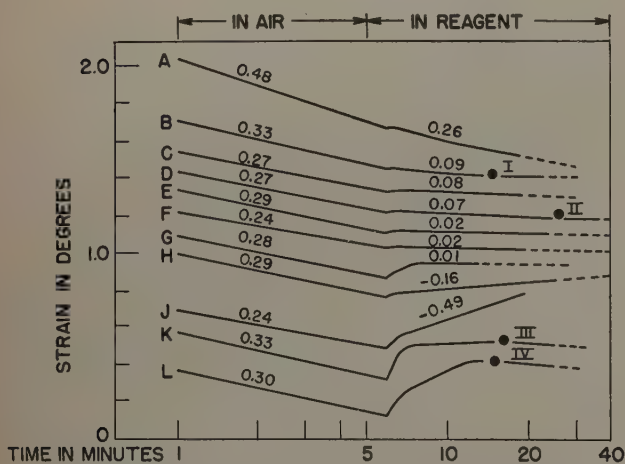


Fig. 6—Effect of a series of reagents on a 5 v chromic acid anodic film. At I and II changed to distilled water, rate became 0.00. At III and IV changed to 2 pct H_3BO_3 plus 0.25 pct NH_4OH solution and rate became 0.08 and 0.14, respectively. The strain rates in air and in the reagent are given beside the curves. Curve and reagent: A—2 pct H_3BO_3 plus 0.25 pct NH_4OH . B—2 pct H_2SO_4 . C—Distilled water. D—3 pct acetic acid. E—3 pct oxalic acid. F—3 pct formic acid. G—25 pct HCl . H—3 pct H_3PO_4 plus 2 pct chromic acid. J—3 pct H_3PO_4 . K—3 pct $NaOH$. L—3 pct NH_4OH .

differing degrees, and the fact that the present technique shows very little difference between the effects of any of these reagents may be attributed to the high purity of the metal used. The oxide film on this material will be much more continuous and stable since it will not contain the oxidation products of the various alloying elements and impurities of commercial alloys.

The effect of 25 pct hydrochloric acid is shown by curve G to be of the same order of magnitude as that of the reagents just discussed, so that here again the oxide film is rather resistant to the reagent, which is to be expected from the fact³ that the oxide film formed by thermal treatment on high purity (99.95 pct) aluminum is relatively insoluble in 25 pct hydrochloric acid. The effect of adding chromic acid to phosphoric acid is shown by curve H when compared with curve J for phosphoric acid alone; the inhibitive action of the chromic acid slows down the rate of attack.

The rapid attack of 3 pct sodium hydroxide is indicated by curve K and by results to be subsequently presented in Fig. 9 which show that pre-etching the film for 9 min in this reagent is sufficient to dissolve it completely. The initial rapid change in strain rate in curve K indicates that most of the attack occurs in the first 2 min. Similar results, presented in curve L, were obtained with 3 pct ammonium hydroxide, although this reagent attacked the film over an 8 to 10 min period.

The magnitude of the transient strain in the reverse direction accompanying a sudden removal of oxide as in curve K should be an index of the intensity of stresses in the oxide layer, therefore an index of the ability of the layer to impede the emergence of dislocations (provided the attack is not so violent as to introduce other effects such as transient heating of the wire.)

Fig. 7 gives the results of a series of measurements carried out on oxide films formed under various conditions on wire specimens previously cleaned in the standard fashion. The curves indicate the effectiveness of these films in causing dislocations to pile up and the rate with which the application of 3 pct phosphoric acid relieved the stresses.

Curves A to E give the results obtained on a series of sulphuric acid and boric acid anodic films. These two anodizing baths are known to give anodic films with different types of structure. The sulphuric acid film is thick and porous, whereas the boric acid film is thin and compact. The extremely high strain rate obtained on curve A on immersion in 3 pct phosphoric acid indicates that the sulphuric acid film is a good barrier for dislocations but is easily and rapidly weakened by immersion in the reagent. This behavior is not changed by sealing in either 5 pct potassium chromate solution having a pH of 3.8, or in distilled water adjusted to a pH of 3.5 with nitric acid. This is surprising since sealing swells and consolidates the film and confers added corrosion resistance to the anodized metal, the presence of chromate in the sealant generally conferring especially good corrosion resistance on the metal. However, as curve D shows, sealing in distilled water gives a very much slower rate of attack by the reagent. Thus it appears that the efficiency of a sealant depends on its pH and is very poor at pH values around 3.8.

Anodic films prepared in boric acid electrolytes are known to be of the compact, nonporous type. It would be expected, therefore, that these would ex-

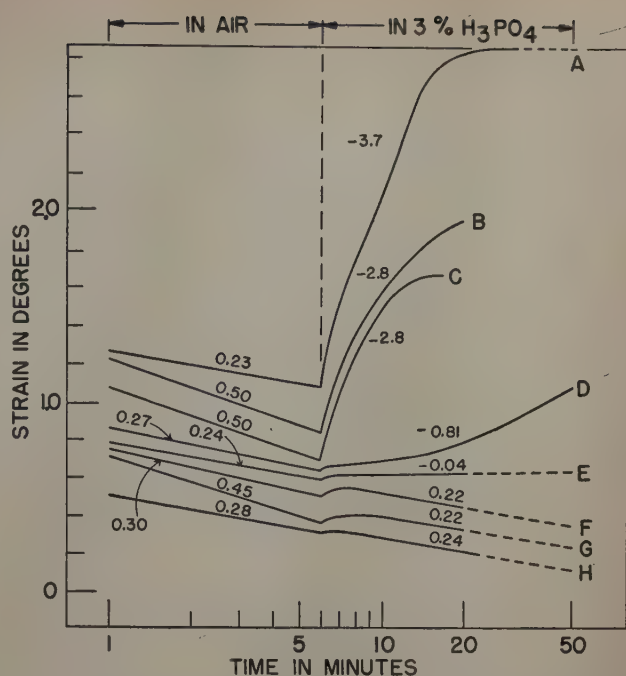


Fig. 7—Effect of phosphoric acid on oxide films formed under a variety of conditions. The strain rates in air and the reagent are given by the appropriate curve. Preparation of oxide films: A—Anodized at 5 v for 5 min in 18 pct H_2SO_4 at $20^\circ C$. B—As in A, then 30 min at $100^\circ C$ in 5 pct $K_2Cr_2O_7$ solution (pH, 3.8). C—As in A, then 30 min at $100^\circ C$ in 0.001 normal HNO_3 (pH, 3.5). D—As in A, then 30 min at $100^\circ C$ in distilled water. E—Anodized for 5 min at 12 v in 2 pct H_3BO_3 plus 0.9 pct NH_4OH solution at $20^\circ C$. F—Oxidized 1 hr in the atmosphere. G—Oxidized $1\frac{1}{2}$ hr at $285^\circ C$. H—Held in distilled water for 26 hr at $20^\circ C$.

hibit a high resistance to 3 pct phosphoric acid; this is in accord with the small change in rate when the etchant is applied in curve E. Another contributing cause of the small magnitude of the effect is doubtless the thinness of the film, for presumably it is less able to block the escape of dislocations during the initial twisting. (When it is desired to discriminate between the two causes, a series of pre-etching experiments can be conducted as was done in the experiments of Fig. 9, discussed later.)

Curves F and G (Fig. 7) were obtained on wires that were annealed $1\frac{1}{2}$ hr at $285^\circ C$, chemically brightened, and then oxidized in air under the con-

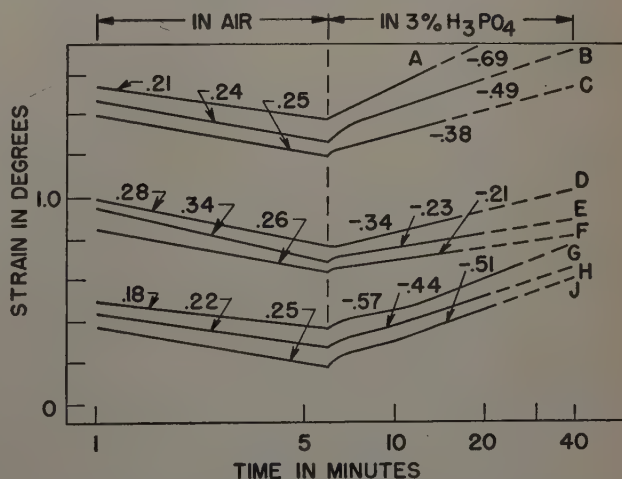


Fig. 8—Effect of pretreating a 5 v chromic acid anodic film in distilled water. The results are given in triplicate. A,B,C: Standard 5 v film without pretreatment. D,E,F: Pretreated 1 hr in water at $20^\circ C$. G,H,J: Pretreated $\frac{1}{2}$ hr in water at $100^\circ C$.

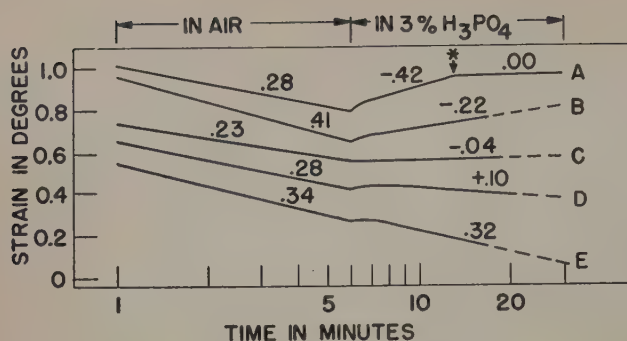


Fig. 9—Effect of pre-etching a 5 v chromic acid film on the strain rates in air and in 5 pct phosphoric acid. A—No pre-etch. *Reagent changed to distilled water. B—Pre-etched 2 min in 3 pct H_3PO_4 . C—Pre-etched 15 min in 3 pct H_3PO_4 . D—Pre-etched 32 min in 3 pct H_3PO_4 . E—Pre-etched 9 min in 3 pct NaOH.

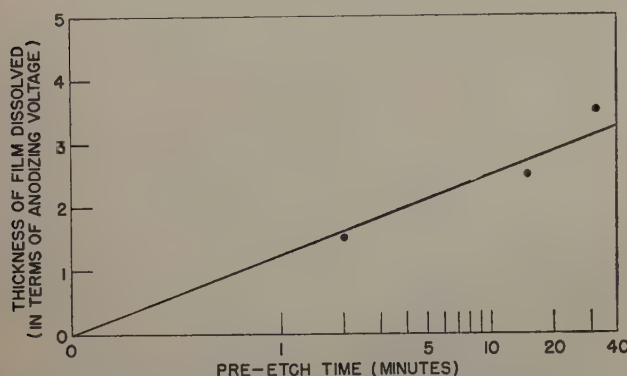


Fig. 10—Rate of attack of an anodic chromic acid film by 3 pct H_3PO_4 .

ditions shown. The thickness of the natural oxide film formed in air at room temperature lies in the range from 10 to 100 Å.^{3,4} Growth of a film is more rapid and its thickness much greater when formed in air at higher temperatures, but comparison of curves F and G suggests that despite its greater thickness a high temperature film is no more effective in causing dislocations to pile up beneath the film than is an air-formed film, owing, presumably, to less adherence to the metal, or to a greater tendency to crack during twisting and to let dislocations escape. The wire tested in curve H was chemically polished and immediately submerged in distilled water for 26 hr. The film formed by this treatment has an effect similar to the air-formed film.

The effect of distilled water on anodic films is reported in Fig. 8. The films were prepared as before on wires annealed 1½ hr at 285°C and chemically polished; anodizing was in a 3 pct chromic acid bath with potential of 5 v. Curves D, E, and F compared with A, B, and C show that 1 hr distilled water at 20°C before twisting reduces the change in strain rate that occurs when 3 pct phosphoric acid is applied to the film. This may be accounted for by solvent action in the water together with a partial conversion of the layer to weaker or less adherent material. Some beta-trihydrate⁵ is doubtless produced, as this is commonly found as a corrosion product when aluminum stands in water. A change in volume accompanying the transformation may also contribute to the weakening.

Curves G, H, and J, giving the effect of a 30 min treatment in distilled water at 100°C, which should produce some alpha-monohydrate in the coating,⁵

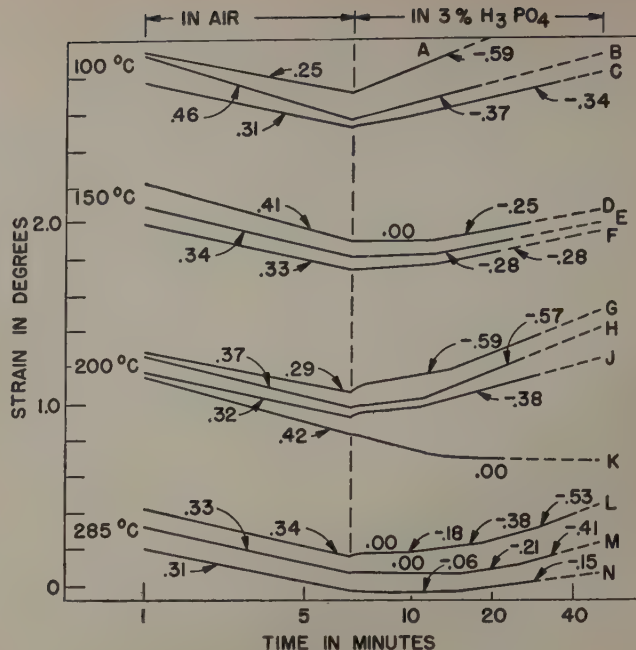


Fig. 11—Effect of annealing 5 v chromic acid anodic film at various temperatures in air. The results are given in triplicate for each annealing temperature. The strain rates for each curve are given in the figure.

resemble curves A, B, and C for the untreated films. The marked change that occurred with the sealing of a sulphuric acid film (Fig. 7) was not duplicated in these experiments on the chromic acid films.

The results of pre-etching are shown in Fig. 9. Wires that had been annealed 1½ hr at 285°C, chemically polished and anodized (3 pct chromic acid, 5 v) were etched for various times in 3 pct phosphoric acid before twisting. The change in strain rate on changing from air to 3 pct phosphoric acid becomes less as the time of pre-etching increases (curves A, B, C, D). These results indicate a gradual thinning or weakening of the film. An approximate idea of the effective thickness left after pre-etching for different times in terms of anodizing voltage to produce an equivalent film can be obtained from the curve of rate in 3 pct phosphoric acid, Fig. 3. If the effective film-thickness dissolved is plotted against the logarithm of the time of etching, a straight line is approximated as shown in Fig. 10. Curve E indicates that 9 min in 3 pct NaOH is more than sufficient to remove the film.

The change from 3 pct phosphoric acid to water in curve A, Fig. 9, as well as the curves of Fig. 6, suggests that the strain rate immediately after a wire with a standard type of film is immersed in one of these reagents is directly related to the rate of attack of that reagent on the film and that a quantitative comparison of rates of attack by different reagents may be had from such tests.

Fig. 11 records the results of annealing anodic films. Wires were annealed, polished, and anodized as in the previous experiments and the anodized wires were then annealed for 1 hr at a series of temperatures. Annealing at 100°C appears to have no deleterious effect on the strength of the film and therefore probably does not cause any changes in the film (curves A, B, C). With annealing above 100°C the change in strain rate in 3 pct phosphoric acid increases after periods of immersion of about

6 min, and similar changes are somewhat more pronounced in films annealed at 285°C. It is presumed that thermal stresses cause the formation of a network of cracks in the anodic film and that at the base of these cracks rapid oxidation will occur. It appears that the furnace-formed oxide under the cracks is attacked at a different rate than the anodic film, so that the rate of untwisting in acid undergoes unusual changes. Since the final slopes of curves D to N vary considerably, it is concluded that there is a wide variation in the degree of alteration of the anodic films during annealing, as might be expected if a rather limited number of crack systems were developed.

Summary

The abnormal after-effect in twisted wires that occurs when untwisting is interrupted by etching can be used to give quantitative information regarding surface films on the wires, if the following variables are controlled: cold work, recovery, recrystallization, and grain growth in the metal prior to twisting; magnitude and duration of the twisting; duration of the initial untwisting prior to etching; nature, temperature, and concentration of the etchant; length and diameter of the wires.

This method was applied to high purity aluminum with various oxide and anodic coatings. The abnormal effect is much greater with the thick, porous type anodic films than with the thin, dense type produced in boric acid or with films formed in air or

water, and increases with increasing anodic film thickness. The normal after-effect rate, however, is independent of this thickness. The rates of attack on a chromic acid anodic film by several different reagents were studied, using as an index the change of rate of untwisting when an etchant is applied. A 2 pct boric acid plus 0.25 pct ammonium hydroxide solution showed the slowest rate of attack, while solutions of sodium hydroxide and of ammonium hydroxide showed the fastest attack among those tried. Adding 2 pct chromic acid to 3 pct phosphoric acid slowed its attack. The rate of attack by water was not altered by adding a wetting agent or by adding ethyl or methyl alcohol.

Sealing a porous-type anodic film in 100°C water slowed the attack of dilute phosphoric acid, but similar treatment in 5 pct $K_2Cr_2O_7$ or in 0.001 normal HNO_3 was relatively ineffective. Annealing anodic films at 100°C in air did not alter their properties, but changes were introduced by annealing at 150° to 285°C.

Acknowledgment

This work was supported in part by Contract N-6ori-02004, U. S. Office of Naval Research.

References

- ¹ C. S. Barrett: *Acta Metallurgica* (1953) **1**, p. 1.
- ² C. S. Barrett: This issue, p. 1652.
- ³ F. Keller and S. D. Edwards: *Pittsburgh International Conference on Surface Reactions* (1948) p. 202.
- ⁴ H. H. Podgurski: Quoted in ref. 3.

Technical Note

Surface Structures on Single Crystals Produced from Melt

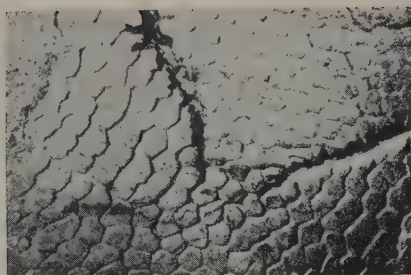
by F. D. Rosi

IN the production of single crystals by the Bridgman method of solidification from the melt in vacuum at a crucible lowering rate of 0.25 in. per hr, a cellular structure was frequently observed in copper and copper-base alloys at the terminal surface of the as-cast crystals (i.e., the surface representing the last portion of the crystal to solidify). The geometrical form of this structure varied from crystal to crystal, but, in general, could be classified as either hexagonal or quadrilateral. Fig. 1 shows examples of this cellular structure, which is similar to that reported by Buerger¹ and, more recently, by Pond and Kessler² and Rutter and Chalmers.³ In the micrographs of Figs. 1b and c, the cubic structure in the alloy crystals is obscured somewhat by excessive surface evaporation in the final stages of solidification.

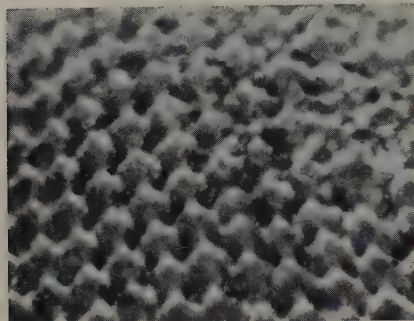
X-ray orientation studies indicate that the traces outlining the various geometrical forms correspond to octahedral planes, which are the planes of greatest reticular density in the face-centered cubic

lattice. It would appear from this that the view first propounded by Bravais,⁴ that the surface energies and normal growth velocities of the different crystal planes are inversely proportional to their reticular densities, applies to this cellular structure, since those surviving are the planes of greatest atomic density. Thus, the observed variation in the geometrical form of this structure in crystals of different orientation is readily understandable from the distribution of the {111} planes in the standard {111}, {110}, and {100} stereographic projections. Depending upon whether the crystal axis (i.e., the direction of crystallization) coincides with a $\langle 111 \rangle$, $\langle 110 \rangle$, or $\langle 100 \rangle$ direction, the cellular structure viewed from a surface perpendicular to the crystal axis will consist of a network of regular hexagons, skewed hexagons (with interfacial angles of 110° and 125°), or cubes, respectively. It follows, moreover, that off-orientations from these principal directions will yield modifications of these three basic geometric configurations. In this connection, it is interesting to note that the bounding planes of the hexagonal structure observed in tin by Rutter and Chalmers³ showed no preferred orientation.

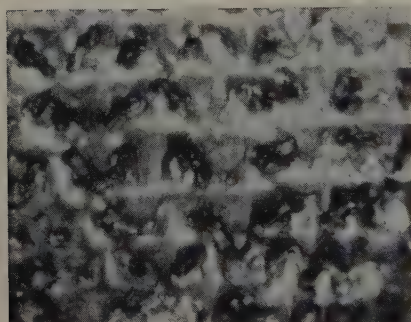
F. D. ROSI, Junior Member AIME, is associated with the Metallurgy Laboratories, Sylvania Electric Products, Inc., Bayside, N. Y.
TN 197E. Manuscript, July 20, 1953.



a—Hexagonal structure in spectroscopic (99.999 pct) Cu. Area reduced slightly for reproduction.



b—Cubic structure in Cu-1 atomic pct Si.



c—Cubic structure in Cu-2 atomic pct Ge.

Fig. 1—Transverse cellular structure observed at terminal surface of single crystals. X10.

In addition to the transverse cellular structure described above, longitudinal striae were observed which closely resemble the line structure reported by Graf,⁵ Pond and Kessler,² and Goss and Weintraub.⁶ The striae appeared as rather thick lines which were found by X-ray analysis to coincide with {100} planes. Moreover, since only those {100} planes were delineated which made a very small angle with the crystal axis, this line structure was most frequently observed in crystals whose axes corresponded closely to a $\langle 100 \rangle$ or $\langle 110 \rangle$.

In agreement with the observations of Smialowski⁷ on zinc and, more recently, Goss⁸ on single crystals of tin, the longitudinal striae were observed only in the alloy crystals and were considerably enhanced by increasing alloying content. This is in sharp contrast to the cellular structure, which was also observed in crystals of highest purity (99.999 Cu).

In consistency with the established crystallography of both the line and cellular structures, the longitudinal striae were observed to form the diagonals to the cubic pattern of the transverse, cellular

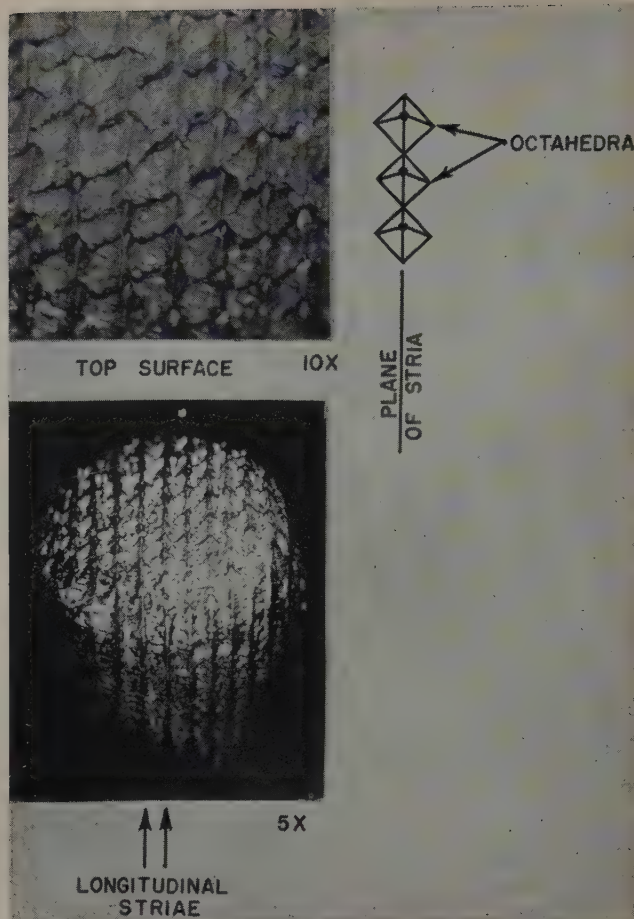


Fig. 2—Relationship between longitudinal line structure with the transverse cellular structure in Cu-2 pct Ge alloy. Area reduced approximately 40 pct for reproduction.

structure in the case of a $\langle 100 \rangle$ orientation (see Fig. 2), and one of the principal axes of the skewed hexagonal pattern for a $\langle 110 \rangle$ orientation.

Acknowledgment

This work is being sponsored in part by the Atomic Energy Commission, Contract AT-30-1, GEN-367.

References

- ¹ M. J. Buerger: The Lineage Structure of Crystals. *Ztsch. Krist.* (1934) **89**, p. 193.
- ² R. B. Pond and S. W. Kessler: Model for Dendrite Growth Form in Metals and Alloys. *Trans. AIME* (1951) **191**, p. 1156; *JOURNAL OF METALS* (December 1951).
- ³ J. W. Rutter and B. Chalmers: A Prismatic Substructure Formed During Solidification of Metals. *Canadian Journal of Physics* (1953) **31**, p. 15.
- ⁴ A. Bravais: *Etudes Cristallographiques*. (1865). Paris. Gauthier-Villars.
- ⁵ L. Graf: About the Structure of Real Crystal—The Formation of Mosaic Structure in Cast, Plastically Deformed and Recrystallized Materials. *Ztsch. Physik* (1943) **73**, p. 121.
- ⁶ A. J. Goss and S. Weintraub: Growth of Single Crystals of Tin from the Melt. *Nature* (London) (1951) **167**, p. 349.
- ⁷ M. Smialowski: On the Mosaic Structure of Metal Crystals. *Wiadomosci. Instytutu Metallurgji i Metaloznawstwa* (Warszawa) (1936) **3**, (4), p. 212.
- ⁸ A. J. Goss: Discussion. *Trans. AIME* (1952) **194**, p. 1187; *JOURNAL OF METALS* (November 1952).

Metals Transactions

January-December 1953

Index to Volume 197

KEY TO PAGE NUMBERS

January	41-88	July	895-942
February	157-204	August	991-1038
February Supplement	213-364	September	1089-1136
March	405-452	September Supplement ..	1141-1268
April	525-572	October	1367-1382
May	633-680	November	1435-1482
May Supplement	685-748	November Supplement ..	1487-1582
June	797-844	December	1631-1662

American Institute of Mining and Metallurgical Engineers
Transactions of the Metals Branch

A

- Absolute Rate Theory Applied to Rate of Growth of Pearlite..... 219
Discussion 1581
Accelerated Solidification in Ingots: Its Influence on Ingot Soundness.... 157
Correction 572
Discussion 1553
Adair, S. E., Jr., Hammond, J. P., and McHargue, C. J.: Effects of Solid Solution Alloying on the Cold-Rolled Texture of Titanium 1199
After-effect measurement and applications to Al 1655
After-Effects in Polycrystalline Cadmium Age Softening of Beta Brass 1240
Aging, low temperature, in Ti alloys..... 178
Ajo concentrates, treatment 633
Albert, P. A.: Habit Plane of Beta in Alpha Titanium 1449
Alexander, B. H., Rosi, F. D., and Dube, C. A.: Mechanism of Plastic Flow in Titanium—Determination of Slip and Twinning Elements 257
Allotropy in the Phase $ZrCr_2$ 304
Alpha Solid-Solution Area of the Cu-Mn-Sn System 723
Aluminum and aluminum alloys: Alnico permanent magnets, effect of macrostructure on 537
Al-3 pct Mg monocrystals, deformation bands in 559
Al-O equilibrium in liquid Fe 173
Al-Si alloys, distribution of Na in 679
coarse grained high purity, inhomogeneity in creep deformation of correlation between creep behavior and resulting structures in alpha solid solutions 324
deformation of high purity Mg in creep compared with Al..... 712
directional properties 431
dynamic formation of slip bands in. flow and fracture characteristics of 24S-T4 as affected by strain thermal history 66
grain boundary attack, in hydrochloric acid and sodium hydroxide..... 911
grain boundary sliding, migration, and intercrystalline failure under creep conditions 305
high purity, importance of Fe in..... 821
influence of Al and Si deoxidation on strain aging of low carbon steel kink band formation during creep at high temperatures 1021
Np-Al intermetallic compounds 1487
residual stresses in 1460
slip and grain boundary sliding in..... 411
stress-strain relations 217
study of grain shape and other applications of stereoscopic micro-radiography. Discussion 1181
subgrain formation 741
subgrain formation during creep..... 717
Discussion 1166
Ti-Al, cold-rolled sheet texture 730
Ti-Al, mechanical properties of 1200
Ti-Cr-Al, phase boundaries 267
torsional after-effect measurement and applications 1561
Aluminum-Oxygen Equilibrium in Liquid Iron 253
1655
173
Amsterdam, M., Rothwarf, F., and Muldaver, L.: Silver-Cadmium Beta and Zeta Phases..... 1458
Anable, W. E., Rasmussen, R. T. C., and Banning, L. H.: Tristage Crystallization Process for Utilizing Western Ferrophosphorus 423
Analyses, chemical, slag-metal samples. 185
Analysis of hydrogen in steel by thermal conductivity method 180
Analysis of Molten-Zone Refining 1531
Ananthanarayanan, N. I., and Libsch, J. F.: Sintering of Ultrafine Ferromagnetic Powders 79
Anantharaman, T. R., and Christian, J. W.: Discussion on Transformation in Cobalt-Nickel Alloys 729
Andersen, J. E., Halpern, J., and Samis, C. S.: Kinetics of the Oxidation of Galena in Sodium Hydroxide Solutions Under Oxygen Pressure 554
Discussion 1556
Anderson, C. T., Kimball, R. W., and Cattoir, F. R.: Effect of Various Elements on Hot-Working Characteristics and Physical Properties of Fe-C Alloys 525
Anderson, E. A., Jilison, D. C., and Dunbar, S. R.: Deformation Mechanisms in Alpha Titanium 1191
Anderson, S., and Bohon, R. L.: Discussion on Thermal Conductivity Method for Analysis of Hydrogen in Steel..... 1551
Anelastic Behavior of Pure Gold Wire... 937
Ang, C-Y., and Wert, C.: Some Properties of Columbium Containing Nitrogen 1032
Annealing: effect on density and hydrogen occlusion of ferrous metals 44
magnetic, Co-Fe alloy 813
Annealing textures: Mo single crystals. 300
Discussion 1569
Zr 288
Anodes, Cu, production in electric arc furnace 197
Antimony and antimony alloys: effect on deposition of Cu 1375
replica method for study of structure of Pb-Sb alloys 55
Arc-Furnace Equipment and Its Operation at the Kennecott Utah Refinery 197
Arc-melting furnace for Cr 64

Arsenic and arsenic alloys: effect on de- position of Cu.....	1375	Binder, I., Moskowitz, D., and Steinitz, R.: System Molybdenum-Boron and Some Properties of the Molybdenum-Borides. Discus- sion.....	747	Cadmium and cadmium alloys: after- effects in polycrystalline.....	1652
Attainment of Equilibrium in Gas-Metal Reactions.....	191	Binder, phase, role in cemented tung- sten carbide-cobalt alloys. Discus- sion.....	746	Ag-Cd beta and zeta phases.....	1458
Discussion.....	1550	Birchenaill, C. E., Davies, M. H., and Simnad, M. T.: A Corrected In- terpretation of the Mechanism of Growth of Magnetite During Oxidation.....	1250	Ag-Cd eutectoid.....	549
Aust, K. T., Maddin, R., and Chen, N. K.: Bending of Molybdenum Single Crystals.....	1477	Birchenaill, C. E., and Derge, G.: Ex- change of Iron Between Liquid Metal and Iron Silicate Slag.....	1648	electrical resistivity of.....	1141
Aust, K. T., and Morral, F. R.: Directional Properties of 2S Aluminum.....	431	Birchenaill, C. E., Himmel, L., and Mehl, R. F.: Self-Diffusion of Iron in Iron Oxides and the Wagner Theory of Oxidation.....	827	single crystals, mechanism of strain hardening.....	1525
Austenite: determination by X-ray methods.....	1539	Birchenaill, C. E., McCabe, C. L.: Vapor Pressure of Silver.....	707	Cadoff, I., and Nielsen, J. P.: Titanium- Carbon Phase Diagram.....	248
diffusion and solubility of boron in.....	1465	Birchenaill, C. E., McCabe, C. L., and Schadel, H. M., Jr.: Vapor Pres- sure of Silver Over Silver- Gold Solid Solutions.....	709	Calcium, diffusion of, in slag.....	1564
effect of carbon on volume fractions and lattice parameters of.....	203	Birchenaill, C. E., and Thomas, D. E.: Concentration Dependence of Diffusion Coefficients in Metallic Solid Solution. Correction.....	1018	Calculation of Interdiffusion Coefficients When Volume Changes Occur.....	1534
effects of sample surface and X-ray diffraction camera geometry on determination of, in hardened steels.....	1529	Bismuth and bismuth alloys: effect on deposition of Cu.....	1375	Calculation of Martensite Nucleus Energy Using the Reaction-Path Model.....	921
retained, determined by X-ray meth- ods.....	87	Bitsianes, G., and Joseph, T. L.: Solid Phase Identification in Partially Reduced Iron Ore.....	1641	Campbell, R. F., and Jensen, W. L.: De- tection of Microcracks in Steel gradients in pearlite.....	1222
stabilization of austenite-martensite reaction in high Cr steel.....	530	Blast furnace, tuyere zone, studies of.....	895	contamination of Si ingots by graphite Cr carbide, grain growth during sin- terling.....	696
Austenite-martensite transformation: effect of Ni and Mo on stabil- ization of.....	922	Blast furnace slag: Mn as indicator of oxidation and desulphurizing power of.....	1451	Cr steel, oxidation, in.....	649
theoretical analysis.....	1503	reduction of Si.....	185	effect of, on volume fractions and lat- tice parameters of retained aus- tenite and martensite.....	203
Austenite-pearlite interface, mechanism of growth.....	220	Bleakney, H. H.: Discussion on Grain Boundary Sliding and Miga- ration and Intercrystalline Failure under Creep Conditions.....	1579	Fe-C alloys, absolute rate theory ap- plied to growth of pearlite in.....	220
Autoradiographs, Al-Si alloys.....	679	Blickwede, D. J.: Effect of Nickel and Molybdenum on Stabilization of the Austenite-Martensite Trans- formation.....	922	effect of elements on hot-working characteristics and physical properties.....	525
Averbach, B. L.: Retained Austenite De- terminations by X-ray Methods.....	87	Kinetics of Galvanizing.....	807	recrystallization kinetics of low car- bon steel. Discussion.....	739
Averbach, B. L., Cohen, M., and Conard, G. P., II: Plastic Bending of Zinc Crystals.....	1036	Bloom, D. S., and Grant, N. J.: Regard- ing Sigma Phase Formation.....	88	solubility in Mo. Correction.....	844
Averbach, B. L., Seigle, L. L., and Cohen, M.: Thermodynamic Properties of Solid Nickel-Gold Alloys. Discussion.....	728	Blowers, soot, description.....	1439	Discussion.....	746
Aziz, P. M., Markson, I., and Barrett, C. S.: Torsional After-Effect Measurement and Applications to Aluminum.....	1655	Bohner, R. L., and Anderson, S.: Discus- sion on Thermal Conductivity Method for Analysis of Hy- drogen in Steel.....	1551	stabilization of austenite-martensite reaction in high Cr steel.....	530
B		Boiler: Cu smelting, design of.....	1435	steel, effect of alloying elements on partition.....	1541
Backofen, W. A., and Hundy, B. B.: Torsion Texture of 70-30 Brass and Armco Iron.....	61	waste heat, to treat combustion gases.....	641	effect of Ni and Mo on stabilization of austenite-martensite trans- formation.....	922
Baes, C. F., Jr., and Kellogg, H. H.: Effect of Dissolved Sulphur on the Surface Tension of Liquid Copper.....	643	Boron and boron alloys: Ago-B ₂ O ₃ sys- tem, thermodynamic properties as slag model.....	1367	influence of rate of deformation on tensile properties of.....	797
Baghouse in zinc smelting.....	1633	diffusion and solubility in iron and steel.....	1463	Ti-C phase diagram.....	248
Bain distortions, transformation by.....	1506	grain boundary films in boron steels.....	445	Discussion.....	1564
Bakelite mounts, effect on mounting Ti alloys in.....	179	Mo-B.....	1537	Ti-Ta-C.....	1205
Ball, C. J. P., et al.: Further Progress in the Development of Mg-Zr Alloys to Give Good Creep and Fatigue Properties Between 500° and 650°F.....	924	Zr-B.....	1117	Ti-rich regions of Ti-C-N and Ti-C-O phase diagrams.....	1498
Balluffi, R. W.: Discussion on Concen- tration Dependence of Diffusion Coefficients in Metallic Solid Solution.....	726	Boswell, F. W. C., Weld, H. M., and Cunningham, R. L.: Observa- tions on Nodular Graphite. Discus- sion.....	738	W-Co-C system. Discussion.....	744
Banning, L. H., Anable, W. E., and Ras- mussen, R. T. C.: Tristage Crystallization Process for Utilizing Western Ferrophosphorus.....	423	Both, E., et al.: Magnetic Annealing of a Co-Fe Alloy.....	813	Carney, D. J., and Rudolph, E. C.: Ex- amination of a High Sulphur Free-Machining Ingot, Bloom and Billet Sections.....	999
Barrett, C. S.: After-Effects in Poly- crystalline Cadmium.....	1652	Boundaries, internal, measurement by random sectioning.....	81	Carr, F. L., et al.: Isothermal Temper Embrittlement of SAE 3140 Steel.....	998
Barrett, C. S., Aziz, P. M., and Markson, I.: Torsional After-Effect Meas- urement and Applications to Aluminum.....	1655	Brass: beta, age softening.....	1240	Carr, F. L., Buffum, D. C., and Jaffe, L. D.: Effect of Grain Size upon Temper Brittleness.....	1147
Barrett, C. S., and Hess, J. B.: Trans- formation in Cobalt-Nickel Al- loys. Discussion.....	729	season cracking.....	408	Carreker, R. P., Jr., Fisher, J. C., and Fullman, R. L.: Simple Devices for Approximating Constant Stress During Tensile Creep Tests.....	657
Bechtold, J. H.: Effects of Temperature on the Flow and Fracture Char- acteristics of Molybdenum.....	1469	70-30, torsion texture of.....	61	Carroll, K. G., Fish, F. M., and Dulis, E. J.: Identification of the Pre- cipitate Accompanying 885°F Embrittlement in Chromium Steels.....	690
Beck, L. H., and Smith, C. S.: Copper- Zinc Constitution Diagram. Re- determined in the Vicinity of the Beta Phase by Means of Quantitative Metallography. Discussion.....	748	Brazing of Ti, filler material for.....	1197	Carwile, N. L., and Geil, G. W.: Effect of Tensile Strain at Low Tem- peratures on Deformation Twin- ning in Ingot Iron.....	213
Beck, P. A.: Discussions on: Cold-Roll- ing and Annealing Textures of Molybdenum Single Crystals.....	1569	Brick, R. M., and Vogel, F. L., Jr.: De- formation of Ferrite Single Crystals.....	700	Cattoir, F. R., Anderson, C. T., and Kimball, R. W.: Effect of Vari- ous Elements on Hot-Working Characteristics and Physical Properties of Fe-C Alloys.....	525
Kinetics of Thermal Reorientations in Cold Rolled Zirconium.....	1573	Bronze, tin, microscopical examination of.....	906	Cech, R. E., and Hollomon, J. H.: Rate of Formation of Isothermal Martensite in Fe-Ni-Mn Alloys.....	685
Kinking in Zinc Single-Crystal Ten- sion Specimens.....	737	Brown, N., and Green, H.: Age Soften- ing of Beta Brass.....	1240	Cerium mischmetal, effect on Mg-Th-Zr alloys.....	927
Recrystallization of a Cold-Rolled Copper Single Crystal.....	1568	Brown, N., Washburn, J., and Parker, E. R.: Relation Between Initial Creep Rate and Resolved Shear Stress in Zinc Single Crystals.....	1229	Chang, H. C., and Grant, N. J.: Grain Boundary Sliding and Migration and Intercrystalline Failure under Creep Conditions.....	305
Becker, J. J., and Hobstetter, J. N.: Orientation Relationships in the Recrystallization of Deformed Copper Single Crystals.....	1235	Buffum, D. C., et al.: Isothermal Temper Embrittlement of SAE 3140 Steel.....	998	Discussion.....	1579
Plastic Deformation of Single Crystals of Copper.....	1231	Buffum, D. C., and Jaffe, L. D.: Some Effects of Microstructure Upon Temper Brittleness.....	1373	Inhomogeneity in Creep Deformation of Coarse Grained High Purity Aluminum.....	1175
Bend Plane Phenomena in the Deforma- tion of Zinc Monocrystals.....	49	Buffum, D. C., Jaffe, L. D., and Carr, F. L.: Effect of Grain Size upon Temper Brittleness.....	1147	Observations of Creep of the Grain Boundary in High Purity Alu- minum. Discussion.....	732
Bend planes at end restraints.....	52	Bunshah, R. F., and Mehl, R. F.: Rate of Propagation of Martensite.....	1251	Change in Ingot Shape During Zone Melting.....	1441
Bending of Molybdenum Single Crystals.....	1477	Burbank, J.: Replica Method for Study of the Structure of Lead-Anti- mony Alloys.....	55	Chaudhuri, A. R., Grant, N. J., and Norton, J. T.: Metallographic Observations of the Deformation of High Purity Magnesium in Creep at 500°F.....	712
Bending, plastic, Zn crystals.....	1036	Burkart, M. W., and Read, T. A.: Dif- fusionless Phase Change in the Indium-Thallium System.....	1516	Chaudhuri, A., Grant, N. J., and Sery, I. S.: Slip and Grain Boundary Sliding as Affected by Grain Size Structure.....	217
Bessemer converter, use of oxygen in. Discussion.....	1551	Burke, J. E., and Seymour, W. E.: Dis- cussion on Kinetics of Thermal Reorientations in Cold Rolled Zirconium.....	1574	Chen, N. K., Aust, K. T., and Maddin, R.: Bending of Molybdenum Single Crystals.....	1477
Bethune, A. W., and Pidgeon, L. M.: Vapor Pressure of ZnS by Cu and Fe Reduction of ZnS by Cu and Fe Discussion.....	804	Burr, A. A., and Ebeling, D. G.: Effects of Microstructure on the Per- formance of Alnico Permanent Magnets.....	537	Chen, N. K., and Maddin, R.: Cold- Rolling and Annealing Textures of Molybdenum Single Crystals.....	300
Beu, K. E.: Notes on the Determination of Retained Austenite by X-Ray Methods.....	1539	Burst formation of martensite in high Cr steel.....	530	Discussion.....	1569
Beu, K. E., and Koistinen, D. P.: Effect of Sample Surface and X-Ray Diffraction Camera Geometry on the Determination of Retained Austenite in Hardened Steels.....	1529	Busby, P. E., Warga, M. E., and Wells, C.: Diffusion and Solubility of Boron in Iron and Steel.....	1463	Plasticity of Columbium Single Crystals.....	1131
Bever, M. B., and Michael, A. B.: On the Distribution of Sodium in Modified Al-Si Alloys.....	679	Buttner, F. H., Udin, H., and Wulff, J.: Determination of the Absolute Grain Boundary Energy of Gold at 1300°K.....	313	Formation of Slip Bands in Aluminum. Discussion.....	733
		Byrkit, J. W.: Operations at New Cor- nelia Copper Smelter of Phelps Dodge Corporation.....	633	Chipman, J., Fulton, J. C., and Grant, N. J.: Reduction of Silicon from Blast Furnace Type Slags.....	185
				Chipman, J., and Goken, N. A.: Alu- minum-Oxygen Equilibrium in Liquid Iron.....	173
				Silicon-Oxygen Equilibrium in Liquid Iron - A Revision.....	1017

Chipman, J., Grant, N. J., and Shields, B. M.: Thermal Conductivity Method for Analysis of Hydrogen in Steel.....	180	Cu-Ni couples, concentration dependence of diffusion coefficients. Correction.....	1018	Decker, B. F., Waterstrat, R. M., and Kasper, J. S.: Formation of Sigma Phase in the Mn-Mo System.....	1476
Discussion.....	1551	Discussion.....	726	Deformation: Al at high temperature, subgrain formation.....	1166
Chipman, J., and Larson, H.: Oxygen Activity in Iron Oxide Slags.....	1089	Cu-Sn and Cu-Sn-P, microscopical examination of.....	906	bands, formation in Al-3 pct Mg mono-crystals during cold rolling.....	559
Chipman, J., Towers, H., and Paris, M.: Diffusion of Calcium Ion in Liquid Slag.....	1455	Cu-Zn constitution diagram. Discussion effect of chloride on deposition of, with As, Sb, and Bi.....	748	cold-rolled Cu single crystal.....	672
Chloride, effect on deposition of Cu.....	1375	effect of dissolved sulphur on surface tension of liquid Cu.....	1375	creep, of coarse grained high purity Al, inhomogeneity in.....	1175
Christian, J. W., and Anantharaman, T. R.: Discussion on Transformation in Cobalt-Nickel Alloys.....	729	electric arc furnace for Cu refining.....	643	effect on recrystallization of Cu single crystals.....	1235
Chromium and chromium alloys: Cr carbide, grain growth during sintering.....	696	electrical resistivity of.....	1144	influence of rate on tensile properties of plain carbon sheet steels.....	797
effect of, on partition of Ni in steels.....	1541	electron microscope study of effect of cold work on subgrain structure of.....	660	high purity Mg in creep at 500°F, metallographic observations.....	712
forging of arc-melted.....	63	energy state of fatigued Cu.....	1558	kink band, in Al.....	1487
in stainless steel.....	1009	operations at New Cornelia smelter.....	633	plastic, Cu single crystals.....	1231
influence on internal friction due to nitrogen in Fe.....	70	oxidation rate of, in oxygen.....	1127	in strain-induced martensite.....	654
Fe-Cr-Co-Ni, rationalization of high temperature properties of.....	1149	single crystals, deformed, orientation relationships in recrystallization of.....	1235	thermodynamic theory of irreversible processes applied to.....	442
metallic oxidation in steel melting.....	649	mechanism of strain hardening.....	1525	Zn monocrytals.....	1217
Ni-Cr, high temperature corrosion in recovery from ferrophosphorus in tris-stage crystallization process.....	844	plastic deformation of.....	1231	process in creep of Mg.....	1123
stabilization of austenite-martensite reaction in high Cr steel.....	428	recrystallization of.....	672	Ti alloys.....	1199
steels, precipitate accompanying 885°F embrittlement.....	530	Discussion.....	1568	twinning in ingot Fe, effect of tensile strain on.....	213
thermal and dilatometric investigation of alloys of Co with.....	690	smelting, furnace and boiler design at Hurley.....	1435	Zn monocrytals, bend plane phenomena.....	49
TiCr ₂ , high temperature modification.....	357	ZnS, reduction by Cu, vapor pressure of Zn in.....	804	Deformation Mechanisms in Alpha Titanium.....	1191
Ti-Cr, aging, low temperature.....	196	Discussion.....	1558	Deformation of Ferrite Single Crystals.....	700
Ti-Cr phase diagram. Discussion.....	743	Zr-Cu system.....	273	Deitz, G. A., and Halpern, V.: Reaction of Silver with Aqueous Solutions of Cyanide and Oxygen.....	1109
Ti-Cr-Al, phase boundaries.....	253	Corrected Interpretation of the Mechanism of Growth of Magnetite During Oxidation.....	1250	Delisle, L.: Electron Microscope Study of the Effect of Cold Work on the Subgrain Structure of Copper.....	660
Ti-Cr-Fe.....	1209	Corrosion: grain boundary, mechanism of high temperature, Ni-Cr alloys.....	917	Densification and Kinetics of Grain Growth During the Sintering of Chromium Carbide.....	696
Ti-Cr-Mo.....	1544	Crafts, W., and Hilty, D. C.: Liquidus Surface of the Fe-S-O System. Discussion.....	844	Density and Hydrogen Occlusion of Some Ferrous Metals.....	44
ZrCr ₂ , allotropic in the phase.....	304	Crafts, W., Hilty, D. C., and Healy, G. W.: Metallic Oxidation in Chromium Steel Melting.....	1549	Deoxidation: influence of Al and Si on strain aging of low carbon steel.....	1021
Zr-Cr.....	279	Crede, J. H., et al.: Magnetic Annealing of a Co-Fe Alloy.....	649	relation of Al-O in steelmaking.....	173
Circular plates, measurement of particle size.....	447	Creep: Al, high purity: kink band formation during, at high temperatures.....	813	Deposition of Cu, effect of chloride on.....	1375
Cobalt and cobalt alloys: binder phase in cemented tungsten carbide-cobalt alloys. Discussion.....	746	subgrain formation during behavior, in alpha solid solutions.....	1487	Derge, G., and Birchenall, C. E.: Exchange of Iron Between Liquid Metal and Iron Silicate Slag.....	1648
Co-Fe alloy, magnetic annealing.....	813	deformation, inhomogeneity in Al.....	1166	Desulphurization, blast furnace slag, Mn as indicator of.....	1451
Co-Ni alloys, transformation in. Discussion.....	729	grain boundary sliding and migration and intercrystalline failure in.....	324	Detection of Microcracks in Steel.....	1222
Fe-Cr-Co-Ni alloys, rationalization of high temperature properties of.....	1149	Discussion.....	1579	Determination of the Absolute Grain Boundary Energy of Gold at 1300°K.....	313
mechanical and magnetic hardness in 10 pct V-Co-Fe alloy.....	349	Mg. Discussion.....	732	Development of Mechanical and Magnetic Hardness in a 10 Pct V-Co-Fe Alloy.....	349
thermal and dilatometric investigation of, with Cr and Mo.....	357	Mg, high-purity, metallographic observation of deformation of.....	712	Diagram of free energy of vaporization of solid and liquid elements.....	656
W-Co-C system. Discussion.....	744	Mg-Zr.....	924	Diffraction analysis: Co-Fe V.....	351
Coercive force, variation with sintering temperature for ultrafine Fe powder compacts.....	80	nature of.....	318	TiAg.....	670
Cohen, M., Averbach, B. L., and Seigle, L. L.: Thermodynamic Properties of Solid Nickel-Gold Alloys. Discussion.....	728	subgrain formation in Al. Discussion rate, Zn single crystals, relation to shear stress.....	1577	Diffraction data: stainless steel.....	340
Cohen, M., Conard, G. P., II, and Averbach, B. L.: Plastic Bending of Zinc Crystals.....	1036	tests, devices for approximating constant stress during tensile creep tests.....	730	TiCr ₂	196
Cohen, M., Wagner, C., and Reynolds, J. E.: Calculation of Interdiffusion Coefficients When Volume Changes Occur.....	1534	Creep Behavior of Extruded Electrolytic Magnesium.....	1229	Ti-Cr-Fe.....	1213
Coke, blast furnace size, study of.....	895	Creep Properties of Commercially Pure Titanium.....	657	Diffraction measurement, V-O alloys.....	293
Correction.....	1018	Crystallization step in tristage crystallization process.....	1121	Diffraction methods, determination of orientation relationships in Zr.....	284
Cold Rolled Texture of Titanium.....	1378	Crystallographic Analysis of the Ductile-Brittle Transition in Body-Centered Cubic Single Crystals.....	331	Diffractions patterns: Cr steel.....	693
Cold Rolling and Annealing Textures of Molybdenum Single Crystals.....	300	Crystallographic Angles for Orthorhombic (Alpha) Uranium.....	425	Cu-Au.....	824
Discussion.....	1569	Crystal orientation, preferential etch for use in optical determination in Ge.....	1650	Np-Al.....	1460
Cold work: effect on Fe.....	44	Crystal structure: oxidized of Fe.....	1190	Ti-C-N.....	1501
electron microscope study of effect on subgrain structure of Cu.....	660	Crystals: Alnico, to study permanent magnet performance.....	438	Discussion.....	1566
Columbium and columbium alloys: plasticity of single crystals.....	1131	single, Cb, plasticity of.....	828	Diffusion, iron.....	832
properties of, containing nitrogen.....	1032	Mo, textures of.....	537	Diffusion, and Solubility of Boron in Iron and Steel.....	1463
Ti-Cb, cold-rolled sheet texture.....	1200	Zn, bend plane phenomena in deformation.....	1131	Diffusion coefficients: calculation of, when volume changes occur.....	1534
Compressive kink bands.....	54	Ti, large grained.....	300	Discussion.....	1018
Conard, G. P., II, Averbach, B. L., and Cohen, M.: Plastic Bending of Zinc Crystals.....	1036	Ti, production.....	49	Diffusion of Calcium Ion in Liquid Slag.....	726
Concentrates, Cu, treatment in New Cornelia smelter.....	633	Zn, plastic bending.....	1191	Diffusionless Phase Change in the Indium-Thallium System.....	1455
Concentration Dependence of Diffusion Coefficients in Metallic Solid Solution. Discussion.....	726	Cubicciotti, D.: Solutions of Metals in Fused Salts.....	258	Dijkstra, L. J., and Sladek, R. J.: Effect of Alloying Elements on the Behavior of Nitrogen in Alpha Iron.....	1516
Correction.....	1018	Cuff, F. B., Grant, N. J., and Floe, C. F.: Titanium-Chromium Phase Diagram. Discussion.....	1036	Discussion.....	69
Concentration Gradients Associated with Growing Pearlite.....	820	Cunningham, R. L., Boswell, F. W. C., and Weld, R. M.: Observations on Nodular Graphite. Discussion on reaction of silver with solutions of.....	1106	Dilatometer.....	1560
Correction.....	1018	Cyanide: reaction of silver with solutions of.....	743	Directional Properties of 2S Aluminum.....	359
Conductivity method of slag control evaluated.....	41		738	Discussion, see under Extractive Metallurgy, Institute of Metals, and Iron and Steel Divisions.....	431
Correction.....	572		1109	Dislocation theory of bend plane formation.....	51
Discussion.....	1552			Dissolution of Ag in cyanide solutions under oxygen pressure.....	1109
Conductivity, thermal, method for analysis of hydrogen in steel.....	180			Distillation, vacuum, desilverized lead bullion.....	991
Constitution diagram. See also Equilibrium diagram and Phase diagram.....				Distribution curves of regular polyhedrons.....	565
Constitution diagram: Co-Mo.....	358			Domagala, R. F., McPherson, D. J., and Hansen, M.: System Zirconium-Chromium.....	279
Cu-Zn. Discussion.....	748			Systems Zirconium-Molybdenum and Zirconium-Wolfram.....	73
Ti-C.....	1206			Discussion.....	747
Ti-Ta-C.....	1206			Dorn, J. E., and Sherby, O. D.: Some Observations on Correlations Between the Creep Behavior and the Resulting Structures in Alpha Solid Solutions.....	324
V-U.....	545			Dowding, J. W., Murphy, R. J., and Grant, N. J.: Manganese as an Indicator of Blast Furnace Slag Oxidation and Desulphurizing Power.....	1451
Constitution of the FeO-Fe ₂ O ₃ -SiO ₂ System at Slagmaking Temperatures.....	1097			Drouard, R., Washburn, J., and Parker, E. R.: Recovery in Single Crystals of Zinc.....	1226
Constitution of Titanium-Rich Ti-Cr-Al Alloys at 1800° and 1400°F.....	253			Dube, C. A., Alexander, B. H., and Rosi, F. D.: Mechanism of Plastic Flow in Titanium—Determination of Slip and Twinning Elements.....	257
Discussion.....	1565				
Contamination of Si ingots.....	653				
Converters, New Cornelia smelter.....	638				
Copper-Zinc Constitution Diagram, Redetermined in the Vicinity of the Beta Phase by Means of Quantitative Metallography. Discussion.....	748				
Copper and copper alloys: Cu-Au alloys, order-disorder transformation in.....	823				
Cu-Mn-Sn system, alpha solid solution area.....	723				

Ductile-brittle transition, crystallographic analysis in body-centered cubic single crystals	1650
Dulis, E. J., Carroll, K. G., and Fisher, R. M.: Identification of the Precipitate Accompanying 885°F Embrittlement in Chromium Steels	690
Dunbar, S. R., Anderson, E. A., and Jillson, D. C.: Deformation Mechanisms in Alpha Titanium	1191
Duwez, P., and Taylor, J. L.: Constitution of Titanium-Rich Ti-Cr-Al Alloys at 1800° and 1400°F	253
Discussion	1565
Dynamic Formation of Slip Bands in Aluminum. Discussion	733

E

Earing characteristics of 2S Al	431
Ebeling, D. G., and Burr, A. A.: Effects of Macrostructure on the Performance of Alnico Permanent Magnets	537
Edwards, E. H., Washburn, J., and Parker, E. R.: Some Observations on the Work Hardening of Metals	1525
Effect of Alloying Elements on the Behavior of Nitrogen in Alpha Iron	69
Discussion	1560
Effect of Carbon on the Volume Fractions and Lattice Parameters of Retained Austenite and Martensite	203
Effect of Chloride on the Deposition of Copper, in the Presence of Arsenic, Antimony, and Bismuth	1375
Effect of Dissolved Sulphur on the Surface Tension of Liquid Copper	643
Effect of Grain Size upon Temper Brittleness	1147
Effect of Manganese on the Activity of Sulphur in Liquid Iron and Iron-Carbon Alloys. Discussion	1549
Effect of Molybdenum and of Nickel on the Rate of Nucleation and the Rate of Growth of Pearlite. Discussion	740
Effect of Nickel and Molybdenum on Stabilization of the Austenite-Martensite Transformation	922
Effect of Small Additions of Oxygen on Lattice Constants and Hardness of Zirconium	344
Effect of Tensile Strain at Low Temperatures on Deformation Twinning in Ingot Iron	213
Effect of Various Elements on Hot-Working Characteristics and Physical Properties of Fe-C Alloys	525
Effects of Macrostructure on the Performance of Alnico Permanent Magnets	537
Effects of Sample Surface and X-Ray Diffraction Camera Geometry on the Determination of Retained Austenite in Hardened Steels	1529
Effects of Solid Solution Alloying on the Cold-Rolled Texture of Titanium	1199
Effects of Temperature on the Flow and Fracture Characteristics of Molybdenum	1469
Electrical equipment used to measure rate of propagation of martensite	1258
Electrical resistance, Cb, effect of nitrogen on	1034
Electrical Resistance of Titanium Metal	903
Electrical Resistivity of Liquid Metals and of Dilute Liquid Metallic Solutions	1141
Electrical resistivity: stainless steel	1104
Ti alloy	1104
Uranium	1238
Electric arc furnace construction for copper refining	197
Electric resistivity measurements, V-Co-Fe alloys	352
Electron Microscope Study of the Effect of Cold Work on the Subgrain Structure of Copper	660
Elliott, R. P., Levinger, B. W., and Rostoker, W.: System Titanium-Chromium-Molybdenum	1544
Elliott, R. P., McPherson, D. J., and Rostoker, W.: Discussion on Titanium-Manganese System	1566
Elliott, R. P., and Rostoker, W.: Structure of the Phase TiMn and the Indexing of Powder Patterns of Sigma-Type Phases	1203
Embrittlement: 885°F, in Cr steels	690
isothermal temper, of SAE 3140 steel	998
Ence, E., Nielsen, J. P., and Margolin, H.: Titanium-Nickel Phase Diagram	243
Eppelsheimer, D. S., and Williams, D. N.: Cold Rolled Texture of Titanium	1378
Equilibrium: between slags and gases	1089
gas-metal reactions	191
Discussion	1550
in liquid Fe, Al-O influence on	173
Si-O in Fe	1017
Equilibrium diagram: see also Constitution diagram and Phase diagram	
Cu-Au	826
Fe-O	1641
Mo-B. Discussion	747
W-Co-C system. Discussion	744
Etch for use in optical determination of Ge crystal orientation	436

Etchant: Bright Dip, use on Al and Al alloys	717
Eutectoid, Ag-Cd	549
Evaluation of the pH and Conductivity Methods of Slag Control	41
Correction	572
Discussion	1552
Evans, J. W.: Free Energy of Vaporization of Metals from 0° to 2000°C	655
Examination of a High Sulphur Free-Machining Ingot, Bloom and Billet Sections	999
Exchange of Iron Between Liquid Metal and Iron Silicate Slags	1648
Extraction replica technique	691
Extractive Metallurgy Division: Discussion: Spokane and Los Angeles Meetings	1556

F

Failure, intercrystalline, under creep conditions	305
Discussion	1579
Farnham, G. S., and Scott, D. A.: Partition of Some Alloying Elements Between Carbide and Ferrite in Steels	1541
Fassell, W. M., Jr., and McKewan, W.: High Pressure Oxidation Rate of Metals—Copper in Oxygen	1127
Fassell, W. M., and Wadsworth, M. E.: Discussion on Kinetics of the Oxidation of Galena in Sodium Hydroxide Solutions under Oxygen Pressure	1556
Fast, J. D., and Meijering, J. L.: Discussion on Effect of Alloying Elements on the Behavior of Nitrogen in Alpha Iron	1560
Fatigue properties, Mg-Zr alloys	924
Ferromagnetic powders, sintering of	79
Ferrophosphorus, trisage crystallization process for	423
Ferrous metals, density and hydrogen occlusion of	44
Few, W. E., and Manning, G. K.: Solubility of Carbon and Oxygen in Molybdenum. Discussion	746
Correction	844
Filler Material for the Brazing of Titanium	1197
Finlay, W. L., et al.: Mechanical Properties of High Purity Ti-Al Alloys	267
Discussion	1561
Fischer, R. B.: Discussions on: Role of the Binder Phase in Cemented Tungsten Carbide-Cobalt Alloys	746
Tungsten-Cobalt-Carbon System	744
Fisher, J. C.: Martensite Nucleation in Substitutional Iron Alloys	918
Fisher, J. C., Fullman, R. L., and Carreker, R. P., Jr.: Simple Devices for Approximating Constant Stress During Tensile Creep Tests	657
Fisher, J. C., and Turnbull, D.: Calculation of Martensite Nucleus Energy Using the Reaction-Path Model	921
Fisher, P. A., et al.: Further Progress in the Development of Mg-Zr Alloys to Give Good Creep and Fatigue Properties Between 500° and 650°F	924
Fisher, R. M., Dulis, E. J., and Carroll, K. G.: Identification of the Precipitate Accompanying 885°F Embrittlement in Chromium Steels	690
Fitterer, G. R.: Some Observations of Slag-Metal Relations in the Acid Open Hearth Steel Furnace	1634
Floe, C. F., Cuff, F. E., and Grant, N. J.: Titanium-Chromium Phase Diagram. Discussion	743
Flow and Fracture Characteristics of the Aluminum Alloy 24S-T4 as Affected by Strain Thermal History	66
Flow characteristics of Mo, effect of temperature on	1469
Flue system, Cu smelter	642
Forging of Arc-Melted Chromium	63
Formation of Deformation Bands in Al-3 Pct Mg Monocrystals during Cold Rolling	559
Formation of Sigma Phase in the Mn-Mo System	1476
Fountain, R. W., and Libsch, J. F.: Development of Mechanical and Magnetic Hardness in a 10 Pct V-Co-Fe Alloy	349
Fracture characteristics: Al alloy 24S-T4 as affected by strain thermal history	66
Mo, effect of temperature on	1469
Free Energy of Vaporization of Metals from 0° to 2000°C	655
Frost, P. D., Parris, W. M., and Hirsch, L. L.: Low Temperature Aging in Titanium Alloys	178
Frye, J. H., Jr., and Stansbury, E. E.: Discussion on Effect of Molybdenum and of Nickel on the Rate of Nucleation and the Rate of Growth of Pearlite	740
Frye, J. H., Jr., Stansbury, E. E., and McElroy, D. L.: Absolute Rate Theory Applied to Rate of Growth of Pearlite	219
Discussion	1581
Fuller, M. L., and Vause, G.: Modifications of the Schulz Technique for the X-Ray Determination of Preferred Orientation in Rolled Metal	1038

Fullman, R. L.: Measurement of Approximately Cylindrical Particles in Opaque Samples	1267
Measurement of Particle Sizes in Opaque Bodies	447
Fullman, R. L., Carreker, R. P., Jr., and Fisher, J. C.: Simple Devices for Approximating Constant Stress During Tensile Creep Tests	657
Fulton, J. C., Grant, N. J., and Chipman, J.: Reduction of Silicon from Blast Furnace Type Slags	185
Funk, C. W.: Discussion on Mechanical Properties of High Purity Ti-Al Alloys	1561
Funk, C. W., and Rowland, J. A.: Alpha Solid-Solution Area of the Cu-Mn-Sn System	723
Furnace: anode, in Cu smelter	640
blast, tuyere zone, studies of	895
Correction	1018
oxidizing, to treat blister Cu	640
reverberatory, Cu smelting, design of	1435
design to treat Cu concentrates	635
Further Progress in the Development of Mg-Zr Alloys to Give Good Creep and Fatigue Properties Between 500° and 650°F	924
Further Studies of the Tuyere Zone of the Blast Furnace	895
Correction	1018

G

Galena, kinetics of oxidation in sodium hydroxide solutions under oxygen pressure	554
Discussion	1556
Galvanizing, kinetics of	807
Gas-liquid metal reactions, equilibrium in	191
Discussion	1550
Geach, G. A., and Slattery, G. F.: Discussion on Systems Zirconium-Molybdenum and Zirconium-Wolfram	747
Geiger counter spectrometer methods for determination of retained austenite	87
Geil, G. W.: Discussion on Microstructure and Mechanical Properties of Iodide Titanium	1562
Geil, G. W., and Carville, N. L.: Effect of Tensile Strain at Low Temperatures on Deformation Twinning in Ingot Iron	213
Geisler, A. H., et al.: Magnetic Annealing of a Co-Fe Alloy	813
Geisler, A. H., Keeler, J. H., and Hubbard, W. R., Jr.: Discussion on Kinetics of Thermal Reorientations in Cold Rolled Zirconium	1574
Germanium and germanium alloys: preferential etch for use in optical determination of crystal orientation of	436
Gervais, A. M., Norton, J. T., and Grant, N. J.: Kink Band Formation in High Purity Aluminum During Creep at High Temperatures	1487
Subgrain Formation in High-Purity Aluminum During Creep at High Temperatures	1166
Gibbons, D. F.: Plastic Deformation of Iron Between 300° and 77.2°K	1245
Giffkins, R. C., and Kelly, J. W.: Discussion on Some Observations of Subgrain Formation During Creep in High Purity Aluminum	731
Gilbert, H. L., Johansen, H. A., and Nelson, R. G.: Forging of Arc-Melted Chromium	63
Gilles, P. W., and Pollock, B. D.: Molybdenum-Boron System	1537
Gilman, J. J.: Plastic Deformation of Rectangular Zinc Monocrystals	1217
Gilman, J. J., and Read, T. A.: Bend Plane Phenomena in the Deformation of Zinc Monocrystals	49
Surface Effects in the Slip and Twinning of Metal Monocrystals. Discussion	735
Glaser, F. W., Moskowitz, D., and Post, B.: Study of Some Binary Hafnium Compounds	1119
Glaser, F. W., and Post, B.: System Zirconium-Boron	1117
Glide plane, ferrite single crystals	703
Gokcen, N. A.: Attainment of Equilibrium in Gas-Metal Reactions	191
Discussion	1550
Thermodynamic Properties of Molybdenum Dioxide	1019
Discussions on: Effect of Manganese on the Activity of Sulphur in Liquid Iron and Iron-Carbon Alloys	1549
Liquidus Surface of the Fe-S-O System	1549
Solubility of Carbon and Oxygen in Molybdenum	746
Correction	844
Vapor Pressure of Zinc in the Reduction of Zn by Cu and Fe	1558
Gokcen, N. A., and Chipman, J.: Aluminum-Oxygen Equilibrium in Liquid Iron	173
Silicon-Oxygen Equilibrium in Liquid Iron—A Revision	1017
Gold and gold alloys: Cu-Au alloys, order-disorder transformation in	823
determination of absolute grain boundary energy of	313
thermodynamic properties of solid Ni-Au alloys. Discussion	728
vapor pressure of Ag over Ag-Au solid solutions	709
wire, anelastic behavior of	937

Fe-Ni-Mn rate of formation of iso-thermal martensite	685	Keller, R. L., and Loria, E. A.: Discussion on Accelerated Solidification in Ingots: Its Influence on Ingot Soundness	1553	Lieberman, D. S., Read, T. A., and Wechsler, M. S.: On the Theory of the Formation of Martensite	1503
FeO-Fe ₂ O ₃ -SiO ₂ constitution at slag-making temperatures	1097	Kellogg, H. H., and Baes, C. F., Jr.: Effect of Dissolved Sulphur on the Surface Tension of Liquid Copper	643	Lillie, C. E., and Stanley, J. K.: Discussion on Recrystallization Kinetics of Low Carbon Steel	739
ferrite single crystals, deformation	700	Kennecott refinery, arc-furnace construction and operation	197	Lime, relation to slag control	41
ingot, effect of tensile strain on deformation twinning in	213	Kessler, H. D., Hansen, M., and Van Thyne, R. J.: System Titanium-Chromium-Iron	1209	Lime-iron oxide slags	1092
kinetics of galvanizing	807	Kessler, H. D., and Van Thyne, R. J.: Discussion on Titanium-Chromium Phase Diagram	744	Liquidus surface diagram, Cr-Mo	363
liquid, Al-O equilibrium in	173	Kessler, H. D., Van Thyne, R. J., and Rostoker, W.: Observations on the Phase TiAg	670	Liquidus Surface of the Fe-S-O System. Discussion	1549
liquid and Fe-C alloys, effect of Mn on activity of sulphur in. Discussion	1549	Kiessling, R.: Discussion on Tungsten Cobalt-Carbon System	745	Liu, S. I., and Ripling, E. J.: Flow and Fracture Characteristics of the Aluminum Alloy 24S-T4 as Affected by Strain Thermal History	66
liquid, Si-O equilibrium	1017	Kimball, R. W., Cattoir, F. R., and Anderson, C. T.: Effect of Various Elements on Hot-Working Characteristics and Physical Properties of Fe-C Alloys	525	Liu, Y. C., and Hibbard, W. R., Jr.: Recrystallization of a Cold-Rolled Copper Single Crystal	672
liquidus surface of Fe-S-O system. Discussion	1549	Kinetics of Galvanizing	807	Discussion	1568
martensite nucleation in	918	Kinetics of slag-metal reactions	1648	Liu, Y. C., and Margolin, H.: Martensite Habit Plane in Quenched Ti-Mn Alloys	667
martensite, rate of propagation of	1251	Kinetics of the Oxidation of Galena in Sodium Hydroxide Solutions Under Oxygen Pressure	554	Load tests, constant	657
mechanical and magnetic hardness in 10 pct V-Co-Fe alloy	349	Discussion	1556	Lord, N. W.: Analysis of Molten-Zone Refining	1531
mechanism of growth of magnetite during oxidation, corrected interpretation	1250	Kinetics of Thermal Reorientations in Cold Rolled Zirconium	284	Loria, E. A., and Keller, R. L.: Discussion on Accelerated Solidification in Ingots: Its Influence on Ingot Soundness	1553
nodular, thermal conductivity of	1016	Discussion	1573	Low Temperature Aging in Titanium Alloys	178
plastic deformation	1245	Kink Band Formation in High Purity Aluminum During Creep at High Temperatures	1487	Lowrie, R.: Mechanical Properties of Intermetallic Compounds at Elevated Temperatures. Discussion	733
preparation of high purity metallic reduction of ZnS by Fe, vapor pressure of Zn in	1443	Kink bands, compressive and tensile	49	Lundin, C. E., McPherson, D. J., and Hansen, M.: System Zirconium-Copper	273
Discussion	1558	Kinking in Zinc Single-Crystal Tension Specimens. Discussion	737	Lustman, B., and McGeary, R. K.: Kinetics of Thermal Reorientations in Cold Rolled Zirconium	284
scaling, observations on	265	Kinking, subgrain boundaries formed by Koh, P. K.: Occurrence of Chi Phase in Molybdenum-Bearing Stainless Steels	339	Discussion	1573
self-diffusion in iron oxides	1570	Koh, P. K.: Discussion on Statistical Grain Structure Studies: Plane Distribution Curves of Regular Polyhedrons	1570	Discussion on Preferred Orientations in Iodide Titanium	1563
sintering ultrafine ferromagnetic powders	79	Koistinen, D. P., and Beu, K. E.: Effects of Sample Surface and X-Ray Diffraction Camera Geometry on the Determination of Retained Austenite in Hardened Steels	1529		
slag-metal relations in open hearth steel furnace	1634	Kuo, K.: Discussion on Tungsten-Cobalt-Carbon System	745		
solids, oxygen activity in	1089				
solid phase identification in partially reduced Fe ore	1641				
Ti-Cr-Fe system	1209				
Iron and Steel Division, Discussion, St. Louis, New York, and Los Angeles Meetings	1549				
Iron and Steel Division, Howe Memorial Lecture, 1953, The Influence of the Rate of Deformation on the Tensile Properties of Some Plain Carbon Sheet Steels by Joseph Winlock	797				
Irreversible processes, applications to physical metallurgy	437				
Isothermal sections: Cu-Mn-Sn	724				
ternary, of iso-activity curves for Si	1100				
Ti-C-N, Ti-C-O, and Ti-N-O	1498				
Ti-Cr-Fe	1210				
Ti-Cr-Mo	1545				
Ti-Ta-C	1206				
Isothermal Temper Embrittlement of SAE 3140 Steel	998				
Isothermal transformation curves for martensite in Fe-Ni-Mn alloy	687				

J		L	
Jaffe, L. D., and Buffum, D. C.: Some Effects of Microstructure Upon Temper Brittleness	1373	Lacombe, P., Lelong, P., and Herenguel, J.: Formation of Deformation Bands in Al-3 Pct Mg Monocrystals during Cold Rolling	559
Jaffe, L. D., Carr, F. L., and Buffum, D. C.: Effect of Grain Size upon Temper Brittleness	1147	Larson, H., and Chipman, J.: Oxygen Activity in Iron Oxide Slags	1089
Jaffe, L. D., et al.: Isothermal Temper Embrittlement of SAE 3140 Steel	998	Lattice constants, Zr, effect of small additions of oxygen on	344
Jaffee, R. I., et al.: Mechanical Properties of High Purity Ti-Al Alloys	267	Lattice defects frozen into an alloy by quenching, decay of	1259
Discussion	1561	Lattice Parameter of Beta Titanium at Room Temperature	195
Jaffee, R. I., Holden, F. C., and Ogden, H. R.: Microstructure and Mechanical Properties of Iodide Titanium	238	Lattice parameters: effect of carbon, in retained austenite and martensite	203
Discussion	1562	on iodide Ti	252
Jaffee, R. I., Maykuth, D. J., and Ogden, H. R.: Titanium-Manganese System	225	Hf compounds	1119
Discussion	1566	Ti-Ta	234
Titanium-Tungsten and Titanium-Tantalum Systems	231	Lattice patterns, Cu-Au	825
Jaffee, R. I., and Ogden, H. R.: Discussion on Titanium-Carbon Phase Diagram	1564	Leaching step in tristage crystallization process	424
Jensen, W. L., and Campbell, R. F.: Detection of Microcracks in Steel	1222	Lead and lead alloys: lead bullion, vacuum desludging, desilverized	991
Jessup, A. C., et al.: Further Progress in the Development of Mg-Zr Alloys to Give Good Creep and Fatigue Properties Between 500° and 650°F	924	replica method for study of structure of Pb-Sb alloys	55
Jillson, D. C., Dunbar, S. R., and Anderson, E. A.: Deformation Mechanisms in Alpha Titanium	1191	Lee, A. E., Jr.: Sintering Zinc Concentrates on the Blackwell 12 by 168 Ft Machine	1631
Johansen, H. A., Nelson, R. G., and Gilbert, H. L.: Forging of Arc-Melted Chromium	63	Leighly, H. P., Walker, H. L., and Marx, J. W.: Recrystallization and Stored Energy	809
Joseph, T. L., and Bitsianes, G.: Solid Phase Identification in Partially Reduced Iron Ore	1641	Lelong, P., Herenguel, J., and Lacombe, P.: Formation of Deformation Bands in Al-3 Pct Mg Monocrystals during Cold Rolling	559
		Lement, E. S., and Das Gupta, S. C.: Stabilization of the Austenite-Martensite Reaction in a High Chromium Steel	530
		Leslie, W. C., and Rickett, R. L.: Influence of Aluminum and Silicon Deoxidation on the Strain Aging of Low-Carbon Steels	1021
		Levinger, B. W.: High Temperature Modification of TiCr ₂	196
		Lattice Parameter of Beta Titanium at Room Temperature	195
		Levinger, B. W., Rostoker, W., and Elliott, R. P.: System Titanium-Chromium-Molybdenum	1544
		Li, C. H., Washburn, J., and Parker, E. R.: Variation of Plastic Properties with Annealing Procedure in Zinc Single Crystals	1223
		Libsch, J. F., and Ananthanarayanan, N. I.: Sintering of Ultrafine Ferromagnetic Powders	79
		Libsch, J. F., and Fountain, R. W.: Development of Mechanical and Magnetic Hardness in a 10 Pct V-Co-Fe Alloy	349
		Lidman, W. G., and Hamjian, H. J.: Densification and Kinetics of Grain Growth During the Sintering of Chromium Carbide	696

K		M	
Kahles, J. F.: Discussion on Absolute Rate Theory Applied to Rate of Growth of Pearlite	1581	Machlin, E. S.: Some Applications of the Thermodynamic Theory of Irreversible Processes to Physical Metallurgy	437
Kasper, J. S., Decker, B. F., and Waterstrat, R. M.: Formation of Sigma Phase in the Mn-Mo System	1476	Mack, D. J., and Speich, G. R.: Silver-Cadmium Eutectoid	549
Keeler, J. H., and Davis, H. M.: Density and Hydrogen Occlusion of Some Ferrous Metals	44	Macrostructure: effects of, on Alnico permanent magnets	537
Keeler, J. H., Hibbard, W. R., Jr., and Decker, B. F.: Textures of Rolled and Annealed Iodide Zirconium	932	steel ingot	1000
Keeler, J. H., Hibbard, W. R., Jr., and Geisler, A. H.: Discussion on Kinetics of Thermal Reorientations in Cold Rolled Zirconium	1574	Maddin, R., and Chen, N. K.: Cold-Rolling and Annealing Textures of Molybdenum Single Crystals	300
		Discussion	1569
		Plasticity of Columbium Single Crystals	1131
		Maddin, R., Chen, N. K., and Aust, K. T.: Bending of Molybdenum Single Crystals	1477
		Magnesia-iron oxide slags	1093
		Magnesium and magnesium alloys: creep behavior of extruded electrolytic creep in Discussion	1121
		deformation bands in Al-3 pct Mg monocrystals	732
		deformation in creep compared with Al	559
		electrical resistivity of Mg-Zr, development of, for good creep and fatigue properties	712
		metallographic observations of deformation in creep at 500°F	1141
		properties of sand cast Mg-Th-Zn-Zr alloys	924
		slip and grain boundary sliding in	712
		Magnetic Annealing of a Co-Fe Alloy	1493
		Magnetic measurements, embrittled steel	217
		Magnetic properties, 10 pct V-Co-Fe alloy	813
		Magnetite: growth mechanism of, during oxidation, corrected interpretation	694
		transport mechanism	349
		Magnets, permanent, Alnico, effect of macrostructure on	828
		Manganese and manganese alloys: Cr-Mn steel slags, recovery from	537
		Cu-Mn-Sn, alpha solid solution area in deoxidizing power in liquid Fe	1013
		effect of, on activity of sulphur in liquid Fe and Fe-C alloys. Discussion	723
		effect on internal friction due to nitrogen in Fe	650
		Fe-Ni-Mn, rate of formation of iso-thermal martensite	1549
		influence on sigma phase	69
		Mn-Mo, formation of sigma phase	83
		oxides, slag-metal relations in open hearth steel furnace	1476
		TiMn phase, structure and pattern of sigma-type phases	1634
		Ti-Mn	1203
		Discussion	225
		Ti-Mn, aging	1566
		Ti-Mn, quenched, martensite habit plane in	178
		Manganese as an Indicator of Blast Furnace Slag Oxidation and Desulphurizing Power	667
		Manning, G. K., and Few, W. E.: Solubility of Carbon and Oxygen in Molybdenum. Discussion	1451
		Correction	746
		Marburg, E.: Accelerated Solidification in Ingots: Its Influence on Ingot Soundness	844
		Correction	157
		Discussion	572
		Margolin, H.: Discussion on Constitution of Titanium-Rich Ti-Cr-Al Alloys at 1800° and 1400°F	1553

Margolin, H., Ence, E., and Nielsen, J. P.: Titanium-Nickel Phase Diagram	243	Mechanical properties: iodide Ti	238	uranium	1238
Margolin, H., and Liu, Y. C.: Martensite Habit Plane in Quenched Ti-Mn Alloys	667	Discussion	1562	V-Co-Fe	353
Margolin, H., and Stone, L.: Titanium-Rich Regions of the Ti-C-N, Ti-C-O, and Ti-N-O Phase Diagrams	1498	2S Al	433	V-O	296
Marin, J., and Wiseman, H. A. B.: Plastic Stress-Strain Relations for Aluminum Alloy 14S-76 Subjected to Combined Tension and Torsion	1181	Mechanism of Plastic Flow in Titanium—Determination of Slip and Twinning Elements	257	V-U	546
Markson, I., Barrett, C. S., and Aziz, P. M.: Torsional After-Effect Measurement and Applications to Aluminum	1655	Mehl, R. F., Birchenall, C. E., and Himmel, L.: Self-Diffusion of Iron in Iron Oxides and the Wagner Theory of Oxidation	827	wustite	832
Martensite: burst formation in high Cr steel	530	Mehl, R. F., and Bunshah, R. F.: Rate of Propagation of Martensite	1251	Zr	287
calculation of nucleus energy of, using reaction-path model	921	Mehl, R. F., Hagel, W. C., and Pound, G. M.: Discussion on Absolute Rate Theory Applied to Rate of Growth of Pearlite	1581	Zr-Cr	933
concentration gradients	820	Mehl, R. F., and Parcel, R. W.: Effect of Molybdenum and of Nickel on the Rate of Nucleation and the Rate of Growth of Pearlite. Discussion	740	Zr-Cu	282
effect of carbon on volume fractions and lattice parameters of	203	Meijering, J. L., and East, J. D.: Discussion on Effect of Alloying Elements on the Behavior of Nitrogen in Alpha Iron	1560	Zr-Mo	76
effect of Ni and Mo on stabilization of austenite-martensite transformation	922	Mercury trap in thermal conductivity method for analysis of hydrogen in steel	181	Zr-W	78
isothermal, rate of formation in Fe-Ni-Mn alloys	685	Metal-gas reactions, equilibrium in	191	Migration, grain boundary, under creep conditions	305
plastic critical temperature in strain-induced	654	Metallic Oxidation in Chromium Steel Melting	649	Discussion	1579
rate of propagation	1251	Metallographic Observations of the Deformation of High-Purity Magnesium in Creep at 500°F	712	Modifications of the Schulz Technique for the X-Ray Determination of Preferred Orientation in Rolled Metal	1038
stabilization of austenite-martensite reaction in high Cr steel	530	Metals: liquid, electrical resistivity of	1141	Mold design, steel ingots	157
theory of the formation of	1503	solutions in fused salts	1106	Molten-zone refining, analysis of	1531
transformation in Ti-Cr-Al alloys	255	Metcalfe, A. G.: Thermal and Dilatometric Investigation of the Alloys of Cobalt with Chromium and Molybdenum	357	Molybdenum and molybdenum alloys: effect of on rate of nucleation and growth of pearlite. Discussion	740
Martensite Habit Plane in Quenched Ti-Mn Alloys	667	Discussions on: Transformation in Cobalt-Nickel Alloys	729	effect of temperature on flow and fracture characteristics	1469
Martensite Nucleation in Substitutional Iron Alloys	918	Tungsten-Cobalt-Carbon System	744	effect on partition of Ni in steels	1541
Martin, J. P., et al.: Magnetic Annealing of a Co-Fe Alloy	813	Metzger, M., and Intrater, J.: Importance of the Iron Content of High-Purity Aluminum	821	effect on stabilization of austenite-martensite transformation	922
Marx, J. W., Leighly, H. P., and Walker, H. L.: Recrystallization and Stored Energy	809	Meyer, H. M., and DeCecco, N. A.: Filler Material for the Brazing of Titanium	1197	influence upon internal friction due to nitrogen in Fe	70
Mash, D. R., and Hall, S. D.: Anelastic Behavior of Pure Gold Wire	937	Michael, A. B., and Bever, M. B.: On the Distribution of Sodium in Modified Al-Si Alloys	679	Mn-Mo, formation of sigma phase	1476
Matzke, E. B.: Discussion on A Study of Grain Shape in an Aluminum Alloy and Other Applications of Stereoscopic Microradiography	741	Michal, E. J., Schuhmann, R., Jr., and Powell, R. G.: Constitution of the FeO-Fe ₂ O ₃ -SiO ₂ System at Slagmaking Temperatures	1097	Mo-bearing stainless steels, chi phase in	339
Maykuth, D. J., et al.: Mechanical Properties of High Purity Ti-Al Alloys	267	Microcracks in steel, detection of	1222	Mo-B	1537
Discussion	1561	Micrographic study, 2S Al	433	molybdenum dioxide, thermodynamic properties of	1019
Maykuth, D. J., Ogden, H. R., and Jaffee, R. I.: Titanium-Manganese System	225	Microradiography, study of grain shape and other uses of stereoscopic microradiography. Discussion	741	Mo-Re	1382
Discussion	1566	Microscopical Examination of Tin Bronzes in the Alpha Range	906	single crystals, bending of	1477
Titanium-Tungsten and Titanium-Tantalum Systems	231	Microstructure and Mechanical Properties of Iodide Titanium	238	cold-rolling and annealing textures	300
Maynor, H. W., Jr., and McHargue, C. J.: Notes on a Molybdenum-Rhenium Alloy	1382	Discussion	1562	Discussion	1569
McCabe, C. L., and Birchenall, C. E.: Vapor Pressure of Silver	707	Microstructure: Ag-Cd	550	solubility of carbon and oxygen in	746
McCabe, C. L., Schadel, H. M., Jr., and Birchenall, C. E.: Vapor Pressure of Silver Over Silver-Gold Solid Solutions	709	Al grain boundary migration	167	Correction	844
McElroy, D. L., Frye, J. H., Jr., and Stansbury, E. E.: Absolute Rate Theory Applied to Rate of Growth of Pearlite	219	Al, high purity. Discussion	731	thermal and dilatometric investigation of alloys of Co with	357
Discussion	1581	Al, kink bands in	1490	Ti-Cr-Mo	1544
McGeary, R. K., and Lustman, B.: Kinetics of Thermal Reorientations in Cold Rolled Zirconium	284	Al, subgrain structure	718	Zr-Mo	73
Discussion	1573	Al-Fe alloys	912	Discussion	747
Discussion on Preferred Orientations in Iodide Titanium	1563	Al-3 pct Mg monocrystal	559	Molybdenum-Boron System	1537
McHargue, C. J., Adair, S. E., Jr., and Hammond, J. P.: Effects of Solid Solution Alloying on the Cold-Rolled Texture of Titanium	1199	Al-Si, autoradiographs	679	Moore, G. A.: Preparation of Metallic Iron of High Purity	1443
McHargue, C. J., and Hammond, J. P.: Preferred Orientations in Iodide Titanium	57	Au, pure	939	Discussion	1449
Discussion	1563	carbon steels	800	Morral, F. R.: Discussion on Mechanical Properties of Intermetallic Compounds at Elevated Temperatures	733
McHargue, C. J., and Maynor, H. W., Jr.: Notes on a Molybdenum-Rhenium Alloy	1382	Cb	1135	Morral, F. R., and Aust, K. T.: Directional Properties of 2S Aluminum	431
McKewan, W., and Fassell, W. M., Jr.: High Pressure Oxidation Rate of Metals—Copper in Oxygen	1127	Cb containing nitrogen	1035	Morris, J. P.: Effect of Manganese on the Activity of Sulphur in Liquid Iron and Iron-Carbon Alloys	1549
McMullin, J. G., and Norton, J. T.: Ternary System Ti-Ta-C	1205	changes observed in nodular graphite. Discussion	738	Discussion on Attainment of Equilibrium in Gas-Metal Reactions	1550
McPherson, D. J., Hansen, M., and Domagala, R. F.: System Zirconium-Chromium	279	chemical replica method for showing	55	Moskowitz, D., Post, B., and Glaser, F. W.: Study of Some Binary Hafnium Compounds	1119
Systems Zirconium-Molybdenum and Zirconium-Wolfram	73	Co, pure	749	Moskowitz, D., Steinitz, R., and Binder, I.: System Molybdenum-Boron and Some Properties of the Molybdenum-Borides. Discussion	747
Discussion	747	Cr carbide	697	Motion pictures, to study, tuyere zone of blast furnace	895
McPherson, D. J., Hansen, M., and Lundin, C. E.: System Zirconium-Copper	273	Cr steel, 885°F embrittlement	691	Muldawer, L., Amsterdam, M., and Rothwarf, F.: Silver-Cadmium Beta and Zeta Phases	1458
McPherson, D. J., Rostoker, W., and Elliott, R. P.: Discussion on Titanium-Manganese System	1566	Cu	660	Murphy, R. J., Grant, N. J., and Dowding, J. W.: Manganese as an Indicator of Blast Furnace Slag Oxidation and Desulphurizing Power	1451
McQuillan, M. K.: Discussion on Titanium-Chromium Phase Diagram	743	Cu single crystals	667, 1232, 1235		
Measurement of Approximately Cylindrical Particles in Opaque Samples	1267	Cu-Mn-Sn system, phases	724	N	
Measurement of Internal Boundaries in Three-Dimensional Structures by Random Sectioning	81	effects on temper brittleness	1373		
Discussion	1561	Fe-Ni-Cr	1152	Nature of the Creep Curve	318
Measurement of Particle Sizes in Opaque Bodies	447	ferrite single crystals, slip lines	705	Discussion	1577
Mechanical Properties of High Purity Ti-Al Alloys	267	galena crystal	555	Nelson, K. E.: Properties of Sand Cast Mg-Th-Zn-Zr Alloys	1493
Discussion	1561	ingot iron specimens after different amounts of strain	214	Nelson, R. G., Gilbert, H. L., and Johansen, H. A.: Forging of Arc-Melted Chromium	63
Mechanical Properties of Intermetallic Compounds at Elevated Temperatures. Discussion	733	iron ore, reduction phases	1646	Neptunium-Aluminum Intermetallic Compounds	1460
		iron scales obtained by oxidation	266	Nesbitt, L. B., Wilson, A. C., Jr., and Tyler, W. W.: Some Low Temperature Properties of Titanium Alloy RC-130-B and Stainless Steel	1104
		Discussion	1570	New Cornelia copper smelter	633
		iron specimens	1247	Newkirk, J. B.: Order-Disorder Transformation in Cu-Au Alloys Near the Composition CuAu	823
		martensite	533	Nickel and nickel alloys: Alnico permanent magnets, effect of macrostructure on performance	537
		martensite, isothermal, formation in Fe-Ni-Mn alloy	688	Co-Ni alloys, transformation in. Discussion	729
		measurement of internal boundaries	81	creep characteristics	318
		Mg. Discussion	733	Cr-Ni steel	1010
		Mg, electrolytic	1124	Cu-Ni couples, concentration dependence of diffusion coefficients. Discussion	726
		Mg, specimens	713	Correction	1018
		Mg-Th-Zn-Zr	1496	effect on rate of nucleation and growth of pearlite. Discussion	740
		Mg-Zn-Th-Zr	929	effect on stabilization of austenite-martensite transformation	922
		Mo	1472	Fe-Cr-Co-Ni, rationalization of high temperature properties of	1149
		Mo-Re alloy	1382	Fe-Ni alloy used to measure rate of propagation of martensite	1251
		NpAl single crystals	1461	Fe-Ni-Mn, rate of formation of isothermal martensite in	685
		quantitative investigation of slip and grain boundary sliding shown by	1267		
		steel ingots	218		
		steel, microcracks in	1555		
		steel, stainless, chi phase	1222		
		Ti	1195		
		TiAg phase	671		
		Ti-C alloys	251, 1499		
		Ti-C-N and Ti-C-O alloys	1215		
		Ti-Cr-Fe	227		
		Ti-Mn	1566		
		Discussion	667		
		Ti-Ni	244		
		Ti-Ta	234		
		Ti-W	232		
		tin bronzes	907		

tween liquid Fe and iron silicate slag	1648	Rolling, formation of deformation bands in Al-3 pct Mg monocrystals during cold	559	Operation at the Kennecott Utah Refinery	197
measurement of diffusion coefficient of calcium ion in molten slags	1455	Rolling textures, Mo single crystals	300	Shear stress: Burgers' expression for	52
sodium fluoride to determine distribution of sodium in modified Al-Si alloys	679	Rosi, F. D.: Surface Structures on Single Crystals Produced from Melt	1661	Zn single crystal, relation to creep rate	1229
Rasmussen, R. T. C., Banning, L. H., and Anable, W. E.: Tristate Crystallization Process for Utilizing Western Ferrophosphorus	423	Rosi, F. D., Dube, C. A., and Alexander, E. H.: Mechanism of Plastic Flow in Titanium—Determination of Slip and Twinning Elements	257	Shepard, O. C.: Discussion on Grain Boundary Sliding and Migration and Intercrystalline Failure under Creep Conditions	1579
Rassbach, H. P., and Saunders, E. R.: Reducing Period in Stainless Steel Melting	1009	Rostoker, W.: Allotropy in the Phase $ZrCr_2$	304	Sherby, O. D., and Dorn, J. E.: Some Observations on Correlations Between the Creep Behavior and the Resulting Structures in Alpha Solid Solutions	324
Rate curves for dissolution of Ag	1111	Rostoker, W., and Elliott, R. P.: Structure of the Phase TiMn and the Indexing of Powder Patterns of Sigma-Type Phases	1203	Shields, B. M., Chipman, J., and Grant, N. J.: Thermal Conductivity Method for Analysis of Hydrogen in Steel	180
Rate of Formation of Isothermal Martensite in Fe-Ni-Mn Alloy	685	Rostoker, W., Elliott, R. P., and Leviner, B. W.: System Titanium-Chromium-Molybdenum	1544	Discussion	1551
Rate of Propagation of Martensite	1251	Rostoker, W., Elliott, R. P., and McPherson, D. J.: Discussion on Titanium-Manganese System	1566	Silicates, dicalcium and tricalcium, related to slag control	41
Rate theory applied to rate of growth of pearlite	219	Rostoker, W., Kessler, H. D., and Van Thyne, R. J.: Observations on the Phase TiAg	670	Silicon and silicon alloys: Al-Si alloys, distribution in	679
Discussion	1581	Roswell, A. E., and Nowick, A. S.: Decay of Lattice Defects Frozen into an Alloy by Quenching	1259	contamination of Si ingots	653
Rationalization of Measured High Temperature Properties of Fe-Cr-Co-Ni Alloys	1149	Rothwarf, F., Muldrew, L., and Amsterdam, M.: Silver-Cadmium Beta and Zeta Phases	1458	equilibrium in gas-metal reactions	191
Rautala, P.: Discussion on System Molybdenum-Boron and Some Properties of the Molybdenum-Borides	747	Rough, F. A., and Saller, H. A.: Vanadium-Uranium Constitutional Diagram	545	exchange of Fe between liquid metal and iron silicate slag	1648
Rautala, P., and Norton, J. T.: Tungsten-Cobalt-Carbon System. Discussion	744	Rowland, J. A., and Funk, C. W.: Alpha Solid-Solution Area of the Cu-Mn-Sn System	723	influence of Al and Si deoxidation on strain aging of low-carbon steel	1021
Reaction of Silver with Aqueous Solutions of Cyanide and Oxygen	1109	Rudolph, E. C., and Carney, D. J.: Examination of a High Sulphur Free-Machining Ingot, Bloom and Billet Sections	999	in slag reduction	1014
Reaction-path model, calculation of martensite nucleus energy with	921	Runnalls, O. J. C.: Neptunium-Aluminum Intermetallic Compounds	1460	lime-silica-iron oxide slags	1094
Reaction-path theory, applied to martensite reaction	530	Russell, R. B.: Crystallographic Angles for Orthorhombic (Alpha) Uranium	1190	reduction from blast furnace type slags silica, slag-metal relations in open hearth steel furnace	1636
Reaction rate equations, galena	558			Silicon-Oxygen Equilibrium in Liquid Iron—A Revision	1017
Read, T. A., and Burkart, M. W.: Diffusionless Phase Change in the Iridium-Thallium System	1516			Silver and silver alloys: Ag-Cd eutectoid	549
Read, T. A., and Gilman, J. J.: Bend Plane Phenomena in the Deformation of Zinc Monocrystals	49			Ag ₂ O-B ₂ O ₃ system, thermodynamic properties as slag model	1367
Surface Effects in the Slip and Twinning of Metal Monocrystals. Discussion	735			decay of lattice defects frozen into an Ag-Zn alloy by quenching	1259
Read, T. A., Wechsler, M. S., and Lieberman, D. S.: On the Theory of the Formation of Martensite	1503			reaction of, with aqueous solutions of cyanide and oxygen	1109
Recovery in Single Crystals of Zinc	1226			TiAg phase	670
Recrystallization and Stored Energy	809			vapor pressure	707
Recrystallization Kinetics of Low Carbon Steel. Discussion	739			over Ag-Au solid solutions	709
Recrystallization of a Cold-Rolled Copper Single Crystal	672			Silver-Cadmium Beta and Zeta Phases	1458
Discussion	1568			Silver-Cadmium Eutectoid	549
Recrystallization: Co-Fe alloy, effect of magnetic field	813			Simnad, M. T., Birchenall, C. E., and Davies, M. H.: A Corrected Interpretation of the Mechanism of Growth of Magnetite During Oxidation	1250
deformed Cu single crystals, orientation relationships in	1235			Simple Devices for Approximating Constant Stress During Tensile Creep Tests	657
Reducing Period in Stainless Steel Melting	1009			Single crystals: Cb, plasticity of	1131
Reduction of Silicon from Blast Furnace Type Slags	185			constant stress during tensile creep tests of	657
Refinery, Kennecott arc-furnace equipment and its operation	197			crystallographic analysis of ductile-brittle transition in	1650
Regarding Sigma Phase Formation	88			Cu, deformed, orientation relationships in the recrystallization of	1235
Reiter, S. F.: Recrystallization Kinetics of Low Carbon Steel. Discussion	739			electron microscope study of effect of cold work on	660
Relation Between Initial Creep Rate and Resolved Shear Stress in Zinc Single Crystals	1229			plastic deformation of	1231
Reorientations, thermal, kinetics of, in cold rolled Zr	284			recrystallization of cold rolled	672
Discussion	1573			Discussion	1568
Replica Method for Study of the Structure of Lead-Antimony Alloys	55			Fe, deformation	1247
Replicas, oxide film, to reveal subgrains in Al	718			ferrite, deformation of	700
Residual Stresses Introduced During Metal Fabrication	405			for study of permanent magnets	537
Retained Austenite Determinations by X-Ray Methods	87			formation of deformation bands in Al-3 pct Mg during cold rolling	559
Revealing the Subgrain Structure of Aluminum	717			In-Th, transformation in	1516
Reynolds, J. E., Cohen, M., and Wagner, C.: Calculation of Interdiffusion Coefficients When Volume Changes Occur	1534			kinking in Zn tension specimens. Discussion	737
Rhenium and rhenium alloys: Mo-Re	1382			metal, slip and twinning. Discussion	735
Rickett, R. L., and Leslie, W. C.: Influence of Aluminum and Silicon Deoxidation on the Strain Aging of Low-Carbon Steels	1021			Mo, bending of	1477
Ripling, E. J., and Liu, S. I.: Flow and Fracture Characteristics of the Aluminum Alloy 24S-T4 as Affected by Strain Thermal History	66			cold-rolling and annealing textures	300
Roast-leach process for recovery of vanadium from ferrophosphorus	423			Discussion	1569
Roasting ferrophosphorus	424			nucleation	809
Roberts, C. S.: Creep Behavior of Extruded Electrolytic Magnesium	1121			strain hardening	1525
Effect of Carbon on the Volume Fractions and Lattice Parameters of Retained Austenite and Martensite	203			surface structures	1661
Discussions on: Nature of the Creep Curve	1577			Zn, bend plane phenomena in deformation of	49
Observations of Creep of the Grain Boundary in High Purity Aluminum	732			plastic bending of	1036
Robertson, W. D., and Scala, E.: Electrical Resistivity of Liquid Metals and of Dilute Liquid Metallic Solutions	1141			plastic deformation of	1217
Robinson, D. L., and Hunter, M. S.: Revealing the Subgrain Structure of Aluminum	717			recovery in	1226
Rods, measurement of particle size	448			relation between creep rate and shear stress in	1229
Rogers, W. T., and Sanchez, L. T.: Use of Oxygen in the Bessemer Converter. Discussion	1551			variation of plastic properties with annealing procedure	1223
Role of the Binder Phase in Cemented Tungsten Carbide-Cobalt Alloys. Discussion	746			Sinnot, M. J.: Thermal Conductivity of Nodular Iron	1016
				Sinnot, M. J., and Kiessel, W. R.: Creep Properties of Commercially Pure Titanium	331
				Sintering, chromium carbide, densification and kinetics of grain growth	696
				Sintering of Ultrafine Ferromagnetic Powders	79
				Sintering Zinc Concentrates on the Blackwell 12 by 163 Ft Machine	1631
				Sladek, R. J., and Dijkstra, L. J.: Effect of Alloying Elements on the Behavior of Nitrogen in Alpha Iron	69
				Discussion	1560
				Slag: Ag ₂ O-B ₂ O ₃ system, thermodynamic properties as model	1367
				blast furnace, Mn as indicator of oxidation and desulphurizing power of	1451
				blast furnace type, reduction of Si	185
				control, evaluation of pH and conductivity methods of	41
				Correction	572
				Discussion	1552
				exchange of Fe between liquid metal and iron silicate slags	1648
				FeO-Fe ₂ O ₃ -SiO ₂ system, constitution at slagmaking temperatures	1097
				ionic theory	1638
				iron oxide, oxygen activity in	1089
				liquid, diffusion of calcium ion in	1455
				reduction period in stainless steel melting	1010
				Slag-metal relations, acid open hearth steel furnace	1634

Slattery, G. F., and Geach, G. A.: Discussion on Systems Zirconium-Molybdenum and Zirconium-Wolfram.....	747	Plane Distribution Curves of Regular Polyhedrons.....	565	liquidus surface of Fe-S-O system. Discussion.....	1549
Sliding, grain boundary, under creep conditions.....	305	Discussion.....	1570	oxidation of galena in sodium hydroxide.....	554
Slip: bands, dynamic formation in Al. Discussion.....	733	Stauss, H. E., and Sandoz, G.: Notes on Contamination of Silicon Ingots.....	653	reduction of ZnS by Cu and Fe, vapor pressure of Zn in.....	804
determination in Ti.....	257	Steel: acid open hearth furnace, slag-metal relations.....	1634	Discussion.....	1558
in metal monocrystals. Discussion.....	735	austenite: determination by X-ray methods.....	1539	Sumsion, H. T., and Seybolt, A. U.: Vanadium-Oxygen Solid Solutions.....	292
lines in Al-3 pct Mg crystals after cold rolling.....	560	effect of sample surface and X-ray diffraction camera geometry on determination of austenite in austenite-martensite reaction, stabilization of high Cr in.....	1529	Surface, measurement of internal Surface Effects in the Slip and Twinning of Metal Monocrystals. Discussion.....	81
Mg specimens.....	713	austenite-martensite transformation, effect of Ni and Mo on stabilization of.....	530	Surface Structures on Single Crystals Produced from Melt.....	1661
Mo single crystals.....	1479	Discussion.....	922	Surface tension of liquid Cu, effect of dissolved sulphur on.....	643
Ti crystals, rotation due to.....	1194	Discussion.....	1551	System $Ag_2O-B_2O_3$; Its Thermodynamic Properties as a Slag Model.....	1367
Slip and cross slip, Cu single crystals.....	1232	boron, diffusion and solubility in.....	1463	System Molybdenum-Boron and Some Properties of the Molybdenum-Borides. Discussion.....	747
Slip and Grain Boundary Sliding as Affected by Grain Size.....	217	Cr, precipitate accompanying 885°F embrittlement in.....	690	System Titanium-Chromium-Iron.....	1209
Slover, E. A.: Hurley Furnace and Boiler Description and Design.....	1435	density and hydrogen occlusion in.....	1455	System Zirconium-Boron.....	1544
Smelter operations, New Cornelia.....	633	diffusion of calcium ion in liquid slag effect of elements on hot-working characteristics and physical properties of Fe-C alloys.....	525	System Zirconium-Chromium.....	279
Smelter, Zn, sintering.....	1631	effect of grain size on temper brittleness of.....	1147	System Zirconium-Copper.....	273
Smith, C. S., and Beck, L. H.: Copper-Zinc Constitution Diagram, Redetermined in the Vicinity of the Beta Phase by Means of Quantitative Metallography. Discussion.....	748	effects of microstructure on temper brittleness.....	1373	Systems Zirconium-Molybdenum and Zirconium-Wolfram.....	73
Smith, C. S., and Gutman, L.: Measurement of Internal Boundaries in Three-Dimensional Structures by Random Sectioning.....	81	high sulphur free-machining ingot, examination of bloom and billet sections.....	999	Discussion.....	747
Discussion.....	1561	ingots, accelerated solidification, influence on soundness.....	157	T	
Smith, C. S., and Williams, W. M.: A Study of Grain Shape in an Aluminum Alloy and Other Applications of Stereoscopic Micro-radiography. Discussion.....	741	Correction.....	572	Takamura, J., and Nishimura, H.: Discussion on Surface Effects in the Slip and Twinning of Metal Monocrystals.....	735
Sodium, distribution in modified Al-Si alloys.....	679	Discussion.....	1553	Tantalum and tantalum alloys: Ti-Ta.....	231
Sodium hydroxide, effect on grain boundaries of Al.....	911	SAE 3140.....	998	Ti-Ta, cold-rolled sheet texture.....	1200
Sodium hydroxide solutions, oxidation of galena in.....	554	low-carbon, influence of Al and Si deoxidation on strain aging.....	1021	Ti-Ta-C.....	1205
Discussion.....	1556	martensite, theory of formation of metallic oxidation in Cr steel melting microcracks in, detection of.....	1222	Taylor, J. L., and Duwez, P.: Constitution of Titanium-Rich Ti-Cr-Al Alloys at 1800° and 1400°F.....	253
Solid Phase Identification in Partially Reduced Iron Ore.....	1641	partition of some alloying elements between carbide and ferrite.....	1541	Discussion.....	1565
Solid solubility, nitrogen in Cb.....	1034	pearlite, concentration gradients associated with.....	820	Temper brittleness: effects of microstructure on.....	1373
Solid solution alloying, effects on cold-rolled texture of Ti.....	1199	plain carbon sheet, influence of rate of deformation on tensile properties of.....	797	steel, effect of grain size on.....	1147
Solid solutions: alpha, creep behavior in Cu-Mn-Sn system.....	324	recrystallization kinetics of low carbon.....	739	Tensile kink bands in Zn monocrystal.....	49
metallic: diffusion coefficients in. Correction.....	1018	Discussion.....	180	Tensile properties: carbon sheet steels, influence of rate of deformation on.....	797
Discussion.....	726	sample storage prior to hydrogen analysis.....	180	high-purity Ti.....	241
rate of decay of lattice defects frozen into Ag-Zn alloy by quenching.....	1259	stainless, low temperature properties.....	1104	Mo, effect of temperature on.....	1471
V-O.....	292	Mo bearing, occurrence of chi phase in.....	339	Tensile strain, effect on deformation twinning in ingot iron.....	213
Solidification, accelerated, in steel ingots and influence on ingot soundness.....	709	reducing period in melting.....	1009	Tensile test data, slip of Zn crystal pairs Ternary System Ti-Ta-C.....	1219
Correction.....	572	thermal conductivity method for analysis of hydrogen in.....	180	Texture: annealed, of iodide titanium.....	58
Discussion.....	1552	Discussion.....	1551	cold rolled: iodide titanium.....	59
Solubility of Carbon and Oxygen in Molybdenum. Discussion.....	746	Steelmaking, evaluation of slag control methods.....	41	Ti, effects of solid solution alloying on.....	1199
Correction.....	844	Correction.....	572	Zr.....	284
Solubilities of metals in their salts and chlorides.....	1106	Discussion.....	1552	hot rolled, iodide titanium.....	59
Solutions of Metals in Fused Salts.....	1106	Steinitz, R., Binder, I., and Moskowitz, D.: System Molybdenum-Boron and Some Properties of the Molybdenum-Borides. Discussion.....	747	iodide titanium, effect of alpha-beta transformation on.....	60
Some Applications of the Thermodynamic Theory of Irreversible Processes to Physical Metallurgy.....	437	Stereoscopic microradiography, study of grain shape and other applications. Discussion.....	741	Mo single crystals.....	300
Some Effects of Microstructure Upon Temper Brittleness.....	1373	Stone, L., and Margolin, H.: Titanium-Rich Regions of the Ti-C-N, Ti-C-O, and Ti-N-O Phase Diagrams.....	1498	sheet, of iodide titanium.....	58
Some Low Temperature Properties of Titanium Alloy RC-130-B and Stainless Steel.....	1104	Strain aging: effect on creep properties of Ti.....	335	torsion, of 70-30 brass and Armco iron wire, of iodide titanium.....	61
Some Observations of Slag-Metal Relations in the Acid Open Hearth Steel Furnace.....	1634	steel, low carbon, influence of Al and Si deoxidation on.....	1021	Textures of Rolled and Annealed Iodide Zirconium.....	932
Some Observations of Subgrain Formation During Creep in High Purity Aluminum. Discussion.....	730	Strain ratios, 2S Al.....	434	Thallium and thallium alloys: In-Th, diffusionless phase change in.....	1516
Some Observations on Correlations Between the Creep Behavior and the Resulting Structures in Alpha Solid Solutions.....	324	Strain thermal history, effect of flow and fracture characteristics on Al alloy 24S-T4.....	66	Thermal and Dilatometric Investigation of the Alloys of Cobalt with Chromium and Molybdenum.....	357
Some Observations on the Work Hardening of Metals.....	1525	Stresses, residual, introduced during metal fabrication.....	405	Thermal Conductivity, Electrical Resistivity, and Thermoelectric Power of Uranium.....	1238
Some Properties of Columbium Containing Nitrogen.....	1032	Stress-strain curves: beta brass.....	1240	Discussion.....	180
Spectrographic analysis: iodide titanium.....	236	Zn crystals.....	1230	Thermal Conductivity of Nodular Iron.....	1016
Spectrometer method for determination of retained austenite.....	229	Stress-strain data, rectangular Zn monocrystals.....	1218	Thermal conductivity: stainless steel.....	1104
Speich, G. R., and Mack, D. J.: Silver-Cadmium Eutectoid.....	549	Structure: bamboo, in grain boundaries of Au.....	313	Ti alloys.....	1104
Speiser, R., and Spretnak, J. W.: Grain Boundary Films in Boron Steels.....	445	coarse grained Al, creep in.....	305	Thermodynamic activities of oxygen and iron in wustite.....	839
Spheres, measurement of particle size.....	447	two and three dimensional, measurement of internal boundaries by random sectioning.....	81	Thermodynamic calculations, Al-O equilibrium in liquid Fe.....	175
Spooner, N., Thomas, J. M., and Thomassen, L.: High Temperature Corrosion in Nickel-Chromium Alloys.....	844	V-O alloys.....	295	Thermodynamic properties, $Ag_2O-B_2O_3$ system, as slag model.....	1367
Spretnak, J. W., and Speiser, R.: Grain Boundary Films in Boron Steels.....	445	Structure of the Phase TMn and the Indexing of Powder Patterns of Sigma-Type Phases.....	1203	Thermodynamic Properties of Molybdenum Dioxide.....	1019
Stabilization of the Austenite-Martensite Reaction in a High Chromium Steel.....	530	Study of Grain Shape in an Aluminum Alloy and Other Applications of Stereoscopic Microradiography. Discussion.....	741	Thermodynamic Properties of Solid Nickel-Gold Alloys. Discussion.....	728
Stanley, J. K., and Lillie, C. R.: Discussion on Recrystallization Kinetics of Low Carbon Steel.....	739	Study of Some Binary Hafnium Compounds.....	1119	Thermodynamic theory of irreversible processes applied to physical metallurgy.....	437
Stansbury, E. E., and Frye, J. H., Jr.: Discussion on Effect of Molybdenum and of Nickel on the Rate of Nucleation and the Rate of Growth of Pearlite.....	740	Subgrain formation: Al, during creep. Discussion.....	730	Thermodynamics of reaction of Ag with cyanide solutions.....	1109
Stansbury, E. E., McElroy, D. L., and Frye, J. H., Jr.: Absolute Rate Theory Applied to Rate of Growth of Pearlite.....	219	Discussion.....	737	Thermoelectric power, uranium.....	1238
Discussion.....	1581	Mg specimens.....	715	Thomas, D. E., and Birchenall, C. E.: Concentration Dependence of Diffusion Coefficients in Metallic Solid Solution. Correction.....	1018
Siarr, C. D.: Notes on the Plastic Critical Temperature in Strain-Induced Martensite Reactions.....	654	Subgrain structure: Al.....	717	Discussion.....	726
Statistical Grain Structure Studies:		Cu, electron microscope study of effect of cold work on.....	660	Thomas, J. M., Thomassen, L., and Spooner, N.: High Temperature Corrosion in Nickel-Chromium Alloys.....	844
		Subgrain Formation in High-Purity Aluminum During Creep at High Temperatures.....	1166	Thomassen, L., Spooner, N., and Thomas, J. M.: High Temperature Corrosion in Nickel-Chromium Alloys.....	844
		Sulphur: dissolved, effect on surface tension of liquid Cu.....	643	Thorium and thorium alloys: creep and fatigue properties of Mg-Zr alloys with.....	924
		effect of Mn on activity of, in liquid Fe and Fe-C alloys. Discussion.....	1549	properties of sand cast Mg-Th-Zn-Zr alloys.....	1493
		effect on hot-working characteristics and physical properties of Fe-C alloys.....	525	Tin and tin alloys: alpha solid solution area in Cu-Mn-Sn systems.....	723
		gas-metal reactions, equilibrium in.....	191	electrical resistivity of tin bronzes in alpha range, microscopical examination of.....	906
				Tin-fusion method for analysis of hydrogen in steel.....	180

Titanium and titanium alloys: aging, low temperature in	178	thermal conductivity, electrical resistivity, and thermoelectric power	1238	Aluminum Alloy and Other Applications of Stereoscopic Micro-radiography. Discussion	741
alpha, deformation mechanism in	1191	V-U constitutional diagram	545	Willis, G. M., and Hennessy, F. L.: System $Ag_2O-B_2O_3$; Its Thermodynamic Properties as a Slag Model	1367
habit plane of beta in	1449	Use of Oxygen in the Bessemer Converter. Discussion	1551	Wilson, A. C., Jr., Wolga, G. J., and Tyler, W. W.: Thermal Conductivity, Electrical Resistivity, and Thermoelectric Power of Uranium	1238
cold rolled texture	1378	V		Wilson, J. B., et al.: Further Progress in the Development of Mg-Zr Alloys to Give Good Creep and Fatigue Properties Between 500° and 650°F	924
creep properties of commercially pure elements	331	Vacuum Dezincing of Desilverized Lead Bullion	991	Winkler, C. A., and Hospadaruk, V.: Effect of Chloride on the Deposition of Copper, in the Presence of Arsenic, Antimony, and Bismuth	1375
determination of slip and twinning effects of solid solution alloying on cold-rolled texture of	1199	Vacuum distillation, dezincing desilverized lead bullion	991	Winlock, J.: The Influence of the Rate of Deformation on the Tensile Properties of Some Plain Carbon Sheet Steel	797
electrical resistance of	903	Vanadium and vanadium alloys: influence upon internal friction due to nitrogen in iron	71	Wiseman, H. A. B., and Marin, J.: Plastic Stress-Strain Relations for Aluminum Alloy 14S-T6 Subjected to Combined Tension and Torsion	1181
filler material for brazing	1197	mechanical and magnetic hardness in 10 pct V-Co-Fe alloy	349	Wolfram. See also Tungsten.	
iodide, mechanical properties	238	recovery from ferrophosphorus	423	Wolfram and wolfram alloys, Zr-W system. Discussion	747
Discussion	1562	V-O solid solutions	292	Wolga, G. J., Tyler, W. W., and Wilson, A. C., Jr.: Thermal Conductivity, Electrical Resistivity, and Thermoelectric Power of Uranium	1238
microstructure	238	V-U constitutional diagram	545	Work hardening of metals	1525
Discussion	1562	Vanadium-Oxygen Solid Solutions	292	Wrazej, W. J.: Observations on Scaling of Iron	265
preferred orientations in	57	Vanadium-Uranium Constitutional Diagram	545	Correction	1570
Discussion	1563	Van Horn, K. R.: Residual Stresses Introduced During Metal Fabrication	405	Wulff, J., Buttner, F. H., and Udin, H.: Determination of the Absolute Grain Boundary Energy of Gold at 1300°K	313
lattice parameter of beta Ti at room temperature	195	Van Thyne, R. J., and Kessler, H. D.: Discussion on Titanium-Chromium Phase Diagram	744	Wyatt, J. L.: Electrical Resistance of Titanium Metal	903
low temperature properties of RC-130-B	1104	Van Thyne, R. J., Kessler, H. D., and Hansen, M.: System Titanium-Chromium-Iron	1209	Wynne, R. H., and Goldberg, C.: Preferential Etch for Use in Optical Determination of Germanium Crystal Orientation	436
mechanism of plastic flow	257	Van Thyne, R. J., Rostoker, W., and Kessler, H. D.: Observations on the Phase TiAg	670	X	
TiAg phase	670	Vapor Pressure of Silver	707	X-ray: determination of preferred orientation in rolled metal, modifications of Schulz technique	1038
Ti-Al, mechanical properties	267	Vapor Pressure of Silver Over Silver-Gold Solid Solutions	709	diffraction camera geometry, effect of, on determination of austenite in hardened steels	1529
Discussion	1561	Vapor Pressure of Zinc in the Reduction of ZnS by Cu and Fe	804	diffraction data. See under Diffraction data.	
Ti-C phase diagram	248	Discussion	1558	examination of iron ore	1645
Ti-Cr, high temperature modification	196	Vaporization of metals, free energy of	655	methods for determination of retained austenite	87
Ti-Cr phase diagram. Discussion	743	Variation of Plastic Properties with Annealing Procedure in Zinc Single Crystals	1223	powder pattern of Mn-Mo sigma	1476
Ti-Cr-Al, phase boundaries	253	Vaux, G., and Fuller, M. L.: Modifications of the Schulz Technique for the X-Ray Determination of Preferred Orientation in Rolled Metal	1038	Y	
Discussion	1565	Vogel, F. L., Jr., and Brick, R. M.: Deformation of Ferrite Single Crystals	700	Yield point, ferrite single crystals	705
Ti-Cr-Fe	1209	W		Z	
Ti-Cr-Mo	1544	Wadsworth, M. E., and Fassell, W. M.: Discussion on Kinetics of the Oxidation of Galena in Sodium Hydroxide Solutions under Oxygen Pressure	1556	Zinc and zinc alloys: bend plane phenomena in deformation of monocrystals	49
TiMn phase, structure and pattern of sigma-type phases	1203	Wagner, C., Reynolds, J. E., and Cohen, M.: Calculation of Interdiffusion Coefficients When Volume Changes Occur	1534	crystals, plastic bending	1036
Ti-Mn, martensite habit plane in quenched	667	Wagner theory of oxidation	827	Cu-Zn constitution diagram. Discussion	748
Ti-Mn	225	Wagstaff, J. B.: Further Studies of the Tuyere Zone of the Blast Furnace	895	decay of lattice defects frozen into an Ag-Zn alloy by quenching	1259
Ti-Ni phase diagram	243	Correction	1018	dezincing, vacuum, of desilverized lead bullion	991
Ti-Ta	231	Walker, H. L., Marx, J. W., and Leighly, H. P.: Recrystallization and Stored Energy	809	electrical resistivity of	1145
Ti-Ta-C	1205	Warga, M. E., Wells, C., and Busby, P. E.: Diffusion and Solubility of Boron in Iron and Steel	1463	kinetics of galvanizing iron	807
Ti-W	231	Washburn, J., and Parker, E. R.: Kinking in Zinc Single-Crystal Tension Specimens. Discussion	737	kinking in single-crystal tension specimens. Discussion	737
Ti-rich regions in Ti-C-N, Ti-C-O, and Ti-N-O phase diagrams	1498	Washburn, J., Parker, E. R., and Brown, N.: Relation Between Initial Creep Rate and Resolved Shear Stress in Zinc Single Crystals	1229	Mg-Th-Zn-Zr, properties of sand cast	1493
Titanium-Carbon Phase Diagram	248	Washburn, J., Parker, E. R., and Droward, R.: Recovery in Single Crystals of Zinc	1226	Mg-Zr, creep and fatigue properties of, with and without Zn	924
Discussion	1564	Washburn, J., Parker, E. R., and Edwards, E. H.: Some Observations on the Work Hardening of Metals	1525	single crystals, mechanism of strain hardening	1525
Titanium-Chromium Phase Diagram	743	Washburn, J., Parker, E. R., and Li, C. H.: Variation of Plastic Properties with Annealing Procedure in Zinc Single Crystals	1223	plastic deformation of	1217
Discussion	743	Waterstrat, R. M., Kasper, J. S., and Decker, B. F.: Formation of Sigma Phase in the Mn-Mo System	1476	recovery in	1226
Titanium-Manganese System	225	Webeler, R., and Welber, B.: Energy State of Fatigued Copper	1558	relation between creep rate and shear stress in	1229
Discussion	1566	Wechsler, M. S., Lieberman, D. S., and Read, T. A.: On the Theory of the Formation of Martensite	1503	variation of plastic properties with annealing procedure	1223
Titanium-Nickel Phase Diagram	243	Welber, B., and Webeler, R.: Energy State of Fatigued Copper	1558	vapor pressure of, in reduction of ZnS by Cu and Fe	804
Titanium-Rich Regions of the Ti-C-N, Ti-C-O, and Ti-N-O Phase Diagrams	1498	Weld, H. M., Cunningham, R. L., and Boswell, F. W. C.: Observations on Nodular Graphite. Discussion	738	Discussion	1558
Titanium-Tungsten and Titanium-Tantalum Systems	231	Wells, C., Busby, P. E., and Warga, M. E.: Diffusion and Solubility of Boron in Iron and Steel	1463	Zinc concentrates, sintering on 12 by 168 ft machine	1631
Torsional After-Effect Measurement and Applications to Aluminum	1655	Wert, C., and Ang, C.-Y.: Some Properties of Columbium Containing Nitrogen	1032	Zirconium and zirconium alloys: compounds, comparison with hafnium	1119
Torsion Texture of 70-30 Brass and Armco Iron	61	Whitehead, D. J., et al.: Further Progress in the Development of Mg-Zr Alloys to Give Good Creep and Fatigue Properties Between 500° and 650°F	924	effect of small additions of oxygen on lattice constants and hardness	344
Towers, H., Paris, M., and Chipman, J.: Diffusion of Calcium Ion in Liquid Slag	1455	Whitton, H. G. G., and Shaw, H. A.: Arc-Furnace Equipment and Its Operation at the Kennebecott Utah Refinery	197	iodide Zr, textures of	932
Transformation: Ag-Cd alloys	550	Williams, D. N., and Eppelsheimer, D. S.: Cold Rolled Texture of Titanium	1378	kinetics of thermal reorientations in cold rolled	284
alpha to beta, effect on sheet texture of iodide titanium	57	Williams, W. M., and Smith, C. S.: A Study of Grain Shape in an		Discussion	1573
austenite-martensite, theoretical analysis of	1503			Mg-Th-Zn-Zr, properties of sand cast	1493
isothermal, austenite to martensite in high Cr steel	530			Mg-Zr, development of, for good creep and fatigue properties	924
curves for martensite in Fe-Ni-Mn alloy	687			Ti-Zr, cold-rolled sheet texture of	1202
order-disorder, in Cu-Au alloys	823			Zr-B	1117
phases Co-Cr and Co-Mo	357			ZrCr ₂ , allotropy in the phase	304
Transformation in Cobalt-Nickel Alloys. Discussion	729			Zr-Cr	279
Transition: ductile-brittle in body-centered cubic single crystals, crystallographic analysis	1650			Zr-Cu	273
Treco, R. M.: Effect of Small Additions of Oxygen on Lattice Constants and Hardness of Zirconium	344			Zr-Mo and Zr-W	73
Tristage Crystallization Process for Utilizing Western Ferrophosphorus	423			Discussion	747
Tungsten and tungsten alloys: binder phase in cemented tungsten carbide-cobalt alloys. Discussion	746			Zone melting, change in ingot shape during	1441
Ti-W system	231			Zone refining, analysis of process	1531
W-Co-C system. Discussion	744				
Zr-W	73				
Tungsten-Cobalt-Carbon System. Discussion	744				
Tungsten. See also Wolfram.					
Turnbull, D., and Fisher, J. C.: Calculation of Martensite Nucleus Energy Using the Reaction-Path Model	921				
Tuyere zone, blast furnace, studies of	895				
Correction	1018				
Twinning: deformation, in ingot iron, effect of tensile strain on	213				
ferrite single crystals	705				
metal monocrystals. Discussion	735				
Mg specimens	713				
Ti crystals	1195				
Ti, determination	257				
Zn monocrystals	1220				
Tyler, W. W., Nesbitt, L. B., and Wilson, A. C., Jr.: Some Low Temperature Properties of Titanium Alloy RC-130-B and Stainless Steel	1104				
Tyler, W. W., Wilson, A. C., Jr., and Wolga, G. J.: Thermal Conductivity, Electrical Resistivity, and Thermoelectric Power of Uranium	1238				
U					
Udin, H., Wulff, J., and Buttner, F. H.: Determination of the Absolute Grain Boundary Energy of Gold at 1300°K	313				
Uranium and uranium alloys: crystallographic angles for orthorhombic shadowcast plastic replicas, chromium steel	1190				
	692				

